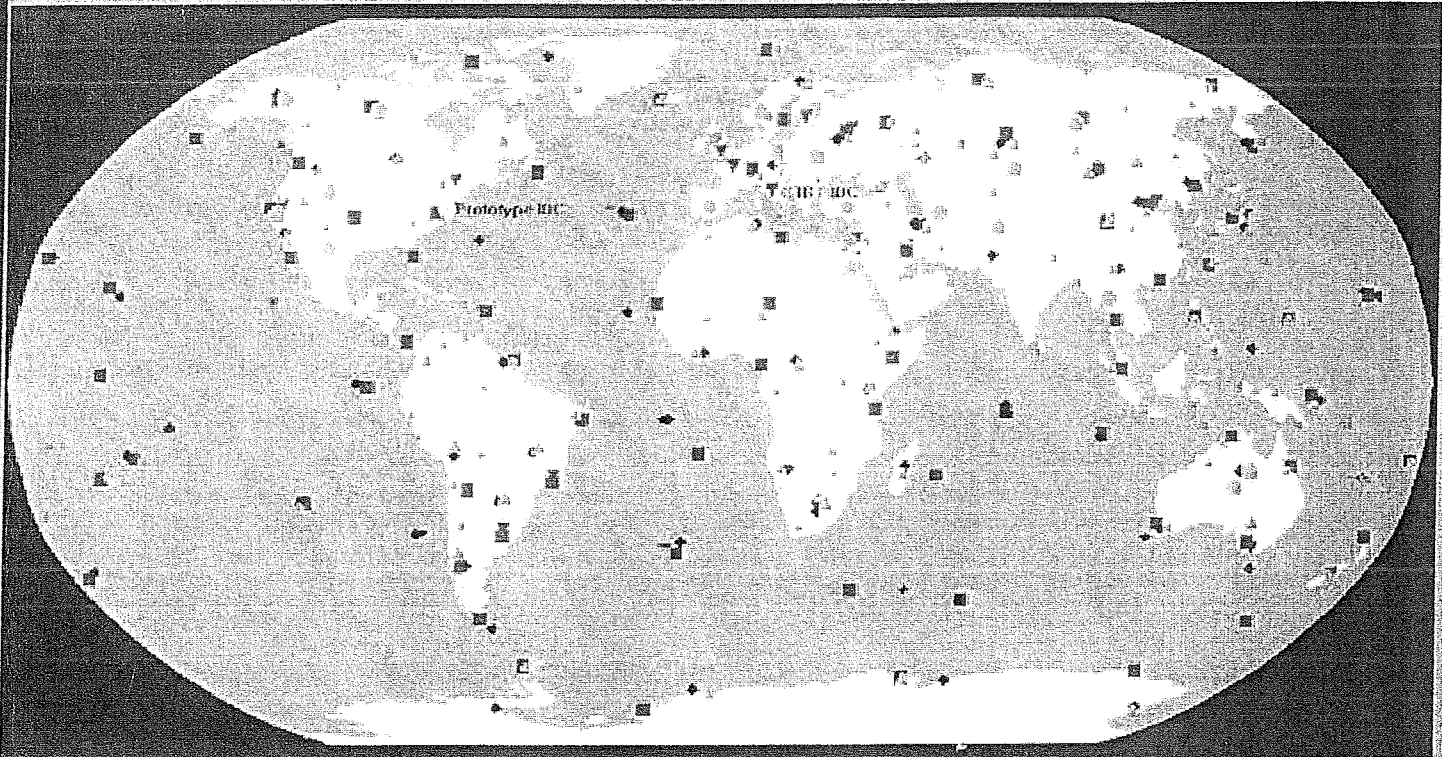
22nd Annual DoD/DOE Seismic Research Symposium

Planning for Verification of and Compliance with the Comprehensive Nuclear-Test-Ban Treaty (CTBT)

Proceedings



VOLUME I

Technical Categories

1. Seismic Research Characterization
3. Seismic Source Characterization
4. Regional Seismic Wave Propagation

VOLUME I - TABLE OF CONTENTS

1. SEISMIC REGIONAL CHARACTERIZATION

01-01 **LLNL'S REGIONAL MODEL CALIBRATION AND BODY-WAVE DISCRIMINATION RESEARCH IN THE FORMER SOVIET UNION USING PEACEFUL NUCLEAR EXPLOSIONS (PNEs)** 3
Joydeep Bhattacharyya, Arthur Rodgers, Jennifer Swenson, Craig Schultz, William Walter, Walter Mooney, and Geoff Clitheroe

01-02 **MONITORING ROUTINE MINE SEISMICITY IN THE CONTERMINOUS UNITED STATES** 13
James W. Dewey and Alena L. Leeds

01-03 **REGIONAL SEISMIC EVENT CHARACTERIZATION USING A BAYESIAN KRIGING APPROACH** 23
Mark Fisk, Steven Bottone and Gary McCartor

01-04 **TWO-DIMENSIONAL FINITE-DIFFERENCE MODELING OF BROADBAND REGIONAL WAVE PROPAGATION PHENOMENA: VALIDATION OF REGIONAL THREE-DIMENSIONAL EARTH MODELS AND PREDICTION OF ANOMALOUS REGIONAL PHASES** 35
Peter Goldstein, Floriana D. Ryall, Michael E. Pasyanos, Craig A. Schultz, and William R. Walter

01-05 **JOINT INVERSION OF RECEIVER FUNCTIONS AND SURFACE-WAVE DISPERSION FOR CRUSTAL STRUCTURE** 43
R.B. Herrmann, C.J. Ammon, and J. Julia

01-06 **LOCATION CALIBRATION OF KAZAKHSTAN BASED ON DTRA (U.S.)-NNC (RoK) JOINT EXPERIMENTS (1997-1999) IN THE FORMER SEMIPALATINSK TEST SITE** 55
Rong-Song Jih and Robert A. Wagner

01-07 **ASSESSING ABILITIES TO ESTIMATE SHORT PERIOD GROUP VELOCITIES IN CENTRAL ASIA** 67
A.L. Levshin, M.H. Ritzwoller, M.P. Barmin, and J.L. Stevens

01-08 **CRUSTAL AND UPPER MANTLE SEISMIC VELOCITY STRUCTURE OF THE FORMER USSR FROM PEACEFUL NUCLEAR EXPLOSIONS (PNEs) AND CHEMICAL EXPLOSION DATA** 77
Walter D. Mooney, Sergei Kostyuchenko, and A.V. Egorkin

01-09 **THE CRUSTAL STRUCTURE AND CTBT MONITORING OF INDIA: NEW INSIGHTS FROM DEEP SEISMIC PROFILING** 89
Walter D. Mooney, P.R. Reddy, V. Vijaya Rao, and D.M. Mall

01-10 **SEISMIC CALIBRATION OF THE EUROPEAN ARCTIC** 99
Svein Mykkeltveit, Frode Ringdal, Conrad Lindholm, and Elena Kremenetskaya

01-11 **REGIONAL CODA MAGNITUDES IN CENTRAL ASIA** 107
W.S. Phillips, H.E. Hartse, and K.M. Mayeda

01-12 **ESTIMATES OF P_n AND S_n ACROSS EURASIA** 115
Michael H. Ritzwoller, Mikhail P. Barmin, Anatoli L. Levshin, Antonio Villaseñor, and E. Robert Engdahl

01-13 **ANALYSIS OF THE NOVEMBER 1999 DEAD SEA CALIBRATION SHOTS** 125
Arthur Rodgers, Stephen Myers, Kevin Mayeda, and William Walter

01-14 **PATH CALIBRATION STUDIES IN AND AROUND THE INDIAN SUBCONTINENT** 135
Chandan K. Saikia, Hong Kie Thio and Bradley B. Woods

01-15 **IMPROVED SURFACE WAVE DETECTION AND MEASUREMENT USING PHASE-MATCHED FILTERING AND IMPROVED REGIONALIZED MODELS** 145
Jeffry L. Stevens and David A. Adams

01-16 **MAPPING LATERAL VARIATIONS IN UPPER MANTLE ATTENUATION USING STACKS OF P AND PP SPECTRA** 155
Linda Warren and Peter M. Shearer

3. SEISMIC SOURCE CHARACTERIZATION

03-01 **SEISMIC CHARACTERIZATION OF THE NOVEMBER 8, 10, AND 11, 1999 DEAD SEA UNDERWATER CHEMICAL CALIBRATION EXPLOSIONS USING CEPSTRAL MODELING AND INVERSION** 161
Douglas R. Baumgardt and Angelina Freeman

03-02 **A GROUND-TRUTH DATABASE FOR CENTRAL CHINA** 173
W. Winston Chan and Xiaoxi Ni

03-03 **MODELING COLLAPSE CHIMNEY AND SPALL ZONE SETTLEMENT AS A SOURCE OF POST-SHOT SUBSIDENCE DETECTED BY SYNTHETIC APERTURE RADAR INTERFEROMETRY** 183
William Foxall

03-04 **AN ANALYSIS OF LARGE MINING BLASTS IN WYOMING AND CENTRAL ASIA** 191
Michael A.H. Hedlin

03-05 **CHARACTERIZATION OF SEISMIC SOURCES** 201
Lane R. Johnson

03-06 **CHARACTERIZATION OF MINING-INDUCED SEISMICITY IN THE WITWATERSRAND BASIN, SOUTH AFRICA** 211
T.H. Jordan, E. Richardson, C. Wright, S. Webb, E. Kgaswane, T. Kwadiba, and R. McRae-Samuel

03-07 **ISOTROPIC AND NONISOTROPIC COMPONENTS OF EARTHQUAKES AND NUCLEAR EXPLOSIONS ON THE LOP NOR TEST SITE** 213
A.L. Levshin, M.H. Ritzwoller, B.G. Bukchin, A.Z. Mostinsky, and A.A. Egorkin

03-08 **SOURCE SPECTRA, MOMENT, AND ENERGY FOR RECENT EASTERN MEDITERRANEAN EARTHQUAKES: CALIBRATION OF INTERNATIONAL MONITORING SYSTEM STATIONS** 223
Kevin M. Mayeda, Abraham Hofstetter, Arthur J. Rodgers, and William R. Walter

03-09 **DEVELOPMENT OF IMPROVED MAGNITUDE MEASURES FOR THE INTERNATIONAL DATA CENTRE** 233
John R. Murphy, Jeffry L. Stevens, Theron J. Bennett, Brian W. Barker, and Ronald W. Cook

03-10 **SEISMIC SOURCE CHARACTERIZATION IN ASIA** 243
George E. Randall and Charles J. Ammon

03-11 **ACOUSTIC FLUIDIZATION OF CRUSHED ROCK BEHIND THE SHOCK FRONT BY DAMAGE-INDUCED SECONDARY SEISMIC RADIATION** 251
Charles G. Sammis

03-12 **NEAR FIELD AND REGIONAL MODELING OF EXPLOSIONS AT THE DEGELEN TEST SITE** 257
J.L. Stevens, N. Rimer, J.R. Murphy, H. Xu, G.G. Kocharyan and B.A. Ivanov

4. REGIONAL SEISMIC WAVE PROPAGATION

04-01 **CRUSTAL PHASE PROPAGATION: DISCRIMINATION AND CORRECTIONS** 271
G. Eli Baker, Mariana Eneva, Jeffry L. Stevens, and Heming Xu

04-02 **THE CONFIDENCE-BUILDING MEASURE ROLE OF SEISMIC CALIBRATION** 281
Leslie A. Casey, John J. Zucca, and W. Scott Phillips

04-03 **EXCITATION AND PROPAGATION OF SHORT-PERIOD SURFACE WAVES IN YOUNG SEAFLOOR** 287
Donald W. Forsyth

04-04 **DYNAMIC FEATURES AND IDENTIFICATION OF REGIONAL SEISMIC SIGNALS FROM DEAD SEA CALIBRATION SHOTS** 295
Yefim Gitterman and Rami Hofstetter

04-05 **DEVELOPMENT OF REGIONAL TRAVEL-TIME TABLES FOR DIFFERENT GEOTECTONIC PROVINCES OF NORTHERN EURASIA** 305
Victor V. Kirichenko and Yury A. Kraev

04-06 **SURFACE WAVE PROPAGATION EFFECTS OBSERVED AT THE SAUDI SEISMIC NETWORK** 317
Gabi Laske and Nathalie Cotte

04-07 **CRUSTAL EFFECTS ON REGIONAL SEISMIC PHASES IN ASEISMIC REGIONS OF NORTHERN EURASIA: CONSTRAINTS FROM PNE RECORDINGS** 327
Igor B. Morozov, Scott B. Smithson, and Elena A. Morozova

04-08 **MULTI-TAPER COHERENCE RECEIVER FUNCTIONS AND P-WAVE SCATTERING WITHIN THE CRUST AND LITHOSPHERE: THE VIEW FROM ARABIA** 337
Jeffrey Park and Vadim Levin

04-09 **REGIONAL SEISMOLOGICAL RESEARCH IN THE MIDDLE EAST IN SUPPORT OF CTBT MONITORING** 347
Eric Sandvol, Dogan Seber, Khaled Al-Damegh, and Muawia Barazangi

04-10 **COMPARISON OF DIFFERENT METHODOLOGIES FOR REGIONAL MAGNITUDE CALCULATION OF EURO-MEDITERRANEAN EARTHQUAKES** 357
Jörg Schlittenhardt

04-11 **Lg WAVE PROPAGATION USING SH AND P AND SV SCREEN PROPAGATORS IN HETEROGENEOUS CRUSTS WITH IRREGULAR TOPOGRAPHY** 359
Ru-Shan Wu, Xiao-Bi Xie, and Xian-Yun Wu

1. Seismic Research Characterization

LLNL'S REGIONAL MODEL CALIBRATION AND BODY-WAVE DISCRIMINATION RESEARCH IN THE FORMER SOVIET UNION USING PEACEFUL NUCLEAR EXPLOSIONS (PNEs)

Joydeep Bhattacharyya, Arthur Rodgers, Jennifer Swenson, Craig Schultz, William Walter
Lawrence Livermore National Laboratory

Walter Mooney and Geoff Clitheroe
United States Geological Survey

Sponsored by U.S. Department of Energy
Office of Nonproliferation Research and Engineering
Office of Defense Nuclear Nonproliferation
National Nuclear Security Administration

Contract No. W-7405-ENG-48

ABSTRACT

Long-range seismic profiles from Peaceful Nuclear Explosions (PNE) in the Former Soviet Union (FSU) provide a unique data set to investigate several important issues in regional Comprehensive Nuclear-Test-Ban Treaty (CTBT) monitoring. The recording station spacing (~ 15 km) allows for extremely dense sampling of the propagation from the source to ≥ 3300 km. This allows us to analyze the waveforms at local, near- and far-regional and teleseismic distances. These data are used to: 1) study the evolution of regional phases and phase amplitude ratios along the profile; 2) infer one-dimensional velocity structure along the profile; and 3) evaluate the spatial correlation of regional and teleseismic travel times and regional phase amplitude ratios. We analyzed waveform data from four PNE's (m_b = 5.1 – 5.6) recorded along profile KRATON, which is an east-west trending profile located in northern Siberia.

Short-period regional discriminants, such as P/S amplitude ratios, will be essential for seismic monitoring of the Comprehensive Nuclear-Test-Ban Treaty (CTBT) at small magnitudes (m_b<4.0). However, P/S amplitude ratios in the short-period band, 0.5 – 5.0 Hz, show some scatter. This scatter is primarily due to propagation and site effects, which arise from variability in the elastic and anelastic structure of the crustal waveguide. Preliminary results show that Pg and Lg propagate efficiently in north Siberia at regional distances. The amplitude ratios show some variability between adjacent stations that are modeled by simple distance trends. The effect of topography, sediment and crustal thickness, and upper mantle discontinuities on these ratios, after removal of the distance trends, will be investigated.

The travel times of the body wave phases recorded on KRATON have been used to compute the one-dimensional structure of the crust and upper mantle in this region. The path-averaged one-dimensional velocity model was computed by minimizing the first arriving P-phase travel-time residuals for all distances (Δ = 300 – 2300 km). A grid search approach was used in the minimization. The most significant features of this model are the negative lid-gradient and a low-velocity zone in the upper mantle between the depths of 100 – 200 km; precise location of the LVZ is poorly constrained by the travel time data. We will extend our investigation to additional PNE lines to further investigate the amplitude and travel-time variations in eastern and central Eurasia.

Finally, the dense station spacing of the PNE profiles allows us to model the spatial correlation of travel times and amplitude ratios through variogram modeling. The statistical analysis suggests that the correlation lengths of the travel-time and amplitude measurements are 12° and 8°, respectively.

This work was performed under the auspices of the U.S. Department of Energy by University of California Lawrence Livermore National Laboratory, under contract No. W-7405-Eng-48. LLNL contribution number UCRL-JC-138991.

Key words: PNE, Former Soviet Union, Seismic Calibration

OBJECTIVE

Peaceful nuclear explosions (PNEs) conducted by the Former Soviet Union (FSU) provide a unique data set to investigate the propagation of high-frequency regional phases for Comprehensive Nuclear-Test-Ban Treaty (CTBT) monitoring. This paper presents our initial results in calibrating the aseismic eastern FSU using PNEs. The PNE data are part of the large dataset of dense, linear, long-range, three-component (at two different instrument gains) profiles recorded by Russian scientists between 1965 - 1988. This dataset gives us a unique tool with which to probe the crust and mantle structure in Northern Eurasia and investigate regional phase phenomenology. In this paper, we will document our analysis in extracting and archiving the KRATON profile in northern Siberia. This dataset consists of waveforms at local, near- and far-regional, and upper mantle distances at nominal station spacing of about 15 km. Travel times of first arriving P-waves are used to develop one-dimensional models. Residuals relative to these models are characterized by their spatial correlation functions (variograms), which is an essential element of travel-time correction surface development using the Bayesian kriging method (*Schultz et al.* 1998). Ratios of high-frequency (0.5-10 Hz) regional phase amplitudes are widely viewed as important seismic discriminants. The distance and path dependence of regional phase amplitudes and amplitude ratios varies regionally because of variations in elastic and anelastic structure of the earth. The scatter introduced by distance and path effects can inhibit identification of explosions from natural seismicity. We employed the dense sampling of the PNE data to investigate the distance and path dependence of regional phase amplitudes. Additionally, the spatial correlation structure of the travel-time and amplitude ratio data is investigated using PNE data sets. Finally, the lateral variations of travel-time residuals, with respect to standard global model *AK135*, and amplitude ratios have been compared to variations of Moho and basement thickness.

RESEARCH ACCOMPLISHED

Introduction

Central and Eastern FSU is largely aseismic; therefore, it is impossible to calibrate these regions with earthquake data. For instance, it is difficult to use natural seismicity, a dataset widely used in most other parts of the world, to estimate these seismic properties. Fortunately, active source seismic data recorded in this region can be used for calibration purposes. During the period extending from January 1965 to September 1988, Russian scientists carried out dense seismic recordings of 122 PNEs. These explosions were carried out at several distinct geological settings and were widely dispersed within the Former Soviet Union (*Sultanov et al.* 1999). At LLNL, we have archived a subset of these PNEs.; namely, data from the profiles QUARTZ, KRATON, KIMBERLITE, METEORITE, and RIFT, which traverse regions of Central and Eastern FSU, are available to us (Figure 1). In total, we have data from 25 PNEs in our database. These profiles cross several different tectonic regions, including the East European Platform, Ural Mountains, West Siberian Platform, Siberian Craton, Altay – Sayan Fold Belt, and the Baikal Rift region. Two of the salient features of the PNE dataset are the closely spaced stations, between 10 – 20 km, and coverage of a wide range of source-to-receiver distances (from near-source to greater than 30°), which allows us to model the propagation and evolution of seismic phases with an extremely high resolution.

Dataset

In this paper, we present our analysis using the data from the KRATON line (Figure 1). This is an east-west trending profile that crosses, for the major part of its length, the Angara Archean craton, the basement core of the East Siberian platform. A significant portion of this profile also crosses the West Siberian Platform, which lies between the Uralides and the Angara craton. The western-most PNE lies on the western edge of the West Siberian basin. The data were digitized from analogue recordings in a 0.5- to 20-Hz band (*Solodilov* 1997). The usable frequency range for the KRATON data is about 0.5 – 10 Hz, though the signal above 5 Hz is low. So, our analysis is carried out in the 0.5- to 5.0-Hz band. For each station, we have three component recordings: vertical, radial and transverse. For each of these components, there are low- and high-gain channels. Since the high-gain channels are frequently clipped, most of the analysis is carried out using the low gain channel. The signal-to-noise ratio of the first arrival is good (*Mechie et al.* 1997); hence, its travel time can be robustly determined. In addition, several regional phases are clearly observed. Teleseismic Pn is clearly observed at distances up to 2000 km. The Pg phase efficiently propagates up to 1500 km. Importantly, we observe a significant difference in the moveout velocities of both Lg and Sn as well as the variation of Lg amplitude laterally. As reported in *Nielsen et al.* (1999), there is a significant scattered ("coda") energy at distances between 1000 – 1500 km.

There were four PNE shots along the KRATON profile, named KRATON1 – KRATON4. The magnitudes for these shots are 5.5, 5.2, 5.1 and 5.6 respectively, and had burial depths between 567 – 886 meters (*Sultanov et al.* 1999). In this paper, we show the results from the KRATON3 shot as the results are similar for the other shots.

Travel-Time Modeling

For each PNE, we have picked the travel times of first arriving *P* wave. Figure 2 shows the residuals of these picks as a function of source-receiver distance. The residuals are computed with respect to the predictions of a standard global model, *AK135* (*Kennett et al.* 1995). As we observe in Figure 2, there is a significant distance-dependent trend in the residuals indicating that *AK135* is inadequate for this region. We estimated a 1-dimensional model for the line. To avoid complications from Pg - Pn crossover in the travel-time curve, we limit our analysis to stations with source-receiver distances being greater than 300 km. The longest source-receiver distance considered for KRATON3 is 2301 km. A grid search algorithm is adopted to identify the model that fits the data the best. The grid-search is carried out in two ways: by varying the crustal structure and by varying the mantle structure. In the former case, modeling technique is similar to that of *Swenson et al.* (2000). Simple crust and upper mantle velocity models are generated by varying the crustal thickness (30 – 55 km), upper crustal Vp (5.5 – 7.0 km/s), lower crustal Vp (6.6 – 8.0 km/s) and the upper mantle Vp (7.9 – 8.1 km/s). The parameters that remain constant are the sediment thickness (= 4 km), sediment Vp (=4 km/s), thickness of the mantle lid (= 25 km) and the P-wave mantle velocity in the mantle lid. The mantle structure is similar to *AK135* below the 410-km discontinuity. A linear gradient, joining the lid velocity to the velocity at 410 km, is used for the rest of the upper mantle. We calculate travel times through each regionalized *P*-wave velocity model using the single-valued *tau-p* formulation similar to that of *Buland and Chapman* (1983) to produce standard travel-time tables. The tables are populated with travel times, parameterized by distance and depth, and a root-mean-square (rms) measure of misfit is adopted. Since the travel-time modeling process is non-linear and the number of model parameters limited, the solution is non-unique. In practice, we have a suite of models that can fit the data equally well. To avoid this ambiguity, we adopt the following procedure. We rank the models based on the rms misfit with the data and select the top 10% of the models; these models fit the data nearly equally well. We then compare these models to the global average model *AK135* and select the model that is closest to *AK135* in shape. In the second-grid search, we keep a uniform crustal velocity but vary its thickness. We allow for more complicated mantle models with changes in the velocity gradient above the transition zone. This allows us to explore the possibility of low-velocity zones (LVZ) in the upper mantle.

We obtain significantly better fits when we allow the mantle structure to deviate away from *AK135*. We show the best fitting one-dimensional velocity model for KRATON3 in Figure 3. Note that we have combined the measurements from both move-out directions (East and West). We plotted the velocity structure of *AK135* for reference. It is clear from Figure 3 that both the crust and uppermost mantle velocities, on average, are faster along KRATON3 compared to the global average. This result is expected in Siberia, which is underlain by Archean crust to the west and Proterozoic crust to the east. The faster velocities are primarily an expression of a stable crustal structure. High-resolution global models have also shown high velocities in the upper mantle going to depths of up to 450 km (*Masters, et al.* (1999).

The travel-time modeling technique described above is adequate for the analysis of data with a global distribution of stations and events where the source-receiver paths encounter a wide range of geological settings. To be consistent in modeling these paths with the same set of models, it is useful to limit the range of possible models. On the other hand, when we have a regional distribution of stations and sources, we can allow ourselves to search over a different set of models that are more appropriate for that region. This is particularly true for KRATON where previous studies by *Solodilov* (1997) and *Nielsen, et al.* (1999) have shown significant low-velocity zones and variations in mantle velocity gradients, respectively. To account for these structures, we now search over models where the mantle velocity gradient is allowed to vary between –0.002 and 0.002. We find that the best models from this set have significantly better fits, i.e., the rms difference between the data and the model predictions is decreased by as much as 40 %. The best fitting model is shown in Figure 3. The most significant feature of this model is the presence of a LVZ in the upper mantle at a depth of 150 – 200 km, similar to the results of *Nielsen, et al.* (1999). Importantly, this model indicates a negative mantle-lid gradient. Figure 4a shows the spatial variation of the travel-time residuals for the best fitting model. We show the topography as a proxy for tectonics. We observe that, though there is no obvious correlation of travel-time variations with station location, we see that in general Western Siberia has negative

residuals compared to Eastern Siberia. This difference might be due to the faster mantle in the west or to the thicker crust observed in Eastern Siberia.

The variance structure of the travel-time picks can give us important insights into the correlation length of regional structures along with robust estimates of measurement errors *Myers and Schultz* (2000). We first compute the mean square differences of all pairs of observations (travel times) as a function of inter-pair distance, i.e., a variogram. We then model this variogram using three statistical parameters: (1) correlation length (range) representing the spatial variability; (2) the background variance (σ_B), representing the overall variability of the data; and (3) the measurement error (σ_M). The measurement error is simply the variance of collocated data, which is the variogram at zero lag. Unlike *Myers and Schultz* (2000), we carry out a shot-specific travel-time analysis. Thus, we will model the variograms for each shot separately. We show the variogram for KRATON3 in Figure 4b where we chose to bin the squared differences in 1° bins. The measurement error for the dataset is 0.06 s, which is low as the source is a single nuclear explosion with well-known location and origin time. The correlation length for KRATON3 is 12° and represents the range at which the data are uncorrelated.

Regional Phase Amplitudes

The amplitudes of regional phases (Pn, Pg, Sn and Lg) in the frequency range 0.5-10 Hz are widely recognized as effective discriminants for distinguishing explosions from natural earthquakes (*Taylor et al,* 1988; *Walter et al,* 1995; *Hartse et al,* 1997). Ratios of regional P- and S-wave phases display distance trends because of differential attenuation and geometric spreading. However, in addition to distance effects, the amplitudes of these phases can vary greatly because of lateral variations in crustal and uppermost mantle structure (both elastic and anelastic). This variability is referred to as path effects. Site effects due to local geology at the recording site can lead to additional variability. After the distance trend is removed, substantial scatter can remain in the ratios because of path effects.

We measured the amplitude ratios Pg/Lg, Pn/Lg and Pn/Sn using the KRATON PNE shots. Amplitude measurements were made in the time domain filtering the traces, windowing the phases and computing the rms amplitude. Individual phases were isolated with group velocity windows (Pn 8.3-7.6 km/s; Pg 6.8-5.8 km/s; Sn 4.6-4.0 km/s & Lg 3.6-3.0 km/s). Problems associated with digitization and band-limited instrument response restrict the usable frequency content of the data. Thus, we simply measured the rms amplitude of each phase in the band 0.5-5 Hz. This is a fairly broad bandwidth. We will investigate if narrower frequency bands can be used with these data.

Figure 5 shows the Pg/Lg, Pn/Lg and Pn/Sn amplitude ratios (0.5-5 Hz) versus distance for the KRATON 3 shot. Linear regression fits to the $\log_{10}$ ratios are plotted along with 1-σ uncertainties. The data are well modeled by the linear trend; however, deviations are apparent. In particular, ratios for the eastern and western stations (relative to the shot location) show different behavior in Figure 5. This behavior reveals that path and site effects impact the observed P/S ratios.

Much effort has been focused on modeling the path effects on regional phases (e.g., *Fan and Lay* 1998; *Rodgers et al, 1*999; *Phillips* 1999). It is now well established that correction surfaces produced by Bayesian kriging (*Schultz et al,* 1998) is the optimal method for representing path effects on regional phases (*Rodgers et al,* 1999; *Phillips* 1999). In order to perform the kriging calculations, it is necessary to characterize the statistical properties and spatial correlation of the data by modeling the variogram. Figure 6 shows a map of the Pg/Lg amplitude ratios of the KRATON 3 shot and the associated variogram. The distance trend of the Pg/Lg ratios was removed revealing the path and site effects. The variogram demonstrates that the data become more poorly correlated as the inter-pair distance increases. We modeled the variogram with a monotonically increasing function that asymptotically approaches the sum of measurement and background variances (Figure 6b). The range (8.4º) governs the rise of the function and represents the range at which the data become uncorrelated. This characteristic range is typical of other regions we have studied (*Rodgers et al,* 1999). The measurement uncertainty (σ_M) is low because the source is a single nuclear explosion. Errors in the variogram measurements (error bars in Figure 6b) are small because the dense station spacing provides many measurement pairs at small inter-station ranges.

CONCLUSIONS AND RECOMMENDATIONS

We document our analyses of the KRATON PNE (shot 3) in northern Siberia. The 1-D travel-time modeling shows a significant low-velocity zone between 150- to 200-km depths. We are developing regionalized 1-D and 2-D travel-time correction models for this region following the technique of *Swenson et al*, (2000). The amplitude ratios show a linear trend with distance. The variogram modeling suggests that the correlation lengths for the travel times are 12° and for the amplitude ratios about 8°. In the future we will investigate the statistical properties of the travel-time and amplitude data. In particular we will consider regional sub-sets of the data and compare the correlation structure of the data in different regions. In order to improve velocity models for travel-time analysis and to understand the behavior of far-regional P, we will model the upper mantle triplication waveforms. We will also investigate the frequency dependence of regional-phase amplitude behavior and document the propagation efficiency of the regional phases as a function of frequency.

REFERENCES

Buland, R., and C. Chapman (1983), The Computation of Seismic Travel Times, *Bulletin Seismological Society of America*, *73* , 1271 - 1302.

Fan, G., and T. Lay (1998), Regionalized Versus Single-Station Waveguide Effects on Seismic Discriminants in Western China, *Bulletin of the Seismological Society of America*, ***88*** , 1260-1274.

Hartse, H., S. Taylor, S. Phillips, and G. Randall (1997), A Preliminary Study of Regional Seismic Discrimination in Central Asia with Emphasis on Western China, *Bulletin of the Seismological Society of America*, ***87***, 551-568.

Kennett, B., E. Engdahl, and R. Buland (1995), Constraints on Seismic Velocities in the Earth from Travel Times, *Geophysical Journal International*, ***122***, 108-124.

Masters G., H. Bolton, and G. Laske (1999), Joint Seismic Tomography for P and S Velocities: How Pervasive are Chemical Anomalies in the Mantle?, *EOS Trans. AGU*, ***80***, S14.

Mechie, J., A. Egorkin, L. Solodilov, K. Fuchs, F. Lorenz, and F. Wenzel (1997), Major Features of the Mantle Velocity Structure Beneath Northern Eurasia from Long-Range Seismic Recordings of Peaceful Nuclear Explosions, in *Upper Mantle Heterogeneties from Active and Passive Seismology*, edited by K. Fuchs, pp. 33 - 50, Kluwer Academic, Netherlands.

Myers, S. and C. Schultz (2000), Improving Sparse Network Seismic Location with Bayesian Kriging and Teleseismically Constrained Calibration Events, *Bulletin of the Seismological Society of America*, ***90***, 199 - 211.

Nielsen, L., H. Thybo, and L. Solodilov (1999), Seismic Tomographic Inversion of Russian PNE Data Along Profile KRATON, *Geophysical Research Letters*, ***26***, 3413 - 3416.

Phillips, W (1999), Empirical Path Correction for Regional Phase Amplitudes, *Bulletin of the Seismological Society of America*, ***89***, 384-393.

Rodgers, A., W. Walter, C. Schultz, S. Myers, and T. Lay (1999), A Comparison of Methodologies for Representing Path Effects on Regional P/S Discriminants, *Bulletin of the Seismological Society of America*, ***89***, 394-408.

Schultz, C., S. Myers, J. Hipp, and C. Young (1998), Stationary Bayesian Kriging: Application of Spatial Corrections to Improve Seismic Detection, Location and Identification, *Bulletin of the Seismological Society of America*, ***88***, 1275-1288.

Solodilov, L. (1997), The GEON Center: 25 years of Implementation of PNE in Studies of Earth's Deep Structure, in *Upper Mantle Heterogeneities from Active and Passive Seismology*, edited by K. Fuchs, pp. 1 - 10, Kluwer Academic Publishers.

Sultanov, D., J. Murphy, and K. Rubenstein (1999), A Seismic Source Summary for Soviet Peaceful Nuclear Explosions, *Bulletin of Seismological Society of America*, ***89***, 640-647.

Swenson, J., C. Schultz, W. Hanley, and S. Myers (2000), Using Radially Heterogeneous and Azimuthally Invariant Travel-Time Models to Improve Seismic Event Location in the Middle East and North Africa, UCRL-JC-135465 abs.

Taylor, S., N. Sherman, and M. Denny (1988), Spectral Discrimination Between NTS Explosions and Western United States Earthquakes at Regional Distances, *Bulletin of the Seismological Society of America*, ***78***, 1563 - 1579.

Walter, W., K. Mayeda, and H. Patton (1995), Phase and Spectral Ratio Discrimination Between NTS Earthquakes and Explosions. Part 1: Empirical Observations, *Bulletin of the Seismological Society of America*, ***85***, 1050 - 1067.

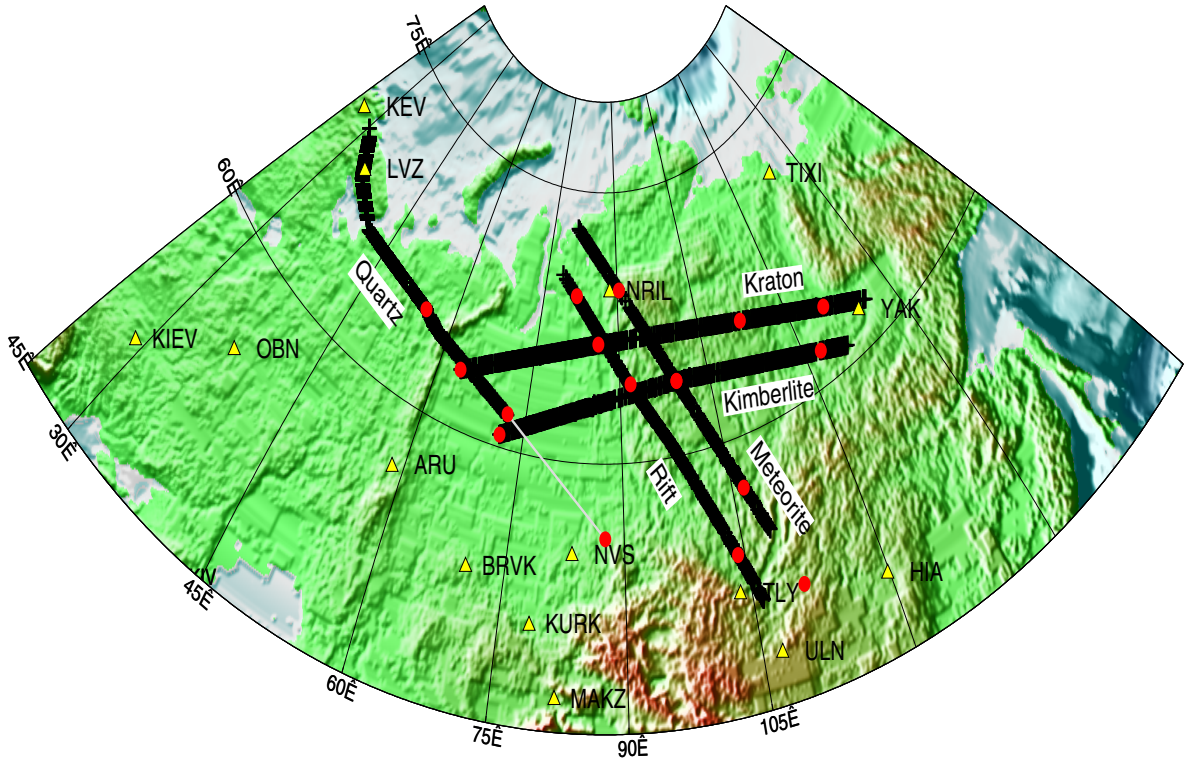


Figure 1. Soviet Peaceful Nuclear Explosion (PNE) datasets available at LLNL. Permanent three component, broadband stations in the region are also shown. The PNE shot points are shown in red circles and PNE stations are shown by +. The permanent stations are shown by the yellow triangles. The names of each PNE profile are indicated.

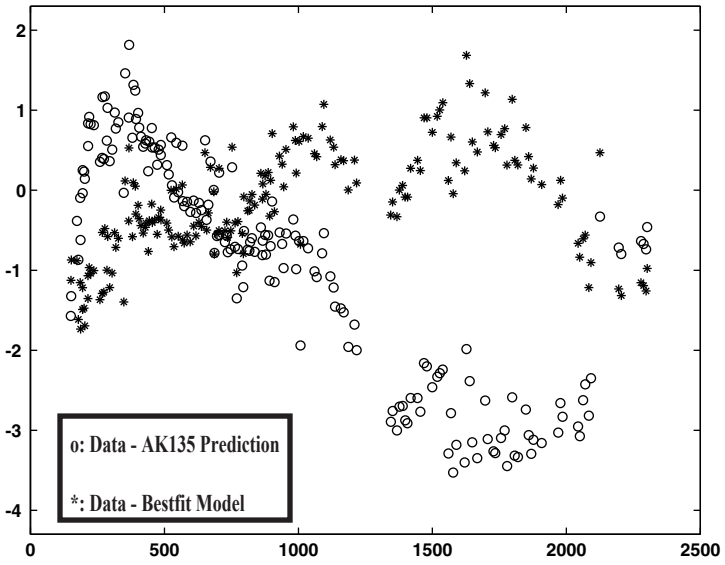


Figure 2. Travel-time residuals as a function of distance range for KRATON3. We observe a strong distance dependence for the AK135 residuals, suggesting that this model cannot adequately explain the data. The distance trends for the bestfit model is much less pronounced. We also see that the amplitude of the misfit is significantly decreased for the bestfit model.

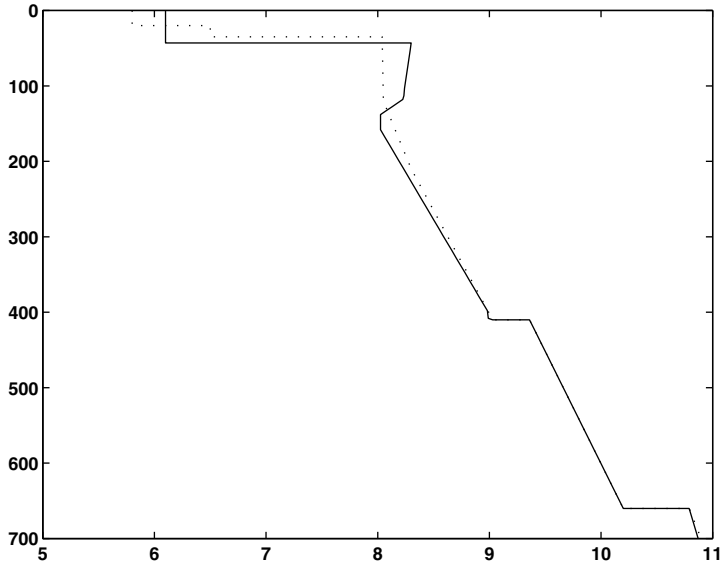


Figure 3. Bestfitting 1-dimensional model for the KRATON3 profile is shown in the solid line. The global reference model, AK135, is shown in the dotted line. The crust and the uppermost mantle is significantly faster for KRATON3 compared to the global average. We also find evidence for a significant low-velocity zone below the mantle lid at depths between 150 - 200 km. Note the negative velocity gradient in the mantle lid.

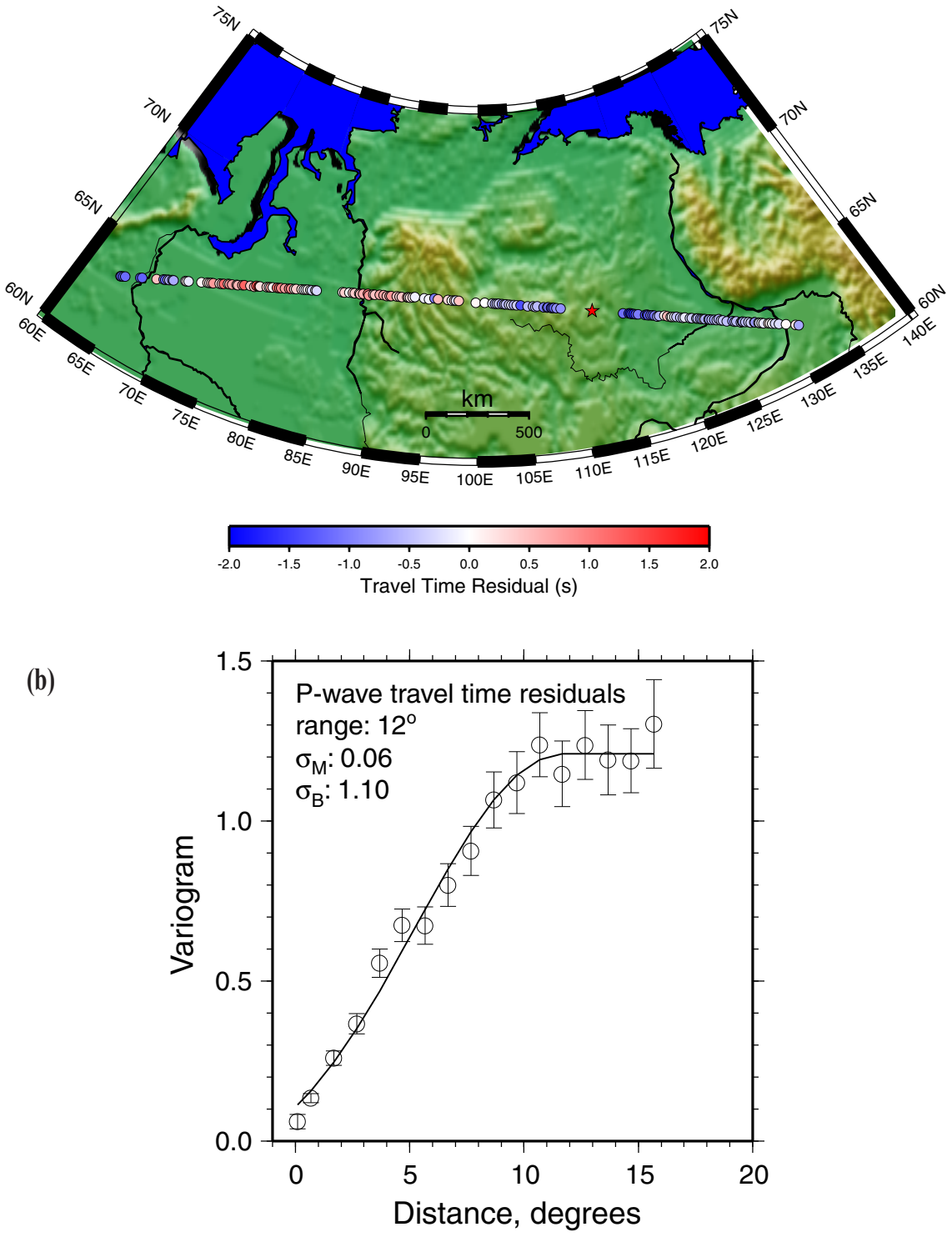


Figure 4. Spatial variation of travel-time residual for the bestfitting 1-D model for KRATON3 (Model_2 as described in text). (a) Map of residuals plotted at station locations on top of topography. Removal of the travel-time predictions of the best-fitting model largely reduces the distance trend revealing path and site effects. We observe faster (negative) residuals for the Eastern stations. (b) Variogram of the travel-time residuals along with our model. The model is parameterized by the range, the measurement error (σ_M) and the background error (σ_B). The range gives us an estimate of the correlation length for the region. The low measurement error indicates the robustness of the travel-time picks.

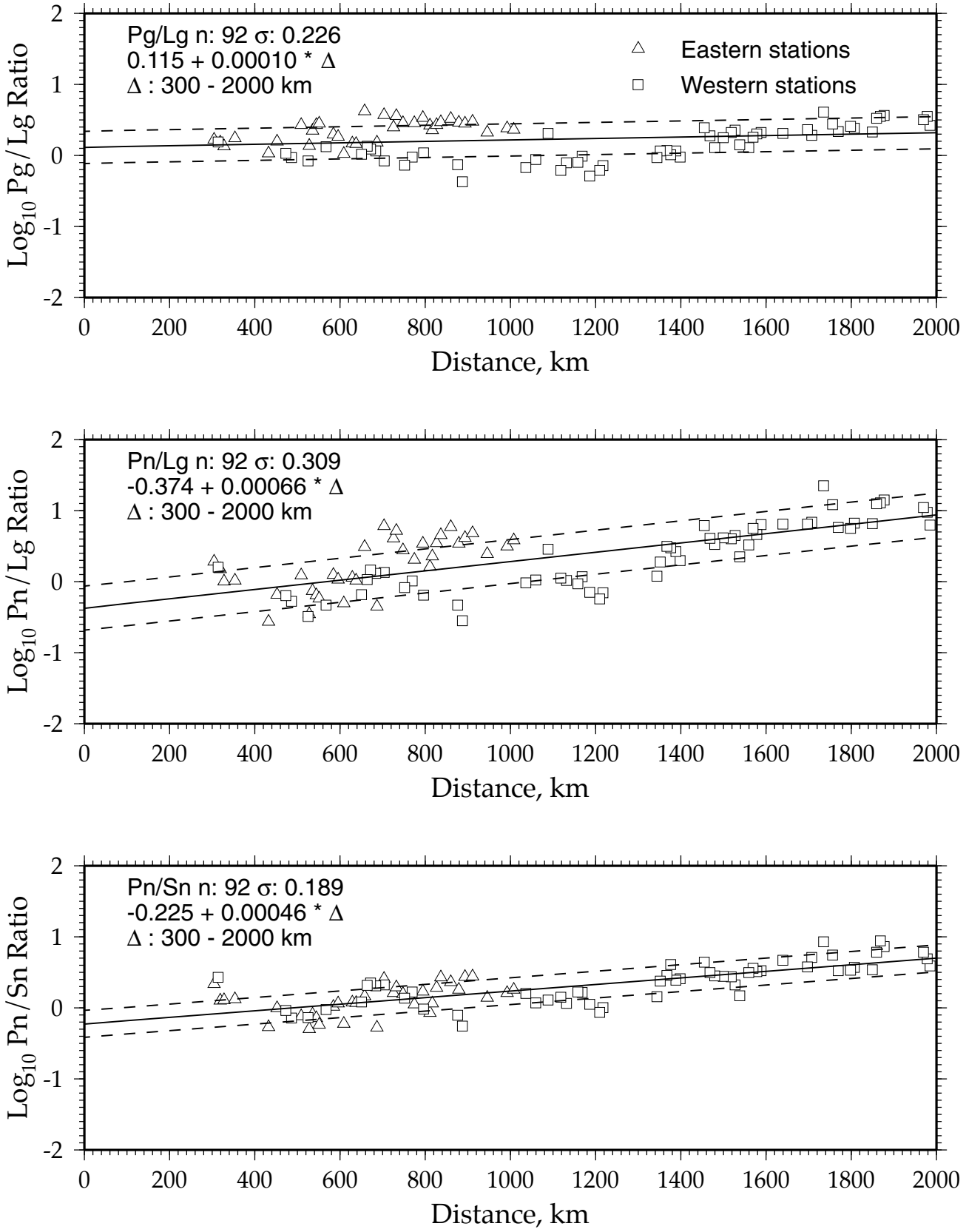


Figure 5. Distance trends of Pg/Lg (top), Pn/Lg (center) and Pn/Sn (bottom). Ratios were taken in the band 0.5-5 Hz. Linear regression fits and 1-σ uncertainties (solid and dashed lines, respectively) are shown. The ratios for eastern and western stations are plotted with triangles and squares, respectively. We considered the ratios with distances between 300-2000 km.

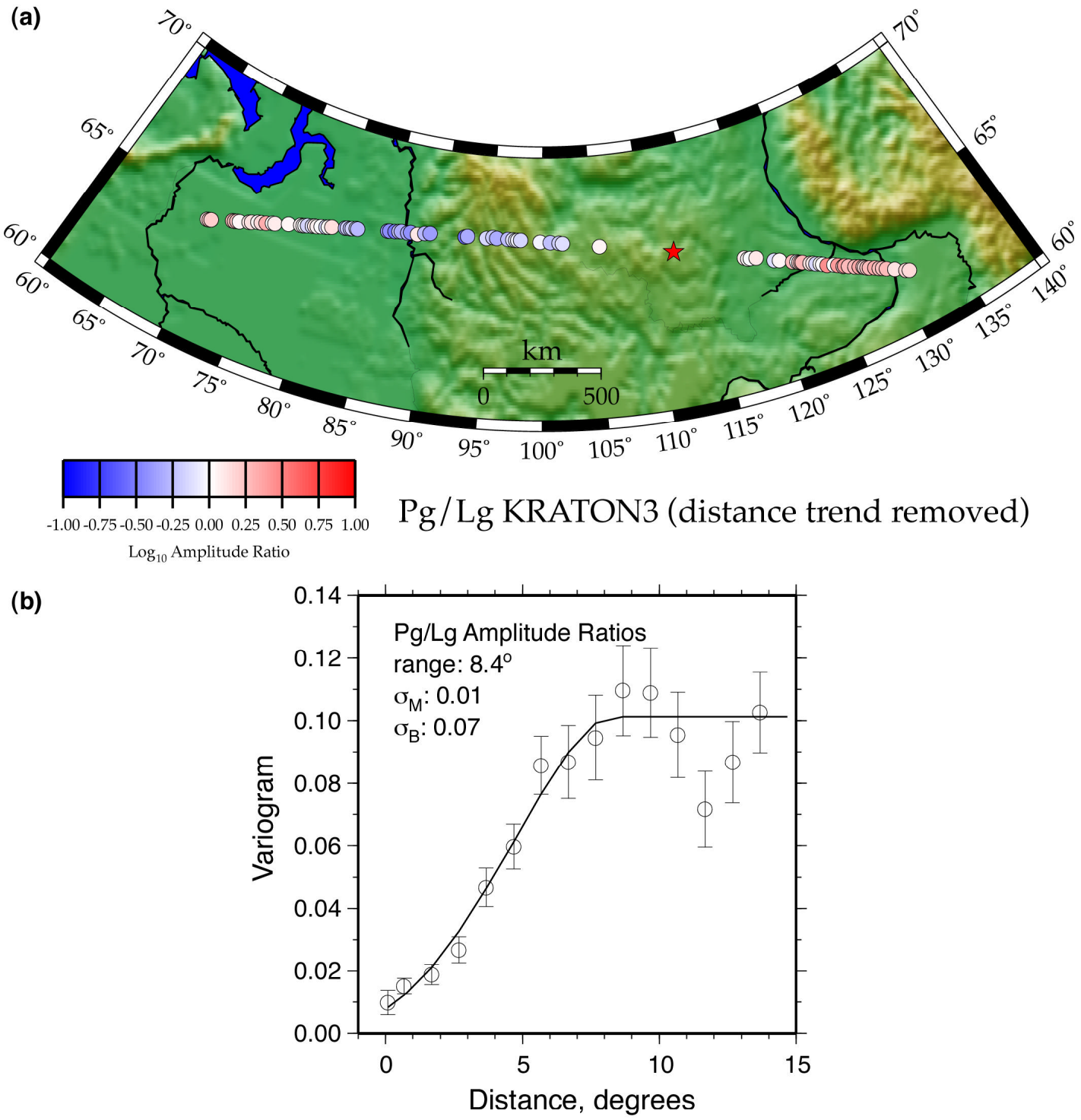


Figure 6. (a) Map of Pg/Lg ratios (0.5-5.0 Hz) for the KRATON3 PNE. Ratios are color coded according to the scale. The distance trend was removed revealing path and site effects. (b) Variogram of the Pg/Lg ratios along with our model. The model is parameterized by a range, the measurement error (σ_M) and the background error (σ_B), similar to that for the travel times.

MONITORING ROUTINE MINE SEISMICITY IN THE CONTERMINOUS UNITED STATES

James W. Dewey and Alena L. Leeds
Adjunct US National Data Center at U.S. Geological Survey (USGS)

Sponsored by U.S. Department of Defense
Defense Threat Reduction Agency

ABSTRACT

We are applying standard U.S. Geological Survey/National Earthquake Information Center (USGS/NEIC) earthquake detection and location methodologies to monitor routine mine seismicity in the conterminous U.S. Our principal goal is to develop knowledge of mining seismicity in districts from which teleseismically recorded mining-associated seismic events might occur. This knowledge would provide a basis for understanding future seismic events from these mining districts that might be located by the International Data Center(IDC) after entry-into-force of the Comprehensive Nuclear-Test-Ban Treaty (CTBT).

Catalogs of routine U.S. mining events are available from May 1997 on the World-Wide Web (http://neic.usgs.gov/neis/mineblast/). Bulletins containing arrival time data are available by anonymous ftp (ftp://ghtftp.cr.usgs.gov/pub/mineblast/). Non-routine mining-events, such as unusually large rockbursts or longwall-collapses, continue to be listed in regular USGS/NEIC media (e.g., http://neic.usgs.gov/current_data.html) if they have magnitudes typical of felt earthquakes; they are not listed in the catalogs of routine mining events.

The cataloged epicenters are calculated from the arrival-times of seismic phases, and their accuracies vary according to the distribution of seismographic stations in the regions in which the mines are located. 90% confidence ellipses on epicentral coordinates are given with the data files on the ftp site. Although the USGS/NEIC does not obtain "ground truth" information from mining companies about most individual mining events, knowledge of mine locations and mining practices enables us to evaluate the reliabilities of the epicenters and confidence ellipses for many regions. The confidence ellipses represent location accuracies quite well for most of the mining districts. Plotting only events with small confidence ellipses dramatically reduces the scatter of epicenters. Problems with the mining-event confidence ellipses are typical of problems associated with confidence ellipses in general: the level of confidence associated with the ellipses must be viewed as being somewhat lower than the nominal 90%; there is evidence of substantial (up to 20 km) location bias for events in a few of the districts; ellipses associated with poorly recorded events are particularly prone to misrepresentation of location accuracy.

The magnitudes routinely assigned to the mining events are based on amplitudes of short-period secondary phases recorded at local and regional distances. For events occurring in the eastern and central U.S. (east of approximately 102□ W longitude), the magnitude is the $m_b(L_g)$ magnitude. For events occurring in the western U.S., the magnitude is a local magnitude that is intended to be equivalent to the M_L magnitude developed by C. F. Richter for Southern California. Because these short-period magnitudes are computed with a different type of data than the teleseismic m_b that is commonly used as the short-period magnitude in the CTBT community, we have made a preliminary attempt to relate our M_L and $m_b(L_g)$ magnitudes to teleseismic m_b. For this we use formulas of Evernden (1967), appropriate for events occurring in western and eastern conterminous U.S. respectively, that enable the calculation of an m_b from regional P-wave amplitude/period data recorded in the U.S. Comparing our M_L with Evernden's "$m_{7.9}$" for western U.S. mining events suggests that our M_L is on average about 0.4 units lower than teleseismic m_b. Comparing our $m_b(L_g)$ with Evernden's "m_{eus}" for eastern U.S. mining events suggests that our $m_b(L_g)$ is also slightly lower, on average, than teleseismic m_b. These attempts to relate our M_L and $m_b(L_g)$ to teleseismic m_b must still be considered very approximate.

The largest magnitude {M_L or $m_b(L_g)$} that we have assigned to a routine mining event is 3.6. Coverage of the U.S. is currently not complete even in the magnitude 3.0 – 3.6 range.

OBJECTIVE

Seismic events associated with the extraction of mineral resources potentially present both problems and opportunities for the implementation of the Comprehensive Nuclear-Test-Ban Treaty (CTBT) (e.g., Heuze and Stump, 1999). The problems arise from the possibility that seismic signals from mine-associated events might be misinterpreted as being from small nuclear explosions. Opportunities arise from the potential of mine-associated events to calibrate the hypocenter determination and magnitude calculation procedures of the International Data Center (IDC). Many mine-associated seismic events are large explosions; the CTBT contains provisions for a State Party to provide information to the Technical Secretariat about the occurrence of large chemical explosions within its territory, as a "Confidence-Building Measure". Mining associated ground-failures present problems and opportunities similar to those presented by large mining explosions.

Explosions from surface mines and quarries and planned longwall collapses from underground mines are frequently detected in the conterminous U.S. by seismographs of the U.S. National Seismograph Network and other cooperating networks, and are recorded in near real-time at the United States Geological Survey National Earthquake Information Center (USGS/NEIC). The USGS/NEIC had historically dealt with routine mining events by identifying them at early stages of analysis and not analyzing them further. Since May 1997, in order to address the potential impact of mine seismicity on the CTBT, the USGS/NEIC has been preparing a monthly catalog entitled "Probable Mining Explosions in the United States" (for March 2000 and earlier) and "Routine Mining Seismicity in the United States" (after March 2000). We view these catalogs as providing a context for understanding U.S. mining-associated seismicity that might be located by the IDC after entry-into-force of the CTBT. The catalogs will also provide information to guide the selection of mines at which calibration experiments (e.g., Heuze and Stump, 1999) might profitably be conducted.

The catalogs are available on the World-Wide Web (http://neic.usgs.gov/neis/mineblast/) and associated bulletins containing arrival-time data and epicenter confidence ellipses are available via "anonymous ftp" (ftp://ghtftp.cr.usgs.gov/pub/mineblast/). Since October, 1999, our website has included a preliminary catalog, a preliminary bulletin with confidence ellipses and arrival times, and a map of routine mine seismicity, all for events occurring within the previous 61 days. Events are typically posted in the preliminary catalogs within several days of their occurrence: the analysis of the events is currently the responsibility of a single analyst, however, and the times to event-postings are longer than several days when the analyst is on leave.

The events listed in "Routine Mining Seismicity in the United States" are those that would have previously been ignored by analysts of the USGS/NEIC once they were identified as having the characteristics of day-to-day mine-associated seismicity. Atypically large longwall roof-collapses and non-planned mining-associated rockbursts and mine collapses have been, and continue to be, reported in regular USGS/NEIC earthquake catalogs if they have magnitudes that are typical of felt earthquakes. The USGS/NEIC receives independent information that some of these atypical events from mining districts are in fact associated with disturbances in mines; these events are then specifically identified in USGS/NEIC files as having been induced events. Atypically large mine-induced events that are not specifically identified as such to the USGS/NEIC will usually be listed as though they were tectonic earthquakes, even if they occur in a district that is known to have had previous mining-induced events. Unusual mining explosions have also occasionally been listed in the regular USGS/NEIC earthquake catalogs. Atypical mining events that are listed in regular earthquake catalogs of the USGS/NEIC are not listed in the catalogs of "Routine Mining Seismicity in the United States." Information on seismic events that have been listed in the regular earthquake catalogs of the USGS/NEIC may be obtained from the main USGS/NEIC website (http://neic.usgs.gov/).

Support for the early development of the catalog of routine mining seismicity was provided by the Arms Control and Disarmament Agency. Support for the ongoing cataloging of mining seismicity and improvements to the cataloging process is provided by the U.S. Department of Defense, Defense Threat Reduction Agency.

RESEARCH ACCOMPLISHED

Monitoring of routine mine seismicity

The epicenters listed in the "Routine Mining Seismicity in the United States" catalogs are calculated from the arrival times of seismic phases recorded at the USGS/NEIC. The completeness of the catalogs and the accuracies of epicenters listed in the catalogs depend on the locations of the recording seismographs with respect to the mines. The locations of seismographs situated within the contiguous U.S. that transmitted data to the USGS/NEIC in June 2000 are shown in Figure 1. The network of transmitting stations has changed somewhat during the period May 1997 – June 2000. In addition, individual stations sometimes have problems that make their data unusable. The completeness and accuracy of the mine-event cataloging therefore vary as a function of time for some of the regions.

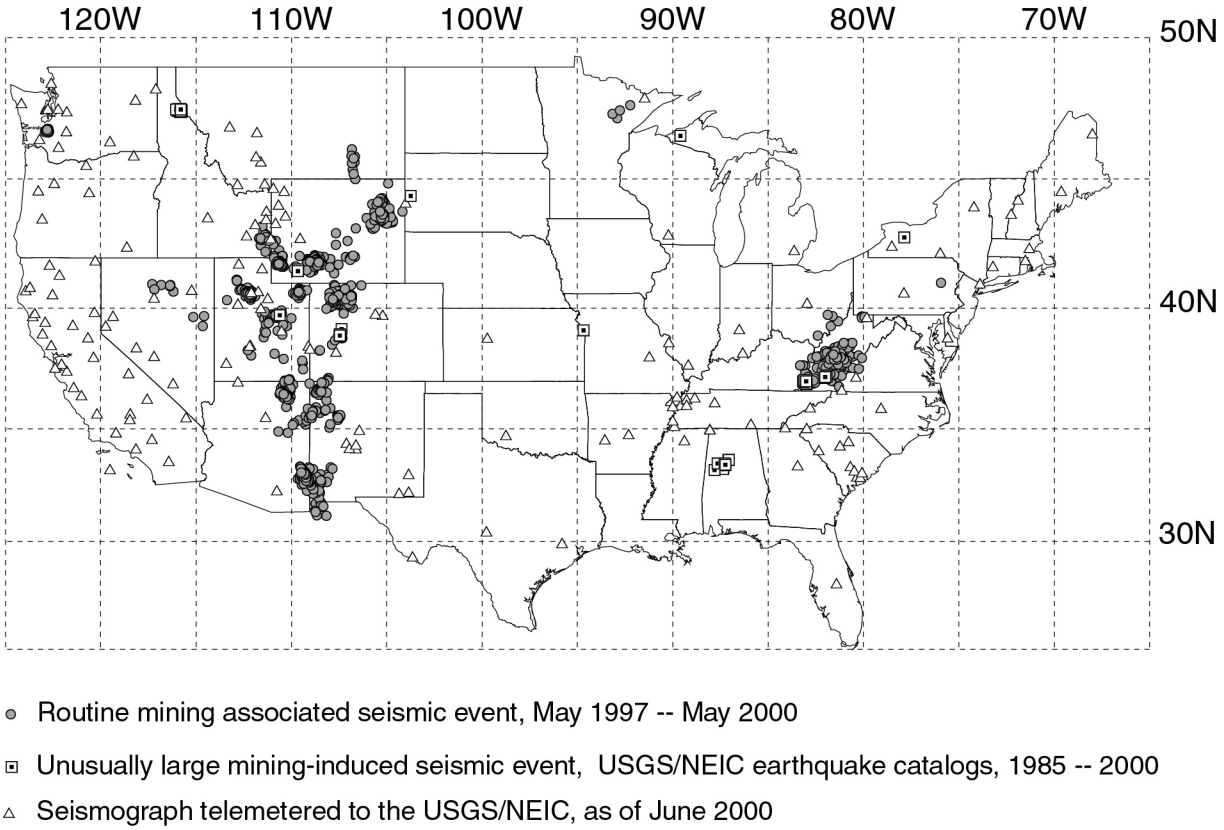


Figure 1. Epicenters of events listed in "Routine Mining Seismicity in the United States" and locations of large mining-induced events listed in regular earthquake catalogs of the USGS/NEIC.

In order to be cataloged, a mine-associated event must have been detected by the automatic event-detector and phase associator used at the USGS/NEIC (this has been the case for over 98 % of the events), or we must have obtained knowledge of the event independently of USGS/NEIC data.

The epicenters of mine-associated events are calculated from the arrival times of first-arriving P-waves, using the Jeffreys-Bullen travel-time tables (Jeffreys and Bullen, 1940). A large majority of arrival-time data used in computing the epicenters are of the P_n phase. Arrivals of the P_n phase from mine-associated events are commonly emersive and of low amplitude, so it is expected that there will be many more gross arrival-time errors than would be expected if arrival-time errors had a Gaussian distribution. Although later arrivals are not formally used in calculating the epicenter, analysts use time-intervals between P_g and S_g arrivals at regional distances to guide their picks of some P_n phases that would not otherwise be picked out of the background noise.

The magnitudes assigned to the events in the "Routine Mining Seismicity in the United States" catalogs are calculated from the amplitudes of local and regional seismic phases. The magnitudes assigned to events that occur east of the Rocky Mountains are $m_b(L_g)$ magnitudes (Nuttli 1973). The magnitudes assigned to events that occur in the western U.S. are M_L magnitudes computed according to the formula of Richter (1935). Unlike the M_L defined by Richter, however, our M_L(GS) are based on amplitudes picked from traces of vertical-component, electronically amplifying seismographs, rather than from the traces of horizontal-component, optically amplifying seismographs. Also, we compute M_L(GS) for seismic events from throughout the western United States, whereas Richter's formula was defined for Southern California, and implicitly incorporates the attenuative properties of Southern California crust and mantle.

The cataloged mining events are identified as such on the basis of their occurring in clusters that have similar sizes and waveforms and that are spatially close to active mining districts.

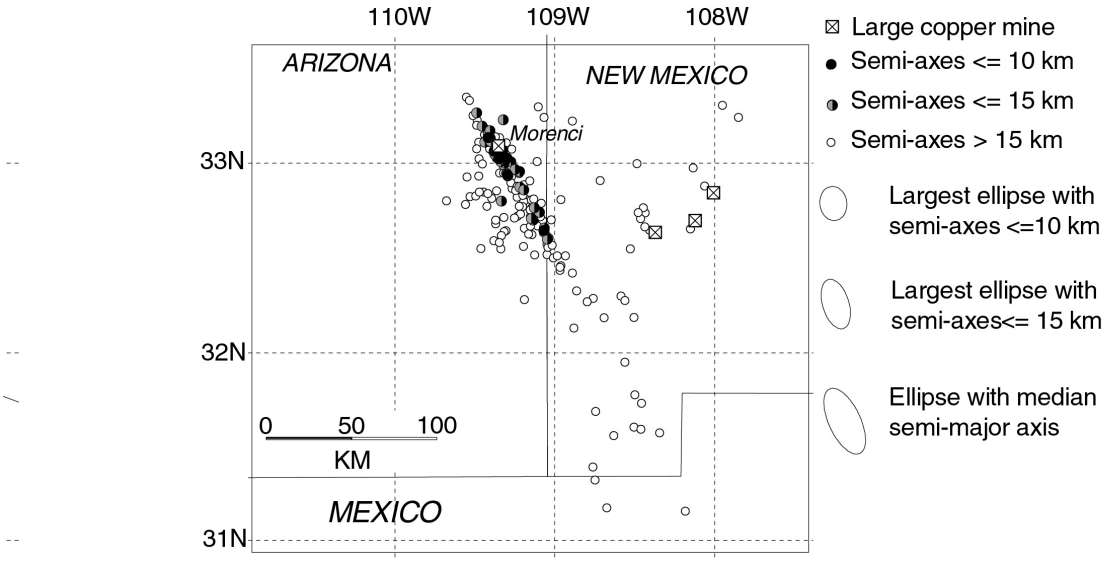


Figure 2. Mine-associated seismicity in southeastern Arizona and adjacent New Mexico. Most of these events probably occurred at Morenci, and many are severely mislocated. Epicenter symbols are distinguished according to the sizes of the associated 90% confidence ellipses.

Completeness of cataloging of mine seismicity

Our goal is to catalog mining events that are large enough that they might be cataloged by the IDC. Empirically, this would correspond to events of M_L(GS) ~ 2.5 in the western U.S. and events of $m_b(L_g)$ about 3.0 in the eastern U.S. We are not now attaining the desired level of completeness. It is noteworthy, for example, that we detected many mining events with $m_b(L_g) > 3.0$ in West Virginia in some months of our study, but none during protracted time-periods when key stations were not operating. In other regions, we have been able to locate some events only

retrospectively, after they were reported in the Reviewed Event Bulletin (REB) of the Prototype International Data Center. Some of the initially missed REB events were actually quite well recorded by seismographs recording at the USGS/NEIC, but they were not found by the USGS/NEIC automatic event-detector. The events in northern Minnesota (Fig. 1), however, could be located only with arrival-time data listed in the REB; these events were recorded by only one of the USGS/NEIC stations. Conversely, some mining districts in the Mountain States are so well monitored by seismographs that we are able to locate many events that are substantially smaller than M_L(GS) 2.5. We deliberately catalog small events from such districts when such cataloging will help understand the nature of the districts' seismicity.

Accuracy of epicenters and the worth of confidence ellipses as measures of epicenter accuracy

Many of the large mines from which we record events are spatially well separated from other large mines, and some closely spaced mines occur in spatially well defined lineations. For these mines, we are able to estimate location accuracies and evaluate the confidence ellipses as measures of epicenter accuracy. The USGS/NEIC does not usually obtain "ground truth" information from mining companies about the locations of individual mining events.

For mines in the middle of regional seismographic networks in Utah and western Washington, it appears that ninety-percent of our epicenters are accurate to within 10 or 15 km. In contrast, for southeastern Arizona (Fig. 2) or southeastern Montana, on the fringes of the area covered by seismographs recording at the USGS/NEIC, an ellipse with a 100-km long semi-axis, centered on the mine, would be necessary to encompass ninety percent of the epicenters of events originating at the mine. Most of the severely mislocated epicenters probably result from a combination of poor azimuthal distribution of recording stations with respect to the epicenter and from gross errors in picking the P_n-phases whose arrival times are used in the epicenter determination process.

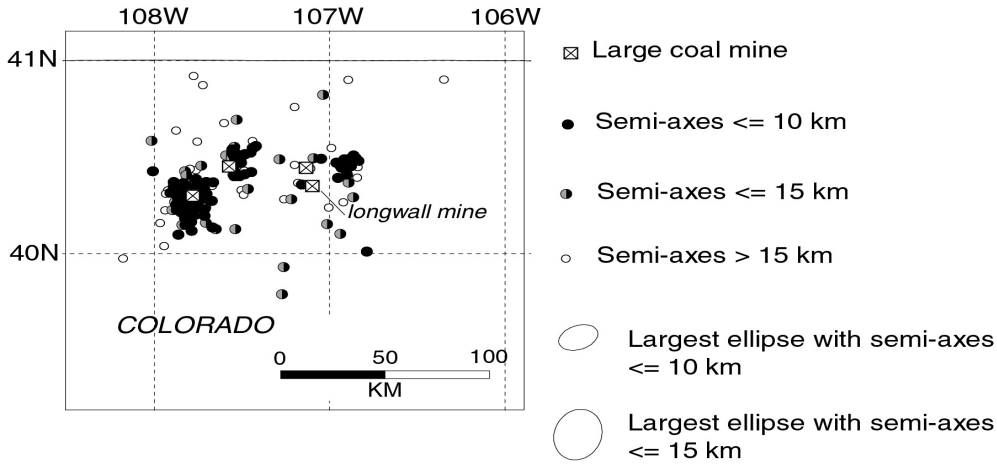


Figure 3. Mine seismicity in northwestern Colorado. With the exception of the longwall mine, the mines shown are surface mines. The longwall-mine events are those whose epicenters are calculated to lie near 40.45N, 106.90W, approximately 20 km ENE of their true positions. Epicenter symbols are distinguished according to the sizes of the associated 90% confidence ellipses.

The nominally 90% confidence ellipses associated with the calculated epicenters have the strengths and weaknesses that are typically associated with such confidence ellipses for events in regions of complex geology that are located with data containing non-Gaussian errors. The strengths are that the ellipses provide information on the relative precision of epicenters within a group of epicenters, and the highly eccentric ellipses do a good job of indicating the directions in which the associated epicenters are most likely to be mislocated (e.g., Fig. 2). The weaknesses are that the level of confidence to be associated with the ellipses is less than the nominal 90% and that the ellipses do not account for bias due to unmodelled velocity structure.

Figure 3 illustrates an intriguing example of bias. Planned roof-collapse events occurring in an underground longwall mine (Walter et al., 1996) are systematically mislocated about 20 km from their true source, whereas explosions occurring in two nearby large surface mines show much less, or no, bias. Such radical differences in bias within a small geographical area seem unlikely to be due to unmodelled velocity structure. The different biases may be due to systematic differences in interpreting phases from the explosion and roof-collapse sources.

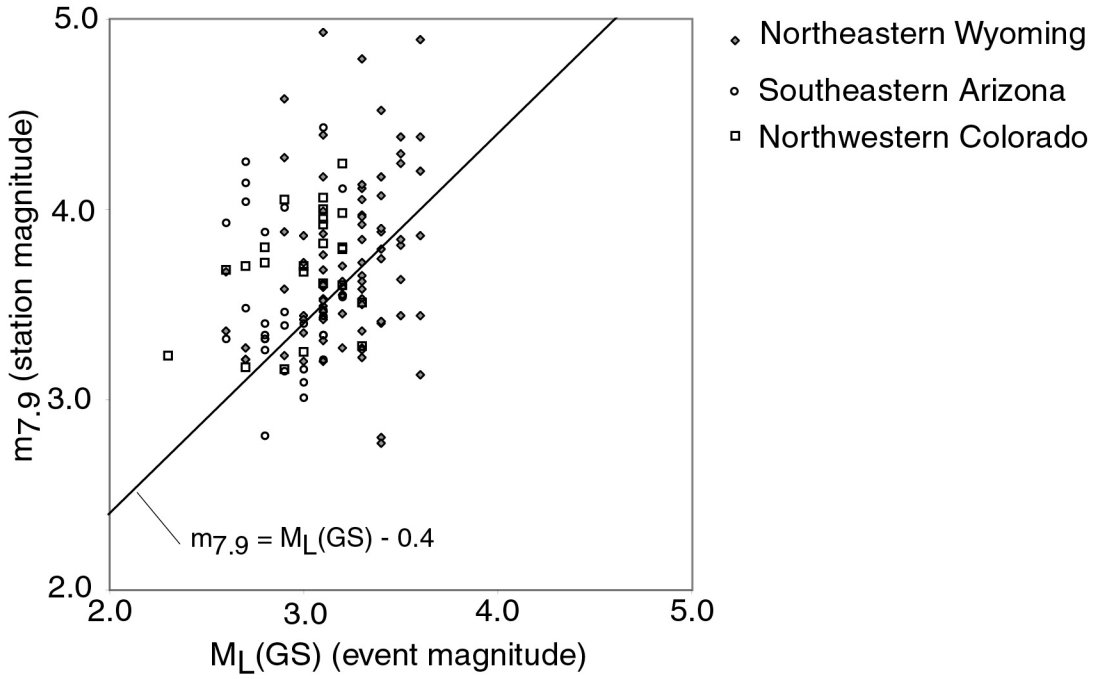


Figure 4. Regional P-wave $m_{7.9}$ (Evernden, 1967) for individual events recorded at individual stations, plotted as a function of the M_L(GS) assigned to the event. All $m_{7.9}$ were obtained at □ > 5□, and most at □ < 10□. Different symbols represent the regions in which the events occurred. The straight line is that of figure 5.

The relationship of $M_L(GS)$ and $m_b(L_g)(GS)$ to teleseismic m_b

The short-period magnitudes that we have assigned to the routine mining seismicity, $M_L(GS)$ and $m_b(L_g)(GS)$, are different than the teleseismic m_b that is the most commonly used short-period magnitude within the CTBT community. The $M_L(GS)$ and $m_b(L_g)(GS)$ are based on amplitudes of short-period secondary waves [S- or surface waves for the $M_L(GS)$ and surface waves for the $m_b(L_g)(GS)$] rather than short-period P-waves, and the $M_L(GS)$ was never explicitly calibrated to agree with teleseismic m_b. None of the events listed in "Routine Mining Seismicity of the United States" have been assigned a teleseismic P-wave m_b that is calculated according to standard USGS/NEIC procedures, because we did not have P-wave amplitude/period data for these events from USGS/NEIC stations at □

> 15□. In order to examine how the M_L(GS) and $m_b(L_g)$(GS) should be interpreted in terms of the teleseismic P-wave m_b, we computed m_b values from P-wave amplitudes/periods recorded at epicentral distances of 5□ < □ < 15□, using regionalized formulas of (Evernden, 1967) that were developed so as to yield magnitude values that are consistent on average with the USGS teleseismic m_b. The P-wave amplitude/period data at 5□ < □ < 15□, used in the computation of short-period body-wave magnitudes according to Evernden's formulas, were extracted from arrival-time data files that are available at the WWW and ftp sites whose addresses are given above.

To western U.S. mining seismic events for which there are P-wave amplitude and phase observations at 5□ < □ < 15□, we assigned Evernden's $m_{7.9}$, which was defined to give values consistent with teleseismic short-period P-wave m_b for events occurring in the western U.S. The individual values of $m_{7.9}$ show large scatter when plotted with respect to M_L(GS) (Fig. 4), but the $m_{7.9}$ are on average higher than the M_L(GS) values that were assigned to the respective mining seismic events. Taking the median value of the $m_{7.9}$ for each M_L(GS), for M_L(GS) having 10 or more $m_{7.9}$ observations in a single region, we find that $m_{7.9}$ are on average about .4 units larger than M_L(GS) (Fig. 5). Assuming that $m_{7.9}$ is an unbiased proxy for teleseismic m_b, figure 5 implies that teleseismic m_b will on average be about .4 units larger than M_L(GS).

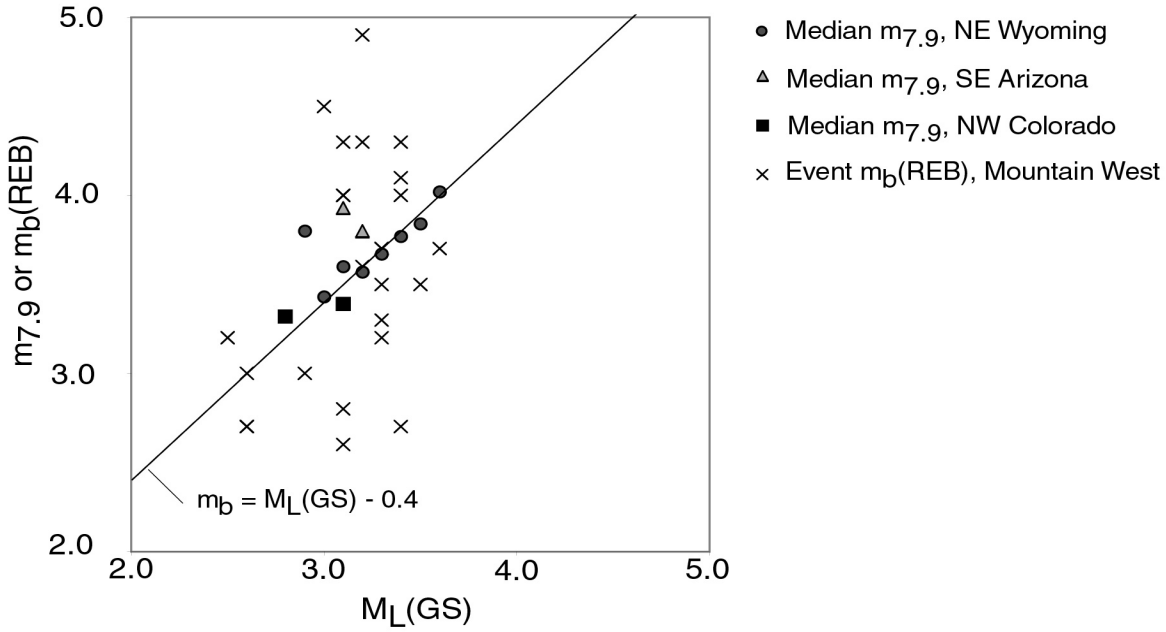


Figure 5. Body wave magnitude as a function of M_L(GS). Median $m_{7.9}$ are based on ten or more observations of $m_{7.9}$ (Evernden, 1967) for each value of M_L(GS). The straight line is an approximate fit by eye to NE Wyoming median values, assuming a slope of 1 for the relationship between $m_{7.9}$ and M_L(GS). The m_b(REB) are those reported for events in the Reviewed Event Bulletin of the Prototype International Data Center.

It would not be surprising if there were a systematic discrepancy between teleseismic m_b and M_L(GS) for the western U.S. mining seismicity. The M_L(GS) and teleseismic m_b have evolved along different paths from their common ancestor [Richter's (1935) original local magnitude], and the partitioning of an explosion's energy into P-waves and secondary waves is likely to be different than the partitioning of an earthquake's energy into P-waves and secondary waves. Keeping in mind the large scatter in the data of figures 4 and 5, and keeping in mind that the $m_{7.9}$ are measured at relatively few of the stations that recorded the mining-induced events, we regard the value of 0.4 as only an approximate measure of systematic difference between teleseismic m_b and M_L(GS) for the western U.S. mining seismicity.

The M_L(GS) appears to be an approximate predictor of the extent to which a regionally recorded mine event will be recorded by stations of the International Monitoring System and listed in the Reviewed Event Bulletin. Figure 6 shows an order-of-magnitude range of M_L(GS) over which Powder River Basin explosions might be listed in the REB, but the number of Powder River Basin explosions listed in the REB, as a fraction of the number of explosions listed in "Routine Mining Seismicity of the U.S.", increases generally as a function M_L(GS). A number of studies (e.g., Anandakrishnan and others, 1997; Carr and Garbin, 1998; Khalturin and others, 1998) have indicated that the maximum amplitude of secondary phases does not scale well with the total charge size of a ripple-fired explosion. Figure 6 suggests that the amount of energy from an explosion that goes into S- and surface waves at regional distances is somewhat indicative of the amount of energy that goes into teleseismic P-waves.

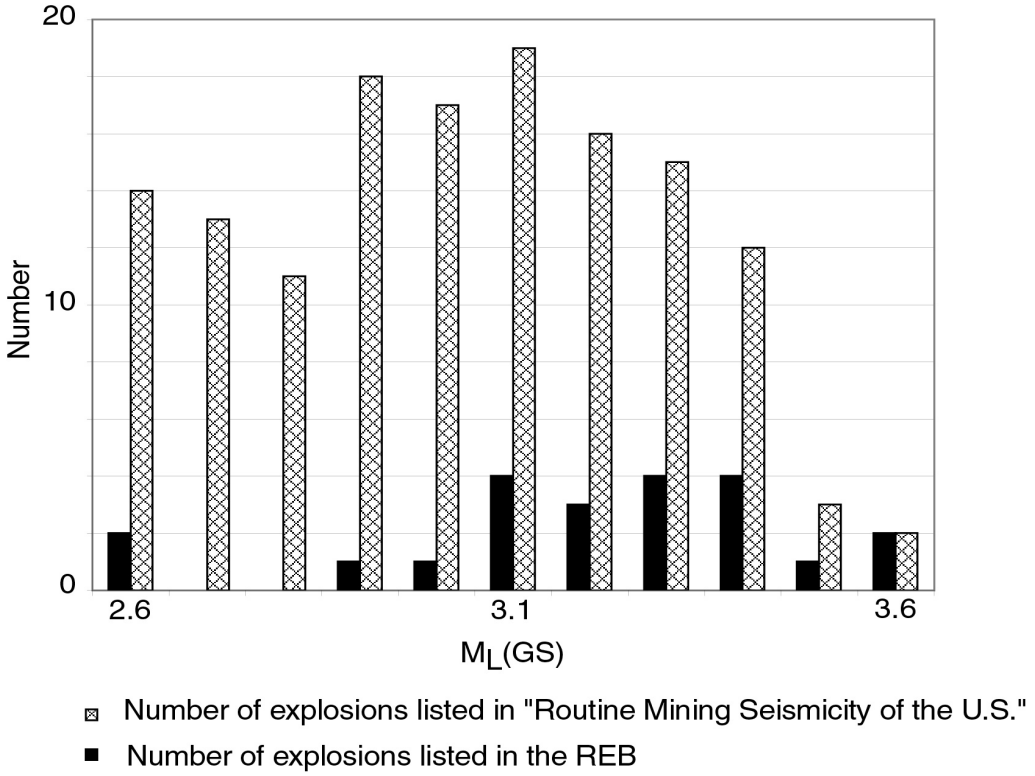


Figure 6. Numbers of events listed in the REB, as a function of M_L(GS), for explosions in the southern Powder River Basin, Wyoming, May 1997 through 20 February 2000.

The arrival-time data files that are available on our WWW and ftp sites contain a handful of P-wave amplitudes/periods from mining events in the eastern U.S., in the distance range 5□ < □ < 15□, from which we can calculate m_{eus} (Evernden, 1967). The m_{eus} is defined so as to be consistent on average with the teleseismic m_b of the USGS for earthquakes in the central and eastern U.S. Assuming that the m_{eus} is an unbiased proxy for teleseismic m_b, the observations suggest (Fig. 7) that the $m_b(L_g)$(GS) may also, like the M_L(GS) in the western U.S., give values that are systematically somewhat lower than teleseismic m_b, but the number of observations is very few and most are from a single station. The $m_b(L_g)$(GS) is based on a formula of Nuttli(1973), which was defined so that $m_b(L_g)$ would yield values equal on average to teleseismic m_b for earthquakes in the central U.S. A discrepancy between $m_b(L_g)$(GS) and m_{eus} (or teleseismic m_b) might be due to differences in excitation of the L_g phase for explosions and earthquakes, or it might be due to attenuation of L_g phases in the central Appalachians being somewhat higher than in the central U.S.

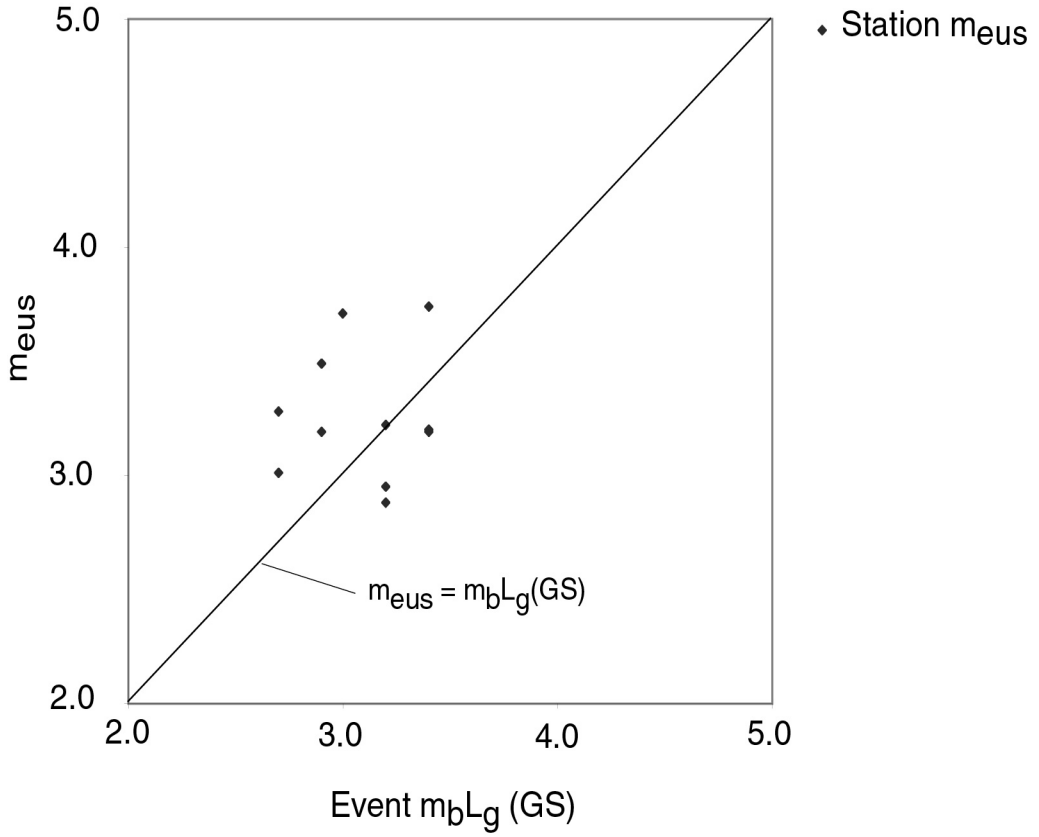


Figure 7. Values of individual station observations of m_{eus} (Evernden, 1967) plotted as a function of the event $m_b(L_g)$(GS), for mining events occurring in the eastern U.S. The line $m_{eus} = m_b(L_g)$(GS) is shown to facilitate comparison of the two magnitude types.

CONCLUDING REMARKS

Since May 1997, we have cataloged approximately 2,000 routine mining-associated seismic events in the U.S. and made the epicenters, epicentral confidence-ellipses, magnitudes, and arrival time data freely available on the WWW and on an anonymous-ftp site. The cataloging of these events provides a context for other States Parties to better understand the nature of U.S. mining-associated seismic events that will occasionally appear in bulletins of the International Data Center.

Our cataloging of mine seismicity has occurred during a time-period in which there have been significant changes in the network of seismographs that record at the USGS/NEIC. Future changes in U.S. seismograph coverage and USGS/NEIC procedures are likely to significantly improve the completeness of coverage and accuracy of epicenter location for regions in which completeness and accuracy are currently poor. These changes include installation of more seismographs in currently poorly monitored areas, improvement of the computer algorithm that automatically detects events and associates arrival-time data with events, and changes in the USGS/NEIC epicenter-computing algorithm that enable secondary phases to be incorporated explicitly into the location process.

REFERENCES

Anandakrishnan, S., Taylor, S.R., and Stump, B.W., 1997, Quantification and characterization of regional seismic signals from cast blasting in mines: a linear elastic model: Geophysical Journal International, v. 131, p. 45-60.

Carr, D.B., and Garbin, H.D., 1998, Discriminating ripple-fired explosions with high-frequency (> 16Hz) data: Bulletin of the Seismological Society of America, v. 88, p. 963-972.

Evernden, J.F., 1967, Magnitude determination at regional and near-regional distances in the United States: Bulletin of the Seismological Society of America, v. 57, p. 591-639.

Heuze, F., and Stump, B. (co-chairs), 1999, Mine Seismicity and the Comprehensive Nuclear-Test-Ban Treaty, Report of a Working Group from Government, Industry, and National Laboratories, Department of Energy Report LA-UR-99-384, 70 pp.

Jeffreys, H., and Bullen, K.E., 1940, Seismological Tables: British Association, Gray-Milne Trust, 50 pp.

Khalturin, V.I., Rautian, T.G., and Richards, P.G., 1998, The seismic signal strength of chemical explosions: Bulletin of the Seismological Society of America, v. 88, p. 1511-1524.

Nuttli, O.W., 1973, Seismic wave attenuation and magnitude relations for eastern North America: Journal of Geophysical Research, v. 78, p. 876-885.

Richter, C.F., 1935, An instrumental earthquake scale: Bulletin of the Seismological Society of America, v. 25, p. 1-32.

Walter, W.R., Hunter, S.L., and Glenn, L.A., 1996, Preliminary report on LLNL Mine Seismicity Deployment at the Twentymile Coal Mine: UCRL-ID-122800, Lawrence Livermore National Laboratory, Livermore, California, 19 pp.

Key Words: Mining related seismicity, location, magnitude

REGIONAL SEISMIC EVENT CHARACTERIZATION USING A BAYESIAN KRIGING APPROACH

Mark Fisk and Steven Bottone, Mission Research Corporation
Gary McCartor, Southern Methodist University

Sponsored by U. S. Department of Defense
Defense Threat Reduction Agency

Contract No. DSWA01-98-C-0152

ABSTRACT

This effort focuses on collecting and analyzing regional seismic data for earthquakes and underground explosions to improve seismic event characterization capabilities with regard to monitoring the Comprehensive Nuclear-Test-Ban Treaty (CTBT). Digital data have now been acquired and processed for 267 regional recordings of 160 underground nuclear (UNE) and chemical (UCE) explosions. The explosion data set includes 99 Nevada Test Site (NTS) UNE's recorded by MNV and KNB; 6 Lop Nor UNE's recorded by NIL, ZAL, ULN, WMQ, BRVK and MAKZ; 22 Semipalatinsk (STS) UNE's recorded by WMQ and BRVK; 6 Novaya Zemlya (NZ) UNE's recorded by ARCES and KEV; and one UNE at the Indian Test Site recorded by NIL. In addition, the set includes 20 Former Soviet Union (FSU) peaceful nuclear explosions (PNE) recorded by BRVK and KEV; and 6 STS UCE's recorded by ZAL and BRVK. (Note: not all of these explosions have recordings by all stations listed.) Over 5300 regional recordings, between 3 and 17 degrees, by existing seismic stations of the International Monitoring System (IMS) are also used in this study. The regional recordings correspond to 4173 presumed earthquakes above mb 3.5 in the Reviewed Event Bulletin (REB) that were processed at the prototype International Data Center (pIDC). Maximum amplitude measurements of Pn, Pg, Sn and Lg have been computed in several frequency bands ranging from 2 Hz up to 14 Hz (depending on the Nyquist frequency of a given station).

The data for the presumed earthquakes have been used to estimate attenuation corrections for Pn/Sn and Pn/Lg amplitude ratios in the 2–4, 4–6, 6–8, and 8–10 Hz passbands for tectonic and stable region types. The regional phase amplitude ratios are further corrected for path variations using a Bayesian Kriging algorithm. A correction surface is determined for each type of amplitude ratio at each station as an optimal linear combination of existing amplitude-ratio data at the station, giving greater weight to data nearer to the location of the event to be corrected. A corresponding uncertainty surface is also estimated in terms of the residual variance of the data and a calibration variance. For well-calibrated locations, the correction converges to the mean of nearby data and the uncertainty converges to the residual variance. For locations far from calibration data, the correction surface converges to the worldwide average, with larger uncertainty due to both residual and calibration variances.

Using these correction and uncertainty surfaces, corrected values of Pn/Smax(6–8 Hz) are then used to define a hypothesis test that fixes the significance level with respect to misclassifying explosions. A score is computed for each event such that events with negative scores are not screened out at the specified significance level. The significance level used here has been set such that none of the available underground explosions are screened out. Events with scores greater than zero are screened out (i.e., are considered to be inconsistent with the hypothesis that the event belongs to the explosion population). Screening rates for earthquakes above mb 3.5 are estimated and improvements in event characterization performance due to Kriging are demonstrated.

OBJECTIVE

This effort focuses on collecting and analyzing regional seismic data for underground explosions and earthquakes to improve seismic event characterization capabilities with regard to monitoring the Comprehensive Nuclear-Test-Ban Treaty (CTBT). Key aspects of this effort include: (i) acquiring regional seismic recordings for underground explosions and earthquakes; (ii) processing the waveforms to measure Pn, Pg, Sn and Lg amplitudes in various frequency bands; (iii) evaluating optimum processing techniques for regional amplitude ratios; (iv) developing a regional event-screening capability, which includes establishing necessary region-specific training sets and distance corrections; and (v) evaluating optimum screening criteria for various regions and comparing explosion and earthquake characteristics in an effort to understand how regional event characterization parameters and screening criteria can be transported to regions for which no explosion data exist.

This work is motivated by the fact that, although depth and Ms:mb are essential methods in the characterization of seismic events, the experimental depth and Ms:mb screening criteria being tested at the prototype International Data Center (pIDC) currently screen out less than 50% of the presumed earthquakes above mb 3.5 in the Reviewed Event Bulletin (REB) (e.g., Fisk et al., 1999b). However, there are a significant number of events in the REB with regional seismic data that can provide additional event-screening performance. Many studies have indicated that ratios of high-frequency, regional seismic phase amplitude ratios can provide adequate separation between underground explosions and earthquakes to aid in monitoring the CTBT (see Fisk et al., 1996, and references therein).

We describe data that have been compiled and processed for 267 regional recordings of 160 underground explosions. These explosions are compared to over 5300 regional waveforms, recorded by existing seismic stations of the International Monitoring System (IMS), for 4173 presumed earthquakes, above mb 3.5, processed at the pIDC. After applying distance corrections that depend on region type (tectonic or stable) to Pn/Sn and Pn/Lg ratios, a Bayesian Kriging algorithm is applied at each station to further correct for path variations. The Kriging algorithm also provides a corresponding uncertainty surface. To characterize the events, we use Pn/Smax in the 6–8 Hz band, where Smax = max(Sn,Lg), which has been corrected for distance and for path variations using the Kriged surface. We apply a hypothesis test, which accounts for the varying uncertainty associated with the Kriged surface, to these data sets to assess whether an event is consistent with the explosion population at a fixed significance level with respect to incorrectly screening out an explosion. A *score* is computed such that events with positive scores are screened out, i.e., are inconsistent with the hypothesis that the event belongs to the explosion population. Events with scores less than or equal to zero are not screened out. At the 0.005 significance level, none of the available explosions are screened out.

RESEARCH ACCOMPLISHED

Regional Explosion Data

We have compiled 267 regional seismic recordings for 160 underground nuclear (UNE), chemical (UCE) and peaceful nuclear (PNE) explosions. Table 1 summarizes our current database of regional explosion recordings, which represent explosions in diverse geological regions at various test sites. These explosions cover a magnitude range of about ML 2.4 to mb 6.2, and a distance range of about 2 to 17 degrees. The regional measurements for the NTS explosions recorded by MNV and KNB were provided by LLNL (Patton and Walter, 1994) and the PNE data recorded by BRVK were provided by Jack Murphy (1998).

The processed data consist of regional phase amplitudes, Pn, Pg, Sn and Lg in the 2–4, 4–6, 6–8, and 8–10 Hz bands. Not all events have complete sets of amplitude ratios. Six of the UNE's conducted on Novaya Zemlya (NZ) were recorded by station KEV and three were recorded by ARCES. Six UNE's occurred at the Lop Nor test site, one recorded by ZAL, four by NIL, two by ULN, one by WMQ, four by BRVK and four by MAKZ. Semipalatinsk (STS) provides 22 UNE's, 21 recorded by WMQ and six by BRVK. There is one UNE at the Indian Test Site recorded by NIL. There are 99 explosions from the Nevada Test Site (NTS), 84 of which have recordings at both MNV and KNB, nine at MNV only, and six at KNB only. In addition, the set includes 20 Former Soviet Union (FSU) PNE's, 16 recorded by BRVK and six by KEV; and 6 STS UCE's, five recorded by ZAL and six by BRVK. A few events in the table do not have either Pn/Sn(6–8 Hz) or Pn/Lg(6–8 Hz) available, and therefore not are used in the screening test described below.

Table 1: Summary of Regional Underground Nuclear Explosion Data

Station	Distance	Magnitude	Test Site	Explosion Dates
KEV	9.4 3.1–19.5	5.52–5.90 4.70–5.50	NZ UNE's FSU PNE's	821011, 841025, 870802, 880507, 881204, 901024 5 (820904–850718)
ARCES	9.9	5.60–5.90	NZ UNE's	880507, 881204, 901024
ZAL	12.2 6.2, 5.5, 5.5 6.0, 6.0	4.71 3.95, n/a, n/a, 3.80, 3.67	Lop Nor UNE STS UCE's	960729 970803, 970831, 970928, 980822, 990925
NIL	14.4–14.7 6.7	5.73, 5.54 5.69, 4.71 5.00	Lop Nor UNE's India UNE	950515, 950817, 960608, 960729 980511
ULN	14.3	5.73, 5.54	Lop Nor UNE's	950515, 950817
WMQ	8.6 2.2	4.6–6.1 4.7	STS UNE's Lop Nor UNE	21 (870606–891004) 880929
BRVK	16.8–16.9 6.2 5.8–6.2 7.2–17.2	6.00,5.73 5.54, 5.69 5.70–7.20 3.95, n/a, n/a, 3.80, n/a, 3.67 4.5–5.8	Lop Nor UNE's STS UNE's STS UCE's FSU PNE's	941007, 950515, 950817, 960608 6 (88023–881217) 970803, 970831, 970928, 980822, 980917, 990925 16 (730815–880906)
MAKZ	6.9–7.2	6.00, 5.73, 5,69, 4.71	Lop Nor UNE's	941007, 950515, 960608, 960729
MNV	1.7–2.2	2.4–5.5	NTS UNE's	93 (1979–1992)
KNB	2.5–2.8	2.6–5.5	NTS UNE's	90 (1979–1992)

Regional Earthquake Data

Over 5300 regional waveforms that were recorded by 52 IMS seismic stations and processed at the pIDC are used in this study. These recordings correspond to 4173 distinct REB events above mb 3.5 that are presumed to be earthquakes. The restriction to mb > 3.5 is used to reduce the possibility of mining blasts contaminating the earthquake data sets. We also limit the events to those with distances beyond 3 degrees to avoid problems of distinguishing Pn and Pg, and to those less than 17 degrees, although regional phase amplitudes are computed at distances up to 20 degrees at the pIDC. In addition, we limit this study to data from IMS stations that have at least 20 or more recordings so that useful training sets may be formed. Figure 1 shows the locations of the 4173 presumed earthquakes and the 160 explosions used in this study. The locations of the 52 IMS stations and 4 non-IMS stations (KEV, WMQ, BRVK and KNB) are included.

Maximum amplitudes of Pn, Pg, Sn and Lg have been measured at the pIDC in the 2–4, 4–6, 6–8, 8–10 and 10–12 Hz bands (depending on the Nyquist frequency of the instrument). For this study, we use Pn/Sn and Pn/Lg in the 6–8 Hz bands that satisfy the signal-to-noise criteria of Pn signal divided by pre-Pn noise greater than 2.0 and S signal divided by pre-S noise greater than 1.2.

In addition to the pIDC data, the earthquake data set also includes 60 recordings by MNV and 75 by KNB of Pn/Lg in the 4–6, 6–8, and 8–10 Hz bands for earthquakes near NTS, processed by LLNL in the same way as the 99 UNE's. These earthquakes are necessary to properly calibrate stations MNV and KNB.

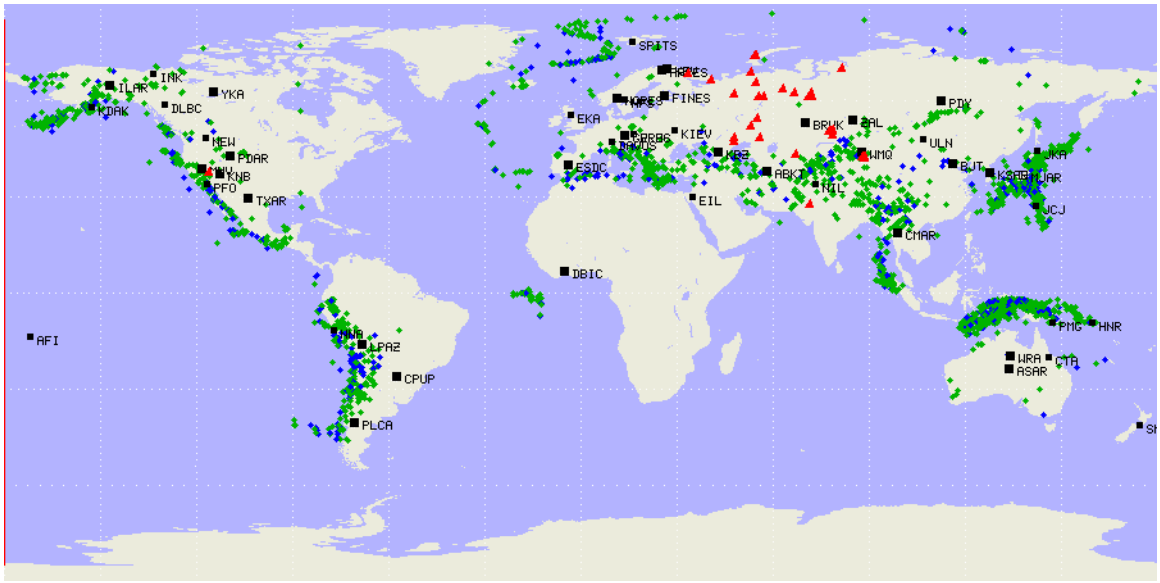


Figure 1. Locations of 160 nuclear explosions (triangles) and 4173 REB earthquakes with mb 3.5 and above. Locations of 52 IMS stations and 4 stations with explosion recordings (KEV, WMQ, BRVK, and KNB) are also shown.

Distance Corrections

The unequal rates of attenuation with distance between regional P and S phases necessitate a correction for distance if amplitude ratios recorded at different distances are to be compared (see Sereno, 1990, Bottone et al., 1997, Fisk et al., 1998, Fisk et al., 1999a and Fisk et al., 2000). P/S distance dependence is modeled by a three-parameter equation of the form

$$\log(\mathrm{P/S}) = a + b\log\Delta + c\Delta\,, \tag{1}$$

where a, b, and c are parameters depending on the particular amplitude ratio (Pn/Lg or Pn/Sn), frequency band and region type. Δ is the epicentral distance. Following Jenkins et al. (1998), we divide the world into tectonic and stable region types and estimate the three coefficients for each region type. We then correct all amplitude ratios at a given station using equation (1) with coefficients estimated using all data located in the appropriate region type. At this point we do not make station-dependent corrections; station dependence will result from Kriging. Figure 2 plots the distance dependence of all REB earthquakes in both the tectonic and stable regions for Pn/Lg(6–8 Hz) and Pn/Sn(6–8 Hz).

Bayesian Kriging

Corrections of regional amplitude ratios using worldwide distance corrections do not depend on station and do not take into account any variations in propagation amplitude that may depend on path differences. One way of treating path variations is Kriging. Kriging has been used to reduce the variance of regional amplitude ratios for earthquake populations (Fan et al., 1999, Rodgers et al., 1999). Ordinary Kriging provides a minimum-mean-square-error prediction (of, in our case, a regional amplitude ratio measured at a particular station) at a given spatial location that is an unbiased linear combination of previously measured data at N separate locations (Cressie, 1993). In Ordinary Kriging the prediction at an unobserved point that is located far from any data points converges to the mean of the available data at that station. For a station that has only data in a subregion with anomalous propagation properties, a prediction in another subregion far removed from this data may be incorrect. In such a subregion we wish for the prediction to converge to a value that is the average over all stations worldwide of the same region type. To achieve this limiting behavior, we generalize the Ordinary Kriging approach using Bayesian methods.

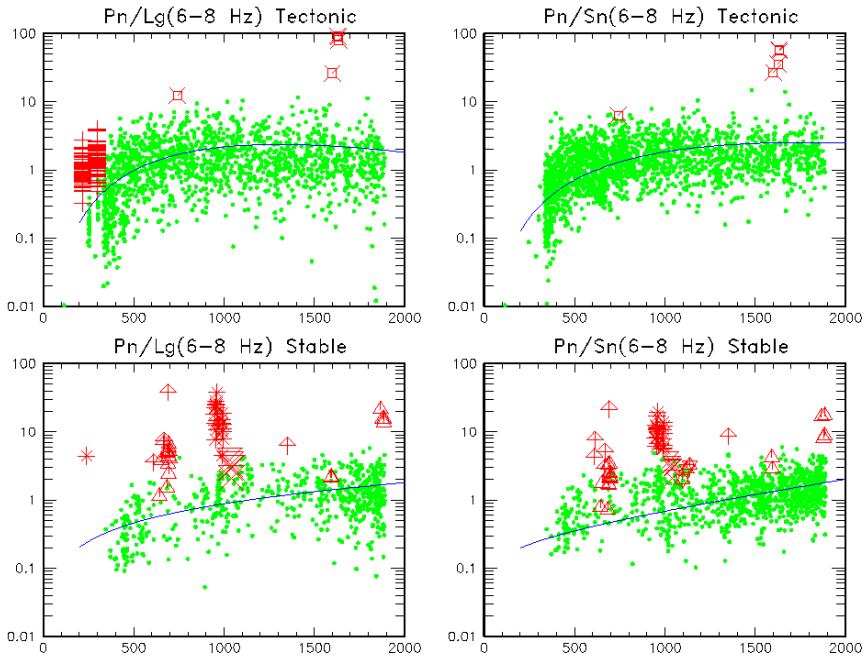


Figure 2. Uncorrected Pn/Lg(6–8 Hz) and Pn/Sn(6–8 Hz) versus distance in km for all REB events and explosions worldwide in tectonic and stable regions. The solid curves are best-fit, three-parameter estimates of the distance dependence for earthquakes.

Suppose we have N data values at locations, $\mathbf{s}_1,\ldots,\mathbf{s}_N$ for a particular regional amplitude ratio, say Pn/Sn(6–8 Hz), recorded by a single station. Let $\mathbf{x}=(x_1,\ldots,x_N)'$ be an N-dimensional data vector where the x_i, $i=1,\ldots,N$, are distance-corrected values of log(P/S), where the distance corrections are relative to the worldwide wide average distance dependence, estimated by using P/S values for data available from all stations. We normalize the data so that the distance-corrected worldwide average is zero.

We assume that data at a given location, $\mathbf{s}_i$, can be modeled by a random variable with a normal distribution, with unknown mean, μ_i, and fixed variance (to be determined), σ_r^2, where σ_r^2 is the same at all locations, that is,

$$x_i \sim N(\mu_i,\sigma_r^2)\,. \tag{2}$$

We also assume that the means of the normal distributions at each location, μ_i, are also normally distributed random variables with zero mean, equal variances, σ_c^2, (to be determined), and correlation between any two μ_i and μ_j dependent only on the distance separating the two locations, that is,

$$\rho_{ij}=\mathrm{corr}(\mu_i,\mu_j)=f(\Delta(\mathbf{s}_i,\mathbf{s}_j))\,, \tag{3}$$

where $\Delta(\mathbf{s}_i,\mathbf{s}_j)$ is the epicentral distance between locations $\mathbf{s}_i$ and $\mathbf{s}_j$. The function f must be a positive definite function (function of positive type), ensuring that the covariance matrix of the random vector of means is positive definite. The form of this function is usually taken to be a known positive definite function with unknown parameters estimated using the available data. We generally use

$$f(\Delta)=\exp(-\Delta/\alpha)\,, \tag{4}$$

where α, the correlation length, is estimated using the data.

We wish to determine an optimal predictor for the mean of an unobserved value located at $\mathbf{s}_0$ given the N data values, $\mathbf{x}$, located at $\mathbf{s}_1,\ldots,\mathbf{s}_N$. We wish to determine the distribution, $p(\mu_0 \mid \mathbf{x})$, of the unknown mean, μ_0, at the unobserved location, $\mathbf{s}_0$, given the data, $\mathbf{x}$. The expected value of this distribution (i.e., the posterior Bayes estimator) could be used as the estimator of μ_0 at that location. Under our assumptions we know $p(x_0, \mathbf{x} \mid \mu_0, \tilde{\mathbf{\imath}})$ and $p(\mu_0, \tilde{\mathbf{\imath}})$, where $\tilde{\mathbf{\imath}} = (\mu_1,\ldots,\mu_N)'$, so we can use Bayes theorem to calculate $p(\mu_0 \mid \mathbf{x})$. Performing the appropriate integrals we get

$$p(\mu_0 \mid \mathbf{x}) \propto \int [\int p(x_0, \mathbf{x} \mid \mu_0, \tilde{\mathbf{\imath}})\, dx_0]\; p(\mu_0, \tilde{\mathbf{\imath}})\, d\tilde{\mathbf{\imath}} \,. \tag{5}$$

Since integrals of normal distributions are normal distributions, $p(\mu_0 \mid \mathbf{x})$ will also be normally distributed, so the proportionality constant need not be determined explicitly. Substituting the appropriate distributions for $p(x_0, \mathbf{x} \mid \mu_0, \tilde{\mathbf{\imath}})$ and $p(\mu_0, \tilde{\mathbf{\imath}})$ as described above and performing the integral over x_0 gives

$$p(\mu_0 \mid \mathbf{x}) \propto \int_{-\infty}^{\infty} \exp\left[-\frac{1}{2}(\mathbf{y} - \tilde{\mathbf{\imath}})' A_1 (\mathbf{y} - \tilde{\mathbf{\imath}})\right] \exp\left[-\frac{1}{2}\tilde{\mathbf{\imath}}'\Sigma^{-1}\tilde{\mathbf{\imath}}\right] d\tilde{\mathbf{\imath}} \,, \tag{6}$$

where $\mathbf{y}$ and $\tilde{\mathbf{\imath}}$ are (N+1)-dimensional vectors given by $\mathbf{y} = (0, \mathbf{x}')'$ and $\tilde{\mathbf{\imath}} = (\mu_0, \tilde{\mathbf{\imath}}')'$, A_1 is an (N+1)-by-(N+1)-dimensional matrix given by

$$A_1 = \frac{1}{\sigma_r^2}\begin{bmatrix} 0 & \mathbf{0} \\ \mathbf{0} & I_N \end{bmatrix}, \tag{7}$$

where I_N is the identity matrix in N dimensions, and Σ is an (N+1)-by-(N+1)-dimensional covariance matrix such that

$$\Sigma_{ij} = \sigma_c^2 \rho_{ij} \,, \qquad i, j = 0,1,\ldots,N \,. \tag{8}$$

The integral in equation (6) can be shown to be proportional to

$$p(\mu_0 \mid \mathbf{x}) \propto \int_{-\infty}^{\infty} \exp\left[-\frac{1}{2}(\tilde{\mathbf{\imath}} - \tilde{\tilde{\mathbf{\imath}}})' S^{-1} (\tilde{\mathbf{\imath}} - \tilde{\tilde{\mathbf{\imath}}})\right] d\tilde{\mathbf{\imath}} \,, \tag{9}$$

where

$$S^{-1} = \Sigma^{-1} + A_1 \tag{10}$$

and

$$\tilde{\tilde{\mathbf{\imath}}} = S\, A_1 \mathbf{y} \,. \tag{11}$$

This integral is easily computed by using the theorem that if a random vector, $\tilde{\mathbf{\imath}}$, is distributed as $N(\tilde{\tilde{\mathbf{\imath}}}, S)$, then the marginal distribution of any set of components of $\tilde{\mathbf{\imath}}$ is multivariate normal with means, variances, and covariances obtained by taking the corresponding components of $\tilde{\tilde{\mathbf{\imath}}}$, and S. This gives

$$p(\mu_0 \mid \mathbf{x}) \propto \exp\left[-\frac{1}{2}(S_{00})^{-1}(\mu_0 - \tilde{\mu}_0)^2\right], \tag{12}$$

or, equivalently, μ_0, given $\mathbf{x}$, is distributed as the normal, $N(\tilde{\mu}_0, \sigma^2)$, where

$$\tilde{\mu}_0 = (S\, A_1 \mathbf{y})_0 \tag{13}$$

and

$$\sigma^2 = S_{00} = [(\Sigma^{-1} + A_1)^{-1}]_{00} \,. \tag{14}$$

A prediction surface, which can also serve as a correction surface, is obtained by computing $\tilde{\mu}_0(\mathbf{s}_0)$ for all values of $\mathbf{s}_0$ within regional distances of the station. An uncertainty surface is given by $\sigma^2(\mathbf{s}_0)$. In principle, such surfaces can be obtained for both earthquakes and explosions at each station, however, due to the scarcity of explosion data, only earthquake surfaces are practical.

An explosion data value, say Pn/Sn(6–8 Hz), at location $\mathbf{s}_0$, can be compared to the earthquake surface by computing the difference $x(\mathbf{s}_0) - \tilde{\mu}_0(\mathbf{s}_0)$. This should be a large positive number if explosions are to be distinguished from earthquakes. Any unknown event at $\mathbf{s}_0$ can also be compared to the surface in the same way, however, if we wish to compare any of the N earthquakes used to determine the surface with a prediction at that location, we must remove that earthquake from the data set and compute a new surface value at that location using the N–1 remaining earthquakes (the leave-one-out procedure). There are three parameters that must be estimated using all available data, σ_c^2, the calibration variance, σ_r^2, the residual variance, and α, the correlation length. Preliminary work suggests that α is typically about 6 degrees, and that σ_c^2 and σ_r^2 are about equal, their sum being equal to the total variance of the data.

Figure 3 shows a typical correction surface at station NIL for distance-corrected log[Pn/Sn(6–8 Hz)], with the corresponding uncertainty surface shown in Figure 4. At locations far from available data, the surface approaches the distance-corrected worldwide average. The locations of nuclear explosions and earthquakes recorded by NIL are depicted by triangles and crosses, respectively. White markers indicate values that are less than the surface, while black markers indicate that the value is greater than the surface. The size of the marker is proportional to the absolute value of the distance from the surface. Thus, very explosion-like values correspond to large black triangles. Figure 4 shows that the uncertainty is lower in areas containing many data points, while it is higher in areas around NIL that are relatively aseismic.

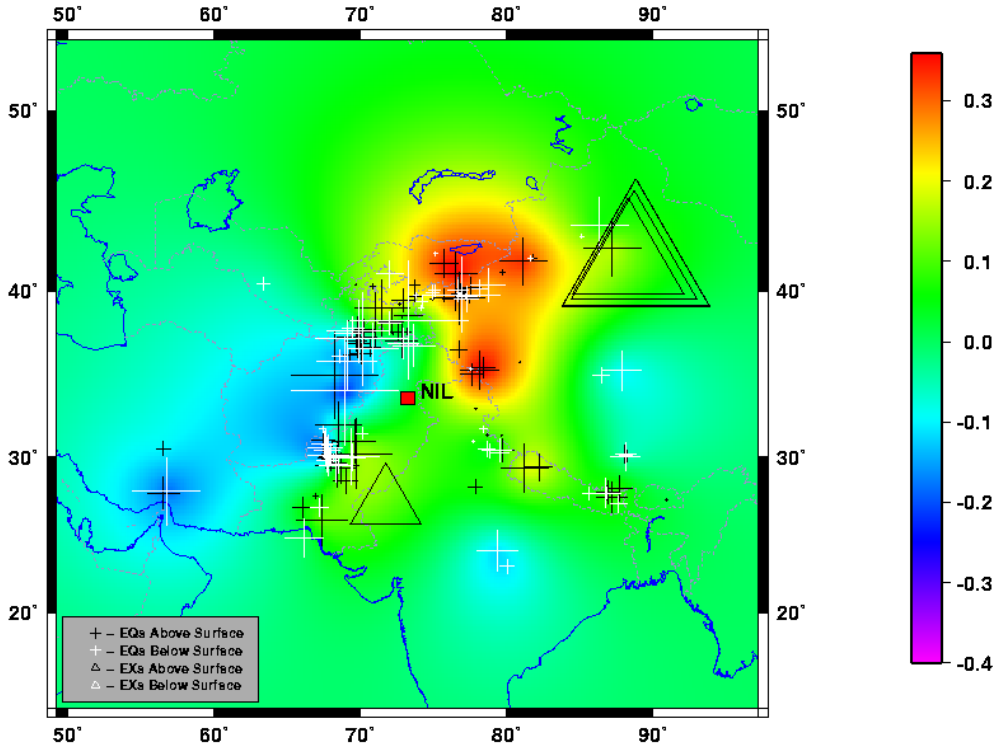


Figure 3. Bayesian Kriged surface for log[Pn/Sn(6–8 Hz)] at NIL. Triangles show locations of nuclear explosions and crosses show the locations of earthquakes. Black (white) markers have values above (below) the surface. Markers size is proportional to the absolute distance from the surface.

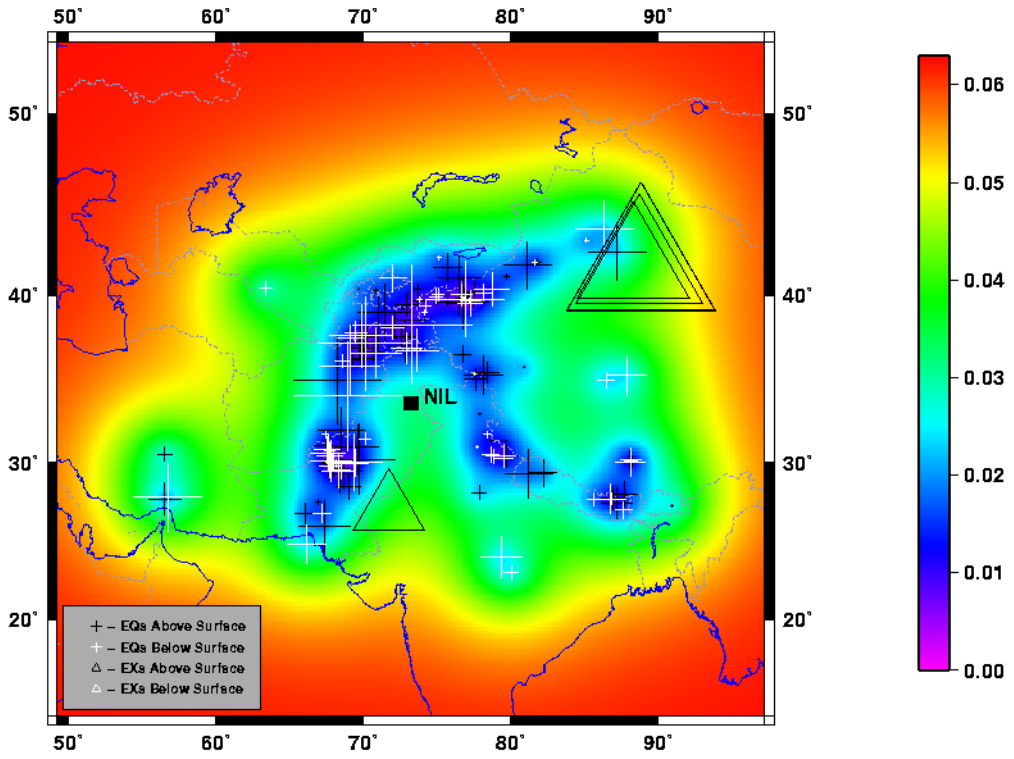


Figure 4. Uncertainty (variance) surface for log[Pn/Sn(6–8 Hz)] at NIL. Triangles show locations of nuclear explosions and crosses show the locations of earthquakes. The markers are the same as Figure 3.

Event-Screening Criterion and Score

An event-screening criterion can be developed from a hypothesis test, using the corrected data and the associated uncertainty, that has a fixed significance level with respect to screening out an explosion. For each station, correction surfaces are calculated for both log[Pn/Sn(6–8 Hz)] and log[Pn/Lg(6–8 Hz)], as well as uncertainty surfaces. To construct a hypothesis test, we define a scaled variable, λ, given by

$$\lambda = \frac{y - \mu_{\mathrm{EX}}}{\sqrt{\sigma^2 + \sigma^2_{\mathrm{r,EQ}}}}, \tag{15}$$

where

$$y = x(\mathbf{s}_0) - \tilde{\mu}_0(\mathbf{s}_0)\,. \tag{16}$$

In Equations (15) and (16), $x(\mathbf{s}_0)$ is the distance-corrected value of log[Pn/Smax(6–8 Hz)] for a test event located at $\mathbf{s}_0$, where Pn/Smax is Pn/Sn if Sn is larger than Lg or Pn/Lg otherwise, $\tilde{\mu}_0(\mathbf{s}_0)$ is the correction surface value at $\mathbf{s}_0$ for Pn/Smax, μ_{EX} is the mean value of y for all explosions in the data set, σ^2 is the uncertainty surface value at $\mathbf{s}_0$, and $\sigma^2_{\mathrm{r,EX}}$ is the residual variance for explosions. If all assumptions are true, then λ should be normally distributed with mean zero and variance one. With this in mind, we define the screening criterion to be

$$\lambda < -z_\alpha\,, \tag{17}$$

where z_α is the (1-α)-percentile of the standard normal distribution, which we usually take as 2.576 for a 0.005 significance level. We also define a regional *score* such that an event is screened out at the α significance level if the score is greater than zero,

$$\text{Score}_R = -\frac{\lambda}{z_\alpha} - 1. \tag{18}$$

We have applied this screening criterion to 140 explosions and 4173 REB events above mb 3.5. For each explosion, the Kriged correction and uncertainty surface values are computed at the explosion location for each station with regional recordings, using all earthquakes available at that station. The value *y*, given by equation (2), is then computed, from which the mean, μ_{EX}, can be estimated. The explosion data is also used to estimate the explosion residual variance, $\sigma^2_{r,EX}$, which we estimate to be $(0.22)^2$. The other estimates used are $\sigma_c = 0.25$, $\sigma_{r,EQ} = 0.25$, and $\alpha = 6.0$ degrees. For each earthquake a Kriged and uncertainty surface is computed at the location of the earthquake by using the remaining earthquakes recorded at that station (using the leave-one-out procedure). The scaled value λ for each event is determined and a score for each event is computed. Those events with positive scores are screened out.

For our data set, none of the 140 explosions are screened out at the 0.005 significance level, while about 73% of the 4173 REB earthquakes are screened out. Figure 5 shows a plot of the scores for all of these earthquakes and explosions. For comparison, Figure 6 shows a plot of distance-corrected log[Pn/Smax(6–8 Hz)] for the same events, before the Kriged corrections were applied. As can be seen from Figure 6, if the explosion with the smallest amplitude ratio had been used as the screening threshold, only about 50% of the earthquakes would have been screened out, showing the improvement resulting from Kriging.

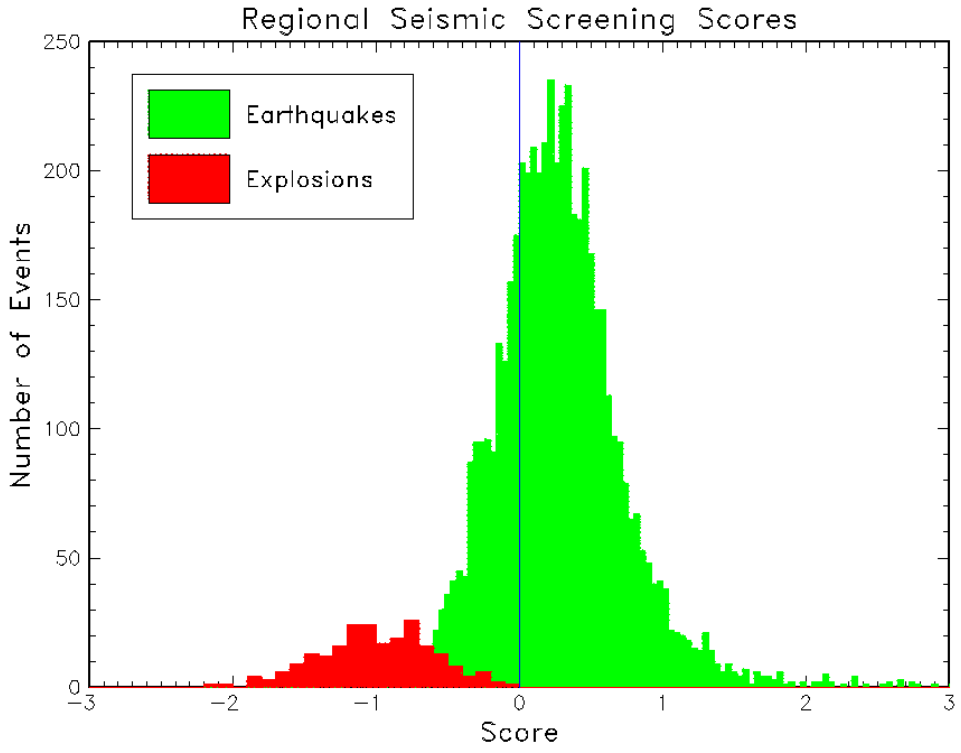


Figure 5. Histograms of regional screening scores for 140 explosions (left) and 4173 earthquakes (right). None of the explosions are screened out (all have scores less than zero using a significance level of 0.005), while 73% of the REB earthquakes are screened out (scores greater than zero).

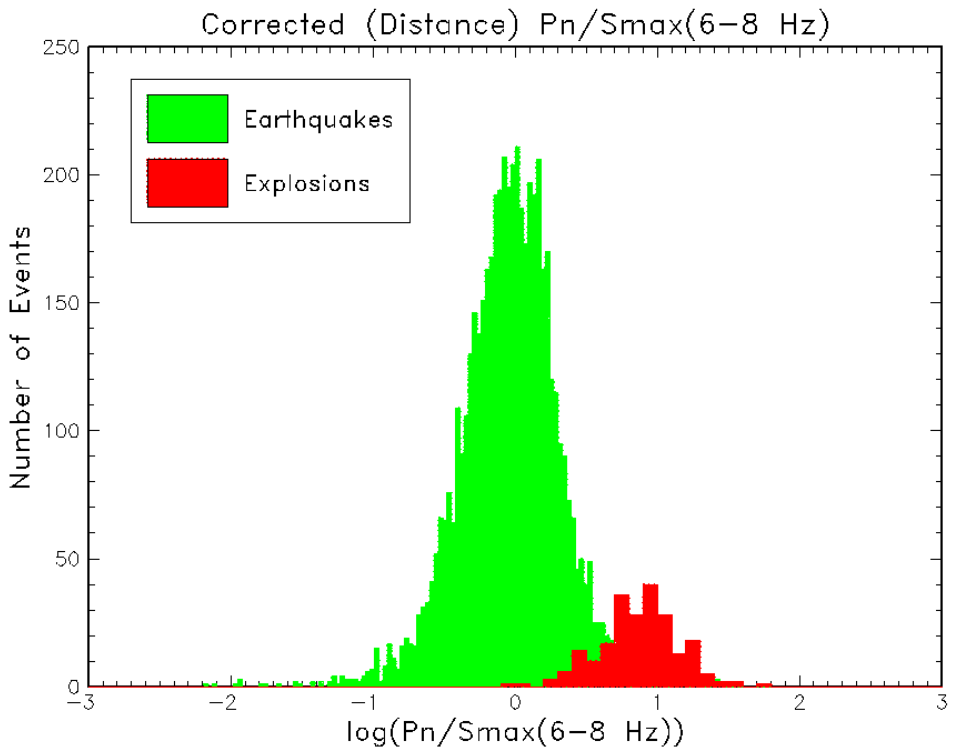


Figure 6. Histograms of log[Pn/Smax(6–8 Hz)] with worldwide distance corrections for 140 explosions (right) and 4173 earthquakes (left). If the explosion with the smallest value were used as a threshold only about 50% of the earthquakes would be screened out.

CONCLUSIONS AND RECOMMENDATIONS

High-frequency, regional seismic P/S amplitude ratios have potential utility to augment the seismic event-screening procedures based on event depth and Ms:mb. Screening performance is generally improved by correcting regional amplitude ratios using spatial techniques, which help account for path variations. In this paper we developed a Bayesian Kriging algorithm that treats subregional variations and accounts for local uncertainty in such a way that in regions far from any calibration data the correction surface approaches the worldwide average and the uncertainty surface approaches maximum uncertainty. Using the screening procedure described in this paper, no available underground explosions were screened out at the Nevada, Lop Nor, Semipalatinsk, Indian, or Novaya Zemlya test sites, while about 73% of REB events above mb 3.5 and with Pn-SNR > 2.0 and S-SNR >1.2 can be screened out, a great improvement over using worldwide distance corrections alone. This screening performance compares favorably with that of Ms:mb. The experimental depth and Ms:mb screening criteria at the pIDC currently screen out less than 50% of REB events above mb 3.5 and about 70% of REB events that have applicable regional data are relatively shallow and do not have an Ms measurement.

There are several potential ways to further improve the regional screening performance. The hypothesis test presented in this paper uses only one screening parameter, namely Pn/Smax(6–8 Hz). Extending the test to include additional amplitude ratios, e.g., Pn/Smax(4–6 Hz) and/or Pn/Smax(8–10 Hz), generally improves screening performance. Another method that may improve performance is multistation averaging, where amplitudes ratios for the same event recorded at more than one station are averaged before applying the hypothesis test. Currently, about 25% of all REB events with regional amplitudes have recordings at two stations or more, a percentage that will increase as more IMS seismic stations come online. Currently, the pIDC measures regional phase amplitudes only on vertical components. Although P/S ratios measured on vertical components show reasonable power for separating earthquakes from explosions, Kim et al. (1997) showed that P/S spectral ratios of rotated, three-component (3-C)

records improve the power. Since most IMS seismic stations have 3-C broadband sensors, the horizontal components should also be considered for event characterization. Preliminary work is this area has shown promise.

Key Words: CTBT monitoring; regional seismic data; event characterization; underground explosions; Bayesian Kriging

REFERENCES

Bottone, S., M. D. Fisk, H. L. Gray, G. D. McCartor, and R. J. Carlson (1997). Initial Regionalization Efforts for the IMS Seismic Network, PL-TR-97-2090, Phillips Laboratory, Hanscom AFB, MA.

Cressie, N. (1993). *Statistics for Spatial Data*, Revised Edition, John Wiley and Sons, Inc., New York.

Fan, G.-W., T. Lay and S. Bottone (1999). Path corrections for source discriminants: A case study at two International Seismic Monitoring stations, submitted to *Pure and Applied Geophysics*.

Fisk, M. D., S. Bottone, R. J. Carlson, H. L. Gray, and G. D. McCartor (1998). Event Characterization Development and Analysis at the Prototype IDC, MRC-R-1548, Mission Research Corporation, Santa Barbara, CA, to appear as a DTRA technical report.

Fisk, M. D., S. Bottone, H. L. Gray, and G. D. McCartor (1999). Event characterization using regional seismic data, *Proceedings of the 21st Seismic Research Symposium*, 427-437.

Fisk, M. D., S. Bottone, and G. D. McCartor (2000). A Seismic Event-Screening Approach Using Regional P/S Amplitude Ratios, MRC-R-1603, Mission Research Corporation, Santa Barbara, CA, to appear as a DTRA technical report.

Fisk, M. D., H. L. Gray, and G. D. McCartor (1996). Regional discrimination without transporting thresholds, *Bull. Seism. Soc. Am.*, **86**, 1545-1558.

Fisk, M. D., D. Jepsen, and J. R. Murphy (1999). Experimental seismic event-screening criteria at the Prototype International Data Center, submitted to *Pure and Applied Geophysics*.

Jenkins, R. D., T. J. Sereno, and D. A. Brumbaugh (1998). Regional Attenuation at PIDC Stations and the Transportability of the S/P Discriminant, AFRL-VS-HA-TR-98-0046, Air Force Research Laboratory, Hanscom Air Force Base, MA.

Kim, Y. K., V. Aharonian, A. L. Lerner-Lam and, P. G. Richards (1997). Discrimination of earthquakes and explosions in southern Russia using regional high-frequency three-component data from IRIS/JSP Caucasus Network, *Bull. Seism. Soc. Am.*, **87**, 569-588.

Murphy, J. R. (1998). Private communication.

Patton, H. J. and W. R. Walter (1994). Private communication.

Rodgers, A. J., W. R. Walter, C. A. Schultz, S. C. Meyers, and T. Lay (1999). A comparison of methodologies for representing path effects on regional P/S discriminants, *Bull. Seism. Soc. Am.*, 89, 394-408.

Sereno, T.J. (1990). Attenuation of Regional Phases in Fennoscandia and Estimates of Arrival Time and Azimuth Uncertainty using Data Recorded by Regional Arrays, SAIC-90/1472, Science Applications International Corporation, San Diego, California.

TWO-DIMENSIONAL FINITE-DIFFERENCE MODELING OF BROADBAND REGIONAL WAVE PROPAGATION PHENOMENA: VALIDATION OF REGIONAL THREE-DIMENSIONAL EARTH MODELS AND PREDICTION OF ANOMALOUS REGIONAL PHASES

Peter Goldstein, Floriana D. Ryall, Michael E. Pasyanos, Craig A. Schultz, and William R. Walter
Lawrence Livermore National Laboratory

Sponsored by U.S. Department of Energy
Office of Nonproliferation Research and Engineering
Office of Defense Nuclear Nonproliferation
National Nuclear Security Administration

Contract No. W-7405-ENG-48

ABSTRACT

An important challenge for seismic monitoring of nuclear explosions at low magnitude to verify a nuclear-test-ban treaty is the development of techniques that use regional phases for detection, location, and identification. In order to use such phases, region-specific earth models and tools are needed that accurately predict features such as travel times, amplitudes, and spectral characteristics. In this paper, we present our efforts to use two-dimensional finite-difference modeling to help develop and validate regional earth models for the Middle East and North Africa and to develop predictive algorithms for identifying anomalous regional phases.

To help develop and validate a model for the Middle East and North Africa, we compare data and finite-difference simulations for selected regions. We show that the proposed three-dimensional regional model is a significant improvement over standard one-dimensional models by comparing features of broadband data and simulations and differences between observed and predicted features such as narrow-band group velocities.

We show how a potential trade-off between source and structure can be avoided by constraining source parameters such as depth, mechanism, and moment/source-time function with independent data.

We also present numerous observations of anomalous timing and amplitude of regional phases and show how incorporation of two-dimensional structure can explain many of these observations. Based on these observations, and the predictive capability of our simulations, we develop a simple model that can accurately predict the timing of such phases.

Key Words: wave propagation, three-dimensional earth models, regional seismic phases

OBJECTIVES

Model Validation and Development

We are comparing data and numerical simulations of regional wave propagation at selected stations in the Middle East and North Africa to validate and improve our regional earth model (MENA1.1, Walter et al., 2000) and begin development of model-based correction surfaces for regional identification and discrimination. For example, we compare data and simulations for events at RAYN, a broadband seismic station in Saudi Arabia (Figure 1).

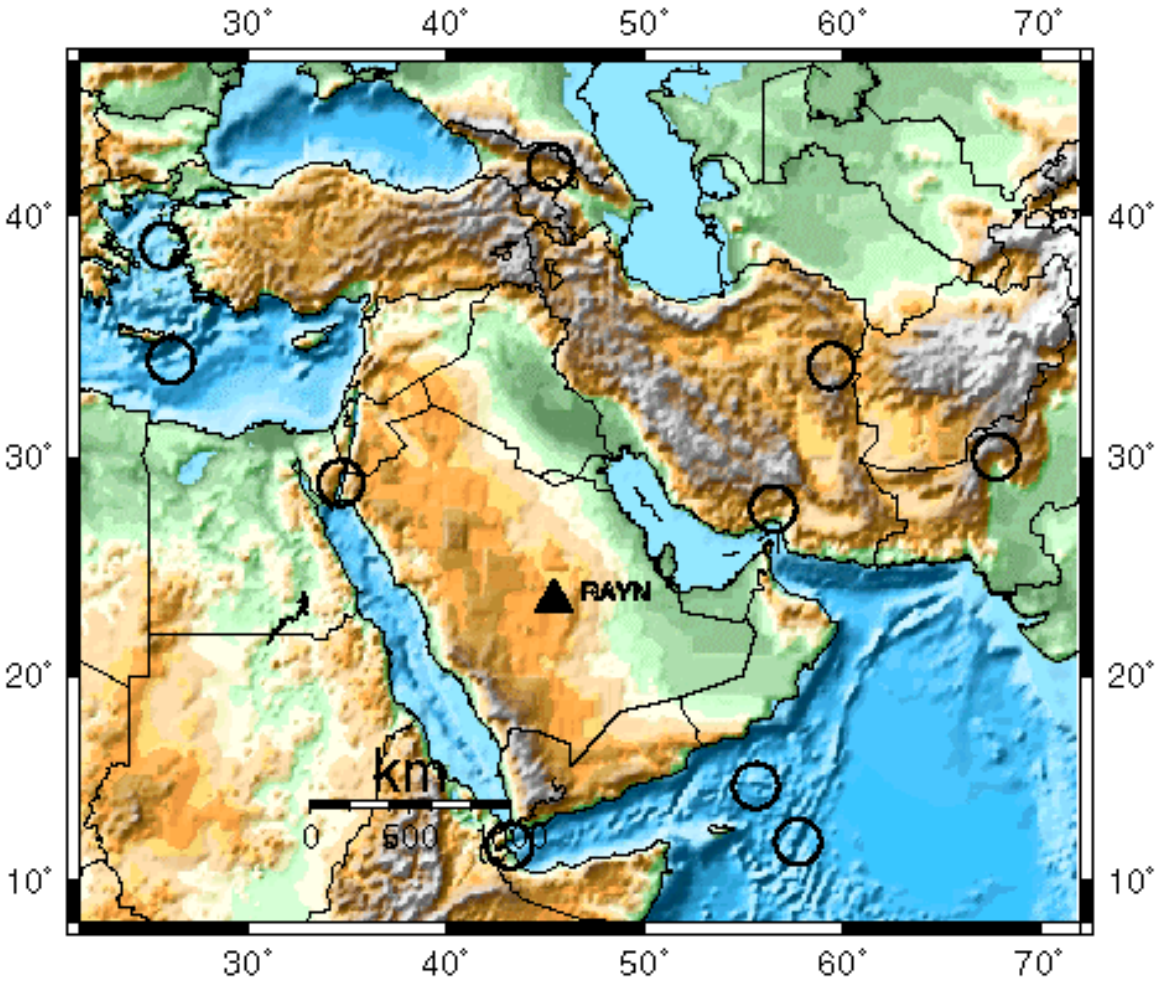


Figure 1, Map of selected events in the vicinity of RAYN. These events are being used to test and validate the MENA model.

Selected cross-sections and waveform comparisons are shown in Figure 2. In comparison to AK135 (the standard one-dimensional earth model used for most monitoring purposes), the MENA model generally produces a much better representation of the observed data. However, in some cases, results for the MENA model are similar to those of AK135 and differ significantly from the observed data. These differences indicate a need for additional calibration.

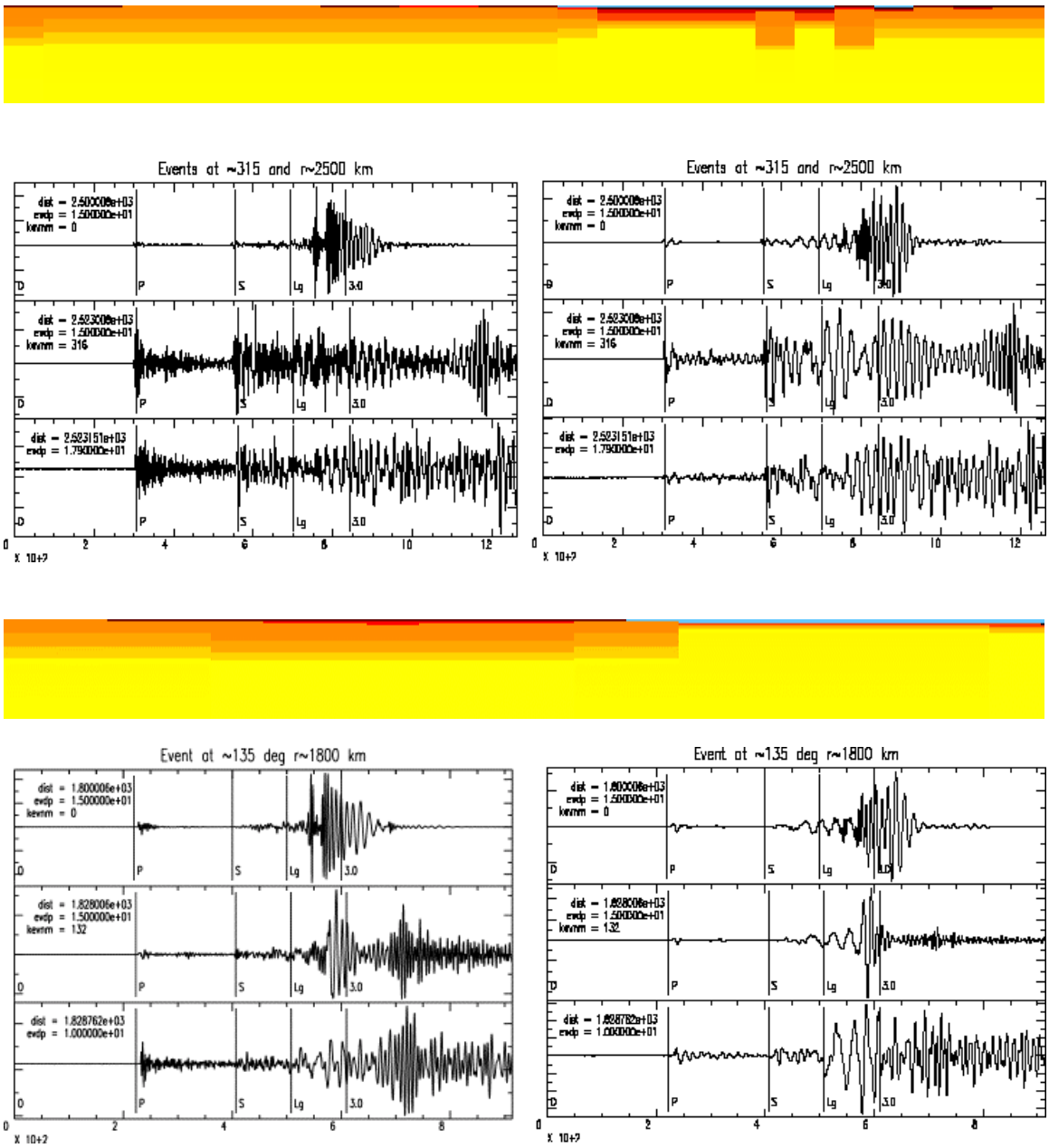
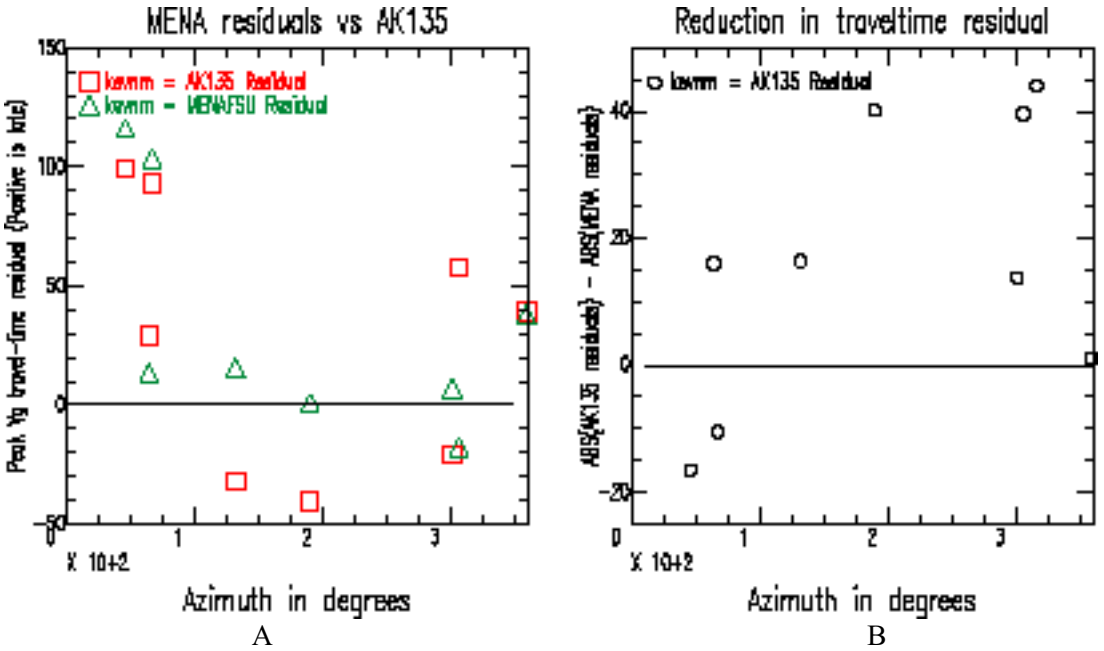


Figure 2. Comparison of data and simulations for earthquakes recorded at RAYN. The top parts of the figure show the Earth cross-section with RAYN at the left edge followed by the data and synthetics for an event at approximately 2500 km. The bottom part of the figure shows the cross-section, data, and synthetics for an event to the southeast at a distance of approximately 1800 km. In each sub panel with waveforms, the top trace is the predicted ground motions based on the AK135 earth model. The middle trace is the ground motion prediction based on the MENA model. The bottom trace is the observed data. The sub panels on the left side are broadband data and synthetics. The sub panels on the right side are narrow band filtered around 20-s period. Visual inspection clearly shows that the MENA model improves upon the conventional AK135 model. This improvement is verified quantitatively by comparing observed and predicted group velocity measurements.

In order to quantify the improvement provided by the MENA model, we compared observed and predicted group velocities (Figure 3). As shown in Figure 3, we found that the MENA model significantly reduced the difference between the observed and predicted group velocities relative to AK135. Furthermore, in cases where it did not reduce the residual it was usually as good as AK135. These discrepancies suggest that additional calibration of the MENA model is warranted.



A B

Figure 3. Comparison of observed and predicted group velocities for the MENA and AK135 models. a) Difference between observed and predicted group velocities for the MENA model (triangles) and AK135 (squares). b) Relative improvement in predicted group velocities (AK135 residual - MENA residuals).

Constraints on Source Parameters

When possible, we try to avoid potential trade-offs between variability due to source parameters and structure, by estimating source mechanism and depth based on a combination of regional, far-regional, and teleseismic data (e.g., Goldstein and Dodge, 1999, Goldstein et al., 2000). Broadband (Approximately 0 to 2 Hz) body waveforms from the far regional and teleseismic data are modeled using generalized ray synthetics. The regional data are modeled at longer periods (approximately 10 to 100 s) using reflectivity. Grid search and simplex algorithms are used to find the best depth and mechanism for both data sets. When available, we also use source parameters estimated by organizations such as the NEIC and Harvard CMT group.

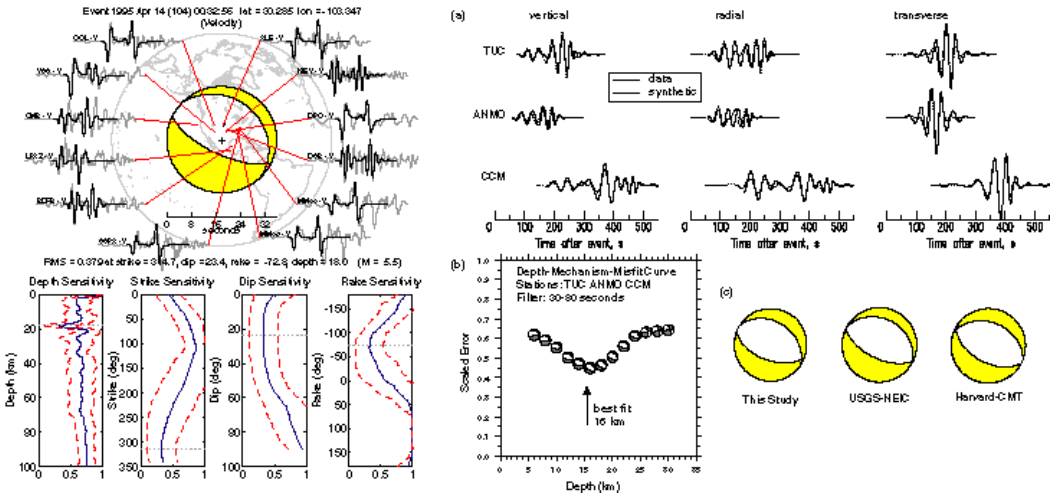


Figure 4. Constraints on source parameters from long-period regional, broadband far-regional, and teleseismic data help reduce uncertainties and trade-offs between source and model parameters. For example, modeling of far-regional and teleseismic bodywave data (left) can provide sharp constraints on depth. Modeling of regional data (right) can provide additional constraints on depth and more accurately constrain mechanism and structure.

Regional Phase Identification

We use numerical simulations of regional wave propagation phenomena to explain and identify anomalous regional S-wave phases (Sx) observed throughout the Middle East and North Africa (Figure 5). Understanding and predicting these anomalous regional phases is important because they can have a significant effect on the performance of regional monitoring techniques.

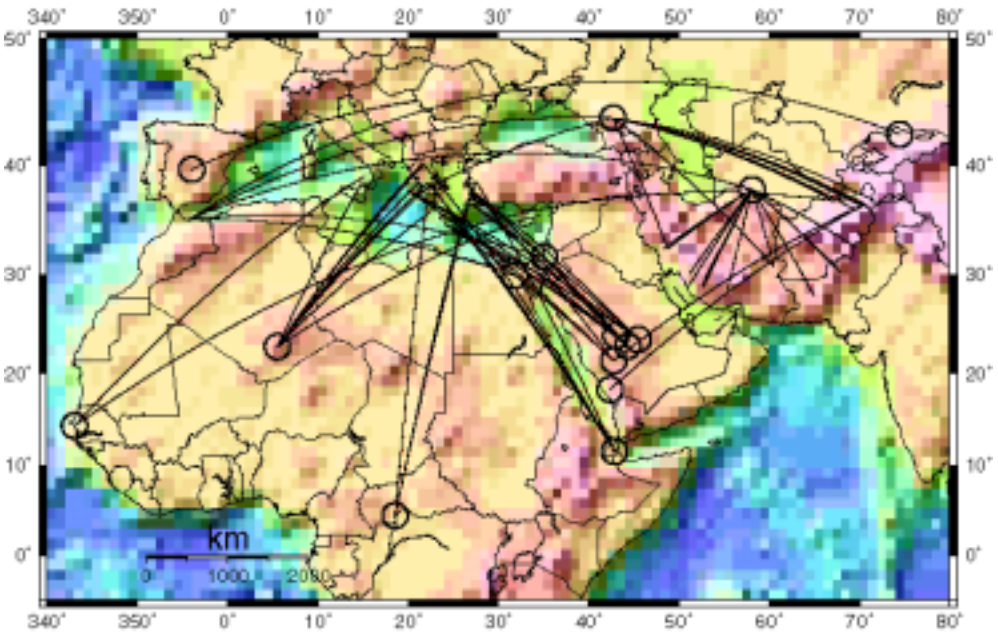


Figure 5, We have observed anomalous, late arriving S-wave phases at numerous stations throughout the Middle East and North Africa. Station locations are indicated as open circles. Event locations are at the tips of the solid lines.

These S phases are considered anomalous and labeled as Sx because they are distinct arrivals with arrival times that differ significantly from what would be predicted for standard regional S phases such as Sn or Lg. They are also consistently observed from event to event at the same station (Figure 6). For example, the Sx phases in Figure 6 have group velocities that are significantly slower than Sn and much too fast to be Lg.

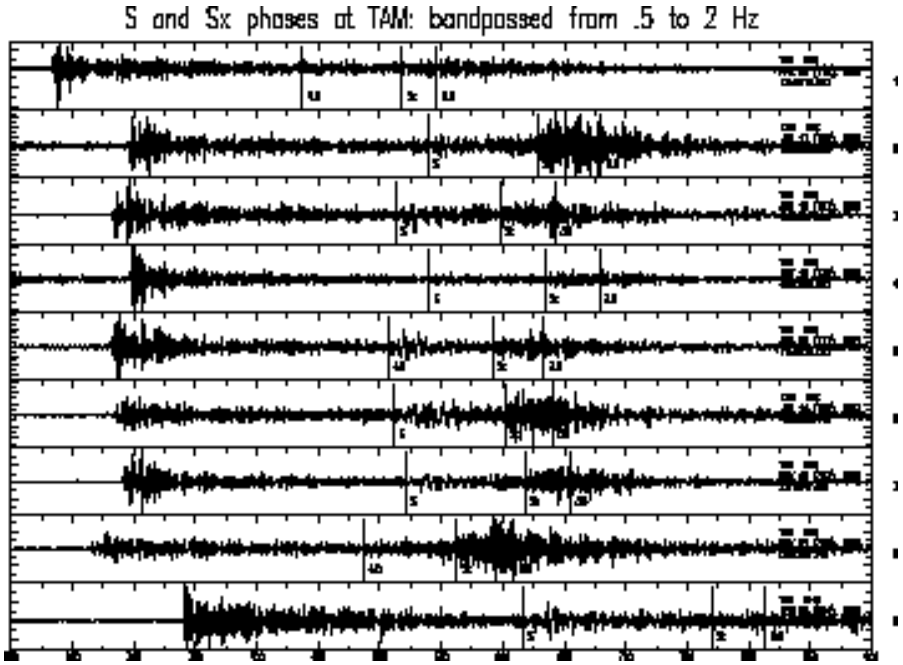


Figure 6. Sx phases recorded on vertical components at TAM. Group velocities of the Sx phases are significantly slower than Sn and much too fast to be Lg.

Based on our simulations, we claim that the Sx phases are conversions from Sn to Lg or Lg to Sn, depending on the geometry of the crust-mantle boundary between the source and receiver. We have developed a simple analytical model, based on the difference in arrival times of the mantle S-waves and anomalous Sx phases, to predict the locations of the conversion points (Figure 7). These conversion points are found to correlate well with sharp changes in the depth of the crust-mantle boundary (Figure 8).

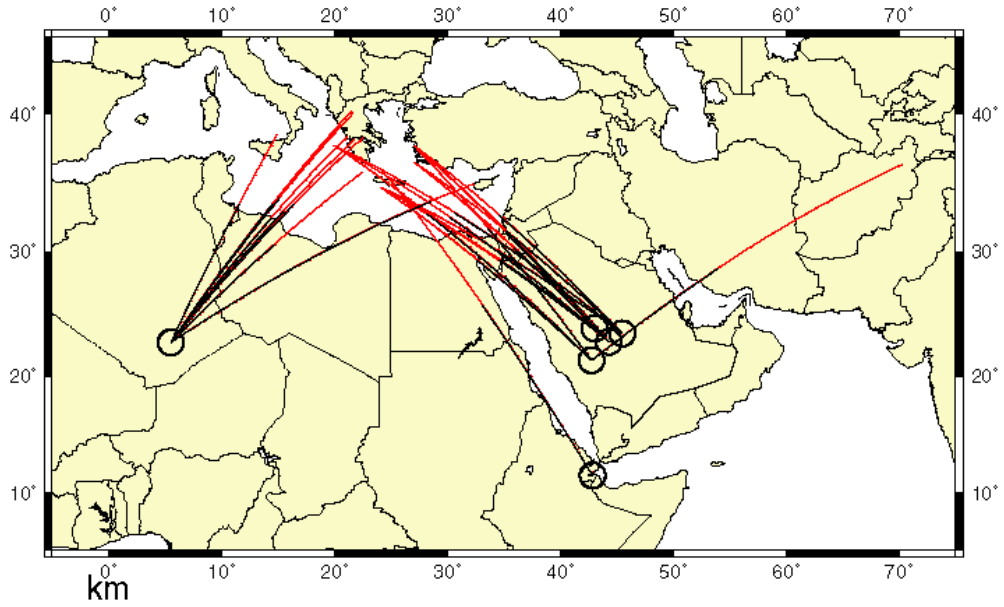


Figure 7. Predicted Sx conversion points based on differences in S and Sx travel times. The bottom ends of the black lines between the station and event pairs indicate the conversion points.

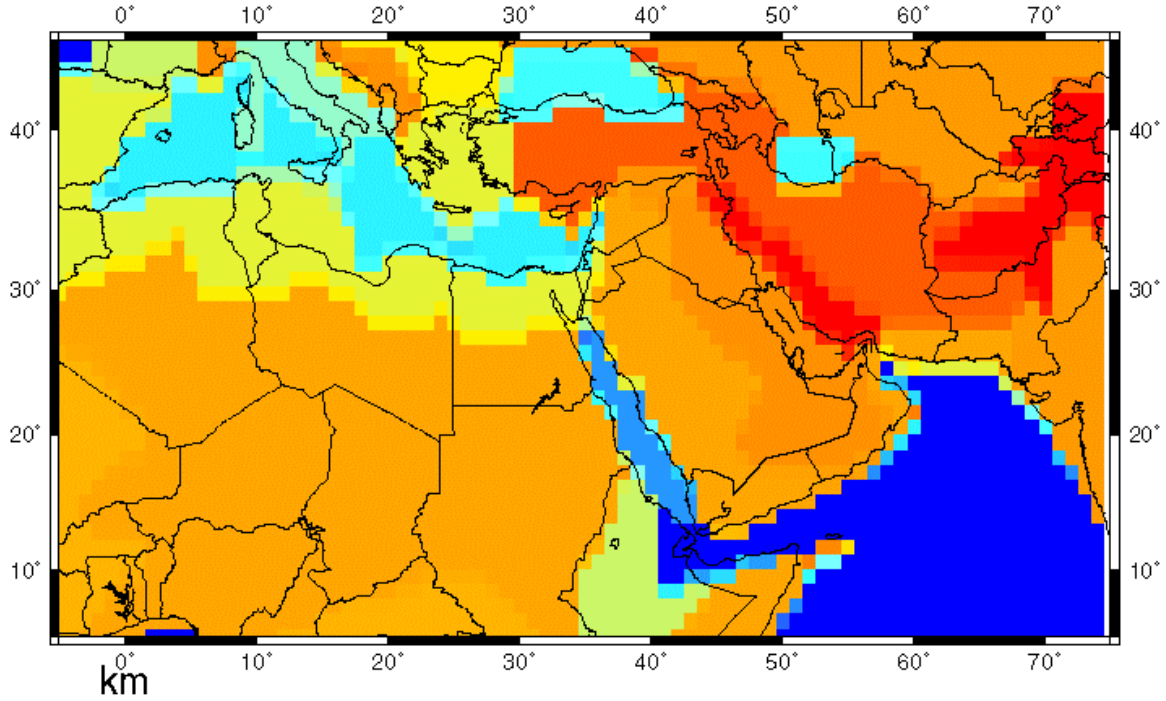


Figure 8. Color-coded map of Moho depth. Upper right (red) areas are deep, and upper left and lower right (blue) areas are shallow. The estimated Sx wave generation points, indicated by the change in line tone in Figure 7, occur at places with rapid changes in crustal thickness.

CONCLUSIONS

We are using two-dimensional finite-difference wave propagation modeling capabilities to help develop and validate a regional model for the Middle East, North Africa, and the former Soviet Union. Based on quantitative comparison of observed and predicted group velocities, we have shown that the MENA model is a significant improvement upon AK135, the conventional model used for monitoring purposes. Qualitative comparison of observed and predicted waveforms also indicates significant improvement.

In order to avoid trade-offs between source and structure, we have developed and are utilizing techniques for estimating source parameters from regional, far-regional, and teleseismic data. These techniques can provide high-resolution constraints on source depth and mechanism.

We have documented anomalous regional S phases (Sx) and shown that a simple model based on conversions at sharp changes in crustal thickness can explain the observed anomalous arrival times. The ability to predict such anomalous phases is important for the development of robust regional monitoring techniques.

REFERENCES

Goldstein, P., and D. Dodge (1999), “Fast And Accurate Depth And Source Mechanism Estimation Using P-Waveform Modeling: A Tool For Special Event Analysis, Event Screening, and Regional Calibration," Geophys. Res. Lett. 26, 2569-2572.

Goldstein, P., D. Dodge, G. Ichinose, A. Rodgers (May 2000), "High Resolution Depth and Source Mechanism Estimation Using a Combination of Regional and Teleseismic Data," Presented at the IRIS 2000 Workshop, Rockport Maine.

Walter, W., M. Pasyanos, J. Bhattacharyya, J. O'Boyle (2000), MENA1.1 – An Updated Geophysical Regionalization of the Middle East and North Africa, UCRL-ID-138079.

JOINT INVERSION OF RECEIVER FUNCTIONS AND SURFACE-WAVE DISPERSION FOR CRUSTAL STRUCTURE

R. B. Herrmann, C. J. Ammon, and J. Julia
Department of Earth and Atmospheric Sciences, Saint Louis University

Sponsored by DSWA

Contract No. DSWA 01-98-C-0160

ABSTRACT

Teleseismic P-wave receiver functions and surface-wave dispersion measurements can be employed to simultaneously infer the shear-wave velocity distribution with depth in the lithosphere. Receiver functions are primarily sensitive to shear-wave velocity contrasts and vertical travel times and surface-wave dispersion measurements are sensitive to vertical shear-wave velocity averages, so that their combination bridges resolution gaps associated with each individual data set.

The inversions are performed using a joint, linearized inversion scheme which accounts for the relative influence of each set of observations, and allows a trade-off between fitting the observations and the smoothness of the model. Additional constraints on mantle structure are also incorporated during the inversion procedure since requiring the data to blend smoothly into an appropriate deep structure affects the estimate of the lower crust velocities, yielding models which are more consistent with expectations than those resulting from unconstrained inversions. We have found that *a priori* knowledge of upper mantle velocities are required to predict the dispersion up to 50 sec period and that stability constraints are required. When dispersion is limited to periods grater than 15 sec *a priori* information on the upper crustal velocities may also be required.

Results of applying this technique to data from different tectonic environments in the Arabian Plate and North America will be presented.

OBJECTIVE

The object of this effort is to implement an efficient algorithm for jointly inverting receiver functions and surface wave dispersion velocities to constraint shear-wave velocity with depth. The benefits of this joint inversion have been shown by several authors [Ozalaybey et al., 1997; Du and Foulger, 1999; Julia et al, 2000]. When no noise is present, the complementary constraints in receiver functions and dispersion observations uniquely characterize the shear-wave velocity variation with depth. Dispersion observations are sensitive to absolute vertical shear-wave velocity averages and the receiver functions are primarily sensitive to shear-wave velocity averages and vertical travel times. Their joint inversion give rise to models where the details constrained by the receiver functions are superimposed to a background velocity model constrained by the dispersion measurements. When noise is contaminating the data the constraints on the model parameters become incompatible, since the noise independently distorts the model imaged by both receiver function and dispersion measurements. The joint inversion, therefore, helps to avoid overinterpreting the data as a result of over-fitting either data set noise.

The utility of this approach in a CTBT framework is that the crustal structure beneath seismograph stations can be assessed. As CTBT monitoring stations are installed, teleseismic waves can be recorded and receiver functions obtained during the initial operation. These estimates together with preexisting dispersion measurements [e.g. Ritzwoller and Levshin, 1998] allow a rapid application of the proposed methodology, so that the S-velocity structure beneath the station can be inferred in the short run. One of the difficult tasks is then assessing estimates of the earth structure models. As in all science the consistency of independent work lends confidence to a result. Some examples are shown below for the Arabian Shield where we

compare velocity models estimated from the joint inversions with those from refraction surveys [Mooney et al., 1985; Prodehl, 1985; Badri, 1991].

Further verification of model suitability is the direct estimation of source properties or construction of phase-match filters using the constructed velocity structures. We believe that this localized structures will permit waveform inversion of regional signals for source identification and will help to produce more accurate filters for signal identification and enhancement, and eventual source identification.

RESEARCH ACCOMPLISHED

We employ a "jumping" algorithm to jointly invert receiver functions and surface-wave dispersion observations for shear-wave velocity. The jumping scheme allows us to implement smoothness constraint in the inversion by minimizing a model roughness norm [Constable et al., 1987] that trade-off with the goodness of fit. Our design of goodness of fit criterion [Julia et al., 2000] takes into account the different units, magnitudes, noise and number of observations of the data and allows to set an influence parameter 'p' before inversion to balance the relative importance of each data set of observations. In particular, a value of p=0 only uses the receiver function data and a value of p=1 only uses the dispersion data.

The system of equations to be inverted is given by

$$\begin{pmatrix} pD_s \\ qD_r \\ sA \end{pmatrix} \vec{x} = \begin{pmatrix} \vec{r}_s \\ \vec{r}_r \\ 0 \end{pmatrix} + \begin{pmatrix} D_s \\ D_r \\ 0 \end{pmatrix} \vec{x}_0$$

where D_s and D_r are the partial derivative matrices for the dispersion measurements and the receiver function estimates, respectively, $\vec{r}_s$ and $\vec{r}_r$ are the corresponding vectors of residuals, $\vec{x}$ is the vector of S-wave velocity, $\vec{x}_0$ is the starting model, and A is a matrix that constructs the second order difference of the model $\vec{x}$. The factor q equals $1-p$ and the factor s balance the trade-off between data fitting and model smoothness.

Additional constraints for upper mantle structure

Additional *a priori* information is required to stabilize the results of our models in the upper mantle. One possibility is to require the deepest layers in our model to be similar to predetermined values, such as PREM. This can be achieved by adding the following set of equations to the original system (1) [Jackson, 1972]

$$W\vec{x} = W\vec{x}_a$$

where $W = (w_{ii})$ is a diagonal matrix of weights and the vector $\vec{x}_a$ contains the *a priori* predefined velocity values. Figure 1 is a comparison between the data only inversion and the velocity constrained inversion for station SODA, in the Arabian Shield, the constraints consisting of forcing our inverted velocity values to be PREM below 55 km depth. The predicted receiver functions are almost unchanged as well as the predicted dispersion velocities at short periods. The sensitivity of the long period range to mantle structure is an important point, since requiring our data to blend smoothly into a more appropriate

deep structure affects our estimate of the lower crust velocities. Therefore, it is important to insure a reasonable upper mantle in the model, not allow the inversion to place an unusual and unlikely structure and simply ignore it because it is unresolved. This example has implications for all narrow band studies of structure.

Application to the Arabian Shield

We employ the methodology described in the preceding section to model receiver functions estimated in the Saudi Arabian Broadband Deployment stations (Figure 2) jointly with group velocities for the fundamental mode of Rayleigh and Love waves, as inferred from an independent tomographic study carried out by Mokhtar et al. [2000]. Receiver function estimates at two overlapping frequency bands are inverted at the same time, jointly with the

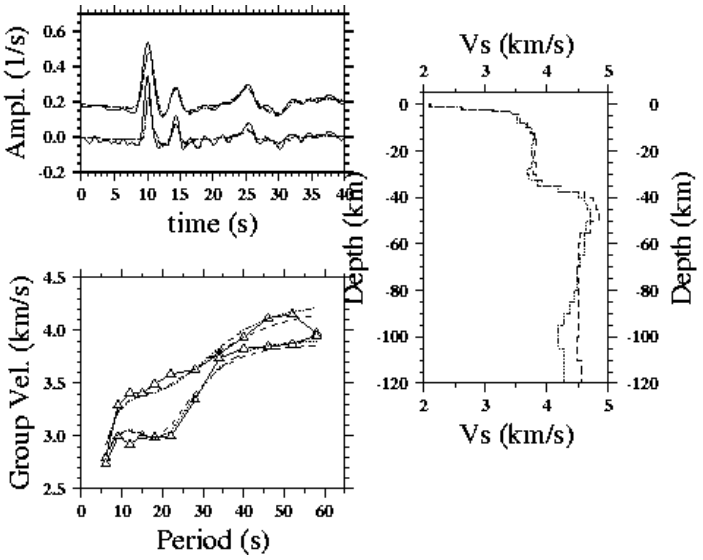


Figure 1: Comparison between the data-only and the constrained inversion results for receiver functions (upper left), dispersion velocities (lower left) and resulting models (right) at station SODA. Solid, dotted and dashed lines correspond to observations, data-only inversion and constrained inversion, respectively.

dispersion observations, to allow a better examination of the transition zones within the structure [Cassidy, 1992]. The data allow analysis to be performed using waves approaching the stations at two different backazimuths, so that evidence for lateral variation is investigated as well. Figures 3, 4 and 5 show the receiver function fits, dispersion velocity fits and resulting models, respectively. In general all the models contain a rapid velocity increase during the few first kilometers below the surface, a lower crust with a rather constant velocity, and a gradational crust-to-mantle transition.

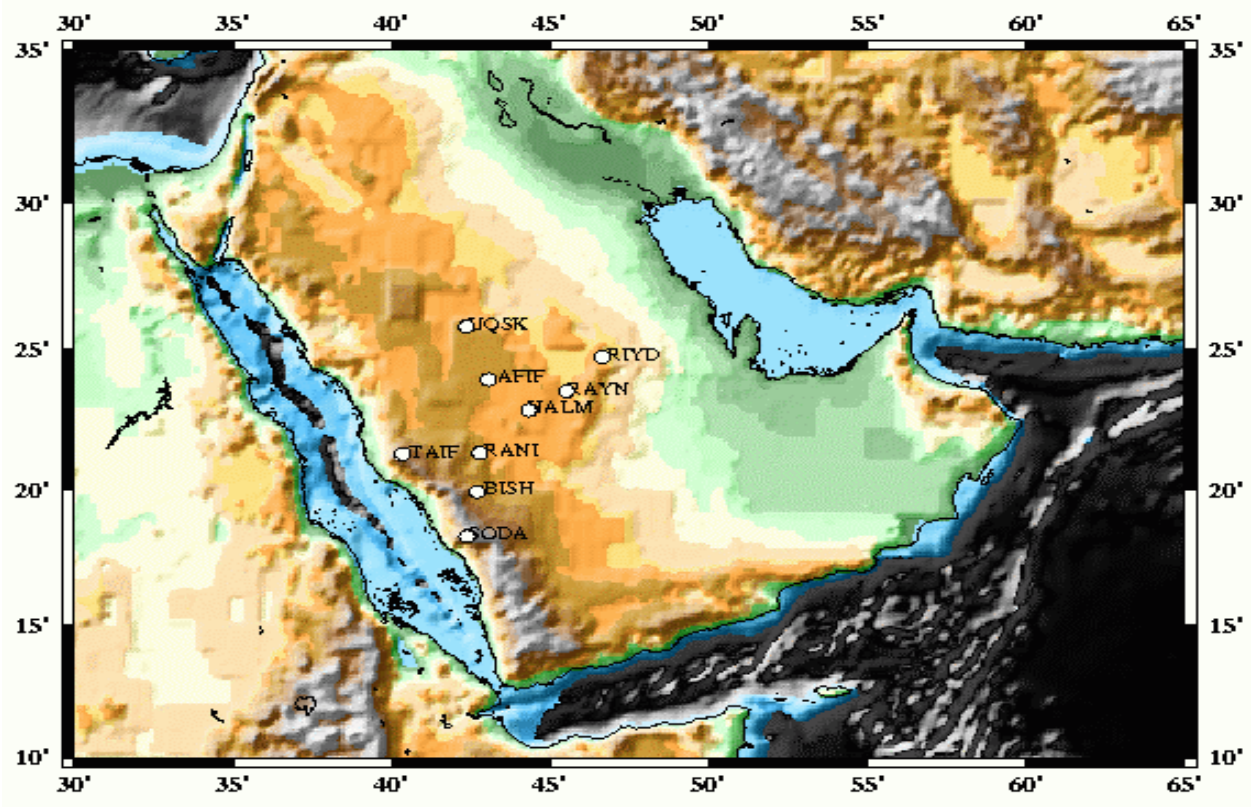


Figure 2: Topographic map of the Arabian Peninsula showing the location of the temporary broadband stations.

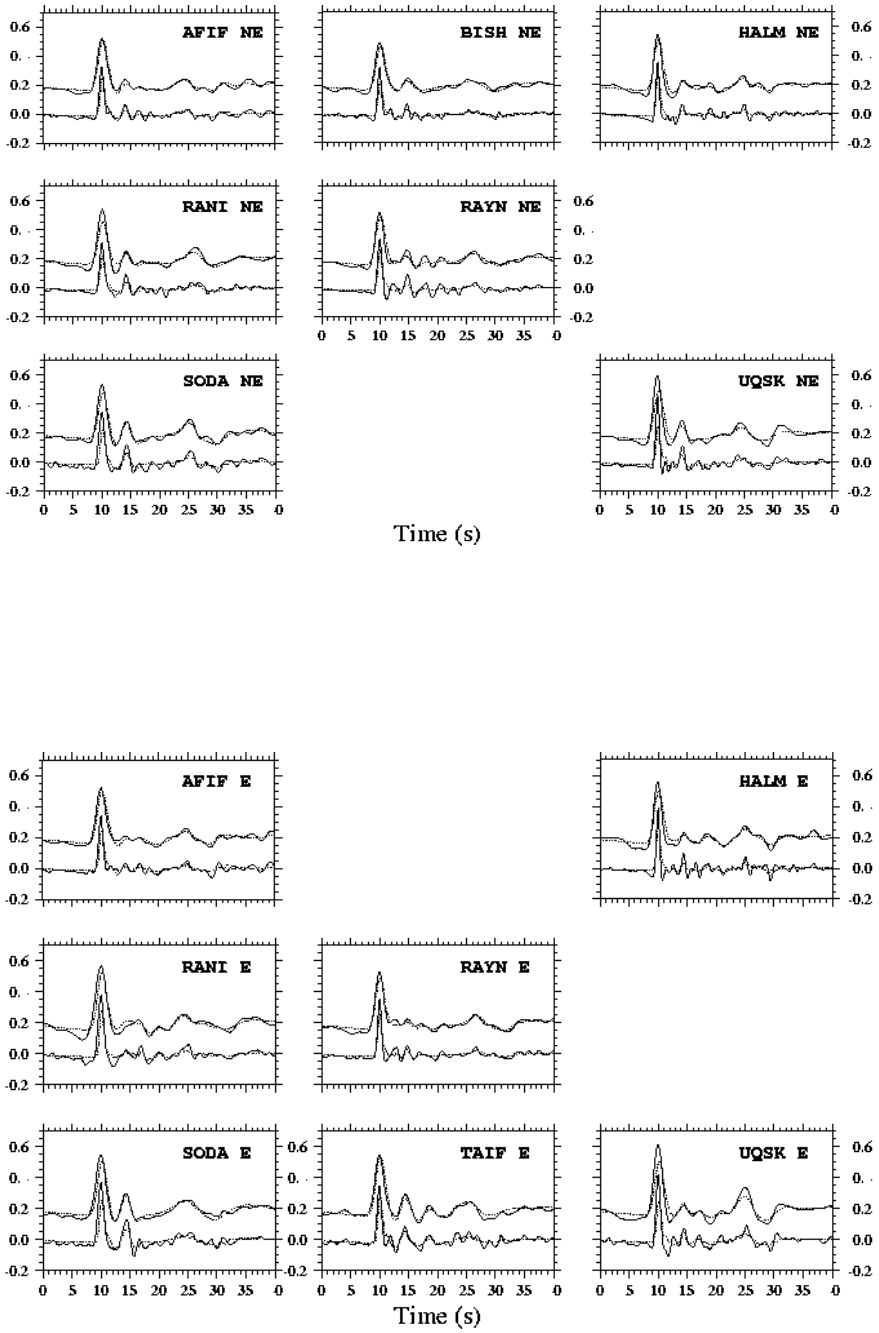


Figure 3: (top) Receiver function waveforms for events approaching NE of the station. (bottom) Receiver function waveforms for events approaching E of the station. Solid and dashed lines are observed and predicted receiver functions, respectively. The station code is shown in the upper right corner.

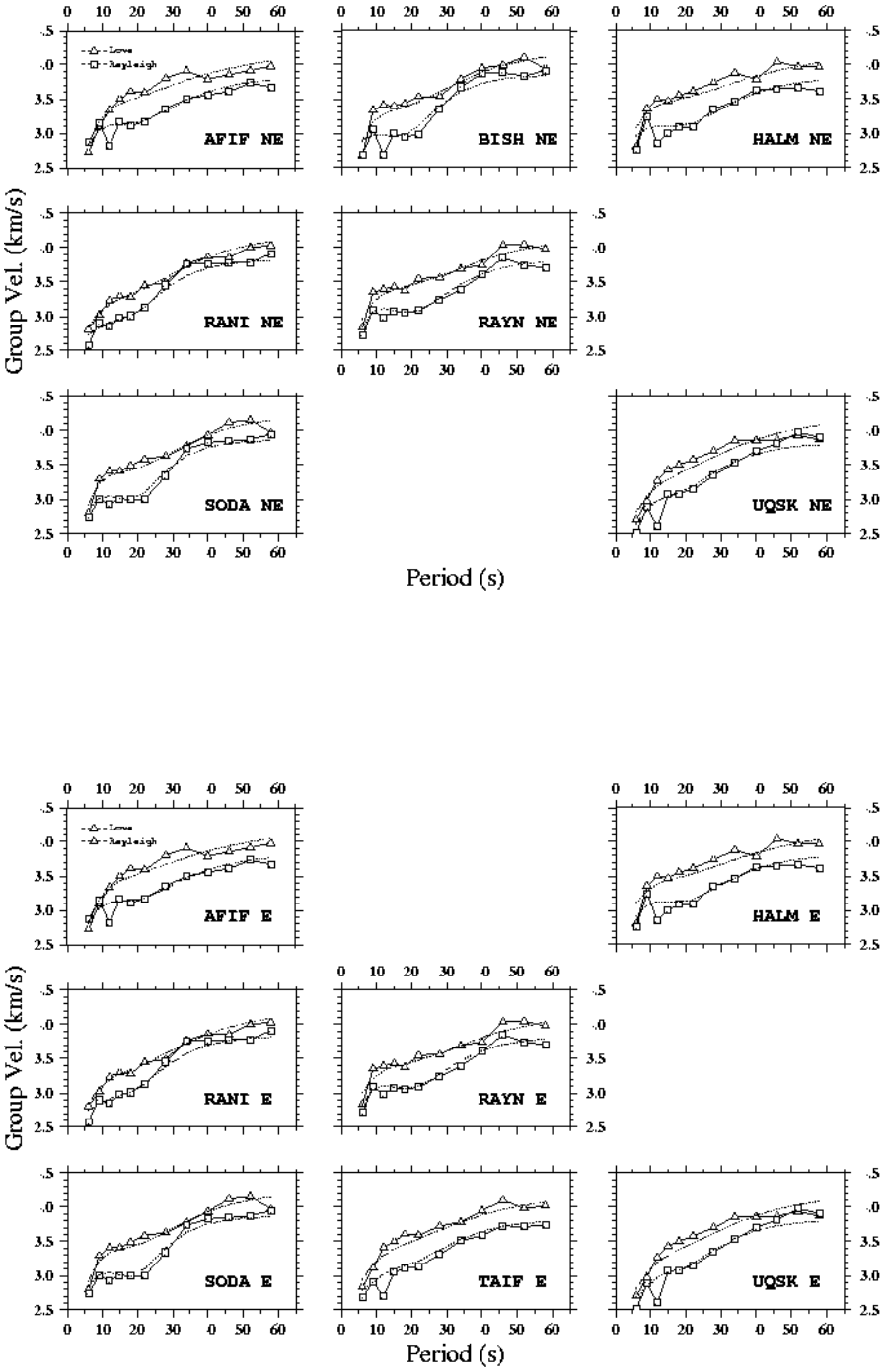


Figure 4: Observed (solid) and predicted (dashed) group velocities at temporary stations in the Arabian Peninsula from the inverted models obtained jointly with the NE (top) and E (bottom) receiver function waveforms. Station codes are labeled in the lower right corner.

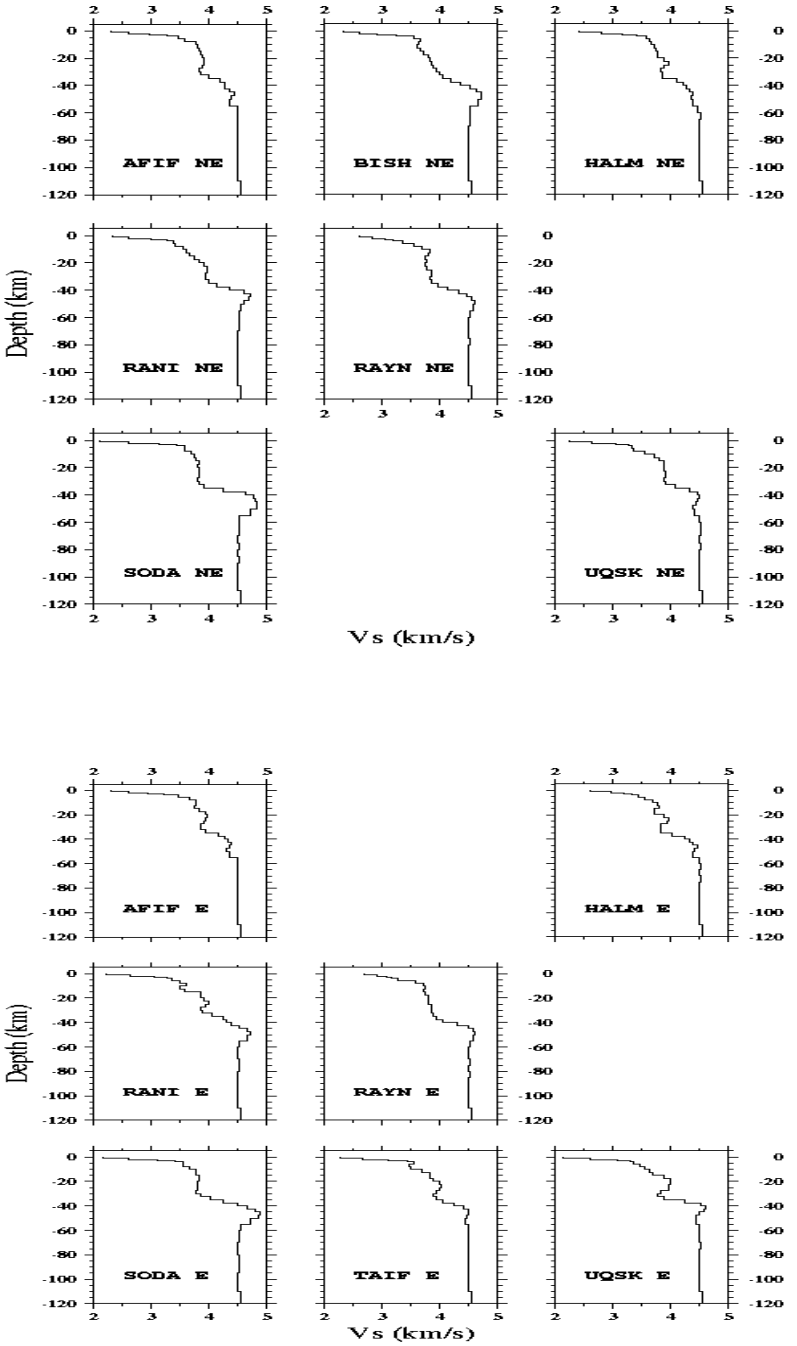


Figure 5: Resulting models obtained from the combination of the dispersion group velocity values and the NE (left) and E (right) receiver functions.

We compare the NE models to the interpretive crustal sections provided by Mooney et al. [1985], Prodehl [1985] and Badri [1991] (Figure 6), by assuming a Poisson's ratio of 0.25. In general our upper mantle is slower, and no one
of the two contrasts inferred in the Mooney et al. [1985] refraction model observed in ours. The upper mantle constraints imposed to our models could be masking such features and could be leading to underestimated velocity values; however, we cannot see strong evidence of such contrasts in our receiver functions and the fit to the high period dispersion velocities is satisfactory. Our crust-to-mantle transition locations and thickness are, in general, in good agreement with those inferred from the refraction models. Beneath HALM and RAYN, however, our inferred crust-to-mantle transitions contrast with a sharp

discontinuity in Mooney et al. [1985] and Badri [1991] interpretations. Actually, a sharper boundary is more consistent with the sharp PpPms phase observed in the receiver function at station HALM, but not at RAYN. The uppermost crust in our models is slower than that inferred from the refraction models; actually, one expects to find low velocity near-surface material as a result of weathering fracture.

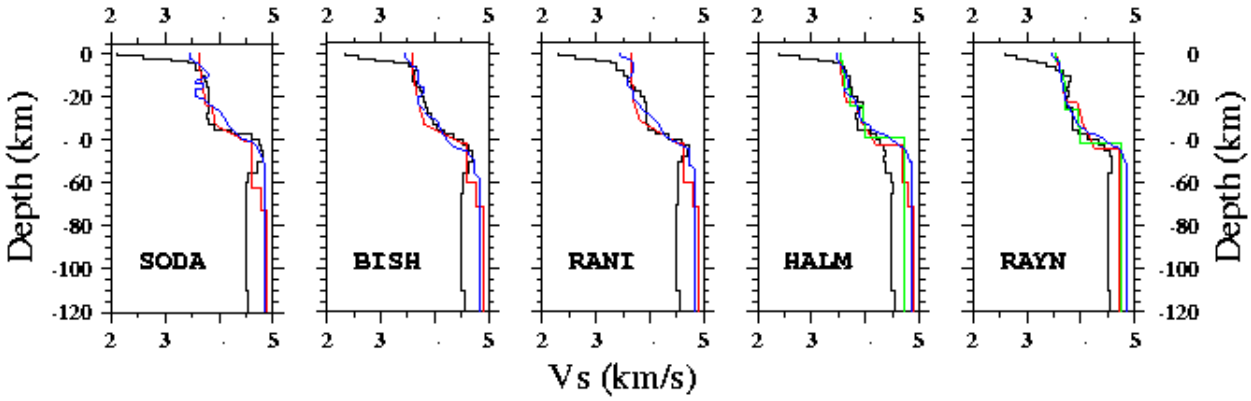


Figure 6: Comparison between the NE resulting models (black) and the refraction profile models from Mooney et al. [1985] (red), Prodehl [1985] (blue) and Badri [1991] (green).

Application to Western US

We also employ the methodology to model receiver functions and dispersion measurements beneath two broad-band stations in North America: ANMO and KNB (Figure 7). In this occasion we invert phase velocity measurements for the fundamental mode of Rayleigh and Love waves with receiver functions at two frequency bands and different ray parameters. As pointed out by Ammon et al. (1990) simultaneous inversion of waveforms with different slowness alone does not appear to be enough to remove the typical depth-velocity ambiguity in receiver function inversions. As in the Arabian Shield, data allow analysis to be performed from various backazimuths; in this application, however, we will focus on the problems posed by the unavailability of short period phase velocity measurements.

Figure 8 shows the velocity constrained inversion results at stations ANMO and KNB, the constraints being the S-wave mantle velocities from TNA model [Grand and Helmberger, 1984]. At station ANMO we observe a significant and unrealistic negative gradient at the uppermost part of the structure which contrasts with the positive and more realistic gradient obtained in the same depth range beneath KNB. This different behavior is probably caused by the different suitability of the starting model (a constant 8 km/s P-wave velocity region over PREM) combined with the lack of constraints from our data. As it happened with the upper mantle structure, this unlikely structure could be trading-off with the remaining of the model, and independent information to constraint that part of the profile could be required. We also observe that some arrivals within the 1-4 s time window are not fitted; these arrivals are associated to upper crust structure, where the inversion procedure has imaged a negative gradient.

Figure 9 shows the inversion results at station ANMO when additional upper crust constraints are considered. The additional constraints simply consist of forcing the uppermost layer to have a S-wave velocity of 2.5 km/s, which is more realistic, and the negative gradient is removed. The fit to the receiver function does not show major changes, and the arrivals in the 1-4 s time window are still not fitted. The match to the dispersion velocities is still good but somewhat underpredicted in the short period range. Additional information from local dispersion velocities or from local S-wave arrivals could provide more realistic constraints. It is important to note, though, that Figure 9 demonstrates that this lack of absolute velocity information in the uppermost structure does trade-off with the remaining of it.

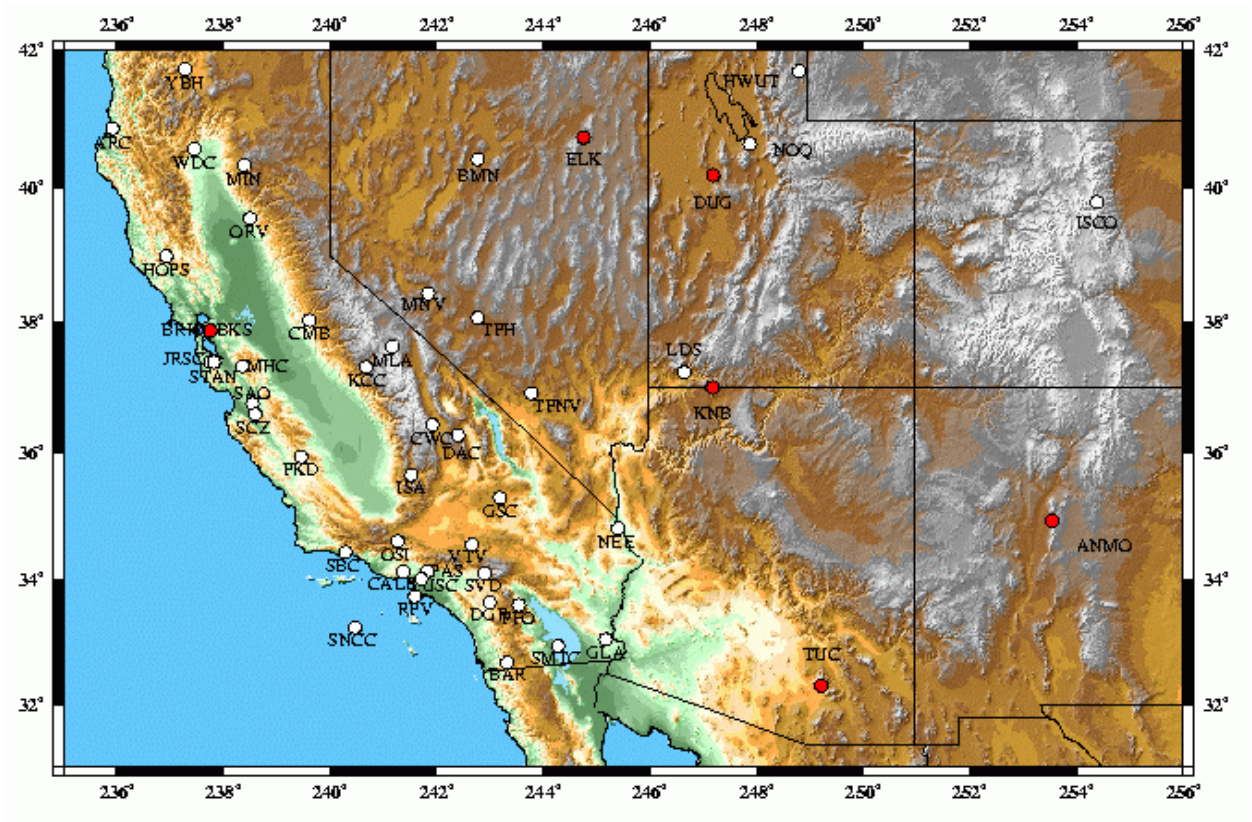


Figure 7: Topographic map of Western U.S. showing the location of various broad-band stations used in our inversions for earth structure.

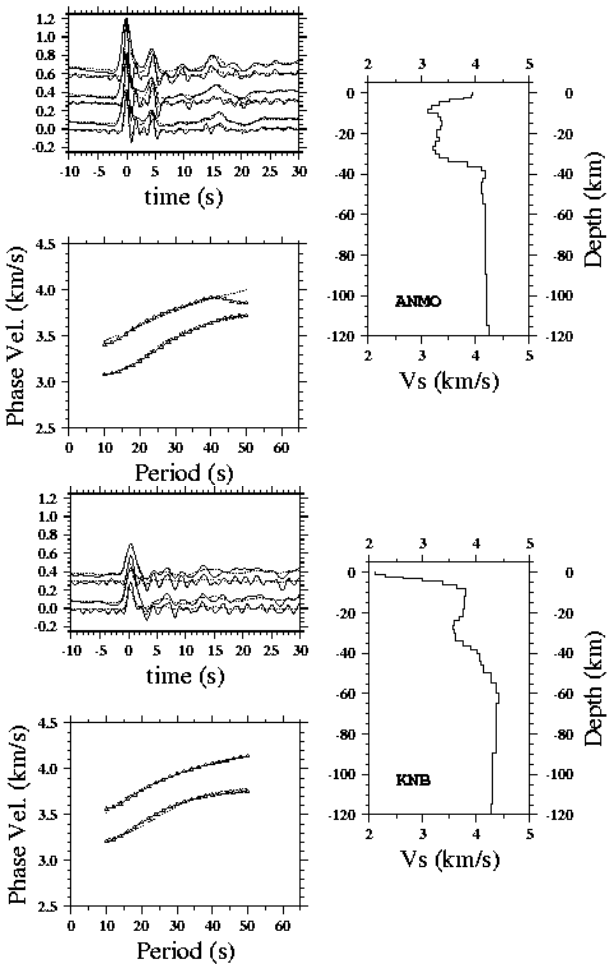


Figure 8: Inversion results at stations ANMO (left) and KNB (right) from the combination of phase-velocity dispersion measurements and receiver functions at different incidence and frequency contents. At ANMO the upper crust is imaged as an unlikely negative gradient as a consequence of the lack of absolute velocity constraints from the short-period dispersion values.

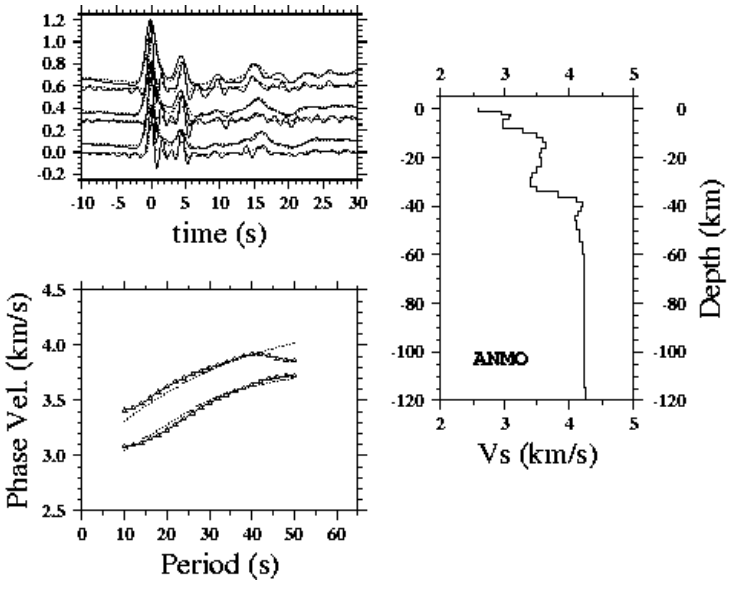


Figure 9: Inversion results for station ANMO forcing the top layer to be 2.5 km/s shear-wave velocity.

CONCLUSIONS AND RECOMMENDATIONS

The combination of surface wave dispersion data and receiver functions provides constraints on the shear velocity of the propagating medium that improve those provided by either of the data sets considered separately, and helps to avoid overinterpretation of single data sets. We also show that this combination cannot unambiguously resolve the fine structure of the upper mantle, although this will depend on the bandwidth considered for the dispersion data set. When no long period information is availble, independent information must be provided during the inversion process to insure a reasonable upper mantle in the model, since allowing the inversion to place an unlikely structure affects the estimates of the lower crust velocities. When no short period dispersion velocities are available, the upper crust velocity information contained in the main peak of the receiver function data may not suffice to constrain that part of earth, and independent constraints may be also required.

Key Words: Surface wave, receiver function, crustal structure, algorithms

REFERENCES

- Badri, M. [1991]. Crustal structure of central Saudi Arabia determined from seismic refraction profiling, *Tectonophysics,* **185,** 357-374.
- Cassidy, J.F. [1992]. Numerical experiments in broadband receiver function analysis, *Bull. Seism. Soc. Am.,* **82,** 1453-1474.
- Constable, S.C.. R.l. Parker, and C.G. Constable [1987]. Occam's inversion: A practical algorithm for generating smooth models from eelctromagnetic sounding data, *Geophysics,* **52,** 289-300.
- Du, Z.J. and G.R. Foulger [1999]. The crustal structure beneath the northwest fjords, Iceland, from receiver functions and surface waves, *Geophys. J. Int.,* **139,** 419-432.
- Grand S.P. and D.V. Helmberger [1984]. Upper mantle shear structure of North America, *Geophys. J. R. astr. Soc.,* **76,** 399-438.
- Julia, J., C.J. Ammon, R.B. Herrmann, and A.M. Correig [2000]. Joint inversion of receiver function and surface-wave dispersion observations, *Geophys. J. Int.* (in press).
- Mooney, W.D., M.E. Gettings, H.R. Blank, and J.H. Healy [1985]. Saudi Arabian seismic-refraction profile: A travel time interpretation of crustal and upper mantle structure, *Tectonophysics,* **111,** 173-246.
- Ozalaybey, S., M.K. Savage, A.F. Sheehan., A.N. Louie, and J.N. Brune [1997]. Shear-wave velocity structure in the northern basin and range province from the combined analysis of receiver functions and surface waves, *Bull. Seism. Soc. Am.,* **87,** 183-189.
- Prodehl C. [1985]. Interpretation of a seismic-refraction survey across the Arabian Shield in western Saudi Arabia, *Tectonophysics,* **111,** 247-282.
- Ritzwoller M.H. and A.L. Levshin [1998]. Eurasian surface wave tomography: Group velocities, *J. Geophys. Res.,* **103,** 4839-4878.

LOCATION CALIBRATION OF KAZAKHSTAN BASED ON DTRA (U.S.)-NNC (RoK) JOINT EXPERIMENTS (1997-1999) IN THE FORMER SEMIPALATINSK TEST SITE

Rong-Song Jih[1] and Robert A. Wagner[2]
1 Sensor and Geotechnical Branch (CPFG), Defense Threat Reduction Agency
2 Largo Geophysics Laboratory, Multimax, Inc.

Sponsored by the Defense Threat Reduction Agency
Seismic R&D Support Desk

ABSTRACT

Defense Threat Reduction Agency [DTRA], U.S.A., and the National Nuclear Center [NNC], Republic of Kazakhstan, jointly conducted a series of large chemical explosions during the summer of 1997 through 1999 at the former Semipalatinsk Test Site [STS] in Eastern Kazakhstan. These experiments were carried out primarily as part of the closing of unused tunnels and shafts at the STS under the Co-operative Threat Reduction Program as regulated in the Nunn-Lugar Bill. These explosions provide an excellent opportunity to test the readiness of some national and international seismic monitoring infrastructure. They also offer a valuable suite of GT0 data for calibrating regional seismographs in the Central Asia with a variety of possible immediate application: improved mapping of seismicity for earthquake hazard reduction, fundamental research in seismology, and nuclear treaty verification. Phase arrival picks of these chemical explosions have been measured off digital waveforms recorded at the Kazakhstan Broadband Network (KZNet), Kyrgiz Network (KNet), Talgar Complex Seismological Expedition [TCSE], and Altai-Sayan Experimental & Methodological Seismological Expedition [ASEMSE]. Region-specific, piecewise linear travel-time curves were derived with standard least-squares regressions:

$TT(Pn) = \Delta / 7.94 + 7.56$ (for $300km \le \Delta < 500km$),
$TT(Pn) = \Delta / 8.13 + 8.79$ (for $500km \le \Delta \le 1{,}000km$),
$TT(Pg) = \Delta / 6.02 + 0.20$ (for $\Delta \le 900km$),
$TT(Sn) = \Delta / 4.69 + 14.98$ (for $\Delta \le 900km$),
$TT(Lg) = \Delta / 3.51 + 0.03$ (for $\Delta \le 1{,}000km$), and
$TT(Rg) = \Delta / 2.99 + 1.86$ (for $\Delta \le 500km$).

Various relevant, independent geophysical information were then utilized to further constrain the thickness of crustal layers. References used include the 3-dimensional Moho and Conrad depths (Zlavdinov, 1974), the heat flow data (Golitsyn and Liatyf-Zade, 1975), a Deep Seismic Sounding [DSS] profile near Karkaralinsk (Antonenko, 1984), USGS open-file reports (Bonham et al., 1980; Leith, 1987ab, 1989), and miscellaneous NRDC-related publications. The KZ40 model derived in this study gives a fairly satisfactory performance in validation tests:

[1] both the mean and median mis-locations are 3-4 km for the 5 GT0 events tested,
[2] the mean and median errors in depth estimates are within 2 km for the 5 GT0 events tested,
[3] the mean and median of RMS residual, which are measures of misfit, are reduced by 50% as compared to those of IASP91 and J-B models, and
[4] the mean and median mis-locations are reduced by 50% as compared to those of IASP91 and J-B models.

These preliminary results suggest that KZ40, being a very simple one-dimensional crustal velocity model, could be adequate for routine location exercise in the eastern half of Kazakhstan and the southwestern part of Siberia. DTRA is currently collaborating with NNC on the last 100-ton shot planned for STS in the summer of 2000. This Ω-3 experiment is meant to destroy the very last unused tunnel in the Degelen Mountain originally excavated for potential nuclear testing by the former U.S.S.R. The additional seismic data from Ω-3 can be used to refine regional 1-dimensional models (such as KZ40) and pave the road for deriving a more sophisticated 3-dimensional representation of the crust of this region. The bilateral cooperation between the U.S.A. and Kazakshtan in executing these Ω-series experiments offers a prototype for how to conduct these experiments that are needed both for calibration purpose and, in other venues, perhaps for confidence building measures as well.

Key Words: Location, calibration, crustal velocity structure.

PROJECT OBJECTIVE

During the Threshold Test Ban Treaty [TTBT] era, seismic monitoring of nuclear tests relied primarily on teleseismic[1] data. The newly signed Comprehensive Nuclear-Test-ban Treaty [CTBT] shifts the focus of seismic monitoring to events with much smaller magnitudes, which may not be recorded at many teleseismic stations. Accordingly, in-country "regional" seismographs become a key ingredient of the verification regime in the treaty provisions. Seismic wave propagation at regional distances is more complex than at teleseismic distances, due to lateral inhomogeneities in the Earth's crust. As a result, determination of region-specific crustal structure - so-called *"calibration"* - is crucial for the CTBT verification. Improved region-specific crustal structure also finds an immediate utility in seismic hazard reduction. Though detailed 3-D structures are ultimately desirable, 1-D models are more appropriate for most location algorithms currently in use. 1-D models also serve as the starting model in deriving more complex and realistic 3-D models.

The objective of this study is to utilize seismic data collected under the recent tunnel / shaft closure experiments in Semipalatinsk Test Site (STS) for calibration of *"Zone 1"* (≤ 1,000km) regional wave propagation in Eastern Kazakhstan. These high explosive experiments were jointly conducted in the summer of 1997 and 1999 by Defense Threat Reduction Agency (DTRA, U.S.A.) and the National Nuclear Center (NNC) of Kazakhstan, under the Cooperative Threat Reduction Program (CTR). Multimax, Inc., a DTRA contractor, merged regional digital seismograms which were scattered at several institutions, and re-measured the phase picks for further analysis. A phased approach of research has been undertaken at DTRA:

[1] Derive the optimal average (*i.e.*, 1-D) crustal velocity model(s) for improved regional location purpose, based on data collected prior to the summer of 1999.

[2] The 1-D model(s) derived with existing data should be validated with independent data set. The Ω-2 of September 1999 and the Ω-3 (scheduled summer 2000) high explosive tests offer the best opportunity to collect seismic data required for such validation tests.

[3] Pending the performance of 1-D model(s) in seismic location exercise, the Source-Specific Station Corrections can be derived to count for the 3-D effect on travel times of various seismic phases.

This paper describes the results obtained so far under the Phase [1] and preliminary results under the Phase [2].

RESEARCH ACCOMPLISHED

Modern Digital Seismographs in Central Asia

Figure 1 is a map showing the IMS seismic stations near the Semipalatinsk Test Site (STS, shown as a shaded patch)[2] as well as all those seismic events reported in the bulletins of International Seismological Center (ISC) between 1987 and 1993. Within 1,000 km of STS, there are two IMS primary stations/sites (blue pentagons in Figure 1): Zalesovo (ZAL, 53.9°N, 84.8°E) and Makanchi (MAK, 46.8°N, 82.0°E); and three auxiliary stations (blue triangles in Figure 1): Borovoye (BRVK, 53.1°N, 70.3°E), Kurchatov (KURK, 50.7°N, 78.6°E), and Ala-Archa (AAK, 42.6°N, 74.5°E). The Lamont Doherty Earth Observatory (LDEO) of Columbia University has been cooperating with several local institutions in Kazakhstan and the southwestern Siberia of Russia on the installation and operation of modern broadband seismographs.[3]

---

[1] So-called *"Zone 3"* in the fifties, which typically refers to distances 2,000km and beyond.

[2] The boundaries of the Semipalatinsk Test Site (STS) were defined and communicated to the U.S. in 1990 upon entry into force of the TTBT. The STS covers an area about 100 km from east to west, and 150 km from north to south (P. G. Richards, personal communications, 1999; See also Khalturin et al., 1999).

[3] LDEO's partners include the Institute of Geophysical Research, National Nuclear Center (NNC), Kazakhstan; Talgar Complex Seismological Expedition (TCSE), Kazakhstan; and Altai-Sayan Experimental & Methodological Seismological Expedition (ASEMSE), Russia. NNC operates Kazakhstan Broadband Network (KZNet), which includes two seismic arrays at Kurchatov and Borovoye. TCSE operates seismographs at Bayanual, Karkaralinsk, and Talgar. ASEMSE operates Yeltsovka (See Appendix A). IRIS supports the Kirghiz Network (KNet), which includes the auxiliary station Ala-Archa

Seismicity Around STS and DTRA-NNC Calibration Events

The seismicity of Eastern Kazakhstan (43°-55°N, 68°-88°E) is much weaker than that of the Tienshan Mountain Range to its south or the Altai Mountain Range to its east (Figure 1). Earthquakes in or around STS have been very rare. The red, gray, and green disks shown in Figure 1 represent shallow (<10km), medium-depth (10-33km), and deep (>33km) seismic events, respectively, based on catalogs published by the International Seismological Center (ISC, in England) between 1987 and 1993. The shallow events in STS shown in Figure 1 are nuclear tests conducted by the U.S.S.R. prior to the signing of CTBT. Deep earthquakes do exist in the Tienshan Mountain, which is about 1,000 km away from the STS. *To calibrate the seismic wave propagation within the stable Kazakh shield, man-made, controlled seismic events would be the best source and any of such opportunities should be embraced and fully exploited.* Six major HE tests have been conducted at the STS during the summer between 1997 and 1999 (Table 1). The biggest shots were of 100 tons, detonated in the tunnels 214 and 160 of Degelen Mountain. The remaining four shots are of 25 tons each. Several teleseismic seismographs have recorded most of these chemical explosions.

Table 1. DTRA-NNC Calibration Events '97-'98

Date	O.T.	N°	E°	Elev	DoB	Charge	Remark
970803	08:07:20.04	49.9412	78.7860	335	50	25	1311*
970831	07:08:38.75	49.8837	78.8148	332	300	25	1381*
970928	07:30:15.13	49.8794	78.8493	329	550	25	1349*
980822	05:00:18.90	49.7667	77.9908	716	0	100	214**
980917	07:19:40.55	49.9810	78.7559	320	30	25	1071
990925	07:00:06.00	49.7819	78.9663	___	___	100	160***

* : Depth-of-Burial Experiments in Balapan. ** : Ω-1 Experiment in Degelen. *** : Ω-2 Experiment in Degelen.

Travel-Time Regression and Additional Geophysical Constraints

Since the source parameters of these HE tests are exactly known - *i.e.*, they are the so-called "GT0" events, the arrival times as well as the distances to seismographs can be accurately measured. Standard least-squares regressions provide the best linear fit of travel times as a function of great circle distance. If non-GT0 events were used, the uncertainty in travel time and/or the distance should be taken into account. This can be accomplished with the Monte-Carlo procedure in which each data point is perturbed according to the pre-defined probability distribution (Jih, 1993). Figures 2 shows results of regressing travel times of Pn and Pg on distance, using the first five events listed in Table 1. The results can be summarized as follows:

$TT(Pn) = \Delta / 7.94 + 7.56, \quad 300km \le \Delta < 500km.$
$TT(Pn) = \Delta / 8.13 + 8.79, \quad 500km \le \Delta \le 1{,}000km.$
$TT(Pg) = \Delta / 6.02 + 0.20, \quad \Delta \le 900km.$
$TT(Sn) = \Delta / 4.69 + 14.98, \quad \Delta \le 900km.$
$TT(Lg) = \Delta / 3.51 + 0.03, \quad \Delta \le 1{,}000km.$
$TT(Rg) = \Delta / 2.99 + 1.86, \quad \Delta \le 500km.$

There are often more than one crustal models whose predicted travel-time curves would match the observed ones. This is exactly the same situation in interpreting the receiver function with crustal models. It is therefore necessary to utilize some independent information, such as the lab measurement of rock composition and velocity *etc.*, to further constrain the crustal model. Previous geophysical studies provide very useful constraints on this region: 3-D Moho and Conrad depths (Zlavdinov, 1974), the heat flow data (Golitsyn and Liatyf-Zade, 1975), DSS profile near Karkaralinsk (Antonenko, 1984), USGS open-file reports (Bonham *et al.*, 1980; Leith, 1987ab,

(AAK). More detailed description of these facilities can be found in Kim et al. (1996).

1989), and other publications (*e.g.*, miscellaneous NRDC-related studies). Combining the velocity regression results (Figure 2) and these geophysical studies, three crustal models, KZ40, KZ45, and KZ50, with crustal thickness of 40, 45, and 50km, respectively, are proposed (Figures 3). The upper mantle velocities of these three models are slightly different, with thicker crust associates with faster P- and S-velocities.

Re-location Results and Metrics of Location Performance

Figure 4 shows the LocSAT locations of the event 970803 using eight different crustal models including JB, IASPEI-91, Southwestern Siberia model (Emanov *et al.*, 1999), a gradient model based on a Deep Seismic Sounding [DSS] profile near the STS (Antonenko, 1984), a discretized version of the DSS model (Leith, 1989), as well as the three models developed in this study: KZ40, KZ45, and KZ50. For each model, the 95% coverage ellipse and RMS residual are printed, along with the absolute error in the origin time, epicenter (measured by mislocation in km), and depth. Six models give excellent depth estimates for this event: JB, IASPEI91, Leith (1989), KZ40, KZ45, and KZ50. Models associated with larger error in depth tend to give larger error in the origin time as well. The majority of models lead to a mislocation of only a few kilometers.

The location performance of each crustal model can be evaluated with five metrics, each being averaged over five events: [1] the size of 95% coverage ellipse, [2] the RMS residual, [3] the rectified error in the origin time, [4] the mislocation, and [5] the rectified error in depth estimate. These 8 by 5 metrics are tabulated in Table 2 (top). The performance can also be measured with the median of the metrics (Table 2, bottom).

The International Seismological Centre [ISC] and the CTBT International Data Center [IDC] in Vienna use the J-B and IASPEI-91 models, respectively, as the baseline model in their routine location operations. The National Earthquake Information Center [NEIC] of US Gelogical Survey has been using the J-B tables for several decades. All the events tested so far move closer to the Ground Truth [GT] locations when KZ-series of region-specific models are used. In fact, both the mean and median mislocation are reduced by more than 50%. Another metric that shows a dramatic improvement is the RMS residual, which is a measure of misfit (in seconds). Smaller RMS residual means better fit. Table 2 indicates that RMS residual also gets a 50% reduction.

Leith (1989) proposes to discretize the gradient crust of Antonenko's (1984) DSS model to get around the same software restriction Thurber (1990) had faced. It is interesting to note that Leith's (1989) model gives a perfect depth estimate for each of the six events. KZ40, KZ45, and KZ50 models perform very well across all five metrics. Models associated with larger error in the depth estimate lead to larger error in origin time as well (*e.g.*, the southwestern Siberia model of Emanov *et al.*, 1999; and the DSS model of Antonenko, 1984).

Table 2. Metrics of Location Performance

Model	μ[C-Elps]	μ[RMS]	μ[Δ(OT)]	μ[Δ(XY)]	μ[Δ(H)]
J-B	143	1.30	1.57	8.82	0.20
IASPEI-91	148	1.36	0.15	8.12	0.20
SW Siberia	170	0.86	1.17	3.44	12.34
Antonenko (1984)	194	0.76	1.98	5.16	17.14
Leith (1989)	177	1.60	0.48	7.38	0.00
KZ40 (this study)	168	0.58	0.31	2.80	0.86
KZ45 (this study)	170	0.56	0.39	3.38	2.56
KZ50 (this study)	171	0.52	0.43	3.74	3.28

μ[X]: mean of metric "X" over five events.

C-Elps: area enclosed by 95% coverage ellipses (km^2). RMS: RMS travel-time residuals (second).

Δ(OT): rectified error in origin time (second). Δ(XY): mislocation in epicenter (km). Δ(H): rectified error in depth (km).

Table 2. Metrics of Location Performance (Continued)

Model	m[C-Elps]	m[RMS]	m[Δ(OT)]	m[Δ(XY)]	m[Δ(H)]
J-B	155	1.30	1.65	9.40	0.10
IASPEI-91	161	1.40	0.13	8.90	0.10
SW Siberia	174	0.80	1.06	4.20	12.50
Antonenko (1984)	221	0.70	1.95	5.10	16.50
Leith (1989)	185	1.70	0.55	7.70	0.00
KZ40 (this study)	173	0.60	0.35	2.90	0.30
KZ45 (this study)	174	0.50	0.36	3.10	0.60
KZ50 (this study)	174	0.50	0.16	3.60	1.60

m[X]: median of metric "X" over five events.

C-Elps: area enclosed by 95% coverage ellipses (km^2). RMS: RMS travel-time residuals (second).

Δ(OT): rectified error in origin time (second). Δ(XY): mislocation in epicenter (km). Δ(H): rectified error in depth (km).

Re-location with IMS Stations Only

The models KZ40, KZ45, and KZ50 are derived with phase readings from events exclusively from the region of study. One would naturally expect regionalized model(s) like these to perform better than do global average models such as IASPEI-91 and J-B, which are not "calibrated" for this specific region. This is indeed the case (see Figure 4). Ideally other events that have not been used in constructing the velocity models should be relocated as an independent check. Alternatively, a sub-optimal check is to re-locate the six events with some phases (stations) excluded. Figure 5 shows the re-location results for the event 990925 with IMS stations only. This is a semi-independent test of the models that can be effortlessly performed at this point - an *ad hoc* measure temporarily used until new data are available for testing. This exercise by itself is also an important test from the CTBT verification point of view. *The IMS stations in this region - Borovoye, Kurchatov, Zalesovo, and Makanchi - appear to be able to locate the 100-ton shot with very reasonable accuracy and precision, provided that region-specific models (such as the KZ-series) are used.*

CONCLUSIONS AND RECOMMENDATIONS

The DOB and Ω-series events provide excellent examples of calibration shots which are needed worldwide for CTBT monitoring. These events provide a prototype for how to conduct these experiments and, could act as an international example of what needs to be done for the CTBT, both for calibration and, in other venues, perhaps for confidence-building measures. Regional and local seismic observations of these shots at different depths-of-burial (DOB) in tunnels, when combined with previous calibration work such as the Nevada Test Site Nonproliferation Experiment and the 1960s Lake Superior experiments, can provide fundamental information on detection thresholds and location calibration in different geological areas. Such a program covering all areas of the world is necessary for the CTBT monitoring regime. During these experiments in STS, one successful - and important - example of instrument deployment and data collection has been set by LDEO of Columbia University under contracts to DTRA and LLNL.

From calibration point of view, the DOB and Ω series experiments offer an excellent opportunity to calibrate the region's propagation properties for many regional and local seismic phases. In addition to phases that are routinely used in regional location exercise, such as Pn, Pg, Sn, and Lg, this study also utilizes the phase PmP. The calibration procedure described in this paper is straightforward and simple to implement. It is a procedure very similar to interpreting the wide-angle refraction profile. The resulting 1-D models appear to be suitable for the shield region of Eastern Kazakshtan. There are indications that these KZ-series crustal velocity models could be applicable to the Southwestern Siberia as well. Emanov *et al.* (1999) use an one-layer simple crustal model to locate events in the Kuzbass-Abakan mining region. Their model gives travel time curves very close to what the KZ-series models would give.

The IMS stations in this region - Borovoye, Kurchatov, Zalesovo, and Makanchi - appear to be able to locate the 100-ton shot with very reasonable accuracy and precision, provided that region-specific models (such as the KZ-series) are used. However, the models developed in this study need to be tested with some really independent data set, *i.e.*, with events that have not been used in deriving the models. A precious opportunity for such tests would be DTRA-NNC's Ω-2 and Ω-3 HE experiments. The Ω-2 experiment of 25 September 1999 also provided an opportunity for on-site inspection team from both DTRA and the CTBTO (in Vienna) to conduct a mock inspection exercise (DTRA, 1999).

This study presents a simple calibration procedure, J_5, which utilizes several GT0 events to derive averaged 1-D crustal model(s). The resulting 1-D crustal model appears to be suitable for regional (≤1,000 km) location purpose in this area which encircles two CTBT primary IMS sites (ZAL, MAK) and three existing auxiliary stations (BRVK, KURK, and AAK). Several metrics shown in the attached Table clearly illustrate how regionalized 1D models (such as KZ45) can improve the location:
[1] the mean and median of RMS residual, which are measures of misfit, are reduced by 50% as compared to those of IASPEI-91 and JB models,
[2] the mean and median mislocation are reduced by 50% as compared to those of IASPEI-91 and JB models,
[3] the mean and median mislocation are 3-4 km for the 5 GT0 events tested,
[4] the mean and median errors in depth estimates are within 2 km for the 5 GT0 events tested.
An alternative approach of utilizing these precious GT0 events is to establish the Source-Specific Station Correction [SSSC] surface for each seismic phase of interest. A follow-up study of comparing the performance of SSSC against 1-D average models in locating events away from STS is planned. A surprising feature of Leith's (1989) discretized model is that it gives the perfect depth estimate for all six events. Why this model performs in this peculiar manner needs to be carefully explored.

ACKNOWLEDGEMENTS

This project is a joint effort of the *Sensor and Geotechnical Applications Branch (CPFG)* of Defense Threat Reduction Agency (DTRA) and Multimax, Inc. Multimax is supported under DTRA contract *DSWA01-98-C-0156* issued by the *Arms Control Technology Division (DTRA/OST).* The analyses of Multimax-furnished phase arrival readings were conducted at the *Seismic R&D Support Desk* of DTRA/CPFG. Additional support for seismo-acoustic data acquisition came from the Bureau of Verification and Compliance (DOS/AC/VC) and DoD Washington Headquarters Services (WHS).

REFERENCES

Antonenko, A. N. (1984). Deep structure of the earth's crust in Kazakhstan (in Russian), Acad. Sci. Kazakh S.S.R., Alma-Ata, 274pp.

Bonham, S., W. J. Dempsey, and J. Rachlin (1980). Geologic environment of the Semipalatinsk area, U.S.S.R. (Preliminary Report), U.S. Geological Survey Report to the Air Force Technical Applications Center, Unpublished (official use only), 46pp.

DTRA (1999). *Connection,* **1-8,** 2, 23.

Emanov, A. F., A. G. Filina, V. I. Khalturin, W.-Y. Kim, and P. G. Richards (1999). Earthquakes and large mining blasts in Southwestern Siberia, Russia, Lamont Doherty Earth Observatory Report, 5pp.

Golitsyn, M. V. and Liatyf-Zade (1975). *Teplovoy rezhim nedr tsentral'nogo Kazakhstana* (the underground thermal regime of central Kazakhstan), *Sovetskaya Geologiya,* **8,** 51-62.

Gorbunova, I. V. (1987). Averaged hodograph of the first P-wave arrivals for the region of Central Asia and Kazakhstan, in *"Earthquakes in the U.S.S.R. in 1987",* Moscow, Nauka Publishing House, 59-63. Lamont Doherty Earth Observatory Report, 9pp.

Jih, R.-S. (1993). Statistical study of Soviet nuclear explosions: data, results, and software tools,

Report TGAL-93-05, Teledyne Geotech Alexandria Laboratory, Alexandria, Virginia. 82pp.

Khalturin, V., T. G. Rautian, and P. G. Richards. (1999). A study of small magnitude seismic events during 1961-1989 on and near the Semipalatinsk Test Site, Kazakhstan, paper submitted to PAGEO.

Kim, W.-Y. (1998). Waveform data information product: calibration explosions at Semipalatinsk Test Site, Kazakhstan, during August and September, 1998. Lamont Doherty Earth Observatory Report, 9pp.

Kim, W.-Y., V. V. Kazakov, A. G. Vanchugov, and D. W. Simpson (1996). Broadband and array observations at low noise sites in Kazakhstan: opportunities for seismic monitoring of a Comprehensive Nuclear-Test-Ban Treaty, in NATO ASI Series, Series E, Vol. 303, 467-483.

Leith, W. (1987a). *Geology of NRDC seismic sites in Eatsern Kazakhstan, U.S.S.R.* U.S. Geological Survey Open-File Report 87-597, Department of Interior, Reston, Virginia, 12pp.

Leith, W. (1987b). Tectonics of Eastern Kazakhstan and implications for seismic source studies in the Shagan River area, in *Proceedings of the 9th annual Seismic Research Symposium,* 15-18 June 1987, Nantucket, MA. 34-38.

Leith, W. (1989). Three-dimensional geological modeling of the Shagan River nuclear test site, in *Proceedings of AFTAC-DARPA Seismic Research Review,* 28-29 November 1989, Patrick AFB, FL. 255.

Nersesov, I. L. and T. G. Rautian (1964). The study of dynamics and kinematics of seismic waves at the profile Pamir - Baikal, *Proc. 8th Assembly European Seism. Comm.,* Budapest, 174-181.

Priestley, K. F., G. Zandt, and G. Randall (1988). Crustal structure in Eastern Kazakhstan, U.S.S.R., from teleseismic receiver functions, *Geophys. Res. Let.,* **15-6,** 613-616.

Ryaboy, V. (1989). Upper mantle structure studies by explosion seismology in the U.S.S.R, *Delphic Associates, Inc. Report,* Falls Church, Virginia, 161pp.

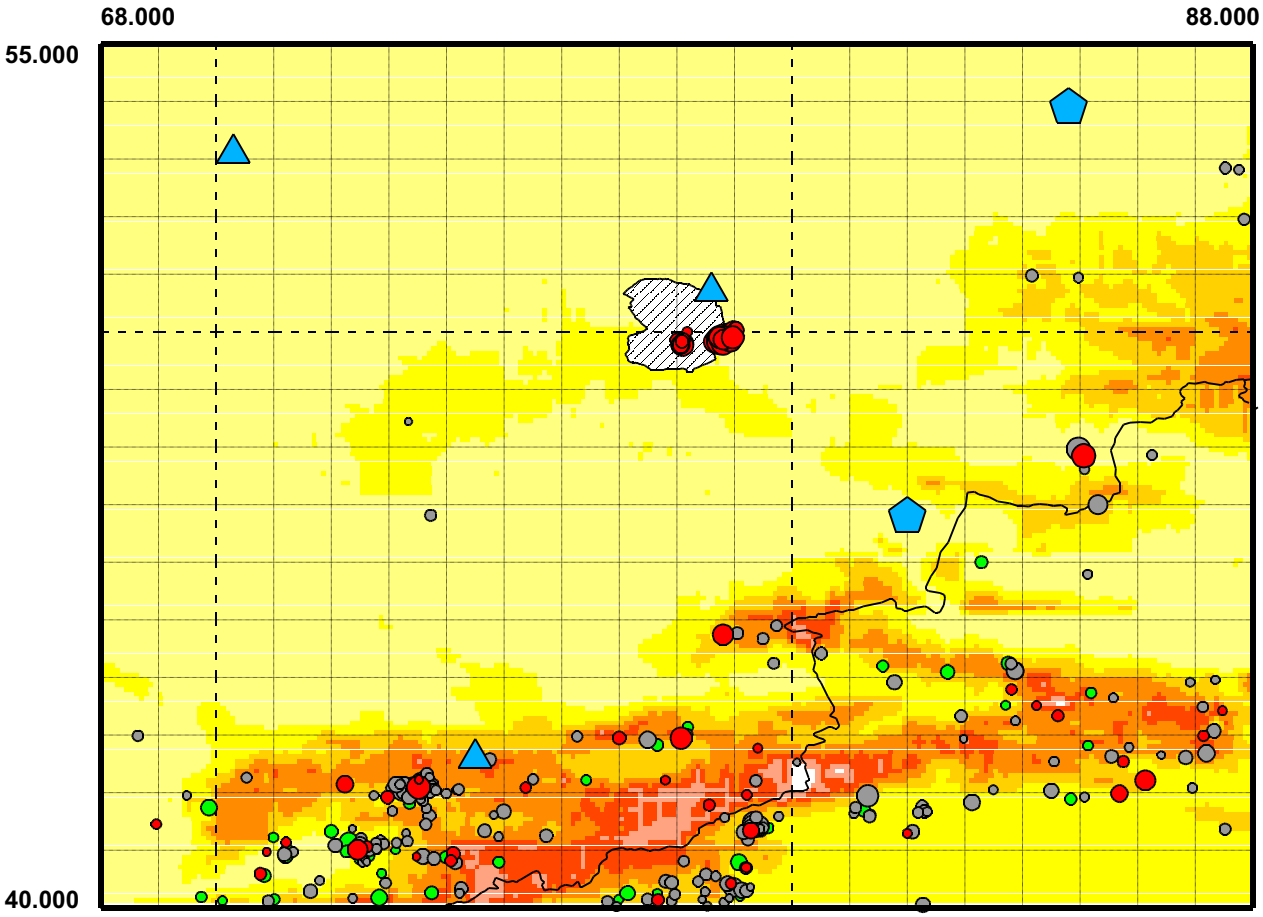
Samygin, S. G. (1974). The Chingiz Fault and its role in the structure of Central Kazakhstan, *Nauka,* Moscow, 208pp.

Thurber, C., H. Given, and J. Berger (1990). Regional seismic event location with a sparse network: application to Eatsern Kazakhstan, U.S.S.R, *J. Geophys. Res.,* **94,** 17767-17780.

Thurber, C. H., H. R. Quin, and P. G. Richards (1993). Accurate locations of nuclear explosions in Balapan, Kazakhstan, 1987 to 1989, *Geophys. Res. Let,* **20,** 399-402.

Zlavdinov, L. Z. (1974). *Izucheniye stroyeniya zemnoy kory po gravimetricheskii dannym* (Study of the structure of the earth's crust from gravity data), *Izd. Nauk. S.S.R.,* 119pp.

ISC SEISMICITY & IMS STATIONS AROUND STS & MAKANCHI



Large & moderate (Ms >= 4.0) events in Central Asia, 1987-1993

304 events with hypocenters/magnitudes published by ISC:

Red: 67 shallow (<= 10km) events, including UNEs in Semipalatinsk

Gray: 184 events of medium depth (10 < H <= 33; Green: 53 deep events (H > 33)

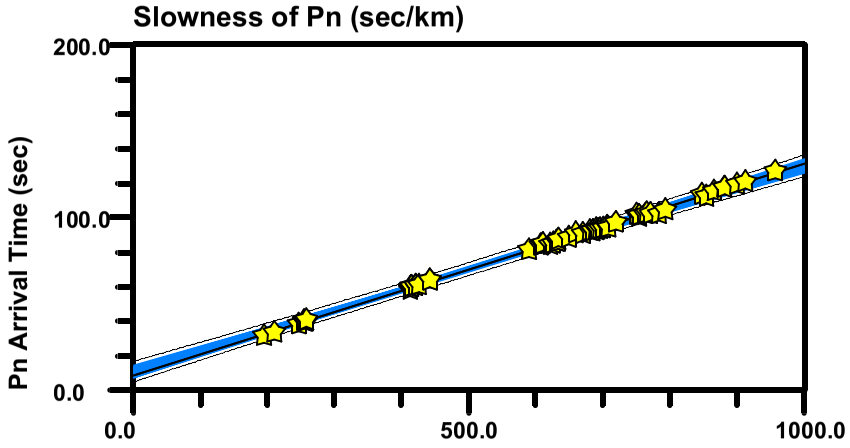
Blue pentagons: IMS primary stations MAK & ZAL

Blue triangles: IMS auxiliary stations AAK, BRVK, KURK

STS (official boundary digitized by Paul G. Richards)

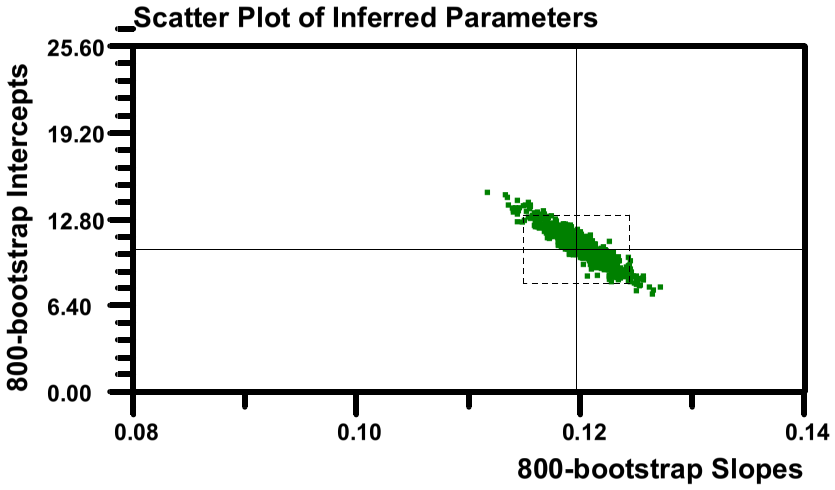
Figure 1

V(Pn) & V(Pg) IN KAZAKHSTAN

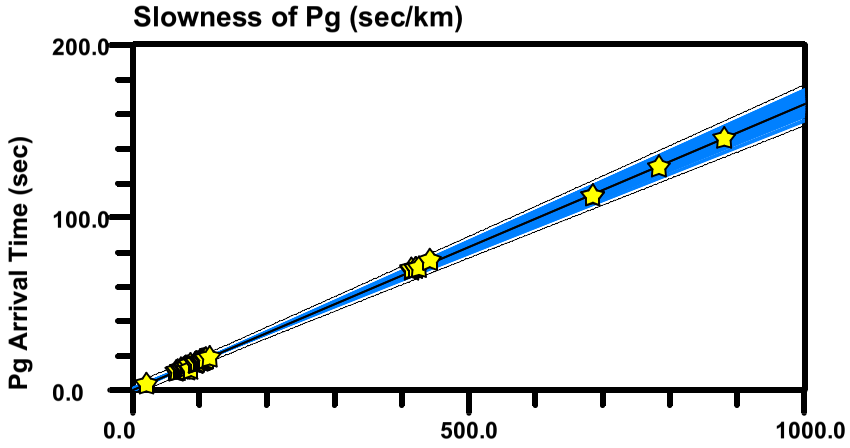


Pn TT-Distance Regression, 55 Arrivals (QC+b)

DWLS (uncertain X & Y): S=0.120(0.002), I=10.571(1.257), 55 data used
OWLS (precise X assumed): S=0.123(0.001), I=8.793(0.337)
Standard LS: S=0.123(0.001), I=8.793(0.337), rho=1.00

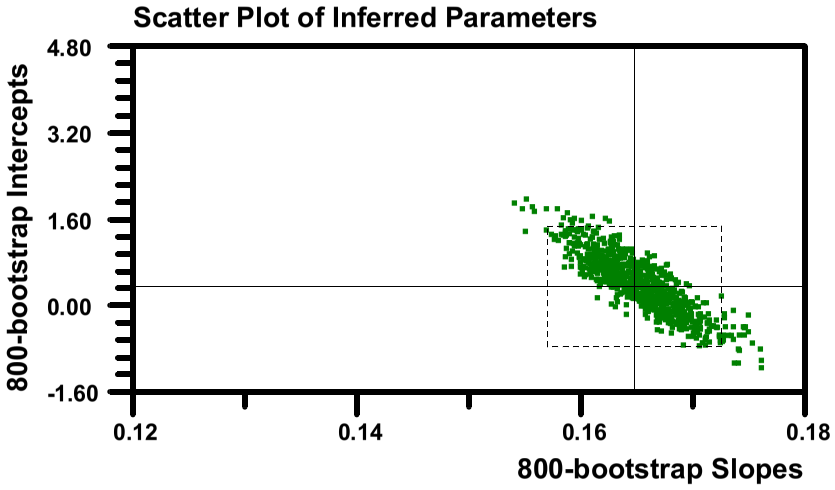


95% confidence interval of slope: 0.120+/-0.005
95% confidence interval of intercept: 10.571+/-2.523
[97.5% quantile of t(53 D.o.F.), 2.007, used]



Pg TT-Distance Regression, 36 Arrivals (QC+b)

DWLS (uncertain X & Y): S=0.165(0.004), I=0.355(0.550), 36 data used
OWLS (precise X assumed): S=0.166(0.001), I=0.197(0.172)
Standard LS: S=0.166(0.001), I=0.197(0.172), rho=1.00



95% confidence interval of slope: 0.165+/-0.008
95% confidence interval of intercept: 0.355+/-1.119
[97.5% quantile of t(34 D.o.F.), 2.034, used]

Figure 2

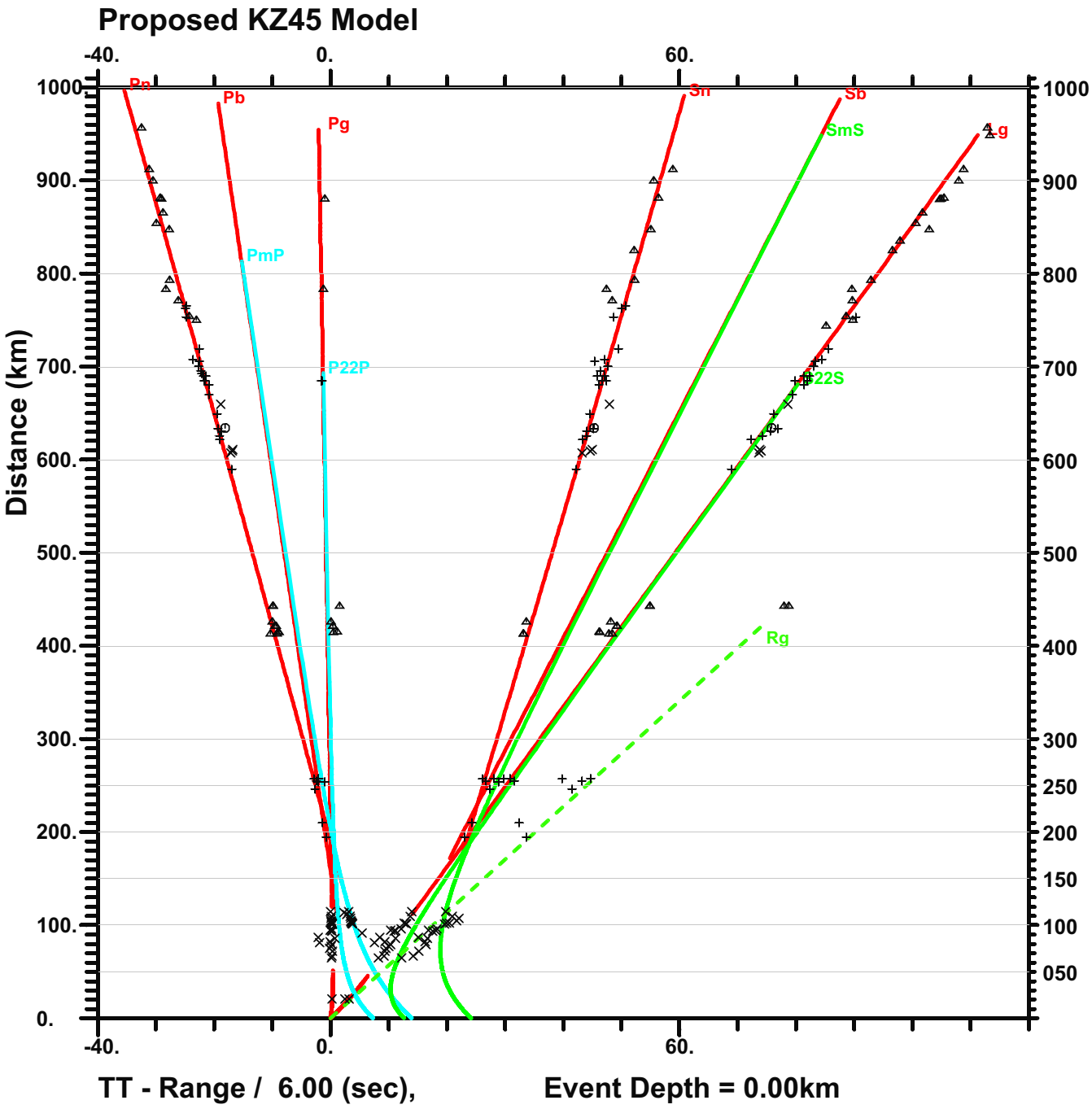
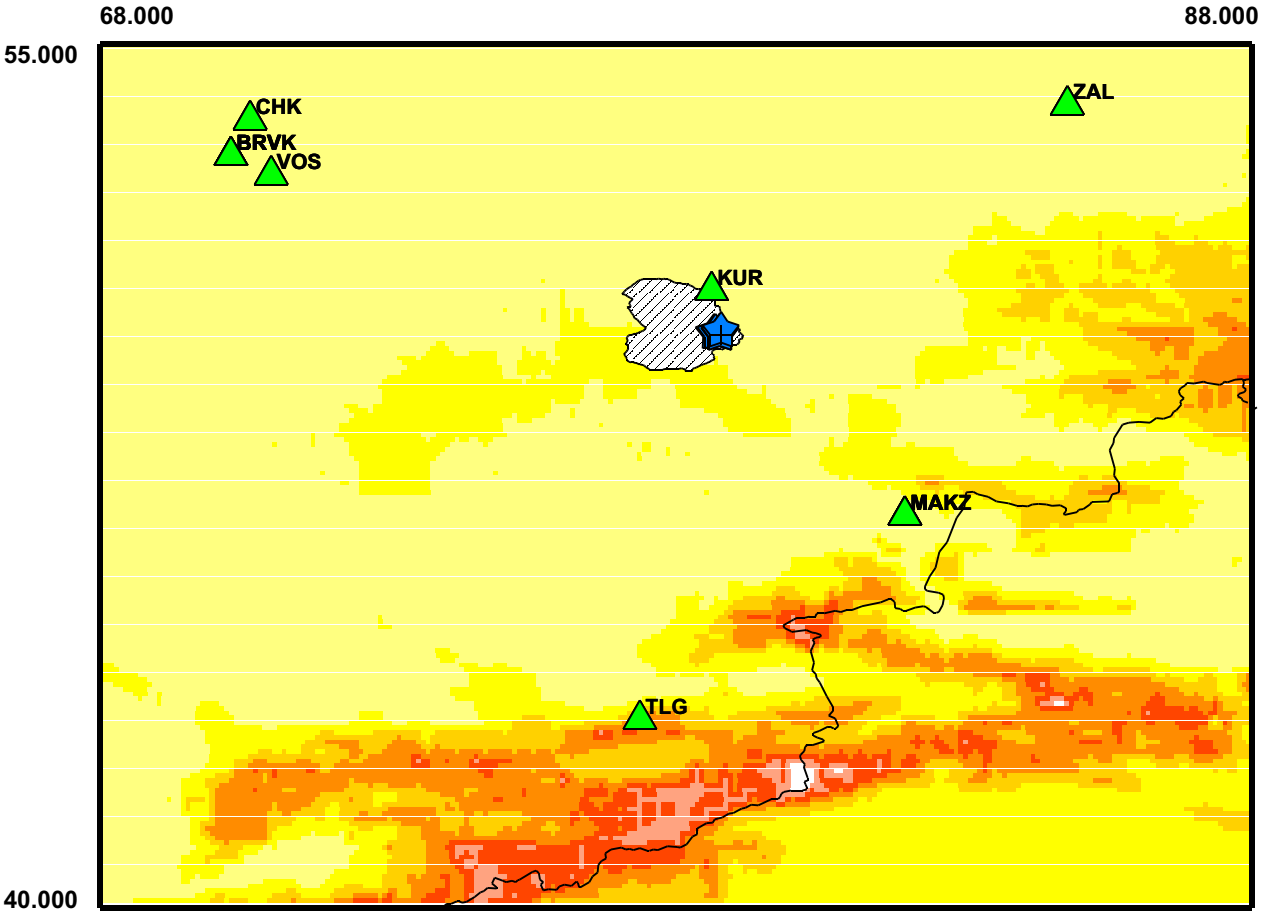

Proposed KZ45 Model
-40.
0.
60.
1000
900.
800.
700.
600.
500.
400.
300.
200.
100.
0.
Distance (km)
Pn
Pb
Pg
PmP
P22P
Sn
Sb
SmS
Lg
S22S
Rg
1000
900
800
700
600
500
400
300
250
200
150
100
050
TT - Range / 6.00 (sec),
Event Depth = 0.00km
Eastern stations
Southern stations
Western stations
Northern stations
Adaquate for 68E-88E, 40N-55N; 1,000 km within STS
0km: 5.40, 3.05; 5-22km: 6.09, 3.53; 22-45km: 6.95, 4.00;
45km: 8.05, 4.60; 205km: 8.35, 4.80

Figure 3

LocSAT Locations of 970803



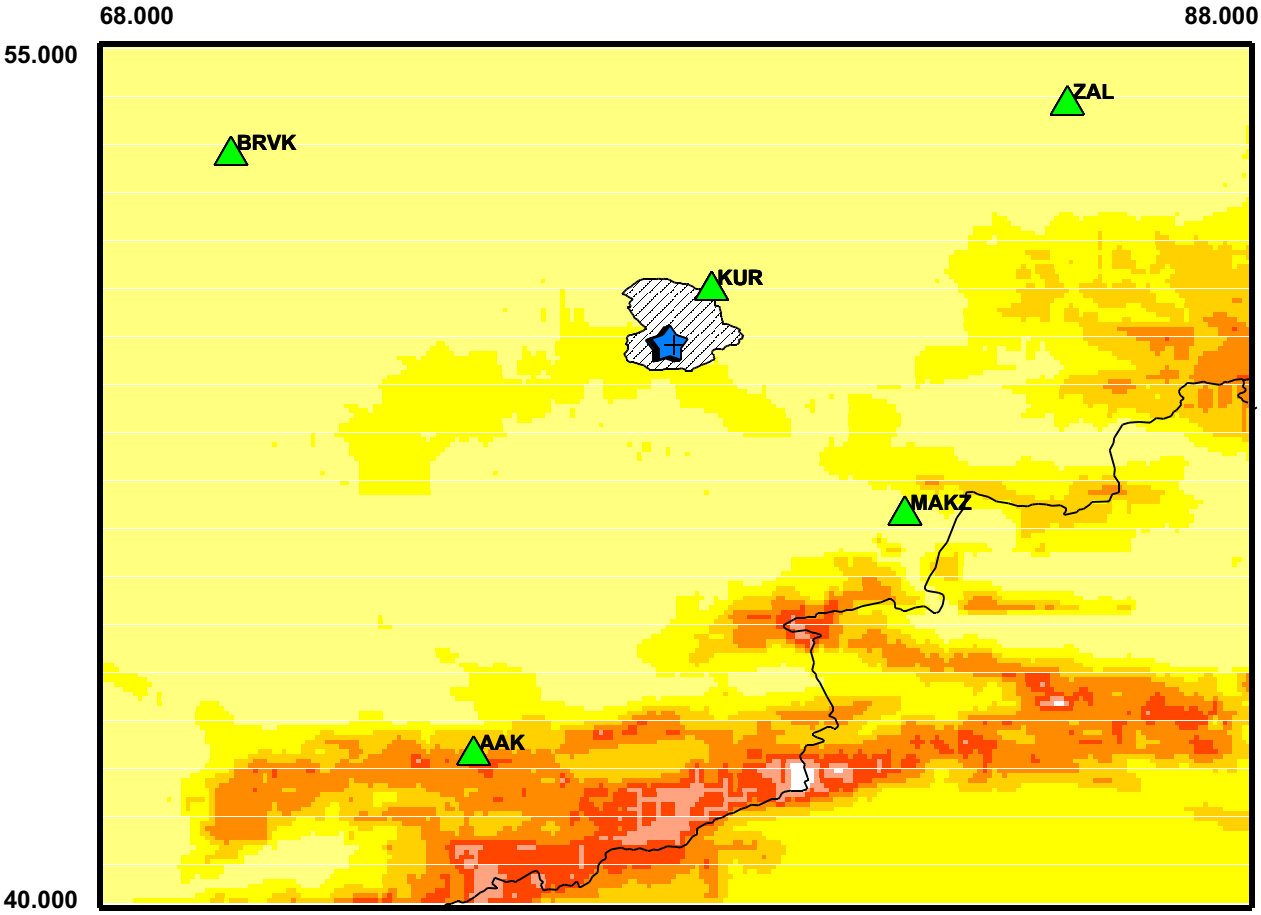
Event 970803, 28 picks, GT info: 0807 20.04 49.9412N 78.7860E 0.05km

J-B model location = 8:7:18.350, 49.976 78.667 0.000
95% C-ellipse=187km^^2, RMS res=1.2s, Error [OT=-1.74s, XY=9.4km, H=-0.1km]
IASPEI91 model location = 8:7:20.044, 49.979 78.694 0.000
95% C-ellipse=192km^^2, RMS res=1.3s, Error [OT=-.04s, XY=7.8km, H=-0.1km]
SW Siberia model (ASEMSE) location = 8:7:21.075, 49.978 78.769 8.401
95% C-ellipse=217km^^2, RMS res=0.7s, Error [OT=1.06s, XY=4.3km, H=8.4km]
DSS (Antonenko, 1984) location = 8:7:21.774, 49.986 78.770 11.959
95% C-ellipse=278km^^2, RMS res=0.6s, Error [OT=1.76s, XY=5.1km, H=11.9km]
Discretized DSS (Leith, 1989) location = 8:7:20.605, 50.013 78.786 0.050
95% C-ellipse=223km^^2, RMS res=1.4s, Error [OT=.56s, XY=8.0km, H=0.0km]
KZ50 (this study) location = 8:7:20.201, 49.964 78.772 0.000
95% C-ellipse=208km^^2, RMS res=0.5s, Error [OT=.16s, XY=2.7km, H=-0.1km]
KZ45 (this study) location = 8:7:20.387, 49.963 78.766 0.000
95% C-ellipse=203km^^2, RMS res=0.5s, Error [OT=.36s, XY=2.8km, H=-0.1km]
KZ40 (this study) location = 8:7:20.427, 49.959 78.759 0.000
95% C-ellipse=201km^^2, RMS res=0.5s, Error [OT=.36s, XY=2.8km, H=-0.1km]

STS (Richards et al., 1999)

Figure 4

LocSAT Locations of 990925.ims



Event 990925.ims, 17 picks, GT info: 0500 6.00 49.7819N 77.9663E 0.00k

J-B model location = 5:0:3.615, 49.753 77.798 0.000
95% C-ellipse=289km^^2, RMS res=1.3s, Error [OT=-2.40s, XY=12.5km, H=0.0km]
IASPEI91 model location = 5:0:5.371, 49.759 77.824 0.000
95% C-ellipse=298km^^2, RMS res=1.5s, Error [OT=-.60s, XY=10.6km, H=0.0km]
SW Siberia model (ASEMSE) location = 5:0:7.445, 49.775 77.879 15.530
95% C-ellipse=323km^^2, RMS res=0.7s, Error [OT=1.40s, XY=6.3km, H=15.5km]
DSS (Antonenko, 1984) location = 5:0:9.974, 49.777 77.896 38.189
95% C-ellipse=387km^^2, RMS res=1.1s, Error [OT=4.00s, XY=5.1km, H=38.2km]
Discretized DSS (Leith, 1989) location = 5:0:6.101, 49.779 77.852 0.000
95% C-ellipse=342km^^2, RMS res=1.8s, Error [OT=.10s, XY=8.2km, H=0.0km]
KZ50 (this study) location = 5:0:6.622, 49.765 77.876 6.686
95% C-ellipse=336km^^2, RMS res=0.4s, Error [OT=.60s, XY=6.8km, H=6.7km]
KZ45 (this study) location = 5:0:6.484, 49.766 77.871 2.811
95% C-ellipse=323km^^2, RMS res=0.4s, Error [OT=.50s, XY=7.1km, H=2.8km]
KZ40 (this study) location = 5:0:6.007, 49.764 77.863 0.000
95% C-ellipse=311km^^2, RMS res=0.5s, Error [OT=0s, XY=7.7km, H=0.0km]

STS (Richards et al., 1999)

Figure 5

ASSESSING ABILITIES TO ESTIMATE SHORT PERIOD GROUP VELOCITIES IN CENTRAL ASIA

A.L. Levshin, M.H. Ritzwoller, M.P. Barmin
Center for Imaging the Earth's Interior, University of Colorado at Boulder

J.L. Stevens
Maxwell Technologies

Sponsored by U.S. Department of Defense
Defense Threat Reduction Agency
Contract No. DTRA01-00-C-0026

ABSTRACT

Our objective is to develop surface wave group velocity maps to periods as low as 8 s across much of Central Asia. Maps previously estimated at CU-B and Maxwell Technologies were confined to periods above about 15 s. Accurate maps at shorter periods would improve signal detection capabilities by advancing signal-to-noise enhancement produced by phase-matched filters. This may permit the extension of surface wave magnitude (M_s) estimates and the $M_s : m_b$ discriminant to periods shorter than 15 s and, hence, to smaller events than current capabilities allow. Significant advances over existing capabilities are possible because data resources in the region of study have improved dramatically in recent years. Our experience shows that shorter period estimates are possible if sufficient care is taken during the measurement procedure. We have begun data acquisition and processing for this purpose, and present preliminary group velocity maps for short periods across Central Asia, together with estimates of spatially variable resolution and amplitude bias. We also project path coverage and resolution estimates for the anticipated data set.

Key words: Central Asia, surface waves, group velocities, $M_s : m_b$ discriminant

OBJECTIVE

The goal of this research is to improve the ability to detect and discriminate small events over wide areas of Central Asia using regional seismic data. We attempt to extend the existing set of Rayleigh and Love wave tomographic group velocity maps to periods shorter than 15 s. Accurate maps at shorter periods would improve signal detection capabilities by advancing signal-to-noise enhancement produced by phase-matched filters. This may permit the extension of surface wave magnitude (M_s) estimates to periods shorter than 15 s and smaller events than current capabilities allow, which is the basis for future tests of $M_s : m_b$ discriminant for these events.

RESEARCH ACCOMPLISHED

Introduction

Seismic calibration of the International Monitoring System (IMS) and other key monitoring stations is critical for effective verification of a Comprehensive Nuclear-Test-Ban Treaty (CTBT). Detection, location, and identification all depend on calibration of source and path effects to ensure maximum efficiency of the IMS to monitor at small magnitudes. The described research that has just started is dedicated to advancing discrimination capabilities for small magnitude events by improving calibration information for surface waves in W. China, Pakistan, N. India, and surrounding areas. The calibration information will be in the form of short period (7 s - 15 s) Rayleigh and Love wave tomographic group velocity maps and station-specific correction surfaces constructed from these maps. Although we have previously provided similar information in the region of study at intermediate periods (15 s - 50 s; e.g., Stevens and McLaughlin, 1997; Ritzwoller *et al.*, 1998; Levshin *et al.*, 1998), the group velocity maps and correction surfaces at short periods will be entirely new. In addition, this new information will be rigorously tested at the CMR Testbed to quantify

the improvement in the ability to estimate surface wave amplitudes and, hence, M_s for smaller events than are currently possible.

The M_s : m_b discriminant and its regional variants are the most reliable transportable means of discriminating earthquakes from explosions (e.g., Stevens and Day, 1985, Stevens and McLaughlin, 2000). To measure surface wave amplitudes accurately in order to estimate M_s is challenging for small magnitude events in which surface waves may not be readily identifiable in raw seismograms. Because amplitude spectra of regionally recorded small magnitude events typically peak below 20 s period (where M_s is usually measured) the regional application of the M_s : m_b discriminant may be improved if M_s were measured at significantly shorter periods; i.e., 8 - 12 s period. To provide these amplitude measurements, it is crucial to be able to reliably detect small amplitude surface waves and accurately measure the corresponding spectral amplitudes. To succeed in both of these efforts requires the ability to predict the group dispersion curves for all source:station paths of interest. It is useful to compress this information into surface wave group travel times or group velocity correction surfaces (e.g., Levshin *et al.*, 1998) from which path corrections can be computed efficiently.

The construction of reliable and robust group velocity maps and correction surfaces at short periods is considerably more challenging than above 15 s period. Because attenuation due to scattering increases at short periods, it is difficult to measure group velocity below 15 s period for paths longer than about 2,500 km. This limits the power of utilizing long paths through the region of study to help homogenize path coverage which has proven so effective in our studies at longer periods. To improve ray coverage using measurements restricted to epicentral distances less than 2,000 - 3,000 km in length implies that it is necessary to process many events smaller in magnitude than those we used previously. Thus, much of the data that we will process will have relatively low signal-to-noise characteristics and great care must be taken in the measurement process. Even with our best efforts, however, short period group velocity maps will not be as reliable or robust as at longer periods, particularly in regions of low station and event coverage such as India. For this reason, we will provide salient information about the quality and reliability of the maps and the group velocity corrections predicted by them.

Maxwell Technologies and the University of Colorado at Boulder are working collaboratively to:

- obtain a new and vastly expanded set of group velocity measurements in the region of study emphasizing measurements between 7 s and 15 s period;
- convert these measurements into group velocity maps and station-specific correction surfaces using both tomographic and model-based methods;
- cross-validate the tomographic and model-based methods to obtain a set of maps and surfaces that are judged most reliable for the area of study;
- embed these maps and surfaces into global maps and surfaces constructed by Maxwell Technologies;
- test and validate the new maps and corrections surfaces with a rigorous set of tests performed on regional data at the CMR Testbed; and
- deliver documentation and reports of all results with the completed maps and surfaces to customers at DoE, CMR, the U.S. NDC, and the IDC.

The final results will be provided in a form that can be easily used within the operational monitoring systems for surface wave identification and phase-matched filtering.

Previous results

The research that we have performed previously in the region of study was primarily dedicated to intermediate periods (15 s - 40 s). It is summarized by Ritzwoller *et al.* (1998) and has been presented at a number of CTBT seismic research symposia (e.g., Levshin and Ritzwoller, 1995a; Levshin *et al.*, 1996, 1997a, 1998; Ritzwoller *et al.*, 1995, 1996) as well as elsewhere (Levshin *et al.*, 1992, 1994, 1997b, 2000a). In our present data set (developed under previous AFTAC, AFOSR, and DSWA funding) we have 850 measurements in the region of study at 10 s period and 3,200 at 15 s period. Figure 1 contrasts path density at periods of 10 s and 15 s for our existing data set. Path density at 15 s is much better than at 10 s partially

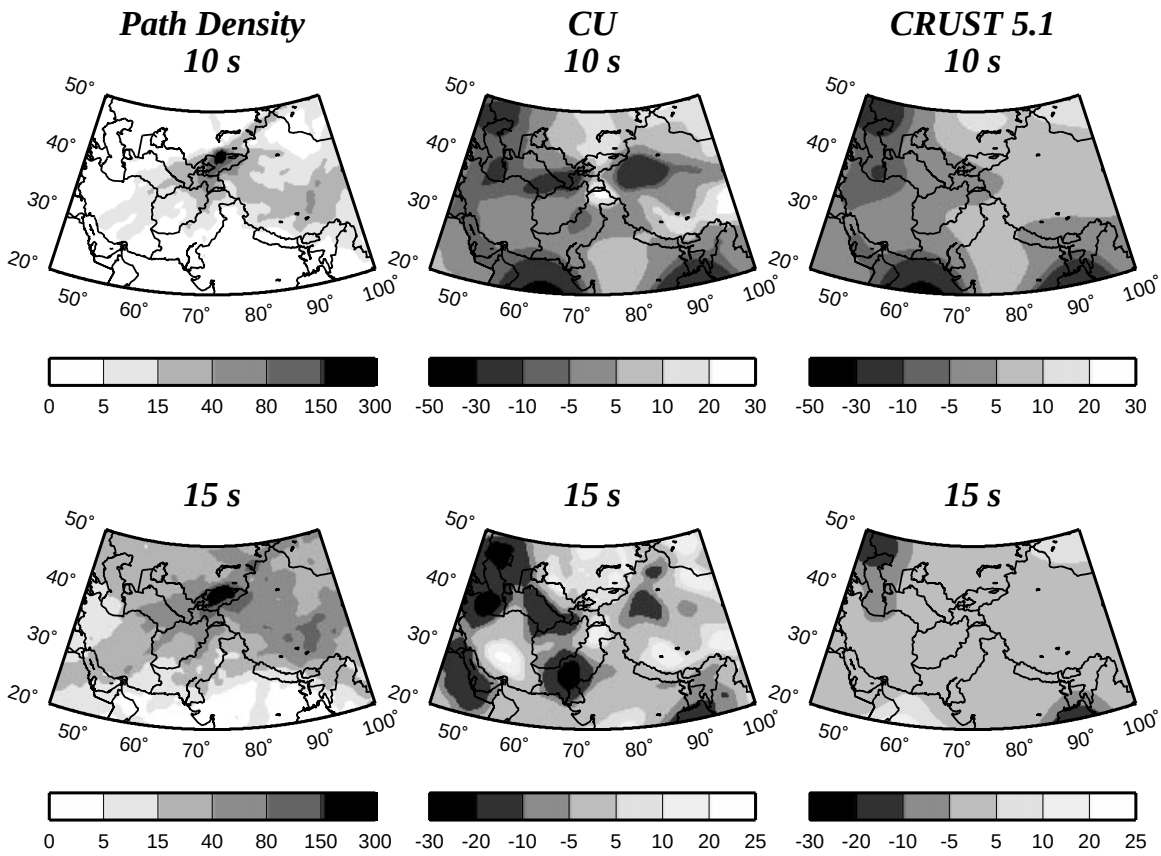


Figure 1: Left Column: Path density for the current data set developed under previous AFOSR, AFTAC, and DSWA funding at 10 s and 15 s periods. Units are number of paths intersecting each $2^\circ \times 2^\circ$ cell ($\sim$50,000 km^2). Middle Column: Our recent Rayleigh wave group velocity maps at 10 s and 15 s periods are presented as perturbation in percent relative to the average across each map. Low velocities are typically sedimentary basins. Right Column: Group velocity maps predicted by a smoothed version of CRUST5.1 (Mooney *et al.*, 1998).

because, at and above 15 s period, measurements can be obtained for paths significantly longer than $\sim$2,000 km, but also because we have not exerted systematic efforts to extract measurements below 15 s period. Clearly, to produce high quality tomographic maps in the region of study at and near 10 s period will require adding more data.

Our tomographic method is discussed by Barmin *et al.* (2000). At each period, we estimate a group velocity perturbation, $\delta U(\theta, \phi)$, relative to an input map, $U_\circ(\theta, \phi)$, which itself may be spatially variable so that group velocity at each spatial point (θ, ϕ) is $U(\theta, \phi) = U_\circ(\theta, \phi) + \delta U(\theta, \phi)$. We typically use a smoothed version of the crustal model CRUST5.1 (Mooney *et al.*, 1998) to compute the input map. We construct $\delta U(\theta, \phi)$ by minimizing the weighted misfit to the data together with both spatial smoothing and model norm regularization constraints. The spatial smoothing constraint determines the wavenumber content of the estimated map. For data that are inhomogeneously distributed, the model norm constraint is very important, and we use path density to determine the strength of this constraint. Where path density is very low (e.g., in the Caspian region at 10 s in Figure 1), $\delta U(\theta, \phi)$ will be strongly damped and constrained to equal the input model.

Figure 1 also presents group velocity tomographic maps at periods of 10 s and 15 s. As discussed above, our tomographic method embeds the tomographic information in an *a priori* model, CRUST5.1, which is also shown in Figure 1 for comparison. The CU and CRUST5.1 maps differ only in those regions where path density is sufficient to allow the CU map to diverge from the *a priori* model. Some means to estimate the quality of group velocity maps are discussed at length by Barmin *et al.* (2000). Two of the most useful

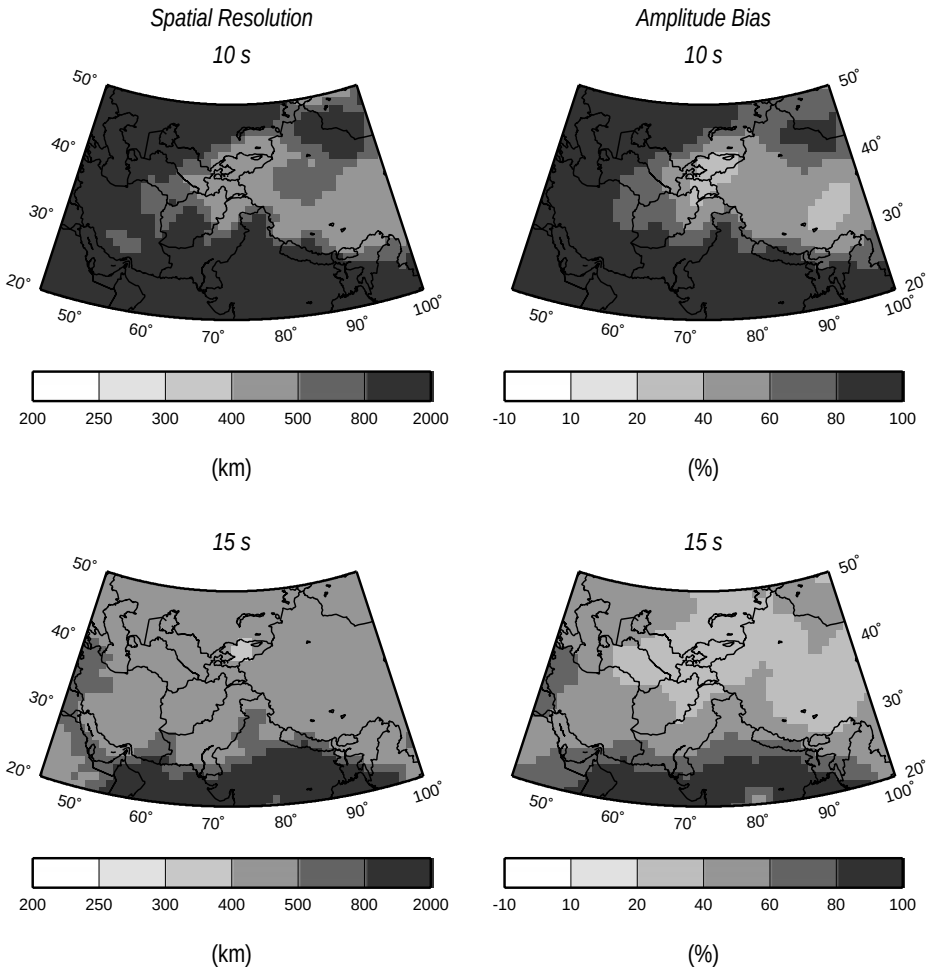


Figure 2: Spatial resolution and amplitude bias estimated for our current data set at periods of 10 s and 15 s. Resolution is in km and amplitude bias is in percent. Note that for amplitude bias, 0% is optimal, and >50% is very big. The salient conclusion is that the current quality of our 15 s maps is much better than the 10 s maps.

qualitative measures are spatially variable resolution and amplitude bias. The estimation of the resolution at a given point on the map is obtained by using the appropriate row of the resolution matrix which characterizes the tomographic image. We define resolution as a radius, σ, of the base of the cone fitted to the resolution function at each point of the grid. To determine the amplitude bias we move a cylindrical perturbation with the 'width', $2\sigma(\theta, \phi)$, around the region of study, perform tomography on the synthetic travel times traced through the test function for the given data set, and investigate the capability to reproduce the test function given the chosen regularization parameters, data characteristics, weighting, etc. Amplitude bias is defined as the relative difference (in percent) of the amplitude of the fit cylinder to the amplitude of the input cylinder at each grid point. Figure 2 presents spatial resolution and amplitude bias of the maps in Figure 1 and contrasts the 10 s and 15 s maps with respect to these measures of map quality.

The quality of the 10 s map is spatially highly variable; west of about the 60°E, north of 45°N, and south of 30° the maps will result almost entirely from the input map, CRUST5.1. The resolution and amplitude bias of the 10 s maps are far worse than at 15 s and major features, such as the Dzungarian Basin in W. China, are entirely missing in Figure 1. Nevertheless, the 10 s map can be considerably improved once systematic efforts are dedicated to adding measurements at and below 10 s period.

Figure 3 presents station specific correction surfaces for the group velocity of the 15 s Rayleigh wave at four stations: AAK, ABKT, WMQ, and WUS (GEOSCOPE station). These surfaces were constructed

by accumulating travel time perturbations through the 15 s map shown in Figure 1 along the great circle linking each point on the group velocity map to the specified station and then assigning that time to the spatial point on the correction surface. Thus, correction surfaces differ strongly for different stations. The group velocity correction for the 15 s Rayleigh wave for the specified station for an event at any location on these maps can simply be read from the map. Because the ray tracing has been done in the construction of the correction surfaces, these maps can be used efficiently, even in real-time, to help identify events (Levshin *et al.*, 2000b). Except for isolated areas that have seen substantial empirical calibration efforts (e.g., much of W. China surrounding Lop Nor), the maps in Figure 3 may be the best correction surfaces currently in existence for the entire region of study. They can be improved considerably, however, at 15 s and below.

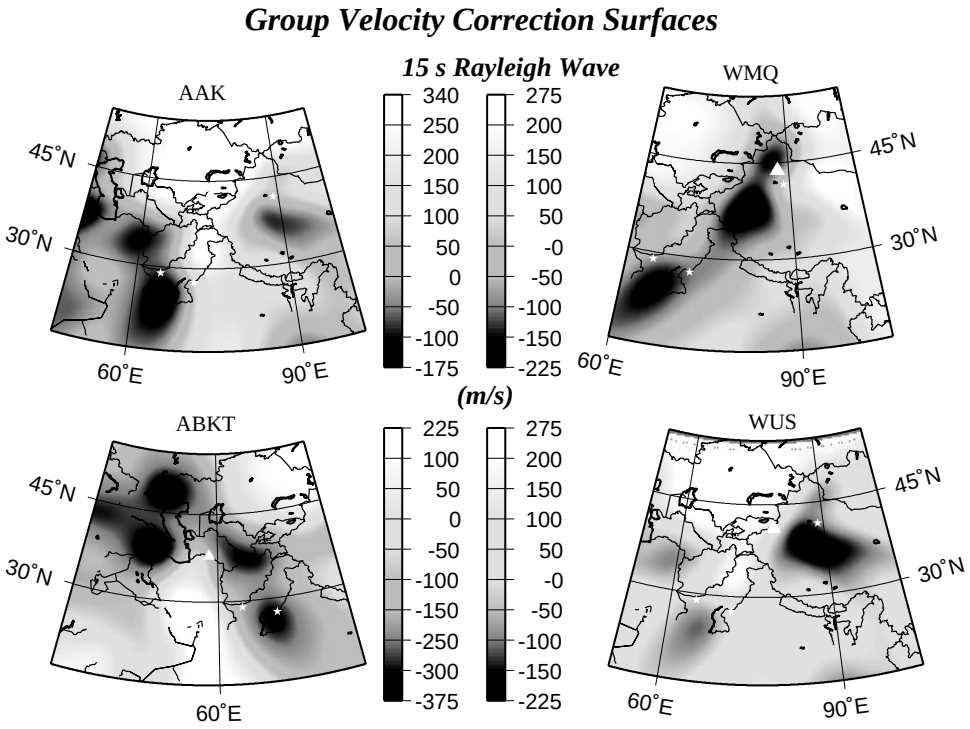


Figure 3: Group velocity station specific correction surfaces for our 15 s Rayleigh wave map shown in Figure 1. The specified stations are indicated on each figure with a triangle, and the Chinese, Pakistani, and Indian test sites are shown with stars.

Recent work done by Maxwell Technologies has focused on techniques for improving surface wave measurements and reducing the surface wave detection threshold, and on development of MAXSURF, the code used at the IDC and PIDC for automatic identification and measurement of surface waves. MAXSURF is responsible for all surface wave processing at the IDC and the PIDC and runs in the processing stream after events have been identified and located. MAXSURF then examines the arrival window where a surface wave would be expected and applies a dispersion test to see if a surface wave can be identified. If so, then the amplitude is measured and stored in the IDC database. Surface waves are identified in the following way: a set of narrow band filters are applied to the data over a set of 8 periods from 16 s to 50 s. A long-period or broadband beam is formed at arrays with the expected azimuth and slowness. The arrival times at each frequency are then compared with predicted arrival times generated from the regionalized group velocity model. Postprocessing techniques have been developed to remove spurious or misassociated arrivals. This type of automatic processing has proven to work very well, and the detection threshold for the IMS network is nearly an order of magnitude lower than the detection threshold for other networks where surface waves are identified visually. Figure 4 shows a comparison of the cumulative distribution of detected arrival amplitudes for the IMS network as reported in the Reviewed Event Bulletin (REB) and the surface

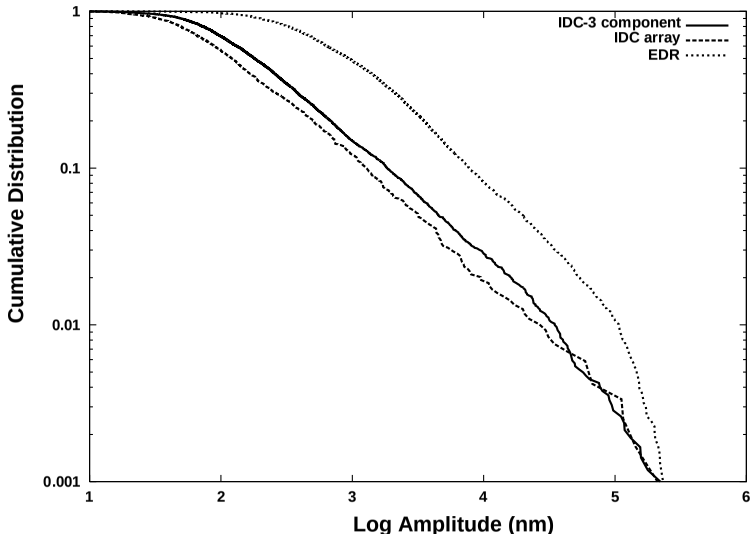


Figure 4: Cumulative distribution of IDC and EDR amplitudes. This figure shows that the IDC detection threshold is approximately one magnitude unit lower than the EDR detection threshold.

waves reported in the Earthquake Data Reports (EDR) produced by the USGS, showing this difference.

This example demonstrates the importance of good group velocity maps. Because surface waves are identified by comparison with predicted arrival times, it is essential that the predicted group velocities are accurate. One way to reduce the threshold further is to increase the frequency band over which surface waves can be measured. The current band of 16 s - 50 s period was found to be a good band for worldwide surface wave data measured at distances of 20-100 degrees, and the global dispersion maps are fairly well defined over this period band. However, at shorter distances, surface waves are dominated by higher frequencies. To improve signal to noise ratio and to measure surface waves at close range, the dispersion test and measurement of surface waves should be performed at higher frequencies. There are currently few measurements available in the 7-15 s period range, and the global group velocity maps are, therefore, not well defined in this band. Good data in this frequency band is required in order to develop the dispersion curves needed for identification of surface waves and phase-matched filtering at regional distances.

Improving Group Velocity Measurements and Maps

The planned work is based on the premise that careful and dedicated efforts devoted to obtaining accurate group velocity measurements at short periods (<15 s) will greatly improve the quality of the 7 s - 15 s group velocity maps, particularly at the short period end. The rationale for this is presented in Figure 5, which shows two frequency-time diagrams for two events of similar magnitude with different path lengths of ~3,000 km and ~1,000 km, respectively. This figure demonstrates the difficulty in obtaining group velocity measurements below periods of about 12 s for paths longer than about 2,000 km. For paths less than about 2,000 km in length, Rayleigh waves can be observed and group velocities estimated regularly to periods of 6 s or 7 s for events with M_s as low as ~4.2 - 4.5 if sufficient care is taken to extract the signal and separate the fundamental mode from Lg, the first overtone, and potential multipaths.

The key to improving tomographic capabilities at short periods is to introduce measurements for paths less than about 2,000 - 2,500 km in length. Fortunately, there are many events in the region of study, although the station distribution is far from optimal. Figure 6 shows the 40 stations (GSN, GEOSCOPE, GEOFON, KNET, KAZNET, CDSN, Saudi Arabian Network) and ~ 1200 earthquakes (PDE; $m_b \geq 4.0$; 1996-1999) from which we will process data in the proposed work. Taking into account that the number of simultaneously operating stations is always substantially less, the number of measurements for this three-year long time interval is expected to be about 15,000. Clustering the group velocity curves will produce 5,000 - 10,000 unique paths. Figure 7 shows the resulting path density if we augment our current data set

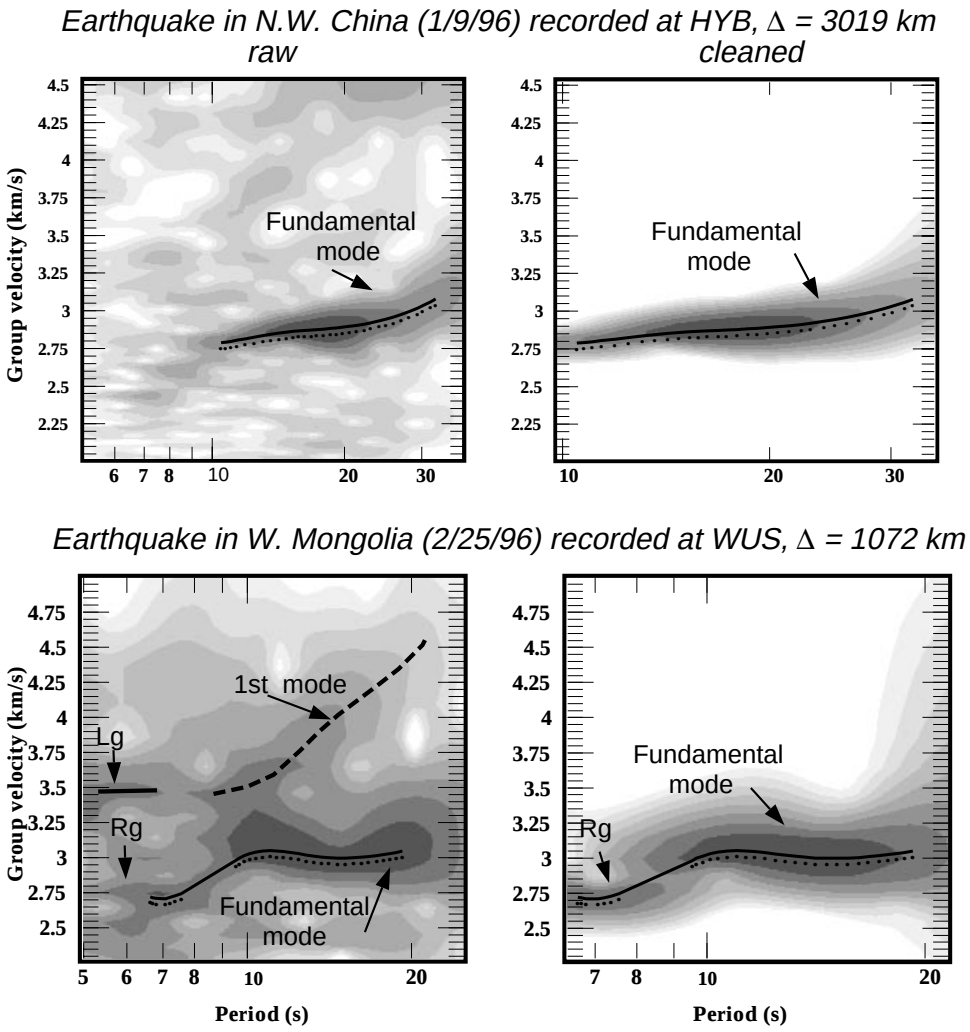


Figure 5: Frequency-time diagrams for two events and paths indicated on the figure. Measurements below about 12 s period are obtained more reliably on shorter paths. (HYB - Hyderabad, India; WUS - Wushi, China).

at the 10 s period (∼850 measurements) with ∼9,900 additional measurements for the stations and events in Figure 6, in which a path is chosen only if meets the following epicentral distance and magnitude criteria: $\Delta \leq$1,500 km if $4.0 \leq m_b \leq 4.2$, $\Delta \leq$1,750 km if $4.2 < m_b \leq 4.4$, and $\Delta \leq$2,000 km if $m_b > 4.4$. From this analysis we expect significant improvement in path coverage in W. China, Pakistan, Afghanistan, Iran, and the surrounding areas. Because of the shortage of both stations and events in India, however, significant improvement in path density in India will be difficult to attain.

The introduction of measurements for the sources and receivers in Figure 6 would have a profound effect on the quality of the Rayleigh wave group velocity maps at and below 10 s period. Figure 8 shows spatial resolution and amplitude bias for the data set described in Figure 6. Resolution and amplitude bias are tremendously improved relative to the 10 s map of Figure 2, but India remains very challenging.

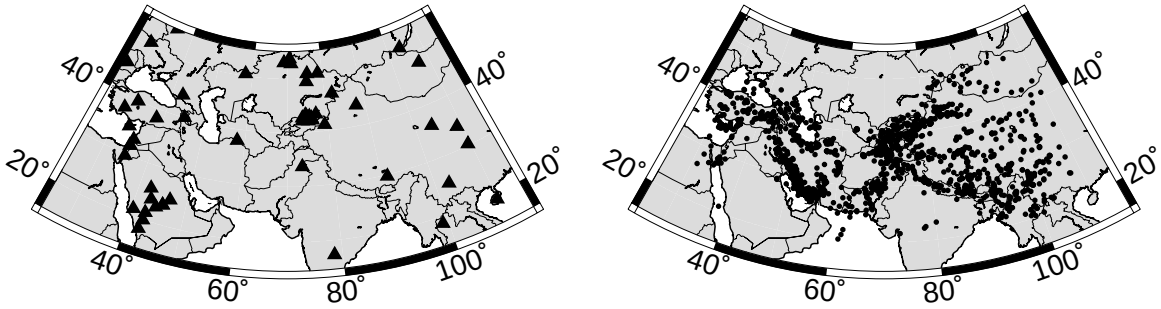


Figure 6: Stations (∼40 from GSN, GEOSCOPE, GEOFON, KNET, KAZNET, CDSN, Saudi Arabia Network) and events (∼1200; PDE $m_b \geq$4.0; 1996 - 1999) to be used in the proposed research.

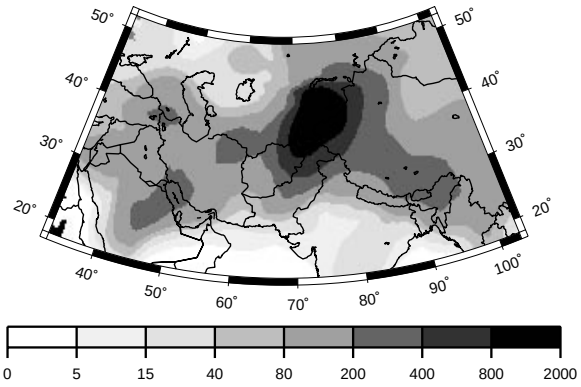


Figure 7: Estimate of the 10 s Rayleigh wave path density (see Figure 1 for definition) that will result from the proposed research; that is, if we augment our current data set at 10 s period (∼850 measurements) with ∼ 15,000 additional measurements for the stations and events in Figure 6 in which a path is chosen only if it meets the following epicentral distance and magnitude criteria: $\Delta \leq$1,500 km if 4.0$\leq m_b \leq$ 4.2, $\Delta \leq$1,750 km if 4.2$< m_b \leq$ 4.4, and $\Delta \leq$2,000 km if $m_b >$ 4.4. Contrast with Figure 1, left column.

CONCLUSIONS AND RECOMMENDATIONS

Work on the described project is in its early stage of acquiring and preprocessing waveform data from various networks: GSN, GEOSCOPE, GEOFON, KNET, KAZNET, Saudi Arabian Network, and CDSN stations following the 1200 events that occurred in 1996-1999 (stations and events in Figure 6). The following stages of the work are planned:

- Obtain group velocity measurements at and above ∼7 s period.
- Produce Rayleigh and Love wave group velocity maps in increments of 1 s from 7 s to 15 s periods for the region of study by the tomographic method. Produce resolution and amplitude bias maps at each wave period.
- Convert the group velocity maps to station specific correction surfaces for IMS and other interesting stations in and adjacent to the region of study.
- Incorporate the group velocity measurements into new global group velocity maps by the model-based method.
- Cross-validate group velocity maps obtained by the tomographic and model-based methods.
- Deliver measurements and maps from CU-B to Maxwell Technologies and customers.
- Test and validate the maps and correction surfaces on IMS data at the CMR Testbed.

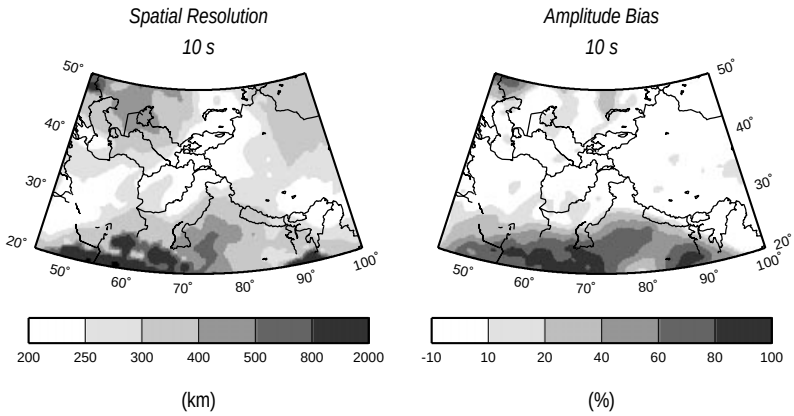


Figure 8: Estimate of the spatial resolution and amplitude bias for the 10 s Rayleigh wave which will arise from the proposed research; i.e., for the paths described in Figure 6. Contrast with the current state in Figure 2. The conclusion from Figures 7 and 8 is that the proposed research is guaranteed to provide substantial improvement in group velocity maps at ~10 s period across most of the region of study. The principal caveat is that India, except for the far north, presents a very challenging target.

REFERENCES

Barmin, M.P., M.H. Ritzwoller, and A.L. Levshin, A fast and reliable method for surface wave tomography, *Pure and Appl. Geophys.*, in press, 2000.

Levshin, A.L., L. Ratnikova, and J. Berger, Peculiarities of surface wave propagation across central Eurasia, *Bull. Seismol. Soc. Am.*, **82**, 2464-2493, 1992.

Levshin, A.L., M.H. Ritzwoller, and L.I. Ratnikova, The nature and cause of polarization anomalies of surface waves crossing northern and central Eurasia, *Geophys. J. Int.*, **117**, 577 - 590, 1994.

Levshin, A.L. and M.H. Ritzwoller, Surface wave group velocity measurements across Eurasia, *17th Seismic Research Symposium on Monitoring a CTBT*, Proceedings, 226 - 236, 1995a.

Levshin, A.L. and M. H. Ritzwoller, Characteristics of surface waves generated by events on and near the Chinese nuclear test site, *Geophys. J. Int.*, **123**, 131 - 149, 1995b.

Levshin, A.L., M.H. Ritzwoller, and S.S. Smith, Group velocity variations across Eurasia, *18th Seismic Research Symposium on Monitoring a CTBT*, Proceedings, 70 - 79, 1996.

Levshin, A.L., M.H. Ritzwoller, L.I. Ratnikova, M. Silitch, R. Kelly, and B. O'Sullivan, Intermediate period group velocity maps across Central Asia and parts of the Middle East, *19th Seismic Research Symposium on Monitoring a CTBT*, Proceedings, 67 - 76, 1997.

Levshin, A.L., M.H. Ritzwoller, M.P. Barmin, A. Villaseñor, and C.A. Padgett, New constraints on the Arctic crust and uppermost mantle: surface wave group velocities, P_n, and S_n, *Phys. Earth. Planet. Int.* (submitted), 2000a.

Levshin, A.L., and M.H. Ritzwoller, Automated detection, extraction, and measurement of regional surface waves, *Pure and Appl. Geophys.*, in press, 2000b.

Mooney, W.D., G. Laske, and G. Masters, CRUST 5.1: A global crustal model at 5° by 5°, *J. Geophys. Res.*, **103**, 727 - 748, 1998.

Ritzwoller, M.H., A.L. Levshin, S.S. Smith, and C.S. Lee, Making accurate continental broad-band surface wave measurements, *17th Seismic Research Symposium on Monitoring a CTBT*, Proceedings, 482-490, 1995.

Ritzwoller, M.H., A.L. Levshin, L.I. Ratnikova, and D.M. Tremblay, High resolution group velocity variations across Central Asia, *18th Seismic Research Symposium on Monitoring a CTBT*, Proceedings, 98 - 107, 1996.

Ritzwoller, M.H., and A.L. Levshin, Eurasian surface wave tomography: Group velocities, *J. Geophys. Res.*, **103**, 4839 - 4878, 1998.

Ritzwoller, M.H., A.L. Levshin, L.I. Ratnikova, and A.A. Egorkin, Intermediate period group velocity maps across Central Asia, Western China, and parts of the Middle East, *Geophys. J. Int.*, **134**, 315-328, 1998.

Stevens, J.L., and S.M. Day, The physical basis for m_b : M_s and variable frequency magnitude methods for earthquake/explosion discrimination, *J. Geophys. Res.*, **90**, 3009-3020, 1985.

Stevens, J.L. and K.L. McLaughlin, Improved methods for regionalized surface wave analysis, *Maxwell Technologies Final Report* submitted to Phillips Laboratory, MFD-TR-97-15887, September, 1997.

Stevens, J.L. and K.L. McLaughlin, Optimization of surface wave identification and measurement, *Pure and Appl. Geophys.*, in press, 2000.

CRUSTAL AND UPPER MANTLE SEISMIC VELOCITY STRUCTURE OF THE FORMER USSR FROM PEACEFUL NUCLEAR EXPLOSIONS (PNEs) AND CHEMICAL EXPLOSION DATA

Walter D. Mooney[1], Sergei Kostyuchenko[2], and A.V. Egorkin[2]

1. U.S. Geological Survey, Earthquake Hazards Team
2. GEON Centre, Moscow, Russia

Sponsored by U.S. Department of Energy
Office of Nonproliferation and National Security
Office of Research and Development

DOE IA No.: DE-AI04-98AL79758

ABSTRACT

In the past forty years, the Ministry of Geology of the former USSR committed vast funds to investigations of the structure of the continental crust and upper mantle by seismic methods. The former USSR is criss-crossed by a network of seismic profiles that are more detailed than in any other part of the world. There are three kinds of profiles: (1) short-range refraction; (2) Deep Seismic Sounding (DSS) profiles; and (3) ultra-long range seismic profiles using Peaceful Nuclear Explosions (PNEs). The main goal of the short-range refraction work was to image sedimentary cover and basement. Measurements were obtained using 48-60 channel analog instruments with 100 m receiver spacing, and seismograms were recorded on photographic paper by the wiggle trace method. The DSS observations were mainly used for crustal studies. The shotpoint spacing was 30-50 km, and three components of ground displacement were recorded. The refracted and reflected compressional (P) and shear waves (S), and converted waves were interpreted. Ultra-long range PNE-sourced profiles provided information on the structure of the crust and upper mantle to a depth of 670 km. For PNE profiles, up to 400 short-period (1.5-20 Hz), three-component seismometers were deployed every 5-10 km to record ground motion. Thirty-nine PNE shots were detonated for these purposes, with intermediate chemical shots spaced at 40-70 km intervals. These chemical shots had charges ranging from 2000 to 5000 kg. The total length of all of these three types of profiles exceeds 80 thousand kilometers. We present a synthesis of these results in the form of updated maps of depth to basement and depth to Moho in Russia.

Key Words: crustal structure, former USSR, seismic refraction, Deep Seismic Sounding, Peaceful Nuclear Explosions

---

OBJECTIVE

To successfully monitor the Comprehensive Nuclear-Test-Ban Treaty (CTBT), accurate models of crustal structure are needed. We present here new, high-quality crustal structure models of the Former Soviet Union.

RESEARCH ACCOMPLISHED

1 Introduction

Seismology is particularly well-suited to measuring the properties of the Earth's crust and uppermost mantle due to the existence of the pronounced variations in seismic wave speeds both with depth and laterally. Seismological studies are capable of imaging structure at high resolution to depths of several tens of kilometers, and moderate resolution to depths of hundreds of kilometers. In the former Soviet Union (FSU),

crustal and uppermost mantle studies have utilized controlled-source seismic-refraction data, including long-range profiles from nuclear sources. These profiles from Peaceful Nuclear Explosions (PNEs) and chemical explosions will be discussed below. Data from controlled sources have many advantages including: 1) the exact time and position of the seismic sources are accurately known; 2) there is no need to rely on either local nor teleseismic events that may occur infrequently and/or have an unsuitable spatial distribution; 3) the recording geometry of the seismic investigation may be planned in relation to the specific geologic target.

A large number of seismic profiles have been collected in the FSU since the early 1950's. An advance in technology has led not only to better instrumentation, but also to improved data processing and interpretation techniques. Useful recent reviews of seismic methods for determining crust and upper mantle structure have been provided by Mooney (1989) and Braile et al. (1995). Giese et al. (1976) summarize older methods of data analysis. Papers that summarize global crustal structure, including the FSU, include: Prodehl (1984), Meissner (1986), Soller et al. (1992), Tanimoto (1995), Pavlenkova (1996), and Mooney et al. (1998). From this, our model of global crustal thickness (Fig. 1) has been greatly refined, and a global average crustal thickness of 39.17 km has been determined (Fig. 2). Another important benefit of seismic profiling has been the cataloging of crustal velocities. The global average crustal velocity has been determined to be 6.45 km/s, and a histogram of average crustal velocity is given in Figure 3. This average crustal velocity implies that the bulk composition of the crust is equivalent to a diorite (Christensen and Mooney, 1995).

A major consideration when discussing seismic data is resolution. General statements about resolution are difficult to make, however, because of the variety in seismic techniques. The quality of a data set is usually considered to be a function of the strength of the signal relative to noise (expressed as signal-to-noise ratio) and the number or density of measurements depending on the number of sources and receivers, and their relative spacing. Generally, there is higher resolution when more closely-spaced data are available. However, physical laws limit the resolution of even a near-perfect data set. The Earth attenuates high frequencies such that signals penetrating deeper will contain relatively low frequencies. Typically, signals traversing the entire crust have peak frequencies of 5-20 Hz resulting in absolute accuracy of depth determination of not better than 2% to 5% of the depth (e.g., 1-2 km for a 40-km-thick crust).

Seismic refraction data provide one of the best sources of information on velocities within the continental lithosphere, but often more information is desired. It is often of interest to determine the composition of the lithosphere, for example, and for this laboratory measurements of the speed of sound in rock specimens believed to have once resided at depth within the lithosphere are compared to refraction data. Lithospheric composition can then be inferred. These studies are reviewed in Holbrook et al. (1992) and Christensen and Mooney (1995).

2 Background

About 32 PNE sources recorded on long-range profiles have been digitized and preserved in the FSU by using hardware provided by German collaborators in 1993. This digitizing system is located in the GEON Center in Moscow and is still operating. The 32 digitized PNEs are along the profiles known as Quartz, Kraton, Kimberlite, Rubin I and II, Meteorite, Rift, and Batholith I and II. An example of PNE data from the Quartz profile is given as Figure 4. These PNE profiles were digitized at 50 samples/s, usually for 10 minutes, depending on the record length of the original analogue field tapes. Thus, the time-window includes reflections from the Earth's core. While it is always possible to redigitize with other parameters, the data from these 32 PNEs can be considered as preserved. In addition, many nuclear shots were fired at Soviet test sites. Some of these shots were recorded on linear profiles or in fan (broadside) geometry. Only a portion of these records have so far been digitized, but more of this work is now being done.

An additional seven PNEs in northern Russia along the profiles Globe (4 PNEs conducted during the first year of the program, 1973), and Horizon (3 PNEs conducted in 1974) have not been digitized. Only paper records exist for these PNEs, and they have not yet been digitized from the paper records.

In southern Russia 5 PNEs along the profiles Region and 3 PNEs on the profiles Meridian have not been digitized because the data tapes are too old (1973-74) and not all tapes are available. Once again, these data are available only on paper records, to limited record times. In summary, some 15 PNEs have not been digitized due to the lack of adequate original field tapes. Conversely, all analogues tapes of PNE data along long-range profiles that can be digitized have already been digitized.

All long-range PNE profiles also had chemical shots with an average spacing of 70 km. These chemical shots have yields of 4,000 to 5,000 kg and were recorded by all stations, with high signal-to-noise ratios to about 200-250 km, and sometimes to greater distances. The recorders on these PNE profiles were at 10 km spacing (as was done for the recording of the PNEs), making these chemical data sparse in terms of resolution of crustal structure. The determination of detailed crustal structure usually requires recorders spaced at 2 km or less. Examples of these record sections for both PNE and chemical-source profiles may be found in Egorkin (1999a, 1999b).

The following chemical shot data have been digitized as of the year 2000: 80 shots on profile Quartz, 40-50 shots on Kraton, 40-50 on Kimberlite, and 40-50 on Rift. The following profiles have chemical shots yet to be digitized: Meteorite, Rubin I and II, and Batholith I and II. Additionally, since deep seismic profiling (refraction profiling) has been carried out in the FSU for more than 50 years, there are a large number of additional chemical shots that are not along PNE profiles that can be digitized. However, all data recorded since 1990 have already been digitized.

The GEON Center has established cooperative research programs with many international institutions, and has shared portions of their data based on common research interests. Among the institutions that have been involved are the U.S. Geological Survey, LLNL, GFZ-Potsdam, University of Karlsruhe, U. Copenhagen, and U. Wyoming. These cooperative agreements have generally involved financial support for the digitizing and duplication of data, the exchange of personnel, and joint publications.

3 Main features of crustal structure of the Former Soviet Union (FSU)

There have been many attempts to synthesize crustal structure both of the FSU and globally in terms of representative crustal cross-sections, and the most important parameters, including crustal thickness, mean crustal velocity, Pn velocity, depth of the Conrad discontinuity (defined as the seismic boundary between upper and middle/lower crust), and the thickness and mean velocities of main crustal layers (sediments, upper, middle and lower crust). This work has recently been done in the FSU to such an extent that new maps of depth to basement and crustal thickness have been produced (Figs. 5 and 6).

The basic features of the crustal structure of the FSU were recognized by the 1960's (Ryaboy, 1966; Kosminskaya, 1968; Pavlenkova, 1973). The seismic velocity distributions vary widely in different geographic localities, and crustal models generally consist of two, three, or more layers separated by velocity discontinuities or gradients. In relatively stable continental regions, the thickness of the crust, as defined by the depth to Moho, is between 30 and 50 km (Fig. 6). Seismic velocities in the upper crustal layer (basement) are usually 5.6-6.3 km/s. At a depth of 10-15 km the seismic velocity increases to 6.4-6.7 km/s. In many stable continental interiors there is a third crustal layer with a velocity of 6.8-7.2 km/s. The seismic velocity below the Moho (Pn velocity) is typically about 8 km/s. The exact nature of the velocity-depth distribution can be quite complex and three-dimensional. The evidence for distinct layers within the continental crust almost exclusively depends on the interpretation of second-arrival phases. In some regions, clear evidence of later arrivals confirms that the velocity increases discontinuously through intermediate layers within the crust. In other regions the velocity may increase gradually with increasing depth, producing no distinct intracrustal reflection.

CONCLUSIONS AND RECOMMENDATIONS

Any new information regarding the seismic structure of the Former Soviet Union would significantly improve the determination of seismic source parameters for the purposes of monitoring the Comprehensive Nuclear-Test-Ban Treaty. As much of the data for the FSU is now available in digital

format, this wealth of new knowledge should be analyzed for greater insight and understanding into the crustal structure of the FSU.

REFERENCES

Braile, L.W., Keller, G.R., Mueller, S., and Prodehl, C., 1995. Seismic techniques. In: Olsen, K.H. (Editor), Continental rifts: Evolution, structure, tectonics. Elsevier, Amsterdam, pp.61-92.

Christensen, N.I. and Mooney, W.D., 1995, Seismic velocity structure and the composition of the continental crust: a global view, J. Geophys. Res., 100, 9761-9788.

Egorkin, A.V., 1999a. Deep Seismic Studies based on three-component recording of ground motions, Izvestiya, Physics of the Solid Earth, 35, 566-585.

Egorkin, A.V., 1999b. Study of the mantle on super long-range geotraverses, Izvestiya, Physics of the Solid Earth, 35, 630-645.

Giese, P., Prodehl, C., and Stein, A. (Editors), 1976. Explosion seismology in central Europe - data and results. Springer, Berlin-Heidelberg-New York: 429 pp.

Holbrook, W.S., Mooney, W.D., and Christensen, N.I., 1992. The seismic velocity structure of the deep continental crust. In: Fountain, D.M., Arculus, R., and Kay, R.W. (Editors), Continental lower crust. Development in Geotectonics, vol. 23, Elsevier, Amsterdam, 1-43.

Kosminskaya, I.P., 1968, The method of Deep Seismic Sounding of the crust and upper mantle, Nauka, Moscow.

Kostyuchenko, S.L., Egorkin, A.V., Solodilov, L.N., Danilova, E.G., and Volkhonina, T.V., 1999. Russian Ministry of Geology map series, GEON Centre, Moscow, Russia.

Mechie, J., Egorkin, A.V., Fuchs, K., Ryberg, T., Solodilov, L., and Wenzel, F., 1993. P-wave mantle velocity structure beneath northern Eurasia from long-range recordings along the profile Quartz, Phys. Earth Planet. Int., 79, 269-286.

Meissner, R., The Continenal Crust: A Geophysical Approach, 426 pp., Academic Press, London, 1986.

Mooney, W.D., 1989. Seismic methods for the determining earthquake source parameters and lithospheric structure. In: Pakiser, L.C., and Mooney, W.D. (Editors): Geophysical framework of the continental United States. Geol. Soc. Am. Memoir 172, 11-34.

Mooney, W.D., Laske, G., and Masters, T.G., 1998. Crust 5.1: a global crustal model at 5□ x 5□. J. Geophys. Res., 103, 727-747.

Pavlenkova N.I., 1973. Wave fields and crustal models of continental type (in Russian). Naukova Dumka, Kiev, 253 pp.

Pavlenkova, N.I., 1996. Crust and upper mantle structure in northern Eurasia from seismic data. Advances in Geophysics, 37, 1-133.

Prodehl, C., 1984. Structure of the earth's crust and upper mantle. In: K.-H. Hellwege (Editor in Chief), Landolt Börnstein New Series: Numerical data and functional relationships in science and technology. Group V, Volume 2a: K. Fuchs and H. Soffel (Editors), Physical properties of the interior of the earth, the moon and the planets, Springer, Berlin-Heidelberg, pp. 97-206.

Ryaboy, V.Z., 1966, Crust and upper mantle structure from DSS profile Kapet-Dag-Aral Sea, Soviet Geology 5, 159-162.

Soller, D.R., Ray, R.D., and Brown, R.D., 1992. A new global crustal thickness model. Tectonics, 1; 125-149.

Tanimoto, T., 1995. Crustal structure of the earth. In: Ahrens, T.J. (Editor), Global Earth Physics: A Handbook of Physical Constants. AGU Ref. Shelf, vol. 1, Am. Geophys. Un., Washington, D.C., p. 214-224.

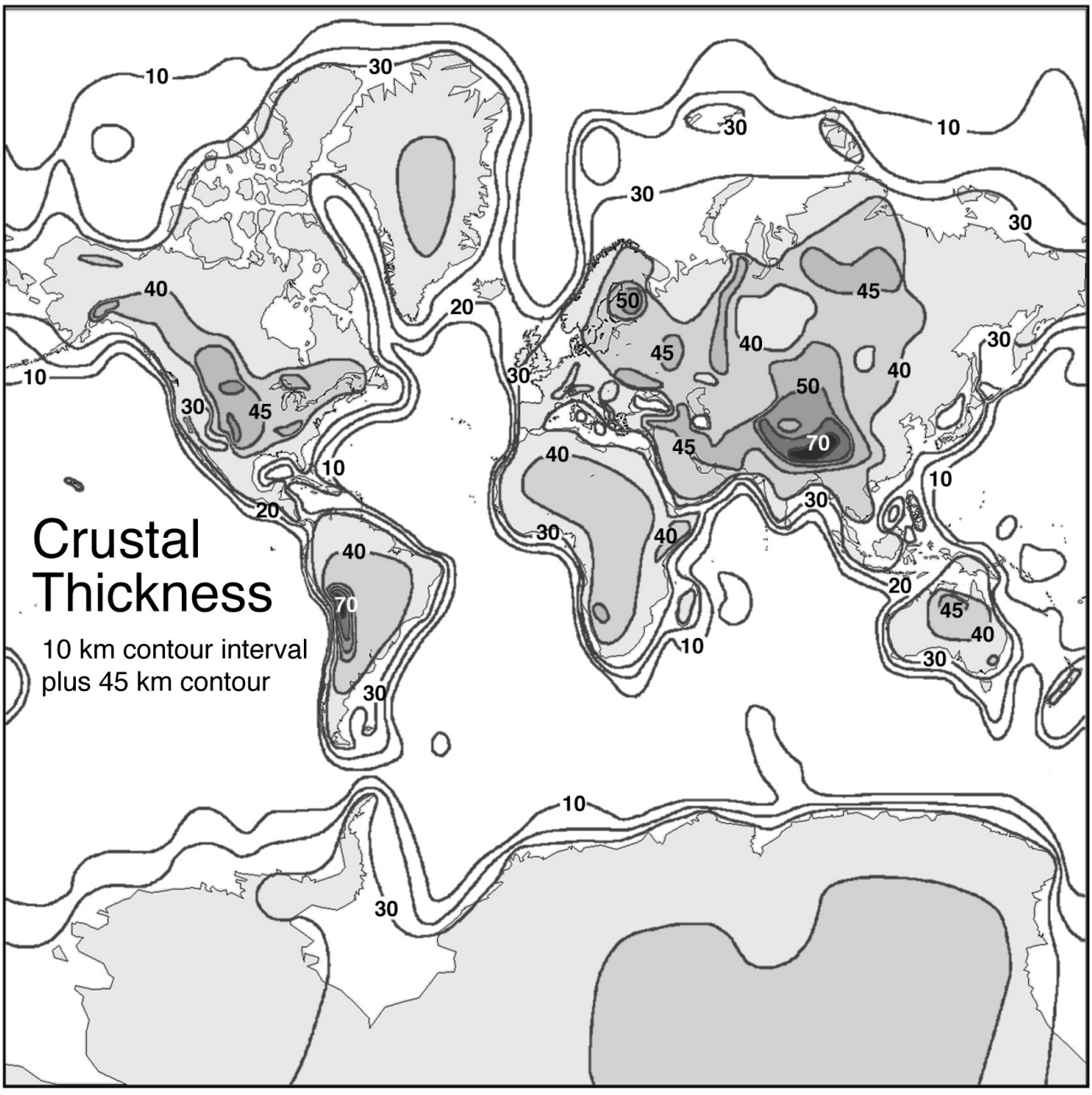


Figure 1. Mercator projection of crustal thickness based on seismic refraction profiles. (From Mooney et al, 1998.)

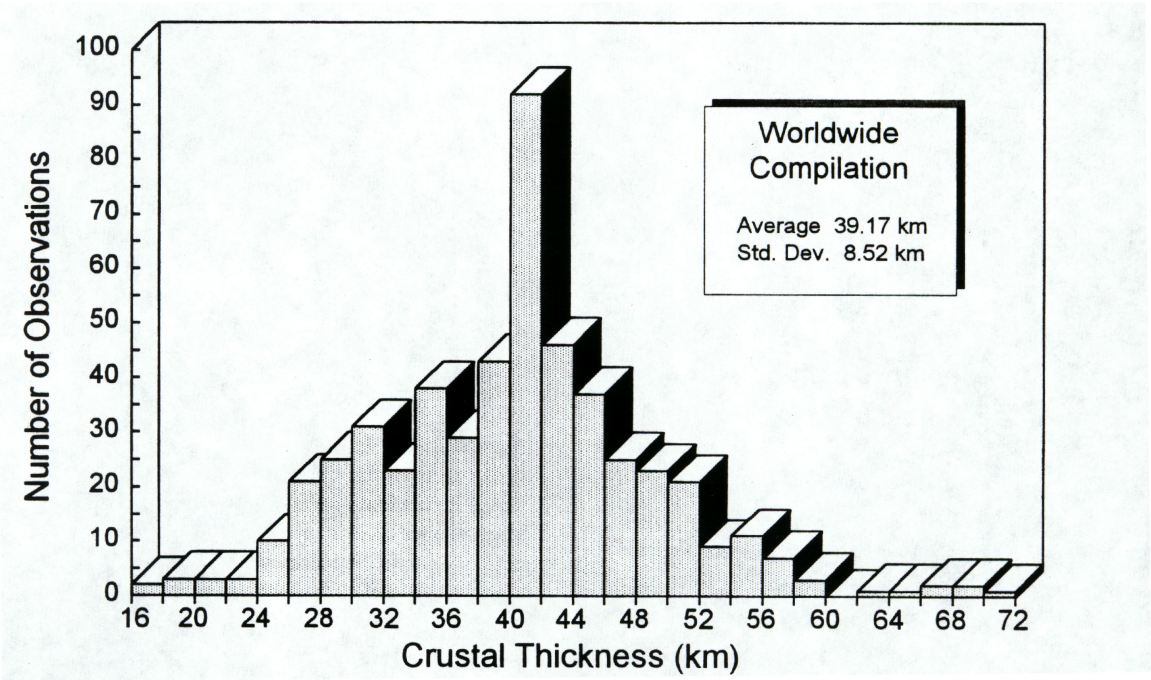


Figure 2. Histogram of thickness of continental crust. (From Christensen and Mooney, 1995)

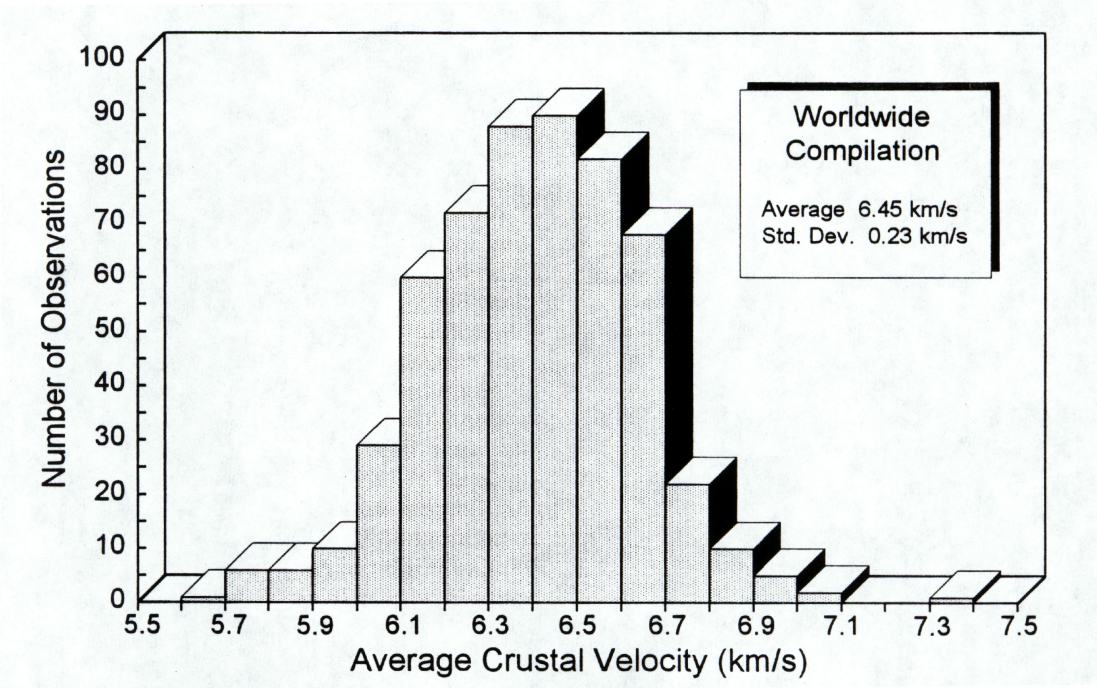


Figure 3. Histogram of average crustal velocity. (From Christensen and Mooney, 1995)

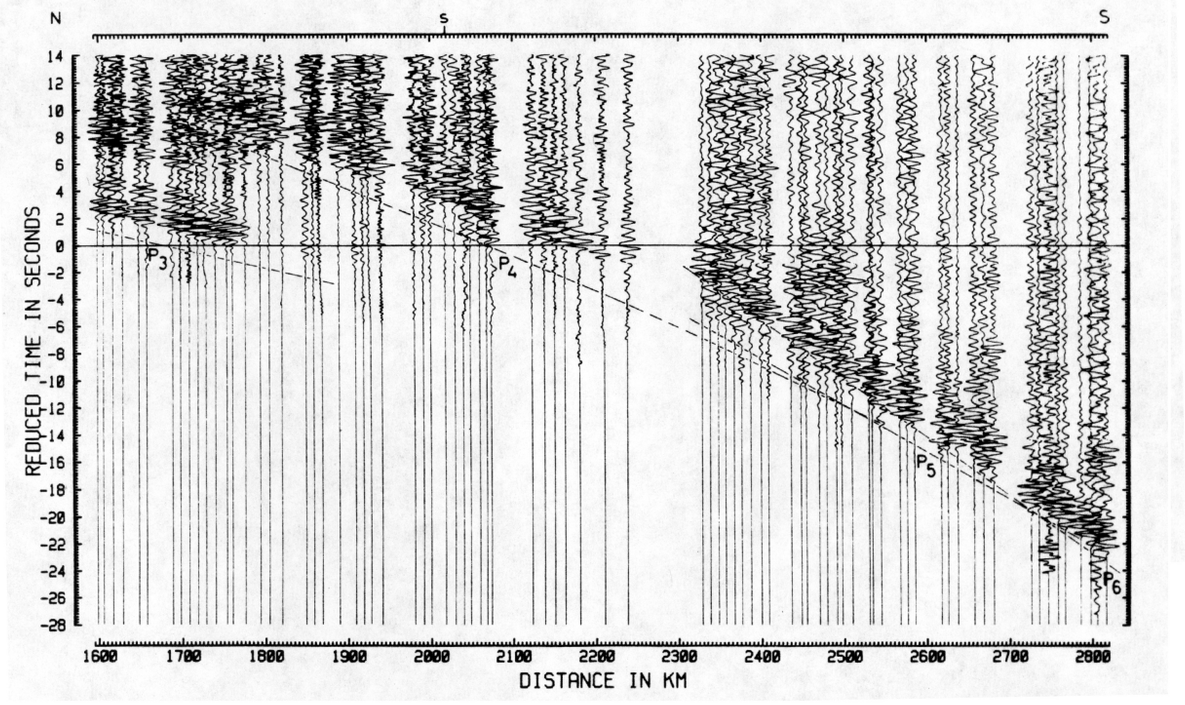


Figure 4. Trace normalized P-wave record section for the vertical component data from the northern PNE recorded along the Quartz profile to the south in the distance range 1600-282 km. Phase P3 from the upper mantle and phases P4, P5, and P6 from the mantle transition zone between 420 and 850 km depth.
(From Mechie et al, 1993)

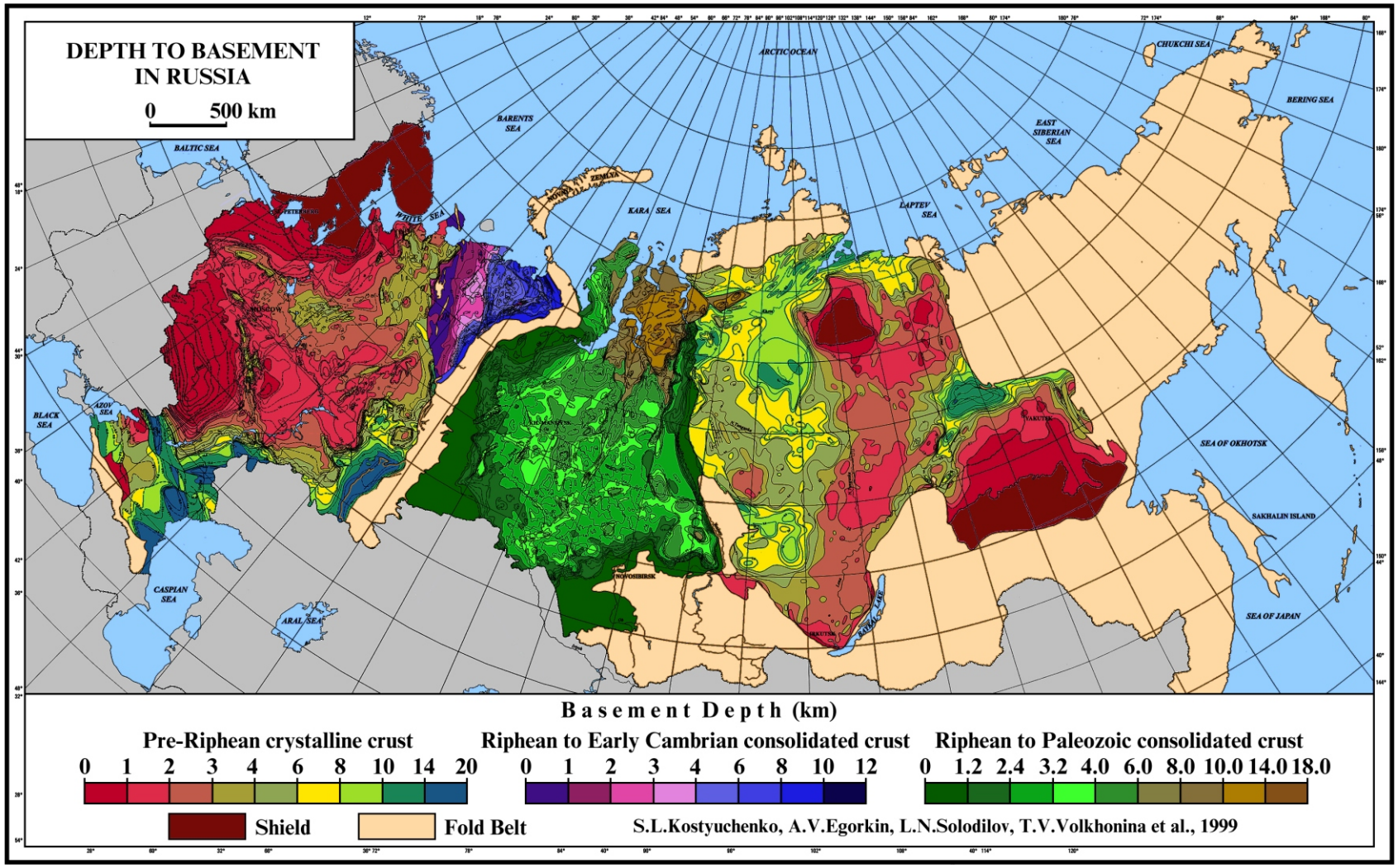


Figure 5. Newly updated map of Russia showing depth to basement produced by S.L. Kostyuchenk et al (1999) of the GEON Centre, Russian Ministry of Natural Resources, Moscow, in cooperation with the U.S. Geological Survey, Menlo Park, California.

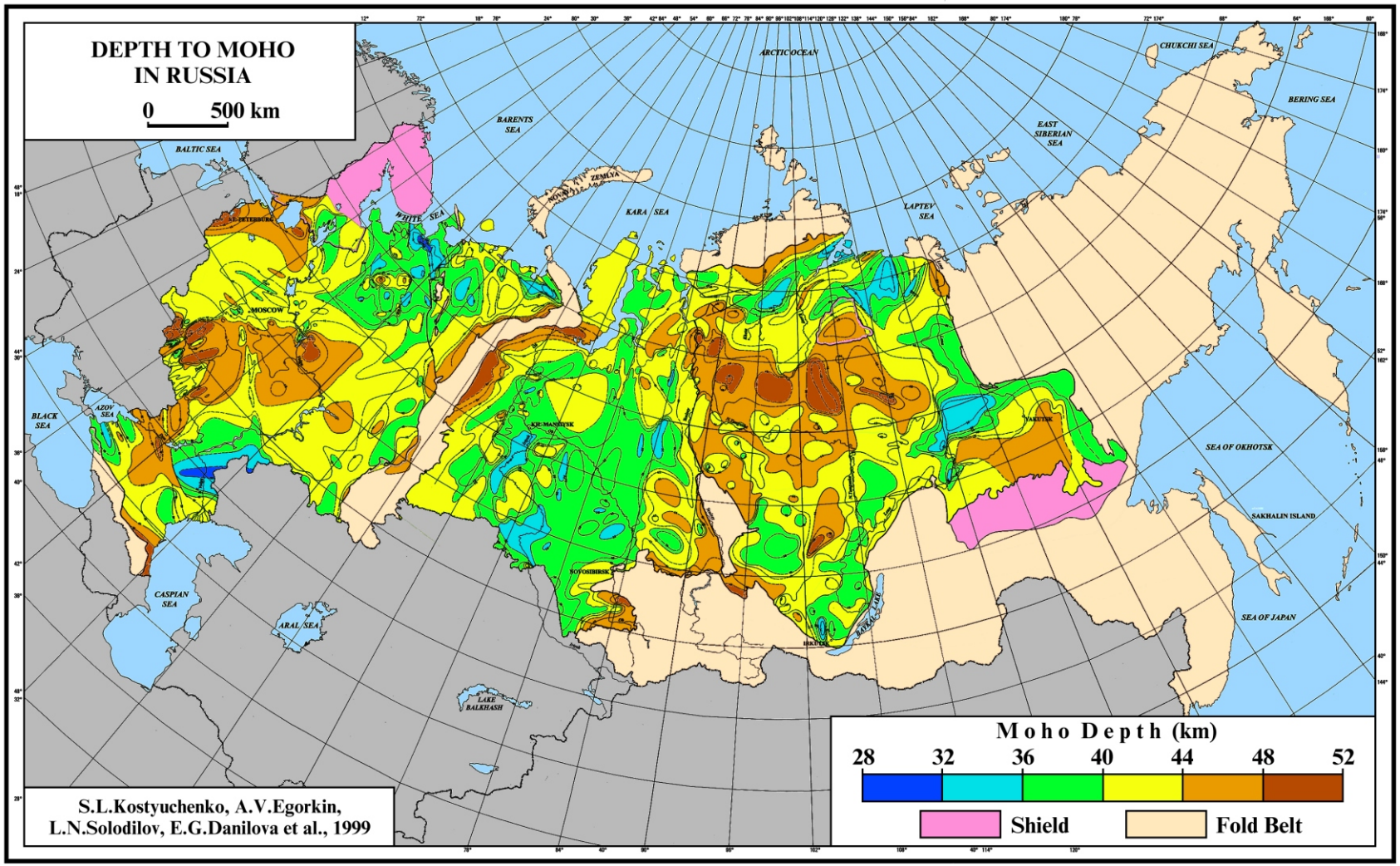


Figure 6. Newly updated map of Russia showing depth to Moho, produced by S.L. Kostyuchenk et al (1999) of the GEON Centre, Russian Ministry of Natural Resources, Moscow, in cooperation with the U.S. Geological Survey, Menlo Park, California.

THE CRUSTAL STRUCTURE AND CTBT MONITORING OF INDIA: NEW INSIGHTS FROM DEEP SEISMIC PROFILING

Walter D. Mooney[1], P.R. Reddy[2], V. Vijaya Rao[2], D.M. Mall[2]

1. U.S. Geological Survey, Earthquake Hazards Team
2. National Geophysical Research Institute, Hyderabad, India

Sponsored by U.S. Department of Energy
Office of Nonproliferation and National Security
Office of Research and Development

DOE IA No.: DE-AI04-98AL79758

ABSTRACT

The nation of India has been collecting seismic data for nearly three decades. However, because it has historically been difficult for Western scientists to access this valuable resource or identify individuals responsible for program development, this information has not readily been made available. In the past year (2000), a collaborative effort began between the National Geophysical Research Institute (NGRI) in Hyderabad, India and the US Geological Survey (USGS) in Menlo Park, CA. Since NGRI is a leading organization for geophysics in India, the scope of this collaborative effort will strengthen our knowledge of crustal structure of India. On a continent-wide scale, it was observed that crustal thickness values range from 35 to 40 km in most of India, with the Himalayas being the biggest exception (thickness about 80 km). We have summarized the internal velocity structure of the crust with crustal columns from throughout India. Crustal structure correlates with geological province, and generally thins at the margins, as a result of the transition from continental to oceanic crust. In addition, we have recently reprocessed newly obtained seismic reflection images and interpreted these results with geological and other geophysical constraints. The deep seismic reflection data was acquired using a recording geometry of 100 m shot/detector spacing, utilizing two DFS-V recording units under master-slave mode. Reprocessing was done using ProMax software at the US Geological Survey in Menlo Park, California. Seismic images across the Central Indian Suture Zone reveal a reflection band from 4 to 19 s (twt) that shallows to the SE. A strong reflection band, at 14 s (twt) (~ 44 km) in the northeast, is interpreted as the Moho. The Moho is not identified continuously along the profile, but is observed as a strong reflector again just before the Central Indian Suture Zone. The divergent reflection fabric across the profile is interpreted as the signature of a collision process between two protocontinents in which buckling of the upper and middle crustal layers took place. Inter-wedging associated with shallow ramp anticlines further support the collision theory. These data, both from seismic reflection and refraction profiling, provide a wealth of information needed for the purposes of seismic monitoring of India.

Key Words: crustal structure, India, seismic reflection, Deep Seismic Sounding

---

OBJECTIVE

High quality regional models of crustal structure are necessary for accurate seismic locations required by the monitoring of the Comprehensive Nuclear-Test-Ban Treaty (CTBT). This paper presents an overview of the crustal structure of India, as well as a newly-interpreted seismic reflection profile through the Central Indian Suture Zone.

RESEARCH ACCOMPLISHED

1 Introduction

The seismic structure of the crust and upper mantle provides critical information regarding lithospheric composition and evolution. There are large variations in fundamental properties, such as crustal thickness, crustal and upper mantle velocity structure, and the depth to the lithospheric / asthenospheric boundary in different tectonic domains. These properties can be interpreted in terms of geological processes that have formed and modified the lithosphere.

India is a geologically complex continent that includes both ancient shields and young mountains (Fig. 1). Seismic reflection and refraction studies have been conducted in different geological and tectonic environments in India. These include: rifts, collisional boundaries, shield and platform areas, and exposed lower crustal granulites. These studies, together with complimentary investigations elsewhere, have provided sufficient insight to understand the geological processes and tectonic features responsible for the evolution of the crust. For a clear view of the subsurface structures in different geological settings, coincident deep seismic reflection and refraction studies provide the most reliable measurements of the structure and physical properties of the crust. This in turn can be useful in monitoring of the Comprehensive Nuclear-Test-Ban-Treaty, as India has recently demonstrated its nuclear capabilities.

2.1 Main Features of the Crustal Structure of Central India

Crustal seismic studies in India were started during 1972. Twenty Deep Seismic Sounding (DSS) profiles have been conducted totaling 6,000 km (Fig. 2). Long range refraction and wide-angle reflection techniques with a dense geophone spacing of 80-200 m and shot point interval of 10-40 km were used in acquiring this data. Kaila and Krishna (1992), Mahadevan (1994) and Reddy et al (1999) provide reviews of Indian continental crustal structure. Estimates of crustal thickness fall into the range of 35-40 km throughout most of the continent, with the biggest exception being the Himalayas that are known to have thicknesses up to 80 km (Mahadevan, 1994). Even here, large lateral variations are suggested, and the thickness of the Himalayas may differ from east to west.

Representative velocity models from the Indian shield are presented in Figure 3. Crustal structure is used to differentiate various portions of the Indian shield. The crust is thicker along the middle of the east coast than along the west coast. Thinning of the crust is probably due to its transition from continental to oceanic at the eastern and south-eastern flanks of the Mahanadi and Bengal basins, respectively. The sharp rise in the Moho from west to east clearly points to the presence of a significantly thinned crust in the eastern and southeastern parts of the Bengal basin. The Cambay basin on the west coast is characterized by an up warp of Moho during the late Cretaceous period, probably representing a transitional type crust as a major source of Deccan trap flows.

The Narmada-Son lineament is the most conspicuous linear geological feature in the Indian Shield after the Himalayas, and has played a significant role in the formation of the crust (Fig. 4). This ancient lineament cuts across central India in a NNE-SSW direction and has been periodically reactivated since the Precambrian. Results from five DSS profiles show a modest variation in crustal thickness from 38-43 km across the lineament. A high velocity of 6.9 km/s at a shallow depth of ~10 km and a 7.3 km/s high velocity layer above the Moho are indicative of magmatic underplating in the region. Recent deep seismic reflection studies (e.g. Reddy et al, 1995) indicate that a continent-continent collision occurred during the Proterozoic Eon and formed a suture between the Dharwar and Bundelkhand cratons. The collisional process is thought to be responsible for the presence of a high velocity layer at shallow depth. The region has repeatedly undergone reactivation since the Proterozoic and presently has a low level of seismic activity. It is also associated with high heat flow.

In general terms, a low average crustal velocity (6.0-6.3 km/s) is indicative of a dominantly felsic composition and a higher average velocity (6.5-6.8 km/s) indicates a more mafic composition. The average crustal velocity for most of the Indian subcontinent, except the basins, is equal to the global average of 6.45 km/s (Christensen and Mooney, 1995; Mooney et al, 1998). This suggests a typical platform / shield crust with a bulk composition equivalent to a diorite.

Crustal reflection studies across the Paleo/Mesoproterozoic Aravalli Delhi Fold Belts in the northwestern Indian shield have revealed crustal scale thrust faults extending down to the Moho and beyond (Fig. 4). A

thick high-velocity (7.3 km/s) lower crust is observed in this region (Tewari et al, 1997). Similar crustal velocity structures are also observed in the Trans-Hudson orogeny (Lucas et al, 1993) of the North American continent. This part of the Indian shield has witnessed two collisional episodes during the end of the Paleo and Mesoproterozoic period, viz. 1800 Ma and 1100 Ma.

Recent investigations of continental and oceanic structure around India show significant variations in the upper mantle structure, with the former being characterized by low Q or low velocity layers and the latter by their absence. In addition, P- and S- wave velocities higher than average global models have led to the inference of lower temperature gradients in the mantle under these areas (Mahadevan, 1994). Models of the upper mantle show a continuous linear increase in P-wave velocity with depth from 8.24 km/s at 55 km followed by a gradient of 0.18 km/s/100 km to a depth of 220 km. The gradient then falls to 0.08 km/s/100 km, arriving at a velocity of 8.62 km/s at 310 km depth (Mahadevan, 1994).

2.2 Presentation of newly processed data from the Central Indian Suture

Seismic reflection data provide the highest resolution image of the internal structure of the crust (Mooney and Meissner, 1992) and provides an estimate of the scattering and attenuation properties of the crust needed for calibrating high-frequency seismic wave propagation. Imaging of the Central Indian Suture (CIS) (Fig. 4), a mega-shear zone, by coincident deep seismic reflection and refraction data shows that there is a distinctly different reflectivity character to the northwest compared with the southeast of the CIS (Fig. 5). Reflections northwest of the CIS are predominently short, and the reflectivity is, in general, only of moderate strength. Toward the CIS, the crust is dominated by long reflections, resembling chevron folds. These folds are similar to cross-sections of structural duplexes, and are usually seen in a compressional environment. Southeast of the CIS, the reflections are longer compared to those in the northwest. The shallow detachments seem to be linked to mid-crustal dipping reflectors that are regarded as ramps.

Time sections show the presence of a strong reflector, commencing at a depth of about 7-8 sec (two way travel time, twt) in the northwest, shallowing up to a depth of 4 sec (twt) near the middle of the profile. This reflector is disrupted close to the CIS by what appears to be reverse-dipping reflectors. Southeast of the CIS, especially from around 6 s to 8 s, one can see a criss-crossing reflection fabric. These two reflectivity characteristics in turn suggest that when the collision occurred (between the Bundelkhand and Deccan proto-continents) buckling of the upper and middle crustal layers of the proto-continents took place, resulting in the western block's lower crustal column subducting below the Deccan proto-continents. Thus, the collision process was of such severe magnitude that the impact was seen in both crustal blocks. The presence of the distinct opposite dipping reflectors, with the CIS zone acting as the divider, also suggests a collisional environment.

The inter-wedging of seismic reflections that are found to be associated with shallow ramp anticlines further supports the collision theory. The available refraction control indicates the presence of a refraction Moho at an average depth of 43 km. This agrees with the reflection Moho that is associated with the deepest set of reflections (at an average depth of 44 km), but is not as distinct as one normally expects. In spite of this, the reflection signatures show that the thrusting and subduction signatures are present at Moho level, with probable thrusting of the Deccan proto-continent over that of the Bundelkhand proto-continent. The dipping reflections across the deep crust and the upper mantle, especially the southeastward dipping branches of deep reflectors, may be regarded as the remnants of former crustal slabs now largely metamorphosed. The presence of a lower crustal, low-velocity zone (which has been inferred from refraction data) further supports the collision theory, as it is evident that the collision resulted in the development of a weak, highly-sheared zone below the midcrustal column.

CONCLUSIONS AND RECOMMENDATIONS

A vast geophysical database can be compiled from extensive seismic profiling which has been carried out in India. Much of this data is slowly becoming available in digital format, and thus can be re-evaluated in terms of the seismic velocity structure and attenuation of the crust and upper mantle. This new data will improve our knowledge of this region of the world, which has recently demonstrated its ability to produce and detonate nuclear weapons. The improved knowledge of the seismic structure, in turn, will enable

significantly improved determinations of seismic source parameters as needed by the Comprehensive Nuclear-Test-Ban Treaty. It is, therefore, imperative that cooperation with American agencies and scientists in India be allowed to continue. Such a reasonable exchange of data will foster new research and cooperative efforts which may lead to more stability in the region.

REFERENCES

Christensen, N.I., and Mooney, W.D., 1995. Seismic velocity structure and composition of the continental crust: A global view, J. Geophys. Res., 100, 9761-9788.

Goodwin, A.M. 1996. Principles of Precambrian Geology. Academic Press. 327 pp.

Kaila, K.L. and Krishna, V.G., 1992. Deep seismic sounding studies in India and major discoveries, In: Ramaseshan, S. Gupta, H.K. (Eds.) Seismology in India: An overview, Current Science, 62, 117-154.

Lucas, S.B., and seven others. 1993. Implications of seismic reflection profiles for the collisional structure of the Proterozoic Trans-Hudson Orogen, In: Seranne, M., Malavieille, J., (Eds.) Late Orogenic extension in mountain belts, Documents - B.R.G.M., 219, 127.

Mahadevan, T.M. 1994. Deep Continental Structure of India: A Review, Geological Society of India Memoir 28, Bangalore, 569 pp.

Mooney, W.D., Laske, G., and Masters, G., 1998. Crust 5.1: A global crustal model at 5° x 5°, J. Geophys. Res., 103, 727-747.

Mooney, W.D., and Meissner, R., 1992. Multigenic origin of crustal reflectivity: A review of seismic reflection profiling of the continental lower crust and Moho. In: Fountain, D.M., Arculus, R., Kay, R.W., (Eds.), Continental Lower Crust. Elsevier, Amsterdam, pp. 45-79.

Reddy, P.R., and eight others, 1995. In: Continental Crust of northwestern and central India, Sinha Roy, S., and Gupta, K.R., (Eds.) Geol. Soc. India Memoir 31, pp. 537-544.

Reddy, P.R., Venkateswarlu, N., Koteswar Rao, P. and Prasad, A.S.S.S.R.S., 1999. Crustal Structure of Peninsular shield, India from DSS studies, Current Science, 77, 1606-1611.

Tewari, H.C., Dixit, M.M., Rao, N.M., Venkateswarlu, N., Vijaya Rao, V., 1997. Crustal thickening under the Paleo/mesoproterozoic Delhi fold belt in the northwestern India: Evidence from deep reflection profiling, Geophys. J. International, 129, 657-668.

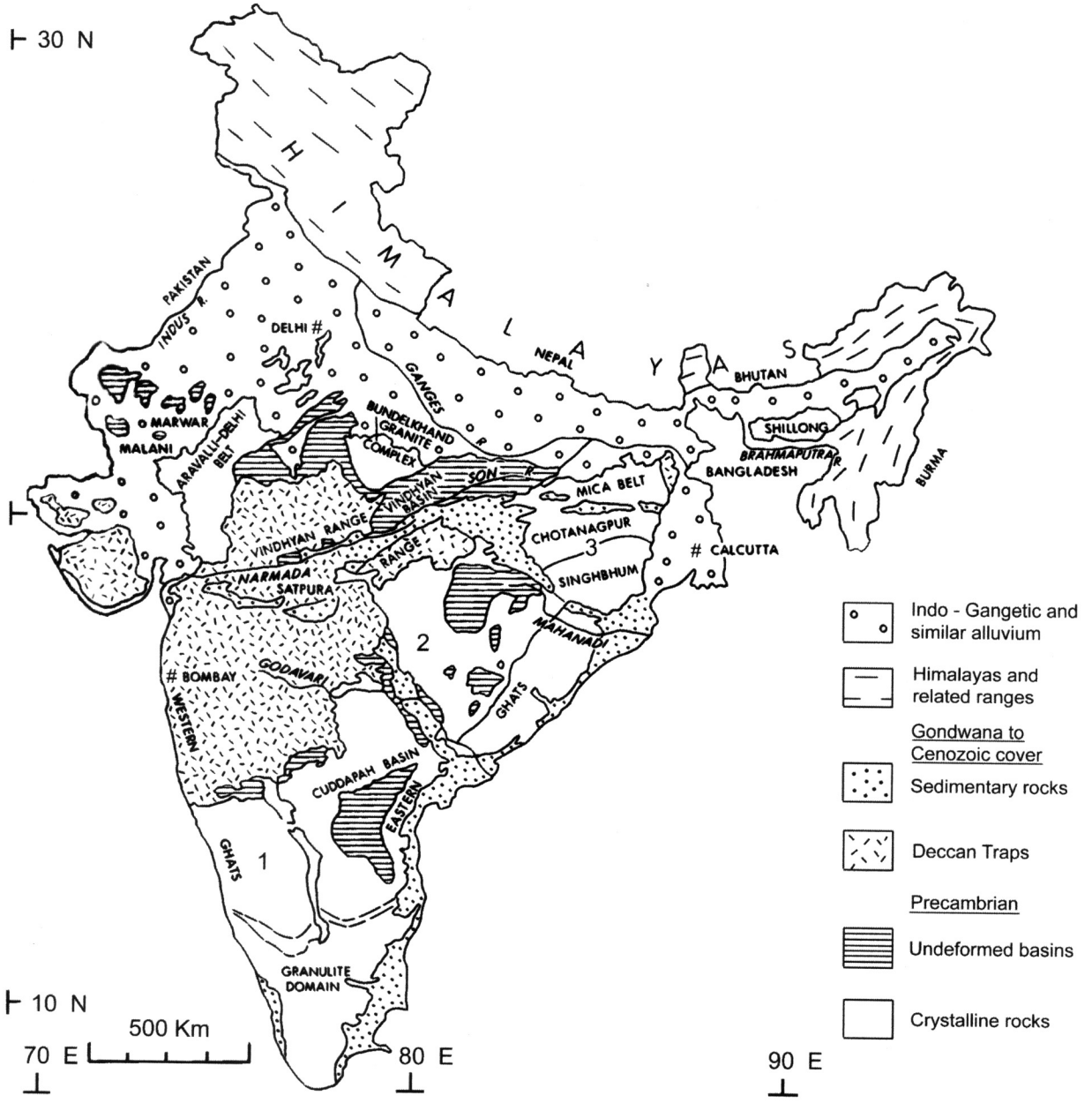


Figure 1. Geological map of India (after Goodwin, 1996)

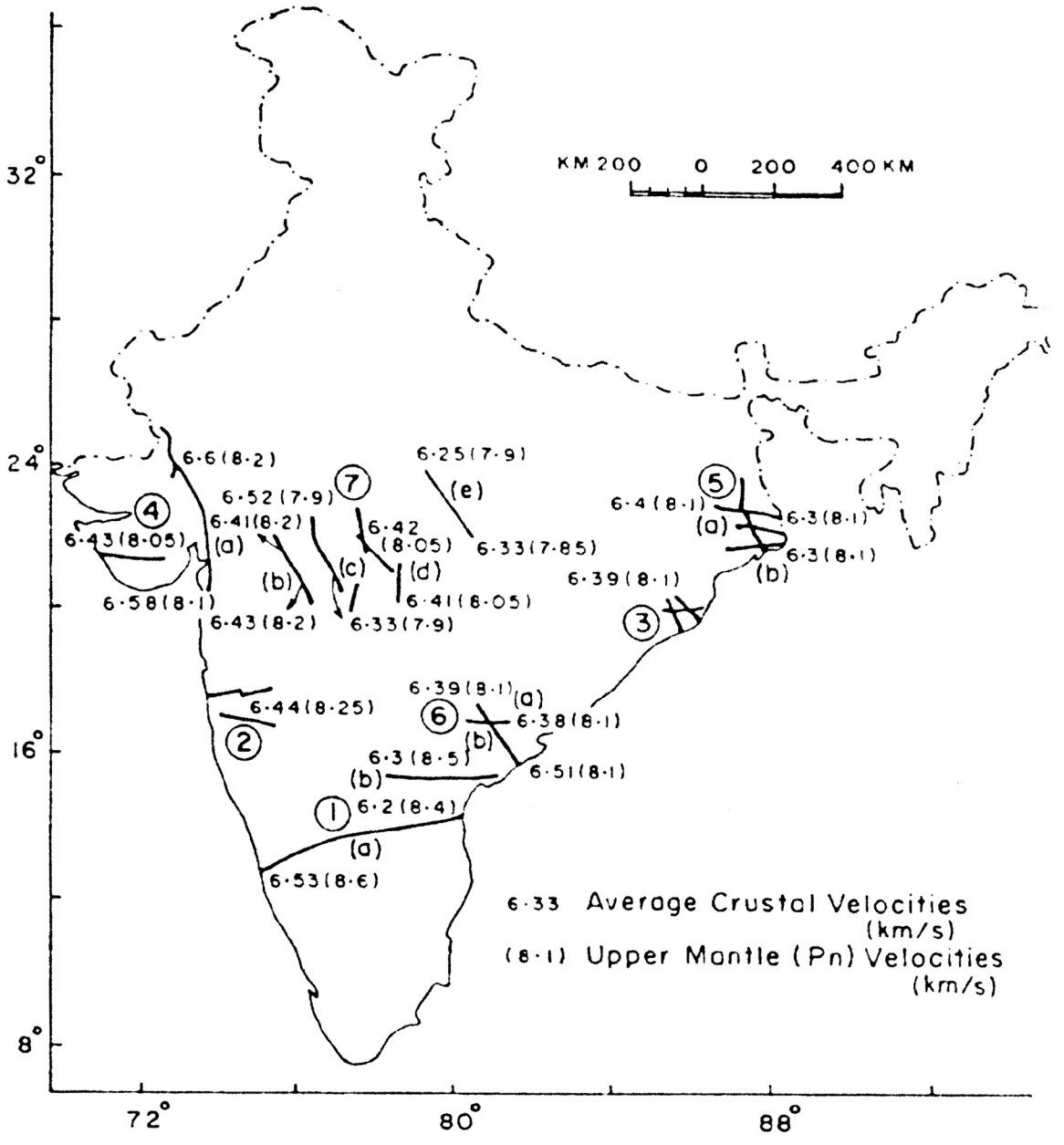


Figure 2. Locations of Deep Seismic Sounding profiles. Circled numbers correspond to seismic velocity depth columns shown in Figure 3.

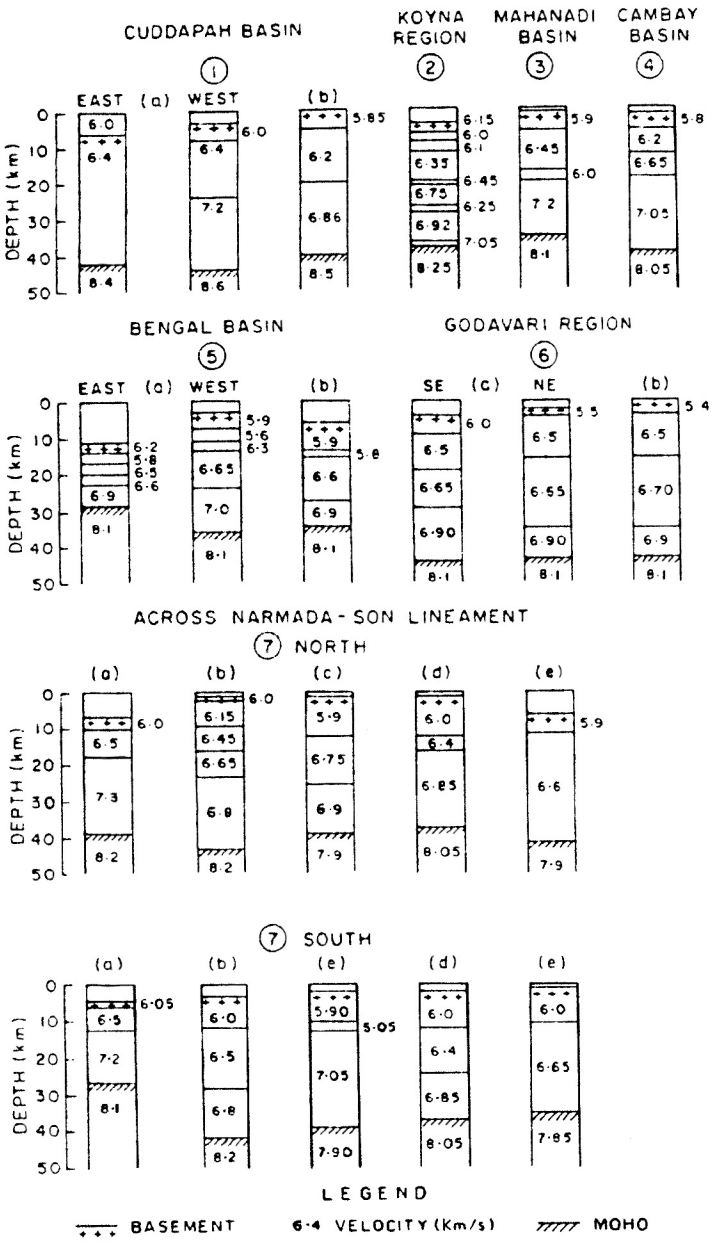


Figure 3. Seismic velocity-depth columns of various regions in the Indian Shield (average crustal and upper mantle velocities along the different DSS profiles shown in Figure 2).

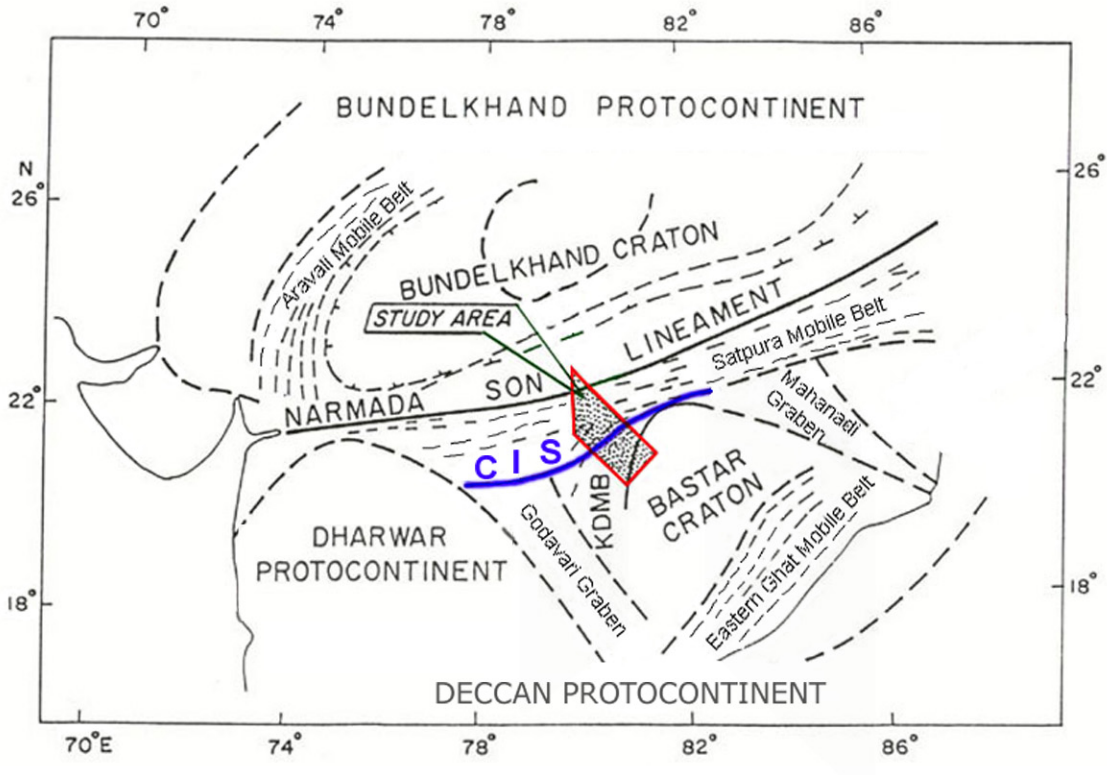


Figure 4. Location map of seismic profile crossing the Central Indian Suture Zone.

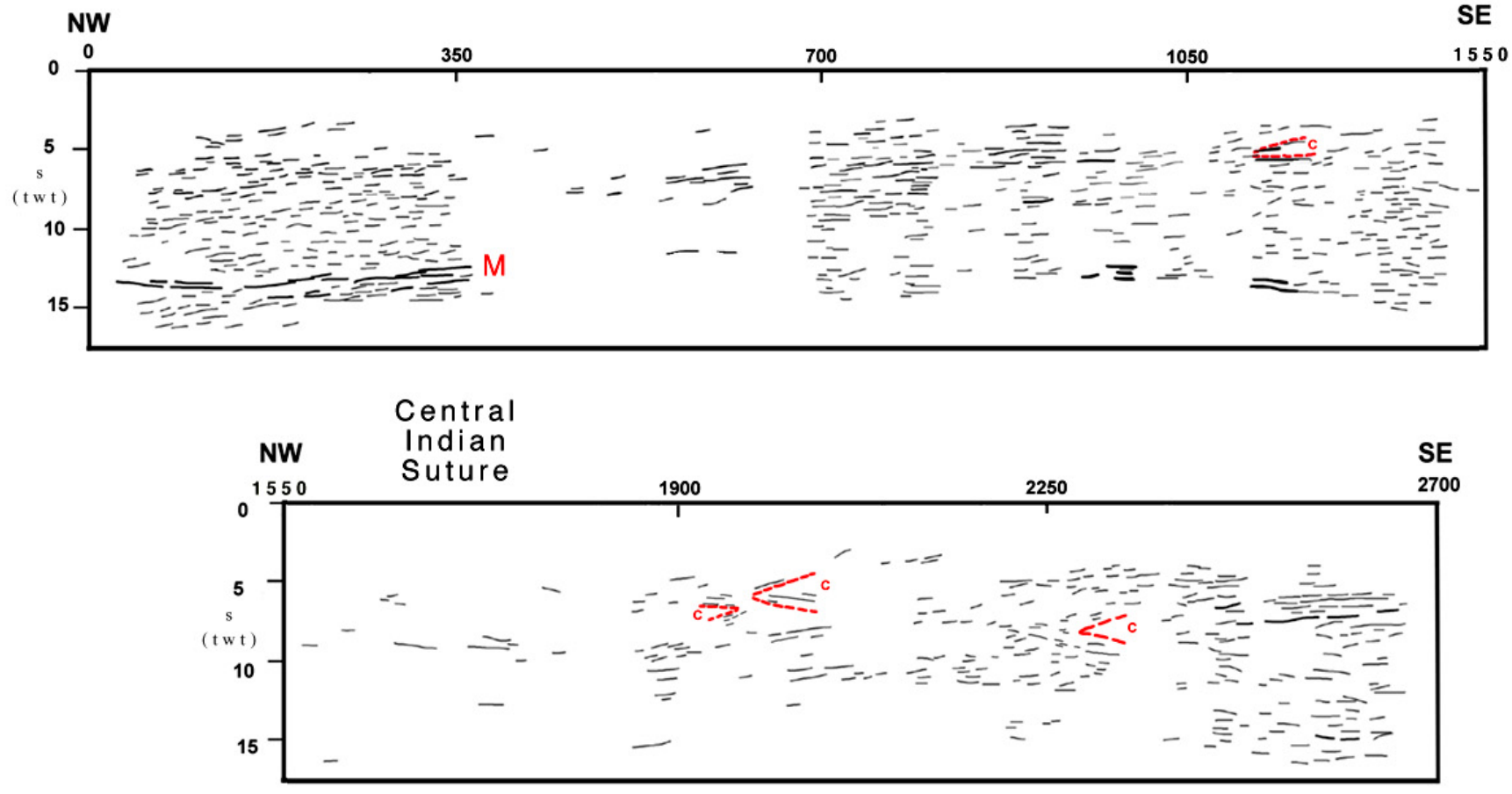


Figure 5. Interpreted profile across the Central Indian Suture Zone. M = Moho, c = inter-wedging (crocodiles). Data were collected and processed by the National Geophysical Research Institute (NGRI), Hyderabad, India (c.f. Reddy et al, 1999)

SEISMIC CALIBRATION OF THE EUROPEAN ARCTIC

Svein Mykkeltveit, Frode Ringdal, Conrad Lindholm, NORSAR
Elena Kremenetskaya, Kola Regional Seismological Centre

Sponsored by U.S. Department of Energy
Office of Nonproliferation Research and Engineering
Office of Defense Nuclear Nonproliferation
National Nuclear Security Administration

Contract No. DE-AC04-99AL66001

ABSTRACT

The purpose of this two-year effort, which started on 1 January 1999, is to support the construction of the U.S. Department of Energy (DOE) Comprehensive Nuclear-Test-Ban Treaty Knowledge Base for detecting, locating and identifying seismic events in the area of northern Fennoscandia, the Kola Peninsula, Novaya Zemlya, and the surrounding waters of the Barents and Kara Seas. The main objectives of the effort are to assemble a set of historical seismic observations suitable for characterizing all aspects of seismic wave propagation and seismic sources in this region, to describe the principal seismic phases observed in the seismograms, and to calibrate the region with respect to seismic wave propagation (travel-times and amplitude-distance relations).

The main emphasis of work on this contract so far has been on data collection. Waveform data have been complied for a range of sources in the European Arctic: Nuclear tests at the Novaya Zemlya test site, peaceful nuclear explosions conducted in the area, earthquakes and presumed underwater explosions from 1970 to the present, and representative blasts from mining operations in the Kola Peninsula, northern Norway, Sweden, Finland and adjacent regions of European Russia. Waveform data collected under this effort have been provided in CSS 3.0 format, with the appropriate metadata included, to DOE through the Lawrence Livermore National Laboratory, to the U.S. Department of Defense through the Center for Monitoring Research, and to the U.S. National Data Center. So far, segmented data for 111 events have been extracted and copied to eight CD ROMs. In addition, a set of seven Exabyte tapes has been produced, containing continuous data in the form of 15-day segments around the origin times of three events that occurred in the Noyaya Zemlya region during 1995-1997. Additional data for events of special interest will be delivered during the year 2000.

The project is a collaborative effort between NORSAR and the Kola Regional Seismological Centre (KRSC) of the Russian Academy of Sciences. The main source of data for this project is the historical waveform archives at NORSAR, containing data from the NORSAR teleseismic array and the network of northern European small-aperture arrays. These data have been supplemented with data provided by KRSC for stations AMD and APA in northwestern Russia.

The work under this contract also includes analysis of the data compiled. So far, a study of the P/S ratio as a regional discriminant in the European Arctic has been conducted. Our conclusion from this study is that the P/S ratio, even at high frequencies is, with present knowledge, not sufficiently stable to be used as a reliable discriminant between earthquakes and explosions. Future application of this discriminant will require extensive regional calibration and detailed station-source corrections. Work continues on other aspects of data analysis, such as a determination of bounds on seismicity in the Kara Sea.

Key Words: data collection, characterization of seismic phases, seismic calibration

OBJECTIVE

This purpose of this research is to support the construction of the DOE CTBT Knowledge Base for detecting, locating and identifying seismic events in the area of northern Fennoscandia, the Kola Peninsula, Novaya

Zemlya, and the surrounding waters of the Barents and Kara Seas. This is done by assembling a set of historical seismic observations suitable for characterizing all aspects of seismic wave propagation and seismic sources in this region, by describing the principal seismic phases observed in the seismograms, and by calibrating the region with respect to seismic wave propagation.

RESEARCH ACCOMPLISHED

Collection and delivery of waveform data

An important aspect of this project is the compilation of a data base of events to be used for calibration purposes. In fulfillment of this goal, waveform data have now been collected for a range of sources in the European Arctic: Nuclear tests at the Novaya Zemlya test site, peaceful nuclear explosions conducted in the area, earthquakes and presumed underwater explosions, and representative blasts from mining operations in the Kola Peninsula, northern Norway, Sweden, Finland, and adjacent regions of European Russia. The basis for the selection of events for inclusion in this data base has been regional and other bulletins covering this area. The bulletin sources have thus included the bulletin of the International Seismological Centre (ISC), the bulletin of the NEIC (USA), the IDC Reviewed Event Bulletin, the NORSAR regional and teleseismic bulletins, and the bulletin of the Kola Regional Seismological Centre.

Table 1 gives an overview of the available digital stations that have formed the primary data source for this project. The table specifies the station type (array, 3C), the station location, the operating organization, and the years during which each station has been in operation. Note that some data from the Hagfors array in Sweden and the GERESS array in Germany have also been included in the data base.

Station	Station Type	Station Location	Operating Organization	Data Availability (in NORSAR's archives)
NORSAR large-aperture array	Array	60.82°N 10.83°E	NORSAR	1971-present
NORESS array	Array	60.73°N 11.54°E	NORSAR	1984-present
ARCESS array	Array	69.53°N 25.51°E	NORSAR	1987-present
Spitsbergen array	Array	78.18°N 16.37°E	NORSAR	1992-present
FINESS array	Array	61.44°N 26.08°E	Univ. of Helsinki	1990-present
Apatity array	Array	67.61°N 32.99°E	KRSC	1992-present
Amderma array	Array, 3C	69.74°N 61.66°E	KRSC	1994-present

Table 1. This table gives an overview of available digital stations that form the primary data source for this project.

The waveform data compiled have been copied to a set of 8 CD-ROMs. CD-ROM No. 1 in this set contains data from 30 underground nuclear test explosions conducted at Novaya Zemlya during 1971-1990 and recorded on the large-aperture NORSAR seismic array. This collection covers all nuclear test explosions on Novaya Zemlya during this time interval, except the m_b 5.7 explosion on 27 September 1978, as the NORSAR array data acquisition system was out of operation on this date. Data recorded at the NORSAR array for a one kiloton chemical explosion conducted on Novaya Zemlya in 1987 are also included. The ray paths from the two Novaya Zemlya test sites to the NORSAR large-aperture array are shown in Fig. 1.

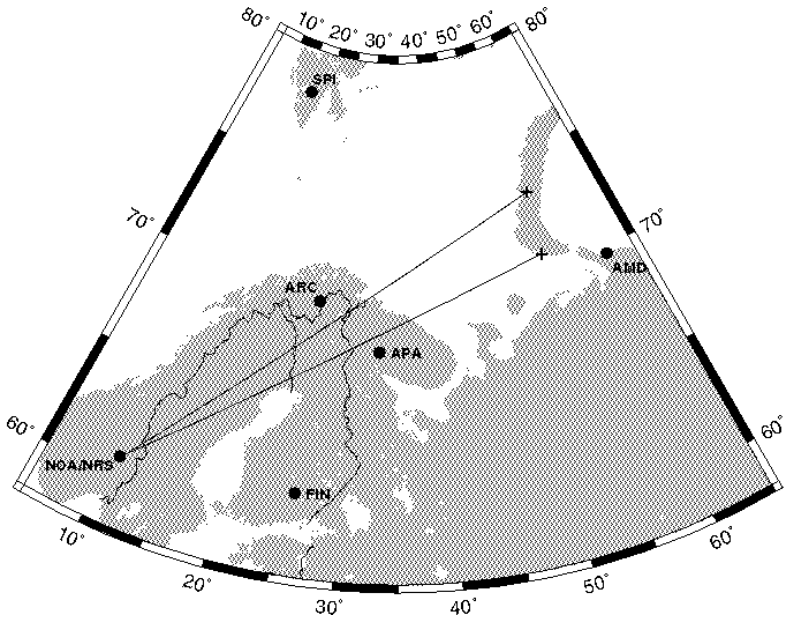


Fig. 1. Ray paths for the Novaya Zemlya events compiled in CD-ROM No. 1.

The data on CD-ROMs Nos. 2-8 comprise all available recordings from 84 seismic events, as collected from the following stations and arrays: Amderma, Apatity, ARCES, FINES, GERES, Hagfors, NORSAR, NORES and SPITS. The data cover the time interval from 1979 through 1998, and have magnitudes ranging from 2.3 to 5.9. These events are shown in Fig. 2.

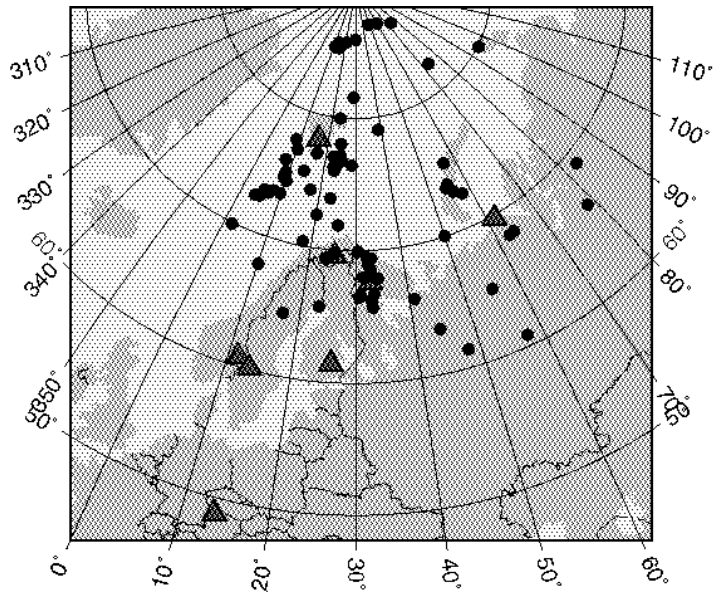


Fig. 2. The map shows the epicenters for the 84 events (filled circles) contained on CD-ROMs Nos. 2-8. The stations for which waveforms are collected are shown as triangles.

An example of the data in this data set is provided in Fig. 3., which shows the NORSAR array recordings from an underwater chemical explosion of 8 tons, set off in the sea at 71.90°N, 25.79°E, and conducted as part of the FENNOLORA deep seismic sounding experiment in 1979.

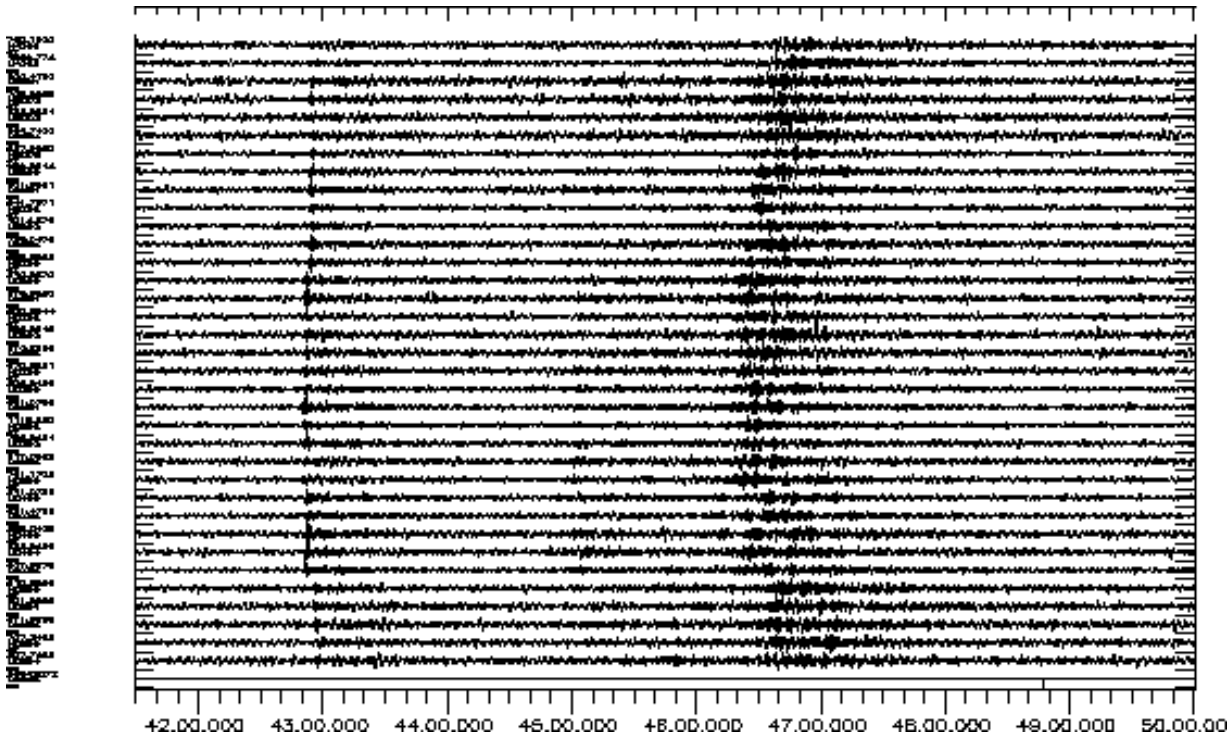


Fig. 3. Data example from the August 17, 1979, event recorded on the 42 short-period channels of the NORSAR array. The source was an underwater chemical explosion of 8 tons, conducted as part of the FENNOLORA deep seismic sounding experiment.

In accordance with the contract, the set of CD-ROMs as described above has been distributed to the US Department of Energy through the Lawrence Livermore National Laboratory, to the US Department of Defense through the Center for Monitoring Research, and to the US National Data Center. All data are in the CSS3.0 format, and appropriate metadata have been provided in accordance with the specifications given by Carr et al (1998). In addition to the segmented data described above, some sample continuous data segnments of lengths up to 15 days have been retrieved from the data archives and provided to the DOE.

P/S ratio as a regional discriminant in the European Arctic

We have used data from seismic stations operated by NORSAR, the Kola Regional Seismological Centre (KRSC) and IRIS to study the characteristics of regional phases in the European Arctic, with emphasis on the P/S ratio discriminant. In particular, we study the variability of the P/S ratio as a function of frequency across various regional arrays. Previous studies using the large-aperture array NORSAR have shown a large variability in P/S ratios for sensors in the array when analyzing a given seismic event. This variability is most pronounced at low frequencies (1-2 Hz), but significant even in the higher frequency range.

It is of interest to investigate this variability across smaller arrays, and we have carried out such studies for mining explosions as well as confirmed earthquakes. The variability of the P/S ratio turns out to be very

significant, even across a small array such as ARCES (diameter 3 km). The main source of this variability comes from the P-wave. Although the standard deviation of the P/S ratio across the arrays is less at higher frequencies, it is still large enough to cause concerns for the effectiveness of P/S as a seismic discriminant in this region. We find that using 3-component data (there are four 3-component stations within the ARCES array), the scatter in P/S ratios is somewhat smaller than when using vertical components alone. However, some caution should be exercised in interpreting this result because of the low number of 3-component sensors.

When assessing data from a regional network for the same event, we find that the P/S amplitude ratio shows large variability for the same source type and similar propagation paths. This effect is most pronounced at relatively low frequencies, but it is also significant at higher frequencies. Our conclusion from this study is that the P/S ratio, even at high frequencies, is with current knowledge not sufficiently stable to be used as a reliable discriminant between earthquakes and explosions. Future application of this discriminant will require extensive regional calibration and detailed station-source corrections.

We have also calculated spectrograms for a set of seismic events of various source types. The most interesting feature observed in the clear evidence of spectral scalloping for an underwater explosion near Murmansk recorded at the ARCES array at a distance of about 300 km. Such spectrograms might contribute useful information in interpreting future seismic events in the region.

Ground truth events

As a separate effort under this contract, waveform data were collected for nine events that occurred in the northern Norway/Kola peninsula region during the interval May-August 1999. These events are well-located earthquakes and mining explosions, and have been classified in accordance with the "Ground Truth" terminology used for the Calibration Database at the Prototype International Data Center (Bondar and North, 1999). The nine events in this database fall within the categories GT1 (three mining explosions), GT2 (two mining explosions), GT5 (3 earthquakes at Revda in the Kola Peninsula) and GT7 (one earthquake at Masi in northern Norway). For these events, waveform data are available from five permanent stations in this area, as well as from the so-called MASI network comprised of 13 broadband stations temporarily deployed in the county of Finnmark, northern Norway, during May-September 1999. These data have been made available on a CD-ROM that has been distributed as described above for previous data deliveries on this project.

Two events in this database of nine ground truth events have been studied in some detail. The locations of these two events are shown in Fig. 4, which also shows the 13 stations of the MASI network.

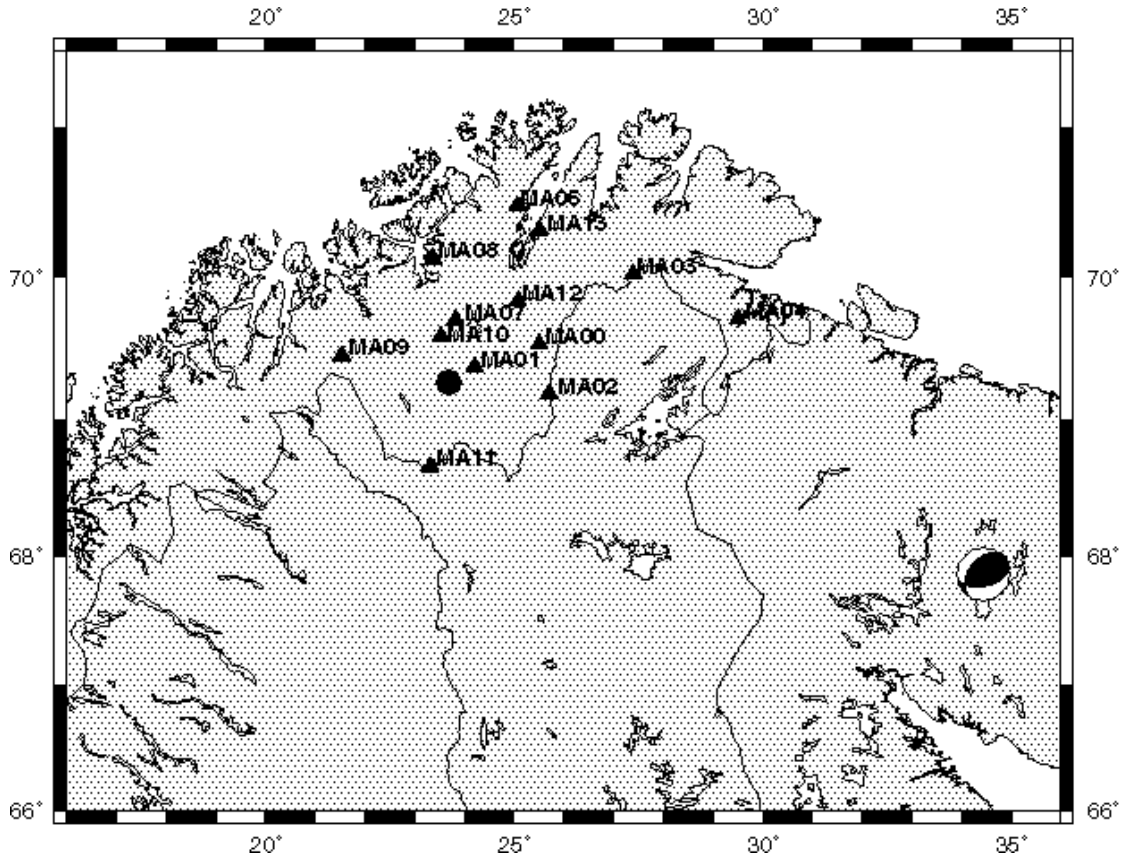


Fig. 4. Map of the 13 MASI stations (triangles) temporarily deployed in Finnmark, northern Norway, during May-September 1999. The dot and the focal plane solution show the positions of the two earthquakes analyzed here (Masi, 22 August 1999, within the MASI network, and Revda, 17 August 1999, in the Kola Peninsula to the east, respectively).

Analysis of the displacement spectra of the MASI network recordings of the 22 August 1999 M_L 2.7 Masi earthquake that occurred within the MASI network, resulted in a relatively high Q of about 1500 in the frequency range 1-10 Hz. The recordings from the Masi earthquake also provided the basis for inferring individual station soil responses (some of the stations of the MASI network were sited on top of thin layers of moraines, whereas others were deployed on solid rock). These results derived from the Masi earthquake records were used to obtain the source spectrum of the Revda M_L 3.9 (M_s 4.2) earthquake of 17 August 1999. The MASI network recordings of this earthquake are shown in Fig. 5. Note that the traces are time-adjusted to align the Rg phases across the network, so that the first Pn onset is outside the frame for the more distantly located stations (at the bottom of the figure).

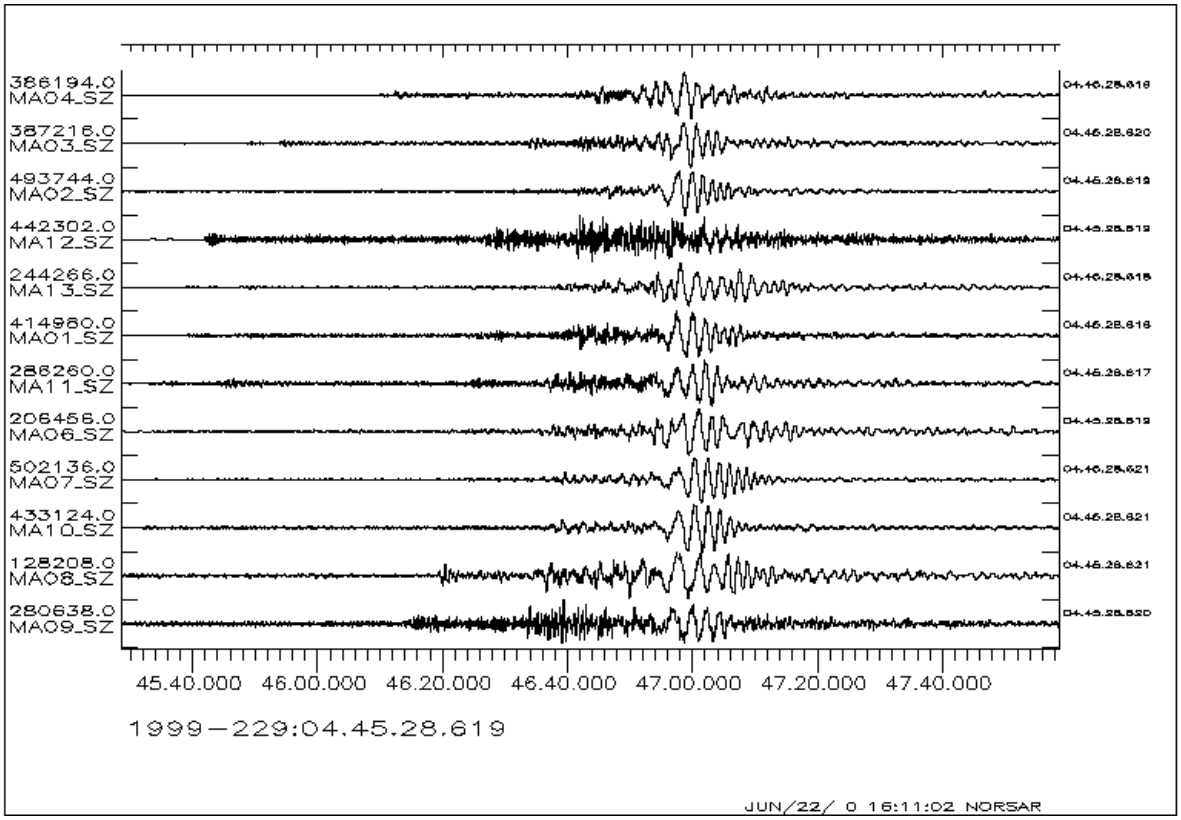


Fig. 5. MASI network recordings of the 17 August 1999 Revda earthquake. The reduction velocity applied is 3.2 km/s in order to align the Rg phase.

The observed spectra for the Revda earthquake can be matched reasonably well with synthetics computed for a circular fault plane of radius 1.6 km, a complete stress drop of 50 bar and a seismic moment of M = 6.7e+22 dyn-cm. The source depth of this earthquake was investigated using a full waveform modelling approach, and the main target in this modelling was the dispersive Rg waves clearly seen in Fig. 5. Matching of synthetic and observed waveforms indicates that the source depth for this event is between 4 and 6 km.

CONCLUSIONS AND RECOMMENDATIONS

Efforts under this contract have resulted in the production of nineCD-ROMs containing data for more than 100 events in the European Arctic, as recorded on arrays and 3-component stations in northern Europe. These data, along with selected continuous data (with data intervals of length up to 15 days), have been made available to the research community. We are in the process of carefully analyzing the events provided in this database in order to ascertain that the events are indeed located within the accuracy estimates given by the various agencies. Our findings in this regard will be provided in future revisions to the database.

The effort also includes some analysis of the data collected. So far, this analysis has focused on the following topics, with results as reported in this paper:

- Study of the P-to-S amplitude ratio as a possible regional discriminant in the European Arctic
- Spetrogram analysis of selected presumed underwater explosions and mining explosions at the Kola Peninsula to identify distinguishing characteristics of these events
- Special analysis for a few events with ground truth information using a comprehensive collection of waveform data to include an extended set of stations in the Fennoscandian-northwestern Russia region.

The work on this project continues with further collection of waveforms for events of special interest, such as new events that have occurred /will occur in the study area, as well as some historical refraction shots undertaken

in the Baltic Sea and surrounding areas. The remaining work also includes the determination of bounds on seismicity in the Kara Sea.

REFERENCES

Bondar, I. & R.G. North (1999): Development of calibration techniques for the Comprehensive Nuclear-Test-Ban-Treaty (CTBT) international monitoring system, *Phys. Earth Planet. Inter., 113*, 11-24.

Carr, D., H. Armstrong, T. Edwards, C. Young & R. Keyser (1998): *Knowledge base metadata handbook*. Draft. Sandia National Laboratories, Albuquerque.

REGIONAL CODA MAGNITUDES IN CENTRAL ASIA

W.S. Phillips and H.E. Hartse
Los Alamos National Laboratory

K.M. Mayeda
Lawrence Livermore National Laboratory

Sponsored by U.S. Department of Energy
Office of Nonproliferation Research and Engineering
Office of Defense Nuclear Nonproliferation
National Nuclear Security Administration

Contract No. W-7405-ENG-36

ABSTRACT

Coda waves are known to be influenced less by path and radiation effects than are direct waves, especially for local earthquakes. This is attributed to the averaging effects of the scattered waves that make up the coda. Furthermore, the duration of coda allows multiple independent measurements to be taken. Thus, coda potentially provide high-precision estimates of source size such as magnitude and moment, with less path bias than direct waves. For purposes of nuclear explosion monitoring, we investigated the use of L_g coda to estimate magnitude at regional distances in central Asia. To do this, we processed coda data for over 3000 recordings made at stations MAKZ, WMQ and LZH. The study area is geologically heterogeneous, and includes Tibet, the Tarim basin, the Tian Shan and platform regions to the north. In tests using 1-Hz data, the scatter between coda amplitude levels obtained from stations WMQ and MAK measured 0.12 (standard deviation in the $\log_{10}$ domain). This is over a factor of 2 lower than the scatter observed for direct L_g. However, in this region, bias enters the coda magnitudes through the effects of lapse time and path. The lapse time bias enters through the inability of standard curves to fit coda decay over long time intervals. We reduce this effect by limiting coda lengths to between 30 and 150 s following the L_g arrival. Coda also showed path dependence similar to direct L_g. We corrected for this using an interpolation (kriging) method. Corrections for lapse time and path had little effect on inter-station scatter because these effects were correlated between stations. We conclude that the early coda yields a more precise measure of event size than does direct L_g, but coda results must still be corrected for path effects in this heterogeneous region.

Key Words: magnitude, regional monitoring, coda.

OBJECTIVES

Monitoring requires reliable moment and magnitude estimates for small events that may only have been observed at a few stations. Here, we test the ability of coda methods to reliably estimate magnitude at regional distances in a geologically heterogeneous portion of central Asia. In particular, we examine non source-related effects on coda amplitudes, such as elapsed time and path, and suggest ways to eliminate them.

RESEARCH ACCOMPLISHED

The stability of coda, with respect to path, has been well documented at local distances. The stability, or uniform coda shape, is consistent with the model of coda as the superposition of waves backscattered from random heterogeneities in the earth's crust and upper mantle (Aki, 1969). Thus, coda reflect path-averaged properties of a given region. The coda stability allows the isolation of relative, radiation-pattern averaged source effects apart from site and path effects. The numerous independent measurements that can be made in the coda result in a high precision, allowing a single station to yield results comparable to a network average. These techniques were combined with an empirical Green's function method to estimate absolute source spectra and study source scaling using data from analog, "spectral analyzing" seismographs (Aki and Chouet, 1975; Chouet et al., 1978; Rautian and Khalturin, 1978; Tsujiura, 1978). In addition, coda duration was found to give stable magnitude estimates (Bisztricsany, 1958) and its use has become widespread in local earthquake network operations. Furthermore, Aki (1980) proposed the use of coda amplitudes, rather than duration, to obtain higher precision magnitude estimates.

Coda methods are successful with dense network, local earthquake data sets because the late, or path-averaged, portion of the coda generally exceeds background noise levels and is readily available for study. The late coda is loosely defined to begin at twice the S-arrival time (Rautian and Khalturin, 1978), taken from observations of the point at which coda shapes begin to coalesce. This poses a problem for the use of coda at regional distances because less data are available at twice the S (or L_g) arrival, so sufficient path averaging may or may not have occurred to make coda useful for estimating source spectra. However, Mayeda (1993) showed that magnitudes of NTS explosions based on regional L_g coda were a factor of 5 more consistent between stations than were magnitudes based on direct L_g. Hartse et al. (1995) demonstrated that spectral ratio discriminants were effective using far local to near regional coda data from NTS explosions and nearby earthquakes. Finally, Mayeda and Walter (1996), showed that the empirical Green's function technique could be used to obtain absolute spectra and study source character using regional coda from western U.S. earthquakes and explosions.

In this study, we apply coda techniques to regional distance, central Asia events recorded at stations MAKZ, WMQ and LZH (Figure 1). We hoped to confirm the stability of coda in this region, or, if not, to work out ways to correct the results so that reliable magnitude estimates can be obtained. To do this, we processed over 3000 records from these stations, obtaining coda decay curves in bands from 20 s to 6 Hz (Figure 1). Here, we present results of analyzing vertical component data in the band 0.7 to 1 Hz.

To calibrate the coda, we follow the method of Mayeda et al., (2000). First, coda decay, b, is determined as a function of distance, Δ,

$$A(t)=A_0\, t^{-0.83} \exp -b(\Delta)t,$$

via a linear fit (Figure 2). We then obtain coda source factors (A_0) by re-fitting the coda decay data with the predicted $b(\Delta)$. The coda source factors are further corrected based on a linear fit of A_0-m_b (PDE) versus distance (Figure 2). Looking for trends in the coda source factors after subtracting an estimate of source size is the technique we will later use to examine other possible effects on the coda. The distance-corrected coda source factors can be converted to magnitude by another linear fit. We plot the raw, distance-corrected coda source factors for events common to MAKZ and WMQ in Figure 3, along with m_b estimates derived from direct L_g. The inter-station scatter of the coda measurement is a factor of 2 lower than that of L_g. The improvement from coda is not as dramatic as in the western U.S. results of Mayeda (1993); however central Asia is one of the most heterogeneous regions on earth, which may present difficulty to the coda method.

We searched for other effects on the coda in this data set. First, we found that the coda length influences the coda source factors (Figure 4) in a way that is consistent with the well-known lapse time effect (Roecker et al., 1982). Coda decay generally does not fit the single scattering model, on which our fitting equation is based, over long time intervals. The coda decays more quickly early on and more slowly, later, which can be due to penetration to higher Q depths (for S coda) or to multiple scattering. This results in a curve-fitting problem and overestimation of coda source factors for long codas. This effect can be corrected for, but the resulting inter-station consistency does not improve (Figure 4). The lack of improvement occurs because corrections are correlated between stations, as shown by stick and histogram diagrams. We address this problem by limiting coda lengths to 30 to 150 s following the L_g arrival in the remainder of the study.

Because we measure the coda so close to the L_g arrival, we might expect path effects to be present in the results. To examine this, we interpolate distance-corrected coda source factors after subtracting m_b (PDE) using kriging (Schultz et al., 1998), (Figure 5). Results show strong laterally varying effects that correlate well with known L_g path effects in this region (Phillips, 1999). Again, these effects can be corrected, but we obtain little improvement in inter-station consistency due to correlated adjustments (Figure 6). To compare coda and direct L_g on the same basis, kriged corrections were generated and applied to the direct L_g results, which show improved inter-station consistency (Figure 6). The path-corrected coda results are now less than a factor of 2 more consistent than those of direct L_g.

Results for events common to WMQ and LZH show higher levels of scatter (Figure 6). After path correction, these coda results are only slightly more consistent than those of direct L_g.

CONCLUSIONS AND RECOMMENDATIONS

Coda estimates show up to a factor of 2 improvement in inter-station consistency relative to direct L_g. This is more likely the result of a higher precision coda estimate, which employs multiple, independent measurements. Path effects are not eliminated in regional coda as well as for local coda. Such path effects can be corrected for using interpolation methods in the same manner as has been previously demonstrated for direct waves. Coda lengths also introduce bias through deficiencies of the fitting equation in light of the lapse time effect on coda decay. This can be accounted for by a more general fitting equation or by limiting the coda interval. The inter-station consistency is often used to demonstrate the ability of coda methods; however, the biases we find are correlated between stations and, thus, have little effect on consistency. Comparing coda results to independently derived moments (Mayeda et al., 2000) is a more effective way to demonstrate the power of coda methods.

REFERENCES

Aki, K. (1969), Analysis of the seismic coda of local earthquakes as scattered waves, *J. Geophys. Res*., **74**, 615-631.

Aki, K., (1980), Physical basis of the duration magnitude and recommended practice for coda magnitude determination, *Proc. 17th Ass. ESC, Budapest*, 73-77.

Aki, K. and B. Chouet (1975), Origin of coda waves: Source, attenuation and scattering effects, *J. Geophys. Res*., **80**, 3322-3342.

Bisztricsany, E.A. (1958), A new method for the determination of the magnitude of earthquakes, *Geofiz. Kozlem.*, **7**, 2.

Chouet, B., K. Aki and M. Tsujirua (1978), Regional variation of the scaling law of earthquake source spectra, *Bull. Seism. Soc. Am*., **68**, 59-79.

Hartse, H.E., W.S. Phillips, M.C. Fehler and L.S. House (1995), Single-station spectral discrimination using coda waves, *Bull. Seism. Soc. Am*., **85**, 1464-1474.

Mayeda, K. (1993), $m_{bLgcoda}$: A stable single station estimator of magnitude, *Bull. Seism. Soc. Am*., **83**, 851-861.

Mayeda, K., A. Hofstetter, W.R. Walter and A. Rodgers (2000), Stable source estimates using regional narrow band coda envelopes: Application to CTBT monitoring and seismic hazard prediction in the Middle East region, *Seism. Res. Lett*., **71**, 209-210.

Mayeda, K. and W.R. Walter (1996), Moment, energy, stress drop and source spectra of western United States earthquakes from regional coda envelopes, *J. Geophys. Res*., **101**, 11195-11208.

Phillips, W.S. (1999), Empirical path corrections for regional phase amplitudes, *Bull. Seism. Soc. Am*., **89**, 384-393.

Rautian, T.G. and V.I. Khalturin (1978), The use of the coda for determination of the earthquake source spectrum, *Bull. Seism. Soc. Am*., **68**, 923-948.

Roecker, S.W., B. Tucker, J. King and D. Hatzfeld (1982), Estimates of Q in Central Asia as a function of frequency and depth using the coda of locally recorded earthquakes, *Bull. Seism. Soc. Am*., **72**, 129-149.

Schultz, C., S. Myers, J. Hipp and C. Young (1998), Nonstationary Bayesian kriging: Application of spatial corrections to improve seismic detection, location and identification, *Bull. Seism. Soc, Am.,* **88**, 1275-1288.

Tsujiura, M. (1978), Spectral analysis of the coda waves from local earthquakes, Bull. Earth. Res. Inst., U. Tokyo, 53, 1-48.

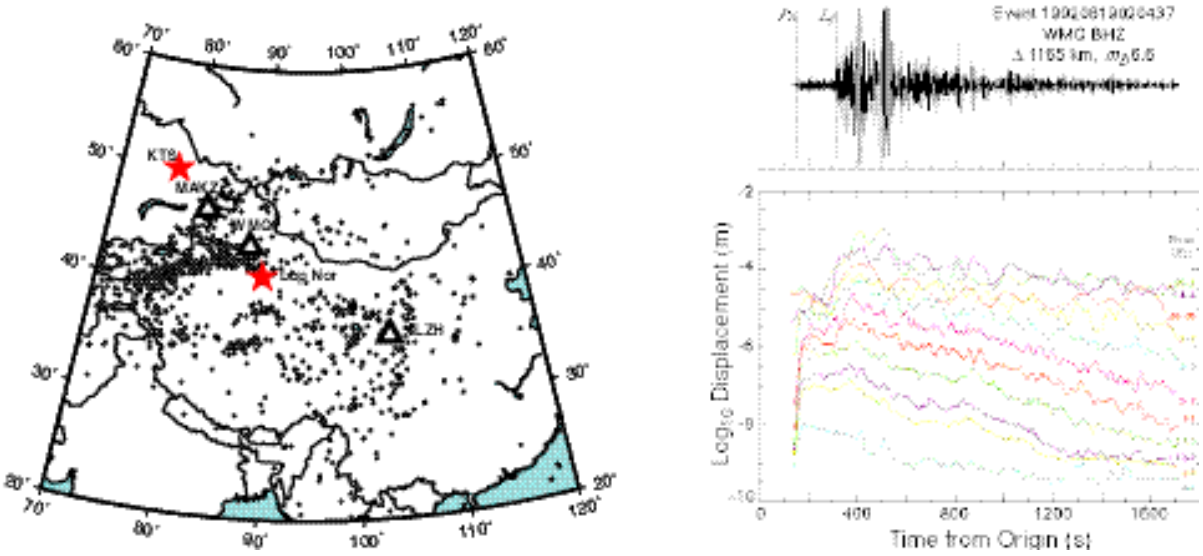


Figure 1. Map showing stations and events used in the study (left) and a sample event with coda decay curves in various bands (right). Energy arriving from a secondary event can be seen at 800 s, illustrating the high level of quality control that must be applied to coda data.

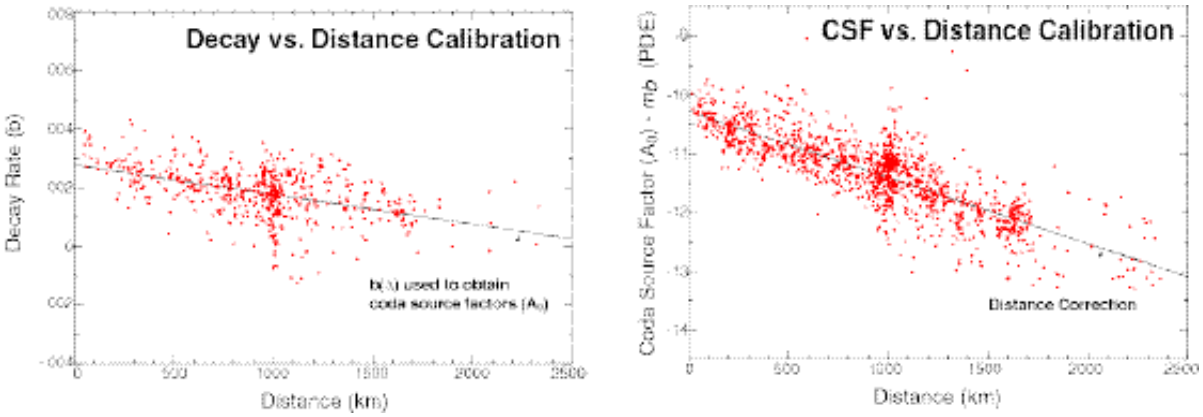


Figure 2. Calibration of 1 Hz band coda data from station WMQ. The temporal decay term is shown versus distance (left) along with a linear fit used to predict decay in the final fit. The fit amplitude or coda source factor is plotted versus distance (right) along with the linear fit used to correct for distance.

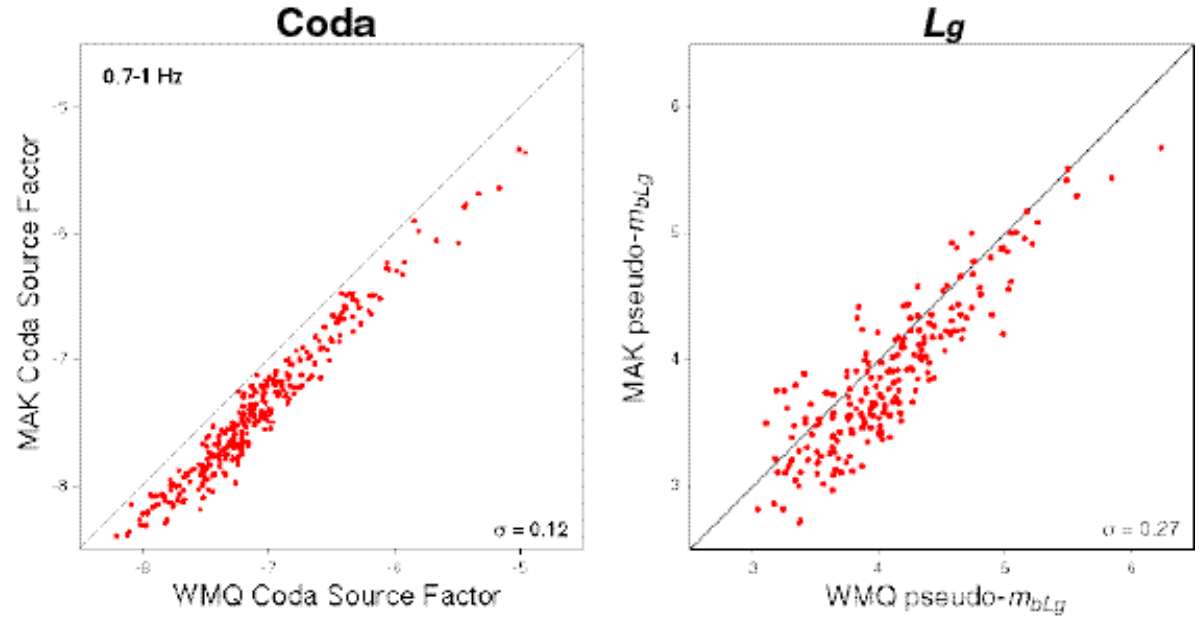


Figure 3. Distance-corrected, 1 Hz coda source factors (left) and m_{bLg} calculated using a Q of 400 (right) for events recorded at MAKZ and WMQ. The σ values give standard deviations of the differences between stations, representing the scatter around the mean offset, which is a site effect. Pseudo refers to slight processing differences from traditional m_{bLg}.

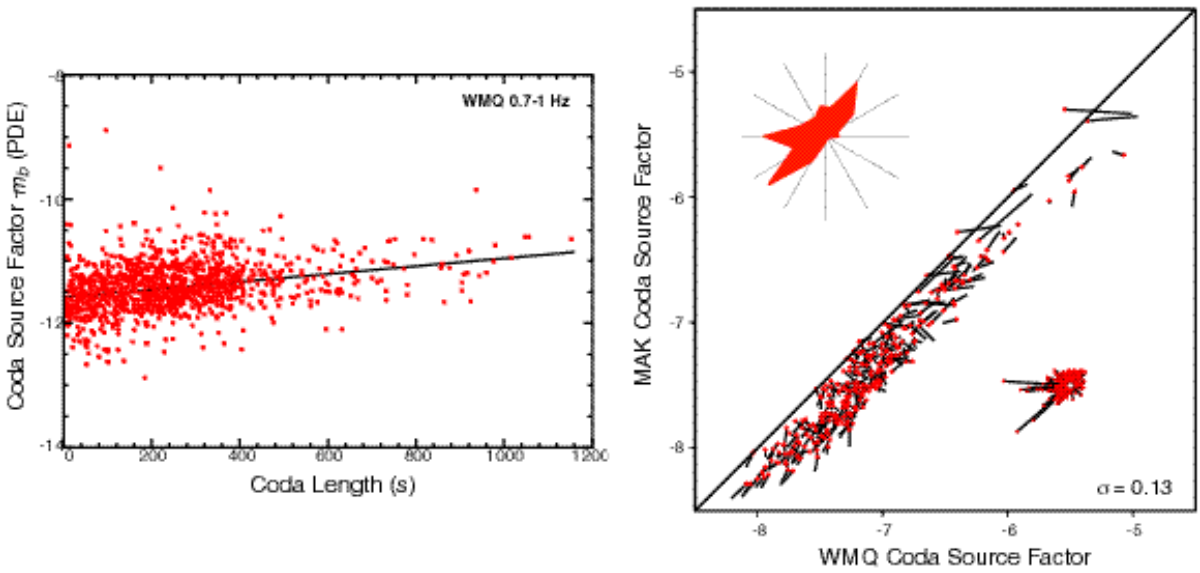


Figure 4. The effect of coda length on distance-corrected coda source factors (left) and corrected values for events recorded at MAKZ and WMQ (right). Open circles represent original values and red dots represent corrected values in the right hand plot. Stick and rose diagrams show that the corrections are somewhat correlated between stations.

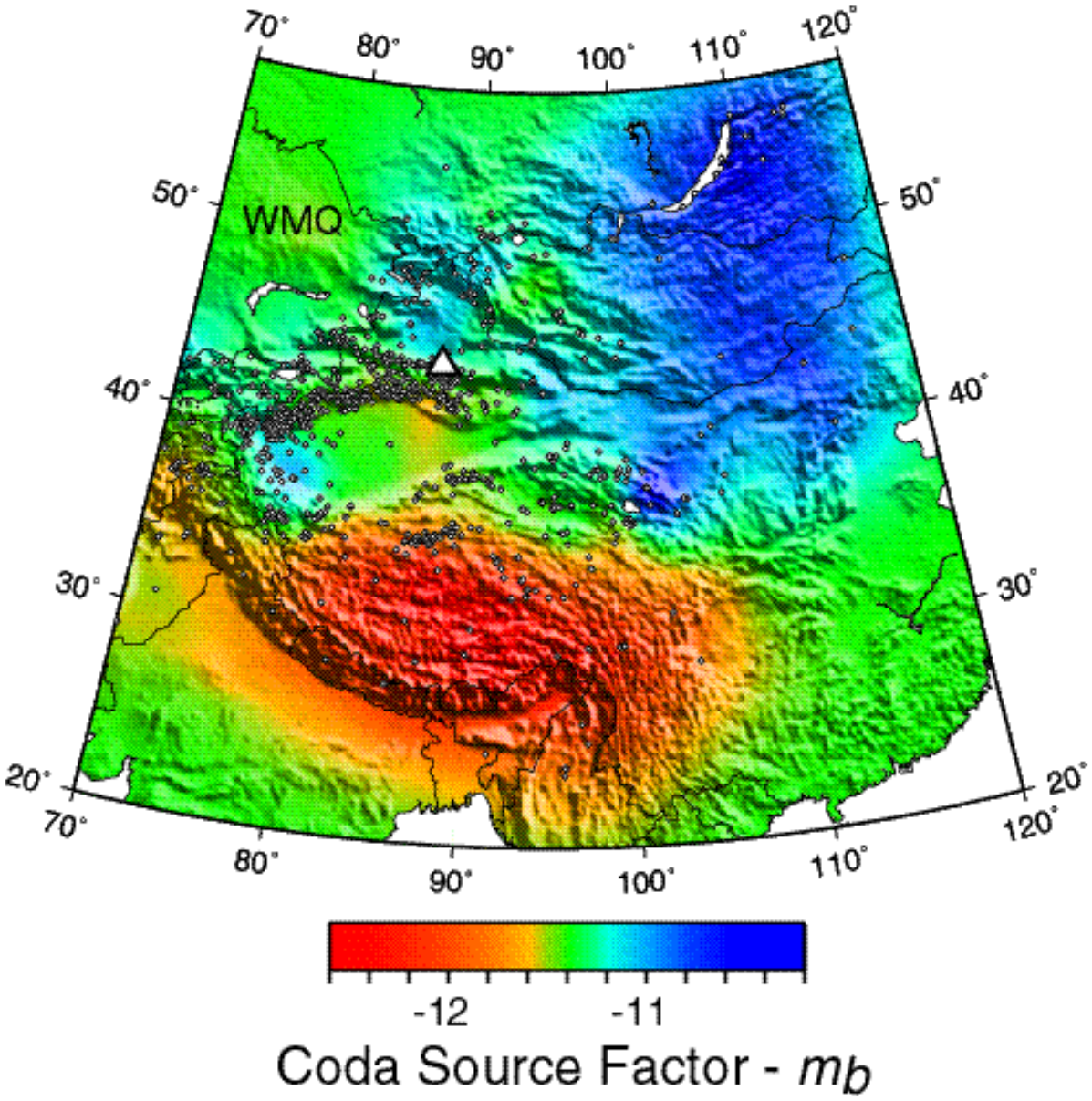


Figure 5. Interpolated (kriged) coda source factors for WMQ, less m_b (PDE), representing path effects on the L_g coda. Events used in the interpolation are shown as open circles. A mean value (green) is indicated in areas where events do not exist. For a particular event, the path correction is calculated by kriging without including that event.

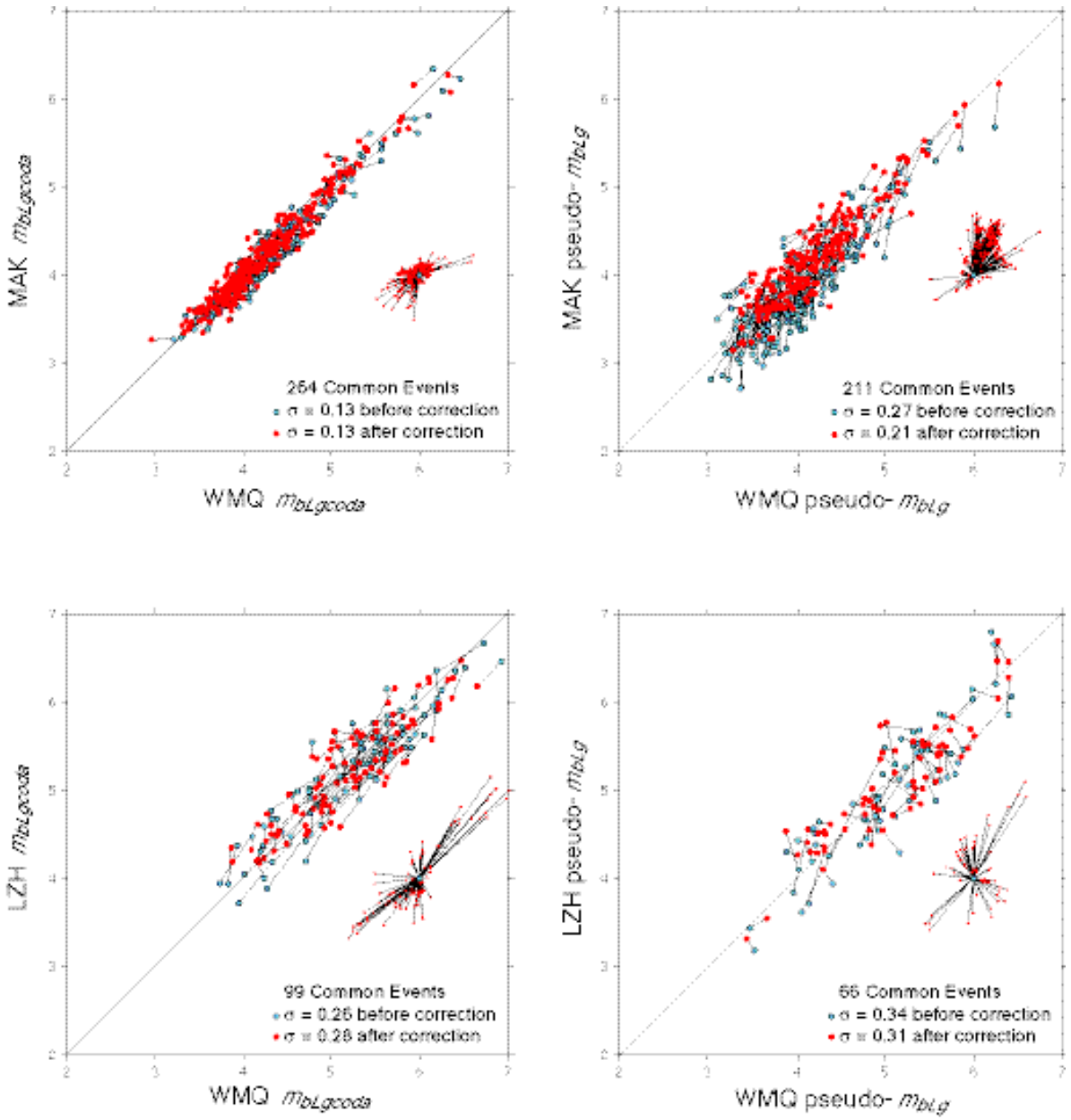


Figure 6. Path correction applied to coda (left) and m_{bLg} (right) for events common to MAKZ and WMQ (top) and LZH and WMQ (bottom). Blue dots represent original values and red dots represent corrected values. Stick diagrams summarize the corrections. Values have been tied to PDE m_b. Site offsets have been removed by the tie to m_b.

ESTIMATES OF P_n AND S_n ACROSS EURASIA

Michael H. Ritzwoller, Mikhail P. Barmin, Anatoli L. Levshin, Antonio Villaseñor, and E. Robert Engdahl

University of Colorado at Boulder

Sponsored by the Defense Threat Reduction Agency
Arms Control Technology Division
Nuclear Treaties Branch

Contract No. DTRA 01-00-C-0013

ABSTRACT

As an intermediate step to producing a integrated P and S model of the crust and upper mantle beneath most of Eurasia to predict regional station specific travel time correction surfaces, we present maps of isotropic P_n and S_n velocities across Eurasia. These maps are constructed using a groomed version of the ISC/NEIC data that are described, in part, by Engdahl et al. (1998). The locations and origin times of the events are replaced with local ground truth locations whenever possible (e.g., Sultanov et al., 1999). We use the tomographic method of Barmin et al. (2000) to estimate P_n and S_n maps on a $1.5^\circ \times 1.5^\circ$ grid, augmented to include station and event static corrections and an epicentral distance or range correction. The starting model is CRUST5.1 (Mooney *et al.*, 1998). We call the P_n and S_n maps together with these corrections the CU P_n/S_n model. Data are used in the inversion if the residual relative to the prediction from the spherical model AK135 (Kennett et al., 1995) is less than 7.5 s for P and 15 s for S, if the event depth is within the crust or less than 50 km deep, if the azimuthal gap to all reporting stations for the event is less than 180 degrees, and if the nominal error ellipse is less than 1000 km^2 in area. We define the phases P_n and S_n as arriving between epicentral distances of 3° and 15°. The resulting data set consists of about $1,600,000$ P_n and $400,000$ S_n travel times inhomogeneously distributed across Eurasia. The P_n and S_n maps compare favorably with recent 3-D models P and S in the uppermost mantle estimated from different data sets (Bijwaard *et al.*, 1998; Villaseñor et al., 2000a) and with recently compiled teleseismic station corrections across the region (Engdahl and Ritzwoller, 2000). The rms misfit to the entire Eurasian data set from the CU P_n/S_n model is 1.8 s for P_n and 3.8 s for S_n. The P_n rms misfit reduces to $\sim$1.7 s for certain high quality subsets of the entire Eurasian data set. We present examples of travel time correction surfaces for several IMS stations or surrogates computed to epicentral distances of 15°. This method will be applied to compute travel time correction surfaces for the remaining IMS stations or surrogates across Eurasia. These correction surfaces will provide an important reference for 3-D models to match and extend.

Key Words: location, Eurasia, P_n, S_n, correction surfaces

OBJECTIVE

The objective of this research is to develop and test a method to produce P_n and S_n station specific travel time correction surfaces across much of Eurasia. This method will be applied systematically to compute correction surfaces for the remaining IMS stations or surrogates across Eurasia to epicentral distances of 15°. These correction surfaces will provide an important reference for emerging 3-D models to match and extend.

RESEARCH ACCOMPLISHED

Introduction

Determination of accurate seismic locations and uncertainties is of prime importance in monitoring the Comprehensive Nuclear Test-Ban Treaty (CTBT). Small magnitude events will only be recorded at a sparse subset of the International Monitoring System (IMS) at regional distances less than 20° - 30°. Sparse network locations are subject to significant bias due to regional variations in the structure of the crust and upper mantle. To meet the goals of the CTBT for these small events, this bias must be substantially reduced in regions of significant structural variability such as that in evidence across much of Eurasia. To do so will require either a model of the 3-D structures or the effects of the structures on the relevant travel-times.

Our ultimate goal is to produce a 3-D P and S model of the crust and uppermost mantle on a $1° \times 1°$ grid beneath N. Africa, the Middle East, and Central Asia that will accurately predict regional travel time variations and improve regional location capabilities. Villaseñor *et al.* (2000a) describe the construction of an S model from surface wave measurements. In order to predict regional S travel times accurately and to convert this model to P, the model will require further calibration using regional body wave travel time data. The study presented here is the first step in this direction. Our approach is not to begin by calibrating the model itself, but rather to calibrate the travel time correction surfaces (e.g., Myers and Schultz, 2000) computed from the model. To do this requires independent estimates of correction surfaces using regional P_n and S_n data. In this paper, we (1) discuss the data set and method used to estimate these correction surfaces, (2) show the first continental scale images of P_n and S_n variations across Eurasia, (3) display the resulting correction surfaces for several IMS surrogate stations, and (4) discuss the fit to the regional phase data.

Data

P_n and S_n travel times are taken from a groomed version of the ISC and NEIC data bases described, in part, by Engdahl *et al.* (1998). ISC travel times are for events that occurred from 1964 through 1997 and NEIC data are from 1998 and 1999. The locations of explosions are replaced with "ground truth" locations whenever possible (e.g., Sultanov et al., 1999). We define the phases P_n and S_n as arriving between epicentral distances of 3° and 15°. At epicentral distances beyond about 10°, however, P_n and S_n may dip into the mantle. The depth of penetration will depend on the radial gradient of velocity, which will vary spatially. Truncation of the data set to include rays only if epicentral distances are less than ∼12°, as in some other studies (e.g., Hearn and James, 1994), severely restricts path coverage in some areas of Eurasia. To utilize longer paths it is desirable to correct for the effect of ray penetration into the uppermost mantle. We discuss the range correction in the next section entitled "Method". This data set totals $3,672,268$ P_n phases and $1,346,676$ S_n phases for $5,418$ stations and 149,929 events worldwide. Data are used in the inversion if the residual relative to the prediction from the spherical model AK135 (Kennett et al., 1995) is less than 7.5 s for P and 15 s for S, if the event depth is within the crust or less than 50 km deep, if the azimuthal gap to all reporting stations for the event is less than 180 degrees, and if the nominal error ellipse is less than 1000 km^2 in area. These selection criteria reduce the data set to $1,636,430$ P_n and $493,734$ S_n phases worldwide. Most of these paths cross Eurasia (0° - 80°N latitude and -10°W - 180°E longitude plus a buffer zone), the numbers being $1,257,052$ for P_n and $422,634$ for S_n.

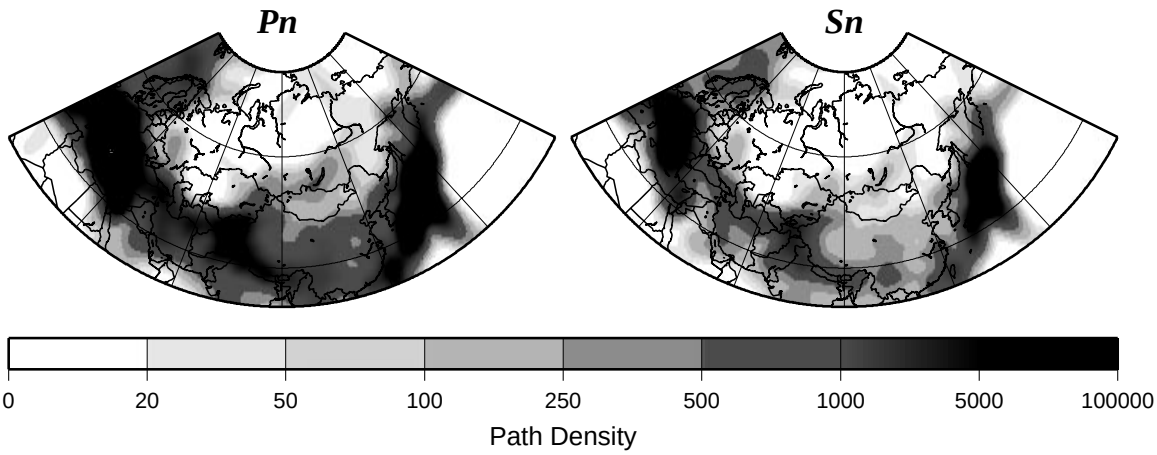


Figure 1: Path density for the P_n and S_n data used here, defined as the number of paths intersecting a $2^\circ \times 2^\circ$ cell ($\sim$50,000km^2). Because path lengths for these phases are by definition short ($< 15^\circ$), paths only exist in regions where both sources and receivers are common. Thus, the path distribution is highly heterogeneous across the region.

Method

The P_n and S_n maps are defined over a two-dimensional surface and, therefore, may be estimated with the same method we developed for surface wave tomography (Barmin *et al.*, 2000). In this method, the model is constructed on an equally spaced grid such that the following figure-of-merit is minimized:

$$(\mathbf{Gm}-\mathbf{d})^T\mathbf{C}^{-1}(\mathbf{Gm}-\mathbf{d}) + \sum_{k=0}^{n}\alpha_k^2||F_k(\mathbf{m})||^2 + \sum_{k=0}^{n}\beta_k^2||H_k(\mathbf{m})||^2, \tag{1}$$

which is a linear combination of data misfit, model roughness, and the amplitude of the perturbation to a reference model. The vector $\mathbf{m}$ represents the estimated model which is a perturbation relative to a reference across the region of interest, $\mathbf{G}$ is the forward operator that computes travel time from the estimated model, $\mathbf{d}$ is the data vector, $\mathbf{C}$ is the data covariance matrix or matrix of data weights, F is a Gaussian smoothing operator, and H is an operator that penalizes the norm of the model in regions of poor path coverage. The spatial smoothing operator is defined over the 2-D model as follows

$$F_k(\mathbf{m}) = m_k(\mathbf{r}) - \int_S S_k(\mathbf{r},\mathbf{r}')m_k(\mathbf{r}')d\mathbf{r}' \ , \tag{2}$$

where S_k is a smoothing kernel:

$$S_k(\mathbf{r},\mathbf{r}') = K_{0k}\exp\left(-\frac{|\mathbf{r}-\mathbf{r}'|^2}{2\sigma_k^2}\right) \tag{3}$$

$$\int_S S_k(\mathbf{r},\mathbf{r}')d\mathbf{r}' = 1, \tag{4}$$

and σ_k is the spatial smoothing width or correlation length. The minimization of the expression in equation (2) explicitly ensures that the estimated model approximates a smoothed version of the model. The maps are estimated on a $1.5^\circ \times 1.5^\circ$ grid across Eurasia.

Barmin *et al.* (2000) discuss tomographic inversions of group and phase velocity data in detail. The inversion for P_n and S_n is essentially the same except that from the reference crustal model we compute source and receiver side Moho penetration points and use these points as the starting and ending points of the ray during inversion. P_n and S_n rays are assumed to be horizontal in a spherical mantle. We have used CRUST5.1 as the reference model in the crust and for P_n and S_n. In addition, we estimate a

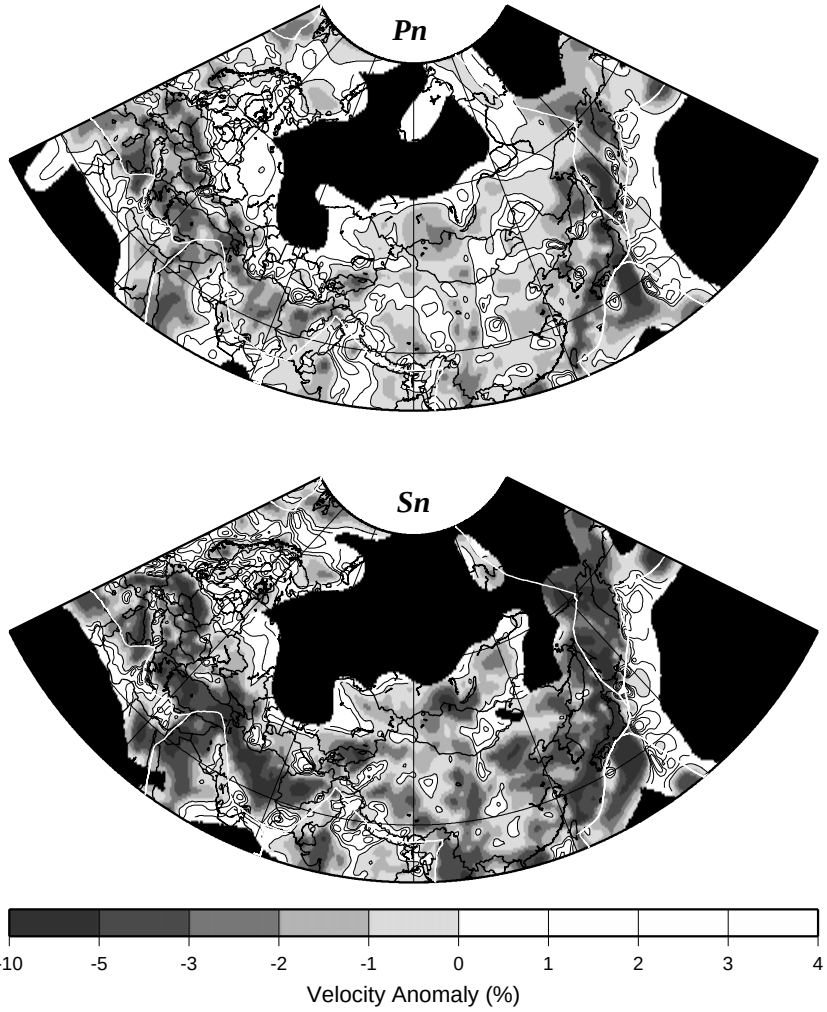


Figure 2: P_n and S_n maps estimated across Eurasia represented as the deviation from the mean across each map in percent. P_n is relative to 8.052 km/s, and S_n is relative to 4.583 km/s. We consider regions in which path density is less than 20 paths/50,000km^2 to be unconstrained by the data, and these regions are shaded black.

range correction and, following Hearn and collaborators (e.g., Hearn and Clayton, 1986; Hearn *et al.*, 1991; Hearn and James, 1994; and elsewhere), we also estimate event and station statics. The range correction is designed to compensate for the fact that rays are not horizontal in the uppermost mantle, but systematically dip further into the mantle as propagation distances increase. This allows us to fit data to greater ranges than is possible without this correction. With this correction, the resulting tomographic maps agree well with those produced with short path data alone (epicentral distances less than 10°) in those regions where tomographic maps can be constructed reliably using only the short path data.

The observed travel time, t_{obs}, is, therefore, modeled as follows:

$$t_{obs} = t_m + t_{crust_sta} + t_{crust_evt} + \delta t_{sta} + \delta t_{evt} + \delta t(\Delta) + \int_p \frac{ds}{v_m}, \tag{5}$$

where t_m is the predicted travel time for horizontal rays through the mantle part of the reference model CRUST5.1, the contributions to the travel time due to the reference crustal model CRUST5.1 on the source and event sides are t_{crust_sta} and t_{crust_evt}, the station and event statics are δt_{sta} and δt_{evt}, $\delta t(\Delta)$ is the distance correction, v_m is the estimated velocity at the top of the mantle, and p denotes the appropriate path linking source and receiver through the mantle. Thus, $t_m, t_{crust_sta}, t_{crust_evt}$, and p are predicted by the

reference model and $\delta t_{sta}, \delta t_{evt}, \delta t(\Delta)$, and v_m are estimated. A static correction is estimated for a station if there are phase picks from at least 7 events made at that station and an event correction is estimated for all events for which there are at least 20 reporting stations. The asymmetry in this condition is due to the fact that there are more physical phenomena modeled with the event static than with the station static (e.g., mislocation, origin time error). The station and event statics are undamped at present.

We will refer to the P_n and S_n maps together with the corrections $\delta t_{sta}, \delta t_{evt}$, and $\delta t(\Delta)$ as the CU P_n/S_n model to distinguish it from our recent 3-D models (e.g., Villaseñor *et al.*, 2000a).

P_n and S_n Tomography

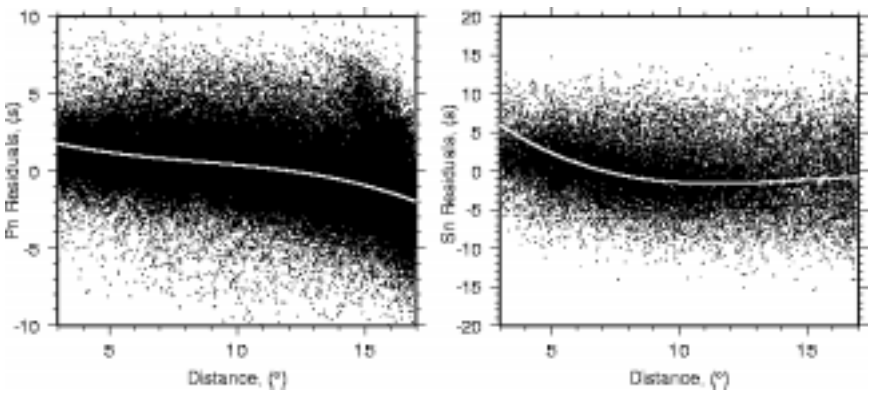


Figure 3: Raw residuals computed for the entire data set using only the P_n and S_n maps shown in Figure 2; these residuals do not include static or range corrections. The white lines are cubic polynomial fits to these data and define the range corrections $\delta t(\Delta)$.

Table 1. Summary of the distribution of station and event statics world-wide.

	P_n		S_n	
static correction	*station (#)*	*event (#)*	*station (#)*	*event (#)*
total	5418	149929	3781	99385
with correction	3295	73587	1780	23737
no correction	2123	76332	2001	75648
max. correction (s)	(-3.78,5.36)	(-6.156,6.89)	(-6.58,10.12)	(-14.56,16.51)
$\# < -2.0$ (s)	4	1396	65	2534
$-2.0 < \# < -1.5$ (s)	14	1884	49	1160
$-1.5 < \# < -1.0$ (s)	57	3781	99	1516
$-2.0 < \# < -0.5$ (s)	177	6801	161	1856
$-0.5 < \# < 0.0$ (s)	580	9890	214	2239
$0.0 < \# < 0.5$ (s)	927	12061	276	2494
$0.5 < \# < 1.0$ (s)	796	12959	231	2358
$1.0 < \# < 1.5$ (s)	425	10913	172	2186
$1.5 < \# < 2.0$ (s)	178	6897	138	1867
$\# > 2.0$ (s)	137	7015	375	5527

The estimated P_n and S_n maps are shown in Figure 2. The velocity anomalies correlate well with known tectonic features and the P_n and S_n maps compare favorably with one another and with the patterns of velocity variations in the 3-D shear velocity model of Villaseñor *et al.* (2000a) and the teleseismic P wave model of Bijwaard and Spakman (1998). Because our tomographic method penalizes the amplitude of the maps in regions of poor data coverage and the estimated maps are perturbations to a reference state, the maps revert to the reference model where data coverage is poor; i.e., less than 15 - 20 paths per each $2^\circ \times 2^\circ$ cell. The areas of poor data coverage are identified as black regions in Figure 2. Both the P_n and S_n maps demonstrate poor coverage across the shield and platform regions of northern Russia and Kazakhstan, in the

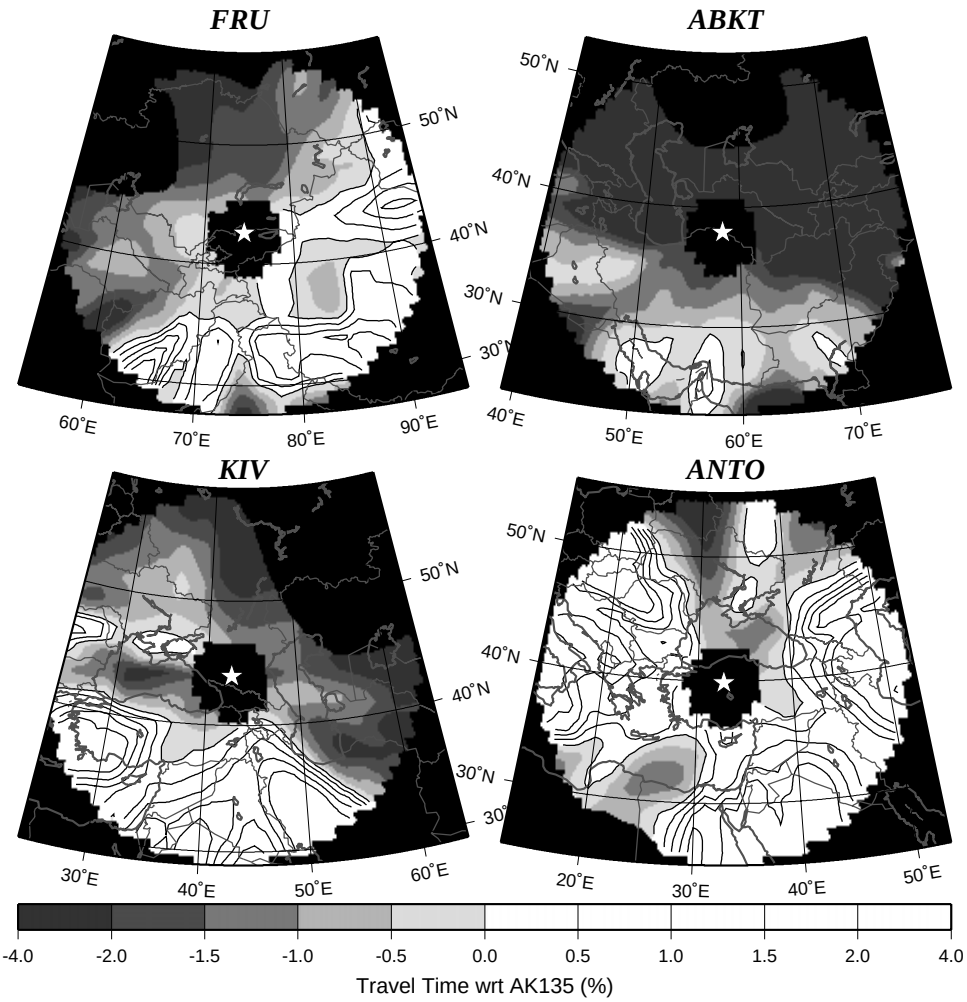


Figure 4: Station specific travel time correction surfaces for P_n for four IMS stations or surrogates (FRU $\rightarrow$ AAK, ANTO $\rightarrow$ BRAR, KIV $\rightarrow$ KBZ). Surfaces exist only where P_n data density is locally greater than 20 paths per 50,000 km^2 and to 15° from the station. Low data density regions are shaded black.

oceans, and across North Africa. Elsewhere the spatial resolution of the maps is estimated to be between 150 - 300 km.

The range correction is shown in Figure 3. This figure shows that mispicks from the triplication from the 400 km discontinuity begin to emerge in the data set at about 15°, which is the reason we have limited the P_n and S_n maps to this distance. The number of S_n picks reduces sharply after about 10°. Station and event statics, δ_{sta} and δ_{evt}, are summarized in Table 1 for the entire data set world-wide. Although for P_n we estimate static corrections only for about 60% of the stations and half of the events world-wide and for S_n the numbers are about 50% and 25%, respectively, the great majority of the measurements emanate from events and are recorded at stations that have static corrections. This is particularly true for P_n, where only 3% of the measurements are made at stations without static corrections and 12% of the measurements are for events without event corrections. For S_n, the numbers are 4% and 33%, respectively. Thus, most measurements have the full complement of corrections applied. Not surprisingly, statics for S_n are typically larger than for P_n and event statics are larger than station statics. This is because S variations in the crust and upper mantle are typically larger than P by about a factor of two and, in addition to compensating for errors in the crustal model, event statics also compensate for mislocations and origin time errors. Event statics also are more effective at reducing rms misfit. Although not shown here, the P_n and S_n station statics are geographically coherent and correlate with one another with a poorly determined S/P ratio of about 1.8.

However, because the statics are determined simultaneously their values are interdependent and difficult to interpret in abstraction from the others. In addition, because we have not constrained the values of the static corrections, in some cases they are probably too large in magnitude, particularly S_n event statics.

Figure 4 displays station specific travel time correction surfaces for several IMS stations or surrogates. These surfaces are for surface sources with the local elevation observed at the station elevation. This differs from correction surfaces as they are commonly displayed in which both the source and station are on the reference ellipsoid. The correction surface for ANTO (Ankara, Turkey) compares favorably with the surfaces from two nearby stations in Turkey (KAS, KVT) reported by Myers and Schultz (2000) using a different method.

Fit to the Data

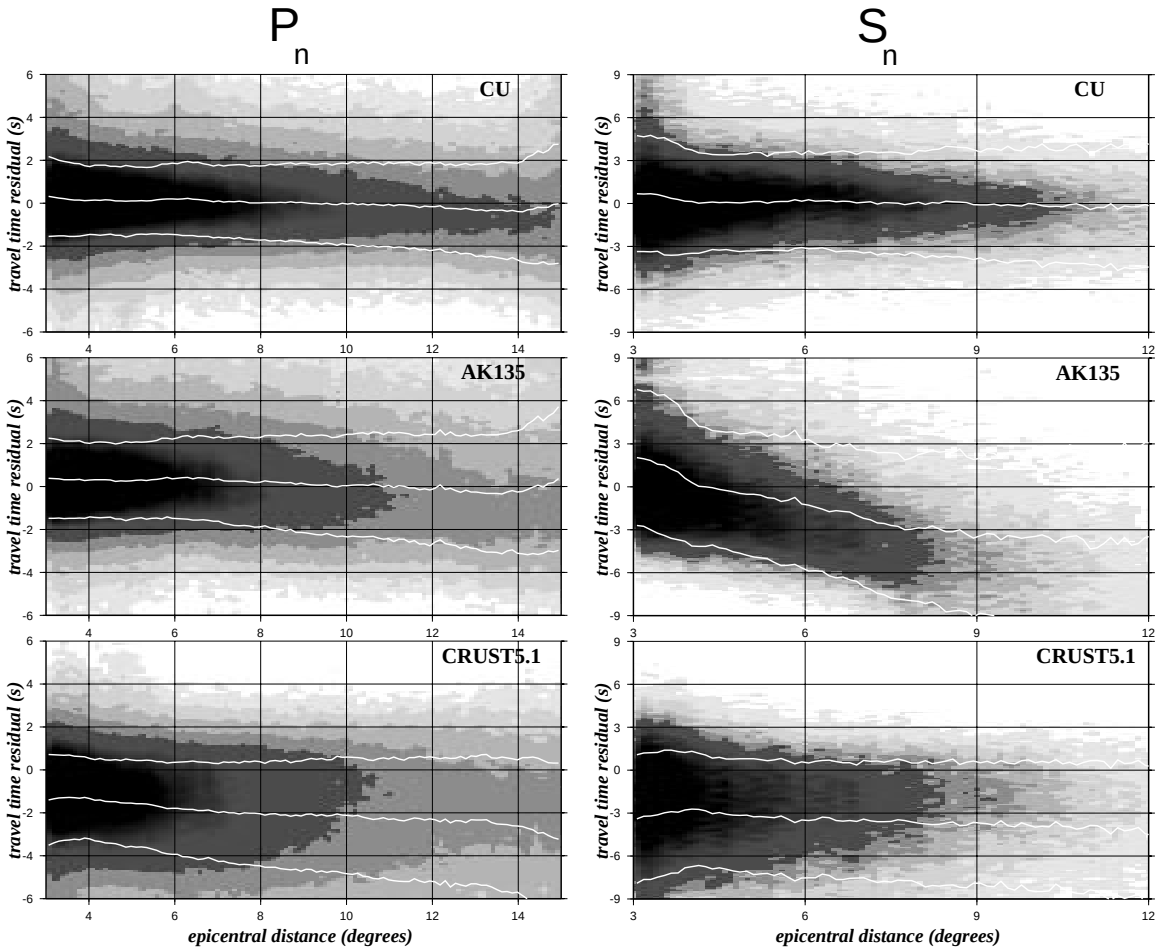


Figure 5: Shaded plots of the density of P_n and S_n travel time residuals (observed - predicted) for the Eurasian data set presented versus epicentral distance. Results for three models are shown: (TOP) the CU P_n/S_n model, (MIDDLE) the spherically symmetric model AK135 (Kennett *et al.*, 1995), and (BOTTOM) the laterally heterogeneous crustal, P_n, and S_n model CRUST5.1 (Mooney *et al.*,1998). Darker shades indicate larger number of residuals and the white lines show the local mean and $\pm 1\sigma$. Means and standard deviations are summarized in Table 2.

Table 2. Summary of misfits to the whole Eurasian data set displayed in Figure 5.

	P_n		S_n	
model	*mean (s)*	σ *(s)*	*mean (s)*	σ *(s)*
CU P_n/S_n	0.06	1.81	0.12	3.83
AK135	0.23	2.06	-0.94	5.36
CRUST5.1	-1.80	2.37	-4.03	5.14

Misfits to the entire Eurasian data set for P_n and S_n are shown in Figure 5 and summary statistics are presented in Table 2. The standard deviation σ reported in Table 2 is computed relative to the mean, so total rms misfit must incorporate the mean. In general, short distance offsets result from errors in the crustal model either in average crustal velocities or Moho depths. Errors in the uppermost mantle velocities manifest themselves as trends with distance. The model AK135 does very well for P. Improvements afforded by the CU P_n/S_n model over AK135 on average begin only after about 8°. However, on average, for both P and S CRUST5.1 is too slow in the crust whereas AK135 is fine for P but too fast for S. CRUST5.1 displays only weak distance trends which indicates that the average upper mantle velocities are reasonable, but AK135 is too slow for S_n, demonstrating a very strong trend. This indicates that uppermost mantle S velocities in AK135 are too slow on average for Eurasia or the depth gradient in the uppermost mantle is not right. The overall rms misfit from our inversions is 1.8 s across all of Eurasia for P_n and approximately twice this value for S_n. These misfit statistics appear to be consistent with those reported by Myers and Schultz (2000) in a study limited to the neighborhood of the Racha earthquake sequence (Caucasus Mountains).

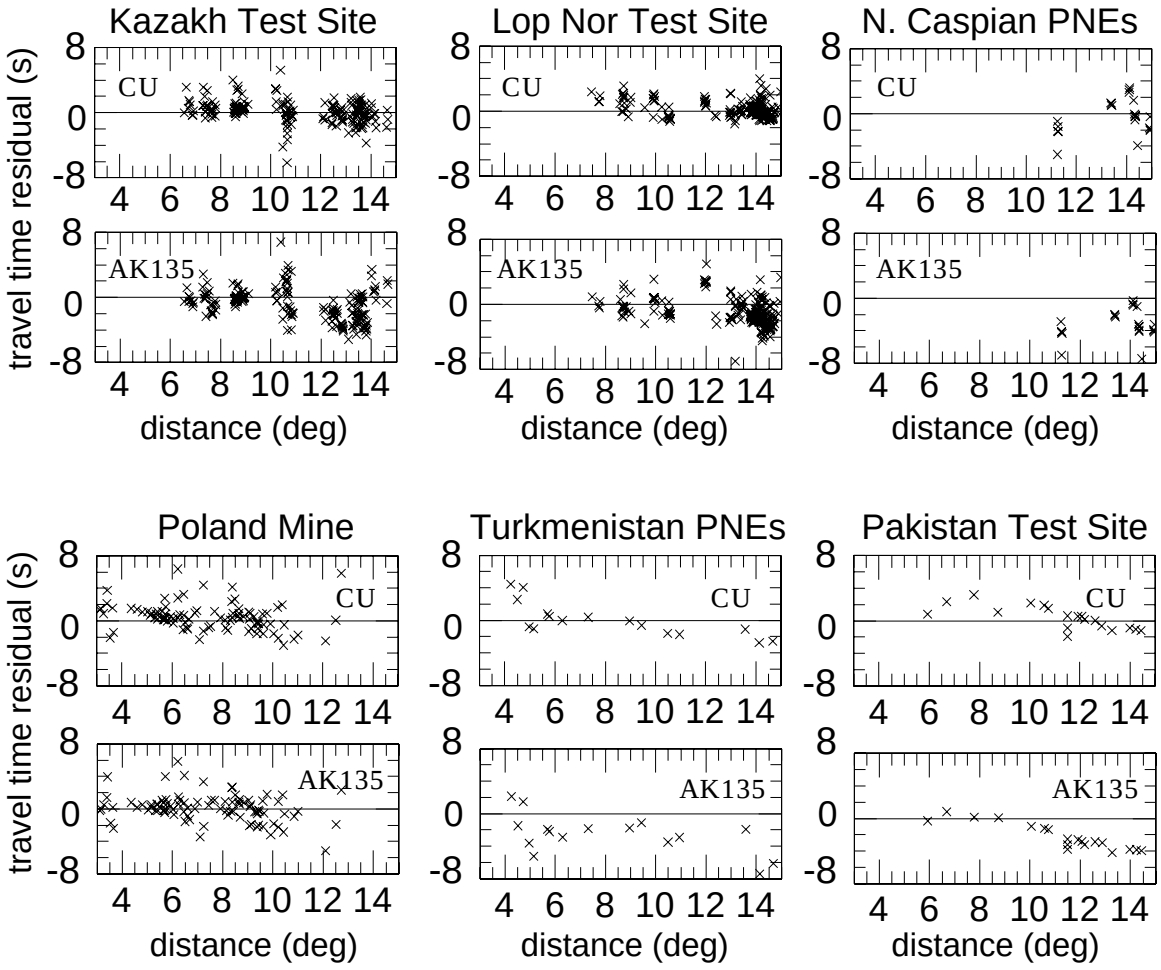


Figure 6: Misfits to P_n and S_n measurements from selected explosions that occurred at six source locations. The upper of each pair of plots for each source location is for the CU P_n/S_n model and the lower of each pair is for the model AK135 Summary statistics are presented in Table 3.

The entire Eurasian data set is very noisy and many locations and origin times are poorly known. A better estimate of expected misfit may come from explosion data in which in many cases the epicenter is well constrained, although the origin times may not be. Figure 6 displays misfits to data from six explosion regions (3 test sites, 2 PNE locations, and 1 large mine) and Table 3 summarizes these data. Only explosions with $m_b \geq 4.6$ as reported in the PDE are used. With the exception of the large mine explosion in south-

western Poland, these events are not observed at enough stations with regional phases to have event statics. The overall misfit of the CU P_n/S_n model to these explosion data is 1.68 s for P_n, which is slightly reduced over the entire Eurasian data set. For events at the three test sites, however, misfit is better than 1.45 s for P and the fit afforded by AK135 is considerably worse. Again, most of the improvement over AK135 delivered by the CU P_n/S_n model comes for paths longer than about 8°. A similar rms misfit of 1.7 s results from a subset of the complete Eurasian data set that consists only of events with $m_b \geq 4.6$ and measurements from events with an event correction measured at stations with a station correction.

Table 3. Summary of misfits to explosion data for P_n displayed in Figure 6.

				rms misfit (s)	
Location	# meas.	# stations	# events	CU P_n/S_n	AK135
Kazakh Test Site	189	18	42	1.38	2.08
Lop Nor Test Site	204	39	19	1.16	1.90
N. Caspian PNEs	22	7	6	2.10	3.72
Pakistan Test Site	19	18	2	1.43	2.72
Poland Mine	92	92	1	1.72	1.68
Turkmenistan PNEs	16	16	1	2.04	3.45
Total	542	-	-	1.68	2.71

CONCLUSIONS AND RECOMMENDATIONS

Conclusions

The method for producing P_n and S_n maps with associated parametric corrections appears to effectively summarize the information in the large groomed ISC/NEIC data base. The P_n and S_n maps correlate well with other high resolution information about structural variations in the uppermost mantle. The station specific travel time correction surfaces computed from the CU P_n/S_n model appear to be robust and fit the data with very low levels of bias at epicentral distances from 3° to 15°. Overall rms misfits across Eurasia for P_n are ~1.8 s and for S_n ~3.8 s and are better for data subsets chosen for their quality (e.g., explosions, large magnitude events, independent information about epicenter location and/or origin time). These misfits are considerably better than those produced by AK135 and CRUST5.1. The correction surfaces will provide an important reference for 3-D models to match and extend.

Recommendations

- **Continued development of the method.** Small modifications to the method may continue to improve the results. For example, although a better starting model of the mantle will not appreciably change the estimated P_n and S_n maps it may help to stablize the static corrections and the range correction. Also, the range correction, which exists to compensate for ray penetration into the mantle, may be improved if it depended on tectonic region because vertical gradients probably vary between tectonic regions.
- **Systematic application of this method to compute station specific travel time correction surfaces across Eurasia.** The method should be applied systematically across all of Eurasia to all IMS stations and surrogates as a reference for future studies.
- **Use of these correction surfaces to calibrate the correction surfaces computed from emerging 3-D models.** The computation of correction surfaces from 3-D models is technically straightforward (e.g., Villaseñor *et al.*, 2000b), but there are practical problems. For example, there are few constraints on variations in crustal velocities across most of Eurasia and the mantle model is probably more accurate in S than in P. Thus, raw predictions from existing models such as that of Villaseñor *et al.* (2000a) are not likely to be as accurate as desired. The correction surfaces shown here will help to calibrate the surfaces computed from 3-D models.

REFERENCES

Barmin, M.P., M.H. Ritzwoller, and A.L. Levshin, A fast and reliable method for surface wave tomography, *Pure and Appl. Geophys.*, in press, 2000.

Bijwaard, H., W. Spakman, and E.R. Engdahl, Closing the gap between regional and global travel time tomography. *J. Geophys. Res.*, **13**, 30055-30078, 1998.

Engdahl, E.R. and M.H. Ritzwoller, Crust and upper mantle P- and S-Wave delay times at Eurasian seismic stations, *Phys. Earth. Planet. Int.*, submitted, 2000.

Engdahl, E.R., R. van der Hilst, and R. Buland, Global teleseismic earthquake relocation with improved travel time and procedures for depth determination, *Bull. Seism. Soc. Am.*, **88**, 722 - 743, 1998.

Hearn, T., N. Beghoul, and M. Barazangi, Tomography of the Western United States from regional arrival times, *J. Geophys. Res.*, **96**, 16369 - 16381, 1991.

Hearn, T.M. and R.W. Clayton, Lateral velocity variations in Souther California. I. Results for the upper crust from P_g waves, *Bull. Seismc. Soc. Am.*, **76**, 495-509, 1986.

Hearn, T.M. and F.N. James, Pn velocities beneath continental collision zones: the Turkish-Iranian plateau, *Geophys. J. Int.*, **117**, 273-283, 1994.

Kennett, B.L.N., E.R. Engdahl, and R.Buland, Constraints on seismic velocities in the Earth from travel times, *Geophys. J. Int.*, **122**, 108-124, 1995.

Mooney, W.D., G. Laske, and G. Masters, CRUST 5.1: A global crustal model at 5 degrees by 5 degrees, *J. Geophys. Res.*, **103**, 727 - 748, 1998.

Myers, S.C. and C.A. Schultz, Improving sparse network seismic location with Bayesian kriging and teleseismically constrained calibration events, *Bull. Seism. Soc. Am.*, **90**, 199 - 211, 2000.

Sultanov, D.D., J.R. Murphy and Kh.D. Rubinstein, A seismic source summary for Soviet peaceful nuclear explosions, *Bull Seism. Soc. Am.*, **89**, 640-647, 1999.

Villaseñor, A., M.H. Ritzwoller, A.L. Levshin, M.P. Barmin, E.R. Engdahl, W. Spakman, and J. Trampert, Shear velocity structure of Central Eurasia from inversion of surface wave velocities, *Phys. Earth Planet. Int.*, submitted, 2000a.

Villaseñor, A., M.H. Ritzwoller, M.P. Barmin, E.R. Engdahl, and A.L. Levshin, Computation of travel times and station correction surfaces in Eurasia using three-dimensional velocity models, this volume, 2000b.

ANALYSIS OF THE NOVEMBER 1999 DEAD SEA CALIBRATION SHOTS

Arthur Rodgers, Stephen Myers, Kevin Mayeda and William Walter
Lawrence Livermore National Laboratory, Livermore, CA 94551 USA

Sponsored by U.S. Department of Energy
Office of Nonproliferation Research and Engineering
Office of Defense Nuclear Nonproliferation
National Nuclear Security Administration

Contract No. W-7405-ENG-48

ABSTRACT

In November 1999 three chemical explosions were conducted in the Dead Sea for the purposes of calibrating the International Monitoring System (IMS) for the Comprehensive Nuclear-Test-Ban Treaty (CTBT). These shots were organized and conducted by the Geophysical Institute of Israel (GII). Large chemical explosions are the most valuable form of ground truth as the location, depth and origin time are very well known. We focus on the two largest shots ($M_W \geq 3.6$) and performed several types of analysis of the regional recordings and travel times of these shots. These data provide valuable new information about the region and offer an opportunity to test monitoring strategies.

1) A crustal and uppermost mantle velocity model was inferred from the travel times of the regional phases: Pn, Pg and Sg. This effort utilized a grid search method to find suitable models of the structure. Results indicate that the crust is relatively thin (32 km) with lower than average crustal velocities (mean V_P = 6.1-6.2 km/s).

2) We located each shot treating the other shot as a calibration explosion. Locations were computed using both station static corrections and kriged correction surfaces. Results show that the locations with static corrections can be better or worse than the locations without corrections. However, the locations with kriged correction surfaces are consistently better than those without corrections or with static corrections because kriging properly accounts for residual statistics.

3) Measures of the S-wave coda for regional events provide a stable estimate of event size (moment magnitude, M_W) and the event source spectrum. S-wave coda envelope amplitudes were calibrated to moments estimated from long-period waveform modeling. We measured moment and body-wave magnitudes and source spectra for many events in the region. The Dead Sea shots show spectral peaking associated with shallow events.

4) Finally, analysis of regional broadband recordings from the Saudi Arabian National Seismic Network reveals spectral scalloping associated with the bubble pulse. The observed bubble pulse periods are consistent with theoretical predictions.

Research performed under the auspices of the U.S. Department of Energy by the Lawrence Livermore National Laboratory under contract W-7405-ENG-48. LLNL contribution UCRL-JC-138997.

Key Words: 1999 Dead Sea Shots, calibration shots, regional velocity models, regional location, regional discrimination

OBJECTIVE

The use of calibration explosions for seismic monitoring of a Comprehensive Nuclear-Test-Ban Treaty (CTBT) provides valuable empirical data and opportunities to test monitoring strategies. Calibration explosions offer a unique set of travel time and explosion source data of the highest quality of ground truth because the source location, depth and origin time are precisely known. For this reason calibration explosions are widely viewed to be the most desirable type of source for empirical calibration.

We analyzed seismic data from the November 1999 Dead Sea Shots to investigate several aspects of regional seismic monitoring. Travel times were used to develop a one-dimensional regional model for event location. Travel time correction methodologies and their effect on event location were tested. Regional S-wave coda moment magnitudes, M_W, scale were computed. Analysis of the source spectrum from S-wave coda waves revealed spectral peaking. This study makes use of the unique data set that the Dead Sea shots provided and demonstrates the importance and potential value of future calibration explosions.

RESEARCH ACCOMPLISHED

This study reports analysis of regional travel-time and waveform data from the November 1999 Dead Sea Shots to address several different aspects of regional seismic monitoring. Each aspect will be presented in its own section. A brief description of the shots follows.

Dead Sea Shots and Regional Seismic Data

In November of 1999, the Geophysical Institute of Israel (GII) conducted three chemical explosions in the Dead Sea. These explosions were conducted to provide calibration data for seismic travel times to stations of the International Monitoring System (IMS) to improve detection and location efforts for CTBT monitoring. Details of the shot locations and origin times are compiled in Table 1. The two largest shots (m_b 3.45 and 3.6) were well observed out to regional distances ($\Delta \geq 500$ km). The Middle East has dense coverage of seismic stations due to the relatively high population density and earthquake hazard along the Gulf of Aqaba-Dead Sea Rift. Stations operated by regional networks in Israel (GII), Jordan (Jordanian Seismic Observatory, JSO), Syria and Saudi Arabia (King Abdulaziz City for Science and Technology, KACST and King Saud University, KSU) were operating during the shots. A map of the shot and station locations is shown in Figure 1.

One-Dimensional Velocity Model Development

The travel times of first-arriving P-waves (Pn and Pg) were used to develop an average one-dimensional velocity model of the crust and uppermost mantle for the region. The P-waves were picked from waveforms from the Jordanian and Saudi Arabian networks. Waveforms were not available for all stations and some waveforms were discarded due to poor signal-to-noise levels. Sn was not clearly observed for these data, including the horizontal components of the KACST network stations. Sn is not expected to propagate efficiently along the paths studied (Kadinsky-Cade et al., 1981; Rodgers et al., 1997). Sg propagated efficiently and was picked when clearly observed.

Firstly, we regressed the travel times of each phase versus distance. Data from both shots were included in this analysis. Both explosions have very similar travel times to each station suggesting that there are not timing errors at the stations between the two shots, although picking the phases can be difficult because of poor signal-to-noise levels. Figure 2a shows the Pn, Pg and Sg travel times versus distance and regression fits for the recordings in Saudi Arabia. The slopes of the Pg and Sg travel times versus distance should reflect the average P- and S-wave velocities of the crust, while the Pn travel-time slope should indicate the average sub-Moho P-wave velocity, assuming the Moho is flat. However, caution must be exercised because two-dimensional structure along the path could bias the results. In fact analysis of seismic refraction data sampling the Sinai Peninsula margin of the Gulf of Aqaba indicates that crust thins from about 30 km north of the Gulf of Aqaba to 20 km at the southern-most tip of the Peninsula (Ginzburg et al., 1979). A low average Pn velocity (7.8 km/s) is reported for the Dead Sea Rift by the seismic refraction

study of Ginzburg et al., (1979) and the Pn tomography study of Hearn and Ni (1994). The absence of short-period Sn propagation in the region and low Pn velocities is consistent with the presence of partial melt in the shallow mantle. A crustal thickness of about 30 km for the Dead Sea region is reported from studies of seismic refraction data (Ginzburg et al., 1979) and teleseismic receiver functions (Sandvol, et al., 1998). Our goal is simply to estimate an adequate one-dimensional velocity model for the region.

We estimated a velocity model from the picked P-wave data shown in Figure 2b using a grid search scheme. A wide range of models was generated and the mean and root-mean square (rms) of the residuals (data minus model prediction) were computed. Models were chosen to minimize the absolute mean residual while also providing good scatter reduction. The sensitivity of travel times to one-dimensional (1D) average velocity structure is certainly non-unique and our goal is to find a range of models that fit the data reasonably well and are consistent with what is already known about the region. By using a grid search technique we avoid problems associated with linearizing the dependence of the data on model parameters, as is required by linear inversion methods. Because the calculation of travel times in a 1D model is fast, the grid search allows us to quickly investigate a wide range of models.

Figure 2c shows the models used in the grid search. We assumed a 2-km-thick sediment layer for all models. The total crustal thickness was varied from 24 to 34 km with a 2-km increment. Three layers composed the crystalline crust: an upper crust (5-km thickness, v_P = 5.0-5.4km/s, 0.1 km/s increment); a middle crust (5 km thickness, v_P = 5.7-6.2km/s, 0.1 km/s increment); and a lower crust (variable thickness, v_P = 6.2-7.0km/s, 0.2 km/s increment). The mantle P-wave velocity was set to 7.8 km/s, consistent with the regression value (Figure 2a).

The best-fitting 1% of the 900 models considered are shown in Figure 2c. The crustal thickness is 32 km for all these models. Upper crustal velocities are poorly constrained. The average crustal P-wave velocity for the best-fitting models is 6.1-6.2 km/s. The model is compiled in Table 2.

Event Relocation: Testing Travel-Time Corrections Methodologies

The two largest Dead Sea shots provide a unique opportunity to test travel time correction methodologies for event location. Each shot was treated as a calibration shot and travel time corrections were computed and applied while locating the other event. In each case we used the reported analyst picks (first-arriving P-waves) from all available regional stations (Figure 1). Two methodologies were used to compute travel-time corrections: station static delays (relative to a one-dimensional model) and kriged correction surfaces (Schultz et al., 1998). Figures 3a and 3b show the ground truth locations, the computed locations without corrections, and with both correction strategies. Results indicate that using the static corrections degraded the location of the Nov. 10 shot compared to the location without corrections. However, the location of the Nov. 11 shot with static corrections is closer to ground truth compared to the location without corrections. The locations with corrections from the kriged surface were closest to ground truth for both events.

The inconsistent behavior of locations using static delay times is due to picking errors. This is illustrated in Figure 3c where we show the individual residuals and kriged travel-time correction surface for both events. In a few cases individual stations have very different residuals, presumably due to inconsistent picking of the arrivals. Despite differences between residuals at a few stations for the two shots, the correction surfaces are generally in good agreement. Fluctuations between nearby data points that arise from picking errors can bias static delay time corrections. Kriging accounts for fluctuations in nearby data points by averaging through the points, leading to a smooth correction surface and more stable corrections.

S-wave Coda Magnitudes

Measurements from the S-wave coda have been shown to provide estimates of the seismic source spectrum and remarkably stable moment magnitudes (Mayeda and Walter, 1996). We measured envelopes of the S-wave coda at the broadband station MRNI in Israel (Figure 4). The estimated source spectra (Figure 4c) are peaked relative to that of a nearby earthquake. Spectral peaking arises from interference notches, Rg-to-S scattering and/or near-source attenuation effects. Yields of the smaller shots are estimated relative to the 5000-kg shot in the low frequency band (0.5-1.5 Hz) band to be 2036-kg and 570-kg for the Nov. 10 and

Nov. 8 shots. Single-station coda body-wave magnitudes, mb, are estimated from the 1-2 Hz band: 3.6, 3.45 and 2.95. Figure 4d shows the source spectra of the three shots scaled by yield. The spectra are similar for frequencies less than 1 Hz, but different for frequencies above 1 Hz. The spectra above 1 Hz do not agree because of source dimensions and bubble pulse interference.

Bubble Pulse Observations

Underwater explosions generate a primary (direct) pulse and secondary pulses associated with the expansion and contraction of a rising gas sphere, called the bubble pulse. Each bubble pulse acts like a secondary source and radiates acoustic energy into the water and this energy subsequently propagates into the solid crust. Due to interference of the direct and bubble pulse excitation, the far-field seismic response should reveal modulation (scalloping) in the spectrum. We observed a very consistent pattern of spectral modulation using the broadband stations of the Saudi National Seismic Network. Figure 5 shows the vertical component spectra and auto-correlations for six stations. Theoretical predictions of the bubble pulse frequency/period reported by GII are 1.72 Hz/0.583 s and 1.26 Hz/0.791 s for the November 10 and 11 shots, respectively. The observed bubble pulse frequencies are in good agreement with their predictions.

CONCLUSIONS AND RECOMMENDATIONS

The Dead Sea Shots provided valuable data for empirical travel-time calibration as well as testing regional seismic monitoring strategies. Unfortunately, the shots were not well recorded by single stations of the International Monitoring System (IMS) at teleseismic distances. Nonetheless, the shots can be used as calibration points for regional velocity models and travel time correction surfaces. We used the travel-times of first-arriving P-waves to estimate a one-dimensional average velocity model for the region. Using the two shots to test travel-time correction strategies for event location, we showed that kriging corrections provide locations closer to ground truth than station-based static delay times. Source spectra inferred from S-wave coda amplitudes show that the shot spectra are peaked below about 2 Hz. Broadband recordings of the shots show spectral scalloping associated with the bubble pulse.

Analysis of regional data from the Dead Sea Shots shows that such calibration shots can be used to successfully calibrate regional seismic travel times and test monitoring strategies. Future experiments can be conducted to advance empirical calibration of new regions.

ACKNOWLEDGEMENTS

AR is grateful to the staffs of KACST and KSU for their hospitality during a visit in November 1999 and for generously sharing waveform data.

REFERENCES

Ginzburg, A., J.Makris, K. Fuchs, C. Prodehl, W. Kaminski and U. Amitai (1979). A seismic study of the crust and upper mantle of the Jordan-Dead Sea Rift and their transition toward the Mediterranean Sea, *J. Geophys. Res*., 84, 1569-1582.

Hearn, T. and J. Ni (1994). Pn velocities beneath continental collision zones: the Turkish-Iranian Plateau, *Geophys. J. Int*., **117**, 273-283.

Kadinsky-Cade, K., M. Barazangi, J. Oliver and B. Issacks (1981). Lateral variations of high-frequency seismic wave propagation at regional distances across the Turkish and Iranian Plateaus, *J. Geophys. Res*., 86, 9377-9396.

Mayeda, K. and W. Walter (1996). Moment, energy, stress drop and source spectra of western United States earthquakes from regional coda envelopes, *J.Geophys.Res.*, **101**, 11,195-11,208.

Rodgers, A., J. Ni and T. Hearn (1997). Propagation characteristics of short-period Sn and Lg in the Middle East, *Bull. Seism. Soc. Am*., 87, 396-413.

Sandvol, E., D. Seber, A. Calvert and M. Barazangi (1998). Grid search modeling of receiver functions: Implications for crustal structure in the Middle East and North Africa, *J. Geophys. Res*., 103, 26,899.

Schultz, C, S. Myers, J. Hipp and C. Young (1998). Nonstationary Bayesian kriging: application of spatial corrections to improve seismic detection, location and identification, *Bull. Seism. Soc. Am.*, **88**, 1275-1288.

Table 1. Ground Truth Locations from Geophysical Institute of Israel

LATITUDE	LONGITUDE	DATE	TIME (GMT)	YIELD (KG TNT)
31.5330	35.4406	Nov. 8, 1999	13:00:00.33	500
31.5338	35.4400	Nov. 10, 1999	13:59:52.210	2060
31.5336	35.4413	Nov. 11, 1999	15:00:00.795	5000

These data were taken from the Geophysical Institute of Israel: http://www.gii.co.il.

Table 2. Preferred Velocity Model for the Region

DEPTH (KM)	THICKNESS(KM)	V_P (KM/S)	V_S (KM/S)
0.0	2	4.50	2.60
2	5	5.00	2.89
7	10	6.10	3.42
17	15	6.80	3.82
32	∞	7.80	4.38

V_P and V_S are the P- and S-wave velocities, respectively.

November 1999 Dead Sea Shots and Regional Seismic Stations

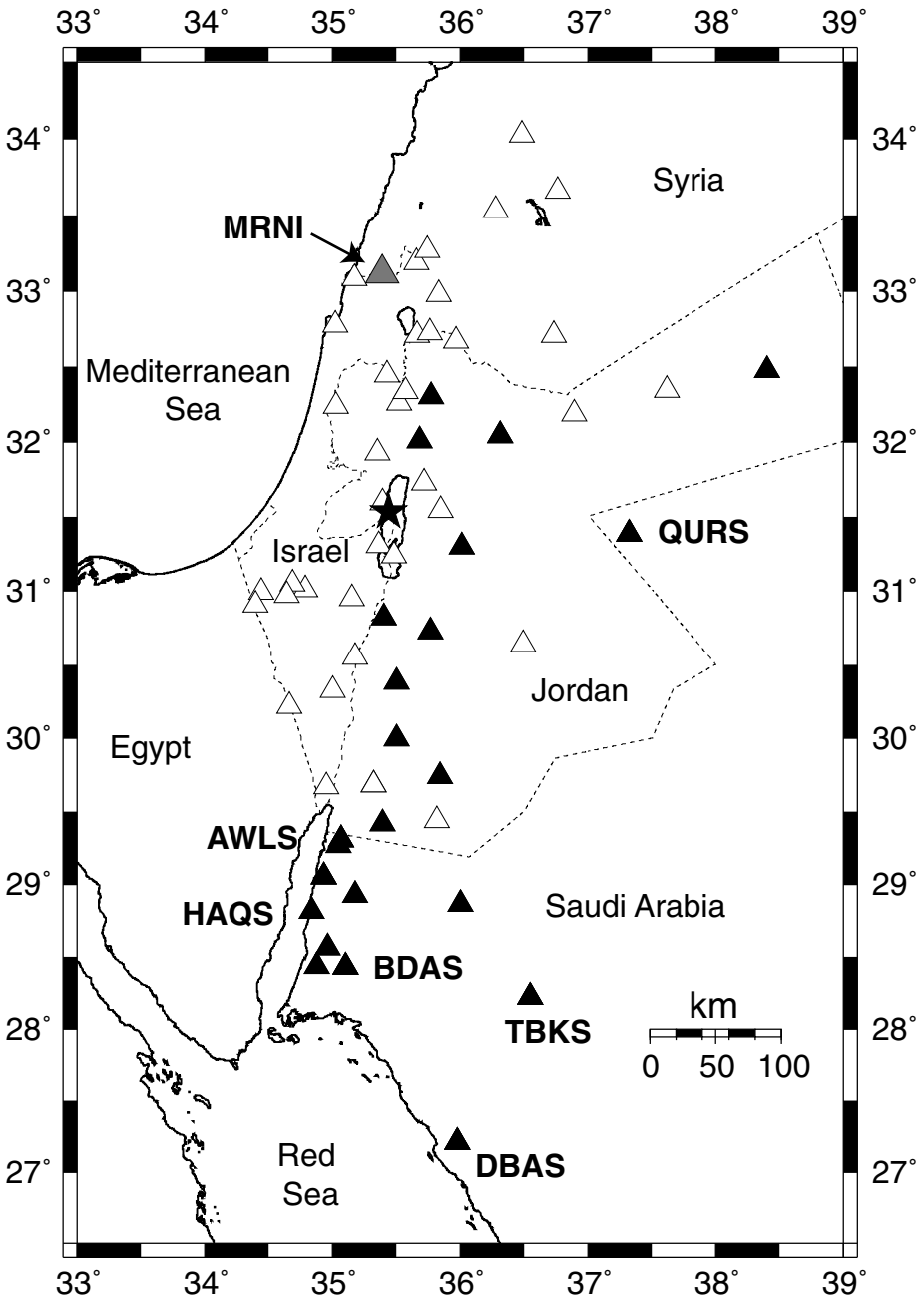


Figure 1. Map of the Dead Sea Shot locations (star) and regional seismic stations reporting P-wave picks (triangles). Black triangles indicate stations for which we had waveform data and picked phase arrivals for velocity model development.

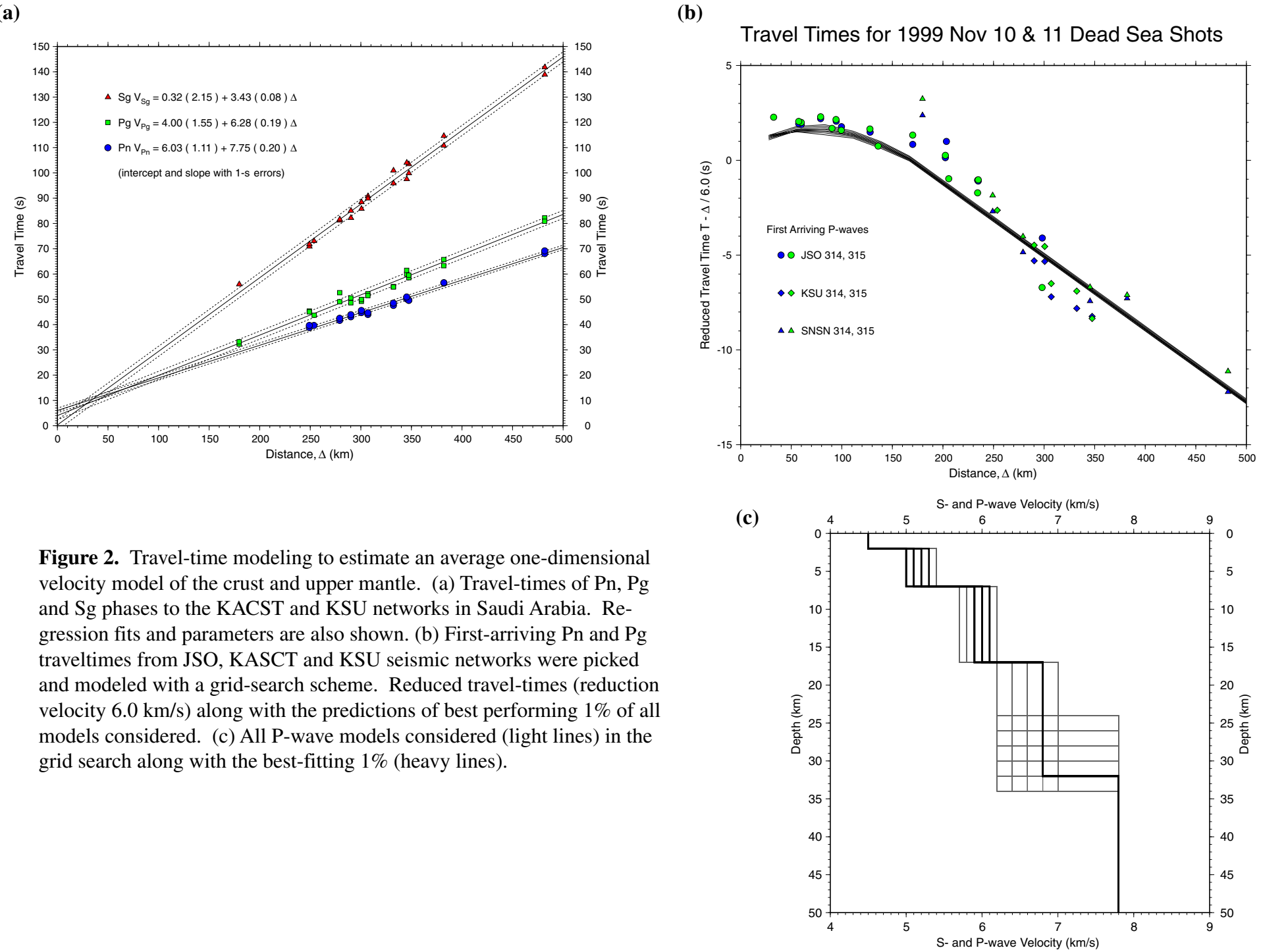


Figure 2. Travel-time modeling to estimate an average one-dimensional velocity model of the crust and upper mantle. (a) Travel-times of Pn, Pg and Sg phases to the KACST and KSU networks in Saudi Arabia. Regression fits and parameters are also shown. (b) First-arriving Pn and Pg traveltimes from JSO, KASCT and KSU seismic networks were picked and modeled with a grid-search scheme. Reduced travel-times (reduction velocity 6.0 km/s) along with the predictions of best performing 1% of all models considered. (c) All P-wave models considered (light lines) in the grid search along with the best-fitting 1% (heavy lines).

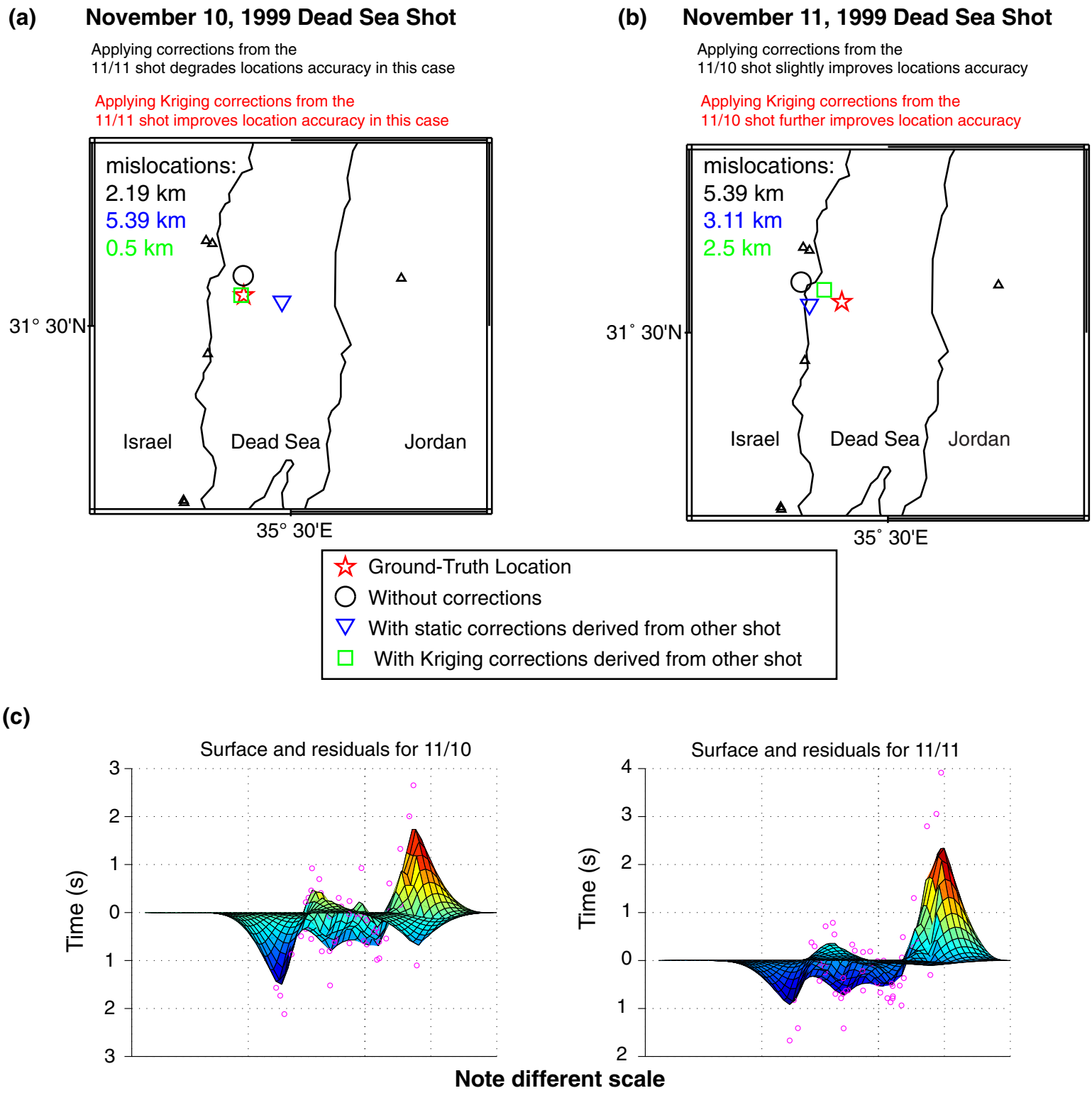
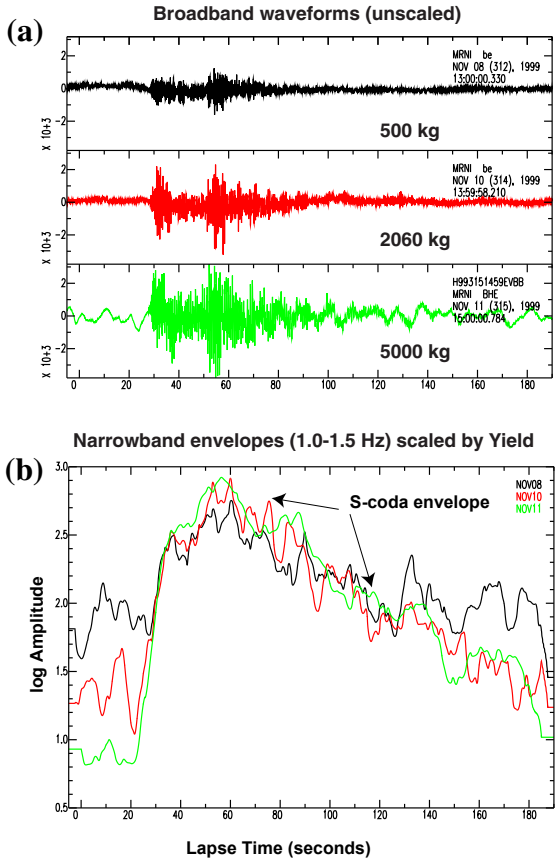
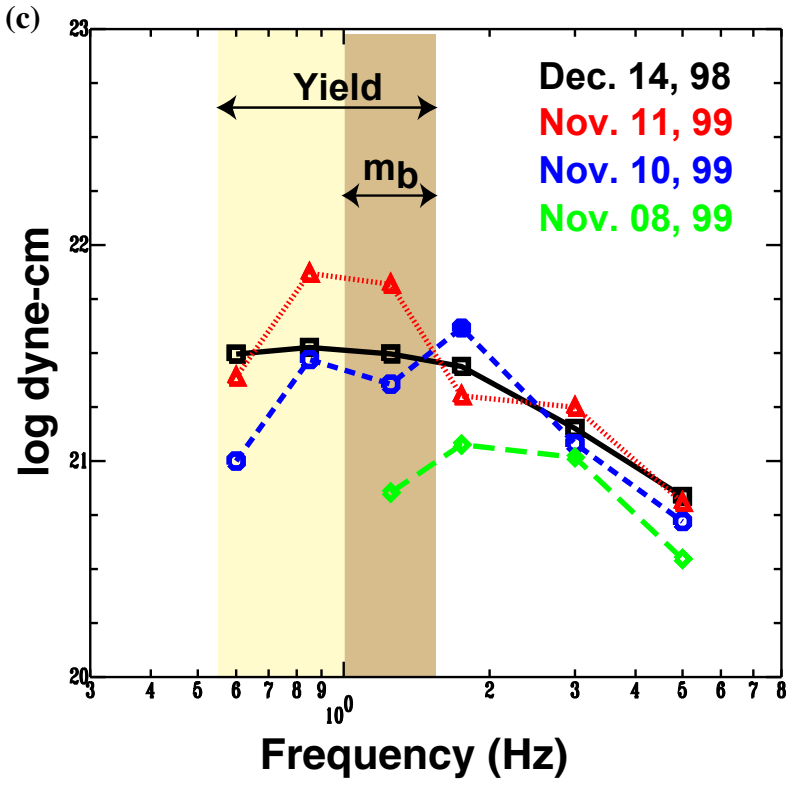


Figure 3. Locations of the (a) November 10, 1999 and (b) November 11, 1999 Dead Sea Shots. Ground truth is shown as the red star. Each shot was located three ways: i) without any path correction (black circle); ii) with static corrections computed as the travel time residual relative to a one-dimensional model (blue triangle); and iii) using travel-time correction computed from the kriging algorithm (green square). The travel-time corrections used to locate each shot were computed from the other shot. (c) Side-view of the travel-time residuals for each shot along with the kriged correction surface. Notice that the patterns of the residuals and the surfaces are very similar, however some residuals at individual stations are not in agreement.





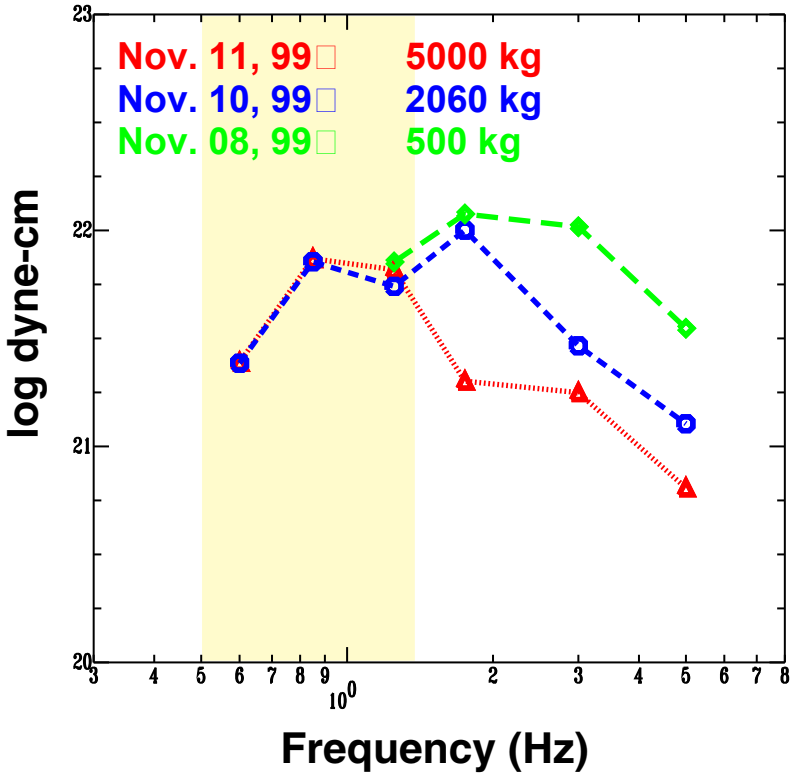


Figure 4. **(a)** Broadband East component waveforms for the three Dead Sea Shots at MRNI (unscaled).

(b) Narrow-band envelopes of the three shots scaled by yield. Notice that the shapes and decay rates of the S-wave coda are quite similar.

(c) Source spectra for the three shots and for an earthquake (M_L 3.6) south of the Dead Sea. Note that the spectrum for each shot is peaked relative to the earthquake spectrum. Spectral peaking arises from interference notches, Rg-to-S scattering and/or near source attenuation effects. Yields of the smaller shots are estimated relative to the 5000 kg shot in the low-frequency band (0.5-1.5 Hz) band to be 2036 kg and 570 kg for the Nov. 10 and Nov. 8 shots. Single-station coda body-wave magnitudes, m_b, are estimated from the 1-2 Hz band: 3.6, 3.45 and 2.95.

(d) Source spectra of the three shots scaled by yield. The spectra are similar for frequencies less than 1.5 Hz, but different for frequencies above 1.5 Hz. This suggests that the corner frequencies of each event are different, possibly due to different effective source diameters.

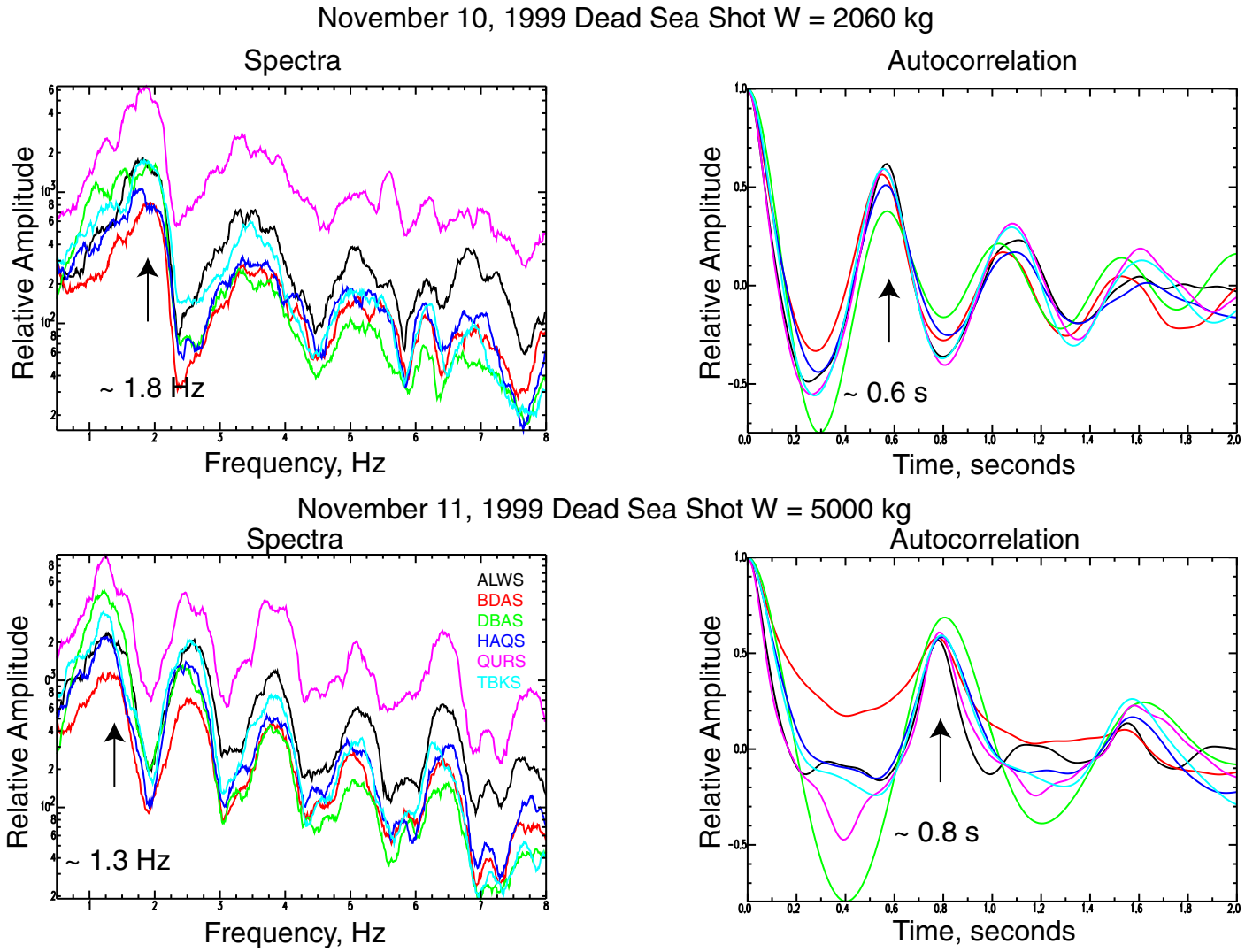


Figure 5. Spectra and auto-correlations of the two largest Dead Sea Shots taken from the vertical component broadband stations of the Saudi National Seismic Network. The scalloping of the spectra (left) is consistent for each shot. Similarly, the auto-correlations (right) of the waveforms are remarkably simlilar. The spectral maxima and peak auto-correlations are consistent with predicted bubble pulse frequencies/periods reported by GII: 1.72 Hz/0.583 s and 1.26 Hz/0.791 s for the November 10 and 11 shots, respectively.

PATH CALIBRATION STUDIES IN AND AROUND THE INDIAN SUBCONTINENT

Chandan K. Saikia, Hong Kie Thio and Bradley B. Woods
URS Group, Inc.

Sponsored by the Defense Threat Reduction Agency

Contract No. DTRA-01-98-C-0146 and DTRA-01-00-C-0033

ABSTRACT

We have developed one-dimensional crustal models for the regions of Peninsular India, northeast India and parts of the northwest Pakistan by modeling regional seismograms recorded up to 12^o distance. We modeled regional seismograms recorded at several stations in the Indian subcontinent, NIL (Nilore, Pakistan) and LSA (Lasha, China). We modeled teleseismic *pP* and *sP* phases to constrain depths and the amplitude variation of the *pP*, *sP* and *P* waves to constrain focal mechanisms of earthquakes. These crustal models are now being used to develop travel-time curves for seismic phases (*P* and *S*) so that they can be used in the seismic event location programs. We have also identified a set of possible GT10 and GT25 events using the data base from the ISC catalog and local contacts. For some events the locations determined using travel times from local networks and regionalized velocity models are found at several tens of kilometers away from the ISC and EHB hypocenters -- especially for small events. Often travel times exhibit residuals relative to a crustal structure used in their locations. To investigate how well this can be calibrated in the region surrounding the Indian subcontinent, we used a few GT10 events from the northeastern India and analyzed their travel times to the seismic stations that operate in the Indian subcontinent. We computed travel-time residuals by subtracting the IASP91 travel times from the observed travel times and by subtracting the IASP91 travel times from the travel times computed for 2D cross-sectional paths obtained from a preliminary 3D model of the region. This 3D model was constructed by placing the crustal model of Mooney and Laske on the mantle structure from Grand's tomographic model extrapolated to P wave velocities using a constant Poisson's ratio. We used a modified shortest path algorithm to calculate these travel times in this study. We computed travel times along many 2D profiles at 10 degree azimuth intervals from the earthquakes and interpolated these travel times to estimate the expected travel times for P waves to a given station using the cubic-spline interpolation method. We also did a similar calculation for travel times from the station GBA to the earthquakes that were identified as GT25 events. We a found a good correlation between the two sets of residuals suggesting that our 3D model of the region is a good initial one for the region.

Objective

The primary objective of this study is to develop crustal models for various regions of the Peninsular India, northeast India and parts of northwest Pakistan. To accomplish this goal we have identified several well located seismic events from the Indian subcontinent and used the arrival times of the impulsive P waves reported in the ISC and local bulletins by the seismic stations operating in regions. In this report we shall present results of regional path models which must be included in the final crustal model of the Indian subcontinent so that reliable theoretical travel times for seismic waves can be computed.

Research Accomplished

In our previous report we discussed preliminary crustal models developed for the northeast and central India. The northeast region of India is characterized by highly complex geology and a high rate of seismicity. In this ongoing investigation we further conducted an investigation of travel times for Pg, P* and Pn waves along various profiles using the time picks from the local networks. A study was conducted at RRL (Regional Research Laboratory, Jorhat) in order to obtain seismic velocities and thicknesses of the upper and lower crust and depth to the Moho discontinuity along the Main Central Thrust (MCT) and Main Boundary Fault (MBF) in the Arunachal Himalaya and the Brahmaputra lineament (BPL) in Assam (Sitaram *et al.*, 2000). The results of this investigation have yielded that the crust of the northeast India is primarily composed of two layers, but with varying thicknesses, along the above three profiles suggesting that the thickness of the Moho depth increases from 45.3±1.4 km to 51.8±1.4 km from the Brahmaputra lineament

towards the north into the MCT. As the crustal structure extends into the Tibet region, the Moho depth increases to about 65 to 70 km as was determined from surface wave analysis (Gupta and Narain, 1967).

The crustal structure of Peninsular India is homogeneous and also consists of two layers above the half space (Saikia et al., 1998; Singh *et al.*, 1999; Saikia, 2000). A great deal of analysis was done using broadband seismograms that were recorded by the modern broadband stations deployed in the Peninsular India from the May 21, 1997 Jabalpur earthquake (origin times: 22h 51m 28.7s, 23.084^{o}N, 80.041^{o}E, h=36 km and M=6, PDE). Figure 1 shows the locations of these broadband stations, shown by triangles, that currently operate in India. Included in this figure are the locations of earthquakes occurring in the stable Indian subcontinent. We used digital seismograms recorded from this earthquake to calibrate the crustal model extending towards HYB (Hyderabad) – a Geoscope station and located 645 km away from the epicenter toward the southwest, BHPL (Bhopal) -- a broadband station operated by the India Meteorological Department (IMD) and is located 271 km west of the epicenter, and BLSP (Bilaspur) which is also a IMD broadband station and is located southeast of the epicenter at a distance of 237 km. The P- and S-wave timings of various phases at these stations required a slight adjustment of the velocity models. Figure 2 shows an example of the agreement between various seismic phases obtained by inverting the recorded data shown by the solid lines (Saikia, 2000). We used a focal depth of 35 km which was obtained by fitting the timings of the teleseismic depth phases, namely the pP and sP waves relative to P (Figure 3). The modeling of the regional refracted sPn and pPn phases relative to the Pn onset up to 15^o away from the epicenter also proved helpful in obtaining its depth.

In addition to working with digital data from this earthquake, we are also using the recorded Pn and Sn timings reported from 24 Indian seismic stations (IMD, 1998). This earthquake also generated 32 aftershocks which were located by the Indian scientists using local crustal models. We have collected the P and S times of these events and are in the process of relocating them using the IASP91 model.

We have further examined the epicenters of earthquakes that occurred in and around the Indian subcontinent during the period from 1964 to 1996 using the phase data published in the ISC catalog. Figure 4 identifies the events that satisfy the criteria of the GT25 and GT10 events (Yang and Romney, 1999). Figure 5 shows the distribution of stations that reported timings to the ISC catalog for these earthquakes. As expected the population of GT10 events decrease significantly and are mostly confined to the northwest Pakistan, Nepal and northeast India. Of these, the events in Nepal and northeast India are more recent because of the local networks that operate in these regions. For many of the events in the northeast India, we have also found in-common earthquakes whose locations are reported in the EHB catalog produced by Engdahl and his co-investigators. For small magnitude events (m_b<4.5) we find that locations published by the local network have moved from the EHB epicenters by several tens of kilometers. It is possible that the EHB locations for these small events are biased because of the crustal model used in locating them and due to the lack of data from local distances.

We have also examined the travel-time residuals using the GT10 locations of several events which occurred in the northeast India. Figure 6a shows the observed residuals for an event which occurred on the September 2, 1990 (m_b=5.2). The small circles represent the observed residuals reported in the ISC catalog at individual stations and are distributed over the entire globe. To investigate how well these residuals correspond to a three-dimensional crustal model of the region, we developed a preliminary model by placing the crustal model of Mooney *et al*. (1998) on the S-wave tomographic model of Grand for the mantle structure. The P-wave model at depth below 100 km was extrapolated using a constant Poisson's ratio. The mantle velocities specified in the crustal model of Mooney *et al*., were extended to a depth of 100 km. Using this composite model we have computed theoretical travel times along profiles at 10^o azimuth intervals from the event using a modified shortest path algorithm. We also computed travel times for the 1D model (IASP91). These travel times were subtracted from the travel times computed using the composite model to compute the theoretical residuals. We used a cubic spline algorithm to interpolate travel times between the nearest two points taken from the profiles. The resulting residuals were used to contour the residual distribution over the study region (Figure 6). Clearly, there is a very good correlation between the observed and the theoretical residuals. Over the Peninsular India, both residuals have similar values, thus demonstrating the potential of our preliminary 3D composite crustal model. Such a model will yield travel-time corrections to relative to the one dimensional IASP91 model for earthquakes, especially of the small sized events, that occur in regions not

been previously calibrated. Empirical estimates of travel-time corrections are generally the most desired data for the purpose of constructing correction surfaces as demonstrated in central Asia (Woods *et al.*, 2000).

A similar investigation conducted for the station Gauribidanur (GBA) in India using the GT25 locations indicated a poor correlation between the observed and the theoretical residuals also computed based on our preliminary 3D model (Figure 6b). This poor correlation strongly suggests that the locations of the GT25 events must be reviewed. We are now extending such station-specific investigations to other stations, namely NIL (Nilore) in Pakistan and DEL (Delhi) and KOD (Kodaikanal) in India.

Conclusions and Recommendations

So far, we have completed developing 1D crustal models for various regions in and around the Indian subcontinent. These models need to be included in our preliminary model of 3D structure of the region. We have collected regional seismograms from earthquakes that span the entire seismicity depth range extending to about 200 km for the earthquakes that occur in the northwest Pakistan around the Pakistani nuclear test site and along the India and Mayanmur border. These seismograms need to be analyzed for identifying characteristics that would separate the deep earthquakes from those that occur at a shallow depth. We have also compiled regional seismograms recorded at LSA, which is a broadband station in China, from earthquakes that occurred in the Indian subcontinent. A preliminary analysis of these waveforms has indicated that they are influenced by the local structure. Although we have succeeded in yielding the observed travel-time residuals from earthquakes in this region using our preliminary composite model, this model should be updated so that time-domain features in the regional seismograms can be simulated using the crustal models. We also found that locations of GT25 events are not reliable because they yield inconsistent travel-time residuals relative to the IASP91 model. For a selected set of events, it is therefore necessary that locations of the GT25 events need improvement. To this end, we propose that regional and teleseismic seismograms are to be analyzed so that depths are reliably estimated in order to relocate them using a fixed depth. This way the trade-off between the depth and the origin time can be significantly reduced and origin times can be improved.

Key words: regional, event location, GT10 and GT25, 1D and 3D models.

References

IMD (India Meteorological Department, 1998). Jabalpur earthquake of 22nd May 1997 and its aftershocks – a consolidated document, 1-70p.

Mooney, W. D., G. Laske and T. G. Masters (1998). CRUST 5.1: A global crustal model at 5^o x 5^o, J. Geophys. Res., 103, 727-747.

Gupta, H. K. and H. Narain (1967). Crustal structure in Himalaya and Tibet plateau region from surface wave dispersion, Bull. Seis. Soc. Am, 57, 235-248.

Saikia, C. K., H. K. Thio, B. B. Woods and D. V. Helmberger (1998). Path calibration and source characterization in the Indian subcontinent and surrounding areas using regional seismograms, 20th Annual Seismic Res. Symp., Proceed. on monitoring a CTBT, 114-126.

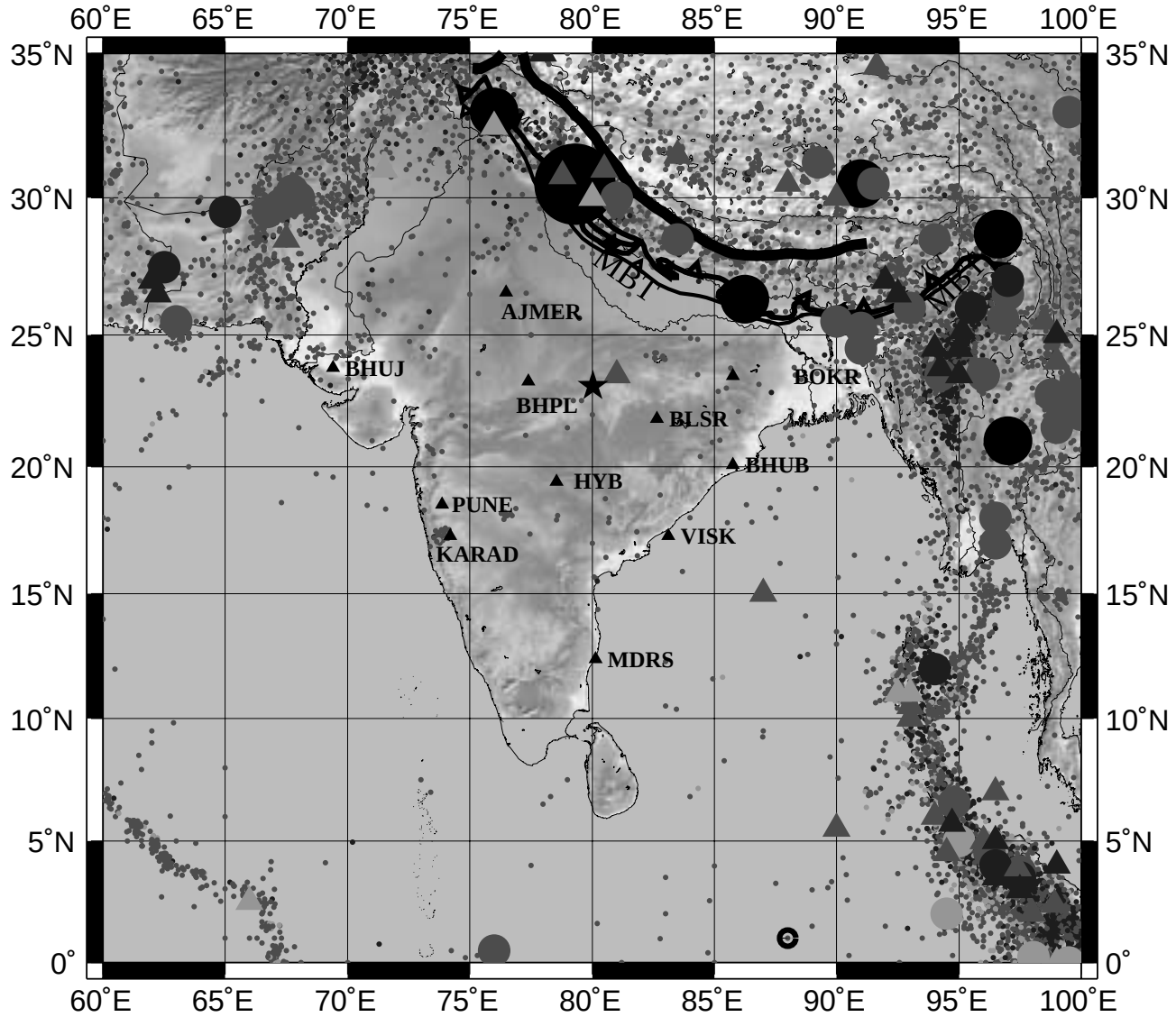
Saikia, C. K. (2000). A method for path calibration using regional and teleseismic broadband seismograms: application to the May 21, 1997 Jabalpur, India earthquake (M_w 5.8), Current Scince, 000-0000.

Singh, S. K., R. S. Dattatrayam, N. M. Shapiro, P. Mandal, J. F. Pacheco and R. K. Midha (1999). Crustal and upper mantle structure of Peninsular India and source parameters of the 21 May 1991, Jabalpur earthquake(Mw 5.8): result from a new regional broadband network, Bull. Seis. Soc. Am., 89, 1631-1641.

Sitaram, M. V. D., D. K. Yadav and K. Goswami (2000). Study on crustal structure beneath Arunachal Himalaya and Assam, Tectonophysic, 000-000.

Woods, B. B., C. K. Saikia and H. K. Thio (2000). Development of source-specific station corrections for regional phases in central Asia, included in this procceeding.

Yang, X. and C. Romney (1999). PIDC ground truth event (GT) database, CMR technical report CMR-99/15 Arlington, VA.



M≥ 8

8 > M ≥7, 0<h≤33km

8>M≥7, 33<h≤70km

8>M≥7, h>70km

7 > M ≥6.5, 0<h≤33km

7>M≥6.5, 33<h≤70km

7>M≥6.5, h>70km

Figure 1. Map showing the locations of broadband stations, shown by triangles, operated by the India Meteorological Department (IMD). Included in this map are the earthquakes occurring in the stable Indian subcontinent.

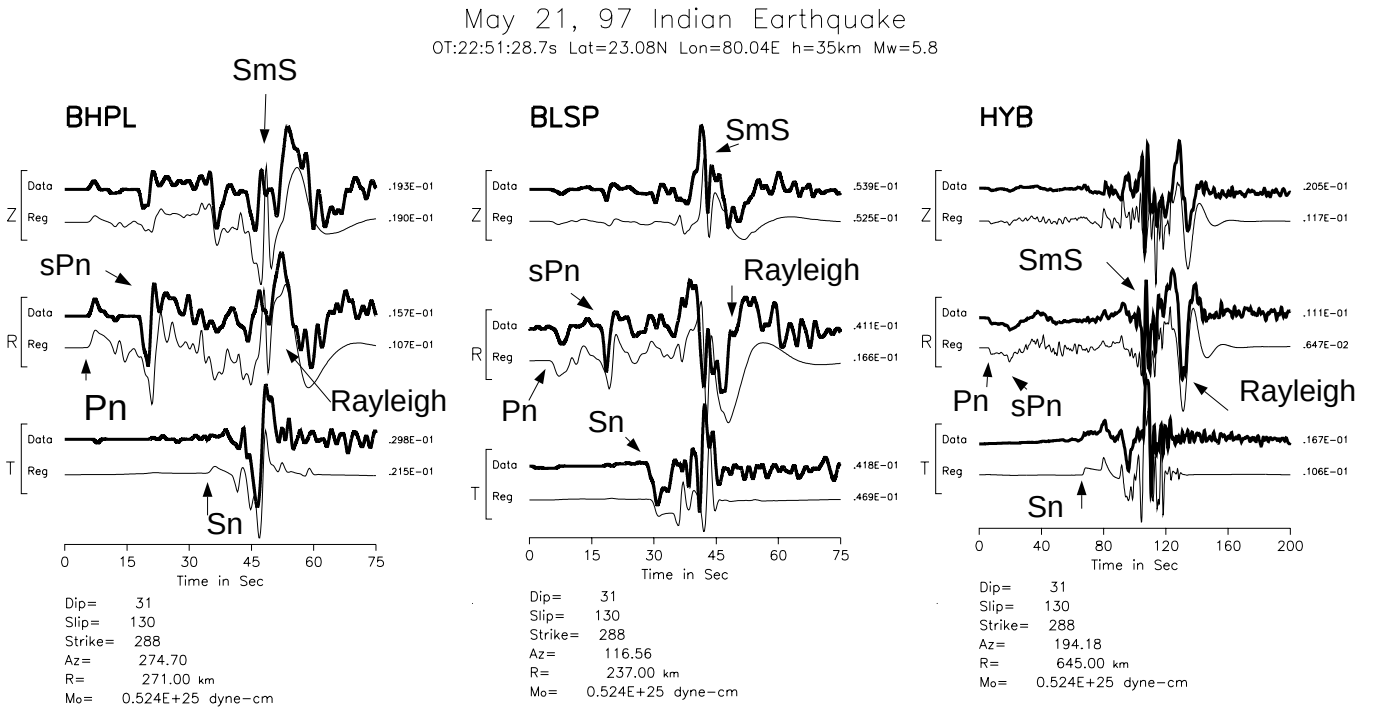


Figure 2. Comparison between the data and the synthetic regional seismograms at stations BHPL (Bhopal), BLSP (Bilaspur) and HYB (Hyderabad). Note the agreement in travel times of sPn, Sn and surface waves relative to the Pn onset. The Pn onsets are aligned in absolute travel times for both the data and synthetics.

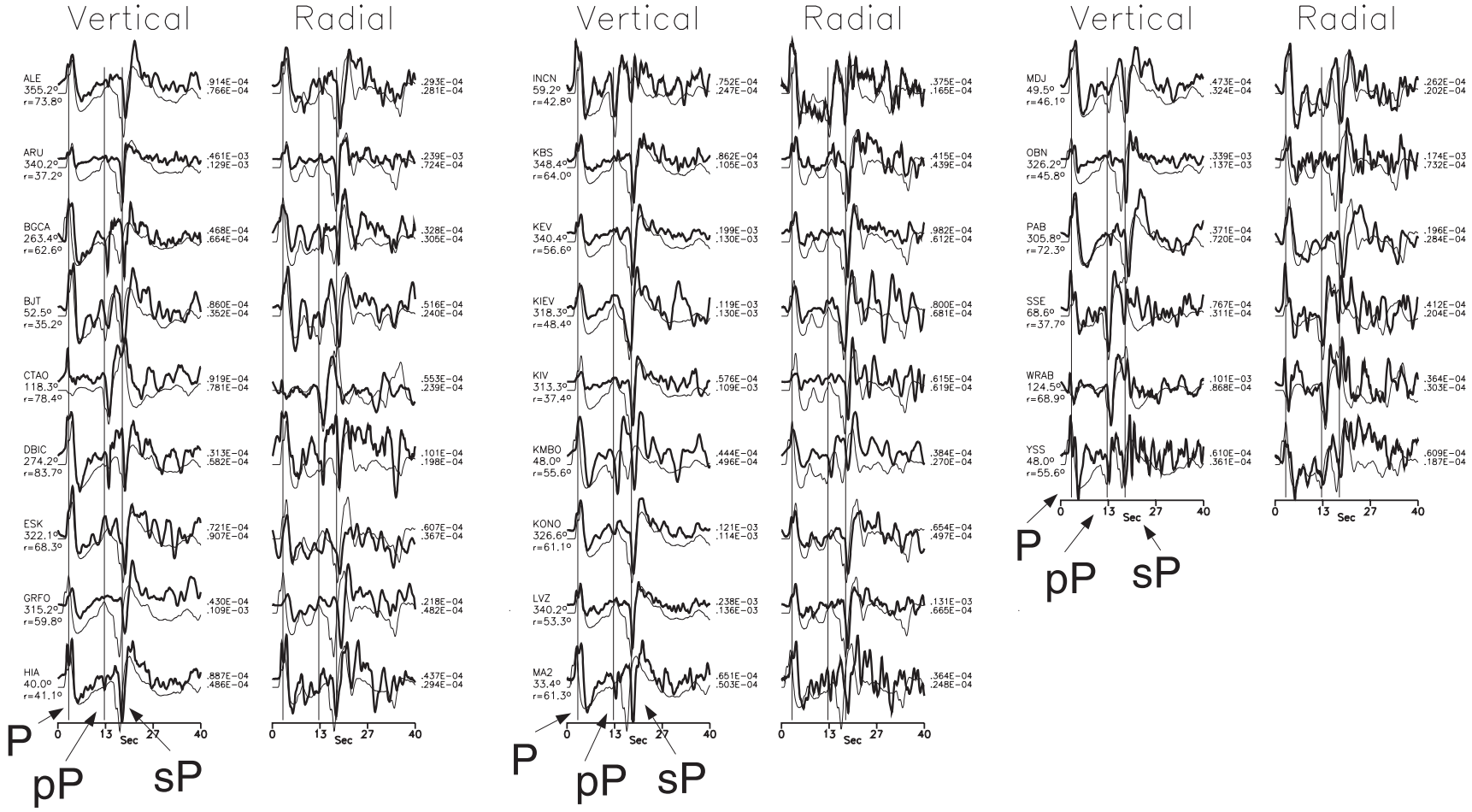

Modeling of Teleseismic Waveforms
97/05/21 22:51:23.088s (23.08N 80.04E)
h=35.0 km Mo=5.88e+24 dyne-cm
Time Delay : 0.0s 0.6s
T.F: (0.1 0.0 0.2s) (0.5 0.0 0.5s)
dip=65.0 rake=68.0 strike=70.0
Vertical
Radial
Vertical
Radial
Vertical
Radial
ALE 355.2° r=73.8°
ARU 340.2° r=37.2°
BGCA 263.4° r=62.6°
BJT 52.5° r=35.2°
CTAO 118.3° r=78.4°
DBIC 274.2° r=83.7°
ESK 322.1° r=68.3°
GRFO 315.2° r=59.8°
HIA 40.0° r=41.1°
INCN 59.2° r=42.8°
KBS 348.4° r=64.0°
KEV 340.4° r=56.6°
KIEV 318.3° r=48.4°
KIV 313.3° r=37.4°
KMBO 48.0° r=55.6°
KONO 326.6° r=61.1°
LVZ 340.2° r=53.3°
MA2 33.4° r=61.3°
MDJ 49.5° r=46.1°
OBN 326.2° r=45.8°
PAB 305.8° r=72.3°
SSE 68.6° r=37.7°
WRAB 124.5° r=68.9°
YSS 48.0° r=55.6°
0 13 27 40
Sec
P
pP
sP

Figure 3

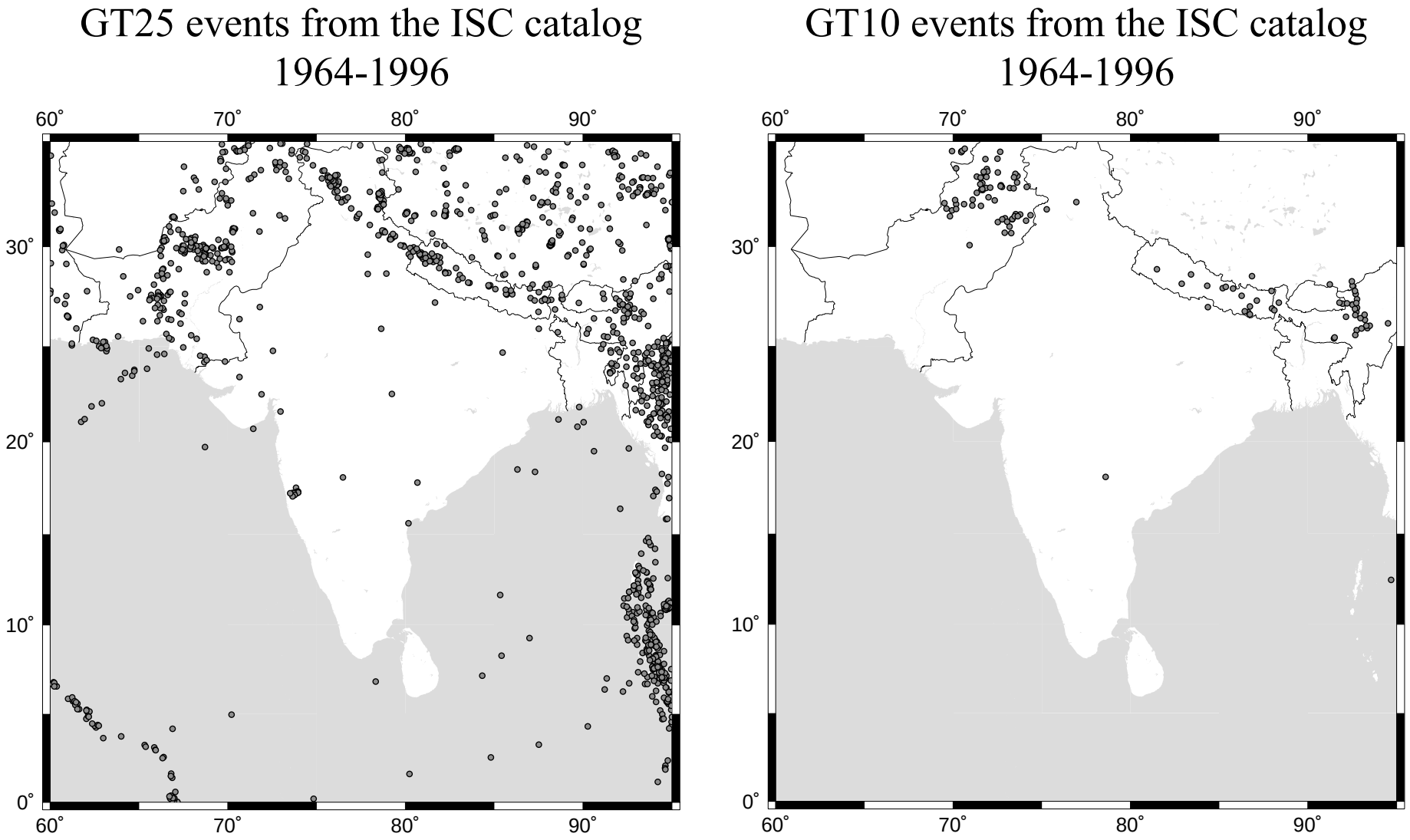


Figure 4. Location of events from the ISC catalog that conform to the GT25 (left panel) and GT10 (right panel) criteria, as discussed in Yang and Romney, 1999.

Location of seismic stations reporting to the ISC

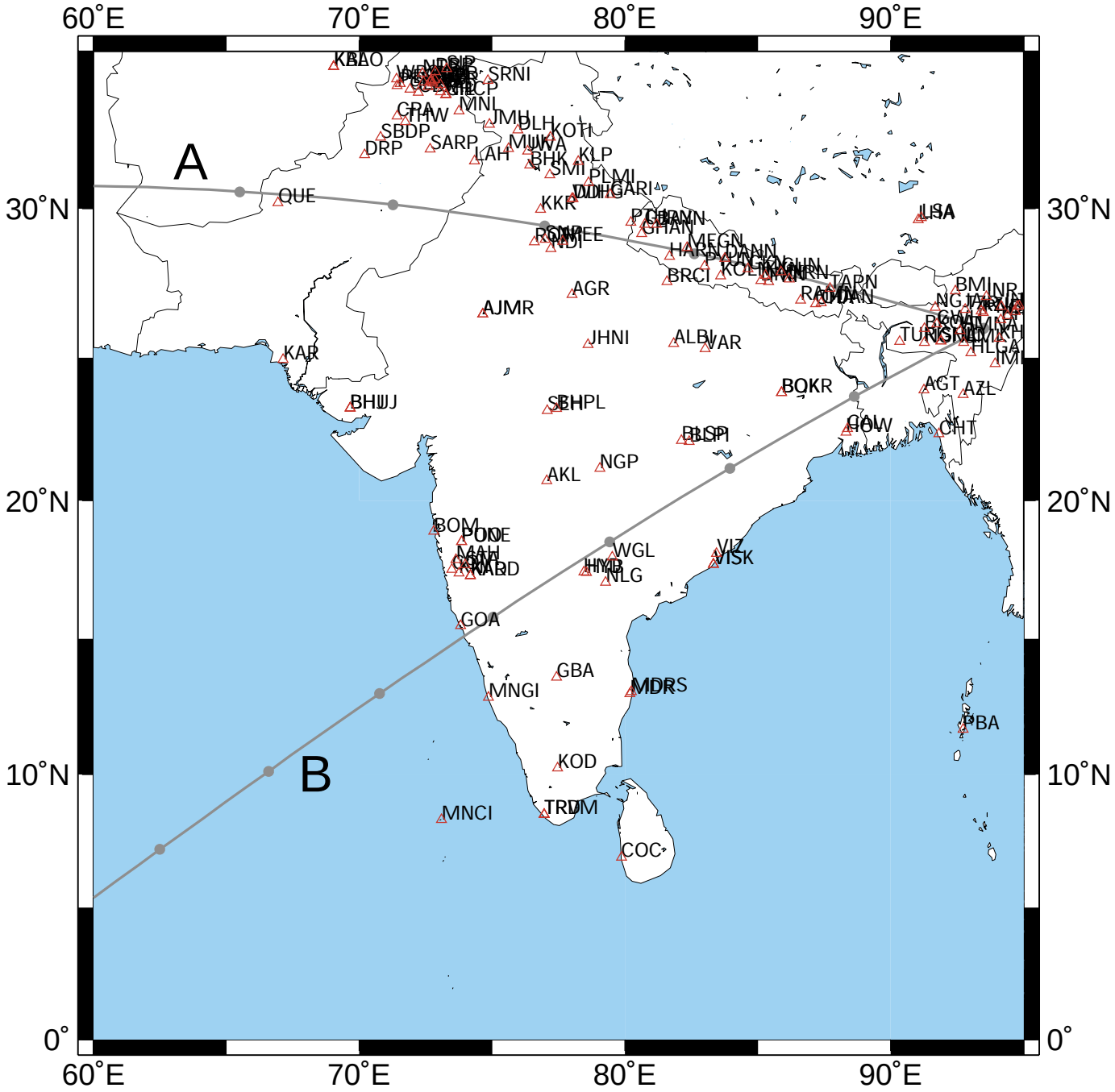


Figure 5. Map of stations on the Indian subcontinent that are included in the ISC bulletins.

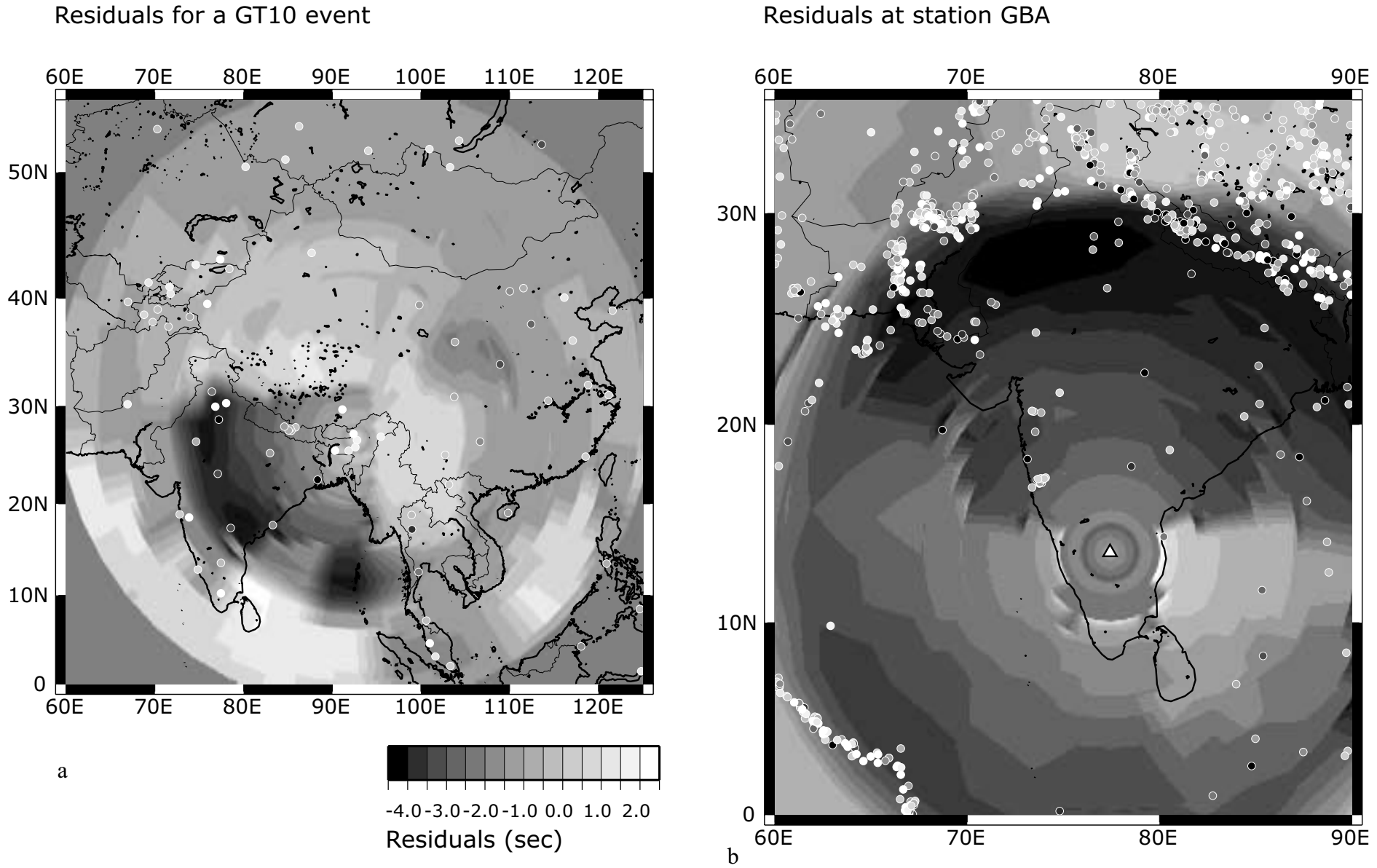


Figure 6. Observed travel-time residuals (dots) plotted on top of maps of synthetic residuals, computed for a composite model based on the Mooney et al (1998) crustal model and the Grand tomographic model below 100 km. The grey shading for the observed and synthetic residuals are identical. a - residuals for a GT10 event in NE India recorded at the ISC stations. b - residuals observed at station GBA for GT10 + GT25 events from the ISC bulletin.

IMPROVED SURFACE WAVE DETECTION AND MEASUREMENT USING PHASE-MATCHED FILTERING AND IMPROVED REGIONALIZED MODELS

Jeffry L. Stevens and David A. Adams
Maxwell Technologies, Systems Division

Sponsored by U. S. Department of Defense
Defense Threat Reduction Agency

Contract No. DSWA01-98-C-0154

ABSTRACT

The goal of this project is to improve the capability to identify and detect surface waves under a Comprehensive Nuclear-Test-Ban Treaty. To date, we have concentrated on two tasks: development of improved regionalized earth models and dispersion curves, and improvements to surface wave processing through implementation of phase-matched filtering and path corrected spectral magnitudes. The first objective is to improve the dispersion curves that are now in use at the International Data Centre (IDC). The global dispersion data set has been expanded and now contains over 248,000 data points. Two global tomographic inversions were performed using this data set. The first inversion used the 149 IDC models as starting models. With the expanded data set regions such as Antarctica and Saudi Arabia where coverage was better were significantly improved. The second inversion increased the number of models to 399 to provide additional degrees of freedom in regions that required them. This inversion significantly improved the data fit in Eurasia and the Middle East. The standard deviation in the error of dispersion curves along paths from the former East Kazakh nuclear test site was reduced by almost a factor of two. We are continuing to make improvements to the models by adding new data, applying constraints where available, and adding models where the data requires them.

Automatic identification of surface waves at the International Data Center is currently performed by narrow-band filtering the data at several frequencies, and then comparing the arrival times with a regionalized dispersion model. We would like to improve the performance of the surface wave detector using phase-matched filtering and are in the process of identifying the optimum procedure for doing so. Some obvious ways of using the phase-matched filtered waveform, such as using an STA/LTA identification technique, do not work as well as the current narrow-band filtering procedure. Narrow band filtering has the advantage of being a very stable method of determining frequency-dependent arrival times. Consequently, we have tried a new approach in which we apply narrow-band filters to the compressed waveform and use a detection test similar to the current test. This allows us to take advantage of the improved signal to noise ratio of the phase-match filtered waveforms, while retaining the robustness of narrow-band filtering for frequency dependent signal identification. After phase-matched filtering, the predicted arrival time is zero at all frequencies, so we test to see if the arrivals are within a time window similar to that used in the existing test. To test the performance of this technique, we added the capability of performing this analysis to Maxpmf, which is a version of the automatic processing code Maxsurf with phase-matched filtering added. We then processed two days of data from the data archive at the PIDC and compared the results with the reviewed event bulletin. The number of detections increased by about 15%. This is a good indication that the method is a significant improvement over current techniques, and we are working on optimizing the technique to obtain further improvements.

Objective

The goal of this project is to improve the capability to identify and detect surface waves under a CTBT in order to improve event screening using the M_s:m_b discriminant. This is being accomplished through development of improved regionalized phase and group velocity models, development of regionalized path corrected spectral magnitudes, and improvement of automated surface wave detection using phase-matched filtering.

Research Accomplished

During the first half of this project we have concentrated primarily on two tasks:

1. Improvement of regionalized global earth models and dispersion curves.
2. Automatic surface wave identification using phase-matched filtering.

There are several tasks to be performed under this contract, and we have focused on these first because 1) all of the tasks require a global earth model and dispersion curves, and optimizing these will improve all other results; and 2) the most immediate practical result of this work will be the improvement of automatic processing of surface waves, and automatic processing of surface waves in turn provides a test of the dispersion curves. In this paper, we first discuss the techniques we have been using to improve the earth models and dispersion curves, and then discuss an improvement to the current surface wave identification procedures using phase-matched filtering.

Development of Regionalized Earth Models

We are developing improved models of earth structure in order to predict surface wave behavior more accurately. These models are important for calculating path corrections for spectral magnitudes, for constructing phase matched filters, and for better prediction of group velocity arrival times used in existence tests in automatic surface wave processing.

Our global models currently consist of 2592 5x5 degree cells, each one associated with a particular model type. There are far fewer model types than cells. Each model type consists of plane layers, each with uniform P and S wave velocities, density and Q, with layers extending to a depth of about 200 km. We treat the S-wave velocities as free parameters which are estimated by tomographic inversion of observations of group and phase velocity dispersion of surface waves. The surface wave dispersion observations come from a variety of surface wave studies and from GSETT3 PIDC data.

Stevens and McLaughlin (2000) describe development of a global earth model with 149 distinct models on a five degree grid that is now used for surface wave identification at the PIDC and IDC. The development used global tomographic inversion of about 90,000 dispersion measurements, using the Crust 5.1 model (Mooney, et al., 1998) as a starting point. This process was continued by Stevens and Adams (1999) who increased the number of data points to more than 164,000 and increased the number of earth model types to 230. We have carried the process still further by increasing the number of model types to 399 and the number of data points to more than 248,000. The total number of free parameters in this case is 5147.

The number of free parameters in the global model can be increased as the number of data points is increased. We describe below procedures for finding new model types. Estimates of S-wave velocities are sensitive to the slower sedimentary layers, especially for higher frequencies. We describe corrections for this effect. Inversions have been performed both with P-wave velocities fixed (by Crust 5.1 or other studies), and with the P-wave velocities constrained by Poisson's ratio, and densities by Birch's Law.

Finding new model types

Addition of new data permits us to increase the number of model types and therefore the total number of free parameters. To select new model types we have been using the results of 2D group velocity tomography to identify cells with the largest perturbations in velocity (Stevens and Adams, 1999). "2D tomography" refers to the more traditional type of tomographic inversion in which we invert observed group velocity dispersion measurements over a narrow frequency band to find the group velocities for each cell on the 5 degree grid. Thus for each of 9 frequency bands we preform a tomographic inversion using the group velocity residuals from the 3D tomographic inversion (inversion for earth structure using both phase and group velocity at all frequencies) as data, and perturbations in the group velocities for each of the 2592 cells as parameters. Cells with large perturbations for several frequency bands are selected as possible candidates for association with new model types. The underlying reason is that cells with the large perturbations are the ones most

constrained, in the 3D inversion, by belonging to a particular type. One problem with this approach is that spurious large perturbations can occur in areas of poor resolution. Therefore, as an additional guide, we now compute resolution matrices of the 2D tomographic systems of equations. Thus well resolved cells with large group velocity perturbations are given new model types and poorly resolved cells with large perturbations are not unless there is other supporting evidence. We are using the Lanczos method of approximating SVDs for sparse matrices described and applied to tomography problems by Vasco *et al.* (1999), and code written by Berry (1992).

Figure 1 shows the diagonal elements of an approximation of the resolution matrix for the 2D tomographic system using group velocity measurements for frequencies above and including 0.025 Hz and below 0.0330 Hz. This approximation is made by computing only the 573 most significant singular values of the SVD out of a possible 2592 (the number of cells) and using the 573 corresponding singular vectors to approximate R, i.e. $R=V_pV_p^T$. V_p is the rectangular 2952x573 submatrix of V where V is defined by the Lanczos decomposition of the full matrix $A=USV^T$.

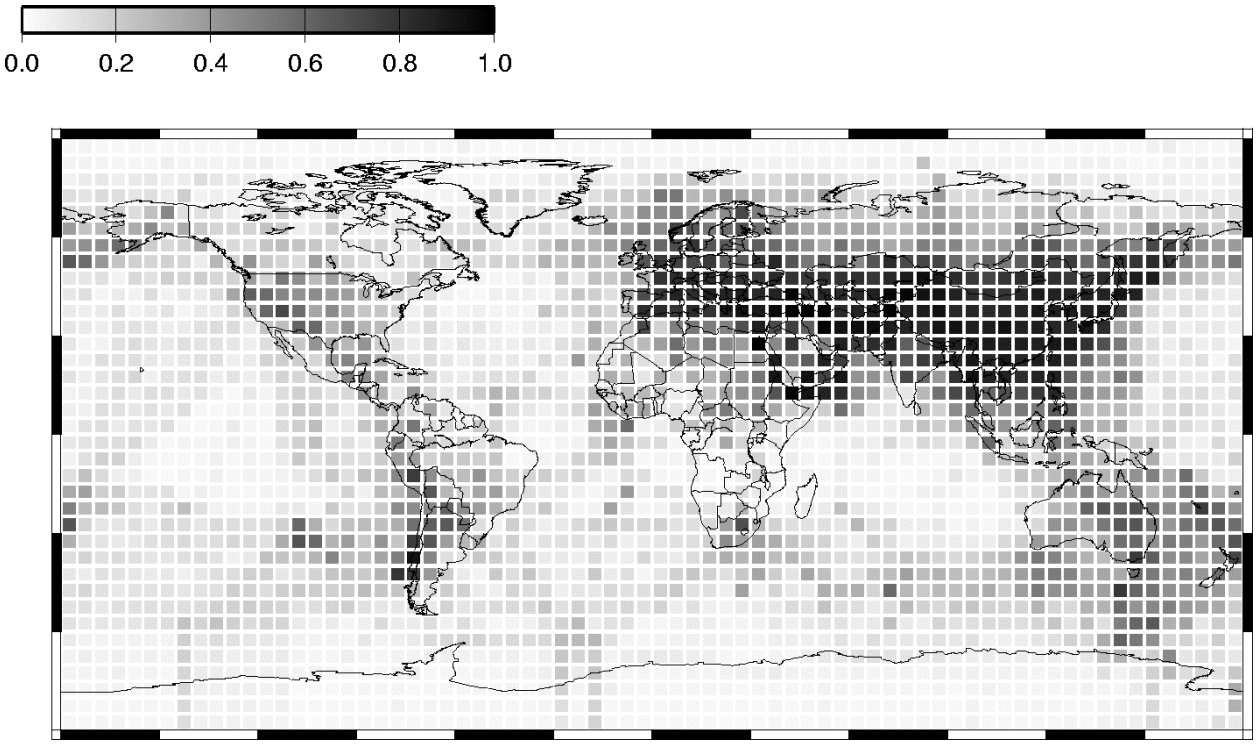


Figure 1. Map of the diagonal elements of the resolution matrix for group velocity measurements in the frequency range 0.025 to .0330 Hz using an approximation of the SVD using the Lanczos method and 573 out of a possible 2592 singular values.

Selection of new model types from resolution calculations

We computed the resolution matrices for the 2D group velocity tomographies for eight frequency bands: below 0.01 Hz, 0.01 to 0.0140 Hz, 0.0140 to 0.0167 Hz, 0.0167 to 0.025 Hz, 0.025 to 0.033 Hz, 0.033 to 0.04 Hz, 0.04 to 0.05 Hz, 0.05 to 0.067 Hz. Those cells associated with diagonal components of resolution matrices greater than 0.6 for 8 frequencies were given new model types. The 0.6 value for a cell means that there is some smearing among other cells but that the true perturbation of the cell contributes the most (60%) to the tomographic value. The new types had the same number of layers and layer thicknesses as the originating types, and the initial parameters were set the same. All of these types are found in Asia and the Middle East.

The addition of these new model types plus those discussed in the following section increases the number of types from 230 to 399 and reduces the weighted standard deviation in data by about 5%.

Selection of new model type for oceanic ridges and the Cocos Plate

Selection of new model types is a fairly complicated process requiring some judgement. Here we give an example of one case that is relatively straightforward because the tomographic results and geophysical constraints provide complementary sets of information. From 2D group velocity tomographies we identified slow regions associated with some oceanic ridges and the Cocos Plate. These observations were used to split a new type A0h from the most populous model type (A0). For each frequency band a 2D group velocity tomography was carried out. The results show an association between slowness perturbation and oceanic ridges which is strongest for the frequency band 0.0167 to 0.025 Hz. This particular slowness perturbation map was chosen to separate A0 type models into two groups of cells with either fast or slow perturbations. The distribution of fast and slow cells is dependent on the slowness value chosen to separate the two groups. In many cases slow type cells were not located at an oceanic ridge. In other cases slow cells were found on a ridge but isolated from other slow cells. Other times a slow group of cells was found at a ridge and was several cells wide. Because the great majority of type A0 cells are not well resolved we relocated some slow cells but never by more than the distance of one cell. For the same reason, we assumed that the ridge types should be in groups only one cell wide, and most single isolated slow cells, especially ones found in plate interiors, were not given the new type. The Cocos Plate now consists of only of cells with the new type. There are many slow types in the interior of the Nazca Plate but we have chosen for now to continue modeling it with the type A0. In the future we may introduce a new Nazca type. Figure 2 shows the locations of cells of the two model types A0 and A0h. After the most recent inversions the A0h velocity structure is slower than the A0 structure between about 10 km and 80 km with a maximum difference of about 1%.

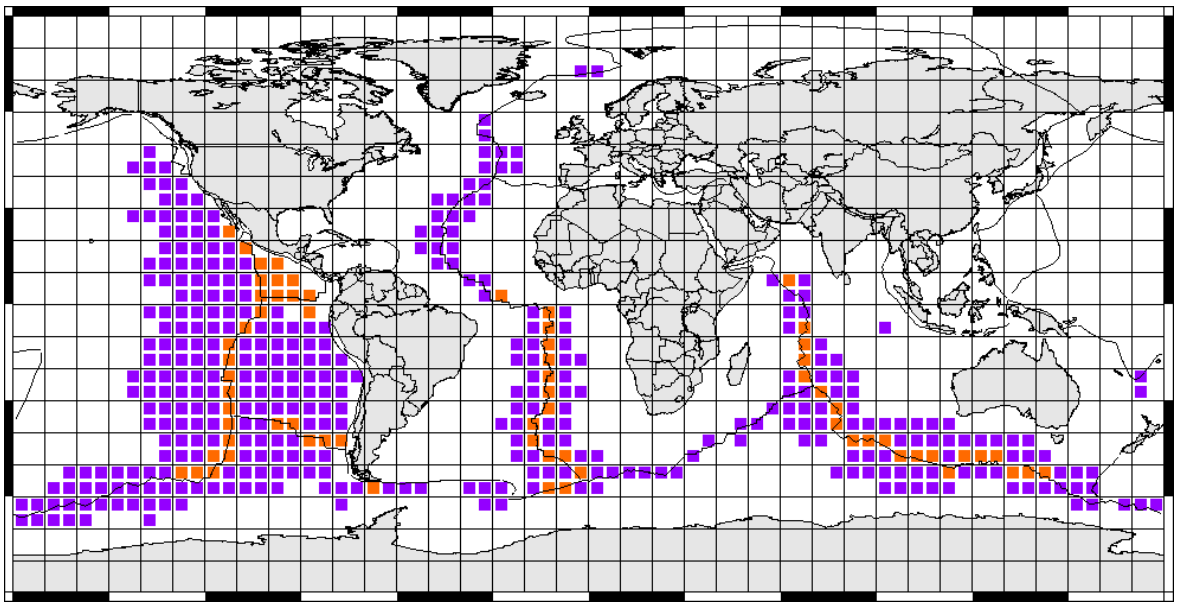


Figure 2. locations of the two model types A0, in purple (or dark gray), and type A0h in orange (or light gray).

Corrections for sedimentary layers and bathymetry

It is important to account for the effects of sediments and, for oceanic model types, the water column. These shallow layers are, in general, too thin to be resolved by the surface wave inversion, yet they do have an effect on the higher frequency parts of the dispersion curves, so these are held fixed when the tomographic inversion is performed. The parameters for the sedimentary layers based on the one degree grid sediment thickness data of Laske and Masters (1997). Their model consists of layer thicknesses, P and S wave velocities and densities

and is still in the process of revision. We use an averaging procedure to incorporate this information into our 5 degree model. Useful information is lost during averaging because the variation of sedimentary parameters within cells can be large. We are in the process of refining this model further, and decreasing the grid spacing to a 1º grid. The surface layers of this model are based on the Laske and Masters sediment maps and high resolution bathymetry maps. The 1º grid will also allow us to define the ocean depths on a finer scale and resolve the ocean/continent boundaries more accurately.

Inversion with fixed Poisson's ratio

The inversions described above used constrained P-wave velocities, fixed to be consistent with the Crust 5.1 models. As the number of models has increased, however, there is increasing inconsistency between the P and S velocities, so the most recent inversions have instead been performed with the P wave velocity and density constrained by the shear velocity. In these inversions, the Poisson's ratio is fixed to 0.25 and the density is governed by Birch's Law. For the inversions with 309 model types the fixed Poisson's ratio models fit the data better with a standard deviation reduction of about 1.5%.

Expanded data set

We have added new dispersion measurements to our data set, the largest consisting of 83,966 phase velocity measurents taken from Curtis et al. (1998) for Eurasia for frequencies between 0.00667 Hz and 0.0385 Hz. This greatly increases the number of phase velocity measurements in the data set. Since group velocities are derived from a derivative of phase velocities, there is a degree of uncertainty in inversion of group velocities that does not exist for phase velocities. Consequently, phase velocities place stronger constraints on the surface wave inversion, and are particularly important at longer periods. Initial inversions of this new data tend to increase the model velocities below about 100 km by a few percent. This brings the total number of data points to be inverted to approximately 248,000. The data set has been derived from a variety of regional and global studies including the following: global surface wave group velocities from earthquakes derived using PIDC GSETT3 data (Stevens and McLaughlin, 1996), augmented with more recent measurements derived from PIDC data; surface wave phase and group velocity dispersion curves from underground nuclear test sites (Stevens, 1986; Stevens and McLaughlin, 1988), calculated from earth models for 270 paths (test site – station combinations) at 10 frequencies between 0.015 and 0.06 Hz; phase and group velocity measurements for western Asia and Saudi Arabia from Mitchell et al.(1996) for 12 paths at 17 frequencies between 0.012 and 0.14 Hz; the global phase velocity model of Ekstrom et al. (1996) for 9 periods between 35 and 150 seconds calculated for each 5 degree grid block from a spherical harmonic expansion of order l=40; group velocity measurements for Eurasia from Ritzwoller et al.(1996) and Levshin et al.(1996) for 20 frequencies between 0.004 and 0.1 Hz with 500 to 5000 paths per frequency; Antarctic and South American group velocity measurements from the University of Colorado (Vdovin et al., 1999; Ritzwoller et al., 1999); and a very large set of dispersion measurements from Saudi Arabia provided by Herrmann and Mokhtar at St. Louis University.

Improvement to data fit

In general, additional data will improve the models primarily in the regions with new data. However, as new data is added, if additional models are not added, the data fit may actually degrade in some regions as the model strains to fit the new data in other regions. One test of the models is to look at the important case of paths from historical nuclear test sites. Tables 1 and 2 show group velocity dispersion residuals and standard deviations in the residuals for periods of 40 seconds and 20 seconds, respectively, for paths from several nuclear test sites. With the expanded data set and 149 models, the results are changed only slightly relative to the inversion with the smaller data set, and in fact the results are degraded slightly for the paths from the test sites. This is because the new data caused larger changes in other areas and with the constraint of the small number of models, the data fit became slightly worse in order to allow larger improvements in the areas with concentrations of new data. With 399 models, however, these constraints are relaxed, and the data fit improves for all test sites, and improves quite dramatically for paths in Asia. In particular the standard deviations of the residuals for paths from the East Kazakh test site are decreased by almost half at 40 seconds and by 25% at 20 seconds.

Table 1. 40 Second Group Velocity % Average Residuals (Standard Deviations)

Source	IDC 5° - 149 Models	#1 - Expanded Data Set	#2 - 399 Models
NTS (59)	0.15 (1.40)	0.22 (1.44)	0.14 (1.20)
East Kazakh (40)	0.80 (2.21)	0.85 (2.45)	0.13 (1.11)
Mururoa (13)	-0.78 (1.43)	-0.73 (1.79)	-0.59 (1.56)
Novaya Zemlya (99)	-0.06 (2.06)	0.01 (2.05)	-0.18 (1.81)
Amchitka (55)	0.25 (1.39)	0.34 (1.39)	0.35 (1.08)

Table 2. 20 Second Group Velocity % Average Residuals (Standard Deviations)

Source	IDC 5°	#1 - Expanded Data Set	#2 - 399 Models
NTS (58)	-0.47 (2.25)	-0.38 (2.23)	-0.30 (1.88)
East Kazakh (40)	-0.75 (1.96)	-0.65 (2.07)	-0.64 (1.44)
Mururoa (11)	0.41 (1.43)	0.41 (1.40)	0.53 (1.36)
Novaya Zemlya (99)	-0.26 (3.61)	-0.23 (3.66)	-0.43 (3.01)
Amchitka (54)	0.83 (3.76)	0.70 (3.74)	0.22 (3.23)

Automatic surface wave processing with phase-matched filtering

Automatic identification of surface waves at the International Data Center is currently performed using the processing program Maxsurf by narrow-band filtering the data at several frequencies and then comparing the arrival times with a regionalized dispersion model. We would like to improve the performance of the surface wave detector by using phase-matched filtering and are in the process of identifying the optimum procedure for doing so. An automatic surface wave processing program, Maxpmf, has been developed which is similar to Maxsurf except that it applies phase-matched filtering to seismograms and calculates path-corrected spectral magnitudes in addition to M_s. Maxpmf integrates a regionalized phase velocity model to generate a phase-matched filter which is used to compress the surface wave waveforms. Figure 3, below, shows an example of waveform compression after application of phase-matched filters to a data set.

Some obvious ways of using the phase-matched filtered waveform, such as using an STA/LTA identification technique, do not work as well as the current narrow-band filtering procedure. Narrow band filtering has the advantage of being a very stable method of determining frequency-dependent arrival times. Consequently, we have tried a new approach in which we apply narrow-band filters to the compressed waveform and use a detection test similar to the current test. This allows us to take advantage of the improved signal to noise ratio of the phase-match filtered waveforms, while retaining the robustness of narrow-band filtering for frequency dependent signal identification. After phase-matched filtering, the predicted arrival time is zero at all frequencies, so we test to see if the arrivals are within a time window similar to that used in the existing test. This is illustrated in Figure 4.

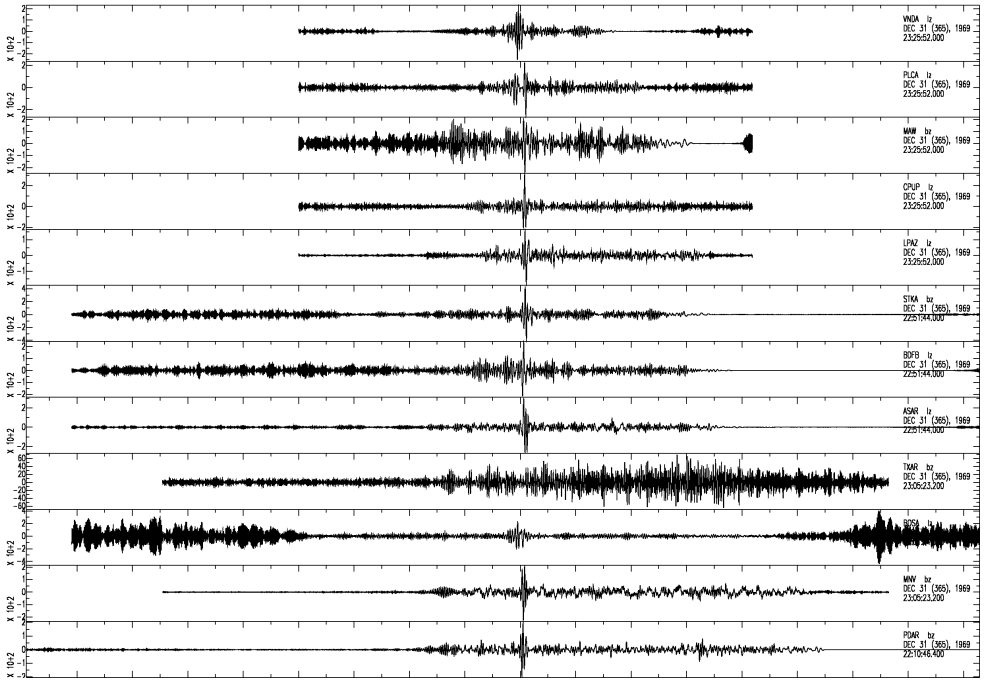


Figure 3. Compressed waveforms after application of phase-matched filters to 12 surface wave seismograms. The data is from an m_b 3.9 South Pacific earthquake that occurred 1997 June 15.

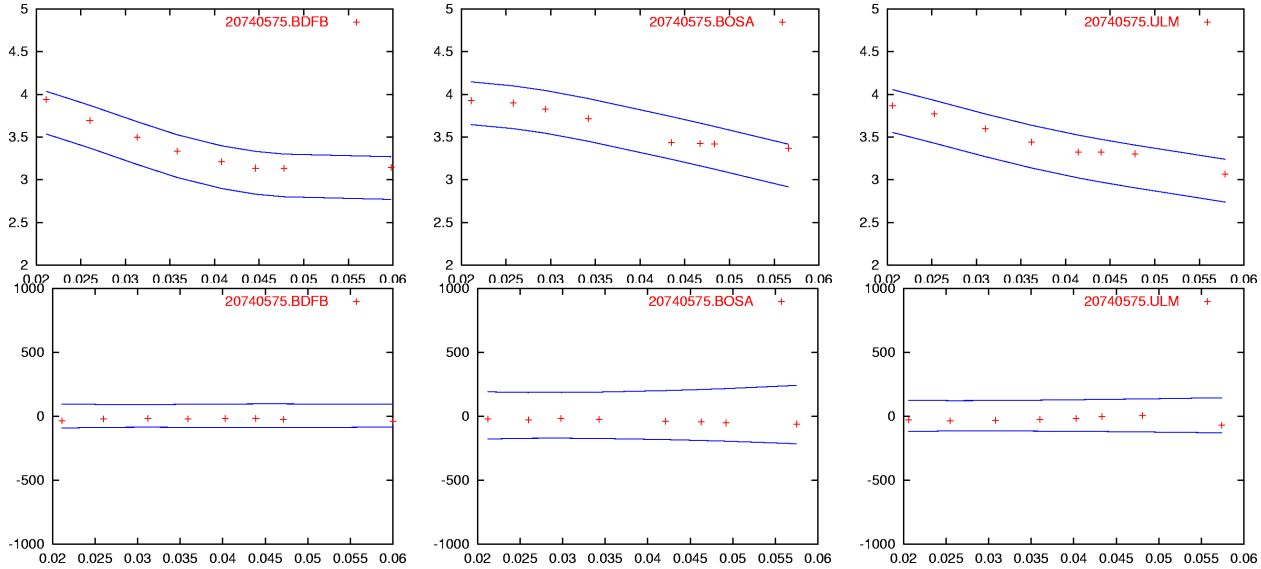


Figure 4. The narrow-band filter detection test (top) compares measured group velocity with a regionalized group velocity model. To improve detection, we phase-match filter the data first, then apply narrow-band filters (bottom). The detection test is applied for the same time interval, but the time is now centered around zero. This example is for an m_b 4.2 South American earthquake observed at BDFB, BOSA, and ULM.

To test the performance of this technique, we added the capability to perform this analysis to Maxpmf, and processed two days of data from the data archive at the PIDC. We then compared the results with the reviewed event bulletin. The number of detections increased by about 15%. This is a good indication that the method is a significant improvement over current techniques, and we are now working on optimizing the technique to obtain further improvements.

CONCLUSIONS AND RECOMMENDATIONS

In this paper, we have described improvements to regionalized dispersion models and phase-matched filtering that are necessary for optimization of surface wave processing under a Comprehensive Nuclear-Test-Ban Treaty. Because the number of events increases rapidly at small magnitudes, a decrease in the threshold of reliable surface wave detection and measurement can greatly reduce the number of unidentified events. Improved surface wave analysis methods can reduce the surface wave magnitude threshold, improve screening capability, and reduce the likelihood of unnecessary on-site inspections under a CTBT. We are continuing to improve the regionalized models and to improve surface wave identification using phase-matched filtering to reduce the threshold for surface wave identification and measurement.

In addition to optimizing procedures for surface wave identification, we are also testing improved procedures for optimizing surface wave measurement. A more stable and reliable measurement of surface wave amplitude than the traditional time domain M_s is the "path corrected spectral magnitude" (Stevens and McLaughlin, 2000; Stevens and Adams, 1999) which corrects the spectral amplitude with a surface wave Green's function and averages over an optimum frequency band. An advantage of the frequency domain processing is that a spectral magnitude of either signal or noise can always be measured over the specified frequency band, while it may not be possible to measure data in a specified frequency band in the time domain. Maxsurf, for example, will reject a seismogram if it can't find a 20 second arrival within the predicted arrival time window. This often occurs at regional distances and there is no reason for such a restriction for spectral magnitudes. Consequently, moments can be measured for regional seismograms in cases where standard M_s measurements cannot be made. During the next year, we will be working to optimize the path corrected spectral magnitude, and will assess the ability of the measurement to improve discrimination.

Acknowledgements

We would like to thank Mike Ritzwoller, Anatoli Levshin and Antonio Villasenor of the University of Colorado, Brian Mitchell and Bob Herrmann of St. Louis University, Goran Ekstrom of Harvard University, Andrew Curtis of Utrecht University, and their coworkers for the use of their data and models in this project**.**

Key Words: surface wave, dispersion curve, phase matched filter, regionalization, moment

REFERENCES

Berry, M. (1992), Large scale singular value computations, *Int. J. Supercomp. Appl., 6, 13-49*.

Curtis, A., J. Trampert, R. Snieder, and B. Dost (1998), Eurasian fundamental mode surface wave phase velocities and their relationship with tectonic structures. *J Geophys. Res., 103 (B11)* 26,919-26,947.

Ekstrom, G., A. M. Dziewonski, G. P. Smith, and W. Su (1996), "Elastic and Inelastic Structure Beneath Eurasia," in *Proceedings of the 18th Annual Seismic Research Symposium on Monitoring a Comprehensive Test Ban Treaty, 4-6 September, 1996*, Phillips Laboratory Report PL-TR-96-2153, July, pp. 309-318, ADA313692.

Herrin, E. and T. Goforth (1977), "Phase-Matched Filtering: Application to the Study of Rayleigh Waves," *Bull. Seism. Soc. Am*., v. 67, pp. 1259-1275.

Laske G., and G. Masters (1997), A Global Digital Map of Sediment Thickness, *EOS Trans. AGU, 78, F483*.

Levshin, A. L., M. H. Ritzwoller, and S. S. Smith (1996), "Group Velocity Variations Across Eurasia," in *Proceedings of the 18th Annual Seismic Research Symposium on Monitoring A Comprehensive Test Ban Treaty, 4-6 September, 1996*, Phillips Laboratory Report PL-TR-96-2153, July, pp. 70-79, ADA313692.

Mitchell, B. J., L. Cong and J. Xie, (1996), "Seismic Attenuation Studies in the Middle East and Southern Asia", St. Louis University Scientific Report No. 1, PL-TR-96-2154, ADA317387.

Mooney, W., G. Laske, and G. Masters (1998), "Crust 5.1: A Global Crustal Model at 5x5 Degrees," *Journal of Geophysical Research*, v. 103, no. B1, pp. 727-747.

Ritzwoller, M. H., A. L. Levshin, L. I. Ratnikova, and D. M. Tremblay (1996), "High Resolution Group Velocity Variations Across Central Asia," in *Proceedings of the 18th Annual Seismic Research Symposium On Monitoring A Comprehensive Test Ban Treaty, 4-6 September, 1996*, Phillips Laboratory Report PL-TR-96-2153, July, pp. 98-107, ADA313692.

Ritzwoller, M.H., O.Y Vdovin, and A.L. Levshin (1999), "Surface wave dispersion across Antarctica: A first look", *Antarctic J. U.S.*, in press.

Stevens, J. L. (1986), "Estimation of Scalar Moments From Explosion-Generated Surface Waves," *Bull. Seism. Soc. Am.*, v. 76, pp. 123-151.

Stevens, J. L., and D. A. Adams (1999), Improved surface wave detection and measurement using phase-matched filtering and improved regionalized models, 1999., *proceedings of the 21st Annual Seismic Research Symposium in Las Vegas, NV,* 274-282.

Stevens, J. L. and K. L. McLaughlin (1996), "Regionalized Maximum Likelihood Surface Wave Analysis," Maxwell Technologies Technical Report submitted to Phillips Laboratory, PL-TR-96-2273, SSS-DTR-96-15562, September, ADA321813.

Stevens, J. L., and K. L. McLaughlin (1988), "Analysis of surface waves from the Novaya Zemlya, Mururoa, and Amchitka test sites, and maximum likelihood estimation of scalar moments from earthquakes and explosions," S-CUBED technical report submitted to Air Force Technical Applications Center, SSS-TR-89-9953, September.

Stevens, J. L. and K. L. McLaughlin (2000), "Optimization of surface wave identification and measurement," *Pure and Applied Geophysics*, in press.

Vasco, D. W., L.R. Johnson, and O. Marques (1999), Global Earth structure: inference and assessment, *Geophys. J. Int.,* 137.

Vdovin, O. Y., J. A. Rial, M. H. Ritzwoller, and A. L. Levshin (1999), "Group-velocity tomography of South America and the surrounding oceans", *Geophys. J. Int.*, 136, 324-330.

MAPPING LATERAL VARIATIONS IN UPPER MANTLE ATTENUATION USING STACKS OF P AND PP SPECTRA

Linda Warren and Peter M. Shearer

Institute of Geophysics and Planetary Physics
Scripps Institution of Oceanography
University of California, San Diego

Sponsored by the National Science Foundation
Grant EAR-9909267

ABSTRACT

Using seismograms from globally-distributed, shallow earthquakes between 1988 and 1998, we compute over 30,000 spectra of P arrivals from epicentral distances of 40° to 80° and PP arrivals from 80° to 160°. We correct each spectrum for the instrument response, an $\omega^{-2.15}$ source model, and a one-dimensional Q_α model (Warren and Shearer, 2000). Next, we stack the logarithms of the P and PP spectra in bins of similar source-receiver range. The stacked log-spectra appear stable between about 0.16 and 0.86 Hz, with noise and/or bias affecting the results at higher frequencies. Since we have multiple sources for each receiver and multiple receivers for each source, we can measure the attenuation beneath each source and receiver by stacking the appropriate P log-spectra. We then correct the PP log-spectra for the appropriate source and receiver-side terms. Since lower mantle attenuation is small, the residual PP log-spectrum approximates attenuation in the upper mantle near the PP bounce point. Using this approach, we produce maps of global variations in average P-wave upper mantle attenuation. These results generally correlate with surface tectonics and previously published Q models. Continents are usually less attenuating than the global average, whereas oceanic regions are more attenuating. Notable exceptions to this pattern include southern Africa (more attenuating than average) and the southwest Pacific (less attenuating than average).

Key Words: Seismic Attenuation, Upper Mantle Structure

OBJECTIVE

The objective of this research is to resolve variations in upper mantle P-wave attenuation by analyzing short-period P and PP spectra. Results of this research will help to establish detection levels for small events and calibrate magnitude versus yield relationships for explosions.

RESEARCH ACCOMPLISHED

Data and Methods

We select our seismograms from the IRIS FARM database between 1988 and 1998. We search the database, which we have filtered and resampled at 5 Hz, for all P arrivals at epicentral distances between 40° and 80° and all PP arrivals between 80° and 160° (i.e., twice the P range interval) from shallow (<50 km depth) earthquakes. Next, after applying a Hanning taper, we compute the spectrum for a 12.8-second-long signal window beginning two seconds before each predicted arrival time and for a 12.8-second-long noise window just preceding this. We select spectra that have average signal-to-noise ratios of two or greater between 0.16 and 0.86 Hz. This results in 18,018 P and 14,287 PP spectra from 1553 events and 151 stations.

Each computed spectrum, $D(f)$, represents the effects of the source $S(f)$, attenuation $A(f)$ and instrument $R(f)$ responses:

$$D(f) = S(f)A(f)R(f)$$

We correct each spectrum for the known instrument response, an $\omega^{-2.15}$ source model (found by Warren and Shearer, 2000, to be appropriate for this data set), and the globally-averaged Q model of Warren and Shearer (2000).

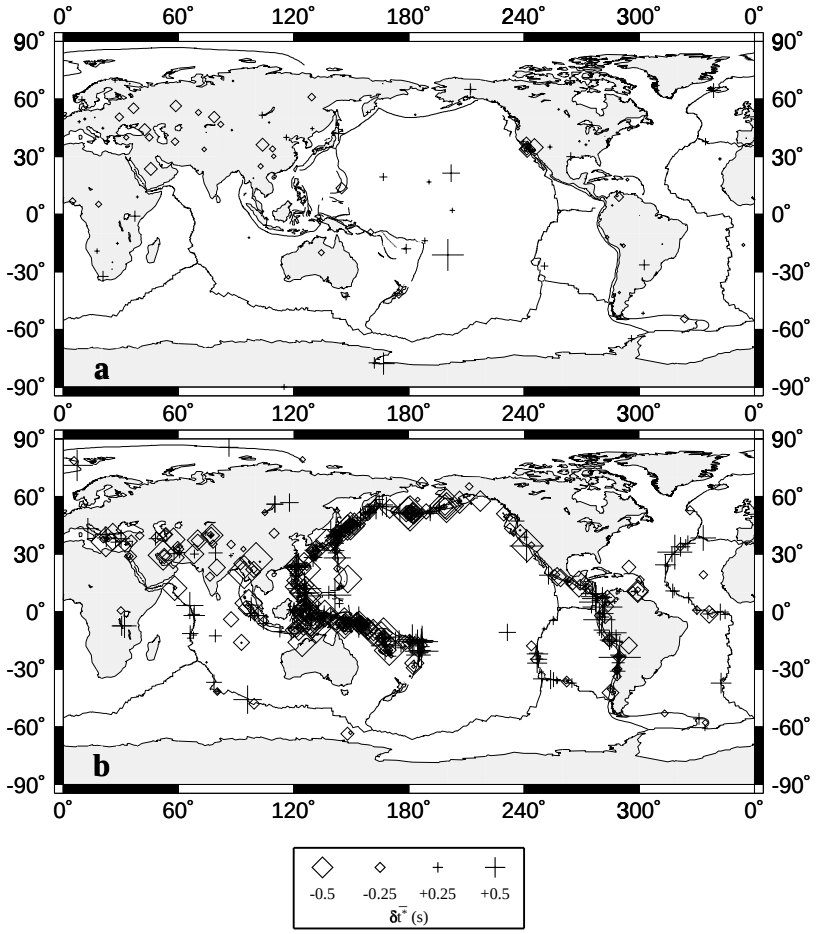


Figure 1. Residual $\overline{t^*}$ measurements for stations (top) and events (bottom)

After these corrections are applied, the remaining spectrum represents deviations from the average attenuation response. The slope of the spectrum allows us to measure how much the wave has decayed along its path. The amplitude decay with frequency is given by $A(f) = A_0 \exp(-\pi f t^*)$ where $t^* = \int dt/Q$. The apparent t^*, termed $\overline{t^*}$, can be measured by fitting a straight line to the spectrum in linear frequency - logarithmic amplitude space:

$$\overline{t^*} = t^* + f\frac{dt^*}{df} = -\frac{1}{\pi}\,\frac{d(\ln A)}{df}$$

When we measure residual $\overline{t^*}$ (which we will refer as $\delta\overline{t^*}$) from the spectrum, positive values indicate that a path is more attenuating than the average while negative values indicate that a path is less attenuating.

Station and Source Terms

We can measure the attenuation beneath each source and receiver by stacking the appropriate P spectra since we have multiple sources for each receiver and multiple receivers for each source. The resulting source-specific response functions include any remaining source spectrum and the effect of near-source attenuation in the upper mantle. The receiver stacks include the site response and near-receiver attenuation in the upper mantle. We measure $\delta\overline{t^*}$ from the slope of the stacked spectra between 0.16 and 0.86 Hz. Maps showing the source and station terms are plotted in Figure 1 and show some coherent patterns. For example, the station and source $\delta\overline{t^*}$ values across Eurasia are mostly negative, indicating that they are on less attenuating material. The variations we see, while relatively small in this region, are probably due to site effects and differences between sources. In other regions, there are much larger variations in $\delta\overline{t^*}$ over relatively small areas.

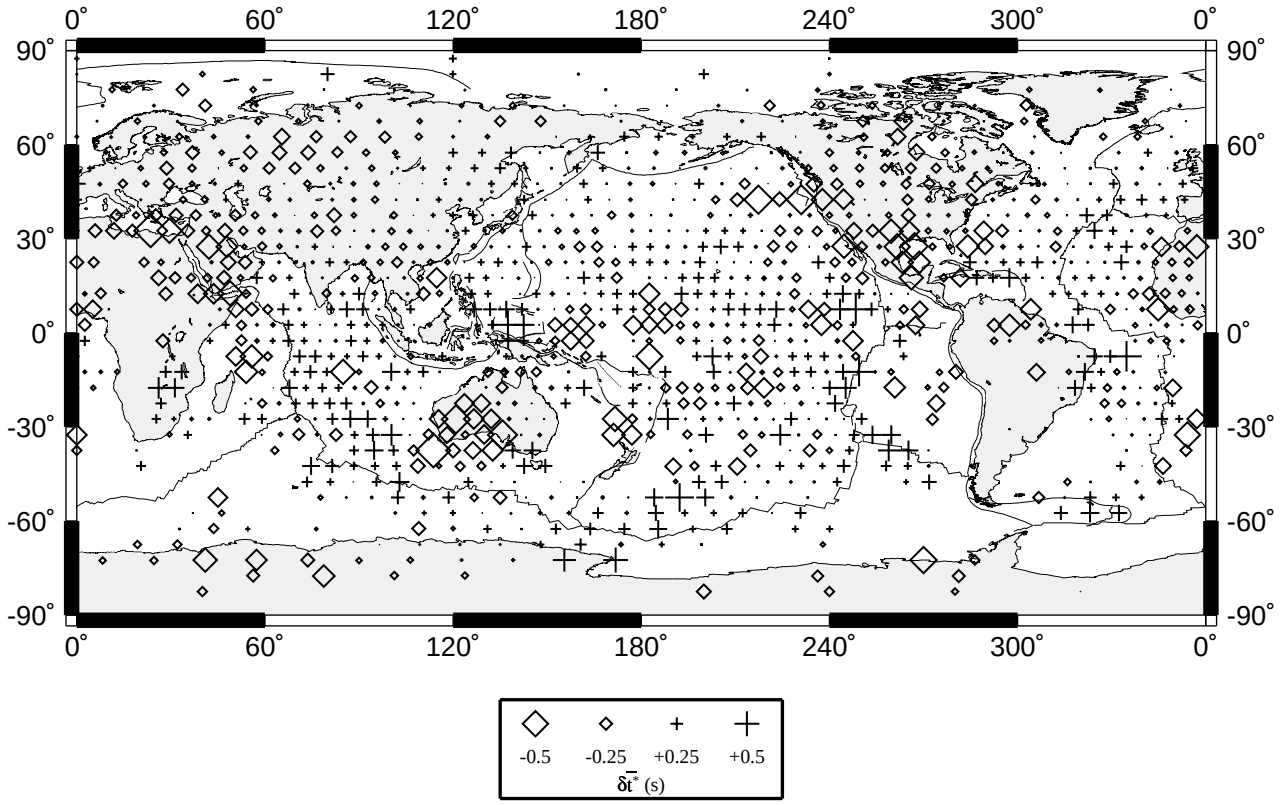


Figure 2. Residual $\overline{t^*}$ measurements averaged in caps of 5° radius at the PP bouncepoints. There are a minimum of 5 measurements in each cap.

Lateral Variations in $\overline{t^*}$

While our station and source terms provide us with a preview of the lateral variations in upper mantle attenuation, they aso reveal that they could be biased by local crustal structures or source differences. Since the PP spectra will be similarly affected, we correct them for the station and source terms. These terms include the propagation response in the upper mantle beneath the stations and earthquakes, so only attenuation accumulated along the rest of the PP path will be left in the spectrum. Since lower-mantle attenuation is small, the remaining spectrum should approximate attenuation near the PP bouncepoint in the upper mantle. We measure $\delta\overline{t^*}$ between 0.16 and 0.86 Hz from the remaining spectrum. Since the individual $\delta\overline{t^*}$ measurements exhibit considerable scatter, we smooth our results be computing the average values within PP bouncepoint caps of 5° radius spaced by 5°. The cap-averaged results are plotted in Figure 2. Larger symbols indicate larger-magnitude variations.

Our results are in general agreement with previous upper mantle Q models (e.g., Romanowicz, 1995; Bhattacharyya et al., 1996). The shields across Eurasia and North America are less attenuating (negative $\delta\overline{t^*}$ values) while more attenuating regions (positive $\delta\overline{t^*}$ values) are found along the mid-ocean-ridge system and in the mid-Pacific. These patterns suggest that the amount of attenuation correlates with the tectonic setting. Indeed, when we bin the caps by tectonic region (following Jordan, 1981) and compute the mean value for each type of region (Figure 3) we see that the mean values follow a pattern consistent with that expected based on their tectonic history. The upper mantle beneath young ocean floor, where hot material is upwelling, is the most attenuating type of region, followed closely by intermediate-age oceans. Old oceans are much less attenuating than young oceans. The least attenuating regions are the old shields and platforms. There are exceptions to these patterns. For example, beneath southern Africa we see a more attenuating region and in the southwest Pacific we see a less attenuating region.

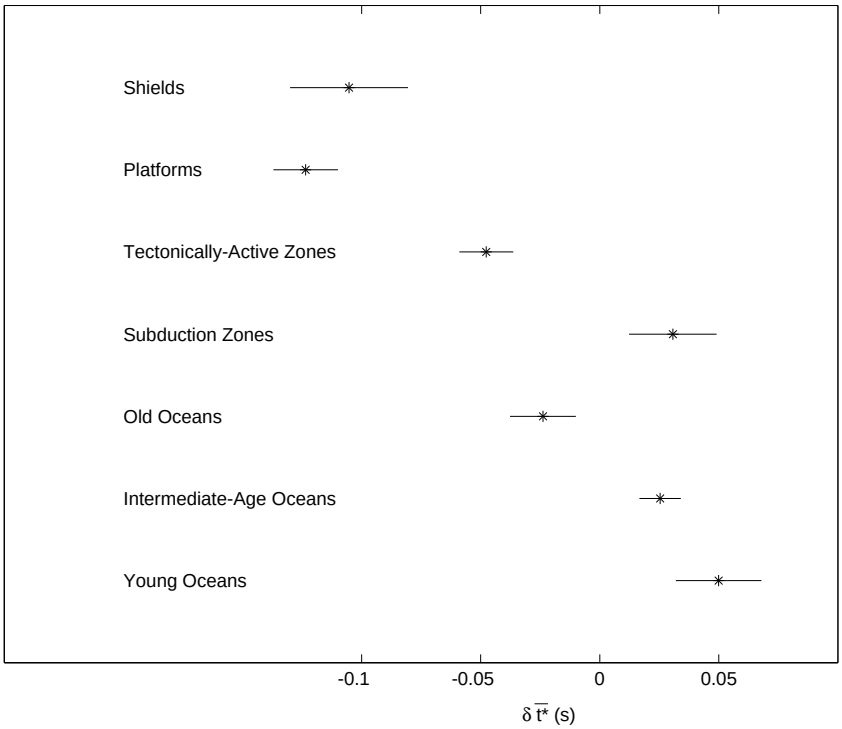


Figure 3. Average residual $\overline{t^*}$ measurements plotted for PP bouncepoints in different tectonic regions. One-standard-error bars are also shown.

CONCLUSIONS AND RECOMMENDATIONS

Variations in upper mantle Q_α can be mapped by analyzing global data sets of short-period P and PP spectra. Given sufficient data, the effects of variations in source spectra and receiver site response can be removed, permitting along-path attenuation to be resolved. Our results are generally consistent with previous studies which show a correlation of upper mantle attenuation structure with tectonic region. Continued research will help to calibrate magnitude versus yield relationships over large parts of the Earth's surface.

REFERENCES

Bhattacharyya, J., G. Masters, and P.M. Shearer, Global lateral variations of shear wave attenuation in the upper mantle, *J. Geophys. Res.*, 101, 22,273–22,289, 1996.

Jordan, T.H., Global tectonic regionalization for seismological data analysis, *Bull. Seismol. Soc. Am.*, 71, 1131–1141, 1981.

Romanowicz, B., A global tomographic model of shear attenuation in the upper mantle, *J. Geophys. Res.*, 100, 12,375–12,394, 1995.

Warren, L.M., and P.M. Shearer, Investigating the frequency dependence of mantle Q by stacking P and PP spectra, *J. Geophys. Res.*, submitted 2000.

3. Seismic Source Characterization

SEISMIC CHARACTERIZATION OF THE NOVEMBER 8, 10, AND 11, 1999 DEAD SEA UNDERWATER CHEMICAL CALIBRATION EXPLOSIONS USING CEPSTRAL MODELING AND INVERSION

Douglas R. Baumgardt and Angelina Freeman
ENSCO, Inc.

Sponsored by U.S. Department of Defense
Defense Threat Reduction Agency
Arms Control Technology Division
Nuclear Treaties Branch

Contract No. DSWA01-98-C-0157

ABSTRACT

We have developed a cepstral simulation and inversion algorithm for analysis of regional seismic recordings of underwater explosions that determines the yield and depth of the explosions. The spectra of seismic recordings of the underwater blasts have strong time-independent spectral scalloping produced by the correlated bubble pulses and echoes of acoustic reflections from the water surface and in the water column. Signed cepstra, computed from the fourier transform of the log-amplitude spectra of regional seismic phases (Pn, Pg, Sn, and Lg), contain positive peaks produced by the bubble pulse correlation and negative peaks from the water-surface reflection. Theoretical cepstra of underwater explosions with assumed depths and yields are computed from simulated time sequences of bubble pressure pulses and water column reflections. The pulses are modeled as minimum-phase wavelets with the amplitudes of the bubble pulses set by the source physics of underwater explosions and the reverberation amplitudes

determined from the assumed reflection coefficients of the surface and bottom of the water column. A prototyped inversion algorithm, that determines explosion depth and yield, matches the synthetic model cepstra to data cepstra, stacked across all seismic phases and channels, by means of exhaustive search and downhill simplex and simulated annealing optimization methods. We have tested this algorithm on seismic recordings of three Defense Threat Reduction Agency's (DTRA) calibration chemical explosions detonated in the Dead Sea on November 8, 10, and 11, 1999. The three explosions all detonated at about 70 m and with yields of 500, 2000, and 5000 kg were recorded at the regional seismic stations EIL and MRNA on the high-frequency channels sampled at 40 Hz. This low bandwidth limits the resolution of short delay signals from water layer bounces but is adequate for resolving the bubble pulses from these events. The cepstral peaks were observed in all of recorded phases, and similar delay times were observed at two different stations for the largest explosion. The cepstral peak quefrencies (time delays) correspond to bubble pulse periods of 400, 550, and 800 ms. We estimate yields 650 ±140kg, 1950±750 kg, and 4200±500 kg for the 500, 2000, and 5000 kg explosions, respectively. Depth estimates of about 80 m from the combination of the bubble pulse period and interpreted surface reflections are not as well resolved, because of the shallow depths of the explosions and the limited bandwidth of the IMS data. However, the results are consistent with the known depths of 70 m. These results show that accuracy of this method is limited by the seismic bandwidth, particularly for small, shallow events. Overall, this study points out the importance of using seismic data for detection and characterization of underwater explosions in inland seas.

OBJECTIVES

The problem of the identification of underwater blasts has gained increased interest recently in the context of the monitoring of the Comprehensive Nuclear Test-Ban Treaty (CTBT) which was opened for signature by the United Nations on 24 September 1996. Annex 1 to the Protocol of the CTBT calls for the installation of an International Monitoring System (IMS) including six hydroacoustic stations and five so-called "T-phase" stations. T-phase stations are seismic sensors located near the coast that can detect hydroacoustic phases converted to seismic phases at the coast. Thus, only 11 stations will be available specifically for monitoring underwater events. If an explosion occurs in the ocean, but near the coast outside of the SOFAR channel, long-range propagation of hydroacoustic signals may be blocked, and there is a possibility that the events may not be easily detected by the IMS assets directed toward the underwater explosions. Because of the relatively larger number of seismic stations, 170 primary plus auxiliary stations, called for the CTBT Protocol for the IMS, near-coast seismic stations may have a better chance of detecting and characterizing underwater events on the continental slopes, outside of the SOFAR channel, or in confined seas. Moreover, early-arriving seismic signals, such as *Pn*, *Pg*, *Sn*, and *Lg*, produced by mode conversion of acoustic waves in the water in the vicinity of the source, may carry more useful information about in-situ source conditions than later arriving T phases that may be affected by propagation path effects in the oceanic water column.

Baumgardt and Der (1998) showed numerous examples of underwater explosions recorded at seismic stations and how they can be best characterized by spectral and cepstral analysis. A simple model for underwater explosions was developed and synthetic cepstra were produced that reproduced most of the essential features of observed underwater explosion cepstra. The main features were bubble pulses, which produce positive cepstral peaks, and the first surface reflection that produces a strong negative cepstral peak. The timing and relative amplitudes of these cepstral peaks provide useful constraints on the depth and yield of underwater explosions.

The following are the objectives of this study:

- Collect appropriate seismic data from explosions and earthquakes in water-covered and nearby areas for study, preferably with corresponding hydroacoustic data that may be used to validate results of calculations.
- Gain an improved understanding of the effects of the water column on the seismic data, and use this understanding to determine parameters such as in the water column/not in the water column, water depth, and others.
- Develop an algorithm to extract information from seismic records of events in and near water-covered areas to aid in monitoring the CTBT.

RESEARCH ACCOMPLISHED

This paper describes the results of our development and application of a spectral and cepstral analysis algorithm described in earlier presentations (Baumgardt, 1999a, Baumgardt and Freeman, 2000) and an annual technical report (Baumgardt, 1999), designed to estimate yield and depth of underwater explosions. In the earlier studies, the results of analysis of presumed underwater explosions detonated in the Norwegian and Baltic Seas were discussed. Estimates of denotation depths and yields of the explosions were presented. However, we had no ground truth information with which to compare the results of our analyses. In November, 1999, under DTRA sponsorship, the Seismology Division of The Geophysical Institute of Israel detonated three chemical explosions in the Dead Sea at a depth of 70 m and with known yields of 500, 2000, and 5000 kg (Gitterman et al., 1999). These events were recorded by two seismic stations of the IMS, Meron (MRNI) and Eilat (EIL), and thus provided us with actual underwater explosions with ground truth which can be used to evaluate the algorithm. In this paper, we review the cepstral analysis and modeling approach, discuss the results of its application to the Dead Sea calibration events, and describe a new graphical user interface (GUI) prototyped in Matlab for the application of the algorithm.

THE DEAD SEA CALIBRATION EXPLOSIONS – NOVEMBER 8, 10, AND 11, 1999

The location and source parameters of the Dead Sea calibration explosions of November 8, 10, and 11, 1999 have been described in detail by Gitterman et al, 1999. Figure 1 shows a map of the location of the explosions and the propagation paths to the two IMS stations, MRNI and EIL.

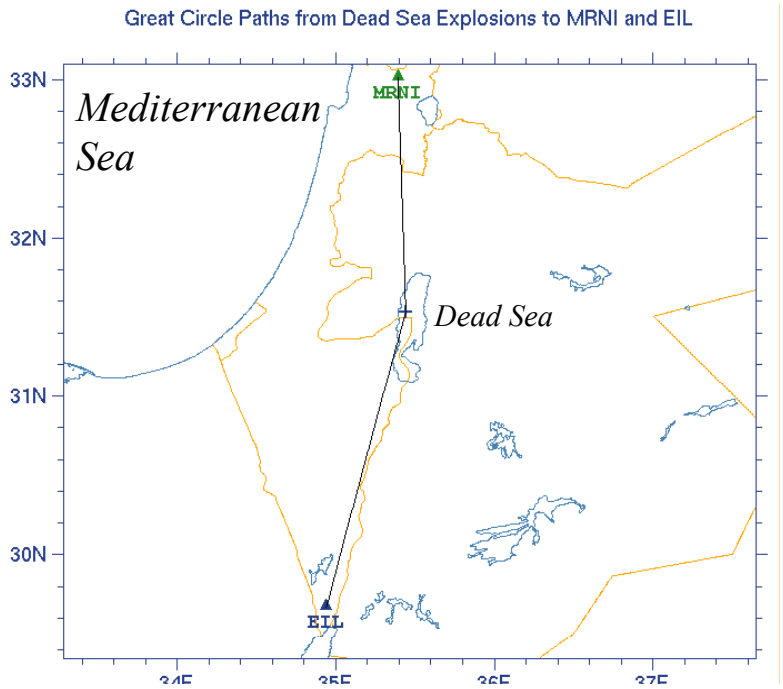


Figure 1: Plot of map of the IMS stations that recorded the calibration explosions in the Dead Sea.

Figures 2 and 3 below show the waveforms of the explosions recorded at EIL and MRNI, respectively, with the phases reported in the Reviewed Event Bulletin (REB) plotted on the waveforms.

It should be noted that the 500 kg event of November 8 was not recorded at EIL. It is notable that these three events had very different waveforms, which are evidently due to the differences in source parameters of the events.

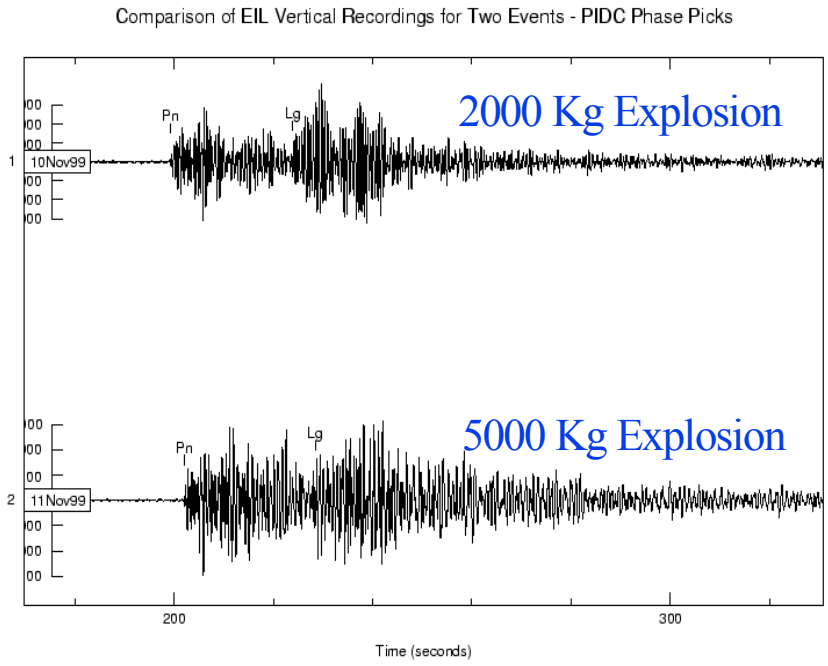


Figure 2: Waveforms of the November 10 and 11, 1999 Dead Sea explosions recorded at EIL.

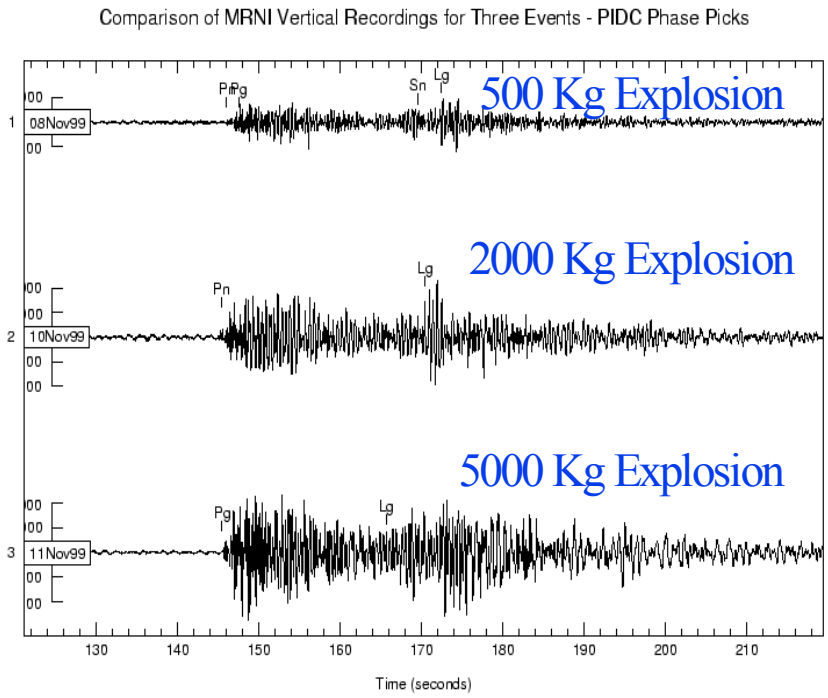


Figure 3: Plots of the MRNI recordings of the November 8, 10, and 11, 1999 Dead Sea Explosions.

CEPSTRAL ANALYSIS

Baumgardt and Zeigler (1988) and Baumgardt and Der (1999) describe the cepstral analysis technique in detail. In brief, the spectra of each of the phases identified in Figures 2 and 3 in a 25 second window are computed and corrected for instrument response and linear trend. A second Fourier transform is then taken of the log of the real part of the spectra, which gives what is called the "cosine" or "signed" cepstrum. The peaks which appear in these cepstra correspond in quefrency (independent variable of the cepstrum) which gives the time delay corresponding to the spectral modulations produced by the explosion bubble pulse and reflection from the free surface.

We have found that averaging, or "stacking", spectra or cepstra, across multiple channels enhances the spectral modulations and cepstral peaks caused by the source and reduces the effects of local site scattering and noise. In our earlier studies of underwater explosions off the coast of Scandinavia (Baumgardt, 1999a,b), we had array data available, and array averaged spectra and cepstra were much improved over those computed for single channel data. For three-component data, such as the IMS stations recordings of the Dead Sea events, array data was not available. However, we have found that stacking cepstra or spectra across the three-component channels (Z, NS, EW) provides more improved results over single channel data. Finally, spectra and cepstra can be stacked across multiple stations that record the event, such as MRNI and EIL for the Dead Sea events.

Stacked cepstra can be computed by either stacking the spectra, and computing the cepstra from the stacked spectra, or by computing cepstra for each channel and stacking the cepstra. We have found little difference in cepstra computed by either spectral or cepstral stacking.

Figures 4 shows the processed spectra and cepstra for the phases recorded at EIL from the 5000 kg explosion of November 11. In this case, the spectra have been stacked across the three components and the cepstra were computed from the stacked spectra.

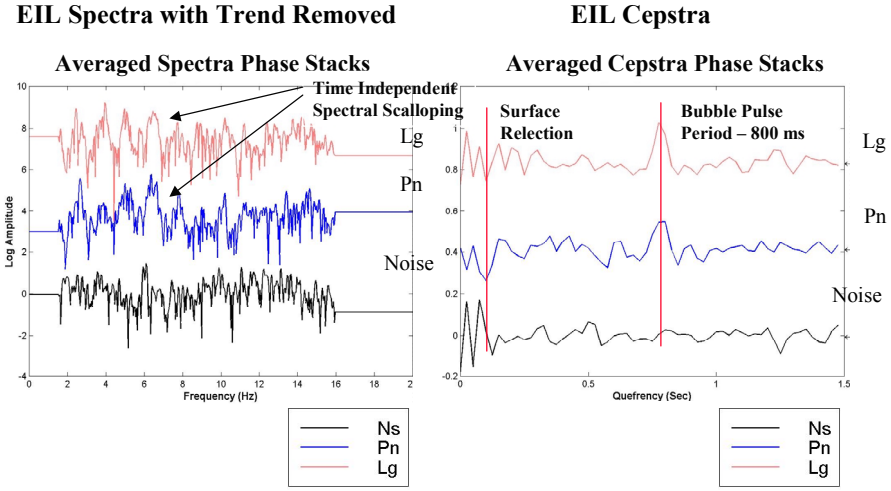


Figure 4: Spectra and cepstra for the EIL recordings of the November 11, 1999 5000 kg Dead Sea Explosion.

The spectra on the left have been processed by removing the instrument response and have been tapered to a flat level on the low and high frequency ends. The spectra are for each of the phases reported by the PIDC for this event (*Pn*, *Lg*) and the noise ahead of the *Pn (Ns)*. The spectra clearly show spectral modulations that appear in all phases but not in the noise, as indicated in the figure. These spectral modulations produce peaks in the cepstra of the two phases as shown on the right of Figure 4. Weak negative peaks at low

quefrency may correspond to reflections from the free surface and the very strong positive peaks are due to the bubble pulse. The estimated bubble pulse period for this event is about 800 ms.

CEPSTRAL MODELING AND INVERSION APPROACH

Spectra of underwater explosions contain very distinct spectral modulation or scalloping in all phases that does not appear in the noise. Spectra of this kind have been shown to be caused by source multiplicity, either due to ripple fire in mine blasts (Baumgardt and Ziegler, 1988) or by water column reverberations and bubble pulses in underwater explosions (Baumgardt and Der, 1998).

We have developed a modeling and inversion algorithm for the characterization of cepstra of underwater blasts which was described by Baumgardt (1999a,b). Because the cepstrum reflects the correlation structure of the source-produced pulses, it is easier to model than the waveforms themselves. The removal of the polynomial trend in the spectra also eliminates the spectral effects of the propagation path and thus, only the source correlation structure is retained in the cepstra. We showed in our earlier study (Baumgardt and Der, 1998) that modeling cepstra does not require information about the propagation path or receiver function, nor does it even require much information about the source time function. Thus, modeling cepstra requires many fewer parameters than modeling waveforms or spectra.

The modeling techniques described by Baumgardt and Der (1998) are used to interpret this event. The model construction is illustrated in Figure 5.

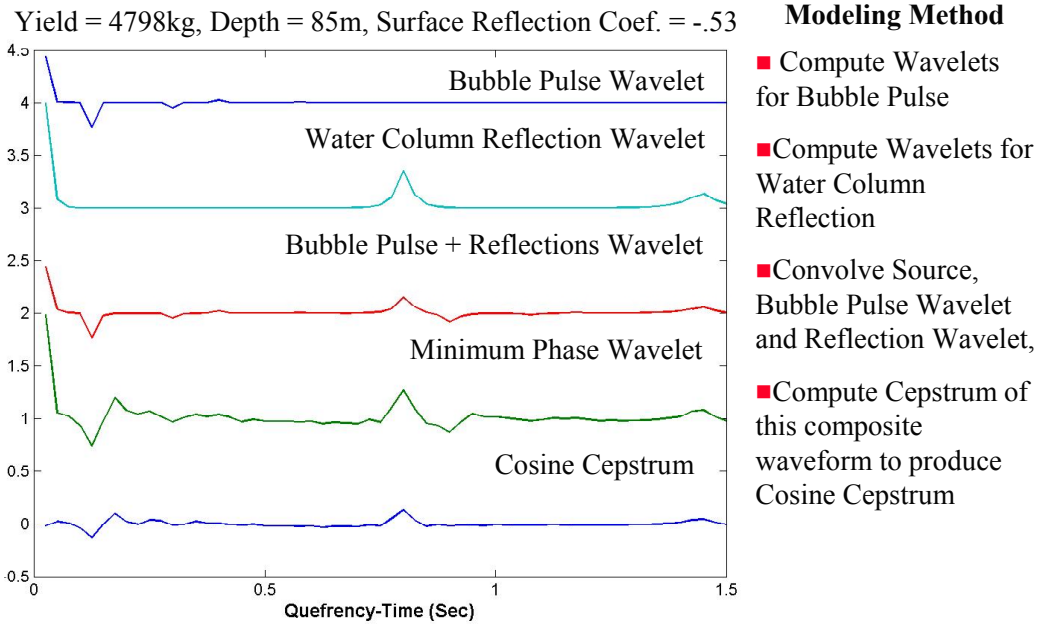


Figure 5: Modeling approach for calculating synthetic cepstra.

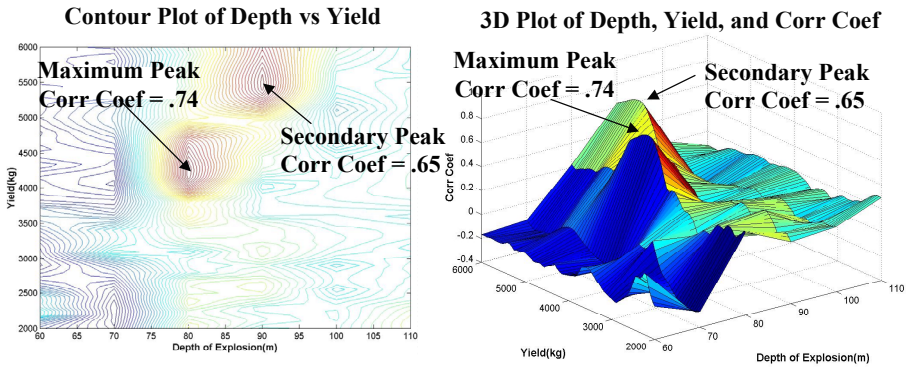
We convolve wavelets for the bubble pulse, shown on top, and water column reverberation, shown as the second trace, for a given assumed yield and depth in the water. The theory for calculating bubble pulse wavelets was taken from the literature and is described by Baumgardt and Der (1998). Other parameters that must be specified include average water column depth, that can be obtained from the bathymetry, and the surface and water bottom reflection coefficients. As in the case of water depth, these parameters can be estimated with some degree of accuracy, but it is also conceivable that they can be inferred from the data.

We assume that the acoustic waves in the water reflect from first-order discontinuities at the bottom and the surface.

We then compute the cepstrum of this composite wavelet, which is shown at the bottom of Figure 5. We also show a minimum phase wavelet reconstruction from the cepstrum which is identical to the original wavelet. This shows that our modeling method assumes minimum phase wavelets.

Finally, we seek a synthetic cepstrum that matches the observed cepstrum. For this purpose, we compute the correlation coefficient between the stacked observed cepstrum and the synthetic cepstrum and seek a cepstrum that provides the highest correlation. We first have considered an exhaustive search method, where the parameter space of blast yield and depth is gridded and synthetic cepstra are computed for each grid point. Then, we correlate the synthetic cepstra at each grid point and compute a correlation coefficient surface over the depth/yield parameter space and look for the peaks in the depth/yield surface.

Figure 6 shows the resultant correlation coefficient surface plotted in contour (left) and as a 3-D surface rendering (right).



Synthetic cepstra are computed for a range of Yield and Depth, and each Synthetic Cepstrum is correlated with the observed cepstra.

Inversion Yield = 4250kg, Depth = 80m	**Actual Yield = 5000kg, Depth = 70m**

Figure 6: Contour plots (left) and 3 D plot (right) of the correlation surface between synthetic cepstra and observed cepstra for the EIL recording of the November 11, 1999 Dead Sea explosion.

Both displays have a distinct peak in the correlation, with a maximum correlation coefficient of 0.74, corresponding to a water depth of 80 m and yield of 4250 kg. The sensitivity to yield is illustrated in Figure 7, which shows the correlation coefficient as a function of yield for the depth of 80 m. The maximum peak was at 4250 kg, but the range covers the true value of 5000 kg. Figure 7 also shows a direct comparison of the observed stack cepstrum and the best-matching synthetic cepstrum. This comparison shows that, although the match is not perfect, reasonably good matches of the essential features, the negative peaks of the water column reflection and the bubble pulses, have been attained.

In addition to the correlation coefficient, we have also used the L1 and L2 norms, described in detail by Baumgardt (1999b). Also, we have experimented with optimal search algorithms for inversion, including the downhill simplex optimal search and simulated annealing methods, along with the exhaustive search method described above, to find the best fitting synthetic cepstrum. Details about optimal search algorithms can be found in Baumgardt (1999b).

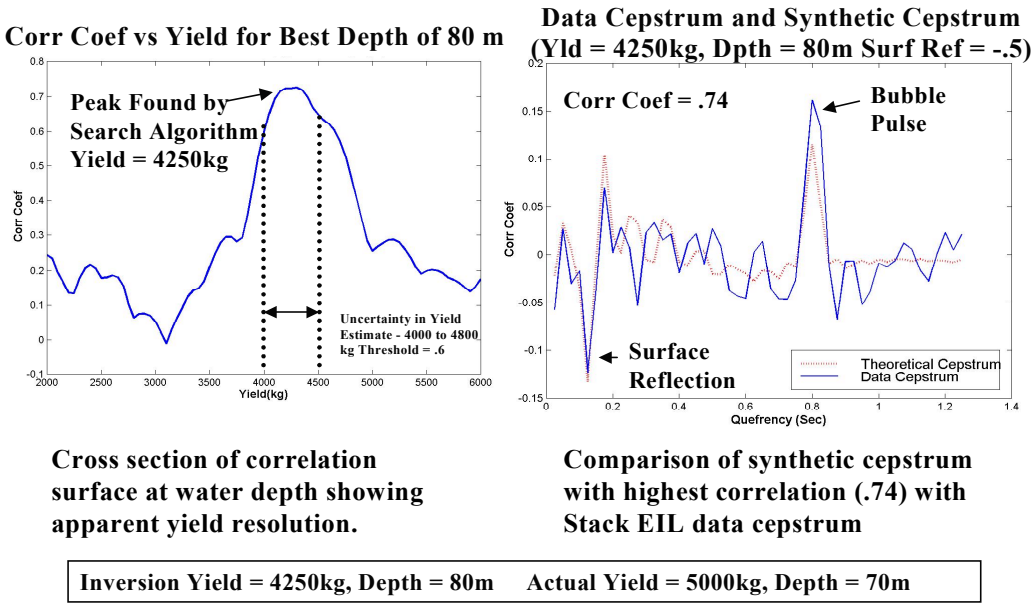


Figure 7: Cross section of the correlation peak (left) and comparison plot of the best matching synthetic and observed cepstra (right).

MATLAB GRAPHICAL USER INTERFACE

We have developed a Graphical User Interface (GUI) to facilitate the user's ease in interfacing with the cepstral simulation and inversion algorithm described above. The GUI for the Cepstral Modeling and Inversion Tool is Windows based, and was designed using Matlab, and can run on either a PC or UNIX workstation. The input data include the standard IDC database flat files (.origin, .arrival, .assoc, .w). The main GUI windows are described below.

The Stations and Channels GUI window (Figure) allows the user to choose the waveform (.w) file to process, and the prefix for the database files associated with the waveform. All of the corresponding stations and channels for the waveform file are displayed, and the user chooses the stations and channels to process. The Save Selection push button saves the parameters chosen for processing the data cepstrum, and the Close push button closes the Stations and Channels GUI window.

The user may compute a data cepstra, using the parameters set in the Stations and Channels GUI window. The parameters for the data cesptra are set in the Process Data GUI window (Figure 9a). The .w file being used is displayed, as well as the inprefix for the database files. The window used (Hanning, Parzen, or Kaiser), window length, and frequency range may be set. The options for noise subtraction, instrument response removal in processing the data cepstra, as well as individual plotting of the stack spectra for each station are available. Also, the polynomial fit degree may be set. The user has the choice of using either a Stacked Spectrum or Stacked Cepstrum method for computing the data cepstra, and the length of the data cepstra may be changed. The user also chooses the directory location for the cepstra files to be saved. When all of the input parameters are set, the user presses the Process Cepstrum button; plots of the data cepstra are displayed, and the cepstra data and necessary variables for the inversion algorithm are saved to the chosen directory. The Close pushbutton closes the Process Cepstrum GUI window.

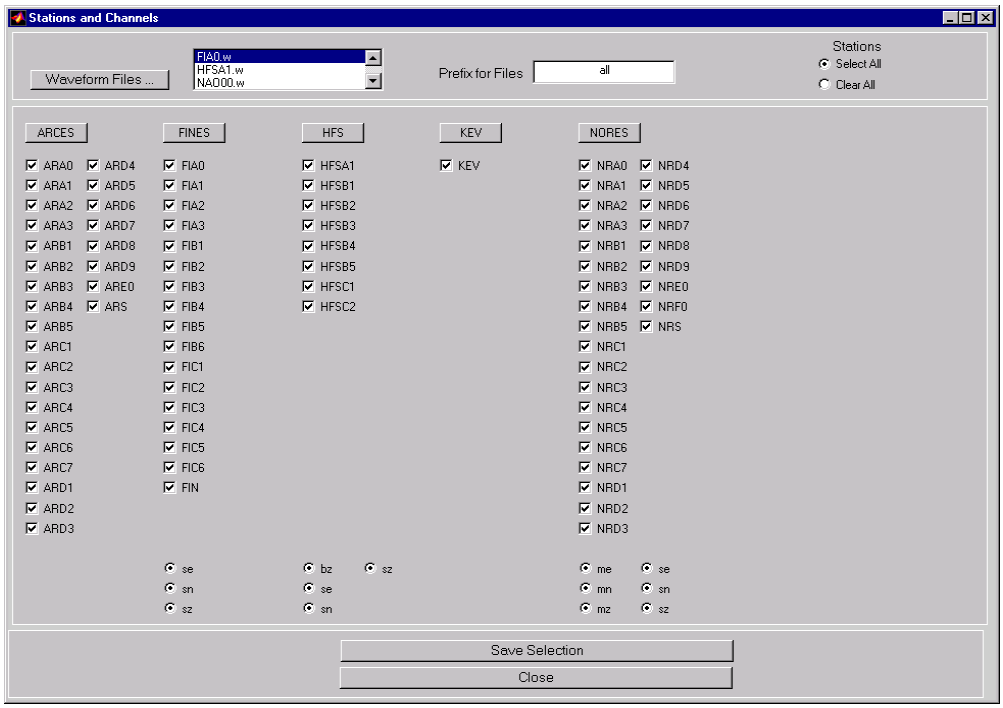


Figure 8: Stations and Channels GUI

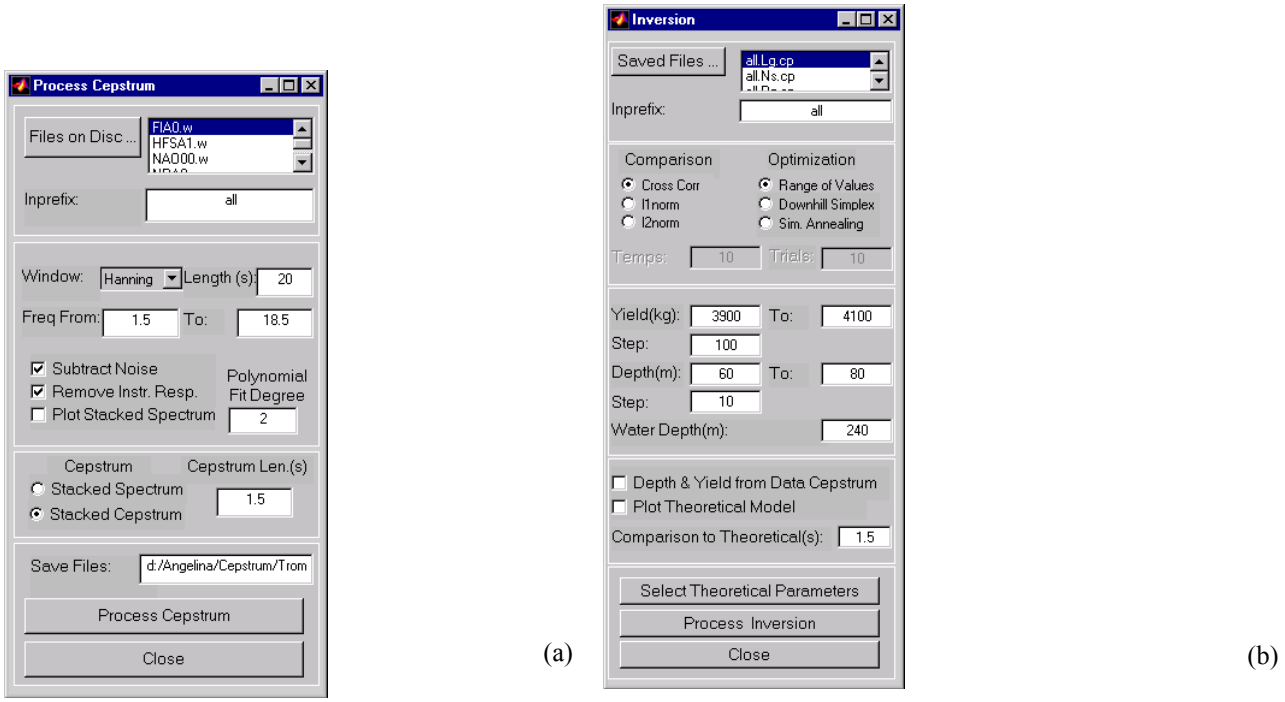


Figure 91: Process Data Cepstrum GUI Window (a) and Inversion GUI Window (b)

The parameters for the inversion of the data cepstrum with the model cepstra are set in the Inversion GUI window (Figure 9b). The saved data cepstra files in the current directory are displayed. However, other data files may be selected. The inprefix may also be edited. A Comparison method for the inversion, either Cross Correlation, L1 Norm, or L2 Norm can be selected by the user. The Optimization method, either Range of Values, Downhill Simplex, or Simulated Annealing is also selected. Choosing the Simulated Annealing method causes the Temperatures and also the Trials edit boxes to become active for the user to edit. If the user selects Range of Values as the Optimization method, the range of yields of the explosion, as well as the steps in yield values are displayed, and may be edited. The same is true for the depths of the explosion. If Downhill Simplex or Simulated Annealing are chosen for the Optimization method, only one edit box for depth, and one edit box for yield is displayed; the user utilizes these to specify the starting values for the Optimizations. It is likewise possible to set the Water Depth at the explosion location.

Checking the Depth and Yield from Data Cepstrum checkbox displays the data cepstrum at the beginning of the inversion process. The user, by clicking on the surface reflection and first bubble pulse, gives the algorithm information for determining a good starting point for depth and yield. This option for initializing depth and yield may be used with all of the optimization methods available. If the Plot Theoretical Model is selected, a figure containing the theoretical cepstrum and its components is displayed during the inversion process. The Select Theoretical Parameters pushbutton opens a GUI window for the theoretical parameters used for cepstral modeling. In this window the surface reflection, bottom reflection, decay constant for bubble pulse, takeoff angle in degrees, number of bubble pulses, and bubble pulse weighting may be edited. The Process Inversion pushbutton runs the inversion with the set parameters. Plots of the data cepstra and of the optimization method are displayed, as is a comparison between the data cepstrum and the best theoretical cepstrum match found by the chosen optimization method.

SUMMARY AND CONCLUSIONS

The results of our analysis of the three Dead Sea events, using the L1 norm fit parameter, are summarized below:

- Bubble Pulse Periods were resolved for all three explosions
  - –November 08, 1999: Bubble Pulse Period = 400 ms
  - –November 10, 1999: Bubble Pulse Period = 550 ms
  - –November 11, 1999: Bubble Pulse Periods = 800 ms
- Exhaustive Search Cepstral Inversion Results Using L1 Norm
  - –November 08, 1999 Actual Yield = 500 kg, Depth = 70 m
    Estimated Yield = 650 kg ± 140 kg (Threshold = .948) at Depth = 80 m
  - –November 10, 1999 Actual Yield = 2000 kg, Depth = 70 m
    Estimated Yield = 1950 kg ± 700 kg (Threshold = .955) at Depth = 80 m
  - –November 11, 1999 Actual Yield = 5000 kg, Depth = 70 m
    Estimated Yield = 4200 kg ± 500 kg (Threshold = .975) at Depth = 80 m

The accuracy of the yield estimates is controlled by the available bandwidth of the data. Large events provide the most accurate estimates since the longer delay times of the bubble pulses require less bandwidth than smaller events. Also, deeper events are resolved more accurately than shallow events for the same reasons – less bandwith is required to resolve the longer delay times of deep events than those of shallow events.

The results of this study indicate that the cepstral analysis and inversion algorithm provides a method for inferring source parameter of underwater explosions using seismic data. As discussed earlier, underwater explosions in regions like the Dead Sea, where acoustic signals do not get into the SOFAR channel of the open ocean, will not be detected by hydroacoustic sensors of the IMS. Thus, it is important that methods like the one described in this paper should be developed for application to seismic data as well as for hydroacoutic data.

Key Words: underwater explosions, yield estimation, discrimination, spectrum, cepstrum, modeling, inversion

REFERENCES

Baumgardt, D.R. (1999a). Seismic characterization of underwater explosions and undersea earthquakes using spectral/cepstral modeling and inversion, in Proceedings of 21 st Seismic Research Symposium, Las Vegas, Nevada, Sept. 21-24, 1999, pp. 352-362.

Baumgardt, D.R. (1999b). Characterization of underwater explosions by spectral/cepstral analysis, modeling, and inversion, Annual Report Submitted to DTRA, Reporting Period: 1 October 1998-30 September 1999, November, 1999, ENSCO, Inc., Springfield, Va.

Baumgardt, D.R. and A. Freeman (2000). Seismic characterization of the November 8, 10, and 11, 1999 Dead Sea underwater chemical calibration explosions using cepstral modeling and inversion, abstract in EOS, Supplement, May 9, 2000, p. s7.

Baumgardt D.R. and Z. Der (1998). Identification of presumed shallow underwater chemical explosions using land-based arrays. *Bull. Seism. Soc. Am.*, 88, 581-595.

Baumgardt, D.R. and K. Ziegler (1988). Spectral evidence of source multiplicity in explosions: application to regional discrimination of earthquakes and explosions, *Bull. Seism. Soc. Am.*, 78, 1773-1795.

Gitterman, Y., V.Pinsky, and A. Shapira (1999). Dead Sea calibration explosions: operations and preliminary data, Progress, Status, and Management Report No. 26, submitted to DTRA, GII Report No. 591/61/97(26), December,1999, Seismology Division, The Geophysical Institute of Israel.

A GROUND-TRUTH DATABASE FOR CENTRAL CHINA

W. Winston Chan and Xiaoxi Ni
Multimax, Inc.

Sponsored by U.S. Department of Energy
Office of Nonproliferation Research and Engineering
Office of Defense Nuclear Nonproliferation
National Nuclear Security Administration

Contract No. DE-FG02-99ER82837

ABSTRACT

We have constructed a ground-truth database consisting of phase-picks data and other geological and geophysical information in Sichuan and Yunnan Provinces in central China. The database includes 1,600 regional seismic events with over 40,000 phase picks recorded by the regional seismic network in central China from 1985 to 1994. The distribution of the seismic events covers the area 97°E to 108°E and 20°N to 40°N, with magnitudes ML= 0.3-6.9 and a maximum depth of 41 km. The data listing in the database is raw data information and contains a comprehensive listing of all phases that were detected. The listed information of the earthquakes includes origin time, epicenter location, magnitude, and focal depth. Major phase picks, such as Pn, Pg, Sg, were reported. Quality control is performed on the raw data, and unreliable picks are discarded. The data are compiled and stored in CSS format. The flat file tables include the origin, arrival, association, and site tables. As part of the effort to construct a comprehensive ground-truth database of central China, other geological and geophysical information such as the seismogenic structure in central China, is also included.

This data set forms the basis of an initial input to a ground-truth database for central China and has been delivered for incorporation into the Knowledge Base developed by the Department of Energy. Analysis of the data has been performed to yield a preliminary velocity model in central China. We performed a three-dimensional (3-D) tomographic inversion in central China by using the phase-picks data in the database. Altogether, 372 events are selected with over 5,900 P-phase arrivals. A five-layer 1-D starting model is chosen according to previous studies in the region. The studied region is divided into 16 by 16 blocks with a resolution of 0.5 degree. A 63% reduction in data variance is achieved after the fifth iteration of the joint inversion of crustal structure with relocation of the events. The results show correlation between the topography and the crustal velocity structure. The resultant crustal model also improves the clustering pattern of the seismic events in the region.

Key Words: ground-truth database, phase arrival time data, tomographic inversion, relocation, China

OBJECTIVE

The current research focuses on collection, processing, and analysis of historical seismic data for central China and assembly of these data in the form of a ground-truth database. As a Phase I feasibility study, we have collected representative ground-truth information for a preliminary analysis of travel times and crustal velocity structure. Seismic wave travel-time data in central China are collected and processed. A preliminary 3-D regional crustal structure in central China is obtained through tomographic inversion. We have also collected geological and geophysical maps of central China. A more extensive data collection and analysis leading to a comprehensive ground-truth database will be conducted in Phase 2.

RESEARCH ACCOMPLISHED

GEOLOGICAL AND GEOPHYSICAL SETTINGS

The central China region is located in a transitional zone between two different continental crusts of eastern and western China. The region is composed of three major tectonic blocks: the Garze block, central

Sichuan block and Aba block. Under regional tectonic movement, these blocks have been subject to strong horizontal compression. The collision and subduction of the Indian and Philippine Sea plates towards the Eurasian plate cause highly active seismicity in central China. The Xianshuihe, Minjiang, Maowen-Tianquan, Anninghe and Zemule faults along the block boundaries are driven by the tectonic movement and produce frequent and strong earthquakes.

The area of Sichuan west to Yaan consists of high mountains and platforms at the edge of the Tibetan Plateau. In the western Sichuan and eastern Tibet area, the topography is very complicated, with outcrop of shale, limestone, igneous rock, and other rocks. East to Yaan are the plain and hilly areas with elevations under 800 m. The Bangonghu-Nujiang, Jinshajiang and Xianshuihe-Xiaojiang fault zones are the major bent structures in central China surrounding the Indian Plate. Geologists believe that these fault zones consist of major faults that cut through the mantle and are the boundaries of the tectonic plates. From the age and range of the rocks in the fault zone, it is obvious that the bent zones become younger from the northeast to the southwest. It is hypothesized that during the long history of geological development, there were many collisions or under-thrusts between the tectonic plates in the southwestern China region. The bent boundaries between the tectonic plates retreated towards the southwest with a certain distance after each collision, and finally reached the present location in the Yaluzangbujiang-Yiluowadijiang zone. There is still active movement in the region, which causes the geological and geophysical activities in the bent zones.

Major geological structures in the central China region include the Sichuan platform syncline and the Longmengshan platform fold zone in the Yangtze Platform, the Kekexilibayankela geosyncline fold zone, the Batangsimo geosyncline fold zone and the kelakunluntanggula geosyncline fold zone in the Kunlunsanjiang fold system, the Gaizenaqu geosyncline fold zone in the Zangzhongnan platform and the Nianqintanggulagaoligong fault uplift zone (Ma, 1989).

SEISMICITY IN CENTRAL CHINA

Seismicity in central China is distributed along orogenic belts. There are the Xianshuihe earthquake belt, Litang earthquake zone and Batang earthquake zone in the region.

1) Xianshuihe earthquake belt: Since 1725, there have occurred 66 earthquakes with M>4.75, among which there were 9 earthquakes with M>7, 10 earthquakes with 6.1<M< 6.9, 26 earthquakes with 5.1<M<6.0 and 21 earthquakes with 4.75<M<5. From the August 1, 1725, Kongding M=7 earthquake to February 6, 1973, M=7.6 Luhuo earthquake, there were 9 earthquakes with M>7 in the region. The Xianshuihe earthquake belt is an active earthquake zone with strong and frequent earthquakes. The focal depths are mostly within 10-20 km. The focal mechanisms show that the stress field has a SW-NE trend and the earthquakes are mainly strike-slip events.

2) Litang earthquake zone: Since the August 24, 1930, M=5.5 Litang earthquake, there have been 9 earthquakes in the zone, among which there were 1 earthquake with M>7 (May 25, 1948 M=7.3 Litang earthquake), 5 earthquakes with 5.1<M<5.9 and 3 earthquakes with M<5.

3) Batang earthquake zone: Since the 1722 M=6 Batang earthquake, there have been 10 earthquakes with M>4.7, among which there were 1 earthquake with M>7 (April 11, 1870 M=7.5 Batang earthquake), 4 earthquakes with 6<M<6.9, and 5 earthquakes with 5<M<5.9. There were 5 earthquakes with M>5.5 in 1989.

PREVIOUS STUDIES ON CRUSTAL STRUCTURE IN CENTRAL CHINA

Regional phases of Pn, Sn, P, and S in central China were investigated by using the broadband digital seismic recordings (Ding et al., 1993) in the Eastern Tibet and Western Sichuan region. Velocities of Pn, Sn, P, S were determined from them. Average velocities of P and S are 5.6-6.0 km/s and 3.3 km/s, respectively, and those of Pn and Sn are 8.17 km/s and 4.6 km/s, respectively. The normal velocities of Pn and Sn in the Tibetan Plateau provide important evidence that both the thermal condition and material in the uppermost mantle of the Tibetan Plateau do not differ very much from those in other normal continents.

The reported velocity of Pn in the Tibetan Plateau varies from 8.0 km/s to 8.4 km/s or higher. Due to the difficulty of picking Sn phase from the seismogram, velocity of Sn in Tibetan Plateau has rarely been reported. Chen and Molnar (1981) and Barazangi and Ni (1982) obtained a value of 4.7 km/s for the velocity of Sn. Zhao and Zeng (1993) obtained another value of 4.55 km/s for Sn velocity. However, most of the previous results were obtained by using Tibetan earthquakes recorded by seismic stations in the neighboring areas. Seismic rays usually travel through a significant portion of non-Tibetan path. Also, a large range of epicentral distance (up to 18°) had been used in those studies.

From Zhao and Xie (1993), an abrupt change of crustal thickness from 79 km in Qiangtang block to 64 km in Songpan block is observed. It agrees very well with the results from teleseismic waveform inversion mentioned above. Less certain is the greater Pn velocity in the uppermost mantle of a narrow belt from Amdo to Golmud (Zhao and Xie, 1993).

GROUND-TRUTH DATABASE OF PHASE PICKS DATA IN CENTRAL CHINA

We have collected seismic data in central China from 1985 to 1994. A database has been constructed with 1,600 seismic events in central China that were recorded by the regional seismic network with over 160 seismic stations operated mainly in Sichuan and Yunnan provinces (Fig. 1). A comprehensive listing of over 40,000 seismic phase arrival time data in Central China are compiled in the database.

The distribution of the seismic events covers the area 97^{o}E to 108^{o}E and 20^{o}N to 40^{o}N, with magnitudes Ml= 0.3-6.9 and a maximum depth of 41km. The data listing in the database is raw data information and contains a comprehensive listing of all phases that were detected. The listed information of the earthquakes includes origin time, epicenter location, magnitude, and focal depth. Major phase picks, such as Pn, Pg, Sg, were reported. The data are compiled and stored in CSS format. The plain text tables include the origin, arrival, association and site tables.

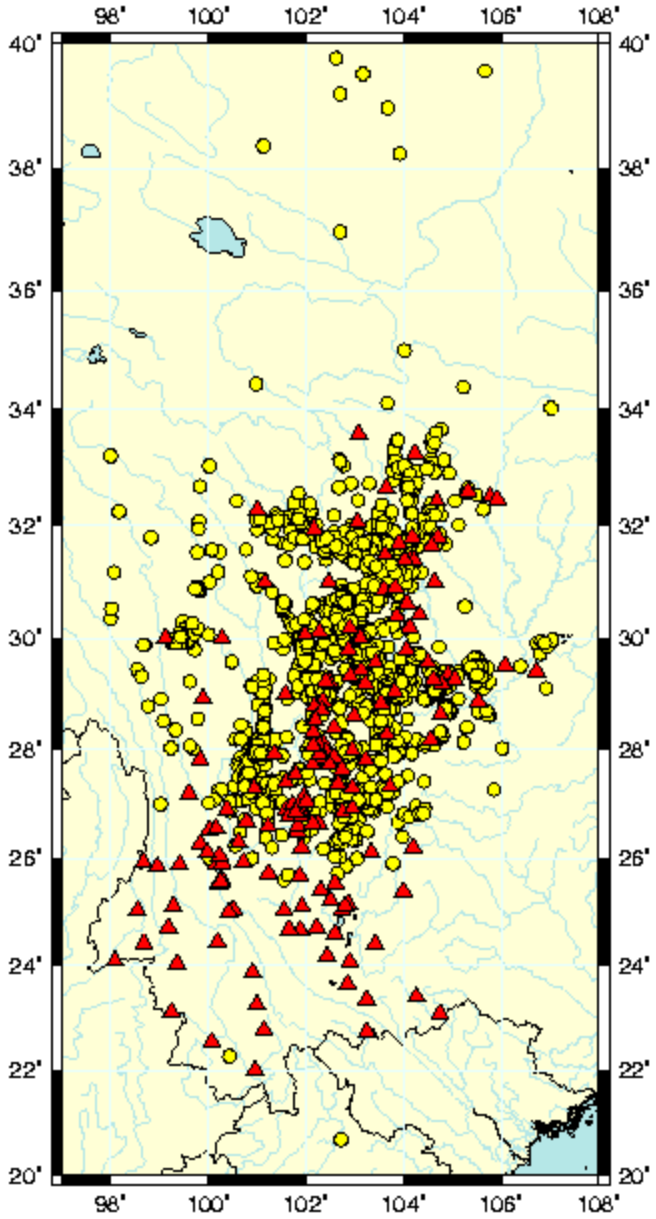


Fig. 1 Location of the seismic events in the central China ground-truth database. The circles denote the seismic events, and the triangles indicate the seismic stations.

Quality control is performed on the raw data. The phase arrival times are verified and validated independently. The arrival times are plotted against the epicentral distances and those that are deviated significantly from the average travel-time curves are regarded as unreliable picks and eliminated from the database. To illustrate the quality of the seismic data after quality control, the phase arrival times are shown in Fig. 2. Overall, the fluctuations in the travel-time curves are limited, which ensures the quality of phase picks data.

This data set forms the basis of an initial input to a ground-truth database for central China and has been delivered for incorporation into the Knowledge Base developed by the Department of Energy. Analysis of the data has been performed to yield preliminary velocity model and event relocation. These data may also be correlated with data obtained from the Chinese Digital Seismic Network (CDSN) to establish ground-truth database information for the region.

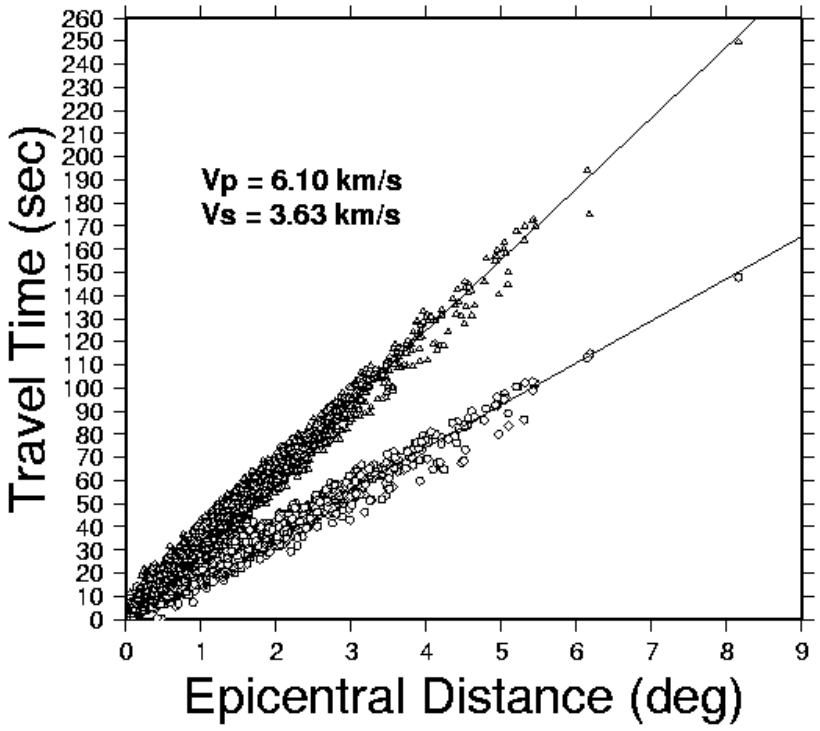


Fig. 2 Pg (circles) and Lg (triangles) travel times against epicentral distance. The P and Lg wave velocities are 6.1 and 3.63 km/sec, respectively.

3-D TOMOGRAPHIC INVERSION

The precise location of seismic events depends on the correctness of the earth model used in the location procedure, especially when dealing with events with small magnitudes that are only recorded in local or regional distances. Lateral heterogeneity can certainly affect the precision of the location of the events. To improve the confidence of the location of seismic events, a three-dimensional regional earth model of high resolution is desirable. The seismic phase picks data collected in central China are used to perform a 3-D tomographic inversion of the regional crustal structure.

We adopt the 3-D tomographic inversion method by Roecker (1987, 1993) and choose 372 seismic events from the compiled database for the 3-D tomographic inversion. The criterion for event selection is based on the density of event distribution in the region. In the central area, where the seismic events prevail, only those that are recorded by at least 20 stations are selected, but in the perimeter area, where the event density is less populated, the criterion is reduced to 5 stations to ensure sufficient coverage of the region. The event location, seismic station location and ray path projection are shown in Fig. 3. The spatial distribution of the events covers central China in the area 97°E-108°E, 24°N-35°N with focal depths up to 41km.

Among the earthquakes adopted for the inversion, large portions of them are located in the central area of the inversion region. Lattice of varying grid sizes is employed to reflect the density of seismic ray coverage where the grid spacing is 0.5 degree in the central area and 2 degrees in the perimeter. The crust in the studied area is divided into 5 layers and each layer is partitioned into 16 x 16 cells (Fig.3).

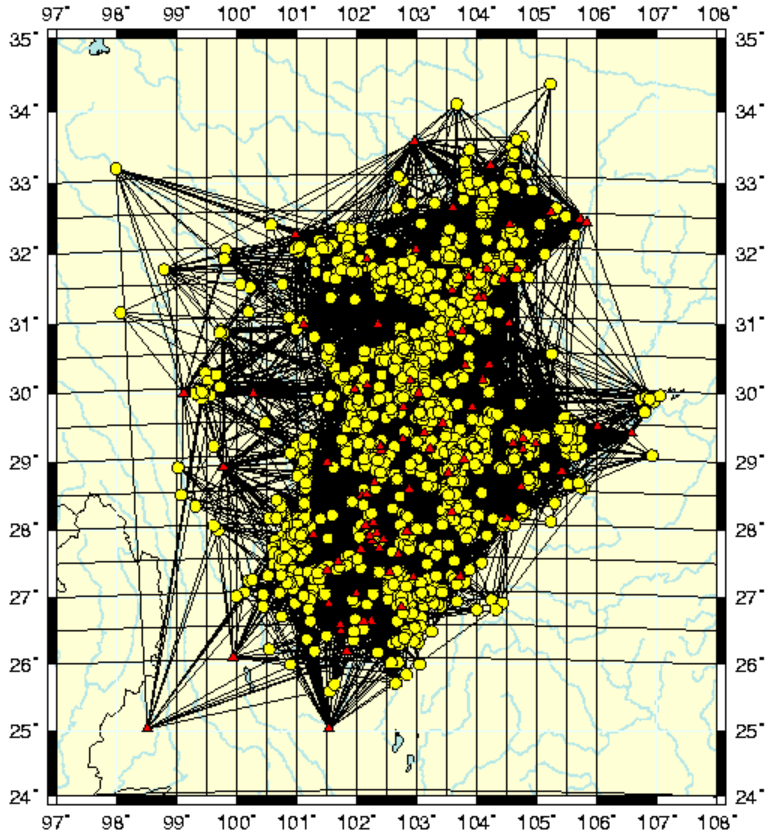


Fig. 3. Ray path projection for the seismic events adopted for the tomographic inversion. The circles denote the seismic events, and the triangles represent the seismic stations. Lattice of different grid sizes is utilized to reflect the density of ray path coverage.

A 1-D starting model of the velocity structure of central China is set up according to the previous seismic profiling in the region (Lin, *et al.,* 1993; Wang, *et al*., 1994). The crust in the region is divided into 5 layers (Table 1).

Table 1 Starting model of crustal structure in central China

Layer	Depth (km)	P-wave velocity (km/s)
1	4.0	4.50
2	14.0	6.00
3	22.0	6.25
4	33.0	6.40
5	45.0	6.70

We perform the tomographic inversion by iteration. In each iteration, the 3-d velocity structure is obtained by inverting the P-wave arrival times. Over 5,900 P-phase arrival times are used in the inversion. After the inversion of the velocity structure, all the events are relocated based on the new 3-D velocity model in a separate step. The new locations of the events are then adopted for the next iteration of tomographic inversion. The iteration is terminated when the improvement of the velocity model is negligible.

The resulting P-wave velocity after the 5th iteration of the tomographic inversion is shown in Fig.4 (a)-(e). Both lateral heterogeneity and vertical variation are observed through the results. The trend of the variation of P-wave velocity in the first layer is found to correlate with the topography and tectonic settings in the region. In the eastern portion of the studied area, the velocity anomaly trends in NNE direction, which is consistent with the geological structures and earthquake faulting in the region. The velocity anomaly generally trends in N-S direction in the central portion and NW direction in the western portion. The same trends are observed in the 2nd layer, but become less evident as it goes further down.

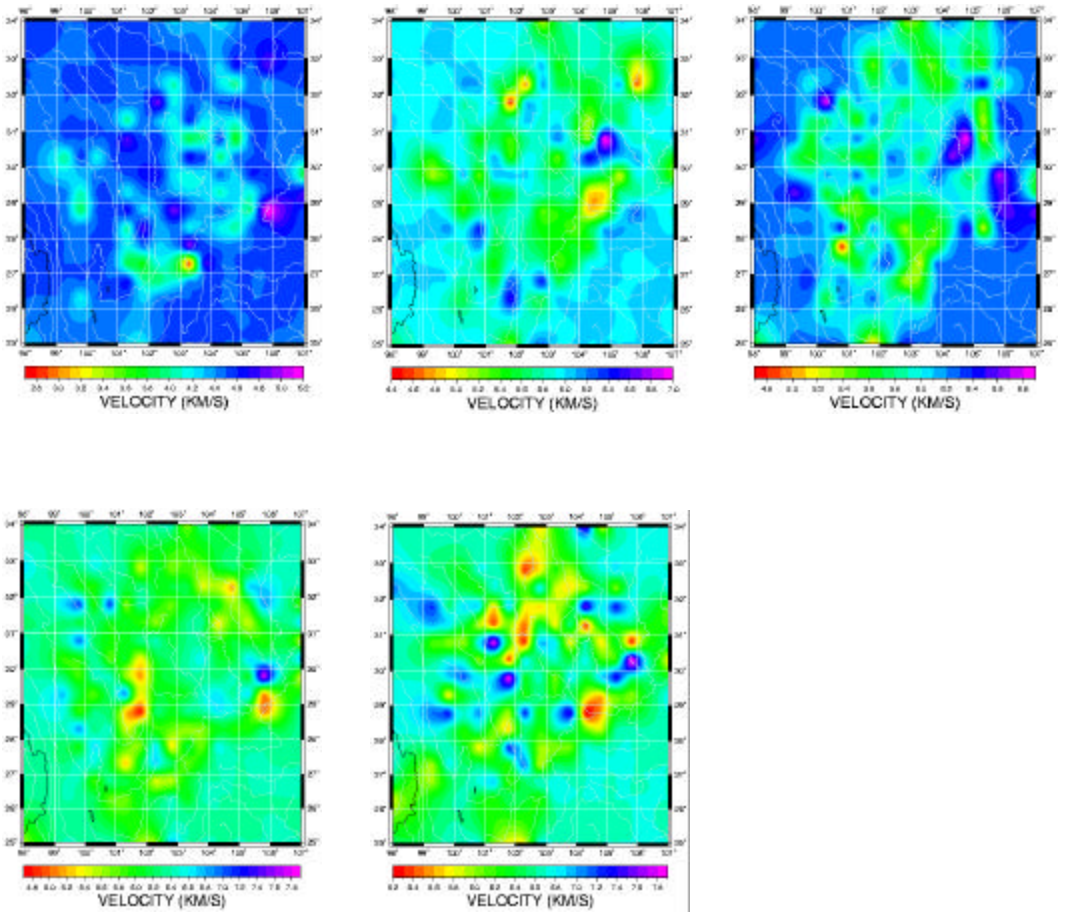
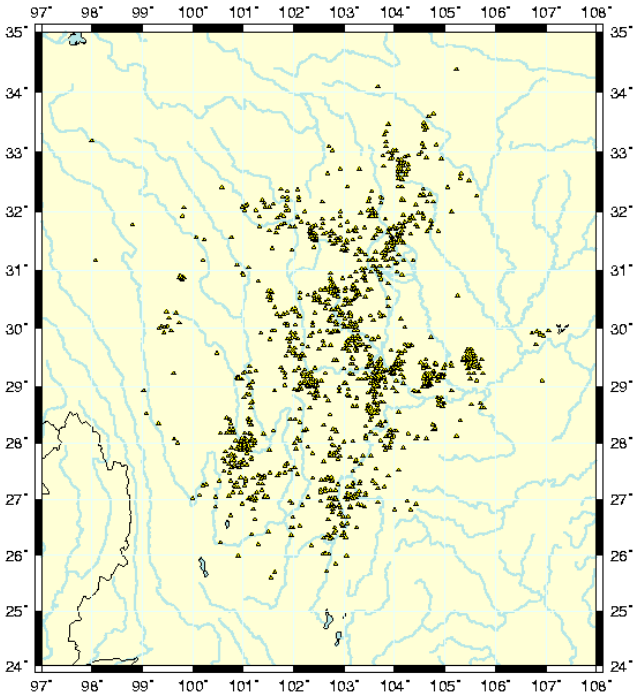


Fig. 4 P-wave velocity after the 5th iteration of tomographic inversion at layers at 4, 14, 22, 33, and 45 km.

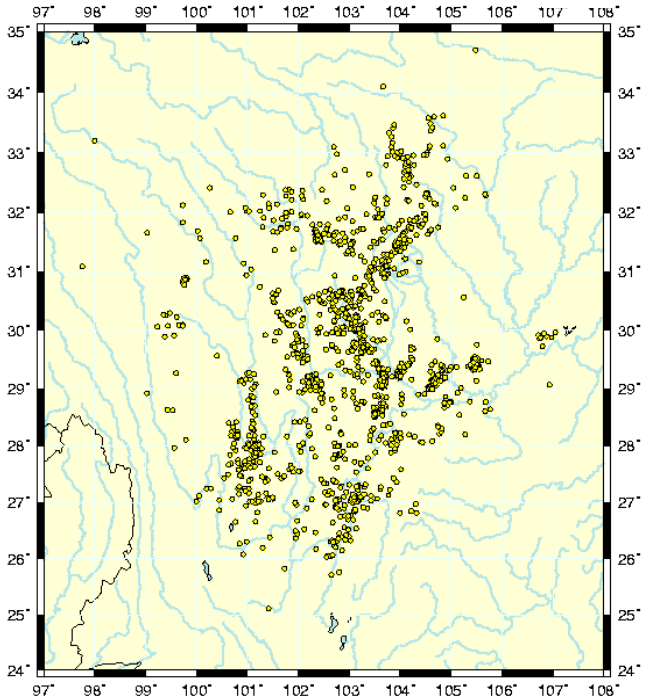
RE-LOCATION OF SEISMIC EVENTS

During the tomographic inversion of the 3-D crustal velocity structure in central China, a 63% reduction of the variance of the travel-time data is achieved after the 5th iteration. The standard error in the re-location of the events is usually less than 2 km in epicenter and less than 5 km in depth. Utilizing the 3-D crustal structure obtained from the inversion, we relocate the seismic events that are recorded by at least 5 stations in the studied region. It is found that the relocated epicenters show improvements in the clustering pattern over the original locations (Fig. 5a, b).

The earthquakes are more concentrated and have a better correlation with the earthquake faults in the region. The result demonstrates the necessity of regional crustal structure of high resolution in relocation of seismic events.



(a)



(b)

Fig. 5 Seismic event epicenter distribution before (a) and after (b) the relocation.

CONCLUSIONS AND RECOMMENDATIONS

This research is aimed at obtaining a database of historical seismological, geophysical, and geological data for central China. By obtaining the local seismic data, better models of the regional crustal structure can be made. We have collected the historical earthquake data in central China recorded by the local and regional seismic networks and constructed a database of phase arrival times. The database consists of 1,600 seismic events from 1985 to 1994 with over 40,000 entries of seismic phase arrival times. The seismic events occurred in central China and the vicinity within an area about 20°x11°. The events were recorded by the local and regional seismic networks operated by the provincial seismic bureaus in central China with over 160 seismic stations. The phase arrival time data are verified and validated independently. Unreliable phase picks that are deviated significantly from the average travel-time curves are discarded. The data are compiled in CSS format. The historical earthquake data provide a unique seismic database for further refinement of the regional crustal structure.

We performed a 3-D tomographic inversion of the crustal structure in central China utilizing the obtained seismic data. Previous research on the crustal structure in central China is analyzed and summarized to set up a 1-D starting model. A total of 372 events and over 5,900 P-phase arrival times are adopted to carry out a tomographic inversion of the crustal velocity structure in the region. The results reveal complex lateral heterogeneity of the crustal structure in central China. We find correlation among the velocity structure, topography and tectonic structures in the region. The resultant 3-D crustal structure improves the clustering pattern of the seismic events.

Recent seismic data from the new digital seismic networks in central China are desirable to enhance the ground-truth database and improve the study of the crustal structure in the region. It is also an interesting research topic to perform the similar study in other areas in China where the high-resolution crustal structure is not well understood yet.

REFERENCES

Barazangi, M. and J. Ni (1982), Velocities and propagation characteristics of Pn and Sn beneath the Himalayan arc and Tibetan Plateau: possible evidence for underthrusting of Indian continental lithosphere beneath Tibet, *Geology*, **10**, 179-185.

Chen, W.P. and P. Molnar (1981), Constraints on the seismic wave velocity structure beneath the Tibetan Plateau and their tectonic implications, *J. Geophys. Res.*, **86**, 5837-5962.

Ding, Z.F., R. S. Zeng, and F. T. Wu (1993), The Pn wave velocities and the relief of Moho in the Tibetan Plateau, *Acta Seismologica Sinica*, **6**, 317-326.

Li, L. and G. Y. Jin (1986), The electronic characteristic and thermal state of the lithosphere in area of Xizang (Tibet) Autonomous Region, Bull. Inst. *Geophys. Geochem. Explor.*, **2**, Geological Publishing House, Beijing, 121-128.

Lin, Z.Y., et al., (1993), A study of the crustal and upper mantle velocity structure in western Yunnan, *Acta Seismologica Sinica*, **15**, 427-440.

Lyon-Caen, H. (1986), Comparison of the upper mantle shear wave velocity structure of the Indian Shield and the Tibetan Plateau and tectonic implications, *Geophys. J. Roy. Astronom. Soc.*, **86**, 727-749.

Ma, X.Y. (Chief Editor) (1989), Lithospheric Dynamics Atlas of China, China Cartographic Publishing House, Beijing.

Molnar, P., Q. P. England, and J. Martinod (1993), Mantle dynamics, uplift of the Tibetan Plateau, and the Indian Monsoon, *Rev. Geophys.*, **31**, 357-396.

Roecker, S.W., Y. H. Yeh, and Y. B. Tsai (1987),Three-dimensional P and S wave velocity structures beneath Taiwan: deep structure beneath an arc-continent collision. *J. Geophys. Res.* , Vol. **92**, No. B10, 10,547-10,570.

Roecker, S.W., T. M. Sabitova, L. P. Vinnik, Y. A. Burmakov, M. I. Golvanov, R. Mamatkanova, and L. Munirova (1993), Three-dimensional elastic wave velocity structure of the western and central Tien Shan. *J. Geophys. Res.* , Vol. **98**, No. B9, 15, 779-15,796.

Wang, C.Y, and X.L. Wang (1994), 3-D velocity structure under Kunming seismic network, *Acta Seismologica Sinica*, **16**, 167-175.

Zeng, R.S. et al. (1993), Three-dimensional seismic velocity structure of the Tibetan Plateau and its eastern neighboring areas with implications to the model of collision between continents, *Acta Seismologica Sinica*, **6**, 251-260.

MODELING COLLAPSE CHIMNEY AND SPALL ZONE SETTLEMENT AS A SOURCE OF POST-SHOT SUBSIDENCE DETECTED BY SYNTHETIC APERTURE RADAR INTERFEROMETRY

William Foxall
Lawrence Livermore National Laboratory

Sponsored by U.S. Department of Energy
Office of Non-Proliferation Research and Engineering
Office of Defense Nuclear Nonproliferation
National Nuclear Security Administration

Contract No. W-7405-ENG-48

ABSTRACT

Ground surface subsidence resulting from the March 1992 JUNCTION underground nuclear test at the Nevada Test Site (NTS) imaged by satellite synthetic aperture radar interferometry (InSAR) wholly occurred during a period of several months after the shot (Vincent et al., 1999) and after the main cavity collapse event. A significant portion of the subsidence associated with the small (less than 20 kt) GALENA and DIVIDER tests probably also occurred after the shots, although the deformation detected in these cases contains additional contributions from coseismic processes, since the radar scenes used to construct the deformation interferogram bracketed these two later events. The dimensions of the areas of subsidence resulting from all three events are too large to be solely accounted for by processes confined to the damage zone in the vicinity of the shot point or the collapse chimney. Rather, the subsidence closely corresponds to the spall dimensions predicted by Patton's (1990) empirical relationship between spall radius and yield. This suggests that gravitational settlement of damaged rock within the spall zone is an important source of post-shot subsidence, in addition to settlement of the rubble within the collapse chimney. These observations illustrate the potential power of InSAR as a tool for Comprehensive Nuclear-Test-Ban Treaty (CTBT) monitoring and on-site inspection in that the relatively broad (~100 m to 1 km) subsidence signatures resulting from small shots detonated at normal depths of burial (or even significantly overburied) are readily detectable within large geographical areas (100 km × 100 km) under favorable observing conditions. Furthermore, the present results demonstrate the flexibility of the technique in that the two routinely gathered satellite radar images used to construct the interferogram need not necessarily capture the event itself, but can cover a time period up to several months following the shot.

In order to explore the power of InSAR to discriminate underground nuclear explosions from other seismic and subsidence events, we model settlement within the chimney and spall zones as three-dimensional distributions of point volume deflation and closing tension crack sources within prescribed subsurface volumes representing the spall and collapse damage zones. We investigate the uniqueness of fitting the InSAR observations by examining the trade-offs among the spatial and strength distributions of the sources, and the overall geometries of the damage zones. Modeling constraints are based on characteristics of collapse chimneys and spall zones deduced from available *in-situ* observations at NTS and elsewhere, analysis and interpretation of near-source ground motion data, and existing results of dynamic modeling of contained underground explosions. We discuss refinements to the modeling approach based on analyses of the mechanics of settlement within damage and rubble zones taken from the fields of mining and geotechnical engineering, and examine the potential of the InSAR technique to detect and discriminate underground nuclear tests in different geological environments.

Key Words: synthetic aperture radar interferometry, detection, source identification, source parameters, modeling

OBJECTIVE

Synthetic aperture radar interferometry (InSAR) imaged ground surface deformation resulting from the March 1992 JUNCTION (m_b5.6) underground nuclear test at the Nevada Test Site (NTS) that occurred over a time interval of months to years, beginning about one month after the event and the collapse of the explosion cavity (Vincent et al., 1999). A significant part of the imaged deformation associated with the Yucca Flat shots GALENA (m_b3.9) and DIVIDER (m_b4.4) most likely also occurred after the events, although in these cases the deformation contains contributions from coseismic and immediate post-shot processes (including cavity collapse and cratering), since the radar scenes used to construct the interferogram bracket the times of the shots. These observations have important implications for the potential of InSAR as a tool for monitoring a Comprehensive Nuclear-Test-Ban Treaty (CTBT) and to aid decision making for on-site inspections. First, the GALENA and DIVIDER observations illustrate that, at least in geological environments similar to Yucca Flat and under favorably arid observing conditions, shots in the magnitude 4 range can be detected, even when, as in these cases, the shots are overburied; second, the deformation signatures enable the shots to be located with an accuracy of a few tens of meters within the large (100 km x 100 km) area covered by a single interferogram; and third, the radar orbits do not necessarily need to capture the shot itself but can be collected up to several months or years after the event, which should prove particularly useful for on-site inspection.

The objective of our research is to develop techniques for inverting InSAR data to characterize underground nuclear tests and to discriminate them from other seismic events. In order to achieve this we first need to construct simple yet viable mechanical models of the sources of the observed deformation caused by well-characterized underground tests at NTS. We can then devise optimal inversion methods that can be applied in the wide variety of geological environments likely to be encountered in CTBT applications. The InSAR data themselves suggest that gravitational settlement within the near-surface spall zone and collapse chimney is the predominant source of long-term post-shot subsidence. In the work described here we conduct elastic modeling of the JUNCTION data to identify the parameters of a settlement source that will control the inversion problem, and examine available constraints on those parameters.

RESEARCH ACCOMPLISHED

InSAR Data

JUNCTION was detonated on 3/26/92 at a depth of 622 m, and was the last nuclear test to be carried out beneath Paute Mesa. Cavity collapse occurred 29 hours after the shot. The collapse chimney did not propagate to the surface, so a crater did not form. Processing of ERS-1 satellite synthetic aperture radar (SAR) data to produce interferograms that image ground deformation at NTS over two time periods, 4/24/92-6/18/93 and 4/24/92-5/26/96, is described fully in Vincent et al. (1999), and the data used here are taken from that study. Figure 1 shows the portion of the 4/24/92-6/18/93 interferogram that images deformation associated with JUNCTION. Since the shot occurred about 1 month before the beginning of the imaging interval, the interferogram captures deformation that occurred only after the event. Each fringe (one color cycle) on the interferogram corresponds to 28 mm of change in path length (range) between the radar and the ground caused by surface deformation. Figure 2 shows displacement (unwrapped phase) cross sections along the major and minor axes of the approximately elliptical deformation pattern. Construction of the cross sections assumes that the range change corresponds entirely to vertical deformation. Figures 1 and 2 show an elliptically shaped subsidence bowl having semi-major and -minor axes of approximately 1.2 and 0.9 km, respectively, and a maximum depth of about 8 cm. The full interferogram reveals deformation signatures coincident with all Paute Mesa tests since 1990, which implies that subsidence resulting from each shot occurs continuously over a period of several years.

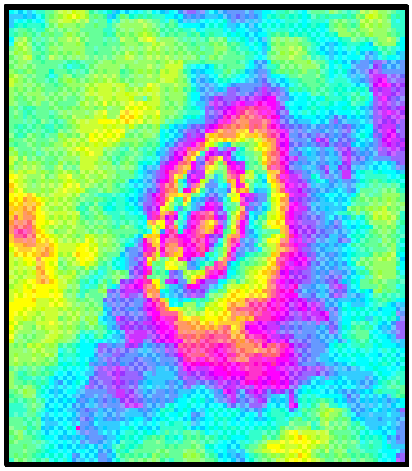


Figure 1: 4/24/92-6/18/93 interferogram imaging ground deformation associated with the JUNCTION event.

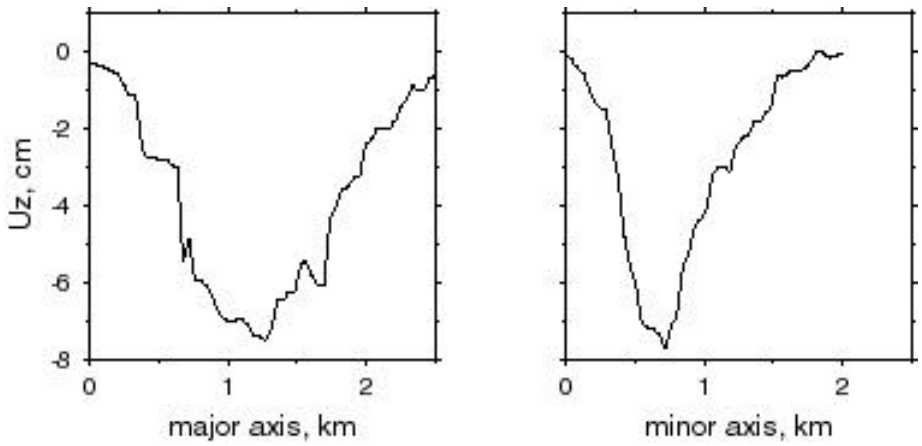


Figure 2: Vertical displacement cross sections (unwrapped phase) along the major and minor axes of the interferogram in Figure 1.

Subsidence Source Models

The most obvious potential source of subsidence following an underground explosion is gravitational settlement of rubble within the collapse chimney and of the intensely fractured rock surrounding the shot point. In general, the chimney is centered on the shot point and has a maximum radius perhaps 15-20% greater than the cavity (e.g. Houser 1969). A zone of intense fracture damage is estimated to extend up to about 5 cavity radii beyond the cavity wall. A cavity radius of about 60 m is estimated for JUNCTION, based the NEIC m_b of 5.5, the m_b-yield relationship of Murphy (1996), and the yield-radius relationship of Terhune and Glenn (1977), which gives a chimney radius of less than 100 m and a damage zone radius of roughly 300 m. The damage radius, therefore, is about three times smaller than the length of the semi-minor axis of the subsidence bowl, which suggests an additional, laterally more extensive source is needed to explain the observed subsidence. The close agreement of the length of the major axis with the maximum radius of spall estimated using Patton's (1990) empirical spall radius-yield relationship for Paute Mesa events leads us to propose gravitational settlement of damaged rock within the near-surface spall zone as this additional source.

Spalling is caused by the down-going tensional wave front produced by reflection at the ground surface of the up-going compressional pulse from a buried explosion (e.g. Eisler and Chilton 1964). Tensile failure of near-surface material occurs where the tensional stress exceeds the sum of the dynamic compressional stress, the overburden and the tensile strength of the material, resulting in detachment and ballistic free-fall of the overlying layer. Spall terminates when the spalled layer falls back under gravity to impact the underlying material. Multiple spalling (Eisler et al. 1966) throughout a range of depths results in a complex spall zone that extends from a few tens of meters below the surface to a maximum depth of a few hundred meters, depending on the yield and depth of the explosion (e.g. Patton, 1990). We propose the following, at present largely heuristic model, to explain how the spall zone can become a source of subsequent subsidence.

It is seems likely that during the interval of ballistic free-fall following spall detachment at any location, rock fragments will became detached from the bottom of the spalled slab and fall back into the spall gap to form a layer of rubble; this is particularly likely considering that multiple spall itself fractures the rock over a large range of scale lengths. The rubble layer will contain significant void space owing to mismatch between the rock fragments (bulking). Bulking (bulking factor= V_D/V , where V_D and V are the volume of the damaged and undamaged rock, respectively) depends on a complex combination of factors, including the shape and size distributions of the fragments - which in turn depend upon the density and orientations of pre-existing fractures - and the rotation of the fragments as they fall, which depends on the width of the spall gap. Much of the newly created void space will be destroyed by compaction at slapdown, but apparently bulking is sufficient either for some of the rubble void space to survive or for yet new void space to be created by imperfect rejoin of the rock across the plane of spall failure. Slapdown itself creates new damage, which is primarily compaction of the underlying material but probably includes shear failure and associated dilatation both above and below the failure plane. Another possible source of void creation is minor spall that results in tensile opening but not in significant ballistic free fall.

We assume that following slapdown, the bulked rock within the spall zone begins to settle under gravity, reducing the void volume. The predominant deformation mechanism is likely to be low-rate, stable frictional sliding (steady-state creep) on inter-block contacts within the fractured and bulked rock mass. We expect that fluid effects involving percolation of surface water play an important role through sub-critical growth of microcracks and/or pore pressure effects. This mechanism also applies to the collapse chimney, where bulking of the chimney rubble has been relatively well studied (e.g. Houser 1969; Hakala 1970), and perhaps also to the zone of compressional damage surrounding the shot point.

Elastic Modeling

Although the mechanism of gravity driven creep outlined above is inelastic, we can simulate void closure using a spatial distribution of dislocation sources associated with a prescribed distribution of volume deflation or closing displacement. We then model the resulting surface deformation by embedding the sources in an elastic half space, under the assumption that the overburden and the spall zone itself respond elastically. For the work described here, we model void closure by point volume deflation sources distributed within a 3-D volume having a prescribed geometry that represents the overall shape of the spall zone. The point source elastic solutions are those of Okada (1992). The purpose of the present phase of modeling is to assess the viability of spall zone settlement as a source of the observed surface subsidence, to evaluate the sensitivity of the surface deformation field to the shape of the spall zone and the distribution of source strength (i.e. amount of void closure), and to examine the trade-off among these parameters. The results of previous observational and modeling studies are used to constrain the selection of model parameters within physically plausible bounds.

Spall Zone Shape

The 3-D shape of the spall zone model, shown in vertical cross-section in Figures 3b and 4b, is based on the results of dynamic 2-D finite difference modeling of the HARZER test by John Rambo (LLNL), as shown in Figure 11 of Patton (1988). Both HARZER and JUNCTION were m_b~5.5 events. HARZER was detonated within 2 km of JUNCTION at about the same depth and in similar geology. The maximum surface range (1.2 km) of the spall zone closely agrees with the estimate from Patton's (1990) empirical relationship, but the maximum spall depth (270 m) is significantly greater. The overall bowl shape of the zone is generally similar to that reported by Stump and Reinke (1987), based on ground motion recordings of small chemical shots in alluvium, and to (unpublished) dynamic models from several other workers. The model shown in Figures 3b and 4b is built from three vertically stacked 3-D layers, each of which has the shape of an inverted elliptical cone (truncated at the apex in the case of the two upper layers). The elliptical horizontal sectional shape was chosen to match the observed deformation pattern, and is discussed further below. Figures 3b and 4b show the distribution of point sources in the layers. The volumetric moment in each layer was distributed uniformly among the point sources. The moments assigned to the layers were then adjusted relative to each other to provide the best fit to cross-sections through the data along the major and minor axes of the observed deformation pattern.

Figures 3a and 4a show the best fit to the data, obtained with a model in which 47%, 47% and 6% of the total volumetric moment of the spall zone is contained in Layers 1,2 and 3, respectively. Therefore, for the geometry constrained by the HARZER results, the model concentrates the void closure towards the center of the spall zone (surface ranges less than approximately one depth of burial [DOB]). The cumulative void closure in this model represents less than 0.1% of the total volume of the spall zone. Note that the uppermost layer is shifted +100 m and +200 m along the major and minor axes, respectively, to fit the asymmetry in the data cross sections. Figure 5 compares the fit obtained from the spall zone model with models representing 70-cm closure of a 150-m diameter void at the top of the collapse chimney (depth 300 m) and 22-cm total void closure within a 600-m diameter damage zone at 620-m depth. The amount of closure in each of the latter models was adjusted to provide the best fit to the data. The spall model produces a significantly better fit. The essential point is that a laterally extensive source with distributed, small amounts of void closure is needed to fit the width of the deformation pattern.

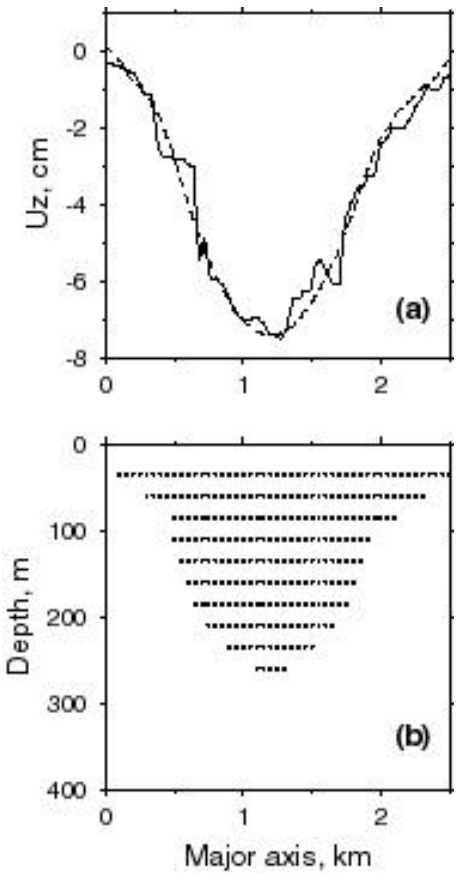


Figure 3: **(a)** Fit of vertical displacement computed (**dashed**) from 3-D spall zone source model to data (**solid**) along major axis of deformation pattern. (**b**) Major axis vertical cross section though uniform distribution of point sources.

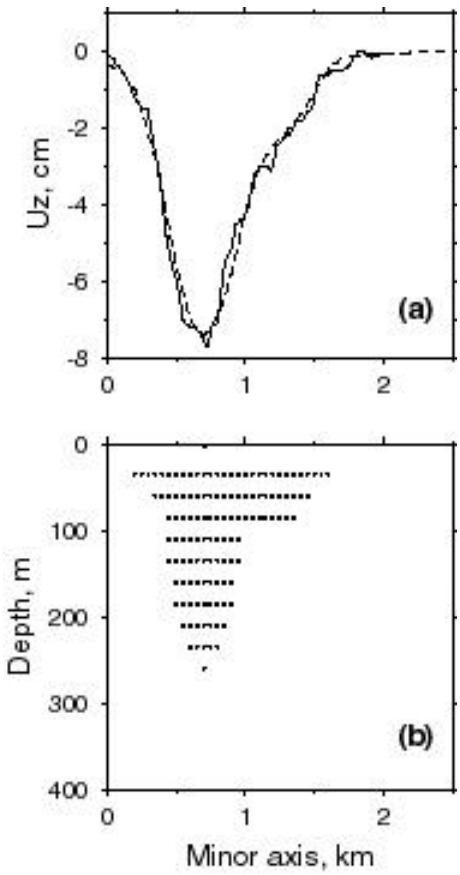


Figure 4: Same as Figure 3 for minor axis of deformation pattern

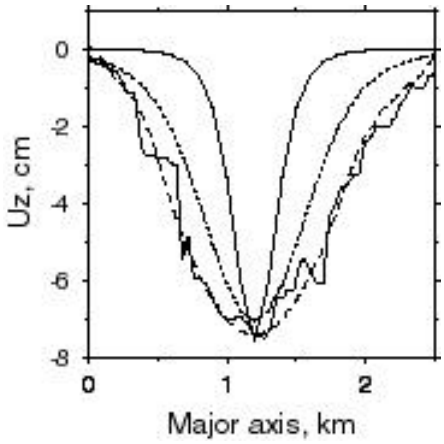


Figure 5: Comparison of data fits for 3-D spall source model (**dashed**), 70-cm closure of 150 m diameter void in collapse chimney at 300-m depth (**solid**), and 22-cm closure within 600-m-diameter damage zone at 620 m depth (**dotted**).

Distribution of Void Volume

Although the depth-integrated spall damage falls off with distance from SGZ as a result of the decreasing maximum depth of spall, it might be expected that the degree of damage would also decay with distance at any given depth. In order to test this possibility an empirical or physical basis is needed to guide the selection of appropriate types of decay laws. So far, we have found very little information about the distribution of damage in spall zones based on direct observations. Some numerical dynamic modeling has carried the calculations through the ballistic interval, but the resulting estimates of residual damage are sensitive to assumed bulking factors, which have large uncertainties. Our initial approach to this problem is based on the work of Stump and Weaver (1992), who proposed a theoretically and empirically based two-stage power law decay of peak spall velocity with distance; the ground motion decays very slowly to a surface range of about 1 DOB and much more rapidly beyond that point. According to simple ballistic theory, the width of the spall gap, $S \propto V_P^2$, where V_P is the peak spall velocity, so bulking should be related to V_P. However, as discussed above, bulking is a complex process, so the form of the relationship between bulking factor and spall velocity is not obvious. In our preliminary assessment we merely assume that void closure volume decays from a maximum at SGZ according to power laws having different exponents on either side of surface range = 1 DOB, and adjust the model to fit the data. For a source layer of given depth and shape, the input model parameters are the point source volumetric moments at SGZ, along the outer periphery of the spall zone, and at surface range = 1 DOB. Figure 6 shows the fit obtained using a single sheet of sources at a depth of 90 m. This preliminary result suggests that the fall off in depth-integrated source strength with range can be represented by a 2-D source having a spatial decay relationship. If, in fact, there is significant decay of source strength with range at constant depth, then there is a potentially strong trade-off between the geometry of the source volume and the assumed decay. Therefore, more work is needed to identify physically appropriate decay laws.

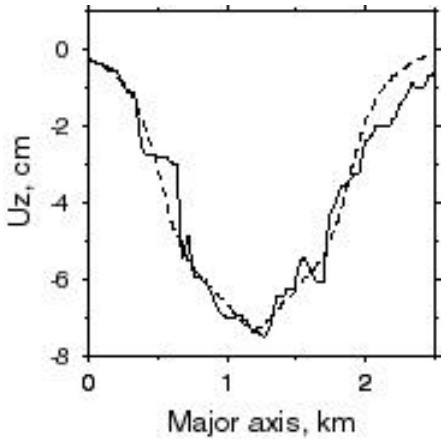


Figure 6: Fit of vertical displacement computed (**dashed**) from single sheet of point sources with two-branch power law decay to data (**solid**) along major axis of deformation pattern.

Two potential causes of the elliptical shape of the surface deformation pattern (Figure 1) are an aspherical explosive source or azimuthally dependent wave propagation effects related to near surface geologic structure. Either would produce a spall zone that is not axially symmetric. Conceivably, an aspherical source could result from the influence of the regional tectonic stress field on cavity growth and shock propagation, but to our knowledge this has not been investigated. Analysis of ground motion data from DIVIDER (Steve Taylor, LANL, unpublished manuscript) shows that nearby faults can have a major influence on spall ground motions and hence on the shape of the spall zone. Specifically, reflections from a fault plane can focus energy inwards towards SGZ and attenuate spall ground motion on the opposite side of the fault. This model appears consistent with the deformation pattern for JUNCTION, where faults striking approximately N-S are mapped 500-700 m on either side of the working point.

CONCLUSIONS AND RECOMMENDATIONS

The simple elastic modeling results presented above demonstrate that gravitational settlement of the damaged rock mass within the near surface spall zone provides a satisfactory explanation of the localized, intermediate to long-term (months to years) subsidence imaged by InSAR following NTS underground nuclear tests. Because likely alternative sources are confined to relatively short ranges around ground zero, they do not produce surface deformation that matches the dimensions of the observed subsidence patterns. In the case of the JUNCTION data analyzed here, good estimates of the shape, dimensions, and depth of the spall zone are provided by well constrained, 2-D (vertical cross-section) finite difference modeling of a nearby test that closely matches the size, depth of burial, and geologic environment of JUNCTION. We obtained a close fit to the InSAR data by extending this spall zone shape to 3-D as three layers, each having the shape of an inverted elliptical cone and a uniform

distribution of point volumetric deflation sources of equal moment. The data fit is quite sensitive to the shape and depth of the spall zone. Relatively modest perturbations to the 2-D shape and depth of the spall zone provided by the finite difference results were needed to fit the data, suggesting that these parameters of the source model can be relatively well constrained. Preliminary results on the distribution of void volume (i.e. source strength) suggest a potential trade off between the geometry of the spall zone and spatial decay of source strength, but are inconclusive. The difficulty lies in finding relations for the decay of source strength with surface range and depth that are supported by data or otherwise physically motivated.

The settlement model we propose is speculative, and detailed study of the damage mechanisms responsible for bulking and void creation in spall zones is needed to verify it. This can be approached by examination of existing dynamic modeling results that run through the slapdown phase. Estimates of bulking factors for specific rock types and geologic environments are likely to be the most uncertain parameters in these calculations. Therefore, additional modeling would probably be necessary, for which it will be important to seek constraint on bulking from the mining and geotechnical fields. A complementary approach will be to explore damage mechanics models that can provide a generalized statistical description of spall zone damage. Most importantly, in order to make the best use of InSAR data on a worldwide basis, it would be desirable to analyze available *in situ* data and modeling results from the widest possible variety of geologic environments. Three-dimensional dynamic modeling would be necessary if the non-axisymmetric shape of deformation fields like that produced by JUNCTION proves to be diagnostically useful. The fact that the net surface deformation produced by NTS explosions is predominantly subsidence might pose a discrimination challenge in that similar deformation patterns could plausibly be caused by mine collapses of similar size.

The elastic modeling presented here is only a crude representation of a complex inelastic settlement process. However, as long as the elastic representation can capture the essential features of the process, such as the cumulative loss of void volume and the equivalent elastic response of the overburden, it is just what is required as the core of a tractable and efficient inverse technique that can be applied in the variety of geological environments CTBT monitoring demands.

ACKNOWLEDGEMENT

This work was performed under the auspices of the U.S. Department of Energy by University of California Lawrence Livermore National Laboratory under contract No. W-7405-Eng-48 for the Office of Research and Development, NN-20, within the Office of NonProliferation and National Security, NN-1.

REFERENCES

Eisler, J., and F. Chilton, (1964) Spalling of the Earth's Surface by Underground Nuclear Explosions, J. Geophys. Res., **69**, 5285-5293.

Eisler, J., F. Chilton, and F. Sauer, (1966) Multiple Subsurface Spalling by Underground Nuclear Explosions, J. Geophys. Res., **71**, 3923-3927.

Hakala, W., (1970) Subsidence Caused by an Underground Nuclear Explosion, Proc., Symposium on Engineering with Nuclear Explosives, Jan. 14-16, 1970, Las Vegas, NV, Am. Nuclear Soc./U.S. Atomic Energy Commission, 1428-1455.

Houser, F., (1969) Subsidence Related to Underground Nuclear Explosions, Nevada Test Site, Bull. Seismol. Soc. Am., **59**, 2231-2251.

Murphy, J., (1996) Types of Seismic Events and Their Source Descriptions, in Monitoring a Comprehensive Test Ban Treaty, E. Husebye and A. Dainty (eds.), Kluwer Academic Publishers, Dordrecht, 225-246.

Okada, Y., (1992) Internal Deformation Due to Shear and Tensile Faults in a Half Space, Bull. Seismol. Soc. Am., **82**, 1018-1040.

Patton, H., (1990) Characterization of Spall from Observed Strong Ground Motions on Mesa, Bull. Seismol. Soc. Am., **80**, 1326-1345.

Patton, H., (1988) Source Models of the Harzer Explosion from Regional Observations of Fundamental- and Higher-Mode Surface Waves, Bull. Seismol. Soc. Am., **78**, 1133-1157.

Stump. B. and R. Reinke, (1987) Experimental Seismology: *In situ* Source experiments, Bull. Seismol. Soc. Am., **77**, 1295-1311.

Stump, B. and T. Weaver, (1992) Physical Models of Spall Ground Motions and the Determination of Spatial Decay Rates, LAUR-92-451, Los Alamos National Laboratory.

Terhune, R and H. Glenn, (1997) Estimate of Earth Media Shear Strength at the Nevada Test Site, UCRL-52358, Lawrence Livermore National Laboratory.

Vincent, P., B. Foxall, and W. Walter, (1999) Analysis, Comparison and Modeling of Radar Interferometry Data of Surface Deformation Signals Associated with Underground Explosions, Mine Collapses and Earthquakes Phase I: Underground Explosions, Nevada Test Site, Proc. 21st Seismic Research Symposium, Las Vegas, NV, 21-24 Sep., 1999, 775-784.

AN ANALYSIS OF LARGE MINING BLASTS IN WYOMING AND CENTRAL ASIA

Michael A.H. Hedlin
Institute of Geophysics and Planetary Physics
University of California, San Diego

Sponsored by
Defense Threat Reduction Agency
Contract No. DSWA01-97-C-0153

ABSTRACT

We have conducted a preliminary analysis of kiloton class, anomalous, mining blasts in Wyoming using IMS seismic data. This research has begun on two fronts. We are examining well documented mine blasts in the Powder River Basin trend in Wyoming using the Pinedale seismic array (PDAR) and the single station ULM. These data are being used with near-regional video, seismic and acoustic data collected by UCSD, LANL, SMU and AFTAC during field experiments in 1996 and 1997. These data are being used to examine differences in the waveforms of mining blasts that are essentially co-located, and detonated with similar planned blasting grids, but for which some have included a significant detonation anomaly (otherwise known as a sympathetic detonation). We are examining coherent and incoherent beams of Pinedale array data in an attempt to detect the large detonations. We are using physical modeling in an attempt to reproduce the waveforms of the anomalous blasts. Our main goal with the modeling is to estimate the explosive yield and timing of the detonation anomalies.

Kiloton class mine blasts are not uncommon in numerous regions worldwide such as Wyoming, Kentucky and, at least historically, the Kuzbass mining region in Russia. Recordings of large blasts in the Kuzbass mining region exhibit time- and frequency-domain characteristics below 10 Hz that are similar to those observed in the Wyoming events. In specific, these features include enhanced surface waves and spectral modulations. We tentatively conclude that the discrimination methods we have found to be useful in Wyoming can also be used in this region. In collaboration with Vitaly Khalturin (LDEO) we are seeking ground truth information on large mining blasts in the Altay-Sayan mining region. This exploratory phase will be followed by physical modeling of the events for which we are able to secure adequate ground truth information.

Key Words: sympathetic detonation, ground truth, spectral modulations

OBJECTIVE

To develop high- and low-frequency seismic techniques to characterize mining explosions and discriminate these events from single explosions and earthquakes. The focus is on mining explosions that detonate as planned and on mining explosions which contain significant detonation anomalies. Our focus has been on spectral modulations and surface waves that will commonly propagate beyond near-regional distances to stations in the IMS monitoring network. We use physical modeling to identify the source processes that give rise to these signals.

This paper summarizes our research on low-frequency signals produced by significant (> 1 kT) anomalous mining explosions in Wyoming. We also report preliminary results from our analysis of Altai-Sayan mine blasts recorded since January 1, 1995 by the IMS seismic station ZAL near Zalesovo, Russia.

RESEARCH ACCOMPLISHED

Wyoming Seismicity

It is not uncommon for mining events to be reported in the PDE catalog. One region where large (> 1 kt of explosive yield) blasts are common is the Powder River Basin coal mining trend in Wyoming. Ther eis little natural seismicity in this area however a plot of event locations taken from the REB shows how mining activity in the Powder River Basin dominates the event catalog (Figure 1). Most of these events were assigned a body were wave magnitude above 3.0 and occurred in the mid day (Figure 2)

All of the large mining events in this catalog used delay-firing and thus a considerable explosive yield is spread out over several seconds and seismic amplitudes are reduced. It is well known that minor deviations from the planned shot pattern are obiquitous. A small subset of these events, however, include a significant detonation anomaly. For reasons as yet not fully understood, a number of shot holes do not detonated at their planned times but detonate simultaneously

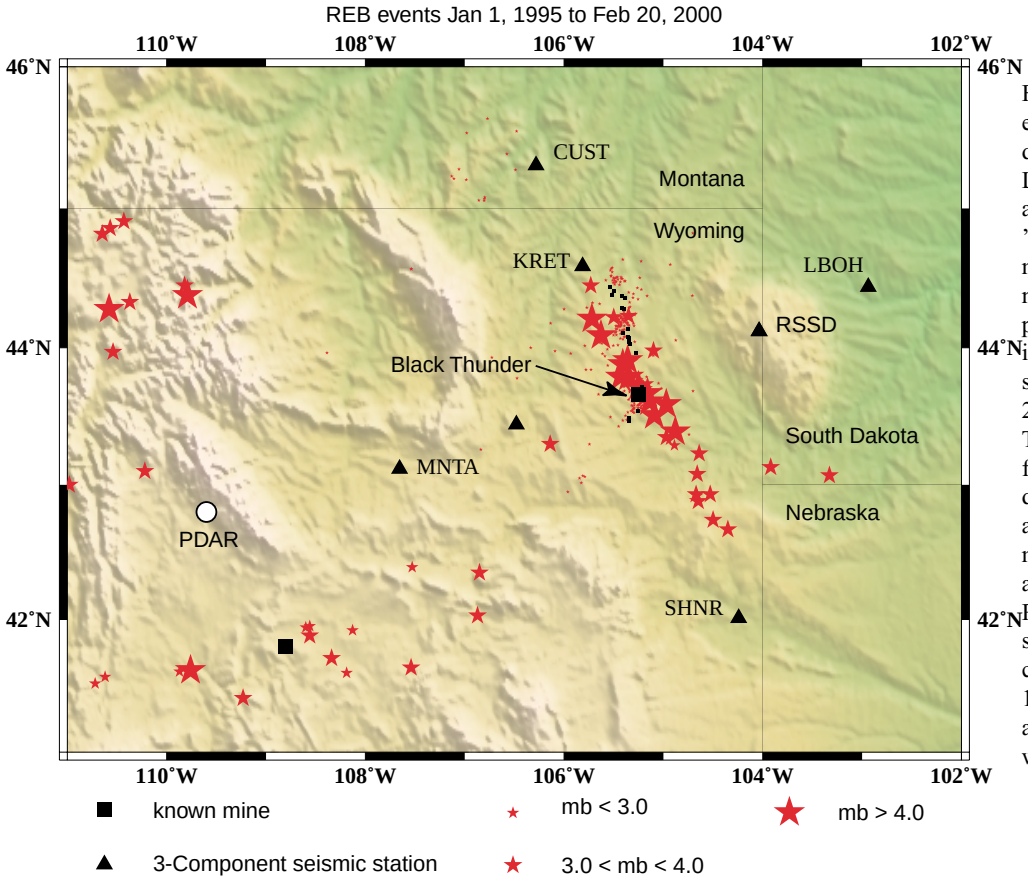


Figure 1. Two regional experiments were conducted in Wyoming by LANL, SMU, AFTAC and UCSD in 1996 and '97. Four broadband seismic stations (3-component STS2's) were deployed in a ring surrounding the Powder River Basin (PRB) at a range of 200 km from the Black Thunder coal mine. A fifth station (KRET) was deployed to the northwest at a range of 100 km. Permanent seismic stations are located at PDAR and RSSD. Mining explosions reported in the PDE catalog between Jan 1, 1995 and Feb 20, 2000 are plotted and correlate well with known mines.

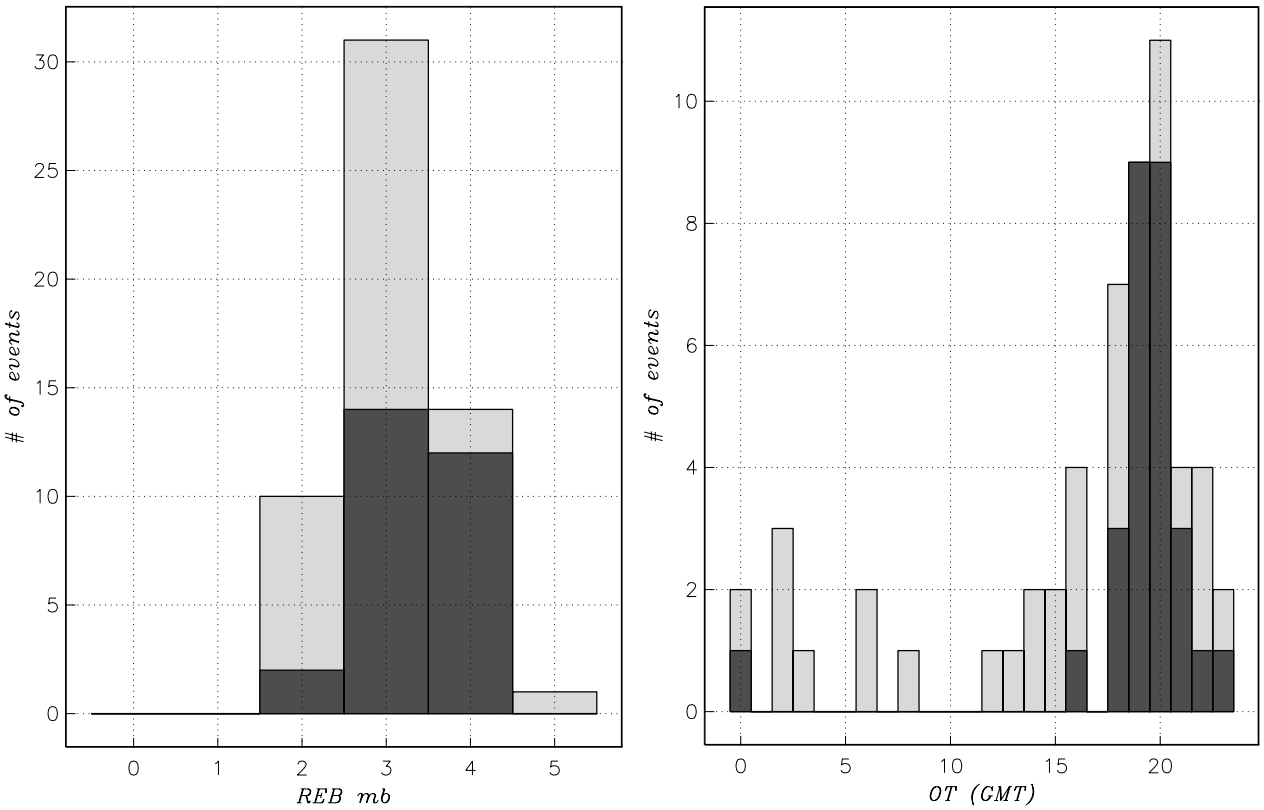


Figure 2. Body wave magnitudes (left) and event origin times (right) as reported in the PDE catalog. Events in these histograms are plotted in Figure 1.

(MARTIN ET AL., 1997). From a monitoring perspective, these events are the most important as the singular release of energy might be regarded by some as the signature of a masked test.

We have investigated these events with the intent of developing the means by which seismic data can be used to identify them as non-nuclear. An important first step in this process is identifying events which are anomalous is to develop the means by which the explosive yield of the sympathetic detonatinon can be constrained.

Analysis of detonation anomalies

Physical modeling of normal, and anomalous, mining blasts can be accomplished given the early work of BARKER ET AL. (1990, 93) and MCLAUGHLIN ET AL. (1994) and recent work by X. Yang who has modified the linear elastic algorithm of ANANDAKRISHNAN ET AL. (1997) and packaged it into an interactive MATLAB package (MineSeis; YANG, 1998). The algorithm assumes the linear superposition of signals from identical single-shot sources composed of isotropic and spall components. Both shooting delays and location differences among individual shots are taken into account in calculating delays of the superposition, although the Green s functions are assumed to change slowly so that a common Green s function is used for all the single shots. We used a reflectivity method to calculate the Green s functions. A 1-dimensional velocity model was used (PRODEHL, 1979; ANANDAKRISHNAN ET AL., 1997).

We have used the MineSeis code to model one event which detonated anomalously. The event occurred on Aug 1, 1996 in the Black Thunder coal mine and involved 2.5 million pounds of ANFO (Hedlin et al., 2000; Figures 3 and 4 in this paper). The event included a significant detonation ~ 1.75 into the shot sequence. The simultaneous detonation boosted the body wave magnitude to 4.0 (PDE catalog). Photos taken from a nearby vantage point (Figure 3) give clear, visual, evidence of a singular detonation within this shot sequence.

Incoherent beams from the Pinedale seismic array (PDAR; Figure 1) reveal a strong resemblance between a 40,000 pound single shot (top trace in Figure 5; Stump et al., 1999) and the August 1 event. The calibration shot compares less well with a routine 4.5 million pound cast blast and one that used 8.3 million pounds but also is known to have included a simultateous detonation (B. Stump personal communication).



FIGURE 3. Three photos of the August 1, 1996 Black Thunder cast blast. The start at 19:33:05 (top), 1.7 seconds later (middle) and the finale at 19:33:09. The significant release of energy into the air resulted from a sympathetic detonation which occurred part way through the shot sequence.

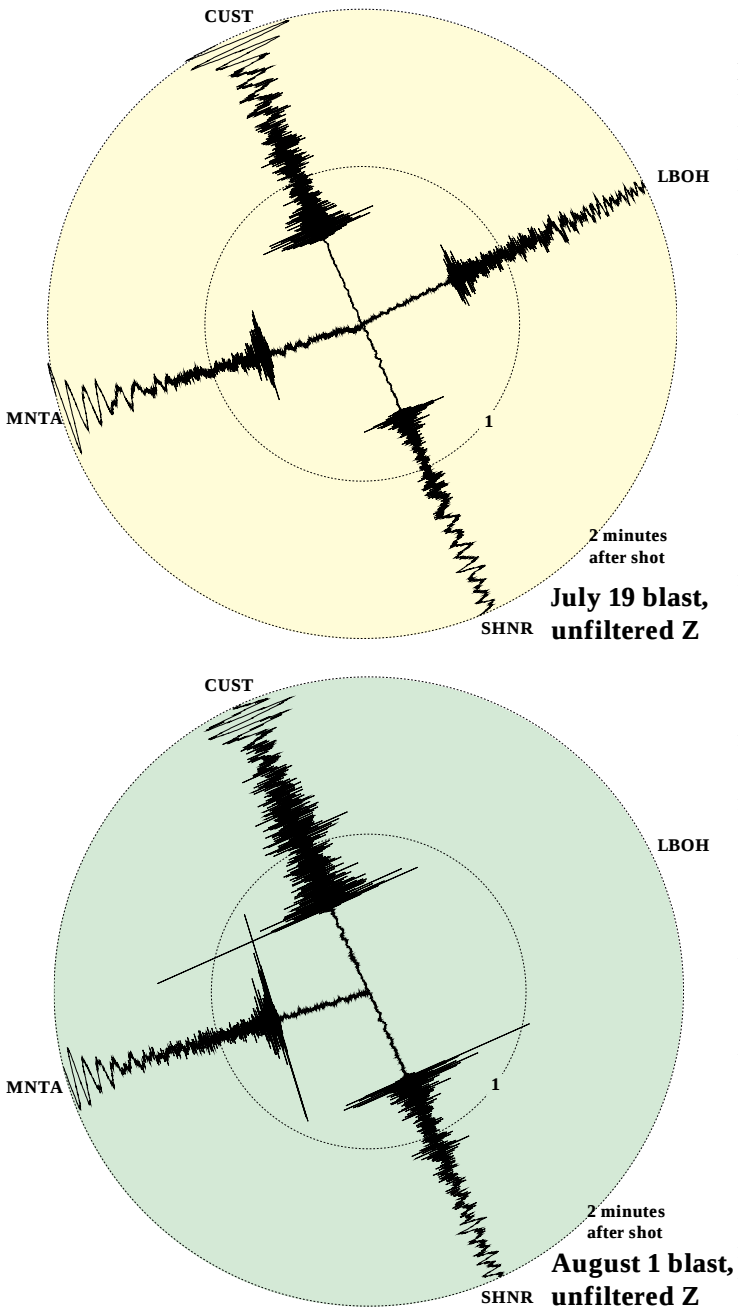


Figure 4. Vertical component recordings of a 4.5 million pound Black Thunder blast (top) and a 2.5 million pound blast at the same mine (bottom). The latter event included a significant detonation anomaly that boosted the body wave magnitude, as reported in the PDE, to 4.0.

Physical modeling of the August 1 event indicates that as few as 5 of the subshots (37,000 pounds total yield) are required to detonate simultaneously in order to explain the boosted body wave am plitudes (Figure 6). This estimate is almost certainly low as the modeling code assumes that all shots are perfectly coupled. The degree of decoupling that results from rock fracturing is, as yet, not well constrained.

Altai-Sayan events

The mines in the Altai-Sayan region in western Siberia produce 100 to 200 blasts each year with a magnitude of 3.5 or above (Khalturin et al., 1997; Figure 7). Of these, ~ 2 each year have a magnitude above 4.0 (Khalturin et al., 1997). This region includes the Kuzbass mine (~ 200 km SE of Novosibirsk) and the Abakan mine. This region is believed to generatethe most energetic seismic signals of all regions in Russia (Khalturin et al., 1997). The mines are believed to be extracting coal. The high magnitudes likely result from shooting entire rows of shots with no delay in each row (Paul Richards pers. comm.).

Stations in the network operated by the Siberian Branch of Russian Academy of Science give a more complete picture of seismicity in this region. Using the empirical relationship between event magnitude and energy class (k) mb = .44K-0.80 (Vitaly Khalturin, personal comm.) we find that a significant number of events in this region are expected to have a body wave magnitude of above 3.0 and that most events occur during local working hours (Figure 9).

Despite having essentially no ground truth information, we have examined events in this region to determine if the methods that appear to be effective in Wyoming also work here. What follows is a preliminary study of 18 events that were recorded at the IMS station ZAL from Jan 1, 1995 to July, 1999. Event and mine locations are shown in Figure 8.

Recordings by the long-period sensor at ZAL reveal that a significant surface wave packet is produced routinely by large mining blasts in this region. The surface wave appears at all ranges to at least 225 km (Figure 10).

The mine blasts also commonly produce significant spectral modulations below 20 Hz (Figure 11). The modulations are typically spaced at

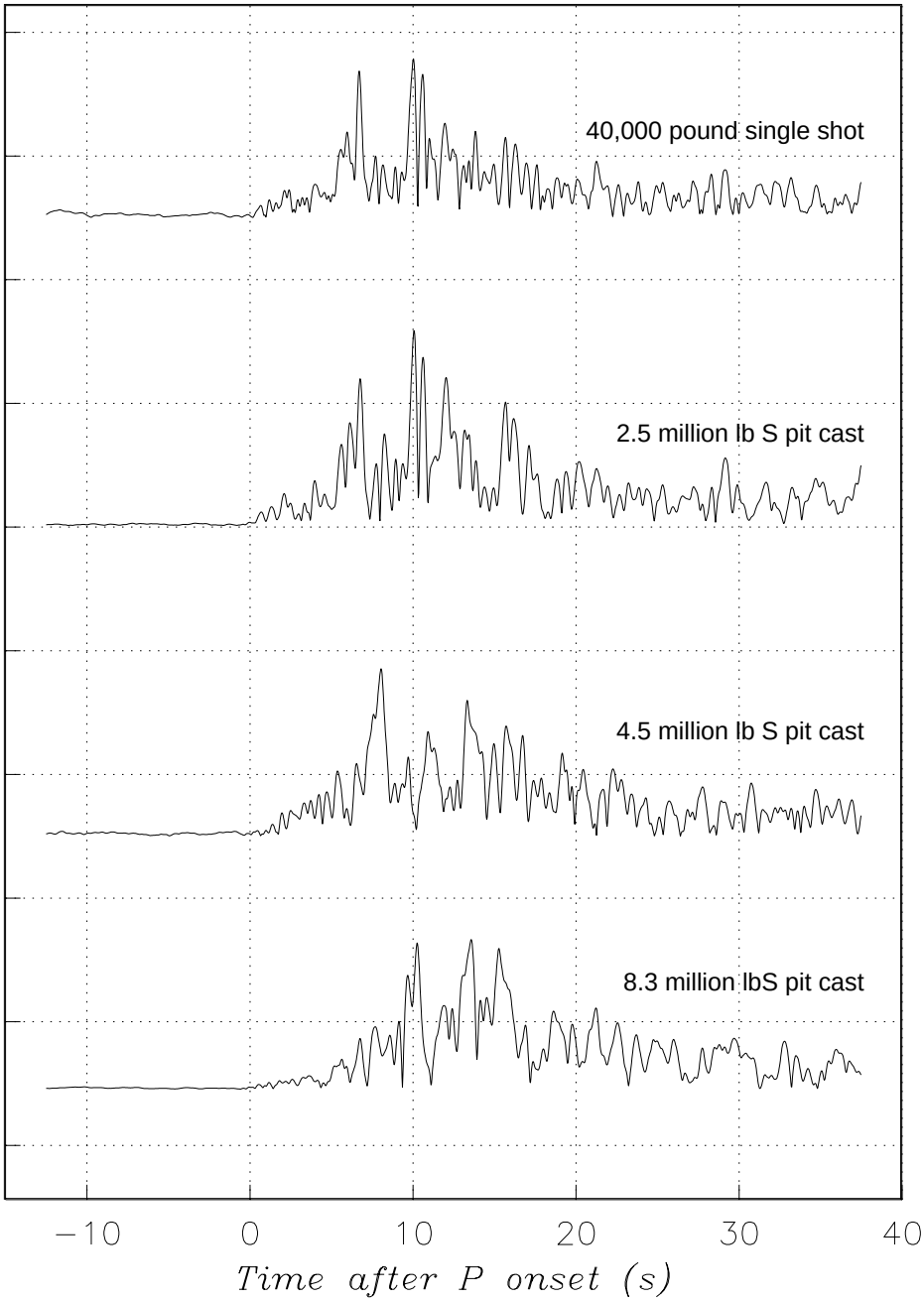


Figure 5. Incoherent beams from events Black Thunder coal mine events recorded by the Pinedale seismic array (PDAR). The top trace is taken from PDAR recordings of a 40,000 calibration sho that occurred in 1995 (PEARSON ET AL., 1995; STUMP, 1995). The next three traces are incoherent beams from large cast blasts. The upper and lower cast blasts are known to have included significant simultaneous detonations. The 2.5 million pound cast blast occurred on Aug 1, 1996 and is discussed in more detail in Hedlin et al. (2000). The incoherent beam from this event is matched, almost exactly, by the beam from the calibration shot indicating the significance of the anomaly. The 4.5 million pound shot (July 19, 1996) is believed to have detonated normally. The 8.3 million pound cast blast has been documented by Stump et al. and is known to have included a detonation anomaly ~ 4 s into the shot sequence - a delay that is seen clearly in the incoherent beams presented here. The weaker correlation of this beam with that taken from the calibration shot suggests a smaller explosive yield in the simultaneous detonation relative to the yield of the overall shot.

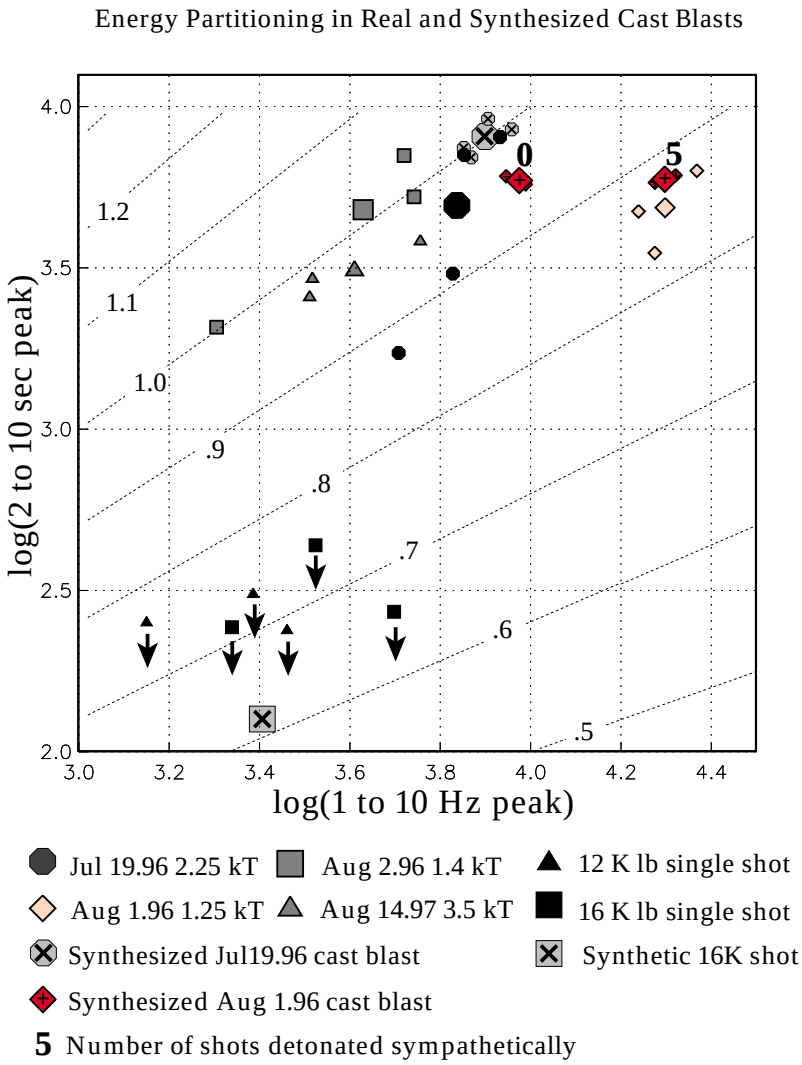


Figure 6. A comparison of 2 to 10 second surface wave and 1 to 10 Hz P wave peak amplitudes using recordings made at a range of 200 km by MNTA, CUST, LBOH & SHNR (Figure 1 in this paper; Hedlin et al., 2000). All events occurred in the Black Thunder coal mine. Each trace is filtered, converted to an envelope and adjusted downward by an amount determined by pre-onset noise. Above are displayed the logarithms of the individual station peak amplitudes. The large symbols represent the network average for each event. Each labeled curve indicates a constant ratio of surface wave to *P* wave amplitude [*i.e.* log(2to10s peak)/log(1to10Hz peak)]. As expected the calibration shots yield essentially no surface wave energy above noise. The downward arrows indicate that the maximum *P* wave amplitude is well constrained but the surface wave amplitude lies below noise. For this reason, no network averages are displayed for these events. The Aug 1.96 cast shot appears as being somewhat explosion-like due to the sympathetic detonation. The sympathetic detonation greatly boosted P wave amplitudes but left the surface waves untouched. Unadjusted amplitudes are plotted as all stations are at the same range from the mine. We also display peak amplitudes from a synthetic version of the July 19 cast blast, from a synthetic 16,000 pound calibration shot and an event that matches the August 1 planned grid but includes 5 shots that detonate simultaneously. The energy partitioning from the synthetic events is in agreement with observations.

~ 5 Hz and suggest an interrow time spacing of ~ 200 msec.

CONCLUSIONS AND RECOMMENDATIONS

We have focused on large mining events in Wyoming as ground truth data in that region is relatively easy to obtain. Several analyses of data from this region indicate that large mining events in this region produce distinctive surface waves and spectral modulations. We have used physical modeling to further the link between these observations and processes at the mine (Hedlin et al., 2000).

From our preliminary analysis of Altai-Sayan mining events we believe that there is strong evidence that the methods that have proven to be effective for characterizinglarge mining events in Wyoming will also be useful in the Kuzbass mining region of Russia. Most Russian mine blasts produce spectral modulations and surface waves that are recorded by the IMS station ZAL. These observations remain tentative as we do not have ground truth information to constrain these events. We have begun a collaboration with Vitaly Khalturin (Lamont) under which we will strive to strengthen communication links between our groups and mining experts in the Kuzbass region.

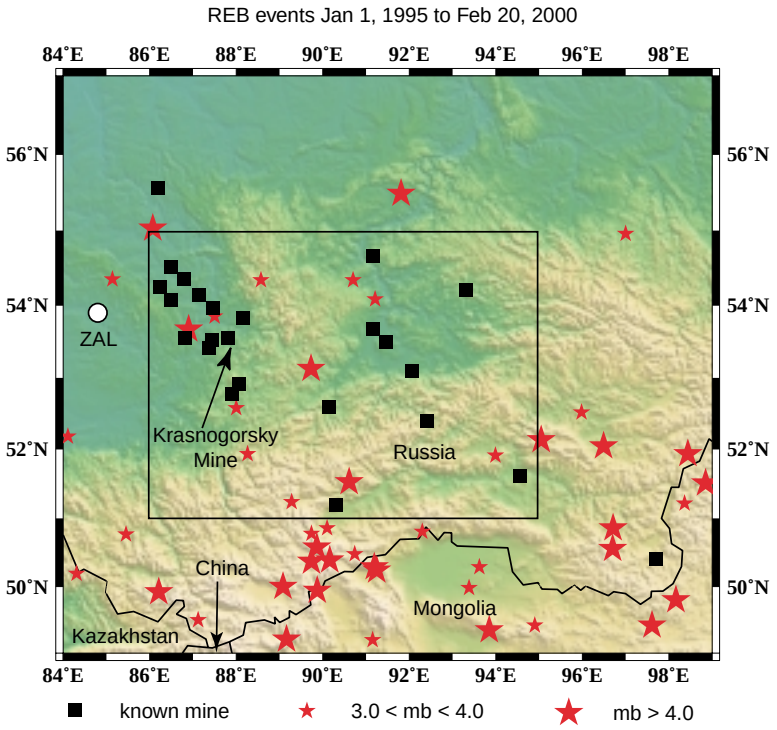


Figure 7. Events reported in the REB catalog between Jan 1, 1995 and Feb 20, 2000 are plotted with known mine locations in the Kuzbass region of Russia. The event locations do not correlate with known mining activity.

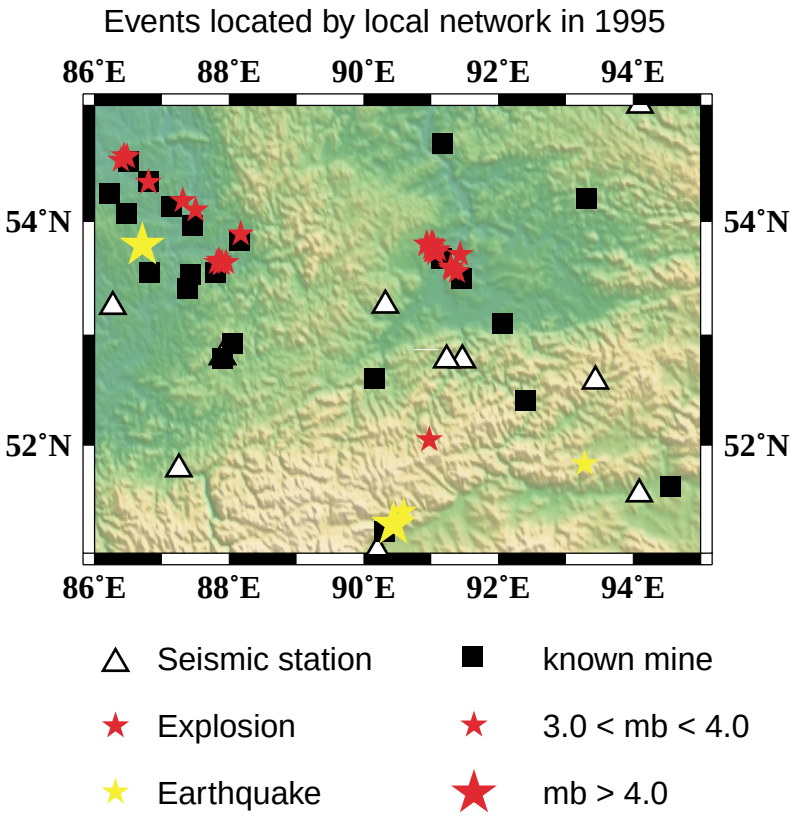


Figure 8. Events detected by the 16 station network in the Kuzbass region. Of the 16 stations, one (ZAL) is part of the IMS. The others are part of the Altay-Sayans Seissmological Expedition of the Siberian Branch of Russian Academy of Science. Body wave magnitudes were estimated from the energy class ratings using .mb = .44K-0.80 (Vitaly Khalturin, personal comm.) Significant events located using the dense network correlate well with known mines. All mine and event locations/magnitudes were generously provided by V. Khalturin.

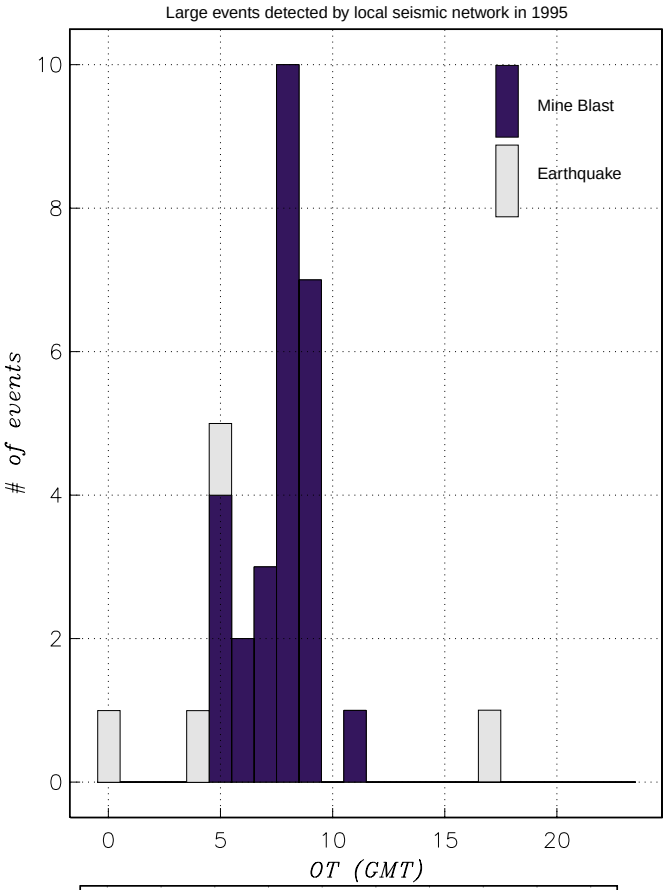


Figure 9. Histogram of origin times of events presented in Figure 8.

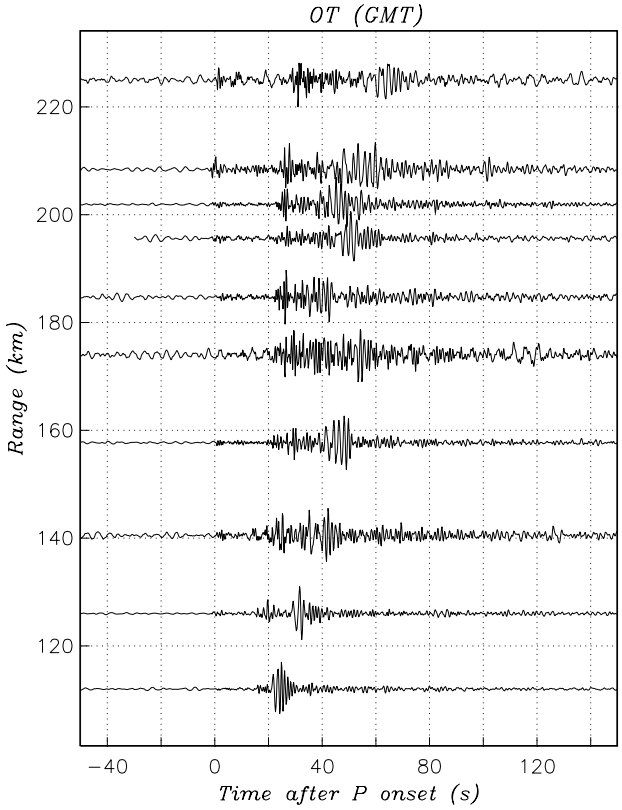


Figure 10. Recordings of Kuzbass mining events made by the MHZ long-period channel at the IMS station ZAL. Large surface waves are seen in most recordings.

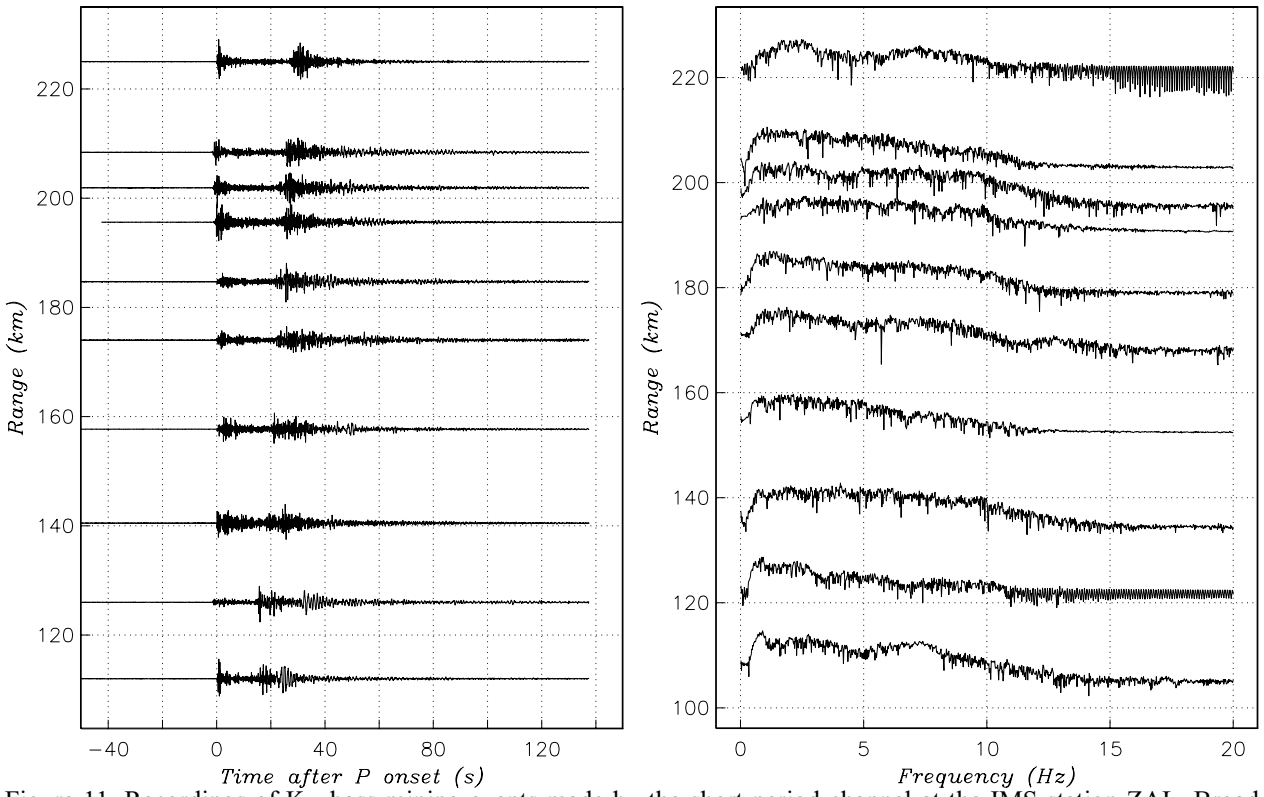


Figure 11. Recordings of Kuzbass mining events made by the short period channel at the IMS station ZAL. Broad spectral modulations are seen most of the events.

REFERENCES

Anandakrishnan, S., Taylor, S.R., and Stump, B.W. (1997), Quantification and characterization of regional seismic signals from cast blasting in mines: A linear elastic model, *Geophysical Journal International,* **131**, 45-60.

Barker, T.G., and Day, S.M. (1990), A simple physical model for spall from nuclear explosions based upon two-dimensional nonlinear numerical simulations, PL report SSS-TR-93-13859.

Barker, T.G., McLaughlin, K.L., Stevens, J.L., and Day, S.M. (1993), Numerical models of quarry blast sources: the effects of the bench, *PL semiannual report, SSS-TR-93-13915.*

Hedlin, M.A.H., Stump, B., Pearson, D.C., and Yang, X. (2000), Identification of mining blaslts at mid- to far-regional distances using low-frequency seismic signals, *in review with PAGEOPH.*

Khalturin, V.I., Rautian, T.G., Richards, P.G., and Kim, W.Y. (1997), Evaluation of chemical explosions and methods of discrimination for practical seismic monitoring of a CTBT, *Phillips Lab. draft Final Report.*

Martin, R., Gross, D., Pearson, C., Stump, B., and Anderson, D. (1997), Black Thunder Coal Mine and Los Alamos experimental study of seismic energy generated by large scale mine blasting, *Proceedings of the twenty-third annual conference on explosives and blasting technique, Las Vegas, Nevada, Feb 2-5, 1997, International Society of Explosive Engineers, Cleveland, Ohio, pp. 1-10.*

McLaughlin, K.L., Barker, T.G., Stevens, J.L., and Day, S.M. (1994), Numerical simulation of quarry blast sources, PL final report SSS-FR-94-14418.

Pearson, D.C., Stump, B.W., Baker, D.F., and Edwards, C.L. (1995), The LANL/LLNL/AFTAC Black Thunder Mine regional mining blast experiment, *17th annual PL/AFOSR/AFTAC/DOE Seism. Res. Symp.*, 562-571.

Prodehl, C. (1979), Crustal structure of the western United States, *US Geological Survey Professional Paper,* 1034.

Stump, B.W. (1995), Practical observations of US mining practices and implications for CTBT monitoring, *Phillips Lab report*, PL-TR-95-2108.

Stump, B.W., and Pearson, D.C. (1997), Comparison of single-fired and delay-fired explosions at regional and local distances, *19th annual Seism. Res. Symp*. 668-677.

Stump, B.W., Pearson, D.C., and Hsu, V. (1999), Empirical scaling relations for contained single-fired chemical explosions and delay-fired mining explosions at regional distances, 1999 SSA meeting.

Yang, X. (1998), MineSeis - A Matlab GUI Program to Calculate Synthetic Seismograms from a Linear, Multi-Shot Blast Source Model, *20th annual Seism. Res. Symp.* 755-764.

CHARACTERIZATION OF SEISMIC SOURCES

Lane R. Johnson
University of California, Berkeley

Sponsored by The Defense Threat Reduction Agency
Arms Control Technology Division
Nuclear Treaties Branch

Contract No. DSWA-97-1-0026

ABSTRACT

The seismic discrimination between weapons tests, industrial explosions, natural earthquakes, and other types of seismic events is limited by an incomplete understanding of the basic physics of the source processes. The problem of quantifying how the generation of elastic waves is related to such factors as mode of energy release, source dimensions, material properties, and stress concentrations is still unsolved for the most part. While a complete solution of this complicated problem may not be possible at the present time, an examination of the similarities and differences between various types of seismic sources could prove useful in the discrimination task. This was one of the objectives of this research effort.

A starting point for the comparison of the different types of seismic sources is the large amounts of empirical data that are summarized in various seismic scaling relationships, such as moment versus yield for contained explosions and stress drop versus moment for natural earthquakes. By converting these scaling relationships for different types of sources to a common form, it is possible to assess whether there are significant differences in the basic source processes. For instance, both contained explosions and natural earthquakes are consistent with a linear relationship between seismic scalar moment and source energy, with the proportionality factor being identical if the efficiency of the earthquake source is taken to be about 0.15%. A recent study of the energy required to generate pseudotachylites suggests that this value of efficiency is not unreasonable. Another approach to the comparison of seismic sources is the consideration of energy density in the source region, which is related to the total energy of the source and its spatial dimensions. Here again recently acquired data suggest that, provided a distinction is made between the initial source dimension and the effective source dimension, the energy densities of different types of sources are more similar than previously thought. This leads to a consideration of such matters as the interaction between the seismic source and the material properties, the degree to which the material properties are modified by the source, and the possibility of secondary sources. These aspects of the problem have been examined by simulating the stress field near different types of seismic sources, comparing the results, and exploring the effect of various source parameters.

Key Words: discrimination, seismic sources, explosions, earthquakes

OBJECTIVES

The scope of this research effort is concerned with the development of an improved understanding of methods for locating and characterizing seismic events in a heterogeneous earth. The general objective is to investigate how improved models for the generation and propagation of elastic waves can help in the evaluation of methods and models currently being used. The work statement for the research contains two primary tasks:

1. Continue the development of analytical and numerical techniques capable of modeling the physical processes that cause the generation of elastic waves by seismic sources. Also continue the development of three-dimensional models of the earth's velocity structure which have sufficient resolution to provide accurate locations of seismic events at regional and teleseismic distances.

2. The modeling capability will be validated against existing data bases and any new data which can be acquired by taking advantage of targets of opportunity to perform broad band recording experiments.

This paper reports on work that has bee done during the past three years on scaling relationships for seismic sources, with particular emphasis on such relationships for small earthquakes. Developing a more complete understanding of these scaling relationships for both contained explosions and natural earthquakes has the potential to provide a more comprehensive theoretical foundation for the methods that are currently being used to monitor a Comprehensive Nuclear-Test-Ban Treaty and perhaps uncover new methods.

RESEARCH ACCOMPLISHED

Haskell (1964) introduced a model of an earthquake as a rupture propagating over a finite section of a fault and provided convenient analytical formulas for the radiated elastic waves. A characteristic of this model in its most simple form is a very uniform release of displacement and stress on the fault surface. Haskell recognized this as a deficiency and suggested that some form of heterogeneity was needed in the distribution of displacement in either time or space. Haskell (1966) and Aki (1967) attempted to model this heterogeneity by describing the acceleration and velocity, respectively, of fault displacement in terms of random functions that were correlated over only limited portions of the fault plane. Brune (1970) considered the time history of displacement on the fault and provided spectral models relating the frequency content of radiated elastic waves to dimensions and stress present on the fault. These models for an earthquake formed the basis for the interpretation of large amounts of observational data in terms of earthquake source parameters, but the emphasis was primarily upon average properties and not much attention was given to the heterogeneity originally explored by Haskell and Aki. Kanamori and Anderson (1975) summarized many of these empirical data and used them to justify scaling laws that related such parameters as fault dimension, stress drop, moment, magnitude, and energy. Emerging from studies of this type was a generally held conviction that the stress drops of most shallow earthquakes was independent of size and generally fell in the range of 10 to 100 bars. Implicit in most of these studies was the assumption that the fault was relatively uniform in terms of material properties and energy release.

A rather different approach to the study of heterogeneity on the fault surface has emerged rather unexpectedly from studies of small repeating earthquakes along the San Andreas fault system in California. Nadeau and Johnson (1998) showed how measurements of moment release rates of these repeating earthquakes could be used to construct scaling relationships between seismic moment, repeat time, fault slip and fault dimension. Their method of interpreting the data does not require the use of any model for the earthquake process and uses the single assumption that slip on the fault at depth is closely related to the measured slip at the surface. The study of Nadeau and McEvilly (1999) provides strong support for this assumption by showing that second order variations of slip in both time and space are strongly correlated between the surface and the depth of the seismogenic zone. The basic scaling relationship obtained by Nadeau and Johnson (1998) relates repeat time of earthquakes T to scalar seismic moment according to the formula

$$T \propto M_o^{\frac{1}{6}} \tag{1}$$

where the fraction $\frac{1}{6}$ is a close approximation to the numerical value of 0.17 which was obtained by regression analysis. This result can also be interpreted in terms of scaling relationships for fault displacement u and fault area A of the form

$$u \propto M_o^{\frac{1}{6}} \tag{2}$$

and

$$A \propto M_o^{\frac{5}{6}} \tag{3}$$

When these relationships are interpreted in terms of stress drops they lead to values in the GPa range, which is not impossible for crustal rocks (Sammis et al., 1999), but much larger than expected values in

the 1 to 10 MPa range. This result, together with the fact that the repeating earthquakes occupy a very small fraction of the fault and are surrounded by regions which appear to be creeping and thus quite weak, argues for a fault which is highly heterogeneous in its strength properties. Alternative interpretations have been recently presented (Anooshehpoor and Brune, 1998, 2000; Sammis and Rice, 2000; Beeler, 2000) which attempt to avoid the need for high stress drops and thus do not require the heterogeneous fault surface.

While one of the strengths of the study by Nadeau and Johnson (1998) was that it did not use a source model that presumed either a homogeneous or heterogeneous fault surface, a full interpretation of the results does require that some type of model be used. Here we introduce such a model and use this model to interpret the data in terms of physical properties and processes on the fault surface. The model introduced here begins with the assumption that strength on the fault surface is highly heterogeneous and attempts to show that such a model is consistent with the scaling relationships presented in Nadeau and Johnson (1998). Only the quasi-static part of the earthquake process is considered here, which extends up to the time that rupture begins.

Consider a planar fault surface lying in the xy plane and let the slip across this surface be denoted by

$$\mathbf{d}(x,y) = d_x(x,y)\hat{\mathbf{x}} + d_y(x,y)\hat{\mathbf{y}} \tag{4}$$

Without loss of generality we will assume that the motion on the fault is in response to a loading traction T_x that acts only in the $\hat{\mathbf{x}}$ direction. Let the slip that would occur if the fault were uniformly weak and creeping uniformly be denoted by $\mathbf{d}_c$. Then the displacement deficit on the fault can be defined as

$$\mathbf{u}(x,y) = \mathbf{d}_c - \mathbf{d}(x,y) \tag{5}$$

At points where the fault slip is keeping up with the applied traction the displacement deficit will be zero.

The fault is considered to be sufficiently weak so that it continually creeps as tectonic stress is applied except on isolated patches which we will call asperities. The asperities are small areas of the fault which are much stronger than the surrounding regions and able to withstand the tectonic stress until a stress limit is reached and rupture occurs. These asperities will be assumed to be circular with radius r_o and area $A_o = \pi r_o^2$. In the static problem being considered here we only consider the situation up to the instant just before the asperities rupture, so there will be no movement on these asperities. Thus the displacement deficit $\mathbf{u}$ will be a maximum at the asperities.

Focus now upon a region of the fault where a group of asperities are close enough together so that they strongly interact. Assume that this group of asperities is roughly in the form of a circle with radius r_a and area $A_a = \pi r_a^2$. The displacement deficit will be the same on all asperities and denoted by u_a. The asperities are assumed to be close enough together so that they prevent almost all motion on the intervening areas between the asperities, and thus the displacement deficit is very close to u_a over the entire area A_a. A solution for elastostatic problem just described can be found in Westmann (1968). The stress on the region A_a where the displacement is u_a is given by

$$\sigma_{xz}(r) = \frac{4\mu u_a}{(2-\nu)\pi}\frac{1}{\sqrt{r_a^2 - r^2}} \tag{6}$$

where $r^2 = x^2 + y^2$, μ is the shear modulus, and ν is Poisson's ratio. The stress on the weak part of the fault outside A_a is assumed to be zero in this solution. However, the displacement caused by the group of asperities does extend outside A_a and in the region $r \geq r_a$ is given by

$$u_x(r,\theta) = \frac{2u_a}{(2-\nu)\pi}[(2-\nu)\sin^{-1}(\frac{r_a}{r}) + \frac{\nu r_a}{r^2}\sqrt{r^2 - r_a^2}\cos(2\theta)] \tag{7}$$

$$u_y(r,\theta) = \frac{2u_a}{(2-\nu)\pi}\frac{\nu r_a}{r^2}\sqrt{r^2 - r_a^2}\sin(2\theta) \tag{8}$$

where θ is the polar angle in the xy plane. We see that the group of asperities is surrounded on the fault plane by a displacement shadow that decays as r^{-1} at distances much greater than r_a. Note that the first

term in the expression for u_x is about 7 times larger than the second term in u_x and the only term in u_y. Thus it will be sufficient in what follows to assume that the displacement deficit within the shadow is given approximately by

$$u_x(r) = \frac{u_a r_a}{r} \tag{9}$$

Next we will assume that the displacement shadow of the group of asperities is terminated when the displacement u_x falls below a critical level denoted by u_c. One can appeal to state variable friction theories to justify the existence of such a critical level of displacement. The radius of the displacement shadow r_c is then given by

$$r_c = \frac{u_a}{u_c} r_a \tag{10}$$

The geometrical picture of the situation on the fault plane is now complete, and it is shown in Figure 1. It will be assumed that $u_a \gg u_c$ and it follows that $r_c \gg r_a$.

Were all of the asperities to rupture and all of the displacement deficit released, the scalar moment of such an event would be approximately

$$M_o = \mu[2\pi \int_0^{r_a} u_a r dr + 2\pi \int_{r_a}^{r_c} \frac{u_a r_a}{r} r dr] = \pi \mu u_a r_a (2r_c - r_a) \approx 2\pi \mu u_a r_a r_c \tag{11}$$

From the expression for stress on the asperity patch (6) it is clear that this stress in not uniform and is greatest near the edge of the patch. Thus, assuming the individual asperities are similar in their properties, one would expect the failure of the asperity patch to begin with the failure of one of those closest to border r_a. This is consistent with the results of Das and Kostrov (1983, 1986) who found that failure of an asperity began on its border and then progressed toward the center. The average stress on one of these border asperities can be evaluated to yield

$$\bar{\sigma}_{max} = \frac{1}{\pi r_o^2} \int_{A_o} \sigma_{xz}(x, y) dx dy = C \frac{u_a}{\sqrt{r_o r_a}} \tag{12}$$

where

$$C = \frac{32\mu}{3\pi^2(2 - \nu)} \tag{13}$$

and it has been assumed that $r_a \gg r_o$ in evaluating the integral. Note that this result is similar to that of Sammis and Rice (2000), who used it to argue for a very weak asperity. Here we use it to argue that when a group of asperities are combined together in close proximity on a fault, they interact in such way as to reduce the stress felt by any individual asperity. In effect, the displacement field is smoothed by the interaction of the asperities, thus reducing displacement gradients, strain, and stress. Assuming that $\bar{\sigma}_{max}$ is a constant that controls the initiation of rupture on the asperity patch, we have

$$u_a = \frac{\bar{\sigma}_{max}}{C} \sqrt{r_o r_a} \tag{14}$$

and then

$$r_c = \frac{\bar{\sigma}_{max}}{C u_c} r_o^{\frac{1}{2}} r_a^{\frac{3}{2}} \tag{15}$$

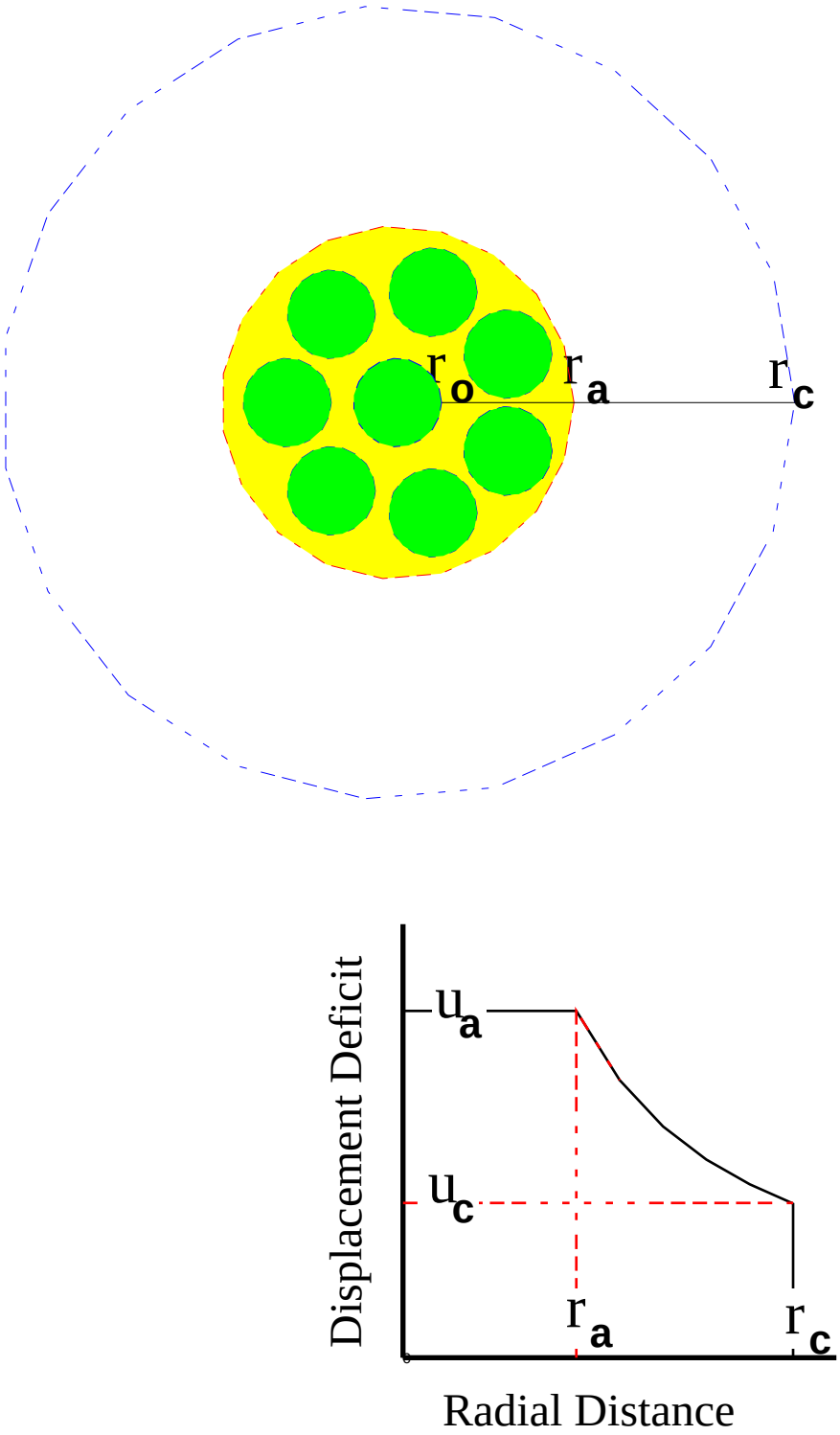


Figure 1: Schematic sketch of the earthquake model consisting of a patch of interacting strong asperities. The upper panel shows a group of asperities having radius r_o with a strong interacting region of radius r_a and surrounded by a displacement shadow that extends out to a radius r_c. The lower panel shows the disiplacement deficit as a function of radial distance from the center of the asperity patch.

The next step is to consider how the results given above change when the size of the asperity patch changes. For this it is convenient to introduce the number n, which is taken to be the number of small asperities in the asperity patch. If the asperities were to add linearly with no interaction, then one would expect that

$$A_a = \pi r_o^2 n \tag{16}$$

which would imply that

$$r_a(n) = r_o n^{\frac{1}{2}} \tag{17}$$

If the asperities were to add with some interaction between them, then we might expect a more general relationship of the form

$$r_a(n) = r_o n^{\kappa} \tag{18}$$

where $\kappa > 1/2$ but is otherwise undetermined at this point.

Now consider what happens when the number of asperities in the patch is increased by one. Then we have

$$r_a(n+1) = (n+1)^{\kappa} r_o \approx r_a(n)(1 + \frac{\kappa}{n}) \tag{19}$$

$$r_c(n+1) \approx r_c(n)(1 + \frac{3\kappa}{2n}) \tag{20}$$

$$u_a(n+1) \approx u_a(n)(1 + \frac{\kappa}{2n}) \tag{21}$$

and finally

$$M_o(n+1) \approx M_o(n)(1 + \frac{3\kappa}{n}) \tag{22}$$

From this last equation we can form the differential equation

$$\frac{d}{dn} M_o(n) = M_o(n) \frac{3\kappa}{n} \tag{23}$$

which has the solution

$$M_o(n) = M_o(1) n^{3\kappa} \tag{24}$$

The same process produces

$$r_a(n) = r_a(1) n^{\kappa} = r_o n^{\kappa} \tag{25}$$

$$r_c(n) = r_c(1) n^{\frac{3}{2}\kappa} = \frac{\hat{\sigma}_{max}}{C} r_o^2 n^{\frac{3}{2}\kappa} \tag{26}$$

$$u_a(n) = u_a(1) n^{\frac{1}{2}\kappa} = \frac{\hat{\sigma}_{max}}{C} r_o n^{\frac{1}{2}\kappa} \tag{27}$$

and from these it is possible to obtain

$$M_o(n) = 2\pi\mu \frac{\hat{\sigma}_{max}^2}{C^2 u_c} r_o^4 n^{3\kappa} \tag{28}$$

These last four equations form a consistent set of parametric equations for all of the geometrical properties of this asperity model of the earthquake process. They are all expressed in terms of the parameter n, which was introduced as the number of asperities involved, but may be considered more generally as a surrogate for the size of the earthquake.

Using the expressions listed above for $r_a(n)$ or $r_c(n)$ one can calculate the areas of the asperity patch or the displacement shadow, respectively. However, neither of these corresponds to the area that was calculated by Nadeau and Johnson (1998). If we define

$$M_o(n) = \mu \tilde{A}(n) u_a(n) \tag{29}$$

then $\tilde{A}(n)$ is an effective area that corresponds to the area calculated by Nadeau and Johnson (1998). It follows that

$$\tilde{A}(n) = A_o(1) n^{\frac{5}{2}\kappa} = 2\pi \frac{\hat{\sigma}_{max}}{C u_c} r_o^3 n^{\frac{5}{2}\kappa} \tag{30}$$

These results for displacement, area, and scalar moment can be expressed in terms of the scaling relationships

$$u_a \propto M_o^{1/6} \tag{31}$$

$$\tilde{A} \propto M_o^{5/6} \tag{32}$$

Assuming that the displacement on the asperities u_a accumulates at a steady rate in time t then we also have

$$t \propto M_o^{1/6} \tag{33}$$

This is the basic observational result presented by Nadeau and Johnson (1998). Note that all of these scaling relationships are independent of the parameter n and the parameter κ, which together control the size of the area where there is strong interaction between the asperities.

Stress drop is a parameter that is commonly used to characterize earthquakes, with conventional thought being that stress drop is independent of earthquake size and in the range of 10 to 100 bars (Kanamori and Anderson, 1975). In the asperity model presented in this paper stress is highly heterogeneous, ranging from infinity (in a mathematical sense) on the border of a single asperity to a very small value in the displacement shadow. This makes it difficult to characterize the stress with a single number, so several available options will be discussed. The only stress that is critical to the theory is the average stress that causes an asperity near the edge of the patch to fail $\bar{\sigma}_{max}$, which was assumed to be a constant material property. This can be compared with the average stress felt by a single isolated asperity

$$\bar{\sigma}_o = \frac{8\mu}{\pi(2-\nu)} \frac{u_a(1)}{r_o} \tag{34}$$

From this we have

$$\bar{\sigma}_{max} = \frac{4}{3\pi} \sqrt{\frac{r_o}{r_a(n)}} \bar{\sigma}_o = \frac{4}{3\pi} n^{-\frac{1}{2}\kappa} \bar{\sigma}_o \tag{35}$$

which shows clearly how interaction of a group of asperities can reduce the maximum stress. Note that it was assumed that $n \gg 1$ in deriving $\bar{\sigma}_{max}$ so this result does not give the correct answer as $n \rightarrow 1$.

Stress drop is commonly calculated using the formula (Kanamori and Anderson, 1975)

$$\Delta\sigma = \frac{7\pi\mu}{16} \frac{\bar{u}}{\bar{r}} \tag{36}$$

where $\bar{u}$ is the average slip over a circular crack of radius $\bar{r}$. Using $u_a(n)$ for $\bar{u}$ and $r_a(n)$ for $\bar{r}$ yields

$$\Delta\sigma_a = \frac{7\pi\mu}{16} \frac{u_a(n)}{r_a(n)} = \frac{21\pi^3(2-\nu)}{512} \hat{\sigma}_{max} \, n^{-\frac{1}{2}\kappa} \tag{37}$$

Still another possibility is to use the formula (Kanamori and Anderson, 1975)

$$\Delta\sigma = \frac{7}{16} \frac{M_o}{\bar{r}^3} \tag{38}$$

Using $r_c(n)$ for $\bar{r}$ yields

$$\Delta\sigma_c = \frac{7}{16}\frac{M_o(n)}{r_c(n)^3} = \frac{28\mu^2}{3\pi(2-\nu)}\ \frac{u_c^2}{\bar{\sigma}_{max} r_o^2}\ n^{-\frac{3}{2}\kappa} \tag{39}$$

The stress drops calculated in Nadeau and Johnson (1998) correspond to taking $u_a(n)$ for $\bar{u}$ and $\sqrt{\tilde{A}(n)/\pi}$ for $\bar{r}$ and this yields

$$\Delta\tilde{\sigma} = \frac{7\pi\mu}{16}\frac{u_a(n)}{\sqrt{\tilde{A}(n)/\pi}} = \frac{7\pi^2\sqrt{3\mu(2-\nu)}}{128}\ \sqrt{\bar{\sigma}_{max}}\ r_o^{-\frac{3}{2}}\ n^{-\frac{3}{4}\kappa} \tag{40}$$

If this result is scaled against moment we obtain

$$\Delta\tilde{\sigma} \propto M_o^{-1/4} \tag{41}$$

which agrees with the empirical result Nadeau and Johnson (1998) obtained.

CONCLUSIONS AND RECOMMENDATIONS

The model of an earthquake that has been presented here is based on the concept of small strong asperities that resist motion on the fault. When a group of these asperities are close enough together so that they can strongly interact, an asperity patch is formed which is stronger than any of the individual asperities and so a greater amount of tectonic displacement can accumulate before failure occurs. The asperity patch is surrounded by a displacement shadow where creep displacement on the weak part of the fault is retarded because of the presence of the asperity patch. The asperity patch ruptures and an earthquake occurs when the stress on one of the asperities, most likely near the border of the patch, reaches its strength limit and fails, which causes a cascade failure of all the other asperities in the patch. At this time the entire displacement deficit associated with the asperity patch, that within both the asperity patch and the surrounding displacement shadow, is released and contributes to the scalar moment of the earthquake. This model depends upon only a few parameters, the radius of the individual asperities r_o, the critical level of displacement that determines the limit of the displacement shadow u_c, the stress level at which an individual asperity will fail $\bar{\sigma}_{max}$, the number of asperities in an asperity patch n, and the exponential factor that controls how the radius of the asperity patch grows with the number of asperities κ. What is rather remakable is that the scaling relationships for displacement, area, and time to failure as a function of moment do not depend upon any of these parameters. They are direct consequences of analytic elastostatic solutions for the exterior crack problem. Another characteristic of this model is that it involves a very heterogeneous stress field that is difficult to characterize in a meaningful way with a single parameter such as stress drop.

REFERENCES

1. Aki, K., Scaling law of seismic spectrum, *J. Geophys. Res.*, **72**, 1217-1231, 1967.

2. Anooshehpoor, A., and J. N. Brune, Quasi-static slip-rate shielding by locked and creeping zones as an explanation for small repeating earthquakes at Parkfield, *EOS, Transactions*, **79**, F594, 1998.

3. Anooshehpoor, A., and J. N. Brune, Quasi-static slip-rate shielding by locked and creeping zones as an explanation for small repeating earthquakes at Parkfield, preprint, 2000.

4. Beeler, N. M., A simple stick-slip and creep-slip model for repeating earthquakes and its implications for micro-earthquakes at Parkfield, preprint, 2000.

5. Brune, J. N., Tectonic stress and the spectra of seismic shear waves from earthquakes, *J. Geophys. Res.*, **75**, 4997–5009, 1970.

6. Das, S., and B. V. Kostrov, Breaking of a single asperity: rupture process and seismic radiation, *J. Geophys. Res.*, **88**, 4277-4288, 1983.

7. Das, S., and B. V. Kostrov, Fracture of a single asperity on a finite fault: a model for weak earthquakes? in *Earthquake Source Mechanisms*, S. Das, J. Boatwright, and C. H. Scholz (eds), Geophys. Monogr. 37, Am. Geophys. Union, 91-96, 1986.

8. Haskell, N. A., Total energy and energy spectral density of elastic wave radiation from propagating faults, *Bull. Seism. Soc. Am.*, **54**, 1811-1841, 1964.

9. Haskell, N. A., Total energy and energy spectral density of elastic wave radiation from propagating faults, Part II, A statistical source model, *Bull. Seism. Soc. Am.*, **56**, 125-140, 1966.

10. Kanamori, H., and D. L. Anderson, Theoretical basis of some empirical relations in seismology, *Bull. Seism. Soc. Am.*, **65**, 1073-1095, 1975.

11. Nadeau, R. M., and L. R. Johnson, Seismological studies at Parkfield VI: Moment release rates and estimates of source parameters for small repeating earthquakes, *Bull. Seism. Soc. Am.*, **88**, 790-814, 1998.

12. Nadeau, R. M., and T. V. McEvilly, Fault slip rates at depth from recurrence intervals of repeating microearthquakes, *Science*, **285**, 718-721, 1999.

13. Sammis, C. G., R. M. Nadeau, and L. R. Johnson, How strong is an asperity? *J. Geophys. Res.*, **104**, 10,609–10,619, 1999.

14. Sammis, C. G., and J. R. Rice, Repeating earthquakes as low-stress-drop events at a border between locked and creeping fault patches, preprint, 2000.

15. Westmann, R. A., Asymmetric mixed boundary-value problems of the elastic half-space, *J. Appl. Mech.*, **32**, 414-417, 1965.

CHARACTERIZATION OF MINING-INDUCED SEISMICITY IN THE WITWATERSRAND BASIN, SOUTH AFRICA

T. H. Jordan and E. Richardson
Department of Earth, Atmospheric and Planetary Sciences, MIT, Cambridge, MA 02139

C. Wright, S. Webb, E. Kgaswane, T. Kwadiba, and R. McRae-Samuel
Bernard Price Institute, University of Witwatersrand, Johannesburg, South Africa

DTRA Contract Number 98-C-0158

ABSTRACT

The objective of this research is to characterize the seismicity of South Africa, with emphasis on understanding the distribution and properties of mining-induced events in the Witwatersrand Basin. The study has focused on the two-year period from April, 1997 to May, 1999, when MIT and the Carnegie Institution of Washington, supported by the U.S. National Science Foundation and in cooperation with the University of Witwatersrand and a number of other research organizations in southern Africa, operated a temporary, 54-station array of broadband, three-component seismometers. This "Kaapvaal" array was distributed on a NE-SW axis from Cape Town, South Africa, to Masvingo, Zimbabwe, for the primary purpose of imaging the deep structure of the South African continent, but it also produced excellent recordings of regional seismicity.

Seismicity and Waveform Catalogs. The following cataloging tasks have been completed or are nearing completion:

1. *Standard Catalog.* In cooperation with the South Africa Council of Geosciences, a catalog of southern African seismicity has been constructed for the two-year period using data from the South African Seismological Network (SANSN) and the Council's standard procedures for associating arrivals and locating events.

2. *Local Mine Catalogs.* Locations, origin times, and magnitudes have been collected for all events with $M_L \geq 2$ from in-mine seismic networks maintained by the following mine operators:

East Rand:	East Rand Proprietary Mine
Central Rand:	West Rand Consolidated, Randfontein Estates, Durban-Roodepoort Deep
West Rand:	Kloof, Libanon, Venterspost
Far West Rand:	Deelkraal, Elandsrand, Western Deep Levels (Tautona, Savuka, Mponeng), Blyvooruitzicht, Doornfontein, Driefontein Consolidated (West & East).
Free State:	Joel, Masimong (Saaiplaas), Bambanani (President Steyn), Matjhabeng (Western Holdings), Harmony, Unisel, St. Helena
Klerksdorp:	Vaal Reefs, Stillfontein, Hartebeestfontein, Buffelsfontein, African Rainbow Minerals

3. *Calibration Catalog.* Events common to the standard and local mine catalogs have been identified and being used to calibrate the performance of SANSN and the Kaapvaal array.

We are currently constructing a catalog of waveforms recorded on the Kaapvaal broadband array, and we plan to use these waveforms in conjunction with the precise locations from the in-mine networks to improve the location and source-modeling procedures in South Africa.

Properties of Mining-Induced Seismicity. We have completed our first detailed study of mining-induced seismicity in the Far West Rand mining district of South Africa. The study was done in cooperation with AngloGold, Ltd., at five of its mines: Deelkraal, Elandsrand, and the three mines of Western Deep Levels (Tautona, Savuka, Mponeng). These mines, which are the deepest in the world, extract ore at 2-4 km and are very seismically active; each is equipped with state-of-the-art, on-reef seismic networks comprising 13-

28 three-component stations that record hundreds of events per day. Based on these data, we have identified two distinct classes of events, designated Type A and Type B. Type A events are tightly development end; they have spectra comparatively enriched in high frequencies, their focal mechanisms often involve isotropic components, and they show an upper magnitude cutoff at $M \sim 0.5$. We interpret these events to be "fracture-dominated" ruptures of competent rock at low normal stress, induced by dynamic stresses during blasting and quasi-static stress perturbations from the excavation and closure of individual stopes.

In contrast, Type B events are temporally and spatially distributed throughout the active mining region. We interpret them to be "friction-dominated" ruptures occurring on existing faults or other weak geologic structures at near-lithostatic normal stresses. They have double-couple focal mechanisms and scaling properties that agree with extrapolations from tectonic earthquakes. For example, the energy/moment ratios for Type B events yield apparent stresses in the range .01-1 MPa with a distinct increase in apparent stress with moment, consistent with the observations of small earthquakes in tectonic environments. Although the data show considerable scatter, the increase in apparent stress scales approximately as $M^{2/3}$. A second important observation is a lower magnitude cutoff in the Type B events at M ~ 0. We interpret this cutoff in terms of a critical patch size for nucleation of shear failure, which yields a critical slip distance $D_c = 10^{-4}$ m. This result is consistent with an upper frequency cutoff, f_{max}, near 200 Hz, which is observed on accelerograms recorded in the near field of large events. The implications of these results for nuclear monitoring in deep-mining environments will be discussed.

ISOTROPIC AND NONISOTROPIC COMPONENTS OF EARTHQUAKES AND NUCLEAR EXPLOSIONS ON THE LOP NOR TEST SITE

A.L. Levshin, M.H. Ritzwoller
Center for Imaging the Earth's Interior, University of Colorado at Boulder

B.G. Bukchin, A.Z. Mostinsky, A.A. Egorkin
International Institute of Earthquake Prediction Theory & Mathematical Geophysics, Moscow, Russia

Sponsored by U.S. Department of Defense
Defense Threat Reduction Agency
Contract No. DSWA01-97-C-0157

ABSTRACT

We test the hypothesis that the existence of an observable isotropic component of the seismic moment tensor can be used as a discriminant to distinguish nuclear explosions from shallow earthquakes. We do this by applying the method described by Bukchin *et al.*, (2000) to a set of data recorded between 1990 and 1996 following events (seven nuclear explosions and three earthquakes) that occurred on the Lop Nor test site in Western China. We represent each source as the sum of an isotropic component at the surface and a non-isotropic, double couple component at an estimated depth. The explosions all possess a significant isotropic component, and the estimated depth of the double-couple component of the moment tensor, presumably the result of tectonic release, lies between 0 and 3 km. For the earthquakes studied, the isotropic component is indistinguishable from zero and the depths of the sources are estimated at 3, 17 and 31 km. The data set we have studied, although very small, suggests that certain source characteristics (namely, double couple depth and the ratio of the isotropic to nonisotropic components of the seismic moment tensor) may prove useful in discriminating explosions from shallow earthquakes. Further work is needed to determine whether these observations hold for explosions at other test sites, to investigate a much larger set of shallow earthquakes located in regions of interest, and to study the robustness of the estimated source parameters as source magnitude and the number of observing stations decrease.

Key words: tectonic release, seismic moment tensor, nuclear explosions, earthquakes, surface waves, discrimination

OBJECTIVE

The objective of the research is to determine if the existence of an observable non-zero isotropic component of seismic moment can be used as a discriminant to distinguish nuclear explosions from shallow earthquakes.

RESEARCH ACCOMPLISHED

Introduction

It has long been known that nearly all underground nuclear explosions have a significant component of nonisotropic seismic radiation (e.g., Press & Archambeau, 1962; Brune & Pomeroy, 1963; Aki & Tsai, 1972; Toksöz & Kehrer, 1972; Helle & Rygg, 1984; Wallace *et al.*, 1985; Walter & Patton, 1990). There appears to be general agreement that the long-period part of the nonisotropic radiation is caused by tectonic release due to existing tectonic stresses in the source region (Mueller & Murphy, 1971; Archambeau, 1972 ; Masse, 1981; Wallace *et al.*, 1985; Day & Stevens, 1986; Stevens, 1986; Day *et al.*, 1987; Patton, 1991; Stevens *et*

al., 1991; Harkrider *et al.*, 1994; Ekström and Richards, 1994; Li *et al.*, 1995).

Most of the experimental studies of tectonic release have concentrated on explosions at the Nevada Test Site and the test sites in Kazakhstan. Burger *et al.* (1986) described the long-period S wave radiation by tectonic release of explosions at Novaya Zemlya. Zhang (1994), Levshin & Ritzwoller (1995), and Wallace & Tinker (1996) studied Chinese nuclear explosions and found that most are accompanied by tectonic release. However, we are unaware of any detailed analysis of the source mechanisms of these events.

Several authors have estimated the relative contributions of the nonisotropic (tectonic release) and isotropic (explosion) components to the resulting seismic moment tensor of explosions (see, for example, Ekström and Richards, 1994). As a rule these estimates have been performed using the assumption that both phenomena occur in the same small volume inside the Earth.

Although the determination of the source mechanism of earthquakes is a routine operation, only a few studies have evaluated the isotropic component of earthquake radiation. This is especially true for weak events that are of the primary interest for discrimination purposes. As is well known, a pure shear dislocation does not radiate an isotropic component. Subsequently, the natural tendency is to constrain the moment tensor solution with the assumption of a zero trace. However, from the point of view of discrimination it is important to determine if a significant isotropic component could appear in unconstrained moment tensor solutions due to some physical phenomena in the source region or due to inaccuracy of measurements and underlying assumptions.

Our approach is, therefore, based on the combination of an isotropic moment tensor at the surface, which models an explosive source, and a pure double couple at an estimated depth, which models tectonic release. We find it useful to express the seismic moment of the double-couple component, M_{0qu}, and the seismic moment of the isotropic component, M_{0ex}, as the total seismic moment M_0 and an angle φ which determines the ratio of the seismic moments of the isotropic and double couple components:

$$M_{0qu} = M_0 \cos\varphi;\ M_{0ex} = M_0 \sin\varphi;\ \tan\varphi = M_{0ex}/M_{0qu}.$$

We call φ the isotropic angle, for want of a better term, because $\varphi = 0$ corresponds to a pure earthquake and $\varphi = 90^\circ$ corresponds to a pure explosion. With this notation and the assumption that the isotropic component of the source occurs at a known depth (usually at or near the surface), the source can then be characterized by six parameters: the seismic moment M_0, the isotropic angle φ, three angles (or two principal axes, **T** (tension) and **P** (compression)) determining the double couple focal mechanism, and the double-couple depth h.

We do this by applying the method described by Bukchin *et al.*, (2000) to a set of data recorded between 1990 and 1996 following events (seven nuclear explosions and three earthquakes) that occurred on the Lop Nor test site in Western China. We determine the source parameters of these events by fitting the polarities of P-wave first arrivals jointly with minimizing the misfit between synthetic and observed Love and Rayleigh surface wave amplitude spectra. We search for the optimal set of parameters by a systematic exploration of parameter space. To characterize the uncertainty of the source parameters, we calculate partial residual functions which describe the minimum misfit as a function of each varying parameter.

Data and Method

We utilized IRIS and GEOSCOPE broadband digital seismograms and the ISC bulletins for 14 events that occurred on the Lop Nor test site in China from 1990 through 1996. Eight of these events are nuclear explosions, the other six are earthquakes. However, only 10 events with high signal-to-noise surface waves recorded at several stations were selected for study. The location of the selected events (7 explosions and 3 earthquakes) is given in Figure 1. The list of stations, with their distances and azimuths from Lop Nor test site are given in Table 1.

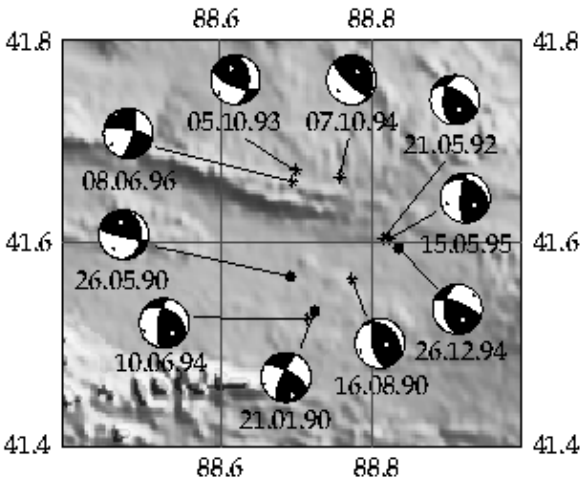


Figure 1: Epicenters and focal mechanisms of earthquakes (circles) and tectonic releases accompanying explosions (stars).

Table 1. Observed Seismograms and Models Used for Surface Wave Calculations for Each Station

Station	Azim. (◦)	Distance (◦)	Model	Station	Azim. (◦)	Distance (◦)	Model
ABKT	271	24	Tectonic	KIV	290	34	Tectonic
ANTO	287	42	Tectonic	KMI	140	20	Tectonic
ARU	317	25	Stable	KONO	320	50	Stable
BNG	260	73	Stable	LZH	111	13	Tectonic
BRVK	319	17	Stable	MA2	43	42	Stable
CHTO	156	24	Stable	MAJO	81	38	Stable
DPC	306	49	Stable	MDJ	70	29	Stable
ENH	118	20	Stable	NIL	242	15	Tectonic
ERM	71	40	Stable	NRIL	0	28	Stable
HIA	60	23	Stable	OBN	310	37	Stable
HYB	204	26	Stable	SEY	38	42	Stable
GNI	282	33	Tectonic	TATO	111	31	Stable
INU	83	38	Stable	TLY	40	14	Tectonic
KEV	333	42	Stable	YAK	36	32	Stable

In our calculations of the theoretical surface wave spectra we used three different models for (1) the structure for the source region, (2) the stations deployed in the stable continental regimes, and (3) the stations in the tectonic regions. For brevity we will call the corresponding models "Lop Nor","Stable", and "Tectonic". Column 4 in Table 1 indicates the model used for each station.

We estimated the source parameters using the spectra of Love and Rayleigh fundamental waves for periods ranging from 20 s to 70 s. Love and Rayleigh fundamental modes were extracted by using frequency-time analysis (FTAN) and floating filtering (e.g., Levshin *et al.*, 1989, 1994). We also analyzed the polarization of filtered surface waves using the technique described in Levshin *et al.*, (1989), Paulssen *et al.*, (1990), Levshin *et al.* (1992, 1994), and Levshin & Ritzwoller (1995). Only records in which the surface wave polarization pattern did not exhibit significant azimuthal anomalies ($\leq 15°$) were used for further analysis.

Results of Inversions

A summary of the inversion results is given in Table 2.

Table 2. Information on the 10 Events Used in the Present Study

Date	Event type	m_b	m_s	Number of records used	Double couple depth (km)	M_0 $(N \cdot m)$	ψ (deg.)	φ (deg.)
21.01.90	earthquake	4.6	-	10	31	$0.15 \cdot 10^{17}$	72	0
26.05.90	earthquake	5.4	-	5	3	$0.42 \cdot 10^{16}$	52	0
26.12.94	earthquake	4.6	-	10	17	$0.15 \cdot 10^{16}$	56	0
16.08.90	explosion	6.2	-	7	1	$0.19 \cdot 10^{17}$	62	10-30
21.05.92	explosion	6.5	5.0	16	3	$0.62 \cdot 10^{17}$	64	10-15
05.10.93	explosion	5.9	4.7	10	0	$0.75 \cdot 10^{16}$	56	0-15
10.06.94	explosion	5.8	-	13	1	$0.52 \cdot 10^{16}$	64	20-40
07.10.94	explosion	6.0	-	11	1	$0.18 \cdot 10^{17}$	60	25-35
15.05.95	explosion	6.1	5.0	9	3	$0.15 \cdot 10^{17}$	62	40-60
08.06.96	explosion	5.9	4.3	12	3	$0.59 \cdot 10^{16}$	58	30-60

ψ is the azimuth of the horizontal compression axis, φ is the isotropic angle, which determines the ratio of the isotropic and nonisotropic (double couple) moments.

Double Couple Depths and Focal Mechanisms

The focal mechanisms for the earthquakes and for the double couple components of the explosions are shown in Figure 1. The double couple depth is well resolved for all events studied and varies from 0 to 3 km for the explosions and for the earthquakes we obtained depths of 3 km, 31 km, and 17 km. The partial residual function of double couple depth is presented in Figure 2 for all events.

The number of surface wave records that we selected for the studied events was admittedly very small (see the column 5 in Table 1), particularly for the earthquakes on the test site. For some events, only a few polarities of P wave first arrivals were available. As a result, the double-couple focal mechanism was very well resolved only for the earthquake on 21.01.90, but for half of the events the principal compression axis, which trends in the SE-NW direction, was resolved well. Fortunately, Gao and Richards (1994) estimated focal mechanisms of several earthquakes in the vicinity of Lop Nor. Considering the focal mechanisms of the studied events, and the solutions obtained by Gao and Richards, we found that while focal mechanisms vary widely, there is a moment tensor characteristic which is quite stable for all events. This characteristic is the orientation of the principal axes of the 2×2 minor of the moment tensor corresponding to the horizontal coordinates $\{M_{xx},\ M_{xy},\ M_{yx},\ M_{yy}\}$. This minor describes the horizontal deformations on the horizontal plane. We found that for all events, horizontal compression is dominant, and the principal horizontal compression axis deviates from the average direction (with an azimuth of 60°) by no more than 12°. The direction of this axis for every event is given in the eighth column in Table 1.

Isotropic Component

These observations allow us to improve the estimates of the isotropic angle φ by assuming that the orientation of the horizontal deformations is a stable characteristic for the region under study. The average direction of horizontal compression is deviated from the fault visible in Figure 1 by about 45°. With this assumption, we applied an *a priori* constraint on the possible double couple focal mechanisms. This constraint was formulated as a condition that the azimuth of the principal compression axis of the horizontal minor of the moment tensor cannot differ from 60° by more than ±45°. This constraint is weak, but reduces the number of possible focal mechanisms in half.

When we applied this constraint, the resolution of the isotropic angle φ defining the seismic moments ratio was improved for three of the seven studied explosions (16.08.90, 05.10.93, and 08.06.96) but the mean

of the curves did not vary appreciably. The curves of partial residual functions of the isotropic angle φ for all explosions are shown in Figure 3. Those for the three earthquakes are displayed in Figure 4. We also applied this method to two earthquakes that occurred in the Gansu province, China (Tianzhu, 1996, $M_s = 4.9$, depth 12 km, and Yongden, 1995, $M_s = 5.4$, depth 6 km). The partial residual functions of the isotropic angle φ are also shown in Figure 4. The explosions, with perhaps one exception (05.10.93), all display substantial non-zero isotropic angles φ ranging from about 10° to 50°, corresponding to M_{0ex}/M_{0qu} ranging from about 20% to 120%. In contrast, the isotropic angles for the earthquakes are all estimated to be approximately 0.

Figure 5 illustrates the effect of adding an isotropic component to the double couple source model for an explosion (on June 10 1994). Theoretical Rayleigh wave amplitude spectra and P wave first arrival polarities are compared here with observations for two different moment tensors. One (a,b) was obtained by minimizing the joint residual for a fixed zero isotropic angle (double couple source model). The other (c, d) is a result of a similar minimization, but for varying isotropic angle (30° is the estimated optimal value). The fit to P wave first arrival polarities is good for both source models, but the fit to Rayleigh wave amplitude spectra is much better in the case of a non-zero isotropic component.

Figure 6 illustrates the effect of adding an isotropic component for the Youngden earthquake. Similar Figure 5, the results for two different moment tensors are presented here. One (a,b) was obtained by minimizing the joint residual for a varying isotropic angle. The other (c, d) is a result of a similar minimization but for a fixed (30°) isotropic angle. In contrast with the previous case the fit is better for a pure double couple source.

CONCLUSIONS AND RECOMMENDATIONS

The results above are consistent with the hypothesis that motivates this study. Namely, that for the events we analyzed on the Lop Nor test site surface wave amplitude spectra combined with polarities of P wave first arrivals can be used to discriminate explosions from earthquakes based on source characteristics alone (a combination of the double couple depth and the ratio of the isotropic to nonisotropic moments). Our recommendations for the further studies are:

- To estimate the applicability of the method for smaller events in the same region based on data from regional networks alone.
- To evaluate if the method is transportable to other regions (Novaya Zemlya, Kazakstan, India and Pakistan).
- In particular, it is important to determine the false alarm rate for earthquakes; that is the percentage of earthquakes that demonstrate a substantial shallow isotropic component.

REFERENCES

Aki, K., and Y. Tsai, The mechanism of Love wave excitation by explosive sources. *J. Geoph. Res.*, **77**, 1452-1475, 1972.

Brune, J. N., and P. W. Pomeroy, Surface wave radiation patterns for under ground nuclear explosions and small-magnitude earthquakes. *J. Geophys. Res.*, **68**, 5005-5028, 1963.

Bukchin, B.G., A.Z. Mostinsky, A.A. Egorkin, A.L. Levshin, M.H. Ritzwoller, Isotropic and Nonisotropic Components of Earthquakes and Nuclear Explosions on the Lop Nor Test Site, China, *Pure and Appl. Geophys.*, in press, 2000.

Burger, R., T. Lay, T. Wallace, and L. Burdick, Evidence of tectonic release in long-period S waves from underground nuclear explosions at the Novaya Zemlya Test sites, *Bull. Seism. Soc. Am.*, **76**, 733-755, 1986.

Day, S.M., and J.L. Stevens, An explanation for apparent time delays in phase-reversed Rayleigh waves from underground nuclear explosions. *Geophys. Res. Lett.*, **13**, 1423-1425, 1986.

Day, S.M., J.T. Cherry, N. Rimer, and J.L. Stevens, Nonlinear model of tectonic release from underground explosions. *Bull. Seism. Soc. Am.*, **77**, 996-1016, 1987.

Ekström, G., and P.G. Richards, Empirical measurements of tectonic moment release in nuclear explosions from teleseismic surface waves and body waves. *Geophys. J. Int.*, **117**, 120-140, 1994.

Gao, L.-P., and P.G. Richards, Studies of earthquakes on and near the Lop Nor, China, nuclear test site. In *Proc. of the 16th Annual Seismic Research Symposium, 7-9 Sept. 1994*, 106-112, Phillips Lab., Directorate of Geophysics, 1994.

Harkrider, D. G., J. L. Stevens, and C. B. Archambeau, Theoretical Rayleig h and Love waves from an explosion in prestressed source regions. *Bull. Sei sm. Soc. Am.*, **84**, 1410-1442, 1994.

Helle, H.B., and E. Rygg, Determination of tectonic release from surface waves generated by nuclear explosions in Eastern Kazakhstan, *Bull. Seism. Soc. Am.*, **74**, 1883-1898, 1984.

Levshin, A.L., Effects of lateral inhomogeneity on surface wave amplitude measurements, *Annales Geophysicae*, **3**, 4, 511-518, 1985.

Levshin, A.L., T.B. Yanovskaya, A.V. Lander, B.G. Bukchin, M.P. Barmin , L.I. Ratnikova, and E.N. Its, *Seismic Surface Waves in Laterally Inhomogeneous Earth*, ed. V. I. Keilis-Borok, Kluwer. Publ., Dordrecht, 1989.

Levshin, A.L., and M.H. Ritzwoller, Charactersistics of surface wave generated by events on and near the Chinese nuclear test site, *Geophys. J. Intl*, **123**, 131-148, 1995.

Li, Y., M.N. Toksoz, and W. Rodi, Source time functions of nuclear explosions and earthquakes in central Asia determined using empirical Green's functions. *J. Geophys. Res.*, **100**, 659-674, 1995.

Masse, R.P., Review of seismic source models for underground nuclear explosions, *Bull. Seism. Soc. Am.*, **71**, 1249-1268, 1981.

Mueller, R.A., and J.R. Murphy, Seismic characteristics of underground nuclear detonations. Part I: Seismic spectrum scaling, *Bull. Seism. Soc. Am.*, **61**, 1675-1692, 1971.

Patton, H.J., Seismic moment estimation and the scaling of the long-period explosion source spectrum. In *Explosion Source Phenomenology, Geophysical Monograph* **65**, *AGU*, ed. S.R. Taylor, H.J. Patton, and P.G. Richards , 171-184, 1991.

Press, F., and C. B. Archambeau, Release of tectonic strain by underground explosions. *J. Geophys. Res.*, **67**, 337-343, 1962.

Stevens, J.L., Estimation of scalar moments from explosion-generated surface waves. *Bull. Seism. Soc. Am.*, **76**, 123-151, 1986.

Stevens, J.L., T.G. Barker, S.M. Day, K.L. McLaughlin, N. Rimer, and B. Shkoller, Simulation of teleseismic body waves, regional seismograms, and Rayleigh wave phase shifts using two-dimensional nonlinear models of explosion sources. In *Explosion Source Phenomenology, Geophysical Monograph* **65**, *AGU*, ed. S.R. Taylor, H.J. Patton, and P.G. Richards, 239-252, 1991.

Toksöz, M.N. and H.H. Kehrer, Tectonic strain release by underground nuclear explosions and its effect on seismic discrimination, *Geophys. J. R. Astr. Soc.*, **31**, 141-161, 1972.

Wallace, T.C., D.V. Helmberger, and G.R. Engen, Evidence of tectonic release from underground nuclear explosions in long-period S waves. *Bull. Seism. Soc. Am.*, **76**, 123-151, 1985.

Wallace, T.C., Body wave observations of tectonic release, In *Explosion Source Phenomenology, Geophysical Monograph* **65**, *AGU*, ed. S.R. Taylor, H.J. Patton, and P.G. Richards, 161-170, 1991.

Wallace, T.C., and M.A. Tinker, The last nuclear weapons test? A brief review of the Chinese nuclear weapons program. *IRIS Newsletter,* **15**, N 3, 1996.

Walter, W.R., and H.J. Patton, Tectonic release from SJVE, *Geophys. Res. Lett.*, **17**, 1517-1520, 1990.

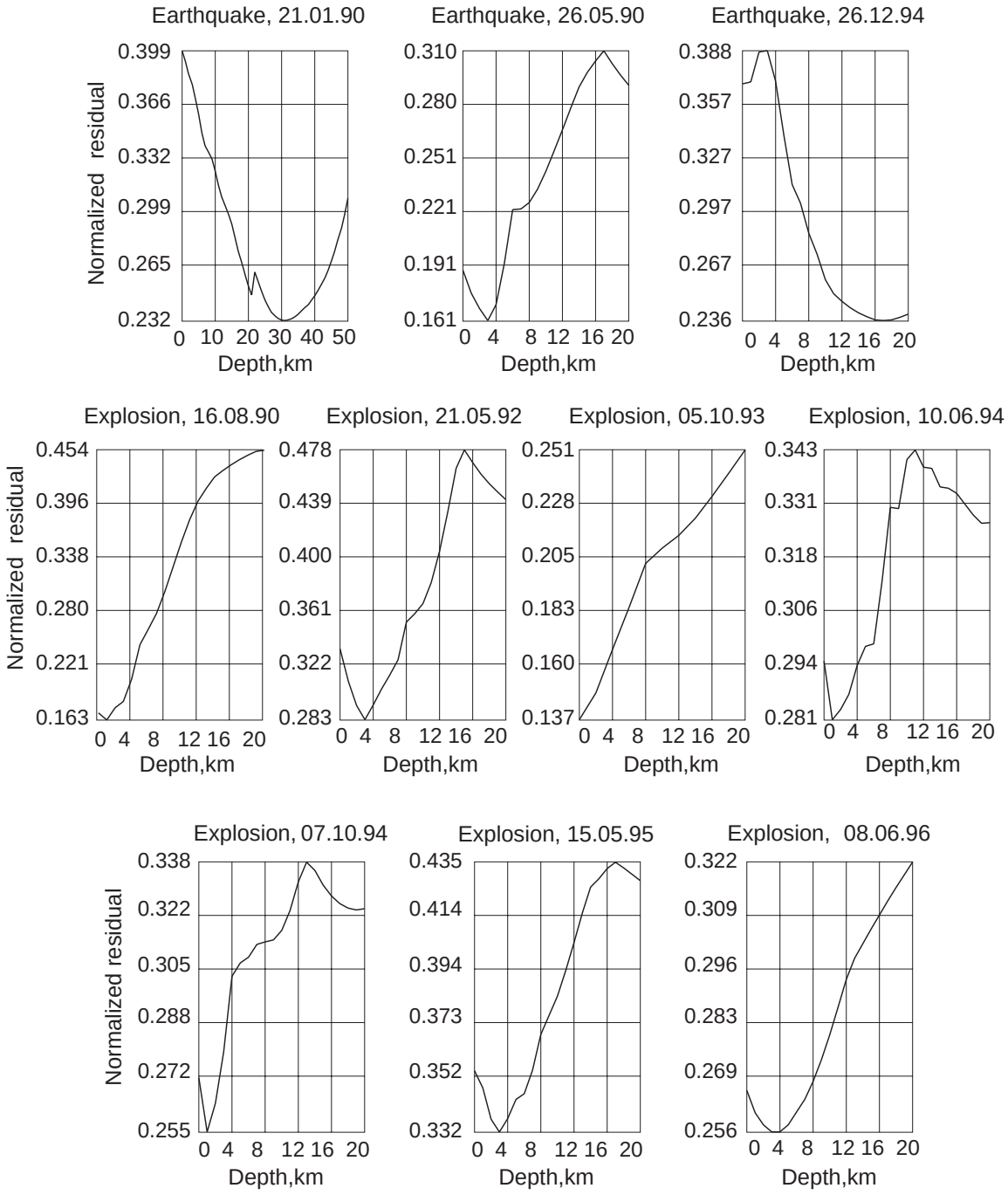


Figure 2. Partial residual functions of the double couple depth *h*.

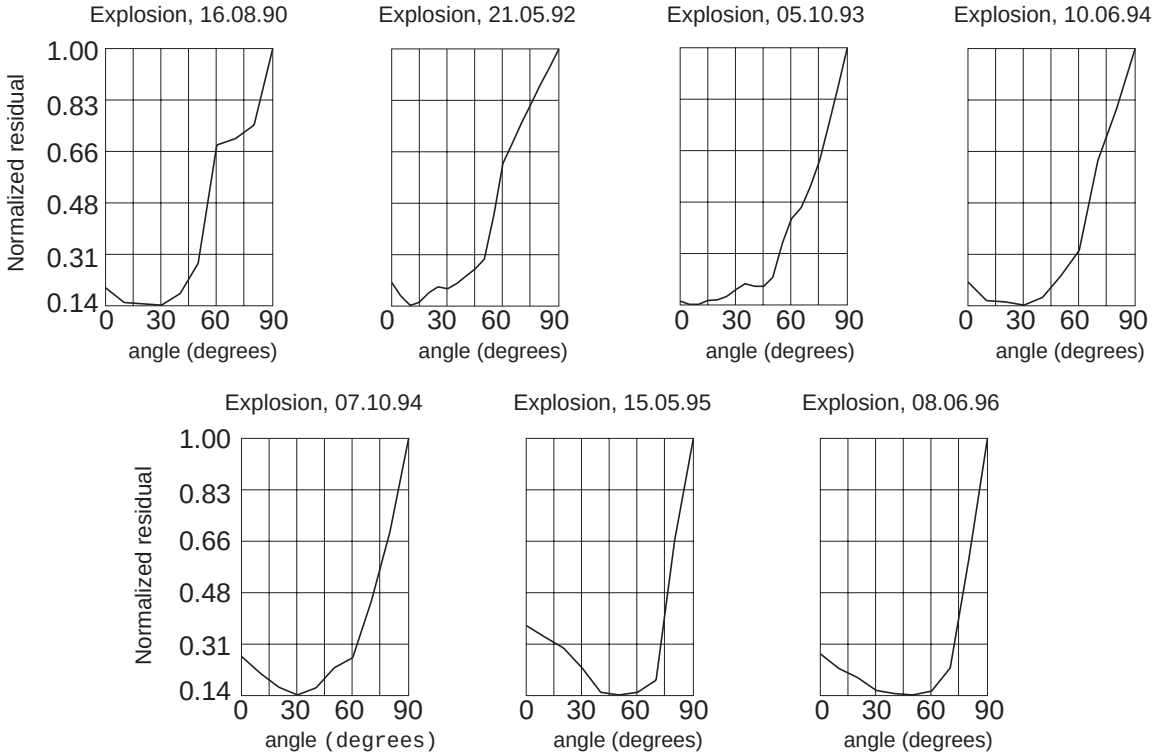


Figure 3. Partial residual functions of isotropic angle for studied explosions.

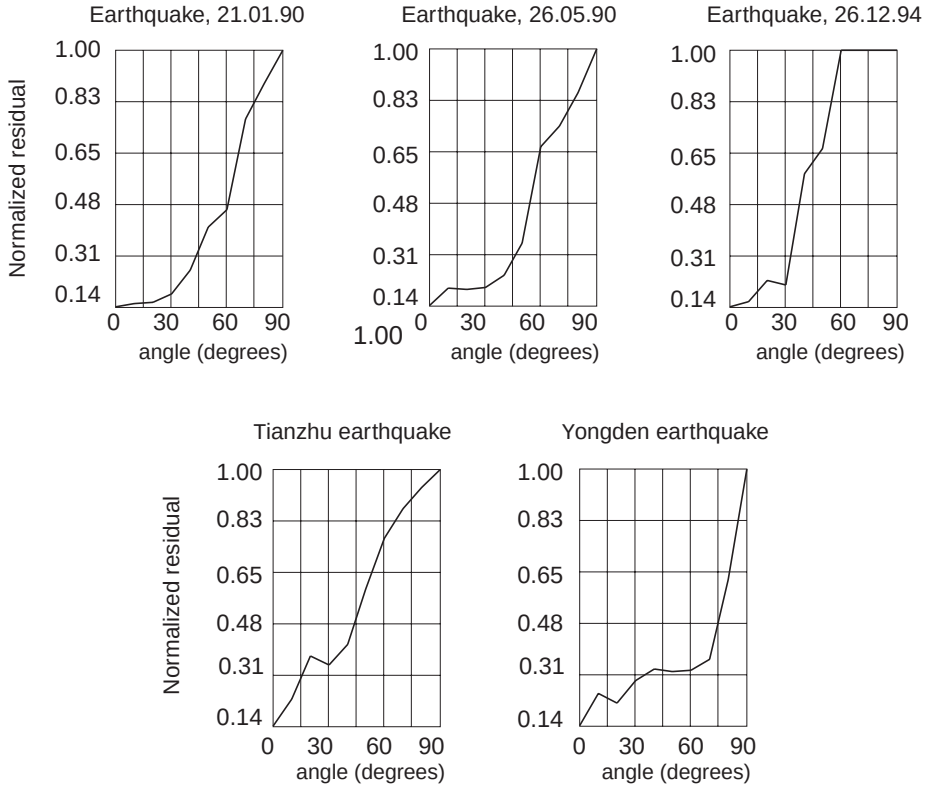


Figure 4. The same as Figure 3, but for the studied earthquakes.

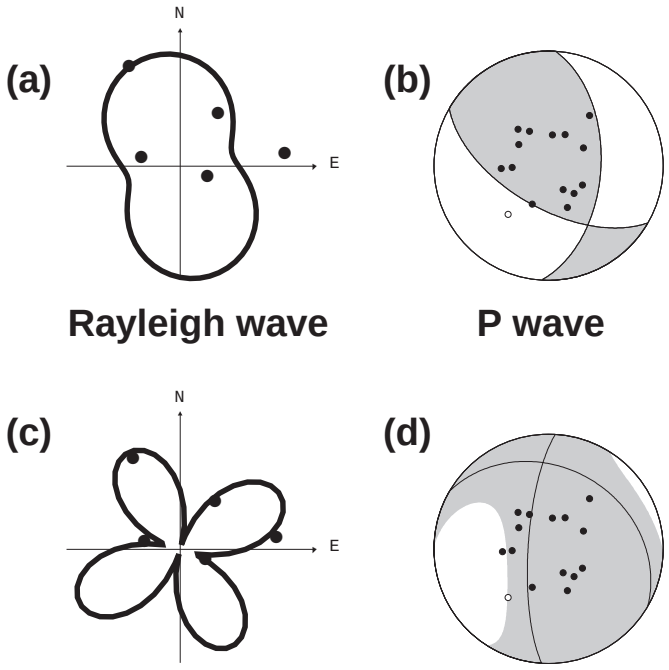


Figure 5. Comparison of observed Rayleigh wave spectral amplitudes at 26 sec period and polarities of first arrivals for the explosion on June 10, 1994 with those predicted for two different source models: (a,b) pure double couple; (c,d) non-zero isotropic component is added.

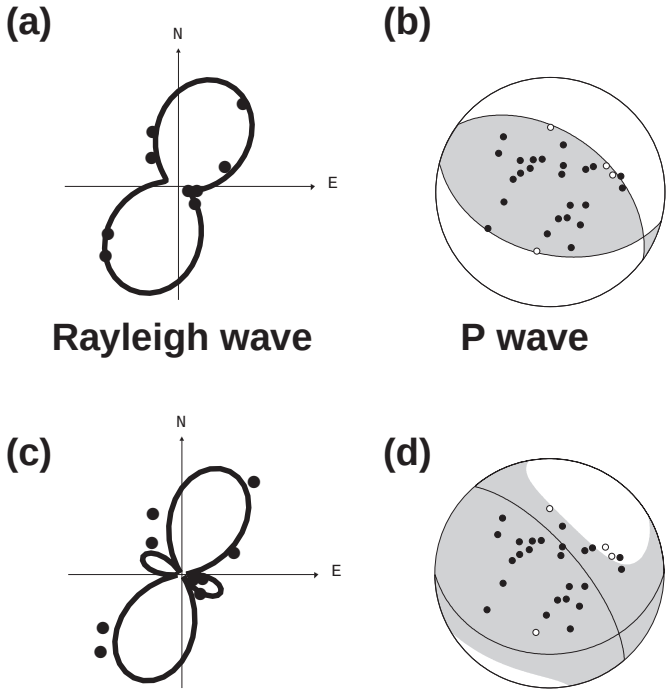


Figure 6. Same as Figure 5, but for the Yongden earthquake in Gansu province, China, on July 21, 1995 and the 50 s period.

SOURCE SPECTRA, MOMENT, AND ENERGY FOR RECENT EASTERN MEDITERRANEAN EARTHQUAKES: CALIBRATION OF INTERNATIONAL MONITORING SYSTEM STATIONS

Kevin M. Mayeda, Abraham Hofstetter,* Arthur J. Rodgers, and William R. Walter
Lawrence Livermore National Laboratory and *Geophysical Institute of Israel

Sponsored by U.S. Department of Energy
Office of Nonproliferation and National Security
Office of Defense Nuclear Nonproliferation
National Nuclear Security Administration

Contract No. W-7405-ENG-48

ABSTRACT

In the past several years there have been several large ($M_w > 7.0$) earthquakes in the eastern Mediterranean region (Gulf of Aqaba, Racha, Adana, etc.), many of which have had aftershock deployments by local seismological organizations. In addition to providing ground truth data (GT << 5 km) that is used in regional location calibration and validation, the waveform data can be used to aid in calibrating regional magnitudes, seismic discriminants, and velocity structure. For small regional events ($m_b << 4.5$), a stable, accurate magnitude is essential in the development of realistic detection threshold curves, proper magnitude and distance amplitude correction processing, formation of an M_s:m_b discriminant, and accurate yield determination of clandestine nuclear explosions.

Our approach provides a stable source spectra from which M_w and m_b can be obtained without regional magnitude biases. Once calibration corrections are obtained for earthquakes, the coda-derived source spectra exhibit strong depth-dependent spectral peaking when the same corrections are applied to explosions at the Nevada Test Site (Mayeda and Walter, 1996), chemical explosions in the recent "Depth of Burial" experiment in Kazahkstan (Myers et al., 1999), and the recent nuclear test in India. For events in the western U.S. we found that total seismic energy, E, scales as $M_o^{0.25}$ resulting in more radiated energy than would be expected under the assumptions of constant stress-drop scaling. Preliminary results for events in the Middle East region also show this behavior, which appears to be the result of intermediate spectra fall-off ($f^{-1.5}$) for frequencies ranging between ~0.1 and 0.8 Hz for the larger events. We developed a Seismic Analysis Code (SAC) coda processing command that reads in an ASCII flat file that contains calibration information specific for a station and surrounding region, then outputs a coda-derived source spectra, moment estimate, and energy estimate.

This is Lawrence Livermore National Laboratory document number UCRL-JC-138990.

Key Words: regional coda waves, moment, energy, SAC

OBJECTIVE

For sparse local and regional seismic networks a stable magnitude is of utmost importance for establishing accurate seismicity catalogs and assessing seismic hazard potential. In the context of network capability, we need accurate magnitudes for construction of detection threshold curves, a crucial element of nuclear test monitoring. In this paper we describe a method of calibrating a region for coda envelope processing using a new routine in SAC. Unlike magnitudes such as M_L, M_d and m_b which are relative, narrowband measures that often have regional biases, our approach can provide a stable absolute source spectra that is corrected for S-to-coda transfer function, scattering, and anelastic attenuation and site effect. Because coda envelope amplitude measurements are not as sensitive to 3-D path heterogeneity and source radiation pattern, the resultant spectra can then be used for stable moment estimation (and hence M_w), traditional short-period magnitudes (i.e., m_b, M_L) and radiated seismic energy, E. There have been numerous scattering studies over the past 3 decades investigating the mechanisms that control coda generation and its decay with time from the origin and dependence upon distance. For our method however, we only use an empirical approach to fit the observed envelopes to obtain an amplitude measure over a range of narrow

frequency bands. We then empirically tie these amplitudes to independently derived moment estimates from calibration events through a simple boot-strapping procedure. Past studies for earthquakes in the western United States showed that a single coda envelope amplitude measurement was roughly equivalent to a 64 station network using direct waves (Mayeda & Walter, 1996). For explosions at the Nevada Test Site (NTS) we found that a 1 Hz single-station coda measurement was roughly equivalent to a 20 station network using direct L_g or P_n (Mayeda, 1993). This is the result of making a time domain measurement over a large length of coda, thereby averaging the combined effects of source radiation pattern, path heterogeneity, and near site random interference, all of which can affect individual phases such as L_g and P_n. The results of the frequency-dependent calibration have been used as input into a newly developed interactive SAC command that forms narrowband envelopes, measures amplitudes, applies region and station-specific corrections, outputs ASCII source information (e.g., M_w, m_b, $\Delta\sigma$, E) and plots the moment-rate spectra. In this paper we describe the calibration method, then apply it to a data set in the Middle East region to estimate seismic moment (and M_w), total radiated seismic energy, and dynamic stress drop (e.g., Orowan) (see Figure 1). We then compare with previous results from the western United States (Kanamori et al., 1993, Mayeda and Walter, 1996).

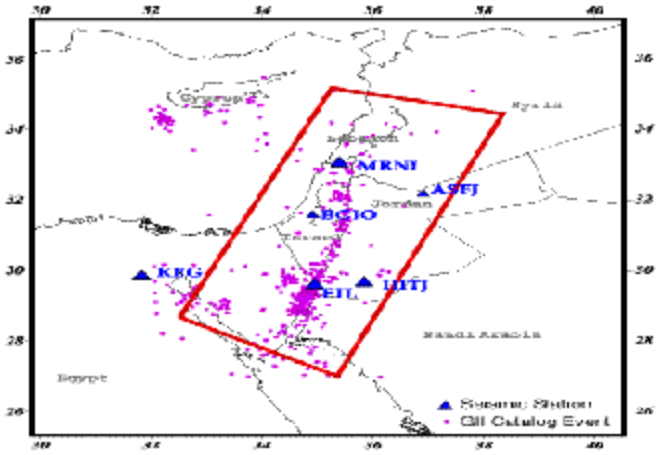


Figure 1. Map showing regions, broadband stations and seismicity from the GI catalog.

RESEARCH ACCOMPLISHED

Synthetic Envelopes

We found that a simple analytic form that resembles the single-scattering model of Aki (1969) generally does a good job at fitting both regional and local coda envelopes. The main difference is that we found that we had better fits by forming the envelopes relative to the S arrival, not the origin time as is done in most scattering models. The analytic expression that we used to fit the observed narrowband envelopes at center frequency f is

$$A_c(f,t \mid x) = A_o \bullet H(t - \tfrac{x}{v(x)}) \bullet (t - \tfrac{x}{v(x)})^{-g} \bullet \exp(-b \bullet (t - \tfrac{x}{v(x)})) \qquad (1)$$

where A_o is a source constant, H is the Heaviside step function, t is the time in seconds from the origin, x is the distance in kilometers, $v(x)$ is the velocity of the peak arrival in km/sec and g and b control the coda decay. It should be noted however that the more complex 2-D and 3-D multiple scattering models could also be used (see Sato and Fehler review, 1999). For our purposes we only want an empirical fit to the data

over a range of distances and frequency bands and thus this simple form is completely adequate for this purpose.

Since we are not explicitly applying a scattering model that has attenuation built into its formulation, we need to find an empirical distance relation for the coda amplitudes. This is preferable since we do not want to make any assumptions about homogeneous coda decay in a region, an assumption commonly made in past coda studies. Instead, we fold in both geometrical spreading and attenuation (whether it be from scattering, absorption, leakage etc.) using a strictly empirical form. We reiterate that we use equation 1 as a means of matching the observed coda envelope shape to extract a coda amplitude measurement. In essence, equation 1 is used as an empirical metric and thus any functional relationship could have been used that fits the data. The steps described in this paper allow one to measure coda envelopes, which are initially in dimensionless units, correct for distance and site effects and tie to an absolute measure. The validation of this approach is simple. We verify that we obtain the same source spectra at different stations and distances for the same event (thus confirming our empirical distance corrections) and then verify that our inferred moments are the same as those that were independently determined from other means such as long-period waveform modeling.

Coda Envelopes

For our data we applied an 8^{th} order, zero-phase (four poles, two passes) Butterworth filter for 13 narrow frequency bands ranging between 0.03 and 8.0 Hz for the two horizontal components. This range of frequency bands was chosen such that we could compute M_w for the Gulf of Aqaba mainshock of November 22, 1995 (M_w 7.1) and measure the high frequencies of some of the smaller aftershocks.

For each component the narrowband envelope at center frequency *f* is of the form:

$$e(t \mid f) = \sqrt{(v(t)^2 + h(t)^2)} \qquad (2)$$

where *v(t)* is one of the bandpass filtered seismograms and *h(t)* is its corresponding Hilbert transform. We then take the $\log_{10}$ of the envelopes, average the two horizontal envelopes, then smooth. Fig. (2) shows an example of a broadband trace and a selection of envelopes in different narrow frequency bands. It is preferable to use the horizontal elements since S-waves have better signal-to-noise ratio and averaging the two provides a smoother envelope than a single component alone. Of course this processing could also be done on a single component such as the vertical but is less desirable.

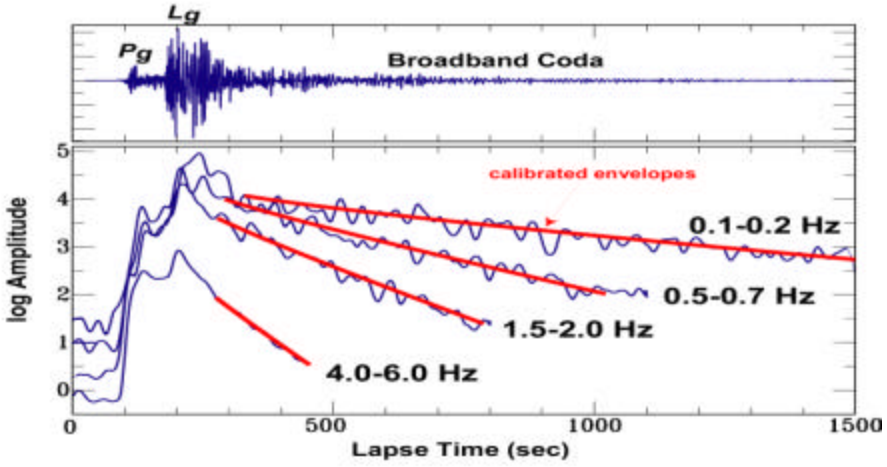


Figure 2. Example of broadband waveform and selected narrowband envelopes along with calibrated envelopes.

Velocity of Direct Phase

After forming narrowband envelopes for all the events, we measure the (phase) velocity of the peak S-arrival for each frequency band and plot versus distance. For the longest periods the peak corresponds to the Rayleigh or Love waves but because we empirically correct for each frequency band, mixing wavetypes makes no difference on the final results as will be shown in the concluding sections. Since our goal is to calibrate both local and regional distance earthquakes, we find that a simple second-order polynomial fits the data at all distances. For each frequency the distant-dependent velocity, *v* is of the form,

$$v(x \mid f) = velorder_0 \; + \; velorder_1 \bullet x \; + \; velorder_2 \bullet x^2 \qquad (3)$$

where *velorder_0*, *velorder_1* and *velorder_2* are constants.

Coda Shape Factors

Now that we know the velocities for each frequency band, we can fit our simple analytic form to find the coda shape parameter *b* which controls the coda decay as measured from the direct S (or L_g) arrival. By rearranging equation 1 and taking the $\log_{10}$ of both sides we get,

$$\log_{10}\left[A_c(f,t \mid x) \bullet (t - \tfrac{x}{v(x)})^g\right] = \log_{10}\left(A_o \bullet H(t - \tfrac{x}{v(x)})\right) - b \bullet (t - \tfrac{x}{v(x)}) \bullet \log(e) \qquad (4)$$

We let *g* vary from 0 to 2 and found that fixing *g* =0.7 fit the data well for the entire frequency range. Coincidentally, this value is consistent with other scattering formulations that consider surface wave and body wave scattering in a full-space. By plotting equation 4 versus $\left(t - \frac{x}{v(x)}\right)$, the slope of the best fitting line is blog(e).

Since we want to fit the coda at all distances we try to measure the coda over a range of distances to determine if *b* is dependent upon distance. For the higher frequencies *b* is strongly distant dependent whereas for frequencies below ~0.5 Hz, the coda shape factor is roughly constant and is smaller (i.e., decays more slowly than the higher frequencies). We find that a simple linear form fits the b values as a function of distance x spanning both local and regional distances,

$$b(x \mid f) = b_o(f) \; + \; hx \qquad (5)$$

where $b_o(f)$ is the intercept value at zero distance at center frequency *f* and η is the slope.

Simple Distance Corrections

For events in the Dead Sea rift and Gulf of Aqaba region, the Geophysical Institute of Israel (GII) routinely performs network locations and assorted magnitudes such as m_b, M_L and M_w. Now that we have the velocities and coda shape factors we set A_o in equation (1) to unity, take the $\log_{10}$ to be consistent with our observed envelopes, then dc shift the synthetic envelopes to fit the observed envelopes using an L-1 norm. The magnitude of the dc shift is the non-dimensional coda amplitude. This amplitude is analogous to a direct wave measure in the sense that a distance and site correction still need to be made. Measuring the coda envelope amplitude over a length of time merely provides a more stable measure than using direct waves which are of short duration and thus considerably more susceptible to interference, source-station heterogeneity, and source radiation pattern. In the following paragraph we empirically find the distance dependence for each frequency band, apply it to the data, then validate by comparing measurements of the same event at two different stations.

For each frequency band we subtract the GII M_L from the amplitude and plot versus distance in kilometers. We try to use events in a narrow magnitude range for each frequency band when determining the distance corrections to avoid potential biases related to corner frequency scaling. For example, using only small

events at short distances and only large events at longer distances would result in very biased curve fitting as opposed to using events of roughly the same size. Up to this point we can now measure distance-corrected coda amplitudes from narrowband envelopes but these are still in dimensionless units. Figure (3a) shows a cartoon of non-dimensional coda spectra for hypothetical earthquakes of various sizes and its corresponding figure shows what the spectra will look like after correcting to an absolute scale. The goal is to correct for S-to-coda transfer function and site effects to obtain a moment-rate spectra. Again, these amplitudes are relative to a source amplitude of 1.0 and are thus in dimensionless units and must be corrected to an absolute scale. The following section describes this crucial series of steps.

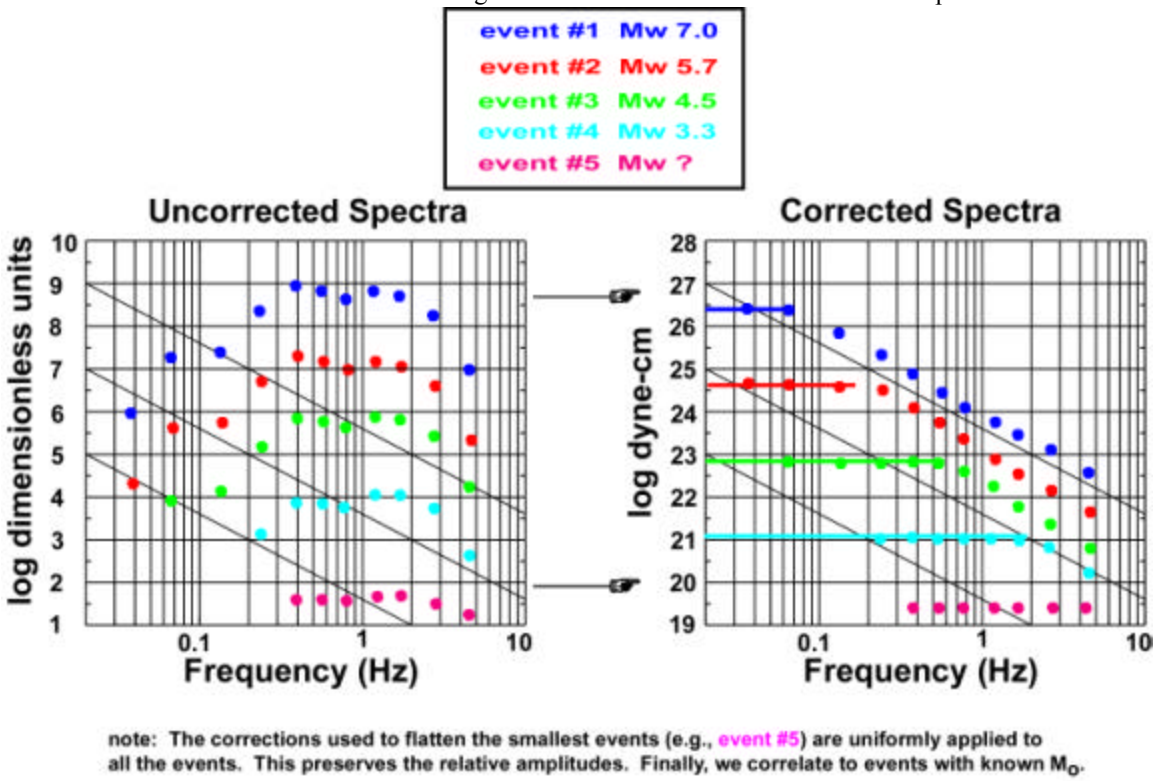


Figure 3a and 3b. Non-dimensional coda amplitude corrected for distance effect only (fig. 3a) for a range of events. Figure 3b shows corrected spectra after tying to independent moments and applying Green's function corrections.

Green's Function and Seismic Moment Corrections

Up to this point we have measured non-dimensional coda envelope amplitudes and corrected for distance. In this section we relate these values to an absolute scale, namely seismic moment to obtain a moment-rate spectrum. Our only assumption is that the S-wave source spectrum is flat below the corner frequency. We purposely underestimate where the corner frequency lies for our set of calibration events to avoid flattening our spectra unrealistically.

We used a 1-D reflectivity code to waveform model a series of events in the region to estimate seismic moment. The only assumption we make is that the source spectrum of these events is flat below the corner frequency. As shown in Figure (3b), we add constants to all amplitudes for each frequency band such that the seismic moments, in a least squares sense, agree with the waveform modeled results. Since these are frequency-dependent corrections, independent of distance, the corrections must be uniformly applied to all distance-corrected amplitudes. Figure (3b) shows that with conservative estimates of the corner frequency, we can flatten the spectra for a range of event sizes. For events that are too small to be waveform modeled ($< \sim M_w$ 3.5), we can still estimate moment using periods less than a few Hertz. For especially small events ($\sim M_w$ 2.5) we can assume they have flat source spectrum at least to 10 Hz. This use of the very small

events is essentially a Green's function correction that allows us to extend the stable coda-derived source spectrum to much smaller events. Therefore, this allows us to find the amplitude corrections for the frequencies between ~2.0 and 8 Hz. Though in figures (3a & 3b) we use just a few events for illustrative purposes, for the actual data we used a number of events of the same relative size to come up with the best set of moment corrections. In our case we instrument deconvolved the traces beforehand and converted to velocity. However, if the instrument did not change over the range of time of study, the moment corrections (which include site and S-to-coda transfer function) could have also included the instrument response.

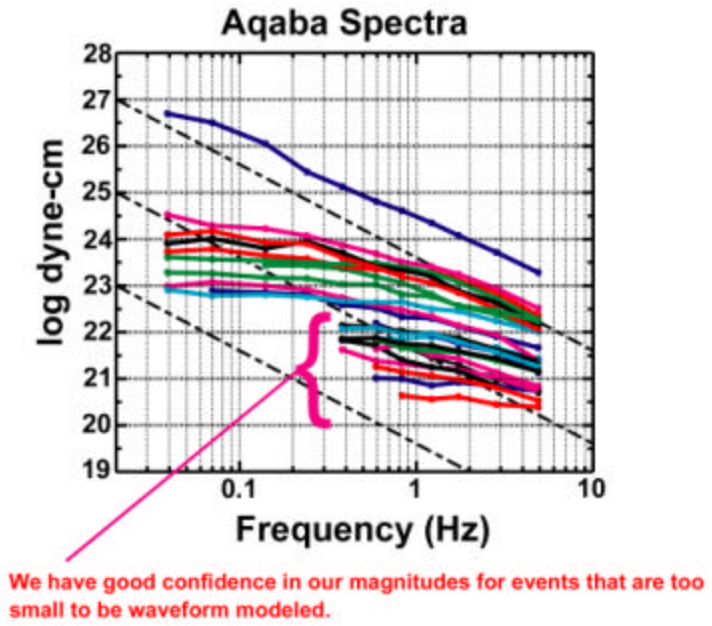


Figure 4. Selected moment-rate spectra for the Gulf of Aqaba sequence.

TESTING & VALIDATION

Figure (4) shows selected source spectra for events in the Gulf of Aqaba region along with some events from the Dead Sea rift at station BGIO. We test for consistency by comparing spectra of the same event at two different stations, in our case, stations BGIO in Israel and KEG in Egypt. Figure (5) shows spectra for two events, one is nodal at BGIO and the other is not. In both cases, the spectra at KEG and BGIO are virtually identical, despite a significant source radiation pattern difference. If we compare individual amplitudes for a large number of events, we also see that the inter-station variation is also very small, comparable to what was observed at NTS.

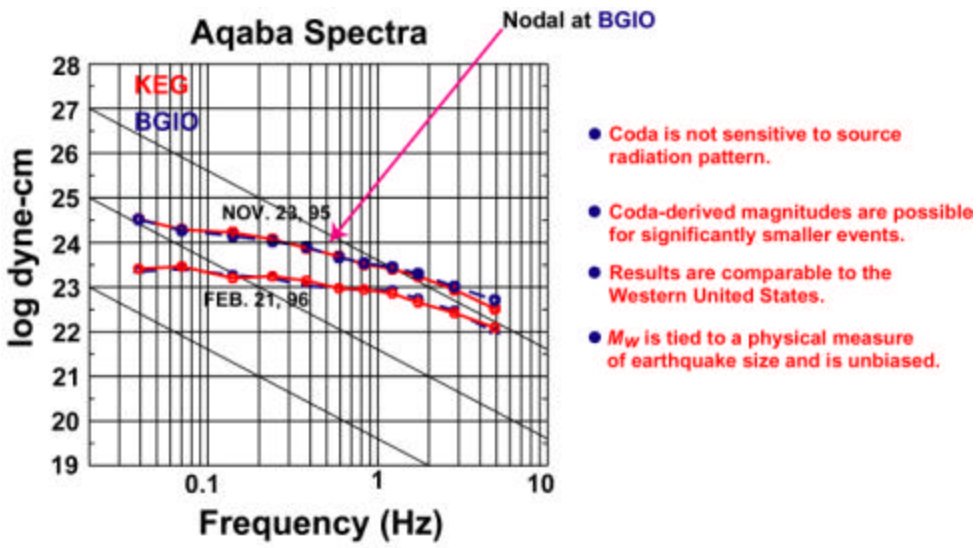


Figure 5. Spectra recorded at KEG and BGIO for the same two events show little variation. Note: The November 23, 1995 aftershock is nodal at BGIO but the coda-derived spectra is the same as the spectra at KEG.

Finally, we verify that our absolute amplitudes are correct by computing M_w from the lowest frequencies of our measured spectra and comparing against independent M_w's. Figure (6) shows that there is good agreement between the two approaches.

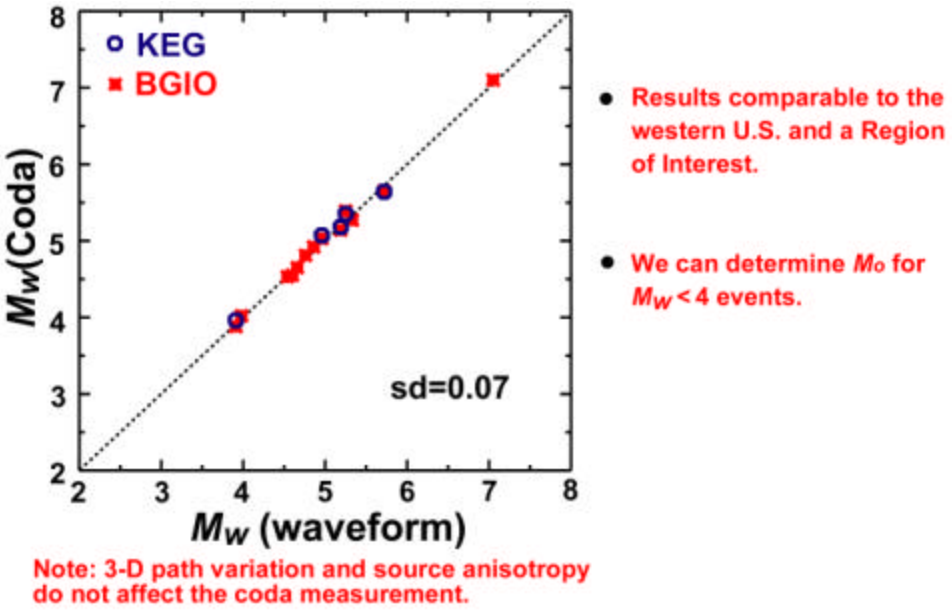


Figure 6. As was found in the western United States, the coda-derived Mw agrees with waveform modelling results.

CONCLUSIONS & RECOMMENDATIONS

Now that we have verified that our spectra are completely corrected back to the S-wave source, we can begin to address a long-standing problem in observational seismology, namely accurate estimation of the radiated seismic energy. For events for which we observe a flat, long-period level (proportional to moment) and decaying high frequencies, we need to extrapolate our observed spectra to f=0 and f= ∞ . Though a majority of the energy is near the corner frequency, for completeness we must do this extrapolation. For the long periods we extend our spectra to f=0 Hz and for the high frequencies, we assume an omega square decay to f= ∞ . Next, we convert our spectra to velocity by dividing by omega, then square and integrate. Only those events for which we have measured at least 70% of the total S-wave energy are used. Finally, we assume a P-wave contribution of energy by multiplying by 1.07. From Figure 7 we see that the Gulf of Aqaba events follow the same trend as those from the western United States.

We have successfully transported a methodology for calibrating stations for regional magnitude to International Monitoring System (IMS) stations in the Middle East region. Resultant source spectra show very small interstation variation as was found in the western U.S. and will allow accurate estimates of Mw and mb for small regional events that cannot be measured teleseismically. We are systematically calibrating all the IMS stations in the region and are tying regional mb's to the teleseismic mb. The coda-derived Mw estimates are being used as input to the joint LANL/LLNL MDAC code for discrimination calibration. The coda methodology has been incorporated into the newest version of SAC that will allow amplitude measurements on narrowband coda envelopes given a calibration flatfile.

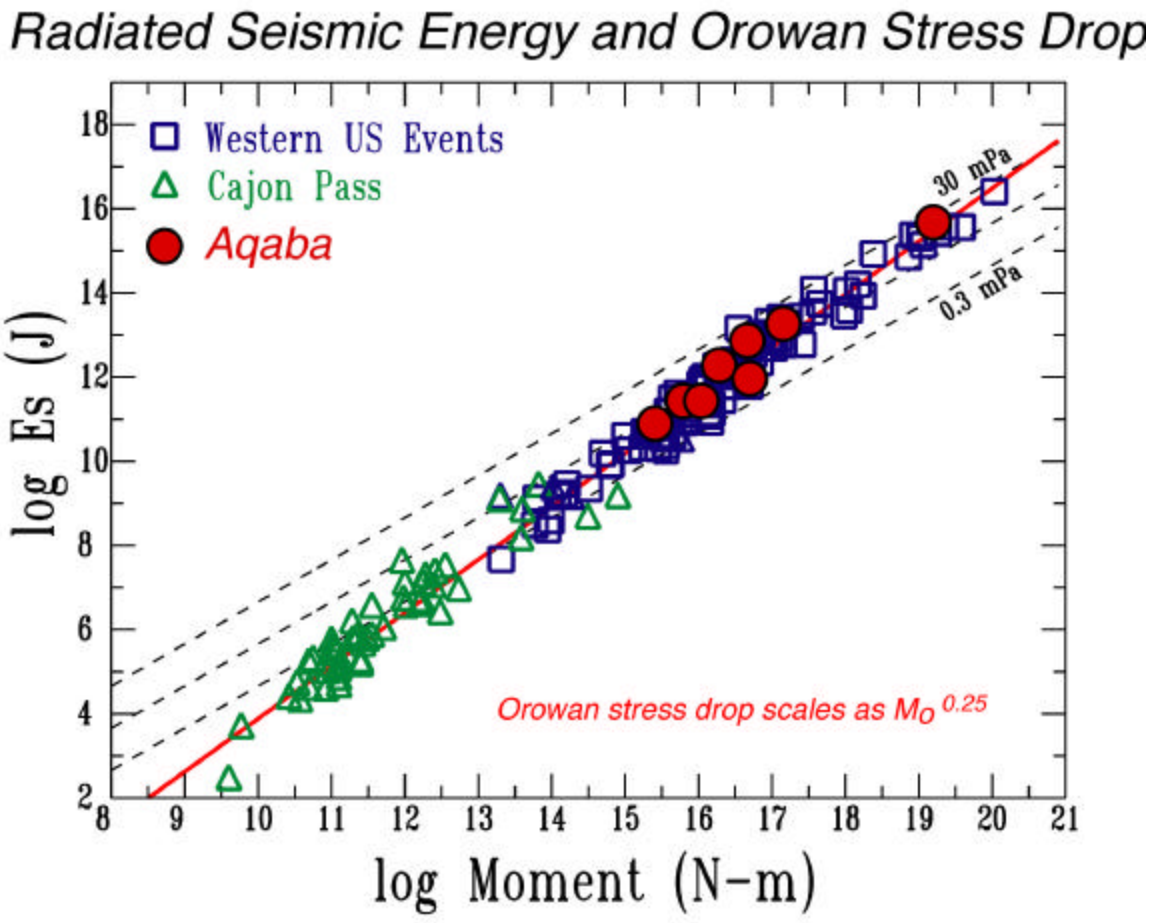


Figure 7. Energy-moment relationship for Aqaba events is in good agreement with results from the western United States.

REFERENCES

Aki, K. (1969), Analysis of the seismic coda of local earthquakes as scattered waves, *J. Geophys. Res*., **74**, 615-631.

Kanamori, J., J. Mori, E. Hauksson, T. H. Heaton, L. K. Hutton, and L. J. Jones (1993), Determination of of earthquake energy release and ML using TERRAscope, BSSA, 83, 330-346.

Mayeda, K., 1993, mb(LgCoda): A stable single station estimator of magnitude, *BSSA*, **83**, 851-861.

Mayeda, K. and W. R. Walter, 1996, Moment, energy, stress drop and source spectra of western United States earthquakes from regional coda envelopes, **101**, *J. Geophys. Res.* 11195-11208.

Myers, S. C., W. R. Walter, K. Mayeda, and L. Glenn (1999), Observations in support of Rg scattering as a source for explosion S waves: Regional and local recordings of the 1997 Kazakhstan Depth of Burial experiment, 89, *BSSA*, 544-549.

DEVELOPMENT OF IMPROVED MAGNITUDE MEASURES FOR THE INTERNATIONAL DATA CENTRE

John R. Murphy, Jeffry L. Stevens, Theron J. Bennett, Brian W. Barker, and Ronald W. Cook
Geophysics Group, Maxwell Technologies, Inc.

Sponsored by the Defense Threat Reduction Agency
Arms Control Technology Division
Nuclear Treaties Branch

Contract No. DASG 60-96-C-0039

ABSTRACT

Many of the most important issues in nuclear test monitoring at the International Data Centre (IDC), such as event screening, depend critically on the details of the definitions of the various magnitude measures to be employed by the IDC and their relations to the classical National Earthquake Information Center, International Seismological Centre, and Air Force Technical Application Center magnitude measures, which have historically been used to assess seismic verification capability. Therefore, it is important that these IDC magnitude measures be well understood and carefully calibrated. During the past year, we have been continuing to refine the IDC m_b and M_S magnitude measures and have initiated an effort to implement an automated L_g-based magnitude measure for application to small, continental seismic events. The effort on m_b has been directed toward incorporation of PKP observations into the generalized m_b determination. A GLM statistical analysis has now been performed on the large sample of PKP amplitude measurements determined from the PIDC IMS station observations to obtain new distance corrections applicable over the PKP distance range. The resulting distance corrections have been compared both with those currently being employed at the IDC and with those previously derived by Lilwall (1987) and some significant differences have been noted. Moreover, the estimated uncertainties in these derived epicentral distance correction factors for PKP have been found to be comparable to or smaller than those previously estimated for the normal teleseismic P distance range. Thus it appears that incorporation of PKP data, will significantly reduce the nominal uncertainties in the network-averaged generalized m_b values for at least some events. Current effort on this task is directed toward the evaluation of the applicability of the previously derived teleseismic P-wave station corrections to PKP observations at those same stations. With regard to the L_g magnitude measure, our goal is to identify an L_g magnitude measure applicable to observations from IMS stations at regional distances which is consistent with the traditional regional magnitude measure, $m_b(L_g)$, and which will be useful for characterizing the sizes of small events observed by the IDC. The L_g magnitude scheme, which we are developing, uses signal measurements in the L_g group velocity window (2.8 km/sec $\leq$ v $\leq$ 3.7 km/sec) from broad-band vertical-component records which have been band-pass filtered in a variety of frequency bands (including a band centered at 1 Hz). We are making several peak and RMS amplitude measures from the L_g window and seeking to identify a stable measurement which is consistent with the traditional L_g magnitude. This effort also requires determination of an appropriate relationship to characterize L_g attenuation in the region surrounding the IMS stations for which the measurements are obtained. For some IMS stations the L_g observations themselves may permit attenuation estimates, but at other stations alternative approaches may be required. We are currently analyzing the observations at selected IMS stations with fairly large samples of L_g detections (e.g. CMAR) to assess consistency between this direct approach and more inferential approaches utilizing L_g attenuation models. Our preliminary results suggest that the L_g attenuation actually observed from regional events surrounding CMAR agrees quite well with models previously derived for this region.

OBJECTIVE

The IDC has the responsibility to characterize and measure seismic sources detected by the global network of stations of the IMS used to monitor the CTBT. The objective of this research program has been to expand and improve the magnitude measurement procedures used to characterize seismic sources at the IDC. We have been seeking to ensure that the magnitudes reported by the IDC are consistent with the definitions of seismic magnitudes and with previous magnitude measures and that they are free of regional biases and biases associated with measurement procedures. We have also been attempting to evaluate new magnitude measures which can help extract as much information as possible about the seismic sources in an automated processing environment.

RESEARCH ACCOMPLISHED

Work on this project has been directed at three distinct seismic magnitude measures: (1) generalized m_b, (2) surface wave magnitude, M_S, and (3) a regional magnitude measure based on Lg. Significant accomplishments have been made during the past year toward developing and refining each of these magnitude measures for use at the IDC.

Generalized m_b – During this past year the effort to revise the IDC m_b estimation procedure has been extended to allow for the incorporation of PKP data. As in our previous analysis (Murphy et al., 1999), a sample of single station m_b observations from some 25,000 REB events was analyzed using a General Linear Model (GLM) in which the single station values, $m_b(i,j,k)$, are represented as a linear combination of the form:

$$m_b(i,j,k) = m(i) + sta(j) + db(k) + e(i,j,k) \qquad (1)$$

where

$m(i)$ = event magnitude
$sta(j)$ = station correction
$db(k)$ = correction to the current PIDC specified dependence on epicentral distance
$e(i,j,k)$ = error term

The system of equations (1) is solved using the Expectation Maximization Algorithm to minimize the residual error, subject to the constraints:

$$\sum_j sta(j) = 0$$

$$\sum_k db(k) = 0 \qquad \text{for } 23^o < D < 92^o \qquad (2)$$

The constraints (2) are employed to retain the average absolute levels of the event magnitudes for comparison purposes. That is, since the absolute levels of the single station magnitudes are set by arbitrary convention, any constant value could be added to all the single station magnitudes without affecting the error term in (1) in any way and, therefore, it is necessary to constrain the absolute levels of the correction terms for comparison purposes.

The final distance corrections determined from the GLM analysis of the subset of shallow focus ($h < 50$ km) events are shown in Figure 1, where they are compared with those currently employed at the PIDC and with those derived by Lilwall (1987) in his analysis of ISC m_b data. As was noted previously, the smoothed GLM estimates of the corrections for epicentral distance are very similar to those employed by the PIDC (i.e Veith/Clawson), and to those estimated by Lilwall, between about 30 and 90 degrees. However, at distances greater than about 95 degrees, the GLM corrections begin to diverge from the other two sets of proposed corrections. Thus, the GLM corrections between about 110 and 140 degrees are consistently lower than those proposed by Lilwall by as much as 0.3 magnitude units, while both the GLM and Lilwall corrections exhibit significantly narrower troughs at the PKP focal point at around 145 degrees than does that associated with the current PIDC correction curve. Therefore, we propose to replace the current PIDC correction curve between 92 and 180 degrees with the smoothed GLM estimate shown in Figure 1.

In order to specify an optimum algorithm for combining single station m_b observations at all distances and obtain a generalized m_b value, it is necessary to first examine the uncertainties in the derived epicentral distance corrections as a function of distance. For this reason, the standard errors of estimate associated with the GLM shallow focus distance correction estimates of Figure 1 are displayed as a function of epicentral distance as a solid line in Figure 2. It can be seen from this figure that, somewhat surprisingly, with the exception of the P diffraction region around 100 degrees, the uncertainties in the distance corrections in the PKP range are quite comparable to those in the normal teleseismic P range between 25 and 95 degrees. Therefore, with the exception of the narrow range between 92 and 103 degrees, we have constrained the standard error of estimate to the average teleseismic P constant value of 0.28 between 23 and 180 degrees, and smoothed the GLM estimates between 92 and 103 degrees to obtain the final teleseismic epicentral distance dependence of the uncertainty represented by the dashed line in Figure 2.

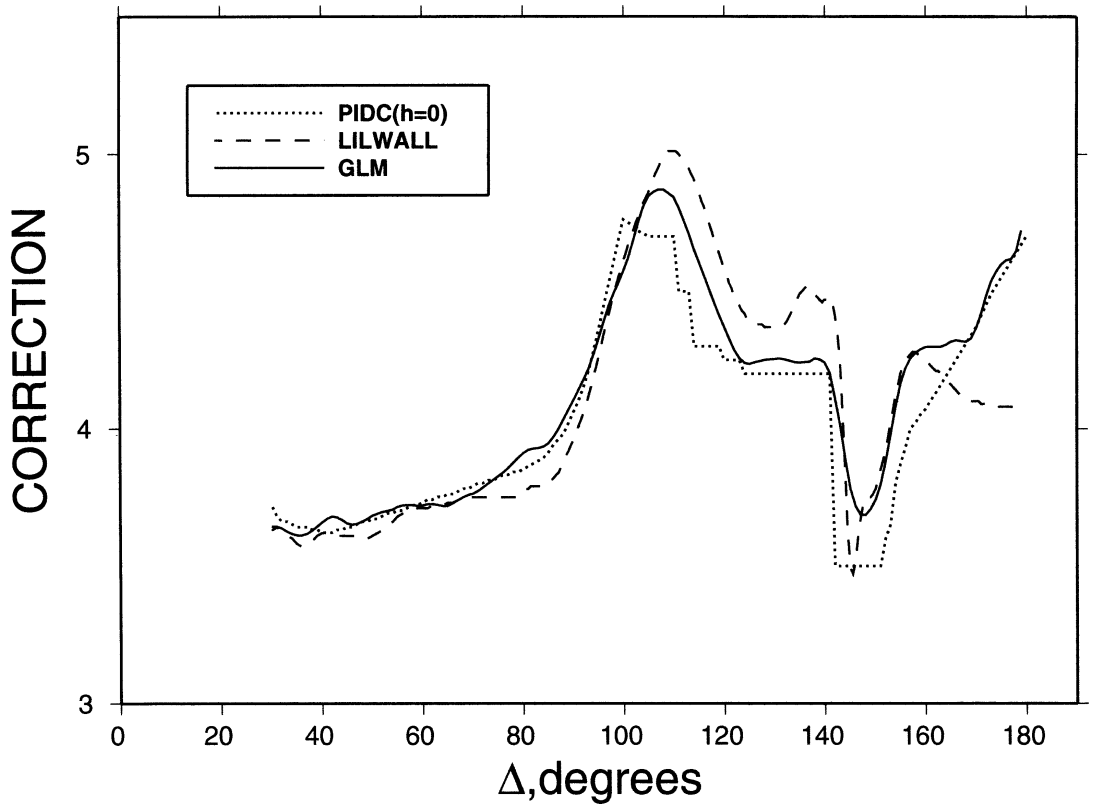


Figure 1. Distance corrections determined from GLM analysis compared to those currently employed at the PIDC and to those derived by Lilwall (1987) in his analysis of ISC data.

The applicability of the m_b station correction factors determined from the previous GLM analysis of the sample of teleseismic P wave data to the PKP observations has also been assessed by comparing these station corrections with the average PKP residuals as a function of distance over the range 100 to 180 degrees. As in our previous analysis of regional P wave data, it has been found that these teleseismic P wave correction factors appear to be generally applicable to the PKP data and produce a significant reduction in variance about the resulting network-averaged m_b values. This fact is illustrated in Figure 3, which shows a comparison of the observed reductions in the standard errors of estimate obtained by applying the station corrections to all the single station P wave data in the distance range from 25 to 180 degrees (left) with those obtained previously for the distance range from 25 to 100 degrees (right). It can be seen that the application of these station correction factors produces comparable reductions in the average standard error of estimate in both cases, corresponding to highly significant reductions of more than 40% in the variance about the resulting network-averaged m_b values. Thus, the station correction factors derived from the teleseismic P wave data appear to be generally applicable over the entire investigated epicentral distance range extending from 2 to 180 degrees. These results are currently being extended to encompass other focal depth ranges of interest.

Regional L_g Magnitude – Although teleseismic magnitude measures are useful for characterizing many of the events observed at the PIDC over the years, it is generally recognized that such magnitudes are not satisfactory for measuring many small events, which may have detected signals at only a few IMS stations. Such events are probably best characterized by observations at regional stations where their signals are strong. During the past year we initiated an effort under this project to identify a regional magnitude measure for use at the IDC. The PIDC has acknowledged the need for regional magnitudes for measuring the size of small events and initially proposed a non-traditional M_L magnitude measure, based on P and P_n observations for stations within 20 degrees of shallow events, to characterize event size. However, this M_L measure has received criticism because it did not correlate very well with teleseismic m_b magnitude measurements. Furthermore, most seismologists prefer a more traditional magnitude scale based on L_g signal amplitude levels measured at regional seismic stations (e.g. $m_b(L_g)$) and taking into account region-dependent attenuation for characterizing the size of small events.

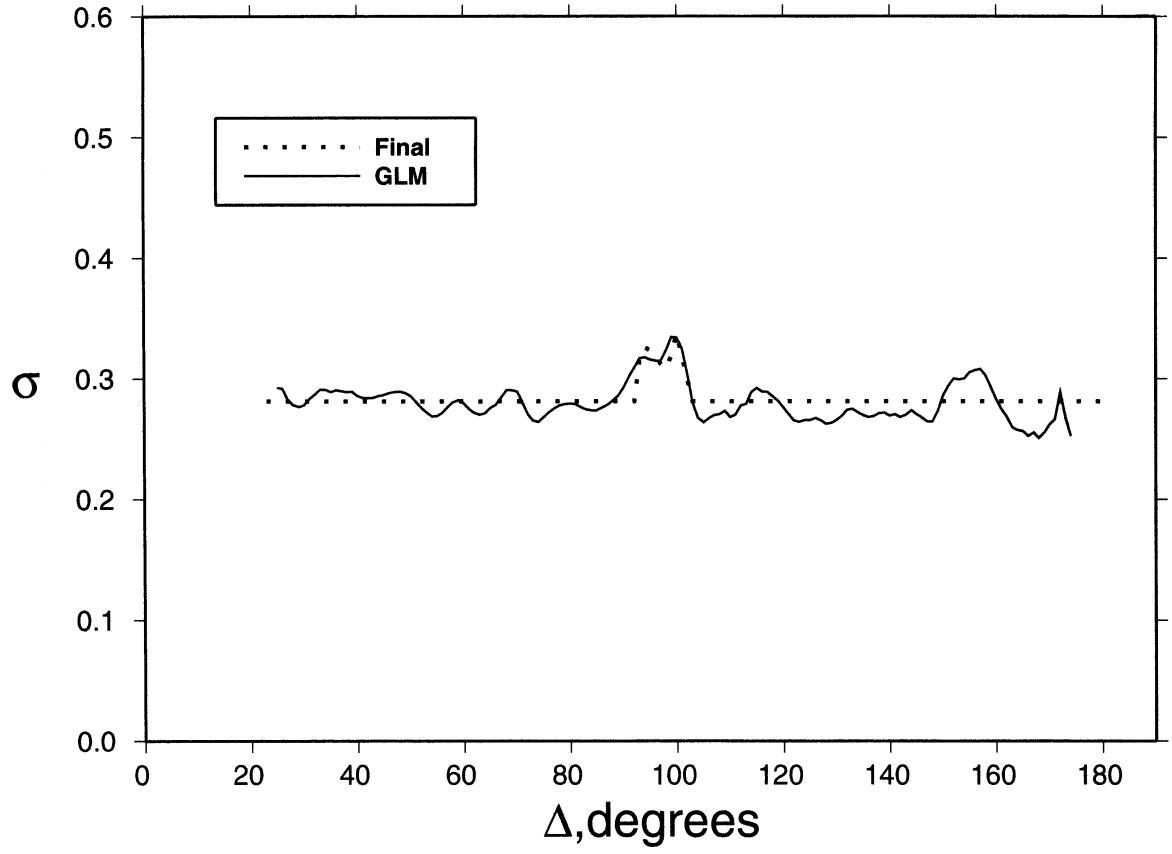


Figure 2. Standard errors of estimate associated with the GLM shallow focus distance correction estimates of Figure 1 compared to our final, smoothed estimate of the uncertainty.

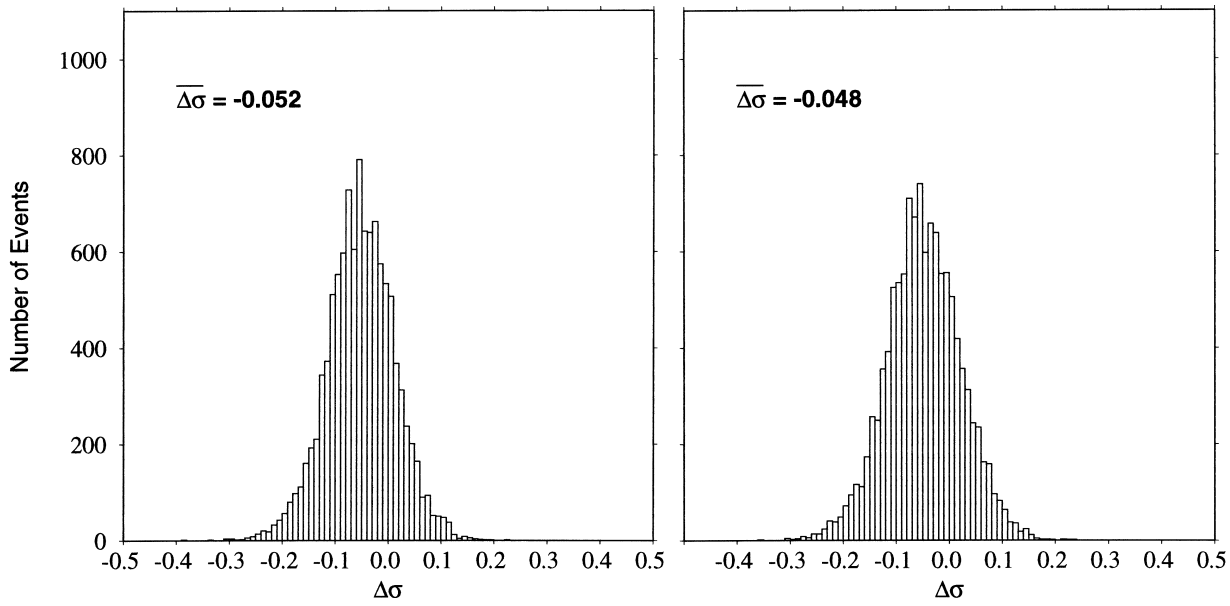


Figure 3. Comparison of the observed reductions in the standard errors of estimate obtained by applying the station corrections to all the single station P wave data in the distance range from 25 to 180 degrees (left) with those obtained for the distance range from 25 to 100 degrees (right).

To meet this objective, we have been conducting some preliminary studies to evaluate a regional magnitude measure, similar to the $m_b(L_g)$ scale defined by Nuttli (1973), which utilizes the amplitude level in a frequency band near 1 Hz measured in the L_g group velocity window and includes corrections for distance based on knowledge of regional L_g attenuation associated with the path-specific propagation. In an effort to broaden the usefulness of this measure, we are also investigating the possibility of measuring the L_g signals in somewhat higher frequency bands for smaller events, which may have larger signal-to-noise ratios at some of the nearer IMS stations.

Similarly to other magnitude measures, the L_g magnitude can be represented as the combination of the logarithm of the measured amplitude, correction factors to account for distance-dependence and station response, and a normalization term to provide some equivalency between scales:

$$m_b(L_g) = \text{Log } A + D(f,R) + S(f) + \text{Log } A_0 \qquad (3)$$

where

A	=	the measured L_g amplitude in a particular frequency (f) band
D(f,R)	=	a correction for signal attenuation with distance, which is frequency dependent
S(f)	=	a station correction, which may be frequency dependent
Log A_0	=	a magnitude normalization term

The Log A_0 term was originally selected by Nuttli to provide agreement between the L_g magnitude scale and the teleseismic m_b magnitude for central North America; however, alternative normalization schemes may be more appropriate for global applications and will be evaluated. We are also investigating a variety of methods for determining the distance correction factor, which would be expected to be strongly path dependent. One option would be to use the observations themselves to define D(f, R) in the region surrounding the individual IMS stations. However, we expect the availability of calibration data to be limited at most IMS stations; so a more indirect approach may be necessary. An alternative is to use a model-based approach to determine L_g attenuation for the source-station path from prior knowledge of L_g propagation characteristics in the region. In particular, there have been a number of studies (cf. Mitchell et al., 1996) covering most continental regions of the world which have determined a Q factor associated with L_g attenuation. It should be possible to use those Q values to determine the L_g attenuation and related distance corrections for the regions around IMS stations. Thus, the correction for L_g amplitude distance dependence can be expressed as the combination of geometric spreading and frequency-dependent attenuation:

$$C_R = \left(\frac{R}{R_N}\right)^{0.833} e^{\pi f \frac{(R - R_N)}{Q v}} \qquad (4)$$

where

R	=	event/station distance
R_N	=	a reference distance for normalization
Q	=	quality factor associated with regional L_g attenuation
v	=	L_g group velocity

and then the magnitude distance correction factor for L_g is just:

$$D(f,R) = \text{Log } C_R \qquad (5)$$

To test the effectiveness of the procedures, we have begun to apply this scheme to the L_g signals at selected IMS stations for events in the REB database at the PIDC during the time period 1995 – Present. For our initial work, we sought a station which had a large number of L_g observations reported for events covering a fairly large range of regional distances. We selected the IMS primary station CMAR in Thailand, for which L_g observations were reported from 240 events (cf. Figure 4). We have retrieved the broadband, vertical-component records at CMAR for these events, as well as some other larger well-recorded events to supplement the CMAR database and provide more uniform coverage over the distance range from 2 to 20 degrees (cf. Figure 5). Each broadband record was filtered using third-order Butterworth filters for several frequency bands including 0.75-1.25 Hz, 1-2 Hz, 2-4 Hz, and others. For each filtered record, amplitude measurements are being made in the L_g group velocity window (from 3.7 km/sec to 2.8 km/sec). We have been measuring peak and RMS averages of the amplitudes over the L_g window, as well as testing a few alternative measures of signal level.

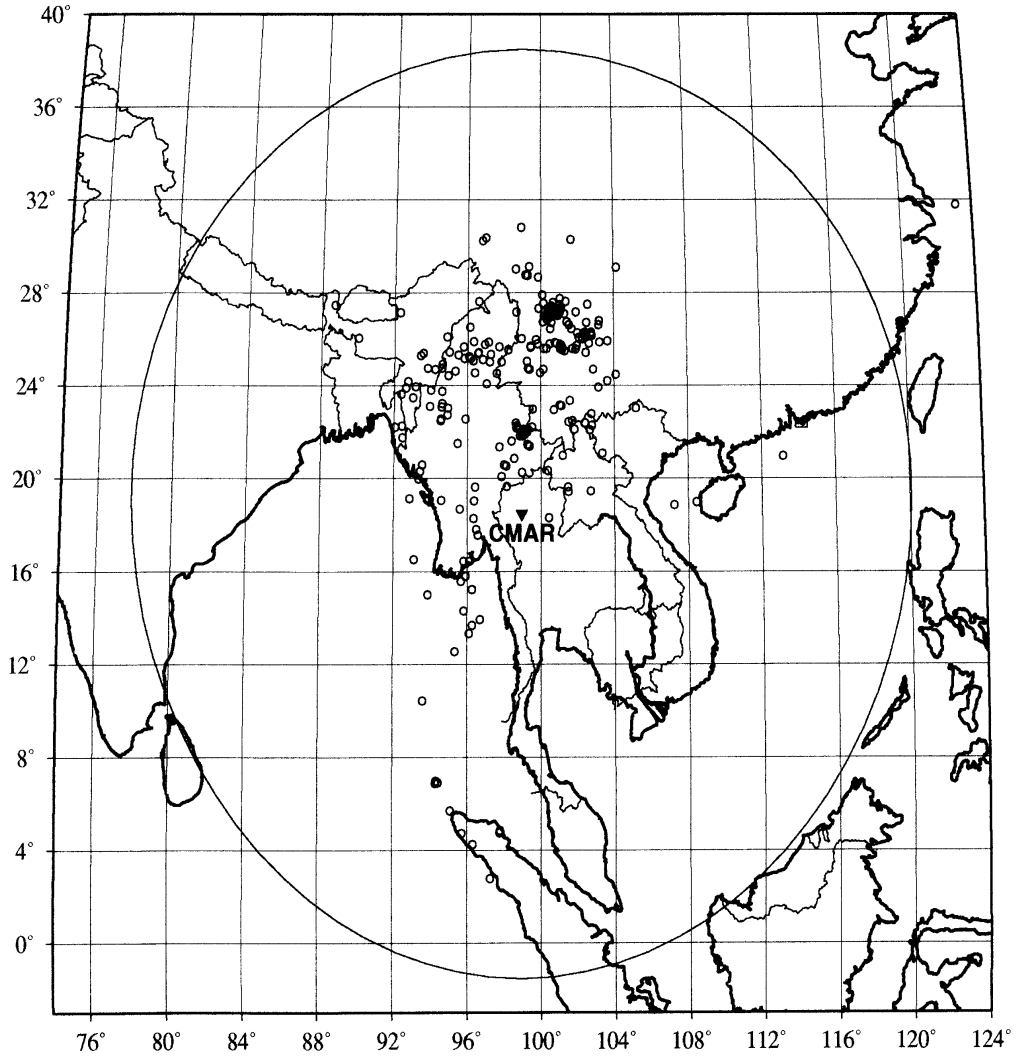


Figure 4. Locations of 242 regional events from the PIDC REB database (1995 – Present) for which Lg signals were reported at the Primary IMS station CMAR in Thailand. Large circle is at 20° from CMAR.

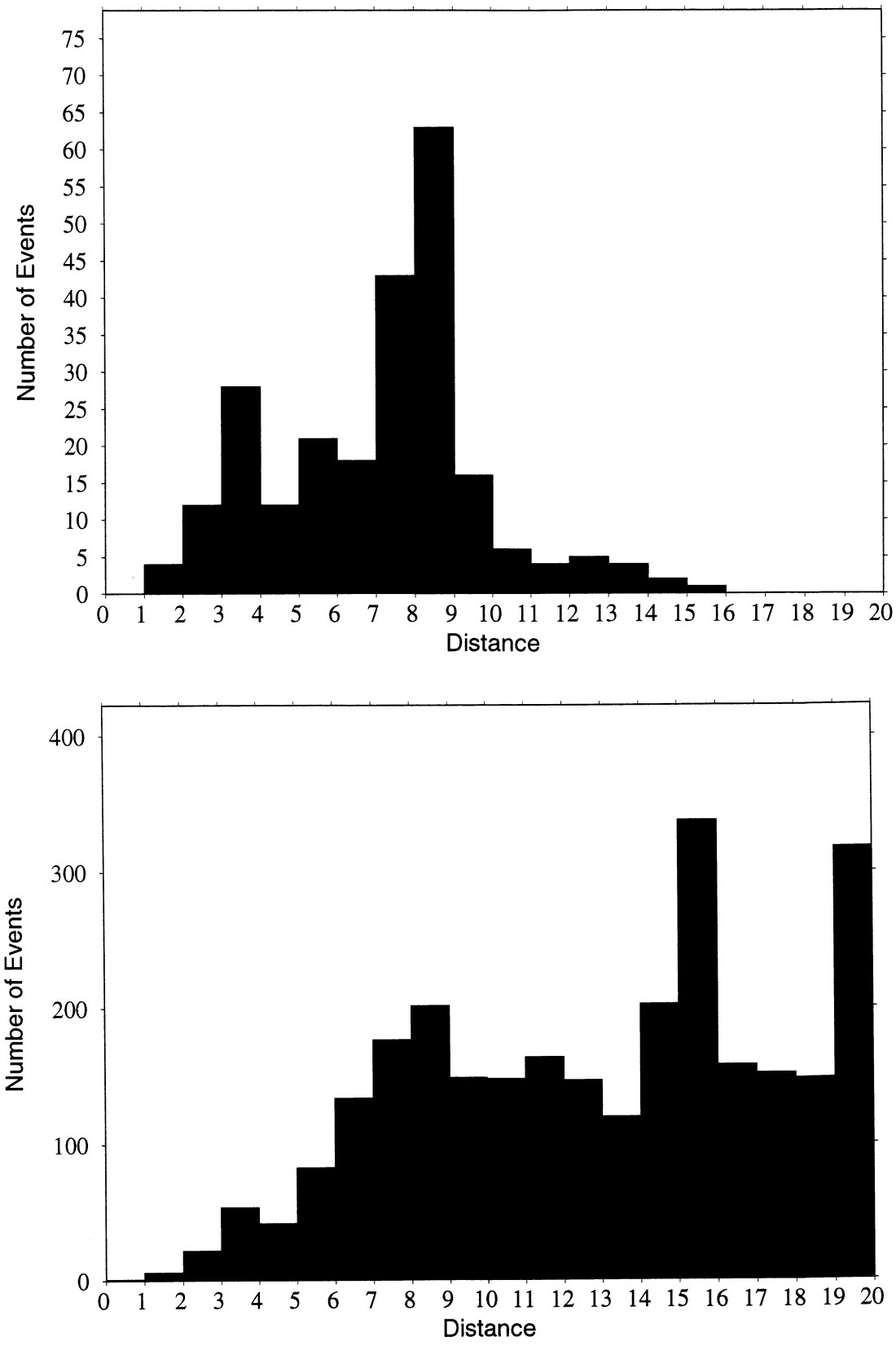


Figure 5. Distributions with respect to epicentral distance of the regional events with Lg signals reported at CMAR (top) and a large sample of 2767 REB events within 20° of CMAR (bottom) from which supplemental data have been selected.

We performed some preliminary analyses on a sample of the measurements at CMAR to determine its consistency with the attenuation model described above. For the limited sample, we found from a multivariate regression analysis that the observations for the 0.75-1.25 Hz passband could be described by a $Q_0 \approx 250$ (i.e. Q at 1 Hz) with a geometric spreading dependence of $R^{-0.83}$. This attenuation appears to be in fairly good agreement with Q_0 results reported by Mitchell et al. (1996) for L_g attenuation in this region; although those studies indicate variation in Q across the region surrounding CMAR, which would imply azimuthal dependence of the L_g magnitude distance correction.

To assess the significance of the azimuthal variations in attenuation and the utility of prior knowledge of L_g attenuation for these kinds of magnitude corrections, we have developed a procedure to determine the total L_g attenuation by summing the effects of Q along the L_g propagation path for a model in which the attenuation varies (e.g. the model of Mitchell et al.). Figure 6 shows the L_g magnitude distance correction term at 1 Hz, combining the effects of the Q model and geometrical spreading, for the region surrounding station CMAR. Although the magnitude correction term appears to be fairly symmetric, there are actually some significant differences at fixed distance as a function of azimuth which are attributable to the Q variations. As would be expected, these are most notable at larger distances where the magnitude correction changes by more than 0.5 magnitude units for events at a distance of 20 degrees over an azimuthal range of about 90 degrees around CMAR. Considering the relatively uniform behavior of the Q model around CMAR compared to some other areas, it seems likely that stronger variations in the L_g magnitude distance corrections should be expected around other IMS stations. These will need to be accounted for in developing reliable L_g magnitude measures for use at the IDC.

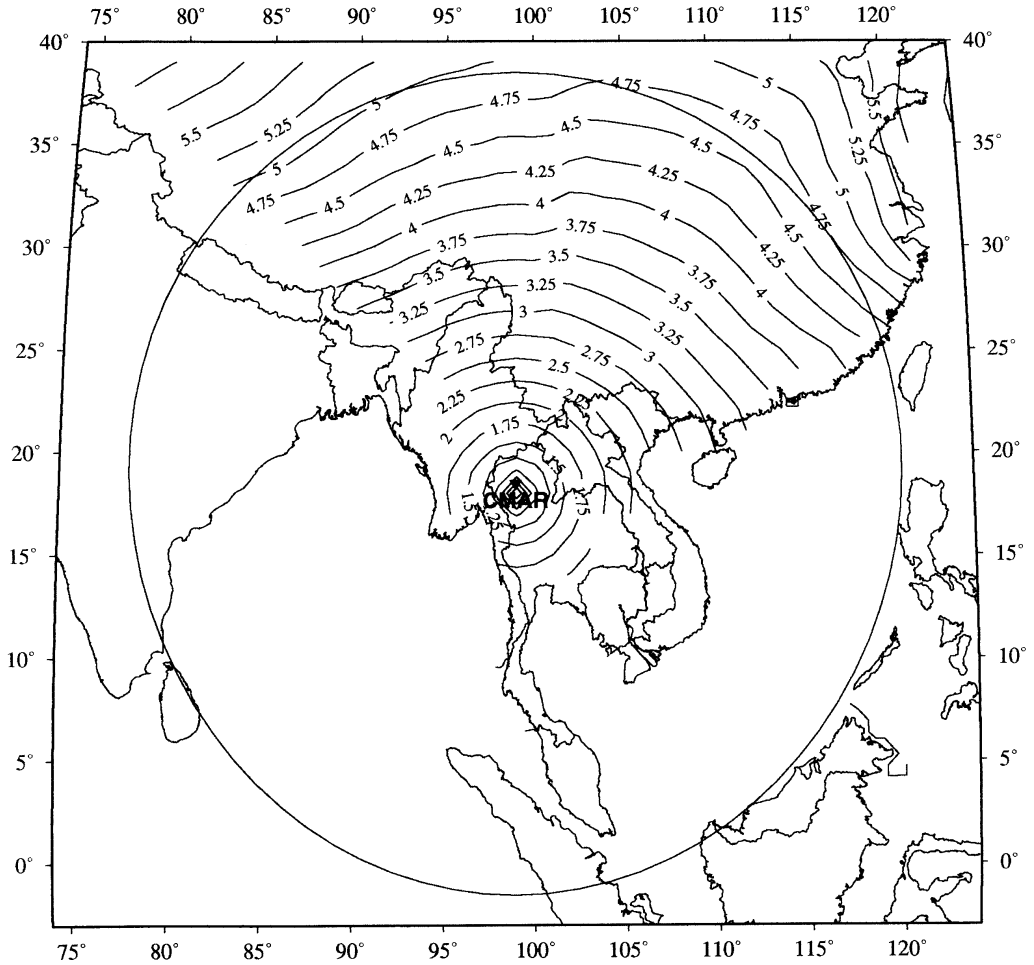


Figure 6. Contour map of Lg magnitude distance correction at 1 Hz predicted for the region surrounding CMAR by combining the effects of geometrical spreading and attenuation based on the regional Q model. Circle is at 20° from CMAR.

Surface Wave Processing – Another element of this project has been the development of improved surface wave processing for M_S magnitude determination at the IDC. A major part of this task has been to provide development and support for automatic surface wave processing using Maxwell's Maxsurf program code. This code has in fact been in place at the PIDC for several years and continues to perform well. We are in the process of completing standard documentation of the software for Maxsurf. In addition, we have developed maximum likelihood M_S station corrections for all available IMS stations, and those are now being used as part of the surface wave magnitude determinations.

CONCLUSIONS AND RECOMMENDATIONS

Significant improvements have been made in magnitude estimation procedures for use at the IDC. Procedures to enhance generalized m_b by incorporating PKP observations have been established and calibrated, and P-wave magnitudes can now be determined over the distance range from 2 to 180 degrees. m_b station corrections for use over the entire range of P wave observations have been developed. Preliminary investigations have been conducted to provide the basis for more traditional regional magnitude measures at the IDC based on L_g observations. Additional studies are needed to establish L_g magnitude distance corrections in the vicinity of IMS stations and to provide the bases for L_g magnitude calibration. Maxsurf has been established as a reliable tool for automatic surface wave processing and M_S estimation. Appropriate M_S station corrections have been determined for use with IMS stations, and these will be refined as new stations become available.

Key Words: seismic, magnitude, PKP, L_g, IDC

REFERENCES

Lilwall, R. C. (1987), "Empirical Amplitude-Distance/Depth Curves for Short-Period P Waves in the Distance Range 20 to 180°," AWRE Report No. O 30/86.

Mitchell, B. J., Y. Pan, and J. K. Xie (1996), "The Variation of L_g Coda Q Across Eurasia and Its Relation to Continental Evolution," PL-TR-96-2154, ADA317387.

Murphy, J. R., J. L. Stevens, T. J. Bennett, B. W. Barker, and R. W. Cook (1999), "Development of Improved Magnitude Measurements for the International Data Centre," Proceedings of the 21st Seismic Research Symposium, Las Vegas, Nevada.

Nuttli, O. W. (1973), "Seismic Wave Attenuation and Magnitude Relations for Eastern North America," J. Geophys. Res. 78, 876-885.

SESIMIC SOURCE CHARACTERIZATION IN ASIA

George E. Randall[1] and Charles J. Ammon[2]

[1]Los Alamos National Laboratory,
[2]Saint Louis University

Sponsored by U.S. Department of Energy
Office of Nonproliferation Research and Engineering
Office of Defense Nuclear Nonproliferation
Nation Nuclear Security Administration

ABSTRACT

A significant challenge of modeling small-to-moderate-size seismic sources is the necessity of relying on short-period signals with long travel paths that are significantly sensitive to earth structure along the path. When the path effects are unknown or difficult to account for, we must rely on components of seismic signals that are minimally dependent on the structure. Although regional surface-wave phase is strongly influenced by structure, surface wave amplitude spectra can be modeled adequately with relatively simple models, and these spectra carry valuable information on source character and depth. Our efforts build on existing seismic source analysis techniques. We directly model regional seismograms where possible but combine those time-domain observations with surface wave amplitude spectra at more distant regional stations. We have used regional seismic data to estimate seismic moment tensors and event depths for characterization of seismic sources in Asia. For larger events in the study (greater than magnitude 5) we have successfully included long-period (approximately 40 seconds period) body-wave trains that can be modeled reliably using simple stratified earth models into our grid search for strike, dip, rake, moment, and depth. Our main focus is to use regional seismic data to estimate seismic source mechanisms, moments, and event depths to characterize seismic sources in Asia. A complete catalog of regionally estimated seismic moments, source mechanisms, and depths will be a useful tool for magnitude calibration and regional characterization. Recent work has suggested possible bias in Harvard CMT moment estimates for events in central Asia (Patton, 1998). Thus, we are particularly interested in constraining seismic moments, which are critical for calibrating regional magnitude scales with global catalogs, and in improving depth estimates for Asian events. In the broader view, accurate seismic source parameters for small-to-moderate size events is a step towards the construction of path-specific or regional, short-period (less than 15 seconds) surface-wave dispersion maps, which are essential for creating matched filters for isolating and analyzing short-period surface waves from small events.

Key Words: seismic source characterization, magnitude calibration, regional characterization, regional wave propagation

OBJECTIVE

We need a catalog of regionally estimated seismic moments, source mechanisms, and depths for magnitude calibration and regional characterization. Recent work has suggested possible bias in Harvard CMT moment estimates for events in central Asia (Patton, 1998). Further modeling studies (Patton and Randall, 2000) suggest that the bias in CMT moment estimates depends on the source mechanism. If we are to develop a catalog of accurate moment estimates, we must refine techniques for regional moment tensor estimation to use all available data. We are focusing on using joint modeling of time domain regional waveforms, regional surface wave spectra, and teleseismic bodywaves. Time domain regional waveform modeling has been a useful tool in Asia (Randall, Ammon & Owens, 1995) when the earth model is suf-

ficiently accurate and the propagation path short enough to accurately characterize the surface wave dispersion. For longer paths, we are jointly modeling the regional surface wave spectra which are less sensitive to the details of the dispersion. The amplitude of the surface wave spectrum is a nonlinear function of the moment tensor estimate, so we have adopted a grid search over strike, dip and rake rather than formulate an iterative nonlinear inversion scheme. Although surface wave spectra are unable to resolve the mechanism polarity, as little as one time domain waveform can resolve the ambiguity.

RESEARCH ACCOMPLISHEMENTS

We are developing a complete catalog of regionally estimated seismic moments, source mechanisms, and depths for Asia and refining techniques for regional moment tensor estimation to develop the catalog. Our present efforts have focused on a number of well recorded regional events which also have CMT (Dziewonski et al., 1983) estimates.

We show some of the work for an event in western China on January 30, 1999, at 41.674N latitude and 88.463E longitude with a 23.3 km. depth. Only station WMQ is close enough to permit regional time domain modeling. The maps in Figure 1 show a polar projection centered on the event, out to 90 degrees distance, and the regional view of the event with paths to stations used to analyze the event. Although there are many more stations at teleseismic distance, for smaller events the signal will only have useful signal to noise at the regional and closer teleseismic stations.

In Figure 2 we show the results of the moment tensor estimation using both the L1 and L2 error norms, and the CMT solution with its best double couple fault planes. The CMT solution shows the moment tensor solution with the shaded region, and the best double couple is shown by the focal planes. The regional solutions are inherently double couple as they are found with a simple grid search over strike, dip and rake. All three solutions have a near horizontal compressional axis and a near vertical tensional axis, although details of the fault planes are apparent.

Figure 3 shows the full waveform regional time domain fits at WMQ, regional surface wave spectral fits at ULN for both vertical Rayleigh and tangential Love waves, and time domain waveforms for vertical component long period body waves including both the P wave and the S wave. For the time domain fits, the bold waveforms are the synthetic and the fine lines are the data. For the spectral fits, the solid curve and the circles are the data and the triangles are the predictions, with errors computed at the discrete frequencies of the circles and triangles. Broadband data and Green's functions are used in the modeling, and both data and Green's functions are filtered in the modeling code to permit simple changes of filter parameters with a single set of waveforms. The WMQ and ULN data have been bandpass filtered from 100 to 20 seconds period; more distant body wave data at HIA and YAK have been bandpass filtered from 50 to 40 seconds period. The results shown are for 25 km. depth which had the minimum error for the range to depths modeled. All Green's function were calculated with a reflectivity algorithm and an earth structure using regional earth models overlying a mantle from the PREM model. This should give results that accurately reflect both regional and teleseismic propagation.

Figure 4 shows a preliminary attempt to model broadband teleseismic P waves for source

depth. The data for the broadband vertical component for station EIL (bold trace) are compared to Green's functions (narrow traces) for depths shown at the right margin of the trace. The Green's function is not meant to accurately represent the moment tensor, but only to show the potential for resolving event depth in addition to the analysis of regional data. In this case, the EIL data suggest a depth between 20 and 25 km. which is comparable to the results of our modeling and the published 23.3 km. depth.

CONCLUSIONS AND RECOMMENDATIONS

We have developed techniques to estimate seismic moment tensors by jointly modeling near regional broadband seismograms, regional surface wave spectra and body waves at far regional and teleseismic distances. We will apply the technique to all events in Asia to build a complete catalog of seismic moment tensor estimates and determine the minimum moment we can expect to accurately model in the region. Well recorded events will also be analyzed for surface wave dispersion and phase matched filters developed for event station paths. Analysis of fundamental mode surface wave spectra using mode isolation based on the dispersion will also be investigated. The dispersion measurement will be included in regional tomographic studies for regionalization of surface wave propagation.

This document is LAUR-00-2583

REFERENCES

Dziewonski, A.M. and J.H. Woodhouse, An experiment in systematic study of global seismicity: Centroid-moment tensor solution for 201 moderate and large earthquakes of 1981, *J. Geophys. Res*, 88, 3247-3271, 1983.

Patton, H.J., Bias in centroid moment tensor for central Asian earthquakes: Evidence from regional surface wave data, *J. Geophys. Res*, 103, 26963-26974, 1998.

Patton, H.J. and G.E. Randall, On the causes of biased estimates of seismic moment for earthquakes in central Asia, submitted to *J. Geophys. Res,* 2000.

Randall, G.E., C.J. Ammon, and T.J. Owens, Moment tensor estimation using regional seismograms from a Tibetan Plateau portable network deployment, *Geophys. Res. Lett.*, 22, 1665-1668, 1995.

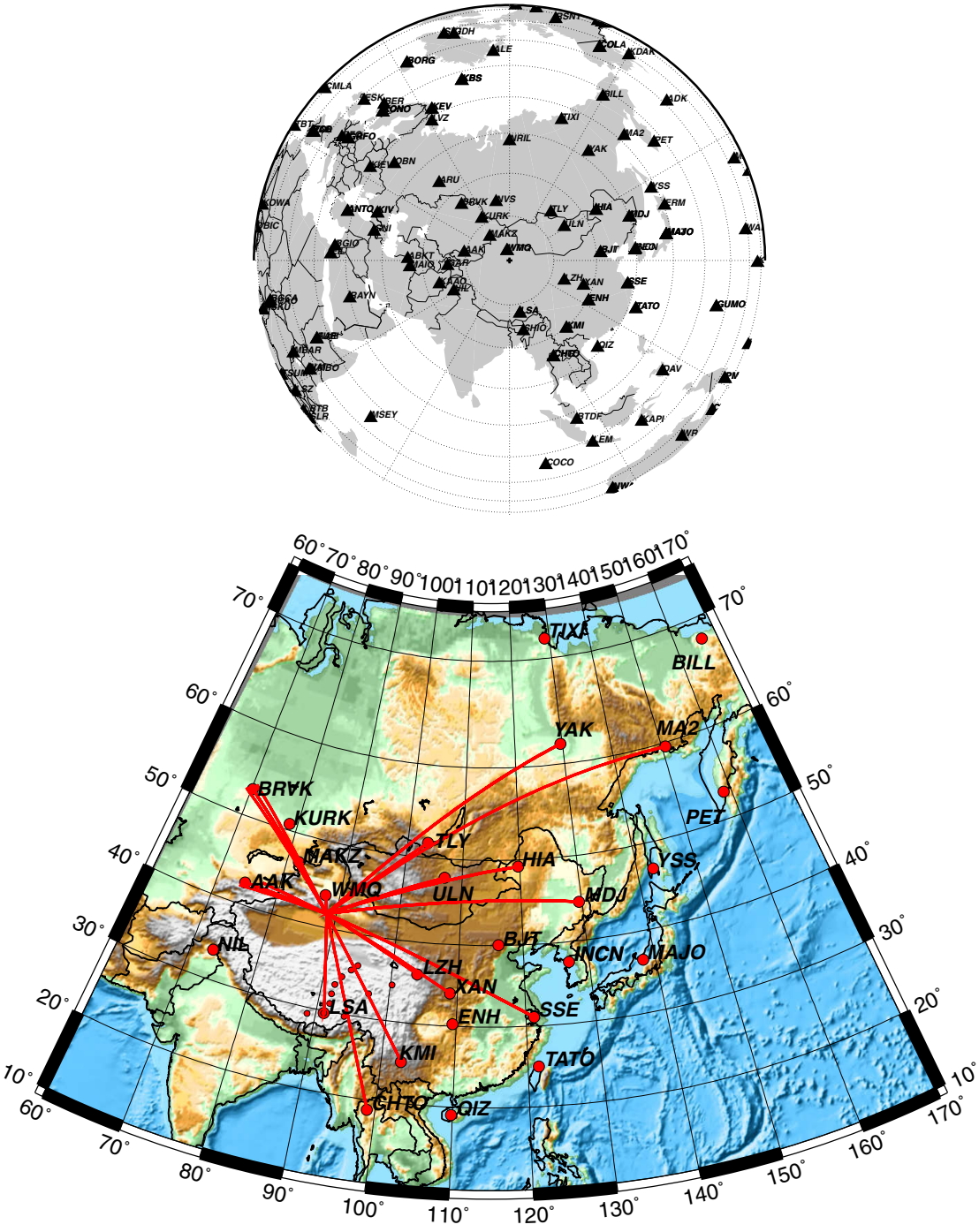


Figure 1. Maps showing teleseismic and regional station distributions with regional paths.

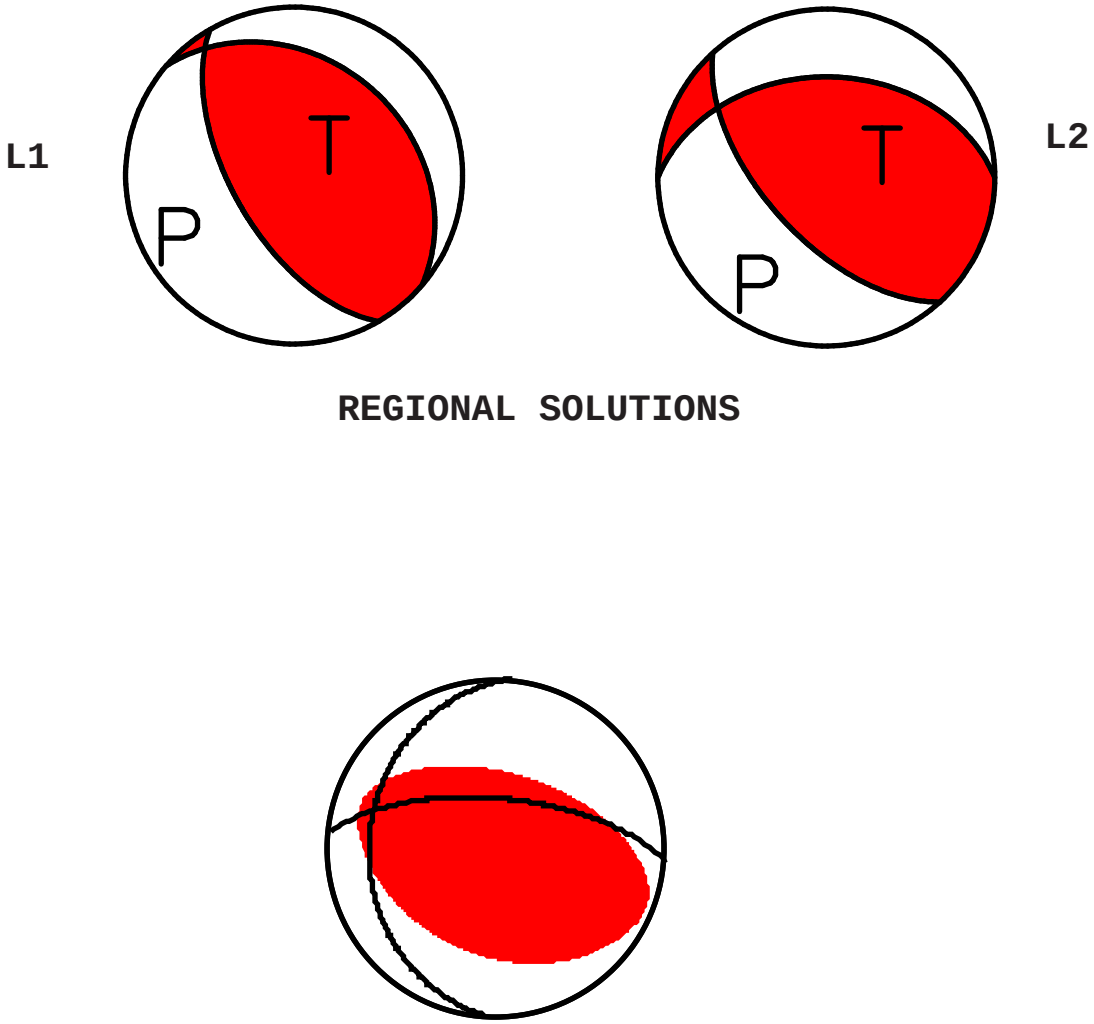


Figure 2. Comparison of regional solutions using L1 and L2 norms for the grid search and the CMT mechanism.

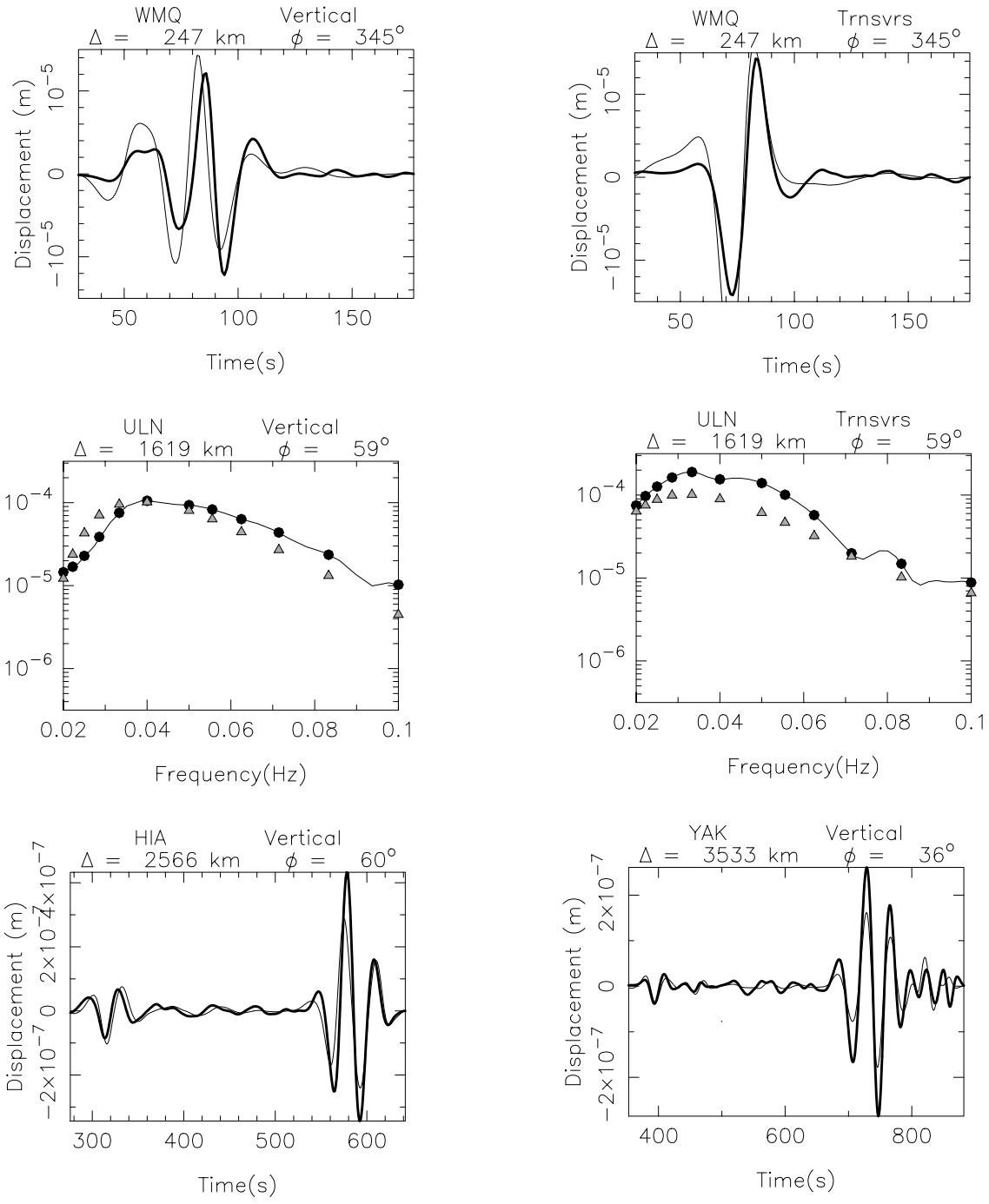


Figure 3. Examples of fits for regional time domain seismograms, regional surface wave spectra, and far regional and teleseismic bodywaves.

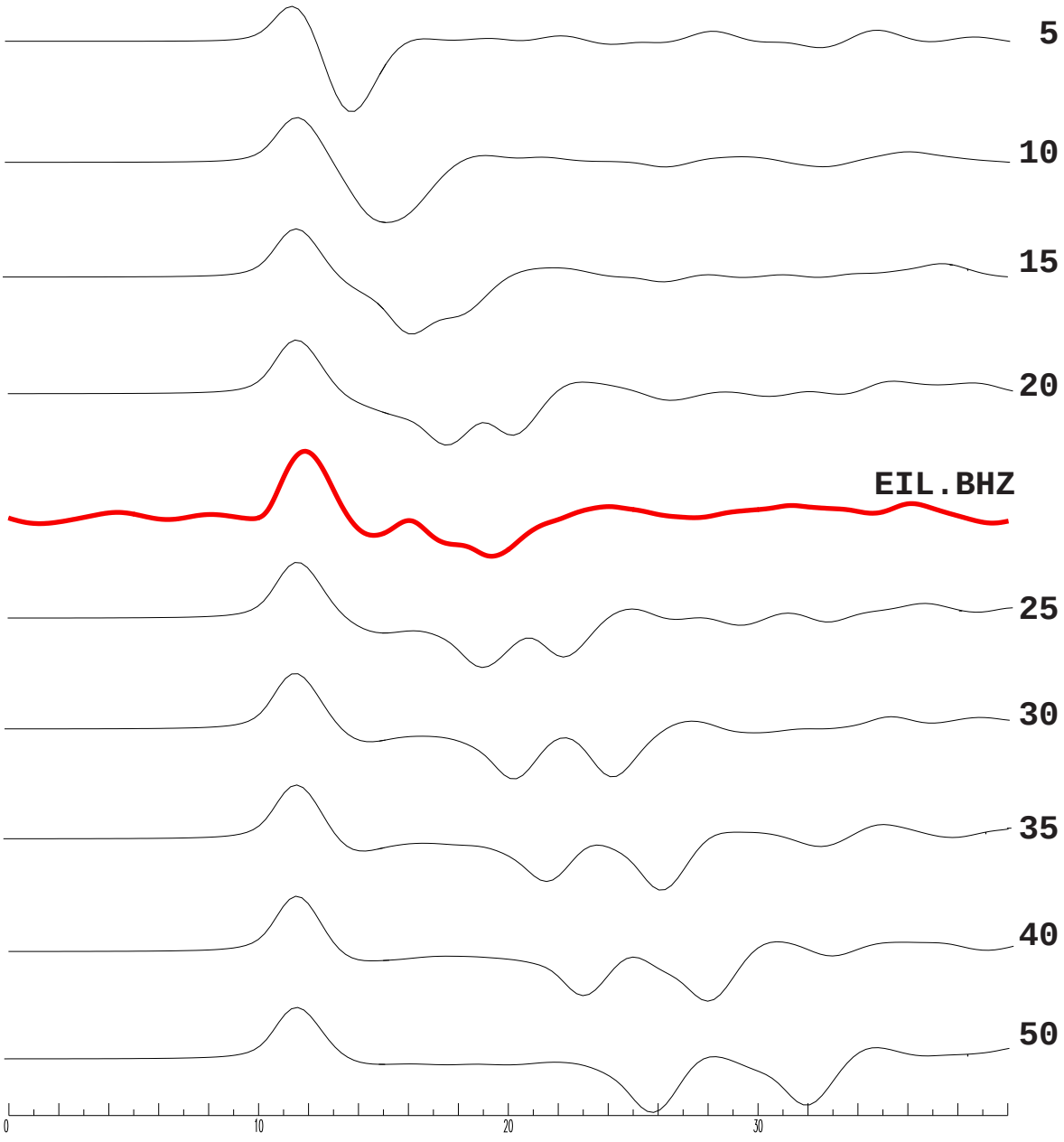


Figure 4. Comparison of observed vertical displacement at EIL and Green's functions calculated for a range of depths.

SESIMIC SOURCE CHARACTERIZATION IN ASIA

George E. Randall[1] and Charles J. Ammon[2]

[1]Los Alamos National Laboratory,
[2]Saint Louis University

Sponsored by U.S. Department of Energy
Office of Nonproliferation Research and Engineering
Office of Defense Nuclear Nonproliferation
Nation Nuclear Security Administration

ABSTRACT

A significant challenge of modeling small-to-moderate-size seismic sources is the necessity of relying on short-period signals with long travel paths that are significantly sensitive to earth structure along the path. When the path effects are unknown or difficult to account for, we must rely on components of seismic signals that are minimally dependent on the structure. Although regional surface-wave phase is strongly influenced by structure, surface wave amplitude spectra can be modeled adequately with relatively simple models, and these spectra carry valuable information on source character and depth. Our efforts build on existing seismic source analysis techniques. We directly model regional seismograms where possible but combine those time-domain observations with surface wave amplitude spectra at more distant regional stations. We have used regional seismic data to estimate seismic moment tensors and event depths for characterization of seismic sources in Asia. For larger events in the study (greater than magnitude 5) we have successfully included long-period (approximately 40 seconds period) body-wave trains that can be modeled reliably using simple stratified earth models into our grid search for strike, dip, rake, moment, and depth. Our main focus is to use regional seismic data to estimate seismic source mechanisms, moments, and event depths to characterize seismic sources in Asia. A complete catalog of regionally estimated seismic moments, source mechanisms, and depths will be a useful tool for magnitude calibration and regional characterization. Recent work has suggested possible bias in Harvard CMT moment estimates for events in central Asia (Patton, 1998). Thus, we are particularly interested in constraining seismic moments, which are critical for calibrating regional magnitude scales with global catalogs, and in improving depth estimates for Asian events. In the broader view, accurate seismic source parameters for small-to-moderate size events is a step towards the construction of path-specific or regional, short-period (less than 15 seconds) surface-wave dispersion maps, which are essential for creating matched filters for isolating and analyzing short-period surface waves from small events.

Key Words: seismic source characterization, magnitude calibration, regional characterization, regional wave propagation

OBJECTIVE

We need a catalog of regionally estimated seismic moments, source mechanisms, and depths for magnitude calibration and regional characterization. Recent work has suggested possible bias in Harvard CMT moment estimates for events in central Asia (Patton, 1998). Further modeling studies (Patton and Randall, 2000) suggest that the bias in CMT moment estimates depends on the source mechanism. If we are to develop a catalog of accurate moment estimates, we must refine techniques for regional moment tensor estimation to use all available data. We are focusing on using joint modeling of time domain regional waveforms, regional surface wave spectra, and teleseismic bodywaves. Time domain regional waveform modeling has been a useful tool in Asia (Randall, Ammon & Owens, 1995) when the earth model is suf-

ficiently accurate and the propagation path short enough to accurately characterize the surface wave dispersion. For longer paths, we are jointly modeling the regional surface wave spectra which are less sensitive to the details of the dispersion. The amplitude of the surface wave spectrum is a nonlinear function of the moment tensor estimate, so we have adopted a grid search over strike, dip and rake rather than formulate an iterative nonlinear inversion scheme. Although surface wave spectra are unable to resolve the mechanism polarity, as little as one time domain waveform can resolve the ambiguity.

RESEARCH ACCOMPLISHEMENTS

We are developing a complete catalog of regionally estimated seismic moments, source mechanisms, and depths for Asia and refining techniques for regional moment tensor estimation to develop the catalog. Our present efforts have focused on a number of well recorded regional events which also have CMT (Dziewonski et al., 1983) estimates.

We show some of the work for an event in western China on January 30, 1999, at 41.674N latitude and 88.463E longitude with a 23.3 km. depth. Only station WMQ is close enough to permit regional time domain modeling. The maps in Figure 1 show a polar projection centered on the event, out to 90 degrees distance, and the regional view of the event with paths to stations used to analyze the event. Although there are many more stations at teleseismic distance, for smaller events the signal will only have useful signal to noise at the regional and closer teleseismic stations.

In Figure 2 we show the results of the moment tensor estimation using both the L1 and L2 error norms, and the CMT solution with its best double couple fault planes. The CMT solution shows the moment tensor solution with the shaded region, and the best double couple is shown by the focal planes. The regional solutions are inherently double couple as they are found with a simple grid search over strike, dip and rake. All three solutions have a near horizontal compressional axis and a near vertical tensional axis, although details of the fault planes are apparent.

Figure 3 shows the full waveform regional time domain fits at WMQ, regional surface wave spectral fits at ULN for both vertical Rayleigh and tangential Love waves, and time domain waveforms for vertical component long period body waves including both the P wave and the S wave. For the time domain fits, the bold waveforms are the synthetic and the fine lines are the data. For the spectral fits, the solid curve and the circles are the data and the triangles are the predictions, with errors computed at the discrete frequencies of the circles and triangles. Broadband data and Green's functions are used in the modeling, and both data and Green's functions are filtered in the modeling code to permit simple changes of filter parameters with a single set of waveforms. The WMQ and ULN data have been bandpass filtered from 100 to 20 seconds period; more distant body wave data at HIA and YAK have been bandpass filtered from 50 to 40 seconds period. The results shown are for 25 km. depth which had the minimum error for the range to depths modeled. All Green's function were calculated with a reflectivity algorithm and an earth structure using regional earth models overlying a mantle from the PREM model. This should give results that accurately reflect both regional and teleseismic propagation.

Figure 4 shows a preliminary attempt to model broadband teleseismic P waves for source

depth. The data for the broadband vertical component for station EIL (bold trace) are compared to Green's functions (narrow traces) for depths shown at the right margin of the trace. The Green's function is not meant to accurately represent the moment tensor, but only to show the potential for resolving event depth in addition to the analysis of regional data. In this case, the EIL data suggest a depth between 20 and 25 km. which is comparable to the results of our modeling and the published 23.3 km. depth.

CONCLUSIONS AND RECOMMENDATIONS

We have developed techniques to estimate seismic moment tensors by jointly modeling near regional broadband seismograms, regional surface wave spectra and body waves at far regional and teleseismic distances. We will apply the technique to all events in Asia to build a complete catalog of seismic moment tensor estimates and determine the minimum moment we can expect to accurately model in the region. Well recorded events will also be analyzed for surface wave dispersion and phase matched filters developed for event station paths. Analysis of fundamental mode surface wave spectra using mode isolation based on the dispersion will also be investigated. The dispersion measurement will be included in regional tomographic studies for regionalization of surface wave propagation.

This document is LAUR-00-2583

REFERENCES

Dziewonski, A.M. and J.H. Woodhouse, An experiment in systematic study of global seismicity: Centroid-moment tensor solution for 201 moderate and large earthquakes of 1981, *J. Geophys. Res*, 88, 3247-3271, 1983.

Patton, H.J., Bias in centroid moment tensor for central Asian earthquakes: Evidence from regional surface wave data, *J. Geophys. Res*, 103, 26963-26974, 1998.

Patton, H.J. and G.E. Randall, On the causes of biased estimates of seismic moment for earthquakes in central Asia, submitted to *J. Geophys. Res,* 2000.

Randall, G.E., C.J. Ammon, and T.J. Owens, Moment tensor estimation using regional seismograms from a Tibetan Plateau portable network deployment, *Geophys. Res. Lett.*, 22, 1665-1668, 1995.

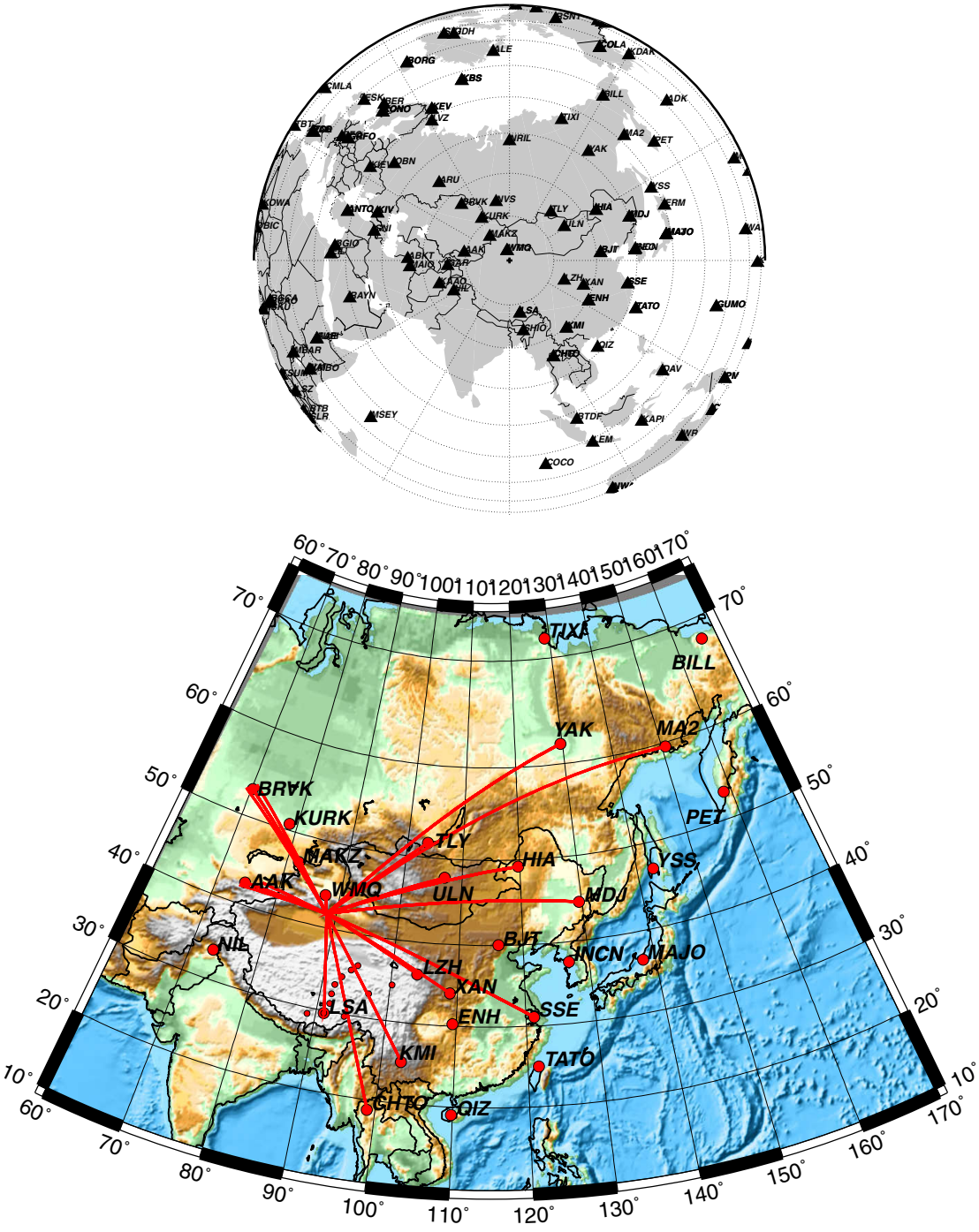


Figure 1. Maps showing teleseismic and regional station distributions with regional paths.

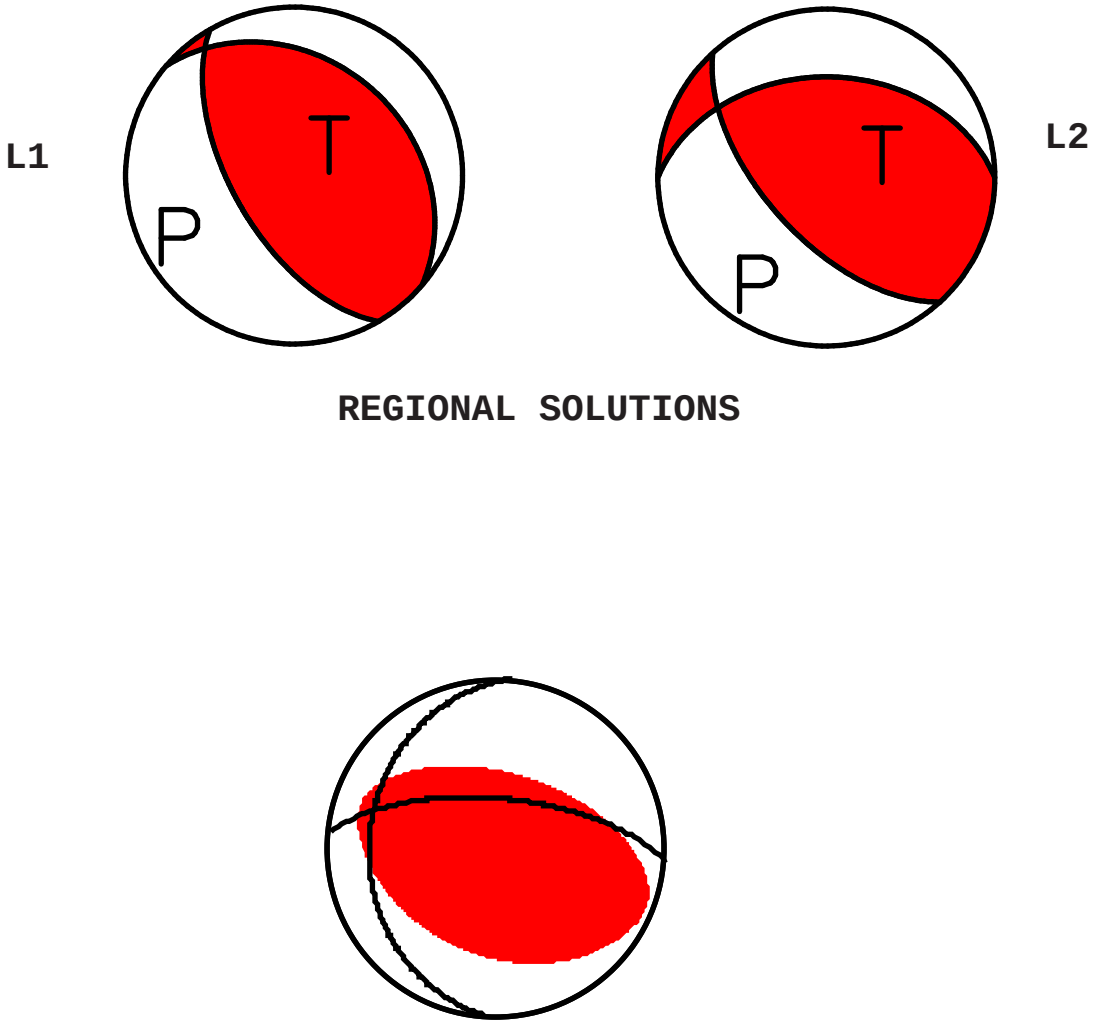


Figure 2. Comparison of regional solutions using L1 and L2 norms for the grid search and the CMT mechanism.

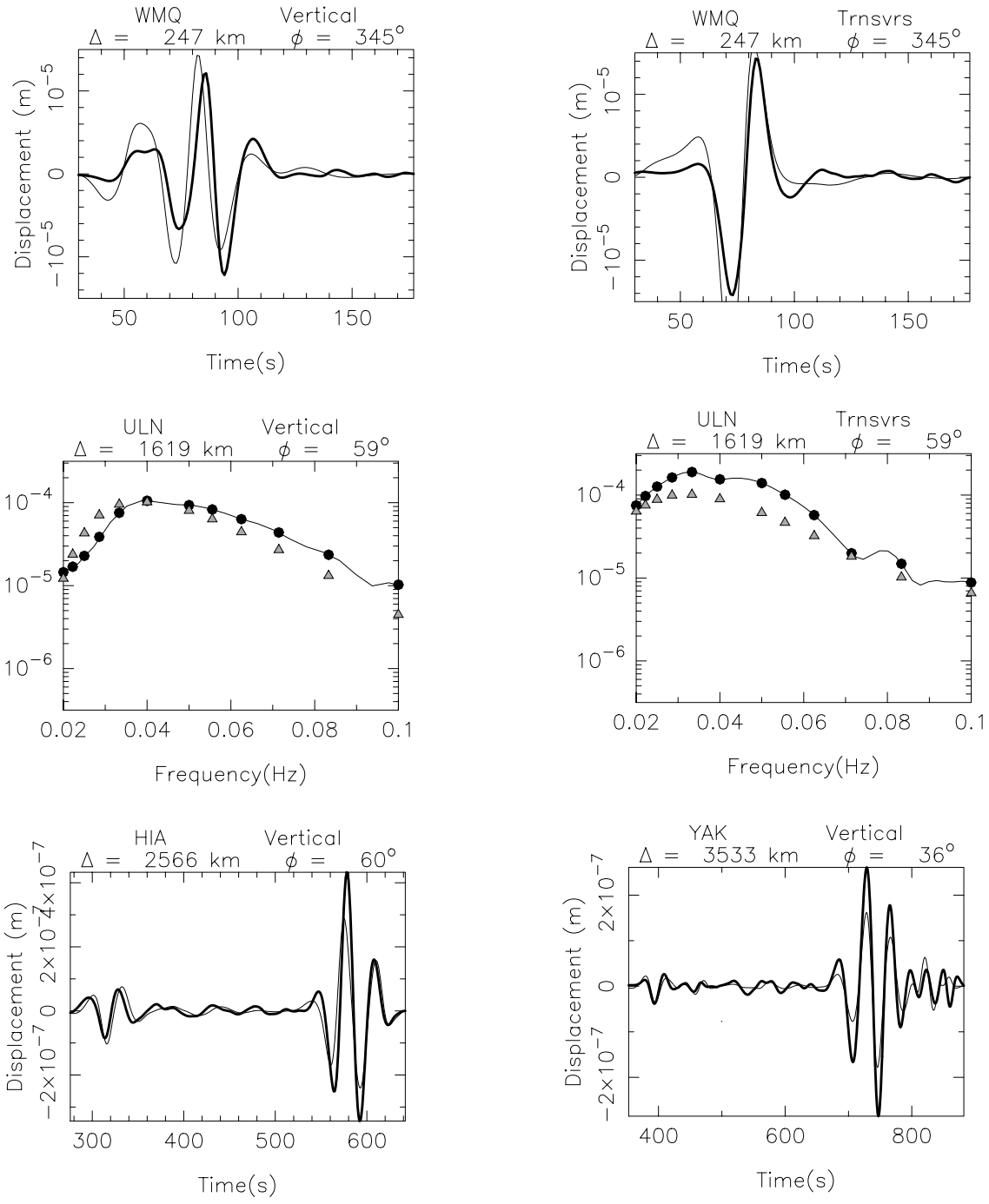


Figure 3. Examples of fits for regional time domain seismograms, regional surface wave spectra, and far regional and teleseismic bodywaves.

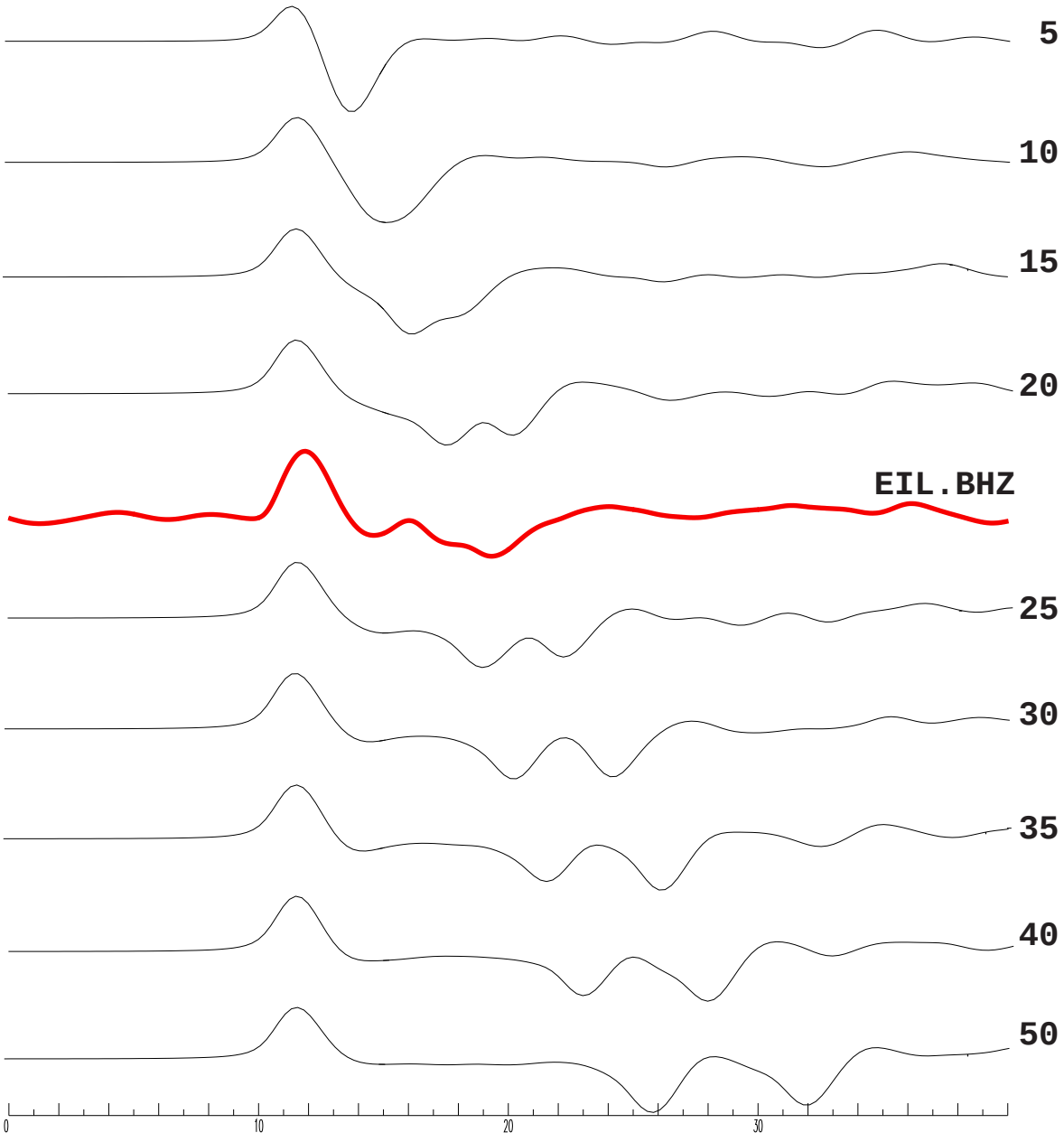


Figure 4. Comparison of observed vertical displacement at EIL and Green's functions calculated for a range of depths.

ACOUSTIC FLUIDIZATION OF CRUSHED ROCK BEHIND THE SHOCK FRONT BY DAMAGE-INDUCED SECONDARY SEISMIC RADIATION

Charles G. Sammis
Department of Earth Sciences
University of Southern California
Los Angeles, CA 90089-0740

Sponsored by DoD (DSWA)
Grant No. DSWA01-97-1-0005

ABSTRACT

Secondary seismic radiation is generated by rock fracture in the "damage zone" of an underground nuclear source and by frictional sliding on preexisting fractures in the "non-linear elastic zone" at larger distances from the shot point. This radiation is important for two reasons: (1) Johnson and Sammis [2000] have shown that it can make an important contribution to the far-field seismic signal, and (2) Sammis [1998] has argued that it can also significantly weaken the granulated rock behind the shock front in the damage zone. This weakening is due to a mechanism called acoustic fluidization originally proposed by Melosh [1979] to explain long-run-out landslides, the fluid morphology of extraterrestrial impact craters, and the low coefficient of effective friction inferred for the San Andreas fault. Such weakening has been shown to be necessary if computer models are to simulate the pulse-broadening observed in the near-field of nuclear explosions in hard rock [Rimer et al., 1987; Rimer et al., 1998]. This paper shows how the secondary radiation calculations of Johnson and Sammis [2000] can be used to calculate the intensity of the high frequency acoustic field behind the shock front and, thereby, to quantitatively assess the strength reduction due to acoustic fluidization.

Key Words: seismic sources, discrimination.

OBJECTIVE

The objective of this research project is to understand the physics of rock fragmentation and subsequent deformation in the source region of a nuclear explosion detonated in crystalline rock. Rock fragmentation in the source region is important because it directly affects the seismic radiation observed in both the near and far field in at least two important ways:

1) The fragmentation process itself generates secondary high-frequency P and S waves that may affect seismic discrimination and yield estimates that use high-frequency local crustal phases.

2) Fragmentation behind the advancing shock front leaves a weakened region that is thought to produce the pulse broadening observed in the far field. A quantitative understanding of this observed pulse broadening is important if the frequency content of the far-field seismic signal is to be used for discrimination and yield estimates.

RESEARCH ACCOMPLISHED

Generation of secondary radiation by the damage process has been modeled by Lane Johnson and the author [Johnson, 1996,1997; Sammis, 1997; Johnson and Sammis, 2000]. They report that secondary seismic energy approaches 10% of the primary radiation.

The micromechanical damage mechanics developed by Ashby and Sammis [1990] has been successfully integrated into the spherically symmetric numerical simulation code at s-cubed through a collaboration between Rimer, Stevens and the author. Rimer et al. [1998]. Although these simulations gave a good description of the extent of the fracture damage near the source (as evidenced by Russian fracture measurements at their hard rock sites), they were unable to explain the observed seismic pulse broadening.

The problem appears to be that while the Ashby and Sammis damage mechanics gives a good description of compressive failure, it does not give an adequate description of the post-failure behavior of the damaged rock. In the s-cubed simulations, it was assumed that the strength of the rock fell to the level given by friction once it failed. This assumption was based on the behavior of granular layers tested under simple shear in the laboratory which are observed to deform according to a simple frictional rheology [Dieterich, 1981; Biegel et al., 1989; Marone and Kilgore, 1993; Sammis and Steacy, 1994;]. However, in order to simulate the observed pulse broadening, Rimer found that he had to reduce the coefficient of friction in the granulated rock to $\mu=0.02$, far below the value of $\mu=0.6$ commonly observed in the laboratory. The problem may lie in the fact that the laboratory measurements of friction in granular layers are made at very low sliding velocities on the order of microns per second whereas deformation rates in the nonlinear region of a nuclear source are very high and dynamic effects may be important.

A physical solution to this dilemma may lie in the "acoustic fluidization" of the granulated rock in the source region. Acoustic fluidization is a phenomenon proposed by Melosh[1979] to explain long run-out landslides on earth and the fluid-like morphology of large extraterrestrial impact craters. Melosh[1996] has recently proposed acoustic fluidization as the mechanism which explains the "heat flow paradox" in which the absence of a heat flow anomaly on the San Andreas fault implies that it slips at a very low effective coefficient of friction. This interpretation is supported by recent computer simulations of faulting in granular medium by Mora and Place [1998].

Acoustic fluidization occurs when high-frequency acoustic energy produces sufficiently large fluctuation in the normal stress between grains that local slip between grains becomes possible at a very low value of the applied stress. The theory developed by Melosh [1979] is necessarily statistical in nature since the stress fluctuations are spatially and temporally distributed throughout the granular medium. The central equation describing the rheology of a fluidized granular medium is

$$\dot{\varepsilon} = \frac{\tau}{\rho\lambda c}\left[\frac{1 - erf\left(s_c / 2^{1/2}\sigma\right)}{1 + erf\left(s_c / 2^{1/2}\sigma\right)}\right] \tag{1}$$

where:

τ = applied shear stress
ρ = density of the granulated rock
λ = wavelength of the acoustic energy
c = P wave velocity in the granulated rock
S_c = critical pressure amplitude in the P wave acoustic field to relieve the overburden pressure ρgh and allow sliding
= $\rho gh - \tau/\mu$
σ = variance of the normally distributed random acoustic P wave field.

Note that the strain rate is linear in the applied stress τ so the fluidized granular rock behaves as a Newtonian fluid with viscosity

$$\eta = \frac{\rho\lambda c}{2}\left[\frac{1 + erf\left(s_c / 2^{1/2}\sigma\right)}{1 - erf\left(s_c / 2^{1/2}\sigma\right)}\right] \tag{2}$$

In a strong acoustic field, $\sigma \approx s_c$ and

$$\eta \approx \rho\lambda c \tag{3}$$

Note that the viscosity is lowest for short wavelength acoustic energy (small λ) and that the low value of the P wave velocity (c) in the highly damaged rock also contributes toward lowering the fluidized viscosity.

There are two questions which must be answered before acoustic fluidization can be considered a viable process in the source region: 1) is a fully fluidized granulated layer weak enough to produce the observed pulse broadening and 2) is the secondary acoustic field strong enough to fully fluidize this layer? We begin with question (1). As a preliminary estimate, take ρ = 3 gm./cm^3, c = 1 km/s as typical values for granulated rock. Assume that the wavelength of the acoustic waves are of the same order as the flaw size that generates them and take λ = 1 cm. If the damaged rock is fully fluidized, the effective viscosity will be $\eta \approx \rho\lambda c = (3)(10^5)(1) = 3x10^5\, P$. The hoop strain during the Hardhat explosion at a distance of r=200 m from the shotpoint was about 7.5x10^{-3} [Rimer et al., 1987]. Since the inflation lasts for about 0.15 s, the strain-rate is about $\dot{\varepsilon} = 5x10^{-2}$ sec^{-1}. If the rock is fully fluidized, the stress required to produce this strain is $\sigma = \eta\dot{\varepsilon} = (3x10^5)(5x10^{-2}) = 1.5x10^4$ dynes/cm^2 ≈ 0.015 bars. Since this is well below the stress level in the granulated layer (Rimer, personal communication), we can conclude that acoustic fluidization can weaken the granulated layer sufficiently to produce the pulse broadening observed at Hardhat.

The second question is more difficult to answer and has been the focus of our current research. As a first step toward calculating the strength of the acoustic field in the granulated zone, Johnson and Sammis [2000] have converted the motions that occur on individual preexisting cracks into seismic moment tensors which may then be used to calculate secondary elastic waves that are radiated into the far field. This crack motion may be separated into sliding motion on the original shear crack that contributes a shear moment per unit volume of

$$m_s = \frac{9}{2}\frac{\lambda+2\mu}{\lambda+\mu}\frac{K_{Ic}}{(\pi a\cos\chi)^{1/2}}\frac{D_0}{\sin\chi\cos^2\chi}\left[\left(\frac{D}{D_0}\right)^{1/3}-1\right]^{1/2} \quad (4)$$

and a tensile opening of the growing "wing cracks" that contributes a tensile moment per unit volume of

$$m_t = \frac{3}{2}\frac{(\lambda+2\mu)^2}{\mu(\lambda+\mu)}\frac{K_{Ic}}{(\pi a\cos\chi)^{1/2}}D_0\left[\left(\frac{D}{D_0}\right)^{1/3}-1\right]^{5/2} \quad (5)$$

In these expressions:

λ and μ = Lame elastic constants
K_{Ic} = Critical stress intensity factor (a material property).
a = Half-length of the preexisting cracks
χ = Geometrical crack orientation factor
D_0 = Initial damage = $\frac{4}{3}\pi(a\cos\chi)^3 N_v$
D = Current damage = $\frac{4}{3}\pi(l+a\cos\chi)^3 N_v$
l = Length of tensile wing cracks
N_v = Number of initial shear cracks per unit volume

While the contribution from an individual crack is small, we found that the combined effect of many cracks in a large region of increased damage can generate secondary waves that are comparable in amplitude to the primary waves generated by the explosion. We performed the numerical integration over the areas of active damage using the following procedure:

- The region surrounding the source was divided into a large number of small volume elements
- The equivalent elastic method [Johnson, 1996, 1997] was used to calculate the principal stresses within each volume element as a function of time.
- The increase in damage (if any) within each volume element was determined using the Ashby and Sammis [1990] theory.
- The increase in damage was converted to a moment tensor using the above equations.
- The displacements at a given receiver location were calculated by summing the contributions from every volume element where there was an increase in damage.
- The vector displacements generated at the receiver location by the secondary waves from all volume elements were summed.

In Johnson and Sammis [2000] we estimated the secondary P and S wave energy in the far field generated by the damage process. We are now working on the high-frequency energy radiated back toward the source. The wavelength of this secondary radiation is determined by the size of the activated flaws that nucleate the damage and can be as short as millimeters. However, this radiation is incoherent and may not propagate beyond the active damage zone. More likely, the wavelength of the secondary radiation that propagates back toward the source will be determined by the width of the active damage zone that must be determined by further modeling. In any event, strong non-linear scattering (which we are also working on) of this inward traveling secondary radiation by the fragmented rock will probably produce the required stochastic acoustic field.

CONCLUSIONS AND RECOMMENDATIONS

Acoustic fluidization appears to be a promising mechanism to weaken the fragmented rock behind the shock front of nuclear explosions detonated in crystalline rock, and thus offers a physical solution to the long-standing mystery of the pulse broadening observed by Rimer et al. [1987]. The nearest natural analog to buried explosions is the formation of a large extraterrestrial craters which show clear morphological

evidence for the fluidization of the fragmented rock in the form of flat crater floors, central peaks, and wave-like ring structures [Melosh and Gaffney, 1983, Melosh et al., 1992].

We have recently developed the theoretical tools required to test the significance of acoustic fluidization in the source region of nuclear explosions. The spatial extent of source fragmentation can be calculated using the damage mechanics developed by Ashby and Sammis [1990] that has been implemented in the s-cubed source code. These calculations can be verified using Russian fracture measurements in hard rock nuclear explosions. The s-cubed code can also estimate the width of the active damage region and hence the dominant wavelength of the secondary radiation. The strength and frequency content of the secondary acoustic emissions from the nucleation and growth of fractures behind the shock front can also be calculated using the techniques developed by Johnson[1996, 1997] and Johnson and Sammis [2000]. We are currently working to put these elements together for a quantitative estimate of the role of acoustic fluidization in the highly damage source region of underground explosions and its effect on the waveforms of seismic radiation in the near and far field.

REFERENCES

Ashby, M.F., and C.G. Sammis, The damage mechanics of brittle solids in compression, PAGEOPH, 133, 489-521, 1990.

Biegel, R.L., C.G. Sammis, and J.H. Dieterich, The frictional properties of a simulated gouge having a fractal particle distribution, J. Structural Geology, 11, 827-846, 1989.

Dieterich, J. H. (1981) Constitutive properties of faults with simulated gouge, in *Mechanical Behavior of Crustal Rocks*., *Geophysical Monograph 24*. American Geophysical Union, 108-120.

Gaffney, E.S., and H.J. Melosh, Noise and target strength degradation accompanying shallow-buried explosions, J. Geophys. Res., 87, 1871-1879, 1982.

Johnson, L.R., The effect of damage on explosion generated waves, Proc. 18th Ann. Seismic Res. Symp, pp 195-198, 1996.

Johnson, L.R., The generation of S waves by explosions, Proc. 19th Ann. Seismic Res. Symp., pp 625-631, 1997.

Johnson, L.R. and C.G. Sammis, Effects of rock damage on seismic waves generated by explosions, PAGEOPH, in press, 2000.

Marone, C. and Kilgore, B. (1993) Scaling of the critical slip distance for seismic faulting with shear strain in fault zones, *Nature*, **362**, 618-621.

Melosh, H.J., Dynamical weakening of faults by acoustic fluidization, Nature, 379, 601-606, 1996.

Melosh, H.J., Acoustic fluidization: A new geologic process, J. Geophys. Res., 84, 7513-7520, 1979.

Melosh, H.J., and E. S. Gaffney, Acoustic fluidization and the scale dependence of impact crater morphology, Proc. 13th Lunar and Planet. Sci. Conf, J. Geophys. Res., 88, supplement, A830-A834, 1983.

Melosh, H.J., E.V. Ryan, and E. Asphaug, Dynamic fragmentation in impacts: hydrocode simulation of laboratory impacts, J. Geophys. Res., 97, 14735-14759, 1992.

Mora, P. and D. Place, Numerical simulation of earthquake faults with gouge: an unflawed explanation of the heat flow paradox, J. Geophysical Res., submitted, 1998.

Rimer, N., J.L. Stevens, and S.M. Day, Effect of pore pressure, fractures, and dilatancy on ground motion in granite, S-Cubed Report SSS-R-87-8670, 1987.

Sammis, C.G., and S.J. Steacy, The micromechanics of friction in a granular layer, PAGEOPH, 142, 777-794, 1994.

Sammis, C.G., Acoustic fluidization in the damage regime of explosions in crystalline rock, Proc. 20th Ann. Seismic Res. Symp., pp 417-421, 1998.

NEAR FIELD AND REGIONAL MODELING OF EXPLOSIONS AT THE DEGELEN TEST SITE

J. L. Stevens, N. Rimer, J. R. Murphy, and H. Xu
Maxwell Technologies, Systems Division

G. G. Kocharyan and B. A. Ivanov
Institute for the Dynamics of the Geospheres, Moscow, Russia

Sponsored by the Defense Threat Reduction Agency
Contract No. DTRA01-00-C-0050

ABSTRACT

Fundamental to the ability to monitor a Comprehensive Nuclear-Test-Ban Treaty is a good understanding of the nuclear explosion source. Considerable research has been done on the nuclear explosion source over the past 30 years, with mixed success. Although empirical and numerical models of explosion sources do a fairly good job of matching observed seismic signals, a good explanation of the physical basis for the explosion source has been elusive. In particular, numerical models of explosion sources developed using laboratory measurements of rock properties fail to predict observed near field ground motion in hardrock. The basic problem is that the strength of the rock measured in the laboratory is much larger than the apparent strength of the rock as determined from the near field ground motion. Furthermore, additional investigation shows that 1) The strength of the rock is not initially low, but rather decreases dynamically as the shock wave passes; and 2) the strength of the rock is reduced to a level well below that predicted for rubbleized rock under hydrostatic dynamic friction.

Maxwell Technologies and the Institute for the Dynamics of the Geospheres (IDG) are in the early stages of a research program directed towards improving the capability to predict the seismic source characteristics of underground explosions in rock. This will be accomplished by development of improved dynamic failure models, constrained by a much better data set than has been available in the past. Near field waveforms are only available from a small number of U.S. nuclear tests, and until recently none have been available from the testing program of the former Soviet Union. IDG now has near field records from at least 10 nuclear explosions at the Degelen test site that will be made available for the project. IDG will also provide near source material properties measurements for all of these events. This unique data set will place strong constraints on the numerical modeling work, as well as providing data from a new and important area to augment our previous data sets which have come primarily from the western United States. In addition, the Russians have data from a seismic line located north of the Degelen test site that was maintained with consistent instrumentation for many years during the Soviet testing program. The 9 seismic stations are spread out at approximately even intervals from the Degelen test site out to a distance of about 150 km. IDG will provide seismic data from these stations for all of the events that have near field records. This provides a rare opportunity to observe and model the seismic wavefield of the explosions as they evolve from the near field of the explosion out to regional distances.

Objective

The objective of this program is to improve the capability to predict the seismic source characteristics of underground explosions in rock. This is to be accomplished by development of improved dynamic failure models which will be constrained by a large unique data set of near field waveforms and parametric data from historic Soviet explosions at the Degelen test site. In addition, we will analyze regional seismic data along a seismic line located north of the Degelen test site that recorded data at 9 stations spaced approximately evenly from the test site to a distance of about 150 km. This project is a collaborative effort between Maxwell Technologies and the Russian Institute for the Dynamics of the Geospheres (IDG).

Research Accomplished

1. Introduction

This joint project between Maxwell Technologies and IDG has just started and still in its organizational stages. This paper therefore describes the background, motivation, and research plan for this project. The main objectives of the project are to obtain a better understanding of the explosion source function, and to model the evolution of the explosion source from the close in hydrodynamic region out to near regional distances. This is being accomplished through modeling of a unique data set of near source and near regional data to be provided by IDG.

Empirical and numerical models of explosion sources do a fairly good job of matching observed seismic signals, however a good explanation of the physical basis for the explosion source is still not satisfactory. In particular, numerical models of explosion sources developed using laboratory measurements of rock properties fail to predict observed near field ground motion in hardrock. This is illustrated in Figure 1, which shows the near field waveforms from the explosion PILEDRIVER together with waveforms from a finite difference calculation of the near field ground motion made using rock properties measured in the laboratory. The basic problem is that the strength of the rock measured in the laboratory is much larger than the apparent strength of the rock as determined from the near field ground motion. Furthermore, additional investigation shows that

1. The strength of the rock is not initially low, but rather decreases dynamically as the shock wave passes.
2. The strength of the rock is reduced to a level well below that predicted for rubbleized rock under hydrostatic dynamic friction.

A number of solutions to these problems have been proposed over the years, including the effective stress model (Rimer, et al, 1984), and various types of damage models. These models all have the characteristic that the material strength is reduced dynamically to a very low level when it fails. The effective stress model says that the weakness comes from water within the rock matrix, and that the broken rock in effect floats on water that is squeezed out of pores or fractures when the rock fails. Although there are questions about the realism of this physical model, it works fairly well to explain the near field waveforms. Figure 2 shows a comparison of the PILEDRIVER waveforms with waveforms calculated using the effective stress model. The agreement is quite good, particularly at the closer two stations. Furthermore, when the PILEDRIVER solution was scaled to the appropriate yield and compared with other US explosions in granite (Hardhat and Shoal), agreement with the observed waveforms was also quite good (Stevens, et al, 1986).

Under a recently completed DTRA contract, Maxwell Technologies worked together with the Russian Institute for the Dynamics of the Geospheres, (IDG) and the University of Southern California, to develop improved micro-mechanical material models. IDG provided extensive measurements of material properties close to nuclear and chemical explosions both before and after the explosions were detonated (Rimer, et al, 1998). In addition, we implemented the damage mechanics model which was developed by Prof. Charles Sammis at the University of Southern California into Maxwell's nonlinear finite difference codes and used this model to simulate the observed explosion damage and a small set of near field waveforms that were also provided by IDG. The results of this work are discussed in detail in the final report (Rimer et al, 1999). The damage model referred to above actually applies to the growth and coalescence of cracks just prior to failure, and does not predict what happens to the rock after failure occurs. Calculations using the damage model followed by a rubbleized model with realistic values of friction did not provide enough strength reduction and thus did not match the near field data. We were more successful in matching the data by dropping the coefficient of friction to very low values (as low as 0.02), but this again leaves the question of what physical mechanism could be responsible for these very low values and corresponding low strength.

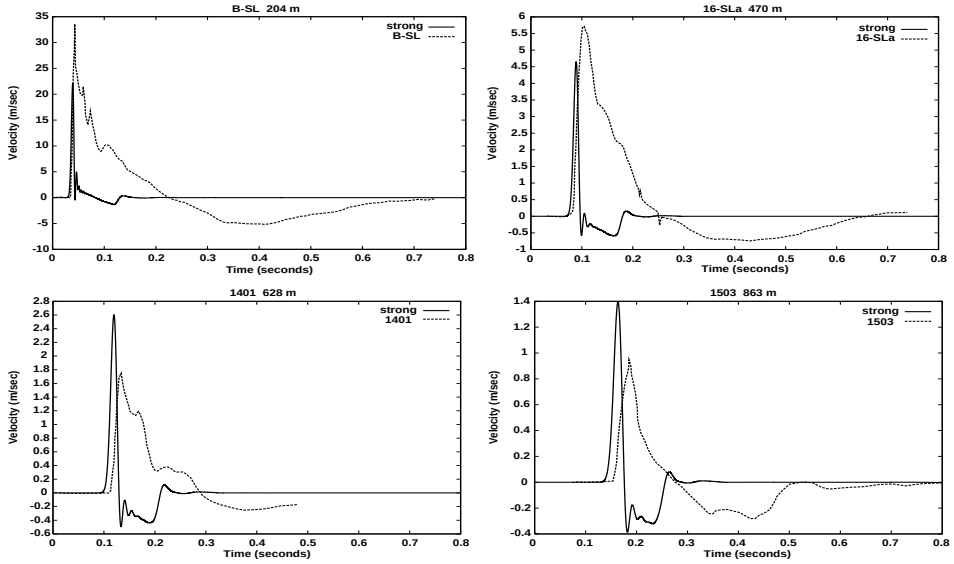


Figure 1. Particle velocity measurements at working point depth from PILEDRIVER compared with data from a calculation using the laboratory strength of granite with no weakening.

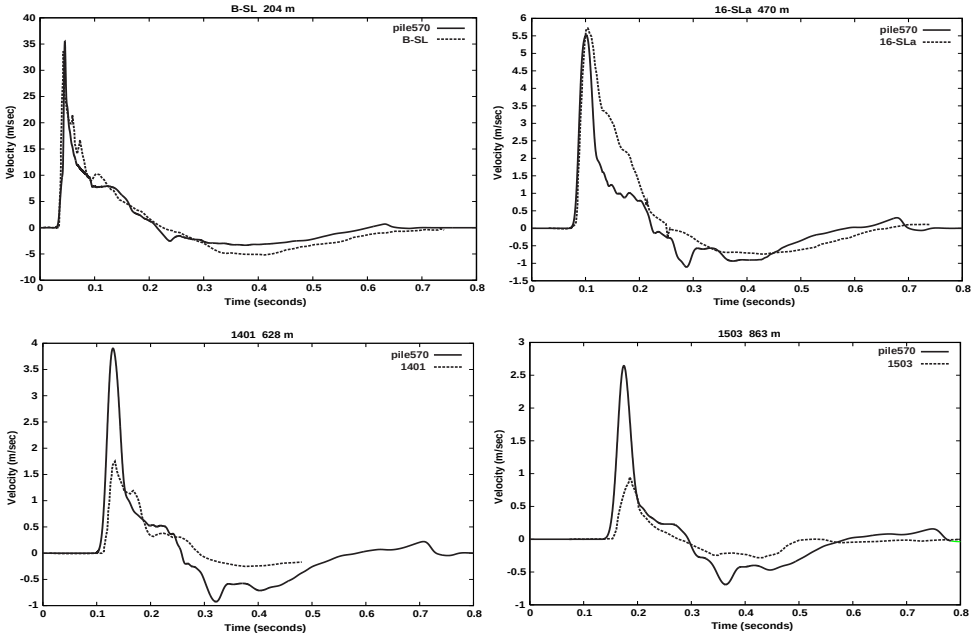


Figure 2. Particle velocity measurements at working point depth from PILEDRIVER compared to numerical simulation pile570 using the effective stress law.

A possible answer initially proposed by Melosh (1979) is "acoustic fluidization". The physics behind this mechanism is that during the fracturing process there is a complex dynamic acoustic wavefield that causes high frequency vibrations in the broken rock. These vibrations cause rapidly changing regions of high and low normal stress, and remove the frictional normal stress from parts of the rock as it moves. Consequently parts of the rock are not confined by the frictional stress and in effect have much lower strength. Acoustic fluidization has been used to explain other phenomena such as landslides and craters (Melosh and Ivanov, 1999), which have been similarly difficult to explain because of anomalously low apparent friction.

The numerical modeling to be accomplished in this project will be constrained by a much better data set than has been available in the past. Near field waveforms are only available from a small number of U.S. nuclear tests, and except for those few referenced above, none have been available from the testing program of the former Soviet Union. IDG has near field records from a number of nuclear explosions at the Degelen test site that will be made available for this project. IDG will also provide near source material properties measurements for all of these events. This unique data set will place strong constraints on the numerical modeling work, as well as providing data from a new and important area to augment our previous data sets which have come primarily from the western United States. In addition, IDG has data from a seismic line located north of the Degelen test site that was maintained with consistent instrumentation for many years during the Soviet testing program. Figure 3 shows a map illustrating the location of the test sites and the seismic stations. The 9 seismic stations are spread out at approximately even intervals from the Degelen test site out to a distance of about 150 km. IDG will provide seismic data from these stations for all of the events that have near field records. This provides a rare opportunity to observe and model the seismic wavefield of the explosions as they evolve from the near field of the explosion out to regional distances. The data that IDG has identified to date for this project are listed in Table 1.

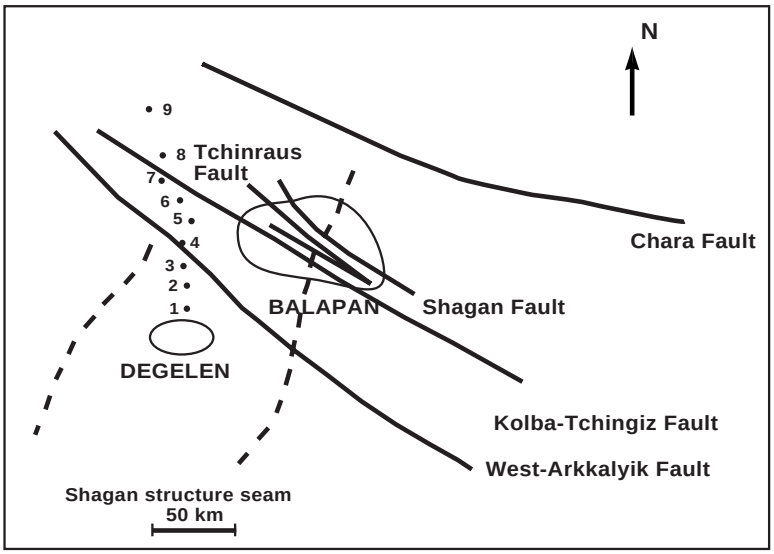


Figure 3. Map showing the locations of the former Soviet Degelen and Balapan test sites, faults, and seismic stations in the region. We will analyze near field waveforms from the Degelen test site, and seismic data recorded at stations 1 through 9 north of the test site for the same events.

2. Numerical Modeling of Explosions

The parameters used in numerical simulations of underground nuclear explosions are constrained by laboratory material properties tests and by direct observations of ground motion from underground explosions. Quasi-static laboratory tests on small rock samples are used to determine the following parameters: density, elastic moduli, pressure-volume (P-V) relation, material strength, porosity, and water content. Of these quantities, the density, moduli, and P-V relation seem to be quite consistent with *insitu* rock properties. In brittle hardrocks such as granite, porosity and water content are more variable *insitu* due to the presence of joints and are therefore less well constrained by laboratory data. Laboratory measurements of strength for brittle hardrocks seem to be very inconsistent with *insitu* strength as inferred by modeling of underground explosions. In particular, finite difference calculations of ground motion in granite, made using the laboratory measurements of shear strength, have invariably given much narrower particle velocity pulses and much smaller displacements than those measured in the field.

Table 1. Degelen events with near field and/or seismic records.

Date	Number of near field records	Distance range, m	Number of seismic records	Distance range, km
1988/04/22	2	69-183	3	57-81
1988/11/23	4	280-475	9	14-83
1987/07/17	14	170-900	7	14.5-84
1987/10/16	4	55-132	8	20-76
1989/10/04	4	45-285	8	16-85
1981/07/17	3	115-310	8	15-80
1965/02/04	4	147-750	9	14-83
1964/05/16	4	150-600	9	13-80
1966/03/20	4	300-600	9	15-84
1966/02/13	4	350-600	9	14-80
1973/12/31	4	110-230		
1974/12/16	4	100-200		
1978/03/26	5	76-270		
1980/06/25	3	155-310		
1982/12/25	4	90-190		
1984/10/18	4	35-110		
1968/07/12	2	80-90		
1968/12/18	3	200-510		
1970/06/28	2	200-240		
1980/09/25	3	100-160		
1971/12/15			9	7.5-85
1987/05/06			9	13-83
1987/12/20			9	13-83
1988/10/18			9	11-77
1989/02/17			9	10-77

Constitutive models have been developed (Rimer and Lie, 1982, Rimer, et al., 1984) which attribute this weaker behavior of *insitu* granite and other rocks under explosive loading to ground-motion-induced rock damage or pore fluid pressure increases. These models have been shown by Day, et al, (1983) and Rimer, et al, (1986), (1987), using one- and two-dimensional calculations, to accurately reproduce the pulse broadening and most other aspects of the ground motion data from U.S. events in granite (PILEDRIVER, for example). The models for granite have since been used to simulate the seismic source function from explosions conducted in the Soviet Union (Stevens, et al, 1991, for example). Figure 2 compares the particle velocity measurements at working point depth from the 62 kt PILEDRIVER event with the results of the pile570 numerical simulation, made using the effective stress model discussed in Rimer, et al (1984, 1998, 1999). Numerical results from pile570 are also in good agreement with the measured cavity radius and with the estimated seismic source function. For this simulation, effective stress model parameters were calibrated to best match the velocity peak and pulse shape at the closest-in gauge station (B-SL). This required a rapid buildup of pore pressure during the loading, leading to a large strength reduction very near the propagating shock front. Note that the pulse shapes at all four stations are rather consistent, with all including a long duration shallow negative velocity pulse. The peak velocities at the two smallest ranges agree very well with the simulation, but the measured peaks at the two larger ranges are a factor of two or more lower than the calculated peaks. The two closest PILEDRIVER gauges were located along roughly a 180 degree different azimuth than the other more distant gauges. However, a connection between possible site anisotropies and the measured ground motions has never been established. It should be noted that the 5.9 kt HARDHAT event, which was detonated in similar rock, near the later PILEDRIVER event, but at a shallower depth of burial, gave particle velocity pulses which were more similar to the PILEDRIVER pulses at the larger ranges. (See Rimer, Stevens, and Day, 1987, for a comparison between the results of the pile570 simulation and the HARDHAT measurements.)

The constitutive models used in these simulations are phenomenological in nature and do not explicitly account for the dynamic response of the *insitu* fractures in the source environment. That is, crystalline rock massifs in the earth's crust are heterogeneous over a wide range of scales from micro-cracks in grains at the micron scale to faults and joints which span many tens of kilometers. It has been observed that this fracture heterogeneity is responsible for nonlinear effects near the source of underground explosions which affect seismic coupling and the resultant seismic waveform. Very near the source, pre-existing cracks nucleate new fractures which granulate the rock, thereby significantly reducing its shear strength and elastic moduli. At greater distances, a network of radial tension cracks are formed which also degrade the mechanical properties of the rock. Even at large distances, movement on pre-existing faults and joints can produce significant deviations from numerical computer simulations which assume a simply connected elastic continuum.

Over the past several years, Professor Sammis and his associates at the University of Southern California have been working to understand the physics and micro-mechanics describing the nucleation and growth of new fractures from pre-existing cracks in crystalline rock under the compressive loading states inherent in laboratory tri-axial compression tests. Similar compressive loading states characterize the shock wave loading near the source of an underground explosion. This work (see Sammis and Ashby, 1988, Ashby and Sammis, 1990, and Sammis, 1991) has resulted in a damage mechanics formulation which is suitable for incorporation into numerical simulation codes. The model introduces a damage parameter, related to the increase in flaw size from its pre-shot average value. Damage accumulates as the flaws extend during the compressive loading and reaches some maximum value at which the rock fails unstably. The model gives no guidance to rock behavior after unstable failure. Incorporation of this damage mechanics formulation into a finite difference code, and subsequent testing and validation of the revised models, were the main topics of Rimer, et al (1998, 1999). Adaptation of the Sammis damage mechanics model for use in the ground motion simulation code is summarized in Rimer, et al (1998). The key input parameter to this model, in addition to the usual elastic moduli, is the average initial flaw size at the rock site. Since unstable compressive failure of a rock element is calculated using the adapted model to occur relatively early in the dynamic motions of interest here, i.e., usually near the propagating shock front, additional modeling was incorporated to complete the description of the stress field after this failure. Limiting the magnitude of deviatoric stresses in a failed rock element through the use of a standard friction law was shown to not provide sufficient strength reduction to simulate the ground motion measurements. In particular, calculated particle velocity time histories were still much narrower than the measured pulses for all reasonable choices of initial flaw size.

The additional strength reduction required to sufficiently broaden the particle velocity pulses was obtained by using a shear damage model originally developed for soft rocks such as tuff, described in Rimer and Proffer (1991). As discussed in Rimer et al (1999), this shear damage model was applied here only for rock elements that had experienced the onset of unstable compressive failure. Thus, a rock element was allowed to undergo significant damage before application of this treatment. The post-failure shear damage model performs an interpolation between the standard coefficient of friction of 0.60 and much lower "effective friction" values of 0.02-0.20 in the friction law used to limit deviatoric stresses. This linear interpolation is based on the maximum shear strain experienced by the failed rock element.

A possible physical mechanism for this strength reduction is the "acoustic fluidization" concept proposed by Melosh (1979) to explain the low strengths (or very low angles of internal friction) apparent in a number of geologic processes, such as seismic faulting, impact crater slumping, and long runout landslides. The main concept of this proposed mechanism is that "sufficiently strong acoustic waves in rock debris can momentarily relieve the static overburden in limited regions of the rock mass, thus allowing sliding to occur in the unloaded region. If this happens frequently enough, flow of the entire rock mass results." In terms of the explosively-induced ground motions of interest here, only the mass of failed or fractured rock, as given by the Sammis damage mechanics formulation, would have the potential for acoustic fluidization. The dynamic fracturing process, by itself, provides enough energy to generate sufficiently strong oscillations post-failure to reduce the "effective normal stress/effective friction" to the low values required in the weak core region near the cavity.

We have not yet developed a first principles relationship between the effective friction coefficient in a (failed) rock element and calculated quantities such as perhaps total energy, kinetic energy, or accumulated damage. The effective friction coefficient for complete damage in the calculations to date is simply an input number, taken from the examples given by Melosh. Most of his examples, however, correspond to far less dynamic situations. For the

explosive induced ground motions of interest here, an effective viscosity approach, rather than the effective friction approach used so far, may prove to be a more physically reasonable treatment.

A series of calculations were made using the Sammis modeling, quantifying the effect of model parameters on particle velocity pulse shapes, cavity radius, and RDP. The simulation which best fits all of the PILEDRIVER ground motion data is Run PD10. Comparisons with measured particle velocities are shown in Figure 4. In contrast with the results of pile570, made with the effective stress model, PD10 provides a much better fit to the PILEDRIVER data at the two larger ranges, while underestimating peak velocities at the closest ranges. Subsequent analyses showed that the timing of the strength reductions for the two models were somewhat different, with the effective stress model providing an earlier reduction than the present damage model. However, calculated cavity radius and RDP with the new model are in as good agreement with the measurements as were those with the more traditional model.

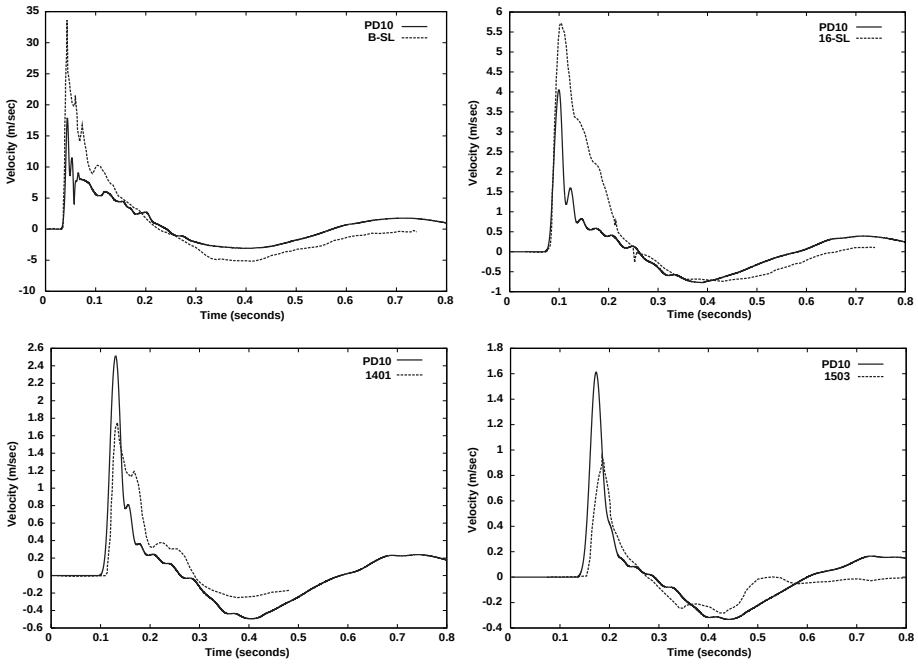


Figure 4. Calculated particle velocity pulses at four ranges for Run PD10 and PILEDRIVER measurements.

The PD10 shear damage model begins the reduction in friction coefficient from the standard coefficient of 0.60 once failed elements experience a maximum shear strain of 0.1% or greater. The reduction to the lower effective friction coefficient of 0.02 for failed rock elements is completed for 3% shear strain or greater. In practice, calculated pulse widths were found not to be very sensitive to an order of magnitude increase in the value of shear strain used to initiate the interpolation since the onset of unstable failure usually occurred at much higher shear strains in the simulations. However, particle velocity pulse widths were sensitive to the choice of shear strain magnitude required for full strength reduction, with lower values of this parameter resulting in longer pulse duration and larger RDP. It is important to emphasize that while the shear damage model (or some other post-failure strength reduction model) is crucial to successful simulation of the ground motion data, it is the micro-mechanical damage mechanics model which primarily determines the size of the central core of weakened rock.

Rimer, et al (1998) also contained extensive data sets on the density and morphology of the near-source fracture sets generated by several large chemical and nuclear explosions detonated in crystalline rock in the Soviet Union. These data, obtained from IDG, consist of comparisons of pre-shot and post-shot fracture densities, aperatures, lengths, and/or P-wave velocities *versus* scaled range ($m/kt^{1/3}$) from 11 explosions (two of these were multiple events).

Included with these *insitu* measurements and observations are average material properties data (densities, porosities, ultrasonic velocities, and unconfined strengths) obtained from laboratory tests on pre-shot core samples from each explosion site. For several of these events, laboratory measurements on post-shot core samples quantified explosion-induced increases in porosity near the cavities. Based on these data sets, the scientists at IDG have also developed empirical relations which scale rock damage with distance and explosive yield. These data place important constraints on nonlinear source models and were used to help validate the damage mechanics formulation.

More recently (Kocharyan, et al, 1998), IDG has also provided near-field dynamic ground motion data, more specifically, radial particle velocities *versus* time at several ranges from three of the underground explosions at Degelen Mountain for which fracture data were presented earlier. In Rimer, et al (1999), comparisons are made between the PILEDRIVER ground motion data and the Degelen data (scaled to the PILEDRIVER explosive yield). Following are some results of these comparisons:

- The Degelen ground motions in general do not show the long duration, shallow negative velocity pulses characteristic of PILEDRIVER and other U.S. events in granite (and other rocks).
- Peak velocities from Degelen events are in good agreement with the PILEDRIVER records at the larger scaled ranges, but are significantly smaller than those at the two closest ranges shown in Figures 1 and 2.
- Positive velocity pulses from the Degelen events, when scaled to PILEDRIVER yield, are of slightly smaller duration than those from PILEDRIVER. This appears consistent with the smaller post-shot cavities reported by IDG, 7-9 scaled meters, versus 10-11 scaled meters for PILEDRIVER.

In contrast to the differences in measured cavity radii and near-field ground motions between the two granite test sites, the seismic evidence (i.e., m_b/yield relations) strongly suggests that the seismic source coupling at the Degelen site is very comparable to that of PILEDRIVER. (See Murphy, 1993.) In general, the granite at the U.S. test site has quite similar material properties to that of the Degelen site. Laboratory measurements for the U.S. rock do show a slightly higher mass density and wave speed, and much lower porosities, 0.1-0.3%, compared to 2-3% for Degelen material. Measured strengths are very similar. Traditional ground motion calculations made with these different material properties do not explain the differences between the ground motion measurements at the two sites. These ground motion differences may be the result of differences in the *insitu* structures of the two granite sites, such as joint, faults, and other fractures, their orientation and spacing.

For the Degelen explosions, where both dynamic ground motion and fracture extent data are available, model parameters were varied to match as much of the data set as possible in order to understand the constraints of these data. The best Degelen calculation, Run DE12, on average, provided a reasonably good simulation of the IDG measurements/observations of particle velocity pulses, cavity radius, and RDP, as well as the increases in porosity and decreases in P-wave velocity as a function of post-shot range from the explosion working point. Figure 5 compares the particle velocity pulses from Run DE12 with the measurements from three Degelen explosions, labeled N1, N8, and N9, all scaled to the PILEDRIVER yield. The simulation is in good agreement with measured peak velocities at five of the six ranges. However, DE12 also shows a second peak or plateau at all six ranges, while such a second signal is readily apparent for only two of the somewhat inconsistent gauge records (although oscillations on three of the other gauge records can be construed as indications of second signals). Large negative pulses, comparable to the simulation, are measured only at some of the larger scaled ranges.

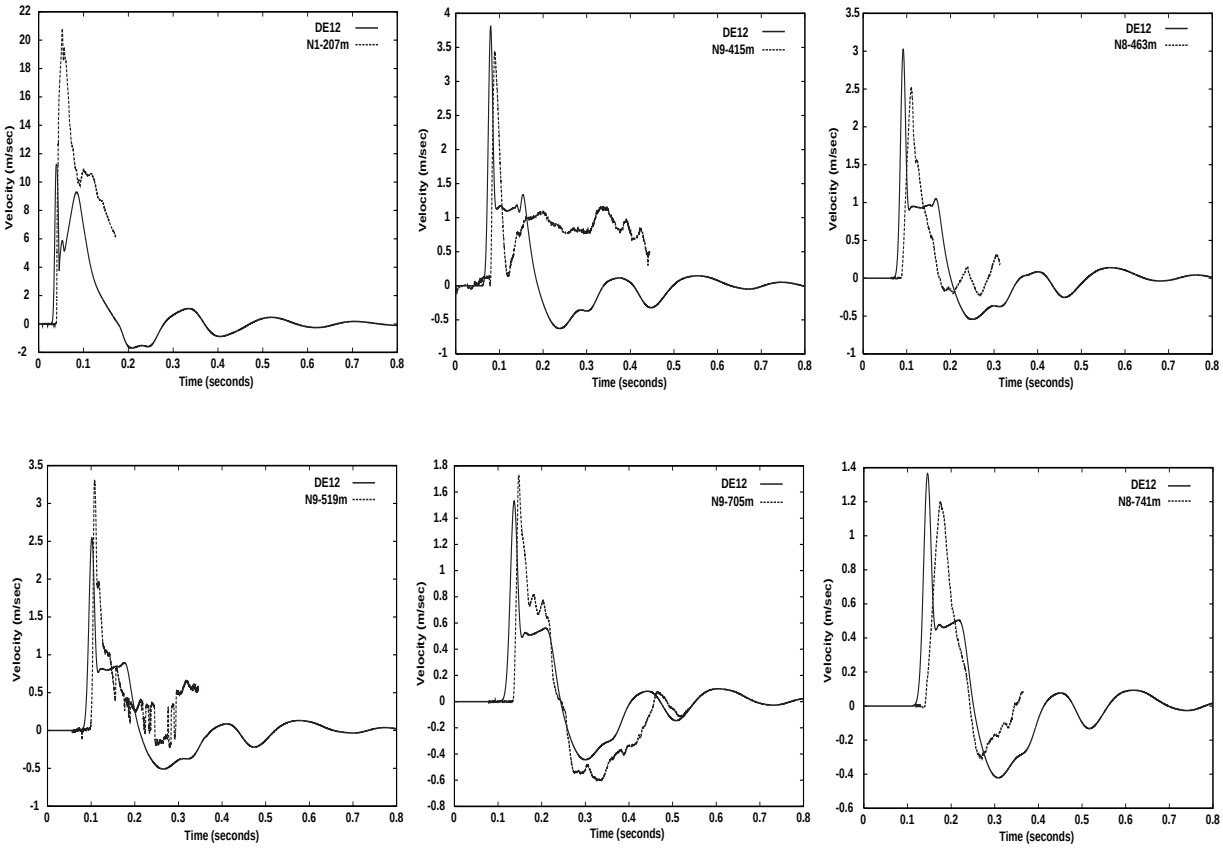


Figure 5. Calculated particle velocity pulses from Run DE12, which includes dilatancy, compared with the Degelen measurements.

In the calculations, the second signal is the result of a dilatant model relating decreases in bulk modulus to increases in the calculated damage parameter. This dilatant model and the non-dilatant model for decreases in shear modulus with damage accumulation are used to simulate the large observed P-wave velocity decreases near the cavity. The dilatant bulk modulus reductions also lead to calculated decreases in mass density (increases in porosity) very near the cavity. P-wave velocities from Run DE12 have been plotted *versus* post-shot range in Figure 6 along with the calculated increases in porosity in the rock near the cavity as a result of the explosion. (An initial porosity of 3% is assumed. Inclusion of this porosity, which was assumed to be crushable only at stress levels in the tens of kilobars, had no significant effect on the calculated pulses.) Comparisons are also shown with the data as reported by IDG. These include both the empirical fit to the post-shot P-wave velocity measurements given by IDG (scaled here to 62 kt) and reported variations in P-wave velocity and porosity data in the most damaged regions of rock surrounding the cavity.

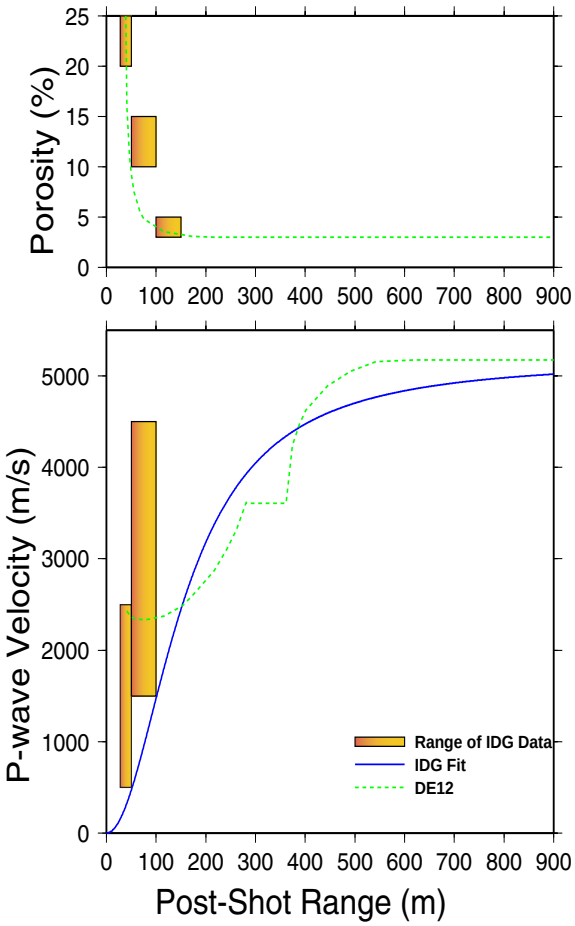


Figure 6. Calculated P-wave velocities and porosities *versus* post-shot range from Run DE12 compared with the data reported by IDG.

Near the cavity, the calculated minimum P-wave velocity of 2335 m/s was well within the variation of the measurements in this region. The slight increase in calculated P-wave velocity close to the cavity wall is not due to increases in calculated bulk or shear modulus. Rather, it results from decreased rock density (increased porosity) in this dilatant region. Further from the cavity, calculated P-wave velocity increases are also well within the data scatter which underlies the IDG empirical fit. The calculation however, shows a plateau in P-wave velocity, or more precisely, a plateau in the accumulated damage which determines the shear and bulk moduli. This plateau, which extends inward from the end of the failed region, encompasses all of the rock elements for which tensile failure was calculated before the onset of unstable compressive failure. At larger ranges, tensile failure was calculated to occur out to approximately the end of the partially damaged region, which in this computational model, also marks the end of post-shot P-wave velocity decreases.

Porosity is calculated to increase from its nominal 3.0 percent initial value only near the cavity. Although the results agree fairly well with the data, Run DE12 shows on average somewhat smaller increases at a given range, with very large porosity (42.5%) calculated only in the grid zone adjacent to the cavity. (As a result of grid rezoning during the calculation, this grid zone actually encompasses the first eight of the initial grid zones.) It is very possible that the very simple model used to introduce dilatancy here is inadequate. However, it is much more likely that the *insitu* rock near the cavity has experienced significant asymmetric block motion which cannot be reproduced using our spherically symmetric code. The calculated RDP and cavity radius from Run DE12 are in good agreement with the observations. Dilatancy in the calculations acts to increase RDP and decrease cavity radius. Although we found it difficult, it may also be possible to simulate the observed RDP and cavity radius without introducing dilatancy by changing other parameters in our constitutive model. Without some dilatancy model however, rock porosity does not increase near the cavity.

In summary, it has been shown in Rimer et al (1999) that most of the available ground motion and damage data from Degelen Mountain explosions in granite may be simulated reasonably well using spherically symmetric calculations with the modified Sammis micro-mechanical damage mechanics model. For reasonable initial flaw size estimates, however, this model predicts compressive failure to roughly a factor of two larger range than the range of intensive failure estimated by IDG from their data analysis. This is not understood as yet. It should be emphasized that simulation of the Degelen ground motion and damage data requires the use of model parameters which are considerably different from those used to simulate the ground motion data from U.S. PILEDRIVER explosion in similar granite. For example, Run DE12 used a damaged effective friction of 0.20 rather than 0.02, and larger shear strain magnitudes (6%) to reach full damage in order to simulate the narrower particle velocity pulses. It is possible that other combinations of model parameters might provide as good a simulation of these Degelen data as those used in Run DE12. Nevertheless, it has been demonstrated that the following model features are important in simulating these data:

- A post-failure damage model gives the central core of weakened rock required to sufficiently widen the particle velocity pulses. The strength of this weakened core is determined by parameters of this damage model.
- Parameters of the micro-mechanical damage mechanics model determine the radial extent of this weakened core.
- Dilatant reductions in bulk modulus are required to simulate the P-wave velocity and porosity measurements.

Key Words: Rock Mechanics, Degelen, explosion, numerical modeling

REFERENCES

Ashby, M.F. and C.G. Sammis (1990), "The Damage Mechanics of Brittle Solids in Compression," PAGEOPH, Vol. 133, No. 3.

Day, S. M., N. Rimer and J. T. Cherry (1983), "Surface Waves from Underground Explosions with Spall: Analysis of Elastic and Nonlinear Source Models," BSSA, 73, pp. 247-264.

Kocharyan, G.G., B.A. Ivanov, and V.N. Kostyuchenko (1998), "Rock Damage and Estimated Seismic Source Parameters of Underground Explosions in Hardrock," Russian Acad. Sci., IDG Final Report on Subcontract 9-11439-KLW, December.

Melosh, H.J. (1979), "Acoustic Fluidization: A New Geologic Process?," J. Geophys. Res., 84, 7513, December.

Melosh, H.J., and B.A. Ivanov (1999), "Impact Crater Collapse," Annual Rev. Earth Planet Science, 27, pp385-415.

Murphy, J.R. (1993),"Comment on 'Q for short-period P waves: is it frequency dependent?' by Alan Douglas", Geophys. J. Int., 113, p535-540.

Rimer, N. and K. Lie (1982), "Numerical Simulation of the Velocity Records from the SRI Grout Spheres Experiments," S-CUBED Topical Report DNA-TR-82-54, September.

Rimer, N., S. M. Day, G. A. Hegemier, H. E. Read, S. K. Garg, and S. Peyton (1984), "Effect of Pore Fluid Pressure on Explosive Ground Motions in Low Porosity Brittle Rocks," S-CUBED Final Report DNA-TR-85-245, July.

Rimer, N., J. L. Stevens, and K. H. Lie (1986), "Effects of Pore Pressure and Fractures on Ground Motion in Granite," S-CUBED Final Report DNA-TR-86-227, June.

Rimer, N., J. L. Stevens, and S.M. Day (1987), "Effects of Pore Pressure, Fractures, and Dilatancy on Ground Motion in Granite," S-CUBED Final Report AFGL-TR-87-0136, April.

Rimer, N. and W. Proffer (1991), "Containment Phenomenology Using a New Shear-Strain-Based Computational Damage Model for Tuff," S-CUBED Technical Report SSS-DTR-91-12612, September, also SSS-DTR-90-11961, October.

Rimer, N., K. Lie, J.L. Stevens, J.R. Murphy, and G.G. Kocharyan (1998), "A Micro-Mechanical Damage Model for Estimating Seismic Source Characteristics of Underground Explosions in Hardrock," Maxwell Technologies Technical Report MFD-DTR-98-15985, January.

Rimer, N., J.L. Stevens, J.R. Murphy, and G.G. Kocharyan (1999), "Estimating Seismic Source Characteristics of Explosions in Hardrock Using a Micro-Mechanical Damage Model," Maxwell Technologies Final Report MTSD-DTR-99-16423, July.

Sammis, C.G. and M.F. Ashby (1988), “The Damage Mechanics of Brittle Solids in Compression,” AFGL-TR-88-0160, July.

Sammis, C.G. (1991), “A Damage Mechanics Source Model for Underground Nuclear Explosions,” PL-TR-91-2103, August.

Stevens, J. L., N. Rimer, and S. M. Day (1986), "Constraints on modeling of underground explosions in granite," S-CUBED annual report to Air Force Geophysics Laboratory, AFGL-TR-86-0264, SSS-R-87-8312, October.

Stevens, J.L., T.G. Barker, E.J. Halda, J.R. Murphy, and N. Rimer (1991), “Simulation of Teleseismic Body Waves from Underground Explosions Beneath Sloping and Flat Surfaces Using Nonlinear Axisymmetric Finite Difference Calculations,” S-CUBED Technical Report DNA-TR-91-5, July.

4. Regional Seismic Wave Propagation

CRUSTAL PHASE PROPAGATION: DISCRIMINATION AND CORRECTIONS

G. Eli Baker, Mariana Eneva, Jeffry L. Stevens, and Heming Xu
Maxwell Technologies, Systems Division

Sponsored by the Defense Threat Reduction Agency
Contract No. DSWA-01-97-C0130

ABSTRACT

The primary objective of this work is to improve the accuracy of discrimination of nuclear explosions from earthquakes, by developing and implementing a transportable path correction algorithm for the Lg/Pg discriminant. A secondary result is the development of a depth discriminant based on Lg group velocity.

A key to understanding Lg and Pg amplitude changes, which can be dramatic over just 10s of kilometers, is using observations of such changes over short distances. We analyze changes in Lg and Pg along short paths between southern California seismic network (SCSN) stations for relationships between propagation and statistics of topography, gravity, and crustal thickness. A second key element of our approach is the use of categorical statistical techniques, which frees us from the common and generally unsupported assumption of a linear relationship between geophysical parameters and propagation. The principle underlying this approach is that distinct crustal or path types that have distinct effects on propagation can be characterized by geophysical parameters. The path types can include directionally dependent parameters. Corrections based on calibrated path types are then transported to uncalibrated areas with similar path types. This approach complements empirical methods that reduce the variance of existing data.

We use an inversion approach to extend the path correction techniques developed in southern California, to global data reported in the Reviewed Event Bulletins (REB), while maintaining the key elements of identifying path types and using short path segments. We divide long source-station paths into short segments, with each segment identified with a particular path type, and then invert for an Lg/Pg ratio correction factor for each path type. This performs comparably to other waveguide method approaches for single stations, but has the advantage of being applicable to multiple stations over a broad region.

Records with Lg or Pg below the background noise level contain important information regarding phase blockage. We use such censored data to determine path corrections and identify blockage. Estimation of Lg and Pg signal-to-noise (S/N) levels based on pre-event noise is common, but leads to inappropriate use of low S/N level measurements. The appropriate noise level to use is that of the pre-phase noise. Using the pre-event noise underestimates the real noise level for Lg and Pg, with the result that noise level measurements of those phases are used as if they were signal. We extend the inversion for path corrections to use low S/N measurements as upper bounds on the phase amplitudes in a Maximum Likelihood estimate, and apply it to the global data reported in the REB with the result that we clearly identify blockage.

We also test and model a depth discriminant based on Lg group velocity. We found in southern California, that Lg from earthquakes and explosions differ in their response to waveguide properties. This suggests that their Lg modal structures differ, which implies that Lg group velocities should differ for earthquakes and explosions. This is confirmed by observations from shallow and non-shallow sources in both SCSN and Israeli network data. The SCSN data consist of 582 high signal-to-noise (S/N) Lg recordings from 10 nuclear explosions, 3 non-shallow earthquakes, and one very shallow earthquake. The Israeli data consist of 630 recordings from 19 quarry blasts and 28 earthquakes, with near-surface to 22 km hypocentral depths. The depth dependent difference in Lg arrival times is significant and so provides a potentially useful depth discriminant. We use modal and finite difference synthetics to model the observations and gain further insight into their origin. Specifically, we examine the frequency-dependent effects on the arrival times of Lg of both modal excitation and Rg-to-Lg scattering in heterogeneous media.

OBJECTIVE

The primary objective of this research program is to improve the accuracy of discrimination of nuclear explosions from earthquakes by developing a transportable path correction algorithm for the Lg/Pg discriminant. A secondary result is the development of a depth discriminant based on Lg group velocity.

RESEARCH ACCOMPLISHED

Introduction

In this paper, we briefly review the development and application of path correction methods based on categorical techniques and southern California data. We focus on the underlying principles and basic results, and refer the reader to Baker and Eneva (1999) and Baker (1998) for details. We then describe the inversion approach used to generalize the method for use with long paths and apply it to data reported in the REB. We discuss the importance of recognizing low S/N data by using pre-phase rather than pre-event noise levels, and the incorporatation of censored data into the inversion. We demonstrate how use of low signal-to-noise level (S/N) measurements in a maximum likelihood estimate identifies Lg blockage, while inappropriate use of the measurements leads to spurious results, and we present results of inversions at a single station and over all of Asia. We conclude with a discussion of a depth discriminant based on Lg travel times. We present observations of late arriving Lg from shallow events in southern California and Israel, and mode and finite-difference modeling of the observations to assess different mechanisms.

Short paths between southern California stations, geophysical parameters, and statistical techniques

We compiled a data set of changes in Lg, Pg, and the Lg/Pg ratio between stations of the southern California seismic network (SCSN) together with statistics of topography, crustal thickness, and the isostatic gravity residual. Statistics used included the mean, median, maximum, minimum, roughness (various measures), average gradient, maximum slope, and second and third moments. Changes in absolute amplitudes of Lg and Pg were obtained by application of corrections for site amplifications, determined by Baker (1997). That permitted us to determine that changes in Lg are significantly larger and are more predictable than those in Pg (Baker, 1998).

We demonstrated (Baker, 1998; Baker and Eneva 1999) that assuming the relationship between propagation and various parameter values is linear will cause some such relationships to be missed altogether, while categorical techniques are appropriate to our assumption of the existence of distinct crustal types (or path types if we want to use directionally dependent parameters). We divided the path segments between stations into five types using cluster analysis and the statistics of parameters listed above, and found that analysis of variance soundly rejects the hypothesis that Lg propagation differences between the crustal types are due to chance (Baker, 1998). Even simple divisions of the crust into types by a single parameter, such as median elevation (in which case we define low, medium, and high elevation crust), is effective at reducing the variance in new data collected in the same area (Baker and Eneva, 1999).

We performed a test in which we clustered short paths between stations together with segments of longer paths between distant stations. We made corrections based solely on the short paths, and applied them to each segment of the long paths. This let us apply corrections based on calibrated areas (the short paths) to some areas without calibration data (some segments of the long paths) but with similar crustal types. The path corrections transported well from the southern Sierra to the Peninsula Range, and from other regions to the Salton Trough, reducing the scatter in the Lg/Pg ratio in both cases. On the other hand, corrections from the southwestern edge of the Mojave Block, when extended to the central and eastern Mojave Block, actually increased the Lg/Pg ratio scatter. In that case, the transport of corrections failed. The crustal types differ in their effects on propagation, but the geophysical parameters used did not distinguish between types. Paleomagnetic data indicates the far western Mojave Block has been strongly rotated relative to the eastern block (e.g. Dokka, 1997), and might have been useful in our study to further distinguish crustal types. This points out the need to thoroughly characterize areas in which corrections are to be extended.

An inversion extending use of short segments of distinct path types to long paths and global data

Previous work on waveguide method-based path corrections average parameters over entire paths (e.g. Rodgers et al., 1999; Lay et al, 1999). Average parameter values may however be misleading. For example, a path half in mountains and half in a basin may have the same average elevation as a path entirely within an high plateau, although the 3 crustal types mentioned likely affect propagation very differently. Thus it is improtant that we continue to base corrections on short path segments. Previous work also has focused on corrections at single stations. For corrections to have a plausible physical basis, they must provide the same correction value for similar paths, even to different stations. To retain the use of short path segments and enable corrections to be made over an entire region utilizing multiple stations, we perform an inversion for correction terms for each crustal type based on the equation $a_i = \sum c_k \bullet d_k$, where a_i is the i^{th} $\log_{10}(Lg/Pg)$ ratio, c_k is the correction term for the k^{th} crustal type, and d_k is the distance of the k^{th} crustal type that makes up the i^{th} event-station path. This can be written in matrix form as

$$\begin{vmatrix} d_{11} & d_{12} & \dots & d_{1n} \\ d_{21} & d_{22} & \dots & d_{2n} \\ . & & & . \\ . & & \dots & . \\ d_{m1} & d_{m2} & \dots & d_{mn} \end{vmatrix} \bullet \begin{vmatrix} c_1 \\ c_2 \\ . \\ . \\ c_n \end{vmatrix} = \begin{vmatrix} a_1 \\ a_2 \\ . \\ . \\ . \\ a_m \end{vmatrix} \qquad (1)$$

and when there are no censored data, can solved as a simple least squares problem. We present an example of this next.

Figure 1 shows the event-station paths from the June 1996 through October 1999 REB, having S/N > 2 for both Lg and Pg. For this very simple test, we divide the crust into types based on increments of sediment thickness (<50 m, 50-200 m, 200-500 m, 500-750 m, 750 m-1 km, 1-2 km, 2-4 km, 4-6 km, 6-8 km, 8-10 km, and > 10 km). Most of the paths cross areas with less than 2 km of sediments, and there are virtually no paths that cross sediments thicker than 6 km. so we effectively fit 8 parameters to 414 Lg/Pg ratios.

In addition to the distance correction, we achieve an 11% σ^2 reduction, and a 24% $SMAD^2$ reduction (the scaled median absolute deviation, SMAD, is the one-norm equivalent of the standard deviation and is a more appropriate measure of scatter for these clearly non-Gaussian distributions). This demonstrates that a small set of correction terms can reduce the Lg/Pg scatter at many stations over a large region.

Recognizing and using censored data to refine path corrections and identify blockage

When a phase is blocked, the measured phase amplitude will be below the pre-phase noise level. Such records are the most important to identifying blockage. When we have such data, the amplitude measured in the phase window is used as an upper bound on the true phase amplitude. Because we use amplitude ratios, we have doubly censored data. When data are censored, we use maximum likelihood estimation to solve equation 1. We present two examples in which this approach identifies areas of blockage. In the first, we use data at a single station to demonstrate the errors that occur when such censoring is not recognized and dealt with appropriately. In the second, we demonstrate the capability of this approach to automatically identify areas of blockage using multiple stations over a larger area.

There are two important issues regarding censored data. The straightforward one is how to analyze it. Bias due to censored data has long been recognized in seismic magnitude estimation (e.g. Ringdal, 1977), and methods of incorporating such data into an inversion are well understood. The more subtle issue for path correction studies appears to be recognizing that data are censored. A surprising and ubiquitous error made in this sort of study is that S/N levels used to select "good" data are determined by comparing amplitudes within Lg and/or Pg signal windows with pre-event noise levels (e.g. Xie and Mitchell, 1990; Lay et al, 1999; Rogers et al, 1999). This is an error. For phase measurements to be plausibly recognized, they must have greater amplitude than the coda of preceding phases. Ignoring this can have serious ramifications, as

the "Lg" measured, for example, may actually represent the amplitude of Pn, Pg, or Sn coda. This undermines the basis for any physical interpretations of results that may be obtained.

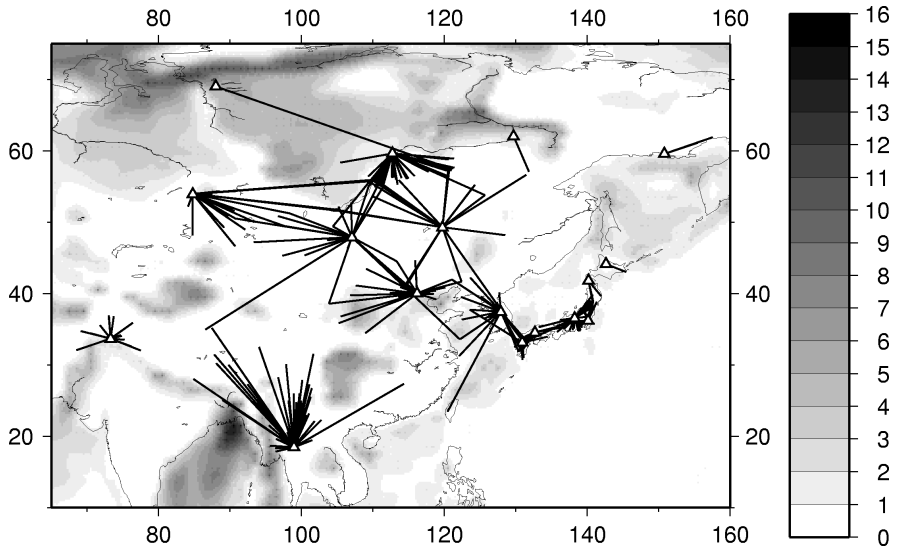


Figure 1: Event-station paths (triangles denote stations) for events with both Lg and Pg S/N > 2 as reported in the June 1996 to Oct. 1999 REB, overlain on a sediment thickness contour map (contour scale is in km).

In the next simple example, we will temporarily neglect the issue of transportability in order to make a single point clearly. That is, we address the effect of using noise level measurements as if they are signal and show how appropriate incorporation of noise level measurements can be used to identify blockage. Thus, although we use the method of dividing the crust into types, we do so very simplistically for just a single station and want to make it clear that we do not suggest that all low elevation crust will block Lg. It is just coincidental that for the paths to this one station, the areas that block Lg are low elevation.

A typical example of waveguide-based path corrections, using data from ZAL, was reported by Lay et al (1999), so we perform a similar analysis using our inverse approach, this time separating crustal types by elevation. We perform the analysis two ways. First, we purposely make the mistake described above. That is, we compare signal amplitudes to pre-event rather than pre-phase noise levels, so that noise level measurements may be used as if they are signal amplitudes. Then we repeat the analysis, but with poor S/N records properly identified as noise level measurements.

From June 1996 through October 1999, the REB reported 433 events with Pn S/N > 2. Of those, only 65 had Lg signal greater than pre-Lg noise. Thus, in our first inversion 85% of the data input as Lg signal measurements really repesent coda amplitudes of earlier phases. The corrections therefore are really due to fitting parameters to the ratio of Pn to Pn, Pg, and/or Sn coda. Both Lay at al (1999) and our first inversion produced an approximately 40% variance reduction due to the distance correction, but only a few percent more for the waveguide based corrections. Figure 2 demonstrates why that is the case. In the top plot, $\log_{10}$(Pn/Lg) is binned for all the data regardless of Lg S/N level, and plotted versus distance (each plot uses 22 points/bin). The large variance reduction with distance is due to the strong relationship demonstrated by this plot. The data however more likely represents the ratio of Pn to Pn coda, rather than Pn to Lg amplitude. The middle plot shows $\log_{10}$(Pn/Lg) of all 433 data points again, plotted vs. mean elevation. There is no apparent relationship, which explains why the waveguide-based corrections provided little further variance reduction. In the bottom plot, we have separated the data into two groups. Recall that all the data have Pn S/N > 2, but now one data set (the upper curve) contains the 368 data points with Lg S/N < 2 (where the noise is pre-Lg noise). For that data set there is still no relationship between mean elevation and relative propagation efficiency. The lower curve is from the 65 data points with Lg S/N > 2. That curve does show a clear relationship between elevation and relative propagation efficiency. The

overall Pn/Lg ratio is of course much smaller, as the noise amplitudes erroneously used as Lg signal amplitude are much larger than the real signal amplitudes. Inversion results are presented in Table 1.

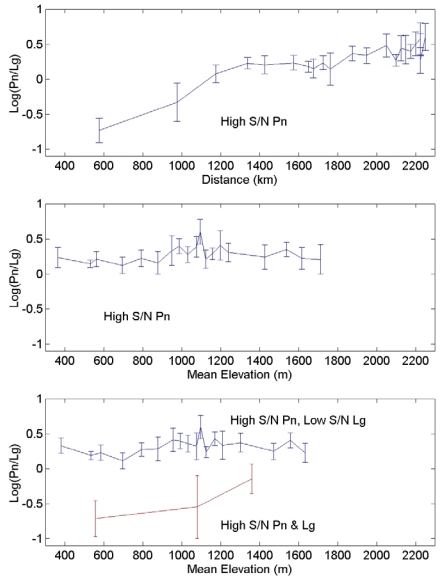


Figure 2: Log_{10}(Pn/Lg) vs. distance (top) and log_{10}(Pn/Lg) vs. mean elevation along the event-station path (middle), both for all data regardless of Lg S/N level In these two cases Lg amplitude may actually reflect amplitude of earlier phase coda. The bottom plot is log_{10}(Pn/Lg) for low S/N Lg (upper curve) and for high S/N Lg (lower curve). All data are binned with 22 data points/bin. The median and two SMAD deviation confidence intervals are plotted.

Crustal Type by Elevation	Noise as Signal	High S/N Only	Censored Data
-.2-.3 km	0.5170	0	-19.9664
.3-.8 km	0.2102	0.025	0.1099
.8-2 km	-0.1165	-0.586	-0.3616
2-3 km	-0.1380	0.224	0.9591
3-4 km	0.6908	0.329	-0.0968
>4 km	0.2481	1.135	0.5170

Table 1: Results of two inversions for path corrections to ZAL. In both, we divide the crust into 6 types based on elevation. As described above (equation 1), we determine the distance each path traverses each crustal type. The important result in this example is the correction term for the lowest elevation crustal type, -200 to 300 meters (top row).

In the 1st inversion, we use Lg noise levels as if they are signal (second column). In that case the large number, relative to other correction terms, (top row) erroneously predicts a small Pn/Lg ratio. In the 2nd inversion, we appropriately use Lg noise levels as upper bounds on signal amplitudes in a maximum likelihood estimate. As an intermediate step, we determine the least squares solution to equation 1 for just the high S/N data. There, the correction term for the lowest elevation group is zero (3rd column), since no paths with good Lg S/N traverse such paths. Finally, when we incorporate the censored data into a maximum likelihood estimate (last column), the correction term for the lowest elevation group is a huge negative number, correctly identifying that crustal type as blocking Lg.

We are not saying that all low elevation paths to all stations, block Lg. Only in this example using data recorded at ZAL to demonstrate the importance of recognizing and appropriately using censored data, do all the low elevation paths happen to block Lg.

The purpose of this final example is to demonstrate that censored data can be used to systematically identify blockage within a large region using multiple stations. To do so, we use a much simpler approach than identifying crustal types. We invert for blockage and relative Pn to Lg attenuation just for latitude-longitude grids. Thus, for this example we are not addressing transportability. This demonstration that maximum likelihood estimation using censored data can identify blockage over a large region sets the stage for future work, which should use more well-defined path types as inversion parameters. For this example, our inversion parameters are simply geographic grid locations, and the data are Lg/Pn amplitude ratios reported in the REB for all the Asian stations from June 1996 through October 1999. We select only data where the paths do not cross oceanic crust. For reasons we do not understand, the REB report a large number of high S/N Lg measurements from event-station paths crossing deep ocean. We do not address this problem here, but remove such data from our inversion data set. This leaves us 1834 measurements. Low S/N level phase amplitudes are treated as upper bounds on the amplitudes. We invert for path effects for all 3°x3° geographic grids that had at least 40 1° long path segments pass through them. Figure 3 shows that

two areas of blockage are identified (darkest tiles). The most northeastern dark area covers a transition from no sediment cover to the east, to a thick (7 km) sedimentary basin to the west. The westernmost dark area corresponds to another thick (7.65 km) sedimentary basin. Thus, despite the coarse spatial averaging of this simple example, two major areas of blockage were automatically identified.

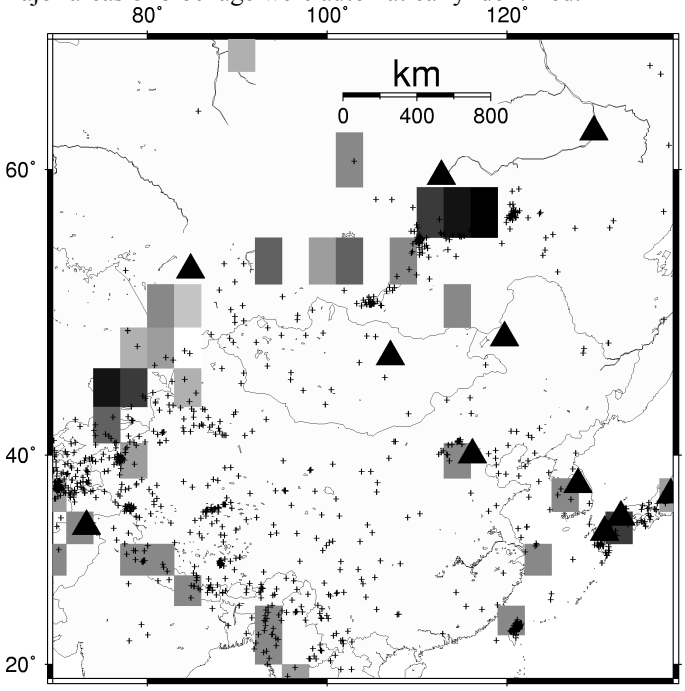


Figure 3: 3x3 degree grids through which passed at least 40, one degree long path segments, along with the locations of 1317 events (dots) and 18 stations (triangles) used in the inversion The important result is that the darkest grid cells were found to block Lg.

Lg arrival times: a resurrected depth discriminant

We noted earlier that Lg propagation effects related to waveguide properties differ in southern California, depending on whether the source is an earthquake or explosion. The simplest explanation for this is that the shallower sources preferentially excite shallowly propagating modes, relative to the deeper sources. If so, we should observe a difference in Lg arrival times. It has long been recognized that Lg arrivals from shallow sources can be delayed relative to Lg from deeper sources. Pomeroy, et al. (1982), for example, listed this depth dependence among possible regional earthquake/explosion discriminants, but abandoned the idea because of the inconsistency of the observations. The data however were analog and typically around 1 Hz or below. We find that the discriminant is much more likely to be successful today with greater bandwidth and digital data permitting better waveform processing techniques. Figure 4 shows two waveforms at 369 km from an earthquake and 340 km from an underground nuclear test at the Nevada Test Site recorded at the same station. The time window defined by group velocities of 3.6 to 3.0 km/second is marked on each record. Notice how much later in the window the Lg arrival from the explosion occurs compared to the arrival of the deeper earthquake.

Figure 4 also illustrates the method used to measure Lg arrival times. Unlike other seismic phases, Lg is not associated with displacements propagating along a well-defined ray path and so there is no distinct model dependent travel-time for the phase and no travel-time residual. Rather, Lg is defined as whatever energy arrives within a particular group velocity window, usually around 3.6 to 3.0 km/sec, and is modeled either as shear waves trapped in the crustal waveguide or as higher mode surface waves. To quantify the relative delay between seismograms, we use the median cumulative amplitude (MCA) of the envelope function of Lg (Figure 4). That is, the MCA is the position that evenly divides the area under the curve of the envelope function into two halves. Because the length of the Lg group velocity window changes with distance, the midpoint is normalized by the window length and is expressed as a fraction of total window length.

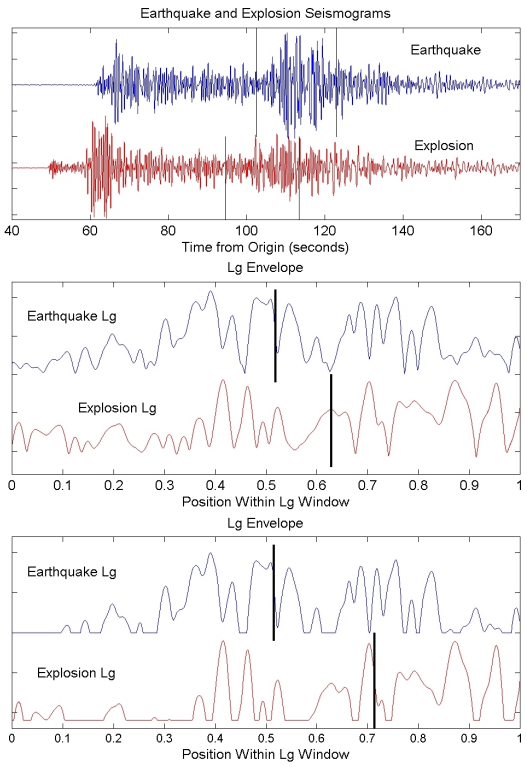


Figure 4. Seismograms (upper plot) from an earthquake at 369 km distance (upper trace) and a nuclear explosion at 340 km distance (lower trace), both recorded at the same station, with the position of the Lg windows bracketed by vertical lines. The envelope functions of just the Lg windows are plotted versus position within the Lg window (middle plot), with the median cumulative amplitude (MCA) positions indicated by vertical lines. Better separation of shallow events occurs when the MCA is determined from only those values of the Lg envelope greater than the mean value of the pre-Lg noise window envelope function (pre-Lg window not shown). The lower plot shows the Lg envelope functions with that correction, and their MCAs (vertical lines).

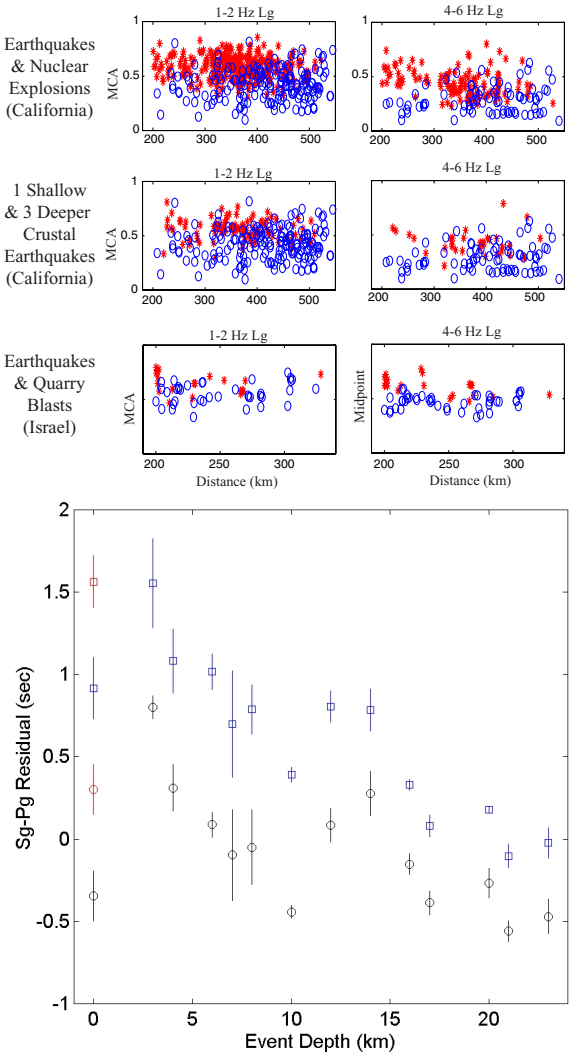


Figure 5. The upper plot shows 3 examples in 2 passbands in which a measure of Lg arrival times (described in Figure 4) is plotted for shallow events (asterisks) and non-shallow earthquakes (circles), vs. distance. The shallow event Lg is always later. The lower plot shows Sg minus Pg residual travel times vs. source depth for 133 local (< 75 km distance) Israeli earthquakes and 33 quarry blasts. The median earthquake Sg minus Pg residuals dencrease with depth throughout the entire seismogenic crust, relative to both IASPEI91 (used by the IMS, squares) and the Israeli velocity model (circles). Quarry blast Sg minus Pg residuals relative to each model are also shown (red, at z=0). This clearly shows that shear wave arrival times depend strongly on source depth throughout the crust. That is, the differences observed at top are not just a near surface effect, but rather, each increment of source depth affects the shear wave travel time

Figure 5 presents observations that demonstrate the effect of depth on S phase arrival times. We found that in all cases - Lg from a very shallow earthquake (1-2 km source depth) vs. non-shallow earthquakes recorded at the SCSN, Lg from NTS nuclear explosions vs. non-shallow earthquakes recorded at the SCSN, and Lg from quarry blasts vs. from 6-22 earthquakes recorded in Israel - the shallow event Lg was slower. No differences were observed in Pg travel times. In addition, for near source observations in Israel, earthquake Sg was delayed relative to Pg as a function of depth from 0 to 22 km deep sources.

Mode synthetic seismograms for sources from 1 to 30 km depth, in 1 km intervals, are shown in Figure 6. There is clearly more energy later in the Lg window of the shallow event seismograms. This observation is quantified in Figure 7, where the MCAs of the Lg windows of the synthetics' envelope functions are plotted vs. source depth. There is also considerably more energy in shallowly propagating modes with lower group velocities than those that bracket the Lg window. In the real Earth, scattering at the surface and by velocity heterogeneities may scatter some of that energy into higher velocity modes. That is essentially the mechanism commonly proposed for the enhancement of Lg by the fundamental mode (e.g. Myers et al, 1999). We examine that mechanism next using finite-difference synthetics.

We use finite-difference modeling to examine the effects of scattering on Lg. This demonstrates how energy may be scattered from Rg to Lg, causing the observed delays of Lg for shallow events. We calculate synthetics for a range of earthquake depths and distances, for both the model of Figure 6 and that same model with random heterogeneities added. The heterogeneities are zero mean Gaussian, with a correlation length of 2.25 km. and a standard deviation of 10% of the velocity in the surface layer, dropping to 7% in the lower crust. The Poisson ratio remains the same as in each layer of the homogeneous model.

Figure 8 shows synthetic seismograms for the homogeneous and heterogeneous models, for earthquakes at 1 km. depth intervals from the surface to the Moho, at 30 km. The Lg window, from 3.6 to 3.0 km/sec group velocity, is outlined by shadowing. The homogeneous model synthetics (left) look much like the mode synthetics, but in this case the fundamental mode is included (labeled Rg). The seismograms are similar those in Figure 6 (the mode synthetics), but have more detail, as the solution is more complete than that of the mode summation. Rg is only generated by very shallow sources and is much larger in the homogeneous model case, as are the higher modes, than for the heterogeneous model (right). Seismograms from propagation through the heterogeneous model have the energy distributed more evenly throughout the record. These simulations demonstrate that Rg to Lg scattering may also be a feasible mechanism for delaying Lg arrivals.

Further observations and modeling support the modal explanation for late arriving Lg from shallow events. In particular, we observe better event separation at higher frequency. This is predicted by the modal explanation, as the modes are more narrowly constrained in depth at higher frequency. The Rg to Lg scattering model however, would predict later Lg at lower frequency, since the higher frequency Rg scatters out away much more rapidly. Near source observations of Israeli quarry blast records confirm this. Below 1 Hz, Rg persists up to 100 km distance from sources and records tend to have energy in either Rg or Lg, but not in both. The mutual exclusivity of Rg and Lg suggests that below 1 Hz, Rg may be a major contributor to Lg. At higher frequencies however, where depth discrimination is stronger, there is no clear Rg beyond 20 km, and no apparent mutual exclusivity between Rg and Lg.

CONCLUSIONS AND RECOMMENDATIONS

Studies using the closely spaced SCSN data identified two factors important to successful transport of waveguide method-based path corrections for Lg to P discriminant values. One is that parameters should not be averaged over entire paths, but rather, long event-station paths should be broken up into small segments. The second is that the assumption of linear relationships between propagation effects and parameter values can miss important relationships, whereas categorical statistics techniques allow us to model propagation based on the assumption that distinct crustal types exist and affect propagation differently from each other. These crustal types can be generalized to path types, so that directional parameters, such as whether the crust in thinning or thickening in the ray direction, can be incorporated.

An inverse method was developed to retain these key elements while determining path corrections for the long event-station paths reported in the REB. It was shown to be effective in an application to all the Asian data reported over 3 years. The method reduces the Lg/Pg scatter for the region using just 8 parameters based on sediment thickness. More refined path type separation, such as the cluster analyses performed for SCSN paths, should be performed. We expect that would provide even greater reductions in scatter.

In the area of path corrections, we recommend for all REB data, that path types be clustered based on statistics of all possible geophysical parameters and censored data be identified and incorporated into the maximum likelihood inversion described here. This will result in a valid map of phase blockage most relevant to IMS stations. This should be performed for as narrow of depth range sources as possible, and refined as more accurate depths and more ground truth data become available. For the path corrections, rigorous error analyses must be performed to assess the accuracy of transportability.

We have made observations of delays in Lg and Sg from shallow events relative to non-shallow events in 2 regions of the world. The delays are large and consistent enough to discriminate depth, with better discrimination at higher frequency. Modeling indicates that the delay is due to excitement of different modes by different depth sources. We recommend that an Lg group velocity discriminant be regionalized for all IMS stations. An effective depth discriminant will depend on accurate regionalized travel time models, and the regionalized discriminant must be rigorously tested using all available ground truth data.

Lg being composed of different modes has profound implications for CTBT monitoring. Path corrections for discriminants, as well as travel times, may not be valid for events at depths other than those of the calibration events. Ensuring the validity of any type of Lg correction surface will depend on our understanding of the source depth effect on Lg and our ability to more accurately assess source depth.

Determination of whether a measurement represents a signal or noise level must be made using pre-phase, not pre-event, noise levels. We have demonstrated that once this is done, noise level measurements incorporated into a maximum likelihood estimate can automatically and accurately identify areas of blockage. We have also demonstrated how the inappropriate use of noise levels as if they are signal amplitudes, a common error, can easily lead to erroneous conclusions.

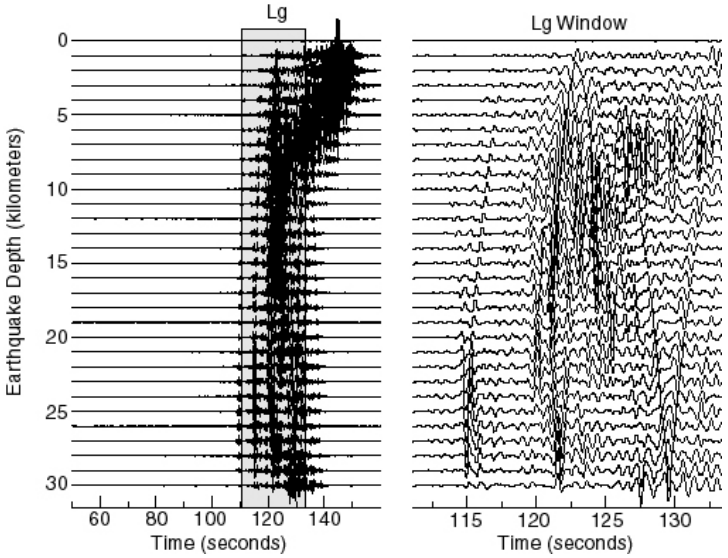


Figure 6: Mode synthetics (sans fundamental mode) at 400 km distance, for a model from the NTS to southern California region (Asad, 1998) and for 0 to 30 km depth sources. Modes excited in shallow layers are larger for shallow sources and so make a greater contribution to later Lg. The left plot shows seismograms from 8.0 to 2.5 km/sec group velocities. The Lg window is shaded. On the right is just the Lg window, from 3.6 to 3.0 km/sec group velocity.

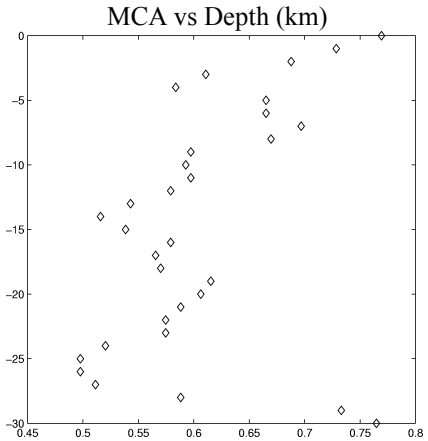


Figure 7: Median cumulative amplitude (MCA) positions of Lg envelope functions, for the seismograms shown in Figure 6). Excitation of different modes is consistent with observed delays of shallow-event Lg.

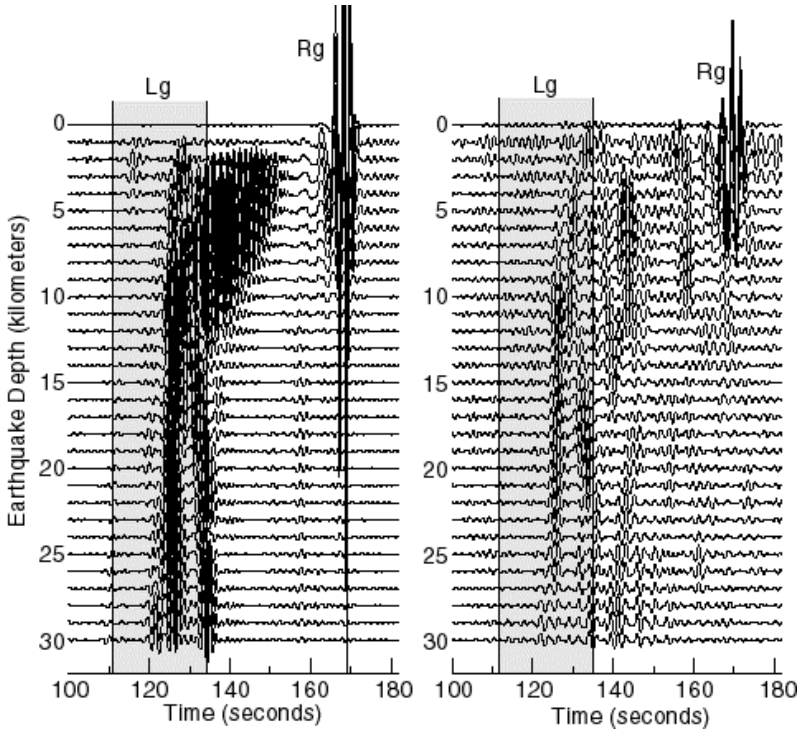


Figure 8: Seismograms at 400 km distance for the homogeneous model (left), and for sources from 0 to 30 km depth, from 4.0 to 2.2 km/sec group velocity, with the Lg window (3.6 to 3.0 km/sec group velocity) indicated by shadowing. The very large Rg for shallow events in the homogeneous model is purposely clipped, to allow more details of the smaller phases to be seen. The right plot shows the same for the heterogeneous model. All traces are plotted on the same scale.

Key Words: discrimination, event depth, blockage, Lg, path correction, propagation

REFERENCES

Asad, Abu Muhammad (1998), Linearized and nonlinear travel time tomography for upper crustal velocity structure of the western Great Basin, Ph.D dissertation, University of Nevada, Reno

Baker, G.E., 1998, Predicting crustal phase propagation efficiency from topography, gravity, and crustal thickness, *Proc. 20th Annl. Seism. Res. Symposium on Monitoring a CTBT*, pp. 153-162

Baker, G.E. and M. Eneva, 1999, Predicting Crustal Phase Propagation from Other Geophysical Parameters, *Proc. 21st Annl. Seism. Res. Symposium on Monitoring a CTBT*, pp. 7-17

Dokka, R. K., 1997, Multiple, large early Miocene vertical axis rotations in the west-central Mojave Desert and implications for the tectonic development of southwestern Cordillera, *GSA Abs. w. Progs,* **29**, p. 279

Lay, T., G. Fan, R.S. Wu, and X.B. Xie, 1999, Path corrections for regional phase discriminants, *Proc. 21st Annl. Seism. Res. Symposium on Monitoring a CTBT*, pp 510-519

Myers, S., W. Walter, K. Mayeda, and L. Glenn, 1999, Observations in support of Rg scattering as a source of explosion S waves: regional and local recordings of the 1997 Kazakhstan depth of burial experiment, *BSSA*, pp. 544-549

Ringdal, F., 1977, Maximum likelihood estimation of seismic event magnitude, *BSSA*, **67**, pp. 789-802

Rodgers, A., W. Walter, C. Schultz, S. Myers, L. Thorne, 1999, A Comparison of Methodologies for Representing Path Effects on Regional P/S Discriminants, *BSSA*, **89**, pp. 394-408

Xie, J. and B.J. Mitchell, 1990, A back projection method for imaging large scale lateral variations in Lg coda Q with application to continental Africa, *Geophys. J.*, **100**, 161-181

THE CONFIDENCE-BUILDING MEASURE ROLE OF SEISMIC CALIBRATION

Leslie A. Casey, John J. Zucca,* and W. Scott Phillips**

U.S. Department of Energy, *Lawrence Livermore National Laboratory, **Los Alamos National Laboratory

**Sponsored by U.S. Department of Energy
Office of Nonproliferation Research and Engineering
Office of Defense Nuclear Nonproliferation
National Nuclear Security Administration**

ABSTRACT

Confidence-Building Measures (CBMs) under the Comprehensive Nuclear-Test-Ban Treaty (CTBT) address the political goal of alleviating compliance concerns raised by chemical explosions and the technical goal of calibrating the International Monitoring System (IMS; ref. Article IV, E, and Part III of the Protocol to the Treaty). The term "calibration" appears in the Treaty associated only with CBMs and On-Site Inspections (OSIs) and has different meanings in each case. For OSI, calibration refers to calibration of the on-site monitoring instruments, whereas, for CBMs, it refers to seismic travel-time corrections for specific paths to improve event location. Calibration of a path is either carried out empirically using known sources or compensated for through earth models. Known sources are called "calibration" or "reference" events and are characterized by information known as ground truth. In practice, the accuracy of the ground truth varies for different types of reference events. Mining explosions or explosions carried out for the express purpose of calibration have the highest degree of accuracy since the location and origin time are known from direct measurement. An example of a calibration event with less accurate ground truth is an earthquake that occurs within a local network with large enough magnitude to be observed regionally. Such events have location accuracy typically less than 5 km. Outside of mining regions and seismically active regions where reference events are plentiful, path calibration will need to be estimated with earth models developed from studies such as seismic refraction experiments. These models will be the result of the integration of all available information and need to be tested—most likely with dedicated calibration experiments—over the region for which they are considered to be valid. Clearly, developing path calibrations is a large effort that requires the cooperation of scientists all over the world.

This paper describes preferred methods of seismic calibration and recommends near-term high-priority courses of action to achieve it.

Key Words: calibration, confidence-building measures, mining explosions

Introduction

Nuclear explosion monitoring capability is fundamentally dependent on the installation of monitoring stations. Currently, the Preparatory Commission (PrepCom) for the Comprehensive Nuclear-Test-Ban Treaty Organization (CTBTO) is installing stations in anticipation of entry-into-force of the Treaty. These stations, especially the seismic ones, will provide the essential detection capability. However, once installed, their potential location capability will not be realized until they are fully calibrated. The Treaty does not require the CTBTO to calibrate the stations. Instead, station calibration is a voluntary activity allowed under the Confidence-Building Measures provision in the Treaty. In a sense, the Treaty can be viewed as a global "neighborhood watch" system, where the CTBTO functions as the eyes and the stations as the ears.

There are many aspects of seismic calibration as evidenced by the several terms needed to describe a seismogram. A seismogram is a recording made by a seismometer of the ground motion from a source propagated through the earth and corrupted by background noise. The waveform model used to describe the observed signal at a given station is a convolution of source, path, and instrument response terms superimposed on additive background noise (from both earth and instrument sources):

$$\text{Seismogram}(t, R, \ldots) = \text{source}(t,\ldots) * \text{path}(t,R,\ldots) * \text{instrument}(t,\ldots) + \text{noise}(\ldots)$$

Many variables contribute to each term; however, with seismic calibration, the primary variables of interest are time (t) and distance (R). The path term represents the impulse response of the earth structure between the location of an equivalent point source and the location of a receiving station. Similarly, the instrument term defines the impulse response of the recording instrument. Finally, the noise term defines the earth noise present at any given site. The path is the only term dependent on the distance between source and receiver, R, and it is the primary source of error in the event location process. Fortunately, much of this error can be reduced through travel-time corrections, which are the primary focus of calibration.

The purpose of this paper's focus on seismic calibration is to highlight the significant role that can be played by the global research community, in particular, on work based on historical and surrogate station data that will allow partial calibration of a station or network in advance of installation. The research role is larger for the seismic community than for the other technical communities supporting ground-based monitoring technologies because of the inhomogeneity of the transmission medium for the seismic signal. In contrast, the hydroacoustic transmission medium, water, is relatively homogeneous. The inhomogeneity of the earth greatly complicates the path term in the above equation. However, unlike radionuclide and infrasound technologies, whose signals depend in part on ever-changing atmospheric wind conditions, the seismic transmission medium is static and, once characterized, is essentially constant, allowing progressive reduction of uncertainty. This progressive nature of seismic calibration makes the long and labor-intensive effort worthwhile.

Seismic Calibration Approaches

Travel-time corrections can be empirical or model based. Empirical calibrations provide more confidence than model-based approaches; however, model-based calibrations are useful when sufficient empirical data are not available to provide corrections across large geographic areas, for example large aseismic regions. Furthermore, the advantages of emperical and model-based approaches can be combined using Bayesian techniques (Schultz et al., 1998).

In the modeling approach, travel times are calculated by tracing rays through two- or three-dimensional earth models of P and S velocities that represent the region being calibrated (Firbas et al., 1998). The P and S velocity models may be derived in a variety of ways, depending on the kind of information available. A hierarchy of techniques has been devised to obtain velocity structure models:

1) Refraction lines provide the most direct estimate;
2) Pn, Sn, teleseismic P and S, and surface wave tomography provide partial constraints over wide regions;
3) Receiver functions provide partial constraints at a single geographic location;
4) Analogy to geophysically similar regions provides a highly uncertain estimate but one that can be applied in the complete absence of data.

The resulting travel times will be more appropriate for the modeled region than those based on a one-dimensional global model. However, both are indirect calibrations and have high uncertainty. For this reason, empirical corrections are preferred where high-quality ground truth about events exists because they are based on actual measurements, and their certainty can be determined.

Ground-Truth Data Drives the Calibration Effort

Empirical travel-time corrections are based on ground truth. Ground-truth events are seismic events for which the type of source and its location in space and time are well known, as are the uncertainties in these parameters. Ground-truth events include well-located earthquakes from global, regional, local, and temporary networks. They also include man-made seismic sources such as mining and other industrial or military explosions, as well as dedicated calibration shots. The most basic ground-truth information includes source type and accurate location and origin time along with error estimates on these quantities. Great care must be taken to obtain accurate error estimates so that appropriate weights can be applied when combining ground-truth information from many sources. In general, ground-truth accuracy trades off with coverage. For example, ground truth from global and regional earthquake catalogs provides the highest levels of coverage but has the largest errors, since earthquake locations are not precisely known. At the other extreme, for example, high ground-truth accuracy but low level of coverage, are dedicated calibration explosions. For such experiments, it is good practice to deploy instruments locally to accurately verify origin time and location. A highly

recommended dedicated calibration shot, known as the reciprocal or inverse calibration shot (Shelton Alexander, private communication, 1999), provides data on many paths simultaneously. In this type of experiment, a large explosion is detonated near an IMS station and recorded at high-priority locations by portable, temporary seismic stations.

As a first step, we suggest beginning the empirical calibration of a given region with ground-truth data from global catalogs. This generally provides reasonable coverage and improvement in accuracy in a cost-effective manner. Higher quality ground-truth information can be added to improve calibration in certain areas or to test the effectiveness of the more common, lower quality information. High-quality ground truth is also critical to evaluate the regional models discussed above.

For global catalog data, studies comparing locations to known ground truth show that an accuracy of $\pm$15 km can be obtained by requiring a certain number of reporting stations within an allowable threshold gap (Sweeney, 1998). These data are referred to as GT15 data, shorthand for ground-truth accuracy of 15 km. This is a significant level of accuracy because it is slightly less than the radius of a 1000-km^2 circle, the 1000 km^2 being the maximum area of an on-site inspection under the CTBT. Regional network locations provide GT5-10 locations, while local networks, for example those deployed during aftershock studies, provide GT5 or better. Additional accuracy can be obtained using locations based on surface rupture from geological or satellite observations to obtain accuracy of GT5 or less. Higher accuracy can be obtained from industrial blasts. These can be described as GT2. Finally, dedicated explosions of tens of meters and millisecond level accuracy have essentially no error and are designated GT0 (Leith and Kluchko, 1998). The Comprehensive Nuclear-Test-Ban Treaty Preparatory Commission recommends that calibration explosions be known to within 100-m location and 0.1-s timing accuracy (PrepCom, 1999).

As the final step, the correction surfaces generated by interpolating ground-truth data must be validated. Dramatic improvements in location quality have been shown in comparisons of locations of the Racha, Georgia, aftershock sequence using a regional array, before and after calibration, based on GT15 data (Figure 3, Myers and Schultz, 2000).

Summary and Recommendations

Calibration of seismic monitoring stations improves confidence in the treaty. Although the Confidence-Building Measures part of the treaty only calls out a subset of calibration activities (i.e., chemical calibration explosions), a wide range of calibration activities has confidence-building value. The Confidence-Building Measures part of the treaty opens the door to contribute to calibration. Indeed, calibration is just beginning to show its value as more stations come online, effectively putting into place a global neighborhood watch system. For seismic methods to operate at their maximum accuracy, regional path travel-time corrections need to be made and applied. These corrections can be calculated from regional geophysical models or, preferably, from empirical calibration event data sets. Empirical calibrations are preferred since they are actual measurements and their

uncertainty can be directly evaluated. The following activities have significant confidence-building value and are recommended to aid seismic calibration:

1) **High-quality ground truth for explosions**. The Treaty already urges States to provide the PTS with such information and data on explosions of 300 tonnes or greater.
2) **Dedicated calibration experiments**. These experiments are needed to validate models and to fill in reference event information. Reciprocal experiments as discussed above are particularly useful.
3) **Local and regional seismic data**. Data from local and regional networks that can locate events within 10 km or better should be made widely available through web sites (for example, the USGS web page entitled Routine United States Mining Seismicity (http://neic.usgs.gov/neis/mineblast/index/html). Such data have confidence-building value by defining the background seismicity for a region.

Guidance is available for use by all researchers. Documents include
1) Guidelines and Reporting Formats for the Implementation of Confidence-Building Measures (PrepCom 9, 1999),
2) Knowledge Base Contributor's Guide (Carr, et al., 2000),
3) The Integration Process Design for Incorporating *Information Products* into the Department of Energy *Knowledge Base* (Moore et al., 2000).

References

Carr, D., S. Moore, H. Armstrong, L. Wilkening, M. Chown, E. Shepherd, T. Edwards, R. Keyser, C. Young, A. Cogbill, J. Aguilar-Chang, A. Velasco, and S. Ruppert (2/00), Knowledge Base Contributor's Guide, SAND2000-0442 (available from http://www.ctbt.rnd.doe.gov).

Firbas, P., K. Fuchs, and W. Mooney (1998), Calibration of Seismograph Network May Meet Test Ban Treaty's Monitoring Needs, Eos Trans. Am. Geophys. Union, 79, 413, 421.

Leith, W. and L. Kluchko (1998), Seismic Experiments, Nuclear Dismantlement Go Hand in Hand in Kazakhstan, Eos Trans. Am. Geophys. Union, 79, 437, 433-444.

Moore, S., H. Armstrong, D. Carr, R. Keyser, E. Shepherd, L. Wilkening, C. Young, M. McCornack, J. Aguilar-Chang, A. Velasco, S. Ruppert, T. Hauk, and C. Schultz (5/3/00), The Integration Process Design for Incorporating *Information Products* into the Department of Energy *Knowledge Base*, SAND2000-0597 (available from http://www.ctbt.rnd.doe.gov/).

Myers, S. and C. Schultz (2000), Improving Sparse-Network Seismic Location with Bayesian Kriging and Teleseismically Constrained Calibration Events, Bull. Seism. Soc. Am., 90, 199-211.

PrepCom 9 (8/30/99), Draft Guidelines and Reporting Formats for the Implementation of Confidence-Building Measures, CTBT/PC-9/1/Annex II, Appendix IV, pp. 26-43, (available from http://www.ctbto.org/).

Schultz, C., S. Myers, J. Hipp, and C. Young (1998), Nonstationary Bayesian Kriging: Application of Spatial Corrections to Improve Seismic Detection, Location and Identification, Bull. Seism. Soc. Am., 1275-1288.

Sweeney, J. (1998), Criteria for Selecting Accurate Event Locations from NEIC and ISC Bulletins, UCRL-JC-130655.

EXCITATION AND PROPAGATION OF SHORT-PERIOD SURFACE WAVES IN YOUNG SEAFLOOR

Donald W. Forsyth

Department of Geological Sciences, Brown University

Sponsored by The Defense Threat Reduction Agency
Arms Control Technology Division
Nuclear Treaties Branch

Contract No. DTRA 01-00-C-0071

ABSTRACT

In seafloor younger than about 20 Ma, the lithosphere is not well-developed and Sn does not propagate efficiently. In young seafloor, however, S waves or normal modes of 3-to-6-s period trapped in the crust are strongly excited by shallow earthquakes and propagate to large distances with little attenuation. Young seafloor typically has few sediments, so there is no low-velocity, low-Q layer at the surface to trap and attenuate these crustal phases. These waves are essentially the equivalent of Lg in continental settings, although because there is no granite in the oceanic crust, they might better be dubbed Lb, with b for basalt. Like T-phases, Sn, and 15-to-20-s period Rayleigh waves, these Lb waves are dispersed and/or scattered arrivals. Unlike these other phases, Lb is close to the microseism peak, yet, because they are so effectively excited by shallow earthquakes and so little attenuated, they stand out above the noise level as one of the most prominent signals on ocean-bottom seismometers (OBS).

In the MELT Experiment, 51 ocean-bottom seismometers were deployed for a period of approximately six months, from November 1995 to May, 1996, in two linear arrays extending about 800 km across the East Pacific Rise at 15 to 18°S. Recordings of regional earthquakes on this array shows that short-period Love and Rayleigh waves (~3-6 s) are excited that travel with velocities characteristic of the upper crust (~ 3 km/s). The Love waves are normally dispersed with continuous frequency variation from 3 s to long periods, but Rayleigh waves appear to have a gap between 12-to-15 s fundamental mode waves with much of their energy concentrated in the water column and the 5-to-6 s higher mode waves. These latter waves, the short-period, crustal surface waves, Lb, show very little attenuation. Even at 3200 km away from an earthquake on the northern East Pacific Rise, they still are a prominent phase, despite lying in the peak of the microseismic noise. The excitation and propagation characteristics of these waves are being explored.

Key Words: Surface waves, attenuation, ocean-bottom seismometers

Introduction

In ocean basins, there are three primary types of seismic waves traveling in low attenuation waveguides that provide good signal-to-noise ratios for small events at large distances: T-phases, Sn, and 15-to-20-s period Rayleigh waves. T-phases, of course, propagate in the SOFAR channel and Sn in the lithospheric mantle. Much of the energy of shorter period Rayleigh waves is concentrated in the water column, which is high Q, and the remainder, except where there are thick sediments, is primarily in the dehydrated, high-Q, lower crust and uppermost mantle. T-phases and 15-to-20-s period Rayleigh waves are efficiently excited by shallow earthquakes and explosions in the oceanic crust and also fall in low-noise windows that are unaffected by oceanic microseisms or long-period, water, gravity waves (Webb, 1998). Thus, these waves are primary candidates for detecting, locating and discriminating explosions from earthquakes in oceanic settings.

Less well known is another type of wave and waveguide in young seafloor. In seafloor younger than about 20 Ma, the lithosphere is not well-developed and Sn does not propagate efficiently. In young seafloor, however, S waves or normal modes of 3-to-6-s period trapped in the crust are strongly excited by shallow earthquakes and propagate to large distances with little attenuation. Young seafloor typically has few sediments, so there is no low-velocity, low-Q layer at the surface to trap and attenuate these crustal phases. These waves are essentially the equivalent of Lg in continental settings, although because there is no granite in the oceanic crust, they might better be dubbed Lb, with b for basalt (or just keep the g for gabbro). Like T-phases, Sn, and 15-to-20-s period Rayleigh waves, these Lb waves are dispersed and/or scattered arrivals. Unlike these other phases, Lb is close to the microseism peak, yet, because they are so effectively excited by shallow earthquakes and so little attenuated, they stand out above the noise level as one of the most prominent signals on ocean-bottom seismometers (OBS).

Data Set

In the MELT Experiment, we deployed 51 ocean-bottom seismometers for a period of approximately six months, from November 1995 to May, 1996 (Forsyth et al., 1998). They were deployed in two linear arrays (Figure 1) extending about 800 km across the East Pacific Rise at 15 to 18°S. During the experiment, we recorded three of the French nuclear tests in Polynesia, several earthquakes at regional distances along the East Pacific Rise, and many teleseismic events (Figure 2). In addition, many very small local events were recorded and located using T-phases. This experiment represents the largest array of ocean-bottom seismometers ever deployed and, at least at the time of the experiment, the longest duration experiment using portable OBSs.

Fifty of the 51 OBSs were equipped with three-component, Mark Products L4C 1-Hz seismometers as well as either a hydrophone or Cox-Webb differential pressure gauge (DPG) to record pressure variations. One was equipped only with a hydrophone. Stable temperatures at the seafloor help make it possible to record long-period signals reliably out to periods of 60 s and more. Several methods for deploying, levelling, filtering and recording were employed by four instrument groups. Data were recorded at either 16 or 32 samples per second, except during the seismic refraction phase of the experiment when higher rates were employed. Instrument response characteristics were derived for each type of instrument and tested by comparing corrected waveforms of earthquakes at adjacent stations. The OBSs operated independently on battery power and no data was transmitted back to the recording ship. After correction for clock drift, the

timing errors are estimated to be less than 0.01 s. After reaching the seafloor, each OBS was located precisely by acoustically ranging to a transponder from the ship, which was navigated using the P-code Global Positioning System (GPS). Locations are estimated to be accurate within about 10 m. At the end of the experiment, acoustic signals were sent to release the weights (anchors) of each OBS. Fifty of the 51 OBSs were recovered. To reduce noise, in three of the four basic OBS designs the seismometer package was deployed separately from the recording package after reaching the seafloor. This mechanical deployment procedure was the most serious instrumental problem in the experiment. The seismometer package did not deploy properly at 20 sites. Seismic records from these OBSs were limited to the waves with pressure components.

This unique data set will provide a good indication of the nature of scattering from regional events by looking at the variability of waveforms from station to station. The aperature is wide enough to the north and south to allow good locations of events at regional distances and long enough to measure apparent attenuation. Propagation characteristics can be estimated both within the array and between the sources and various elements of the array.

Example Seismograms

Figure 3 shows seismograms from an earthquake at the northern end of the Easter microplate at a distance of about 660 km, filtered in different bands. At regional distances, the distinction between surface waves and body waves is blurred, but there is clear dispersion on the transverse component between waves of ≥ 10 s period that predominantly arrive at times corresponding to mantle shear velocities (~4 km/s beneath young seafloor) and waves of period ≤ 5 s that travel with velocities characteristic of the upper crust (~ 3 km/s). Following the simply dispersed portion of the seismogram is a long train or coda of scattered, short-period surface waves. The dispersed part is predominantly Love waves on the transverse component, but there is a Rayleigh wave component at the shorter periods that shows up on the vertical component, presumably consisting of higher mode waves trapped in the crust.

There is a window (Figure 4) in the pressure noise field between the microseism peak and the pressure variations associated with long-period internal gravity waves that allows the longer Rayleigh waves to be detected. In 3 km of water, the window lies between about 10 and 30 s; in shallower water, the window closes because the depth of penetration of the gravity waves is roughly proportional to period. The short-period, crustal surface waves, Lb, show very little attenuation as long as they propagate in regions with little sediment. At 3200 km away from an earthquake on the northern East Pacific Rise, they still are a prominent phase (Figure 5) at 5 s period, despite lying in the peak of the microseismic noise (Figure 4).

Excitation of Seismic and Hydroacoustic Waves in Oceanic Environment

Our expectation is that the combination of relative excitation of T-phases, Lb, and 15-to-20 s Rayleigh waves will prove to be a powerful discriminant between explosions and shallow earthquakes in the same manner as standard Ms:mb or MLg:mb discriminants on land. We will explore that possibility first with empirical comparisons with the recordings of the French tests and the earthquakes on the array of MELT Experiment OBSs. To understand the results, we will model excitation and propagation of the waves; first with standard reflectivity and normal mode codes for a layered earth, then with a 3-D numerical code to

understand the role of lateral heterogeneities in crustal structure and water depth. We will concentrate primarily on exploring the effect of crustal heterogeneities on the propagation of the Lb phase.

One of our goals is to determine effective attenuation coefficients as a function of frequency. We suspect that Lb is effectively excited only by very shallow events in oceanic crust, because the velocities indicate that it is primarily a crustal phase. Part of our task will be to see how well it is excited by events in subduction zones along the Cocos and Nazca plate boundaries. We also do not know how well it is transmitted in older seafloor, where alteration may decrease Q in the basaltic crust and the buildup of sediments may trap and attenuate the waves. We have seen short-period signals of this type from East Pacific Rise events recorded on continental stations near the west coast of South America, but have not explored this phenomenom systematically in terms of propagation efficiency as a function of age of seafloor or sediment thickness.

References

Forsyth, D.W., S.C. Webb, L.M. Dorman, Y. Shen, Phase velocities of Rayleigh waves in the MELT Experiment on the East Pacific Rise, Science, 280, 1235-1238, 1998.

Webb, S.C., Broadband seismology and noise under the ocean, Rev. Geophys., 36, 105-142, 1998.

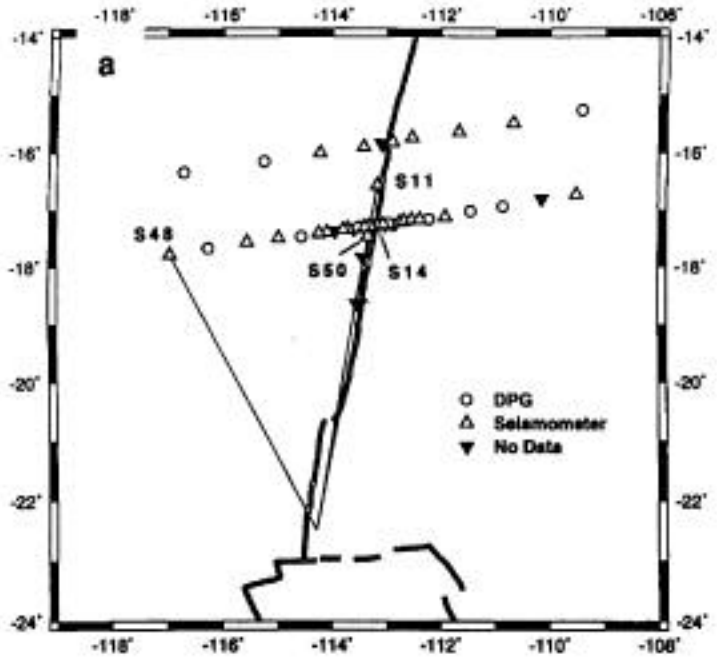


Figure 1. Location of ocean-bottom seismometers (OBSs) in the MELT Experiment. Plate boundaries of the East Pacific Rise and Easter Microplate are shown as double-wide lines. Epicenter of source of seismograms in Fig. 3 is shown just north of microplate.

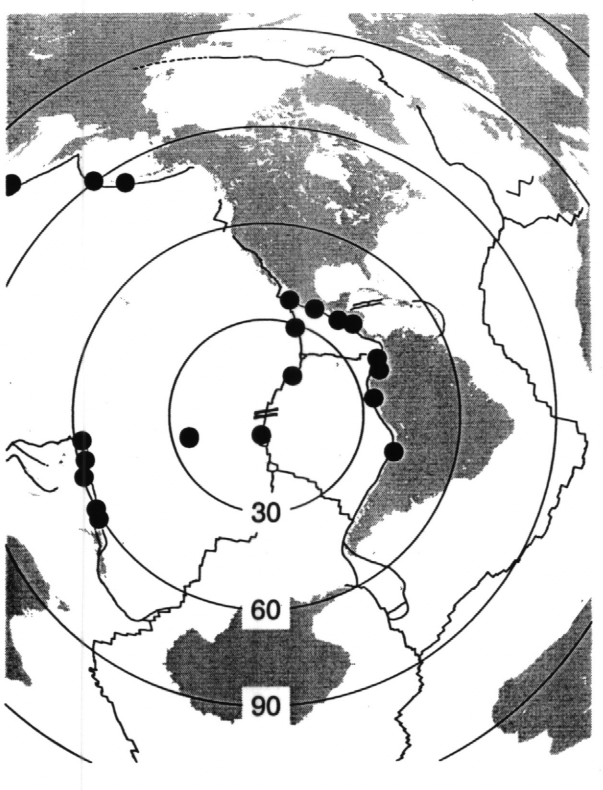


Figure 2. Location of the array and some of the events recorded during the ~ 6-month recording period of the MELT Experiment.

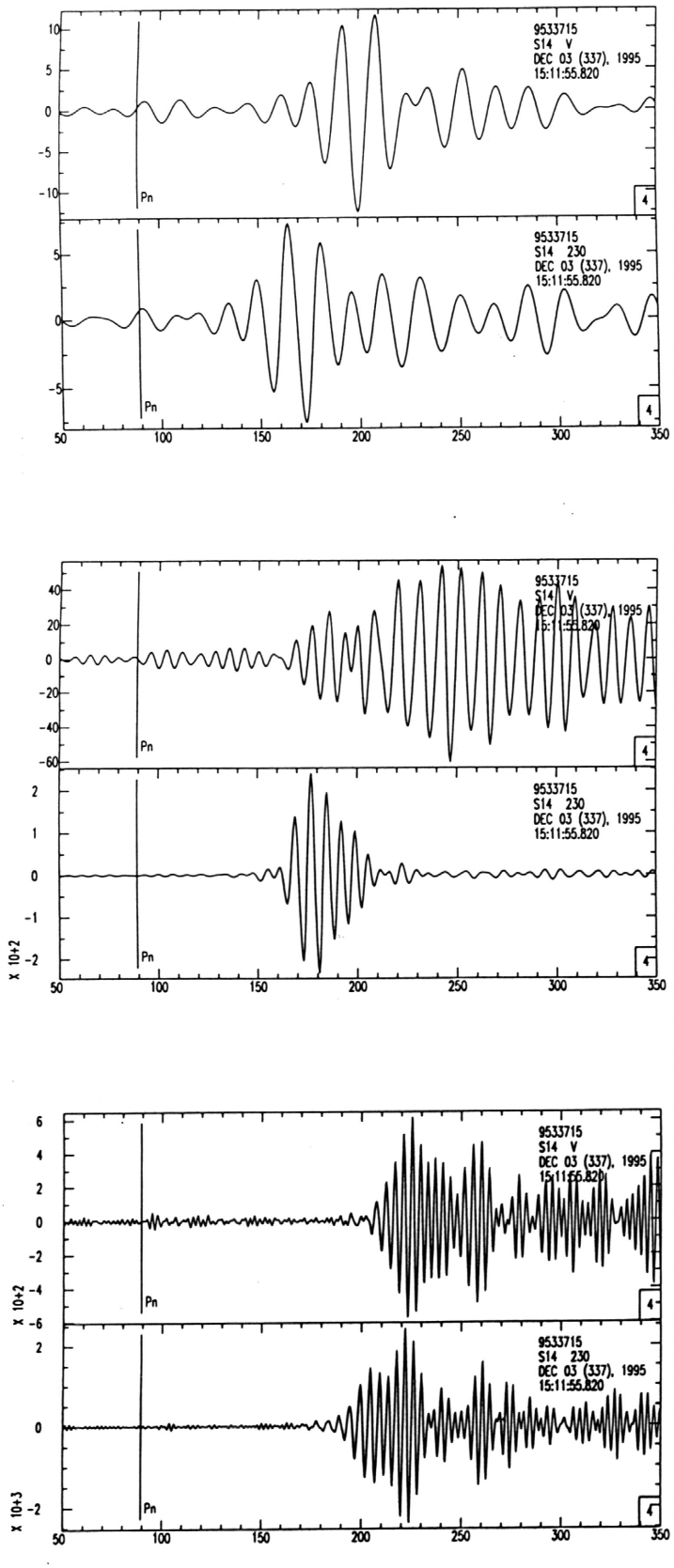


Figure 3. Seismograms recorded on an OBS 660 km from an earthquake at the northern end of the Easter microplate (mb 4.7). Upper record in each pair is the vertical component, lower record the transverse component. Top pair, filtered from 0.04 to 0.07 Hz, middle pair from 0.08 to 0.15, bottom pair from 0.15 to 0.5 Hz. Separate vertical scale for each panel. Note that at long periods (top panel), the vertical component is twice as large as the horizontal (fundamental mode Rayleigh wave dominates the vertical component), but at shorter periods, the horizontal component is much larger. Middle panel shows highly dispersed Rayleigh wave on the vertical component, due to water layer and dispersion of Love wave in transition from a mantle to a crustal phase. Energy at short periods (bottom panel) must be trapped in crust; 220 s corresponds to group velocity of 3 km/s. Horizontal component to about 230 s appears to be simply dispersed, fundamental mode Love wave; later arrivals seem to be scattered, multiple arrivals. Vertical component at short periods must be composed of higher mode Rayleigh waves. Collectively we are calling this packet of energy Lb.

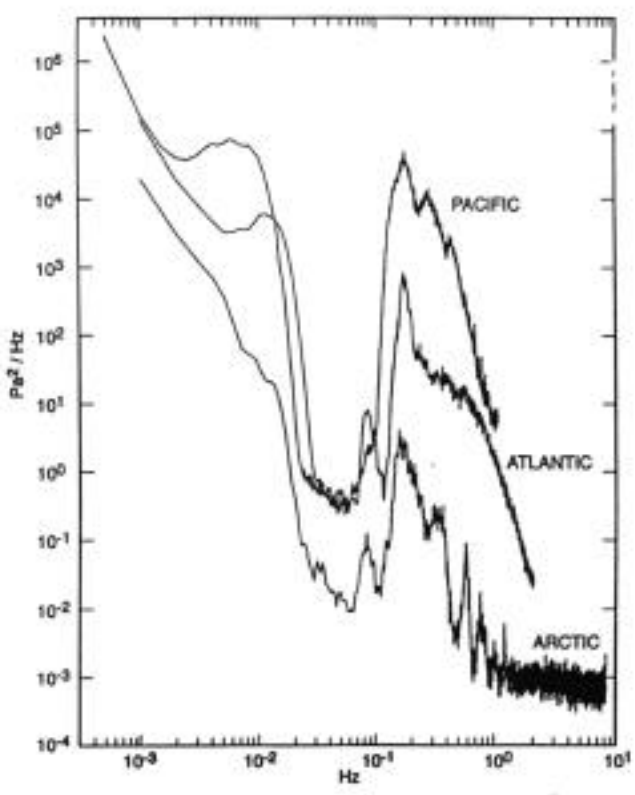


Figure 4. Comparison of noise spectra for pressure component in different oceans (from Webb, 1998). Note "hole" that allows Rayleigh waves and other signals to be detected in the 0.03-0.10 Hz frequency band.

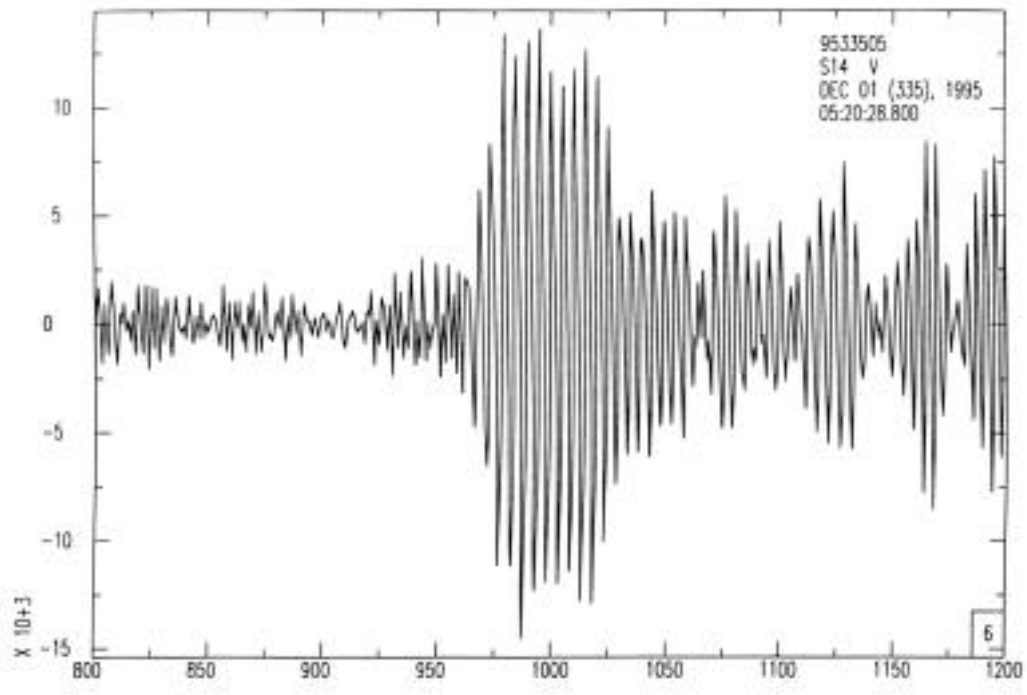


Figure 6. Vertical component seismogram on an OBS at a distance of 3195 km from an earthquake on the northern EPR. Bandpass filtered with corners at 0.15 and 0.5 Hz. The 5-to-6 s energy forms a prominent phase that is highly dispersed and scattered. It begins at an arrival time equivalent to a group velocity of about 3.3 km/s, equivalent to typical lower crustal shear wave velocities, and almost the same onset velocity for same period as the vertical record in figure 3, despite traveling in seafloor of somewhat greater average age.

DYNAMIC FEATURES AND IDENTIFICATION OF REGIONAL SEISMIC SIGNALS FROM DEAD SEA CALIBRATION SHOTS

Yefim Gitterman and Rami Hofstetter

Geophysical Institute of Israel

Sponsored by The Defense Threat Reduction Agency

Contract No.DSWA01-97-C-0151

ABSTRACT

Three large-scale underwater chemical explosions were conducted on November 8-11, 1999 in the Dead Sea. One of the main objectives of the experiment was to provide data for source characterization to improve the IMS detection, location and discrimination capabilities.

The explosions were recorded by the Israel Seismic Network (ISN) including 23 short-period (SP) stations, two auxiliary IMS broadband (BB) stations MRNI and EIL, BB station JER, and three temporary BB stations deployed at sites of the planned Israeli CNF stations.

The magnitude values, determined from SP recordings, fit well the empirical relationship obtained from previous explosions: $M_L = 0.285 + \log_{10}W(kg)$, confirming a high seismic efficiency of the shots. The efficiency was also estimated by determination of energy of seismic waves recorded at local seismic stations relative to the explosives energy.

A clear spectral modulation, caused by the bubble pulsation effect, is observed in all SP and BB seismograms. The bubble periods, determined from the harmonic series on smoothed spectra of ISN seismograms, are in good agreement with the modified Willis' (1963) empirical equation: $T_b=2.1*W^{1/3}/(P_0+d*\square)^{5/6}$, where P_0 is the pressure at the sea level (10.778 m of water column), the shot depth d=70 m, water density $\square$=1.236g/cm^3.

Date	Charge W, kg	Local (duration) magnitude M_L		Bubble period T_b, sec	
		Predicted	Observed	Predicted	Observed
08.11.99	500	3.0	3.1	0.367	0.383
10.11.99	2060	3.6	3.6	0.589	0.561
11.11.99	5000	4.0	3.9	0.791	0.782

Identification of the seismic signals from underwater explosions is based on spectral features of recordings: spectra coherency at different stations, due to the bubbling modulation and low-frequency seismic energy. Discrimination analysis was done by spectral energy ratio (1-3Hz)/(6-8Hz) and semblance (1-12Hz) characteristics, using local SP and BB stations data of the explosions and nearby earthquakes with comparable magnitudes. The methods provided reliable discrimination between earthquakes and explosions in the Dead Sea region.

Key words : Dead Sea explosions, seismic energy, spectra, bubble periods, semblance, spectral ratio

OBJECTIVE

The primary objective of this study is to characterize the specific seismic source for the Dead Sea calibration underwater explosions in a short distance range, to estimate the seismic efficiency of the shots, to investigate dynamic features of radiated seismic waves and provide a preliminary discrimination analysis of the explosions and nearby earthquakes.

RESEARCH ACCOMPLISHED

Local station data. The charge parameters and Ground Truth Information are presented in Gitterman and Shapira (2000). The explosions were recorded by the Israel Seismic Network (ISN), consisting of 23 SP stations, two auxiliary IMS stations MRNI and EIL, and CNF station JER (Jerusalem). Three temporary (surrogate) BB stations were deployed at sites of planned CNF stations (AMZI, MMLI and DIM). Temporary short-period seismic stations were placed along the Dead Sea coast, at the Mineral Beach (HOF, the closest point), and in the hotel area, Ein-Bokek (CRL): two 3C stations on the Hotel Carlton building and two 3C stations on the ground near the Hotel. Station locations are shown on the map on Fig. 1 Data of several Jordanian stations, presented also on the map, were obtained on-line at the Geophysical Institute of Israel.

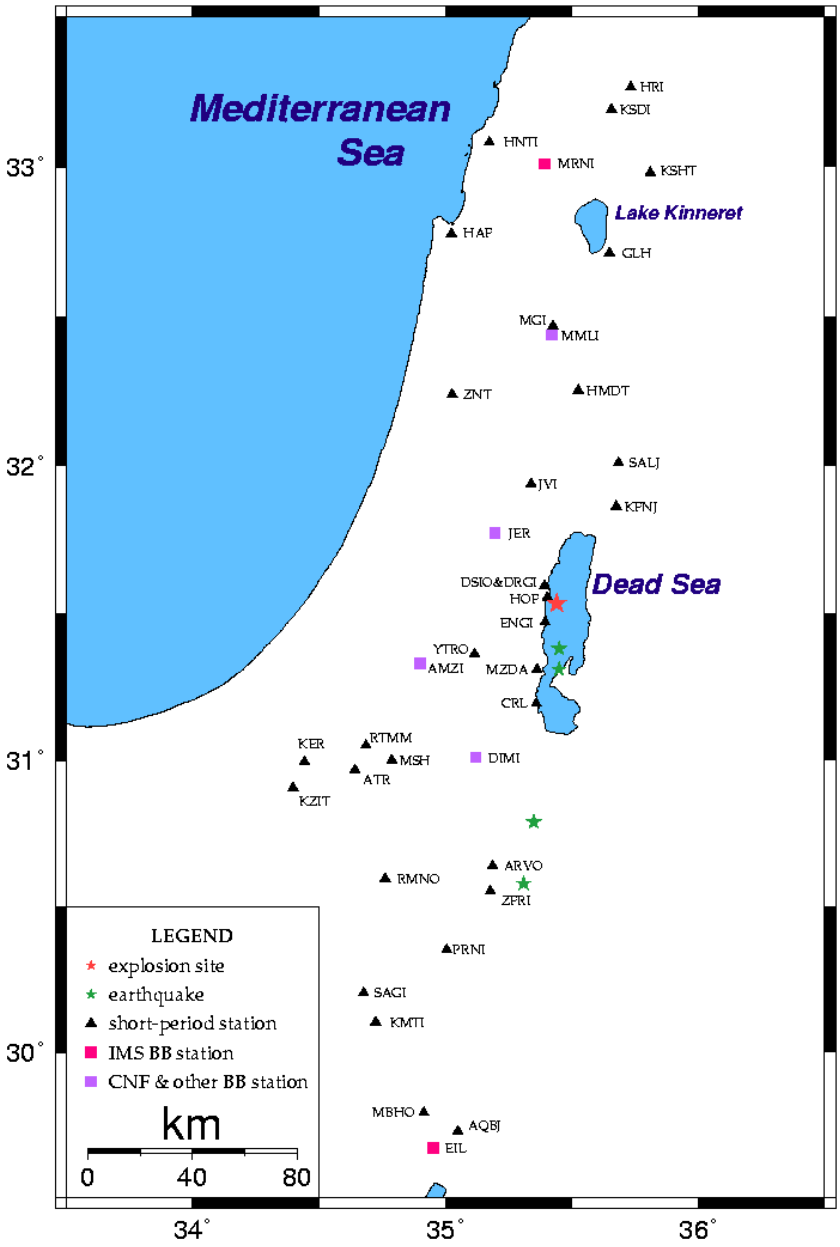


Fig. 1. Location of Israel and Jordanian seismic stations recorded the explosions.

Near-field observations. Several strong motion sensors were installed along the west coast of the Dead Sea. The maximal Peak Ground Acceleration, 0.0769g, was observed at the Mineral Beach at distance 4.2 km (Fig. 2).

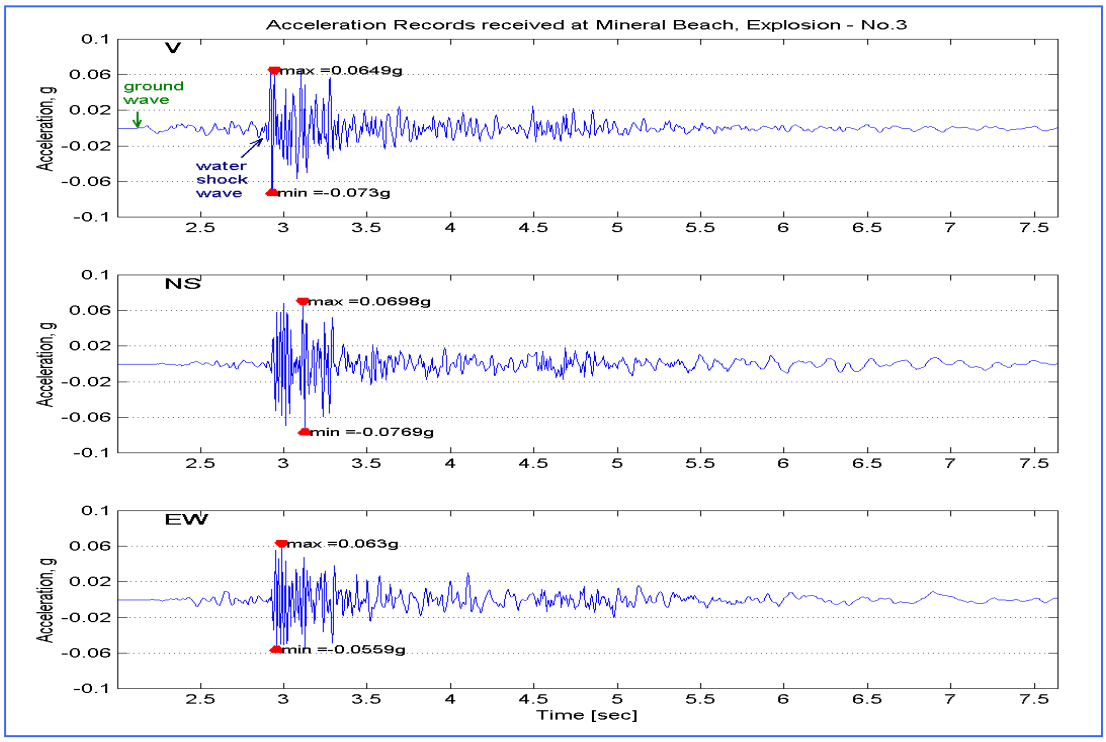


Fig.2. Accelerograms observed at Mineral Beach from the 5000 kg shot.

The high-frequency (about 40-55 Hz) and high-amplitude seismic waves, recorded by an accelerometer A-800, located in a few meters from the shore, are generated by the shock wave - sea shelf interaction. It is evident from the joint recording of a seismometer co-located with the A-800 and a nearby hydrophone placed in water (Fig.3).

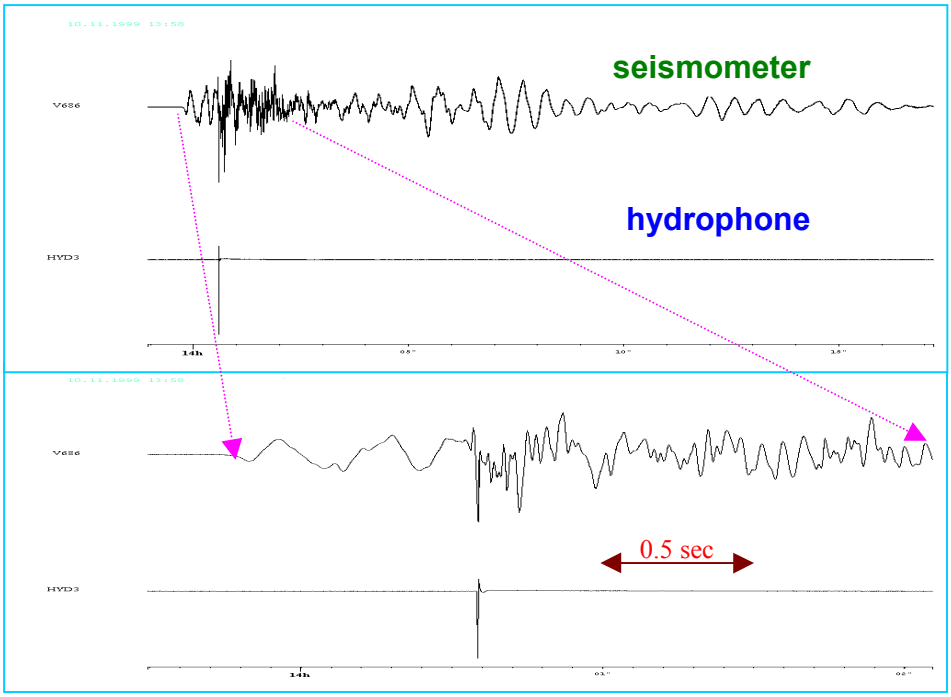


Fig. 3. Seismometer and hydrophone recording at Mineral Beach of the 2000 kg explosion.

Seismic efficiency. An increase of explosion charge weight causes an appropriate rise of radiated seismic energy, and corresponding magnitudes and signal amplitudes, as well as signal periods and wavelengths. Two small test shots (25 kg), conducted two weeks before the main series at the same location and depth, are also considered.

Table 1. Comparison of predicted and observed local magnitudes and fundamental frequencies of the calibration explosions in the Dead Sea (depth d ~ 70m).

ChargeW, kg	Local (ISN based) magnitude M_L		Frequency f_b, Hz / Bubble period T_b, sec		
	Predicted (Eq. 1)	Measured	Predicted (Eq. 3)	Measured	
				average from ISN spectral maxima	from autocorrelation analysis of IMS stations (CMR event Report, 1999)
25 (two shots)	1.7	1.7 1.9	7.20/0.139	6.50/0.154	-
500	3.0	3.1	2.72/0.367	2.61/0.383	2.70/0.37
2060	3.6	3.6	1.70/0.589	1.78/0.561	1.82/0.55
5000	4.0	3.9	1.26/0.791	1.28/0.782	1.30/0.77

Observed local (duration) magnitudes (Table 1), determined from short-period ISN recordings, correspond well to the values predicted at the design stage of the experiment by the empirical relationship (Gitterman, 1998):

$$M=0.285+\log_{10}(W, \text{kg}) \quad (1)$$

based on the 1993 series of small scale Dead Sea shots (Gitterman et al., 1998). The high magnitudes under relatively low charge weights confirm a high seismic efficiency of underwater explosions in the Dead Sea, significantly exceeding the upper limit curve for all known chemical and nuclear explosions in hard rock (Khalturin et al., 1997), presented on Fig. 4. The observed magnitudes and amplitudes of seismic waves verify that the whole charge was properly detonated in all cases.

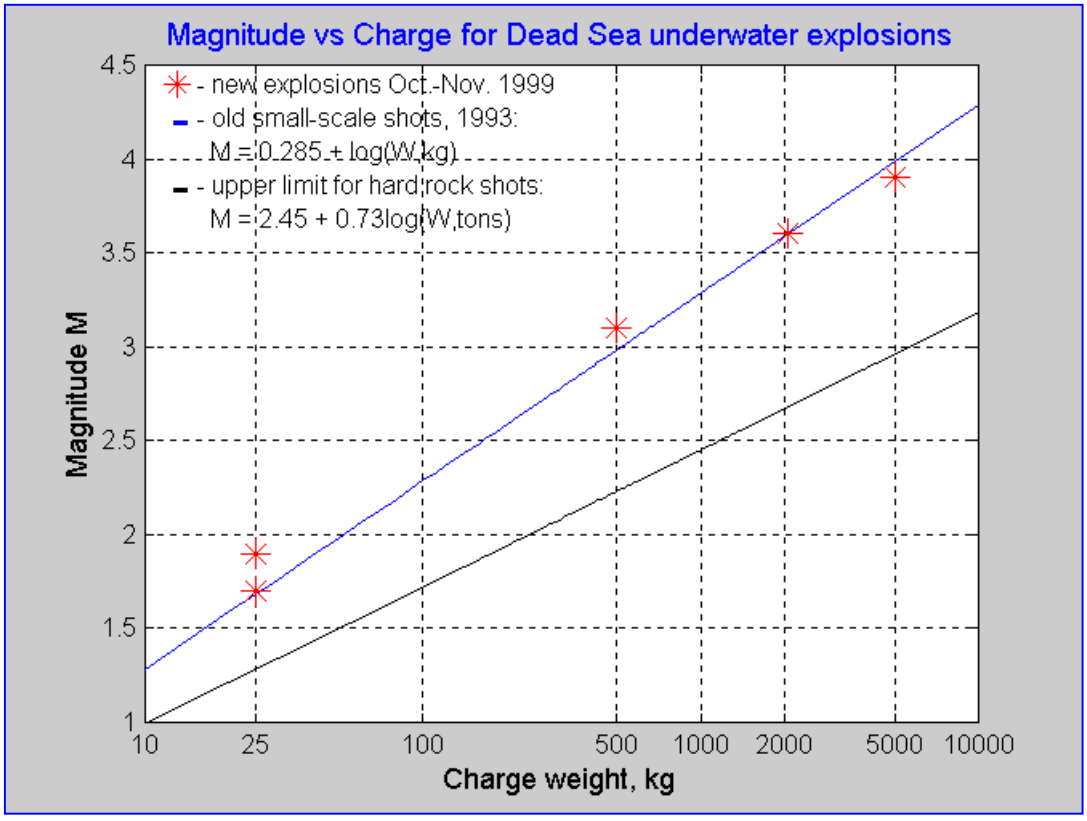


Fig. 4. Magnitude versus charge weight for the Dead Sea explosions.

Some features of seismic amplitudes and waveforms for the three explosions, observed at stations located at different distances and azimuths, are shown on Fig. 5.

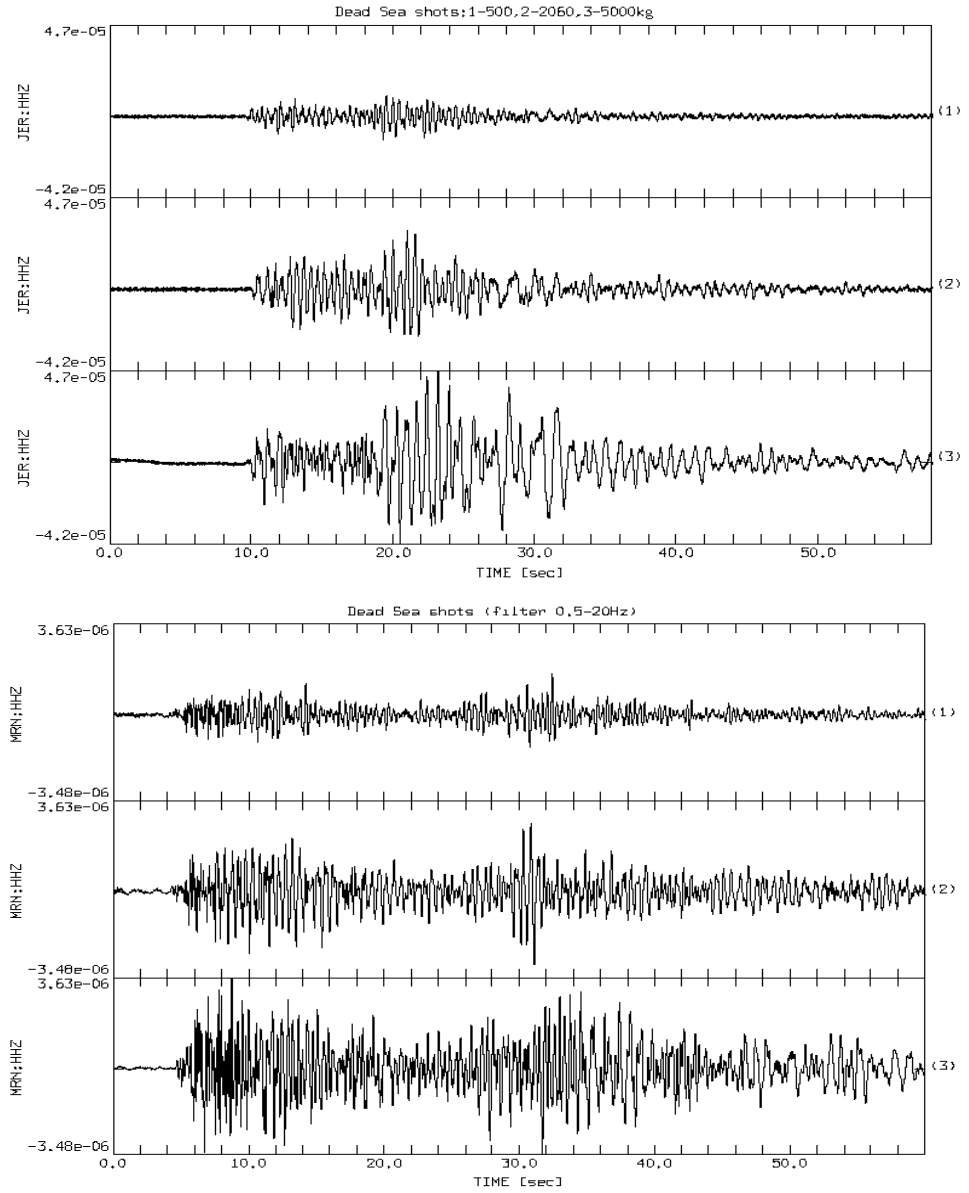


Fig. 5. Signal enhancement at BB stations JER (r=35 km) and MRNI (r=164 km) with the charge increase.

The explosion seismic efficiency was also estimated by determination of energy of seismic waves recorded at local seismic stations relative to the explosives energy. The energy release of an earthquake is an important physical quantity that describes the earthquake. Kanamori et al. (1993) presented a method for the estimation of the seismic energy, based on time-domain integration, of local and regional velocity-squared seismograms observed at TERRAscope in Southern California. They were able to obtain reliable energy estimation, since the propagation effect is of minor importance at short distances. Recently, Mayeda and Walter (1996) proposed to estimate the energy from the coda envelops using broad band data at different frequency ranges. The method of Mayeda and Walter (1996) seems to be better than that of Kanamori et al. (1993). Calibration of the region is now in progress, and once it is being achieved, a refinement of the results is expected when applying the method of Mayeda and Walter (1996). In the presented research we used the method of Kanamori et al. (1993) to estimate the seismic energy of the Dead Sea explosions.

Hofstetter and Shapira (2000) estimated the attenuation function in the short period frequency range (0.5 Hz to 10 Hz)

$$A(R) = (1.850 \pm 0.005)\ logR + (0.00460 \pm 0.00005)R\ loge + 0.05 \qquad (2)$$

where R is the hypocentral distance $R^2 = \Delta^2 + h^2$ in the distance range of $50 \le R \le 1500$ km, Δ is the epicentral distance, h is the source depth which is close to zero in our case. The standard deviation is 0.24 (or uncertainty factor of 1.7). The function (2) was utilized for estimation of the seismic energy for the Dead Sea shots, observed at several 3C short period and broad band stations of the Israel Seismic Network, including IMS and CNF stations (see Fig. 1), located at different distances (range 50-211 km) and azimuths. Fig. 6 shows the seismic efficiency, estimated as:

$$Efficiency = \frac{seismic\ \ energy}{Explosives\ \ energy}$$

where, according to the manufacturer's specification, the energy of the used Chen Amon explosives is given by $1000\text{cal/gr} = 4.2\times10^{13}$ erg/kg. The efficiency values for different stations are averaged, and the variance is also shown for different shots.

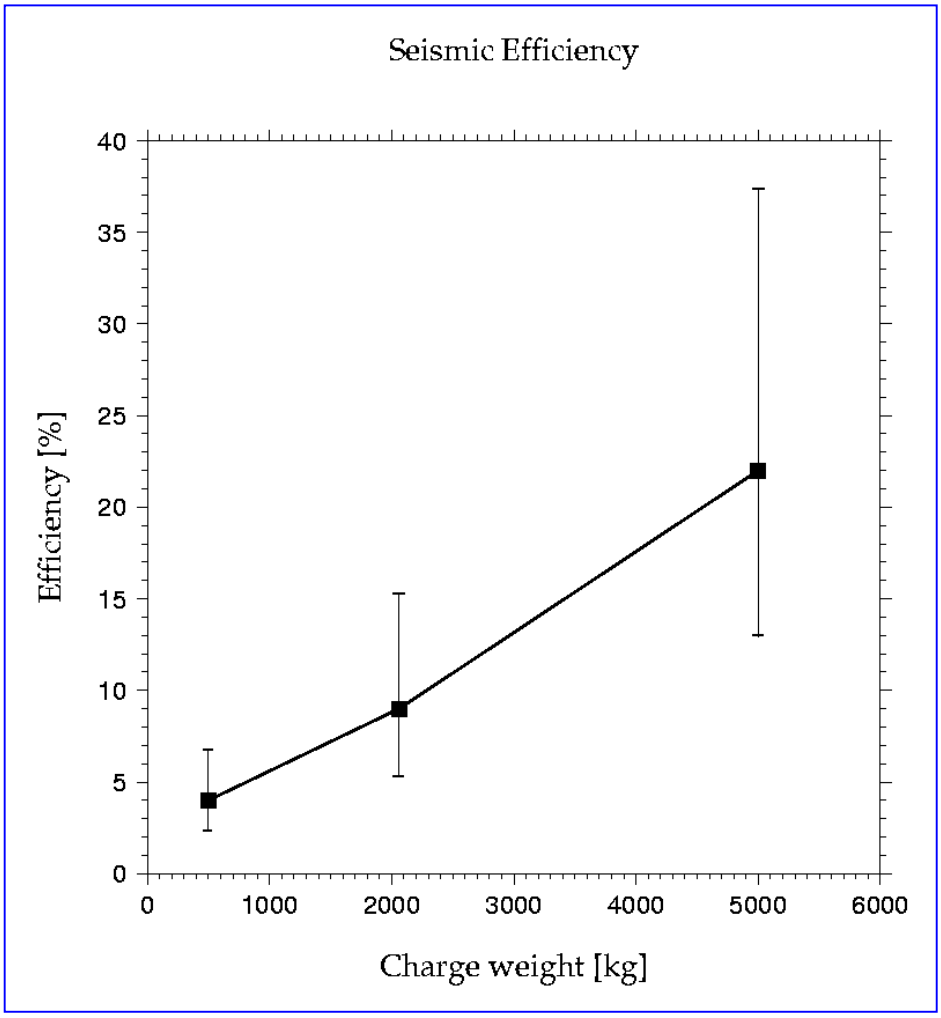


Fig. 6. Seismic efficiency of the Dead Sea calibration underwater explosions estimated from seismograms of local short period and broad band stations, located in the distance range 50-200 km.

Evidently, a large part of the explosives energy was released with uprising hot gases in the detonation vicinity, and the energy of initially radiated seismic waves was either absorbed or scattered in the media along the propagation path to a station. But it is obvious that the efficiency of the underwater explosions in the Dead Sea (especially for the largest explosions 5000 kg), is much higher than that for similar hard-rock shots, which as known reaches a few percents only (see also Fig. 4).

We suppose that the efficiency values for the shots 500 kg and 2060 kg are underestimated, nevertheless the increase trend corresponds to a lesser scattering of seismic energy on the crust inhomogeneities and a lower intrinsic dissipation of seismic energy for longer wavelengths from larger shots.

Bubbling effect and spectral modulation. The prominent azimuth and distance independent spectral modulation, caused by the bubble pulsation effect, is presented in all SP and BB seismograms. The clear frequency banding is observed in smoothed amplitude spectra of the whole signal (50-60 sec) and in spectrograms (see examples on Figures 7 and 8).

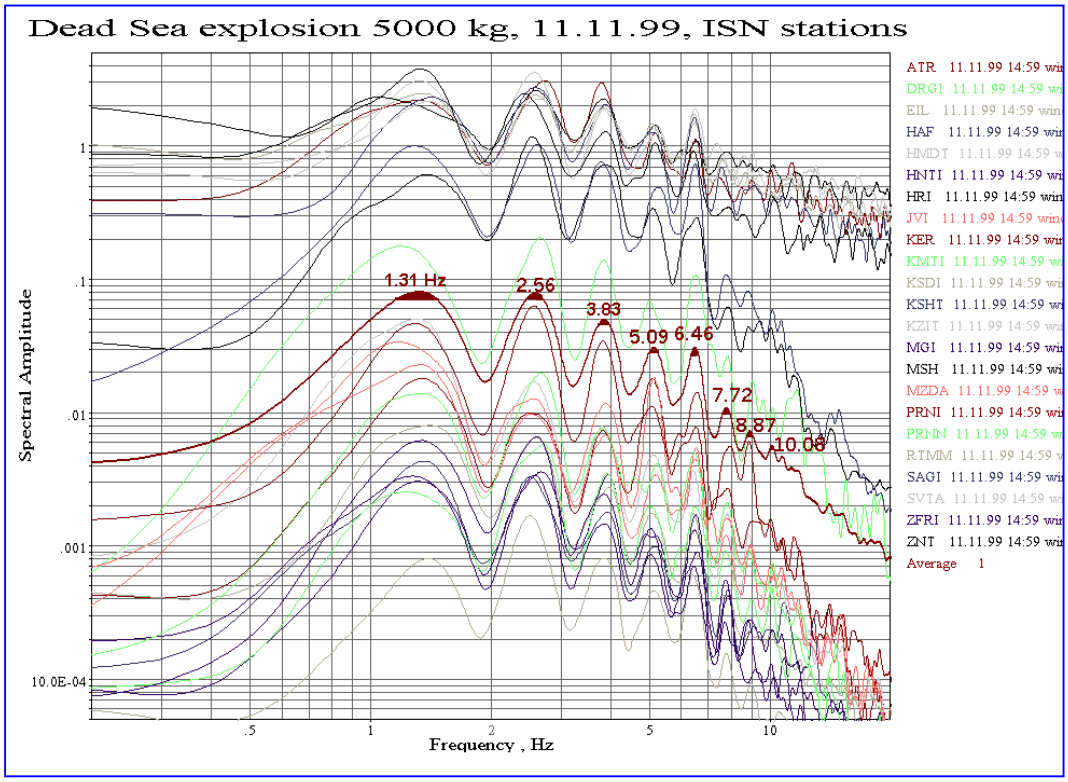


Fig. 7. Determination of the bubble frequency from smoothed averaged spectra of ISN seismograms.

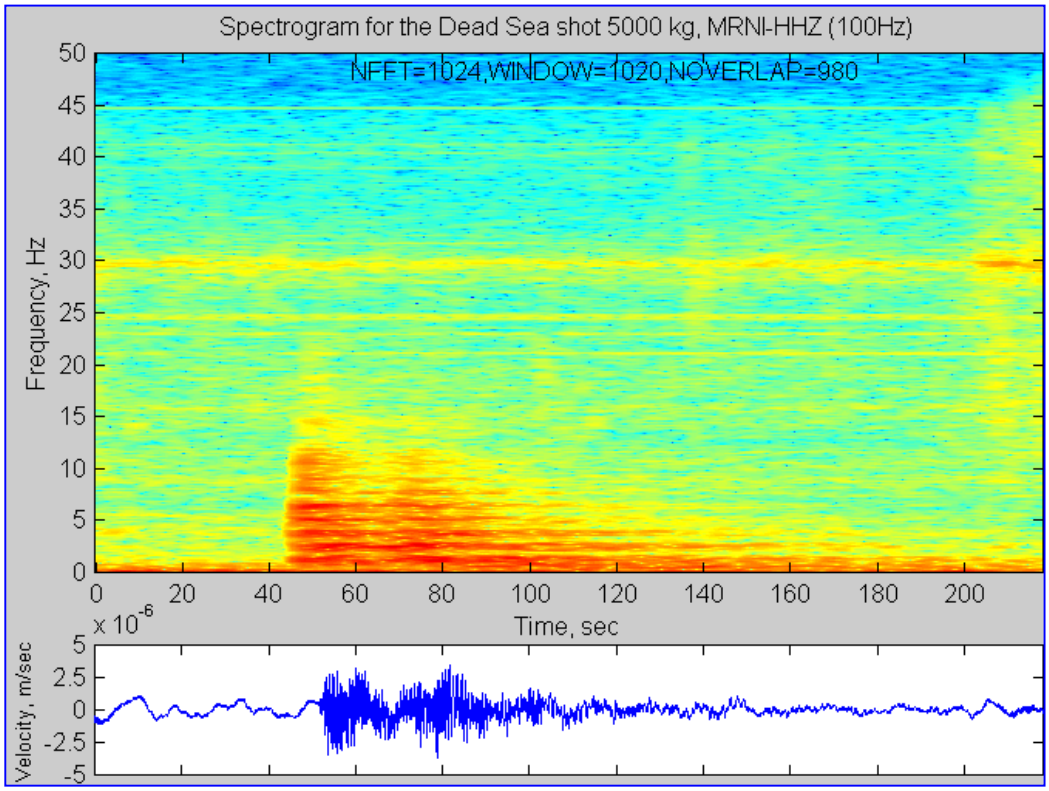


Fig. 8. Spectrogram of the largest explosion recorded at the BB IMS station MRNI (vertical component) with 100 sps (time windows 10.2 sec, shift 0.4 sec).

Spectrograms demonstrate time-independent spectral modulation with at least eight harmonic strips observed in the initial part of seismogram. The high-frequency strips are disappearing with time increasing. The low-frequency (less than 1 Hz) energy belongs to the coda of an earthquake in Turkey preceding the explosion. Obtained spectra and spectrograms show no energy at frequencies more than 10-12 Hz.

The bubble periods (and bubble frequencies), determined from the harmonic series in smoothed spectra of ISN seismograms (Fig. 7), are in good agreement with the modified Willis' (1963) empirical equation (see Table 1):

$$T_b = 2.1 * W^{1/3}/(P_0 + d * \square)^{5/6} \qquad f_b = 1/T_b \qquad (3)$$

where P_0 is the barometric pressure at the level of the Dead Sea (792 mm mercury or 10.778 m of water column during the experiment), the shot depth d = 70 m, water density $\square$=1.236g/cm^3. The observed periods are also consistent with estimations obtained from hydrophone recordings (Gitterman and Shapira, 2000), and from autocorrelation analysis of IMS stations (CMR Event Report, 1999).

Discrimination analysis. We tested the spectral classification method (Gitterman et al., 1998), which includes application to seismograms at different network stations of two spectral statistics: a) energy ratio in low and high frequency windows, averaged for several stations; b) semblance, characterizing coherency of spectral curves at network stations.

The method was applied to vertical ISN and 3C Broad Band (EIL, JER and MRNI) records of the three calibration explosions in the Dead Sea and of four earthquakes close in magnitude, location and time occurrence to the explosions. The earthquake parameters are presented in Table 2, and all analyzed events and recording stations are shown on Fig.1.

Table 2. List of earthquakes of October-November 1999, close in location and magnitude to the Dead Sea calibration shots.

Date year/month/day/hour/min/sec	Magn. M_L	X, km	Y, km	Depth, km	Latit.	Long.	Region
1999 10 04 02 04 37.6	2.8	192.4	80.2	22	31.31	35.45	Arad
1999 10 07 03 50 26.8	2.9	179.8	-0.6	9	30.58	35.31	Arava
1999 11 16 02 39 15.5	3.4	192.3	87.7	21	31.38	35.45	Arad
1999 11 16 16 57 45.0	2.7	183.0	21.7	15	30.79	35.35	Arava

Time windows of 30-40 sec, containing the whole signal, were used. The spectra are smoothed in frequency windows about 0.7 Hz, energy ratio was calculated for the (1-3 Hz)/(6-8 Hz) ranges, and semblance for the (1-12 Hz) range. For BB data the semblance is calculated in 1-9 Hz range, because only 20Hz records are available for some earthquakes.

Identification of underwater explosions is based on spectral features of recordings: spectra coherency at different stations, due to the bubbling modulation and low-frequency seismic energy. Figures 9-10 show coherent and relatively low-frequency spectra for the explosions, and non-regular and high-frequency spectra for the earthquakes. The different spectral patterns provided clear separation of the two populations of seismic events in the two-parametric space, shown on Fig. 11.

The spectral methods for discrimination between earthquakes and underwater explosions provided reliable automated identification of the Dead Sea explosions. These observations correspond well to the results from the previous series of smaller underwater explosions (16-304 kg) conducted along a profile in the Dead Sea in 1993 (Gitterman et al., 1998). In the following we are going to conduct the similar spectral discrimination analysis using data obtained at more distant short-period and BB stations.

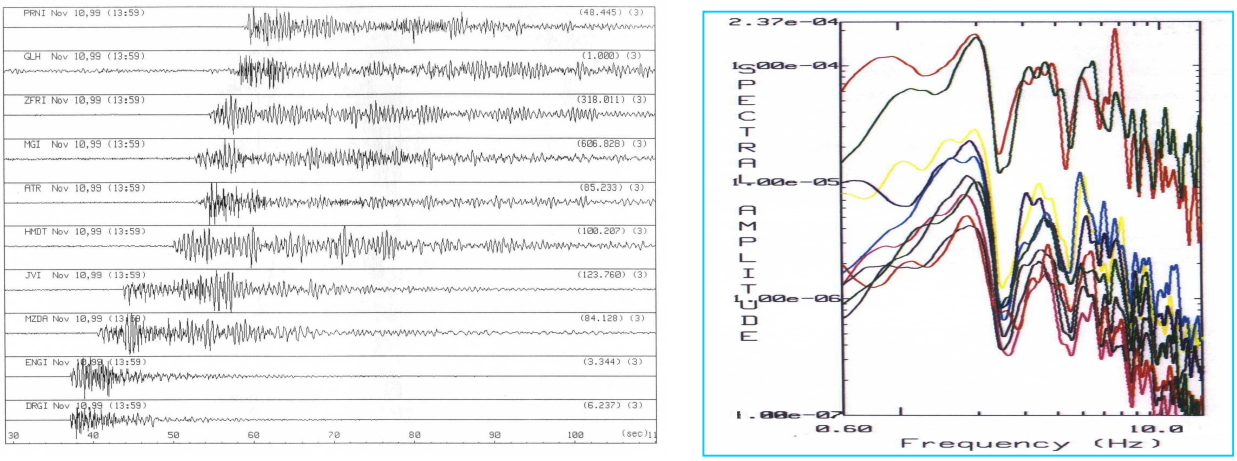


Fig. 9. Sample seismogram and spectral patterns at different ISN stations for the Dead Sea shot 2060 kg.

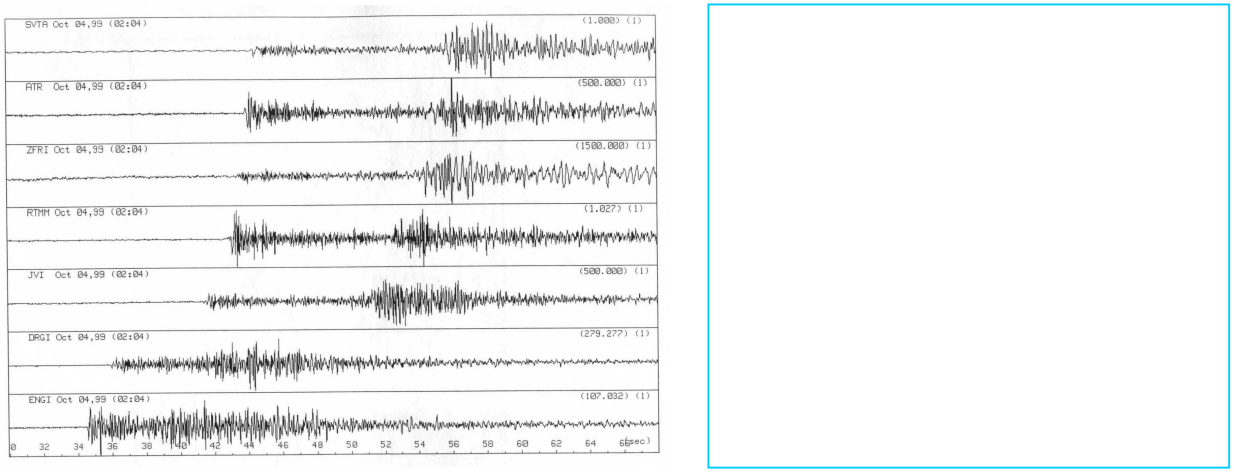


Fig. 10. Sample seismogram and spectral patterns at different ISN stations for the closest to the explosion site earthquake on 4.10.99.

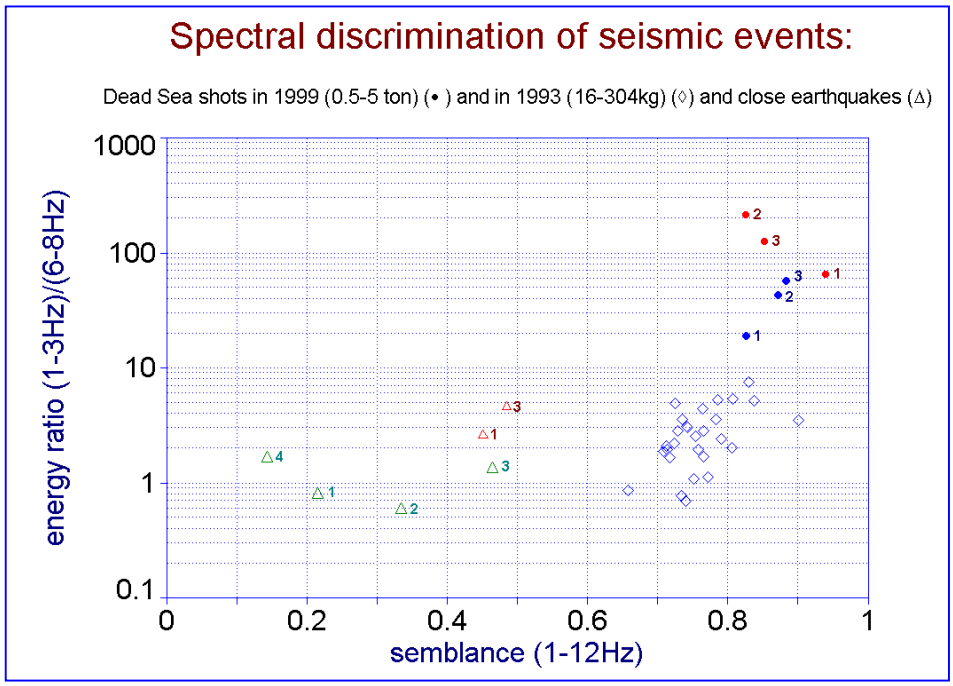


Fig. 11. Discrimination results for the Dead Sea explosions (•) and nearby earthquakes (Δ), based on ISN short-period recordings, and BB stations EIL, JER and MRNI (shown by red color, where semblance is calculated in 1-9 Hz range, because for some earthquakes only 20Hz records were available).

CONCLUSIONS AND RECOMMENDATIONS

The high magnitudes under relatively low charge weights confirm a high seismic efficiency of underwater explosions in the Dead Sea, significantly exceeding the upper limit curve for all known chemical and nuclear explosions in hard rock. The observed magnitudes and amplitudes of seismic waves verify that the whole charge was properly detonated in all cases. Our primary estimations of the seismic efficiency were justified, and the expected magnitude (about 4) was reached. Further work in estimating the seismic energy of the Dead Sea explosions is needed by the method, based on the coda envelops using broad band data at different frequency ranges.

A prominent spectral modulation (azimuth- and time-independent), caused by the bubble pulsation effect, is observed in all SP and BB seismograms, presented by the clear frequency banding in smoothed amplitude spectra of the whole signal and in spectrograms. The bubble periods, determined from the harmonic series on smoothed spectra of ISN seismograms, are in good agreement with the known empirical equation.

A preliminary discrimination analysis based on spectral energy ratio and semblance characteristics, using local short-period stations recordings of the explosions and nearby earthquakes with comparable magnitudes. Due to the specific features of seismic waves from the underwater explosions (spectra coherency at different stations, caused by the bubbling modulation, and low-frequency seismic energy), the analysis provided reliable separation between earthquakes and explosions in the Dead Sea region. Further analysis is needed including more distant seismic stations.

REFERENCES

Event Report – Dead Sea Calibration Explosions, 1999/11/08-1999/11/11, Issued: November, 1999, Center for Monitoring Research, Arlington.

Gitterman, Y., Z. Ben Avraham and A.Ginzburg, 1998. Spectral analysis of underwater explosions in the Dead Sea. Geophys. J. Int., 134, 460-472.

Gitterman Y., 1998. Magnitude-yield correlation and amplitude attenuation of chemical explosions in the Middle East. Proceedings of the 20th Annual Seismic Research Symposium on Monitoring a Comprehensive Nuclear Test Ban Treaty, Santa Fe, Sept.21-23, 1998, 302-311.

Gitterman, Y., V.Pinsky and A.Shapira, 1998. Spectral classification methods in monitoring small local events by the Israel seismic network. Journal of Seismology, 2: 237-256.

Gitterman, Y. and A. Shapira, 2000. Audio-visual and hydroacoustic observations of the Dead Sea calibration experiment, Proceedings of the 22nd Annual Seismic Research Symposium on Monitoring a Comprehensive Nuclear Test Ban Treaty, this volume.

Hofstetter, A. and Shapira, A., 2000. Determination of earthquake energy release in the Eastern Mediterranean region, Geophys. J. Int., in press.

Kanamori, H., Mori, J., Hauksson, E., Heaton, T., Hutton, K. and Jones, L., 1993. Determination of earthquakes energy release and M_L using TERRAscope, Bull. seism. Soc. Am., 83, 330-346.

Khalturin, V., T. Rautian, P. Richards and W-Y. Kim, 1997. Evaluation of chemical explosions and methods of discrimination for practical seismic monitoring of a CTBT, Report AFRL-VS-HA-TR-98-0012.

Mayeda, K. and Walter, R., 1996. Moment, energy, stress drop, and source spectra of Western United States earthquakes from regional coda envelopes, J. Geophys. Res., 101, 11195-11208.

Willis, D.E., 1963. Seismic measurements of large underwater shots, Bull. Seism. Soc. Am., 53, 789.

DEVELOPMENT OF REGIONAL TRAVEL-TIME TABLES FOR DIFFERENT GEOTECTONIC PROVINCES OF NORTHERN EURASIA

Victor V. Kirichenko and Yury A. Kraev
Western Services Corporation
Under subcontract to
Science Applications International Corporation

Sponsored by The Defense Threat Reduction Agency
Arms Control Technology Division
Nuclear Treaties Branch

Contract No. DSWA01-98-C-0029

ABSTRACT

During the last two years, new regional travel-time tables for different provinces of Northern Eurasia were developed in the framework of the Seismoacoustic Research for CTBT Monitoring project. This project is being performed by SAIC and its subcontractors: the Western Services Corporation, the Geophysical Survey of the Russian Academy of Sciences (RAS) and Complex Seismological Expedition (CSE) of the Joint Institute of Physics of the Earth of the RAS. One of the main objectives of the project is to calibrate travel times for regional seismic waves travelling to the seismic stations of the Russian Academy of Sciences included in the Comprehensive Nuclear-Test-Ban Treaty International Monitoring System (IMS).

The development of regional travel-time tables is based on the published data of origin times and locations of nuclear explosions as calibration sources. The data are from peaceful nuclear explosions on the territory of the former Soviet Union as well as underground nuclear tests at the Semipalatinsk test site, Amchitka Island, and the French Test Site in the Sahara. Values of arrival times for major regional seismic phases (Pn/P, Pg, Sn/S and Lg) were measured, analyzed and collected from the stations of the Geophysical Survey and Complex Seismological Expedition.

The territory of Northern Eurasia was subdivided into 11 provinces based on the results of the analysis of Pn travel times as well recently published papers on seismic and tectonic regionalization of Northern Eurasia. At the 22nd Seismic Research Symposium we present newly developed travel-time tables for the following provinces: Central-East-European territory, Cenozoic Folded Regions (Balkan and Carpathian mountains, Crimea-Caucasus-Kopet-Dagh, Tyan Shan), Ural folded region, West-Siberian platform, Kazakh massif, Altai and Sayan mountains, Siberian platform, Baikal rift zone, North East territory and Chukot Peninsula. For all the developed travel-time tables, modeling errors were calculated and their comparison with the IASPEI-91 tables is presented. The newly developed regional travel-time tables differ substantially from the IASPEI-91 travel-time tables. For the Pn seismic phase at distances of 1,500 - 2,000 km, the deviations from the IASPEI-91 travel-time tables are as follows: -8 to -10 sec for the Central-East-European territory, West-Siberian and Siberian platforms; -4 to -5 sec for the Ural folded region, the Kazakh massif and the Baikal rift zone and -2 to +4 sec for the Cenozoic folded regions and Altai and Sayan mountains. For the Sn phase at the same distances, the deviations from the IASPEI-91 travel-time tables are, respectively: -15 to -20 sec, -8 to-10 sec and -5 to +5 sec. For the Pg phase, travelling in the Earth's crust, the deviations from the IASPEI-91 travel-time tables may be subdivided into two groups of provinces as follows: 1) platforms, Paleozoic massifs and Baikal rift zone and 2) Cenozoic folded regions and Altai and Sayan mountains. For the first group the deviations are from -3 to -5 sec at the distances of 700 - 1,000 km. For the second group travel times are consistent with the IASPEI-91 travel-time tables. Travel times for the Lg phase have large deviations even for geotectonically homogeneous provinces and are almost the same for the studied provinces. At the current stage of studies we accepted the value of 3.55 km/sec for the apparent velocity of Lg phase for all the studied provinces. In general, modeling errors for the newly developed travel-time tables are lower then those for the IASPEI-91 tables.

The newly developed travel-time tables as well as their modeling errors were used for tests on re-location of historical underground nuclear explosions at the territory of the former Soviet Union. We used seismic records of the stations included in the IMS or those stations, which are located not farther than 300 km from the IMS stations within geotectonically homogeneous regions. A comparison between the mislocation estimates for the newly developed travel-time tables and the IASPEI -91 travel-time tables is presented.

OBJECTIVE

This work represents the results of a continued effort to develop regional travel-time tables for different geotectonic provinces of Northern Eurasia. The overall objective is to calibrate travel times for regional seismic waves travelling to the seismic stations of the Russian Academy of Sciences included in the Comprehensive Nuclear-Test-Ban Treaty International Monitoring System (IMS). The newly developed travel-time tables may be directly used to improve seismic event location as well as to test and to validate 3D travel-time models currently being developed.

RESEARCH ACCOMPLISHED

Regionalization

The regionalization of the territory of the Northern Eurasia was carried out on the basis of recent seismicity studies (Seismicity and Seismic Zoning of Northern Eurasia, 1993 and 1995), geological and tectonic features of deep structures (Deep Structure, 1991; Pavlenkova, 1996) as well as taking into account the results of our analysis of Pn travel times. For presentation of our results, the territory of the Northern Eurasia was subdivided into 11 provinces: Central-East-European territory, Cenozoic folded regions, Ural folded region, West-Siberian platform, Kazakh massif, Altai and Sayan region, Siberian platform, Baikal rift zone, Amur and Maritime territory, North East territory and Chukot Peninsula, Kamchatka-Kuril-Sakhalin region. The polygon vertices for the specific provinces are presented in Table 1. Figure 1 presents the regionalization of the territory of Northern Eurasia.

Calibration Events

It is obvious that underground nuclear explosions with announced data on time origins, locations and depths are the most appropriate calibration events. For the purposes of the IMS seismic calibration in Northern Eurasia underground nuclear explosions conducted at the territory of the former Soviet Union (peaceful nuclear explosions, Semipalatinsk Test Site (STS) and Novaya Zemlya Test Site), in the Sahara desert (France) and on Amchitka Island (USA) were chosen due to their appropriate relative location to the territory of the Northern Eurasia. Recently published data on peaceful nuclear explosions (PNEs) in the USSR (Sultanov et al, 1999) as well as previously and recently published data on nuclear underground tests at the Semipalatinsk Test Site (Bocharov et al, 1989; Adushkin et al, 1997; Belyashova, 1999), on Amchitka Island (Springer et al, 1971 and Springer et al, 1975) and in the Sahara desert (Duclaux et al, 1972) allowed the development of a database using well-characterized calibration events. Calibration events of the GT0 category were primarily used for the development of regional travel-time tables.

Data on Travel Times

Data resources were formed on the basis of seismic observations conducted during the time framework of 1965 - 1990 by the Geophysical Survey (GS) of the RAS and the Complex Seismological Expedition (CSE) of the Joint Institute of Physics of the Earth of the RAS. Values of arrival times for major regional seismic phases (Pn/P, Pg, Sn/S and Lg) were measured, analyzed and collected.

The total number of the GS's stations used for the purposes of seismic calibration is about 400. The total number of the CSE's stations used for the purposes of seismic calibration is about 200. Data of seismic observations of the RAS's institutions was added by the data of about 300 station in the Northern Eurasia providing data to the International Seismological Center.

Results

The regional travel-time curves were constructed using linear regression of the experimental travel time data using one or two linear regressions for the residual standard deviation minimization. Modeling errors were calculated as standard deviations of the experimental data from the estimated lines in a 2-degree moving window with a 50 % overlap. The basic equation and the parameters of the developed travel-time tables are presented in the Table 2. Modeling errors for the developed travel-time tables are presented in the Table 3. The newly developed regional travel-time tables differ substantially from the IASPEI-91 travel-time tables (see the Abstract). Figures 2, 3 and 4 represents the comparison of the Pn, Sn, Pg and Lg reduced travel-time curves for: (1) Central-East-European territory, West-Siberian platform, Siberian platform, (2) Ural folded region, Kazakh massif, Baikal rift zone, (3) Cenozoic folded regions, Altai and Sayan region, North-East territory and Chukot Peninsula and IASPEI-91. We grouped the aforementioned provinces taking into account the similarity of Pn and Sn reduced travel-time tables.

Tests on Relocation

We have located 21 historical underground nuclear explosions at the STS with published ground truth time of origins and locations (Bocharov et al, 1989) using the IASPEI-91 travel-time tables. Then, we relocated the aforementioned set of the explosions using the newly developed travel-time tables. We used the network of eight regional seismic stations included in the IMS (ZAL, MAK, NRI, GEYT, BRVK, ARU, AAK, TLY) or those stations, which are located not farther than 300 km from the IMS stations within geotectonically homogeneous regions. The aforementioned stations are located at the range of 6^O to 20^O from the underground nuclear explosions. The defining phases were: Pn, Sn, Pg and Lg. LocSat, provided by DTRA's Center for Monitoring Research (CMR), was used for the relocation tests.

The testing and validation metrics are as follows:

- 90% of events moved closer to the GT epicenters with an average improvement of 8.7 km and a median improvement of 7.0 km;
- 76% of events moved closer to the GT epicenters by 20% or more with an average improvement of 7.2 km and median improvement of 7.0 km;
- 10% of events moved away from GT epicenters with an average deterioration of 7.8 km and a median deterioration of 7.8 km;
- the same 10% of events moved away from GT epicenters by 20% or more;
- average mislocations by using the IASPEI-91 travel-time tables and the regional travel-time tables are 18.9 km and 8.2 km, respectively;
- median mislocations by using the IASPEI-91 travel-time tables and the regional travel-time tables are 14.9km and 7.9 km, respectively;
- 33% of GT epicenters are within the calculated 90% uncertainty ellipses by using the IASPEI-91 travel-time tables and 80% of GT epicenters are within the calculated 90% uncertainty ellipses by using the regional travel-time tables;
- average uncertainty ellipse area is 442 km^2 for the IASPEI-91 travel-time tables and 327 km^2 for the regional travel-time tables;
- median uncertainty ellipse area is 408 km^2 for the IASPEI-91 travel-time tables and 313 km^2 for the regional travel-time tables;
- average and median decrease of 90% uncertainty ellipse size is 115 km^2 and 103 km^2, respectively;
- average bias in origin time estimation is 1.1 sec with an associated standard deviation of 1.0 sec (median bias is 1.1 sec) for the IASPEI-91 travel-time tables and -0.5 sec with an associated standard deviation of 0.8 sec (median bias is -0.4 sec) for the regional travel-time tables.

CONCLUSIONS AND RECOMMENDATIONS

1. The regional travel-time tables for the different geotectonic provinces of the Northern Eurasia were newly developed and compared with the IASPEI-91 tables. The developed regional travel-time tables differ substantially from the IASPEI-91 travel-time tables.
2. Validation testing using ground truth data related to the underground nuclear explosions at the STS shows that estimates of event locations and time origins are significantly improved and location error ellipses are substantially reduced using the newly developed travel-time tables.
3. At the final stage of the project performance we are planning to complete the development of regional travel-time tables for the remaining geotectonic provinces of the Northern Eurasia, to clarify the previously developed travel-time tables taking into account still coming travel-time data from our subcontractors and to continue relocation tests using ground truth time of origins and locations for underground nuclear explosions at the territory of the USSR and DetSSSC's software developed at the CMR (Xioping Yang et al, 1998).

Key Words: Seismic Regional Characterization, Location Calibration.

REFERENCES

Adushkin, V.V., V.A. An, V.M. Ovchinnikov and D.N. Krasnoshchekov, A jump of the Density on the Outer-Inner Core Boundary from the Observations of PkiKP Waves on the distance about 6 ^{O}, Transactions of the RAS, Vol. 354, No. 3,1997.

Belyashova, N.N. National Nuclear Center of Kazakhstan Republic, Table of Locations of Balapan Nuclear Explosions Newly Mapped by NNCKR, Calibration Workshop, 12-14 January 1999, Oslo, Norway.

Bocharov, V.S., S.A. Zelentsov and V.N. Mikhailov, Characteristics of 92 Underground Nuclear Explosions at the Semipalatinsk Test Site, Atomnaya Energiya, Vol. 87, No. 3, 1989.

Deep Structure of the USSR Territory. Moscow. Nauka Publishing House, 1991 (in Russian).

Duclaux, F., M.L. Michaud, Conditions Experimentals des Tirs Nucleaires Souterains Francais au Sahara, R. Acad. Sc., Paris, Vol. 270,Serie B, 189-192,1972.

Pavlenkova N.I., Crust and Upper Mantle Structure in Northern Eurasia from Seismic Data. Advances in Geophysics, Vol. 37, Academic Press, 1996.

Seismicity and Seismic Zoning of Northern Eurasia. Vol. 1. Moscow: IPE RAS,1993 (in Russian).

Seismicity and Seismic Zoning of Northern Eurasia. Vol. 2-3. Moscow: UIPE RAS,1995 (in Russian).

Springer, D.L. and R.L. Kinnaman, Seismic Source Summary for U.S. Underground Nuclear Explosions, 1961-1970. Bull. Seim. Soc. Am., Vol.61, 1073-1098, 1971, and Seismic Source Summary for U.S. Underground Nuclear Explosions, 1971-1973. Bull. Seim. Soc. Am., Vol.65, 343-349, 1975.

Sultanov, D.D., J.R. Murphy, and Kh.D. Rubinstein, A Seismic Source Summary for Soviet Peaceful Nuclear Explosions, Bull. Seim. Soc. Am., Vol.89, No.3, 1999.

Xioping Yang, Keith McLaughlin, Robert North, SSSCs for Regional Phases at IMS Stations in North America and Fennoscandia, Technical Report CMR-98/46.

Table 1. Regionalization of Northern Eurasia

Region No.	Region name	Polygon Vertices, Lat. (deg. N) - Long. (deg. E)			
I	Central-East-European territory	72-6 48-56	72-48 48-12	70-48 52-12	70-56 52-6
II	Cenozoic folded regions	48-12 40-90 32-72	48-62 40-78 32-42	46-62 38-78 36-42	46-90 38-72 36-12
III	Ural folded region	78-48 48-62	78-72 48-56	74-72 70-56	74-62 70-48
IV	West-Siberian platform	78-72 58-86 74-62	78-102 58-82 74-72	70-102 54-82	70-86 54-62
V	Kazakh massif	54-62	54-82	46-82	46-62
VI	Altai and Sayan region	58-82	58-104	46-104	46-82
VII	Siberian platform	78-102 54-138 58-104	78-132 54-114 58-86	64-132 60-114 70-86	64-138 60-104 70-102
VIII	Baikal rift zone	60-104	60-114	48-114	48-104
IX	Amur and Maritime territory	54-114	54-142	42-142	42-114
X	North East territory And Chukot Peninsula	76-132 60-156 64-132	76-168W 58-156 76-132	60-168W 58-138	60-168 64-138
XI	Kamchatka-Kuril-Sakhalin region	60-156 48-162 54-142	60-168 48-156 54-138	52-168 42-156 58-138	52-162 42-142 58-156

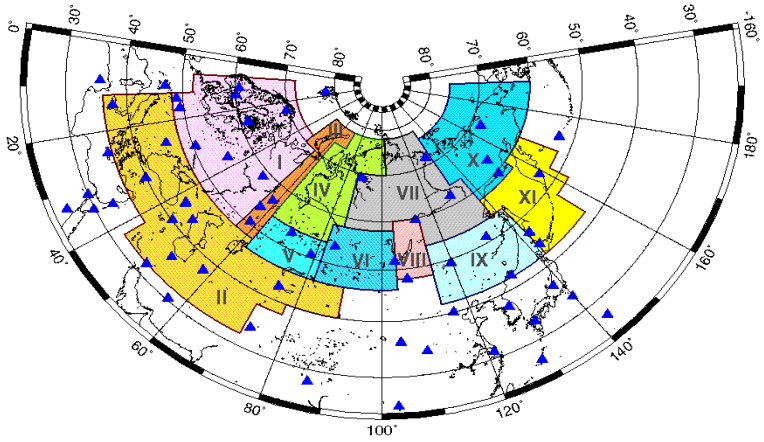


Figure 1. Regionalization of Northern Eurasia
I. Central-East-European territory II. Cenozoic folded regions III. Ural folded region IV. West-Siberian platform V. Kazakh massif VI. Altai and Sayan regions VII. Siberian platform VIII. Baikal rift zone IX. Amur and Maritime territory X. North East territory and Chukot Peninsula XI. Kamchatka-Kuril-Sakhalin region, - IMS stations

Table 2. Parameters of the Developed Travel-Time Curves (Depth = 0 km)

Basic Equation: $T\text{-}R/V_{red} = (A \pm \sigma_A) - (B \pm \sigma_B) \times R$

Phase	Range, km	V_{red}, km/sec	A	σ_A	B	σ_B	N	r	SD, sec
I. Central-East-European territory									
Pn	250-1150	8.0	8.15	0.37	0.0044	0.0004	75	0.80	0.8
	1151-2500	8.0	14.63	0.39	0.0098	0.0002	288	0.93	1.5
Sn	250-2500	4.62	15.76	0.75	0.0058	0.0005	235	0.59	3.4
Pg	250-1300	6.0	0.64	0.67	0.0062	0.0006	75	0.75	1.6
Lg	250-2500	3.5	-2.25	1.28	0.0016	0.0009	167	0.13	5.0
II. Cenozoic folded regions									
Pn	200-1800	8.0	8.79	0.36	0.0033	0.0003	224	0.59	1.9
Sn	250-2000	4.62	12.12	1.23	-0.0020	0.0012	84	0.18	4.4
Pg	250-1200	6.0	1.25	1.19	0.0056	0.0016	57	0.43	2.4
Lg	200-2200	3.5	0.87	1.63	0.0045	0.0016	85	0.29	5.3
III. Ural folded region									
Pn	250-2000	8.0	8.23	0.40	0.0048	0.0004	59	0.87	1.2
Sn	250-2000	4.62	12.86	1.22	-0.0002	0.0011	53	0.03	3.3
Pg	250-1200	6.0	-0.60	1.06	0.0047	0.0014	35	0.50	1.8
Lg	200-2200	3.5	-2.08	1.21	0.0018	0.0012	38	0.24	3.1
IV. West-Siberian platform									
Pn	250-2300	8.0	8.84	0.54	0.0065	0.0004	89	0.90	1.7
Sn	300-2200	4.62	15.69	1.27	0.0036	0.0009	86	0.38	4.1
Pg	250-1200	6.0	-0.54	1.45	0.0052	0.0016	42	0.46	2.3
Lg	250-2200	3.5	-1.62	1.49	0.0034	0.0011	82	0.33	4.8
V. Kazakh massif									
Pn	250–777	8.0	8.11	0.39	0.0026	0.0006	57	0.51	1.0
	778-2200	8.0	10.71	0.68	0.0061	0.0004	74	0.87	1.3
Sn	250-2000	4.62	15.96	0.86	0.0037	0.0007	82	0.49	2.9
Pg	300-1200	6.0	0.28	1.28	0.0045	0.0016	28	0.49	1.9
Lg	250-2300	3.5	-2.24	1.17	0.0027	0.0010	86	0.28	4.2
VI. Altai and Sayan region									
Pn	250-1600	8.0	8.40	0.62	0.0010	0.0008	62	0.23	1.6
Sn	300-2200	4.62	13.25	1.60	-0.0007	0.0011	57	0.08	4.2
Pg	300-1200	6.0	-0.93	3.05	0.0026	0.0031	25	0.17	3.3
Lg	250-2200	3.5	-6.60	1.47	-0.0020	2.1013	99	0.21	4.2
VII. Siberian platform									
Pn	250-2300	8.0	9.83	0.39	0.0069	0.0002	206	0.90	1.4
Sn	600-2300	4.62	16.99	1.04	0.0067	0.0006	174	0.64	3.0
Pg	300-1300	6.0	-0.90	1.54	0.0055	0.0014	29	0.60	1.9
Lg	250-2500	3.5	-3.51	1.18	0.00002	0.0007	189	0.03	4.0
IX. Baikal rift zone									
Pn	400-2000	8.0	6.83	0.59	0.0032	0.0006	282	0.87	1.3
Sn	400-2000	4.62	12.36	1.04	0.0008	0.0007	178	0.61	3.3
Pg	400-1200	6.0	-0.89	1.32	0.0037	0.0017	121	0.53	1.8
Lg	400-2500	3.5	-6.41	0.59	-0.0020	0.0004	245	0.34	4.0
XI. North East territory and Chukot Peninsula									
Pn	350-2000	8.0	9.97	0.79	0.0044	0.0006	27	0.85	1.5
Sn	500-2200	4.62	6.62	2.48	-0.0050	0.0018	17	0.58	4.0
Pg	500-1200	6.0	1.56	2.31	0.0051	0.0023	7	0.69	2.0
Lg	400-2500	3.5	-0.99	2.42	-0.0013	0.0014	17	0.23	4.0

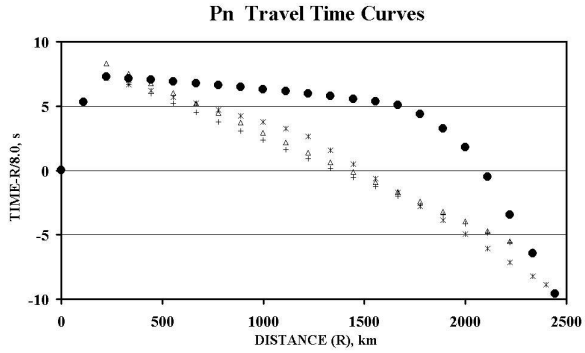
Note: **T - travel time, sec; R - epicentral distance, km; V_{red} - reduction velocity, km/sec;**
N - data set; r - correlation coefficient; SD - residual standard deviation, sec.

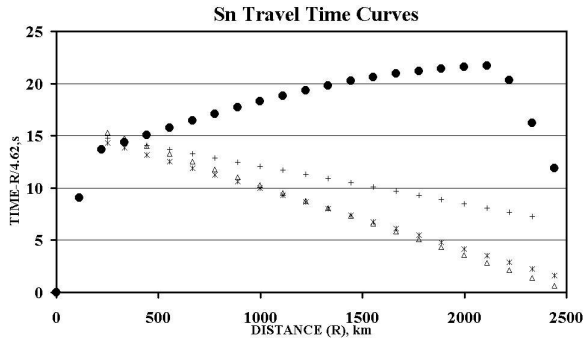
Table 3. Modeling Errors for the Eurasian Geotectonic Provinces

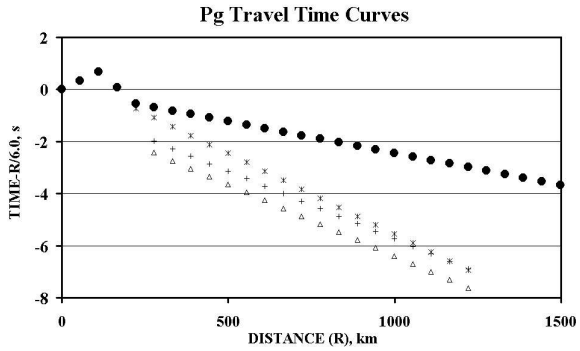
Dis-tance, deg.	I. Central-East-European territory				II. Cenozoic folded regions				III. Ural folded region				IV. West –Siberian platform				V. Kazakh massif			
	Modeling Error, sec				Modeling Error, sec				Modeling Error, sec				Modeling Error, sec				Modeling Error, sec			
	Pn	**Pg**	**Sn**	**Lg**	**Pn**	**Pg**	**Sn**	**Lg**	**Pn**	**Pg**	**Sn**	**Lg**	**Pn**	**Pg**	**Sn**	**Lg**	**Pn**	**Pg**	**Sn**	**Lg**
3	0.5	0.9	3.8	4.5	0.4	1.9	3.8	4.6	0.8	1.9	3.7	3.2	1.8	2.1	1.8	3.9	0.9	1.7	2.6	2.0
4	0.4	1.0	3.9	4.7	1.3	2.9	3.9	4.3	0.6	2.0	2.2	3.5	1.8	2.2	1.2	3.7	0.8	1.8	1.1	3.1
5	0.9	1.7	2.9	6.7	1.2	3.0	2.9	4.8	1.0	1.9	2.2	3.4	1.7	3.2	4.9	4.7	0.6	2.1	1.8	4.1
6	0.9	1.6	2.6	7.0	1.2	1.9	2.6	3.9	1.4	1.8	2.6	3.4	1.7	3.3	7.0	1.8	0.7	2.2	2.3	5.0
7	0.6	1.3	2.9	5.7	1.2	1.7	2.9	3.9	1.5	2.9	2.9	2.9	1.7	2.6	3.7	4.4	1.0	2.4	3.2	4.4
8	0.7	1.0	3.4	2.6	1.8	2.3	3.4	5.4	0.6	2.0	4.7	3.0	1.7	2.5	4.4	3.7	1.3	2.2	4.6	2.9
9	0.8	1.4	3.3	3.8	2.1	3.2	3.3	6.6	1.1	1.2	4.3	4.6	1.4	2.2	4.0	4.1	1.5	1.4	4.8	5.0
10	1.2	1.7	3.9	4.4	1.8	3.0	3.9	5.8	1.6		2.4	6.9	1.3	2.0	2.9	5.0	1.2		3.1	4.7
11	1.2	1.7	3.4	5.1	2.1		3.4	7.3	1.6		2.7	3.9	1.5		3.4	5.9	0.9		2.7	4.4
12	1.4		2.9	5.7	2.2		2.9	9.2	1.5		4.7	3.6	1.5		4.1	4.6	0.9		2.7	5.2
13	1.6		3.5	4.5	1.9		3.5	6.0	1.4		4.4	4.0	1.4		5.1	4.5	0.8		3.0	5.1
14	1.0		3.8	4.7	2.3		3.8	4.3	1.4		4.3	4.3	2.2		5.2	7.5	0.8		3.0	3.3
15	1.3		3.7	5.5	2.6		3.7	5.5	1.4		3.8	5.5	2.8		3.5	6.5	1.5		2.8	4.1
16	1.5		3.0	5.8	2.4		3.0	5.1	1.1		2.3	5.1	2.1		3.8	4.6	1.6		3.2	4.5
17	1.3		3.0	6.3	2.4		3.0	6.3	1.0		3.0	6.3	1.6		5.3	4.4	1.5			6.5
18	1.2		3.5	7.1			3.5	7.1	0.5		3.5		1.8		6.8	4.1	1.7			
19	1.5		2.7	7.1			2.7	7.1			2.7		1.0		2.9	7.0				
20	1.5		3.2	3.7			3.2	3.7			3.2		0.9							

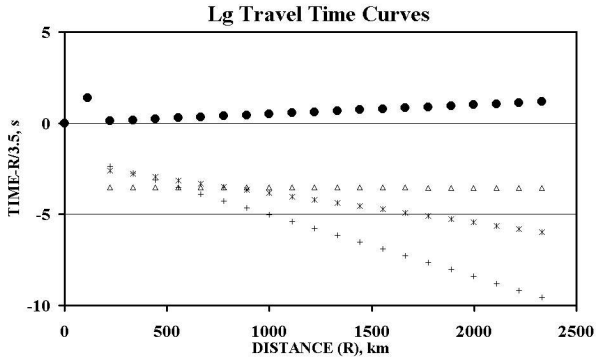
Table 3 (continued)

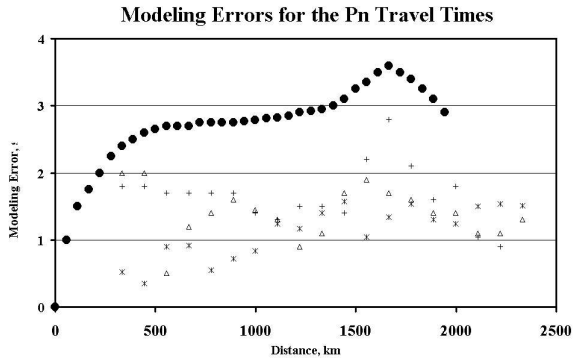
Dis-tance deg.	VI. Altai and Sayan region				VII. Siberian platform				VIII. Baikal rift zone				X. North East territory and Chukot Peninsula			
	Modeling Error, sec				Modeling Error, sec				Modeling Error, sec				Modeling Error, sec			
	Pn	**Pg**	**Sn**	**Lg**	**Pn**	**Pg**	**Sn**	**Lg**	**Pn**	**Pg**	**Sn**	**Lg**	**Pn**	**Pg**	**Sn**	**Lg**
3	1.0	2.0	2.7	3.5	2.0	3.0	3.0	4.5	1.3	1.2	1.9	3.6	0.5			
4	1.0	2.5	2.9	3.1	2.0	2.5	2.5	4.2	1.2	2.0	1.8	2.9	1.4			
5	1.1	3.6	3.3	3.2	0.5	2.2	3.9	4.0	1.2	1.9	2.2	3.1	1.4			
6	0.9	4.5	3.7	3.0	1.2	2.4	2.3	3.7	1.2	1.6	2.1	2.9	1.5			
7	1.5	4.6	3.0	3.5	1.4	2.3	3.0	3.8	1.2	1.2	2.6	3.0	1.0			
8	1.8	3.5	2.8	3.4	1.6	2.3	4.0	3.6	1.1	1.5	3.2	3.3	0.8			
9	1.7	3.1	3.4	4.0	1.5	2.0	4.1	5.2	1.6	2.1	3.2	3.9	1.0			
10	1.9	3.1	3.7	3.6	1.3	1.8	3.1	5.7	1.6		3.6	4.4	1.7			
11	2.3		5.2	5.0	0.9	1.6	2.8	3.9	1.3		3.6	4.5	1.1			
12	3.1		5.7	6.5	1.1		2.9	3.1	1.4		3.9	4.1	1.1			
13	2.4		4.4	5.3	1.7		3.3	3.9	1.3		4.9	3.4	1.4			
14	1.0		4.7	4.1	1.9		4.3	4.1	1.1		5.1	3.5	1.5			
15	0.8		5.8	3.5	1.7		4.3	3.7	2.1		5.3	4.3	1.6			
16			6.1	4.6	1.6		3.2	4.0	2.6		5.0	4.4	1.4			
17			4.6	5.2	1.4		2.9	3.9	2.1			4.2	2.3			
18			4.7	6.2	1.4		2.9	3.4								
19			4.0	6.7	1.1		2.2	3.3								
20					1.1		2.1	3.9								

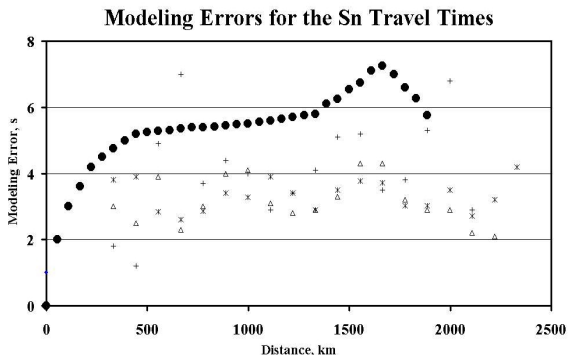


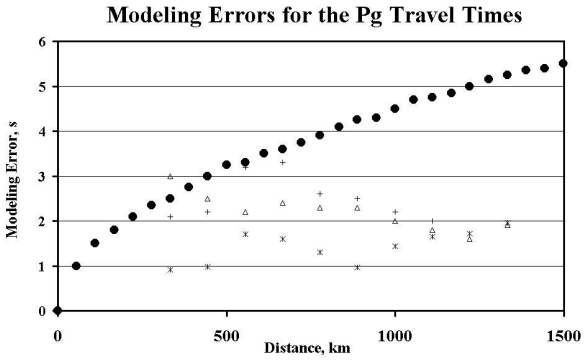












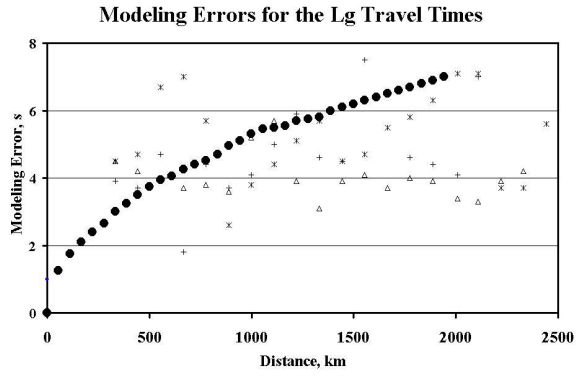


Figure 2. Comparison of Pn, Sn, Pg and Lg reduced travel-time curves and modeling errors for Central-East-European territory (+), West-Siberian platform (*), Siberian platform (□) and IASPEI-91 (□).

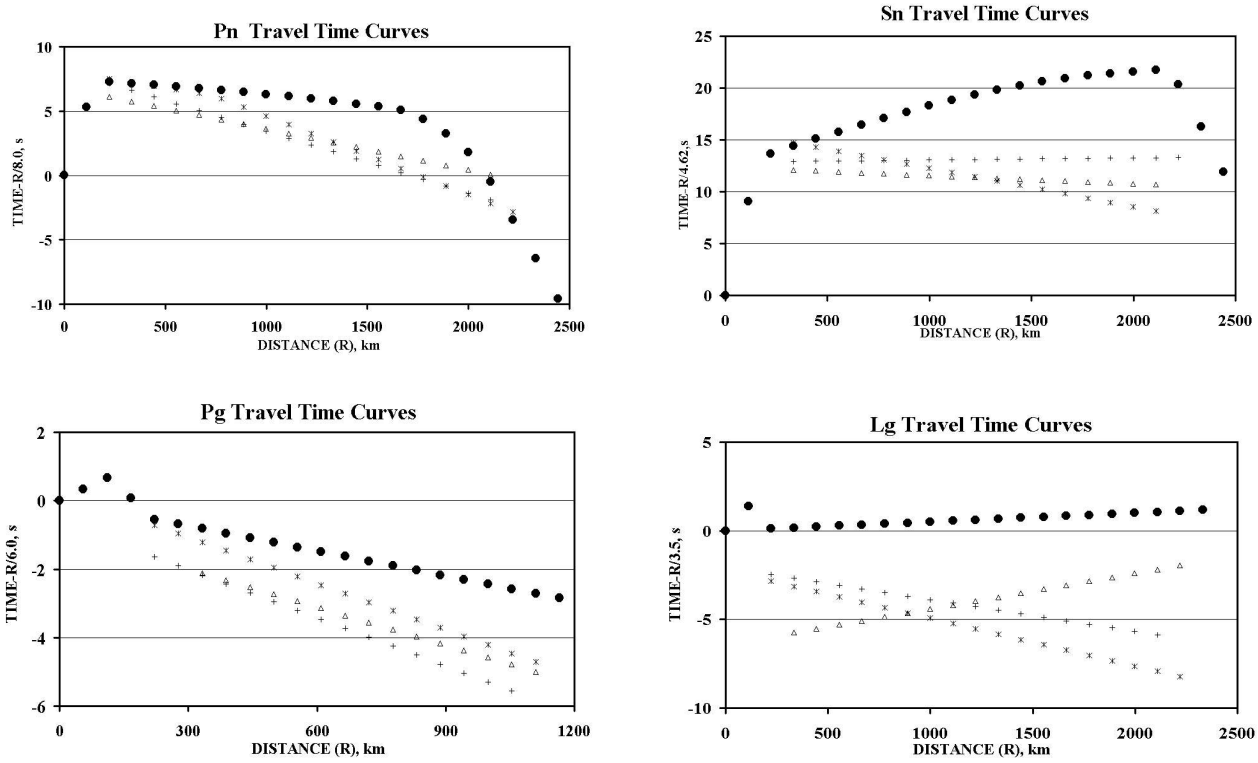


Figure 3. Comparison of Pn, Sn, Pg and Lg reduced travel-time curves and modeling errors for Ural folded region (+), Kazakh massif (*), Baikal rift zone (□) and IASPEI-91 (□).

SURFACE WAVE PROPAGATION EFFECTS OBSERVED AT THE SAUDI SEISMIC NETWORK

Gabi Laske and Nathalie Cotte

Cecil H. and Ida M. Green Institute of Geophysics and Planetary Physics, La Jolla

Sponsored by The Defense Threat Reduction Agency
Through SAIC Subcontract Number: 44000025260

ABSTRACT

Global surface wave arrival angles (also called polarization data) are extremely useful data to constrain the short-wavelength structure in global surface wave phase velocity maps. This paper investigates the feasibility of using such data on a more regional scale to validate regional models. We measure the arrival angles at the Saudi Arabian Seismic Network and compare them with predictions calculated using published phase velocity maps. We find large discrepancies between data and existing maps and demonstrate the great potential such data have to constrain the regional structure around the Saudi Arabian Peninsula. A by-product of our procedure is the retrieval of the misalignment of the horizontal components of the seismic sensor. We find a significant misalignment of approximately 4 degrees for the seismometer at station AFIF.

Key Words: Seismic Surface Waves, Western Asia, Saudi Network, Arrival Angles, Surface Wave Dispersion, Model Validation

OBJECTIVE

The objective of this research is to investigate techniques and surface wave datasets to validated regional crustal and upper mantle models. Special attention is dedicated to assess the feasibility of using arrival angle data in this process. This project concentrates on waves propagating in the area covering Western Asia, Near East, Eastern Europe and Northern Africa.

RESEARCH ACCOMPLISHED

Introduction

Under the new SAIC consortium grant DTRA01-PRDA-99-01, a group of University affiliates work with SAIC to compile a new high-resolution crust and upper mantle model for Western Asia and Northern Africa. This initiative is driven by both factors the need of the seismic monitoring community for a model that is more accurate than what is currently available and the recent vast increase of a variety of regional seismic data. While all the traditionally used databases will go into the modelling process, ranging from crustal refraction seismic data bases to dispersion measurements for short- and intermediate-period regional and semi-regional surface waves, some others will not be considered. Among these are surface wave arrival angles, also called polarization data. The reasons why such data are usually not considered in regional (and global) modelling are many-fold and include the comparably large difficulty to obtain precise measurements, the dependence on horizontal component records, the increased sensitivity to noise and the complexity of the theoretical framework to interpret the measurements.

Since polarization data are more sensitive to small-scale structure than surface wave dispersion data are, it seems natural to use such data in the validation process of a newly developed model. In this paper, we investigate the feasibility of this endeavor. While our database is routinely updated to include data from all broad-band stations available for the Western Asian and Northern African Region, the study presented here concentrates on observations obtained at the Saudi Arabian Seismic Network (Figure 1). This network was installed by colleagues Frank Vernon and Rob Mellors at Scripps (Vernon et a., 1996) and was operational from December 1995 through February 1997 (Table 1).

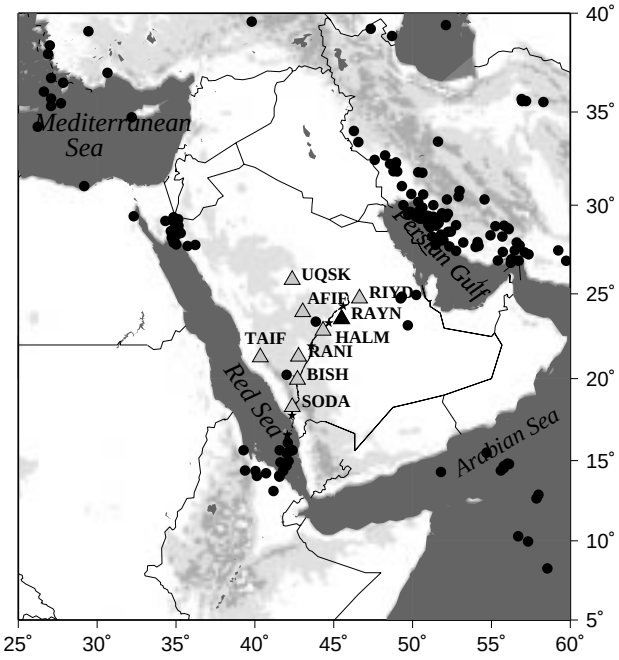


Figure 1. Map of the temporary Saudi Arabian Seismic Broadband Network (triangles). BISH was operational from November to December 1995, while station RAYN became the permanent IRIS/IDA station in June 1996 (see also Table 1). The circles are regional events recorded by the network between November 1995 and May 1996.

Table 1. The Saudi Arabian Seismic Network

Station	Latitude	Longitude	Start	End	Location
AFIF	23.9310	43.0400	95.327	97.055	Afif
BISH	19.9228	42.6901	95.322	95.338	Bisha
HALM	22.8454	44.3173	95.327	97.055	Hadabat Al-Mahri
RANI	21.3116	42.7761	95.338	97.058	Raniyah
RAYN	23.5220	45.5008	95.337	96.160	Ar Rayn
RIYD	24.7220	46.6430	96.069	97.060	Riyadh
SODA	18.2921	42.3769	95.338	97.058	Al-Soda
TAIF	21.2810	40.3490	96.158	96.240	Taif
UQSK	25.7890	42.3600	96.161	97.055	Uqlats Sakur

A useful by-product of the investigation of polarization data is the retrieval of the misalignment of the horizontal components. Significant misalignment of more than 5 degrees has been found at global broad-band stations (Laske, 1995; Laske and Masters, 1996) which has often later been confirmed and corrected by the network operators. For example, a previously unknown significant deviation of the north-component from true North could be corrected at station AAK -- a key station for the seismic monitoring community -- in January 1994 after we detected a misalignment in our dataset. In this paper, we present the misalignment of the horizontal components found for the stations of the Saudi Seismic Network.

Peculiar Waveforms in the Surface Wave Database

Our current database for the Saudi Arabian Seismic Network includes surface wave waveforms for all shallow large events (source depth less than 150 km; seismic moment greater than $4x10^{18}$ Nm). These events typically have surface wave magnitudes Ms=6.2 and larger. We also include smaller events (with seismic moments greater than

$5x10^{17}$ Nm) for epicentral distances smaller than 95 degrees for which the surface wave magnitudes are typically 5.2 and larger. Our database has yet to be augmented with the smaller regional events (e.g. as shown in Figure 1) but now has 176 shallow, mainly teleseismic events. The raw 40 Hz data which are available at the IRIS/DMC are initially decimated to 1 Hz data and low-pass filtered at 37 s. All 3-component records are also corrected for instrumental effects and the horizontal components are rotated into radial and transverse components. In the processed 3-component records, we often notice a surprisingly large signal on the transverse component, at the same time as the fundamental mode Rayleigh wave train but significantly later than the expected time for the fundamental mode Love wave. This is especially the case for events occurring in the Kuril Islands region (Figure 2).

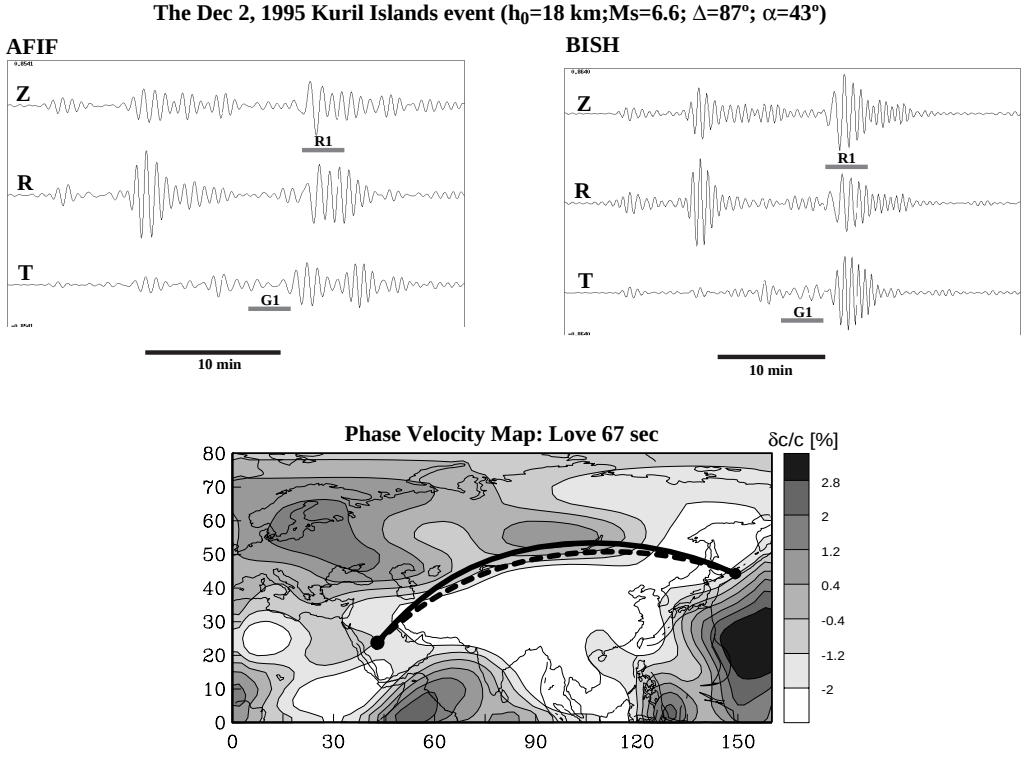


Figure 2. top: Three-component records at stations AFIF and BISH of the Dec 2, 1995 (95.336) Kurils Islands event. Note the strong signal on the transverse component at the theoretical Rayleigh wave arrival time (R1). Also note the lack of signal at the time predicted for the Love wave to arrive (G1) and the difference of signal between stations AFIF and BISH. The seismograms were low--pass filtered for periods longer than 37s.
bottom: A section from the global phase velocity map of Laske and Masters (1996) for Love waves at 67 s. Also shown is the source-receiver great circle (dashed) and the actual ray (solid) resulting from a ray tracing calculation using this map. The ray diverts up to 3 degrees from the great circle and the arrival angle predicted at the receiver is -6 degrees.

Tests with synthetic seismograms show that events in the Kuril Islands with source mechanisms similar to that of the Dec 2, 1995 event produce only little fundamental mode Love wave energy on the transverse components at the Saudi Array. We therefore suspect that the observed signal is composed of either delayed scattered Love waves or accelerated short-period Rayleigh waves that were refracted into faster regions adjacent to the great-circle path between the source and receiver. Multi-pathing effects would therefore "rotate" the seismic wave packets for Rayleigh and Love waves from the expected radial and transverse components. To test our hypothesis, we perform 2D ray tracing calculations using the phase velocity maps that are available in the literature. For estimating the effects at long and short periods we compare the calculations for the phase velocity maps of Ekstrom et al. (1997) and of Laske and Masters (1996) at different periods. The map in Figure 2 represents the "average case" around 65 s for which lateral heterogeneity diverts the ray path up to 3 degrees away from the source-receiver great circle. The arrival angle at station AFIF is about 6 degrees if looking toward the source. Lateral refraction is less at longer periods where heterogeneity is more dominated by long-wavelength structure (the arrival angle at 100 s is 2 degrees)

and gets stronger for shorter periods (the arrival angle at 35 s is 7.5 degrees). We also use the linear path integral approximation of Woodhouse and Wong (1986) to predict arrival angles. For 35 s we obtain an angle of 14.5 degrees which is significantly different from the ray tracing angle. Discrepancies of this magnitude are usually indicative for significant multi-pathing effects between source and receiver so that both theoretical values are invalid and a polarization measurement from the corresponding seismogram cannot be interpreted in terms of a wave propagating along a single ray.

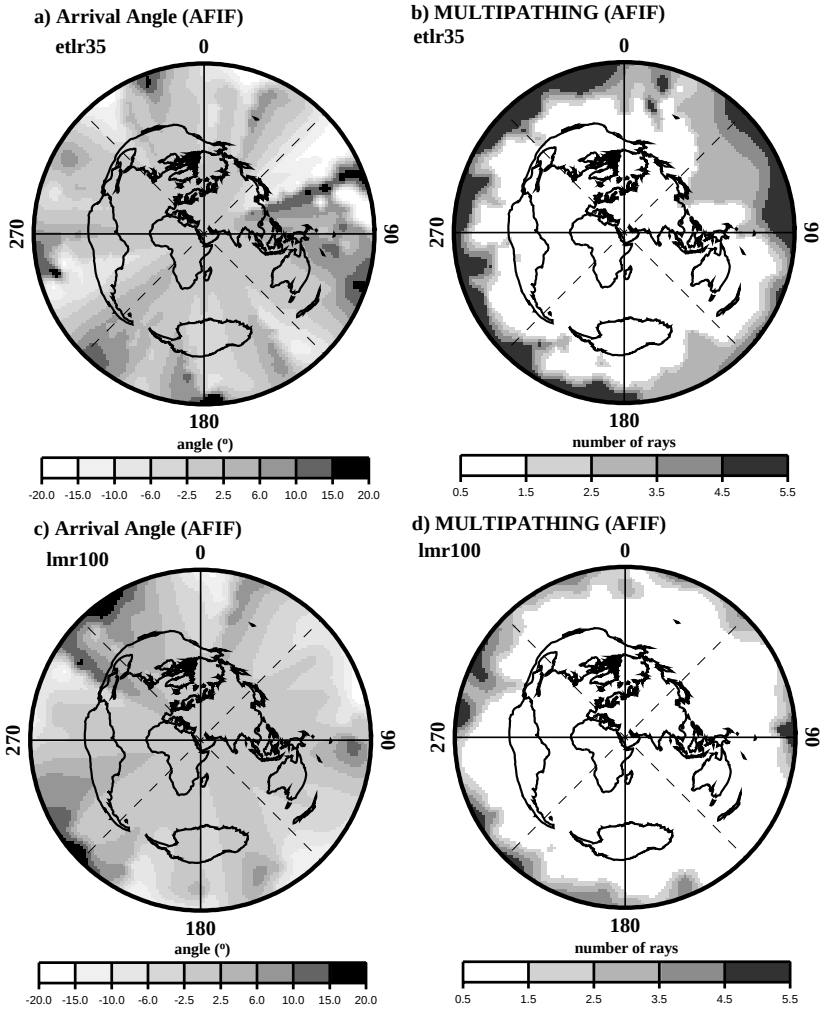


Figure 3. Ray tracing maps obtained by using the global phase velocity maps of Ekstrom et al. (1997) for 35 s (etlr35) and Laske and Masters (1996) for 100 s (lmr100). The maps are drawn in polar representation and were obtained by tracing rays from fictitious source locations on a 5x5 degree grid to station AFIF at the center. a)+c) Plotted are the ray tracing angles for models etlr35 and lmr100 obtained for each fictitious source at its source location. b)+d) Multi-pathing expressed as the number of rays arriving within less than a wave period. Considerable multi-pathing is found for events in the Kuril Islands region for short periods, while for long periods this effect as well as off-great circle arrival angles are moderate.

In Figure 3, we demonstrate the severity of multi-pathing for the case of station AFIF. We use the FD ray tracer of Farra (1990) to calculate arrival angles as well as estimate the strength of multi-pathing by counting the rays that come in at the same time within a period. Calculations are performed with fictitious sources on a 5x5 degree grid. We notice strong multi-pathing and large predicted arrival angles for fictitious events occurring near the Kuril Islands. As expected, the effect is much weaker for longer periods for which the phase velocity maps contain significantly less short-wavelength structure. From this experiment we conclude that arrival angles measured for

short periods at the Saudi Arabian Seismic network for events occurring in the Kuril Island regions cannot be used in the modelling of seismic structure.

Polarization Angles-Station Misorientation

Using the multi-taper technique of Laske et al. (1994a), we are able to obtain 384 high-precision arrival angles for 83 of the 176 events at each period between 250 and 60s and 204 angles at each period between 60 and 40s for 48 additional events. Table 2 summarizes the number of measurements for both Love and Rayleigh waves for each station and some examples of measurements are shown in Figure 4. Values at all periods are usually to within 25 degrees of the great circle direction but the variance in the data increases significantly as periods get shorter (not shown). The observed arrival angles at station AFIF are peculiar. For both Love and Rayleigh wave the angles concentrate around -5 degrees. Less strong but also obvious is a similar clustering of the data at station SODA. The relative stability of these mean values may encourage the data analyst to adopt them as an underlying misrotation of the horizontal components. However, some contribution to the mean in the data may come from lateral heterogeneity. This is especially true for stations with only few measurements. In order to avoid mapping component misalignment into seismic heterogeneity and vice versa we prefer to include a component misalignment as additional model parameters in a joint inversion for structure (Laske, 1995). The relationship between polarization angles and component misalignment is non-linear but can easily be linearized and solved for in an iterative procedure in which only 1 or 2 iterations are necessary for the system to converge. The joint inversion of the new polarization data observed at the Saudi Network is performed with the augmented global database of Laske and Masters (1996), for long-wavelength structure up to harmonic degree 12. To increase the accuracy of the determined component-misalignment, we perform similar inversions for at least 6 cases which are typically 3 periods in the long-period band (250-100s) for both Rayleigh and Love waves and then average the results. We use only long periods because the increasing contribution from short-wavelength structure could induce a bias at shorter periods, especially for stations with uneven data coverage.

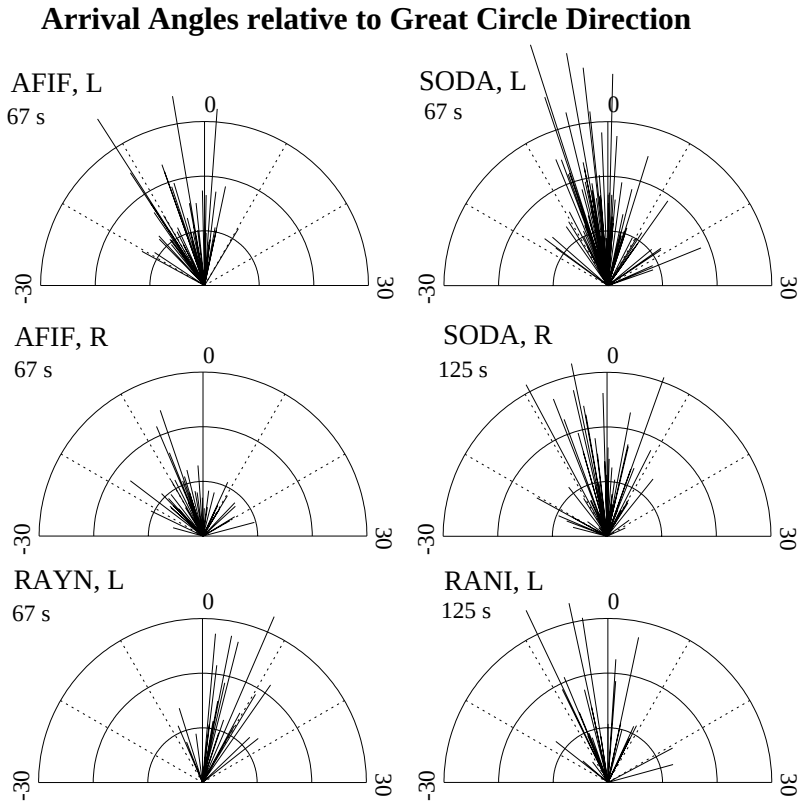


Figure 4. Polarization angles at stations AFIF, SODA, RAYN and RANI for Rayleigh (R) and Love (L) waves at 67 s and 125 s period. The plots show rose diagrams, where the polar angle is the off-great circle arrival angle and the

length of the plotted vector is the reciprocal error bar. Accurate measurements with small error bars tend to stick out of the cluster of observations. At stations AFIF, many of the measurements cluster at about -5 degrees. This is observed for both Love and Rayleigh waves at all frequencies. The horizontal components at this site were likely to be misaligned.

Table 2. Component Misalignment Expressed as Apparent North

Station	# Rayleigh	# Love	Apparent North [deg]	Comment
AFIF	64	57	-4.22 +/- 0.66	
BISH	5	5	0.52 +/- 1.35	uncertain; stolen after 2 weeks
HALM	35	38	-1.65 +/- 0.84	
RANI	34	35	-2.76 +/- 0.96	
RAYN	29	25	1.71 +/- 0.87	
RIYD	5	14	0.70 +/- 1.34	uncertain; late installation
SODA	83	93	-2.72 +/- 0.54	
TAIF	16	18	-4.01 +/- 1.66	uncertain; late installation
UQSK	15	17	-4.04 +/- 2.52	uncertain; late installation

Table 2 summarizes the component misalignment that we obtain for the stations of the Saudi Network. Though the of amount of data at each station is relatively low as compared to those for permanent broad-band stations of the global seismic network, we obtain stable results at at least 4 of the 9 stations (AFIF, RANI, RAYN and SODA). Note that the components at station AFIF are significantly rotated with respect to true North by approximately 4 degrees. Stations SODA and RANI also have significant misalignment though it is smaller than at station AFIF. The misalignment at these three stations implies that the systems are rotated clockwise from true North, while the components at RAYN are rotated anti-clockwise. The number of data at stations BISH, RIYD and TAIF is relatively low which is reflected in the larger error bar for the misalignment. However, the misalignment at station TAIF is at least 2.5 degrees. The value for station UQSK is somewhat uncertain as the few available measurement have large error bars and Love and Rayleigh wave angles seem inconsistent. It is important to recognize that the polarization data have to be corrected for component misalignment in these cases as predictions using existing high-resolution global phase velocity maps are typically within 5 degrees from the source-receiver great circle, hence of the same magnitude.

Polarization Angles -- Compatibility with Existing Dispersion Maps

After the polarization data have been corrected for component misalignment, the data can now be used to validate an existing model or be used jointly with other data in an inversion for a new model. To test whether the data are consistent with currently existing models, we compare the arrival angles at various periods with the predictions calculated for a particular phase velocity map. We chose the linear path integral approximation of Woodhouse and Wong (1986) as theoretical framework to interpret the measured arrival angles as an integral of the transverse gradient of phase velocity perturbation along the source-receiver great circle. The phase velocity maps we test are those of Laske and Masters (1996) (L&M), Ekstrom et al. (1997) (ET&L), Trampert and Woodhouse (1995) (T&W) and their updated version (Trampert and Woodhouse, 1996). All maps are available on the WWW or through anonymous ftp and are expanded in surface spherical harmonics where the truncation level varies. The L&M maps are expanded up to l=24, while the maps of ET&L and T&W are truncated at l=36 or l=40. We find that the short-wavelength structure in the ET&L and T&W maps for harmonic degree 25 and above generally increases the misfit of the data so we truncate all maps for the comparison in Table 3 at l=24, while maintaining the original truncation in Figure 5. We should also note that the linear theoretical framework to interpret polarization data starts to break down if significant large-amplitude structure at l=36 is present (Laske et al., 1994b; Wang and Dahlen, 1995). We find that the different maps for similar periods can give very different variance reductions though the maps look rather similar (Table 3, Figure 5). For example, our polarization data are reasonably consistent with the T&W Rayleigh wave phase velocity maps at 100 and 67 s but are clearly inconsistent with the Love wave maps of the same authors. It is

interesting to note that the updated version of 1996 fairs much worse than the 1995 version, possibly due to the fact that the 1996 maps contain more incompatible short-wavelength structure (l=10-24) than the 1995 maps. Our polarization data are also inconsistent with the L&M maps. We can achieve a significantly better fit to the data with variance reductions up to 40% when we include the new data in a joint inversion with the global polarization and dispersion dataset of Laske and Masters (1996) for new phase velocity maps. An example is shown in Figure 5.

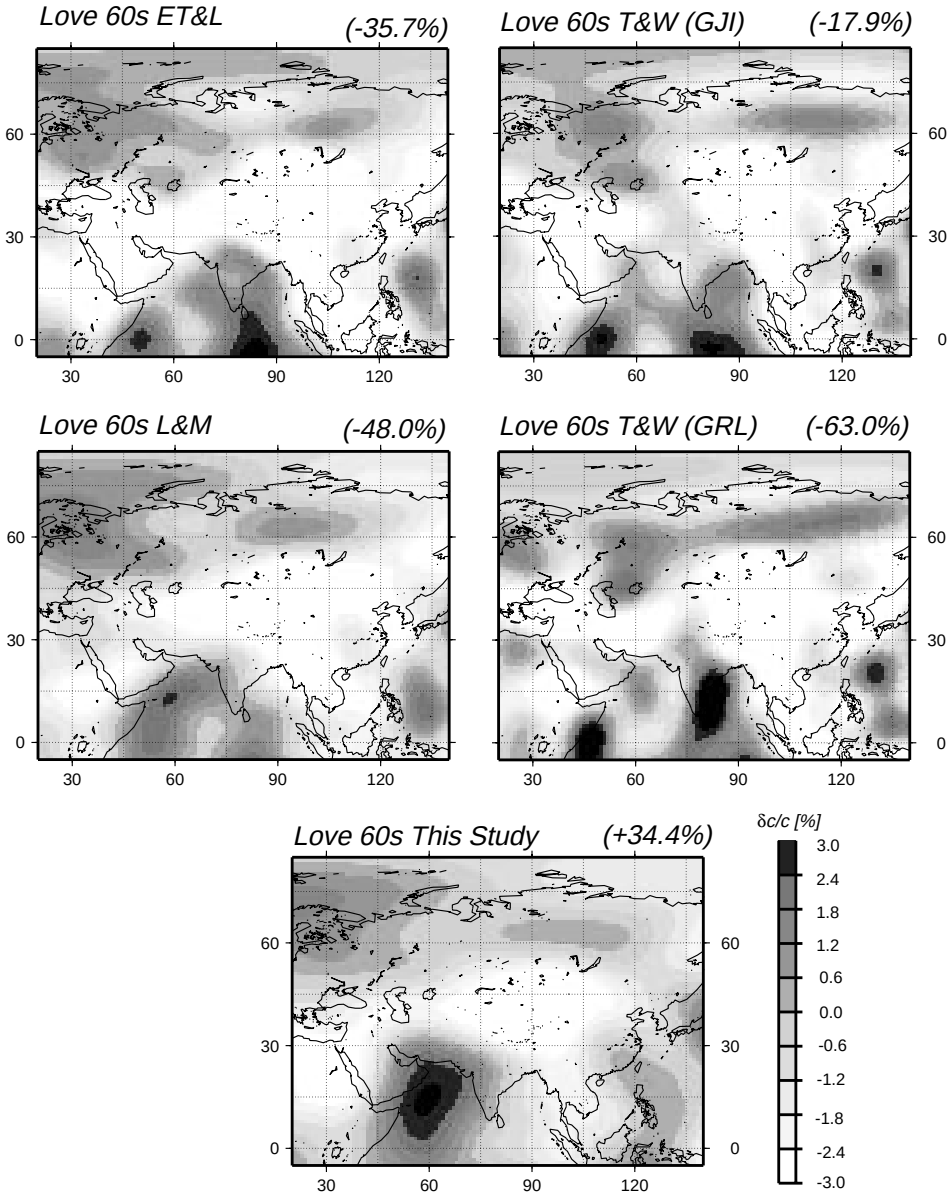


Figure 5. Sections of the global phase velocity maps of Ekstrom, Tromp and Larson (1997) (ET&L), Trampert and Woodhouse (T&W; 95=GJI; 96=GRL) and Laske and Masters (1996) for Love waves at 60 sec (L&M). All maps are expanded in surface spherical harmonics, with different truncation levels (ET&L: l=36; T&W: l=40; L&M: l=24). The lower panel shows a map obtained from a joint inversion of the L&M dataset and the new arrival angle data of the Saudi Seismic Network. Note that the new data require significant changes in regional structure to be well fit (the number in the right upper corners list the variance reduction for each map).

Obviously, the new data require a significant enhancement of structure to the southeast of the Saudi Arabian Peninsula. Also note that changes in the model can occur as far the Philippines. We want to stress that the data

coverage of the L&M dataset is significantly poorer than that of the ET&L dataset (about 1/3) and that the map shown in Figure 5 should not be regarded as a new model for the Eurasian region. We are also currently measuring arrival angles across the array using a wavefront fitting technique that was successfully applied to intermediate-period data recorded in the French Alps (Cotte et al., 2000). A possible discrepancy with the polarization data introduced in this paper could point either toward the complexity of the approaching wavefront, inconsistencies in the polarization dataset and local anisotropy. Obviously, this project is ongoing research but we want to summarize by pointing out the great potential of a dataset of high-precision polarization measurements to constrain structure on a regional scale.

Table 3. Variance Reduction for the Saudi Polarization Data

Data Type	L&M	ET&L	T&W 95	T&W 96
R 150s	6	13	21	-2
R 100s	-17	20	29	23
R 67s	-62	-6	24	28
R 50s	0	-10	-	-
R 40s	-	-5	-21	-27
L 150s	-9	-6	-15	-53
L 100s	-44	-5	-4	-42
L 67s	-48	-36	-18	-63
L 50s	12	9	-	-
L 40s	-	2	1	-36

CONCLUSION AND RECOMMENDATIONS

We have described our current catalog of arrival angle measurements (also called polarization data) at the Saudi Arabian Seismic Network and we have demonstrated the great potential of such a dataset for

a) re-calibrating the orientation of horizontal components

b) validating existing models using such data

While sifting our database for outliers we produced ray tracing maps for stations at the Saudi Network. Such maps are invaluable tools to identify source regions that are likely to be the origin of travel paths that suffer from severe multi-pathing effects, for a given station. Not only should polarization measurements for such events be discarded a priori as outliers. Dispersion measurements, especially measurements of group travel time can also strongly be affected by distortions in the spectral amplitudes that are caused by focusing-defocusing effects. For the case of the Saudi Arabian Seismic Network, we should obviously discard all polarization data for events occurring in the Kuril Islands region and we should also investigate the consistency of dispersion measurements for the corresponding seismic records very carefully when modelling Earth structure or locating events.

It is important to realize that the ray tracing maps vary strongly from station to station within the Western Asian/Northern African region and also vary as a function of period. We typically identify less critical source regions for longer periods (about 100s) than for shorter periods (35s) since longer period surface waves are less affected by relatively shallow (i.e crustal) short-wavelength structure. A particular source region may display multi-pathing for one station but not for another. For example, waveforms recorded for the Kuril Islands events that were so peculiar for the Saudi Array will most likely not suffer from multi-pathing effects at IRIS/IDA stations AAK and ABKT as indicated in Figure 6. On the other hand, Macquarie Ridge events will likely produce distorted short-period surface wave packets at station AAK. The same is true for events in the Solomon/Fiji/Tonga subduction system recorded at station ABKT. Also worth mentioning is the fact that multi-pathing can occur for events significantly closer than 90 degrees, an epicentral distance cut-off that is typically used in regional surface wave tomography. We therefore recommend to

c) produce ray tracing maps for individual stations to evaluate a potential bias in surface wave polarization and dispersion data caused by focusing-defocusing effects.

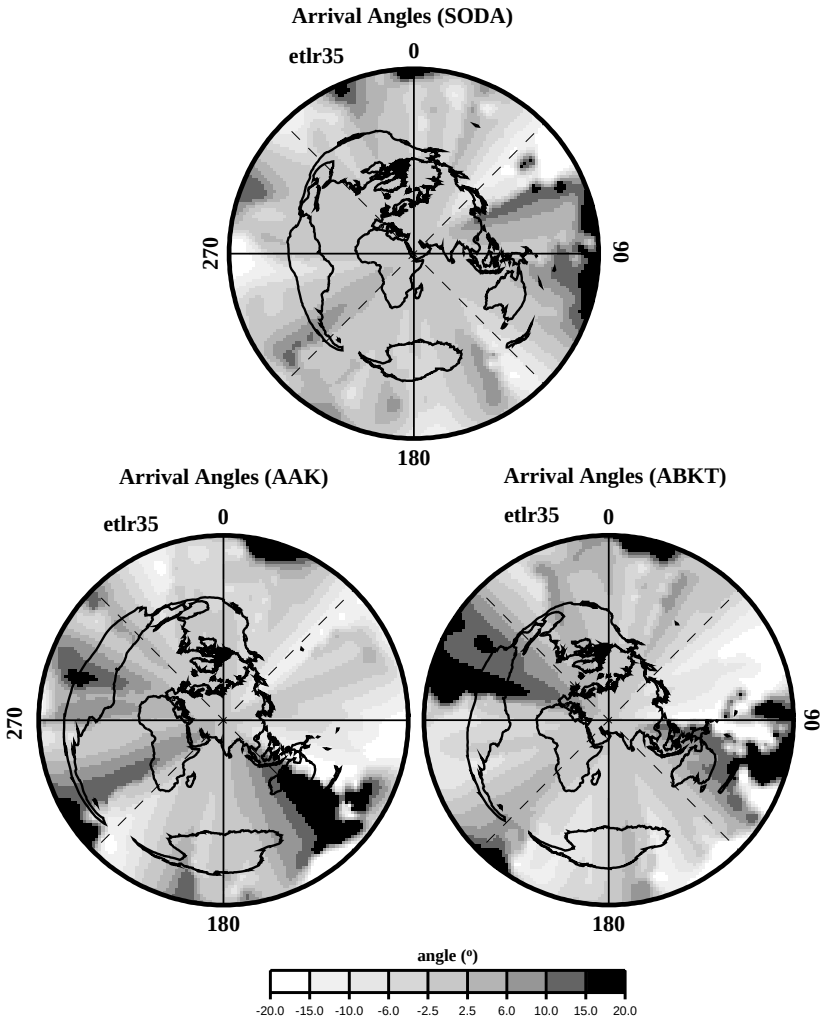


Figure 6. Ray tracing maps obtained with global phase velocity maps of Ekstrom et al. (1997) for 35 s (etlr35) for the Saudi Seismic station SODA and the IRIS/IDA stations AAK and ABKT. For details see Figure 3. Note that the maps look quite different for the relatively close stations AAK and ABKT.

REFERENCES

Cotte N., Pedersen H.A., Campillo M., Farra V. and Cansi Y., 2000. Off-great circle propagation of intermediate period surface waves as observed on a dense array in the French Alps, *Geophys. J. Int*., in press.

Ekstrom, G., J. Tromp, and E.W. Larson, 1997. Measurements and models of global models of surface wave propagation, *J. Geophys. Res*., **102**, 8137—8157.

Farra, V., 1990. Amplitude computation in heterogeneous media by ray perturbation theory: a finite element approach, *Geophys. J. Int*., **103**, 341—354.

Laske, G., G. Masters, and W. Zurn, 1994a. Frequency-dependent polarization measurements of long-period surface waves and their implications for global phase-velocity maps, *Phys. Earth Planet. Int*., **84**, 111-137.

Laske, G., G. Masters, and J. Um, 1994b. Phase, amplitude and polarization of surface waves and the fine-scale structure of global dispersion maps, *EOS Trans. AGU*, **75**, F 476.

Laske, G., 1995. Global observation of off-great circle propagation of long-period surface waves, *Geophys. J. Int*., **123**, 245—259.

Laske, G., and G. Masters, 1996. Constraints on global phase velocity maps by long-period polarization data, *J. Geophys. Re*s., **101**, 16,059--16,075.

Trampert, J., and J.H. Woodhouse, 1995. Global phase velocity maps of Love and Rayleigh waves between 40 and 150 seconds, *Geophys. J. Int*., **122**, 675—690.

Trampert, J., and J.H. Woodhouse, 1996. High-resolution global phase velocity distribution, *Geophys. Res. Let.*, **23**, 21—24.

Vernon, F., R.J. Mellors, J. Berger, A.M. Al-Amri, and J. Zollweg, 1996. Initial results from the deployment of broad-band seismometers in the Saudi Arabian Shield, *Proceedings of the 18th Seismic Research Symposium on Monitoring a Comprehensive Test Ban Treaty*, 4-6 Sept, Annapolis, Maryland, 108—117.

Wang, Z., and F.A. Dahlen, 1995. Spherical-spline parameterization of three-dimensional Earth models, *Geophys. Res. Lett*., **22**, 3099—3102.

Woodhouse, J.H., and Y.K. Wong, 1986. Amplitude, phase and path anomalies of mantle waves, *Geophys. J. R. Astron. Soc*., **87**, 753—773.



CRUSTAL EFFECTS ON REGIONAL SEISMIC PHASES IN ASEISMIC REGIONS OF NORTHERN EURASIA: CONSTRAINTS FROM PNE RECORDINGS

Igor B. Morozov, Scott B. Smithson, and Elena A. Morozova

Department of Geology and Geophysics, University of Wyoming, PO Box 3006, Laramie, WY, 82071-3006

Sponsored by U.S. Department of Defense
Defense Threat Reduction Agency

Grant No. DSWA01-98-0015

ABSTRACT

The University of Wyoming database of seismic recordings of Peaceful Nuclear Explosions (PNEs) has been recently extended to 19 PNEs recorded along 7 long-range refraction/reflection profiles: QUARTZ, CRATON, KIMBERLITE, RIFT, METEORITE, and RUBY (2 lines). These profiles form a grid traversing the East European Platform, the Ural Mountains, the West Siberian Basin, the Baikal Rift, and the Siberian craton in two directions,., and include dense and reversed linear as well as fan PNE recordings (RUBY). Dense, 3-component recordings along subparallel and crossing profiles provide us with unique opportunities to study large-scale propagation effects of regional seismic phases, allow detailed examination of the regional seismic phases, correlation between the individual PNE records and with geologic and tectonic features.

In this report, we extend traditional, travel-time analysis of PNE arrivals to amplitude and waveform inversion and show how short-period PNE recordings are used to constrain the effects of crustal structure on seismic arrivals within 1000 - 3000 km ranges. These new constraints include (1) characterization of crustal attenuation through coda measurements and (2) imaging of the crustal structure using receiver function techniques. Both of these factors are of primary importance for modeling of crustal-guided phases, such as the P_g and L_g,

Energy-balance considerations in three dimensions show that an extensive coda is inherent to all *P*-wave phases. This coda can be explained by crustal scattering and is a result of effectively areal excitation of short-period scattered waves (P_g, S_g, L_g, R_g) within the crust by the waves incident from the mantle, or, conversely, by generation of mantle phases from crustal-guided waves within a distributed source region. The resulting estimates of coda Q range between Q=380 near 2 Hz and Q=430 around 5 Hz and can be associated with crustal attenuation. Our coda model also explains the observed build-up of the arrival amplitude with time and the apparent lack of a pronounced coda of body-wave arrivals from the mantle transition zone. We "deconvolve" the overlapping codas of the arrivals and extract their true relative amplitudes. These coda-free amplitudes could potentially be used in improved seismic discriminants.

In order to constrain the principal crustal structures from regional and teleseismic PNE arrivals, we show that scattering and P/S conversions within the crust cause reverberations in the waveforms of *P*-wave arrivals. Stacking of receiver functions of first arrivals results in consistent images of the basement along the PNE profiles. In another consequence, variation of the sediment/basement contact is a major factor influencing the complexity of PNE arrivals that may influence both amplitude and frequency characteristics of seismic discriminants.

This study demonstrates that amplitudes and waveforms of PNE records provide valuable quantitative constraints on crustal structure for the analysis of the propagation of L_g and other phases and for development and calibration of regional seismic discriminants.

Key Words: Peaceful Nuclear Explosions, Russian Eurasia, Crust, Scattering, Attenuation, Receiver Functions

OBJECTIVE

During the past several years, supported by the grants from the Air Force Office for Scientific Research (F49620-94-1-0134 and F49620-94-A-0134) and from the Defense Threat Reduction Agency (DSWA01-98-0015) the University of Wyoming has acquired an impressive data set of seismic recordings of Peaceful Nuclear Explosion along a grid of linear profiles in Northern Eurasia (Figure 1). These unique seismic data are being investigated for their potential use in CTBT monitoring.

Until recently, apart from observations of *Lg* and *S* waves and their amplitude measurements (Morozov et al., 1997, 1999), PNE records were analyzed primarily as wide-angle seismic data, with an emphasis on travel-time modeling and inversion. In this report, we focus our attention on the amplitude and waveform pattern of the PNE wavefield and investigate applicability and usefulness of coda amplitude measurements and receiver function techniques traditionally employed in teleseismic studies. Our objective in the following is to demonstrate that (1) these methods allow constraining variations of the depth of the basement and crustal attenuation – crustal features that are critical for *Lg* modeling and seismic path calibration, and (2) accounting for coda effects allows obtaining coda-free amplitudes of secondary phases (P_g, *PP*, *S*, L_g) that could be used in improved seismic discriminants.

RESEARCH ACCOMPLISHED

Of the seven PNE lines in Figure 1, QUARTZ has been studied the best, with detailed crustal and upper

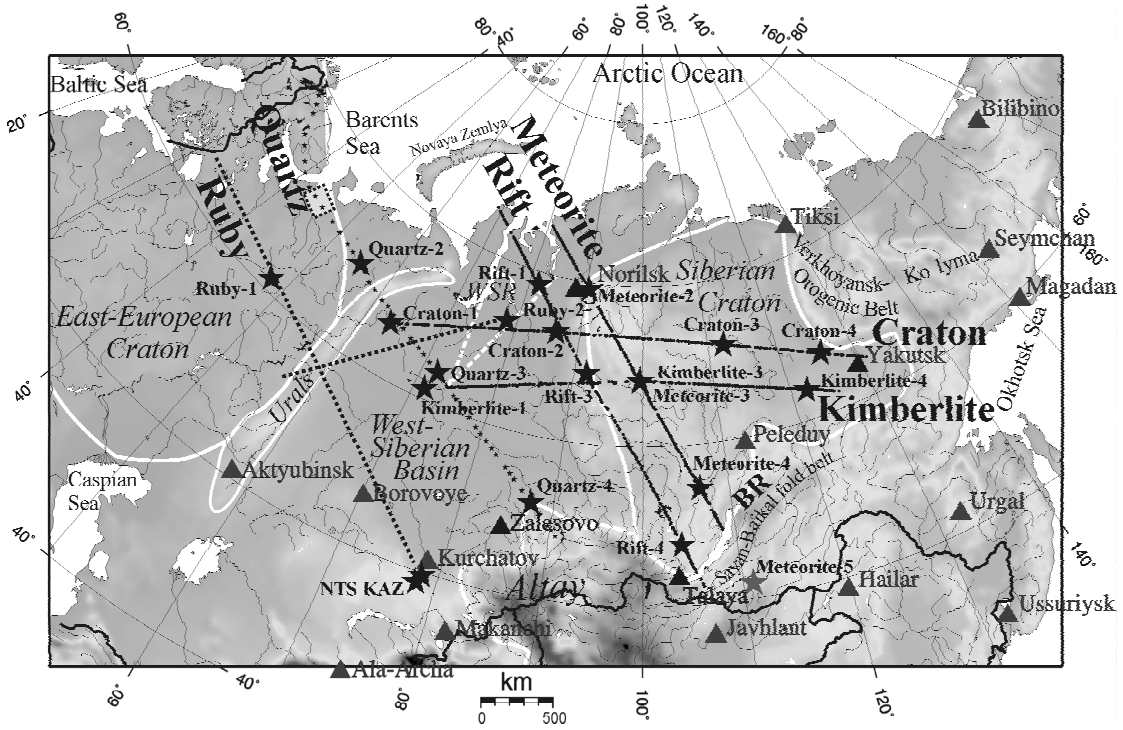


Figure 1 DSS PNE profiles under study at the University of Wyoming: QUARTZ, CRATON, KIMBERLITE, RIFT, METERORITE, and RUBY (two lines, obtained recently). Large stars are the PNEs, small stars (for profile QUARTZ only) are the chemical explosions. Profile RUBY is shown schematically. The coordinates and other parameters of the PNEs used in these profiles were reported by Sultanov et al. (1999). Major tectonic units are indicated in white contours (WSR – West Siberian Rift, BR – Baikal Rift).. Note the extent of systematic, continuous profiling, with PNEs detonated at the nodes of a 2-D recording grid. Also note that the profiles are close to some of the IMS stations (labeled triangles). The study of crustal effects presented here was performed for profile QUARTZ. The box NW of PNE QUARTZ 2 indicates the area where crustal attenuation was measured using coda amplitude analysis.

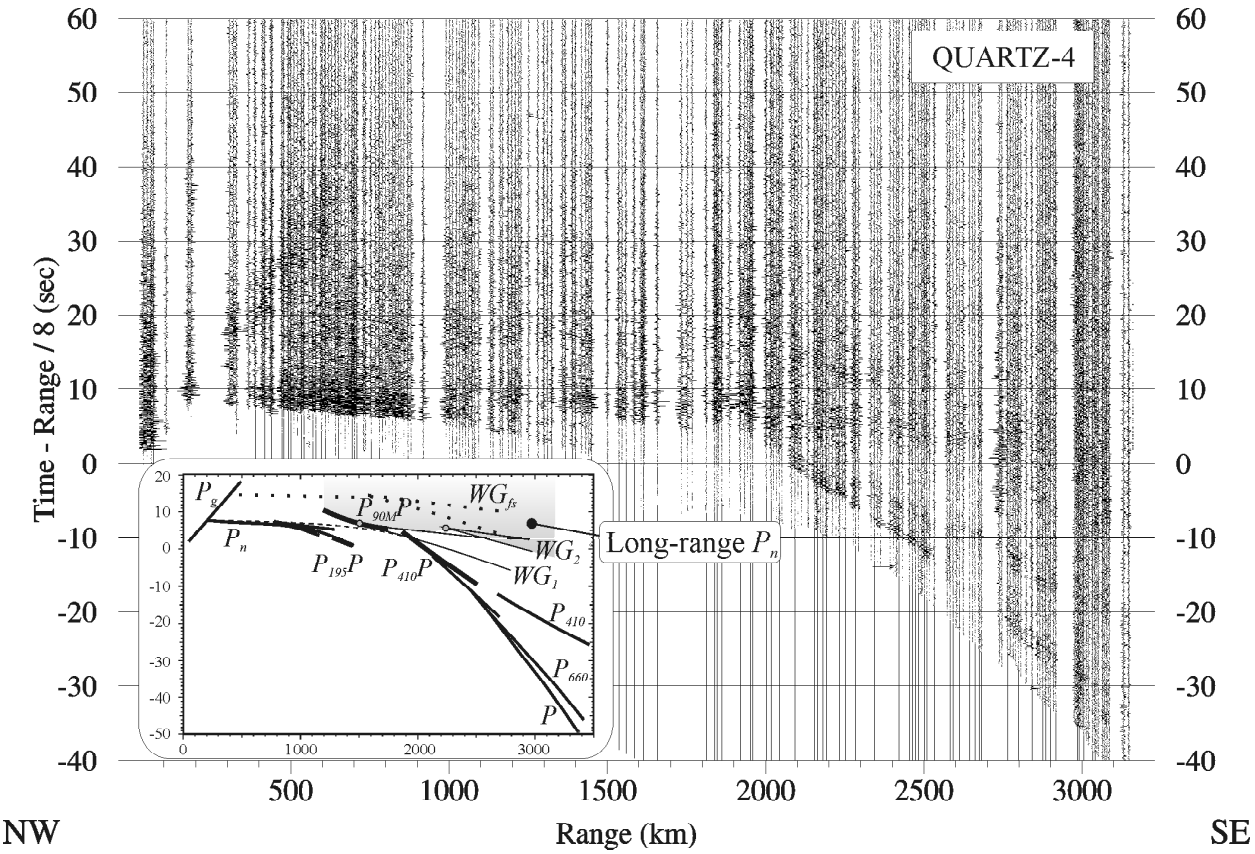


Figure 2 Vertical-component record from PNE QUARTZ-4 (Figure 1). Inset shows a sketch of typical refracted, reflected arrivals and their multiples identified in the PNE wave pattern. Note the strong second phases in the record. The long-range P_n phase (shaded in the inset) consists of arrivals forming a strong band of energy propagating to 3000 km at a group velocity between 8.0 – 8.1 km/s, with a faster branch at 8.5 km/s beyond 2700 km (Morozov *et al.*, 1998a). Note the unusually high energy of the arrivals in the primary P_n branch supporting the interpretation of the long-range P_n as a series of Moho and free-surface multiples of P_n and P_N (labeled *WG* and WG_{fs}). Also note that the long-range P_n phase is strong and is followed by a coda extending beyond the ends of records shown here.

mantle models developed, and this profile will be used in the following analysis. For our interpretation of the amplitude character of a "typical" PNE wavefield (Figure 2), we extract amplitude decay curves from several seismic records from PNE QUARTZ-4 (often also referred to as PNE 323) and CRATON (Figure 1 and Figure 3), between the offsets of 2000 – 2500 km. At these offsets, the separation of the phases provides the best illustration of the PNE energy pattern (Figure 2). The energy in the PNE wavefield at this distance appears to build up for 20 – 30 s after the first arrivals, followed by an extensive coda that can be observed for 100 – 150 s (Figure 3). Both the high amplitudes of the WG phases and the coda are surprising and must be understood in the context of future amplitude modeling of PNE records. Specifically, we will need to explain two features of the recorded distribution of PNE energy in Figure 3:

1) The long-duration codas of the observed codas of PNE arrivals. The coda of the free-surface multiple *PP* (WG_{fs} in our notation) appears much stronger than the coda of $P_{410}P$ reflections of nearly the same amplitude.

2) The apparent excess in the amplitudes of the WG phases compared to the reflections from the transition zone. Recent 1-D modeling (Mechie *et al.*, 1993; Morozova *et al.*, 1999).showed much lower amplitudes.

1. Coda decay rate of the PNE arrivals

A simple physical model of the coda allows us to obtain meaningful estimates of crustal attenuation quality factor (Q) and of the relative amplitudes of the arrivals without presently impractical 3-D finite-difference modeling. Our approach follows coda models accepted in teleseismic array observations (e.g., Greenfield, 1971; Bannister et al., 1990; Dainty, 1990; Gupta et al., 1991) and is based on two main observations. Firstly, waves propagating through the mantle and incident on the crust at high apparent velocity form a source of scattered energy different from the point-source model commonly used in coda estimates. Thus a correct coda model must take into account the distributed character of its excitation. Secondly, despite their apparent difference, we postulate that *all* the mantle arrivals could have similar coda patterns. Due to their long extent, these codas overlap contributing to the stepwise increase in energy seen in Figure 3. Decomposition of the recorded amplitude pattern allows us to obtain the true relation between the amplitudes of the onsets of the different PNE phases and their codas.

Figure 3 shows that the two *WG* multiples forming the long-range P_n are clearly distinct in the character of their codas. The first, Moho multiple labeled *WG* in Figure 2 is followed by a coda that dominates the record after high-pass filtering. However, in the low-frequency band, the strongest phase is the free-surface P_n multiple (WG_{fs}) followed by its coda. The higher amplitude of the WG_{fs} event is consistent with higher reflectivity of the free surface compared to the Moho. Also, the longer and low-frequency coda of WG_{fs} suggests a predominance of surface waves that propagate efficiently at lower frequencies and are progressively more attenuated as the frequency increases; this observation thus points to predominantly crustal origin of the coda.

Previous measurements of coda decay rate (Ryberg *et al*., 1995; Ryberg and Wenzel 1999) resulted in very high Q values over 1000 - 2000. However, we suggest that these values of Q might be overestimated from the use of a coda power decay rate (Aki and Chouet, 1975):

$$P(t) \propto t^{-\zeta} e^{-\omega t / Q}, \qquad (1)$$

where t is the time after the arrival, ω is the frequency. In expression (1), the factor $t^{-\zeta}$ with $\zeta \geq 1$ describes the geometric spreading of the waves forming the coda, and the quality factor Q corresponds to the attenuation. Ryberg and Wenzel (1999) used a preset value of $\zeta = 2$ assuming body-wave nature of the coda waves and a point source. However, as pointed out by Morozov *et al*. (1998a), the energy of the coda of the long-range PNE phases is better described by a relation (1) with $\zeta \approx 1.0$ for the higher-frequency coda and $\zeta \approx 0.9$ for the lower-frequency coda, with $Q=\infty$. This ambiguity in the determination of the attenuation factor Q using equation (1) illustrates the importance of a correct model of geometrical spreading. The tendency of the geometric spreading parameter ζ to values lower than 1 when $Q=\infty$ shows that formula (1) may not be applicable to the coda decay rate of the long-range PNE arrivals.

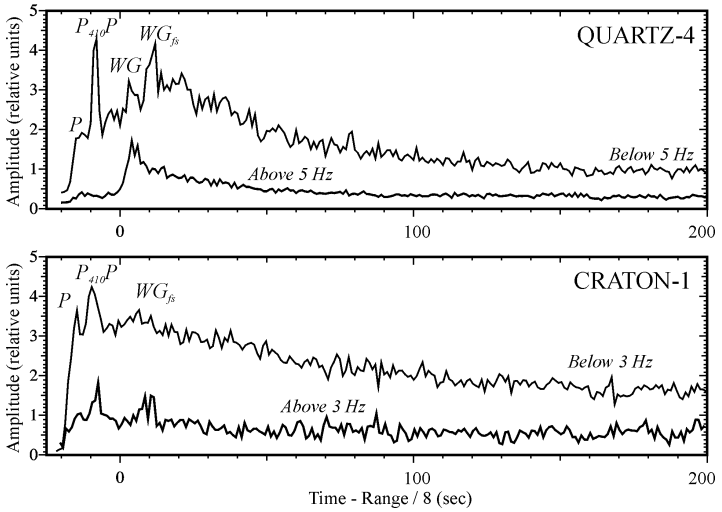


Figure 3 Amplitude of the high-frequency and low-frequency (filter corner frequency is 5 Hz for QUARTZ and 3HZ for CRATON) records within the offset range 2500 - 2600 km from PNE QUARTZ-4 and CRATON-1 (modified from Morozov and Smithson, in press). Time reduction is 8 km/s, and 7 three-component instantaneous trace amplitude records were averaged within a 2-s sliding time window and within the offset range (Morozov and Smithson, 1996) was used. First arrivals, a reflection from the 410-km discontinuity, and two whispering-gallery phases (*WG* and WG_{fs}) are indicated. Note the difference of the codas following the free-surface multiple refraction WG_{fs} at low frequencies and the Moho multiple *WG* at high frequencies. Note the about 150-sec long codas following the arrivals; also note the differences in these codas between the high- and low-pass filtered records and also between the PNEs.

Assuming predominantly crustal origin of the coda waves, coda amplitudes of PNE arrivals in Figure 2 can be explained readily once we take into account that seismic waves propagating through the mantle and entering the crust form a source of scattered waves that is different from a point source implied by relation (1). High apparent velocity of the incident waves (8 – 10 km/s) exceeds the velocity of the crustal-guided waves (3.5 – 5.5 km/s) generated through conversions on the Moho, on the basement, on surface topography, and on other velocity heterogeneities. Note that the most efficiently propagating phases within the crust (in the frequency range 0.5 - 10 Hz), post-critically reflected *S* waves, or L_g (Campillo, 1987), tend to the lower limit of this velocity range.

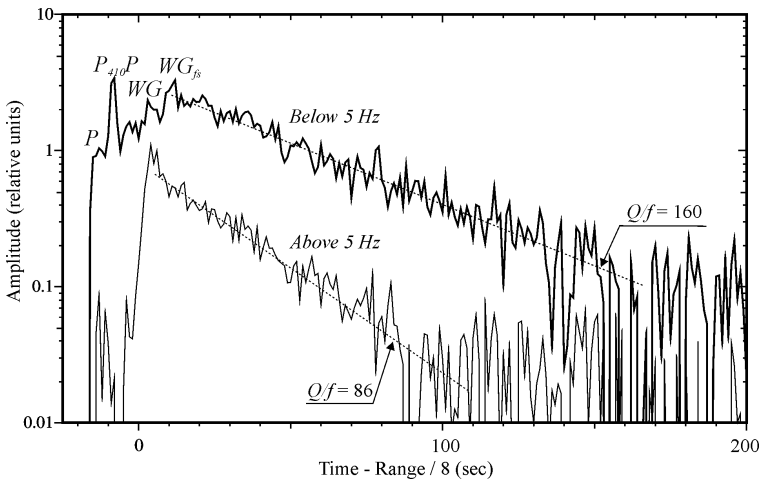


Figure 4 The same amplitudes as in Figure 3 plotted in logarithmic scale. Straight lines correspond to the relation (2) with $Q \approx 320$ for the low-frequency curve (at approximately 2 Hz) and $Q \approx 430$ for high frequency (at 5 Hz). Background noise estimated from a time window between 300- 350 s of the records was subtracted from both records prior to taking logarithm.

Since the apparent velocities of the incident mantle waves are much higher than the velocity of crustal-guided phases, we can approximate the generation of scattered energy within the crust and on the Moho as nearly simultaneous. The area of this distributed source of scattered energy increases with time, and thus the geometric spreading in coda decay cancels out and the entire decay of coda amplitude is due to the crustal attenuation:

$$P(t) \propto \tilde{P}(t) = e^{-\omega t/Q}. \qquad (2)$$

For more detail on the derivation of this coda power decay relation, see Morozov and Smithson (in press); a similar relation for coda energy was also obtained by Dainty (1985).

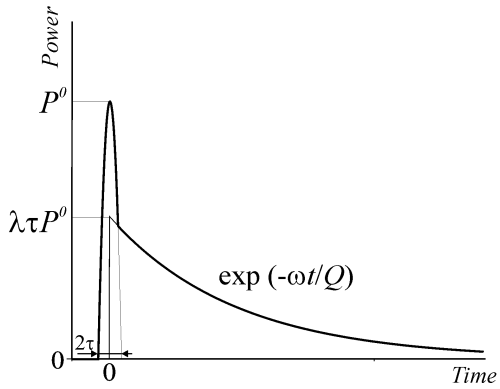


Figure 5 A model of intensity variation with time for a PNE event (see equations (3)). The energy of the primary event is approximated by a parabolic function and is characterized by its peak power P^0 and duration τ. The coda is parameterized by its coupling to the primary event λ and by its decay rate ω/Q defined in relation (2).

Relation (2) shows that the coda power decay law is purely exponential, in good agreement with the data throughout the entire observed duration of the coda. These linear trends of $\ln P(t)$ are consistent with log-RMS coda shapes of Semipalatinsk nuclear explosions presented by Baumgardt (1985). From this relation frequency-dependent *Q* can be easily estimated (Figure 4), resulting in values ranging from Q=320 near 2 Hz and Q=430 around 5 Hz. These values above suggest a dependence of $Q \approx 270 \cdot f^{0.3}$. and further confirm our association of the arrival PNE coda effects with crustal, preferably $P \rightarrow L_g$ or $L_g \rightarrow P$ scattering (Singh and Herrmann, 1983; Dainty, 1990). The comparatively low values of *Q* might be related to the effect of the thick sedimentary cover of the Pechora basin sampled by the part of the profile used in this analysis (Morozova *et al*., 1999).

2. True amplitudes of PNE phases

Since second arrivals ride on top of the codas of the earlier phases, the PNE record section exhibits a characteristic energy buildup, with the onsets of later phases appearing stronger than they are in reality. For the use

of these amplitudes in seismic discriminants, more stable estimates would apparently arise from the amplitudes that are free from such crustal contributions. As we show below, such "coda-free" amplitudes can be obtained by "deconvolving" the observed averaged amplitude.

In a simplified approach to such deconvolution, we again start from the localized amplitude decay curves shown in Figure 3, and model each of the events as a superposition of a primary arrival and of its coda (Figure 5). We assume that coda power follows the time dependence (2) and is proportional to the total energy of the primary phase. This approximation leads to a two-parameter amplitude decay model for each of the four arrivals labeled in Figure 3:

$$P(t-t^0)=\begin{cases} 0, & t<t^0, \\ \lambda P^0 \tau \tilde{P}(t-t^0), & t \geq t^0, \end{cases} \qquad (3)$$

where t^0 is the onset time, P^0 is the squared amplitude of the onset, τ is the estimated duration of the primary phase (so that $P^0\tau$ measures its total energy), and λ is the relative coda amplitude parameter. Since we assume that the mechanism of scattering is common for all arrivals, λ is the same for P, $P_{410}P$, WG, and WG_{fs}.

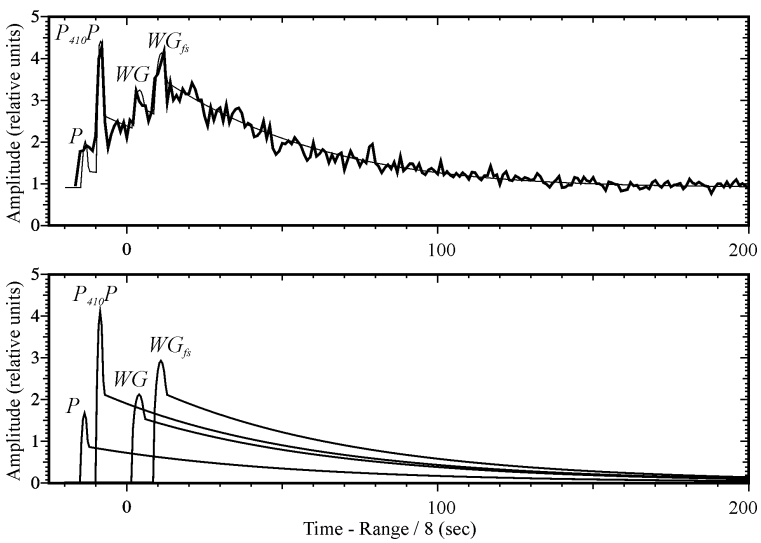


Figure 6 *Top*: Coda amplitude decay model for frequencies below 5 Hz. Thick line is the low-frequency amplitude from Figure 3, thin line shows the modelled amplitude shown in Figure 6. Note that crustal scattering and a simple approximation of coda power (1) explain the observed coda build-up by the subsequent *P*, $P_{410}P$, *WG*, and WG_{fs} arrivals. *Bottom*: Amplitudes and codas of the four separate arrivals forming the total coda energy. Note that this decomposed section is dominated by the reflection $P_{410}P$. Also compare the amplitude of *WG* in this plot to the high-frequency WG coda in Figure 3 and note that *WG* is stronger at lower frequencies, as expected.

By varying the parameters describing the amplitudes of the four arrivals in Figure 3, we obtained the coda-free amplitudes of these arrivals (Figure 6): $A_P \approx 1.7$, $A_{P410P} \approx 4.1$, $A_{WG} \approx 2.1$, $A_{WGfs} \approx 2.9$, $\lambda \approx 0.22$. During this joint inversion of the energy envoelopes, we also found that a value of Q=380 better describes the observed pattern of overlapping codas than the value of Q=320 estimated from the cumulative linear trend in Figure 4.

Figure 6 shows that the simple model (3) describes the observed amplitude pattern satisfactorily throughout the entire recording time range. As expected, the strongest phase in the deconvolved amplitude pattern in the bottom of Figure 6 is the reflection from the 410-km discontinuity. Note that because of increased attenuation below about 150-km depth (Morozov *et al*., 1998a, b), the arrivals from the mantle transition zone are very weak in the high-pass filtered records and they do not boost the apparent WG energy (Figure 3).

3. Mantle waveguide focusing under the profiles QUARTZ and RUBY?

As the argument above shows, the energies of secondary phases including the long-range P_n appear stronger than they are in reality due to their enhancement by the codas of the earlier phases. However, even after our amplitude correction, the amplitudes of the WG modes, and in particular, their total energy (Figure 6, bottom) are still significantly higher than expected from 1-D modeling (Mechie *et al*., 1993; Morozova *et al*., 1999). At longer ranges, high amplitudes of the surface multiples of P_n in this region are also indicated by the observations of a very strong *PP* phase (corresponding to the first phase in the WG_{fs} group in our notation) from the Semipalatinsk nuclear explosions (Baumgardt, 1985, 1990).

As a solution to this controversy, we suggest that high amplitudes of the waves guided within the lithosphere could be their focusing under the northern part of the East European Platform. This region has a mantle structure that is distinctly different from that of the West Siberian basin (Mechie et al., 1997; Morozova et al., 1999). The unusually high amplitudes of the long-range P_n have been observed only on the profiles QUARTZ and RUBIN traversing the East European platform (Ryberg et al., 1995), and the strong *PP* phase was also identified along a the path close to that of the profile RUBIN (Figure 1; Baumgardt, 1985). On the contrary, our preliminary study suggests that the long-range P_n is much weaker and crustal attenuation is somewhat lower under the Siberian craton .

Although still qualitative, the above argument is supported by an observation that not only the *WG* arrivals but also their primary phases P_n, and P_N (the latter are refractions and reflections from regional seismic boundaries between 90 – 140 km depth; cf. Pavlenkova, 1996; Morozova *et al*., 1999) are very strong between the offsets of about 300 – 800 km (Figure 2). Such strong amplitudes should be due to high energy of the source and to the velocity gradient and reflectivity observed within the lithosphere (Morozova *et al*., 1999). After a reflection from the Moho and free surface, this near-critical energy could form the observed strong waveguide arrivals (WG in Figure 3).

The high amplitudes of multiple refractions (*PP* and *WG*) could be explained by the effects of crustal, Moho, and lithospheric heterogeneity favoring propagation of energy within the top 150 – 200 km of the mantle under the northern part of the East European platform and under the West Siberian basin (Figure 1). Among these effects are the strong velocity gradient and reflecting boundaries in the uppermost mantle (Morozova *et al*., 1999). As demonstrated by Kennett (1987), within the ranges of PNE profiles (20° to 30°) layered structures within the mantle may act as a wave-guide contributing significantly to the *P*-wave coda.

Baumgardt (1985) also suggested that focusing could explain the high-amplitude *PP* in NORSAR recordings of the Semipalatinsk nuclear explosions. In particular, near-receiver focusing was required to account for the variations of *PP* amplitude across the array. In contrast to this observation, QUARTZ records show consistent and strong WG phases within the entire offset range and suggest that reflective lithosphere with vertical velocity gradient and favorable source conditions should be responsible for the overall character of the wavefield. Near-receiver scattering manifests itself in reduced coherency between the adjacent seismograms.

The unusually strong P_n and WG phases observed in QUARTZ records could support the observations of coda flattening between 310 – 450 sec after the teleseismic *P*-wave arrival in the recordings of Semipalatinsk explosions at NORSAR (Baumgardt, 1985, 1990). In a detailed study, Baumgardt (1990) showed that this part of the coda consisted primarily of L_g and S_n modes, with minor amounts of P_n energy and no detectable teleseismic *P* contribution. He interpreted this coda flattening as a result of $P_n \rightarrow L_g$ scattering under the Urals. This explanation, which appears to be the only reasonable model of the observed coda, also implies that the P_n is strong and carries enough energy to reverse the decay of the *P*-wave coda.

4. The nature of the PNE arrival coda

Since our coda decay model in equation (2) is dictated simply by the scattering geometry and by the principle of conservation of energy, it should be applicable to other observations of scattering at regional and teleseismic distances. Indeed, in a teleseismic study of underground nuclear explosions at Novaya Zemlya, Greenfield (1971) interpreted the observed coda as a result of near-source $R_g \rightarrow P$ scattering and pointed out that without crustal attenuation, the coda energy would have been constant. Dainty (1990) suggested that for Kazakh nuclear tests recorded at NORESS, about half of the coda energy consisted of near-source $L_g \rightarrow P$ scattering, and another half was represented by $P \rightarrow L_g$ scattering near the seismic array, with an energy decay law similar to derived above (Dainty, 1985). Baumgardt (1985, 1990) used incoherent beams and continuous "polar scans" to identify variations in coda decay and mode content within 200 – 400 sec of the teleseismic *P*-wave codas.

The codas of the WG phases and, as we suggested above, of all the other *P*-wave phases are not due to anomalously low crustal attenuation and to a tuned, narrow-band, highly scattering uppermost mantle as suggested by Ryberg *et al*. (1995) or by Ryberg and Wenzel (1999). On the contrary, we favor the traditional interpretation of the coda as a result of crustal scattering of the waves incident from the mantle and propagating at high apparent velocities. The reciprocity principle complements this mechanism by its counterpart in which strong crustal-guided waves (P_g, S_g, L_g, R_g) generated by the PNE are scattered on crustal heterogeneities producing secondary phases propagating through the mantle and feeding the observed coda (Dainty, 1985, 1990).

The observed difference between the amplitude dependencies of the records at lower and higher frequencies (Figure 3) is very significant. Similarly to the deep *P*-wave phases, the WG_{fs} arrival and its coda are low in their high-frequency content. Compared to *WG*, WG_{fs} is similar but travels two additional passes through the crust, and thus the disappearance of WG_{fs} in the high-pass filtered record should be related to crustal attenuation. Also, the increased *Q* at higher frequencies (Figure 4) and its regional variations (Figure 3) suggests that the low-frequency coda contains more surface waves sampling the sedimentary, lower-*Q* parts of the upper crust. Therefore, the difference between *WG* and WG_{fs} also points to a crustal nature of the coda.

An important implication of our coda model is that only a three-dimensional (3-D) analysis of scattering can yield reasonable quantitative estimates of the dynamic properties of the PNE wavefield. Although 3-D or 2-D modeling of PNE short-period records using realistic crustal and mantle models is at present not practical, it appears that interpretations of scattering based exclusively on 1-D simulations (Tittgemeyer, 1996; Ryberg and Wenzel, 1999) might become misleading. On the contrary, energy balance considerations consistent with the accepted teleseismic coda models and utilizing the true, 3-D view of the process of wave propagation allow us to explain the behavior of the coda and to unravel the amplitude relations between the observed PNE phases.

5. Using receiver functions to map crustal basement

In another application of the new, amplitude and waveform analysis of PNE records, we computed receiver function sections by deconvolving the vertical-component record of each PNE seismogram from profile QUARTZ from the corresponding inline component. The receiver function sections from the three QUARTZ PNEs were stacked and correlated with the detailed crustal model derived earlier (Morozova et al., 1999; Figure 7); in this model, the depths to the basement were obtained from industry reflection and borehole data and was provided by the Center GEON, Moscow.

A comparison (Figure 7, middle) of the detailed picks of the crustal basement with the receiver function image shows that although the Moho P/S conversion cannot be correlated in the receiver function stack, the basement is well pronounced as a *P* to *S* converted arriving 1 – 2 sec after the first arrivals. Although such conversions generally contribute to the complexity of the first-arrival waveforms and cannot be picked directly, deconvolution reveals the variations of the depth of the basement with substantial detail. Among possible implications of this observation, we suggest that (1) receiver functions computed using the 3-component recordings of PNE first arrivals can be used to constrain such important structural features of the crust as the depth to the basement, and (2) it shows that P/S conversions on the basement and other resonances within the sediments contribute to the complexity and amplitudes of the first (and presumably all other) arrivals. Both of these conclusions should be considered carefully during modeling of Lg propagation in realistic crustal structures like the one presented in Figure 7, top.

CONCLUSIONS AND RECOMMENDATIONS

Based an analysis of amplitude envelopes of the records from the profile QUARTZ, we arrived at both a consistent explanation of the character of PNE arrival coda as well as at a realistic estimate of its decay rate, in contrast to some of the previous results (Ryberg *et al*., 1995; Tittgemeyer *et al*., 1996; Ryberg and Wenzel, 1999). The key points of our coda model of PNE arrivals are:

1) A long coda detectable to 100 – 150 sec in DSS records follows every PNE arrival at an offset range over 2000 km;

2) Codas of the long-range arrivals are due to scattering within the crust of the primary PNE arrivals propagating at high apparent velocities thus leading to distributed coda excitation and reduced geometric spreading;

3) The codas of the PNE arrivals build up energy within the record section leading to an increased energy within the *PP* time window. This amplitude pattern of the records was inverted for true amplitude relations between the arrivals.

As a result of our PNE coda model, we obtained estimates of coda *Q* ranging between Q_0=380 near 2 Hz and Q_0=430 around 5 Hz. These values correspond to the values generally associated with the crust (including the sedimentary rocks) and suggest that the crust could be the source of the extensive coda pattern observed in PNE

records (Figure 3). As our study shows, the amplitude pattern of the PNE records throughout their full length can be explained quantitatively by body- and guided waves within the upper mantle and by (predominantly) crustal scattering.

Using receiver function analysis of PNE arrivals, we show that scattering and P/S conversions within the crust cause reverberations in the waveforms of *P*-wave arrivals. Stacked receiver functions of first arrivals produced a consistent images of the basement along the PNE profile QUARTZ. This technique could potentially be used for imaging crustal basement along other PNE and conventional-explosion profiles with 3-component recordings.

REFERENCES

Aki, K. and B. Chouet (1975). Origin of coda waves: source, attenuation, and scattering effects, *J. Geophys. Res.,* 80*,* 3,322-3,342.

Bannister, S. G., E. S. Husebye, and B. O. Ruud (1990). Teleseismic *P* coda analyzed by three-component and array techniques: deterministic location of topographic *P*-to-*Rg* scattering near the NORESS array, *BSSA*, 80, 1969-1986.

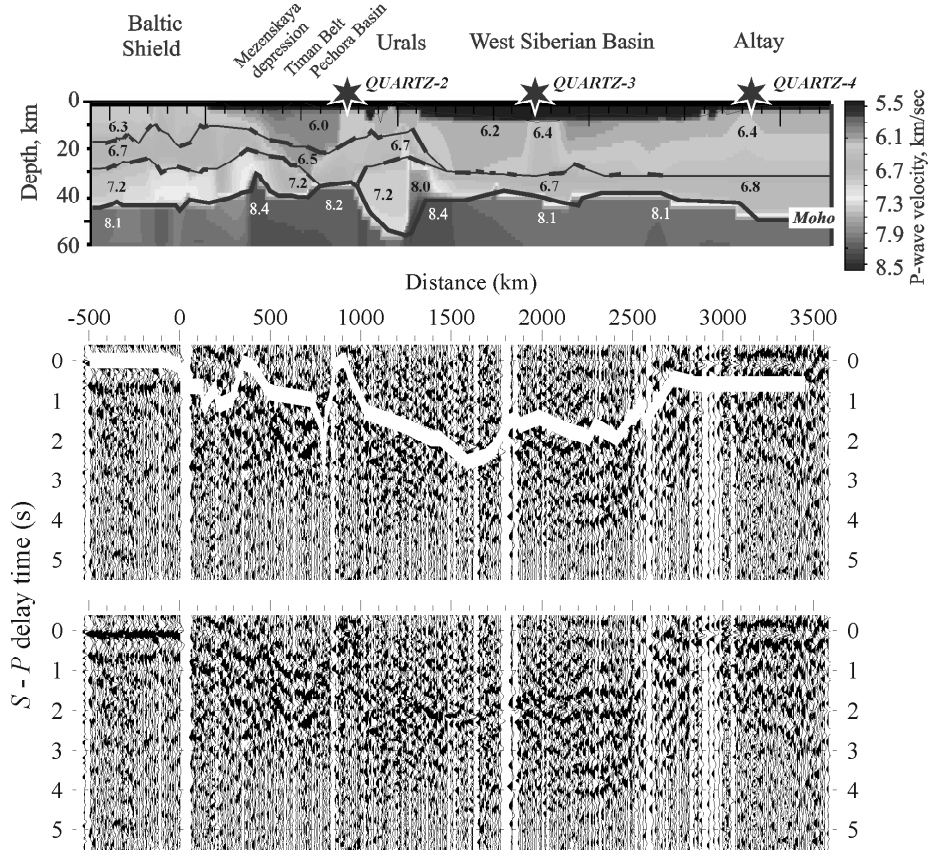


Figure 7 Mapping the crustal basement using receiver functions. *Top*: detailed crustal and uppermost mantle velocity model from profile QUARTZ (same as in Fig. 2). *Middle* and *bottom*: interpreted and uniterpreted stacked receiver function sections from the three QUARTZ PNEs. The white line in the middle plot is the zoomed in profile of the basement from our crustal model scaled to *S – P* wave delay time. Note the good fit of the basement depth with the stacked receiver function. Also note that such a detailed basement profile cannot be obtained from a travel-time interpretation of QUARTZ data (it was derived from industry reflection, higher-resolution DSS, and borehole data, and provided by GEON), but, remarkably, it wss obtained here from the PNE data alone.

Baumgardt, D. R. (1985). Comparative analysis of teleseismic *P* coda and *Lg* waves from underground nuclear explosions in Russia, *Bull. Seism. Soc., Am*., 75, 1413-1433.

Baumgardt, D. R. (1990). Investigation of teleseismic *Lg* blockage and scattering using regional arrays, *Bull. Seism. Soc., Am*., 80, 2261-2281.

Campillo, M. (1987). *Lg* wave propagation in a laterally varying crust and the distribution of the apparent quality factor in central France, *J. Geophys. Res.,* 92, 12604-12614.

Dainty, A. M. (1985). Air Force Geophysical Laboratory Report, AFGL-TF-86-0218.

Dainty, A. M. (1990). Studies of coda using array and three-component processing, *PAGEOPH*, 132, 221-244.

Greenfield, R. J. (1971). Short-period *P*-wave generation by Rayleigh-wave scattering at Novaya Zemlya, *JGR*, 76, 7988-8002.

Gupta, I.N., T. W. McElfresh, and R. A. Wagner (1991). Near-source scattering of Rayleigh to *P* in teleseismic arrivals from Pahute Mesa (NTS shots, in: Taylor, S. R., H. J. Patton, and P. G. Richards (Eds.), Explosion Source Phenomenology, *AGU Geophys. Monograph*, 65, 151 - 160.

Kennett, B. L. N. (1987). Observational and theoretical constraints on crustal and upper mantle heterogeneity, *Phys. Earth Planet. Interiors*, 47, 319-332.

Mechie, J., A. V. Egorkin, K. Fuchs, T. Ryberg, L. Solodilov, and F. Wenzel (1993). P-wave velocity structure beneath northern Eurasia from long-range recordings along the profile Quartz, *Phys. Earth Planet Inter*., 79, 269-286.

Mechie, J., A. V. Egorkin, L. Solodilov, K. Fuchs, F. Lorenz, and F. Wenzel (1997). Major features of the mantle velocity structure beneath northern Eurasia from long-range seismic recordings of peaceful nuclear explosions, *in:* Fuchs, K. (Ed.) Upper mantle heterogeneities from active and passive seismology, pp. 33-50, Kluwer Academic Publ., Dordrecht.

Morozov, I. B. Comment on "High-frequency wave propagation in the uppermost mantle" by T. Ryberg and F. Wenzel, *J. Geophys. Res*., in press.

Morozov, I., B., E. A. Morozova, and S. B. Smithson, (1997). Observation of *Lg* and *S* wave propagation along the ultra-long profile "Quartz", Russia, *in:* Fuchs, K. (Ed.) Upper mantle heterogeneities from active and passive seismology, Kluwer, pp. 147-154.

Morozov, I., B., E. A. Morozova, and S. B. Smithson, (1998a). On the nature of the teleseismic *Pn* phase observed in the recordings from the ultra-long profile "Quartz", Russia, *Bull. Seism. Soc. Am.*, 88, 62-73.

Morozov, I., B., E. A. Morozova, and S. B. Smithson, (1999). Preliminary characterization of l_g phase propagation from Peaceful Nuclear Explosions in Siberia, Russia, 21 DoD/DoE Seismic Research Symposium, Las Vegas, NV, September, 1999.

Morozov, I., B., E. A. Morozova, S. B. Smithson, and L. N. Solodilov (1998b). 2-D image of seismic attenuation beneath the Deep Seismic Sounding profile QUARTZ, Russia, *Pure Appl. Geoph*, 153, 311-343.

Morozova, E. A., I. B. Morozov, S. B. Smithson, and L. N. Solodilov (1999). Heterogeneity of the uppermost mantle beneath the ultra-long range profile "Quartz," Russian Eurasia, *J. Geophys. Res*., 104 (B9), 20,329-20,348.

Ryberg, T., and F. Wenzel (1999). High-frequency wave propagation in the uppermost mantle, *J. Geophys. Res.,* 104*,* 10,655-10,666.

Ryberg, T., K. Fuchs, A. V. Egorkin, and L. Solodilov (1995). Observations of high-frequency teleseismic P_n on the long-range Quartz profile across northern Eurasia, *J. Geophys. Res.,* 100*,* 18151-18163.

Singh, S., and R. B. Herrmann (1983). Regionalization of crustal coda *Q* in the Continental United States, *J. Geophys. Res*., 88, 527-538.

Sultanov, D. D., J. R. Murphy, and Kh. D. Rubinstein, 1999. A seismic source summary for Soviet Peaceful Nuclear Explosions, *Bull. Seism. Soc. Am.,* 89, 640-647.

Tittgemeyer, M., F. Wenzel, K. Fuchs, and T. Ryberg (1996). Wave propagation in a multiple-scattering upper mantle—observations and modeling, *Geophys. J. Int.,* 127, 492-502.

MULTI−TAPER COHERENCE RECEIVER FUNCTIONS AND P−WAVE SCATTERING WITHIN THE CRUST AND LITHOSPHERE: THE VIEW FROM ARABIA

Jeffrey Park, Vadim Levin
Department of Geology and Geophysics, Yale University

Sponsored by U. S. Department of Defense
Defense Threat Reduction Agency
Arms Control Technology Center
Contract No. DSWA01−98−011

ABSTRACT

We apply a new receiver function (RF) inversion technique that uses multi−taper coherence estimates instead of spectral division. The multi−taper spectrum estimates are leakage resistant, so that low−amplitude portions of the *P*−wave spectrum can contribute usefully to the RF estimate. The coherence between vertical and horizontal components can be used to obtain a frequency−dependent uncertainty for the RF, which is very useful for weighting RF stacks.

Teleseismic RFs for Global Seismographic Network station RAYN on the eastern edge of the Arabian Shield contain a strong converted−phase P_Hs that we believe arises from the Hales discontinuity at the depth of ~70 km. The RAYN RFs also indicate that a similar zone borders the crust−mantle transition at ~40km. Synthetic seismograms computed in simple one−dimensional anisotropic models help us explore the range of scenarios that would match observed receiver functions. The RFs require, assuming hexagonal anisotropy, a tilted symmetry axis with a north−south strike. In our preferred model the anisotropic zones are bounded by sharp discontinuities at the top and by smooth gradients below. The gradients extend downward from the Moho and the Hales discontinuities. Within both anisotropic zones the symmetry axes, indicative of fabric in the olivine−dominated upper mantle rock, are oriented along the N−S direction (±10°), and are tilted 50° toward the south. We propose that these regions of coherent fabric within the upper mantle represent the development of shear zones during the late Proterozoic continent−continent collision, when the the Ar−Rayn tectonic block was involved in an episode of northward "escape" along the northern flank of the Najd fault system.

P waves from regional−distance earthquakes are complex and reverberatory, as would be expected from a combination of head waves, post−critical crustal reflections and shallow−incident *P* from the upper mantle. Nevertheless, regional−distance RFs for GSN stations RAYN and ANTO show some agreement with teleseismic RFs. At RAYN the moveout of the Moho−converted Ps phase, relative to direct P, follows well the predictions of the IASP91 earth model. The Moho−converted Ps phase shows complexity associated with the transition−zone triplication near Δ=20° and constant delay (zero moveout) as Δ−−>0, consistent with conversion from P_n. Similar behavior is seen at ANTO for events that arrive from the west. For eastern backazimuths the ANTO RFs show features whose moveout is negative as Δ−−>0. This moveout is poorly fit by reverberations in flat layers or by direct scattering from a dipping interface, but is consistent with a topographic scatterer a few 10s of km eastward of the ANTO site. Regional receiver functions may therefore be useful in judging whether teleseismic RFs at a particular station are suitable candidates for a 1−D velocity structure inversion. Synthetic seismograms of regional *P* phases, computed with a locked−mode reflectivity approach, confirm many of the observed features of the RAYN and ANTO regional receiver functions.

Key Words:

P waves, receiver function, Arabian Shield, continental lithosphere, seismic anisotropy, scattered waves, regional seismic wave propagation

OBJECTIVE

Proper detection and discrimination of seismic waves from suspected clandestine explosions is best accomplished when the wave−propagation characteristics of the Earth between the source and the seismometer are well−known. Teleseismic body waves from earthquakes and explosive sources experience scattering as they travel upwards through the uppermost mantle and crust. Regional body waves experience scattering as they travel through the crustal waveguide. The objective of this research project is to use variations in the elastic anisotropy of the crust and uppermost mantle to describe the scattering that is observed in seismic data. Many models for seismic scattering invoke a statistical 3−D distribution of small−scale anomalies in isotropic *P* and *S* seismic velocities e.g., the phase−screen approach (Wu, 1994) or finite−difference computations (e.g. Levander and Hollinger, 1992). The motivation for using anisotropy is threefold. First, fairly modest fluctuations in anisotropic properties can cause significant conversion of *P* (compressional) motion to *S* (shear) motion in propagating seismic waves. Second, numerical experiments have shown that flat−layered anisotropic media can cause large scattered wavetrains in both surface waves (Park, 1996) and body waves (Levin and Park, 1997; 1998; Savage, 1998). Third, elastic anisotropy, as a material property of rocks, seems to be the rule rather than the exception, caused by aligned cracks (Hudson, 1981), by lattice−preferred mineral orientation within rocks (Babuska and Cara, 1991), and by fine−layering (Helbig, 1994). Large−scale 3−D velocity structures are not necessary to create a P−coda or an extended surface−wave signal, at least in theory. If a 1−D anisotropic seismic−velocity structure can usefully represent much of the scattered seismic energy in an incoming signal at a particular seismic observatory, there are practical benefits. An analyst, faced with a complex seismic signal to interpret, would likely need to know fewer parameters of earth structure local to the station, and may run simpler synthetic seismogram codes to reproduce the data.

Although this research focusses on developing anisotropic models for crustal seismic velocities, the receiver functions themselves are useful in the verification and monitoring of a Comprehensive Nuclear−Test−Ban Treaty (CTBT). Receiver functions represent empirically the scattering of compressional (*P*−wave) to shear (*S*−wave) energy at particular seismic stations. Since explosions radiate an surfeit of P−wave energy relative to earthquakes, the conversion of *P* to *S* energy makes the discrimination problem more difficult. Receiver functions can be useful empirically if they explain a significant fraction of scattering in seismic records, even if no simple earth−structure model can explain them.

RESEARCH ACCOMPLISHED

A key objective of this research is to determine whether layered anisotropy is pervasive in the crust and has a strong influence on body−wave coda. Computational modeling (Cassidy, 1992; Kosarev et al 1994; Levin and Park, 1997; 1998; Savage, 1998) demonstrates that both anisotropy and dipping interfaces cause predictable variations in *P*−to−*S* scattered energy, dependent on the incoming direction of the *P*−wave −− its angle of incidence (or equivalently, its slowness *p*), and its back−azimuth angle ϕ. The *P*−to−*SH* energy scattered to the transverse−horizontal component of motion is particularly diagnostic, as its amplitude is predicted to reverse from positive to negative, and vice versa, in a lobate pattern with back−azimuth ϕ. We have analysed seismic data from several permanent seismic observatories to study the back−azimuth dependence of receiver functions.

Receiver Functions From Multiple−Taper Spectral Correlation Estimates.

The simplest way to estimate a receiver function (RF) is by spectral division, a ratio of Fourier transforms for the different components: $H_R(f) = Y_R(f)/Y_Z(f)$ and $H_T(f) = Y_T(f)/Y_Z(f)$. Here $Y_Z(f)$, $Y_R(f)$, and $Y_T(f)$ are the Fourier spectra of the vertical, radial and transverse seismic components, respectively. An inverse Fourier transform converts spectral−domain receiver functions $H_R(f)$ and $H_T(f)$ into a prediction filter of *Ps* scattered waves. RFs are typically contaminated by the "scattered" wave field, the portion of the *P*−wave coda that arises from multiple scattering and conversion in a strongly heterogeneous crust (Abers, 1998). In this study we apply a new RF−estimation technique (Park and Levin, 2000a) that uses multiple−taper spectral correlation estimates (Vernon et al 1991) instead of spectral ratios.

The multitaper RF algorithm has two distinct advantages. First, it estimates the receiver functions $H_R(f)$ and $H_T(f)$ only from the portion of the horizontal motion that is correlated (in a narrow frequency band) with the vertical motion. Second, the relative proportion of uncorrelated horizontal motion, as quantified by the spectral coherences $C_R(f)$ and $C_T(f)$, is used to estimate the uncertainty of $H_R(f)$ and $H_T(f)$. (High coherence

implies low uncertainty.) These uncertainties can be used to weight RF−estimates from different earthquakes when estimating a composite, or "stacked," receiver function in the frequency domain. There is no formal uncertainty estimate for the time−domain multitaper RF, but an informal assessment can be made from the acausal part of the RF i.e. the amplitude of $H_R(t)$, $H_T(t)$ for $t<0$. In our experience with real data, the coherence between horizontal and vertical motion in a P coda is highly frequency dependent, and the pattern of frequency dependence can vary greatly from event to event. Therefore the use of uncertainty−based weights in multiple−record RF estimation is important. With stacking, much higher−frequency RFs can be resolved (Figure 1), well over $f=1$ Hz. For geologic applications, this allows much finer depth resolution to determine e.g., the thickness of the Moho transition. For CTBT monitoring, this allows us to characterize deterministic seismic scattering at frequencies of nonproliferation interest.

We have applied our new RF technique to GSN station PET (Petropavlovsk−Kamchatsky, Russia), ARU (Arti, Russia), YSS (Yuzhno−Sakhalinsk, Russia, ADK (Adak, Alaska), MAJO (Matsushiro, Japan), COL (College, Alaska) and COR (Corvallis, Oregon) (Park and Levin, 2000a; Yuan et al 1999). We have focussed particularly on data recorded at two important GSN stations in the Middle East, RAYN (Ar Rayn, Saudi, Arabia) and ANTO (Ankara, Turkey) (Levin and Park 2000; Park and Levin 2000b; see Figure 2).

Shear zones in the Proterozoic lithosphere of the Arabian Shield and the nature of the Hales discontinuity.

Seismic velocity discontinuities are commonly found within the upper 100 km of the mantle lithosphere, with great variability in their depth, lateral extent, and the polarity of velocity jump. Among the more commonly observed is the "80 km" or Hales discontinuity, identified in a variety of tectonic environments (Hales, 1969; Pavlenkova, 1996; Bostock, 1997), and sometimes associated with seismic anisotropy. Anisotropy is associated with the crust−mantle transition, and with another anomalous region ~70 km deep, which we interpret as containing the Hales discontinuity. Azimuthal patterns and frequency dependence of pulse shapes of observed *P−SH* converted waves (Figure 3) suggest that both zones are bound by discontinuities in anisotropic properties on one side, and by smooth gradients on another. In our preferred model anisotropic zones extend downward from the Moho and the Hales discontinuities (Figure 4). Within both zones the anisotropic symmetry axes, indicative of systematic fabric in the olivine−dominated upper mantle material, are oriented along the N−S direction (±10°), and are tilted 50° to the south.

We interpret our findings as evidence for thin shear zones within the mantle lithosphere, developed after the assembly of the Arabian Shield during a late Proterozoic continent−continent collision (Figure 5). Post−collisional tectonics created the Najd fault system and involved the Ar−Rayn block in an "escape tectonics" episode along the trajectory that would be close to present−day N−S direction. Preservation of these shear zones for ~500 My within the upper mantle is in good agreement with geochemical evidence for common tectonic history of the crust and upper mantle composing the Arabian Shield.

Although recognised globally, the details of the Hales discontinuity appear to be tied to the tectonic history of a specific location (Arabian shield, Slave craton). Therefore, a single origin of this seismic feature, analogous to the mineral phase changes at 420− and 670−km depth, may be hard to constrain. Rather, we hypothesize that the typical depth range of the Hales discontinuity (60−90 km) is where tectonic events often leave their "marks" in the continental lithosphere, perhaps indicating the minimum thickness of the stiff mantle lid in orogenic events. Proterozoic stretch marks from similar dynamics may be preserved within the shallow lithosphere of the Arabian Shield. The receiver function study of Sandvol et al. (1998a) suggests a variable depth to an interface in the Hales depth range across the southeastern portion of the Shield, but does not analyze the transverse component. Our experience with RAYN, for which Sandvol et al. (1998a) reported no P_{Hs} phase, suggests that the azimuthal dependence of the transverse RF is a crucial constraint on the relict strains embedded within continental lithosphere.

Receiver Functions From Near−Teleseismic and Regional P Waves.

The extended codas of regional P waves, suggestive of intense scattering, discourage their analysis with traditional receiver−function (RF) estimation algorithms. However, reflectivity seismograms using a locked mode approximation demonstrate that the extended nature of regional *P* can be simulated with a 1−D model, for which off−path− and back−scattering is absent (Park and Levin, 2000b). Complex scattering is surely present in real data from regional distances, but spectral cross−correlation mitigates its influence on receiver−function estimation. Using multiple−taper spectral cross−correlation, stable receiver functions (RFs) can be estimated from regional and near−teleseismic *P* waves (Park and Levin, 2000b). Resolution of *Ps* converted energy is greatly improved by averaging single−event RFs in the frequency domain in narrow epicentral−distance bins.

Stations RAYN and ANTO represent, to some extent, the extremes of what one might expect in receiver−function studies. RAYN lies atop a stable shield with minimal sediment cover, and primary *Ps* conversions from the Moho are readily retrievable from reverbatory shallow−incidence regional and near−teleseismic *P* waves (Figure 6). Although sited on hard rock, ANTO lies within a river valley in an actively deforming region, close to the active North Anatolian fault system. For events from the east to ANTO, the *Ps* conversions at f>1 Hz appear to be strongly influenced by shallow 3−D structures (Figure 7). In particular, some negative pulses in the RFs move out to shorter delays as Δ−−>0, a behavior we find easiest to model with *P*−*P* and *P*−*S* scattering from a surface or near−surface obstacle 20−30 km eastward of ANTO (Figure 8). For events from the west to ANTO, Moho−converted *Ps* energy is easier to identify in the regional RFs. For both stations the radial RFs estimated from regional *P* agree well with the radial RFs from teleseismic *P*. This implies that some features in the teleseismic receiver functions for ANTO, as estimated from eastern backazimuths, may actually represent topographic scattering rather than *Ps* conversions from deep crustal and mantle interfaces. We conclude that receiver functions from regional *P* are useful to check the suitability of teleseismic receiver functions for 1−D structure inversion.

A strong east−west asymmetry in the ANTO regional−*P* receiver functions is consistent with previous observations of regional−wave propagation. Rodgers et al. (1997) and Gok et al. (2000) report inefficient S_n and *Lg* propagation for regional−distance events from the east and southeast to ANTO, and efficient propagation from the west. East of ANTO lie the Turkish and Iranian plateaus, characterized by Cong and Mitchell (1998) as having depressed shear velocities and high attenuation (Q<100 in the crust). Regional waves from the east traverse a continental collisional zone extending from central Anatolia through the Zagros mountains in southwest Iran. Broadband stations GNI (Garni, Armenia) and TBZ (Trabzon, Turkey) lie within this collision zone in eastern Anatolia. Sandvol et al. (1998b) and Cakir et al. (2000), report complex receiver functions for, respectively, GNI and TBZ, and derive models from the radial RFs with low−velocity zones in the shallow mantle. If low velocities and low Q imply subsolidus temperatures and partial melt, as suggested by Cong and Mitchell (1998) and Cakir et al. (2000), the propagation of regional phases would likely be disrupted.

Regional RFs for RAYN and for western backazimuths at ANTO show complexity in the inferred Moho *Ps* phase near Δ=20°. This appears to be consistent with (1) the triplication of *P* associated with velocity gradients in the mantle transition zone, and (2) a merging of teleseismic and regional *P*, both of which imply overlapping phases with distinct incidence angles and (therefore) distinct Ps delay times relative to direct *P*. Many of the general features of regional *P* receiver functions are confirmed with receiver functions estimated from synthetic seismograms, computed using a locked−mode approximation with a anisotropic reflectivity code. The reverberative nature of P_n and P_g phases leads to complex radial RFs with small "acausal" pulses and a train of causal pulses whose amplitude varies strongly with epicentral distance and with the details of crustal structure, all in the absence of lateral structure. Using a simple reflectivity code with an upgoing plane−wave predicts significant *P*−to−*SH* conversion at the Moho at near−horizontal incidence, but locked−mode synthetics suggest that regional−*P*−to−*SH* conversion is very weak for modest levels of anisotropy. In the context of 1−D models, it appears possible to generate nonnegligible transverse motion in regional *P* with shallow, but not anisotropy near the Moho. However, *P*−to−*SH* conversion is not as large in our synthetics as would appear to be the case in data from RAYN and ANTO. Either shallow crustal anisotropy is much larger than ~5% or else scattering from 2−D and 3−D structures is pervasive in the observed phases.

CONCLUSIONS AND RECOMMENDATIONS

A significant proportion of the scattered wave field, even at *f>1* Hz, appears to be characterized by a predictable series of *P*−to−*S* conversions by horizontal or near−horizontal interfaces in the crust and shallow mantle. These converted phases typically have polarity changes with back−azimuth that are consistent with elastic anisotropy as the cause of *P*−to−*S* scattering. Our investigations suggest that the continental mantle, in some locales, possesses thin layers (10−20 km) of sheared rock, from past tectonic events, that cause *P*−to−*S* scattering.

Not all scattering can be predicted by a receiver function, of course. Often a large proportion of the scattered wave field on the horizontal components is incoherent with the vertical component. Poor coherence biases normal RF estimators, but is alleviated by the new multiple−taper receiver−function estimator we have developed.

We recommend continued use of back−azimuth and range−dependent receiver functions to characterize scattering at broadband seismic monitoring stations within the verification system of the CTBT. Data analysis from our preliminary suite of stations suggests that a 1−D anisotropic crustal structure is appropriate

for modeling a significant portion of crustal scattering in teleseismic signals. Receiver function analysis is applicable to regional and near−teleseismic *P* in some cases (RAYN and ANTO from the west, but not ANTO from the east). This suggests that new methods to characterize regional−distance scattering empirically may be fruitful. Further work should focus on data from other continental regions. Application of multiple−taper coherence methods to the study of scattered waves in seismic array data should be pursued.

REFERENCES

Abers, G. A., Array measurements of phases used in receiver−function calculations; importance of scattering. **Bull. Seism. Soc. Amer., 87**, 313−318, 1998.

Babuska, V., and Cara, M., **Seismic Anisotropy in the Earth**, Kluwer Academic, Dordrecht, 1991.

Bostock, M. G., Anisotropic upper−mantle stratigraphy and architecture of the Slave craton, **Nature, 390**, 393−395, 1997.

Cakir, O., Erduran, M., Cinar, H., and Yilmazturk, A., Forward modelling receiver functions for crustal structure beneath station TBZ (Trabzon, Turkey), **Geophys. J. Int., 140**, 341−356, 2000.

Cassidy, J. F., Numerical experiments in broadband receiver function analysis, **Bull. Seism. Soc. Amer., 82**, 1453−1474, 1992.

Cong, L., and Mitchell, B. J., Seismic velocity and Q structure of the Middle Eastern crust and upper mantle from surface wave dispersion and attenuation, **Pure Appl. Geophys., 153**, 503−538, 1998.

Gok, R., Turkelli, N., Sandvol, E., Seber, D. and Barazangi, M., Regional wave propagation in Turkey and surrounding regions, **Geophys. Res. Letts. 27**, 429−432, 2000.

Helbig, K., **Foundations of Anisotropy for Exploration Seismics**, Pergammon/Elsevier Science, Oxford, 1994.

Hudson, J. A., Wave speeds and attenuation of elastic waves in material containing cracks, **Geophys. J. Roy. Astron. Soc., 64**, 133−150, 1981.

Kosarev, G. L., Makeyeva, L. I. and Vinnik, L. P., Anisotropy of the mantle inferred from observations of P to S converted waves, **Geophys. J. Roy. Astron. Soc., 76**, 209−220, 1984.

Levander, A. R., and Hollinger, K., Small−scale heterogeneity and large−scale velocity structure of the continental crust, **J. Geophys. Res., 97,** 8797−8804, 1992.

Hales, A. L., A seismic discontinuity in the lithosphere. **Earth Planet. Sci. Letts., 7**, 44−46, 1969.

Levin, V., and J. Park, P−SH conversions in a flat−layered medium with anisotropy of arbitrary orientation, **Geophys. J. Int., 131**, 253−266, 1997.

Levin, V., and J. Park, A P−SH conversion in layered media with hexagonally symmetric anisotropy: A cookbook, **Pure and Applied Geophysics, 151**, 669−697, 1998.

Levin, V. and Park, J., Shear zones in the Proterozoic lithosphere of the Arabian Shield and the nature of the Hales discontinuity, **Tectonophysics**, in press, 2000.

Park, J., Surface waves in layered anisotropic structures, **Geophys. J. Int., 126**, 173−184, 1996.

Park, J. and Levin, V., Receiver functions from multiple−taper spectral correlation estimates, **Bull. Seism. Soc. Amer.**, submitted 2000a.

Park, J. and Levin, V., Receiver functions From regional P waves, **Geophys. J. Int.**, submitted 2000b.

Pavlenkova, N. I., General features of the uppermost mantle stratification from long−range seismic profiles. **Tectonophysics**, 264, 261−278, 1996.

Rodgers, A. J., Ni, J. F., Hearn, T. M., Propagation characteristics of short−period Sn and Lg in the Middle East, **Bull. Seism. Soc. Amer., 87**, 396−413, 1997.

Sandvol, E., Seber, D., Barazangi, M., Vernon, F. L., Mellors, R., and Al−Amri, A., Lithospheric seismic velocity discontinuities beneath the Arabian Shield. **Geophys. Res. Letts., 25**, 2873−2876, 1998a.

Sandvol, E., Seber, D., Calvert, A., and Barazangi, M., Grid search modeling of receiver functions; i crustal structure in the Middle East and North Africa, **J. Geophys. Res., 103**, 26899−26917, 1998b.

Savage, M., Lower crustal anisotropy or dipping boundaries? Effects on receiver functions and a case study in New Zealand, **J. Geophys. Res., 103**, 15069−15087, 1998.

Vernon, F. L., J. Fletcher, L. Carroll, A. Chave and E. Sembrera, Coherence of seismic body waves from local events as measured by a small−aperture array, **J. Geophys. Res., 96,** 11981−11996, 1991.

Wu, R.−S., Wide−angle elastic wave one−way propagation in heterogeneous media and an elastic wave complex screen method, **J. Geophys. Res., 99**, 751−766, 1994.

Yuan, H., J. Park and V. Levin, P−to−S converted phases from subducted slabs in the Northwest Pacific, **EOS Trans. AGU**, Fall Supplement, 80, F720, 1999.

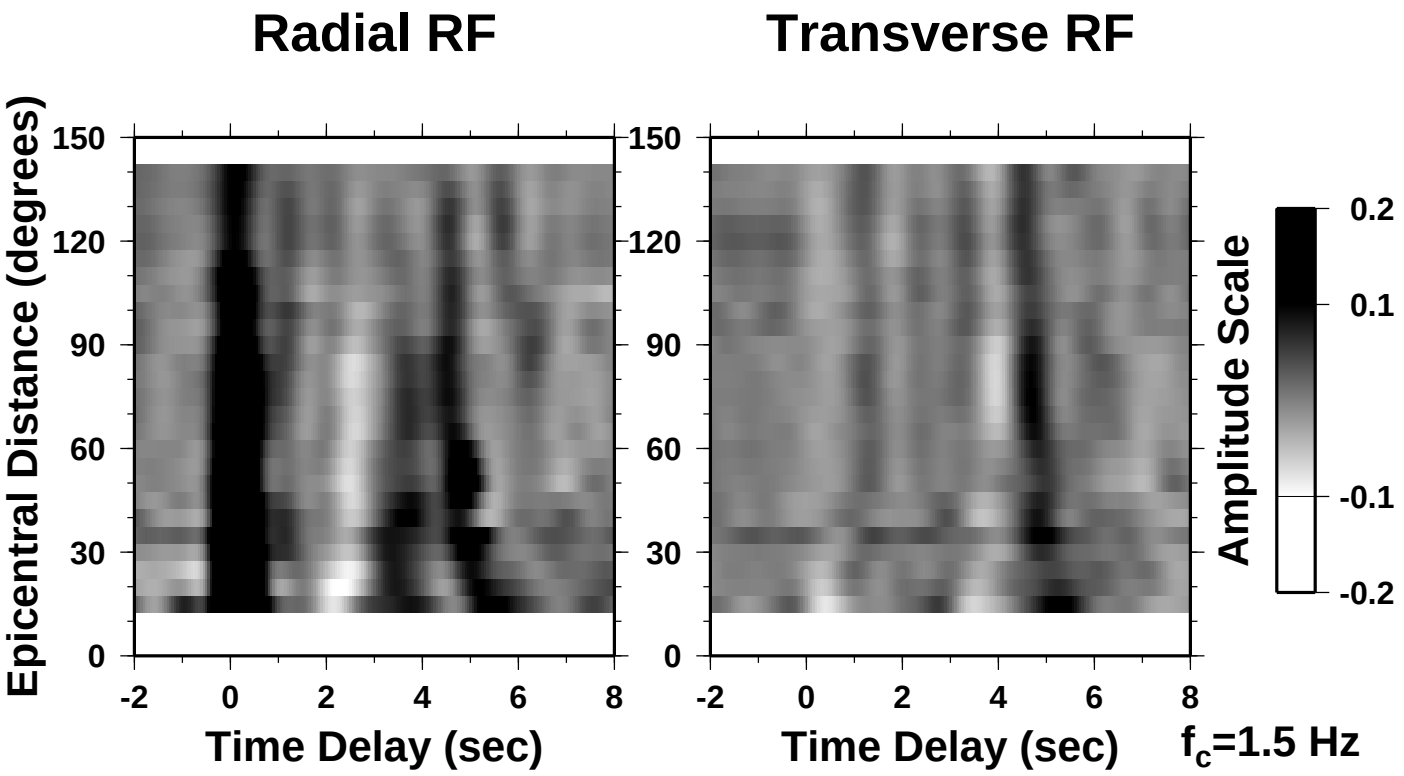
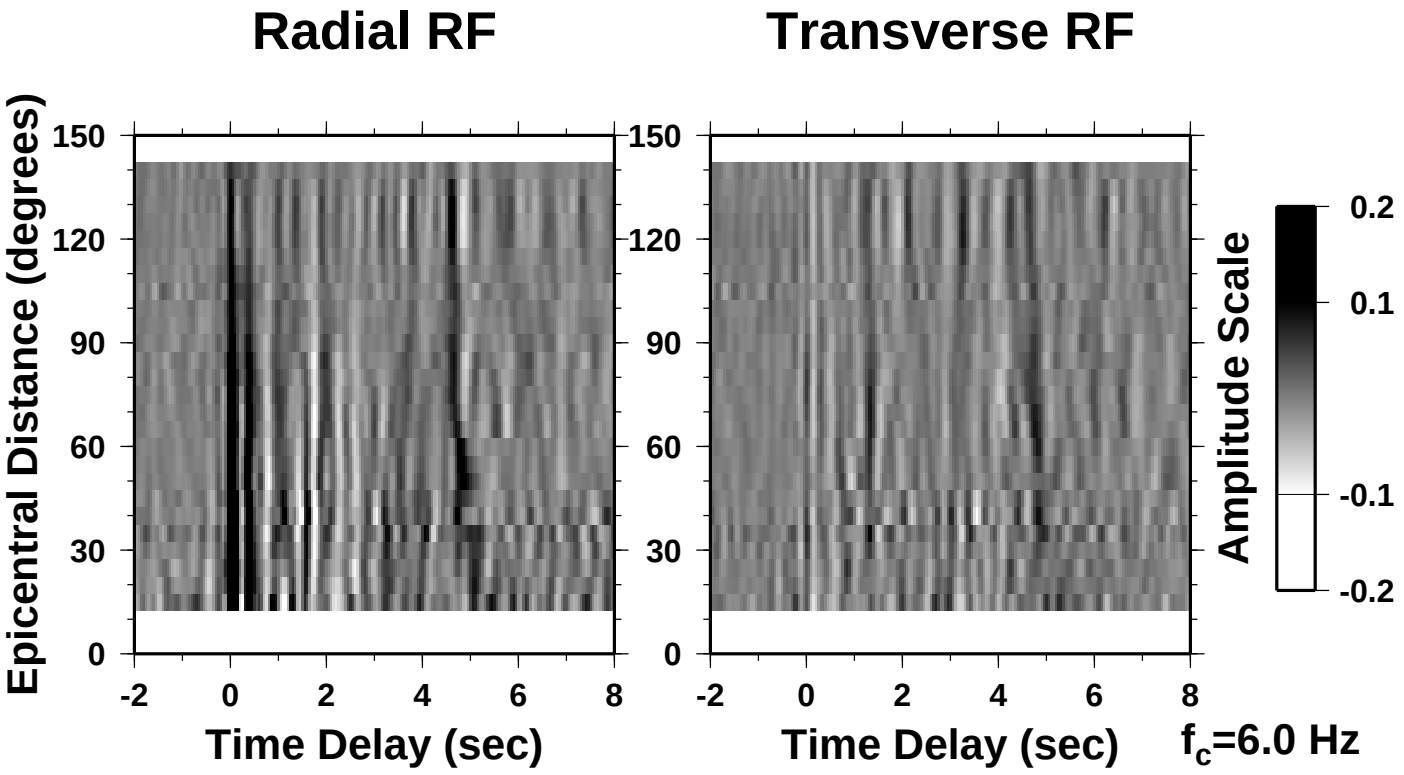


Figure 1. Grey-shade plots of composite receiver-functions at ARU (Arti, Russia) for frequency cutoffs f_c=1.5 Hz (above) and f_c=6.0 Hz (below), plotted against epicentral distance Δ. Only events in the back-azimuth range 50˚-150˚ contribute to the composite RFs. Over 200 P-coda are stacked in the images.



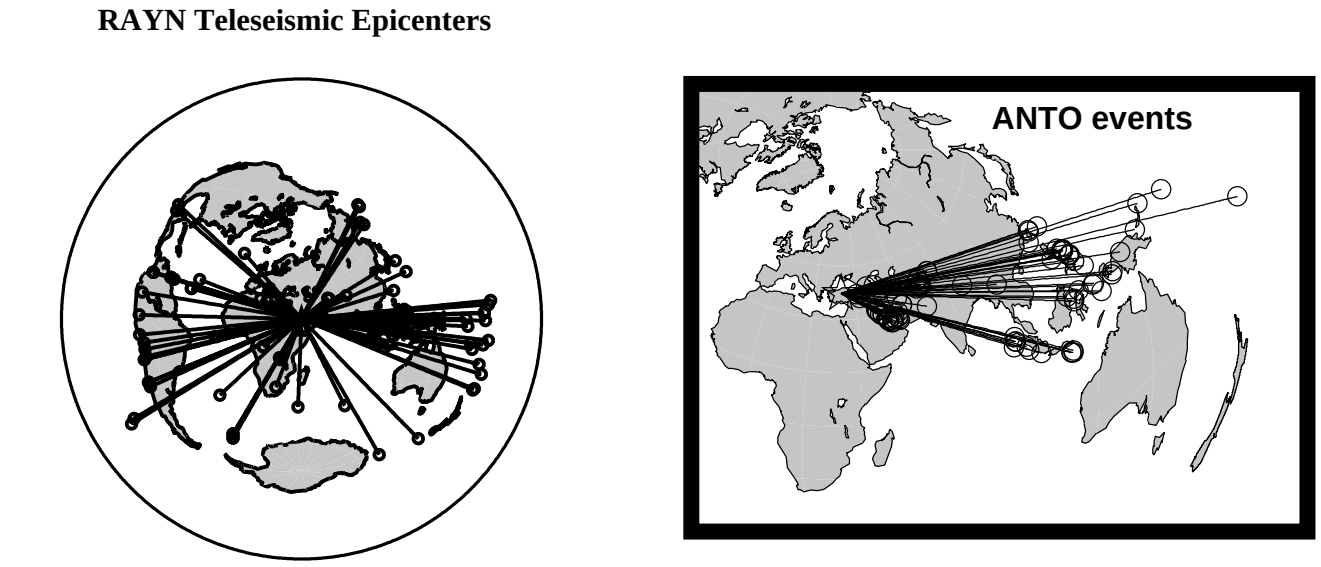


Figure 2. Events for Middle East stations. Regional earthquakes are analyzed in a narrow back-azimuth sector.

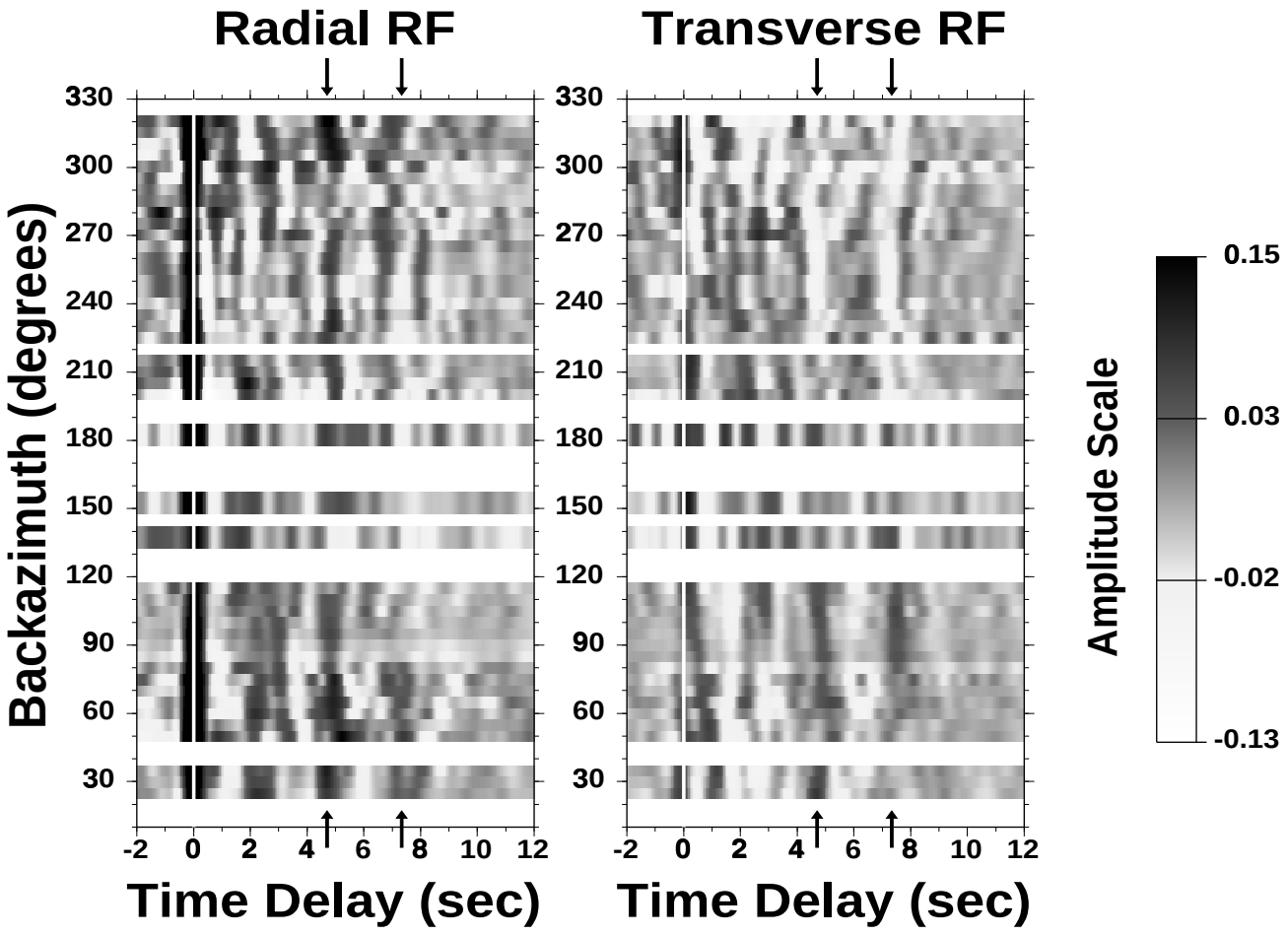
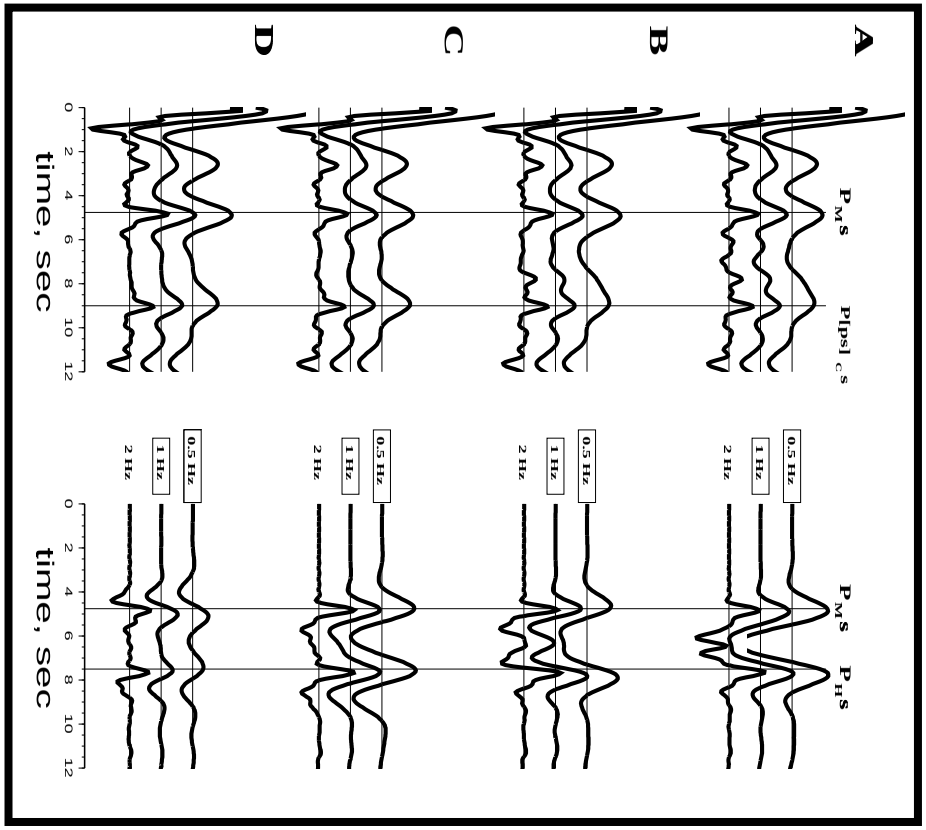
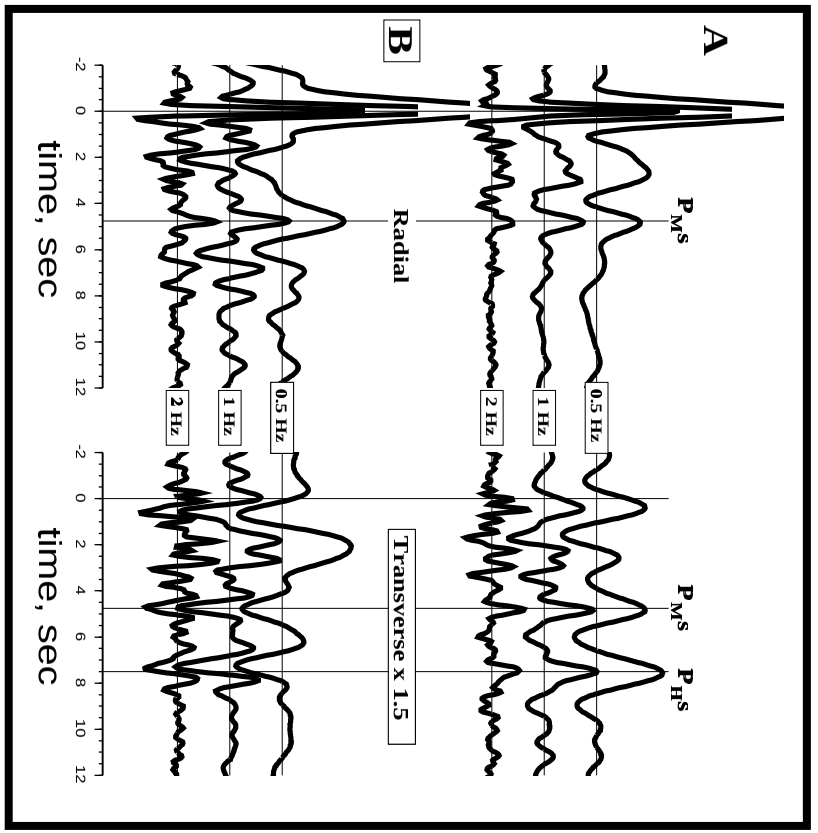


Figure 3. RAYN receiver functions as a function of back-azimuth. Data include direct P, PKP, and Pdiff phases observed between spring 1997 and summer 1999. RF spectra are lowpassed (effectively) at 1 Hz (fc=2.0 Hz). The converted phases Pms and PHs are indicated by arrows at roughly 4.8 and 7.2-sec delay. Note the polarity changes in the transverse RFs for these phases. Conversions from the east have positive amplitude, conversions from the west are negative.





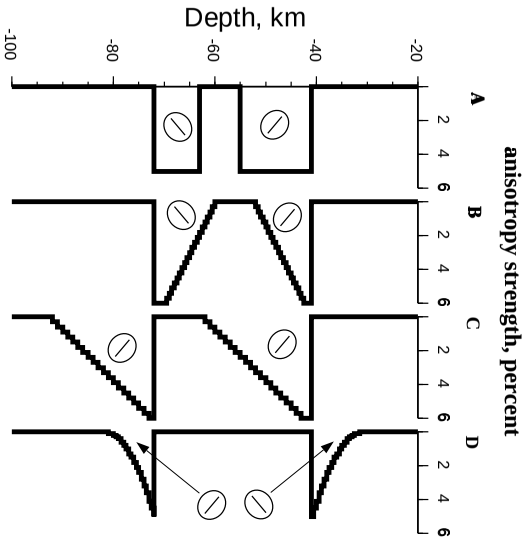


Figure 4. Upper Left: Composite RAYN RFs for narrow backazimuthal ranges for a variety of cutoff frequencies. The eastern stack (A) includes data from backazimuths 75°–107°; The western stack (B) includes data from backazimths 255°–285°. P_Ms is clear in all frequencies on both radial and transverse components, while P_Hs is primarily seen on the transverse component. Time-alignment of P_Hs is better at high frequencies. Lower Right: Vertical profiles of anisotropy strength in the models we tested for RAYN RFs. Coffee-bean symbols show the orientation of symmetry axis of anisotropy. Symmetry-axis tilt (from the vertical) toward the south is indicated by a symbol that tips to the left. Lower Left: Synthetic RFs for a P wave incident from the east. The 2-Hz receiver functions for Model C provide the best match to the one-sided pulses on the RAYN RFs from eastern backazimuths. Model D, with a slightly different anisotropic gradient beneath the Hales discontinuity, matches better the P_Hs pulse from western backazimuths.

Figure 5. Schematic diagram illustrating the development of shear zones within the upper mantle beneath the Ar Rayn terrane of the Arabian Shield, during an episode of northward "tectonic escape" in the late Proterozoic. Arrows beneath the Moho and Hales discontinuities indicate the location and direction of lattice-preferred orientation in olivine grains suggested by Model C.

Figure 6. Regional and near-teleseismic RAYN receiver functions, averaged in 4° epicentral-distance bins in the frequency domains with uncertainty handicaps. Results for short-period data (40 sps) are shown for eastern backazimuths, with frequency cutoff $f = 10$ Hz. Superimposed delay curves are computed for the Ps converted phases that would arise from a Moho at 41 km depth for incoming P and P_n waves using the phase velocities of the IASPEI91 model.

6

Figure 7. ANTO receiver functions, averaged in 10° epicentral-distance bins in the frequency domains with uncertainty handicaps. Results for events from eastern backazimuths are shown, with frequency cutoff $f = 3$ Hz. The thin solid lines indicate predicted Ps arrival delays computed from the RAYN crustal model, from a midcrustal interface, the Moho and a hypothetical Hale discontinuity. The RF traces are shaded on the negative side to highlight features whose delays decrease as $\Delta \to 0$. Note the continuity of RF pulses from teleseismic to regional distances, especially at short delay times.

7

Figure 8. Moveout curves for simple scenarios of Ps scattering, using an upgoing plane-wave slowness from the IASPEI91 earth model. The Moho depth is taken to be 40 km beneath a hypothetical station, and crustal V_P and V_S are 6.0 and $6/\sqrt{3}$, respectively. The mantle V_P is 8.0 km/sec. Curve "FM" indicates Ps delays for a flat Moho. Curve "DM" indicates Ps delays for a Moho that dips 40°, with direct-P approaching from the updip side. Curves "S" and "SS" in the left panel indicate P_{DS} and Ps_{DS} phases that convert and reflect, respectively, from a shallow interface D. Curves "SP" and "SS" in the right panel indicate the arrivals of P and S waves, respectively, from a surface scatterer 30 km from the station, between source and receiver. Only the surface scatterer causes negative moveout as $\Delta \to 0$ similar to ANTO RF features in Figure 7.

REGIONAL SEISMOLOGICAL RESEARCH IN THE MIDDLE EAST IN SUPPORT OF CTBT MONITORING

Eric Sandvol, Dogan Seber, Khaled Al-Damegh, and Muawia Barazangi
Institute for the Study of the Continents (INSTOC), Cornell University

Sponsored by the Defense Threat Reduction Agency
Arms Control Technology Division
Nuclear Treaties Branch

Grant No. DSWA 01-97-1-0006

ABSTRACT

In order to decipher the character and pattern of regional seismic phase propagation we have continued to compile a large data set of regional and local seismograms recorded in the Middle East. We have mapped zones of blockage, inefficient, and efficient propagation for Lg and Sn. Two tomographic techniques have been developed in order to objectively determine regions of efficient and inefficient regional phase propagation. We have found that regional wave propagation in this region is very complex; hence the station density from our data set in this region is invaluable. We have collected data from Saudi Arabia, Oman, Turkey and Syria in order to further improve our resolution of our wave propagation tomographic models. Furthermore, this quantity of data will allow us to isolate the source, site, and path effects in the generation of Lg, Sg, and Pg.

We have also continued our study of crustal and upper-most mantle structure in the Middle East using receiver function interpretation and grid search waveform modeling. Data from our ongoing broadband experiment in eastern Turkey combined with three-component short period receiver functions in Syria have begun to give us an accurate idea of crustal thickness in the northern portion of the Middle East. We also plan to calculate receiver functions in Saudi Arabia in order to map crustal thickness variations across the Arabian Shield. We also have begun to collect all available travel time observations in the Middle East in order to accurately determine the mantle P and S-wave velocity structure. We have initially focused on Pn travel time tomography. This work will provide important new reliable models of variations in upper mantle seismic wave velocities. All of the above results will be integrated in the Cornell GIS system.

Key Words: Regional wave propagation, crustal velocity, upper mantle velocity, Middle East, CTBT

OBJECTIVE

The CTBT requires the development of credible strategies for effective monitoring, including the ability to detect, locate, discriminate, and characterize any suspect events for any region on earth. In order to accomplish this task necessary models and fundamental observations concerning seismic event location and regional wave propagation are required. Examples of such critical models are travel time models for individual IMS stations that can be used to correct for three-dimensional variations in seismic velocity structure. One dimensional travel time models are not sufficient for regions that contain substantial lateral variations in crustal thickness and uppermost mantle velocity. Furthermore, observations are required for the propagation of several key regional phases in the Middle East and North Africa since current knowledge is insufficient to accurately characterize regional wave propagation in this complex region. New seismological data are required to constrain both travel time and wave propagation models of very low yield events at regional distances. In order to make our final results available to the monitoring community we will include our data and results on the Middle East and North Africa into the Cornell GIS database.

Our objective is to expand the existing geophysical/seismological information and to provide new knowledge of the Middle East and North Africa using data from both short period national networks as well as broadband temporary and global networks. In this paper we give two examples of techniques and observations that are critical to improving seismic event location and discrimination in the Middle East and North Africa.

RESEARCH ACCOMPLISHED

Regional Wave Propagation in the Middle East

Research on seismic wave propagation in the Middle East has demonstrated the necessity for a large number of seismic stations to be used to accurately characterize Lg and Sn behavior in this region (Figure 1). We have compiled a large data set of regional and local seismograms recorded in the Middle East. We have used this data set to decipher the character and pattern of regional seismic wave propagation. We have mapped zones of blockage as well as inefficient and efficient propagation for Lg, Pg, and Sn throughout the Middle East. Two tomographic techniques have been developed to objectively determine regions of lithospheric attenuation in the Middle East. The first technique used Lg/Pg ratios to characterize crustal attenuation as well as to determine the path effects on this commonly used discriminant. The second technique used discrete Sn propagation efficiencies that we defined after examining over 4000 seismograms. This technique allowed us to map the regions of inefficient and efficient Sn propagation in the Middle East.

We observe evidence for a significant increase in Lg attenuation relative to Pg across the Bitlis suture and the Zagros fold and thrust belt, corresponding to the boundary between the Arabian and Eurasian plates (Figures 2a,

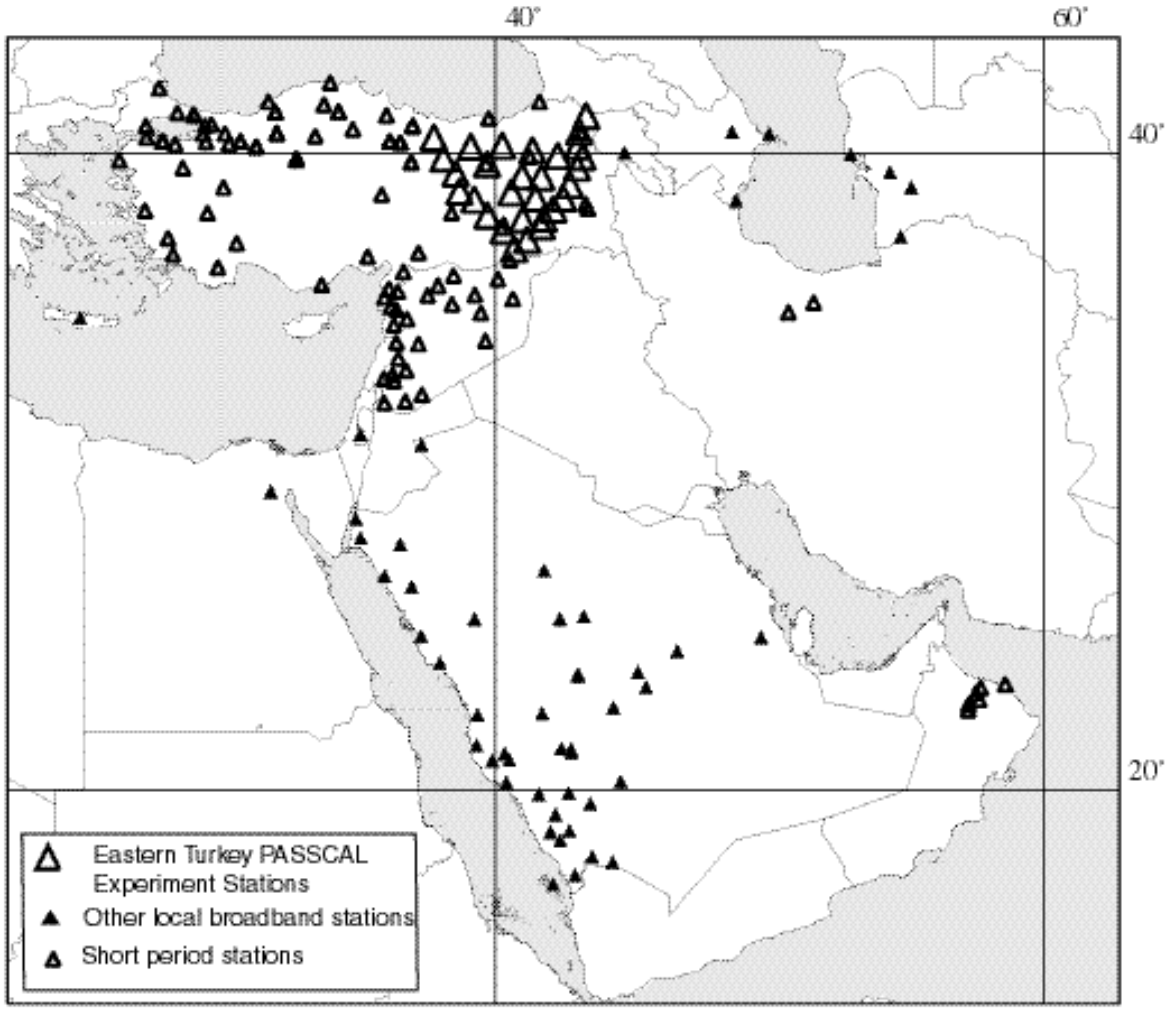


Figure 1. A map showing the seismic stations contained Cornell's seismic waveform database in the Middle East.

b, c). Generally Lg was blocked when the ray paths crossed either of these major tectonic boundaries. We also observed Lg blockage in the Mediterranean and southern Caspian Seas. We also found that within the Middle East, Lg propagation is most efficient in the Arabian Shield and in eastern Jordan and Syria in a region known as the Rutbah uplift. This region is thought to have very little variation in crustal thickness or variation in the thickness of the sedimentary cover. Our tomographic method assumes that variations in Lg/Pg ratios are due to path effects (Sandvol et al., 2000), neglecting possible differences in Lg excitation relative to Pg for different size or types of seismic events. We are currently creating a database in the Middle East large enough to allow us to simultaneously solve for the source and path effects.

We have also investigated the frequency dependence of Lg attenuation in the Middle East. We bandpass filter each of the regional seismograms for a given frequency band prior to calculating the Lg/Pg ratios. These

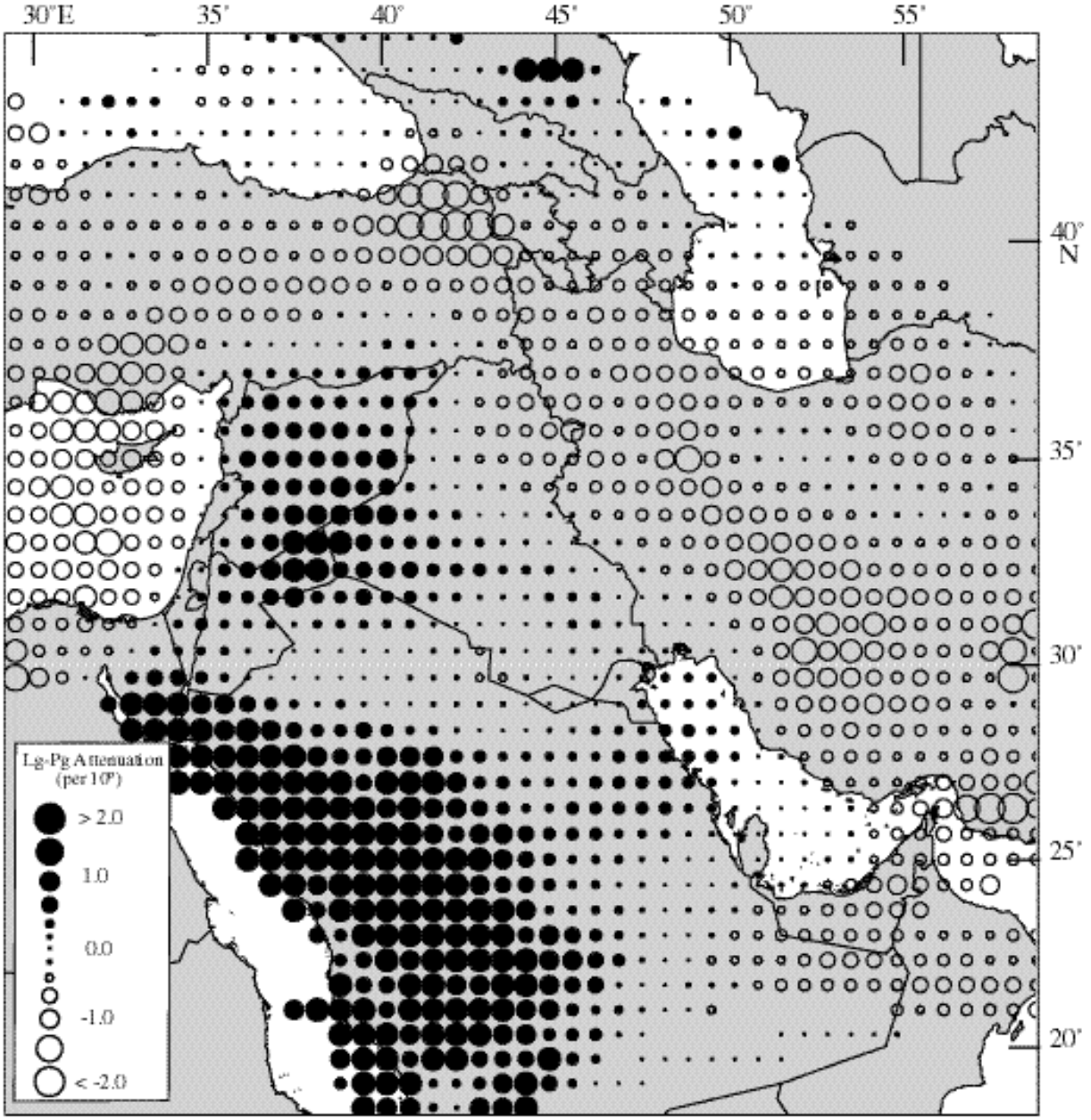


Figure 2a. A map showing the Lg/Pg ratio tomographic model for frequencies between 0.5 and 2 Hz. This image is based upon approximately 4400 regional waveforms.

filtered amplitude ratios are used to create our Lg/Pg tomographic model for that given frequency band. In general we have found only a small frequency dependence of Lg/Pg amplitude ratios in the Middle East. The difference that is observed between the lower and higher frequencies can be attributed to lower signal to noise ratio at the 2 to 4 Hz and the smaller number of events that satisfy our signal to noise criteria.

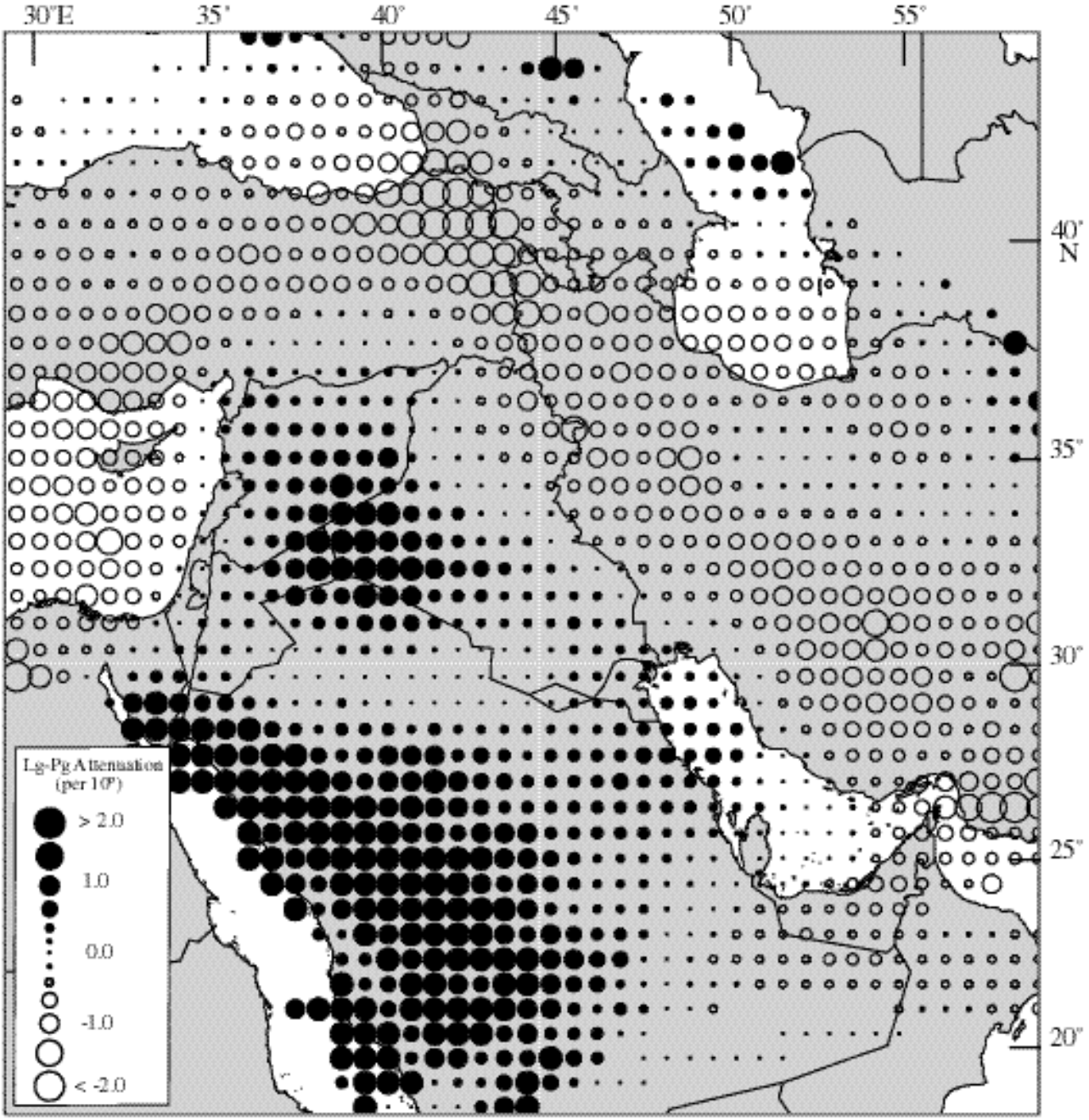


Figure 2b. A map showing the Lg/Pg ratio tomographic model for frequencies between 1 and 3 Hz.

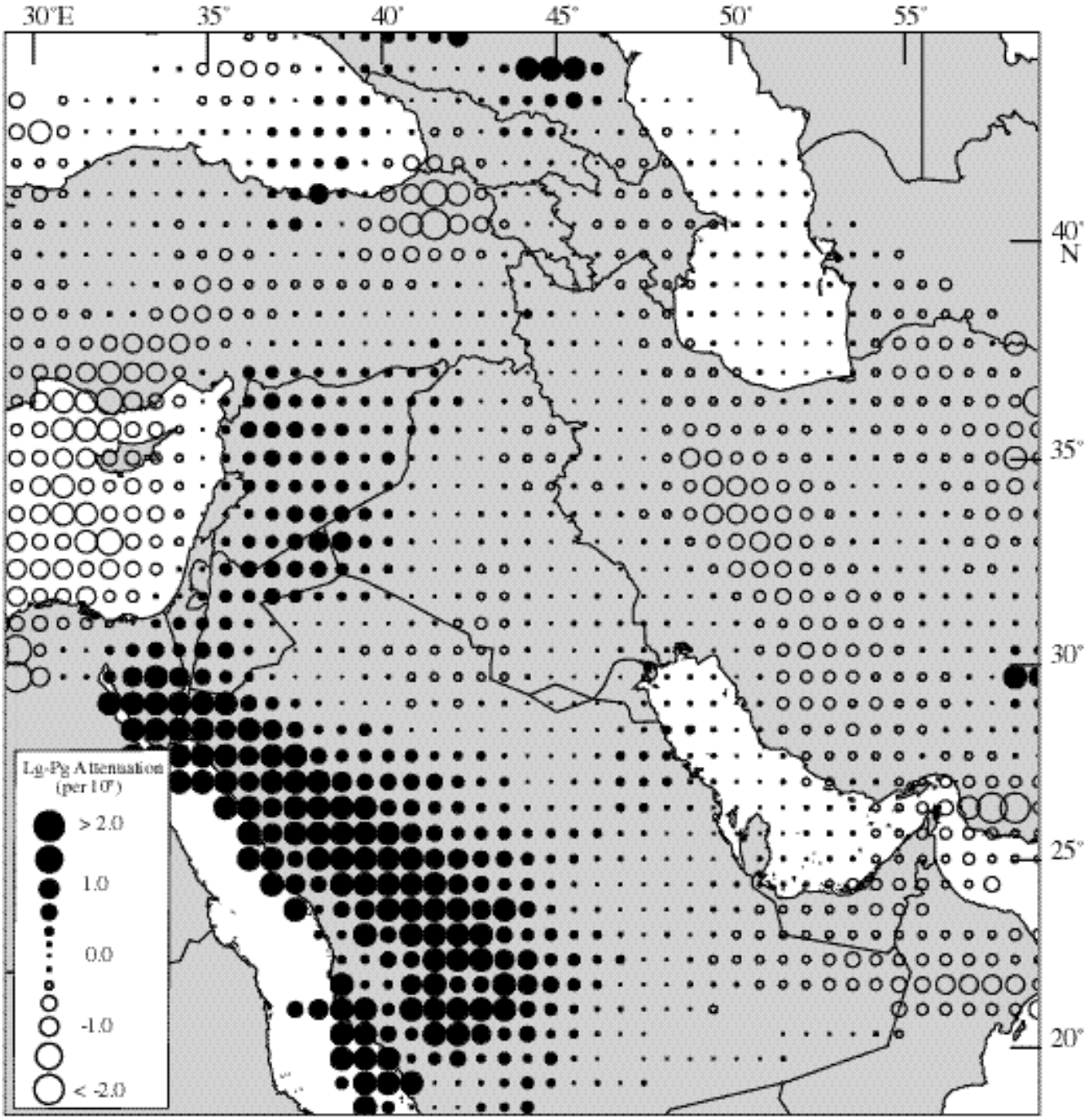


Figure 2c. A map showing the Lg/Pg ratio tomographic model for frequencies between 2 and 4 Hz.

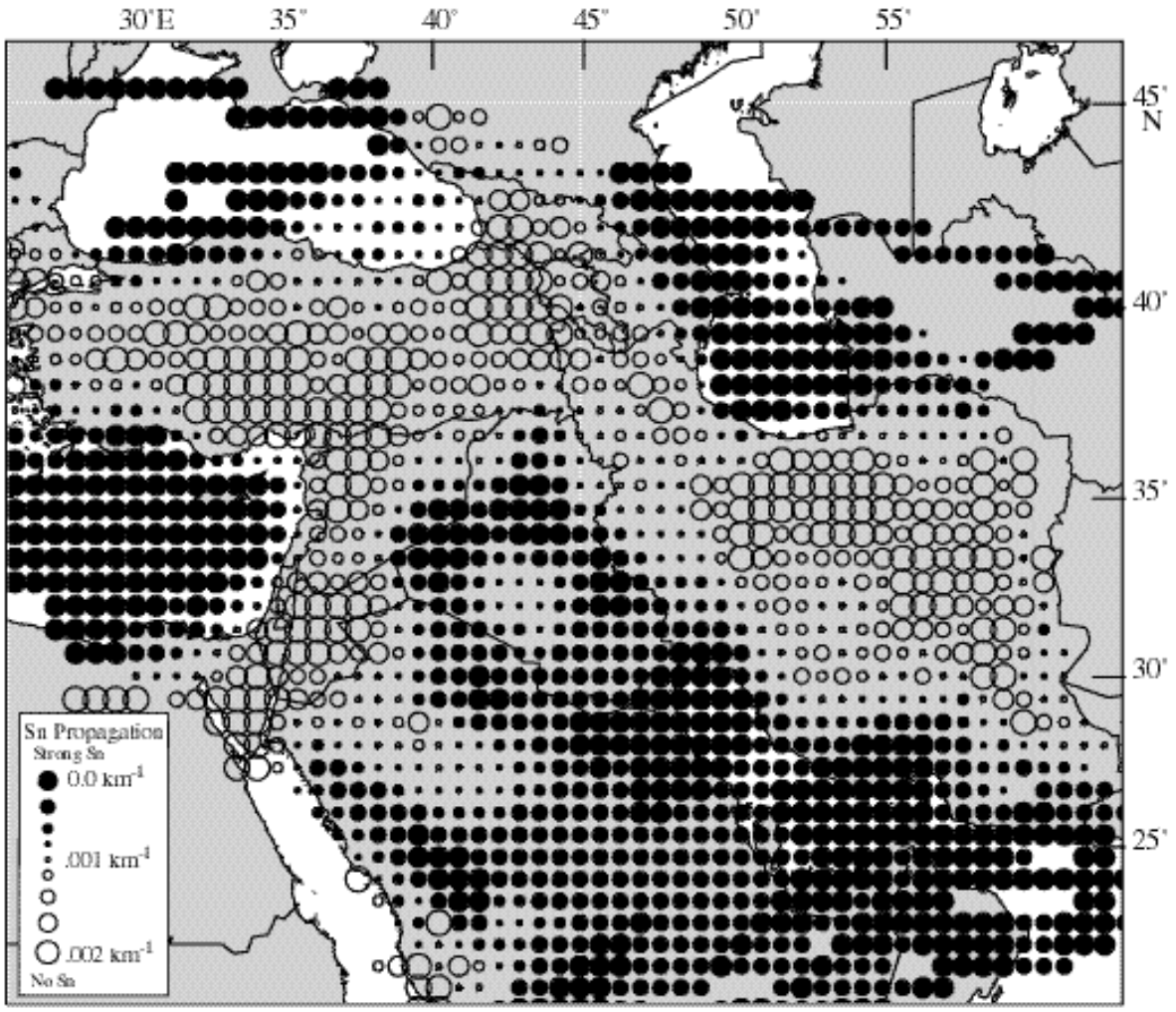


Figure 3. A map showing a tomographic model of Sn propagation efficiency in the Middle East. The model parameters in this image are the reciprocal of the Sn extinction path length. This image is based upon approximately 4200 regional waveforms.

We also observed a zone of inefficient Sn propagation along the Dead Sea fault system (Figure 3) that coincides with low Pn velocities along most of the Dead Sea fault system and with previous observations of poor Sn propagation in the Gulf of Aqaba (Rodgers et al., 1997). Our observations indicate that in the northern portion of the Arabian plate (south of the Bitlis suture) there is also a zone of inefficient Sn propagation that would not have been predicted from prior measurements of Pn velocities. However, existing Pn tomographic models have relatively poor ray coverage for much of the eastern portion of the Dead Sea fault system. We have begun to collect phase data from the Syrian National Seismic Network and our temporary PASSCAL array in eastern Turkey in order to obtain a better uppermost mantle velocity model for this region.

Crustal Structure in the Middle East

We are continuing to utilize a grid search modeling of receiver functions in the Middle East to help improve current Moho maps in the region (Sandvol et al., 1999). We have modeled receiver functions calculated from the ILPA array and found a low velocity zone at station IR7 located near the Alborz mountains (Figure 4). We have also obtained a velocity model for IR1 located 50 kilometers to the west of the Alborz mountains. We found a relatively similar crustal thickness as was observed at station IR1 (Figure 4). We have also begun to model receiver functions at station ABKT (Turkmenistan) and NIL (Pakistan). At station ABKT we have found evidence for a strong lateral heterogeneity in the crustal structure.

Preliminary receiver functions were also calculated from three component short period data from the Syrian National Seismic Network (SNSN). We were able to stack receiver functions for four of the six stations in the SNSN. The other two three-component stations were too noisy for receiver function analysis. Our preliminary receiver function analysis has indicated that there is a significant increase in crustal thickness along the northern margin of the Palmyride fold and thrust belt. This observation is consistent with a very sharp change in the gravity data in this region, however it is not consistent with the relatively small topographic signature of the Palmyride mountain belt. In order to verify this initial observation more quality three component data will need to be collect in Syria.

We have also calculated several preliminary receiver function profiles using the broadband three component data that we have collected from the ongoing eastern Turkey PASSCAL seismic experiment. We deployed 29 stations in October of 1999 and plan to dismantle the array in April of 2001. Our initial receiver function analysis indicates that there is no significant change in crustal thickness across the Bitlis suture. In easternmost Turkey, north of Lake Van we observe very rapid increases in crustal thickness over less than 50 km. These observations, however, are very preliminary and more data processing is required to insure that our models are robust.

CONCLUSIONS AND RECOMMENDATIONS

Our study of regional wave propagation demonstrates that there are dramatic variations in Lg and Sn propagation in the Middle East. Furthermore, using Lg/Pg ratio tomography can, for the most part, determine the path effects on Lg/Pg ratio calculations and thereby is a method for isolating the source effects on Lg/Pg amplitude ratios. We have also begun to further improve our crustal thickness maps using receiver function inversions of stations in Syria, Iran, Turkmenistan and Pakistan. We have found important variations in crustal structure throughout these regions. It is essential for both discrimination and location research to have a reliable lithospheric velocity model for the Middle East.

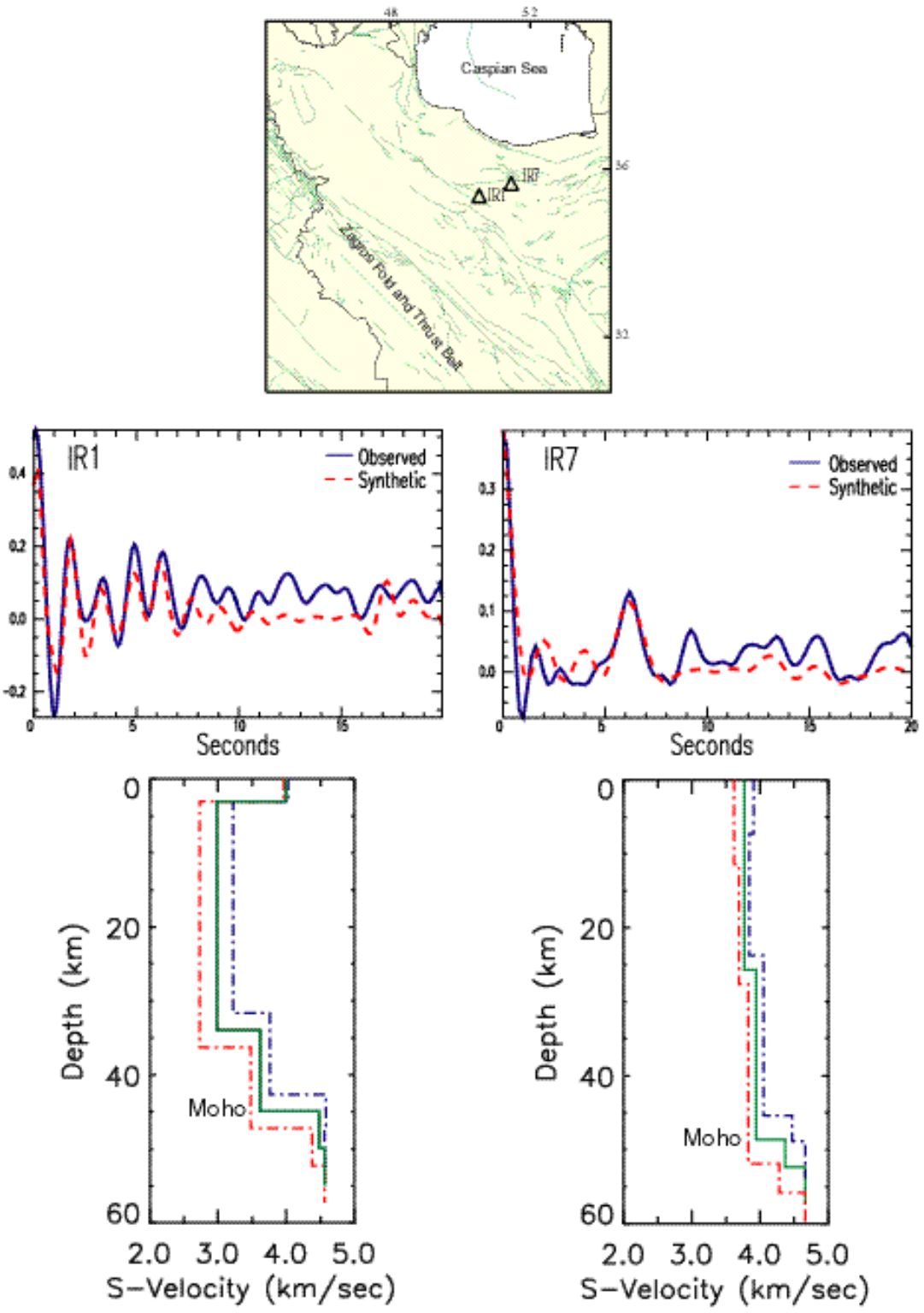


Figure 4. Velocity models derived from grid search modeling of receiver functions for the two three component stations in the ILPA array. Note the large low velocity zone beneath station IR1.

REFERENCES

Hearn T. and Ni, J., Pn velocities beneath continental collision zones: The Turkish-Iranian Plateau, Geophys. J. Int., vol. 117, 273-283, 1994.

Rodgers, A., Ni, J., and Hearn, T., Propagation characteristics of short period Sn and Lg in the Middle East, Bull. Seism. Soc. Amer., vol. 87, 396-413, 1997.

Sandvol, E., Seber, D., Calvert, A., and Barazangi, M., Grid search modeling of receiver functions: implications for crustal structure in the Middle East., Journ. Geophys. Res., vol. 108, p. 26899-26917, 1998.

Sandvol, E., Al-Damegh, K., Clavert, A., Seber, D., Barazangi, M., Mohamad, R., Gok, R., Turkelli, N., and Gurbuz, C., Tomographic imaging of Lg and Sn propagation in the Middle East, Pure and Applied Geophys., in press.

COMPARISON OF DIFFERENT METHODOLOGIES FOR REGIONAL MAGNITUDE CALCULATION OF EURO-MEDITERRANEAN EARTHQUAKES

Jörg Schlittenhardt

Federal Institute for Geosciences and Natural Resources (BGR), Germany

ABSTRACT

Based on the data of the German Regional Seismic Network (GRSN) the reliability of several types of magnitudes in the regional distance range is investigated to derive a consistent method for a unified magnitude scale, intended to be used for a European seismic reference bulletin. As this bulletin will include many small events with body-wave magnitude below m_b 4.0, for the calibration of regional magnitude scales, variations in the source corner frequency as a function of event magnitude have to be considered to take into account non-linear relations between the magnitude scales.

For the magnitude comparison European earthquakes with tightly clustered epicenters are used as reference data set to eliminate a possible amplitude/frequency bias caused by travel path effects. For the calculation of various proposed regional magnitudes (M_L, $m_b(P_n)$, $m_b(Lg)$, log rms(Lg), M_0 based regional magnitude) only events with independent teleseismic estimates of the earthquake size are used. Results from this test of the relative performance of the different regional magnitude scales using GRSN recordings of the 1997 Umbria-Marche, central Italy, earthquake sequence will be presented.

For 38 earthquakes of the Umbria-Marche sequence three types of regional magnitudes were calculated for the GRSN station WET. The relative performance of the three different magnitude scales is evaluated by linear regression against network m_b body wave magnitudes. The standard deviation *S.D.* and the slope S is used for assessing the reliability of the Lg based magnitudes relative to a reference magnitude set. The best result is obtained for rms m_{lg} in terms of both S and *S.D.*. However, the differences are only slight for M_L and $m_b(Lg)$.- A similar comparison was made for the three magnitudes with the M_0-values as a reference. Here the *S.D.* values are clearly smaller, but again the rms m_{Lg} magnitude gave the best results.

Based on a method proposed by Bolt & Herrariz (1983) a calibration relation M_0- relating seismic moment and measurements (amplitude and coda decay time) from regional seismograms was calculated, using 14 earthquakes with independent seismic moments. This equation can now be used to calculate M_0 for other earthquakes of the Umbria-Marche sequence for which no seismic moment estimates exist. Additionally, results from a newly derived $m_b(P_n)$ scale for Euro-Mediterranean earthquakes and a regional comparison to results from the Western United States will be presented.

Key Words: Seismic wave propagation, regional phases, seismic regionalization, earthquake location, seismic magnitude

Lg WAVE PROPAGATION USING SH AND P AND SV SCREEN PROPAGATORS IN HETEROGENEOUS CRUSTS WITH IRREGULAR TOPOGRAPHY

Ru-Shan Wu, Xiao-Bi Xie and Xian-Yun Wu
Institute of Tectonics, University of California, Santa Cruz

Sponsored by U.S. Department of Defense
Defense Threat Reduction Agency

Contract No. DSWAO 1 -97-1-0004

ABSTRACT

This study is aimed at development and application of new wave propagation and modeling methods for regional waves in heterogeneous crustal waveguides using one-way wave approximation. The half-space generalized screen propagators (GSP) for both SH and P-SV waves have taken the free surface into the formulation and adopt a fast dual domain implementation. The method is several orders of magnitude faster than finite-difference method with a similar accuracy for certain problems. It has been used for the simulation of wave propagation for high-frequency waves (1-25Hz) to a regional distance (greater than 1000km).

In this year, we further develop the method in two fronts. First, we extend the SH GSP method to treat irregular surface topography by incorporating a coordinate transform into the method. It is demonstrated that our new approach has superior wide-angle response to surface topography over the PE (parabolic equation) method. The efficiency of the screen propagator approach makes it very promising for long distance Lg simulation. For a test model with a propagation distance of 250km and a dominant frequency of 1Hz, the screen method took about 35 minutes, while the boundary element method took about 72 hours. For longer propagation distances and higher frequencies, the factor of saving could be huge.

Second, we developed a P-SV screen propagator for crustal waveguides with flat surfaces. This is the major task of this year. Free surface reflection and conversion have been incorporated into the screen propagator theory. Numerical tests have been done against the wavenumber integration and finite-difference calculations. The results demonstrated the feasibility of the approach.

Finally, numerical simulations have been conducted for various crustal waveguide structures, including deterministic structures, small-scale random heterogeneities and random rough surfaces. Influences of random heterogeneities and rough surfaces on Lg amplitude attenuation and Lg coda formation have been studied.

INSTRUCTION

Short-period regional phases (P_n, P_g, S_n, L_g, etc.) play an important role for both discrimination and yield estimation procedures for monitoring the Comprehensive Nuclear-Test-Ban Treaty (CTBT). Amplitude ratios of short-period P wave energy (P_n, P_g) to S wave energy (S_n, L_g) have emerged as particularly promising discriminants, especially at frequencies above 3Hz (Walter et al., 1995; Taylor, 1996; Hartse et al., 1997; Fan and Lay, 1998). Regional phases mainly propagate in the crustal waveguide and the uppermost mantle. A wide variety of observational and theoretical studies show that the structure and multi-scale heterogeneities of the crustal wave guide and uppermost mantle strongly affect the regional phases in waveform properties and amplitudes (Kennett, 1986, 1989; Zhang et al., 1994; Fan and Lay, 1998). However, due to the complexity involved in regional phase propagation and limit of capability of the existing analysis and simulation approaches, the mechanism of excitation and propagation of regional phases is still not appreciated. In these investigations, numerical approaches for simulating regional phases are very useful.

In the crustal waveguide environment, major wave energy is carried by forward propagating waves, including forward scattered waves, therefore neglecting backscattered waves in the propagation will not change the main features of regional waves in most cases. Based on the concept, a generalized screen propagator method (GSP) based on one-way wave equation has been developed by Wu (1994), Wu, Jin and Xie (1999a) and has been successfully used to simulate SH Lg waves in the complex crustal waveguide and investigate the energy partitioning of Lg waves (Wu, Jin and Xie, 1999b). Wu, Xie and Wu (1999) further extended the GSP method to treat complex crustal waveguides with irregular or rough topography by incorporating a surface topographic transformation into the method. For a test model with propagation distance of 250km, dominant operating frequency of 1Hz, the BE (boundary element) method took about 72 hours, while the screen method took only 35 minutes with the same accuracy. For longer propagation distances and higher frequencies, the factor of saving could be huge.

Based on the success of Lg propagation using SH screen propagators, in this paper we extend the screen propagator method to P-SV Lg wave propagation. As the first step we apply the complex screen method to a flat, heterogeneous half space. Unlike SH wave, the image method can not be used to account for the effect of free surface. We incorporate the reflection coefficient calculations of elastic waves on free surface into the complex screen method for the effect of free surface on P-SV waves. Comparison of synthetic seismograms calculated by the complex screen method and wavenumber integration method for an elastic half-space shows feasibility and validity of the approach. Synthetic seismograms for elastic layered model and a laterally varying crustal waveguide are conducted and compared with wavenumber integration method and finite difference method, respectively. The results demonstrate that the complex screen method can be used to model regional phases containing P_n, P_g, S_n and L_g.

METHODOLOGY

Figure 1 illustrates the principle of the method. The screen method is a forward matching algorithm. To avoid the energy increase caused by the repetitive application of reflection calculation, we extend the model in vertical direction from free surface, and the extended part has the parameters of background medium. The complex screen method will be applied to such an extended model for elastic wave simulation. For each forward step we apply the reflection calculation to the incident field (only to upgoing waves) to get the reflections and conversions from free surface. Figure 1 also shows such a process by an upgoing ray from source. Knowing the reflections and

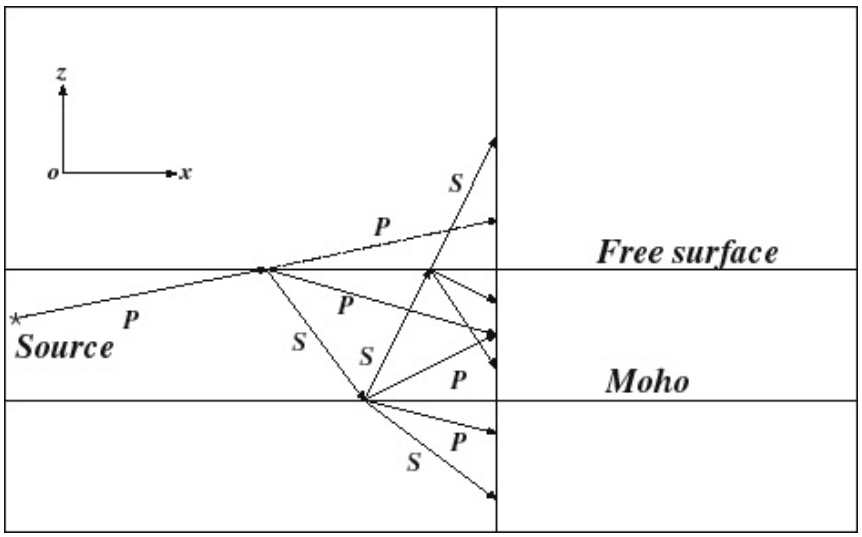


Figure 1. Illustration of the screen method

conversions, we can calculate the scattered field of the reflected fields using the complex screen method and then combine the scattered field into the incident field to obtain new incident field. In the following, a simple description of the complex screen method and reflection coefficient formulas will be given.

COMPLEX SCREEN APPROXIMATION FOR ELASTIC WAVES

A complete derivation of the complex screen method for modeling elastic waves can be seen in Wu's papers (Wu, 1994, 1996). A short review of the method for forescattering is given in this section. Suppose that the parameters of the elastic medium and the total wave field can be expressed as

$$\rho(\mathrm{x}) = \rho_0 + \delta\rho(\mathrm{x})$$
$$\alpha(\mathrm{x}) = \alpha_0 + \delta\alpha(\mathrm{x})$$
$$\beta(\mathrm{x}) = \beta_0 + \delta\beta(\mathrm{x})$$

and

$$u(\mathrm{x}) = u_0 + \mathrm{U}(\mathrm{x})$$

where ρ_0, α_0 and β_0 are the parameters of the background medium, $\delta\rho(\mathrm{x})$, $\delta\alpha(\mathrm{x})$ and $\delta\beta(\mathrm{x})$ are the corresponding perturbations, u_0 and $\mathrm{U}(\mathrm{x})$ are the incident field and the scattered field, $\mathrm{x} = x\mathrm{e}_x + z\mathrm{e}_z$ is a 2-D position vector in Cartesian coordinates. We take e_x to be the primary propagation direction perpendicular to the thin slab. The incident field u_0 at x_0, i.e., the entrance of the thin slab, can be decomposed into plane P and S waves

$$u_0(\mathrm{x}) = \frac{1}{4\pi^2}\int dk\left[u_0^P(k,x_0) + u_0^S(k,x_0)\right]e^{ikz} \tag{1}$$

where k is the transverse wavenumber of plane waves. Superscripts P and S denote P and S waves, respectively. The forward propagated field is composed of primary wave and forward scattered P and S waves. Therefore, at x_1 the exit of the thin slab, it can be expressed as

$$u_f(z,x_1) = \frac{1}{4\pi^2}\int dk\left[u_f^P(k,x_1) + u_f^S(k,x_1)\right]e^{ikz} \tag{2}$$

where

$$u_f^P(z,x_1) = \left\{e^{i\gamma_\alpha \Delta x}u_0^P(k,x_0) + u_f^{PP}(k,x_1) + u_f^{SP}(k,x_1)\right\} \tag{3}$$

$$u_f^S(z,x_1) = \left\{e^{i\gamma_\beta \Delta x}u_0^S(k,x_0) + u_f^{SS}(k,x_1) + u_f^{PS}(k,x_1)\right\} \tag{4}$$

where $\gamma_\alpha = (k_\alpha^2 - k^2)^{1/2}$ and $\gamma_\beta = (k_\beta^2 - k^2)^{1/2}$ are the x components (propagating wavenumber) of P and S wavenumbers in the background medium. $k_\alpha = \omega/\alpha$ and $k_\beta = \omega/\beta$ are P and S wavenumbers, α and β are P and S velocities of the background medium. $\Delta x = x_1 - x_0$ is the thickness of thin slab. Subscripts f denotes forward scatterings, and PP, PS, SP and SS indicate the scattering between different wave types. The scattering and conversion coefficients U_f^{PP}, U_f^{PS}, U_f^{SP} and U_f^{SS} can be calculated by the complex screen approximation (Wu, 1994,1996).

REFLECTIONS FOR P-SV WAVES

Suppose that a plane P (or S) wave is traveling in the background medium at a angle of i (or j) with respect to x (see Fig. 1). The reflection coefficients of the displacement at the free surface can be written as (Aki and Richard, 1984)

$$\hat{P}\overset{\vee}{P} = \frac{-\left(\frac{1}{\beta_0^2}-2p^2\right)^2 + 4p^2\frac{\cos i}{\alpha_0}\frac{\cos j}{\beta_0}}{\left(\frac{1}{\beta_0^2}-2p^2\right)^2 + 4p^2\frac{\cos i}{\alpha_0}\frac{\cos j}{\beta_0}}\exp\left\{-2i\omega\frac{\cos i}{\alpha_0}z_{free}\right\} \tag{5}$$

$$\hat{P}\overset{\vee}{S} = \frac{4\frac{\beta_0}{\alpha_0}p\frac{\cos i}{\alpha_0}\left(\frac{1}{\beta_0^2}-2p^2\right)}{\left(\frac{1}{\beta_0^2}-2p^2\right)^2 + 4p^2\frac{\cos i}{\alpha_0}\frac{\cos j}{\beta_0}}\exp\left\{-i\omega\left(\frac{\cos i}{\alpha_0}+\frac{\cos j}{\beta_0}\right)z_{free}\right\} \tag{6}$$

$$\hat{S}\overset{\vee}{P} = \frac{4\frac{\beta_0}{\alpha_0}p\frac{\cos j}{\beta_0}\left(\frac{1}{\beta_0^2}-2p^2\right)}{\left(\frac{1}{\beta_0^2}-2p^2\right)^2 + 4p^2\frac{\cos i}{\alpha_0}\frac{\cos j}{\beta_0}}\exp\left\{-i\omega\left(\frac{\cos i}{\alpha_0}+\frac{\cos j}{\beta_0}\right)z_{free}\right\} \tag{7}$$

$$\hat{S}\overset{\vee}{S} = \frac{\left(\frac{1}{\beta_0^2}-2p^2\right)^2 - 4p^2\frac{\cos i}{\alpha_0}\frac{\cos j}{\beta_0}}{\left(\frac{1}{\beta_0^2}-2p^2\right)^2 + 4p^2\frac{\cos i}{\alpha_0}\frac{\cos j}{\beta_0}}\exp\left\{-2i\omega\frac{\cos j}{\beta_0}z_{free}\right\} \tag{8}$$

where z_{free} denotes the free surface location. p is ray parameter which is $\frac{\sin i}{\alpha_0}$ for P wave incidence, and $\frac{\sin j}{\beta_0}$ for S wave incidence. The symbol " $\wedge$ " and " $\vee$ " denote upgoing and downgoing waves, respectively. From the screen method, the incident P wave at $x = x_0$ can be expressed as a superposition of plane waves

$$u_0^P(z, x_0) = \frac{1}{4\pi^2}\int dk u_0^P(k, x_0)e^{ikz} \tag{9}$$

Applying the reflection coefficient formulation (5-8) to the upgoing waves in eq. (9), the reflected P and S waves can be expressed by

$$u_x^{PP}(z, x_0) = \frac{1}{4\pi^2}\int dk \mid u_0^P(k, x_0) \mid \hat{P}\overset{\vee}{P}\frac{\gamma_\alpha}{k_\alpha}e^{-ikz} \tag{10}$$

$$u_z^{PP}(z, x_0) = -\frac{1}{4\pi^2}\int dk \mid u_0^P(k, x_0) \mid \hat{P}\overset{\vee}{P}\frac{k}{k_\alpha}e^{-ikz} \tag{11}$$

$$u_x^{PS}(z, x_0) = \frac{1}{4\pi^2}\int dk \mid u_0^P(k, x_0) \mid \hat{P}\overset{\vee}{S}\frac{k^{PS}}{k_\beta}e^{-ik^{PS}z} \tag{12}$$

$$u_z^{PS}(z, x_0) = \frac{1}{4\pi^2}\int dk \mid u_0^P(k, x_0) \mid \hat{P}\overset{\vee}{S}\frac{\gamma_\beta}{k_\beta}e^{-ik^{PS}z} \tag{13}$$

where k^{PS} is transverse wavenumber of the converted S wave, using Snell's law, $k^{PS} = \sqrt{k_\beta^2 - k_\alpha^2 + k^2}$. $|u_0^P(k, x_0)|$ is the amplitude of incident P wave with transverse wavenumber k. In the same way, the reflected P and S waves due to the incident plane S wave can be obtained by

$$u_x^{SP}(z, x_0) = \frac{1}{4\pi^2}\int dk \,|u_0^S(k, x_0)|\, \hat{S}\check{P}\frac{\gamma_\alpha}{k_\alpha} e^{-ik^{SP}z} \tag{14}$$

$$u_z^{SP}(z, x_0) = -\frac{1}{4\pi^2}\int dk \,|u_0^S(k, x_0)|\, \hat{S}\check{P}\frac{k^{SP}}{k_\alpha} e^{-ik^{SP}z} \tag{15}$$

$$u_x^{SS}(z, x_0) = \frac{1}{4\pi^2}\int dk \,|u_0^S(k, x_0)|\, \hat{S}\check{S}\frac{k}{k_\beta} e^{-ikz} \tag{16}$$

$$u_z^{SS}(z, x_0) = \frac{1}{4\pi^2}\int dk \,|u_0^S(k, x_0)|\, \hat{S}\check{S}\frac{\gamma_\beta}{k_\beta} e^{-ikz} \tag{17}$$

where k^{SP} is the transverse wavenumber of the converted P wave, $k^{SP} = \sqrt{k_\alpha^2 - k_\beta^2 + k^2}$. $|u_0^S(k, x_0)|$ is the amplitude of incident S wave with transverse wavenumber k. We can calculate all of the reflected waves using eqs. (10-17), once the incident fields u_0^{P} and u_0^{S} are known. It is not difficult to see that eqs (10-11, 16-17), i.e., the reflected waves of the same type waves, can be implemented by FFT. However, eqs (12-15), i.e., the reflected converted can not be directly implemented by FFT because the nonlinear relationship exists between k and k^{PS} for P-S (or k^{SP} for S-P). Although we can obtain uniform samples with respect to k and k^{PS} (or k^{SP}) by complex variable interpolation, the noise due to the interpolation is so strong that the accumulated errors increase fast for multiple step propagation. In this study, the direct calculations of the summation integrals are performed for the converted reflections. The implementation of eqs (12-15) by summation is not much slower than by FFT because only limited summation is required where the conversion coefficients are not zero.

NUMERICAL EXAMPLES

To test the accuracy and ability of the complex screen method used as a propagator for crustal wave guides with flat surfaces, several numerical examples have been conducted and compared with those calculated by wavenumber integration method and finite difference method. For the screen method, the spatial intervals in x and z directions are $\Delta x = \Delta z = 0.25km$. To reduce the effects of boundary reflection and large-angle waves, two smooth window functions are applied in space domain and wavenumber domain, respectively. The vertical components of displacement in all figures shown in this paper are multiplied by 2.

Figure 2 shows synthetic seismograms calculated by the screen method (solid) and wavenumber integration method (dashed) for an elastic half-space. (a) is the vertical component of the displacement and (b) is the horizontal component. The homogeneous elastic half-space has $\alpha = 4km/s$, $\beta = 2.5km/s$ and $\rho = 2.5g/cm^3$. An explosive source is located at 16km depth and has dominant frequency of 1Hz. The size of the extended model used is 1024×528. The first 4 receivers are placed along free surface and have the offset of $100 - 124km$, and the last 5 receivers are placed in vertical direction and have the vertical depth $0 - 32km$. From Figure 2 the reflection and conversion by free surface are in excellent agreement. It is also shown that the use of direct summation over incident waves for converted waves (P-S or S-P) avoids the strong noise caused due to the complex variable interpolation in wavenumber domain.

Figure 3 shows synthetic seismograms along a vertical profile at the distance of $80km$ calculated by the screen method (solid) and wavenumber integration method (dashed) for a 2-layered half-space model ($56km$). The parameters for two elastic layers are $\alpha_1 = 6.8km/s$, $\beta_1 = 3.5km/s$, $\rho_1 = 3.5g/cm^3$,

$\alpha_2 = 8.16 km/s$, $\beta_2 = 4.2 km/s$ and $\rho_2 = 3.5 g/cm^3$. An explosive source is 28km depth and has a dominant frequency of $0.5 Hz$. The size of the extended model is 1024×320. From figure 3 the results from the two methods are in excellent agreement up to wide-angle reflections. The reflections from free surface are angle-dependent and agree exactly with those calculated by wavenumber integration method. The multiple reflections of S waves behind travel time of $40 \sec$. from interface have near 90^0 incident angle to screens and can not be modeled accurately by the screen method. However, the multiples can not survive in the wave guide and do not contribute much to Lg waves.

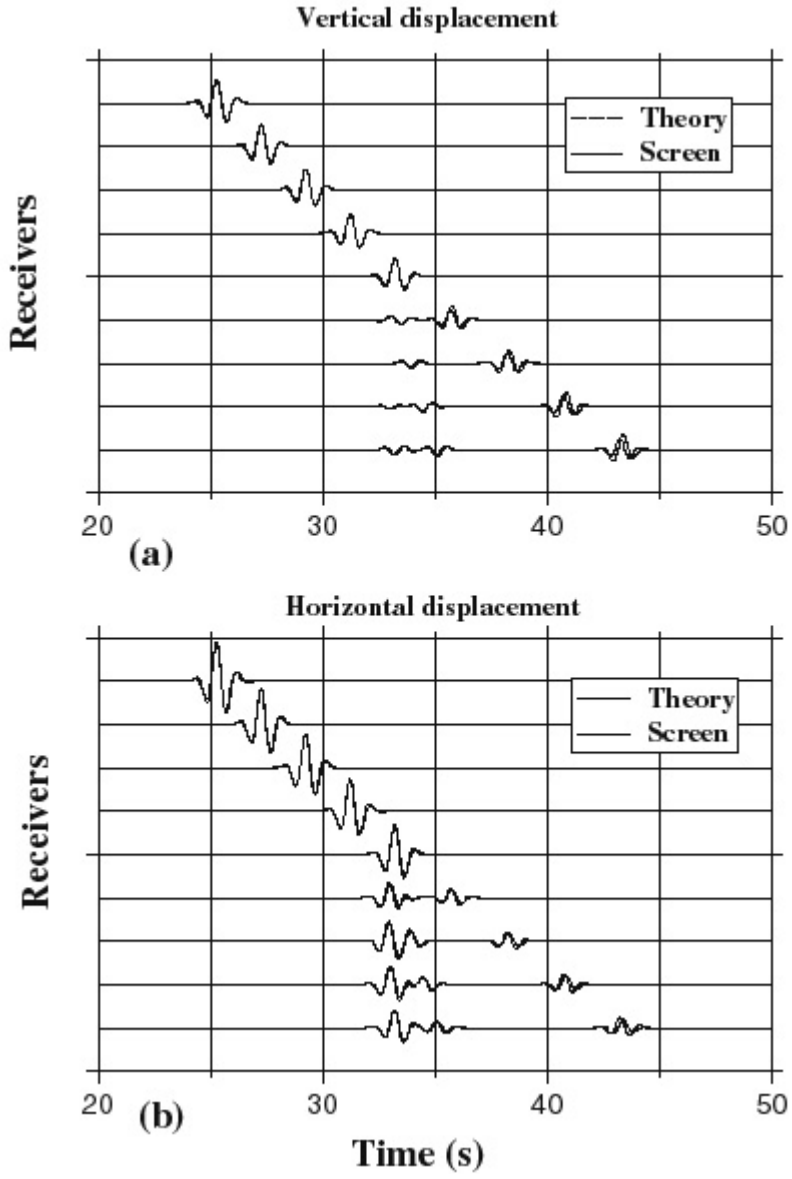


Figure 2. Synthetic seismograms calculated by the screen method (solid) and wavenumber integration (dashed) for an elastic half-space. (a) is the vertical component of the displacement, (b) is the horizontal component. An explosive source is located at $16 km$ depth and has a dominant frequency of $1 Hz$. The first 4 receivers are placed along free surface, and the last 5 receivers are placed in vertical direction.

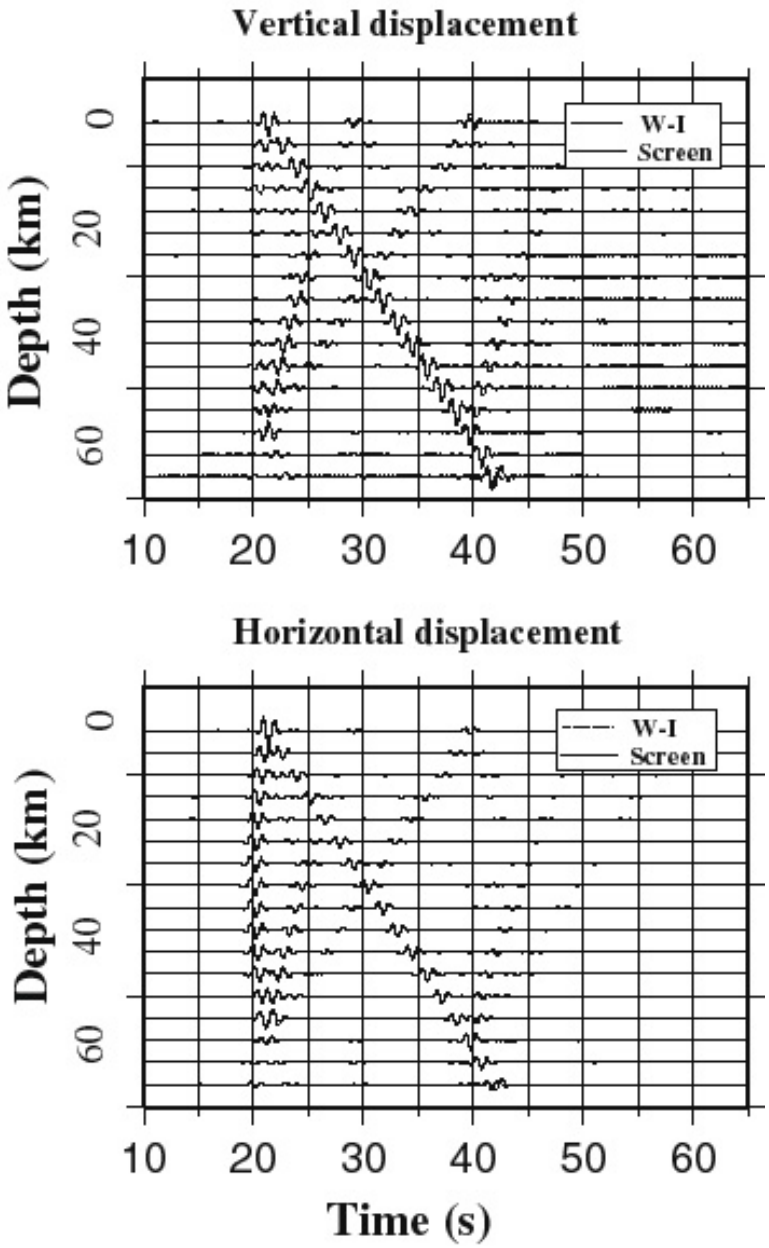


FIGURE 3. Synthetic seismograms along a vertical profile at the distance of $80km$ **calculated by the screen method (solid) and wavenumber integration method (dashed) for a 2 layered model (** $56km$ **). The source depth is** $28km$ **and its dominant frequency is** $0.5Hz$ **.**

Figure 4 shows a laterally varying crustal model. The geometry of the model and the parameters are also given in Figure 4. The source is located at $16km$ depth and has a dominant frequency of $1Hz$. The comparison of synthetic seismograms along vertical profile at the distance of $200km$ calculated by the complex screen method (solid) and finite difference method (dashed) is shown in Figure 5. Excellent

agreement can be seen. While finite difference method took 51 hours on a single processor of SUN Workstation, the complex screen method took only 0.6 hour.

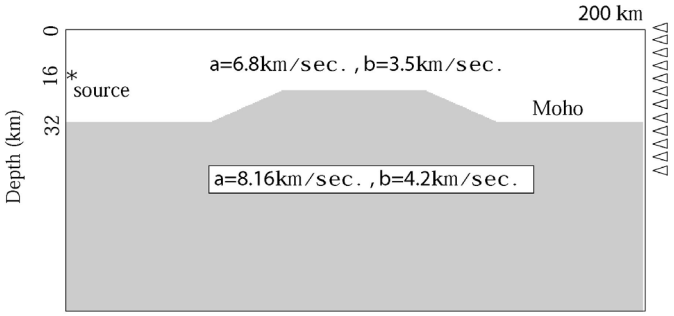


Figure 4. A thinning crustal model

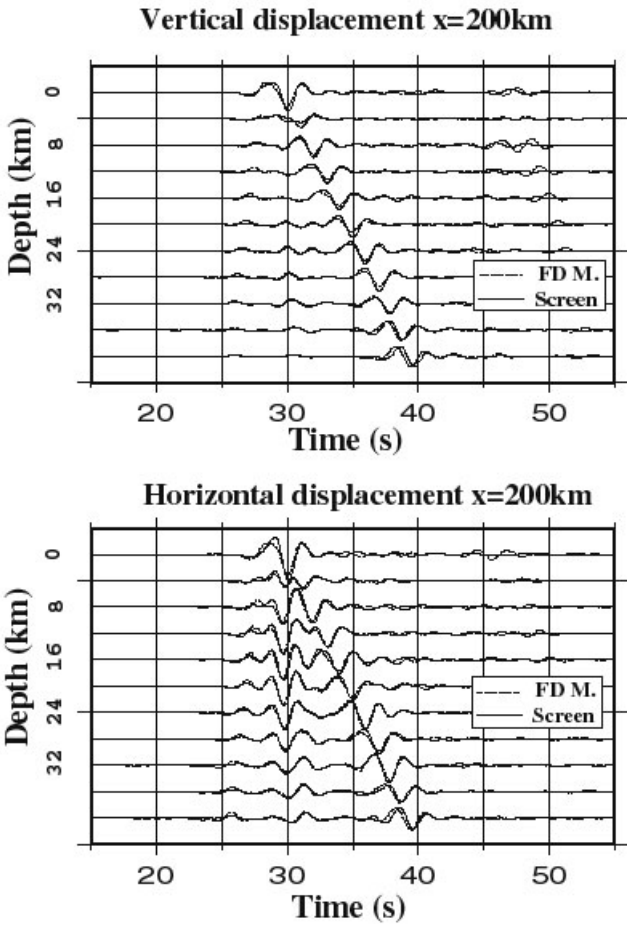


Figure 5. Synthetic seismograms along a vertical profile at the distance of $200km$ **calculated by the screen method (solid) and finite difference method (dashed) for a thinning crustal model (** $32km$ **). The source depth is** $16km$ **and its dominant frequency is** $0.5Hz$ **.**

CONCLUSIONS

This paper is part of the study aimed at development and application of a new wave propagation and modeling method for regional waves in heterogeneous crustal wave guides using one-way wave approximation. In this paper we extend the complex screen method to 2D P-SV problems for regional phase simulation by incorporating the reflection coefficient formulas on free surface into the method. The comparison of synthetic seismograms calculated by the complex screen method and by wavenumber integration method and finite difference method shows feasibility and validity of this extension. For a test model with a propagation distance of $80km$ and a dominant frequency of $0.5Hz$, finite difference method took 51 hours, while the complex screen method took 0.6 hour. The complex screen method is 85 times faster than finite difference method. For longer propagation distance and higher frequencies, the factor of saving could be huge. By this extension, our ability of simulating regional phases will be greatly enhanced. It makes us possible to simulate path effects in different regions for various discriminants in the monitoring system, such as P_n / L_g, S_n / L_g, etc.

Key Words: seismic wave propagation, crustal structure, discrimination

References

Aki, K. and P.G., Richards, 1980, Quantitative seismology: Theory and Methods, *Vol. 1 and 2*, W.H. Freeman, New York.

Fan, G.W. and T. Lay, 1998, Statistical analysis of irregular wave-guide influences on regional seismic discriminants in China, *Bull. Seis. Soc. Am.,88*, 74-88.

Hartse, H.E., S.R., Taylor, W.S., Phillips, and G.E., Randall, 1997, A preliminary study of regional seismic discrimination in central Asia with emphasis on western China, *Bull. Seis. Soc. Am., 87*, 551-568.

Kennett, B.L.N., 1986, *Lg* waves and structural boundaries, *Bull. Seis. Soc. Am., 76*, 1133-1141.

Kennett, B.L.N., 1989, On the nature of regional seismic phases---I. Phase representations for P_n, P_g, S_n, L_g, *Geophys. J. 98*, 447-456.

Taylor, S.R., 1996, Analysis of high frequency P_n / L_g ratios from NTS explosions and western U.S. earthquakes, *Bull. Seis. Soc. Am., 86*, 1042-1053.

Walter, W.R., K.M., Mayeda, and H. Patton, 1995, Phase and spectral ratio discrimination between NTS earthquakes and explosions. Part I: Empirical observations, *Bull. Seis. Soc. Am., 85*, 1050-1067.

Wu, R.S., 1994, Wide-angle elastic wave one-way propagator in heterogeneous media and an elastic wave complex-screen method, *J. Geophys. Res*., 99, 751-766.

Wu, R.S., S. Jin, and X.B., Xie, 1998a, Seismic wave propagation and scattering in heterogeneous crustal waveguides using screen propagators: I *SH* waves. Submitted to *Bull. Seis. Soc. Am.*

Wu, R.S., S. Jin, and X.B. Xie, 1998b, Energy partition and attenuation of Lg waves by numerical simulations using screen propagators, submitted to *Phys. Earth and Planet. Inter.*

Wu, R.S., X.B., Xie, and X.Y., Wu, 1999, Lg wave simulations in heterogeneous crusts with irregular topography using half-space screen propagators, *Proc. of the 18th Annual SRS on Monitoring CTBT*

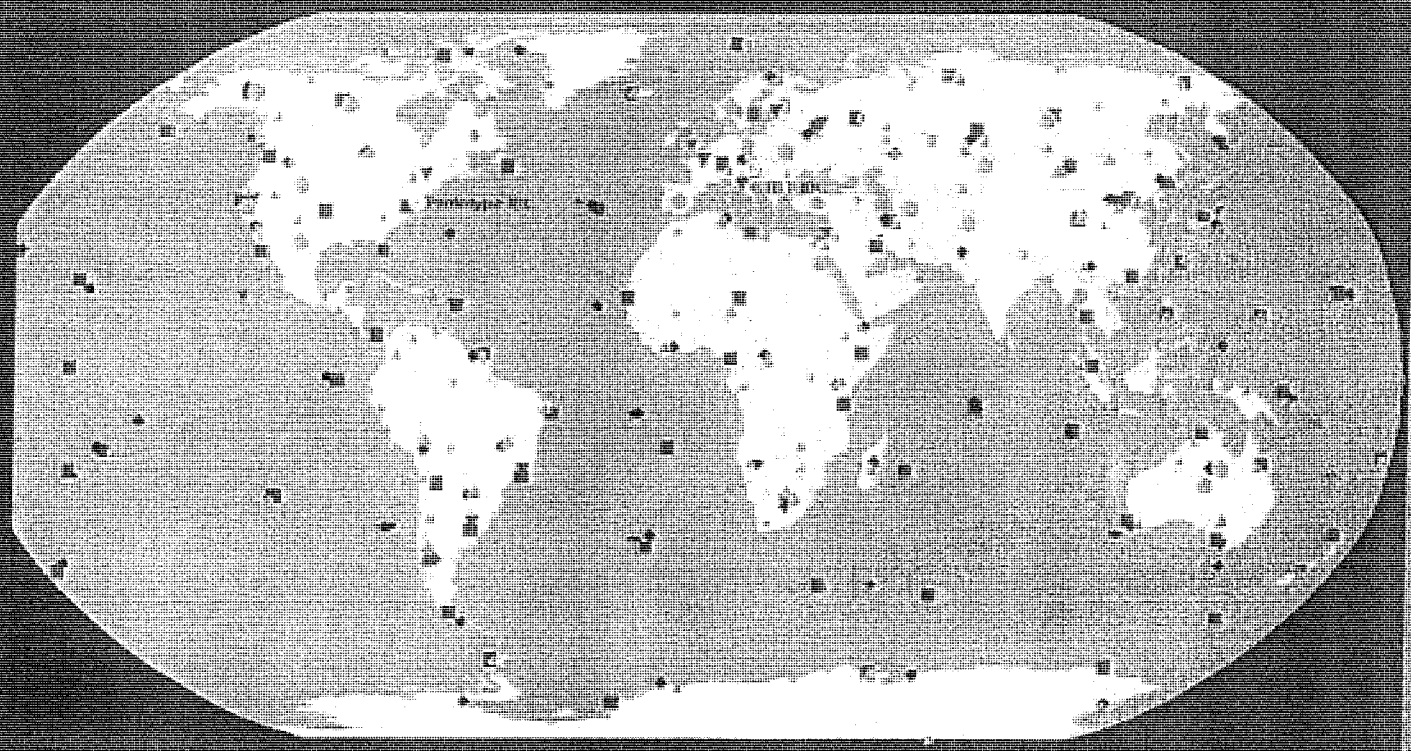
Xie, X.B. and Z.X. Yao, 1988, *P-SV* wave responses for a point-source in two-dimensional heterogeneous media: finite difference method, *Chinese J. Geophys., 31*,473-493.

Zhang, T.-R., S. Schwartz, and T. Lay, 1994, Multivariate analysis of waveguide effects on short-period regional wave propagation in Eurasia and its application in seismic discrimination, *J. Geophys. Res*., 99, 21929-21945.

22nd Annual DoD/DOE Seismic Research Symposium

Planning for Verification of and Compliance with the Comprehensive Nuclear-Test-Ban Treaty (CTBT)

Proceedings



VOLUME II

Technical Category

2. Seismic Event Detection, Location and Identification Methods

VOLUME II - TABLE OF CONTENTS

2. SEISMIC EVENT DETECTION, LOCATION, AND IDENTIFICATION METHODS

02-01 **APPLICATION OF REGULARIZED DISCRIMINATION ANALYSIS TO REGIONAL SEISMIC EVENT IDENTIFICATION** 3
Dale N. Anderson and Steven R. Taylor

02-02 **A NEW JOINT *P* AND *S* VELOCITY MODEL OF THE MANTLE PARAMETERIZED IN CUBIC B-SPLINES** 15
Michael Antolik, Göran Ekström, Adam M. Dziewonski, Yu J. Gu, Jian-feng Pan, and Lapo Boschi

02-04 **UTILIZING RESULTS FROM INSAR TO DEVELOP SEISMIC LOCATION BENCHMARKS AND IMPLICATIONS FOR SEISMIC SOURCE STUDIES** 25
Michael L. Begnaud, Aaron A. Velasco, and Lee K. Steck

02-05 **REGIONAL SIGNAL CHARACTERISTICS FOR USE IN SCREENING SEISMIC EVENTS IN ROCKBURST AREAS** 33
Theron J. Bennett, Margaret E. Marshall, and Ronald W. Cook

02-06 **EMPIRICAL ANALYSIS OF A 3-D PAKISTAN REGIONALIZED VELOCITY MODEL FOR IMPROVED SEISMIC EVENT LOCATIONS** 43
Michelle Bernard-Johnson, Shirley Rieven, Carolynn Vincent, Delaine Reiter, and William Rodi

02-07 **APPLICATION OF A CEPSTRAL F-STATISTIC FOR IMPROVED DEPTH ESTIMATION** 53
Jessie Bonner, Delaine Reiter, and Bob Shumway

02-08 **USING THE *F*-DETECTOR TO HELP INTERPRET *P*-SEISMOGRAMS RECORDED BY SEISMOMETER ARRAYS** 63
David Bowers

02-09 **UPPER MANTLE STRUCTURE OF NORTHERN EURASIA** 73
Geoff Clitheroe and Walter D. Mooney

02-10 **SEISMIC TRAVEL TIMES TO AREA 1 IMS STATIONS IN 3-D EARTH MODELS BY DYNAMIC RAY TRACING** 81
Vernon F. Cormier

02-11 **PROBABILISTIC INTEGRATION OF SEISMIC, HYDROACOUSTIC AND INFRASONIC DATA USING THE DEMPSTER-SHAFER RULES FOR COMBINING EVIDENCE** 91
Zoltan A. Der, Matthew W. McGarvey, and Robert H. Shumway

02-12 **ESTIMATION OF DEPTH AND ATTENUATION OF EARTHQUAKES IN BOLIVIA** 103
Lawrence A. Drake

02-13 **IDENTIFICATION AND VALIDATION OF REFERENCE EVENTS WITHIN THE AREA BEING REGIONALLY MONITORED BY IMS STATIONS IN ASIA AND NORTH AFRICA** 113
E.R. Engdahl and Eric A. Bergman

02-14 **2-D SIGNAL DETECTORS FOR 3-COMPONENT SEISMIC RECORDINGS** 121
Eystein S. Husebye and Yuri V. Fedorenko

02-15 **THREE-DIMENSIONAL *A PRIORI* MODEL CONSTRAINTS AND UNCERTAINTIES FOR IMPROVING SEISMIC LOCATION** 129
Megan P. Flanagan, Stephen C. Myers, Craig A. Schultz, Michael E. Pasyanos, and Joydeep Bhattacharyya

02-16 **REGIONAL SEISMIC EVENT DISCRIMINATION IN SIBERIA** 137
Hans E. Hartse

02-17 **AN INTERESTING REGIONAL SEISMIC EVENT FROM QINGHAI PROVINCE, CHINA** 147
Hans E. Hartse and Aaron A. Velasco

02-18 **TOMOGRAPHY AND LOCATION PROBLEMS IN CHINA USING REGIONAL TRAVEL-TIME DATA** 155
Thomas M. Hearn and James F. Ni

02-19 **ADAPTIVE TECHNIQUES FOR ESTIMATING AND LOCATING SMALL EVENTS USING REGIONAL WAVEFORM DATA** 161
Don V. Helmberger, Chen Ji, and Brian Savage

02-20 **THE NEVADA SEISMIC ARRAY (NVAR) REGIONAL SEISMO-ACOUSTIC STUDIES** 171
Eugene Herrin, Ileana Tibuleac, Paul Golden, and Gordon G. Sorrells

02-21 **IN SITU MONITORING OF LOCAL SEISMICITY** 181
Eystein S. Husebye and Yuri V. Fedorenko

02-22 **USE OF DEPTH PHASES IN EVENT SCREENING** 191
David Jepsen and Spiro Spiliopoulos

02-23 **ANALYSIS OF REGIONAL SEISMIC DATA FOR UNDERGROUND EXPLOSIONS** 201
Won-Young Kim, Mark Fisk, and Steven Bottone

02-24 **PATH CORRECTIONS FOR REGIONAL PHASE DISCRIMINANTS** 211
Thorne Lay, Guangwei Fan, and Jiajun Zhang

02-25 **A MINE EXPLOSION SOURCE PHENOMENOLOGY EXPERIMENT** 219
James F. Lewkowicz, Jessie L. Bonner and Alfredo Urzua

02-26 **EVENT RELOCATIONS AND SEISMIC CALIBRATION IN NORTHEAST RUSSIA** 223
Kevin G. Mackey and Kazuya Fujita

02-27 **PHENOMENOLOGY RESEARCH USING PAST NEVADA TEST SITE EXPLOSION AND EARTHQUAKE DATA** 233
Kevin M. Mayeda, Michael E. Pasyanos, Jennifer O'Boyle, Stephen C. Myers, William R. Walter, and Peter Goldstein

02-28 **APPLICATION OF SOVIET PNE DATA TO THE IMPROVEMENT OF SEISMIC MONITORING CAPABILITY** 237
John R. Murphy, Jamil D. Sultanov, Brian W. Barker, Ivan O. Kitov, and Margaret E. Marshall

02-29 **IMPROVED FOCAL DEPTH DETERMINATION FOR USE IN CTBT MONITORING** 245
John R. Murphy, Ronald W. Cook, and William L. Rodi

02-30 **SEISMIC CALIBRATION OF GROUP 1 IMS STATIONS IN EASTERN ASIA FOR IMPROVED IDC EVENT LOCATION** 255
John R. Murphy, Jeffry L. Stevens, M. Nafi Toksoz, William L. Rodi, Jamil D. Sultanov, Ivan O. Kitov, James F. Lewkowicz, and Jessie L. Bonner

02-31 **THE USE OF IMPERFECT CALIBRATION FOR SEISMIC LOCATION** 265
Stephen C. Myers and Craig A. Schultz

02-32 **BODY-WAVE MAGNITUDES AND LOCATIONS OF PRESUMED EXPLOSIONS AT THE CHINESE TEST SITE, 1967-1996** 273
Aoife O'Mongain, Alan Douglas, and John B. Young

02-33 **SURFACE WAVE IDENTIFICATION RESEARCH IN THE MIDDLE EAST AND NORTH AFRICA** 283
Michael E. Pasyanos, Peter Goldstein, William R. Walter, and Arthur Rodgers

02-34 **M_S : m_b RELATIONSHIPS FOR SMALL MAGNITUDE EVENTS: OBSERVATIONS AND PHYSICAL BASIS FOR m_b BASED ON REGIONAL PHASES** 293
Howard J. Patton

02-35 **DETECTION AND LOCATION OF THE DEAD SEA SHOTS USING ADVANCED PROCESSING TECHNIQUES** 301
Vladimir Pinsky, Avi Shapira, Yefim Gitterman and Alona Malitzky

02-36 **SINGLE STATION EVENT LOCATION: EPICENTRAL DISTANCE, BEARING, AND FOCAL DEPTH** 311
Jay Pulliam, Cliff Frohlich, and Ben Phillips

02-37 **A PLAN FOR SEISMIC LOCATION CALIBRATION OF 30 IMS STATIONS IN EASTERN ASIA** 321
Paul G. Richards, Won-Young Kim, and Vitaly I. Khalturin

02-38 **RESEARCH IN REGIONAL SEISMIC MONITORING** 329
F. Ringdal, E. Kremenetskaya, V. Asming, T. Kværna and J. Schweitzer

02-39 **GRID-SEARCH TECHNIQUES FOR SEISMIC EVENT LOCATION** 339
William Rodi and M. Nafi Toksöz

02-40 **IMS CALIBRATION IN NORTH AMERICA AND NORTHWESTERN EURASIA UTILIZING 3-D CRUSTAL AND UPPER MANTLE VELOCITY MODELS TO REFINE LOCATION OF REGIONAL SEISMIC EVENTS** 349
Russian Federation / United States Calibration Working Group

02-41 **SOURCE SPECIFIC STATION CORRECTIONS (SSSCS) FOR INTERNATIONAL MONITORING SYSTEM (IMS) SEISMIC STATIONS IN NORTH AFRICA, MIDDLE EAST AND WESTERN ASIA** 359
Group - 2 Consortium; SAIC, University of Colorado, Harvard University, University of California San Diego, Multimax, and Geophysical Institute of Israel

02-42 **INTEGRATING DIVERSE CALIBRATION PRODUCTS TO IMPROVE SEISMIC LOCATION** 369
Craig A. Schultz, Stephen C. Myers, Jennifer L. Swenson, Megan P. Flanagan, Michael E. Pasyanos, and Joydeep Bhattacharyya

02-43 **IDENTIFICATION, ASSOCIATION, AND ANALYSIS OF RAYLEIGH WAVES IN THE CONTEXT OF CTBT MONITORING** 377
Neil D. Selby

02-44 **IMPROVING GLOBAL SEISMIC EVENT LOCATIONS USING SOURCE-RECEIVER RECIPROCITY** 387
Peter M. Shearer

02-45 **REDUCING SYSTEMATIC ERRORS FOR SEISMIC EVENT LOCATIONS IN ANISOTROPIC REGIONAL STRUCTURES** 397
Gideon P. Smith and Douglas A. Wiens

02-46 **IMPROVED VELOCITY MODELS IN WESTERN CHINA FOR TWO- AND THREE-DIMENSIONAL FINITE DIFFERENCE MODELING** 405
L.K. Steck, C.R. Bradley, and L.E. Jones

02-47 **REGIONAL MODEL CALIBRATION FOR IMPROVING SEISMIC LOCATION** 415
Jennifer L. Swenson, Craig A. Schultz, and Stephen C. Myers

02-48 **ASSESSING EVENT LOCATION CAPABILITY WITH GROUND TRUTH EVENTS AT THE DEGELEN MOUNTAIN TEST SITE, KAZAKHSTAN** 425
Clifford Thurber, Chad Trabant, and Renate Hartog

02-49 **METHODS FOR THE IMS REGIONAL KINEMATIC CALIBRATION** 433
Nikolai A. Vasiliev

02-50 **REGIONAL BODY-WAVE DISCRIMINATION RESEARCH** 443
William R. Walter, Arthur Rodgers, Kevin Mayeda, and Steven Taylor

02-51 **COMPUTATION OF TRAVEL TIMES AND STATION CORRECTION SURFACES IN EURASIA USING THREE DIMENSIONAL VELOCITY MODELS** 453
A. Villaseñor, M.H. Ritzwoller, M.P. Barmin, E.R. Engdahl, and A.L. Levshin

02-52 **EXTENDING REGIONAL WAVE FORM MODELING TO SHORTER PERIODS TO IMPROVE THE LOCATION AND IDENTIFICATION OF SMALL SEISMIC SOURCES** 463
Bradley B. Woods, Chandan K. Saikia, and Hong Kie Thio

02-53 **EXCITATION AND ATTENUATION OF REGIONAL WAVES, AND MAGNITUDE DEPENDENCE OF PN/LG RATIOS IN EASTERN EURASIA** 471
Jiakang Xie

02-54 **MAXIMUM SPECTRAL ENERGY ARRIVAL TIME OF RAYLEIGH WAVES FOR ACCURATE EPICENTER DETERMINATION AND LOCATION ERROR REDUCTION** 481
Nazieh K. Yacoub

2. Seismic Event Detection, Location and Identification Methods

APPLICATION OF REGULARIZED DISCRIMINATION ANALYSIS TO REGIONAL SEISMIC EVENT IDENTIFICATION

Dale N. Anderson and Steven R. Taylor

Pacific Northwest National Laboratory
Los Alamos National Laboratory

Sponsored by U.S. Department of Energy
Office of Nonproliferation Research and Engineering
Office of Defense Nuclear Nonproliferation
National Nuclear Security Administration

Contract No. DE-AC06-76RLO-1830
Contract No. W-7405-ENG-36

ABSTRACT

We present a generalized multivariate seismic event identification method, Regularized Discrimination Analysis (RDA) [Friedman 1989], that can be applied to a large number of regional discriminants. RDA is readily adaptable to an outlier or classical identification approach to regional seismic identification. RDA is designed to address the problems associated with linear (LDA) and quadratic (QDA) discrimination in small-sample, high-dimensional settings. RDA includes LDA, QDA and Euclidean distance based nearest neighbor discrimination in its parameterization. RDA can be used to transition from an outlier analysis approach to seismic identification to classical discrimination as quality explosion calibration data are collected. Further, RDA provides the statistical structure to model highly correlated seismic measurements. We demonstrate the importance of including the correlation structure between seismic measurements in event identification. Not including this correlation structure in any identification framework can aggravate identification errors and give an erroneous impression of capability. With RDA, a large number of amplitudes from a Magnitude and Distance Amplitude Correction (MDAC) analysis [see Taylor et al. 1999] can be used and no a priori sub-selection of amplitudes (or discriminants) is necessary.

Key Words: discrimination, singular covariance matrix, outlier analysis.

OBJECTIVE

Not accounting for the dependence between individual seismic discriminants in any identification process can aggravate identification errors and give an erroneous impression of capability. For example, weight is positively correlated with height. An individual who is 6 feet tall and weighs 120 lb. might reasonably be viewed as unusual. However, taken alone, it is not unusual to find someone who is 6 feet tall, nor is it unusual for someone to weigh 120 lb. It is the inconsistency with the correlated behavior of height and weight that makes a 6 foot, 120-lb. person an *outlier*.

Two discriminants with a strong positive correlation provide redundant information about the source of a seismic event (strongly correlated discriminants vary, in a probabilistic sense, together). For example, if X and Y are discriminants and the correlation between X and Y is ρ, then the variance of $X+Y$ is

$$Var(X+Y) = \sigma_X{}^2 + \sigma_Y{}^2 + 2\rho\sigma_X\sigma_Y. \qquad (1)$$

The $Var(X+Y)$ increases linearly in ρ. It is reasonable to conjecture that many regional discriminants will be positively correlated. Combining correlated discriminants with a sum, and computing the variance as if they are uncorrelated, may not be a good aggregation method. For a measured event discriminant $X = x$, a p-value can be computed as the conditional probability of observing a discriminant value equal to or more extreme than x. It is important to note that a p-value is a random variable because it is a function of a random variable. For observed discriminants X and Y, we can compute the p-values p_x and p_y and then aggregate this marginal information

with the product $p_{Aggregate} = p_x\, p_y$. However, aggregating with a product can also be dangerous. For example, for bivariate normal random variables X, Y the variance of the product XY is

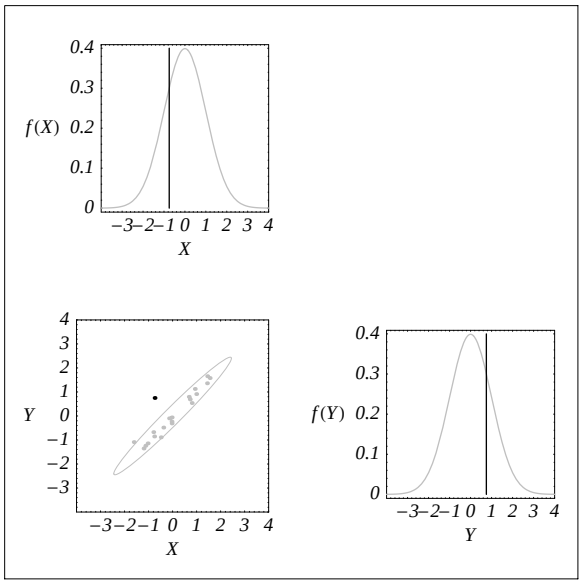
$$Var(XY) = \mu_Y{}^2\sigma_X{}^2 + \mu_X{}^2\sigma_Y{}^2 + 2\rho\mu_X\mu_Y\sigma_X\sigma_Y + (1+\rho^2)\sigma_X{}^2\sigma_Y{}^2. \qquad (2)$$

Here, the linear correlation between X and Y is ρ. $Var(XY)$ is a polynomial in ρ with no real-valued zeros ($Var(XY) > 0$) and a minimum at one of the values 1, -1 or $-\mu_X\mu_Y/\sigma_X\sigma_Y$. Values of ρ that increase $Var(XY)$ are governed by $-\mu_X\mu_Y/\sigma_X\sigma_Y$. This dependence will propagate into p-value calculations as well.

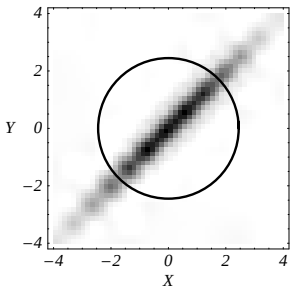
One of the main points of this paper is that seismic discriminants should be aggregated, to the best degree possible, with a statistical likelihood or probability model. A likelihood-based approach to combining discriminants provides a rigorous method to properly account for correlation between discriminants. The most desirable event identification framework would be composed of discriminants that are independent of each other, yet strongly indicative of the source of a seismic event. Independent discriminants contribute in a purely additive (orthogonal) way to the identification of an event, and never carry redundant information. For example, a principal components analysis (PCA) can be used to construct linear combinations of amplitudes that are orthogonal. In the traditional application of PCA, a subset (dimension reduction) of these linear combinations is used to construct a discrimination rule. The use of PCA in discrimination analysis has no limiting statistical deficiencies; however, we feel that the PCA approach presents some seismological concerns. Any feature selection analysis on amplitudes, including PCA, defacto constructs discriminants that may or may not have a known physical basis. Thus, the primary two or three PCA linear combinations may not be the best discriminants for a Mahalanobis distance based discrimination rule (see McLachlan, 1992, page 197 for a statistical basis for this observation.).

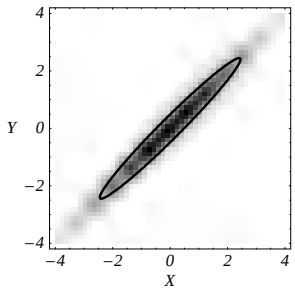
In the regional setting, a PCA will likely be based on earthquake data with no explosion data. This means that the PCA linear projections may do a poor job of combining explosion amplitude information, because $\Sigma_{EX} \neq \Sigma_{EQ}$ (in other words, important earthquake versus explosion discriminants may not be included in the final PCA linear amplitude combinations). If all the PCA linear combinations from Σ_{EQ} are used in an outlier analysis, then there will be no loss of information; however, this approach is conceptually equivalent to the regularized discrimination analysis (RDA) we present. RDA does not construct potentially controversial linear combinations as in a PCA. In a regional setting, the goal of independent discriminants, without a PCA type analysis is probably not possible because different seismic phases may share similar apparent source spectra and may overlap in time (e.g., Lg spectra may be contaminated by Sn coda). Figure 1 illustrates a fabricated model for two discriminants X and Y.

Figure 1a gives the bivariate ellipsoid that encloses 95% of the data from a particular source (the gray points). The Gaussian curves on the top and right sides of Figure 1a are the marginal densities for this model. The black point on the graph is clearly not a member of the population of gray points. However, neither of the marginal representations indicates that this point is unusual. Figures 1b and 1c show a transition from the region (black) that will include most all of the gray data to an outlier region. The circle, superimposed on Figure 1b, represents a source elimination rule that is constructed by assuming no correlation between X and Y. The ellipse, superimposed on Figure 1c, represents a source elimination rule that is constructed with the inclusion of correlation between X and Y. The most disturbing observation is the potential for identification errors when the no-correlation rule is used. In this case, the region outside of a decision rule defines false alarms and the darker region interior to a decision rule defines missed-explosions.



a)





b) c)

Figure 1. Fabricated model for discriminants X and Y and correlation and no-correlation based decision rules.

OUTLIER DETECTION ANALYSIS

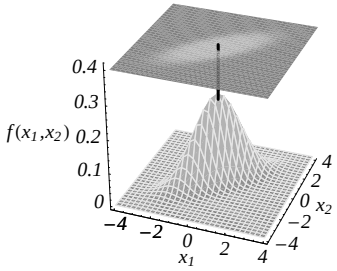
The methodology for outlier detection in the seismic context is well established (see Fisk et al. 1996; Taylor and Hartse 1997). Classical multipopulation discrimination methodologies may not be well suited to nuclear test monitoring for two main reasons. First, existing or planned seismic stations that will be used for monitoring have little or no nuclear explosion data on which to adequately characterize the statistical distribution of the nuclear explosion population. Note that industrial mining explosions are not necessarily a good surrogate upon which to base discriminants for nuclear explosions. Secondly, even if a set of nuclear explosion data exists, it is likely to be limited; that is, a small number of events, from a given test site, detonated under standard containment conditions (as opposed to potential evasive conditions). Such nuclear explosion data may not be suitable for deriving population statistics used in broad-area monitoring. Comparison of nuclear explosion data from different test sites or even from within a single test site (e.g. Nevada Test Site) illustrates the complexities of near-source nonlinear material properties and emplacement conditions on seismic discriminants (see Taylor 1991; Taylor and Denny 1991).

As noted in Fisk et al. (1996), for a large number of calibration earthquakes, the likelihood ratio outlier test statistic is essentially the multivariate normal density function (MVN(μ_{EQ}, Σ_{EQ})). Specifically, for a vector of discriminants $\mathbf{x}$, if

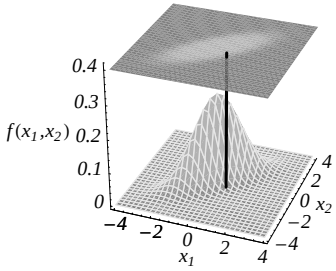
$$f_{\mathbf{X}}(\mathbf{x}) = \left|2\pi\Sigma_{EQ}\right|^{-1/2} \exp\left\{-\frac{(\mathbf{x}-\mu_{EQ})'\,\Sigma_{EQ}^{-1}\,(\mathbf{x}-\mu_{EQ})}{2}\right\} \qquad (3)$$

is close to zero, then the data $\mathbf{x}$ indicate outlier, otherwise earthquake. Here, μ_{EQ} and Σ_{EQ} are estimated with the calibration data, thus establishing the outlier rule for future events. The term close to zero is defined by a critical value ξ that serves as a point of reference for evaluated values of $f_{\mathbf{X}}(\mathbf{x})$, and is determined by the tolerable false-outlier rate α. If μ_{EQ} and Σ_{EQ} are assumed known and $\mathbf{x}$ is a vector of p variables then

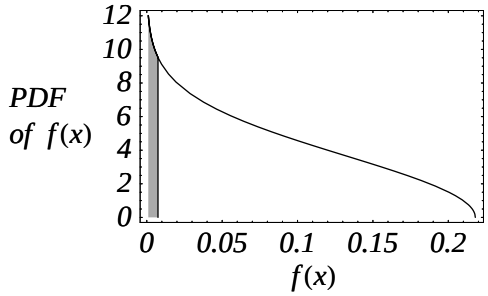
$$P\left(f_{\mathbf{X}}(\mathbf{x}) < \xi\right) = P\left((\mathbf{x}-\mu_{EQ})' \Sigma_{EQ}^{-1} (\mathbf{x}-\mu_{EQ}) > -2 \ln(\xi \sqrt{\left|2\pi\Sigma_{EQ}\right|}\right). \quad (3.a)$$



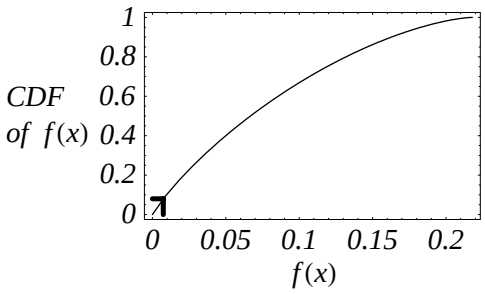
a) Discriminants x_1 and x_2 are interior to a $(1-\alpha)$% probability region which translates to a large likelihood value.



b) Discriminants x_1 and x_2 are outlier to a $(1-\alpha)$% probability region which translates to a likelihood value near zero.



c) Typical probability density function (PDF) of $f_{\mathbf{X}}(\mathbf{x})$ with a α% false-outlier region.



d) Typical cumulative distribution function (CDF) of $f_{\mathbf{X}}(\mathbf{x})$ with a α% false-outlier region defining the value of ξ.

Figure 2. Likelihood-based outlier rule. The rule is illustrated in two dimensions with discriminants x_1 and x_2. The rule is easily extended to p dimensions with a p dimensional likelihood function.

The random variable $(\mathbf{x}-\mu_{EQ})' \Sigma_{EQ}^{-1} (\mathbf{x}-\mu_{EQ})$ follows a chi-squared distribution with p degrees of freedom (Rencher 1998, Theorem 2.2F), thus

$$P\left(f_{\mathbf{X}}(\mathbf{x}) < \xi\right) = 1 - F_{\chi_p^2}\left(-2 \ln(\xi \sqrt{\left|2\pi\Sigma_{EQ}\right|}\right); \xi \in \left(0, 1 \sqrt{\left|2\pi\Sigma_{EQ}\right|}\right], \quad (3.b)$$

where $F_{\chi^2_p}(x)$ is the chi-squared cumulative distribution function with p degrees of freedom. To determine the value of ξ we solve for ξ in the equation $P\left(f_{\mathbf{X}}(\mathbf{x}) < \xi\right) = 1 - F_{\chi^2_p}\left(-2\ln(\xi\sqrt{|2\pi\Sigma_{EQ}|}\right) = \alpha$. Thus an outlier rule based on $f_{\mathbf{X}}(\mathbf{x})$ is equivalent to an outlier rule based on $(\mathbf{x}-\mu_{EQ})'\Sigma_{EQ}^{-1}(\mathbf{x}-\mu_{EQ})$. The outlier rule $f_{\mathbf{X}}(\mathbf{x})$, in two dimensions, is illustrated in Figure 2. Note that this rule is a one-sided test. In this paper, we use an outlier rule based on Equation 3 and illustrated in Figure 2.

RIDGE DISCRIMINATION AND REGULARIZED DISCRIMINANT ANALYSIS

The optimal regional discrimination method needs to be stable, robust and simple, and it should have a well-grounded physical basis. As regional seismic research continues, an optimal regional discrimination method will be developed. Ultimately, that method may use only two or three features from a seismic wave. *What is currently desirable is a technique that properly aggregates all available seismic information from a suite of phase measurements.* Classical discrimination does this because it is essentially based on the formation of a likelihood ratio, and statistical likelihood functions can properly combine phase amplitudes.

In the Gaussian case, the likelihood requires a covariance matrix of the phase amplitudes, and as discussed above these phase amplitudes may be strongly correlated. This will lead to a near singular covariance matrix that in turn will give a likelihood function with unstable statistical properties. There has been some very useful research on this problem within the statistics community (see Smidt and McDonald 1976; DiPillo 1976, 1977, and 1979; Randles et al. 1978; Loh 1995,1997; and Campbell 1980). In general terms, this research studied the utility of a ridge adjustment to the covariance matrix in discrimination analysis. Aki and Richards (1980) describe this type of adjustment as the stochastic inverse in seismological inverse problems. This adjustment is also similar to damped least squares (Aki and Richards 1980). In the statistical literature this approach is known as ridge discrimination. In a preliminary study, we have embedded these ideas into the event source elimination approach to regional discrimination. Our initial studies have produced some positive results.

Ridge Discrimination

Ridge discrimination was proposed as a method of addressing the problem of near-singular covariance matrices in Gaussian linear (LDA) and quadratic (QDA) discrimination. In ridge discrimination, the covariance matrix of the k^{th} group, used in a LDA or QDA application, is an additive combination of the sample covariance and the identity matrix. The weighting in this addition is governed by a smoothing parameter λ. A common λ is used across all groups. Formally, the ridge discrimination covariance matrix for the k^{th} group is

$$\Sigma_k(\lambda) = (1-\lambda)\,\mathbf{S}_k + \lambda\frac{tr(\mathbf{S}_k)}{p}\,\mathbf{I}\;;\;\lambda\in[0,1]. \qquad (4)$$

Here, $tr(\mathbf{S}_k)$ is the trace of the sample covariance matrix $\mathbf{S}_k$ and p is the dimension of the amplitude vector. The covariance matrix $\Sigma_k(\lambda)$ is essentially formed by adding a λ proportion of the average eigenvalue of $\mathbf{S}_k$ to the diagonal elements of $\mathbf{S}_k$. Equation 4 is equivalent to Equation 12.132 in Aki and Richards (1980) with ε (Aki and Richards) and λ playing analogous roles.

As a preliminary study of this approach, we have performed a leave-one-out Monte Carlo outlier analysis with highly correlated regional discriminant data. This type of Monte Carlo study can also be used to select optimal features for outlier detection. First, we fix a value of λ. With n earthquake events, a leave-one-out cross-validation involves n steps. For step i, the i^{th} event was removed from the earthquake data. This event was used as the test case and all other earthquake data were used to construct the covariance $\mathbf{S}_{EQ}$ and the mean $\bar{\mathbf{x}}_{EQ}$. We then construct the covariance $\Sigma_{EQ}(\lambda)$. The $\mathbf{S}_{EQ}$ and $\bar{\mathbf{x}}_{EQ}$ are then used to generate a large number of simulated discriminants, and for each simulated data point we evaluate the multivariate normal (MVN) density using $\Sigma_{EQ}(\lambda)$ and $\bar{\mathbf{x}}_{EQ}$ (i.e., MVN($\bar{\mathbf{x}}_{EQ}, \Sigma_{EQ}(\lambda)$)). We need to do this because we use the MVN($\mu_{EQ}, \Sigma_{EQ}(\lambda)$) density as the outlier rule and these simulated data can be used to define a critical value ξ for the rule. The value ξ serves as the critical value to classify an event as earthquake or outlier. In our study, we use the 5^{th} percentile (α=0.05) of the MVN($\bar{\mathbf{x}}_{EQ}, \Sigma_{EQ}(\lambda)$) density values, gotten from the simulated discriminants, for the critical value ξ.

If the MVN($\bar{\mathbf{x}}_{EQ}, \Sigma_{EQ}(\lambda)$) density is greater than ξ, when evaluated with discriminants from an unknown event, then we would conclude the event is an earthquake. If the MVN($\bar{\mathbf{x}}_{EQ}, \Sigma_{EQ}(\lambda)$) density is smaller then ξ, then the data are in the extreme regions of the density support and we would call the event an outlier. We evaluate the test case with this rule. Repeating this process for all n of the earthquake data gives a leave-one-out cross-validated error rate for the fixed λ value. We then fix another value of λ and repeat the cross-validation analysis.

The data used in this preliminary study consist of amplitudes of Pn, Pg, Sn and Lg taken in seven different frequency bands and corrected for source and propagation effects (see Taylor et al. 1999). The data consist of 412 earthquakes and 4 explosions. For each source, the data are normalized to the low frequency Lg.

Four sets of seven amplitudes are analyzed in this paper. The seven amplitudes were selected from the twenty-seven amplitudes (28-1=27, low frequency Lg was used to normalize the amplitudes). Additionally this data set has four explosions that were used as test cases in all of the steps of the cross-validation study. In our study, we compute a cross-validated false-outlier rate; however, we cannot reasonably estimate a missed-explosion rate because we have only the four explosions.

We have noted that a very small value of λ can be used to get a covariance $\Sigma_{EQ}(\lambda)$ with an acceptable condition number (ratio of max to min eigenvalues). In Figure 3, we summarize the distribution of the test values $f_{\mathbf{X}}(\mathbf{x})$ with trade-off plots. The ordinate is the 5th percentile of $f_{\mathbf{X}}(\mathbf{x})$ evaluated at each test amplitude data point and the abscissa is the interquartile range (IQR) of $f_{\mathbf{X}}(\mathbf{x})$. Each point is labeled with its corresponding λ value. Because all of the test values are computed from earthquake amplitudes, we want a distribution of test values that will optimally indicate earthquake. In terms of the trade-off plots in Figure 3, we want the 5th percentile of the outlier test statistic, $f_{\mathbf{X}}(\mathbf{x})$, to be as large as possible. Note that a small increase in the value of λ from zero generally decreases the IQR and increases the 5th percentile up to an optimum. These are desirable distributional properties because these two features indicate that the distribution is shifting away from zero and the variability of the distribution is decreasing. This property is further illustrated with fabricated boxplots in Figure 4, and a summary plot with regional data in Figure 5. Eventually the λ values cause the 5th percentile to move toward zero with a continued mild decrease in the IQR. Again, this is not desirable because small test values indicate outlier. The main points in this discussion are that a mild increase in λ away from zero will give a covariance $\Sigma_{EQ}(\lambda)$ with an acceptable condition number, and that there is an optimal value of λ that gives test value ($f_{\mathbf{X}}(\mathbf{x})$) distribution properties that minimize false-outlier rates. As shown in Figure 5, for an optimal λ, the ability to detect the explosions as outliers to the earthquake population is excellent. Thus in this preliminary study, we have observed that λ can have an optimal value that achieves, in the mean square error sense, a minimal false-outlier rate. Other research in support of this observation can be found in Peck et al. (1988). These methods show promise as a way to address the problem of high correlation among seismic discrimination measurements. Ridge discrimination is especially appealing when it is generalized to regularized discrimination analysis.

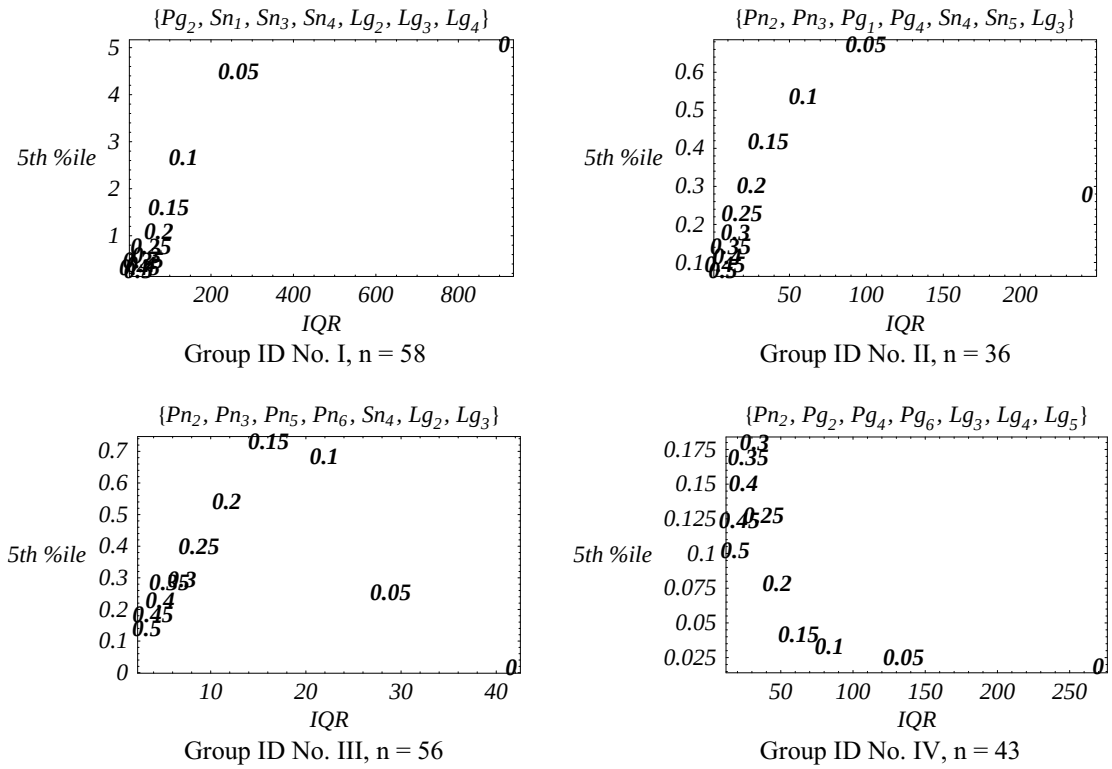


Figure 3. Trade-off plots of the test value data (MVN($\mu_{EQ}, \Sigma_{EQ}(\lambda)$)) evaluated with the cross-validation earthquake amplitudes. The value of λ appears in red, and the number (n) of cross-validation data used to construct the plot appears at the bottom of pair of plots.

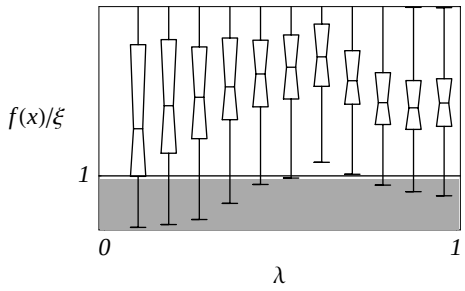


Figure 4. Illustration of the distributional properties of the test statistic $f_{\mathbf{X}}(\mathbf{x})$ as a function of λ. An increase in the value of λ away from zero generally decreases the IQR and increases the 5th percentile up to an optimum. These are desirable distributional properties because these two features indicate that the distribution is shifting away from zero and the variability of the distribution is decreasing. Eventually the λ values cause the 5th percentile to move toward zero with a continued mild decrease in the IQR. The shaded region represents the critical region that defines outlier.

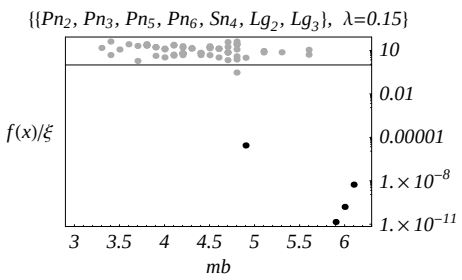


Figure 5. Test statistic $f_{\mathbf{X}}(\mathbf{x})$ plotted against *mb* for Group No. III in Figure 3. In this summary plot, all earthquake events were used to estimate μ_{EQ} and $\Sigma_{EQ}(\lambda)$. The optimal λ value is 0.15. Based on these data, this value will give a minimum IQR and a 5th percentile that is optimally above zero.

Regularized Discrimination Analysis

Regularized discrimination analysis (RDA) was proposed by Friedman (1989) as a method of discrimination to address applications with highly correlated discriminants and small training samples for some classification groups. Friedman s generalization of ridge discrimination involves the construction of a weighted-average covariance matrix

$$\mathbf{S}_k(\gamma) = (1-\gamma)\,\mathbf{S}_k + \gamma\,\mathbf{S}\,;\ \gamma \in \mathbf{[0,1]}. \qquad (5)$$

Here, $\mathbf{S}_k$ is the computed covariance matrix for kth group, and $\mathbf{S}$ is the pooled covariance matrix. Note that $\mathbf{S}_k$ may be singular due to a small number of training data or strongly correlated variables for the kth group. $\mathbf{S}_k(\gamma = 0)$ is computed from the kth group data alone (QDA) and $\mathbf{S}_k(\gamma = 1)$ is a pooled covariance (LDA). RDA uses a two-parameter formulation of a covariance matrix in forming discrimination rules. With $\mathbf{S}_k(\gamma)$ defined above, the RDA covariance matrix is

$$\Sigma_k(\lambda,\gamma) = (1-\lambda)\,\mathbf{S}_k(\gamma) + \lambda\,\frac{tr(\mathbf{S}_k(\gamma))}{p}\,\mathbf{I}\,;\ \lambda \in \mathbf{[0,1]},\ \gamma \in \mathbf{[0,1]}. \qquad (6)$$

Note that this is simply the ridge discrimination formulation with $\mathbf{S}_k$ replaced by $\mathbf{S}_k(\gamma)$. Here, λ and γ are the same values across all groups. Higbee s (1994) generalization allows λ and γ to change from group to group.

RDA theory can potentially be integrated into an outlier analysis approach to event identification or used as a classical seismic discrimination method. For outlier analysis, pooling ($\mathbf{S}$) could potentially occur across seismic stations within a geophysically homogeneous region. Here, each station may have observed a small number of seismic events. An RDA type covariance would be constructed for each station (Equation 6). We are researching techniques of optimally choosing values for λ and γ for $\Sigma_k(\lambda,\gamma)$ when only earthquake data are available.

There are some very appealing features of RDA. As noted in Friedman (1989), RDA reduces to quadratic discrimination for values of $\lambda = 0$, and $\gamma = 0$. For $\lambda = 0$, and $\gamma = 1$ RDA reduces to linear discrimination. Other extremes in the RDA parameters give nearest neighbor and weighted nearest neighbor type discrimination methods. In the nearest neighbor case, $\lambda = 1$, and $\gamma = 1$ which gives $\Sigma_k(1,1) = tr(\mathbf{S})/p\ \mathbf{I} = \omega\ \mathbf{I}$, ω a constant. For the weighted nearest neighbor case, $\lambda = 1$, and $\gamma = 0$ which gives $\Sigma_k(1,0) = tr(\mathbf{S}_k)/p\ \mathbf{I} = \omega_k\ \mathbf{I}$, ω_k a constant. In both of these cases, the discrimination function is based on Euclidean distance rather than Mahalanobis distance. However in the weighted nearest neighbor case the kth term in the discrimination function, corresponding to the kth group, is weighted with ω_k. These observations are summarized in Figure 6. RDA also addresses some of the inadequacies with QDA. In particular, QDA usually requires larger sample sizes than LDA and is quite sensitive to model violations (Friedman 1989).

RDA provides a rich and adaptable family of discrimination methods that appear to be very applicable to the regional seismic problem. RDA readily provides a statistical framework to use MDAC amplitudes (see Taylor et al.

1999) in regional seismic discrimination. We also note that the $\Sigma_k(\lambda,\gamma)$ can be used as the covariance matrix in negative evidence methods (Anderson et al. 1999). In fact, RDA can be the foundation for any enhanced discrimination framework that is based on the use of statistical likelihood functions. For the classical discrimination problem (calibration data for all seismic sources), optimal values of λ, and γ are identified with cross-validated error rates. The details of this procedure can be found in Friedman (1989).

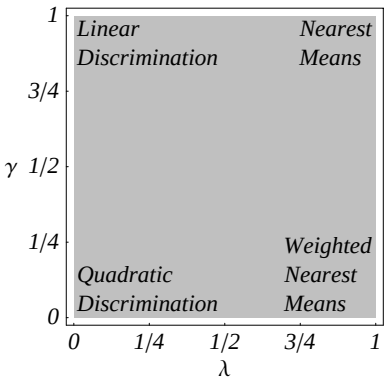


Figure 6. The relationship between regularized discrimination analysis (RDA) and some other classical discrimination methods.

CONCLUSIONS AND FURTHER DEVELOPMENTS

We have illustrated the importance of properly modeling the correlation structure of seismic measurements in the seismic event identification problem. If this correlation is not captured in the mathematics of a discrimination method, then both false-alarm and missed-explosion rates can be aggravated. Empirically we have noted that the false-alarm errors can be seriously increased when discriminant correlations are not properly modeled. In the regional discrimination problem, seismic measurements will be strongly correlated (e.g., Lg spectra may be contaminated by Sn coda and amplitudes may be constructed with frequency bands that overlap). This poses another problem in that an estimate of a covariance matrix for these measurements will be near singular. The true, unknown covariance matrix is itself near singular. Ridge discrimination and its generalization, RDA, provide a statistical method that can perform well in the presence of highly correlated seismic measurements. These methods properly combine measurements through a covariance matrix and are mathematically adaptable to a variety of regional seismic identification settings. We believe that regularized discrimination provides a reasonable solution to the regional discrimination problem and provides the flexibility to adapt to a future maturation of seismic event identification.

If an outlier detection algorithm is based on the use of statistical likelihood functions, then in an operational setting, missing data may be accounted for using detection thresholds with negative evidence methods (Anderson et al. 1999). However, outlier detectors are constructed with ground truth earthquake data, which can have left-censored data due to poor signal-to-noise, particularly at high frequencies. Woodward et.al (1999) show the utility of filling missing ground truth earthquake data with the EM algorithm with a marked decrease in error rates. Anderson and Phillips (1999) have developed an approach to incorporate censoring thresholds associated with missing spatial data into Kriging parameter estimates. We are adapting the work of Woodward et.al (1999) and Anderson and Phillips (1999) to the outlier detector approach presented in this paper. In particular, future developments include;

- the development of methods to incorporate amplitude censoring thresholds into the EM algorithm to fill missing earthquake training data,
- the development of a method of optimally choosing the RDA parameters λ and γ using only earthquake training data (RDA concepts integrated into outlier analysis),
- the comparison of optimal λ and γ determined with explosion and earthquake training data with optimal λ and γ determined only with earthquake training data.

REFERENCES

Aki, K. and P.G. Richards (1980). *Quantitative Seismology: Theory and Methods*. W.H. Freeman and Company, San Francisco.

Anderson, D.N., S.R. Taylor and K.K. Anderson (1999). Discrimination Information in Phase Amplitude Thresholds with Application to Western China Regional Data , *Bulletin of the Seismological Society of America*, 89, pp. 648-656.

Anderson, K.K. and W.S. Phillips. (1999). A Simple Procedure for Kriging Left-Censored Data. , PNNL-SA-31023, Pacific Northwest National Laboratory, Richland, Washington.

Campbell, N.A. (1980). Shrunken Estimators in Discriminant and Canonical Variate Analysis , *Applied Statistics* , 29, pp. 5-14.

Clemen, R.T. and R.L. Winkler (1985). Limits for the precision and value of information from dependent sources , *Operations Research*, 33, pp. 427-442.

DiPillo, P.J. (1976). The Application of Bias to Discriminant Analysis , *Communications in Statistics — Theory and Methods*, A5(9), pp. 843-854.

DiPillo, P.J. (1977). Further Application of Bias to Discriminant Analysis , *Communications in Statistics — Theory and Methods*, A6(10), pp. 933-943.

DiPillo, P.J. (1979). Biased Discriminant Analysis: Evaluation of the Optimum Probability of Misclassification , *Communications in Statistics — Theory and Methods*, A8(14), pp. 1447-1457.

Fisk, M.D., H.L. Gray, and G.D. McCartor (1996). Regional Event Discrimination without Transporting Thresholds , *Bulletin of the Seismological Society of America*, 86, pp. 1545-1558.

Friedman, J.H. (1989). Regularized Discriminant Analysis , *Journal of the American Statistical Association*, 84, pp. 165-175.

Higbee, K.T. (1994). Variably Regularized Discriminant Analysis , *Proceedings of the Statistical Computing Section*., American Statistical Association, Alexandria, Virginia. pp. 263-268.

Lehmann, E.L. (1983). *Theory of Point Estimation*. John Wiley & Sons, New York.

Loh, Wei-Liem. (1995). On Linear Discriminant Analysis with Adaptive Ridge Classification Rules , *Journal of Multivariate Analysis*, 53, pp. 264-278.

Loh, Wei-Liem. (1997). Linear Discrimination with Adaptive Ridge Classification Rules , *Journal of Multivariate Analysis*, 62, pp. 169-180.

McLachlan, G.J. (1992). *Discriminant Analysis and Statistical Pattern Recognition*. John Wiley & Sons, New York.

Morrison, D.G. and D.C. Schmittlein (1991). How many forecasters do you really have? Mahalanobis provides the intuition for the surprising Clemen and Winkler result , *Operations Research*, 39, pp. 519-523.

Peck, R., L.W. Jennings and D.M. Young (1988). A Comparison of Several Biased Estimators for Improving the Expected Error Rate of the Sample Quadratic Discriminant Function , *J. Statist. Comput. Simul.*, 29, pp. 143-156.

Randles, R.H., J.D. Broffitt, J.S. Ramberg and R.V. Hogg (1978). Generalized Linear and Quadratic Discriminant Functions Using Robust Estimates , *Journal of the American Statistical Association*, 73, pp. 564-568.

Rencher, A.C. (1998). *Multivariate Statistical Inference and Applications*. John Wiley & Sons, New York.

Smidt, R.K. and L.L. McDonald (1976). Ridge Discriminant Analysis , University of Wyoming Department of Statistics, Technical Report No. 108, Laramie, Wyoming.

Taylor, S.R. (1991). Regional seismic observations from NTS explosions, in Explosion Source Phenomenology , *AGU Monograph 65*, Taylor, S.R., H.J. Patton , and P.G. Richards, eds., pp. 185-196.

Taylor, S.R., and M.D. Denny (1991), An Analysis of Spectral Differences Between NTS and Shagan River Nuclear Explosions , *J. Geophys. Res.*, 96, pp. 6237-6245.

Taylor, S.R., and H.E. Hartse (1997). An Evaluation of Generalized Likelihood Ratio Outlier Detection to Identification of Seismic Events in Western China , *Bulletin of the Seismological Society of America*, 87, pp. 824-831.

Taylor, S.R., A.A. Velasco, H.E. Hartse, W.S. Phillips, W.R. Walter, and A.J. Rodgers (1999), Amplitude Corrections for Regional Seismic Discriminants. , LAUR-99-3040, Los Alamos National Laboratory, Los Alamos, New Mexico.

Woodward, W.A., S.R. Sain, H.L. Gray, and M.D. Fisk (1999). Outlier Testing When Some Data are Missing , *21st Seismic Research Symposium*., 21-24 September, Las Vegas, Nevada., U.S. Departments of Energy and Defense, pp. 674-682.

A NEW JOINT P AND S VELOCITY MODEL OF THE MANTLE PARAMETERIZED IN CUBIC B-SPLINES

Michael Antolik, Göran Ekström, Adam M. Dziewonski, Yu J. Gu, Jian-feng Pan, and Lapo Boschi
Department of Earth and Planetary Sciences, Harvard University
Cambridge, MA 02138

Contract No.: DSWA01-97-C-0124

Abstract

The objective of the project is to develop and improve upon three-dimensional (3-D) seismic velocity models of the Earth and to utilize such models for improving the locations of events recorded at regional and teleseismic distances. Our previous experiments performed using 3-D models of varying resolution show that the accuracy of event location with respect to ground truth does not necessarily improve with an increasing number of free parameters in a model. One reason for this may be the lack of waveform data used for constructing recent high-resolution models, since the maximum sensitivity of seismic travel times to structure is in the middle to lower mantle. In this paper we develop a new joint, P and S velocity model parameterized in terms of radial and horizontal cubic splines, using a combination of direct and differential travel times and surface wave phase measurements. The accuracy of the travel time data has been improved by relocating the events using a previously existing 3-D mantle P wave model. The cubic spline parameterization conveniently allows more detailed models to be inserted within it for use of regional phases in event location. Our preliminary model shows substantial differences in compressional velocity in the uppermost mantle compared with previous models. In conjunction with the model development, we are collecting new reference events with accurate locations, among them earthquakes on mid-ocean ridges and transforms, using a constrained inversion technique.

Key words: Event location; seismic tomography; mantle heterogeneity

Objective

The aim of this project is to ultimately improve the locations of earthquakes and other seismically recorded events in order to enhance the ability to monitor the Comprehensive Nuclear-Test-Ban-Treaty (CTBT). Our strategy is based on developing new, detailed 3-D models of the mantle, with an emphasis on P wave structure. This involves the construction of global high-resolution models with more detail in certain areas where particularly good data coverage is available. A second, subsidiary objective concerns the development of additional techniques used in locating events teleseismically and regionally with sparse datasets, and with assessing the improvement in accuracy afforded by the new techniques and models. We have previously studied the location accuracy obtained by some previously existing mantle P wave models [*Antolik et al.*, 2000]. Here we describe the development of a new joint P and S wave velocity model of the mantle, using a diverse and improved data set of travel times and surface wave phase velocity measurements.

Research Accomplished

The accuracy of event location with respect to ground truth is not a simple function of the number of free parameters or "resolution" of a particular velocity model. This was reported by *Antolik et al.* [2000], where they tested four existing P wave models. Two of these models, S&P12/WM13 (hereafter referred to as SP12) [*Su and Dziewonski*, 1993] and MK12WM13 [*Su and Dziewonski*, 1997] were parameterized in terms of relatively low-order spherical harmonic functions. The other two models, that of *van der Hilst et*

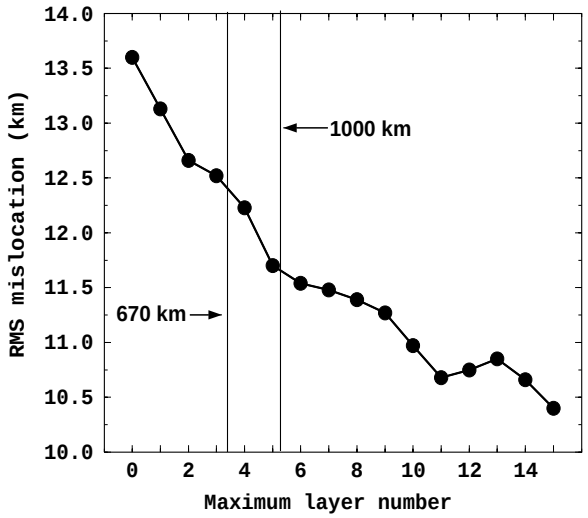


Figure 1: Root mean square mislocation obtained from locating a set of nuclear explosions with known locations using model corrections from BDP98 corresponding to layers only shallower than a certain depth. Each layer is slightly less than 200 km thick and are numbered in ascending order from the top to the bottom of the mantle. The depths of 670 km and 1000 km are indicated by the vertical lines. The data point for layer 0 is equivalent to locating the events in the reference 1-D model PREM (no layers from BDP98 were used). The majority of the improvement in location accuracy is obtained by considering only those layers above 1000 km.

al. [1997] (HWE97) and *Boschi and Dziewonski* [1999] (BDP98), were parameterized in terms of constant-

velocity blocks with horizontal dimensions of 2° and 5°, respectively, and contain nearly an order of magnitude more free parameters. Surprisingly, the best locations were provided by model SP12 even though the models with higher resolution provide a better fit to the travel time residuals. These tests were performed using a well-calibrated set of explosions and earthquakes [*Kennett and Engdahl*, 1991] and datasets consisting of a limited number of teleseismic phases in order to simulate global location of small events by the International Monitoring System (IMS) seismic network. Model SP12 provided consistently smaller magnitude mislocations than the other three models.

There are several possible reasons for this result. The parameterization most often chosen for newer, high-resolution models is typically that of blocks with constant velocities [e.g., *Boschi and Dziewonski*, 1999; *Vasco and Johnson*, 1998; *Grand et al.*, 1997]. These models therefore introduce artificial lateral discontinuities into the structure and may induce an unrealistic shape in long-wavelength anomalies. A lack of correlation between new, high-resolution Earth models and earlier longer wavelength models has previously been noted [*Grand et al.*, 1997]. Another issue is the coverage of the data sets used in the inversion problem. Because of the very large number of parameters used to define the higher resolution models, most of these models make use of a somewhat limited data set (for example, only phase travel times) in order to reduce the size of the necessary computer resources (memory and CPU time). This may result in a relative lack of resolution in certain areas of the mantle (particularly at shallow depths) to which teleseismic phase travel times are not sensitive. As an example, we show in Figure 1 the mislocation obtained from a group of explosions using only a subset of the layers of model BDP98 as a correction to PREM. Nearly all of the improvement in the locations is obtained by considering depths above 1000 km, which shows that resolution of the shallow mantle is most critical to teleseismic event location. Models which do not recover the upper mantle structure well will not provide the most accurate locations.

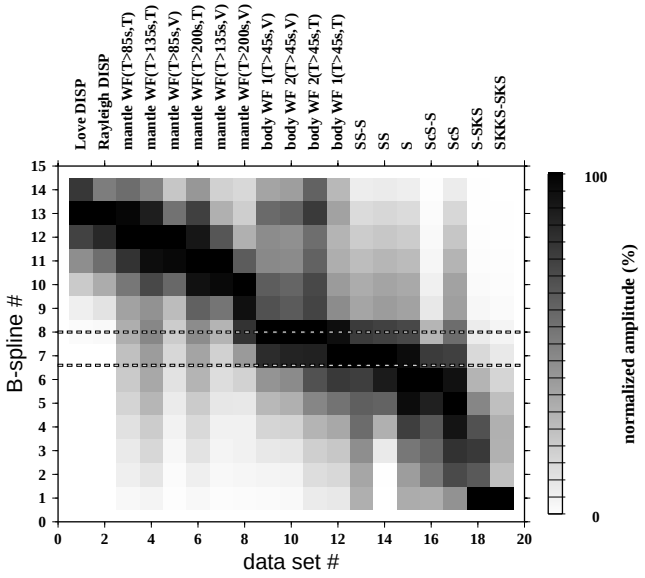


Figure 2: Diagram showing the average amplitide of the diagonal elements of an inner product matrix for an inversion for shear wave velocity [*Gu et al.*, 2000]. Each cell corresponds to that portion of the matrix describing sensitivity of a particular data set used (listed at the top) to one of the radial B-splines of the model. The splines are numbered in ascending order from the CMB to the top of the mantle (i.e., spline 1 has maximum amplitude near the CMB, see Figure 4). A higher normalized amplitude indicates greater sensitivity of a dataset to the coefficients of a radial spline.

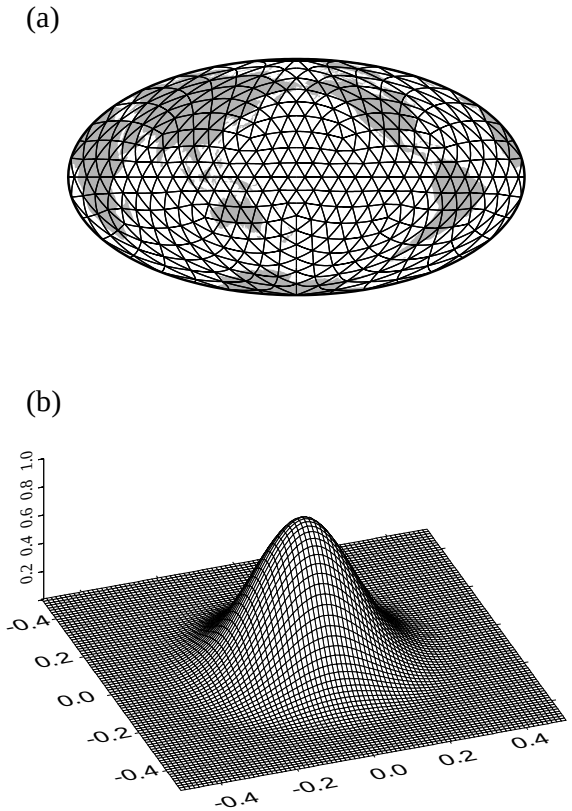


Figure 3: (a) Horizontal parameterization of the global model. The Earth's surface is divided into 362 equal-area triangles. Each knot location corresponds to the center of a spherical B-spline. (b) A 3-D view of a spherical B-spline used in the lateral expansion. The spline function is localized, axially symmetric, and has been normalized to 1.

It is therefore important to use data in tomographic inversions which have maximum sensitivity to upper mantle structure. Figure 2 shows the average value of the diagonal elements of an inner product matrix used in an inversion for S wave velocity [*Gu et al.,* 2000]. Maximum sensitivity to the upper mantle is provided by the use of surface wave dispersion measurements and body and surface waveforms with periods longer than 45 s. Differential and direct travel times are mostly sensitive to lower mantle structure. For a P wave inversion Figure 2 would be similar, without the Love wave measurements and with the travel times for corresponding P phases substituted. In deriving our new global mantle model, we have therefore made use of a variety of datasets.

For the model parameterization we choose a combination of spherical and radial B-splines. Horizontally, the spherical splines are centered at 362 uniformly distributed knots (Figure 3). The number of free parameters is close to that involved in a degree-18 spherical harmonic expansion. Perturbations to PREM in both P and S velocity are represented by

$$\frac{\delta v(r,\theta,\phi)}{v_\circ} = \sum_{i,j} C_{ij} S_j(\theta,\phi) \cdot B_i(r) \tag{1}$$

where r, θ, and ϕ are radius, colatitude, and longitude, respectively, S_j is the jth spherical spline, and B_i the ith radial spline. C_{ij} are the model coefficients to be determined. The mathematical form of the S_j is given in *Wang and Dahlen* [1995]. A 3-D view of one of the spherical spline functions is shown in Figure 3b. The maximum amplitude is localized to the vicinity of the central knot. The spline approach thus combines

some of the advantages of using a local, block parameterization with the advantage of producing a smooth model.

Radially, the parameterization consists of 14 cubic B-splines distributed non-uniformly with depth (Figure 4). The local support of B-splines allows for fast computation since only neighboring splines are needed to compute the value of the model at a given point. The second derivatives of the splines vanish at both ends. We use the split parameterization of *Gu et al.* [2000] in which the radial splines are split at the boundary between the upper and lower mantle (670 km) in order to detect possible sharp changes in velocity variations across this depth. Six B-splines are used for the upper mantle portion and 8 for the lower mantle.

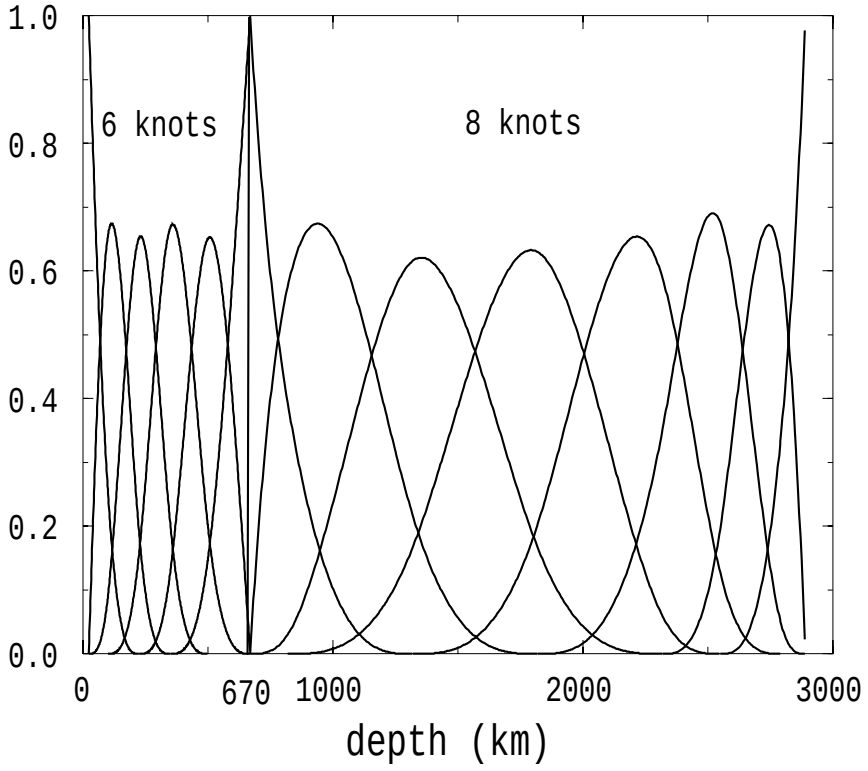


Figure 4: Split radial B-splines used for parameterization of the global model. Two sets of splines are used: 6 for the upper mantle and 8 for the lower mantle. This parameterization provides higher nominal resolution near the 670-km discontinuity.

We are currently using a large of number of datasets in the inversions as well as developing others for future use. The compressional velocity model is determined by travel times of direct P and core phases (PKP, PcP) to improve resolution in the lowermost mantle. These datasets were adopted from those of *Engdahl et al.* [1998] but have been improved through relocation of the earthquakes in a 3-D model (SP12). The travel times were then formed into summary rays with sources at the center of 2° x 2° cells. Events deeper than 50 km were grouped by depth into bins with a thickness of 100 km. Events whose epicenter moved more than 1° from the location published by *Engdahl et al.* [1998] were discarded. The total number of summary rays is 626,073 for P, 215,590 for PKP, and 68,473 for PcP. We also make use of the Love and Rayleigh wave dispersion measurements published by *Ekström et al.* [1997] in the period range 35-150 s, which have their maximum sensitivity in the upper 200-300 km of the mantle. These were previously used by *Ekström and Dziewonski* [1998] to derive a 3-D model of mantle shear wave velocity expanded in

spherical harmonics up to degree 20 as part of an earlier phase of this project. For shear velocity inversions, we also use the direct and differential travel time datasets described in *Su et al.* [1994]. They consist of approximately 45,000 measurements of S, SS, ScS, SS - S, S - SKS, ScS - S, and $SKKS$ - SKS travel times. Future models will also include the extensive dataset of body and surface waveforms compiled over the years at Harvard.

We solve the inverse problem by non-linear, iterative least-squares analysis. The equations are of the form

$$\delta \mathbf{d}_0 = \mathbf{A}\delta\mathbf{x} \tag{2}$$

where $\delta\mathbf{x}$ is the perturbation in the model from the previous iteration, $\delta\mathbf{d}_0$ is the corresponding unexplained portion of the data vector, and $\mathbf{A}$ is the kernel matrix. For the final iteration, we require that

$$|\mathbf{A}\delta\mathbf{x} - \delta\mathbf{d}_0|^2 + \lambda^2|\delta\mathbf{x}|^2 + \eta^2 g^2 = min \tag{3}$$

where λ and η are damping factors and g^2 is the integrated squared gradient of the model:

$$g^2 = \int_\Omega \int_{r_{cmb}}^{r_{moho}} |\bigtriangledown (\delta v/v_0)|^2 dr d\Omega. \tag{4}$$

The least-squares model solution at each iteration is computed by the method of Cholesky factorization [*Trefethen and Bau*, 1997].

An initial P wave velocity model is shown in Figure 5. With respect to model BDP98, the new model shows higher amplitude velocity perturbations in the upper mantle, which may be the result of the 3-D relocation of the sources prior to inversion. Use of the surface wave measurements produces lower velocities throughout the eastern and central Pacific than are observed using travel times alone. At the bottom of the mantle, the new model has slightly lower amplitude than BDP98 and much lower amplitude than model SP12, especially in the southern hemisphere. This may be partly due to the relatively coarse separation of the radial splines in the lower mantle in this parameterization. Since, as noted above, the upper mantle is most critical for accurate earthquake location, the new model may improve upon the location accuracy provided by BDP98 and other high-resolution models. Our new models will be tested using the dataset of calibration events compiled at Harvard and other institutions.

Constraining earthquake locations on mid-ocean ridges and transforms

In addition to the construction of more detailed and accurate global velocity models, we have focused our efforts on building a larger database of reference or "ground-truth" events to be used for model calibration. So far, the geographical distribution of events with locations known to an accuracy of 5 km or better is extremely limited. Many of these events are nuclear explosions and are concentrated in only a few source regions, making comprehensive testing of velocity models and calibration of new seismic stations very difficult. We are experimenting with relocation of events on remote plate boundaries using a technique which constrains the location to a point along the plate boundary. For example, by limiting the process to only large events for which a Centroid Moment Tensor (CMT) solution exists, an assessment can be made as to whether an event should be located along a mid-ocean ridge segment or an adjacent transform fault based on its focal mechanism. We then perform a transformation of coordinates into the system defined by the pole of rotation between the two plates, such that the ridge or transform fault lies along a parallel or meridian. We use accurate bathymetry to determine the precise location and trend of the boundary [*Smith and Sandwell*, 1997]. In the subsequent location process, the coordinate (latitude or longitude) which corresponds to the plate boundary is held fixed. In this way, we are able to develop a master set of events which can then be used to relocate other smaller events in the same region.

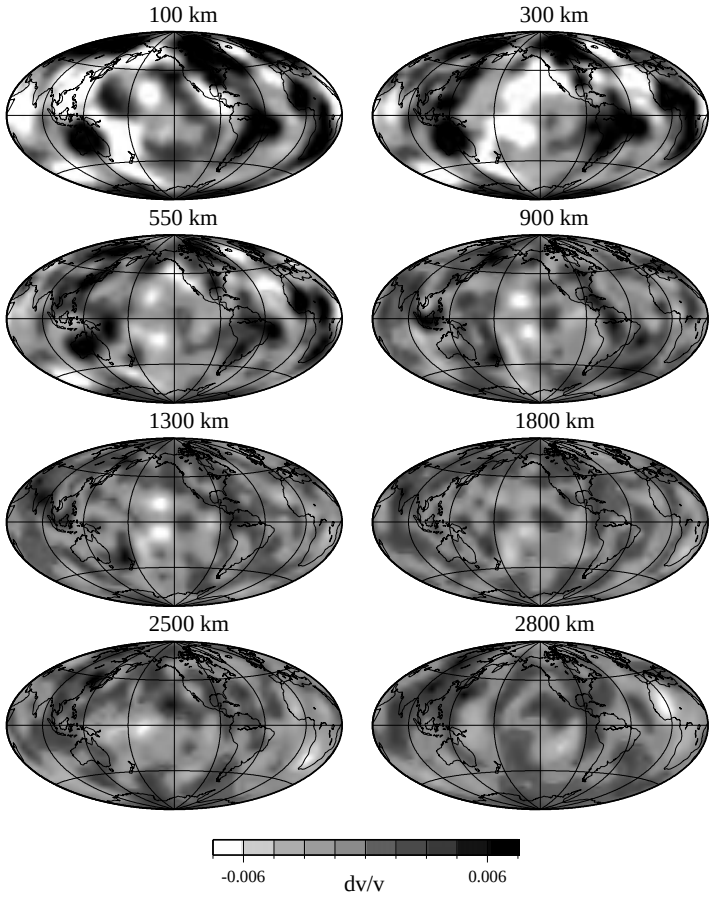


Figure 5: Model of P wave velocity at various depths obtained in joint inversion of compressional and shear velocity using travel times and surface wave phase velocities. Scale shows fractional velocity perturbation from PREM.

We have thus far compiled a catalog of these events along most of the transform faults in the Atlantic, Pacific, and Indian oceans. Figure 6 shows the relocation of events along the Romanche Fracture Zone (RFZ) in the central Atlantic. The top panel shows the ISC locations of events in the CMT catalog. After relocation (middle panel), the strike-slip earthquakes associated with the RFZ lie along the trend defined by the bathymetry. The ISC locations are systematically displaced to the south relative to the RFZ, and the apparent mislocations are as large as 40 km. The results obtained thus far are promising but require extensive testing to determine the accuracy of the relocations.

Conclusions and Recommendations

Although the current generation of global velocity models provides substantial improvement over 1-D velocity models for teleseismic earthquake location [*Smith and Ekström*, 1996; *Antolik et al.*, 2000], there is still much room for improvement. The consistent accurate location of small events to within the area specified for on-site inspection under the CTBT (1000 km^2) will likely require the use of regional phases in addition to teleseismic travel times, and also possibly consideration of anisotropy or arrival angle data. To this end, we are developing new global models which combine a local parameterization with the advantages

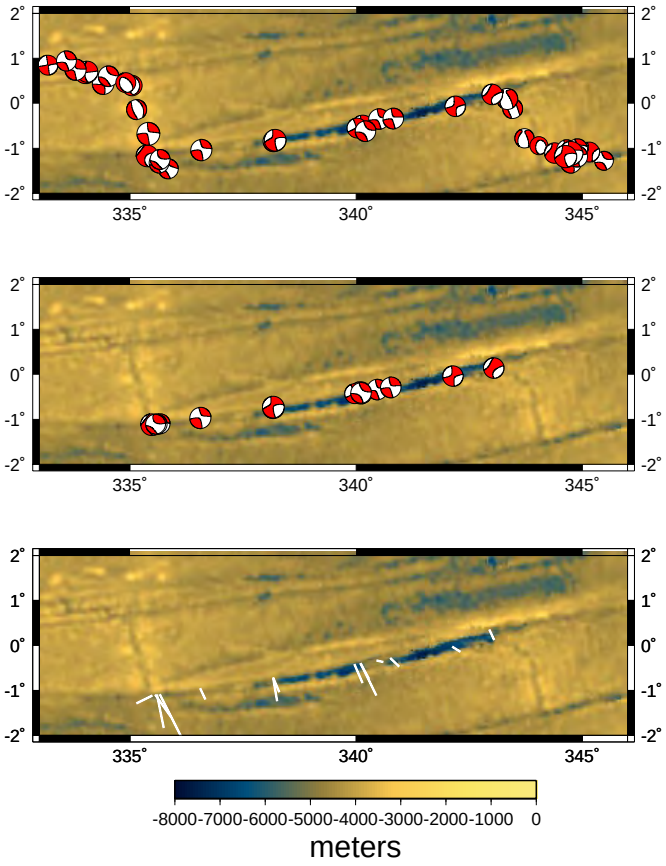


Figure 6: Relocation of earthquakes along the Romanche Fracture Zone in the central Atlantic. The top panel shows the focal mechanisms of large earthquakes in the region plotted at their ISC locations. After identification of the strike-slip events to be constrained to the RFZ, these events are relocated after coordinate transformation (middle panel). The bottom panel shows the change in location of these same events, multiplied by a factor of 2.5. Bathymetry is taken from *Smith and Sandwell* [1997].

of smoothness over large distances. This will enable straightforward replacement of portions of the global model by a more detailed model covering a particular region. The smooth parameterization will allow simple computation of 3-D raypaths.

Testing of new global and regional velocity models, as well as calibration of newer IMS stations, will benefit from the compilation of reference events in remote regions. Our database of relocated events on mid-ocean plate boundaries will also enable construction of more accurate travel time and phase velocity datasets.

References

Antolik, M., G. Ekström, and A. M. Dziewonski, Global event location with full and sparse datasets using three-dimensional models of mantle P wave velocity, *Pure Appl. Geophys.*, in press, 2000.

Boschi, L. and A. M. Dziewonski, "High" and "low" resolution images of the Earth's mantle: Implications of different approaches to tomographic modeling, *J. Geophys. Res., 104*, 25,567-25,594, 1999.

Ekström, G., and A. M. Dziewonski, The unique anisotropy of the Pacific upper mantle, *Nature, 394*, 168-172, 1998.

Ekström, G., J. Tromp, and E. W. F. Larson, Measurements and global models of surface wave propagation, *J. Geophys. Res., 102*, 8137-8157, 1997.

Engdahl, E. R., R. D. van der Hilst, and R. P. Buland, Global teleseismic earthquake relocation with improved travel times and procedures for depth determination, *Bull. Seism. Soc. Am., 88*, 722-743, 1998.

Grand, S. P., R. D. van der Hilst, and S. Widiyantoro, Global seismic tomography: A snapshot of convection in the Earth, *GSA Today, 7*(4), 1-7, 1997.

Gu, Y. J., A. M. Dziewonski, W. Su, and G. Ekström, Shear velocity model of the mantle and discontinuities in the pattern of lateral heterogeneities, submitted to *J. Geophys. Res.*, 2000.

Kennett, B. L. N., and E. R. Engdahl, Traveltimes for global earthquake location and phase identification, *Geophys. J. Int., 105*, 429-465, 1991.

Smith, G. P., and G. Ekström, Improving teleseismic event locations using a three-dimensional earth model, *Bull. Seism. Soc. Am., 86*,, 788-796, 1996.

Smith, W. H. F., and D. T. Sandwell, Global sea floor topography from satellite altimetry and ship depth soundings, *Science, 277*, 1956-1962, 1997.

Su, W. and A. M. Dziewonski, Joint 3-D inversion for P- and S-velocity in the mantle, *EOS, 74*, 557, 1993.

Su, W. and A. M. Dziewonski, Simultaneous inversion for 3-D variations in shear and bulk velocity in the mantle, *Phys. Earth Planet. Inter., 100*, 135-156, 1997.

Su, W., R. L. Woodward, and A. M. Dziewonski, Degree-12 model of shear velocity heterogeneity in the mantle, *J. Geophys. Res., 99*, 6,945-6,980, 1994.

Trefethen, L. N., and D. Bau, *Numerical Linear Algebra*, Soc. for Ind. and Appl. Math., Philadelphia, PA, 1997.

van der Hilst, R. D., S. Widiyantoro, and E. R. Engdahl, Evidence for deep mantle circulation from global tomography, *Nature, 386*, 578-584, 1997.

Vasco, D. W. and L. R. Johnson, Whole Earth structure estimated from seismic arrival times, *J. Geophys. Res., 103*, 2633-2671, 1998.

Wang, Z., and F. Dahlen, Spherical-spline parameterization of three-dimensional Earth models, *Geophys. Res. Lett., 22*, 3,099-3,102, 1995.

UTILIZING RESULTS FROM INSAR TO DEVELOP SEISMIC LOCATION BENCHMARKS AND IMPLICATIONS FOR SEISMIC SOURCE STUDIES

Michael L. Begnaud, Aaron A. Velasco, Lee K. Steck
Los Alamos National Laboratory

Sponsored by the U.S. Department of Energy
Office of Nonproliferation and National Security
Office of Defense Nuclear Nonproliferation
National Nuclear Security Administration

Contract No. W-7405-ENG-36

ABSTRACT:

Obtaining accurate seismic event locations is one of the most important goals for monitoring detonations of underground nuclear tests. This is a particular challenge at small magnitudes where the number of recording stations may be less than 20. Although many different procedures are being developed to improve seismic location, most procedures suffer from inadequate testing against accurate information about a seismic event. Events with well-defined attributes, such as latitude, longitude, depth, and origin time, are commonly referred to as ground truth (GT). Ground truth comes in many forms and with many different levels of accuracy.

Interferometric Synthetic Aperture Radar (InSAR) can provide independent and accurate information (ground truth) regarding ground surface deformation and/or rupture. Relating surface deformation to seismic events is trivial when events are large and create a significant surface rupture, such as for the M_w = 7.5 event that occurred in the remote northern region of the Tibetan plateau in 1997. The event, which was a vertical strike slip event, appeared anomalous in nature due to the lack of large aftershocks and had an associated surface rupture of over 180 km that was identified and modeled using InSAR. The east-west orientation of the fault rupture provides excellent ground truth for latitude, but is of limited use for longitude. However, a secondary rupture occurred 50 km south of the mainshock rupture trace that can provide ground truth with accuracy within 5 km.

The smaller, 5-km-long secondary rupture presents a challenge for relating the deformation to a seismic event. The rupture is believed to have a thrust mechanism; the dip of the fault allows for some separation between the secondary rupture trace and its associated event epicenter, although not as much as is currently observed from catalog locations. Few events within the time period of the InSAR analysis are candidates for the secondary rupture. Of these, we have identified six possible secondary rupture events (*mb* range = 3.7-4.8, with two magnitudes not reported), based on synthetic tests and residual analysis. All of the candidate events are scattered about the main and secondary rupture. A Joint Hypocenter Determination (JHD) approach applied to the aftershocks using global picks was not able to identify the secondary event. We added regional data and used propagation path corrections to reduce scatter and remove the 20-km bias seen in the mainshock location. After preliminary analysis using several different velocity models, none of the candidate events proved to relocate on the surface trace of the secondary rupture. However, one event (*mb* = not reported) moved from a starting distance of ~106 km to a relocated distance of ~28 km from the secondary rupture, the only candidate event to relocate in relative proximity to the secondary rupture.

Key Words: InSAR, ground truth, seismic location

OBJECTIVE

One of the most important goals for monitoring detonations of underground nuclear tests is obtaining accurate seismic event locations, particularly for small magnitude events where the number of recording stations may be less than 20. Although many different procedures are being developed to improve seismic location, most procedures suffer from inadequate testing against accurate information about a seismic event. Interferometric Synthetic Aperture Radar (InSAR) can provide independent and accurate information (ground truth) regarding ground surface deformation and/or rupture. Identifying the secondary event within the Tibet aftershock sequence would provide a small ground truth event, a valuable calibration point in this region. We can also use the event to validate the regional location methods, velocity models, and empirical calibration approaches being used for CTBT monitoring.

RESEARCH ACCOMPLISHED

The verifiability of a Comprehensive Nuclear-Test-Ban Treaty (CTBT) depends on the ability to effectively monitor small magnitude (< 4) events, with an implicit goal of locating seismic events within a contiguous area smaller than 1000 km^2. Although many different procedures are being developed to improve seismic location, most procedures suffer from inadequate testing against accurate information about a seismic event. Events with well-defined attributes, such as latitude, longitude, depth, and origin time, are commonly referred to as ground truth (GT). Ground truth comes in many forms and with many different levels of accuracy. Nuclear tests, mining explosions, or specific calibration explosions have all been used to assess event locations. Deployments of seismic instruments to record and locate aftershock sequences can also give a level of accuracy much greater than sparse global networks of stations (Myers and Schultz, 2000).

A large (M_w = 7.5) earthquake occurred in a remote northern region of the Tibetan plateau. The event was a vertical strike slip event and appeared anomalous in nature due to the lack of large aftershocks (Velasco *et al.*, 2000). The event had an associated surface rupture that was identified and modeled using Interferometric Synthetic Aperture Radar (InSAR) (Peltzer *et al.*, 1999). InSAR can provide independent and accurate information (ground truth) regarding ground surface deformation and/or rupture. The Tibetan mainshock created a surface rupture of over 180 km in length (Figure 1), and occurred on a previously mapped fault that was determined using SPOT imagery (Tapponnier and Molnar, 1977). Focal mechanisms are shown for the Tibet mainshock event (Velasco *et al.*, 2000) and a 1973 Ms=6.9 event west of the Tibet mainshock (Molnar and Chen, 1983). The east-west orientation of the fault rupture provides excellent ground truth for latitude, but is of limited use for longitude. However, a secondary rupture, which occurred 50 km south of the mainshock rupture trace (Peltzer *et al.*, 1999), can provide ground truth with accuracy within 5 km.

Relating surface deformation to seismic events is trivial when events are large and create significant surface rupture, such as the mainshock. However, the smaller secondary rupture presents a challenge. This 5-km-long rupture is believed to have a thrust mechanism (Peltzer, G., personal communication), which implies that the earthquake/ aftershock that generated it may be near but not necessarily on the surface trace of the fault. Identifying the secondary event within the aftershock sequence would provide a small ground-truth event, a valuable calibration point in this region. We can also use the event to validate the regional location methods, velocity models, and empirical calibration approaches being used for CTBT monitoring. Furthermore, InSAR is providing unique insight for anelasticity in the crust, and co-locating an event may reveal unique insight into the rupture. In this paper, we focus on identifying the secondary rupture by adding more regional data, attempting to use S-phases, creating synthetic tests, using various velocity models, and hypothesis testing.

Data and Velocity Models

Figure 1 shows the global USGS event locations prior to the Tibetan mainshock, after the mainshock during a time period in which the InSAR was performed, and until March 1999. Few events within the time period of the InSAR analysis are candidates for the secondary rupture. All of the events are scattered and biased south of the rupture, with a 20-km bias for the mainshock location (Steck *et al.*, 2000). A Joint Hypocenter Determination (JHD) approach (Dewey, 1983) applied to the aftershocks using global picks was not able to identify the secondary event (Velasco *et al.*, 2000).

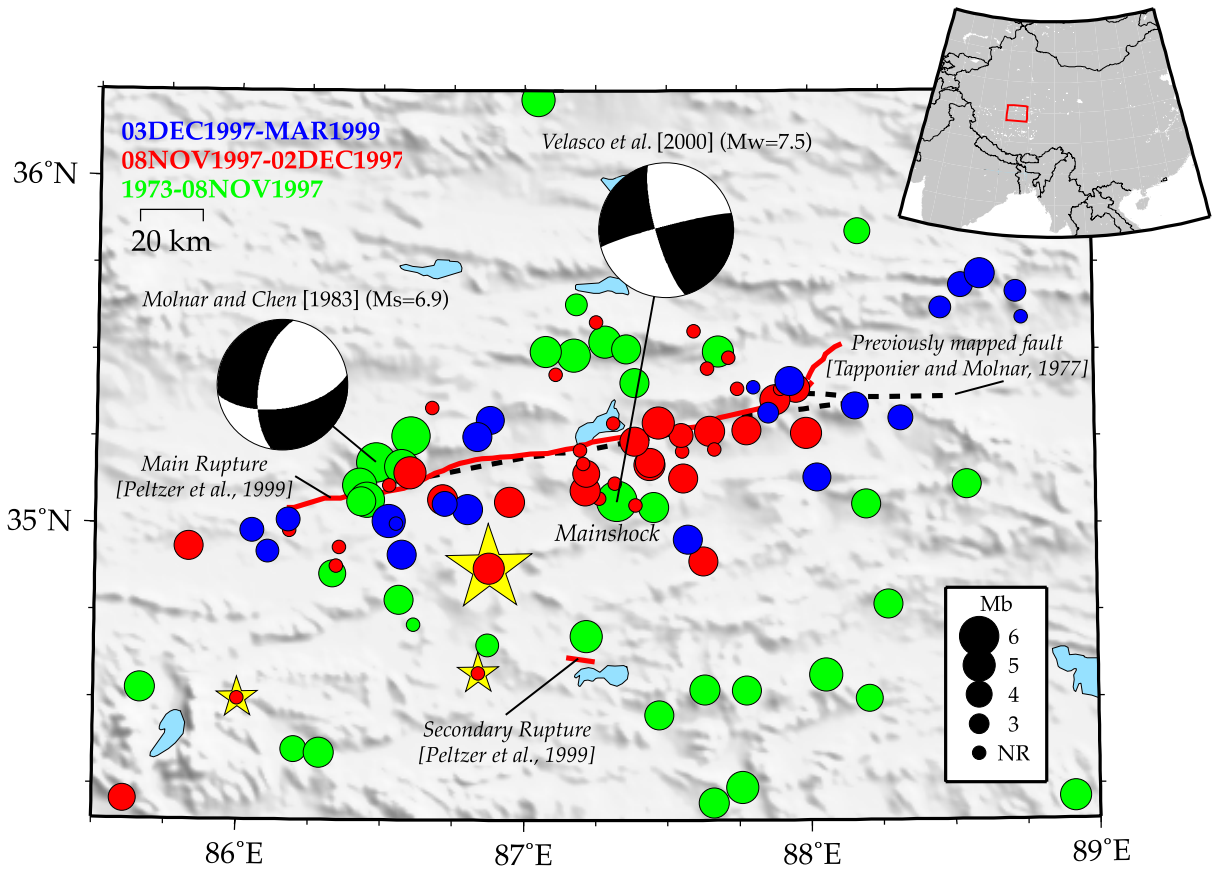


Figure 1. United States Geological Survey (USGS) catalog locations for the area around the Manyi/Tibet earthquake (Mw=7.5) on 08NOV1997. Shown are events before and including the mainshock (green), events between the mainshock and the second satellite pass used to create the InSAR image for the center section of the main rupture (red), and events after the second satellite pass through March 1999 (blue). The epicenters between the mainshock and second satellite pass are possible candidates for an event that occurred during the secondary rupture (red line ~50 km south of main rupture), three of which were chosen as the most likely candidates (highlighted). Focal mechanisms are shown for the Manyi mainshock event (Velasco *et al.*, 2000) and a 1973 Ms=6.9 event west of the Manyi mainshock (Molnar and Chen, 1983).

We use the global catalog as a guide to obtain waveform data from the IRIS database for a set of digital seismic stations within 30 degrees of the mainshock. We individually pick regional travel-time data for all of the aftershocks of this Tibetan earthquake, pick all regional phases than can be identified (Pn, Pg, Sn, Lg), and explore the use of S-phases for location. We merge these regional picks with the global catalog picks from the Reviewed Event Bulletin (REB) developed by the prototype International Data Center (pIDC) and the USGS Earthquake Data Reports (EDR).

For the seismic event relocation procedure (described below), two types of errors are used to provide weighting of the arrivals for the inversions: modeling and measurement errors. Measurement error is the error associated with the travel-time picks, and can be estimated using signal-to-noise ratio (SNR) criteria. However, many of the global picks do not include signal-to-noise ratio (*snr*) information. Furthermore, arrival times from global catalogs can have varied quality. For many arrival times reported to the USGS catalogs of the Chinese Digital Station Network (CDSN), travel times can have round-off or truncated reported times (Steck *et al.*, 2000). Thus, for consistency and for handling the uncertainty of the travel-time picks, we assign measurement errors for regional *P*- and *S*-waves to be

1.0 s and 2.0 s, respectively. For the global catalog times, we assign the measurement errors for *P*- and *S*-waves to be 2.0 s and 3.0 s, respectively.

Modeling error, which is the error associated with the inadequacy of the velocity models to account for earth structure, affects the error ellipse estimation. For 1-D velocity models, the modeling error can be parameterized as a function of radial distance. We use the regional models from previous studies and the modeling errors that we developed for those models using teleseismic locations (Jih, 1998; Li and Mooney, 1998; Steck *et al.*, 2000). We also calculate travel times for *S* phases for these same 1-D velocity models, and add a Tibetan model (Jih, 1998).

This region has some of the most dramatic crustal structure in the world, making 1-D velocity models particularly inadequate. Furthermore, for seismic events in the regional context, the number of observing stations is small and the SNRs of seismic phases can be low, contributing to location errors. Therefore, we also employ 2-D travel-time corrections (or propagation path corrections - PPCs) based on residuals for regional 1-D velocity models that were developed using a kriging interpolation algorithm (Schultz *et al.*, 1998; Steck *et al.*, 2000). The advantage of using the kriging algorithm is that travel-time corrections and modeling error can both be estimated. The use of these 2-D travel-time corrections removes the 20-km location bias observed for the Tibet mainshock event (Steck *et al.*, 2000).

Synthetic Tests and Relocation Procedure

The location algorithm is based on a Geiger method implemented using the EvLoc algorithm (Bratt and Bache, 1988; Nagy, 1996). The method has been modified to include 2-D kriged travel-time correction surfaces (Schultz *et al.*, 1998). To assess whether we have adequate azimuthal station coverage to obtain precise locations on the fault, we perform a suite of synthetic tests using the station and phase information that we have for the aftershocks. We select several events of various magnitudes and place them on the main and secondary ruptures to generate synthetic arrival data. Using our measurement error criteria as discussed above, we perform inversions to check that we obtain the synthetic locations. We then add gaussian noise (dependent on estimated pick and model error) to the picks, and perform the relocations. We perform this set of inversions ten times, with each run generating gaussian noise for the picks (Figure 2). This was done to test how well events could be constrained on the ruptures given normal arrival pick errors, with the velocity model known.

To assess the lateral resolution that we are obtaining, we fix the depth. We calculate the average mislocation for the suite of synthetic relocations to be ~5 km. Thus, given any noise in our data sets, we can expect to be within 5 km of the actual epicenter at best. This number, of course, will vary per event. Furthermore, we discover that our error ellipse estimates appear to be slightly low, as two of the ten events lie outside of the 90% error ellipse. Thus, we find that for events in the region, we should be able to obtain locations within 5 km of the fault given adequate data, and that we are slightly underestimating the error ellipses.

We attempted to include S phases as a means of improving the relocations for all the events shown in Figure 1 that had *S-wave* picks (Figure 3). PPCs were used for P phases in the locations. When including the S phases, many of the events could not be relocated due to residual restrictions (Figure 3a). Also, the mainshock location displays the southern bias observed in the catalog location. When S phases are excluded (Figure 3b), the mainshock is located on the main surface rupture. The location bias observed when including the S phases is not surprising given that there are no PPCs currently calculated for the S-wave models. Thus, we decided not to use S phases for relocating any of the candidate secondary rupture events.

Search for Secondary Rupture Event

As the first step in determining the candidate events for the secondary rupture, we determined which of the events from the EDR catalog were within the time period for the InSAR satellite pass and after the mainshock (08 NOV1997 - 02 DEC 1997) (Peltzer *et al.*, 1999). Of the events located near the main and secondary ruptures, 42 were possible candidates for the secondary rupture (Figure 1).

We placed the 42 candidate events on the secondary rupture, fixed the location and depth (3 km), and relocated using the IASP91 velocity model. The resulting values for the standard error for one observation (SDOBS) were analyzed to find the minimum values. Those events with low SDOBS values would become the best candidates for the secondary rupture. We chose a value of 3.0 s for SDOBS as a first cut for the 42 candidate events, leaving 11 events for further analysis.

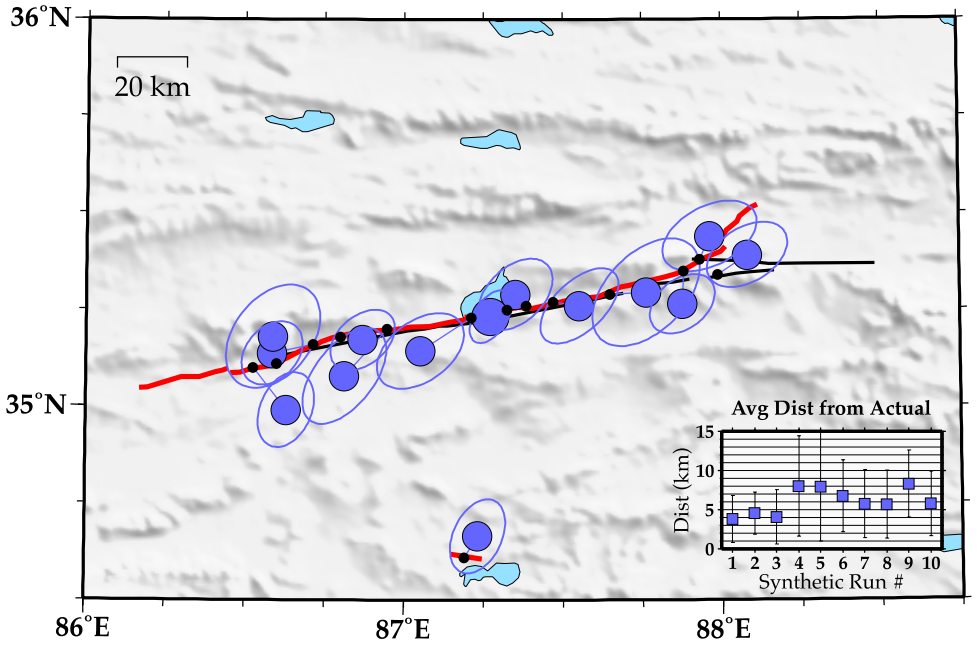


Figure 2. Relocations and 90% error ellipses for synthetic data. Data generated for select events around and including the main Manyi event on 08NOV1997. Selected events were placed on the main and secondary ruptures (black dots) to generate synthetic arrival data with added gaussian noise. This was done to test how well events could be constrained on the ruptures given normal arrival pick errors, with the velocity model known. Depth fixed at 33 km. Inset: Average distance from actual synthetic origin for ten synthetic location runs.

Of the 11 events above, we determined which had the lowest average residuals. We limited this analysis to only regional stations with 2-D travel-time correction surfaces. We calculated which events had the greatest percentage of phase residuals below 4.0 s, since the events all have differing number of defining phases. Any events with less than five regional defining stations before relocation and less than 50% of phases with absolute residuals below 4.0 s were discarded. We also tried to limit the remaining events to those with a relatively large percentage of manually repicked phases, leaving six candidate events. We further limited the remaining candidate events by discarding events that were obviously at too great a distance to be associated with the secondary rupture, which left three events (Figure 1).

We estimated the size of the event that caused the secondary rupture to be between M_w = 4.8-5.1, using the equation for moment magnitude (Lay and Wallace, 1995). The secondary rupture is ~5 km in length and has a displacement measured at least 0.1 m. The magnitude range was determined using a range of rupture depths from 1-5 km. After analyzing the waveforms of the three candidate events, we were able to discard one event based on the low SNR of the first arrivals at relatively near stations (MAKZ and LSA).

In order to investigate the two remaining candidate events (Figure 1), we analyzed waveforms for the first P arrivals and the Rayleigh waves for station MAKZ (Figure 4). The P arrivals display a similarity suggesting a common mechanism. We filtered the waveforms between 15 and 30 s to analyze the Rayleigh waves. Offset in the Rayleigh waves suggests a separation of ~29 km between the two events, relative to station MAKZ. The catalog locations display this approximate relative separation, as should any relocations.

Relocation Results

The relocations for the two remaining candidate events are shown in Figure 3. We relocated the events using three different global and regional velocity models [IASP91, SSB (Jih, 1998), and TIBET (Jih, 1998)], PPCs when available (the TIBET model does not have calculated PPC surfaces), and a depth fixed at 3 km. To show relative

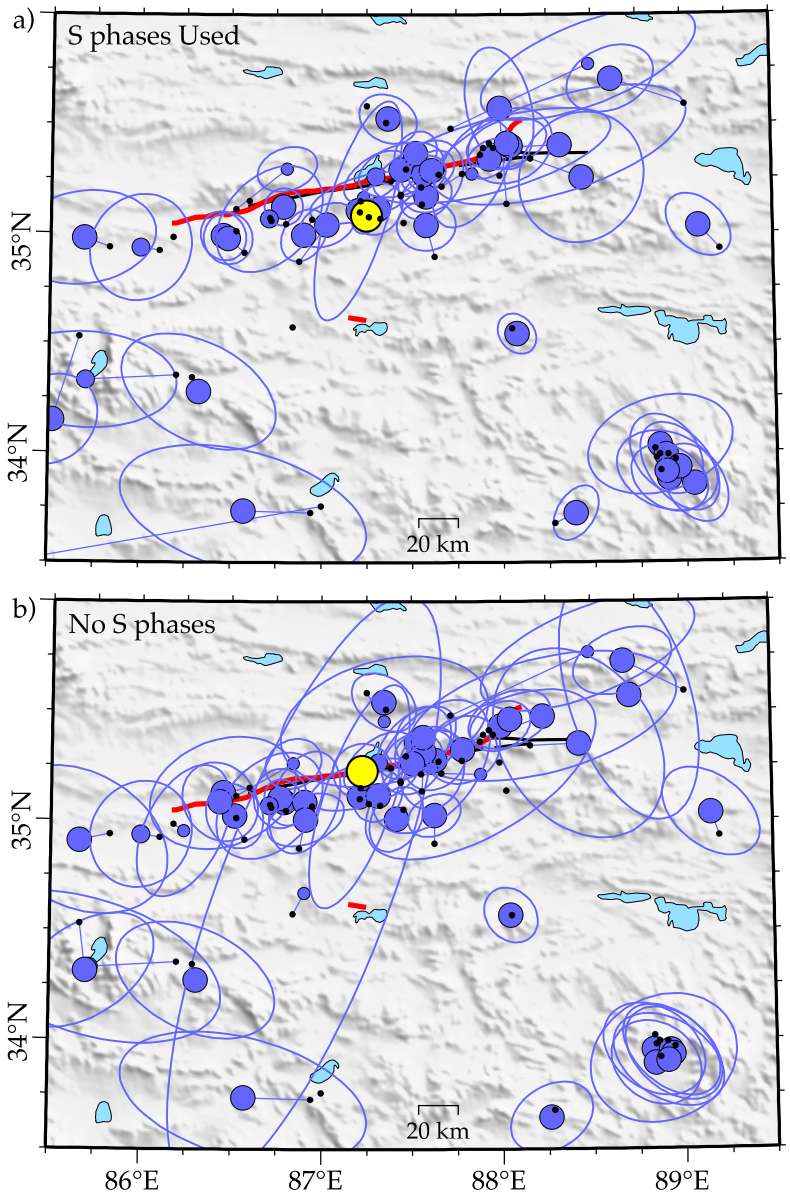


Figure 3. Relocations and error ellipses for EDR catalog locations around the 08NOV1997 Tibet mainshock only for those events which had S phases. 2-D travel-time corrections were used. Catalog locations are shown as black dots. a) S phases included in the relocation. Using S phases in the relocations does not correct for the southern bias in the mainshock (yellow). Several events were not relocated due to residual restrictions. b) Relocations without including S phases. The mainshock relocates to the trace of the main rupture.

relocation differences between the candidate events, we restricted the stations used in the relocation to those common to both events.

The relocations appear to migrate towards the main rupture surface instead of the secondary rupture surface. The SSB model actually shifted the 19NOV1997 event to the main rupture surface trace. The above suggests that both candidate events were, most likely, located on or near the main rupture. The 90% error ellipses for the relocations also do not encompass any part of the secondary rupture. The relative distances between the relocated events are

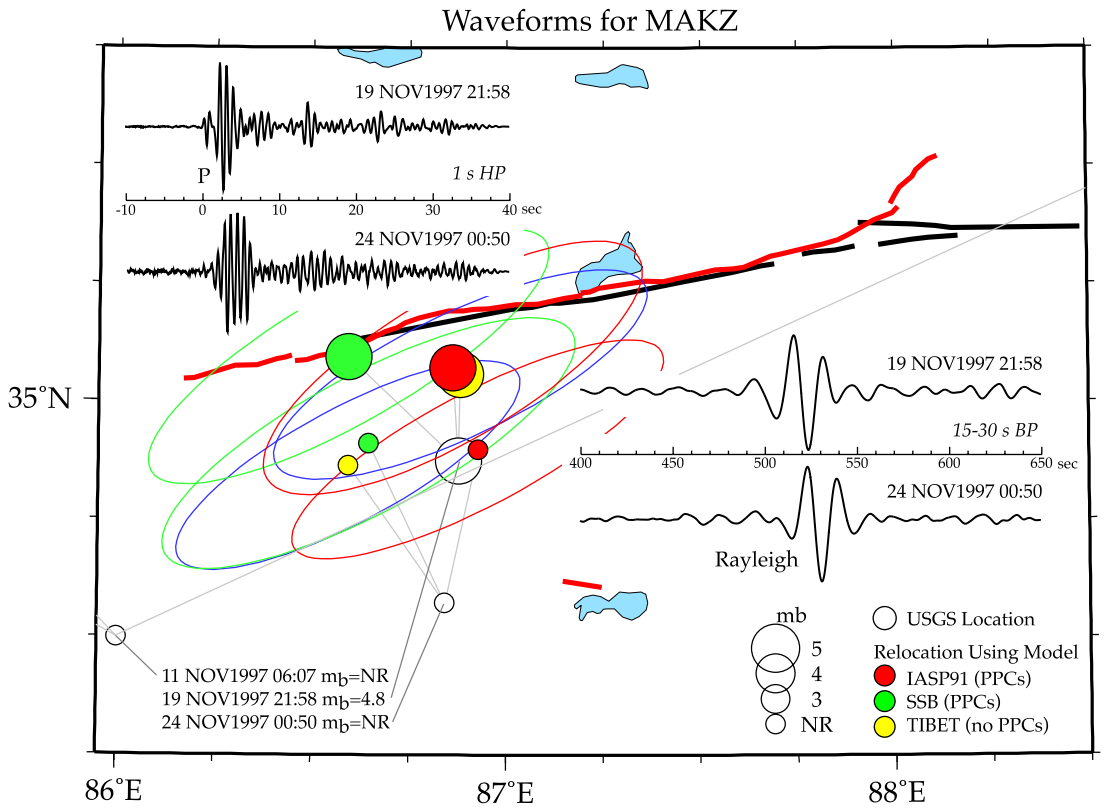


Figure 4. Catalog locations, relocations, and 90% confidence ellipses for two possible secondary rupture events. Both occurred during the appropriate time window (08NOV1997-02DEC1997). Relocations were determined using propagation path corrections (PPCs) when available and only those stations common to both events (i.e., ASAR, CMAR, FINES, GERES, HYB, LSA, MAKZ, SHL, WRA). IASP91 (red), SSB (green) (Jih, 1998), and TIBET (blue) (Jih, 1998) velocity models were used for the relocations. A third candidate event (lower left) was discarded due to low signal-to-noise ratio and relocation instability. Waveforms are shown for station MAKZ around the P (top left, 1-sec high-pass filter, time-aligned on P arrival) and Rayleigh arrivals (right, 15-30 sec band-pass filter, absolute time). The P-waves display a similarity suggesting a common mechanism. The offset in the Rayleigh waves indicates a separation of ~29 km between the two events, relative to station MAKZ. The relocated epicenters display this approximate separation. This suggests that neither event is related to the secondary rupture.

consistent with the ~29 km separation indicated by the Rayleigh wave offset. This again suggests that the candidate events are not associated with the secondary rupture.

We also relocated the candidate event above that was discarded due to lower than desired SNR at nearby stations. Using regional stations only with PPCs, the event relocated from ~106 km to ~28 km from the secondary rupture, the only event to relocate in relative proximity to the secondary rupture. However, when limiting the stations used to those common for the two candidate events above, the event relocated off the view of Figure 3, with one velocity model relocating the event far east, and the other two models relocating the event far west. Although this event did relocate near the secondary rupture, its instability precludes us from identifying it as the secondary rupture event. The lack of any candidate events to relocate close to the secondary rupture suggests that the secondary rupture was aseismic in nature or, most likely, coseismic with the mainshock event.

CONCLUSIONS AND RECOMMENDATIONS

InSAR can be a valuable tool for ground-truth tests of event locations, particularly for those associated with CTBT studies. InSAR has already been successfully used as a ground-truth test for the relocation of the Tibet mainshock using 2-D travel-time corrections, removing the 20-km location bias (Steck *et al.*, 2000). We were able to limit the possible secondary rupture events by using synthetic tests with events restricted to the rupture trace identified by InSAR. InSAR also provides a means of estimating magnitude by providing information on fault displacement and area. Using this information, we were able to estimate the magnitude for a secondary rupture event at M_w = 4.8-5.1 which should have been detected by stations within regional distances. Analysis of the travel time residuals and the relocation results suggests that no cataloged event can be associated with the secondary rupture. Thus, the secondary rupture was aseismic in nature or, most likely, coseismic with the mainshock.

REFERENCES

Bratt, S. R., and T. C. Bache (1988). Locating events with a sparse network of regional arrays, *Bull. Seism. Soc. Am.* **78**, 780-798.

Dewey, J. W. (1983). Relocation of instrumentally recorded pre-1974 earthquakes in the South Carolina region, in *Studies related to the Charleston, South Carolina, earthquake of 1886*, G. S. Gohn (Editor), *U. S. Geological Survey Professional Paper 1313*, Q1-Q9.

Jih, R.-S. (1998). Location calibration efforts in China, in *Proc. of the 20th Annual Seismic Research Symposium,* 12.

Lay, T., and T. C. Wallace (1995). *Modern global seismology*, Academic Press, San Diego, California, 521 pp.

Li, S., and W. D. Mooney (1998). Crustal structure of China from deep seismic sounding profiles, in *Proc. of the 7th international symposium on Deep seismic profiling of the continents, Tectonophysics,* **288***,* 105-113.

Molnar, P., and W.-P. Chen (1983). Focal depth and fault plane solutions of earthquakes under the Tibetan Plateau, *J. Geophys. Res.* **88**, 1180-1196.

Myers, S. C. and C. A. Schultz (2000). Improving sparse network seismic location with Bayesian kriging and teleseismically constrained calibration events, *Bull. Seism. Soc. Am.* **90**, 199-211.

Nagy, W. (1996). New region-dependent travel-time handling facilities at the IDC: Functionality, testing, and implementation details, *SAIC Tech Rep. 96/1179*, 57 pp.

Peltzer, G., F. Crampé, and G. King (1999). Evidence of nonlinear elasticity of the crust from the Mw7.6 Manyi (Tibet) earthquake, *Science* **286**, 272-276.

Schultz, C. A., S. C. Myers, J. Hipp, and C. J. Young (1998). Nonstationary Bayesian kriging; a predictive technique to generate spatial corrections for seismic detection, location, and identification, *Bull. Seism. Soc. Am.* **88**, 1275-1288.

Steck, L. K., A. A. Velasco, A. H. Cogbill, and H. J. Patton (2000). Improving regional seismic event location in China, *Pure & Appl. Geophys.* in press.

Tapponnier, P. and P. Molnar (1977). Active faulting and tectonics in China, *J. Geophys. Res.* **82**, 2905-2930.

Velasco, A. A., C. J. Ammon, and S. L. Beck (2000). Broadband source modeling of the November 8, 1997 Tibet (Mw = 7.5) earthquake and its tectonic implications, *J. Geophys. Res.* in press.

REGIONAL SIGNAL CHARACTERISTICS FOR USE IN SCREENING SEISMIC EVENTS IN ROCKBURST AREAS

Theron J. Bennett, Margaret E. Marshall, and Ronald W. Cook
Maxwell Technologies, Inc.

Sponsored by The Defense Threat Reduction Agency
Arms Control Technology Division
Nuclear Treaties Branch

Contract No. DSWA01-98-C-0153

ABSTRACT

Because of their shallow focal depths, small magnitudes, and often anomalous focal mechanisms, rockbursts may sometimes be difficult to discriminate from other seismic source types. The goals of this research project are to improve CTBT monitoring capability in the vicinity of rockburst areas by carefully analyzing the characteristics of rockburst sources and signals and to develop better regional discrimination techniques for these events using International Monitoring System (IMS) station observations. To accomplish this objective we have collected PIDC data from more than 1000 events in the vicinity (within 50 km) of 35 known historical rockburst sites worldwide for the five year time period starting at the beginning of 1995; 27 other sites of historical rockburst produced no events in the REB during this time period. Based on these REB data, the most active rockburst areas were found to be in Poland, the Kola Peninsula in northern Russia, and South Africa; but rockburst areas in North America, Germany, Tajikistan, and Japan have also been investigated. Although the majority of these events had REB magnitudes in the range $3 \le m_b \le 4$, very few (n = 5) were "screened" by the nominal screening procedures at the PIDC. A somewhat larger number (n = 49) were "not-screened," but most were "not considered" or had "insufficient data" for screening. We have analyzed the PIDC screening results for these rockburst events in detail, and they indicate that teleseismic discrimination procedures are not likely to be effective for screening these rockburst sources. However, there does appear to be some evidence that regional signals recorded by IMS stations from events in these rockburst areas may have differences related to source type. We are, therefore, focusing on several regional phase signal measurements; and we have been developing parametric measures, which have been indicated in some prior regional discrimination studies, to evaluate their potential value for screening and event identification in rockurst areas. For use in these studies, waveform data have been retrieved from regional (Δ less than about 20°) IMS stations for event samples from each of the 35 historical rockburst areas described above. For several more active areas (like Poland and South Africa) larger data samples have been retrieved to analyze variability in the regional signals between events. The regional discriminant measures being investigated include L_g/P ratios, L_g spectral ratios, regional LP signals, and regional phase complexity. We have also been seeking to establish better ground truth for events in some of the rockburst areas. In particular, several events in the western U.S. are known, from local seismic network operations, to be associated with mine collapses, mine explosions, and earthquake activity in Utah and Wyoming. We have retrieved IMS station records from several of these events and are comparing signal characteristics between these different source types and also with older recordings of NTS explosions recorded for similar paths, and at some common stations, to help define source-related differences. We hope to establish similar ground truth for some of the other more-active historical rockburst source areas.

OBJECTIVE

Rockbursts present several unique challenges for seismic discrimination and event screening in the CTBT monitoring environment. Rockbursts are located in approximately the same depth range as nuclear tests, so depth discriminants are likely to be ineffective. Some rockburst mechanisms produce relatively weak long-period surface waves which could negate screening based on M_S-vs-m_b. Since many rockbursts are small, their screening is likely to depend heavily on observations from a few regional stations. The current studies will identify rockburst regions with respect to their significance to CTBT monitoring and focus on the performance of three promising discriminant measures for use in IDC event screening in those regions. The research program includes the following elements: (1) systematic collection of IDC data for events in known rockburst areas worldwide, (2) determination of S/P or L_g/P ratios for events from rockburst areas, (3) measurement and analyses of complexity of regional signals from evens in rockburst areas, (4) determination of LP surface-wave excitation for events in

rockburst areas, (5) relation of the range of behavior of observed signal characteristics to those expected from reported rockburst and other source mechanisms, and (6) prediction of seismic signal and discrimination behavior for significant rockburst areas worldwide.

RESEARCH ACCOMPLISHED

In prior reports on rockbursts, we have noted that mining-induced seismic activity occurs in mining regions all over the world. In assessing what impact these events have on CTBT monitoring at the IDC/PIDC, we have first identified where historical rockbursts (including all types of mining-induced events) have occurred and then looked more closely at the events reported in the PIDC REB bulletins in the vicinity of those locations for the time period 1995 – Present. Figure 1 shows 104 locations worldwide where we have found reports of apparent mining-induced seismic activity. This is an increase of about 40 locations from the map which we previously published (cf. Bennett et al., 1999), and will no doubt continue to grow. The majority of the new locations, which we have identified, are in the U.S. or Canada; this is at least partly because information on mining activity in these areas is more readily available. In many cases, the new locations represent refinements of old locations where we have now identified separate mines with associated induced activity (e.g. in Ontario Province, Canada). However, in some cases the mine locations may be significantly separated; so it is probably better to keep a more complete list. The mapped locations also include a few new areas where mining-induced activity has been reported (e.g. Alaska, western Washington, and Vancouver Island). 1122 events are included in the PIDC REB bulletins within 50 km of 43 historical rockburst locations; these locations are shown as closed circles on the map. It should be noted that, while no REB events have occurred in the vicinity of the remaining 61 historical rockburst locations, there are small seismic events (below the REB threshold) occurring in many of these areas. There is also a potential for somewhat larger mining-induced events in most areas. Most of the 1122 REB events near the historical rockburst sites occur in just a few areas: (1) three areas in Poland, (2) a mining area on the Kola peninsula in Russia, and (3) five areas in the gold mining region of South Africa. However, a few other broader scale mining areas have been the locations of several REB events; these include several mining areas in North America, Germany, Tajikistan, and Japan. The majority of the REB events from the rockburst areas have magnitudes in the range 3 – 4.

Nominal PIDC screening procedures fail to provide event discrimination for almost all events in rockburst areas. Less than 0.5 % of the more than 1000 events from the seven mining areas denoted above are "screened out" by the nominal procedures based on event focal depth and M_S-versus-m_b; that is, these events cannot be reliably designated as earthquake-like by the nominal criteria. This is probably to be expected, since most events in these rockburst areas occur at shallow depths and many seem to be inefficient in generating LP surface waves (cf. Bennett and McLaughlin, 1997). At last year's meeting, we presented detailed analyses of the actual discriminant measures for 5 events, which were "screened out," and 49 events, which were "not screened," from these seven areas. However, it is probably more significant that the large majority of the REB events from these mining areas are categorized as having "insufficient data" or "not considered." Although 90% of the REB events in these areas had magnitudes greater than 3.0, some have M_L but no m_b; and about half would fall below the somewhat arbitrary cutoff of $m_b \geq 3.5$ to be considered for PIDC screening. For most events in these areas, there is no indication of focal depth; and LP surface wave magnitudes have not been measured. So, in general the data available at IMS stations for applying the nominal teleseismic screening procedures are not adequate for characterization of events from most rockburst areas.

Because many rockbursts are small, the strongest seismic signals are often those recorded at regional stations. By comparing IMS station observations for events from the vicinity of historical rockbursts with similar observations from outside those areas, we have found some systematic differences in several regional signal parametric measurements, which are routinely determined at the PIDC/IDC. For example, observations of short-period/long-period (SP/LP) energy ratios seem to indicate that events from rockburst areas have more high-frequency energy relative to low-frequency energy than events from outside those areas. Assuming that events from the rockburst areas are more likely to be rockbursts and those from outside the areas are more likely to be earthquakes, this result may have implications for source characterization of regional events. We also found that on average L_g/P_n and S_n/P_n ratios in several different frequency bands appeared to be systematically larger for events from within rockburst areas compared to events outside. There were also indication in the L_g spectral ratios that events from rockburst areas tended to generate relatively more high-frequency L_g than sources outside the areas. We have also been looking into two other measurements which may be useful for characterizing rockburst events at regional distances:

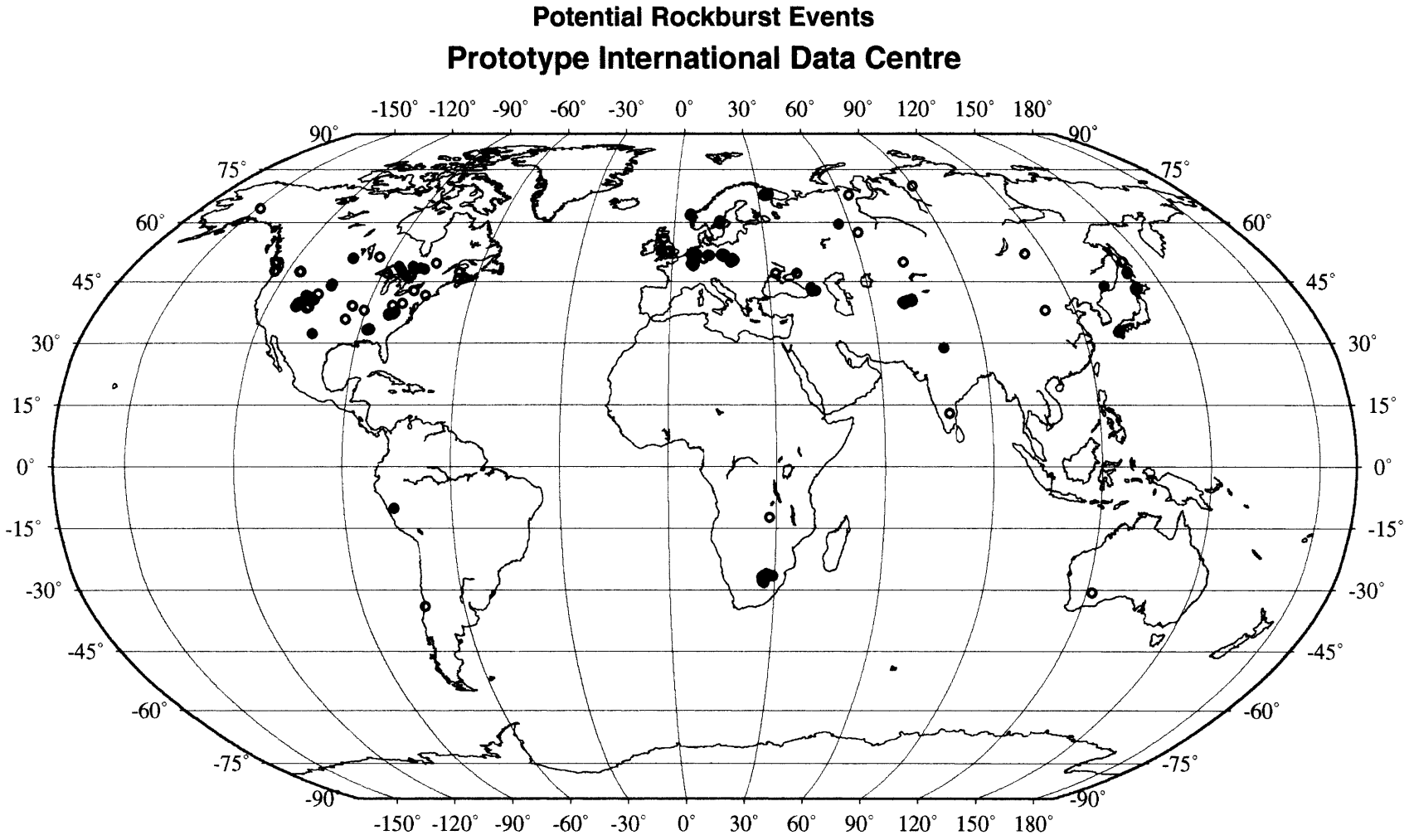


Figure 1. Locations of 104 historical rockburst areas worldwide. 1122 PIDC REB events have occurred within 50 km of 43 sites (closed circles) but no REB events at other sites (open circles).

regional P-wave complexity and regional LP signals. We have made some systematic measurements on the regional P signals recorded at IMS and other stations for selected events in some more-active rockburst areas and compared signal duration and envelope characteristics with similar measurements for other source types in the same region at comparable distances. We are currently analyzing these results to identify any differences. To analyze regional LP signals, we have attempted to isolate low-frequency surface-wave signals on the broadband IMS station recordings for several events from selected rockburst areas using low-frequency band-pass filters. Although we have recovered some reasonable LP signals for some small rockburst events, the signal-to-noise levels are often small; and comparisons between events may not be reliable. More robust signal processing schemes may be required to determine reliable LP surface-wave signals from these small regional events.

To better understand the variability between rockburst sources and to evaluate potential regional discriminant measures more completely, we have been attempting to develop improved ground truth for events in several areas. One of the most active rockburst areas in North America is the Wasatch Plateau-Book Cliffs coal mining area in southern Utah (cf. Arabasz and Wyss, 1999). Events as large as 4 M_L occur in association with longwall mining in this area; and several events from this area are included in the PIDC REB (cf. Figure 2). This area of the western U.S. is particularly interesting for seismic event discrimination because it includes a variety of seismic source types (viz. rockbursts, mineblasts, nuclear tests, and earthquakes) recorded at similar distances and in similar propagation environments. In addition to the Utah rockbursts, a trona mining area just north of the Utah border in southwestern Wyoming has been the site of several mine collapses, including one of the largest induced mining events ever in North America (a 5.2 m_b event on 1995/02/03). In addition to the mining-induced activity, there is significant commercial blasting activity associated with mines in northwestern Colorado, southwestern and eastern Wyoming, and southern Montana. Many of these have been large enough to be included in the REB. Natural earthquake activity extending along the Wasatch front and other areas of the southern Basin and Range provide alternative source types for comparison. Finally, nuclear tests at NTS, recorded in some cases at seismic stations common to the PIDC and at similar distances, provide a unique database for careful comparison of regional seismic signal characteristics from the different source types important to CTBT monitoring. It is also noteworthy that we have excellent ground truth information for many of these events from the local seismic network operated by the University of Utah, as well as from reports on blasting activity at U.S. mines now being reported by the USGS. As a result, we are able to associate individual mine tremor events in Utah with specific mines. The event locations we show in Figure 2 are, except for nuclear tests, the PIDC REB locations. For most events we have alternative ground truth locations based on the local network information which in some cases show large differences compared to the REB. For example, there is a 1999 mineblast plotted in the south-central Utah rockburst area in Figure 2, which based on USGS ground truth information actually occurred more than 300 km to the south in northern Arizona. For each of the ground truth events in Figure 2, we are collecting the available IMS station waveform data, as well as other regional waveforms for some of the older nuclear tests; and these will be used to test and analyze the potential regional discriminant measures described above.

Another example of improved ground truth information for events in one of the more active rockburst areas is shown in Figure 3. Europe has several notable historical rockburst areas, including some that produce large and numerous seismic events. As noted previously, there are two very active mining areas in Poland: (1) in the vicinity of copper mines near Lubin (at about 51.5° N 16.0° E) and (2) at coal mines in Upper Silesia (centered near 50.5° N 19.0° E). These sources produce the largest number of REB events in the vicinity of known rockburst areas and have included large events with magnitudes as great as 5 m_b, although the largest since the start of the PIDC REB bulletins has only been 4.2 m_b. Another site of a large mining-induced event is in eastern Germany near Völkershausen, where a 5.4 m_b event occurred at a potash mine in 1989; however, this site has been relatively quiet since and has contributed little to the REB events list. In fact, in the REB there are several much more active rockburst areas in the Ruhr valley mines of western Germany (near 51.5° N 7.0° E), where events have reached 3.5 m_b, and in southwestern Germany near the French border (at about 49.0° N 6.5° E), where event magnitudes have reached 4.2 M_L. For each of these areas, there is fairly good coverage by local seismic networks; and we have been using information compiled by the Federal Institute for Geosciences and Natural Resources in Hanover, Germany (BGR) and by the Institute of Geophysics of the Polish Academy of Sciences to establish better ground truth for many of the PIDC REB events. As can be seen on the map in Figure 3, in addition to the rockbursts there are

numerous chemical explosions (e.g. near the Germany/Poland border and within Poland) and earthquake sources for which we are developing better ground truth information. For each of these events, we are also retrieving the available regional IMS station data for comparing and testing the potential regional discriminant measures for use in event screening at the PIDC/IDC.

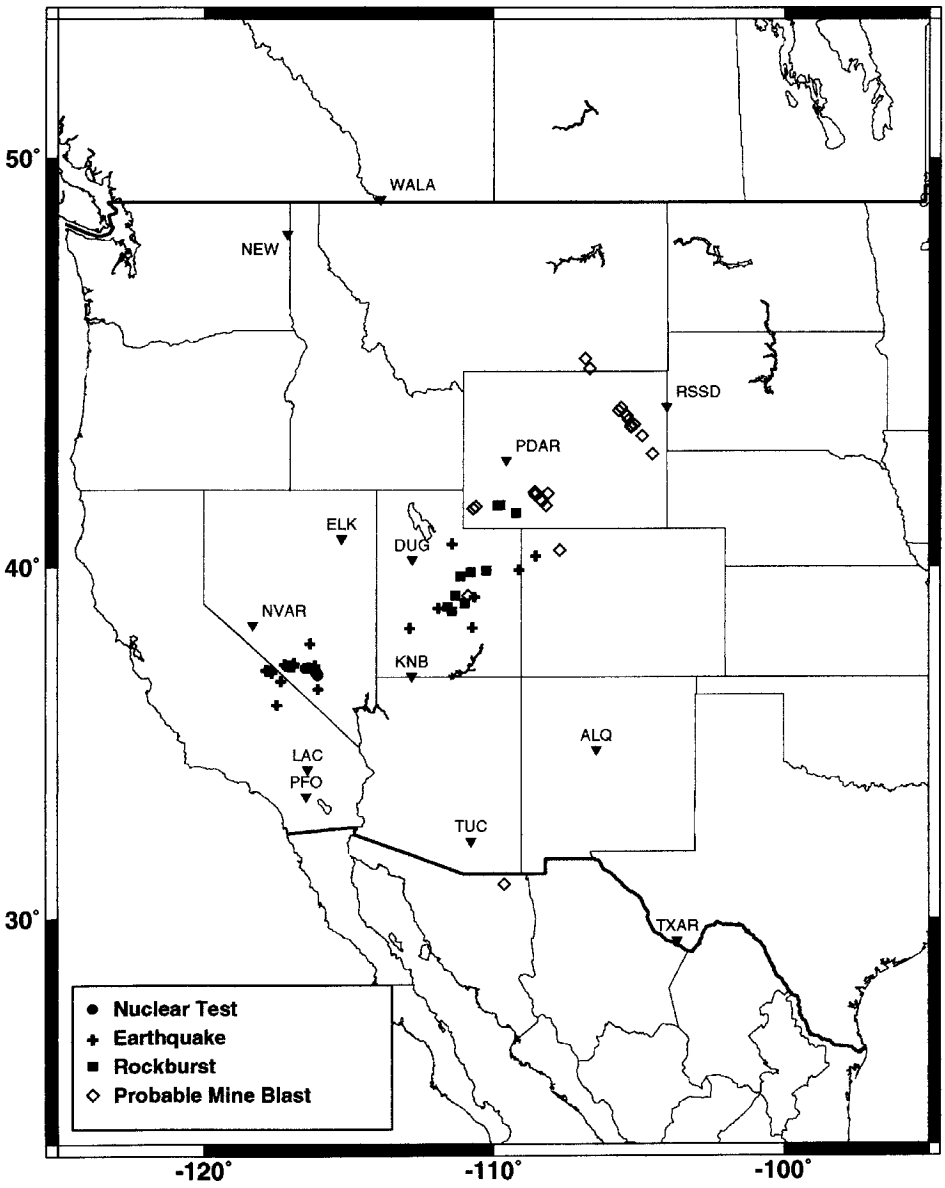


Figure 2. Locations of selected rockbursts, explosions and earthquakes recorded at the PIDC and other regional stations in the western U.S.

We have begun testing of the variability of regional discriminant measures for some of the events in the western U.S. shown in Figure 2 above. One of the most promising regional discriminant measures for use in event screening has been P/S or P/L_g amplitude ratios based on observations at regional stations (cf. Taylor et al., 1988; Bennett et al., 1992; Fisk et al., 1999). Bennett et al. (1996) suggested that there might also be systematic differences in the L_g/P ratios between rockbursts or mine tremors and underground nuclear tests. This is illustrated in Figure 4 where we compare the ratios for rockbursts in three different source areas with nuclear tests in two source areas. Although the results appear mixed at low frequencies, at higher frequencies the L_g/P ratios are on average larger for the rockburst events than for the nuclear tests.

To evaluate the reliability of this discriminant for event screening, it is necessary to have some idea of its variability between events. We have been looking at the regional phase signals at IMS stations for several of the Utah rockbursts and comparing them to similar measurements for other source types recorded at similar distances. Figure 5 shows the L_g/P amplitude ratios in different frequency bands for mine tremors at three coal mines compared to a Wyoming mine blast, a Utah earthquake, and the GORBEA nuclear test. It can first be noted that there is significant variability (about a factor of 4) in the ratios for several frequency bands

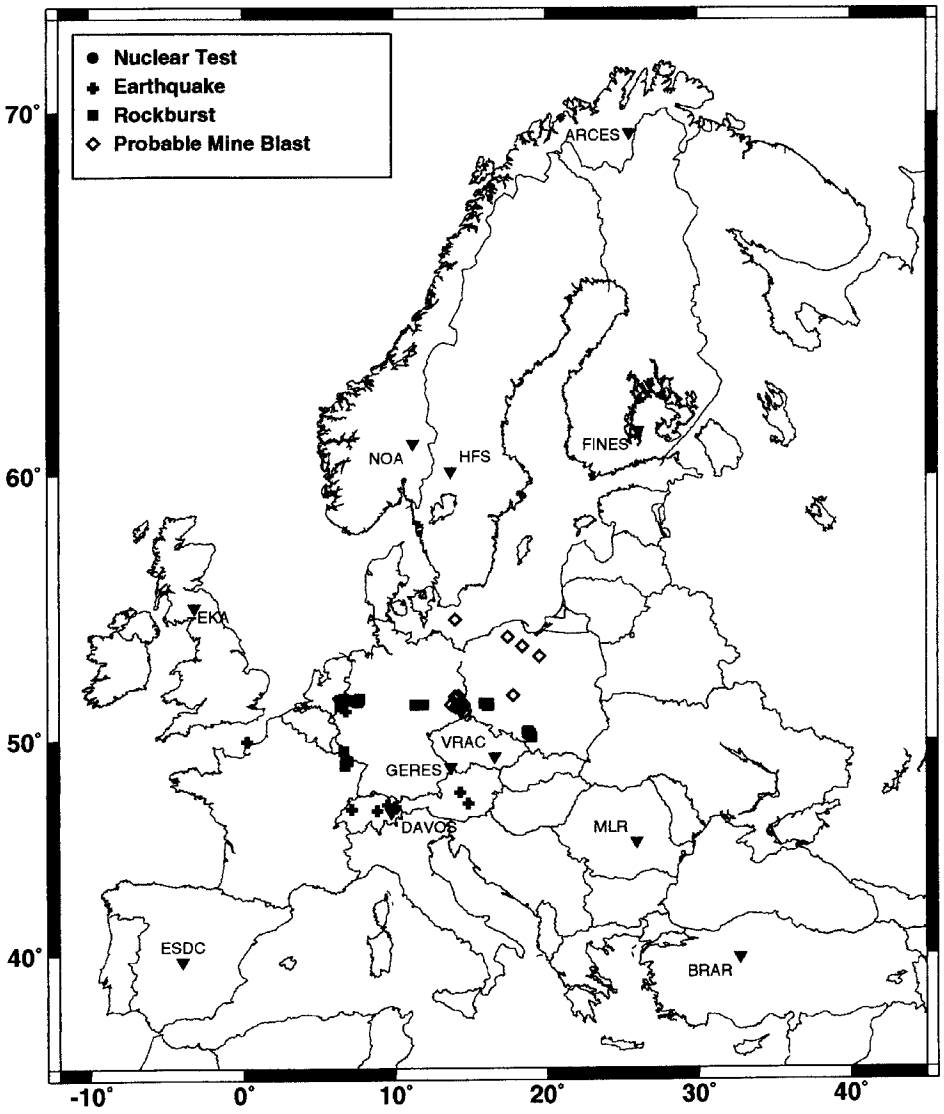


Figure 3. Locations of selected rockbursts, explosions and earthquakes recorded at the PIDC regional stations in Europe.

between the mining-induced events at different mines. Although further study is needed, this would appear to be a source effect and not a propagation effect, since the paths don't vary much between these events. It is also rather remarkable that the L_g/P_g ratios (shown in the top plot) are actually quite large for the nuclear test; in fact, the ratios for the nuclear test at high frequencies are almost as large as for the earthquake and larger than those for the mine tremors and mineblast. The L_g/P_n ratios (shown in the bottom plot) tend to be lower for the nuclear test; at high frequencies the ratios for the nuclear test and the mineblast tend to be similar and about a factor of two lower than the Utah earthquake and the Willow Creek mining-induced event. However, there is no discernible difference at high frequencies between the L_g/P_n ratios for the

Skyline mining-induced event and the nuclear test and mineblast. The behavior of the L_g/P ratios for GORBEA seems to be anomalous compared to the average behavior for NTS events, which we showed in Figure 4; this needs to be looked at more closely. We expect to see some differences in the L_g/P ratios between mining-induced events because of the effects of differences in mining practice on source mechanism (cf. Bennett and McLaughlin, 1997); we intend to investigate these differences with more observations from these mines and in other mining areas where we have good ground truth information. Alternative regional signal measurements need to be studied more thoroughly for application to cases where the L_g/P discriminant and associated screening procedures do not work.

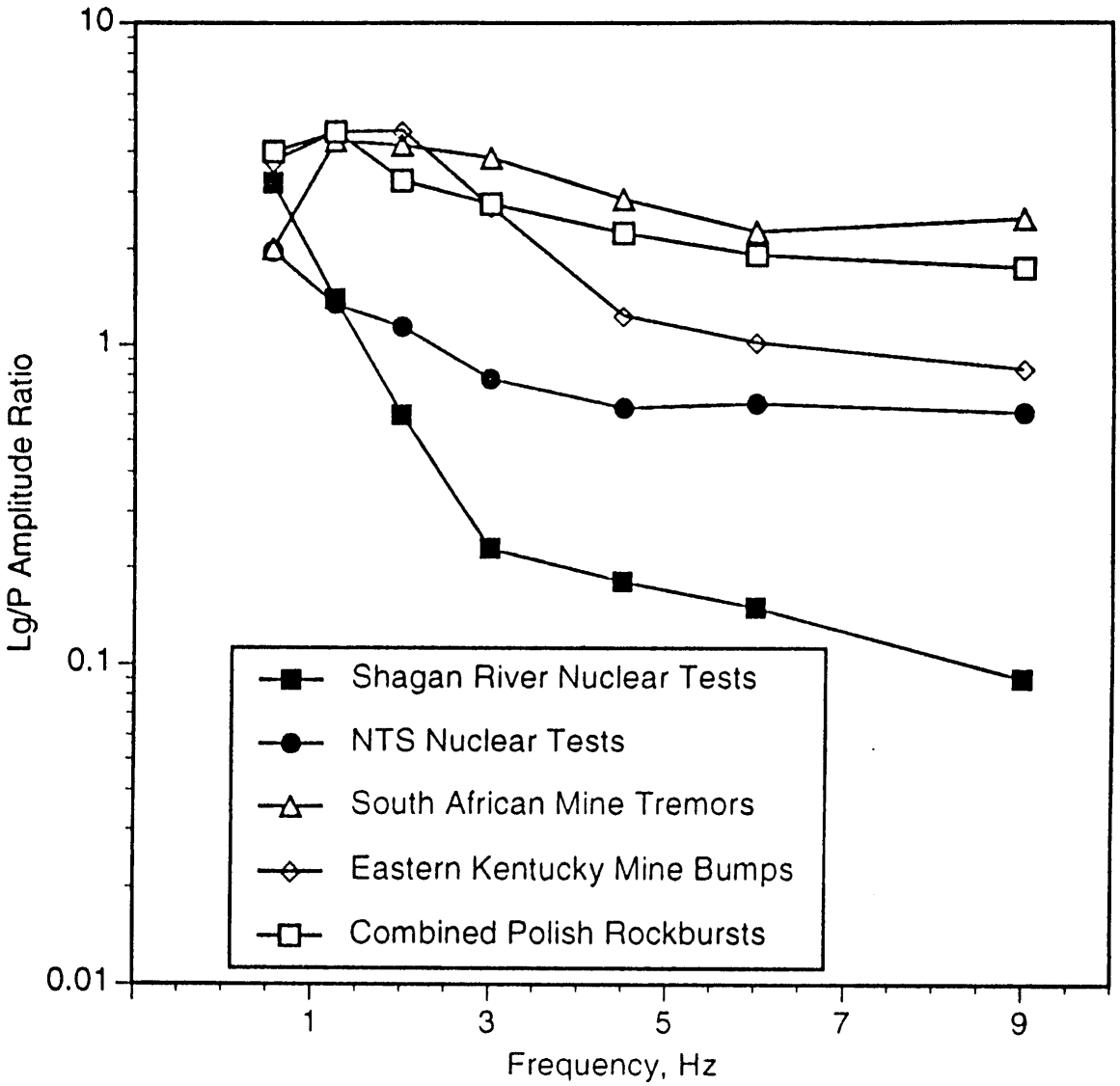


Figure 4. Comparison of Lg/P ratios in different frequency bands for rockbursts from three different source areas with average Lg/P ratios for nuclear explosion tests at NTS and Shagan River (cf. Bennett et al., 1996).

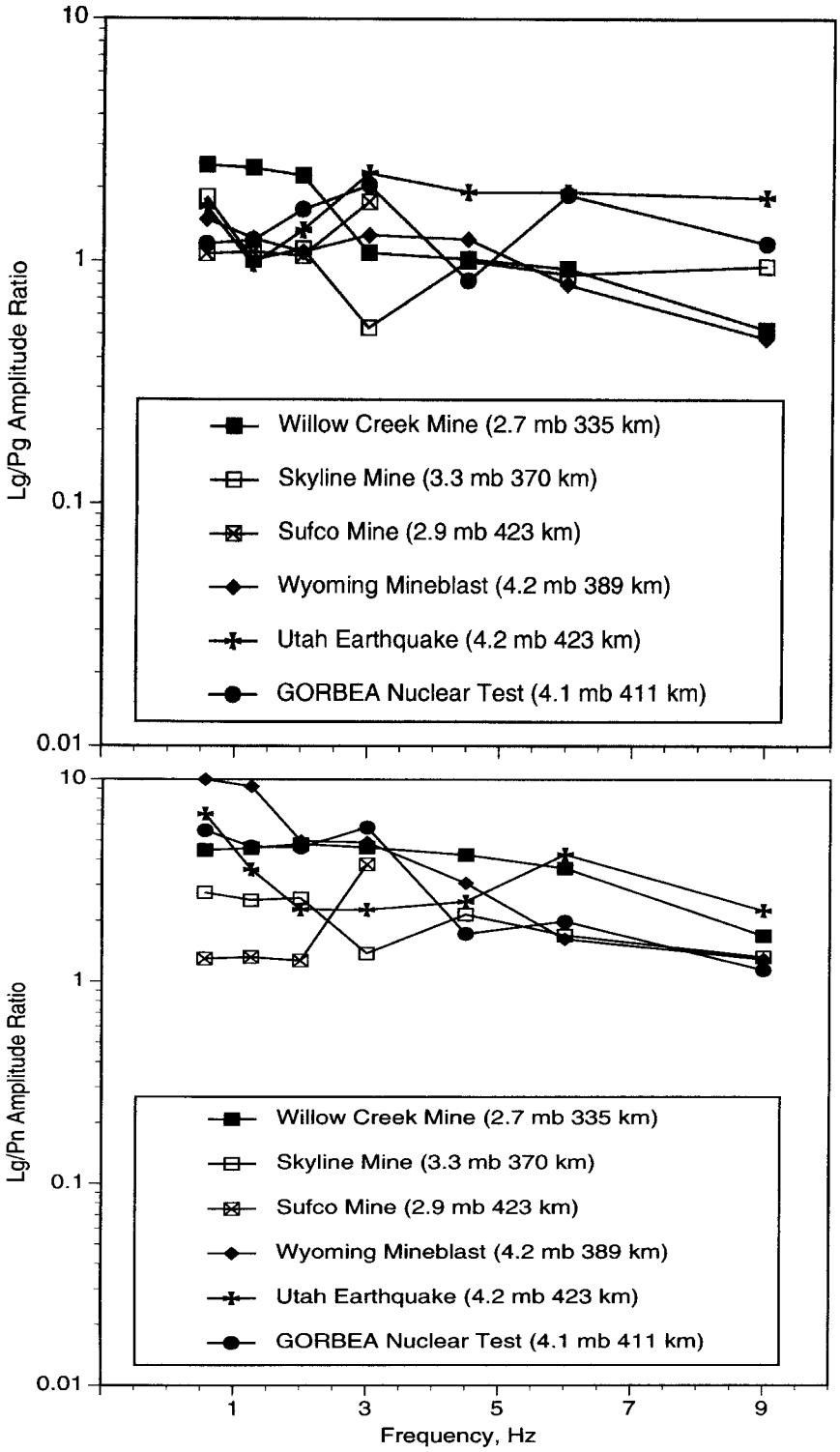


Figure 5. Comparison of Lg/Pg (top) and Lg/Pn (bottom) ratios in different frequency bands for several Utah mine tremors, a Wyoming mineblast, a Utah earthquake, and an NTS nuclear test recorded at similar regional distances.

CONCLUSIONS AND RECOMMENDATIONS

Rockbursts occur in mining areas throughout the world; and, although they are often small, there is a potential for larger events in most rockburst areas. Nominal PIDC/IDC screening procedures almost always fail in rockburst regions; the reason for failure is usually that the IMS station data at teleseismic distances are insufficient. Regional stations usually provide the strongest seismic signals from small rockburst events, and there appear to be some systematic differences in a variety of regional signal parametric measurements at IMS stations between rockburst and non-rockburst regions worldwide. We are continuing to investigate these and some other regional signal characteristics observed at IMS stations for selected events in a variety of rockburst areas where we have good ground truth. For one such area in the western U.S., where there is good ground truth for rockbursts, mineblasts, earthquakes, and nuclear explosions recorded at similar distances and similar stations, some preliminary results for screening with regional L_g/P ratios appear less promising than originally hoped. Further analyses and improved understanding of the variability in regional signal characteristics between events and between source regions are needed.

Key Words: seismic, screening, discrimination, regional, CTBT, PIDC, IDC, IMS

REFERENCES

Arabasz, W. J., and M. Wyss (1999), "Spatially-Varying b-Values in Coal-Mining Seismicity in Utah: Inferred Influence of Heterogeneity and Stress Differences on Local Mean Magnitude," Paper Presented at the 1999 Fall Annual Meeting of the American Geophysical Union.

Bennett, T. J., A. K. Campanella, J. F. Scheimer, and J. R. Murphy (1992), "Demonstration of Regional Discrimination of Eurasian Seismic Evnets Using Observations at Soviet IRIS and CDSN Stations," PL-TR-92-2090, ADA253275.

Bennett, T. J., M. E. Marshall, B. W. Barker, K. L. McLaughlin (1996), "Investigations of the Seismic Discrimination of Rockbursts," PL-TR-96-2184.

Bennett, T. J., and K. L. McLaughlin (1997), "Seismic Characteristics and Mechanisms of Rockbursts for Use in Seismic Discrimination," in Rockbursts and Seismicity in Mines, edited by S. J. Gibowicz and S. Lasocki, 61-66.

Bennett, T. J., M. E. Marshall, and R. W. Cook (1999), "Screening of Seismic Events in Rockburst Areas," Proceedings of the 21st Seismic Research Symposium, Las Vegas, 363- 373.

Fisk, M., S. Bottone, H. Gray, and G. McCartor (1999), "Event Characterization Using Regional Seismic Data," Proceedings of the 21st Seismic Research Symposium, Las Vegas, 427-437.

Taylor, S. R., N. W. Sherman, and M. D. Denny (1988), "Spectral Discrimination Between NTS Explosions and Western United States Earthquakes at Regional Distances," Bull. Seism. Soc. Am., 78, 1563-1579.

EMPIRICAL ANALYSIS OF A 3−D PAKISTAN REGIONALIZED VELOCITY MODEL FOR IMPROVED SEISMIC EVENT LOCATIONS

Michelle Bernard−Johnson, Shirley Rieven, Carolynn Vincent, Delaine Reiter,
Weston Geophysical

William Rodi,
Earth Resources Laboratory, Massachusetts Institute of Technology

Sponsored by U.S. Department of Defense
Defense Threat Reduction Agency
Contract No. DSWA01−98−C−0143

ABSTRACT

The objective of this project is to improve regional event location in Pakistan and the surrounding regions by developing a 3−D velocity model for the crust and upper mantle. The CTBT goal of 1000 km^2 location accuracy for small events is dependent upon the availability of such models, which can be used to compute accurate travel times of regional seismic phases. Our approach is to refine an *a priori* 3−D velocity model through joint nonlinear tomography and multiple event location applied to regional earthquake arrival time data. Previously, we presented our *a priori* model, which is constructed on a 1°−by−1° grid to a depth of approximately 100 km. The preliminary model exhibits complex structural variation in the Pakistan region with crustal thickness ranging from 25 km to 75 km, a clear deviation from 1−D global models such as the IASP91 model (Kennett and Engdahl, 1991).

We have generated 3−D *P*, *Pg* and *Pn* travel time tables at regional distances by applying the finite−difference raytracing method of Podvin and Lecomte (1991) to our *a priori* model. To test our model empirically, we have relocated a suite of 44 Calibration Event Bulletin events using *P* and *Pn* arrival times from 14 stations in the Pakistan region, reported to the International Seismological Centre (ISC). Locations obtained with the IASP91 travel time tables were compared to locations obtained with our 3−D travel time tables. While our 3−D model results in smaller rms residuals for 29 of 44 events, the tests are not definitive since ground−truth locations are not available and the depths of the events are poorly constrained by the regional data.

We are currently expanding our database to include 55,000 phase arrivals from over 4000 events recorded at 77 stations in the study region, which we are expanding to include additional parts of southwest India. The arrival time picks at these and teleseismic stations were reassociated, and the events relocated, by Engdahl *et al.* (1998), leading to high quality location estimates. Approximately ten percent of the event locations are classified as GT5 (5 km location accuracy) or better. Using the reassociated *P* times at the regional stations, we intend to relocate a subset of the events using both the IASP91 and our 3−D travel time tables. A more extensive evaluation of our 3−D model will then be possible by comparing rms residuals, as well as comparing our locations to those obtained by Engdahl *et al.* Furthermore, the residuals resulting with our 3−D tables will comprise the primary data set for tomographic updating of our *a priori* model. We are analyzing the spatial pattern of these residuals and raypath coverage in anticipation of performing the 3−D tomography.

Key Words: seismic, 3−D velocity model, location, Pakistan, tomography

OBJECTIVE

Precise location of seismic events in the context of the Comprehensive Nuclear−Test−Ban Treaty (CTBT) requires accurate velocity models. The purpose of this research is to construct a regional velocity model of the crust and upper mantle structure to improve seismic event locations for the area between 25 and 40 degrees North and 55 and 80 degrees East. This area lies between the eastern border of Iran and the western edge of the Tibetan Plateau. To date we have developed a database of regional seismic events and supplemental information that will be used to construct and refine the velocity model through the application of tomographic techniques. We generate travel times through the region using a finite difference travel time modeling algorithm (Podvin and Lecomte , 1991) and use our grid search algorithm for 3−D hypocenter relocation. We are developing a joint inversion technique that uses multiple event relocation (incorporating input from our database of phase arrivals) to constrain iterative perturbations of the velocity model. This joint inversion will provide the ‘‘best’’ fit, in the least−squares sense, between the observed and predicted arrival times. The end result will be a refined 3−D velocity model and improved multiple hypocenter estimates. In this report we describe the progress we have made towards building a high quality regional model during the second year of this three year project.

RESEARCH ACCOMPLISHED

Phase Arrival Database and 3−D Velocity Model Development and Testing

Two primary objectives during the first two years of this project have been to collect and refine a high quality database of phase arrivals and to develop a good 3−D preliminary velocity model over the region. Both the database and the 3−D velocity model can be used in tomographic studies as well as other related projects. During this reporting period we have addressed gaps in the ray−coverage over Pakistan by expanding our study area boundaries to the West (covering areas of Iran), North (including areas of Uzbekistan, Kyrgyzstan and Kazahkstan) and East (China and portions of northern India) where additional data were readily available. We are also expanding our region to the South to include areas of northwestern India. Below we detail some of the development and testing of the phase arrival database and 3−D velocity model that has occurred during the previous year.

Travel Time Database Improvements

Our initial effort to establish a database of regional phase arrivals began with the acquisition of bulletin data for approximately 700 seismic events. These phase arrivals were obtained from three online sources, including the Prototype International Data Center (pIDC), the International Seismological Centre (ISC), and the Incorporated Research Institutes for Seismology (IRIS). During the early stages of our research, we used these data to identify a set of test events that would contribute the "observables" portion of our input data and also provide a set of validation events. Because these events have been located by multiple organizations, the redundancy of hypocenter estimates and the availability of depth phase data provided a measure of the accuracy of the combined event catalog. Upon comparison of different estimates, it became apparent that the relative quality of the location estimates exhibited significant variation, particularly in depth. The pIDC reported very few ground truth (GT) events with location accuracies better than 25km (GT25). This lack of validation events presents a significant challenge in establishing a demonstrable advantage in using a 3−D model over the standard 1−D models currently used. In this performance period, we have investigated methods of addressing these concerns, and give details of some of these procedures later in the paper.

We have expanded our in−house database of phase arrivals by incorporating the results of very recent hypocenter relocation studies. In particular, we compared the relative hypocenter accuracies of the ISC catalog with those reported by Engdahl *et al*. (1998). In that study, the authors reassociated the ISC arrivals and then relocated the events using the AK135 velocity model. Our original database reflected the hypocentral estimates as reported only by the three locating agencies previously noted. For instance, the pIDC’s Ground Truth Database for the Pakistan region identified only 60 GT events during its period of data availability. Of those, only 7 are reported as being located with hypocenter accuracies better than GT 25 (one event, the 1974 Indian nuclear test, is listed as a GT0, while six events are classified as GT1, including the 1998 India and Pakistan nuclear tests). By comparison, the Engdahl *et al*. (1998) results report 2,181 events qualifying as GT10 or better (including 8 explosions), of which there are 426 events qualifying as GT 5 or better. The availability of these additional well located events improves our ability to verify the quality of our tomographically derived velocity model. In addition, the Engdahl

et al. (1998) database offers an additional advantage, because P waves were reclassified as Pn when appropriate. This provides an important data distinction that we take advantage of, since in our method we invert for these secondary arrivals using independently derived travel time calculations.

In summary, our database has expanded from 7,599 phase arrivals to 54,770 P, P*n*, and P*g* arrivals. These events are distributed in depth, with the predominant proportion (76.5 percent) being located within the top 100 km of the Earth's surface. The magnitudes of these events range from a high of 6.5 (m_b) to a minimum of 3.0. More than 80 percent of these events have at least 10 regional stations reporting phase arrivals A total of 77 regional stations contributed arrivals to the expanded database. We are currently in the process of evaluating the azimuthal gaps for these events. We will continue our effort to identify, evaluate and incorporate phase data from events with high quality location estimates . To ensure an independent test of our tomographic model, we will establish a set of our highest quality events to be used solely for verification purposes.. The remainder will be used in the tomographic inversion.

Velocity Model Improvements

High density, well distributed ray coverage is crucial to the success of a tomographic inversion, because it constrains the possible velocities for large portions of the model grid. We have increased the size of our study area to incorporate rays that travel significant distances within our contractual region but are not contained entirely within it. This increase in sudy size has required the collection of additional geologic and geophysical information to expand the model to the South into sections of India. There are a number of stations in this region that will provide travel times through the southeastern quadrant where the southwestern portion of the Indus Suture defines the convergence of the Indian plate with the Eurasian plate. Incorporating rays that cross this region is especially important for the purposes of CTBT monitoring because seismic events that occur near test sites would propagate rays through this region. Accurate hypocenter location estimates would rely heavily on the quality of the velocity model available for this region. In the following sections we cover some of the procedures we have implemented to test the validity of our input 3−D regional velocity model.

Velocity Model Testing Using Reciprocity

On 14 Feb 1977, a magnitude 5.2 earthquake (Table 1) occurred in the region near Nilore, Pakistan. The event forms an interesting test of reciprocity for the velocity model near station NIL. We collected arrival time data from 24 stations within our model region that recorded the event, and then compared the observed travel time residuals at these stations, with respect to the Jeffreys−Bullen (JB) global model, to the predicted travel time residuals computed using our preliminary 3−D model (Figure 1). The results show that our 3−D model predicts the regionally observed travel times better than the JB model by a factor of 1.5. We expect that the largest residuals between the predicted and observed travel times (Figure 2) will decrease following a full tomographic inversion of our dataset.

Date	***OT***	***Lat***	***Long***	***Depth (km)***	***Mag***
14 Feb 1977	00:22:38	33.5967	73.2669	27	5.2

Table 1. ISC Origin data for an earthquake that occurred beneath station NIL. The ISC listed the depth as 27 km; however, detailed aftershock studies in the epicentral region suggest the 14 Feb 1977 main shock occurred at a depth of 12−20 km (Seeber and Armbruster, 1979). To accommodate this depth range, we computed the SSSC for station NIL at 15 km.

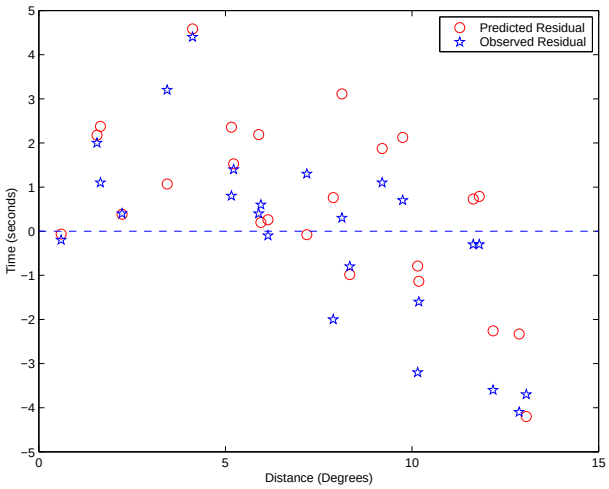


Figure 1. Observed P*g* and P*n* travel times at 24 regional stations that recorded the 14 Feb 1977 event underneath NIL. The predicted travel times were calculated using the Weston 3−D velocity model for Pakistan and were found to model the observed data by a factor of 1.5 times better than the fit provided by the Jeffreys−Bullen model.

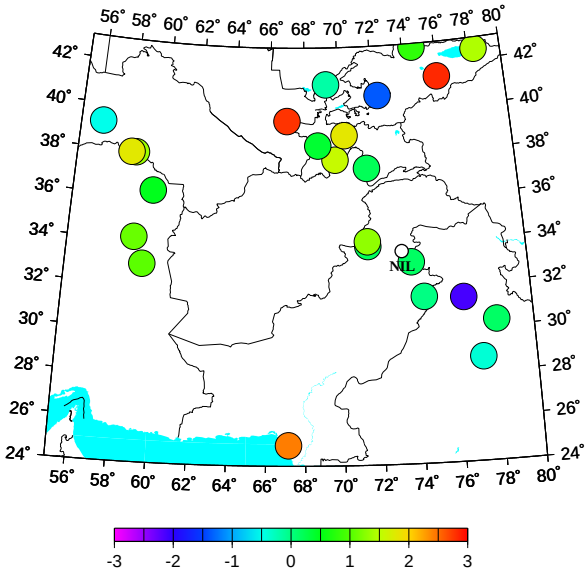


Figure 2 Difference between observed and predicted travel times as plotted at the stations that recorded the Nilore (NIL) earthquake.

Velocity Model Testing Using Jackknifing

We are interested in establishing a baseline understanding of how our preliminary input model performs in comparison to the 1−D IASP91 model. Comparing rms travel time residuals from event locations using the two different models has shown inconsistent results. The jackknife method of estimating error (Efron and Gong, 1983) provides another comparison of location performance between our 3−D model and IASP91. In this method, we relocate each event multiple times (as many times as there are observed phase arrivals in the inversion), and for each relocation, we exclude one phase arrival. Inspecting the spatial distribution of all of the relocation estimates provides a measure of how each data point affects the inversion. Large changes in the hypocenter introduced by a particular datum can indicate either poor quality phase picking or it can indicate a poor model along that ray path. A good model and well picked data would produce a full set of relocation estimates that are tightly clustered.

We applied the jackknife method to four events from the Engdahl *et al.*(1998) database. These 4 events are a

subset of 200 that we used for a pre−tomographic analysis test case discussed later in this paper. The results of the 4−event jackknife study are shown in Figure 3. Events 1 and 2 have 24 and 22 arrivals, respectively, and show smaller hypocenter changes relative to events 3 and 4 which have only 10 arrivals. The rms residuals for events 1 and 3 were smaller for our 3−D model (0.923 s and 1.196 s, respectively) than for the IASP91 model (1.071 s and 1.594 s). For event 2, the residuals were similar (0.844 versus 0.883). The residual for event 4 is larger in the 3−D model case (1.572 s) than in the IASP91 case (1.414 s). The results of the jackknife tests indicate that, in all cases, our 3−D model produces smaller relocation scatter than does the IASP91 model (See Table 2 for scatter values). This indicates that even our initial 3−D model produces a more robust fit to the observed data than does the 1−D model, and a 3−D model improved by tomographic inversion should perform even better.

EVENT ID	***3−D Epicenter Scatter (KM)***	***IASP91 Epicenter Scatter (km)***	***3−D Depth scatter (km)***	***IASP91 Depth scatter (km)***	***Number of Data***
1	0.6750	0.7375	1.6083	1.9542	24
2	0.5636	0.6227	1.2772	1.2864	22
3	8.2600	12.610	27.810	48.790	10
4	4.3600	4.7500	5.7000	7.9900	10

Table 2. Results of the jackknife study of four events from the Engdahl et al. (1998) database. The values indicate average scatter.

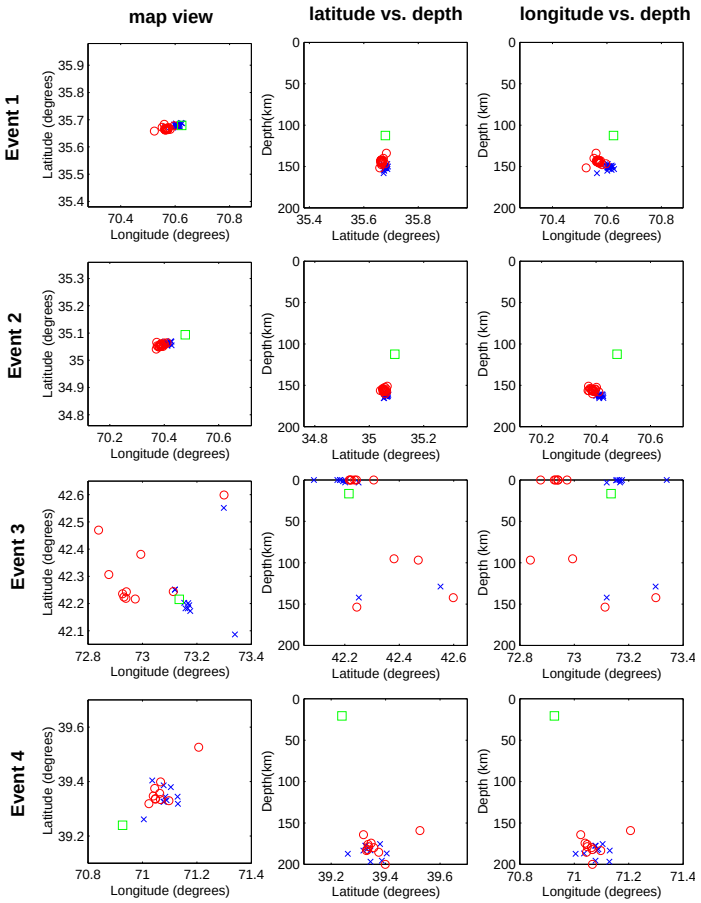


Figure 3. Jackknife test results for four events. "X"s represent 3−D model hypocenters, "o"s represent 1−D IASP91 model hypocenters. Singular squares represent the hypocenters calculated by Engdahl *et al.* (1998) using the AK135 model.

Preliminary Tomographic Analysis

Figure 4 illustrates the five main components in our tomographic inversion method that have either been completed or are in development. The "Condition Model" function transforms input velocity models into the proper format for the inversion. Converting from spherical to Cartesian coordinates produces a station−centered sub−grid which, in part, reduces errors introduced by the coordinate transformation. This module reparameterizes the velocity model to reduce the size of the tomographic inversion and constrain the inversion to geologically realistic solutions. The "Predict travel time" function produces travel time tables for each station. Using a finite difference implementation of Huygen's principle (Podvin and Lecomte, 1991; Lomax, 1999), we

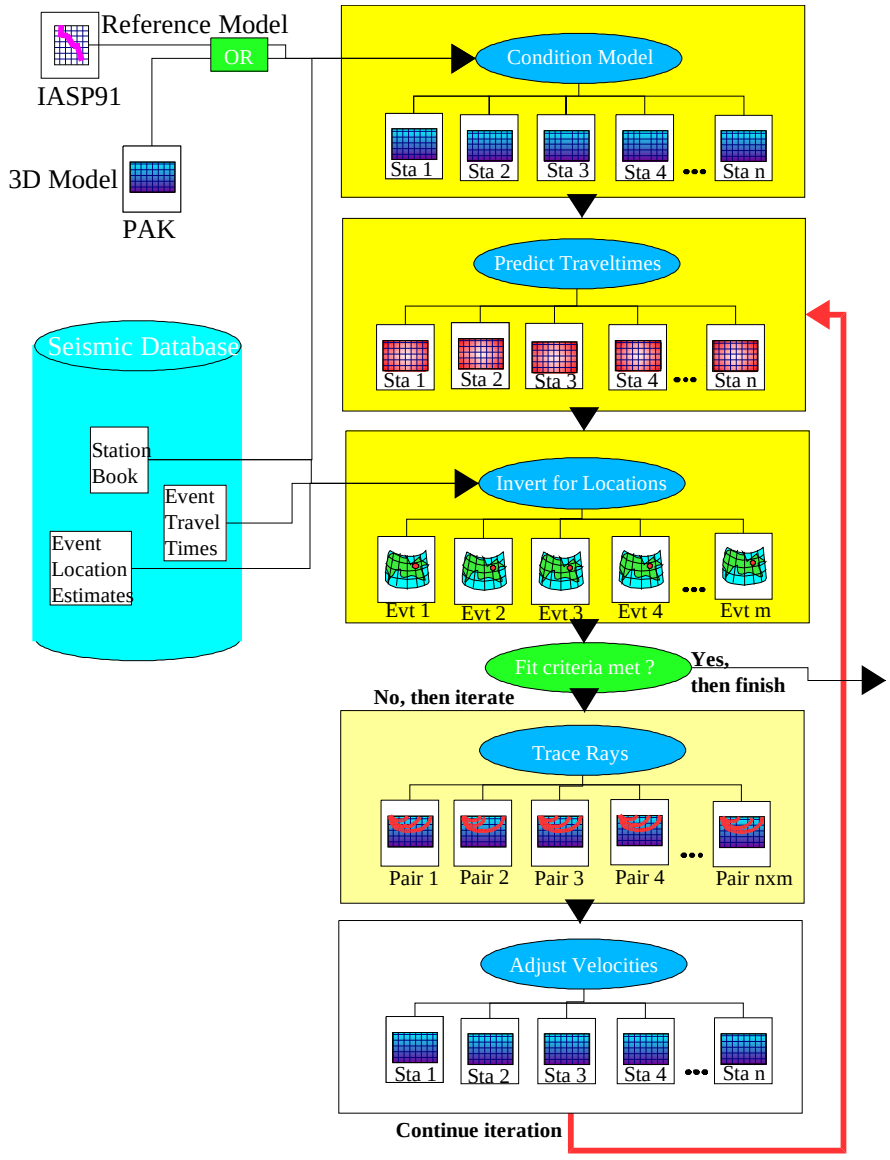


Figure 4: Schematic overview of joint tomographic inversion for a 3−D velocity model and improved seismic event hypocenters. The degree of completion of a particular function is indicated by the shading of the block, where lighter shades indicate modules which require further development.

Our 3−D grid search algorithm ("Invert for location") produces hypocenters for each event in the tomographic inversion. More specifically, it obtains the maximum likelihood estimate (MLE) of the hypocentral parameters and the probability density function scale factor by searching a grid of solution hypocenters through subsets of increasing fineness. The final MLE of the hypocenter is taken as the solution achieving the largest likelihood among all the points of the grids searched. We used this algorithm to generate the estimates shown in the jackknife test discussed previously.

In order to use the Podvin and Lecomte (1991) travel time estimation method as the forward modeling core of the tomographic inversion, we are expanding its functionality to include the generation of accurate spatial coordinates of the rays as they travel from the source to the receiver. The lack of accurate ray coordinates is a deficiency in the original version of the original that must be remedied prior to performing tomographic inversion. The improved ray tracing module will produce ray coordinates for each input station/event phase arrival time, which will be recalculated after every update of the velocity model until the fit to the data falls below a predetermined threshold criteria.

In any inversion, a reasonable guess of the velocity structure in the starting model is very important . To test the appropriateness of our 3−D *a priori* model, we relocated a set of 44 Calibration Event Bulletin events using arrival times form 14 regional stations. In this analysis, our 3−D model resulted in smaller rms residuals for 66 percent of the events. Since ground truth locations are not available for these events and the depths are poorly constrained by the regional data, further analysis was performed on a larger data set. In an extension of this study, we relocated 200 events from the Engdahl *et al.* (1998) database using our current 3−D model (Fiugre 5).

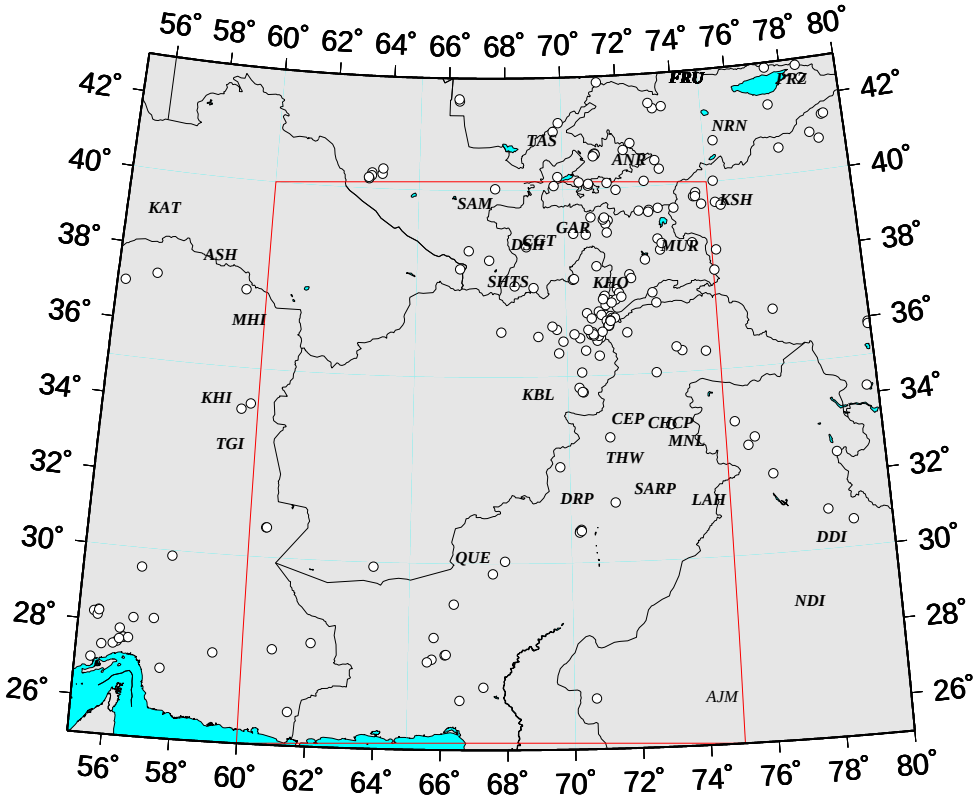


Figure 5. A set of 200 events from the Engdahl *et al.* (1998) database used in an preliminary test of our tomographic inversion plan.

We chose events that were reported in the catalog to have standard error in position of less than or equal to 5 km, as determined from the diagonal elements of the covariance matrix (Engdahl *et al.*, 1998). The event list was further narrowed to optimize spatial distribution and to exclude deep events (maximum depth was 163 km). A subset of thirty regional stations, also selected for optimal spatial distribution as well as for quantity of data reported in the bulletin for each station, was used to locate each event. We relocated each event with the Weston

3−D velocity model of Pakistan and then with the 1−D IASP91 model. This test was performed for three different cases relative to the Engdahl *et al.* (1998) hypocenter solution: (1) constrained to a 10 km radius in X−Y space and +/− 20 km in Z, (2) a fixed depth constrained to +/− 5 km, but free in X−Y space, and (3) a free solution in all directions.

The hypocenter solution for the 3−D model has a smaller rms residual for approximately 75% of the events in both variations of the constrained cases (1 and 2) and it has smaller residuals for just over 60% of the events in the free solution (3) (see Table 3). Average standard error reductions for the set of events are also shown to be 130−170% greater than average standard error increases for the 3−D hypocenter solutions compared with the 1−D solutions. These results show that the 3−D model is generally fitting the data better than the 1−D model. A smaller rms error can be an indication of a better location; however, 3−D structures may introduce biases that lead to smaller rms errors. Therefore, small rms residuals are not an absolute indicator of a better location. Other tests (such as jackknifing, as discussed in the previous section) are required to demonstrate that locations calculated using the 3−D model are more accurate than the 1−D solutions.

Location Constraints	**No. of 3−D Events with smaller rms residuals than 1−D**	**No. of 3−D Events with larger rms residuals than 1−D**	**Average Standard Error Reduction**	**Average Standard Error Increase**
Case 1: XYZ*	148	51	0.4042	0.2098
Case 2: Z	148	52	0.3920	0.2298
Case 3: None	121	79	0.2766	0.2118

**One best hypocenter solution was found outside our model region and was removed from this evaluation*

Table 3. Comparison of rms residuals for preliminary tomographic analysis of 200 events from the Engdahl, et al. (1998) database. These events were relocated using both the 3−D regional model and the 1−D reference IASP91 model. Three different hypocenter contraint conditions were imposed on the inversion.

To obtain a preview of the magnitude and spatial distribution of travel time residuals over the model space, we plotted the residuals for each station−event pair at the great−circle midpoint of the ray. This is only an informal spatial approximation, as the residuals are distributed over the entire raypath. Therefore, interpretations and conclusions drawn from this representation of the results are limited and must take the nature of the midpoint approximation into consideration. We can see from Figures 6 and 7 that locations determined using the 3−D model result in overall smaller residuals than those determined by the IASP91 model. In both cases, the magnitudes and sign of the residuals appear to exhibit a spatial correlation across some regions. For most regions, it appears that the 3−D model already does a better job of approximating the true velocity structure than IASP91, as expected. However, we anticipate that full implementation of the tomographic inversion, which will update the *a priori* model along the full raypath between each station and event, will improve the regions that are less well constrained in the preliminary model. This initial test demonstrates the functionality of the majority of components required for tomographic inversion. It also produces a "preview" of the spatial distribution of travel time residuals over the model space.

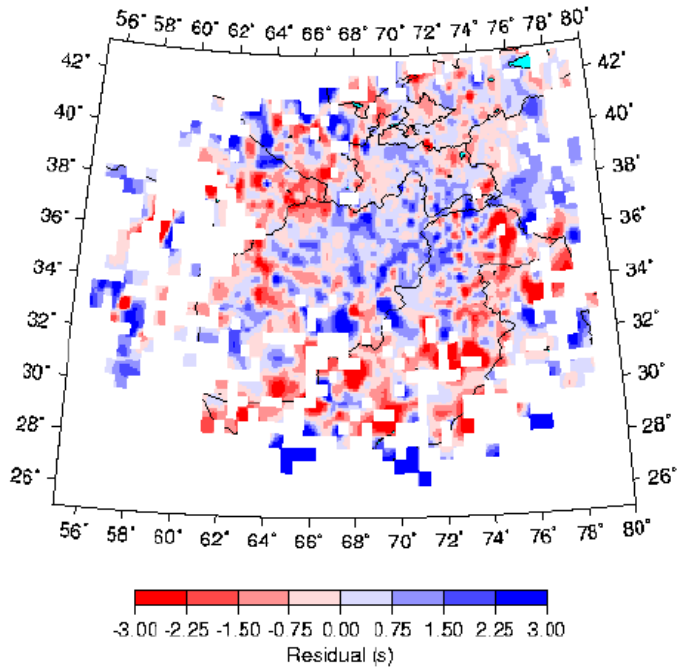


Figure 6. Residuals of 200 events relocated using the Weston 3−D velocity model of Pakistan. The solutions were constrained to within a 10 km radius in XY space and to +/− 20 km in depth of the Engdahl *et al.* (1998) solutions. Residuals are plotted at the great circle midpoint of the raypath and are averaged for points located within a 9 km grid spacing. Areas not resolved from this small set of the data are white. Large residuals (either positive or negative) are indicated in dark shades, whereas light shades indicate residuals approaching zero. Highs and lows are indicated by either a"+" or "−" sign..

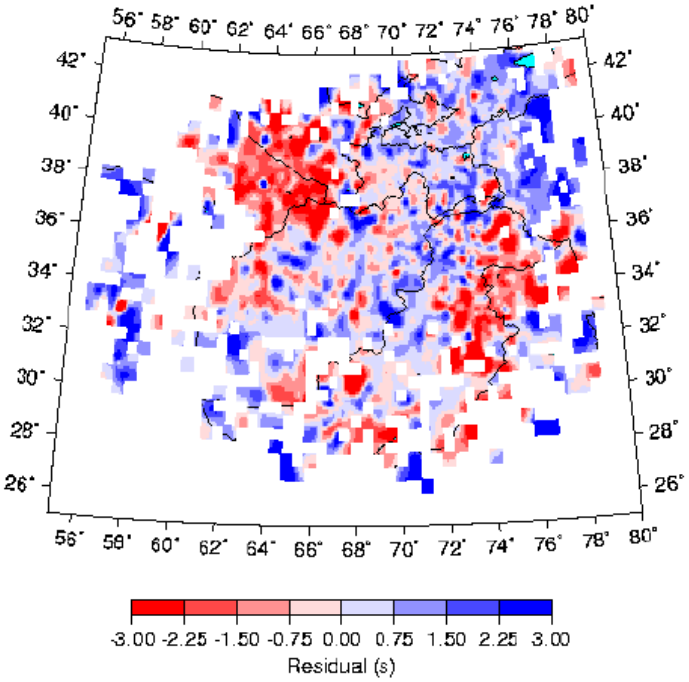


Figure 7. Residuals from the same set of events shown in Figure 6 relocated using the IASP91 1−D travel time tables.

CONCLUSIONS AND RECOMMENDATIONS

During the past year we have made significant progress towards producing a fully 3−D tomographic velocity model of the Pakistan region and surrounding areas. We have completed the development and testing of a 3−D starting velocity model and have established a database of seismic events that we are using as the input travel times to the inversion. We continue to evaluate the quality of each of our input data sets to ensure the highest quality data is available for our inversion. In this paper we have described the functionality and demonstrated the application of key computational modules necessary to support the final tomographic inversion. In each case, we have completed various performance tests on the computational accuracy.

Work to be completed during the final year of this contract includes the final development and implementation of the joint inversion technique and establishment of appropriate convergence criteria. Once these modules are completed and tested, we will perform a full tomographic inversion to produce an accurate regional 3−D velocity model for the Pakistan region and the consequent improved hypocenter estimates.

REFERENCES

Efron, B. and Gong, G. 1983. A Leisurely Look at the Bootstrap, the Jackknife, and Cross−Validation. *The American Statistician.* **v.** 37. No. 1, pp. 36−48.

Engdahl E. R., van der Hilst, R., and Buland, R. 1998. Global teleseismic earthquake relocation with improved travel times and procedures for depth determination, Bull. Seism. Soc. Amer., 88 (3), p. 722−743.

Jeffreys, H. and Bullen K.E. 1940. Seismological Tables, British Association for the Advancement of Science, London.

Kennett, B.L.N. and Engdahl, E.R. 1991. travel times for global earthquake location and phase identification. *Geophys. J. Int.*. **v**. 105. pp. 429−465.

Kennett B. L. N.,Engdahl, E.R., and Buland,R. 1995. Constraints on seismic velocities in the earth from travel times, Geophys. J. Int., 122, p. 108−124.

Lomax, A. 1999. Probabilistic, Non−Linear Earthquake Location in 3−D Media. An online guide to software for probabilistic, non−linear earthquake location in 3−D velocity structures.

Podvin, P. and Lecomte, I. 1991. Finite difference computation of traveltimes in very contrasted velocity models: a massively parallel approach and its associated tools. *Geophys. J. Int.* **v.** 105. pp 271−284.

Seeber, L. and Armbruster, J., 1979. Seismicity of the Hazara Arc in northern Pakistan: decollement vs basement faulting, in Geodynamics of Pakistan, , pp. 131−142. Geological Survey of Pakistan.

APPLICATION OF A CEPSTRAL F−STATISTIC FOR IMPROVED DEPTH ESTIMATION

Jessie Bonner, Delaine Reiter, Weston Geophysical
Bob Shumway, University of California at Davis

Sponsored by U.S. Department of Defense
Defense Threat Reduction Agency
Contract No. DSWA01−98−C−0142

ABSTRACT

A definitive way to rule out seismic events as possible nuclear tests is to accurately determine the source depth. However, the determination of depth for regionally recorded events remains one of the most challenging problems for regional seismic monitoring. Cepstral techniques are used to detect echoes in a signal (such as the depth phases pP and sP) and have been utilized in the past for seismic depth determination by Alexander (1996), Bennett *et al.* (1989) and Kemerait (1982). To further test the cepstral technique, we formulated a cepstral F−statistic found by using a classical approach to detecting a signal in N stationarily correlated time series (Shumway, 1971). We have also implemented techniques to window and taper the cepstra that decrease significantly the number of false alarms in the F−statistic. To help with the interpretation of the F−statistic, we perform the analysis using data recorded on multiple arrays and look for correlations in peaks of the cepstra.

We first performed the cepstral F−statistic analysis on a set of 32 events from the pIDC REB on 12 Feb 2000 to determine the usefulness of the technique on teleseismic data where the P waves are often less complicated by path effects, focal mechanism, and coda complexity than regional signals. Using the cepstral F−stat, we were able to determine depths for 16 of the 32 events. For eight other events, the SNR was too small for analysis, while the remaining eight events were possibly too shallow for resolution of a depth phase (< 8 km). The technique determined depths ranging from 10 km to 90 km for seven of 17 events that the pIDC had fixed to 0.0 km. For pIDC m_b magnitudes less than 3.8, there is a significant amount of scatter in the depths reported by the pIDC, the USGS, and those calculated by the cepstral analysis. The scatter is reduced at magnitudes greater than 3.8. For events with magnitude greater than 4.0, the average difference between the USGS and Weston cepstral depths is less than 25 km, while the mean difference between the pIDC and Weston depths is approximately 35 km.

We also tested the cepstral F−statistic method using a combination of teleseismic and regional data by determining focal depths for earthquakes in Central America and northern South America using TXAR, PDAR, ILAR, NVAR, and YKA data. The USGS located 29 events within the study region between 05 May 2000 and 15 June 2000, and 21 of the depths were constrained to 33 km. The USGS did not use depth phases for any of the events to determine the focal depth. We were able to determine depths for 26, while two were too small for analysis and a third had two plausible depths. We found that the median depth determined from the cepstral analysis was 31 km which is in agreement with the nominal USGS depth of 33km, however, there were several events in which the USGS and Weston cepstral depths disagreed significantly (e.g. 110 km for one event with a visible pP). We observed that a significant amount of the scatter in the cepstral depths is the result of the analysis at regional distances. By comparing depths calculated by teleseismic arrays separately from depths determined by regional arrays, we observed that the scatter averages approximately 9 km for events with magnitude 4 and decreases about 4 km per magnitude unit up to our maximum magnitude studied of 5.2. Thus, for larger events (m_b > 5), the depths obtained by regional and teleseismic analysis should be within 5 km of each other. For small events, which are of particular interest in areas of high monitoring concern, the scatter may prove to be too large for the cepstral F−statistic to be used in an operational capacity on regional data.

Key Words: seismic, depth estimation, cepstral, F−statistic

OBJECTIVE

The primary objective of this research is to establish the operational usefulness of cepstral techniques to determine the depth of a seismic event. To accomplish this objective, we have developed a statistical criterion to accompany cepstral estimates of seismic depth phase delay times. The statistical measure, or cepstral F−statistic, provides a measure of the significance of a particular peak in the cepstrum. We have applied the technique to data from the Prototype International Data Center (pIDC) Reviewed Event Bulletin (REB) and from the United States Geological Survey (USGS) bulletin, and the results show the method is highly successful for teleseismic distances, slightly less reliable at far−regional distances, and problematic at distances less than 10° from the source.

RESEARCH ACCOMPLISHED

Cepstral techniques are used to detect echoes in a signal using simple Fourier transform processing methods. They have been used in such diverse applications as speech analysis, image processing and radar data analysis (Bogert et al., 1963; Childers et al., 1977). The cepstrum is defined as the Fourier transform of the log of the spectrum of a time domain signal (Oppenheim and Schafer, 1975), and was designed to help analyze the periodicity that occurs in the power spectrum when echoes are present in the original signal. In principle, cepstral analysis can be used to detect the periodicity of scalloping in the seismic spectrum that is due to the interference of the direct (*P*) and depth (*pP* and/or *sP*) phases. This periodicity is directly related to the depth phase delay time, which is in turn directly related to focal depth. Cepstral techniques have been utilized in the past for seismic depth determination (Alexander, 1996; Bennett et al., 1989; Kemerait, 1982), but the results have been mixed, and the operational capability of the method has never been established. To improve the method, we have formulated a cepstral F−statistic (Shumway et al., 1998) that attaches statistical significance to peaks in the cepstrum. The F−statistic is found using a classical approach to detecting a signal in N stationarily correlated time series (Shumway, 1971). Testing the hypothesis $S(d) = 0$, where S is the signal transform at delay time d, leads to an F−statistic given by

$$F_{2,2(N-1)}(d) = (N-1)\frac{SCB(d)}{SCE(d)},$$

which can be interpreted as a signal−to−noise ratio. The subscripts refer to an F distribution with 2 and 2(N−1) degrees of freedom. In this instance, the signal consists of the spectrum of the stacked log spectra, or *beam cepstrum (SCB)*, defined as

$$SCB(d) = N\left|\overline{Q}(d)\right|^2$$

where

$$\overline{Q}(d) = N^{-1}\sum_{j=1}^{N} Q_j(d),$$

is the mean Fourier transform of the log spectra. The noise is defined as the *error cepstrum (SCE):*

$$SCE(d) = \sum_{j=1}^{N}\left|Q_j(d) - \overline{Q}(d)\right|^2$$

$$= SCT(d) - SCB(d),$$

where *SCT(d)* is the *total stacked cepstrum,*

$$SCT(d) = \sum_{j=1}^{N} \left| Q_j(d) \right|^2 .$$

The error cepstrum is a measure of the extent to which the individual channel or window transforms differ from the mean transform. The beam and total cepstra are computed from multiple windows of data, which can be extracted from elements in an array. Note that the total stacked cepstrum (*SCT(d)*) is equivalent to the sum−stack proposed by Alexander et al. (1995), which is computed by simply adding up the cepstra of individual windows. Our tests have shown that the sum−stack will not reflect the common signal components as well as either the beam cepstrum or the F−statistic. In the following paragraphs, we describe the methods used to implement this procedure.

Preprocessing. We have found that bandpass filtering the data prior to processing helps accentuate the cepstral peaks. Currently, we employ a 3−pole, Butterworth bandpass filter between 0.6 and 4 Hz to the demeaned data. For arrays such as CMAR and KSAR, high−frequency cultural noise may prompt lowering the hi−cut frequency to 2 Hz for optimum peak enhancement. The improvement in the cepstral peaks comes from the increase in the signal to noise (SNR) ratio brought on by filtering along with the smoothing of the P−wave caused by the relatively narrow band. The filtering also removes long period noise and signals that complicate the cepstra as well.

Cepstral Analysis. The P wave arrival and coda are windowed and the log−power spectrum of each window of data is calculated. The log spectrum is detrended with a cubic spline (Shumway, 1997) to remove the Fourier component of the spectra that is not due to possible depth phases. Reiter and Shumway (1999) noted that noise in the high frequency part of the spectra often obscures peaks in the cepstrum that are due to true signal echoes. To overcome this high frequency noise, we use cosine tapered windows to extract only the signal portion of the spectra. Since most teleseismic signals are in the 1−2 Hz bandwidth, the window usually was chosen between zero and 2−3 Hz. For regional signals, the bandwidth is increased to between 3−4 Hz. The results of this method decrease significantly the number of false peaks seen in the cepstral F−statistic. The cepstra of the raw data are now ready to be calculated by taking the Fourier transform of the windowed and detrended log power spectra. We calculate the following three cepstral quantities.

Beam Cepstra (**SCB**) = cepstra of summed windowed and detrended log spectra
Total Cepstra (**SCT**) = sum of individual cepstra
Cepstral F−statistic = (N−1) **SCB**/(**SCT**−**SCB**)

The results of these calculations on a teleseism recorded at ILAR are shown in Figure 1. For this event, there are four large peaks that are visible in all three cepstra at 5.1, 9.5, 11.8, and 19.5 seconds (the time scale refers to delay times in seconds i.e. pP−P or sP−P). The most obvious choice for the pP phase based upon visual inspection of the seismogram (Figure 2) would be the largest cepstral F−statistic peak at 5.1 seconds. Upon analysis of the cepstral F−stat, caution should be exerted when picking large peaks that may be created by random processes that cause the beam and total cepstra to have similar values at certain points. This results in large amplitude spikes in the F−statistic that are not the result of echos in the signal. Thus the peaks in the F−statistic should be picked while examining the beam and total cepstra for co−located peaks. For the analysis of this example event as well as the others we determined the three largest peaks above the confidence line and recorded for depth analysis.

Peak Correlation. In some cases, only a single peak may exhibit an amplitude above the 99% confidence level. However, in most cases (e.g. Figure 1) there will be numerous peaks that may result from pP or sP depth phases, secondary arrivals not associated with depth phases (e.g. PcP), arrivals from other earthquakes, and/or noise. Thus, we feel it is difficult for an accurate depth determination to be based upon the cepstral F−statistic peak produced by analysis of a single array. Instead, we compute the cepstra for several arrays so that a comparison of F−statistic peaks between arrays can be completed. The analyst will overlay the F−statistics from all arrays and search for correlations in the peaks to determine if more than two arrays are noting similar delays. If so, we use the IASP91 (Kennett and Engdahl, 1991) standard earth model to compute depths based upon the delays. The depths calculated at each array were averaged together to give a source depth that was then compared with the

USGS and pIDC data. The results of our comparisons will be discussed in the following sections.

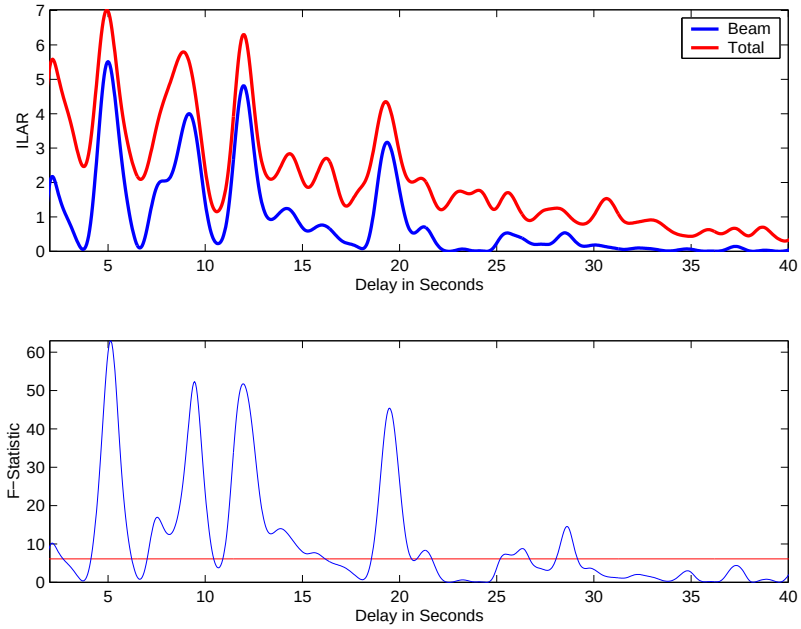


Figure 1. (Upper) Beam and total cepstra for a Central American earthquake recorded at ILAR. (Lower) Cepstral F−statistic with 99% confidence line shown in red.

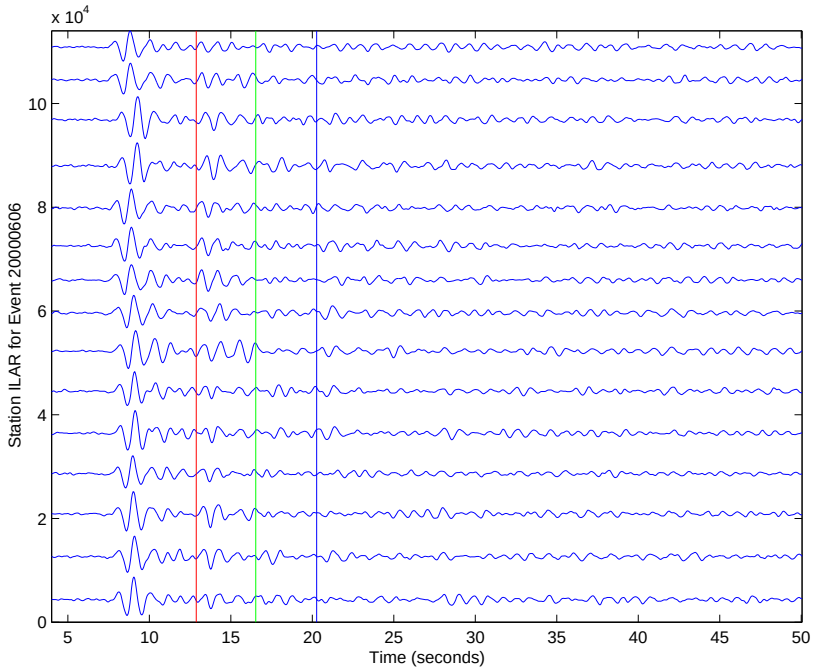


Figure 2. Seismograms recorded at ILAR for an event in central America. The P wave is followed by another arrival approximately 5 seconds later that may be pP based upon the reverse polarity. The red, green, and blue lines mark the largest, second largest, and third largest peaks, respectively, in the cepstral F−statistic.

Application of the Technique At Teleseismic Distances. To examine the usefulness of our technique at teleseismic distances, we determined depths for a number of events using the cepstral F−statistic method (referred throughout as the Weston method) and compared our cepstral depths to depths determined by the pIDC and USGS. We picked February 12, 2000 at random and downloaded the REB from the pIDC. For this day, 32 events were located (Figure 3) by the pIDC while the USGS computed locations for 26 of the 32 events. Because the F−statistic requires beaming individual elements from an array, we downloaded data from CMAR, KSAR, TXAR, NVAR, PDAR, ILAR, and YKA when available. The data was converted from GSE2.0 to SAC and read into memory in SAC2000. Using the new Matlab routine in SAC, we copied the data from the SAC workspace into the Matlab environment where the cepstral analysis was performed. The cepstral analysis requires a signal−to−noise ratio (SNR) greater than 4 to obtain statistically valid peaks that may be correlated between arrays. When the SNR is low, we find many peaks in the cepstral F−statistic that are not associated with depth phases. For the events analyzed thus far, a pIDC mb > 3.8 seems to be sufficient for teleseismic analysis at more than 2 arrays. However, if the event was only recorded at CMAR or KSAR or other arrays where background noise is high, the threshold for cepstral analysis may be raised to mb > 4.0.

Using the Cepstral analysis, we were able to determine depths for 16 of the 32 events. Of the other 16 events, the SNR was too small for analysis for eight events, while the remaining eight were too shallow for a depth phase (< 8 km) or the depth phase was not observed. For the 32 events (note the USGS had only located 26 of the events to date), the pIDC had fixed the depths of 17 of these events to 0.0 km. The Weston cepstral technique obtained depths for seven of these fixed−depth events ranging from 10 to 90 km. Figure 4 shows the depths reported by the USGS and pIDC (with error bars for the pIDC) and the Weston cepstral depths with associated error. Figure 5 is a plot of the residuals (Weston Cepstral Depth−USGS and Weston−pIDC) for the events. For magnitudes less than 3.8, there is a significant amount of scatter in the residuals between the depths calculated by the two groups and the cepstral analysis. The scatter is reduced at magnitudes greater than 3.8. For events with magnitude > 4.0, the average difference between the USGS and Weston cepstral depths is less than 25 km, while the difference between pIDC and Weston depths is near 35 km.

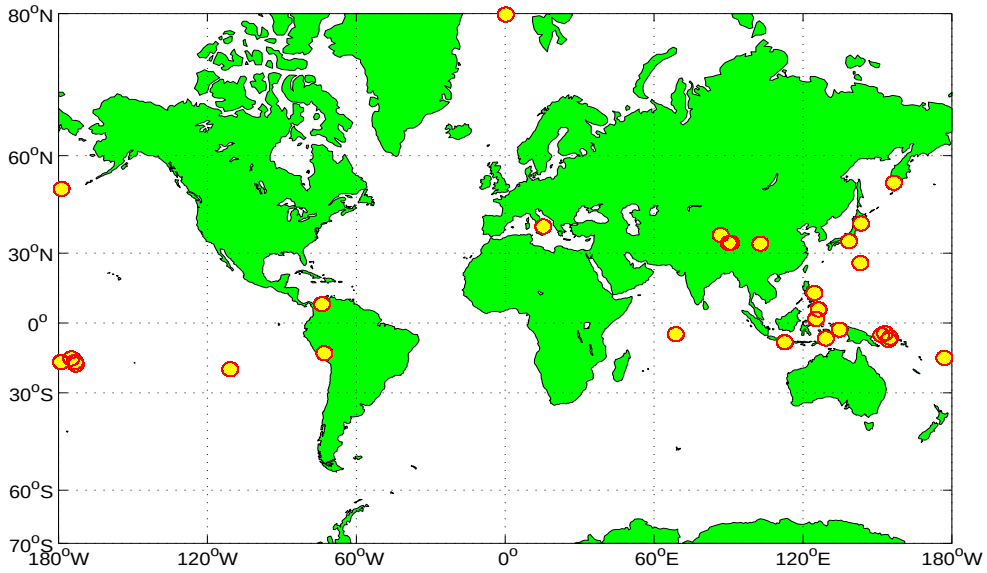


Figure 3. Location of the pIDC REB events for 12 Feb 2000.

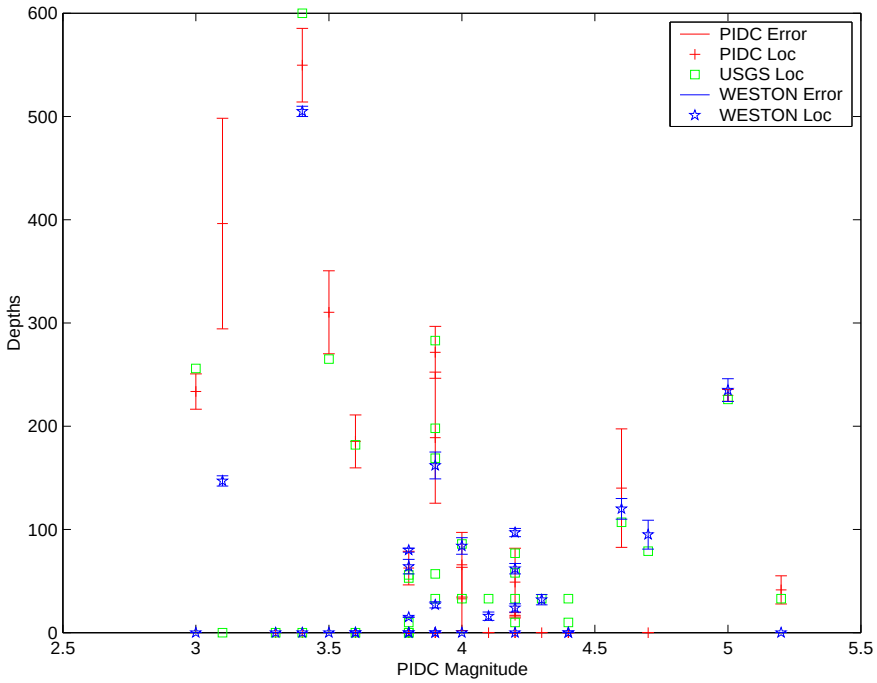


Figure 4. Comparison of depths (and errors) reported by the pIDC and USGS for 32 events on 12 Feb 2000. The depths and scatter as determined by the Weston cepstral F−statistic analysis are also shown.

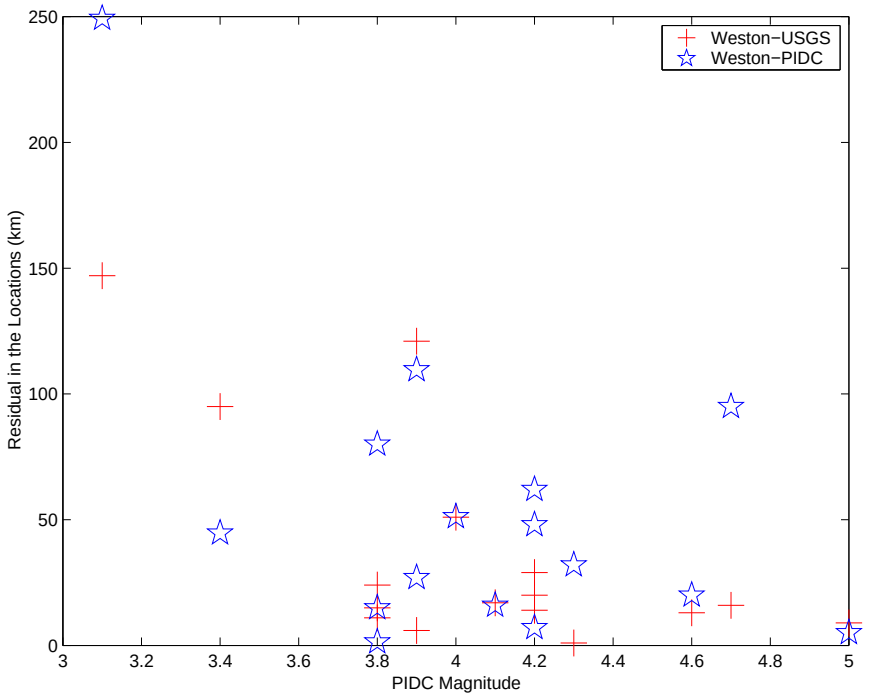


Figure 5. Residuals for depths calculated by the Cepstral technique and the USGS and pIDC reported depths.

Application at Teleseismic and Regional Distances. The cepstral F−statistic technique was applied to 29 events located by the USGS in Central America and northern South America between 05 May 2000 and 15 June 2000. While this region has little or no significance to treaty monitoring, it does have an abundance of earthquakes with a wide range of depths recorded at regional and teleseismic distances. The event characteristics and the results of the analysis are shown in Table I and the locations are shown in Figure 6. For Event No. 20000530, we were not able to determine a reliable depth due to its small magnitude that resulted in poor SNR at TXAR and no signal at NVAR, PDAR, ILAR, and YKA. For events 20000516 and 20000608_3, we were only able to determine depths based upon a single array due to small magnitude and lack of data availability, respectively. Figure 7 shows the Weston depths and error in comparison to the USGS depths. As of the publication of this manuscript, we still had not received the pIDC depths for events located during this time period. Of the 28 events for which Weston depths were calculated, the USGS had fixed the depths of 21 of the events to 33 km. For two additional events, the USGS had constrained the depths to 10 and 20 km. None of the depths reported by the USGS for these events were constructed using depth phases. For 25 of 26 events, we were able to determine a single depth that corresponded to several statistically significant peaks in the cepstral analysis noted on multiple arrays. For Event 20000615, we found two depths (192.5 and 89.25) that were feasible. For 25 of 29 events, TXAR was located at regional distances to the earthquakes ($10° < \Delta < 20°$) allowing for an interesting comparison of the cepstral analysis at regional and teleseismic distances. Of these 25 events, there were six (6) events (24%) for which a stable depth could not be estimated based upon the TXAR analysis. The reasons for the failure of the method included small amplitude Pn arrivals, complicated secondary phases such as Pg, and the interplay of the crossover between the P and Pn phases near approximately 16−20°. When comparing the TXAR depths with the depths calculated from the other arrays, we find that a significant amount of the standard deviation in the Weston cepstral depths comes from the analysis at the regional distances (Figure 8).

Weston Event No.	Year	Month	Data	Origin Time	Lat	Long	Depth	Magnitude	Type		Cepstral Dept	Mean	Med	STD	Range	Min	Max
20000505	2000	5	5	143449	11.93	−86.18	103	4.1			5 (2 sP−P)	64	62	5.1	12	60	72
20000510	2000	5	10	155742.27	16.22	−96.86	33	4.5	mb	GS	10 (6 sP−P)	31.4	29	6.5	19	24	43
20000511_1	2000	5	11	174045.82	16.15	−97.93	33	4.5	mb	GS	7 (2 sP−P)	18	16	4.4	12	12	24
20000511_2	2000	5	11	175826.45	16.28	−97.98	33	4.8	mb	GS	6 (1 sP−P)	18	17.5	2.3	6	16	22
20000513	2000	5	13	112719.52	14.57	−93.29	33	4	mb	GS	8 (3 sP−P)	54.6	53.5	6.2	14	48	62
20000514_1	2000	5	14	90019.88	18.11	−102.7	33	4.8	mb	GS	6 (2 sP−P)	25.3	25	1.9	5	23	28
20000514_2	2000	5	14	152437.13	14.11	−92.76	33	4.4	mb	GS	5	34.2	31	9.8	22	25	47
20000515_1	2000	5	15	72606.61	16.91	−100.6	33	4.2	mb	GS	6 (3 sP−P)	26.3	27	2.5	7	22	29
20000515_2	2000	5	15	104710.76	13.19	−91.11	33	4.3	mb	GS	6 (2 sP−P)	35.2	34	7.3	17	29	46
20000516	2000	5	16	81900.6	11.68	−86.93	20	4.2			1	75?	N/A	N/A	N/A	N/A	N/A
20000519	2000	5	19	224212.06	14.06	−92.49	33	4.3	mb	GS	6	20.5	21	5.8	16	11	27
20000521	2000	5	21	5317.21	16.48	−97.9	33	4.5	mb	GS	5	17.2	17	3.4	10	12	22
20000523	2000	5	23	163645.69	2.06	−78.39	33	5	mb	GS	5 (2 sP−P)	31	32	2.8	6	28	34
20000524_1	2000	5	24	103602.13	2.24	−79.52	33	4.4	mb	GS	5 (1 sP−P)	21.6	22	0.9	2	20	22
20000524_2	2000	5	24	202833.84	13.53	−91.21	33	4.4	mb	GS	5 (1 sP−P)	34.5	33	8.2	19	27	46
20000524_3	2000	5	24	231416.67	14.38	−92.76	79	4.6	mb	GS	4	22.5	22	2.1	5	20	25
20000527	2000	5	27	73500.68	11.67	−86.98	72	5	mb	GS	5	51.4	48	9.4	25	42	67
20000528	2000	5	28	50150.17	11.52	−87.04	33	4.6	mb	GS	5	35.4	35	3.6	9	31	40
20000530	2000	5	30	132918.08	5.7	−77.37	33	4	mb	GS							
20000603_1	2000	6	3	75736.34	16.16	−94.2	33	5	mb	GS	10 (5 sP−P)	112.2	107.5	15.4	46	94	140
20000603_2	2000	6	3	123944.1	15.33	−104.85	10	4.2	mb	GS	7 (2 sP−P)	23.1	22	3.2	10	18	28
20000606_1	2000	6	6	170316.72	16.25	−97.09	33	4.3	mb	GS	8 (4 sP−P)	33.4	30	6.3	16	24	40
20000606_2	2000	6	6	182541.15	19.01	−103.83	125	4.4	mb	GS	7 (4 sP−P)	17.5	16	3.5	13	22	9
20000607	2000	6	7	52018.93	10.56	−86.41	33	4.3	mb	GS	5 (2 sP−P)	35.4	35	5.4	13	29	44
20000608_1	2000	6	8	80810.27	14.3	−92.07	33	5.2	mb	GS	5	24.5	24.5	2.1	5	22	27
20000608_2	2000	6	8	130130.31	14.1	−91.9	33	4.5	mb	GS	5	23.5	22.5	3.1	7	20	27
20000608_3	2000	6	8	153339.59	14.29	−92.06	33	5	mb	GS	1	24?	N/A	N/A	N/A	N/A	N/A
20000613	2000	6	13	171119.9	14.01	−92.27	33	4.4	mb	GS	7 (3 sP−P)	22.3	22	3.1	9	16	25
20000615	2000	6	15	34813.79	12.84	−87.92	209.6	4.6	mb	GS	2	192.5	192.5	23.3	33	176	209
											4 (2 sP−P)	89.25	85.5	10.9	24	81	105

Table I. Depths for USGS located events in central America using the cepstral F−statistic analysis.

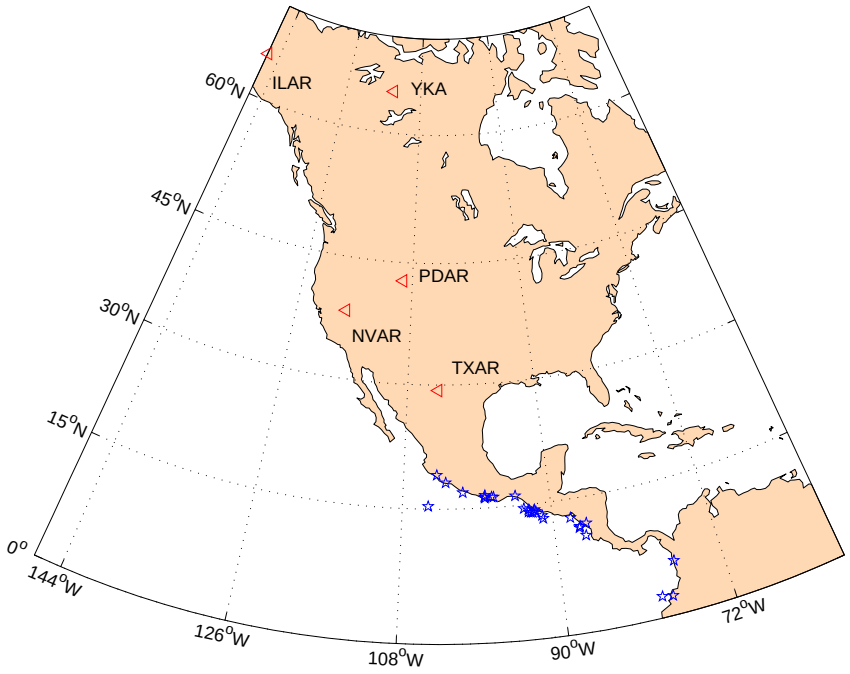


Figure 6. USGS locations of the events in Central America and northern South America that were used to evaluate the cepstral F−statistic method at both teleseismic and regional distances. Also shown are the arrays used in the cepstral F−statistic analysis.

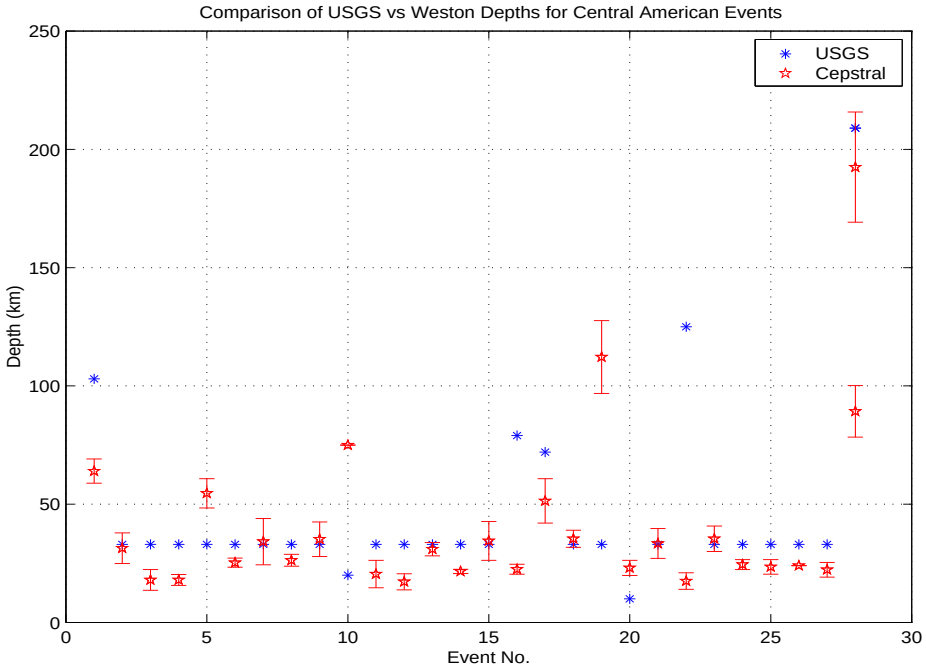


Figure 7. A comparison of the Weston cepstral depths and scatter with the USGS depths for 28 events in Central and northern South America.

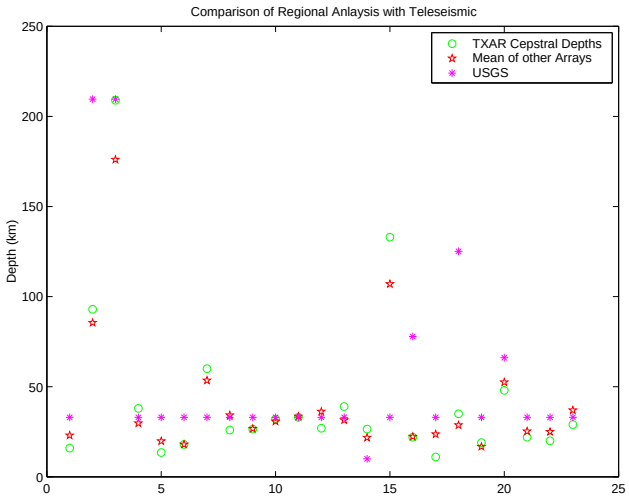


Figure 8. A comparison of the Weston cepstral depths using TXAR only (green circle), using all arrays but TXAR (red stars), and the USGS depths (magenta astericks).

We also note that the difference between the Weston cepstral depths using TXAR only and the depths obtained from the other arrays decreases in general as a function of magnitude (approximately 4 km per unit magnitude). The obvious interpretation for the magnitude dependence is the fact that the Pn and pPn arrivals are larger and more easily identified by the cepstral technique for greater magnitude events. This presents a difficult problem in that a main reason to use the regional arrays would be to determine depths for small regional events since larger events will be recorded at teleseismic distances where the cepstral analysis is more straightforward and successful.

Near−Regional Analysis. Our initial work with near−regional data (< 10°) has shown the analysis is even further complicated by the complexity of the seismograms. As an example, we completed the cepstral F−statistic analysis on copper mining explosions from Arizona as recorded at TXAR and found we were getting statistically valid peaks for surface detonated events. These peaks (Figure 9) were found to be caused by PnPn and Pg arrivals thus indicating the difficulty with using the Weston method at these distances.

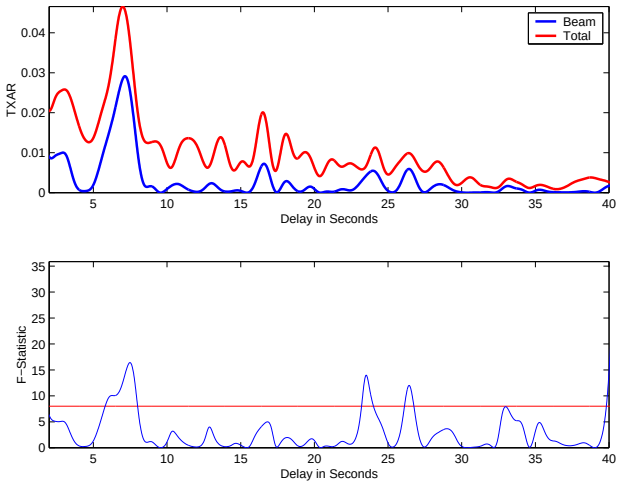


Figure 9. Cepstra for a delay−fired surface explosion in Arizona as recorded at TXAR (Δ = 6.2°). The peaks in the cepstra are the result of secondary P arrivals such as PnPn and Pg, and are not the result of depth phases.

CONCLUSIONS

We have formulated a cepstral focal depth estimation technique that provides a statistical estimate of the significance of the peaks in the stacked cepstrum. This significance measure has been missing in previous cepstral estimates of focal depth. During the past year, we have examined the usefulness of the technique on a variety of different datasets at both teleseismic and regional distances. Our results show that the method is highly successful for teleseismic distances, slightly less reliable at far−regional distances, and problematic at distances less than 10° from the source. The variability in the far−regional cepstral depths seem to be dependent upon signal bandwidth and the magnitude of the event. For small events, which are of particular interest in areas of high monitoring concern, the scatter may prove to be too large for the cepstral F−statistic to be used in an operational capacity on regional data.

The question remains as to "Whose depths are more reliable? The USGS, pIDC, or Weston's cepstral depths? This is very much a valid question, however, we believe that the cepstral F−statistic provides a statistically valid and robust means for determining focal depths. Based upon our procedure that searches for peaks that correlate between arrays, we do not rely on measurements made at a single station, but instead search for agreement amongst all the data. Our future work will focus on detailed datasets where the systematic error in the focal depths is GT5 or better to answer part of this question as to the reliability of the technique. We will continue to develop methods to automate the entire procedure as well as attempt to incorporate additional tests of the validity of the peaks in the cepstral F−statistic. Our continued major focus during the final stages of this project will be on the operational potential of this method for seismic depth estimation.

REFERENCES

Alexander, S. S. (1996), A new method for determining source depth from a single regional station, *Seismic Res. Ltrs*., **67**, p. 63.

Alexander, S. S., R. C. Hsu, S. L. Karl, I. N. Gupta and D. H. Salzberg (1995), New techniques for estimating source depth and other diagnostic source characteristics of shallow events from regional observations of P, Lg and Rg signals, Report No. PL−TR−95−2108, Phillips Laboratory, Directorate of geophysics, Air Force Materiel Command, Hanscom AFB, MA 01731−3010. ADA 310037.

Bennett, T. J., B. W. Barker, K. L. McLaughlin, and J. R. Murphy (1989), Regional discrimination of quarry blasts, earthquakes and underground nuclear explosions, Final Report GL−TR−89−0114, Geophysics Laboratory, Hanscom Air Force Base, MA.

Bogert, B. P., M. J. R. Healy and J. W. Tukey (1963), The quefrency analysis of time series for echoes: cepstrum, pseudo−autocovariance, cross−cepstrum and saphe cracking, in *Proceedings of a Symposium on Time Series Analysis*, ed. M. Rosenblatt, John Wiley and Sons, Inc., New York.

Childers, D. G., D. P. Skinner, and R. C. Kemerait (1977), The cepstrum: a guide to processing, *Proc. of the IEEE*, **65**, p. 1428−1443.

Goldstein, P. and D. Dodge (1998), Depth and mechanism estimation using waveform modeling, in Proceedings of the 20th Annual Seismic Research Symposium on Monitoring a Comprehensive Test Ban Treaty (CTBT), p. 238−247.

Kemerait, R. C. and A. F. Sutton (1982), A multidimensional approach to seismic event depth estimation, in *Geoexploration*, **20**, p. 113−130.

Kennett B. L. N. and E. R. Engdahl (1991), Traveltimes for global earthquake location and phase identification, *Geophys. J. Int.*, **105**, p. 429−465.

Oppenheim, A. V., and R. W. Schafer (1975), *Digital Signal Processing*, Prentice Hall, New York.

Reiter, D. and R. H. Shumway (1999), Improved Seismic Event Depth Estimation Using Cepstral Analysis, *Weston Geophysical Scientific Report WBCA6.*

Shumway, R. H. (1971), On detecting a signal in N stationarily correlated noise series, *Technometrics*, **10**, p. 523−534.

Shumway, R. H., D. R. Baumgardt and Z. A. Der (1998), A cepstral F−statistic for detecting delay−fired seismic signals, *Technometrics*, **40**, p. 100−110.

Woodgold, C. R. D. (1999), Wide−aperture beamforming of depth phases by timescale contraction, *Bull. Seis. Soc. Am.*, 89, p. 165−177.

USING THE F-DETECTOR TO HELP INTERPRET P-SEISMOGRAMS RECORDED BY SEISMOMETER ARRAYS

David Bowers
AWE Blacknest
Sponsored by United Kingdom Ministry of Defence

ABSTRACT

The F-detector was first suggested by Melton & Bailey (1957) and its effectiveness was demonstrated by Blandford (1974), using data from the short-period seismometer array at the Tonto Forest Observatory. For an array of N seismometers, the F-detector output is the time-averaged power on the beam divided by N-times the time-averaged variance of the individual channels about the beam. F is robust in that it is resistant to spikes and to signals arriving off the desired beam. However, while F is commonly used as a detector for infrasound signals, the short-term average divided by the long-term average (STA/LTA) has been preferred for the detection of seismic signals.

One reason why STA/LTA-type detectors are ubiquitous may be that when seismic-phase detection algorithms were originally developed the computing power was not available to calculate F. Another reason is that when the noise is correlated between array elements F is sub-optimal and the STA/LTA detector was found to be as effective as F.

Whether correlated noise is observed depends on the design of the seismometer array and on the properties of the noise. For small-aperture arrays ($\sim$ 2 km) 1 Hz noise is generally highly correlated between seismometers. However, for medium-aperture arrays ($\sim$ 10-20 km), such as EKA, YKA and WRA, the 1 Hz noise-correlation is generally low (average cross-correlation coefficient < 0.15). Under conditions of low noise-correlation the statistical distribution of F approximates to the non-central F-distribution. Thus, an approximate probability can be attributed to a postulated signal detection, under the hypothesis of a chosen signal-to-noise ratio (SNR). These appealing properties of F suggest that it may be more effective than STA/LTA-type detectors, at least for medium aperture arrays with low noise-correlation.

Here we consider an alternative application of F and demonstrate that this is a useful tool when interpreting array seismograms. We show examples where the F-trace and associated probability are helpful in confirming that a signal is real. We have found this to be particularly useful for 'special event' analysis, for example, detecting P at ASAR from the 100 tonne chemical explosion on August 22, 1998 in East Kazakhstan. We also show that F is an effective tool for helping to identify surface reflections (pP and sP) on teleseismic P-seismograms – phases that are important for determining the depth of a seismic source.

During the process of reviewing associated (and missed) detections from an automatic system, analysts are often faced with the difficult task of deciding whether a signal really exists, especially at low SNR. Clearly F and the associated probability have the potential to help analysts in the routine identification of seismic-phases during the review process.

Key Words: Seismometer Arrays, P-Seismograms, F-Detector, Special Event Analysis.

OBJECTIVE

To assess whether a trace based on the F-detector has the potential to help the analyst identify body wave phases, such as P, and surface reflections (pP and sP). Correct identification of P, pP and sP is of importance if the Comprehensive Nuclear-Test-Ban Treaty (CTBT) is to be verified using P seismograms recorded at long range.

RESEARCH ACCOMPLISHED

Introduction

Under the CTBT an analyst reviewed bulletin of seismic disturbances (REB) will be produced by the IDC (International Data Centre) using data from the seismic component of the International Monitoring System (IMS). The treaty also requires 'event screening' of the REB, that is producing a subset of seismic disturbances in the REB that can be identified as earthquakes with confidence.

One of the most effective methods of identifying an earthquake is to show that the disturbance is deeper than the maximum depth current emplacement technology will allow an explosive device to be buried (say > 10 km). This requires a reliable estimate of the depth, which is often not possible using travel times alone (especially for intra-crustal earthquakes). The time difference between teleseismic P and the associated surface reflections (pP and sP) is one of the most reliable methods for estimating the depth of a seismic source. However, the success of the method relies critically on identifying correctly P and associated surface reflections.

For deep sources (say ≥ 50 km) the moveout of $pP - P$ and/or $sP - P$ times with distance may be used to help confirm the identification of the surface reflections. For example, J.R. Murphy (*written comm.*) suggests at least 1.5 s moveout, between the $pP - P$ times at the nearest and farthest stations, to confirm that pP has been identified correctly, and that the source is really ≥ 50 km deep. However, this requires identification of candidate pP phases and accurate reading of the onset of P and pP – not an easy task as, (1) the onset of pP is often masked by the P coda, (2) pP can be weak, and (3) sP may be strong and confused with pP. Also, the pulse shape of pP and sP is often different from P for deep sources, making identification difficult on seismograms recorded by narrow band seismograph systems. Such problems may also affect the results of Woodgold (1999), who applied a wide-aperture beamforming technique to identify pP on data from the Canadian National Seismograph Network, using time scale contraction based on model $pP - P$ moveout.

One way to confirm that P, pP and sP have been identified correctly on a number of seismograms from the same seismic disturbance is to search for orientations of the double couple (earthquake) source that produce pP/P and sP/P ratios that are similar to those formed by the candidate phases (allowing for uncertainty in the observed amplitudes). Pearce (1977, 1980) formalised this procedure as the relative amplitude method. If after applying the method, orientations of a double couple are consistent with the observed amplitude ratios, then the hypotheses that the seismic disturbance is an earthquake, and that the candidate P and surface reflections have been identified correctly, are supported. The above relies on the fact that fortuitous compatibility of the amplitude ratios with a double-couple source, resulting from false identification of the candidate phases at even a small number of stations, is extremely unlikely (Pearce & Rogers 1995).

When a seismic disturbance is recorded at only a small number of stations (say less than four), then care must be taken to ensure that other seismic phases (such as S-to-P conversions at the Moho for intra-crustal sources) are not mistaken for surface reflections (Bowers *et al.* 2000). Maps showing the Moho depth and Poisson's ratio (which governs the $sP - pP$ time) for the structure in the epicentral region, can be used to increase confidence in the correct identification of the surface reflections (Bowers *et al.* 2000).

There will be many seismic disturbances that are too small to generate surface waves that can be detected by the IMS. For some of these disturbances regional discriminants may well be inconclusive. Then the only data available for 'special event' analysis will be teleseismic P, recorded by a few of the more sensitive seismometer arrays within the IMS. Douglas *et al.* (1999) demonstrated, for the 100 t chemical explosion in Kazakhstan on August 22, 1998, that the absence of surface reflections on a number of P seismograms,

well distributed in distance and azimuth, can be used to infer that the seismic source is shallow. In the absence of any other information to indicate the non-nuclear origin of the disturbance, an on-site inspection is required to confirm that the source is not a violation of the CTBT.

The key factor in all of the above methods for identifying earthquakes and possible treaty violations is the ability to confirm the presence, or absence, of P and surface reflections. Here, we consider the F-detector output for an array of seismometers. Arrays are superior to single stations in that they can be 'steered' to enhance energy with a specific vector slowness. The most common array processing is 'delay-and-sum', or beamforming, which not only increases the SNR, but also suppresses signal-generated noise in the vicinity of the receiver (Key 1968). We argue that a trace showing some measure of the coherency of P energy across the array, such as F, displayed with the beamformed seismogram is of help in interpreting the seismogram in terms of candidate P, pP and sP.

Further, the F-trace may be of use to IDC analysts during the process of reviewing associated detections (and missed detections) from an automatic system (based on a tuned STA/LTA). Then analysts are often faced with the difficult task of deciding whether a signal really exists, especially at low SNR.

The F-Detector

The F-detector was first suggested by Melton & Bailey (1957). Representing the outputs, at time t, of an N-element seismometer array as $u_i(t)$, the beam can be written as,

$$\hat{u}(t) = (1/N) \sum_{i=1}^{N} u_i(t). \tag{1}$$

F is approximated by (Blandford 1974),

$$F \approx \frac{N-1}{N} \frac{\sum_{t=1}^{M} \hat{u}(t)^2}{\sum_{t=1}^{M} \sum_{i=1}^{N} (u_i(t) - \hat{u}(t))^2}, \tag{2}$$

where, the summation $t = 1, \ldots, M$ represents averaging over a 'box car' time window, T of M-samples. In words, F is approximately the time averaged power on the beam divided by N times the time averaged variance of the individual channels from the beam.

F can also be written as (e.g. Blandford 1974),

$$F \approx (N-1) \frac{\sum_{t=1}^{M} \hat{u}(t)^2}{\frac{1}{N} \sum_{t=1}^{M} \sum_{i=1}^{N} u_i(t)^2 - \sum_{t=1}^{M} \hat{u}(t)^2}, \tag{3}$$

which is simpler to compute. The expression is exact if the signal and noise are white. As Blandford (1974) points out, when a signal arrives with similar vector-slowness to the beam, F increases because, (1) the beam power in the numerator increases, and (2) the denominator in reduced to the residual noise (in this way F checks that the signal is recorded by several seismometers). If a signal arrives from a significantly different vector-slowness to the beam, F will be reduced as the denominator increases faster than the numerator. Also, F is robust in that it is resistant to data spikes, and so should be superior to a standard STA/LTA detector.

F Signal Hypothesis

The F signal hypothesis (Blandford 1974) assumes that on each channel of the array there is, (I) identical, deterministic signals, and (II) independent, Gaussian, and identically distributed noise with a stationary autocorrelation (the noise need only be stationary over the time window surrounding the signal). If (I) and (II) are satisfied then F has a non-central F-distribution $F(N_1, N_2, \lambda)$. With,

$$\begin{aligned} N_1 &= 2\,B\,T \\ N_2 &= N_1(N-1) \\ \lambda &= 2\,B\,T\,R^2, \end{aligned}$$

where, N_1 and N_2 are the degrees of freedom, λ is the non-centrality parameter, B is the bandwidth in Hz, T is the time window (s), and R^2 is the ratio of the signal and noise power on the beam.

Abramowitz & Stegun [p. 948, eqn 26.6.26] (1964) give an approximation for the probability of the non-central F-distribution,

$$P(F'|N_1, N_2, \lambda) \approx P(F|N_1^*, N_2), \tag{4}$$

where,

$$\begin{aligned} F &= \frac{N_1}{N_1 + \lambda} F' \\ N_1^* &= \frac{(N_1 + \lambda)^2}{N_1 + 2\lambda}. \end{aligned}$$

Thus, the probability of $F'(N_1, N_2, \lambda)$ can be easily computed using a numerical recipe for $F(N_1^*, N_2)$ and the approximation in Equation 4.

Relationship with Semblance

The semblance of an N-element array, over an M-sample window is defined as (e.g. Neidell & Taner 1971),

$$S = \frac{\sum_{t=1}^{M} \left[\sum_{i=1}^{N} u_i(t)\right]^2}{N \sum_{t=1}^{M} \sum_{i=1}^{N} u_i(t)^2}. \tag{5}$$

Thus, S is the power on the beam divided by the average power of the channels used to form the beam, each averaged over an M-sample time window.

Douze & Laster (1979) note that,

$$F = \frac{S}{1 - S} (N - 1), \tag{6}$$

thus F can be easily determined once S has been computed.

Practical Considerations

One of the most appealing properties of F is the ability to test a hypothesis that a signal exists with a given SNR. However, the interpretation of the probability associated with F from teleseismic P signals, recorded at seismometer arrays, depends on the validity of the F signal hypothesis assumptions (I) and (II) above.

For assumption (I) to be approximately satisfied the signal coherence across the array needs to be high. In general, the cross-correlation between signals from two seismometers in an array decreases with increasing distance, but this relationship also depends on the signal passband, the site conditions at each seismometer and the structure of the crust and upper mantle beneath the array. For assumption (II) to be approximately satisfied requires that the noise coherence across the array be low. In general, noise cross-correlation decreases with increasing distance between the seismometers in an array (e.g. Blandford & Clark 1975). Thus, there is a trade-off between the validity of assumptions (I) and (II) and the spacing between the seismometers in the array.

Early experiments using the F-detector, such as that at the 19-element, 2.9 km aperture array, at CPO (Cumberland Plateau Observatory) with a minimum seismometer spacing of 0.3 km, found that strongly correlated noise, at about 1 Hz, resulted in poor agreement between the false alarm rate predicted by theory and that observed (Edwards *et al.* 1967). Blandford (1974) reports on the implementation of the F-detector at the 37 element array at TFO (Tonto Forest Observatory) with a minimum seismometer spacing of 4 km. Blandford (1974) found low average noise cross-correlations between seismometers at TFO in the signal passband, and showed that the F-detector behaves as predicted by theory. Presumably the average signal cross-correlations at TFO are high to achieve agreement between observation and theory.

Based on the TFO experiment we might expect that large-aperture (> 30 km) seismometer arrays with a minimum seismometer spacing of 4 km to be near optimal to satisfy the F signal hypothesis assumptions.

	Example 1	**Example 2**
Source region	East of Honshu, Japan	East Kazakhstan
Date	1997 07 09	1998 08 22
Origin Time (UT)	09:36:08.7	05:00:18.7
Lat. (°N)	35.461	49.756
Lon. (°E)	140.174	77.827
Depth (km)	70.6±4.9	0
Az. Gap (°)	108	199
m_b	4.6	3.8

Table 1: REB source parameters for our two examples.

Unfortunately, the only large-aperture array in the IMS is at NORSAR (Norway), which while having low average noise cross-correlation, also has poor signal cross-correlation (Frazier 1972). Here, we show examples of signals recorded by medium-aperture (10–20 km) arrays, with a minimum seismometer spacing of 1–2 km, where the average signal cross-correlation is high. We show that while the average noise cross-correlation is not zero, it is low, suggesting that the probability of F may be interpreted semi-quantitatively, and used as guide to an analyst to help decide whether a signal exists.

We consider two seismic disturbances as examples (Table 1); the first to show how the F trace and the associated probability can help in the identification of surface reflections (pP and sP), and the second to show how these traces can help with 'special event' analysis. To control the bandwidth B we bandpass filter the time-shifted N-channel data (for the vector slowness under consideration) using a two-pass 4-pole Butterworth filter. The passband and window length T (also used for the STA window) seems intuitively to depend on the characteristics of the signal (Blandford 1974) – typically we use a 2 s window. The LTA noise window is set to 50 s. Since our algorithm for calculating the probability of F only allows integer values for the degrees of freedom, N_1 we follow Blandford (1974) and round down to the nearest integer. The values for the semblance, F, probability and STA/LTA traces refer to the mid-point of the time window T.

We report the maximum average cross-correlation for the STA window $\max(\hat{c})$, and the average noise cross-correlation for the LTA window, $\hat{c}$(LTA). Average cross-correlations are calculated using z-transformed cross-correlation coefficients for each independent pair of seismometers in the array (VanDecar & Crosson 1990, Lilwall 1991).

Example 1: July 9, 1997 East of Honshu, Japan

We process seismograms from three medium-aperture arrays (WRA, YKA and EKA) to show how the F-trace and probability can help in the identification of P and the surface reflections pP and sP. Table 2 shows the processing parameters used for the three array seismograms presented in Fig. 1. Each seismogram is formed by beamforming using the vector slowness calculated from the REB hypocentre and the IASPEI 1991 model (Kennett 1991). The average noise correlations, $\hat{c}$(LTA) are low (< 0.15), while for these seismograms because the SNR is high, the maximum of the average cross-correlation, $\max(\hat{c})$ is also high (> 0.90) indicating good signal coherence across the array in the 0.5–3.0 Hz passband. The probability trace in Fig. 1 indicates the probability of F under the hypothesis that R (the square root of the ratio of the signal and noise power on the beam) is that indicated in Table 2. Note that here we have normalised the WRA amplitudes to unity (and inverted one channel), as there are calibration problems for these data.

On the semblance, F, probability and STA/LTA traces there are precursors to the P onset. These are due to the time window T covering both noise and the first half-cycle, or so, of the signal. At YKA this first half cycle has the highest semblance, presumably because signal generated noise in the vicinity of the receiver degrades the semblance after the P onset. This effect becomes apparent under conditions of high SNR (when precursors due to the two-pass filtering also have to be considered).

At first sight, interpretation of these seismograms in terms of P, pP and sP is not straight forward if following the IDC analyst instructions (Anonymous 1998), as the highest amplitude arrivals after the P

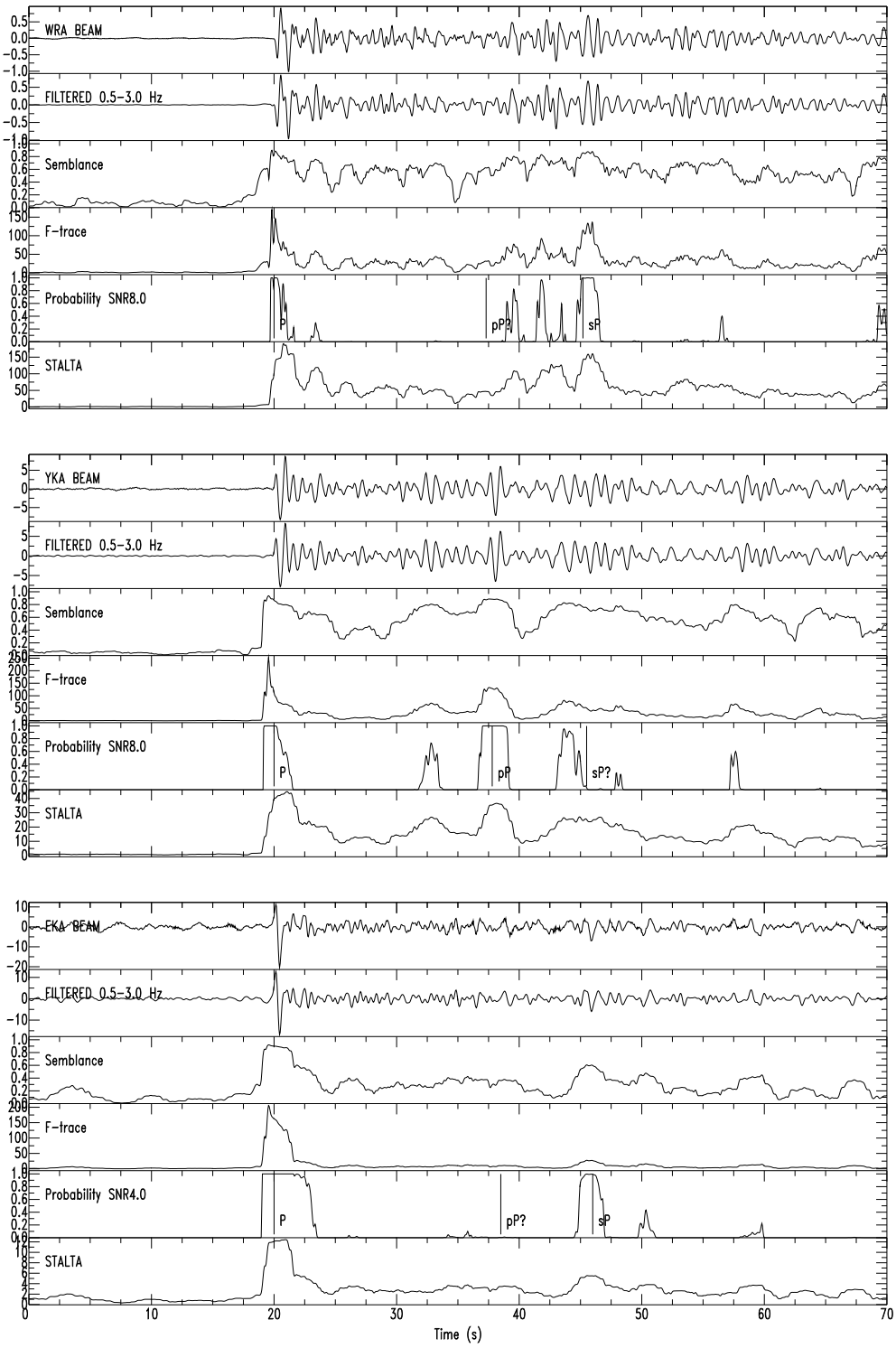


Figure 1: Seismograms and associated traces from the July 9, 1997 earthquake east of Honshu, Japan. The picks on the probability trace are the predicted times relative to the P onset for a depth of 67 km in the IASPEI 1991 model. The processing parameters are given in Table 2.

Station	Δ	Az	PV	BB	B	T	$\hat{c}$(LTA)	max($\hat{c}$)	R	$h = 67$ km	
	(°)	(°)	(km s^{-1})	(°)	(Hz)	(s)				$pP - P$	$sP - P$
WRA	55.4	186.7	15.5	5.8	$3.0 - 0.5$	2.0	0.047	0.933	8.0	17.3	25.2
YKA	65.7	29.5	17.3	300.2	$3.0 - 0.5$	2.0	0.082	0.951	8.0	17.8	25.5
EKA	84.3	339.9	22.0	29.3	$3.0 - 0.5$	2.0	0.128	0.929	4.0	18.5	26.0

Table 2: F processing parameters for Example 1. Δ: distance. Az: Azimuth. PV: phase velocity. BB: Backbearing. $\hat{c}$(LTA): average cross-correlation of the LTA time window. max($\hat{c}$): maximum of the average cross-correlation. h: depth used to predict the time difference between phases using the IASPEI 1991 model.

onset (at 20 s) show little similarity to the pulse shape of direct P. The exception is perhaps the arrival at about 38 s at YKA (which we interpret as pP with opposite polarity to P). The EKA seismogram appears simple, with small coda amplitude compared with direct P. WRA shows a series of pulses starting about 19 s after the P onset. The first of these could be pP, if so this suggests our interpretation of pP at YKA is incorrect as WRA is closer to the epicentre than YKA (Table 2), and 1-D earth models predict increasing $pP - P$ times with distance at long range.

Based on our initial interpretation that the pulse at about 38 s at YKA is pP, we calculate $pP - P$ and $sP - P$ times (using the IASPEI 1991 model) and find a good fit for a source depth of 67 km. The predicted relative $pP - P$ and $sP - P$ times are shown on the probability traces in Fig. 1. Where the probability is highest (approaching unity) corresponds closely to the predicted times for pP at YKA, and for sP at WRA and EKA. Close examination of the WRA and EKA seismograms around the predicted sP time does indeed show a weak, but distinct, arrival. Since the probability of F is high (say $> 90\%$) around the predicted sP time (and low surrounding this local maxima) suggests that this energy has the expected vector slowness for sP, and supports our initial identification of pP at YKA. We have indicated predicted arrivals that have a probability below 90% by appending a '?' to that pick. Of course, the apparent absence of pP at WRA and EKA may be due to either the orientation of the double couple (earthquake) source (pP could be near a minimum in the radiation pattern), or to defocusing of pP energy by above-source structure.

At WRA the $sP - P$ time may be about 1 s longer than predicted. Similarly, the probability trace for YKA suggests there may be a possible sP about 1.5 s before the predicted $sP - P$ time. Differences between observed and predicted $pP - P$ and $sP - P$ times of about 5% are perhaps not surprising given the heterogeneous structure expected above the slab in the subduction zone. However, the predicted moveout (Table 2) of $pP - P$ is 1.2 s between WRA and EKA, whereas the difference between the predicted $pP - P$ times and those inferred from the probability trace appears to be up to about 2 s. Thus, attempts to detect the diagnostic moveout of $pP - P$ (and $sP - P$) times may well fail as the moveout signal could be masked by heterogeneity in the above-source P and S wave speeds.

The $pP - P$ times in the REB are 24.5 s and 19.3 s, for YKA and WRA respectively. The $pP - P$ time for YKA in the REB is close to that inferred as possible sP from the probability trace, suggesting a misassociation. The REB $pP - P$ time at WRA corresponds to a local peak in the probability trace (of about 80%) that is about 2 s later than that predicted for a depth of 67 km. The probability trace for WRA in Fig. 1 shows a series of local maxima preceding the peak we have associated with sP. A similar unassociated probability peak is seen between P and pP on the YKA trace. Both WRA and YKA have azimuths that are sub-parallel to the subducting slab, so these unassociated arrivals may be due to effects such as S-to-P conversions, multi-pathed energy due to the slab, and focusing and scattering by heterogeneous structure in the source region. Analysis of F and the probability trace for signals recorded by medium-aperture arrays may help us to increase our understanding of these phases (and of scattered phases recorded by dense seismometer networks in general).

A comparison of the different traces suggests that the STA/LTA trace is qualitatively similar to F at WRA, but that F has better resolution than the STA/LTA for the YKA and EKA seismograms. However, it is clear that the probability trace is the most useful trace as it allows semi-quantitative statements to be made as to the statistical significance of each associated surface reflection. Our confidence that a probability

peak from a given array is a real surface reflection is increased if peaks are found near predicted pP and sP times at other arrays.

Example 2: August 22, 1998 East Kazakhstan

Here we show how F and the associated probability can be used to test if a weak signal has been detected. P-waves from the 100 t chemical explosion in East Kazakhstan are reported in the REB from only six stations at long range ($> 30°$). The large azimuth gap (199°) is a result of no signals being reported from the south and east. For 'special event' analysis, seismic disturbances that may be considered possible treaty violations, good azimuthal coverage is desirable for, (1) reliable location, and (2) the application of the relative amplitude method to identify shallow (i.e. suspicious) disturbances (e.g. Douglas *et al.* 1999).

Fig. 2 shows the P seismograms and associated traces from two array stations, ILAR and ASAR. No detection is reported from ASAR in the REB. The ILAR filtered array beam shows a clear, simple P signal at the time reported in the REB, whereas the filtered beam at ASAR shows a possible signal at about 58 s (60 s is the time predicted using the REB location and origin time and the IASPEI 1991 model). However, there is a similar signal on the filtered beam at ASAR at about 34 s. The probability of the 34 s phase is about 40%, whereas that at 58 s is about 80%, suggesting that the 58 s signal is real (plus it is at about the expected time). Further, the probability traces in Fig. 2 confirm that the ILAR and ASAR seismograms from the East Kazakhstan explosion are simple (Douglas *et al.* 1999).

CONCLUSIONS AND RECOMMENDATIONS

Our main conclusions are listed below.

- For the medium-aperture seismometer arrays considered the average noise cross-correlations are low, and average signal cross-correlations are high, suggesting that the conditions for the F signal hypothesis are approximately met. Thus, the probability of F can be interpreted semi-quantitatively.
- The probability of F is shown to be useful for identifying weak P signals with a given vector slowness, recorded by medium-aperture arrays. This is found to be useful for identifying weak signals for 'special event' analysis, and for identifying surface reflections (pP and sP).
- Our example demonstrates that observed $pP-P$ and $sP-P$ times can differ from those predicted by the IASPEI 1991 model by up to about 2 s. Thus, the moveout of $pP-P$ and $sP-P$ times, expected to increase with increasing distance, may be masked by variations in the observed times from those predicted. The differences between observed and predicted times are consistent with variations in the above-source P and S wave speeds of up to about 10%.

We recommend that the F-trace and associated probability should be implemented as a tool to help analysts at the IDC identify P, pP and sP (and other body wave phases). Such a tool would also help analysts during the process of reviewing associated (and unassociated) detections from an automatic system, and in the process of identifying signals that have been missed by an automatic system.

Present computing power is such that there may be a case for replacing the current STA/LTA detector by F in the current IDC automatic detection processing for medium-aperture seismometer arrays in the IMS.

Further research is required to determine the P and S wave speed variations in the above-source region of deep earthquakes (the region above the subducting slab). If large variations are confirmed then the use of the moveout of $pP-P$ and $sP-P$ times as a method of confirming that surface reflections are real needs to be reconsidered.

Acknowledgments

I thank Bob Blandford for many stimulating discussions on the properties of the F-detector.

Station	Δ (°)	Az (°)	PV (km s^{-1})	BB (°)	B (Hz)	T (s)	$\hat{c}$(LTA)	max($\hat{c}$)	R
ILAR	60.7	20.2	16.3	328.4	1.0–3.0	2.0	0.073	0.690	3.0
ASAR	88.4	130.4	23.5	327.4	1.5–3.0	1.5	0.036	0.237	1.5

Table 3: F processing parameters for Example 2.

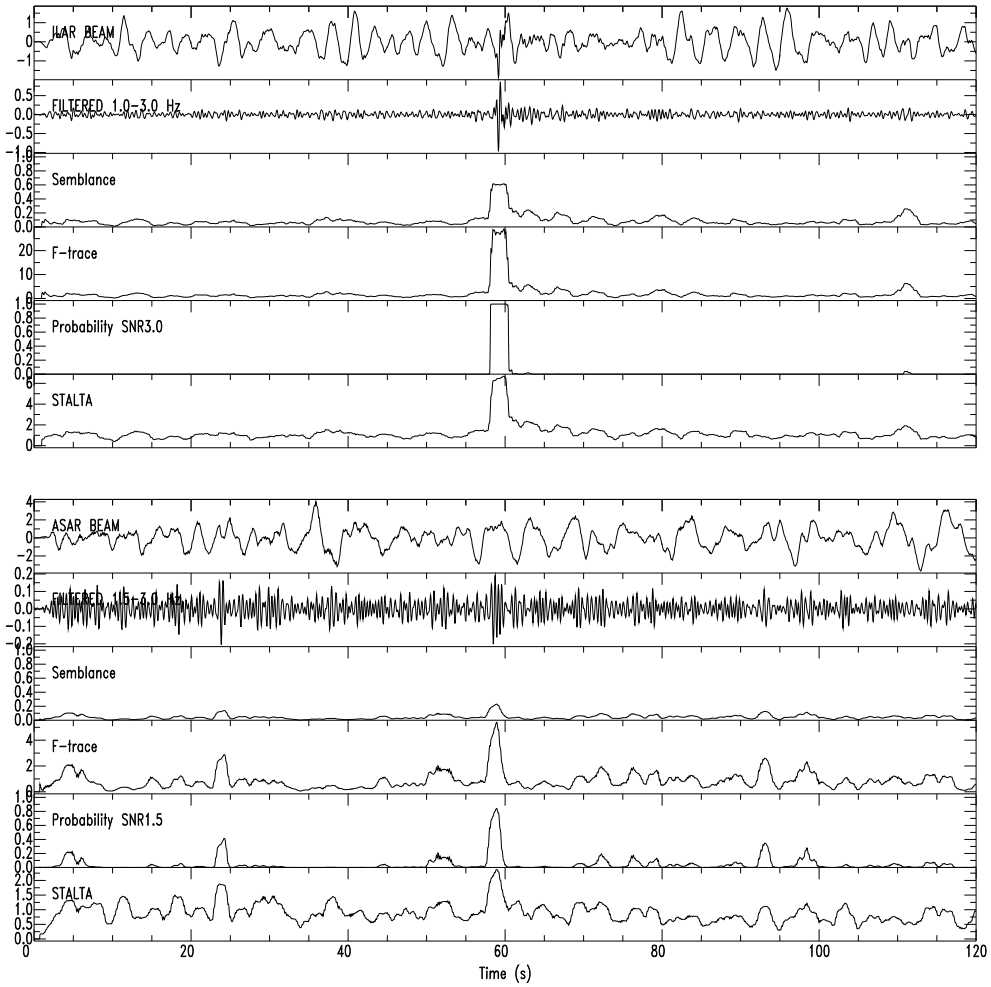


Figure 2: Seismograms and associated traces from the August 22, 1998 100 t chemical explosion in East Kazakhstan. The processing parameters used are given in Table 3.

REFERENCES

Anonymous (1998). Analyst instructions for seismic, hydroacoustic and infrasonic data, IDC documentation – technical instructions, IDC6.2.5, 61-62.

Abramowitz, A. & Stegun, I.A. (1964). Handbook of mathematical functions, Appl. Math. Ser. No. 55, National Bureau of Standards.

Blandford, R.R. (1974). An automatic event detector at the Tonto Forest seismic observatory, *Geophysics*, **39**, 633-643.

Blandford, R.R. & Clark, D.M. (1975). A note on seismic array design, *Bull. seism. Soc. Am.*, **65**, 787-791.

Bowers, D., Pearce, R.G., & Douglas, A. (2000). Using regional geophysical databases to facilitate the identification of surface reflections on P-seismograms, *Geophy. J. Int.*, in press.

Douglas, A., Bowers, D., Marshall, P.D., Young, J.B., Porter, D. & Wallis, N.J. (1999). Putting Nuclear-Test Monitoring to the Test, *Nature*, **398**, 474-475

Douze, E.J. & Laster S.J. (1979). Statistics of semblance, *Geophysics*, **44**, 1999-2003.

Edwards, J.P., Benno, S.A., & Creasey, G. (1967). Evaluation of the CPO auxiliary processor. *CPO Special Report No. 5*, Texas Instruments Sci. Serv. Div.

Frazier, C.W. (1972). Short-period amplitude and waveform studies at NORSAR, in *Seismic Discrimination Semi-Annual Technical Summary*, Lincoln Laboratory, MIT.

Kennett, B.L.N. (1991). *IASPEI Seismological Tables*, Research School of Earth Sciences, Australian National University, Canberra, Australia.

Key, F.A. (1968). Some observations of signal generated noise, *Geophys. J. R. astr. Soc.*, **15**, 377-392.

Lilwall, R.C. (1991). The detection and location of near-regional seismic disturbances by the Eskdalemuir array: a study using noise and signal correlations, AWE Report O-20/90, HMSO, London.

Melton, R.S. & Bailey, L.F. (1957). Multiple signal correlators, *Geophysics*, **22**, 565-588.

Neidell, N.S. & Taner, M.T. (1971). Semblance and other coherency measures for multichannel data, *Geophysics*, **36**, 482-497.

Pearce, R.G. (1977). Fault plane solutions using relative amplitudes of P and pP, *Geophys. J. R. astr. Soc.* **50**, 381-394.

Pearce, R.G. (1980). Fault plane solutions using relative amplitudes of P and surface reflections: further studies, *Geophys. J. R. astr. Soc.* **60**, 459-487.

Pearce, R.G. & Rogers, R.M. (1995). Seismic source discrimination at teleseismic distances using radiation patterns: concepts and feasibility study, AWE Report No. O-4/94. HMSO, London.

VanDecar, J.C. & Crosson, R.S. (1990). Determination of teleseismic relative phase arrival times using multichannel cross-correlation and least squares. *Bull. seis. Soc. Am.*, **80**, 150-169.

Woodgold, C.R.D. (1999). Wide-aperture beamforming of depth phases by timescale contraction, *Bull. seis. Soc. Am.*, **89**, 165-177.

PROBABILISTIC INTEGRATION OF SEISMIC, HYDROACOUSTIC AND INFRASONIC DATA USING THE DEMPSTER-SHAFER RULES FOR COMBINING EVIDENCE

Zoltan A. Der[1], Matthew W. McGarvey[1] and Robert H. Shumway[2]
[1]Ensco Inc, Springfield VA.
[2]University of California at Davis, Davis CA.

Sponsored by ; Defense Threat Reduction Agency

Contract DSWA01-98-C-0145

1.0. ABSTRACT

Identification of suspicious events as nuclear explosions or events of other types is commonly based on incomplete and contradictory data. Although in CTBT monitoring most of the evidence comes from seismic sources, other types of data (hydoacoustic, infrasonic) are often helpful in the classifying an event. The major issue is the manner of merging information from such diverse sources. During this work the Dempster-Shafer (DS) calculus has been implemented as a vehicle for merging information in multi-discriminant schemes. The main motivation for this was that, unlike full Bayesian calculus, DS does not require full knowledge of the conditional probabilities and priors in the problem, the algorithm accepts various combinations of joint probability estimates, and it can merge the information from various independent source regardless of the order of the merging of the data. The final outcome of such calculations is an evidential interval consisting of the support (evidence for) and the plausibility (1-the support against) of simple and composite propositions. Propositions (hypotheses in the parlance of DS) are either simple (the event is an earthquake) or composite, (the event is some kind of explosion). The development of the solutions can be followed as the algorithm processes the various discriminants successively.

In the application of the DS calculus the key inputs are probability masses derived for the various propositions (simple or composite) appropriate to the various (seismic and non-seismic) discriminants. We incorporated several approaches from the general pattern-recognition literature into the estimation of probability masses. Since the seismic discriminants use various aspects of seismograms they can be assumed to furnish independent information as required by the merging process in DS calculus. The same is true for other types of discriminants. The total process is being implemented in MATLAB and includes a graphical user interface. We have found that the output of the process imitates human reasoning quite well for various hypothetical scenarios.

2.0. OBJECTIVES

The objective of this project is to develop a system for event identification by merging information from various seismic, infrasonic and hydroacoustic sources to be used in a practical system for routine discrimination. The basis of the system is formed by the Dempster-Shafer (e.g. Shafer 1976) algorithms which are prominently suitable for combining information from discriminants involving overlapping hypotheses, conflicting and incomplete data. It can also accept rules if stated in terms of stated probabilities (e.g. Dillard 1982).

3 RESEARCH ACCOMPLISHED

3.1 Background

Identifying various types of observed events in the context of a Comprehensive Nuclear Test Ban Treaty (CNTBT) is a classical pattern recognition and data fusion problem. The actual task involves the collection of available observations and the application of various proven discriminants based on previous data.

Presently, the latter come mostly from seismic observations, but other types of data, such as hydroacoustic, infrasonic and radionucleide observations, may contribute. Although considerable work devoted to the statistics of individual discriminants, very little has been done on the joint analyses of multiple discriminants. Moreover, no practical, systematic procedures exist for the merging of information from multiple discriminants especially if these are not very efficient individually (such as the Lg/P discriminant,). Classical Bayesian methods for assessing evidence from multiple sources require the knowledge of the joint statistical distributions of all the quantities measured. This often includes prior probabilities of various hypotheses for which indifferent priors, i.e. assuming that all hypotheses are equally likely, are often employed. In practice, joint distributions and priors are commonly not available, and arbitrary assumptions about them may bias the results.

The DS process of merging evidence from two knowledge source is illustrated in **Figure 1.**. For any knowledge source (discriminant)here may be simple or compound propositions (connected by logical OR's) which are normalized such that they sum to unity. Thus these quantities cannot be called probabilities in the exact sense. Probability weights (masses) are assigned to each proposition. In Figure 1 the probability masses belonging to various combinations of hypotheses are shown along the vertical and horizontal axis, respectively, for the two knowledge sources. We form a product matrix of probability masses and attribute each product to the intersections of the sets in the compound propositions from the two knowledge sources. If these do not overlap, then the product is attributed to the null set. Subsequently, the products corresponding to the same combinations of propositions are summed and the results are divided by the complement of the product masses attributed to the null set. Finally the probability masses attributed to the same subsets of propositions are summed. It can be shown that results will again sum to unity as required by the DS method. There are two main probabilities in DS calculus. The support for a proposition is the sum of all probability masses that contain the proposition and the plausibility is unity minus all the probability masses that support its negation. The interval between these two quantities is termed the evidential interval.

It is a property of the DS method that the final results do not depend on the order of combination. Moreover, even though algorithms for merging multiple sources were developed, the final result will be the same as that obtained by chaining the merging process by merging only two knowledge sources at each step, i.e. merging the result of the last step with the probability masses from the next knowledge source (**Figure 2**). These properties are, of course, to be expected for any reasonable algorithm for merging evidence. Nevertheless, the intermediate results will strongly depend on the order of the consideration of various types of evidence. For instance, if we merge all the evidence favoring a given proposition first, the probability mass for it will reach high values, only to be diminished when unfavorable evidence is merged later.

3.2. Work accomplished

During this project

a) We have built a Dempster-Shafer inference engine in MATLAB complete with user interfaces
b) Implemented various algorithms from the pattern recognition literature to estimate probability masses directly from the previously analyzed data in the region of study.
c) Tested and evaluated the behavior of the system with synthetic data using various realistic scenarios
d) We have added algorithms to evaluate the uncertainties in the results by repeating the calculations iteratively using perturbed probability masses

The final product is a practical system designed to evaluate new events by automatically comparing them to pre-existing data from the same region. Most of the remaining work involves the development of rules and statistical-pattern recognition analyses to be stated in terms of probabilities to be entered into the fusion process.

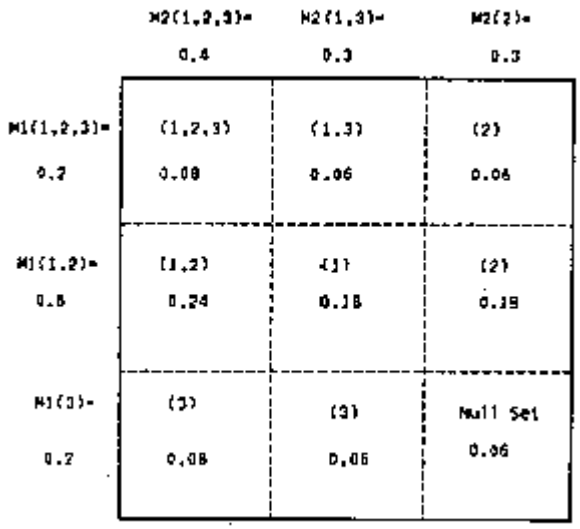


Figure 1. A numerical example for merging evidence from two knowledge sources (discriminants). The two sets of probability masses are shown along the two axes with their assignments to propositions 1,2,3 in parentheses. Note the assignment of cross products.

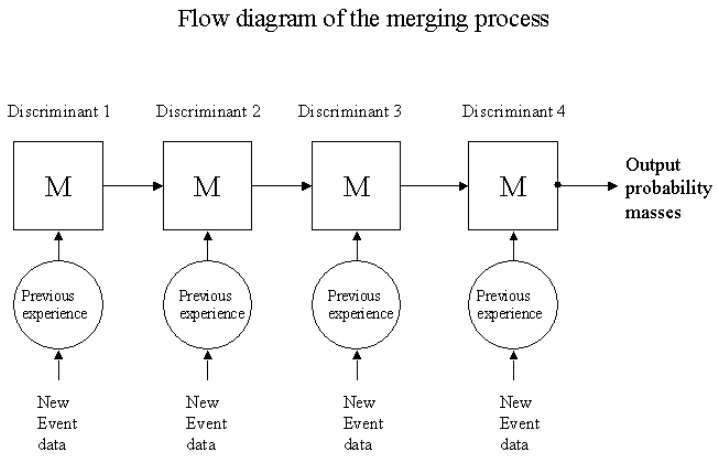


Figure 2. The probability masses from successive knowledge sources are merged chainwise, the order is immaterial. If the overlap of propositions in the discriminants are chosen appropriately at the final step we shall have probability masses assigned to all simple propositions (i.e. the discriminants are able to separate all of these).

3.3. SIMULATIONS OF THE REASONING PROCESS.

3.3.1. Discriminants

We have implemented a simple prototype demonstration system for identifying seismic events that incorporates the following discriminants.

1) P wave complexity
2) Modulation
3) S/P spectral ratios
4) Lg-P spectral ratios
5) Ms-mb
6) Lg spectral ratio
7) Location
8) Hydroacoustic detection
9) Infrasonic detection

The individual discriminants is our simulations have assumed properties that are based on previous experience and physical insight. A few examples of these are described briefly below.

P wave complexity has been found to be effective in dicriminating earthquakes from quarry blasts in Scandinavia (Blandford 1993). P wave from earthquakes tend to have more gradual onset of amplitudes that explosions. These observations were made visually. In order to parametrize complexity we have computed the ratio of the first moment of the seismogram Pn power centered on the arrival time to that of the total power all within the time interval between the arrival time and two seconds after the arrival. This gave us a complexity parameter of 0.7 for impulsive arrivals that decayed after the arrival, 0.9 for arrivals that started abruptly but remained at constant amplitude and 1.5 for arrivals that built up gradually (as unity minus exp(at)) in amplitude from arrival onset within the following 2 second interval. We assumed that these characteristics has a considerable overlap, because P waves from many earthquakes in other regions are quite impulsive too.

Spectral modulation distinguishes single explosions and earthquakes from multiple mining explosions and underwater explosions. The cause for spectral modulation in multiple mining explosions is ripple firing (Baumgardt and Ziegler 1986, Smith 1993, Kim et al 1994) while spectra of underwater explosions are modulated because of multiple bubble pulses and water reverberations (Baumgardt and Der 1999). This discriminant was parametrized as the maximum cepstral amplitude, this spectral modulation parameter varied between zero to 0.7 in our simulations, the latter value was assigned as the mean value for underwater explosions and quarry blasts. Low values of these parameter were assigned to earthquakes and single explosions. Moderate amount of overlap between these two groups of population was assumed in our simulations. Other, equally efficient, possibilities for modulation-based discriminants exist however (Hedlin 1998).

Sn/Pn spectral ratios are commonly given as vectors of values for various frequency bands, the remarks with regards to the reduction of dimensionality made above apply to this discriminant as well. Because their values depend only weakly on frequency the values in various bands but are similar for the same events these can be combined to form a univariate discriminant. This can be accomplished by the standard procedure of computing the covariance matrix between the vector components for a large data set (containing all kind of events) and projecting the individual event vectors along the eigenvector corresponding to the largest eigenvalue. This is done in the system automatically for this types of discriminants. Sn/Pn discriminant tends to separate single explosions on one hand from earthquakes and multiple mining explosions (Sereno et al 1998). Some studies indicate that mine bursts are less earthquake-like than most earthquakes, and multiple explosions (quarry blasts) are also intermediate in character.

Ms-mb. This is a member of a family of discriminants that essentially compare the spectral energy of seismograms in the short and long period bands. Its various versions (mb-ML, mb-M0) are effective discriminants that can separate earthquakes from all kinds of explosions over wide magnitude ranges. For

this discriminant we have incorporated the following features; we assumed that the Mb for quarry blast was slightly lower than for single blasts (the P waveforms from various sub-explosions destructively interfere) thus making the Ms-mb values more earthquake-like. Mine bursts were also assumed to be more earthquake-like.

Intelligent systems for monitoring also apply numerous rules, besides standard discriminants, in assessing the nature of an event. Although many of such rules are formulated a deterministic decisions, many of these can be recast in forms of probability statements and thus integrated into our data fusion scheme.

Instead of probability mass assignments based on the statistical of pattern analyses of previous evidence, which may not exist at all, one may have to make probability mass assignments based on some physical models. These may take the form 'if we have not detected a hydroacoustic signal happens then we assign the probability mass to Proposition 4 of .2 and .7 to the combination of Propositions 1,2,3,5'. These probability mass assignments can then be combined the same way as those derived before.

3.3.3. Propositions.

With regards to event type the following single propositions (with their abbreviations) were assumed;

1) Single explosion on land…….EX
2) Single underwater explosion…..……UWX
3) Mining explosion (multiple)……QB
4) Mine burst……MB
5) Earthquake……EQ

Note that nuclear explosions are not mentioned as a separate category in this case. It is not possible to discriminate nuclear explosions from large single chemical explosions using the discriminants listed here, as evidenced by the studies of the large chemical explosion NPE. Individual discriminants such as those described above are generally not able to separate the individual probability masses appropriate to all these propositions. For instance, Ms-mb is able to separate most explosions from earthquakes, but may not be able to attribute proability masses to each type of explosion. Moreover spectral modulation is a property of both underwater explosions and quarry blasts. Thus the problem is posed in the manner of the combination of simple and/or compound propositions as shown in Figure 1.

3.3.4. Methods for the estimation of probability masses

In all cases the discriminants will provide probability masses to the DS fusion process based on past experience in the region. The computation of the probability masses, i. e. relative weights of the applicable single or compound propositions, can be accomplished by the use of the various classification methods described in the pattern recognition literature.

Mathematically, the most expedient way to define probability masses is to fit Gaussian probability densities to pre-existing data sets, previous experience, from the same region. The Gaussian probability densities of these distributions at the parameter values corresponding to the new event may be used as probability weights in such a scheme. In using Gaussian statistics we are not attempting to decide at each step which of the relevant propositions are the most likely, but only to provide relative weight in the combination process. Naturally, the sums of probability masses, which will be incomplete with regards to all the possible propositions, will have to be normalized to unity prior to entering into the DS fusion process.

If the parameter populations are distinctly non-Gaussian, however, then one has to use other methods for computing probability masses. The pattern recognition literature provides numerous approaches to the problem, it includes methods such as the nearest neighbor classification, potential functions, smoothed empirical distributions and neural networks (e.g. Tou and Gonzalez 1974, Theodoridis and Koutroumbas 1999). We are in the process of implementing several of ones briefly described below. These provide options in the processing flow that the operator may chose.

Another issue is the questions of which of the discriminants can be considered as independent pieces of information. The Dempster-Shafer formalism used in our work requires that the information merged from

various sources be independent. Clearly, the M0-mb and related discriminants and hydroacoustic data can be considered to be independent pieces of information since they were derived from different sensors. The same is true for the Pn/Sn spectral ratios vs Lg spectral ratios since they were derived from different parts of seismograms. The case of Sn/Pn and Lg/Pn ratios is less clear, since they both involve the Pn spectra. In this work we shall still treat them as independent pieces of information since both also involve different parts of the seismograms. On the other hand, the numerous values of the same kinds of spectral ratios (such as Sn/Pn) in various frequency bands are clearly not independent , since they tend to be similar for a given events and depend only slightly from frequency, and thus seem to furnish the same kind of information. For such redundant information that a reduction in the dimensionality by combining such evidence is appropriate. Typically it can be shown by eigenanalysis that the information is almost entirely contained in the first few eigencomponents (often in one!) and thus spectral ratio information over numerous frequency bands can be stated in terms of one or two variables.

3.5. A few examples.

In order to demonstrate the workings of the system, we have generated synthetic data and 'previous experience' for the set of discriminants listed above. In order to have sufficient realism in these simulations, the synthetic data were made conform with the published results by a number of investigators (Li et al 1996, Sereno et al 1998, Fisk 1994, Fisk et al 1994, Bennett et al 1994, Barker 1996, Barker et al 1993). In most areas no results are available for all the discriminants above. In actual applications, ideally, standardized reference data sets should be accumulated within geophysically well defined regions. The 'new data' for one synthetic set displays consistently the properties of a single explosion. The other set has contradictory characteristics in the various discriminants. We must remind the reader, however, that these are totally made-up data.

As we mentioned before, the various discriminants are used to separate various sets (combined propositions) of event types. These sets often overlap but are not identical for the various discriminants. This allows one to compute the probability masses for the simple propositions. For instance, applying the Ms-mb discriminant may resolve the question whether a given event is an earthquake, but will provide much less information about the type of explosion one is examining. Modulation is commonly more characteristic explosions, quarry blasts and underwater explosions, than earthquakes, but an observation of a hydroacoustic signal and location in a water-covered area will lead to the decision that it is an underwater explosion. The application of multiple discriminants that use various sets of propositions is actually needed to identify the probability masses for the single propositions. In some cases the set of discriminants available for an event may not be sufficient to identify it as one of the event types listed above. In such cases only a combined proposition (such as it is some kind of explosion) can be proven. In order to prove decisively that an event is a nuclear, rather than chemical, explosion some corroboration in the form of radionucleide release is needed, although the location and event size may be a factor in the decision.

Working with the first set, we show the Ms-mb data and the data point in **Figure 3** (top). The Sn/Pn spectral ratio data is assumed to be available for five frequencies (Figure 1 bottom). The latter is reduced to a single dimensional Gaussian distribution in the process as described above. As we step through the various discriminants the probability mass for the proposition 1 (EX single explosion) steadily increases (**Figure 4**), but starts at low values because the single proposition of EX has not been isolated yet. On the other hand, the probability mass for the proposition 5 (EQ earthquake) starts at a higher value, since the first discriminant gives a probability mass to it, and steadily diminishes as more and more evidence is merged contradicting it (Figure 2).

Note that after the application of the first few discriminants the inferred probability masses for some of the single proposition of EX remains low. This is because these discriminants can separate only subsets of single propositions and provide no information about the probabilities of the single proposition such as those listed above for explosions.

The second data set, combined with the same 'previous experience' was designed to give much less consistent result (displays of the system for the contradictory discriminants Ms-mb and Sn/Pn spectral ratios are shown in **Figure 5**). The history of the proposition 1 (EX) shows an increase for modulation and

Sn/Pn which support it, followed by a sharp decline as conflicting data for the Lg/Pg spectral ratios, Ms-mb and Lg spectral ratios are merged. The best fit is to the properties of a mine tremor but with a low probability.

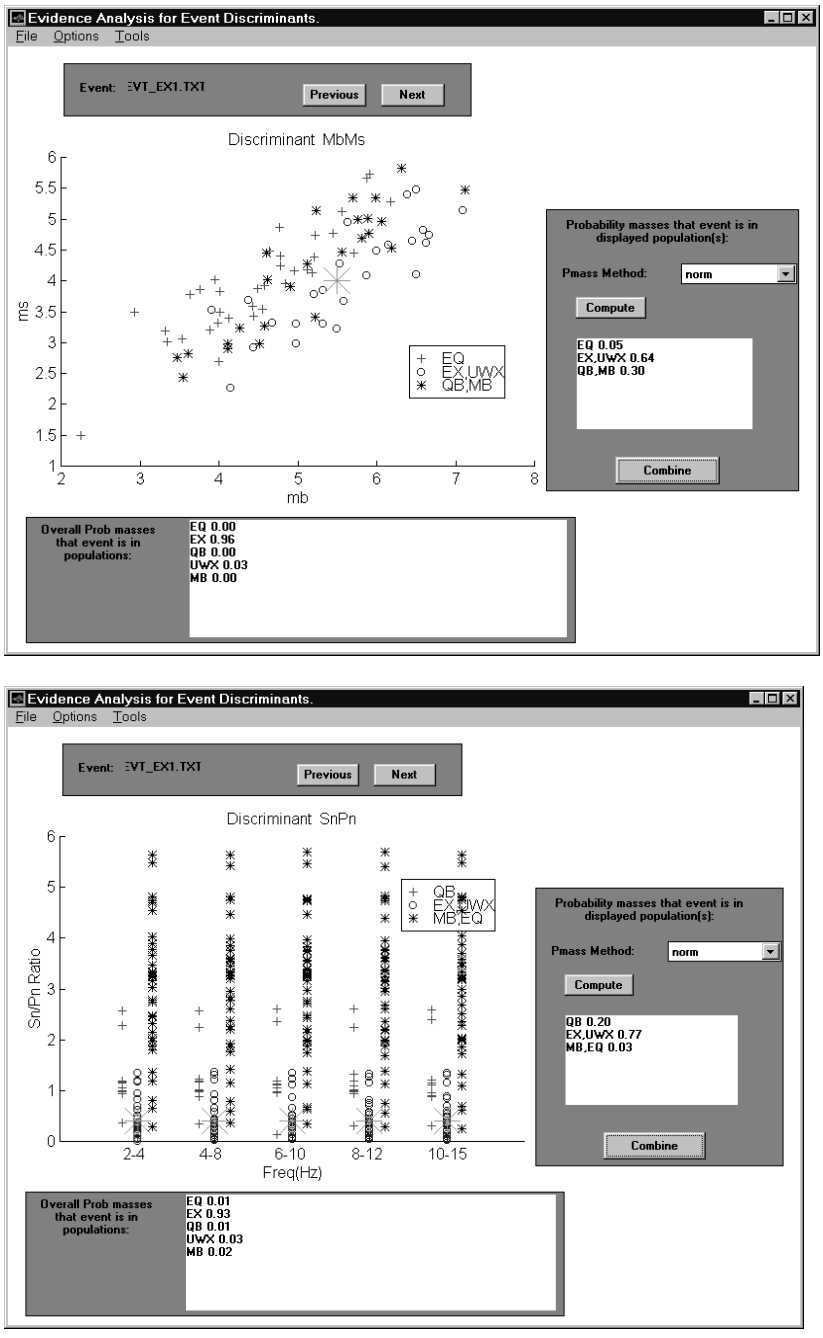


Figure 3. Synthetic Ms-mb (top) and Sn/Pn spectral ratio (bottom) populations. The Ms-mb were assumed to be well separated for earthquakes and single explosions but mixed for quarry blasts and mine bursts. The large stars correspond to the assumed data. The panels show the GUI presentation, allowing the combination of evidence (Compute button), changing of the method for computation of probability masses.

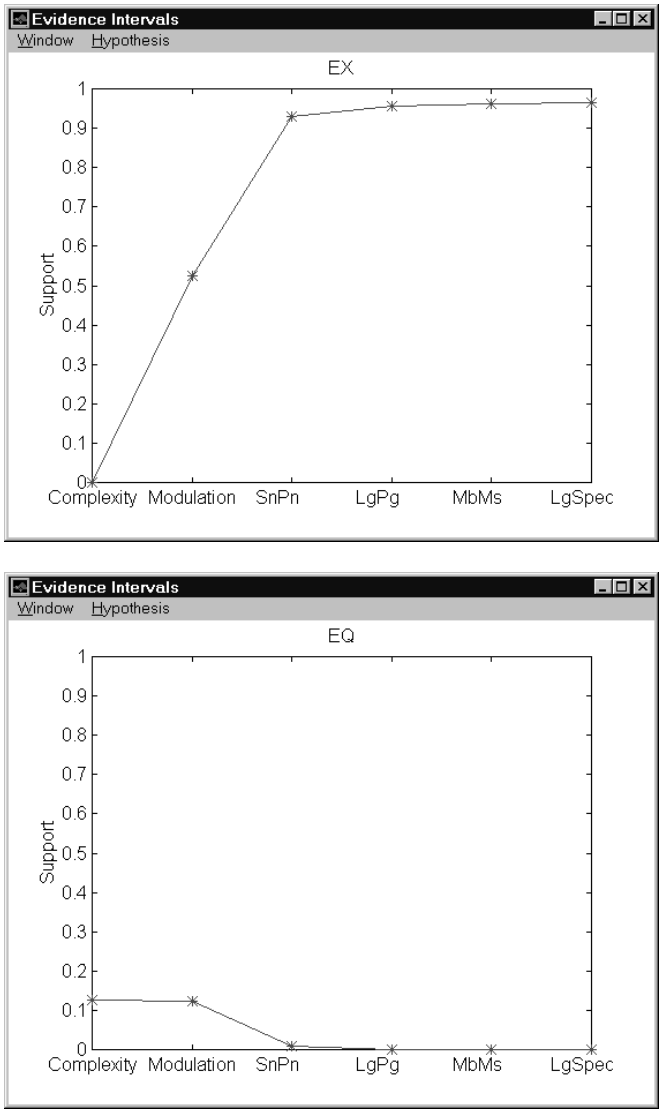


Figure 4. The time histories of supports for the #1 proposition (EX single explosion) and those for the proposition #5 (EQ earthquake). Note the monotonous increase of the first and the decrease of the second. This is due to the fact that all the data support proposition #1.

.

.

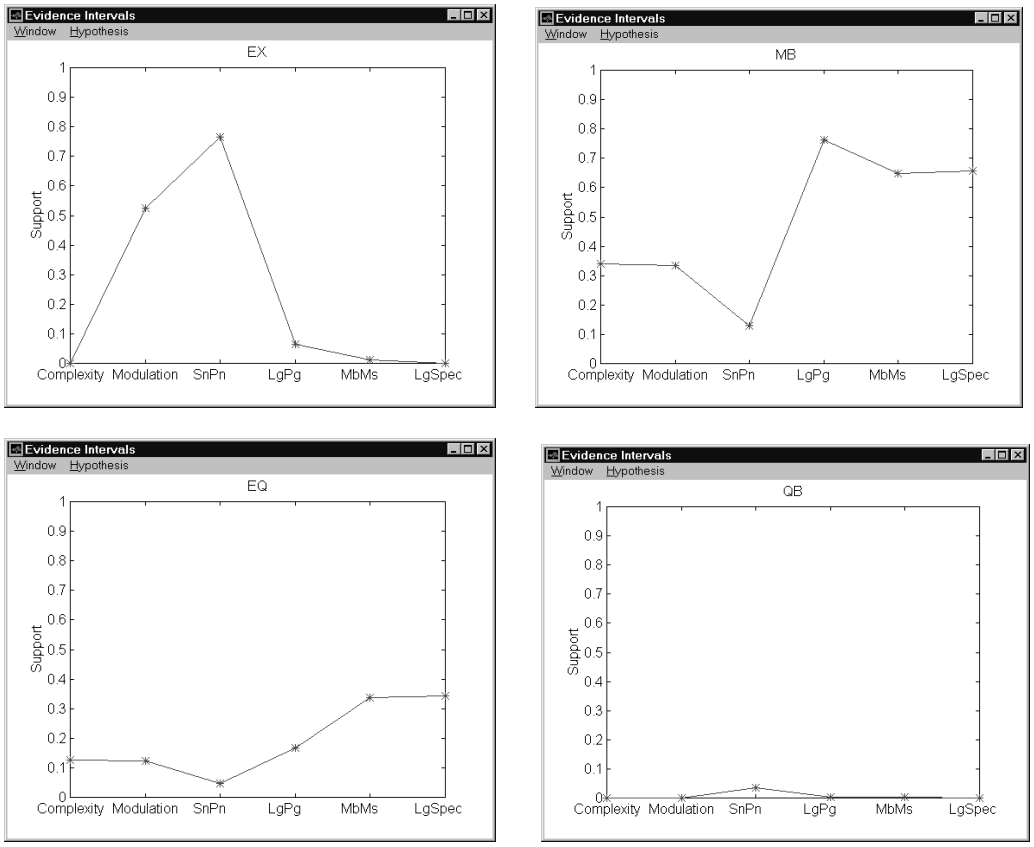


Figure 5. The time histories of supports (support) for the #1 proposition (EX single explosion), #4 (MT mine tremor), #5 (EQ earthquake) and #2 (QB quarry blast or multiple explosion) for the second set of assumed data. Because of the conflicting data the support for each is changing non-monotonously and none reach a high value.

Figure 5 shows the time histories of support for a case where the data were inconsistent with any of the single propositions. In such cases the support fluctuates, increases where the data are consistent with a proposition, only to decrease again when new, contradictory evidence is introduced.

Assessment of the uncertainties in the results of the DS merging process.

We have added some important new features to the DS process by incorporating the uncertainties in the estimated probability masses. The estimates of the probability masses from the acquired empirical data in a given region are point estimates giving no hint of their uncertainties. Consequently, the final results of the merging process may be severely biased or unreliable. It is a simple matter, however, to estimate the uncertainties in these probability masses by resampling schemes such as bootstrap or jackknife (Efron 1982). Such schemes would be quite helpful in cases where the 'previous experience' consist if small data sets. It does not add much to the computing time if the probability masses are perturbed using their estimated uncertainties and the merging process is repeated many times in a Monte-Carlo scheme. The results will then be populations of probability mass estimates for the various propositions and will give a much better assessment of the given discrimination problem.

This addition to the algorithm enables the user to relate new data to the previous experience in the region in a more quantitative manner. The results thus obtained reflect the uncertainties due to scatter in the empirical data and the limitations imposed by sparse data sets. **Figure 6** shows a synthetic example of the merging procedure using a Monte-Carlo scheme where the computation was repeated many times with randomly perturbed probability masses. Since all discrimination problems involve relatively small amounts of data, this calculation can easily be done on small computers.

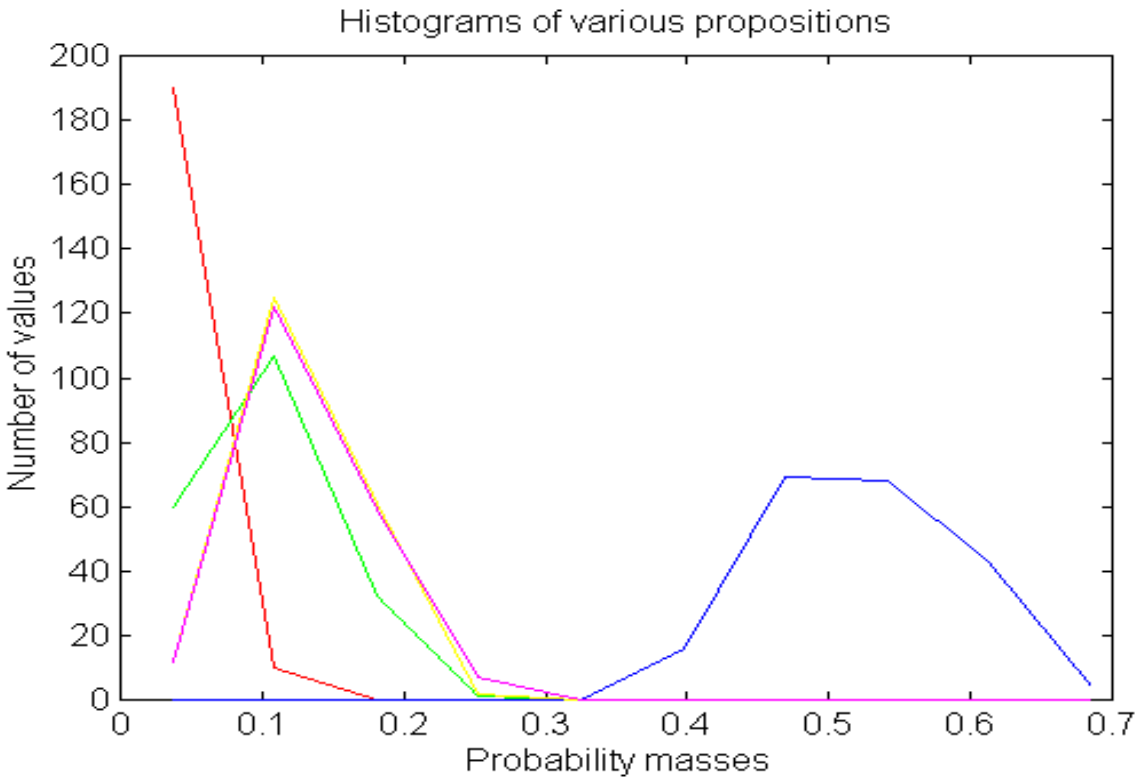


Figure 6. Populations of probability masses for four propositions, one very unlikely, two about equally unlikely and one the most probable. The populations were generated by randomly perturbing the original probability masses.

4.0. CONCLUSIONS AND RECOMMENDATIONS

The work presented shows that the DS rules for combining evidence from multiple independent sources provide a good framework for identifying events on the basis of various types of seismic, infrasonic and hydroacoustic observations. The methodology easily accommodates incomplete and contradictory data and overlapping sets of single propositions. The development of belief and plausibility estimates as more discriminants are added reflect the internal consistency of the data set. In the cases where conflicting pieces of information must be reconciled a widening of the evidential interval and the lowering of belief indicates a reduction in the reliability of the conclusions.

The results shown above demonstrate that the DS calculus is eminently suitable for merging information from various discriminants and it simulates the human reasoning process quite well. The relatively low computational efficiency of the DS process relative to other methods is immaterial in nuclear monitoring where speed of computation is not an issue.

Key Words; nuclear monitoring, data fusion, discrimination, inference

5.0. REFERENCES

Barker, T.G., McLaughlin, K.L. and J.L. Stevens (1993), Numerical simulation of quarry blast sources. Maxwell Laboratories, S-Cubed, La Jolla, CA. Technical Report prepared for Phillips Laboratory, Kirtland AFB, NM.

Barker, T. G. (1996), XNICE: A system for assessing network identification performance. PL-TR-96-2087. Prepared for the Phillips Laboratory. Hanscom AFB, MA, by S-Cubed, Division of Maxwell Laboratories, La Jolla, CA.

Baumgardt, D.R. and K. A. Ziegler (1988). Spectral evidence for source multiplicity in explosions, application to regional discrimination of earthquakes and explosions,
Bull. Seism. Soc. Am. 78, 1773-1795.

Baumgardt, D. R., and Der, Z. A. (1998), Identification of presumed shallow underwater chemical explosions using land-based regional arrays. Bull. Seism. Soc. Am., 88, 581-595.

Bennett, T. J., Marshall, M. E., McLaughlin, K. L., Barker, B. W. and J. R. Murphy (1994), Seismic investigations of rockbursts. Proceedings of the 18-th Annual Seismic Research Symposium on Monitoring a Comprehensive test Ban Treaty. Annapolis, MD.

Blandford, R. R. (1993), Discrimination of earthquakes and explosions at regional distance using complexity. AFTAC-TR-93-044. Air Force Technical Applications Center, Patrick AFB, FL.

Cleckner, W. H. (1985), Tactical Evidential Reasoning: An application of the Dempster-Shafer theory of evidence. M.S. Thesis. Naval Postgraduate School, Monterey, CA.

Dempster, A. P. (1968), A generalization of Bayesian inference. J. Roy. Stat. Soc., Series B., 30, 205-247.

Dillard, R. A. (1982), Computing probability masses in rule-based systems. Technical Document 545, Naval Ocean Systems Center, San Diego, CA.

Dillard, R. A. (1983), Computing confidences in tactical rule-based systems by using the Dempster-Shafer theory. Technical Document 649, Naval Ocean Systems Center, San Diego, CA.

Efron, B. (1982), The Jacknife, the Bootstrap and Other Resampling Plans. CBMS-NSF Regional Conference Series in Applied Mathematics.

Fisk, M. D. (1994), Identification and event characterization; Getting down to outliers. CTBT Monitoring Technologies Conference, San Diego, CA.

Fisk, M. D., Gray, H. L. and McCartor, G. L. (1994), Statistical framework for seismic event discrimination and preliminary assessment of CTBT monitoring capability. CTBT Monitoring Technologies Conference, San Diego, CA.

Hedlin, M. A. (1998), A global test of a time-frequency small-event discriminant. Bull. Seism. Soc. Am., 88, 973-988.

Kim, W.Y., Simpson, D.W. and P.G. Richards (1994), High frequency spectra and regional phases from earthquakes and chemical explosions..Bull. Seism. Soc. Am., 84, 1365-1386.

Li, Y., Toksöz, M. N., and Rodi, W. L. (1996), Discrimination of small earthquakes and explosions. Proceedings of the 18-th Annual Seismic Research Symposium on Monitoring a Comprehensive test Ban Treaty. Annapolis, MD.

Marchard, P. (1996), Graphics and GUIs with MATLAB. CRC Press.

Ryall, A., S., Baumgardt, D. R., Fisk, M. D., and Riviere-Barbier, F. (1996), Resolving regional discrimiantion problems. In "Monitoring a Comprehensive Test Ban Treaty.", NATO ASI Series, Series E: Applied Sciences. Kluwer Academic Publishers.

Sereno, T. J., Jenkins, R. D. and Bache, T. C. (1998), Discrimination of Asian explosions with range-corrected S/P ratios. In Proceeding of the 2—th Annual Seismic Research Symposium on Monitoring a Comprehensive Test Ban Treaty. Santa Fe, NM.

Shafer, G. (1976), A Mathematical Theory of Evidence. Princeton University Press.

Smith, A.T. (1993), Discrimination of explosions from simultaneous mining blasts. Bull. Seism. Soc. Am., 83, 160-179.

Tou, J. T.,, and Gonzalez, R. C. (1974), Pattern Recognition Principles. Addison-Wesley.

ESTIMATION OF DEPTH AND ATTENUATION OF EARTHQUAKES IN BOLIVIA

Lawrence A. Drake
Observatorio San Calixto, Bolivia

Sponsored by U.S. Department of Defense
Defense Threat Reduction Agency and Air Force Technical Applications Center
Contract No.: F49620-97-1-0214

ABSTRACT

It is well known that, without depth phases or phases from a few nearby seismograph stations, the depths of many events cannot be accurately determined and must be assigned. This is especially true in regions of subduction. Carefully drawn intensity maps of 11 felt earthquakes in Bolivia have been examined and the depths of these earthquakes have been determined from the Kövesligethy formula

$$I_0 - I_n = a \log (r_n/h) + b(r_n - h)$$

where r_n is the mean hypocentral distance to the closest points of intensity I_n, h is depth, a and b are constants and I_n is less than I_0. With the depths of the earthquakes determined, the approximate horizontal acceleration caused by them has been found to be

$$\log a_h = 0.35\ M_w - 0.54 \log (r/h) - 0.0036\ (r - h), \quad h < 70 \text{ km}$$

$$\log a_h = 0.33\ M_w - 1.38 \log (r/h), \quad 70 \text{ km} <= h < 150 \text{ km}$$

$$\log a_h = 0.30\ M_w - 1.50 \log (r/h), \quad 150 \text{ km} <= h < 330 \text{ km}$$

$$\log a_h = 0.21\ M_w - 1.85 \log (r/h), \quad 330 \text{ km} <= h$$

where r is hypocentral distance and M_w is moment magnitude. The attenuation corresponding to these accelerations has been compared with that for P waves of Richter (1958) and of Veith and Clawson (1972), and with that for P_g and L_g waves for France of Campillo and Plantet (1991). With the seismic array around Cochabamba in central Bolivia operating, locations of seismic events and observations of attenuation in Bolivia have been much improved.

Key Words: Anelasticity, attenuation, Bolivia, earthquake intensity, earthquake location.

OBJECTIVE

It is well known that, without depth phases or phases from a few nearby seismograph stations, the depths of many events cannot be accurately determined and must be assigned (Eisenberg et al., 1989). Regional strucures, such as downgoing slabs, can severely bias depth estimation when only regional and teleseismic P arrivals are used to determine the hypocenter (Engdahl et al., 1998). The region of Bolivia is unusual in that it includes a downgoing slab, the Nazca plate from the west, at about 8 cm/a (Norabuena et al.,1998; 1999; Kendrick et al., 1999), and a mid-crustal décollement in the east, of the Subandean fold-thrust belt into the Brazil Shield, at about 1 cm/a (Gubbels et al., 1993; Lamb et al., 1997). If the depth estimation of a seismic event is wrong, and the seismic stations are not uniformly distributed relative to the epicenter of the event, the estimation of the epicenter of the event will be wrong also. The Comprehensive Nuclear-Test-Ban Treaty requires the location of seismic events to approximately plus or minus 17.8 km ("a benchmark value of 17 km", Wüster et al., 2000). In 1996, at the 90% confidence level, the equivalent circle areas for the m_b (Preliminary Determination of Epicenters) 4-4.5 magnitude range was about 8000 km^2 (Wüster et al., 2000). This area corresponds to a location accuracy of approximately plus or minus 50.5 km^2. Also, in a monitoring context, depth is important as a potential screening parameter for indubitably natural seismic events (Wüster et al., 2000). Hence, it is important for the monitoring of the Comprehensive Nuclear-Test-Ban Treaty to improve the estimation of the depths of seismic events. Also, the International Data Centre,

operated by the Provisional Technical Secretariat (Comprehensive Nuclear-Test-Ban Treaty (CTBT), 1997, p. 14), provides estimates of the magnitude of all of the seismic events that it lists. Hence, it is important to examine the attenuation of seismic waves in the region of Bolivia and to compare this attenuation with that observed for compressional and shear waves in other parts of the world.

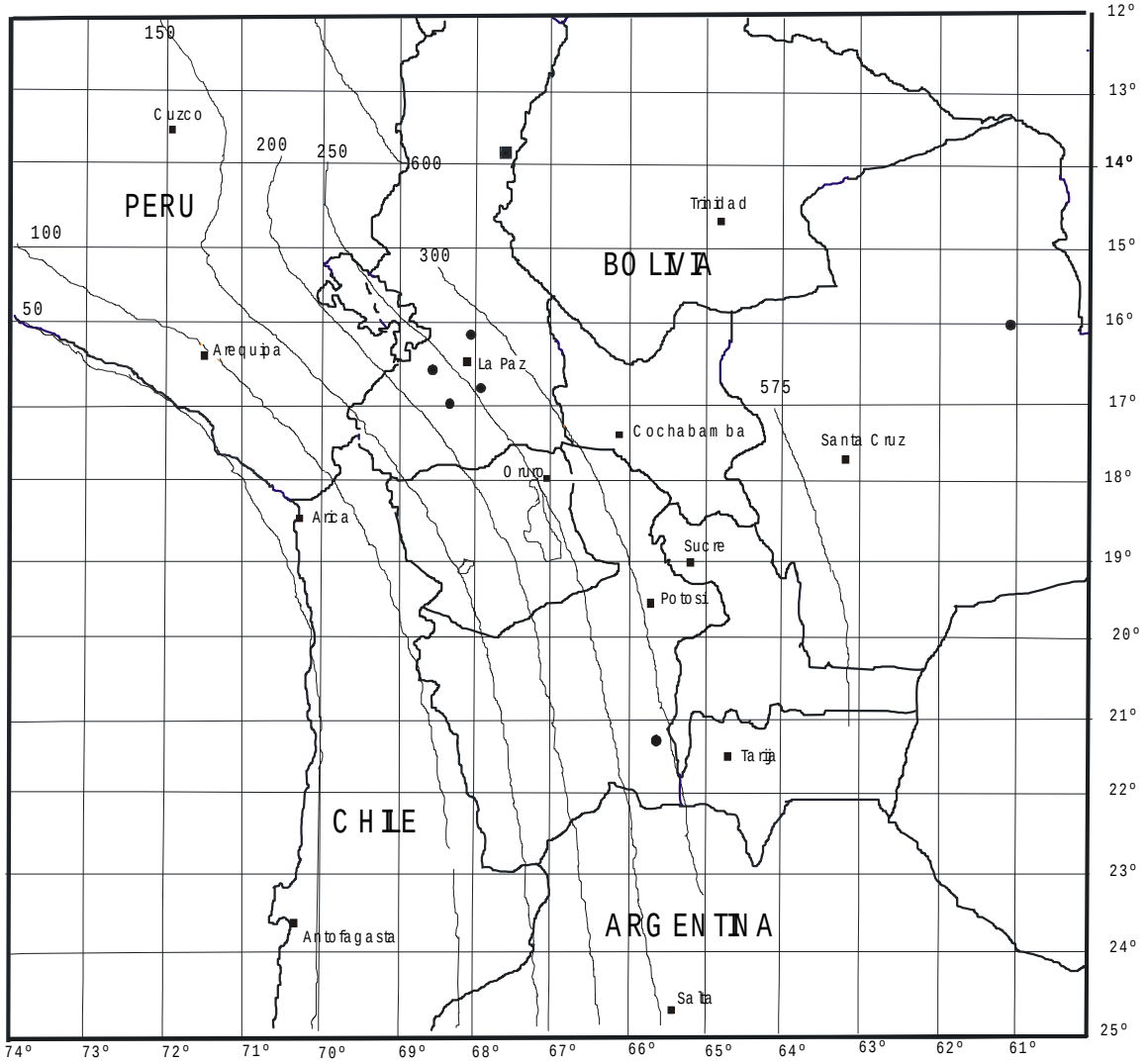


Figure 1. Seismic stations in Bolivia operated by Observatorio San Calixto. Three stations are close to the city of Cochabamba. Contours of the Nazca plate are shown, as well as the epicenter of the earthquake of 9 June 1994 of latitude –13.87, longitude –67.51, depth 677 km and Mw = 8.2 (Vega, 1994; Cabré and Vega, 1995).

RESEARCH ACCOMPLISHED

The region of Bolivia, with the seismic stations at present operating and the depth contours of the Nazca plate (Cahill and Isacks, 1993), is shown in Figure 1. The coordinates of the seismic stations are tabulated

in Table 1. Because of the theft of the radio and battery from the station Cerro Ichu Kkollu, the seismometer has been moved temporarily to the central station, Colegio Juan XXIII.

In order to determine the depths of earthquakes in the region of Bolivia more reliably, a study has been made of isoseismals of 10 shallow Bolivian earthquakes (Rodríguez and Vega, 1976a; 1976b; Vega, 1997) and, for comparison, of six other damaging earthquakes in other parts of the world (Tocher, 1960; Ergin, 1969; Bolt, 1993a, p. 271; Maley and Cloud, 1973; Berlin, 1980, 2, pp. 137-142; Procházková et al.; 1979; Berardi et al., 1981; Bolt, 1993b, pp. 166-172). This study was based on the formula of Kövesligethy (Ergin, 1969) and on the principle of Ambraseys and Adams (1996): "It is hard to neglect the evidence of a well-defined area of high intensity."

After the revision the depths of the 10 shallow Bolivian earthquakes, the isoseismals of these earthquakes were used, together with those of the Vrancea, Romania, earthquake of 1977 (Kondorskaya et al., 1979; Radu et al., 1979), and those of the deep Colombian earthquake of 1970 (Catalog of Earthquakes for South America: Colombia, 1985; Furumoto, 1977) and those of the deep Bolivian earthquake of 1994 (Vega, 1994; Cabré and Vega, 1995), to derive expressions for acceleration in the region of Bolivia as a function of moment magnitude (M_w) of an earthquake, its depth and epicentral distance from it.

Table 1. Seismic stations operated by Observatorio San Calixto

Name	Code	Date	Latitude S	Longitude W	Altitude m	Component
La Paz, Milluni	LPAZ	1993-….	16º17’16.6” (16º.2879)	68º07’50.4” (68º.1307)	4740	BB-Z-NS-EW SP-Z
Zongo	BOA	1972 -….	16º16’09.7” (16º.2694)	68º07’26.5” (68º.1240)	4397	SP-Z-NS-EW
Banderani	BOB	1975-….	16º08’39.6” (16º.1443)	68º07’58.4” (68º.1329)	3960	SP-Z
Gloria	BOD	1986 -….	16º38’14.6” (16º.6374)	68º35’53.2” (68º.5981)	4230	SP-Z
Chanca	BOE	1982 -….	16º48’45.7” (16º.8127)	67º58’55.6” (67º.9821)	4325	SP-Z
Collana	BOF	1993 -….	16º57’14.4” (16º.9540)	68º20’16.8” (68º.3380)	4480	SP-Z
San Ignacio	SIV	1990 -….	15º59’28.7” (15º.9913)	61º04’19.9” (61º.0722)	520	SP-Z
Mochará	MOCB	1993 -….	21º15’01.5” (21º.2504)	65º38’16.8” (65º.6380)	3580	SP-Z
Bombeo	BBO	1998-....	17º39’27” (17º.6575)	66º27’27” (66º.4575)	3821	SP-Z-NS-EW
Apacheta	APC	1998-....	17º21’32” (17º.3589)	66º01’30” (66º.0250)	3676	SP-Z-NS-EW
Cerro Ichu Kkollu	IKK	1998-....	17º15’02” (17º.2506)	66º19’32” (66º.3256)	4612	SP-Z-NS-EW
Colegio Juan XXIII		1998-....	17º22’31.7” (17º.3755)	66º11’33.7” (66º.1927)	2599	Central station

Isoseismal estimations usually do not note the effect of soft soil. For example, in a study of the the ground motion induced in the city of Rome by the Fucino (Italy) earthquake of 13 January 1915, it was recognized that the presence of a near-surface layer of rigid material is not sufficient to classify a location as a “hard-rock site” when the rigid material has a sedimentary complex below it (Fäh et al., 1993). Also, it is well known that, in the Kobe earthquake of 1995, the fault was in the mountains west and southwest of Kobe and that the high intensities were over the soil of Kobe to the east and northeast of the fault (Furumura and Koketsu, 1998). Care has been taken to allow for this effect, both in the estimation of the depth of the

earthquakes and in the use of the expressions that have been derived for acceleration (Reiter, 1990; pp. 147-163).

In a recent study of 356 earthquakes in Greece, Albania, former Yugoslavia and Turkey, Papazachos and Papaioannou (1997; 1998; Trifunac, 1998) used, as the formula of Kövesligethy (cf. Ergin, 1969):

$$I_o - I_n = 1.6135 \log (1 + x_n^2/h^2) + 0.0033((x_n^2 + h^2)^{1/2} - h)$$

where I_o is the maximum intensity, I_n is less than I_o, x_n is the minimum mean radius of the area of intensity I_n and h is depth of the earthquake. For x = 90 km and h = 22 km, this formula becomes:

$$I_o - I_n = 3.6 \log(r_n/h) = 1.8 \log (1 + x_n^2/h^2)$$

where 3.6 is the Kövesligethy coefficient and $r_n^2 = x_n^2 + h^2$. For explosions in the region of Lakes Michigan and Superior, Howell (1966) and Willis and DeNoyer (1966) found that the absorption varies between 3×10^{-4} f Hz/km and 6×10^{-3} f Hz/km, where f is frequency. Nuttli (1973) noted that absorption was not much different in California and central and eastern U.S. at epicentral distances below 100 km, and Berlin (1980, 1, p. 81) noted that, for epicentral distances below 100 km, the absorption term is usually omitted.

The 10 shallow Bolivian earthquakes, the earthquake of intermediate depth near Vrancia, Romania, of March 1977 (Kondorskaya et al., 1979; Radu et al., 1979), the large deep Peru-Colombia earthquake of July 1970 (Catalog of Earthquakes for South America: Colombia, 1985; Furumoto, 1977), the large deep Bolivian earthquake of June 1994 (Vega, 1994; Cabré and Vega, 1995), and six other shallow damaging earthquakes in other parts of the world are listed in Table 2. Times, epicenters and depths were taken from the International Seismological Summary or from the Bulletin of the International Seismological Centre. If the time and hypocenter were not listed for an earthquake, they were estimated from La Paz readings and the pattern of the isoseismals. For the Totora earthquake of 22 May 1998, they were taken from the Preliminary Determination of Epicenters. Moment magnitudes were estimated from the moments of the earthquakes, if they were available, or were estimated from magnitude relations (Ambraseys and Adams, 1996; Giardini et al., 1997).

Table 2. Earthquakes according to international agencies

Date	Time	Latitude	Longitude	Depth	Mw
d m yr	h m s	deg.	deg.	km	
24 02 1947	17 31 36.0	-15.50	-68.80	65.0	6.4 Consata
28 03 1948	01 30 07.0	-18.91	-65.34	13.8	6.1 Sucre
26 08 1957	11 28 52.0	-18.74	-63.73	33.0	6.1 Postrer Valle
29 02 1960	23 40 16.0	30.57	-09.43	2.0	6.0 Agadir
31 07 1970	17 08 05.4	-01.50	-72.60	648.8	8.2 Peru-Colombia
09 02 1971	14 00 40.6	34.40	-118.43	9.0	6.5 San Fernando
12 05 1972	17 16 38.0	-17.46	-66.90	107.0	5.0 Tiquipaya
06 09 1975	09 20 12.0	38.51	40.77	32.0	6.7 Lice
22 02 1976	08 09 22.7	-18.33	-65.35	41.0	5.4 Quiroga
06 05 1976	20 00 12.5	46.35	13.26	11.2	6.5 Friuli
30 06 1976	17 16 58.0	-18.40	-66.90	73.0	4.7 Arque
04 03 1977	19 21 54.1	45.83	26.72	99.0	7.5 Vrancea
23 11 1980	18 34 52.2	40.86	15.33	0.0	6.7 Campania-Lucania
23 07 1981	13 51 28.5	-17.03	-65.12	53.0	5.0 Chimoré
09 05 1986	16 23 48.8	-17.17	-65.62	13.0	5.9 Villa Barrientos
18 10 1989	00 04 14.8	37.06	-121.79	12.5	6.9 Loma Prieta
09 06 1994	00 33 16.7	-13.87	-67.51	677.0	8.2 Reyes-Rurrenabaque
06 11 1995	02 18 43.5	-19.10	-68.31	57.0	5.4 Cumujo
22 05 1998	04 48 50.4	-17.73	-65.43	24.0	6.5 Totora

For each earthquake, trial values of the Kövesligethy coefficient were assumed of 3.6, 4.0, 4.5 and 5.0 (cf. Ergin, 1969) and the depth of the earthquake was found which gave the best correlation with the minimum mean radiuses of the intensity regions. For the six earthquakes outside Bolivia, these depths and the corresponding correlation coefficients are tabulated in Table 3.

Because the vertical extent of the fault plane for these earthquakes is probably of the order of 15 or 20 km (Bolt, 1993b, p. 168) and because the most probable depth of the source of intensity is probably not the depth of the rupture that caused the initial P, there are differences in the depths in Tables 2 and 3. Because of the presence of the ocean or a sea, there is poor correlation with the minimum mean radiuses of the intensity for the earthquakes of Agadir, San Fernando, Campania-Lucania and Loma Prieta. For the earthquake of Lice, in central Turkey in 1975, the International Seismological Centre clearly had little depth control (cf. Berlin (1980, 2, p. 137). The faults of the San Fernando (Bolt, 1993a, p. 218) and Campania-Lucania (Pantosti and Valensise, 1990) earthquakes caused surface breaks.

For the 10 earthquakes in Bolivia, epicenters and depths revised from the isoseismals are tabulated in Table 4. For the Tiquipaya earthquake of 1972, the hypocenter of the International Seismological Centre appears to be 84 km WSW of the hypocenter from the isoseismals, and 99 km deeper. For the very shallow Arque earthquake of 1976, the hypocenter of the International Seismological Centre appears to be 83 km SW of the hypocenter from the isoseismals, and 70 km deeper. As late as 1995, for the Cumujo earthquake, the hypocenter of the International Seismological Centre appears to be 16 km NE of the hypocenter from the isoseismals, and 48 km deeper.

Table 3. Revised depths and correlations with isoseismals

Agadir	San Fernando	Lice	Friuli	Campania-Lucania	Loma Prieta
6.2 km	6.1 km	4.1 km	5.2 km	8.6 km	25.2 km
0.95974	0.96975	0.99961	0.99982	0.98717	0.97953

Table 4. Revised locations of Bolivian earthquakes

Date	Time	Latitude	Longitude	Depth	Mw
d m yr	h m s	deg.	deg.	km	
24 02 1947	17 31 36.0	-15.30	-68.58	23.1	6.4 Consata
28 03 1948	01 30 07.0	-18.91	-65.34	13.8	6.1 Sucre
26 08 1957	11 28 52.0	-18.51	-63.79	18.8	6.1 Postrer Valle
12 05 1972	17 16 38.0	-17.38	-66.11	8.3	5.0 Tiquipaya
22 02 1976	08 09 22.7	-18.43	-65.16	8.2	5.4 Quiroga
30 06 1976	17 16 58.0	-17.84	-66.38	2.9	4.7 Arque
23 07 1981	13 51 28.5	-16.97	-64.98	5.8	5.0 Chimoré
09 05 1986	16 23 48.8	-17.02	-65.47	20.2	5.9 Villa Barrientos
06 11 1995	02 18 43.5	-19.22	-68.40	8.5	5.4 Cumujo
22 05 1998	04 48 50.4	-17.85	-65.16	5.9	6.5 Totora

From the the re-determined depths of the 10 shallow Bolivian earthquakes, from the well-known depth of the Vrancea, Romania, earthquake, from the well-known depths of the Colombian earthquake of 1970 and of the Bolivian earthquake of 1994, from their isoseismal patterns, and from the relation of horizontal acceleration (a_H, cm/s^2) with intensity (I) of Murphy and O'Brien (1977; $\log a_H = (I + 1)/4$), the following relations for horizontal acceleration as a function of moment magnitude (M_w), hypocentral distance (r) and depth (h) were found:

$$\log a_h = 0.35\ M_w - 0.54 \log (r/h) - 0.0036\ (r - h), \quad h < 70 \text{ km}$$

$$\log a_h = 0.33\ M_w - 1.38 \log (r/h), \quad 70 \text{ km} <= h < 150 \text{ km}$$

$$\log a_h = 0.30\ M_w - 1.50 \log (r/h), \quad 150 \text{ km} <= h < 330 \text{ km}$$

$$\log a_h = 0.21\ M_w - 1.85 \log (r/h), \quad 330 \text{ km} <= h$$

The attenuation of the displacement that might correspond with these horizontal accelerations is compared with that for P waves of Richter (1958, p. 688; surface focus, cf. Veith and Clawson, 1972) and of Veith and Clawson (1972; depth of focus, 15 km), and with that for P_g and L_g waves for France of Campillo and Plantet (1991; Campillo et al., 1984; 1985) in Table 5 for an earthquake of M_w or m_b equal to 5 for distances of 2° to 10°. M_w is taken to be equal to m_b up to magnitude 5.2 (Giardini et al., 1997, for the Mediterranean region). Displacements in Table 5 are centre to peak in nanometres and the period used is 0.5 s, commonly observed for local earthquakes in Bolivia. Because the conversion from acceleration to displacement depends on the square of the frequency, in the third row of Table 5, the frequency (Hz) is given that makes the displacements corresponding to the $\log_{10}$ of the horizontal acceleration in row 2 of Table 5 equal to the displacements corresponding to the attenuation of Veith and Clawson (1972) in row 5 of Table 5. These frequencies appear to be large, compared to a period of 0.5 s. However, the accelerations from which they are calculated are consistent with intensities and accelerations expected from earthquakes of given magnitudes (Richter, 1958, p. 353; Trifunac and Brady, 1975; Murphy and O'Brien; 1977). The displacements of Veith and Clawson (1972; cf. their Figure 1) for an event of surface focus are larger than those of Richter (1958) for distances of 2° to 10°. The P_g attenuation of Campillo and Plantet (1991), corresponding to the displacements given in row 6 of Table 5, is normalized to that of Veith and Clawson (1972) at 2° (surface focus). The L_g attenuation of Campillo and Plantet (1991), corresponding to the displacements given in row 7 of Table 5, is normalized to the attenuation between distances of 250 km and 750 km used in the French location program used at present in Bolivia, and the period used is 1.08 s, consistent with this attenuation.

Table 5. Horizontal accelerations and displacements

Distance km	222.4	333.6	444.8	556	667.2	778.4	889.6	1000.8	1112
log ah	.369	-.126	-.593	-1.046	-1.489	-1.925	-2.357	-2.784	-3.209
Hz	52.7	34.7	30.3	22.9	16.2	11.2	7.5	4.8	3.1
Richter	158.1	79.2	39.7	19.9	12.9	8.3	5.4	3.5	2.5
V-C	212.8	157.7	70.5	43.4	31.5	23.9	19.9	17.7	16.1
Pg	212.8	83.5	39.3	20.3	11.1	6.4	3.8	2.3	1.4
Lg	721.9	378.9	219.0	133.5	84.2	54.4	35.8	23.8	16.0

Attenuation for earthquakes from a depth of 100 km to a depth of 700 km has been revised from digital data (Nolet et al., 1998a; 1998b; 1998c; Veith, 1998). Dewey (1999) noted that the m_b-formula-independent bias between magnitudes estimated by the U.S. Geological Survey and those estimated by the Prototype International Data Center is about 0.3, $4.5 <= m_b < 5.5$. Murphy and McLaughlin (1998) show data that imply, for earthquakes of depth less than 50 km, from 1982 to 1994, m_b estimated by the U.S. Geological Survey corresponded to M_w of 5.27, and, after 1994, to M_w of 5.34. These findings disagree with observations from the Mediterranean region (Giardini et al., 1997). Murphy and McLaughlin (1998) also show that, for earthquakes with a depth greater than 20 km, "if it is assumed that the Harvard moments provide unbiased estimates of source size", for magnitudes estimated by the U.S. Geological Survey, down to a depth of 160 km, there is a bias of 0.3 units, and, from depths of 160 km to 350 km, there is a bias of 0.2 units; for magnitudes estimated by the Prototype International Data Center, from depths of 200 km to 350 km, the negative bias changes from zero to -0.1, and, from depths of 450 km to 650 km, it is -0.3.

CONCLUSIONS AND RECOMMENDATIONS

Depths of 10 Bolivian earthquakes have been revised and formulas have been derived for the horizontal accelerations to be expected on hard soil at various distances from earthquakes of various depths in the region of Bolivia. The attenuation of the displacement that might correspond with these horizontal accelerations from a distance of 2° to a distance of 10° has been compared with that for P waves of Richter

(1958) and of Veith and Clawson (1972), and with that for P_g and L_g waves for France of Campillo and Plantet (1991). It will be worth plotting the attenuations of Richter (1958) and of Veith and Clawson (1972) and comparing them with those found from digital data for earthquakes from a depth of 100 km to a depth of 700 km (Nolet et al., 1998a).

We are having trouble with our southern stations. Time at the stations near Cochabamba cannot be read, and the station Mochará appears to be too far southwest of the satellite over the Atlantic Ocean to transmit its data. We are arranging to receive via internet data from Chile and northern Argentina: without these data, our stations, practically in a straight line from La Paz to San Ignacio de Velasco, are useless for local locations. Work has been done (Beck et al, 1996; Zandt et al., 1996; Myers et al., 1998; Chmielowski et al., 1999; Swenson et al., 1999), and is being done, particularly by the method of receiver functions (Langston, 1979; Ammon et al., 1990) on the structure of the Andes. We are continuing investigation on the propagation of Love and Rayleigh waves across irregular structures (Bolt and Drake, 1986; Drake and Bolt, 1989; Drake, 1989; Meier and Malischewsky, 2000) by the finite element method.

REFERENCES

Ambraseys, N.N. and R.D. Adams, 1996. Large-magnitude central American earthquakes. Geophys. J. Int. 127, 665-692.

Ammon, C.J., G.E. Randall and G. Zandt, 1990. On the nonuniqueness of receiver function inversions. J. Geophys. Res. 95, 15303-15318.

Beck, S.L., G. Zandt, S.C. Myers, T.C. Wallace, P.G. Silver and L.A. Drake,1996. Crustal-thickness variations in the central Andes. Geology 24, 407-410.

Berardi, R., A. Berenzi and F. Capozza, 1981. Campania-Lucania Earthquake on 23 November 1980: Accelerometric Recordings of the Main Quake and Relating Processing. Report presented to the Annual Meeting of the Geodynamic Project on: Italy's Seismicity -Status of Scientific Know-How and Seismic Standards Quality. Udine, 103 pp.

Berlin, G.L., 1980. Earthquakes and the Urban Environment (2 vols). CRC Press, Boca Raton, Florida.

Bolt, B.A., 1993a. Earthquakes. Freeman, New York.

Bolt, B.A., 1993b. Earthquakes and Geological Discovery. Scientific American Library, New York.

Bolt, B.A. and L.A. Drake, 1986. Love mode dispersion across subduction zones by finite element modelling. Geophys. J. R. Astr. Soc. 84, 515-528.

Cabré, R. and A. Vega, 1995. Sismo boliviano del 9 de junio de 1994. Revista Técnica de YPFB (Yacimientos Petrolíferos Fiscales Bolivia) 16(1-2), 5-8.

Campillo, M. and J.-L. Plantet, 1991. Frequency dependence and spatial distribution of seismic attenuation in France: experimental results and possible interpretations. Phys. Earth Planet. Int. 67, 48-64.

Campillo, M., M. Bouchon and B. Massinet, 1984. Theoretical study of the excitation, spectral characteristics and geometrical attenuation of regional seismic phases. Bull. Seism. Soc. Am.74, 79-90.

Campillo, M., J.-L. Plantet and M. Bouchon, 1985. Frequency dependent attenuation in the crust beneath central France from Lg waves: data analysis and numerical modelling. Bull. Seism. Soc. Am.75, 1395-1411.

Catalog of Earthquakes for South America: Colombia, 1985. Centro Regional de Sismología para América del Sur (vol. 4, B.L. Askew and S.T. Algermissen, eds), Lima, Peru.

Chmielowski, J. and G. Zandt, 1999. The central Andean Altiplano-Puna magma body. Geophys. Res. Lett. 26, 783-786.

Comprehensive Nuclear-Test-Ban Treaty (CTBT), 1997. Preparatory Commission for the Comprehensive Nuclear-Test-Ban Treaty Organization. Austria, V.97-28276.

Dewey, J.W., 1999. On the PIDC/USGS mb discrepancy. Seism. Res. Lett. 70, 211-212.

Drake, L.A., 1989. Love and Rayleigh waves in irregular structures. In Observatory Seismology: A Centennial Symposium for the Berkeley Seismographic Stations (J.J. Litehiser, ed.). University of California Press, Berkeley, pp. 333-346.

Drake, L.A. and B.A. Bolt, 1989. Finite element modelling of surface wave transmission across regions of subduction. Geophys. J. Int. 98, 271-279.

Eisenberg, A., D. Comte and M. Pardo, 1989. The need for local arrays in mapping the lithosphere. In Observatory Seismology: A Centennial Symposium for the Berkeley Seismographic Stations (J.J. Liteheiser, ed.). University of California, Berkeley, pp. 187-198.

Engdahl, E.R., R. van der Hilst and R. Buland, 1998. Global teleseismic earthquake relocation with improved travel times and procedures for depth determination. Bull. Seism. Soc. Am. 88, 722-743.

Ergin, K., 1969. Observed intensity-epicentral distance relations in earthquakes. Bull. Seism. Soc. Am. 59, 1227-1238.

Fäh, D., C. Iodice, P. Suhadolc, and G.F. Panza, 1993. A new method for the realistic estimation of seismic ground motion in megacities: the case of Rome. Earthquake Spectra 9, 643-668.

Furumoto, M., 1977. Spacio-temporal history of the deep Colombia earthquake of 1970. Phys. Earth Planet. Int. 15, 1-12.

Furumura, T. and K. Koketsu, 1998. Specific distribution of ground motion during the 1995 Kobe earthquake and its generation mechanism. Geophys. Res. Lett. 25, 785-788.

Giardini, D., M. di Donato and E. Boschi, 1997. Calibration of magnitude scales for earthquakes of the Mediterranean. J. Seism. 1, 161-180.

Gubbels, T.L., B.L. Isacks and E. Farrar, 1993. High-level surfaces, plateau uplift, and foreland development, Bolivian central Andes. Geology 21, 695-698.

Howell, B.F., 1966. Lake Superior seismic experiment: frequency spectra and absorption. In The Earth beneath the Continents. American Geophysical Union Geophysical Monograph 10 (J.S. Steinhart and T.J. Smith, eds), pp. 227-233.

Kendrick, E.C., M. Bevis, R.F. Smalley, O. Cifuentes and F. Galban, 1999. Current rates of convergence across the central Andes: estimates from continuous GPS observations. Geophys. Res. Lett. 26, 541-544.

Kondorskaya, N.V., O.N. Solonieva, A.I. Zakharova, T.B. Yanovskaya, L.S. Chepkunas and L.N. Pavlova, 1979. The earthquake of March 4, 1977, its recording pecularities and source parameters. Tectonophys. 53, 203-215.

Lamb, S., L. Hoke, L. Kennan and J. Dewey, 1997. Cenozoic evolution of the Central Andes in Bolivia and northern Chile. In Orogeny Through Time (J.-P. Burg and M. Ford, eds). Geol. Soc. Spec. Publ. 121, 237-264.

Langston, C.A., 1979. Structure under Mount Rainier, Washington, inferred from teleseismic body waves. J. Geophys. Res. 84, 4749-4762.

Maley, R.P. and W.K. Cloud, 1973. Strong-motion accelerograph records. In San Fernando, California, Earthquake of February 9, 1971 (L.M. Murphy, scientific coordinator). National Oceanic and Atmospheric Administration, Washington, pp. 325-348.

Meier, T. and P.G. Malischewsky, 2000. Approximation of surface wave mode conversion at a passive continental margin by a mode-matching technique. Geophys. J. Int. 141, 12-24.

Murphy, J.R. and K.L. McLaughlin, 1998. Comment on "Empirical determination of depth-distance corrections for m_b and M_w from Global Seismograph Network stations" by Guust Nolet, Steve Krueger and Robert M. Clouser. Geophys. Res. Lett. 25, 4269-4270.

Murphy, J.R. and L.J. O'Brien, 1977. The correlation of peak ground acceleration amplitude with seismic intensity and other physical parameters. Bull. Seism. Soc. Am. 67, 877-915.

Myers, S.C., S. Beck, G. Zandt and T. Wallace, 1998. Lithospheric-scale structure across the Bolivian Andes from tomographic images of velocity and attenuation for P and S waves. J. Geophys. Res. 103, 21233-21252.

Nolet, G., S. Krueger and R.M. Clouser, 1998a. Empirical determination of depth-distance corrections for m_b and M_w from Global Seismograph Network stations. Geophys. Res. Lett. 25, 1451-1454.

Nolet, G., S. Krueger and R.M. Clouser, 1998b. Reply. Geophys. Res. Lett. 25, 4243-4244.

Nolet, G., S. Krueger and R.M. Clouser, 1998c. Reply. Geophys. Res. Lett. 25, 4271-4272.

Norabuena, E., L. Leffler-Griffin, A. Mao, T. Dixon, S. Stein, I. Selwyn Sacks, L. Ocola and M. Ellis, 1998. Space geodetic observations of Nazca-South America convergence across the central Andes. Science 279, 358-362.

Norabuena, E.O., T.H. Dixon, S. Stein and C.G.A. Harrison, 1999. Decelerating Nazca-South America and Nazca-Pacific plate motions. Geophys. Res. Lett. 26, 3405-3408.

Nuttli, O.W., 1973. Seismic wave attenuation and magnitude relations for eastern North America. J. Geophys. Res. 78, 876-885.

Pantosti, D. and G. Valensise, 1990. Faulting mechanism and complexity of the November 23, 1980, Campania-Lucania earthquake, inferred from surface observations. J. Geophys. Res. 95, 15319-15341.

Papazachos, C. and Ch. Papaioannou, 1997. The macroseismic field of the Balkan area. J. Seism. 1, 181-201.

Papazachos, C. and Ch. Papaioannou, 1998. Further information on the macroseismic field in the Balkan area. J. Seism. 2, 363-375.

Procházková, D., Z. Schenková and V. Kárník, 1979. Macroseismic fields of the main Friuli shocks of 1976. Tectonophys. 53, 249-259.

Radu, C., V. Kárník, G. Polonic, D. Procházková and Z. Schenková, 1979. Isoseismal map of the Vrancia earthquake of March 4, 1977. Tectonophys. 53, 187-193.

Reiter, L., 1990. Earthquake Hazard Analysis. Colombia University Press, New York.

Richter, C.F., 1958. Elementary Seismology. Freeman, San Francisco.

Rodríguez, R. and A. Vega, 1976a. El terremoto del 12 de mayo de 1972 en Cochabamba. Revista geofísica, Instituto Panamericano de Geografía e Historia 5, 161-171.

Rodríguez, R. and A. Vega, 1976b. Sismo del 22 de febrero de 1,976 en el sur de Cochabamba. Publication No. 27, Observatorio San Calixto, La Paz, Bolivia.

Swenson, J.L., S.L. Beck and G. Zandt, 1999. Regional distance shear-coupled PL propagation within the northern Altiplano, central Andes. Geophys. J. Int. 139, 743-753.

Tocher, D., 1960. Seismological notes. Bull. Seism. Soc. Am. 50, 323-330.

Trifunac, M.D., 1998. Comment on 'The macroseismic field of the Balkan area' by C. Papazachos and Ch. Papaioannou. J. Seism. 2, 359-362.

Trifunac, M.D., and A.G. Brady. 1975. On the correlation of seismic intensity scales with the peaks of recorded ground motion. Bull. Seism. Soc. Am. 65, 139-162.

Vega, A.J., 1994. El gran terremoto profundo del día 9 de junio de 1994 en el norte de la República de Bolivia. Revista Geofísica, Instituto Panamericano de Geografía e Historia 40, 39-55.

Vega, A., 1997. Terremoto en Cumujo, Provincia Atahuallpa de Oruro. Revista Geofísica, Instituto Panamericano de Geografía e Historia 46, 17-36.

Veith, K.F., 1998. Comment on "Empirical determination of depth-distance corrections for m_b and M_w from global seismograph network stations". Geophys. Res. Lett. 25, 4241-4242.

Willis, D.E. and J.M. DeNoyer, 1966. Seismic attenuation and spectral measurements from the Lake Superior experiment. In The Earth beneath the Continents. American Geophysical Union Geophysical Monograph 10 (J.S. Steinhart and T.J. Smith, eds), pp. 218-226.

Wüster, J., F. Rivière, R. Crusem, J.-L. Plantet, B. Massinon and Y. Caristan, 2000. GSETT-3: evaluation of the detection and location capabilities of an experimental global seismic monitoring system. Bull. Seism. Soc Am. 90, 166-186.

Zandt, G., S.L. Beck, S.R. Ruppert, C.J. Ammon, D. Rock, E. Minaya, T.C. Wallace and P.G. Silver, 1996. Anomalous crust of the Bolivian Altiplano, central Andes: constraints from broadband regional seismic waveforms. Geophys. Res. Lett. 23, 1159-1162.

IDENTIFICATION AND VALIDATION OF REFERENCE EVENTS WITHIN THE AREA BEING REGIONALLY MONITORED BY IMS STATIONS IN ASIA AND NORTH AFRICA

E. R. Engdahl and Eric A. Bergman

University of Colorado

Sponsored by The Defense Threat Reduction Agency
Arms Control Technology Division
Nuclear Treaties Branch

Contract No. DTRA01-00-C-0032

ABSTRACT

High-resolution cluster analysis is applied to explosions and earthquake sequences in Asia and North Africa for which one or more of the associated events is known to an accuracy of 5 km or better (GT5). In particular, we analyze phase data reported to the ISC and NEIC for the 1997 Ghaen-Birjand earthquake sequence in eastern Iran and the 1997 Jiashi swarm in western China. In both cases, reference event data is available from short-term portable seismograph deployments following the initiation of seismic activity in those regions. For the cluster analyses we used 92 events of the Iran sequence and 123 events of the Jiashi swarm, ranging in magnitude from 3.4 to 7.1. The analyses produce new locations (relative to the centroid) and 90% confidence ellipses that sharpen the spatial relationship of the earthquakes to known faults and modes of deformation in these regions. Shifting the centroid to match reference event locations produces source-station path corrections (to ak135) for regional seismic phases recorded by IMS and surrogate stations in Asia. The standard error of these path corrections is typically only a few tenths of seconds. Hence, these data can be used to validate 3-D models and to support the calculation of travel-time curves and source-specific station corrections for the Asian and north African regions.

Key Words: Reference Events, Cluster Analysis, Path Corrections

OBJECTIVE

The primary objective of this research effort is to develop a comprehensive reference event database with validated travel-time information for regional seismic phases recorded by IMS and surrogate stations in Asia and North Africa. This database can be used to support the calculation of regional travel-time curves and source-specific station corrections.

RESEARCH ACCOMPLISHED

Method

Validation of potential reference events is performed in two steps. First, ISC/NEIC reported phase arrival times from event clusters are used to perform some simple tests of location uncertainties using the EHB location algorithm (Engdahl et al., 1998). Second, further analysis of the events is performed by multiple event relocation (cluster) analysis using the method of Hypocentroidal Decomposition (HDC; Jordan and Sverdrup, 1981) HDC is used because it makes maximal use of all available data and it carries the a priori error budget through the analysis in a completely rigorous manner. Results of the cluster analysis may reveal the effects of small-scale lateral heterogeneities (on the order of tens of kilometers), perhaps requiring (data permitting) further sub-division of the original cluster into sub-clusters for separate analyses. A final product of this validation process for an event cluster (or sub-clusters) is a set of source-station path corrections for each phase reported, with statistics. These corrections can then be used in developing calibration correction surfaces for individual IMS and surrogate stations.

Application

In this report, we analyze phase data reported to the ISC and NEIC for the 1997 Ghaen-Birjand earthquake sequence in eastern Iran and the 1997 Jiashi swarm in western China. Nearly all the events in this study have magnitudes of 3.5 or greater. In both cases, reference event data is available from short-term portable seismograph deployments following the initiation of seismic activity. For the cluster analyses we used 92 events of the Iran sequence and 123 events of the Jiashi swarm, ranging in magnitude from 3.4 to 7.1. The analyses produce new locations which are defined by "cluster vectors" in space and origin time, relative to the centroid which is then located in the traditional manner to yield absolute locations and origin times. If one or more reference events are included in the cluster, the centroid can be shifted to provide the optimal match to the reference locations, which brings all events in the cluster into close alignment with "ground truth". The expanded set of corrected hypocenters is then available to calculate source-station path corrections relative to the Earth model ak135 (Kennett et al., 1995) for regional seismic phases recorded by IMS and surrogate stations in Asia.

Iran Sequence

On May 10, 1997, a damaging multiple event (called the Ghaen-Birjand earthquake) occurred in a region of high seismicity at the boundary of the Lut Block in eastern Iran. The Geophysics Institute at Tehran University reported that the quake was accompanied by a surface rupture which included three segments with a total length of 113 km or (by excluding inter-segment distances) a length of 87 km. The spatial and temporal distribution of aftershocks revealed two barriers along the fault line at inter-segment distances. Five months later the second period of aftershock activity began along the southern end of the surface rupture while the northern part was quiescent.

Phase data was reported to ISC and NEIC for 92 events near the fault traces of this earthquake through 1999, but only three of these events were larger than mb 4.9. Nevertheless, we were able to successfully perform a cluster analysis of the data set. Plotted in Figure 1 are the HDC locations of 42 events in the sequence that have 90% confidence ellipses with areas equivalent to that of a circle with radius 10 km. The correlation of our HDC locations to mapped faults in the region, perhaps with only a slight northerly bias, is remarkable. We are collaborating with the researchers in Tehran who carried out the field study of this sequence to obtain more information about any of the events in the HDC analysis which were well-recorded by the temporary deployment of portable seismographs following the main shock, in order to

establish as many reference locations for this cluster as possible. Nevertheless, it is instructive to estimate Pn source-station path corrections from residuals computed with respect to our HDC locations. Because of outlier residuals, we use a robust median statistics approach to estimate the median, spread and standard error of Pn residuals at each reporting station using an algorithm programmed by R. Buland (personal communication). In Figure 2 are plotted the more reliable of these medians for 16 stations at distances up to 20 degrees from the source region of the sequence. The range of these Pn corrections which are based entirely on HDC locations is about +/- 4sec and they seem to be spatially correlated.

Jiashi Swarm

In 1997 a strong earthquake swarm occurred in an intraplate region of western China (Jiashi county) at the edge of the Tarim basin. In the 10 months following the onset of this activity phase data were reported to ISC and NEIC for 123 events within a small area (50 x 50 km) of the region. Of these 123 events, 113 were mb 3.5 or larger, with 8 larger than mb 4.9. A temporary deployment of 3 portable seismographs within distances of less than 30 km from events in the swarm captured an mb 4.7event in the swarm. Data from these stations and other permanent stations at distances less than 250 km from the source were used by Chinese scientists to locate this event using a local crustal model. Hence, it qualifies as a reference event. A cluster analysis of the swarm produced HDC locations for 57 events that have 90% confidence ellipses with areas equivalent to that of a circle with radius 5 km. These HDC locations were shifted by moving the centroid of the cluster so that the HDC location of the reference event matched the ground truth location. The resulting high resolution locations are plotted in Figure 3. The pattern of epicenters is confined to a small region but does not appear to display any lineation that would indicate that the events belong to a single fault. Focal mechanisms of the larger swarm events indicate both strike slip and normal faulting, which, in combination with the pattern of epicenters, is consistent with a complex, diffuse pattern of deformation.

As we did for the Iran sequence, we estimate the median, spread and standard error of Pn residuals at each reporting station and plot the more reliable median estimates for 57 stations at distances up to 20 degrees from the source region of the swarm. However, in the case of the Jiashi swarm, we use residuals based on HDC locations which have been shifted to match the reference event. The shift required is 10.4 km at an azimuth of 18° and a surprisingly large change in origin time, 2.8 seconds earlier. The medians plotted in Figure 4 are quite large, ranging from +8 to -3 sec, suggesting a possible error in the origin time of the reference event. To better understand the problem we plot in Figure 5a medians based on residuals for unshifted HDC locations and in Figure 5b medians based on reference event locations for Lop Nor explosions (nearly 900 km from the Jiashi source region) estimated using cluster analysis (JED) by Terry Wallace (personal communication). The comparison is not conclusive but the possibility of a problem in the origin time estimate for the Jiashi swarm reference event seems likely. Additional information, such as the arrival times and crustal model used to locate the reference event will be needed before these corrections can be validated. We are attempting to confirm the reliability of the reference location with the researchers who conducted the aftershock study.

CONCLUSIONS AND RECOMMENDATIONS

High-resolution cluster analysis is being applied to earthquake sequences in Asia and North Africa for which one or more of the associated events is known to an accuracy of 5 km or better (GT5). In particular, we analyze phase data reported to the ISC and NEIC for the 1997 Ghaen-Birjand earthquake sequence in eastern Iran and the 1997 Jiashi swarm in western China. In both cases, reference event data is available from short-term portable seismograph deployments following the initiation of seismic activity in those regions. For the cluster analyses we used 92 events of the Iran sequence and 123 events of the Jiashi swarm, ranging in magnitude from 3.4 to 7.1. The analyses produce new locations (relative to the centroid) and 90% confidence ellipses that in the case of the Iran sequence sharpen the spatial relationship of the earthquakes to known faults in that regions. Shifting the centroid to match a reference event location for the Jiashi swarm event produces source-station path corrections relative to ak135 of regional Pn phases recorded by stations in Asia. The standard deviation of these path corrections is typically only a few tenths of seconds. Hence, these data can eventually be used to validate 3-D models and to support the calculation of travel-time curves and source-specific station corrections for the Asian region.

Our initial work with the candidate "reference events" in the two regions suggests that considerable care must be taken to ensure reliable results. Many aftershock studies and temporary seismograph deployments in remote areas suffer from logistical, operational, and analytical difficulties which may compromise the quality of the computed locations. Such problems are seldom apparent in published papers and abstracts. In many cases it will be necessary to gain access to raw data and analysis records—and most importantly, to gain the cooperation of the original researchers— to confirm the reliability of "reference events" offered by the seismological community in these regions.

REFERENCES

Engdahl, E. R., R.D. Van der Hilst and R.P. Buland, Global teleseismic earthquake relocation with improved travel times and procedures for depth determination, Bull. Seism. Soc. Amer., 88, 722-743, 1998.

Jordan, T.H. and K.A. Sverdrup,. Teleseismic location techniques and their application to earthquake clusters in the south-central Pacific, Bull. Seis. Soc. Amer., 71, 1105-1130, 1981.

Kennett, B. L. N., E.R. Engdahl and R.P. Buland, Constraints on seismic velocities in the Earth from traveltimes, Geophys. J. Int., 122, 108-124, 1995.

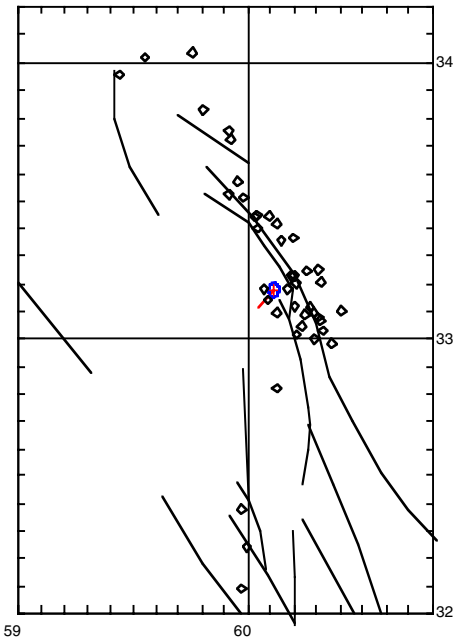


Figure 1. Map of the Ghaen-Birjand region in eastern Iran showing major mapped fault traces. Epicenters of 42 of the best-located events (area of 90% confidence ellipse less than 314 km^2, equivalent to a circle with 10 km radius) based on HDC analysis of the 1997 earthquake sequence are shown. Tics are 0.1 deg.

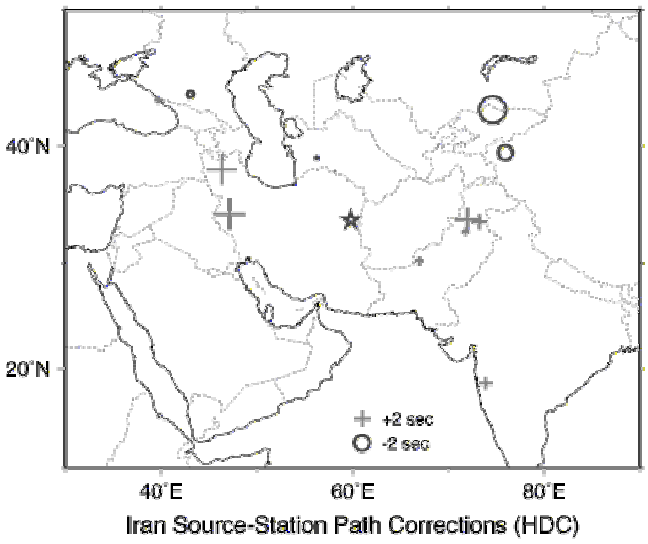


Figure 2. Source-station Pn path corrections based on median residuals to stations using HDC locations. Only stations which observed at least 5 Pn arrivals and with standard errors of less than 0.5 sec are plotted. Star is location of Ghaen-Birjand mainshock.

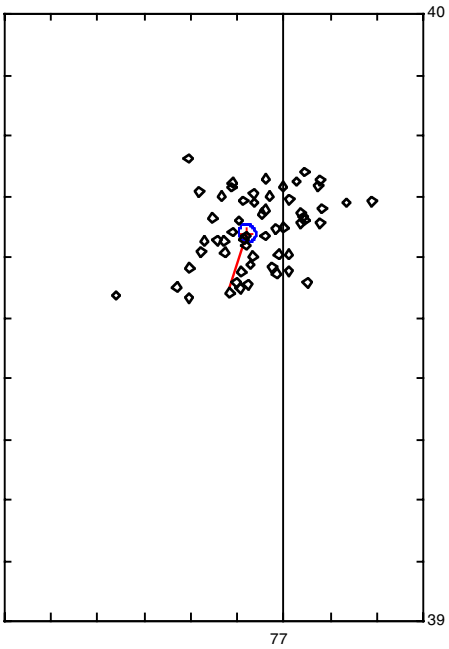


Figure 3. Locations of the 57 best-located members (area of 90% confidence ellipse less 78 km^2, equivalent to a circle with 5 km radius) of the 1997 Jiashi swarm in western China. Relative locations from HDC analysis, with the entire cluster is shifted in space and time (10.4 km at an azimuth of 18°; 2.8 second earlier origin time) from the HDC solution to best match the one cluster event for which a reference location is available. Tics are in 0.1 deg.

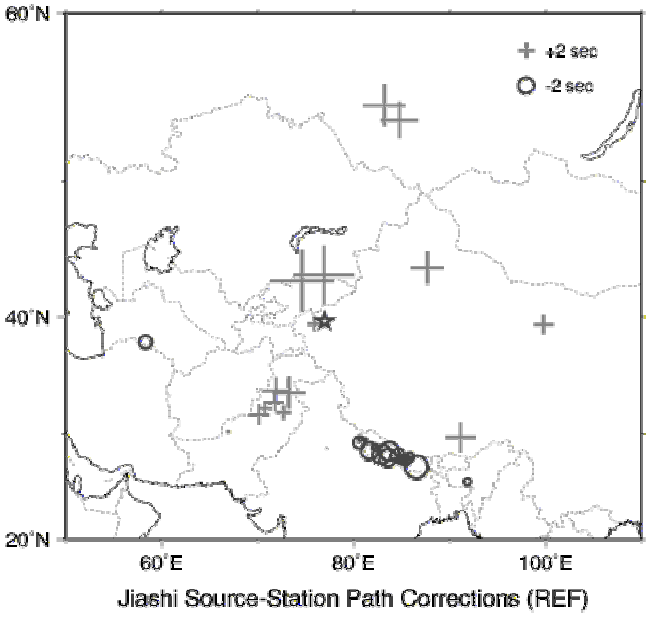


Figure 4. Source-station Pn path corrections based on median residuals to stations using HDC locations with the centroid shifted to bring the cluster into agreement with the reference event (star). Only stations which observed at least 5 Pn arrivals and with standard errors of less than 0.5 sec are plotted.

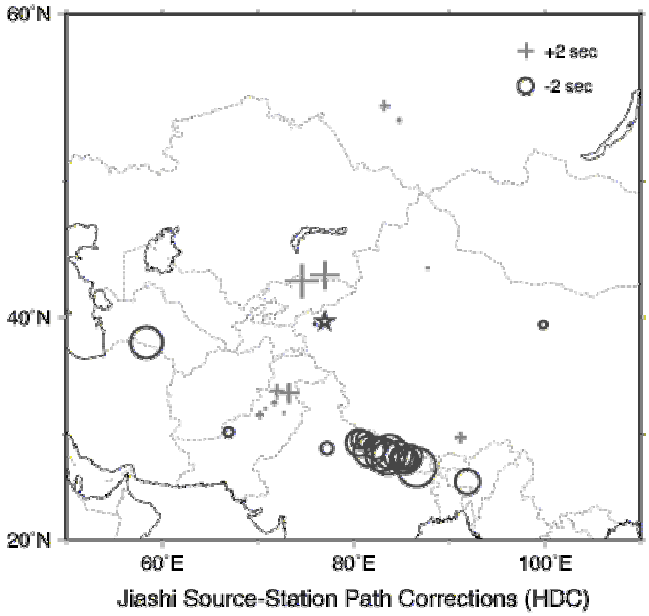


Figure 5a. Source-station Pn path corrections based on median residuals to stations using HDC locations. Only stations which observed at least 5 Pn arrivals and with standard errors of less than 0.5 sec are plotted. Star is location of reference event.

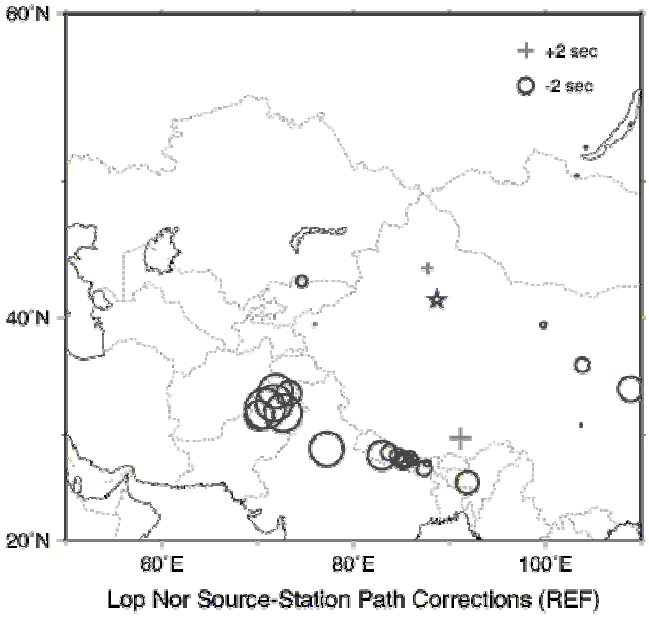


Figure 5b. Source-station Pn path corrections based on median residuals to stations using well determined Lop Nor explosion locations. Only stations which observed at least 5 Pn arrivals and with standard errors of less than 0.5 sec are plotted. Star is location of Lop Nor test site.

2-D SIGNAL DETECTORS FOR 3-COMPONENT SEISMIC RECORDINGS

Eystein S. Husebye and Yuri V. Fedorenko

Institute of Solid Earth Physics, University of Bergen, Norway

Sponsored by The Defense Threat Reduction Agency
Arms Control Technology Division
Nuclear Treaties Branch

Contract No. DSWA 01-98-C-0159

ABSTRACT

Despite much ingenuity in research of optimal signal detector design the simple and universal used STA/LTA detector has a performance literally 'second-to-none' to other often more advanced detectors. In other words, continued research in this field may be considered a bit futile. Our undertaking here has been motivated by some strange observational phenomenon in analysis of seismic recordings from national Norway network stations namely that apparently strong events were not recorded albeit easily visible in corresponding local records. The other, mentally puzzling attitude among seismologists, is that only 1-D detectors (Z-component) are used while at local and regional distance ranges horizontal components often exhibit the strongest not necessarily P-waves signal amplitudes. We are investigating both of these signal phenomena with goal of improving signal detection in a CTBT IMS context.

The two major reasons for non-detected signals are apparently i) a gradual P-amplitude increase (typical of many mid-oceanic events) and ii) spiky records. In the former case, a lag of 5 - 10 sec between the STA and LTA windows respectively often suffice while in the latter case the STA/LTA detector per se is not robust enough to handle spikes. These may naturally be removed by a simple spike filter preceding in time the detector operation but this is not always done. Anyway, the station TRO (Tromsoe, N.Norway) has a poor signal detection performance which is obviously related to a spiky operational environment (housed in a big building). Introducing a Kolmogorov-Smirnov (K-S) type detector where the test statistic is tied to the non-parametric K-S-distribution (not power as for the STA/LTA) signal detection increased significantly. However, not unexpectedly in a non-spiky environment the latter detector had a superior performance.

2-D signal detectors where the test statistics incorporate information extracted from both the vertical and horizontal seismometers are not much discussed in the literature despite often strong signals on the latter components. A prerequisite for 2-D detectors is that i) waveforms are at best weakly correlated between components and ii) also envelopes should be weakly correlated. We have tested both of these assumption on real data (3-C records from the ARCESS array) and found them valid in the frequency ranges 2 - 8 Hz and 1 - 10 Hz respectively. For higher frequencies correlation is strong between all components implying some instrumental defects. So far we have only tried a crude 2-D detector that is a combination of two 1-D STA/LTA detectors on the vertical and horizontal components. For local and regional signals the 2-D test statistics cluster along the diagonal between 'vertical and horizontal' axes while spikes etc are clearly along a single axis. The first 2 stations here, at Ask near Bergen and at Petrozavodsk NW Russia, become operational 10 July, 2000, Data quality and on-line detector performances are comparable or better than standard seismograph stations which costs are an order of magnitude higher than ours at less than $ 1000 each.

Key words: 1-D and 2-D signal detectors, spiky records, Kolmogorov-Smirnov detector, false alarm rates, novel 3-comp. seismograph cost $<$ $ 1000.

OBJECTIVE

The fundamental task of observational seismology is real time monitoring of earthquake activities and equally important providing high quality data for the research community. During the pioneering years, say 1900 - 1970, universities commonly deployed and operated local and national networks. Not so any more due to increasing costs and sophistication of network operations for which tasks academic institutions are not well suited. In other words, modern seismograph networks including routine bulletin works are mainly handled by various kind of national and governmental agencies like IRIS, ISC, USGS and UN/CTBTO. These agencies provide excellent bulletin and/or earthquake waveform services but are less convenient for specialized research needs like extended time testing of signal detectors and automated event location algorithms. For the latter experiments, an obvious advantage would be to have our own station/network operation which by itself is challenging tasks in terms of low station costs and flexibilities in data managements.

In this work, we first give details on some specific design features on our novel stations which now produce continuous, high-quality seismic recordings. These data are in turn used to check and verify previous theoretical detector design findings which were based on synthetic signals and Gaussian noise waveforms. Of particular interest is naturally the usefulness of 2-D detectors which incorporate jointly both horizontal and vertical components signal parameters in their test statistics.

RESEARCH ACCOMPLISHED

NOVEL SEISMOGRAPH DESIGN

As mentioned, our efforts are motivated by the need for extensive testing of signal detectors and signal source recognition in a flexible manner and not to reinvent the seismograph. Hence, we have used standard, inexpensive instrument components but naturally some modifications are introduced for enhanced performances. Details are as follow:

- Seismometer; We use small, cheap geophones GS-11D (US $ 60/each from Geo Space Corporation, Houston, TX) with natural undamped frequency at 4.5 Hz. However, in combination with an elaborated preamplifier an approximately flat acceleration response is achieved in the 0.5 - 40 Hz frequency range (Fig. 1) which is adequate for short period (SP) signal recordings.

- 19 bits A/D converter - effective spike suppression and quantization noise reduction by oversampling. Our experience indicates that most of spikes in seismic recordings above 8-10 Hz are produced by impulsive noise coming from power lines. Such kind of noise is suppressed in the A/D converter which design includes careful grounding separation. Digital data acquisition systems always use a limited number of bits for signal representation. Recently, costly and precise 24-bits A/D have been introduced into seismograph stations which is sort of sampling "overkill". The reason being that there is no customary preamplifiers or commutators with a dynamic range close to 24-bits. Anyway, it is a well known fact that low-pass filtering of quantization noise improves the accuracy of the A/D-converter. We have taken advantage of this thus in effect converting the standard 16-bits one to a 19-bits A/D-converter (Fig. 2) deemed adequate for SP seismic recording systems. Presently the primary sampling rate is 3150 Hz for each channel, while output sampling rate is 50 Hz.

- Timing - "soft" system time adjusting. Presently we use an accurate GPS clock which controls the data acquisition system time. Even if GPS looses the satellites for a short while, for instance, a few minutes, the time error may exceed the sampling period. If the GPS clock adjusts system time instantly after it regain the satellites, number of samples per second may differ from the preset sampling rate. "Soft" system time adjusting helps us to avoid such situation. The cost of the GPS is about $ 300 but a much cheaper (approx. $ 50) radio clock is under consideration.

- CPU and data storage. We use an inexpensive CPU unit (Intel 486 or Intel 586 at a cost of $ 150) which is adequate for signal detection processing in several frequency bands. Via modem/phone detected signal parameters can be transmitted to the Hub while continuous waveform storage is

on a 8 Gigabyte disk (cost about $ 80). Accessing waveform data at the station site via the Web is under consideration albeit we hope that parameterized signal data would suffice for preliminary bulletin production.

Total hardware cost for the above, novel SP 3C seismograph stations is less than $ 1000 even when using the GPS clock while the recording performances match or are even better that of the site-sharing ASK station. Cost comparison is very favorable for our station as the price of just a single seismometer is at least $ 1500. The idea of using inexpensive geophones to mimic responses of standard but costly seismometers via transfer function modeling is not entirely new in seismology (Barzilai et al., 1998) since obviously the Earth is spatially undersampled in this regard. Besides the requirement of cheap instrumentation, station siting and operation should also be inexpensive. A pilot experiment here is installation of one of our station at a local high school where the students would access and analyze their station recordings plus those of other "school" stations on Internet. In this way, we ensure low operational costs retaining participant access to to all data without any additional hardware cost for us.

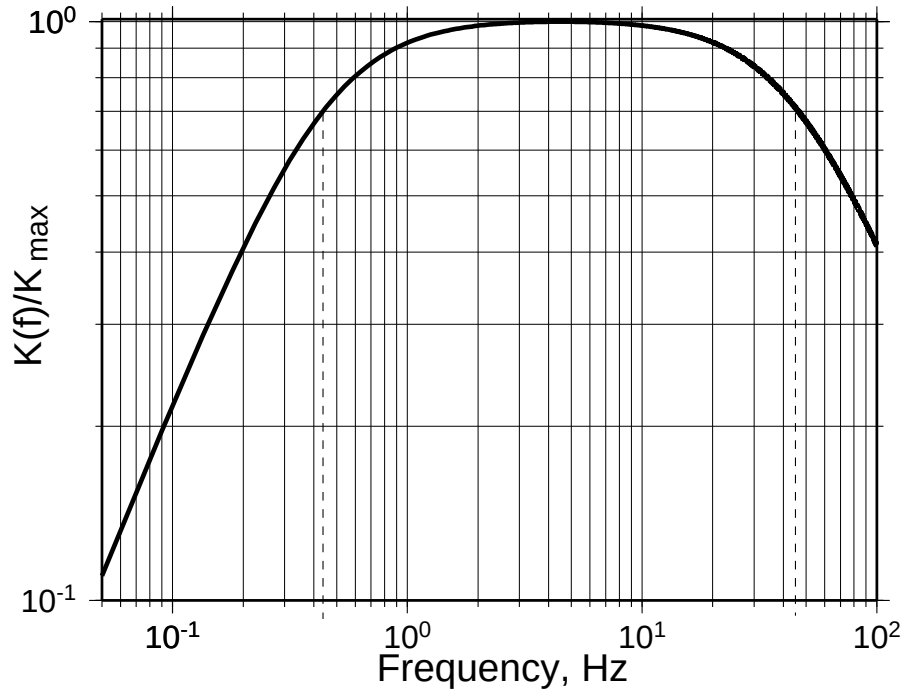


Fig. 1. Approximately flat acceleration response for the GS-11D geophone in combination with our own designed preamplifier. In essence, low-cost geophone transformed to high-cost short period seismometer by smart "response" hardware.

SIGNAL DETECTOR DESIGN

In previous works, Fedorenko et al., 1998, Fedorenko et al., 1999, Husebye and Fedorenko, 1999, we have demonstrated that the wavelet transform may be a more suitable tool than the FFT for signal detection, phase pickings and signal source recognition. This in turn requires that the ambient noise is white which is equivalent to an approximate flat seismometer acceleration response curve. Since most instruments in use measures ground velocities the noise spectra are in general non-flat as shown in Fig. 3 for the ARCESS array center seismometer. To overcome this drawback in the context of signal detection our preamplifier is designed in such a manner as to modify our ground velocity measuring geophones to produce seismometer ground acceleration motions which in case of noise give approximately white spectra (Fig. 3) in the frequency range 1.5 - 20 Hz. The spectral hump at lower frequencies, due to relatively strong microseisms, are in practice of no consequences as this part is removed by bandpass filtering in the detector processor.

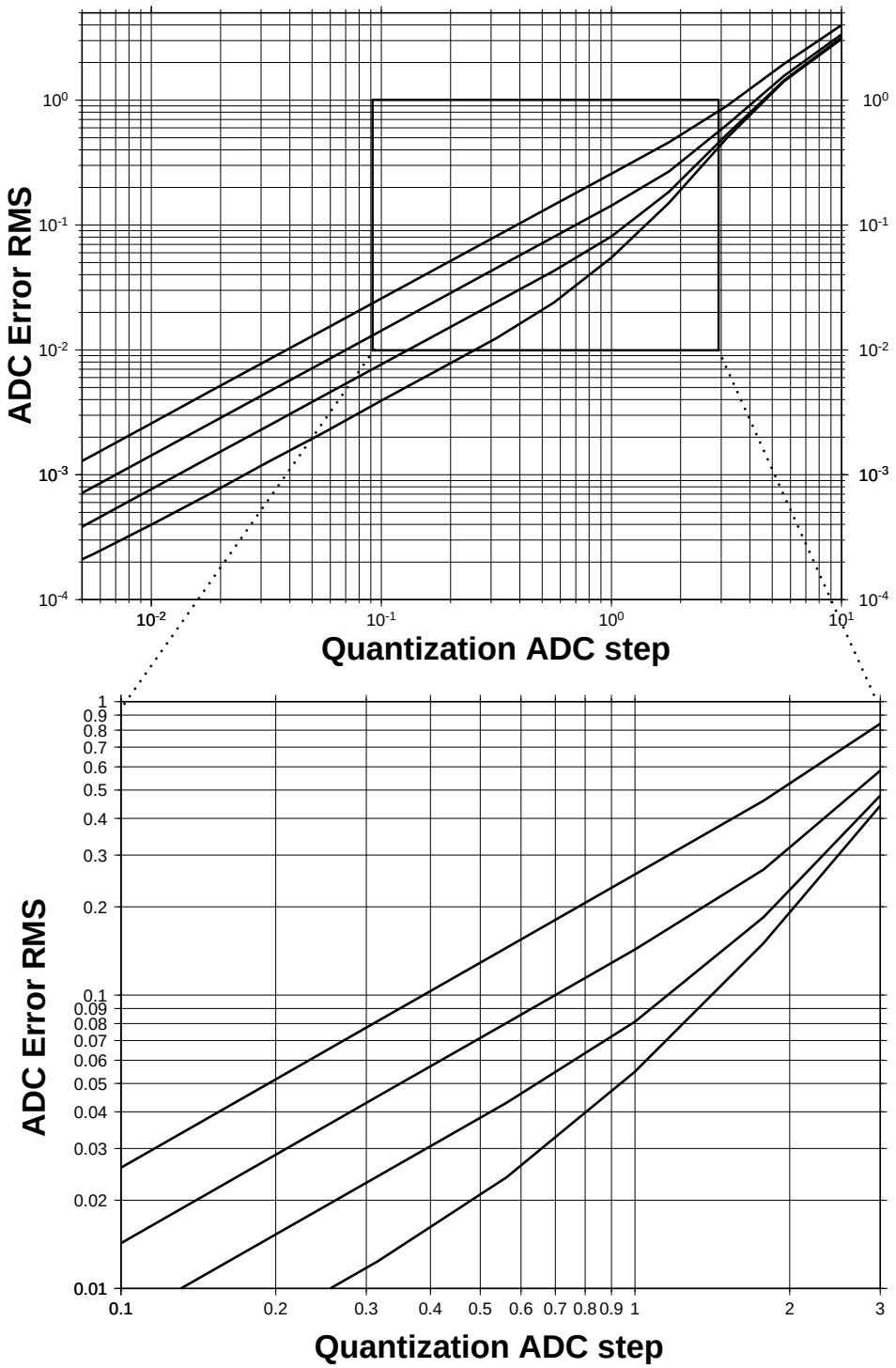


Fig. 2. Quantization noise reduction by oversampling. Upper line at both panels represents ADC (A/D converter) output noise without oversampling, $f_s/f_{\text{out}} = 1$. The next lines correspond to oversampling $f_s/f_{\text{out}} = [4,\ 16,\ 64]$, respectively. Notice that quantization error with oversampling by 64 is approximately 8 times lower (3 bits gain) than without oversampling. Quantization ADC steps are in units of noise standard deviation, ADC error RMS is $\left[\frac{1}{L-1}\sum_{j=1}^{L}(n_j - n_j^q)^2\right]^{1/2}$ where n_j is the initial noise, n_j^q is the quantized noise and L is number of samples in the noise realization.

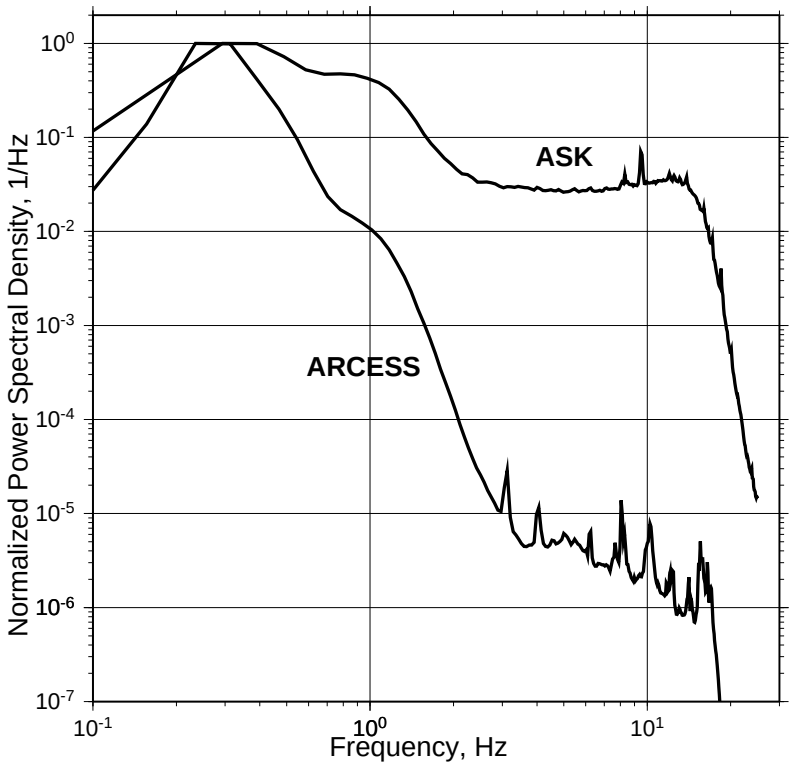


Fig. 3. Normalized power spectral density for ARCESS 3C center station (winter time) and our novel station at ASK (summer time) - in both cases Z-components. Since the noise level in winter is high the normalization gives low level of the high frequency noise at ARCESS. Note, that above 2 Hz the ARCESS spectra follows approximately $1/f$ slope while ASK spectra is almost flat in this frequency range.

In our more theoretical detector studies (Fedorenko and Husebye, 1999) we found that the popular STA/LTA detector has an excellent performance in comparison to many other detectors including the non-parametric Kolmogorov-Smirnov one. It was one exception here namely in case of spiky records often caused by electrical outgauges in buildings were station is housed. Naturally, other kind of electrical disturbances may cause spikes in the recordings. In such cases the STA/LTA detector become literally blinded while the KS-detector was little affected. Instead safeguarding here in terms of 2 different detector systems we build-in a spike 'killer' in the A/D-converter ensuring spike-free records prior to signal detection per se.

The basic requirement here is noise independency between components and the validity of this assumption is demonstrated in Fig. 4. As can be seen, there is no significant noise coherency even at low microseism frequencies (f $<$ 0.5 Hz). In typical signal detector passbands within 2 - 15 Hz the noise coherency is truly small being less than 0.02 units. Besides component independency also valid for component envelopes the noise appears to be Gausssian as presumed in our theoretical detector study. The above results imply that a 2-D detector should outperform the conventional 1-D STA/LTA detector foremost because more signal information is incorporated in the test statistics.

Our 2-D signal detector operates in the three frequency bands which coincide with the corresponding frequency bands in wavelet transforms, namely 1.5625 - 3.125 Hz, 3.125 - 6.25 Hz and 6.25 - 12.5 Hz. The first step is data preparation prior to the detection process itself using IIR (Infinite Impulse Response) Butterworth filters of order 6 to obtain filtered time histories for the $x_k(t)$ (**N**), $y_k(t)$ (**E**), $z_k(t)$ (**Z**) for our 3 frequency bands $k = 1, 2, 3$. The 2-D detector is modeled after the 1-D STA/LTA detector which in the former case is defined as:

$$\begin{aligned} \mathrm{STAH}_k(t) &= \mathrm{IIRF}_{\mathrm{STA}} \left(x_k(t)^2 + y_k(t)^2 \right)^{1/2} \\ \mathrm{STAV}_k(t) &= \mathrm{IIRF}_{\mathrm{STA}} \left(|z_k(t)| \right) \end{aligned}$$

where H=horizontal and V= vertical, $\mathrm{IIRF}_{\mathrm{STA}}$ defines Bessel low pass IIR filter of order 3 with cut-off at 0.5 Hz. The LTAH and LTAV are defined in a similar manner but with a frequency cut-off at 1/300 sec. The combination of Butterworth prefiltering and Bessel type of filters for forming the STA and LTA test statistics are motivated by the need of suppressing side-lobe detections that is false alarms caused by noise triggering (Steinert et al., 1975).

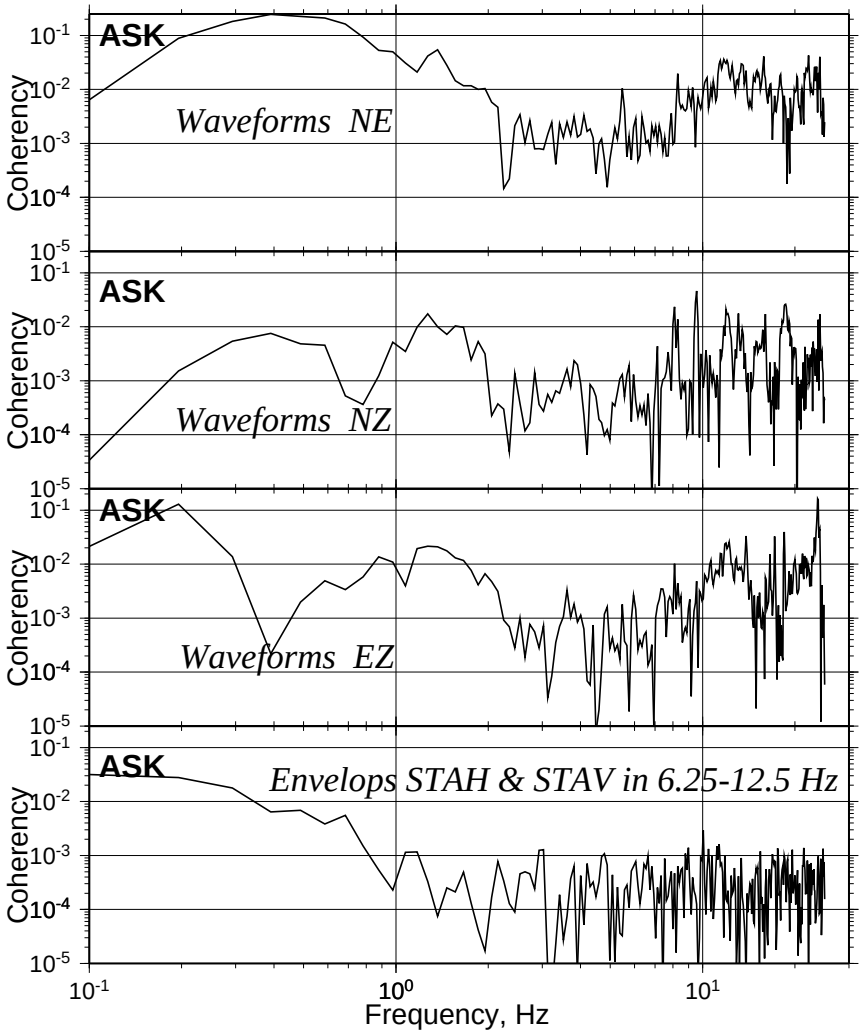


Fig. 4. Observed noise coherency between 3-component waveforms and STAH and STAV envelops. This is original noise waveforms recorded by our novel ASK station of length 60 min presumably free of signals. Coherency at levels of 0.01 or less give component independency for the ambient noise field. Also note that similar results were obtained when noise waveforms were replaced by the corresponding envelopes, in this case the coherency is less than 0.001. In the STA/LTA 2D detector the test statistics are the noise and signal envelopes.

Anyway, we may consider $\mathrm{STAH}_k(t)$ and $\mathrm{STAV}_k(t)$ as approximate envelopes of horizontal $a_h(t)$ and vertical $a_z(t)$ acceleration components in the given frequency bands while $\mathrm{LTAH}_k(t)$ and $\mathrm{LTAV}_k(t)$ are estimates of RMS of the ambient noise. Also, this LTA definition is coincident with the parameter used for record "denoising" in our wavelet processing scheme for picking automatically P- and S-phase onsets (Husebye and Fedorenko, 1999). In order to keep them from being affected by the seismic signal we freeze these values while the detector is in the detection state.

The 2-D detector is taken to be ratio $R_k(t)$ between the STA and LTA that is:

$$R_k(t) = \frac{\left[\mathrm{STAH}_k^2(t) + \mathrm{STAV}_k^2(t)\right]^{1/2}}{\left[\mathrm{LTAH}_k^2(t) + \mathrm{LTAV}_k^2(t)\right]^{1/2}}$$

A signal detection is declared whenever any $R_k(t)$ exceeds a preset threshold currently set at 4.0 for all 3 bands. This setting is rather conservative since we so far have not observed any clear false alarms. Depending on signal shape and duration the detector may be triggered several times during signal "passage". An independent trig requires a time lag of minimum 2 sec while detection state is defined as a time lag less than 60 sec between the last trigger events. We naturally count no of triggs during detection state as this parameter is useful for differentiating between earthquakes and explosions (most 8 triggs) while man made signals like marine air gun activities, human walking near the site etc. often produce more than 20 triggs.

The horizontal and vertical acceleration envelopes are used to obtain the estimate of an acceleration envelop $a_k^{\mathrm{env}}(t)$ and of an apparent incidence angle θ_k

$$\begin{aligned} a_k^{\mathrm{env}}(t) &= \left[\mathrm{STAH}_k^2(t) + \mathrm{STAV}_k^2(t)\right]^{1/2} \\ \theta_k(t) &= \arcsin\left[\mathrm{STAH}_k(t)/a_k^{\mathrm{env}}(t)\right] \end{aligned}$$

Seismic events have $10 < \theta_k(t) < 60$ while spikes and non-seismic events often lay outside this diapason.

RESULTS

Our novel 3-comp. station is co-located with the ASK station of the NSN for easy site access and direct comparison of detector performances. Phase pickings are approximately coincident in time while waveforms are not directly comparable due to velocity versus acceleration responses of these two stations. Neither is detector output directly comparable since the ASK station (SEISAN software; p. comm. J. Havskov) use a 1-D detector tied to the vertical component and just one filter band of 2 - 8 Hz. In other words, our detector has a superior performance to that of the standard ASK station. Up to now station operation has been smooth the only nuisances being extensive testing of air guns in nearby fjords. These signals can cause triggerings every 10 - 15 sec for many hours at a time but easily recognized as such via the trigger counter. The detection parameter "apparent angle of incidence" is observationally limited to the interval $10° - 60°$ for earthquakes and chemical explosions. This implies that horizontal components record parts of the P-wave field even for teleseismic events making 2-D detectors superior to those based on vertical components only. For arrays where vertical sensors are dominant (only four 3-Comp. stations in ARCESS) 2-D detectors are of less interest unless the latter ones are used for detecting Lg and Rg-waves. The conservative threshold setting of 4.0 ensure no false alarms due to noise triggering. To lower threshold value, for Gaussian noise a threshold of 2.4 would be acceptable, we would produce many more detections of air gun signals and nearby human activity signals. Such events are of no scientific interest so better removed in this manner that is by a conservative threshold setting.

CONCLUSIONS AND RECOMMENDATIONS

Based on the results presented above our conclusions are:

- It is feasible to build and deploy low cost seismograph stations providing short period seismic record quality comparable if not better than that stemming from conventional, relative high-cost stations.
- Controlling your own station sitings and operations give clear research advantages regarding signal detector research and event location experiments.
- Our novel 2-D signal detector has a performance clearly superior to that of 1-D STA/LTA detectors. For array where most sensors are vertical only the advantages of 2-D detectors are likely to be marginal. Only exception is using the few 3-comp. array stations (only 4 in the ARCESS array) for detecting Lg- and Rg-waves.

Our recommendations are:

- 2-D type detectors should be installed in all 3-comp. stations in the seismic part of the IMS/CTBTO global monitoring system due to its superiority relative to 1-D detectors. For array stations 2-D detectors would be of limit usefulness.
- For event location research local network data are a must. We have demonstrated here that such networks are affordable even for low cost research budgets. Main design elements in our novel stations is replacing costly seismometers with low-cost geophones but retaining in the latter case seismometer response characteristics.
- Event locations; with many stations recordings at hand from dense networks envelope waveform inversion for retrieving source parameters should be feasible. With the above signal and instrumentation accomplishments we would focus our future research on these problems.

REFERENCES

Barzilai, A., T. VanZandt, T. Pike, S. Manion, and T. Kenny, "Improving the Performance of a Geophone through Capacitive Position Sensing and Feedback," Conference Proceedings, American Society of Mechanical Engineers International Congress, Nov. 1998.

Fedorenko, Yu. V., E. S. Husebye, B. Heincke and B. O. Ruud, 1998. Recognizing explosion sites without seismogramm readings: neural network analysis of envelope–transformed multistation SP recordings 3–6 Hz. Geophys. J. Int., 133, F1–F6.

Fedorenko, Yu. V., E. S. Husebye and B. O. Ruud, 1999. Explosion site recognition; neural net discriminator using three-component stations. Phys. Earth Planet. Int., 113, 131-142.

Fedorenko, Yu. V. and E. S. Husebye, 1999. Simulating Seismic Signal Detectors. Proceedings of the 21st Seismic Research Symposium, Las Vegas, Nevada, Vol. 1, p. 419-426.

Husebye, E. S. and Yu. V. Fedorenko, 1999. First breaks - automatic phase picking of P- and S- onsets in seismic records. Proceedings of the 21st Seismic Research Symposium, Las Vegas, Nevada, Vol. 1, p. 466-475.

Steinert, O., E.S. Husebye and H. Gjøystdal, 1975. Event detection false alarm rate and noise stability at NORSAR. J. Geophys., 41, 289-302.

THREE-DIMENSIONAL *A PRIORI* MODEL CONSTRAINTS AND UNCERTAINTIES FOR IMPROVING SEISMIC LOCATION

Megan P. Flanagan, Stephen C. Myers, Craig A. Schultz, Michael E. Pasyanos, and Joydeep Bhattacharyya
Lawrence Livermore National Laboratory

Sponsored by the U.S. Department of Energy
Office of Nonproliferation and National Security
Office of Defense Nuclear Nonproliferation
National Nuclear Security Administration

Contract No. W-7405-ENG-48

ABSTRACT

Accurate seismic event location is key to monitoring the Comprehensive Nuclear-Test-Ban Treaty (CTBT) and is largely dependent on our understanding of the crust and mantle velocity structure. This is particularly challenging in aseismic regions, devoid of calibration data, which leads us to rely on *a priori* constraints on the velocities. We investigate our ability to improve seismic event location in the Middle East, North Africa, and the Former Soviet Union (ME/NA/FSU) by using *a priori* three-dimensional (3-D) velocity models in lieu of more commonly used one-dimensional (1-D) models. Event locations based on 1-D models are often biased, as they do not account for significant travel-time variations that result from heterogeneous crust and mantle; it follows that 3-D velocity models have the potential to reduce this bias. Here, we develop a composite 3-D model for the ME/NA/FSU regions. This fully 3-D model is an amalgamation of studies ranging from seismic reflection to geophysical analogy. Our *a priori* model specifies geographic boundaries and velocity structures based on geology, tectonics, and seismicity and information taken from published literature, namely a global sediment thickness map of 1^o resolution (Laske and Masters, 1997), a regionalized crustal model based on geology and tectonics (Sweeney and Walter, 1998; Bhattacharyya et al., 2000; Walter et al., 2000), and regionalized upper mantle (RUM) models developed from teleseismic travel times (Gudmundsson and Sambridge, 1998). The components of this model were chosen for the complementary structures they provide. The 1^o sediment map and regionalized crustal model provide detailed structures and boundaries not available in the more coarse 5^o models used for global-scale studies. The RUM models offer improved resolution over global tomography, most notably above depths of 300 km where heterogeneity is greatest; however, we plan to test other published upper mantle models of both *P*- and *S*-wave velocity.

We compute travel times through this integrated model for comparison with other standard 1-D models, as our goal is to evaluate whether the 3-D model can better predict the observed travel times. The arrival times are computed through the model using a 3-D finite-difference technique and are then compared with a declustered set of ISC *P* arrival times (Engdahl et al., 1998). Our ME/NA/FSU model predicts the *P* and *Pn* travel times very well, as measured by variance reduction, for three stations we tested: ARU, KVT, and GAR; these predicted times also resemble some patterns seen in *Pn* tomography models of this region. Such tests will allow us to identify parts of the model that may need modification.

We also compute model-based correction surfaces for each station in the ME/NA/FSU regions that can be used as additional constraints in our event location algorithm to determine the improvement provided by using 3-D models. We use this method to relocate a set of ground truth events: the 1991 Racha aftershock sequence which was investigated by Myers and Schultz (2000) using empirical kriged correction surfaces and a 1-D velocity model. They find an epicenter mislocation bias of 42 km when no corrections are applied and that this mislocation is reduced to 13 km when their empirically derived correction surfaces are included. We relocate this same set of events using our model-based correction surfaces and produce a mislocation bias of only 26 km, a significant improvement. We are currently implementing methods to quantify uncertainties on the model-based corrections which will be required to compute representative error ellipses for the new locations. We also plan to combine both the model-based and empirical correction techniques to achieve the best improvement in location. This test case demonstrates the power of using 3-D velocity models to improve location capability for small, regionally recorded events. This example also shows how the model-based approach holds great potential for improving locations in aseismic regions where it may not be possible to compute empirical correction surfaces.

Key Words: travel time corrections, model-based correction surfaces, 3-D velocity model, event location

OBJECTIVE

High quality regional velocity models are necessary for accurate seismic locations required for monitoring the Comprehensive Nuclear-Test-Ban Treaty (CTBT). A common approach to seismic location has been to use a one-dimensional (1-D) velocity model and apply source-specific station corrections to remove bias due to three-dimensional (3-D) Earth structure. Such corrections yield more accurate travel-time predictions and hence more accurate location of the seismic event; however, they do not provide source-specific uncertainties for the new locations.

Empirical kriged corrections and other model optimization methods are well suited to improve travel-time prediction in areas where ground truth (GT) events are available; however, vast portions of the ME/NA/FSU are devoid of GT events (*e.g.*, North Africa, Russia). In order to improve travel-time prediction at regional and near teleseismic distances in regions without GT calibration, we have developed the *a priori* 3-D velocity model MENAFSU1.0. We seek to validate our *a priori* 3-D velocity model MENAFSU1.0 and use this model to locate a regionally recorded set of GT events. The new locations are compared to those computed using a 1-D velocity model and empirically derived kriged correction surfaces, and the improvement in location using our model-based correction surfaces is demonstrated in an end-to-end case study.

RESEARCH ACCOMPLISHED

Middle East, North Africa, and Former Soviet Union 3-D velocity model (MENAFSU1.0)

This regionalized model is a preliminary set of geophysically distinct regions that can be used for estimating travel-times, surface wave dispersion, and discrimination properties particularly in aseismic regions where calibration data is sparse. The model can also provide a platform for assessing progress in seismic location, discrimination, detection—the entire calibration process—and aid in determining the priority and planning of calibration

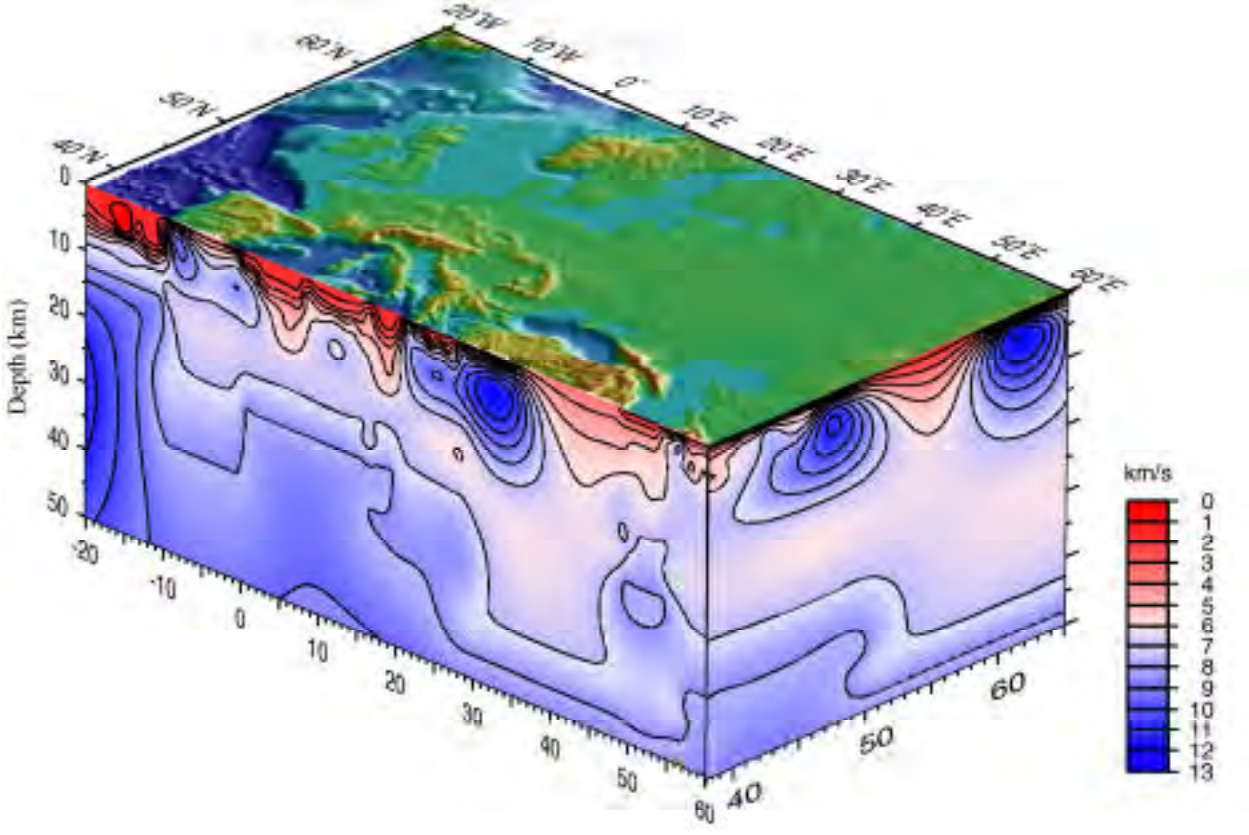


Figure 1. Cross-section of *P*-wave velocities from our 3-dimensional MENAFSU1.0 model.

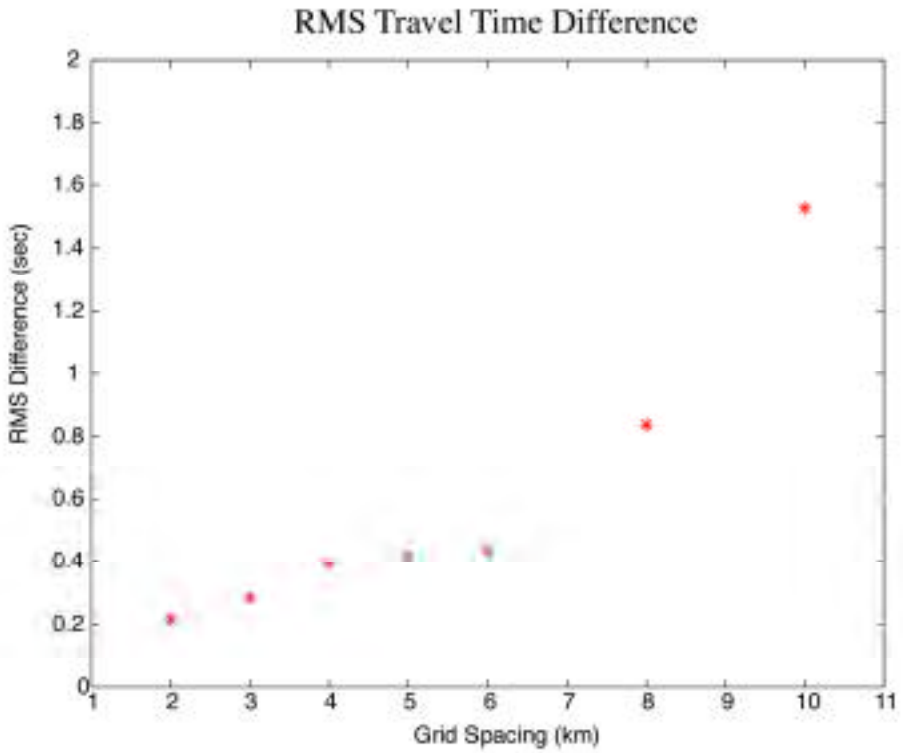


Figure 2a. The RMS travel time difference is reduced when a smaller grid spacing is used in the 3-D finite difference computation; this RMS error is the difference between travel time calculated through the FD code and that calculated using a 1-D ray-tracer (CalcTT) through the *AK135* velocity model.

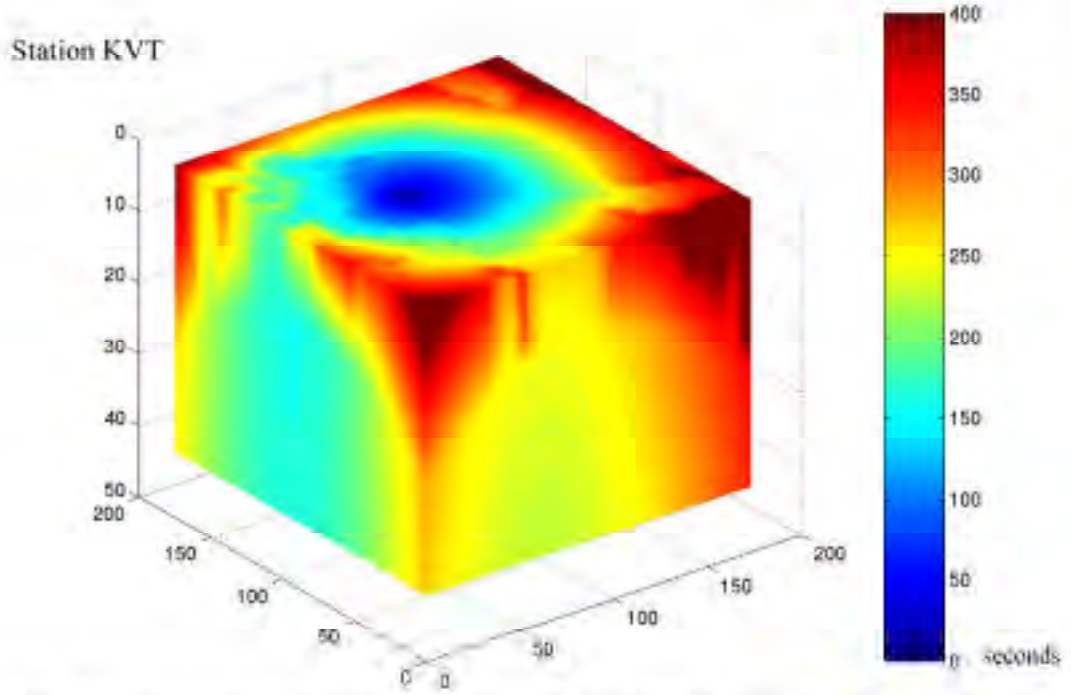


Figure 2b. This volume of travel times is the output from the 3-D finite difference calculation. The 3-D velocity structure causes the travel times to be asymmetric about the station KVT, which is located at zero time (bright blue spot in center). Arrival times for *P* and *Pn* phases for specific source-station paths are extracted from this volume by interpolation. Note the axes are units of 10 km, and the colors are time in seconds.

experiments. Our goal is to build a reference model for the region that can be used in making model-based correction surfaces. This model has been used to derive predictions of surface wave dispersion curves and regional travel times for comparison with data. In addition, empirical observations are being used to further refine the background geophysical model. The MENAFSU1.0 model specifies geographic boundaries and velocity structures based on geology, tectonics, and seismicity. This regionalization serves as a starting point, and we expect to refine and improve upon it based on such tests as predicting *P* and *Pn* travel times (presented here) as well as surface wave velocities. As the model improves and demonstrates some predictive power, it may evolve into a base model for tomographic inversions as well as a reference model for other CTBT-related research efforts.

The entire area is divided into 31 regions selected primarily on the basis of seismicity patterns, tectonic history, crustal thickness, and crustal velocity (Bhattacharyya et al., 2000; Walter et al., 2000). Each region is composed of 7 homogeneous layers for water, unconsolidated and consolidated sediments, upper crust, middle crust, lower crust, and upper mantle half-space, following the specifications of Mooney et al. (1998) in their 5^o resolution model *CRUST5.1*. We have stripped off and replaced the sediments with a high-resolution 1^o sediment model (Laske and Masters, 1997) and have discretized all 31 regions into 1^o latitude and longitude blocks while the depth layers remain variable in thickness. A representative cross-section of the velocity model is shown in Figure 1. We have added a regionalized upper mantle model below the *Pn, Sn* velocity layers. Of the many upper mantle models available, we have chosen initially to use the *RUM* (Regionalized Upper Mantle) model of Gudmundsson and Sambridge (1998). This model is attractive for two reasons; first it follows a similar regionalization procedure as was used for the crust except applied to the mantle. Second, it is based on deviations from *AK135* (Kennett et al., 1995) which is our basis for calculating travel times.

The MENAFSU1.0 velocity model is an amalgamation of geophysical and geological studies, constituting a self-consistent 3-dimensional Earth model for the crust and upper mantle. Because the MENAFSU model is 3-D, region-specific velocity structure, it can be characterized more accurately than 1- or 2-D models. While this model comprises *P*-wave, *S*-wave, density, and attenuation, we use only the *P*-wave structures at this time.

Finite Difference Travel-Time Calculations

We use an algorithm originally developed by Vidale (1988) and further refined by Hole and Zelt (1995) which uses a finite difference (FD) approximation to the Eikonal equation to compute first arrival travel times through regularly gridded velocity structures. This technique approximates Huygen's principle by propagating wavefronts radially outward from a point source using each grid (or time) node as a secondary source for each successive grid node. This procedure is more efficient and accurate than ray tracing as it is able to account for sharp velocity gradients which can produce different propagation modes (*e.g.*, refracted and diffracted body waves, head waves) in addition to direct phases. Furthermore, because the travel times are computed for every grid point in the volume, the code is much faster than tracing rays from a single event to a large number of receivers. In fact, we use the principle of reciprocity by placing the source point at the seismic station location and interpolate the travel times computed at each grid node to match the exact earthquake location (Flanagan et al., 1999).

We modify the original code in two ways. First, we adapt it to read in 3-D velocity models instead of 1-D such that it can compute times through our MENAFSU1.0 (or any custom 3-D) model. Second, we apply a Cartesian to spherical coordinate transformation to the source and receiver locations that are input to the code (K. Koper, personal communication, 1999). These modifications are necessary as we need to compute travel times out to regional and near-teleseismic distances (~13° to 30°) while the original FD algorithm operates in Cartesian coordinates, which are accurate only for distances of up to 300 km in the Earth. To account for the curvature of the Earth one option is to apply an Earth flattening transformation; however, this is only strictly valid for 1-D velocity models and not for our 3-D model. We develop the spherical coordinate transformation scheme in which we parameterize a spherical surface inside the Cartesian volume of grid nodes. Here, the source and receiver positions and velocity model are known in spherical coordinates, and they are transformed into the Cartesian system as input to the FD code. The finite difference operators remain unchanged, and the output is converted to spherical coordinates as well.

The FD algorithm requires our velocity model to be discretized on to an equally spaced grid; this requires fine sampling, by linear interpolation, of our 1° by 1° velocity model. This procedure results in the loss of some resolution with depth (*e.g.*, some sediment layers may be thinner than the grid size) and an oversampling of lateral structure as the velocities in the shallower part of the model vary more rapidly with depth than they do laterally.

Our fully 3-D code is run in a volume of dimensions of roughly 30° by 30° laterally and 800 to 1000 km deep with a grid spacing of 3 km; the exact latitude-longitude bounds of the volume vary with each station. The grid spacing is determined empirically as a trade-off between the accuracy of the travel-time prediction and computer memory limitations as both the velocity grid (or slowness) and the travel-time grid must be held in memory simultaneously. Our current resources limit us to grids with about 350 million nodes which requires approximately 4 Gbytes of computer memory. After a number of tests running the code with incrementally smaller grid sizes and comparing the resulting travel times with those computed using a simple 1-D ray tracer, we find that a grid spacing of 3 km provides a reasonable accuracy as shown in Figure 2a. Accuracy and errors of the FD code arise from grid boundary effects and from the discrete approximation of the differencing algorithm. These accuracies are being evaluated through convergence tests and through careful comparisons with known solutions; currently the RMS errors appear to be less than 0.5 seconds (Figure 2a). Absolute errors and accuracy are being derived in seismic areas where we can statistically assess the ability of this *a priori* model to predict data.

The outputs from the FD code are two 3-D volumes: one of the *P*-wave velocity at each grid node and one of the *P* arrival time at each node; an example of the travel-time volume is shown in Figure 2b as computed for station KVT. We perform two runs for each station of interest, once using the MENAFSU1.0 and once using the global reference model *AK135*; we then compare times from each of these volumes for the same source-station paths.

Validation of Travel-Time Improvement

To test the predictive power of the MENAFSU1.0 model, we compute the median residuals between the observed *P* and P_n arrivals at each station and the arrivals predicted by both our MENAFSU1.0 model and the *AK135*. We use *P* and P_n travel-time picks from a relocated subset of earthquakes in the ISC Bulletin (Engdahl et al., 1998) which have been further processed with a declustering algorithm. This entails filtering spatial data with the goal of consolidating heavily clustered points into small collections of representative data points with associated uncertainties. This technique is intended to reduce the extremely large set of arrival times into a smaller more manageable data set with minimal loss of information. As part of the process, outliers within data clusters are removed and the uncertainty estimates for the improved data set are provided.

Travel-time residuals are computed by interpolating between grid nodes to calculate the predicted arrival time for an exact source-station path. This is done for both the MENAFSU1.0 travel-time volume and the *AK135* travel-time volume, and each predicted time is subtracted from the observed arrival time. These residuals (observed - predicted time) for station ARU and KVT are shown in histogram form in Figure 3. The 3-D MENAFSU1.0 model predicts the observations very well, showing a significant variance reduction, while for others it does not improve the fit given by the *AK135*. This procedure will help us identify regions where the model needs to be improved

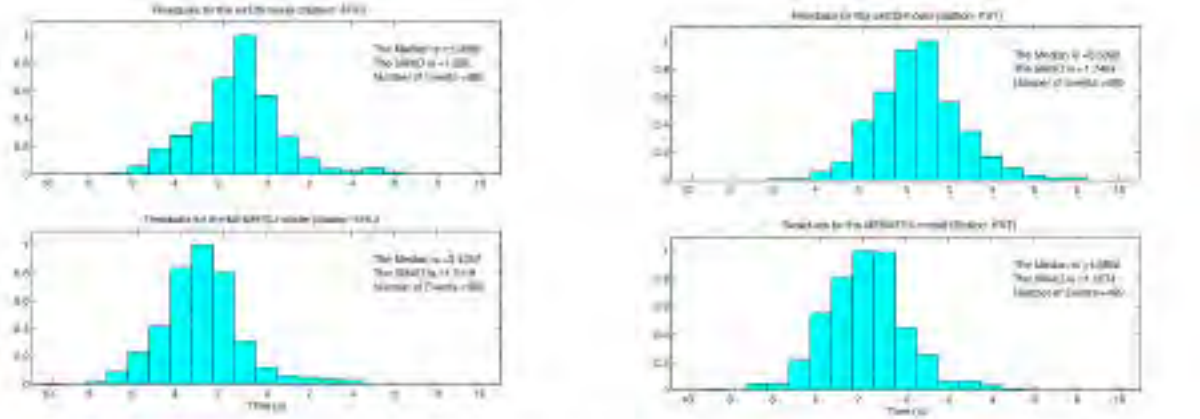


Figure 3. Travel-time validation for the MENAFSU1.0 model at example stations ARU and KVT. In general, travel-time variance for the MENAFSU1.0 model is reduced compared to the *AK135* model. In some instances the mean of the distribution is displaced from zero; however, this may be due to optimization of event origin times relative to the *AK135* model.

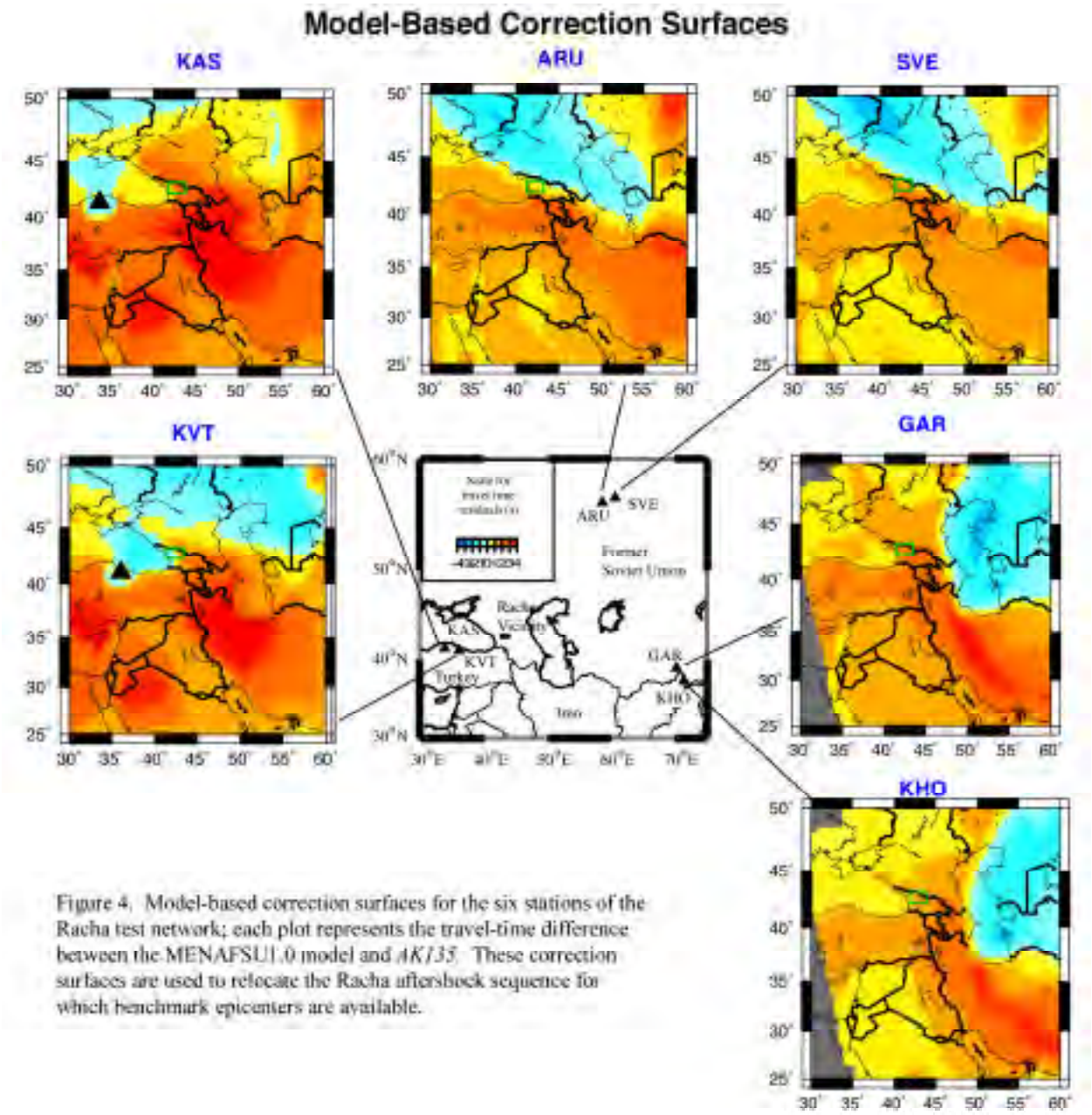


Figure 4. Model-based correction surfaces for the six stations of the Racha test network; each plot represents the travel-time difference between the MENAFSU1.0 model and *AK135*. These correction surfaces are used to relocate the Racha aftershock sequence for which benchmark epicenters are available.

Model-Based Correction Surfaces

To compute model-based correction surfaces we subtract the *AK135* predicted time from the MENAFSU predicted time along a regular grid in latitude, longitude and at a depth of 10 km. Examples of these surfaces are shown in Figure 4 for the six stations we will use in our relocation test described below. Each correction surface provides station-specific travel-time corrections for regional to near-teleseismic distances providing improved accuracy and precision for travel-time predictions. We find travel time differences of up to 6 sec relative to *AK135*, most in areas of very thick crust or sediment (blue indicates fast regions and red indicates slow). Note the patterns in these correction surfaces correlate with the structural features in the MENAFSU1.0 model; fast predictions are seen to the north on the Russian platform while slow anomalies are seen at the southern Caspian as well as eastern Turkey and the southern Caucasus.

Next we determine the improvement provided by the 3-D models by relocating a set of ground truth events. We use the model-based correction surfaces computed for six stations (KAS, KVT, GAR, KHO, ARU, and SVE)

comprising the test network which recorded the 1991 Racha aftershock sequence; these surfaces are plotted in Figure 4. The fast and slow residual patterns seen in these correction surfaces show strong similarities to the patterns seen in the empirical kriged correction surfaces based on 1-D velocity models Myers and Schultz (2000).

Improving Location: The 1991 Racha Aftershock Sequence

The improvement in seismic location that is gained by using our *a priori* 3-D velocity model is the ultimate test of this method's utility. We use a set of GT2 locations determined using regionally recorded aftershocks in the region of Racha, Georgia. These GT locations are then compared with our locations computed using our model-based correction surfaces, and we assess the degree to which our 3-D velocity model accounts for some of the differences that are indicated by the path corrections and spatial differences in arrival times to each of the six stations (Flanagan,et al., 2000).

In a previous study, Myers and Schultz (2000) demonstrated location improvement using Modified Bayesian Kriging (MBK) to compute empirical correction surfaces for the sparse 6-station test network. The MBK correction surfaces for the test-network stations are based on high-quality teleseismically constrained hypocenters throughout the Middle East (Engdahl et al., 1998). The 1991 Racha events are then relocated with and without the aid of MBK correction surfaces, and the resulting epicenters are compared to the benchmark GT2 locations determined from a dense local deployment of seismic sensors. When no travel-time correction is applied, the mean horizontal distance between the local and test network locations is 42 km, and there is a distinct bias in sparse-network locations towards the north-northwest. The mean difference between local and sparse network locations is reduced to 13 km when the empirical corrections are applied and the bias in location is significantly reduced (Figure 5, center).

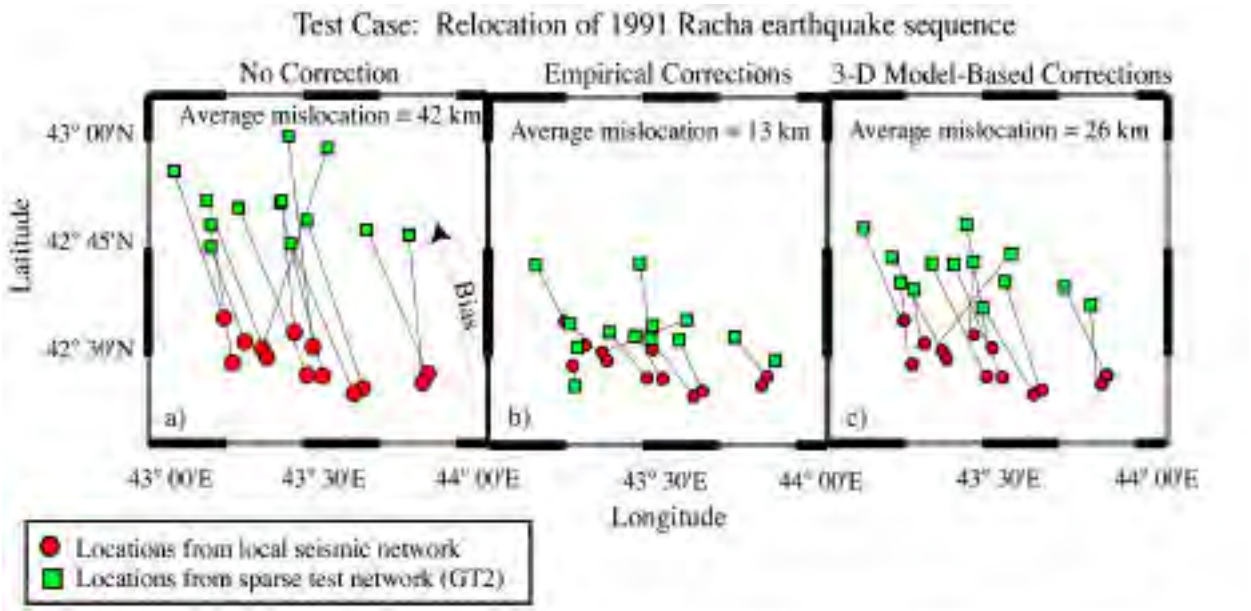


Figure 5. Location bias is significantly reduced when either empirically dervived or 3-D model-based corrections

Next we relocate the Racha events with and without our new model-based correction surfaces (shown in Figure 4) as constraints, and the resulting epicenters are compared to benchmark GT2 locations. The mean difference between the benchmark and test network locations is reduced from 42 km to 26.6 km when the model-based corrections are applied, and the bias in location is significantly reduced (Figure 5, right). This reduction is almost as large as that achieved when the empirical kriged correction surfaces are applied. We are currently implementing methods to derive uncertainty estimates for the model-based correction surfaces which will be required to compute representative error ellipses for the new locations. Since our *a priori* MENAFSU1.0 model does not have

uncertainties associated with it, we must use the misfit between the observed travel times and those predicted from our model as a measure of uncertainty (see Figure 3).

This test case demonstrates the power of 3-D model-based corrections to improve location of small, regionally recorded events. This model-based approach shows enormous potential for improving location in aseismic regions, where GT events are not available. However, this relocation of the Racha sequence should be viewed with caution as we continue to test and evaluate the predictive power of the MENAFSU1.0 velocity model in other regions.

CONCLUSIONS AND RECOMMENDATIONS

Empirically derived correction surfaces are applicable where GT events exist, but extrapolation of travel-time corrections from GT events is quickly damped to the background statistics of the *AK135* model in regions where there are no data to constrain the corrections. Therefore, model-based corrections, which are shown here, are better suited to improve travel-time prediction and thus location capability in areas devoid of GT events.
The test case relocation of the 1991 Racha sequence should be viewed as a one-point validation of our 3-D model. Additional validation of the predictive power of the MENAFSU1.0 velocities is being actively pursued in other high-quality GT regions. Further testing of the FD code for grid size *vs.* accuracy of the predicted travel time is underway as we investigate variable grid spacing techniques to allow us to compute times for smaller grid spacing and geographic areas larger than 30°. We are also compiling a large data set of shear wave arrival times to test and validate the *S*-wave velocity structure of MENAFSU1.0 as our FD code can easily compute first arrival times for shear waves.

This work was performed under the auspices of the U.S. Department of Energy by University of California Lawrence Livermore National Laboratory under contract No. W-7405-Eng-48 for the Office of Research and Development, NN-20, within the Office of Nonproliferation and National Security, NN-1. LLNL contribution UCRL-JC-138984.

REFERENCES

Bhattacharyya, J., W. Walter, M. Flanagan, J. O'Boyle and M. Pasyanos, (2000) , Preliminary Definition of Geophysical Regions in Western Eurasia, UCRL-ID-138402.

Engdahl, E.R., R. van der Hilst, and R. Buland, (1988) Global Teleseismic Earthquake Relocation with Improved Travel Times and Procedures for Depth Determination, *Bull. Seismol.. Soc. Am., 88*, 722-743.

Flanagan, M. P., C. A. Schultz, and L. J. Hutchings, (1999) Development of 3-D Crust and Upper Mantle Velocity Models to Improve Seismic Event Location, AGU Fall Meeting, San Francisco, CA, *EOS Trans. Am. Geophys. Un., 80*, p. F656.

Flanagan, M. P., S. C. Myers, M. E. Pasyanos, C. A. Schultz, W. R. Walter, K. D. Koper, (2000) Improving Regional Event Locations in the Middle East by Incorporating Model Based Correction Surfaces Derived from 3-D Velocity Structures, SSA Spring Meeting, San Diego, CA, *Seismol. Res. Lett., 71*, p. 184.

Gudmundsson, O., and M. Sambridge, A Regionalized Upper Mantle (RUM) Seismic Model, (1998) *J. Geophys. Res., 103*, 7121-7136.

Hole, J.A. and B.C. Zelt, 3-D Finite Difference Reflection Travel Times, (1995) *Geophys. J. Int., 121*, 427-434.

Kennett, B.J.N., E.R. Engdahl and R. Buland, (1995) Constraints on Seismic Velocities in the Earth from Travel Times, *Geophys. J. Int, 122*, 108-124.

Laske, G. and T.G. Masters, (1997) A Global Digital Map of Sediment Thickness, *EOS Trans. AGU, 78*, F483.

Mooney, W. D., G. Laske, and T. G. Masters, (1998) CRUST 5.1: A global crustal model at 5° X 5°, *J. of Geophys. Res., 103*, 727-747.

Myers, S.C., and Schultz, C.A., (2000) Improving Sparse Network Seismic Location with Bayesian Kriging and Teleseismically Constrained Calibration Events, *Bull. Seismol. Soc. Am., 90*, 199-211.

Sweeney, J. and W. R. Walter, (1998) Preliminary Definition of Geophysical Regions for the Middle East and North Africa, UCRL-ID-132899.

Vidale, J., (1988) Finite-difference Calculation of Travel Times, *Bull. Seismol. Soc. Am., 78*, 2062-2076.

Walter, W.R., M.E. Pasyanos, J. Bhattacharyya and J. O'Boyle, (2000) MENA 1.1 – An Updated Geophysical Regionalization of the Middle East and North Africa, UCRL-ID-138079.

REGIONAL SEISMIC EVENT DISCRIMINATION IN SIBERIA

Hans E. Hartse

Los Alamos National Laboratory

Sponsored by U.S. Department of Energy
Office of Nonproliferation Research and Engineering
Office of Defense Nuclear Nonproliferation
National Nuclear Security Administration

Contract No. W-7405-ENG-36

ABSTRACT

In July and August of 1987, three Peaceful Nuclear Explosions (PNEs) were detonated in the northern Baikal Rift. These PNEs, each near m_b 5.0, were recorded at teleseismic distances and are listed in global seismic bulletins. Broadband and short-period sensors were being digitized at Chinese Digital Seismic Network (CDSN) station HIA during that summer (at event-station distances of about 1450 km). As HIA will become an International Monitoring System (IMS) primary array, these PNEs provide an excellent opportunity to test and calibrate regional, short-period discriminants in preparation for future test-ban monitoring. Hence, we retrieved HIA records of the explosions from the IRIS Data Management Center (DMC) along with about 400 additional presumed earthquakes from central Siberia, eastern Mongolia, and northeastern China. Binning event origin times into time-of-day histograms indicates uniform event distribution throughout the 24-hour day. We therefore concluded that the event catalogs (PDE and REB) used for data retrieval were not contaminated with industrial explosions.

We tested short-period discriminants by measuring root-mean-square (RMS) amplitudes of P_n, P_g, S_n, and L_g phases and then formed amplitude ratios using several frequency band measurements between 1 and 6 Hz. For most events, event-station distances are between 400 and 1600 km from HIA, with P_n being the first arrival. P_g and S_n are generally difficult to identify as distinct arrivals. L_g is the strongest secondary arrival. After correcting ratios for distance effect, the P_n/L_g ratios at frequencies above 3 Hz separate the explosions from the earthquakes. The P_n/L_g cross-spectral ratios (P_n above 3 Hz and L_g near 1 Hz) also separate the explosions from the earthquakes. Although it does not separate the explosions and earthquakes quite as well as the P_n/L_g ratios, the L_g spectral ratio appears to be a potentially useful discriminant, just as it has been recognized as a useful regional discriminant in the western United States. Of course more explosions will need to be measured before firmer conclusions can be reached regarding the L_g spectral ratio in Siberia.

Key Words: discrimination, seismic sources, regional seismology

OBJECTIVE

Over the past several years seismic verification research has emphasized the analysis of seismograms recorded at regional distances (between about 200 and 2000 km). The primary objective of this research has been to lower magnitude levels at which events can be detected, located, and identified. Our efforts have been directed at regional event identification in Asia. To date we have primarily relied on known nuclear tests from a few test sites to build data sets of nuclear explosion seismograms. There are, however, a few Soviet Peaceful Nuclear Explosion (PNE) seismograms that were digitally recorded at regional distances by the Chinese Digital Seismic Network (CDSN) during the late 1980's, and these records present additional opportunities to test discriminants.

In this paper, we examine regional broadband digital data recorded at CDSN station HIA in northeast China. Three PNEs detonated in Siberia were recorded at HIA during the summer of 1987 at event-station distances of about 1450 km. Many regional earthquakes have been recorded at HIA from throughout northeast China, Mongolia, and Siberia. As HIA is scheduled to become an International Monitoring System (IMS) array, our primary objective here is to test short-period regional body wave discriminants in Siberia as we have done elsewhere in Asia (Hartse et al., 1997).

RESEARCH ACCOMPLISHED

We obtained all waveforms for this study from the IRIS Data Management Center (DMC). All data were recorded at CDSN station HIA between the years 1987 and 1999 (Figure 1). From the 1980s until late 1994, HIA BH (20 sps) and SH (40 sps) components were operated in a triggered mode. In more recent years, SH and BH data have been acquired continuously. All events presented here fall within a box bounded from 44^o to 70^o north latitude and from 102^o to 140^o east longitude (Figure 1).

We obtained most of our data based on origin times reported in USGS PDE, pIDC REB, and SSB (Gao and Richards, 1994) event catalogs. The PNE event information from 1987 is listed in PDE and ISC catalogs, and we obtained additional information in Table 1 from Sultanov et al. (1999). In total, we assembled waveforms of about 400 earthquakes ranging in magnitude (m_b) from near 2.5 to near 6.5. The August 1987 Neva 2 explosion (Table 1) triggered the SH components at HIA with the P_n arrival, and it triggered the BH components at HIA with the L_g and surface wave arrivals. All three Neva 2 explosion records are shown in Figure 2 with a bandpass filter from 0.75 to 6 Hz applied. These waveforms are dominated by a strong L_g arrival. P_n is somewhat impulsive, but weak when considering these events are all near m_b 5.0 in size. P_g and S_n phases are generally poorly developed for earthquakes from Siberia and the explosions share these same characteristics.

To test for the presence of mining explosions within our presumed earthquake data set, we binned the numbers of events occurring within 4 sub-regions by hour of day (Figure 3). If significant numbers of mining explosions were present, we expected to see more events during daylight hours than during hours of darkness. Daylight hours in Siberia fall between about 0 hours and 14 hours GMT. We see no increase in event origin times during these hours. Hence, we conclude that our earthquake data set is not significantly contaminated by mining explosions. The large number of events occurring between hour 16 and 17 on the Stanovoy histogram is related to two m_b 5.5 earthquakes that occurred within one minute of each other on March 21, 1999, followed by several aftershocks.

Before making any measurements we corrected each seismogram for instrument response into units of displacement in meters. After manually picking each regional phase arrival, we bandpass filter, cut appropriate data windows, and measure the RMS amplitude (in the Log_{10} domain) for Pn, Pg, Sn, Lg, and pre-phase noise. We made time-domain phase amplitude measurements in several one-octave filter bands from 0.5-1 Hz up to 6-8 Hz. More details of our amplitude measurements are given in Hartse et al. (1997).

We tested several regional short-period discriminants. by forming amplitude ratios, removing the ratio-distance trend, and then plotting the corrected amplitude ratios versus magnitude. Before forming any amplitude ratio we test each phase amplitude to confirm that it exceeds pre-phase noise by at least a factor of 1.2. Figure 4, an L_g spectral ratio, shows the ratio-distance trend at the top and the discrimination plot on the bottom.

The L_g spectral ratio has long been identified as a viable discriminant for the western United States (Bennett and Murphy, 1986; Taylor et al., 1988). However, Hartse et al. (1997) found that the L_g spectral ratio did not separate Kazakh test site explosions from regional earthquakes recorded at station WMQ. For Siberia, and with a limited explosion data set, we find that the L_g spectral ratio separates the regional earthquake and explosion populations recorded at HIA. This result is more similar to results from the western United States than to other regions of Asia.

Figure 5 shows P_n/L_g ratios that also separate the explosions from the earthquakes. These ratios seem to work well in all regions of Asia where L_g is present (Hartse et al., 1997; Taylor et al., 2000), including Siberia. The dominant presence of L_g on the regional seismograms from Siberia help make these P_n/L_g discriminants and the L_g spectral ratio discriminant especially attractive because L_g can be observed over long distances at low magnitude levels. Figure 6 helps show why the P_n/L_g ratio works well in Siberia. The explosion records (red) filtered at 4-8 Hz have P_n and L_g amplitudes that are about equal, while the earthquake records (green and yellow) are dominated by L_g energy in all bands.

The P_n spectral ratio (top, Figure 7) does not separate the event populations as well as the L_g spectral ratio or the P_n/L_g ratios, but the explosions are near the top of the earthquake population. Hence, the P_n spectral ratio appears to perform in Siberia about as well as it has been observed to perform elsewhere in Asia (Hartse et al., 1997). The P_n/S_n ratios also apparently perform quite well in Siberia (bottom, Figure 7). However, S_n for small Siberian events is often in the P-coda noise and can not be measured.

CONCLUSIONS AND RECOMMENDATIONS

From this preliminary examination of discrimination performance in Siberia, we believe the outlook for successful regional event identification is quite promising. The regional P/S discriminants perform well, just as they do elsewhere in Asia. The exceptional strength of L_g recorded at distances of over 1000 km and for events smaller than m_b 4, will allow more and smaller events to be evaluated compared to the more tectonically active regions of Asia where S-wave attenuation is stronger.

We did not anticipate the good discrimination performance of the L_g spectral ratio. Perhaps the separation of the Neva 2 PNEs from regional earthquakes using the L_g spectral ratio is in some way related to the depth of burial for each PNE (between about 800 and 1500 m). The performance of this discriminant in Siberia should be studied more closely, because, if it can be documented as reliable, the exceptional propagation of L_g will allow for the L_g spectral ratio to be applied to many small events at distances of 1000 km or more.

REFERENCES

Bennett, T. and J. Murphy, Analysis of seismic discrimination using regional data from western United States events, *Bull. Seis. Soc. Am.*, 76, 1069-1086, 1986.

Gao, L. and P. G. Richards, Studies of earthquakes on and near the Lop Nor, China, nuclear test site, *Proceedings of the 16th Annual DARPA/AF Seismic Research Symposium*, 106-112, 1994.

Hartse, H.E., S.R. Taylor, W.S. Phillips, and G.E. Randall, Regional event discrimination in central Asia with emphasis on western China, *Bull. Seism. Soc. Am.*, 87, 551-568, 1997.

Sultanov, D.D., J.R. Murphy, and Kh.D. Rubinstein, A seismic source summary for Soviet Peaceful Nuclear Explosions, *Bull. Seismol. Soc. Am.*, 89, 640-647, 1999.

Taylor, S. R., N. W. Sherman, and M. D. Denny, Spectral discrimination between NTS explosions and western United States earthquakes at regional distances, *Bull. Seis. Soc. Am.*, 78, 1563-1579, 1988.

Taylor, S.R., A.A. Velasco, H.E. Hartse, W. S. Phillips, W.R. Walter, Amplitude corrections for regional seismic discriminants, Los Alamos National Laboratory, Los Alamos, NM, LAUR-99-3040, in press *PAGEOPH*, 2000.

Table 1. Neva 2 PNE Information

Name	*Date (ymd)*	*Time (hr:mn:sc)*	*Lat (^oN)*	*Lon (^oE)*	*Depth (m)*	*Material*	*Yield (ktons)*	*m_b (ISC)*
Neva 2-1	19870707	00:00:00.0	61.50	112.85	1502	limestone	15 (13)	5.1
Neva 2-2	19870724	02:00:00.0	61.45	112.80	1515	limestone	15 (13)	5.1
Neva 2-3	19870812	01:30:00.5	61.45	112.80	815	salt	3.2	5.0

Information in this table is from Sultanov et al. (1999). Yields are from official reports and yields in parentheses are estimates from other sources.

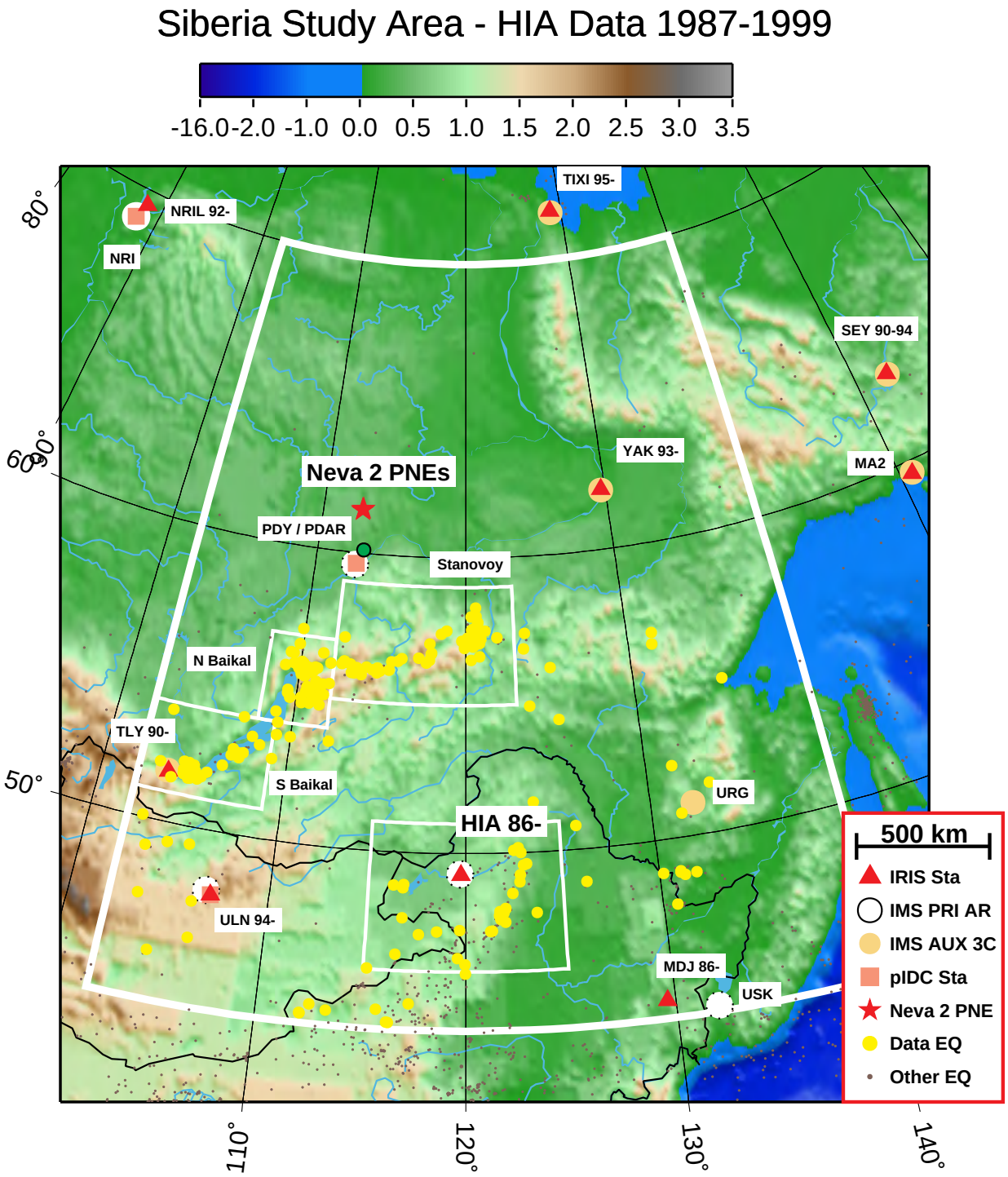


Figure 1. Study area map showing station HIA, other regional stations, and locations of events used in this study. The green circle near PDY represents the earthquake in our data set that is nearest to the "Neva 2" PNE locations. HIA recorded all three "Neva" PNEs detonated during the summer of 1987. The small white boxes outline sub-regions that we examined for evidence of mine-related seismicity. See Figure 3 for more details.

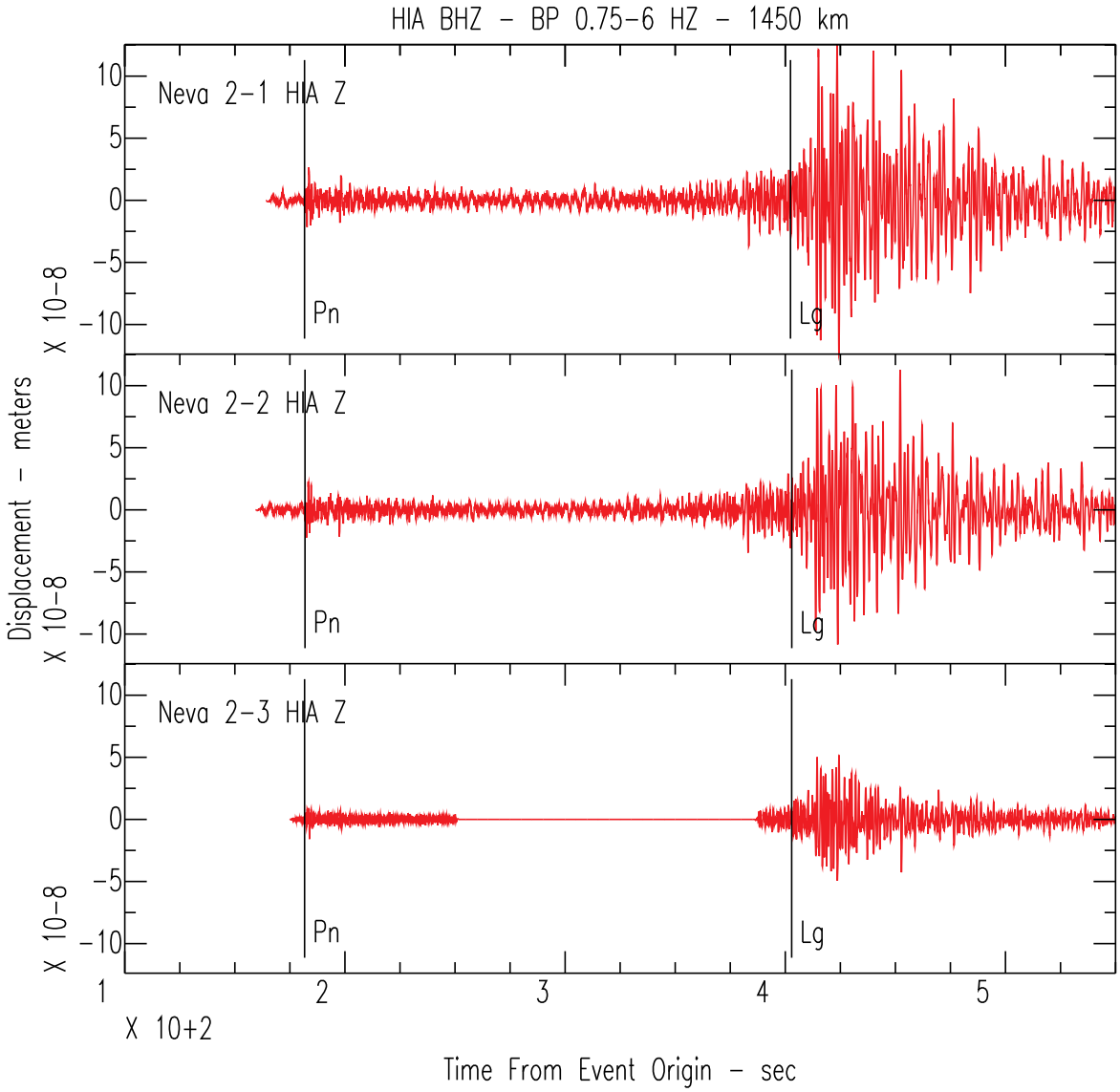


Figure 2. The "Neva 2" PNE records from station HIA bandpass filtered between 0.75 and 6 Hz. Only the P_n and L_g phases from the Neva 2-3 explosion triggered the event detector at HIA. Regional waveforms of Siberian seismic events generally have moderately weak P_n, weak to missing P_g and S_n, and a strong L_g. All three PNEs have m_b (ISC) values near 5.0. Table 1 presents more information on each explosion.

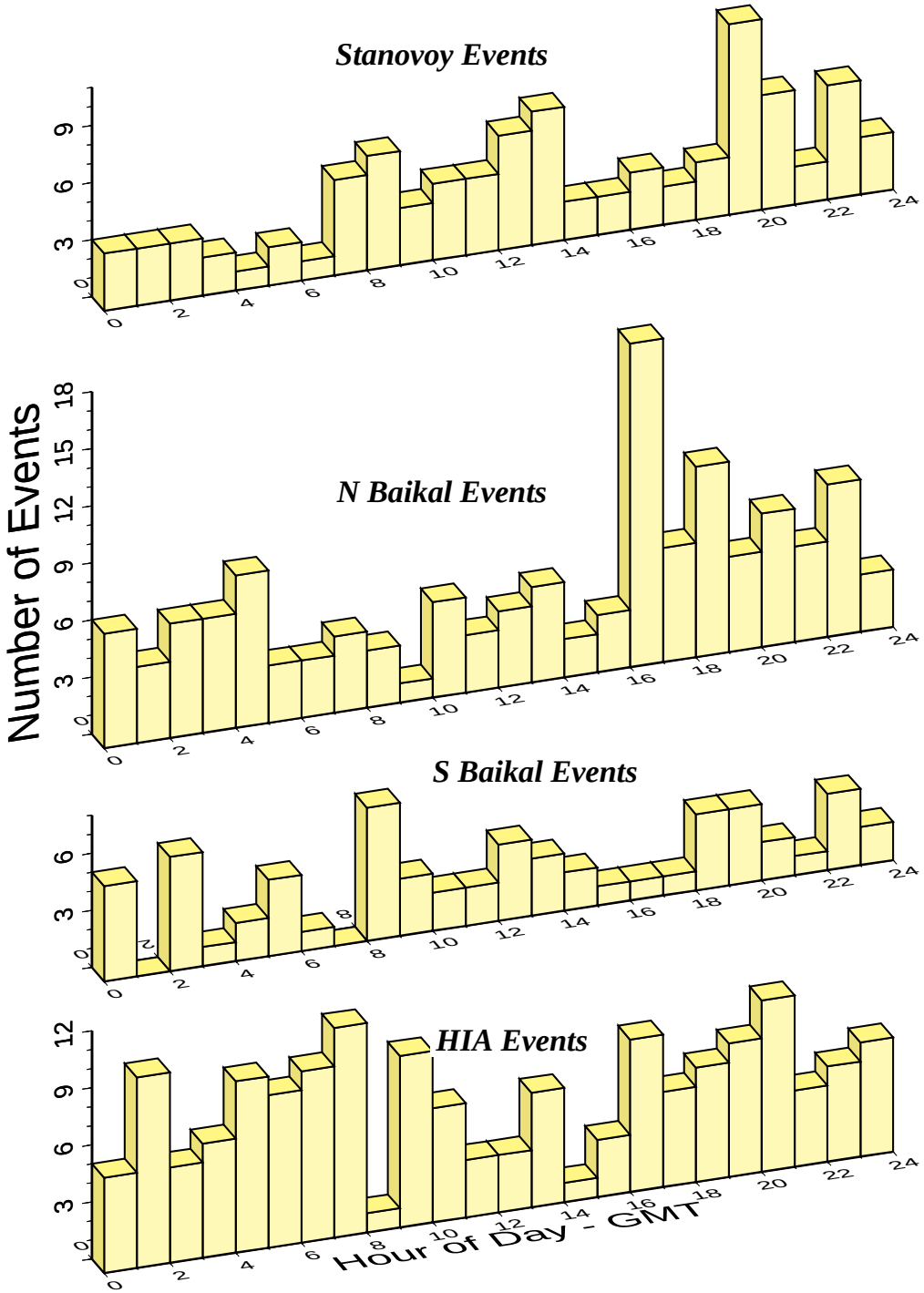


Figure 3. Number of events versus hour of day histograms for the presumed earthquakes that we analyzed in this study. Each sub-region outlined in white and labeled in Figure 1 corresponds to each histogram shown here. Daylight hours should be between 0 and 14 GMT. We see no evidence of increased seismicity during daylight hours in any of these subregions, and, hence, conclude that our data are not significantly contaminated by mining explosions. The large number of events occurring between hour 16 and 17 on the Stanovoy histogram is related to two m_b 5.5 earthquakes that occurred within one minute of each other on March 21, 1999, followed by several aftershocks.

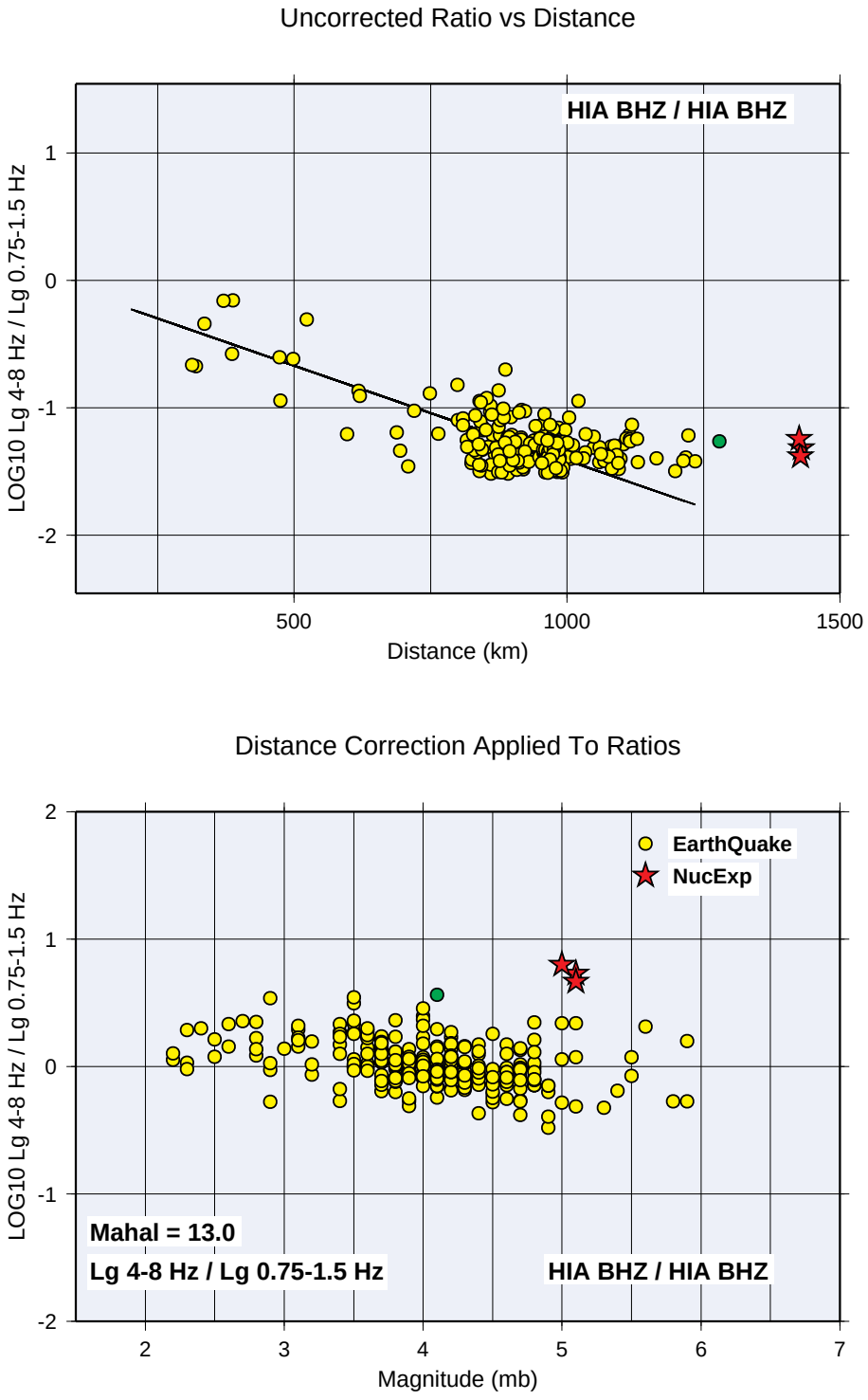


Figure 4. L_g spectral ratio discriminant for Siberian events. The top shows the ratio-distance trend of the earthquake population and the bottom is the distance-corrected ratio versus magnitude discrimination plot. The green dot represents the earthquake that occurred nearest the PNE locations. This discriminant separates the PNEs from the earthquakes, which we had not previously observed with regional events from near the Lop Nor and Kazakh test sites.

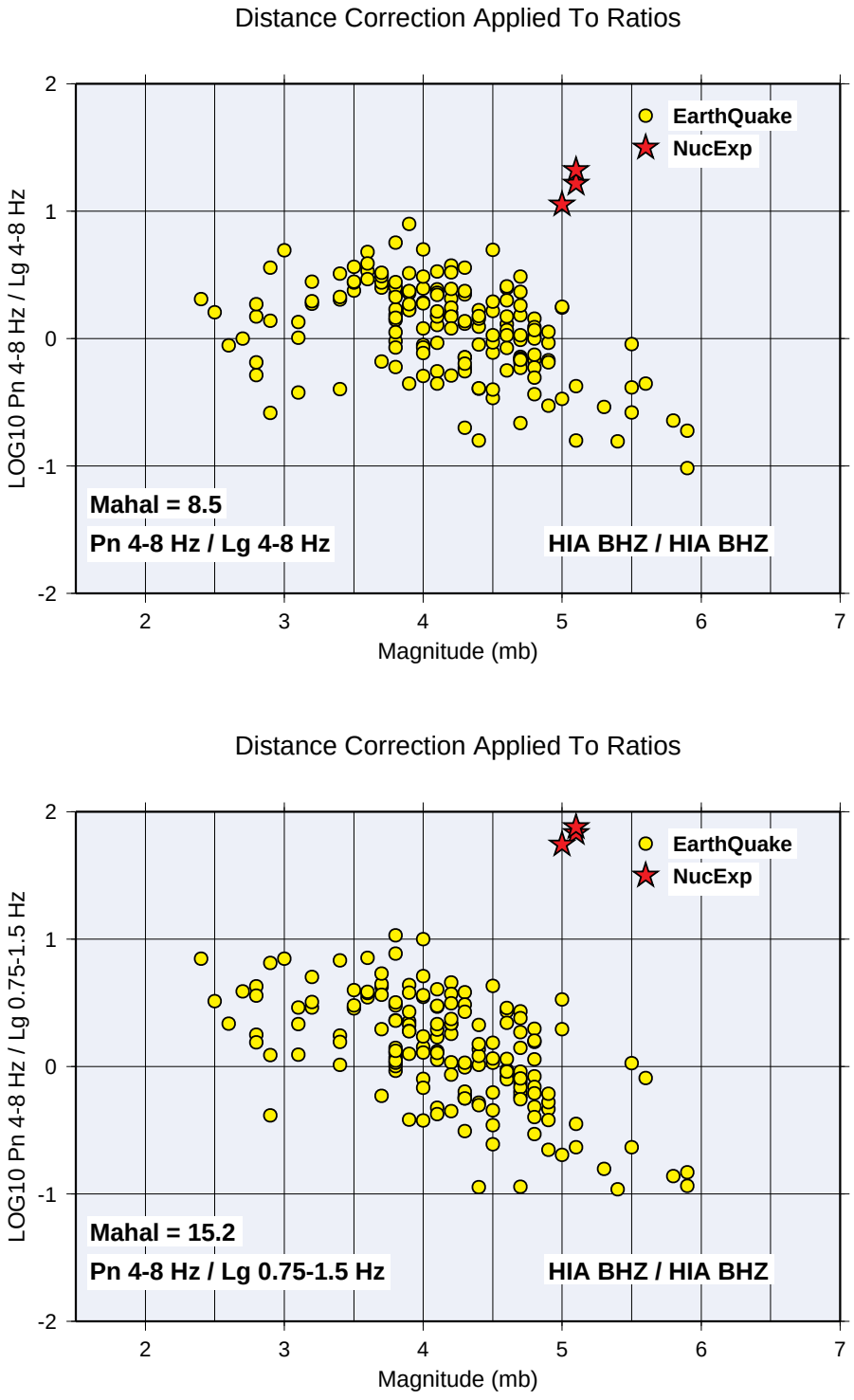


Figure 5. P_n/L_g ratio versus magnitude discriminants for Siberian events. The top shows the 4-8 Hz P_n/L_g ratio and the bottom shows that P_n(4-8 Hz)/L_g(0.75-1.5 Hz) ratio. Distance corrections have been applied. Both ratios separate the explosions from the earthquakes, as we have previously observed in other regions of Asia.

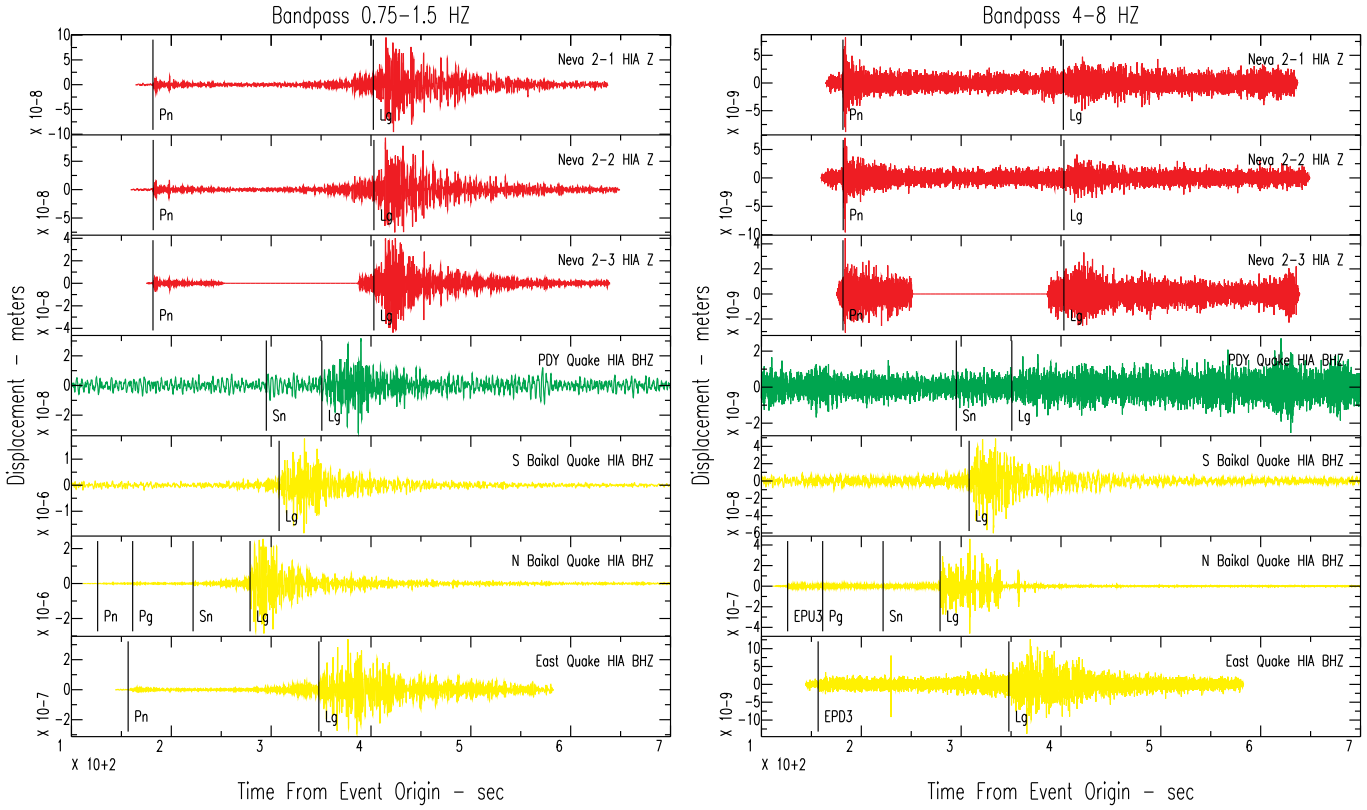


Figure 6. Explanation for the success of the P_n / L_g discriminants shown in Figure 5. The "Neva 2" PNE records bandpass filtered between 0.75 and 6 Hz (on left in red) have a slightly impulsive P_n arrival, but appear quite similar compared to the earthquakes (in green and yellow). However, in the 4- to 8-Hz band, the "Neva 2" records display P_n and L_g amplitudes that are about equal, while the earthquakes have L_g amplitudes that are much larger than their P_n amplitudes.

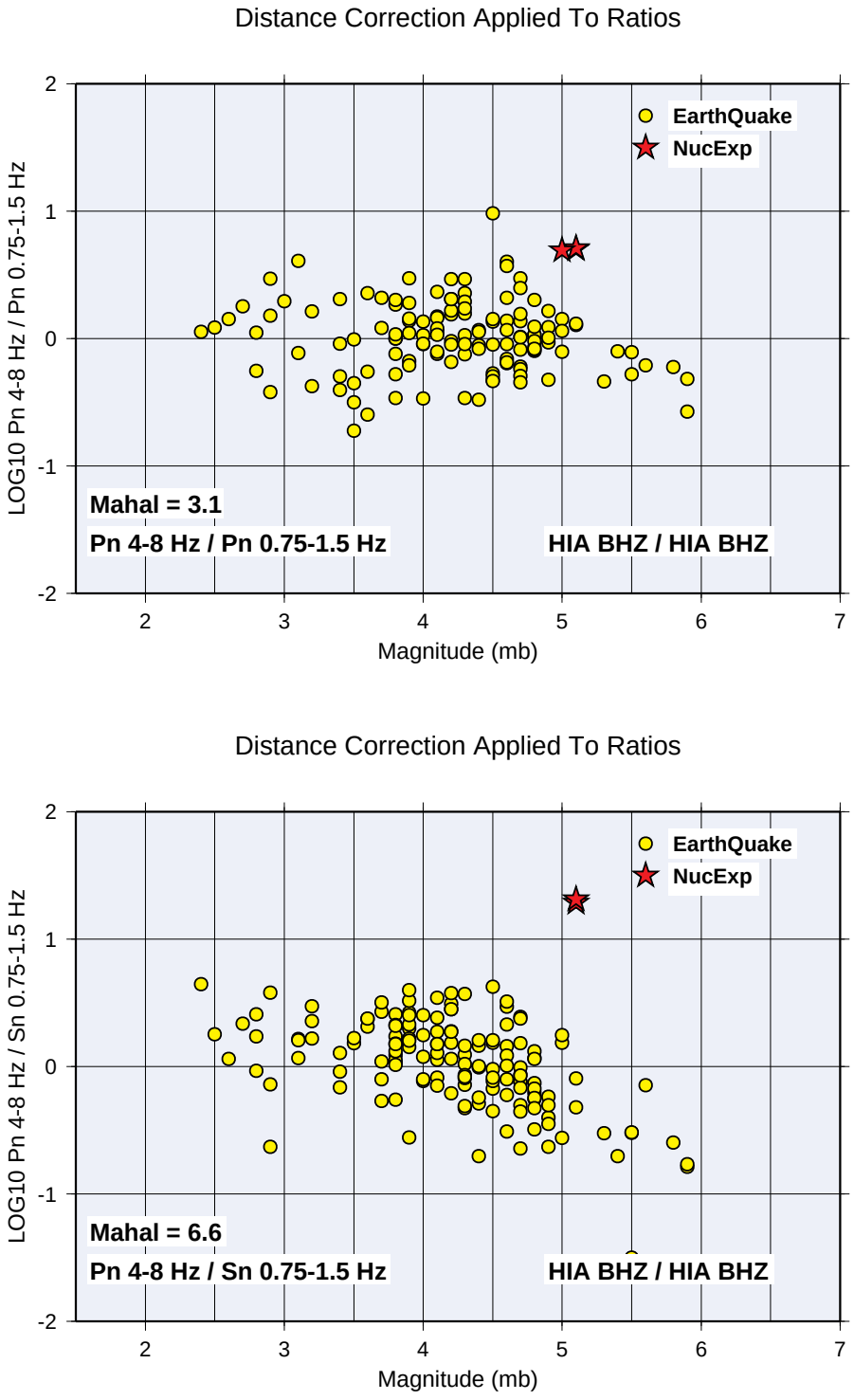


Figure 7. P_n spectral ratio and the P_n(4-8 Hz)/S_n(0.75-1.5 Hz) ratio versus magnitude. Distance corrections have been applied. Both ratios separate the explosions from the earthquakes, but not quite as well as ratios that use L_g. The primary drawback of these ratios is that P_n is often a weak phase, and S_n is a poorly developed phase in Siberia. Hence, signal-to-noise problems often eliminate many smaller regional events from consideration when applying these discriminants.

AN INTERESTING REGIONAL SEISMIC EVENT FROM QINGHAI PROVINCE, CHINA

Hans E. Hartse and Aaron A. Velasco

Los Alamos National Laboratory

Sponsored by U.S. Department of Energy
Office of Nonproliferation Research and Engineering
Office of Defense Nuclear Nonproliferation
National Nuclear Security Administration

Contract No. W-7405-ENG-36

ABSTRACT

We anticipate that regional seismology will play a key role in future monitoring for potential underground nuclear tests. Understanding the regional characteristics of wave propagation, including source, path, and site effects, will be required before such monitoring becomes routine. To prepare for such monitoring, we have been studying many seismic events from central Asia recorded at regional distances. Here we report on one particularly interesting event from Qinghai Province, China that provides a good example of why a comprehensive regionalization effort is required for successful monitoring.

On December 6, 1997, a seismic event with m_b near 4.5 occurred in a mountainous region (over 4000 meters elevation) of the east-central Qinghai Province, China. The event was detected and located by the prototype International Data Centre (pIDC) and by the National Earthquake Information Center (NEIC). Both organizations fixed the depth when estimating the event's location. The pIDC estimated an m_b of 4.2 and an M_S (using only 2 stations) of 3.4. Using the pIDC m_b:M_S event screening criteria this event falls within the earthquake population. From the regional waveforms for this event we observe, in general, that signal-to-noise ratios are poor for body waves at frequencies above about 2 Hz, except at stations WMQ (1350 km) and MAKZ (2000 km). Rayleigh and Love waves at periods between about 15 and 25 seconds generally have good signal-to-noise ratios at most regional stations. We merged arrival times from regional stations with times from the NEIC and pIDC bulletins and relocated the event. Our relocation moved the event about 10 km farther south, but we could not constrain depth.

At WMQ we observe that P_n above 1 Hz is exceptionally strong relative to the shear phases S_n and L_g, and P_n is also unusually strong relative to the Love and Rayleigh waves. From our experience with regional short-period discriminants in central Asia, we interpret such characteristics as indicative of an explosion. To better understand this event we modeled the Rayleigh and Love waves to estimate source parameters (moment, depth, source mechanism). We found a best-fit source model of a strike-slip double-couple earthquake with a source depth of near 20 km and an approximate seismic moment of 1.76×10^{16} Nm (M_w = 4.8). The strong P_n amplitude at WMQ may be attributed to the focal mechanism, rupture directivity, and energy focusing at the crust-mantle boundary along the path from the source region to WMQ. In summary, this earthquake provides a good example of how the relationship among source, path, and site effects must be understood in preparation for regional seismic monitoring.

Key Words: discrimination, seismic sources, regional seismology

OBJECTIVE

Over the past several years seismic verification research has emphasized the analysis of seismograms recorded at regional distances (between about 200 and 2000 km). The primary objective of this research has been to lower magnitude levels at which events can be detected, located, and identified. Our efforts have been directed at regional event identification in Asia. While conducting seismic regionalization research we have come across an

interesting seismic event from Qinghai Province, China (Figure 1). The short-period body wave characteristics of this event are quite explosion-like, while the long-period characteristics are more similar to an earthquake. Below, we present a detailed analysis of this event. Our objective is to show how careful regionalization and discrimination research efforts are necessary for the future successful monitoring of nuclear-test-ban treaties.

RESEARCH ACCOMPLISHED

Observations

On December 6, 1997, at near 04h53m GMT, a seismic event occurred in a mountainous region of the east-central Qinghai Province, China (Figure 1). The event was detected and located by the prototype International Data Centre (pIDC) and by the United States Geologic Survey National Earthquake Information Center (NEIC). Both organizations used only teleseismic records when estimating the event's location, and neither organization attempted to estimate an event depth. The pIDC assigned an m_b of 4.2 and an M_S (using only 2 stations) of 3.4. The NEIC assigned an m_b of 4.5. We merged arrival times from regional stations with times from the NEIC and pIDC bulletins and relocated the event. Our relocation moved the event about 10 km farther south, but we could not constrain depth. Because the Qinghai Province is seismically active, and because this event was small enough that it was not associated with any damage reports, it generated little seismological interest. Further, the event did not occur near any nuclear test site, and thus was of little interest to the nuclear test monitoring community.

During routine processing of regional data recorded at station WMQ, we noticed that this event had unusually strong P_n amplitude relative to the S-phase amplitudes, suggesting a possible explosion source. Hence, we gathered additional waveforms, primarily form Chinese Digital Seismic Network (CDSN) stations, for further analysis. Unfortunately, stations LZH and and XAN were not operating on December 6, 1997 (Figure 1). In general, signal-to-noise ratios are low for body waves at frequencies above about 2 Hz, except at stations WMQ (1350 km) and MAKZ (2000 km) (Figure 2, top). Figure 2 (bottom) compares the 06 December event with a similarly sized earthquake that occurred in June 1988 only 16 km from the Qinghai event. The P_n(4-8 Hz) amplitude of the Qinghai event is much larger than the S_n(0.75-1.5 Hz) amplitude, while the S_n amplitude of the 1988 earthquake is greater than its corresponding P_n amplitude.

Rayleigh and Love waves at periods between about 15 and 25 seconds generally have good signal-to-noise ratios at most regional stations for the Qinghai event (Figure 3). Large nuclear explosions in Asia have been known to generate strong Love waves (Walter and Patton, 1990; Wallace, 1991) through tectonic release. Hence, observing both Rayleigh and Love waves for a given event can not necessarily rule out the possibility of an explosion source. From an initial examination of the surface waves, we can only assume that the event was not an unusually deep earthquake.

Forming P_n/S_n discrimination ratios using WMQ measurements (details found in Hartse et al., 1997) emphasizes the unusually strong P_n energy of this event (Figure 4, top). Note that the Qinghai event falls high on the ratio plot and within the population of Kazakh Test Site (KTS) explosions. Furthermore, the other presumed earthquakes from the Qinghai area (squares) do not display these characteristics. As suggested by the strong Rayleigh waves, however, the pIDC m_b:M_S event screening criteria place the Qinghai event within the Asian earthquake population (Figure 4, bottom).

Summarizing the waveform observations, the short-period data (where it exceeds noise levels) suggests the Qinghai event may be an explosion, while the regional surface wave data imply the event is a crustal-depth earthquake, but the surface wave data do not absolutely rule out an explosion source. Possible explanations for these observations could include some combination of these factors: (1) some type of a large mining explosion, (2) an earthquake with an unusual source radiation pattern, (3) unusually strong S_n and L_g attenuation (or phase blockages) along the path to WMQ, (4) unusual focusing of P_n energy due to the geometry of the crust-mantle boundary along the path to WMQ. To better understand this event, we used surface waves to estimate source parameters. We present the surface wave inversion results below.

Surface Wave Source Inversion

Although there are many approaches to source inversions using regional data (e.g., Dreger and Helmberger, 1993; Ritsema and Lay, 1993), we use the approach outlined by Randall et al. (1995), where we deconvolve the instrument response, window, and filter the data prior to the source inversions. We refine the filtering process by performing a phase-matched filter instead of a typical bandpass (Herrin and Goforth, 1977). Summarizing, our

approach is as follows: we remove the instrument response, perform phase-matched filtering, calculate a suite a synthetics for chosen regional velocity models, time shift the seismograms, and then invert for the moment tensor. We further explore the uniqueness of the solutions by performing a focal mechanism grid search.

We obtained a major double-couple solution with strike, dip, and rake of 190° ±5°, 71° ±10°, and -27° ±5°, respectively. The errors reflect the formal inversion uncertainty, but we later explored how unique this solution is with a grid search technique. The moment is 1.76×10^{16} Nm (M_w = 4.8) with a 16% non-double couple component. This moment estimate is uncertain given the different elastic parameters for different models. We plot the normalized L2 error as a function of depth (Figure 5, top), and find the depth estimate to be between 15 and 20 km. We also plot the focal mechanism at the minimum. For this solution, we obtain an excellent fit to the data for both Love and Rayleigh waves, except for BJT. We underestimate the amplitude at BJT, but match the dispersion characteristics adequately.

Figure 5 (bottom) compares our moment tensor solution with the moment tensor solutions of two larger earthquakes from the Qinghai Province. The moment tensor solutions for the larger events indicate thrust mechanisms. This is in contrast to our strike-slip mechanism for the 06 December event. We know that the larger events occurred about 50 km northeast of the 06 December event. The June 1988 earthquake, with waveforms shown in the bottom of Figure 2, occurred much closer to the 06 December event. We plan to analyze the regional surface waves of the June 1988 earthquake and compare its focal mechanism to those mechanisms shown in Figure 5.

CONCLUSIONS AND RECOMMENDATIONS

Because we were able to use regional surface waves to obtain a stable long-period moment tensor solution with little non-double component, we can conclude that the 06 December 1997 event from Qinghai Province is most likely an earthquake. The unusually strong high-frequency P_n amplitude at WMQ may be due to one or many contributing factors. These include enrichment of P_n high frequencies due to rupture directivity, and possibly path effects that focus some of the P_n energy beneath station WMQ. We still do not fully understand this event, and we do not have a complete explanation for why the relative P_n/S_n ratios of the 06 December 1997 event and the June 1988 event are so different (Figure 2, bottom). For future work, we will analyze the surface waves of the June 1988 event to learn more about its focal mechanism.

This event highlights the difficulties of monitoring small magnitude events in the context of a nuclear-test-ban treaty. Clearly, there will be some small earthquakes that will appear explosion-like on some discriminants. Combining several discriminants is an obvious solution to the event identification problem. We have shown that regional surface waves can prove to be important for event analysis. Furthermore, requirements for successful regional monitoring include well-calibrated paths, special processing techniques such as phase-matched filtering, and source modeling capabilities. Thus, regional discrimination must incorporate a range of tools, techniques, and data types to be robust.

REFERENCES

Dreger, D. S., and D. V. Helmberger, Determination of source parameters at regional distances with three-component sparse network data, *J. Geophys. Res., 98*, 8107-8125, 1993.

Hartse, H.E., S.R. Taylor, W.S. Phillips, and G.E. Randall, Regional event discrimination in central Asia with emphasis on western China, *Bull. Seism. Soc. Am., 87*, 551-568, 1997.

Herrin, E. and T. Goforth, Phase-matched filters: application to the study of Rayleigh waves, *Bull. Seismol. Soc. Am. 63*, 663-671, 1977.

Randall, G. R., C. J. Ammon and T. J. Owens, Moment-tensor estimation using regional seismograms from a Tibetan Plateau portable network deployment, *Geophys. Res. Lett., 22*, 1665-1668, 1995.

Ritsema, J., and T. Lay, Rapid source mechanism determination of large ($M_w \geq 5$) earthquakes in the western United States, *Geophys. Res. Lett., 20*, 1611-1614, 1993.

Wallace, T. C., Body wave observations of tectonic release, in *Explosion Source Phenomenology, AGU Monograph 65*, S. R. Taylor, H. J. Patton, and P. G. Richards, Editors, American Geophysical Union, Washington D.C., 161-170, 1991.

Walter, W. R. and H. J. Patton, Tectonic release from the Soviet Joint Verification Experiment, *Geophys. Res. Lett.*, 17, 1517-1520, 1990.

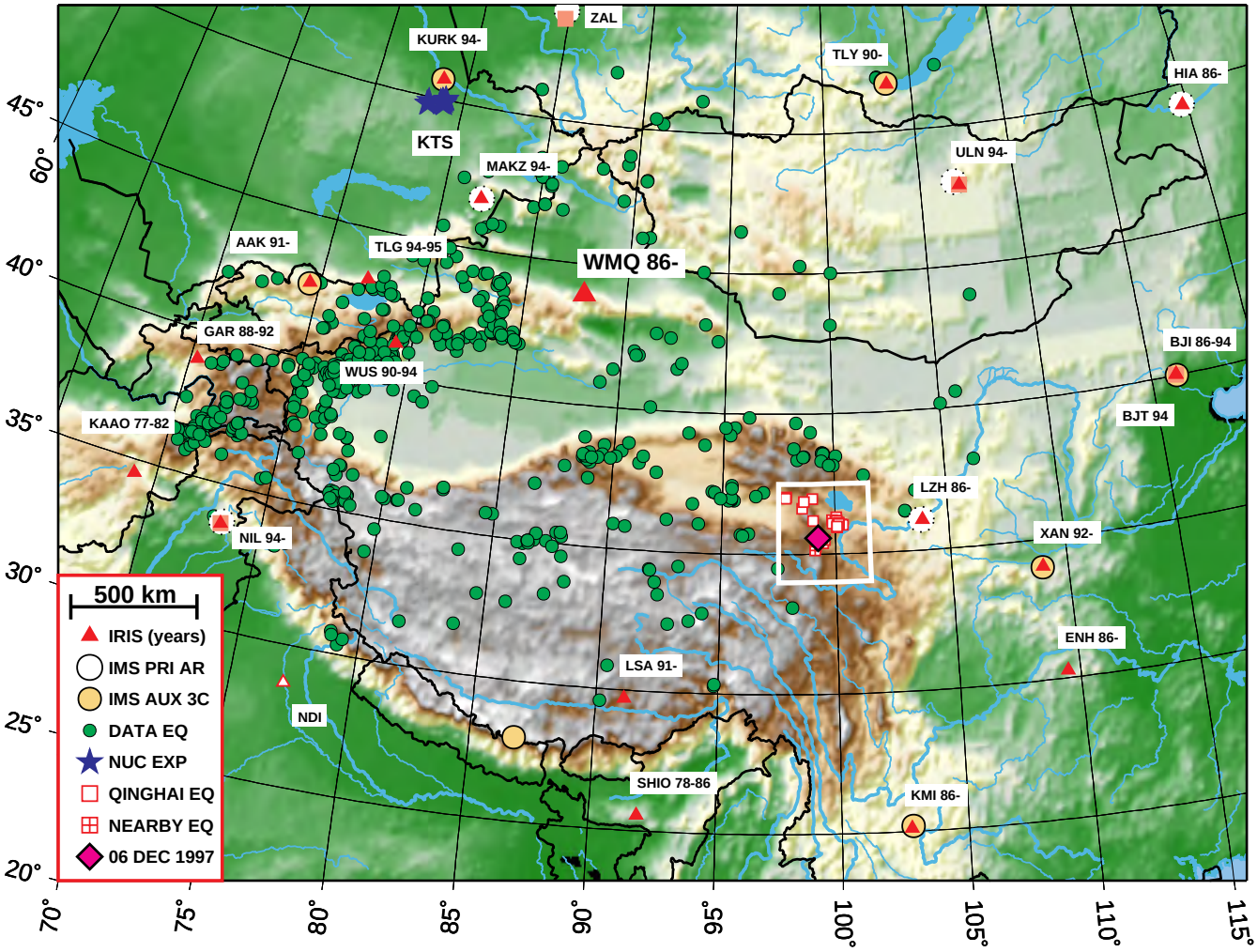


Figure 1. Map of central Asia showing Qinghai area inside white box. Stations LZH and XAN were not operational on 06 December 1997, when the Qinghai event (magenta diamond) occurred. We have primarily analyzed short-period waveforms recorded at WMQ, and surface wave data from the Qinghai event recorded at several regional stations. Earthquake locations are represented by green circles and red squares, and nuclear explosion locations are represented by blue stars from the Kazakh test site (KTS).

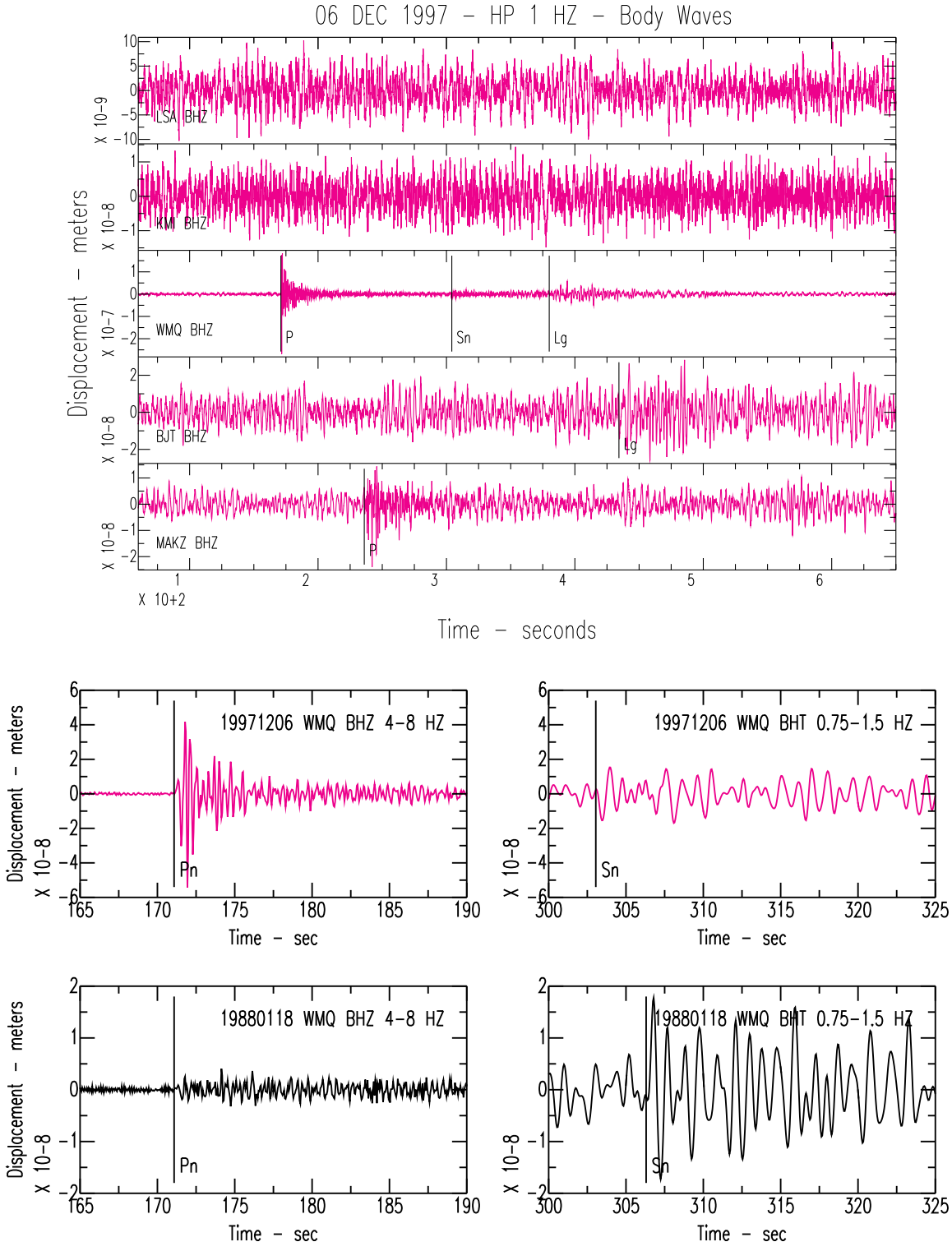


Figure 2. Regional body wave record section (top) of the Qinghai event as observed at stations LSA, KMI, WMQ, BJT, and MAKZ. With the exception of WMQ, most regional phase amplitudes fall within the background noise. The four bottom panels compare WMQ records of P_n and S_n from the Qinghai event to a similarly sized, nearby (16 km) earthquake from June 1988 (black traces). Note the unusually strong P_n amplitude of the Qinghai event relative to the S_n amplitude. Because of such a strong P_n amplitude, the Qinghai event falls within the explosion population on station WMQ P_n/S_n discrimination plots.

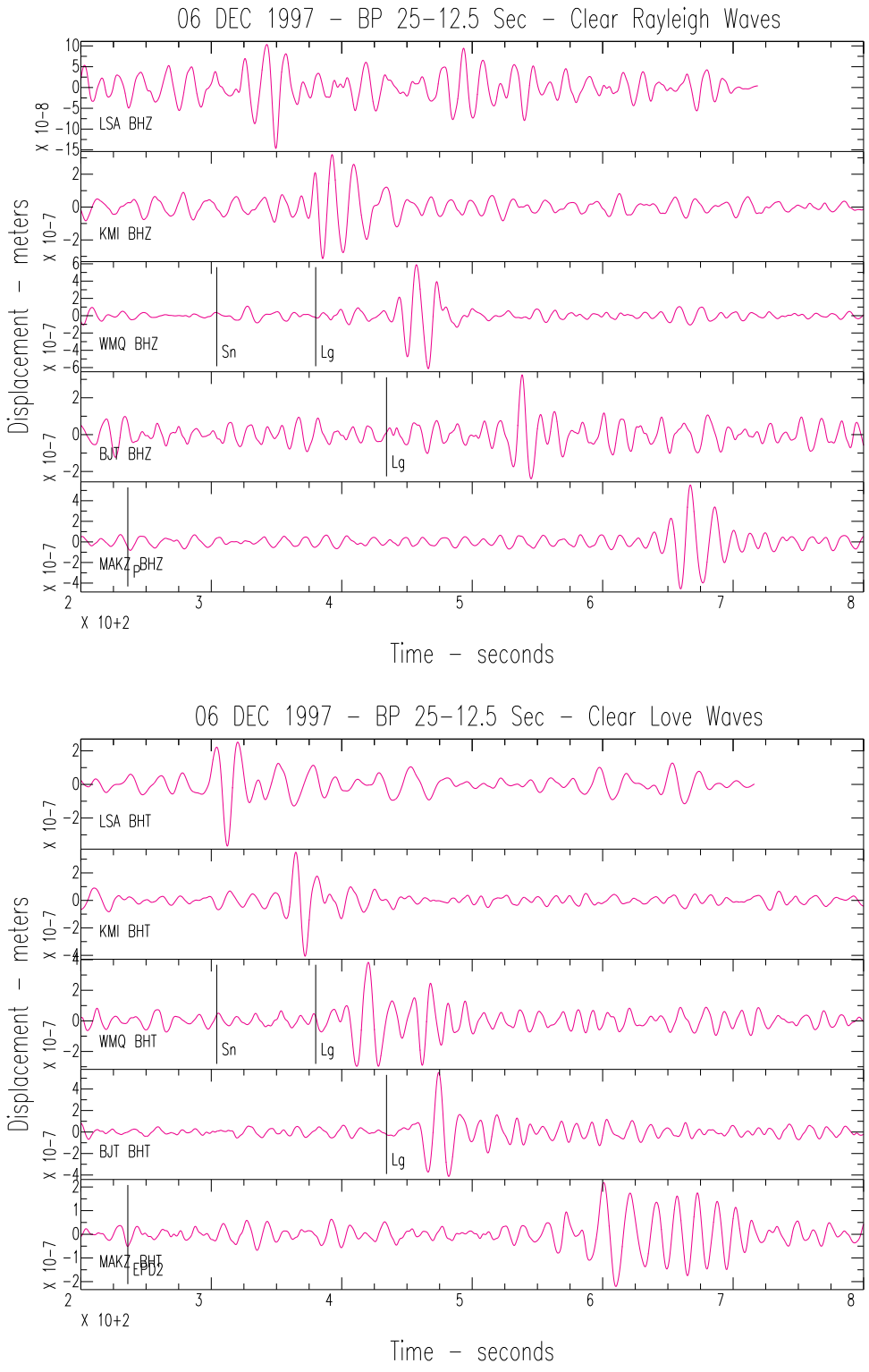


Figure 3. Regional surface wave record sections of the Qinghai event as observed at stations LSA, KMI, WMQ, BJT, and MAKZ. Clear Rayleigh waves (top) and clear Love waves (bottom) are observed at all stations. The strong surface waves of the Qinghai event suggest an earthquake source.

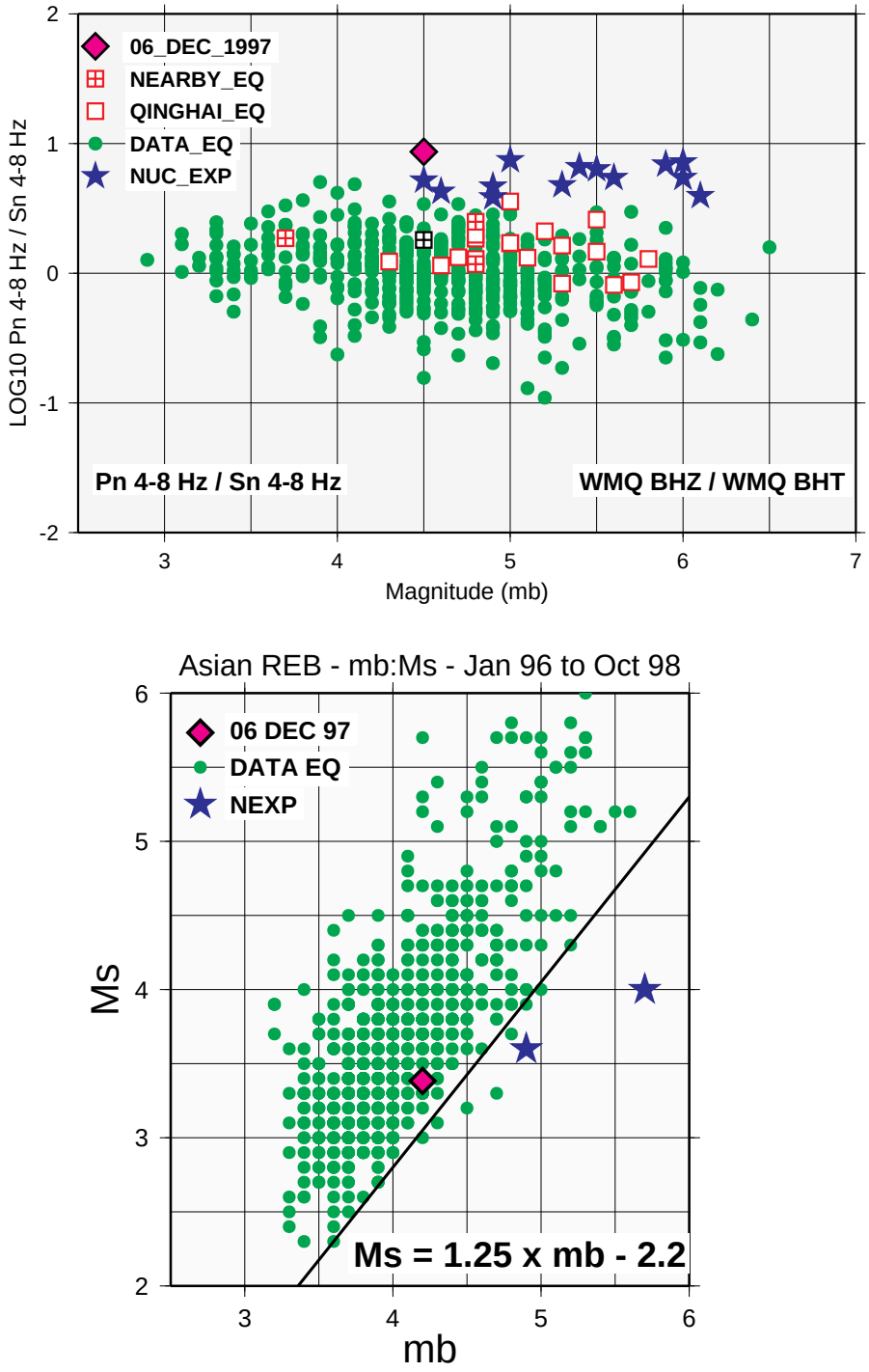


Figure 4. P_n/S_n ratio versus magnitude (top) for regional data recorded at station WMQ, and the teleseismic m_b:M_S relationship (bottom) based on the prototype International Data Center Reviewed Event Bulletin for Asian events between January 1996 and October 1998. Note that the Qinghai event (diamond) falls within the Kazakh test site explosion population at top, and it is distinctly separated from the other nearby Qinghai earthquakes (squares). The black square, well within the earthquake population, represents the June 1988 earthquake with WMQ waveforms shown in Figure 2. Note, however, that the Qinghai event falls within the earthquake population when surface wave magnitudes are considered as shown on the m_b:M_S plot (bottom).

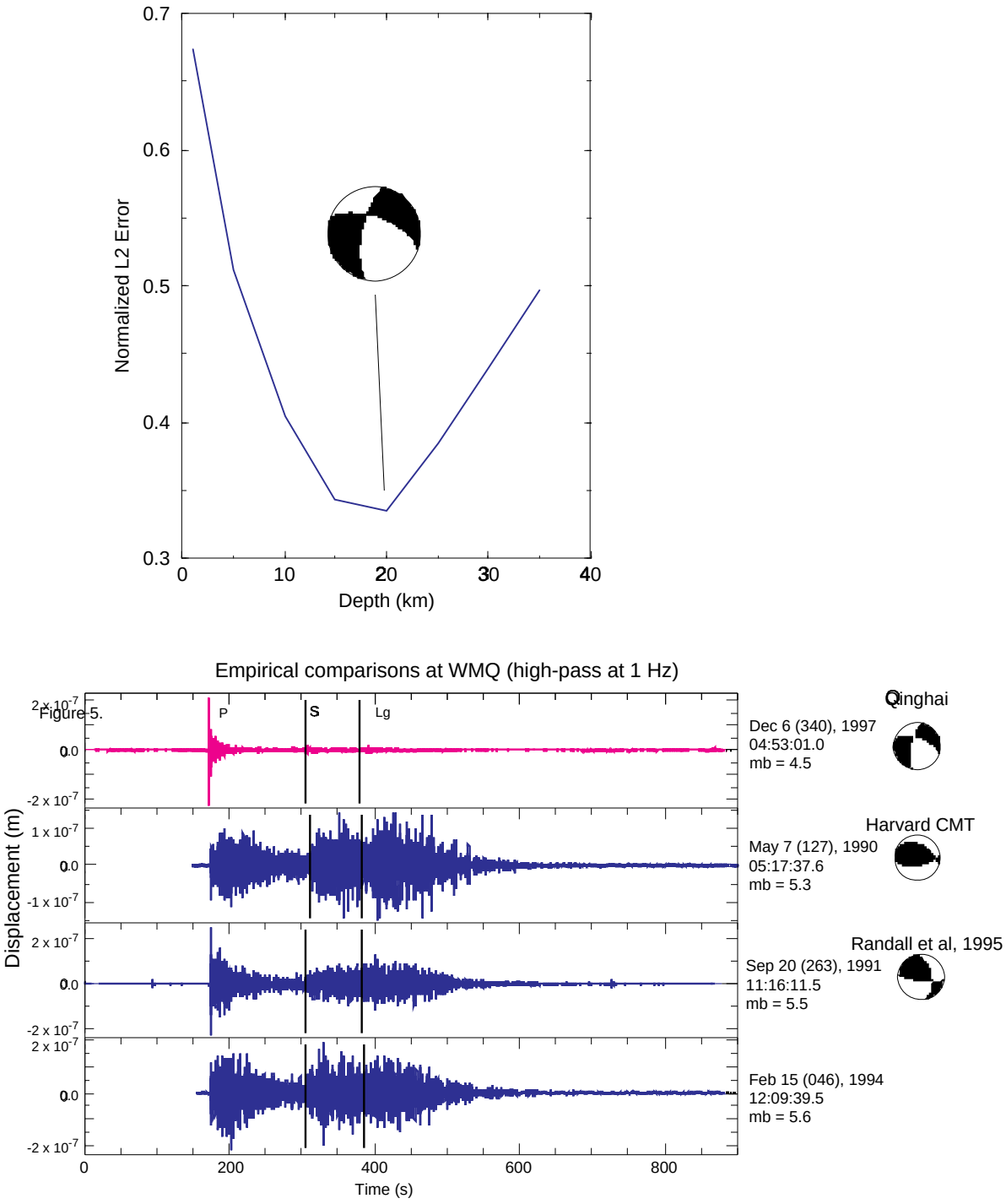


Figure 5.

Figure 5. Error versus depth of our best-fit moment tensor solution for the Qinghai event (top). This solution was found by modeling regional Rayleigh and Love waves shown in Figure 3. Shown at bottom are the short-period waveforms and moment tensor solutions for the Qinghai event and other events from the Qinghai area. The Qinghai event is dominated by strike-slip motion while the other events are dominated by thrust motion.

TOMOGRAPHY AND LOCATION PROBLEMS IN CHINA USING REGIONAL TRAVEL-TIME DATA

Thomas M. Hearn and James F. Ni

New Mexico State University, Physics Department

Sponsored by The Defense Threat Reduction Agency
Arms Control Technology Division
Nuclear Treaties Branch

Contract No. DTRA01-99-C-0016

ABSTRACT

Phase data from the Annual Bulletin of Chinese Earthquakes (ABCE) are being collected and used for tomographic inversion and event location problems within China. So far, we have seven years of data in computer form and six more in catalog form. Current efforts focus on regional tomography of China, comparing locations between the ABCE and other earthquake catalogs, and developing station corrections for IMS stations in and around China.

We used the Pn phase data from the ABCE catalog to image the uppermost mantle velocity and anisotropy structure beneath China. Raypaths cover most of central and eastern China; coverage in western China and Tibet is poor. The data quality is exceptional, with Pn phases routinely identified and picked for distances from 1.5 to 9 degrees. Over 25,000 arrivals have been used in the Pn tomography algorithm. The average uppermost mantle velocity beneath China is 8.0 km/s. The Tarim, Junggar, Tsidam, and Sichaun basins have the highest Pn velocities (over 8.2 km/s). These places are cratonic terrains that were accreted to southern Asia before the Indian-Asian collision. The high velocities imply higher density mantle that may have aided in the development of these basins. The eastern Tien Shan has normal Pn velocities of 8.0 to 8.1 km/s. Pn velocity beneath Tibet decreases from south to north as previous studies have also found. Late station delays in and around Tibet attest to its 70 km thick crust. Along the southeastern Tibet margin, low Pn velocities are found suggesting that high temperatures and possible partial melt exist in the uppermost mantle there. A region of high anisotropy surrounds Tibet. Eastern China has lower Pn velocities and thinner crust as a result of Cenozoic extension of eastern China. A very low Pn velocity (<7.7 km/s) is found north of Hainan Island. This feature may be related to the opening of the South China Sea.

We compared event locations between the ABCE and the PIDC catalogs for our only year of overlap, 1995. The ABCE locations are located with many local stations and can be expected to be better than the teleseismic locations. On average, ABCE and PIDC locations differ by 0.95 degrees. For the same events, estimated errors from the PIDC locations average 0.76 degrees. Several events were mislocated in excess of 4 degrees due to a lack of reporting stations and poor azimuthal coverage. The 1995 location capability of the PIDC was not sufficient to locate Chinese events within the 1000 sq-km region required by the CTBT. Better station coverage and calibration are needed to achieve this goal.

Key Words: China, Tomography, Pn

OBJECTIVE

NMSU seismologists, in conjunction with seismologists from the Institute of Geophysics of the China Seismological Bureau (IG/CSB), seek to collect seismic data to calibrate International Monitoring System stations in China and to document regional phase propagation characteristics in China. We are approaching these problems through regional tomography, characterization of regional wave propagation, station calibration, and an analysis of current location capabilities in China (Figure 1).

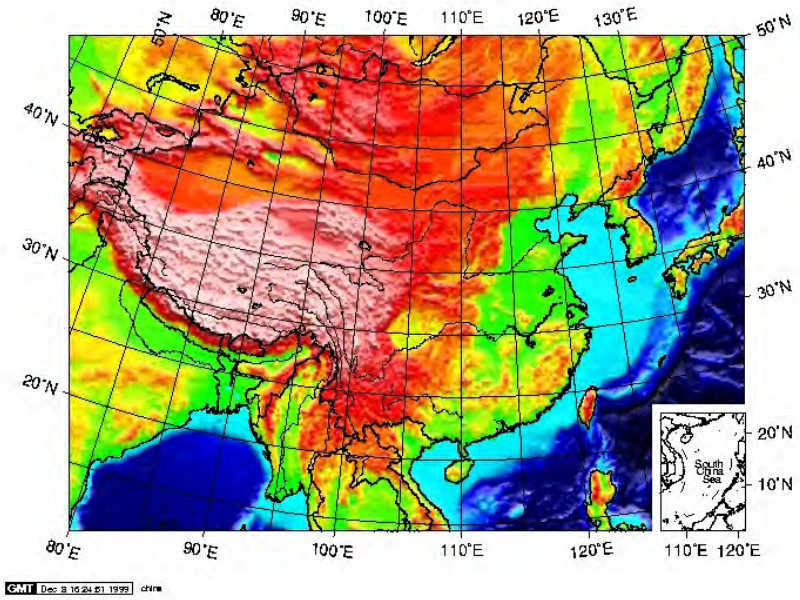


Figure 1 - Shaded topography of China.

RESEARCH ACCOMPLISHED

Data collection

Our data set of the Annual Bulletin of Chinese Earthquakes (ABCE) consists of both paper catalogs and digital data sets provided by our colleagues from the China Seismological Bureau (CSB). Paper catalogs span 1983 to 1995; 1991 to 1995 were also given to us in digital form. The 1986 and 1987 catalogs were typed into the computer and work on other catalogs proceeding. The data quality from the ABCE is exceptional, with Pn phases routinely identified and picked for distances of up to 9 degrees [Figure 2]. Pn arrivals form the linear first-arrival portion of the travel-time curve between distances of 200 to past 1500 km.

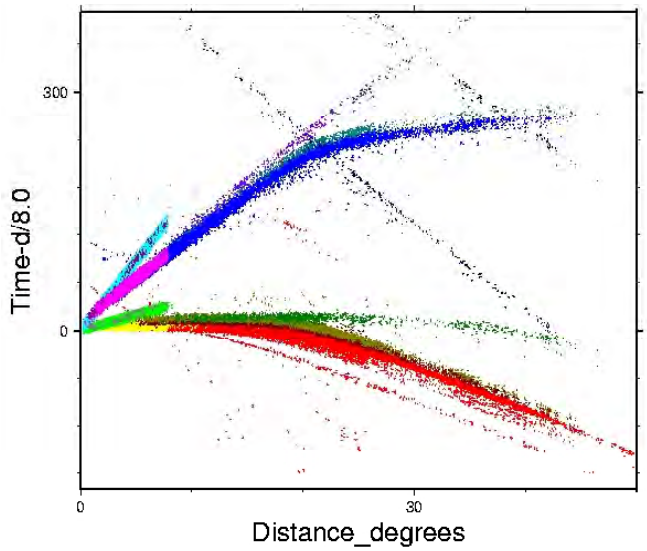


Figure 2 - P-wave first arrival travel times from the Chinese bulletins (ABCE) for 1991 through 1995. Pg, Pn and a distant P branch are clearly visible. The ABCE routinely identifies arrivals as Pg, Pn, P, PP, pP, Sg, Sn, S, SS, sS, sP, PcP, S11, ScS, P11, ScP, PcS.

Pn tomography beneath China

We have applied the Pn tomography algorithm of Hearn [1999] to Pn data from the ABCE to image the P-wave velocity and anisotropy at the surface of the mantle. Raypaths for these data cover most of central and eastern China; coverage in western China and Tibet is poorer, but we are now beginning to include data from other sources to remedy this. We used raypaths between 1.8 and 15 degrees distance and only stations and events with more than 9 arrivals at them. The final Pn data contains over 115,000 arrivals that span most of China [Figure 3].

The inversion yields an average Pn velocity of 8.05 km/s for all of China. Additional travel time studies have also been made by plotting out travel time curves for three different regions of China. We found the apparent velocities for these regions to be:

Region	Pg velocity	Pn velocity
Huabei	6.19	7.94
Tianshan	6.28	8.02
Sichuan	6.08	7.86

Figure 4 shows the regionally varying Pn velocities and anisotropy from the inversion. The Tarim, Tsidam, and western Sichaun basins have the highest Pn velocities. These places may be cratonic terrains that were accreted to southern Asia before the Indian-Asian collision. The high velocities also represent higher density mantle that may have aided in the development of these basins. Pn velocity beneath Tibet decreases from south to north as has been found in previous Tibet studies [McNamara, 1997]. This suggests that the subducted Indian plate ends somewhere beneath central Tibet. Eastern China has much lower Pn velocities. Along the southeastern Tibet margin, low Pn velocities are found suggesting that high temperatures and possible partial melt exists in the mantle there. Anisotropy is shown in Figure 5 by short line segments oriented along the fast anisotropy direction. Major regions of anisotropy are beneath the eastern Himalayan syntaxis, Sichuan Basin and Taiwan. Our resolution in the velocity and anisotropy is between two and three degrees. Because anisotropy can vary on shorter distance scales, much of it remains unresolved.

Both station and event delays represent the combined effect of crustal velocity and thickness [Figures 6 and 7]. Event delays, however, are also susceptible to errors in origin time or depth in the event location. In most Pn tomography studies [e.g. Hearn, 1999], these errors create such scatter in the event

delays that they are of little use. This is not the case for the ABCE data, and it indicates that events in China are exceptionally well located.

The delays can be interpreted as a rough map of crustal thickness in China. For a constant velocity crust, 1 second of delay time represents approximately 10 km of crustal thickening. Late station and event delays in Tibet then imply that the crust there is 30 to 40 km thicker than the crust in eastern China. Events north of the Tarim Basin and in the Tien Shan also show late delays indicating crust that is 10 to 20 km thicker than eastern China. A thin crust is also apparent on the southeast margin of Tibet where extension is occurring.

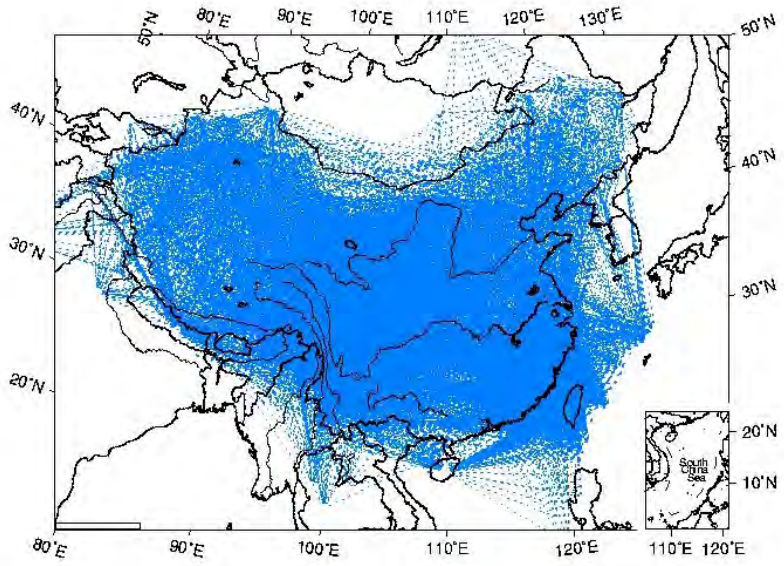


Figure 3 - Pn raypaths used in the tomography. Distances were restricted to 1.8 to 15 degrees. About 25,000 raypaths are shown.

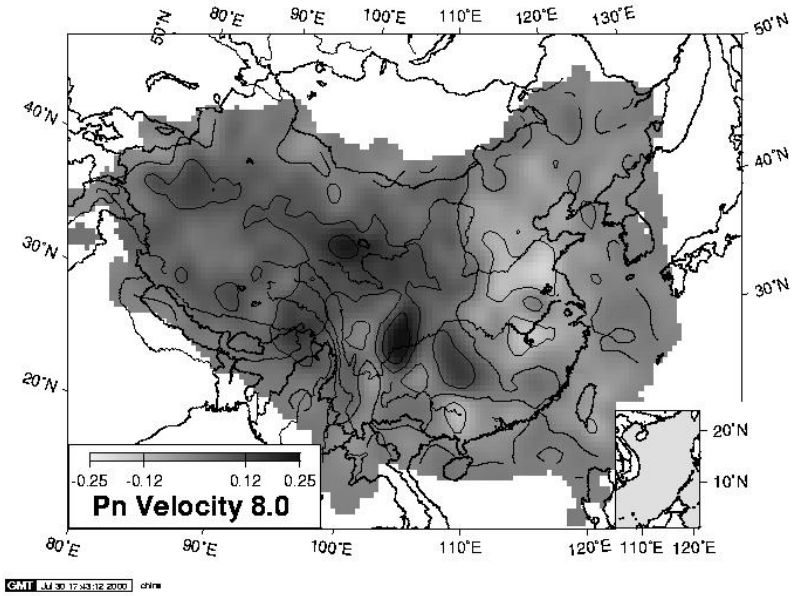


Figure 4 - Pn velocity beneath China. Shades represent variations from a mean Pn velocity of 8.0 km/s. The Tarim, Tsidam, and western Sichaun basins have the highest Pn velocities. These places may be cratonic terrains that were accreted to southern Asia before the Indian-Asian collision. Eastern China has lower Pn velocities.

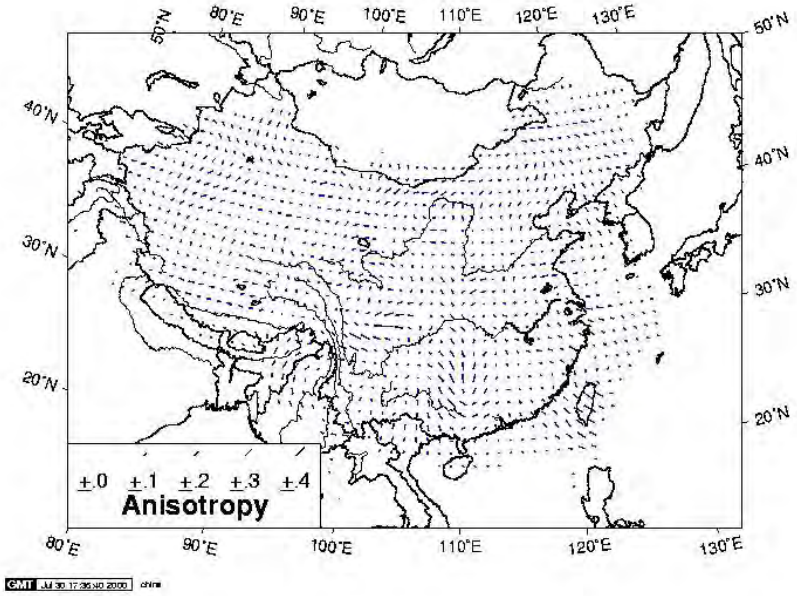


Figure 5 - Pn anisotropy beneath china. Line segments show the orientation of the anisotropic fast direction; line lengths show the magnitude of the anisotropy.

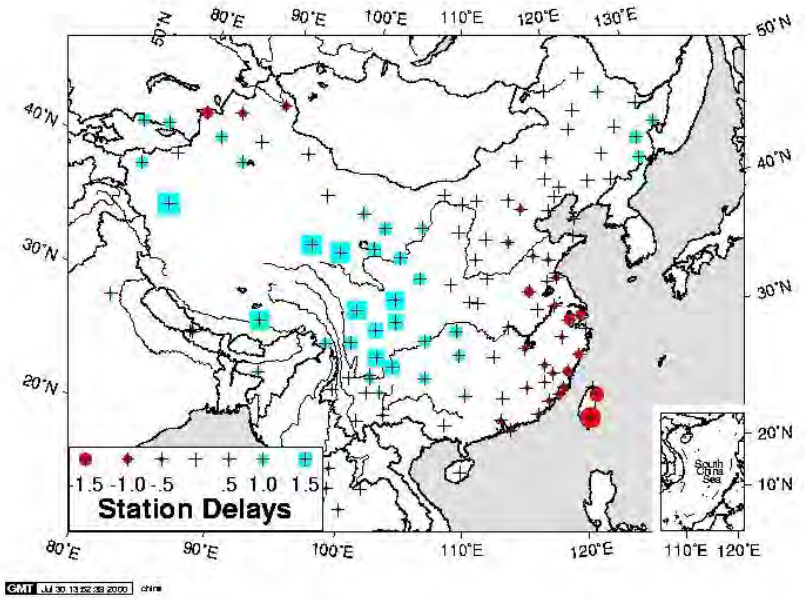


Figure 6 - Station delays beneath China (zero-mean). These delays depend on both crustal thickness and crustal velocity. For a constant velocity crust, one second of delay corresponds to about 10 km of crustal thickening. Late arrivals in Lhasa, Tibet, and around the edges of the Tibetan Plateau result from the 70 km thick crust. Early delays in the east and in Taiwan are the result of thinner crust.

ADAPTIVE TECHNIQUES FOR ESTIMATING AND LOCATING SMALL EVENTS USING REGIONAL WAVEFORM DATA

Don V. Helmberger, Chen Ji, and Brian Savage
Seismological Laboratory
California Institute of Technology

Sponsored by The Defense Threat Reduction Agency
Arms Control Technology Center
Nuclear Treaties Branch

Grant Number DSWA01-98-1-0010

ABSTRACT

Attempts at locating and identifying small events could benefit greatly from a better appreciation of regional seismograms. Essentially, we need more information from the few regional seismograms available than just arrival times and amplitude ratios. Here we discuss a method of estimating source parameters using as few as one broadband station in conjunction with travel-time and polarities from at least one more station. The method employs an adaptive grid-search of matching three-component waveform records against synthetics to establish source location and depth. The basic matching procedure contains a trade-off of source mechanism with location. The better the constraint on mechanism and depth, the better the location. It appears that refined depths and origin times can be obtained for GT5 events if the first-motion polarities are available to constrain the focal plane. The locations of GT10 and GT25 and EHB (Engdahl, Kennett, and Buland) events can also be improved if CMT's and other independent depth estimates are available.

Preliminary results applied to the PASSCAl data recorded in Pakistan and Tibet (China) and TriNet (CAL) proved highly effective when locating events located approximately between two stations. If both stations have usable three-component data, we can determine depth and source mechanism and refine the location. If we assume the mechanism and depth are known (Master Reference Event), we can relocate the event using just one broadband station and the *P*-wave arrival time pick from the other, or we can refine the crustal model. We find good agreement when testing these results against those from the entire array.

Crustal complexities can change the separation between key phases (*Pnl*, *Snl* and surface waves) which may require some calibration for maximum sensitivity. In many situations, distortions in wave-shapes may be severe enough to require 2D and 3D Green's functions. To accomplish this objective, we are developing an adaptive method for recovering 2D structure using Waveform Tomography. Our approach uses individual generalized rays computed from a layered model. The model is divided into blocks with variable velocity perturbations such that ray responses are allowed to shift relative to each other to maximize synthetic waveform fits to data. An efficient simulated annealing algorithm is employed in this search. The technique is applied to a collection of 25 aftershocks (Landers EQ) as recorded at two stations, GSC and PFO, separated by about 200 km which bracket the event population along the Landers fault system. The events are assumed to have known mechanisms and epicenters, but both their depths and origin times are allowed to vary. The results indicate considerable variation, especially in the top layer (up to ± 13%) which mirrors surface geology. A similar experiment involving a profile of observations across Tibet indicates substantial deep crustal variation. But given such large changes in velocities requires regeneration of the ray responses and the process repeated. Presently, we are at this stage of development.

Key Words: Crustal calibration; Source estimation.

OBJECTIVES AND SIGNIFICANCE

Global seismic monitoring requires improved locations of events and reliable capabilities to discriminate nuclear explosions from earthquakes. In this section, we will review some of the fundamental problems facing this global monitoring and how our efforts will produce improvements in location and discrimination.

Several recent review meetings addressing the Comprehensive Nuclear Test Ban Treaty (CTBT) have started with the basic difficulty in location. After two years of Review Event Bulletin (REB), North reported on GSETT-3

that REB 90% confidence ellipses contain the national network event locations less than half of the time. "Thus an appropriate means of implementing path-dependent teleseismic travel times, and of transitioning from these to regional travel time curves, will need to be developed." The strategy discussed at the Oslo Workshop held in 1999 and adopted by the pIDC is to implement procedures for such calibrations. Essentially, this is a bottom-up approach where one attempts to expand coverage from global to regional. The key to this procedure is the quality of nationally located events and ground truth (GT) methodology. The ground truth phenomenology developed around the location problem is based on the first-order need for a good XY-location and developing compatibility with global estimates.

Since it has proven difficult to determine event depth and origin time independently, the methodology tends to side-step this problem by assuming surface sources. GT1 and GT2 man-made events are obviously excellent locations but generally do not apply in most regions with no previous testing experience. Thus, we need to be concerned with the REB and GT10 and GT25 events of less accurate locations. GT10 events come from local networks and are selected from existing bulletins (CEB, NEIC, and ISC) provided that at least three IMS stations report the event. They must be recorded by at least 5 stations within a distance of 3° and have coverage consisting less than a 180° azimuthal gap at a distance less than 5°. The CEB is a pIDC's Calibration Event Catalog which is growing rapidly, now at over 2200 events. Its event location accuracy is assumed to be somewhere between GT10 and GT25. This appears to be the same accuracy expected in the relocated ISC data set of about 8,000 events [Engdahl *et al*., 1998], referred as EHB.

In general, majority of local seismic networks in many seismically active regions operates exclusively with short-period vertical component instruments. Hypocentral locations are often determined by using regional and local *P*- and *S*-wave travel times picked from this type of network and focal mechanisms are determined using the first-motion polarities. Various National Data Centers (NDC) provide these locations as ground truth locations for their datasets. Most local arrays still operate short-period Wood-Anderson types of instruments (usually the vertical component only) at relatively high gain. The emphasis was on determining the locations of buried fault zone by recording a large number of small events. The recordings go off the scale for any sizeable events (M>5), and thus events recorded teleseismically are not well recorded in the faulting region except for strong-motion instruments. Only in recent events with modern equipment have we learned about the complexity of faulting. These recent studies have suggested that the location from a short-period array is usually not the location of the asperity producing the teleseismic signal. Fortunately, the mechanism of the initial break is typically the same as the larger sub-events and is reliably recorded by the direction in which the vertical record goes off-scale. Thus, the focal mechanisms are still quite useful, especially for calibration size events (3.5<M<5.5). However, a major problem is that focal mechanisms are dependent on velocity model and particularly the take-off angle and depth. Depths are usually estimated from local *S*- and *P*-wave arrival time picks. But recent studies [Savage and Helmberger, 1999] indicates that the phase routinely picked as given in the Caltech-USGS bulletin appear to be *sP*, a phase that leaves the source as the *S* wave and reflects off the free-surface and travels to the station as a *P* wave. This phase is relatively strong on the vertical component and has been studied extensively in recent years. It is particularly obvious for deep events as noted by Zhao and Helmberger [1993] in their study of Pamir-Hindu Kush events, and Saikia *et al*. [1996] in other regions. This misidentification of *S*, using short-period methodology, leads to hypocentral depths that are on average too shallow and appears to explain the disparity in results comparing the depths from the Southern California Seismic Network (SCSN) catalog with waveform inversion. In particular, Zhu and Helmberger [1996b] found an average focal depth of 5.6±4.4 km from SCSN vs. depth of 11.9±3.7 km from waveforms for a population of 355 events with magnitude >3.5. Since strike-slip events do not have nodes in the vertical plane (independent of take-off angle), they should not show a disparity in focal mechanisms between the first-motion results and the waveform results which appear to be the case for the Landers aftershocks [Jones and Helmberger, 1998]. However, Northridge aftershocks do show this difficulty for those events listed as shallow in SCSN [Song and Helmberger, 1997]. This issue is presently being addressed in Japan and is probably a global problem, and must be addressed at individual arrays usually on the scarce-side in most countries.

In the last few years, real-time systems are being developed to monitor seismic activity for rapid notification and rapid damage assessment. The TriNet system now under development in southern California is an example where the recent Hector Mine earthquake was reported on the web within minutes, including the mechanism and direction of rupture. Because of the growing global concern with loss of life and damage during catastrophic earthquakes, many countries from other tectonic regions are starting to address the issue of the earthquake hazards. Thus, we can expect a period of transition where a combination of short-period instruments with a few sparse broadband instruments will be the only resource to obtain accurate locations of seismic events, basically the situation facing monitoring in many regions.

We are contributing our efforts to this process by a series of user-friendly software package that allow a mixed

set of travel times and polarities from short-period instruments, normally included in local catalog, and waveform data to better constrain earthquake source parameters, including location, depth, origin time, and mechanism. These codes will be made available to anyone on our web site. They would be developed and tested on the present seismic networks in southern California and China (Cooperative Program starting this summer, Lupei Zhu). A demonstration of this procedure will be given at the CTBT Annual meeting (2000).

SOUTHERN CALIFORNIA – A TEST BED FOR TECHNIQUE DEVELOPMENT

Earthquake occurrence in southern California has been one of the highest in the world. Over 500 seismic stations now exist with about 150 broadband stations similar to those of the IMS. Thus, we have a natural laboratory to observe seismic wave complexity generated by different types of earthquakes in variety of tectonic settings. We will begin by displaying some interesting observations followed by our modest attempts at explaining some of the details (Figure 1).

One of the simplest profiles of data is displayed in the lower panel, on the left. The middle section displays synthetics for a simple 1D model, just the standard California model with an 8 km transition zone from crust-to-mantle, Ji and Helmberger (1999). The basic long-period *Pn*, *pPn*, and *sPn* emerge from the *PmP* (*Pg*) and depth phases. The former features are expanded in scale and replotted in velocity on the right. These depth phases are generally quite well behaved and have been used to model most of the events occurring in the western United States. Thus, the relative stability of these phases can be exploited to help constrain source properties. However, there are some complex paths such as displayed in the upper profile that requires much more effort to explain. Those arrivals with very weak *Pn*'s (SVD, DGR, PLM, GOR, and DAR) are sampling the midpoints between Death Valley and the Panamint Range. They also contain a large second arrival, about 1.5 secs back, which can be modeled as a reflected-refracted arrival from a low-velocity-zone structure, see diagram below map, Ji and Helmberger (1999). The upper-mantle structure farther to the west is dominated by the rapid development of a high-velocity lid, with a strong gradient between eastern and western California, Melbourne and Helmberger (2000). Methods for inverting observed waveforms containing such complexities for structures are under development with some progress reported on in Helmberger *et al*. (2000) as presented at the meeting.

REVIEW OF SOURCE ESTIMATION

Significant progress has been made recently in retrieving source mechanisms from regional broadband seismograms. A consequence is that the magnitude threshold of events that can be analyzed has been lowered to less than 4 [Zhu and Helmberger, 1996b]. Because of the frequent occurrence and relatively simple source functions of earthquakes in the magnitude range of 4 to 5, their waveforms are ideal for calibrating path effects and investigating regional structures.

An application of this method is displayed in Figure 2. The alignment displayed is produced by cross-correlation which is controlled by the strongest arrival, Rayleigh waves. Thus, fitting whole records automatically is determined by the ratio of Rayleigh waves to Love waves. However, there is considerable information in the extended *Pnl* in terms of *P*, *pP*, and *sP* as there is in the teleseismic waveform modeling. To use this information, we model the beginning of the *Pnl* portion separately as in Figure 2. Fortunately, they are generally compatible as indicated by the above numerical experiment. These results suggest that a great deal of information is embedded in waveforms if used properly and the structure is simple. The adaptive grid-search code is ideal for adding outside constraints as displayed in the upper right-hand corner of Figure 2. Using the *P* polarities of the TERRAscope stations and the GSC waveforms, we obtained excellent results. Generally, we cycle through depth and pick the best fit with lowest misfit error, h =11~km. This depth agrees well with the teleseismic depth phases, namely *sP* (Wald, 1992). The individual depth phases in the regional data, *pPmP*, *sPmP*, *sSmS* are quite obvious at higher frequency as pointed out by Helmberger *et al*., 1992. The depth sensitivity from regional displacement waveforms (>150 km) comes from two features. The shape of the *Pnl* is controlled by the separation of *PmP* from its depth phases, *pPmP* and *sPmP*. The other depth constraint comes from the amplitude of the *Pnl* to surface waves. Strong surface waves suggest a shallow depth. It is quite common that the result from a single station agrees quite well with the network solution [Zhao and Helmberger, 1993, 1994; Dreger and Helmberger, 1991]. It is particularly important in sparse networks to use this method, so that the *Pnl* is not overruled by the details of the Rayleigh waves.

REGIONAL EARTHQUAKE STUDIES IN SOUTHEASTERN ASIA AND RECOMMENDATION

In a study by Zhu *et al*. [1997], we established the ability of two permanent stations, NIL (Nilore) in Pakistan and AAK in Kyrgyzstan, to locate and determine source characteristics of events in the Pamir-Hindu Kush region. In the winter of 1992, a temporary PASSCAL array (PAKN) was deployed in the northern Pakistan, which is very close to NIL. To calibrate the paths of events to AAK and NIL, we selected twelve events, 6 deep and 6 shallow,

and determined a very simple two-layer crustal models which seems to fit most of the recording throughout the highlands formed by the continental collision zone including Tibet. A library of Green's functions is then computed as a function of depth and distance as in California. For crustal events, the amplitude of the surface waves are very large for the shallow events (h = 10 km) so that the amplitude ratio of the *Pnl* to surface waves proves quite diagnostic of depth as discussed earlier. As the source moves into the mantle, the high-frequency signals trapped by the crustal waveguide disappears. The waveshapes become increasingly simple as the focal depth increases, essentially reducing to just *P*-waves and *S*-waves. However, there is still important information about polarity and relative strengths.

The above Green's functions are used to find fits to observations by applying an adaptive grid-search as described earlier. An example of fit to a Tibetan event, assuming these same Green's functions, is shown in Figure 3b using data from the 1991-1992 PASSCAL experiment. The procedure was used to study 50 events occurring during this time period (Figure 3a). Details are given in Zhu [1998] showing that most events are shallower than reported by the ISC and CMT's (when reported). Many of these events are not seen teleseismically and some are badly located as displayed in Figure 4a. Some deep events also occur in southern Tibet as reported by Zhu and Helmberger (1996a].

In Figure 4, we introduce a new type of relocation process, where we use one station (LHSA, see Figure 3b) and one travel time pick at another station (TUNL) which is close to a permanent short-period station. We assume that the mechanism and depth are known (Event 222, Figure 3) and test for location resolvability. We search a relatively large area (250 km by 200 km) with a 10 km grid spacing. The waveform misfit error as a function of location is shown in gray scale. The error surface has alternating troughs (dark areas) and ridges (light areas) simply because the surface waves in the data are in and out of phase with synthetics as the epicentral distance changes. They essentially lie along circles centered at the broadband stations (LHSA in this case). There is no well-defined minimum to constrain the event location using the waveform alone. However, by using the *P* arrival time at another station (TUNL), we added additional constraint on the event location. Combining the waveform misfit and arrival time gives the "best" location, which is close to the network location. As discussed in Helmberger and Zhu [1997], this event probably qualifies as GT5 since it is very well recorded by the array (Figure 3).

In conclusion, we have reviewed some of our efforts in improving locations and depth estimation through the use of waveform modeling. We think that some of these methods will prove useful in improving monitoring in remote regions.

REFERENCES

Bent, A. L., and D. V. Helmberger, Seismic characteristics of earthquakes along the offshore extension of the Western Transverse Ranges, California, Bull. Seismol. Soc. Am., Vol. 81(2), 399-422, 1991.

Dreger, Douglas S. and D. V. Helmberger, Source parameters of the Sierra Madre earthquake from regional and local body waves, *Geophys. Res. Lett.*, **18**, No. 11, 2015-2018, 1991.

Engdahl, E. R., R. van der Hilst, and R. Buland, Global teleseismic earthquake relocation with improved travel times and procedures for depth determination, *Bull. Seismol. Soc. Am.*, **88** (3), 722-743, 1998.

Helmberger, D. V., and G. R. Engen, Modeling regional love waves; Imperial Valley to Pasadena, *Bull. Seismol. Soc. Am.*, **79**(4), 1194-1209, 1989.

Helmberger, D. V., and G. R. Engen, Modeling the long-period body waves from shallow earthquakes at regional ranges, *Bull. Seismol. Soc. Am.*, **70**, 1699-1714, 1980.

Helmberger, D. V., X. J. Song, and L. Zhu (2000), Crustal Complexity from Regional Waveform Tomography: Landers Aftershocks, *JGR*, in press.

Ji, Chen, and D. V. Helmberger, Modeling regional seismograms, *Eos Trans. AGU*, **80**, Fall Meeting Suppl., 1999.

Ji, Chen, D. V. Helmberger, and D. J. Wald (2000), Basin Structure Estimation by Forward and Inversion Methods, *BSSA*, in press.

Jones, Laura E. and D. V. Helmberger, Earthquake Source Parameters and Fault Kinematics in the Eastern California Shear Zone, *Bull. Seismol. Soc. Am.*, **88**, No. 6, 1337-1352, 1998.

Langston, C. A., The SsPmp phase in regional wave propagation, *Bull. Seismol. Soc. Am.*, **86**, 133-143, 1996.

Melbourne, T. and D. V. Helmberger (2000), Lithospheric Control of Plate Boundary Deformation, *Science* (submitted).

Saikia, C. K., B. B. Woods, L. Zhu, H. K. Thio, and D. V. Helmberger, Path calibration, source estimation and regional discrimination for the Middle-East: Application to the Hindu-Kush region, *Scientific Report No. 1*, Phillips Lab, PL-TR-96-2069, 1996.

Saikia, C. K., H. K. Thio, B. B. Woods, X. Song, L. Zhu, and D. V. Helmberger, Path calibration, source estimation

and regional discrimination for the Middle-East and western Mediterranean, *Scientific Report No. 2*, Phillips Lab, PL-TR-96-2307, 1996.

Saikia, C. K. and D. V. Helmberger, A frequency wave number algorithm to compute up- and down-going wave fields from a buried seismic source, *BSSA*, **87,** 987-998, 1997.

Savage, B., and D. V. Helmberger, Fault dimensions from broadband networks (Abstract), *Eos Trans. AGU*, **80**, Fall Meeting Suppl., 1999.

Song, Xi J., L. E. Jones, and D. V. Helmberger, Source characteristics of the 17 January 1994 Northridge, California Earthquake from Regional Broadband Modeling, *Bull. Seismol. Soc. Am.* **85,** no. 6, 1591-1603, 1995.

Song, Xi J. and D. V. Helmberger, Broadband modeling of regional seismograms: the Basin and Range crustal structure, *Geophys. J. Int.* **125,** 15-29, 1996.

Song, X. and D. V. Helmberger, Source estimation of finite faults from broadband regional networks, *Bull. Seismol. Soc. Am.*, **86,** 797-804, 1996.

Song, Xi J. and D. V. Helmberger, Waveform Tomography and Pseudo Green's functions, *BSSA*, **88**, 304-312, 1997.

Song, X., and D. V. Helmberger, Northridge aftershocks, a source study with TERRAscope data, *Bull. Seismol. Soc. Am*., **87**(4), 1024-1034, 1997.

Wald, D. J., Strong motion and broadband teleseismic analysis of the 1991 Sierra Madre, California, Earthquake, *J. Geophys. Res*., **97**, 11,033-11,046, 1992.

Wallace, T. C. and D. V. Helmberger, Determining source parameters of moderate-sized earthquakes from regional waveforms, *Phys. Earth Planet. Interiors*, **30**, 185-196, 1982.

Wen, Lianxing and D. V. Helmberger, Propagational corrections for basin structure: Landers earthquake, *Bull. Seismol. Soc. Am.*, **87,** No. 4, 782-787, 1997.

Zhao, L. S., and D. V. Helmberger, Source retrieval from broadband regional seismograms: Hindu Kush region, *Phys. Earth Planet. Inter*., **78**, 69-95, 1993.

Zhao, L. S., and D. V. Helmberger, Source estimation from broadband regional seismograms, *Bull. Seismol. Soc. Am.*, **84**, 91-104, 1994.

Zhao, L. S., and D. V. Helmberger, Regional moments, energy levels, and a new discriminant, *PAGEOPH*, **146**, 281-304, 1996.

Zhu, Lupei and D. V. Helmberger, Advancement in Source Estimation Techniques Using Broadband Regional Seismograms, *Bull. Seismol. Soc. Am.*, **86,** No. 5, 1634-1641, 1996.

Zhu, L. and D. V. Helmberger, Intermediate depth earthquakes beneath the India-Tibet collision zone, *GRL*, **23,** 435-438, 1996.

Zhu, L., D. V. Helmberger, C. K. Saikia, and B. B. Woods, Regional waveform calibration in the Pamir-Hindu Kush region, *J. Geophys. Res*., **102**, B10, 22,799-22,813, 1997.

Zhu, L., and D. V. Helmberger, Significant Moho relief across the northern margin of the Tibetan Plateau, *Science*, **281**, 1170-1172, 1998.

Zhu, L. (1998), Broadband waveform modeling and its application to the lithosphere structure of the Tibetan Plateau, Ph.D. Thesis, California Institute of Technology, Pasadena, California.

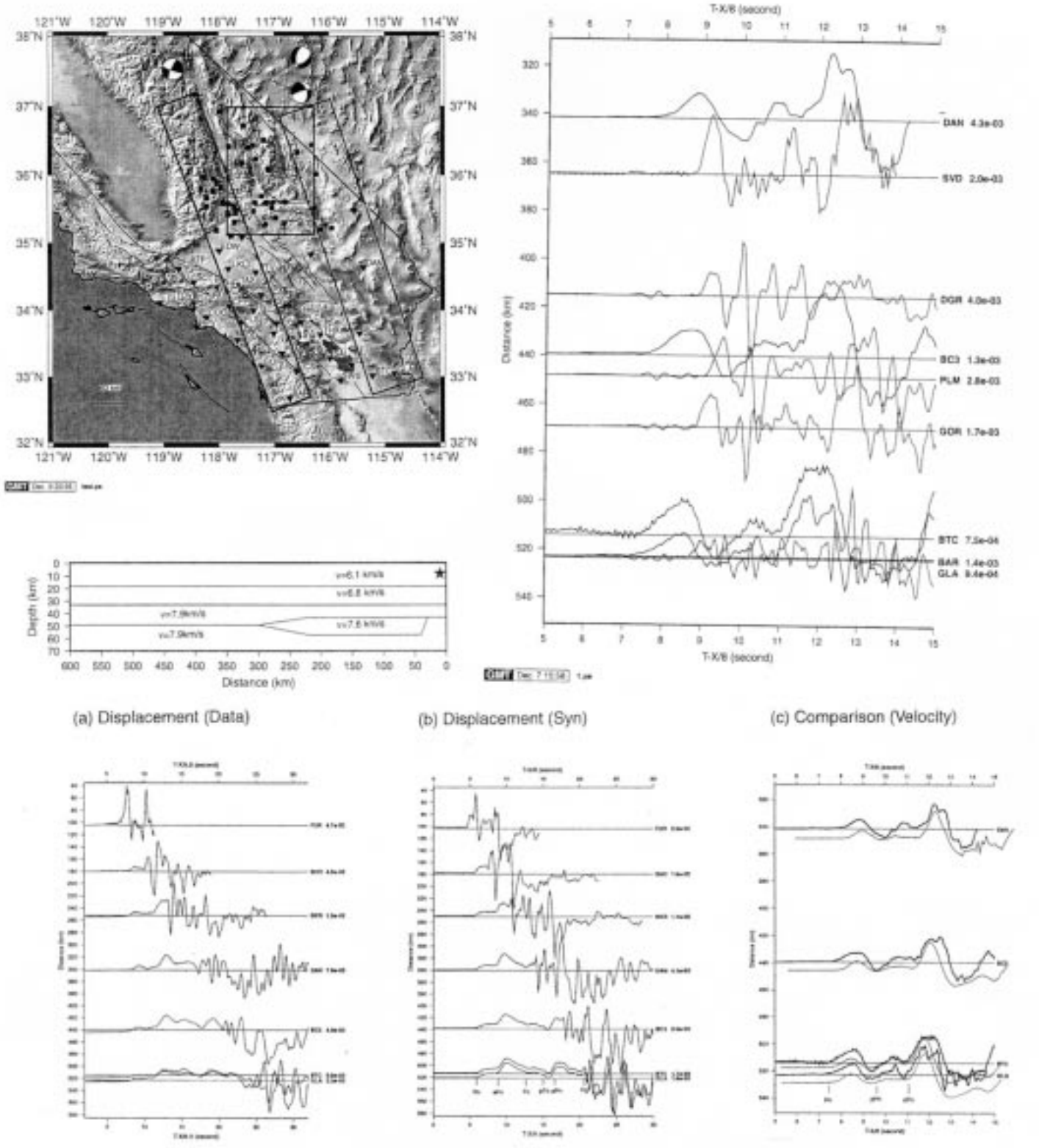


Figure 1. Upper panel (a) displays the locations of TriNet stations relative to events. The P_{nl} (extended P-waves) obtained in the easternmost box are relatively simple (black) while those sampling beneath the Panamint Range (between Death Valley and the Sierras) are late and complex (gray). The traces in gray require a complicated upper-mantle structure (see box) as discussed by Chen Ji and Helmberger (1999). Lower panel (b) displays modeling (1D) appropriate for the structure beneath the eastern block.

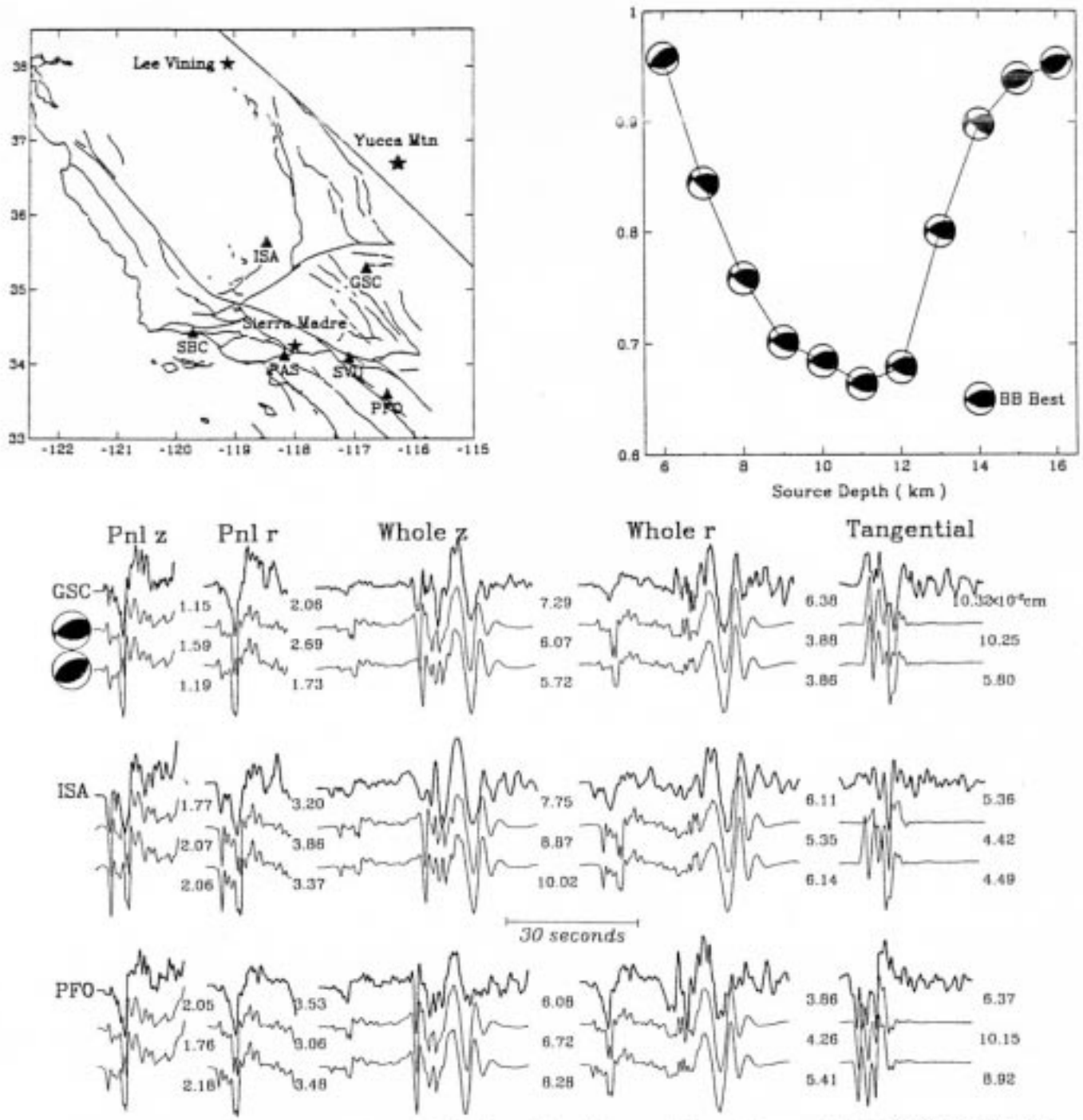


Figure 2. Comparison of Sierra Madre broadband observations at three stations (GSC, ISA, and PFO) with synthetics generated by estimating the fault parameters. Three windows of observed waveforms are used, namely, the beginning portion P_{nl} (first two columns), the Rayleigh waves or whole recording (middle two columns), and the tangential (column on the right). The corresponding Green's functions are shifted in time for best alignment and used to estimate strike, dip, and rake. The amplitude determine the seismic moment (numbers indicate peak amplitudes in cm). The bottom trace of each set corresponds to the source estimation using only the P_{nl} columns and the middle traces correspond to using all 5 columns. Both solutions yield the same moment of 3. X 10^{24} ergs. Single station solutions and various combinations of the data sets using P polarities are discussed in Zhao and Helmberger (1993).

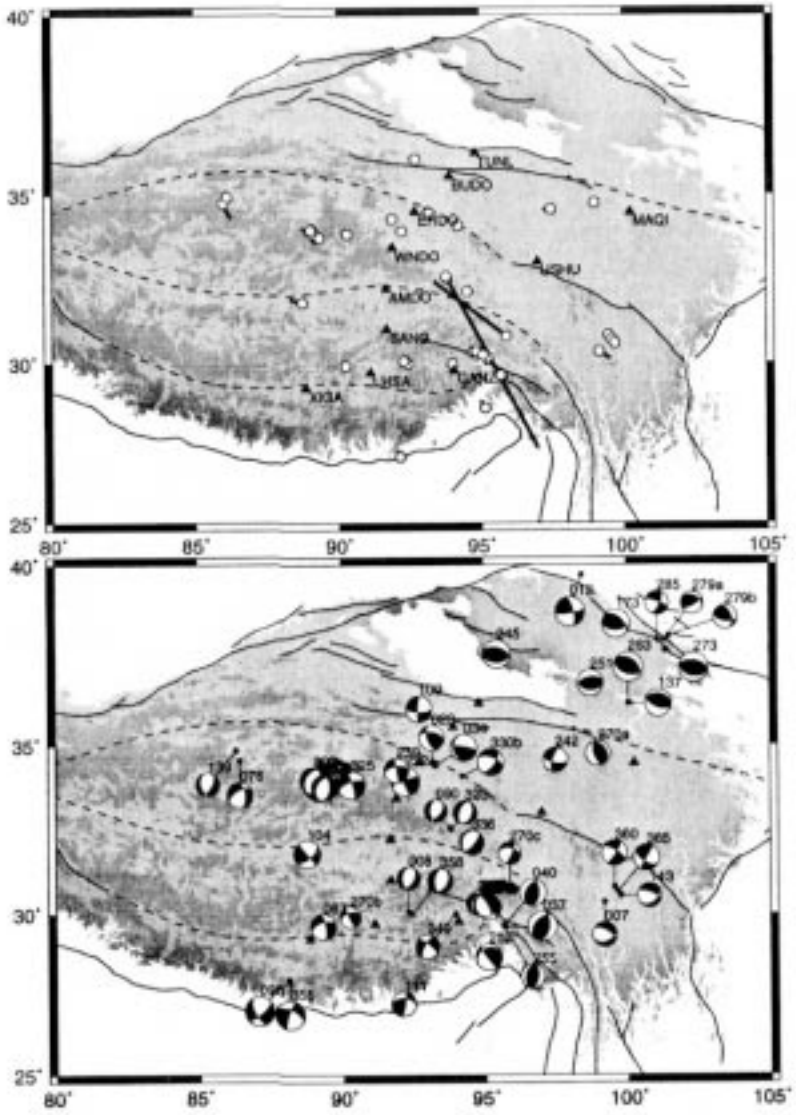


Figure 3a. Upper map displays the event mislocations relative to ISC estimates. Some of these (Mw<4) moved several degrees. Source mechanisms of earthquakes in Tibet and surrounding areas determined from inverting their broadband regional waveforms. All earthquakes are found to be located in the upper crust, between 5 and 30 km, except three events (Events 355, 095, and 067) in southern Tibet that lie at depths between 70 and 80 km.

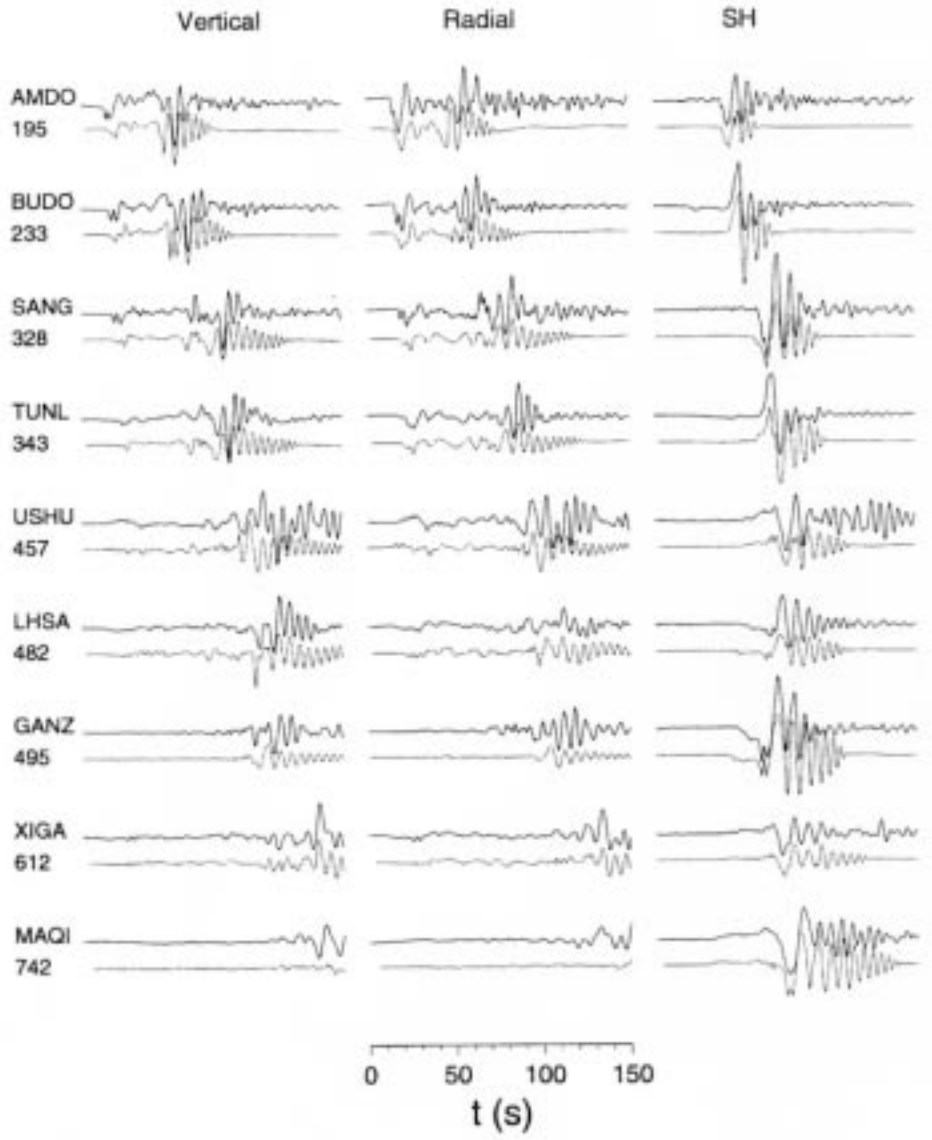


Figure 3b. Displacement waveform fit of a crustal event (Event 222), see map on the left produced by the waveform inversion. Each trace is multiplied by the square root of its epicentral distance (indicated by the number below the station name) to account for the surface wave amplitude decay with distance. This event had a Mw = 4.7 and a depth of 10 km.

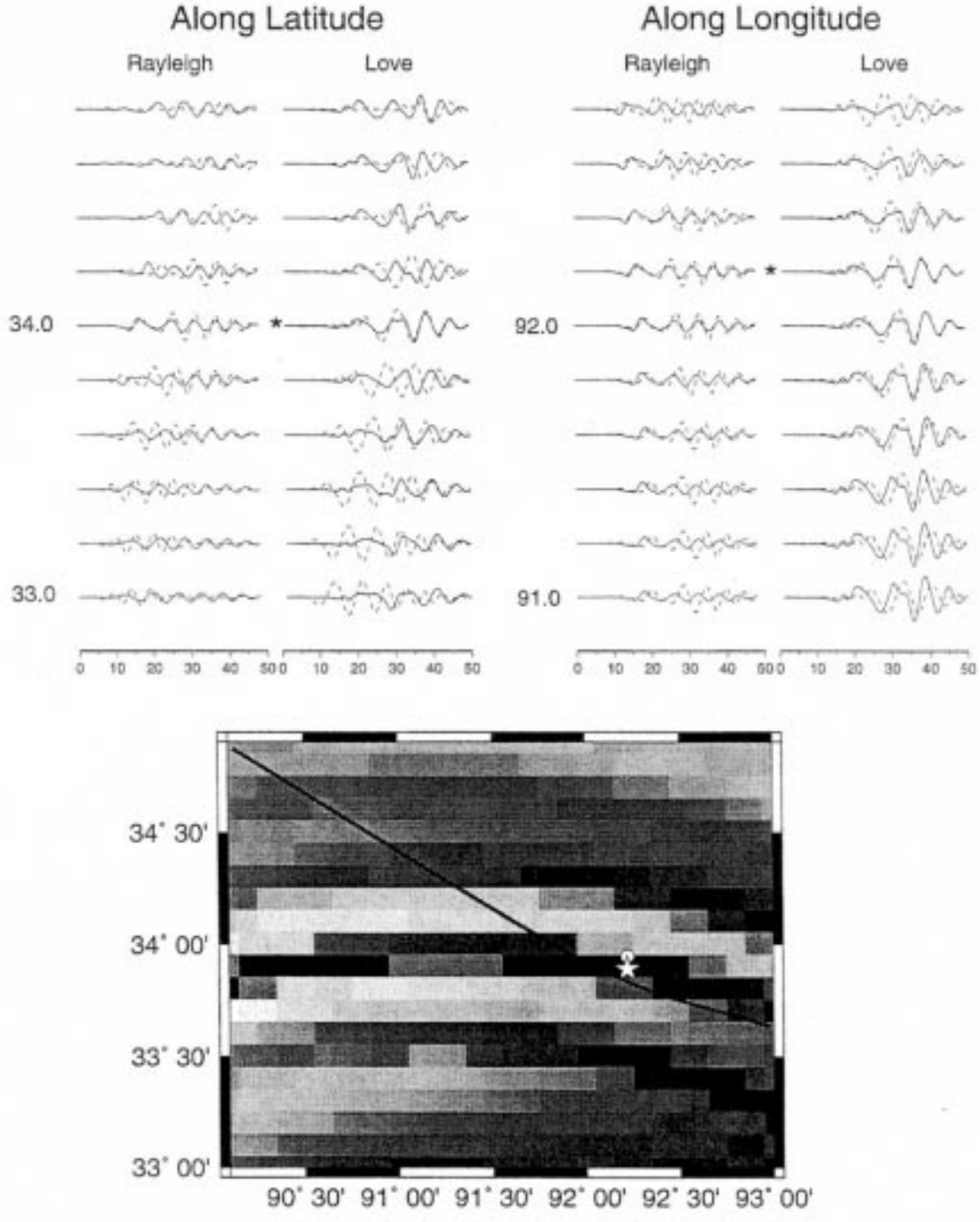


Figure 4. The bottom panel shows the waveform misfit error as a function of event location in gray scale (dark represents the minimum and white represents the maximum). The broadband station (LHSA) which provides the waveform in velocity is located in the south (see Figure 3a). Solid line represents possible event location to satisfy arrival time constraints at LHSA and another station to the north (TUNL).

THE NEVADA SEISMIC ARRAY (NVAR)
REGIONAL SEISMO-ACOUSTIC STUDIES

Eugene Herrin, Ileana Tibuleac and Paul Golden, Southern Methodist University
Gordon G. Sorrells, Seismic Diagnostics, Inc

Sponsored by Defense Threat Reduction Agency
Contract No. DSW-AOI-97-I-0024

ABSTRACT

Studies are underway at the Southern Methodist University Geophysics Laboratory to identify seismo-acoustic sources located at regional distances from the Nevada Seismic Array (NVAR). The objective of this project is to evaluate the seismo-acoustic method for the identification of mine blasts as well as other type of vented explosions. The studies involve the processing and analysis of regional seismic and seismo-acoustic data acquired at NVAR during selected daily intervals for a period of one year. Our assessment of the initial results of the studies show that NVAR is surrounded by regional seismo-acoustic sources The most active seismo-acoustic source is found near Hawthorne, NV where sequences of signals are generated several times aweek. In addition, multiple seismo-acoustic sources are located within the Carlin/Battle Mountains gold mining district in northcentral NV. Occasional seismo-acoustic signal generated by sources in western Utah and northwestern Arizona were also observed. Additional studies are underway to calibrate NVAR to locate events on the Nevada Test Site.

Key Words; Seismo-acoustic, array, regional monitoring, infrasound

OBJECTIVES

The objectives of the research projects whose initial results are summarized below are to:

- evaluate the seismo-acoustic method for the identification of mine blasts as well as other type of vented explosions.
- calibrate NVAR to locate events on the Nevada Test Site

RESEARCH ACCOMPLISHMENTS

Seismo-Acoustic Studies NVAR is well suited to be the focus for studies of seismo-acoustic phenomena. It is virtually surrounded, at regional distances by more than 60 active major mines. In addition, a US Navy ordnance disposal depot is located 30-40 km southwest of the array and there are multiple possible seismo-acoustic sources on the Nellis AFB Bombing and Gunnery Range, approximately 150-200 km southeast of the array. Thus, the first task of the NVAR seismo- acoustic study is simply to identify and select a subset of these sites for future detailed surveillance. The following procedures were implemented to carry out this task.

The NVAR seismic array data are continuously reviewed to identify and select regional events with “good” signal to noise ratios (SNRs) for inclusion in an experimental data set. The review is constrained to data recorded on normal workdays between the hours of 12:00 PM and 6:00 PM local time. The anticipated effect of this constraint is to maximize the percentage of commercially generated seismo-acoustic events in the data set. Approximate epicenters and origin times are calculated for each selected event using array back azimuth and S-P range estimates. A 0.25-0.34 km/s group velocity window is also calculated for each event. The NVAR infrasound and seismic data are then searched within the group velocity windows to identify possible associated infrasound signals. An association is declared if an infrasound signal is detected within the group velocity window and its back azimuth is within 15° of back azimuth of the prior seismic event. Potential seismo-acoustic sources are then identified by evidence of correlated temporal and spatial clustering, as well as by the occurrence of one or more seismic events with an associated infrasound signal within the apparent time-space cluster. The results of the application of these methods to data acquired at NVAR from 1April99 to 30June99 are summarized in the following paragraphs.

Over 500 of the regional seismic events detected at NVAR during the 91 day period beginning 1April99 were found to satisfy the SNR and occurrence time constraints described in the previous paragraphs. Figure 1 is a histogram illustrating the distribution of the occurrence times of these events, referenced to the local time base. Notice that the distribution is distinctly bimodal with significant clusters occurring in the 12-1 PM and the 3-4 PM time periods. Miners typically blast at or near the end of work shifts. The shifts usually end at noon or at the end of the normal workday. We believe that this practice accounts for the bimodal structure of the histogram seen in Figure 1. If this is the correct interpretation it then follows that that the regional seismic activity seen at NVAR on a typical workday afternoon is largely the result of mine blasts.

The spatial distribution of the regional seismic events in the experimental data set is illustrated in Figure 2. . The red dots seen on this map locate the event epicenters. The yellow triangle identifies the location of the center element of NVAR. The Polygon located southeast of the array outlines the boundaries of the Nevada Test Site (NTS). The dense cluster of epicenters enclosed by the ellipse centered a few hundred kilometers north-northeast of the array merits some further comment. The area enclosed by the ellipse roughly coincides with the Carlin /Battle Mountain Gold Mining Complex. There are at least seven major mines currently active within this Complex. The seismic activity generated by blasting at one of these mines (the Carlin East Open Pit) has been studied by Jarpe et al (1996). Their data shows that blasting activity at this site generates seismic events with magnitudes m_b >1 at a rate of the order of a few per week. If the blasting activity at other major mines in the Complex is comparable to that found at the Carlin East Open Pit, then it is reasonable to assume that the majority of the events whose epicenters are enclosed by the ellipse are the result of mine blasts.

The epicenters seen in Figure 2 are color coded according to their daily occurrence time in Figure 3. The epicenters of the events that occurred during the two peak daily activity periods (see Figure 1) are shown in red. The epicenters that occurred at other times during the workday afternoon are shown in green. It is seen from Figure 3 that the majority of the events that locate within the Carlin /Battle Mountain Complex occur during the peak daily activity periods. This result lends additional support to the assumption that the majority of the seismic activity within the Complex is generated by mine blasts. It is also worth noting that the dimensions of the peak daily activity clusters that occur in the Complex substantially exceed any uncertainties in the individual epicenter estimates. Consequently, the dense concentration of epicenters in this region is believed to be the result of blasting activity at multiple mine sites.

Twenty-eight seismic events in the experimental data set were found to have associated infrasound signals. The distribution of their occurrence time coded epicenters is shown separately in Figure 4. While the population of regional seismo-acoustic events in the experimental data set is currently too sparse to provide any conclusive evidence of significant temporal or spatial clustering, there are some interesting properties that deserve further comment. First, note that the seismo-acoustic locations are well distributed in azimuth about NVAR and a few detections have been made at ranges greater than 500 kilometers. This result encourages us to believe that continued sampling using the procedures outlined above will yield a population of events that can be used to comprehensively evaluate the seismo-acoustic method of blast identification. Secondly, it is worth noting that the occurrence times of the seismo-acoustic events are approximately equally divided between the peak daily activity periods and off-peak time periods. This result suggests that vented explosive processes other than routine mine blasting may play a significant role in generating the regional seismic signals seen on workday afternoons at NVAR. Finally, the occurrence of seven of the events in the Carlin /Battle Mountain Complex confirm that at least some of the events in this region are indeed the result of mine blasts. It should also be noted that incipient seismo-acoustic clusters appear to be emerging at a site about 150 kilometers east of NVAR and at one near Mammoth Lake CA about 100 km south of the array. A quick inspection of Figure 2 shows that tight seismic epicenter clusters characterize both sites. These areas will be given further attention during the future expansion of the experimental data set.

A swarm of locally generated seismo-acoustic signals are recorded several times a week at NVAR. The swarms invariably originate at a point some 50-60 km southwest of the array and their duration is usually 3-5 minutes. An example of the records of a typical swarm is shown in Figure 5. In this figure, the code, sz, identifies the record from an element of the NVAR seismic array. The code, sd, identifies the record

from an element of the infrasound array. Notice that while the seismic signals overlap, forming a complex wave train, it is clear from the infrasound records that the swarm in this particular case, consists of nine discrete events. We believe that swarms of this type are generated by the disposal of obsolescent ammunition at a site associated with routine operations at the Hawthorne Naval Ordnance Depot. The occurrence of strong "air-coupled" waves following the seismic signals should also be noted. These observations illustrate that that "air-coupled" wave data can be used in the absence of available infrasound observations to aid in the identification of local or regional seismo-acoustic sources.

Infrasound signals that cannot be associated with a seismic source are practically a daily occurrence at NVAR. Since a study of their properties is outside the scope of the current investigation, their occurrences are not normally logged into the experimental data set. Nevertheless, one type of unassociated infrasound signal has attracted our attention. It appears in a swarm-like pattern containing 10-12 discrete signals. The swarm may last for 10-15 minutes and the source is invariably located southeast of the array. An example of some of the signals in one of the detected infrasound swarms is illustrated in Figure 6. The absence of a corresponding seismic swarm suggests that the signals are the result of air blasts or possibly poorly coupled surface blasts. The fact that the Nellis AFB Bombing and Gunnery Range is also found south east of NVAR suggests that they may be a by-product of military training exercises that routinely take place on the Range.

Calibration Studies at NVAR The NVAR (Mina, Nevada) seismic array was calibrated for regional and teleseismic events. Back azimuth and phase velocity estimates were calculated using the crosscorrelation method. The database included 553 events, well located by NEIC, between March and December 1999 with $6.6 > m_b > 2.7$ and epicentral distance between 110 and 11225 *km*.
Elevation differences of up to 0.4 *km* and complicated geology made static corrections for each array element necessary. We used 57 core phases (*PKP, PKKP, PcP*) to determine static time corrections.
No pattern was observed in the back azimuth and phase velocity residuals as a function of azimuth at NVAR.
Detection capability and location accuracy at NVAR (Mina, Nevada array) was assessed using a sequence of 553 earthquakes ($M_L < 4.4$) that occurred from 07/31/1999 to 09/26/1999 near Scotty's Junction, about 60 km west of the Nevada Test Site. Based on the analysis of these data the 90% detection level for *Pg* was found to be 1.4 *nm* for a normal noise environment. 16 events ($M_L > 3.2$) in the sequence were identified as having similar location and source mechanism by crosscorrelation of their waveforms with a large, well located event. Backazimuth was calculated for each of these events using a crosscorrelation method (Tibuleac and Herrin, 1997). Epicentral distance was estimated using *Lg - Pg* arrival time differences. Arrival times for the *Pg* and *Lg* phases were determined using wavelet decomposition methods (Tibuleac and Herrin, 1999). The standard deviation for calculated epicentral distance was 2.8 *km*. The standard deviation for calculated backazimuth was 0.94 *deg*rees. This translates to a standard deviation of 2.6 *km* at a distance of 157 *km* (the distance from NVAR to Scotty's Junction).
Extrapolation of these results implies the 90% detection threshold at NVAR for events on NTS is less than 2.0 local magnitude units as determined by the University of Nevada at Reno. Using only the NVAR array for epicentral location we obtained an extrapolated 90% coverage area of less than 180 km^2 for events at NTS.

REFERENCES

Jarpe, S. P., B. Moran, P. Goldstein, and L. A. Glenn, 1996, The implications of mining practice in an open-pit gold mine for monitoring a Comprehensive Test Ban Treaty: Lawrence Livermore Report, UCRL-ID-123017, 28 p.
Sorrells, Gordon G., Eugene Herrin, and Jessie L. Bonner, 1997 Construction of Regional Ground Truth Databases Using Seismic and Infrasound Data, *Seis. Res. Lett.*, **68**, 743-752.
Tibuleac and Herrin, (1997), Calibration Studies at TXAR, *Seis. Res. Lett.*, **68**, 353 - 365.
Tibuleac and Herrin, (1999), An Automatic Method for Determination of *Lg* Arrival Times Using Wavelet Transforms, *Seis. Res. Lett.*, **70**, 577 - 595.

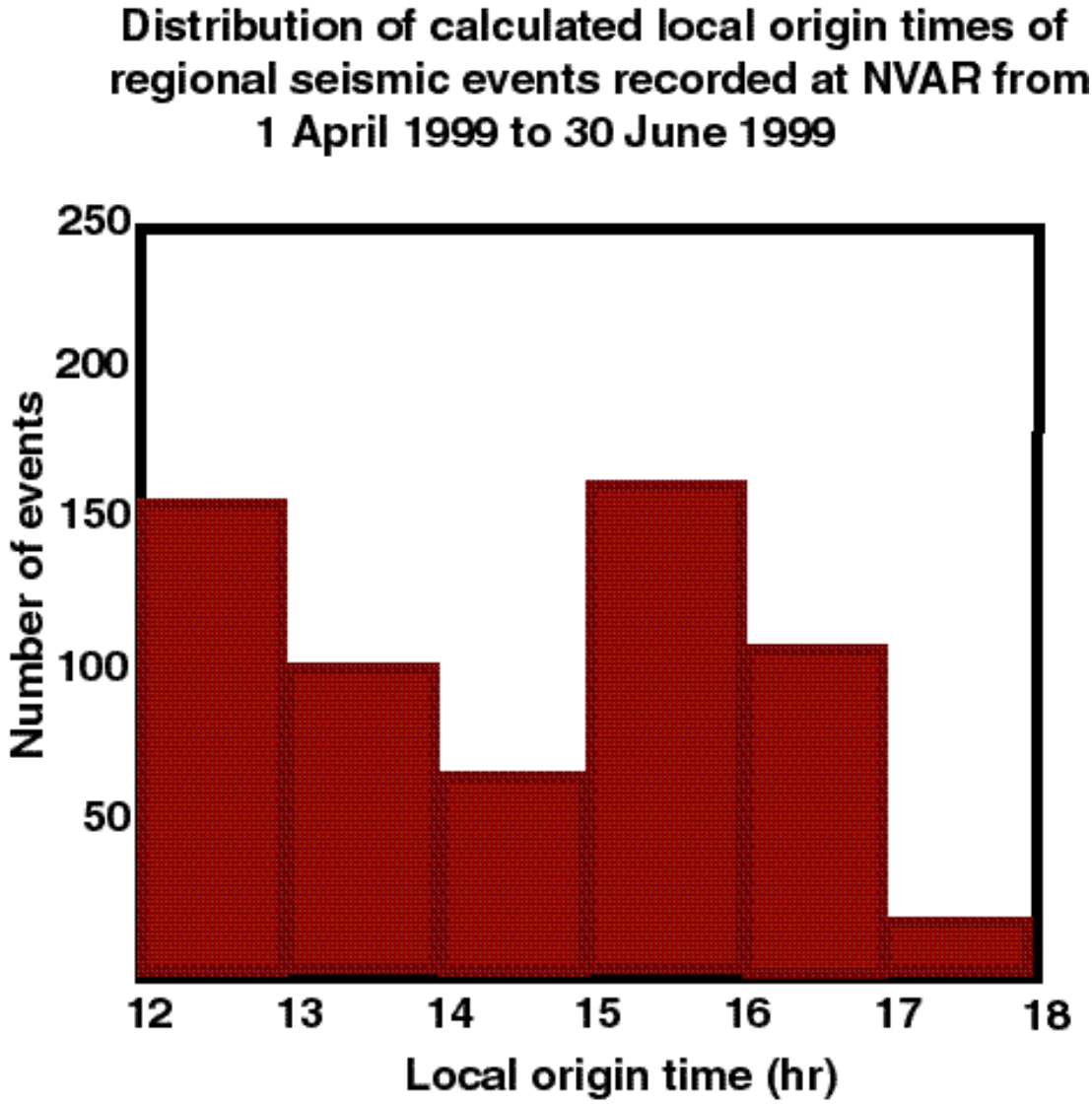


Figure 1. A histogram illustrating the distribution of daily occurrence times of regional seismic events detected on workday afternoons at NVAR from 1 April 1999 to 30 June 1999.

Epicenters of regional seismic events detected at NVAR between 1 April 1999 - 30 June 1999 with local origin time between 12.00 and 18.00.

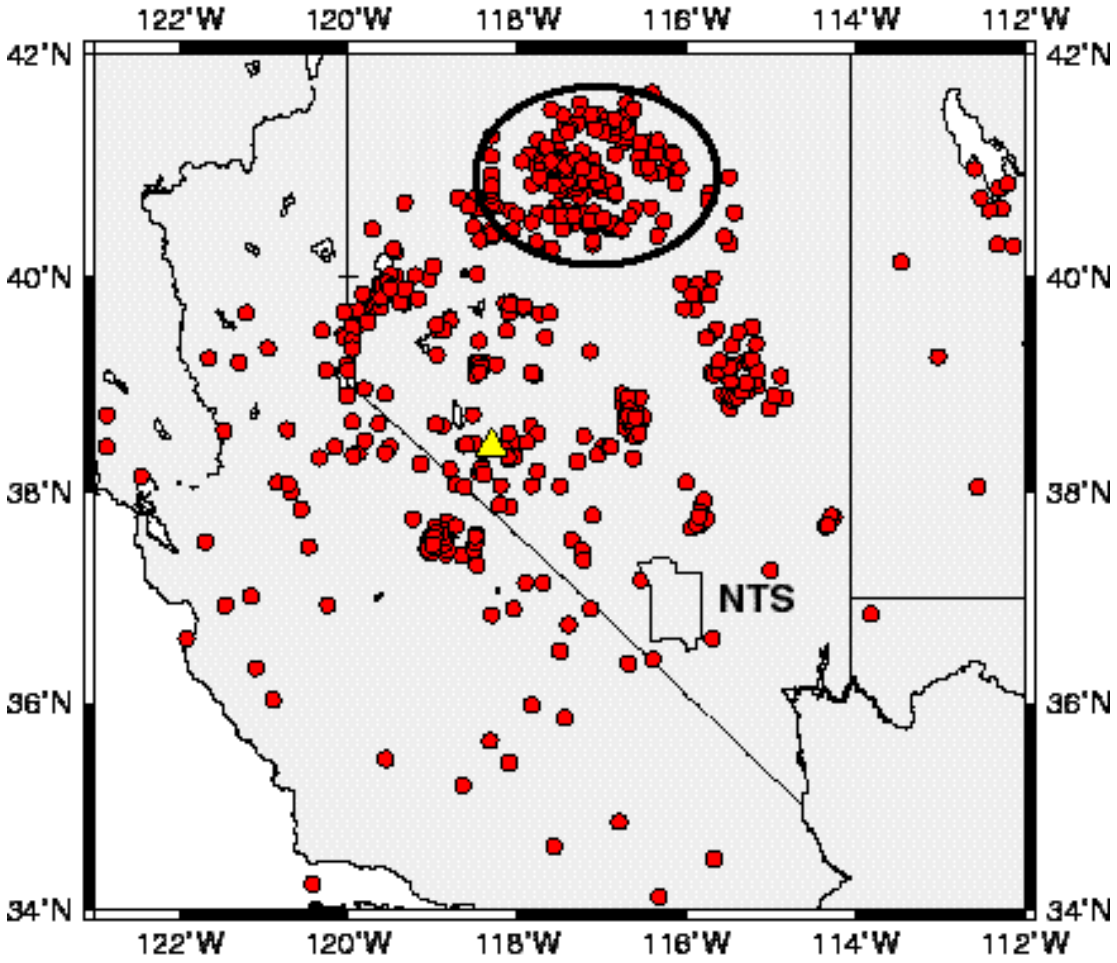


Figure 2. A map illustrating the spatial distribution of the epicenters of regional seismic events detected on workday afternoons at NVAR from 1 April 1999 to 30 June 1999.

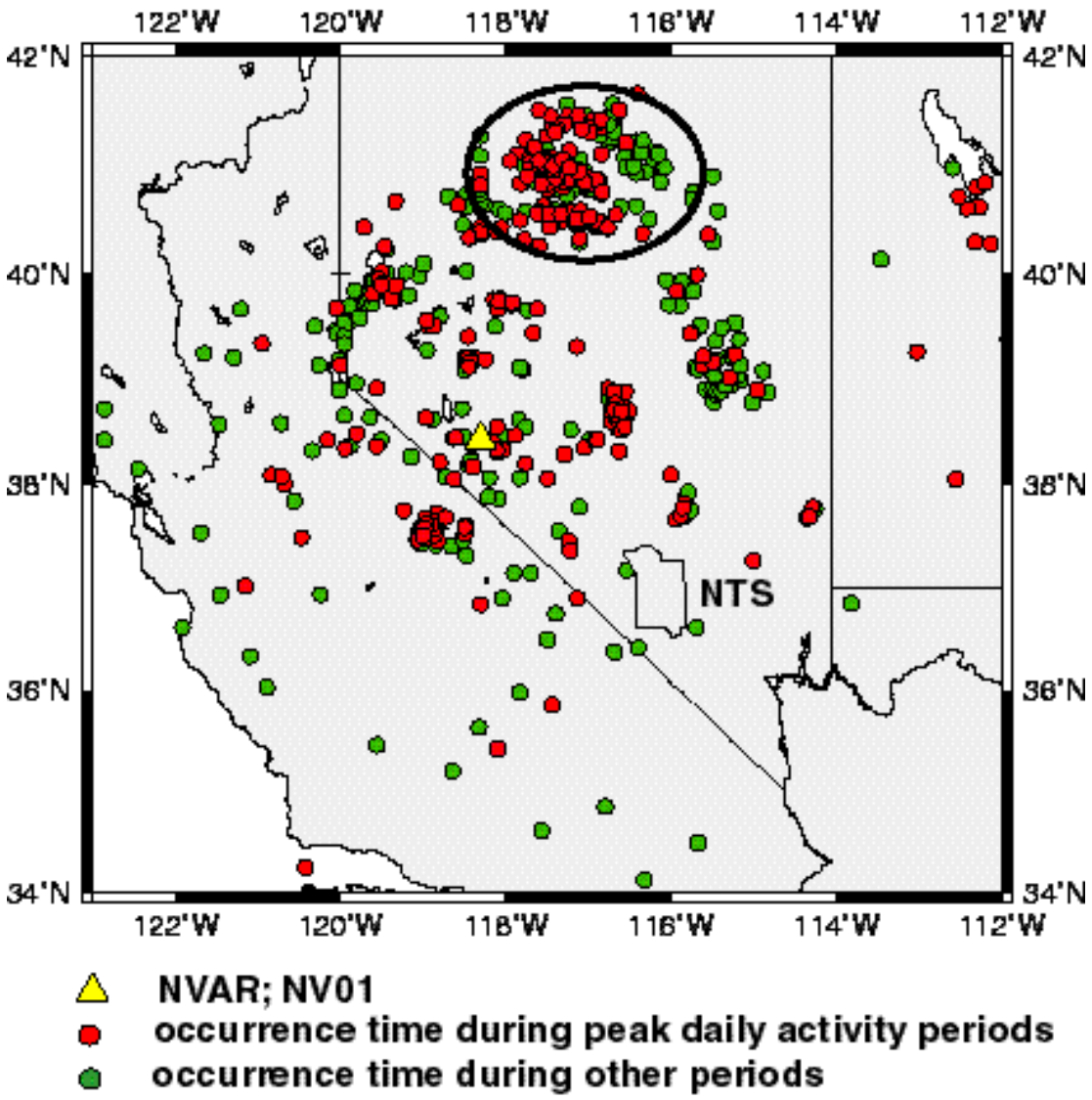


Figure 3. A map illustrating the spatial distribution of the occurrence time coded epicenters of regional seismic events detected on workday afternoons at NVAR from 1 April 1999 to 30 June 1999.

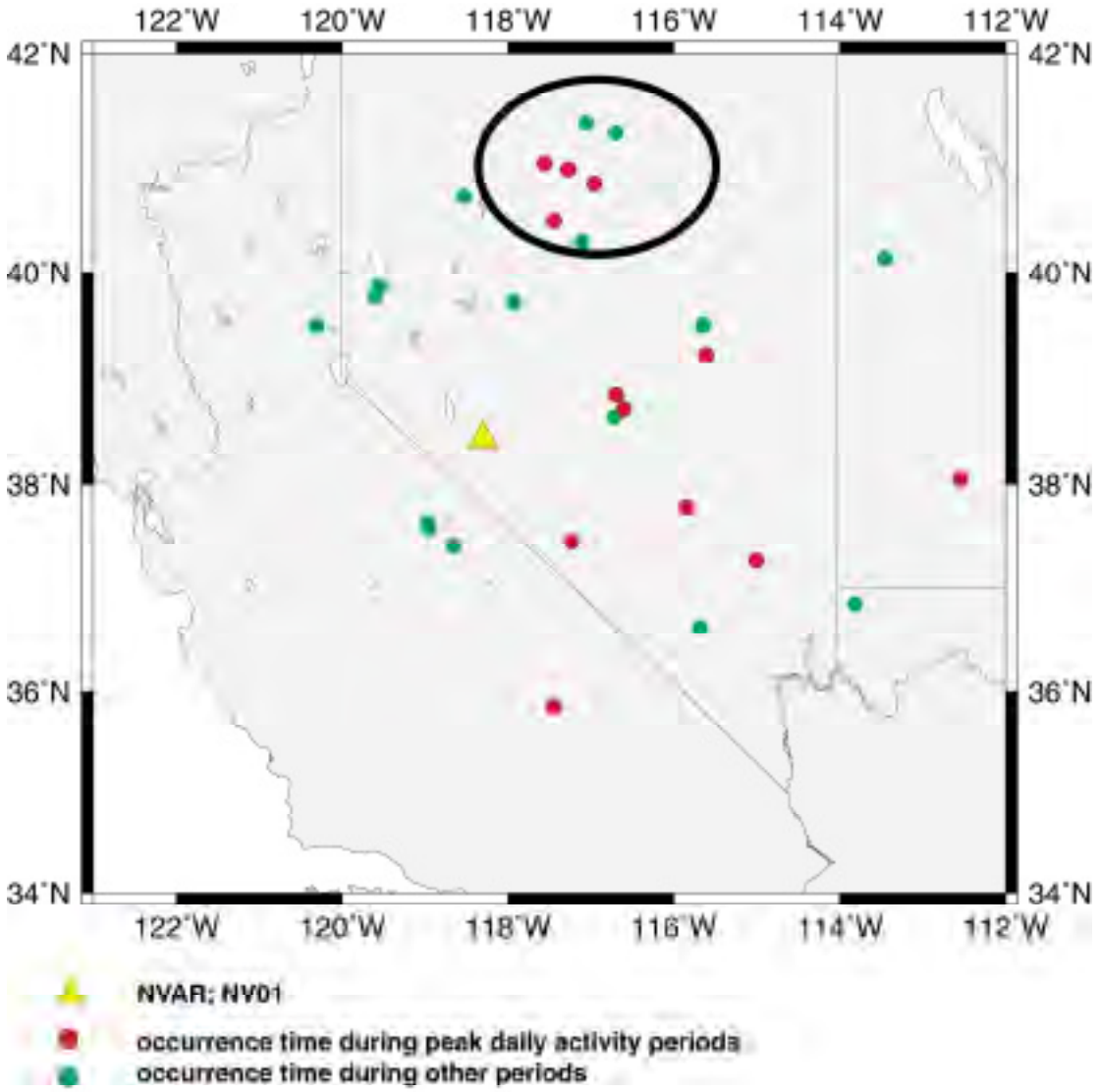


Figure 4. Spatial distribution of the occurrence time coded epicenters of regional seismo-acoustic events detected on workday afternoons at NVAR between 1 April 1999 - 30 June 1999

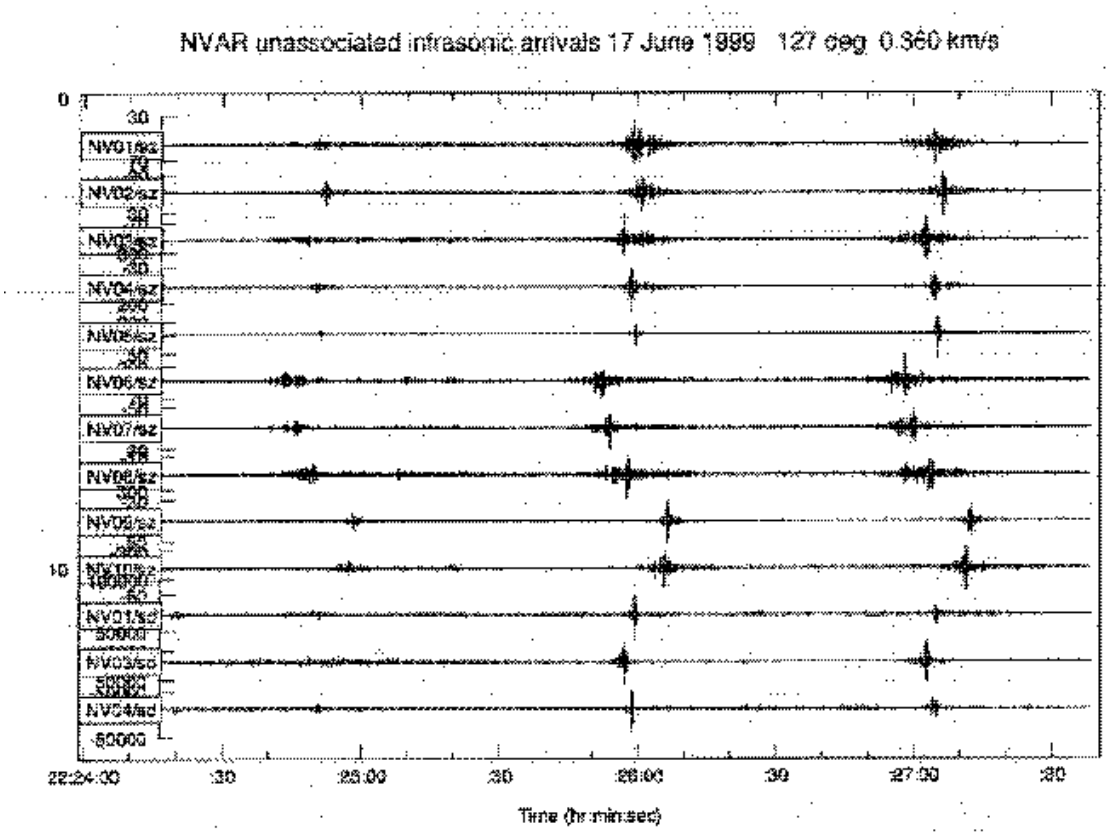


Figure 5. An example seismogram of a locally generated seismo-acoustic swarm detected at NVAR.

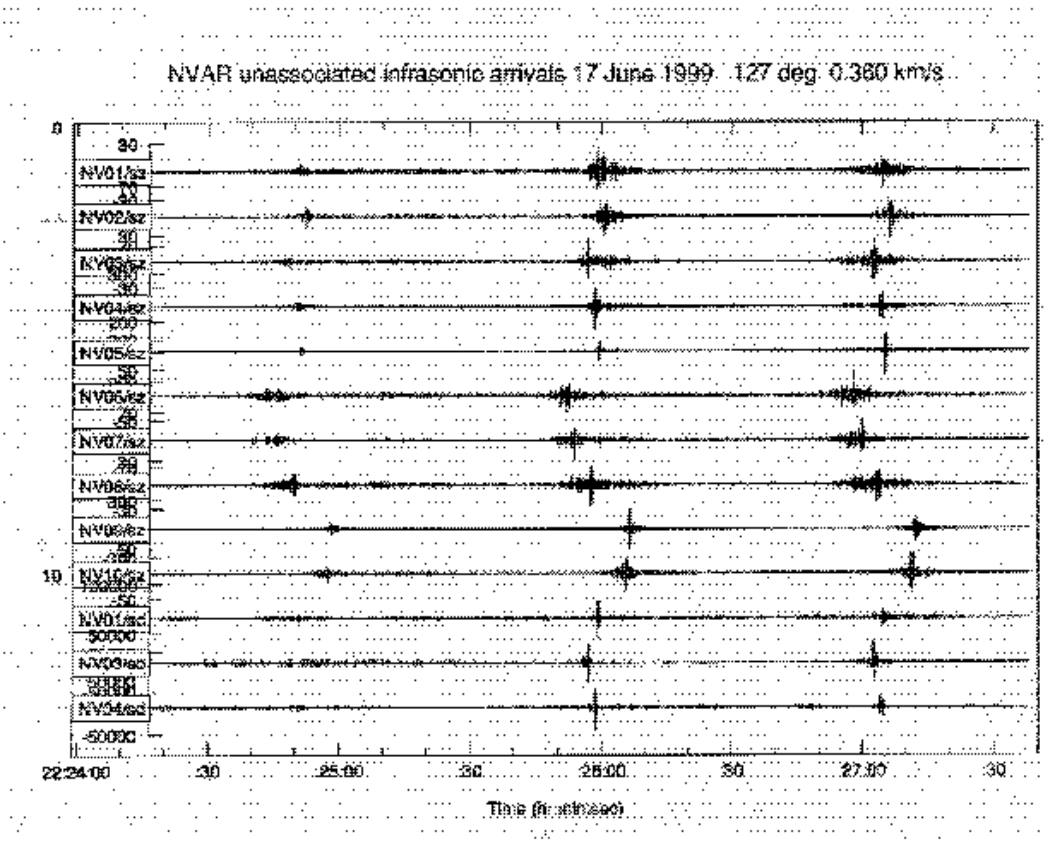


Figure 6. An example seimogram of an infrasonic swarm detected at NVAR.

IN SITU MONITORING OF LOCAL SEISMICITY

Eystein S. Husebye and Yuri V. Fedorenko

Institute of Solid Earth Physics, University of Bergen, Norway

Sponsored by The Defense Threat Reduction Agency
Arms Control Technology Division
Nuclear Treaties Branch

Contract No. DSWA 01-98-C-0159

ABSTRACT An essential element of CTBT IMS monitoring is accurate epicenter locations. Recently, focus is on the IASPEI 1991 travel time tables which are not adequate for global usages due to strong upper mantle velocity variations in many regions. Related problems are network configurations (too few reporting stations) and persistent identification and pickings of secondary phases. For small array records, phase velocities can be estimated via f-k analysis but still differentiations between Pg-, PmP- and Pn-phases and likewise Sn- and Lg-phases remain problematic. In the latter case the issue is whether ray theory is adequate for describing wave propagation in the crustal wave guide.

We are considering two approaches to the above problems; namely i) to analyze existing monitoring performances using NORSAR GBF-bulletin data including use of close-in station records from the Khibiny and ii) event discrimination in W. Norway. The GFB data cover 1999 and the total no of events were 7793 mainly stemming from Kiruna, Sweden (3544), Khibiny, Kola (956) and Zapolarny, Kola (325). To our surprise, there is no strong correlation between event occurrences and time-of-day nor day-of-week. The only exception here is Kiruna with a strong concentration of explosions at midnight hours. By taking first and second order derivatives of spatial histograms (seismicity plot) it is easy to identify the above mining areas particularly through the curvature plot. The events areal coverage for the respective mining areas amount to an aperture about 1° so accuracy is not unreasonable since bulletin production is automated. However, the strongest curvature are found for areas close to specific mine locations so we test this concept on other parts of Fennoscandia like W. Norway in order to locate the many quarries in industrialized areas. Simply, delete events in areas exhibiting small curvature. We would also see if we in this manner may better outline active faults through earthquake occurrences. A close scrutiny of some Khibiny mine explosions comparing epicenter determinations using our new Nansen station records and the listings from the Kola Seismological Center, Apatity gave locations difference close to 30 km in the extreme although epicenter distances were less than 60 km. In other words, travel time tables are not the lone cause of occasionally poor event locations. An alternative to formal epicenter determination procedures is to use waveforms instead of individual P- and S-phases. We have with base in the Nansen station tried a large number of schemes using the covariance matrix based on the 3-component recordings but really have problems in consistently recognizing signals from a specific mine. For W. Norway we used 10 years of manually produced bulletins subjecting these event listings to cluster analysis as well. As for N. Fennoscandia & Kola large land areas are almost void of earthquakes so many hundreds of bulletin events are exclusively explosions. Likewise, in off-shore areas reported events are exclusively earthquakes. However, in the intermediate coastal areas we have mix of earthquakes and explosions in the event population not easily separable by cluster analysis alone. Reason being harbor construction works which may take place at any hour of the day. A confusing aspect of the bulletin event listings is that non-zero focal depth estimates are no proof of an earthquake source.

Both for Fennoscandia & Kola and W. Norway cluster analysis have proved very efficient in isolating space-time stationary source areas areas from which explosion signals dominate in the event listings. Most of these signal sources are besides easily recognizable as such through signal envelope analysis using ANN source discrimination schemes.

Key words: Epicenter location, mine explosions, waveform classifier, Bayes statistics, Khibiny, N. Fennoscandia, Kola, W. Norway .

OBJECTIVE

A seismic monitoring nuisance is the national network recordings of numerous chemical explosions in many countries. These events are of marginal scientific interest but on the other hand constitute the same processing and analyst loads as in case of earthquake recordings. In the context of the CTBTO/IMS global monitoring system it is highly desirable to eliminate these local explosion recordings to prevent system overloading both on national and IMS networks levels. In case of the IMS this is done by i) requiring at least 3 alpha station/array reports or ii) event magnitude being less than 3.5 units. On local network levels small earthquakes are of prime research interest at least in aseismic countries so the explosion/earthquake discrimination problems persists down to small event magnitudes. Naturally, there has been many and successful local discrimination studies using primarily the Pn/Lg-discriminant (Blandford, 1996; Dowla, 1996; Shapira et al, 1996) but such analysis are seldom integrated in daily processing tasks. An important part of the discrimination problem is that of establishing reliable ground truth data bases which are not always simple in areas where occurring earthquakes (EQs) constitute only a few percent of the event population. The ultimate solution here is to tie EQ occurrence only to those felt and/or those with m_b magnitude exceeding 3.0. Another aspect of explosion identification is the often poor network epicenter locations capabilities producing diffuse seismicity patterns typical of natural EQ occurrence. In any country, use of explosive charges exceeding a few tonne of dynamite is strictly regulated so recordable explosions are confined to very small areas. In this study, we investigate event distribution in Fennoscandia and NW Russia (Kola) as reported by Norsar through their bulletins for the time period Oct, 98 - Oct, 99 based on their generalized beamforming technique for automatic epicenter determination. The Norsar array network as used, comprises the regional arrays Noress (N), Arcess (N), Hagfors (S), Finessa (SF) and the 2 miniarrays Spitsbergen (N) and Apatity (RU). The accuracy of epicenter locations depends both on geometry and no of reporting arrays which here are not quantified in terms of mislocation probabilities. As a complement to the Fennoscandia & Kola study we have also investigated the event distribution in W. Norway. The data used are 10 years of bulletin listings 01/01/90 - 31/12/99. For this area the epicenter locations are far more accurate due a relatively dense local network operated by the University of Bergen and analyst inspections of recordings.

RESEARCH ACCOMPLISHED

BULLETIN SCREENING

We started with the classical approach that is plotting event occurrence as functions of time of day and day of week for the 3 active mining areas Kiruna (S), Khibiny (RU) and Zapolarny (RU) (Fig. 1). It is somewhat surprising that the event occurrence are reasonably flat with exception of Kiruna where midnight explosions dominate. If we subtract the events in the 3 mining areas from the total event population and then fitting a plane to the histogram surface we obtained the probability density function (p.d.f.) $p(x, y, t) \sim 10^{-6}$ km^{-2}year^{-1}. Even for an area of 1000 km^2 the probability for earthquake (EQ) occurrence is extremely small. Similar area and histogram plots for W. Norway are shown in Fig. 5. In this area the event distributions are more complicated as off-shore areas are obviously earthquake prone.

PROBABILITIES OF EARTHQUAKES IN THE EXPLOSION POPULATIONS

In some of our previous studies (Fedorenko et al., 1998; Fedorenko et al., 1999) we restricted our discrimination research to recognize seismic signals (envelopes) from specific mines and quarries. Basic assumption was that signal waveforms were time and spatial stationary which in practice appeared to be valid. However, using quarry blast signals for which exact ground truth information was lacking our recognition scheme become less accurate. In other words, can we quantify the p.d.f. of selecting learning sets correctly from ground truth data bases? We have used the above data set from N. Fennoscandia and Kola for such an experiment. This area is suitable for such experiments since very, very few earthquakes appear to occur here.

As a mean to screen out explosions automatically a Neural Network (NN) scheme may be used. Previously, we have shown that such algorithms when applied to multistation or multicomponent waveform recordings exhibit well defined epicenter location accuracies. Let the function describing it be $A(\varphi, \lambda)$ where φ, λ are latitude and longitude, or $A(x, y)$ with x and y being distances in km. This function shows the relative number of events "passing through" the NN algorithm. If the width of $A(x, y)$ is reasonably small, the explosion recognition may be very reliable just using their spatial positions. For example, the

Kiruna (KIR) cluster contains 3544 events while the complete area shown in the figure contains 7793 events. The three main mines clusters together include [3544 (KIR) + 956 (KHI) + 325 (ZAP)] = 4825 events where KHI=Khibiny and ZAP = Zapolarny. Therefore, only 2968 events (38 %) lay outside these 3 clusters. Such cluster distributions can be 'sharpened' by computing first (gradient) and second (curvature) order spatial derivatives of event distributions as demonstrated in Fig. 2. As a supplement here individual mining operations in Khibiny are shown in Fig. 3. The Nansen (NKK) station near Kirovsk record many mining explosions which occasionally trigger avalanches in winter times. Let location ability of the NN algorithm be twice wider than the cluster shape and be expressed as a 2D Gaussian

$$A(x,y) = A_0 \exp\left\{-\frac{1}{2(1-r^2)}\left[\frac{(x-x_0)^2}{2\sigma_1^2} - 2r\frac{(x-x_0)(y-y_0)}{\sigma_1\sigma_2} + \frac{(y-y_0)^2}{2\sigma_2^2}\right]\right\}$$

with $\sigma_1 \approx \sigma_2 = 60$ km. The parameter A_0 is assumed to be 1, but may be smaller. The earthquake p.d.f. $p_q(x,y,t)$ is almost constant in time, $p_q(x,y,t) = p_q = 0.8 \cdot 10^{-6}$ km^{-2} year^{-1}; the last figure came from the "trend plane" (Fig. 4), where the plane surface was fitted to the remaining events after the clusters are removed. We can calculate the number of earthquakes N_{qpass} and explosions $N_{xpass} = N_{total} - N_{qpass}$ "passing through" the NN algorithm in unit time (here 1 year) as $N_{qpass} = \int_{\infty}^{\infty} A(x,y)p_q dxdy$. For example, taking the EQ p.d.f. for Kiruna as $p_q = 0.8 \cdot 10^{-6}$ year^{-1}km^{-2} which gives $N_{qpass} \approx 2 \cdot 10^{-2}$ year^{-1} for this cluster. Now we can calculate the probability of wrongly identifying an earthquake as an explosion at KIR. For mutually independent events Q and X, $Q \bigcap X = 0$ and $Q \bigcup X = 1$, where Q stands for "recorded event is an earthquake" and likewise X - "recorded event is an explosion", so we obtain

$$P(Q) = \frac{N_{qpass}}{N_{total}}.$$

For KIR $N_{total} = 3544$ year^{-1} which gives $P(Q) = 2 \cdot 10^{-2}/3544 = 5.6 \cdot 10^{-6}$. Such a probability of earthquake occurrence is almost negligible, hence we can use a simple decision rule: Take all events from this cluster to be explosions, the corresponding probability of error $P(Q) \approx 5.6 \cdot 10^{-4}\%$.

Further refinements are feasible using the distribution of explosions over time, say local time of day. Recall Bayes theorem for Q and X; $Q \bigcap X = 0$ and $Q \bigcup X = 1$, then

$$P(Q|B) = \frac{P(Q) \cdot P(B|Q)}{P(Q) \cdot P(B|Q) + P(X) \cdot P(B|X)}$$

B defines "event in specific time interval (in our case hour)" , $P(Q)$ and $P(X)$ as before the probability of an earthquake and explosion, respectively and $P(Q|B)$ - probability of an earthquake within a hour interval for a given day of week. Also $P(B|Q)$ - probability of an earthquake to occur at a specific hour is taken to be $1/24$ assuming that the occurrence of earthquakes does not depend on time of day. Similarly, $P(B|X)$ is a probability of an explosion to occur in a given hour which is obtainable from the results given above. On this basis we calculate the probability to recognize earthquakes as explosions from the Kiruna cluster in the local hours 0-1 and 4-5. From the daily distribution (Fig. 1) we obtain

$$\begin{aligned} P(B|X)_{0-1} &= [1 - P(Q)]\,\frac{586}{3544} = 0.16535 \\ P(B|X)_{4-5} &= [1 - P(Q)]\,\frac{18}{3544} = 0.005079 \end{aligned}$$

Using Bayes formula we obtain eventually

$$\begin{aligned} P(Q|\text{event in } 0-1) &= \frac{5.6 \cdot 10^{-6} \cdot (1/24)}{5.6 \cdot 10^{-6} \cdot (1/24) + (1 - 5.6 \cdot 10^{-6}) \cdot 0.1635} = 1.43 \cdot 10^{-6} \\ P(Q|\text{event in } 4-5) &= \frac{5.6 \cdot 10^{-6} \cdot (1/24)}{5.6 \cdot 10^{-6} \cdot (1/24) + (1 - 5.6 \cdot 10^{-6}) \cdot 0.0050790} = 4.59 \cdot 10^{-5} \end{aligned}$$

As demonstrated above, exploiting the fine structure of daily event distribution we obtain improved error estimates. These results clearly implies that in N. Fennoscandia & Kola the CTBT source discrimination problem is mainly that of differentiating between numerous chemical (mining) explosion and nuclear explosions since the probability of earthquake occurrence is small indeed.

CLUSTER REMOVAL IN PRACTICE

In summary, the above cluster removal is simple:

- make 2D histogram of all events from bulletins for the area of interest;
- calculate slopes using spatial derivatives of histogram and its curvature (Laplacian);
- sort slopes and curvature in descending order;
- set percentage of area assumed to be under clusters, e.g. 20%;
- remove first 20% of cells in slopes and curvature sorted list;
- put smooth surface on the remaining cells providing an estimate of EQs p.d.f.;
- fit polynomial trend to the above surface.

This trend will be average estimate of earthquake p.d.f. over the area of study.

W. NORWAY EVENT DISTRIBUTION

A display in the form of event occurrence per unit area (km^2) and time (10 years = 01/01/90 - 31/12/99) is given in Fig. 5. As map inserts are shown time of day distributions for the 6 boxed areas having the highest event activities. Area 1 encloses the Titania mine which shooting practices are exceptionally time-space stationary. Practically all events take place in 2 subsequent hour intervals; two because semiannual changes between summer/winter times. Locally, this kind of knowledge is apparently non-existent since analyst continues to read P- and S-arrivals for every explosion. It will suffice to read just one P-arrival for origin time as epicenter is known to nearest kilometer. The Area 2 and 3 stem from road construction work (undersea tunnel) and harbor construction work, respectively. In the latter area, relatively many events are given non-zero focal depths in the bulletin listings. However, we do not consider these depth estimates as proof of events being earthquakes. In Area 4 (Bergen district) a large number of major construction works have taken place during the last decade including bridges, underground oil storages and major harbor works. Better spatial resolution should be obtainable using shorter time periods of say 2 years. Area 5 (off-shore) is obviously earthquake prone in view of the approximately flat hour-of-day distribution. Also, naval exercises do not involve use of WW 2 types of heavy depth charges any more so explosion sources at sea is very infrequent today. However, there are obviously some explosions within this population which we would attempt to identify in a subsequent study. Road construction works (undersea tunneling) account for almost all events in Area 6 in 1991/92.

Adapting the cluster analysis technique described above we proceeded as follows; firstly the basic assumption is that explosion events are clustered in the sense of steep curvatures and sharp gradients and hence are removed using a corresponding 0/1 spatial weighting. Note, any assumptions regarding flat/non-flat earthquake/explosion occurrence distributions as a function of time of day is not incorporated here. Then, a smooth surface is fitted to the residual presumably spatial earthquake distribution given a p.d.f. maximal value in the Area 5 $\sim$ $0.05\,km^{-2}\,year^{-1}$. The validity of this estimated can be tested on selected areas like Area 1 in Fig. 5; over the time interval of 10 years about 6 EQ (one every 4th hour) should have occurred in the Titania area but this is obviously not the case. Similar results are found for many smaller areas in particular east of longitude 5.0° East. On this basis we refined our analysis; in essence we found that off-shore areas are exclusively earthquakes while between 4 - 6 E and 58 - 63 N we have mixed populations while further east explosion events are dominant. In other words, the assumption of uniform EQ p.d.f. for the whole area (Fig. 5 map) is only valid as a first approximation. In the mentioned area with mixed EQ/explosion population, the open pit mine Titania (Area 1; Fig. 5) produce event waveforms which are easily recognized as such (Fedorenko et al, 1999). Spatial cluster analysis for W. Norway did not work too well here simply because the very spiky event distribution and relatively small number of events. For Kola such distributions are smoother due to the accumulation of several mines in a small area and also due to lesser accuracy in epicenter locations. For W. Norway we replaced the curvature and gradient mapping with a rather crude spatial event plot that is eliminating all events between 04 a.m. - 08 p.m. (retaining nocturnal events only) as shown in Fig. 6. In other words, EQ occurrence is confined to a narrow N/S-trending zone in the coastal areas and as mentioned those off-shore. Also, 15 felt EQs are reported for this area in the 1990/99 reporting period.

The really difficult events are underwater harbor works since explosions here could take place at any hour and sometimes preferably at night due to shipping traffic. Pure statistical means in assuming EQ only off-shore W. Norway and explosion only like in Kola would probably be better than actual discriminant analysis where error rates of a few per cent is common. However, in the area of mixed populations the tedious work of introducing waveform diagnostics would be needed. As student work, we will start to undertake discriminant analysis initially using the explosion signal recognition approach.

CONCLUSIONS AND RECOMMENDATIONS

Albeit some details remain in our studies of Norsar and University of Bergen event listings we have confidence in the following conclusions.

- Event populations in N. Fennoscandia and Kola (NW Russia) are completely dominated by mining explosion clusters in Kiruna, Khibiny and Zapolarny.
- A combination of trend and cluster analysis give that the p.d.f. of EQ occurrences in these mining areas is negligible so in a CTBT context the discriminant problem is confined to chemical versus nuclear explosions.
- Similar results are obtained for W. Norway although here off-shore areas are exclusively earthquakes. However, in coastal areas explosions dominate but EQ occurrences cannot be ignored.
- Our space-time cluster analysis is well suited for limiting explosion source areas and thereby identifying events which should be useful for more elaborated source discrimination studies using event waveforms and their corresponding envelope transforms.

Recommendations: The results obtained suggest that aseismic regions like Fennoscandia and NW Russia can be monitored in more efficient ways than presently done. Reason being that too few seismic stations are used so due epicenter inaccuracies spatial event plots exhibit similarities to seismicity mapping. By deploying many more inexpensive seismic stations more accurate event locations would be feasible and moreover explosion source signal recognition would be feasible as part of automated event processing. Fedorenko and Husebye (ibid) demonstrate that inexpensive 3-comp. geophones can be operated as a high quality seismograph station (cost less than US $ 1000) and besides local high schools appear to be enthusiastic about operating such stations.

REFERENCES

Blandford, R.R., 1996. Regional seismic event discrimination. In E.S. Husebye and A.M. Dainty (eds). Monitoring a Comprehensive Test Ban Treaty. Kluwer Acad. Publ., Dordrecht, The Netherlands, 689 - 720.

Dowla, F.U., 1996. Neural networks in seismic discrimination. In E.S. Husebye and A.M. Dainty (eds). Monitoring a Comprehensive Test Ban Treaty. Kluwer Acad. Publ., Dordrecht, The Netherlands, 777 - 790.

Fedorenko, Yu. V., E. S. Husebye, B. Heincke and B. O. Ruud, 1998. Recognizing explosion sites without seismogramm readings: neural network analysis of envelope–transformed multistation SP recordings 3-6 Hz. Geophys. J. Int., 133, F1-F6.

Fedorenko, Yu. V., E. S. Husebye and B. O. Ruud, 1999. Explosion site recognition; neural net discriminator using three-component stations. Phys. Earth Planet. Int., 113, 131-142.

Fedorenko, Yu. V. and E.S. Husebye, 2000. 2-D signal detectors for 3-component seismic recordings. Proceed. 22nd Seismic Res. Symp., New Orleans, LA, Sep. 2000.

Shapira, A., Y. Gitterman and V. Pinsky, 1996. Discrimination of seismic sources using the Israel Seismic Network. Proceed. 18Th Seismic Research Symp., Annapolis, MD, Sep. 1996, 612 - 621.

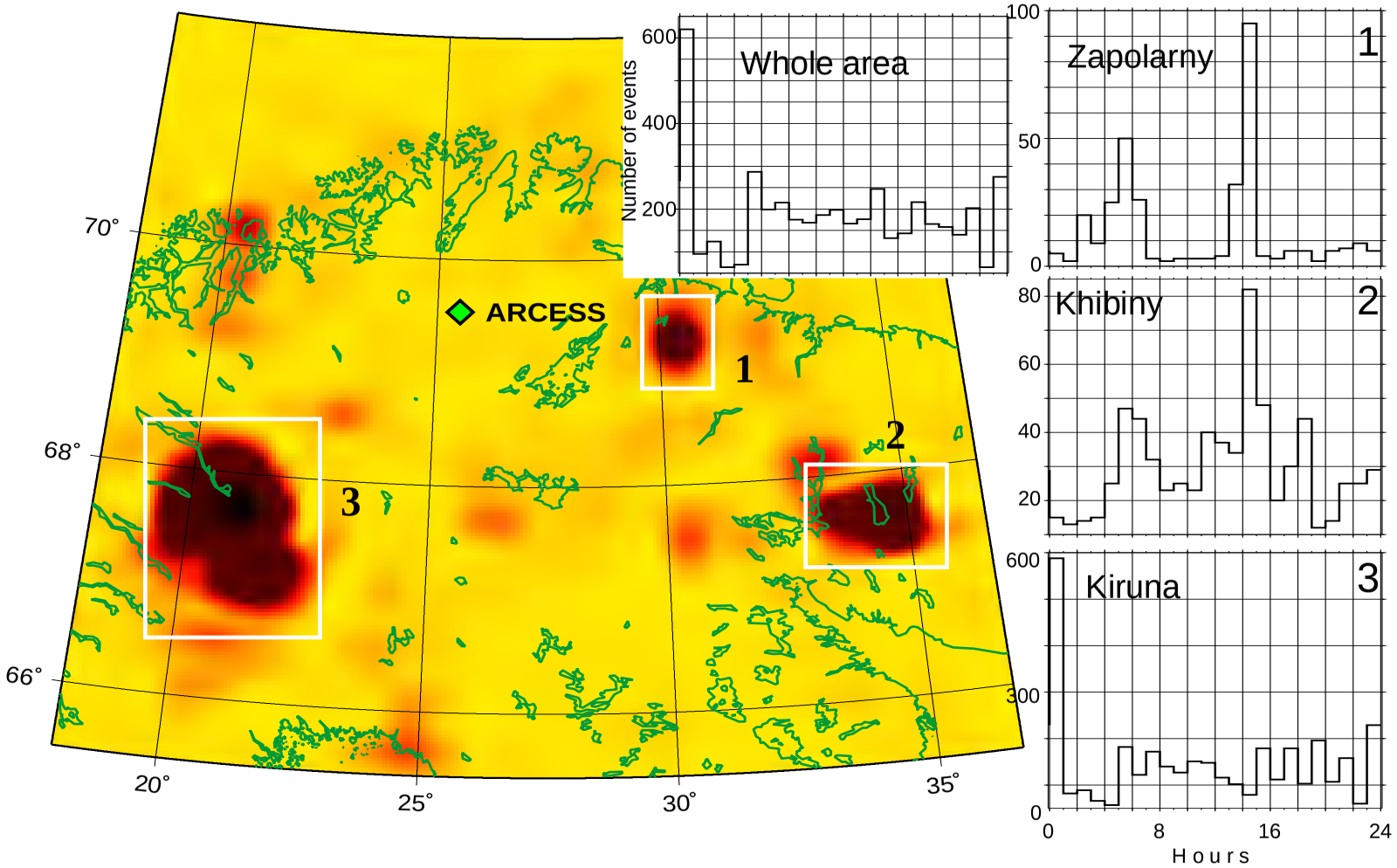


Fig. 1. Event distribution in Fennoscandia and NW Russia (Kola) as reported by Norsar through their bulletins for the time period Oct, 98 - Oct, 99 based on their generalized beamforming technique for automatic epicenter determinations.

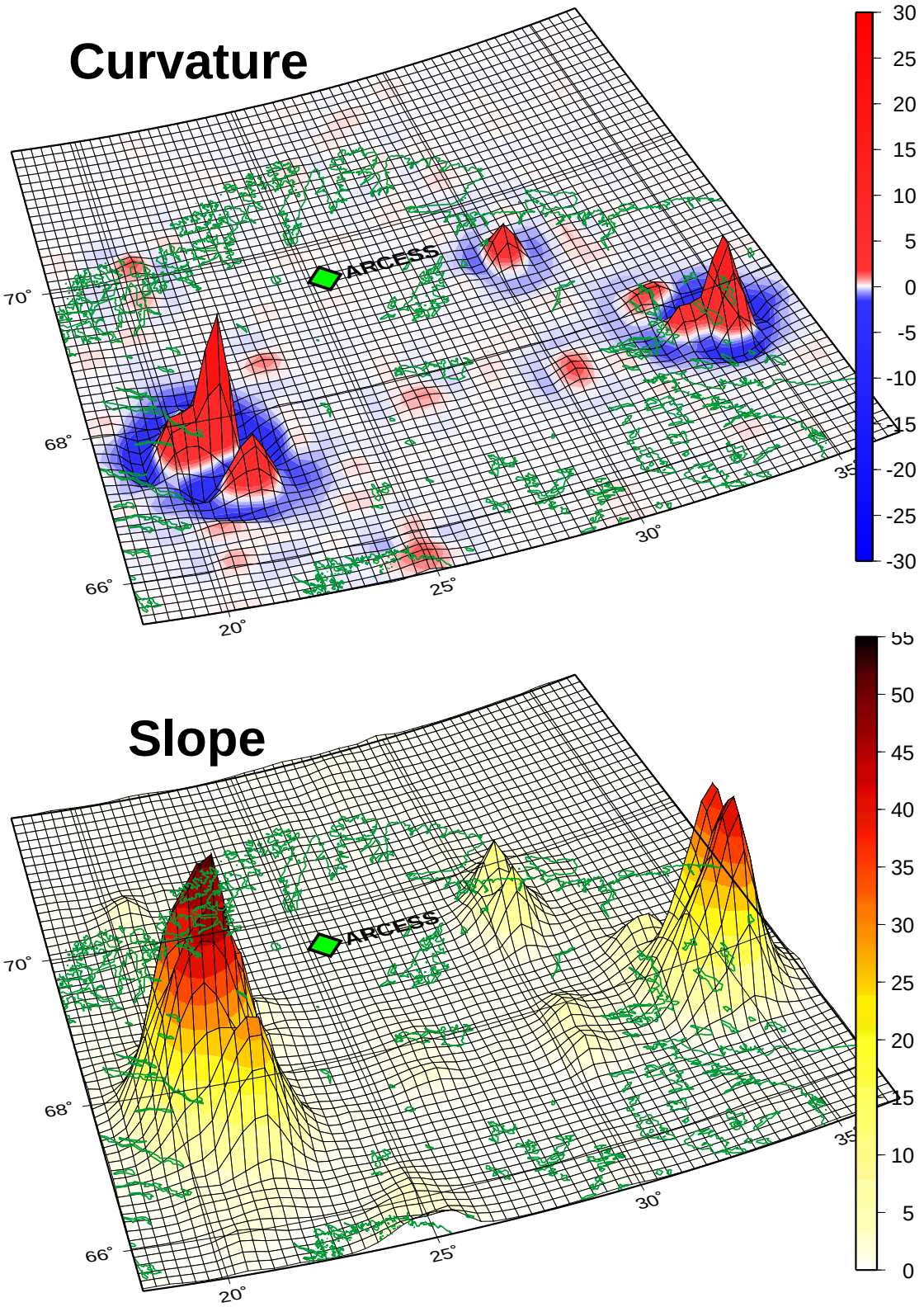


Fig. 2. First (gradient) and second (curvature) order spatial derivatives of event distributions.

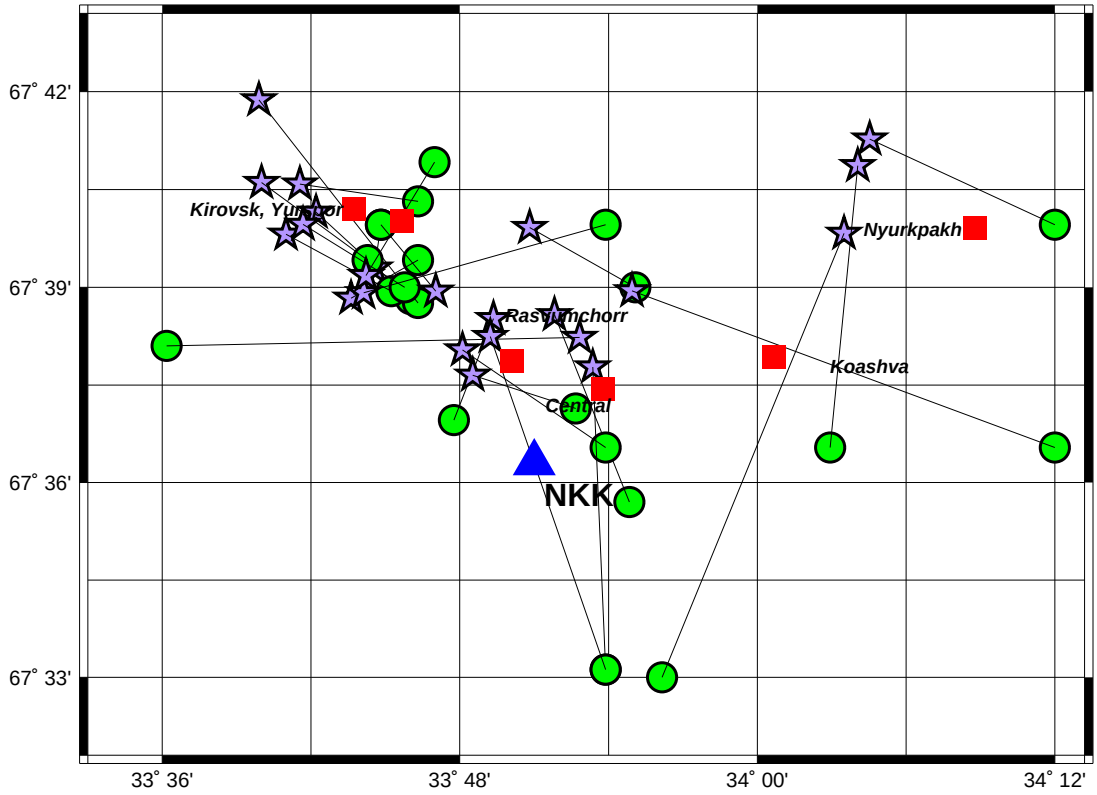


Fig. 3. Individual mining operations in Khibiny located by NKK seismic station. Sqares indicate active mines, stars and circles indicate epicenter locations by us and Kola Regional Seismological Centre respectively.

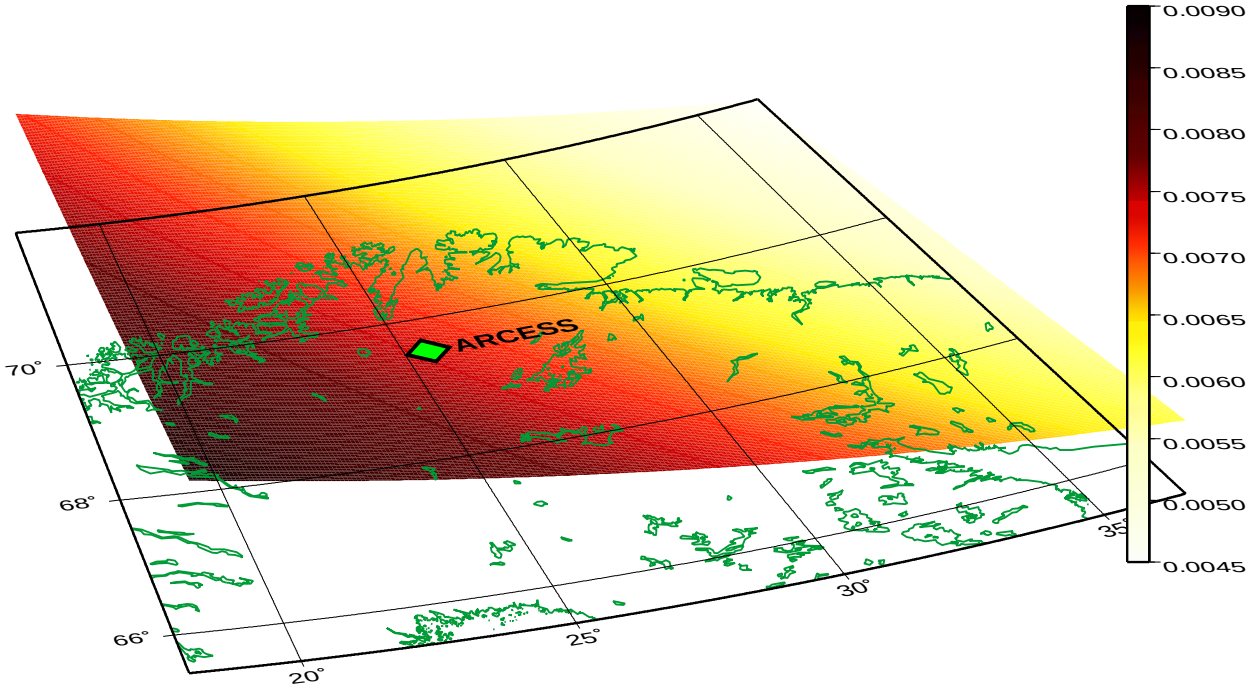


Fig. 4. Plane surface fitted to the remaining events p.d.f. after the clusters are removed; the probability of EQ occurence in this region is negligible.

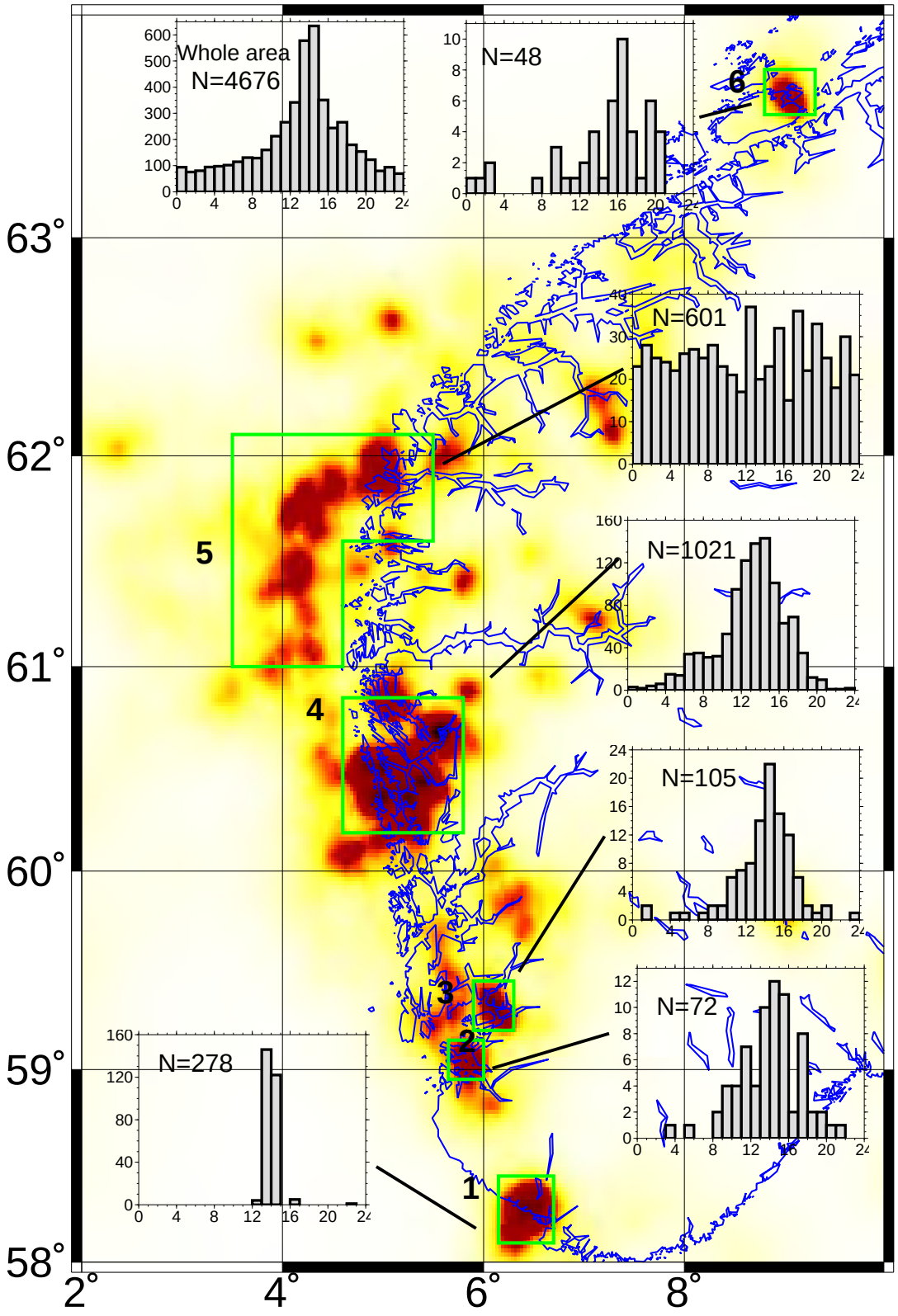


Fig. 5. The event distribution in W. Norway. The data used are 10 years of bulletin listings 01/01/90 - 31/12/99. For this area the epicenter locations are far more accurate due a relatively dense local network operated by the University of Bergen and analyst inspections of recordings.

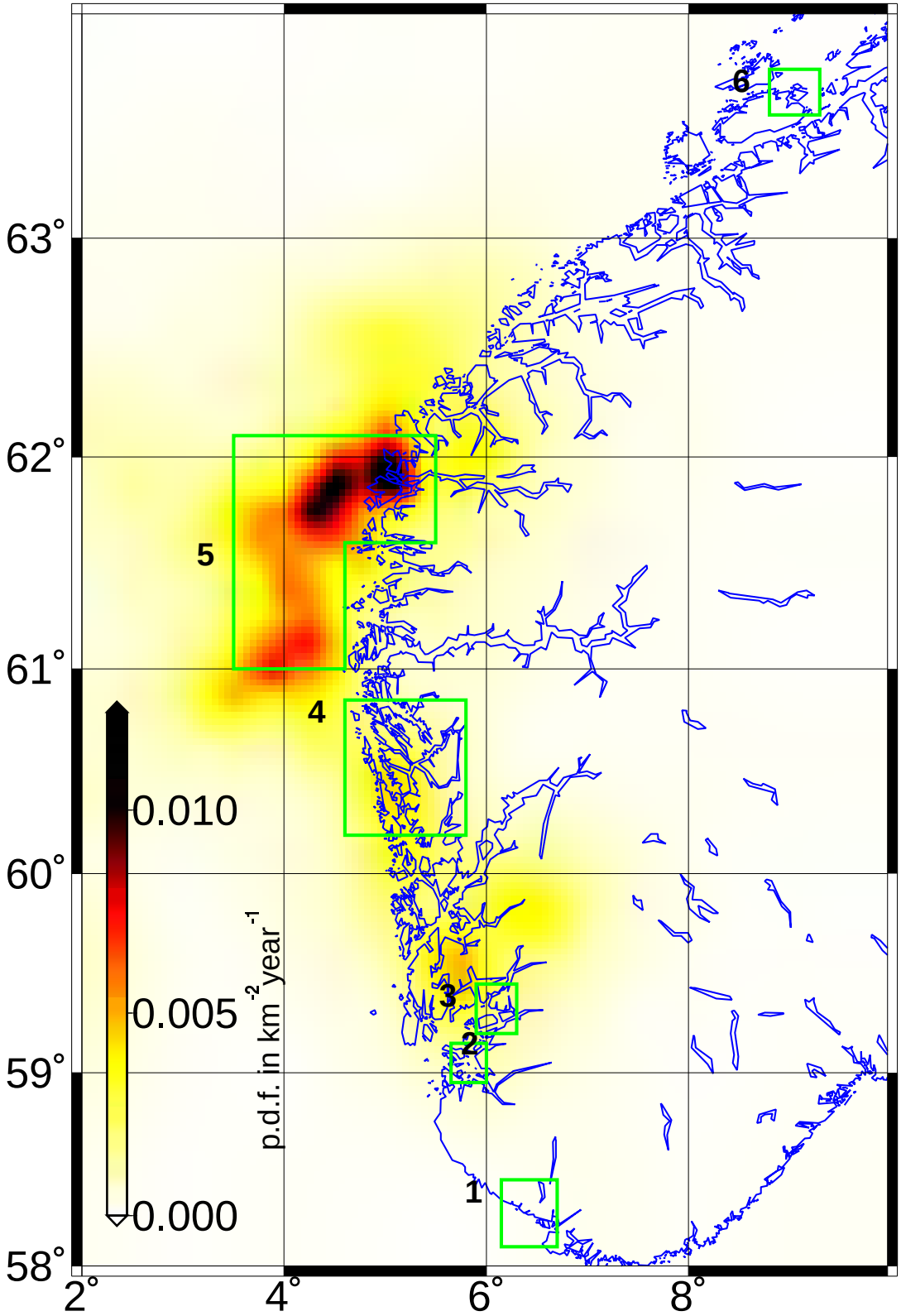


Fig. 6. Noctural (8 p.m. - 6 a.m.) event distribution for W. Norway outlining a narrow coastal seismicity zone from 59N/6E - 62N/4E.

USE OF DEPTH PHASES IN EVENT SCREENING

David Jepsen and Spiro Spiliopoulos
Australian Geological Survey Organisation

Sponsored by Defense Threat Reduction Agency
Arms Control Technology Division
Nuclear Treaties Branch

Contract No. DTRA01-99-C-0002

ABSTRACT

Accurate identification of depth phases is essential in improving the performance of the event screening process. In the first Release of event screening software, the rules for depth phases were insufficient, in that events that had inappropriate depth phase picks could satisfy the depth phase criteria. To strengthen the depth phase criteria so there is more confidence in the results, a new set of constraints were examined. The uncertainty in pP and sP onset times and the variability in the earth's velocity structure were the main factors that had to be accounted for. As a result, the existing criteria of a minimum moveout of 1.5 seconds and at least 3 associated depth phases, had to be extended to include minimum allowable pP-P and sP-P times and a SNR threshold of 2. The application of these new criteria is quite severe, resulting in no events less than 50km and only 20% of all depth phase solutions being screened out. On the otherhand one can be quite confident that no shallow events are screened out.

Much depth phase information is being discarded using these stringent criteria. Research into an independent technique to determine whether the depth-phase solutions are reliable is being investigated. The relative amplitude method (Pearce algorithm), is being employed to search for double couple focal mechanism solutions that are consistent with the amplitudes of P, pP and sP phases associated with the event. The existence or non-existence of these solutions is an indicator of the validity of the depth phase picks.

1. Introduction

If an event is confidently deeper than a depth threshold for which it is feasible with existing technology to test an underground nuclear explosion, then it is very likely to be of natural seismic origin. Thus, focal depth is one of the key characteristics used to distinguish earthquakes from underground nuclear explosions. Currently, at the PIDC about 11% of the REB events above mb3.5 have depths determined by depth phases. Compared to the ISC and other bulletins, this percentage is low. Development of improved techniques and procedures at the PIDC to identify and verify more depth phases, will assist in screening out more natural seismic events based on event depth.

There are currently no methods at the PIDC to actually validate the depth phase picks. In the first Release of depth screening criteria, there were simply criteria in terms of the number of depth phases and the amount of moveout of pP-P travel times with distance. These intended to eliminate cases for which the depth phases were too few in number or without expected moveout behaviour to be considered reliable. Based on a study by Jepsen and Fisk (1999), these criteria appear to function as intended for most cases. However there are known REB events with erroneous depth phase picks that satisfy the criteria. In this paper, research on more robust depth phase criteria is described. Although the new criteria is not foolproof, they are set conservatively such that one can be quite confident that no shallow events are screened out.

Much depth phase information is being discarded using these stringent criteria. Research into an independent technique to determine whether the depth-phase solutions are reliable is being investigated and is described in this paper. The relative amplitude method (Pearce algorithm), is being employed to search for double couple focal mechanism solutions that are consistent with the amplitudes of P, pP and sP phases associated with the event. The existence or non-existence of these solutions is an indicator of the validity of the depth phase picks.

2. Current depth event screening criteria

The depth screening criterion recommended by the IDC Technical Experts Group on Event Screening, May 1999, and which is in the Release 3 IDC software, is as follows (see CTBT/WGB/TL-2/31). An event will be screened out if:

$$\hat{D} - 2\sigma_D > 10km$$

where

$$2\sigma_D = 2\sqrt{s}_{zz} + k,$$

The value of k depends on whether depth phase criteria are met:

k = 0km for depth-phase solutions
k = 20km otherwise

Comparisons of REB depth estimates with those of the PDE and local bulletins has shown that REB depth estimates exhibit significant regional biases and that the depth uncertainties do not adequately reflect all of the model and random errors. As an interim approach, a constant term k has been introduced to account for errors not adequately represented by s_{zz}. It has been shown by Jepsen and Fisk (1999) that the value of k=40km in Release 2 could be reduced to 20km and still provide the appropriate coverage at the specified level of confidence.

It was recommended that the depth screening criteria be applied to all events in the REB with mb >= 3.5, and for which depth estimates were not constrained by an analyst. This criterion, including the two-sigma term, is equivalent to requiring that the 97.5% one-sided confidence interval is entirely deeper than 10km.

For events with depth-phase solutions, additional depth-phase validation criteria need to be satisfied before the event can be tested for screening. The Release 3 depth phase screening criteria consists of:

- Number of depth phases (ndp) >= 3
- ΔT(pP-P) >=1.5 seconds for stations between 25 & 100 degrees
- Signal-to-noise = 2.0 for pP and sP, based on peak-to-trough amplitude measurements;
- t(pP-P) > 12.9 &/or t(sP-P) > 19 seconds at the nearest station beyond 25 degrees;

These criteria are an extension of the Release 2 criteria that only required the event to satisfy the first two criterion.

Significant concern was noted by the Experts regarding potential misidentification of depth phases, particularly by inexperienced analysts. Improvements to analyst procedures and guidelines for depth phase identification has been set up to minimise these problems.

3. Evaluation and implications of depth-phase validation criteria

Fisk et al. (1999) found several events for which the pIDC analysts mis-identified depth phases, leading to over-estimated depths in the REB. For some cases, the depth-phase criteria were not satisfied, either because there were less than three depth phases or because the moveout of pP-P was less than 1.5 seconds. Thus, these events were not screened out as being deep. However, some cases were found with erroneous depth phases for which the depth-phase validation criteria were satisfied. For example, an event in the Vanuatu Islands region on 97/04/27 has a PDE depth estimate of 42km, while the REB provides a depth estimate of 82km, based on 8 depth phases and pP-P moveout of more than 1.5 seconds. It is clear from the examination of the seismic waveforms in figure 1 that although depth phases are clearly present, the pP arrivals were picked too late in the wavetrain by the analyst. Other similar examples have been described by Jepsen and Fisk (1999), Murphy and Cook (1998), and Bowers (1999). Consequently, new depth phase validation criteria needed to be examined.

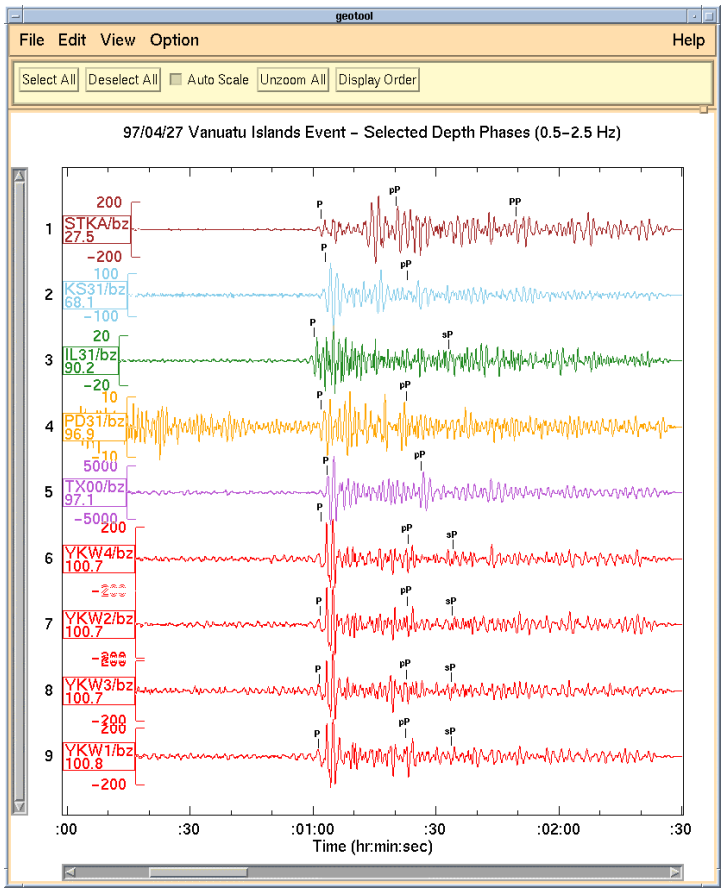


Figure 1: Bandpassed-filtered waveforms for an event in the Vanuatu Islands region. Analyst picks of depth phases were mis-identified too late in the waveforms, leading to a REB depth estimate that was too deep for this event by about 40km.

3.1 Evaluation results

To evaluate the depth-phase criteria the following questions were addressed:

(i) Is the existing moveout criterion appropriate?
(ii) Is a monotonically increasing moveout criteria necessary and/or useful?
(iii) What is an appropriate signal-to-noise ratio (SNR) that should be required for depth phases?
(iv) What is an acceptable uncertainty in the timing errors of depth phase picks?

In order to perform this study, pIDC and IRIS waveform data from 10 medium-sized earthquakes (mb 5.5-5.9), with depths ranging from 40 to 600km were used. For each event, onset times and amplitudes of P, pP and sP were picked. In most cases the raw waveform had to be deconvolved to broadband displacement before a clear depth phase was observable. A measure of the pre-signal amplitude for depth phases (in the 5 seconds preceding the signal) was also measured for determining SNR.

In general it was found that it was difficult to pick precise arrival onsets. Emergent onsets and precursory effects of filtering were the main factors. The raw (upper) and deconvolved waveforms (lower) from several IMS stations of the deep Fijian event on the 29th March 1998, shown in figure 2, clearly show these problems. On the raw waveforms the pP phases are both barely visible and emergent, but when the traces are deconvolved the pPs are more striking but precursory effects are introduced. As a consequence, many events displayed a large scatter in the pP-P and sP-P times. For example, the sP picks of the 4 January 1998 REB event shown in figure 3 span the distance range 40 - 140 degrees, with a maximum scatter of 3 seconds in the distance range 50-90 degrees. The dashed line on the figure represents the theoretical moveout (based on Iaspei91 travel times) expected for an event at

45km depth, and the lines either side represent 1 second deviations to the theoretical. Although there is a large scatter in the sP-P times, the depth phases fit very well with the assigned depth. Two hundred depth phases were picked for the 10 events, and on average the average residual of the moveout to the Iaspei91 travel time model was 0.7 seconds. It was suggested by Bowers (1999) that more accurate pP-P and sP-P times could be obtained by picking the times of the maximum peaks of the P, pP and sP. Certainly this was the case for the deep Hindu Kush event he showed, but this was not case for the majority of events.

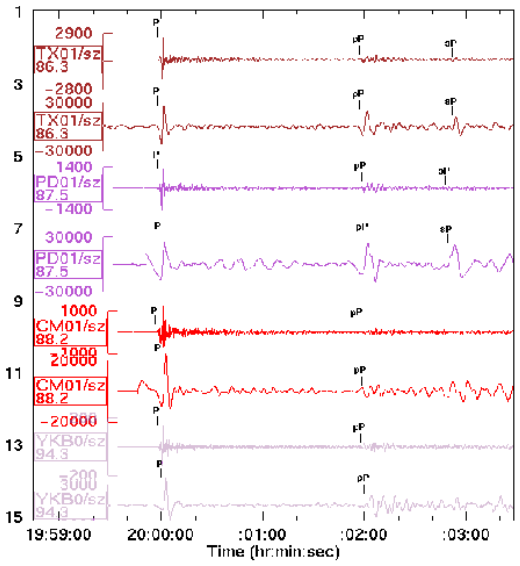


Figure 2: Raw (upper) and deconvolved waveforms (lower) at IMS stations: TXAR, PDAR, CMAR, YKA of the deep Fijian event on 29/03/1998.

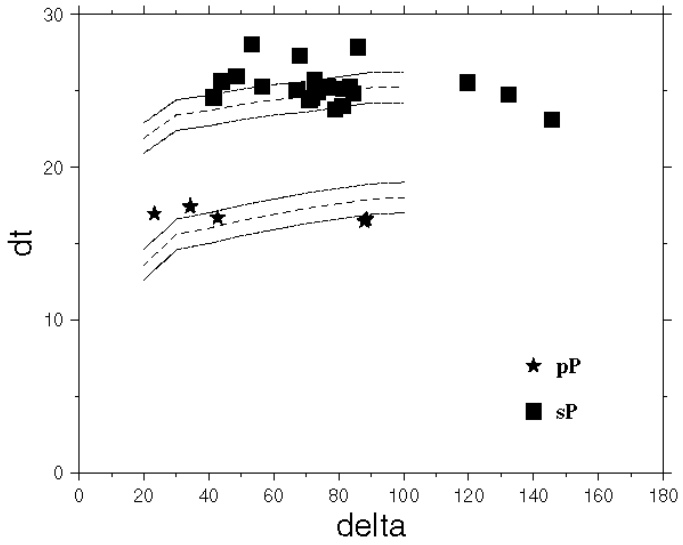


Figure 3:Travel time differences of pP-P (stars) and sP-P (squares) versus distance for a 04/01/98 REB event. The dashed lines represent the expected moveout, while the solid lines represent one-second deviations.

Another clear result was that the moveout typically increased monotonically with distance. However due to the scatter in pP-P and sP-P times this was not often seen for shallow events where the slope in the moveout is of the same order as the possible scatter (eg. an event at depth 50km, the expected moveout is 1.8 and 2.9 seconds for pP-P and sP-P respectively over the distance 30 to 90 degrees). In the case of the deep Fijian event, shown in figure 4 a large number of pP and sP's were observed and both clearly show the monotonically increasing moveout trend.

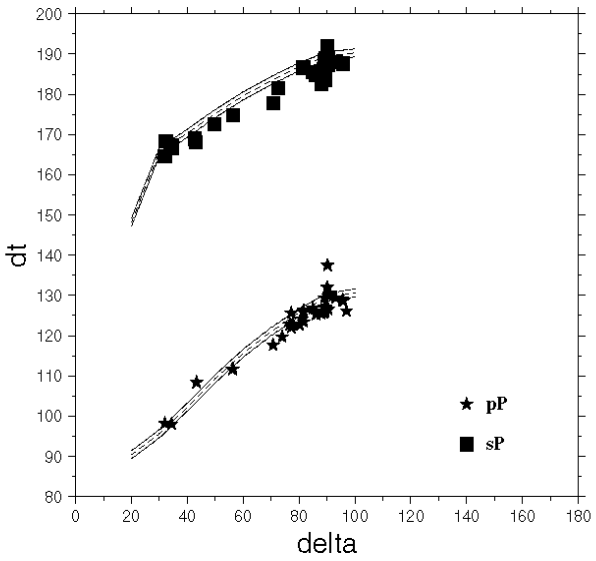


Figure 4: Travel time differences of pP-P (stars) and sP-P (squares) versus distance for the deep Fijian REB event on 29/03/98.

The intended use of the existing moveout criteria is to ensure that double explosions will not be screened out. Also it will assist in eliminating screening of events where an analyst may have overzealously picked any signal as a depth phase as long it satisfied a constant pP-P or sP-P time difference for all distances (some cases are known to exist). This criteria is equivalent to not screening out depth-phase events shallower than 50km. However with the large scatter of pP-P and sP-P times, it is possible that shallow events can be screened if they satisfy the 1.5 second moveout criteria. The histogram in figure 5 shows those REB events during 1998 that would be screened out by this criterion. In fact, 138 shallow depth-phase solutions (10km < depths < 50km) in this period were screened out. Since none of these events were shallower than 10km, serious screening errors were not made in these cases. However, this illustrates that there is certainly cause for concern and suggests that additional improvements in the depth-phase validation criteria are needed.

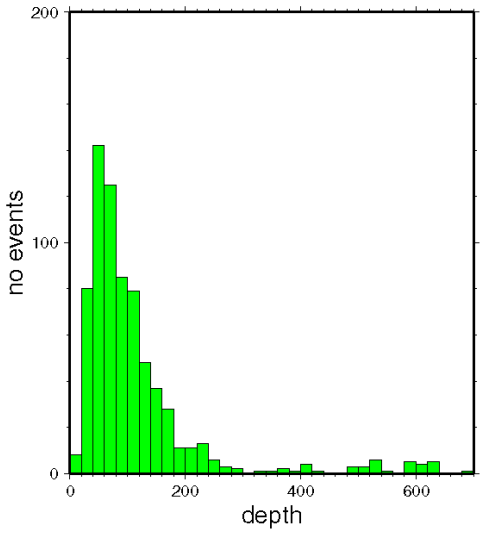


Figure 5: Histogram of depth-phase solutions in the REB during 1998 that were screened out with the existing (Release 2) criteria.

A potential improvement investigated is the criteria that pP-P > 12.9s or sP-P > 19.0s at the nearest station beyond 25 degrees. These criteria are equivalent to requiring focal depths deeper than 50km (as is the pP-P moveout criterion of 1.5s). The advantage of including these criteria is that the absolute times (12.9s for pP-P and 19.0s for sP-P) are considerably larger than the average timing errors of 0.7s, hence would provide an additional consistency check that is not as sensitive to timing errors. Results indicate that these criteria do not significantly reduce the number of events (> 50km) to which the depth screening criteria can be applied.

So the Release 2 moveout criteria (moveout >= 1 sec and ndp >=3) can be strengthened by employing two additional criteria: (i) pP-P > 12.9sec & (ii) sP-P > 19.0 sec**.** As a result no event less than 50km nor any event deeper that does not satisfy the moveout rule will be screened out. This restricts the use of depth phases of shallow events but is necessary to be confident that the screening criteria are working appropriately.

The depth-phase criteria could also be strengthened by: (1) ensuring that mis-timed depth-phase picks (with large timing residuals) are thrown out; (2) requiring that clear depth phases with SNR > 2 are used. Currently a 2 second residual is allowed by the location algorithm at the pIDC for depth phase picks. This ensures that mis-timed depth phase picks are thrown out and it ensures a monotonically increasing moveout with a maximum allowable residual of 2 seconds. However it was found that many depth-phase solutions (~40) were found which had associated depth phases with residuals greater than 2 seconds. This indicates that the pIDC location algorithm or rules employed by the analyst should be reviewed.

As expected, by varying the allowable residuals and the number of depth phases required for all depth phase solutions (> 50km) in the REB during 1998, the number of events screened out increased with residual size and decreased with the required number of depth phases (see table 1). Ensuring only a 2 second residual for each depth phase and that there are at least 3 depth phases associated, results in a few less events being screened out than with the existing criteria (543 to 582). The difference is due to some 39 events exceeding the allowable residual of 2 seconds. Further study is needed to assess appropriate restrictions on the allowable timing residuals. Another result was that depth phases with a SNR >= 2 were quite obvious and amounted to 90% of the depth phases analysed.

No. depth phases	Residual 1 sec	Residual 2 sec	Residual 3 sec
ndp >= 3	487	**533**	**543**
ndp >= 4	348	417	425
ndp >= 5	257	316	327

Table 1. Number of events with depth-phase solutions that could be screened out for various values of allowable residuals and number of depth phases.

3.2 Implications

These criteria are conservative in that no shallow events (< 50km) with depth phases are screened out. Application of these criteria to all REB events in the 2nd half of 1999, it is found that only 128 out of 661 events with depth phases are screened out (see figure 6). Although not foolproof, one can feel quite confident that no shallow events are screened out. It should be noted that the depth-phase criteria described above test for physical consistency of the depth phases, and are primarily intended to prevent the depth screening criteria from being applied to depth-phase solutions with erroneous depth-phase picks. However, they do not actually validate that the phases that were picked are truly depth phases nor do they assist in identifying more valid depth phases.

To utilise much of the depth phase information bring thrown out above, the relative amplitude method is being trialed to investigate an approach to validate the depth phase picks.

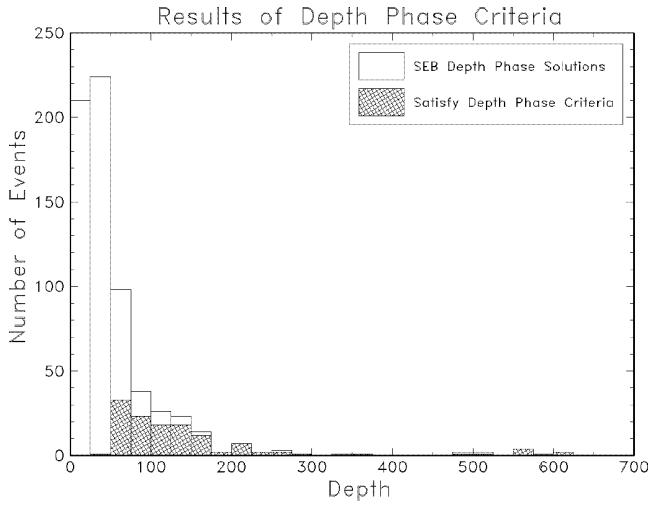


Figure 6: Histogram of total number of depth phase solutions and those that satisfy the depth phase criteria, in 25km depth bins.

4. Relative Amplitude Technique

The relative amplitude technique (RAMP) developed by Pearce (1977) can be used to calculate and validate source mechanism solutions for seismic events, since the impulse on the recorded seismogram is proportional to the amplitude of the pulse (for simple earthquakes with mb < 5.5 recorded at short period, and for simple deep and larger earthquakes recorded at long period). Pearce (1994) noted that the relative polarities and amplitudes of P and associated depth phases depended on three factors: (i) the direction of emergence from the source; (ii) the relative attenuation (of the short depth-surface two-way path); and (iii) the source type and orientation (i.e. the source radiation pattern). The relative attenuation can be accounted for by including an above source structure in the processing. Hence the presence of a number of stations (at varying emergence angles and azimuths), can then be used to fix on the source radiation pattern of the event. RAMP searches the strike-slip-dip parameter space using the relative amplitudes and polarities of P, pP and sP and/or the 3 components of S, at a number of stations, to determine the range of moment tensor solutions that are consistent with the input data.

Although there may be some evidence for earthquakes with components of non-double couple mechanisms (Frohlich, 1994), many studies have convincingly shown that seismic source mechanisms, apart from shallow volcanic events, can be described by double couple mechanisms. RAMP can then be used in a restricted way, by only allowing double couple mechanisms to be formed, to determine the focal mechanism of the event. Pearce & Rogers (1989) showed that the use of P and depth phase picks at three strategically positioned stations, could form a well constrained source mechanism. In this study, RAMP is used to test whether each event forms a well constrained double couple solution, and so validate whether the depth phases picked by analysts are correct or not. This will provide a check that is independent of current depth phase screening criteria which is only related to the relative times of the first arrival and associated depth phases.

4.1 Data and Processing

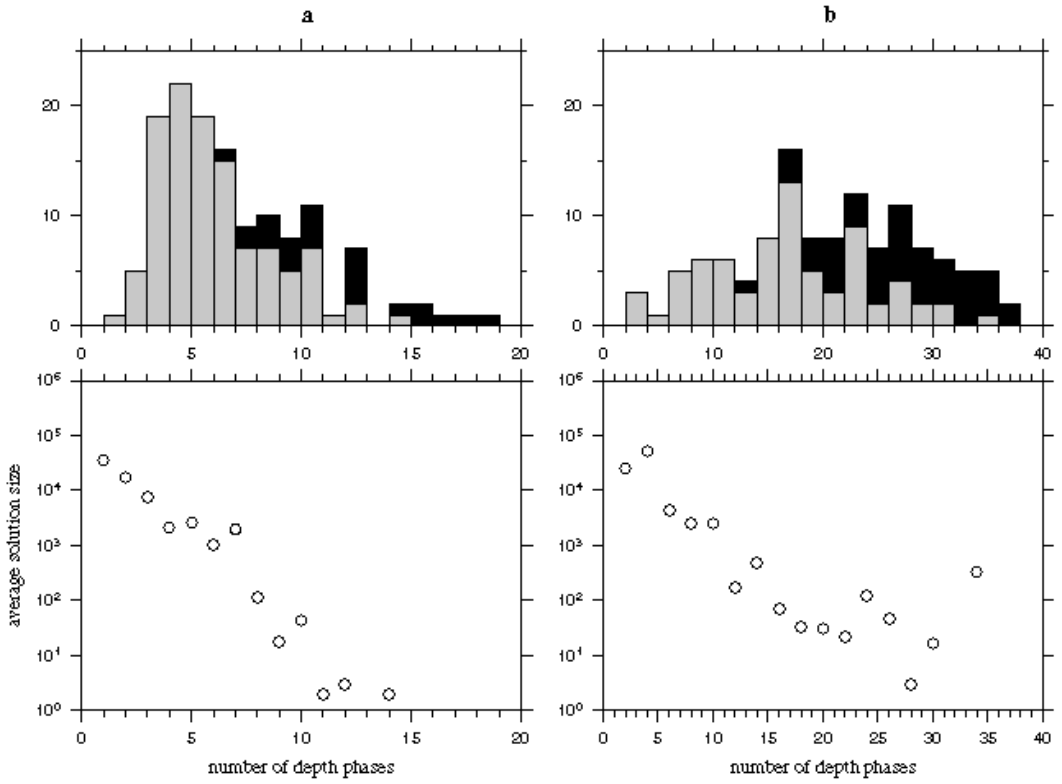
A restricted dataset of the 661 REB depth phase events from the 2nd half of 1999 was chosen to evaluate the applicability of RAMP. Only depth phase events with depths between 50 and 100km were used in this study (136 in total), since depth phase picks for shallower events are more likely to be in error and deep events would suffer from the need to make allowances for anelastic attenuation along the whole propagation path.

Full application of RAMP requires both the relative amplitudes and polarities of P and its associated depth phases. It was difficult to measure the relative polarity for most of these events, so in the processing this was left undetermined. As a result this allowed many more combinations of solutions to form, of which a number were redundant. As noted above, the amplitudes of observed phases can be affected by attenuation along the short depth-

surface two-way path, but also by seismic noise, complex pulse shape, interfering arrivals and the instrument response. A 33% uncertainty has been imposed on the amplitudes to encompass these variations. If very strict (i.e. small) uncertainties are imposed, RAMP will quite often fail to form events. On the otherhand if the uncertainty is too large the events may not form well-constrained solutions.

A 5*5*5 degree strike-dip-slip parameter space has been chosen for this study. This grid size allows RAMP to process quickly while being dense enough so solutions can be formed. There are 93312 possible solutions.

Two different approaches of applying RAMP to the dataset were tested. The first method solely involved the amplitude information contained in the REB and was trialed to see whether RAMP could be used as an effective tool. Since most of the events had only a small number of depth phases and the amplitudes were not calculated in the same or equivalent short-period filter band, these events were not expected to form many well constrained events. Secondly a more comprehensive application of RAMP was tested. This involved measuring amplitudes (in 0.8-4.0Hz filter band) of observed depth phases and calculating maximum amplitudes of the waveform data in time windows where the depth phases were expected based on the REB depth of the event. In this process the complete waveforms are being utilised. In both processes, the relative amplitudes at one station were allowed to be incompatible in the forming of solutions.



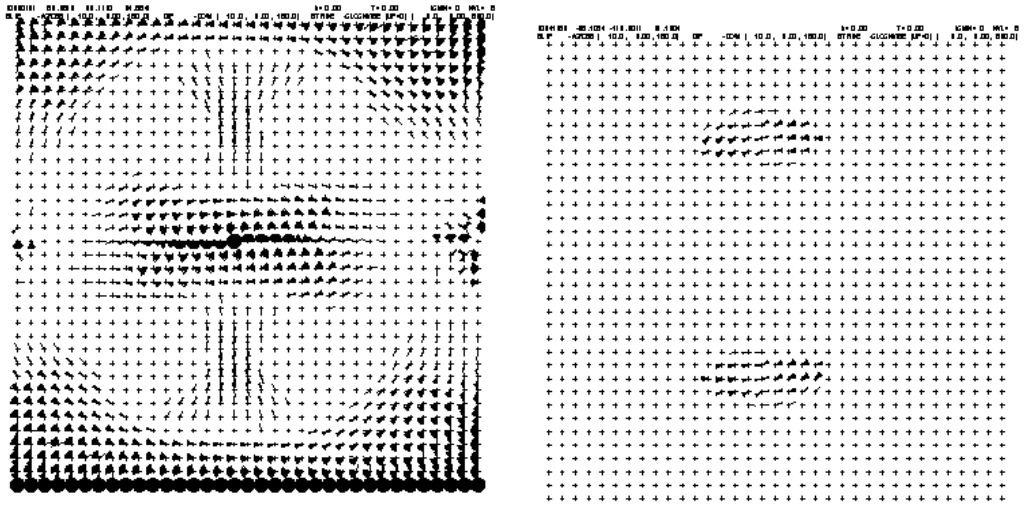
Figures 7a&b: Average solution size, histogram of events with solutions (grey) and without solutions (black) versus number of depth phases, for a) trial run; b) comprehensive run.

4.2 Results

For the trial run, double couple solutions were formed for 111 out of the 136 events. The solution size varied from 1 to 35874. Whereas in the more comprehensive run, 73 out of 123 events processed formed double couple solutions, with solution size varying from 1 to 53146. Figures 7a&b show the average solution size, and a histogram of the number of events with or without solutions, both versus the number of depth phases (ndp). In both cases, the average solution size decreases with npd phases used. The drop off rate is much faster in fig. 7a

than fig. 7b due to the fact that the extra depth phase information used in fig. 7b (maximum amplitudes in the expected depth phase time intervals) are less constrained than amplitudes of the observed depth-phases, and in the trial run more stations are contributing depth phase information at a given ndp than in the comprehensive run. However the average solution size is offset by the shift in the number of depth phases available for processing.

There are more failures in the second run, as shown in the histogram of figure 7b, but there appears to be an equal or greater number of events that have a solution size less than 500, which is the level chosen in this study at which an event is termed well constrained. This limit was determined through careful examination of the distribution of solutions calculated for the 136 events. Figures 8 a & b show the solutions determined for a poorly constrained event in Southern Greece and a well constrained Fijian event. The poorly constrained event in fig. 8a has 10064 solutions and no clear mechanism at all. The well-constrained event, fig. 8b has 402 possible solutions divided into two mirrored regions. The symmetry of solutions is a feature of not constraining the polarities of the phases. Where available, the solutions have been compared with CMT solutions. Only one event, the 26 August 1999 Philippines event had an available CMT solution, and the solutions determined by RAMP were in agreement.



a **b**

Figures 8 a & b: Double couple solutions consistent with the input data for the a) poorly constrained southern Greek event and the b) well-constrained Fijian event. The dip, slip are on the vertical and horizontal axes respectively, and the azimuth of the strike for consistent solutions is shown as a vector plotted at each dip-slip position.

4.3 Screening with RAMP

If the depth phases for an event can be confidently validated by RAMP in that the event has a well-constrained double couple mechanism, then it can be screened out. In table 2 the number of events that formed solutions those with well-constrained mechanisms is given. Fifty-seven out of the 123 events processed would be screened out in the comprehensive run, which is slightly better than results from the trial run. This compares well with the results of the Release 3 depth-phase criteria, where 55 events are screened out. Also it has an added advantage that the depth phases are validated.

	Number of events	Number of events with at least one solution	Number of events with a well constrained solution (500)
Trial run	36	11	2
Comprehensive run	23	13	7

Table 2: Results of the number of events processed, with solutions, and well-constrained solutions for the trial and comprehensive runs.

The trial run was applied to all the depth-phase events less than 50km, and it was found that 186 out of 434 depth-phase events formed well-constrained solutions. The impact of applying RAMP to these events could mean that approximately 50% of the events with depths < 50km, may now be screened out.

5. Future Work

To propose RAMP as an event screening tool a number of tasks need to be researched:

- Determine the appropriate screening level for a well-constrained solution. Both theoretical estimates of solution size with various network configurations, and comparisons to GroundTruth data need to be examined.
- Can significant improvements to the solutions be gained by attempting to read or automatically determine the relative polarities. Will this be a burden on the analysts?
- Test RAMP on the full suite of 661 depth phase events.
- Can the mis-labelling of depth phases over many stations (pP as sP or sP as pP) form well-constrained solutions? If so, what is their consequence?

6. Conclusions

Confidence in depth-phase solutions can be improved by imposing criteria on the relative timing and relative amplitudes of the P and depth phases. RAMP has shown that it could be an effective tool for event screening. However the definition of a well-constrained event needs to be more rigorously determined. Further improvements can probably be gained by fine tuning the use of RAMP on depth phase solutions. The current depth-phase criteria based on moveout and SNR will need to be reviewed in light of these results.

7. References

Bowers, D. (1999). Depth Phase Identification for Event Screening: Future Improvements, *Proceedings of the IDC Technical Experts Meeting on Seismic-Acoustic Event Screening*, 21-25 May 1999, Vienna, Austria.

CTBT/WGB/TL-2/31. Report of the IDC Technical Experts Meeting on Seismic-Acoustic Event Screening, 21-25 May, 1999.

Frohlich, C. (1994). Earthquakes with Non-Double-Couple Mechanisms, *Science*, **264**, 804-809.

Jepsen, D. and M. D. Fisk (1999). Evaluation of PIDC Depth Estimates, *Proceedings of the IDC Technical Experts Meeting on Seismic-Acoustic Event Screening*, 21-25 May 1999, Vienna, Austria.

Murphy, J. R. and R. W. Cook (1998). A Preliminary Analysis of PIDC Focal Depth Determination in the Northern Hindu Kush Region, Maxwell Technologies Technical Note, Reston, VA.

Pearce, R. G. (1977). Fault plane solutions using relative amplitudes of P and pP, *Geophys J. R. astr. Soc.*, **50**, 381-394.

Pearce, R.G. and R. M. Rogers (1989). Determination of Earthquake Moment Tensors From Teleseismic Relative Amplitude Observations, *Journal of Geophys. Res.*, **94**, 775-786.

ANALYSIS OF REGIONAL SEISMIC DATA FOR UNDERGROUND EXPLOSIONS

Won-Young Kim
Lamont-Doherty Earth Observatory of Columbia University

Mark Fisk and Steven Bottone
Mission Research Corporation

Sponsored by The Defense Threat Reduction Agency
Arms Control Technology Division
Nuclear Treaties Branch

Contract No. DSWA01-98-C-0152

ABSTRACT

In recent years, numerous regional seismic event discrimination studies have shown that the high-frequency (usually greater than 3–4 Hz), *P/S* spectral amplitude ratios of regional *P* (*Pg* or *Pn*) and *S* (*Sg*, *Sn* or *Lg*) waves observed at distance range from few kilometers up to about 2,000 kilometers, provide an efficient method to classify regional earthquakes, quarry blasts and underground nuclear explosions. The high-frequency *P/S* spectral ratios of vertical-component records, *P/S* spectral ratios of rotated, three-component regional records, as well as the *P/S* spectral ratio of the three-component regional records corrected for the free surface effect have been used depending upon the availability of data. The distance correction is also applied to *P/S* ratios which improves significantly the discrimination power of *P/S* ratios over uncorrected ratios, particularly if the events have data from wide distance ranges (*e.g.*, 3 to 17 degrees). Distance corrected and network averaged *P/S* spectral ratios provide transportability of the spectral ratio method to various regions worldwide. However, the *P/S* spectral ratio method is region dependent and we must find the best phases, frequency bands, and distance corrections for each region by using training data set with wide distance range, azimuthal coverage, and event size. There are many regions worldwide where there are lack of training data set. In this study, we focus on data collection and analysis of such regions – Novaya Zemlya, Russia and Semipalatinsk Test Site, Kazakstan, for evaluating the *P/S* ratios for regional seismic discrimination for CTBT monitoring.

We analyzed regional data from earthquakes, peaceful nuclear explosions, underground nuclear test around Novaya Zemlya, Russia to evaluate applicability of *P/S* ratio discriminant. In this region, data are available from the past underground nuclear explosions with magnitude $m_b(P)$ range from 4.5 to 6.5, while the useful earthquake data are limited to $m_b(P)$ 3.5 – 4.5. We report our analysis of the regional data to examine possible size (magnitude) dependence of regional high-frequency *P/S* spectral amplitude ratios as reported by Ringdal *et al*. (1999) for signals recorded at NORSAR from the Novaya Zemlya underground nuclear explosions. We also collected and analyzed regional data around Semipalatinsk Test Site, Kazakstan, where there are limited data available from few earthquakes. The regional data from the recent calibration explosions in Balapan and Degelen Mt. at various depth of burials are analyzed to shed light on whether the reported magnitude dependence of regional high-frequency *P/S* spectral amplitude ratios are due to yields of the explosions, or due to efficiency of *S* wave excitation from various burial depths of the sources.

OBJECTIVE

We seek practical methods of discrimination between different types of sources, in Novaya Zemlya, E. Kazakstan and W. China by using high-frequency *P/S* spectral amplitude ratios at regional distances. In particular we address the problems, for CTBT monitoring, posed by small, low-magnitude events, $m_b(P)$ smaller than 4.

RESEARCH ACCOMPLISHED

Recently, Ringdal *et al*. (1999) reported that *P/S* spectral amplitude ratios from 16 Novaya Zemlya

Key Words: CTBT monitoring; regional seismic discrimination; underground explosions

underground nuclear tests recorded at a low-gain vertical channel of NORSAR (Norwegian Seismic Array) appeared to be dependent upon the event size, and argued that comparing the *P/S* ratios of large underground nuclear tests (UNT) and small earthquakes could give rise misleading conclusions on event identification. The result of their study has some significance in applying the *P/S* ratios for classifying the explosions from earthquakes using the regional records in regions with few known small earthquakes and large UNTs in the past. For instance, Novaya Zemlya as well as Semipalatinsk Test Site in eastern Kazakstan regions had numerous UNTs ranging from magnitude $m_b(P)$ 4.5 to 6.5, while very few small earthquakes with magnitude range approximately $m_b(P)$ 3.5 to 4.5 have occurred around these test site regions. In particular, the *P/S* spectral ratios of the regional records from the Kara Sea event on August 17, 1997 have been analyzed by Richards & Kim (1997) using the data recorded at KEV (Kevo, Finland; Δ = 1040-1127 km, AZ=261-266°). Richards & Kim (1997) reported that the event is likely an earthquake based upon its location and the *P/S* ratios in the frequency band 3-8 Hz, and indicated that high-frequency *P/S* ratio is an efficient method to discriminate earthquakes and explosions around Novaya Zemlya test site.

In the following, we examine apparent magnitude dependence reported by Ringdal *et al*. (1999) in an effort to shed light on seismic event identification using the high-frequency *P/S* ratios of regional phases. We report further, on the *P/S* ratios of seismic records at regional distances from numbers of underground nuclear tests at Novaya Zemlya and Lop Nor Chinese test sites with different magnitudes.

Records from Novaya Zemlya Underground Nuclear Tests Recorded at NORSAR

We obtained waveform data recorded on a low-gain channel (NAO01) at NORSAR from 17 UNT from Novaya Zemlya used by Ringdal *et al*. (1999). The magnitude ranges of these UNT are from $m_b(P)$ 3.8 to 6.0 (see Table 1). The vertical records from selected events are plotted in Figure 1. Waveform data from the smallest event on Aug. 26, 1984 ($m_b(P)$=3.8) show extremely poor signal-to-noise ratio, in particular, there are no discernible *S* wave energy on the trace (Fig. 1), while the data from the event on Oct. 1, 1981 ($m_b(P)$ =5.97) have digitizing noise. Although the locations of the UNT's (Lilwall & Marshall, 1986; Marshall et al., 1994) are very close from each other (epicentral distance range of 2271 to 2287 km from NAO01 site), there are considerable variation on *S* wave amplitudes (group velocity between 4.5 and 3.5 km/sec) among the traces. The waveform data show that *S* wave amplitudes, starting from *Sn* arrival down to arrivals with group velocity 3.5 km/sec, are stronger on the traces from smaller events (e.g., Oct. 9, 1977 $m_b(P)$ =4.36 & May 7, 1988, $m_b(P)$=5.58),while *S* wave amplitudes are weaker relative to *P* waves on the traces from the large magnitude events (e.g., Aug. 10, 1978, $m_b(P)$ = 6.00). Since the source to station paths for these UNTs to NAO01 site are very similar, variations of these relative amplitude of *S* waves from UNTs might be due to the sources.

For Novaya Zemlya test site, the term underground nuclear explosions (UNEs) that we generally use should be distinguished from underground nuclear tests (UNTs), since each one of these "test" actually consisted of multiple UNEs carried out with some time delays in separate tunnels. When the time delays among the multiple explosions are long enough and when more than one explosions of a test have comparable yields, then these seismic events are known as "double" event (e.g., Oct. 18, 1979 and Oct. 11, 1980). Most of these tests may have complex shot patterns and depth of burials of each explosion. According to Mikhailov (1997), all of these underground nuclear tests consisted of multiple explosions in tunnels, except the two smallest tests on Oct. 9, 1977 and Aug. 26, 1984 which were listed as single explosion tests.

We analyzed waveform data from 15 UNTs at Novaya Zemlya test site. *Pn/Sn* spectral ratios are calculated for each discrete frequency band 1 through 5 Hz in order to examine the characteristics of the *Pn/Sn* ratios of these events. *Pn/Sn* ratios of these events in the frequency band 1 to 4 Hz are plotted in Figure 2. The regression of *Pn/Sn* ratios against magnitudes yield a slope of 0.14 with a standard deviation (σ) of 0.13 at 1 Hz, while the slopes and standard deviations at other frequencies are: 0.37 and σ =0.10 at 2 Hz, 0.23 and σ =0.13 at 3 Hz, and 0.04 and σ=0.11 at 4 Hz, respectively. Hence, the slope is the greatest at around 2 Hz, and suggests apparent magnitude dependence of the *Pn/Sn* ratios. However, the slopes are small at other frequencies and considering other factors such as depth of burials and complex shot patterns of these UNTs which might cause different efficiency of *S* wave excitation from each test, this may be considered "apparent" magnitude dependence of *Pn/Sn* ratio. Note also that these slopes of the regression are strongly affected by only two low magnitude events. In any case, relatively low *Pn/Sn* ratios at around 2 Hz from the two smaller UNTs may be caused by stronger *S* amplitudes relative to *P* wave at around 2 Hz from the single UNE.

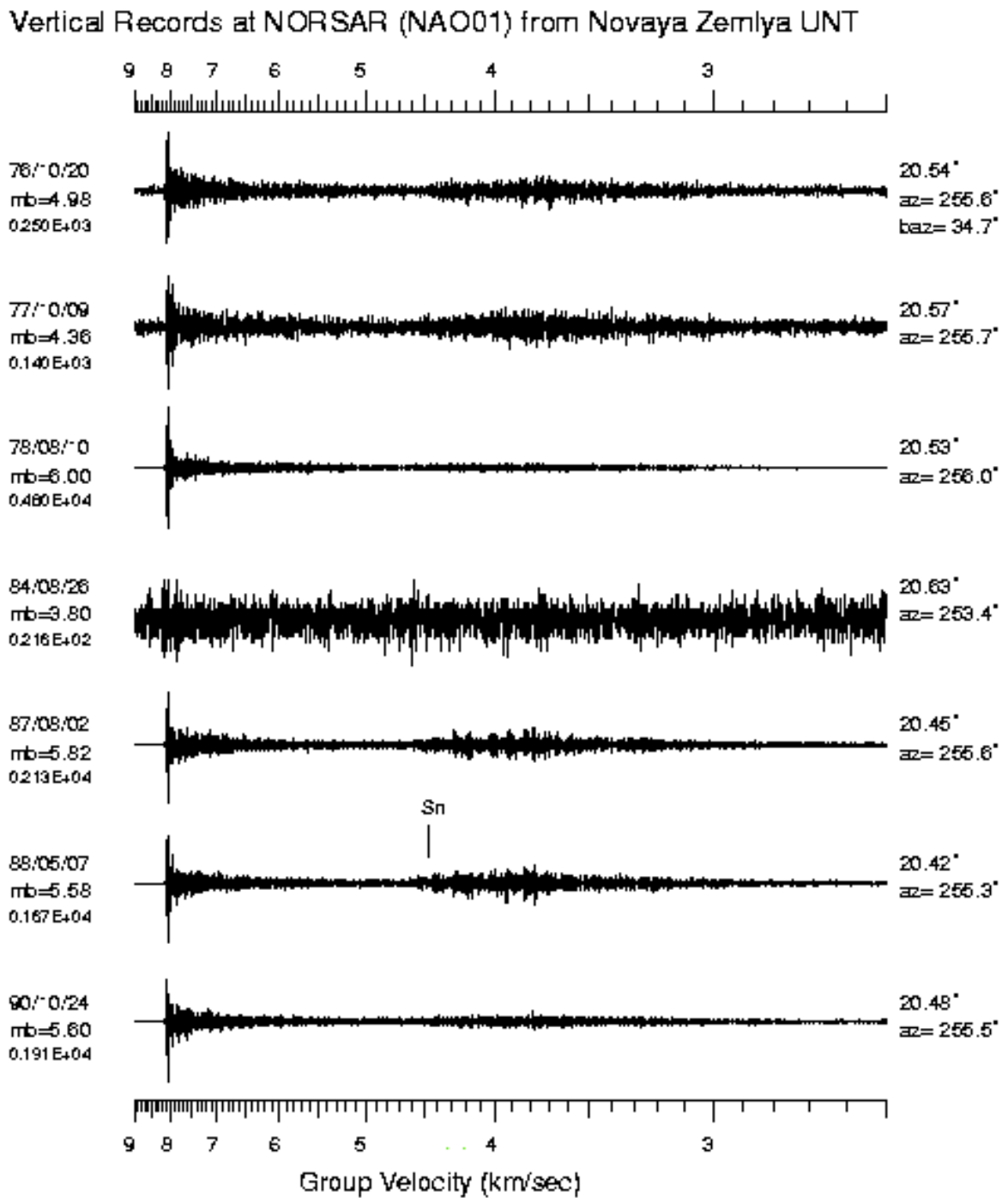


Fig.1 Selected waveform data from Novaya Zemlya underground nuclear tests recorded at a low-gain vertical channel (NAO01) at NORSAR. Events have magnitude, $m_b(P)$ 3.8 to 6.0 and epicentral distance ranges from 2271 to 2287 km with an average azimuth of 256°. Traces are plotted with group velocity in km/sec and the event id and magnitude for each event is indicated at the beginning of each trace.

Table 1. Novaya Zemlya Underground Nuclear Tests Recorded at NORSAR*

Origin time		Lat	Long	Magnitude		
Year-Mo-Da	(hh:mm:sec)	(°N)	(°E)	$m_b(P)$	N Obs.	Remarks
1976-Oct-20	07:59:58.07	73.398	54.821	4.98	39	
1977-Sep-01	02:59:57.97	73.339	54.628	5.66	84	
1977-Oct-09	10:59:58.12	73.409	54.936	4.36	28	
1978-Aug-10	07:59:57.93	73.291	54.892	6.00	91	
1979-Sep-24	03:29:58.75	73.343	54.681	5.77	104	
1979-Oct-18	07:09:58.75	73.316	54.825	5.79	91	double
1980-Oct-11	07:09:57.47	73.336	54.949	5.76	80	double
1981-Oct-01	12:14:57.23	73.304	54.827	5.97	100	bad data
1982-Oct-11	07:14:58.63	73.339	54.617	5.58	87	
1983-Aug-18	16:09:58.90	73.354	54.983	5.91	96	
1983-Sep-25	13:09:58.22	73.328	54.550	5.77	105	
1984-Aug-26	03:30:00.0	74.1	53.8	3.80	NAO	poor S/N
1984-Oct-25	06:29:58.12	73.355	54.999	5.82	104	
1987-Aug-02	02:00:00.20	73.326	54.611	5.82	99	
1988-May-07	22:49:58.34	73.314	54.562	5.58	92	
1988-Dec-04	05:19:53.30	73.366	55.010	5.89	94	
1990-Oct-24	14:57:58.45	73.331	54.766	5.60	0	

* Epicenter and magnitude from the report on Novaya Zemlya by Marshall et al. (1994).

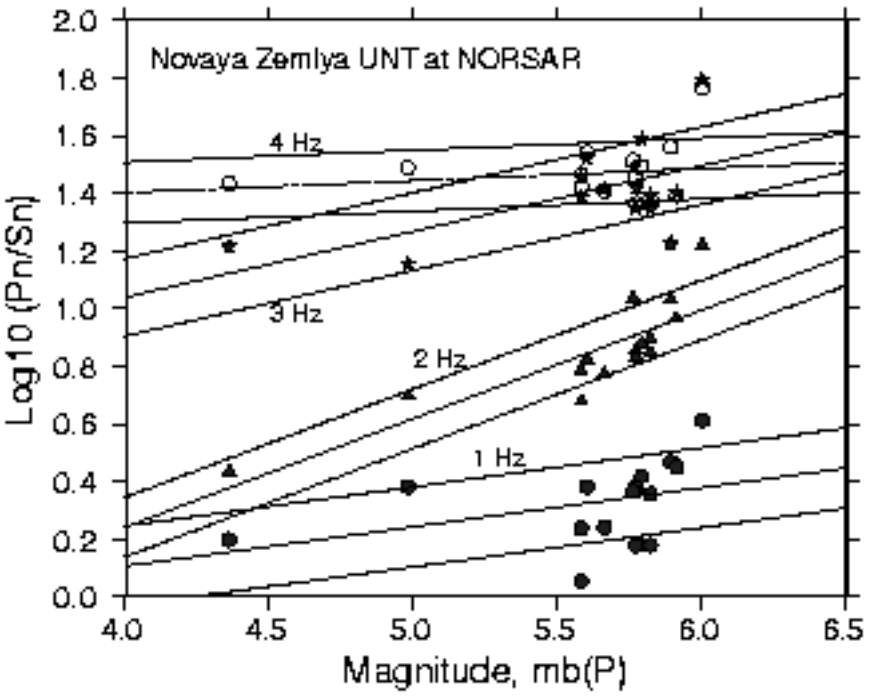


Fig. 2 Log_{10} (*Pn/Sn*) spectral ratios of each event are plotted against magnitudes for frequencies 1 to 4 Hz. The *Pn/Sn* ratios in the frequency bands 1–4 Hz indicates a weak magnitude dependence of *Pn/Sn* ratios. The slope (thick line) and the standard deviation (±2σ) of the regression (dotted lines) are plotted for reference.

Records from Lop Nor Underground Nuclear Tests at BRVK

We collected digital seismic records from 13 Chinese underground nuclear tests at Lop Nor recorded at BRVK (Borovoye) in northern Kazakstan. The data set include the first known underground nuclear test at Lop Nor on Sept. 22, 1969 and are the most records available at a single site at regional distances (see Table 2). Records from the UNT on Sept. 22, 1969 had only P waves, while records from three events had poor resolution. Hence, records from nine UNTs from Lop Nor at BRVK (Δ=1844–1895 km, AZ=319°) have been analyzed to examine if there is any indication of magnitude dependence of *P/S* spectral amplitude ratios among these events. The magnitude of these events ranges from $m_b(P)$ 4.9 to 6.2 and vertical component waveform data are shown in Figure 3. Records are plotted with group velocity in km/sec and magnitude is indicated at the beginning of each trace. BB indicate broadband signals from the new instrument (STS-2 sensors), while TSG-KS indicate signals recorded by STsR-TSG KS system (Kim & Ekström, 1996). The vertical records show clear *Sn* and *Lg* waves (Fig. 3), but note that *Sn* and *Lg* waves are less well excited by the smallest event on July 29, 1996 ($m_b(P)$=4.9), which is opposite to the case of records from Novaya Zemlya UNTs discussed in the previous section (Fig. 1).

The results of *Pn/Lg* spectral ratios are plotted against magnitude in Figure 4. The *Pn/Lg* ratios in the frequency bands 1-4 Hz indicates a very weak magnitude dependence of *P/S* ratios. The regression of Log_{10} (*Pn/Lg*) against magnitude yields a slope of 0.12 to 0.15 and a standard deviation of 0.07 to 0.10 in the frequency bands, 1–2 Hz and 3–4 Hz, respectively.

Table 2. Underground Nuclear Tests at Lop Nor Test Site Recorded at BRVK & MAK

Origin time		Lat	Long	Magnitude			
YearMoDa	(hh:mm:sec)	(°N)	(°E)	$m_b(P)$	M_S	Site	Remark
1969-09-22	16:14:58.8	41.386	88.296	5.2		H	P wave only
1976-10-17	05:00:03.7	41.649	88.161	4.9		H	poor resolution
1983-10-06	10:00:02.8	41.566	88.766	5.5	4.2	V	
1984-10-03	05:59:57.8	41.602	88.730	5.4		V	
1984-12-19	06:00:04.2	41.680	88.443	4.7	4.2		poor resolution
1987-06-05	04:59:58.3	41.584	88.737	6.2	4.7	V	poor resolution
1990-08-16	04:59:57.6	41.564	88.770	6.2	4.4	V	
1993-10-05	01:59:56.6	41.667	88.695	5.9	4.8		
1994-10-07	03:25:58.1	41.662	88.753	6.0			
1995-05-15	04:05:57.8	41.603	88.820	6.1	5.0		
1995-08-17	00:59:57.7	41.559	88.800	6.1			
1996-06-08	02:55:57.9	41.657	88.690	5.9	4.3		
1996-07-29	01:48:57.8	41.824	88.420	4.9			

Records from Lop Nor Underground Nuclear Tests Recorded at MAK

We analyzed digital seismic records from four latest Chinese underground nuclear tests at Lop Nor recorded at MAK (Makanchi) in northeastern Kazakstan. MAK is the nearest broadband seismographic station from Lop Nor outside of China. MAK is located about 755–796 km from the Lop Nor explosions with an azimuth of about 319° (Kim *et al*., 1996). The magnitude of these events ranges from $m_b(P)$ 4.9 to 6.1. The vertical component waveform data are shown in Figure 5. The event id, magnitude and zero-to-peak amplitude in micrometer/sec is indicated at the beginning of each trace. The vertical records from the four UNTs show considerable difference on *Lg* waves excitation (Fig. 5). *Lg* waves are well excited from the strongest UNT on May 15, 1996 ($m_b(P)$=6.1), while *Lg* waves are least excited by the smallest event on July 29, 1996 ($m_b(P)$=4.9). Although records from only four events are available, the excitation of shear wave energy from the Lop Nor UNTs are similar to the case of BRVK, but it is opposite to the case of records at NORSAR from Novaya Zemlya UNTs discussed in the previous section.

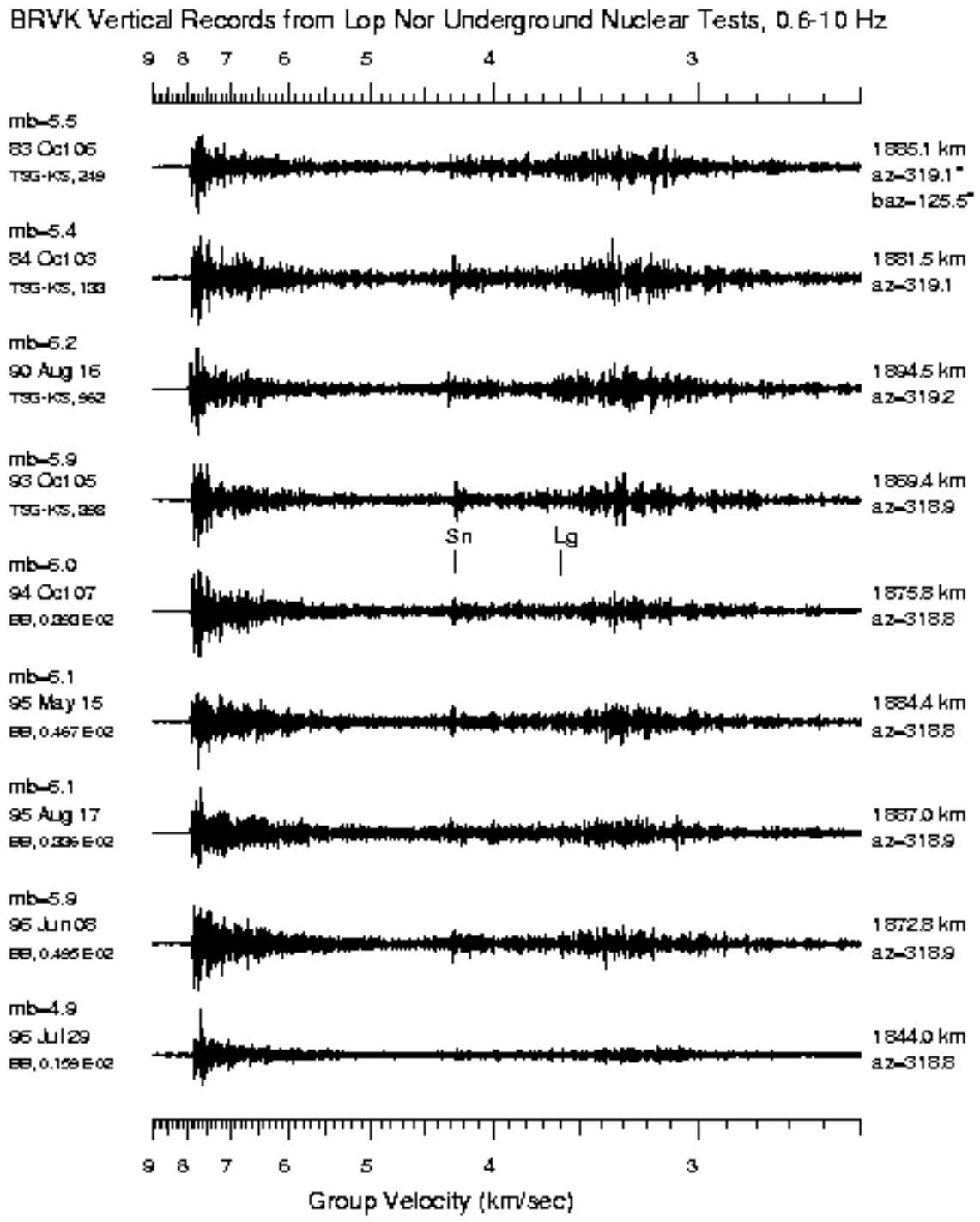


Fig. 3 Vertical component records at BRVK in northern Kazakstan from underground nuclear tests from Lop Nor. Records are plotted with group velocity in km/sec and magnitude, $m_b(P)$, of each event is indicated at the beginning of each trace. BB indicate broadband signals from the new instrument (STS-2 sensors), while TSG-KS indicate signals recorded by STsR-TSG KS system with SKM-3 sensor.

The Log_{10}(*Pn/Lg*) spectral ratios are plotted against magnitude in Figure 5. The *Pn/Lg* ratios in the frequency bands 1-7 Hz indicates no magnitude dependence of *P/S* ratios. Even the *P/S* ratios in the frequency bands 3-5 Hz indicates a negative slope against magnitude, which is due to the strong *P* wave spectral peak at this frequency band on signal from the event on July 29, 1996 (Figure 5). The results of this analysis suggest that the magnitude dependence of *P/S* ratios is not supported from this data set. Obviously, poor signal to noise ratios of *S* waves from weak UNTs at Novaya Zemlya recorded at NORSAR at far regional distances ($\Delta \approx 2280$ km) might caused "apparent" magnitude dependence of *P/S* ratios.

CONCLUSIONS AND RECOMMENDATIONS

Pn/Sn spectral amplitude ratios of vertical-component records from 15 UNTs at Novaya Zemlya test site recorded at NORSAR (Δ = 2271–2287 km) show "apparent" magnitude dependence at certain frequency. *Pn/Sn* ratios of these events in the frequency band 1 to 4 Hz suggests that the magnitude dependence reported by Ringdal et al. (1999) is pronounced at around 2 Hz. This is may be due to a relatively low *Pn/Sn* ratios at around 2 Hz from the two smallest UNTs may be caused by stronger *S* amplitudes relative to *P* wave at around 2 Hz from the single UNE carried out for the two UNTs. Further, at frequencies 1, 3 and 4 Hz, size dependency of *Pn/Sn* ratios appear to be weak.

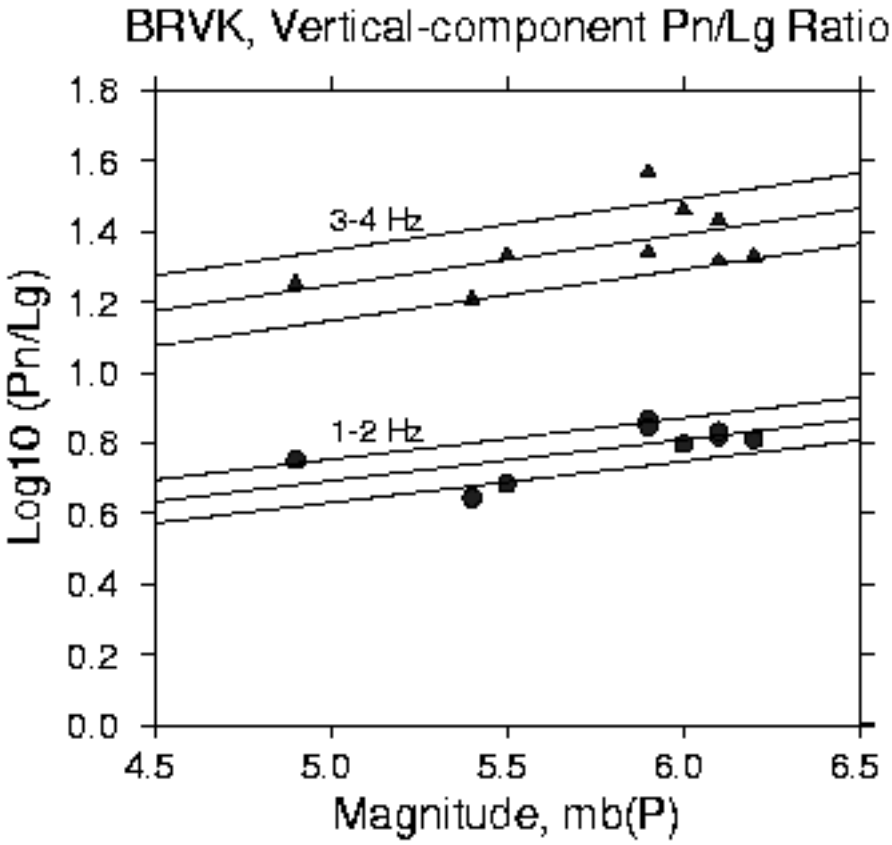


Fig. 4 Log_{10} (*Pn/Lg*) spectral ratios of each event are plotted against magnitudes for frequency band 1-2 Hz and 3-4 Hz. *Pn/Lg* ratios in the frequency bands 1-4 Hz indicate a very weak magnitude dependence of *Pn/Lg* ratios. The slope (thick line) and the standard deviation ($\pm 2\sigma$) of the regression (dotted lines) are plotted.

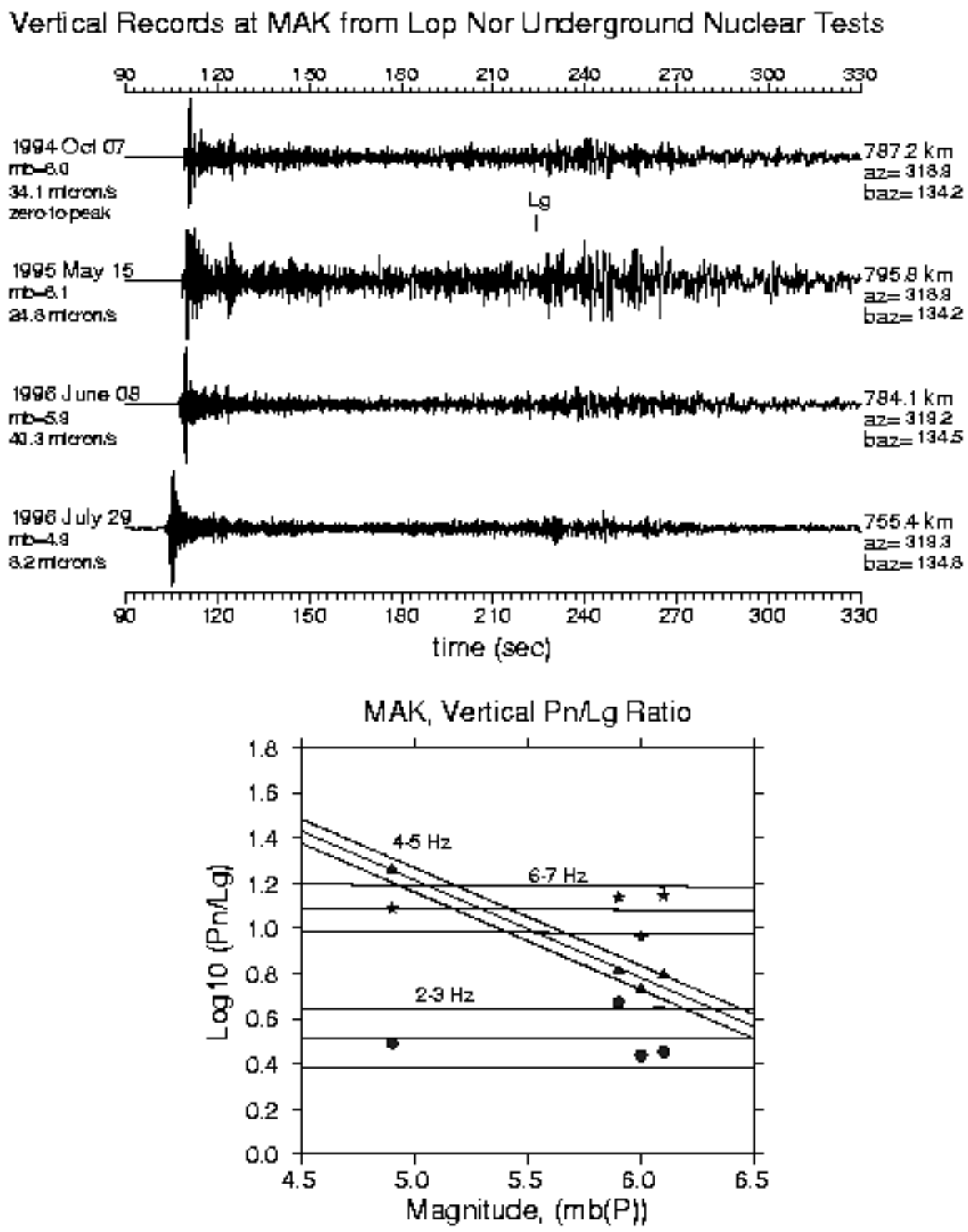


Fig. 5 (*upper panel*) Vertical records from four Chinese underground nuclear tests at Lop Nor recorded at MAK (Makanchi). Event id, magnitude and zero-to-peak amplitude in micrometer/sec is indicated at the beginning of each trace. Notice the considerable variation of *Lg* waves excitation from each event. (*lower panel*) $\mathrm{Log}_{10}(Pn/Lg)$ spectral ratios at three frequency bands are plotted against magnitude. Notice a negative slope at 4-5 Hz band, which is due to strong *P* wave spectral peak at this frequency on signal from the event on July 29, 1996.

Pn/Lg spectral amplitude ratios of vertical-component records from nine UNTs – magnitude ranges of $m_b(P)$ 4.9 to 6.2, at Lop Nor recorded at BRVK (Δ = 1844–1895 km, AZ = 319°) indicate that there is no clear magnitude dependence of *P/S* spectral amplitude ratios among these events (Fig. 4). We observed that *Sn* and *Lg* waves are less well excited by the smallest event on July 29, 1996 ($m_b(P)$=4.9), which is opposite to the case of records from Novaya Zemlya UNTs at NORSAR (Fig. 1).

Pn/Lg spectral amplitude ratios of vertical-component records from four Chinese underground nuclear tests at Lop Nor recorded at MAK (Makanchi) show no magnitude dependence of *P/S* ratios (Fig. 5). MAK is located about 755–796 km from the Lop Nor explosions with an azimuth of about 319°. The vertical records from the four UNTs show considerable difference on *Lg* waves excitation (Fig. 5). *Lg* waves are well excited from the strongest UNT on May 15, 1996 ($m_b(P)$=6.1), while *Lg* waves are least well excited by the smallest event on July 29, 1996 ($m_b(P)$=4.9). Although records from only four events are available for analysis, the excitation of shear wave energy from the Lop Nor UNTs at MAK are opposite to the case of records at NORSAR from Novaya Zemlya UNTs. The *Pn/Lg* ratios in the frequency bands 4–5 Hz even show a negative slope against magnitude, which is due to the strong *P* wave spectral peak at this frequency band on signal from the smallest event on July 29, 1996 (Figure 5).

The results of this study suggest that the magnitude dependence of *P/S* ratios is not supported by the regional data set we analyzed. Obviously, poor signal to noise ratios of *S* waves from weak UNTs at Novaya Zemlya recorded at NORSAR at far regional distances ($\Delta \approx 2280$ km) , as well as spectral peaks in the source spectra at a particular frequency for low-magnitude events might have caused "apparent" magnitude dependence of *P/S* ratios.

High-frequency, three-component *P/S* spectral amplitude ratios of regional signals have been successfully applied to identify earthquakes signals from explosions (e.g., Kim *et al*. 1997). We recommend to use three-component *P/S* ratios whenever possible. We also collected waveform data from UNTs at Semipalatinsk test site and from PNEs (peaceful nuclear explosions) carried out by former Soviet Union for additional studies to examine further the magnitude dependence of *P/S* ratios as well as to improve discrimination between different types of sources using high-frequency *P/S* spectral amplitude ratios at regional distances. In particular we will address the problems posed by small, low-magnitude events for CTBT monitoring.

REFERENCES

Kim, W. Y., V. Aharonian, A. L. Lerner-Lam and P. G. Richards, Discrimination of earthquakes and explosions in southern Russia using regional high-frequency three-component data from the IRIS/JSP Caucasus Network, *Bulletin of the Seismological Society of America*, **87**, 569-588, 1997.

Kim, W. Y., V. Kazakov, A. Vanchugov and D. Simpson, Broadband and array observations at low noise sites in Kazakhstan: Opportunities for seismic monitoring of a Comprehensive Test Ban Treaty, in E. Husebye and A. M. Dainty (eds.), *Monitoring a Comprehensive Test Ban Treaty*, Kluwer Academic Publishers, 467–482, 1995.

Kim, W. Y. and G. Ekström, Instrument responses of digital seismographs at Borovoye, Kazakhstan by inversion of transient calibration pulses, *Bulletin of the Seismological Society of America*, **86**, 191–203, 1996.

Lilwall, R.C. and P. D. Marshall, Body wave magnitude and locations of Soviet underground explosions at the Novaya Zemlya test site, Atomic Weapons Research Establishment Report No. O17/86, HMSO, London, 1986.

Marshall, P.D., D. Porter, J.B. Young, and P.A. Peachell, Analysis of short-period seismograms from explosions at the Novaya Zemlya test site in Russia, Atomic Weapons Research Establishment Report No. O2/94, HMSO, London, 1994.

Mikhailov, V.N., *USSR Nuclear Tests: general characteristics, goals and organization of nuclear tests in the USSR*, edited by Mikhailov in Russian, Moscow, IZDAT, 1997.

Richards, Paul G. and Won-Young Kim, Testing the nuclear test-ban treaty, *Nature*, Vol. **389**, pp. 781–782, 23 October 1997.

Ringdal, F., Study of low-magnitude seismic events near the Novaya Zemlya nuclear test site, *Bull. Seism. Soc. Am.*, **87**, 1563-1575, 1997.

Ringdal, F., T. Kvørna, J. Schweitzer, E. Kremenetskaya and V. Asming, Research in Regional Seismic Monitorng, Proc. 21st Seismic Research Symposium: Technologies for Monitoring the Comprehensive Nuclear-Test-Ban Treaty, 21-24 Sept. 1999, Las Vegas, Nevada, 607-615, 1999.

PATH CORRECTIONS FOR REGIONAL PHASE DISCRIMINANTS

Thorne Lay, Guangwei Fan, and Jiajun Zhang

Earth Sciences Department and Institute of Tectonics
University of California, Santa Cruz

Sponsored by The Defense Threat Reduction Agency
Arms Control Technology Division
Nuclear Treaties Branch

Contract No. DTRA 01-98-C-0161-P00001

ABSTRACT

In order to utilize regional seismic phases for reliable source identification, it is essential to account for wave propagation effects that may obscure the subtle differences in source radiation for distinct source types. Recent work has established three main approaches to the problem of characterizing and correcting regional phases for propagation effects: empirical methods based on parametric dependence on path properties such as pathlength or crustal waveguide parameters, empirical interpolation methods such as cap-averaging and Kriging for station-dependent source region correction surfaces, and waveform modeling methods based on complete waveform synthesis for one-, two-, or three-dimensional crustal models. Empirically based methods remain the most viable general approach, as model based methods are still greatly limited by our wave propagation techniques and by lack of independent constraints on three-dimensional waveguide structure. Kriging and waveguide parameter regressions for frequency dependent regional phase amplitude ratio measurements for International Seismic Monitoring Stations, NIL and ZAL were conducted in the first year of this study. The data have a large amount of scatter, much of which is attributed to wave propagation effects; however, propagation corrections are limited by our understanding of source induced scatter and by effects of partial or total blockage of regional phases. We have addressed the issue of source induced scatter by analysis of a well-controlled data set of regional recordings of shallow earthquakes with reasonably well-determined focal mechanisms. By using events in very close proximity with varying depth and/or focal mechanisms recorded on common paths, we have isolated source-related contributions to variance in regional seismic discriminant measurements involving P/S-type ratios (e.g., Pn/Lg, Pg/Lg, Pn/Sg, and Pg/Sg) for earthquakes in southern California and southern Nevada. Broadband waveforms for earthquakes near the Nevada Test Site (NTS) and in southern California recorded at stations of the Livermore NTS Network (LNN), the Caltech TERRAscope Network, and the Berkeley Digital Seismic Network (BDSN) are used to obtain the seismic discriminant measurements. Pn/Lg and Pg/Lg spectral amplitude ratios for various frequency bands between 0.5 and 10 Hz from vertical velocity waveforms are computed for 17 tightly located clusters of earthquakes. For each cluster, we examine the correlations between observed Pn/Lg and Pg/Lg ratios and estimated source depths or previously determined source mechanisms. Focal mechanism predictions do not match the observations well, likely due to refraction and directivity effects that overwhelm the point-source radiation pattern. However, the data do show significant scatter that is clearly not attributable to varying path structure. Source depth effects show weak trends, with events shallower than 3 kilometers having enhanced Pg/Lg and Pn/Lg ratios that contribute to the overall scatter. Depth dependence is of great concern, as it undermines the empirical approaches to path correction. Variance estimates for logarithmic amplitude ratios normalized by mean amplitude ratios vary from 0.01 to 0.05 for different phase pairs, and there is strong dependence on propagation distance. These variance parameters appear to be suitable for use in spatial interpolations of observed P/S type ratios for a specific unidentified event path. With respect to blockage effects, we have undertaken a specific study of blockage associated with Lg phases traversing the northern margin of Tibet. Using observations at WMQ, we explore the spatial variation of Lg transmission across the Plateau, manifested in large corner frequency shifts and disappearance of the Lg signal. The corner frequency shift shows systematic evolution with transit length in the Plateau, indicating that there is progressive, not discrete, blockage of the wavefield, and this is likely due to the anomalous crustal properties of Northern Tibet. Correction using

Kriging or parametric regression does not appear to be sufficiently accurate for safe incorporation of the discriminants into event identification procedures.

Key Words: seismic discriminants, regional seismic phases, amplitude corrections, regional wave propagation

OBJECTIVE

One of the major challenges confronting seismic monitoring of the Comprehensive Nuclear-Test-Ban Treaty (CTBT) is discriminating the seismic signals of small underground explosions from those produced by other sources. There is tremendous regional variability in short-period signals from all sources, and the characteristics that define the source type may be subtle, easily overwhelmed by propagation complexities in the heterogeneous crust. Reliable regional seismic discriminants must have sufficiently small scatter in the background earthquake population that rare single-shot explosion events will produce diagnostic outlying measurements. That component of the scatter caused by propagation effects can be reduced by path corrections of varying sophistication. We are seeking to develop and test various approaches to reduce the scatter in regional discriminant populations, using numerous observations in Eurasia (China, Russia, and Southeast Asia, in particular) and the Middle East collected under this and a previous PL/DOE-funded effort. Multi-variate regressions of various path attributes (to assess which parametric path characterizations are significant), spatial representations of the path influences such as kriging (to enable interpolation to a unique path for a suspect event), and tests of significance of the corrections (ability to tighten up scatter in discriminant measures to a useful extent) are all being considered in our effort to develop a unified strategy for discriminant calibration that will transport into the operational regime and lead to high confidence discrimination. Basic understanding of the causes and statistical nature of source-related scatter in discriminant measurements is also being pursued, for the purpose of establishing intrinsic thresholds for propagation corrections.

RESEARCH ACCOMPLISHED

The second year of our research project has involved work on two critical problems that have emerged in the course of seeking a robust propagation correction procedure. These are the problems of source-mechanism and source-depth related scatter and phase blockage. We have conducted two separate investigations of these issues, as their resolution is required for developing an integrated approach to discriminant processing.

Seismic recordings at regional distances tend to be very complex due to the superposition of energy traveling on multiple paths within the crustal waveguide, compounded by source radiation pattern and source depths effects. The waveform complexities result in substantial scatter in various regional discriminant measurements that are designed to measure attributes diagnostic of the source type. This becomes a particular problem for isolated stations in tectonically complex areas with great variation in path and earthquake properties. For CTBT monitoring, identification of rare explosion signals becomes a statistical problem of recognizing measurements with explosion attributes as outliers in a population of corresponding measurements for earthquake signals. Reduction of the scatter in the reference earthquake population is essential for high confidence outlier detection (e.g., Fisk, 1994). Scatter in regional discriminant measurements associated with path propagation effects is typically suppressed by empirical means such as distance corrections, attenuation corrections, spatial averaging of event populations by methods such as cap-averaging and kriging (e.g., Schultz et al., 1998; Phillips, 1998; Hartse et al., 1998; Rodgers et al., 1999) or regression on waveguide parameters such as crustal thickness and elevation (e.g., Fan and Lay, 1998a). When such methods are applied, there is always a question of how much of the scatter can really be attributed to propagation effects, versus source effects? Corrections that reduce all of the variance would likely map source induced scatter into erroneous path corrections, potentially giving poor performance of the discriminant for the next unknown event in the region. A firm statistical basis for separating correctable path contributions from intrinsically non-correctable (other than by simple methods such as azimuthal averaging, which is seldom viable in the CTBT monitoring context) source contributions is needed. There are many examples in the literature of individual regional distance waveform anomalies attributed to source depth or focal mechanism effects, typically for nearby events recorded on the same path, but as yet there has not been a thorough statistical analysis of the variance contributed by source effects that can guide efforts in path correction.

In our efforts in quantifying source radiation pattern and source depth effects, the following strategy evolved for isolating the near source contributions and seeking to quantify them. We used three sets of events, each comprises one or more clusters of earthquakes with accurate locations within a few kilometers of one another. For the first and second sets of events, we seek clusters of small earthquakes with known focal mechanisms. The events in the first set are aftershocks of the 29 June 1992 Little Skull Mountain earthquake (Mw=5.7) near NTS and are located in a single cluster. The events in the second and third sets are earthquakes located in Southern California, which comprise three and seventeen clusters, respectively. The focal mechanisms

and depths for all the events in the second set were determined by Thio and Kanamori (1995). The third set of events is the extended events set, which includes the second set of events as well as events for which focal mechanisms are not available and the magnitudes are small. The hypocentral parameters of the events in the third set are from the Southern California Earthquake Center (SCEC) catalog. Hereinafter we will refer to these event sets as the LSM-Events set, TK-Events set, and SCEC-Events set.

Because events in a given cluster are located within a few km from the center of the cluster, regional recordings several hundred kilometers away should share common propagation structure. Propagation effects can still vary in a common structure as a result of source depth effects intermingled with source radiation effects. Multipathing effects are expected to be complex and frequency dependent and cause focal-mechanism dependent wave propagation with partitioning between various paths for a given type of wave depending on source radiation pattern.

We began with analysis of the first set of events, for which radiation pattern variations among various events can be estimated using the focal mechanisms determined previously. The focal mechanisms and source depths can be used to predict synthetic P/S amplitude ratios for specific discriminants to assess how deterministic the scatter observed in the discriminants is. For events with similar source depths and focal mechanisms, the scatter observed in regional discriminant measures for these common paths can be used to define the statistical variance in earthquake measurements that we expect to have to deal with, as a function of distance and frequency. We can correlate the scatter with source depth and radiation pattern variations to further quantify the contributions from specific source properties.

The strategy is illustrated in Figure 1 for aftershocks of the Little Skull Mountain earthquake. Focal mechanisms and relative source depths are available for these events from Harmsen (1994) and Meremonte et al. (1995), and discriminant measurements are from Walter et al. (1995). We compared data with focal mechanism predictions for the Little Skull Mountain events, finding little correlation between observed and predicted P/S ratios for most stations, but some stations do indicate systematic variations with source depth. Figure 1 shows that there is moderate variability in mechanism type, which is primarily normal faulting with the exception of two strike slip events. For station MNV Pg/Lg measurements range over a factor of 4, while Pn/Lg measurements vary over a factor of 2.5; the scatter is larger for both phases for station KNB. The magnitude of the scatter does not vary much with frequency, and correlations between frequency bands are relatively high for Pn/Lg at station KNB, but low for other ratios at KNB and MNV. Predicted P/S ratios obtained by integration of the focal mechanisms over appropriate take-off angles and azimuths show weak correlations with the observed amplitude variations for MNV (Figure 1) as well as KNB (not shown here). For MNV the variation of predicted ratios for Pg/Lg is comparable to that for observed ratios, while for Pn/Lg the variation of predicted ratios is a factor of two larger than that for measurements. Little correlation with depth was found for the Pg/Lg and Pn/Lg measurements as well.

Given that the Little Skull Mountain events have substantial uncertainty in focal mechanism, we sought to find other clusters of earthquakes with known mechanisms recorded at regional distances by broadband stations. Southern California provides numerous earthquake clusters for which the focal mechanisms have been determined by broadband waveform inversions (e.g., Thio and Kanamori, 1995). Figure 2 shows locations of a total of 17 clusters of Southern California earthquakes and broadband stations used in this study. The events in the clusters occurred in 1992-1998 and were located at regional distances from the stations (100-1100 km). Some of the events have known focal mechanisms and belong to both the TK-Events and SCEC-Events sets, while others do not have known focal mechanisms and are included only in the SCEC-Events set.The clusters comprise 350 earthquakes with magnitudes ranging between 3.5 and 7.0 (there are 210, 93, 38, 15, and 3 events with magnitudes less than 4.0, 4.0-4.5, 4.5-5.0, 5.0-5.5, 5.5 and larger, respectively). Each cluster includes 40-70 earthquakes that were located within 10 km from the center of the cluster. Some of the clusters are closely located and named with similar identifications; events in A-clusters are associated with the earthquake sequence of Northridge of 17 January 1994 (Mw=6.7); B-clusters for the Joshua Tree sequence of 23 April 1992 (Mw=6.1) and Landers sequence of 28 June 1992 (Mw=7.3); C-clusters for the Big Bear sequence of 28 June, 1992 (Mw=6.2).

One of the main difficulties encountered in this analysis involves the windowing of regional phases at these relatively close distances of less than 200 km, particularly when source depths vary from 5 to 15 km. The problem is that as the source depth increases, the depth phases may move out of one group velocity window (say, for Pn) and into another (say, for Pg), thus causing contamination of the energy measures computed for the separate phases. This is difficult to account for in the prediction of amplitudes by focal mechanism integration.

In order to 'tune' the integrations to better reflect the actual contributions from phases for different source depths, we constructed regional distance synthetics for various source/receiver geometries using the range in source depths and focal mechanisms of the observations. Then we found ranges of radiation pattern integrations that provide reasonably good predictions of the observed relative amplitudes in the Pn, Pg, and Lg windows. This guided us to incorporate sPn contributions to the Pn window for shallow events and Sg contributions to the Pg window (S waves that come out from the source, convert to P, and then arrive in the Pg window). We found quite good predictability at distances of 220 to 400 km, but shorter distance windows are very problematic due to the short time windows and overlapping of depth phases.

Using our refined radiation pattern integration criteria, we further analyzed three clusters of events (clusters A1, B1, and C1); each cluster comprises events located within a 10 km radius, recorded at several TERRAscope and BDSN stations, and had diverse focal mechanisms. The correlations with focal mechanism predictions and source depth are generally found to be weak, certainly much lower than for synthetic predictions. Yet the scatter in the observations is very substantial, and it presumably does reflect either a source effect or some remarkable sensitivity to the precise travel path taken.

We further analyze characteristics of Pg/Lg and Pn/Lg measurements for events in the SCEC-set, which comprises all the events in the 17 earthquake clusters (Figures 2). This is the extended events set from the TK-set, with focal mechanisms for most events here are not known. The corresponding data are broadband waveforms recorded at eleven BDSN and seven TERRAscope stations. For each cluster we calculated Pn/Lg and Pg/Lg spectral amplitude ratios for various frequency bands between 0.5 and 10 Hz (the frequency passbands span 0.5-1, 1-2, 2-4, 4-6, 6-8, and 8-10 Hz) using vertical velocity waveforms. Then, to characterize the scatter of the observed Pn/Lg and Pg/Lg measurements for the cluster we computed the variance, mean, minimum, and maximum of the amplitude ratios for all the events in the cluster.

With the exception of Pn/Lg measurements for cluster A1 events, all the Pn/Lg and Pg/Lg measurements span in the range from -0.5 and 0.5 in the 10 base logarithm. A weak correlation between observed P/S ratios with source depth suggests some relationship between source depth and Pg/Lg and Pn/Lg measurements. The weak correlation indicates that Pg/Lg and Pn/Lg measurements are more sensitive to source radiation pattern or the precise location of each event in the cluster. Figure 3 shows the distribution parameters of Pg/Lg, for the 2-4 Hz passband for all the station-cluster pairs used in this study. Figures 3 shows that there are considerable differences between scatter of the distribution parameters; the scatter for epicentral distances of 100-300 km is much larger than that for longer distances; the distribution parameters tend to become small in absolute value at large distances. This distance dependence may be important for Kriging applications.

In this analysis for various station-cluster pairs we found little correlation between P/Lg measurements and source depth for Little Skull Mountain events and TK-set events. This presumably reflects some remarkable sensitivity to the effect of source radiation pattern (including focal-mechanism dependent wave propagation) and the precise location of each event in a cluster (including location dependent wave excitation and propagation). Because effects of source radiation pattern and wave propagation on Pn/Lg and Pg/Lg ratios vary among stations located in different azimuths and distances, the effects are expected to be reduced by stacking (averaging) the ratios for various stations. Therefore the stacking procedure allows us to examine the effects of source depth on observed Pn/Lg and Pg/Lg ratios for events in various clusters. In calculation of the station averaged ratio it is desirable to use stations that are azimuthally well distributed. However, most stations used here are distributed to the north or northwest of the event cluster, and there are usually a few stations with good SNR for small events with magnitudes less than 4. Therefore, we expect that much of the effects of source radiation pattern and wave propagation remain in the station averaged ratios calculated using our data set, in particular, for the Pn/Lg ratio; the effects are large for the depth range where only small events are included in our events set.

We examined the depth distribution of the station averaged Pg/Lg and Pn/Lg measurements for events in each cluster. The station averaged Pg/Lg or Pn/Lg ratio for each event was plotted in logarithm against the depth of the event, normalized with the average value for all the events in the cluster. For A-cluster events, which comprise the largest events set used in this study, negative logarithmic Pg/Lg ratios for events near the free surface indicate large Lg excitations relative to Pg in comparison to events with other depths; the logarithmic Pg/Lg and Pn/Lg are positive and have relative maxima at depths less than 3 km and minima at depths between 3 and 5 km; below 5 km the overall trend of Pg/Lg and Pn/Lg is increasing with depth. Large Lg excitations for shallow events are also found for C- and D-cluster events, but not for B-cluster events. Since the events in A-, C-, and D-clusters occurred in basin-like structures in contrast with B-cluster events, the large Lg excitations may be caused by surface geology and/or topography associated with the basin structures for clusters A, C, and D. An overall trend of increasing Pg/Lg and Pn/Lg for depths below 5 km is also found for events in clusters B, D, and

F, which suggests that deep events excite stronger Pg and Pn waves and weaker Lg waves than shallow events. The Pg/Lg and Pn/Lg minima at depths between 3 and 5 km are also found for B-cluster events, which may correspond to large Lg excitations in comparison with events at other depths. The minima may indicate discontinuities of material properties, a situation similar to the free surface, which are favorable for Lg excitations.

One of the main observations of this analysis is that there is little correlation between observed and predicted P/S ratios for most stations for the Little Skull Mountain events and Southern California events, for which focal mechanisms were determined previously. This is caused primarily by our inability to predicted P/S ratios for realistic structures between source and station, although we found quite good correlation between computed P/S ratios using waveforms computed from the reflectivity methods and point-source radiation pattern integrations. Another source of the weak correlation is the limitation of point-source radiation pattern integrations. Although this analysis has not been encouraging with respect to isolating deterministic focal mechanism contributions to the scatter in discriminant measures for Little Skull Mountain and California earthquakes, further examination of the source mechanisms effects on regional signals in diverse regions of the world is necessary. There may be possible explanations for the weak correlation between observed and predicted focal-mechanism-dependent scatters, with the limitation of point-source radiation pattern integrations being a likely source of inaccuracy. Even small events can have directivity effects and complex weighting of the specific arrivals at a given range that are difficult to account for. It is also possible that the source mechanisms for many of the small events are very poor, and this likely to be true for the source depths (even in a densely-instrumented region such as California).

The second part of our effort this year has been to improve our understanding of continental Lg blockage. Lg is sensitive to the laterally heterogeneous velocity structure and changes in crustal discontinuities and crustal thickness. Usually, Lg can be described as a superposition of many higher modes or trapped postcritical S reverberations. Blockage of Lg was first observed for travel paths involving segments of oceanic crust (Press and Ewing, 1952). Lg blockage also was noted in continental areas with large changes in crustal thickness, such as the mountain belts in central Asia (Ruzaikin et al., 1977). It is believed that scattering of Lg energy from fractures within the crust may be a major cause of strong Lg attenuation in tectonically active regions. It is also possible that the lack of continuous waveguide in areas with significant variations of crustal thickness may result in strong attenuation of Lg.

For most parts of the Asian continent, Lg is observed, however, Lg blockage is reported for paths crossing the Tibetan Plateau (Ni and Barazangi, 1983; McNamara et al., 1996; Rapine et al., 1997). Qualitative analysis of Lg propagation efficiency relative to P-wave coda reveals that Lg signals are attenuated within central Tibet and along its southern boundary (Ni and Barazangi, 1983; Rapine et al., 1997). Using data recorded at 11 broadband stations around Tibet, it is found that Lg is generated inside the Plateau, and can propagate to distances of at least 600 km; however, for the paths crossing the Himalayan and Kunlun mountains Lg is either blocked or strongly attenuated (McNamara et al., 1996).

In this study, we used regional waveforms recorded at a broadband station WMQ to investigate energy partitioning of Lg, as defined by a group velocity of 3.6 to 3.0 km sec^{-1}. We analyze 81 earthquakes with magnitudes of 4.4 □ m_b □ 6.4, that occurred between 1987 and 1998 in the Tibetan Plateau and around its margins (Figure 4). The recorded seismograms show great variability in broadband waveform complexity on different paths. For events prior to the middle of 1997, we use source parameters given by the International Seismological Centre (ISC) bulletin, for later events we use source parameters provided by the USGS Preliminary Determination of Epicenters (PDE) catalog. Only events with focal depths less than 45 km are condsidered in this study. All events used have signal-to-noise ratios greater than 2 based on the measurements for Pn signals and pre-Pn noise. Because all events are recorded at a single station, the site effects and instrument response are not concerns in evaluation of attenuation of Lg energy.

To quantifying Lg attenuation and blockage effects, we first visually examine all vertical seismograms to see how Lg is manifested. We measure the corner frequency (f_c) of the amplitude spectra for each event, and use corner frequency as a parameter to demonstrate the degree of relative attenuation of Lg energy. For the events located near the northern margin of the Tibetan Plateau, Lg has large amplitude and a corner frequency of 1 – 2 Hz. The Lg energy decays slowly at frequencies higher than 2 Hz and more rapidly after 5 Hz. Figure 5a shows velocity spectrum for an event that is located close to the northern margin of the plateau. The signal-to-noise ratio is high at frequencies up to 10 Hz. A comparison with amplitude spectra for events outside the Plateau at similar distances and approximately equal seismic moment indicates that Lg is very normal for events near the northern margin. This is consistent with the observation that Lg from events northeast of the Plateau can be

recorded at seismic stations near the northern edge of the Plateau for about 200 km (McNamara et al., 1996). It is also supported by a numerical simulation of Lg wave propagation, which shows that a Moho step does not cause Lg blockage (Gibson and Campillo, 1994).

In contrast, for the events that are located near the Himalayan mountains, Lg wave is very weak or entirely absent. Corresponding corner frequencies for amplitude spectra are observed to be lower, usually ranging between 0.2 ~ 0.4 Hz. Since observable Lg is generated by the source within the Plateau (McNamara et al., 1996), the lack of Lg energy and low corner frequencies indicates a strong attenuation of Lg energy at frequencies between 0.3 ~ 0.5 and up to 1 Hz along the paths crossing through the Plateau (see Figure 5b). In general, a good signal-to-noise ratio is expected at frequencies below 3 ~ 5 Hz. On a profile crossing the Tibetan Plateau, the corner frequency of the amplitude spectra decreases systematically with distance. Figure 6a shows the corner frequency of the amplitude spectra as a function of the path length. There is a shift in linear trend as the back azimuth changes. We performed linear regression analysis to investigate which physical factor is the most important contributor to Lg extinction. Although low Q beneath the plateau is certainly a very important candidate (Ruzaikin et al., 1977), we only consider topographic features and waveguide structure in our analysis due to the limited availability of information. Regression analysis shows that corner frequency of Lg amplitude spectra has a strong negative correlation with the topography measures of the Tibetan Plateau (as high as 0.92 ~ 0.94), such as mean elevation along the paths (see Figure 6b) or the travel distance over the plateau above a certain elevation. At the same time, there is little evidence for a relationship between the corner frequency and the event magnitude or type of the faulting. The absence of Lg energy can be attributed to the effects of partial path within the Plateau. While this is a progressive path effect, the effect is so overwhelming that correction is difficult and inaccurate.

CONCLUSIONS AND RECOMMENDATIONS

We have explored two fundamental problems that challenge efforts to develop an integrated strategy to discriminant processing. We have empirically characterized the frequency dependence and distance dependence of variance in regional discriminant measures for events in California. The intrinsic scatter is substantial, and represents the combined effects of focal mechanism and source depth. These results can be applied for improved kriging procedures and for better understanding the limitations of path correction procedures. Central Asia, an area of great interest for CTBT monitoring, has long been recognized as a region with regional phase blockage, for either Sn or Lg arrivals. We have systematically explored the phenomenon of blockage associated with the Tibet Plateau, for the purpose of assessing whether blockage is progressive, discrete or correctable.

REFERENCES

Fan, G. and T. Lay, Statistical analysis of irregular wave-guide influences on regional seismic discriminants in China, *Bull. Seism. Soc. Am., 88*, 74-88, 1998a.

Fisk, M. D., Identification and event characterization - getting down to the outliers, in *Proceedings of the ARPA CTBT monitoring technologies conference*, 26-29 September 1994, San Diego, CA, 1994.

Gibson, R.L., and M. Campillo, Numerical simulation of high- and low-frequency Lg-wave propagation, *Geophys. J. Int., 118*, 47-56, 1994.

Harmsen, S. C., The Little Skull Mountain, Nevada, earthquake of 29 June 1992: Aftershock focal mechanisms and tectonic stress field implications, *Bull. Seism. Soc. Am., 84*, 1484-1505, 1994.

Hartse, H. E, R. A. Flores, and P. A. Johnson, Correcting regional seismic discriminants for path effects in western China, *Bull. Seism. Soc. Am., 88*, 596-608, 1998.

McNamara, D.E., T.J. Owens, and W.R. Walter, Propagation characteristics of L_g across the Tibetan plateau, *Bull. Seism. Soc. Am., 86*, 457-469, 1996.

Meremonte, M., J. Gomberg, and E. Cranswick, Constraints on the 29 June 1992 Little Skull mountain, Nevada, earthquake sequence provided by robust hypocenter estimates, *Bull. Seism. Soc. Am., 85*, 1039-1049, 1995.

Ni, J., and M. Barazangi, High-frequency seismic wave propagation beneath the Indian Shield, Himalayan Arc, Tibetan Plateau and surrounding regions: high uppermost mantle velocities and efficient S_n propagation beneath Tibet, *Geophys. J. R. astr. Soc., 72*, 665-689, 1983.

Phillips, W. S, Empirical path corrections for regional-phase amplitudes, *Bull. Seism. Soc. Am., 89*, 384-393, 1999.

Press, F., and M. Ewing, Two slow surface waves across North America, *Bull. Seism. Soc. Am., 42*, 219-228, 1952.

Rapine, R.R., J.F. Ni, and T.M. Hearn, Regional wave propagation in China and its surrounding regions, *Bull. Seism. Soc. Am., 87*, 1622-1636, 1997.

Rodgers, A. J, W. R. Walter, C. A. Schultz, S. C. Myers, and others, A comparison of methodologies for representing path effects on regional P/S discriminants, *Bull. Seism. Soc. Am., 89*, 394-408, 1999.

Ruzaikin, A.I., V. Nersesov,, and P. Molnar, Propagation of Lg and lateral variations in crustal structure in Asia, *J. Geophys. Res*., *82*, 307-316, 1977.

Schultz, C. A., S. C. Myers, J. Hipp, and C. J. Young, Nonstationary Bayesian kriging: A predictive technique to generate spatial corrections for seismic detection, location, and identification, *Bull. Seism. Soc. Am., 88*, 1275-1288, 1998.

Thio, H.-K., and H. Kanamori, Moment tensor inversions for local earthquakes using surface waves recorded at TERRAscope, *Bull. Seism. Soc. Am., 85*, 1021-1038, 1995.

Walter, W., K. Mayeda, and H. Patton, Phase and spectral ratio discrimination between NTS earthquakes and explosions, Part 1, Empirical observations, *Bull. Seism. Soc. Am., 85*, 1050-1067, 1995.

A MINE EXPLOSION SOURCE PHENOMENOLOGY EXPERIMENT

James F. Lewkowicz, Jessie L. Bonner and Alfredo Urzua, Weston Geophysical

Sponsored by the U.S. Department of Energy
Office of Nonproliferation Research and Engineering
Office of Defense Nuclear Nonproliferation
National Nuclear Security Administration

Contract No. DE-AC04-1999AL66423

ABTRACT

The seismic and acoustic discrimination of large surface and underground mine blasts, including mine collapses and rock bursts, continues to be a difficult scientific problem (Report of a Working Group from Government, Industry and National Laboratories, 1999). Under a Comprehensive Nuclear-Test-Ban Treaty monitoring regime the discrimination of signals from such large mine blasts may be ambiguous. The difficulty is due, in part, to the lack of complete understanding of the source models for the seismic and acoustic signals, the fact that mines operate in both soft and hard rock environments, use different blasting techniques and signals from such activities will most likely be recorded regionally, which are difficult to interpret. Alternatively, if controlled mine blast experiments could be performed, in close collaboration with the mining industry, significant knowledge could be gleaned to reduce the chance of false alarms from such mining activities and, hopefully, provide the mining industry with useful information to conduct more cost-effective blasting operations. In addition, these experiments could also be used to provide important empirical calibration information for the International Monitoring System (IMS). It is important to conduct such experiments in the full spectrum of mining locales and geographical regions, including both hard and soft rock environments. One of the goals of this effort is to engage the mining industry in a variety of collaborative experimental field efforts in which both the seismic monitoring community and mining industry benefit from the resulting exchange of ideas and information.

In concert with the above, a controlled mining experiment was suggested by Walter *et al.*, 1999, in which a surface delayed-fired production explosion and a buried single explosion (zero delay) are collocated and detonated simultaneously. This experiment would provide valuable insight into answering important scientific issues related to source phenomenology, depth of burial effects, and regional effects on seismic wave propagation and useful IMS calibration information.

As part of its effort, Weston Geophysical has arranged, in principle, the collaboration of a major mining company, to conduct the experiment described by Walter *et al.*, at one of its hard rock mines in South America. As part of the collaboration, the mining company has agreed to pay all expenses related to detonating the controlled blasts. The mine under consideration routinely conducts both surface (open pit) and below ground (block caving) operations. The company has made available extensive information regarding its mining operations, detailed geological information and will provide major logistical support to participants at its mine during the experiment. In addition, it will allow participants access into the mine for the purposes of recording both seismic, acoustic and video near - source data. Also, the mine is located in a geographic area that is extremely interesting from a scientific perspective in terms of tectonics and earthquake activity. Consequently, numerous scientific experiments will be taking place at regional distances from the mine, supported by other funding agencies, which can be leveraged by all parties to enhance the results from individual efforts.

OBJECTIVES

The objective is to identify and develop cooperative targets of opportunity with the mining industry that will result in field experiments to seismically calibrate the International Monitoring System (IMS), reduce the ambiguity of identifying seismic signals from mines and, at the same time, be of use to the mining industry to improve its blasting techniques. These cooperative experiments will involve monitoring mine blasts of routine production explosions, e.g., delay or ripple fired, and in certain instances conducting and monitoring mine explosions designed to answer specific technical questions. It is also stressed that an inherent goal of this effort is to develop a symbiotic

relationship with the mining industry to provide mining engineers information that will be useful in their design and execution of production blasts and for the seismic monitoring research community to improve discrimination capability.

The Preparatory Commission (PrepCom) of the Comprehensive Nuclear-Test Ban Treaty Organization, under the auspices of Working Group B (CTBTO/WGB), has identified the need for highly focused research to provide regionalized travel times to improve seismic event location methods to be used in the International Data Centre (PrepCom, 1999). Regional seismic calibration will be useful to help reduce event location uncertainty and improve the location accuracy. WGB has recommended the enhancement of existing ground truth databases through the collection of pertinent information such as may be provided by chemical mining explosions and well-recorded earthquakes. It also suggested that mining explosions that may be recorded on more than one IMS station should be given priority and cooperation with the mining industry is encouraged in order to obtain detailed information on the mining explosion characteristics such as its explosive size, spatial and temporal distribution. There are numerous other reasons to study mining explosions in the context of treaty monitoring. For example, the identification of large chemical mining explosions may be problematical under certain conditions as no validated seismic discriminants exist for mine blasts. Also, a field experiment has been proposed (Walter *et al*., 2000) to aid in determining the differences in source phenomenology between a surface production mine explosion and a buried fully contained nuclear test. Such an experiment would also address long-standing nuclear test evasion concerns regarding the possible "masking" of an underground nuclear explosion within the confines of a working mine.

The objective of this research is twofold: (1) implement the recommendations of the CTBTO's WGB to develop improved empirical travel times needed to calibrate the IMS and (2) to decrease the ambiguity of seismic signals from mining operations. Progress towards both of these goals may be achieved by executing the field experiment proposed by Walter *et al.* Such an experiment should ideally be carried out within an active mine that routinely conducts both surface and underground operations at the same location. A large copper mine meeting these criteria has been identified within 100 kilometers of Santiago, Chile. The seismic signals from explosions at this mine could be recorded at numerous IMS stations, including primary and auxiliary stations and both infrasound and hydroacoustic stations within the southern part of the continent.

The mining company has agreed, in principle, to conduct collocated surface and underground explosions, pay for the explosives, preparation of the shots and the associated logistics. It will further cooperate by allowing the installation of near source instrumentation within the mine, providing information on the mine's geology and rock properties and detailed information related to the characteristics of its production blasts.

As noted earlier, operations at this copper mine consist of both open pit and underground extraction. The underground extraction is performed using block caving, as well as mechanical extraction, depending on the degree of rock fracture. The mine's operations are conducted at an elevation of 3500-4000 meters. Adverse weather conditions during part of the year dictate that all extraction processes and operations take place below the surface. Because the mine conducts very extensive operations below the surface, it provides ample opportunity to conduct an experiment of the type described by Walter *et al*., i.e., a collocated surface delay fired production explosion at a location just above a single fired fully contained explosion. There are a myriad of abandoned tunnels and drifts at various depths that provide an opportunity for conducting such collocated explosion pairs. Existing operations allow for the explosions to be located directly above one another, i.e., the open pit is currently directly above the block caving extraction process, see Figure 1. The experiment is currently being planned to take place in early 2002. As production continues, the geometry of the experiment could be altered but, hopefully, not significantly. The draft test plan, which is still evolving, calls for seismic instrumentation to be installed within the mine's boundaries, generally within five kilometers of the explosions. Approximately 5-7 sites would be occupied in the mine. These data will provide detailed information to formulate a seismic source model for the explosions. Another critical aspect of the test plan would be to acquire regional seismograms to improve knowledge of how the geology affects the radiated seismic energy. A number of international research efforts are currently underway or being planned to record data in the Andes. By cooperating with these other groups, e.g., the Universidad de Chile and University of Arizona, resources would be leveraged. For example, the University of Arizona (S. Beck and T. Wallace, private communication, 2000) will be conducting an extensive field deployment and has agreed, in principle, to cooperate by allowing use of its communication links and other resources, including instrument deployment at regional distances, as logistics permit. Plans are currently being made to finalize the test plan for this experiment in order to conduct the experiment in early 2002.

REFERENCES

Department of Energy (1999), Report of a Working Group from Government, Industry and National Laboratories, Mine Seismicity and the Comprehensive Nuclear-Test Ban Treaty, Report Nos. LA-UR-99-384 and UCRL-ID-132897.

PrepCom (1999), Recommendation for Seismic Event Location Calibration Development, CTBTO/WGB/TL-2/18, 1-12 February 1999.

Walter, William R., Denny, M., and Pearson, C., (1999), A Mining/Contained Explosion Source Phenomenology Experiment, Draft Manuscript.

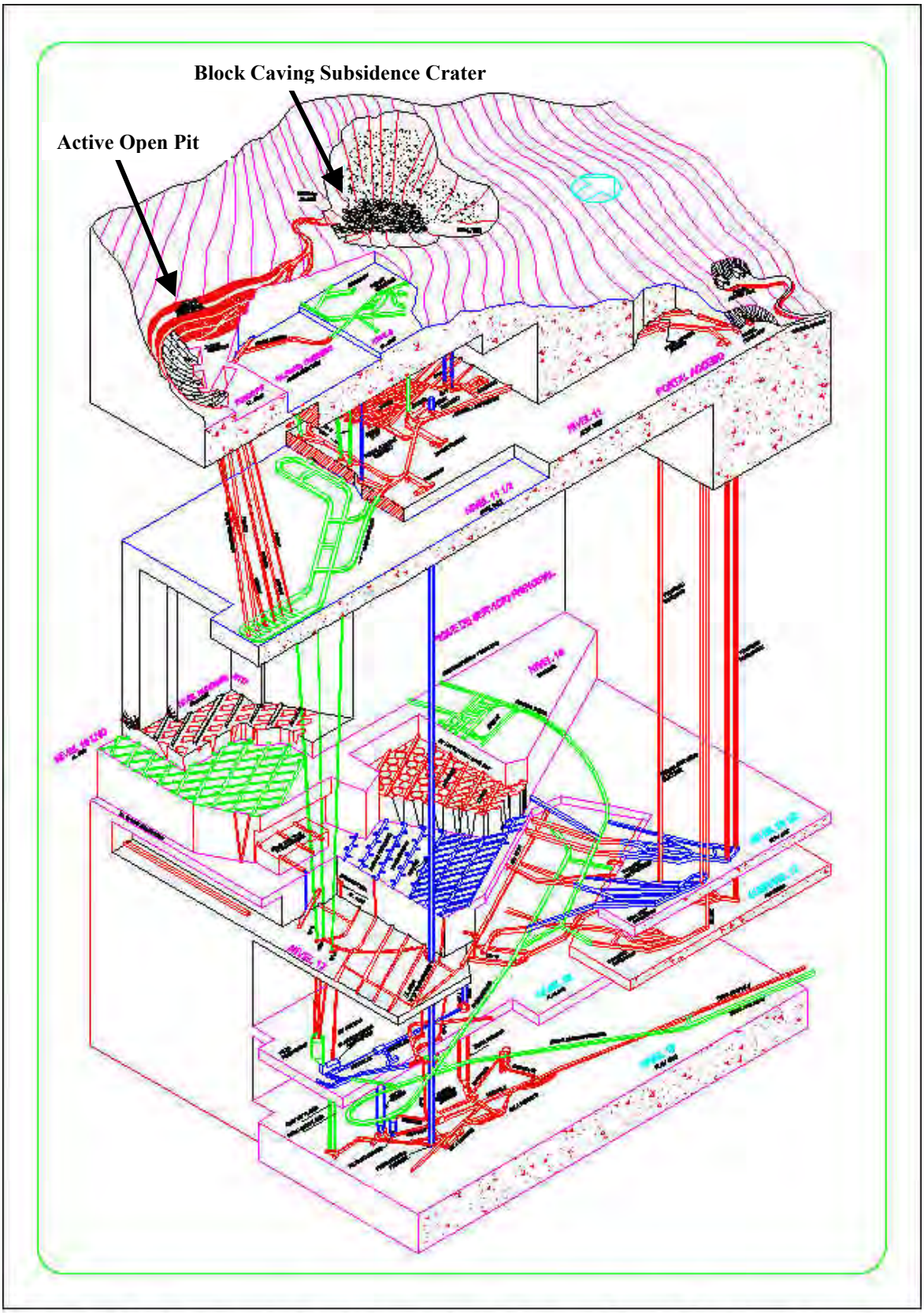


Figure 1. This figure shows the open pit operation which is collocated above the block caving operations. The close proximity of the open pit and the subsidence crater from block caving operations can be seen.

EVENT RELOCATIONS AND SEISMIC CALIBRATION IN NORTHEAST RUSSIA

Kevin G. Mackey and Kazuya Fujita

Department of Geological Sciences, Michigan State University

Sponsored by The Defense Threat Reduction Agency
Arms Control Technology Division
Nuclear Treaties Branch

Contract DTRA01-98-C-0168

ABSTRACT

In effort to obtain ground truth classifications in support of Comprehensive Nuclear-Test-Ban Treaty monitoring for continental regions of northeastern Russia, we have relocated approximately 100 seismic events reported in the International Seismological Centre (ISC) catalog, which occurred from 1970 through 1996. ISC solutions for this region utilize data from very few local or regional stations. In this study, we have supplemented ISC data with local and regional () < 20E) arrivals from Russian regional seismic networks. Supplemental data normally include Pn, Sn, Pg, and Sg phase arrivals. Pg and Sg phases are often reported out to 1,000 km, well beyond the Pn/Pg crossover distance. Relocations were computed using a least squares method utilizing Pn, Pg, and Sg arrivals. For the Pg and Sg crustal phases, locally calibrated velocities were utilized. The J-B travel-time curve was used for Pn arrivals, as it results in overall reduced RMS residuals when compared to the IASPEI 91 tables and generally agrees with the average crustal and upper mantle seis mic velocities and crustal thickness. Only stations within 20^{o} were used in the relocations.

Most of our relocations differ by about 30 km or less relative to ISC parameters, with some exceptions being considerably more (one event moved 500 km). Overall locations appear to improve: locations occurring within aftershock sequences cluster tighter, and event alignment with known active faults improves. There is no consistent pattern to the azimuth of change in epicenters from ISC to our relocations. However, locally, or within aftershock sequences, there is a consistent bias in the in the epicenter shift. No specific areas stand out as having large differences between ISC and our solutions.

In order to further improve calibration capabilities in northeast Russia, we have deployed a small network of digital seismic stations in the Magadan region, concentrated primarily in the Kolyma gold mining district. The stations currently have a spacing of about 200-250 km and are located in close proximity to areas of tectonic seismicity as well as active mining with associated explosions. Both microearthquakes and mine blasts are well recorded by our network. Expansion of the network is currently in progress.

Key Words: seismic regionalization, calibration, location, seismic sources

OBJECTIVE

The objective of our research is to improve epicentral coordinates to better locate and identify ground truth seismic events in northeast Russia in support of Comprehensive Nuclear-Test-Ban Treaty (CTBT) monitoring. Northeast Russia is a tectonically complex region formed by the amalgamation of a large number of terranes of various origins in the Mesozoic and Cenozoic (Fig 1; Nokleberg et al., 1994). Thus, the crustal structure and seismic velocities are expected to vary considerably within the region. In addition, a presumed Pliocene rift system, the Moma rift, crosses the continental part of northeast Russia, while the Arctic Ocean shelf is traversed by the currently active Laptev Sea rift system (e.g., Fujita et al., 1990; Drachev et al., 1998). These rift systems have also perturbed the crust resulting in lower seismic velocities and thinner crustal thicknesses (e.g., Kogan, 1974; Mackey et al., 1998).

To accomplish our objectives, we have calculated travel-time curves specific to discrete cells in the study area. These individual travel-time curves were then used to relocate seismic events, both explosions and earthquakes, and compare them to known mining sites or epicenters calculated by international agencies (e.g., the International Seismological Centre, ISC), as well as Russian determined epicenters.

These velocity calibrations and relocations are based on a computerized database containing phase arrival times from approximately 10,000 historic earthquakes that have been located by several regional seismic networks in northeastern Russia, generally covering the past 30 years. Each network has utilized different location methodology, travel-time curves, and phase data (see Mackey and Fujita, 1999). Thus hypocenter determinations throughout the study area can be improved by using a standardized methodology, calibrated travel-time curves, and combining phase data from adjoining networks. In this paper, the larger events in the study area are relocated in conjunction with developing best-fit crustal travel-time curves.

This study will aid in improving ground truth information and in the identification of seismic sources throughout the study area.

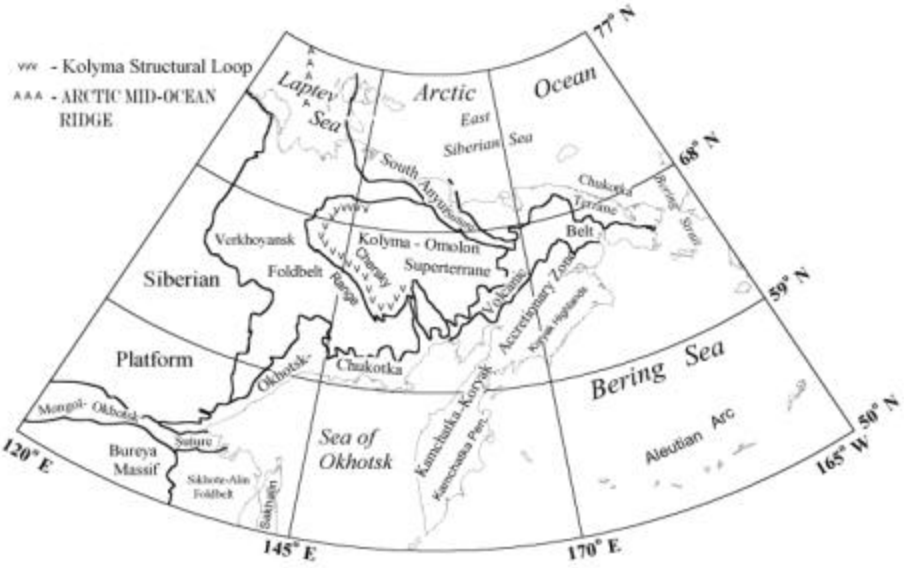


Figure 1. Index map and geologic provinces of northeast Russia.

RESEARCH PERFORMED

Relocations using Russian phase data

The basic location routine used is a least squares best fit routine, modified for this study to accept multiple phases, specifically Pg, Pn, and Sg. Sn arrivals are not used, as the data are considerably noisier than the other phases.

Throughout the study area, many geologic and tectonic environments exist. Combined with the physical vastness of the region, this makes it likely that no single velocity or travel-time curve will reflect actual seismic velocities for any particular phase. In order to overcome this problem, the study area was broken into cells, and the best fitting velocities were determined by minimizing the sum of event RMS residuals through trial of multiple travel time curves. Cell sizes are generally 3^o north-south by 5^o east-west, although this was adjusted in areas with sparse activity in order to increase the number of useable events. For any given block, only events containing Pn phase arrivals (generally 2 or more) were used. This selects only the larger events, which contain more arrivals and have better azimuthal coverage of receiving stations. The number of selected events ranged from 5 to over one hundred, with a few exceptions.

Travel-time curves for Pg and Sg phases were calculated assuming a flat-earth-straight-ray approach. This is reasonable because Pg and Sg phases are confined to relatively short distances in the crust, thus the distance traveled between epicenter and station is considered equivalent to the surface distance. For hypocenters at depth, the travel path is assumed to be the hypotenuse of the triangle made by the depth and the surface distance. Event depths are restricted to a maximum of 33 km, as all events are assumed crustal in nature. Events for which depth tends above the surface are restricted to 0 km.

In order to determine the best crustal velocities for locating events within a given cell, the selected events are first located with crustal velocities 'guessed' for the region. The velocities used in the guess were generally the best-fit velocities from an adjacent cell. The resulting output is analyzed for high residual arrivals, generally those greater than 3.5 seconds. High residuals are generally a result of either typographical errors, misassociated phases, or bad time picks. Typographical errors and misassociated phases are corrected if possible, while bad time picks are omitted from use in further locations. Events having many high residual arrivals such that it was impossible to get a reasonably good location and events with four or fewer recording stations are omitted from further analysis. Overall, less than 5% of the originally selected events were omitted in the study area.

In order to determine the better fitting travel-time curve to use for Pn arrivals in the location procedure, the Jeffreys-Bullen (JB; Jeffreys and Bullen, 1970) P wave travel-time curve was compared to the IASPEI 91 (I-91) curve by Kennett (1991). Results for test regions in the Amur, northern Yakutia, Magadan, and Chukotka regions indicate that the JB table does a better job of fitting the Pn arrivals in the region. Therefore, the JB table was used in all relocations computed in this study.

Following removal of large residual time picks and correction of misassociated phases, the remaining selected events for a given block were located multiple times using different crustal velocities. A total of 1309 earthquakes were relocated in 44 geographic cells. Crustal velocities tested for each block range from 5.875 km/sec to 6.350 km/sec in 0.025 km/sec increments for Pg, and 3.470 km/sec to 3.650 km/sec in 0.020 km/sec increments for Sg. In this manner, the crustal velocities that best fit the events in the cell were found. The newly found best fitting velocity for each cell was then used to relocate the events a second time. After locating with the new velocity, any additional high residual arrivals were omitted or corrected. Arrivals with residuals over 3.0 seconds were removed. Arrivals with lower residuals were occasionally removed if the station was very close to the epicenter, or if a single residual had a value several times larger than all others for a particular event and 'stood out'. If any arrivals were removed or had phase associations changed, the events in the cell were again subjected to a search for the best-fit crustal velocities. Final Pg crustal velocities for each cell are shown on Figure 2. The distribution of Sg velocities shows a nearly identical pattern. Crustal velocities in northern Yakutia were somewhat problematic, with adjacent cells alternating between high and low velocities, which indicated that the original cell size used was exceeding the geographical scale of the velocity variations. Therefore, locations and calibrations for Yakutia north of 66^o were performed using a 5^o x 3^o moving window, shifting the window in 1^o increments. For each cell, the best fitting crustal velocities were determined by trial of multiple Pg and Sg velocities as discussed above. This resulted in a similar velocity structure as determined earlier, but with greatly smoothed velocity shifts (Figure 2).

Velocity Structure

Crustal velocities determined in the location process correlate well with the regional tectonic provinces. Generally the highest velocities (Pg velocities ranging from 6.225 to 6.300 km/s and Sg from 3.61 to 3.65 km/s) occur in the western portion of the study region, which is part of the Siberian platform. Elevated crustal velocities in the Siberian platform are consistent with seismic studies conducted by Suvorov et al. (1999), where Pg velocities were generally found to range from 6.2 - 6.3 km/s. South of the Siberian platform, velocities decrease across the Mongol - Okhotsk suture (Figures 1 and 2). This velocity decrease is consistent with with the results of Suvorov

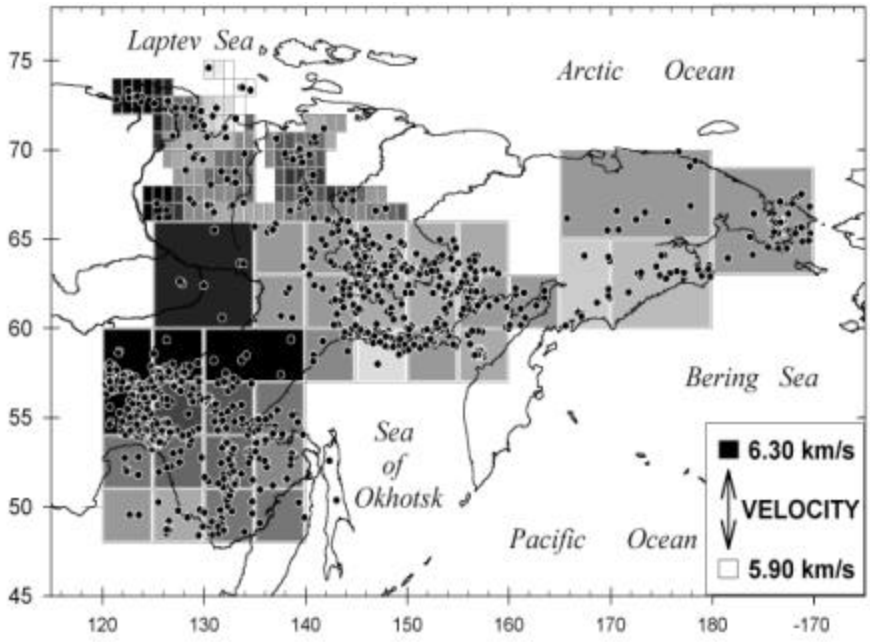


Figure 2. Grid of calibrated Pg velocities. Epicenters are shown for reference.

and Kornilova (1985). Velocities also drop sharply in the Verkhoyansk foldbelt, along the eastern edge of the Siberian platform. From the Verkhoyansk foldbelt and east through the Mesozoic terrane assemblages (Kolyma - Omolon Superterrane) to the Bering Strait, crustal velocities are consistently in the 6.00 - 6.05 km/s range, and Sg velocities in the 3.51 - 3.55 km/s range, with only a few cells deviating slightly. The final analysis for velocities in northern Yakutia indicates that the highest velocities are associated with the Siberian platform along the western edge of the region. The lowest velocities occur in the Laptev Sea and correspond to active rifting along the extension of the Arctic Mid-Ocean Ridge. The velocity shifts in northern Yakutia are probably a result of rapidly changing velocity gradients associated with presently and recently active rifting adjacent to the Siberian platform and other older tectonic structures. The low velocity region in the Laptev Sea extends into the continent, where it generally follows the strike of the grabens outlined in Fujita et al. (1990).

Location Improvements

The newly determined velocities in each cell were used in the final relocation of events. Plots comparing original and relocated epicenters show clear improvement of relative locations relative to the Russian network solutions. It is expected that an improvement in event locations will result in better defined lineations in the seismicity as earthquakes occur along faults, and that clusters of events would concentrate into smaller areas for near-point sources, such as aftershock sequences. In the Amur region, the seismicity trend extending through the Zeya basin becomes clearer and seismicity clusters tighten throughout the region (Figure 3). Relocated epicenters in the Magadan region show a tightening of several clusters of seismicity and a slightly improved lineation of events along the trace of the Ulakhan fault (Figure 4). The cluster near 62^{o} N x 157^{o} E is due to an aftershock sequence following an event on February 11, 1987. Clusters of seismicity in the eastern portion of Chukotka are reduced to much smaller lineations.

Travel-time curves resulting from the relocated events also show a distinct improvement. Figure 5 compares travel-time curves for one cell in the Magadan region. The level of scatter is reduced for all phases using the relocations, consistent with improved hypocenter parameters.

Comparison with ISC Epicenters

About 100 events among those that we relocated are listed in the ISC Bulletin. Most (90%) of our relocations differ by less than 45 km relative to the ISC parameters, with a few being significantly different (one event with poor station coverage in the ISC moved 500 km). As noted, our locations are likely to be an improvement

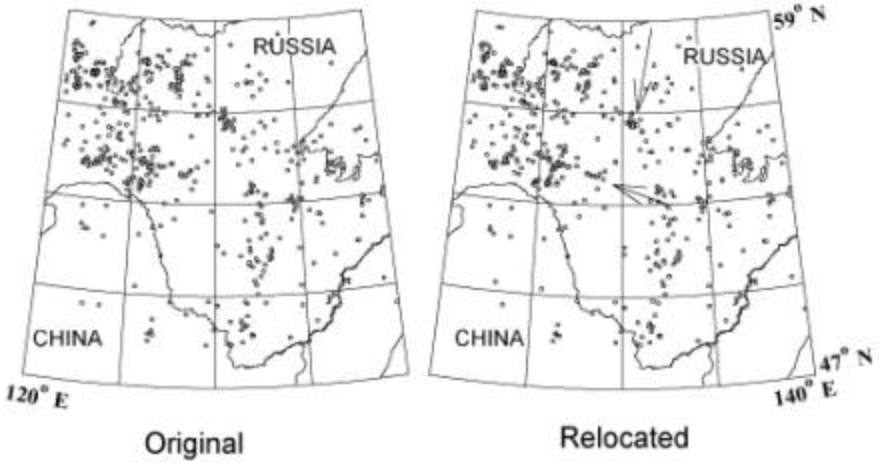


Figure 3. Original vs. relocated epicenters for the Amur region.

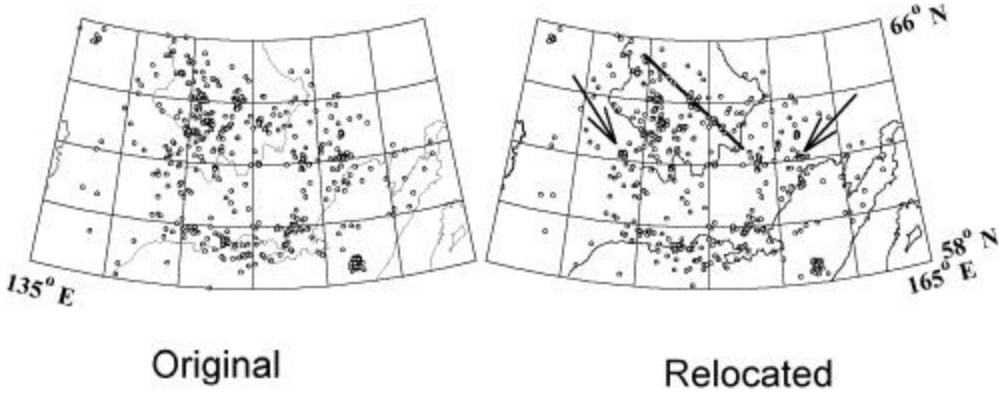


Figure 4. Original vs. relocated epicenters for the Magadan region. Ulakhan fault is shown by a heavy line.

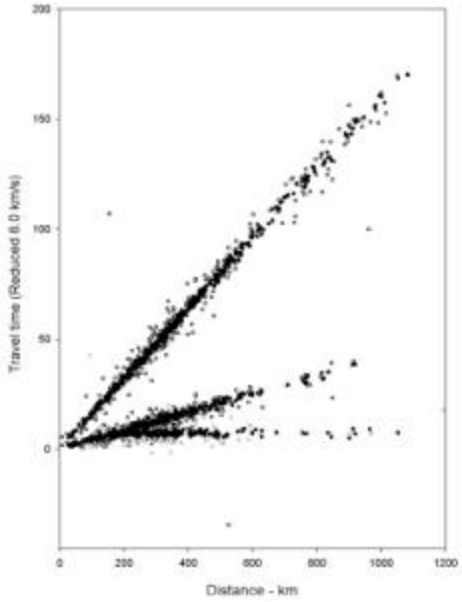


Figure 5. Travel-time curve for the region 60-63°N x 145-150°E comparing original (open circles) with relocated event parameters (closed circles). Note the significant reduction in scatter of data points. Sn data are omitted.

due to the large number of local phases utilized. However, there is no large-scale spatial pattern to the azimuth or magnitude of change in epicenters calculated by ISC relative to our relocations (Figures 6 and 7).

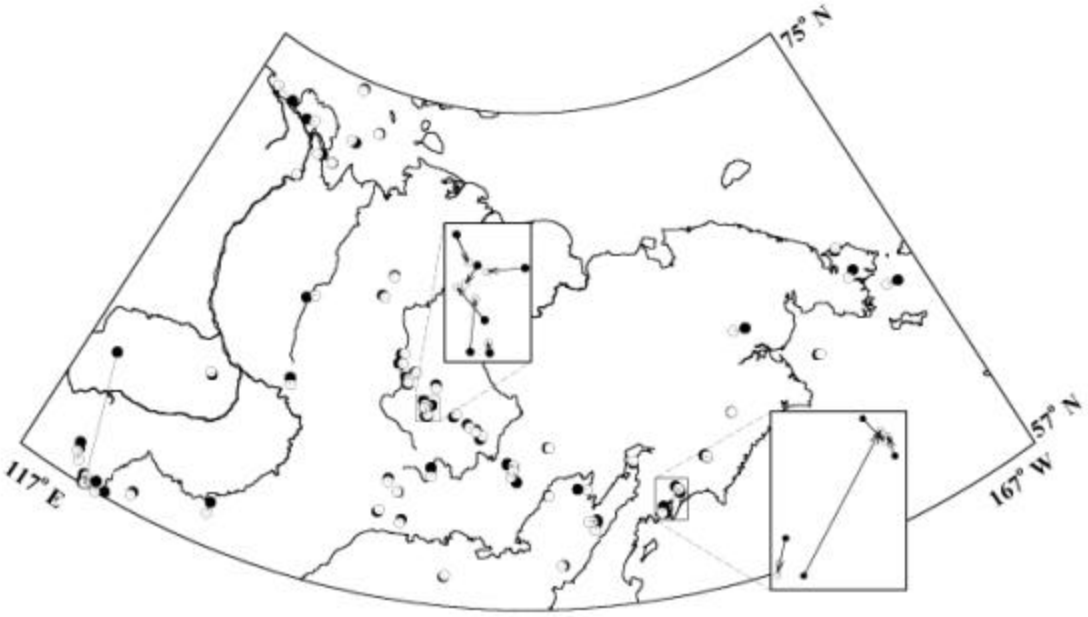


Figure 6. Comparison of ISC epicenters (solid) and relocated epicenters (open) using local data for the northern portion of the study area. Connecting lines show magnitude of displacement. Note that relocations cluster better than ISC determined epicenters (insets).

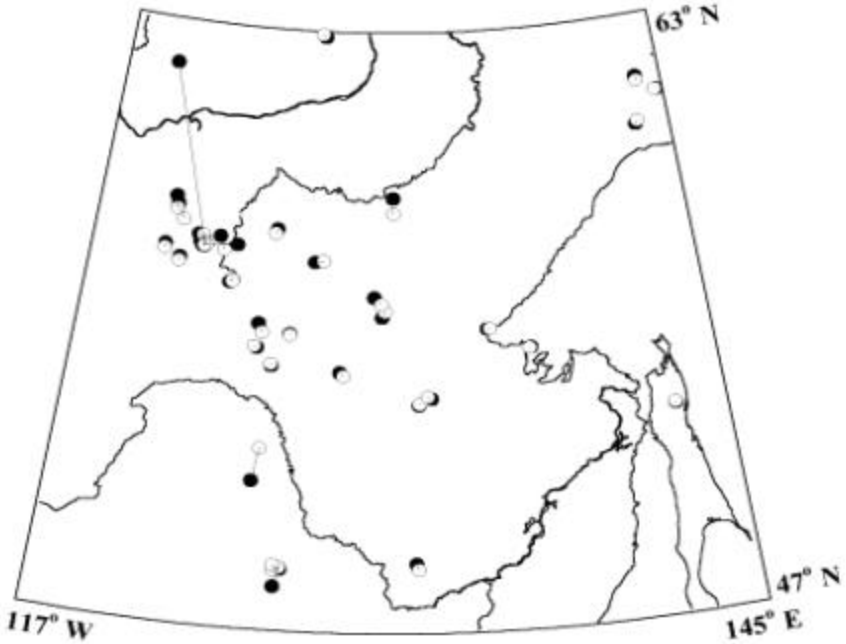


Figure 7. Comparison of ISC (solid) and relocated epicenters (open) using local data for the Amur region. Connecting lines show magnitude of displacement. Note that relocations cluster better than ISC determined epicenters.

Although there are some areas where there appears to be some consistent bias (e.g., the larger events in Chukotka, the Laptev Sea, and also perhaps in the north-central Verkhoyansk Range), the most consistent bias in the in the epicenter shift is "radial" with aftershocks and other events tending to move into tighter clusters (see insets,

Fig. 6). No specific areas stand out as having large differences between ISC and our solutions. Examination of events whose locations have the greatest differences, by more than 45 km, indicate that our relocations are much better than the ISC solutions, with a few exceptions at the edges of our study area.

ISC solutions are generally worse where they have no close stations, or the stations fall into a narrow azimuthal range. Similarly, a few of our solutions at the edges of our study area are worse because we have a narrow azimuthal range, which may also affect our travel-time curve calibrations.

An area where we show clear improvement is Chukotka, where our relocations use both the Russian and American data, hence providing excellent azimuthal coverage. We also locate aftershocks better; generally our solutions fall in closer proximity to the mainshock, as we have larger numbers of close stations. Given the magnitude of even the largest events, M < 7, aftershock areas are not expected to be large. The area where our solutions may have some problems is in the Laptev Sea where, due to our criteria for not using stations greater than 25°, we do not have good azimuthal coverage to the north and the seismic velocities in the crust appear to vary relatively rapidly (Fig. 2).

Based on a preliminary sampling of events we believe that our solutions are better than those reported by the ISC due the increased number of close-in stations, the relatively good azimuthal distribution in most of our study area, and the use of calibrated travel-time curves. We feel that many events meet GT10 criteria, and a reasonable number may qualify as GT5. Additional careful analysis of individual solutions may lead to further improvements in our ability to obtain ground-truth values.

Regional network deployment

In the summer of 1999, we began a program to develop seismic discriminants for CTBT monitoring by converting existing photopaper analog stations in the Magadan and Yakutsk networks to digital data acquisition. At present, we have deployed seven stations in northeast Russia, most in the Magadan region (Figure 8). All stations are 3 component, with three stations recording broadband instruments (Seymchan - STS-1, Okhotsk - Guralp CMG-40T, and Anadyr - CMG-40T). The remaining stations use short-period Russian seismometers (SKM-3 or SM3-KV). All seismometer outputs are digitized at 30 samples per second with 24-bit resolution and logged on a PC. In addition, we are supplementing our digital data with records from the IRIS station at Magadan, MA2, and other regional analog photopaper stations.



Figure 8. Map of the Magadan region showing locations of digital seismic stations deployed in 1999 and 2000 (closed triangles). Also shown are supporting analog stations (open triangles) and future mine deployment sites (circles).

We are presently beginning the process of identifying and analyzing the local earthquakes and explosions in the digital data. Two of our stations are located in active mining regions, which supports acquisition of ground truth data directly useful for calibration of the IMS Alternate stations Magadan (MA2) and Seymchan (SEY).

Figure 9 shows a mine blast near Susuman, which was recorded at Seymchan, Magadan and other regional stations. Figure 10 is a sample record of a local earthquake. In addition to locally occurring events, several hundred regional and teleseismic events have also been recorded at the deployed stations.

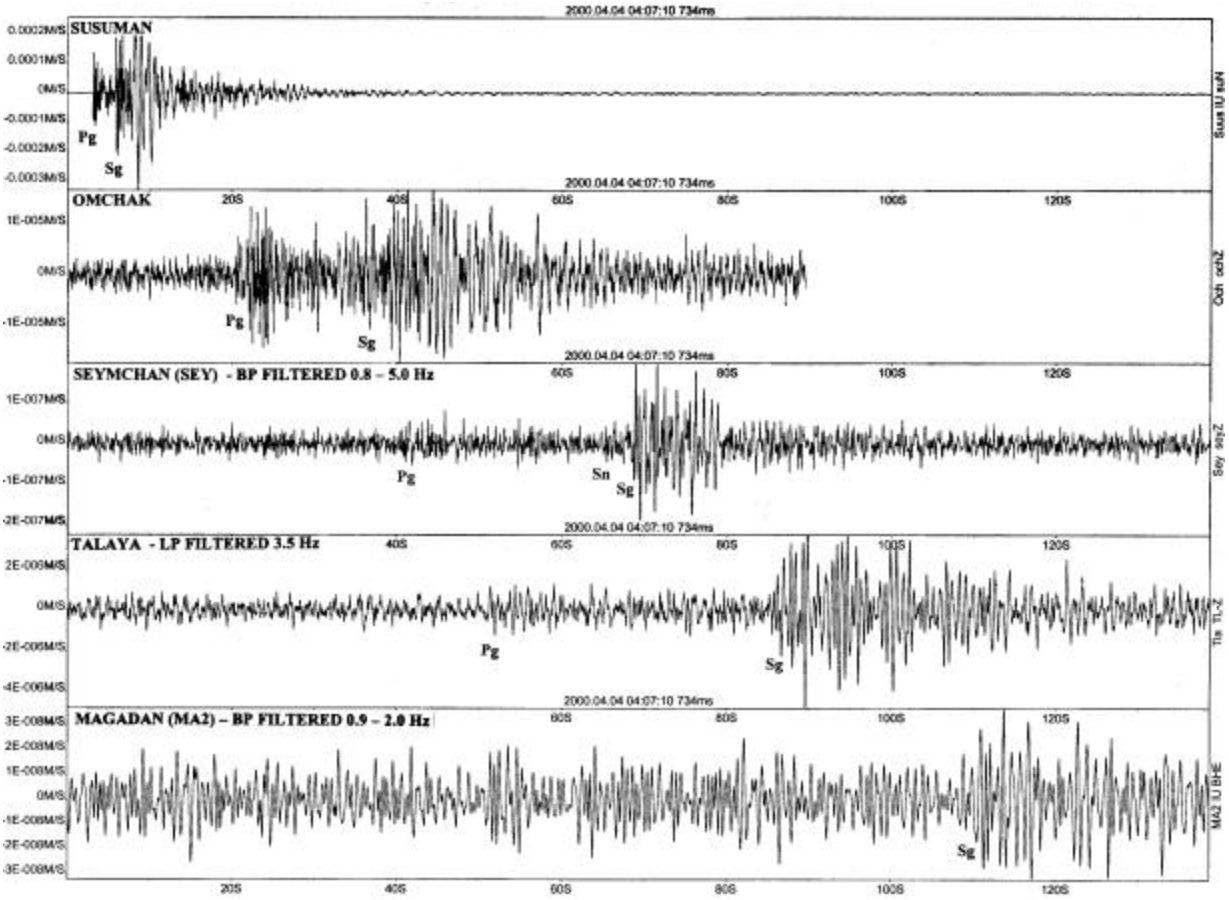


Figure 9. Sample seismograms from an April 4, 2000 mine blast as recorded by five stations in northeast Russia. The blast occurred approximately 25 km northeast of Susuman, and was recorded at the IMS alternate stations Seymchan (SEY; see middle trace) and Magadan (MA2; see lower trace).

CONCLUSIONS

By determining locally calibrated travel-time curves and relocating regional earthquakes recorded by regional networks operating in northeast Russia, we have greatly improved epicenters relative to both the original Russian determination and the ISC Bulletin. Nominal errors are less than 10 km and, with most events having good azimuthal coverage and several stations within several hundred kilometers reporting both P and S arrivals, many of these events may meet GT5 criteria. In order to improve our ability to obtain ground truth events, we have deployed a network of digital stations in the Magadan District, including at or near mines. The data from this deployment is currently under analysis.

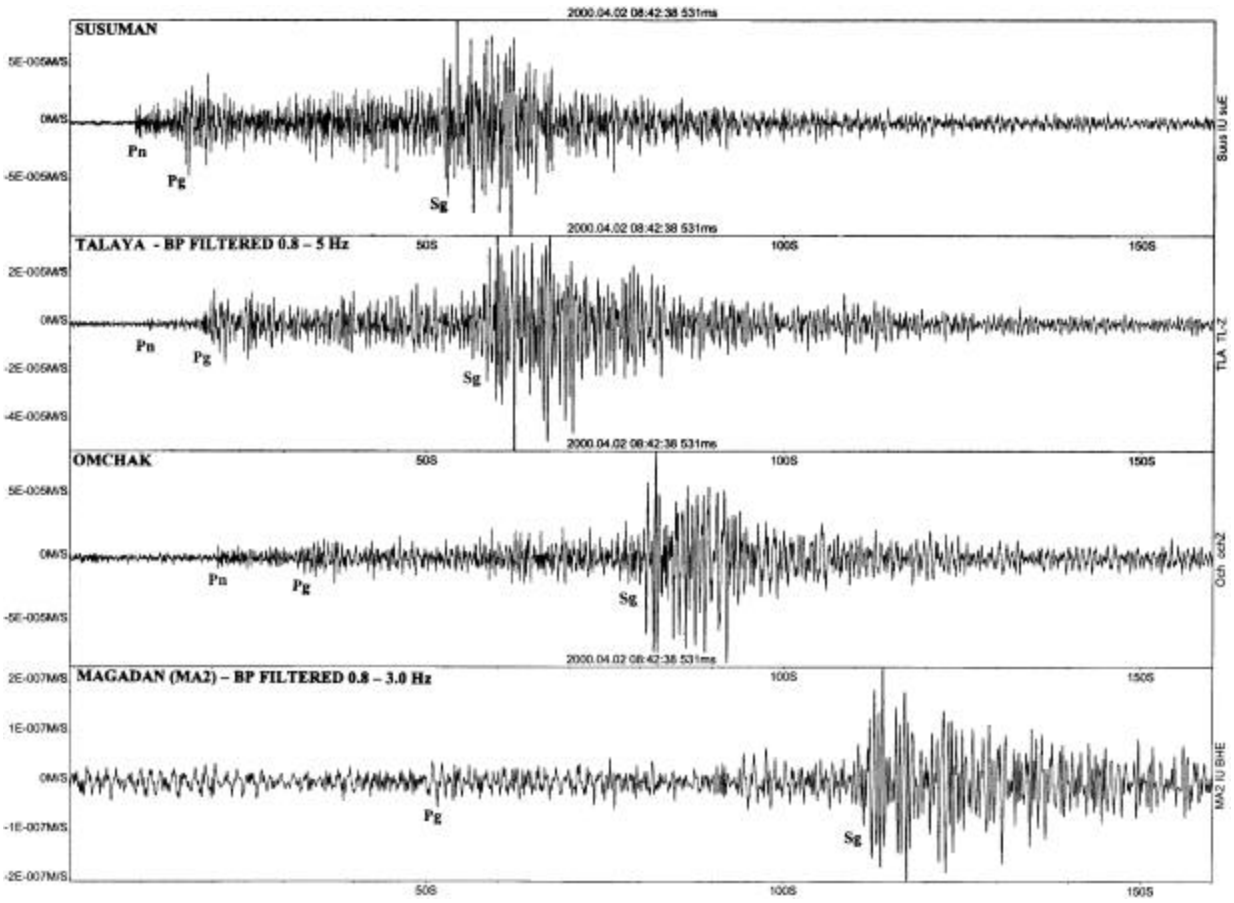


Figure 10. Sample seismograms depicting a local earthquake as recorded by stations of our network in northeast Russia. This event occurred on April 02, 2000, at approximately 63.9°N x 154.1°E.

REFERENCES

Drachev, S., Savostin, L. A., Groshev, V. G., and Bruni, I. E., 1998, Structure and geology of the continental shelf of the Laptev Sea, Eastern Russian Arctic: *Tectonophysics*, v. 298, p. 357-393.

Fujita, K., Cambray, F.W., and Velbel, M.A., 1990, Tectonics of the Laptev Sea and Moma rift systems, northeast USSR: *Marine Geology*, v. 93, p. 95-118.

Jeffreys, H., and Bullen, K.E., 1970, *Seismological Tables*: Office of the British Association, London, 50 pp.

Kennett, B.N.L., 1991, *IASPEI 1991 Seismological Talbes*: Research School of Earth Sciences, Australian National University, Canberra, 167 pp.

Kogan, M. L., 1974, Conducting seismic work of the CMRW-DSS on oceanic ice on the shelves of the Arctic seas (example of work in the Laptev Sea): *Geofizicheskie Metody Razvedki v Arktiki*, vyp. 9, p. 33-38.

Mackey, K.G., and Fujita, K., 1999, The northeast Russia seismicity database and explosion contamination of the Russian earthquake catalog: in *Proceedings of the 21st Seismic Research Symposium: Technologies for Monitoring The Comprehensive Nuclear-Test-Ban Treaty, 21-24 September, 1999, Las Vegas, Nevada,* v. 1, p. 151-161.

Mackey, K.G., Fujita, K., and Ruff, L.J., 1998, Crustal thickness of northeast Russia: *Tectonophysics*, v. 284, p. 283-297.

Nokleberg, W.L., Parfenov, L.M., Monger, J.W.H., Baranov, B.V., Byalobzhesky, S.G., Bunbtzen, T.K., Feeney, T.D., Fujita, K., Gordey, S.P., Grantz, A., Khanchuk, A.I., Natal'in, B.A., Natapov, L.M., Norton, I.O., Patton, W.W., Jr., Plafker, G., Scholl, D.W., Sokolov, S.D., Sosunov, G.M., Stone, D.B., Tabor, R.W., Tsukanov, N.V., Vallier, T.L., Wakita, K., 1994, *Circum-North Pacific tectonostratigraphic terrane map*: U. S. Geological Survey Open-File Report 94-714, 221 pp., 5 plates.

Suvorov, V.D., and Kornilova, Z.A., 1985, Deep structure of the Aldan shield according to near earthquake data: *Soviet Geology and Geophysics*, v. 26 (2), p. 79-84.

Suvorov, V.D., Parasotka, B.S., and Chernyi, S.D., 1999, Deep seismic sounding studies in Yakutia: *Izvestia, Physics of the Solid Earth*, v. 35 (7-8), p. 612-629.

PHENOMENOLOGY RESEARCH USING PAST NEVADA TEST SITE EXPLOSION AND EARTHQUAKE DATA

Kevin M. Mayeda, Michael E. Pasyanos, Jennifer O'Boyle Stephen C. Myers,
William R. Walter, and Peter Goldstein
Lawrence Livermore National Laboratory

Sponsored by the U.S. Department of Energy
Office of Nonproliferation and National Security
Office of Defense Nuclear Nonproliferation
National Nuclear Security Administration

Contract No. W-7405-ENG-48

ABSTRACT

We use regional waveform data from the Nevada Test Site (NTS) to investigate phenomenological relationships between recorded amplitude and explosion yield as well as test regional depth estimation procedures. Our goal is to better understand the performance of seismic observables in other regions of monitoring interest, especially at small magnitudes (m_b<<4.5). Some of the topics we are studying include: stable yield estimation, depth estimation, and M_s:m_b performance. We use Lawrence Livermore National Laboratory's NTS explosion database, which consists of several hundred events ranging from ~200- to ~1500-m depth and yields ranging from a few tenths of a kiloton to the megaton range. In addition to the broadband explosion data, we have a large dataset of well-located earthquakes on the test site with depths ranging from 2 to 17 km and magnitudes ranging between M_W 1.5 and 5.7.

For yield estimation the relation between teleseismic body wave magnitude (m_b) and nuclear explosion yield has been studied extensively over the past several decades for a number of test sites for large (>1 kt) explosions. In this paper we will look at broadband coda, P_g, and L_g from over 260 nuclear explosions to study yield estimation capability by comparing F-factors. For monitoring compliance with a CTBT, small events that are recorded only at regional distances will be used to estimate magnitude and equivalent yield. Past coda studies show that coda-derived magnitudes of earthquakes and explosions are more stable than any direct phase method, including $m_b(L_g)$. In fact, single-station coda measurements can be equivalent to a network average of at least ten direct phase measurements over a broad range of frequencies.

In regions where the depth estimate is poorly constrained, other regional methods have been proposed to estimate depth. These include time-domain measures of P-wave complexity, cepstral peaking, and more recently spectral peaking from R_g-to-S scattering. Myers et al. (1999) and Mayeda and Walter (1996) showed that strong spectral peaking in the S-wave and coda were likely due to R_g-to-S scattering in the near-source region. We propose a side-by-side comparison of these techniques in a region with excellent ground truth, namely NTS. We will investigate to what extent cepstral peaking, coda spectra peaking, and complexity provide a reliable depth estimate.

Finally, a number of large regional studies computing surface wave dispersion curves throughout the globe will be used to push the M_s measurements to smaller magnitude by the use of phase-matched filters. For larger teleseismically recorded events, we will test to see if the M_s:m_b trends for explosions and earthquakes continue to separate at small magnitudes at regional distances.

Although NTS is unique from other test sites in its geologic characteristics, this dataset of explosions and earthquakes is ideal for a number of reasons: (1) continuous recordings from high-quality broadband stations, (2) ground truth information that far exceeds any other area, (3) path and site effects that are virtually common for all events, and (4) wide range in depth, source size, and material properties. Because our goal is phenomenological in scope, we will use these results to guide our interpretations and assess our capability in other areas of monitoring interest.

Research performed under the auspices of the U.S. Department of Energy at the Lawrence Livermore National Laboratory under contract number W-7405-ENG-48. This is LLNL contribution UCRL-JC-138995

Key Words: yield estimation, depth estimation, Ms:mb, regional coda waves, NTS, phenomenology

OBJECTIVE

We are in the process of testing a number of regional seismic techniques on ground-truth data from the Nevada Test Site in order to better understand how they will work in regions where we lack ground truth. For example, we have studied magnitude-yield relationships using the regional phases such as Pg, Lg and Lg coda for ~250 nuclear explosions over a broad range yield, depth, and source material property to ascertain the best measure for yield estimation. For large explosions recorded teleseismically the discriminant of choice is the Ms:mb discriminant but there have been very few regional studies to verify the continued separability at small magnitudes. Finally, because NTS has both shallow (<2 km) depth earthquakes and normal crustal depth earthquakes we are testing the cepstral techniques which claim depth estimation capability.

RESEARCH ACCOMPLISHED

Depth

Coda spectral peaking has been observed for NTS explosions (Figure 1a) as well as during the recent Depth-of-Burial explosions in Kazakhstan (Myers et al., 1999). We hypothesize that the spectral peaking is the result of depth-dependent excitation of Rg which scatters into S. To test this we plotted the location of the spectral peak versus the depth of burial and the scaled depth (depth/yield**0.333) in Figures 1c & 1d. We see that there is a good correspondence between peak frequency and depth of burial but not for scaled depth. Another test of our ground-truth data is to apply a cepstral peak algorithm to rigorously test the methodology.

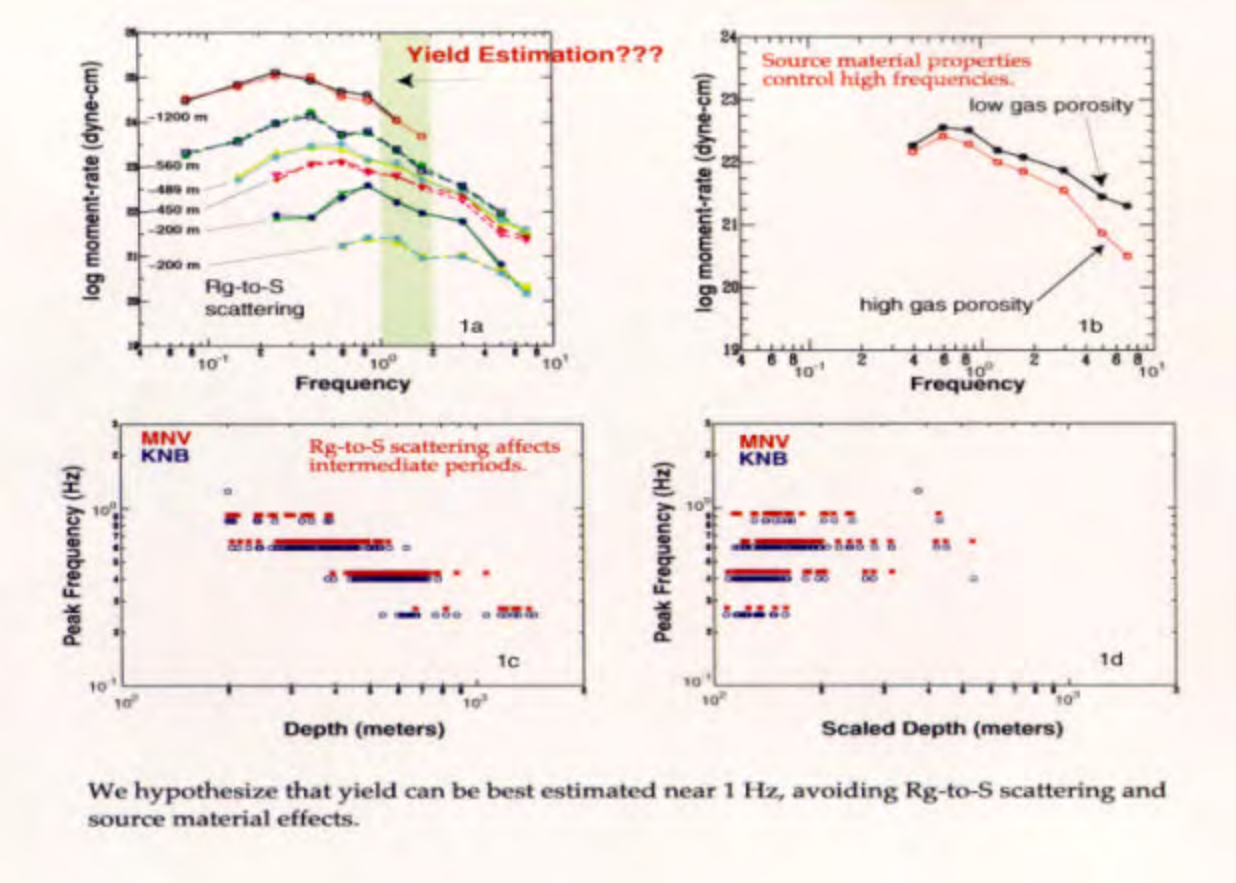


Figure 1.

Yield Estimation

We have measured Pg, Lg and coda amplitudes in multiple frequency bands (0.1<f<6.0 Hz) and plotted against official yield for roughly 250 nuclear explosions at NTS. Upon separating the populations into those fired in high-

strength/low gas porosity material versus low strength/high gas porosity material, we found that in high-strength material the F-value using the coda at ~1 Hz was 1.80 whereas Pg and Lg were roughly 33% larger (Figure 2). For frequencies below ~1 Hz, spectral peaking related to Rg-to-S scattering caused an increase in the F-value and for high frequencies (f>~3 Hz) the source material effects strongly influenced the spectral decay (Figure 1b). We are now applying this technique to other IMS stations in the Middle East, former Soviet Union, and north Africa.

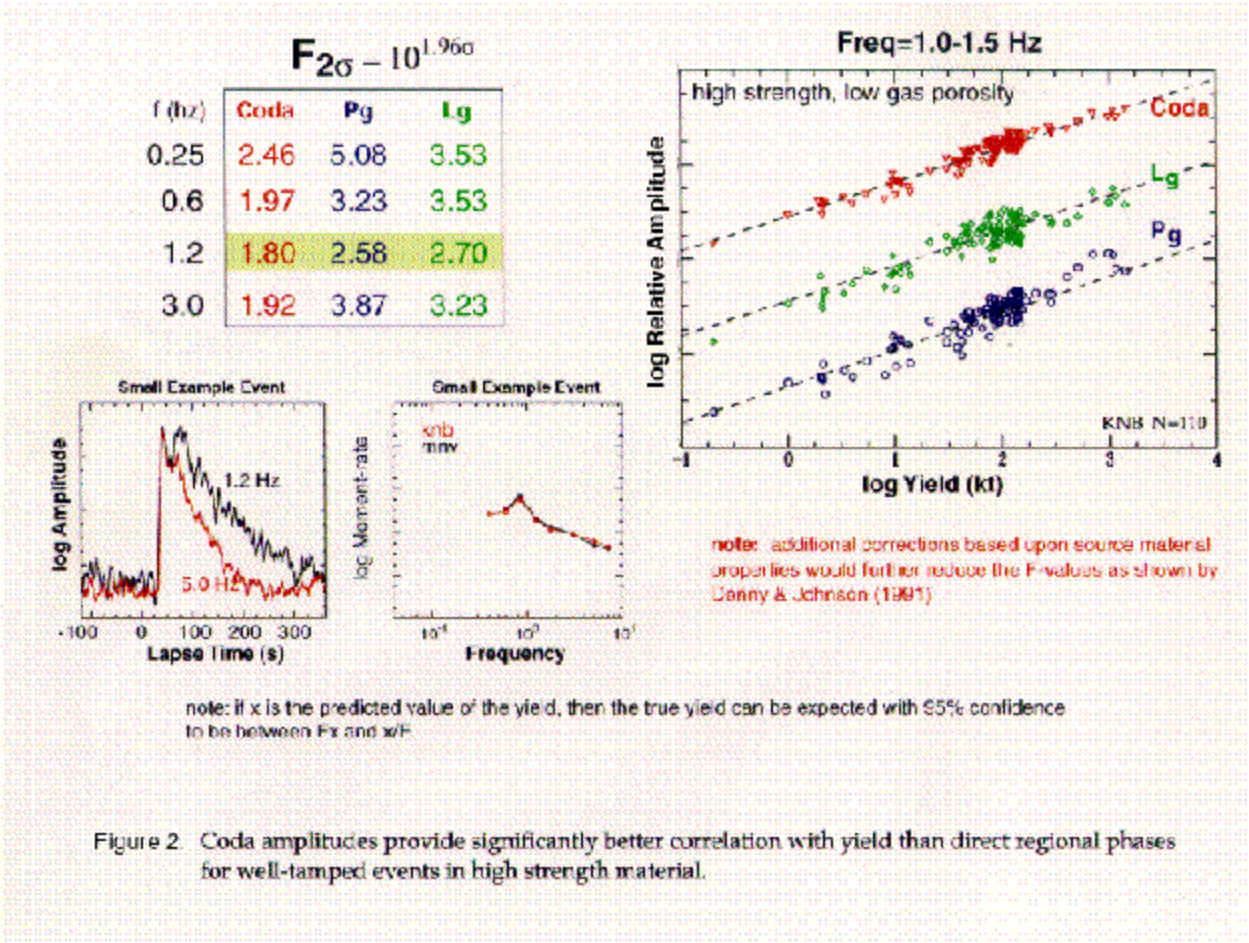


Figure 2. Coda amplitudes provide significantly better correlation with yield than direct regional phases for well-tamped events in high strength material.

Coda

Narrowband coda measurements have been shown to provide the most stable source size estimate of any of the regional phases. For small magnitude events the length of available coda will be small and be asymptotic to the direct S arrival. We are testing the interstation variance using two LLNL stations, KNB and MNV, for common events at NTS as a function of the coda window length. We hope to obtain a mapping of error versus window length so that in areas where we only have one coda measurement, we can place an error estimate.

Ms:mb

We are using large explosions recorded at LLNL's regional broadband stations to form match-filters to estimate Ms for the smaller explosions and earthquakes from the NTS region. Figure 3 shows the teleseismic Ms:mb separation works for events in the Middle East and North Africa region and it is our goal to test this at small magnitudes at regional distances for the Western United States. See also Pasyanos et al. in this session.

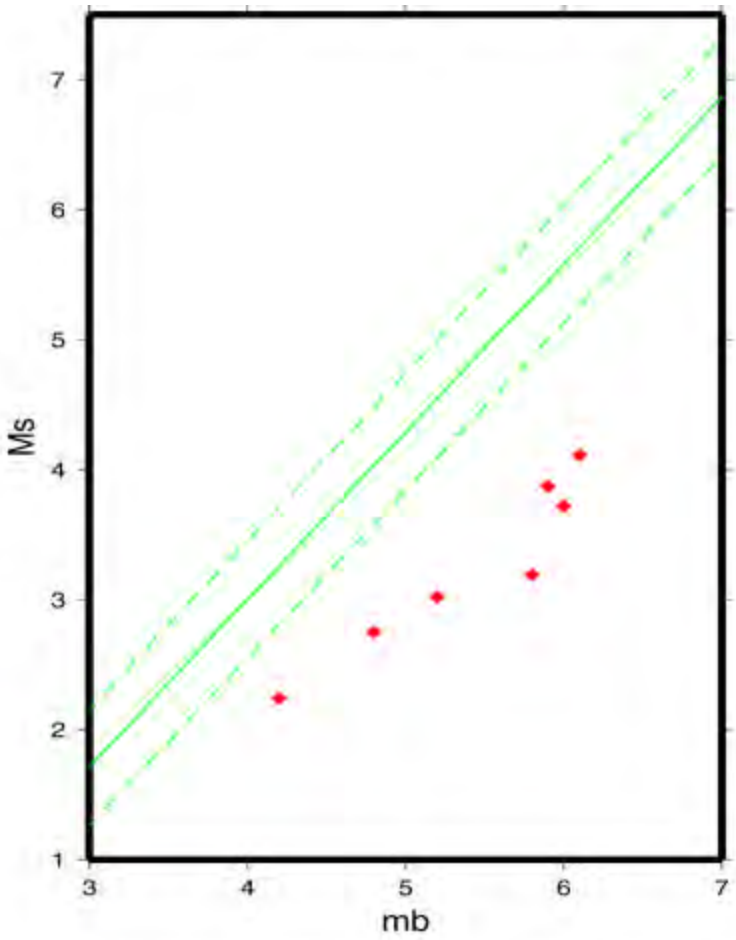


Figure 3. Plot of mb vs. Ms for events which have been phase-matched filtered using the group velocities predicted from the surface wave tomography. The best fitting regression of the earthquakes (not shown) and one standard deviation are shown by the solid and dashed green lines. Explosions are indicated by the red diamonds (see Pasyanos et al. this session).

CONCLUSIONS and RECOMMENDATIONS

The NTS dataset of explosions and earthquakes can guide us in the interpretation of regional seismic techniques in other regions where we lack ground truth data. We are extending the yield and Mw:mb studies to Borovoye Peaceful Nuclear Explosion (PNE) data as well as other regions of monitoring interest.

REFERENCES

Mayeda, K. and W.R. Walter (1996), Moment, energy, stress drop and source spectra of western United States earthquakes from regional coda envelopes, **101**, *J. Geophys. Res.*, 11195-11208.

Myers, S.C., W.R. Walter, K. Mayeda, and L. Glenn (1999), Observations in support of Rg scattering as a source for explosion S waves: Regional and local recordings of the 1997 Kazakhstan Depth of Burial experiment, 89, *BSSA*, 544-549.

APPLICATION OF SOVIET PNE DATA TO THE IMPROVEMENT OF SEISMIC MONITORING CAPABILITY

John R. Murphy, Jamil D. Sultanov*, Brian W. Barker, Ivan O. Kitov*, Margaret E. Marshall
Geophysics Group, Maxwell Technologies, Inc.
*Institute for Dynamics of the Geospheres, Russian Academy of Science

Sponsored by the Defense Threat Reduction Agency
Arms Control Technology Division
Nuclear Treaties Branch

Contract No. DSWA01-97-C-0126

ABSTRACT

In order to discriminate the regional seismic signals produced by underground nuclear explosions from those produced by earthquakes, rockbursts, and conventional mining explosions of comparable magnitude, it is necessary to know the ranges of signal variations that can be expected as a function of source type and propagation path conditions over the entire ranges of these conditions which may be encountered in global test monitoring of the Comprehensive Nuclear-Test-Ban Treaty. For this reason, Maxwell Technologies and the Russian Institute for Dynamics of the Geospheres (IDG) have been working on a joint research program to improve regional discrimination capability through analyses of seismic data recorded from Soviet Peaceful Nuclear Explosion (PNE) events. During the past year the effort on this project has continued to focus on discrimination analyses of regional seismic data recorded from Soviet PNE tests and on a comparison of the characteristics of U.S. and Soviet explosion aftershocks. The discrimination research has centered on an analysis of regional seismic data recorded from Soviet PNE tests at both the Borovoye and selected other Soviet stations. Analyses of the Borovoye data have revealed that some of the Soviet PNE tests can't be reliably identified as nuclear explosions using the nominal high frequency L_g/P_n spectral ratio discriminant currently being tested at the IDC. In fact, these Borovoye PNE discriminant values have been found to constitute some of the most anomalous explosion L_g/P_n ratios in the large discrimination database assembled by Fisk (1999). This analysis is currently being extended to incorporate data recorded from 12 Soviet PNE events at a number of temporary stations which were deployed in the 200-700 km distance range from these tests. These high resolution data have been digitized at the IDG and are currently being processed to determine high frequency L_g/P_n discriminant ratio values which can be compared with those determined from data recorded at the Borovoye station, to further test the applicability of this proposed IDC regional discriminant. The analysis of explosion aftershocks has been directed toward an assessment of their potential applicability to onsite inspections under the CTBT. That is, given the existing uncertainties in IDC seismic locations, it will generally be necessary to initially employ a number of monitoring technologies in an attempt to zero in on the event location for onsite inspection purposes, and one of the primary techniques proposed for this purpose is the seismic detection of explosion induced aftershocks by temporary regional stations deployed for that purpose (Zucca et al., 1996). In order for this approach to be useful and reliable, it is necessary to have quantitative understanding of the dependence of aftershock activity on the explosion source characteristics. Most of the current state of knowledge regarding such explosion aftershocks is based on experience with explosions conducted at nominal containment depths at a few U.S. and Soviet nuclear weapons test sites. Thus, it is not clear how representative this experience is for the monitoring of small, deeply buried explosions in the variety of tectonic and geologic environments which must be considered in global monitoring of the CTBT. Aftershock monitoring data recorded from the more diverse Soviet PNE tests can help to supplement these test site data to provide a more extensive experience base for use in defining onsite inspection strategy. Current effort on this phase of the project is directed toward the characterization of aftershock sequences observed following both Soviet PNE and weapons tests at designated test sites. These studies encompass analyses of aftershock information from 15 Semipalatinsk, 10 Novaya Zemlya, and 12 Soviet PNE tests conducted at a variety of locations throughout the FSU.

OBJECTIVES

Under this research program, scientists from Maxwell Technologies, Inc. and the Russian Institute for Dynamics of the Geospheres (IDG) are using seismic data recorded from Soviet Peaceful Nuclear Explosions (PNE) and nearby Central Asian earthquakes and chemical explosions to better define the limitations of existing operational capabilities with respect to the global seismic monitoring required by the Comprehensive Nuclear-Test-Ban Treaty (CTBT). The objectives of this program are to expand our recently completed analysis of regional seismic data recorded from Soviet PNE events to incorporate seismic data from nearby earthquakes and large chemical explosions, and to use these data to directly test the utility of different regional discriminants over the widest possible ranges of source and propagation path conditions.

RESEARCH ACCOMPLISHMENTS

During the past year, work on this project has been directed toward the continuation of the discrimination analysis of broadband seismic data recorded from Soviet PNE events, a comparison of near-regional seismic data recorded from nearby chemical and nuclear explosions at the Soviet Degelen Mountain test site and an analysis of aftershock monitoring data collected following a number of Soviet PNE tests. Figure 1 shows the map locations of Soviet PNE tests for which broadband, digital seismic data have now been collected and analyzed to further evaluate the high frequency (6-8 Hz) Pn/Lg spectral ratio discriminant currently being tested at the PIDC. These data provide a

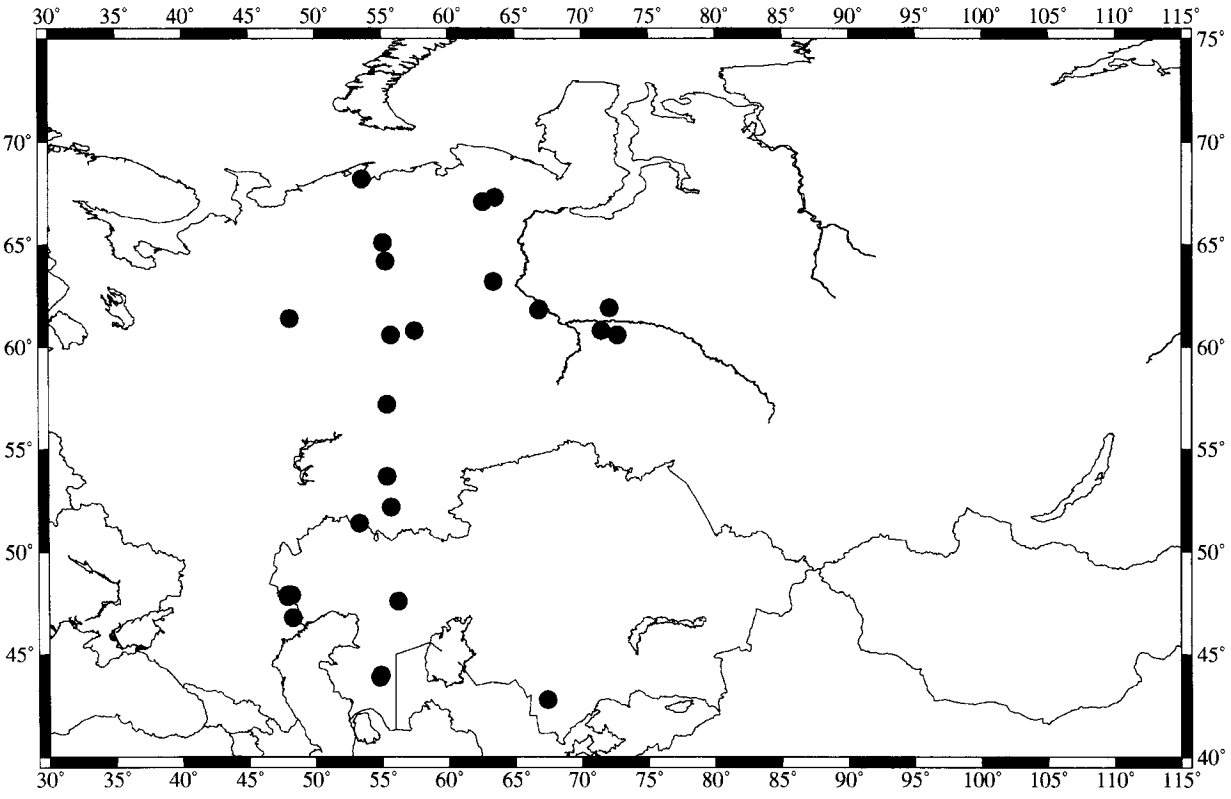


Figure 1. Map locations of Soviet PNE events for which high frequency (6-8 Hz) Pn/Lg spectral ratio discriminant values have been estimated from recorded regional seismic data.

valuable supplement to the previously analyzed nuclear test site data in that they encompass a wide range of source media (salt, limestone, granite, sandstone/shale, clay, chalk) and sample a variety of different regional propagation paths. Moreover, these PNE events are predominantly low yield (average yield = 9 kt), overburied (average scaled depth = 425m/kt$^{1/3}$) explosions of the type which are of greatest concern in CTBT monitoring. The 6-8 Hz Pn/Lg discriminant ratio values determined from broadband regional recordings of these PNE events are plotted in Figure 2, where they are compared with the corresponding mean and 2σ bounds on the REB earthquake population analyzed by Fisk et al (1999). It can be seen that the means of the two populations are well separated, although the two distributions overlap to some extent, as has been noted previously by Fisk et al (1999) in their analyses of data recorded from nuclear explosions at the various weapons test sites. However, several of the Soviet PNE spectral discriminant values shown in Figure 2 constitute the lowest explosion discriminant values observed to date, with values approaching the mean of the REB earthquake population. Preliminary analysis of the geographical distribution of the PNE events contributing these apparently anomalous values suggest that they may be affected by unusual propagation conditions. In any case, these results indicate that the high frequency Pn/Lg spectral ratio discriminant will have to be carefully calibrated for applications at previously untested sites.

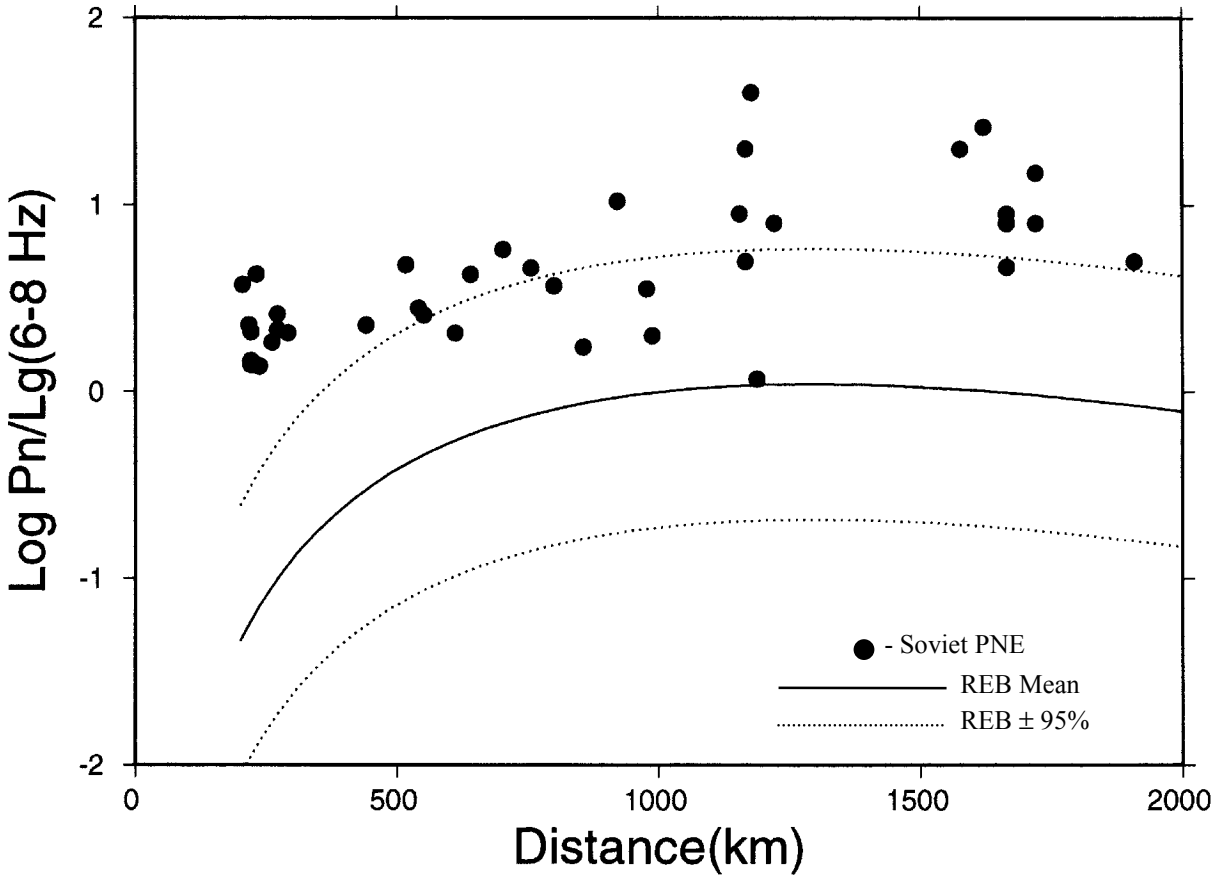


Figure 2. Comparison of 6-8 Hz Pn/Lg discriminant ratio values determined from broadband regional recordings of the Soviet PNE events of Figure 1 with the corresponding mean and 2σ bounds on the REB earthquake population analyzed by Fisk et al (1999).

The analysis of seismic signal generation by chemical (CE) and nuclear (NE) explosions has focused on comparisons of near-regional seismic data recorded from two nearby explosions conducted at the Degelen Mountain area of the Semipalatinsk test site. A sketch showing the relative locations and configurations of these two explosions is shown in Figure 3 where it can be seen that they were separated by less than one kilometer. The CE test was conducted first, on June 5, 1961 and consisted of 150 tons of fully tamped ammonium nitrate detonated in a rectangular chamber. The companion NE test was conducted at nearly the same depth four months later on October 11, 1961 and had a yield of 1.1kt. Broadband seismic data were recorded from both events at stations located at distances of 39 and 84 km from the Degelen site. The vertical component recordings from the two events at the 39 km station are shown in Figure 4 where it can be seen that they are fairly similar, although, as might be expected, the initial P wave arrival from the NE event is more impulsive and simple than that from the CE event. It can be also be seen that the moveout of the Rayleigh wave arrival with respect to the initial P arrival is greater for the NE event than for the CE event, which turns out be consistent with the 1 km separation of the two explosions shown in Figure 3. More surprising is the fact that when this relative delay is accounted for, it can be seen that the two Rayleigh wave arrivals are 180° out of phase, with that from the CE event appearing to be phase reversed with respect to that expected from a nominal explosion source. This phase reversal can also be seen on the 84 km recordings and may indicate that significant tectonic release accompanied the CE event. If this hypothesis is correct, then it may be that there was no significant strain energy remaining to be released by the subsequent, nearby NE event, which could provide a plausible explanation for the relative Rayleigh wave phase reversal between the two explosions.

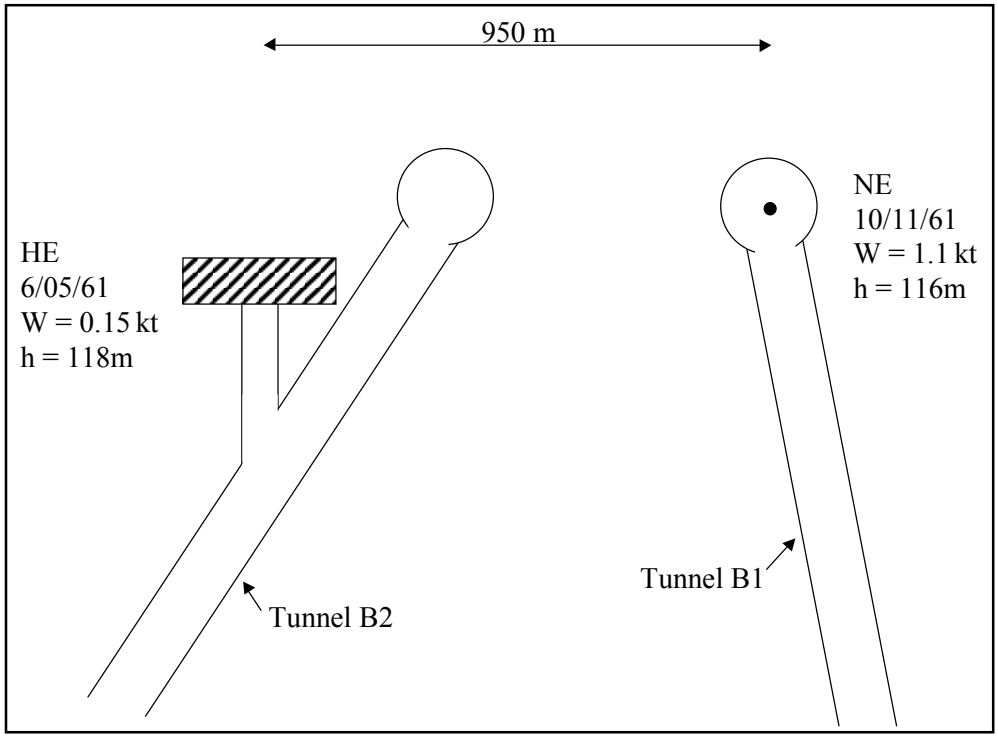


Figure 3. Schematic diagram showing the source configurations for the nearby 150 ton CE and 1.1 kt NE events detonated at Degelen Mountain in 1961.

The average NE/CE spectral ratios determined from the P and S wave time windows, as well as the total vertical component recordings at the 39 and 84 km stations are compared in Figure 5 where it can be seen that they are all roughly independent of frequency over the range from 1 to 20 Hz, with average values ranging from about 7 to 10, which is roughly consistent with the direct ratio of the two yields (i.e. 7.3). Thus, in this case, it does not appear that the seismic coupling of the CE event was greater than that of an NE event of comparable yield by the often quoted factor of two. Moreover, it is surprising that the spectral ratios appear to be independent of frequency in that the nominal source corner frequency of the 1.1 kt NE event is on the order of 5 Hz, while that of the 150 ton CE event

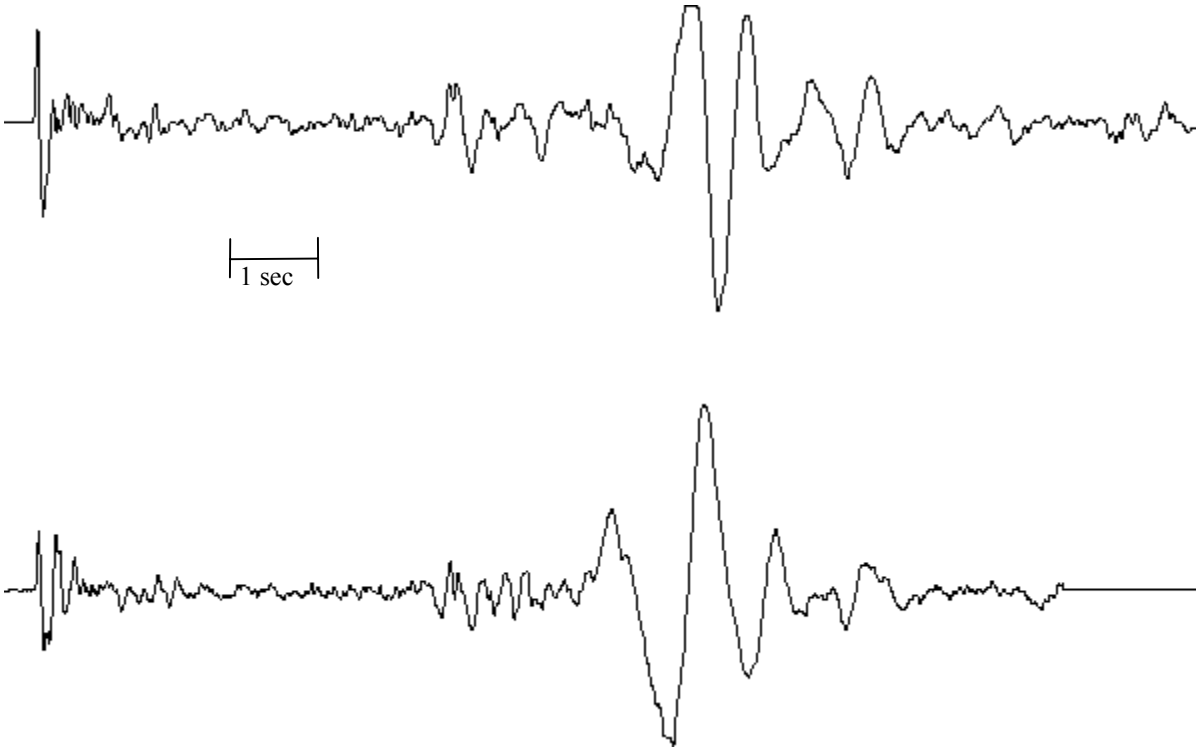


Figure 4. Comparison of vertical component recordings of the Degelen Mountain CE and NE events observed at a near-regional station at a range of 39 km. Note that the Rayleigh wave arrival from the CE event appears to be phase reversed with respect to that from the NE event.

should be approximately a factor of two larger. It follows that, in terms of conventional explosion source theory, the spectral ratios would in fact be expected to decrease significantly between 5 and 10 Hz. Thus, it may be that both the amplitude level and frequency content of the CE seismic source have been affected by tectonic release. It will be necessary to recover and analyze the free-field data recorded from these explosions to conclusively test this hypothesis.

With regard to the third topic of our current research, it is well known that most underground nuclear explosions are followed by aftershocks which can be associated with either the cavity collapse process or with the triggering of tectonic strain release by the explosions. In fact, the detection of such aftershocks is one of the primary techniques proposed for the location of clandestine underground nuclear tests under the onsite inspection regime of the CTBT (Zucca et al, 1996). In order for this approach to be useful and reliable, it is necessary to have quantitative understanding of the dependence of aftershock activity on the explosion source characteristics. Most of the current state of knowledge regarding such explosion aftershocks is based on experience with explosions conducted at nominal containment depths at a few U.S. and Soviet nuclear weapons test sites. Thus, it is not clear how representative this experience is for the monitoring of small, deeply buried explosions in the variety of tectonic and geologic environments which must be considered in global monitoring of the CTBT. Aftershock monitoring data recorded from the more diverse Soviet PNE tests can help to supplement these test site data to provide a more extensive experience base for use in defining onsite inspection strategy. Therefore, an initial sample of 13 Soviet PNE events for which aftershock monitoring was carried out has been selected for analysis. The map locations of these explosions are shown in Figure 6 where it can be seen that they are broadly distributed across the territories of the former Soviet Union. The location symbols on this figure distinguish between those PNE events for which aftershocks were observed and those for which no aftershocks were detected. Note that, in contrast to NTS

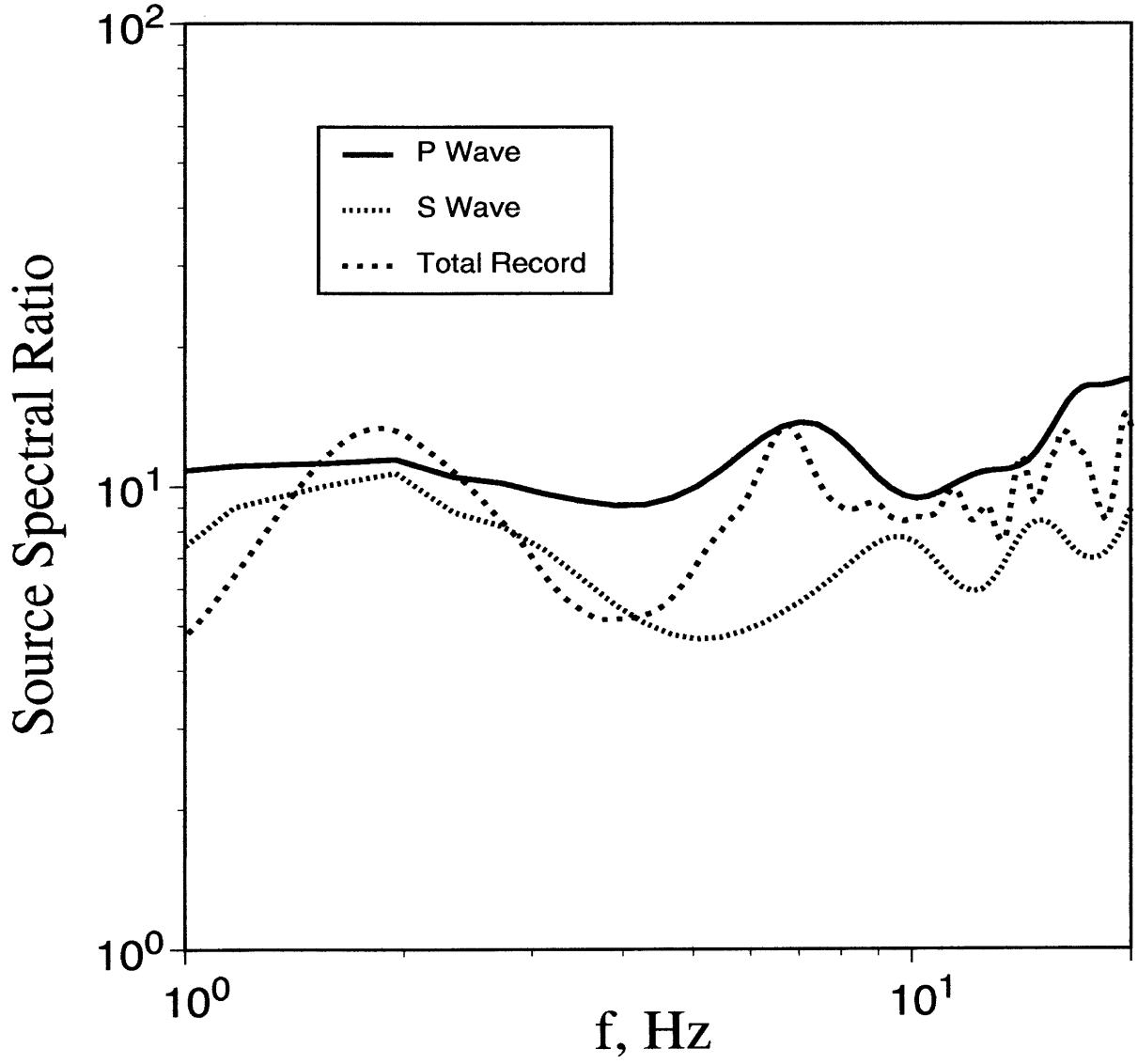


Figure 5. Average Degelen NE/CE source spectral ratios determined from data recorded at the 39 km and 84 km stations.

experience, there are a significant number of Soviet PNE events for which no aftershock activity was detected. The source parameters of these 13 PNE events are listed in Table 1 where it can be seen that the explosions for which no aftershocks were observed encompass a wide variety of source media, yields and depths of burial, although most are significantly overburied relative to the nominal nuclear test site scaled depth of burial criterion. However, the four PNE events of Table 1 for which aftershocks were observed were also low yield, overburied explosions, so these can not be the only factors controlling the occurrence of aftershocks. For each of the four PNE events for which aftershocks were observed, the dependence of aftershock frequency of occurrence and magnitude on elapsed time after the explosion was investigated in detail. It was found that for two of the explosions (Helium-3 and Quartz-4) the aftershock activity ceased completely within 8 hours after the explosion, while those from Ruby-1 ceased within 20 hours and those from Kama-1 ceased within 67 hours. Thus only one of these 13 PNE events triggered aftershock activity which might conceivably have been detected by seismic monitoring associated with an onsite inspection. These results are currently being compared with other observations from nuclear tests at weapons test sites in the U.S. and Former Soviet Union in an attempt to better quantify the probability of their detection under a CTBT onsite inspection regime.

Table 1. Source Parameters of Soviet PNE Events Analyzed For Explosion-Induced Aftershocks

Aftershocks Observed

DATE	NAME	LAT, N	LON, E	YIELD, kt	h, m	EDIUM
7/08/74	Kama-1	53.7	55.1	10	2123	limestone
9/17/84	Quartz-4	55.8	87.5	10	557	granite
4/19/87	Helium-3	60.6	57.2	3.2	2015	limestone
9/06/88	Ruby-1	61.4	48.1	7.5	793	anhydrite

No Observed Aftershocks

DATE	NAME	LAT, N	LON, E	YIELD, kt	h, m	EDIUM
12/06/69	Mangyshlak-1	43.9	54.8	31	407	chalk
6/25/70	Magistral	52.2	55.7	2.3	702	salt
12/12/70	Mangyshlak-2	43.8	54.9	85	497	chalk
12/23/70	Mangyshlak-3	44.0	54.9	75	740	clay
12/22/71	Azgir 3-1	47.9	48.1	64	986	salt
4/11/72	Crater	37.3	62.1	14	1720	limestone
9/30/73	Sapphire-2	51.7	54.6	6.6	1145	salt
8/10/77	Meterorite-5	51.0	111.0	8.5	494	granite
9/10/77	Meterorite-4	44.0	54.9	75	740	clay

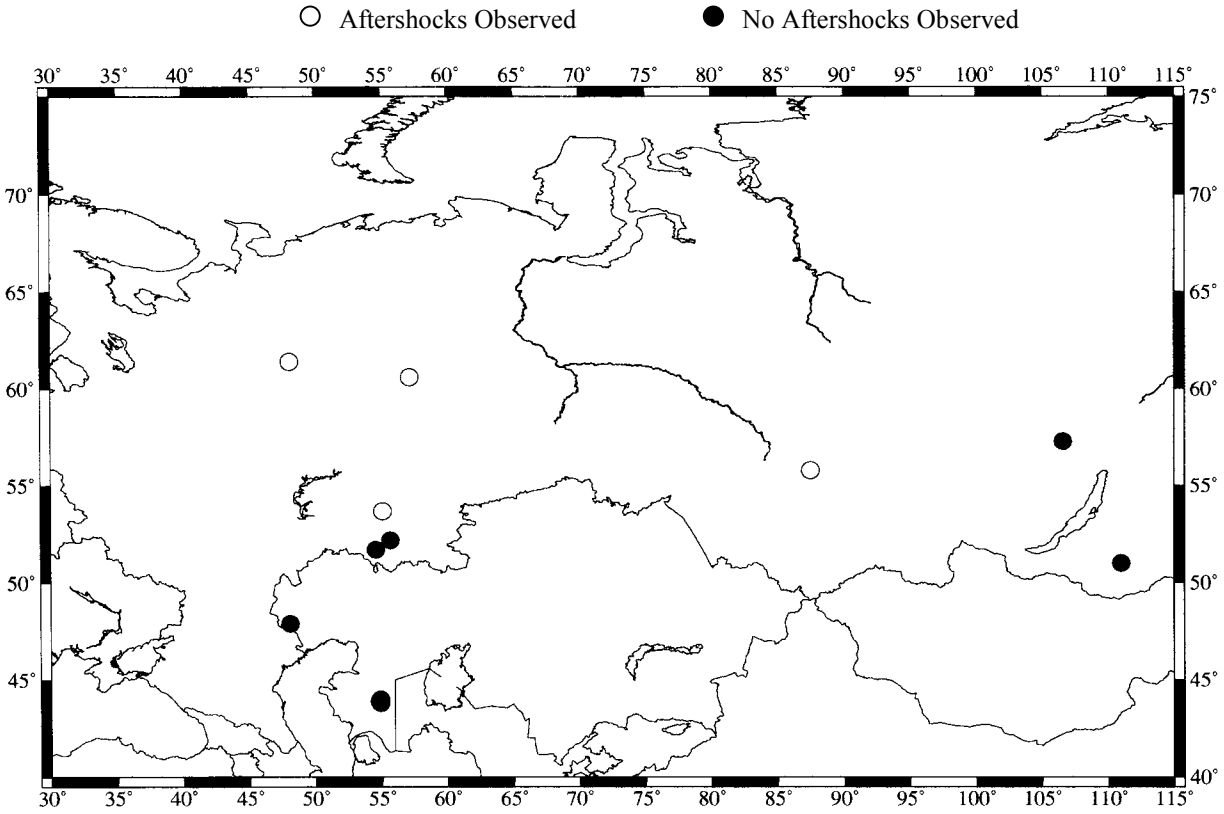


Figure 6. Map locations of Soviet PNE events for which onsite monitoring for aftershock activity was carried out.

CONCLUSIONS AND RECOMMENDATIONS

A three year study has now been completed in which data recorded from Soviet PNE events have been analyzed to assess their implications with respect to the identification of clandestine underground nuclear tests under the CTBT. A seismic source summary for Soviet PNE events has been published (Sultanov et al, 1999) which lists the best currently available source parameters for 122 PNE experiments conducted between 1965 and 1988. In addition, broadband regional seismic data recorded from a number of these PNE events and nearby earthquakes at the Borovoye station and other temporary stations have been systematically analyzed to quantify regional discrimination capability with respect to such events. The results of these analyses have indicated that, while the conventional high frequency S/P discriminants generally separate these explosion and earthquake populations, there is evidence that additional research will be required before low yield, overburied explosions in hardrock media can be consistently identified with high confidence using such discriminants. A comparison of near-regional seismic signals recorded from nearby CE and NE events at Degelen Mountain has also been completed and evidence has been found which indicates that tectonic release may also affect the seismic source characteristics of CE events, further complicating the seismic discrimination of these two types of tamped underground explosions. Finally, the results of near-field aftershock monitoring of a number of Soviet PNE events have been reviewed and it has been found that a surprisingly large number either produced no detectable aftershocks or produced brief aftershock sequences which ceased within 20 hours after the explosion. Such experience will have to be considered in evaluations of the reliability of aftershock monitoring to identify clandestine underground nuclear test locations during possible onsite inspections under the CTBT.

Key Words: seismic, discrimination, regional, Soviet PNE, Borovoye, aftershocks

REFERENCES

Fisk, M., S. Bottone, H. Gray and G. McCartor (1999), "Event Characterization Using Regional Seismic Data", Proceedings of the 21st Seismic Research Symposium: Technologies for Monitoring the Comprehensive Nuclear-Test-Ban Treaty, LA-UR-99-4700.

Sultanov, D. D., J. R. Murphy and Kh. D. Rubinstein (1999), "A Seismic Source Summary For Peaceful Nuclear Explosions," *Bull. Seism. Soc. Am., 89*, pp. 640-647.

Zucca, J. J., C. Carrigan, P. Goldstein, S. Jarpe, J. Sweeney, W. L. Pickles and B. Wright (1996), "Signatures of Testing: On-Site Inspection Technologies" in Monitoring a Comprehensive Test Ban Treaty, Proceedings of the NATO Advanced Study Institute, Kluwer Academic Publishers.

IMPROVED FOCAL DEPTH DETERMINATION FOR USE IN CTBT MONITORING

John R. Murphy and Ronald W. Cook
Geophysics Group, Maxwell Technologies, Inc.

William L. Rodi
Earth Resources Laboratory, Massachusetts Institute of Technology

Sponsored by the Defense Threat Reduction Agency
Arms Control Technology Division
Nuclear Treaties Branch

Contract No. DSWA01-97-C-0127

ABSTRACT

Seismic event location remains as one of the most important discriminants for separating natural tectonic and explosive events. However, in order to be useful for discrimination purposes, the uncertainties associated with seismic locations must be well defined and reliable, and this has proven to be difficult to accomplish to the required degree of accuracy. In particular, high-confidence estimation of focal depths remains as an outstanding monitoring problem. During the past year, we have continued to pursue a research program which is directed toward the development of improved detection and identification procedures for the depth phases pP and sP, as well as with formulation of a new algorithm for computing more reliable confidence intervals on focal depth estimates determined from P-wave first arrival times. With regard to depth phase identification , we have continued to investigate the utility of the fully automatic network stacking algorithm which maps the IDC post-P detection times at a station into candidate depth phases using the pP - P and sP – P delay times predicted by the IASPEI travel-time tables for that epicentral distance and then combines the individual station results as a function of candidate source depth. This automatic algorithm has now been applied to data from about 150 REB events in the Hindu Kush and in the Hokkaido and central Honshu regions of Japan. Prominent candidate pP and sP peaks have been identified in the resulting network detections stacks for a majority of these events, including some with m_b values as low as 3.7 and depths as shallow as 50km. Current effort on this phase of the project centers on the incorporation of the Pearce algorithm (Pearce, 1977; 1980) into the depth phase identification procedure. In this approach, the relative amplitudes of P and any candidate pP and sP phases are determined for the various observing stations and processed by the Pearce algorithm to define the range of earthquake focal mechanisms which is consistent with these relative amplitude observations. This permits the relative amplitude characteristics of candidate depth phases to be assessed for consistency with the predictions for characteristic earthquake focal mechanisms in that source region, thereby greatly increasing the confidence in the depth phase identification. The investigation of improved confidence intervals on focal depth estimation determined from P-wave first arrival times has also continued, with Monte Carlo simulations being used to define precise confidence regions corresponding to generalized model assumptions. This model is currently being carefully evaluated using data from earthquakes for which the focal depths are well constrained by verified depth phase observations and is being extended to include the formulation of an hypothesis test which will be suitable for event screening purposes.

OBJECTIVES

The objectives of this research program are to determine more reliable estimates of the uncertainties associated with the different focal depth estimation procedures and to increase the number of events which can be identified as earthquakes on the basis of focal depth through the implementation of new and improved analysis tools. This is being accomplished through the development of improved procedures for identifying and using the teleseismic depth phases pP and sP, the incorporation of regional S-P based origin

time constraints into an improved depth estimation algorithm and the development of more robust statistical hypothesis tests for use in event screening.

RESEARCH ACCOMPLISHMENTS

During the past year, work on this project has continued to focus on the development of improved tools for detection and identification of the depth phases pP and sP and on the continuation of the evaluation of a new algorithm for computing more reliable confidence intervals on focal depths determined from P wave first arrival times alone. With regard to depth phase identification, we have now completed an analysis of IMS data recorded from approximately 150 REB events located in the Hindu Kush, Hokkaido and central Honshu regions outlined in Figure 1. These data have been analyzed using a fully automated network stacking algorithm which employs signal analysis procedures similar to those originally proposed by Israelsson (1994) and more recently applied to a sample of Canadian data by Woodgold (1999). In this approach post-P arrivals observed at each station for a given event are mapped from functions of delay time to functions of source depth using the pP-P or sP-P delay times predicted by the IASPEI travel time tables for the various station distances. These functions of depth for all the stations in the detecting network are then added together to identify arrivals consistent with the predicted depth phase moveouts over the entire range of potential source depths. This transformation is illustrated in Figure 3, which shows the predicted pP moveout with respect to P as a function of source depth for two different epicentral distances. Using such predicted moveout curves, the observed delay times of all post-P arrivals with respect to P can be translated into equivalent focal depths under the hypotheses that they are either pP or sP arrivals. Those arrivals which are consistent with such hypotheses should then show up as peaks on the stacked network depth function. In the present application, difficulties associated with the variability of observed short-period signals between the widely separated IMS stations are avoided by stacking unit amplitude boxcar functions centered on the post-P detection times which are automatically determined at each station by the IDC front end signal processing procedures.

Some typical results of applying this network stacking algorithm to detection data from selected earthquakes in the Hindu Kush, Hokkaido and central Honshu regions are presented in Figures 3-5, respectively, where it can be seen that in each case there is a prominent peak near the corresponding REB depth which would be readily identified as a candidate pP depth phase. This procedure has now been systematically applied to all 150 REB events in our selected sample, and it has been found that prominent candidate pP and/or sP peaks can generally be identified in the resulting network stacks for a majority of these earthquakes, including some with mb values as low as 3.7 and depths as shallow as 50km. Thus, it appears that the proposed network stacking algorithm is effective at providing fully automated detection of candidate pP and sP arrivals at IMS network stations.

Of course, the automatic process described above only considers the consistency in timing of detections across the network and subsequent analyst review would be required to confirm the depth phase identification with high confidence. We have been investigating the feasibility of using the information inherent in the observed relative amplitudes of the various P arrivals at different stations to increase the confidence in the identification of such candidate depth phases. In this approach, the recorded short-period waveforms corresponding to the stations for which the automatic detections have been stacked are first presented to the analyst aligned on the time corresponding to the candidate depth phase peak under investigation. Such a display of the P wave data recorded from the Hindu Kush earthquake of 1995/08/17 is presented in Figure 6, where it can be seen that there are indeed some prominent arrivals at the predicted pP times corresponding to this candidate depth phase peak. Also shown on this figure are the annotated relative P and pP amplitude values which have been interactively estimated by an analyst. It has been shown by Bob Pearce of the IDC (Pearce, 1977; 1980) that such relative amplitude data can be systematically evaluated to identify the range of earthquake focal mechanisms which is theoretically consistent with the observations, and such information can potentially lead to greatly increased confidence in depth phase identification. That is, in principal, candidate depth phase amplitude data from an event under investigation can be used to define a range of permissible focal mechanisms consistent with these observations, and the compatibility of these focal mechanisms with the known regional tectonics can be assessed to further test the credibility of the proposed phase identification. One source of such regional

tectonic information is the historical Harvard centroid moment tensor (CMT) catalog, solutions from which are summarized for our selected Hindu Kush study area in Figure 7.

As an example of this validation process, the observed relative amplitude data from the Hindu Kush earthquake of Figure 6 have been processed using the RAMP code developed by Pearce (1980) to identify the range of permissible focal mechanism solutions which are theoretically consistent with these observed P/pP amplitude ratios. The resulting range of permissible solutions is graphically summarized in Figure 8 (left), where these solutions are compared with the range of focal mechanisms corresponding to the observed historical Harvard CMT solutions for the Hindu Kush region (right) from Figure 7. It can be seen that , in this case, a number of permissible solutions inferred from the phase amplitude rations for this event are consistent with historical CMT solutions for this region, which greatly increases the confidence of the identification of this candidate depth phase as pP.

With regard to focal depth estimates based on P wave first arrivals alone, we previously developed an approach to computing confidence intervals on focal depth that accounts for such complexities as nonlinearity of traveltime as a function of focal depth, uncertainty in the variance of arrival time picks, and errors in traveltime tables ("modeling errors"). Our approach defines a confidence interval as the set of focal depths that cannot be rejected at a given confidence level, using a likelihood ratio test statistic in the rejection test. To avoid linearity assumptions, Monte Carlo simulation is used to estimate the needed distribution of the test statistic. We are now extending our algorithm to perform a focal-depth discrimination test. For this test, the null hypothesis is that the focal depth is anywhere in the interval 0 to 10 km, in contrast to considering each individual depth as in the computation of confidence intervals. The test statistic is still taken to be a likelihood ratio, whose distribution is inferred by simulation. The result of the computation is the highest confidence level at which $0 < z < 10$ km can be rejected. If this level is sufficiently high (e.g., > 95%), a shallow focus can be rejected for the purposes of discrimination. We are currently applying our proposed focal depth discriminant to events in the northern and southern portions of our Hindu Kush study region, taking into account the uncertainty in the traveltime correction at station NIL.

CONCLUSIONS AND RECOMMENDATIONS

A research investigation directed toward the development of improved tools for detection and identification of the depth phases pP and sP and the evaluation of a new procedure for computing more reliable confidence intervals on focal depth estimates based on P wave first arrival times alone has now been largely completed. A principal result of this investigation has been the development and testing of a fully automatic algorithm for stacking raw IMS detection data to identify candidate depth phases for further review by the IDC analyst. This automatic algorithm has now been applied to data from about 150 REB events in the Hindu Kush, Hokkaido and Honshu regions. Prominent candidate pP and sP peaks have been identified in the resulting network detection stacks for a majority of these events, including some with m_b values as low as 3.7 and depths as shallow as 50 km. We conclude that this new automatic network stacking algorithm holds promise for providing a useful tool which could be used by IDC analysts to make more frequent and more reliable depth phase picks for use in event screening. Most recently, we have been extending this automatic procedure to permit the analyst to review any candidate depth phases and to assess their consistency with what is known about the regional tectonic environment in which the event occurred. In particular, the Pearce algorithm is being used to define the permissible range of focal mechanisms consistent with the relative amplitudes of P and any candidate pP and sP phases for a particular event, and these solutions are being compared with the range of observed focal mechanisms for that source region as represented by the historical Harvard CMT solutions. Initial tests of this evaluation procedure indicate that it can provide confirming evidence which could significantly increase the confidence in depth phase identification. It is our recommendation that these procedures be further refined and then tested in the IDC operational environment using the PIDC testbed. With regard to the determination of improved confidence intervals on depth, a more rigorous statistical method based on Monte Carlo simulation and grid search has now been implemented as is currently being evaluated using data recorded from Hindu Kush earthquakes with well-constrained focal depths.

Key Words: seismic, focal depth, discrimination, prototype International Data Centre, Hindu Kush

REFERENCES

Israelsson, H. (1994), "Stacking of Waveforms for Depth Estimation," Center for Seismic Studies Final Report C95-02

Pearce, R. G. (1977), "Fault Plane Solutions Using Relative Amplitudes of P and pP", Geophys. J. R. Astron. Soc., 50, 381-394

Pearce, R. G. (1980), "Fault Plane Solutions Using Relative Amplitudes of P and Surface Reflections: Further Studies", Geophys. J. R. Astron. Soc., 60, 459-487.

Woodgold, C.R.D. (1999), "Wide Aperture Beamforming of Depth Phases by Timescale Contraction." Bull. Seism. Soc. Am., 89, pp.165-177.

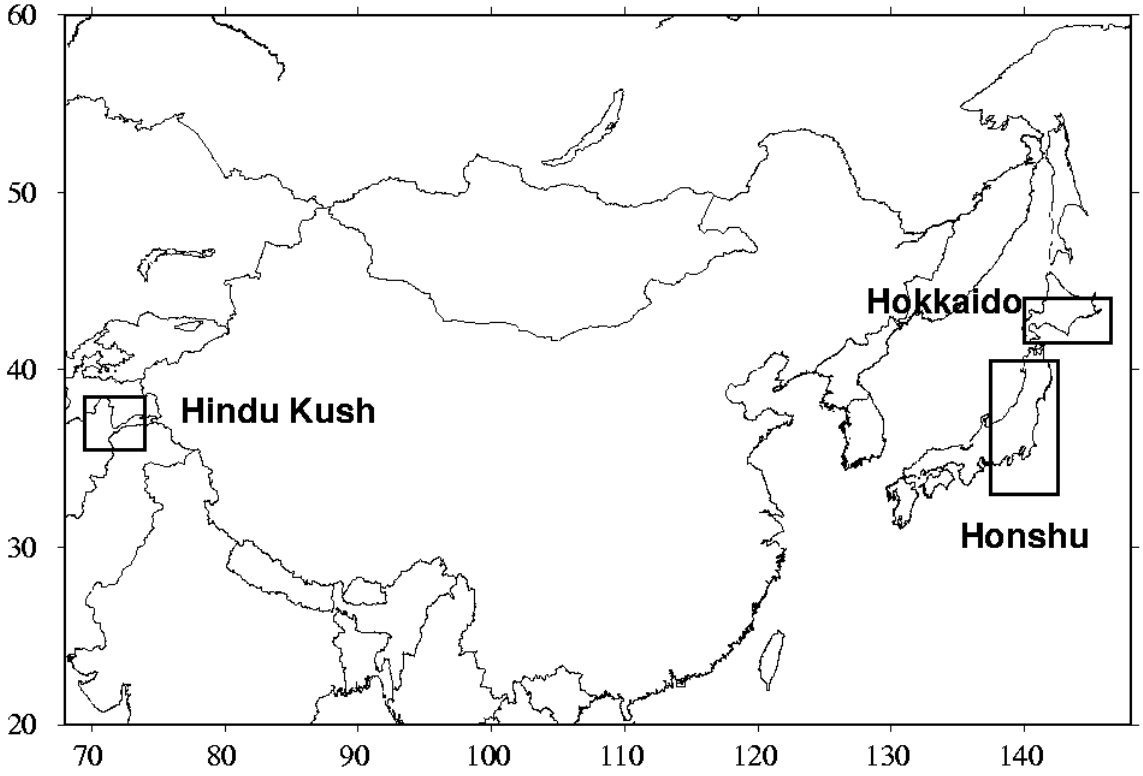


Figure 1. Map locations of the events in the Hindu Kush, Hokkaido and central Honshu regions used in the evaluation of the depth phase stacking algorithm.

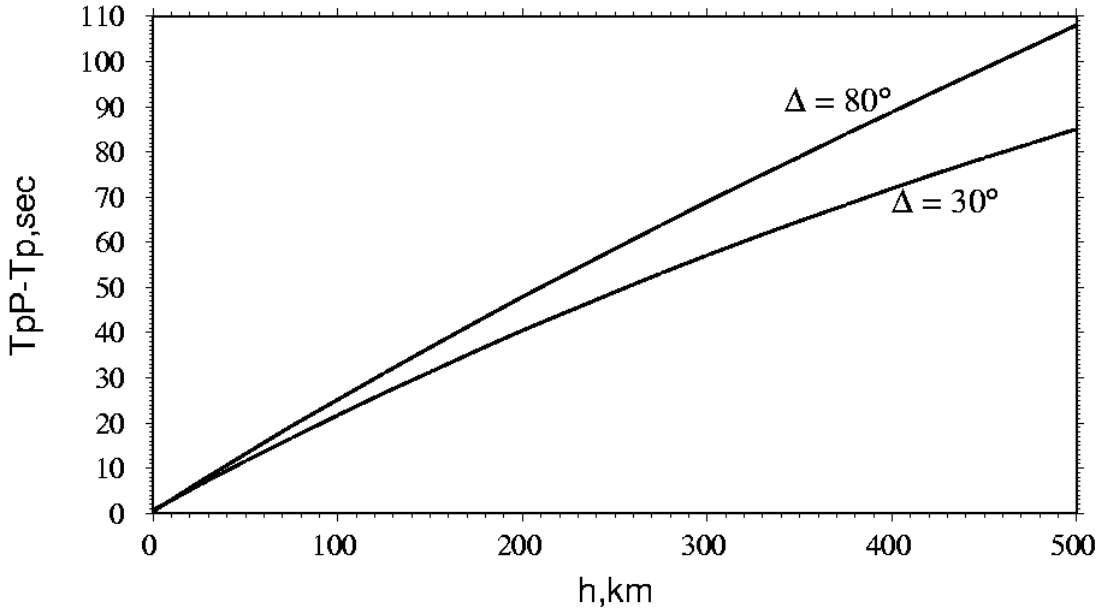


Figure 2. pP-P moveout times as a function of focal depth at fixed epicentral distances of of 30 and 80 degrees.

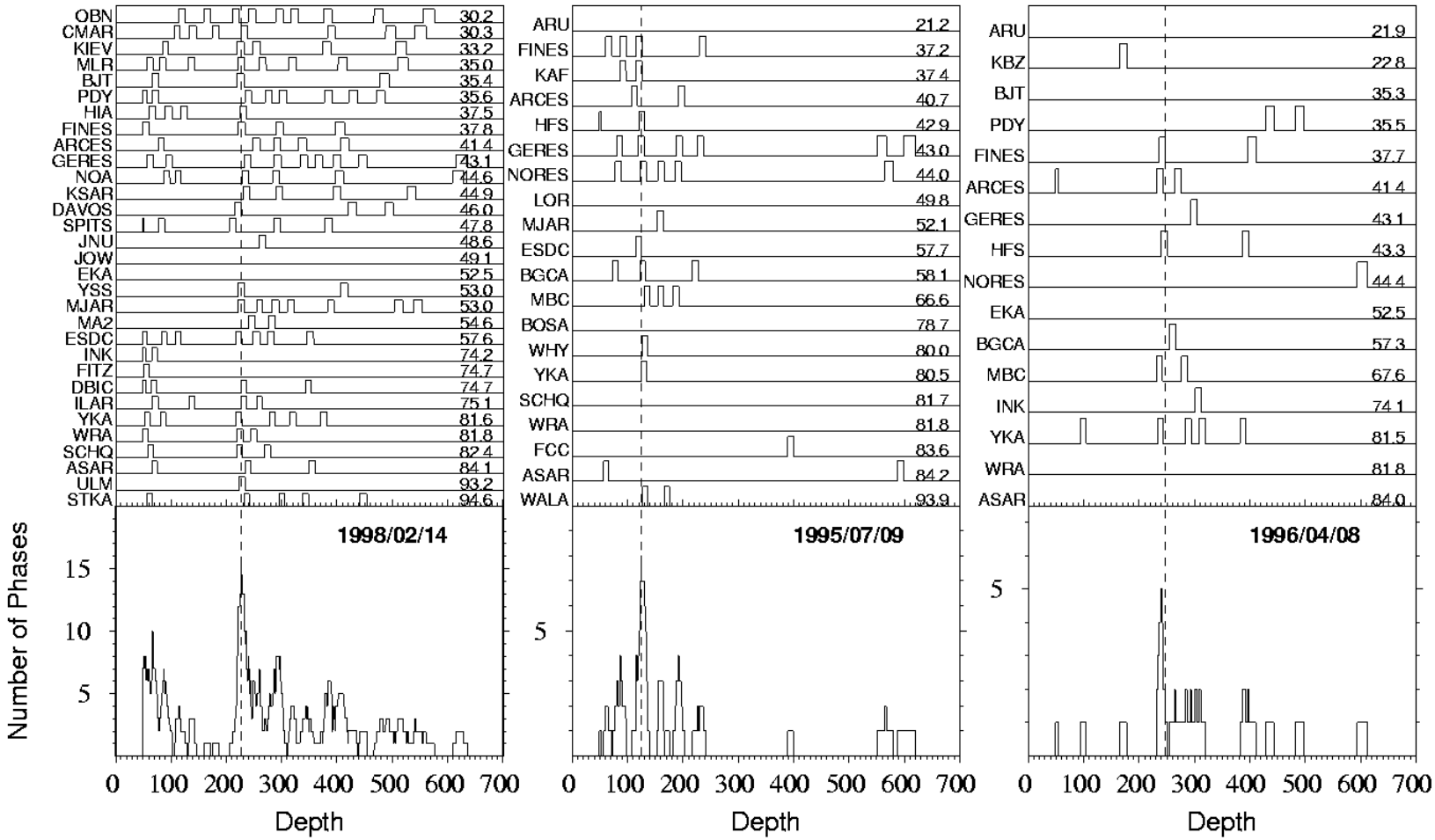


Figure 3. Network detection stacks of pP for the Hindu Kush earthquakes of 1998/02/14 (m_b = 5.03), 1995/07/09 (m_b = 4.40) and 1996/04/08 (m_b = 4.04). Note the prominent peaks near the corresponding REB depths which are indicated by the dashed vertical lines on these figures.

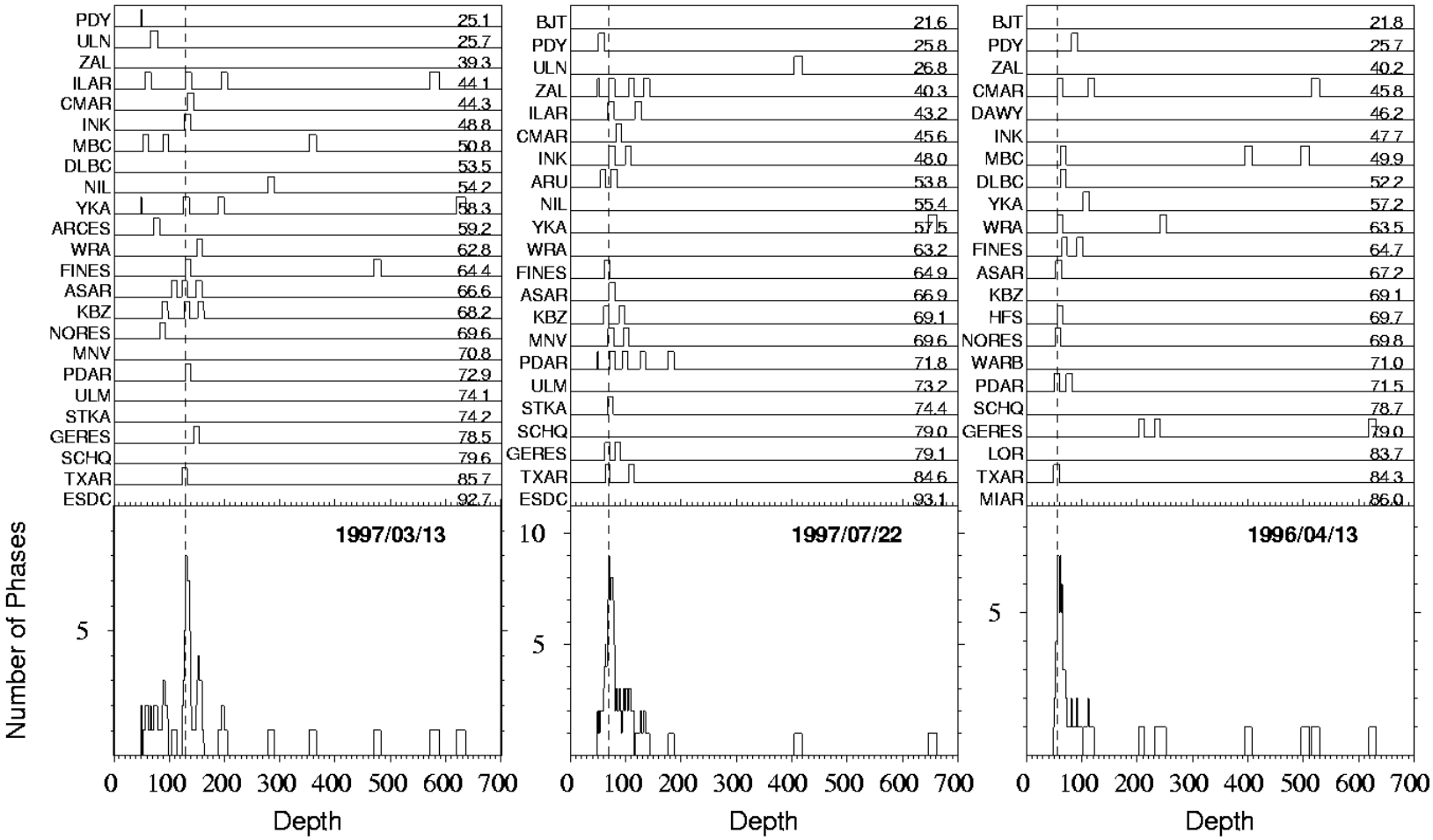


Figure 4. Network detection stacks of pP for the Hokkaido earthquakes of 1997/03/13 (m_b = 4.34), 1997/07/22 (m_b = 3.97) and 1996/04/13 (m_b = 3.82). Note the prominent peaks near the corresponding REB depths which are indicated by the dashed vertical lines on these figures.

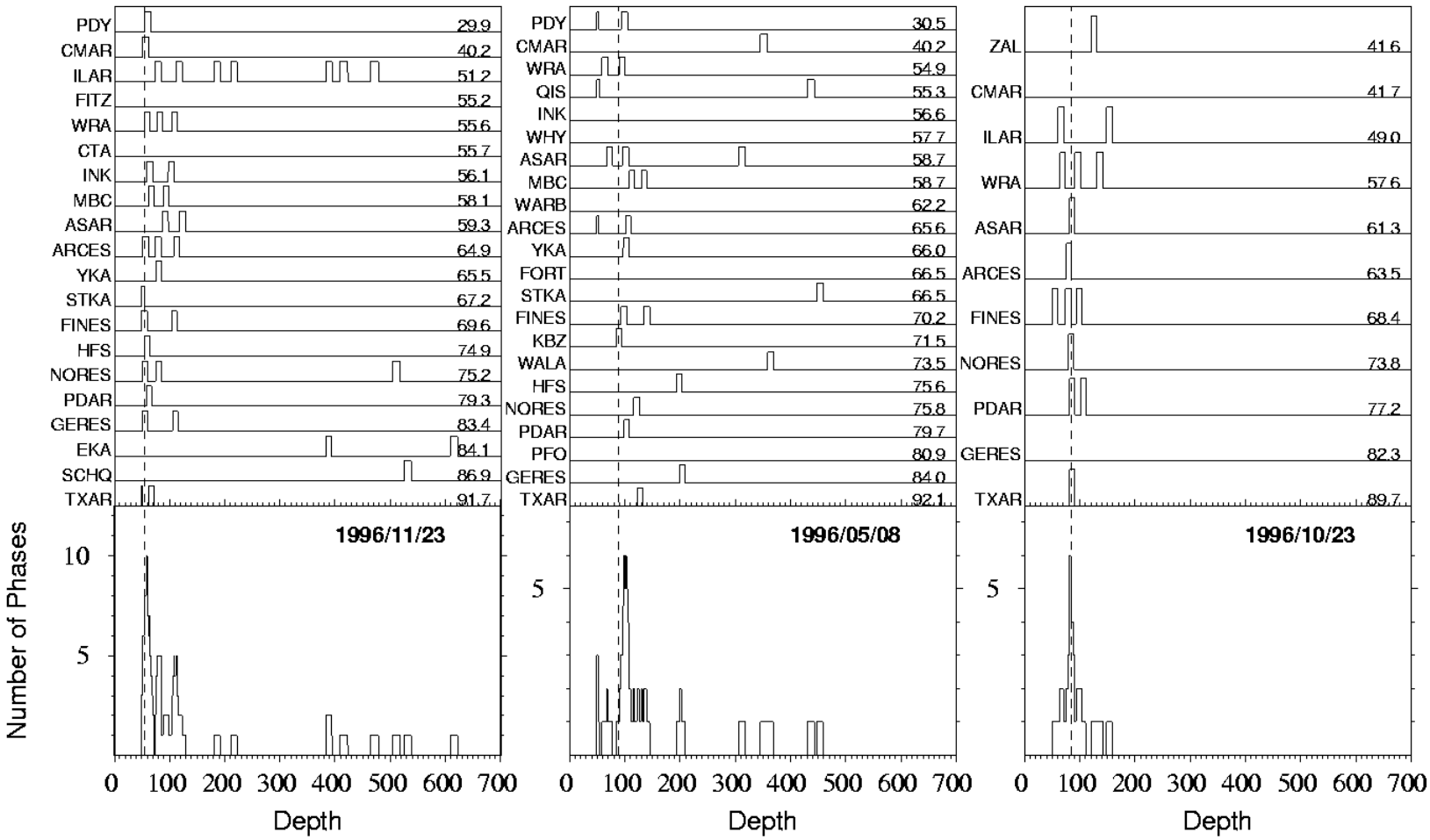


Figure 5. Network detection stacks of pP for the central Honshu earthquakes of 1996/11/23(m_b = 4.32), 1996/05/08 (m_b = 3.86) and 1996/10/23 (m_b = 3.79). Note the prominent peaks near the corresponding REB depths which are indicated by the dashed vertical lines on these figures.

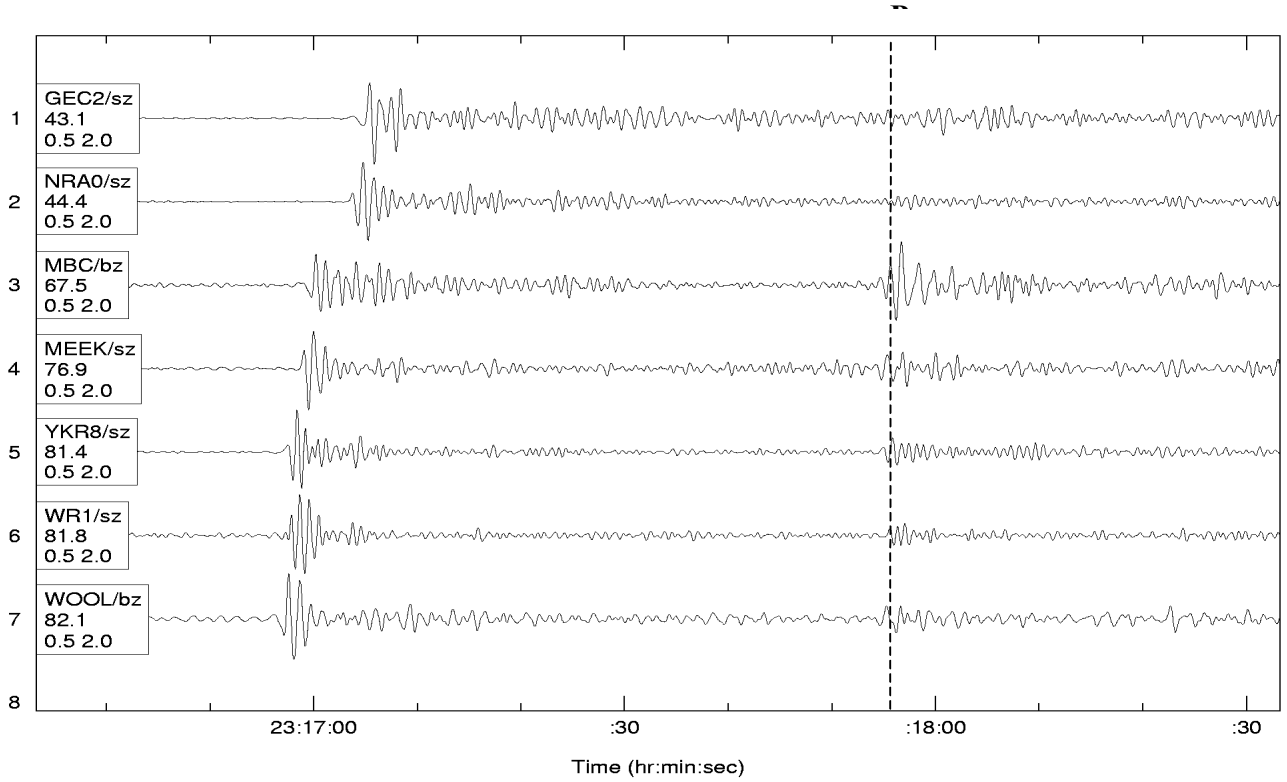


Figure 6. Vertical component teleseismic recordings of the Hindu Kush earthquake of 1995/08/17, shown aligned on the candidate pP phase arrival time identified by the network stacking algorithm. The annotated numerical values on each trace denote the relative amplitudes of P and pP to be used as input to the Pearce focal mechanism code RAMP.

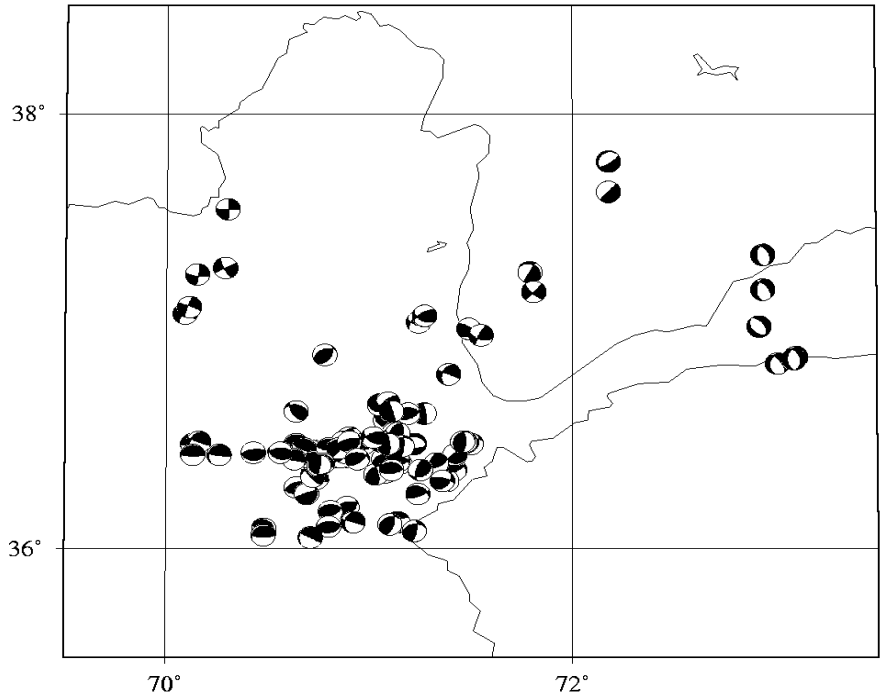


Figure 7. Harvard CMT focal mechanism solutions for historical earthquakes in the Hindu Kush region.

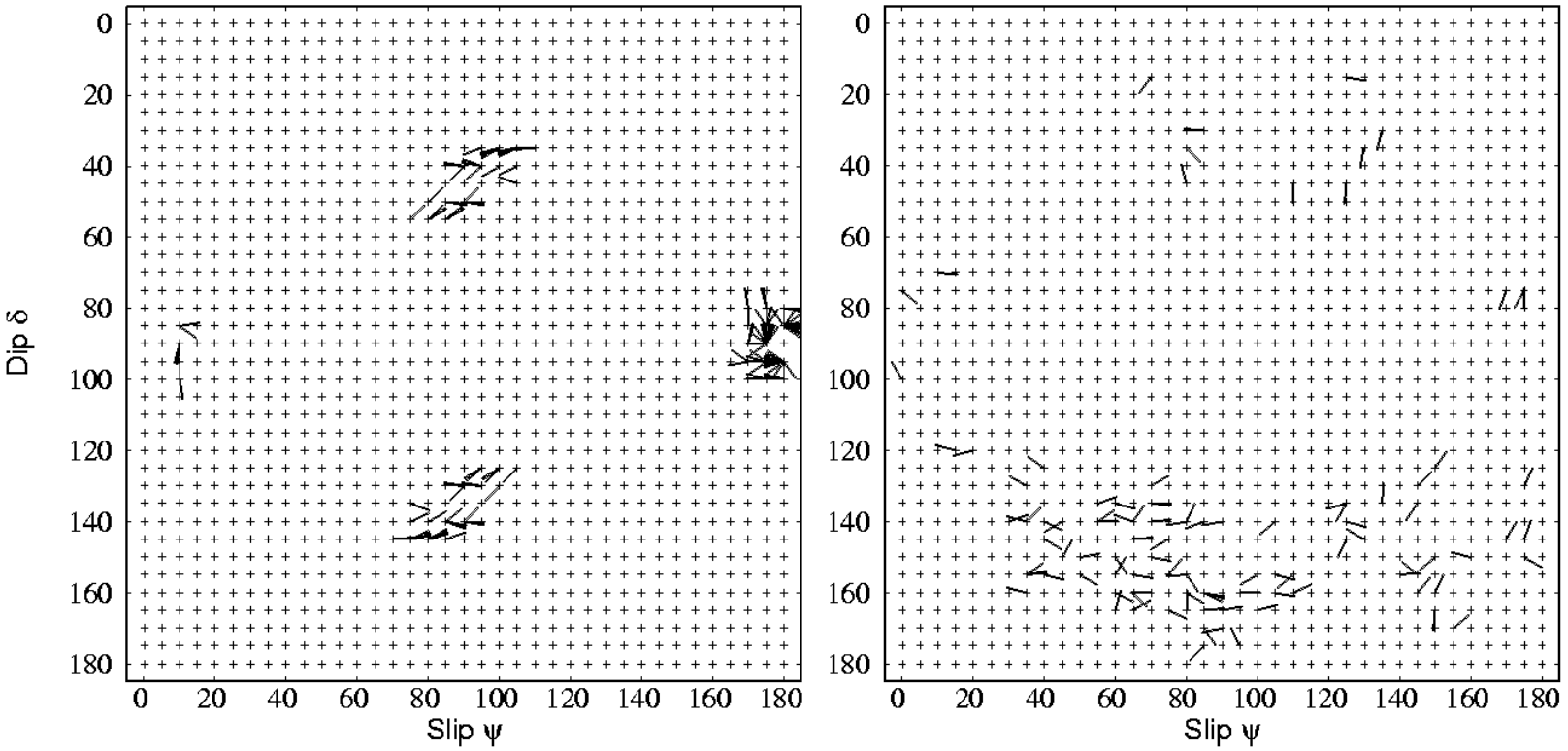


Figure 8. Comparison of permissible focal mechanism solutions for the Hindu Kush earthquake of 1995/08/17 determined by the RAMP code from the observed P/pP amplitude ratios (left) with the historical Harvard CMT solutions for earthquakes in this region (right). The orientations of the line segments representing the individual solutions indicate the strikes of the focal mechanisms, measured clockwise from north.

M_s : m_b RELATIONSHIPS FOR SMALL MAGNITUDE EVENTS: OBSERVATIONS AND PHYSICAL BASIS FOR m_b BASED ON REGIONAL PHASES

Howard J. Patton
Los Alamos National Laboratory

Sponsored by U.S. Department of Energy
Office of Nonproliferation Research and Engineering
Office of Defense Nuclear Nonproliferation
National Nuclear Security Administration

Contract No. W-7405-ENG-36

ABSTRACT

To address the challenge of small event monitoring for the Comprehensive Nuclear-Test-Ban Treaty (CTBT), there is great interest to extend the successful teleseismic m_b-M_s discriminant to regional-distance applications. Among the outstanding issues are (1) how well can we expect the discriminant to perform for regional data as a function of source size and (2) what is the physical basis behind its performance. In a recent paper Patton (2000), M_w: m_b scaling relationships for Pn and Lg waves with 1-s periods were developed for earthquakes and explosions located in distinct tectonic regions and geologic materials around the world. Among a number of findings of that study is the result that m_b(Pn) for explosions scales at a significantly higher rate than m_b(Lg) in the M_w range ~3.5 - 6.0. On the other hand, Pn and Lg scaling rates do not differ for earthquakes. On plots of M_s versus m_b(Pn), the scaling results suggest that earthquake and explosion populations converge at M_s ~ 1 -2, while populations may or may not converge on plots of M_s versus m_b(Lg), and show better separation at small magnitudes. Observations of regional M_s for small-yield explosions at the Nevada Test Site (NTS) confirm the scaling predictions. Thus, m_b based on regional shear phases may serve as a better m_b-M_s discriminant than m_b based on regional compressional phases, a surprising conclusion. These findings certainly cannot be explained by simple theories of the explosion source, and I propose a physical model combining well-established scaling models and the latest understanding of Lg generation by underground nuclear explosions.

Key Words: discrimination, regional monitoring, physical basis, regional phases

OBJECTIVE

The objective of this project is (1) to characterize m_b-M_s scaling for earthquakes and explosions using regional-distance observations and (2) to provide a physical basis for the scaling and for discrimination performance at small magnitudes. One of the greatest challenges of monitoring a CTBT is discriminating man-made seismic events from natural events at low source strengths, and this project seeks an understanding of the potential at small magnitudes using extensions of the m_b-M_s discriminant to regional data.

RESEARCH ACCOMPLISHED

A recent study of regional scaling relations found that m_b(Pn) scales at a higher rate than m_b(Lg) on plots of M_w versus m_b for explosions detonated at NTS (Patton, 2000). Scaling relations for explosions at Semipalatinsk and other hard-rock test sites suggested similar differences between Pn and Lg scaling rates, but the data sets were smaller and showed more scatter than NTS observations, and as a result, estimates of scaling rates were less certain. In contrast to explosions, earthquakes did not show differences in scaling rates for Pn and

Lg waves. In this paper, I provide further evidence that source scaling of 1-Hz Pn and Lg waves is different for NTS explosions, and I propose a physical model to explain why this might be. The verification significance of this work relates to characterization of m_b-M_s scaling and to the discrimination potential at small magnitudes. This characterization is the subject of current research, but some tentative results will be examined.

Both m_b(Pn) and m_b(Lg) were measured for most explosions conducted at NTS in order to develop better technologies for estimating seismic yield (e.g., Nuttli, 1986; Patton, 1988; Vergino and Mensing, 1990). Of special interest to this project is the frequently overlooked fact that yield-scaling reported for Lg and Pn waves differed for explosions detonated in tuff, as summarized in the table below.

Table 1: Yield-scaling results for NTS explosions (after Patton; Vergino and Mensing)

Phase	Test Region	Intercept	Yield Slope	Gas Porosity Slope
Lg	Yucca, AWT	3.52	0.96*	–
Lg	Yucca, AWT	4.13	0.75	–0.025
Lg	Yucca & Pahute, BWT	4.18	0.76*	–
Pn	So. Yucca, AWT & BWT	3.84	0.91	–0.027
Pn	Pahute, AWT & BWT	3.87	0.91	–0.027

* Yield slope when gas porosity is left out of the regression model.

Patton (1988) found that after accounting for the effects of gas porosity, yield scaling of 1-Hz Lg waves for explosions above the water table (AWT) is the same as it is for explosions below the water table (BWT). The same effect of gas porosity is seen for Pn waves (Vergino and Mensing), but the slope on log yield, 0.91, is significantly greater than it is for Lg waves, 0.76. Thus, Pn scaling rates with official yield are 20% higher than they are for Lg waves. For comparison, estimates of scaling slopes on plots of M_w versus m_b for NTS explosions are 1.37 ± 0.03 and 1.22 ± 0.03 for Pn and Lg waves, respectively (Patton, 2000), a 12% difference.

Direct comparisons of m_b(Pn) and m_b(Lg) should also reveal differences in scaling for NTS explosions. Figure 1 shows such a plot for 243 explosions ranging ~3 orders of magnitude in yield. A linear regression yields a slope of 1.13 ± 0.02. In other words, m_b(Pn) scales at a rate 13% higher than Lg waves. This estimate is about the same percentage as the one obtained from M_w versus m_b data, which used explosions detonated in a variety of media, just as Figure 1 does. The yield-scaling results in Table 1 pertain just to explosions fired in tuff and rhyolite. In any case, summarizing for NTS explosions, scaling rates are not the same for regional phases based on compressional (Pn) and shear wave (Lg) phases, as various scaling relationships reveal that rates for Pn are ~13 to 20% higher than they are for Lg.

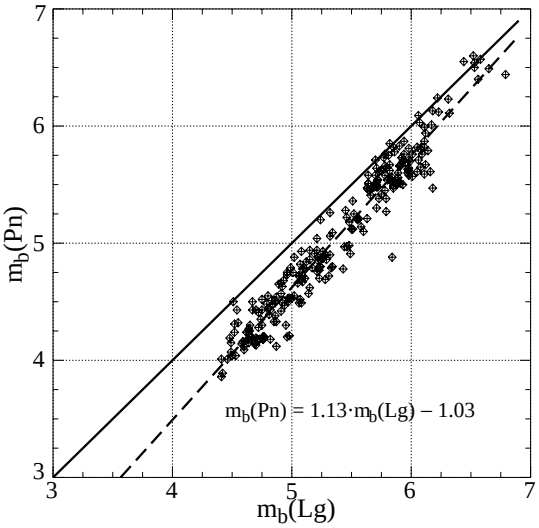


Figure 1. Regional m_b for NTS explosions. Dash line is a regression fit to the data; solid line represents equality.

A Physical Model. In this sub-section, a model combining the basic tenets of the Mueller-Murphy model (Mueller and Murphy, 1971; M-M) with recent insights into Lg generation by underground explosions is proposed to explain the differences in source scaling between Pn and Lg waves. In this development, I use the concept of an "effective" source function. An effective source function combines the features of a traditional source function with the effects of complex wave propagation on seismic wave generation. In this case, the propagation effects occur so close to the source that it is impossible to separate them in far-field data from intrinsic source properties. An example of such propagation effects is near-field Rg-to-S scattering. Gupta *et al*. (1992) proposed that this scattering mechanism is particularly effective for generating low-frequency crustal S waves (< 2 Hz) by explosions because of their shallow depth of burial and efficient Rg excitation characteristics. Subsequent research, both observational (Patton and Taylor, 1995; Gupta *et al*., 1997; Myers *et al*., 1999) and synthetic (e.g., Jih, 1993; 1995), has supported this proposed mechanism. The model of Rg-to-S scattering has undergone some refinements with subsequent research. In particular, excitation nulls observed in spectral amplitudes of Lg waves (Patton and Taylor, 1995; Gupta *et al*., 1997) were interpreted to be caused by the imprint of Rg source spectra excited by a compensated linear vector dipole (CLVD). These nulls are related to focal depth of the CLVD source, which is a kinematic description of spall phenomena occurring in the geologic strata over the explosion point source. Thus, while the explosion source is an efficient source of Rg waves, spallation, which reaches to the free surface and has a centroid depth even shallower than the explosion, appears to be even more efficient generating Rg waves that scatter into 1-Hz Lg observed in the far-field. Another key observation is that effects of Rg-to-P scattering are absent in the spectra of Pg waves from underground explosions (Patton and Taylor, 1995), suggesting that this mechanism plays a lesser role in the excitation of regional P waves.

Based on this evidence, I argue that differences in scaling rates of Pn and Lg waves might be caused by the fact that effective source functions for these phases are not similar, nor do they scale alike. The model I will develop is illustrated in the figure below.

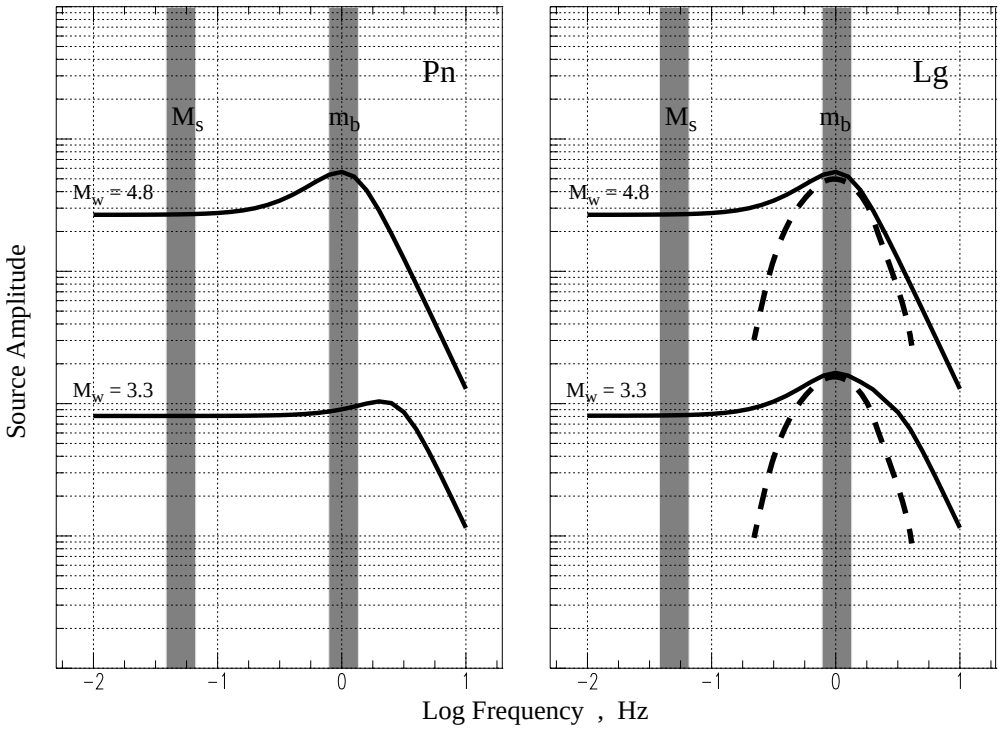


Figure 2. Effective Pn and Lg source functions for explosions with yields of 100 and 1 kt (solid lines) and idealized Rg-to-S scattering functions (dash lines). For illustration purposes, the Lg source function at 100 kt is simply the M-M spectrum plotted for Pn waves, while for 1 kt, it is a hybrid formed by vertically shifting the 100-kt spectrum down, interpolating, and suturing the 1-kt M-M spectrum at ~3 Hz.

The Pn source functions are represented by M-M spectra for 100 and 1 kt explosions in granite with P-wave speeds, α, of 5 km/s, S-wave speeds, β, of 3 km/s, and density, ρ, 2.5 g/cm^3. As source size decreases, the spectral overshoot moves out of the 1-Hz band to higher frequencies. Lg effective source functions are modeled as a composite of the M-M spectrum and a narrow band spectrum representing the contribution of Rg-to-S scattering. While the M-M spectrum scales with source size, the scattering spectrum does not because it is a property of the near-source velocity medium. The bump in Lg spectra is hypothesized to persist at small yields for frequencies near 1 Hz, because Rg-to-S scattering is strong in this band for large and small events.

To relate this model to observations of scaling differences, an analytical expression is needed for the slope, $\Delta m_b(Pn)/\Delta M_w$. First note that

$$M_w \sim 2/3 \cdot \log M_o \sim 2 \cdot (\log \Psi_\infty + \log I_\alpha) / 3 \quad ,$$

and

$$\Delta M_w = 2 \cdot (\Delta\log \Psi_\infty + \Delta\log I_\alpha) / 3 \quad \text{and} \quad I_\alpha = \rho\alpha^2 \quad ,$$

where M_o is the seismic moment of an explosion, which equals $4\pi I_\alpha \Psi_\infty$ (Aki *et al.*, 1974), and Ψ_∞ is the static level of the reduced displacement potential (RDP). I_α is referred to as source medium "impedance." Second, using equation 4.88 of Aki and Richards (1980), we can relate the far-field amplitude, A(f), to the source function, S(f), as follows

$$m_b(Pn) \sim \log A(1\ Hz) \sim \log S(1) - 1/2 \cdot \log \alpha I_\alpha \quad ,$$

and

$$\Delta m_b(Pn) = \Delta\log S(1) - 1/2 \cdot \Delta\log \alpha I_\alpha \quad ,$$

where Pn propagates as a body wave in the mantle and S(1) refers to the source amplitude in the 1-Hz band. Therefore, an analytical expression for the scaling rate of Pn waves is

$$\Delta m_b(Pn)/\Delta M_w = 3/2 \cdot \frac{\Delta\log S(1) - 1/2 \cdot \Delta\log \alpha I_\alpha}{\Delta\log \Psi_\infty + \Delta\log I_\alpha} \quad . \qquad (1)$$

Invoking the Mueller and Murphy source model and letting A be Ψ_∞ for a 1-kt explosion, then $AW^{0.76}$ is Ψ_∞ for a W-kt explosion. If B is amplitude of the source function in the 1-Hz band for a 1-kt explosion, then $BKW^{0.76}$ is the amplitude for a W-kt explosion, where K is a measure of overshoot in the source function. Thus, in the range of 1 to W kt, the scaling rate can be written in terms of overshoot parameter K and yield W,

$$\Delta m_b(Pn)/\Delta M_w = 3/2 \cdot \frac{\log K + 0.76 \cdot \log W - 1/2 \cdot \Delta\log \alpha I_\alpha}{0.76 \cdot \log W + \Delta\log I_\alpha} \quad , \qquad (2)$$

where $\Delta\log I_\alpha$ is the logarithm of impedance ratio, $I_\alpha{}^W/I_\alpha{}^1$, and superscripts refer to explosion yields.

A similar development is followed to derive an expression for $\Delta m_b(Lg)/\Delta M_w$, except the source is a composite of the explosion and Rg-to-S scattering. Equation (1) above is assumed to apply to Lg waves also, and the scaling of Ψ_∞ obeys the M-M model, just as it does for Pn waves. The development departs from that of Pn waves for the 1-Hz band, where B' is amplitude of the explosion source function, and Φ is amplitude from Rg-to-S scattering. Patton (1990) found that the strength of the spall source (which is proportional to the mass of spalled material) scales as $W^{0.75}$, very nearly the same scaling as Ψ_∞ of the explosion. It follows then that amplitudes for the composite source are $B' + \Phi$ for a 1-kt explosion and $[KB' + \Phi]W^{0.76}$ for a W-kt explosion, assuming linear superposition of the explosion and Rg-to-S sources. The scaling rate for Lg waves can be written in terms of W, K and a new parameter, K′,

$$\Delta m_b(Lg)/\Delta M_w = 3/2 \cdot \frac{\log (K+K'-1)/K' + 0.76 \cdot \log W - 1/2 \cdot \Delta\log \alpha I_\alpha}{0.76 \cdot \log W + \Delta\log I_\alpha} \quad , \qquad (3)$$

where $K' = 1 + \Phi / B'$. For $K' \geq 2$, the source amplitude due to scattering is as large as or larger than the amplitude of the explosion source function. In the following sub-section, I calculate the range of acceptable models as a function of the material parameter I_α under the constraints imposed by measured scaling rates for Pn and Lg waves and associated uncertainties.

Solution Subspace. Figure 3 shows solutions for K and K′ in the subspace where the central value of $\Delta m_b(Pn)/\Delta M_w$, 1.37, is assumed. Acceptable solutions are bounded by 2-σ errors on the estimate of Lg scaling slope. The plot spans reasonable values for the overshoot parameter K, based on realizations of M-M source functions for media at NTS and yields of ~100 kt. Notice that many solutions give $K' > 2$, indicating Lg source amplitudes from Rg-to-S scattering are larger than source amplitudes from the explosion. However, many solutions have unrealistically large K′ values, especially for smaller impedance ratios, where solution space shows rapid increases of K′ values. In order to constrain solution space further, knowledge of an appropriate range for the source impedance ratio is needed for NTS. This is readily available from a large measurement data base that was developed and maintained by weapon laboratories for nuclear test containment studies.

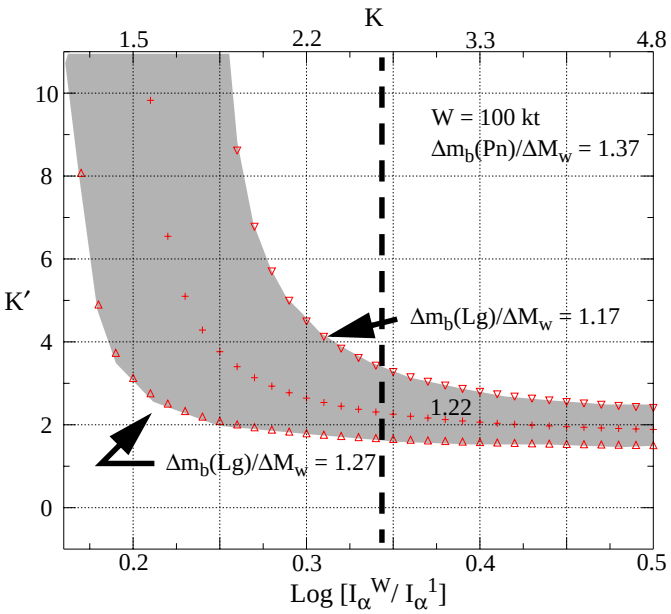


Figure 3. Acceptable solutions (or source models) are located in the shaded region. The central value on Lg scaling rate, 1.22, is the locus of points shown by plus symbols.

Rather than using *in-situ* measurements of working point densities and P-wave speeds, I chose to compute source impedance with a method that gives a better measure of what seismic waves "feel" in the source region. Details were presented in a poster at the 22nd Annual Seismic Research Symposium 12-15 September 2000, but the basic approach is to use measurements of seismic moment M_o and cavity radii (from the containment data base), and calculate "far-field" estimates of I_α using Aki *et al*'s famous equation, $M_o = 4\pi I_\alpha \Psi_\infty$. The results show relationships for I_α between explosions conducted in different media that are expected (e.g. estimates of I_α for dry alluvium are much smaller than for wet tuff). An estimate of I_α^1 was found by taking an average of all data for W < 5 kt, and an estimate of I_α^W was found by taking an average of all data for 50 < W < 200 kt. The log ratio, I_α^W / I_α^1, is 0.34, which is plotted as a vertical dash line in Figure 3. This result is probably a reasonable estimate for M_w-m_b observations used to determine scaling rates of Pn and Lg waves.

For log impedance ratios near 0.35, solution space does not show large variations in K′ as the solution curves are generally flat. Values of K′ are quite reasonable, and the majority of solutions have $K' > 2$. This is consistent with the hypothesis that Rg-to-S scattering is an important mechanism for generating 1-Hz Lg waves from underground nuclear explosions. Under this hypothesis, differences in Pn and Lg scaling rates are caused by effective source functions with dis-similar shapes and scaling behavior. The composite source gives a shallower slope because the bump in Lg spectra from Rg-to-S scattering persists for small yields, while it scales out of the 1-Hz band with decreasing yield in the M-M model used for Pn waves.

Implications for m_b-M_s Discrimination. The teleseismic m_b-M_s discriminant is very effective, and its physical basis is well understood (e.g. Stevens and Day, 1985). There is much interest to extend the discriminant to regional-distance applications for monitoring smaller events than teleseismic data can record. The physical

model proposed in this paper builds on our understanding of the explosion source and regional phase excitation. It provides a basis for predicting regional m_b scaling at small magnitudes. Based on the results for NTS, there is reason to believe that, unlike the teleseismic m_b-M_s, the best regional discriminant might be one which utilizes amplitudes of shear-wave phases, such as Lg, for the m_b, not compressional phases.

This project is in the early stages developing data sets to test m_b-M_s scaling predictions at small magnitudes. Part of this work involves developing technologies and calibrating regions for regional M_s determinations; efforts at universities and the lab are well underway for western China and surrounding areas. Plots of regional m_b-M_s for Pn and Lg waves are shown below (Figure 4) as examples of some preliminary data sets I have compiled.

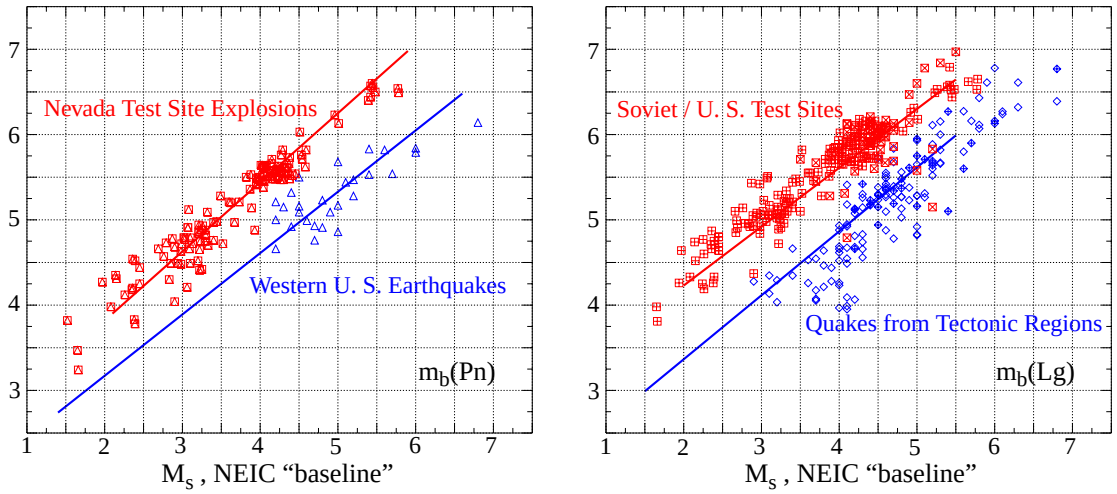


Figure 4. Plots of regional m_b versus M_s for areas in western U. S. and Eurasia. Pn data are just from the western U. S., while transportability of Nuttli's m_b(Lg) enables data from both areas to be plotted on the same graph (Patton, 2000). Measurements of M_s include regional and teleseismic data, and are reduced to a common baseline. Solid lines for earthquake and explosion populations are predictions from M_w versus m_b scaling models.

I have exploited the intrinsic transportability of Nuttli's m_b(Lg) to plot explosion data from NTS, Semipalatinsk, and Novaya Zemlya and earthquake data from tectonic regions of North America and southern Eurasia on a single graph. This is not possible with m_b(Pn) because it has been tied to teleseismic m_b(P) on a region by region basis, and it is well known that m_b(P) shows significant variations worldwide due to regional bias. The results to date are very preliminary, but there is some indication that source populations are better separated at small magnitudes for Lg than they are for Pn, consistent with the scaling models.

CONCLUSIONS AND RECOMMENDATIONS

A major conclusion to date is that m_b(Pn) and m_b(Lg) based on 1-Hz amplitudes show significantly different scaling rates for NTS explosions. This is supported by the analysis of large numbers of regional m_b observations with respect to (1) yield scaling, (2) M_o scaling, and (3) relative scaling of the respective magnitudes over a wide range of source size. A physical model which explains different scaling rates draws on the hypothesis that effective source functions for Lg waves are a composite of two sources, the explosion and near-source Rg-to-S scattering, while Pn waves are generated only by the explosion. Consequently, the shape and scaling behavior of effective source functions for Pn and Lg waves are dis-similar. In light of the evidence that earthquakes do not show differences in scaling rates, I argue that regional m_b-M_s discrimination may perform better for m_b based on shear-waves (Lg) in contrast to traditional compressional-wave based m_b.

A key question is whether or not P-wave scaling differs from Lg at other test sites around the world, especially

those with hard rock. At this point, it is difficult to say because the existing data are limited in quantity and range of source size. This question is important to resolve because it will address issues about the variability of regional m_b-M_s performance and further test our understanding of its physical basis. The latest evidence I have on this score is presented in the poster at the 22nd Annual Seismic Research Symposium.

This is report no. LA-UR-00-3437 of the Los Alamos National Laboratory, Los Alamos, NM 87545.

REFERENCES

Aki, K. and P. Richards (1980), *Quantitative Seismology: Theory and Methods*. W. H. Freeman and Company, San Francisco, CA.

Aki, K., M. Bouchon, and P. Reasenberg (1974), Seismic source function for an underground nuclear explosion. *Bull. Seismol. Soc. Am.* 64, 131-148.

Gupta, I. N., W. Chan and R. Wagner (1992), A comparison of regional phases from underground nuclear explosions at East Kazakh and Nevada Test Sites. *Bull. Seismol. Soc. Am.* 82, 352-382.

Gupta, I. N., T. Zhang, and R. Wagner (1997), Low-frequency Lg from NTS and Kazakh nuclear explosions--Observations and interpretations. *Bull. Seismol. Soc. Am.* 87, 1115-1125.

Jih, R.-S. (1993), Statistical characterization of rugged propagation paths with application to Rg scattering study. Report No. TGAL-93-06, Teledyne Geotech, Alexandria, VA.

Jih, R.-S. (1995), Numerical investigation of relative contributions of Rg scattering and incomplete dissipation to Lg excitation, in *Proceedings of the 17th Annual Seismic Research Symposium*, James F. Lewkowicz, Jeanne M. McPhetres, and Delaine T. Reiter, editors, Phillips Laboratory Report No. PL-TR-95-2108.

Mueller, R. and J. Murphy (1971), Seismic characteristics of underground nuclear detonations, Part 1: Seismic spectrum scaling. *Bull. Seismol. Soc. Am.* 61, 1675-1692.

Myers, S., W. Walter, K. Mayeda and L. Glenn (1999), Observations in support of Rg scattering as a source for explosion S waves: Regional and local recordings of the 1997 Kazakhstan depth of burial experiment. *Bull. Seismol. Soc. Am.* 89, 544-549.

Nuttli, O. (1986), Yield estimates of Nevada Test Site explosions obtained from seismic Lg waves. *J. Geophys. Res.* 91, 2137-2151.

Patton, H. (1988), Application of Nuttli's method to estimate yield of Nevada Test Site explosions recorded on Lawrence Livermore National Laboratory's digital seismic system. *Bull. Seismol. Soc. Am.* 78, 1759-1772.

Patton, H. (1990), Characterization of spall from observed strong ground motions on Pahute Mesa. *Bull. Seismol. Soc. Am.* 80, 1326-1345.

Patton, H. (2000), Regional magnitude scaling, transportability, and M_s : m_b discrimination at small magnitudes. accepted for publication in *Pure Appl. Geophys.*, special volume on *Monitoring the Comprehensive Nuclear-Test-Ban Treaty.*

Patton, H. and S. Taylor (1995), Analysis of Lg spectral ratios from NTS explosions: Implications for the source mechanisms of spall and the generation of Lg waves. *Bull. Seismol. Soc. Am.* 85, 220-236.

Stevens, J. and S. Day (1985), The physical basis of m_b : M_s and variable frequency magnitude methods for earthquake/explosion discrimination. *J. Geophys. Res.* 90, 3009-3020.

Vergino, E. and R. Mensing (1990), Yield estimation using regional m_b(Pn). *Bull. Seismol. Soc. Am.* 80, 656-674.

SEISMIC CALIBRATION OF GROUP 1 IMS STATIONS IN EASTERN ASIA FOR IMPROVED IDC EVENT LOCATION

John R. Murphy and Jeffry L. Stevens
Geophysics Group, Maxwell Technologies, Inc.

M. Nafi Toksoz and William L. Rodi
Earth Resources Laboratory, MIT

Jamil D. Sultanov and Ivan O. Kitov
Institute for Dynamics of the Geospheres

James F. Lewkowicz and Jessie L. Bonner
Weston Geophysical Corporation

Sponsored by The Defense Threat Reduction Agency
Arms Control Technology Division
Nuclear Treaties Branch

Contract No. DTRA-00-C-0024

ABSTRACT

A Consortium of institutions which includes Maxwell Technologies, Inc., Massachusetts Institute of Technology's Earth Resources Laboratory (ERL), Weston Geophysical Corporation, the Russian Institute for Dynamics of the Geospheres (IDG), the Department of Geophysics of Peking University, and the Seismological Bureau of Sichuan Province has been assembled to conduct a research program directed toward the seismic travel time calibration of the 30 Group 1 IMS stations of eastern Asia. A carefully crafted scientific approach to this complex problem has been formulated in which rigorous seismological and statistical analyses of 3-D velocity models established for the regions surrounding the IMS stations of interest will be formally integrated with unique calibration data sets which will be provided by our international Consortium members to provide robust estimates of source-region specific station corrections (SSSCs), together with quantitative measures of the uncertainties in those estimates. A rationale for assigning priorities to the IMS stations to be investigated has been established, and a staged program of deliverables has been formulated in which preliminary calibration results for these priority stations will be provided six months after contract award and updated and refined on a regular basis throughout the three year performance period. We are currently assembling a preliminary 3-D velocity model of the entire region which is composed of a global background model on a 5°-by-5° grid (Stevens and McLaughlin, 1999), supplemented by more detailed models in regions where they are available. At the present time, such detailed models have been identified for a large portion of the Former Soviet Union (FSU) for which Deep Seismic Sounding (DSS) data have been used to define a 3-D velocity model of the crust and upper mantle on a roughly 40km-by-40km grid (Shchukin, 1989), and for an approximately 20°-by-20° area centered on the Pakistan/Afghanistan region for which a 3-D velocity model has been defined on a 1°-by-1° grid (Bernard et al., 1999). Regional phase travel times through these 3-D velocity models are being computed using the Podvin and Lecomte (1991) finite difference algorithm to obtain preliminary SSSC estimates with respect to the IDC default IASPEI91 model for each of the 30 Group 1 IMS stations. These preliminary estimates will be tested and refined using the various calibration data sets which are being assembled for this study. These include a unique set of regional arrival time data at 60 FSU permanent network stations from some 40 Soviet PNE tests, as well as 50 Semipalatinsk and Novaya Zemlya explosions with precisely known locations and origin times, including a number of stations which are either at or very near to Group 1 IMS station locations. The resulting SSSCs will then be thoroughly tested to quantify improvements to event locations in terms of uncertainty and location errors relative to the known locations of selected regional ground truth events. Our ultimate objective is to provide the IDC with the enhanced location capability which will be required to meet the CTBT monitoring objectives for this large Group 1 IMS station region.

OBJECTIVES

The purpose of this effort is to develop improved 3-D velocity models, Site-Specific Station Corrections (SSSCs), and Slowness-Azimuth Station Corrections (SASCs) for eastern Asia, to demonstrate the effectiveness of these models and corrections in improving locations of seismic events, to evaluate the uncertainties associated with these improved models and corrections, and to install these models and corrections at the Prototype International Data Centre (PIDC) of the Comprehensive Nuclear-Test-Ban Treaty (CTBT) located at the Center for Monitoring Research (CMR) and evaluate their performance. The specific objectives are fourfold. The first is to collect appropriate calibration data and seismic events occurring in and around the calibration region. The second is to use these data to refine the regional velocity models and to define and refine SSSCs and SASCs for the 30 IMS stations within the region. The third is to use the new velocity models and SSSCs and SASCs with calibration data ["Ground Truth" (GT) data] to evaluate the location capabilities of the system. The fourth is to implement the SSSCs and SASCs into the location system at PIDC/CMR and to work with the CMR staff to evaluate their performance in that operational environment.

RESEARCH ACCOMPLISHMENTS

The determination of accurate seismic locations for detected events is one of the most important functions of the IDC because location plays such a key role in CTBT verification. Thus, for example, under the CTBT, the areas to be designated for potential onsite inspections are limited to 1000 km^2; and, consequently, this value has been adopted as the minimum performance requirement for uncertainties in IDC seismic locations. However, it has proven difficult to demonstrate that this level of accuracy can be routinely achieved, particularly for small events recorded by limited numbers of IMS stations. The principal reason for this difficulty is that the earth is laterally heterogeneous over a very broad range of length scales; and, therefore, travel time curves based on radially symmetric earth models, such as the standard IASPEI91 model employed at the IDC, can be seriously in error for some source and station locations. This problem is particularly acute at regional distances where the propagation paths of the seismic phases used in location are predominantly confined to the crust and upper mantle portions of the Earth which exhibit the greatest regional variability. Since many of the small seismic events which are of primary concern in CTBT monitoring will have to be located using regional seismic data, such variability places significant limitations on currently achievable location accuracy. It follows that in order to establish a robust CTBT monitoring capability, it will first be necessary to calibrate the IMS stations to account for such systematic deviations from the nominal travel time curves.

We are in the early stages of a three year program which has the objective of calibrating the 30 Group 1 IMS stations of eastern Asia. The map locations of these stations are shown in Figure 1, where it is indicated that they are composed of 11 primary and 19 secondary stations. It can be seen from Figure 1 that regional coverage circles extending to 2000 km radius surrounding these stations would encompass most of the Asian continent, with overlapping, multiple station coverage in most areas. Thus, the area under investigation is very large indeed. Of this total of 30 stations, 13 are currently active IMS stations and 7 more are in close proximity to permanent network stations for which significant historical calibration data are available. This subset of 20 stations has been designated as the "Priority 1" stations for the purposes of our investigation.

Our overall approach to this problem centers on the formulation of a 3-D velocity model of the region which can be used to define corrections to the default IASPEI91 model currently employed at the IDC. Thus, an initial velocity model is defined from currently available information and is then refined by performing joint tomography and multiple event locations using arrival time data collected for this region. Once an optimum average model has been developed, source-specific empirical travel time corrections for each station will be determined by interpolating between observed calibration event residuals relative to this 3-D model. Model-based travel times determined by ray tracing through the 3-D velocity model will then be combined with these empirical corrections to generate 3-D travel time tables for each Group 1 IMS station, and these predicted travel times will be differenced against the corresponding IASPEI91 travel times to define the required SSSCs as a function of source location around each station. This process will then be iterated to incorporate data from additional calibration events as they become available and the final models will be validated based on relocation experiments conducted using travel time data recorded from ground truth calibration events in the region.

Our preliminary model for the Group 1 region is a composite of three models: the long-period models of Stevens and Adams (1999) (model LP), the preliminary model of Bernard et al. (1999) for the Pakistan region (model OPM) and the Deep Seismic Sounding models for the former Soviet Union (model DSS). Each of these models is defined on a regular latitude/longitude grid of laterally homogeneous cells. The cells of model LP are 5 degrees by 5 degrees and cover the entire globe. The cells of model OPM are 1 degree by 1 degree and cover 24.5 degrees N to 43.5 degrees N in latitude and 54.5 degrees E to 80.5 degrees E in longitude. The DSS model cells are 0.3333 degrees wide in latitude and 0.5 degrees wide in longitude and cover 40 N to 72.33 N latitude and 30 to 140 degrees E longitude. Many of the DSS cells, however, are not defined. Each cell of each model is associated with a layered velocity versus depth profile. The LP profiles extend to 600 km depth. The OPM and DSS profiles extend to 30 km below the Moho depth, which is generally different for different cells. The areas covered by these three models are identified on the map in Figure 2, where the annotations in the 5 by 5 degree background model denote the different 1-D velocity models inferred by Stevens and Adams (1999) from their tomographic inversion analyses of observed IMS surface wave data.

The three models were assembled in hierarchy as follows. First, a master rectangular grid of latitude/longitude cells was constructed having variable cell dimensions and containing all the cell boundaries of the three input models. Each cell of the master grid was assigned a composite velocity profile defined to be the appropriate LP profile with the shallower depths replaced by an OPM profile or DSS profile, when either is defined. For a small number of master cells, both OPM and DSS profiles are defined; and we allowed the latter to take precedence. If the deepest velocity of a DSS or OPM profile exceeds the LP velocity at that depth, the velocities of LP layers below that depth were raised to this value. We point out that the master model, like LP, has profiles which vary from cell to cell in the number of total layers, number of crustal layers, etc.

The raytracing algorithm requires a grid of constant-velocity, cubic cells in a Cartesian coordinate system. We constructed such a grid for each station, extending 2000 km north, south, east and west of the station, and to a depth of 600 km. The cell size was 5 km. For each vertical column of cells in the Cartesian raytracing grid, we mapped the horizontal coordinates of the center of the column to a latitude and longitude, based on a sterographic projection centered at the station. This latitude and longitude is then located in the composite velocity model and the velocity profile at this point is extracted. The velocity profile is then translated into a uniform 5 km layering by calculating layer velocities that preserve the vertical travel time to each interface. This translation is done in conjunction with an earth-flattening transformation, which extends the legitimacy of Cartesian raytracing to greater distances from the station. The re-layered velocity profile defines the cell velocities for a column of the raytracing grid.

Ray tracing through this complex 3-D velocity model is being carried out using a code based on the finite difference algorithm of Podvin and Lecomte (1991). There are several advantages to using this approach in the current application. First, it permits the inclusion of secondary arrivals in the location problem; and secondly, it improves on previous modeling methods by being able to accommodate very large velocity contrasts of arbitrary shape, as high as 10:1. It is particularly convenient for estimation of SSSCs in that transmitted and diffracted body waves, as well as head waves, can be readily modeled for each possible hypocentral location in a Cartesian grid centered on a particular station. A first arrival criterion is then used to choose among the various types of waves to create the travel time tables. This algorithm has been extensively tested against a variety of models, including that corresponding to IASPEI91, and found to be accurate to better than 0.5 seconds over the entire range of source to station distances of interest in this project.

It is well known that there are extensive portions of the study area shown in Figure 1 which are essentially aseismic and, therefore, cannot be effectively calibrated using earthquake data alone. Fortunately, however, the U.S.S.R. did conduct an extensive series of PNE tests at widely dispersed locations throughout the territories of the FSU for which precise locations and origin times are now available (Sultanov et al., 1999). Travel time data from these explosions were observed at numerous stations of the U.S.S.R. permanent seismic network, and these data obviously constitute a primary resource for the calibration of Group 1 IMS stations in the FSU. Figure 3 shows the map locations of the approximately 60 U.S.S.R. permanent network stations for which travel time data are currently available from Soviet nuclear tests. Although all of these stations can provide ground truth data useful for calibrating subsurface velocity models for the region, there is a subset of 8 of them which are either at or very near to Group 1 IMS station locations; and these will obviously provide very important data

for use in model validation studies. Particularly notable among these is the Borovoye station (BRVK) in Kazakhstan for which an exceptionally accurate

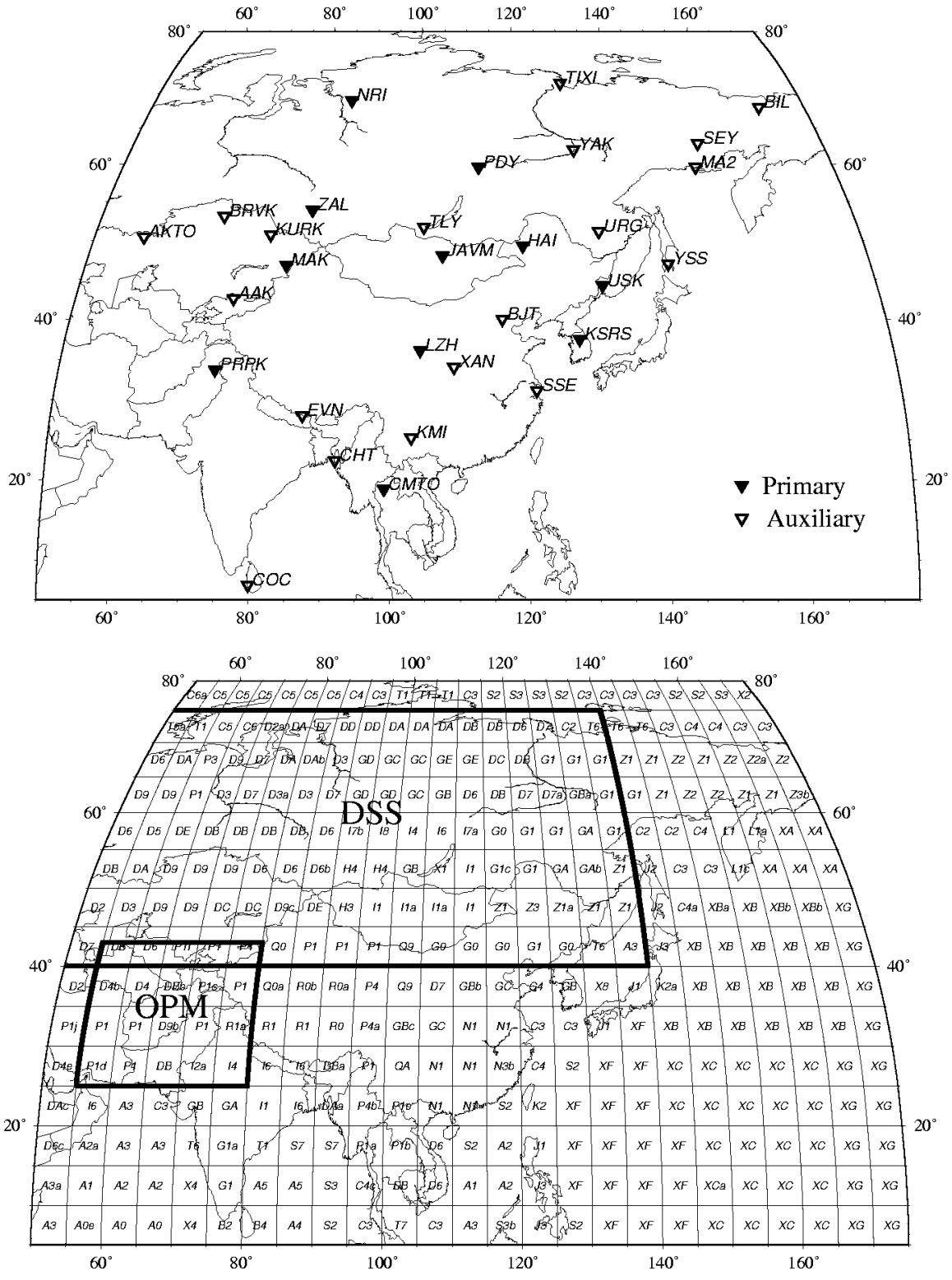


Figure 2.Map showing preliminary velocity models for Eastern Asia. The background model on the uniform 5 by 5 grid is the surface wave based model of Stevens and Adams (1999).

calibration database of regional ground truth data is available from over 100 nuclear explosions. This fact is illustrated in Figure 4 which shows the locations of underground nuclear tests within about 20° of the Borovoye station, together with the observed P wave travel time residuals with respect to IASPEI at BRVK for each test location. It can be seen from this figure that these regional calibration events are very well distributed about the BRVK station and that the observed travel time residuals with respect to IASPEI show a very complex pattern varying from about –8.0 to +1.0 seconds. It is probably fair to say that there is no other IMS station location for which a comparable amount of well distributed ground truth travel time data is currently available. Consequently, we have chosen to use BRVK as our benchmark station for the testing and evaluation of all of our calibration procedures.

As an initial test of our modeling procedures, we have estimated a preliminary SSSC for station BRVK by ray tracing through a 3-D DSS velocity model covering the region out to 20° around that station. Since DSS Pn velocities are not currently available for this entire area, we have adopted an upper mantle Pn velocity model which is consistent with the average observed PNE arrival times as a function of distance at BRVK for this initial application. A grayscale plot of the resulting surface focus SSSC is shown in Figure 5 where it can be seen that the preliminary 3-D velocity model predicts a complex pattern of corrections with respect to IASPEI, with a total range of variation extending from about –7.9 to +2.7 seconds. The extent to which this model predicts the observed PNE ground truth residuals of Figure 4 is illustrated in Figure 6, which shows the corresponding residuals computed with respect to the travel times predicted by the 3-D DSS velocity model. It can be seen that the residuals with respect to this latter model are greatly reduced relative to those of Figure 4, with the majority of residual values falling in the range of about ±1.5 seconds. This fact is illustrated more clearly in Figure 7, where the travel time residuals from Figures 4 and 6 are compared on an event by event basis. It can be seen that, while the residuals with respect to the original IASPEI model show an average bias of approximately –3.7 sec, those computed with respect to the DSS model are essentially unbiased, showing an average value of only –0.1 seconds. Moreover, the standard deviation of the residuals decreases from about 2.2 to 1.7 seconds in going from the IASPEI to the DSS model, indicating that the DSS model not only eliminates the average bias, but also accounts for more of the site specific variations between individual events. Thus, although further refinements are clearly required, the initial results obtained using the 3-D DSS velocity model are encouraging. We are currently proceeding to apply these same modeling procedures to the estimation of preliminary SSSCs for all 20 of our Priority 1 stations.

CONCLUSIONS AND RECOMMENDATIONS

We are in the early stages of a comprehensive program to calibrate the 30 Group 1 IMS stations of eastern Asia in an attempt to improve IDC seismic location capability in this area. A preliminary, composite 3-D velocity model for the entire region has now been formulated and an efficient finite difference ray tracing code for computing travel times through such models has been implemented and tested. A preliminary ground truth database consisting of arrival time observations at approximately 60 stations of the U.S.S.R. permanent seismic network from Soviet PNE tests has been assembled, including data at a number of stations which are either at or very near to Group 1 IMS station locations. Among these is the Borovoye station BRVK for which an exceptionally well distributed ground truth data set of regional arrival time observations from Soviet PNE events is available for testing of proposed calibration procedures. Initial tests of a 3-D, DSS-based velocity model for the region around station BRVK have been encouraging in that they indicate that such a model can account for virtually all of the observed travel time bias and a significant amount of the site to site variability associated with the predictions of the IDC default IASPEI91 model. Current efforts are directed toward the estimation of preliminary SSSCs for the subset of 20 Group 1 IMS stations which have been designated as the highest priority for calibration.

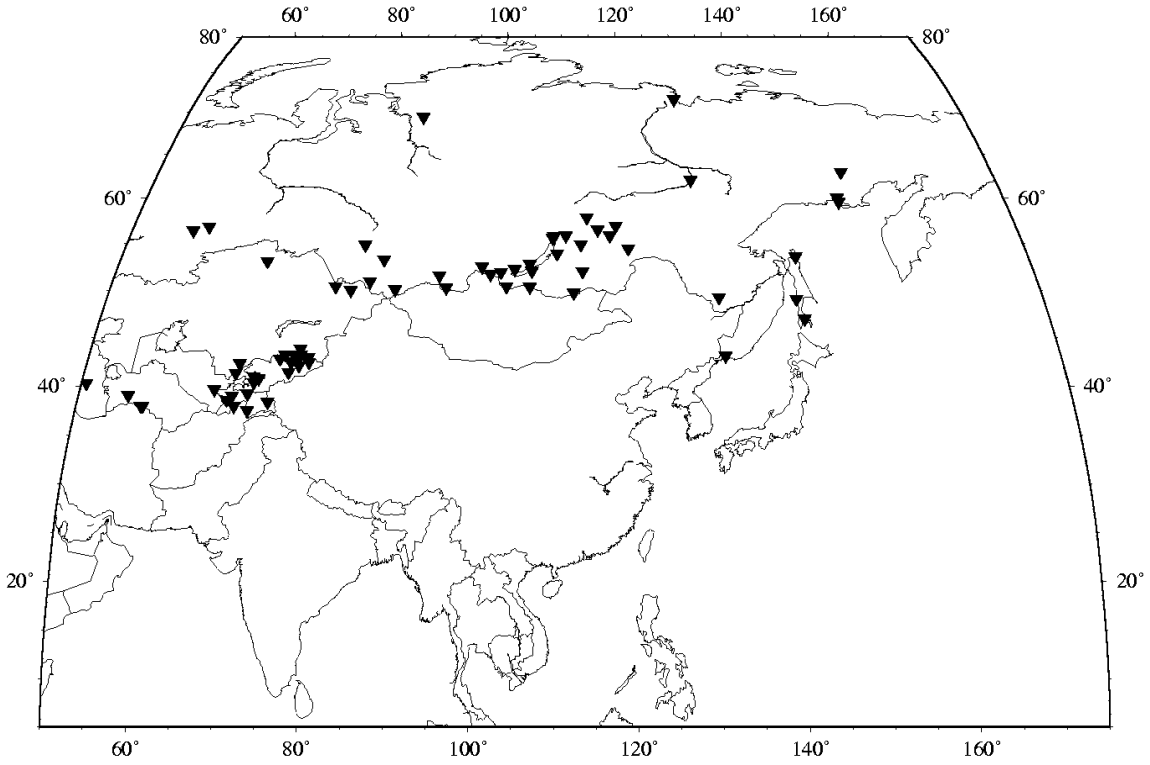


Figure 3. Map locations of U.S.S.R. permanent network stations for which travel time data are currently available from Soviet nuclear tests.

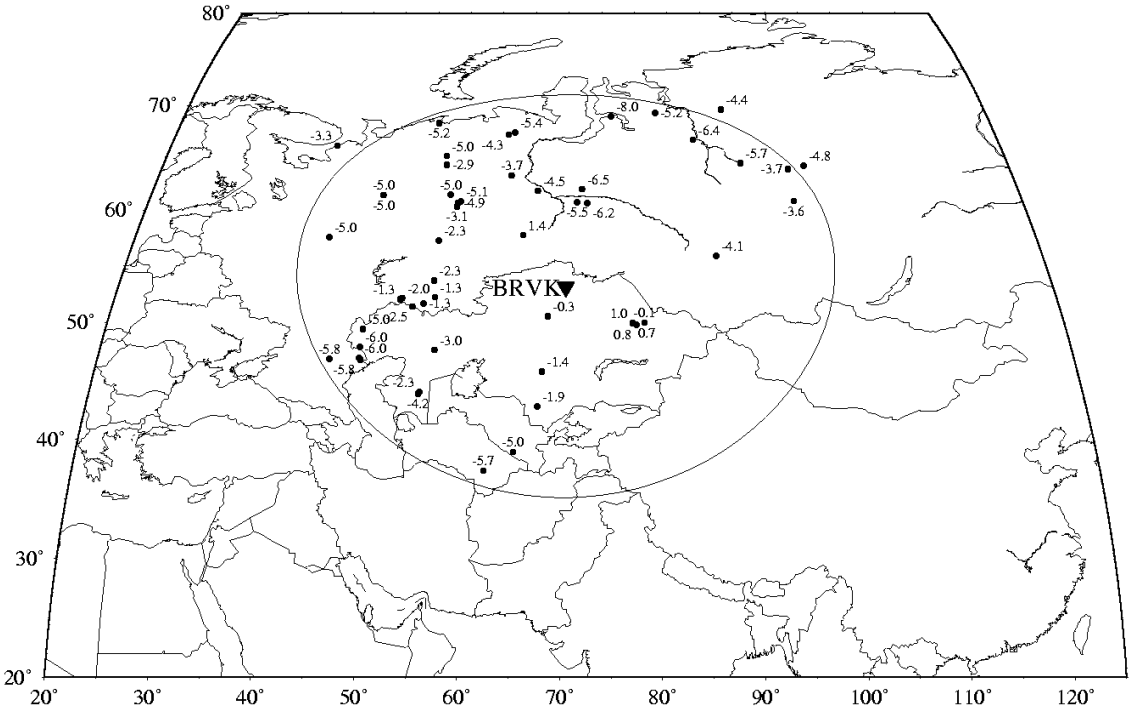


Figure 4.Map locations of regional distance underground nuclear tests recorded at IMS station location BRVK, together with associated observed travel time residuals with respect to IASPEI. The oval line marks a constant epicentral distance of 20° from BRVK.

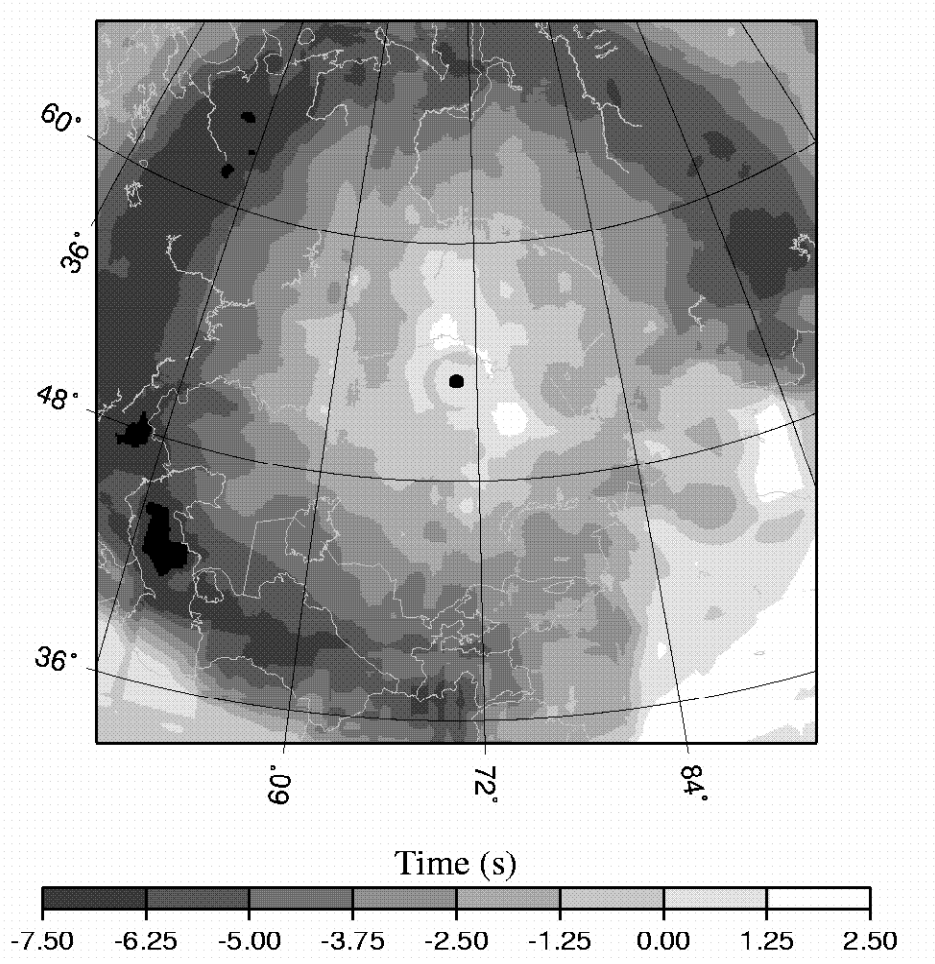


Figure 5. Surface focus SSSC for the Borovoye station computed using the DSS based 3-D velocity model for the surrounding region. Differential arrival times are computed with respect to the IDC default IASPEI91 model.

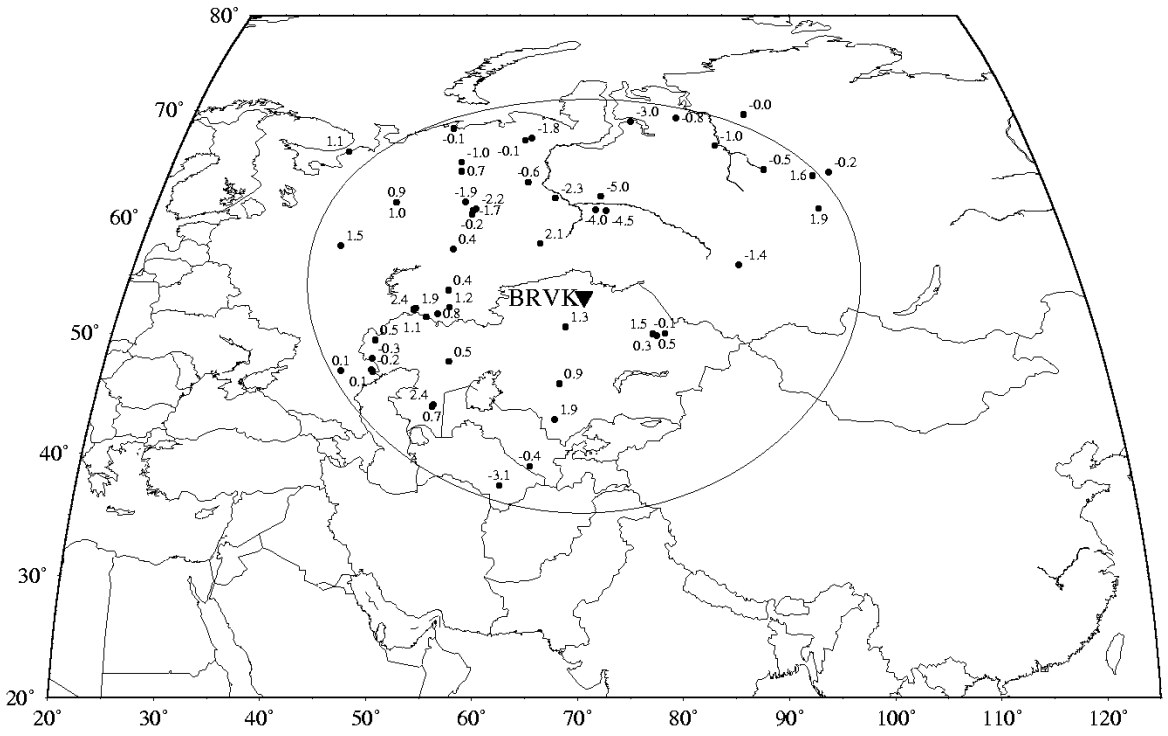


Figure 6. P wave travel time residuals for PNE ground truth events recorded at the BRVK station, computed with respect to the travel times predicted by the DSS based 3-D velocity model for the surrounding region.

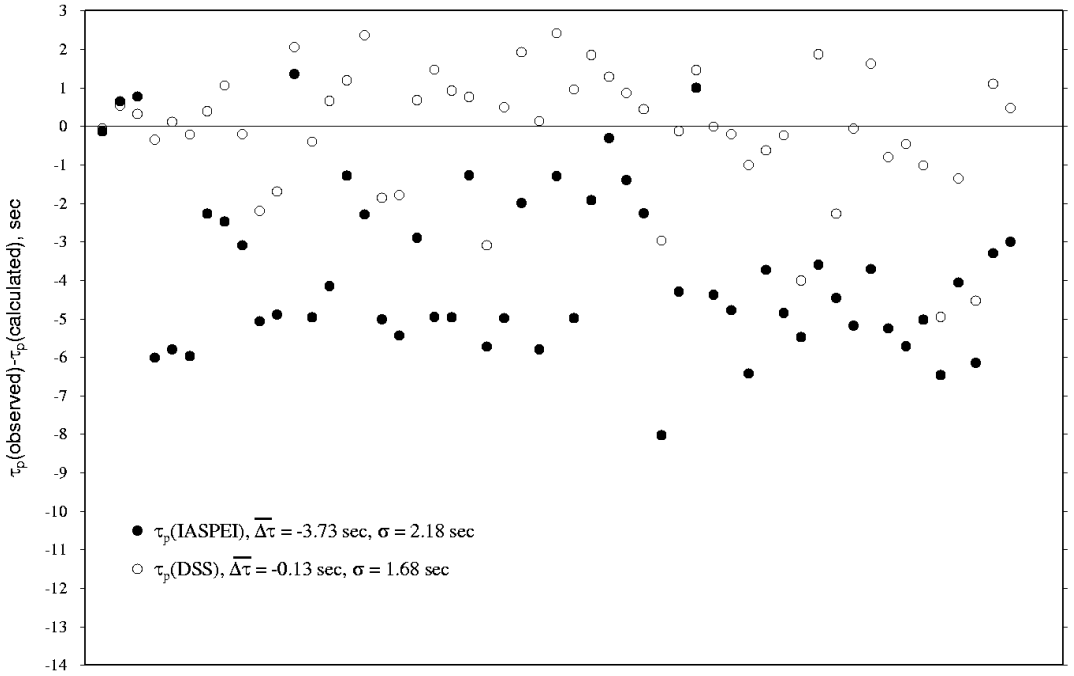


Figure 7. Comparison of P wave travel time residuals for PNE events recorded at the BRVK station, computed with respect to the IASPEI 91 and 3-D DSS velocity models, respectively.

Key Words: seismic, location, calibration, IMS, DSS, Soviet PNE, 3-D velocity models, SSSC

REFERENCES

Bernard, Michelle, Delaine Reiter, Shirley Rieven and William Rodi (1999), "Development of a 3-D Model for Improved Seismic Event Location in the Pakistan/India Region", Proceedings of the 21st Annual Seismic Research Symposium.

Podvin, P., and I. Lecomte (1991), "Finite Difference Computation of Traveltimes in Very Contrasted Velocity Models: A Massively Parallel Approach and Its Associated Tools," *Geophys. J. Int*. **105**, pp. 271-284.

Stevens, Jeffry L. and David A. Adams (1999), "Improved Methods for Regionalized Surface Wave Analysis", Proceedings of the 21st Annual Seismic Research Symposium.

Sultanov, D. D., J. R. Murphy and Kh. D. Rubinstein (1999), "A Seismic Source Summary For Peaceful Nuclear Explosions," *Bull. Seism. Soc. Am., 89*, pp. 640-647.

THE USE OF IMPERFECT CALIBRATION FOR SEISMIC LOCATION

Stephen C. Myers and Craig A. Schultz
Lawrence Livermore National Laboratory

Sponsored by U.S. Department of Energy
Office of Nonproliferation Research and Engineering
Office of Defense Nuclear Nonproliferation
National Nuclear Security Administration

Contract No. W-7405_ENG-48

ABSTRACT

Efforts to more effectively monitor nuclear explosions include the calibration of travel times along specific paths. Benchmark events are used to improve travel-time prediction by 1) improving models, 2) determining travel times empirically, or 3) using a hybrid approach. Even velocity models that are determined using geophysical analogy (i.e. models determined without the direct use of calibration data) require validation with calibration events. Ideally, the locations and origin times of calibration events would be perfectly known. However, the existing set of perfectly known events is spatially limited and many of these events occurred prior to the installation of current monitoring stations, thus limiting their usefulness. There are, however, large numbers of well (but not perfectly) located events that are spatially distributed, and many of these events may be used for calibration.

Identifying the utility and limitations of the spatially distributed set of imperfect calibration data is of paramount importance to the calibration effort. In order to develop guidelines for calibration utility, we examine the uncertainty and correlation of location parameters under several network configurations that are commonly used to produce calibration-grade locations. We then map these calibration uncertainties through location procedures with network configurations that are likely in monitoring situations. By examining the ramifications of depth and origin-time uncertainty, we expand on previous studies that focus strictly on epicenter accuracy. Particular attention is given to examples where calibration events are determined with teleseismic or local networks and monitoring is accomplished with a regional network.

Key Words: location, seismic regionalization, calibration

OBJECTIVE

We aim to analyze the utility and limitations of imperfect calibration data when applied to common monitoring situations. The most desirable set of calibration events would have little or no uncertainty in either hypocenter or origin time. However, such "perfect" calibration events are achieved through dedicated calibration explosions and the cost of developing a perfect calibration data set over a broad geographic region would be prohibitive. Therefore, a practical approach to the calibration of seismic location includes the use of events that are located with high – but not necessarily perfect – accuracy.

Highly accurate calibration events are generally earthquakes that are 1) well recorded with a regional to global network or 2) located to high accuracy with a dense local network. When the locating network is well distributed around an event, a high-accuracy location can be achieved, and these events can be used to calibrate travel times to permanent monitoring stations. However, even when the best network configuration is available, uncertainties in source location parameters can reduce calibration utility. We aim to track how uncertainties in earthquake ground-truth sources propagate through the calibration process, and identify limitations of using earthquake data for calibration.

RESEARCH ACCOMPLISHED

Accurate representation of calibration uncertainties includes mapping the uncertainty of calibration-event source parameters through the calibration process. This study examines how uncertainties and correlations in calibration-event location and origin time (we will refer to these parameters as source parameters) propagate through the calibration process. We begin by examining the correlation matrix for calibration-event source parameters determined with a regional to teleseismic network. We then examine calibration events that are located with a local network. An analytical expression for the propagation of source and travel-path uncertainties is derived, so that the importance of each term is identified. Additionally, an earthquake data set is used to empirically test the effect that location uncertainty has on calibration estimates. Of particular importance to this study are 1) the commonly noted correlation between event depth and origin-time parameters and 2) the way in which this correlation maps into travel-time calibration and subsequent seismic location.

Test Data Set

Throughout this study we refer to a test data set consisting of 111 events from the ISC catalogue. These events are recorded from regional to teleseismic distance and meet the criteria of at least 50 defining arrivals with a maximum azimuthal gap in station coverage of 90°. Sweeney (1998) found that events meeting these criteria are generally within 20 km of known locations. Some test events far surpass the above criteria and others barely meet the criteria. Furthermore, the events are geographically distributed throughout Eurasia and North Africa (Figure 1). Because this data set represents a wide range in station geometry and ray paths cover a diversity of tectonic provinces, location parameter uncertainties and correlations that are common to the test data set as a whole may be generally applied to other regional/global-network locations.

Trade off between event depth and origin time (regional/teleseismic network)

Common network configurations for monitoring and for the determination of calibration events include stations at regional to teleseismic distance. For monitoring, the set of stations is likely to be sparse (due to small source size) and for calibration the network is necessarily extensive (otherwise the above criteria are not met). The trade-off between event depth and origin time is evident from analysis of the location system of equations. The determination of earthquake locations is an inverse problem of the form:

$$Ax = r \qquad [1]$$

Where A is an Nx4 matrix of travel-time partial derivatives with respect to the four location parameters (N is the number of observations), x is a 4x1 vector of the change in location parameters, and r is an Nx1 vector of travel-time residuals. Equation [1] is a linearization of a non-linear problem, so [1] is iterated until a stable solution is found.

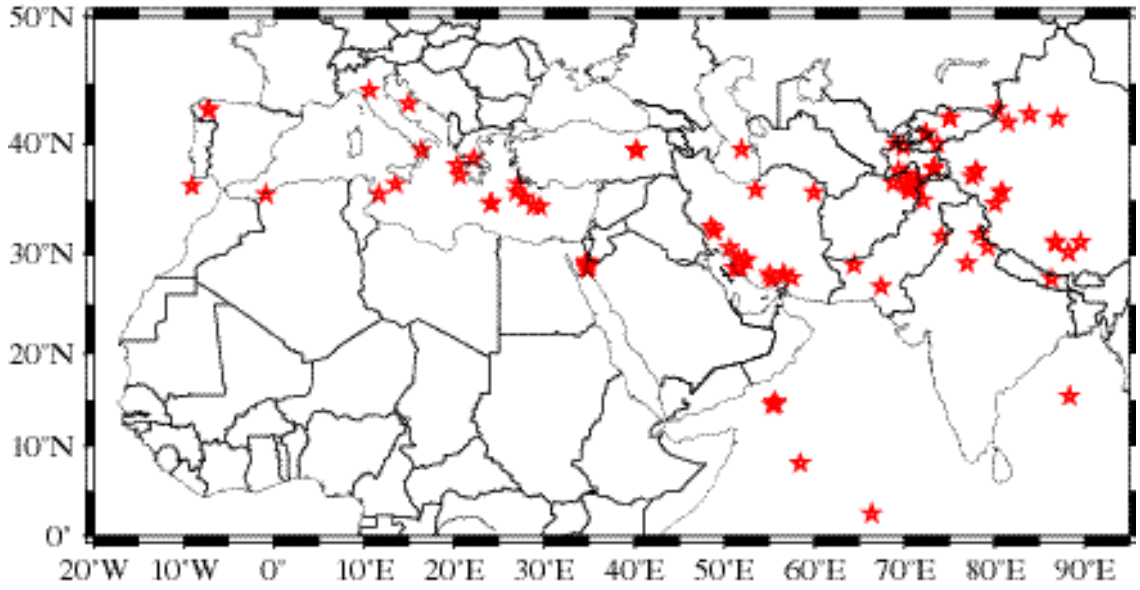


Figure 1. Epicenters of 111 test events are shown by stars. These globally recorded events meet the criteria of 50 defining phases and maximum azimuthal gap of 90°. In order to test how the trade-off between event depth and origin time effects calibration, travel-time residuals are calculated for test events with depths fixed at 0 and at 30 km. The depths reported in the ISC catalogue range from 0 to 174 km.

For events located with a regional to teleseismic network, the resolution of event depth and origin time parameters is poor. Figure 2 shows the average *A* martix for 111 test events. The pertinent features of Figure 2 are that partial derivatives for the horizontal components of event location are widely varying and uncorrelated, whereas the partial derivatives with respect to event depth are nearly identical for each arrival. Because the vertical partial derivatives are nearly constant and partial derivatives for origin time are always equal to one, the column vectors of partial derivatives representing depth and origin time are nearly linear combinations of one another. Therefore, there will be little resolution between origin time and event depth. The correlation between source parameters is further investigated by computing the model correlation matrix for the average *A* matrix (Figure 3). Again, the horizontal components of location are uncorrelated with other source parameters, whereas origin time and depth are almost perfectly correlated.

It is important to note that the above analysis does not include depth phases. Of the crustal events in the test data set, depth phases were not identified in the International Seismic Center (ISC) catalogue. Because depth phases are rarely identifiable as distinct arrivals for crustal events at regional to teleseismic distance, we believe that this analysis is representative of both calibration and monitoring situations for which local data are not available. We note that some subcrustal events are included so that a broad range of true event depth is considered.

Origin-time bias (local network)

Locations derived from a local network, such as an aftershock study, can have well-determined hypocenters with uncorrelated depth and origin-time parameters. Because of this superior hypocenter accuracy, these events are highly desirable for calibration of monitoring stations. Although existing hypocenters determined with a local network do not provide the spatial coverage afforded by events determined with regional to teleseismic networks, these events can provide important high-accuracy calibrations at specific geographic locations.

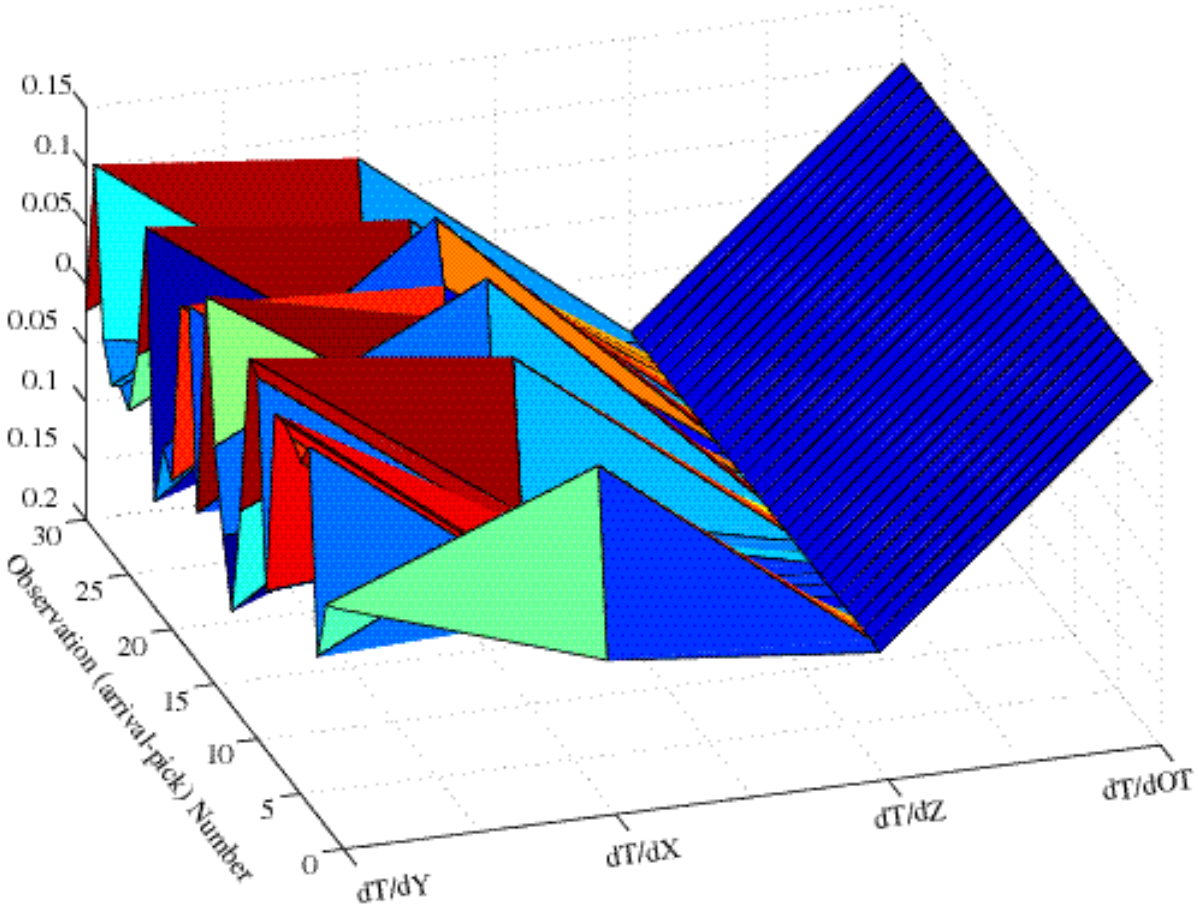


Figure 2 Partial derivative matrix for a typical event located with a regional to teleseismic network. Note that the partial derivatives with respect to depth (Z) and origin time (OT) are nearly linear combinations of one another, so there will be little or no resolution between depth and origin time. The number of observations is cut to 30 and the values of the origin-time partial derivatives are scaled down from their value of 1, so that matrix features are clear. See text for discussion.

Unfortunately, origin times for events determined with local networks are not beyond reproach. The most significant source of origin-time error can be systematic travel-time prediction errors due to velocity model inaccuracies. Several studies demonstrate that origin times for events located with a local network can be biased by systematic travel-time prediction errors (e.g. Pavlis, 1986), even when a “best estimate” of local velocity structure is used.

The consequence for calibration is that origin time bias is directly mapped into travel-time corrections (i.e. residuals). If a bias between observed and predicted travel time is well resolved (i.e. origin time bias is minimal), then an overall bias between observed and predicted travel-times is important calibration information. However, because the magnitude of the origin-time bias is unknown for most local studies, we may inadvertently propagate origin-time bias into calibrations by using origin times from local studies.

To further complicate matters, origin-time bias is likely to change from locale to locale. If the bias for one aftershock study is not the same as a neighboring study, then travel-time corrections derived from the two locales

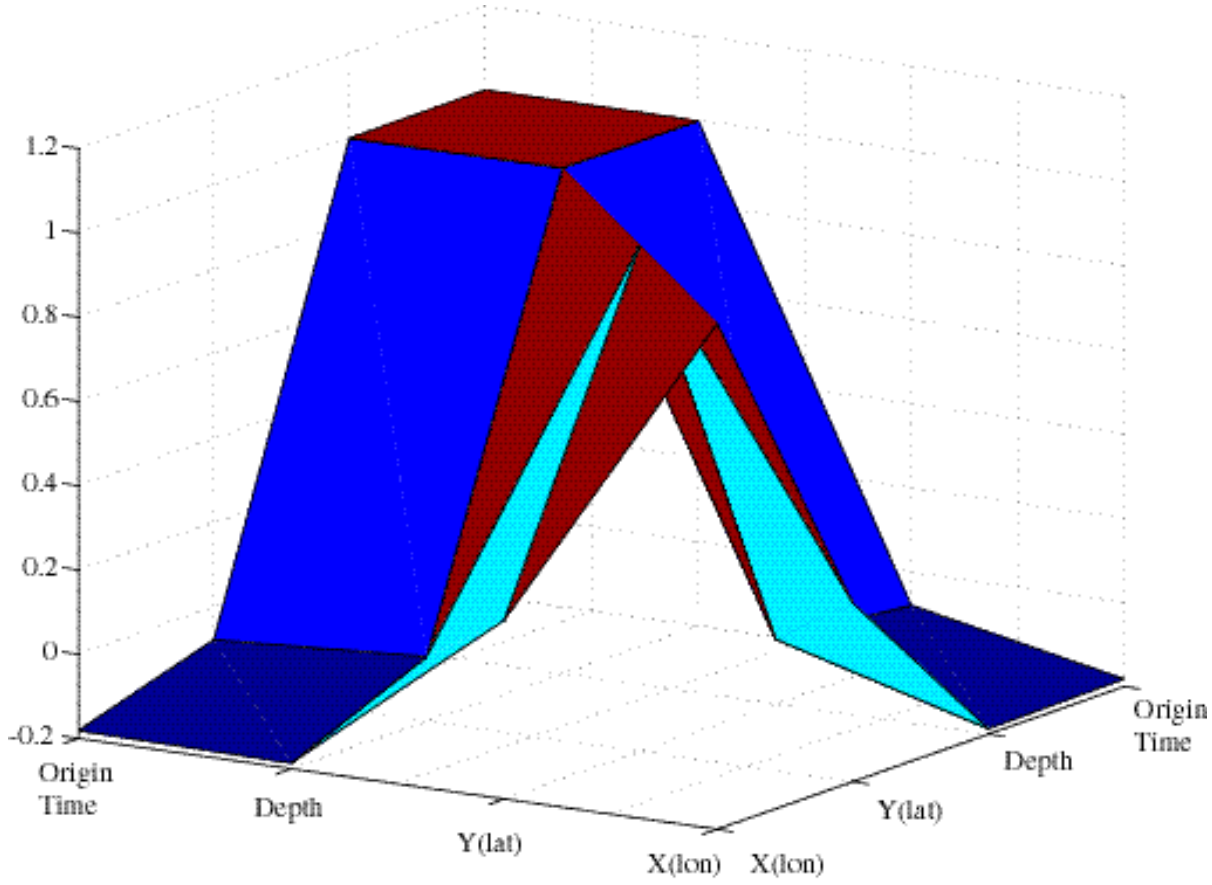


Figure 3
Averaged model correlation matrix for 111 events determined with a regional to teleseismic network. Horizontal components of event location are not significantly correlated with other parameters, whereas, the correlation between event depth and origin time is almost perfect. The correlation matrix demonstrates the trade-off between origin time and depth.

will not be compatible. When viewed as a geographic surface of travel-time residuals, there will be a discontinuity between the two local studies. In other words, combining local studies with differing origin-time biases results in geographically non-stationary calibration bias.

One way to insure a zero-mean origin-time residual (remove origin-time bias) is to fix the hypocenter -- as determined with a local network -- and recalculate the origin time relative to the velocity model that is to be calibrated. However, numerous regional to teleseismic stations must be used, and the local stations must be omitted when determining the new origin time. If local stations are included, then bulk differences between the crustal portion of the regional velocity model and each local velocity structure will again result in non-stationary origin-time bias. As discussed above, when the local stations are removed there is almost perfect correlation between

origin time and depth. Therefore, even though the new origin time is not biased, it is not well resolved and a strong trade-off between origin time and event depth persists.

From the above discussion it would appear that origin time is difficult to pin down. Because the travel-time residual is the observed arrival time minus the sum of origin time and predicted travel time, it is not obvious how travel-time calibration can be derived from earthquake data sets.

How important is it to resolve the origin-time and depth of a calibration event?
Travel-time calculation is separable into vertical and horizontal components. The basic travel-time equation for a surface focus in a layered media is

$$t = Xp + 2\sum_{i=1}^{N} h_i \eta_i \qquad \eta_i = \left(1 - v_i^2 p^2\right)^{1/2} / v_i \qquad [2]$$

where t is travel time, X is horizontal distance, p is ray parameter (horizontal slowness), h_i is the thickness of each layer, η_i is vertical slowness, v_i is the velocity of layer i, and N is the number of layers from the surface to the bottoming depth of the ray. There are direct analogies to continuous velocity structures, but we present the discrete case for simplicity. For a non-surface focus, layers entirely above the focus only contribute once to the vertical slowness component (the up-going ray) and the layer containing the event contributes once for the up-going ray with a fractional contribution to account for the path from the focus to the bottom of the layer.

In order to isolate the effects of various portions of the travel path and calibration event parameters, we derive the variance of the travel-time residual by substituting a two-layer velocity model (equation [2]) into the travel-time residual equation (t_{res}=$t_{observed}$-$t_{predicted}$). We then expand the square of the right-hand-side of the resulting equation. Because the expected value of the travel-time residual is zero (re-computing the origin time forces the average residual to be zero) the distribution of the travel-time calibrations is described by the variance of the travel-time residuals. From the previous section we know that the only correlated source parameters are origin time and depth, and from equation [2] we see that event depth only affects the vertical component of travel time. Therefore, we find that the only correlated parameters in the travel-time residual equation are those for event depth, event origin time, and the vertical component of travel time, and the variance of t_{res} reduces to:

$$\sigma_{res}^2 = \sigma_{to}^2 + \sigma_X^2 + \sigma_z^2 + \sigma_O^2 - 2\rho_{Oz}\sigma_O\sigma_z \qquad [3]$$

where σ^2_{res}, σ^2_{to}, σ^2_X, σ^2_z, σ^2_O are variances for the travel-time residual, arrival-time pick, horizontal travel time, vertical travel time, and origin time, respectively, and ρ_{oz} is the correlation coefficient between origin time and the vertical travel time. We know from the previous section that ρ_{oz} is approximately one. Therefore, if σ_z and σ_O are equal, then uncertainty in depth and origin time have no effect on the travel-time residual (calibration) distribution. Although σ_z and σ_O are generally not equal, the last term of equation [3] will tend to minimize the effect of event origin time and depth errors on the travel-time residual.

We empirically test the importance of event depth using the aforementioned test data set. The best origin time is determined with each epicenter fixed at the ISC epicenter and event depth set to zero. This procedure is repeated with event depth set to 30 km.

Figure 4a,b shows the distribution of the absolute value of the mean travel-time residual for each event when event depth is set to 0 and 30, respectively. So each occurrence in the distributions shown in Figure 4a,b is the mean absolute value of travel-time residuals for one event. We note that the sum of the squared errors is approximately equal for each event when depth is fixed at the surface and 30 km, so neither depth is necessarily preferred by the data. To make Figure 4c we first compute the difference between travel-time residuals at each station for a single event. For each event we find the average of the absolute value of these differences, and Figure 4c is the distribution over all events.

Figure 4c shows that on average, the expected difference in travel-time residual resulting from fixing the depth of an event at a grossly incorrect depth is about 0.34 seconds. The maximum computed error for the same scenario is 0.62 seconds. Considering that the calculated difference in travel time between a surface and 30-km-depth event is about

3.3 seconds (6 km/s crust), these results support the analytically derived prediction that correlation between origin time and event depth will tend to negate errors in depth. Comparing Figure 4c to Figures 4a,b, it is evident that errors resulting from incorrect event depth are a small component (~20%) of the overall residual distribution; the mean value of the distributions in Figure 4a,b are 1.81 and 1.72 seconds, respectively, compared to a mean value of 0.34 seconds resulting from different event depths.

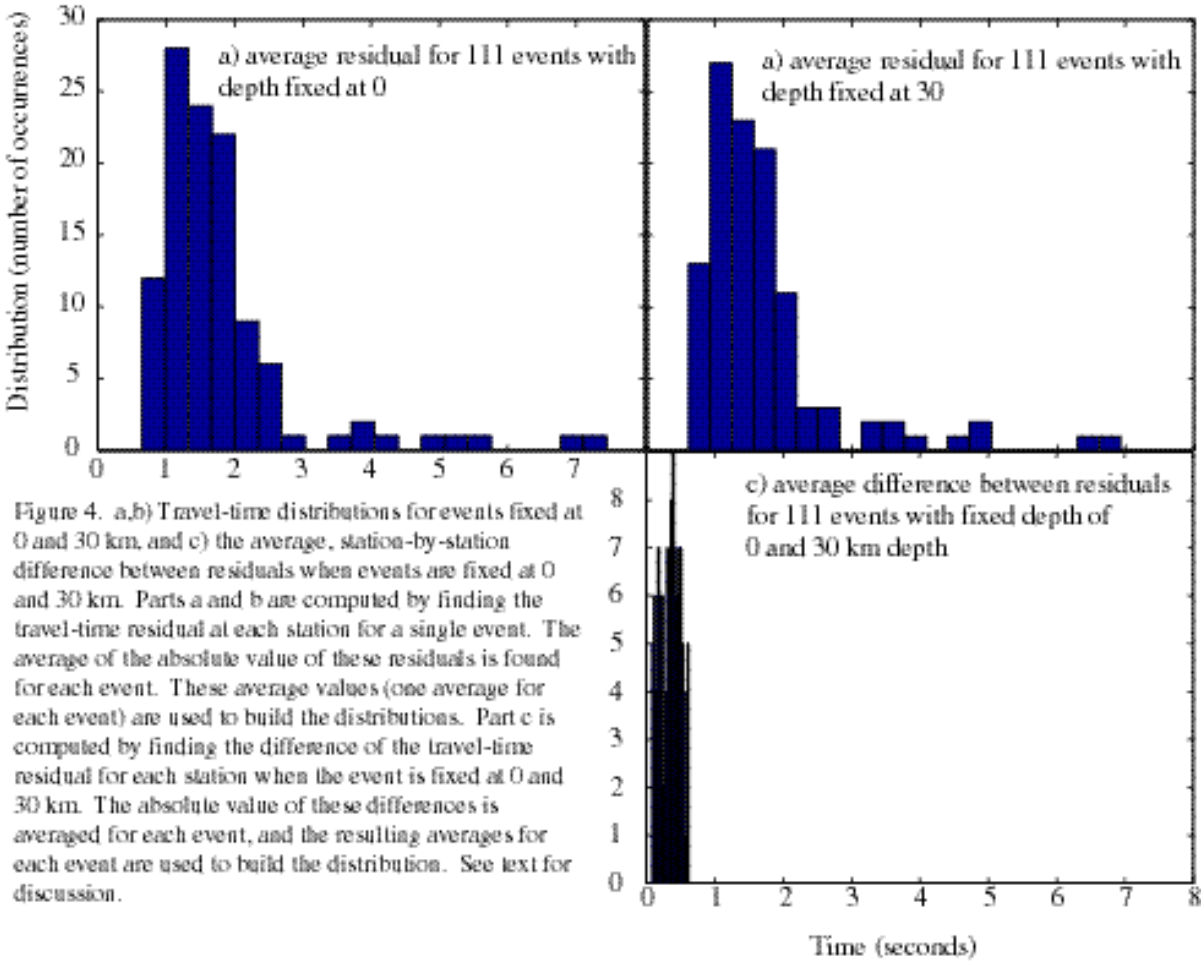


Figure 4. a,b) Travel-time distributions for events fixed at 0 and 30 km, and c) the average, station-by-station difference between residuals when events are fixed at 0 and 30 km. Parts a and b are computed by finding the travel-time residual at each station for a single event. The average of the absolute value of these residuals is found for each event. These average values (one average for each event) are used to build the distributions. Part c is computed by finding the difference of the travel-time residual for each station when the event is fixed at 0 and 30 km. The absolute value of these differences is averaged for each event, and the resulting averages for each event are used to build the distribution. See text for discussion.

Another component of the residual distribution is picking error. Under the best circumstances, the standard deviation of picking error is about 0.25 seconds for first arrivals, and more typically the standard deviation of picking error is 0.5 to 1.0 second (F. Ryall, personal communication). Therefore, errors introduced by calibration-event depth inaccuracies are likely to be less than picking error. Only when picking error is small does the variance of picking and event-depth error become approximately equal.

Separability of calibration into vertical and horizontal slowness

From the calibration standpoint, it is the correction of model errors that we would like to extract from the travel-time residuals. Commonly, travel-time residuals for a well-recorded event have a structured spatial (geographic) pattern, although incoherent noise from random processes like picking error can blur the pattern. It is the underlying spatial pattern that represents the systematic travel-time error due to velocity-model inaccuracies. Techniques such as non-stationary Bayesian kriging (Schultz et al., 1998) are demonstrated to effectively extract model error from a spatially distributed set of travel-time residuals (Myers and Schultz, 2000). However, given the trade-off between origin time and depth, we would like to know just what we are calibrating when we extract model error from the pattern of earthquake travel-time residuals.

From the correlation between the vertical component of travel time and event origin time (Equation [3]), it is clear that recalculating the origin time absorbs much of the near-event model inaccuracy in vertical slowness. Physically, we interpret this finding to mean that near-source velocity anomalies and errors in event depth have the effect of slowing or advancing seismic arrivals at regional to teleseismic stations by approximately the same amount of time. In the location process, equally shifting the time of all network arrivals maps into a change in origin time. Conversely, Equation [2] shows that the variance in horizontal slowness is not diminished by correlation with other parameters. So, neither origin time nor other source parameters can absorb inaccuracies in horizontal slowness. Therefore, we conclude that near-source vertical slowness anomalies and errors in event depth play a minimal role in affecting the spatial (geographic) pattern of travel-time residuals, and the dominant parameter affecting the spatial pattern of regional travel-time residuals is variations in horizontal slowness from the base velocity model.

CONCLUSIONS AND RECOMMENDATIONS

Spatial coverage of travel-time calibration events can be vastly improved if earthquakes are used to augment the catalogue of explosion sources. Unlike dedicated calibration explosions, source parameters of earthquakes are not perfectly known. Although earthquake source-parameter uncertainties present some limitations, we find that useful calibration information can be extracted from earthquake data sets.

The origin times and depths of earthquake calibration events are typically poorly known, and a strong correlation between origin time and depth exists. In contrast, event latitude and longitude are typically well resolved, and these horizontal location parameters are not correlated with other source parameters. As a result, earthquake data sets are most useful for calibrating horizontal slowness. This is fortunate, because horizontal slowness is the critical parameter in most monitoring situations. Because clandestine tests are unlikely to occur near a local network, depth estimates will rely on surface reflections, and surface reflections are not likely to be separable from the direct pulse for a shallow event. Unfortunately, the absence of surface-reflected waves cannot be used as evidence for a surface focus, and a location based on sparse regional recordings will be poorly resolved in depth. Poor vertical resolution commonly requires event depth to be fixed during the solution of source parameters, and when event depth is fixed, calibration of horizontal slowness becomes far more important than calibration of vertical slowness.

Although the depth of calibration events can be well constrained by using a local network, event origin time can remain suspect due to systematic local-velocity-model inaccuracies. Furthermore, the origin-time bias is generally different for each local study. Local studies can be tied together by re-computing origin times using arrivals from regional to teleseismic stations. However, local stations must be removed from this process (see above), resulting in diminished resolution of near-source vertical slowness calibration. We note that similar origin time issues arise when origin times for nuclear explosions with perfectly known hypocenters are estimated using seismic arrivals. Based on the empirical difference of travel-time residuals for events that are fixed at different crustal depths, we find that using accurate event depth information can account for as much as 20% of a typical travel-time correction. Therefore, if both excellent depth resolution of calibration events is available and the monitoring network and recorded phases provide resolution of event depth, then use of 3-dimensional travel-time corrections can have utility.

REFERENCES

Myers, S., C. Schultz (2000). Improving Sparse Network Location with Bayesian kriging and Teleseismically Constrained Calibration Events, *Bull. Seismol. Soc. Am.*, **90**, 199-211.

Pavlis, G. (1986). Appraising Earthquake Hypocenter Location Errors: A Complete, Practical Approach for Single-Event Locations, *Bull. Seismol. Soc. Am.*, **76**, 1699-1717.

Sweeney, J. (1998). Criteria for Selecting Accurate Event Locations from NEIC and ISC Bulletins, UCRL-JC-130655.

Schultz, C.., S. Myers, J. Hipp, C. Young (1998). Nonstationary Bayesian kriging: A Predictive Technique to Generate Corrections for Detection, Location, and Discrimination, *Bull. Seismol. Soc. Am.*, **88**, 1275-1288.

BODY-WAVE MAGNITUDES AND LOCATIONS OF PRESUMED EXPLOSIONS AT THE CHINESE TEST SITE, 1967-1996

Aoife O'Mongain (1), Alan Douglas, John B. Young

AWE Blacknest

(1) on placement from the British Geological Survey

Sponsored by United Kingdom Ministry of Defence

ABSTRACT

For nearly 40 years the forensic seismology group at Blacknest have published estimates of the basic parameters of presumed explosions (epicentre, origin time, body-wave magnitude) determined using state-of-the-art methods from bulletin data (usually the International Seismological Centre (ISC) bulletin). These basic parameters are widely considered to be some of the most reliable estimates that are freely available. However, not all presumed explosions have been analysed.

Here, we estimate the epicentres and body-wave magnitudes of presumed underground explosions at the Chinese test site in Xinjiang Province using ISC bulletin data, supplemented by P-onset times measured from data recorded by the four UK-type seismometer arrays (EKA, GBA, WRA, YKA). The epicentres are estimated using Joint Epicentre Determination. The body-wave magnitudes are calculated using the Joint Maximum-Likelihood method. This work builds on an earlier report that reviewed epicentres and body-wave magnitudes for 17 presumed Chinese explosions fired between 1967 and 1989. A further 11 presumed explosions, dated from 1990 to 1996, are analysed to complete the set.

The estimates of the epicentres of the presumed explosions suggest that a number of different regions exist within the test site. The seismograms at each of the UK-type arrays for these presumed explosions appear to display common features which may relate to specific regions of the test site. Here, we attempt to distinguish the different areas of the test site using the P-wave characteristics observed at the 4 UK-type arrays.

Key Words

Location, body-wave magnitudes, Xinjiang Province, P-wave characteristics, UK-type seismometer arrays

OBJECTIVE

The objective of this research is to provide reliable magnitude and location estimates for underground explosions at the Chinese test site. From the epicentre relocations we can assess how accurately epicentres can be located and demonstrate how well the onset times are read for explosions. We expect the seismograms from explosions to be simple but this study illustrates that they are often complex and highly variable, even for test areas within less than one hundred kilometres of each other. It is important to investigate this variability in order to use complexity as a discriminant.

RESEARCH ACCOMPLISHED

Introduction

Using P times and amplitude observations taken from the bulletins of the International Seismological Centre (ISC), Douglas et al (1993) obtain estimates of the body-wave magnitudes (m_b), epicentres and origin times of 17 Chinese explosions that took place between 1967 and 1989; 7 being fired in the atmosphere at the Lop Nor site, and 10 underground at the Singer site.

Since 1989 11 more presumed underground explosions have been reported from the Singer site in the ISC bulletins. Here we extend the work of Douglas et al (1993) and give estimates of magnitudes and locations for all 21 presumed underground tests (Table 1 lists these tests). In addition to the bulletin data taken from the ISC, some experiments are described on epicentre estimation using the P onset times read as part of this study from the recordings of the four UK-type arrays (EKA, GBA, WRA, and YKA). The purpose of the experiments is to see how well epicentres can be estimated using carefully read onset times from small numbers of stations, as compared to those using bulletin data from large numbers of stations. The distance, azimuth and back-azimuth of the arrays from the Singer site is given in Table 2.

The epicentres and origin times are re-calculated using joint epicentre determination (JED; Douglas 1967). Estimating epicentres and station terms simultaneously for groups of explosions gives better estimates of relative positions than is possible when each disturbance is considered individually. Given the true location of at least one explosion, the best estimates of absolute position can be found.

The magnitudes are estimated by the joint maximum-likelihood (JML) method of Lilwall (1986) and Lilwall and Neary (1985), which makes allowance for the detection thresholds of the recording stations. As magnitude decreases, then increasingly, below average amplitudes are not reported because they are below the detection threshold. As a result of this the mean magnitude estimated from the detecting stations is biased high. However, the maximum-likelihood magnitude m_b^{ML} should be unbiased.

Table 1 lists the 21 underground explosions for which times and amplitudes are published by the ISC and shows which of the explosions were recorded by the UK-type arrays. Douglas et al (1993) show that there are three separate test areas within the Singer site, here referred to as the Northern (N), Eastern (E) and South-Western (SW) areas. The area in which each explosion took place is given in Table 1 with the ISC m_b and m_b^{ML}.

Douglas et al (1993) suggest, from an analysis of the topography of the area, that the Northern and South-Western test areas are in mountainous regions, whereas the Eastern area is in a region of little relief. Matzko (1994) suggests that the explosions in the Eastern area were fired at the bottom of shafts. As the Northern and South-Western areas are in mountains, it may be that the explosions in these region were fired in tunnels driven into the hillsides (Douglas et al 1993)

Epicentre Relocations

Figure 1 shows the ISC epicentres for the 21 explosions and Figure 2 the JED results obtained using the ISC times. The JED estimates obtained using only the onsets read from the recordings at the UK-type arrays are also shown in Figure 2. Some recordings required an optimum frequency filter (Douglas 1997) to reduce low frequency noise and give a more reliable estimate of the onset time. The 4 May 1983 and 29 September 1988 explosions are not included in the analysis of the array data because

Explosion #	Date	YKA	EKA	WRA	GBA	ISC	m_b^{ML}	Test Area
1	690922	*	*	*	*	5.2	5.10	SW
2	751027	*	*	N	*	5.0	4.80	SW
3	761017	*	*	*	*	4.9	4.84	N
4	781014	*	*	-	*	4.9	4.54	E
5	830504	*	-	-	*	4.5	4.08	N
6	831006	*	*	N	*	5.5	5.45	E
7	841003	*	*	*	*	5.4	5.18	E
8	841219	*	N	*	*	4.7	4.38	N
9	870605	O	*	*	*	6.2	6.22	E
10	880929	*	-	*	-	4.6	4.34	N
11	900526	N	*	*	*	5.5	5.26	E
12	900816	*	*	*	*	6.2	6.13	E
13	920521	*	*	O	*	6.5	6.58	E
14	920925	*	*	*	*	5.0	4.58	N
15	931005	N	*	*	*	5.9	5.84	E
16	940610	*	*	*	*	5.8	5.71	E
17	941007	*	*	*	*	5.9	5.82	E
18	950515	*	*	*	*	6.0	6.05	E
19	950817	*	*	*	*	5.9	5.97	E
20	960608	*	*	*	*	5.7	5.72	E
21	960729	*	*	*	*	4.7	4.24	N

Table 1: Presumed underground explosions at the Singer Test Site. A '*' indicates which arrays recorded each explosion. '-' denotes that a phase was not detected for a particular explosion at that array, 'O' means that the station was overloaded for this explosion and 'N' denotes that there was no data available for this explosion. Also given are the bodywave magnitudes taken from the ISC bulletin and the maximum-likelihood magnitude m_b^{ML} estimated here.

GBA			
Test Area	Epicentral Distance(°)	Azimuth(°)	Back-Azimuth(°)
Northern	29.56	201.9	16.7
South Western	29.21	202.0	16.9
Eastern	29.53	202.7	17.3
EKA			
Test Area	Epicentral Distance(°)	Azimuth(°)	Back-Azimuth(°)
Northern	57.82	317.6	62.2
South Western	58.05	317.7	62.5
Eastern	58.11	317.7	62.1
YKA			
Test Area	Epicentral Distance(°)	Azimuth(°)	Back-Azimuth(°)
Northern	74.53	10.8	342.4
South Western	74.89	10.8	342.3
Eastern	74.62	11.0	342.0
WRA			
Test Area	Epicentral Distance(°)	Azimuth(°)	Back-Azimuth(°)
Northern	74.66	135.4	326.0
South Western	74.44	135.3	325.7
Eastern	74.36	135.7	326.1

Table 2: Epicentral distance, azimuth and back-azimuth to each of the UK-type arrays from each of the test areas. The angles are measured from the centre of the test areas, taken to be 41.55N 88.72E for the Eastern Test area, 41.70N 88.35E for the Northern test area and 41.34N 88.28E for the South Western test area.

there are not enough observations for a stable epicentre to be estimated. For all of the JED estimates the epicentres of the explosions of 6 October 1983 and 3 October 1984 were restrained to the locations published by Matzko (1994), on the assumption that these are the true locations. All JED depths were restrained to zero. Table 3 gives the location and origin time results of both the array and ISC JED runs.

The ISC epicentres (Figure 1) do not clearly separate into test areas within the Singer site whereas the JED results, both using ISC data and array data, (Figure 2) do show three distinct areas. Table 1 shows that most of the explosions have been at the Eastern test area and that these are usually larger in magnitude than those in the other two areas.

The results using the array observations (Figure 2) show that, even though the number of stations is small (four), the three test areas can be resolved when the onsets are reliably read. The variance of the array observations is over 50 times smaller than that of the ISC data which is highly significant (Table 4).

The hypothesis that all the epicentres at the Northern area had in effect a common epicentre was tested. It was found that the difference between the estimated epicentres and a common epicentre is significant at the 4.5% level. A similar test for the Eastern area shows that the hypothesis that the explosions have a common epicentre must be rejected (epicentre shifts are significant at less than the 0.005% level).

Magnitude Estimates

The m_b^{ML} estimates are derived from the amplitude and period observations given in the ISC bulletins, using the amplitude-distance curve of Lilwall (1987). The station thresholds used are the same as those used by Douglas (1993) - as a first pass, the thresholds for 1989 have been assumed to stay constant up to 1996. The estimates of m_b^{ML} must therefore be taken to be preliminary until the assumptions made about the thresholds for the period 1990-1996 have been checked.

The variation in signal characteristics with both m_b^{ML} and areas within the Singer site are now being investigated. Inspection of the recordings from the UK-type arrays shows that the P seismograms differ

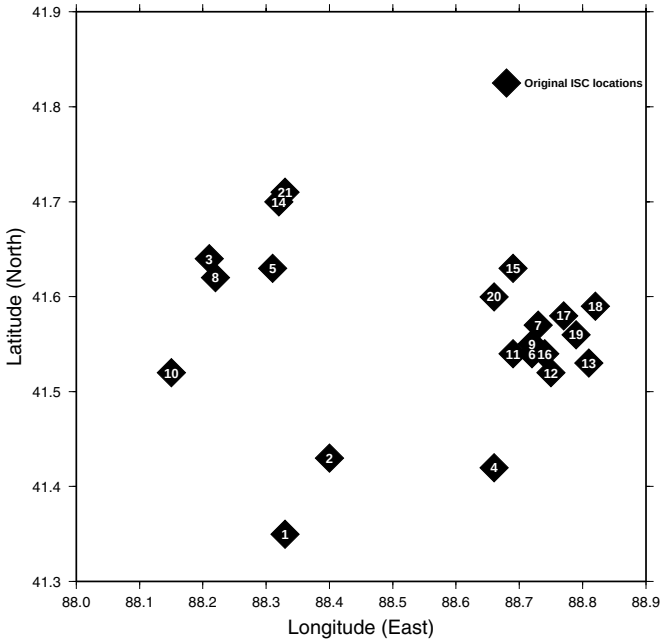


Figure 1: Original ISC coordinates for the underground tests at Singer. The numbers are the 'explosion #' given in Table 1.

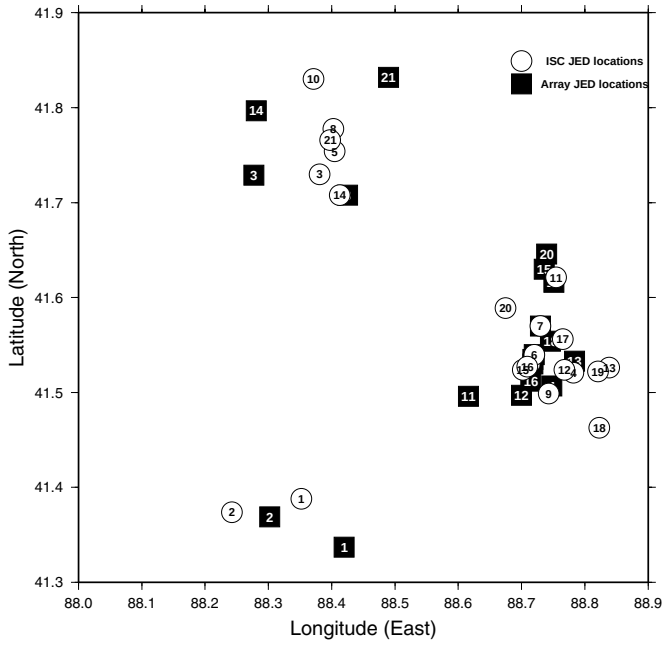


Figure 2: ISC JED relocations (circles) and the array JED relocations (squares). The numbers are the 'explosion #' given in Table 1.

Array JED results				
Explosion #	Date	Origin Time	Latitude	Longitude
1	690922	16:15:01.41±0.50	41.337N±8.5	88.420E±10.1
2	751027	0:59:59.94±0.57	41.369N±7.5	88.302E±13.9
3	761017	5:00:00.99±0.56	41.729N±7.5	88.277E±13.7
4	781014	0:59:59.69±0.57	41.507N±7.6	88.748E±13.8
6	831006	10:00:00.00±0.00	41.540N±0.0	88.720E±0.0
7	841003	6:00:00.00±0.00	41.570N±0.0	88.730E±0.0
8	841219	6:00:00.23±0.47	41.708N±8.3	88.425E±12.2
9	870605	5:00:00.37±0.40	41.535N±6.9	88.718E±9.3
11	900526	7:59:59.93±0.50	41.496N±8.5	88.616E±10.0
12	900816	4:59:59.79±0.40	41.497N±6.9	88.700E±9.3
13	920521	4:59:59.69±0.40	41.533N±6.9	88.784E±9.2
14	920925	8:00:01.04±0.39	41.797N±6.9	88.281E±9.3
15	931005	1:59:58.71±0.50	41.630N±8.5	88.736E±0.0
16	940610	6:26:00.15±0.40	41.512N±6.9	88.715E±9.3
17	941007	3:26:00.33±0.40	41.616N±6.9	88.751E±9.2
18	950515	4:06:00.17±0.40	41.554N±6.9	88.746E±9.3
19	950817	1:00:00.15±0.40	41.530N±6.9	88.718E±9.3
10	960608	2:56:00.34±0.40	41.646N±6.9	88.740E±9.2
21	960729	1:49:00.54±0.40	41.832N±6.9	88.490E±9.3
ISC JED results				
Explosion #	Date	Origin Time	Latitude	Longitude
1	690922	16:15:01.06±0.67	41.388N±2.2	88.352E±10.1
2	751027	1:00:00.60±1.20	41.374N±6.6	88.242E±18.9
3	761017	5:00:00.98±0.88	41.730N±3.3	88.381E±13.1
4	781014	0:59:59.83±0.86	41.521N±3.4	88.782E±12.6
5	830504	5:00:00.49±1.80	41.754N±1.4	88.405E±22.6
6	831006	10:00:00.00±0.00	41.540N±0.0	88.720E±0.0
7	841003	6:00:00.00±0.00	41.570N±0.0	88.730E±0.0
8	841219	6:00:00.63±0.71	41.778N±1.4	88.402E±8.4
9	870605	5:00:00.04±0.36	41.499N±7.6	88.743E±5.6
10	880929	7:00:00.50±0.90	41.830N±5.2	88.371E±9.2
11	900526	8:00:00.31±0.41	41.621N±8.4	88.755E±5.3
12	900816	4:59:59.67±0.34	41.524N±7.2	88.768E±4.8
13	920521	4:59:59.27±0.33	41.526N±7.3	88.839E±4.7
14	920925	8:00:00.40±0.47	41.708N±8.9	88.413E±6.3
15	931005	1:59:58.22±0.35	41.524N±7.8	88.702E±4.9
16	940610	6:26:00.22±0.36	41.527N±7.6	88.709E±4.9
17	941007	3:25:59.90±0.35	41.556N±7.4	88.765E±4.9
18	950515	4:05:59.36±0.35	41.463N±7.3	88.823E±5.0
19	950817	0:59:59.65±0.38	41.522N±7.6	88.821E±5.4
10	960608	2:55:59.92±0.38	41.589N±7.6	88.675E±5.4
21	960729	1:48:59.92±0.49	41.766N±8.9	88.398E±7.0

Table 3: JED results of location and origin time for both the array and ISC JED runs. The location confidence limits are given in kilometres.

JED run	No. of Explosions	Stan. Dev.	Variance	DoF	Restrained explosions
All Test areas					
ISC	28	2.0413	4.1670	5204	831006 and 841003
4 Arrays	23	0.2774	0.0770	13	831006 and 841003

Table 4: Results from the ISC and array JED runs using all underground explosions from the Singer test site.

for the three test areas. These differences are particularly clear on the GBA seismograms (Figure 3). The differences seem most likely to be due to lateral variations in structure near the test site but the details of this variation have still to be examined.

Other evidence of differences in near source effects of the three test areas is shown in such features as the period of the first P arrival. Figure 4 shows the period against m_b^{ML} for all GBA recordings. For the Northern area the period has a wide range even though the range of m_b^{ML} is small, whereas the periods for explosions at the Eastern area show the clear systematic increase with m_b^{ML} that might be expected as the corner frequency of the P pulse should decrease with yield and hence magnitude.

Figure 5 shows that there is a large discrepancy between the GBA station magnitudes and the station magnitudes at the other arrays, especially for the Eastern test area explosions. The rms values, however, show much better correlation (Figure 6), indicating that anomalous P-wave amplitudes can produce suspect station magnitude results, while rms values are more stable. The complexity of the GBA seismograms appears to be due to a reduction in the amplitude of the first arrival rather than an increase in the coda amplitude as seen in Figure 5 and Figure 6.

CONCLUSIONS AND RECOMMENDATIONS

The experiments using JED show that well-read onset times from four array stations are sufficient to resolve the distribution of epicentres into three separate test areas. It is to be hoped that the onset times measured at the IDC for explosions and published in the REBs can achieve similar accuracy.

To try and further improve the JED locations the array observations will be merged with those from the ISC and JED estimates will be obtained with the two sets of observations weighted appropriately. We also intend to analyse the REB onset times that are available for the four of the Singer tests to estimate the errors in the times. Further work is needed to investigate the anomalous P amplitudes at GBA and a large phase that is visible 20 seconds after the onset on the GBA recordings of the Eastern explosions only.

To improve the m_b^{ML} estimates, the maximum likelihood magnitudes will be recomputed, once the station threshold values have been determined for the time period from 1990-1996.

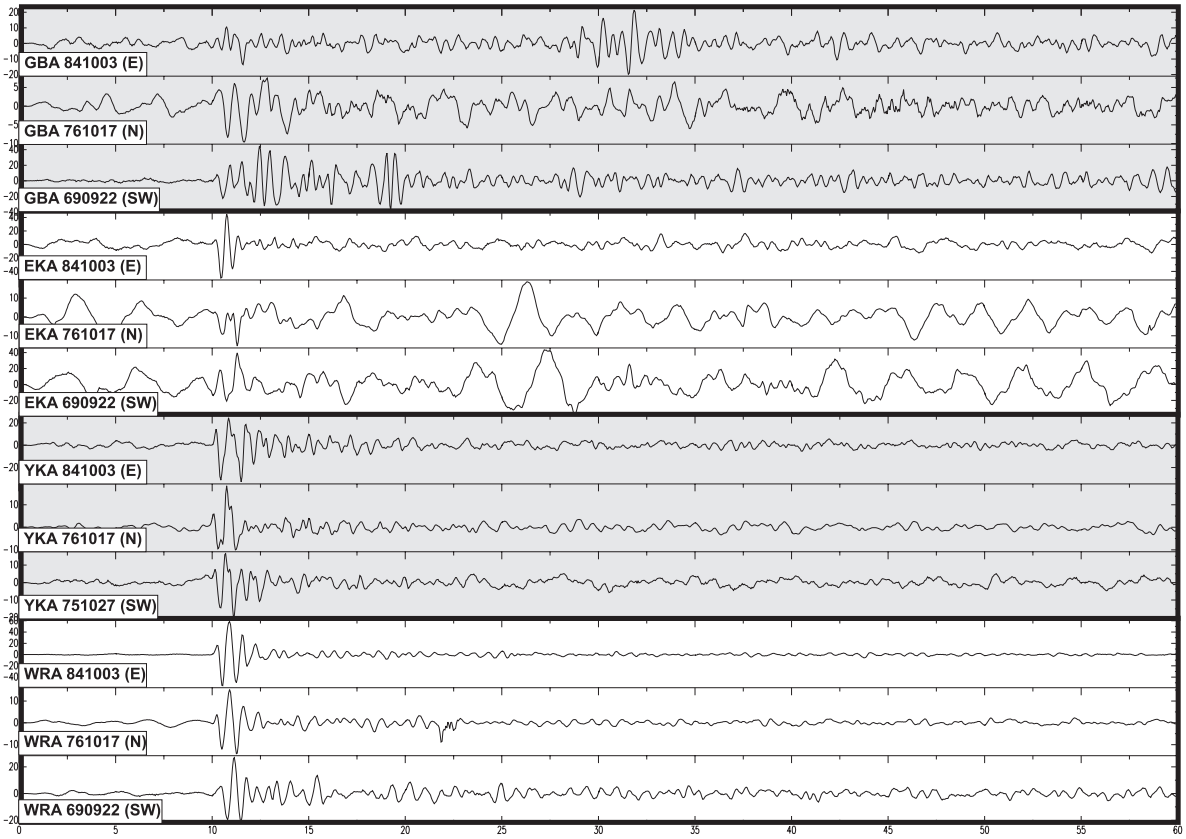


Figure 3: Unfiltered P beams from GBA, EKA, YKA and WRA for explosions of similar magnitude from the three test areas.

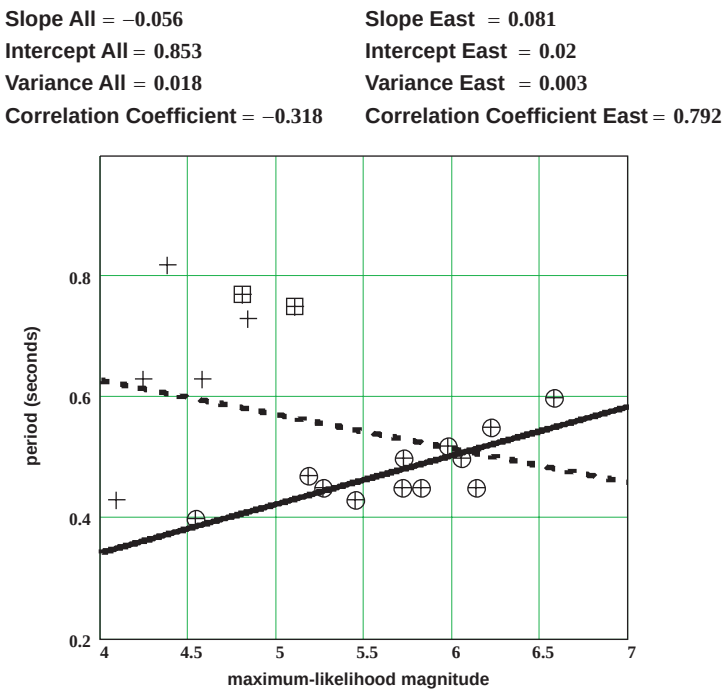


Figure 4: Period against m_b^{ML} for all explosions recorded at GBA. Two least squares lines are shown, the dashed line illustrates the estimate for all of the tests whereas the solid line is for the Eastern test area only.

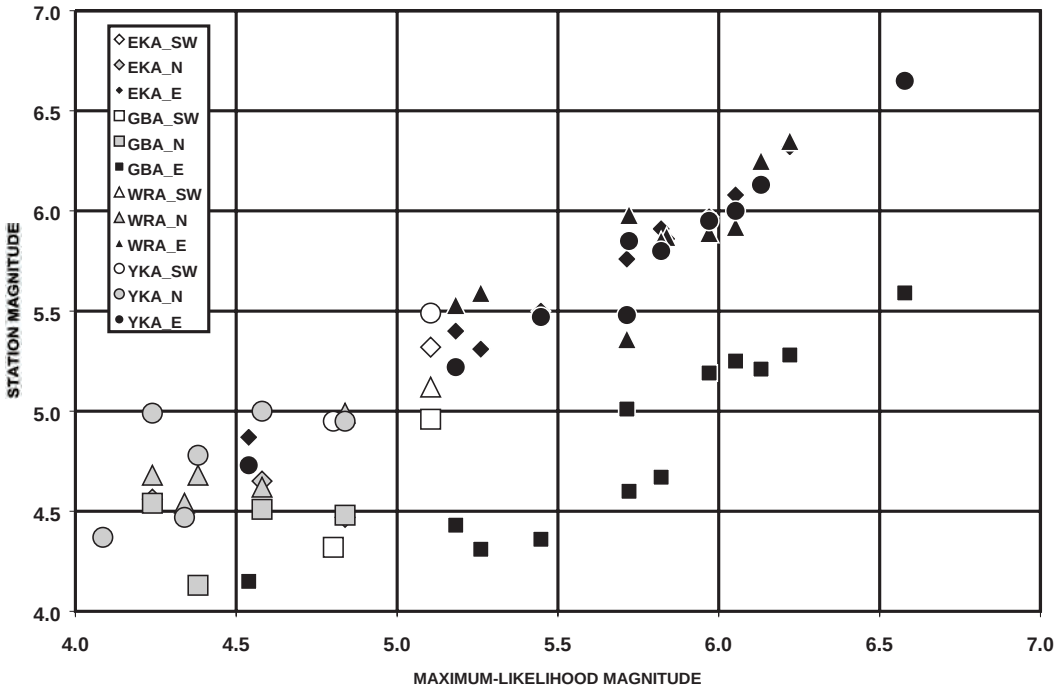


Figure 5: Station magnitude values for all arrays and all test areas. Note the anomalous GBA_E values.

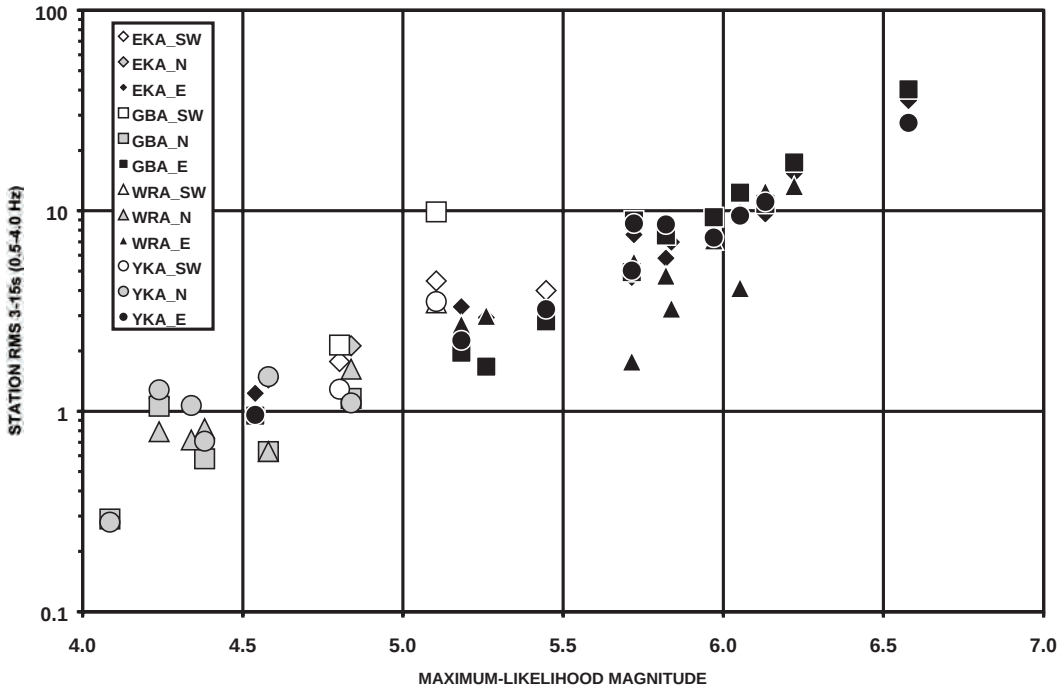


Figure 6: Station rms values for all arrays and all test areas for a time window from 3-15 seconds after the onset time. Note that all the arrays show similar values, even GBA_E.

REFERENCES

Douglas, A. (1967). Joint Epicentre Determination. *Nature*, **215**, 47-48.

Douglas, A. (1997). Bandpass filtering to reduce noise on seismograms: Is there a better way?. *Bull. Seis. Soc. Am.*, **87**, 770-777.

Douglas, A., Marshall, *P*.D., & Jones, K.H. (1993). Body-wave magnitudes and locations of explosions at the Chinese test site, 1967-1989. AWE Report No. O-12/93. HMSO, London.

Lilwall, R.C. (1986). Some simulation studies of seismic magnitude estimators. AWE Report No. O-22/86. HMSO, London.

Lilwall, R.C. (1987). Empirical amplitude-distance/depth curves for short-period P waves in the distance range 20 to 180°. AWE Report No. O-30/86. HMSO, London.

Lilwall, R.C. & Neary, J.M. (1985). Redetermination of body-wave magnitudes (m_b) for the period 1965-81 using ISC bulletin data. AWE Report No. O-21/85. HMSO, London.

Matzko, R. (1994). Geology of the Chinese nuclear test site near Lop Nor, Xinjiang Uygur Autonomous Region, China. *Eng. Geol.*, **36**, 173-181.

SURFACE WAVE IDENTIFICATION RESEARCH IN THE MIDDLE EAST AND NORTH AFRICA

Michael E. Pasyanos, Peter Goldstein, William R. Walter and Arthur Rodgers
Lawrence Livermore National Laboratory

Sponsored by U.S. Department of Energy
Office of Nonproliferation and National Security
Office of Research and Development
Nuclear National Security Administration

Contract No. W-7405-ENG-48

ABSTRACT

We are in the process of making improvements in surface wave identification throughout the Middle East and North Africa. Seismic surface waves have long played an important role in nuclear explosion monitoring by providing both information about the lithosphere they pass through and the source that generated them. We have made high-resolution group velocity maps of the Middle East and North Africa using the tomographic inversion of more than 10,000 individual path measurements. These maps provide valuable constraints on models of the underlying structure of the region. The maps also provide estimates of expected phase of new events that can be used in phase-match filters to compress the expected signal and thus improve the signal-to-noise ratio. Of very high interest is improving the performance of the traditional M_S:m_b discriminant and extending the discriminant down to events with smaller magnitude that are recorded at closer regional distances. This paper directly addresses the improvement that phase match filters bring to the estimation of the surface wave magnitude, M_S. We have estimated M_S for over 8000 events at 30 stations, both with and without the use of phase match filters, and have found a marked improvement in our ability to discriminate between earthquakes and explosions.

When considering smaller magnitude events, however, several other problems emerge. In our analysis, for example, deep events can flag as "explosion-like" using the m_b:M_S discriminant, since they are also inefficient generators of surface waves. If unidentified as deep events or classified as "normal" depth events, they can contaminate the actual distribution of surface wave magnitudes (and their derived discriminants) for shallow earthquakes. It is clearly very important to independently identify the source depth of these events in order to avoid misclassifying them. One possible method is through the use of waveform modeling. In order to be effective, however, we need to have reasonable estimates of local earth structure. We are also making use of a combined regional and teleseismic technique to provide constraints on source and structure. Far regional and teleseismic data provide high-resolution estimates of depth, while regional data help constrain the mechanism and structure.

Research performed under the auspices of the U.S. Department of Energy at the Lawrence Livermore National Laboratory under contract number W-7405-ENG-48.

Key Words: identification, surface waves, group velocity, discrimination, Middle East, North Africa

OBJECTIVE

The purpose of this study is to use surface waves to improve the identification of events throughout the Middle East and North Africa (MENA). We have calculated surface wave magnitude (Ms) from data in the LLNL MENA waveform database by measuring the amplitude of the surface wave train in specific period ranges. Amplitudes are then converted to magnitudes by a scale that accounts for factors such as period, attenuation, geometrical spreading, etc. Regional determinations of this parameter have proved difficult due to factors such as unsuitable magnitude algorithms, poor signal-to-noise, and propagation complications. We have tried to overcome some of these obstacles by using phase-matched filtering on the raw waveform and a surface wave magnitude algorithm suitable for regional distances.

Surface wave magnitude is an accurate measure of the long-period and shear-wave energy of a seismic event. It is generally used in conjunction with other magnitude estimates to form a discriminant. M_S:m_b is a well-known, important, and reliable discriminant between earthquakes and explosions. By calculating regional surface wave magnitudes, we hope to extend the threshold of the M_S:m_b discriminant down to lower magnitude levels. Discrimination between earthquakes and explosions is important to monitoring the Comprehensive Nuclear-Test-Ban Treaty.

RESEARCH ACCOMPLISHED

Surface wave magnitudes

We have selected all available waveform data for shallow (depth < = 50 km) events greater than or equal to m_b 3.5 from the LLNL MENA waveform database recorded at selected stations. A map of the stations and events used is shown in Figure 1. Stations are indicated by triangles. Events with only one or two single station measurements are shown in open circles. Events recorded with acceptable signal-to-noise ratio at three or more stations are shown in closed circles. Explosions, regardless of the number of recording stations, are indicated by the closed diamonds. Amplitude measurements are made by taking vertical waveforms containing surface waves and deconvolving them to ground displacement. The displacement traces are then bandpass filtered over a selected period range, usually around 20 seconds. The maximum amplitude and period of the surface wave is then measured.

In addition to making amplitude measurements on raw traces, we also measured amplitudes on traces that had been phase-matched filtered. The filtering routine compresses the signal using the input group velocity profile, eliminates any spurious energy occurring outside of the allowable frequency-time windows, and redisperses the cleaned signal. Phase-matched filter estimates are determined from surface wave group velocity estimates (Pasyanos et al., 2000). In previous studies (Pasyanos et al., 1999), we have also compared the results made using the high-resolution tomography in the Middle East to other estimates from a global surface wave model (Stevens and McLaughlin, 1997) and a 1-D global earth model PREM (Dziewonski and Anderson, 1981). Amplitude measurements are corrected for factors such as attenuation, geometrical spreading, and the period of the measurement in order to yield magnitude. Traditionally, M_S measurements (i.e. Gutenberg, IASPEI) are only made at teleseismic distances (Δ > 20°). Several methods have been developed to make regional surface wave measurements. We employ the formula of Rezapour and Pearce (1998), given as:

$$M_S = \log(A/T)_{max} + 1/3 \log(\Delta) + 1/2 \log(\sin \Delta) + 0.0046\,\Delta + 5.370$$

where A is amplitude, T is period, and Δ is distance in degrees.

Single station measurements for a given event are then combined in order to produce an overall magnitude for the event. We test three combination methods. The first is a network average, determined by calculating the mean of the individual measurements. Uncertainty is given as the standard deviation of the measurements. The second method that we test uses a maximum likelihood method to compensate for the self-censoring of data that occurs near the noise floor. Here we use the signal-to-noise ratio as a weighting function for the magnitude measurements. The third method that we used simply uses the maximum of the individual measurements as the event magnitude. The uncertainty used is the difference between the maximum measurement and the mean. While the second methodology will consistently overestimate magnitudes relative to the first method, this value might produce a better discriminant, the reasoning being that an observation of a large surface wave should not be down-weighted by other observations with small or non-existent surface waves. We have excluded any single station measurements derived from amplitudes with signal-to-noise ratios less than 0.65. While it may seem counterproductive to include any measurements with a signal-to-noise ratio of less than 1.0 (or higher), we choose to keep events near the threshold since it is the absence of surface wave signal which is the discriminant. Although events with very low signal-to-noise ratios (< 0.65) will have such small weights in the maximum likelihood method as not to significantly influence the event magnitude, they have been completely removed so as not to contaminate single station measurements or magnitude estimates made using the other (mean and maximum) methods, where the effect would be severe.

Overall, we have made over 49,000 amplitude estimates for over 8,000 events at 30 stations using 4 different methods (without phase-matched filtering and with phase-matched filtering using three different models). Consequently, we have made over 8,000 single-station magnitude estimates with acceptable signal-to-noise ratio. This results in a total of 7,000 earthquakes with 2 or more stations and about 6,000 earthquakes with 3 or more stations, along with 8 explosions. In conjunction with other high-frequency magnitude estimates (i.e. m_b), M_S forms an important discriminant between earthquakes and explosions. In order to test and validate our results, we have taken the measured surface wave magnitudes for a particular station and compared them against m_b measurements taken from the USGS PDE catalog. Figure 2 shows plots of M_S:m_b for events which have been phase-matched filtered using the group velocities predicted from the surface wave tomography. Event magnitudes have been calculated using the maximum likelihood method. Explosions are indicated by the blue diamonds. For a given m_b, explosions produce M_S measurements that are low. The best fitting regression of the measurements is shown by the solid line. We calculate our discriminant by subtracting from the measured surface wave magnitude the surface wave magnitude expected from the body wave magnitude, as determined from the regression line in Figure 2. Explosions generally have M_S measurements between one and two magnitude units lower than earthquakes with a similar body wave magnitude.

We perform a simple statistical analysis on both the earthquakes and explosions to estimate the mean and variance of the discriminant in the two populations (Figure 3a). From the statistics of the two populations, we can now generate receiver operator curves. A receiver operator curve quantifies the probabilities of misidentifying events with a particular discriminant, either as an explosion misclassified as an earthquake (missed violation) or as an earthquake misclassified as an explosion (false alarm). The receiver operator curve is asymmetric due to the unequal variances in the earthquake and explosion populations. Figure 3b shows the corresponding receiver operator curve for the two statistical populations. The equiprobable point is defined as the point on the curve where the missed violation rate and the false alarm rate are equivalent. Without phase-matched filtering and maximum likelihood we have an equiprobable point of 0.116 or 11.6%. Using maximum likelihood, the equiprobable point increases slightly to 0.128 or 12.8%. When we use phase-matched filtering without maximum likelihood, the equiprobable point drops to 0.080 or 8.0%. Finally, using phase-matched filtering and maximum likelihood, we find an equiprobable point of 0.080 or 8.0%. This is the solid curve shown in Figure 3b. The dashed curve corresponds to the equiprobable line with no phase matched filtering. This quantifies the improvement in M_S-m_b discrimination provided by phase-matched filtering using the LLNL group velocity maps and correction surfaces. We expect that phase-matched filtering will become of premium importance for the smallest magnitude events.

Investigating anomalous events

Differences in surface wave and body wave magnitudes can be caused by a number of factors. Events with deep source depths do not effectively generate surface waves and will flag as anomalous events. Some events in this database from the Hindu Kush and Zagros regions that were tagged with nominal source depths (i.e. 10 km, 33 km) fall into this category (see Figure 4). Since their source depths can often be determined independently by other means, they can be ruled out as explosions by other means. If these deep events can be systematically identified and removed from the earthquake population, we would expect to see even greater separation between the two populations.

Figure 5 shows a plot of the M_S:m_b discriminant as a function of catalog source depth. Earthquakes are illustrated by the triangles and explosions by the stars. There are a couple of features to note. First, there is a clear trend in the discriminant with depth. This trend is unsurprising since we expect deeper events to be less efficient producers of surface waves than shallower events, and this is reflected here. The trend results in about a 1.0 unit difference in the discriminant between 0 and 50 km depth. Secondly, with the exception of the Pakistani explosion which occurred in the coda of a large nearby shallow earthquake in Afghanistan, the explosions separate well from the earthquake population, particularly with respect to other shallow events. Finally, we can see the large scatter from earthquakes where the depth was unknown, but arbitrarily set to a particular depth by a geophysicist. These are represented by the large bands occurring at 5 km, 10 km, and especially at 33 km. In these cases, most of the events that are indicated as explosion-like are probably deep events, especially in light of the fact that most of these events are happening in areas where deep events are known to occur. For example, if the trend that we are seeing in the discriminant continues to deeper events, then a mislocation in source depth from 130 km to 33 km could make a difference of about 2 units in the discriminant, bringing those events back into the middle of the population. Even a mislocation of about 50 km in depth would clearly put the event back into the scatter in the earthquake population.

Figure 6 is an example of an event in the Hindu Kush region that had a 33 km source depth and an anomalously low M_S. Waveform modeling was performed on data at station NIL, located about 150 km south of the event. We suspected that this event might be deep, causing the large discrepancy in magnitudes. Results from the waveform modeling indicate otherwise, suggesting a source depth of about 25 km. Another possible explanation for the anomaly is that the attenuation relationship used in the Rezapour and Pearce magnitude formula might not be appropriate for all areas. The thick crust in the Hindu Kush region differs significantly from the global average for the crust. This effect is particularly critical when we are considering events located close in to the seismic stations, as we are in this particular case. Several other possibilities exist. One is that the m_b for this event is significantly overestimated, producing a larger m_b-M_S discrepancy. For an m_b 5.0 event, this earthquake did not produce very large signals at regional recording stations. In addition to being close, several of the nearest stations also appear to be nodal for the Rayleigh wave, as station NIL is in Figure 6. This would also cause an underestimate of M_S. We would like to estimate the source depth of as many of these events with constrained depth as possible and, if necessary, to properly remove them from the earthquake population. There are still a number of unresolved questions of why many of the events in particular regions are anomalous. Sorting out these issues is an active research area.

CONCLUSIONS AND RECOMMENDATIONS

Using surface wave magnitudes in discriminants has long been important in identifying seismic events. By employing techniques such as phase-matched filtering that has been based on high-resolution tomographic studies, we can begin to also apply this capability to smaller, regional events. As our understanding of regional earth structure improves, we can expect to see continued improvement in regional discriminants using surface waves. As illustrated in our study, it is imperative to the success of this discriminant to be able to independently identify and remove deeper events that also flag as “explosion-like.” While large events often have clear indications of the source depth, such as depth phases, these signals are often obscured for smaller events. We are considering several methodologies to help us in this endeavor.

REFERENCES

Dziewonski, A. and D. Anderson, Preliminary Reference Earth Model, Phys. Earth. Planet. Int., 25, 297-356, 1981.

Pasyanos, M.E., W.R. Walter, S.R. Ford, S.E.Hazler, Improving mb:Ms Discrimination using Phase Matched Filters Derived from Regional Group Velocity Tomography, 21st Seismic Research Symposium, September 21-24, 1999, Las Vegas, NV.

Pasyanos, M.E., W.R. Walter, and S.E. Hazler, Surface wave dispersion study of the Middle East and North Africa for Monitoring the Comprehensive Nuclear-Test-Ban Treaty, LLNL Report UCRL-JC-133973, submitted to Pure and Applied Geophysics, 2000.

Rezapour, M. and R.G. Pearce, Bias in Surface-Wave Magnitude Ms due to Inadequate Distance Corrections, Bull. Seism. Soc. Am., 88, 43-61, 1998.

Stevens, J. and K. McLaughlin, Improved methods for regionalized surface wave analysis, Final Report PL-TR-97-2135, Phillips Laboratory, Directorate of Geophysics, AFMC, Hanscom AFB, 26 pp., 1997.

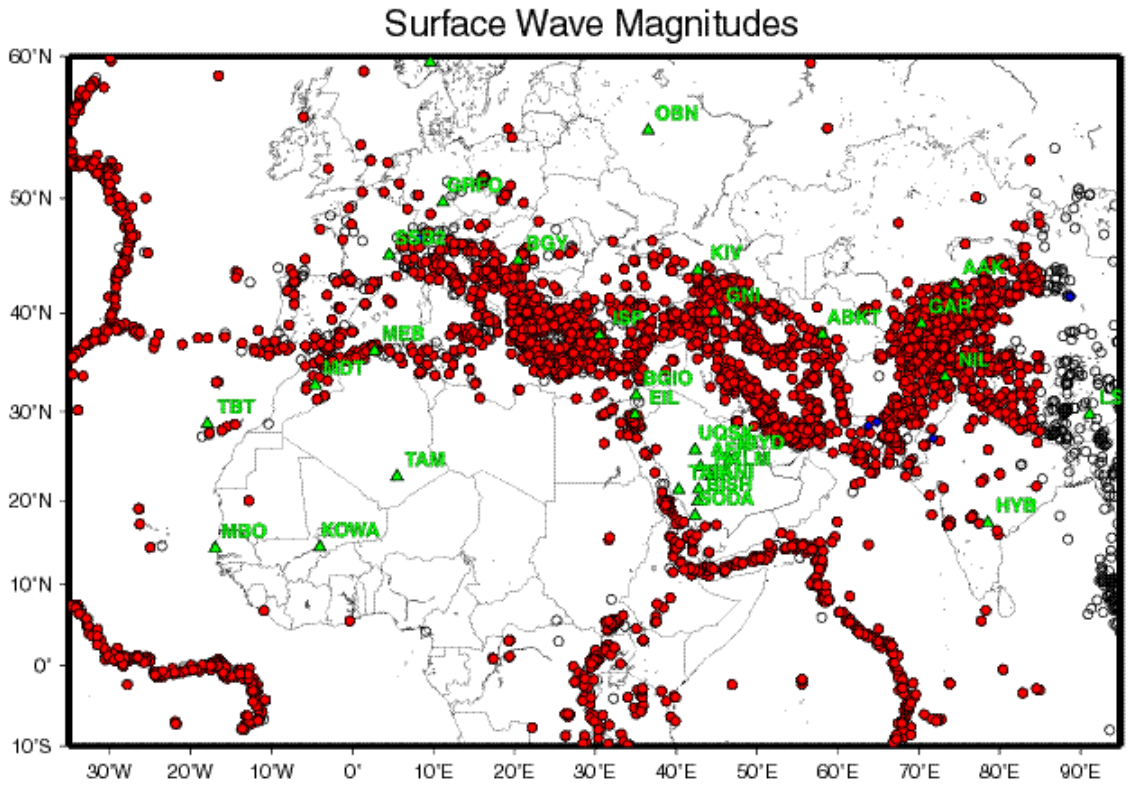


Figure 1. Events and stations used for surface wave magnitudes. Stations are indicated by triangles. Events are shown by circles, explosions are indicated by the solid diamonds.

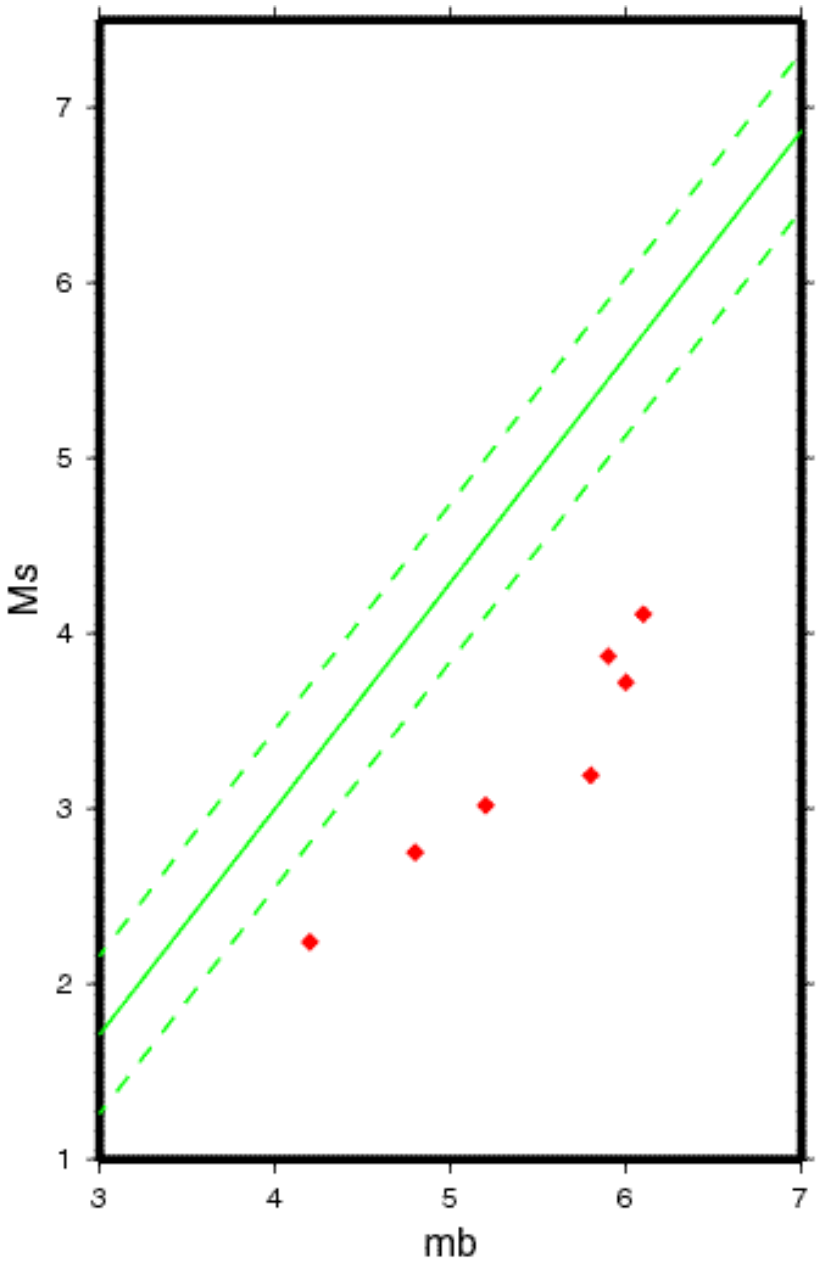


Figure 2. Plot of mb vs. Ms for events which have been phase-matched filtered using the group velocities predicted from the surface wave tomography. The best fitting regression of the earthquakes (not shown) and one standard deviation are shown by the solid and dashed green lines. Explosions are indicated by the red diamonds.

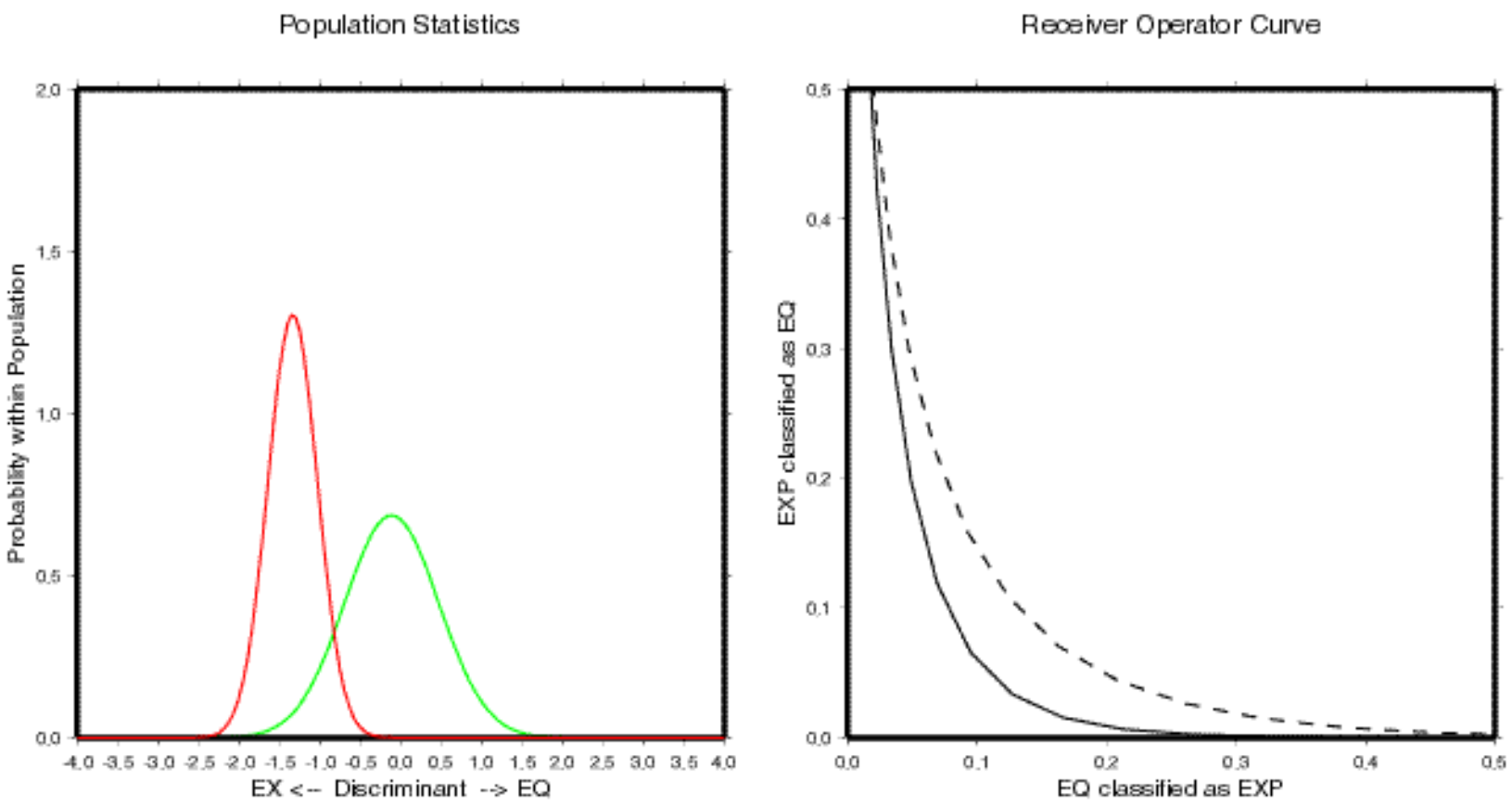


Figure 3. Separation of the discriminant for the earthquake (green curve) and explosion (red curve) populations and the receiver operator curves derived from the statistics of the discrimant for the two populations. The solid curve corresponds to the receiver operator curve with phase-matched filtering and the dashed line corresponds to the reciver operator curve with no phase-matched filtering.

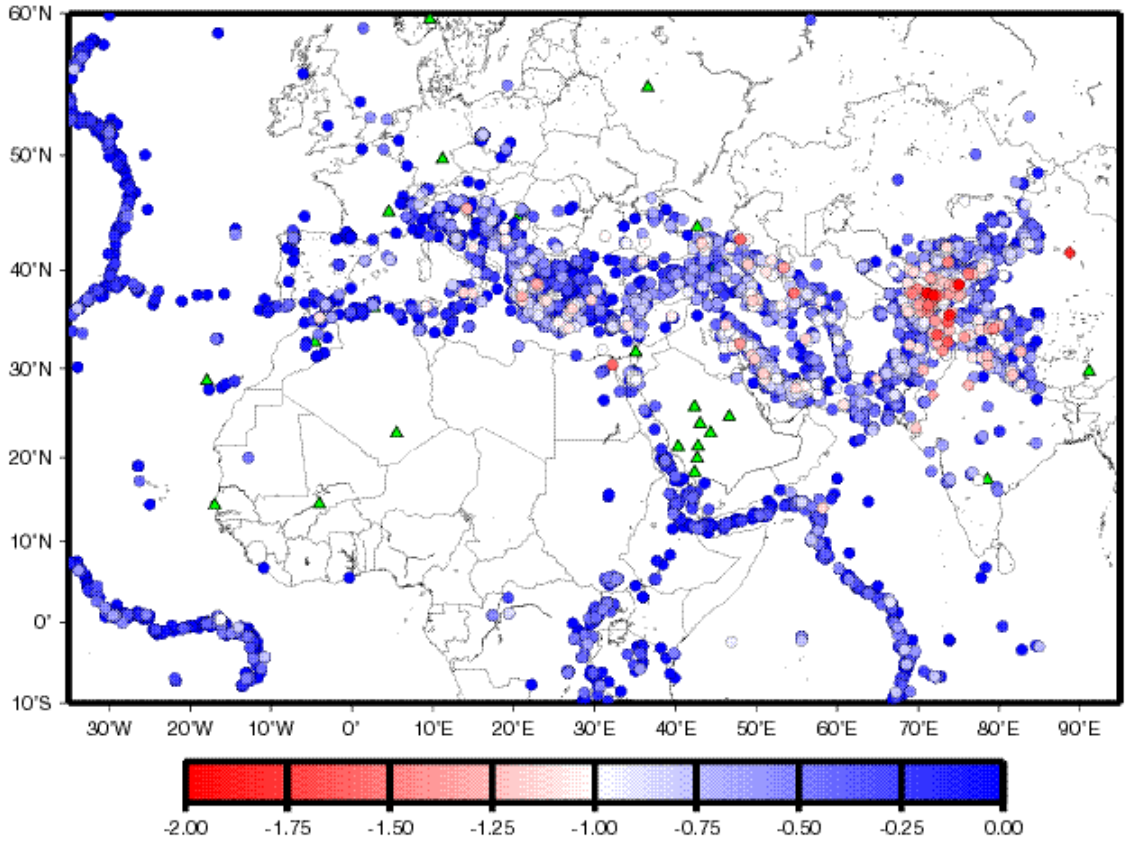


Figure 4. Map view of events color coded by Ms:mb discriminant. Earthquake-like events are shown in blue shades, explosion-like events are in red shades. Stations are shown as green triangles.

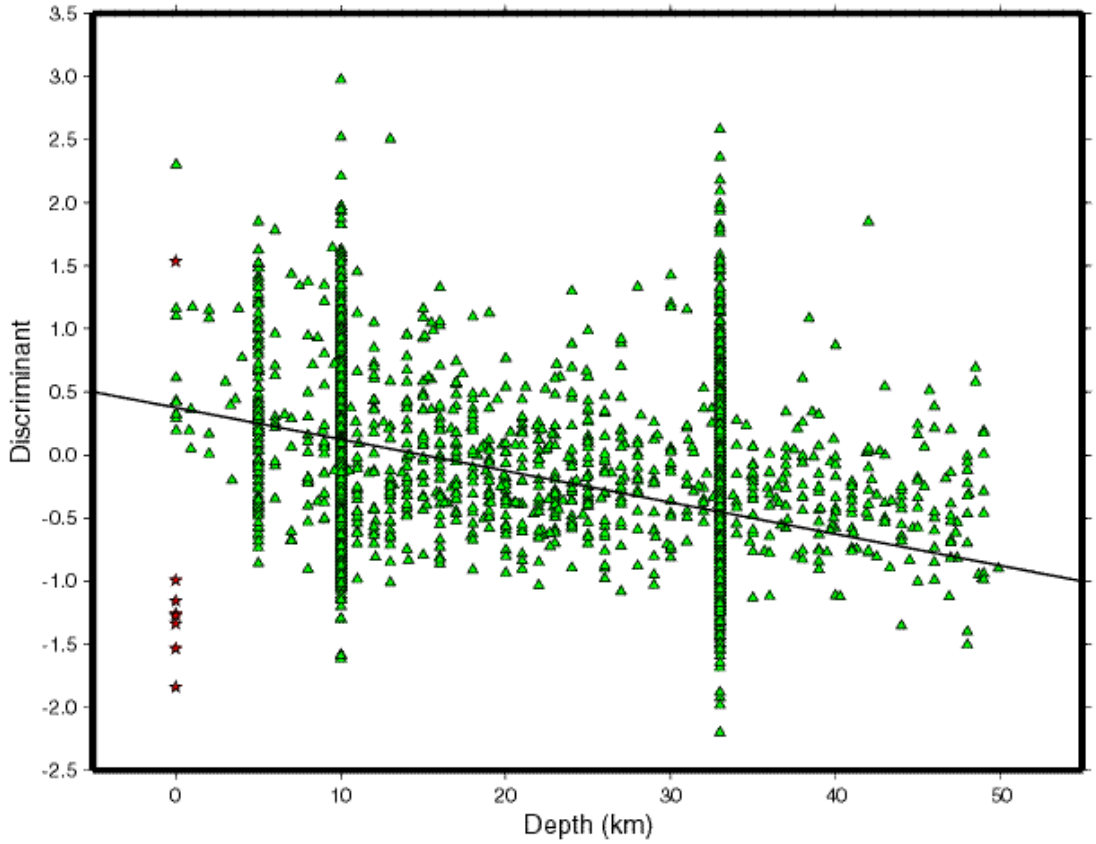
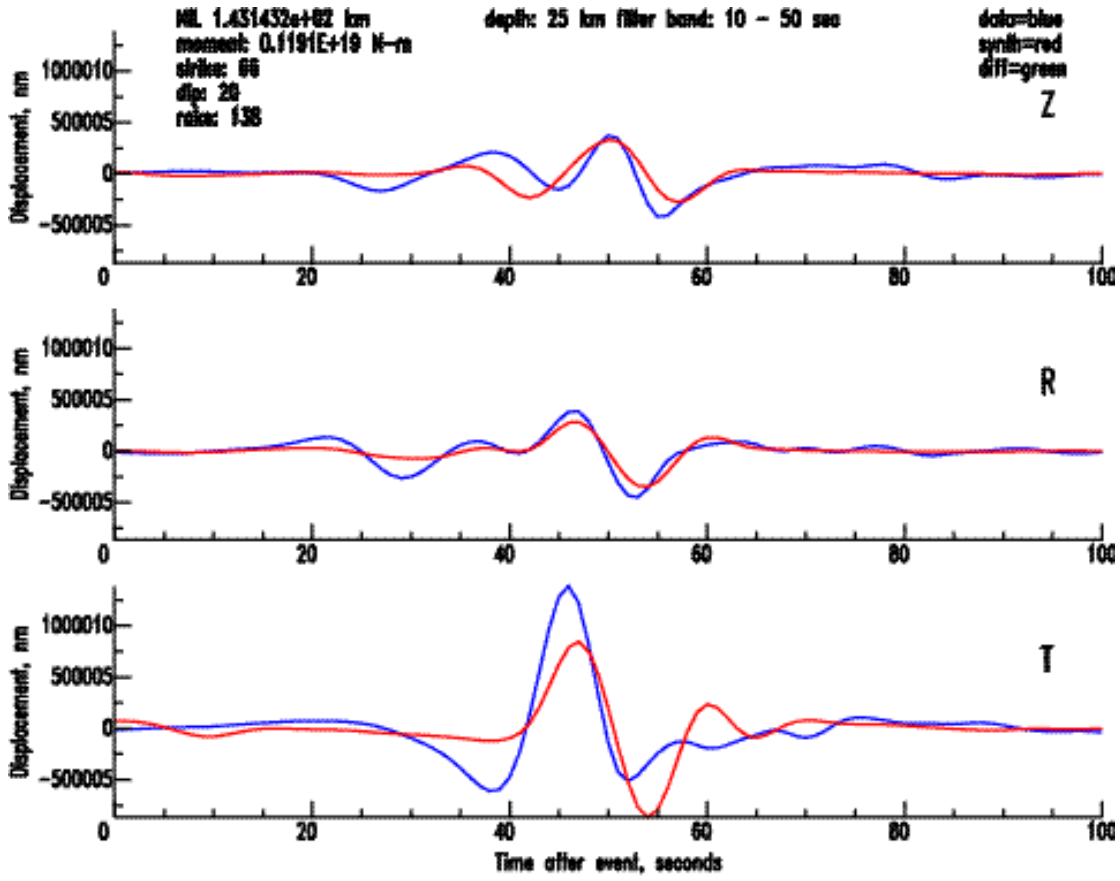


Figure 5. Discriminant plotted as a function of source depth. Earthquakes are illustrated by green triangles, explosions by the red stars. Large scattering in the discriminant are found where the depths are fixed at 5 km, 10 km, and especially at 33 km.



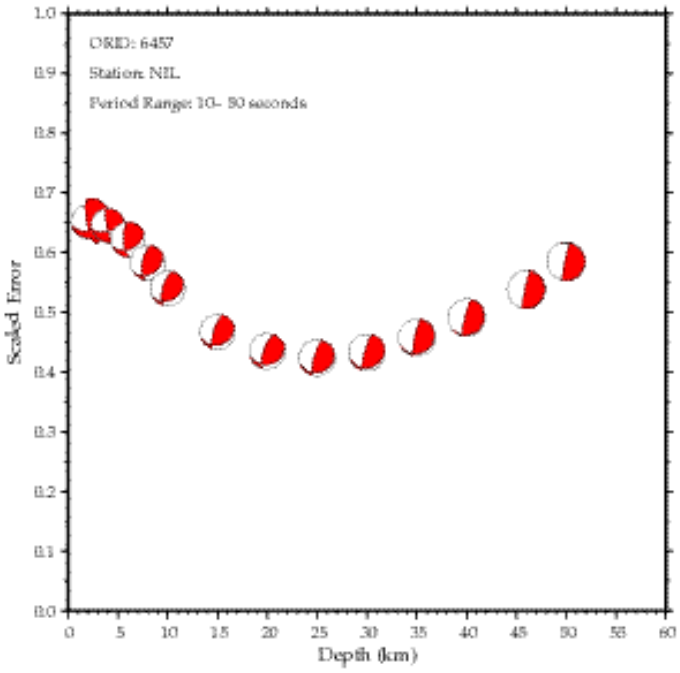


Figure 6. Waveform modeling results for an anomalous event in the Hindu Kush.

M_s : m_b RELATIONSHIPS FOR SMALL MAGNITUDE EVENTS: OBSERVATIONS AND PHYSICAL BASIS FOR m_b BASED ON REGIONAL PHASES

Howard J. Patton
Los Alamos National Laboratory

Sponsored by U.S. Department of Energy
Office of Nonproliferation Research and Engineering
Office of Defense Nuclear Nonproliferation
National Nuclear Security Administration

Contract No. W-7405-ENG-36

ABSTRACT

To address the challenge of small event monitoring for the Comprehensive Nuclear-Test-Ban Treaty (CTBT), there is great interest to extend the successful teleseismic m_b-M_s discriminant to regional-distance applications. Among the outstanding issues are (1) how well can we expect the discriminant to perform for regional data as a function of source size and (2) what is the physical basis behind its performance. In a recent paper Patton (2000), M_w: m_b scaling relationships for Pn and Lg waves with 1-s periods were developed for earthquakes and explosions located in distinct tectonic regions and geologic materials around the world. Among a number of findings of that study is the result that m_b(Pn) for explosions scales at a significantly higher rate than m_b(Lg) in the M_w range ~3.5 - 6.0. On the other hand, Pn and Lg scaling rates do not differ for earthquakes. On plots of M_s versus m_b(Pn), the scaling results suggest that earthquake and explosion populations converge at M_s ~ 1 -2, while populations may or may not converge on plots of M_s versus m_b(Lg), and show better separation at small magnitudes. Observations of regional M_s for small-yield explosions at the Nevada Test Site (NTS) confirm the scaling predictions. Thus, m_b based on regional shear phases may serve as a better m_b-M_s discriminant than m_b based on regional compressional phases, a surprising conclusion. These findings certainly cannot be explained by simple theories of the explosion source, and I propose a physical model combining well-established scaling models and the latest understanding of Lg generation by underground nuclear explosions.

Key Words: discrimination, regional monitoring, physical basis, regional phases

OBJECTIVE

The objective of this project is (1) to characterize m_b-M_s scaling for earthquakes and explosions using regional-distance observations and (2) to provide a physical basis for the scaling and for discrimination performance at small magnitudes. One of the greatest challenges of monitoring a CTBT is discriminating man-made seismic events from natural events at low source strengths, and this project seeks an understanding of the potential at small magnitudes using extensions of the m_b-M_s discriminant to regional data.

RESEARCH ACCOMPLISHED

A recent study of regional scaling relations found that m_b(Pn) scales at a higher rate than m_b(Lg) on plots of M_w versus m_b for explosions detonated at NTS (Patton, 2000). Scaling relations for explosions at Semipalatinsk and other hard-rock test sites suggested similar differences between Pn and Lg scaling rates, but the data sets were smaller and showed more scatter than NTS observations, and as a result, estimates of scaling rates were less certain. In contrast to explosions, earthquakes did not show differences in scaling rates for Pn and

Lg waves. In this paper, I provide further evidence that source scaling of 1-Hz Pn and Lg waves is different for NTS explosions, and I propose a physical model to explain why this might be. The verification significance of this work relates to characterization of m_b-M_s scaling and to the discrimination potential at small magnitudes. This characterization is the subject of current research, but some tentative results will be examined.

Both m_b(Pn) and m_b(Lg) were measured for most explosions conducted at NTS in order to develop better technologies for estimating seismic yield (e.g., Nuttli, 1986; Patton, 1988; Vergino and Mensing, 1990). Of special interest to this project is the frequently overlooked fact that yield-scaling reported for Lg and Pn waves differed for explosions detonated in tuff, as summarized in the table below.

Table 1: Yield-scaling results for NTS explosions (after Patton; Vergino and Mensing)

Phase	Test Region	Intercept	Yield Slope	Gas Porosity Slope
Lg	Yucca, AWT	3.52	0.96*	–
Lg	Yucca, AWT	4.13	0.75	–0.025
Lg	Yucca & Pahute, BWT	4.18	0.76*	–
Pn	So. Yucca, AWT & BWT	3.84	0.91	–0.027
Pn	Pahute, AWT & BWT	3.87	0.91	–0.027

* Yield slope when gas porosity is left out of the regression model.

Patton (1988) found that after accounting for the effects of gas porosity, yield scaling of 1-Hz Lg waves for explosions above the water table (AWT) is the same as it is for explosions below the water table (BWT). The same effect of gas porosity is seen for Pn waves (Vergino and Mensing), but the slope on log yield, 0.91, is significantly greater than it is for Lg waves, 0.76. Thus, Pn scaling rates with official yield are 20% higher than they are for Lg waves. For comparison, estimates of scaling slopes on plots of M_w versus m_b for NTS explosions are 1.37 ± 0.03 and 1.22 ± 0.03 for Pn and Lg waves, respectively (Patton, 2000), a 12% difference.

Direct comparisons of m_b(Pn) and m_b(Lg) should also reveal differences in scaling for NTS explosions. Figure 1 shows such a plot for 243 explosions ranging ~3 orders of magnitude in yield. A linear regression yields a slope of 1.13 ± 0.02. In other words, m_b(Pn) scales at a rate 13% higher than Lg waves. This estimate is about the same percentage as the one obtained from M_w versus m_b data, which used explosions detonated in a variety of media, just as Figure 1 does. The yield-scaling results in Table 1 pertain just to explosions fired in tuff and rhyolite. In any case, summarizing for NTS explosions, scaling rates are not the same for regional phases based on compressional (Pn) and shear wave (Lg) phases, as various scaling relationships reveal that rates for Pn are ~13 to 20% higher than they are for Lg.

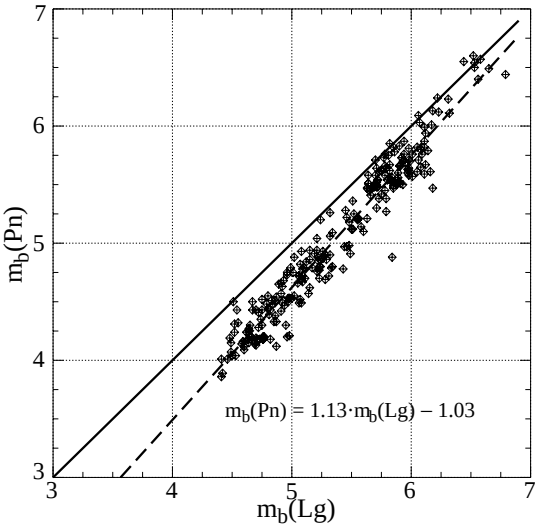


Figure 1. Regional m_b for NTS explosions. Dash line is a regression fit to the data; solid line represents equality.

A Physical Model. In this sub-section, a model combining the basic tenets of the Mueller-Murphy model (Mueller and Murphy, 1971; M-M) with recent insights into Lg generation by underground explosions is proposed to explain the differences in source scaling between Pn and Lg waves. In this development, I use the concept of an "effective" source function. An effective source function combines the features of a traditional source function with the effects of complex wave propagation on seismic wave generation. In this case, the propagation effects occur so close to the source that it is impossible to separate them in far-field data from intrinsic source properties. An example of such propagation effects is near-field Rg-to-S scattering. Gupta *et al*. (1992) proposed that this scattering mechanism is particularly effective for generating low-frequency crustal S waves (< 2 Hz) by explosions because of their shallow depth of burial and efficient Rg excitation characteristics. Subsequent research, both observational (Patton and Taylor, 1995; Gupta *et al*., 1997; Myers *et al*., 1999) and synthetic (e.g., Jih, 1993; 1995), has supported this proposed mechanism. The model of Rg-to-S scattering has undergone some refinements with subsequent research. In particular, excitation nulls observed in spectral amplitudes of Lg waves (Patton and Taylor, 1995; Gupta *et al*., 1997) were interpreted to be caused by the imprint of Rg source spectra excited by a compensated linear vector dipole (CLVD). These nulls are related to focal depth of the CLVD source, which is a kinematic description of spall phenomena occurring in the geologic strata over the explosion point source. Thus, while the explosion source is an efficient source of Rg waves, spallation, which reaches to the free surface and has a centroid depth even shallower than the explosion, appears to be even more efficient generating Rg waves that scatter into 1-Hz Lg observed in the far-field. Another key observation is that effects of Rg-to-P scattering are absent in the spectra of Pg waves from underground explosions (Patton and Taylor, 1995), suggesting that this mechanism plays a lesser role in the excitation of regional P waves.

Based on this evidence, I argue that differences in scaling rates of Pn and Lg waves might be caused by the fact that effective source functions for these phases are not similar, nor do they scale alike. The model I will develop is illustrated in the figure below.

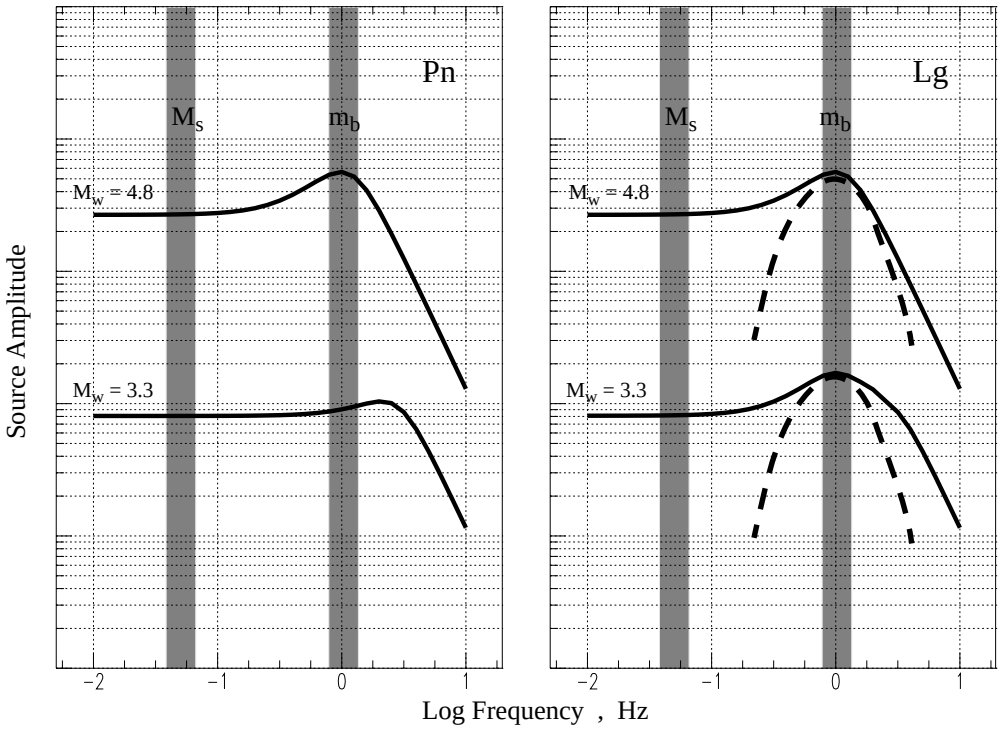


Figure 2. Effective Pn and Lg source functions for explosions with yields of 100 and 1 kt (solid lines) and idealized Rg-to-S scattering functions (dash lines). For illustration purposes, the Lg source function at 100 kt is simply the M-M spectrum plotted for Pn waves, while for 1 kt, it is a hybrid formed by vertically shifting the 100-kt spectrum down, interpolating, and suturing the 1-kt M-M spectrum at ~3 Hz.

The Pn source functions are represented by M-M spectra for 100 and 1 kt explosions in granite with P-wave speeds, α, of 5 km/s, S-wave speeds, β, of 3 km/s, and density, ρ, 2.5 g/cm^3. As source size decreases, the spectral overshoot moves out of the 1-Hz band to higher frequencies. Lg effective source functions are modeled as a composite of the M-M spectrum and a narrow band spectrum representing the contribution of Rg-to-S scattering. While the M-M spectrum scales with source size, the scattering spectrum does not because it is a property of the near-source velocity medium. The bump in Lg spectra is hypothesized to persist at small yields for frequencies near 1 Hz, because Rg-to-S scattering is strong in this band for large and small events.

To relate this model to observations of scaling differences, an analytical expression is needed for the slope, $\Delta m_b(Pn)/\Delta M_w$. First note that

$$M_w \sim 2/3 \cdot \log M_o \sim 2 \cdot (\log \Psi_\infty + \log I_\alpha) / 3 \quad ,$$

and

$$\Delta M_w = 2 \cdot (\Delta\log \Psi_\infty + \Delta\log I_\alpha) / 3 \quad \text{and} \quad I_\alpha = \rho\alpha^2 \quad ,$$

where M_o is the seismic moment of an explosion, which equals $4\pi I_\alpha \Psi_\infty$ (Aki *et al.*, 1974), and Ψ_∞ is the static level of the reduced displacement potential (RDP). I_α is referred to as source medium "impedance." Second, using equation 4.88 of Aki and Richards (1980), we can relate the far-field amplitude, A(f), to the source function, S(f), as follows

$$m_b(Pn) \sim \log A(1\ Hz) \sim \log S(1) - 1/2 \cdot \log \alpha I_\alpha \quad ,$$

and

$$\Delta m_b(Pn) = \Delta\log S(1) - 1/2 \cdot \Delta\log \alpha I_\alpha \quad ,$$

where Pn propagates as a body wave in the mantle and S(1) refers to the source amplitude in the 1-Hz band. Therefore, an analytical expression for the scaling rate of Pn waves is

$$\Delta m_b(Pn)/\Delta M_w = 3/2 \cdot \frac{\Delta\log S(1) - 1/2 \cdot \Delta\log \alpha I_\alpha}{\Delta\log \Psi_\infty + \Delta\log I_\alpha} \quad . \qquad (1)$$

Invoking the Mueller and Murphy source model and letting A be Ψ_∞ for a 1-kt explosion, then $AW^{0.76}$ is Ψ_∞ for a W-kt explosion. If B is amplitude of the source function in the 1-Hz band for a 1-kt explosion, then $BKW^{0.76}$ is the amplitude for a W-kt explosion, where K is a measure of overshoot in the source function. Thus, in the range of 1 to W kt, the scaling rate can be written in terms of overshoot parameter K and yield W,

$$\Delta m_b(Pn)/\Delta M_w = 3/2 \cdot \frac{\log K + 0.76 \cdot \log W - 1/2 \cdot \Delta\log \alpha I_\alpha}{0.76 \cdot \log W + \Delta\log I_\alpha} \quad , \qquad (2)$$

where $\Delta\log I_\alpha$ is the logarithm of impedance ratio, $I_\alpha{}^W/I_\alpha{}^1$, and superscripts refer to explosion yields.

A similar development is followed to derive an expression for $\Delta m_b(Lg)/\Delta M_w$, except the source is a composite of the explosion and Rg-to-S scattering. Equation (1) above is assumed to apply to Lg waves also, and the scaling of Ψ_∞ obeys the M-M model, just as it does for Pn waves. The development departs from that of Pn waves for the 1-Hz band, where B' is amplitude of the explosion source function, and Φ is amplitude from Rg-to-S scattering. Patton (1990) found that the strength of the spall source (which is proportional to the mass of spalled material) scales as $W^{0.75}$, very nearly the same scaling as Ψ_∞ of the explosion. It follows then that amplitudes for the composite source are $B' + \Phi$ for a 1-kt explosion and $[KB' + \Phi]W^{0.76}$ for a W-kt explosion, assuming linear superposition of the explosion and Rg-to-S sources. The scaling rate for Lg waves can be written in terms of W, K and a new parameter, K′,

$$\Delta m_b(Lg)/\Delta M_w = 3/2 \cdot \frac{\log (K+K'-1)/K' + 0.76 \cdot \log W - 1/2 \cdot \Delta\log \alpha I_\alpha}{0.76 \cdot \log W + \Delta\log I_\alpha} \quad , \qquad (3)$$

where $K' = 1 + \Phi / B'$. For $K' \geq 2$, the source amplitude due to scattering is as large as or larger than the amplitude of the explosion source function. In the following sub-section, I calculate the range of acceptable models as a function of the material parameter I_α under the constraints imposed by measured scaling rates for Pn and Lg waves and associated uncertainties.

Solution Subspace. Figure 3 shows solutions for K and K′ in the subspace where the central value of $\Delta m_b(Pn)/\Delta M_w$, 1.37, is assumed. Acceptable solutions are bounded by 2-σ errors on the estimate of Lg scaling slope. The plot spans reasonable values for the overshoot parameter K, based on realizations of M-M source functions for media at NTS and yields of ~100 kt. Notice that many solutions give $K' > 2$, indicating Lg source amplitudes from Rg-to-S scattering are larger than source amplitudes from the explosion. However, many solutions have unrealistically large K′ values, especially for smaller impedance ratios, where solution space shows rapid increases of K′ values. In order to constrain solution space further, knowledge of an appropriate range for the source impedance ratio is needed for NTS. This is readily available from a large measurement data base that was developed and maintained by weapon laboratories for nuclear test containment studies.

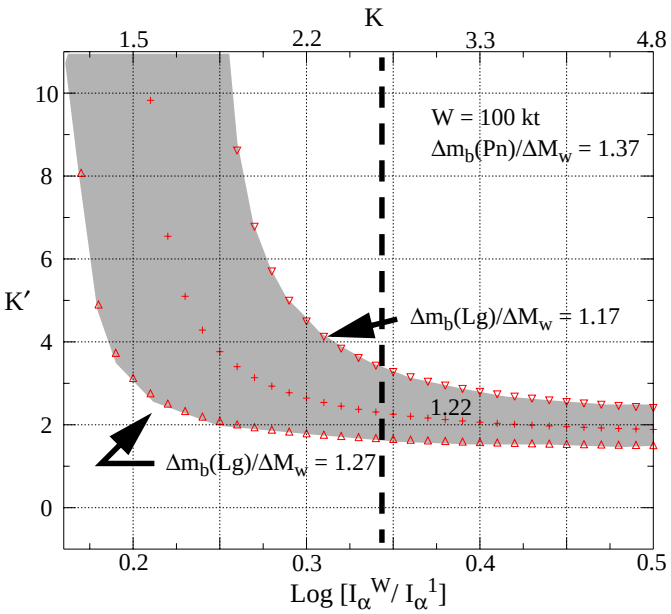


Figure 3. Acceptable solutions (or source models) are located in the shaded region. The central value on Lg scaling rate, 1.22, is the locus of points shown by plus symbols.

Rather than using *in-situ* measurements of working point densities and P-wave speeds, I chose to compute source impedance with a method that gives a better measure of what seismic waves "feel" in the source region. Details were presented in a poster at the 22nd Annual Seismic Research Symposium 12-15 September 2000, but the basic approach is to use measurements of seismic moment M_o and cavity radii (from the containment data base), and calculate "far-field" estimates of I_α using Aki *et al*'s famous equation, $M_o = 4\pi I_\alpha \Psi_\infty$. The results show relationships for I_α between explosions conducted in different media that are expected (e.g. estimates of I_α for dry alluvium are much smaller than for wet tuff). An estimate of I_α^1 was found by taking an average of all data for W < 5 kt, and an estimate of I_α^W was found by taking an average of all data for 50 < W < 200 kt. The log ratio, I_α^W / I_α^1, is 0.34, which is plotted as a vertical dash line in Figure 3. This result is probably a reasonable estimate for M_w-m_b observations used to determine scaling rates of Pn and Lg waves.

For log impedance ratios near 0.35, solution space does not show large variations in K′ as the solution curves are generally flat. Values of K′ are quite reasonable, and the majority of solutions have $K' > 2$. This is consistent with the hypothesis that Rg-to-S scattering is an important mechanism for generating 1-Hz Lg waves from underground nuclear explosions. Under this hypothesis, differences in Pn and Lg scaling rates are caused by effective source functions with dis-similar shapes and scaling behavior. The composite source gives a shallower slope because the bump in Lg spectra from Rg-to-S scattering persists for small yields, while it scales out of the 1-Hz band with decreasing yield in the M-M model used for Pn waves.

Implications for m_b-M_s Discrimination. The teleseismic m_b-M_s discriminant is very effective, and its physical basis is well understood (e.g. Stevens and Day, 1985). There is much interest to extend the discriminant to regional-distance applications for monitoring smaller events than teleseismic data can record. The physical

model proposed in this paper builds on our understanding of the explosion source and regional phase excitation. It provides a basis for predicting regional m_b scaling at small magnitudes. Based on the results for NTS, there is reason to believe that, unlike the teleseismic m_b-M_s, the best regional discriminant might be one which utilizes amplitudes of shear-wave phases, such as Lg, for the m_b, not compressional phases.

This project is in the early stages developing data sets to test m_b-M_s scaling predictions at small magnitudes. Part of this work involves developing technologies and calibrating regions for regional M_s determinations; efforts at universities and the lab are well underway for western China and surrounding areas. Plots of regional m_b-M_s for Pn and Lg waves are shown below (Figure 4) as examples of some preliminary data sets I have compiled.

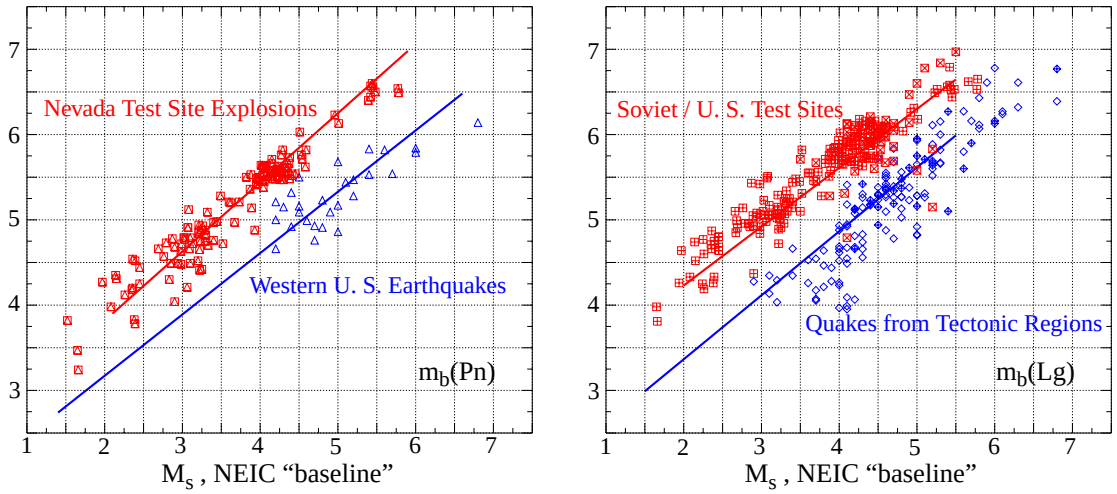


Figure 4. Plots of regional m_b versus M_s for areas in western U. S. and Eurasia. Pn data are just from the western U. S., while transportability of Nuttli's m_b(Lg) enables data from both areas to be plotted on the same graph (Patton, 2000). Measurements of M_s include regional and teleseismic data, and are reduced to a common baseline. Solid lines for earthquake and explosion populations are predictions from M_w versus m_b scaling models.

I have exploited the intrinsic transportability of Nuttli's m_b(Lg) to plot explosion data from NTS, Semipalatinsk, and Novaya Zemlya and earthquake data from tectonic regions of North America and southern Eurasia on a single graph. This is not possible with m_b(Pn) because it has been tied to teleseismic m_b(P) on a region by region basis, and it is well known that m_b(P) shows significant variations worldwide due to regional bias. The results to date are very preliminary, but there is some indication that source populations are better separated at small magnitudes for Lg than they are for Pn, consistent with the scaling models.

CONCLUSIONS AND RECOMMENDATIONS

A major conclusion to date is that m_b(Pn) and m_b(Lg) based on 1-Hz amplitudes show significantly different scaling rates for NTS explosions. This is supported by the analysis of large numbers of regional m_b observations with respect to (1) yield scaling, (2) M_o scaling, and (3) relative scaling of the respective magnitudes over a wide range of source size. A physical model which explains different scaling rates draws on the hypothesis that effective source functions for Lg waves are a composite of two sources, the explosion and near-source Rg-to-S scattering, while Pn waves are generated only by the explosion. Consequently, the shape and scaling behavior of effective source functions for Pn and Lg waves are dis-similar. In light of the evidence that earthquakes do not show differences in scaling rates, I argue that regional m_b-M_s discrimination may perform better for m_b based on shear-waves (Lg) in contrast to traditional compressional-wave based m_b.

A key question is whether or not P-wave scaling differs from Lg at other test sites around the world, especially

those with hard rock. At this point, it is difficult to say because the existing data are limited in quantity and range of source size. This question is important to resolve because it will address issues about the variability of regional m_b-M_s performance and further test our understanding of its physical basis. The latest evidence I have on this score is presented in the poster at the 22nd Annual Seismic Research Symposium.

This is report no. LA-UR-00-3437 of the Los Alamos National Laboratory, Los Alamos, NM 87545.

REFERENCES

Aki, K. and P. Richards (1980), *Quantitative Seismology: Theory and Methods*. W. H. Freeman and Company, San Francisco, CA.

Aki, K., M. Bouchon, and P. Reasenberg (1974), Seismic source function for an underground nuclear explosion. *Bull. Seismol. Soc. Am.* 64, 131-148.

Gupta, I. N., W. Chan and R. Wagner (1992), A comparison of regional phases from underground nuclear explosions at East Kazakh and Nevada Test Sites. *Bull. Seismol. Soc. Am.* 82, 352-382.

Gupta, I. N., T. Zhang, and R. Wagner (1997), Low-frequency Lg from NTS and Kazakh nuclear explosions--Observations and interpretations. *Bull. Seismol. Soc. Am.* 87, 1115-1125.

Jih, R.-S. (1993), Statistical characterization of rugged propagation paths with application to Rg scattering study. Report No. TGAL-93-06, Teledyne Geotech, Alexandria, VA.

Jih, R.-S. (1995), Numerical investigation of relative contributions of Rg scattering and incomplete dissipation to Lg excitation, in *Proceedings of the 17th Annual Seismic Research Symposium*, James F. Lewkowicz, Jeanne M. McPhetres, and Delaine T. Reiter, editors, Phillips Laboratory Report No. PL-TR-95-2108.

Mueller, R. and J. Murphy (1971), Seismic characteristics of underground nuclear detonations, Part 1: Seismic spectrum scaling. *Bull. Seismol. Soc. Am.* 61, 1675-1692.

Myers, S., W. Walter, K. Mayeda and L. Glenn (1999), Observations in support of Rg scattering as a source for explosion S waves: Regional and local recordings of the 1997 Kazakhstan depth of burial experiment. *Bull. Seismol. Soc. Am.* 89, 544-549.

Nuttli, O. (1986), Yield estimates of Nevada Test Site explosions obtained from seismic Lg waves. *J. Geophys. Res.* 91, 2137-2151.

Patton, H. (1988), Application of Nuttli's method to estimate yield of Nevada Test Site explosions recorded on Lawrence Livermore National Laboratory's digital seismic system. *Bull. Seismol. Soc. Am.* 78, 1759-1772.

Patton, H. (1990), Characterization of spall from observed strong ground motions on Pahute Mesa. *Bull. Seismol. Soc. Am.* 80, 1326-1345.

Patton, H. (2000), Regional magnitude scaling, transportability, and M_s : m_b discrimination at small magnitudes. accepted for publication in *Pure Appl. Geophys.*, special volume on *Monitoring the Comprehensive Nuclear-Test-Ban Treaty.*

Patton, H. and S. Taylor (1995), Analysis of Lg spectral ratios from NTS explosions: Implications for the source mechanisms of spall and the generation of Lg waves. *Bull. Seismol. Soc. Am.* 85, 220-236.

Stevens, J. and S. Day (1985), The physical basis of m_b : M_s and variable frequency magnitude methods for earthquake/explosion discrimination. *J. Geophys. Res.* 90, 3009-3020.

Vergino, E. and R. Mensing (1990), Yield estimation using regional m_b(Pn). *Bull. Seismol. Soc. Am.* 80, 656-674.

DETECTION AND LOCATION OF THE DEAD SEA SHOTS USING ADVANCED PROCESSING TECHNIQUES.

Vladimir Pinsky, Avi Shapira, Yefim Gitterman and Alona Malitzky

Geophysical Institute of Israel

Sponsored by The Defense Threat Reduction Agency

Contract No.DSWA01-97-C-0151

ABSTRACT

Seismic data of the Dead Sea calibration experiment, which provided Ground Truth source parameters, were used in studying advanced signal processing methods. The data set includes recordings of the SP stations of the Israel Seismic Network (ISN), the EILAT Experimental Seismic Array (EILESA) and the IMS primary station GERESS. There were no detection problems at ISN and Cypriot stations (r<500 km), equipped by the simplest STA/LTA algorithm. Meanwhile, low SNR at the GERESS (R=2400 km) did not allow to detect even the largest explosion by the routine automatic procedure.

We applied Adaptive Optimal Group Filter (AOGF) (Kushnir, 1995) method to the GERESS recordings, containing the explosion signal. The algorithm is based on computation of the preceding noise spectral matrix and theoretically provides undisturbed output signal with maximum SNR. The tool facilitated event detection, and yielded accurate estimations of the apparent velocity (±1 km/sec) and back azimuth ($\pm 2^0$). Equivalent results were obtained by the Maximum Likelihood Technique (MLT) (Bohme, 1995) – the highly sensitive moving window spectral analyzer of array data, destined mainly for the detection of multiple signals.

The same techniques were applied to the recordings of the EILESA – 8 station short period micro-array temporally deployed in the vicinity of the IMS BB station EIL. The algorithms provided satisfactory azimuth and velocity determination in spite of the poor array configuration. However, the estimates exhibited significant temporal variations of azimuth and apparent velocity attributed to heterogeneity of the upper crust.

Using ISN and CSN manual P picks for the three calibration explosions the best-fit 4 layer stratified model was evaluated for 500 km distance range, providing residual RMS = 0.2 sec The scatter of residuals didn't reveal systematic azimuth dependency. Then we applied robust automatic locator (Pinsky, 1999), developed in the frame of the contract, to the ISN recordings of the three events. The locator is the two stage procedure, using envelope location at the first stage to estimate the time intervals for the P, S first arrivals to the network stations. The second stage comprises automatic picking of the P, S first arrivals with robust fitting of the picks (eliminating outliers) to the travel time model. The results of the automatic location appeared close to the real epicenter and for the case of the best-fit model even better than the analyst solution, based on the conventional local model.

Key Words: Dead Sea explosions, automatic detection, location, parameter estimation, travel time.

OBJECTIVE

The major tasks of the CTBT monitoring are detection and location of seismic sources. Calibration explosions, such as the three detonated in the Dead Sea, serve the task providing travel time and azimuth corrections for tuning the IMS and other seismic networks and testing the assigned software. The main objective of this work was analysis of the waveforms from the Dead Sea calibration explosions at different recording systems and investigation of the travel times and behavior of several sophisticated algorithms for detection, location and parameter estimation using these recordings.

RESEARCH ACCOMPLISHED

1. Application of the Adaptive Optimal Group Filer (AOGF).

The main source parameters of the three Dead Sea explosions are presented in the Table 1. Signals of all the explosions were recorded with good SNR by all the stations within 500 km from the source: the Israel Seismic Network, Cyprus and Jordan seismic networks, CNF stations, BB IMS stations EIL and MRNI, so that there were no detection problems even for the simplest STA/LTA algorithm. The largest 5 t explosion was detected at GERESS (2400 km) as a weak signal, extracted though after careful pre-filtering. However, for many stations and arrays at R > 800 km (for example BRAR, Turkey) the signal is impossible to extract. This indicates practical distance and region limits for detection the explosive source of $m_b = 4$ from the Dead Sea area.

Table 1. Main parameters of the Dead Sea explosions.

Date	Origin time (O.T.), GMT	Coordinates	Total charge, t	Comments
8.11.99	13:00:00.33	31.5330N 35.4406E	0.5	Measurement accuracy: coordinates – 50 m, origin time – 5 msec
10.11.99	13:59:58.21	31.5338N 35.4400E	2.06	
11.11.99	15:00:00.795	31.5336N 35.4413E	5	

Main power of the signal is concentrated between 0.8 and 1.5 Hz, that doesn't change much with distance and provides good SNR at GERESS in this frequency band. Therefore, using this frequency band or close to it for GERESS recordings it was possible to estimate rather accurately azimuth and apparent velocity (the true Az=128.5 °, Vel.=12.15 km/sec), using usual wideband F-K analysis technique. Fig. 1. illustrates the estimates (we used for the analysis Kushnir & Haikin SNDA package) as maximum of the statistic at Az=132.5 °, Vel.= 12.32 km/sec for 0.8-1.8 Hz and Az=128.3 °, Vel.= 15.46 km/sec for 1.1-1.4 Hz frequency band respectively. We applied Adaptive Optimal Group Filter (AOGF) method (Kushnir, 1995) to the GERESS recordings, containing the explosion signal. The algorithm is based on computation of vector $\boldsymbol{R(f)}$ at each frequency *f:*

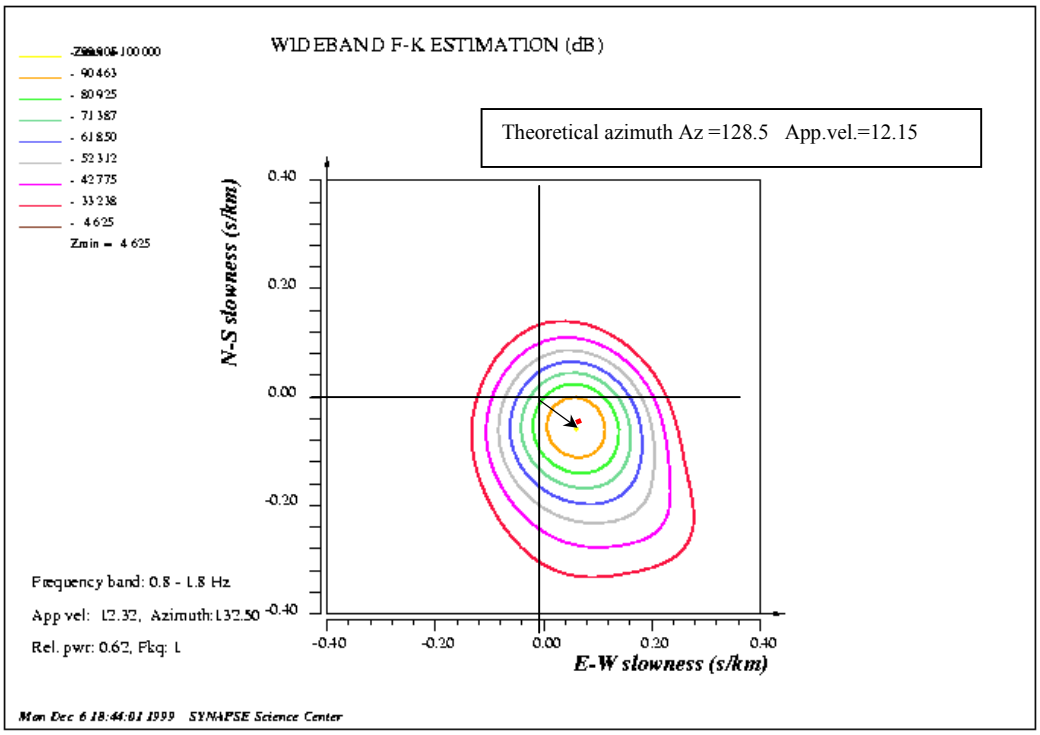
$$\boldsymbol{R^*(f)} = [\boldsymbol{H^*(f)\, F^{-1}(f)\, H(f)}]^{-1}\, \boldsymbol{H^*(f)\, F^{-1}(f)}, \qquad (1)$$

where $\boldsymbol{H(f)}$ is a vector of the array response with element $\boldsymbol{h_n(f) = \exp(-2\pi i f \tau_n)}$, $\boldsymbol{n=1,\ldots,N}$, $\boldsymbol{F(f)}$ is a matrix spectral density of the array noise. In the algorithm the $\boldsymbol{F(f)}$ matrix is estimated from the noise, preceding the signal.

The algorithm theoretically provides undisturbed output signal with maximum SNR for the true staring azimuth and apparent velocity. This property of AOGF is used in the SNDA (Seismic Network Data Analysis) package (Kushnir, Haikin, 1996) for Adaptive F-K analysis (AF-K). The AF-K (Fig. 2) results in Az=126.9°, Vel.=10.0 km/sec in the frequency band (0.8-1.5 Hz). In all cases the time interval used for the analyses was equal 5 sec.

For the signal extraction we applied SNDA version of the AOGF to the GERESS 25 channels recordings with staring azimuth Az=123.8° and apparent velocity Vel.=12.3 km/sec, filtered in the 1-3 Hz interval. The results of the AOGF and BEAM are shown on Fig.3 together with traces of the GERESS channel GED9 (with the best SNR). From the Fig. 3 we see that the AOGF has a slight advantage over the BEAM here.

a



b

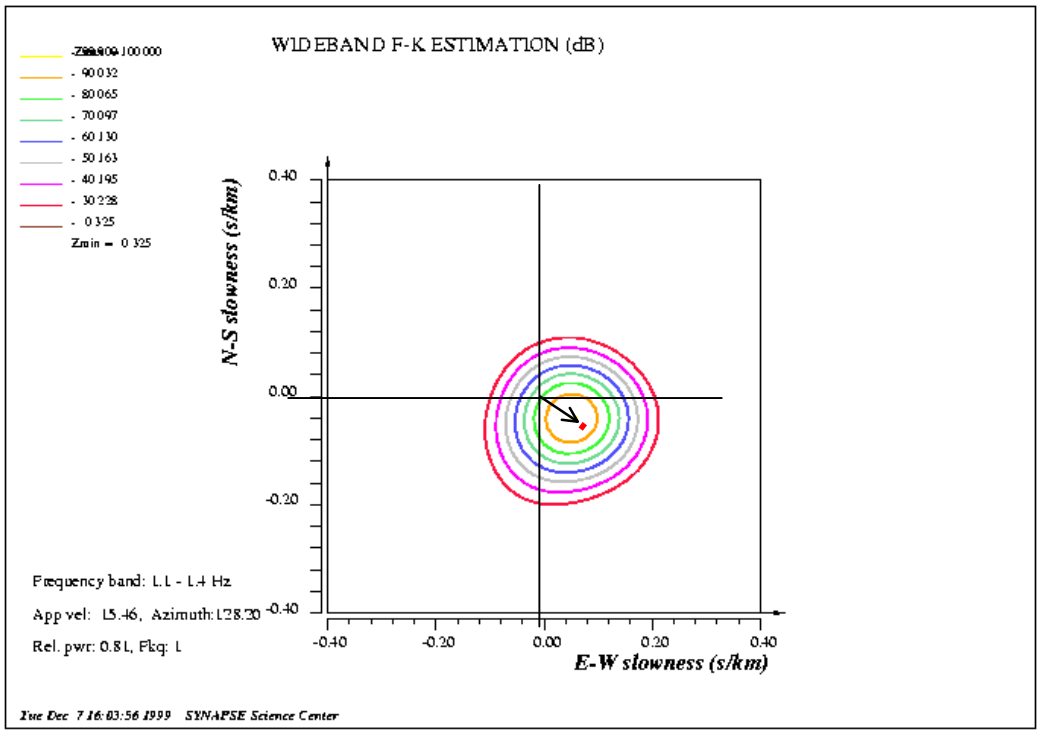


Fig.1. F-K analysis of the GERESS Dead Sea explosion on 99.11.11 by wideband conventional F-K in 0.8-1.8 Hz band (a), and 1.2-1.4 Hz band (b).

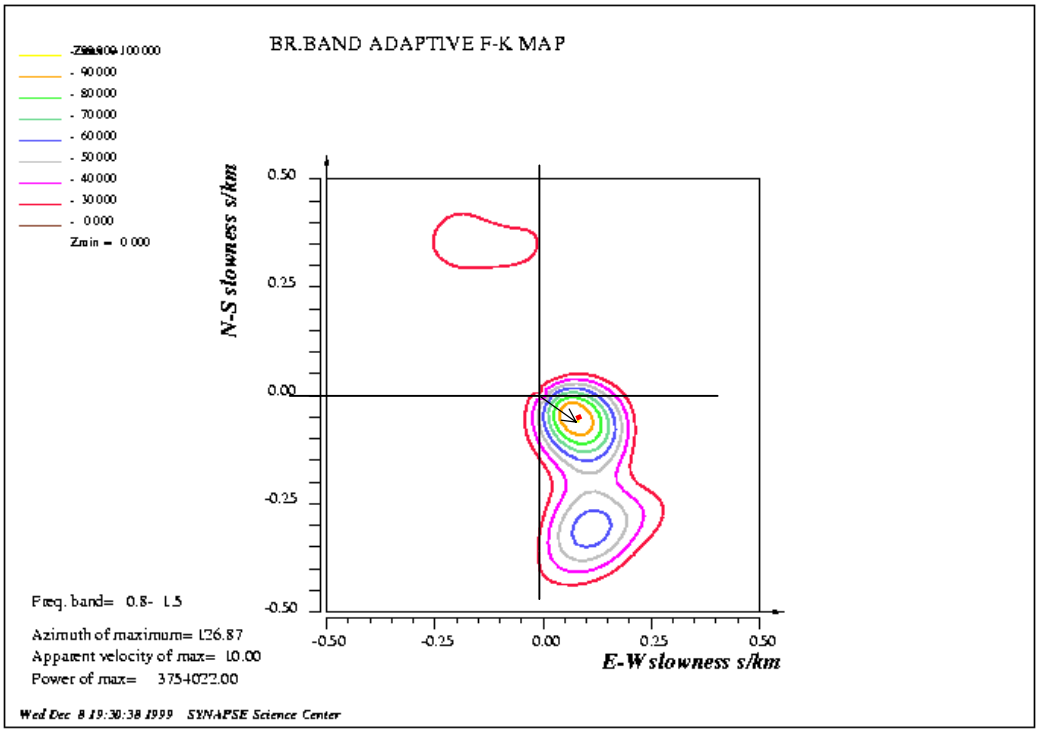


Fig.2. The AF-K slowness analysis of the GERESS Dead Sea explosion on 99.11.11 in 0.8-1.5 Hz band.

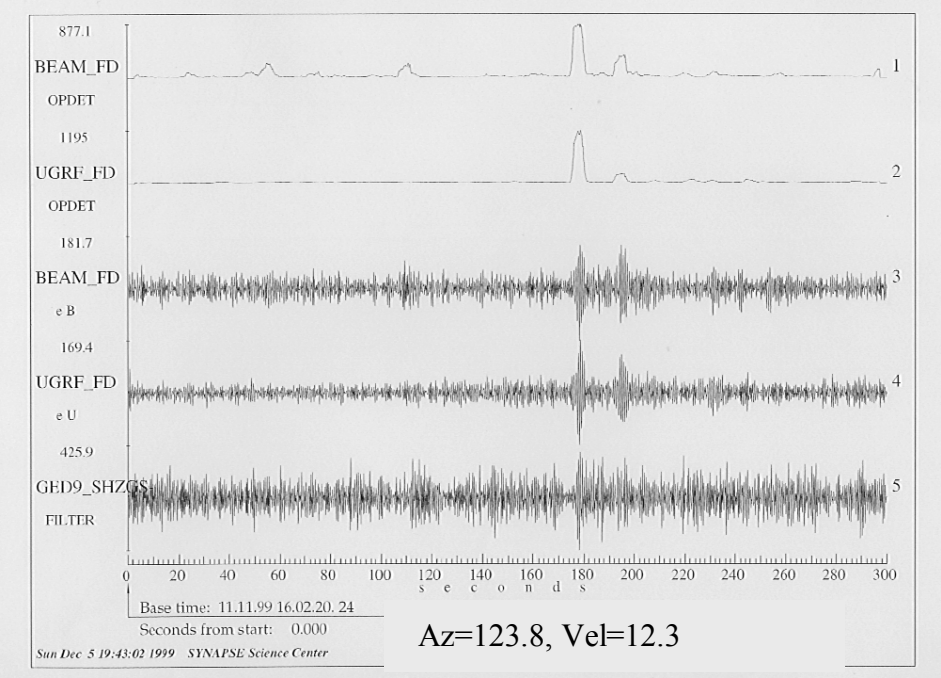


Fig.3. Application of the AOGF to the GERESS Dead Sea explosion recordings. The AOGF (UGRF – Undisturbed GRoup Filter) trace (4) is compared to the beam and GED9 channel recordings in the (1-3 Hz) frequency range. The 1C traces of the Optimal Detector for the beam and UGRF are at the top.

2. Application of the Maximum Likelihood Techniques.

A novel approach for ***M*** dimensional array signal detection and parameter estimation is a Maximum Likelihood Technique of Böhme (1995). The algorithm is destined for recognition of multiple seismic phases arriving to an array with ***m*** different azimuths and apparent velocities, which are distinguished in the procedure by a statistical projection method. The analysis is based on the frequency domain ***SNR(f, t)*** estimation, within time domain moving window. We introduced some simplification of the method resulting in statistics ***FM(t)*** and ***fm(t),*** with directly computed probability distributions, that are theoretically known in the case of white background noise. These statistics are defined as follows:

$$F(f_i, \vec{\xi}_m) = \max_{\xi_1,\ldots,\xi_m} SNR_m(f_i)$$
$$FM(t) = \max_{i=1,\ldots,P} F(f_i, \vec{\xi}_m)$$
$$fm(t) = \min_{i=1,\ldots,P} F(f_i, \vec{\xi}_m) \qquad (2)$$

The probability distributions of the ***FM(t)*** and ***fm(t)*** statistics are defined via the standard ***F*** probability distribution function

$$1-\alpha = P\{FM \le \kappa_m^{\alpha}\} = U(\kappa_m^{\alpha})^P$$
$$1-\beta = P\{fm \le \kappa_{m+1}^{\beta}\} = 1-(1-U(\kappa_{m+1}^{\beta}))^P \qquad (3)$$

where f_i is the i-th FFT frequency $i = 1,\ldots,p$; 2D vector $\mathbf{k}$ is slowness, $U=F_{2p,2p(M-m-1)}$ denotes standard Fisher distribution with given degrees of freedom; , . – given probabilities of false alarm for each of the statistics: maximum ***FM(t)*** and minimum ***fm(t)*** respectively.

The results of application of the method to the GERESS recordings of the Dead Sea explosion signal is demonstrated in the Table 2 and on Fig. 4 (a, b), showing five subplots: 1) seismogram and theoretical P arrival (arrow), 2) moving window statistics of the ***FM(t)*** and ***fm(t)***, 3) number of the detected sources ***N(t),*** 4)azimuth estimates ***Az(t)*** and 5) apparent velocity ***Vel(t).*** The sequential test with test level α = 0.01is carried out over each seismogram sliding window of 3.2 sec length and of 0.5 sec shift unit. The seismograms are pre-filtered in the several indicated below frequency bands. .

Table 2. Results of MLTM processing of GERESS recordings for the Dead Sea 5 t shot
(distance: 23.84 deg., P-arrival time: 15:05:15.6).

Estimation	Filter	Azimuth, degree	Apparent Velocity, km/sec
Theory (IASPEI91)	-	128.5	12.14
IDC (Beamforming)	narrow BP	127	10
MLTM algorithm	No filter	135.3	12.7
	0.8-1.8 Hz	132.7	13.3
	0.8-1.5 Hz	137.7	14.5
	1.1-1.4 Hz	129.9	15.4

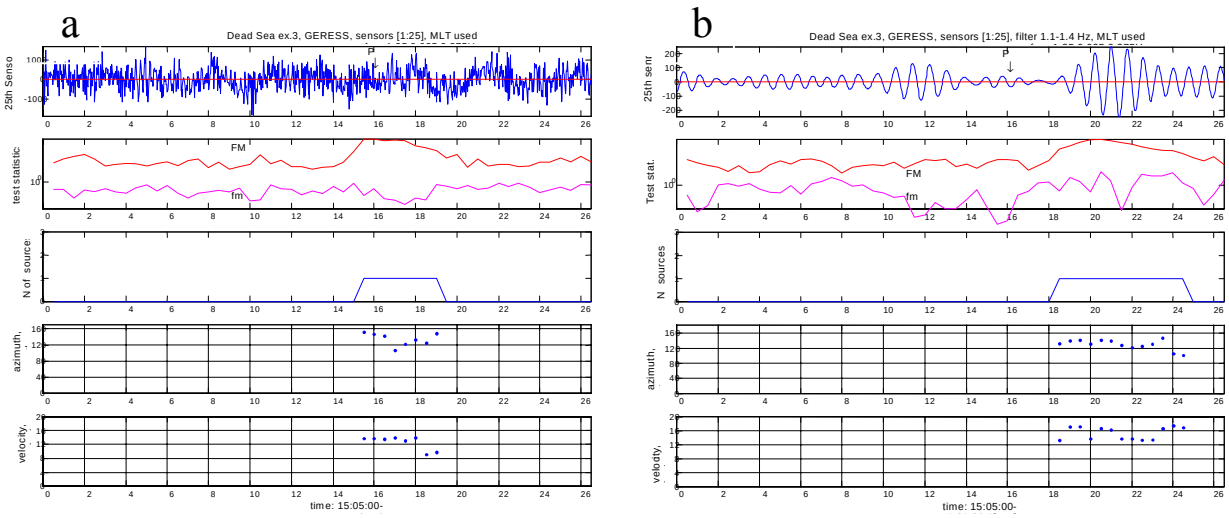


Fig. 4. MLTM processing for the Dead Sea shot with no pre-filtering (a) and BP filtering in 1.1-1.4 Hz (b).

3. Application of the MLTM to the EILESA.

The Eilat Experimental Seismic Array (EILESA), was established in 1998, 15 km to the north of the town of Eilat. It consists of 13 short-period (L4C seismometer) stations, including a reference 3-C station inside the 200 m long tunnel, co-located with the BB station EIL (Fig. 5a.). Eight of the array stations recorded the last of the explosions situated at a. distance of 255 km and azimuth 16^{o} (Fig. 5b). The MLT was applied with 21 even frequency bins in the 1.17-8.98 Hz range. The false alarm rate $\alpha_1 = 0.01$, $\alpha_2 = 0.02$. The moving window length is 128 points (50 Hz sampling rate) shifting by 20 samples for each time bin. The results are demonstrated on Fig.6, which show that there is detection of one source in true P wave arrival time, but the detection lasts continuously 5 sec only. Then it stops possibly due to the destroying of the signal coherency by the scattered waves. The azimuth estimates vary in time beginning from the negative values and decreasing down to –18^{o}. Then they rise up to12^{o}. Probably the effect is due to the wave diffraction caused by a heterogeneity. The apparent velocity estimate, high in the beginning, decreases gradually, and finally reaches the true 6 km/sec level, where it oscillates.

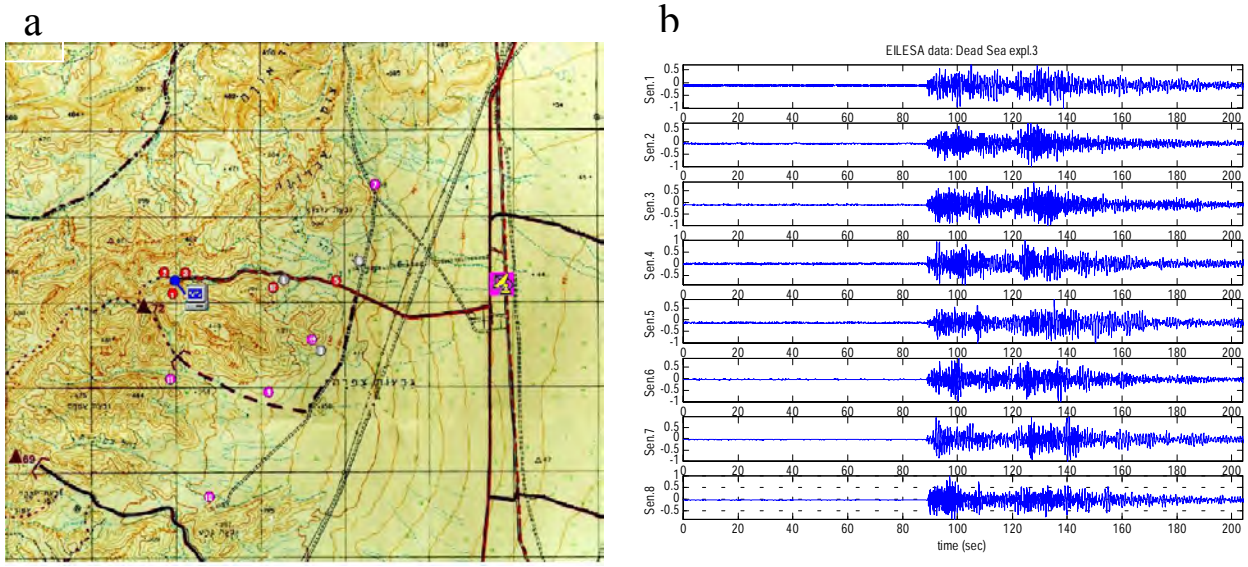


Fig. 5. 13 element EILESA array. Configuration (a), the 5 t Dead Sea explosion recordings at R=255 km and Az=16 ^{o} (b).

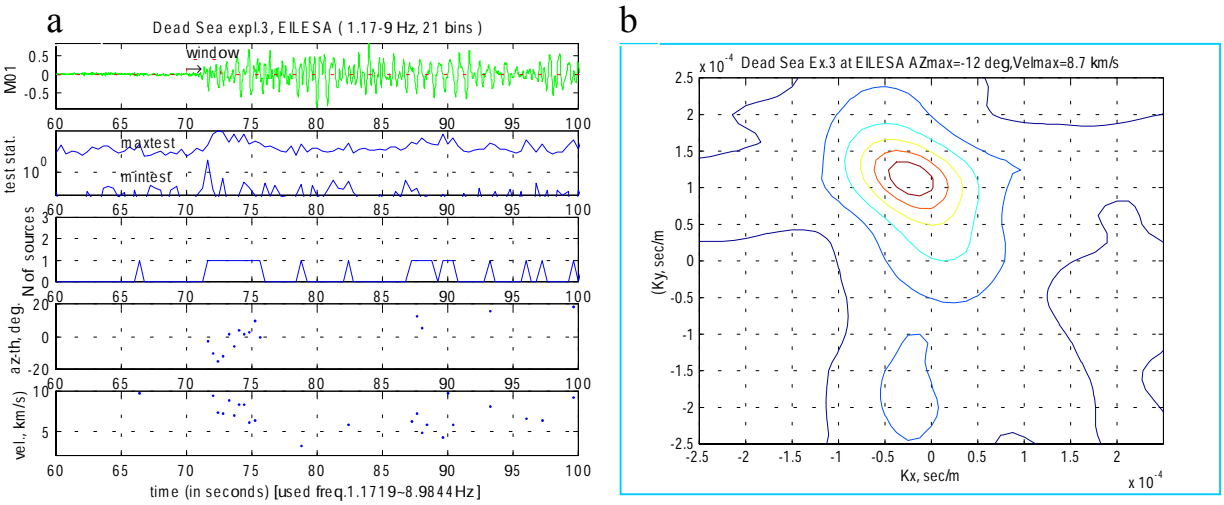


Fig. 6. The Dead Sea explosion record by the EILESA array and the MLTM detection and parameter estimation (a). Values of the FM statistic versus slowness *(Kx, Ky)* for the 72 sec time point (b). The maximum of the statistic corresponds to the Az = -12 ^{o}, Vel = 8.7 km/sec.

4. Evaluation of the travel-time model using the Dead Sea explosions data.

One of the main goals of the Dead Sea experiment is calibration of the IMS and other stations in the area. The true known source location and ignition time provide unique opportunity for measuring exact real travel times. All the explosion's P waves were observable all over the Israel and Jordan seismic networks (ISN and JSN) in the distance range 8 – 240 km and also at Cyprus up to 500 km. We measured P travel times for the three explosions and noticed that for the most of stations they fell in rather small 0.2 sec time interval. The picks were then compared to the travel times (see Fig. 7) corresponding to the two velocity models: the 3-layer and the 4-layer one. The 3-layer model was in use for the ISN location purpose previously (Seismological Bulletin No.11, 1992) (see Table 3), and the 4-layer is the present one (Table 4). For some of the picks there are considerable deviations in the both cases.

Then, we looked for the model better matching our P pickings. The four layer stratified model was chosen from visual inspection of the data and the best fit depths and velocities were obtained by the least-square method according to full-range scanning within given parameter intervals. After that the result was further improved by application of the Levenberg-Markvardt optimization procedure. Most of Jordan stations (see, for example, LISJ,KFNJ, SALJ on Fig. 7.) show delays of ~0.7 sec from the ISN best-fit travel time curve for the reason which is still to be clarified. Probably, this is due to the leap of media properties from one to another side of the Jordan fault or simply, this is due to the watch problems. Thus, the outliers were excluded from the optimization procedure and only matching well N = 80 observations were selected. Final residuals $dt_j=T_{obs,j}-T_{calc,j}$ $,j=1,\ldots N$ have RMS=0.201 sec compared to RMS=0.32 and RMS=0.71 for the two models mentioned above respectively. The notable feature of the best-fit model (Table 5) is a ~1 km thicker layer of the sediments with average Vp=3.77 km/sec, providing relatively large delays of the P waves at the closer stations (< 10 km). The model agrees also to the parameters obtained in the joint hypocenter determination procedure (see Table 6) (Dr. N. Rabinowitz, personal communication).

We tried to examine the travel time dependency on azimuth by computation of the deviations from the best-fit model for the different stations. There is known thickening of the crust in the Southeastern direction, so the azimuth dependant deviation from the best-fit model was expected. Unfortunately, the azimuth coverage is not representative in the East-Western direction and thus the data we have didn't allow us to notice the effect.

Table 3. Velocity model used previously.

Thickness, km	Vp, km/sec	Vs, km/sec
2.1	3.5	2.0
10.6	5.7	3.2
15.5	6.4	3.6
	7.9	4.4

Table 4. Present Velocity model.

Thickness, km	Vp, km/sec	Vs, km/sec
2.56	4.36	2.45
7.2	5.51	3.10
21.64	6.23	3.50
100	7.95	4.46
	8.15	4.60

Table 5. Best-fit velocity model

Thickness, km	Vp, km/sec	Vs, km/sec
3.35	3.77	2.12
3.18	6.00	3.37
12.16	6.11	3.43
13.77	6.73	3.78
	7.88	4.43

Table 6. Joint Epicenter Solution model

Thickness, km	Vp
2	3.03
3	5.60
5	6.21
5	6.39
6	6.61
7	7.05
17	7.61
20	8.10

5. Automatic picking and location of the explosions.

We applied robust automatic locator (Pinsky, 1999), developed in the frame of the contract, to the ISN and JSN recordings of the three events, using the best-fit velocity model. The locator is the two-stage procedure, using envelope location at the first stage to estimate the time intervals for the P, S first arrivals to the network stations. The second stage comprises automatic picking of the P, S first arrivals with robust fitting of the picks (automatically eliminating outliers) to the travel time model. The results of the automatic location are presented in the Table 7 together with true coordinates and manual-picking location results. The latter are due to the conventional velocity model used (Table 4.). The results show accurate location in the automatic case and a somewhat shifting for manual picking due to the conventional model imperfection.

Table 7. Location of the Dead Sea explosions by an analyst and the automatic locator.

Date	Charge, kg	M_L	AXES	GPS, km	Analyst Solution, km	ERROR km	Automatic Locator, km	ERROR, km
08.11.99	500	3.1	X Y H	191.957 104.594 0.5	188.20 105.6 2	-3.76 1.00 2	192.3 103.9 0	0.3 -0.6 -0.5
10.11.99	2000	3.6	X Y H	191.897 104.686 0.5	190.4 104.5 3	1.50 -0.19 3	191.9 104.1 1	0.0 0.6 0.5
11.11.99	5000	3.9	X Y H	192.023 104.661 0.5	191.1 103.7 2	-0.92 0.96 2	192. 104.7 5	0. 0. 4.5

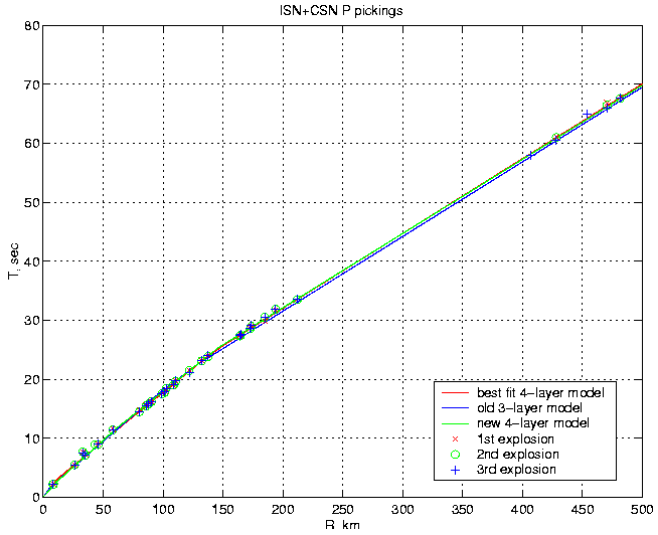


Fig. 7. P travel times for the three stratified models and the P picks for the three explosions.

SINGLE STATION EVENT LOCATION: EPICENTRAL DISTANCE, BEARING, AND FOCAL DEPTH

Jay Pulliam, Cliff Frohlich, and Ben Phillips
Institute for Geophysics, The University of Texas at Austin

Sponsored by the Defense Special Weapons Agency
Contract No. DSWA-01-97-0016

ABSTRACT

The most sensitive and reliable methods for locating small-magnitude regional seismic events using records from a single, three-component station require knowledge of the near-station and along-path crustal structure. Unfortunately, obtaining information about crustal structure is time-consuming and may be costly. Furthermore, different location methods may be required depending on the lateral complexity of the crust. Here we address a simpler problem: How often can single-station methods accurately determine event-station bearing and distance information if no information about crustal structure is available?

- Neither bearing nor distance determination was generally possible for signals if the SNR was less than about 2.0; bearing determination was most successful at most stations if signals were high-pass filtered with a cut-off frequency of about 0.5 Hz.
- Bearing determination for low-magnitude signals was possible even if they had no impulsive P phases if covariance methods were applied to the entire P-to-S time window.
- For signals with SNR > 2.0, there were clear differences between stations with respect to how well they could determine bearing direction. At many 'good' stations, 66% of the bearings determined by the 2-D covariance method were within about 6^o-10^o of the expected bearing; at many other stations, the 66^{th} percentile of the bearings was 10^o-30^o.
- There were no obvious differences in the geographic or tectonic character of 'good' and 'other' stations.

Our original method for determining event-station distance relied solely on the ratios of short-term and long-term averages to find S-P times and thus distance; this method was able to determine distances to within 20 km of the true distance for only 10% of the records we studied. Currently, we are revising the phase=identification method to incorporate information about signal polarization.

Methods specifically designed for determining focal depths of events in sparsely-instrumented regions are rare. Here we apply a method for determining the focal depths of small- to moderate-sized earthquakes via waveform correlation between radial and vertical components of relatively high-frequency (1-5 Hz) seismic data recorded at a single three-component station and their synthetic counterparts. In addition to our waveform correlation method, which minimizes the complicating effects of the source time function and focal mechanism, we have begun to explore a strategy that exploits the expected simplicity of source time functions for small magnitude tectonic events and explosions. In this study we modify the deconvolution method of Christensen and Ruff (1984) and evaluate its applicability for focal depth determination at regional distances through a series of synthetic experiments.

OBJECTIVE

We are trying to develop, apply, and evaluate methods for locating seismic events using only a single, broadband, three-component seismographic station. Most of our work has been directed toward estimating the bearing and distance to and the focal depth of small-magnitude events located at regional distances from a station using full waveform data. A large percentage of seismic events could be identified as tectonic in origin if either or both the epicenter and/or focal depth were reasonably well-constrained. While approaches that use travel times and/or waveform data from several stations are well-developed, there are many regions of the world in which station coverage is sparse and small-magnitude events are often recorded by only one station, if at all.

RESEARCH ACCOMPLISHED

Single-Station Epicenter Location Without Special Knowledge of Crustal Structure

The bulk of our research effort has concerned developing location methods that rely on the comparison of observed and synthetic seismograms, and thus require knowledge of near-station crustal structure. However, to evaluate how much these methods improve location capabilities, we have also applied more simplistic methods to determine station event bearing and distance that require no knowledge of structure.

We therefore collected about 3800 three-component, digital waveforms for seismic events with reported magnitudes of 3.0-4.5 recorded at about 104 different stations distributed around the world. This search procedure produced records with highly variable amplitudes, including many low-SNR records in which the seismic signal was indistinguishable from the background. A preliminary analysis indicated that we could seldom obtain station-event bearings when the SNR for the time interval between P and S was less than about 2.0. Success rates for bearing determination were highest when the waveforms were high-pass filtered with a corner period T_F of about 2.0 sec. The restricted data set of records with SNR exceeding 2.0 included 1287 station-event pairs and included data from a broad variety of geographic and tectonic environments.

To determine station-event bearing, we used a 2-D method that separately determined the bearing axis (bearing angle mod 180°) and the bearing direction (see Magotra et al., 1987; Walck and Chael, 1991; Pulliam and Frohlich, 1998; 1999). We evaluated station-event bearing for the 1287 records for which SNR exceeded 2.0, applying the method to a 20-40-second interval beginning with the P arrival and ending prior to the arrival of S. To determine the event-station distance, we compared short-term and long-term signal averages to determine the time-separation between the onset times T_1 and T_2 of the two highest-amplitude portions of the waveform, and assigned a distance assuming that (T_2-T_1) corresponded to the S-P time interval.

These methods, which incorporate no information about regional crustal structure, were only partially successful at determining station-event bearing and distance. For the 1287 events, we obtained bearings within ±10° of the correct value for 54%, and within ±20° for 72%. For distance, the method was unable to determine any S-P interval for 41% of the signals; for the remaining 760 signals, the station-event distance was within ±20 km for 18%, and within ±50 km for 44%.

These low success rate suggest that it will be important develop location methods that incorporate information about regional crustal structure. Because the results indicate signals within P-to-S time interval generally are polarized along the event-station direction, we believe we can significantly improve station-event distance determination rates by developing a distance algorithm that incorporates both polarization and signal-to-noise information. However, even with these improvements it seems likely that a significant fraction of events will be mislocated unless more sophisticated algorithms that incorporate information about regional structure are developed.

Single-station Focal Depth Determination

We have presented results previously regarding the determination of event focal depths via waveform correlation to synthetic seismograms (Frohlich and Pulliam, 1999; Pulliam and Frohlich, 1998, 1999, 2000; Pulliam et al., 1997). We have recently focused on a new method for focal depth determination that makes use of the expected simplicity and short duration of source time functions for small-magnitude regional events. Christensen and Ruff (1984) presented a method for determining focal depths of large-magnitude, teleseismic events by deconvolving simple synthetic Green functions from the data to isolate the source time function. They show that when the incorrect depth is used for the Green functions, a complicated, oscillatory source time function of relatively long duration results. Using the correct focal depth for the Green functions produces a simpler and more realistic source time function of shorter duration. We seek to extend this method to small-magnitude, shallow seismic events recorded at regional distances and address several complicating issues through simulation with synthetic Green functions and various crustal structures. These issues include: the tradeoff between the source time function and focal depth, the required accuracy of the crustal model, the effects of the (presumably unknown) focal mechanism on the deconvolution and focal depth results, and the measure of source time function "simplicity" that points most reliably to the correct focal depth.

Tradeoff Between Source Time Function and Focal Depth

To explore the tradeoff between the source time function and estimates of focal depth we computed Green functions for a layer over a half-space model for a suite of focal depths from 0-15 km in increments of 2.5 km using a reflectivity method (Fig. 1). To illustrate the method we first construct synthetic radial and vertical component data by convolving Green functions for a 45 degree dip-slip fault with a source time function (Fig. 2). The source depth is 5 km. When each of the Green functions shown in Figure 1 is deconvolved from the synthetic data shown in Figure 2, the correct source time function is retrieved only for the correct focal depth of 5 km (Figure 3). Note that a similar function (with opposite polarity) also appears at the 5 km focal depth for the vertical strike-slip fault. In contrast, other source depths show a time lag for the source pulse plus a great deal of noise. This result indicates the tradeoff between origin time and the form of the source time function vs. focal depth. Since the estimate of origin time depends on crustal velocities as well as focal depth, the keys to reducing the ambiguity between the origin time and focal depth lie in the form of the source time function and the relative amplitudes of the source function and later parts of the seismogram. To construct a criterion for choosing the proper source time function we must make some assumptions about the source. For many sources of interest to CTBT discrimination—small-magnitude tectonic events and explosions—we expect the source time function to be relatively compact, short in duration, and "simple", i.e., impulsive and unimodal, compared to large-magnitude shallow events that have large rupture surfaces. This suggests a criterion that favors compactness and high relative amplitudes early in the record compared to later parts of the record. After evaluating a number of candidates, we determined that a ratio of the norm of the deconvolved record's first 10 seconds divided by a the norm of the following 10 seconds was the most effective criterion. The maximum of this ratio of norms shoud indicate the correct focal depth. Figure 4 plots this ratio of norms as a function of focal depth for each of the fundamental faults, as computed for each of the deconvolved records shown in Figure 3. Radial and vertical components are computed separately, so their results are to some extent independent and a highly peaked function that is consistent result between the two components suggests minimal tradeoff and high confidence in the focal depth estimate. Note that, since each seismogram is produced by a single fault that resembles just one of the fundamental faults most closely, one should not expect a peak for each of the fundamental faults. Note, for example, that in Figure 3 the vertical dip-slip fault produces poor results after deconvolution. This poor result is reflected in the ratio of norms for the vertical dip-slip fault in Figure 4 (solid line).

Effect of Focal Mechanism on Deconvolution Results

An event's focal mechanism changes the amplitude and polarity of each phase, which can complicate the deconvolution procedure. While it may be possible to find focal mechanisms for small-magnitude events with a single station, thereby allowing accurate modeling of seismograms, it may not be practical to do so, or to depend on the ability to do so. Regardless, it is instructive to examine the sensitivity of focal depth results to variations in the focal mechanism. Figure 5 shows one focal mechanism, in which the fault has a strike of 0°, dip of 10°, slip of 155°. The azimuth to the station is indicated by the thick solid line for each component. When the data shown in Figure 5 are deconvolved from the Green functions shown in Figure 1, the results (Figure 6) are more complex and less definitive than when the focal mechanism matches one of the fundamental faults (as in Figure 3). The noise in each record is of considerably higher amplitude (relative to the source pulse) and the source pulse distortion is more pronounced for all but the correct source depth. However, the "source simplicity" criterion is able to identify the correct focal depth, albeit with a norm ratio that is an order of magnitude smaller the the norm ratio in Figure 4. Figures 8-11 show focal depth results for deconvolutions of various focal mechanisms. All of these examples have "signal norm to noise norm" ratios between 1 and 8, compared to 20 for the first (ideal) case and all these depth functions are less peaked, indicating lesser depth resolution. However, only the vertical component of the last case (Figure 11) shows a real ambiguity in choosing the correct depth. Obviously, focal mechanisms in which critical phases exactly on nodal lines will not produce reliable results.

Effect of Inaccurate Crustal Velocity Model

To test the dependence of focal depth determinations on accurate knowledge of the crustal model, we conducted an experiment intended to mimic a potential procedure for finding focal depths with real data when we have limited information about the crustal structure in the vicinity of a seismographic station. We constructed a fairly complicated velocity model consisting of eight crustal layers on top of PREM (Fig. 12) and computed synthetic teleseismic data for a variety of focal mechanisms, focal depths, and epicentral distances (30°-70°). We applied the SORVEC crustal receiver function method (Zhao and Frohlich, 1996; Zhao et al., 1996) to these data while specifying search limits that allowed models of various complexity: from three to seven layers with wide search

bounds for individual layers' thicknesses and shear and compressional wave velocities. This step produced a set of models (Fig. 12) that have similar bulk characteristics (average velocities and crustal thicknesses) but which differ in number of layers and the seismic velocities of each layer. These approximations are intended to represent estimates of crustal structure obtained using real data, which tend to match the real Earth in some characteristics (e.g., average crustal velocity, depth to Moho, etc.) but which fail to match finer details. The question we wish to answer is "How significantly can the model used to compute Green functions differ from the actual Earth and still produce accurate focal depth estimates via the "source simplicity" criterion?"

To address this question we compute suites of "reference" Green functions for each model, comparable to Figure 1, for an epicentral distance of 200 km and deconvolve each from "data" seismograms constructed using the original, eight-layer velocity model, the source time function shown in Figure 2, and various focal mechanisms. The resulting focal depth estimates are shown in Figures 13-17. Note the progressive loss of resolution as the model becomes less and less detailed and deviates more and more from the true, eight-layer model. If more depth increments had been used to compute Green functions, the depth functions in Figures 4, 7-11, and 13-17 would be smoother curves, with a less obvious peak. The choice of focal depth would therefore be less obvious and one's confidence in each focal depth estimate would diminish with successively less refined (and less accurate) models. This exercise demonstrates a tradeoff between the accuracy of the crustal model used to generate Green functions and depth resolution of event foci. Note also the drop in the ratio of norms between the seven-layer model (Figure 13) and the six-layer model (Figure 14), and continued decreases with each successive figure.

CONCLUSIONS AND RECOMMENDATIONS

The deconvolution method that relies on a "source simplicity" criterion presented here shows promise for discrimination between explosions and tectonic events. Christensen and Ruff (1984) make a strong case for the deconvolution method's effectiveness when applied to large-magnitude, deeper events recorded at teleseismic distances. Additional complications arise in extending the method to small-magnitude, shallow events recorded at regional distances. These include: poor signal-to-noise ratios, relatively high amplitudes of scattered waves that complicate the seismograms, a tradeoff between depth resolution and accuracy of the crustal model. Specifically, the following conclusions may be gleaned from our synthetic experiments:

- Successful application depends strongly on the accuracy of a crustal model's bulk characteristics but depends only weakly on details of the model, such as the number of layers and velocities of each layer.
- In contrast, knowledge of an event's focal mechanism is not critical; the simultaneous deconvolution of Green functions for the three fundamental fault types leads to accurate focal depth results.
- There is a fundamental tradeoff between depth resolution of event foci and accuracy of the crustal models used to compute Green functions. However, models that match the bulk characteristics of the real Earth may serve to identify the correct focal depth. But in all cases, confidence in the focal depth estimate wll be enhanced by greater accuracy of the crustal model.

Lastly, we observe that the "source simplicity" method, like the waveform correlation method, depends on full waveform information, as opposed to travel times. It is the pulse distortion of the improperly deconvolved data that allows some reconciliation (however imperfect) of the focal depth vs. origin time/source time function tradeoff. Given the need to understand certain aspects of crustal velocity structure well, attention should be focused on developing practical methods for modeling crustal velocities.

Key Words: Single-station location, focal depth determination, regional seismology

REFERENCES

Christensen, D. H., and L. J. Ruff (1984). Analysis of the trade-off between hypocentral depth and source time function, *Bull. Seismol. Soc. Am.*, **75**, 1637-1656.

Frohlich, C., and J. Pulliam (1999). Single-station location of seismic events: A review, and a plea for more research, *Phys. Earth Planet. Int.*, **113**, 277-291.

Magotra, N., N. Ahmed and E. Chael (1987). Seismic event detection and source location using single-station (three-component) data, *Bull. Seismol. Soc. Am.*, **77**, 958-971.

Pulliam, J., and C. Frohlich (2000). Determining Earthquake Focal Depths with a Single Seismographic Station at Regional Distances, submitted to *Bull. Seis. Soc Am.*, May 2000.

Pulliam, J., and C. Frohlich (1999). Accuracy and uncertainty in single-station event location, in *Proc. 21st Ann. Seismic Res. Symp., vol. I.,* tech. rept. No. LA-UR-99-4700, Dept. Defense, Arlington, Va., pp. 589-598.

Pulliam, J., and C. Frohlich, Case Studies of Event Location with a Single Station, *Proceedings of the 20th Annual Seismic Research Symposium on Monitoring a Comprehensive Test Ban Treaty*, J. Fantroy, D. Heatley, J.Warren, F. Chavez, and C. Meade (edit.), Santa Fe, N.M., 275-285, 1998.

Pulliam, J., C. Frohlich and S.P. Grand (1997). Factors controlling single-station seismic event location, *Proceedings of the 19th Annual Seismic Research Symposium on Monitoring a Comprehensive Test Ban Treaty*, M.J. Shore, R.S. Jih, A. Dainty, and J. Erwin (edit.), Orlando, FL, pp. 272-280.

Walck, M. C. and E. P. Chael (1991). Optimal backazimuth estimation for three-component recordings of regional seismic events, *Bull. Seismol. Soc. Am.,* **81**, 643-666.

Zhao, L.-S., and C. Frohlich (1996). Teleseismic body waveforms and receiver structures beneath seismic stations, *Geophys. J. Int.,* **124**, 525-540.

Zhao, L.-S., Sen, M. K., Stoffa, P. L., and C. Frohlich (1996). Application of very fast simulated annealing to the determination of the crustal structure beneath Tibet, *Geophys. J. Int., 125*, 355-370.

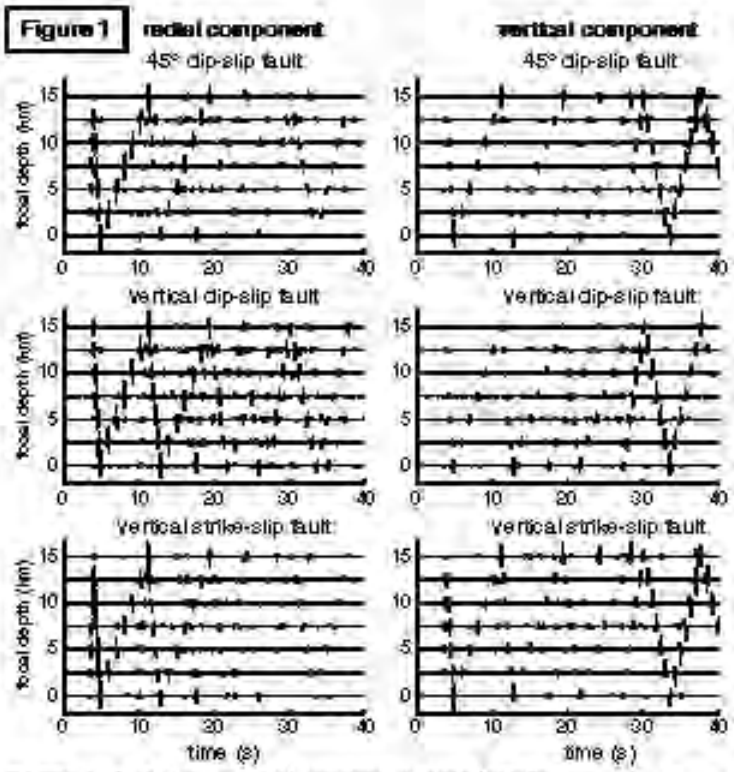
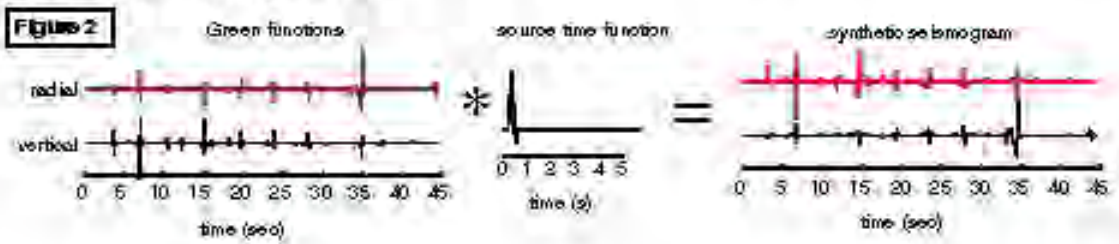


Figure 1. Radial and vertical component Green functions for three fundamental faults and focal depths of 0 to 15 km in increments of 2.5 km. These were computed using a reflectivity method and a simple layer over a half-space velocity model. The epicentral distance is 100 km.

Figure 2. Synthetic seismograms are constructed by convolving a source time function with the Green functions from Figure 1 for a 45° dip-slip fault and a focal depth of 5 km.



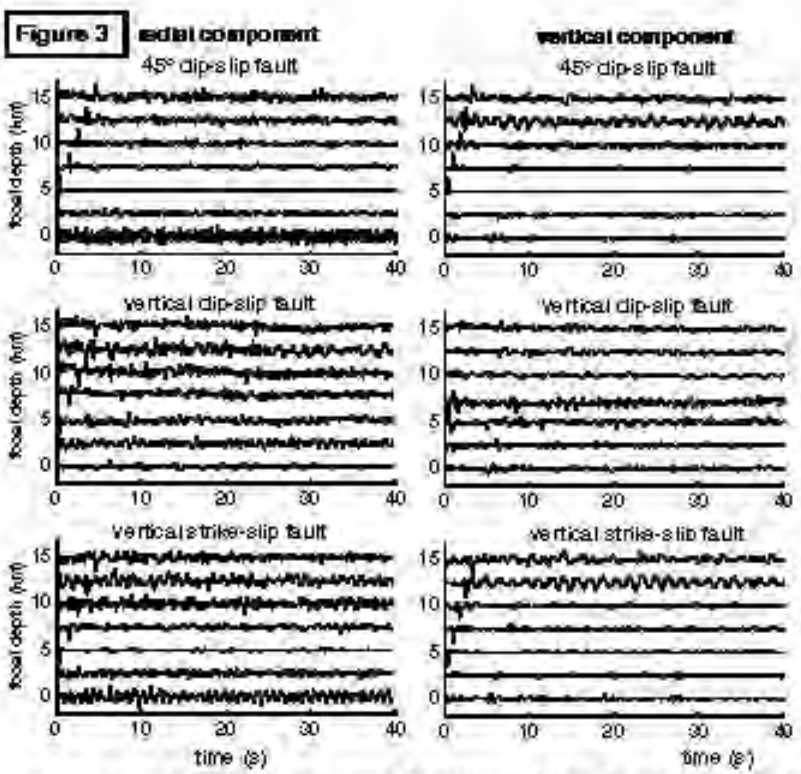


Figure 3. The Green functions shown in Figure 1 are each deconvolved from the synthetic data shown in Figure 2. The result for the correct focal depth and fault type is simply the input source time function shown in Figure 2 (45° dip-slip fault and focal depth of 5 km) but results for other focal depths and fault types are more complex. The familiar tradeoff between origin time (onset of source time function) and focal depth is indicated by the increasing time lag for increasing focal depth but the more useful properties are the distortion of the pulses retrieved by the deconvolution and the relative amplitudes of the source pulse and the following noise.

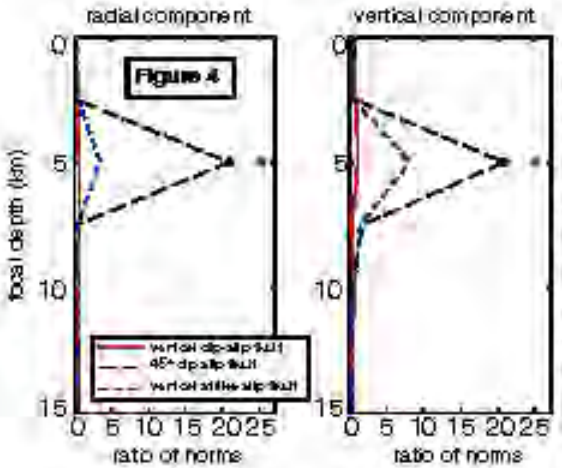


Figure 4. The correct pulse (by construction, in this case) is compact, short in duration, and has a large amplitude ratio when compared to later parts of the record. A criterion that favors these characteristics can be devised that is essentially the ratio between the norms of the record's first 10 seconds and the following 10 seconds. When plotted as a function of focal depth for each fault type, this ratio achieves a maximum at the correct focal depth. Obviously, inaccurate estimates of crustal structure and various focal mechanisms will degrade the strongly peaked ratio of norms and will thereby degrade depth resolution. The square at right indicates the correct focal depth.

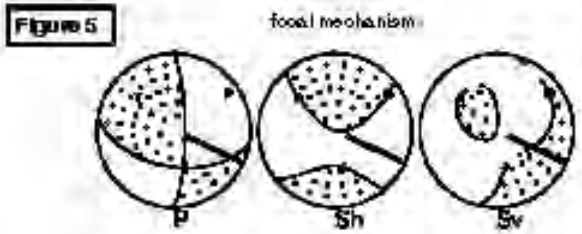
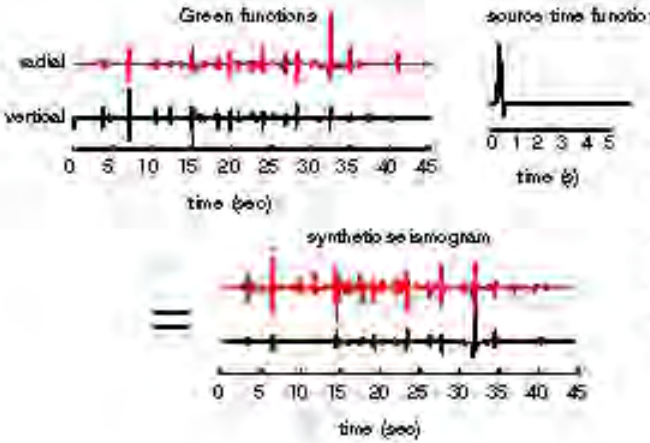


Figure 5. An example of the potentially complicating effect of a focal mechanism that differs from those of the fundamental faults. Synthetic data are again constructed but this time they incorporate the focal mechanism shown.

Figure 6. When the Green functions shown in Figure 1 are deconvolved from the data shown in Figure 5, a more complicated set of traces results. Noise is large in amplitude and the pulse distortion is more pronounced for all but the correct focal depth.



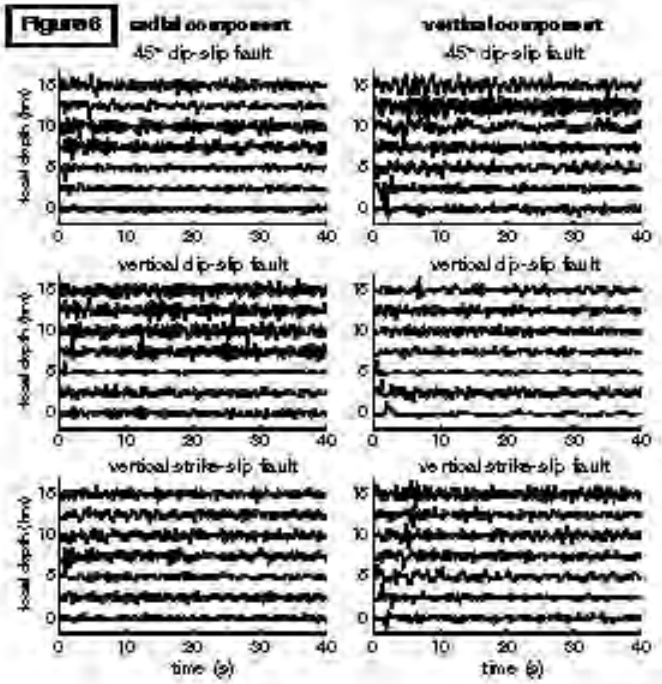
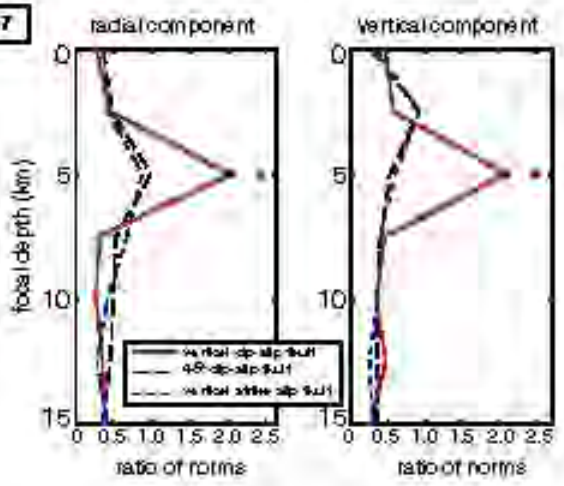
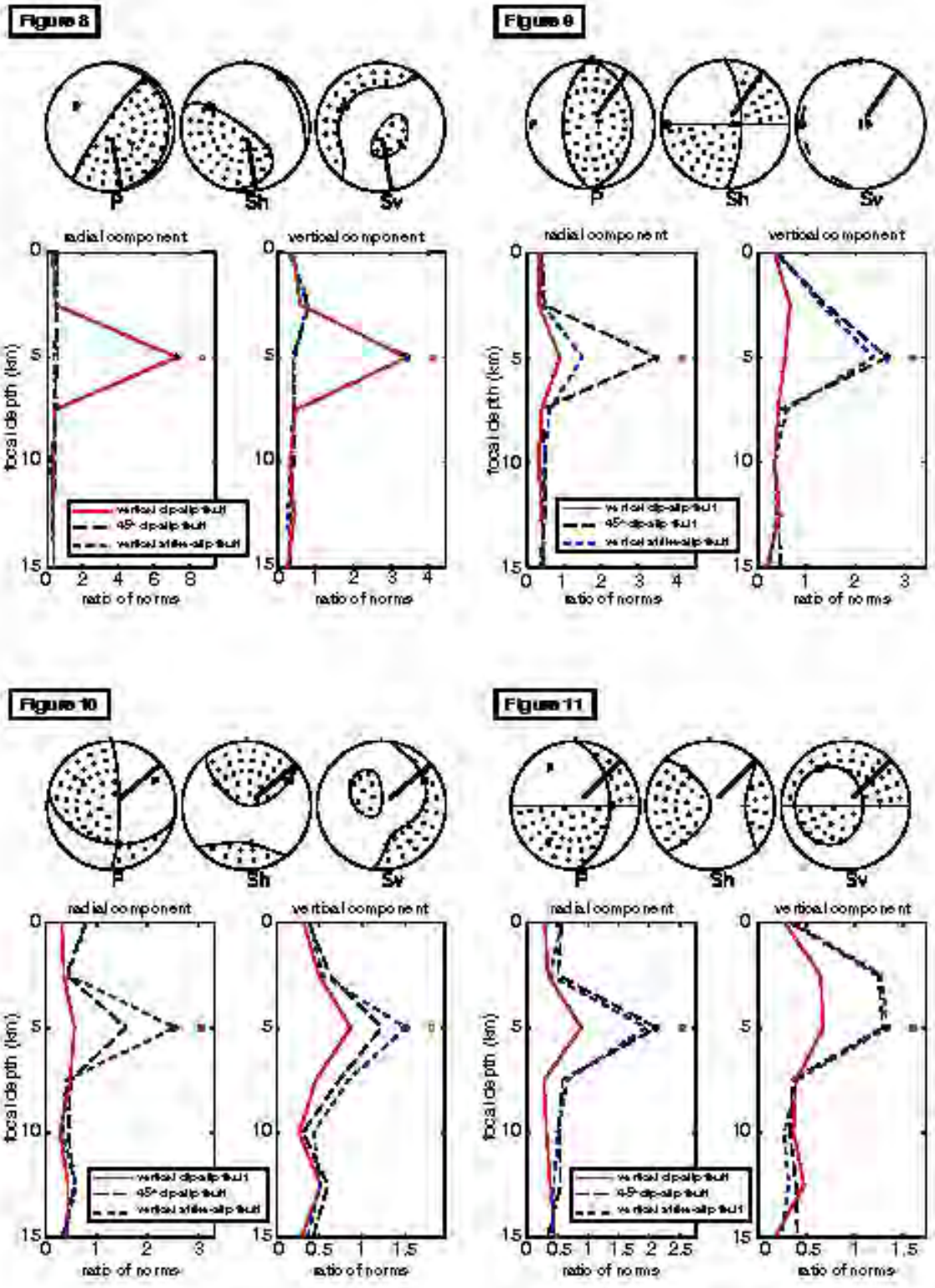


Figure 7. Note the much lower values for the ratio of norms compared to Figure 4, in which the focal mechanism of the data matched one of the fundamental faults. Nevertheless, a distinct peak identifies the correct focal depth and the focal depth resolution ("spread" or "peakedness" of the norm function through depth) is comparable.





Figures 8-11. Various focal mechanism and their effects on the focal depth criterion. Note that in some cases the depth resolution is degraded (e.g., Figure 11), in which case the choice of focal depth is ambiguous. See the text for further discussion of depth resolution and confidence.

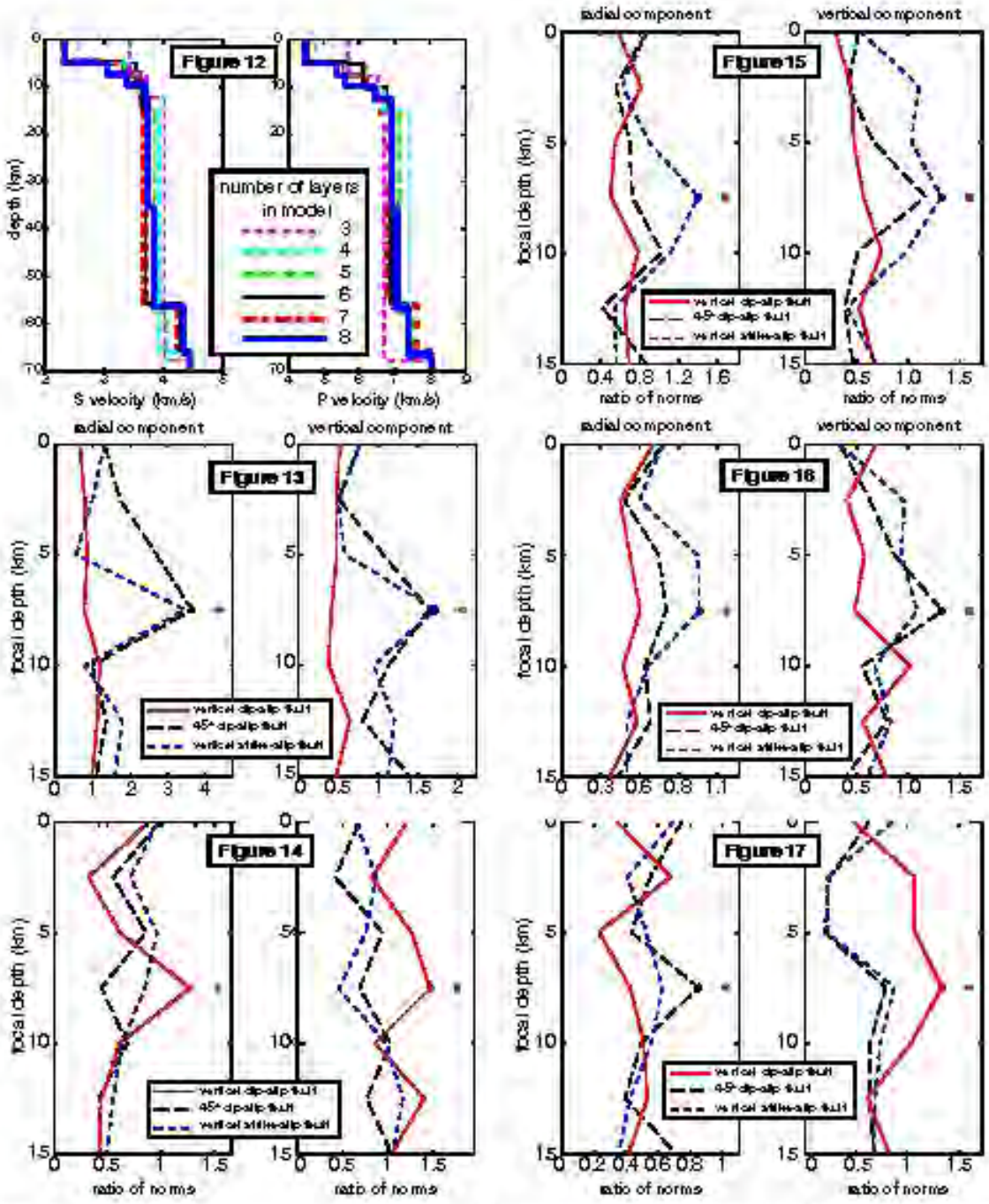


Figure 12. Velocity models obtained by applying the SORVEC method (Zhao and Frohlich, 1996) to synthetic synthetic seismograms computed for teleseismic distances (30°-70°) using an eight-layer crustal model over PREM. Wide search bounds were prescribed for layer thicknesses and for compressional and shear wave velocities but the number of layers allowed was successively limited to seven, six, five, four, and three.

Figures 13-17. Results of deconvolving data constructed using the Green functions of h=7.5 km depth computed using the eight-layer velocity model (Fig. 12), the source time function shown in Figure 2 and various focal mechanisms from the models shown in Figure 12 that approximate the eight-layer input model in bulk characteristics but which lack similar levels of detail. Results for the "source simplicity" criterion are shown formodels with seven layers (Fig. 13), six layers (Fig. 14), five layers (Fig. 15), four layers (Fig. 16), and three layers (Fig. 17). These approximations are intended to represent estimates of crustal structure obtained using real data, which tend to match the real Earth in some characteristics (e.g. average crustal velocity, depth to Mohorn, etc.) but which fail to match finer details. This series illustrates a tradeoff between depth resolution of event foci and accuracy of the reference crustal model.

A PLAN FOR SEISMIC LOCATION CALIBRATION OF 30 IMS STATIONS IN EASTERN ASIA

Paul G. Richards, Won-Young Kim, Vitaly I. Khalturin
Lamont-Doherty Earth Observatory of Columbia University

Sponsored by the Defense Threat Reduction Agency
Arms Control Technology Division
Nuclear Treaties Branch

Contract No. DTRA01-00-C-0031

ABSTRACT

In March 2000, a collaborative academic-industry research consortium comprised of five institutions started an integrated series of projects, all with the goal of improving the capability to locate seismic events based on data acquired by International Monitoring System (IMS) stations in Eastern Asia. The focus of this effort is to develop and deliver validated high-resolution travel time grids for operational use in support of the location estimates made by the International Data Centre (IDC) of the Comprehensive Test Ban Treaty Organization. These are to be used for for the specified stations to locate on the order of a hundred events per day around the world. The basic approach is to use thousands of so-called "ground truth" seismic events in Eastern Asia that have been accurately located by regional or local networks. These will be used to obtain the travel times of key seismic phases from any point in the region to any of the 30 IMS stations that are the focus of the project. These travel-times will in general be a function of distance and azimuth --- and depth. They must be determined as a continuous function of postion, from the empirical discrete ground truth data; and they must be demonstrated to improve location estimates of new events, over the estimates obtained on the basis of current procedures (typically, based on the Earth model IASP91).

In the first project, the Lamont-Doherty Earth Observatory of Columbia University will contribute numerous newly-obtained ground truth locations in Eastern Asia whose errors are thought to be of the order of five km or better (so-called GT5 events) and that are expected to be large enough for detection at IMS stations. In most cases these events are recent enough for inclusion in the Reviewed Event Bulletin of the PIDC (since 1995). In the second project, the University of Wyoming will contribute observed travel times for about 3000 three-component recordings at stations widely deployed in the Soviet era to detect regional waves from 21 nuclear explosions carried out during the Deep Seismic Sounding program. This dataset is an invaluable resource for thorough calibration of major aseismic regions in Russia and Central Asia. We expect to be able to find analog seismograms for several of these 21 nuclear explosions, as recorded at Eastern Asia stations now identified as part of the IMS, or at stations that were operated at sites close to the IMS station locations. Our consortium personnel at the University of Wyoming are Scott Smithson, Elena Morozova, and Igor Morozov.

In the third project, Mission Research Corporation will derive and test travel time surfaces, for IMS stations, that fit the GT data and Calibration Event Bulletin data. The lead person at MRC for the consortium is Mark Fisk. URS Greiner Woodward Clyde will contribute some ground truth data for India, Nepal, Pakistan, and much 1D and 2D modeling experience; the University of Connecticut will contribute 3D modeling experience. Both these organizations, and Wyoming and Lamont, will work together in Project 4 to provide expected travel times to 30 IMS station locations in Eastern Asia. In this fourth project, detailed studies of a small percentage of our claimed GT5 events will be carried out for purposes of validation of their location quality. The consortium lead person at URS Greiner is Chandan Saikia, and at the University of Connecticut is Vernon Cormier. Mission Research Corporation will package all of the products of the consortium for delivery to the Center for Monitoring Research in the fifth project, including quantitative evaluation of location improvements. In the sixth project, an Experts Group Review process will provide overall guidance. In this work, a group of consultants will meet with consortium members at Lamont for a few days each year. They will give advice on GT events and on how to use phase picks of GT events to provide improved location estimates for events recorded regionally at IMS stations in East Asia.

OBJECTIVE

This project is intended to assist the International Data Centre to improve the accuracy of estimates of the location of seismic events — and to reduce the uncertainty of such estimates — on the basis of an interpretation of the arrival times of standard seismic waves observed at 30 stations of the International Monitoring System located in Eastern Asia. Such improvement is needed, to meet the goals of the IDC in supplying the location estimates that could be the basis of an on-site inspection request.

To see what accuracy is needed, we may quote the CTBT Protocol, Part II, ¶3:

"The area of an on-site inspection shall be continuous and its size shall not exceed 1000 square kilometers. There shall be no linear dimension greater than 50 kilometers in any direction."

Also, ¶41(b) states (with reference to an OSI request) that the proposed boundaries of the area to be inspected are to be specified on a map in accordance with ¶3.

RESEARCH ACCOMPLISHED

At this time of writing our project has been running for about 4 of an anticipated 36 months. So far, we have identified and obtained a number of relevant ground truth datasets in Eastern Asia; and we have begun the work of obtaining accurate travel times (for different phases, as a function of distance, azimuth, depth) for six stations in Central Asia.

In subsections that follow, we give a general rationale for this type of work (improvements in global bulletins of seismicity); a summary of the main method we are using; an overall timetable for the project; and some specifics concerning the first group of stations for which we expect to report results.

RATIONALE

Major users of seismic data include:

- the national and international groups now being organized to monitor compliance with the Comprehensive Nuclear Test-Ban Treaty
- researchers who improve our knowledge of Earth's internal structure and the physics of earthquake processes; and
- those engaged in earthquake engineering and earthquake hazard mitigation.

Although the most basic data in seismology for all these users are seismograms, in practice the great majority of those who work with seismic data do not use seismograms directly. Instead they mostly use data products derived from seismograms. The most important of these products, are bulletins of seismicity.

In the last 20 years there have been enormous improvements in the quality and quantity of seismograms, associated with the development of broadband feedback sensors and techniques of digital recording to permit high dynamic range across wide bands of frequency. There is ongoing revolutionary improvement in access to seismogram data, as satellite communications and the Internet spread even to remote locations. It has therefore been frustrating to find that the quality of the principal data product derived from seismograms acquired internationally, the global bulletin of seismicity, has not yet seen the types of radical improvement needed by any of the user communities, listed above.

The US Geological Survey (USGS) and the International Seismological Centre (ISC) publish their bulletins months to years in arrears, using volunteered data, and methods of analysis that essentially have not changed for sixty years. These are very useful bulletins, and their quality has greatly improved because of the increased number of reported signal detections. The Reviewed Event Bulletin (REB) of the CTBT monitoring community, produced since 1995 January 01 by GSETT-3 and the PIDC and now by the IDC in Vienna, is vastly improved over the other global bulletins in its timeliness of publication. However, both the REB location estimates, and the estimates of their uncertainty (error ellipses), require improvement.

It appears that the principal reason for inaccuracies in the REB locations is lack of a sufficiently good model of Earth structure, and specifically of travel time information. It is desirable to calibrate each IMS station so that in effect the location of a new event can be located with reference to another event, whose location is known accurately and which, preferably, is not far from the new event. By using a sufficiently large number of calibration events, whose location is accurately known and whose signals are detected reliably at IMS stations, it is possible to generate a station-based travel time surface (a function of distance and azimuth), for each seismic phase. Different surfaces are needed for different event depths. For CTBT monitoring, the most important surface is that for zero depth.

As noted in the report of the first Oslo Workshop on IMS Location Calibration (January 1999, which led to the paper CTBT/WGB/TL - 2/18):
"such calibration is necessary in order to significantly improve the location precision of internationally reporting earthquake agencies,"
and
"no attempt has so far been made to include such corrections in routine location processing on a global scale."
Our consortium project will carry out such an approach to calibration for 30 IMS stations.

SUMMARY OF METHOD

The IMS stations in East Asia which are the subject of this project, are listed in Table 1, and shown in Figure 1, with station coordinates as originally given in Annex 1 to the CTBT Protocol. Not all of these sites currently have operational IMS stations. However, in some cases there are non-IMS stations which are operating at or near the IMS site, and in other cases stations have operated near the IMS site in the past. In general we refer to such non-IMS stations as surrogate stations. Their data may be used to assist in building up the necessary station-based travel-time data set for purposes of obtaining the types of travel-time surface needed at the IDC for every IMS station site.

Code	Country	Station Name	Lat	Long
PS12	China	Hailar	49.27	119.74
PS13	China	Lanzhou	36.09	103.84
PS23	Kazakhstan	Makanchi	46.80	82.00
PS25	Mongolia	Javhlant	47.99	106.77
PS29	Pakistan	Pari	33.65	73.25
PS31	Republic of Korea	Wonju	37.50	127.90
PS33	Russian Federation	Zalesovo	53.94	84.81
PS34	Russian Federation	Norilsk	69.40	88.10
PS35	Russian Federation	Peleduy	59.63	112.70
PS37	Russian Federation	Ussuriysk	44.28	132.08
PS41	Thailand	Chiang Mai	18.80	99.00
AS7	Bangladesh	Chittagong	22.40	91.80
AS20	China	Baijiatuan	40.02	116.17
AS21	China	Kunming	25.15	102.75
AS22	China	Sheshan	31.10	121.19
AS23	China	Xi'an	34.04	108.92
AS57	Kazakhstan	Borovoye	53.06	70.28
AS58	Kazakhstan	Kurchatov	50.72	78.62
AS59	Kazakhstan	Aktyubinsk	50.40	58.00
AS60	Kyrgyzstan	Ala-Archa	42.64	74.49
AS68	Nepal	Everest	27.96	86.82
AS86	Russian Federation	Seymchan	62.93	152.37
AS87	Russian Federation	Talaya	51.68	103.64
AS88	Russian Federation	Yakutsk	62.01	129.43
AS89	Russian Federation	Urgal	51.10	132.36
AS90	Russian Federation	Bilibino	68.04	166.37
AS91	Russian Federation	Tiksi	71.66	128.87
AS92	Russian Federation	Yuzhno-Sakhalinsk	46.95	142.75
AS93	Russian Federation	Magadan	59.58	150.78
AS100	Sri Lanka	Colombo	6.90	79.90

Table 1. IMS stations in Eastern Asia. A TBD Primary station (PS20) and a TBD Auxiliary station (AS39) may eventually be negotiated in Eastern Asia.

Table 2 lists our present knowledge of the availability of data at each of the 30 IMS sites in Table 1, whether or not there is an IMS station currently operating at the site. In the case where no IMS station is operating, we list some appropriate surrogate stations. Our basic approach will be to acquire lists of reliably located seismic events in Eastern Asia, preferably occurring since the beginning of publication of the REB on January 1, 1995 and large enough to be included in the REB. From such events, preferably of GT5 quality or better, we shall obtain the picked arrival times at IMS stations and thus build up a set of station-based travel-times for events of accurately known location.

For each major set of event locations that we plan to use for IMS station calibration, an extensive validation effort will be made. We plan to do this by acquiring waveform data and phase-pick data for a subset of the events, from as many stations as possible. From such data we shall make our own location estimates, including waveform studies of the depth, in order to validate our conclusions as to the quality of the locations. For the major aseismic areas of Eastern Asia (for example, for much of the northern part of this region, which is in Russia), such an approach cannot be used. However, we are fortunate in that major reflection/refraction profiles were carried out in this region during the Soviet era, in the Deep Seismic Sounding program (DSS). Extensive DSS data will be analyzed in our consortium project by the University of Wyoming. Specifically, arrival times will be picked, and interpreted to generate 2D and 3D regional models and hence travel-times to IMS station sites in Russia.

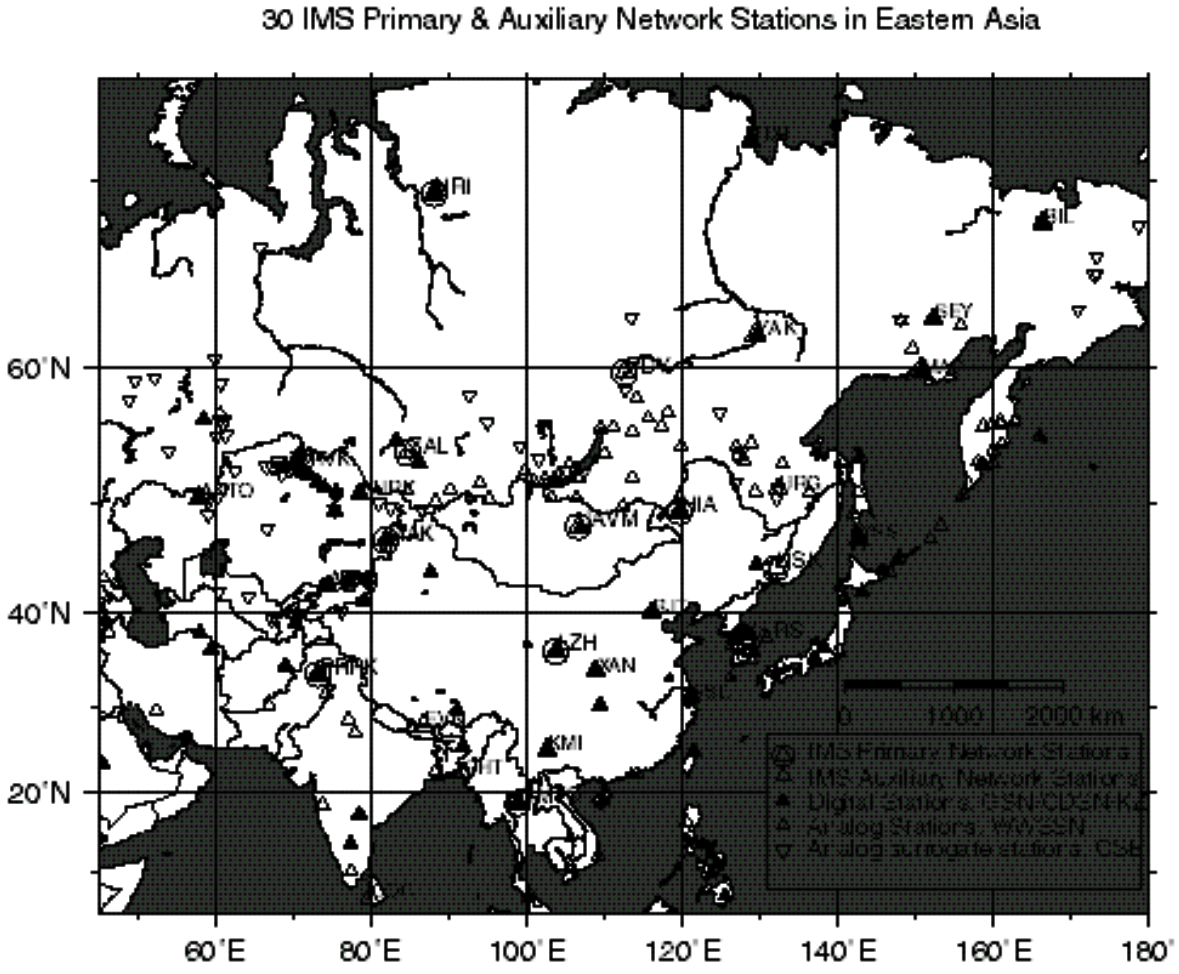


Figure 1. IMS primary and auxiliary stations in our project, and surrogate station locations.

Code			Phase data	Digital waveform data		Analog waveform data
IMS	**ISC**	**PIDC**	**Operator**	**Operation**	**Source**	
HIA		HIA	CDSN	1986/07-	DMC/IDC	
LZH	LZH		CDSN	1986/06-	DMC	
MAK			KZ/GSN	1994/07-	LDEO	
JAVM	ULN	ULN	GSN (ULN)	1994/11-	DMC	
PRPK	NIL	NIL	GSN (NIL)	1994/12-	DMC	
KSRS		KSAR	KIGAM	1995/01-	IDC/KIGAM	
ZAL	NVS, ELT		ZAL IDC (ZAL)	1995/01	IDC+ELT (1998/08-, LDEO)	
NRI	NRI	NRI	GSN (NRIL)	1992/12-	DMC/IDC	1964-, Obninsk
PDY	BOD	PDY	IDC	1995/01-	IDC	
USK	VLA		CDSN (MDJ)	1986/10-	DMC	
CMTO	CHG,CHTO		GSN (CHTO)	1992/09-	DMC	
CHT	SHL,HOW		GSN (SHIO)		DMC	HOW, SHL/WWSSN (LDEO)
BJT	PEK,BJI	BJT	CDSN (BJI)	1986/07-	DMC	
KMI	KMI		CDSN (KMI)	1986/06-	DMC	
SSE	SSE		CDSN (SSE)	1986/06-	DMC	
XAN	XAN		CDSN (XAN)	1992/11-	DMC	
BRVK			KZ/GSN	1994/07-	LDEO	
KURK			KZ/GSN	1994/07-	LDEO	
AKTO			KZ	1994/09-	LDEO	
AAK	FRU		GSN (AAK)	1990/10-	DMC	
EVN	DMN,KKN			1991/06-11	ING	
SEY	SEY		GS/GSRAS	1990/09-	DMC/GS	1969- Magadan
TLY	IRK		GSN/GSRAS	1990/10-	DMC	1964- Irkutsk
YAK	YAK	YAK	GSN/GSRAS	1993/08-	DMC	
URG					Sogda 75/01-76/10 CSE	
BIL	ILT		GSN/GSRAS	1995/08-	DMC	Bilibino 64- Magadan
TIXI	TIK		GSN/GSRAS	1995/08-	DMC	1964- Obninsk
YSS	YSS		GSN/GSRAS	1992/05-	DMC	
MA2	MAG,MGD		GSN/GSRAS	1993/09-	DMC	1964- Magadan
COC	KOD		AWRE (GBA)			KOD 1964-'90 WWSSN LDEO

Table 2. A summary of information on data (picks, waveforms) at 30 IMS sites, listing the operating IMS stations, and surrogate stations, useful for acquiring phase picks and waveforms for stations in Table 1.

Station operators are:
GSN = Global Seismographic Network;
CDSN = Chinese Digital Seismographic Network;
KZ = Kazakhstan Broadband Seismographic Network (NNC, RK/LDEO);
GS = GeoScope;
GSRAS = Geophysical Survey, Russian Academy of Sciences
Data sources are:
IDC = International Data Centre for IMS;
DMC = IRIS Data Management Center
ING = The National Institute of Geophysics, Italy

The AWRE operation of GBA has ended, with this station handed over to local operation, but much relevant data for this station is easily available.

We note that a sophisticated modeling effort is the only way to set up the required travel time grid for each IMS station, in two important cases: from large aseismic regions; and to IMS station locations where no station or nearby surrogate now exists. But we are well aware that it would be inappropriate for the IDC to rely for its monitoring operations on purely 3D calculations in a 3D model. Therefore we shall make great efforts to search for appropriate validation, to the extent possible, of any predicted effects on travel times caused by 3D structure. It is here that a search for data from old analog stations can play a key role. We are familiar with analog stations all over the former Soviet Union which operated during the period 1965 — 1990 at locations that were selected in 1996 to become the sites of modern instrumentation (IMS); and we plan to track down old data from these stations (see Table 2), and to

work with scientists in Russia and Central Asia to analyze them. This work will bring together old analog data at fixed stations, the special DSS field data, modern waveform data, and the full sophistication of modeling in 1D, 2D, and 3D structures.

OVERALL TIMETABLE

The thirty IMS stations we are studying in Eastern Asia can be grouped geographically into five regions, and the consortium expects to propose to the Configuration Control Board of the Center for Monitoring Studies, on travel-time grids for IMS sites, in the following sequence of regions:

Central Asia (MAK, BRVK, KURK, AAK, AKTO, ZAL) ~ year two, first quarter
China (HIA, LZH, JAVM, BJT, KMI, SSE, XAN) ~ year two, fourth quarter
Korea (KSRS) ~ year three, second quarter
Russia (NRI, PDY, USK, SEY, TLY, YAK, URG, BIL, TIXI, YSS, MAG) ~ year three, fourth quarter
Indian subcontinent (PRPK, CHT, EVN, COC) and CMTO ~ year three, fourth quarter

SOME SPECIFICS CONCERNING THE FIRST GROUP OF STATIONS

As noted above, the first set of stations for which we plan to deliver the necessary station-specific travel time information is MAK, BRVK, KURK, AAK, AKTO, ZAL. These Central Asian stations are indicated in Figure 2. It may be possible to include additional stations, such as NIL (surrogate for PRPK — noting that NIL has been picked by the PIDC in recent years), and possibly some stations in China. It would appear that the work of documenting improvements in event location can be done better if the travel-time information is supplied for a larger number of stations. In the case of Central Asia stations, such travel times will be obtained in our project on the basis of (a) early studies based mainly on earthquake data (e.g. the work of Nersesov and Rautian, using stations of the Complex Seismological Expedition), (b) Deep Seismic Sounding, and (c) recent studies of nuclear and chemical explosions. We are also using (d) an empirical approach in which phases are picked at IMS stations, for so-called Ground Truth events whose location is known quite accurately on the basis of additional data, obtained for example from local and regional networks.

Of the IMS stations in and near Kazakhstan that we are now studying, only ZAL has been contributing data to the PIDC or IDC. Thus phases at ZAL, and only at ZAL, have been picked for numerous events in our GT datasets in recent years. Under a joint program between the National Nuclear Centre of the Republic of Kazakhstan and the Lamont-Doherty Earth Observatory of Columbia University in New York, Kazakhstan stations AKTO, BRVK, KURK and MAK have operated with high quality sensors and digital recording throughout the period of full-time production of the REB. Station AAK has also operated throughout this period (i.e., since 1995 January 1), and continuous data from all these stations are easily available. Since these stations have not yet contributed data to the PIDC/IDC as yet, it will be necessary to obtain picks at these stations for many events in our GT datasets.

With these picks, we shall first have to go through a process of re-creating REB locations with the Central Asia station picks included, using the same travel times (*iasp91*) that have been used for this region by the PIDC. Second, we shall go through an iterative process of (a) developing stations-specific travel-times, (b) re-locating events, and (c) documenting improvements in the resulting event locations (as compared to those in the re-created REB). It is only on the basis of demonstrated improvements in event locations, that stations-specific travel-times will be acceptable and used for improved event location in future.

Because of the excellent signal-to-noise ratio of Kazakhstan stations, in particular of BRVK, KURK, MAK, it is likely that they will detect signals for a large fraction of global seismicity reported by the IDC. The impact that Kazakhstan IMS stations will have on the REB (when these stations are eventually included in the IMS) will be significantly greater if station-specific travel-times are available for them *ab initio*.

CONCLUSIONS AND RECOMMENDATIONS

It appears that the Reviewed Event Bulletin of the International Data Centre will be the first bulletin of global seismicity to be published using stations for which arrival times are interpreted with station-specific travel time information. Such an approach is potentially a major improvement upon current practice. Our work is to provide such station-specific information for thirty stations of the International Monitoring System in Eastern Asia.

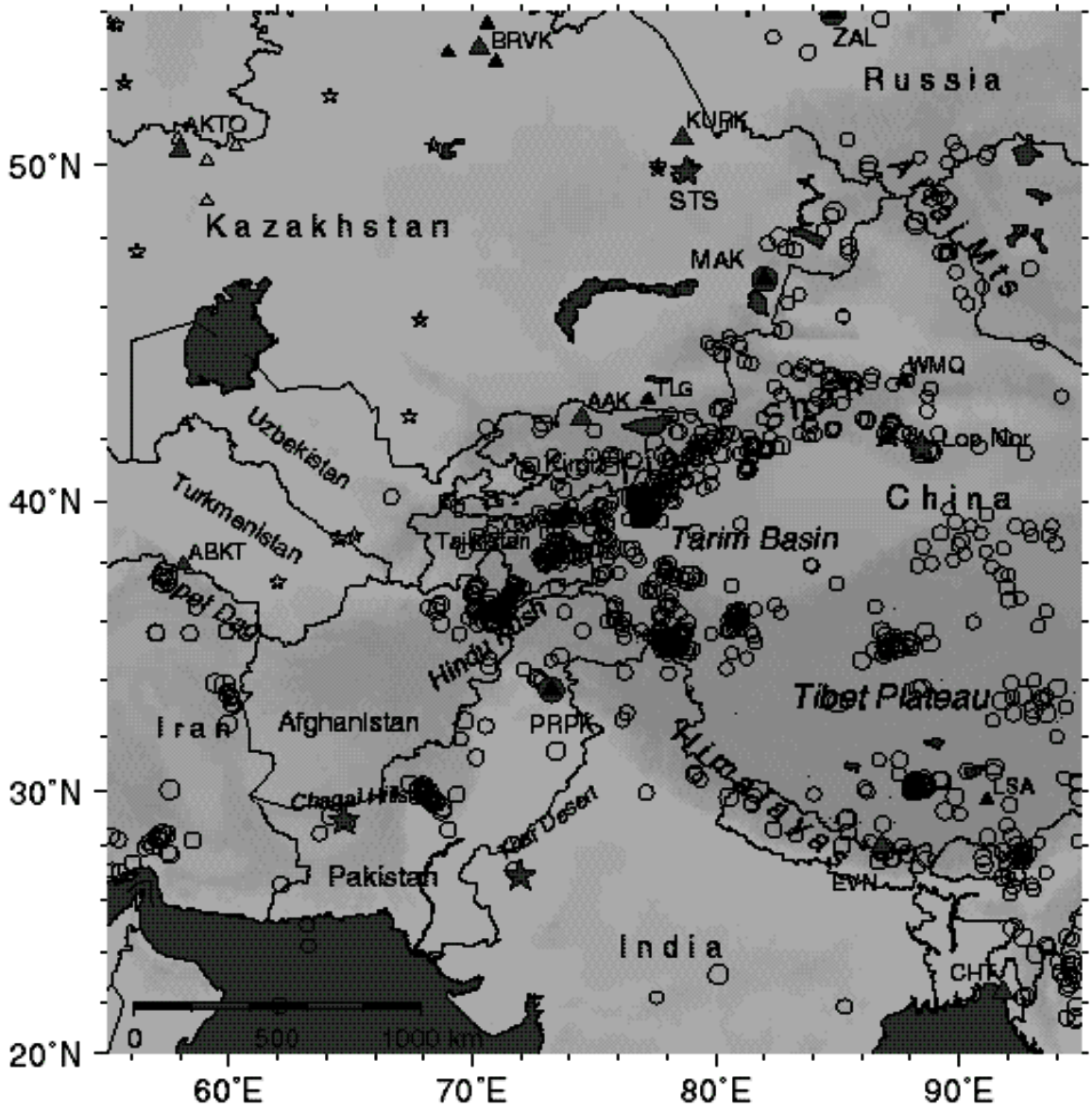


Figure 2. Central Asia map showing locations of IMS primary stations (circle with black triangle), auxiliary stations (white triangle), other digital stations (black triangle), analog stations (open triangle), underground nuclear explosion test sites (big star), and PNEs (small star). Circles are used to indicate GT events.

We do not know as yet whether the desired degree of improvement in location accuracy (for seismic events published in the REB) can be achieved on the basis of phase picks and station-specific travel times. This question should be examined on an annual basis for the next few years. Recognizing that eventually it may be appropriate to use methods based on whole waveforms (such methods have been demonstrated to lead to remarkably accurate event locations in regional bulletins that document dense seismicity, for example in parts of California), we recommend that research also be carried out using waveform-based methods in the context of global bulletin publication (at least, for areas which are seismically most active).

Key Words CTBT, earthquake location, seismicity bulletins

RESEARCH IN REGIONAL SEISMIC MONITORING

F. Ringdal[1)], E. Kremenetskaya[2)], V. Asming[2)], T. Kværna[1)] and J. Schweitzer[1)]
[1)] NORSAR, Kjeller, Norway
[2)] KRSC, Apatity, Russia

Sponsored by the Department of Defense

Contract No. F08650-06-C-0001

ABSTRACT

During the last decades, a network of sensitive regional arrays has been installed in northern Europe in preparation for the global seismic monitoring network under the Comprehensive Nuclear-Test-Ban treaty (CTBT). This regional network, which comprises stations in Fennoscandia, Spitsbergen and NW Russia provides a detection capability for the European Arctic that is close to $m_b = 2.5$, using the Generalized Beamforming (GBF) method for automatic phase association and initial location estimates. We have continued our studies to use data from the regional networks operated by the Kola Regional Seismological Centre (KRSC) and NORSAR to assess the seismicity and characteristics of regional phases of the Barents/Kara Sea region, as well as the application to seismic event screening.

We have studied the seismicity (i.e. seismic events apart from confirmed nuclear explosions) of the Western Russia/ Novaya Zemlya region for the past 25 years, and found an average of less than one seismic event per year exceeding m_b 3.5. Thus, the event occurrence in this region is so low that no event of m_b 3.5 and greater located in this region should be screened out in the IDC screening process. The same consideration could apply in some other regions of the world, and the study of detailed seismicity patterns is an important part of the further screening developments.

In discrimination studies, our results for the European Arctic show that the P/S discriminant should be applied with great caution in this region, and further research is required. The regional M_S:m_b discriminant has considerable promise, and the shorter-period energy available in surface waves recorded at regional distances can be exploited in improving the monitoring capabilities during periods with strong interfering surface waves from large distant earthquakes.

We recommend that the current efforts to improve m_b determinations and to reconcile the current m_b values with the "historic" magnitude scale be continued. A project to apply maximum-likelihood techniques to reassess the m_b of past seismic events should be undertaken.

We have analyzed data from the Eurobridge profiling experiment which comprised a 1130 km seismic refraction profile crossing the Baltic Shield in the northwest and the Ukrainian Shield in the southeast. We have investigated in detail observed deviations in P-wave travel times from those predictions by the Fennoscandian crustal and upper mantle velocity model. Our study has revealed several instances of documented timing errors at the various arrays. An important outcome of this study is the development of a method to identify possible timing anomalies at IMS stations. This method could be useful both in validating calibration data and in providing a tool for continuously checking the timing accuracy and consistency of IMS stations.

We have also analyzed data from some recent profiling experiments near the Spitsbergen array in order to improve the calibration of this station. Not unexpectedly, the study has demonstrated that the crust and uppermost mantle around the SPITS station is very heterogeneous. However, with the exact travel times available through this study for different azimuths in the range 0-3 degrees, the location and detection processing of local and near-regional events at SPITS will be considerably improved.

The location calibration effort will continue to be an important part of our work. The recommendations provided in the paper CTBT/WGB/TL-2/49 should be followed up by the international community, and the progress of this work will be reviewed in a planned workshop in Oslo in 2001.

OBJECTIVE

This work represents a continued effort in seismic monitoring, with emphasis on studying earthquakes and explosions in the Barents/Kara Sea region, which includes the Russian nuclear test site at Novaya Zemlya. The overall objective is to characterize the seismicity of this region, to investigate the detection and location capability of regional seismic networks and to study various methods for screening and identifying seismic events in order to improve monitoring of the Comprehensive Test Ban Treaty. An important part of the work is contributions toward the international effort to provide regional location calibration of the International Monitoring System.

RESEARCH ACCOMPLISHED

INTRODUCTION

NORSAR and Kola Regional Seismological Centre (KRSC) of the Russian Academy of Sciences have for many years cooperated in the continuous monitoring of seismic events in North-West Russia and adjacent sea areas. The research has been based on data from a network of sensitive regional arrays which has been installed in northern Europe during the last decade in preparation for the CTBT monitoring network. This regional network, which comprises stations in Fennoscandia, Spitsbergen and NW Russia (see Figure 1) provides a detection capability for the Barents/Kara Sea region that is close to $m_b = 2.5$ (Ringdal, 1997).

The research carried out during this effort is documented in detail in several contributions contained in the NORSAR Semiannual Technical Summaries. In the present paper we will limit the discussions to some recent results of interest in the context of applying screening criteria to seismic events in the European Arctic and within the location calibration effort currently underway for the International Monitoring System (IMS). We also report on some recent developments in monitoring mining events in the Kola Peninsula.

SCREENING

The development of event screening criteria is one of the main tasks of the expert work currently conducted by Working Group B of the Preparatory Commission for the Comprehensive Nuclear-Test-Ban Treaty (CTBT). The purpose of event screening is to "screen out" events that are thought to be consistent with natural causes (such as earthquakes), so that detailed analysis can be focused on those events that are truly of interest for monitoring purposes. The current seismic screening procedure employed at the International Data Centre (IDC) is applied only for seismic events exceeding a m_b threshold of 3.5, and focuses on two criteria: event focal depth and M_s:m_b. These are considered to be the most robust criteria currently available, but have the disadvantage that they are difficult to apply to small events or events recorded only by few stations. Other criteria, such as the high-frequency P/S ratio, hold the promise of being applicable at much lower event magnitudes, and this is currently an area of active research (see e.g. Ringdal et.al., 2000).

The purpose of screening is not to identify events, but rather to limit as far as possible the number of events that need to be subjected to special analysis. It might be argued that in some regions of the world, seismic events exceeding m_b 3.5 are so infrequent that any particular screening criteria based on signal characteristics may be superfluous. We have studied the region comprising Western Russia and Novaya Zemlya, including the surrounding parts of the Barents and Kara Seas in this perspective. Our recommendation, as detailed below, is that the event occurrence in this region is so low that no event of m_b 3.5 and greater located in this region should be screened out. This would exclude the possibility of accidentally missing events of potential monitoring interest, and at the same time improve confidence that the treaty is adhered to.

Seismicity of the European Arctic

The seismicity of the Barents/Kara sea region has previously been discussed by Ringdal (1997). Nuclear and chemical explosions were conducted at Novaya Zemlya until 1990, and in addition a number of PNEs were carried out in Western Russia until 1988. We have carried out a detailed study of the seismicity of Western Russia, including the Ural Mountains and the Novaya Zemlya region. Our emphasis has been on collecting information on available seismic events (in addition to the confirmed nuclear explosions) for a region bounded by 50-78 deg North, 30-65 deg East, and with m_b of 3.5 or greater. This is of interest in the screening process at the IDC, since the current event screening criteria are applied only to events above this magnitude.

Table 1: Seismic events with m_b at least 3.5 during 1975-2000 in the region 50-78N, 30-65E. Confirmed nuclear explosions are not included.

No	Date/time	Location	mb (MLE)	Comment/Reference
1	15.11.78/ 08.30.00	73.40 N, 55.00 E	3.6	obably chemical explosion, Novaya Zemlya ingdal, 1997)
2	10.04.81/ 19.43.33	68.76 N, 36.96 E	4.4	rthquake, felt in Murmansk, Kola Peninsula
3	01.08.86/ 13.56.3	72.945 N, 56.549 E	4.3	assified as earthquake by Marshall et.al. (1989)
4	26.02.87/ 00.18.21	60.10N, 60.20 E	4.1	ockburst in Sevuralboksitruda mine, 50m of tunne stroyed, 150 cubic m rock volume (VNIMI, 1989
5	16.04.89/ 06.34.4	67.67 N, 33.73 E	3.5	rthquake in Kirovsk mine, faulting observed, 3 fl tunnels (total 200m) destroyed (Kremenetskaya a sming, 1995)
6	14.05.89/ 11.46.56	50.84 N, 51.24 E	4.3	EIC/PDE
7	28.05.90/ 00.35.48	55.17 N, 58.72 E	4.3	llapse of Kurbazakskaya mine of shnouralboksitruda, 450 000 sq. m area affected omakin and Yunusov, 1993)
8	28.05.90/ 02.41.28	55.17 N, 58.72 E	4.4	e preceding event. Reference: Lomakin and Yunu 993)
9	16.06.90/ 12.43.2	68.52 N, 33.09 E	4.0	rthquake, felt in Murmansk, Kola Peninsula
10	05.01.95/ 12.46.01	59.60 N, 56.65 E	4.5	llapse at the Silvinit salt mine near Solikamsk. 3 0 sq.m. area affected.
11	10.06.96/ 17.16.47	59.74 N, 43.11 E	3.7	EB (PIDC)
12	13.06.96/ 19.22.38	75.2 N, 56.7 E	3.5	cated by Ringdal et. al. (1997)
13	16.08.97/ 02.11.00	72.510 N, 57.550 E	3.5	assified as earthquake by Richards and Kim (199
14	17.08.99/ 04.44.36	67.885 N, 34.532 E	4.3	rthquake/collapse, mine Umbozero of Sevredmet 0 000 sq.m area affected. 50 cubic m rock volum ver changed course
15	18.01.00/ 04.05.32	58.06 N, 49.42 E	3.5	EB (PIDC)

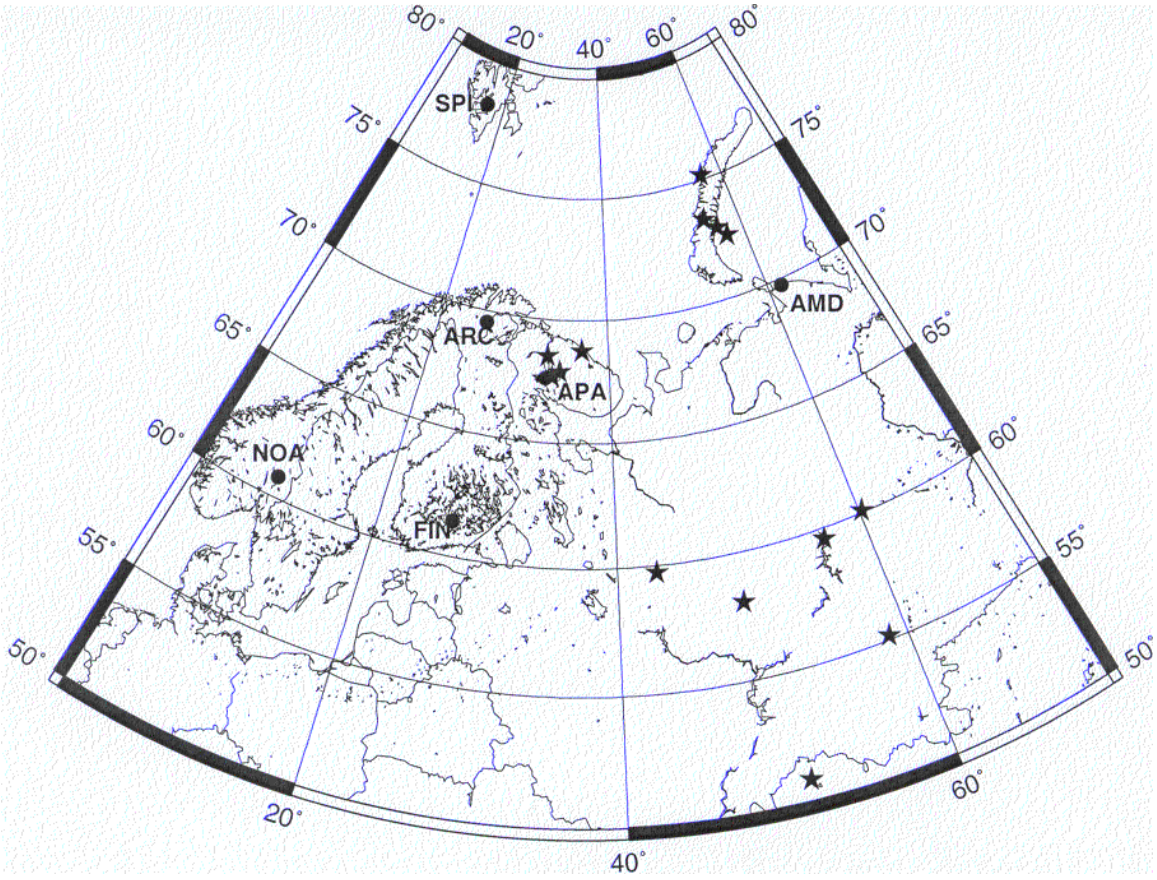


Fig.1 Map showing the regional network operated by NORSAR and KRSC. The map also shows the location of the events in Table 1, which comprises all known events 1975-2000 (apart from nuclear explosions) with m_b of 3.5 or greater in a region bounded by 50-78 deg North, 30-65 deg East.

In this compilation, we have used available international bulletins (ISC, USGS/NEIC, PIDC) together with the regional bulletins issued by NORSAR and KRSC. We have re-assessed the m_b estimates, making use of the maximum-likelihood method developed by Ringdal (1986) as well as the regional magnitudes provided by NORSAR and KRSC, adjusted to world-wide m_b. We have attempted to make our magnitude estimates consistent with "historic" world-wide m_b, as opposed to the current values which have been shown to have a slight negative bias relative to the traditional estimates.

The result of this compilation is listed in Table 1, which covers the 25-year time interval 1975-2000 (see also Figure 1). Only 15 reported seismic events (not counting confirmed nuclear explosions) have exceeded magnitude 3.5 in this period, i.e. less than one event per year on the average. We note that the detectability of the current global network is sufficiently high so that we consider this catalog to be essentially complete since 1990, but a few small events may certainly have been missed for the earlier years. Nevertheless, the average occurrence of events of m_b=3.5 or greater in this region seems to be at most 1 event per year. It thus appears that any screening of seismic events above magnitude 3.5 in this region is superfluous, so it is currently not necessary to develop screening criteria for this region. This could of course change if the screening is applied at a lower magnitude threshold in the future.

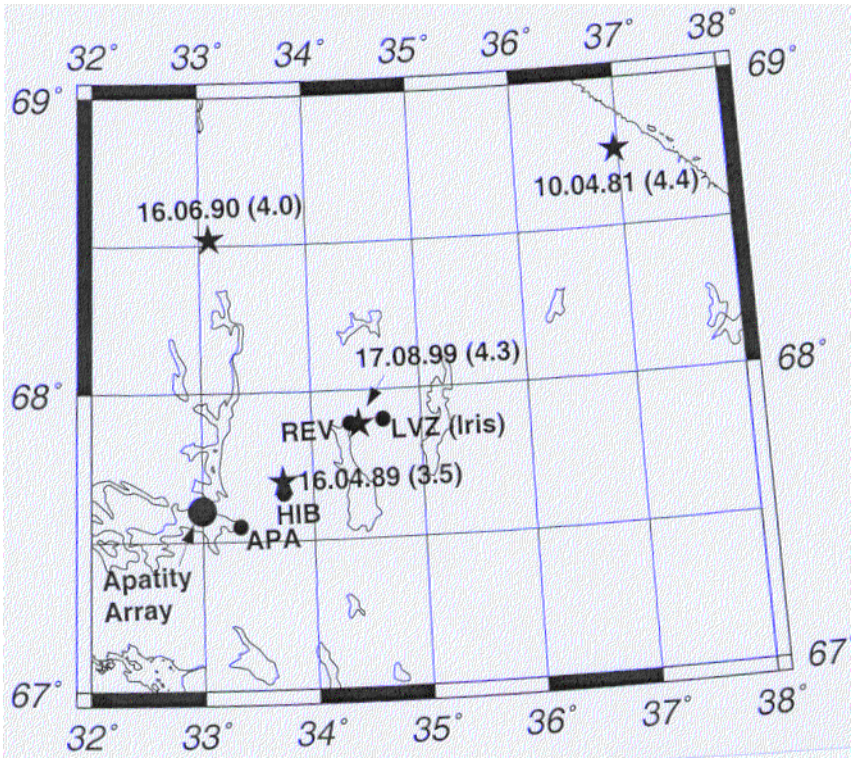


Fig. 2. Station network operated by KRSC in the Kola Peninsula. Two new stations (HIB and REV) have been deployed in 2000. The locations of those seismic events in Table 1 which occurred in the Kola Peninsula are also indicated.

It is interesting to note, as explained in Table 1, that many of the events are associated with mining activity (i.e. collapses, rockbursts or earthquakes inside known mines). This means that true tectonic earthquakes of m_b=3.5 or greater in this region are very rare indeed. Any significant seismic event located by the IDC inside this region should be subject to special analysis, as part of the confidence-building process that is essential in CTBT verification.

We might note that other parts of the European Arctic have a much higher level of natural seismicity than the Western Russia/Novaya Zemlya region discussed above. For example, there are many significant earthquakes in the intraplate areas of Fennoscandia, and the seismicity is of course even higher along the tectonic plate boundary areas, such as the North Atlantic Ridge, Spitsbergen and the Lomonosov Ridge.

Study of P/S ratios

A paper by Ringdal et. al. (2000) discusses the application of the P/S ratio for discriminating seismic events in the European Arctic. It is shown that the P/S ratios of Novaya Zemlya nuclear explosions measured in the 1-3 Hz filter band scale with magnitude, indicating a need for caution and further research when applying P/S discriminants. Using mainly data from the large NORSAR array, the authors note that observed P/S amplitude ratios in the European Arctic shows large variability for the same source type and similar propagation paths, even when considering closely spaced observation points. This effect is most pronounced at far-regional distances and relatively low frequencies (typically 1-3 Hz), but it is also significant on closer recordings (around 10 degrees) and at higher frequencies (up to about 8 Hz). The conclusion from the study is that the P/S ratio at high frequencies (e.g. 6-8 Hz) shows promise as a discriminant between low-magnitude earthquakes and explosions in the European Arctic, but its application will require further research, including extensive regional calibration and detailed station-source corrections. Such research should also focus on combining the P/S ratio with other short-period discriminant, such as complexity and spectral ratios.

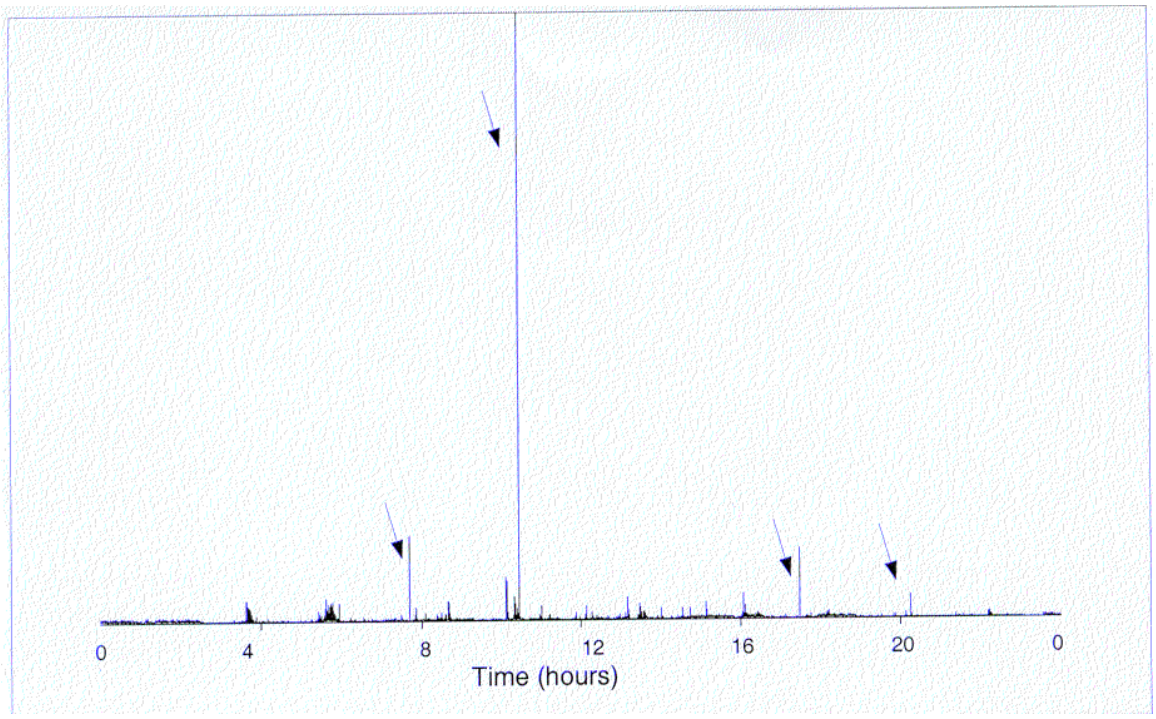


Fig 3. STA trace (filter 4-12 Hz) for station REV in the Kola Peninsula. The data cover the 24 hours of 12 April 2000. The arrows mark detected microearthquakes in the Revda mine (magnitudes 0.0-1.0)

Study of Regional M_s:m_b

A paper by Kremenetskaya et. al. (2000) describes the historical archive of regional long-period data (on analog form) available at KRSC since 1970 for the station APA in Apatity, Kola Peninsula. Since the station APA is situated at a regional distance from the Novaya Zemlya test site, these recordings provide a unique source for studying the performance of M_s:m_b at regional distances for the European Arctic. Selected seismograms from APA have been digitized, and the quality of the analog recordings at this station is demonstrated by comparing recordings from a modern broad-band seismometer at the same place to signals digitized from the analog equipment.

In the paper, it is further shown that the APA surface wave recordings, normalized for distance and magnitude, provide an encouraging degree of separation between earthquakes and explosions in the European Arctic. It is demonstrated that this separation can be achieved in a wide frequency band (at least 10-25 seconds period), and the authors note that this gives promise for applying the M_s:m_b discriminant down to lower magnitudes and at lower signal periods than is possible using teleseismic recordings. They also note that the shorter-period energy available in surface waves recorded at regional distances can be exploited in improving the monitoring capabilities during periods with strong interfering surface waves from large distant earthquakes.

NETWORK DEVELOPMENTS

Kola network and earthquake studies

On 17 August 1999, only 4 hours after the large earthquake in Turkey, an earthquake of m_b=4.3 occurred in a mining area in Revda, Kola Peninsula. This is the largest seismic event in Kola for almost 20 years, and has been the subject of considerable interest. The earthquake, which was associated with a large mine collapse in the Lovozero Massif, was preceded by numerous foreshocks several months in advance, and was followed by several aftershocks.

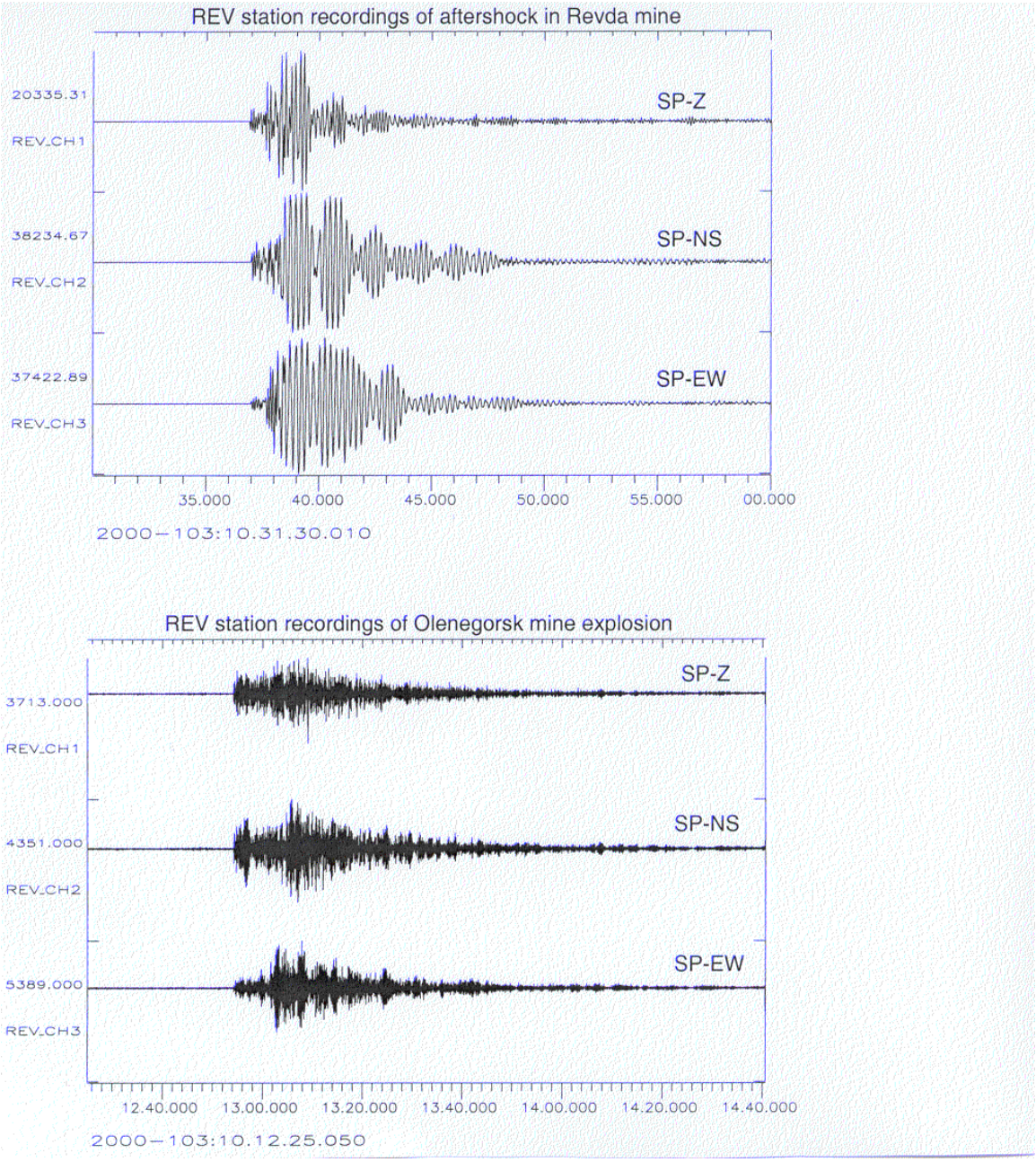


Fig.4. REV 3-component short period recordings on an aftershock in the Revda mine (top) and a mining explosion in the Olenegorsk mine 50 km away (bottom). Note the strong Rg phases on the top traces.

KRSC installed in early 2000 3-component seismic stations in the Khibiny Massif (HIB) and in Revda (REV) - see Fig. 2. The station at Revda was deployed for the purpose of studying the aftershocks of the 17 August 1999 event, and the station in Khibiny had as its main purpose to enable improved locations and origin times for seismic events in the Khibiny mines. An example of a one-day STA trace for the Revda station is shown in Figure 3. This trace could be seen as a simple version of the Threshold Monitoring technique applied to this mining site, and most of the peaks on the trace are in fact associated with the Revda mine. Examples of recordings for two of the peaks are shown in Figure 4 (for an aftershock at Revda and a mining explosion in Olenegorsk).

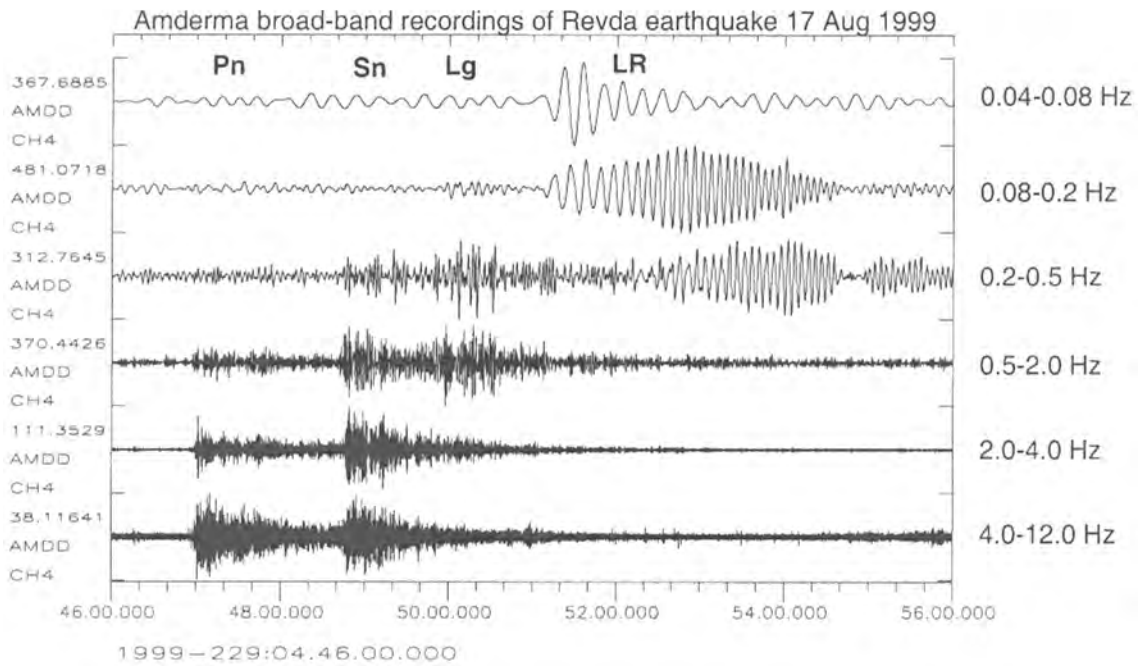


Fig.5. Amderma broad-band vertical channel recording of the Revda earthquake of 17 August 1999. The traces are filtered in several different bands. The distance from the event to the station is approximately 10 degrees.

Amderma station

The seismic station at Amderma is a key monitoring resource for the Kara Sea region. In 1999, KRSC installed a broadband 3-component seismometer (Guralp) at this site, and implemented a dial-up mechanism to enable rapid retrieval of data of special interest. An example of data retrieved in this way for the 17 August 1999 Revda event is shown in Figure 5. We note the strong surface waves recorded for this event, and in particular the high Rayleigh wave energy in the frequency band near 0.1 Hz (10 seconds period) is noteworthy. The prominence of energy at these high frequencies and their possible usefulness in regional M_s:m_b discrimination has been pointed out by Kremenetskaya et al (2000). Otherwise, the traces show a feature which is common for many paths in the European Arctic: The Pn and Sn phase are dominant at frequencies above 2 Hz, whereas the Lg phase is strongest near 1 Hz.

LOCATION CALIBRATION

Eurobridge profile

We have analyzed data from the Eurobridge profiling experiment which comprised a 1130 km seismic refraction profile crossing the Baltic Shield in the northwest and the Ukrainian Shield in the southeast. There were three series of shots, one in 1995 and two in 1996. Observations of these explosions at the Fennoscandian arrays provide an opportunity to check the accuracy of the travel-time tables in use at NORSAR for Fennoscandia. At the same time, these refraction shots provide a useful extension to the pIDC ground-truth database. P-phases from most of the Eurobridge shots were observed at the FINES, HAGFORS and NORES arrays, and even at the more distant ARCES array as many as 12 out of the 29 events were seen. We have investigated in detail observed deviations in P-wave travel times from those predictions by the Fennoscandian crustal and upper mantle velocity model. Our study has revealed several instances of documented timing errors at the various arrays. Even when accounting for these timing errors, there remains a considerable scatter in the travel times as compared to the theoretical model. The interpretation of these anomalies in terms of crustal and upper mantle structure is not obvious. An important outcome of this study is the development of a method to identify possible timing anomalies at IMS stations. This method could be useful both in validating calibration data and in providing a tool for continuously checking the timing accuracy and consistency of IMS stations.

Calibrating the Spitsbergen array

We have analyzed data from some recent profiling experiments near the Spitsbergen array in order to improve the calibration of this station. Data from airgun shots in the water as well as small underwater explosions of 25 to 50 kg conventional explosives could be observed at distances up to 350 km when using the double-beam technique for SNR enhancement. Not unexpectedly, the study has demonstrated that the crust and uppermost mantle around the SPITS station is very heterogeneous. However, with the exact travel times available through this study for different azimuths in the range 0-3 degrees, the location and detection processing of local and near-regional events at SPITS will be considerably improved. This is particularly important because there are large numbers of local events recorded at SPITS every day, and a correct location and phase identification will help eliminate these phases from interfering in the GBF process for network association and event definition analysis.

Oslo Workshop on location calibration

A workshop was held in Oslo, Norway during 20-24 March 2000 in support of the global seismic event location calibration effort currently being undertaken by PrepCom's Working Group B in Vienna. Among the contributions were recent results provided by NORSAR and KRSC of our joint regional calibration effort in the European Arctic, which has resulted in much improved travel-time models for the Barents region. We show that the Barents model, which is known to give accurate locations in the Fennoscandian and NW Russia area, can be successfully applied to the more general northern Eurasia region. The recommendations from this workshop have been provided in the paper CTBT/ WGB/TL-2/49, issued by Working Group B of the CTBTO Preparatory Commission.

CONCLUSIONS AND RECOMMENDATIONS

The seismicity of the Western Russia/Novaya Zemlya region is very low, with an average of less than one seismic event per year exceeding m_b 3.5. Thus, the event occurrence in this region is so low that no event of m_b 3.5 and greater located in this region should be screened out in the IDC event screening process. This would exclude the possibility of accidentally missing events of potential monitoring interest, and at the same time allow for special analysis of all significant events in this region. This would contribute to improved confidence building with respect to treaty adherence. We consider that the same consideration could apply in some other regions of the world, and the study of detailed seismicity patterns is an important part of the further screening developments.
Our results for the European Arctic show that the P/S discriminant should be applied with great caution in this region, and further research is required. The regional M_S:m_b discriminant has considerable promise, and the shorter-period energy available in surface waves recorded at regional distances can be exploited in improving the monitoring capabilities during periods with strong interfering surface waves from large distant earthquakes.

We recommend that the current efforts to improve m_b determinations and to reconcile the current m_b values with "historic" magnitude scale be continued. A project to apply maximum-likelihood techniques to reassess the m_b of past seismic events should be undertaken.

The location calibration effort will continue to be an important part of our work. The recommendations provided in the paper CTBT/WGB/TL-2/49 should be followed up by the international community, and the progress of this work will be reviewed in a planned workshop in Oslo in 2001.

Key Words: Detection, Location, Discrimination, Screening, Seismic Data Analysis

REFERENCES

Kremenetskaya, E. and V. Asming (1995). Induced seismicity in the Khibiny Massif (Kola Peninsula). *PAGEOPH, 145 No. 1*, 29-37.

Kremenetskaya, E.Asming, V. and F. Ringdal (1999). Seismic location calibration of the Barents region. *Semi-annual Technical Summary 1 October 1998 - 31 March 1999*, NORSAR Sci. Rep. 2-98/99, Kjeller, Norway.

Lomakin,V.S. and Ph.Ph.Yunusov (1993). Effective methods for seismological observations in mines. In: *Prediction and prevention of rock bursts in ore deposit.* Apatity, Kola Science Centre, Mining Institute, pp.73-76 (in Russian).

Kremenetskaya, E.Asming, V. and F. Ringdal (2000). Study of regional surface waves and frequency-dependent Ms:mb discrimination in the European Arctic, submitted to *PAGEOPH Special Issue on CTBT Monitoring.*

Marshall, P.D., R.C. Stewart and R.C. Lilwall (1989): The seismic disturbance on 1986 August 1 near Novaya Zemlya: a source of concern? *Geophys. J.*, 98, 565-573.

Richards, P.G. and Won-Young Kim (1997). Test-ban Treaty monitoring tested, *Nature*, 389, 781-782.

Ringdal, F. (1986). Study of magnitudes, seismicity and earthquake detectability using a global network, *Bull. Seism. Soc. Am*. 76, 1641-1659.

Ringdal, F. (1997): Study of low-magnitude seismic events near the Novaya Zemlya nuclear test site, *Bull. Seism. Soc. Am. 87 No. 6*, 1563-1575.

Ringdal, F., E.Kremenetskaya, V.Asming, T.Kvœrna, J. Fyen, J. Schweitzer (1998). Seismic monitoring of the Barents/Kara Sea Region. *Proceedings from the 20th Annual Seismic Research Symposium on CTBT Monitoring, September 21-23, 1998*

Ringdal, F., T.Kvœrna, E.Kremenetskaya, V.Asming (1997). The seismic event near Novaya Zemlya on 16 August 1997. *Semiannual Technical Summary 1 April - 30 September 1997*, NORSAR Sci. Rep. 1-97/98, Kjeller, Norway.

Ringdal, F., E.Kremenetskaya and V. Asming (2000): Observed characteristics of regional seismic phases and implications for P/S discrimination in the European Arctic, submitted to *PAGEOPH Special Issue on CTBT Monitoring*.

VNIMI - State Scientific Research Institute for Mining Geomechanics (1989): Catalog of rockbursts in ore and non-ore deposits. Leningrad, VNIMI, 1989, 189pp (in Russian).

GRID-SEARCH TECHNIQUES FOR SEISMIC EVENT LOCATION

William Rodi and M. Nafi Toksöz
Earth Resources Laboratory
Massachusetts Institute of Technology

Sponsored by The Defense Threat Reduction Agency
Arms Control Technology Division
Nuclear Treaties Branch
Contract pending

U.C. Lawrence Livermore National Laboratory
Subcontract No. B506161

ABSTRACT

We are developing a new algorithm for seismic event location to address particular problems of importance in monitoring the Comprehensive Nuclear-Test-Ban Treaty, including the assessment of location accuracy and increasing the number of seismic phases used for location. Our approach is formulated within a maximum-likelihood estimation framework and implemented numerically with grid-search and Monte Carlo techniques. It obtains globally optimal hypocentral estimates and non-ellipsoidal confidence regions that do not depend on the usual assumption of local linearity of the forward problem. The approach accommodates such complexities as 3-D traveltime tables, non-Gaussian data errors, and general types of parameter constraints. Specific problems we are addressing are (1) extension of our uncertainty analysis to account more realistically for the effects of modeling errors (errors in traveltime tables), which traditionally have not been distinguished from random picking errors in the determination of location confidence regions; (2) incorporation of azimuth and slowness data, in addition to arrival times, into the maximum-likelihood framework; and (3) integration of phase association into the event location algorithm in order to perform these tasks simultaneously with a grid-search approach. We present examples of our event location algorithm applied to data from the International Monitoring System, illustrating the effects of nonlinearity on hypocentral confidence regions determined from sparse data sets.

Key words: seismic, event location, confidence region, grid search, CTBT

OBJECTIVE

Over the past decade, grid search has gained popularity as an inversion algorithm for seismic event location, owing to its simplicity of implementation and ability to find globally optimal hypocentral estimates. Unlike the traditional iterative methods, grid search easily accommodates problem complexities such as general error models (non-Gaussian), nonlinear parameter constraints, and multiple data types (azimuth and slowness in addition to arrival times). One of the early applications of the method was the work of Sambridge and Kennett (1986), who applied a directed grid-search technique to teleseismic location. Recently, Dreger *et al.* (1998) applied grid search to problems of event location with sparse regional networks, an important situation in CTBT monitoring. Previous applications of grid search in event location were formulated to minimize a "data misfit" function with respect to hypocentral parameters. Contours of this function were recognized to approximate the boundaries of confidence regions, to which confidence levels could be assigned within certain linear approximations and under the assumption of Gaussian errors (Wilcock and Toomey, 1991).

We are developing a more general algorithm for event location that uses grid search to maximize a general likelihood function. Maximum likelihood estimation theory provides a formal framework for non-Gaussian error assumptions and for combining diverse types of data and prior information on parameters. In addition, our algorithm replaces approximate, analytical formulas for confidence levels with Monte Carlo simulation, which is not restricted by the Gaussian assumption and which accounts fully for nonlinearity of the forward problem and parameter constraints. Other enhancements in progress or planned for the near future include the incorporation of azimuth and slowness data, a more complete treatment of the errors in traveltime tables sued for forward modeling, and integration of seismic phase association tasks into our grid-search algorithm in an attempt to constrain event locations with more seismic phases. Our objective is improved location accuracy and more realistic analyses of location error for small, sparsely recorded events.

RESEARCH ACCOMPLISHED

Maximum Likelihood Formulation

The hypocentral parameters of a seismic event are a three-dimensional position vector $\mathbf{x}$ and an origin time t. Let $\mathbf{d} = (d_1, d_2 \ldots, d_n)$ be an n-dimensional vector of arrival times picked from various seismic phases at a seismic network. The event location problem may be expressed as

$$d_i = t + T_i(\mathbf{x}) + e_i, \quad i = 1, \ldots, n \tag{1}$$

where T_i is a traveltime function (traveltime table) for the ith datum and e_i is an error with respect to this function. The index i counts over both stations and phase types (P, S, etc.), including only those combinations that have been actually observed (i.e., completeness of data coverage is not assumed).

We assume the errors are statistically independent and, following Billings *et al.* (1994), that each is distributed with a "generalized Gaussian" probability density function (p.d.f.) given by

$$\mathrm{pdf}(e_i) = \frac{1}{K\sigma_i} \exp\left\{ -\frac{1}{p} \left| \frac{e_i}{\sigma_i} \right|^p \right\} \tag{2}$$

where $K = 2p^{1/p}\Gamma(1 + 1/p)$ and Γ is the gamma function. When $p = 2$, then e_i is normally distributed with zero mean and variance $(\sigma_i)^2$. When $p = 1$, it is exponentially distributed. We assume that the scale parameters σ_i are known in a relative sense and write

$$\sigma_i = \sigma\nu_i \tag{3}$$

where the ν_i are known but the universal scale parameter, σ, is not.

The joint p.d.f. of the n data is the product of the error p.d.f.'s. Considered as a function of the unknown parameters ($\mathbf{x}$, t and σ) this joint p.d.f. is a *likelihood* function, which we denote as $L(\mathbf{x}, t, \sigma; \mathbf{d})$. It is convenient to deal with the negative logarithm of likelihood, which we denote as Λ. This is given by

$$\begin{aligned} \Lambda(\mathbf{x}, t, \sigma; \mathbf{d}) &\equiv -\log L(\mathbf{x}, t, \sigma; \mathbf{d}) \\ &= \sum_{i=1}^{n} \log \nu_i + n \log K + n \log \sigma + \frac{1}{p\sigma^p} \Psi(\mathbf{x}, t; \mathbf{d}) \end{aligned} \tag{4}$$

Here, Ψ is a 'data misfit' function defined as

$$\Psi(\mathbf{x}, t; \mathbf{d}) = \sum_{i=1}^{n} |d_i - t - T_i(\mathbf{x})|^p / (\nu_i)^p. \tag{5}$$

The maximum likelihood estimates of the unknowns are the values that maximize L or, equivalently, *minimize* Λ. We denote these estimates as $\mathbf{x}_{ml}$, t_{ml}, and σ_{ml}. The maximization may be subjected to prior constraints on the parameters. In our current algorithm, we assume hard upper and lower bounds on focal depth (z) and the p.d.f. scale factor:

$$0 \leq z \leq z^{max} \tag{6}$$

$$\sigma^{min} \leq \sigma \leq \sigma^{max}. \tag{7}$$

We allow latitude and longitude to be anywhere on the globe, or restricted to within a given distance of a given geographic location. We place no constraint on origin time.

Given its structure, Λ is amenable to a hierarchical minimization with respect to the unknown parameters, leading to minimization subproblems of lower dimension than the original problem. We define a "reduced" objective function which, for each fixed hypocenter, is minimum with respect to t and σ (subject to prior constraints on σ):

$$\widetilde{\Lambda}(\mathbf{x};\mathbf{d}) = \min_{t,\sigma} \Lambda(\mathbf{x}, t, \sigma; \mathbf{d}). \tag{8}$$

The location problem reduces to minimization of $\widetilde{\Lambda}$.

Grid Search

Our current grid search algorithm obtains the maximum likelihood estimates of the hypocentral parameters ($\mathbf{x}_{ml}$ and t_{ml}) and the p.d.f. scale parameter (σ_{ml}), as defined in the previous section. The algorithm computes the reduced objective function, $\widetilde{\Lambda}$ in equation (8), at each point in a 3-D grid of hypocenters. Following previous workers, the hypocenter grid is constructed dynamically through a process of successive refinement. Our procedure for grid refinement resembles that of the 'neighborhood' search algorithm developed by Sambridge (1999). The first grid covers the entire globe and from 0 to 700 km in depth at coarse spacing: 100 km in depth, 9 degrees in latitude, and 9 degrees in longitude near the equator and increasing at higher latitudes. On each pass of grid refinement, nodes are added as neighbors of a subset of grid points comprising the "best" (smallest $\widetilde{\Lambda}$) points tested thus far. Neighbors are placed at one-third the grid-spacing of the previous pass. The size of the grid subset chosen for refinement is reduced on each pass. The search ends when the grid spacing is less than 0.3 km.

Non-Ellipsoidal Confidence Regions

A confidence region on the hypocenter of an event is defined classically in terms of a statistic, τ, that is a function of the data vector, $\mathbf{d}$, and the hypocenter, $\mathbf{x}$. A confidence region at confidence level $1-\alpha$ comprises those values of $\mathbf{x}$ satisfying the inequality

$$\mathrm{cdf}(\tau(\mathbf{d},\mathbf{x})) \leq 1-\alpha. \tag{9}$$

Here, cdf denotes the cumulative distribution function of a random variable.

Flinn (1965) defined hypocentral confidence regions for the case of Gaussian errors ($p=2$) and no prior bounds on σ ($\sigma^{min}=0$, $\sigma^{max}=\infty$). Evernden (1969) treated the case with σ completely known ($\sigma = \sigma^{min} = \sigma^{max} = \sigma_{ml}$), while Jordan and Sverdrup (1981) generalized these two results to account for partial prior knowledge of σ. The statistic used by each of these workers can be expressed in our notation as

$$\tau(\mathbf{d},\mathbf{x}) = \frac{\widetilde{\Psi}(\mathbf{x};d) - \widetilde{\Psi}(\mathbf{x}_{ml};d)}{\sigma^2_{ml}} \tag{10}$$

where $\widetilde{\Psi}$ is the "reduced" data misfit function (Ψ minimized with respect to t for each fixed $\mathbf{x}$). Under the approximation that the traveltime functions, $T_i(\mathbf{x})$, are locally linear near $\mathbf{x} = \mathbf{x}_{ml}$, the probability distribution of τ does not depend on any of the unknown parameters ($\mathbf{x}$, t or σ), and a confidence region takes the form

$$\widetilde{\Psi}(\mathbf{x};\mathbf{d}) - \widetilde{\Psi}(\mathbf{x}_{ml};\mathbf{d}) \leq \sigma_{ml}^2 C_\alpha \tag{11}$$

where C_α is a constant. Under the linearity assumption, this equation defines a hyper-ellipsoid in hypocenter space. Flinn (1965), Evernden (1969), and Jordan and Sverdrup (1981) derive different values of C_α based on differing assumptions about σ.

To test the linear approximation, Wilcock and Toomey (1991) computed non-ellipsoidal confidence regions directly from equation (11). This equation implies that each surface of constant data misfit, $\widetilde{\Psi}(\mathbf{x};\mathbf{d})$, is the boundary of a confidence region for some level of confidence, $1-\alpha$. They directly sampled $\widetilde{\Psi}(\mathbf{x};\mathbf{d})$ on a grid of hypocenters to map the non-ellipsoidal confidence region for a fixed confidence level, thus taking the major effect of nonlinearity into account. However, the approach of Wilcock and Toomey (1991) ignores another effect of nonlinearity: the probability distribution of τ may depend on the true values of the unknown parameters. This effect can be caused by the use of nonlinear constraints on the parameters, as in eqs. (6) and (7), as well as by nonlinearity of the traveltime functions. Moreover, they did not consider the case of non-Gaussian errors.

We have generalized the approach of Wilcock and Toomey as follows. We define a test statistic as the logarithm of a likelihood ratio:

$$\begin{aligned}\tau(\mathbf{d},\mathbf{x}) &= \log\left[\frac{\max_{\mathbf{x},t,\sigma} L(\mathbf{x},t,\sigma;\mathbf{d})}{\max_{t,\sigma} L(\mathbf{x},t,\sigma,\mathbf{d})}\right] \\ &= \widetilde{\Lambda}(\mathbf{x};\mathbf{d}) - \widetilde{\Lambda}(\mathbf{x}_{ml};\mathbf{d}).\end{aligned} \tag{12}$$

That is, τ differences our reduced objective function between $\mathbf{x}$ and the maximum likelihood solution, $\mathbf{x}_{ml}$. This statistic is equivalent to the ones used by Flinn and Evernden under their respective assumptions about σ, but accommodates arbitrary constraints on the parameters and non-Gaussian error distributions. Letting $\mathbf{x} = (x, y, z)$, the statistic for a 2-D confidence region on the event epicenter, (x, y), is given by

$$\tau(\mathbf{d},x,y) = \min_z \widetilde{\Lambda}(\mathbf{x};\mathbf{d}) - \widetilde{\Lambda}(\mathbf{x}_{ml};\mathbf{d}) \tag{13}$$

and for a confidence interval on focal depth is

$$\tau(\mathbf{d},z) = \min_{x,y} \widetilde{\Lambda}(\mathbf{x};\mathbf{d}) - \widetilde{\Lambda}(\mathbf{x}_{ml};\mathbf{d}). \tag{14}$$

Confidence regions using these log-likelihood statistics could still be defined via the inequality of equation (9), except this inequality presumes that the distribution (c.d.f.) of τ does not depend on the true values of the parameters. We assume the main dependence is on focal depth and σ, and write the c.d.f. of τ as $\mathrm{cdf}(\tau; z, \sigma)$. We generalize the inequality of equation (9) to use the c.d.f. of τ that is minimum with respect to the true parameters. Thus, the hypocentral confidence region is given by

$$\min_\sigma \mathrm{cdf}(\tau(\mathbf{d},\mathbf{x}); z, \sigma) \leq 1-\alpha. \tag{15}$$

The epicentral one is

$$\min_{\sigma,z} \mathrm{cdf}(\tau(\mathbf{d},x,y); z, \sigma) \leq 1-\alpha, \tag{16}$$

and the focal depth confidence interval is

$$\min_{\sigma} \mathrm{cdf}(\tau(\mathbf{d}, z); z, \sigma) \leq 1 - \alpha. \tag{17}$$

With these definitions, a confidence region will include the true value of the parameter *at least* $100(1-\alpha)$ percent of the time.

Confidence Regions Via Monte Carlo Sampling

We outline the technique for hypocentral confidence regions. The basic idea is to estimate the c.d.f. of the test statistic τ by simulation, i.e. computing τ for many randomly generated samples of the error vector. We generate each error, e_i^{mc}, using a pseudo-random number generator in accordance with the assumed error distribution (eqs. (2)–(3)) for some given "true" σ. Then, for given true hypocentral parameters, $\mathbf{x}$ and t, synthetic data are calculated as

$$d_i^{mc} = t + T_i(\mathbf{x}) + e_i^{mc}. \tag{18}$$

We apply our grid search algorithm to these data to obtain the m.l. hypocenter, $\mathbf{x}_{ml}^{mc}$. Plugging this into the formula for τ,

$$\tau(\mathbf{d}^{mc}, \mathbf{x}) = \widetilde{\Lambda}(\mathbf{x}; \mathbf{d}^{mc}) - \widetilde{\Lambda}(\mathbf{x}_{ml}^{mc}; \mathbf{d}^{mc}). \tag{19}$$

we obtain one sample from $\mathrm{cdf}(\tau; z, \sigma)$. We compare this sample to the observed value of the statistic, $\tau(\mathbf{d}, \mathbf{x})$, obtained from the real data. We count a rejection of $\mathbf{x}$ if

$$\tau(d^{mc}, \mathbf{x}) < \tau(\mathbf{d}, \mathbf{x}). \tag{20}$$

The fraction of rejections after many Monte Carlo trials yields an estimate of $\mathrm{cdf}(\tau(\mathbf{d}, \mathbf{x}); z, \sigma)$. Performing this simulation for multiple values of σ and then minimizing amongst them gives the *lowest* confidence level such that the confidence region includes $\mathbf{x}$. The process for depth confidence intervals and epicenter confidence regions proceeds in the same manner, except that in the latter case the simulation is performed for multiple values of true depth as well as σ, and the confidence level is minimized over both.

Examples With IMS Data

We illustrate our grid-search/Monte Carlo event location algorithm on two events from the Prototype International Data Center (PIDC) Reviewed Event Bulletin (REB). The first is event number 20354875, which occurred 1 March 1999 near Crete and was assigned a magnitude of $m_b = 3.9$. The International Monitoring System (IMS) location is based on five arrival times: Pn at stations BRAR ($\Delta = 7.2°$) and KVAR ($\Delta = 15.7°$), and P at BGCA ($\Delta = 30.6°$), ARCES ($\Delta = 34.5°$) and DBIC ($\Delta = 40.0°$). We applied our grid-search location algorithm to this event using the IASPEI91 traveltime tables and with no elevation or path corrections applied to the data. Arrival time errors were assumed to be Gaussian ($p = 2$) with standard deviation (σ) bounded between 0.5 and 1.5 seconds.

Figure 1 displays confidence level as a function of event location, computed via Monte Carlo simulation. The simulations were performed with three hypothesized "true" values of σ and 6 values of focal depth. The number of error realizations for each σ and z was 300. The top left panel displays confidence level as a function of event depth. The two points where the curve intersects a given confidence level are the end-points of the focal depth confidence interval at that level. The

90% confidence interval on the focal depth of this event is 34 to 92 km, while the 95% interval is 0 to 101 km. The IMS solution fixed the depth to zero.

The upper right panels show cross-sections of confidence levels on the 3-D hypocenter. In each plot, a contour of constant confidence level outlines the boundary of the hypocentral confidence region at that level. The REB solution for the hypocenter is plotted as a circle. We see that the hypocentral confidence regions display significant departure from ellipsoidal behavior. Significantly, the effect is to stretch the confidence regions towards the earth's surface, making it more difficult to reject a shallow focus.

The bottom panels are confidence level as a function of event epicenter, whose contours define epicentral confidence regions at various levels. In the bottom left panel, depth is unconstrained ($z \geq 0$) as in the usual definition of an epicentral confidence region. We see that these confidence regions are close to ellipsoidal and indicate roughly the same epicentral uncertainty as the REB, which reports semi-axes of 57 and 22 km for the 90% confidence ellipse. In the lower right panel, depth is constrained to be shallow ($0 \leq z \leq 10$ km). The title above the plot indicates that a shallow focus can be rejected with a confidence of 83%. However, the plot shows that this low confidence pertains only to a small epicentral region, much smaller than the epicentral confidence region for unconstrained depth (lower left). Thus, the epicenter pertinent to a shallow focus event is much better determined.

A second example of Monte Carlo confidence regions is shown in Figure 2. These are for an $m_b = 3.7$ event in the Afghanistan-Tajikistan border region (17 March 1999, event no. 20380677 from PIDC). The data set comprised five P wave arrival times, all teleseismic except station NIL ($\Delta = 5.1°$). The REB solution reports semi-axes of 92 and 33 km for the 90% confidence region on epicenter. This is consistent with but somewhat larger than the epicentral uncertainty implied in the lower left panel. The REB confidence interval on depth is 35 to 130 km, compared to our smaller 52 to 116 km confidence interval (upper left panel of Figure 2). Our smaller location uncertainties may be due to a more optimistic assumption about data errors (0.5 to 1.5 s) than used in the IMS location algorithm. Looking at the lower right panel, we see that a shallow focus is rejected with 98% confidence, and essentially with 100% confidence outside an elliptical region northeast of the unconstrained solution.

CONCLUSIONS AND RECOMMENDATIONS

We have developed a general theoretical and computational framework for finding event location estimates and confidence regions, relaxing some of the assumptions currently used in the routine processing of IMS data. In particular, we do not assume local linearity of forward problem (traveltime vs. hypocenter) in the computation of confidence regions, and we accommodate fairly general error models and parameter constraints. Our preliminary tests show consistency with IMS results reported in the Reviewed Event Bulletin, but also some noticeable departures from the ellipsoidal confidence regions computed by IMS when small data sets are used.

Currently we are incorporating azimuth and slowness data into our formulation and algorithms. Such data are routinely used in IMS processing and can provide important constraints on sparsely recorded, small events. We are beginning to address some additional, difficult problems of importance in CTBT monitoring. One is the effect of errors in station corrections and traveltime tables ("modeling" errors) on location accuracy. In current location algorithms, modeling errors are accounted by inflating the variances assigned to the data, thus assuming they are random and independent between stations and phases. We will investigate more realistic treatments of these errors that are consistent with empirical analyses of traveltime residuals and calibration studies. The second problem to address is unassociated and mis-associated seismic phases. Our goal is to

integrate key elements of seismic phase association into the process of event location in an attempt to constrain locations with more data and, accordingly, leave fewer unassociated phases in the arrival bulletins. Our maximum likelihood formulations and grid-search approach to event location provides a flexible framework for addressing these problems.

References

[1] Billings, S.D., M.S. Sambridge and B.L.N. Kennett, 1994, Errors in hypocenter location: picking, model and magnitude dependence, *Bull. Seism. Soc. Am., 84,* 1978–1990.

[2] Dreger, D., R. Uhrhammer, M. Pasyanos, J. Franck and V. Romanowicz, 1998, Regional and far-regional earthquake locations and source parameters using sparse broadband networks: a test on the Ridgecrest sequence, *Bull. Seism. Soc. Am., 88,* 1353–1362.

[3] Evernden, J.F., 1969, Identification of earthquakes and explosions by use of teleseismic data, *J. Geophys. Res., 74,* 3828–3856.

[4] Flinn, E.A., 1965, Confidence regions and error determinations for seismic event location, *Rev. Geophys., 3,* 157–185.

[5] Jordan, T.H. and K.A. Sverdrup, 1981, Teleseismic location techniques and their application to earthquake clusters in the south-central Pacific, *Bull. Seism. Soc. Am., 71,* 1105–1130.

[6] Sambridge, M., 1999, Geophysical inversion with a neighbourhood algorithm—1. Searching a parameter space, *Geophys. J. Int., 138,* 479–494.

[7] Sambridge, M.S. and B.L.N. Kennett, 1986, A novel method of hypocentre location, *Geophys. J.R. astr. Soc., 87,* 679–697.

[8] Wilcock, W.S.D. and D.R. Toomey, 1991, Estimating hypocentral uncertainties for marine microearthquake surveys: a comparison of the generalized inverse and grid search methods, *Marine Geophysical Researches, 13,* 161–171.

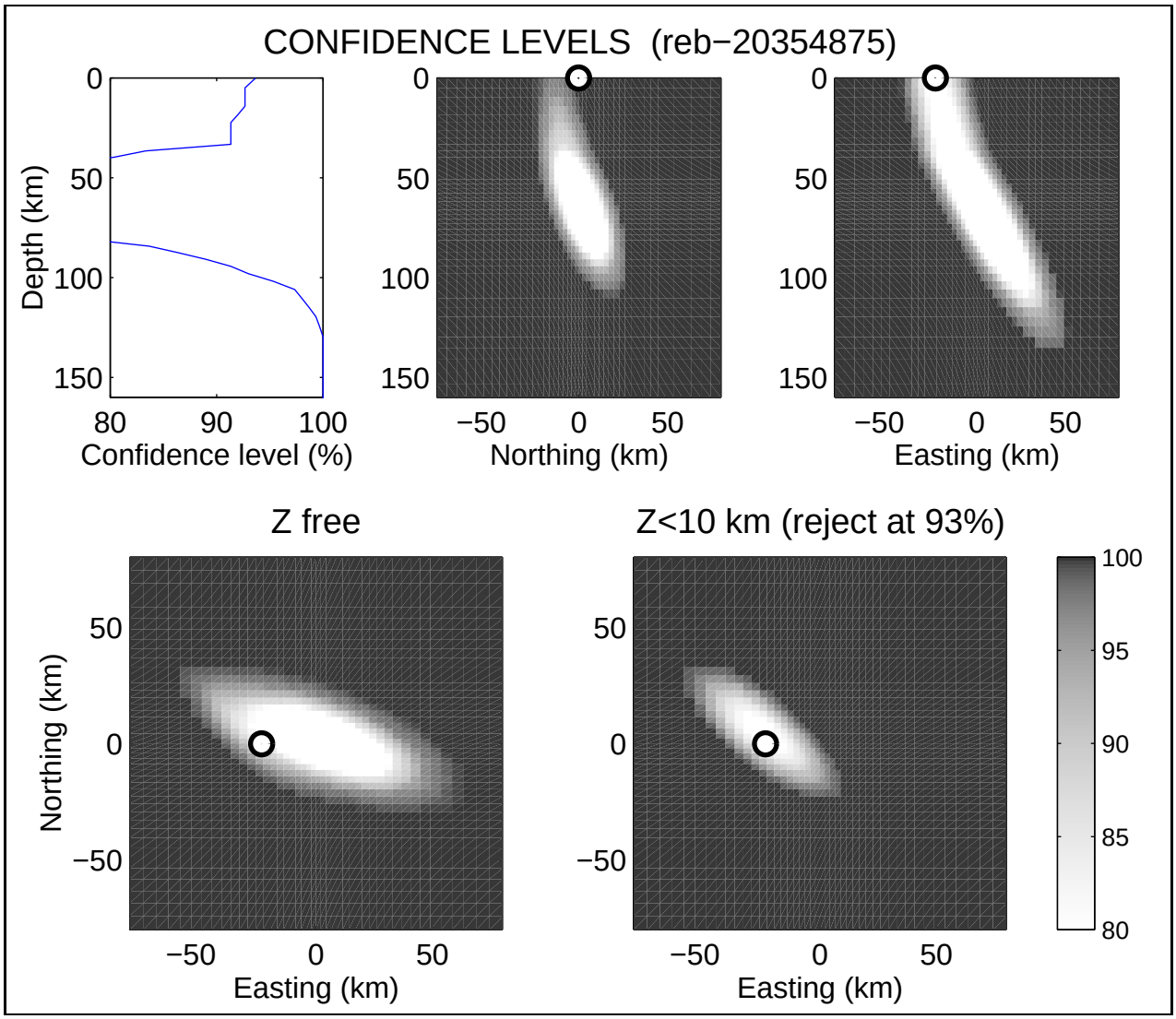


Figure 1: Confidence level vs. location for an $m_b = 3.9$ event near Crete (1 March 1999, event no. 20354875 from PIDC). *Top left:* Confidence level vs. focal depth. *Top center and right:* cross-sections of confidence level vs. hypocenter. *Bottom left:* Confidence level vs. epicenter. *Bottom right:* Confidence level vs. epicenter with focal depth constrained between 0 and 10 km. In the top images, each contour of constant confidence level intersects the boundary of the 3-D hypocentral confidence region at that level. Contours in the bottom images are the boundaries of epicentral confidence regions. Note that confidence levels below 80% are all displayed with white. The circles mark the event hypocenter reported in the Reviewed Event Bulletin.

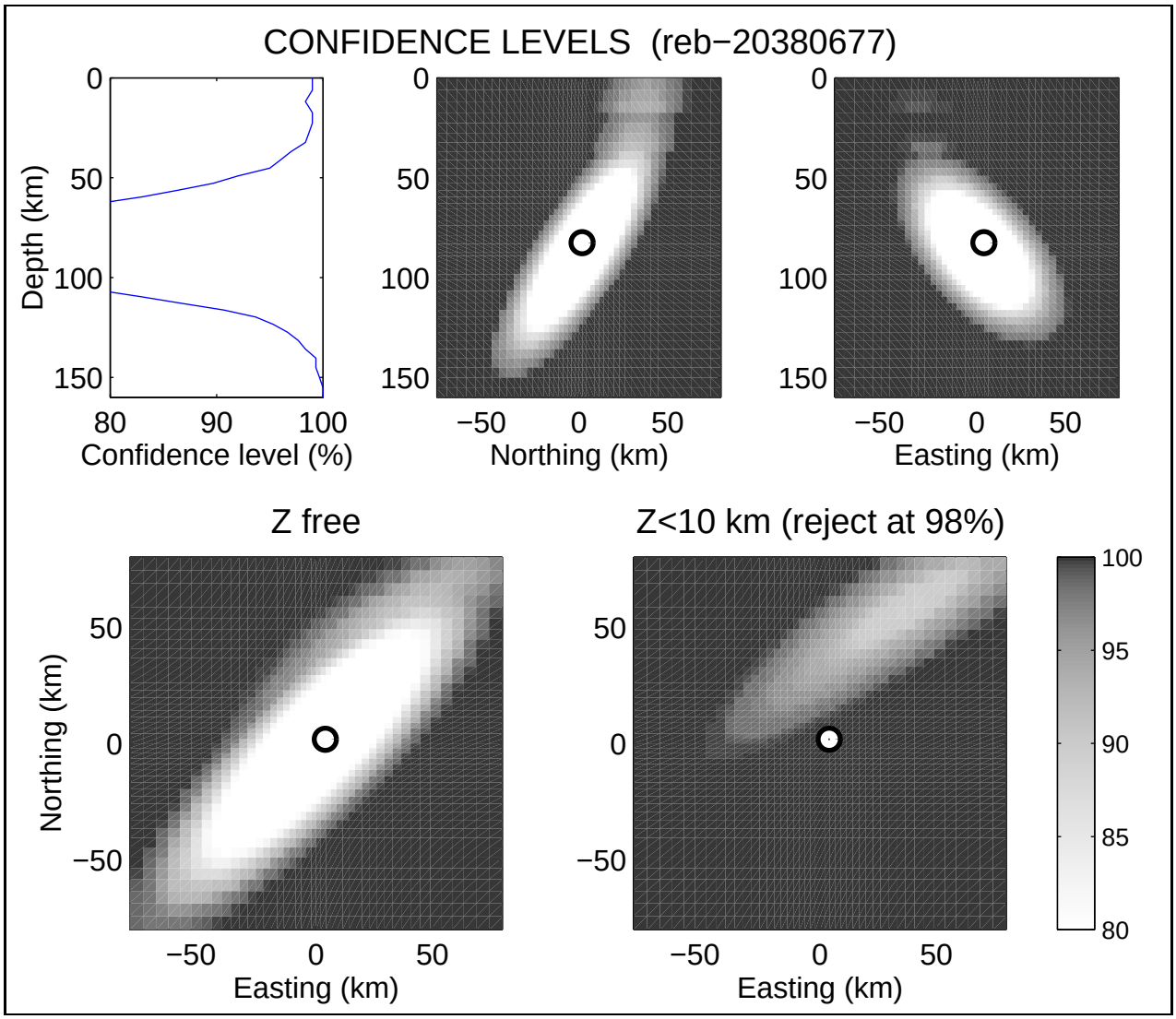


Figure 2: Confidence level vs. location for an $m_b = 3.7$ event in the Afghanistan-Tajikistan border region (17 March 1999, event no. 20380677 from PIDC). The figure is in the same format as Figure 1. Contours of constant confidence level correspond to confidence regions on the hypocenter (top images) and epicenter (bottom images). The circles mark the event hypocenter reported in the Reviewed Event Bulletin.

IMS CALIBRATION IN NORTH AMERICA AND NORTHWESTERN EURASIA UTILIZING 3-D CRUSTAL AND UPPER MANTLE VELOCITY MODELS TO REFINE LOCATION OF REGIONAL SEISMIC EVENTS

Russian Federation / United States Calibration Working Group
Contact Person: Vladislav Ryaboy

Center for Monitoring Research

Sponsored by The Defense Threat Reduction Agency
Arms Control Technology Division
Nuclear Treaties Branch
Contract No. DSWA01-98-C-0032

ABSTRACT

This work was performed within the United States/Russian Federation Joint Research Program of Seismic Calibration of the International Monitoring System (IMS) in Northern Eurasia and North America. The parties to this program are the Nuclear Treaty Programs Office (NTPO), Department of Defense (DOD), USA and the Special Monitoring Service (SMS) of the Ministry of Defense (MOD), Russian Federation. A RF/US working group (WG) has been established to coordinate the joint research program, and the current membership is given below. The main objective of the calibration effort is to improve the IMS location accuracy of the regional seismic events within North America and Northwestern Eurasia (west of the Ural Mountains) using calibration datasets exchanged between the US and RF to derive Source-Specific Station Corrections (SSSCs) from 3-D crustal and upper mantle velocity models. 3-D modeling software developed by P. Firbas was used to compute SSSCs from 3-D crustal and upper mantle models for Pn, Sn, and Pg phases within North America and for Pn within Northwestern Eurasia. We described the 3-D velocity models used for calculations of the Pn and Pg travel times at the 21st Seismic Research Symposium (Las Vegas, Nevada, 1999) and at the 2nd Workshop on IMS Location Calibration in Oslo, Norway. The 3-D velocity models for Sn-waves were calculated from the Pn model using the relationship for Vp/Vs vs. depth from the AK-135 model of Kennett et al. SSSCs were calculated for the regional phases Pn, Pg, and Sn out to distances of 20 degrees, 10 degrees, and 20 degrees, respectively, for 22 IMS stations and 4 additional stations in North America and for 26 IMS stations and 9 additional stations in Northwestern Eurasia.

These SSSCs, with their estimated modeling errors, were applied to relocate 9 large chemical and nuclear explosions with known locations and origin times detonated within various tectonic provinces of Northwestern Eurasia and an independent set of 10 chemical explosions detonated within different regions of North America. The validation results are preliminary, but we generally find that the model-based SSSCs produce significantly improved location accuracies and reduced confidence ellipses for GT0 and GT2 events in the cases where it can be shown that the analysis data are accurate. Results of relocation experiments for selected events located in different regions of North America and Northwestrn Eurasia clearly indicate that our model-derived SSSCs and estimated modeling errors improved the average location accuracy compared to the IASPEI-91 tables from 25.9 km to 5.7 km for North America and from 28.1 km to 9.3 km for Northwestern Eurasia, and decreased the 90% error ellipse area for all events from 3,840 km^2 to 817 km^2 and from 6,512 km^2 to 1,284 km^2, respectively. The error ellipses contained the ground-truth locations for all events we tested at the 90% confidence level. Our study demonstrates the promise of the application of the 3-D travel-time modeling approach for deriving bias corrections to improve regional seismic event locations.

The RF members of the WG: Colonel Vyacheslav Gordon (chairman), Colonel Vitaly Shishkov, Lt. Colonel Dmitry Bobrov, and Dr., Prof. Marat Mamsurov. The US members of the WG: Dr. Anton Dainty (chairman), Dr. Douglas Baumgardt, Mr. John Murphy, Dr. Robert North, and Dr. Vladislav Ryaboy.

Key Words: location, calibration, IMS, 3-D crustal and Upper mantle velocity models, Pn, Sn, and Pg waves.

OBJECTIVE

This paper presents results from the Russian Federation / United States Joint Research Program of Seismic Calibration of the International Monitoring System in Northern Eurasia and North America during 1999-2000. The participants in this program are the Nuclear Treaty Programs Office, Department of Defense, USA, and the Special Monitoring Service of the Ministry of Defense, RF. To date the Joint Program has focused on collection and interpretation of data from large chemical and nuclear explosions with known location and origin time to improve regional seismic event location by the IMS in western areas of Northern Eurasia and North America.

A location accuracy of 1000 km^2 in continental areas is desirable for the IMS based on the limitation of On-Site Inspections to this area under the CTBT. However, this accuracy often cannot be achieved with globally averaged travel-times because of large variations of travel-times of regional phases. These travel-time variations are mainly caused by lateral velocity variations in the crust and upper mantle. To achieve the CTBT goal of 1000 km^2 location accuracy the IMS has to be calibrated, i.e., travel-times of seismic waves used in the location must take into account the 3-D structure of the Earth (Firbas, Peshkov, and Ryaboy, 1997). Regional seismic event location accuracy is critically dependent on the joint contribution of several factors, including seismic network configuration, errors in arrival time measurements, phase (mis)identification, and accuracy of reference travel-time curves based on crustal and upper mantle velocity structure. Seismic event locations based on regional 1-D velocity models can have errors caused by travel-time variations within different major tectonic provinces and by ray paths crossing boundaries between tectonic provinces with different crustal and upper mantle velocity structures. Seismic event locations based on 3-D velocity models have the potential to overcome these limitations. The main objectives of this paper are the following:

- Regionalization of western areas of Northern Eurasia and North America based on tectonic and seismic data.
- Seismic travel-time data collection and analysis.
- Deriving 3-D velocity models and source-specific station corrections (SSSCs).
- Regional seismic event relocation to demonstrate the improvement in location accuracy.

RESEARCH ACCOMPLISHED

The 3-D approach for the IMS calibration includes the following main steps:

- Regionalization based on tectonic data, travel-times, and crustal and upper mantle velocity structures;
- Collection and analysis of Pn travel-times;
- Collection and analysis of 1-D crustal and upper mantle velocity-depth sections;
- Development of a 3- crustal and upper mantle velocity model;
- Computation up to distance of 20 degrees of Source-Station Specific Corrections (SSSCs) for seismic stations using the 3-D crustal and upper mantle velocity model for the Pn wave (Northern Eurasia, western part) and for Pn, Sn, and Pg waves (North America);
- Regional seismic event relocation to demonstrate the improvement in location accuracy.

These steps are described further in this paper.

Tectonic maps of North America and Northern Eurasia were taken as a starting point for delineating various tectonic provinces. These maps were simplified and digitized to allow more reliable interpolation and comparison of seismic data (travel times of seismic waves, crustal and upper mantle velocity models, location of seismic stations and seismic events) for different tectonic provinces (Figure 1, top; Figure 2, top) and to help create a 3-D starting velocity model of the crust and upper mantle for North America and Northern Eurasia. Detailed seismic studies of the Earth's crust and upper mantle have been carried out in most regions of Northern Eurasia and North America and published in numerous reports, papers, and monographs (e.g. Pakiser and Mooney, 1989; Pavlenkova 1996; Romanowicz, 1979; Van der Lee and Nolet, 1997; and many other published works). The crust and upper mantle velocity structure varies most strongly between western areas of North America and the Pre-Cambrian platform.When crossing the boundary from west to east between these tectonic provinces, values of mean velocity in

the crust, Moho depth, and Pn velocity increase from approximately 6.2-6.3 km/s, 30-35 km, and 7.7-7.9 km/s to 6.5-6.6 km/s, 40-50 km, and 8.1-8.2 km/s, respectively. The crustal thickness (Moho depth) within Northern Eurasia varies from 55-60 km beneath the Ural mountains to 32-35 km beneath the North Caspian sedimentary basin. Crossing the boundaries between the Pre-Cambrian platforms (East-European and Siberian) and the young Paleozoic platforms (Timan-Pechora and West-Siberian platforms) is typically accompanied by a decrease of crustal thickness from approximately 45-50 km to 35-40 km, respectively. In general the crustal thickness decreases towards the Arctic ocean. Pn velocity within Northern Eurasia varies from approximately 7.8-8.0 km/s to 8.4 km/s and greater. The largest values of Pn velocity are found beneath the East-European and Siberian Pre-Cambrian platforms (8.1-8.4 km/s and greater.

Eight nuclear and large chemical explosions with known locations and origin time in North America (Figure 1, top) and 24 nuclear and large chemical explosions in Northern Eurasia (Figure 2, top) were selected to serve as events for location calibration, i.e., the travel-time corrections were derived from seismic recordings of them. Analysis of explosion seismology observations shows that the Pn travel-time variations are caused by lateral inhomogeneities of the Earth's crust and upper mantle velocity structure, on both large and small scales. In the development of our 3-D models of North America and Northern Eurasia we started fitting the large scale anomalies first. Where necessary, we continued to fit smaller scale anomalies. Both types of anomalies had to be taken into account to achieve accurate location of regional seismic events as required by the IMS calibration task. The computer program "sssc" (Firbas, 2000) was used to compute SSSCs for Pn, Pg, and Sn travel-times up to distance 20 deg, 8 deg, and 20 deg, respectively, from the 3-D earth velocity model. The goal was to define 3-D crustal and and upper mantle velocity models capable of predicting Pn travel-times with an accuracy of approximately 1.0-1.5 sec (r.m.s.). The simplest 3-D velocity models were sought from a family of 3-D models that simultaneously fit the observed Pn travel-times for all calibration events. Figure 1 (bottom) and Figure 2 (bottom) show the upper mantle regionalization for North America and Northern Eurasia, and numbers on these Figures refers to numbers on the velocity models of Figure 3 (top) and Figure 3 (bottom), respectively.

Long-range seismic profile observations can be used very effectively for IMS calibration. Figure 4 (top) and Figure 4 (bottom) compare observed and calculated Pn travel-time curves for the Fennolora long-range profile in Scandinavia (Figure 2, top) (using the preliminary 3-D model, revision 2.2). These Figures show that observed Pn travel-times within the Baltic shield at shot points B and I fit Pn travel-times calculated for our 3-D model (revision 2.2) with r.m.s. 0.58 sec and 0.71 sec, respectively. Similar results were obtained for Pn travel-times along Early Rise long-range profiles in North America. The 3-D velocity models developed for North America (revision 5.0) and for Northern Eurasia (revision 2.0) were used to produce maps of SSSCs for IMS stations and other stations needed for the relocation experiments. Figure 5 (top) and Figure 5 (bottom) show, as an example, the SSSC maps calculated for Pn and Sn waves, respectively, for the TXAR IMS station. This station is located near the boundary between the tectonically active western regions of North America and the Pre-Cambrian platform. The SSSCs computed for Pn waves varied from +5 seconds to -5 seconds for western USA and the North American Pre-Cambrian platform, respectively. SSSC variations for Sn waves are more pronounced. SSSCs were calculated in Northern Eurasia only for Pn waves.

The purpose of relocation experiments in this work is to evaluate the influence of SSSCs for Pn, Pg, and Sn phases in North America and SSSCs for Pn waves in Northern Eurasia for regional seismic event locations. We tested location accuracy by using SSSCs inferred from the 3-D model along with the estimated modeling and measurement errors to relocate test events with known location and compare the results with locations based on the IASPEI-91 travel-times. Careful Pn travel-time and waveform analyses were performed to identify and eliminate outliers. The LocSAT program was used for seismic event relocation experiments. Results of relocation experiments for selected GT0 or GT2 events showed that application of SSSCs did not improve locations of outliers. Results of relocation experiments for 31 selected events with known location located in different regions of Northern Eurasia and North America clearly indicate that the 3-D model-derived SSSCs and estimated modeling errors improved location accuracy and decreased 90% error ellipse area.

CONCLUSIONS AND RECOMMENDATIONS

Northern Eurasia

1. Pn travel-times recorded from nuclear and large chemical explosions within western areas of Northern Eurasia were collected and carefully analyzed for IMS calibration. Pn travel-time anomalies were recorded and plotted.

2. A preliminary version of a 3-D crustal and upper mantle velocity model of Northern Eurasia (western areas) (version 2.0) was developed and evaluated by comparison of observed and calculated Pn travel-times.

3. SSSCs for the Pn phase were calculated for IMS stations and several additional stations up to distance 20 deg in Northern Eurasia using the 3-D crustal and upper mantle velocity model.

4. These SSSCs, along with estimated modeling and measurement errors, were used to relocate a set of nuclear and large chemical explosions detonated within western areas of Northern Eurasia and recorded at regional distances. Utilization of the SSSCs resulted in a substantial improvement in seismic event location accuracy and a significant decrease of error ellipse area in comparison with location based on the IASPEI-91 travel-time tables. Mean mislocations for nine nuclear and chemical explosions were decreased from 28.1 km to 9.3 km, and mean error ellipse area decreased from 6,512.3 km^2 to 1,284.3 km^2 using IASPEI-91 travel-times and SSSCs(3-D), respectively. The ground truth locations (GT) are inside the error ellipses at 90% confidence level for all of the calibration events for both using IASPEI-91 travel-times and SSSCs(3-D).

North America.

1. The application of SSSCs(3-D) with estimated modeling error for Pn, Pg, and Sn phases for the preliminary 3-D velocity model of North America derived in this study (version 5.0) led to a clear improvement in seismic event location accuracy and a substantial decrease in error ellipse area compared to locations based on the IASPEI-91 travel-times. For 100% of the calibration events relocated using SSSCs(3-D) for Pn phase only and for all selected test events relocated using Pn, Pg, and Sn phases the ground truth locations (GT) are inside the error ellipses calculated at 90% confidence level. This confirms that the 3-D model used for North America is able to predict travel time variations with high accuracy.

2. The average distance between true and calculated epicenters decreased using Pn waves only from 19.4 km (IASPEI-91 travel times) to 5.7 km (SSSCs(3-D) for all 12 events analyzed. Similar relocation experiments using SSSCs for Pn, Pg, and Sn phases for another set of 10 GT0 or GT2 events improved location accuracy from 25.9 km to 5.7 km on average and decreased mean 90% error ellipse area from 3,840 km^2 to 817 km^2 while preserving 100% coverage. The improvement in accuracy of epicenter locations and decrease of error ellipse areas while keeping true locations inside the computed error ellipses shows the promise of the 3-D crustal and upper mantle velocity model approach for regional seismic event locations.

3. The validation results obtained show that model-based SSSCs produce significantly improved location accuracies and reduced confidence ellipses in cases where it can be shown that analysis data are accurate.

In accordance with the Joint US/RF research program of the IMS seismic calibration, our main recommendations for North America and Northern Eurasia include:

North America:

- Continuation of collection, documentation and analysis of data relevant to the IMS calibration for Alaska, Canada, Greenland and neighboring oceanic regions with the aim of extending and improving the 3-D velocity model of North America;

- Continuation of relocation experiments using additional calibration events with known location and origin time;

Northern Eurasia:

- Extension of the work to Siberia, the Far East and southern regions of the former Soviet Union territory in Northern Eurasia;

- Continuation of collection, documentation and analysis of data relevant to the IMS calibration for Siberia, the Far East and southern regions of the former Soviet Union territory in Northern Eurasia;

- Continuation of work to improve the 3-D velocity model of Northern Eurasia;

- Calculation and validation of SSSCs for other regional phases: Sn, Pg, and Lg;

- Continuation of relocation experiments using additional calibration events with known location and origin time.

REFERENCES

Firbas, P., A.B. Peshkov, and V. Ryaboy. From IASP-91 global model to a 3-D model for CTBT monitoring. In: Upper Mantle Heterogeneities from Active and Passive Seismology (Edited by K. Fuchs), Kluwer, 199-214, 1997.

Firbas, P., Location calibration based on 3-D modeling. In: Advances in Seismic Event Location (Thurber, C.H. and Rabinovitz, N. - editors). Kluwer, 135-162. (2000, In print).

Kennett, B.L.N. (editor). IASPEI 1991 Seismological Tables, Australian National University, 167 p., 1991.

Kennett, B.L.N., E.R. Engdahl, and R. Buland, Constraints on seismic velocities in the Earth from traveltimes. Geophys. J. Int., 122, 108-124, 1995.

Pakiser, L.C., and Mooney, W.D., (editors), (1989), *Geophysical framework of the continental United States.* Geological Society of America, Memoir 172, 826 p.

Pavlenkova, N.I. (1996). *Crust and upper mantle structure in Northern Eurasia from seismic data.* Advances in geophysics, v. 37, Academic Press, 1-121.

Romanowicz, B.A.(1979), *Seismic structure of the upper mantle beneath the United States by three-dimensional inversion of body wave arrival times,* Geophys. J. R. Astr. Soc., *57*, 479-506.

van der Lee, S., and Nolet, G. (1997a), *Seismic image of the subducted trailing fragments of the Farallon plate,* Nature, vol. 386, 266-269.

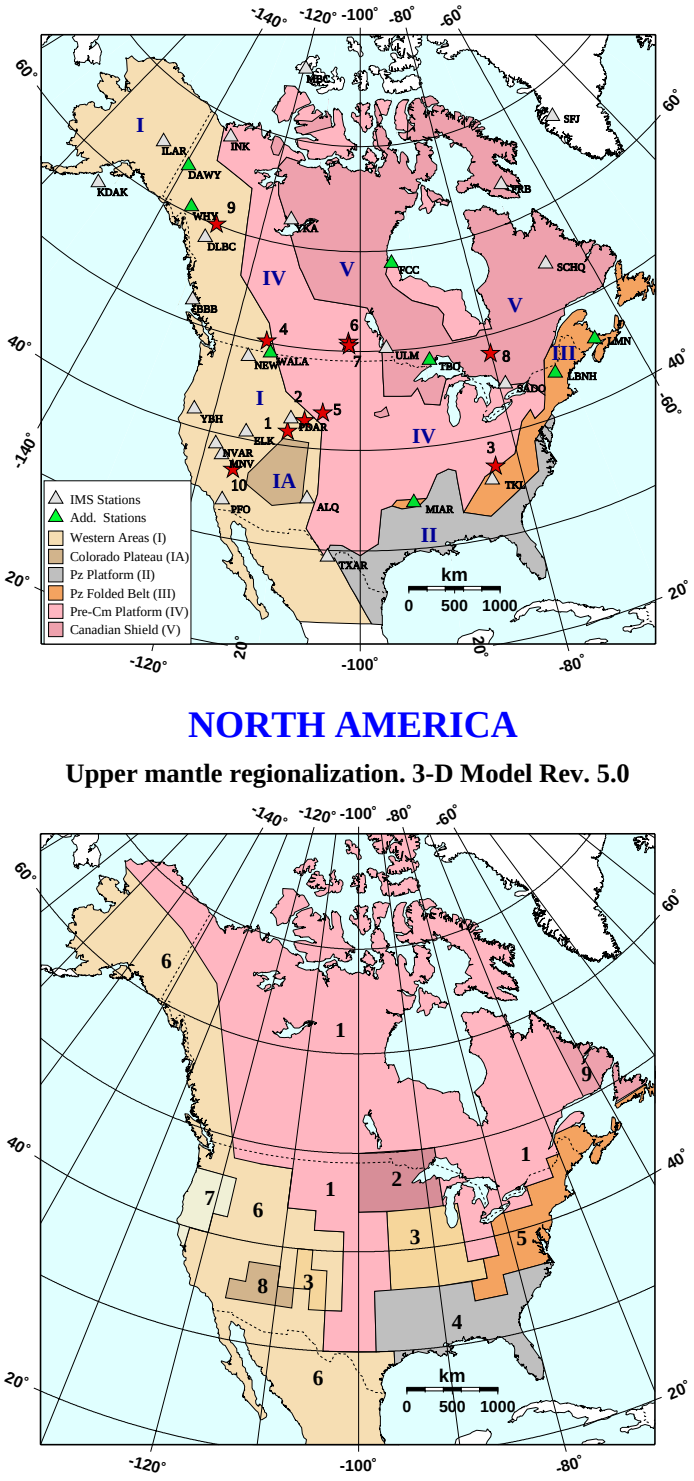
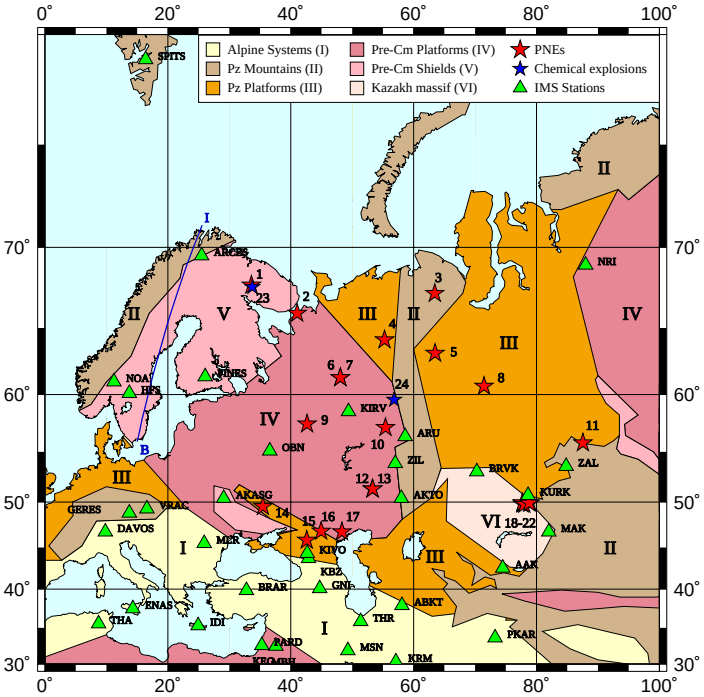


Figure 1. North America. Tectonic map and network used for relocation experiments (top) and upper mantle P-velocity regionalization (bottom). Stars are true locations of GT0 or GT2 events. Numbers on the regionalization map refer to numbers on the velocity models in Figure 3 (top).

NORTHERN EURASIA (western areas)

IMS Stations, Main Tectonic Provinces and Calibration Events Used



UPPER MANTLE REGIONALIZATION

Model (Rev. 2.0)

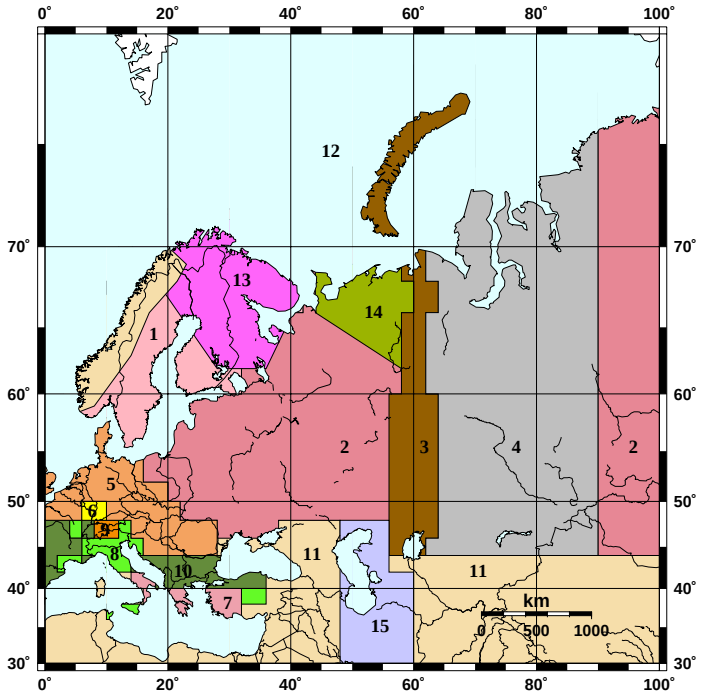


Figure 2. Western areas of Northern Eurasia. Tectonic map (top) and map of the upper mantle P-velocity regionalization. Stars are explosions used in this work. Numbers on the regionalization map (bottom) refer to numbers on the velocity models in Figure 3.

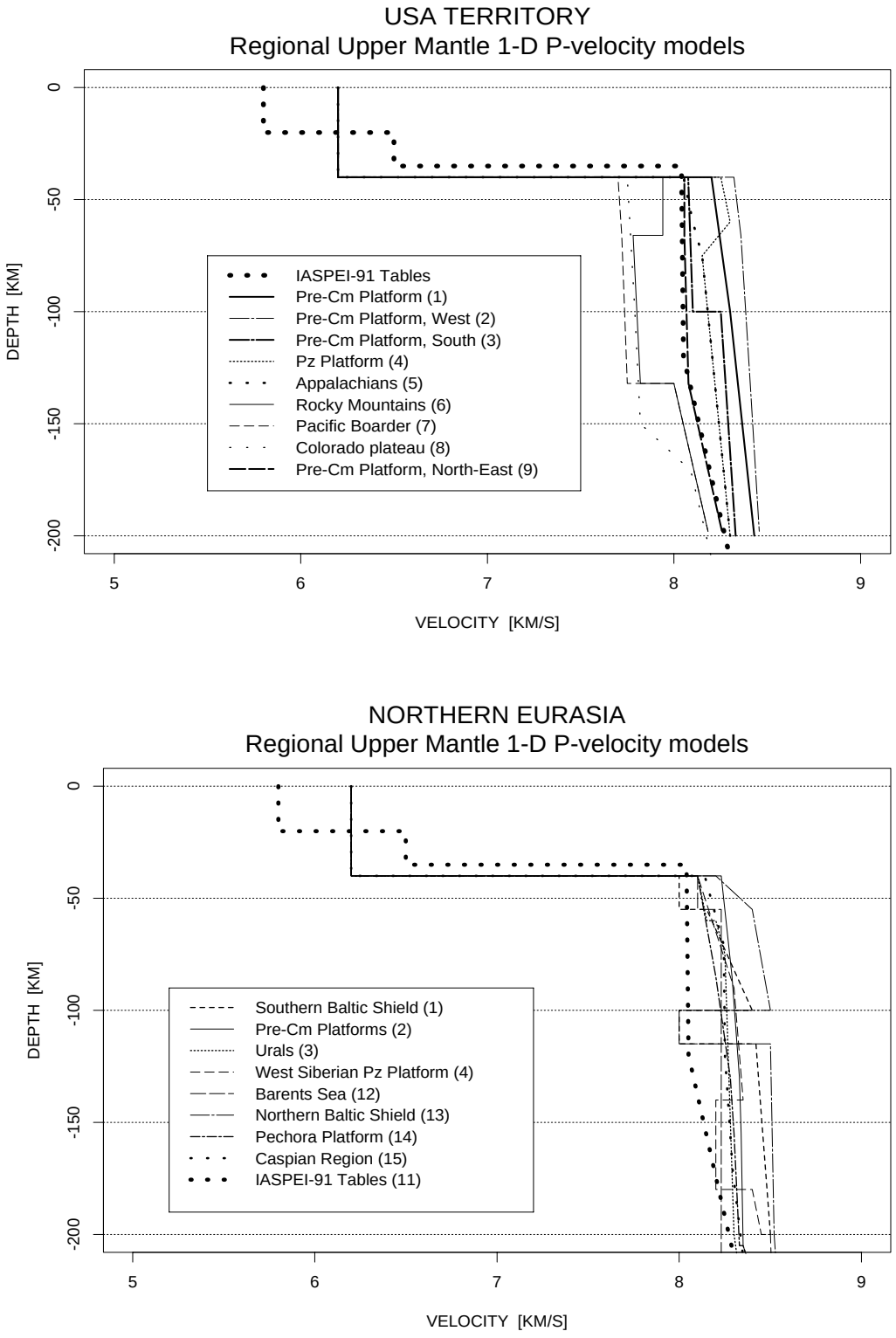


Figure 3. Regional upper mantle 1-D P-velocity models of North America (top) and Northern Eurasia (bottom).

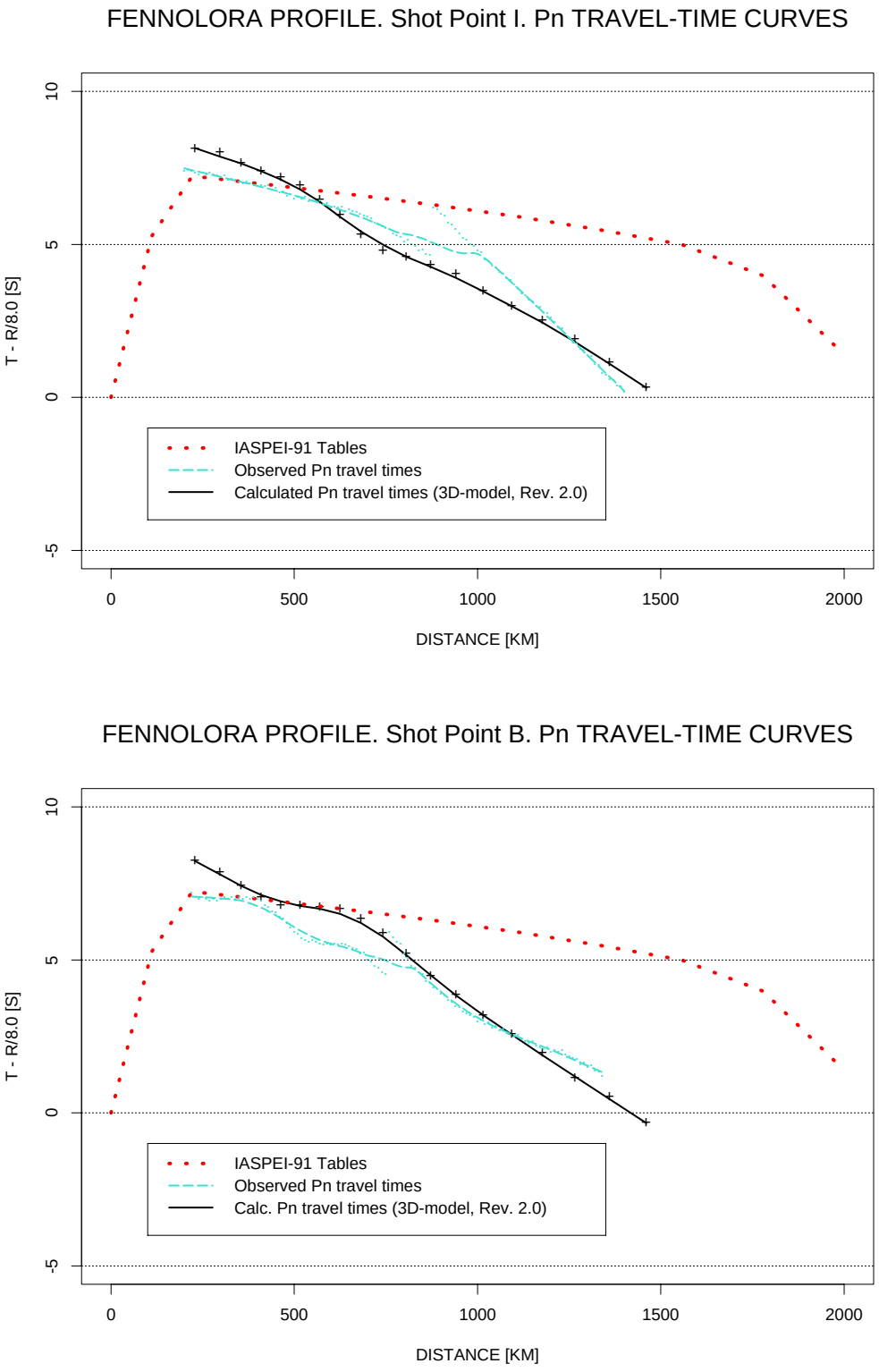
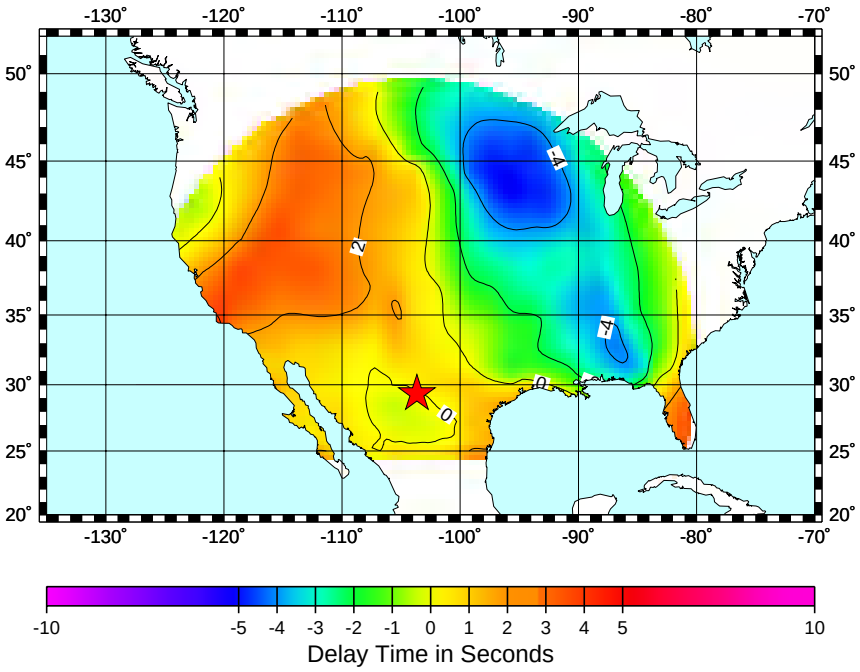


Figure 4. Baltic Shield. Comparison of observed and calculated Pn travel-time curves for 3-D model, revision 2.2, shot points I (top) and B (bottom) of the Fennolora profile. Shot points I and B are located on northern and southern ends of the Fennolora profile, respectively (Figure 2, top). Crosses are calculated Pn travel times. Dashed and solid lines are smoothed observed and calculated Pn travel-time curves, respectively.



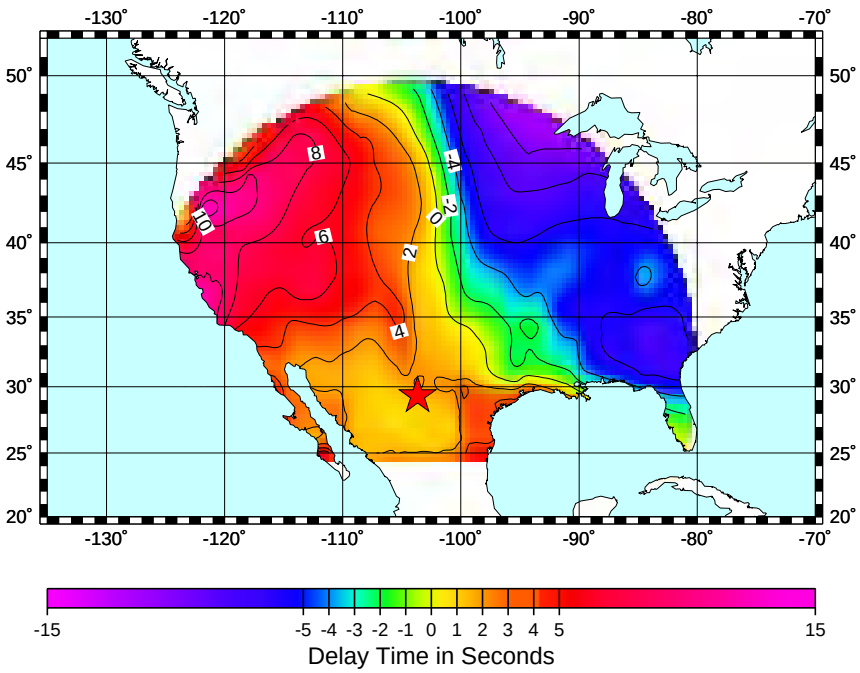


Figure 5. SSSCs calculated for Pn (top) and Sn (bottom) phases using 3-D model, revision 5.0, for the TAXAR station (star).

SOURCE SPECIFIC STATION CORRECTIONS (SSSCS) FOR INTERNATIONAL MONITORING SYSTEM (IMS) SEISMIC STATIONS IN NORTH AFRICA, MIDDLE EAST AND WESTERN ASIA

Group - 2 Consortium

SAIC, University of Colorado, Harvard University, University of California San Diego, Multimax, and Geophysical Institute of Israel

Sponsored by The Defense Threat Reduction Agency
Arms Control Technology Division
Nuclear Treaties Branch

Contract No. DTRA01-00-C-0013

ABSTRACT

To date, IDC regional travel time corrections have been successfully implemented for Fennoscandia and North America. Corrections and associated modeling errors to Pn, Pg, Sn, and Lg IASPEI91 travel time tables are specified on 1 by 1 degree latitude and longitude "source specific" grids within 20 degrees of each International Monitoring System (IMS) station. International Data Center (IDC) location software is configured to read and apply these grids when locating events in the Reviewed Event Bulletin (REB). In order to develop regional travel time corrections for IMS stations in North Africa, Middle East, and Western Asia, a consortium was formed of experts in IDC software integration/testing/validation, regional/global body/surface-wave tomography, tectonic regionalization, 3D ray-tracing, and ground truth (GT) data collection with the goal to improve location accuracy and precision while maintaining honest 90% coverage ellipses.

The three-year R&D program will provide Source Specific Station Corrections (SSSCs) for all IMS primary and auxiliary seismic stations in the region. Corrections will be developed, tested, and validated in two phases. A preliminary set of SSSCs will be delivered and tested by late 2001. A refined set of SSSCs will be delivered and tested by early 2003. The preliminary set will develop corrections for surface sources only based on an initial preliminary regionalization and set of crustal and upper mantle models. The 3D model will be based on a hierarchy of global 3D models, regional models, and tectonic regionalization. Travel times will be computed by 3D ray tracing from each station to a grid of source locations. Modeling errors for the initial correction set may be conservatively large. Meanwhile, a concerted effort has begun to gather ground truth (GT) location data in the region for validation. All GT origins, GT arrivals, velocity models, regionalizations, SSSCs, and metadata will be delivered for testing and validation. The preliminary set of SSSCs will focus the research team on problem areas and issues. GT data collection and analysis will continue throughout the entire program. Problem areas and technical issues will be addressed to refine models and GT data collection for a second and final delivery.

OBJECTIVE

The objective of this research is to develop, test, validate and deliver source specific station corrections (SSSC) for regional phases (Pn, Sn, Pg, Lg) up to 20-degree epicentral distances for International Monitoring System (IMS) stations in North Africa, the Mediterranean, Middle East and West Asia. It is expected that regional SSSCs will improve locations by both decreasing individual absolute errors (bias) and improving precision (reduce error ellipses) w.r.t. current IDC practice.

RESEARCH ACCOMPLISHED

Introduction

Improvements both in seismic location and accuracy are crucial for monitoring the Comprehensive Nuclear-Test-Ban Treaty (CTBT). The development and application of regional SSSCs for IMS stations in Fennoscandia and North America (Yang et al., 2000d, Yang et al., 2000e) have demonstrated that path

dependent corrections relative to the default IASPEI91 travel times are capable of improving event locations and reducing uncertainties. To further develop and validate regional SSSCs for IMS stations in North Africa, the Mediterranean, Middle East and West Asia, a consortium, called "Group 2" has been formed. The Group 2 consortium consists of scientists from SAIC, Harvard University, University of Colorado Boulder, University of California San Diego, Multimax and the Geophysical Institute of Israel with broad expertise in collection and maintenance of ground truth data, tectonic regionalization, construction of global and regional 3D models, computation of travel-times in 3D media, joint hypocenter determination (JHD) as well as testing, validation and integration of mission critical software.

The IDC software uses the IASPEI91 tables in its location module to obtain predicted travel times for a suite of seismic phases in various distance and depth ranges. However, the IASPEI91 travel times, being 1D global averages, can considerably deviate from true travel times at regional distances. The difference can be as much as 5-10 seconds. This not only affects event locations but often results in very large coverage ellipses because the estimated travel time uncertainties (modeling errors) incorporate the large discrepancy between predicted and true travel times. The application of SSSCs is expected to improve locations and reduce the size of error ellipses while still maintaining 90% coverage level, owing to the better travel time and modeling error estimates. SSSCs are path dependent travel time corrections relative to the default IASPEI91 tables for a given phase at a station. They are specified on a rectangular latitude/longitude grid, where both a correction and a modeling error are assigned to each grid point.

The Group 2 consortium will follow model-based approaches to constructing SSSCs. Ground truth data will be used for validation purposes only. Figure 1 shows the IMS stations (black triangles), together with a circle of 20-degree radius around the stations, for which the Group 2 is responsible. The envelope of these circles depicts the consortium's primary region of interest.

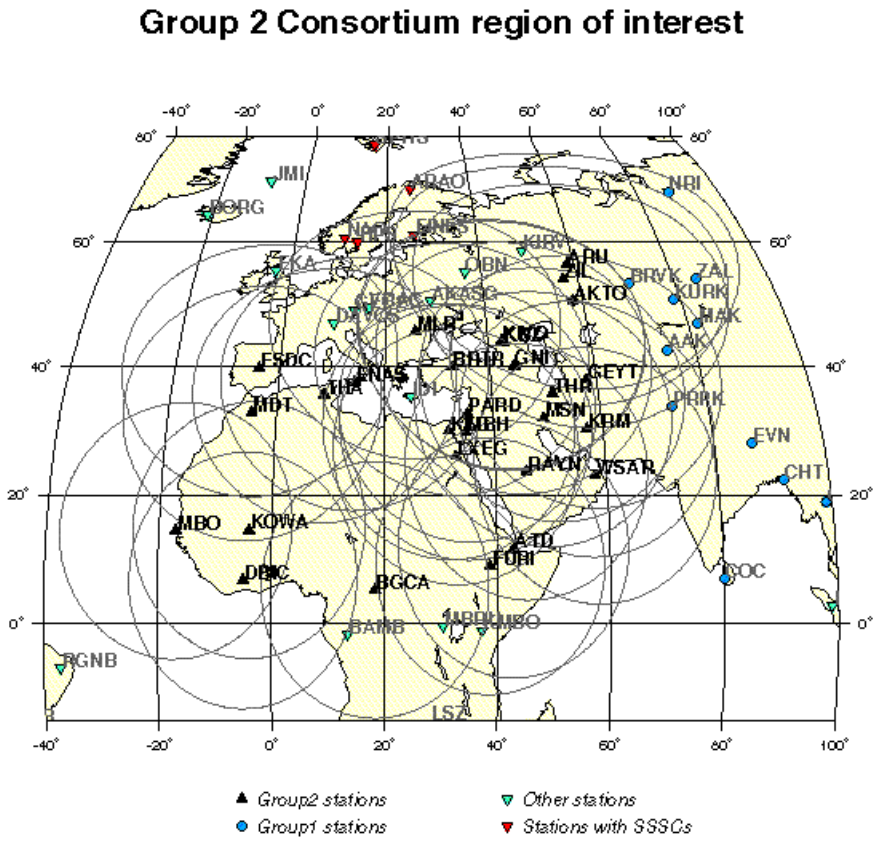


Figure 1. Group 2 region of interest. Group 2 IMS stations (black triangles) are drawn with their surrounding 20-degree circle. Note the overlap with Group 1 stations (blue circles). Other IMS stations are plotted as inverted triangles.

Travel time corrections will be developed, tested and validated in two phases over three years. In the first phase preliminary corrections will be developed based on readily available models for the region of interest. The second phase will provide a refined set of corrections utilizing improved models, error estimates and algorithms. Construction of improved 3D hybrid models (a combination of global and regional velocity models) from which travel times are derived via 3D ray tracing will be the primary focus of the consortium.

The validation of the corrections will be based on reference events with location accuracy of 5 km or better. Collection and validation of such reference events will be an ongoing major effort throughout the entire project. Validation of the SSSCs requires that the locations meet specified metrics in order to demonstrate improvements when the corrections are applied.

Ground truth data collection

In order to test and validate the model based corrections it is essential to obtain a set of reliable reference events spread over the region of interest. Since the expected improvement in location is on the order of 10 km, the location of reference events should be known within 5 km accuracy or better. Besides events with exactly known hypocenters, such as nuclear explosions and calibration shots, events can also be selected from seismic bulletins, provided that their location meets the following criteria:

- 10 or more stations at $\Delta < 250$ km
- 10 or more time-defining phases
- minimum distance of recording stations <= 30 km
- largest azimuthal gap < 120 degrees

and desirably:

- magnitude > 3.5
- depth < 35 km
- phases recorded at IMS stations or surrogates
- first arrivals recorded beyond 250 km

Although the above criteria are similar to those developed for GT10 or better events (Dewey and Kork, 2000), they appear to be stringent enough that events meeting the above requirements will be located better than 5 km. The selected events will be subject to further expert review within the consortium.

Reference events are selected from the CMR Nuclear Explosion and Ground Truth databases (Bondár et al., 2000, Yang et al., 2000a, Yang et al., 2000b), the CMR Calibration event bulletin (Yang et al., 2000c), the PIDC/IDC REB, the NEIC and ISC bulletins (Engdahl et al., 1998) as well as national and local network bulletins in the region. Chemical explosions identified with a mine or a quarry can also be accepted if the size of the quarry does not exceed 5 km. Figure 2 shows the set of reference events we have collected so far. This effort will continue throughout the 3-year program.

When testing and validating the models, it is irrelevant which stations recorded the event, therefore phase arrivals are collected from all the recording stations through established contacts with local network operators. We follow the principle that reference events used for the validation of the models will not be used in the validation of SSSCs.

As part of a cross-validation procedure empirically derived path-dependent corrections obtained from Joint Hypocenter Determination (Douglas, 1967, Dewey, 1991) will be compared to model based SSSCs. To perform this task, event clusters, recorded by IMS stations, their surrogates as well as other well established teleseismic stations are collected. Station corrections and statistical scatter of clusters will be used as one source of information in estimating model errors.

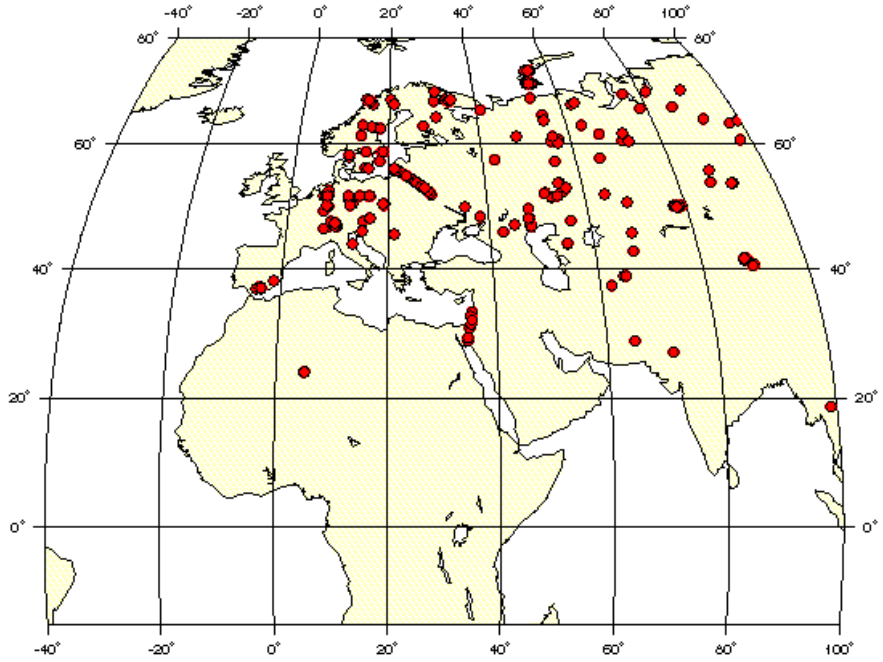


Figure 2. Reference events located with 5 km accuracy or better in the region of interest.

Model construction

Currently available global 3D models, although they adequately describe the gross features of the Earth, have not yet the resolution (especially in the crust and uppermost mantle) required for regional calibration. Therefore one of our main objectives is to construct a 3D hybrid velocity model that has sufficient resolution to generate path dependent travel times on a 1 by 1 degree grid. To accomplish this goal we will combine global mantle P and S models (Boschi and Dziewonski, 1999, Bijwaard et al., 1998) with global and regionalized uppermost mantle (Gudmundsson and Sambridge, 1998), crust and sedimentary models (Mooney et al., 1998, Laske and Masters, 1997, Seeber et al., 1997) as well as local and regional crust models. New 1 by 1 degree sedimentary models under development will also be utilized.

Figs. 3 and 4 provide a comparison between P and S global models in the Middle East region. The P wave velocity model was obtained from P-wave tomography (Bijwaard et al., 1998), while the S model is derived from surface wave tomography (Villasenor et al., 2000). Fig. 5 shows preliminary correction surfaces calculated from the S model. A hybrid model can optimally exploit the advantages of different methods.

In some regions the best achievable calibration information is limited to regionalized travel time curves or local velocity models. However, even in those regions we will apply rigorous 3D ray tracing. The hybrid 3D model will be constantly refined as it is tested against ground truth data and empirical regionalized travel time curves until an acceptable fit is achieved.

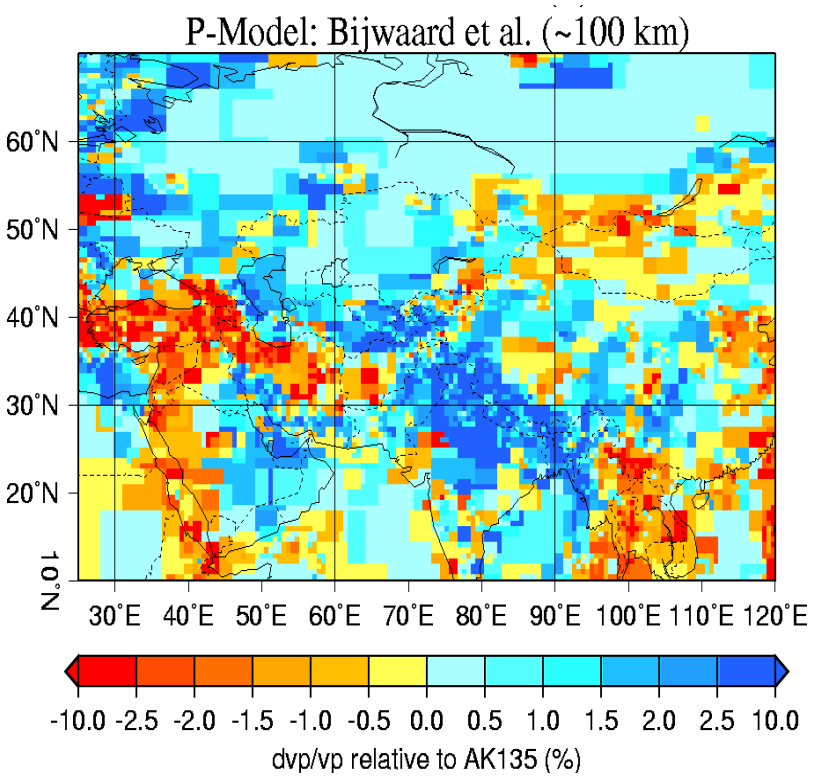


Figure 3. P wave velocity model (Bijwaard et al., 1998) at 100 km depth in the Middle East region relative to AK135.

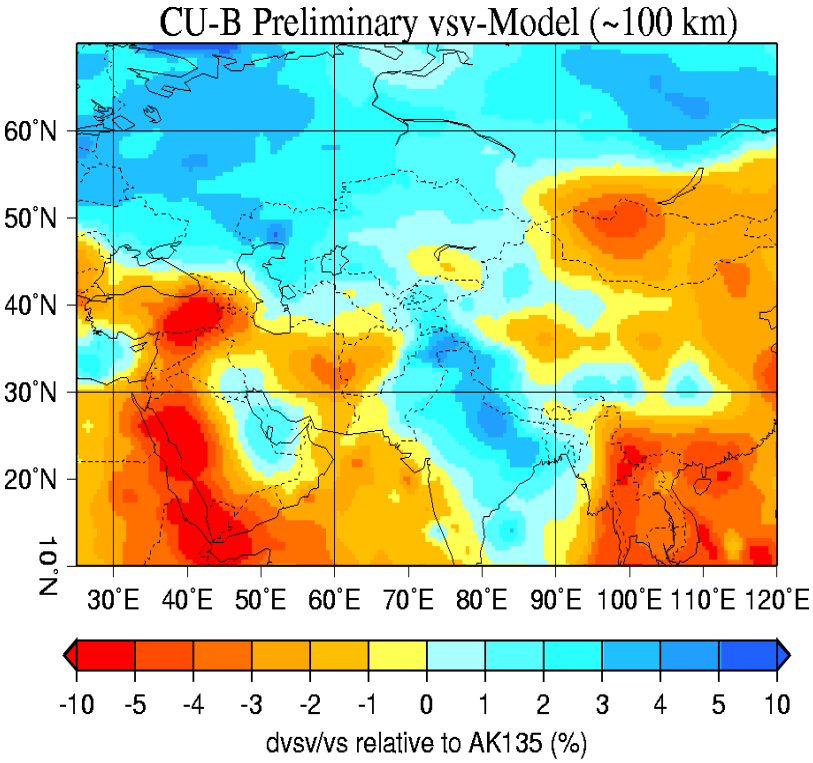


Figure 4. S wave velocity model at 100 km depth in the Middle East region relative to AK135 (Villasenor et al., 2000).

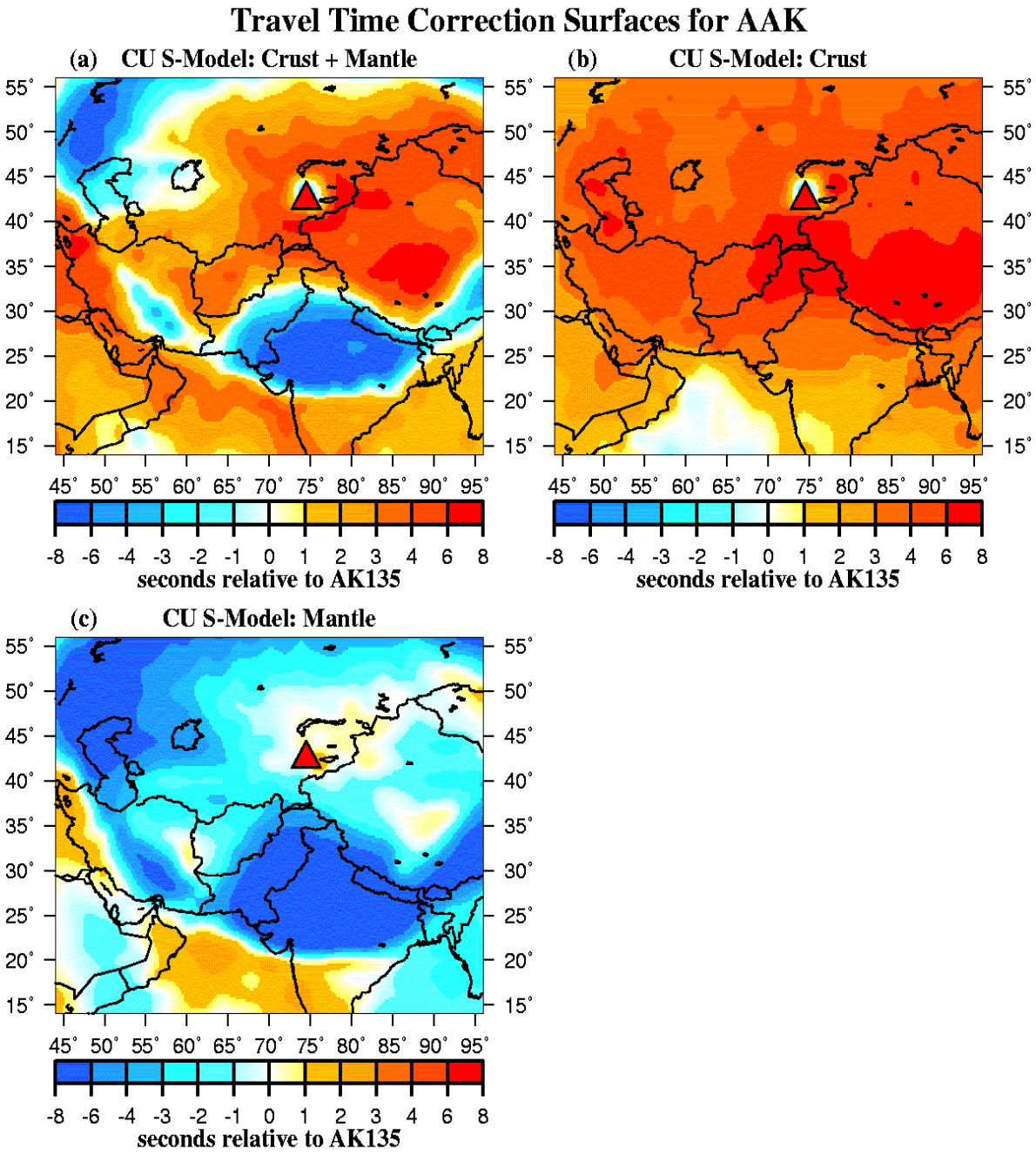


Figure 5. Preliminary correction surfaces calculated by 3D ray tracing through the S wave velocity (Villasenor et al., 2000).

One important aspect of the model construction is the estimation of modeling errors at each grid point, i.e. the uncertainty in the predicted travel times. The modeling errors will be estimated from the scatter of travel times caused by small perturbations in the model parameters, as well as from the comparison of travel times obtained by different ray tracing algorithms and empirical JHD station corrections. The modeling errors must be conservative enough to ensure actual 90% ellipse coverage.

CONCLUSIONS AND RECOMMENDATIONS

Testing and validation plan

Testing and validation requires a representative set of reference events. Previous studies (Bondár et al., 1998, Yang et al., 2000d) have shown that SSSC testing results are ambiguous when limited to GT10 events (events located with 10 km accuracy). Thus, only GT5 or better events will be used for validation testing. Reference events that were used in the model development will not be used in the validation procedures. Validation requires proof that location accuracies are improved as well as the 90% ellipse coverage is maintained.

Validation testing consists of two stages: off-line unit testing and integration testing. Off-line unit tests are designed to quantitatively measure the improvements in location, uncertainties and coverage when corrections are applied with respect to default travel time tables. Validation tests will be conducted in accordance with the recommendations of the CTBT Working Group B Location Calibration Expert Group (CTBT/WGB/TL-2/18, CTBT/WGB/TL-2/48) and the procedures established in past CMR calibration efforts (Bondár and North, 1999, Bondár et al, 1999, Yang et al., 2000e). We will provide the metrics recommended in CTBT/WGB/TL-2/18:

- the median mislocation of GT events should be significantly reduced
- mislocation should be reduced by 20% or more for the majority of the events
- median confidence ellipses should be reduced in area, and the coverage (percentage of GT events lying within the confidence ellipse) should be the same or better
- confidence ellipses should be reduced by 20% or more for the majority of the events
- fit, as expressed by residuals or their variance, should be similar or better

Besides those recommended by WGB we may construct additional metrics to measure the performance of the SSSCs (for instance, we will require that the ellipse coverage be consistent with the confidence level).

Integration tests will be carried out on the CMR R&D Test Bed in order to ensure that the new tables added to the system will not negatively influence the overall performance of the full IDC software suite.

Time schedule

The three-year project is divided into two major phases. Starting in March 2000, Phase 1 (0-18 months) will provide a set of preliminary SSSCs based on the initial models. In this phase SSSCs will be computed for sources at 10 km depth, in order to avoid projecting the effects of low velocity sedimentary layers into the deeper crust and upper mantle propagation. Slowness and azimuth corrections will not be addressed at this stage. Phase 1 schedule is outlined as follows:

- Phase 1- Preliminary Corrections (0-18 months)
  Select methodologies, models and data
  Develop 3D models, regional TT curves and event clusters
  Construct SSSCs
  Testing, validation and documentation
  Integration testing on CMR R&D test bed
  Deliver preliminary corrections

The IDC software will not be capable of utilizing full SSSC depth dependence until the end of the scheduled program. Therefore initial Phase 1 SSSCs will be provided for a source depth of 10 km consistent with those already developed for Fennoscandia and North America. Shallow crustal structure will be included at each station, however it is undesirable to map shallow crustal structure into corrections for the mid crust and upper mantle. In Phase 2 special attention will be given to areas of deep seismicity (h>50 km) such as Romania and parts of the Mediterranean.

Phase 2 (12-36 months), beginning in 2001, will provide the final, refined set of corrections. During this phase knowledge acquisition will be focused on gaps in models and GT events identified during Phase 1. Model based slowness and azimuth corrections will be compared to empirical slowness-azimuth station corrections (SASCs), and if they are proven superior to empirical corrections, they will be included in the Phase 2 products. The overlap between Phase 1 and Phase 2 allows us to address problems identified during Phase 1 at an early stage. The outline of Phase 2 schedule largely follows the Phase 1 plan:

- Phase 2- Refined Corrections (12-36 months)
  Select revised methodologies, models and data
  Develop 3D models, regional TT curves and event clusters
  Construct improved SSSCs including source depth
  Construct and examine model based source specific SASCs
  Testing, validation and documentation
  Integration testing on CMR R&D test bed
  Deliver refined corrections

Deliverables

The consortium will deliver the following products:

- SSSCs (Source Specific Station Corrections)
- Possibly SASCs (Slowness and Azimuth Station Corrections)

Validated travel time, slowness and azimuth corrections will be provided for each IMS stations within the region of interest over a horizontal grid of 1 degree or less for the regional phases Pn, Pg, Sn and Lg up to 20-degree epicentral distances. The corrections will be based on velocity models, possibly combined with empirical ground truth observations. The corrections in each grid point will be accompanied with estimated uncertainties.

- 3D Velocity models

  The 3D models, from which the delivered SSSCs and SASCs are derived, will also be delivered.
- Reference events

  Ground truth data collected for the testing, evaluation and validation of the models and corrections will be incorporated in CMR databases with event origins and station arrivals.
- Documentation

  Technical reports will be prepared to provide appropriate documentation for each of the above products.

Group 2 Consortium members

SAIC (Science Applications International Corporation)
Keith McLaughlin (scatter@cmr.gov), Robert North (north@cmr.gov), István Bondár (ibondar@cmr.gov), Hans Israelsson (hans@cmr.gov), Xiaoping Yang (xiaoping@cmr.gov), Victor Kirichenko (kirichenko@wsc.ru), Yury Kraev (kraev@wsc.ru)
University of Colorado at Boulder
Robert Engdahl (engdahl@merckx.colorado.edu), Michael Ritzwoller (ritzwoll@merckx.colorado.edu), Anatoly Levshin (levshin@merckx.colorado.edu), Antonio Villasenor (antoniov@ciei.colorado.edu)
Harvard University
Adam Dziewonski (dziewons@seismology.harvard.edu), Goran Ekström (ekstrom@seismology.harvard.edu), Michael Antolik (antolik@seismology.harvard.edu)
University of California at San Diego
Gabriele Laske (gabi@mahi.ucsd.edu), Jonathan Berger (jberger@igpp.ucsd.edu)
Multimax
Winston Chan (wchan@multimax.com), Indra Gupta (gupta@multimax.com), Wilmer Rivers (wilmer@multimax.com), Robert Wagner (wagner@multimax.com)

Geophysical Institute of Israel
Avi Shapira (avi@iprg.energy.gov.il) , Abraham Hofstetter (rami@iprg.energy.gov.il)

Key Words: Seismic Location Calibration, Ground Truth

REFERENCES

Bijwaard, H., W. Spakman and E.R. Engdahl, Closing the gap between regional and global travel time tomography, *J. Geophys. Res.*, **103**, 30055-30078, 1998.

Bondár, I., X. Yang, K. McLaughlin, R.G. North, V. Ryaboy and W. Nagy, Source specific station corrections for regional phases at IMS stations in North America and Fennoscandia, *EOS*, **79**, No. 45, 555, 1998.

Bondár, I., R.G. North and G. Beall, Teleseismic slowness-azimuth station corrections for the International Monitoring System seismic network, *Bull. Seism. Soc. Am.*, **89**, 989-1003, 1999.

Bondár, I. and R.G. North, Development of calibration techniques for potential use by the CTBT International Monitoring System, *Phys. Earth Planet. Int.*, **113**, 11-24, 1999.

Bondár, I., X. Yang, R.G. North and C. Romney, Location Calibration Data for CTBT Monitoring at the Prototype International Data Center, *Pure and Appl. Geophys.*, in press, 2000.

Boschi, L. and A.M. Dziewonski, High and low-resolution images of the Earth's mantle: Implications of different approaches to tomographic modeling, *J. Geophys. Res.*, **104**, 25567-25594, 1999.

Dewey, J.W. and J. Kork, Selection of earthquakes for calibration events in the United States, *Proceedings of the 2nd Workshop Location Calibration, IDC Technical Experts Group on Location Calibration*, Oslo, Norway, 20-24 March, 2000.

Dewey, J.W., Joint epicenter determination for earthquakes occurring over several decades: a case history from Northern Algeria, *in: Seismicity, Seismotectonics and Seismic Risk of the Ibero-Maghreb Region*, eds.: J. Mezcua and A. Udias, Instituto Geografico Nacional, Monografia No. 8, Madrid, Spain, 51-63, 1991.

Douglas, A. Joint epicentre determination, *Nature*, **215**, 47-48, 1967.

Engdahl, E.R., R. van der Hilst and R. Buland, Global teleseismic earthquake relocation with improved travel time and procedures for depth determination, *Bull. Seism. Soc. Am.* **88**, 722-743, 1998.

Gudmundsson, O. and M. Sambridge, A regionalized upper mantle (RUM) seismic model, *J. Geophys. Res.*, **103**, 7121-7136, 1998

Laske, G. and G. Masters, A global digital map of sediment thickness, *EOS Trans.* AGU, 78, F483, 1997.

Mooney, W.D., G. Laske and G. Masters, CRUST5.1: A global crustal model at 5x5, *J. Geophys. Res.*, **103**, 727-747, 1998

Seeber, D., M. Vallve, E.A. Sandvol, D.N. Steer and M. Barazangi, Middle East tectonics; applications of geographic information systems (GIS), *GSA Today*, **7**, 1-6, 1997.

Villasenor, A., M.H. Ritzwoller, A.L. Levshin, M.P. Barmin, E.R. Engdahl, W. Spakman and J. Trampert, Shear velocity structure of Central Eurasia from inversion of surface wave velocities, submitted to *Phys. Earth Planet. Int.*,, 2000.

Yang, X., R.G. North and C. Romney, PIDC Nuclear explosion database (Revision 3), *Center for Monitoring Research*, Technical Report CMR-00/16, 2000a.

Yang, X., I. Bondár and C. Romney, PIDC Ground truth event (GT) database (Revision 1), *Center for Monitoring Research*, Technical Report CMR-00/15, 2000b.

Yang, X., I. Bondár and K. McLaughlin, PIDC Calibration Event Bulletin (CEB) Database (Revision 1), *Center for Monitoring Research*, Technical Report, CMR-00/17, 2000c.

Yang, X., I. Bondár, K. McLaughlin, and R.G. North, Source specific station corrections for regional phases at Fennoscandian stations, *Pure and Appl. Geophys*., in press, 2000d.

Yang, X., I. Bondár, K. McLaughlin, R.G. North and W. Nagy, Path-dependent travel-time corrections for the International Monitoring System in North America, submitted to *Bull. Seism. Soc. Am*., 2000e.

INTEGRATING DIVERSE CALIBRATION PRODUCTS TO IMPROVE SEISMIC LOCATION

Craig A. Schultz, Steven C. Myers, Jennifer L. Swenson, Megan P. Flanagan,
Michael E. Pasyanos, and Joydeep Bhattacharyya
Lawrence Livermore National Laboratory

Sponsored by U.S. Department of Energy
Office of Nonproliferation Research and Engineering
Office of Defense Nuclear Nonproliferation
National Nuclear Security Administration

Contract No. W-7405-ENG-48

ABSTRACT

The monitoring of nuclear explosions on a global basis requires accurate event locations. As an example, under the Comprehensive Nuclear-Test-Ban Treaty, the size of an on-site inspection search area is 1,000 square kilometers or approximately 17 km accuracy, assuming a circular area. Achieving this level of accuracy is a significant challenge for small events that are recorded using a sparse regional network. In such cases, the travel time of seismic energy is strongly affected by crustal and upper mantle heterogeneity and large biases can result. This can lead to large systematic errors in location and, more importantly, to invalid error bounds associated with location estimates. Corrections can be developed and integrated to correct for these biases. These path corrections take the form of both three-dimensional model corrections along with three-dimensional empirically based travel-time corrections. LLNL is currently working to integrate a diverse set of velocity model and empirically based travel-time products that are provided internally by the DOE laboratories and externally through contracts into one consistent and validated calibration set.

To perform this task, we have developed a hybrid approach that uses three-dimensional model corrections for a region and then empirically uses reference events when available to improve these path corrections. This empirical approach starts with the best *a priori* three-dimensional velocity model that is produced for a local region and uses this as a baseline correction. When multiple competing models are provided from various sources for a local region, uncertainties in the models are compared against each other using our ground truth data and our analysts picks. Based on the results of this comparison an optimal model is selected. We are in the process of combining three-dimensional models on a region-by-region basis and integrating the uncertainties to form a global correction set. Our Bayesian kriging approach then combines the set of optimal models and their statistics with empirical calibrations to give an optimal three-dimensional *a posteriori* calibration estimate. In regions where there is limited or no coverage by reference events, travel-time corrections are based primarily on the model. The integrated *a priori* model is particularly important in these areas. In regions with adequate calibration events, the corrections are based primarily on these events. We demonstrate improvement in event location through the reduction of regional bias. In regions with sparse or no ground truth, the *a priori* model will need to be spot-validated with the use of dedicated calibration experiments or through the use of mining explosions, where available.

Key Words: calibration, product integration, event location, reference events, model corrections, validation

OBJECTIVE

The monitoring of nuclear explosions on a global basis requires accurate event locations. Unfortunately, crustal and upper mantle velocity anomalies often lead to systematic travel-time anomalies that in many cases lead to large systematic errors in location estimates. Typically these velocity anomalies are not accounted for in the location process and the predicted errors misrepresent the true uncertainty of the event location. At Livermore, we are working to implement a unified framework that combines empirical-based and model-based path corrections to remove bias from the location problem. Our framework will incorporate any combination of *a priori* and *a posteriori* one-dimensional, two-dimensional, and three-dimensional models. These models that are derived from a variety of sources including external contracts, are combined with our empirically based travel time corrections. The errors are then propagated into our coverage ellipse estimates. This paper focuses on the Livermore effort to integrate a diverse set of three-dimensional velocity model and empirical based travel-time products into one consistent and validated calibration set.

RESEARCH ACCOMPLISHED

We continue to work closely with Sandia National Laboratories (SNL) to implement a framework that allows us to design, build, integrate, and visualize calibrations that are produced from our own internal DOE research and that provided through research associated with external contracts. This is not an entirely new project. Instead, it is the natural extension of our empirical and modeling calibration efforts over the past five years. A large part of our effort at Livermore has been concerned with generating standardized detection, travel-time, and amplitude correction volumes on a regional basis. The tessellated output of the correction volumes combines a set of sub-regions into one global correction set. The global set of integrated corrections is then fed directly into the appropriate detection, location, and discrimination algorithms and leads to the primary improvement in our ability to locate and discriminate events. In our framework, we address four core issues.

Knowledge Base Product Visualization. We are working to provide improved end-to-end visualization of all calibration events (i.e. ground truth events), their uncertainties, constructed models, empirically kriged surfaces on a region-by-region basis. We can now provide a completely integrated demonstration of the DOE laboratories' geographic regionalization.

Direct Calibration Modification. We are working to visualize, access, and potentially alter within any geographic subregion the calibration events, statistics, model, and/or kriged surfaces, if required. Subregions can be rapidly redefined. This may be especially useful when adding calibration information in regions where a subset of calibrations and uncertainties need to be added after the fact and in an efficient fashion.

External Product Integration. This process allows the laboratories to identify geographic subregions that correspond to regions covered by external contractors. Contract research provided to Livermore within a geographic subregion can be seamlessly incorporated into the DOE KB. Product integrators assess uncertainties in contributed calibrations and compare these uncertainties with our internal models and with other contributions from external contractors in the region. The optimal model is selected and assigned to that sub-region.

DOE Coordinated Analysis. This process standardizes DOE calibration efforts into one single format and access tool. Use of this tool ensures the seamless coordination and integration of projects. Sub-regions can be easily merged at boundaries and models can be altered to properly merge analyses made by different laboratories in regions that overlap. This process is fully auditable.

This framework is being developed in multiple phases. The first phase involves standardizing the suite of statistical, kriging, modeling and tessellation tools that have been developed by LLNL and SNL over the past two years.

Framework for Integrating Calibrations

The overall goal of our framework is to provide a flexible, interactive environment in which an analyst can produce, test, and manage calibration information for seismic stations. This framework focuses on providing accurate characterizations of location uncertainty given the highly nonstationary and regionally varying nature of seismic travel time, azimuth, and slowness.

To account for variations in regional structure, our framework is designed to account for dramatic variations in travel-times and amplitudes that occur over relatively short distances in the crust - variations that can lead to significant errors in event location. Figure 1 gives a general overview of how we accurately account for these errors. We begin by cataloging well constrained - both in location and source characteristics - historic earthquakes and explosions in the DOE KB and use these events to spatially map their amplitude and travel-time changes as a function of geographic coordinate. This acts as the data set that we use to both test our internal DOE models and any external models developed by contractors. These data are also used to assign and validate the uncertainties associated with the models (Hanley and Schultz, 2000). As more events occur over time, the two-dimensional and three-dimensional velocity models are continually refined and our ability to account for crustal effects is improved (Flanagan et al., 1999; Swenson et al., 1999; Flanagan et al., 2000;). However, one quickly realizes that model prediction will never be perfect. By its very nature, a model of the earth is underdetermined by the observational data and, thus, gives only an average estimate of the true earth structure. More precisely, if one tried to predict the travel time or amplitude of an event that was used to develop the model, one could not recover its exact characteristics. To provide an accurate characterization, we have developed a set of innovative statistical techniques and algorithms that work together with the model to empirically predict and propagate the travel-time or amplitude correction along with its uncertainties (Schultz and Myers, 1998; Myers and Schultz, 1999; Myers and Schultz, 2000).

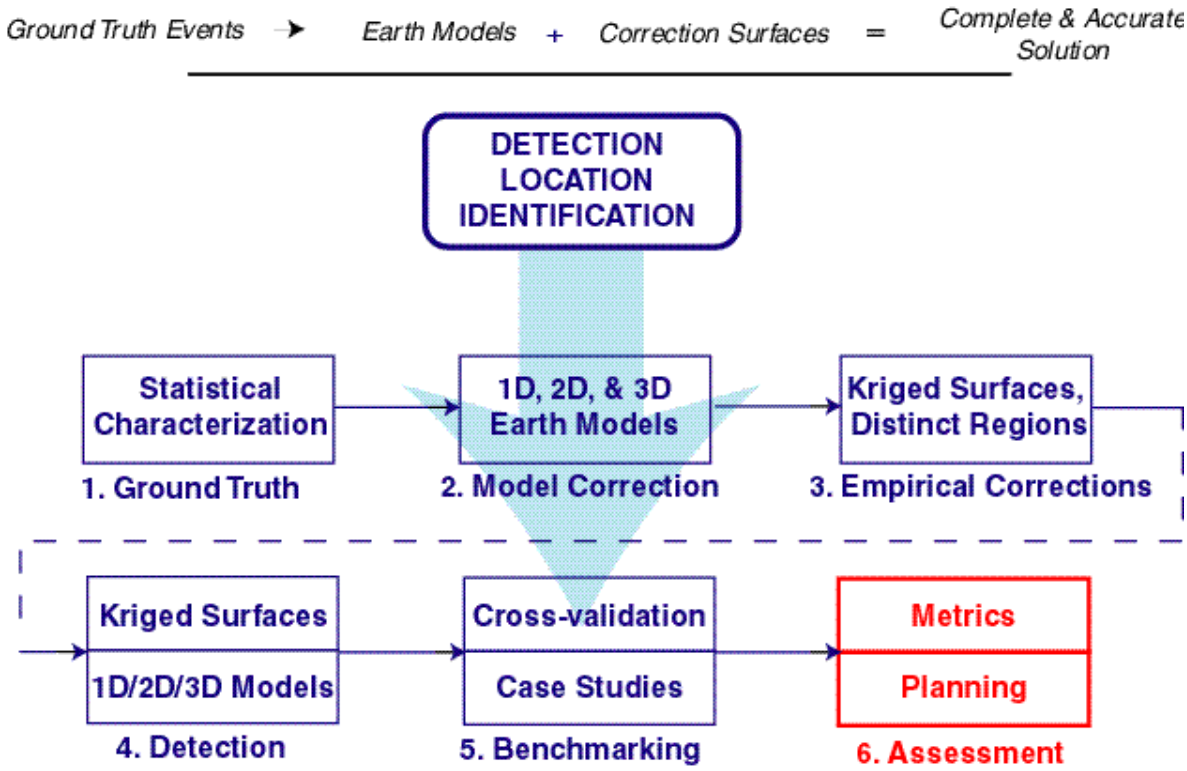


Figure 1: Developing a comprehensive framework for location.

Methodology for Diverse Calibration Integration

Producing calibration information for a region involves the creation of calibration surfaces and/or tessellations for all the stations within the region. This requires the production and refinement of dozens of subregions, both model- and statistical-based. Producing these entities is inherently an interactive process in which the researcher must

observe the effect of changes, and use that feedback to decide whether continued modification is required. Figure 2 shows the general structure of a calibration set in our approach.

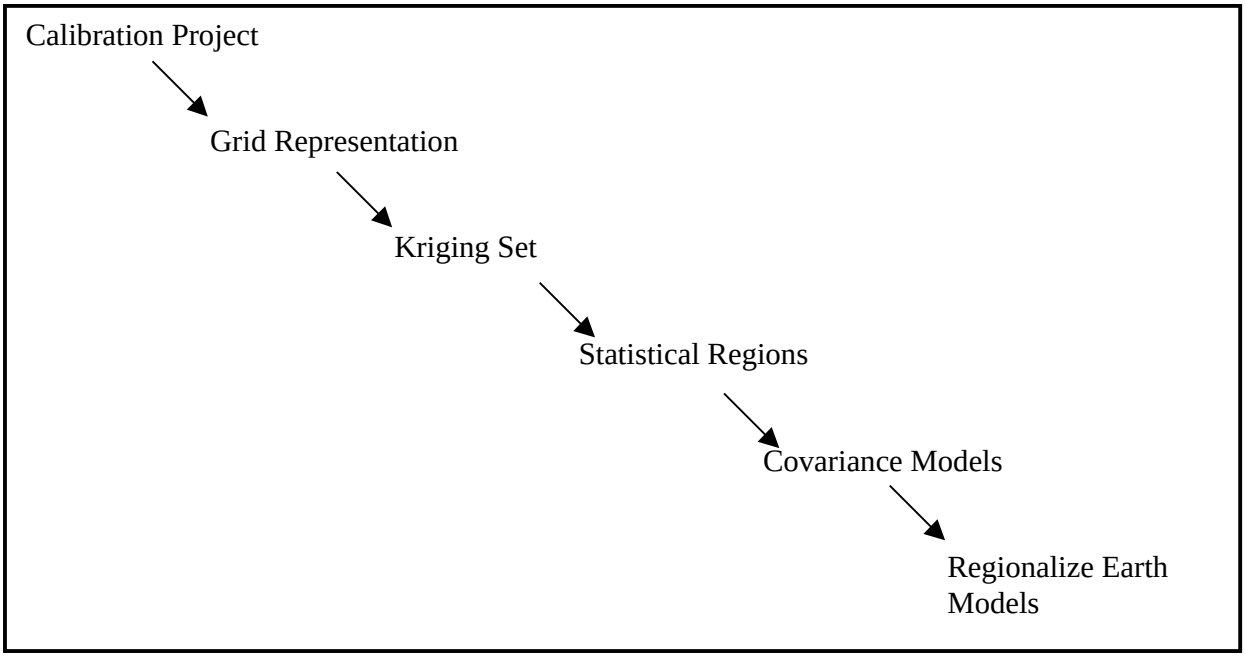


Figure 2: General structure of how calibrations are integrated to form both location and amplitude corrections.

The framework we have designed handles multiple mesh (tessellation) and station-phase-attribute surfaces at once. For each correction surface, a suite of algorithms is incorporated to spatially reduce the dimensionality of the data we integrate while retaining all pertinent calibration information. Distinct calibration data quality groups are spatially associated within geographic subregions. These subregions are created and edited in terms of their boundaries. Various trends and velocity models can be removed within each subregion, as shown in Figure 3. Outlier removal is supported but not encouraged. Statistical tests, graphical methods, and analyst discretion (which may be arbitrary) are supported as methods to identify outliers.

Data with similar spatial statistics are grouped within statistical regions (Figure 4). Statistical regions are completely independent of kriging regions, so statistical regions may overlap any number of kriging regions. However, it may be common for statistical and kriging regions to have identical boundaries. Statistical analysis consists of stationary or non-stationary, isotropic or anisotropic variogram two-dimensional and three-dimensional modeling. In the future, more general statistical modeling will be incorporated. Incorporating non-parametric non-stationary, anisotropy, and/or co-variograms (mixing data sets) are some of the options that work towards increased variogram generality. Variograms are then assigned to a specific kriging region. After assigning variograms to all regions with both DOE calibration data and external contract data integrated, the data set can be kriged.

It may be desirable to krig on any number of optimally spaced (regular, irregular) grids (e.g. tessellation). The grids may be optimized for one kriged surface or a collection of surfaces. If tessellation is chosen, the bounds of the tessellation and the lowest density spacing are specified to ensure accuracy at all times. A collection of surfaces over which the tessellation is optimized must also be specified. The resulting tessellation (node and triangle information) is saved so subsequent surfaces can be kriged on the same mesh.

Using this process we are able to assure that realistic modeling uncertainties are assigned and propagated on a regional basis. Calibration data and models from a diverse set of sources including the laboratories and contracting

universities can be integrated into one correction surface suite and the uncertainties are standardized on a global scale. We continue to validate this process with newly acquired ground truth events and refine it as required.

CONCLUSIONS AND RECOMMENDATIONS

In general, we have developed a hybrid approach to location that uses three-dimensional model corrections for a region and then uses reference events when available to improve the path correction. Our approach is to select the best *a priori* three-dimensional velocity model that is produced for a local region and then use this as a baseline correction. When multiple models are produced for a local region, uncertainties in the models will be compared against each other using ground truth data and an optimal model will be chosen. We are working towards implementing a calibration integration process of combining three-dimensional models on a region-by-region basis and integrating the uncertainties to form a global correction set. The Bayesian kriging prediction combines the optimal model combination and its statistics with the empirical calibrations to give an optimal *a posteriori* calibration estimate. The result, as shown in Figure 5, is improved location estimates and robust location uncertainties that show significant improvement in calibrated regions (Schultz and Myers, 1999; Schultz et al., 1999).

To aid this process we have developed a general framework to provide a flexible, interactive environment in which a researcher can produce, test, and manage calibration information for seismic stations. This approach allows a general statistical analysis on a regional basis and results in a self consistent global calibration set.

References

Flanagan, M., Schultz, C., Myers, S.C., Pasyanos, M., Walter, WR, 2000, Improving regional event locations in the Middle East by incorporating model based correction surfaces derived from 3-d velocity structures, *Seismological Society of America 94th Annual Meeting.*

Flanagan, MP, Schultz, CA, Hutchings, L, 1999, Development of 3-D crust and upper mantle velocity models to improve seismic event location, *Fall American Geophysical Union Meeting.*

Hanley, WG, Schultz, CA, Myers, SC, 1999, Statistical analysis of travel time residuals applied to the analysis of station quality, *Seismological Society of America 94th Annual Meeting.*

Myers, SC, Schultz, CA, 2000, Improving Sparse Network Seismic Location with Bayesian Kriging and Teleseismically Constrained Calibration Events, *Bull. Seism. Soc. Am.*, 90, 199-211

Myers, S.C., Schultz, CA, 1999, Improvement in seismic location using non-stationary Bayesian kriging, *Seismological Society of America 94th Annual Meeting.*

Schultz, CA, Myers, SC, Flanagan, M, Swenson, J, Hanley, J, Pasyanos, M, 1999, Improving seismic event location through calibration of the International Monitoring System, *21st Seismic Research Symposium Technologies for Monitoring the Comprehensive Nuclear Test Ban Treaty.*.

Schultz, CA, Myers, SC, 1998, Nonstationary Bayesian Kriging: A predictive technique to generate spatial corrections for seismic detection, location, and identification, *Bull. Seism. Soc. Am*., 88, 1275-1288.

Swenson, JL, Schultz, CA, Hanley, WG, 1999, Using radially heterogeneous and azimuthally invariant travel-time models to improve seismic location in the Middle East and North Africa, *Fall American Geophysical Union Meeting.*

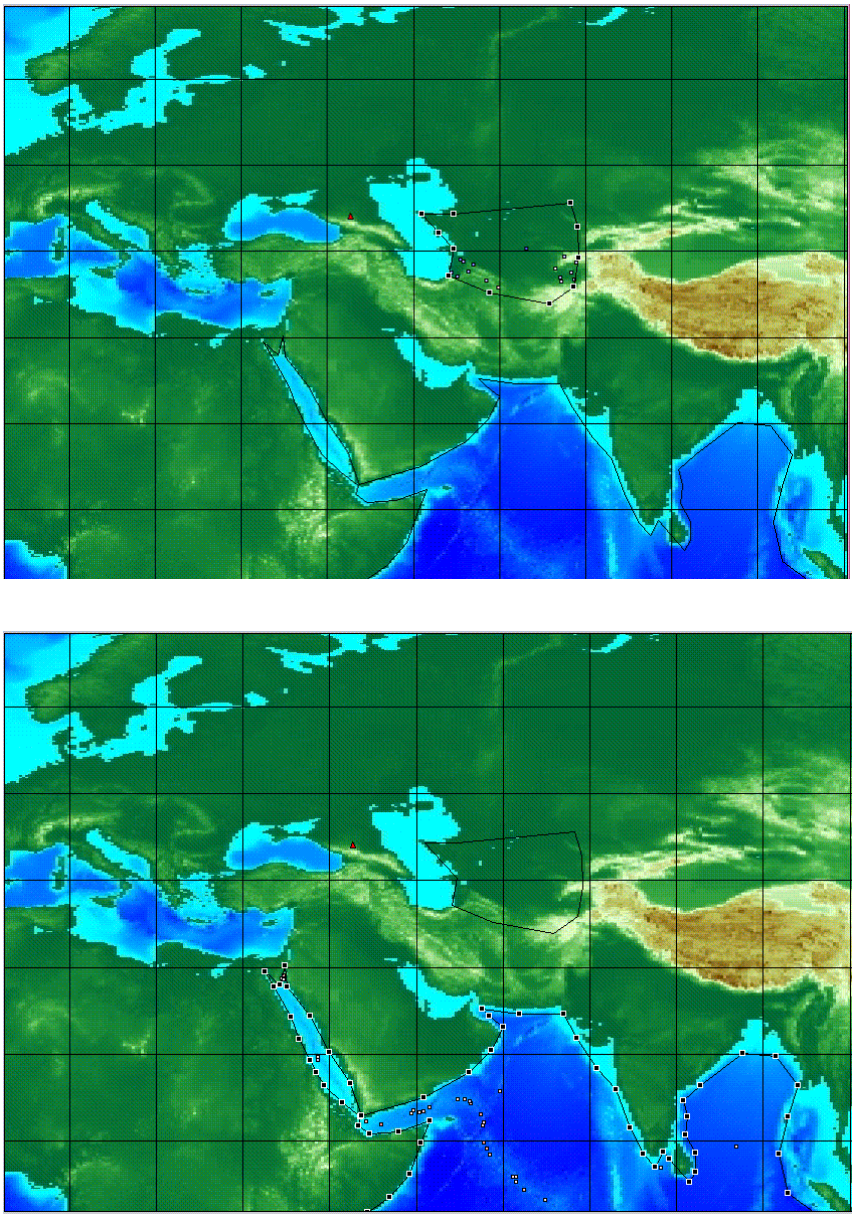
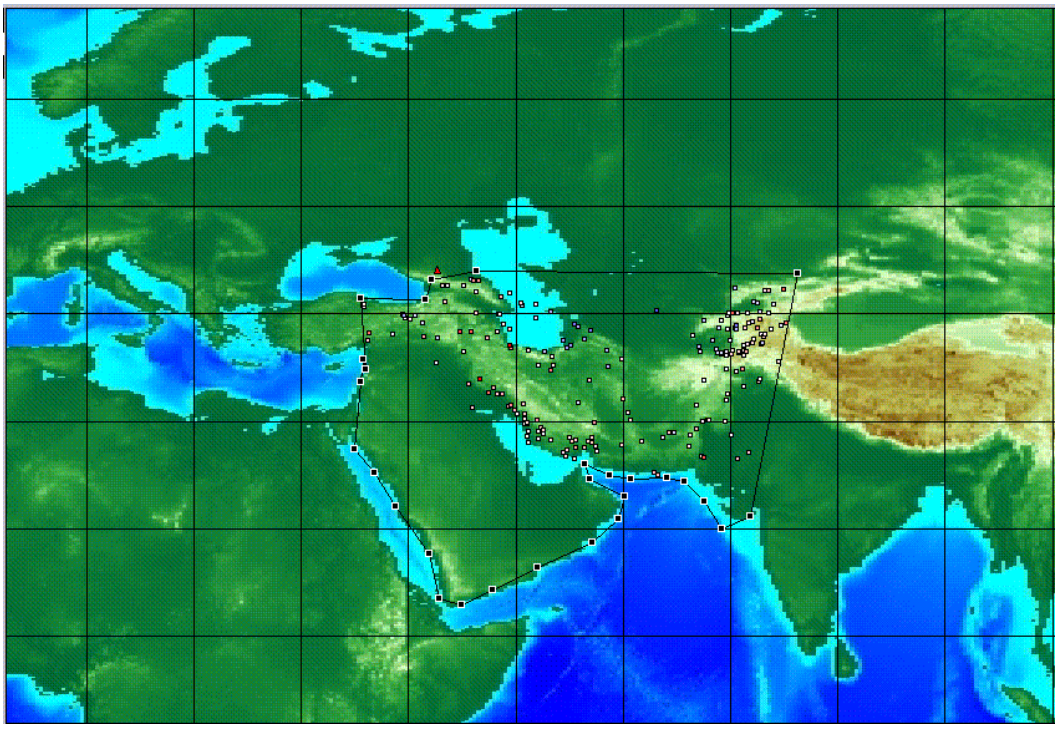
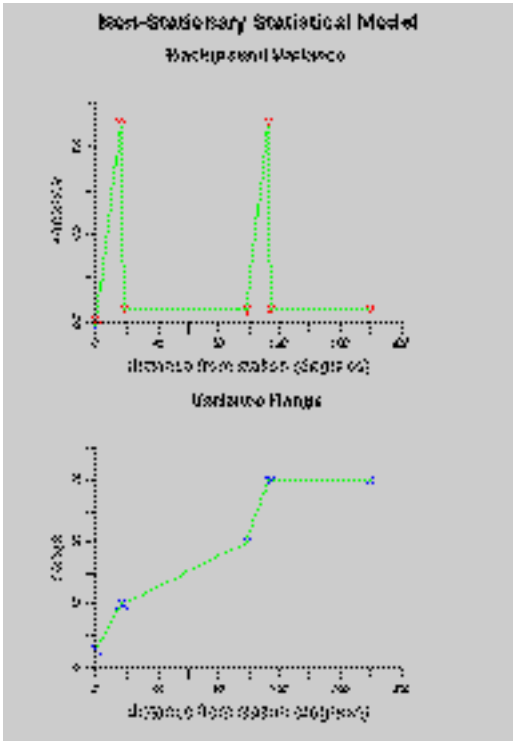


Figure 3: Two examples of integrated model subregions, the first (highlighted with squares) is a fast velocity zone east of the Caspian, while the second is an oceanic subregion that is represented by an oceanic model.





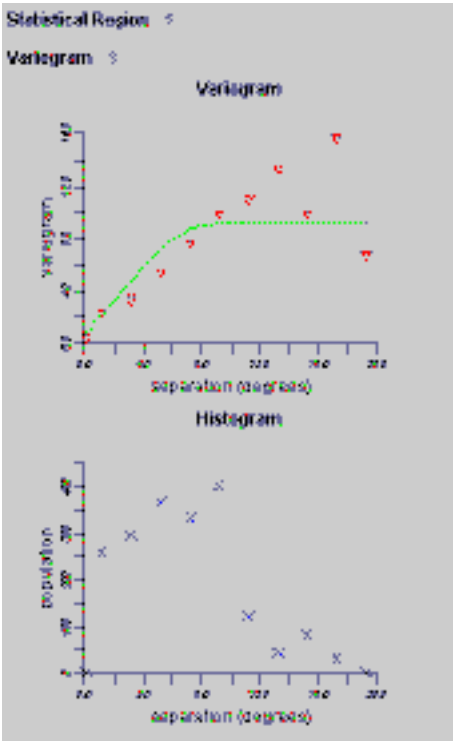


Figure 4: Statistical subregions where the statistics of data and model products provided by external contracts are integrated into one statistical model and a self-consistent set of statistics is applied. This assures accurate uncertainty estimates as an end product.

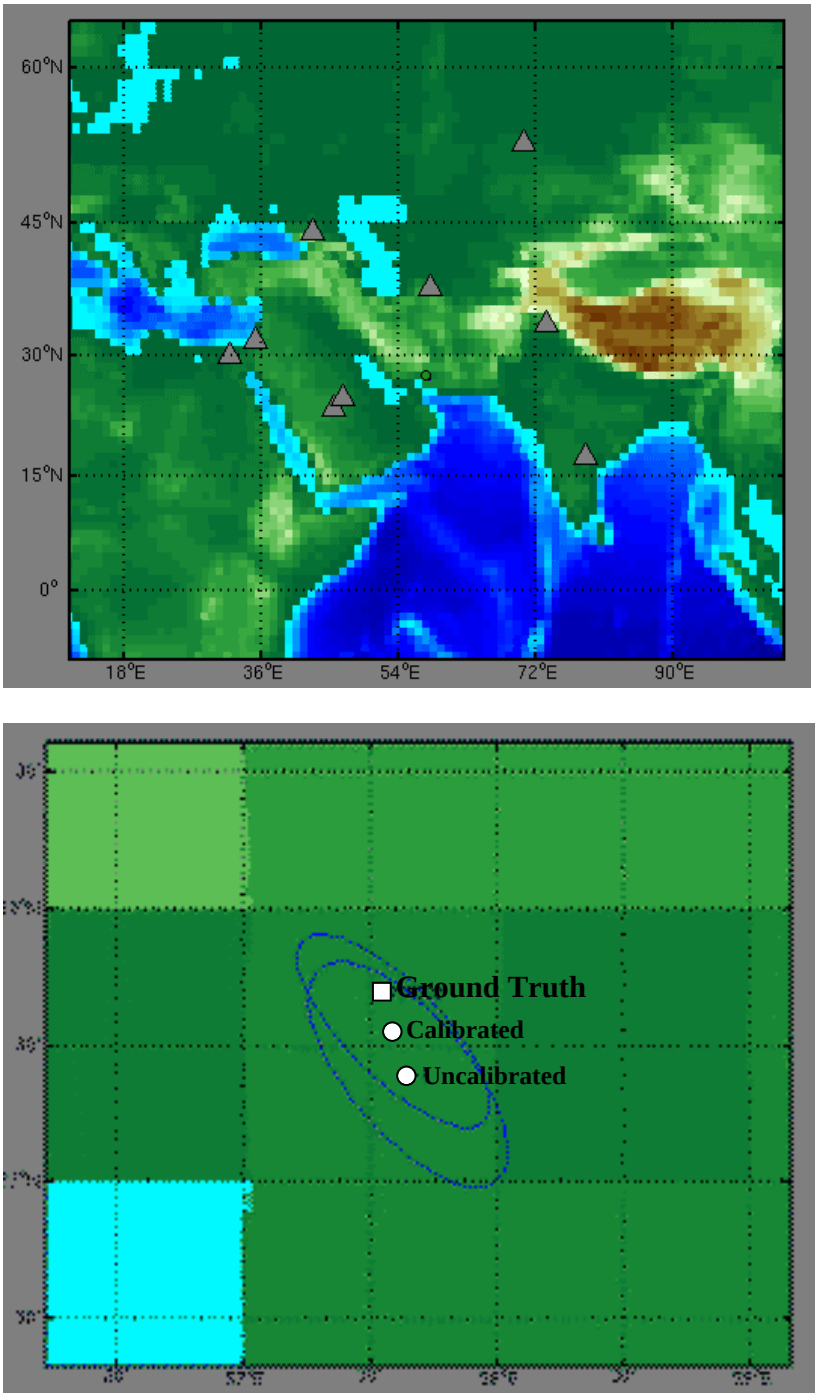


Figure 5: Given the regional station configuration (above) the location and ellipse for a seismic location is shown in the Middle East (below). There is a clear migration of the location towards the known ground truth point and the size of the ellipse is reduced by calibration.

INTEGRATING DIVERSE CALIBRATION PRODUCTS TO IMPROVE SEISMIC LOCATION

Craig A. Schultz, Steven C. Myers, Jennifer L. Swenson, Megan P. Flanagan,
Michael E. Pasyanos, and Joydeep Bhattacharyya
Lawrence Livermore National Laboratory

Sponsored by U.S. Department of Energy
Office of Nonproliferation Research and Engineering
Office of Defense Nuclear Nonproliferation
National Nuclear Security Administration

Contract No. W-7405-ENG-48

ABSTRACT

The monitoring of nuclear explosions on a global basis requires accurate event locations. As an example, under the Comprehensive Nuclear-Test-Ban Treaty, the size of an on-site inspection search area is 1,000 square kilometers or approximately 17 km accuracy, assuming a circular area. Achieving this level of accuracy is a significant challenge for small events that are recorded using a sparse regional network. In such cases, the travel time of seismic energy is strongly affected by crustal and upper mantle heterogeneity and large biases can result. This can lead to large systematic errors in location and, more importantly, to invalid error bounds associated with location estimates. Corrections can be developed and integrated to correct for these biases. These path corrections take the form of both three-dimensional model corrections along with three-dimensional empirically based travel-time corrections. LLNL is currently working to integrate a diverse set of velocity model and empirically based travel-time products that are provided internally by the DOE laboratories and externally through contracts into one consistent and validated calibration set.

To perform this task, we have developed a hybrid approach that uses three-dimensional model corrections for a region and then empirically uses reference events when available to improve these path corrections. This empirical approach starts with the best *a priori* three-dimensional velocity model that is produced for a local region and uses this as a baseline correction. When multiple competing models are provided from various sources for a local region, uncertainties in the models are compared against each other using our ground truth data and our analysts picks. Based on the results of this comparison an optimal model is selected. We are in the process of combining three-dimensional models on a region-by-region basis and integrating the uncertainties to form a global correction set. Our Bayesian kriging approach then combines the set of optimal models and their statistics with empirical calibrations to give an optimal three-dimensional *a posteriori* calibration estimate. In regions where there is limited or no coverage by reference events, travel-time corrections are based primarily on the model. The integrated *a priori* model is particularly important in these areas. In regions with adequate calibration events, the corrections are based primarily on these events. We demonstrate improvement in event location through the reduction of regional bias. In regions with sparse or no ground truth, the *a priori* model will need to be spot-validated with the use of dedicated calibration experiments or through the use of mining explosions, where available.

Key Words: calibration, product integration, event location, reference events, model corrections, validation

OBJECTIVE

The monitoring of nuclear explosions on a global basis requires accurate event locations. Unfortunately, crustal and upper mantle velocity anomalies often lead to systematic travel-time anomalies that in many cases lead to large systematic errors in location estimates. Typically these velocity anomalies are not accounted for in the location process and the predicted errors misrepresent the true uncertainty of the event location. At Livermore, we are working to implement a unified framework that combines empirical-based and model-based path corrections to remove bias from the location problem. Our framework will incorporate any combination of *a priori* and *a posteriori* one-dimensional, two-dimensional, and three-dimensional models. These models that are derived from a variety of sources including external contracts, are combined with our empirically based travel time corrections. The errors are then propagated into our coverage ellipse estimates. This paper focuses on the Livermore effort to integrate a diverse set of three-dimensional velocity model and empirical based travel-time products into one consistent and validated calibration set.

RESEARCH ACCOMPLISHED

We continue to work closely with Sandia National Laboratories (SNL) to implement a framework that allows us to design, build, integrate, and visualize calibrations that are produced from our own internal DOE research and that provided through research associated with external contracts. This is not an entirely new project. Instead, it is the natural extension of our empirical and modeling calibration efforts over the past five years. A large part of our effort at Livermore has been concerned with generating standardized detection, travel-time, and amplitude correction volumes on a regional basis. The tessellated output of the correction volumes combines a set of sub-regions into one global correction set. The global set of integrated corrections is then fed directly into the appropriate detection, location, and discrimination algorithms and leads to the primary improvement in our ability to locate and discriminate events. In our framework, we address four core issues.

Knowledge Base Product Visualization. We are working to provide improved end-to-end visualization of all calibration events (i.e. ground truth events), their uncertainties, constructed models, empirically kriged surfaces on a region-by-region basis. We can now provide a completely integrated demonstration of the DOE laboratories' geographic regionalization.

Direct Calibration Modification. We are working to visualize, access, and potentially alter within any geographic subregion the calibration events, statistics, model, and/or kriged surfaces, if required. Subregions can be rapidly redefined. This may be especially useful when adding calibration information in regions where a subset of calibrations and uncertainties need to be added after the fact and in an efficient fashion.

External Product Integration. This process allows the laboratories to identify geographic subregions that correspond to regions covered by external contractors. Contract research provided to Livermore within a geographic subregion can be seamlessly incorporated into the DOE KB. Product integrators assess uncertainties in contributed calibrations and compare these uncertainties with our internal models and with other contributions from external contractors in the region. The optimal model is selected and assigned to that sub-region.

DOE Coordinated Analysis. This process standardizes DOE calibration efforts into one single format and access tool. Use of this tool ensures the seamless coordination and integration of projects. Sub-regions can be easily merged at boundaries and models can be altered to properly merge analyses made by different laboratories in regions that overlap. This process is fully auditable.

This framework is being developed in multiple phases. The first phase involves standardizing the suite of statistical, kriging, modeling and tessellation tools that have been developed by LLNL and SNL over the past two years.

Framework for Integrating Calibrations

The overall goal of our framework is to provide a flexible, interactive environment in which an analyst can produce, test, and manage calibration information for seismic stations. This framework focuses on providing accurate characterizations of location uncertainty given the highly nonstationary and regionally varying nature of seismic travel time, azimuth, and slowness.

To account for variations in regional structure, our framework is designed to account for dramatic variations in travel-times and amplitudes that occur over relatively short distances in the crust - variations that can lead to significant errors in event location. Figure 1 gives a general overview of how we accurately account for these errors. We begin by cataloging well constrained - both in location and source characteristics - historic earthquakes and explosions in the DOE KB and use these events to spatially map their amplitude and travel-time changes as a function of geographic coordinate. This acts as the data set that we use to both test our internal DOE models and any external models developed by contractors. These data are also used to assign and validate the uncertainties associated with the models (Hanley and Schultz, 2000). As more events occur over time, the two-dimensional and three-dimensional velocity models are continually refined and our ability to account for crustal effects is improved (Flanagan et al., 1999; Swenson et al., 1999; Flanagan et al., 2000;). However, one quickly realizes that model prediction will never be perfect. By its very nature, a model of the earth is underdetermined by the observational data and, thus, gives only an average estimate of the true earth structure. More precisely, if one tried to predict the travel time or amplitude of an event that was used to develop the model, one could not recover its exact characteristics. To provide an accurate characterization, we have developed a set of innovative statistical techniques and algorithms that work together with the model to empirically predict and propagate the travel-time or amplitude correction along with its uncertainties (Schultz and Myers, 1998; Myers and Schultz, 1999; Myers and Schultz, 2000).

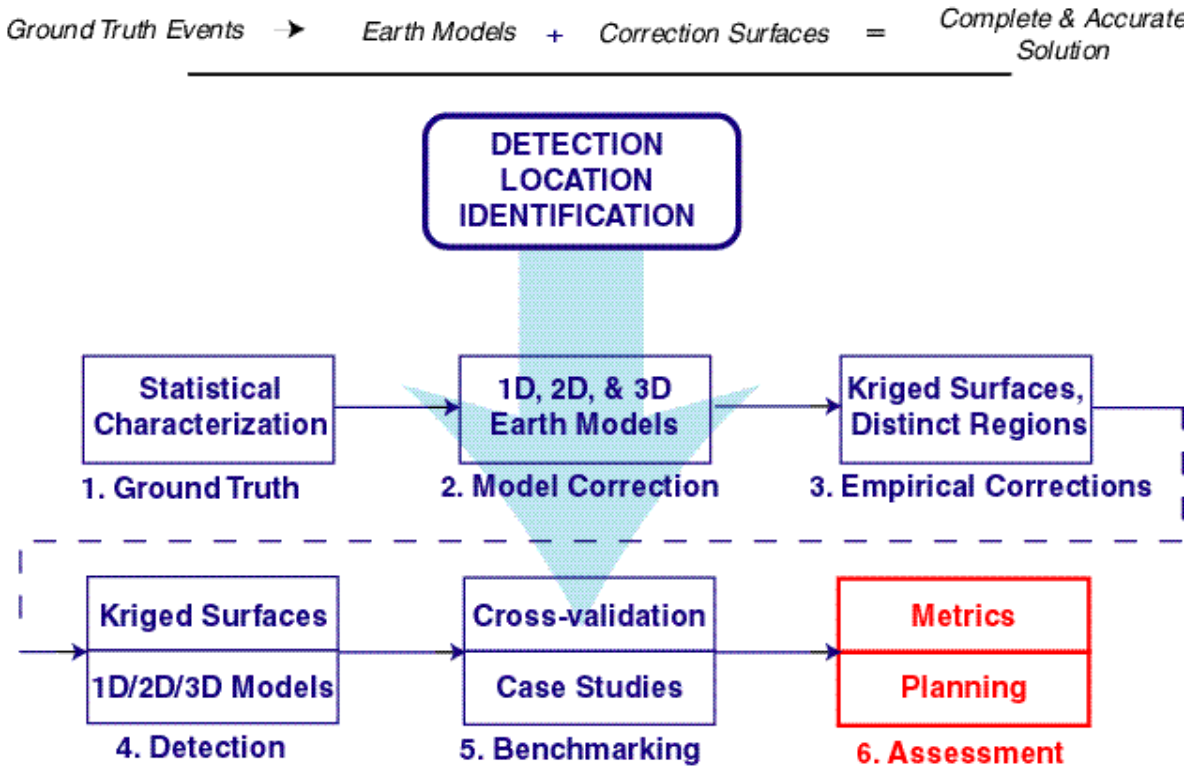


Figure 1: Developing a comprehensive framework for location.

Methodology for Diverse Calibration Integration

Producing calibration information for a region involves the creation of calibration surfaces and/or tessellations for all the stations within the region. This requires the production and refinement of dozens of subregions, both model- and statistical-based. Producing these entities is inherently an interactive process in which the researcher must

observe the effect of changes, and use that feedback to decide whether continued modification is required. Figure 2 shows the general structure of a calibration set in our approach.

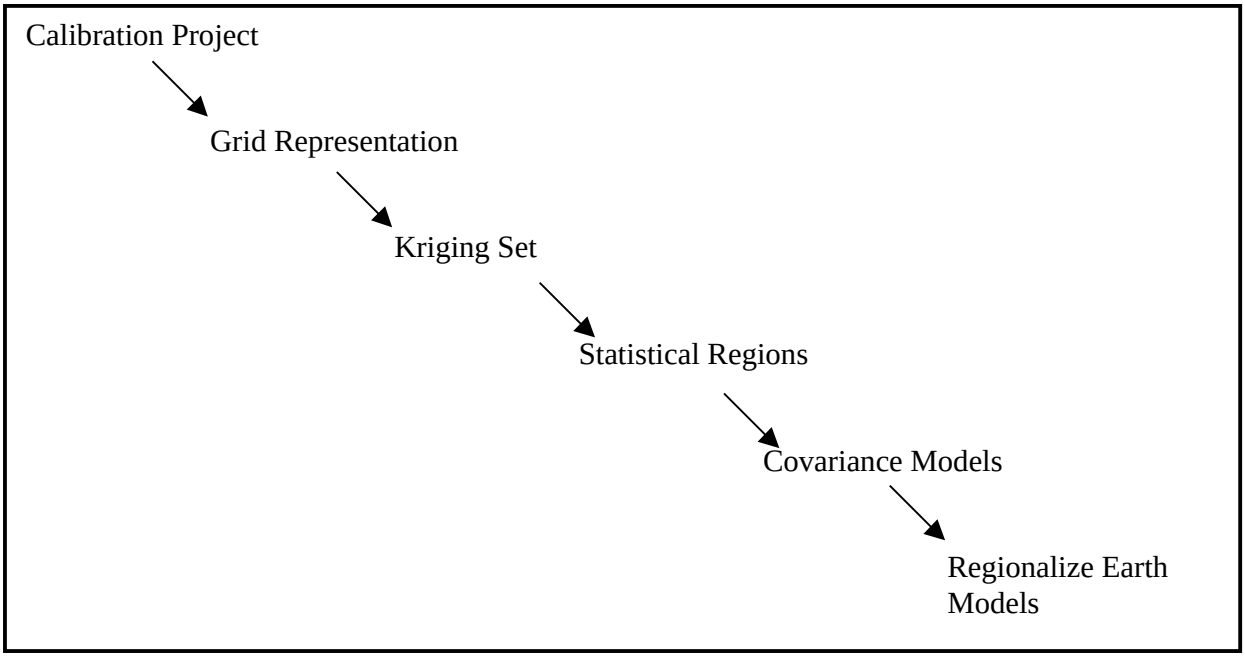


Figure 2: General structure of how calibrations are integrated to form both location and amplitude corrections.

The framework we have designed handles multiple mesh (tessellation) and station-phase-attribute surfaces at once. For each correction surface, a suite of algorithms is incorporated to spatially reduce the dimensionality of the data we integrate while retaining all pertinent calibration information. Distinct calibration data quality groups are spatially associated within geographic subregions. These subregions are created and edited in terms of their boundaries. Various trends and velocity models can be removed within each subregion, as shown in Figure 3. Outlier removal is supported but not encouraged. Statistical tests, graphical methods, and analyst discretion (which may be arbitrary) are supported as methods to identify outliers.

Data with similar spatial statistics are grouped within statistical regions (Figure 4). Statistical regions are completely independent of kriging regions, so statistical regions may overlap any number of kriging regions. However, it may be common for statistical and kriging regions to have identical boundaries. Statistical analysis consists of stationary or non-stationary, isotropic or anisotropic variogram two-dimensional and three-dimensional modeling. In the future, more general statistical modeling will be incorporated. Incorporating non-parametric non-stationary, anisotropy, and/or co-variograms (mixing data sets) are some of the options that work towards increased variogram generality. Variograms are then assigned to a specific kriging region. After assigning variograms to all regions with both DOE calibration data and external contract data integrated, the data set can be kriged.

It may be desirable to krig on any number of optimally spaced (regular, irregular) grids (e.g. tessellation). The grids may be optimized for one kriged surface or a collection of surfaces. If tessellation is chosen, the bounds of the tessellation and the lowest density spacing are specified to ensure accuracy at all times. A collection of surfaces over which the tessellation is optimized must also be specified. The resulting tessellation (node and triangle information) is saved so subsequent surfaces can be kriged on the same mesh.

Using this process we are able to assure that realistic modeling uncertainties are assigned and propagated on a regional basis. Calibration data and models from a diverse set of sources including the laboratories and contracting

universities can be integrated into one correction surface suite and the uncertainties are standardized on a global scale. We continue to validate this process with newly acquired ground truth events and refine it as required.

CONCLUSIONS AND RECOMMENDATIONS

In general, we have developed a hybrid approach to location that uses three-dimensional model corrections for a region and then uses reference events when available to improve the path correction. Our approach is to select the best *a priori* three-dimensional velocity model that is produced for a local region and then use this as a baseline correction. When multiple models are produced for a local region, uncertainties in the models will be compared against each other using ground truth data and an optimal model will be chosen. We are working towards implementing a calibration integration process of combining three-dimensional models on a region-by-region basis and integrating the uncertainties to form a global correction set. The Bayesian kriging prediction combines the optimal model combination and its statistics with the empirical calibrations to give an optimal *a posteriori* calibration estimate. The result, as shown in Figure 5, is improved location estimates and robust location uncertainties that show significant improvement in calibrated regions (Schultz and Myers, 1999; Schultz et al., 1999).

To aid this process we have developed a general framework to provide a flexible, interactive environment in which a researcher can produce, test, and manage calibration information for seismic stations. This approach allows a general statistical analysis on a regional basis and results in a self consistent global calibration set.

References

Flanagan, M., Schultz, C., Myers, S.C., Pasyanos, M., Walter, WR, 2000, Improving regional event locations in the Middle East by incorporating model based correction surfaces derived from 3-d velocity structures, *Seismological Society of America 94th Annual Meeting.*

Flanagan, MP, Schultz, CA, Hutchings, L, 1999, Development of 3-D crust and upper mantle velocity models to improve seismic event location, *Fall American Geophysical Union Meeting.*

Hanley, WG, Schultz, CA, Myers, SC, 1999, Statistical analysis of travel time residuals applied to the analysis of station quality, *Seismological Society of America 94th Annual Meeting.*

Myers, SC, Schultz, CA, 2000, Improving Sparse Network Seismic Location with Bayesian Kriging and Teleseismically Constrained Calibration Events, *Bull. Seism. Soc. Am.*, 90, 199-211

Myers, S.C., Schultz, CA, 1999, Improvement in seismic location using non-stationary Bayesian kriging, *Seismological Society of America 94th Annual Meeting.*

Schultz, CA, Myers, SC, Flanagan, M, Swenson, J, Hanley, J, Pasyanos, M, 1999, Improving seismic event location through calibration of the International Monitoring System, *21st Seismic Research Symposium Technologies for Monitoring the Comprehensive Nuclear Test Ban Treaty.*.

Schultz, CA, Myers, SC, 1998, Nonstationary Bayesian Kriging: A predictive technique to generate spatial corrections for seismic detection, location, and identification, *Bull. Seism. Soc. Am*., 88, 1275-1288.

Swenson, JL, Schultz, CA, Hanley, WG, 1999, Using radially heterogeneous and azimuthally invariant travel-time models to improve seismic location in the Middle East and North Africa, *Fall American Geophysical Union Meeting.*

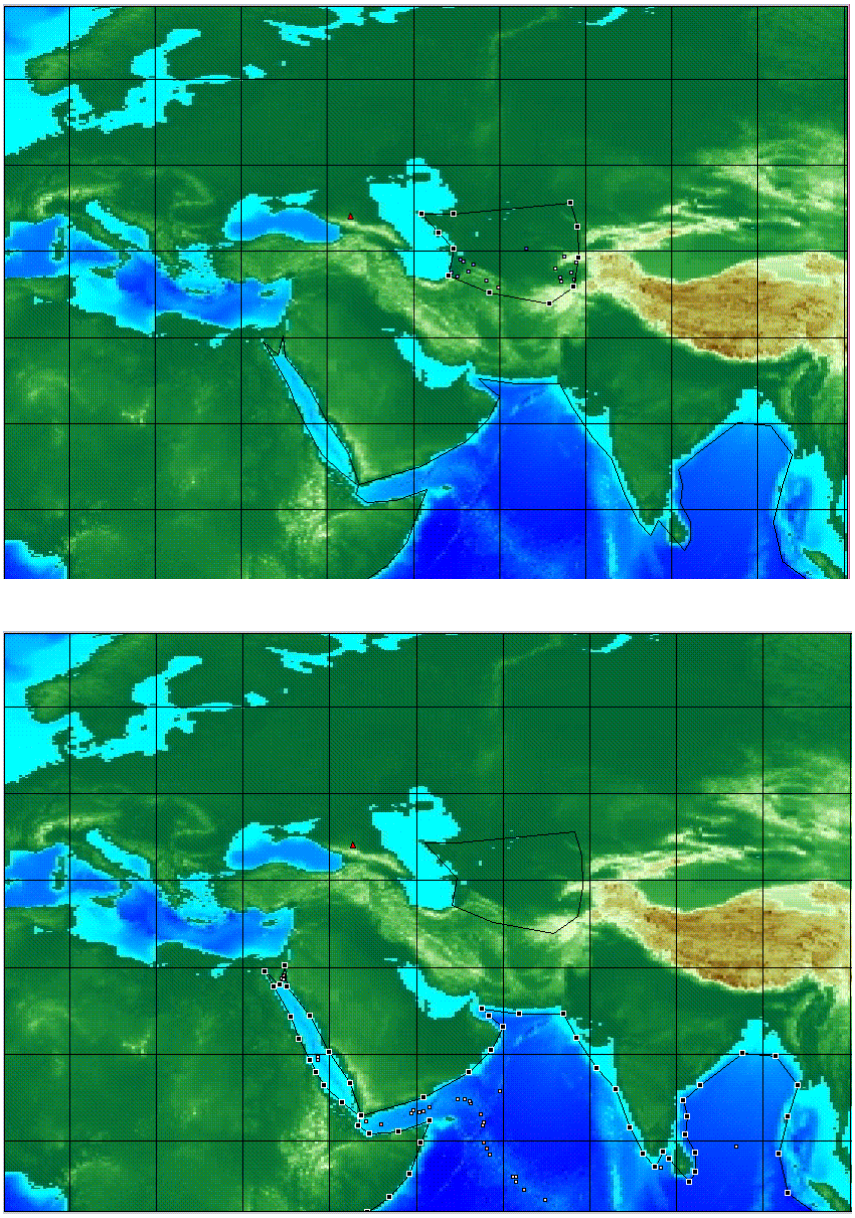
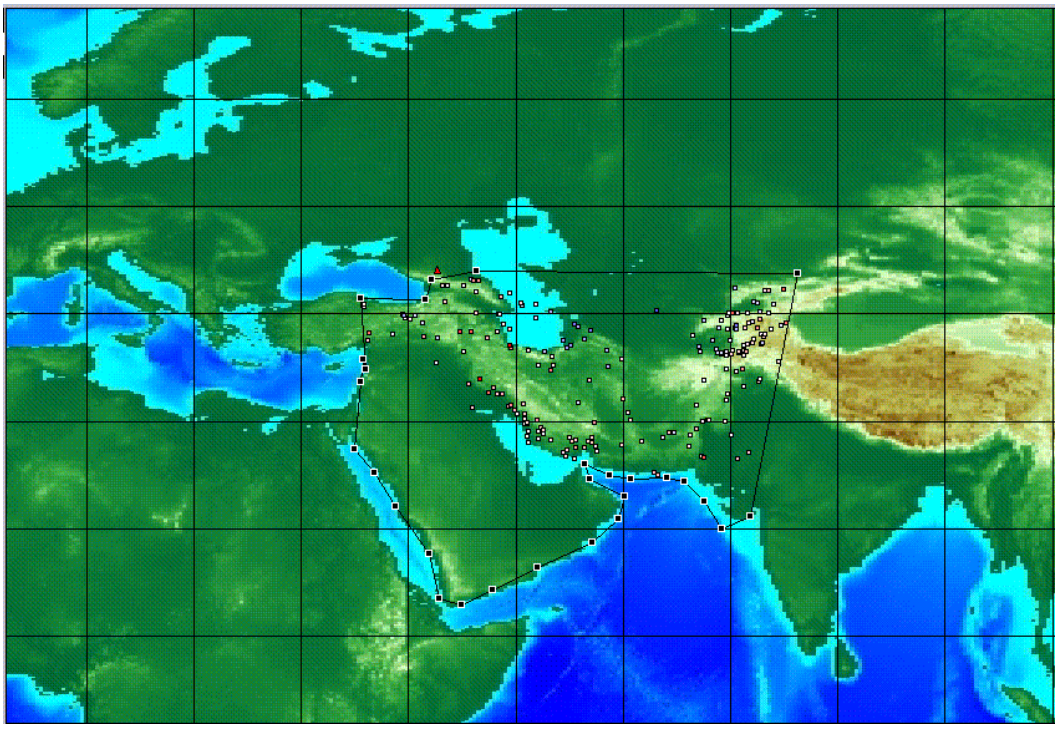
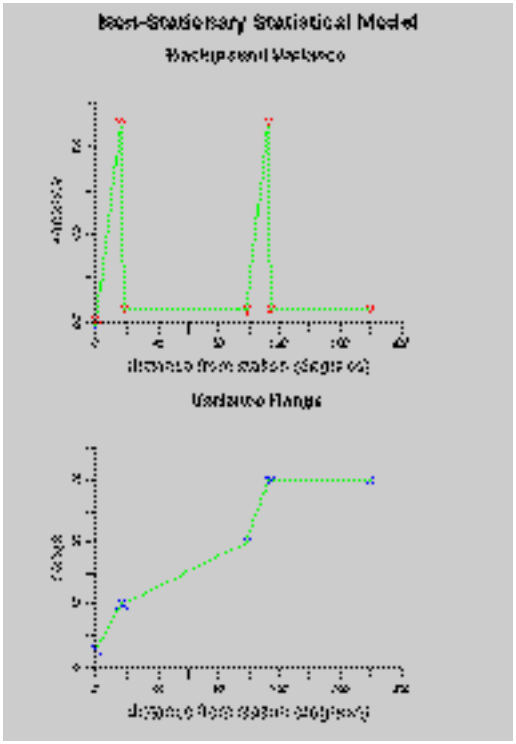


Figure 3: Two examples of integrated model subregions, the first (highlighted with squares) is a fast velocity zone east of the Caspian, while the second is an oceanic subregion that is represented by an oceanic model.





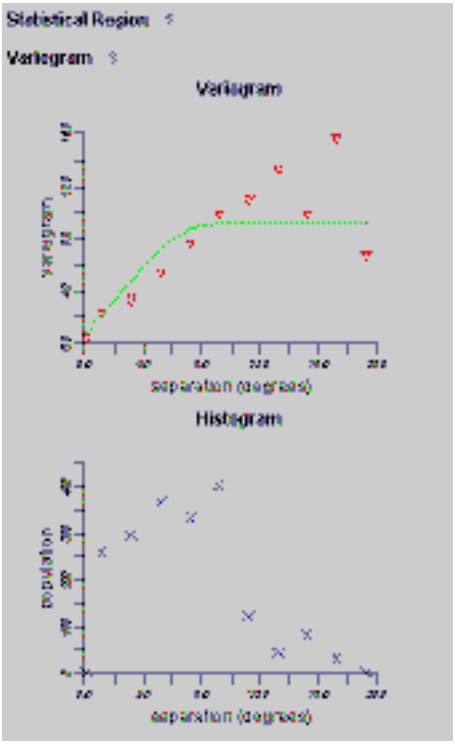


Figure 4: Statistical subregions where the statistics of data and model products provided by external contracts are integrated into one statistical model and a self-consistent set of statistics is applied. This assures accurate uncertainty estimates as an end product.

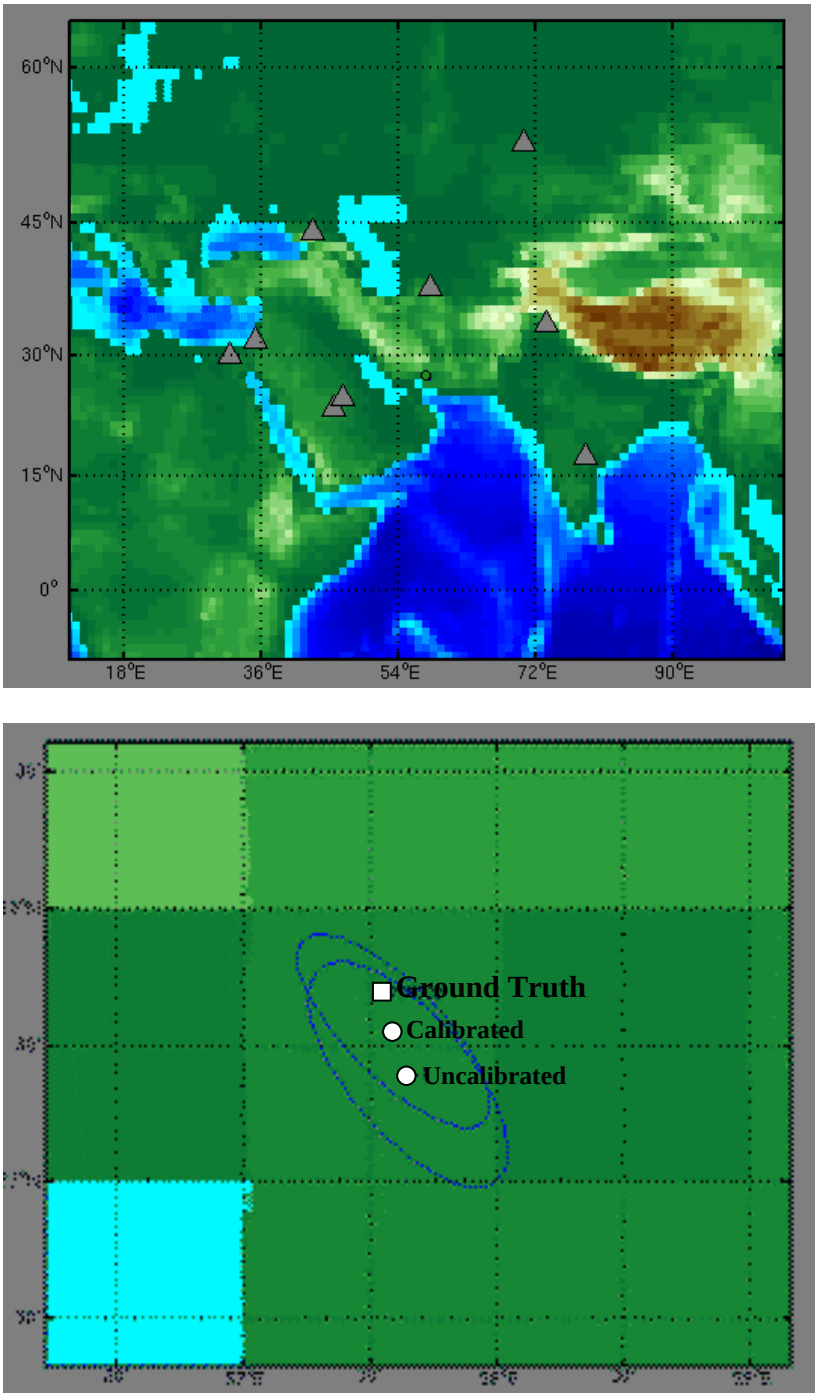


Figure 5: Given the regional station configuration (above) the location and ellipse for a seismic location is shown in the Middle East (below). There is a clear migration of the location towards the known ground truth point and the size of the ellipse is reduced by calibration.

IDENTIFICATION, ASSOCIATION AND ANALYSIS OF RAYLEIGH WAVES IN THE CONTEXT OF CTBT MONITORING

Neil D. Selby
AWE Blacknest
Sponsored by United Kingdom Ministry of Defence

ABSTRACT

The correct identification and association of Rayleigh waves is vital within the context of the CTBT because of the use of the body-wave to surface wave magnitude ratio $m_b : M_S$ as a discrimination method. Rayleigh waves can be identified by their dispersion characteristics (the variation in group speed with frequency) and their elliptical polarization in the plane of propagation. Classically, Rayleigh waves are associated with a seismic disturbance by calculating the angle from which the wave arrives at a recording station (the 'back-azimuth'). Recently, two approaches to the detection of Rayleigh waves have been proposed (North and Woodgold, 1994; Chael, 1997) which rely on Rayleigh wave dispersion and polarization characteristics respectively.

Currently, the identification of Rayleigh waves at the IDC relies on software developed using the methodology of North and Woodgold (1994) and the group speed model of Stevens and McLaughlin (1996). The REB records the arrival time (and residual from the model), an amplitude measurement and consequent calculated M_S. Back-azimuths are also measured and recorded in the REB, although these are not used in associating a Rayleigh wave with a given seismic disturbance.

I present an analysis of Rayleigh wave detections in the REB for 1999 that shows that there is a very wide residual distribution for both arrival times and back-azimuths. For back-azimuths, only 55% of measurements lie within 30° of the great circle path. I also show that the accuracy of back-azimuth measurement varies at each station in the Primary IMS network, which may be a function of station locations, station noise levels and possible mis-orientation of horizontal components. There are a number of reasons why measured back-azimuths may vary from the great-circle between source and receiver. Earth structure can cause such deviations, but these are unlikely to be more than 30°. It may be that a Rayleigh wave associated with a different seismic disturbance has been selected in error, or it may be that the data is simply too noisy to make an accurate measurement. Finally, the processing of the data and the measurement technique applied may be sub-optimal.

In order to investigate the reasons for the large errors in back-azimuth seen in the REB I analyse data from a selection of events from January, 1999. The results of this analysis show that the large majority of back-azimuths, from a range of earthquake magnitudes and epicentre-station distances, can be measured to within 30° of the great-circle path. In those instances where such accuracy cannot be achieved, it is doubtful that the correct Rayleigh wave has been identified. For about 10% of paths, (including all the reports from one seismic disturbance) I can detect no Rayleigh wave at all despite the presence of an M_S measurement in the REB. This is potentially of grave consequence if $m_b : M_S$ is to be used as a discriminant between earthquakes and explosions.

Key Words: Rayleigh waves, Back-azimuth, M_S.

OBJECTIVE

To assess the analysis by the International Data Centre (IDC) of Rayleigh waves observed at seismic stations of the International Monitoring System (IMS) and to determine whether the levels of identification and association achieved can be improved upon.

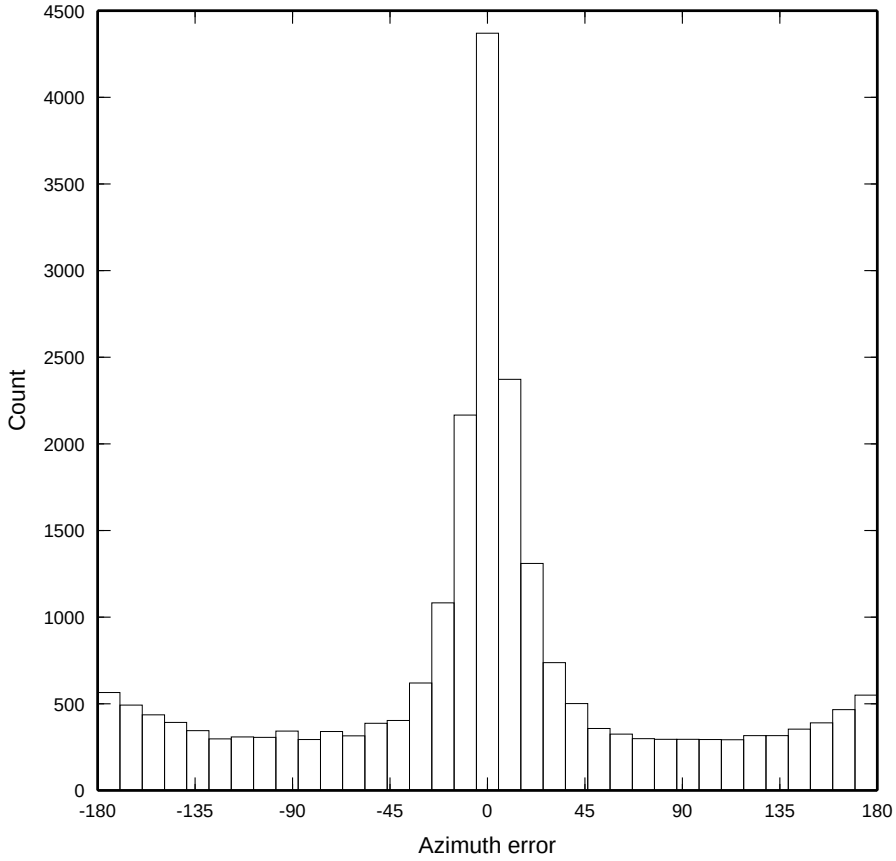


Figure 1: Distribution of back-azimuth residuals for Rayleigh wave observations in the REB 1 January 1999 - 25 November 1999.

RESEARCH ACCOMPLISHED

A brief perusal of the Reviewed Event Bulletin (REB) produced until February 2000 by the prototype International Data Centre (pIDC), Arlington, Virginia, USA and since that date by the IDC in Vienna, Austria, shows that the observations of Rayleigh wave (LR) phases often have large back-azimuth and arrival time residuals. Users of the REB may be drawn to the conclusion that observations with these large residuals should be treated with caution. It is important that all observations of LR in the REB can be relied upon, since the value of M_S, obtained from the measurement of Rayleigh wave amplitude, is used in an important screening criterion, the body-wave/surface-wave magnitude ratio, $m_b : M_S$. This study investigates the reliability of both the identification and association of Rayleigh waves in the REB. Here I use the term 'identification' to mean the detection of a Rayleigh particle motion and the term 'association' to mean the connection of an identified Rayleigh wave with a known epicentre, established using body-wave measurements.

Review of REB LR reports

To investigate the reliability of the back-azimuth measurements given in the REB I collated all LR reports for the period 1 January 1999 - 25 November 1999. Fig. 1 shows the distribution of the reported azimuth residual for the 22 934 observations. Approximately 45% of the residuals are greater than 30°. Earth structure can cause Rayleigh waves to deviate from the great-circle path (see, for example; Woodhouse and Wong, 1986; Laske, 1995; Bungum and Capon, 1974) but I believe that ±30° is a generous margin which should encompass the back-azimuth of all first arriving wave-packets at the frequencies and path

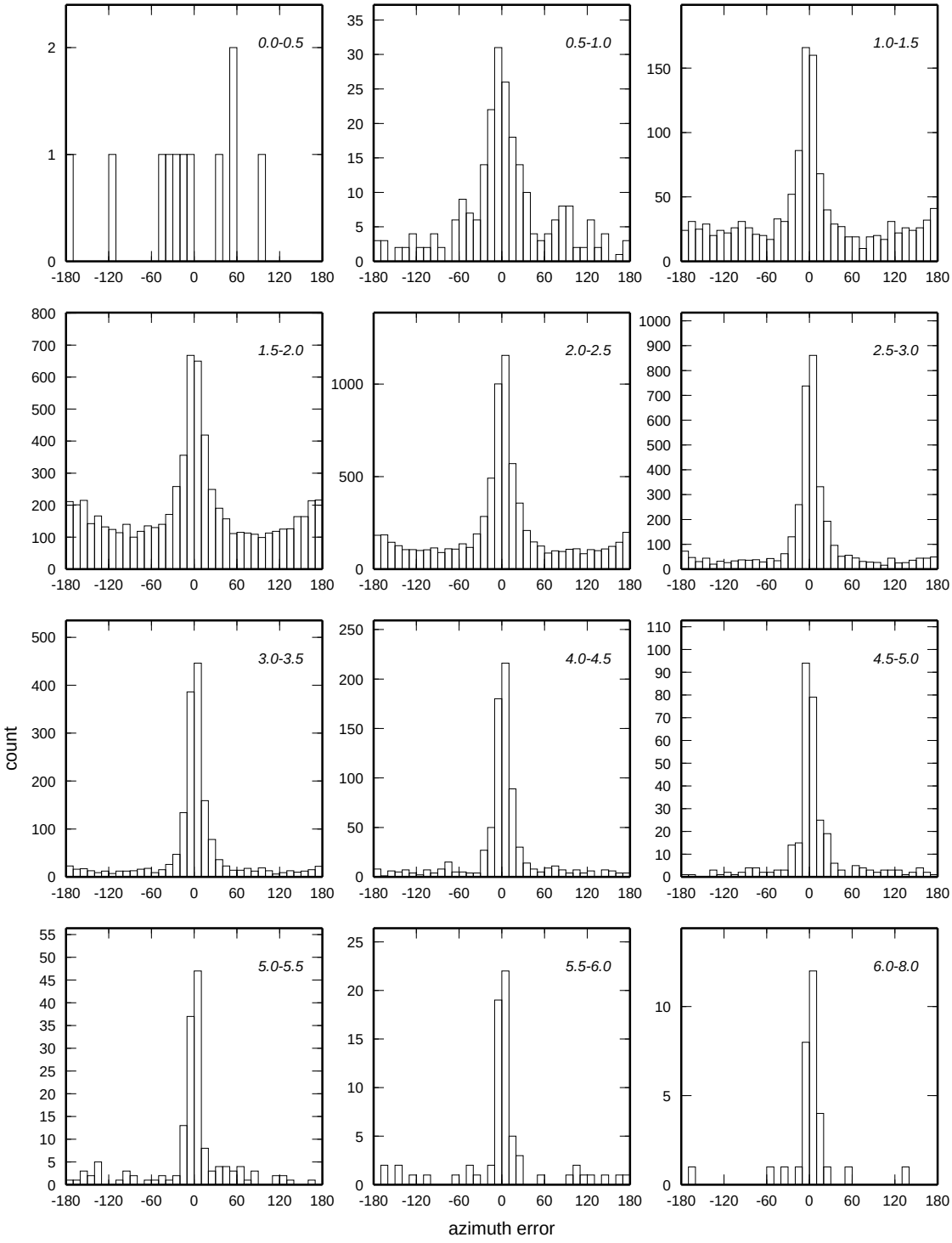


Figure 2: Azimuth error plotted against log (measured amplitude)

Station	Error	Station	Error	Station	Error	Station	Error
ARCES	+15	CMAR	+5	MAW	-10	PLCA	0
BDFB	-5	DBIC	-20	MNV	+20	SCHQ	0
BGCA	-10	ESDC	0	NOA	0	ULM	0
BJT	+5	HIA	0	NRIS	T	YKA	-5
BOSA	0	ILAR	+20	PDAR	+5	ZAL	T
BRAR	-15	KSAR	0	PDY	T		

Table 1: Stations used in this study and systematic error at each station. T=triaxial seismometer.

Event no.	Date	Time	Location	Lat	Long	Ms	LR
20276833	1999/01/01	09:05:46	SUDAN	4.33N	31.41E	3.5	4
20277798	1999/01/02	17:55:04	SICHUAN, CHINA	27.29N	101.12E	3.9	8
20279693	1999/01/04	11:09:57	SE SIBERIA	57.45N	123.63E	3.2	3
20281441	1999/01/05	18:27:41	ETHIOPIA	6.23N	37.62E	3.6	4
20288809	1999/01/13	04:36:19	VENEZUELA	9.99N	63.83W	3.8	2
20291674	1999/01/14	22:45:15	NW CAUCASUS	41.10N	44.00E	4.2	13
20291760	1999/01/15	10:16:35	CRETE	34.65N	26.37E	3.3	4
20291801	1999/01/15	13:45:57	IRAN-IRAQ	35.47N	45.25E	3.1	2
20293318	1999/01/17	19:32:13	ITALY	39.09N	17.33E	4.2	12
20299300	1999/01/22	02:36:23	SE SIBERIA	57.24N	120.60E	3.3	1
20300510	1999/01/22	22:48:01	SUDAN	5.06N	32.31E	3.4	4
20304734	1999/01/25	18:19:15	COLOMBIA	4.41N	75.56W	5.7	11
20307458	1999/01/27	19:07:54	LAKE BAYKAL	55.92N	110.52E	2.8	2
20307707	1999/01/27	21:24:28	CHILE	40.48S	72.15W	4.2	3
20309281	1999/01/28	22:28:11	ZAMBIA	15.76S	26.42E	3.4	2
20310643	1999/01/29	18:42:32	CALIFORNIA	28.10N	112.08W	3.8	10
20313853	1999/01/31	08:16:01	E CAUCASUS	43.05N	46.96E	3.5	7
20314536	1999/02/01	04:52:41	S. ZEMLYA	85.51N	86.45E	4.6	12

Table 2: Earthquakes used in this study. Event number in the pIDC REB catalogue, Date, Time, Location, Latitude, Longitude, Surface wave magnitude (Ms), number of associated Rayleigh waves (LR).

lengths under investigation. Consequently we must assume that the back-azimuth residuals of these 45% must be due to one of four causes: mis-alignment of the horizontal components at a station; measurement of a mis-associated or mis-identified Rayleigh wave; a poor application of the measurement technique; or it may be that back-azimuth measurement to within the accuracy required is not possible.

Figure 2 shows the distribution of back-azimuth error partitioned by the logarithm of the measured Rayleigh amplitude reported in the REB. Note that the vertical scale is different in each panel. It is clear that at high amplitudes back-azimuths are measured accurately, as would be expected since these measurements will have a high signal-to-noise ratio. However, the poorest distribution is not at the lowest amplitudes. A possible explanation for this is that small amplitude Rayleigh waves cannot be detected at the noisiest stations and so are not reported.

Investigation of systematic station residuals

Wang and Stead (1998) carried out an analysis of back-azimuth residuals for body-wave phases recorded at three-component stations. Elsewhere (Selby, 1999), I have carried out an analysis of each station which listed LR observations during the study period. In Fig. 3 I show examples of the back-azimuth residual distribution at four stations. The character of this distribution is different at each station. HIA, which appears to be one of the most reliable IMS stations for LR detection and association has a narrow peak centred on zero (i.e. the great-circle back-azimuth). CMAR has a broader central peak which is also

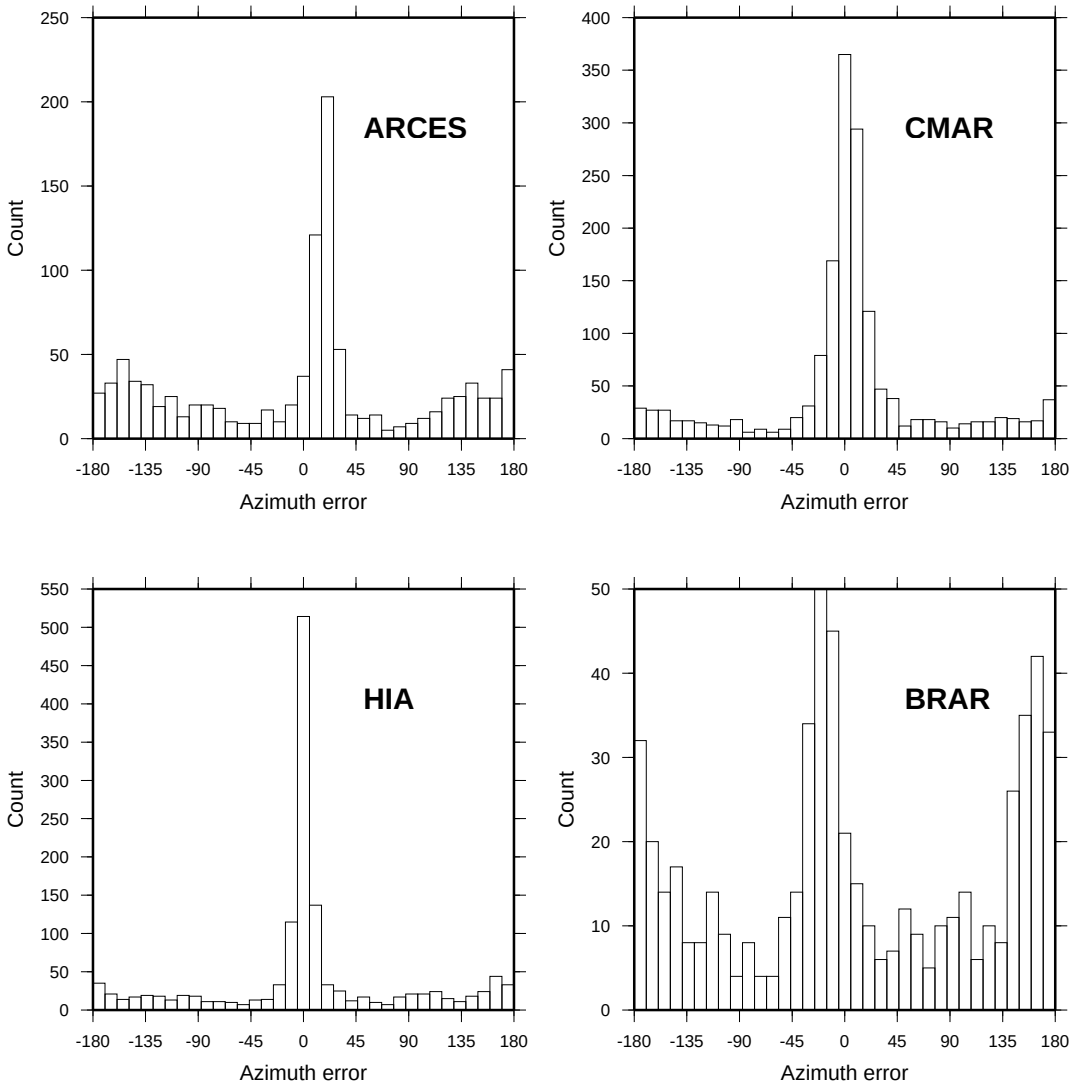


Figure 3: Back-azimuth residual distributions for IMS stations ARCES (1037 measurements), CMAR (1598 measurements), HIA (1371 measurements) and BRAR (576 measurements)

centred on zero. ARCES shows a higher level of background, random residuals and its central peak is offset from zero. At BRAR, although there are fewer observations, the distribution of residuals is uneven and shows two major peaks. Because the pattern of residual distribution is so different at every station it is rather hard to decide on the cause of systematic errors. Some stations show large peaks which are simply offset from zero, perhaps suggesting a simple misalignment of horizontal components, whereas at other stations there may be more complex problems. Because it is not known whether these errors are due to station misalignment or to other factors (such as structure at the station) and also because the error distributions are not normal, I choose not to make a fully accurate measurement of this systematic error. In my view each station should be checked for mis-alignment rather than assumptions made based on averaging of remote data. Re-enforcing this view is the fact that the findings of Wang and Stead (1998), based on body-wave data, do not always agree with my results. However, the errors estimated do perhaps indicate which stations require investigation. The stations NRIS, PDY and ZAL in Russia are triaxial (rather than conventional three component). Assessment of pIDC REB back-azimuth reports from these stations show that there is no straight-forward relationship between observed and predicted azimuth at these stations. Wang and Stead (1998) explain how these distributions are related to the alignment of the

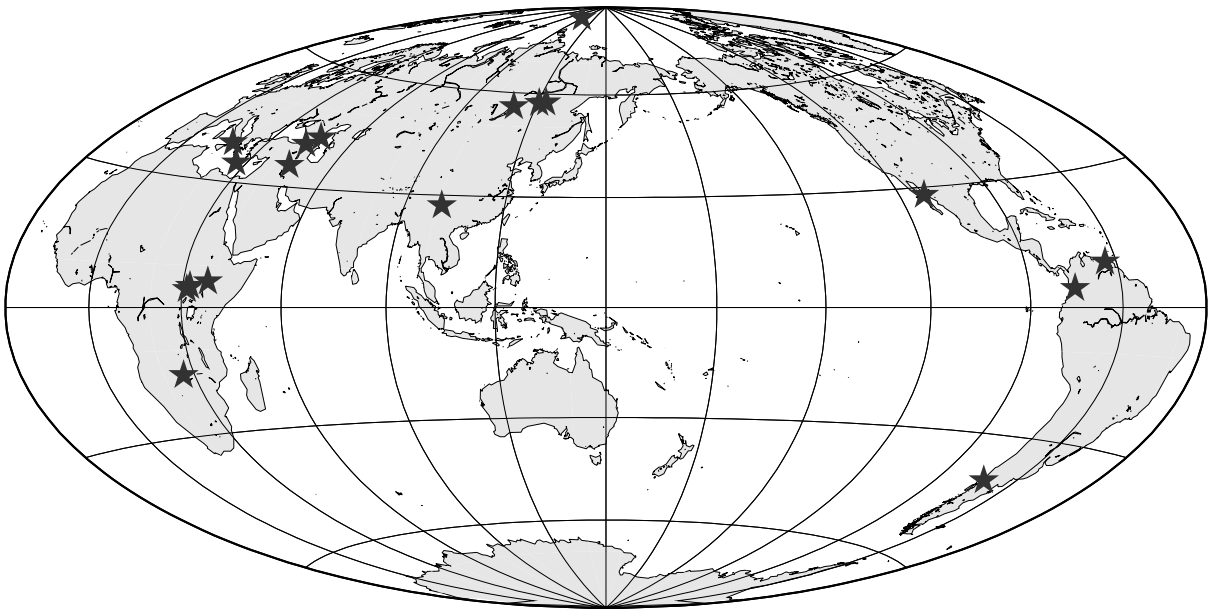


Figure 4: Distribution of events used in this study

triaxial components, but since I are not concerned here with the orientation of station components I proceed no further with these stations. In table 1 I show the approximate systematic error observed at each station.

Analysis of a selection of waveforms

In order to determine the sources of error in the REB LR back-azimuth reports I analyze data from a selection of earthquakes from 1 January 1999 - 1 February 1999. 18 earthquakes with 105 associated LR reports were selected. Table 2 lists the selected earthquakes, their locations and the number of IMS stations reporting LR. The location of these earthquakes is shown in Fig. 4. The earthquakes were chosen to have epicentres on shore or close to the continental edge, to be shallow (REB depth 0km) and cover a range of magnitudes. Data were acquired for each path for a time window starting at the origin time of the earthquake and ending 30 minutes or one hour later, depending on the epicentre-station distance. A multiple taper dispersion plot (Dziewonski *et al.*, 1969; Dziewonski and Hales, 1972) is produced for the vertical component and from this time and frequency windows are selected. The back-azimuth is calculated from the cross-correlation of the Hilbert transformed vertical and radial components (see, for example, Chael, 1997). Elsewhere (Selby, 2000) the analysis of these data is described in more detail. Fig. 5 shows a comparison of measured back-azimuth and geometric (great-circle) back-azimuth for paths for which I was able to make a measurement. The dotted lines show the $\pm 30°$ error bounds. The grey squares are the pIDC

Case	N	%
Back-azimuth measured to within 30°	74	70.5
Back-azimuth measured, error greater than 30°	2	1.9
No Rayleigh wave found	8	7.6
Rayleigh wave on vertical component only	2	1.9
Data incomplete or faulty	8	7.6
Data not retrieved	4	3.8
Triaxial, not processed	7	6.7

Table 3: Summary of the results of this study

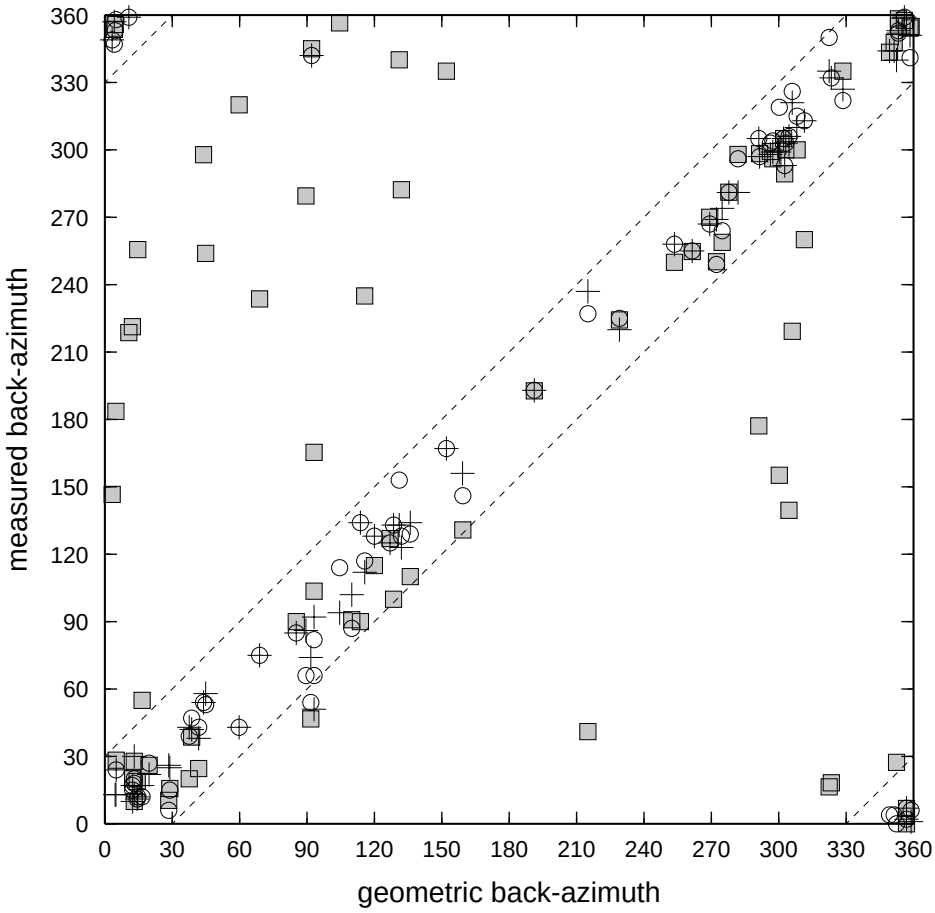


Figure 5: Observed back-azimuth plotted against geometric back-azimuth. Filled squares: PIDC measurements. Open circles: this study. Crosses: This study plus correction for station systematic error.

measurements given in the REB. There is a large scatter. Open circles show the measurements made in this study and the crosses these measurements adjusted using the station systematic errors in Table 1. It is clear that for the large majority of paths included in this study it is possible to make sufficiently accurate back-azimuth measurements to associate an observed Rayleigh wave with the epicentre. In Fig. 5 only two measurements lie outside the 30° error bounds. On further inspection (Selby, 2000) these turn out not to be the correct waveforms. Fig. 5 shows clearly that the systematic station errors discussed earlier do not form a major part of the back-azimuth residuals observed. It also shows that where a Rayleigh wave has been identified correctly it has also been associated correctly. Hence the large azimuth residuals must be due to poor processing of the data or a poor measurement technique.

CONCLUSIONS AND RECOMMENDATIONS

Table 3 shows the final results of the waveform analysis. Of the 105 waveforms for which the back-azimuth was measured, 74 gave an answer within ±30° of the great-circle back-azimuth. Only two gave an error greater than 30°, and further examination showed that these were unlikely to be correctly identified or associated Rayleigh waves. More worrying is that for 8 paths I was unable to detect a Rayleigh wave at all. For a further two paths there may have been a suspicion of a Rayleigh wave on the vertical component only, but this is not certain. In particular, for one earthquake (REB event 20281441, Ethiopia, see Table 2) I was unable to detect any Rayleigh waves at all, suggesting that the REB quoted M_s for this earthquake is meaningless. I found no examples of genuine Rayleigh waves associated with the wrong event, which

indicates that the global model used by the pIDC (Stevens and McLaughlin 1996, 1997) is effective as a dispersion test. However, measurement of noise to give a surface wave magnitude is clearly undesirable. Any automated routine used for verification must only identify and associate definite Rayleigh waves. It seems clear from this study that a dispersion test alone cannot do this if the signal-to-noise ratio is low, sometimes, M_s may be measured from noise rather than the correct Rayleigh wave. It is of course difficult to design an automated routine which can achieve the same reliability as analyst review, but any algorithm must only find and measure Rayleigh waves where an analyst would see them. In these circumstances it seems that a routine must include the following elements

- a dispersion test
- a test for degree of polarization
- a back-azimuth measurement
- a signal-to-noise ratio test.

The algorithm should be able to select a time window and frequency band for which the signal-to-noise ratio is good, which shows the correct dispersion, is correctly polarized and has the right back-azimuth.

To conclude, polarization and back-azimuth measurements can be made to within the desired accuracy for Rayleigh waves at periods useful to verification. If a back-azimuth estimate cannot be made with a high level of coherence or if the azimuth is incorrect, then there must be doubt about whether the correct waveform has been identified and it should not be used to measure surface wave magnitude.

REFERENCES

Bungum, H. and J. Capon, (1974). Coda pattern and multi-path propagation of Rayleigh waves at NORSAR. *Phys. Earth Planet. Inter.*, **9**, 111-127.

Chael, E. P. (1997). An automated Rayleigh-Wave Detection Algorithm. *Bull. seism. Soc. Amer.*, **87**, 157-163.

Dziewonski, A. M. and A. L. Hales (1972). Numerical analysis of dispersed seismic waves. *Methods in Computational Physics*, **11**, *Seismology: Surface Waves and Earth Oscillations*, 39-85.

Dziewonski, A. M., S. Bloch and M. Landisman (1969). A technique for the analysis of transient seismic signals. *Bull. seism. Soc. Amer.*, **59**, 427-444.

Laske, G., (1995). Global observation of off-great circle propagation of long period surface waves. *Geophys. J. Int.*, **123**, 245-259.

North, R. G. and C. R. D. Woodgold (1994). Automated detection and association of surface waves. *Annali Di Geofisica*, **XXXVII**, 301-308.

Selby, N. D. (1999). Rayleigh wave (LR) reports in the Reviewed Event Bulletin (REB) of the prototype International Data Centre (pIDC): 01/01/1999-25/11/1999.
AWE Blacknest internal note DFS/AG/396.

Selby, N. D. (2000). Association of Rayleigh waves using back-azimuth measurements, application to Test Ban verification. *Bull. seism. Soc. Amer.*, in review.

Stevens, J. L. and K. L. McLaughlin, (1996). Regionalized maximum likelihood surface wave analysis, Maxwell Technologies Technical Report submitted to Phillips Laboratory, PL-TR-96-2273, SSS-DTR-96-15562, September.

Stevens, J. L. and K. L. McLaughlin (1997). Improved methods for regionalized surface wave analysis. *Proceedings of the 19th Annual Seismic Research Symposium on Monitoring a Comprehensive Test Ban Treaty*, 171-180.

Wang, J. and R. Stead (1998). Remote checking of channel status for 3C seismic stations at the PIDC. Technical Report CMR-98/11.

Woodhouse, J. H. and Wong Y. K., (1986). Amplitude, phase and path anomalies of mantle waves, *Geophys. J. R. Astron. Soc.*, **87**, 753-773.

IMPROVING GLOBAL SEISMIC EVENT LOCATIONS USING SOURCE-RECEIVER RECIPROCITY

Peter M. Shearer

Institute of Geophysics and Planetary Physics
Scripps Institution of Oceanography
University of California, San Diego

Sponsored by The Defense Threat Reduction Agency
Contract DSWA01-98-1-0005

ABSTRACT

The leading source of error in seismic event locations is travel time perturbations caused by three-dimensional Earth structure. The reciprocity of travel times between sources and receivers provides a method for testing the effectiveness of empirical methods for improving event locations that rely on nearby calibration events of known location. We apply this approach to travel time residuals obtained by Engdahl *et al.* (1998) for almost 100,000 teleseismic events. By analyzing the residual patterns at thousands of seismic stations of known location, we characterize the spatial coherence of station/event mislocation vectors. We find that, on average, calibration events are likely to improve locations only if they are located within 100 to 150 km of the target events. For 84 events of known location, we find that applying source-receiver reciprocity can significantly reduce location errors by correcting for the teleseismic residual pattern observed at stations close to the target events. These results have implications for efforts to improve event locations for nuclear explosion monitoring purposes.

Key Words: Seismic, Event Location, Source-Receiver Reciprocity

OBJECTIVE

The objective of this research is to experiment with new methods to improve seismic event locations, in support of monitoring efforts for the Comprehensive Nuclear Test Ban Treaty.

RESEARCH ACCOMPLISHED

Introduction

Improving seismic event locations is an important part of research to support nuclear test verification efforts. A goal of programs to monitor the Comprehensive Nuclear Test Ban Treaty (CTBT) is to achieve high-confidence absolute location uncertainties of less than 1000 km^2 (National Research Council, 1997). Errors in absolute event location in routine location methods using reference one-dimensional velocity models are typically dominated by the biasing effects of three-dimensional structure. Two main approaches have been applied to account for 3-D structure, both in teleseismic and regional event location problems. In the first, improved velocity models of the crust and mantle are developed that more correctly predict the seismic travel times used by the location algorithm. This includes models of crustal thickness variations, upper mantle *Pn* velocities, and full 3-D mantle tomography models. For example, Lienert (1997) demonstrated that a locally determined velocity model for regional phases in the western United States could improve the location accuracy of explosions at the Nuclear Test Site (NTS) in Nevada. Smith and Ekström (1996) showed that the rms location errors for 108 global events of known location could be improved by using a 3-D mantle model. Although this approach has achieved some success, global velocity models are still too smooth to fully account for the sharp local velocity changes that in many cases may dominate the location errors.

An alternative method is to apply empirical travel time corrections based on the residuals observed for calibration events of known locations. Because travel times to nearby events are likely to have similar patterns of residuals, their locations can be improved by using these station corrections, even if the details of the

underlying 3-D velocity structure remain unknown. This approach would be straightforward if the "ground truth" events were in exactly the same places as the target events. However, in practice this is rarely the case, so considerable effort has gone into devising ways to interpolate the residuals between calibration events to create station correction "surfaces" that can be used to locate events at arbitrary locations (e.g., Cogbill and Steck, 1997; Schultz *et al.*, 1998). A fundamental difficulty of this approach is the sparse coverage of calibration events in many parts of the world.

In principle, due to reciprocity of travel times between sources and receivers, the residuals observed at seismic stations (which of course have known locations) from distant events provide information that could be used to improve the locations of nearby events as measured by distant stations. Here, we experiment with this approach to characterize how rapidly mislocation vectors change with position and to test whether source-receiver reciprocity can significantly improve global event locations. We use the recent teleseismic relocation effort of Engdahl *et al.* (1998) for nearly 100,000 events from 1964 to 1995 as a starting point, although the same approach could also be applied to regional or local event data. To test the accuracy of our locations, we examine the ground truth events tabulated by Smith and Ekström (1996).

We find that the scatter in computed station "mislocation vectors" is comparable to that seen in the ground truth events, suggesting that station locations can serve as a proxy for calibration events. Station mislocation vectors typically change rapidly over short scales; the correlation distance of station mislocation vectors is less than ∼150 km, suggesting that, on average, calibration events are only useful for improving teleseismic event locations if they are located within 150 km of the target event. For 84 of the ground truth events, there is a suitable seismic station within this distance. For these events, median location errors are reduced compared to the original Engdahl *et al.* (1998) locations when travel time corrections are applied based on source-receiver reciprocity.

Data and preliminary processing

Engdahl *et al.* (1998) (henceforth termed EHB) devoted considerable effort to produce a cleaner version of the phase data collected by the International Seismological Center (ISC) and to relocate nearly 100,000 events (1964 to 1995) using an improved 1-D velocity model, later arriving phases, ellipticity corrections, and azimuth independent "patch" corrections to account for station terms. The EHB locations are widely recognized as one of the best sets of teleseismic event locations. For 104 ground truth events (both explosions and earthquakes) from Smith and Ekström (1996), the EHB mislocation rms, average and median are 10.5 km, 9.0 km and 8.1 km, respectively. These numbers compare quite favorably to the best overall results (rms = 13.2 km) obtained by Smith and Ekström (1996) using a 3-D Earth model and azimuthally varying station terms. At least some of the differences between the EHB and Smith and Ekström locations may be attributed to the inclusion of regional phase data in the EHB results (Smith and Ekström used data only at ranges greater than 30°).

We use the EHB location residuals as a starting point for our relocation efforts. We first relocate the events using the L1-norm, source-specific station term (SSST) approach of Richards-Dinger and Shearer (2000). The L1-norm may have some advantages in earthquake location due to its robustness with respect to outliers in the data (e.g., Kennett, 1992; Shearer, 1997). However, the EHB data are sufficiently clean that it is unlikely that the L1-norm makes much difference in this case compared to conventional least-squares approaches. To simply our algorithm, we use only P, Pn, pP, pwP, S, Sn, and sS arrivals (no core phases). We use the iasp91 (Kennett and Endahl, 1991) velocity model. We compute SSST corrections using an iterative procedure based on the median station residuals from the 20 closest events to each target event (see Richards-Dinger and Shearer, 2000, for more details). This method should improve the relative location accuracy among nearby events but does nothing to improve the absolute location accuracy of event clusters.

The SSST locations for 99,715 EHB events are available via anonymous ftp to mahi.ucsd.edu in the directory /pub/EHB_SSST. The SSST locations for 104 Smith and Ekström (1996) test events show a modest improvement over the original EHB locations; the mislocation rms, average and median are 10.1 km, 8.4 km and 7.5 km, respectively. In some regions the SSST locations appear to cluster more clearly into linear features that the EHB locations, but the improvement, if any, is generally very slight. A comparison

between the EHB locations and the SSST locations is shown in Figure 1 for earthquakes in the vicinity of the Mendocino Triple Junction off the coast of California and Oregon.

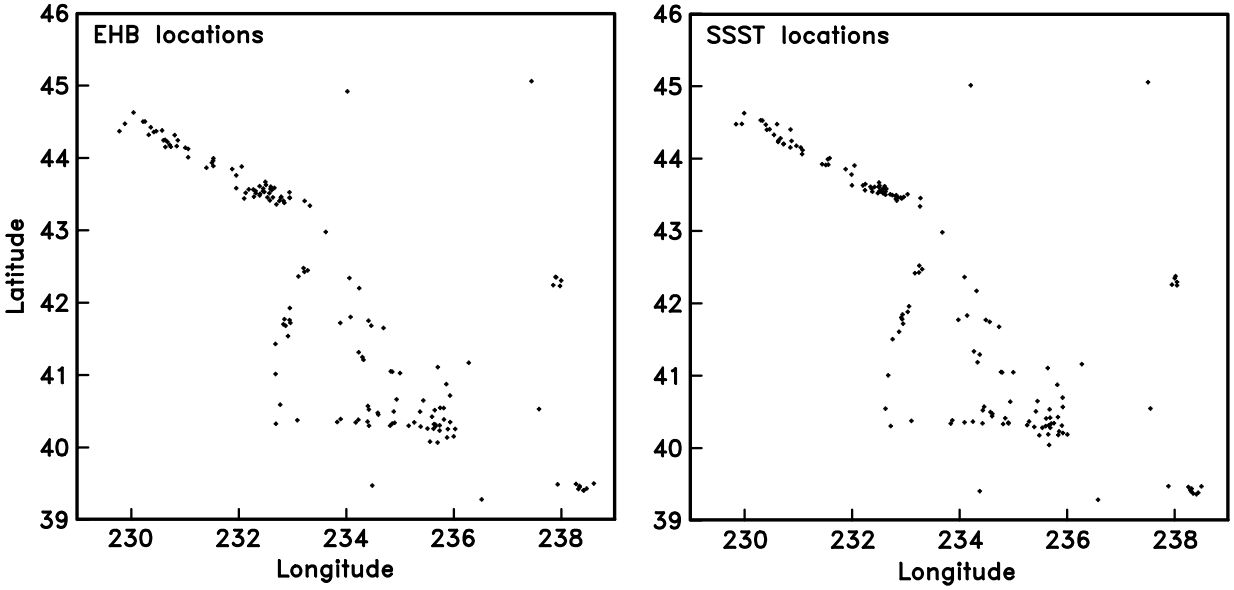


Figure 1. Earthquakes near the Mendocino Triple Junction (offshore northern California and Oregon) as located by (left) Engdahl *et al.* (1998) and (right) the source-specific station term (SSST) method.

Source-receiver reciprocity and station relocation

The reciprocity of travel times between sources and receivers means that the travel time from a source to a receiver is identical to the travel time that would be measured if there were a source at the station and a receiver at the event (see Figure 2). In practice, earthquakes or explosions are never located in exactly the same places as seismic stations. However, if a station is located close enough to a target event, then the teleseismic residual pattern observed at the station should be correlated to the residual pattern seen at the event. In this case, seismic stations could serve as proxies for ground truth events. The potential advantage of this approach is that there are data available for stations in many areas that are aseismic or currently lack ground truth events. If source-receiver reciprocity could be invoked, then these stations could be used to calibrate event locations in these areas.

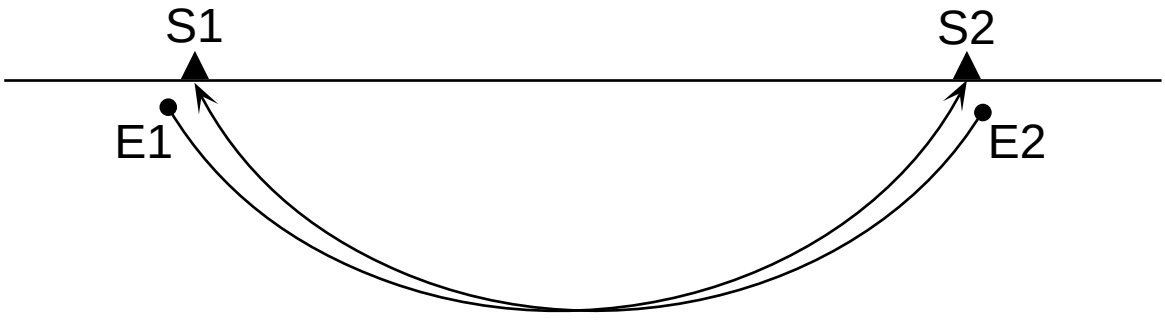


Figure 2. Source-receiver reciprocity implies that the travel time residual for a ray path from event E1 to station S2 will be approximately the same as the residual from source E2 to station S1, provided the corresponding events and stations are sufficiently close together.

To examine source-receiver reciprocity in the EHB data set, we first relocate the stations to see if they move significantly compared to their known locations. Our starting point is the residuals for the SSST locations (see above). We fix the event locations and origin times and adjust the station locations to give the

best L1-norm fit to the travel times. We consider only changes in the latitude and longitude of the stations; we do not permit depth variations. We use both P and S arrivals when available; many stations have only P picks. To even out the very non-uniform event coverage, we compute summary ray residuals based on 10° bins in range and azimuth. One might object at this point by pointing out that because the true event locations are unknown, the station relocation procedure is not completely reciprocal to the event location procedure (which uses stations of known locations). Biases in the event locations might thus feed back into the station locations. However, this will only occur if the residuals resulting from the event mislocations have a systematic degree-one component around the target station. As we will see later, it appears that the strongest contributor to event mislocations is near-source structure. In most cases, therefore, the biasing effects of event mislocation on our station relocation method will be minimized by averaging over a wide range of azimuths.

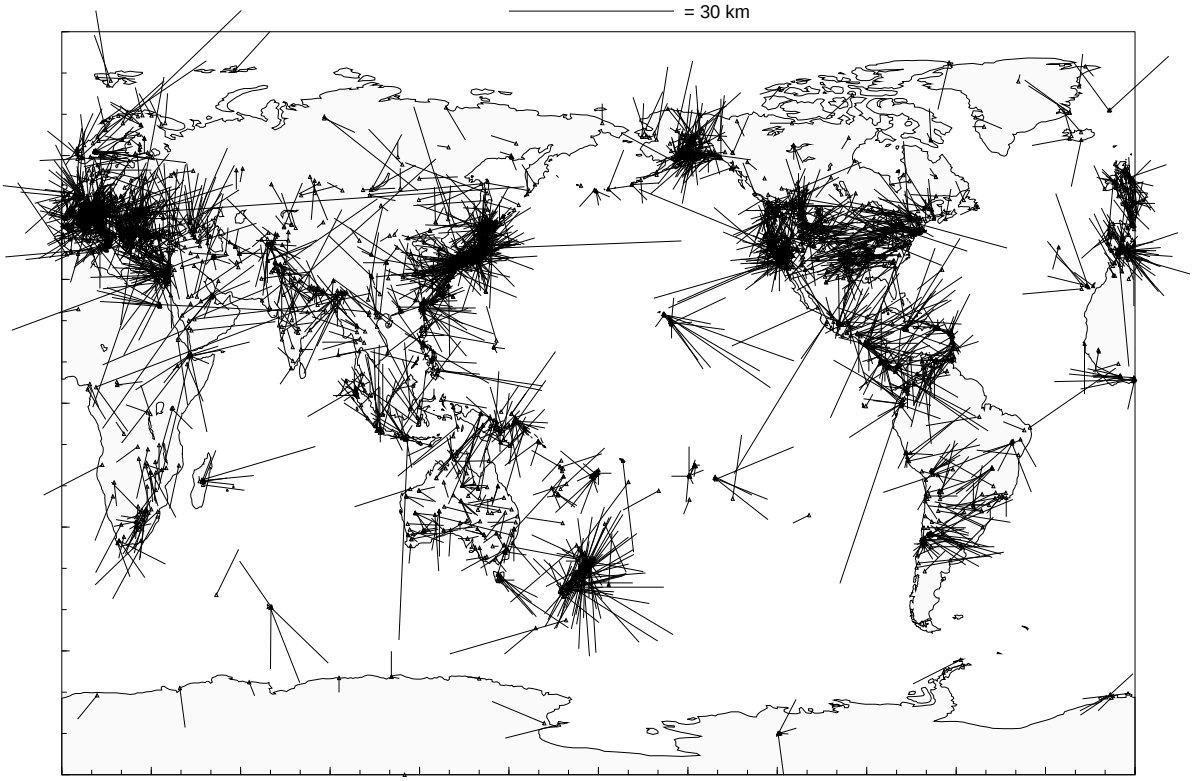


Figure 3. Mislocation vectors for 3004 global seismic stations as relocated using travel time residuals to distant events (see text). The true station locations are shown as triangles; the lines are drawn in the direction of the relocated stations. The lengths of the vectors are highly exaggerated; for reference a 30-km mislocation vector is shown above the plot.

We restrict our analysis to stations that recorded at least 100 events, from at least 10 different summary-ray source bins, and with no more than a 90° gap between summary ray azimuths. The resulting mislocation vectors for 3004 stations are plotted in Figure 3. The mislocation rms, average and median are 8.2 km, 6.2 km and 5.0 km, respectively. These station location errors are 13% to 33% less than the corresponding errors for the 104 calibration events in the SSST locations. The smaller errors in the station locations may be a result of: (1) differences in the station distribution compared to the 104 calibration events, (2) the fixed depth of the stations in the relocation procedure compared to the floating depths permitted in the event relocations, and/or (3) some of the residuals used in the station relocations being absorbed in event mislocations (see preceding paragraph). However, regardless of the exact size of the station mislocation vectors, it is instructive to to examine their directions and their degree of spatial coherence. This is illustrated in Figure 4, which shows the station mislocation vectors in detail across part of Europe.

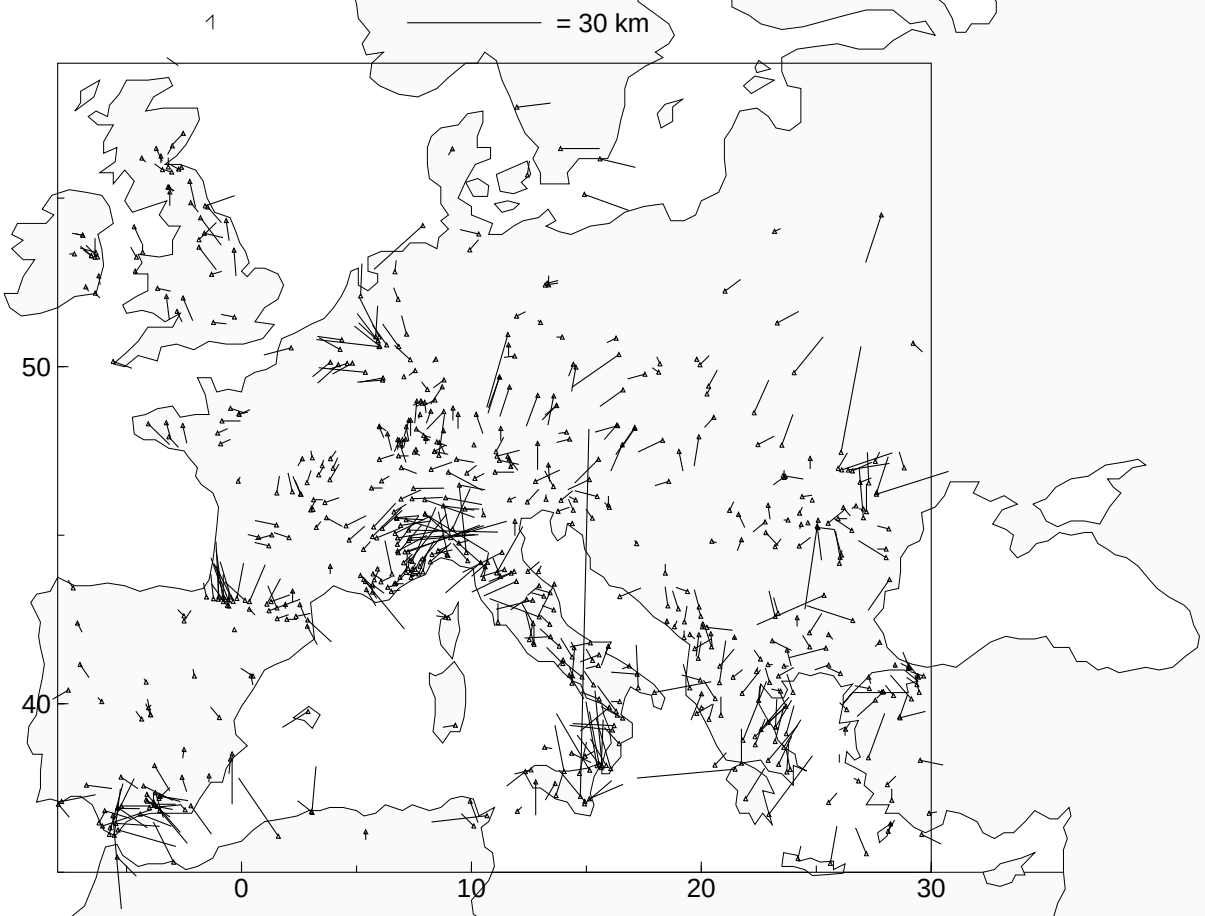


Figure 4. A closeup of station mislocation vectors in Europe. The true station locations are shown as triangles; the lines are drawn in the direction of the relocated stations. The lengths of the vectors are highly exaggerated; for reference a 30-km mislocation vector is shown above the plot.

The station mislocation vectors are correlated among nearby stations but often exhibit sharp changes over very short length scales. For example, notice the group of four southward pointing vectors in northwestern France (48°N, 3°W), about 150 km west of a group of six eastward pointing vectors (48°N, 0°E). Even greater incoherence in the station mislocation vectors can be seen across parts of Great Britain and Italy. The degree of spatial coherence of the mislocation vectors may be quantified by plotting the difference between pairs of mislocation vectors as a function of station spacing (Figure 5).

As one might expect, this plot shows considerable scatter. The globally averaged properties become clearer when the 50th (median) and 90th percentiles are plotted for 10-km averaging bins in station separation. The mislocation vector difference is reduced as the station pairs become close together but this effect only becomes significant for station separations of less than ∼300 km. For comparison, the dashed lines in Figure 5 show the 50th and 90th percentiles of the lengths of the individual station mislocation vectors.

When a calibration event is used to improve the location of a target event, a key question is how close the calibration event needs to be in order to significantly improve the target event location. We can address this question for teleseismic events on a global scale by using our station mislocation vectors as a proxy for event mislocation vectors. Thus, if we had travel time data from a station of unknown location we could attempt to improve our initial estimate for the station location by subtracting the mislocation vector for a nearby "ground truth" station. Figure 5 shows that, on average, this will only lead to an improvement in the station location if the calibration station is within 100 to 150 km of the target station. Further, the average improvement in the station location is fairly modest (less than 30%) even at much closer station spacing.

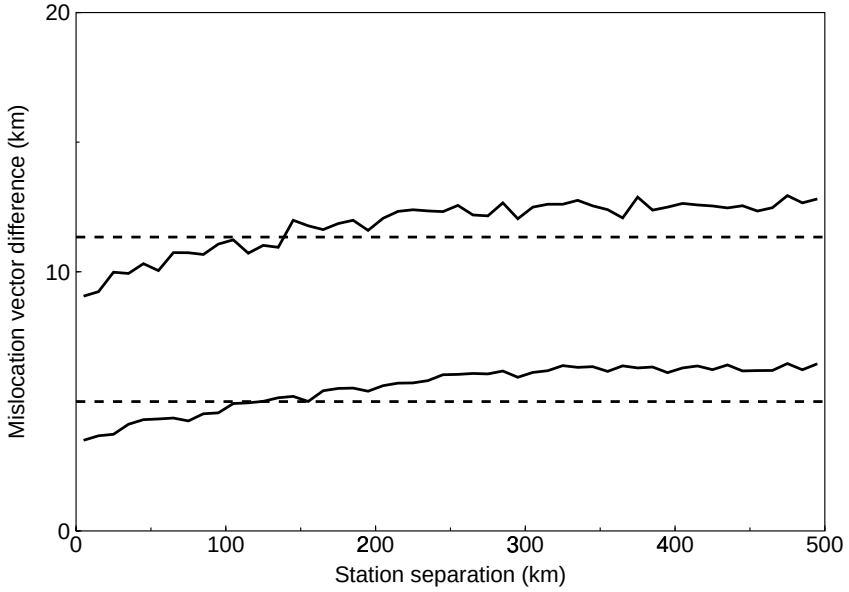


Figure 5. The difference in global station mislocation vector pairs plotted as a function of the distance between the true station locations. The solid lines show the 50th and 90th percentiles of the data, as binned in 10 km increments. The dashed lines show the 50th and 90th percentiles of the individual station mislocation vector lengths.

This is not to say that there are no regions where the station mislocation vectors show greater spatial coherence than the global average (presumably areas with relatively small local velocity perturbations). In these regions, calibration stations could be useful at distances greater than 150 km. But there also exist regions where the mislocation vector coherence is less than the global average. Calibration stations in these areas would only be useful if they were extremely close to the target stations.

Note that the observed residual patterns between stations are likely to be correlated at station separations far greater than 150 km, due to velocity perturbations near the distant source regions. It is only the degree-one part of the residual pattern that controls the station mislocation vectors. This part of the residual pattern appears to be dominated by local structures and can vary rapidly over minor changes in the station locations.

Of course, the true locations of seismic stations are already known so this analysis is useful only to the extent that is provides information relevant to the event location problem. In the next section, we compare the station mislocation vectors to mislocation vectors for the 104 ground truth events and test to see if the event locations can be improved by using travel time data from nearby stations.

Using source-receiver reciprocity to improve event locations

Figure 6 shows mislocation vectors for our SSST relocations of 104 ground truth events from Smith and Ekström (1996) compared to the station mislocation vectors discussed in the previous section. In some areas the event mislocation vectors correlate with nearby station mislocation vectors. For example in Figure 6, two events in the western United States (near 40°N, 252°E) are mislocated in the northeast direction, in approximate agreement with the mislocations of stations to the east and west of the events (stations to the south don't agree as well).

In other areas, however, the event mislocation vectors disagree with the trend of nearby station vectors (or the station vectors may be so incoherent that no clear conclusion may be drawn). At least some of the discrepancies between event and station mislocation vectors may arise from the mismatch between the surface stations and earthquakes at depth. Also, the distribution of events around the stations will differ from the distribution of stations around the events, so one would not necessarily expect the mislocation vectors to be exactly the same.

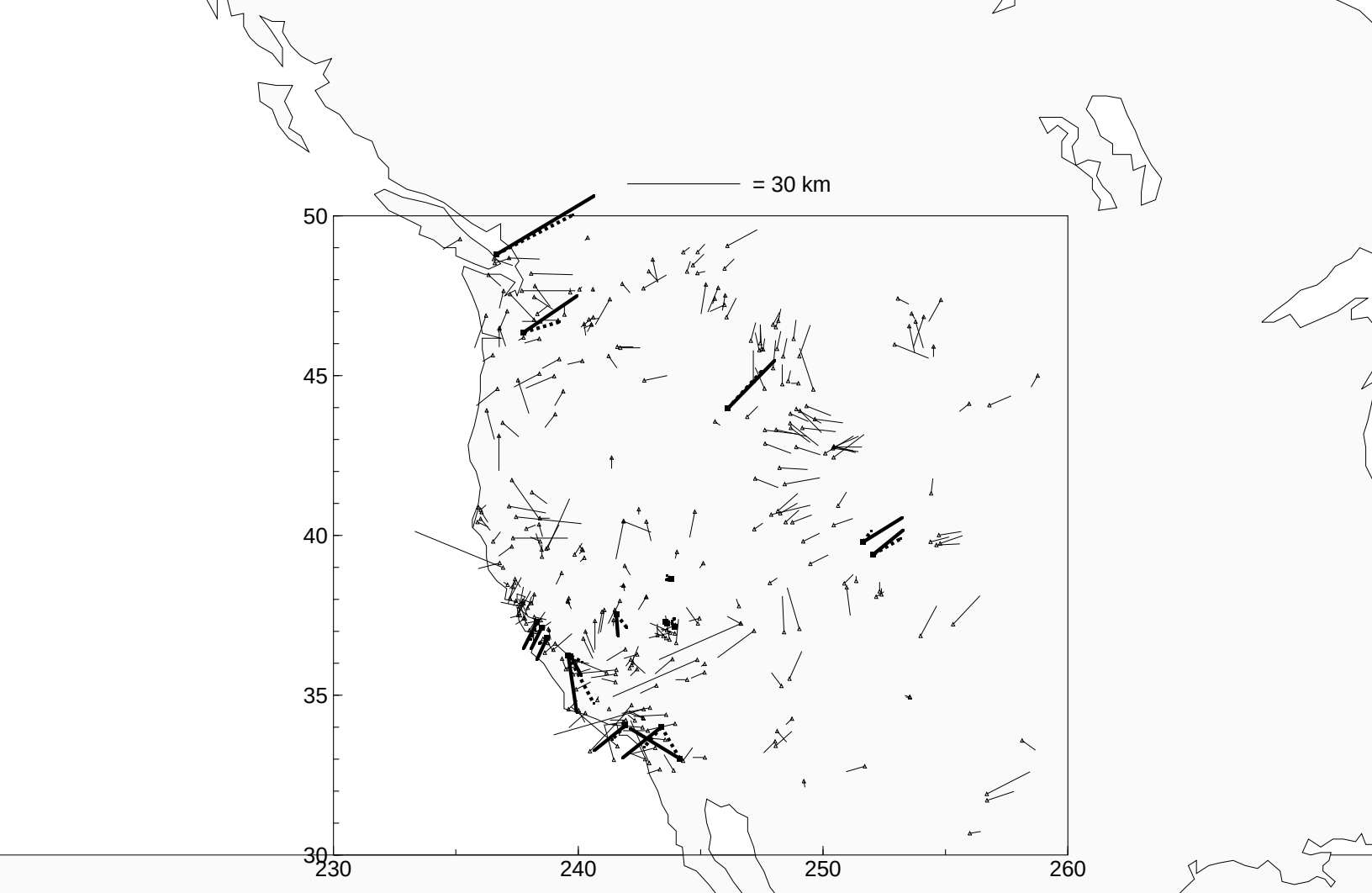


Figure 6. A closeup of station mislocation vectors (thin lines) in the western United States, compared to event mislocation vectors for ground truth events (thick lines). The SSST station mislocation vectors are shown as the solid thick lines; the mislocation vectors following application of corrections based on source-receiver reciprocity are shown as the dashed thick lines. The lengths of the vectors are highly exaggerated; for reference a 30-km mislocation vector is shown above the plot.

To more precisely apply source-receiver reciprocity in the case of target events with nearby stations, we attempted to improve the event locations by using the following procedure: We used only those target events for which there were nearby stations within 150 km, restricting our relocations to 84 of the ground truth events. For these stations, we then searched for distant events within 10° of a distant station that recorded the target event. Next, we computed the median residual for that distant station to apply as a correction in locating the target event. While we only relocated 84 events using this method, it was necessary to have access to residuals from most of the other events in the EHB data set in order to compute all of these path corrections.

The corrected ground truth mislocation vectors are plotted as dashed lines in Figure 6 for comparison to the original SSST mislocation vectors (solid lines). In the majority of cases the errors in the locations are reduced, although in a few examples the errors are increased. For the 84 events, the original EHB mislocation rms, average and median were 11.3 km, 9.8 km and 8.8 km, respectively. The SSST mislocation rms, average and median were 10.8 km, 9.0 km and 7.7 km. Following relocation using source-receiver reciprocity to the teleseismic residual patterns at nearby stations, these numbers were reduced to 9.1 km, 7.8 km and 6.6 km. The improvement compared to the SSST locations is fairly modest (about 15%), but consistent with the suggestion of Figure 5 that large improvement in locations will be achieved only if the station/event spacing is much smaller than 150 km.

CONCLUSIONS AND RECOMMENDATIONS

Source-receiver reciprocity can be used to gain insight into the effectiveness of using ground truth calibration events to improve teleseismic event locations. Perhaps our most significant result is that station mislocation vectors change rapidly over fairly short distances, with a globally averaged correlation length of about 150 km. This has sobering implications for the use of calibration events to improve teleseismic event location because source-receiver reciprocity implies that event mislocation vectors will behave in a similar fashion. In most regions, calibration events at distances greater than 150 km probably will have little or no benefit in improving the location of a target event (and may worsen the location). Interpolation of "correction surfaces" among calibration events will only be useful in teleseismic event location if the calibration events are spaced closely enough that their mislocation vectors are spatially correlated.

In regions where calibration events are missing, sparse, or poorly recorded, seismic stations could be used as substitutes for calibration events. These could be existing or archived stations, or new station deployments specifically designed for this purpose. All that is necessary is for these stations to record travel times at a range of event azimuths and ranges that are comparable to the station distribution used to locate the nearby events of interest. Because stations are restricted to the near-surface, reciprocity will be achieved most closely for shallow events, i.e., those that will be of greatest interest for CTBT monitoring purposes. In areas of little or no natural seismicity, it may be cheaper and politically easier to field temporary station deployments than to arrange for calibration explosions.

In principle, the effect of source-receiver reciprocity is naturally accounted for in tomographic inversions for three-dimensional Earth structure. However, as Smith and Ekström (1996) have shown, these models are currently of limited effectiveness in improving event locations. Our results suggest that the scale length of the heterogeneity that dominates teleseismic event mislocations is much smaller than the typical resolution of the tomographic models.

Our study examined both regional (e.g., Pn and Sn) and teleseismic phase data from the EHB data set. We also experimented with using only teleseismic arrivals at source-receiver ranges greater than 30°in hopes of minimizing location biases associated with the strong velocities heterogeneities in the crust and uppermost mantle. However, in this case the average location accuracy was reduced somewhat compared to the results obtained when the entire data set was used. The station mislocation vectors exhibited similar behavior to that shown here; on average the mislocation vectors were correlated only for station separations less than ∼150 km. Thus, it does not appear that the range of applicability of calibration events can be extended by using data only at longer source-receiver distances.

Our analysis was focused on teleseismic locations but many of the same concepts could be applied to purely regional location problems for smaller events, an increasing focus for CTBT monitoring efforts. The principles of source-receiver reciprocity apply at all length scales.

Acknowledgments

We thank Bob Engdahl for sending the EHB locations and residuals.

REFERENCES

Cogbill, A. and L. Steck, Use of propagation path corrections to improve regional event locations in western China, *EOS Trans. AGU (Fall Meeting Suppl.)*, **78(46)**, F445, 1997.

Engdahl, E.R., R. van der Hilst and R. Buland, Global teleseismic earthquake location with improved travel times and procedures for depth determination, *Bull. Seismol. Soc. Am.*, **88**, 722-743, 1998.

Kennett, B.L.N., Locating oceanic earthquakes—The influence of regional models and location criteria, *Geophys. J. Int.*, **108**, 848–854, 1992.

Kennett, B.L.N. and E.R. Engdahl, Travel times for global earthquake location and phase identification, *Geophys. J. Int.*, **105**, 429–465, 1991.

Lienert, B.R., Assessment of earthquake location accuracy and confidence region estimates using known nuclear tests, *Bull. Seismol. Soc. Am.*, **87**, 1150–1157, 1997.

National Research Council, *Research required to support comprehensive nuclear test ban treaty monitoring*, National Academy Press, Washington, D.C., 1997.

Richards-Dinger, K.B. and P.M. Shearer, Earthquake locations in southern California obtained using source-specific station terms, *J. Geophys. Res.*, **105**, 10,939–10,960, 2000.

Schultz, C., S. Myers, J. Hipp and C. Young, Nonstationary bayesian kriging: A predictive technique to generate spatial corrections for seismic detection, location, and identification, *Bull. Seismol. Soc. Am.*, **88**, 1275–1288, 1998.

Shearer, P.M., Improving local earthquake locations using the L1 norm and waveform cross-correlation: Application to the Whittier Narrows, California, aftershock sequence, *J. Geophys. Res.*, **102**, 8269–8283, 1997.

Smith, G.P. and G. Ekström, Improving teleseismic events locations using a three-dimensional Earth model, *Bull. Seismol. Soc. Am.*, **86**, 788–796, 1996.

REDUCING SYSTEMATIC ERRORS FOR SEISMIC EVENT LOCATIONS IN ANISOTROPIC REGIONAL STRUCTURES

Gideon P. Smith and Douglas A. Wiens
Dept Earth & Planetary Sciences, Washington University

Sponsored by the Defense Threat Reduction Agency

Contract No. Pending

ABSTRACT

In CTBT applications many events of interest are only detected at regional distances. Providing more accurate prediction of P-wave propagation at regional distances is therefore of particular importance in seismic event location. At such distances (2□-14□) the phase Pn is the seismic phase that is most frequently reported and which thus controls the location accuracy. We are working on reducing systematic errors in Pn travel-times and thus seismic event location at regional distances.

In recent work the P.I. has mapped lateral and anisotropic variations in Pn velocities beneath continents across the globe (Smith and Ekstrom, 1999). This work provides the most comprehensive and possibly most accurate mapping of anisotropic Pn velocities available to date. While the lateral variations in Pn velocities that were mapped were strong, and are likely to contribute to improved location capabilities, strong (up to 10%) anisotropic signatures were also observed. The horizontally travelling Pn phase should therefore accumulate large travel time residuals due to both heterogeneity and anisotropy, which would result in large systematic location errors. The question remains whether this new mapping can provide, in a practical sense, significant reductions in systematic event mislocation at the regional scale. Preliminary results indicate that, even in areas of good station coverage, a distinct difference in location is obtained using anisotropic models.

OBJECTIVE

In CTBT applications many events of interest are only detected at regional distances. Our objective is identification and reduction of systematic errors in the location of events determined using regional seismic data. At such distances (2□-14□) the phase Pn is the seismic phase that is most commonly reported and which thus controls the location accuracy. In order to accurately locate seismic events, whether natural or artificial, by traditional travel-time methods one must first be able to accurately predict arrival times. Historically travel-times have been calculated using one-dimensional seismic velocity models (e.g. Jeffreys and Bullen, 1940; Herrin et al., 1968; Herrin and Taggart, 1968; Herrin, 1968; Dziewonski and Anderson, 1981; Kennett and Engdahl, 1991). However, the Earth is composed of rocks which vary laterally at varying length scales (e.g. Crosson, 1976; Engdahl et al., 1977, 1982; Engdahl and Billington, 1986; Dziewonski, 1984; Su and Dziewonski, 1993) and can be anisotropic (e.g. Christensen, 1966; Kumazawa and Anderson, 1969; Hess, 1964; Raitt et al., 1969; Forsyth, 1975; Tanimoto and Anderson, 1984), resulting in travel-times which do not match those predicted by these one-dimensional velocity profiles. In addition, at regional length scales global Earth models, which are largely based on long-period surface waves and vertically arriving body waves, provide poor first arrival travel-time predictions. Providing more accurate prediction of P-wave propagation at regional distances is therefore of particular importance in event location. When attempting to satisfy the location requirements of the CTBT it is essential to obtain the most accurate location possible, with the minimum necessary computing time

The question remains as to whether the current generation of regional models can usefully contribute to relocation problems. While it has already been well established that variations in regional phases such as Pn can lead to large mislocations of the epicenter (Herrin and Taggart, 1962), progress has been slow in routinely applying regional models to locations for global catalogs. This is probably because most of the Pn velocity models produced are of a highly local nature (e.g. Hess, 1964; Raitt et al., 1969; Bamford, 1977; Fuchs, 1977; Hirn, 1977; Vetter and Minster, 1981), and no systematic global mapping of Pn velocities has been attempted. In addition although azimuthal anisotropy is a known feature of Pn

propagation (e.g. Beghoul and Barazangi, 1990; Hearn, 1996), most previous studies of Pn anisotropy have not mapped lateral variations in azimuthal anisotropy, but instead produced, if anything, a single estimate for an entire region.

In recent work the P.I. has mapped lateral and anisotropic variations in Pn velocities beneath continents across the globe (Smith and Ekstrom, 1999). This work represents the most comprehensive and possibly the most accurate mapping of anisotropic Pn velocities available to date. This provides the first opportunity to truly test the possibility of applying an anisotropic Pn velocity model to calculation of travel-times to improve regional locations for events distributed in different parts of the world. The question remains whether this new mapping can provide, in a practical application, significant reductions in systematic event location at the regional scale. Our work is aimed at applying this new mapping of Pn anisotropic structure to investigate the possible systematic errors produced by lateral heterogeneity and azimuthal anisotropy

RESEARCH ACCOMPLISHED

As a preliminary investigation we have already implemented a grid search relocation algorithm and applied this to the Pn mapping of Smith and Ekstrom (1999) to test for systematic errors in location. In this study we have taken several events in western Europe as we have good mapping of both Pn velocities and anisotropy in this area. Figure 1 shows the lateral variations in Pn velocities of Western Europe extracted from our dataset. Figure 2 shows the fast azimuths of the Pn anisotropy from our model.

In this preliminary relocation experiment we use travel-time data from the ISC database. The ISC location is used as a first estimate. The fit of travel times is then calculated for this location and for a set of points on a rectangular grid at 10-km spacing. The minimum in the rms of the travel times is then selected as the new location estimate and the travel-time misfits recalculated using a smaller grid spacing. This is repeated until the travel-time misfit appears to converge. This procedure has been performed for a selection of earthquake events for isotropic, laterally heterogeneous, and anisotropic structures. In this preliminary test for systematic effects great-circle raypaths were used. The results of this can be seen in Figure 3.

Figure 3(a) shows the relocation vector of the events using laterally varying Pn velocities. The base of the arrow lies at the location found with an isotropic model. The arrow points in the direction of the location found by use of the laterally varying Pn velocities. The arrow length is proportional to the distance between the two locations, and a 10 km displacement is shown for scale. Similarly, Figure 3(b) compares the relocation vector of the events when using azimuthally anisotropic Pn velocities. Again the base of each arrow lies at the location found with an isotropic model.

With these events “ground truth” is not known and so comparison to a “true” location is not possible. However, what is demonstrated is a noticeable systematic difference between the locations found with the different models. In both cases the revised locations have moved away from stations where the model predicts a fast traveltime anomaly, and towards stations where the traveltime anomaly would be slow. If we assume that the anisotropic locations are the most accurate, being based on the most detailed model, this would suggest that failure to account for anisotropic structure introduces significant systematic errors.

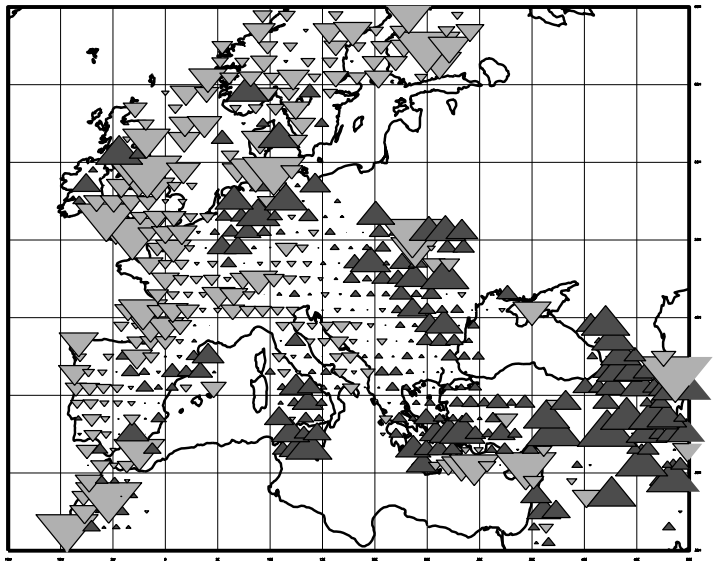


Figure 1: Lateral variations in the isotropic Pn velocity across Western Europe. Upward pointing triangles are slow, downward pointing triangles are fast. The size of the triangle is proportional to the anomaly. Values are in the range 7.8 to 8.4 km/s.

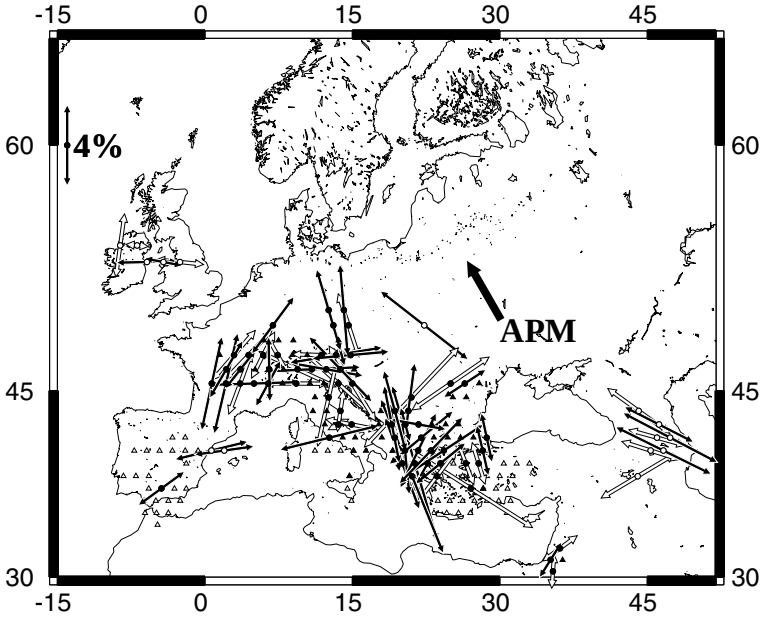


Figure 2: Pn anisotropy results for Western Europe. The center of each symmetric arrow pair is plotted at the center of the cap. Arrows point in the direction of fast Pn propagation and are proportional to the strength of anisotropy. Black arrows are higher quality estimates. Black and white center points indicate 1.5° and 3° radius caps respectively. Triangles show the location of null results. The absolute plate motion vector is also shown (Minster and Jordan, 1978).

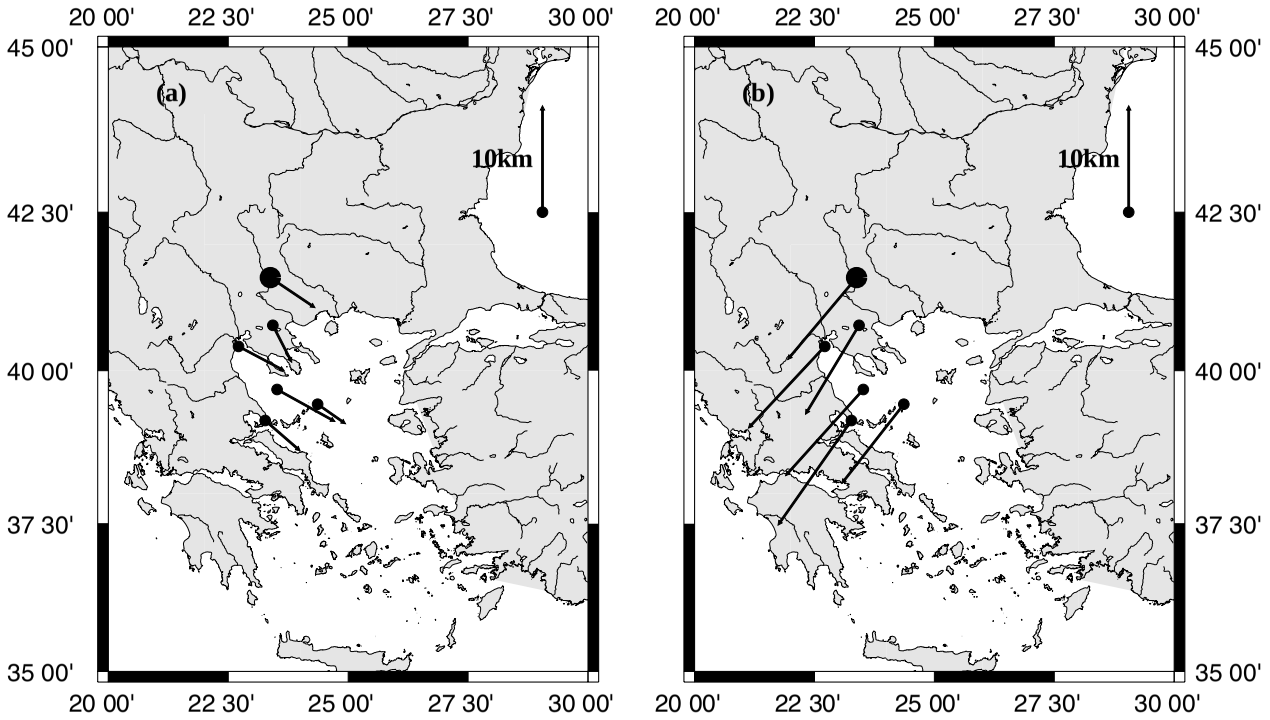


Figure 3: (a) Relocation vectors of the events using laterally varying Pn velocities. The base of the arrow lies at the location found with an isotropic model. The arrow points in the direction of the location found by use of the laterally varying Pn velocities. The arrow length is proportional to the distance between the two locations, and a 10 km displacement is shown for scale. (b) Relocation vectors of the events when using azimuthally anisotropic Pn velocities. Again the base of each arrow lies at the location found with an isotropic model.

Comparing Figures 3(a) and (b) a distinct difference in relocation azimuth is also observed, suggesting that when only lateral heterogenity in Pn velocities is considered significant systematic errors may still be introduced. The change in location for these events is larger when including anisotropy (Figure 3(b)) in this case averaging approximately 10 km.

This example is expected to be an example of minimum effect as the station coverage for this region is good. In areas with much poorer azimuthal coverage the location may be entirely controlled by the anisotropy. This may be seen by considering the strength of anisotropy observed. The average Pn anisotropy observed is about 6%. If we take an isotropic (average) Pn velocity of say 7.9 km/s then 6% anisotropy corresponds to a maximum anisotropic velocity of 8.4 km/s. If we use Pn observations over 2□-11□ and apply the isotropic velocity value we can achieve maximum travel-time misfits (assuming propagation along either the fast or slow directions) of 1.6 to 8.8 s, corresponding to mislocations of 12.7 to 69.7 km. Obviously in most real situations it is unlikely that the only propagation will be along the fast or slow axis but this gives some indication of the effect anisotropic structure could have in areas where azimuthal coverage is poor. Proper application of an anisotropic Pn velocity model should remove such errors.

CONCLUSIONS AND RECOMMENDATIONS

In order to establish whether relocation using our anisotropic Pn velocity model does infact translate into a reduction in relocation errors we must have some benchmark by which to test our relocations. One way of establishing whether errors have been reduced is to perform relocations of events where the hypocentral parameters of the event are already known, and have not been derived from seismological data. Ideal examples of this type of event are explosion events, such as peaceful nuclear explosions (PNEs). The first step in our future work will be to establish a list of events for which we have independent estimates of the hypocentral parameters. Our preliminary dataset for this will be the list already published by the author in earlier work (Smith and Ekstrom, 1996, table 1) which includes 26 explosions in various geographic locations. We are however working at expanding this list. For example, at present we are recovering all of the travel-times from the Gnome experiment (Carder, 1962). This was a PNE that was detonated in New Mexico in 1962, prior to the establishment of the modern ISC database. This large event was recorded by an unprecedented number of stations across the U.S. and should provide useful test data for our study. In future we hope to be able to incorporate more recent "ground truth" events, catalogs of which are currently being compiled by several researchers in response to the CTBT challenge. For these more recent events we will use the actual arrival time data published on the web by the IDC, thus testing in a manner as close to actual IDC operations as possible the capability of our methods as applied to the IMS monitoring network stations.

The second stage in future work will be to develop and test a method of applying the anisotropic Pn velocity model to calculation of arrival times and event locations. Clearly the lateral heterogeneity and azimuthal anisotropy in our model could produce deviations from a great-circle ray-path from event to station which may be equally as important as the anomalies themselves in influencing travel-times. However, calculation of such ray-path anomalies is likely to be a computational involved process and therefore not necessarily one that would be practicable for monitoring efforts. Part of this project will therefore involve investigation of the importance of such raypath anomalies.

To achieve this we will perform and compare relocations using a variety of models and approximations. These will include isotropic Pn velocity models, Pn models incorporating lateral heterogeneity but no anisotropy, and also our full anisotropic Pn velocity model. Relocations will be performed using both great-circle raypaths as well as raypaths calculated using the anisotropic model. In this way we will be able to quantify the various levels of improvement possible to help determine if the reduction in the error ellipse provided by accurately accounting for raypath deviations is worthwhile given the additional computational requirements.

Our preliminary work will examine the relocation of test events within North America as the locations of PNEs in this region are well known, and the Pn velocity and anisotropy is well sampled. However, at all stages testing will be undertaken with the practical operating procedures and challenges of the IDC in mind.

For this reason we will make maximum use of phase data from stations contributing to the IMS, apply our methods to as diverse a range of geographic locations and situations as possible, and statistically quantify the degree of improvement for the additional cost in computational time. In this manner we hope to maximize the practical usefulness of the product of our research for monitoring purposes.

Key Words: Pn, anisotropy, regional phases, CTBT, relocation.

References

Bamford, D., 1977. Pn velocity anisotropy in a continental upper mantle, Geophys. J. Roy. Astron. Soc., 49, 29-48.

Beghoul, N., and M. Barazangi, 1990. Azimuthal anisotropy of velocity in the mantle lid beneath the Basin and Range, Nature, 348, 536-538.

Carder, D.S., 1962. The Gnome Symposium. Bull. Seism. Soc. Am., 52, 977-979.

Christensen, N. I., 1966. Elasticity of ultrabasic rocks. J. Geophys. Res., 71, 5921-5932.

Crosson, R. S., 1976. Crustal structure modeling of earthquake data 1. Simultaneous least squares estimation of hypocenter and velocity parameters, J. Geophys. Res., 81, 3036-3046.

Dziewonski, A. M, 1984. Mapping the lower mantle: determination of lateral heterogeneity in P velocity up to degree and order 6, J. Geophys. Res., 89, 5929-5952.

Dziewonski, A. M., and D. L. Anderson, 1981. Preliminary Reference Earth Model. Phys. Earth and Planet. Int., 25, 297-356..

Engdahl, E. R., and S. Billington, 1986. Focal depth determination of Central Aleutian Earthquakes, Bull. Seism. Soc. Am., 76, 77-93.

Engdahl, E. R., N. H. Sleep, and M.-T. Lin, 1977. Plate effects in North Pacific subduction zones, Tectonophys., 37, 95-116.

Forsyth, D. W, The early structural evolution and anisotropy of the oceanic upper mantle, Geophys. J. Roy. Astr. Soc., 43, 103—162, 1975

Fuchs, K., 1977. Seismic anisotropy of the subcrustal lithosphere as evidence for dynamical processes in the upper mantle, Geophys. J. Roy. Astron. Soc., 49, 167-179.

Hearn, T., 1996. Anisotropic Pn tomography in the Western United States, J. Geophys. Res., 101, 8403-8414.

Herrin, E., 1968. Seismological tables for P-phases, Bull. Seism. Soc. Am., 60, 461-489.

Herrin, E. and J. Taggart, 1968. Regional variations in P travel times. Bull. Seism. Soc. Am., 58, 1325-1337.

Herrin, E. and J. Taggart, 1962. Regional Variations in Pn velocity and their effect on the location of epicenters, Bull. Seism. Soc. Am., 52, 1037-1046.

Herrin, E., W. Tucker, J. Taggart, D. W. Gordon, and J. L. Lobdell, 1968. Estimation of surface focus P travel times, Bull. Seism. Soc. Am., 58, 1273-1291.

Hess, H. H, Seismic anisotropy of the uppermost mantle under oceans, Nature, 203, 629—631,1964

Hirn, A., 1977. Anisotropy of the continental upper mantle: possible evidence from explosion seismology, Geophys. J. Roy. Astron. Soc., 49, 49-58.

Jeffreys, H. and K. E. Bullen, 1940. Seismological Tables, British Association for the advancement of Science, London.

Kennett, B. L. N., and E. R. Engdahl, 1991. Traveltimes for global earthquake location and phase identification, Geophys. J. Int., 105, 429-465.

Kumazawa, M., and O. L. Anderson, 1969. Elastic moduli, pressure derivatives, and temperature derivatives of single crystal olivine and single crystal forsterite, J. Geophs. Res., 74, 5961-5972.

Raitt, R. W., G. G. Shor Jr., T. J. G. Francis, and G. B. Morris, Anisotropy of the Pacific upper mantle, J. Geophys. Res., 74, 3095--3109, 1969

Smith, Gideon P., and Goran Ekstrom, 1999. A global study of Pn anisotropy beneath continents, *J. Geophys. Res., 99*, NO. B12, 23,787-23,800.

Smith, Gideon P., and Goran Ekstrom, 1996. Improving teleseismic event locations using a 3-dimensional Earth model, *Bull. Seism. Soc. Am., 86,* 788-796.

Smith, Gideon P., and Goran Ekstrom, 1996b. Regional Phases in global Earth models, abstarct EOS Trans., 77, Fall Meet. Suppl., F489.

Su. W. and A. M. Dziewonski, 1993. Joint 3-D inversion for P- and S- velocity in the mantle, EOS, 74, 557.

Tanimoto, T. and D. L. Anderson, Mapping convection in the mantle, Geophys. Res. Lett., 11, 287--290, 1984

Vetter, U., and J.-B. Minster, 1981. Pn velocity anisotropy in southern California, Bull. Seis. Soc. Am., 71, 1511-1530.

IMPROVED VELOCITY MODELS IN WESTERN CHINA FOR TWO- AND THREE-DIMENSIONAL FINITE DIFFERENCE MODELING

L. K. Steck, C. R. Bradley, and L. E. Jones
Los Alamos National Laboratory

Sponsored by the U.S. Department of Energy
Office of Nonproliferation and National Security
Office of Defense Nuclear Nonproliferation
National Nuclear Security Administration

Contract No. W-7405-ENG-36

ABSTRACT

In order to improve our understanding of the tectonics of western China, we are developing methods for creating improved three-dimensional (3-D) lithospheric structural models for the region. Stratamodel®, a computational toolbox for modeling fully heterogeneous rock properties in 3-D and ArcInfo, a widely accepted surface mapping routine, form the framework within which we build our models. To explore the accuracy of our new velocity structures, we compare synthetic seismograms from a full-waveform finite difference algorithm with regional data available from the IRIS-DMC for seismic events in western China. In this paper, we present seismogram modeling results from an earthquake in the Xinjiang province of western China, demonstrate improvements to previous velocity models, and describe the scheme we are using to create 2-- and 3-D velocity models for western China.

On January 30, 1999, at 03:51:07 GMT an earthquake occurred at 41.67 W, 88.46 N near the Lop Nor test site in western China. Using an anelastic finite difference code, we model the records from this event at the stations AAK, MAKZ and WMQ. Preliminary two-dimensional models were obtained for each source-receiver path from the Cornell Database, and these are fused with appropriate one-dimensional velocity models from published receiver function work or our own surface wave inversions. For each source-receiver path, the Cornell Database provides a topography profile, a depth-to-basement (or basin) profile, and a Moho profile. To date we have not included topography effects in our modeling.

The Cornell Database contains two surfaces that define the interfaces between the basin and crust, and the crust and Moho. These interfaces form the primary structural divisions in the Arc-Info data set. The structural model is then improved with the addition of geophysical province models. The specific path from source to receiver is then forward modeled and the velocity model refined. The ultimate goal of the model maker is to provide a tool for building 2-D and 3-D gridded velocity models for travel-time and full waveform seismic estimates.

Given that any particular source receiver combination may cross several geophysical provinces, full waveform modeling is incorporated to model the specific path effects on the waveform. We have modeled both elastic and anelastic realizations of the crust for several events, and present a memory-efficient scheme for modeling the effects of Q in three dimensions.

Key Words: velocity model, tectonics, finite difference, wave propagation

OBJECTIVES

One of the fundamental problems facing discrimination and location of earthquakes and explosions is creating accurate structural models for the lithosphere. Path effects on the seismic waveform can obscure spectral and time domain discrimination indices and poor velocity models generate ambiguity in event depth and location.

It has been our objective over the last year to generate a methodology for providing improved velocity models for western China and to test this methodology via the method of finite difference waveform modeling. Our specific objectives are:

1) Provide a method for generating improved velocity models by incorporation of 1-D and 2-D velocity models into an algorithm to merge these models into a 3-D structure.
2) Generate an interface for extracting these models into a useful form for either ray tracing or full waveform modeling.
3) Test the accuracy of the models via finite difference and travel time calculations for known earthquake and explosion paths.
4) Perfect a memory-efficient method for simulating intrinsic attenuation (Q) in the lithosphere for full waveform simulation.

To date, we have addressed items (1) and (2) through two commercial software systems: Stratamodel®, a software package designed to incorporate several types of structural information for the creation of a global 3-D lithospheric model, and ArcInfo®, a data base algorithm we are using to pass lithologic surfaces to the waveform or travel-time modeler.

We have selected an event from January 30, 1999, that occurred near Lop Nor in western China to test our wave propagation algorithms and the accuracy of the velocity model maker. The results of our analysis follow.

RESEARCH ACCOMPLISHED

Finite difference modeling of the 1999 January 30 earthquake near Xinjiang Province, western China

On January 30, 1999, at 03:51:07 GMT, an earthquake occurred at 41.67 W, 88.46 N. Using an anelastic finite difference code, we model the records from this event at stations AAK, MAKZ, and WMQ. Preliminary 2-D models were obtained for each source-receiver profile from the Cornell Database, and these are fused with appropriate 1-D velocity models from published receiver function work or our own surface wave inversions. The Cornell Database contains two 3-D structures from which 2-D profiles can be obtained: a "Eurasia" model (EU) and the University of Colorado (CUB) dataset. The latter is derived from inversion of surface wave data and is thus appropriate for modeling longer period energy. Both the EU and CUB models are comprised of 3-D "topography", "depth to basement" and "depth to Moho" information. To date we have not included topography effects in our modeling. We compare results from 2-D profiles obtained from the EU and CUB to synthetics from purely one-dimensional models. For each source-receiver path presented here, our synthetics comprise a bandwidth from roughly 0.02 Hz to 1.0 Hz.

Station WMQ

Station WMQ, at roughly 247-km epicentral distance, is located on the northern edge of the Tarim basin (Figure 1). Seismograms at WMQ were modeled using the CUB and the EU basement and Moho profiles, along with several simple 1-D models. The primary velocity structure used for this source-receiver profile is based on a 7-layer modified Tien-Shan model (Kosarev et al., 1993) over a mantle half-space. Velocities for a 1-D, 3-layer average Tien-Shan model were, in turn, a simplification of this primary velocity model. Both velocity models are given in Table I. Several alterations to the 7-layer model were made, including removing the crustal low-velocity zones and thinning the crust by about 10 km. None of the source/velocity model combinations tried were able to fit both the body and surface waves simultaneously. The TW and GER2a models fit the body wave arrival times and polarities well, particularly for the prominent depth phase and Lg. The surface waves are not well matched with this source model. In contrast, the CMT and GER1 models fit the surface waves well, but did not match the polarities of the body waves. The GER1, GER2, and CMT depths appear to be too deep by about 5 km, based on depth phase arrival time and waveform matching. The depth phase arrival time and polarity are consistent with it being an sP. Figure 2 compares several of our models for WMQ.

Station MAKZ

We model station MAKZ, at 770-km epicentral distance, with a similar modified Kosarev structure since its source-receiver path passes primarily through the Tien Shan fold and thrust belt (Figure 1). Crustal thickness along the profile varies from about 42 km to nearly 50 km and Moho depth increases gently from the source end of the profile to the receiver end, of whether the complex **EU** or simpler **CUB** basement and Moho are used. A seven-layer structure based on the Kosarev model (reference above), a simplified average three-layer (*basin, basement*, and *mantle*) structure, and a model based on phase velocity inversion work by Curtis and Woodhouse (1997) were tested.

The 7-layer Kosarev model (Table I) was fused with depth to basement and Moho information from the EU and CUB datasets, while the 3-layer 'average' model was tested for the CUB profile only. Results for the Kosarev model and CMT solution show reasonably good fits to the body wave data, but, as we observed at station WMQ, surface waves appear phase shifted. The 3-layer average Tien Shan model, coupled with the CU basement and Moho structures, produced similar results.

The modified Curtis and Woodhouse model produced surface waves that were obviously fast by more than 10 seconds for both the TCW and GER source mechanisms. Note that the TCW source produces body waves of incorrect polarity and unusual complexity on the radial component. The GER source produces correct polarities for the body waves, and a more distinct 'beating' on both the vertical and radial component; a feature observed in the data.

All velocity models produce, with varying degrees of success, a waveform feature in the Lg phase that resembles 'beating'. The presence of this feature in the synthetics may be due to the 2-dimensional nature of the modeled Moho structure.

Table I: Velocity Structures

(Modified) Kosarev Model Kosarev et al., 1993	depth	Pvel	Svel	density
	0.0	**4.19**	**2.42**	**2.44**
	5.0	**5.83**	**3.37**	**2.72**
	10.0	**5.60**	**3.11**	**2.72 LVZ**
	20.0	**6.12**	**3.54**	**2.78**
	30.0	**6.21**	**3.59**	**2.82**
	40.0	**7.09**	**4.10**	**2.97**
	Mantle	**7.80**	**4.51**	**3.37**
Average Tienshan Model				
	0 – 5	**4.19**	**2.42**	**2.44**
	5 – 50	**6.205**	**3.587**	**2.82**
	Mantle	**7.61**	**4.40**	**3.28**
(Modified) Curtis and Woodhouse Model Curtis and Woodhouse, 1998				
	0 - 5	**5.93**	**3.43**	**2.768**
	5 – 50	**6.17**	**3.57**	**2.88**
	Mantle	**8.11**	**4.69**	**3.65**

Modeling the Lithosphere of Western China

Discrimination and location of earthquakes and explosions depend on the source model but also depend on the effects to the seismic waveform as it propagates through the crust. The problem of creating accurate structural models for the crust is difficult in regions where data are sparse or non-existent. We have chosen to use Stratamodel, a toolbox created by Landmark Graphics Corporation, to model the 3-D lithospheric properties. The algorithm incorporates known published data and interpolates or extrapolates properties based on a set of arithmetic or geostatistical rules.

It has been our objective over the last year to generate a methodology for providing improved velocity models for western China and to test this methodology via the method of finite difference waveform modeling. Below we discuss the data sets we are using and the method for their incorporation into Stratamodel to create better models of the lithosphere.

Stratamodel

Stratamodel, which models heterogeneous rock and fluid properties in three dimensions for geological analysis and visualization, was originally designed to model oil and gas reservoirs. We have reformatted our data sets for western China to mimic Stratamodel's required format.

There are three types of models required by Stratamodel in order to create a full 3-D model of the lithosphere: 1) the Stratigraphic Framework Model, 2) the Well Model and 3) the Attribute Model.

Stratigraphic Framework Model

Gridded horizons, layer boundaries, and detailed reservoir characterizations (typically well data) form the basis for Stratamodel's 3-D modeling. The gridded horizons we have chosen are to the topography, basin and Moho surfaces accessible via the Cornell database (http://www.atlas.geo.cornell.edu/ima.html). Figure 3 shows the basin and Moho relief from the IPE Cornell data set. Previous modeling studies of path effects through western China (e.g., Jones et. al, 1998; Bradley and Jones, 1998) have used these surfaces as a framework around which individual crustal models (e.g. Romanowitz, 1982; Kosarev et al., 1993; Curtis and Woodhouse, 1997; Jih, 1998; Mahdi and Pavlis, 1998) have been inserted in a "layercake" manner for the particular region of interest.

These data surfaces divide the lithosphere into sequences that have undergone distinct geophysical processes in time, pressure, and temperature and logically should be treated differently by the model creation process. These surfaces are the reference for the stratigraphic framework in the lithospheric model. These surfaces dictate the cell resolution of the initial model and subdivide the model into geophysically independent sequences. These sequences are the basin (and topography) structure, crustal structure, and Moho or lower lithosphere structure. The "well" model controls layering within each of these sequences.

Well Model

In an oil reservoir there may typically be well data to enhance the information on the geostratigraphy. In a similar vein, there are many detailed studies of regions of interest in western China, some encompassing extensive regions (Jih, 1998; Li and Mooney, 1998; Mooney, 1999). These individual studies provide 1-D and 2-D information about specific geophysical provinces. Figure 4 shows the geophysical provinces we have chosen for the initial model of western China. There are 33 distinct provinces, each of which has a 1-D structural model associated with it. The preliminary velocity models were derived from Jih, 1998, and Li and Mooney, 1998. Currently there are fifteen 1-D models for the 33 provinces so there is some redundancy, but we have allowed for expansion when our knowledge of the crust improves.

The 1-D structural models are treated in Stratamodel like wells. They provide the detailed information for the sub-layering within each sequence. This information is called the "attribute" model.

Attribute Model

Once the stratigraphic framework is built to describe structure and stratigraphy and well models is in place for the correlation of individual provinces, the attribute model must be defined. The attribute model describes how the geophysical rock parameters are distributed throughout the model grid. This distribution can be based on simple mathematical relations or higher order geostatistical parameters.

Within each model cell, the search radius, the mathematical bias relative to the "well" data and the interpolation scheme, determines the attributes associated with it. For our current model, we are calculating Vp, Vs, density, and the intrinsic attenuation coefficients for P-waves, Qp, and S-waves, Qs.

The Model

The stratigraphic framework defined by the Cornell surfaces and the well data defined within each geophysical province have given an initial lithospheric model for China. Each sequence defined by the topography, basin and Moho surfaces has been subdivided by four layers (Figure 5). The number of layers in the crustal sequence was chosen to match the models presented in Mooney, 1999. The basin and lower lithosphere layering will be improved as more data are incorporated into the model. In Figure 5 the topography and two orthogonal cross sections through the model are displayed. In the basins, the layering is assumed to be proportional. This forces the layers within the basin to pinch out as the basins shallow. Within the crust and lower crust, the layers follow the top of the sequences that define them. The resulting model follows structural trends more closely than simple "layercake" models.

The well data are shown in Figure 6 for the 33 provinces used in this model. The effect of the wells is to bias the nearby model cells with information from the physical province. Each sequence is independent of the others. This forces the cells that lie within a sequence to use only well data lying between the surfaces that define that sequence. Currently, the weighting scheme for the cell attribute is a simple inverse distance weighted average of the well data and a search radius from each cell equal to half the total model size.

Future models will refine the weighting scheme and well density to more strictly enforce the transition from province to province in the geophysical model. With the current model we are performing full waveform modeling and travel-time tests to determine the accuracy of the model.

CONCLUSIONS AND RECOMMENDATIONS

We have performed 2-D modeling of an event near Xinjiang, China at stations AAK, MAK and WMQ. Depending on our choice of focal mechanism, we have achieved a good fit for the body wave phases, event depth and surface waves. No single mechanism fits all of these features simultaneously. We conclude that path effects on the recorded waveform are not yet being fully simulated and that better crustal models need to be developed. These are our recommendations.

1) A robust model-making method is critical to address the need for 2-D and 3-D structure in the simulation of path effects on the recorded waveform.

2) Validation through modeling of the velocity structure should include full 3-D simulation, and there may be a need for intrinsic attenuation in the simulations.

REFERENCES

Bradley, C. and E. Jones (1998), Modeling propagation effects from explosions in western China and India, *Proceedings of the 20th Annual Seismic Research Symposium on Monitoring a CTBT*, Santa Fe, NM.

Bradley, C. and S. Day, (2000), Elastic Coarse-Graining of Memory Variables: Memory Efficient Q: Simulation for Finite Difference Methods, submitted to *Bull. Seism. Soc. Am.*, (LA-UR-99-719.

Curtis, A. and J. H. Woodhouse (1997), Crust and upper mantle shear velocity structure beneath the Tibetan plateau and surrounding regions from interevent surface wave phase velocity inversions, *J. Geophys. Res.,* 102(B6), 11,789-11,813.

Day, S. (1998), Efficient simulation of constant Q using coarse-grained memory variables. *Bull. Seism. Soc. Am.,* 88(4) 1051-1062.

Day, S. and B. Minster, (1984), Numerical simulation of attenuated wavefields using a Padé approximant method, *Geophysical J. Roy. Astr. Soc*., 78, 105-118.

Dziewonski, A., A. Bloch, and M. Landisman (1969), A technique for the analysis of transient seismic signals, *Bull. Seism. Soc. Am.,* 59(1), 427-444.

Jih, Rong-Song, Location Calibration efforts in China (1998), in *Proceedings of the 20th Annual Seismic Research Symposium in Monitoring a Comprehensive Test Ban Treaty,* Santa Fe NM.

Jones, E., C. Bradley, F. App, R. Bos, and H. Patton (1998), Modeling seismic propagation from large scale structural features in western China. Los Alamos National Laboratory Memorandum, LA -UR-97-4186.

Kosarev, G., N. Petersen, L. Vinnik, and S. Roecker (1993), Receiver functions for the Tien Shan analog broadband network: Contrasts in the evolution of structure across the Talasso-Fergano fault. *J. Geophys. Res*., 98(3), 4437-4448.

Li, S., and W. D. Mooney (1998), Crustal Structure of China from Deep Sounding Profiles, *Tectonophysics,* 288, pp 105-113.

Mahdi, H., and G. Pavlis (1998), Velocity variations in the crust and upper mantle beneath the Tien Shan inferred from Rayleigh wave dispersion: Implications for tectonic and dynamic processes. *J.. Geophys. Res., 103(B2*) , 2693-2703.

Mooney, W. D., Crustal and Upper Mantle Structures of China and Adjacent Areas: Interim Report (9/28/99): Data Compilation and Results, DOE ID DE-A104-98AL79758.

Romanowitz, B., Constraints on the structure of the Tibet Plateau from pure path phase velocities of Love and Rayleigh waves. *J. Geophys. Res*., 87(B8), 6865-6883, 1982.

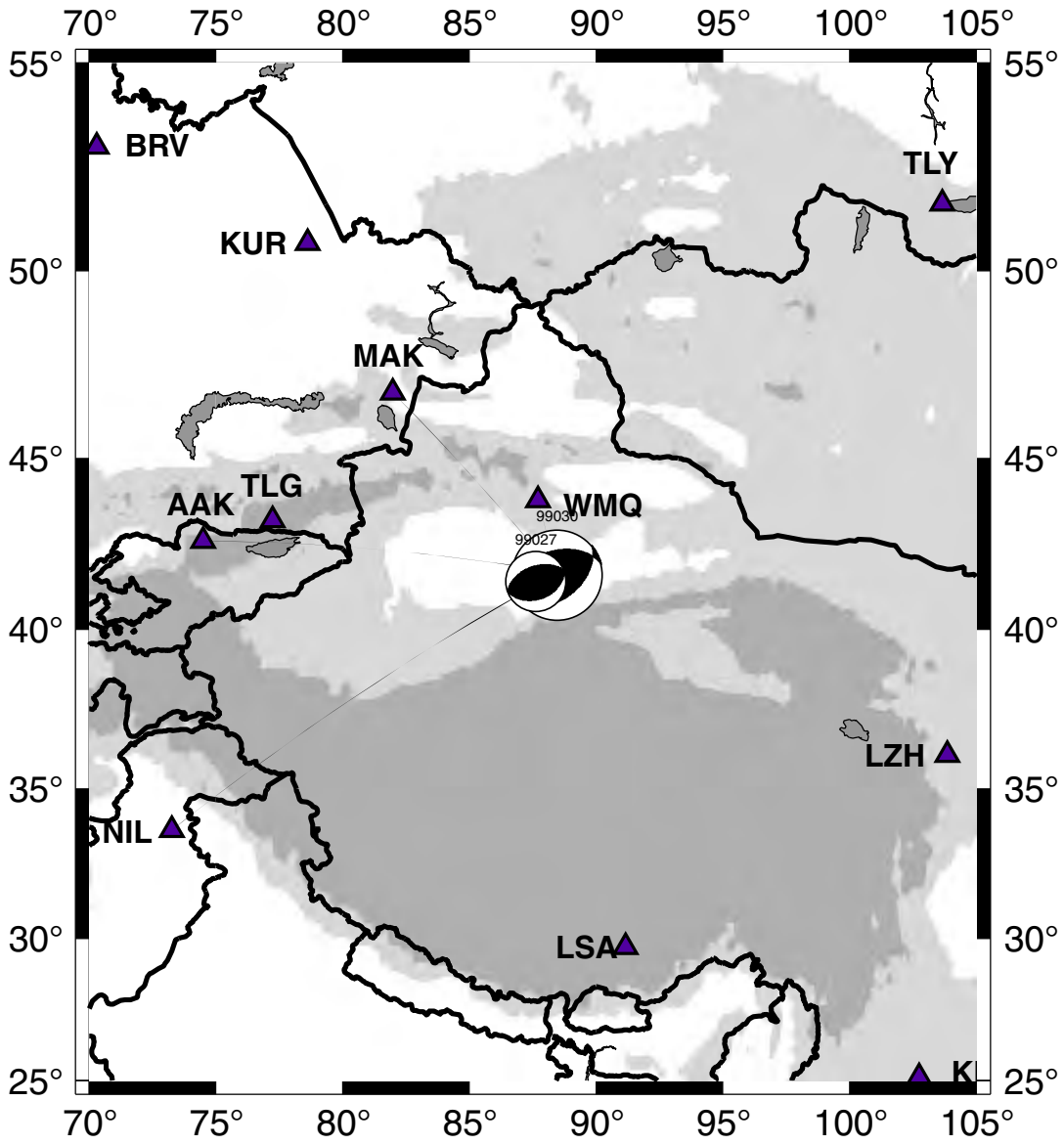


Figure 1: Map of source region for the 30 January 1999 event. Focal mechanisms are shown as predominantly thrust component. Stations modeled are indicated by the back azimuth lines shown.

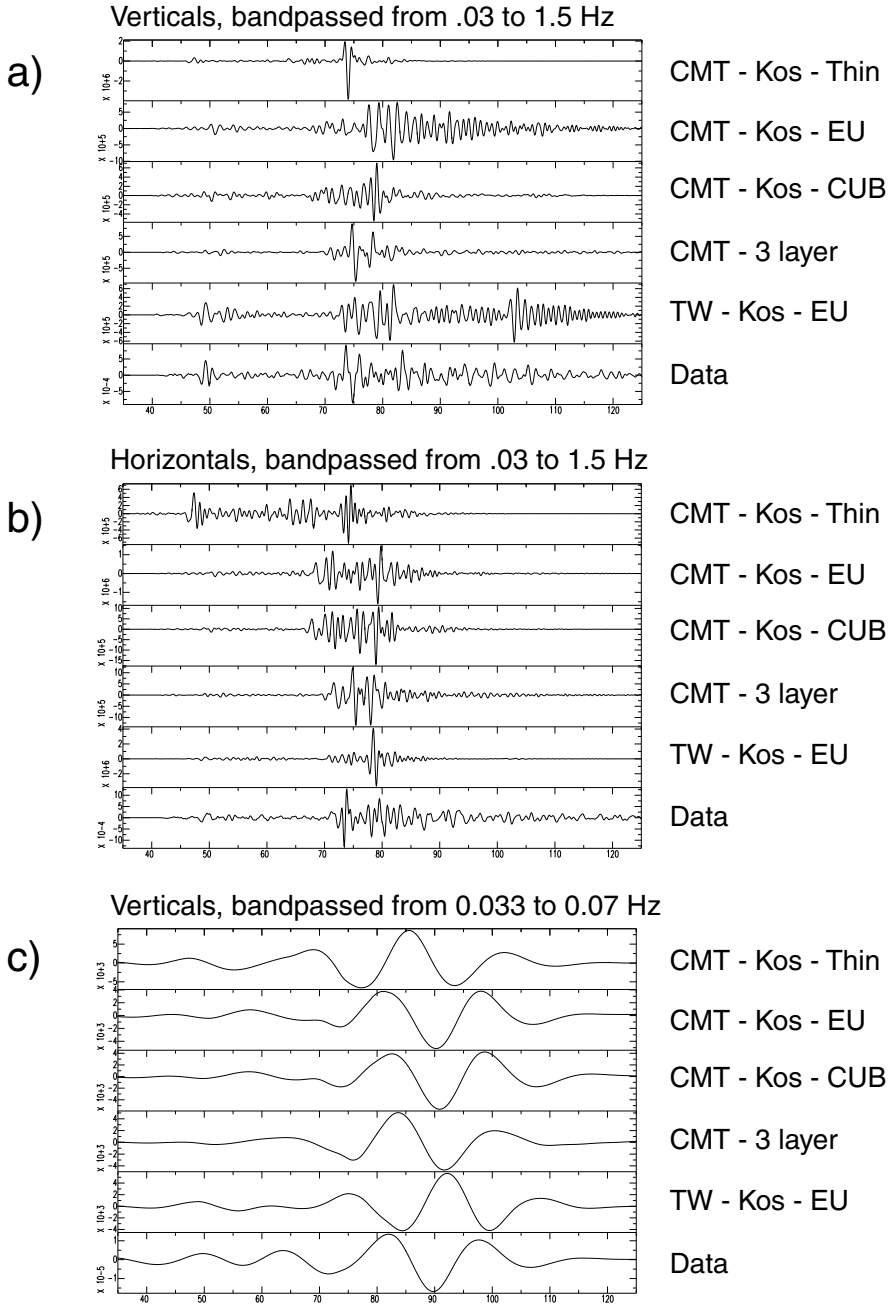


Figure 2. This shows (a) vertical, (b) radial, and (c) long-period vertical synthetic waveforms for several source/velocity model combinations. Instrument-corrected velocity data are shown with the synthetics. The source model and velocity model are indicated, along with the type (if any) of depth-to-basement and depth-to-moho information. The 'Thin' velocity model is an abbreviated flat-layer Kosarev model with a 40-km-thick crust (no EU or CUB information used). The '3-layer' model is an average Kosarev model with 3 flat layers.

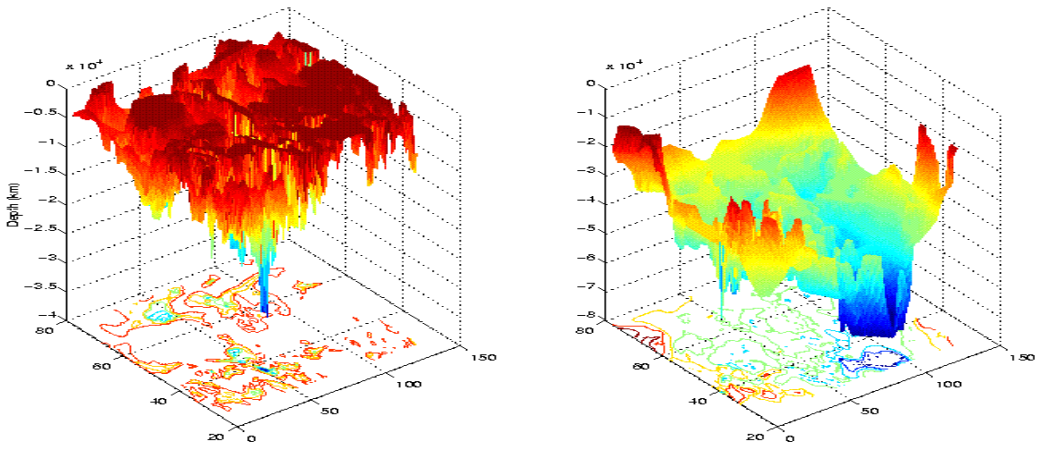


Figure 3. The IPE basement and Moho surfaces from Cornell. These surfaces are used to define the initial lithospheric sequences. Layering within the sequences is dictated by 1-D models describing distinct geophysical provinces.

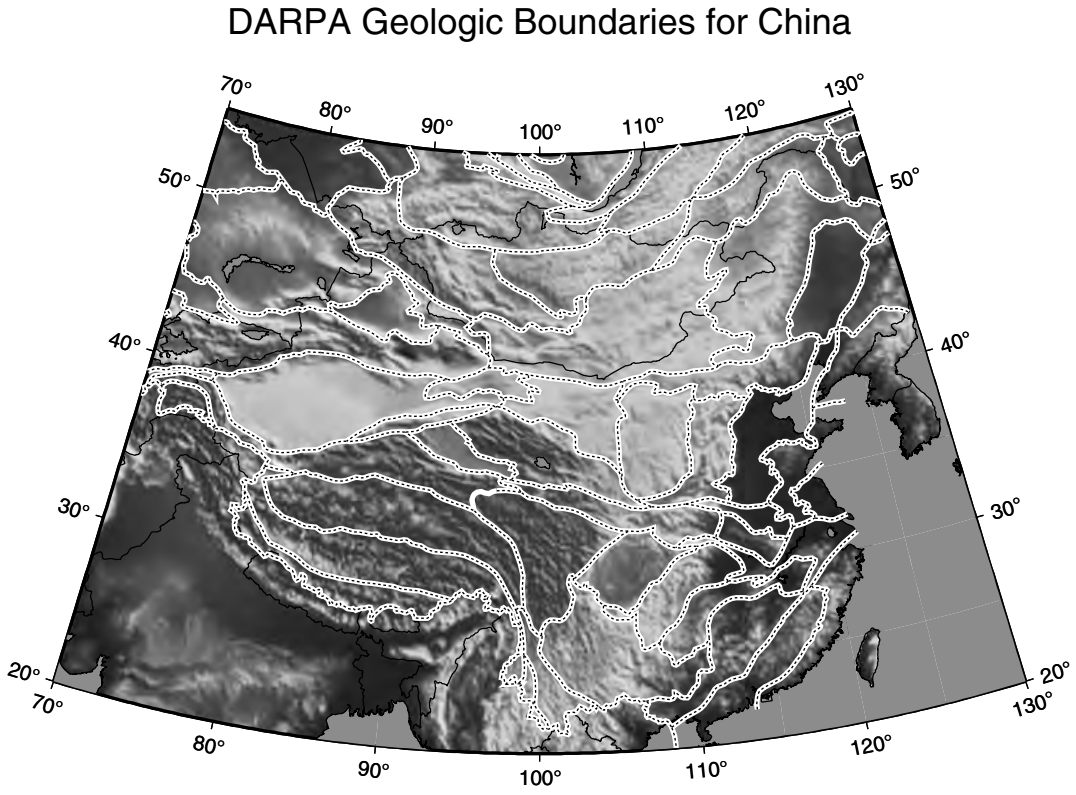


Figure 4. Defense Advanced Research Project Agency (DARPA) boundaries used in the initial velocity model. These 33 geophysical provinces have a 1-D velocity model associated (not necessarily unique) and are used to enforce a structural change in the model generated by Stratamodel.

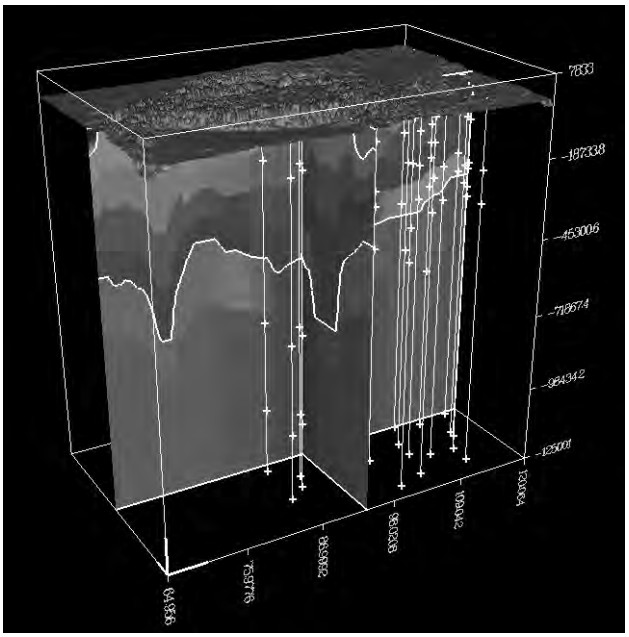


Figure 5. Velocity model for China from Latitude 22 N to 56 N, Longitude 65 E to 130 E. Topography shown as the uppermost surface. Two orthogonal cross sections show the depth and detail of the current model: 12 heterogeneous layes in 3 sequences, depth extent 125 km.

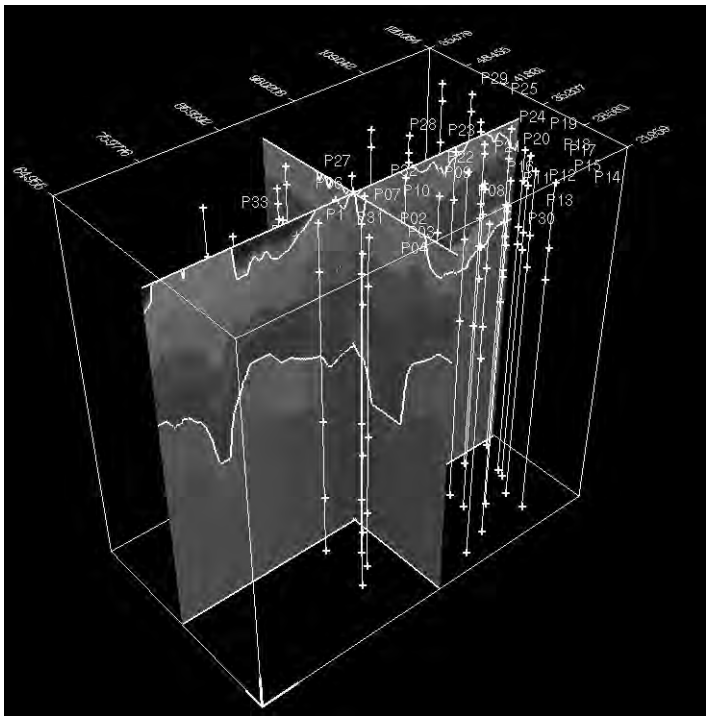


Figure 6. The topography has been stripped away from figure 4 to show the layer sequences in more detail. The 33 1-D velocity models are shown in as "wells".

REGIONAL MODEL CALIBRATION FOR IMPROVING SEISMIC LOCATION

Jennifer L. Swenson, Craig A. Schultz, and Stephen C. Myers

Lawrence Livermore National Laboratory

Sponsored by the U.S. Department of Energy
Office of Nonproliferation and National Security
Office of Defense Nuclear Nonproliferation
National Nuclear Security Administration

Contract No. W-7405-ENG-48

ABSTRACT

Accurate seismic event location is integral to the effective monitoring of the Comprehensive Nuclear-Test-Ban Treaty (CTBT), as well as being a fundamental component of earthquake source characterization. To account for the effects of crustal and mantle structure on seismic travel times, and to improve seismic event location in the Middle East and North Africa (MENA), we are developing a set of radially heterogeneous and azimuthally invariant travel-time models of the crust and upper mantle for each MENA seismic station.

We begin by developing an average one-dimensional velocity model that minimizes the *P*-phase travel-time residuals from regional through teleseismic distance at each station. To do this we (1) generate a suite of 1-D velocity models of the earth, (2) compute travel times through the 1-D models using a *tau-p* formulation to produce standard travel-time tables, and (3) minimize the root-mean-square (rms) residuals between the *P*-phase arrivals predicted by each model and a groomed set of ISC *P*-phase arrival times (Engdahl et al., 1998). Once we have an average one-dimensional velocity model that minimizes the *P*-phase travel-time residuals for all distances, we repeat steps 1 through 3, systematically perturbing the travel-time model and using a grid search procedure to optimize models within regional, upper mantle, and teleseismic distance ranges. Regionalized models are combined into one two-dimensional model, using indicator functions and smoother methodologies to reduce distance and depth discontinuity artifacts between the individual models.

Preliminary results of this study at a subset of MENA stations show that we are improving predictability with these models. Cross-validating the travel-time predictions with an independent data set demonstrates a marked reduction in the variance of the travel-time model error distributions. We demonstrate the improvement provided by these 2-D models by relocating the 1991 Racha aftershock sequence. We will extend our investigation to additional MENA stations, and will use our model in tandem with nonstationary empirical corrections (nonstationary Bayesian kriging) to further improve our ability to accurately predict travel times and locate seismic events in this region.

Key Words: 2-D models, travel times, kriging, seismic event location

OBJECTIVE

An accurate velocity model of the earth is a fundamental component of seismic event location. Global velocity models such as *ak135* (Kennett *et al.*, 1995) minimize a set of worldwide travel-time residuals and are primarily meant for prediction of teleseismic travel-times. However, global models are often inadequate for prediction of travel times at regional and near teleseismic distances, where the effect of crustal and mantle structure on seismic travel times is considerable. In order to improve the travel-time predictions at regional and near teleseismic distances in the Middle East and North Africa (MENA), we are developing two-dimensional, station-specific velocity models that are optimized to predict travel times. We will use our travel-time models at each station in tandem with nonstationary spatial corrections (nonstationary Bayesian kriging) to further improve our capability to accurately locate all seismic events in this region.

RESEARCH ACCOMPLISHED

Data

We focus our initial travel-time modeling efforts on 27 of the International Monitoring System (IMS) seismic stations in the Middle East and North Africa. The locations of the IMS stations used in this study are shown in Figure 1. The data we use are a set of *P*-phase arrival times from earthquakes recorded at those each of those stations. The earthquakes are a relocated subset of those contained in the *ISC Bulletin* (Engdahl *et al*., 1998). To minimize the error introduced by a misidentification of phase arrival time, we use only high-confidence *P*-phase picks. The data set has also been declustered - a statistical grooming procedure that reduces the impact of outliers, enhances numerical stability, and lessens computation demands. We divide the groomed data set into a modeling data set and a cross-validation data set. The cross-validation data set represents 10% of the total data set.

Method

For the purposes of this study, the data are parsed into three earthquake-station distance ranges: regional (1º-13º), upper mantle (13º-30º), and teleseismic (30º-90º). Sensitivity analyses were performed to identify those properties of the crust and mantle to which seismic travel times in each distance range were most influenced. Of the 11 properties investigated in the sensitivity analyses, crustal thickness, upper and lower crustal *P*-wave velocity and upper mantle velocity had the largest effect on travel-times. The eight model parameters we use to describe model space are listed below in Table 1. We develop an adaptive grid search method that efficiently samples the space of reasonable models, allowing the four most influential model parameters (as identified in the sensitivity analyses) to vary.

Table 1: Grid search model parameters of the 1-D velocity models

MODEL PARAMETERS VARIED IN THE GRID SEARCH
Crustal thickness 30-55 km
Crustal *P*-wave velocity
Upper crust 5.5-7.0 km/s
Lower crust 6.6-8.0 km/s
Upper mantle velocity 7.9-8.1 km/s
ADDITIONAL MODEL PARAMETERS
Sediment thickness 4 km
Sediment *P*-wave velocity 4 km/s
Thickness of mantle lid 25 km
P-wave velocity gradient in the mantle lid 0

We calculate travel times through each regionalized *P*-wave velocity model using a ray-tracer that employs the single-valued *tau-p* formulation similar to that of Buland and Chapman (1983). An earth-flattening transformation is used to account for the sphericity of the earth, which preserves the kinematic properties of the rays. The resulting travel-time tables are populated with travel times, parameterized by distance and depth.

To test the predictive power of each model, we compute the root-mean-square and mean residuals between the declustered *P*-phase arrivals at each station and the arrivals predicted by each 1-D regionalized model. We repeat the calculation for the declustered *P*-phase arrivals at each station and the arrivals predicted by the *ak135* model (Kennett *et al.*, 1995). To compute these residuals we interpolate between grid nodes to calculate the predicted travel time for the earthquake-station path. Then each predicted time is subtracted from the observed arrival time. We find that a suite of models predict the travel-time arrivals equally well. To further optimize our models, the 50 models that provide the lowest rms residuals are further minimized against the *ak135* model. The model that most closely approximates *ak135* is designated as the preferred model.

The preferred one-dimensional regional models are then merged into one two-dimensional model over the entire distance range of the model, from regional out to teleseismic distances (Figure 2). Merging is accomplished using indicator functions to reduce distance and depth discontinuity artifacts between the individual models (Figure 2). The result is a radially heterogeneous and azimuthally invariant travel-time model of both the crust and upper mantle. This methodology provides optimal models for the three distinct ray-bottoming depths, allowing increased predictability and a smooth travel-time curve.

To test the predictive power of the 2-D models, we compute the rms and mean residuals between the declustered *P*-phase arrivals at each station and the arrivals predicted by both the optimized 2-D model and the *ak135* model. Station-specific analyses of the capability of our 2-D models to predict the observations help us identify regions where the model needs to be improved or alternative models need to be applied.

There are several caveats associated with our technique that merit mention. First, since the travel-time modeling process is non-linear and the number of model parameters is limited, the solution is non-unique. In addition, these two-dimensional models are azimuthally invariant and radially segmented to facilitate statistical averaging. As a result, the models do not account for azimuthal changes in structure and can only account for average changes in radial structure. Our two-dimensional models are thus likely to have better predictive power in areas with dense GT event coverage. Stations with small azimuthal deviations benefit most from these corrections. To predict corrections in aseismic regions, three-dimensional models will likely be required.

Results

For the majority of the 27 IMS stations for which we have computed 2-D models, our 2-D model predicts the observations very well, showing significant variance reduction; for a small number of stations, the 2-D model only slightly reduces the variance. We have selected four IMS MENA stations to illustrate in more detail our method and results: *AAE* (Addis Ababa, Egypt), *ANTO* (Ankara, Turkey), *AQU* (Abruzzo, Italy) and *TBT* (Canarias, Spain) (Figure 1). The results from these individual stations are fairly representative of results from the remainder of stations included in our initial modeling study.

The map in the upper-right-hand corner of Figure 3 shows the azimuthal distribution of a typical modeling data set. This particular data set was recorded at station *AAE*. The data have been parsed into three earthquake-station distance ranges: regional (white circles; 1º-13º), upper mantle (gray circles; 13º-30º), and teleseismic (black circles; 30º-90º).

We tested the predictive power of each *P*-wave velocity model at stations *AAE, ANTO, AQU* and *TBT* by computing the rms and mean residuals between the declustered *P*-phase arrivals at each station and the arrivals predicted by each 1-D regionalized model. We repeat the calculation for the declustered *P*-phase arrivals at each station and the arrivals predicted by the *ak135* model (Kennett *et al.*, 1995). The 50 models that provide the lowest rms residuals are further minimized against the *ak135* model. For each station, the model that most closely approximates *ak135* is designated as the preferred model. This piece-wise optimization of the travel-time curve markedly improves predictability, especially at regional and teleseismic distances.

Figure 3 shows a cartoon illustrating our preferred regionalized models at station *AAE*. *P*-wave velocity *versus* depth profiles for each distance range at each station are shown in Figure 4. The preferred one-dimensional regional models are then merged into one two-dimensional model over the entire distance rage of the model, from regional out to teleseismic distances (Figure 2). The profiles in Figure 4 all display some distance and depth discontinuity artifacts between the individual models, illustrating the importance of using indicator functions when merging the regionalized models into one 2-D model.

To test the predictive power of the 2-D models, we compute the rms and mean residuals between the declustered *P*-phase arrivals at each station and the arrivals predicted by both the optimized 2-D model and the *ak135* model. Those results are shown in Tables 2a and 2b below.

Table 2a: rms residuals (seconds squared)

STATION	data *vs ak135*	data *vs* best 2-D model	Reduction
AAE	2.67838	2.05136	23%
ANTO	2.16813	1.68400	22%
AQU	2.13796	1.76301	18%
TBT	2.76454	1.69335	39%

Table 2b: mean residuals (seconds)

STATION	data *vs ak135*	data *vs* best 2-D model	Improvement
AAE	2.12126	0.86341	59%
ANTO	1.18942	-0.00094	92%
AQU	1.22124	-0.02453	96%
TBT	0.99596	-0.25633	74%

Histograms of the distribution of residuals are shown in Figure 5. Table 2 and Figure 5 demonstrate a clear reduction in travel-time variance between *ak135* and our preferred 2-D models. In addition, our 2-D models provide a mean residual closer to 0. These results suggest that we are improving predictability with these models.

CONCLUSIONS AND RECOMMENDATIONS

Summary

An accurate velocity model of the earth is a fundamental component of seismic event location, which in turn is integral to the effective monitoring of the Comprehensive Nuclear-Test-Ban Treaty (CTBT). Because global velocity models can be inadequate for prediction of travel times at regional and near teleseismic distances, we are developing two-dimensional, station-specific velocity models that are optimized to predict travel times for IMS stations in the Middle East and North Africa.

We develop an adaptive grid search method that efficiently samples the space of reasonable *P*-wave velocity models of the earth. Optimized 1-D regionalized models for each IMS station are better able to predict travel-time arrivals than *ak135*. Regionalized models are being mathematically combined into one 2-D model, using indicator functions and smoother methodologies to reduce distance and depth discontinuity artifacts between individual models. We find that this piece-wise optimization of the travel-time curve improves predictability, especially at regional and near teleseismic distances.

Further research

These are preliminary results from an initial set of IMS seismic stations; we are in the process of incorporating the remainder of the IMS stations into our study. A station-specific analysis of the capability of our 2-D models to predict the observations will help us identify regions where the model needs to be improved or alternative models need to be applied. We will further optimize our regionalized models by performing a finer adaptive grid search centered near the residual lows identified in our initial analysis. We will also experiment with those additional model parameters we have identified as mechanisms to fine tune the model, such as positive and negative velocity gradients in the upper mantle.

We will test the predictive capability of each 2-D model by cross-validating the data. Our cross-validation data set at each station consists of 10% of the groomed modeling data set. We expect that cross-validating the travel-time predictions by using arrivals from this set of independently located events will demonstrate a marked reduction in the variance of the travel-time model error distributions.

A subset of events from the 1991 Racha earthquake sequence recorded at stations *KAS*, *ARU*, *SVE*, *KVT*, *GAR*, and *KHO* will be used to demonstrate improvement in earthquake location using our 2-D models over our 1-D models and over a generalized earth model such as *ak135*.

Finally, we will use our travel-time models at each station in tandem with nonstationary spatial corrections (nonstationary Bayesian kriging) to further improve our capability to accurately locate all seismic events in this region.

This work was performed under the auspices of the U.S. Department of Energy by University of California Lawrence Livermore National Laboratory under contract No. W-7405-Eng-48 for the Office of Research and Development, NN-20, within the Office of Nonproliferation and National Security, NN-1. LLNL contribution UCRL-JC-138983.

REFERENCES

Buland, R. and C. Chapman. The computation of seismic travel times, *Bull. Seism. Soc. Am.*, *73*, 1271-1302, 1983.

Engdahl, E.R., R. van der Hilst, and R. Buland, Global teleseismic earthquake relocation with improved travel times and procedures for depth determination, *Bull. Seism. Soc. Am.*, *88*, 722-743, 1998.

Kennett, B.L.N., E.R. Engdahl, and R. Buland. Constraint on seismic velocities in the earth from travel-times, *Geophys. J. Int.*, *122*, 108-124, 1995.

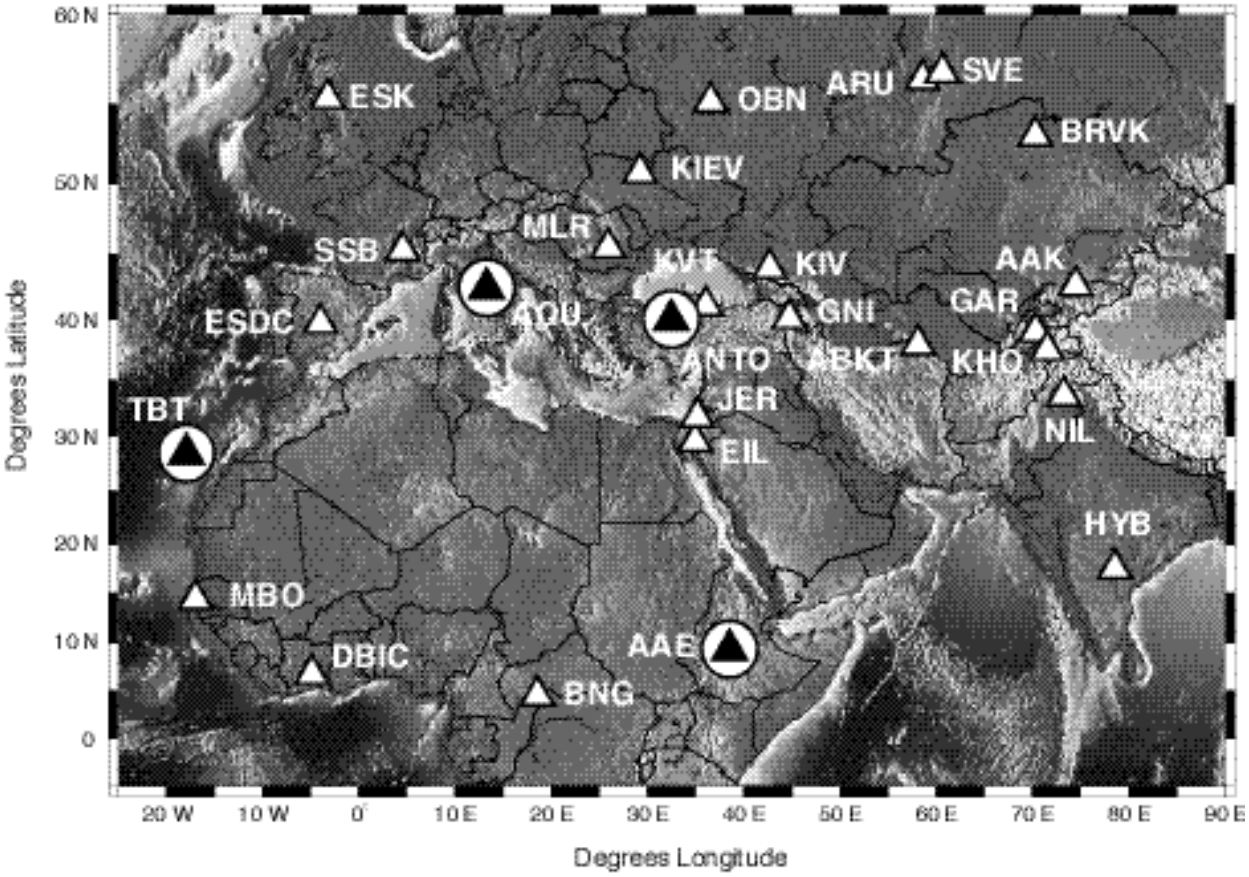


Figure 1: Location of the 27 International Monitoring System (IMS) seismic stations in the Middle East and North Africa for which we have developed 2-D travel-time models. We will present detailed modeling results from the four IMS stations highlighted by the encircled triangles.

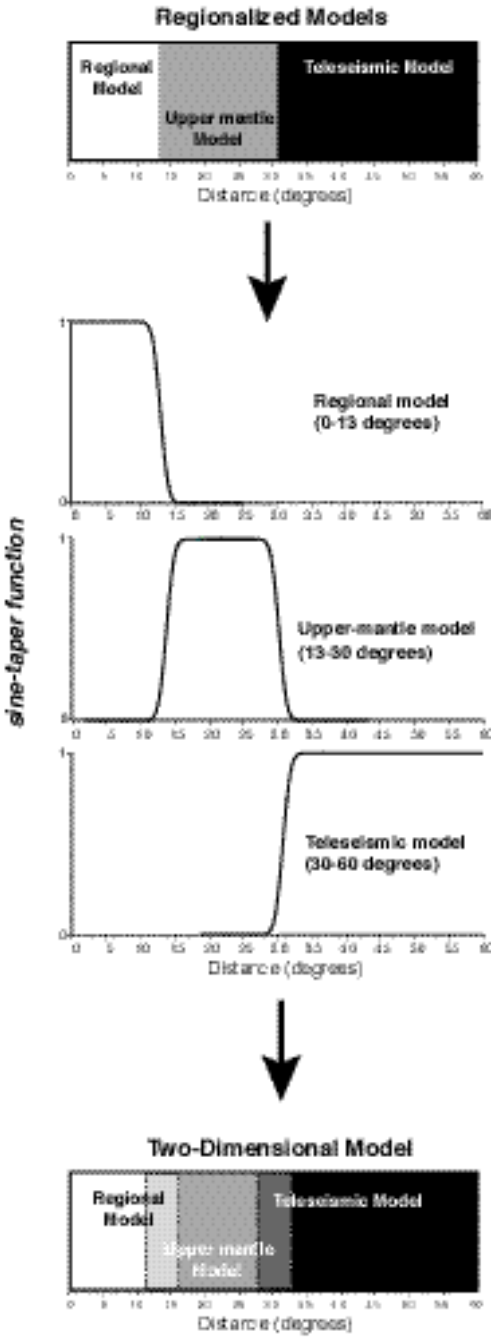


Figure 2: Cartoon depicting the merging of regionalized 1-D models into a 2-D model. Merging is accomplished using indicator functions to reduce distance and depth discontinuity artifacts between the individual models. The result is a radially heterogeneous and azimuthally invariant (see Figure 3) travel-time model of the crust and upper mantle. This methodology provides optimal models for the three distinct ray-bottoming depths, allowing increased predictability and a smooth travel-time curve.

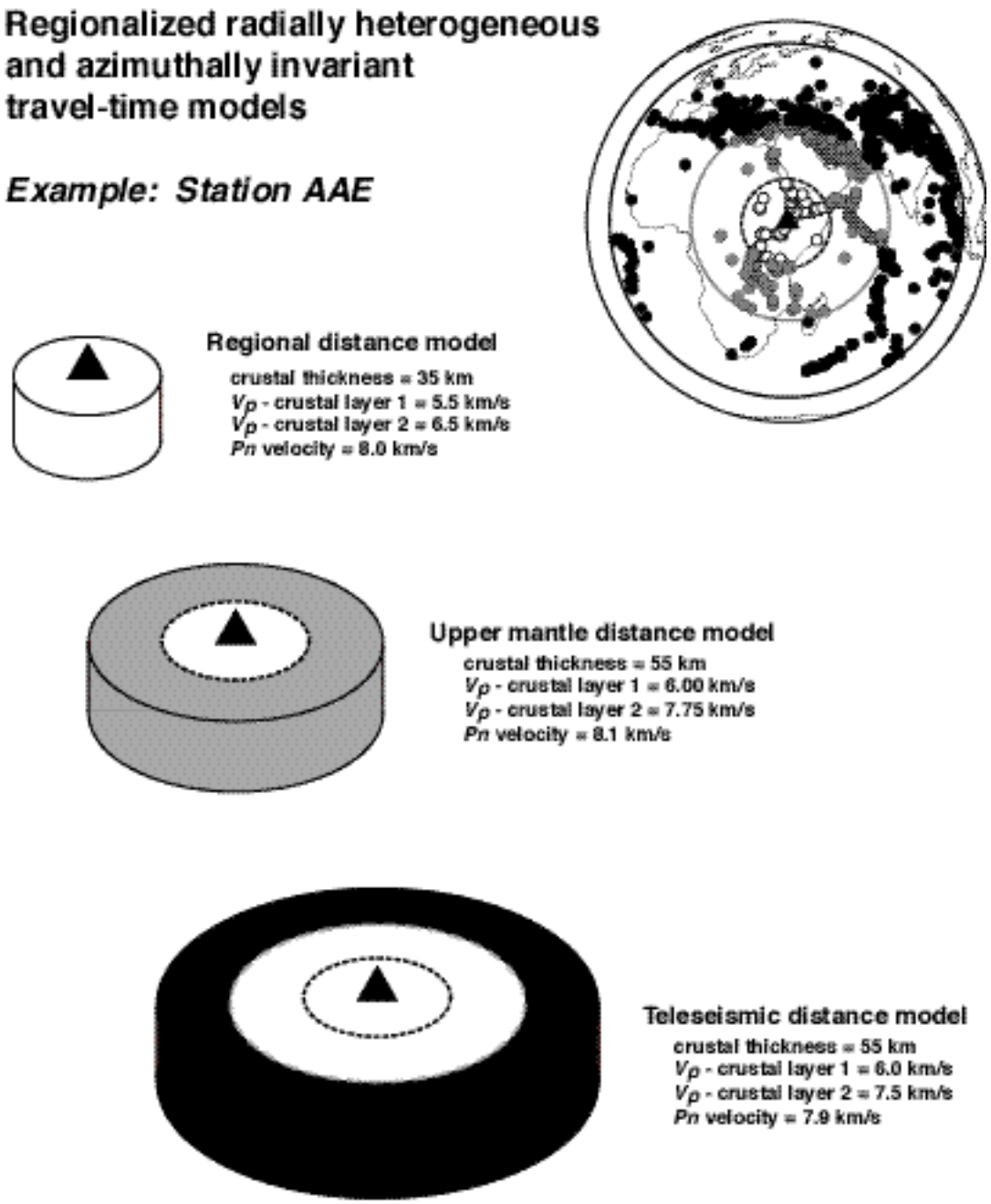


Figure 3: The map in the upper-right-hand corner shows the azimuthal distribution of a typical modeling data set. This particular data set was recorded at station *AAE*. The data have been parsed into three earthquake-station distance ranges: regional (white circles; 1°-13°), upper mantle (gray circles; 13°-30°), and teleseismic (30°-90°). This figure also illustrates the best regionalized radially heterogeneous and azimuthally invariant travel-time models at the IMS seismic station *AAE*.

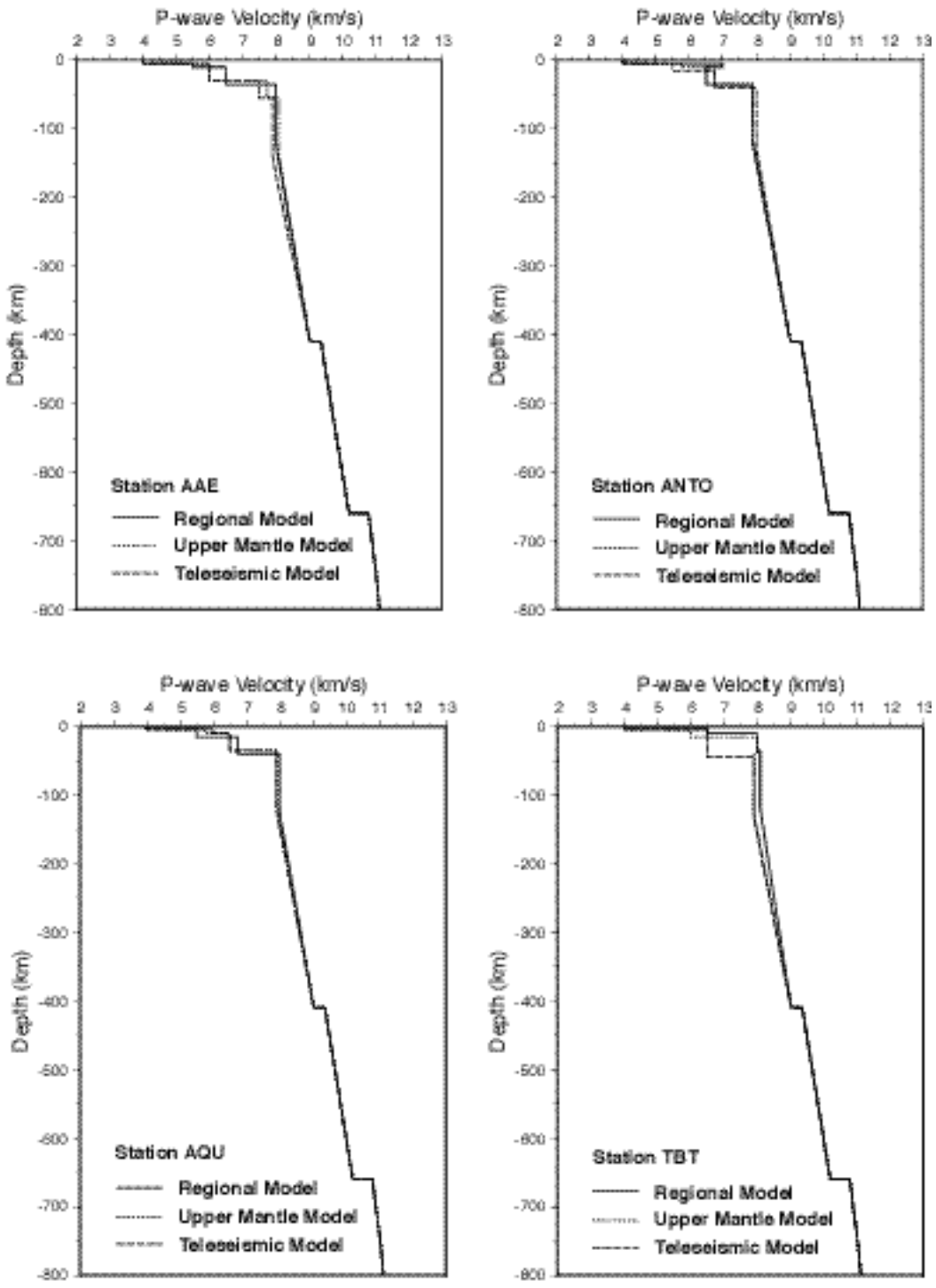


Figure 4: Preferred regionalized models for stations *AAE*, *ANTO*, *AQU*, and *TBT*. The *P*-wave velocity *versus* depth profiles for each distance range at each station are shown. The solid line corresponds to the regional-distance model; finely dashed line corresponds to the upper mantle-distance model; coarsely dashed line corresponds to the teleseismic-distance model.

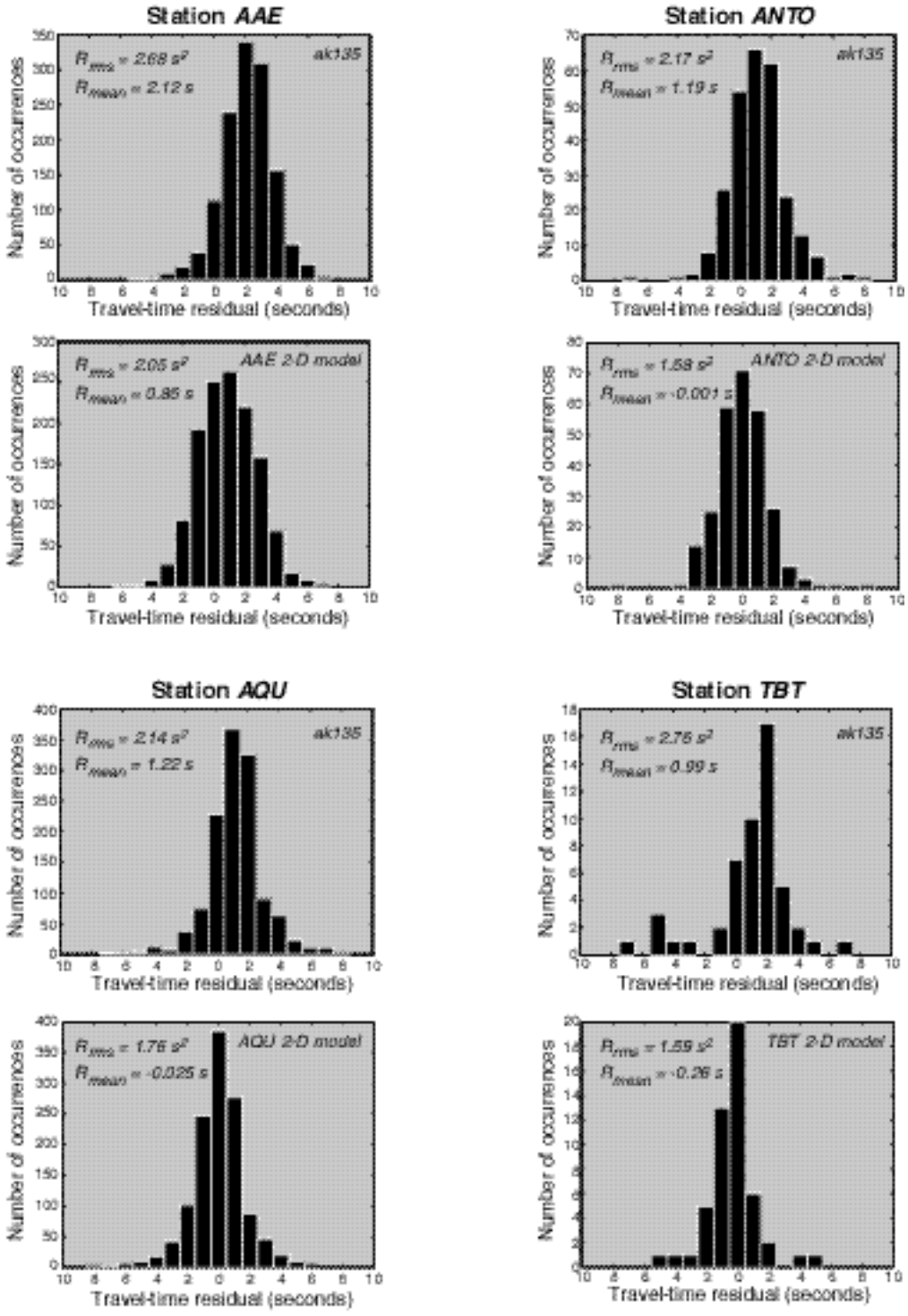


Figure 5: Distribution of travel-time residuals predicted by a global velocity model (*ak135*) and 2-D models computed for IMS seismic stations *AAE*, *ANTO*, *AQU*, and *TBT*. R_{rms} = rms residual (seconds squared); R_{mean} = mean residual (seconds).

ASSESSING EVENT LOCATION CAPABILITY WITH GROUND TRUTH EVENTS AT THE DEGELEN MOUNTAIN TEST SITE, KAZAKHSTAN

Clifford Thurber, Chad Trabant, and Renate Hartog
Department of Geology and Geophysics, University of Wisconsin-Madison

Sponsored by the Defense Threat Reduction Agency
Arms Control Technology Division
Nuclear Treaties Branch

Contract No. DSWA01-98-1-0008

ABSTRACT

We are investigating seismic event location capability in Kazakhstan using first-P arrivals from nuclear explosions with relatively precise or exact ground truth information. We use a waveform cross-correlation (WCC) method to determine high-precision relative arrival times. We then use the improved arrival times to examine several issues regarding location accuracy and precision. Since the true explosion locations are known precisely, we can evaluate both relative (joint hypocenter determination, JHD) and absolute (single-event) location capability. Aspects we are currently investigating include relative and absolute location accuracy, in particular using sparse regional-distance observations, the spatial variability of derived source-specific station corrections (that is, path corrections), and the influence of global heterogeneity on absolute location accuracy.

We have combined information from several sources in order to establish adequate ground truth information for Degelen Mountain. Locations and origin times for 68 Degelen explosions were published by Bocharov et al. (1989). Tunnel portal coordinates for all Degelen explosions were released as part of a tunnel closure project (Leith, 1998). In addition, we obtained sections of a map showing all of the Degelen tunnels, albeit with some apparent distortions and no coordinates (W. Leith, pers. comm.). By combining the true portal coordinates with the tunnel maps, we were able to determine approximately the complete location and geometry of all the tunnels. Using the Bocharov et al. (1989) ground truth information, we then verified our estimated tunnel geometry for those events, and determined that the explosions all took place at essentially the tunnel ends. We then adopted the other tunnel ends as our best estimates of the locations for the remaining Degelen explosions.

We were able to obtain sufficient digital data for 19 Degelen explosions to carry out our WCC-JHD analysis. Each event had between 4 and 17 observations. Using all the digital data and fixing one event location at ground truth, we can locate the other 18 with a mean mislocation of only 2 km. If we restrict the data to stations within 40°, resulting in only 7 usable events with between 3 and 8 observations, fixing one location and solving for the other 6 yields an average mislocation of about 7 km. We have also carried out single-event locations using our WCC data. If no station corrections are applied, the mean mislocation is about 12 km, with a significant southward location bias. Using the station corrections derived from our JHD analysis, the mean mislocation decreases to about 2 km.

For location using path corrections to be accurate and effective in practice, the rate at which the corrections change with changing source location must be relatively modest. Otherwise, the standard interpolation and extrapolation approach will yield erroneous results. We compared the sets of JHD path corrections we derived for events at Degelen with our previous results for Balapan. The corrections are very highly correlated ($r = 0.98$) with a linear least-squares fit slope of 0.97 and an intercept of 0.3 s. This might suggest that the corrections should be readily transportable between the two nearby regions. However, we find that using the Balapan corrections to locate Degelen events results in a mean mislocation of about 5 km, with a general bias to the northeast. Examining the path correction differences more closely, we find that they have a strong azimuthal pattern. This effect could possibly be due to either local or global heterogeneity.

We are also investigating the contributions of global 3-D structure to mislocation. We present the preliminary results of an analysis of single-event location accuracy using a high-resolution global 3-D model. The resulting location accuracy using the 3-D model does not approach that obtained using JHD-derived path corrections.

OBJECTIVE

We are carrying out investigations of seismic event location capability using events that have ground truth information to allow a direct assessment of actual location errors and computed precision estimates. The objectives are to determine the most effective approaches for precise and accurate event location for CTBT monitoring purposes. Waveform cross-correlation methods have been applied to determine more accurate relative arrival times for available digital seismic data from nuclear explosions at Degelen Mountain, Kazakhstan. These arrival times, along with the original bulletin times, are used for a comparison of two strategies for improving absolute location accuracy and reducing estimated location uncertainty, one "calibration-based" and the other "model-based." The calibration-based approach involves joint hypocenter determination (JHD), including the estimation of path corrections. The model-based approach involves the use of a global three-dimensional (3D) velocity model to provide improved travel time estimates.

RESEARCH ACCOMPLISHED

All of the Degelen Mountain nuclear tests were conducted in tunnels that had been bored roughly horizontal into the mountain. Excellent sources of Degelen Mountain ground truth information exist for tunnel entrances, or portals (Leith, 1998), but few sources exist for coordinates of the explosions aside from Bocharov et al. (1989). Bocharov et al. (1989) only reports ground truth for events between 1961 and 1972. Unfortunately, the events for which sufficient waveform data for cross-correlation are available occurred between 1977 and 1988. In order to bridge this gap and establish adequate ground truth for many of the later explosions, we obtained two maps of the Degelen Mountain tunnel complex (W. Leith, pers. comm.). One map is larger and composed of four different map sections, the other is smaller and a single sheet. We were informed that the smaller map should be considered less accurate, therefore we used the larger sectioned map for the ground truth estimate. The large map illustrates many of the reported Degelen Mountain tunnels, albeit with some apparent distortions and no coordinates. An absolute framework for the large map is determined by overlaying GPS-estimated tunnel portal locations of Leith (1998). The approximate locations and orientations of all tunnels on the map sections are then determined by digitizing the tunnel portals and ends. Our estimate for the locations of all tunnels on the map sections is shown in Figure 1. Tunnel labels used in the figure correspond to those listed from the KNNC Tunnel Data Volumes in Leith (1998). Even though very good locations are known for the tunnel portals, this process was deemed necessary because most explosions probably occurred at, or much closer to, the tunnel ends as opposed to tunnel portals.

In order to test our ground truth estimates, our tunnel portal estimates are compared to the GPS-determined portals of Leith (1998). The 142 portals corresponding to Leith (1998) compared well, with a median difference of 77 meters. For this comparison there were 6 notably large differences (larger than 900 meters) between the map-based estimate and the locations in Leith (1998). The tunnels in question are those labeled 104, 151, 152, 200M-bis, 806, and E-2 in Figure 1. All 6 of the discrepant portals appear in the same general location, relative to the other tunnels, on both the large and small maps. Additionally, one of them (tunnel E-2) has a tunnel end, based on our estimate, that corresponds to one of the Bocharov et al. (1989) reported explosion locations (event 680929). Because of this, we believe the map-based estimate to be generally closer to the true portal location for these 6 tunnels. The source of the discrepancy is currently under investigation.

To further test our ground truth estimates, our tunnel locations are compared to explosion locations reported by Bocharov et al. (1989). Bocharov et al. (1989) reported locations of 53 events that occurred in 46 different tunnels on our maps. All of these events located very close to our estimates of their corresponding tunnels with the majority at the ends of the estimated tunnels. Based on the close proximity of Bocharov et al. (1989) reported events to the ends of our estimated tunnels and the assumption that tests could not be conducted farther into a tunnel than the previous test was conducted, it follows that the first detonation in a tunnel was usually at the tunnel end. These initial tunnel explosions, determined by the chronological order of tests in a given tunnel, had a median distance of 80 meters from their corresponding tunnel end. In the case where multiple explosions occurred in a single tunnel, each event location was equally close to their corresponding tunnels. Approximately 75% of the events listed in Leith (1998) occurred in unique tunnels. Unfortunately, given current information, we cannot determine where multiple detonations in a single tunnel occurred. Since most tunnels only had one explosion that was most likely at the tunnel end, and the mean tunnel length was only 685 meters, the tunnel ends are adopted as our ground truth estimate for events that were not reported by Bocharov et al. (1989).

Origin times for the 84 Degelen Mountain events in the ISC catalog not reported by Bocharov et al. (1989) are refined using published ground truth locations and our map-based ground truth location estimates, origin times reported by Bocharov et al. (1989), and ISC catalog arrival times. The objective is to restrain a portion of the origin times in order to sufficiently constrain the remaining origin times to give very good absolute estimates. This procedure involves applying JHD with epicenters restrained to ground truth estimates and only the origin times reported by Bocharov et al. (1989) restrained. The JHD technique then solves solely for path corrections and the remaining unrestrained origin times relative to our reference velocity model ak135.

To evaluate this procedure, a data set is constructed from only the 68 Degelen Mountain events reported by Bocharov et al. (1989). With the event epicenters restrained to their absolute locations, the origin times are restrained in different ratios to test the accuracy with which the unrestrained origin times can be recovered. With 23 of 68 origin times restrained, all of the remaining origin times are recovered within 0.4 seconds with an RMS error of 0.13 seconds. The same recovery is observed when 46 of 68 origin times are restrained. Based on this exercise, the origin times estimated in this manner are assumed to be within 0.4 seconds of their true values. The resulting origin times for each event are listed in Table 1 along with 95% confidence limits and our map-based location estimates.

JHD is applied to relocate the events using 144 cross-correlation (C-C) derived teleseismic and regional arrival times from 19 nuclear explosions at Degelen Mountain. The initial locations for these events are set to the ground truth estimate described above. Each event had between 4 and 17 observations. For all of the Degelen Mountain relocation analyses, event 870717 is restrained as the master event. This event was chosen because it had a relatively large number of observations (12) and the largest magnitude (6.4 mb) of the group as reported in the pIDC's Nuclear Explosion Database (NEDB). Most events relocated to within 3 km of our ground truth estimate, and all relocated to within 4.5 km, with a mean mislocation of 2.0 km (Figure 2). All 95% confidence ellipses covered less than 16.5 km^2, with most being less than 8 km^2, and a mean coverage of 6.6 km^2. Only 5 of the 18 relocated events had confidence ellipses that covered their ground truth location estimate. This underestimation of location uncertainties is expected given the very small number of observations (Evernden, 1969) and is a well-known problem in such location scenarios. No correlation exists between azimuthal gap and mislocation for our locations using waveform cross-correlation picks, despite having a large average azimuthal gap of 146°. This is contrary to the trend observed by Thurber and Engdahl (2000) wherein mislocation increases with increasing azimuthal gap using worldwide ground truth events and ISC data. We attribute this difference to the accuracy of our arrival times.

In a more realistic CTBT-like monitoring situation, far fewer events would normally be available for JHD and the event magnitudes would most likely be small, resulting in observations being made only out to regional distances or slightly beyond. This scenario is especially challenging for seismic location due to the fact that regional seismic phases pass through significant portions of the Earth's crust and uppermost mantle, which have a laterally heterogeneous velocity structure that is poorly represented by our 1-D reference velocity model. In order to investigate location capability in such a situation, the full C-C Degelen Mountain data set is limited to phases arriving from less than 40° epicentral distance. Imposing this limitation eliminates 12 events because they have less than 3 observations, and reduces the number of observations to between 3 and 8 for the 7 remaining events. Again, 870717 is chosen as the master event. As expected, both mislocations and uncertainties increase substantially for the unrestrained 6 events (Figure 3). The mean mislocation is 7.43 km with the largest being 15.4 km. Four of the events have associated 95% confidence ellipses covering less than 570 km^2, well within the CTBT 1000 km^2 goal. The other two events have ellipses covering 1730 and 8869 km^2, which is not surprising as each event had only three observations. The average azimuthal gap for this "regional" data set is 165°.

We also use the software package LocSAT of the International Data Centre to locate the explosions in the 1-D reference earth model ak135 both without and with station corrections. The station corrections were obtained from our JHD of explosions at Degelen Mountain and Balapan. We test to what extent these two sets of station corrections are transportable; can we use them to locate events that occurred in the general vicinity of the two sites? To be able to compare the locations estimated using both sets of corrections, we only include stations for which both corrections are available, that is, stations that recorded at least three Balapan and three Degelen Mountain explosions. Using only the resulting set of twenty stations, the number of observations per event ranges from 4 to 16, and is 8 on average. The azimuthal gap ranges from 90° to 240°, with an average gap of 190°.

Figure 4 shows the ground truth locations (solid dots) and our estimated locations (open squares) of Degelen Mountain explosions without and with station corrections. On the top (Figure 4a) we show our estimates without using any station corrections. A systematic bias of the estimated locations is evident; the median mislocation distance is 14.4 km. When we apply the source region specific station corrections for Degelen (middle, Figure 4b) we obtain much improved locations, with the median mislocation distance reduced to 2.7 km. Note that if we do not restrict the data set to stations that have observations of both Balapan and Degelen Mountain explosions, the median mislocation distances are11.8 km without and 1.7 km with station corrections, respectively.

There is a strong linear correlation between the Degelen Mountain and Balapan station corrections, suggesting that the station corrections might be transportable. Degelen Mountain corrections are systematically 0.3 s larger than the Balapan corrections. This offset could be due to a difference in structure beneath the two sites, for example a different crustal structure, however, it could also be due to a difference in the origin time estimates used in the JHD procedure. The estimated origin times are assumed accurate to within 0.4 seconds, so we cannot resolve whether the offset is due to structure or not. However, when we plot the difference between the two station corrections as a function of azimuth to the station, a smoothly varying pattern, resembling a sinusoid, becomes apparent. Indeed, if we locate Degelen Mountain events using the Balapan corrections, the estimated locations are slightly displaced

towards Balapan (Figure 4c). We interpret these systematic mislocations as due to a difference in structure between Degelen Mountain and Balapan. However, the median mislocation distance is only 4.7 km, still a significant improvement compared to just locating in ak135 with no station corrections (Figure 4a).

We also evaluate how well we can locate the Degelen explosions when we use a recent 3D global P wave velocity model, BSE [Bijwaard et al., 1998]. A subset of the events have relatively small mislocations (15 km or less), but the rest have substantially larger mislocations (> 20 km). When we only use teleseismic data, these large mislocations are substantially decreased. Thus, the global model reproduces teleseismic travel times much better than regional travel times, which is not surprising. However, even when only teleseismic data are used, a systematic mislocation to the west-northwest is apparent.

CONCLUSIONS AND RECOMMENDATIONS

Ground truth information is a key to evaluating seismic event location capability. For the Degelen Mountain explosions, where we have developed high-quality ground truth information, the improved arrival times from cross-correlation analysis and appropriate path corrections yield excellent relative (JHD) and absolute (single-event) location results, even from sparse stations at relatively close distances with large azimuthal gaps. In both cases, we obtain location accuracies that are adequate for CTBT monitoring. Path corrections vary modestly from the adjacent Balapan area, but the variations are enough to cause significant location bias if corrections from one site are applied to the other. Preliminary locations using an existing global 3-D model are much less accurate, but the accuracy can be improved substanitally if regional-distance data are excluded. The calibration-based approach yields superior accuracy, but the model-based approach should be more transportable.

Key Words: Location, Ground Truth, Corrections, Calibration, Waveform Cross-Correlation

REFERENCES

Bijwaard, H., W. Spakman, and E. R. Engdahl, 1998. Closing the gap between regional and global travel time tomography, J. Geophys. Res., 103, 30,055-30,078.

Bocharov, V. S., S. A. Zelentsov, and V. N. Mikhailov, 1989. Characteristics of 96 underground nuclear explosions at the Semipalatinsk test site, Atomnaya Energiya, 67.

Leith, W., 1998. Degelen nuclear test and tunnel data, Technical Memorandum dated June 26, 1998, to the Defense Threat Reduction Agency, contract DNA001-95-C-1079.

Thurber, C. H., and E. R. Engdahl, 2000. Advances in global seismic event location, in C. Thurber and N. Rabinowitz (editors), Advances in Seismic Event Location, Kluwer Academic Publishers, in press.

Table 1. 152 ISC-reported Degelen Mountain nuclear explosions including our estimated origin times and their uncertainties (+/- value, 95% confidence), ground truth location estimates, and body-wave magnitudes (pIDC). The first 68 events are from Bocharov et al. (1989).

YRMODAHRMN	SEC	+/-	LATITUD	LONGITU	MAG
640315	8 0 0.4	0.00	49.8160	78.0752	6.2
640516	6 059.8	0.00	49.8077	78.1020	6.2
640719	6 0 0.6	0.00	49.8091	78.0929	6.0
641116	6 0 0.2	0.00	49.8087	78.1334	6.1
650303	61459.4	0.00	49.8247	78.0527	6.0
650511	640 0.2	0.00	49.7702	77.9943	5.2
650617	345 0.0	0.00	49.8284	78.0669	5.8
650729	3 5 0.2	0.00	49.7797	77.9981	4.5
650917	4 0 0.1	0.00	49.8116	78.1467	5.6
651008	6 0 0.4	0.00	49.8259	78.1114	5.8
651121	458 0.0	0.00	49.8192	78.0636	6.1
651224	5 0 0.2	0.00	49.8045	78.1067	5.2
660213	458 0.1	0.00	49.8089	78.1210	6.5
660320	550 0.3	0.00	49.7616	78.0239	6.2
660421	358 0.1	0.00	49.8097	78.1000	5.4
660507	358 0.2	0.00	49.7429	78.1050	4.8
660629	658 0.5	0.00	49.8344	78.0734	5.6
660721	358 0.0	0.00	49.7367	78.0970	5.9
660805	35759.6	0.00	49.7643	78.0424	6.1
660819	35259.9	0.00	49.8271	78.1088	5.1
660907	35159.7	0.00	49.8288	78.0637	4.8
661019	35759.9	0.00	49.7471	78.0205	6.3
661203	5 2 0.2	0.00	49.7469	78.0334	4.9
670130	4 159.5	0.00	49.7674	77.9914	4.8
670226	35759.8	0.00	49.7457	78.0823	6.6
670325	558 1.1	0.00	49.7536	78.0630	5.9
670420	4 8 0.0	0.00	49.7416	78.1054	6.3
670528	4 759.6	0.00	49.7564	78.0169	6.2
670629	25659.9	0.00	49.8167	78.0490	5.3
670715	32659.9	0.00	49.8359	78.1182	6.0
670804	658 0.3	0.00	49.7603	78.0555	5.8
671017	5 4 0.2	0.00	49.7809	78.0038	6.1
671030	6 4 0.0	0.00	49.7944	78.0079	6.0
671208	6 359.8	0.00	49.8171	78.1638	5.4
680107	34659.9	0.00	49.7544	78.0309	5.3
680424	103559.7	0.00	49.8452	78.1032	5.0
680611	3 559.7	0.00	49.7930	78.1451	5.8
680712	12 8 0.0	0.00	49.7547	78.0899	5.9
680820	4 559.6	0.00	49.8226	78.0774	4.8
680905	4 559.6	0.00	49.7416	78.0756	6.2
680929	343 0.0	0.00	49.8120	78.1219	6.3
681109	254 0.1	0.00	49.8005	78.1391	4.9
681218	5 159.7	0.00	49.7459	78.0920	5.7
690307	82659.8	0.00	49.8215	78.0627	6.3
690516	4 259.7	0.00	49.7594	78.0758	6.0
690704	24659.6	0.00	49.7460	78.1113	6.0
690723	247 0.2	0.00	49.8156	78.1296	6.1
690911	4 2 0.0	0.00	49.7763	77.9967	5.0
691001	4 259.9	0.00	49.7825	78.0983	5.9
691229	4 2 0.0	0.00	49.7337	78.1022	5.1
700129	7 3 0.0	0.00	49.7956	78.1239	5.9
700327	5 259.6	0.00	49.7478	77.9990	5.4
700628	158 0.0	0.00	49.8015	78.1068	6.2
700724	357 0.0	0.00	49.8097	78.1284	5.8
700906	4 259.9	0.00	49.7597	78.0054	6.0
701217	7 1 0.0	0.00	49.7456	78.0992	6.1
710322	433 0.3	0.00	49.7985	78.1090	6.0
710425	33259.9	0.00	49.7685	78.0339	6.4
710525	4 3 0.4	0.00	49.8016	78.1388	5.2
711129	6 259.9	0.00	49.7434	78.0785	5.5
711215	75259.8	0.00	49.8264	77.9973	4.9
711230	621 0.2	0.00	49.7600	78.0371	5.8
720310	45659.8	0.00	49.7453	78.1197	5.8
720328	422 0.1	0.00	49.7331	78.0757	5.6
720607	128 0.0	0.00	49.8267	78.1155	5.7
720706	1 3 0.0	0.00	49.7375	78.1101	4.8
720816	31659.8	0.00	49.7655	78.0588	5.6
721210	427 0.0	0.00	49.8194	78.0582	6.0
730216	5 3 0.0	0.05	49.8061	78.1034	5.6
730710	127 0.1	0.05	49.7730	78.0451	5.4
731026	427 0.1	0.05	49.7469	78.1320	5.3
740130	457 0.1	0.08	49.8158	78.0401	5.4
740516	3 3 0.1	0.05	49.7459	78.0374	5.3
740710	257 0.0	0.05	49.7791	78.1027	5.3
740913	3 259.9	0.06	49.7653	78.0549	5.2
741216	623 0.0	0.07	49.7598	78.0754	5.0
741216	641 0.3	0.07	49.8329	78.0318	4.8
750220	533 0.1	0.04	49.7965	78.0093	5.7
750311	543 0.0	0.05	49.7462	78.1060	5.4
750608	327 0.0	0.05	49.7606	78.0125	5.5
750807	357 0.0	0.05	49.8038	78.1234	5.2
751213	457 0.0	0.06	49.8076	78.1144	5.1
760115	447 0.0	0.06	49.8120	78.1576	5.3
760421	458 0.1	0.06	49.7462	78.1060	5.1
760519	257 0.2	0.08	49.7770	78.0009	5.0
760723	233 0.0	0.06	49.7492	78.0617	5.1
761030	457 0.1	0.10	49.8285	78.0516	4.9
761230	357 0.2	0.06	49.7686	78.0331	5.2
770329	357 0.0	0.05	49.7704	78.0136	5.4
770425	4 7 0.1	0.06	49.8076	78.1144	5.1
770730	157 0.1	0.05	49.7500	78.0399	5.3
770817	42659.9	0.06	49.8200	78.1400	5.1
771029	3 7 0.0	0.04	49.8265	78.0801	5.6
771226	4 259.9	0.07	49.8038	78.1234	4.9
780326	357 0.0	0.04	49.7643	77.9993	5.6
780422	3 7 0.0	0.04	49.7469	78.1251	5.3
780529	45660.0	0.07	49.7986	78.1022	4.7
780728	24659.9	0.04	49.7488	78.0893	5.7
780829	23659.9	0.05	49.8074	78.1091	5.2
780920	5 3 0.1	0.13	49.7934	78.1447	4.3
781015	537 0.1	0.05	49.7395	78.1127	5.2
781031	417 0.1	0.05	49.7875	78.0974	5.2
781129	433 0.0	0.05	49.7826	78.0073	5.3
781214	443 0.1	0.09	49.8061	78.1034	4.8
781220	43259.9	0.08	49.8169	78.0542	4.7
790506	317 0.1	0.05	49.7643	77.9993	5.2
790531	555 0.0	0.05	49.8265	78.0801	5.3
790718	317 3.3	0.06	49.7791	78.1027	5.2
790927	413 0.2	0.11	49.7500	78.0399	4.5
791018	417 0.1	0.05	49.8200	78.1003	5.2

Table 1 (continued)

YRMODAHRMN	SEC	+/-	LATITUD	LONGITU	MAG
791130	453 0.6	0.09	49.7794	78.0953	4.5
791221	442 0.1	0.09	49.7957	78.1230	4.7
800410	4 7 0.2	0.06	49.7780	78.0547	5.3
800522	357 0.1	0.04	49.7739	78.0287	5.8
800731	333 0.1	0.05	49.7955	78.0907	5.5
800925	62112.9	0.08	49.7855	78.0805	4.9
810630	15715.3	0.05	49.7669	78.0744	5.4
810717	23718.1	0.05	49.8064	78.1352	5.3
810814	22715.2	0.06	49.7587	78.0565	5.3
811120	457 5.1	0.06	49.7401	78.0965	5.2
811222	431 5.4	0.07	49.8267	78.0757	5.1
820219	35613.4	0.05	49.8136	78.0319	5.4
820625	2 3 7.0	0.07	49.7749	78.0996	5.0
820823	243 6.7	0.08	49.7473	78.0331	5.0
820921	257 3.1	0.05	49.7839	78.1347	5.5
821225	423 8.4	0.10	49.7763	78.0280	4.9
830330	41710.1	0.09	49.7810	78.0413	5.0
830412	341 8.2	0.08	49.7910	78.0807	5.0
830530	33347.1	0.04	49.7439	78.1127	5.5
830624	25613.8	0.08	49.7459	78.0374	5.0
830911	63313.1	0.10	49.7854	78.0806	4.9
831129	219 8.8	0.05	49.7355	78.0994	5.5
831226	429 9.2	0.04	49.7975	78.1036	5.7
840415	31711.5	0.04	49.7499	78.0824	5.9
840909	259 8.7	0.06	49.8060	78.0997	5.1
841018	457 8.3	0.11	49.7328	78.0987	4.5
841123	355 7.5	0.10	49.8176	78.0551	4.7
850725	311 9.1	0.06	49.8157	78.0096	5.3
870226	45824.3	0.04	49.8299	78.0835	5.4
870403	11712.3	0.04	49.7467	78.1162	7.3
870506	4 2 8.0	0.04	49.7742	77.9986	6.1
870606	237 9.2	0.04	49.8327	78.0704	5.4
870717	117 9.1	0.03	49.7664	78.0287	6.4
870918	232 8.9	0.20	49.8060	78.0997	4.4
871016	6 6 7.0	0.15	49.7313	78.0906	4.6
871220	255 9.1	0.07	49.7742	77.9986	5.2
880206	419 8.9	0.10	49.7664	78.0287	4.8
880422	930 9.3	0.07	49.7942	78.1000	5.1
881018	340 9.1	0.07	49.7799	78.0079	5.2
881123	357 9.0	0.04	49.7726	78.0378	5.6
890217	4 1 9.1	0.05	49.8235	78.0680	5.3
891004	1130 0.1	0.09	49.7498	78.0117	5.2

Figure 1. Tunnel portals (triangles) (Leith, 1998) and actual (Bocharov et al., 1989) or estimated (this study) ground-truth explosion locations (circles) for Degelen Mountain.

Figure 2. Degelen Mountain JHD mislocations and 95% confidence ellipses for 19 events using all digital data.

Figure 3. Degelen Mountain JHD mislocations and 95% confidence ellipses for 7 events (one fixed) using stations within 40°.

Figure 4. Estimated (open squares) and ground truth (solid circles) locations of 19 Degelen Mountain explosions, using only stations (20) that recorded at least three Balapan and three Degelen Mountain

explosions. a) Without station corrections, b) with station corrections obtained from Degelen Mountain data, and c) with station corrections obtained from Balapan data.

METHODS FOR THE IMS REGIONAL KINEMATIC CALIBRATION

Nikolai A. Vasiliev

Laboratory of Experimental Geophysics
Joint Institute of Physics of the Earth
Russian Academy of Sciences

ABSTRACT

Among the problems related to CTBT a very important role belongs to the calibration of the regional travel times (regional kinematic calibration). The success in solving this task would significantly improve the accuracy of the weak seismic event location by the system. The methods that are applied to perform this kind of calibration are assumed in the present paper. All these methods can be broken into two principal groups: methods for direct calibration and those utilizing the velocity model of the media that is to be developed in an intermediate stage.

Direct methods are used to construct the time correction surfaces making use of previously learned seismological experience (regional travel time tables) or directly employing the experimental data. The first approach represents the try to perform the task through the linear combination of regional travel time tables (godographs) and their errors. Another technique is a kind of spatial interpolation of the regional observations for given station.

Indirect methods solve the calibration problem in two steps. Initially the 3-D velocity model of the media is being produced by the inversion of the observations. Afterwards the field of travel times is generated on the base of the velocity model. Methods inside the group differ depending upon what way is chosen for the reverse kinematic problem solution. Currently the velocity models are being built by "try-and-drop" technique or by tomographic inversion. The tomographic P-models developed till now do not possess the horizontal resolution enough to be successfully applied in a regional scale. The main reason of poor lateral resolution for the uppermost mantle comes from low amount and uneven distribution of regional P-wave observations used to produce the global tomographic models. The reliability of 3-D model constructed by "try-and-drop" method is unknown but its using is still reasonable unless enough data for the area to be calibrated have been collected.

Some investigators make the attempts to supplement the basic data by newly collected regional P-observations; others try to employ the S-models constructed on the base of the surface wave or the channel wave observations. The "try-and-drop" technique can be assumed as the attempt to compensate the lack of data by experience and intuition of the scientist.

The success of the efforts is defined by the availability of the regional P-wave observations and by proper choosing the method corresponding to the volume and geographic distribution of the data set. When and where the collected data density and geometry reach the definite threshold the seismic tomography will be able to resolve the problem of regional kinematic calibration in a comprehensive and optimal in given sense manner. In a meanwhile the composition of data availability, data distribution, geologic and tectonic complexity, and knowledge about the region define some role for each of calibration methods assumed.

OBJECTIVE

The quantitative target of the CTBT seismic monitoring is expressed by the requisite upper bound area of the 90% error ellipse around the detected seismic event. This area must be not more than 1000 km^2. Nevertheless the first evaluation of the IMS effectiveness revealed that the real results rarely fit 1000 km^2 requirement especially for the weak events that are mostly detected by the regional stations (within 2000 km circle around the event). Currently several methods to perform the regional kinematic calibration are being developed and the task of their classification rises. Such classification is aimed at better understanding the limitation of the methods and outlining the relevant areas of their application.

RESEARCH ACCOMPLISHED

All the methods related to the problem could be divided into two main parts. The first group constructs travel time corrections directly from observational data. The second group is characterized by two-stage way of solving the problem: the velocity model of the media is the result of the first step in which the reverse kinematic problem is being solved.

Methods for direct estimation of the regional travel times

Let us call direct that methods which aimed at producing the travel time corrections directly from experimental observations passing over the building the intermediate velocity model of the media. Depending upon the scale of the region the next types of corrections can be recognized.

Bulk corrections are those independent upon the azimuth and distance. They reflect features of crust and upper mantle underlying the seismic station.

Regional corrections are expressed by the regional travel time tables or godographs that are constructed for regions of the homogeneous tectonic structure of the upper layers of the Earth. Usually such godographs are calculated and utilized for a regional seismic network; their usage is helpful, but often it is impossible to track back a source of their appearance. We also put to this category the corrections developed for the relatively small areas when these areas are assumed to be homogenous. An example can be extracted from the history of nuclear explosion monitoring. The testing areas of the nuclear test sites were studied carefully enough to develop separate time corrections for them (Pahute Mesa and Yucca Flat inside Nevada Test Site of USA, Balapan and Degelen at the Semipalatinsk Test Site of former USSR, Mururoa and Fangataufa at the Pacific Test Site of France).

Continuos correction fields (point corrections, Source-Specific Station Corrections) are produced by different techniques of a spatial interpolation of experimental observations or regional travel time tables. The correction for new event inside the area covered by the correction surface is defined by the vertical projection of hypocenter to the surface.

The third type of corrections seems to be one of the highest importance for the monitoring the CTBT. Currently inside this group two main methods are being developed. The first (Proportional Godograph Method) is based on the knowledge of the travel time tables for the homogenous regions composing the complex terrain. The second approach is grounded on the direct using of the experimental data to construct the correction surface. The Kriging method is the most developed representative of the latter approach.

The Proportional Godograph Method

According to approach proposed by I. Bondar et. al., 1998, given a seismic ray intersects several homogeneous regions having their own travel time tables, the estimation for the total travel time is expressed as a weighted travel time table with the weights being proportional to the lengths of particular surface projections of the ray inside each region.

This estimation works good for a head wave model when seismic wave velocities are independent upon the depth and the travel in the crust is taken into account. Nevertheless the authors suggested this formulae for the real media since the shape of the experimental travel time - distances plots for regional distances is close to linear.

The Proportional Godograph Method (PGM) is very attractive to application for the kinematic calibration at least because it allows usage the many years experience of seismological observations expressed in regional travel time tables.

The calibration of some territory by this method includes the next steps.

1. Defining the homogenous regions composing the calibrated area;
2. Collecting all available information on the 1-D models (in time and velocity domains) related to given regions; data analysis and choosing the single model for each elementary province;
3. Regionalization that is positioning the borderlines between the elementary provinces;

4. The correction surface calculations;
5. An evaluation of corrections on the ground of the calibration events relocation.

The example of PGM application is described in the paper of Yang et. al., 1999. The method was used for the waves Pg, Pn, Sn, and Lg for the IMS American stations.

The reliable correction evaluation was made using 21 calibration events of known coordinates with the accuracy not worse than 2 km. The calculated epicenters uptrend takes place with 9.7 km median improvement for the events with enhanced epicenters and 4.7 km median deterioration for epicenters shifted out of the true event. The special attention was paid for two earthquakes located inside the Nevada Test Site. The corrections have worked out positively for both cases: the resulted deviation from the true epicenter is as small as 7-8 km. The good news is that the error ellipse area decreased from 1760 to 910 km^2. The negative effect is that the error ellipse coverage (the percentage of calibration events covered by the ellipse) went back from 84% to 74%. We can suggest that the underestimation of the modeling error is responsible for the both effects: the deviation of individual travel time tables from the median characterizes the scatter of mean for different populations rather than the general population scatter.

PGM is already in use for IMS calibration while its methodical error is still to be studied. We have investigated PGM by mean of Pn raytracing (program code "beam87" written by V. Cerveny, 1985). The case of compound media consisted of high-speed "platform", low-speed "tectonically-active" regions, and transmission zone between two regions was assumed. Separately we studied the PGM behavior for the different sharpness of the border between two regions [Vasiliev, 2000].

The PGM appears to be biased and sensitive to the epicenter distance and the distance between the source and media-dividing border. The biases vary from -0.3 s to +0.6s.

We investigated the influence of the regionalization error i.e. the error of location the borderline between different regions. PGM transfers this kind of error proportionally. For the border with transmission zone of 100 km width and distance event - border of 700 km each 100 km in error of border positioning causes PGM bias of 0.3 s ... 0.4 s for stations at epicenter distances 300...1700 km

Modeling for borders of different transmission widths reveals that PGM does not experience the notable dependency upon the sharpness of the border between two regions.

The behavior and quantitative scale of the PGM error allows its practical usage when the error is taken into account. We proposed the approach to do so by introducing both bias and pseudo scatter.

Kriging

The various procedures to construct the surface including scattered points are being widely applied in the mapping and visualization of geophysical data. Some of these are: 2-D bicubic interpolation, an adjustable tension continuous curvature surface gridding algorithm [Smith and Wessel, 1990], a "nearest neighbor" gridding [Smith and Wessel, 1999].

The latter algorithm employs the weighted mean taken through the points inside the correlation radii. Its realization in the GMT package [Smith and Wessel, 1999] additionally takes into account the individual measurement errors.

More developed weighted algorithm constitutes the ground of so called Kriging method. The main feature of the latter is the simultaneous producing of two surfaces: for travel time corrections and for their errors. This method is in practical use for geophysical field surfaces generation for knowledge database of USA Department of Energy developed for the needs of the CTBT [Hipp, 1997], [Young, 1998], [Schultz, 1998]. The Kriging has to satisfy the next requirements:

- To manage the different quality of the data;
- To make user able to effect the weight of each observation;
- To account spatial distribution of the background values for both the time corrections and their errors.

In the most modern release Kriging uses so called variogram reciprocal as the weight of the experimental datum. The variogram is the function assigned to the each station and is based on the correlation of the travel time deviation dependent upon the event-station distance. For stationary case, when the statistics of the process do not vary from point to point, the variogram is equal to background dispersion out of the correlation radii. Inside the circle of this radii the variogram equals to correlation of the observations in the different points subtracted from 1.

The complex regions that include high- and low-velocity provinces are of the most interest from kinematic calibration point of view. For these cases the background statistics vary from point to point and the procedure of Nonstationery Bayesian Kriging has been proposed [Schultz et. al, 1998]. In brief, the latter allows to come to different background models (travel time bias and dispersion) for different tectonic provinces.

The application of the Nonstationery Bayesian Kriging procedure is described in [Myers et. al., 1998] and includes the next steps.

1. One must collect sufficient for each station calibration event database. The number and density of such events are defined by the correlation radii. The latter value for the tectonic regimes is around 2 –3 deg. The authors of the assumed paper use teleseismically located events for calibration database. Selected events fit the next conditions:
   - The azimuth coverage is not less than 270;
   - The number of defining phases is not less than 50.
2. Following Sweeney, 1996 it is accepted that the conditions above guarantee the deviation of the calculated location from the true epicenter not more than 20 km with a 90% reliability.
3. The variogram for each station is constructed.
4. So called declusterization aimed at increasing the calculation effectiveness is to be done. This action averages the experimental observations inside the cell of size defined by condition that the correlation between observation of events occurred inside the circle of this radii is not less than 0.95 (usually about 50 km).
5. The travel time and modeling errors surfaces are constructed.
6. The evaluation of the calculated corrections is made using the set of checkpoints.

The application example of Kriging used to locate the earthquake swarm in Racha region (Armenia) by six IMS stations displays the sufficient enhancement of the calculated epicenters. The average error decreases from 51 km to 14-19 km [Myers et. al., 1998].

The features of the Kriging that limit its application are the next:
- The need to have big training population for each station;
- Relatively small area being calibrated by the method;
- Non portability of the calibration results from one station to others.

These requirements make the calibration scale of the Kriging pretty narrow when comparing to other known calibration methods. The most perspective area of Kriging seems to be the control of the test sites. It worth noting that while these places constitute only negligible part of the Earth surface, the monitoring practice learns us that the test sites are the points of the special attention and sensitivity especially when some event occurs in their vicinities.

Methods for travel time corrections estimation through the velocity model of the media

These methods assume solutions the reverse and afterwards the direct kinematic problem. On the first stage one has to build a velocity model for the media using the observation data. On the second step the correction surface around a station is generated from the velocity model. Doubtlessly, this approach serves to mutual enrichment of the geophysics and the seismological practice when is being applied correctly.

The methods can be divided into two groups depending upon what way is used to solve the reverse kinematic problem: whether it is the try-and-drop method for selection of the model or the tomography is used for this.

Try-and-drop method for the velocity model selection

This method of the velocity model selection comes from the Deep Seismic Sounding (DSS). It consists in selection the only model from the variety of physically valid models. The selected model should provide the minimum deviation from the observed data. For direct kinematic problem solution the separate task is the development of a software working with a global 3-D velocity model of the Earth crust and the uppermost mantle.

Petr Firbas has developed such software, has chosen the necessary resolution for crust and mantle, selected the initial models, and made the tentative adjustment of the model. He also calculated the tentative correction surfaces for the European IMS stations [Firbas et. al., 1997a,b,c]. The program deals with the global models of the Earth crust and the Moho discontinuity of 5 x 5 deg. resolution, and the mantle model of 2 x 2 deg. resolution. The composing background models are:

- The Earth crust model CRUST 5.1 [Mooney, Laskey, and Masters., 1998];
- The mantle model RUM [Gudmundsson and Sambridge, 1998] based on the upper mantle regionalization according to the rock ages and corresponding 1-D velocity models for each type of the tectonic provinces.

As velocity models for the definite regions become more developed they lay over the background model. The application results for North America and for some part of Northern Eurasia are described by Ryaboy et. al., 1998, 1999. Authors suppose that the Moho depth variations as well as the Earth crust velocity structure do not affect notably the travel times at the regional distances. On this ground the focused attention is paid to searching the uppermost mantle velocity model. To perform the regional kinematic calibration 8 PNEs inside USA terrain and 8 PNEs carried in the European Russia have been used. The information about the sources is known exactly.

In the every iteration of the whole procedure the next steps are to be done manually:

- The regionalization is introduced on the first step or is corrected on the succeeding steps; the new regions having specific 1-D velocity structure come into play if necessary;
- The parameters of 1-D velocity models are varied for the regions lying along the ray path surface projection;
- The direct kinematic problem is being solved for the newly adjusted complex model;
- The time correction surface is evaluated by comparison against the observation data.

These actions are being repeated for each explosion until the discrepancy between the model-generated travel times and observed data reaches about 1 second for each event after what one has to deal with the next explosion. After the complex model is corrected event by event (first pass of the inner loop is completed) one has to return to the first explosion because the 1-second difference between the model and experiment can become upset by the model changes involved by succeeding explosions. The procedure stops when the complex model fits experimental data for all the explosions.

The 1.5 second convergence in term of residual mean square was achieved for North America after 45 iterations (i.e. after 45 outer loop repetitions). The background 3-D model RUM contained only 4 typical 1-D velocity models for the continent. The resulted 3-D model includes 5 more mantle types, the borderlines and the models for the initial 4 elementary models have been changed sufficiently. The travel time deviations from IASPEI-91 vary from -5 s to +5 s that corresponds to the North America observation experience.

The calibration of the Northern Eurasia by this method is in the very beginning. There were carried out only 5 iterations; the discrepancies between the complex 3-D model and observations stay still as high as 2-3 seconds for some regions.

The evaluation of the IMS station correction fields modelled by this method was made using only few events. The corrections application leads to improvement of calculated epicenters while the statistics presented in the papers cannot be assumed as sufficient.

The try-and-drop selection method suffers from several unresolved limitations.

1. The model adjustment procedure allows too much subjectivity. The density of the data available is not even comparable to that of DSS where the method comes from. The investigator's fantasy becomes almost fully unleashed and the resulted model inevitably brings the authors understanding of the mantle structure in a fare more degree than the experimental data influence;
2. The combination of the huge labor-intensity and non-reproduction of the resulted 3-D model make the using of this very questionable;
3. There are no independent data to evaluate the corrections: the total number of 1-D model parameters is so big that all the regional experimental data are to be used for the 3-D model adjustment. In fact the model is evaluated using the residual mean square term characterizing the convergence to already used observations instead of using the control population.

We can suggest that the success of the first steps in this direction can be explained by availability and using of widely spread PNEs data, and on the other hand by good choice of the terrain to begin the calibration. North America consists of sharply divided two parts: low-velocity Western tectonic province and high-velocity Eastern platform. For such area one can expect the improvement in the event location even after simplest differentiation when comparing to global IASPEI-91 velocity model.

Transmission seismic tomography application to the problem of the regional kinematic calibration

The particularities of the regional kinematic calibration from point of view of the tomography application consists in the next:

- Relatively thin layer including the Earth crust and uppermost 100...400 km of the mantle is being investigated;
- Anomalies to be revealed are lateral; their amplitude is high (up to 5% of average velocity in the media);
- Characteristic size of heterogeneity is small (tens of km) comparing to the required global scale of the solution;
- P-velocity structure is of the main importance for the location improvement.

The problem occupies its specific place in a hierarchy of structure heterogeneity and earlier has never been solved in such a big scale by the tomographic method. At a time there is no P-velocity global model for the uppermost mantle that would directly allow to solve the regional kinematic problem.

Currently the tomographic approach to calibration is being developed by the geophysics working with the entire mantle P-velocity models and by investigators dealing with other than P wave velocity models for the lithosphere.

P-wave tomography

Kennett, 1998 analyzed the status of the P-velocity models development for upper mantle. He recognizes 3 kinds of approximation for such models; the order of the approximation depends upon the model ability to predict the velocity anomalies.

Author proposed to assume the RUM model [Gudmundson, Sambridge, 1998] as the 0-approximation. This model consists of 9 1-D velocity models corresponded to the different tectonic types of the continents and oceans. The geometry of the tectonic provinces is outlined by the seismic activity pattern and geological and tectonic structures on the Earth surface. The main merit of the model is its global scale. According to Kennett RUM is able to explain some 15% of velocity anomalies that is one third of the full tomography predictability.

The model developed by van der Hilst, Widiantoro, and Engdal, 1997 can be accepted as the model of the first approximation. The model was resulted from the tomography using the averaged rays between clusters of events and groups of neighboring stations. The approach stabilizes the result but smoothes the velocity anomalies. The model has resolution of 2 x 2 deg. on the surface and 100 km in the depth for the best covered terrain. The poor resolution and reliability occurs for oceans as well as for Africa, Eurasia, Antarctica, South America.

The tomographic model of Widiyantoro, 1997 is assumed to be the second approximation. The amount and quality of the data were sufficiently increased compared to the observation ground of the van der Hilst et. al. model. The events were relocated using pP phases; all available at that time ISC data were used (around 7,000,000 P-waves). No clusterization was employed. For the areas of highest data density the model resolution is 1 x 1 deg. and layer thickness of 50-75 km. The authors managed to build the velocity structure for as many as 14 regions, the patches are joined to construct the global 3-D P-velocity model of the mantle.

The second approximation differs from the first one by its resolution power, by amplitude of heterogeneity revealed, and by the coverage: the less detailed model describes the heterogeneity of lower amplitude but it is of wider coverage. The common feature of both tomographic P-models is defined by the very steep rays in the uppermost mantle used for the inversion. This leads to impossibility to resolve the low-scale lateral velocity anomalies, very uneven mosaic coverage defined by natural seismic activity and distribution of stations reporting to ISC.

Ekstrom et. al., 1998 analyzed the real resolution power of the modern tomographic P- models in sight of regional kinematic calibration. The analysis include some of the models assumed by Kennett. The starting point of analysis is the tomographic model of Su, Dziewonski, 1993 describing the large-scale mantle P-velocity heterogeneity on the ground of the spherical parameterization. Usage the model for the nuclear tests location [Smith, Ekstrom, 1996] sufficiently improved the calculated epicenters (the location error decreased by 40%) for the explosions situated inside the stable platforms. The same time relocation using this model does not work positively for the explosions located at the edges of platform where the lithospheric heterogeneity prevails, and the predictability of the model is poor.

To resolve smaller details of the velocity structure the block parameterization instead of spherical one should be involved. After this action far more unknown parameters to be estimated by an inversion appear, and the problem is usually regularized by different ways. Ekstrom et. al., 1998 tried to answer the question whether the real resolution power improves for the models of block parameterization comparing to those of spherical structure. Analysis of the block models [van der Hilst, Widiantoro, Engdal, 1997] and [Boschi, Dziewonski, 1998] comparing with the spherical harmonic model of Su and Dziewonski, 1997 led to the conclusion that the resolution power for formers increases indeed. Authors also stated that the inversion algorithm does not effect the result (SIRT and LSQR have been compared). Another important result is that the models of high resolution preserve the positive features of low-resolution models: the former can predict the big-scale low-amplitude velocity anomalies that are the base of the teleseismic travel time corrections. The latter means that the tomographic approach has a potential to perform the kinematic calibration in a comprehensive manner.

Authors came to the general conclusion that the uppermost mantle models of good lateral resolution should be built on the base of the regional data when the rays are sub-horizontal.

The same paper demonstrates the practical tomographic approach to study the uppermost mantle lateral heterogeneity. All the regional Pn phases stored at the ISC database at the time of study for the event-station distances from 2 to 11 deg. were used. The requirement serves to provide the head wave model workability. The "two station" technique [Berghoul, Barazangi, 1989] has been applied to estimate the P-velocity in the uppermost mantle under the stations. For circular area of radii 1 – 2 deg. around the stations the estimations for Pn velocity and velocity anisotropy have been obtained. We believe that the main results from the practical part of this paper are the next:

- The areas where the regional kinematic calibration can be performed using the earthquake data were outlined. One can expect the increase in ISC data volume and quality; this will necessary enhance the prediction power of the velocity model but will not spread the model to the stable platform regions.
- The anisotropy is notable and can be up to 5% of average Pn velocity. It has been proven the correlation between the anisotropy "fast" axis and the direction of the mountain chains at least in Europe. In other words one has to bear in mind this result when developing the 3-D velocity model covering the modern tectonic regimes: in fact the well pronounced anisotropy introduces 4th dimension into the model.

Tomography employing waves of the other types than P

Ritzwoller et. al., 1999 try to apply the S-velocity tomography to develop the P-velocity model. The well known advantages of the S-models comes from the observation base. Such models are usually deduced from the channel or surface wave data that spread horizontally and far from the epicenter therefore the S-models reflect the lateral heterogeneity of the uppermost mantle and are of wide (even global) coverage.

The authors develop the S-model on the base of group and phase velocity maps of LR and LQ waves for period range from 15 s to 20 s. Each particular 1-D model has 8 parameters to be adjusted (for each layer: thickness, average velocity , and velocity gradient) and are defined down to 400 km depth. All available information about the velocity structure for a given region is used for setting the best starting approximation and restrictions on the variability of parameters.

Authors pointed out good correlation between the revealed S-velocity anomalies, the tectonic structure, and the P-model of a low resolution [Bijwaard, 1998].The S-model conversion into the P-model is planned to be done on the future steps of a study. Nevertheless we assume such conversion as very doubtful. The main obstacle - an ambiguous relation between P and S velocities especially complicated in the uppermost mantle - could not be overcame by anyone so far while the whole row of continental and even global S-models is known.

We would propose to try developing the "SBPV" method (S-Borders, P-Velocity) that employs the tomographic S-model to construct the spatial border of the tectonic provinces. In turn the velocity structure of the province would be set from the P-wave tomography with the static borders.

CONCLUSIONS AND RECOMMENDATIONS

The simultaneous development of direct and indirect methods for calibration has sense as these approaches complement each other.

The success of the calibration efforts is defined by the trade-off between the complexity of the region to be calibrated and the amount and the geographic distribution of the data available. The relation of this type should be assigned to each region and will change with time. On the base of such relation the optimal calibration method could be chosen.

We also assume that to make the solution of the calibration problem more manageable some research laboratory should possess the technical ability to try all the tools being developed and to access all the data being collected.

Key Words: International Monitoring System, seismic calibration, regional kinematic calibration, 3-D P-velocity model.

REFERENCES

Berghoul, N., M. Barazangi (1989), Mapping high Pn velocity beneath the Colorado Plateau constrains uplift models, J. Geophys. Res., 94, 7083 - 7104.

Bijwaard, H., W. Spakman, E.R. Engdahl (1998), Closing the gap between regional and global travel time tomography, J. Geophys. Res. 103, 30055 - 30078.

Bondar, I., X. Yang, K. McLaughlin, R. North, V. Ryaboy, and W. Nagy (1998), Source Specific Station Corrections for regional phases at IMS stations in North America and Fennoscandia, EOS Trans. AGU, 79(45), Fall Meet. Supple., F839.

Bondar, I, V. Ryaboy (1997), Regional travel-time tables for the Baltic shield region, Center for Monitoring Research, Technical report CMR-97/24, 3-5.

Boschi, L., A.M. Dziewonski (1998), Long and short wavelength images of the Earth's mantle, EOS, Trans. Am. Geophys. Soc., S220, 79.

Braile, L.W., W.J. Hinze, R.R.B. von Frese, and R.G. Keller (1989), Seismic properties of the crust and uppermost mantle of the conterminous United States and adjacent Canada, Memoir-Geol. Soc. Am., 172, 655-680

Cerveny, V. (1985), Gaussian beam synthetic seismograms, J. Geophys., 58, 44-72.

Ekstrom, G., A.M. Dziewonski, M. Antolik, L. Boshi, G.P. Smith (1998), Research addressing the problem of seismic event location at teleseismic and regional distances, Proceedings of the 20th Annual Seismic Research Symposium on monitoring a CTBT, 229-237.

Firbas, P., A.B. Peshkov, V. Ryaboy (1997a), From IASP-91 global model to a 3-D model for CTBT monitoring. In: Upper mantle heterogeneities from active and passive seismology (Edited by K. Fuchs), Kluwer, 199-214.

Firbas, P. (1997b), IMS Calibration: 3-D Travel-Time Modeling for Europe, Center for Monitoring Research, Technical report CMR-97/02.

Firbas, P. (1997c), Program SSSC for Computation of Station-Source Specific Time Corrections for 3-D Velocity Models, Center for Monitoring Research, Technical report CMR-97/08.

Gudmundsson, O., M. Sambridge (1998), A regionalized upper mantle (RUM) seismic model, J. Geophys. Res., 103, B4, 7121-7136.

van der Hilst R.D., S. Widiantoro, E.R. Engdahl E.R. (1997), Evidence for deep mantle circulation from global tomography, Nature, 286, 578-584.

Hipp, J., C. Young, and R. Keyser, (1997) Travel-time correction surface generation for the DOE knowledge base, Proceedings of the 19th Annual Seismic Research Symposium on monitoring a CTBT, 231-241.

Joint Russian-U.S.A. Scientific Program on IMS Calibration in North America and Northern (1998), Status Report 2, 9-12, 33-34

Kennett, B.L.N. (editor), (1991) IASPEI 1991 Seismological Tables, Research School of Earth Sciences Australian National University

Kennett, B.L.N. (1997), 3-D structure from seismic tomography - implications for event location, Proceedings of the 19thAnnual Seismic Research Symposium on monitoring a CTBT, 51-56.

Mooney, W.D., G. Laskey, T.G. Masters (1998), Crust 5.1: A global crustal model at 5 x 5 deg., J. Geophys. Res., 103, B1, 727-747, 1998.

Myers, S., C. Schultz (1998) Demonstrating improvement in seismic source location using Bayesian kriging: a case study of the 1991 Racha aftershock sequence, Proceedings of the 20th Annual Seismic Research Symposium on monitoring a CTBT, 54 - 62.

Ritzwoller M.H., M.P. Barmin, A. Villasenor, A.L. Levshin, E.R. Engdahl, (1999), Construction of a 3-D P and S model of the crust and upper mantle to improve regional locations in W. China, Central Asia, and parts of the Middle East, Proceedings of the 21th Annual Seismic Research Symposium on monitoring a CTBT, 229-237.

Ryaboy, V. (1998), Evaluation of the IMS location accuracy of large chemical and nuclear explosions in Northern Eurasia and North America using regional and global Pn travel-time tables, Proceedings of the 20th Annual Seismic Research Symposium on monitoring a CTBT, 92-101.

Ryaboy, V. (1999), Development of 3-D crustal and upper mantle velocity models of Northern Eurasia and North America to refine location of regional seismic events, Proceedings of the 21st Annual Seismic Research Symposium on monitoring a CTBT, 616-625.

Schultz, C.A., S.C. Myers, S D. Ruppert, A.J. Rodgers, J. Hipp, C. Young, (1998) Nonstationary Bayesian kriging: application of spatial corrections to improve seismic detection, location, and discrimination, Proceedings of the 20th Annual Seismic Research Symposium on monitoring a CTBT, 115-123.

Smith G.P., Ekstrom, G. (1996),Improving teleseismic event locations using a three-dimensional Earth model, Bull. Seism. Soc. Am., 86, 788-796.

Smith, W.H.F, and P. Wessel, (1990), Gridding with continuous curvature splines in tension, Geophysics, 55, 293-305.

Smith, W.H.F, and P. Wessel, (1999) The Generic Mapping Tools Version 3.3.1. Technical Reference and Cookbook, http://imina.soest.hawaii.edu/gmt/, 77

Su, W., A.M. Dziewonski (1993), Joint 3-D inversion for P- and S-velocity in the mantle, EOS, Trans. Am. Geophys. Soc., 74, 557.

Sweeney, J.(1998), Criteria for selecting accurate event locations from NEIC and ISC bulletins, Lawrence Livermore National Laboratory, UCRL-JC-130655.

Vasiliev, N. (2000), Proportional Godograph Method and Raytracing, Joint Institute of Physics of the Earth, Laboratory of Experimental Geophysics, Technical Report IFZ/EG-001/2000.

Widiyantoro, S.(1997), Studies of seismic tomography on regional and global scale, Ph.D. Thesis, Australian National University.

Yang, X., K. McLaughlin, R. North (1999), Source-Specific Station Corrections for regional phases at International Monitoring System stations, Proceedings of the 21th Annual Seismic Research Symposium on monitoring a CTBT, 333-337.

Young, C.J., J.R. Hipp, E. Shepherd, and S. G. Moore (1998) The DOE model for improving seismic event locations using travel time corrections: description and demonstration, Proceedings of the 20th Annual Seismic Research Symposium on monitoring a CTBT, 773-781.

REGIONAL BODY-WAVE DISCRIMINATION RESEARCH

William R. Walter, Arthur Rodgers, Kevin Mayeda and Steve Taylor*
Lawrence Livermore National Laboratory and *Los Alamos National Laboratory

Sponsored by U.S. Department of Energy
Office of Nonproliferation Research and Engineering
Office of Defense Nuclear Nonproliferation
National Nuclear Security Administration

Contract No. W-7405-ENG-48

ABSTRACT

Monitoring the world for potential nuclear explosions requires identifying them by their expected seismic signatures and discriminating them from earthquakes and other sources of seismic waves. Large events (approximately m_b > 4.0) can often be successfully identified by the M_S:m_b discriminant. In order to monitor small events (approximately m_b < 4.0) short-period regional waveform data recorded within 2000 km will be needed because of poor signal-to-noise at large distances and/or long-periods. Many studies have shown that short-period (0.5-10 Hz) regional body wave phases (e.g. Pn, Pg, Sn, Lg and coda) have excellent discrimination power down to very small magnitudes when used at various nuclear tests sites. In order to broaden the application of these regional body wave techniques, we are developing size-, distance- and location-based corrections to apply to the regional data to allow wider data comparison and better discrimination performance.

Building on prior work (e.g. Taylor et al. 1999, Rodgers and Walter, 2000), we are developing a revised Magnitude and Distance Amplitude Correction (MDAC) procedure. The procedure makes use of the very stable moment magnitude determinations from regional coda envelopes (see Mayeda et al, this Symposium) to provide an independent size estimate. Using a Brune (1970) style omega-squared source spectral model, we parameterize the source in terms of apparent stress and its scaling with moment. For the distance corrections we parameterize in terms of geometrical spreading, and frequency-dependent attenuation. In addition there are constants associated with velocities, densities and a phase- and frequency-dependent site effect. Using this relatively simple model we can remove much of the magnitude and distance trends from the regional data. We use a grid-search technique to explore the model space with more emphasis on removing the magnitude and distance trends than in fitting the observable spectra perfectly. Two-dimensional path effects are currently corrected by kriging the MDAC residuals but they could also be addressed through location-dependent attenuation models if available.

Using earthquake and explosion data from the Nevada Test Site and India we show that the revised MDAC correction and kriging of the residuals can significantly improve phase and spectral ratio discrimination performance. In addition by correcting the regional amplitudes we allow maximum flexibility in exploring and creating new combinations of regional phases which may have even better discrimination potential. Finally the corrected regional amplitudes provide critical information on the detection of regional phases, which is another important factor in the overall estimation of discrimination capability.

Key Words: seismic, regional, discrimination, explosion identification, short-period body waves

OBJECTIVES

Monitoring the world for potential nuclear explosions such as for the Comprehensive Nuclear-Test-Ban Treaty (CTBT) requires characterizing seismic events and discriminating between earthquakes, mining activities and banned nuclear tests. We are developing, testing and refining size, distance and location based regional seismic amplitude corrections to facilitate the comparison of all events that are recorded at a particular seismic station. These corrections, calibrated for each station, reduce amplitude measurement scatter and improve discrimination performance. We test the methods on well known (ground truth) datasets in the U.S. and then apply them to the uncalibrated stations in Eurasia, Africa and other regions of interest to improve underground nuclear test monitoring capability.

RESEARCH ACCOMPLISHED

As part of the overall Department of Energy Ground-based Nuclear Explosion Monitoring (GNEM) program, we continue to pursue a comprehensive research effort to improve our capabilities to seismically characterize and discriminate underground nuclear tests from other natural and man-made sources of seismicity. To reduce the monitoring magnitude threshold we make use of regional body wave data and calibrate each seismic station. Our goals are to reduce the variance and improve the separation between earthquakes and explosion populations by accounting for the effects of propagation and differential source size. Building on prior work (e.g. Taylor et al., 2000; Rodgers and Walter, 2000) we are developing a revised Magnitude and Distance Amplitude Correction (MDAC) procedure. Here we briefly review the problem and previous work and then discuss the revised MDAC technique.

Context and NTS Examples

In recent years many studies at nuclear test sites have demonstrated that particular ratios of the amplitudes of regional phases (Pn, Pg, Sn, Lg and coda) have the power to separate explosions from earthquakes, particularly at high frequencies (e.g. Walter et al. 1995, Hartse et al., 1997). For example, Figure 1 shows the comparison of a Nevada Test Site (NTS) nuclear explosion at Rainier Mesa with a nearby earthquake. These events have epicenters within a few kilometers of each other and are nearly the same size or magnitude. The waveforms on the right-hand side of the figure show the differences in the regional phase amplitudes, particularly Lg at 6-8 Hz, as seen at the regional station MNV (a broadband element of the International Monitoring System (IMS) primary array at NVAR). The large contrast in regional phase amplitudes between the two types of events is due to differences in the depth, focal mechanism, source spectra and the medium properties. The exact partitioning of each of these differences in the overall contrast in regional phase amplitudes remains an area of vigorous research. It is clear, however, that if we can account for propagation and source size effects, these physical differences provide a clear basis for effective discrimination techniques.

One such discriminant is the ratio of 6-8 Hz Pn amplitudes to 6-8 Hz Lg amplitudes. In Figure 2 we show the effectiveness of this discriminant for a set of NTS earthquakes and explosions described in detail in Walter et al., 1995 (see Figure 6a in that paper). The relatively large Pn phases and weak Lg amplitudes from the explosions lead to large 6-8 Hz Pn/Lg values for these events relative to the earthquakes. For normal depth earthquakes there is almost no overlap with the explosions. Because there is a good physical basis for earthquake and explosion discrimination we expect this discriminant to be effective for future events on or near NTS. The largest events to occur at NTS since the original study of Walter et al. (1995) was completed was the Frenchman Flat sequence that occurred in January 1999 (K. Smith, pers. Comm.). There were four events larger than magnitude 3.5 with the largest event having an Mw of 4.8 (Walter and Mayeda, 1999). We have processed them using the same techniques as in Walter et al., (1995) and they are plotted for comparison with the original events in Figure 2. Note that they plot within the normal earthquake population and continue to discriminate from the explosions. This gives us confidence we can identify any future events at NTS using these calibrated measurements

Because the events in Figure 2 are all within 50 km or so of each other, and situated within a similar crustal structure and tectonic setting, we expect relatively little difference in the path effects between these events and the stations MNV and KNB. Also because this discriminant measure uses phases at the same frequency band, we expect little or no dependence on source size or magnitude. This allows us to compare all these events together without source or path corrections. If we chose to compare two regional phase amplitudes at different frequencies, such as 1-2Hz Lg to 6-8 Hz Lg, then there is a strong magnitude effect because of the different spectral corner frequencies for small and large events (e.g. Walter and Priestley, 1991, Taylor and Denny, 1991). We show this example in Figure 3 based on the Walter et al., (1995) NTS data (see Figure 8a in the original paper). Note that a magnitude 3 explosion

and a magnitude 5 earthquake have very similar values for the Lg 1-2/6-8 Hz ratio, leading to an ineffective discriminant unless the magnitude difference is accounted for.

We can model the magnitude dependence of regional phase spectral ratios by accounting for the corner frequency differences using a spectral model such as Brune (1970) for earthquakes and Denny and Goodman (1990) for explosions. For explosions we additionally note that events in unsaturated, high gas porosity material above the water table have steeper (f^{-3}) spectral fall off at frequencies above the corner frequency than earthquakes or explosions in saturated material (f^{-2}) do. This is reflected in the model as shown at the top right hand side of Figure 3. The material property effect also can affect the corner frequency scaling as illustrated. A second effect, the scattering and conversion of Rg to S waves (e.g. Myers et al., 1999) introduces an additional frequency dependence to explosion S-wave spectra as shown at the bottom right of Figure 3. Taking all these effects together we can model the behavior of the spectral ratio discriminant reasonably well as shown by the model curves in Figure 3.

Now we are ready to address the question of analyzing new events, which may be located far from any reference explosion data and of a quite different magnitude than any previous explosions. In this case we need to correct for the different paths traveled by the event and the different source spectral scaling introduced by the magnitude differences. Previously we have done this both by correcting the amplitudes (e.g. Taylor et al., 2000) and by correcting the discriminant ratios (Rodgers and Walter, 2000). We have demonstrated that the two techniques give identical answers when carefully done. While the ratios have some advantages in the stability of the search for optimal corrections (since ratios cancel a number of terms), the amplitude correction is more general and has utility for estimating the detectability of regional phases as well. Therefore we will focus on corrections to amplitudes. Here we will briefly review the Magnitude and Distance Amplitude Corrections (MDAC) procedure (Taylor et al., 2000) and describe some revisions that we are starting to implement.

Revised MDAC

The basic MDAC procedure involves estimating and removing a simple theoretical earthquake spectrum from the data to remove any magnitude and distance trends in the regional phase amplitudes and any discriminants formed from those amplitudes (Taylor et al., 2000). The observed regional phase spectra are modeled as:

$$P(f,R) = I(f)\, S(f)\, G(f,R)\, A(f,R) \qquad (1)$$

where f is frequency and R is distance and:

I(f) is the instrument response,
S(f) is the source spectrum from the Brune (1970) model,
G(f,R) is the earth response, modeled as proportional to Site(f) R^{η},
A(f,R) is the apparent attenuation, modeled as $e^{(-\pi f R/Q(f)c)}$,

c is the velocity of the phase and Q(f) is the frequency dependent quality factor.

In addition the source spectrum depends upon the seismic moment and stress drop and can have additional complications due to non-constant stress drop scaling and differential P/S corner frequency effects that we will discuss later. We require the different phases for the same event recorded at the same station to have the same moment values and any other source parameters, such as stress drop or corner frequencies to be related to each other. This effectively imposes some of the ratio constraints discussed in Rodgers and Walter (2000) on the amplitudes and improves discrimination performance. While such models of observed spectra are certainly oversimplified, they have proven track records of providing good first-order fits to real earthquakes. In addition they also provide simple theoretical models to use in aseismic areas.

To estimate the source spectrum we first need an estimate of the seismic moment. In the revised MDAC procedure we take advantage of the very stable moment magnitude determinations from regional coda envelopes (see Mayeda et al., this volume). The coda-based technique provides an accurate and independent estimate of moment from as few as one station. Using a direct measure of moment also eliminates the need to scale from other magnitudes such as m_b to moment eliminating two fitting parameters from the original formulation (Taylor et al, 2000). The combination of using the more stable coda measure and eliminating two free parameters should reduce scatter in the resulting correction.

We show an example of the revised MDAC fits using the coda-based moment magnitudes (M_w) in Figure 4 for three NTS earthquake Lg spectra recorded at KNB. The earthquakes are the June 1992 Little Skull Mountain mainshock and two aftershocks and cover two orders of magnitude in size. The M_w values were calculated in a previous study by Mayeda and Walter (1996) using the regional coda technique at two stations, MNV and KNB. The left-hand side of Figure 4 shows that using a constant stress drop model does not fit all the data simultaneously. In this case we used a Brune stress drop of 30 bars, which provides a good fit to the mainshock but not the smaller aftershocks. The aftershocks require lower stress drops to match the observed spectra, consistent with the observations of Mayeda and Walter (1996) using the coda-based source spectra determinations. A problem with non-constant stress drop scaling is that the Brune (1970) model is specifically set up as constant stress drop model. Taylor et al. (2000) have implemented a non-constant scaling, which we used in Figure 4, but at a cost of the stress drop becoming a non-physical parameter. This means we can no longer interpret a stress drop in terms of bars in the non-constant scaling case. This is somewhat unsatisfactory both theoretically and practically when we want to use the MDAC formulation in regions without data where parameters like stress drop may be determined from models.

In the second revision to MDAC we reformulate the Brune (1970) source spectrum in more general terms. The Brune (1970) spectral shape is given by:

$$S(f) = S_o / (1 + (f/f_c)^2) \qquad (2)$$

where S_o is the zero frequency spectral level and f_c is the corner frequency. We parameterize S_o using the seismic moment and the well known relationship between them (e.g. Aki and Richards, 1980):

$$S_o = R_{\theta\varphi} M_o / (4\pi\rho_r\rho_s c_s^5 c_r)^{1/2} \qquad (3)$$

where $R_{\theta\varphi}$ is the radiation pattern coefficient appropriate to the given wave type, ρ is the density, c is the velocity of the given wave type and the subscripts r and s refer to the receiver and source region respectively. Note we have removed the geometrical spreading term to a separate G(f,R) function in equation (1). To parameterize the corner frequency, we reformulate the stress drop in terms of a more general stress parameter, the apparent stress (e.g. Wyss, 1970):

$$\sigma_a = \mu E / M_o \qquad (4)$$

where E is the seismically radiated energy and μ is the rigidity. The seismically radiated energy in any particular wave type with velocity c and a spectrum given by equation (2) can be determined by integrating to find (Walter and Brune, 1993):

$$E_c = \pi\rho_r c_r S_o 2 f_c^3 = R_{\theta\varphi}^2 M_o^2 f_c^3 / (16\pi\rho_s c_s^5) \qquad (5)$$

where we used equation (3) to put it in terms of seismic moment. Note again we have removed the geometrical spreading term since it appears separately in G(f,R). Equation (5) can now be used with equation (4) to determine the corner frequency scaling for a particular phase.

To keep the source parameters related we want to use a single apparent stress parameter for each event and therefore we sum the energy from all the regional phases (e.g. Pn, Pg, Sn and Lg) to find the total radiated body-wave energy to put into equation (4). For simplicity we group the P-waves and S-waves together and use an additional parameter to link the P- and S wave corner frequencies:

$$f_{c\alpha} = x f_{c\beta} \qquad (6)$$

where subscripts α and β denote P- and S-wave corner frequencies and x is the scale factor. For the Brune (1970) model x is the ratio of the wave velocities, but other studies have shown that the corner frequencies are more equal (x=1), by including this parameter we allow maximum flexibility. We treat the energy radiated as the simple sum of P and S wave energy and use equations (4), (5) and (6) to solve for the S–wave corner frequency:

$$f_{c\beta} = (k\sigma_a / M_o)^{1/3} \qquad \text{where } k = 16\pi\rho_s / (\mu(x^3 R_{\theta\varphi\alpha}^2/\alpha_s^5 + R_{\theta\varphi\beta}^2/\beta_s^5)) \qquad (7)$$

so that for constant apparent stress the corner frequency scales as $M_o^{-1/3}$ as in the Brune (1970) model. This formulation using equation (7) allows us to put in physical non-constant apparent stress scaling by changing the apparent stress with moment. Now for example we can use the quarter root scaling observed by Mayeda and Walter

(1996) for Western U.S. earthquakes to improve the spectral fits. For example the earthquakes in Figure 4 have apparent stress values ranging from 196 bars for the mainshock to 20 for the smaller aftershock and we have agreement between the coda determined values and those in the revised MDAC. Equations 1-7 with the independent coda determined seismic moments constitute the revised MDAC procedure.

So far we have used the revised MDAC to correct for trends in Magnitude and Distance, but there are also variations due to the spatial variability of events, for example events occurring in very different tectonic regions. We account for much of this effect empirically by kriging the MDAC residuals using the Bayesian technique developed by Schultz et al, (1998) and shown to be very effective for discriminants (e.g. Rodgers et al., 1999). However in cases where empirical data is lacking, we want to allow the apparent attenuation function to vary spatially as well. This way we can make use of a prior information such as that produced by attenuation tomography (e.g. Phillips et al., 2000), or other geophysical studies. Allowing the attenuation to become a function of location is the last part of the revised MDAC procedure. Finally, by removing the magnitude and distance trends from the data, we allow the combination of individual measures, to form a multivariate discriminants that can be significantly more effective than the best individual measure (e.g. Taylor, 1996).

CONCLUSIONS AND RECOMMENDATIONS

Regional discrimination algorithms require calibration at each seismic station to be used for nuclear explosion monitoring. We have developed a revised Magnitude and Distance Amplitude Correction procedure to remove source size and path effects from regional body-wave phases. This allows the comparison of any new regional events recorded at a calibrated station with all available reference data and models. This also facilities the combination of individual measures to form multivariate discriminants that can have significantly better performance. We will show that this revised MDAC improves regional earthquake and explosion discrimination on a test set of events in the western U.S. and other regions of the world. Calibrating seismic stations for monitoring the CTBT is a challenging task that will require processing large amounts of data, and collaboration with government, academic and industry researchers and incorporation of the extensive R&D results both within and outside of DOE.

ACKNOWLEDGEMENTS

This work performed under the auspices of the U.S. Department of Energy by the Lawrence Livermore National Laboratory under contract W-7405-ENG-48. UCRL-JC-138998.

REFERENCES

Aki, K. and P. G. Richards, (1980). *Quantitative Seismology*, W. H. Freeman, New York.

Brune, J., (1970). Tectonic stress and the spectra from seismic shear waves earthquakes, *J. Geophys. Res*., **75**, 4997-5009.

Denny, M. D. and D. M. Goodman, (1990). A case study of the seismic source functions SALMON and STERLING reevaluated, *J. Geophys. Res. 95*, 19,705-19,723.

Hartse, H., S. R. Taylor, W. S. Phillips, and G. E. Randall, (1997). A preliminary study of regional seismic discrimination in Central Asia with an emphasis on Western China*, Bull. Seism. Soc. Am.* **87**, 551-568.

Mayeda, K. M. and W. R. Walter, (1996). Moment, energy, stress drop and source spectra of Western U.S. earthquakes from regional coda envelopes, *J. Geophys. Res*., **10***1*, 11,195-11,208.

Myers, S. C., W. R. Walter, K. Mayeda and L. Glenn, (1999). Observations in support of Rg scattering as a source for explosion S waves: regional and local recordings of the 1997 Kazakhstan depth of burial experiment, *Bull. Seism. Soc. Am. 89*, 544-549.

Phillips, W. S., H. E. Hartse, S. R. Taylor, A. A. Velasco and G. E. Randall, (2000). Regional phase amplitude ratio tomography for seismic verification, Los Alamos National laboratory, LAUR-99-1904, submitted to *Pure. App. Geophys*.

Rodgers, A. J., W. R. Walter, C. Schultz and S. Myers, (1999). A comparison of methodologies for representing path effects on regional P/S discriminants, *Bull. Seism. Soc. Am. 89*, 394-408.

Rodgers, A. J. and W. R. Walter, (2000). Seismic Discrimination of the May 11, 1998 Indian Nuclear Test with Short-Period Regional Data From Station NIL (Nilore, Pakistan), submitted to PAGEOPH.

Schultz, C., S. Myers, J. Hipp, and C. Young, (1998). Nonstationary Bayesian kriging: application of spatial corrections to improve seismic detection, location and identification, *Bull. Seism. Soc. Am., 88*, 1275-1288.

Taylor, S. and M. Denny, (1991). An analysis of spectral differences between NTS and Shagan River nuclear explosions, *J. Geophys. Res.*, **96**, 6237-6245.

Taylor, S., (1996). Analysis of high-frequency Pg/Lg ratios from NTS explosions and Western U.S. earthquakes, *Bull. Seism. Soc. Am., 86*, 1042-1053.

Taylor, S., A. Velasco, H. Hartse, W. S. Philips, W. R. Walter, and A. Rodgers, (2000). Amplitude corrections for regional discrimination, submitted to *Pure. App. Geophys.,* 2000

Walter, W., and K. Priestley, (1991). High-frequency P wave spectra from explosions and earthquakes, in *Explosion Source Phenomenology*, ed. S. Taylor, H. Patton and P. Richards, American Geophysical Union Monograph.

Walter, W. R. and J. N. Brune, (1993). Spectra of seismic radiation from a tensile crack, *J. Geophys. Res., 98*, 4449-4459.

Walter, W. R., K. Mayeda, and H. J. Patton, (1995). Phase and spectral ratio discrimination between NTS earthquakes and explosions Part 1: Empirical observations, *Bull. Seism. Soc. Am.,* **85**., 1050-1067.

Walter, W. R. and K. Mayeda, (1999). LLNL Nevada test site seismic event report, Bulletin 99-02, Lawrence Livermore National Laboratory UCRL-MI-133002-99-02.

Wyss, M., (1970). Stress estimates of South American shallow and deep earthquakes, *J. Geophys. Res., 75*, 1529-1544.

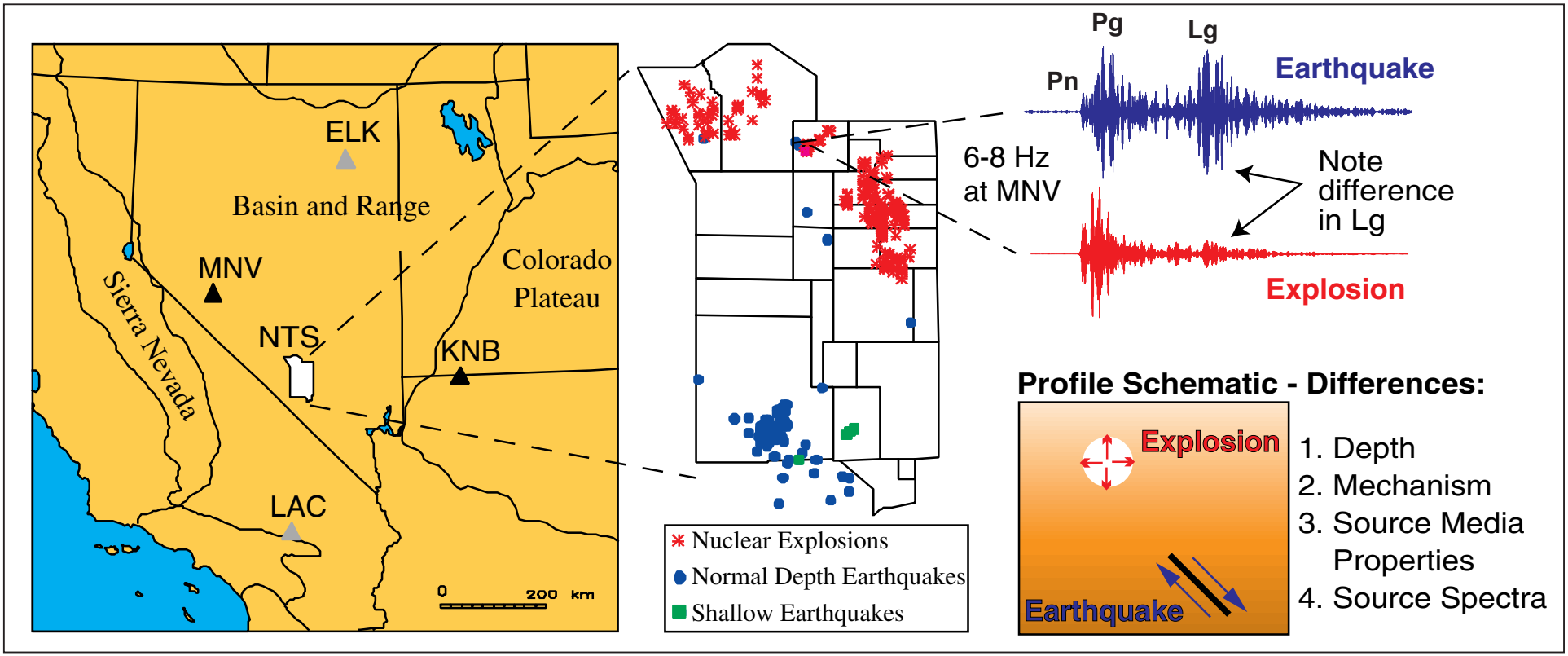


Fig. 1. An example of regional body-wave discrimination at the Nevada Test Site (NTS). The left-hand map shows the location of NTS in relation to the regional seismic stations MNV (Mina, Nevada) and KNB (Kanab, Utah), part of the four station LLNL NTS network. The expansion of NTS (center) shows the location of about 50 earthquakes and 120 explosions used in an earlier discrimination study by Walter et al. (1995). The top left-hand seismograms compare an earthquake and an explosion of similar size and with very closely located epicenters. Note that at this high-frequency passband of 6-8 Hz, there is a significant difference in the Lg amplitude compared with the Pn or Pg amplitudes between the two events. These relative phase amplitude differences are caused by differences in depth, mechanism, source medium properties and source spectra as outlined on the lower left. These physical differences lead to the ability to discriminate earthquakes from explosions for nearly co-located, equal size events. To compare events of different sizes and locations, we must account for source size and path effects, which is the subject of this paper.

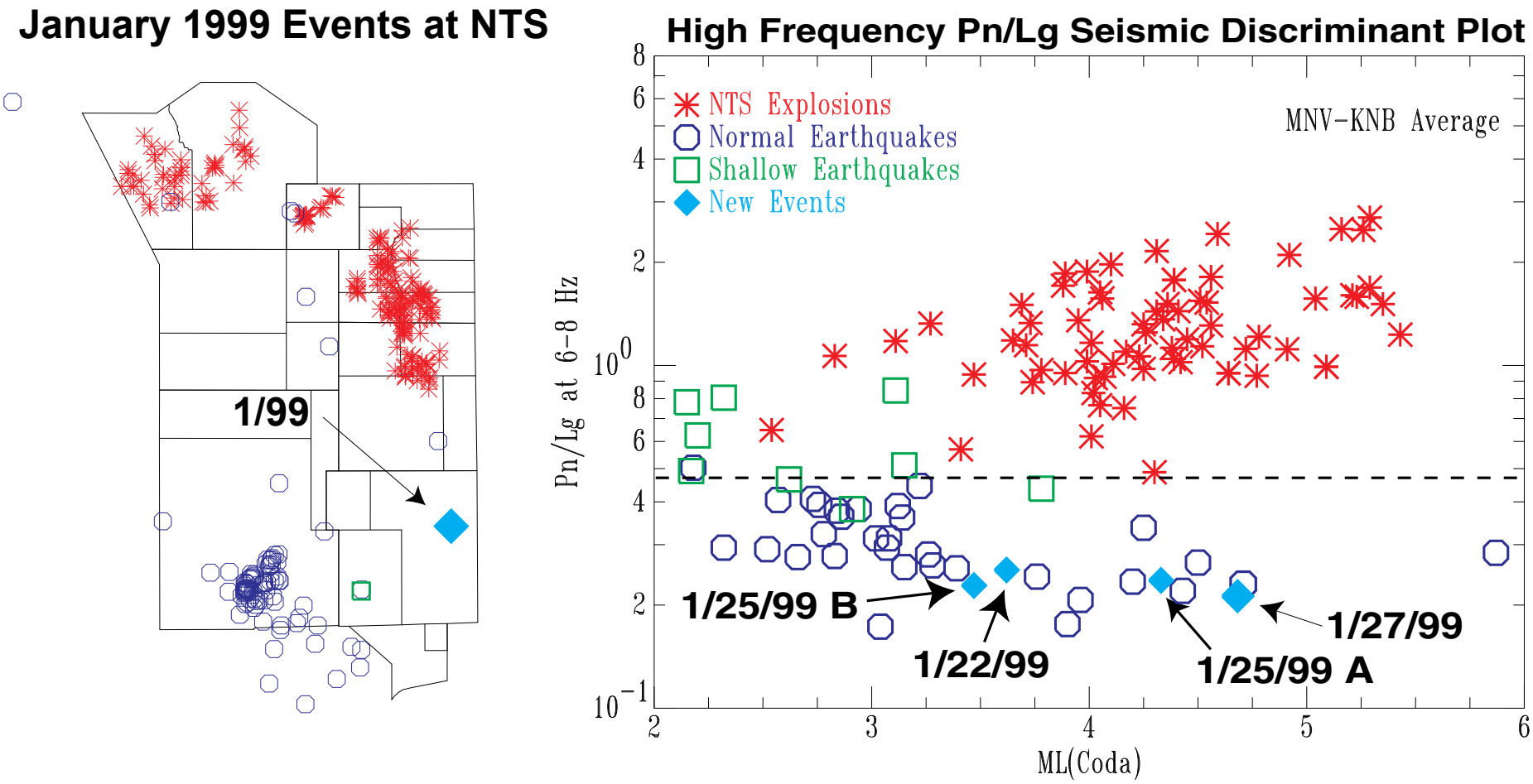


Fig. 2. An example of discrimination results for recent NTS earthquakes compared with historical data from an earlier study. The left-hand map shows the location of the events, the right-hand plot shows the 6-8 Hz Pn/Lg discriminant averaged over values from MNV and KNB (both must exist and pass signal-to-noise tests). The base plot is after Figure 6 of Walter et al. (1995). Note the almost complete separation of normal depth earthquakes and explosions. In January 1999 a vigorous earthquake sequence occurred in the Frenchman flat region of NTS, with four events over moment magnitude 3.5, the largest Mw=4.8 (Walter and Mayeda, 1999). This is the largest earthquake to occur at NTS since the 1992 Little Skull Mountain events. Processing these new events in the same manner as in the earlier study we find they plot in the earthquake population and discriminate well from the explosions. This gives us confidence in our ability to identify new earthquakes at NTS using our calibrated discriminants.

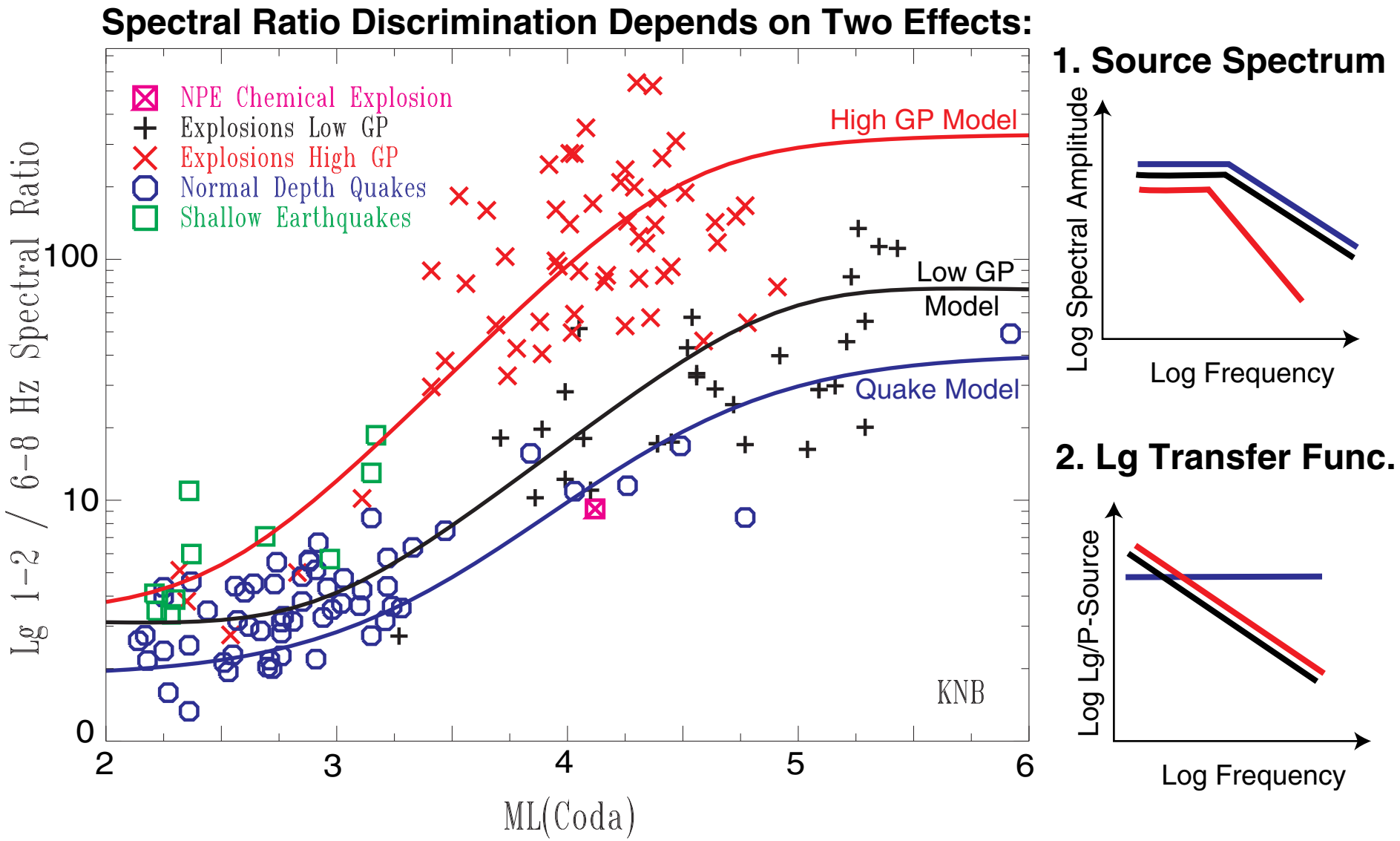


Fig. 3. An example of the magnitude dependence of ratios using amplitudes in different frequency bands. The left-hand plot shows the Lg 1-2/6-8 Hz spectral ratio after Figure 8a of Walter et al., (1995). We model the spectral ratio values using two effects. First we use source spectral models for the earthquakes and explosions. The earthquakes and low gas porosity (GP) explosions have high-frequency fall off as f^{-2} while the high gas porosity events have steeper f^{-3} fall off at high frequencies. As the two frequency measures at 1-2 Hz and 6-8 Hz move from both being on the flat part of the spectrum for small magnitude events to both being on the falling-off part of the spectrum for large magnitude events, they trace out a characteristic sigmoid shape as shown in the model curves. This is the magnitude dependence we seek to remove with the MDAC procedure. In addition the explosion models are offset from the earthquakes due to the second effect, the scattering and conversion of Rg and P energy to Lg energy. This is a frequency dependent transfer function (e.g. Myers et al., 1999) and depends on the shallow depth of the explosions and the velocity structure and other near-source effects.

An example of MDAC fits to Lg spectra from the 1992 Little Skull Mountain sequence at the Nevada Test Site: Mainshock and two aftershocks.

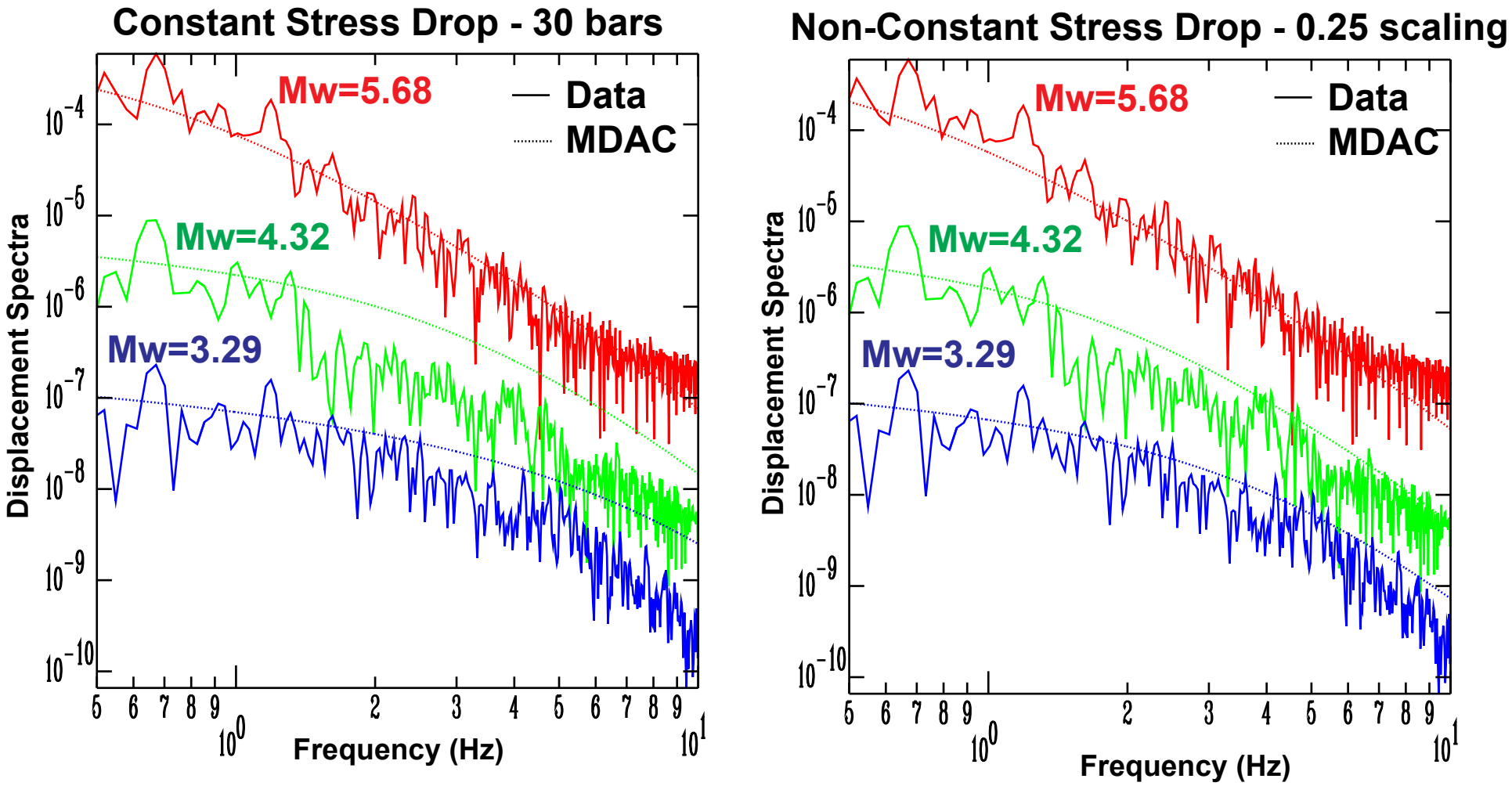


Fig. 4. Example of MDAC Lg spectral fits to three NTS earthquakes recorded at station KNB. The largest event is the June 29, 1992, Little Skull Mountain mainshock, and the smaller events are two aftershocks. The moment magnitudes come from a study by Mayeda and Walter (1996) that used regional coda envelopes and a set of corrections to determine source spectra, moments and stress drops of a number of Western U.S. earthquakes. We tried fitting these events with both constant stress drop models (left) and quarter root stress drop scaling (right). Note the quarter root scaling produces better fits and is consistent with the independent coda results of Mayeda and Walter (1996).

COMPUTATION OF TRAVEL TIMES AND STATION CORRECTION SURFACES IN EURASIA USING THREE DIMENSIONAL VELOCITY MODELS

A. Villaseñor, M.H. Ritzwoller, M.P. Barmin, E.R. Engdahl, and A.L. Levshin

Department of Physics, University of Colorado, Campus Box 390, Boulder, CO 80309

Sponsored by The Defense Threat Reduction Agency
Arms Control Technology Division
Nuclear Treaties Branch

Contract No. DTRA01-99-C-0019

ABSTRACT

We have investigated the performance of a variety of travel time computation methods for application in highly heterogeneous three-dimensional (3-D) velocity structures, such as those found in Central Eurasia. Recent 3-D models of the crust and upper mantle beneath Central Eurasia (e.g., Villaseñor et al., 2000) contain sharp vertical and horizontal velocity contrasts and thin layers which complicate the accurate computation of travel times.

Techniques based on ray-perturbation theory or the graph method (e.g., Pulliam and Snieder, 1996; Nolet and Moser, 1993) do not appear to work well when the velocity anomalies are large relative to the reference model. In these cases the reference ray can be very different from the minimum-time ray, and the methods fail to converge rapidly and in some cases do not converge at all to the global minimum.

Ray shooting and finite-difference algorithms are more computationally expensive, but provide accurate results in the presence of large velocity contrasts. In the ray-shooting method, the model is parameterized in terms of smooth polynomials in all directions. Ray-shooting methods are normally implemented only in 2-D (e.g., Červený and Pšenčík, 1988), and do not consider propagation paths off the sagittal plane. The finite difference method computes travel times for first-arriving phases for the entire model (e.g., Podvin and Lecomte, 1991). Rays are obtained afterward by back-tracing from any point inside the model (receiver) to the source. This method is 3-D and the model is parameterized in terms of constant-velocity cubic cells. The accuracy of the travel times is determined by the cell size. Computer memory effectively limits the minimum cell size for a given region but this constraint can be overcome by computing travel times in 2-D.

Ray shooting and finite difference methods produce similar travel times, but differences can locally be greater than 1 s largely due to the differences in model parameterization between the two methods. We report estimates of uncertainties in travel times and station correction surfaces between these two methods and also discuss the effect of computing travel times in 2-D rather than in 3-D.

For IMS stations in Central Eurasia we present travel time correction surfaces relative to the 1-D model ak135 predicted by the 3-D velocity model of Villaseñor et al. (2000). At epicentral distances less than about 10 degrees, the character of the correction surfaces is dominated by the difference in crustal thickness between the 3-D model and ak135. Beyond 5-10 degrees, velocity variations in the uppermost mantle become increasingly important.

Key Words: Travel times, ray tracing, source-specific station corrections, SSSC.

OBJECTIVE

The objective of this research is to evaluate methods for computing travel times at regional distances for three dimensional velocity models, and assess their usefulness to produce model-predicted source-specific station corrections (SSSCs) for IMS stations in Central Eurasia.

RESEARCH ACCOMPLISHED

Introduction

Locating low magnitude events with the accuracy required by CTBT monitoring is a challenging task. These events are normally recorded only at regional distances, where the effect of crustal and upper mantle structure on seismic travel times is important. One-dimensional (1-D), radially-symmetric models such as iasp91 (Kennett and Engdahl, 1991) or ak135 (Kennett et al., 1995) cannot predict travel times accurately for local and regional distances. A method to account for the effects of lateral heterogeneity at a given station is to construct source-specific station corrections or SSSCs. Empirical SSSCs can be constructed in regions where calibration data such as explosions and/or well located earthquakes are available (e.g., Bondár et al., 1999). Unfortunately this is normally not the case, and large regions of the Earth have little or no calibration data. For these regions, SSSCs can be obtained using available regional and/or global velocity models. To obtain these model-predicted SSSCs, rays have to be traced through the model, from each station to points on a specified rectangular latitude/longitude grid, within a given distance from the station (normally 20 degrees). Therefore, accurate and efficient methods to calculate travel times in 3-D velocity models are required.

Computation of travel times in heterogeneous media is a complicated problem. This complexity is illustrated by the large number of methodologies developed, and by the fact that each one has its advantages and shortcomings (for a review see for example Červený, 1987). We have restricted this study to three families of methods: ray bending, ray shooting, and finite difference methods. Bending methods are generally fast and work well for smoothly varying velocity models, but may converge toward local travel time minima. Shooting methods work better for more heterogeneous models, but at the expense of computation time, and they cannot trace rays in shadow zones. Finite difference methods can provide very accurate results even in presence of extreme velocity variations, but require small cell sizes. Finite difference methods normally produce travel times for first arriving phases, and not for later phases.

The two bending codes tested in this study are described by Bijwaard and Spakman (1999). The first code is an implementation of the graph method by Nolet and Moser (1993) based on the work of Moser (1991). The second code is based on ray perturbation theory, and was developed by Pulliam and Snieder (1996) based on the original implementation of Snieder and Sambridge (1993). Both codes perform 3-D ray tracing and work well for models with small velocity perturbations (e.g. Bijwaard et al., 1998). However, they do not work with other models (e.g., Villaseñor et al., 2000) that contain sharp vertical discontinuities, thin layers, and large lateral velocity variations. These two codes have not been used in the results presented in this study.

We have also tested the ray shooting code of Červený and Pšenčík (1988). This is a 2-D method, for laterally-varying layered models. The geometry of the layers is described in terms of splines. Computations are made in a cartesian (flat Earth) reference system, and applying an earth-flattening transformation.

Finally we have tested the finite difference technique of Podvin and Lecomte (1991). This method can be used both in 3-D and 2-D. The model is parameterized in terms of cubic constant-velocity cells. Therefore, models described using a spherical parameterization have to be mapped into a cartesian reference system, resulting in some inefficiency in the amount of memory required to store the model. Travel time wavefronts and not rays are computed in this method. Rays can be obtained a posteriori by backtracking towards the source following the normal direction to the wavefronts.

Accuracy tests

We have conducted tests to evaluate the performance and accuracy of the ray shooting and finite difference methods. First we test these methods against theoretical travel times for the one-dimensional, radially-symmetric model ak135 (Kennett et al., 1995). Second we compare the results of both methods in 2-D, using vertical cross-sections of the S model of Villaseñor et al. (2000), and finally we compare the performance of 2-D versus full 3-D travel times.

To evaluate the accuracy of the ray shooting and finite difference methods, we compare their results with theoretical travel times (Buland and Chapman, 1983) for ak135. The results of these comparisons are shown in Figure 1. In

this case the ray shooting method is very precise, better that 0.1 s. The accuracy of the finite difference method depends on the cell size. For a cell size of 1 x 1 km the precision is also better than 0.1 s. If the cell size is increased to 2 x 2 km the precision is still better that 0.25 second, but some artifacts caused by the finite difference model parameterization (2 x 2 km constant velocity cells) can be seen. When the first arrival changes from Pg to Pn (at approximately 1.5 degrees) there is a baseline shift of 0.1 s (Figure 1). This shift is caused because Moho depth in the finite difference model parameterization of 2 x 2 km cells is 36 km, instead of 35 km in ak135.

We have compared the 2-D ray shooting method and the finite difference method using two great-circle vertical cross sections through the S model of Villaseñor et al. (2000) for Central Eurasia. This model is transversely isotropic in the uppermost mantle, but for this test we have used the v_{SV} component of the model, which is better constrained than v_{SH}. The differences between travel times using both methods for the two great circle paths considered are shown in Figure 2. The differences are on the order of 2 seconds, much larger than the tests performed with the 1-D model ak135. We find that these differences are caused by the way the 3-D model is translated into the internal parameterization of each travel time code. In some other cases, not shown here, the differences are much larger, and caused by the failure of the ray-shooting method to find the minimum travel time ray path. In most cases, modifying the parameters that control the accuracy of the ray shooting solution eliminates these problems, but at the expense of longer computation time. On the other hand, the finite difference method is very fast and efficient, and always provides the first arrival time even in presence of extreme velocity contrasts (Podvin and Lecomte, 1991).

Finally we have investigated the importance of full 3-D travel time computation versus computations in 2-D. For this test we only use the finite-difference method of Podvin and Lecomte (1991) because the ray shooting code is strictly 2-D. To evaluate the differences between 3-D and 2-D travel times we have considered two profiles through the S model of Villaseñor et al. (2000). Figure 3 shows the differences between the computed 3-D and 2-D travel times. These differences are small (less than 2 seconds), and similar in magnitude to the differences between both 2-D codes shown in Figure 2. Full 3-D ray-tracing is important for non-linear tomography studies, allowing to obtain improved, more focused velocity models (Bijwaard and Spakman, 2000; Widiyantoro et al., 2000), but for the model considered here and for regional distances it is not necessary for computing travel times and SSSCs with sufficient precision. This is probably because the model we have used is more heterogeneous vertically (with thin layers and sharp velocity contrasts) than laterally, and therefore off-great circle propagation is not very important.

Effects of the reference model on the computation of SSSCs

Global velocity models obtained by inversion of large datasets of arrival times of seismic phases (e.g., Bijwaard et al., 1988), are normally described as perturbations to 1-D models such as iasp91 or ak135. These 3-D models provide high resolution in regions with high density of earthquakes and stations but contain large gaps in regions where seismicity is low and/or stations do not exist. On the other hand, models that use surface wave and normal mode data have lower resolution than models based on body waves, but their coverage is more homogeneous. These models are normally described as perturbations relative to PREM (Dziewonski and Anderson, 1981)

There are some significant differences between PREM and ak135 in the crust and upper mantle. PREM is designed as an average Earth model, and contains a 3 km thick water layer, with Moho located at 24.4 km depth. The crust in ak135 is of continental type (because most of seismic stations are located on continents), with a Moho depth of 35 km. In the uppermost mantle, between Moho and 220 km, PREM is transversely isotropic, and exhibits a well-developed low velocity zone, while ak135 is isotropic and lacks a low velocity zone, although the velocity gradient in the uppermost mantle is very small for both P and S. In the upper mantle PREM has a velocity discontinuity at 220 km depth which is much sharper for P than for S. This discontinuity is absent in ak135. Finally the transition zone is 20 km thicker for PREM (400 – 670 km) than for ak135 (410 – 660 km).

These differences between PREM and ak135 obviously translate into different travel times at regional distances, as shown in Figure 4. We have calculated the difference in travel times between PREM and ak135 for a source located at 40 km depth, and for receivers also at 40 km depth. This has been done to avoid additional complications by differences in crustal structure. Therefore, the curves shown in Figure 4 represent the effect of differences in upper mantle and transition zone structure between the two models. Immediately below Moho v_{PH} for PREM is larger than v_P for ak135. As a result PREM travel times for v_{PH} are faster (smaller) than ak135, and this can be observed as

increasingly negative values in Figure 4 (top panel, solid line). The difference in travel time reaches a minimum of approximately –3 s at distances of 14 degrees, and then decreases to 0 at 25 degrees. The situation is reversed for PREM v_{PV}. Immediately below Moho v_{PV} for PREM is slightly smaller v_P for ak135 and this results in positive values, indicating that travel times for PREM v_{PV} are slower (larger) than ak135 (top panel, dashed line). The same pattern can be observed for S wave travel times (Figure 4, bottom). In this case the differences in travel times are larger (-8 s for PREM v_{SH}) and the maximum values of the differences occur at different distances (e.g., at 19 degrees for PREM v_{SH}).

SSSCs are normally referred to iasp91 or ak135 (for the purpose of regional travel times both models are identical) but many global and regional models are expressed as perturbations relative to PREM. Because of the differences in travel times between PREM and ak135 we must expect artifacts in the SSSCs that are caused by the choice of the reference model, in addition to features due to lateral heterogeneity. Figure 5a shows the SSSC relative to ak135 for auxiliary IMS station AAK (Ala-Archa, Kyrgyzstan) computed from the S model of Villaseñor et al. (2000). At epicentral distances less than about 10 degrees, the character of the correction surface is dominated by the difference in crustal thickness between the 3-D model and ak135. The crust in Central Eurasia is thicker than 35 km, and this results in positive station corrections (slower travel times than ak135). Beyond 5-10 degrees, velocity variations in the uppermost mantle become increasingly important. High velocities in the Indian craton produce large negative corrections (faster travel times than ak135). This effect can also be observed in the East European platform, north of the Caspian Sea. On top of these features caused by lateral heterogeneity there is a ring of negative values, centered on the station and with a radius of approximately 20 degrees. As shown in Figure 4, this ring can be explained by the differences between our upper mantle model (which uses PREM as reference model) and ak135.

To avoid these artifacts, the SSSCs can be calculated relative to the model beneath the station, instead of relative to iasp91 or ak135. This guarantees that the velocity discontinuities of the 3-D model and reference model are located exactly at the same depths. Figure 5b shows the results of applying this procedure to AAK. The ring with negative values has disappeared, the shape of the correction surface is smoother and better correlated with the features of the 3-D model. Figure 5c shows the difference between the two correction surfaces obtained for AAK (Figures 5a and 5b). This clearly illustrates that the ring is an artifact caused by the choice of the reference model.

CONCLUSIONS AND RECOMMENDATIONS

We have tested the performance of travel time codes based on ray bending, ray shooting and finite differences for computing model-predicted SSSCs. For three-dimensional Earth models with large lateral and vertical velocity variations ray shooting and finite differences provide the best results.

For laterally heterogeneous models, the differences in computed travel times between different codes can be rather large (up to 2 seconds for regional distances). In some cases this can be caused by poor performance of one the methods (for example not being able to find the minimum travel time path, and converging to a local minimum). However, in the examples presented here, the differences are caused by differences in the internal model parameterization of each travel time code. These differences can be even larger if the influence of model uncertainties on the computation of travel times is considered.

Full 3-D ray tracing is important for non-linear tomography studies, allowing to obtain improved, more focused velocity models. However, 3-D travel times are not necessary for computing regional SSSCs. Tests indicate that, for models like the ones used in this study, travel time differences between 2-D and 3-D ray tracing are similar in magnitude to differences between travel time codes. In the future, when higher-resolution, more heterogeneous models become available, 3-D ray tracing may be required.

The choice of the reference model is extremely important for determining the features of model-predicted SSSCs. To ensure smoothly varying SSSCs, the 3-D model should have the upper mantle and transition zone discontinuities at the same depth as the reference model. Otherwise, the computed SSSCs may display large artifacts, that manifest as circular features (positive or negative in sign) centered on the station. These artifacts can be eliminated by using the model beneath the station as the reference model for the computation of the SSSCs.

Finally, methods need to be developed to evaluate the uncertainties of travel times and SSSCs based upon the uncertainties in the travel time methods and in the 3-D velocity models.

REFERENCES

Bijwaard, H., and W. Spakman, Fast kinematic ray tracing of first- and later-arriving global seismic phases, Geophys. J. Int., 139, 359-369, 1999.

Bijwaard, H., and W. Spakman, Non-linear global P-wave tomography by iterated linearized inversion, Geophys. J. Int., 141, 71-82, 2000.

Bijwaard, H., Spakman, W., and Engdahl, E.R., Closing the gap between regional and global travel time tomography, J. Geophys. Res., 103, 30055-30078, 1998.

Bondár, I., X. Yang, K. McLaughlin, R.G. North, V. Ryaboy, and W. Nagy, Source specific station corrections for regional phases at IMS stations in North America and Fennoscandia, Eos Trans. AGU, 79, 555, 1999.

Buland, R., and C.H. Chapman, The computation of seismic travel times, Bull. Seism. Soc. Am., 73, 1271-1302, 1983.

Červený, V., Ray tracing algorithms in three-dimensional laterally varying layered structures, in: Seismic Tomography, edited by G. Nolet, pp. 99-133, Reidel, Dordrecht, The Netherlands, 1987.

Červený, V., and I. Pšenčík,, Numerical modeling of seismic wave fields in 2-D laterally varying layered structures by the ray method, in Seismological Algorithms, Academic Press, London, 1988.

Dziewonski, A.M., and D.L. Anderson, Preliminary reference Earth model, Phys. Earth Planet. Inter., 25, 297-356, 1981.

Engdahl, E.R., R. van der Hilst, and R. Buland, Global teleseismic earthquake relocation with improved travel times and procedures for depth determination, Bull. Seism. Soc. Am., 88, 722-743, 1998.

Engdahl, E.R., and M.H. Ritzwoller, Crust and upper mantle P- and S-wave delay times at Eurasian seismic stations, Phys. Earth Planet. Int., submitted, 2000.

Kennett, B.L.N., and E.R. Engdahl, Travel times for global earthquake location and phase identification, Geophys. J. Int., 105, 429-465, 1991.

Kennett, B.L.N., E.R. Engdahl, and R. Buland, Constraints on seismic velocities in the Earth from travel times, Geophys. J. Int., 122, 108-124, 1995.

Moser, T.J., Shortest path calculation of seismic rays, Geophysics, 56, 59-67, 1991.

Nolet, G., and T.J. Moser, Teleseismic delay times in a 3-D Earth and a new look at the S discrepancy, Geophys. J. Int., 114, 185-195, 1993.

Podvin, P., and Lecomte, I., Finite difference computation of travel times in very contrasted velocity models: a massively parallel approach and its associated tools, Geophys. J. Int., 105, 271-284, 1991.

Pulliam J., and R.K. Snieder, Fast, efficient calculation of rays and travel times with ray perturbation theory, J. Acoust. Soc. Am., 99, 383-391, 1996.

Snieder, R.K., and M. Sambridge, The ambiguity in ray perturbation theory, J. Geophys. Res., 98, 22021-22034, 1993.

Villaseñor, A., M.H. Ritzwoller, A.L. Levshin, M.P. Barmin, E.R. Engdahl, W. Spakman and J. Trampert, Shear velocity structure of Central Eurasia from inversion of surface wave velocities, Phys. Earth Planet Int., submitted, 2000.

Widiyantoro, S., A. Gorbatov, B.L.N. Kennett, and Y. Fukao, Improving global shear wave traveltime tomography using three-dimensional ray tracing and iterative inversion, Geophys. J. Int., 141, 747-758, 2000.

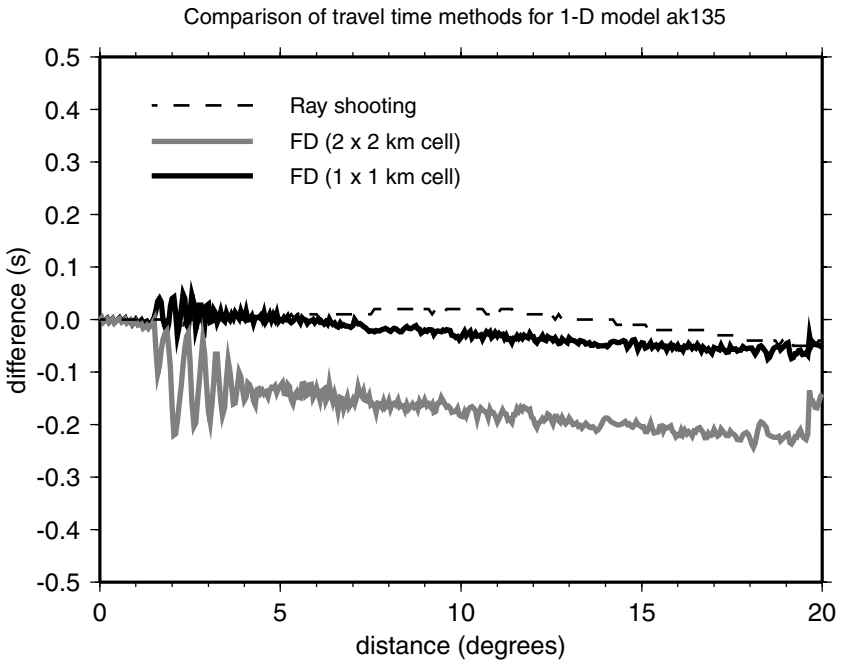


Figure 1. Differences between computed travel times using different methods and theoretical arrival times for the one dimensional model ak135. Thick black line for the finite difference method with 1 x 1 km cells, thick gray line for the same method with 2 x 2 km cells, and dashed line for the ray-shooting method.

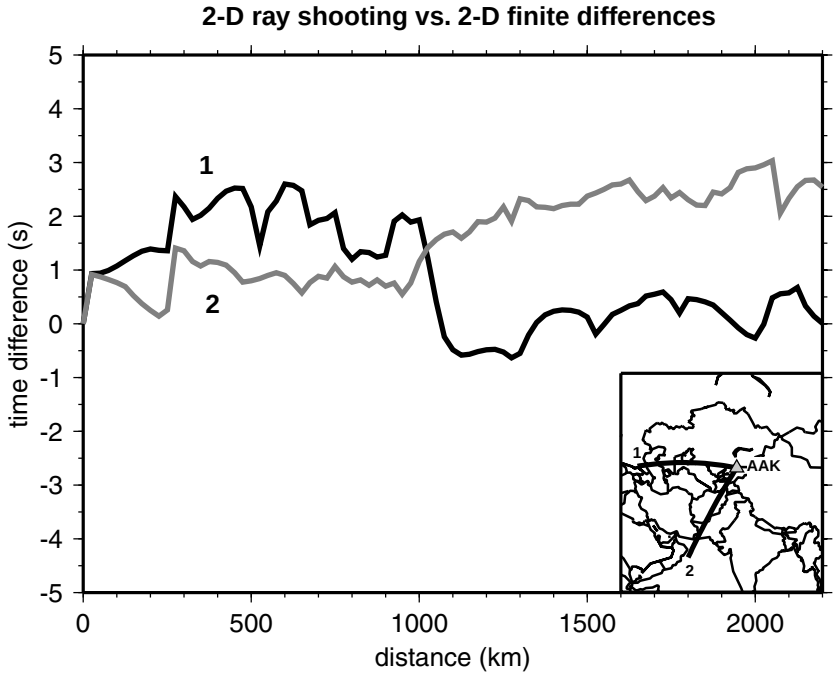


Figure 2. Differences between travel times computed using the 2-D ray shooting and the 2-D finite difference methods for two great circle cross sections through the vSV model of Villaseæor et al. (2000). The starting point of both great circle cross sections is IMS station AAK (Ala-Archa, Kyrgyzstan). The curves represent the ray-shooting travel time minus the finite difference travel time. Map inset shows the location of the two cross sections.

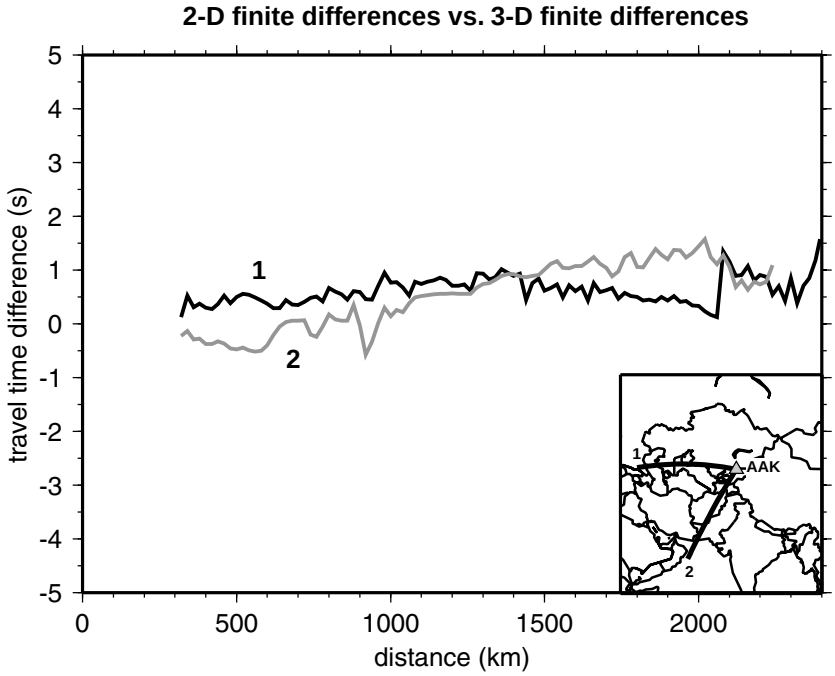


Figure 3. Differences between computed travel times along two great circle cross sections through the vSV model of Villaseæor et al. (2000) using the finite difference method in 2-D and 3-D. The starting point of both cross sections is IMS station AAK (Ala-Archa, Kyrgyzstan). Each curve represents the 2-D travel time minus the 3-D travel time. Map inset shows the location of the two cross sections.

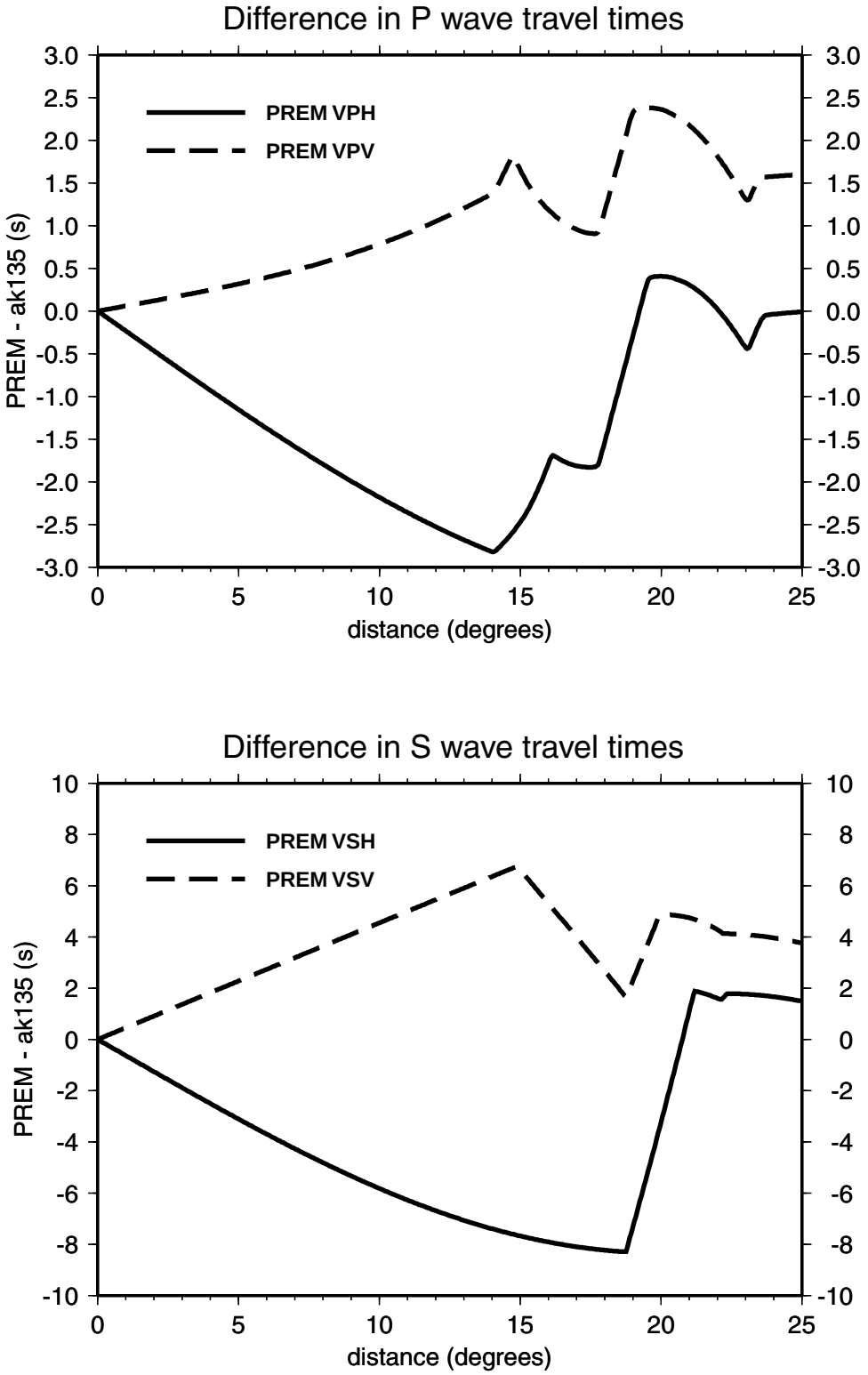


Figure 4. Travel time differences between 1-D models PREM and ak135 for regional distances. Top panel shows differences in P-wave traveltimes, and bottom panel shows differences in S-wave travel times.

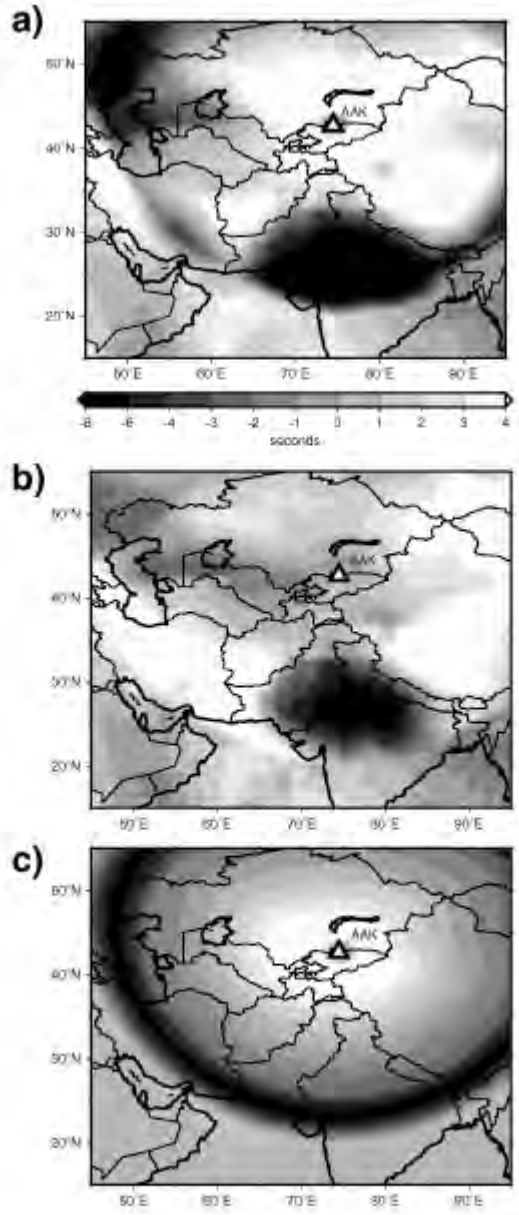


Figure 5. SSSCs for IMS station AAK (Ala-Archa, Kyrgyzstan) for the vSV model of Villaseñor et al. (2000). a) correction surface relative to ak135, b) relative to the model beneath the station, and c) difference between the two SSSCs.

EXTENDING REGIONAL WAVE FORM MODELING TO SHORTER PERIODS TO IMPROVE THE LOCATION AND IDENTIFICATION OF SMALL SEISMIC SOURCES

Bradley B. Woods, Chandan K. Saikia, and Hong Kie Thio

URS Greiner Woodward-Clyde

Sponsored by Defense Threat Reduction Agency

Contract No. DTRA 01-98-C-0151

ABSTRACT

In an effort to improve the location of small seismic events near known test sites, we are determining source-station specific corrections (SSSC's) for regional P, S and Lg phases recorded at IMS stations within 20^0 of these locals, in particular the central Asian test sites of Lop Nor and Semipalantinsk. To this end, we are calculating travel-time residuals between phase arrival information from various sources -- CEB and ISC values as well as direct waveform picks -- and IASP91 predictions using available ground-truth data for events in and near these test sites. These residuals are then averaged for each station to determine the empirical SSSC's. Ground-truth data for these events vary in accuracy; in particular, the level of ground truth for more recent Lop Nor explosions, which are the only ones recorded by many of the newer IMS stations, is not well constrained, being GT25 locations from the Reviewed and Calibration Event Bulletins (REB and CEB). As accurate hypocentral information is crucial to obtaining well-calibrated travel-time corrections, we re-evaluated these more poorly constrained ground-truth data. We found that the ISC locations were quite similar to those of GT5 Lop Nor events which were determined from joint epicenter determinations (JED). For $m_b \geq 5$ explosions the average difference in epicentral locations is 2.9 km, with the maximum being 5.5 km; and differences in origin time being 0.1 sec on average, with the maximum being 0.3 sec. Epicentral errors for these ISC locations are small, being less than 5 km. Discrepancies and errors are significantly larger for the smaller ($m_b \leq 4.7$) explosions, and are assumed to be due to SNR phase picking problems and fewer observations used to determine locations. Consequently the ISC teleseismic locations for $m_b \geq 5$ explosions can be considered to be of GT5 quality. We compared the ISC and GT25 (CEB) locations of the four available 1995+ Lop Nor explosions -- those occurring in the operating period of most of the present IMS stations in the region -- to ascertain how accurate the CEB locations actually are. The difference in epicentral location, on average, is 11.3 km with the maximum being 18.4 km; the average differential origin time is 1.4 s, with the maximum being 1.7 s. These differences are larger than those between the GT-5 and ISC locations. As the ISC locations are fairly consistently determined over time and use a large number of observations (200+), their values are considered robust and more accurate than the CEB values, which are determined from far fewer observations. Furthermore, travel-time corrections were determined for ISC reporting stations which observed both the 1995+ and earlier (1980-1994) GT5 events. Three sets of corrections were calculated: one using the GT5 locations for the earlier (1994-) events and the other two using the ISC or CEB locations for the more recent (1995+) events. The 1994- GT5 and 1995+ ISC location-based corrections are quite similar in value, whereas the 1994- GT5 and 1995+ CEB location-based corrections are significantly different. Therefore we used the ISC locations for these 1995+ events to establish SSSC's for regional P phases. The 1995+ explosions were then relocated using IMS phase information both with and without SSSC's, and compared these hypocenters to the ISC, or assumed GT, values. The average difference in location is 6.6 km and 17.4 km respectively for the corrected and uncorrected locations, with error-ellipse axes being only marginally smaller (5%) for the corrected locations.

Key Words:

Regional Location, Travel-time Calibration, SSSC's

OBJECTIVE

We are developing techniques to better locate and characterize small (mb< 4.5) seismic events, particularly for regions surrounding known nuclear test sites. Such events are of particular interest to the CTBT monitoring community, and reliably locating and identifying them is of paramount concern. Events of this size are usually only observed regionally (Δ < 20°) as was the case of the August 16, 1997 Kara Sea event (Israelson *et al.*, 1997). Consequently we are concentrating on improving location capabilities for stations within 20° of test sites in central Asia. Attempts at developing improved 1-D models for these purposes has proven difficult, in part, no doubt, due to the laterally varying nature of the crustal structure in the region. Therefore we have more recently concentrated on determining source-specific station corrections (SSSC's) for IMS stations relative to specific test sites; this scheme is particularly well suited to the problem at hand, that is to determine empirical travel-time corrections for a relatively small geographic region centered about a point with several master events. To determine SSSC's it is important to have accurate ground truth (GT) information regarding the location of master events used in determining the travel-time calibrations, or residuals; therefore the accuracy of GT hypocenters must be verified as well. These SSSC's, which are determined for the IASP91 global travel-time model using the location code LocSAT, used by the IDC, can be directly applied to future operational location determinations for events in this area.

RESEARCH ACCOMPLISHED

We are determining SSSC's for IMS stations within 20° of nuclear test sites in central Asia; the work described here pertains specifically to the Lop Nor test site. Unfortunately, for this region there are no GT-10, or better, events in the PIDC GT Event Database (Yang and Romney, 1999) for the period in which most of the IMS stations, or their surrogates, have been operating. Therefore it was first necessary to develop a set of alternative "quasi-GT" events for calibration purposes; in particular we wished to make use of the 1995 and 1996 Lop Nor explosions as they were well recorded by the IMS stations in the region. We first compared ISC and CEB (The PIDC's Calibration Event Bulletin) locations for these events and found significant differences in the epicenters and origin times; Table 1 provides these comparisons. The average difference between the ISC and CEB locations is 11.4 km, and the ISC origin times (OT) are, on average, 1.43 seconds earlier than the CEB OT's. Thus further analysis was needed to determine which set of locations were more accurate and should be used to determine travel-time calibrations; although the error ellipses for the ISC locations are a factor of 2-3 smaller, suggesting they are better constrained.

To this end we compared ISC locations for Nor explosions from the early 1990's and the 1980's with their GT-5 locations and OT's, which were taken from a joint epicentral determination study by Gupta (1995) using master events with locations determined by satellite imagery. Table 2 compares these two sets of locations as well as providing other relevant information; the last column, the number of observations, refers to the number of picks used to determine the ISC location for each event. For the larger ($m_b \geq 5.0$) events the locations and OT's are quite similar, being, on average, less than 2.9 km and 0.1 s apart, respectively. The differences are significantly larger for the smaller ($m_b \leq 4.7$) events. These relationships are shown graphically in Figure 1 in which the difference in epicentral location are plotted vs. m_b, and the number of observations. From these results it seems appropriate to take ISC locations of the larger explosions, particularly those determined with more than 100 observations, as comparable to GT-5 events.

The next step was to establish the effectiveness of SSSC's for known GT-5 events before determining corrections for the later (1995+) ersatz GT-5 events. For this we used the 9 events given in Table 2 and their ISC P-wave picks from stations within 25°; this distance range was chosen so as to provide more adequate station coverage, particularly for the less well recorded, older events. As these events vary in number of observations as well as azimuthal coverage (see Figure 2), the location results for them should give an indication of the limitations of this method. Locations were determined using the LocSAT code (Nagy and Bratt, 1991) and the IASP91 model (Kennett and Engdahl, 1991). P-wave residuals were calculated relative to the GT-5 hypocenters and OT's, and averaged for each station; individual residuals which were over 1.5 standard deviations from the average station value were determined to be spurious and removed, and the average station residual, or correction, was recalculated.

These events were then relocated separately using the corrected and uncorrected arrival times; the results are given in figure 2. The corrected locations are significantly closer in distance to the GT-5 locations —usually by a factor of two or more —and on par with the ISC locations; the poorest corrected relocations, as would be expected, correspond to events with the fewest observations and poorer azimuthal coverage. Thus the travel-time correction procedure applied here provides more accurate locations and, consequently, justifies applying the same methodology to the IMS stations in this region.

Corrections were then determined in the same fashion for the IMS alpha and beta stations within 25° of the Lop Nor test site using the ISC hypocenters; for this no distinction was made between alpha and beta station, and, in a few cases, surrogate ISC stations and their arrival picks were used to make up for non-reporting IMS stations. The mislocations relative to the ISC hypocenters are plotted in Figure 3. The corrected relocations are 2-4 times closer to the ISC epicenters, taken to be GT, than the uncorrected relocations, and are on par with, or better than the CEB locations assuming that the ISC locations are more accurate. Clearly if the CEB locations were used as GT, the corrected relocated events would be closer to these locations as well. For the case of using observations out to 25° degrees, the mislocations are less than 5km relative to the ISC epicenters, whereas the the mislocations are between 5 to 10 km using observations out to 20°. The former use between 9 to 13 observations while the latter only use between 4-8 observations, with a corresponding degradation in azimuthal coverage. Figure 4 provides map-view comparisons of the locations for these events. None of the uncorrected location error ellipses overlap with the ISC location, whereas the ISC locations all lie within the corrected location 90% error ellipse for that event.

CONCLUSIONS AND RECOMMENDATIONS

P-wave SSSC's were determined for IMS and ISC stations within 25° of the Lop Nor test site, an area in which GT-5 events are available, thus making this method viable. Regional relocations using these corrections provided significantly improved epicenters, relative to the GT epicenters, compared to uncorrected relocations using the same set of stations; the GT locations lie within the 90% confidence intervals for the corrected relocations, which is not the case for the uncorrected relocations. These SSSC's for IMS stations can be directly incorporated into IDC location routines for this particular geographic region, *i.e.* within several hundred kilometers of the GT-5 epicenters used as master events. This same methodology can be applied to other regions with such GT information, particularly known nuclear test sites. Further, it was found for the set of explosions examined here that ISC locations based on 100+ observations were very close to GT-5 locations. This suggests that in some cases ISC events can be used as GT events for travel-time calibrations. This possibility needs to be examineded for the case of earthquakes.

REFERENCES

Gupta, V., 1995. Locating nuclear explosions at the Chinese test site near Lop Nor, *Science and Global Sec.*, **5**, pp. 205-244.

Israelsson, H., M. D. Fisk, X. Yang, and R. G. North, 1997. The August 16, 1997 event in the Kara Sea, *CMR Technical Report*, CMR-97/38, Alexandria, VA.

Kennett, B. L. N., and E. R. Engdahl, 1991. Traveltimes for global earthquake location and phase identification, *Geophys. J. Int.*, **105**, pp. 429-465.

Yang, X. and C. Romney, 1999. PIDC Ground Truth Database, *CMR Technical Report,* CMR-99/15, Alexandria, VA.

Table 1

Comparison of GT (CEB) and ISC Locations and Origin Times					
Event Julian Date	m_b (ISC)	ΔR (km)	Δ *O.T.*† (sec)	Smaj, Smin CEB (km)	Smaj, Smin ISC (km)
95135	6.0	18.4	1.6	8.7, 8.0	2.4, 2.3
95229	5.9	9.6	1.2	9.3, 7.8	2.4, 2.3
96160	5.7	9.1	1.2	7.4, 6.6	2.8, 2.4
96211	4.7	8.2	1.7	9.4, 7.8	4.5, 3.2

†: Δ *O.T.* > 0: ISC earlier

Table 2

Comparison of GT(JED) and ISC Locations and Origin Times				
Event Julian Date	m_b (ISC)	ΔR (km)	Δ *O.T.*† (sec)	Num. Obs.
92269	5.0	2.2	0.3	110
92142	6.5	3.5	0.1	710
90228	6.2	1.1	0.0	598
90146	5.5	3.4	0.0	276
88273	4.6	33.6	-4.0	25
87156	6.2	3.6	-0.2	491
84354	4.7	21.4	-4.5	43
84277	5.4	5.5	0.1	76
83279	5.5	1.0	0.1	54

†: Δ *O.T.* > 0: ISC earlier

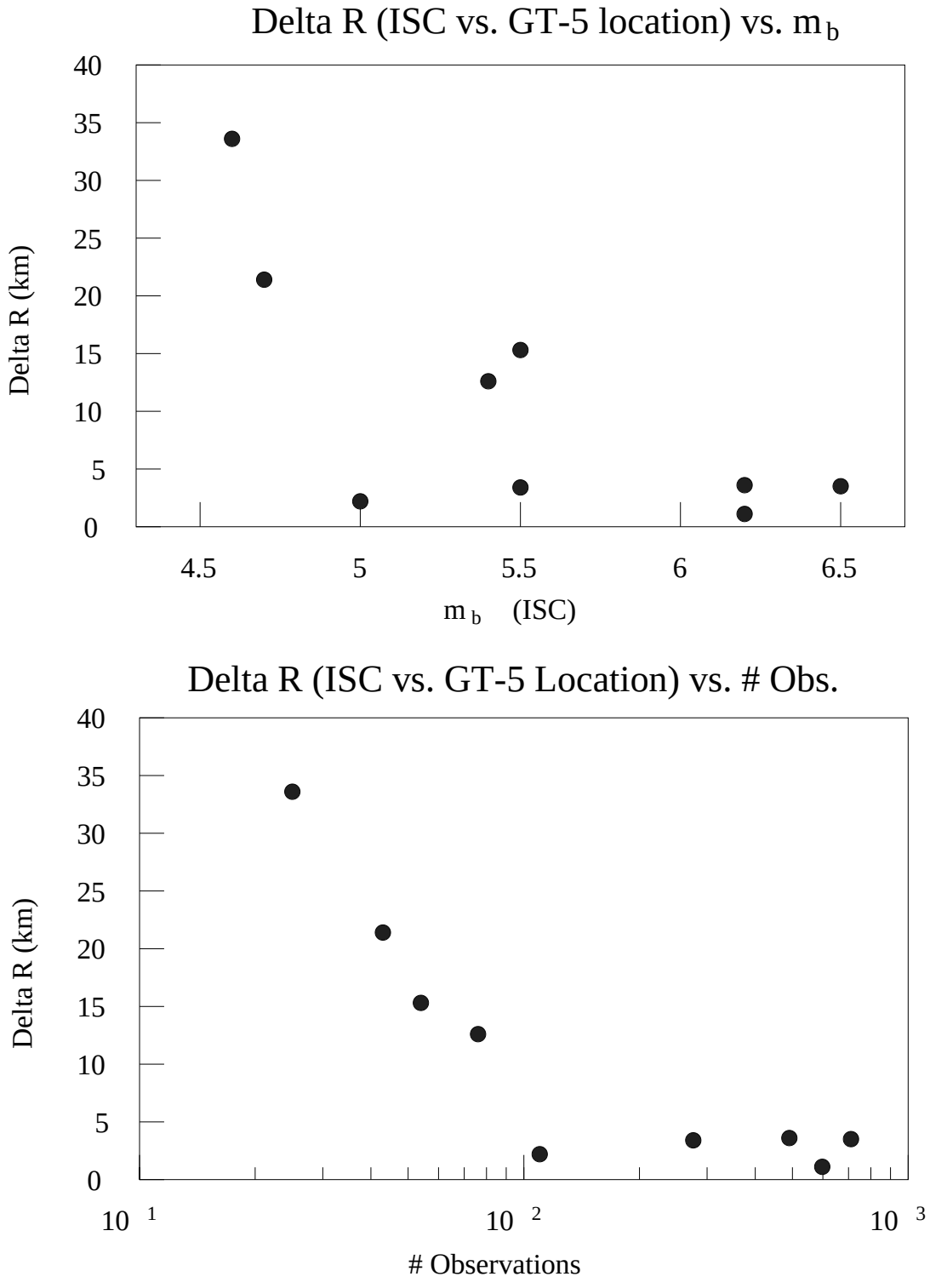


Figure 1. Relative location of ISC epicenters with respect to GT-5 locations for Lop Nor explosions: (top) vs. m_b(ISC); (bottom) vs. number of observations used to determine the ISC location.

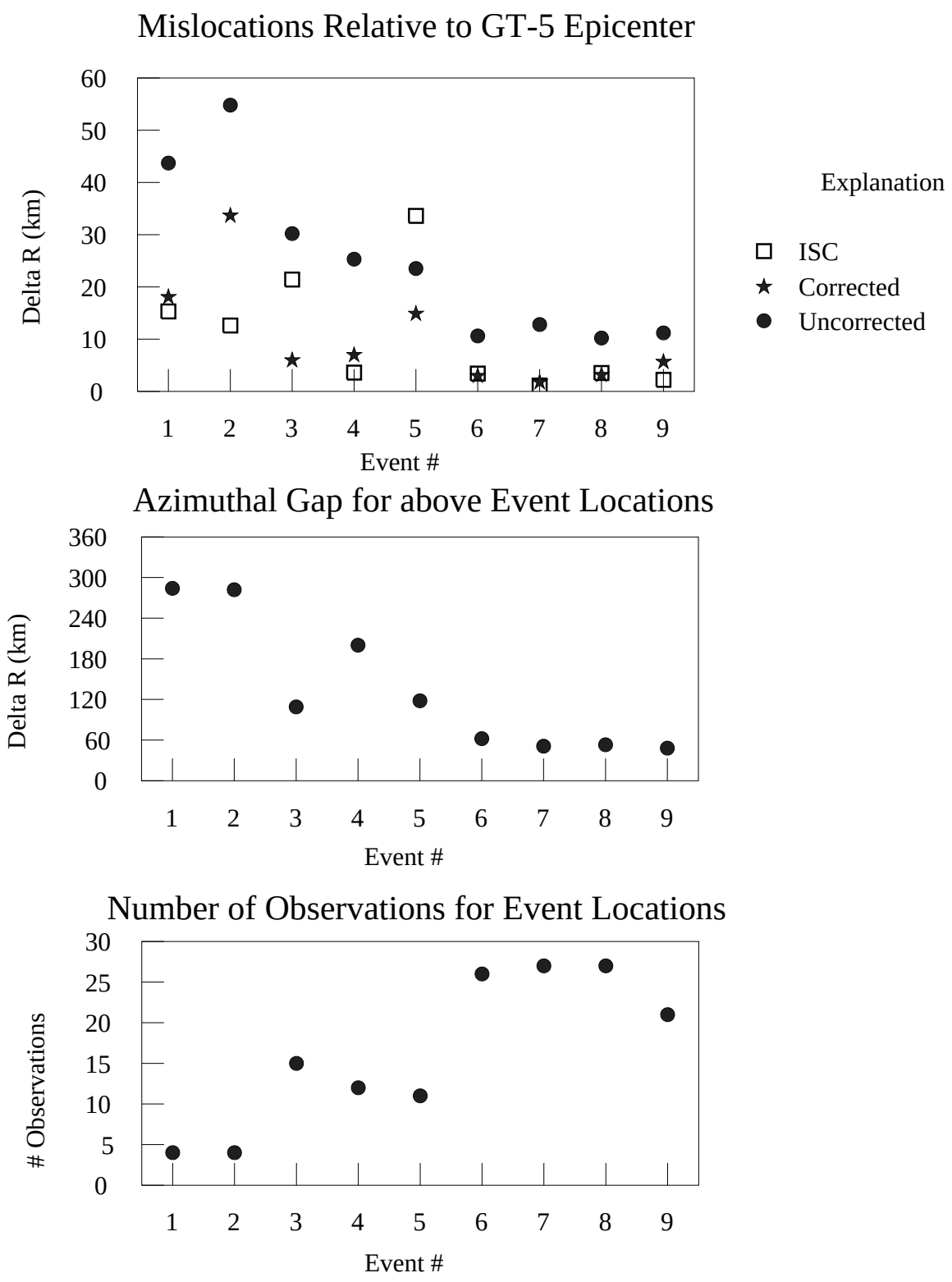


Figure 2. (top) Comparison of locations relative to GT-5 epicenters for regional corrected (star), uncorrected (circle), and ISC (open square) values; (middle) maximum azimuthal gap for the above regional locations; (bottom) number of observations used for the above regional locations

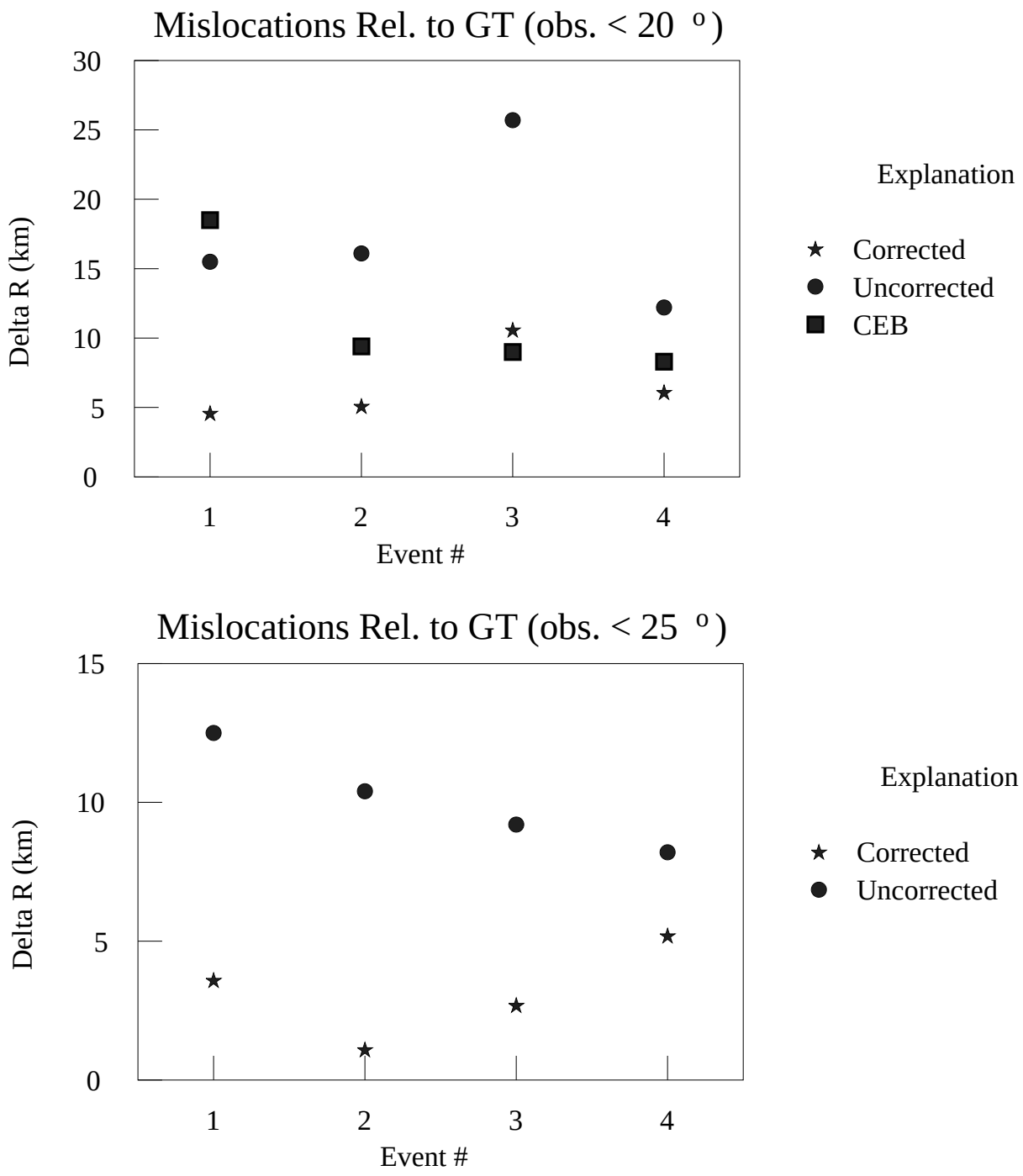


Figure 3. Comparison of locations relative to GT-5 (ISC) epicenters for regional corrected (star), uncorrected (circle), and CEB (square) values; the top figure is for locations using observations within 20^{o}, while the bottom figure is for locations using observations within 25^{o}.

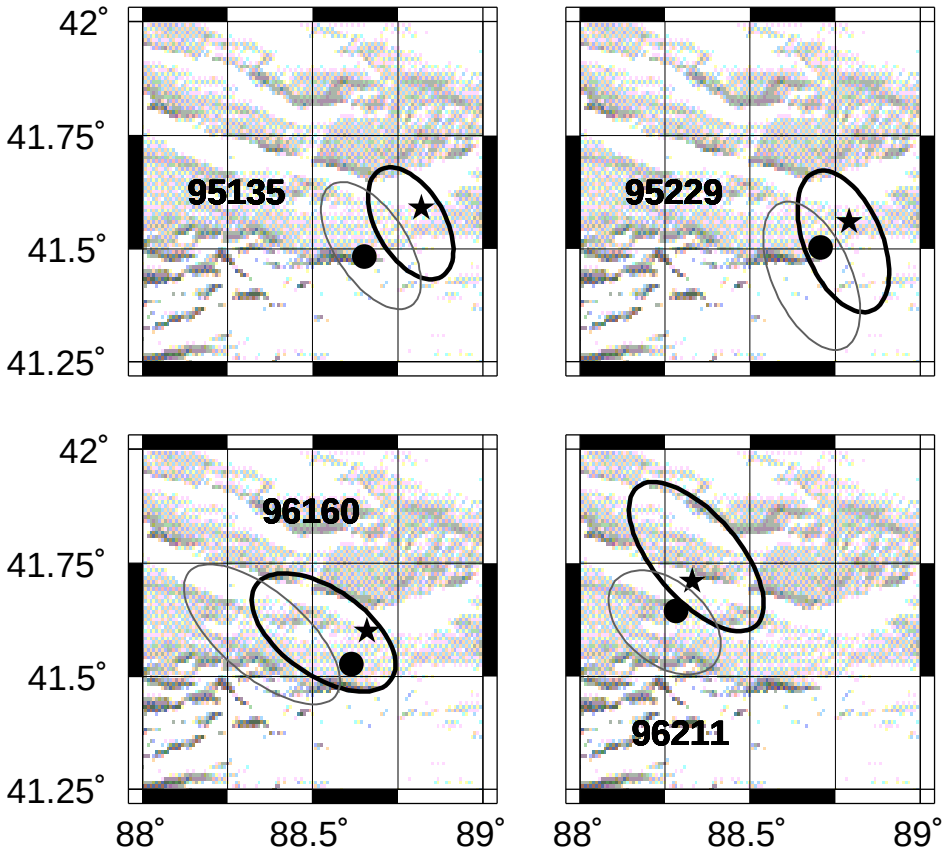


Figure 4. Map projections of ISC (star) and CEB (circle) locations, along with the corrected (thicker, darker line) and uncorrected (thinner, lighter line) regional ($\Delta<20^{o}$) location 90% confidence-level error ellipses, for 4 Lop Nor explosions (Julian date is given in each panel). The ISC locations were taken as GT for the purpose of determining the SSSC's used in the corrected regional locations.

EXCITATION AND ATTENUATION OF REGIONAL WAVES, AND MAGNITUDE DEPENDENCE OF PN/LG RATIOS IN EASTERN EURASIA

Jiakang Xie, Lamont-Doherty Earth Observatory of Columbia University

Sponsored by The Defense Threat Reduction Agency
Contract No. DSWA01-98-1-0006 and DSWA01-98-1-0009

ABSTRACT

In the past one and half years I have been processing large amount of regional/teleseismic data from IRIS, CDSN, GBA, Kyrghizstan and Kazakhstan network stations in eastern Eurasia. Fourier spectra of Pn, Lg and Pg waves were computed for many events/paths to study characteristics of seismic sources and path attenuations. Estimations of source spectral parameters and path attenuation were difficult for all wave types. I have used various methods to tackle the difficulties, including the standard two-station method for Q measurement, the reversed two-station method of Chun et al. (1987) for Q measurement, the empirical Green's function method for measuring source rise times, and the simultaneous Bayesian inversion method for source-path spectral parameters by Xie (1993, 1998, 1999).

It is well known that seismic source parameters, such as magnitude, seismic moment and corner frequency tend to scale with one another. Xie and Patton (1999) obtained details of these scalings for each wave types (Pn and Lg), and source types (underground nuclear explosions and earthquakes) in central Asia. These scalings, and an spectral overshoot in explosion-excited Pn and Lg waves, make the Pn/Lg spectral ratios from explosions differ from those from earthquakes in a frequency-dependent manner. For a given event size, there is a frequence band in which the Pn/Lg spectral ratios from both source types differ the most, resulting in an optimal frequency band for the ratios to be used for a discrimination purpose. This optimal frequency band is dependent on the corner frequencies derived using Pn and Lg. For events with smaller magnitudes or seismic moments, the Pn and Lg corner frequencies become higher, causing the optimal frequency band to shift higher.

Until recently, the analyses of explosions in central Asia were conducted only for a limited magnitude range (about 5.0 to 6.0). A new analysis have been conducted using data from a large Lop Nor explosion (mb=6.6 on May 21, 1992) and a small Kazakhstan explosion (mb=3.8 on Aug. 22, 1998). Special efforts have been made to make Q estimates in this and previous analyses consistent with each other. The new analysis validates the previously proposed source spectral scaling relationships and the magnitude dependence of Pn/Lg spectral ratios in a wider magnitude range. Observed Pn/Lg ratios from the two new explosions clearly support the magnitude dependence of the Pn/Lg ratio. In particular, they show that attempts of discriminating explosions from earthquakes using Pn/Lg spectral ratios, when the magnitude dependence is ignored, may fail. Since the spectral scalings and spectral overshoot are expected to hold for other high-frequency phases, a magnitude dependence should also be present for other types of phase spectral ratios.

Key Words:Seismic Sources, Q, Eastern Eurasia, Explosion Discrimination, P/Lg ratios

OBJECTIVE

There are two ultimate objectives of this research: (1) We wish to quantify path attenuation of regional waves in continental areas, such as Eurasia, by developing digital, tomographic Q maps. (2) We wish to quantify the difference in the excitations of various regional waves, so that we may achieve better, quantitative understanding and criterion of the P/Lg spectral ratio discriminant of explosions. There proposed research is composed of several tasks. The first is to further improve the inverse method for simultaneous determination of source seismic moment (M_0), corner frequency (f_c) and path-variable Q_0 and η (Q at 1 hz and its power-law frequency dependence, respectively) using regional wave spectra. The second task is to apply the improved inverse method to Lg, Pn, Pg and Sg spectra from many earthquakes and explosions in Eurasia to estimate source M_0, f_c and path Q_0, η. The third task is input the measured Q values to a computerized tomographic algorithm, to obtain laterally varying Q maps for Lg and other regional waves. The fourth task is analyze source spectral scaling and other source spectral characteristics of seismic events, such as the amount of spectral overshoot of explosions, to explore when, how and why the P/Lg spectral ratios can be used to discriminate explosions from earthquakes.

This research provides important input to the implementation of a Comprehensive Nuclear-Test-Ban Treaty. The tomographic Q maps can be used for the calculation of source spectral characteristics of any future seismic event to infer the nature and size of the event. These Q maps can also be used for estimating the detection threshold of the existing seismic stations located within the area studied. The source spectral behavior inferred from this study will help to understand if, when and how the P/Lg amplitude ratio can be used to discriminate explosions from earthquakes.

RESEARCH ACCOMPLISHED

Processing of Lg, Pg and Pn spectra in eastern Eurasia

In the past one and half years I have been processing large amount of regional/teleseismic data from IRIS, CDSN, Kyrghizstan, Kazakhstan and GBA network stations in eastern Eurasia. Fourier spectra of Pn, Lg and Pg waves were computed for many events/paths to study characteristics of seismic sources and path attenuations. Fig. 1 shows the path coverage by these spectra.

The spectra have been used to derive path-variable Q at 1 Hz and its power-law frequency dependence, as well as source spectral parameters for each wave type. It is well known that estimations of source spectral parameters and path Q were difficult. I have used various methods to tackle the difficulties, including (1) the standard two-station method for Q measurement, (2) the reversed two-station method of Chun et al. (1987) for Q measurement, (3) the empirical Green's function method for measuring source rise times which can be converted to corner frequencies, and (4) the simultaneous Bayesian inversion methods for source-path spectral parameters by Xie (1993, 1998, 1999). Examples of applications of methods (2), (3) and (4) are shown in Figs. 2 through 4.

The magnitude dependence of Pn/Lg ratios

Xie and Patton (1999; here after referred to as XP99) developed source spectral scaling relationships for the excitations of Pn and Lg by underground nuclear explosions and

earthquakes in central Asia. Interesting features of these source spectral scalings include that (1) for explosions, seismic moments estimated using Pn are systematically larger than those estimated using Lg, (2) for both explosions and earthquakes Pn corner frequencies are systematically higher, by a factor of 3-4, than the Lg corner frequencies at the same moment level; (3) both Pn and Lg excitations by explosions exhibit spectral overshoot, whose effect appears to be more pronounced for Pn than for Lg. These features make the Pn/Lg spectral ratios from explosions differ from those from earthquakes at any fixed magnitude level in a frequency-dependent manner. As shown in Figs. 11 and 12 of XP99, at lower frequencies the Pn/Lg ratios from explosions tend to be higher than those from earthquakes at the same magnitude, but the difference can be relatively small. In a intermediate frequency range the Pn/Lg ratios from both explosions and earthquakes grow with frequency, but the growth is faster for the ratios from explosions than those from earthquakes. As a result, the Pn/Lg ratios from the two source types become more separated. Beyond certain high frequency limit the Pn/Lg ratios from both source types stop to grow, and the separation remain roughly unchanged with increasing frequency. Therefore there is a frequence band in which the Pn/Lg spectral ratios from explosions differ the most from those from earthquakes, resulting in an optimal frequency band for the ratios to be used for a discrimination purpose. This optimal frequency band is dependent on the corner frequencies derived using Pn and Lg. For events with smaller magnitudes or seismic moments, the Pn and Lg corner frequencies become higher, causing the optimal frequency band to shift higher.

A limitation of the work by XP99 is that the explosions used only cover a limited magnitude range (about 5.0 to 6.0). A new analysis have been conducted using data from a large, "megaton" Lop Nor explosion (mb=6.6 on May 21, 1992) and a small Kazakhstan explosion (mb=3.8 on Aug. 22, 1998). Fig. 5 shows locations of these two explosions. Q values have been obtained by XP99 for paths between the Lop Nor test site and KNET stations, and for the two-station path between stations MAK and KURK. The latter path runs very close to the path between the Kazakhstan explosion and station MAK in Fig. 5. Therefore I can use the Q values obtained in XP99 as a priori knowledge to inversions of the two new explosions, and avoid complications caused by inconsistent path Q corrections.

I obtained M_0, f_c values for Pn and Lg from both new explosions. Figs. 6 and 7 show the new scalings developed by adding these new values:

$$\log M_0 = 9.70(\pm 0.25) + 1.13(\pm 0.04)\, m_b \quad \text{for } Pn \text{ from explosions}, \tag{1}$$

$$\log M_0 = 9.26(\pm 0.45) + 1.12(\pm 0.07)\, m_b \quad \text{for } Lg \text{ from explosions}; \tag{2}$$

$$\log M_0 = 18.16(\pm 0.36) - 4.33(\pm 0.44) \log f_c \quad \text{for } Pn \text{ from explosions}; \tag{3}$$

$$\log M_0 = 15.18(\pm 0.22) - 3.80(\pm 0.26) \log f_c \quad \text{for } Lg \text{ from explosions}. \tag{4}$$

Note scaling relationships in equations (1), (2), (3) and (4) differ only slightly from the respective scalings (equations (16), (17), (20) and (21)) in XP99, developed without the two new explosions. Thus the analysis of the new explosions validates spectral scaling relationships in XP99. In Fig. 8, I replot the statistically expected Pn/Lg spectral ratios for different source types and magnitudes over an generic central Asian path, first shown in XP99 (Fig. 12), and the observed Pn/Lg spectral ratios for explosions and earthquakes in XP99. The statistical simulation fits the observation very well. Pn/Lg ratios for the newly analyzed, "megaton" and 100-ton explosions are also shown in Fig. 8 (thick curves in grey). These ratios are the observed ratios corrected for the new path-avaraged Q values that differ from those of the generic path. As

predicted by the scaling relationships, the two new ratios are similar in shape to the previous ratios from explosions, but are shifted along the frequency axis toward lower frequencies and higher frequencies for the "megaton" and 100-ton explosions, respectively, owing to the lower and higher f_c values.

Interestingly, between 1 and 10 Hz the 100-ton ratio in Fig. 8 falls into the earthquake population of XP99 because of the magnitude dependence. This is a good example of how ignoring the magnitude dependence can cause a false event identification using the Pn/Lg spectral ratio.

CONCLUSIONS AND RECOMMENDATIONS

I have been processing spectra of Pn, Pg and Lg waves from numerous paths in eastern Eurasia. When complete, the spectra will be used to invert for path-variable Q values and source M_0 and f_c values for the events involved. These will be used for tomographic regionalizations of Q, and for deriving or modifying source scaling relationships for explosions and earthquakes.

New analysis of a large, "megaton" and a small, hundred-ton explosions validated the source spectral scalings for explosions by Xie and Patton (1999) in a much wider magnitude range, and confirmed the magnitude-dependence of Pn/Lg ratio from explosions. I have demonstrated clearly that attempts of discriminating explosions from earthquakes using Pn/Lg spectral ratios, when the magnitude dependence is ignored, may fail. Since the spectral scalings and spectral overshoot are expected to hold for other high-frequency phases, a magnitude dependence should also be present for other types of phase spectral ratios in central Asia. At least for that region, future discrimination should incorporate the magnitude dependence. Future work using similar methodology is needed to see whether the magnitude dependence is a generally phenomenon in other continental areas.

References

Chun, K. G.F. West, R.J. Kokoski and C. Samson, 1987. A novel technique for measuring Lg attenuation - Results from eastern Canada between 1 to 10 Hz, *Bull. Seism. Soc. Am.*, **77**, 398-419.

Xie, J. 1993. Simultaneous inversion of source spectra and path Q using Lg with applications to three Semipalatinsk explosions, *Bull. Seism. Soc. Am.*, **83**, 1547-1562.

Xie, J., 1998. Spectral inversion using Lg from earthquakes: Improvement of the method with applications to the 1995, western Texas earthquake sequence, *Bull. Seism. Soc. Am.*, **88**, 1525-1537.

Xie, J., 1999. Excitation and attenuation of regional waves from recent seismic events in China, *Proc. 21st Seis. Res. Symposium: Technologies for Monitoring the Comprehensive Test Ban Treaty*, U.S. Dept. of Defense and U.S. Dept. of Energy, LA-UR-99-4700, pp. 323-332.

Xie, J. and H. Patton, 1999. Regional Phase Excitation and Propagation in the Lop Nor Region of Central Asia and Implications for the Physical Basis of P/Lg Discriminants, *J. Geophys. Res.*, **104**, 941-954.

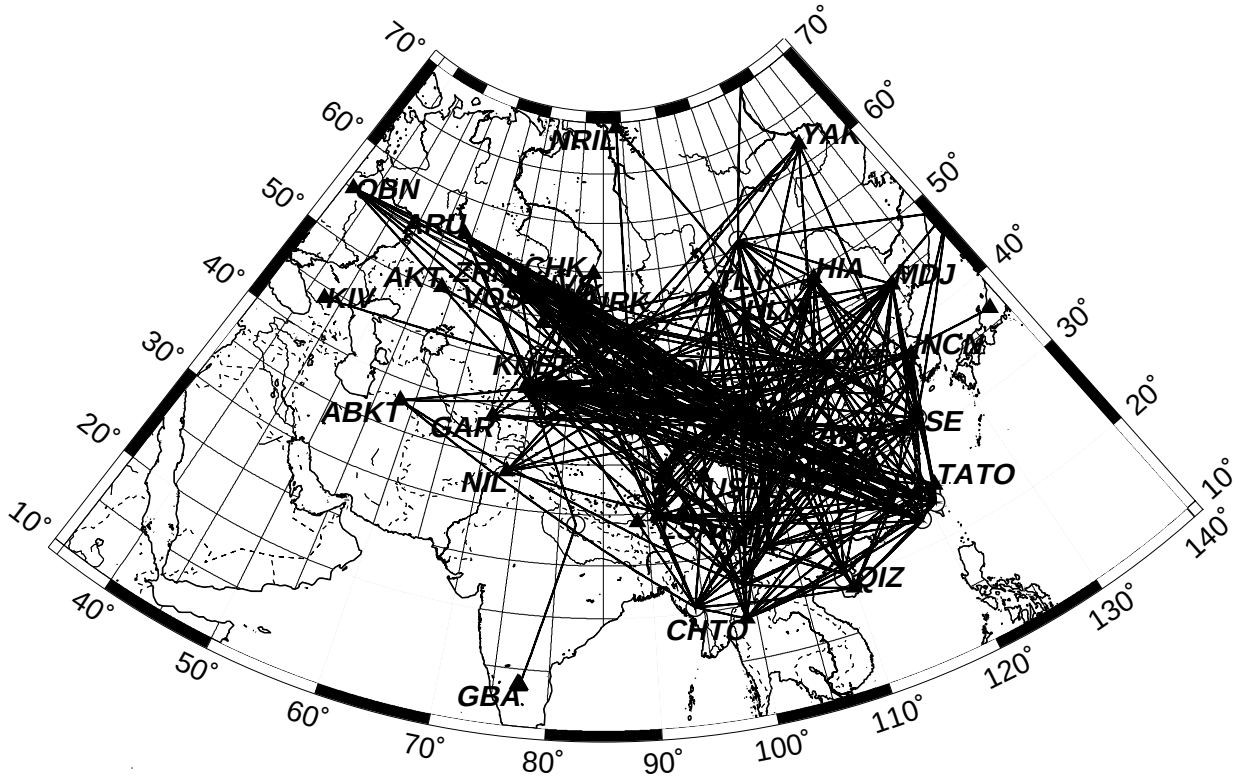


Fig. 1. Map showing path coverage by Lg, Pg and Pn spectra obtained in this study as of July, 2000.

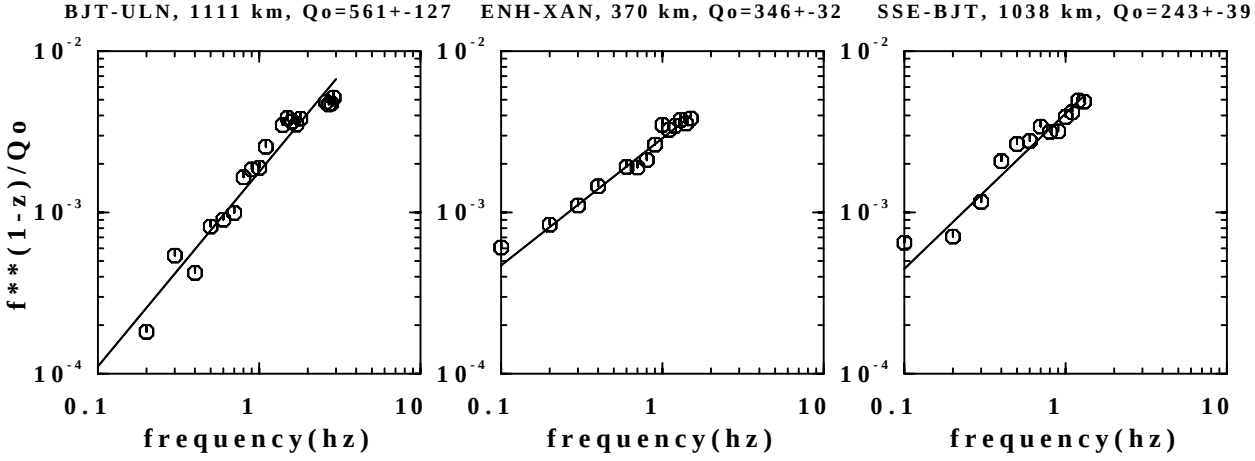


Fig. 2. Examples of inter-station Lg Q measurements using reversed two-station spectral ratios (Chun *et al.*, 1987). Station pair, inter-station distance and Q_0 values are indicated on the top of the panels.

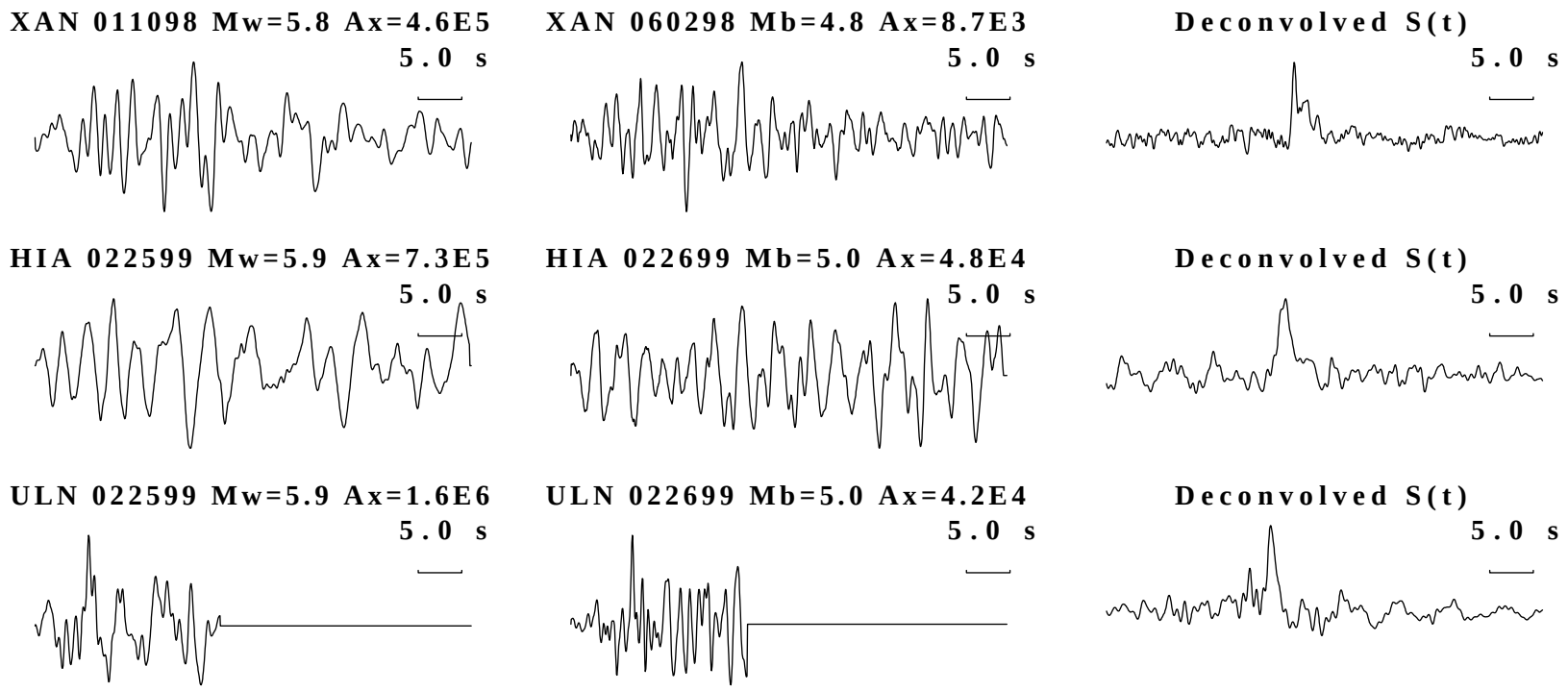


Fig. 3. Examples of the empirical Green's function (EGF) deconvolution. Each row shows Lg waveforms from a pair of large and small (EGF) events, observed at the same station (left and middle traces, respectively), and the deconvolved trace (right trace) from which a rise time can be measured. Station name, event date, event M_W or M_b and maximum amplitude in digital count are indicated on the top of the Lg waveforms. The epicentral distances involved are (from top to bottom rows): 956.4 km (XAN to 011098) 1087.4 km (HIA to 022599) and 445.1 km (ULN to 022599).

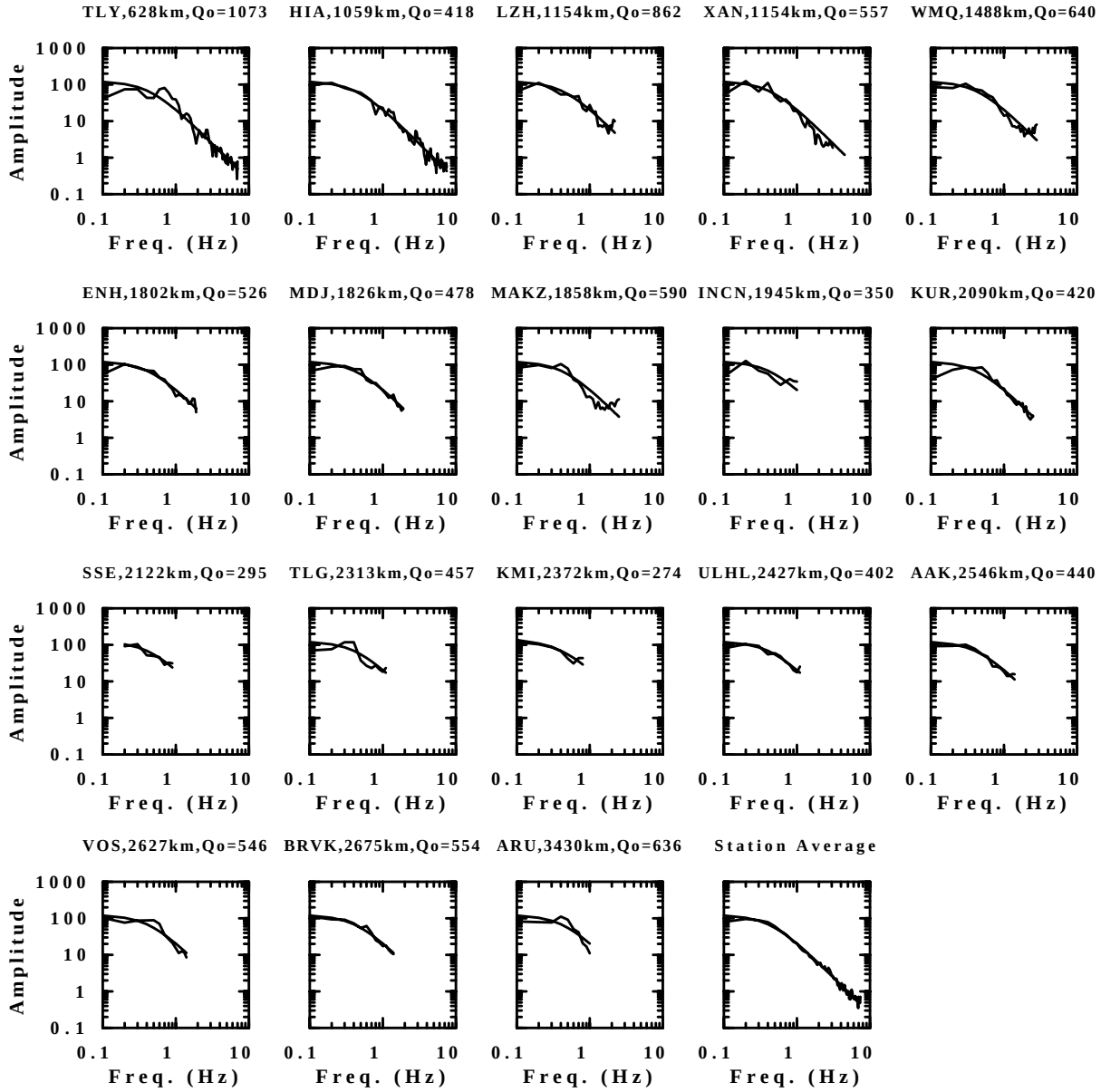


Fig. 4. Synthetic Lg source spectra for 18 broad-band stations recording the 09/24/98 Mongolian earthquake, versus the observed. The lower right panel is the station average. The synthetic spectra are calculated using the best-fit source model of ($M_0 = 1.26 \times 10^{17}$ N m, $f_c = 0.44$ Hz), obtained during the inversion with the Bayesian method (Xie, 1993, 1998, 1999). Station code, distance and Q_0 values obtained during the inversion are written on the top of the panels. The observed source spectra are ground motion spectra with the effects of path Q removed. The unit of the amplitude is the same as that of Figure 7 of Xie (1998).

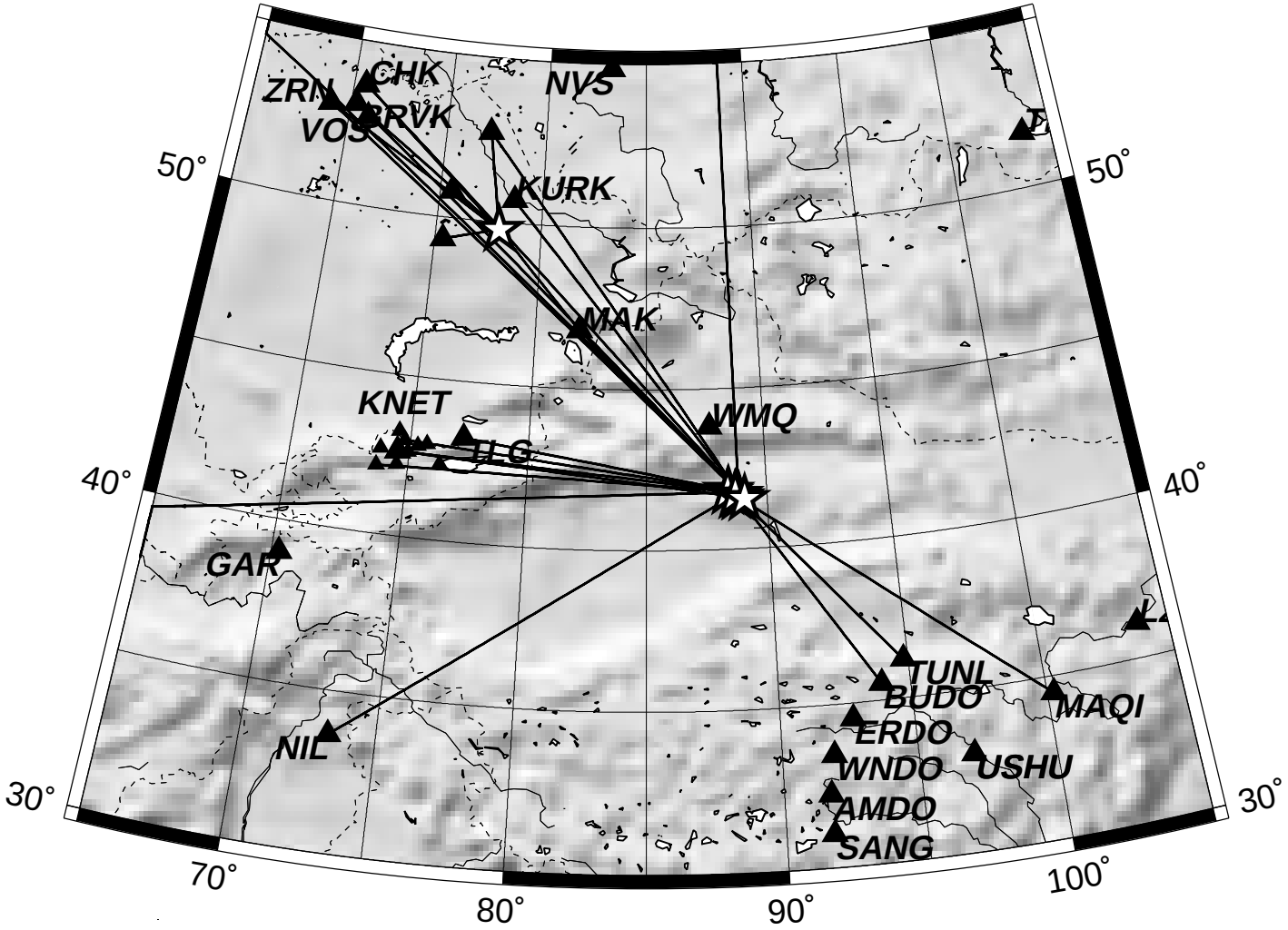


Fig. 5. Locations of the explosions in the Lop Nor and Kazakhstan test sites (stars) and recording stations (triangles). Stations in the southeast portion of the map are temporary stations deployed in the Tibetan Plateau Passcal experiment (1991-1992). Note that the path from the 100-ton, Kazakhstan explosion (star just south of station KURK) to station MAK runs very close to the two-station path between KURK and MAK in Xie and Patton (1999).

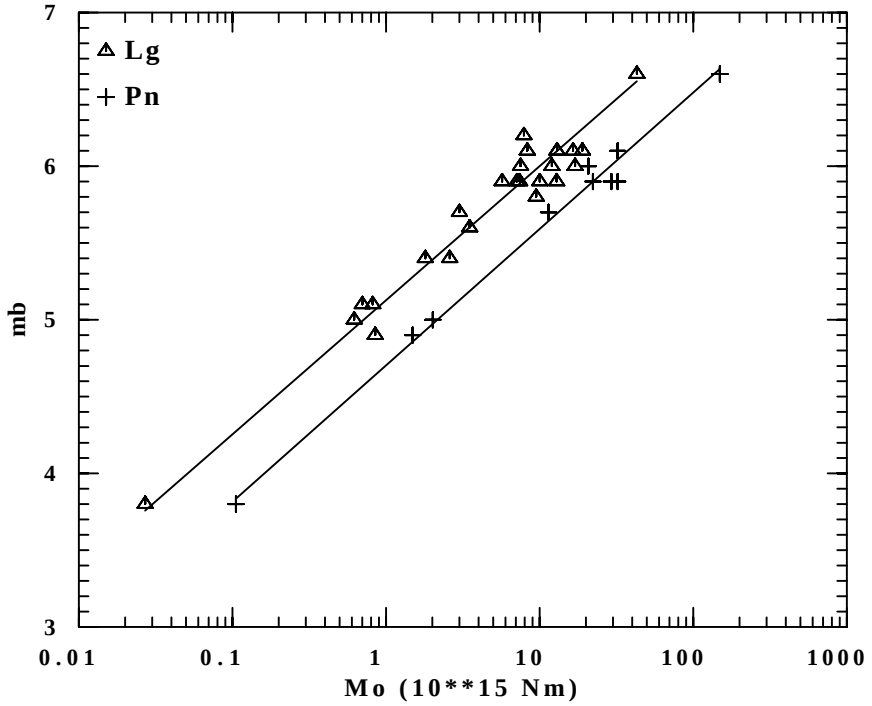


Fig. 6. m_b versus logarithm of M_0 for explosions in central Asia. Results for the 052192, "megaton" and 082298, 100-ton explosions are included, expanding the magnitude range of a previous study by Xie and Patton (1999, Fig. 7).

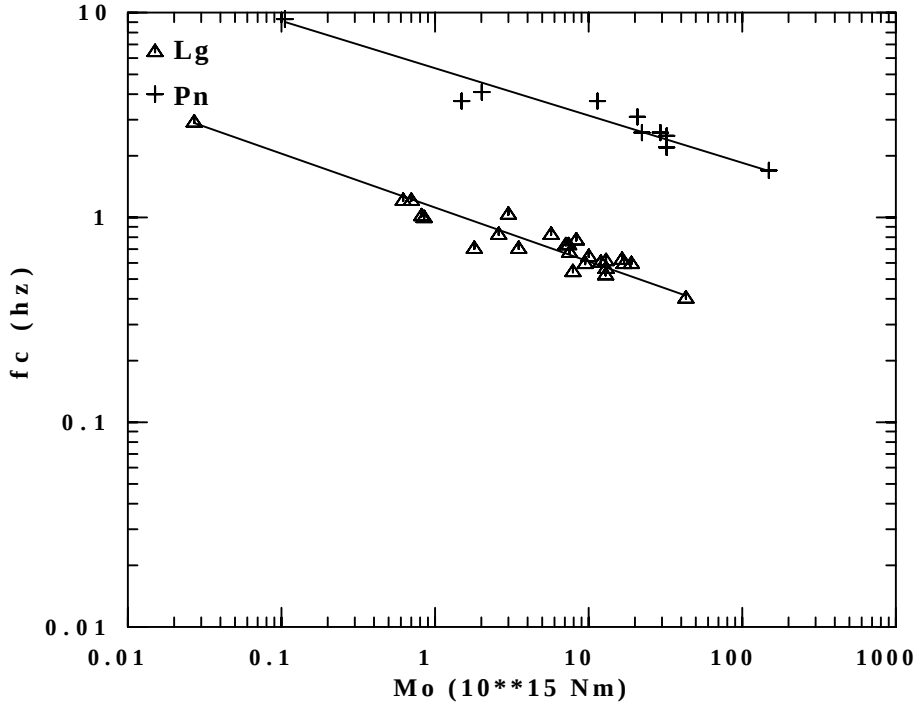


Fig. 7. f_c versus M_0 for explosions in central Asia. This figure is an expansion of Fig. 9 of Xie & Patton (1999) by adding M_0 and f_c values of the "megaton" and 100-ton explosions.

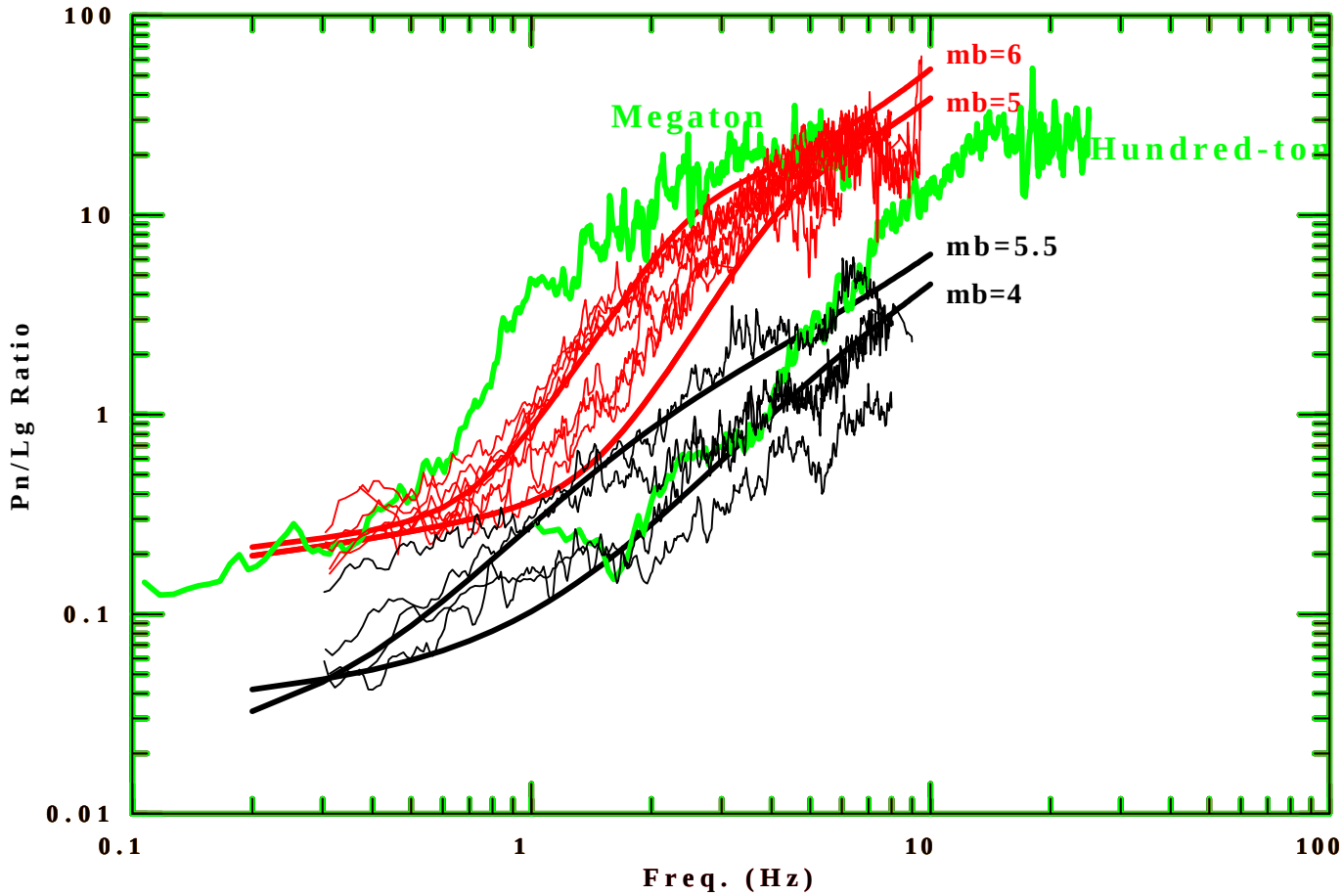


Fig. 8. Pn/Lg spectral ratios. Thick smooth curves are statistically predicted ratios using the source scaling relationships and generic path Q_{Lg} and Q_{Pn} models, for explosions with two m_b values (6 and 5) and earthquakes with two m_b values (5.5 and 4), respectively. Thin, fluctuating curves are the observed ratios for explosions and earthquakes obtained by Xie & Patton (1999, Fig. 12). Thick grey curves are observed ratios from the 052192, "megaton" and 082298, 100-ton explosions. The latter curve is corrected for its Q_{Lg} and Q_{Pn} values that differ from the generic path.

MAXIMUM SPECTRAL ENERGY ARRIVAL TIME OF RAYLEIGH WAVES FOR ACCURATE EPICENTER DETERMINATION AND LOCATION ERROR REDUCTION

Nazieh K. Yacoub
Research Division, Nuclear Treaty Monitoring Directorate
Air Force Technical Applications Center

ABSTRACT

Maximum spectral energy (MSE) is defined as the most energetic signal in prescribed frequency and velocity windows characteristic to a seismic phase and is computed by means of the Fast Fourier Transform (FFT) and the Multiple Filter Analysis (MFA). MSE arrival times for Rayleigh waves are computed in the period window 17 to 23 seconds and in the velocity window 2.8 to 3.2 kilometers/second (km/sec). These arrival times and a constant velocity model of 3.0 km/sec are used in a hypocenter computer program to evaluate location error, *i.e.*, mislocation vector.

Epicenter locations for selected nuclear explosions from the Nevada Test Site (NTS) are determined by the Rayleigh waves MSE arrival times. The same explosions are also located by the conventional P-wave first-break arrival times, listed in the International Seismic Center (ISC) Bulletin. Explosion selection is restrained by the availability of both arrival times from the same set of stations common to each explosion. This limited the study to only seven nuclear explosions; each has 12 or more digital seismograms with corresponding P-wave first-break arrivals listed in the ISC Bulletin. The study is confined to NTS explosions, since for these there are published locations against which to compute the location errors. All such errors of epicenter location computed from MSE arrivals are less than those of epicenter locations from first-break arrivals. The location error for the seven explosions, calculated by the MSE arrivals, is half that calculated by the P-wave first-break arrivals.

INTRODUCTION

The conventional seismic event location is based on measuring the arrival times of impulsive phases with sharp, clear onsets at several stations. The goodness of a determined epicenter depends on factors including the velocity model, the sharpness for the P-wave first break, and the accuracy of measuring the first break onset time. Velocity models are subject to error due to the unaccounted variations of geological structures and rock physical properties along the propagation path. Such variations are more apparent at regional distances where the body wave path is confined to the earth's crust, as pointed out by Herrin and Taggart (1962). At teleseismic distances velocity variations over the propagation path are minimized for body waves because of the short distances travelled by these waves in the earth's crust. This facilitated the development of global travel time tables for body-waves, such as the IASPEI (International Association of Seismology and the Physics of the Earth's Interior) Tables, Herrin 68-Tables, JB (Jeffrey-Bullen) Tables, etc. The availability of these tables makes teleseismic body waves the primary tool for locating seismic events.

Surface waves, and some regional phases, are non-impulsive and propagate along or through the earth with nearly constant velocities much slower than P-wave velocities. For surface focus seismic sources, the apparent P-wave velocity ranges from 8.2 to 24.4 km/sec in the distance range 10 to 100 degrees. These velocities are 3 to 8 times faster than the 3.0 km/sec of Rayleigh waves propagating through continental and shallow oceanic crusts. A similar argument applies to Love waves. The Lg regional phase travels with a velocity of about 3.5 km/sec (Nuttli, 1972, and Ewing *et al.*, 1957), which is less than half the apparent velocity for P-wave at 10 degrees. The constant and low velocities of these phases simplifies the location procedure. However, these phases show no onset time and cannot be used for epicenter determination by current methodologies.

The first attempt to locate seismic events using Rayleigh waves was done by von Seggren (1970). By cross-correlating a Rayleigh wave train with another Rayleigh wave train of a well-located event (reference event) from the same region, he was able to determined the relative travel-time based on the correlation trace peak. He used three pairs of US nuclear explosions: Jorum-Boxcar, Faultless-Boxcar, and Milrow-Long Shot. For example, the mislocation vector magnitude for the Boxcar explosion using the Jorum explosion as the reference event is 34.4 km based on Rayleigh waves, and 29 km based on body waves which was reduced to 8.3 km by using relative travel times, *i.e.*, travel time residuals. Similar results were obtained for the other pairs.

A timing method is proposed that replaces onset arrival times in the hypocenter determination procedure with the arrival times for seismic signal amplitudes. These amplitudes are functions of the source's energy, and are used in detection, source characterization, magnitude measurement, attenuation, etc., but not in source location. MSE reflects the most energy for a seismic phase, and is measured within its characteristic frequency and velocity

windows. Yacoub (1982) used amplitude averaging for the maximum energy of Rayleigh waves within the period range 17 to 23 seconds to estimate Rayleigh wave spectral magnitudes. Although the method was successful in magnitude estimation, as reflected by the reduction in the network magnitude standard deviation, the arrival times for these averaged magnitudes failed to reduce the location error. Yacoub (1994a, 1996, and 1998b) forsakes amplitude averaging for the most energetic signal in frequency and velocity windows characteristic to the seismic phases. This proved to be successful in measuring Rayleigh wave spectral magnitudes which showed lower network magnitude standard deviation than the corresponding time domain magnitude, M_S (Yacoub, 1998b). MSE was also successful in locating nuclear explosions using Rayleigh waves (Yacoub, 1994b, 1996, and 1999), and P-waves (Yacoub, 1997, 1996, and 1998b). The average location error against the ground truth computed by the spectral timing, either for Rayleigh wave or for P-waves, is reduced to half that computed by P-wave first-break timing.

Seven nuclear explosions, from NTS, are located using arrival times for the Rayleigh wave maximum energy, assuming constant velocity model of 3 km/sec. These explosions are located by the conventional method using P-wave first-break arrival times listed in the ISC Bulletin, and the Herrin (1968) travel-time tables for surface focus. In both methods of timing the location parameters are determined by the same computer program for epicenter estimation using arrival times as recorded by stations from the World Wide Seismic Station Network (WWSSN), Global Seismic Network (GDSN), and the Canadian Seismic Network (CSN).

MAXIMUM SPECTRAL ENERGY

Maximum spectral energy is defined as the most energetic signal in prescribed frequency and velocity windows which uniquely characterize a seismic phase. For example, the P-wave energy peaks in a bandpass 0.7 to 1.4 Hertz (Hz), and in a velocity window ±3 to 5 seconds from P-wave travel-time table predicted arrival. For the regional Lg phase, the energy peaks in a frequency window 0.8 to 1.2 Hz, and a velocity window 3.4 to 3.6 km/sec (Nuttli, 1972, and Ewing *et al.*, 1957). For the Rayleigh and the Love waves, the energy peaks in a period range 17 to 23 seconds, and a velocity window 2.8 to 3.2 km/sec for Rayleigh waves, and 3.3 to 3.7 km/sec for Love waves (Yacoub, 1998b).

MSE is computed by means of the Fast Fourier Transform (FFT) and the Multiple Filter Analysis (MFA), developed by Dziewonski *et al*. (1969). MFA is performed by passing seismogram spectra through a set of narrow-band Gaussian filters at selected center frequencies within the frequency window for the seismic phase. Inverse Fourier Transform (IFT) is applied to each center frequency which produces a complex time domain function. The sum of the squares for the real and the imaginary parts defines the spectral energy. The most of these energies is the maximum energy for the center frequency of the Gaussian filter, and the maximum of these maxima characterizes the MSE whose arrival time is computed and, is used in the hypocenter location.

VELOCITY MODEL

Reliable velocity models are required to locate seismic sources. Since body waves are the primary phase for seismic location, their velocity models are continuously updated with the availability of new data. However, this is not the case with surface waves. The most extensive work done to establish global group velocity models is the classical work by Oliver (1962), which is based on earthquake-generated surface waves. He showed that in the period range 17 to 23 seconds Rayleigh waves travel with a group velocity of 3.0 km/sec through continental crusts and 3.5 km/sec through oceanic crusts.

Yacoub (1994a) used Multiple Filter Analysis techniques to study velocity and frequency characteristics of surface waves maximum spectral energy. Over 5000 long period digital seismograms generated by 215 nuclear explosions at US, Peoples Republic of China (PRC), and the former Union of Soviet Socialist Republics (USSR) test sites were processed. These seismograms are recorded by stations from the WWSSN, the CSN, GDSN, and the US Atomic Energy Detection System (USAEDS). The study showed that maximum spectral energy propagates with a velocity between 2.8 and 3.2 km/sec for Rayleigh waves and between 3.3 to 3.7 km/sec for Love waves, and occurs in the period range 17 to 23 seconds for both waves with the energy dropping by more than an order of magnitude outside the period window 15 to 30 seconds. Propagation paths, for these waves, cover the Northern Hemisphere and cross most types of crustal structures with the exception of very deep oceanic crusts. Yacoub (1998b) developed a travel time curve for Rayleigh waves that propagated in continental, tectonic, and oceanic crusts. Figure 1 shows an azimuthal-equidistant projection for some of the stations used and their great circle paths from NTS. Note the various crustal structures crossed by the propagation paths. The travel time distance scatter diagram, shown in Figure 2, is based on 500 arrivals generated by nuclear explosions at various test sites. The correlation model, where both variables have equal error, gives a slope of 3.0 ± 0.017 km/sec, which is an average group velocity for all paths, including paths shown in Figure 1. The correlation coefficient for the data is 0.998, which is reflected by the low scatter around the correlation line. Note that the scatter of the data around the correlation line is very small at distances below 4000 km and becomes more

pronounced beyond that distance. The increase in the scatter could be attributed to multipath effect or propagation in higher velocity layers, or both, since it is equally distributed on both sides of the correlation line.

EPICENTER DETERMINATION

Rayleigh wave long period digital seismograms, for selected nuclear explosions from the NTS, are processed to compute the arrival times of their MSE, within the period window 17 to 23 seconds and the velocity window 2.8 to 3.3 km/sec. The same explosions are located by the conventional P-wave first-breaks arrival times, listed in the ISC Bulletin. Explosion selection is conditioned by the availability of P-wave arrival times and digital LP seismograms from the WWSSN, CSN, and GDSN common to each explosion. This limited the study to only seven nuclear explosions; each has 12 or more digital LP seismograms with corresponding P-wave first-break arrivals. The study is confined to NTS explosions, since for these there are published locations against which to compute the location errors.

These arrival times are used in a hypocenter computer program to determine the source epicenter. Velocity models used by the program are a constant velocity model of 3.0 km/sec for Rayleigh wave location and the Herrin (1968) Travel Time Tables for P-wave location. In cases for stations with large travel time residuals for either P- or Rayleigh-waves, the station is restrained from both data sets to maintain identical networks. Following is an example of epicenter determination.

The Hearts nuclear explosion, 6 September 1979, Yucca Flat, NTS, has 42 digital seismograms. Twenty of these have first-break arrival times listed in the ISC Bulletin. However, one station, ALE, was rejected by the program because of high residuals, so the station is restrained from both solutions. Figure 3a depicts a sample of the original seismograms from stations PHC, STJ, KBS, and KEV. Plotted on the seismograms are the velocity window 2.7 to 3.3 km/sec and the 3.0 km/sec Rayleigh waves velocity marker. This sample represents a typical dispersed Rayleigh wave, shown by PHC, and highly contaminated seismograms as shown by the rest of the seismograms. The use of these noisy seismograms demonstrate the robustness of the MFA to extract the proper signal and allow for measuring the arrival time for the maximum spectral energy as depicted in Figure 3b. This figure shows the filtered seismogram at the period with the most energy. The arrival time for maximum spectral energy is annotated above the red inverted arrow, on top of the velocity window box. Azimuthal distribution for the network is shown in Figure 4a, and Figure 4b depicts the mislocation vector for the determined epicenters. The ground truth is shown with the red star, P-wave determined epicenter and the mislocation vector are shown by the green square and the green line, respectively, and the MSE determined epicenter and the mislocation vectors are shown by blue circle and blue line, respectively. The location error is 18.32 km for the P-wave onset timing, and 11.15 km for Rayleigh waves MSE timing.

Figures 4, 5, 6, 7, 8, and 9 depict in a similar manner the results for the determined epicenters for nuclear explosions Backbeach, Scantling, Lowball, Mizzen, Strake, and Sheepshead.

RESULTS

Results for Rayleigh wave and P-wave location errors for the seven explosions are shown in Table 1 and by the bar chart in Figure 10. The table and the figure depict the mislocation vector magnitudes between the determined epicenters and the actual locations as determined from Rayleigh wave MSE timing and P-wave onset timing. The location error determined from Rayleigh wave MSE timing shows a reduction in the location error of between 40 to 70 percent of that determined from P-wave first-break timing. On the average the mislocation vector magnitude determined by the Rayleigh wave MSE timing is 13 km, and that determined by P-wave onset timing is 29 km, which is about a 55-percent reduction.

CONCLUSIONS

Robustness of the maximum spectral energy timing method for Rayleigh wave seismic location is manifest in its consistently greater location accuracy compared to the P-wave onset timing method.

Maximum spectral energy arrival times allow for the use of non-impulsive phases such as Rayleigh waves to locate epicenters without resort to the relative location method.

ACKNOWLEDGMENTS

The author expresses his thanks to Dr. Eugene Smart for his encouragement and editorial comments.

REFERENCES

Anstey, N.A. (1977). *Seismic Interpretation: The Physical Aspects*, The International Human Resources Development Corporation, Boston, 625pp

Dziewonski, A., S. Block, and M. Landisman (1969). A technique for analysis of transient seismic signals, *Bull.*

Seism. Soc. Am. **59**, 427-444.
Farnbach, J.S. (1975). The complex envelope in seismic signal analysis, *Bull. Seism. Soc. Am.* **65**, 952-961.
Ewing, W.M., W.S. Jardetzky, and F. Press (1957). *Elastic Waves in Layered Media*, McGraw-Hill, New York. 380 pp.
Herrin, E., and J. Taggart (1962). Regional variations in Pn velocity and their effect on the location of epicenters, *Bull. Seism. Soc. Am.* **52**, 1037-1046.
Herrin, E. (1968). Introduction to "1968 Seismological Tables for P Phases", *Bull. Seism. Soc. Am*. **58**, 1193-1241.
Herrin, E., and T. Goforth (1977). Phase-Matched Filters: Application to Study of Rayleigh Waves, *Bull. Seism. Soc. Am*. **67**, 1259-1275.
Herrmann, R.B. (1973). Some aspects of bandpass filtering of surface waves, *Bull. Seism. Soc. Am.* **63**, 663-671.
Nuttli, O. (1972). Seismic wave attenuation and magnitude relations for Eastern North America, *J. Geophys. Res*. **79**, 876-885.
Oliver, J. (1962). A summary of observed seismic wave dispersion, *Bull. Seism. Soc. Am*. **52**, p81-86.
Tanner, M.T., F. Koehler, and R.E. Sheriff (1979). Complex seismic trace analysis, *Geophysics* **44**, 1041-1063.
Unger, R. (1981). The instantaneous amplitude, phase and frequency in seismic event detection, timing and identification, *Proc. NATO, Identification of Seismic Sources-Earthquakes or Underground Explosions*, E.S. Husebye and S. Mykkeltveit (Editors), D. Reidel Publishing Company, Dordrecht, The Netherlands, 649-662.
von Seggren, D. (1970). Relative location of explosions using surface waves, Seismic Data Laboratory Report no. 259, Teledyne Geotech, 17pp
Yacoub, N.K. (1982). "Instantaneous Amplitudes": A new method to measure seismic magnitude, *Bull. Seism. Soc. Am.* **73**, 1345-1355.
Yacoub, N.K. (1994a). Spectral Magnitude: An alternative to long period time domain magnitude for seismic nuclear explosions monitoring, Seism. Soc. Am., 89th Annual Meeting, 5-7 April 1994, Pasadena, CA, Abstract, *Seismological Research Letters* **65**, 1. p71.
Yacoub, N.K. (1994b). Epicenter determination using the arrival time of maximum energy for Rayleigh Waves, Seism. Soc. Am., 66th Eastern Section Meeting, 16-18 October 1994, Columbia, NC, *Seismological Research Letters* **65**, n3/4, p 231.
Yacoub, N.K. (1996). Maximum Spectral Energy Arrival Time for Epicenter Determination. Part I: Rayleigh Waves, Abstract, Seism. Soc. Am., 91nd. Annual Meeting, 1-3 April 1996, Saint Louis, MO, *Seismological Research Letters*.
Yacoub, N.K. (1997). Maximum spectral energy timing method for epicenter determination and location errors reduction. Part II: P-Waves, Seism. Soc. Am., 92nd Annual Meeting, 9-11 April 1997, Honolulu, HI, *Seismological Research Letters* **68**, n2, p 309.
Yacoub, N.K. (1998a). Maximum Spectral Energy Timing Method for Epicenter Determination and Location Errors Reduction. Part II: P-Waves, Abstract, Seism. Soc. Am., 93rd Annual Meeting, 16-18 March 1998, Boulder, CO, *Seismological Research Letters*.
Yacoub, N.K. (1998b). Maximum spectral energy for seismic magnitude estimation. Paper I: Rayleigh Waves, *Bull. Seism. Soc. Am.* **88**, 952-962.
Yacoub, N.K. (1999). Maximum spectral energy arrival time of Rayleigh Waves for epicenter determination and location error reduction, Abstract, Seism. Soc. Am., 94th Annual Meeting, 3-5 May 1999, Seattle, WA, *Seismological Research Letters.*

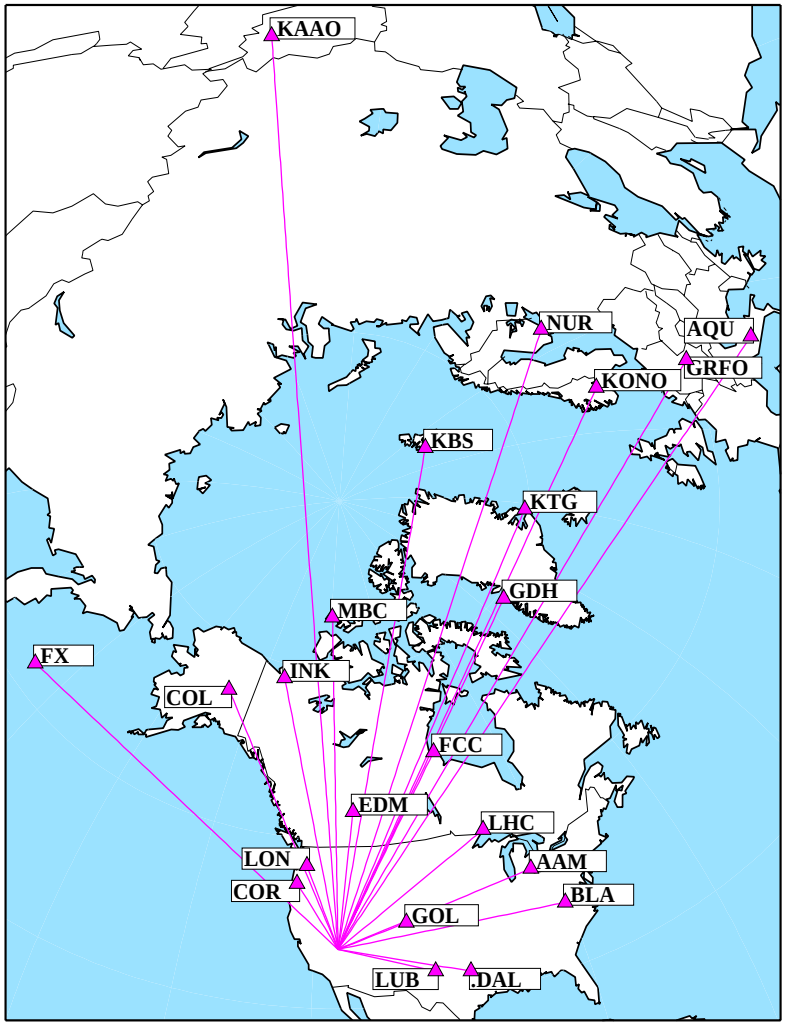


Figure 1. Azimuthal-Equidistant projection for the propagation paths between the Nevada Test Site and some of the seismic stations used in the study of the group velocity of Rayleigh wave maximum spectral energy. Note the various crustal structures crossed by the propagation paths such as the path to station KAAO and FX. No digital data are available from South America or South Pacific. From Yacoub (1998b).

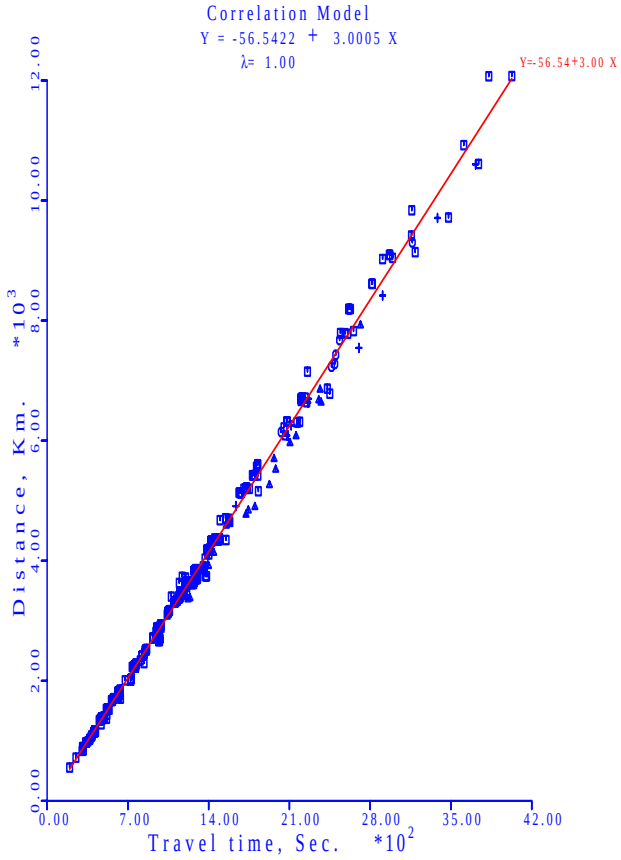


Figure 2. Scatter diagram for Rayleigh wave maximum energy travel time versus distance. Five hundred travel times at several seismic stations from various test sites are shown with different symbols. The travel times represent the arrivals for the maximum spectral energy in the period window 17 to 23 seconds. Note the slight increase in the scatter with distance, which could be attributed to longer path other than the assumed great circle, and the excellent fit at distances less than 4000 km. The slope for the curve is 2.99 ± 0.02 which represents the average group velocity. The different symbols represent the different test sites: squares for

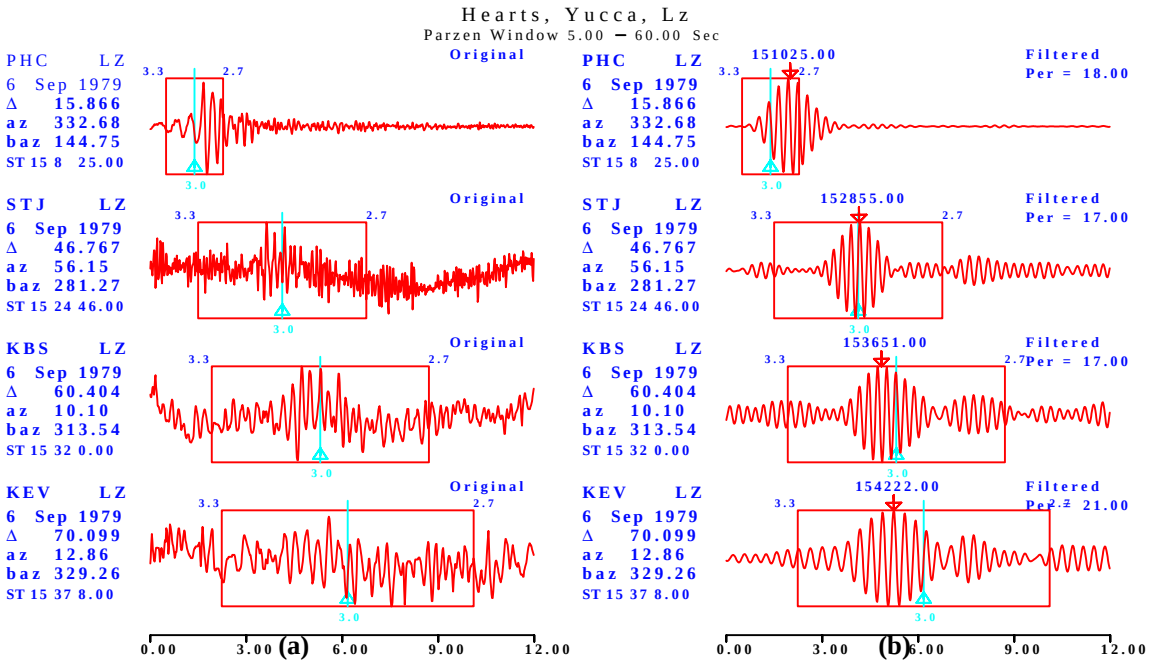


Figure 3. (a) Shown are sample seismograms generated by Hearts nuclear explosion. Each seismogram shows the velocity windows that encompass the Rayleigh wave and the 3.0 km velocity arrival. (b) Shown are the filtered seismograms with the most energy in the period range 17 to 23 seconds. The maximum energy is

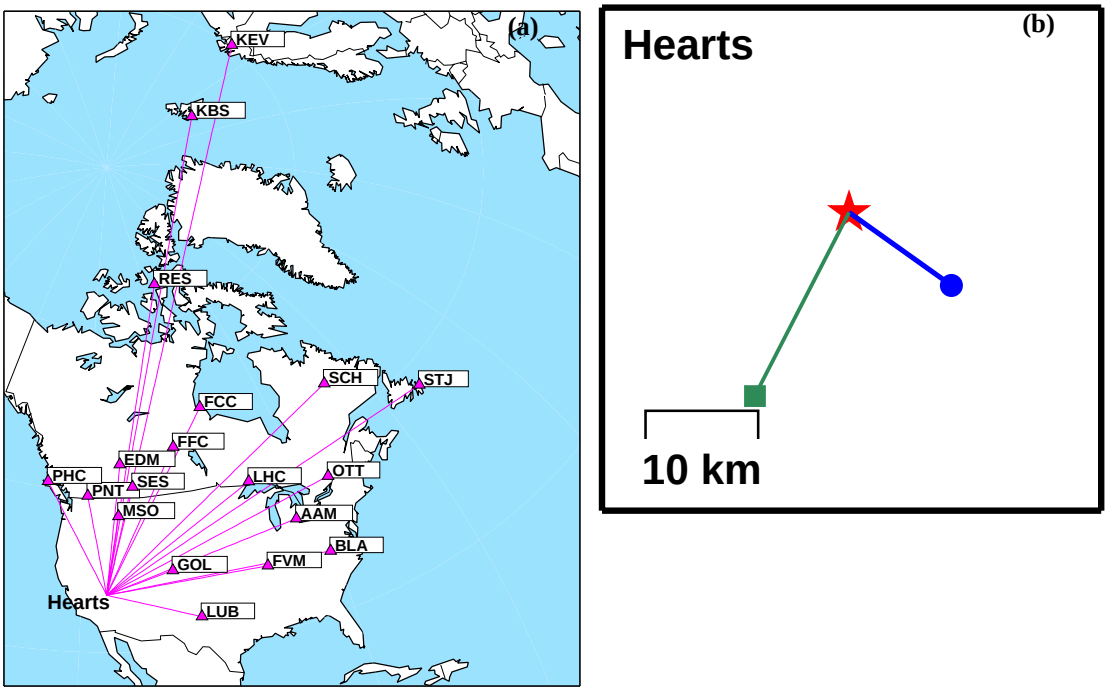


Figure 4. Nuclear explosion Hearts, 6 September 1979. Figure (a) depicts the azimuthal distribution for the network and their great circle path to the actual location for the explosion used to determine the epicenter by P-wave arrival times and Rayleigh waves maximum spectral energy arrival times. Figure (b) depicts the mislocation vectors for the determined epicenters. ★ shows the actual location, ■ shows the P-wave location, and ● shows the Rayleigh wave location. Here the location error for P-wave is 18.32 km and for Rayleigh MSE is 11.2 km.

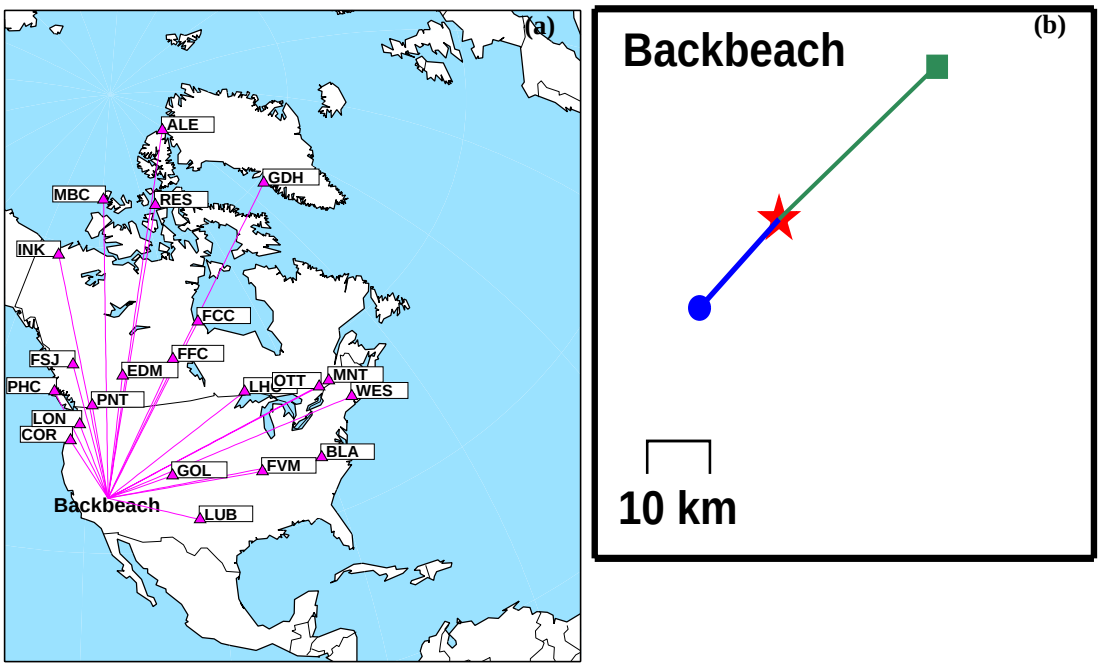


Figure 5. Nuclear explosion Backbeach, 11 April 1978. Figure (a) depicts the azimuthal distribution for the network and their great circle path to the actual location for the explosion used to determine the epicenter by P-wave arrival times and Rayleigh waves maximum spectral energy arrival times. Figure (b) depicts the mislocation vectors for the determined epicenters. ★ shows the actual location, ■ shows the P-wave location, and ● shows the Rayleigh wave location. Here the location error for P-wave is 33.1 km and for Rayleigh MSE is 9.7 km.

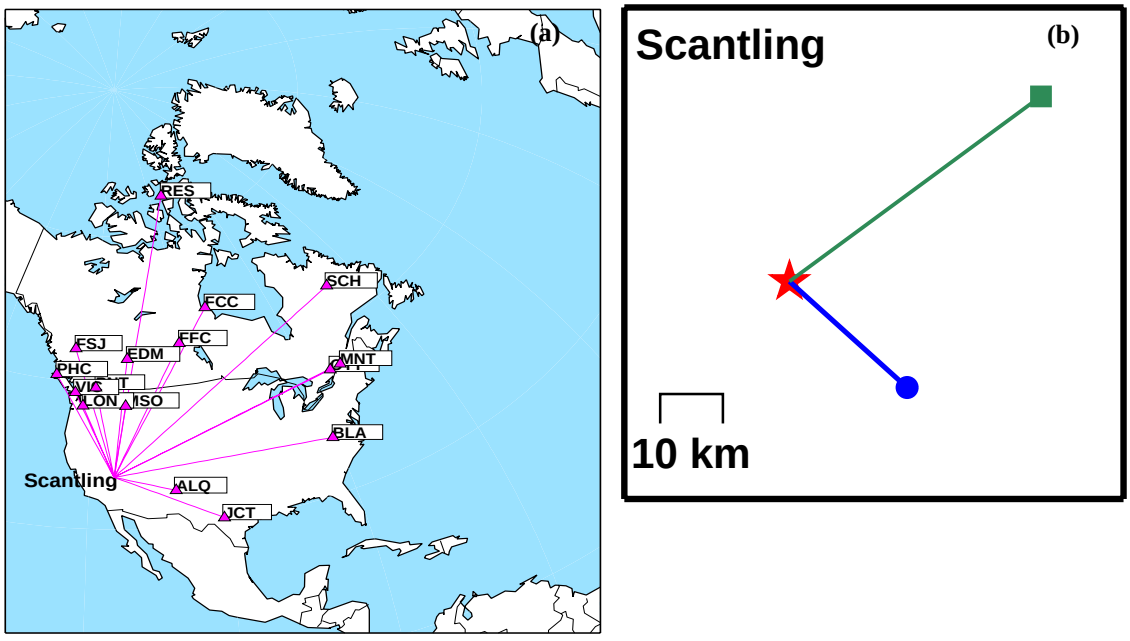


Figure 6. Nuclear explosion Scantling, 19 August 1977. Figure (a) depicts the azimuthal distribution for the network and their great circle path to the actual location for the explosion used to determine the epicenter by P-wave arrival times and Rayleigh waves maximum spectral energy arrival times. Figure (b) depicts the mislocation vectors for the determined epicenters. ★ shows the actual location, ■ shows the P-wave location, and ● shows the Rayleigh wave location. Here the location error for P-wave is 49.9 km and for Rayleigh MSE is 25.1 km.

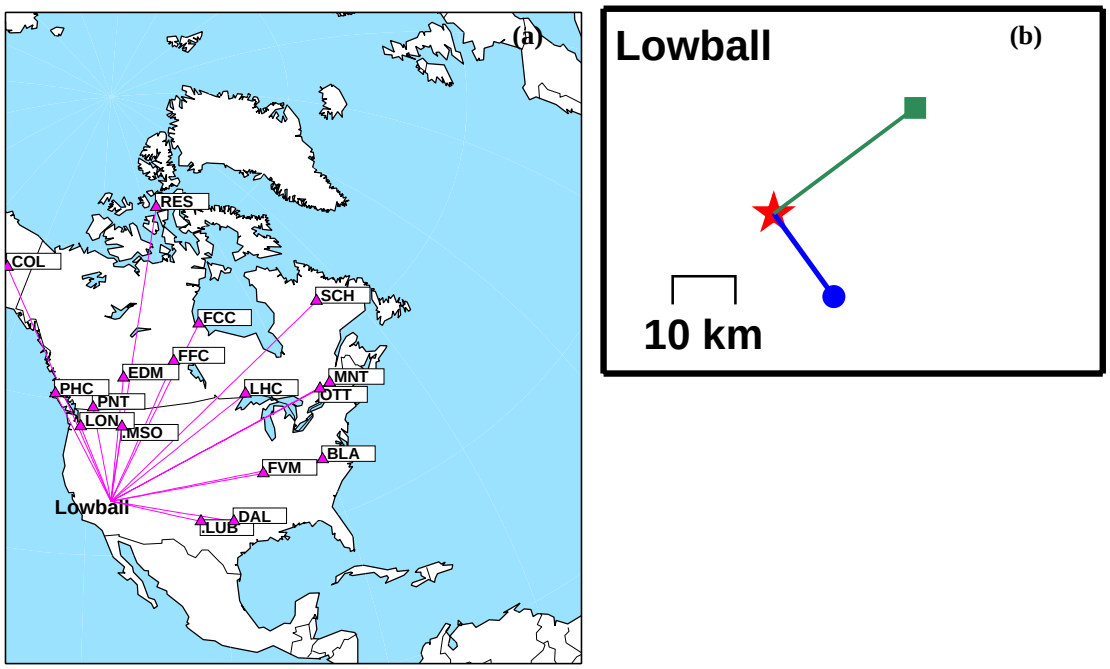


Figure 7. Nuclear explosion Lowball, 12 July 1978. Figure (a) depicts the azimuthal distribution for the network and their great circle path to the actual location for the explosion used to determine the epicenter by P-wave arrival times and Rayleigh waves maximum spectral energy arrival times. Figure (b) depicts the mislocation vectors for the determined epicenters. ★ shows the actual location, ■ shows the P-wave location, and ● shows the Rayleigh wave location. Here the location error for P-wave is 28.3 km and for Rayleigh MSE is 16.3 km.

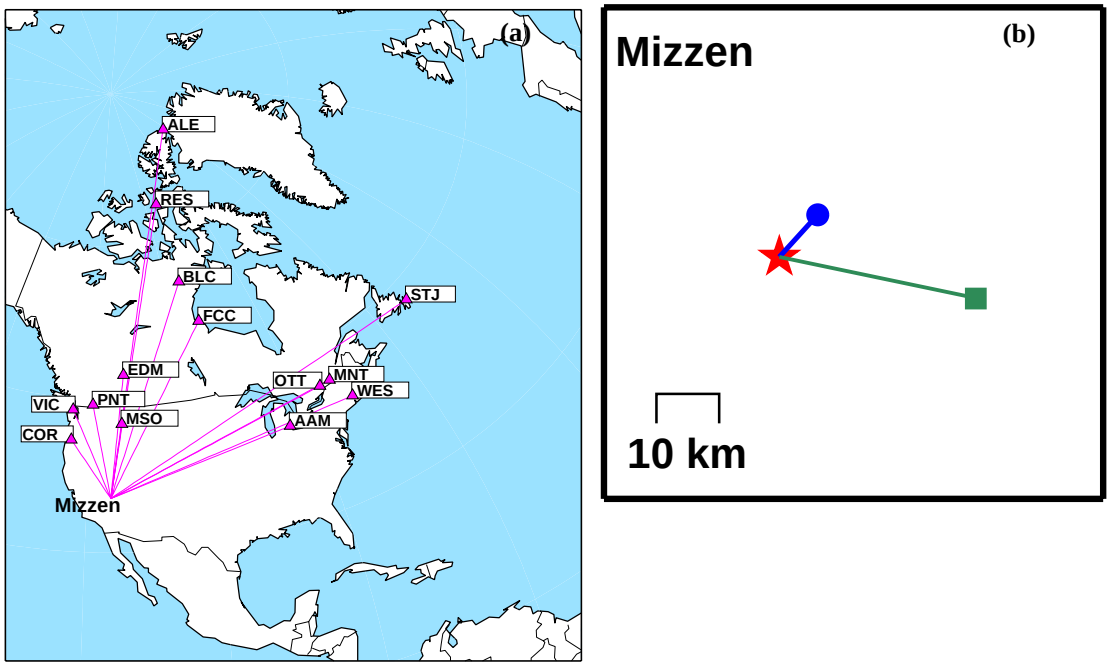


Figure 8. Nuclear explosion Mizzen, 3 June 1975. Figure (a) depicts the azimuthal distribution for the network and their great circle path to the actual location for the explosion used to determine the epicenter by P-wave arrival times and Rayleigh waves maximum spectral energy arrival times. Figure (b) depicts the mislocation vectors for the determined epicenters. ★ shows the actual location, ■ shows the P-wave location, and ● shows the Rayleigh wave location. Here the location error for P-wave is 32.0 km and for Rayleigh MSE is 9.3 km.

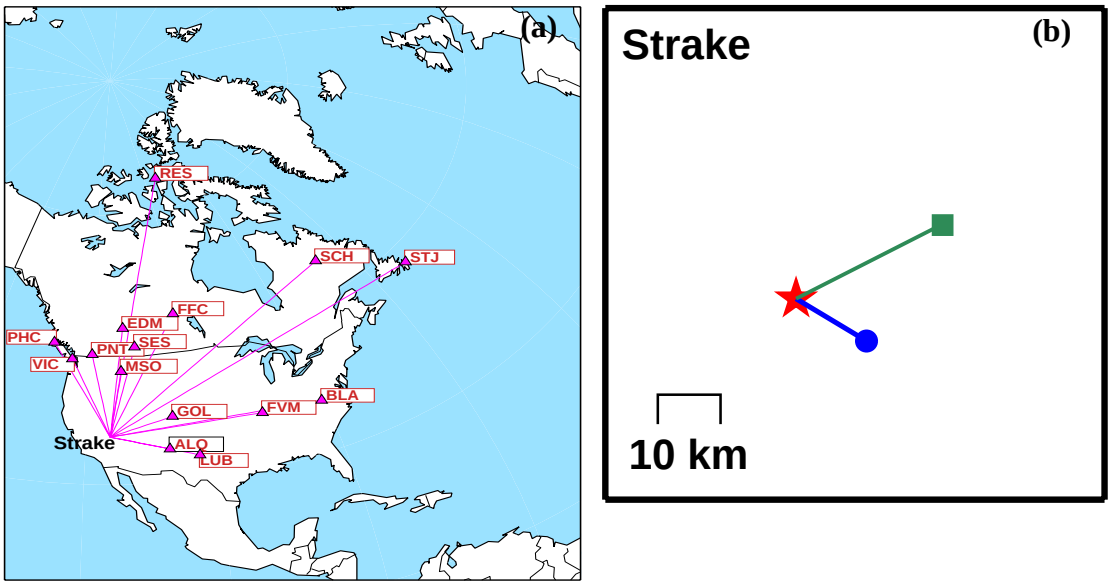


Figure 9. Nuclear explosion Strake, 4 August 1977. Figure (a) depicts the azimuthal distribution for the network and their great circle path to the actual location for the explosion used to determine the epicenter by P-wave arrival times and Rayleigh waves maximum spectral energy arrival times. Figure (b) depicts the mislocation vectors for the determined epicenters. ★ shows the actual location, ■ shows the P-wave location, and ● shows the Rayleigh wave location. Here the location error for P-wave is 26.1 km and for Rayleigh MSE is 13.0 km.

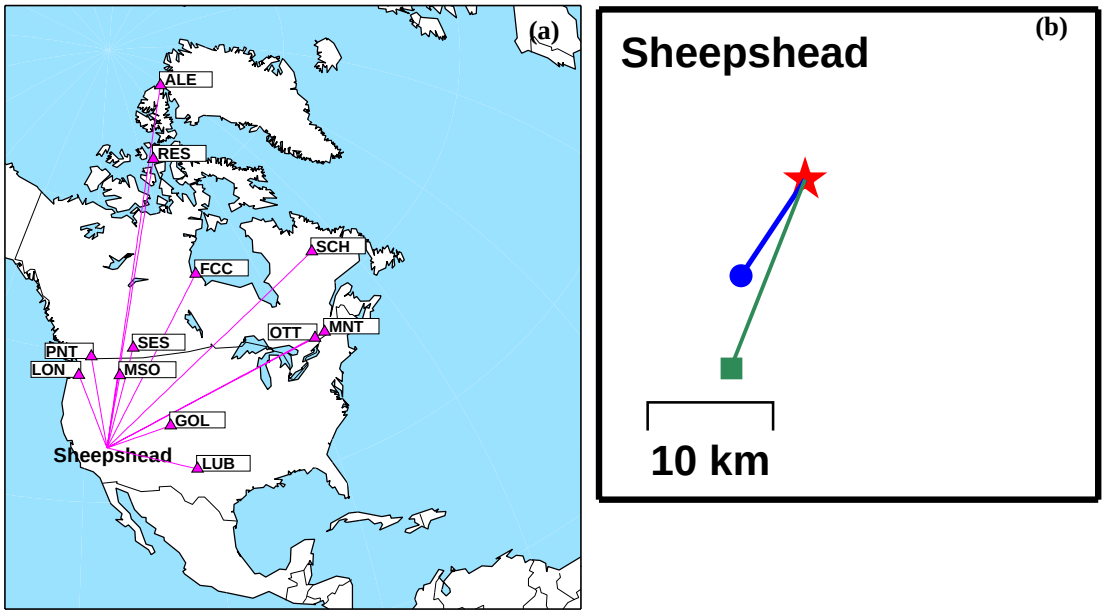


Figure 10. Nuclear explosion Sheepshead, 16 September 1979. Figure (a) depicts the azimuthal distribution for the network and their great circle path to the actual location for the explosion used to determine the epicenter by P-wave arrival times and Rayleigh waves maximum spectral energy arrival times. Figure (b) depicts the mislocation vectors for the determined epicenters. ★ shows the actual location, ■ shows the P-wave location, and ● shows the Rayleigh wave location. Here the location error for P-wave is 16.1 km and for Rayleigh MSE is 9.2 km.

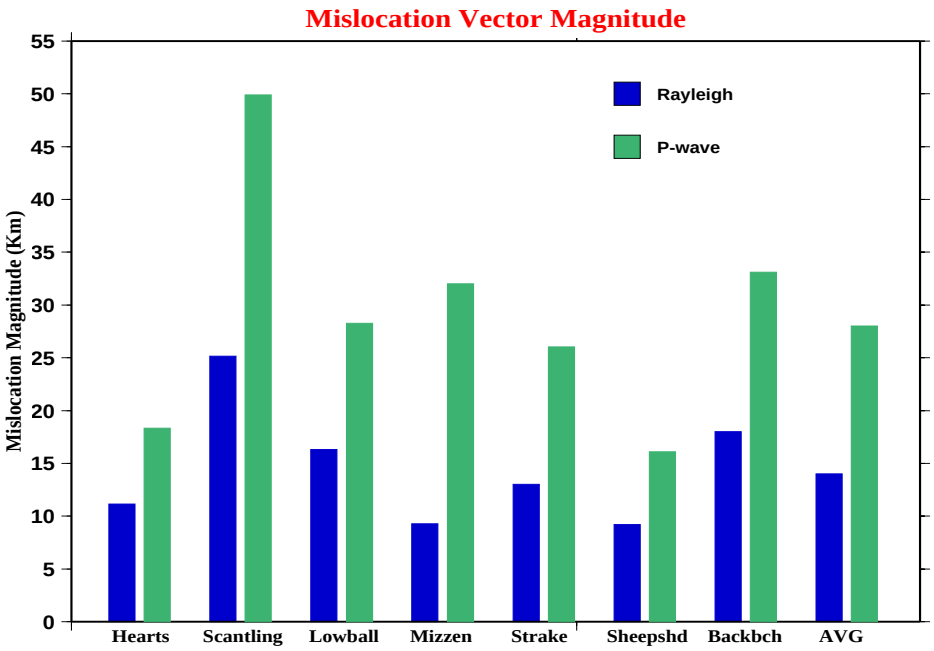


Figure 11. Bar chart showing mislocation vector magnitudes for six presumed nuclear explosions from Yucca, Pahute Test Site, and their averages, as indicated under each group of bars. Numerical values are given in Table 3.

- Represents location error for epicenters computed from P-wave conventional timing method.
- Represents location error for epicenters computed from Rayleigh wave maximum energy spectral timing method.

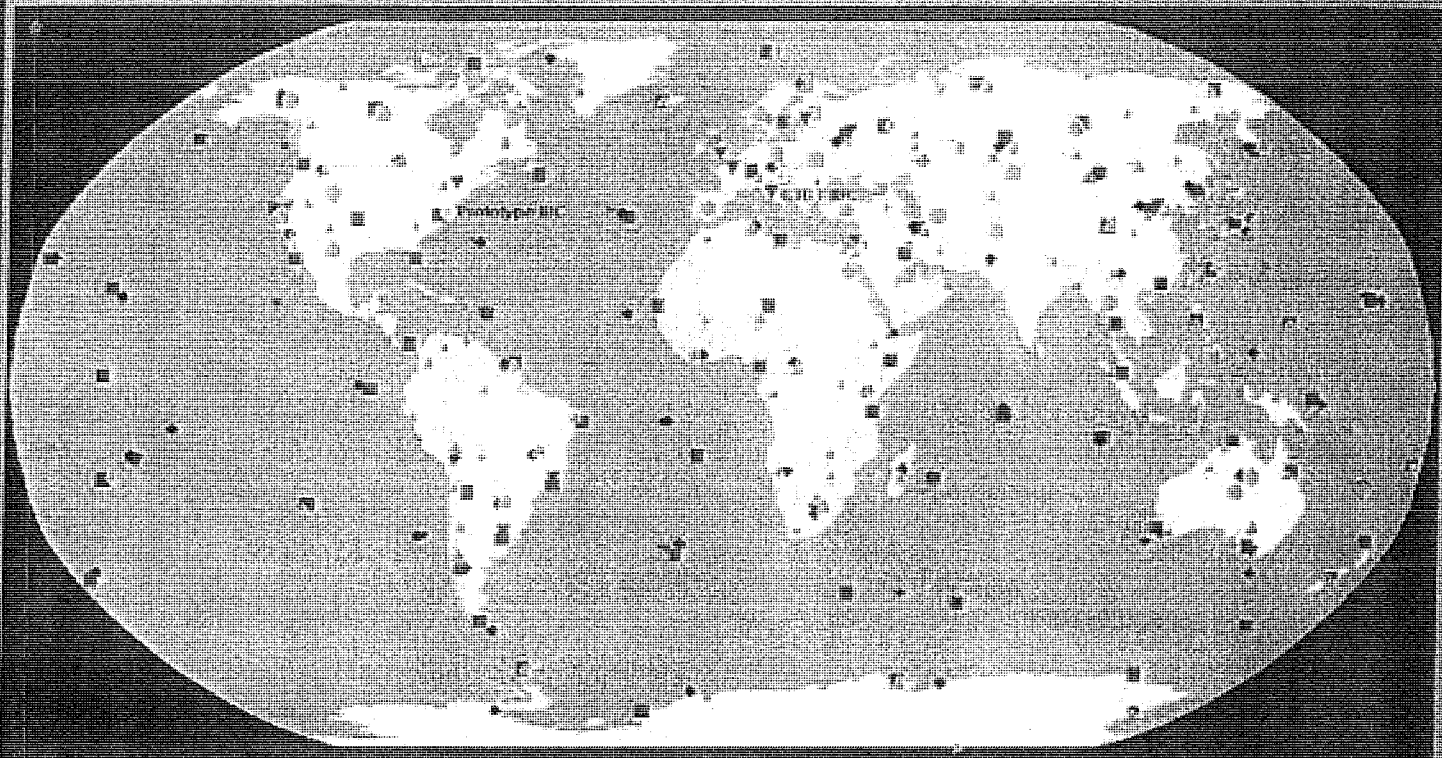
Table 1: Mislocation Vector Magnitudes

Event	No STA	Location Error, Km		Reduction%
		LR	P	
Hearts	19	11.2	18.3	39%
Backbeach	19	9.7	33.1	71%
Scantling	18	25.1	49.9	49%
Lowball	17	16.3	28.3	42%
Mizzen	14	9.8	32.0	71%
Strake	14	13.0	26.0	50%
Sheepshead	12	9.2	16.1	42%
Averages		13±6	29±11	55%

22nd Annual DoD/DOE Seismic Research Symposium

Planning for Verification of and Compliance with the Comprehensive Nuclear-Test-Ban Treaty (CTBT)

Proceedings



VOLUME III

Technical Categories

5. Hydroacoustic Monitoring
6. Radionuclide Monitoring
7. Infrasound Monitoring
8. Data Processing and Analysis
9. International Monitoring System
10. Other

VOLUME III - TABLE OF CONTENTS

5. HYDROACOUSTIC MONITORING

05-01 **DETECTION OF T-PHASES AT ISLAND SEISMIC STATIONS: DEPENDENCE ON SEAFLOOR SLOPE, SEISMIC VELOCITY AND ROUGHNESS** 3
Catherine D. de Groot-Hedlin and John A. Orcutt

05-02 **LONG RANGE LOCALIZATION OF IMPULSIVE SOURCES IN THE ATMOSPHERE AND OCEAN FROM FOCUS REGIONS IN SINGLE ELEMENT SPECTROGRAMS** 13
Gerald L. D'Spain, William A. Kuperman, John A. Orcutt, and Michael A.H. Hedlin

05-03 **EFFECT OF CHARGE DEPTH IN RUSSIAN HYDROACOUSTIC DATA FROM NUCLEAR AND HE EXPLOSIONS** 17
Mariana Eneva, Jeffry L. Stevens, Jack Murphy, and Boris D. Khristoforov

05-04 **AUDIO-VISUAL AND HYDROACOUSTIC OBSERVATIONS OF THE DEAD SEA CALIBRATION EXPERIMENT** 29
Yefim Gitterman and Avi Shapira

05-05 **CALIBRATION OF HYDROPHONE STATIONS: LESSONS LEARNED FROM THE ASCENSION ISLAND EXPERIMENT** 41
Philip E. Harben and Arthur J. Rodgers

05-06 **THE HYDROACOUSTIC NETWORK, INTERNATIONAL MONITORING SYSTEM: STATUS AND PLANS** 51
Martin Lawrence, Marta Galindo, Patrick Grenard, and John Newton

05-08 **DISCRIMINATION CRITERIA FOR SOURCES OF T PHASES RECORDED IN FRENCH POLYNESIA** 55
Emile A. Okal and Jacques Talandier

05-09 **INDIAN OCEAN HYDROACOUSTIC WAVE PROPAGATION CHARACTERISTICS** 57
Pierre-Franck Piserchia and Pierre-Mathieu Dordain

05-10 **HYDROACOUSTIC CALIBRATION WITH IMPLODING GLASS SPHERES** 65
Jay J. Pulli and Phil Harben

05-11 **MODELING LONG-RANGE HYDROACOUSTIC REFLECTIONS IN THE ATLANTIC AND PACIFIC OCEANS** 75
Jay J. Pulli, Zachary Upton, Rob Gibson, and Ted Farrell

05-12 **T-PHASE OBSERVATIONS FROM THE MAY 1999 ASCENSION ISLAND EXPERIMENT** 85
Arthur Rodgers and Philip Harben

05-13 **FINITE DIFFERENCE MODELING OF T-PHASE PROPAGATION FROM OCEAN TO LAND** 95
Jeffry L. Stevens, G. Eli Baker, Heming Xu, Gerald D'Spain and Lewis P. Berger

6. RADIONUCLIDE MONITORING

06-01 **THE DOE AUTOMATED RADIOXENON SAMPLER-ANALYZER (ARSA) BETA-GAMMA COINCIDENCE SPECTROMETER DATA ANALYZER** 107
T.R. Heimbigner, T.W. Bowyer, J.I.McIntyre, K.H. Abel, J.C.Hayes, M.E. Panisko, and W.K. Pitts

06-02 **RADIONUCLIDE LABORATORY SUPPORT FOR THE COMPREHENSIVE NUCLEAR-TEST-BAN TREATY INTERNATIONAL MONITORING SYSTEM** 115
Pamela D. Greenlaw and Colin G. Sanderson

06-03 **RADIONUCLIDE OPERATIONAL RESEARCH & DEVELOPMENT** 121
Harry S. Miley, Dale N. Anderson, Richard J. Arthur, J. Edward Ellis, Tom W. Heimbigner, Gary R. Kiebel, and Robert C. Thompson

06-04 **AUTOMATIC AND INTERACTIVE ANALYSIS SOFTWARE FOR BETA-GAMMA COINCIDENCE SYSTEMS USED IN CTBT MONITORING** 129
J. Rynes, K.M.F. Biegalski, P. Donohoe, and S. Biegalski

06-05 **TESTING FOR OUTLIERS IN RADIONUCLIDE DATA** 139
Barbara Zhao, Wayne A. Woodward, H.L. Gray, and Mark D. Fisk

7. INFRASOUND MONITORING

07-01 **AN ALTERNATIVE CTBT INFRASOUND SENSOR USING PVDF PIEZOCABLE** 151
Steven Africk

07-02 **TUNING OF AUTOMATIC SIGNAL DETECTION ALGORITHMS FOR IMS STYLE INFRASOUND ARRAYS** 153
David J. Brown, Charles N. Katz, Jin Wang, and Rodney W. Whitaker

07-03 **STATISTICAL PERFORMANCE MEASURES OF THE HWM-93 AND MSISE-90 EMPIRICAL ATMOSPHERIC MODELS AND THE RELATION TO INFRASONIC CTBT MONITORING** 161
Douglas P. Drob and J.M. Picone

07-04 **INSTALLATION AND PRE-CERTIFICATION OF CTBT STATION IS59, HAWAII** 171
Milton Garcés and Henry Bass

07-05 **CHARACTERIZATION OF PREDICTED INFRASONIC PHASES FOR IS59, HAWAII** 181
Milton Garcés, Colin Potter, Douglas Drob, Michael Picone, Roger Hansen and Kent Lindquist

07-06 **THE INFRASOUND ANALYSIS TOOL KIT *INFRAMAP*: CAPABILITIES, ENHANCEMENTS AND APPLICATIONS** 191
Robert Gibson and David Norris

07-07 **EVALUATION OF INFRASONIC SPATIAL FILTERS** 199
Michael A.H. Hedlin, Jon Berger, and Mark Zumberge

07-08 **INFRASOUND SENSOR MODELS AND EVALUATION** 209
Richard P. Kromer and Timothy S. McDonald

07-09 **INFRASOUND DETECTION OF ROCKET LAUNCHES** 219
Keith L. McLaughlin, Anna Gault, and David J. Brown

07-10 **OPERATION OF A PROTOTYPE CTBT INFRASOUND ARRAY IN ARCTIC ALASKA** 231
John V. Olson and Charles R. Wilson

07-11 **ON THE ANALYSIS OF THE SPATIAL AND TEMPORAL STRUCTURE OF NATURAL INFRASOUND SIGNALS** 239
John V. Olson, Charles R. Wilson, and Curt A.L. Szuberla

07-12 **DETECTION AND LOCATION CAPABILITIES OF MULTIPLE INFRASOUND ARRAYS** 247
Robert H. Shumway

07-13 **INFRASOUND MODELING USING SOVIET EXPLOSION DATA AND INSTRUMENT DESIGN CRITERIA FROM EXPERIMENTS AND SIMULATIONS** 259
Jeffry L. Stevens, David A. Adams, G. Eli Baker, Heming Xu, John R. Murphy, Igor Divnov and V.N. Bourchik

07-14 **THE ROLE OF GROUND TRUTH IN IMPROVED IDENTIFICATION OF MINING EXPLOSION SIGNALS: UTILIZATION OF CALIBRATION EXPLOSIONS AND ACOUSTIC SIGNALS** 271
Brian Stump and Chris Hayward

07-15 **A SMALL APERTURE SEISMO-ACOUSTIC ARRAY: Signal Assessment** 281
Brian Stump, Chris Hayward, Sara Mihan House, Myung-Soon Jun, and Jeong-Soo Jeon

07-16 **PROGRESS ON THE ESTABLISHMENT OF THE CTBT IMS INFRASOUND NETWORK** 291
A. Veloso, D. Christie, P. Campus, M. Bell, A. Langlois, E. Demirovic, and P. Martysevich

07-17 **AN OPTICAL FIBER INFRASOUND SENSOR** 293
Jonathan Berger, Richard Hilt, Eric Husmann, Scott Nooner, Ruedi Widmer-Schnidrig, and Mark Zumberge

8. DATA PROCESSING AND ANALYSIS

08-01 **MIDDLE EAST AND NORTH AFRICA DATABASE DEVELOPMENT AND RESEARCH TO POPULATE THE DOE KNOWLEDGE BASE** 305
Muawia Barazangi, Dogan Seber, Eric Sandvol, Francisco Gomez, Christine Sandvol, and Carrie Brindisi

08-03 **AUTOMATIC INTERPRETATION OF REGIONAL SHORT PERIOD SEISMIC SIGNALS USING THE CUSUM-SA ALGORITHMS** 317
Zoltan A. Der, Matthew W. McGarvey, and Robert H. Shumway

08-04 **REDUCING INFORMATION OVERLOAD IN LARGE SEISMIC DATA SETS** 327
Jeff Hampton, Chris Young, John Merchant, Dorthe Carr, and Julio Aguilar-Chang

08-05 **FORMATION OF GROUND TRUTH DATABASES AND OTHER STUDIES FOR REGIONAL SEISMIC RESEARCH** 337
Ivan Henson, Indra Gupta, and Robert Wagner

08-06 **REGIONAL SEISMIC THRESHOLD MONITORING** 347
T. Kværna, F. Ringdal, J. Schweitzer, and L. Taylor

08-07 **THE GSETT-3 EXPERIMENT AND THE PROTOTYPE INTERNATIONAL DATA CENTER** 357
Robert G. North and Richard J. Stead

08-08 **DEVELOPMENT OF AUTOMATED MOMENT TENSOR SOFTWARE AT THE PROTOTYPE INTERNATIONAL DATA CENTER** 365
Douglas Dreger, Barbara Romanowicz, and Jeffry Stevens

08-09 **LLNL MIDDLE EAST AND NORTH AFRICA AND FORMER SOVIET UNION RESEARCH DATABASE** 375
Jennifer L. O'Boyle, Stanley D. Ruppert, Teresa F. Hauk, Doug Dodge, and Mike Firpo

08-10 **SURFACE WAVE SIMULATION AND PROCESSING WITH MATSEIS** 385
Beverly D. Thompson, Eric P. Chael, Chris J. Young, William R. Walter, and Michael E. Pasyanos

9. INTERNATIONAL MONITORING SYSTEM

09-01 **THE PRIMARY SEISMIC NETWORK, INTERNATIONAL MONITORING SYSTEM: STATUS AND PLANS** 395
H. Given, L. Astiz, S. Barrientos, S. Bereza, C. Ebeling, M. Hfaiedh, G. Perez, R. Stewart, Y. Starovoit, N. Tavener, and M. Yamamoto

09-02 **CERTIFICATION OF U.S. INTERNATIONAL MONITORING SYSTEM STATIONS** 397
Preston B. Herrington, Randy K. Rembold, J. Mark Harris, and Richard P. Kromer

09-03 **COMPARISON OF PIDC AND IDC EVENT BULLETINS** 403
Hans Israelsson

10. OTHER TOPICS

10-01 **MIGRATION OF RESEARCH RESULTS INTO OPERATIONAL MONITORING SYSTEMS** 413
Leslie A. Casey, Ellen R. Shepherd, Aaron A. Velasco, and Stan D. Ruppert

10-02 **DELIVERING RESEARCH RESULTS TO THE DTRA CMR R&D TESTBED** 419
David H. Salzberg, Robert L. Woodward, and Robert G. North

10-03 **GLOBAL AND REGIONAL GIS DATABASE DEVELOPMENT IN SUPPORT OF CTBT MONITORING** 429
Dogan Seber, Eric Sandvol, Christine Sandvol, Carrie Brindisi, and Muawia Barazangi

10-04 **SEISMIC CATALOGUE COMPLETENESS AND ACCURACY** 439
Terry Wallace, Frank Vernon, and Gary Pavlis

10-05 **A TESTBED FOR NUCLEAR EXPLOSION MONITORING RESEARCH AND DEVELOPMENT** 441
Robert L. Woodward, David H. Salzberg, and Robert G. North

5. Hydroacoustic Monitoring

DETECTION OF T-PHASES AT ISLAND SEISMIC STATIONS: DEPENDENCE ON SEAFLOOR SLOPE, SEISMIC VELOCITY AND ROUGHNESS

Catherine D. de Groot-Hedlin, John A. Orcutt
Scripps Institution of Oceanography,

Sponsored by The Defense Threat Reduction Agency
Arms Control Technology Division
Nuclear Treaties Branch

Contract # DSWA01-98-0004

ABSTRACT

The hydroacoustic segment of the International Monitoring System (IMS) currently being installed for use in verifying compliance with the Comprehensive Nuclear Test Ban Treaty (CTBT), will consist of six hydrophone stations and five supplemental T-phase stations. The ability to detect acoustic signals at T-phase stations relies on an understanding of the acoustic to seismic coupling mechanisms. In this paper, we model upslope propagation of acoustic energy at a sloping wedge using an elastic parabolic equation (PE) modeling method. We synthesize both vertical and horizontal displacement waveforms for broadband sources, and show that the signal amplitudes are strongly dependent on the properties of the offshore slope. For all slope types, the signal amplitudes at onshore seismic stations decrease rapidly with increasing frequency. This decrease with frequency is most pronounced for sources with high mode number content at a shallow sloping wedge. Finally, we show that a significant amount of energy can be lost to surface shear waves at the sloping wedge. We investigate the dependence of surface shear wave excitation on seafloor roughness.

Key words: hydroacoustics, acoustic to seismic transmission

OBJECTIVE

The hydroacoustic component of the International Monitoring System (IMS), currently being installed for use in verifying compliance with the Comprehensive Nuclear Test Ban Treaty (CTBT), will consist of six hydrophone stations and five supplemental T-phase stations (Lawrence and Grenard, 1998). The T-phase stations, which will be located on islands where acoustic transmission is partially blocked, will each be equiped with one to three seismometers designed to detect seismic phases generated by conversion of hydroacoustic waves at the island boundary. Although the T-phase stations are significantly less sensitive than hydrophones to ocean-borne acoustic energy, because of the relatively high attenuation of the seismic phase within the crust, their anticipated lower cost makes their use desirable.

There are several physical processes that can impede routine discrimination between underwater explosions and naturally-occuring events. For instance, at T-phase stations, discriminants based on spectral characteristics are hindered by the frequency dependent attenuation of seismic energy within the crust, which makes detection of high frequency T-phases difficult. A further difficulty with T-phase stations is that signal amplitudes depend on the azimuth of the arriving T-phase (Hanson, 1998) and may vary with physical parameters at the land/ocean interface, such as seismic velocities or slope gradients. Thus, accurate calibration of T-phase stations requires a better understanding of acoustic to seismic conversion at the island boundary. In this paper, we describe acoustic to seismic coupling in terms of the upslope propagation of acoustic modes impinging on a sloping wedge. We demonstrate the effect of slope and bottom velocity on predicted waveforms using PE modelling, and show that the results are in agreement with acoustic mode theory.

RESEARCH ACCOMPLISHED

We have examined the effect on the recorded signal of several physical parameters, including the slope of the ocean/shore boundary, the modal content of the incoming acoustic phase, and the distance between the seismic station and shoreline.

We model acoustic to seismic coupling along a sloping wedge using an elastic parabolic equation (PE) code developed by Collins (1993), which allows for simultaneous computation of compressional potential and vertical displacement, u_z. We examine the compressional potential and u_z for four scenarios, with varying slope angles and source depths. In each case, the velocity model is as shown in figure 1, and computations are performed for a range of frequencies between 2 and 24Hz. Both the seafloor and land section of the model feature a 1km thick "sedimentary" layer, with a P-velocity of 1800m/sec, over a faster basement. The distance between the source and the "shoreline", (*i.e.,* where the

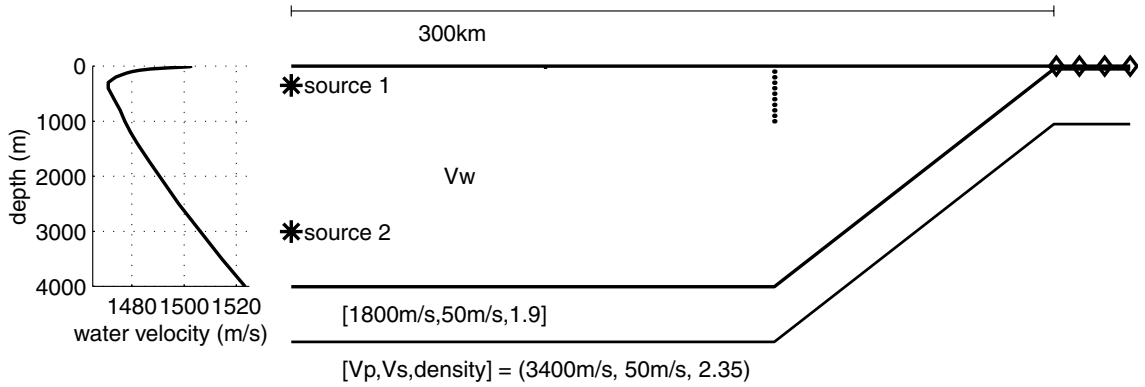


Figure 1 Environmental model for PE computations. The water velocity profile used for all computations is shown at left. The diamonds denote seismometer locations, recording vertical displacement, and the asterisks denote the 2 source locations used in the modeling. The position of a vertical hydrophone array is marked by the dotted line**.**

ocean depth decreases to zero) is fixed at 300km for all computations. The P-wave attenuation is set to 0.1 dB/wavelength and the S-wave attenuation is set to 1 dB/wavelength. The water depth is constant at 4 km up to the base of the slope. The model is extended 30 km past the shoreline to model the effects of transmission loss with distance inland. The S velocity was held at a very low value, 50 m/sec, to limit the analysis to coupling of acoustic energy to P waves.

The dB loss in compressional potential for a source at 350 m depth, is shown as a function of depth and range from the source in figure 2 for a slope of 2°. Results for a 2Hz source are shown above and for 24 Hz, below. At both frequencies, some energy couples into the basement within the first 50 km. As the ocean depth decreases, acoustic energy is absorbed into the seafloor at different ranges corresponding approximately to the modal cutoff depths. Some energy couples into beams that radiate directly into the basement; the remainder becomes trapped in the sediment layer and propagates along this attenuative waveguide to the land. For the 2 Hz source, the ranges corresponding to low order mode cutoff depths are indicated by regions of significant intensity in the bottom. For the 24 Hz source, much of the energy is trapped within the top 1km of the ocean, and couples into the waveguide very near the shoreline.

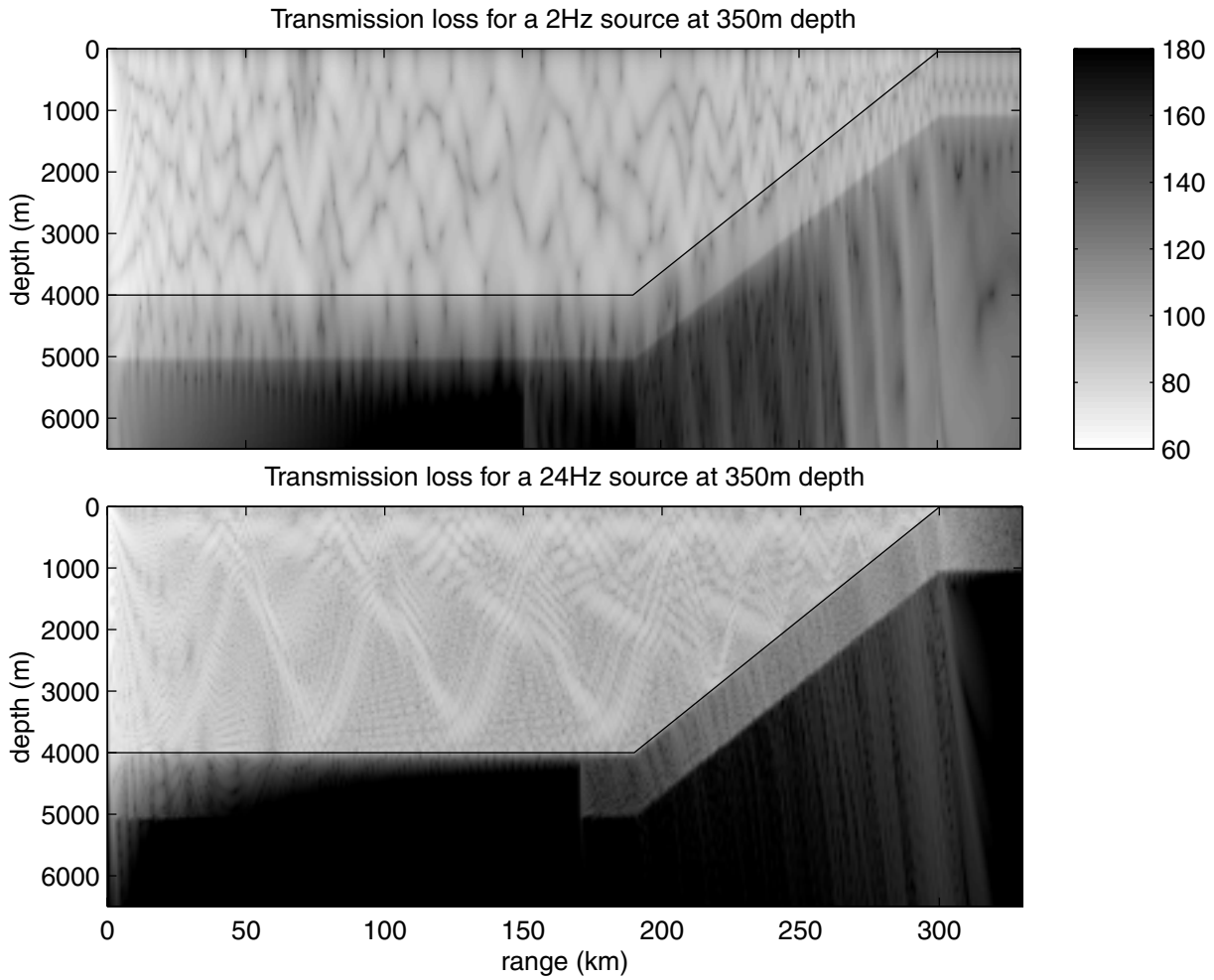


Figure 2 Transmission loss plots for a 2Hz (top) and 24Hz (bottom) source at 350m depth, for a 2° slope.

The decrease in $u_z(z=0)$ as a function of range from the source, is shown in figure 3, for 2 Hz, 8 Hz and 24 Hz sources. For each source, u_z decreases almost linearly with distance beyond the range at which the ocean depth vanishes. The decrease is most rapid at high frequencies, as shown, since the attenuation (in dB) is nearly linear with frequency within the bottom.

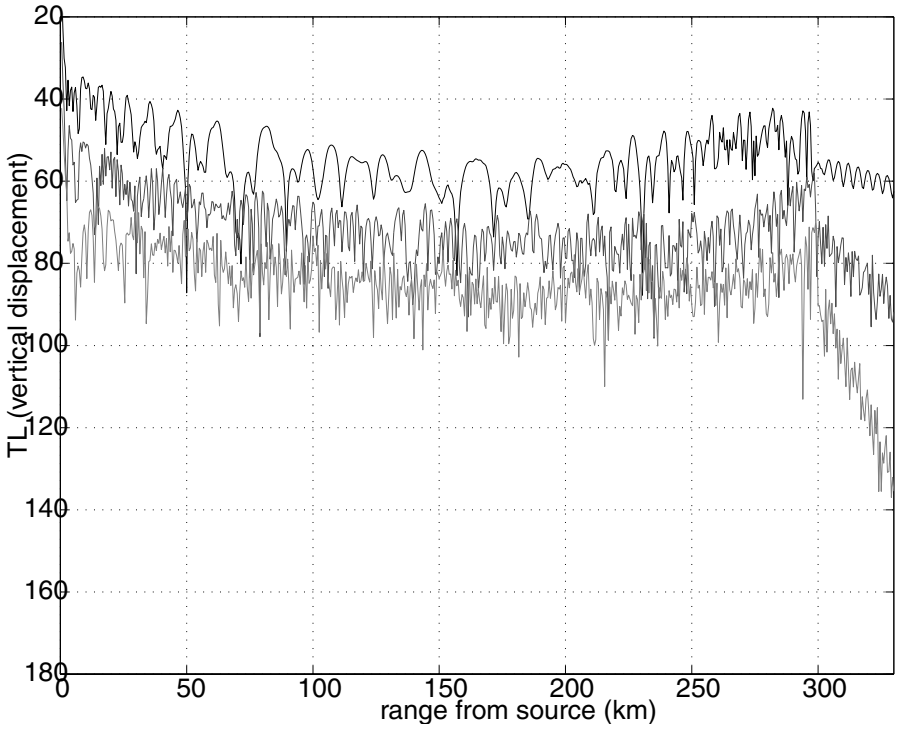


Figure 3 Decrease in vertical displacement (in dB) for 2 Hz (black), 8 Hz (gray), and 24 Hz (light gray) sources at 350 m depth.

For comparison, the decrease in potential energy for an identical model, but with a source at 3000 m depth, is shown in figure 4 for frequencies of 2 Hz and 24 Hz. In this case, the results for 2Hz are nearly identical to those above, but at 24 Hz frequencies, the acoustic energy within the ocean propagates as surface interacting rays, which then couple into the waveguide at a distance of greater than 10km from the shore. The decrease in $u_z(z=0)$ as a function of range from the source is shown in figure 5, at frequencies of 2, 8 and 24Hz. As shown, the results are nearly identical to those for the shallow source at 2Hz. However, the total dB loss in u_z is much greater at high frequencies as compared to the results for the shallow source, since the path length through the attenuative waveguide is longer.

The frequency dependence of the recorded signals at varying distances inland is summarized in figure 6, for the sources at 350m and 3000m depth. As shown, signal strengths at 2Hz are nearly identical at the 2 source depths, but the falloff in amplitude with increasing frequency is far more severe for the deep source than for the shallow source. In comparison, the average dB loss in the compressional potential at a vertical hydophone array at a range of 190km from the source is nearly uniform as a function of frequency.

The attenuation in u_z may be interpreted in terms of the acoustic modes excited by the source. Since acoustic energy propagates in the ocean with negligible transmission loss, the signal amplitudes recorded at T-phase stations will decrease with increasing distance traveled by the converted seismic phase. For a simple wedge model, the depth, and

hence, range at which the acoustic energy becomes trapped in the sediment waveguide depends on slope of the wedge, as well as the modal composition and frequency of the source. The depth at which a given mode couples into the bottom is given approximately by the cutoff depth for a Pekeris waveguide (Pekeris, 1948), *i.e.*

$$d_m = (m\text{-}0.5)\, c_1\, c_2 / (2f(c_2^2 - c_1^2)^{1/2}), \qquad (1)$$

where m is the mode number, f is the frequency of the source, and c_1 and c_2 are the velocities of the fluid layer and fluid halfspace, respectively. For a slope of angle α, the range from the shore at which the acoustic mode couples to the seismic mode is given approximately by $d_m/\tan(\alpha)$. Thus, the lowest order modes at any given frequency couple to seismic waves nearest to the shore, so the recorded amplitude at a T-phase station will depend on the mode content of the acoustic signal, particularly at high frequencies that are strongly attenuated by propagation through land.

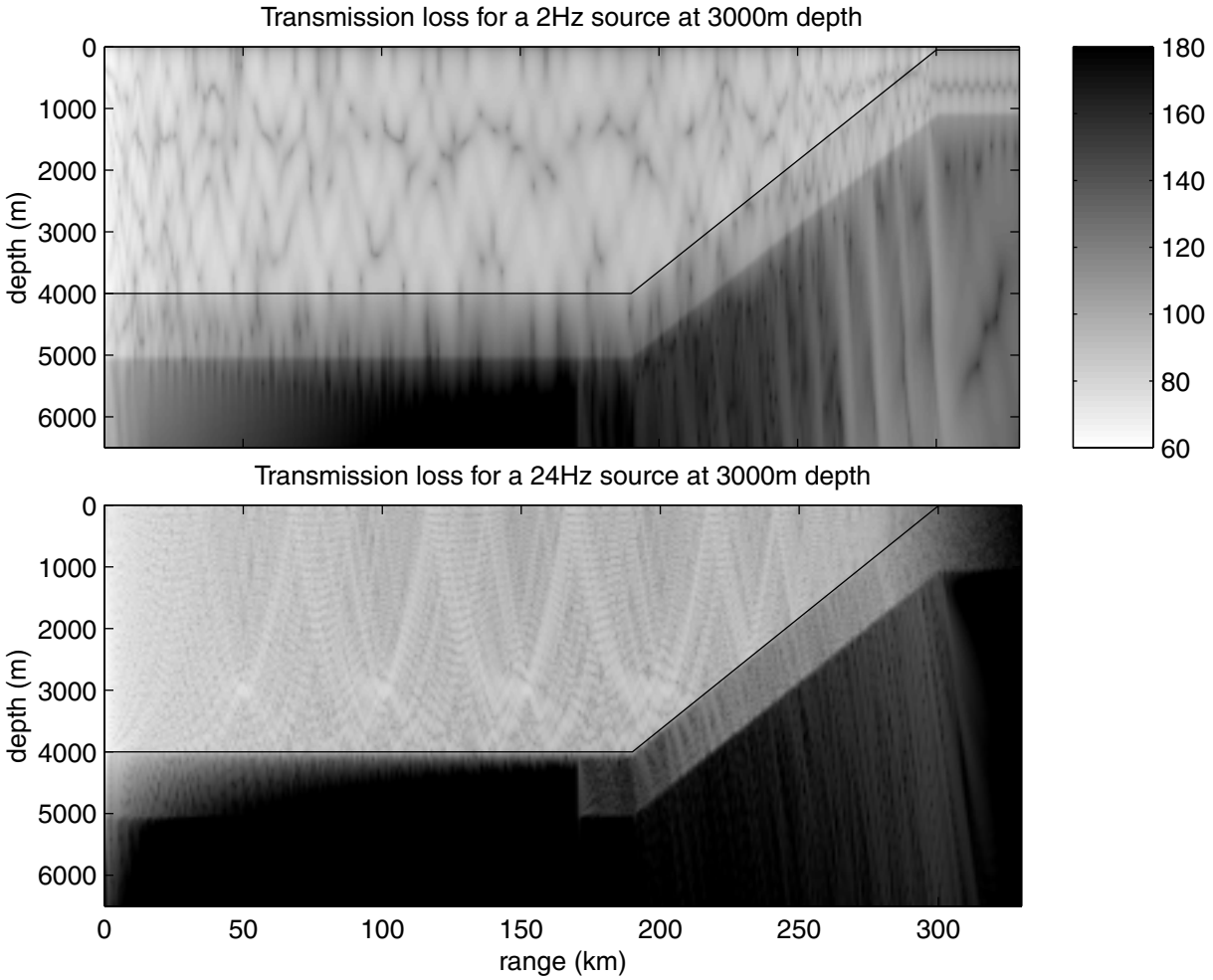


Figure 4 As in figure 2, but for a source at 3000 m depth.

Figure 7 shows several discrete normal modes that exist in the flat region of the model at 2Hz (a) and 24Hz (b). A particular mode can be excited only if the modal depth function at the source is non-zero, thus at 2Hz, the lowest order modes can be excited by both shallow and deep sources. At 24Hz, low order modes can be excited only by the shallow source. Figure 8 shows the approximate amplitude wave-number spectra excited by the 2Hz and 24Hz sources at depths of 350 and 3000m. As shown, the first 10 modes are not excited by the deep 24Hz source, thus coupling takes place much further from the shoreline and is hence attenuated far more than for the shallow source. On the other hand, since the modal composition of lower frequency sources is less strongly dependent on depth, and since intrinsic attenuation is

not as severe at low frequency, recorded T-phases are correctly predicted to be less strongly influenced by the modal composition of the source.

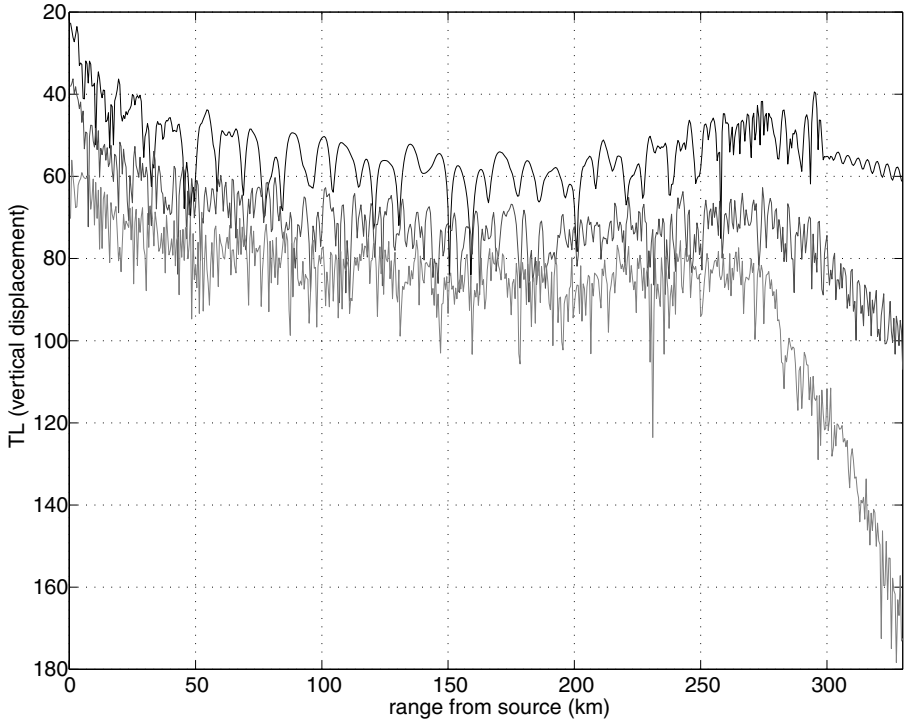


Figure 5 As in figure 3, but for a source at 3000 m depth.

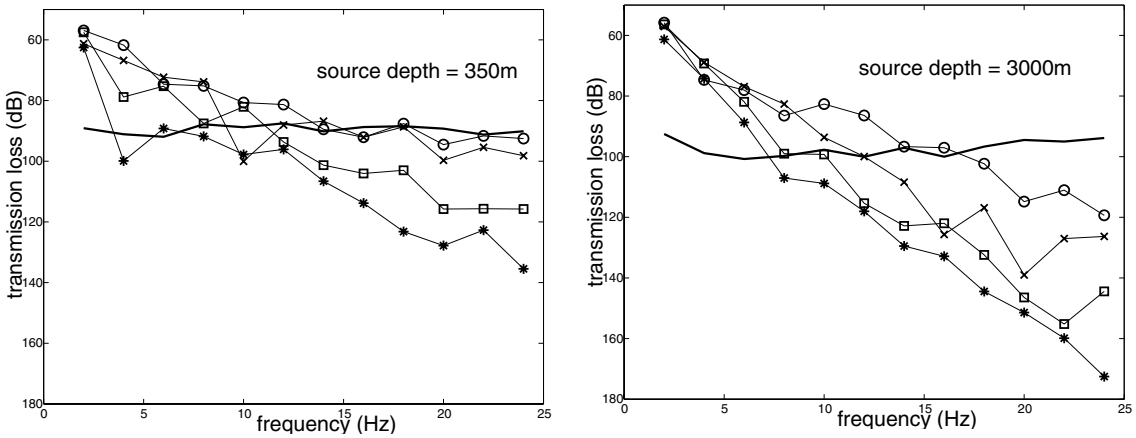


Figure 6 The dB loss in u_z as a function of frequency for sites located 1 km (circles), 10 km (x'es), 20 km (squares), and 30 km (asterisks) inland. a) results for a source at the sound channel minimum incident on a 2^o slope. b) results for a source below the reciprocal depth incident incident on a 2^o slope. The average transmission loss in compressional potential to a vertical array extending from 100-900 m depth at a range of 190 km from the source is shown for comparison, and is marked by the heavy lines.

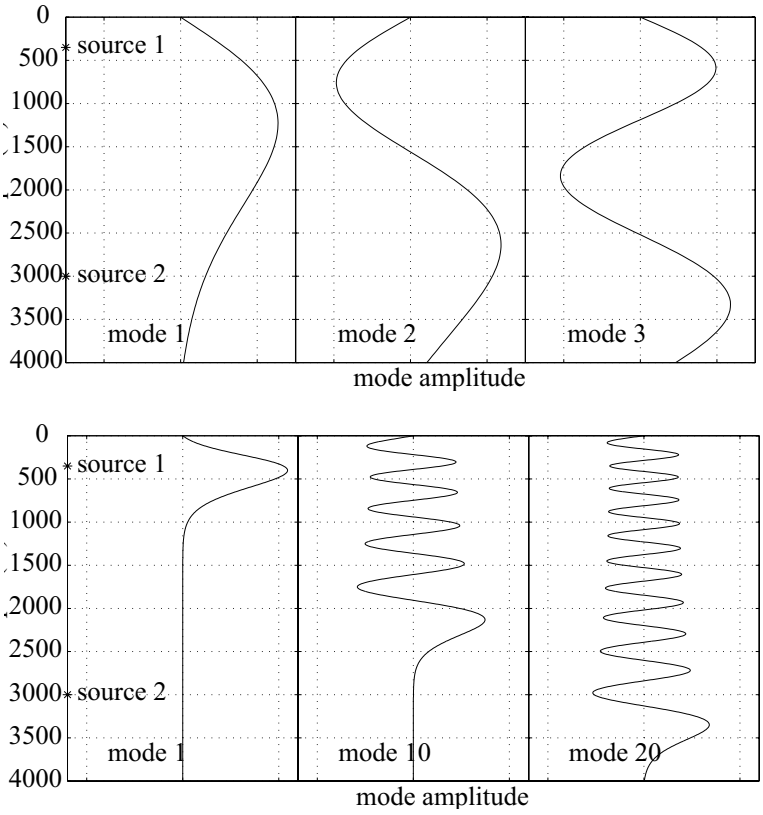


Figure 7 Several modal depth functions in the flat part of the ocean for a) 2 Hz, and b) 24 Hz.

Since low order modes are cutoff at shallow depths near the shore, the effect of slope angle on the recorded signal is expected to be small, in the frequency domain, for sources composed primarily of low order modes. Figure 9a summarizes the frequency dependence of the signals for onshore stations, for a model with a 6.6° slope. As predicted, the decrease in signal strength as a function of frequency is similar to that of the 2° slope, as shown in figure 6a. Conversely, for sources which generate high order modes, the effect of slope is expected to be significant, since the path length through the attenuative waveguide is much shorter for steeper slopes. This is confirmed by the results shown in figure 9b. Comparing these results with those of figure 6b, for a 2° slope, it can be seen that the signal decreases much more slowly as a function of frequency for the steeper slope.

Finally, it should be noted that, although the effect of slope on total transmission loss is small for low order modes, this does not negate the possibility that detection of T-phases depends on slope. As shown by Jensen and Kuperman (1980), each mode couples over a narrow depth range at about the cutoff frequency. This corresponds to a narrower distance range for a steep slope than at a shallow one, thus, as discussed in de Groot-Hedlin and Orcutt (1999), the duration of any given mode mode may be greater at a shallow slope than at a steep one, and its amplitude correspondingly lower.

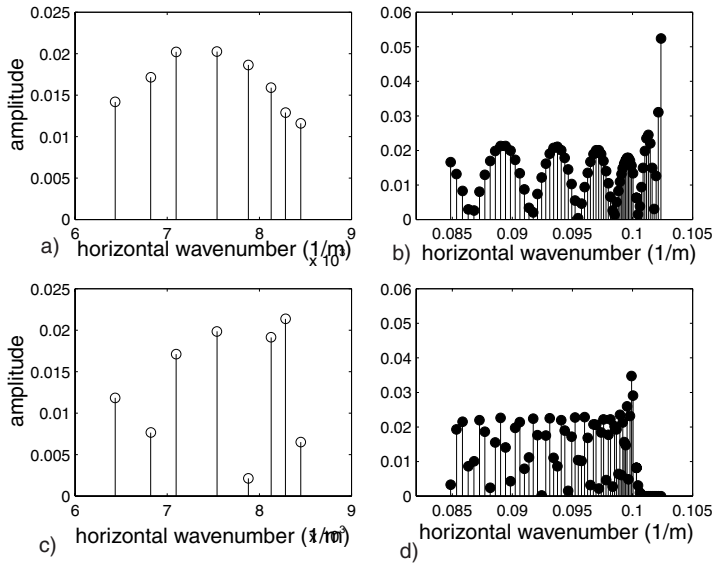


Figure 8 Approximate pressure wave-number spectra for a source at 350 m depth at a) 2 Hz and b) 24 Hz, and for a source at 3000 m at c) 2 Hz and d) 24 Hz. We show only the peaks corresponding to the normal modes of the ocean waveguide.

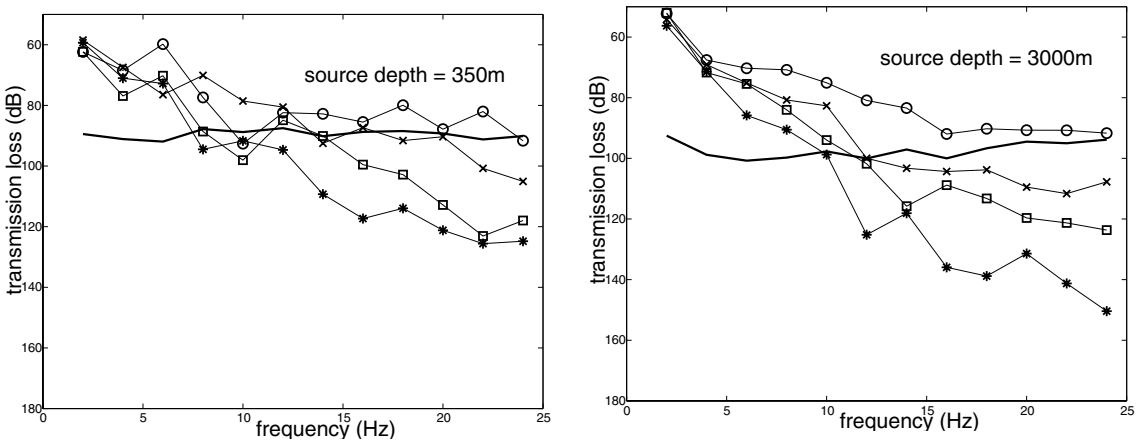


Figure 9 As in figure 6, but for a model with a steeper slope of 6.6°.

In comparison, for a model with significant shear velocity in the bottom, much of the T-phase energy is converted to surface waves, which propagate along the ocean, seafloor boundary, and are rapidly attenuated. Vertical displacement losses for a model with a (constant) seafloor P-wave velocity of 2400m/sec and S-save velocity of 1200m/sec are shown in figure 10, for a frequency of 5Hz. The displacements along the surface are shown in detail figure 11. As shown, surface waves are attenuated rapidly with distance along the coast.

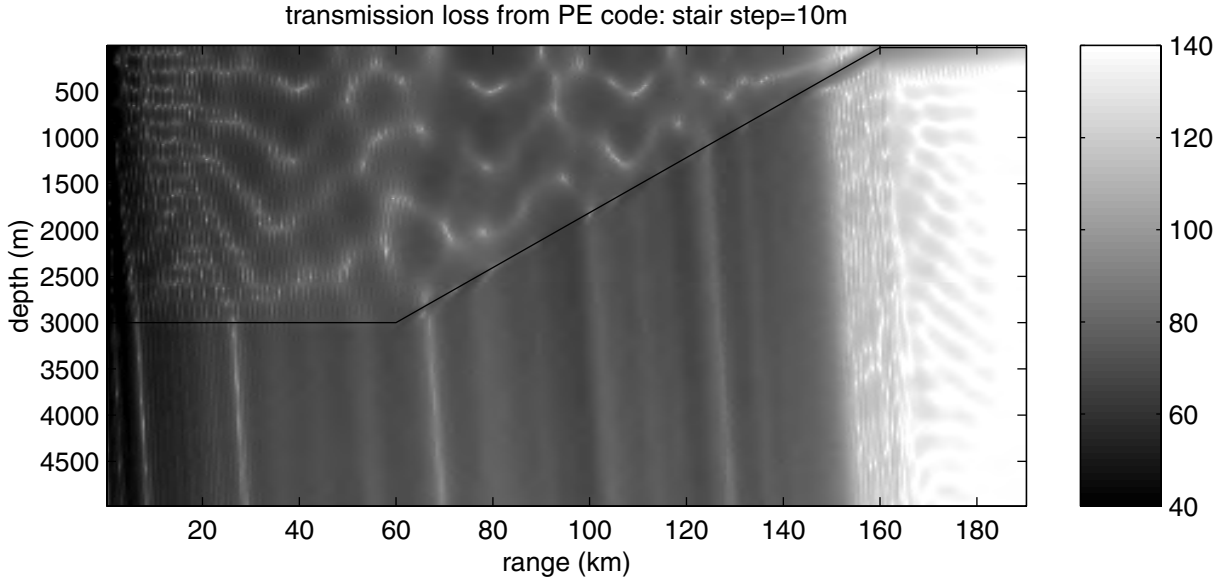


Figure 10 Transmission loss at f=5Hz for model with seafloor P-velocity of 2400m/sec and S-velocity of 1200m/sec. The water velocity profile is shown in figure 1. The source is 350m, i.e. at the sound channel minimum.

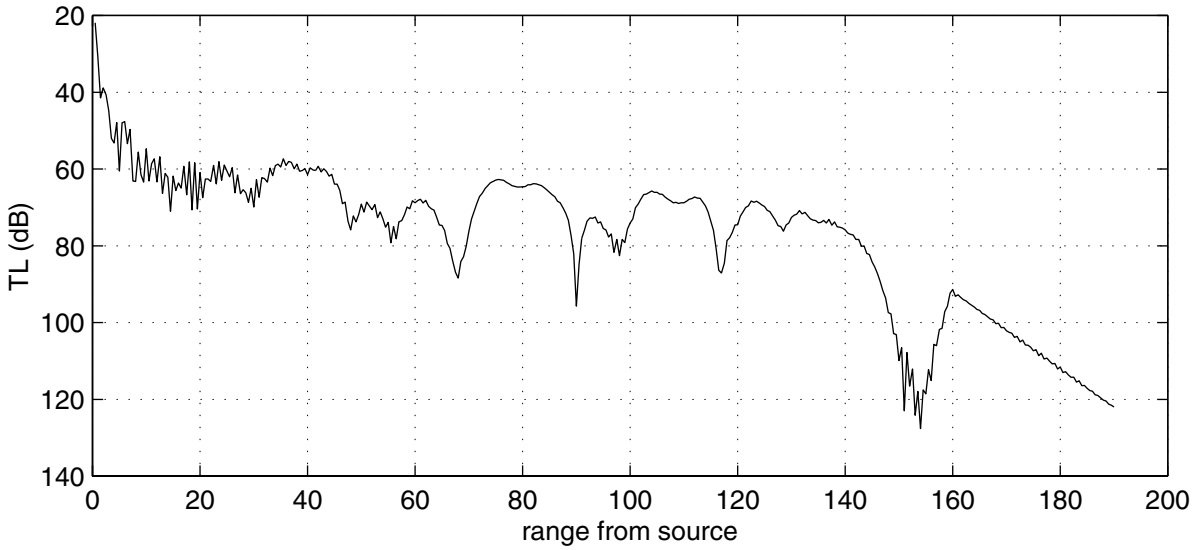


Figure 11 Loss in vertical displacement along the surface for elastic seafloor.

CONCLUSIONS

The transformation of acoustic to seismic modes can also be described in terms of mode coupling. Low modes couple to the seafloor at shallow depths, and higher order modes couple into seismic energy at increasing depths, and hence ranges from the coast. Since attenuation increases both with increasing frequency and with distance propagated through the attenuative crust, T-phase signal amplitudes decrease most rapidly with increasing frequency for sources comprised of high order acoustic modes coupling to seismic energy near a shallow coastline.

REFERENCES

Collins, M.D., An energy conserving parabolic equation for elastic media, *J.Acoust.Soc.Am*., **94**, 975-982, 1995.

de Groot-Hedlin, C.D., and J.A. Orcutt, Excitation of T-phases by seafloor scattering, submitted to *J. Acoust. Soc. Am.,* 1999.

Hanson, J.A., Seismic and hydroacoustic investigations near Ascension Island, *Ph.D. thesis, UCSD*, 1998.

Jensen, F.B. and W.A. Kuperman, Sound propagation in a wedge-shaped ocean with a penetrable bottom, *J. Acoust. Soc. Am.,* **67**, 1564-1566, 1980.

Lawrence, M.W., and P. Grenard, Hydroacoustic Monitoring System for the Comprehensive Nuclear Test Ban Treaty, IEEE, p694-697, 1998.

Pekeris, C.L., Theory of propagation of explosive sournd in shallow water, Geol. Soc. Am. Mem., **27**, 1948.

LONG RANGE LOCALIZATION OF IMPULSIVE SOURCES IN THE ATMOSPHERE AND OCEAN FROM FOCUS REGIONS IN SINGLE ELEMENT SPECTROGRAMS

Gerald L. D'Spain, William A. Kuperman,
John A. Orcutt, and Michael A. H. Hedlin

Scripps Institution of Oceanography,
University of California, San Diego

Sponsored by the Defense Threat Reduction Agency

Contract Numbers DTRA01-00-C-0061 and DTRA01-00-C-0084

ABSTRACT

Waveguide propagation often displays transitions from one type of propagation to another as the mode number (or the take-off angle from a ray theory point of view) increases. An example of such a transition occurs when the boundary of the waveguide changes from being formed by refraction to being formed by reflection. When these transitions occur, they can result in broadband focusing of energy. These focus regions are observable in time series and in single element spectrograms. By measuring the difference in arrival times between these focus regions and knowing the group velocities involved, the range to a long-range impulsive source can be estimated, in the same way that time-of-arrival differences between seismic phases in single station seismograms are used to estimate epicentral distances. Examples of such broadband focusing in low-frequency acoustic propagation in the ocean and infrasonic propagation in the atmosphere are presented in this paper.

OBJECTIVE

The two programs whose contract numbers are listed above just started in July of this year. The first program is in the area of Infrasound Monitoring and the second is in Hydroacoustic Monitoring. The objectives of both projects are to use physics-based signal (and array, if applicable) processing techniques to locate and discriminate signals of interest to the International Monitoring System (IMS) for the Comprehensive Nuclear-Test-Ban Treaty (CTBT). Both research programs will involve theoretical development, numerical modeling, and comparisons of predictions with data from IMS, and IMS-like, stations to understand the benefits and limitations of various approaches. The purpose of this paper is to describe one of the physics-based techniques for estimating the range to a long-range impulsive source that will be investigated in these programs.

RESEARCH ACCOMPLISHED

Because both of these programs just started, the focus of this paper is to present some of the ideas behind the work to be undertaken. Part A is devoted to spectral focusing in ocean acoustic propagation and Part B discusses infrasound propagation in a canonical atmosphere.

A. Deep Ocean Sound Propagation

The first two authors of this paper are the Principal Investigators on "Long Range Localization of Impulsive Sources from Phase/Group Speed Transition Markers in Single Hydrophone Spectrograms", the new program in Hydroacoustic Monitoring at the Marine Physical Laboratory (MPL). The work in this project will expand upon the results to appear in Kuperman, D'Spain, and Heaney, 2000. Fig. 1 shows a spectrogram from the data collected by the shallowest element of the vertical hydrophone line array deployed during the Acoustic Thermometry of Ocean Climate (ATOC) program (ATOC Consortium, 1998; Colosi et al, 1999; Worcester et al, 1999). The ATOC signals have a bandwidth from 60 to 90 Hz, at the upper end of the frequency band of interest in hydroacoustic monitoring component of the IMS. Two broadband arrivals, separated in arrival time by around 5 s, can be clearly seen in the figure. The 3.5 Mm

path over which this energy traveled is shown in Fig. 2 (Path "1"). Taking into account the receiver depth and calculating the effective group speeds for these two spectral focus regions, the time difference can be used to estimate the range to the source to within about 10 percent.

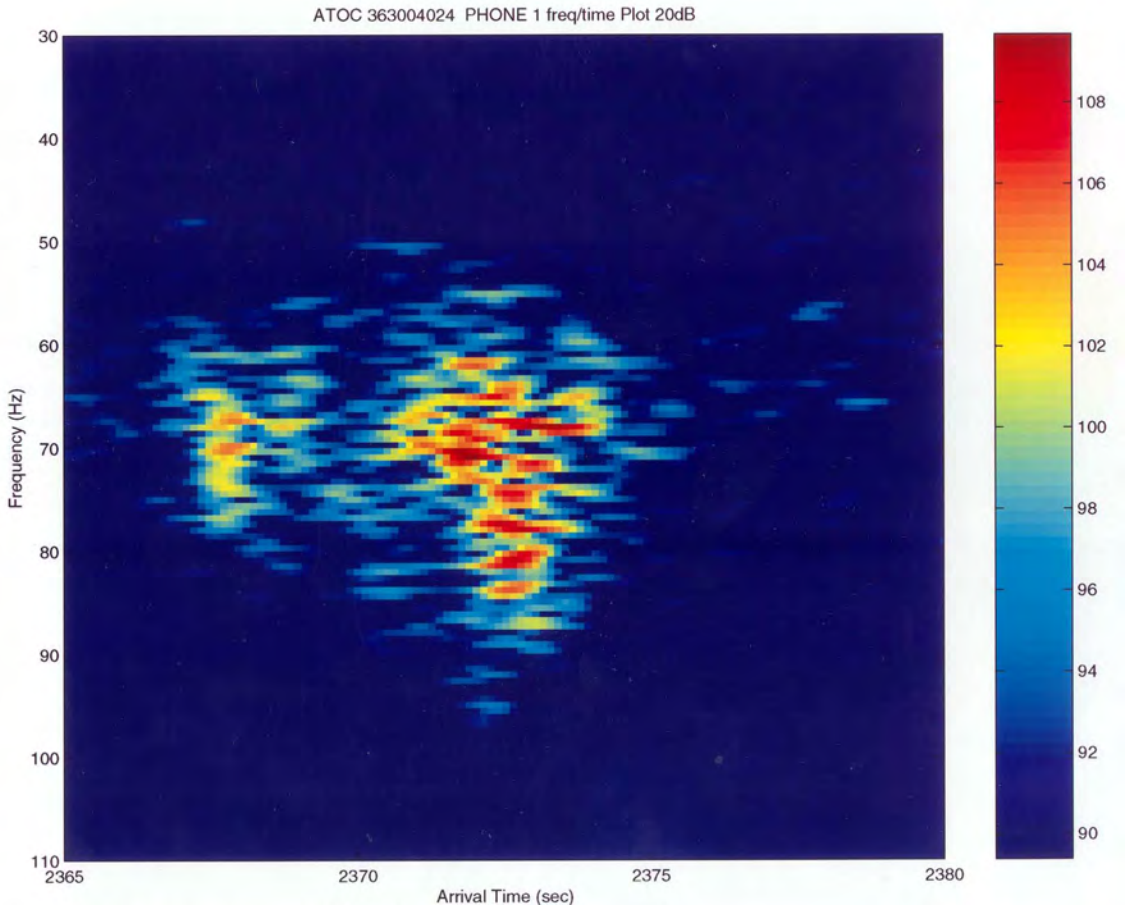


Figure 1. A spectrogram from the data from a single hydrophone collected during an Acoustic Thermometry of Ocean Climate (ATOC) transmission, after matched-filtering the received signal with the transmitted maximal length sequence (m-sequence) signal.

The focus regions in Fig. 1 are due to a combination of two effects. The first effect is the well-known broadband focusing that occurs at the extrema of the dispersion curves for a given mode of propagation. Examples of this type of focusing are the Airy phases associated with the minima in mode group velocity dispersion curves in shallow waveguide propagation and the G-waves in seismology arising from the characteristics of long-period Love wave dispersion (Aki and Richards, 1980). The second effect is related to the phenomenon of "weakly divergent bundle of rays" (WDBR) discussed in Brekhovskikh, Goncharov, and Kurtepov, 1995. The WDBR effect occurs when, from a ray theory point of view, an extremum exists in the ray cycle distance as a function of the ray take-off angle at the source. Only those rays associated with such extrema need to be considered when modeling received sound fields over megameter propagation distances in the ocean (Brekhovskikh, Goncharov, and Kurtepov, 1995). From a normal mode point of view, the extrema appear in the mode group velocity curves as a function of mode phase velocity (or equivalently mode number) at a single frequency. Under the WKB approximation, focusing across frequency at a given mode coincides with focusing across mode number at a given frequency. However, as frequency decreases, the WKB approximation breaks down so that these two focusing effects become

separate phenomena. They are intimately related to the concept of waveguide invariants (Chuprov, 1982; Brekhovskikh and Lysanov, 1991; D'Spain and Kuperman, 1999).

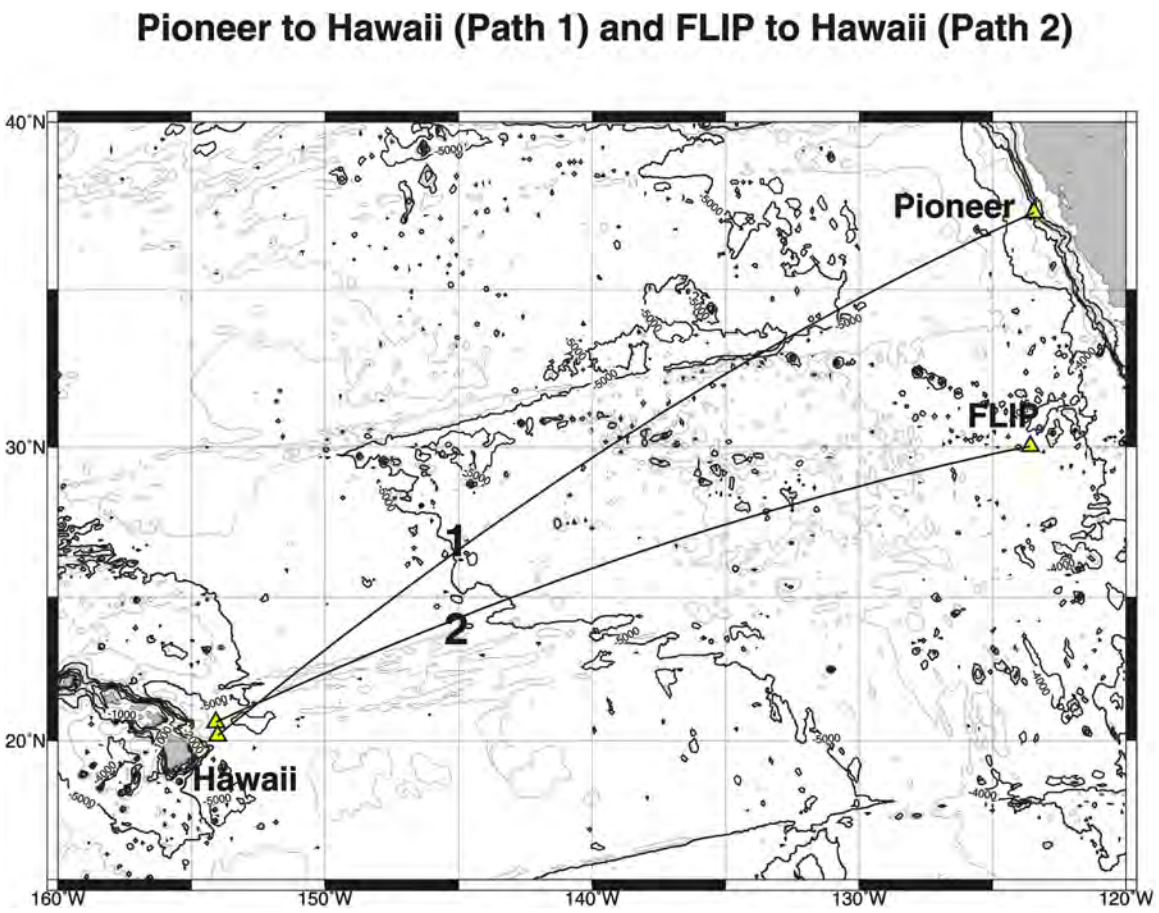


Figure 2. A map of the Northeast Pacific Ocean with superimposed ocean bathymetry contours showing two great circle paths. The path labeled "1" corresponds to the ATOC path from the source at Pioneer Seamount to the vertical receiving array off the northeast coast of Kauai and is the path traveled by the signal plotted in Fig. 1. Path "2" is that of the Acoustic Engineering Test (AET), also part of the ATOC program.

Fig. 3 shows a plot of the "effective" mode group velocity (i.e., inverse of range-averaged group slowness assuming adiabatic mode propagation) as a function of phase velocity at the receiver location for the ATOC Path 1 in Fig. 2. Curves for each of the integral frequencies from 60 to 90 Hz are plotted so that the two focusing effects can be examined simultaneously. These curves were calculated using the Kraken normal mode code (Porter, 1995), freely distributed at the Ocean Acoustics Library web site (http://oalib.saic.com/) with input environmental information extracted from an ocean climatology data base. Several plateaus occur at places where the curves also are tightly bunched together, indicating a simultaneous combination of broadband focusing and WDBR effects. The two plateaus, one at a phase velocity of about 1495 m/s (and effective group velocity of about 1482.5 m/s) and the other at 1523 m/s, are those that presumably give rise to the two focus regions in the single element spectrogram in Fig. 1 since these corresponding mode groups appear to be the ones most effectively excited/received by the source/receiver depth combination.

EFFECT OF CHARGE DEPTH IN RUSSIAN HYDROACOUSTIC DATA FROM NUCLEAR AND HE EXPLOSIONS

Mariana Eneva, Jeffry L. Stevens, and Jack Murphy
Maxwell Technologies/Systems Division

Boris D. Khristoforov
Institute for Dynamics of the Geospheres, Russian Academy of Sciences

Sponsored by the Defense Threat Reduction Agency
Contract No. DSWA01-97-C-0166

ABSTRACT

In a collaborative effort to understand better the coupling of energy from explosions near the water surface, we examine and analyze unique hydroacoustic data from the Russian archives. This is important to CTBT monitoring, because the hydroacoustic energy from such blasts is greatly diminished by comparison with deeply immersed charges. The data include peak pressure measurements and hydrophone records from nuclear explosions, as well as a comprehensive digitized data set from 100-kg TNT explosions in a reservoir. Our work includes the continued use of the REFMS code for modeling of shock-wave reflection and refraction in multi-layered ocean and ocean bottoms. We also study relevant Russian publications reporting on the HE experiments and make comparisons with existing relationships depicting the dependence of the coupling coefficient on charge depth/height.

A number of near-surface nuclear blasts were carried out in the shallow waters ($\leq$ 60 m) of the Bay of Chernaya (Novaya Zemlya) in the late 50's and early 60's. Data is available from three of these explosions. The first underwater nuclear blast (October 10, 1957) was reported with yield of 10 kt and charge depth of 30 m. Seven peak-pressure measurements are available from this explosion, which average about 300 kg/cm^2 at a 235-m distance and sensor depths 10 to 50 m. Hydrophone records from the two other nuclear blasts (October 23 and 27, 1961) are available at much larger distances, 35 km to 160 km, at sensor depths of 1 m above the bottom. These records show levels of sound pressure measured in three different bands from low to high frequencies. The records from the first of these nuclear explosions, of yield 4.8 kt and charge depth 20 m, indicate peak levels of sound pressure between 103 dB and 125 dB. The records from the second 1961 nuclear explosion, of 16-kt yield and height above water 1.1 m, show levels between 90 dB and 130 dB, with the pressure of the direct shock wave being diminished to ~4% of the pressure that would have been observed in boundless water. Distinct arrivals are seen for both 1961 blasts, such as direct shock waves in water (T-phase), refractions in the crust and the bottom layers, and signals corresponding to sound speed of shock waves in air.

Continuing our earlier analysis of pressure-time histories from the 100-kg TNT experiments in a reservoir, we are using the latest REFMS version to model the digitized hydroacoustic measurements from twelve explosions with charge depths from 0 to 2.75 m. In addition to pressure data, the complete data set now includes impulse and energy data as well. The modeling results match the peak-pressure observations rather well, especially in mid-pool, where the measurements suggest free-water-like environment. The estimated pressure coupling coefficients for the shallowest charges, in the range of 30 to 70%, are compared with existing relationships. We find that while these relationships predict coupling to be independent of distance to sensor, our estimates based on the Russian HE data decrease with distance. This suggests that the coupling is more complex than in theory and may have to be adjusted for more accurate modeling of the effect of charge depth.

OBJECTIVE

The objective of this work is to analyze and model unique historical Russian data including hydroacoustic measurements from nuclear explosions in Novaya Zemlya and 100-kg TNT experiments in a reservoir of

water. The purpose is to evaluate decoupling of energy as a function of explosion depth, thus contributing to CTBT verification.

RESEARCH ACCOMPLISHED

Introduction

Understanding the difference in coupling from deep underwater explosions versus shallow and near surface explosions is of significant interest to CTBT verification. The reason is that while even small deep explosions generate signals easily observable at great distances in the world sound channel, shallow and surface explosions produce signals of significantly diminished energy. Therefore finding, analyzing and modeling hydroacoustic data featuring various combinations of explosion depths and distances to sensors, can be very useful in evaluating and modeling the difference in the effects of fully-immersed and shallow charges.

Unique historical Russian hydroacoustic data has become recently available from 100-kg TNT explosions conducted at various depths in a reservoir (Kozachenko and Khristoforov, 1970; Korobeinikov and Khristoforov, 1976) and from underwater and above- water nuclear explosions in the shallow Bay of Chernaya, Novaya Zemlya, detonated in 1957 and 1961 (*USSR Nuclear Weapons Tests and Peaceful Nuclear Explosions 1949 through 1990*, 1996). Eneva et al. (1999) have analyzed earlier pressure records from the 100-kg TNT data showing up to 60-70% decrease in peak pressure between half-immersed (0-m depth) and fully immersed charges, as well as several peak-pressure measurements from the 1957 underwater nuclear explosion. These data were modeled using a numerical code from the Computational Aids provided by DSWA (Stephens and Kelley, 1996). It was derived from a more comprehensive code for modeling of surface reflections, and bottom reflections and refractions due to sound-velocity gradients, known as REFMS. Details on the code can be found in Britt (1986) and more recent *REFMS User's Guides*. It is also discussed at some length in *Handbook of Nuclear Weapon Effects* (1996) – further referred to as *EM-1*. REFMS uses spherical wavefronts and finite-element calculations taking into account deviations from acoustic properties, i.e., nonlinear effects. It has been extensively validated and found in many cases to predict the underwater shock-wave environment with accuracy better than or comparable with hydrodynamic computations. This is significant, because the latter require much greater computer and labor resources. Still, REFMS is valid in relatively weakly nonlinear regimes and cannot replace hydrocodes in highly nonlinear environments. In our earlier work (Eneva et al., 1999), many of the measurements in the Russian experiments were predicted very well with REFMS, thus providing further validation of the code. These data and predictions were also compared with results from LLNL hydrodynamic calculations (Clarke et al., 1995). It was found that rates of change in peak pressures as charge depth increases in the Russian data are very similar to that predicted by REFMS, and somewhat similar to the LLNL predictions. However, the LLNL calculations for nuclear explosions were found to be much more similar to the high-explosive (HE) predictions of REFMS than to the nuclear REFMS calculations. The latter reach full coupling for much shallower explosion depths than in the hydrodynamic modeling; see Figures 6 and 7 in Eneva et al. (1999). In any case, these different approaches to modeling are not directly comparable and the relevance of small-scale HE tests to the study of the effect of charge depth of nuclear underwater explosions is not well understood.

Here we present results from the continuation of the above studies. We can now add archival records from one more underwater explosion and one above-water nuclear blast. Also, we now have the complete digitized data set from the twenty-nine 100-kg TNT experiments, including time histories of pressure and impulse (222 hydroacoustic records each, 36 records in air, and 50 in ground), and shock-wave parameters (peak pressures, specific impulse, pulse duration, and energy estimates). We have analyzed and modeled the hydroacoustic data from twelve experiments performed in a full reservoir (3-m water level). These are more relevant analogues for our purpose, as we seek to evaluate the effect of shallow explosions in relatively deep water, from which signals are likely to propagate to large distances in the SOFAR channel. In contrast, signals from explosions in shallow water are greatly diminished and are unlikely to reach the sound channel at above-noise level. Thus the remaining seventeen 100-kg TNT tests, carried out in very

shallow water (1-m and 0.5-m water level), are not considered at this time. We continue to apply REFMS modeling to the observations where possible, using its latest, 1999 version.

Nuclear Explosions in the Bay of Chernaya, Novaya Zemlya

Several underwater and above-water nuclear explosions of torpedoes have been carried out in the Bay of Chernaya during the period September 1955 - August 1962. Data are currently available for two of the underwater and one of the above-water explosions. Their location is shown on the map of the Bay of Chernaya in Figure 1. The torpedoes were launched from submarines in the vicinity of the strait connecting the bay with Barents Sea. In all three cases the geographic co-ordinates noted in the archival materials were the same - 70.70^0N and 54.67^0E. However, their locations must have not been exactly identical, as the reported depths of the bottom under the blasts differ. More details about these nuclear blasts are shown in Table 1 (*USSR Nuclear Weapons Tests and Peaceful Nuclear Explosions 1949 through 1990*, 1996). Yield values in parentheses represent different estimates in the literature.

Table 1. Archival data from three nuclear explosions in 1957 and 1961.

Date & Moscow time	Yield [kt]	Depth/ Height Expl. [m]	Depth Bottom Under Expl. [m]	Distance to Sensors [km]	Depth Bottom Under Sensors [m]	Depth Sensors [m]	Available Data/ Type of Sensor
10/10/57 09:54:32	10	30 under	≤ 60	0.235	≤ 60	10-50	peak-pressure measurements/MID-3
10/23/61 13:30:47	4.8 (4)	20 under	47	34.84	50	49	sound, infra/hydrophones
				104.9	60	59	sound/hydrophones
10/27/61 11:30:26.6	16 (17.5)	1.1 above	59	34.84	50	49	sound, infra, ultra/ hydrophones
				160.5	45	44	infra/hydrophone

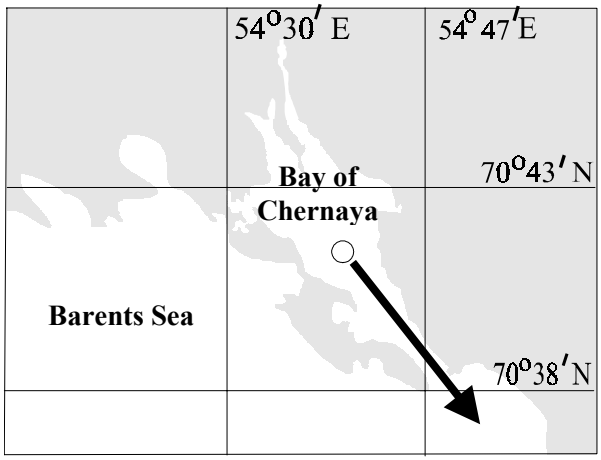
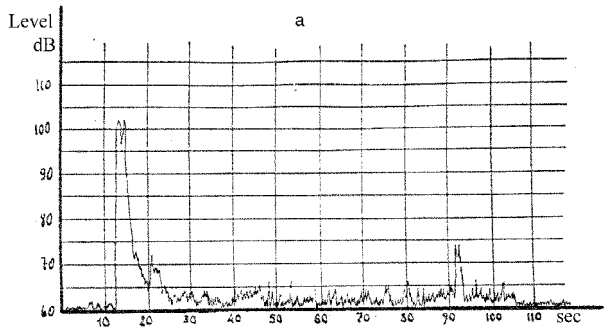


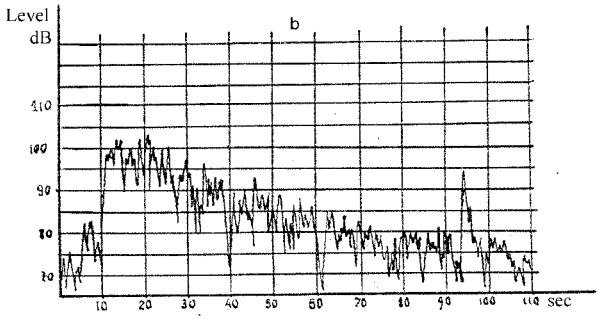
Figure 1. Map of the Bay of Chernaya (Novaya Zemlya). Circle shows location of two underwater and one above-water explosions (1957-1961). Arrow indicates direction to sensor locations, where long-

The measurements from the 1957 explosion were in the near field, while the hydroacoustic signals from the 1961 blasts were recorded at much larger distances. The exact geographic co-ordinates of the sensor locations are not available, but it is known for the 1961 explosions that measurements were taken along a line originating at the blast location and passing through the narrow strait connecting the bay with Barents Sea. The hydrophones were suspended at 1 m above the bottom in the case of the 1961 blasts and at various depths in the case of the 1957 explosion. The Russian archives cite sound velocity of 1430 m/s, characteristic for low-salinity water.

The peak-pressure measurements in the near field (235 m) from the 1957 underwater explosion were made at seven depths, using four to six sensors at each depth. Based on the average of these measurements (~300 kg/cm^2) as compared with REFMS-predicted values and data from the 100-kg TNT experiments, Eneva et al. (1999)

suggested that the explosion yield was probably not larger than 5 to 6 kt, versus the reported 10 kt (*USSR Nuclear Weapons Tests and Peaceful Nuclear Explosions 1949 through 1990*, 1996). More details can be

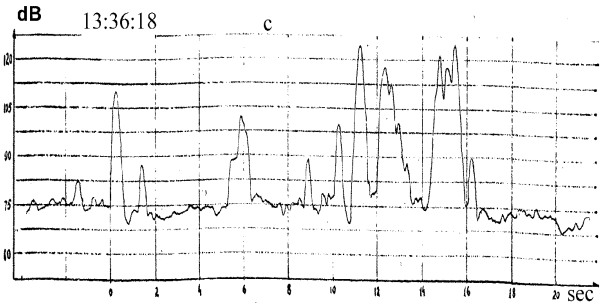




found in our earlier publication.

The hydroacoustic signals from the 1961 explosions were recorded with hydrophones suspended from ships at different distances (see Table 1), much further than the sensors used for the 1957 underwater explosion. Three channels with different filters were used, referred to as "sound", "infrasound", and "ultrasound" in the Russian archives. The **a** espond to frequency bands 60-10,000 Hz, 5-100 Hz 8-100 kHz, respectively. The records in **b** es 2 to 5 are of somewhat compromised quality, as t ere scanned from the archival materials. The level of sound pressure in these figures is shown in dB (decibels), better suited to represent small pressures. As a reminder, the pressure level p in the units of dB is given by 20 x $\log_{10}(p/p_0)$, where $p_0 = 2 \times 10^{-4}$ dyn/cm^2 = 2 x 10^{-5} Pa = 2 x 10^{-10} kg/cm^2 = 0 dB, is the threshold of audibility. Thus, 1 μbar = 1 dyn/cm^2 = 0.1 Pa = 74 dB, 1 mbar = 134 dB, and 100 mbar = 174 dB (e.g., a normal conversation is about 60 dB). An equivalent illustration of the dB-unit is in terms of intensity level (or energy), 10 x $\log_{10}(E/E_0)$, where the hearing threshold is $E_0 = 10^{-12}$ watts/m^2.

Figures 2 and 3 show records from the underwater 1961 explosion at two distances and in different frequency bands. In Fig. 2a (35-km distance), the time of explosion is placed at 0 s. The pre-signal noise levels are ~60 dB in the sound band of frequencies and ~70-80 dB in the infrasound band. The maximum signal levels in both cases reach 102-103 dB. As could be expected, attenuation is much less in the lower frequencies (Fig. 2b). Three distinct arrivals are observed in the sound band (Fig. 2a) – at ~12 s, ~21 s, and ~92 s. The corresponding effective sound velocities are ~2900 m/s, ~1660 m/s, and ~380 m/s, respectively. Thus the first arrival likely represents a wave reflected from the top of the crust and passing through the layer of deposits on the bottom. The low-velocity third arrival may indicate propagation of shock wave in air, which can travel at larger velocities than that of regular acoustic waves. For such an arrival to be observed, the shock wave in air from the explosion plume must have propagated through an air sound channel and then refracted towards the water. As to the second arrival, it is a few seconds earlier than a direct shock hydroacoustic wave (T-phase) at 1430 m/s would arrive (i.e., at ~24.4 s). While such a phase is not seen in the higher-frequency band (Fig. 2a), the lower-frequency record (Fig. 2b) indicates substantial energy around 24.4 s, in a pack with earlier and later arrivals. Compared with the higher-frequency record (Fig. 2a), the onset of the first arrival is earlier in the low-frequency band (~10 s, or a velocity of ~3500 m/s), while the third arrival is later (~93-94s, or velocity of ~370-375 m/s).



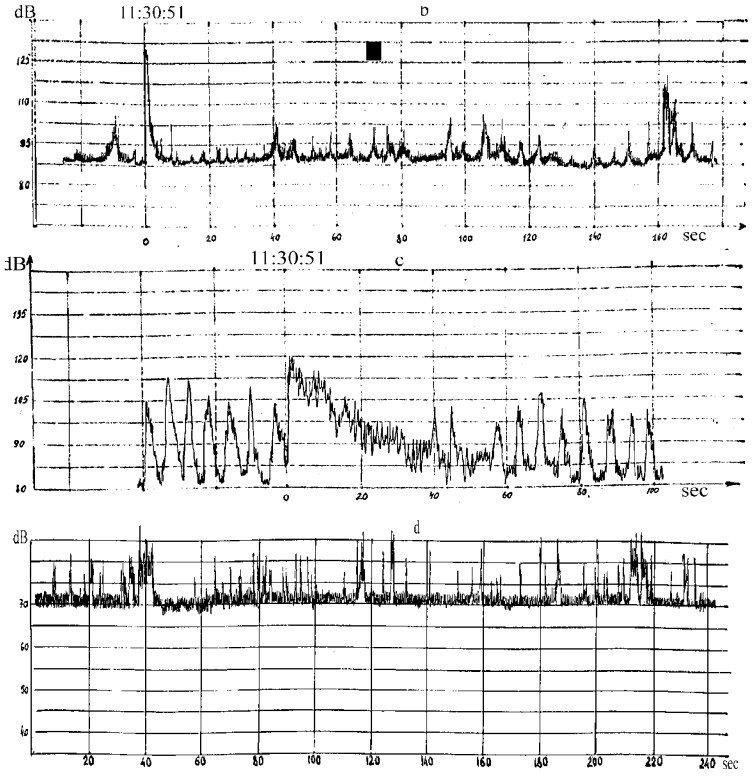


Figure 3 shows the available short portion (~25 s) of the record made in the sound band of frequencies, at a distance of ~105 km from the underwater 1961 explosion. The noise level is at ~75 dB, while the signal level reaches ~125 dB. The horizontal axis has its 0 at 13:36:18 Moscow time; i.e., 331 s after the time of explosion. Thus the earliest arrival observed on this record may have propagated mostly in air with a velocity of ~317 m/s. More energy is observed later, arriving at velocities ~310 m/s.

Figures 4 and 5 show records from the above-water 1961 nuclear explosion of 16-kt yield at two distances. The records in Fig. 4 have been made in the same location as the records from the underwater explosion, at a distance of ~35 km. The pre-signal noise levels were higher than four days earlier prior to the underwater explosion - ~90 dB, ~110 dB, and ~73 dB in the sound, infrasound, and ultrasound bands, respectively. Maximum signal levels in the three bands were ~130 dB, ~120 dB, and ~90 dB. The sound, infrasound, and ultrasound records have their 0's on the time axes at 11:30:51 Moscow time, which is 24.4 s after the time of explosion (see Table 1). The direct shock wave (T-phase) is clearly seen, with corresponding significantly stronger attenuation for the higher frequencies (Fig. 4a). A smaller arrival ~12 s earlier in the sound record, is likely to be of the same type as the first arrival in the records from the underwater explosion, i.e., reflected in the crust and passing through the sediments on the bottom. It is not seen, however, in the infrasound record (Fig. 4b). The sound record also reveals a distinct slow phase at ~162 s (+24.4 s), i.e. ~ 3 min after the explosion. The available portion of the infrasound record is too short to see a corresponding signal. The ultrasound record shown in Fig. 4c is the longest (~ 4 min). The distinct phases in the ultrasound band around 40 s (+24.4 s), i.e. ~ 1 min after the explosion, may correspond to the lower-frequency signals around the same time in Fig. 4a and 4b. As high frequencies attenuate much faster than the lower frequencies, the arrivals in Fig. 4c appear more emergent than in Fig. 4a-b.

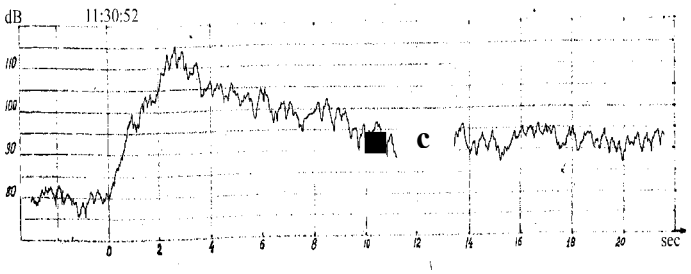


Figure 5 shows the available short portion of an infrasound record from the above-water 1961 nuclear explosion made at ~160-km distance. The pre-signal noise level is ~83 dB, while the signal level reaches ~115 dB. The 0 of the time axis is at 11:30:52 Moscow time, which is 25.4 s after explosion. The arrival seen at this time has traveled with an effective speed of ~6320 m/s, indicating likely reflection from the crust-mantle transition zone.

In an attempt to put these observations in perspective, we searched for relevant literature discussing coupling for shallow and above-water explosions. The *EM-1* (1996) manual lists relationships between pressure coupling coefficients and depth/height of blast, derived from theory of radiation hydrodynamics for low-yield non-radiative (<1 kt), high-yield radiative (>20 kt), and intermediate-yield (1 to 20 kt) nuclear sources. The coupling coefficient, ε, is given as a function of scaled charge depth, and is used to estimate the direct shock-wave peak pressure, $P_{max} = A\varepsilon/R^n$, where A = f(n), n = f(h), R is distance, and h is sensor depth; n approaches 1.13 for deep sensors (i.e., in free water), but is much larger for shallow sensors, in order to account for faster decrease of peak pressure with distance. Using a different approach, Clarke et al. (1995) at LLNL simulated the shock wave from a 1-kt nuclear explosion at 10 km, using a combination of a hydrodynamic code for the strong-shock calculations in the near field (distances <300 m) and a weak-shock calculation for the far field. Because of the very different set-up of the problem, comparisons with the *EM-1* relationships are likely inappropriate. One important difference is that in the LLNL calculations, full coupling is reached at a very large depth, 1000 m/kt$^{1/3}$, while in the *EM-1* relationships the coupling coefficients were set to 1 (i.e., to full coupling) at a very small charge depth, 4.5 m/kt$^{1/3}$. One might assume that these estimates (seemingly at two extremes) should be comparable at least for 0-m/kt$^{1/3}$ charge depth (i.e., half-immersed charges). For such explosions, we calculated from the *EM-1* relationships ε = 0.2, 0.162, 0.11, and 0.057 for 1 kt, 5kt, 10 kt, and 16 kt, respectively. From the Clarke et al.'s pressure estimates, we calculated ε = 0.041, which is close only to the 16-kt *EM-1* estimate, but is very different from the *EM-1* estimate for 1 kt. This illustrates the difficulty when attempting to bring together even results from two different modeling approaches, let alone observations and predictions.

For a 1.1-m charge height above water of the 16-kt 1961 explosion (0.44-m/kt$^{1/3}$ scaled height), we calculate ε = 0.0412 from the *EM-1* relationships. Compared with 0.057 for a half-immersed charge, the difference is not large for this yield. Incidentally, the LLNL estimate, 0.041, is the same (only it is for a 1-kt yield). Thus the peak pressure of the direct shock wave from this explosion might be expected to be ~4 % of the pressure that would be measured from a deep charge. Using further the *EM-1* relationships, and converting the estimates in dB, we calculate that the free-water pressure levels from a 16-kt nuclear explosion are 158 dB at 35 km and 143 dB at 160 km. A 4 %-coefficient reduces these to 130 dB and 115 dB, respectively; the former is in excellent agreement with the level observed at 35 km in Fig. 4a, while the latter cannot be verified as the direct wave at 160 km arrives much later than the time window shown in Fig. 5.

The 4.8-kt 1961 underwater explosion at 20-m depth (~12-m/kt$^{1/3}$ scaled depth) cannot be viewed in light of the *EM-1* coupling coefficients, because full coupling is assumed for such depths. Using the LLNL pressure estimates, we estimate that ε might be ~10%, interpolating between 0.041 for 0 m/kt$^{1/3}$ and 0.176 for 20 m/kt$^{1/3}$ (no pressure estimates available in between). This is a very crude estimate, especially because the LLNL calculations are only for 1 kt at 10 km. The free-water direct shock-wave pressure for this explosion are 154 dB at 35 km and 143 dB at 105 km. Thus the free-water estimate at 105 km for a 4.8-kt explosion is the same as the estimate for a 16-kt explosion at 160 km (see previous paragraph), which might have influenced the particular choices of yields and distances in the Russian tests. A ~10% coupling coefficient would reduce the pressure levels to 134 dB and 123 dB at the two distances. There is no observation in this time window at 105 km, but the observed level for the direct shock wave at 35 km is only ~100 dB in the infrasound record around ~24.4 s (Fig. 2b); this translates into an observed coupling coefficient of only 0.2%. Even lower level, < 70dB, is seen in the sound record at this time (Fig. 2a). As to the pressure level of ~103 dB observed for the arrivals reflected from the crust (~10-12 s at 35 km), it is the same as for the other 1961 explosion, given the difference in yields (4.8 kt vs. 16 kt) and positions in respect to the water surface (under and above); compare Fig. 2a (~12 s on the time axis) and 4a (~ −10 s on that time axis).

In addition to the arrivals of clearer origin discussed above, Figures 2 to 5 show phases likely due to multiple hydroacoustic reflections from the bottom, water surface and surrounding margins, known also as reverberations (*EM-1*, 1996). Due to much more efficient attenuation at higher frequencies, reverberations are relatively short-lived for frequencies exceeding 300 Hz. Shot Swordfish is cited in *EM-1* (1996) as the only nuclear explosion from which reverberation measurements were made at long ranges, but numerous

such measurements exist from HE explosions. Once in the water however, it does not matter in terms of reverberations if the energy originates from nuclear or HE sources.

In the 50's and 60's, the nuclear explosions in the Bay of Chernaya demonstrated the potential for a cover-up in shallow basins and reservoirs. Radioactive contamination stayed mostly in the bay and was not detected in the open sea. The acoustic waves from such explosions cannot reach the world sound channel at above-noise level and do not produce gas bubble phases as deep-water explosions do. The hydroacoustic energy is rather small by comparison with the energy transmitted in the air and the ground. Such explosions are thus not easily detectable with hydroacoustic means and could have posed a significant detection problem at that time. Today such nuclear blasts would be easily detected with the seismic network for CTBT monitoring. The closest U.S. analogues of these underwater explosions have been conducted in the West Pacific - Baker (1946, yield 23 kt, explosion depth 27 m, bottom depth 54 m) and Umbrella (1958, yield 8 kt, explosion on the bottom, bottom depth 45 m). All other U.S. underwater nuclear explosions have taken place in open-water, deep basins.

HE Explosions of 100-kg TNT in a Reservoir

Eneva et al. (1999) have reported earlier on some aspects of the 100-kg TNT reservoir explosions. These 1956 tests have been described and analyzed in several earlier Russian publications (e.g., Kozachenko and Khristoforov, 1970; Korobeinikov and Khristoforov, 1976). Twenty-nine 100-kg TNT experiments (charge radius ~0.25 m) were performed in a reservoir of length 87 m, depth 3 m, and width 25 to 55 m from bottom to top. Comprehensive measurements of shock wave time-histories and parameters (peak pressures, specific impulse and pulse duration) were made at various distances in water, air and ground. Most of the experiment configurations were applied twice, taking measurements at 7.5 m and 22.5 m from one of the explosions, and at 15 m and 30 m from the other. Sensor depths were varied from 0.25 m to 2.75 m, charge depths from 0 m (half-immersed) to 2.75 m, and water level from 3 m to 0.5 m. The bottom consisted of a layer of air-saturated sand, with a very low sound velocity (270 m/s), which for all practical purposes had an effect similar to the air above the water surface. These experiment configurations led to the observation of both regular and irregular reflections from the water surface and the bottom, depending on the locations of explosions and sensors. Eneva et al.'s work has been now extended to include analysis and modeling of additional shock wave parameters, such as positive pulse duration, and impulse and specific energy of the positive pulse. The latest 1999 REFMS version has been used to predict the measurements of shock-wave parameters.

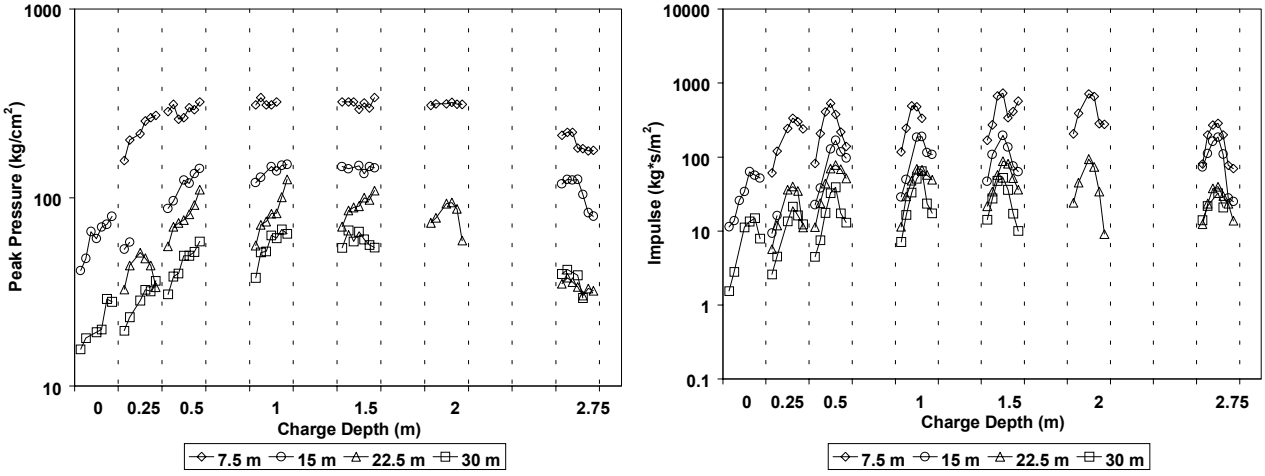
Impulse, pulse duration, and energy in boundless (free) water have been discussed in the classic work of Cole (1948). The pressure of the shock wave P (overpressure above the hydrostatic pressure), as a function of time t after arrival of the shock wave, is given by $P(t) = P_{max}e^{-t/\theta}$, where P_{max} is the initial peak pressure, and θ is so-called time constant, i.e., the time over which the pressure-time history can be approximated with an exponential decay. For many purposes, the effect of a shock wave depends on the time-integral of pressure, or impulse, more significantly than on the detailed form of pressure change with time. The specific impulse of unit area of the shock wavefront, up to a time τ after its arrival, is given by $I(\tau) = \int_0^\tau P(t)\,dt$. Another significant measure of the shock wave is energy flux density, E_f, representing the energy flux across unit area of a fixed surface normal to the direction of propagation (often referred to as energy flux, or simply energy); $E_f(\tau) \sim \int_0^\tau P^2(t)\,dt$. All these parameters can be represented by power laws $\sim 1/R^\alpha$, where R is distance from source and α is a constant. The empirical relationships given by Cole (1948) for HE charges of TNT, after modification of the units, are as follows:

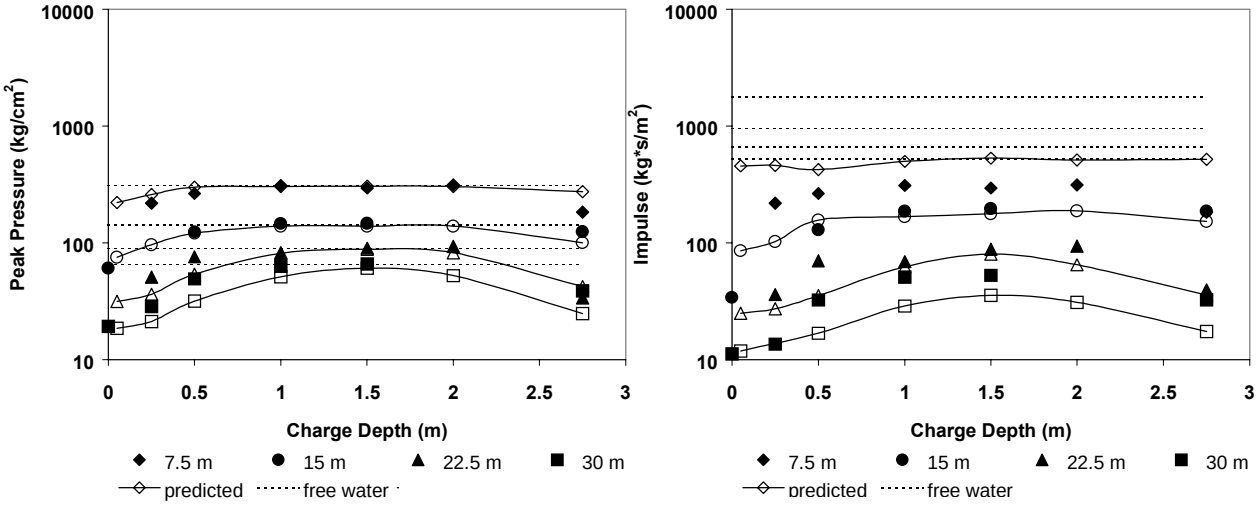
$$P_{max} = 533(W^{1/3}/R)^{1.13} \qquad I = 588\ W^{1/3}(W^{1/3}/R)^{0.89} \qquad E_f = 8300\ W^{1/3}\ (W^{1/3}/R)^{2.05}, \tag{1}$$

where W is yield in kg (100-kg TNT in this case), and the impulse and energy flux are estimated in time $\tau = 6.6\theta$. The units in eq. (1) are m for distance, kg/cm^2 for pressure, kg$*$s/m^2 for impulse, and kg$*$m/m^2 for energy flux. These relationships show that the peak pressure decreases with distance faster than an

inversely proportional relationship (i.e., than acoustic approximation would imply), while the energy decreases faster than inversely proportional to the square root of the distance.

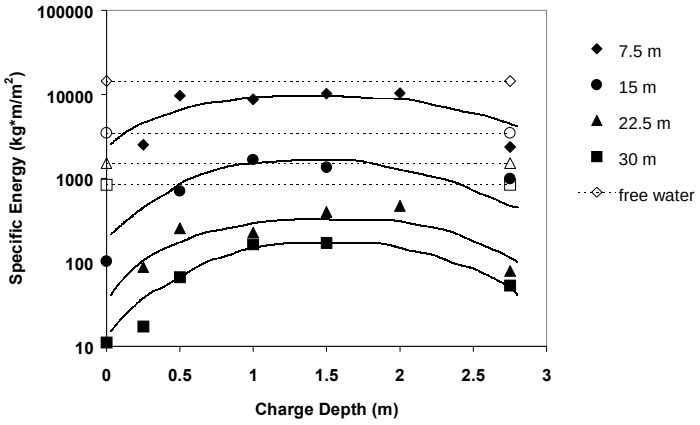
Figure 6 shows the peak-pressure and specific-impulse measurements from the twelve experiments, versus charge depth. The impulse is estimated over the duration τ_+ of the positive phase of the shock wave. The dependence of positive pulse duration, τ_+, on explosion depth is similar to that of the impulse and is not shown. Data on measurement errors have not been found in the archives yet, but thirteen of the measurements at sensor depth 1.5 m have been taken by two different sensors for a given explosion and distance. The discrepancies between these are the smallest for the peak pressures (3.3% on average and not larger than 12.5%), larger for the pulse duration (9% on average, but as large as 33% in one case), and the largest for the impulse (14% on average, and as large as 28% in one case). The semi-symmetric appearance





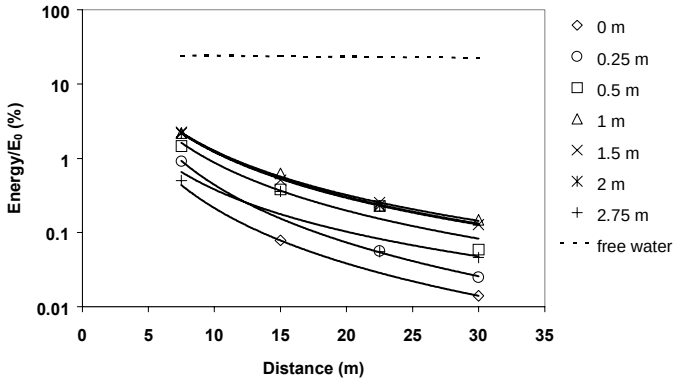
of the overall dependence of peak pressure on charge depth is due to the similar sound velocities of air and the sand on the bottom. Thus in the following we will mostly refer to results down to mid-pool depth. Fig. 6 shows a number of features of peak pressures: increase with charge depth, reaching maximum values around mid-pool; decrease with distance; mostly increase with sensor depth for any given shallow charge depth, but nearly constant values for mid-pool charge depths (especially closer to the explosions, at 7.5-m distance). The impulse also shows general increase with charge depth and decrease with distance. However, for any given explosion depth, the dependence on sensor depth is nearly symmetrical, with maximum reached around 1.5-m depth (mid-pool). This effect is due to reflections from the water surface and the bottom, which reduce the positive pulse duration, and therefore the impulse, when measurements are taken near the two boundaries. Kozachenko and Khristoforov (1970) have suggested semi-empirical formulae to fit the observations shown in Fig. 6, representing the shock-wave parameters through the free-water estimates in eq. (1) above, after application of certain correction factors. These correction factors are rather complicated functions of distance, sensor depth, and charge depths, and are not shown here.

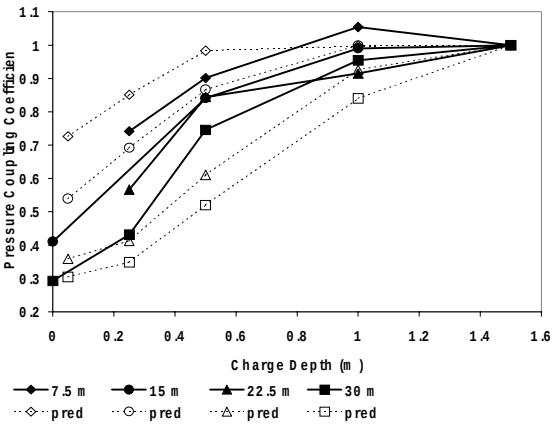
Since measurements at 1.5-m depth are least affected by the boundaries, Figure 7 shows peak pressure and impulse measured at this depth, as a function of charge depth. Compared with peak-pressures from the REFMS modeling, the observed pressures indicate very good agreement in the near field (7.5 m and 15 m) and poorer fit further from the source. However, the fit is very good for charge depths around mid-pool at all distances. The impulse measurements agree with the REFMS predictions at mid-distances (15 m and 22.5 m), but appear rather overestimated closer to the source (7.5-m distance) and somewhat underestimated further from the source (30-m distance), except for small charge depths. These discrepancies may be related to additional reflections from the walls of the reservoir, not modeled at present. Fig. 7 also shows estimates in boundless water calculated from eq. (1). While observed and REFMS-predicted peak pressures fit these calculations very well for mid-reservoir charge depths, the impulse measurements are much lower. The reason for this is that pulse duration is undercut due to reflections from the boundaries, thus significantly reducing the impulse as compared with boundless water. As an example, note that the REFMS-predicted values at 7.5-m, already quite higher than the observations, are comparable with the free-water calculations at four times larger distances (30 m). These results show that in terms of peak pressures (but not impulse), explosions and measurements at depth of ~1.5-m approximate very well a free-water environment.



Similarly, specific energy of positive pulse, E_+, measured at 1.5-m depth, is shown in Figure 8. These estimates are compared with calculations of the energy density flux in eq. (1), showing increasing departure for larger distances. Figure 9 shows the dependence of shock-wave energy, as a portion of total energy of explosion (418 x 10^5 kg∗m = 418 MJ for 100-kg TNT), on distance to sensor. The shock-wave energy in this case is calculated as $2\pi R \int_0^H E_+(h)\, dh$, where h is sensor depth, $E_+(0) = 0$ and H is the maximum sensor depth (2.75 m in these experiments). At 23-24%, the free-water estimates in Fig. 9 are much higher than the observed values, which exceed 1 to 2% only in the near field, and are measured at hundreds of a per cent further from the source. A distinct dependence on charge depth is indicated; for any given distance, these estimates are generally lowest for half-immersed charges (0-m depth), higher for 0.25-m and 2.75-m depths closer to the boundaries, still higher for 0.5-m depth, and the highest for mid-pool charge depths (1 m, 1.5 m, and 2 m).

Finally, Figure 10 shows what could be considered as a coupling coefficient in terms of pressure, versus charge depth. This coefficient is estimated by dividing the peak pressures from various charge depths by the pressure from a mid-pool explosion, best approximating a boundless-water environment. All measurements are taken at mid-pool, i.e., at 1.5-m depth. It is evident that these coefficients decrease as the charge approaches the surface, and the rate of this decrease is faster for larger distances. The character of the REFMS-predicted changes is the same, but a good match between observations and predictions is only seen at 15-m distance, i.e., neither too close nor too far from the source. In general, the REFMS modeling overestimates the observations in the near field (7.5 m and 15 m), possibly because in the real reservoir more energy is lost to reflections in the reservoir walls. Conversely, further from the source (22.5 and 30 m), peak pressures tend to decrease with charge depth more slowly than predicted, except perhaps on the surface (half-immersed charges).





In addition to the relationships for pressure coupling coefficients from nuclear explosions, *EM-1* (1996) also lists a simpler relationship for HE explosions of all sizes. These coefficients are much higher and change much more slowly with charge depth, than those for nuclear blasts. The small charge depth of 4.5 m/kt$^{1/3}$, for which full coupling is assumed in the *EM-1* manual, translates into less than 0.25 m in the 100-kg TNT case, using a scaling

factor of 0.046416 = $(0.0001 \text{ kt})^{1/3}$. Thus, only the observations from a half-immersed charge (0-m depth), ε = 0.41 at 15 m and ε = 0.29 at 30 m, can be compared with the analogous *EM-1* HE estimate of ε = 0.89 at 0 $\text{m/kt}^{1/3}$. Thus, our data not only show significantly smaller estimates for ε, but also reveal a dependence on distance that is absent in the *EM-1* relationships.

CONCLUSIONS AND RECOMMENDATIONS

Unique historic Russian data sets from three nuclear explosions in the shallow waters of the Bay of Chernaya (Novaya Zemlya) and 100-kg TNT reservoir explosions have been examined and analyzed for the purpose of characterizing the effect of charge depth on the hydroacoustic signals. This is of interest to CTBT monitoring because of the diminished signal levels from shallow explosions as compared to fully immersed charges. We have made various estimates to compare with existing relationships describing the coupling of hydroacoustic energy. We have also modeled the small-scale HE explosions, using the REFMS code for modeling of shock waves in water. The hydrophone records from the nuclear explosions recorded near and further from the source, shed light on the type of arrivals and pressure levels observed from such explosions. In particular, the pressure level of direct shock wave from the 1961 above-water blast appears diminished to about 4% of the free-water pressure at 35 km, in agreement with existing coupling relationships. The pressure levels from the underwater nuclear explosions are less well understood in this respect. The 100-kg TNT experiments and the REFMS-predicted peak pressures indicate coupling coefficients in the range of 30 to 70 % for half-immersed charges, depending on distance, gradually increasing to full coupling in mid-pool, where the conditions can be approximated with free-water regime.

These observations and results suggest that the effect of charge depth on the hydroacoustic shock-wave energy is more complicated than currently accounted for by existing relationships. Thus these relationships may have to be adjusted, while the relevance of the effect of charge depth in small-scale HE shallow experiments to the effect of depth of nuclear explosions needs further investigation.

ACKNOWLEDGEMENTS

We thank Bob Britt (SAIC) and Bob Thrun (NSWC) for providing the latest version of the REFMS code. Bob Britt was also very helpful with explanations of this software. Norton Rimer (Maxwell) is thanked for discussions and Chuck Wilson (Maxwell) has continued to advise us on the relevant literature.

REFERENCES

Eneva, M., J.L. Stevens, J. Murphy, B.D. Khristoforov, and V.V. Adushkin, Analysis of Russian hydroacoustic data for CTBT verification, in *Proc. 21st Seis. Res. Symp., 21-24 Sep., 1999*, Dept. Defense LA-UR-99-4700, 25-35, 1999. (Also accepted for publication in *Pure Appl. Geophys.*, 2001).

Britt, J.R., *Shock Wave Reflection and Refraction in Multi-Layered Ocean/Ocean Bottom – A User's Manual for the REFM Code*, SAIC, DNA TR-86-49, January 1986 (U).

Clarke, D.B., J.W. White, and D.B. Harris, *Hydroacoustic Coupling Calculations for Underwater and Near-Surface Explosions*, Lawrence Livermore National Laboratory, UCRL-ID-122098, 1995.

Cole, R.H., *Underwater Explosions*, Princeton University Press, Princeton, New Jersey, 1948.

Handbook of Nuclear Weapon Effects: Calculational Tools Abstracted from DSWA's Effects Manual One (EM-1), ed. J. Northrop, DSWA, pp. 736, 1996 (U).

Korobeinikov, V.P. and B.D. Khristoforov, Underwater explosions: Summary of Science and Technology, *Hydromechanics* **9**, 54-119, 1976 [in Russian].

Kozachenko, L.S. and B.D. Khristoforov, Shock waves in a shallow-water reservoir, *J. Appl. Mech. Tech. Phys.* **4**, 166-171, 1970 [in Russian].

Stephens, T. and C.S. Kelly, Computational Aids Update, *Science & Technology Digest*, August, 42-43, 1996.

USSR Nuclear Weapons Tests and Peaceful Nuclear Explosions 1949 through 1990, Ministry of the Russian Federation for Atomic Energy, ISBN 5-85165-062-1, pp. 63, 1996.

AUDIO-VISUAL AND HYDROACOUSTIC OBSERVATIONS OF THE DEAD SEA CALIBRATION EXPERIMENT

Yefim Gitterman and Avi Shapira

Geophysical Institute of Israel

Sponsored by the Defense Threat Reduction Agency

Contract No.DSWA01-97-C-0151

ABSTRACT

Three chemical charges of 500, 2060 and 5000 kg were detonated in November, 1999 in the Dead Sea at water depth of about 70 m (480 m below the ocean level). The main objective of the experiment was to calibrate the seismic travel times at local and regional distances.

Using a specially designed recording system and GPS measurements, it was possible to provide an accuracy of 5 milliseconds for the detonation time and few meters for the location. However, the actual location accuracy was reduced to 50 meters due to strong variable undercurrents and winds in the Dead Sea.

The source parameters of the explosions are:

Date	Origin Time (GMT)	Coordinates	Charge, kg	Magnitude	
				M_L	m_b
08.11.99	13:00:00.330	31°31'58.804"N 35°26'26.242"E	500	3.1	-
10.11.99	13:59:58.210	31°32'01.800"N 35°26'24.000"E	2060	3.6	-
11.11.99	15:00:00.795	31°32'00.995"N 35°26'28.760"E	5000	3.9	4.1

(Note: The GII is not estimating m_b magnitudes for event of m_b<4.0)

The experiment was video taped. The video and audio tracks provide a "live" presentation of interesting effects such as the "cavitation hat", arrivals of the shock waves and the bubble pulsations at the raft, where the camera was placed, and water uplift at the detonation point. The video clips also provide a rough estimation of the shock wave propagation time to the surface and to the raft and contribute to verification of the charge depth and explosion-to-raft distance.

One of the main objectives of the explosions was to characterize the specific seismic source by observation of radiated energy in the close vicinity. Two piezoelectric sensors, located at a distance of about 700 m from the shot point and at water depth of 25-30 m, provided unique pressure measurements of the water shock waves. The measured peak pressures significantly exceeded the expected values from an equal TNT charge in ocean water due to enhanced acoustic impedance of the supersaline Dead Sea water. Analysis of different phases and arrival times on the records provided identification of surface ("ghost") and bottom reflections and contributed to the verification of the experiment configuration. The shock wave energy was calculated utilizing the wave energy flux density equation, recorded pressure-time functions and unusual properties (density and acoustic velocity) of the Dead Sea water. The energy percentage was estimated relative to the energy of the explosive material used in the experiment.

This is not the first time that explosions have been carried out in the Dead Sea; it is, however, the first time that a seismic source with an equivalent magnitude of about 4.0 on the Richter scale has been artificially generated in the area. Unique observations of underwater shot phenomena and shock waves in the particular Dead Sea water were obtained. The experiment is also unique for this region since it has precise information on coordinates and origin time of an explosion being recorded over 2500 km beyond the borders of Israel.

Key Words: Dead Sea, underwater explosion, travel time calibration, audio-video clip, water shock wave

OBJECTIVE

The overall objective of the Dead Sea explosions was to calibrate the seismic travel times at local and regional distances in the Middle East and East Mediterranean region, to calibrate regional and IMS stations and provide data for the improvement of the CTBT monitoring capabilities with the IMS.
The specific objectives of the presented research relate to quantifying the coupling and the specific seismic source characterization of the explosions, including analysis of audio and video recordings, observation of radiated energy in close vicinity and measuring shock wave pressure in the unique Dead Sea settings.

RESEARCH ACCOMPLISHED

1. Charge design and detonation technique. Based on results of preliminary small test explosions of 25 kg at depths 70-100 m, it was decided to use a combined detonation technique: electric fuses and detonating cord (fuse) with multiple initiation points, and to limit the charges to the depth of 70 m. Parameters of the explosions are presented in Table 1. The charge unit design is shown on Figure 1. Sample photographs of the charges are presented in Figure 2. The primer blasting agent, CHEN AMON explosive, based on Ammonium Nitrate, has density 1.3-1.4 gr/cm^3, which is higher than the Dead Sea water density 1.236 gr/cm^3 (Anati, 1997), and detonation velocity 5500 m/sec. The Rotex detonating fuse (cord) 10,5 was used, which detonates at a velocity higher than 6500 m/sec.

2. Measurement of origin times and coordinates. In the first shot, a small seismic sensor was attached to the charge and provided accurate determination of the origin time. During the second shot, the sensor got disconnected from the recording system, and the O.T. estimation is based on measuring the relative propagation time of shock waves to piezoelectric sensors (see Chapter 4 below) and the absolute GPS time of the waves arrival to a hydrophone, co-located with the sensors. For the largest explosion we recorded the exact moment of detonating electric fuses, connected to detonating cord, which initiated the charge. The finite detonation time of the cord of the length of about 70-75 m is estimated to be 10 msec (~ 70m/7000m/sec), was also considered. The timing in the recording system was continuously synchronized with GPS. Using 500 samples per second digitizer, we obtain accuracy better than 5 msec.

The differential GPS system "Magellan" provided an accuracy of few meters in determining the location coordinates. Nevertheless, due to strong variable underwater currents and winds in the Dead Sea (especially during the second shot), we estimate the actual accuracy to be about 50 m, corresponding to possible drifting of the charge around the anchor.

Table 1. Parameters of the calibration underwater explosions in the Dead Sea, charge depth H=70-73m, the sea depth ~260 m (Ground Truth Information rank GT0).

Date	Origin time (O.T.), GMT	Location, GPS Magellan	Total charge kg	Charge components, kg			Initiation of the charge (using electric fuse - EF, and detonating cord - DC)	Comments
				chen amon	Accelerator			
					Red chen	TNT +PETN		
08.11	13:00:00.33	31.5330N 35.4406E	500	410	60	30	EF connected to DC on the water surface and at depth near the charge	
10.11	13:59:58.21	31.5338N 35.4400E	2060	1640	240	180	EF connected to DC (length about 70-75 m) on the water surface	After detonation failure on 9.11, two additional TNT units were submerged (10.11) near the main charge
11.11	15:00:00.80	31.5336N 35.4413E	5000	4460	360	180	EF connected to DC (length about 70-75 m) on the water surface	An impressive water uplift about 15 m was observed 5-7 sec after the detonation

3. Audio-visual records of the explosions. The experiment was video taped. A home camera was placed on the raft that was hosting all measurement equipment and the initiation systems, at a distance of several hundred meters from the shots. The video and audio tracks provided observations and rough time measurements of interesting physical phenomena, such as a "cavitation hat", arrivals of the shock waves and the bubble pulsations near the raft. The video clips also provided a rough estimation of the shock wave propagation time to the surface and to the raft and contribute to verification of the charge depth and explosion-to-raft distance.

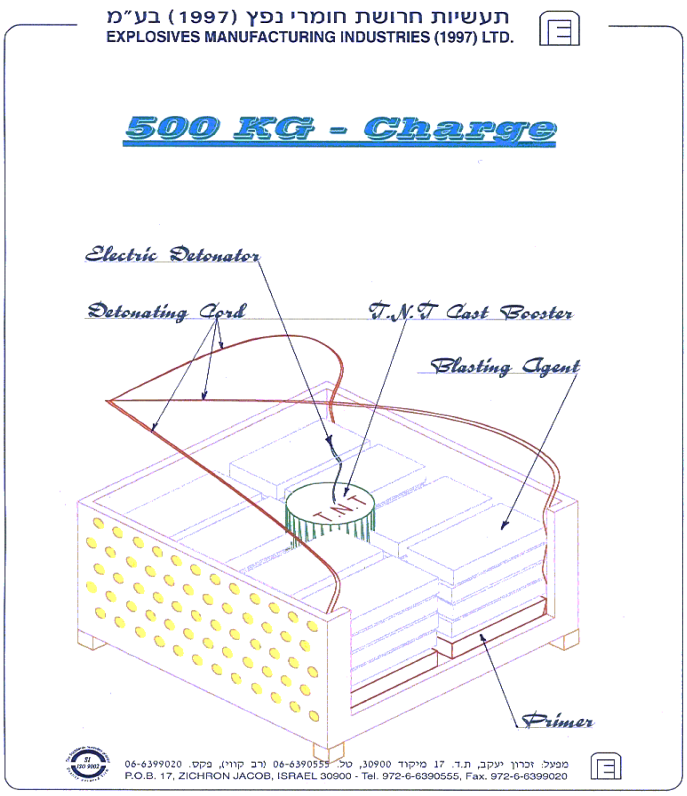


Fig. 1. Design of the charge unit, containing 500 kg of explosives for the explosion on 8.11.99 and 10.11.99 (total of 4 units), and 833 kg for 11.11.99 (total of 6 units).

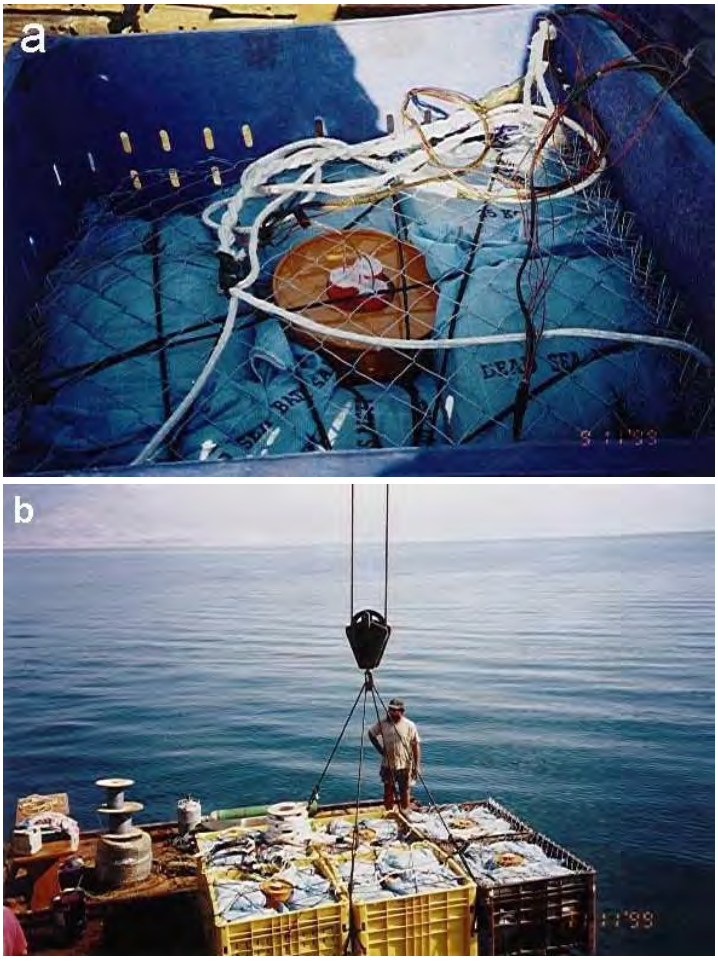


Fig. 2. Sample photographs of the charges of the three explosions: (a) the 500 kg charge unit was used also for the 2060 kg charge; (b) the 5000 kg charge consisted of six units of about 833 kg each.

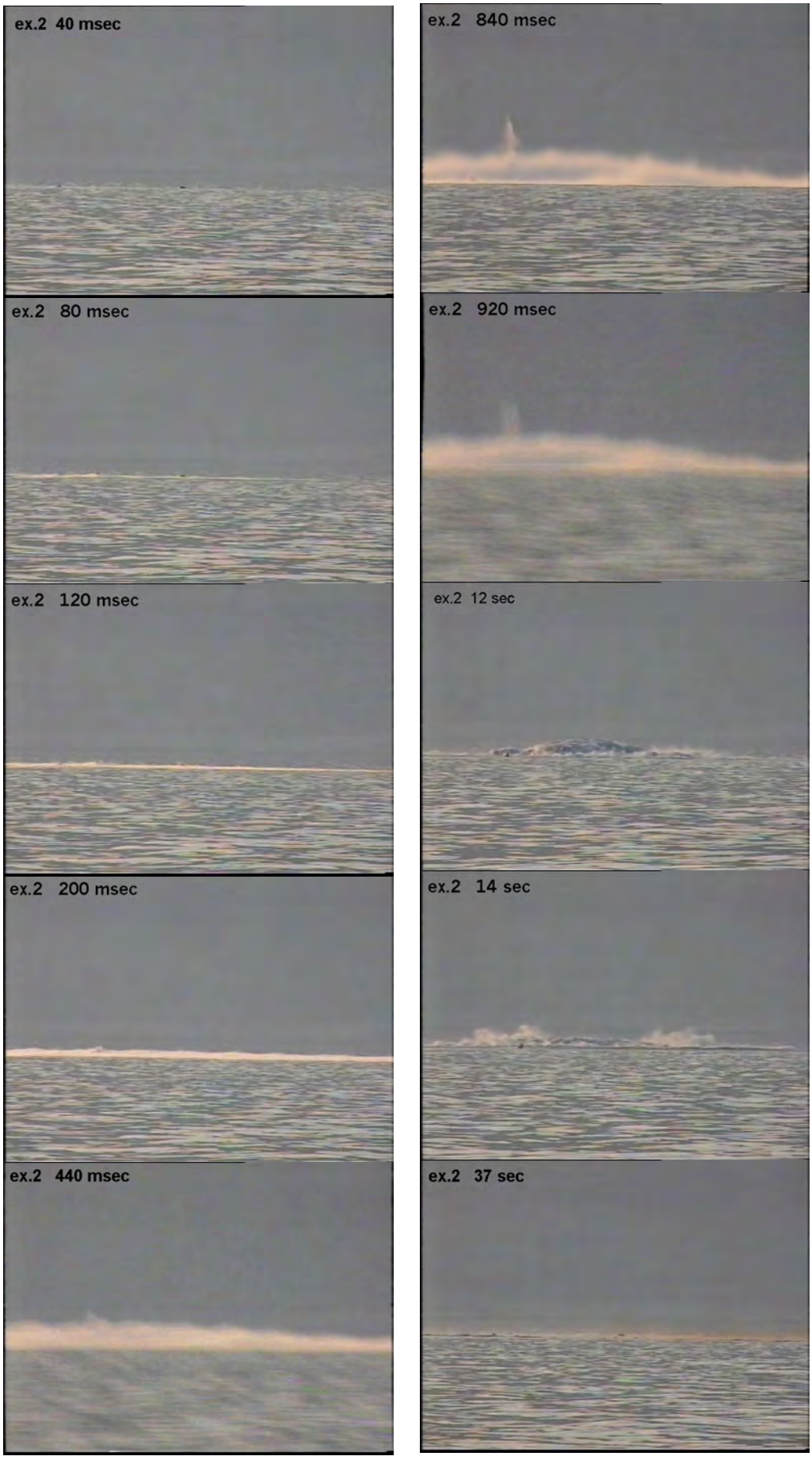


Fig.3. Snapshots from the video-record of the 2060 kg explosion

The video-recording rate is 25 fps (frames per second). This rate facilitates time measurement accuracy of about 40 msec. Figure 3 shows snapshots of the 2060 kg explosion, where following phenomena can be observed:

a) "Cavitation hat", created when the direct shock wave arrivals to the water surface. An initial sign of the cavitation strip can be revealed at about 40 msec after initiation, ant this estimation fits well the propagation time t_c = 70m/1770m/s = 0.0395 sec. The frames 80, 120 and 200 msec show an evolution of the cavitation process;
b) The camera went out of focus by the shock wave impact upon the raft at about 440 msec after detonation, yielding an estimation that the raft distance from the shot is ~775 m. This estimation corresponds well to the estimation obtained from hydroacoustic recordings (see Table 3);
c) The focus' distortion is repeated after ~0.5 sec (at the 920 msec snapshot) due to the gas bubble pulsation, which is close to the predicted and measured from seismic spectra bubble pulse period (Table 3);
d) Water uplift by the gases rise, in the time window 9-14 sec;
e) Appearance of yellow gases – explosive's detonation products, during 35-40 sec, in the area displaced to the right from the epicenter. These displaced gases are also an evidence to the strong underwater currents in the Dead Sea, which prevented location accuracy better than 50 m of the charge .

The video-record of the largest explosion 5000 kg has the impressive audio-track providing several specific audible signals, produced by the gas bubble pulsation, with intervals little less than 1.0 sec. It corresponds well to the estimation made from seismic records, of the bubble pulse period of about 0.8 sec (Table 3).

15 sec. videoclip of the 5000 kg shot

ex3_15sec.mpg

4. Types of water shock waves. The water pressures were measured by Sadwin Engineering Consultancy using type 138A01 piezoelectric underwater blast sensors manufactured by PCB Piezotronics. The pressure-time history was recorded by a computer system with 250 kHz response for each channel used. The record duration was only 0.7 sec due to some restrictions of computer memory and disc space. The full record of the largest explosion is plotted on Fig.4. The measurement gage was located at the distance of about 600 m and at the depth of 30 m.

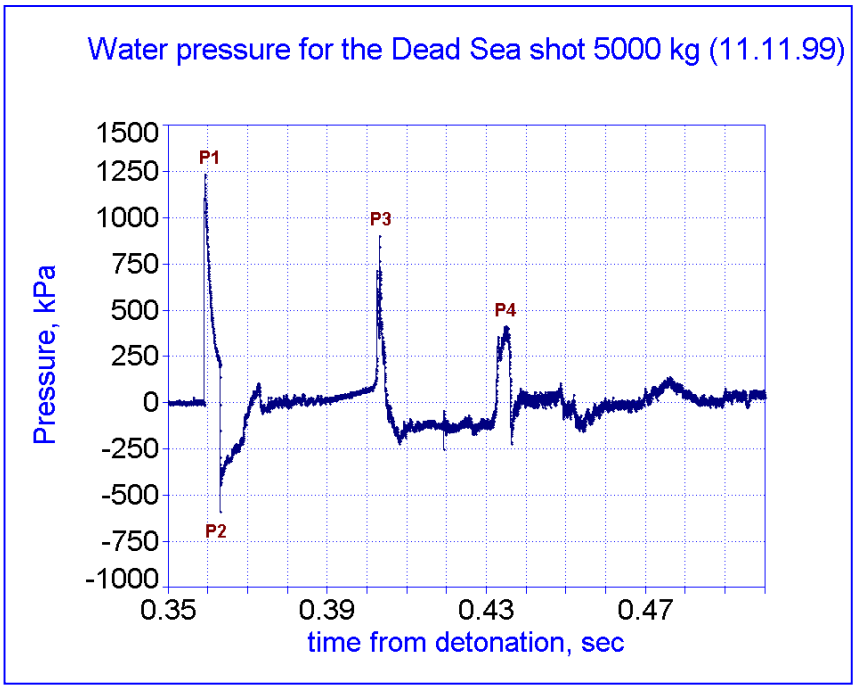


Fig.4. Pressure-time history of the largest explosion.

The primary or direct wave P1, and surface-reflected P2 waves can be easily identified, whereas interpretation of P3 and P4 phases meets some difficulties discussed in Chapter 5 below.

The cepstral simulation and inversion algorithm for analysis of regional seismic recordings of underwater explosions (Baumgardt, 2000) allows to separate out the band modulation of the surface reflection, yielding a negative cepstral peak at about 0.15 seconds period from the narrow band (20 Hz) EIL and MRNI seismic data of the Dead Sea shots. The optimal search inversions program returned very low values of the best matching reflection coefficient, sometimes on the order of -0.3 to -0.4 (D. Baumgardt, personal communication), which corresponds in some way to the water pressure measurements (Fig.4) showing the amplitude of the surface reflected wave about half of that of the primary shock wave amplitude.

The acoustic velocity in the Dead Sea has a high value C_w = 1770.6 m/sec (Anati, 1997), supporting the interpretation that the 0.15 sec cepstral peak is caused by the surface reflection. The fundamental frequency in this case is $f_r = C_w /(4*h)$ = 1770.6/(4*70) = 6.32Hz, and period is 0.158 sec, fitting well to the cepstral peak. In the ISN spectra, this surface reflection maximum is merged with the 5th harmonic of the bubble fundamental frequency $f_{b5} = f_b*5$ = 1.28∗5 = 6.4 Hz, causing enhanced maximums at about 6.46 Hz.

5. Verification of distances and depths. Based on the experiment configuration and arrival times of different phases measured from recordings of the shock waves, we tried to verify estimations of the source-sensor distance r, charge depth h and sea depth H in the shot point area. Travel times of different phases as measured from recordings of piezoelectric sensors and auxiliary hydrophones (which allowed kinematic estimations only) are presented in Table 2.

Table 2. Arrival (travel) times of different water shock waves.

Charge, kg	Sensor type	Sensor depth, h_s, m	Arrival time from the initiation moment, sec					
			Direct wave P1, t_d	Surface reflected P2, t_s	P3 t_3	P4 t_4	1st bubble pulse	2nd bubble pulse
500	hydroph.	2	0.510	-	-	-	0.931	1.289
2060	hydroph.	2	-	-	-	-	1.095	1.602
	piezoel.	30	0.44546	0.44854	-	-	-	-
		25	0.45933	046180	-	-	-	-
5000	hydroph.	2	0.349*	-	-	-	1.147	1.922
	piezoel.	30	0.35915	0.36304	0.40248	0.432	-	-

* - time from the charge detonation moment

The required parameters were estimated from combinations of simple kinematic equations, under the assumption that the shock wave velocity is constant along the whole propagation path (C_w = 1770.6 m/s):

$$r_i/C_w = t_i - \Delta t \qquad (1)$$

where index *i* corresponds to different waves, r_i is the propagation path and depends on ***h*** and ***H***, t_i is the arrival time (relative the initiation moment), and Δt is a delay of a shot caused by the detonation cord with unknown length and detonation velocity (>6500 m/sec), which connects the initiation point on the water surface and the charge at depth.

The detailed bathymetric map of the Dead Sea (Hall, 1993) shows (see Fig. 5), that the sea depth in the experiment area is ***H***=260-265 m.

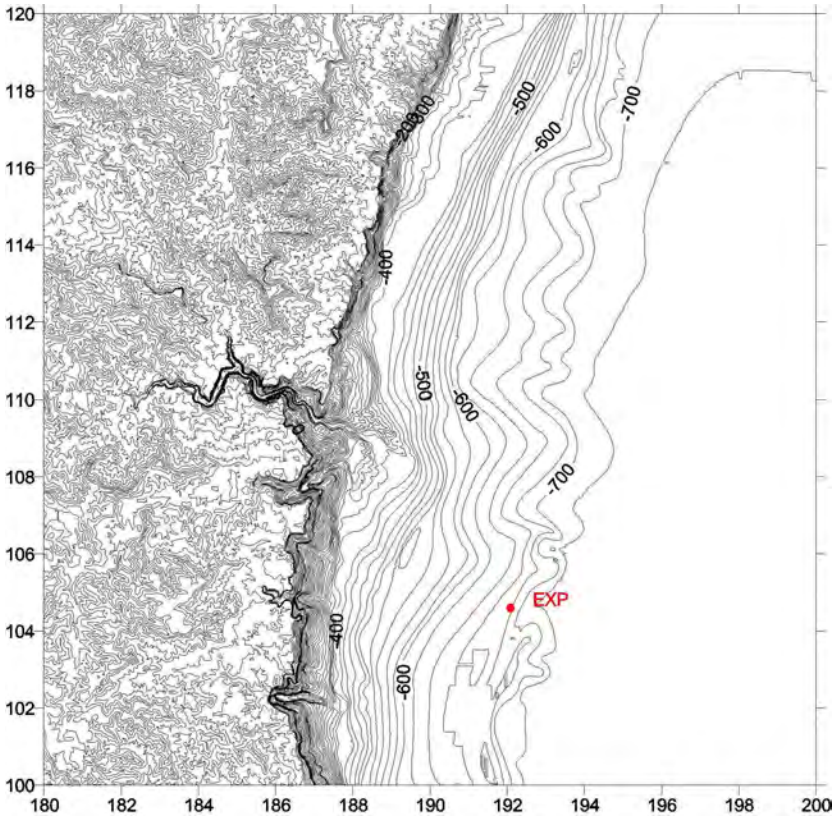


Fig.5. Bathymetric chart of the Dead Sea and the explosion site. The water surface level is -415 m.

The phase analysis results can be summarized as follows:

1. For both shots 2 and 3 the estimated delay Δt is 0.010 sec, a reasonable value considering the detonation cord length of about 70-75 m and detonation velocity 7000-7500 m/s. It is confirmed by a similar time difference of the direct wave arrivals to the hydrophone and the piezoelectric sensors during shot 3 (see Table 2).
2. The interpretation of phase P3 (see also Fig. 6) as the bottom-transmitted wave and P4 as the bottom-reflected wave, provides the sea depth estimate ***H***=265 m, which corresponds well to the batymetric map estimation. However, the very high amplitudes and short duration of phase P3 contradict the theoretical description of the bottom-transmitted wave as a slow-raising and low amplitude wave, and correspond much better to the bottom-reflected wave (see, for example, USACE, 1991). Thus this interpretation is based only on kinematic features of the observed phases.
3. The interpretation of phase P3 as the bottom-reflected wave and P4 as the surface-bottom reflection provide a rather different estimate of the sea depth ***H***=212 m. This interpretation is based on both kinematic and dynamic features of the observed waves, but is in disagreement with the batymetric map (another discrepancy is that surface-bottom reflection should be negative due to reflection from the water surface). The difference can not be related to estimation errors, and at the moment we can not provide any reasonable explanation and make a choice between the two interpretations.
4. The bubble period was estimated as the average time interval between the 1st and 2nd bubble pulses.
5. The distance values are very close to the preliminary estimations (Progress Report No. 26, 1999). A little increased charge depth estimation ***h***=73.5 m for the 5000 kg shot seems to be reasonable, possibly due to long-drown rope and a charge-center shift.

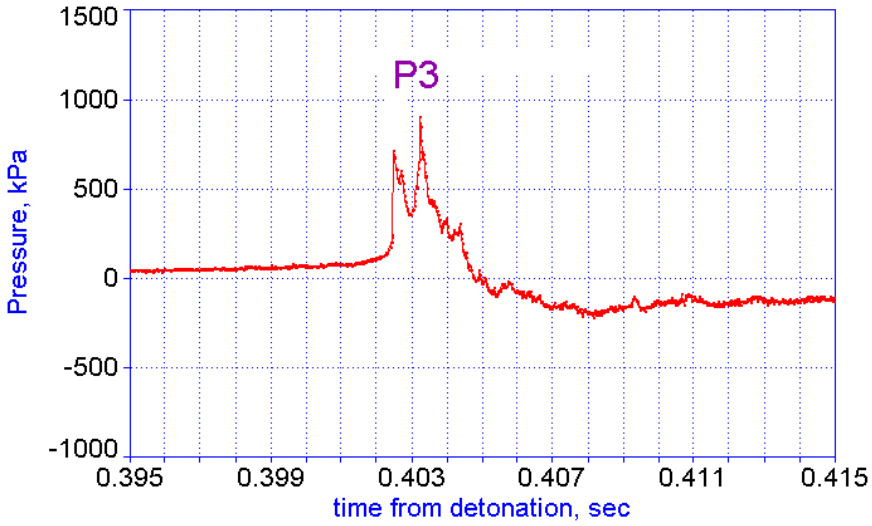


Fig. 6. Complex form of the P3 phase for the shot 5000 kg.

Obtained estimates of the shot configuration parameters and the bubble period are presented in Table 3.

Table 3. Shot configuration parameters and bubble periods estimated from shock wave travel times.

Charge, kg	Shot depth ***h***, m	Sea depth, ***H***, m	Hypocentral distance ***r***, m	Bubble period T_b, sec	Comments
500	-	-	900	0.390	no precise piezoelectric measurements
2060	70	-	770, 795	0.578	***r*** is for two gages separated by 25 m
5000	73.5	265 (or 212)	618	0.782	***H*** estimate depends on phase interpretation

6. Enhanced peak pressures. For the largest shot of 5000 kg, the main blasting agent CHEN AMON was about 97% of the total charge weight (see Table 1). According to the manufacturer estimation the explosive energy is about 80% of TNT. Nevertheless, the measured peak pressures significantly exceeded the expected values from an equal TNT charge in ocean water (see Table 4, Fig. 7).

USACE (1991) and Joachim and Welch (1997), in a form similar to that provided by Cole (1948), give the relationships:

$$P(t) = P_m e^{-(t-ta)/Q} \quad (2)$$

$$P_m\,(MPa) = 53.1\,(W^{1/3}_{(kg)}/R_{(m)})^{1.13} \quad (3)$$

$$t_a = r/C_w \quad (4)$$

$$Q_{(s)} = 9.2*10^{-5}\,W^{1/3}\,R_s^{0.18} \quad (5)$$

$$R_s\,(m/kq^{1/3}) = r/W^{1/3} \quad (6)$$

where P_m is the peak pressure, t_a is the arrival time, Q is the time constant, W is the equivalent weight, in kg, of TNT, detonated in ocean/lake water, r is the lateral distance in m, C_w is the sonic velocity in water, m/sec.

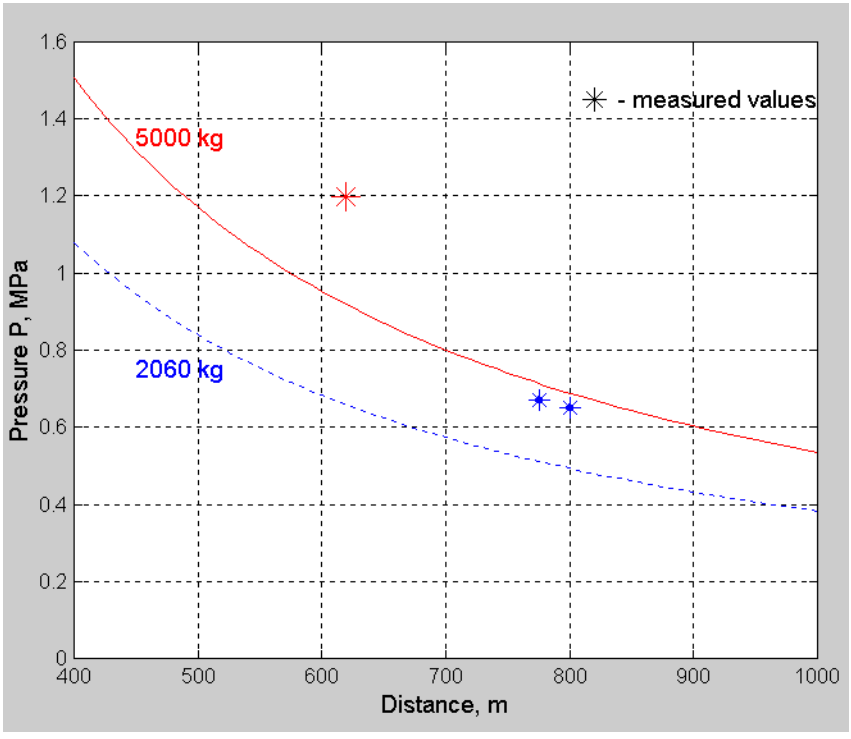


Fig. 7. Peak water pressure vs distance for underwater explosions of TNT in the ocean water and measurements of the Dead Sea shots.

The peak pressure values in Table 4 and Fig. 7 are calculated by Eq. 3. This observation of the enhanced pressures for the Dead Sea shots can be attributed to the acoustic impedance of the supersaline Dead Sea water being about 40% higher than in the ocean and, thus, yielding a much stronger shock waves impact (see also Eq. 7).

Table 4. Parameters of the shock waves for the explosions on 10.11.99 and 11.11.99.

Explosive weight, kg	Distance R, m	Sensor depth, m	Peak pressure, kPa		
			Estimated from eq.(3)	Measured	Ratio measured/estimated
2060	770	30	515	672	1.30
	795	25	496	654	1.32

5000	618	30	922	1230	1.33

7. Estimation of the shock wave energy. Shock wave energy flux density is calculated as (Cole, 1948):

$$E_{DS} = Z_{DS}^{-1}\int P^2(t)dt \qquad (7)$$

where Z_{DS} is the Dead Sea water acoustic impedance, $Z_{DS}=\rho_{DS}*C_{DS}$ =1236kg/m^3×1770m/sec, and P(t) is the curve-fit equation (see Fig. 8) with estimated time constant Q_{DS} = 0.0018458 sec:

$$P_{DS}(t) = 1.23*\exp[-(t-0.3592)/Q_{DS}] \quad \text{(in MPa)} \qquad (8)$$

Integral in (7) is calculated from the arrival time t_a=0.3592 sec to $t=t_a+6.7Q$ (Cole, 1948).

The full shock wave energy can be calculated (at distance r=618 m) as:

$$E_{DS} = \frac{1}{Zw}\int_{t_a}^{t_a+6.7Q}(10^3\times 1230\times\exp(-(t-0.3592)/Q))^2\,dt = 1219\ joul/m^2$$

$$E_s = E_{DS}\times 4\pi r^2 = 0.585\times 10^{17}\ \text{erg}$$

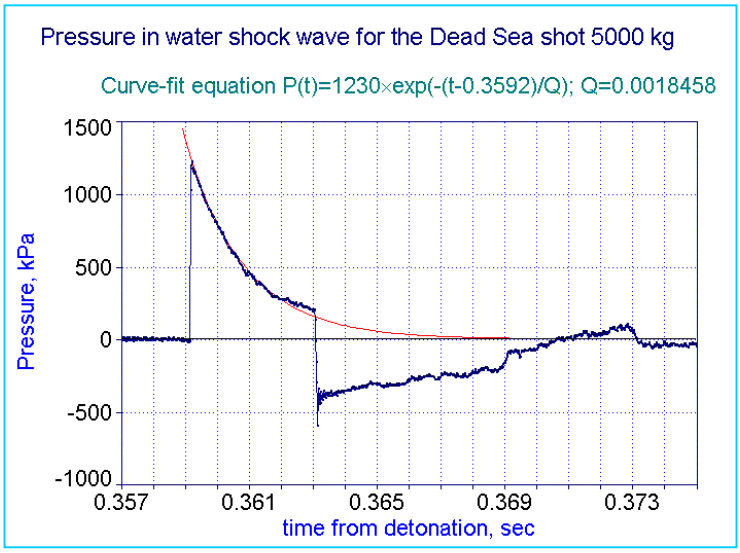


Fig.8. Primary and surface-reflected shock waves and the curve-fit equation.

Specific energy of the explosive CHEN AMON, used in the experiment, according to the manufacturer specifications: 1000 cal/gr = 4.2×10^{13} erg/kg, and the full explosive energy is: E_e=2.1×10^{17} erg. Then the share energy estimate for the primary shock wave is estimated to be

$$E_s/E_e = 27.5\%$$

8. Preliminary estimation of the TNT equivalent. It is assumed that the primary shock wave energy flux for the Dead Sea shot (W=5000 kg of CHEN AMON) E_{DS} equals the shock wave energy flux E_{OC} for the "equivalent" TNT charge W_T exploded in the ocean water:

$$E_{DS} = E_{OC} \qquad (9)$$

The value E_{OC} is calculated from Eq. (3,5,7):

$$E_{OC} = Z_{OC}^{-1}\int[53.1(W_T^{1/3}/r)^{1.13}\exp(-t/Q_{OC})]^2dt \qquad (10)$$

where the impedance for the ocean water is Z_{OC}=1030kg/m^3*1536m/sec, and Q_{OC} depends on W_T, as in Eq. (5). The value E_{DS} is calculated from Eq. (7,8):

$$E_{DS} = Z_{DS}^{-1}\int[1.23*\exp(-t/Q_{DS})]^2dt \qquad (11)$$

Finally, the TNT equivalent to the 5000 kg charge of CHEN AMON exploded in the Dead Sea is determined from Eq.(9-11) as:

$W_T = 4010$ kg

This value corresponds to the manufacturer estimation of the explosive CHEN AMON energy as about 80% of TNT.

CONCLUSIONS AND RECOMMENDATIONS

The video and audio tracks present interesting phenomena such as the "cavitation hat", arrivals of the shock waves and the bubble pulsations at the raft, and water uplift at the detonation point. The video clips also provid a rough estimation of the shock wave propagation time to the surface and to the raft and contribut to verification of the charge depth and explosion-to-raft distance.

The measured peak pressures significantly exceed the expected values from an equal TNT charge in ocean water due to enhanced acoustic impedance of the super saline Dead Sea water. Analysis of different phases and arrival times on the records enables the identification of surface ("ghost") and bottom reflections and contributed to the verification of the experiment configuration. The shock wave energy was calculated utilizing the wave energy flux density equation, recorded pressure-time functions specific for the Dead Sea water. These observations could also provide preliminary estimations of the shock energy share relative to the explosive energy, and TNT equivalent of the shots.

This is not the first time that explosions have been carried out in the Dead Sea; it is, however, the first time that a seismic source with an equivalent magnitude of about 4.0 on the Richter scale has been artificially generated in the area. The experiment is also unique for this region since it has precise source information of a seismic event that was recorded over 2500 km beyond the borders of Israel.

ACKNOWLEDGEMENTS

Many individuals and institutions supported the Dead Sea calibration experiment and contributed to its success at different stages. Special thanks to Dr. A. Dainty of the DTRA of the US Department of Defense, for full financial and diplomatic support of the experiment in the politically high-sensitive area. Thanks to Eng. E.Hausirer of Explosive Manufacturing Industries (1997) Ltd, Israel, for crucial assistance during the experiment. The Earth Sciences Research Administration of the Israel Ministry of National Infrastructures donated the piezoelectric sensors for measuring water shock waves. Thanks to the Israel Atomic Energy Commission and to the Arms Control Division of the Ministry of Defense, Israel, for their great support. Thanks to Dr. M. Abelson of the Geological Survey of Israel who provided an elaborated report about a potential environmental impact of the planned explosions. Special thanks to the Israel Defense Forces and the Police of Israel for their assistance in conducting the explosions. The management and numerous personnel of the Geophysical Institute of Israel provided financial and technical support throughout the experiment.

REFERENCES

Anati, D.A., 1997. The hydrography of a hypersaline lake. In: The Dead Sea (The Lake and its setting). Ed. T.M. Niemi, Z. Ben-Avraham and J.R. Gat.

Baumgardt, D., 2000. Seismic Characterization of the November 8, 10, and 11, 1999 Dead Sea Underwater Chemical Calibration Explosions Using Cepstral Modeling and Inversion, Spring 2000 AGU meeting, Washington.

Cole, R. H., 1948. Underwater explosions, Princeton University Press, 1948.

Dead Sea Calibration explosions: Operations and Preliminary Data, 1999. Progress Report No.26 on Contract No. DSWA01-97-C-0151, GII Report No. 591/61/97(26), December, 1999.

Hall, J. K., 1993. The GSI Digital Terrain Model (DTM) completed. In: R. Bogoch and Y. Eshet (eds.), GSI Current Research: V., Jerusalem, 47-50.

Joachim, C. E. and C. R. Welch, 1997, Underwater shocks from blasting, In: Proceedings of the 23rd Annual Conference on Explosive and Blasting Technique, Las Vegas, Nevada. International Society of Explosive Engineers, Cleveland, OH, 526-536.

U.S Army, Corps of Engineers (USACE), 1991. Underwater blast monitoring. Engineer Technical Letter No. 1110-8-11 (FR). Washington, D.C. 9p.

CALIBRATION OF HYDROPHONE STATIONS: LESSONS LEARNED FROM THE ASCENSION ISLAND EXPERIMENT

Philip E. Harben and Arthur J. Rodgers
Lawrence Livermore National Laboratory

Sponsored by U.S. Department of Energy
Office of Nonproliferation Research and Engineering
Office of Defense Nuclear Nonproliferation
National Nuclear Security Administration

Contract No. W-7405-ENG-48

ABSTRACT

Calibration of hydroacoustic stations for nuclear explosion monitoring is important for increasing monitoring capability and confidence from newly installed stations and from existing stations. Calibration of hydroacoustic stations is herein defined as the near-field precision location of the hydrophones and determination of the amplitude response; and the regional-scale calibration of acoustic travel times, bathymetric shadowing, diffraction, and reflection as recorded at a particular station. An important type of calibration not considered here is ocean-basin–scale calibration of a hydroacoustic monitoring system.

To understand how to best conduct hydroacoustic station calibrations, an experiment was conducted in May 1999 at Ascension Island in the South Atlantic Ocean. The experiment made use of a British oceanographic research vessel towing an airgun array and collected data over three Missile Impact Location System (MILS) hydrophones that were in use by the National Data Center (NDC) and the prototype International Data Centre (pIDC). From the towed airgun data, we were able to determine the location for each of the three hydrophones to accuracy better than 100 meters in latitude, longitude, and depth. The agreement with the nominal locations was excellent in depth and to within 1 kilometer in latitude and longitude. The depths determined for the hydrophones and the ocean bottom depths determined from the ship's sonar system force the conclusion that all three hydrophones are located at or near the ocean bottom. Amplitude frequency response of the hydrophones was also calibrated using a calibrated, temporarily deployed hydrophone to determine the airgun source function. With the source function known, the amplitude and phase response of the hydrophones could be deconvolved from the recorded waveforms provided a "pure" source waveform arrival is identified on the recording. Unfortunately, since the hydrophones are located near the ocean bottom, the recording is contaminated by reflections and scattered energy, making a reliable deconvolution impossible. Instead, peak-to-peak amplitudes were used at the dominant source energy to determine clip levels and calibration factors (in pascals at 10 Hz) for each of the three hydrophones. Consistency was confirmed using background hydroacoustic noise.

Imploding sphere sources were tested as a potential method to couple hydroacoustic energy directly into the Sound Fixing and Ranging (SOFAR) channel (at a nominal depth of 700 meters) without the use of explosives. Tests near Ascension Island and off the Pacific coast of California have demonstrated that imploding spheres can be made to fail at prescribed depths and that the signals are similar in amplitude and frequency content to about 1 lb. of high explosive. Although the source has promise as an alternative to small explosions, like explosives, most of the acoustic energy is at frequencies above that of the hydroacoustic monitoring band for nuclear explosions (1–50 Hz).

The use of towed airguns for the near-field precision location and amplitude calibration of hydrophones is ideal. The precision of the source location and timing, the ease of obtaining a planned source shot geometry and numerous shots, and the relatively low-frequency content of the source (i.e., in the CTBT monitoring band) cannot be equaled with air-dropped explosives or most other methods. If the hydrophones are located on the ocean bottom, in situ calibration is very difficult, ideally requiring a co-located, calibrated hydrophone at each hydrophone needing calibration. This will not be necessary with the new floated hydrophone stations since a "pure" recording of the source will be possible. Imploding spheres and small explosive sources in the Sound Fixing and Ranging (SOFAR) channel need further evaluation as regional calibration sources due to the relatively high-frequency content of the source.

Key Words: T-phase, hydroacoustic

OBJECTIVE

Hydroacoustic monitoring for the Comprehensive Nuclear-Test-Ban Treaty (CTBT) has made use of some existing hydroacoustic stations not necessarily intended to be used for the purpose of CTBT monitoring. Some of these systems are very old with poor knowledge of the sensor calibrations and location in the ocean. New hydroacoustic stations, such as Diego Garcia, would benefit from an in-field experimental calibration. The calibrations of T-phase stations -- seismic stations on an island that conduct hydroacoustic monitoring for the CTBT through T-phase signals -- are also poorly understood, making it difficult to utilize such stations effectively in a network of monitoring stations. Finally, although many recognize the possible benefits of joint analysis of different monitoring technologies such as seismic, hydroacoustic, and infrasound, little effort has been expended on this topic, in part because there is not much data of this type to analyze and in part because it is not clear exactly how to analyze it.

The Ascension Island Experiment, conducted in May 1999, was an attempt to gather data that could be used to understand all of these technical issues. The experiment would specifically locate and calibrate the CTBT hydroacoustic monitoring station at Ascension Island, help determine how to calibrate T-phase stations, and would leave behind a continuous monitoring system consisting of nearly co-located seismic, hydroacoustic, and infrasound stations. It represented an experiment of opportunity through collaboration and cost sharing. Participant institutions included Lawrence Livermore National Laboratory, Cambridge University, Naval Research Laboratory, Scripps Institute of Oceanography, Los Alamos National Laboratory, the Provisional Secretariat, and the Center for Monitoring Research. This paper focuses on the most important objective of the Ascension Island Experiment; hydroacoustic station calibration. We present the analysis of the Ascension Island data to determine precision in-situ hydrophone locations, to calibrate a hydrophone monitoring system response using an airgun source, and the use of a safe deep water hydroacoustic source based on the implosion of a glass sphere for future long-range calibrations.

RESEARCH ACCOMPLISHED

The J.C. Ross, an icebreaker class oceanographic research ship belonging to the British Antarctic Survey, was hired for 4 days of airgun shooting around the waters of Ascension Island (Minshull, 1999). The ship was equipped with an 11-airgun array with a total shooting volume of over 6000 cubic inches. The track of the ship during airgun shooting is shown in Figure 1 with blowups in the immediate vicinity of the nominal locations of the Ascension hydrophones. During most of the shooting near the hydrophones, a single 1000 cubic inch airgun was used. The same airgun was fired over a temporary, calibrated hydrophone, providing the source characterization required for determining the calibration factors for the Ascension hydrophones. In addition, imploding spheres were tested during this cruise but the results presented here are for a subsequent test off the coast of California.

The ship track was determined by an on-board differential Global Positioning System (GPS) that archives time and position to 1 millisecond and 1 meter accuracy, respectively. For the analysis that follows, the ship track file was corrected to account for the difference in the position of the GPS ship antenna with respect to the towed airgun. The airgun position accuracy is estimated at 10 meters. Airgun depth was also corrected. The airgun depth is nominally 5 meters when the single gun was fired around ASC26 and 20 meters depth at the other hydrophones, when the full airgun array was deployed. The depth position accuracy is estimated to be 5 meters.

Experimental Determination of Hydrophone Locations:

In all, 35 airgun shots were used to determine a new location for ASC26. The direct arrival times were picked for each of the 35 shots and subtracted from the known shot zero-time to get a direct path traveltime from the airgun to the hydrophone for each shot. The corresponding travel times were compared with that determined by a ray tracing code that uses the nominal sound speed profile in the region and season (Levitus et al, 1994) at 1m-depth increments. The ray tracing code determines means and root-mean-square (RMS) residuals from all the shot locations for a specific trial hydrophone location in a 3-D grid. The procedure is applied to every trial location in the grid with increments of 55 meters in latitude and longitude and 3 meters in depth. A grid search routine then looks for the trial location in the
3-D grid with a minimum RMS value. The latitude and longitude with the minimum RMS value is taken as the location of the hydrophone. The depth of the hydrophone is determined by examining the means at each depth with the same latitude and longitude corresponding to the minimum RMS value. The depth closest to having a zero-mean

is taken as the best depth.

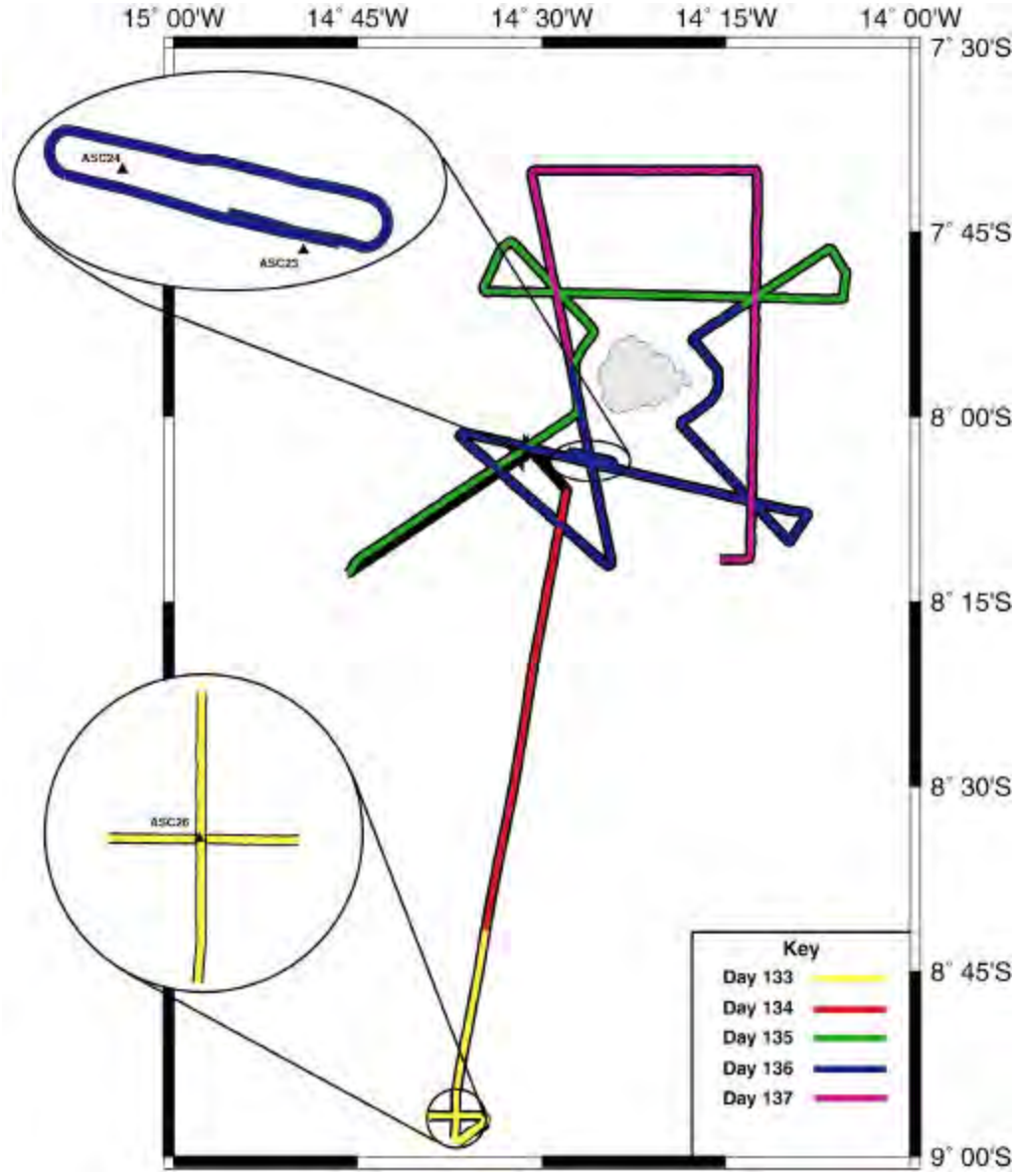


Figure 1. The J.C.Ross ship track during airgun shooting in the waters around Ascension Island. The blow-ups show the track in the immediate vicinity of the three hydrophones and plots their nominal location.

The results for ASC26 are summarized in Figure 2 by showing the individual airgun shots, old and new locations for the hydrophone, bathymetry data determined by the J.C. Ross along the ship track, and the raw airgun waveforms recorded by ASC26 and aligned with the ship position for that airgun shot. The raw waveform data clearly indicates a hydrophone location consistent with that determined by the location analysis procedure. Furthermore, the bathymetry values determined by the J.C. Ross are consistent with the 1.66-km depth determined for the hydrophone from the airgun data provided the hydrophone is located on or near the ocean bottom. The original 1957 installation report (Western Electric, 1961) gives the depth of ASC26 as 1.66 km with no mention of a floated hydrophone system, consistent with the airgun data and J.C. Ross bathymetry.

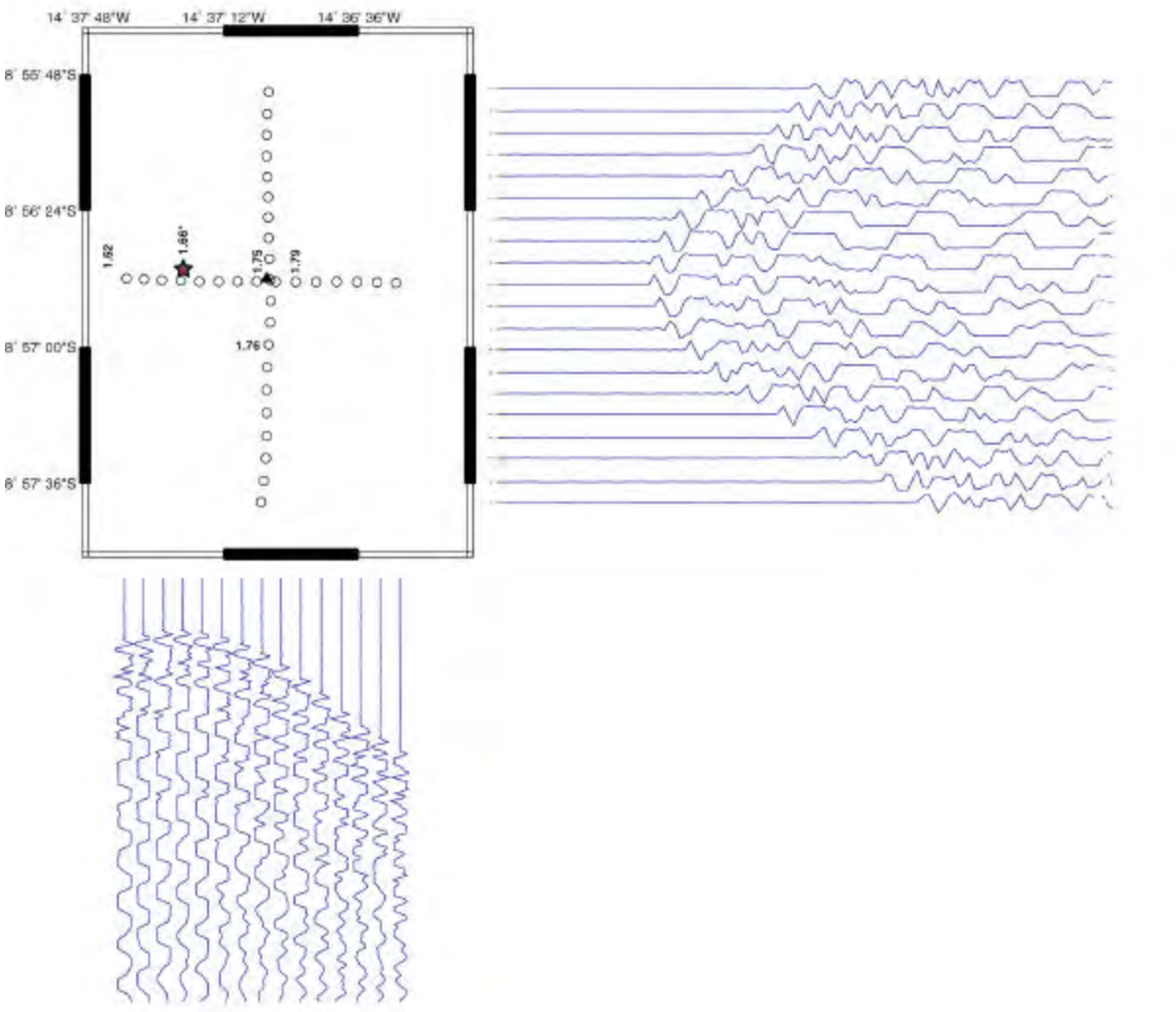


Figure 2. The old (black triangle) and new (red star) location for ASC26. The open circles are the locations of each airgun shot. The numbers associated with some circles are the ocean bottom depths in kilometers as determined by ship sonar. The 1.66-km depth is associated with the new location. The waveforms aligned with each shotpoint are the raw airgun signals recorded by ASC26 for that shot, beginning at shot time. The raw data clearly suggests the new location.

The racetrack pattern around ASC23 and ASC24 resulted in a large number of airgun shots in the vicinity of both hydrophones. Although all the data was initially used in the location analyses, an improvement in the mean and RMS fits was observed when direct traveltime paths greater than 1 second were omitted from the analyses. Consequently, the locations for ASC23 and ASC24 were conducted with all airgun shots that had less than a 1 second traveltime (e.g. were less than 1.5 kilometers from the hydrophone). The reasons for the higher RMS values using all the airgun data could be due to errors introduced by complications in the direct arrival by shadowing from bathymetric features and errors in the ray tracing routine and the sound speed profile, all of which are compounded by lower angle ray paths. Using the same procedure as outlined for ASC26, the ASC23 and ASC24 locations were determined using 46 airgun shots and 35 airgun shots respectively (Figure omitted due to paper length limitations). The bathymetry in the region shows considerable variability but is consistent with hydrophones that are near to the ocean floor. Traveltimes of reflected phases from ship locations nearest the hydrophones also point to a hydrophone depth that is very near the ocean bottom.

The three Ascension Island hydrophones presently in use by the NDC and pIDC have been located to an accuracy of at least 100 meters in latitude, longitude, and depth (Harben et al, 1999). It is clear from the hydrophone depths determined by the airgun shootings, the bathymetry determined by the J.C. Ross, and the original 1957 installation document that the hydrophones are located on or near the ocean bottom. The new locations are all less than a kilometer from the old locations, indicating that the old locations were more accurate than expected. Furthermore, the new depths are within 10 meters of the nominal locations.

A towed marine airgun with precision timing and differential GPS logging capability is a good method for determining the position of in-place hydrophones. Other methods to determine hydrophone locations such as air-dropped Signal Underwater Source (SUS) charges would have difficulty matching the precision of an airgun because the inherent SUS location and zero time errors are larger, the pattern of SUS charges is more difficult to control, and the number of charges used has practical and cost-driven limitations. Small implosive sources such as lightbulbs have been used from ships as hydrophone calibration sources and may be useful in location, though precision position determination and ease in deploying a large number of sources needs to be studied. It is not necessary to have as large or as capable a ship as the J.C. Ross to accomplish a location survey using airguns since it only requires a relatively small single airgun with precision timing and location. Such a system could be temporarily mounted on a relatively small ship near the survey location to minimize cost.

Determining Hydrophone Calibrations:

A temporary calibrated hydrophone moored at 925 meters depth was used to record the waveforms from a 1000 cubic inch airgun to determine the airgun source function. By repeated firings, the source function reproducibility was tested and shown to be highly repeatable. The source function for the airgun was determined using the direct phase recordings corrected by the known instrument response. The source was found to have a peak amplitude of 751 kPa at 1 meter, consistent with manufacturer specifications. Because all three Ascension hydrophones are located near the ocean floor, it was not possible to simply deconvolve the projected measured source function from the signals measured at the Ascension hydrophones to determine the hydrophone monitoring system amplitude and phase response. The direct arrival phase at the hydrophones was contaminated by nearly time-coincident bottom reflections and scattering (and to a lesser extent by Stoneley waves). Consequently, a procedure was developed to determine a calibration factor for each hydrophone, which is shown below for ASC26 Harben et al, Feb. 2000).

The recordings of the 1000 cubic inch airgun shots near ASC26 are best viewed in record section as shown in Figure 3. The record section proceeds from the recorded waveform of the airgun shot closest to ASC26 (top at 1.81 km) to the airgun shot farthest away (bottom at 8.63 km). The distances shown are direct acoustic path ranges and record sections plot each shot at an even spacing below the previous shot though the range between shots is not linear (particularly when the airgun is nearest the hydrophone). The record section clearly shows a number of phase arrivals. The Stoneley wave, traveling along the ocean-sediment interface, is ahead of the direct path acoustic wave but is small enough in amplitude that the coda does not significantly contaminate amplitude measurements and arrival picks of the direct hydroacoustic phase. The coda of the direct phase exhibits ringing for the closest airgun shots. The ringing corresponds to a clipped signal. We do not know if the signal clipping and ringing is due to the sensor or to system electronics. The ringing could also be the result of mechanical motion of the hydrophone cable system at high acoustic signal levels. The reflected phases are single (1st) and double (2nd) reflections off the free surface. As the source-receiver range increases, the direct arrival amplitude falls below clipping level and exhibits the peak-to-peak amplitude fall-off with distance expected by predictions based on directivity effects due to reflection off the free surface and geometrical spreading. By projecting the known source signal level to the range that clipping ceased, a clip level in Pascals for each of the hydrophone systems as well as a maximum signal level for linear system response could be determined.

The procedure for determining a calibration factor starts by determining an analysis window of source-receiver ranges. The ranges are chosen so that the minimum range is beyond the ranges that exhibit clipping (4.4 km for ASC26) and the maximum range is before the signal-to-noise ratio becomes too low for accurate peak amplitude measurements (7.5 km for ASC26). For each airgun shot record in the range analysis window, the peak-to peak direct arrival amplitude is measured in raw counts. By projecting the source function to the range and conditions (i.e. accounting for directivity and spreading due to geometry but not attenuation which is negligible at these frequencies and ranges) of each airgun shot, the expected source level in Pascals is determined for that shot geometry. The

calibration factor (in counts / Pascal) is then determined by dividing the measured peak-to-peak amplitude by the projected source level for each shot and averaging over all shots in the range analysis window. It should be noted that the bulk of the airgun acoustic energy is centered at 10 Hz. All calibration factors and corrections were therefore conducted at 10 Hz and do not necessarily apply to acoustic frequencies more than an octave above or below 10 Hz.

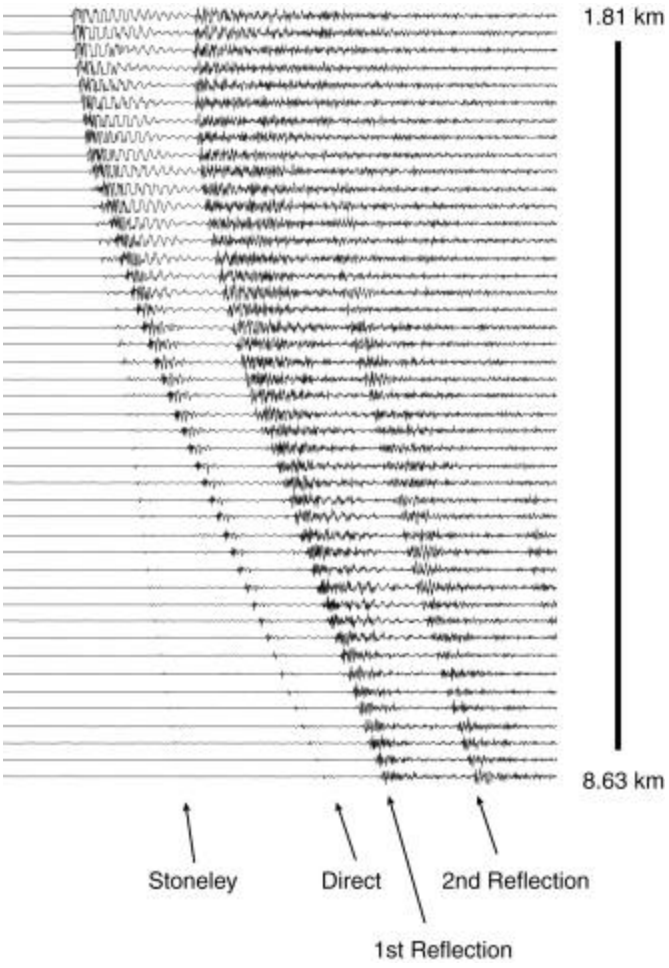


Figure 3. Record section for ASC26 with airgun shots nominally 150 meters apart. As the ship sails away from the hydrophone we see normal move-out and the development of distinct phases as labeled.

The results for the clip levels, the maximum levels with linear response, and the 10-Hz calibration factors for the three Ascension hydrophones are shown in the table below. The calibration factors were applied to a 5-minute noise period measured at each station and found to be self-consistent.

Hydrophone Name	Counts per Pascal (Ct/Pa)	Clip Level (Pa)	Max. Linear Level (Pa)
ASC26	3.5×10^5	29	20
ASC24	1.7×10^4	120	88
ASC23	8.8×10^4	102	68

A highly repeatable source like an airgun should be able to provide for effective amplitude and phase response calibration provided the hydrophone used to measure the source function and the hydrophone to be calibrated are able to measure a portion of the direct phase before scattered and reflected wave phases arrive. Another calibration strategy is to locate a calibrated hydrophone as near as possible to the hydrophone with unknown instrument

response. In this case, ambient background noise measurements may be sufficient to deconvolve an instrument response using the calibrated hydrophone as the "source function". In the case of ocean bottom hydrophones, this is probably the only means to obtain a full amplitude and phase response curve. Newly install floated hydrophone stations, on the other hand, will probably be easy to calibrate using a direct deconvolution of the projected source function.

Imploding Sphere Sources for Long-Range Calibration:

One way to accomplish long-range calibrations is to detonate a large number of small (1-2 lbs of high explosive) charges within the SOFAR axis on various tracks in an ocean basin, recording the signals at all operational hydroacoustic stations. Although pressure-detonated explosives are a simple, reliable, and flexible method to generate an impulsive hydroacoustic source at a desired depth, safety procedures, specialized training, and local regulations preclude their use on most ships. This leaves few alternatives as SOFAR axis sources, since airgun and most other seismic marine sources are designed for use only at shallow depths. Imploding spheres have a relatively long history of specialized use and are a potential acoustic source at mid-ocean depths and below; but they have not been deemed reliable because they fail well below or above the desired depth or do not fail catastrophically at all. If imploding spheres can be made reliable and can deliver an adequate signal for long range calibration, the method has the distinct advantage of having no stored energy at the surface and therefore no shipboard safety concerns and no special shipboard equipment requirements for deployment. This advantage allows for the possibility of deploying the spheres from a wide variety of ships on cruises for other purposes, thereby minimizing the costs associated with ground truth data collection. The need for an inexpensive source at the SOFAR axis that does not have the hazard and safety procedure problems of explosives was recognized in the recent International Workshop on Hydroacoustic Monitoring for the CTBT that met in Tahiti late September, 1999 (CTBTO/PTS/DASE, 1999). The workshop findings identify acoustic source development as a technical issue and advocate an approach to the problem that addresses the safety issue and the need for low-cost expendable sources.

An imploding source exploits the pressure difference between an enclosed volume of gas at nominal atmospheric pressure and the external water pressure at the implosion depth. A sudden catastrophic failure of the containing vessel leaves the relatively low-pressure gas bubble exposed to relatively high-pressure water and a rapid implosion ensues. The implosion momentum collapses the bubble radius to less than that required for an equilibrium pressure balance. At the instant of minimum bubble radius, the bubble begins expanding and radiates a positive acoustic pressure spike. This oscillation can continue for a few cycles, each with successively reduced pressure spikes as energy is dissipated and the bubble approaches a static equilibrium pressure. The process is similar to the bubble pulses seen from subsurface explosions, the gas globe from the explosion oscillating about the equilibrium pressure. One distinct difference is that in the case of underwater explosions there is an initial shock wave caused by ignition of the explosive and creation of the expanding gas globe consisting of explosion gas products. There is no such analog in an implosion. Another important difference is the relatively cold low-pressure gas inside the sphere compared to the high temperature dense explosive gas products in the gas globe. The bubble collapse details of the two cases cannot be directly compared.

If a glass sphere is of sufficient volume to produce the desired source signal level and has sufficient wall thickness to survive the water pressures in the operational depth range, the sphere failure must be initiated by some controlled method at a predetermined depth. Such a mechanical implosion initiation device was designed to crack the sphere at a preset depth, herein referred to as the "spherecracker" (Boro and Harben, 1999). The spherecracker was designed to be rugged enough to be reusable, heavy enough to sink the whole assembly loaded with the sphere, and without stored energy at the surface. In addition, use of inexpensive materials from standard stock was also a goal so that the spherecracker cost is low enough to allow for a use-once option in deployment. The device is shown in Figure 4 and consists of two orthogonal cut-out plates that hold the sphere and a cylinder-piston-ram assembly that punches a hole in the sphere. A rupture disk attached to one end of the cylinder assembly is calibrated to fail within 5% of the failure pressure, 1000 psi in our tests. Failure of the rupture disk results in an inrush of high-pressure water into the air-filled piston chamber, driving the piston -- and attached ram -- towards the glass sphere. The Custom Glass Shop, a Division of Kontes Glass Company (CGS) made the spheres. The spheres are a special order modification of a standard 22-liter laboratory boiling flask. The wall thickness is nominally 0.64 cm (0.25 inches) but, since each sphere is hand blown, the wall thickness can vary considerably. Our concern with these spheres was their survival at nominal SOFAR axis depths. Initial tests were conducted without the spherecracker to assure that the spheres would survive to SOFAR depths.



Figure 4. The spherecracker is shown on the right in the lowering orientation. The glass sphere is shown on the left atop a laboratory beaker.

An opportunity to conduct a field test with a CGS sphere and spherecracker came in February 2000. The spherecracker was loaded aboard the Research Vessel (R.V.) Sproul and tested west of San Diego CA at water depths around 1200 meters. The spherecracker was loaded with a 22-liter CGS glass sphere and was lowered until a 1000 psi rupture disk failed. After initiating a successful implosion, the spherecracker was recovered undamaged. By reloading the device with a new pressure disk and glass sphere, it could be used repeatedly. The impulsive hydroacoustic signal recorded from the implosion allowed accurate determinations of hydrophone depth, implosion depth and water depth from the surface reflected, bottom reflected, and 2nd bottom reflected phases, respectively (Harben et al, May 2000). The implosion occurred at 685 meters depth. The implosion signal was felt on the ship and recorded by a calibrated hydrophone suspended 13 meters deep. The recorded signal shown in Figure 5 was of short duration (less than 5 msec) and with a small bubble pulse about 2 msec after the main collapse. The event starts with a rarefaction as the sphere shatters and collapses. The large compressional pressure spike following the rarefaction occurs when the collapse reaches a minimum volume and reverses (begins expanding). The waveform was projected back to 1 meter by multiplying the hydrophone output by the distance of the hydrophone from the implosion, 672 meters. The peak pressure from the implosion is slightly larger than that from 1 lb of TNT at the depth of the test (Urick, 1983). The source does not show any appreciable acoustic energy above background levels for frequencies below about 50 Hz. Above 50 Hz the source amplitude rises to a broad maximum at frequencies between 200 and 800 Hz. There is a relatively shallow high frequency roll-off of the source energy between 1 kHz and 10 kHz whereas the noise rolls off more steeply in this band. The consequence is that the signal-to-noise ratio is highest at about 10 kHz.

Long-range propagation of signals from small (1-2 lb) explosions within the SOFAR has been amply demonstrated (Harben et al, May 2000). Since the imploding sphere source within the SOFAR has a peak pressure amplitude similar to that of a small (1 lb) explosion and similar frequency content, it is reasonable to assume that the imploding sphere source signal will propagate for long distances within the SOFAR. The pressure amplitude spectra of the imploding sphere source shows that the bulk of the acoustic energy is well above the frequency band that is used for nuclear explosion monitoring (nominally 1-80 Hz). This means that travel times, shadowing, diffraction, reflections, etc. would be calibrated at frequencies starting at the high end of the nuclear explosion monitoring band and extending beyond it. For some parameters (e.g. travel time) this may be acceptable but for others (e.g.

shadowing) it may lead to inaccuracies. Potential methods do exist to excite lower frequencies from the imploding sphere. By increasing the volume of the sphere, imploding the sphere at a shallower depth, or through the use of multiple spheres simultaneously imploded, lower frequency energy can be excited.

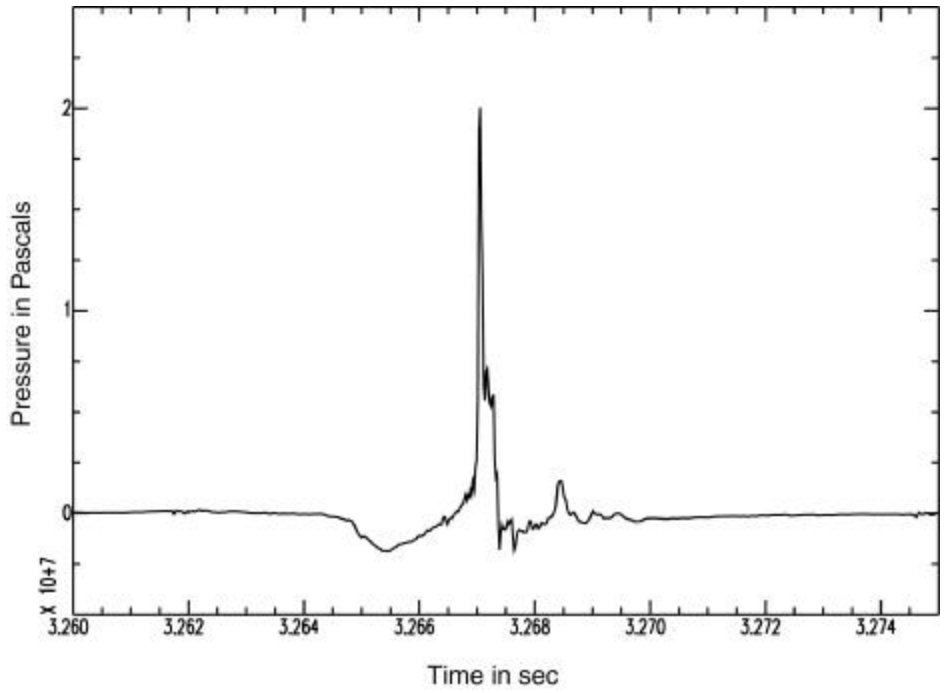


Figure 5. The calibrated pressure-time history of the implosion as recorded by a shallow ship-suspended hydrophone and projected back to 1 meter.

CONCLUSIONS AND RECOMMENDATIONS

It is clear that a towed airgun system with good timing and location control can accurately determine hydrophone location and calibration, provided the hydrophone is floated a sufficient distance from the ocean bottom so that a "pure" recording of the direct phase can be recorded before reflected phases arrive. Such calibrations are crucial in verifying location (and current drift limits) and in establishing the full in-field system response in physical units of pressure. Such calibrations should be conducted at every hydroacoustic station in the monitoring network.

Long-range calibrations that attempt to determine hydroacoustic features such as travel times, shadowing, reflections, etc. in the region of a station, or even for a whole ocean basin, have not yet been attempted. The Ascension experiment began that effort by developing an imploding sphere source and by evaluating airguns as longer-range SOFAR guided sources (Hanson and Harben, 2000). The next step is to actually conduct a regional scale calibration experiment using imploding spheres and an airgun source, comparing the two and determining how to conduct such calibrations on a routine basis.

The Diego Garcia hydroacoustic station has recently been installed and is an ideal candidate for the next in-field calibration site. From the experience gained at Ascension Island, the local calibration of Diego Garcia would best be accomplished using a towed airgun system. This would provide the most accurate measurements of hydrophone locations and of the system amplitude and phase response. Diego Garcia would also be a prime site for further experimentation with imploding spheres and airguns to calibrate longer range travel times and determine bathymetric and island shadowing at a station where little is known at present. Future calibrations are in order for Crozet Island and other upgraded and new hydroacoustic stations as they come on-line.

ACKNOWLEDGEMENTS

A large number of individuals and institutions made the Ascension Island Experiment possible. Donna Blackman of Scripps Institute of Oceanography was a crucial catalyst for the experiment and provided assistance in the field and with data analysis. Tim Minshull, at Southampton University, England planned and coordinated the ship use, the airgun configuration and operation, and the overall specifics of the cruise. Vicki Childers and John Brozena from the Naval Research Laboratory provided partial financial support of the cruise and assisted in the field. Marta Galindo and Martin Lawrence of the PTS provided financial support for the temporary OBH deployments and field assistance. Keith McLaughlin and Ann Gault, CMR, provided all hydrophone data during the experiment and useful information on station history. Don Rock at LLNL installed the temporary seismic stations and ran the synergy experiment. Rod Whitaker and Tom Sandoval of LANL sited and installed the infrasound station for the synergy experiment. Jay Pulli and Ted Farrell of BBN Inc. assisted with MILS data during the cruise and collaborated with imploding sphere investigations. Jeff Hanson of SAIC provided insightful suggestions during the planning phase of the experiment and in data analysis. Jenny Hollfelder of LLNL assisted with ship track file corrections and report figures. Carl Boro at LLNL designed and machined the sphere implosion mechanism. Leroy Dorman of the Scripps Institute of Oceanography tested the imploding sphere off the west coast of California.

REFERENCES

Boro, C. and P.E. Harben, 1999, *Sphere Implosion Initiation Device*, Record of Invention IL-10551, University of California, LLNL Patent Group.

CGS, a Division of Kontes Glass Co., 1022 Spruce St., Vineland, NJ, (800) 682-6644.

Hanson, J.A. and P.E. Harben, *Acoustic-to-Seismic Wave Coupling Study at Ascension Island*, Proc. SSA Annual Mtg., April, 2000.

Harben, P.E., J.R. Hollfelder, and A.J. Rodgers, *Experimentally Determined Coordinates for Three MILS Hydrophones near Ascension Island*, UCRL-ID-136507, November, 1999.

Harben, P.E., D.K. Blackman, A.J. Rodgers, C. Turpin, and J.R. Hollfelder, *Calibration Factors for Three MILS Hydrophones Near Ascension Island*, UCRL-ID-138036, Feb., 2000.

Harben, P.E., C.Boro, L. Dorman, and J. Pulli, *Use of Imploding Spheres: An Alternative to Explosives As Acoustic Sources At Mid-Latitude SOFAR Channel Depths*, UCRL-ID-139032, May, 2000.

Informal Workshop on Hydroacoustics: Programme and Abstracts, Sponsored by CTBTO/PTS and the DASE, Papeete, Tahiti, French Polynesia, Sept. 27 - Oct. 1, 1999.

Levitus, S., T. Boyer, J. Antonov, R. Burgett, and M. Conkright, *World Ocean Atlas*, NOAA/NESDIS, Silver Springs, Maryland, 1994.

Minshull, T. A., *Cruise Report: RRS James Clark Ross 42*, University of Southampton School of Ocean and Earth Science, 1999.

SEA Cable Installation MILS Areas 9, 11, and 12, Western Electric Company
North Carolina Works, Winston Salem, NC, Contract Order NObsr 64554,
Effective Date 1 February 1958, Publication date 15 November 1961.

Urick, R.J., *Principles of Underwater Sound*, Peninsula Publishing, Los Altos, CA., Copyright 1983.

THE HYDROACOUSTIC NETWORK, INTERNATIONAL MONITORING SYSTEM: STATUS AND PLANS

Martin Lawrence, Marta Galindo, Patrick Grenard, John Newton

Hydroacoustic Monitoring Section, International Monitoring System Division, Provisional Technical Secretariat, Preparatory Commission for the Comprehensive Nuclear-Test-Ban Treaty Organization

ABSTRACT

The hydroacoustic network is one of the monitoring networks of the International Monitoring System (IMS) established under the Comprehensive Nuclear-Test-Ban Treaty. The Signatory States of the Comprehensive Nuclear-Test-Ban Treaty have formed a Preparatory Commission to oversee Treaty-related activities until the Treaty enters into force. The Preparatory Commission has established technical requirements, certification standards, and draft operational practices for the hydroacoustic network. The Hydroacoustic Monitoring Section of the IMS Division of the Preparatory Commission's Provisional Technical Secretariat is responsible for the establishment, certification, and operation of the hydroacoustic stations according to Commission's requirements and standards.

The IMS hydroacoustic network, designed to monitor the major world oceans, contains eleven stations located with an emphasis on the vast ocean areas of the Southern Hemisphere. Two quite different sensing techniques are employed in the hydroacoustic network; hydrophone sensors, which effectively cover large ocean areas, but are quite complex and expensive, and seismic detectors on small islands which are less effective, but considerably simpler and cheaper.

At the introduction of the CTBT, three of the planned hydroacoustic network stations existed, leaving the remaining eight stations to be totally new installations. However, the upgrades required to bring the existing stations up to the specified standard are such that the work required on these stations will be similar to that for new installations. The establishment of each hydroacoustic station requires a survey to ensure the suitability of the site and to assist with installation planning, followed by the installation of new equipment, and then a period of testing leading finally to certification that the station meets the specified standards. Site surveys have been completed, or are underway, for seven of the stations and two additional surveys are planned to begin during 2000. Equipment has been installed at two new hydrophone stations and one new island seismometer station. Work is underway on the installation of another hydrophone station.

Key Words: International Monitoring System, Hydroacoustic

THE HYDROACOUSTIC NETWORK, INTERNATIONAL MONITORING SYSTEM: STATUS AND PLANS

Martin Lawrence, Marta Galindo, Patrick Grenard, John Newton

Hydroacoustic Monitoring Section, International Monitoring System Division, Provisional Technical Secretariat, Preparatory Commission for the Comprehensive Nuclear-Test-Ban Treaty Organization

INTRODUCTION

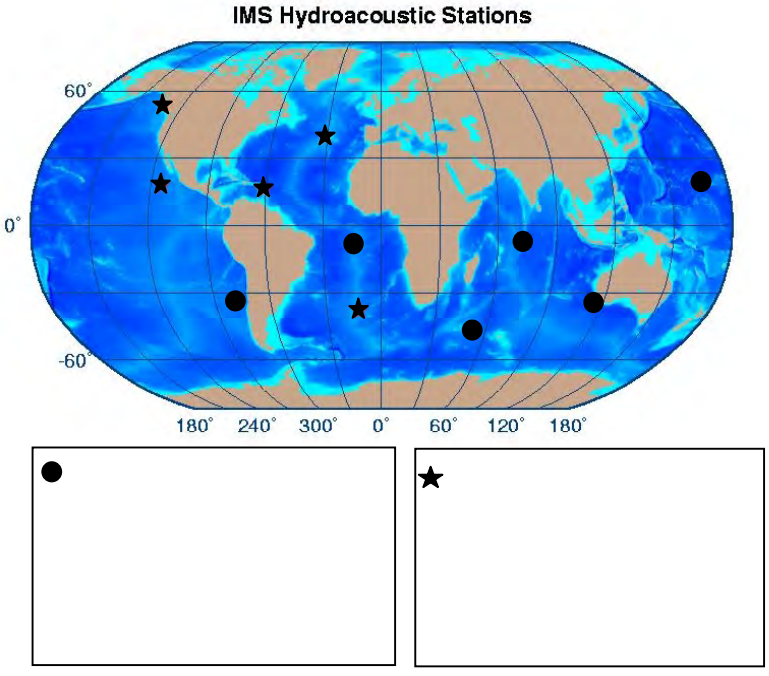
The hydroacoustic network is one of the monitoring networks of the International Monitoring System (IMS) established under the Comprehensive Nuclear-Test-Ban Treaty. The Signatory States of the Comprehensive Nuclear-Test-Ban Treaty have formed a Preparatory Commission to oversee Treaty-related activities until the Treaty enters into force. The Preparatory Commission has established technical requirements, certification standards, and draft operational practices for the hydroacoustic network. The Hydroacoustic Monitoring Section of the IMS Division of the Preparatory Commission's Provisional Technical Secretariat is responsible for the establishment, certification, and operation of the hydroacoustic stations according to Commission's requirements and standards.

The IMS hydroacoustic network, designed to monitor the major world oceans, contains eleven stations located with an emphasis on the vast ocean areas of the Southern Hemisphere. Two quite different sensing techniques are employed in the hydroacoustic network; hydrophone sensors, which effectively cover large ocean areas, but are quite complex and expensive, and seismic detectors on small islands which are less effective, but considerably simpler and cheaper.

This paper presents a brief overview of the IMS hydroacoustic network and describes the two types of stations, namely the T-phase and hydrophone stations. The present status of the network implementation is outlined. Examples of station data are used to show the typical noise background and the types of signals expected.

THE HYDROACOUSTIC NETWORK

The existence of the SOFAR channel (Sound Fixing and Ranging) makes the ocean a remarkably efficient medium for the transmission of sound energy. Thus the signal generated by an explosion occurring in the water, above water in the low atmosphere, or underground near shore will be detected effectively even at long distances by sensors located in the SOFAR channel.

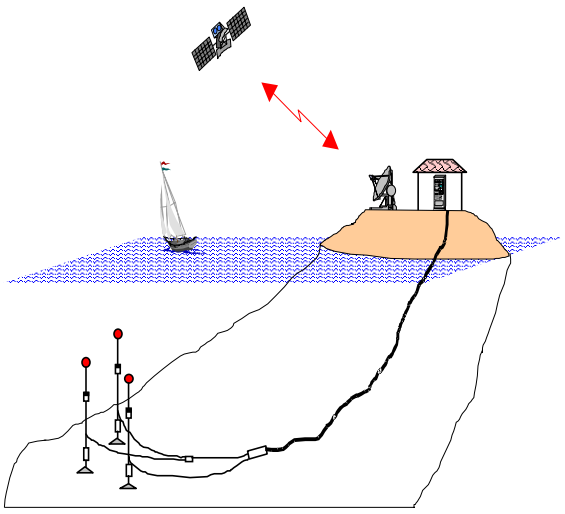


In order to detect the acoustic energy ducted through the SOFAR channel a network composed of 11 hydroacoustic stations is being implemented. Six stations will be equipped with hydrophone sensors. The other five hydroacoustic stations are located on small, steep-sloped islands and will make use of seismic sensors to detect waterborne energy, which is converted to a seismic wave at the boundary of the island. This type of propagation has long been known to the

seismic community as T-phase propagation. T-phase stations are not as effective in detecting and identifying hydroacoustic signals from explosions, but they are considerably less expensive than hydrophone stations. The mixture of hydrophone and T-phase stations selected for the IMS hydroacoustic network was chosen to provide a cost-effective compromise. The network is shown on the map, in which the stations are listed in order from west to east.

HYDROPHONE STATIONS

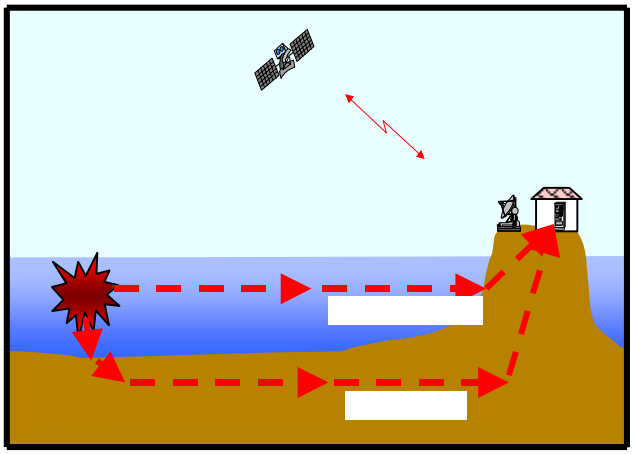
All hydrophone stations, except for Cape Leeuwin, are located on relatively small islands. They generally consist of two undersea trunk cables, each with three hydrophone sensors. To avoid bathymetric blockage by the island, cables and sensors are deployed on opposite shores of the island. Each hydrophone sensor has an independent wet-end digitizer. The digital signals are transmitted to the shore facility via a non-repeatered fiber optic cable for processing and transmission by satellite to the IDC in Vienna (see figure).



The hydrophone sensors are placed at or near the axis of the SOFAR channel, using a subsurface float and an ocean-bottom anchor. In order to provide the station with some directional capabilities, the three hydrophones are placed in a triangular configuration and each sensor is separated horizontally by a distance of approximately two kilometers.

T-PHASE STATIONS

A T-phase station uses seismometers that are located to detect seismic waves generated by the coupling of waterborne energy along the flanks of the island. Each station is composed of one to three seismometers and a data acquisition system. As in the case of the hydrophone stations, the data are formatted and transmitted by satellite in real time to the IDC. The figure shows, in schematic form, a typical T-Phase Station including the seismic and hydroacoustic signal paths from an underwater event, the shore facility (sensor) and the satellite link to the IDC in Vienna.



STATION STATUS AND PLANS

The establishment of each IMS hydroacoustic station requires a survey to ensure the suitability of the site and to assist with installation planning, followed by the installation of new equipment, and then a period of testing leading finally to certification that the station meets the specified standards.

A brief description follows of the station status and plans for each of the eleven stations of the hydroacoustic network.

HA01 Cape Leeuwin
This station is a totally new hydrophone based station, situated at the south-west corner of Australia. It will have a single triplet of hydrophones (all other hydrophone stations have two triplets). The site survey for this station is complete. Manufacture is underway, with installation expected around April 2001.

HA02 Queen Charlotte Islands
This is a T-phase station that existed before the CTBT was opened for signature. It is situated off the Pacific coast of Canada. However, the station needs a substantial upgrade to bring it to CTBT specifications. The field work for the site survey is complete. The site survey report is in preparation. Installation is planned to take place in 2001.

HA03 Juan Fernandez Island
This station is a totally new hydrophone based station, situated off the coast of Chile. Proposals for performing the site survey are currently being examined. Installation is planned to take place in 2003.

HA04 Crozet Island
This station is a totally new hydrophone based station, situated in the French Austral Territories in the south-west of the Indian Ocean. The site survey and manufacture for this station are complete. The shore facility and the underwater cable are installed, as are one triplet of hydrophones. Completion of the installation is planned to take place in January 2001.

HA05 Guadeloupe
This is a totally new T-phase station, situated in the French Antilles. It will have two 3-component broad-band seismometers, one on Desirade and one on Martinique. The site survey for this station is complete. Installation of one seismometer is complete and data is being sent to Vienna. Installation of the other seismometer is planned to take place in September 2000.

HA06 Socorro Island
This is a totally new T-phase station, situated off the Pacific coast of Mexico. The site survey for this station is complete. The site survey results are currently being examined in detail, in particular to decide on whether to have 2 or 3 seismometers and also on exactly where to locate them. Installation is planned to take place in 2001.

HA07 Flores Island
This is a totally new T-phase station, situated in the Azores in the northern Atlantic Ocean. The field work for the site survey for this station is complete. The site survey report is in preparation. Installation is planned to take place in 2002.

HA08 Chagos Archipelago
This station is a totally new hydrophone based station, situated at Diego Garcia in the northern Indian Ocean. The site survey and manufacture for this station are complete. The station was installed in April 2000. The communications link to Vienna should be complete in September 2000.

HA09 Tristan da Cunha
This is a totally new T-phase station, situated in the southern Atlantic Ocean. Proposals for performing the site survey are currently being examined. Installation is planned to take place in 2003.

HA10 Ascension Island
This is a hydrophone based station that existed before the CTBT was opened for signature. It is situated in the mid Atlantic Ocean. Unfortunately a cable break has made this station inoperative. Further, the station needs a substantial upgrade to bring it to CTBT specifications. Work is expected to begin in 2001, leading to installation in 2003.

HA11 Wake Island
This is a hydrophone based station that existed before the CTBT was opened for signature. It is situated in the north-west Pacific Ocean. However, the station needs a substantial upgrade to bring it to CTBT specifications. Work is expected to begin in 2002, leading to installation in 2004.

DISCRIMINATION CRITERIA FOR SOURCES OF T PHASES RECORDED IN FRENCH POLYNESIA

Emile A. Okal, Northwestern University
Jacques Talandier

Sponsored by the Department of Defense
Defense Threat Reduction Agency

Grant Number DSWAOI-98-1-0007

ABSTRACT

We use a dataset of 150 digital records of T phases from 71 sources obtained on seismometers of the Polynesian Seismic Network to define a discriminant separating earthquake and explosion sources. It uses the maximum amplitude of recorded ground velocity, measured on its envelope (e_{Max} ; in microns/second), and the duration of the phase measured at 1/3 of maximum amplitude ($tau_{1/3}$; in seconds). Earthquake sources and man-made explosions are effectively separated in a log-log space by the straight line

(1) $\log_{10}(e_{Max}) = 4.9 * \log_{10}(tau_{1/3}) - 4.1$

We are motivated by the observation that other criteria, both in the time and frequency domains, fail to reliably separate the populations of the various kinds of events. In particular, we define a class of intraplate earthquakes, mainly located in the vicinity of active centers of volcanism, whose T phases feature many characteristics reminiscent of explosions, rather than of plate boundary earthquakes.

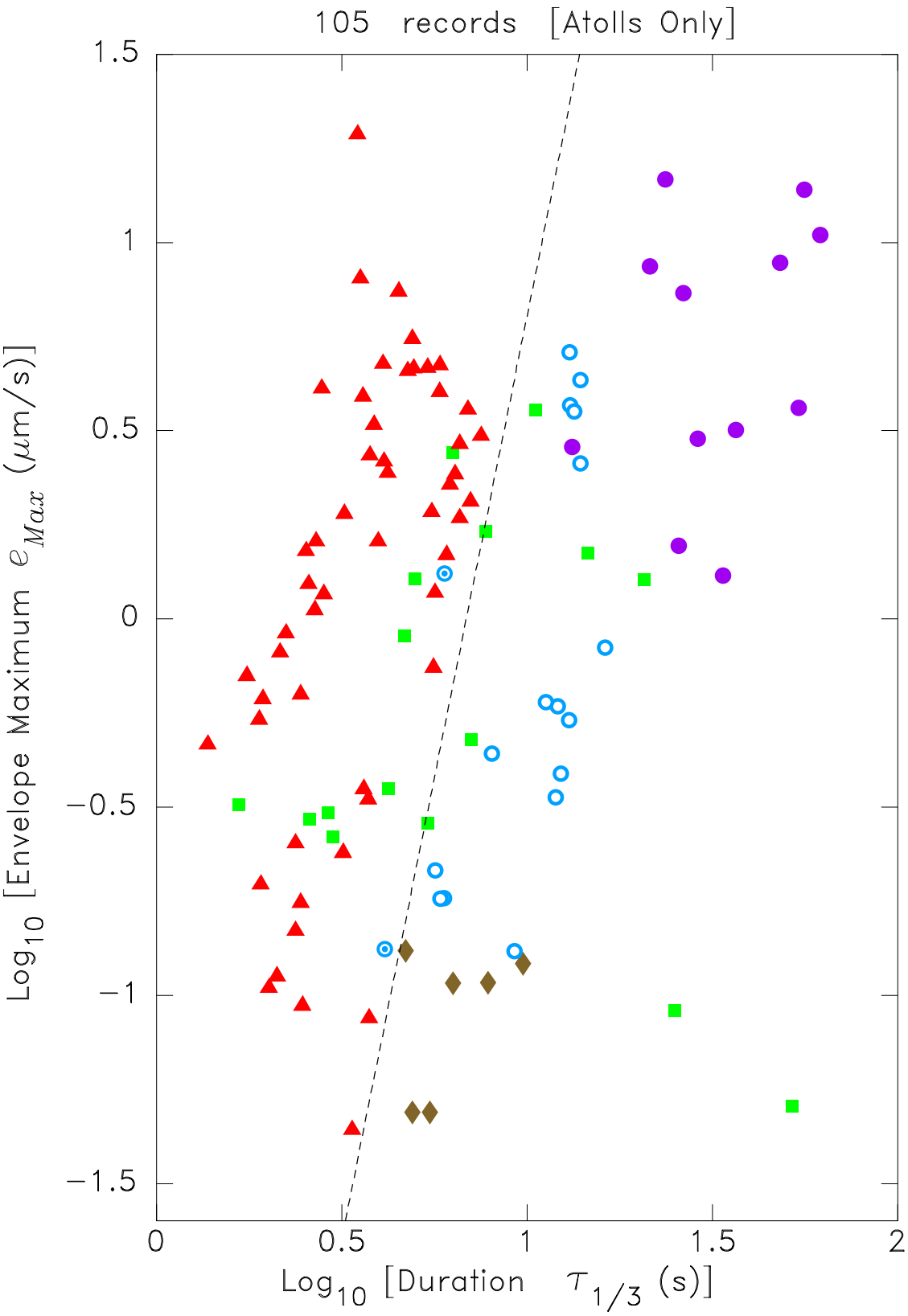
In the frequency domain, we studied systematically such parameters as mean frequency of the signal, maximum frequency of the signal, and width of spectrum, as well as the ratio of energy contained in the lower and higher parts of the seismic spectrum. In most instances, we observe that the highest and lowest values of the properties investigated indeed belong to different classes of sources. However, there is a field of average values where no discrimination is possible, in particular because intraplate earthquakes tend to exhibit properties typical of explosions (notably higher-frequency spectra). Thus the parameters listed above cannot be used as reliable discriminants.

In the time domain, we similarly investigated the rise time and fall time of the envelope of the signal, as well as its total duration, with very similar conclusions, namely that the longest signals, and those rising fastest were indeed generated by explosions, while the slower-rising or longer-lasting ones were generated by plate boundary earthquakes. However, there are intraplate earthquakes occupying an intermediate field and making the use of such discriminants unreliable. We also tested the higher statistical moments -- skewness and kurtosis -- applied to the envelope of the waveshapes, with totally similar conclusions, namely they discriminate efficiently between the end-members of the populations, but cannot resolve the center field, which is occupied by a mixture of explosions and intraplate earthquakes.

On the other hand, we find that the discriminant (1), when applied to T phases recorded at atoll stations, successfully separates explosions, which plot above the straight line (1), from earthquakes (both plate boundary and intraplate), which plot below the line. The only exception is a small earthquake at the volcanic island of Mehetia in Polynesia, which is marginally misidentified, and a record of a Hawaiian earthquake at one Polynesian station, which is correctly identified at another station. An important aspect of the performance of (1) as a discriminant is that it misses no explosion in our dataset. We emphasize that the performance of (1) as a discriminant can be degraded if records are taken at stations located on high islands, rather than on atolls. The reason is that the propagation of the converted seismic wave from the conversion point to the station can significantly affect the time domain characteristics of the waveshape of the final T phase. Also, T phases recorded from episodes of volcanic activity cannot be reliably discriminated from man-made explosions; this is probably due to the explosive nature of some volcanic sources. We will present a possible interpretation of the origin of the discriminant (1) in terms of scaled properties of seismic and explosive sources.

Key words: T-phases, hydroacoustics, explosions, discriminants

NOTE: This paper is currently in press in PAGEOPH.



The duration-amplitude discriminant. This figure plots the envelope maximum e_{Max} as a function of signal duration measured at 1/3 of maximum, $\tau_{1/3}$. The following symbols are used to differentiate the various sources: *Solid circles:* Subduction earthquakes; *Open Circles:* Midplate earthquakes; *Solid squares:* Explosive volcanic events; *Triangles:* Man-made explosions; *Diamonds:* Presumed firing of missiles. The two bull's eye symbols showing the only misidentified midplate earthquakes The dashed line is the proposed separator. This figure includes only records obtained at atoll stations.

INDIAN OCEAN HYDROACOUSTIC WAVE PROPAGATION CHARACTERISTICS

Pierre-Franck Piserchia, Pierre-Mathieu Dordain
CEA/DIF – Département Anlayse, Surveillance, Environnement, France

Sponsor
Commissariat à l'Energie Atomique (CEA), France

ABSTRACT

The channeling efficiency of the Deep Sound Channel (often referred as the Sofar channel) allows long range propagation of hydroacoustic waves over a few thousands of kilometers. Strong T-waves, referring to a third arrival on seismic waves, are commonly observed on underwater receivers (hydrophones stations) and on coastal receivers (T-phase stations), when an oceanic earthquake or an underwater explosion occurs, even for small events. Consequently, to insure the verification of the Comprehensive Nuclear-Test-Ban Treaty (CTBT), the hydroacoustic network of the International Monitoring System (IMS) uses five T-phase stations and six hydrophones. At the end of 2001, three hydrophone stations -HA1 at Cape Leeuwin, HA4 at Crozet, and HA8 at Diego Garcia will continuously send their data to the IMS. These data will also be available at National Data Centers. Then, using these data it will be possible 1) to refine the network detection capability 2) to estimate the network localization precision and 3) to estimate the transmission loss of the hydroacoustic propagation and the hydroacoustic-to-seismic conversion at the T-phase stations. To prepare this evaluation, we are studying the underwater propagation in the region of the Indian Ocean and in the South Atlantic Ocean using modeling approaches.

The first part of this paper gives a general view of the variation of the bathymetry, the sound speed propagation and the Sofar channel axis in the Indian Ocean. In particular, it is shown that there is a strong sound speed profile variation, from the North to South Indian Ocean, due to a cold water front coming from the Sub-Antarctic Ocean. In a second part, three areas are defined in the region of the Indian Ocean and in the Antarctic Ocean. In each of them, a typical sound speed profile has been considered to estimate numerically the underwater transmission loss characteristics. The underwater blockage effect due to underwater seamounts are also investigated in this part. In the three regions previously defined, this approach allows us to propose a basic formulation of the transmission loss (TL in dB) :

$$TL(f_s, z_s, r) = A_o(f_s, z_s) + 10 \cdot \log(r) + B(f_s, z_s) + \alpha(f_s) \cdot (r - 1)$$

where f_s, z_s, r are respectively the frequency, the depth, the distance of the underwater source and α is the absorption coefficient. These laws could give a good and simple characterization of the transmission loss and can be used to estimate quickly the source charge weight from an hydroacoustic record of an underwater blast. In this preliminary study, A_o and B are estimated numerically using a parabolic equation technique in the frequency domain. In the discussion, we investigate the number of record points and source localization which are necessary to provide a good estimation of A_o and B.

Objective:

At the end of 2001, three hydrophone stations (Figure 1). -HA1 at Cape Leeuwin, HA4 at Crozet, HA8 at Diego Garcia - will continuously send their data to the IMS. These data will also be available at National Data Centers. Then, using these data it will be possible 1) to refine the network detection capability 2) to estimate the network localization precision and 3) to estimate the transmission loss. The objective of this research is to study the underwater propagation in the region of the Indian Ocean using modeling approaches to prepare an experimental evaluation of the IMS hydroacoustic network in the Indian Ocean. We are in particular investigating the transmission loss and blockage effects due to sea mounts or underwater plateaus.

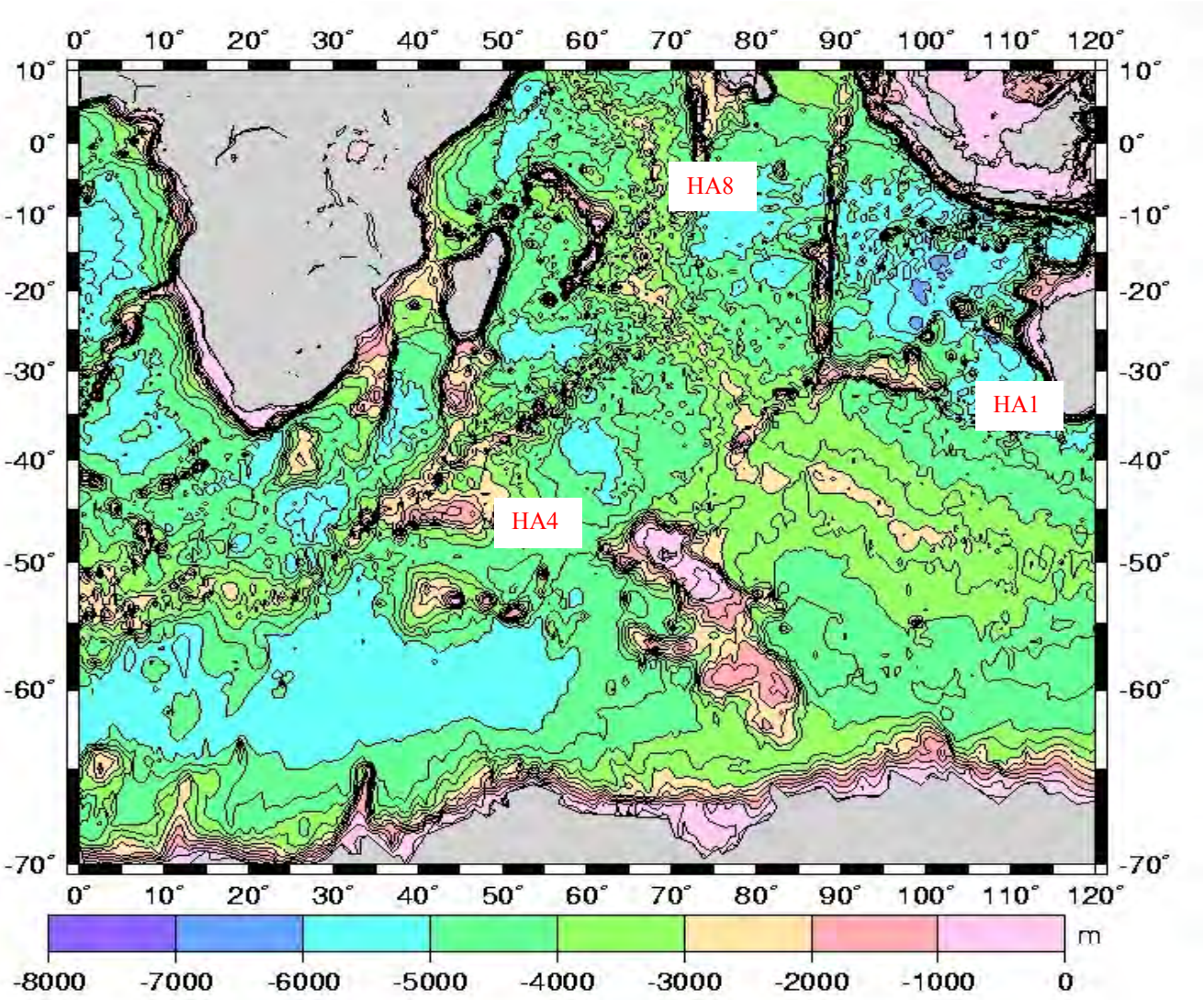


Figure 1 : Indian Ocean map. Three hydrophone stations participate to the International Monitoring System in the Indian Ocean -HA1 at Cape Leeuwin, HA4 at Crozet, HA8 at Diego Garcia.

Research accomplished :

The first part of this paper gives a general view of the variation of the bathymetry, the sound speed propagation and the Sofar channel axis in the Indian Ocean. In the second part, we investigate numerically the underwater transmission loss.

Overview of the Indian Ocean main characteristics

Hydroacoustic wave propagation in an ocean is mainly controlled by the velocity variation with respect to depth and range. It is well known that the velocity increases with temperature, salinity and depth. In the Indian Ocean, bands of equal temperatures run east-west. Water temperature is the highest along the equator, because there Earth is most warmed by solar radiation, and become cooler toward Antarctica (Figure 2). Because the temperature decreases with depth, the velocity decays rapidly with depth down to a minimum at the Sofar channel axis. Below this depth, the velocity increases quite linearly with the hydroacoustic pressure. Due to this variations, bands of equal sound speed run east-west and there is a strong sound speed variation on the Sofar channel axis, from about 1500 m/s in the North to 1455 m/s in South Indian Ocean. In our study, we have considered three different types of sound speed profiles (Figure 2).

Hydroacoustic wave propagation in an ocean is also controlled by the bathymetry variation (Figure 1) along the wave path. The Indian Ocean basin is the shallowest of the two other major basins because it is the youngest. This basin has five important ridges that may block hydroacoustic wave propagation. It has three active mid-ocean ridges : the Southwest Indian Ridge, the Southeast Indian Ridge and the Mid-Indian Ridge where there is the strongest seismic activity and two inactive volcanic ridges : the Chagos-Laccadive Plateau and the Ninetyeast Ridge. The large Kerguelen Plateau has also some regional seismic activity.

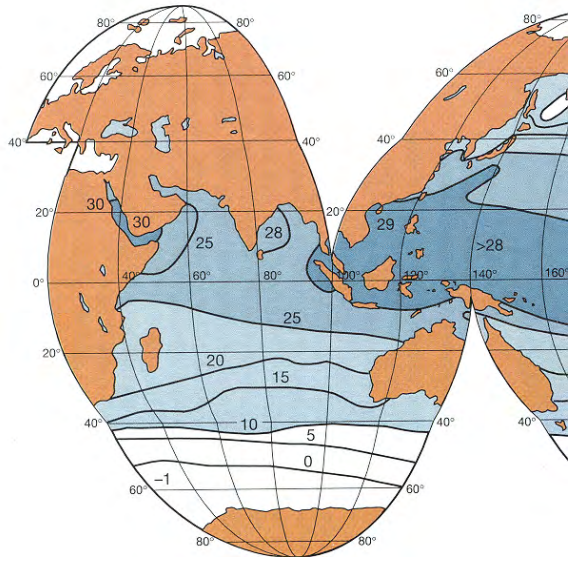


Figure 2 : Ocean surface temperatures (from Gross et al., 1996). In the Indian Ocean, bands of equal temperatures run east-west. Water temperatures are the highest along the equator, because there Earth is most warmed by solar radiation, and become cooler toward Antarctica. Note the presence of a cold water front at the latitude 40°.

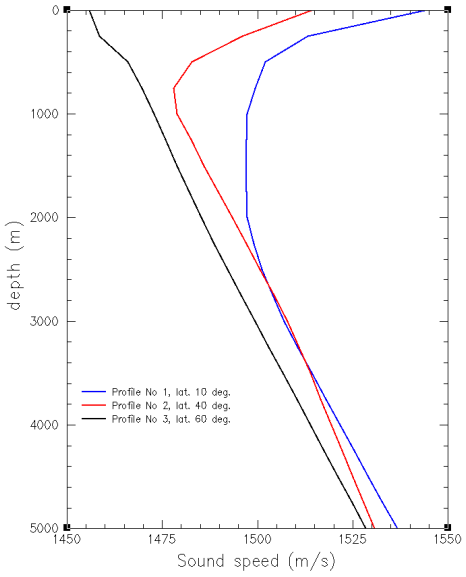


Figure 3 : Ocean Indian sound speed variation. The Sofar channel axis depth decreases from North (blue profile) to South (black profile) to reach the sea surface. Note a strong sound speed variation on the Sofar channel axis, from about 1500 m/s in the North to 1455 m/s in the South.

Transmission loss estimation from modeling

Our strategy

After an underwater explosion occurs, only a portion of energy is trapped in the Sofar channel (Piserchia et al, 1998) allowing propagation of waves over large distances without any reflection losses at sea flour and sea surface. As we will see in this paper, the trapped energy flux depends on the Sofar channel characteristics, the source depth and the source frequency. It is well known, that the transmission loss of this energy is mainly due to the geometrical attenuation, blockage effects and absorption. To investigate the roles played by the source and Sofar characteristics as well as the blockage effects, the basic transmission loss formulation (TL in dB ref. 1 m):

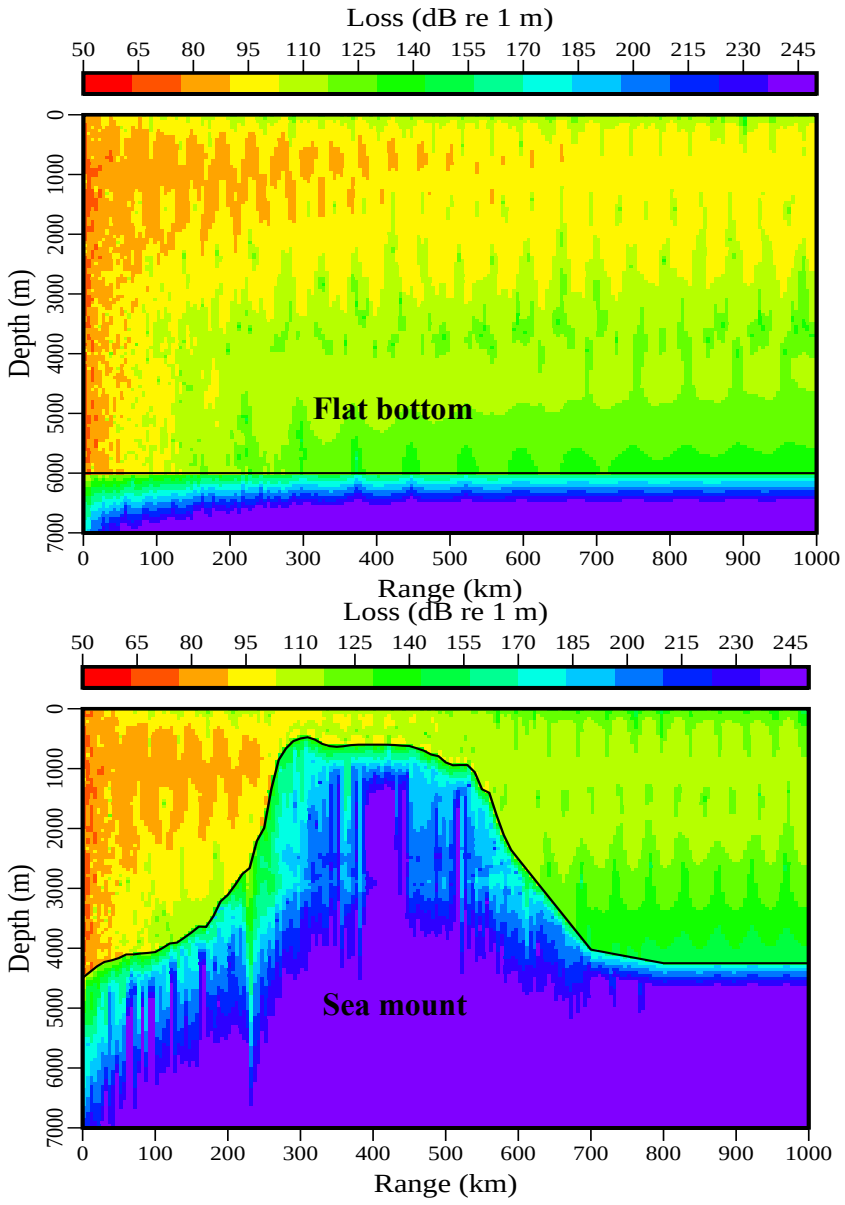


Figure 4 : Two cases of underwater propagation using the profile n°2. A 10 Hz isotropic source is located on the Sofar channel axis at 800 m in a flat bottom ocean in the first case and in front of a sea mount in the second case. These two color images of the transmission loss have been computed by the

code RAMS. In the first case, the transmission loss (in dB ref. 1 m) can be approximated by TL = 35 + 10 log(r) whereas in the second case we obtain TL = 35 + 10 log(r) + 15.

$$TL(f_s, z_s, r) = A_o(f_s, z_s) + 10 \cdot \log(r) + B(f_s, z_s) \quad (1)$$

as been considered. The source may vary with depth and frequency and the receiver is always considered to be on the Sofar channel axis. f_s, z_s, r are respectively the frequency (in Hertz), the depth (in meter), the distance (in meter) of the underwater source.

A0 represents the trapped energy at 1m in Sofar channel. *A0* decreases when the trapped energy increases. The second term *10 log(r)* represents the attenuation due to the cylindrical spreading. The second parameter *B* represents additional attenuations due to blockage effects. In this preliminary study, *A0* and *B* were numerically estimated in the three previous regions we defined. The code RAMS is used to solve the Helmoltz equation using the parabolic equation approximation in the frequency domain (Collins, 1993). In a first step, we computed the transmission loss in the three regions. Then, in a second step, *A0* and *B* are computed minimizing the difference between the numerical estimation and our formulation (1).

Numerical results

Tables 1 and 2 represent the numerical estimation of *A0* in two regions located in the north of the cold water front. In these two regions, *A0* is evaluated with a standard deviation error lower than 5 dB. In both cases, when the source is on the Sofar channel axis respectively at 1500 m (profile n°1) and 800 m (profile n°2), *A0* reaches a minimum equal to 38 dB and 35 dB. We re-find the well known property that the transmission loss is minimum when the source is on the Sofar Channel axis. When the source goes closer to the Sofar channel limits near the surface (at 100 m) or the sea bottom (at 5000 m), *A0* and therefore the transmission loss can increase up to 13 dB at 10 Hz. This additional loss is all the more important that the frequency is low. In the frequency range 5 to 15 Hz, this additional loss is always higher than 10 dB. An under evaluation of 10 dB of the level would lead to an under charge weight estimation of a factor 10. Table 3 gives the results we obtained in the Antarctic Ocean. In this region, because the minimum sound speed zone is at the sea surface, there are reflections losses. *A0* must be interpreted cautiously because our modeling do not take into account of these losses.

Variation A_0 of with the source location and frequency

Profile n°1	Zs=100 m	Zs=500 m	Zs=800 m	Zs=1500 m	Zs=5000 m
5 Hz	53 dB	42 dB	41 dB	38 dB	57 dB
10 Hz	51 dB	42 dB	41 dB	38 dB	49 dB
15 Hz	50 dB	42 dB	41 dB	38 dB	48 dB

Tab. 1 : A_0 estimation in the region n°1 at the North of the Indian Ocean. The minimum sound speed zone is close to 1500 m.

Profile n°2	Zs=100 m	Zs=500 m	Zs=800 m	Zs=1500 m	Zs=5000 m
5 Hz	52 dB	39 dB	35 dB	39 dB	57 dB
10 Hz	48 dB	39 dB	35 dB	40 dB	49 dB
15 Hz	46 dB	39 dB	36 dB	41 dB	48 dB

Tab. 2 : A_0 estimation in the region n°2 at the South of the Indian Ocean. The minimum sound speed zone is close to 800 m.

Profile n°3	Zs=100 m	Zs=500 m	Zs=800 m	Zs=1500 m	Zs=5000 m
5 Hz	45 dB	35 dB	35 dB	38 dB	53 dB
10 Hz	38 dB	33 dB	38 dB	44 dB	48 dB
15 Hz	35 dB	37 dB	40 dB	39 dB	47 dB

Tab. 3 : A_0 estimation in the region n°3 in the Antarctic Ocean.

These results demonstrate that it is important to know the variation of the transmission loss with the source depth variation in each regions of the Indian Ocean. They have been obtain considering a flat bottom ocean. As it has been said in a previous part the Indian Ocean basin has five important ridges that could generate hydroacoustic wave blockage effects. As an illustration of these effects, Figure 4, gives two cases of underwater propagation using the profile n°2. A 10 Hz isotropic source is located on the Sofar channel axis in a flat ocean bottom in the first case and in a front of a sea mount in the second case. In the first example, the transmission loss can be approximated by TL = 35 + 10 log(r) whereas in the second example we obtain TL = 35 + 10 log(r) + 15. The additional increased of 15 dB is due the blockage effects of the sea mount. Figure 5 illustrates an other example of underwater blockage due to a sea mount. The transmission loss after the sea mount is compared with the transmission loss in a flat ocean sea bottom. In this example, it is shown that the addition loss increases with the frequency decayed from 5 dB at 5 Hz to 15 dB at 15 Hz. An under estimation of 15 dB of the source level could lead to an under charge weight evaluation of a factor 30.

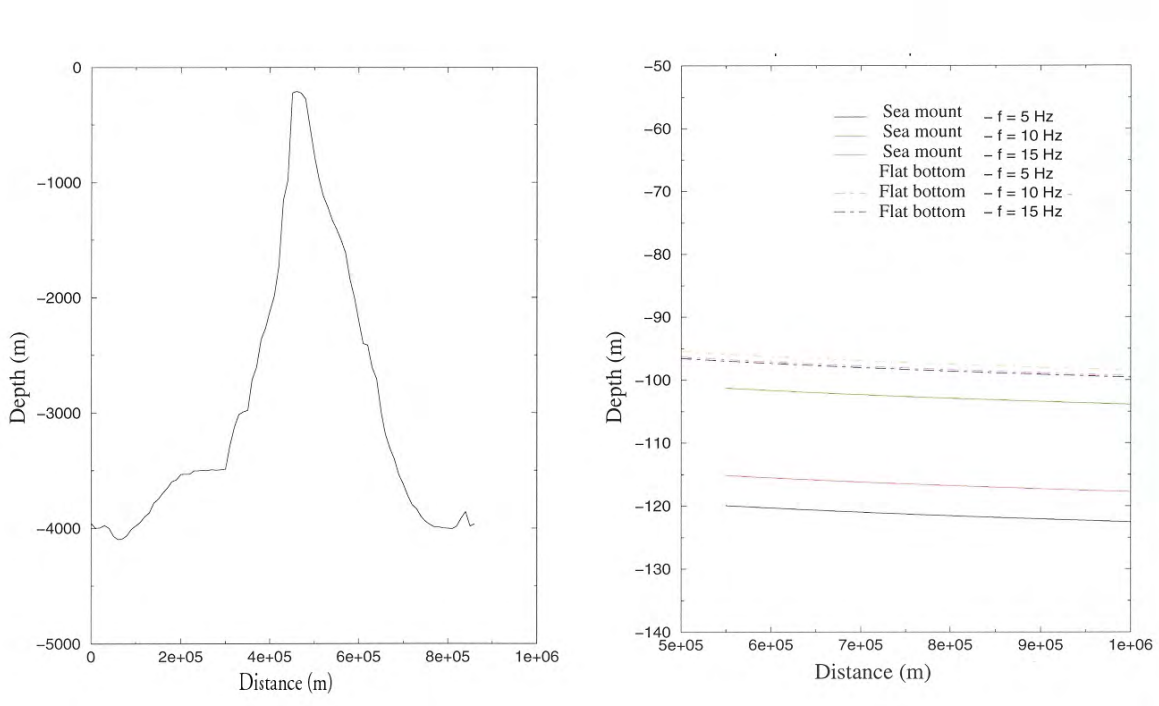


Figure 5 : Blockage effects due to an underwater sea mount. The source is located in front of the sea mount on the Sofar channel axis. The figure on the right represents the transmission loss variation with range and frequency behind the sea mount.

Discussion

We investigated numerically the number of record points and source localization which are necessary to provide a good estimation of *A0* and *B*. In this paper, the transmission loss was computed every 500 m by the code RAMS. Then in a second step, *A0* was evaluated to minimize the difference between the numerical estimation and our formulation (1). In a numerical parameterized study, we found that a distance between points smaller than 400 km and more than three points of records are needed to insure an acceptable error lower than 5 dB on the *A0* calculation.

Conclusions and Recommendations :

As it has been recommended at the *Tahiti Hydroacoustic Workshop* (organized by CTBTO and CEA/DASE in September 1999), we believe that it is necessary to calibrate the hydroacoustic network of the International Monitoring System in the Indian Ocean. This study demonstrates that the transmission loss may vary with the source depth and from one region of the Indian Ocean to an other. This is the reason why we believe that the transmission loss should be studied carefully in particular to validate model calculations used to estimated source levels. During the definition of the calibration experiment, we recommend to also investigate source geometry to analyze transmission loss phenomena and blockage effects.

Key Words : T-phase, hydroacoustic, Indian Ocean propagation, transmission loss

References :

Collins, M.D., A higher-order energy-conserving parabolic equation for range-dependent ocean depth, sound speed, and density, J. Acoust. Soc. Am., 101, 1068-1075, 1993.

CTBTO/PTS, CEA/DASE, Informal workshop on “hydroacoustics”, French Polynesia Tahiti, Conference proceeding, September 1999.

Gross, M. G., Gross, E.. *Oceaography*, seventh edition, NJ : Prentice Hall, 1996.

Levitus, S., Boyer, T. Antonov, J., Burgett, R., and Conkright, M., World Ocean Atlas 1994, NOAA/NESDIS, Silver Springs, Maryland, 1994.

Piserchia, P.-F, Rodrigues, D., Virieux J., Gaffet S., Detection of underwater explosions from very long range records, Oceans’98 , Nice, Conference proceeding, vol. 2, 698-702, 1998.

HYDROACOUSTIC CALIBRATION WITH IMPLODING GLASS SPHERES

Jay J. Pulli[1] and Phil Harben[2]

[1]BBN Technologies; [2]Lawrence Livermore National Laboratory

Sponsored by U.S. Department of Energy
Office of Nonproliferation Research and Engineering
Office of Defense Nuclear Nonproliferation
National Nuclear Security Administration

Subcontract Number B334423

ABSTRACT

Calibration and validation of acoustic source and propagation models plays an important role in the hydroacoustic component of Comprehensive Nuclear-Test-Ban Treaty (CTBT) monitoring. This validation requires that we have a loud acoustic source with sufficient low-frequency energy that could be easily deployed in the Sound Fixing and Ranging (SOFAR) channel. SUS charges (Signal Underwater Source, 0.82 kg of explosive) have been used for this purpose for years, but safety and environmental concerns make these sources impractical. Light bulbs with sinkers have long been used as shallow acoustic sources, but are too small for the purposes stated. Here we describe investigations into the use of thin-walled glass spheres as calibration sources.

Since glass becomes stronger under pressure, a method is needed to reliably initiate the failure of the sphere at a specified depth. A prototype-smashing device, called a "spherecracker", was designed for this purpose. It consists of a 4-inch-diameter piston with a 1/4-inch diameter ram. The end cap on the device's cylinder tapers to a 1-inch diameter opening with a rupture disk calibrated to fail within 5% of the failure pressure. The ram initiates failure by punching a hole into the glass sphere.

In March 1999 we conducted an experiment with a 10-inch-diameter glass sphere at Dabob Bay, Washington. The sphere was tethered and lowered to a depth of 600 ft. A metal pipe was then slid down the tether line as a smashing device. This implosion produced a pressure pulse with peak amplitude of 9×10^{11} μPa at 1 meter and duration of 1 msec. The signal was recorded at a sampling rate of 100 kHz, and the spectrum shows energy from 50-50000 Hz. The low-frequency source level is approximately 200 dB re 1-uPa.

In February 2000 a test was conducted with a 22-liter glass sphere off the coast of San Diego at a depth of 685 meters in water that was 1200 meters deep. The Research Vessel (R. V.) Sproul was used to deploy the sphere. Implosion was initiated by the spherecracker. This implosion produced a pressure pulse with peak amplitude of 2×10^{13} μPa at 1 meter and duration of 1 msec. The signal was recorded at a sampling rate of 48 kHz, and the spectrum shows energy from 50-20000 Hz. The low frequency source level is approximately 190 dB re 1-uPa.

Included in this paper are long-range hydroacoustic propagation predictions using the program HydroCAM with each of these source measurements.

Key Words: Hydroacoustics, calibration, sources, glass spheres

OBJECTIVE

The objective of this work has been to investigate the feasibility of using imploding glass spheres as deep-water acoustic sources for calibration experiments under the hydroacoustic component of nuclear explosion monitoring. Like its counterpart in seismic monitoring, hydroacoustic monitoring requires ground truth for both model validation and the interpretation of observed data. Explosive charges have long been used for this purpose, but safety and environmental concerns often preclude their use for research, especially by university groups. Airgun sources, typically used for oil and gas exploration, operate near the surface and are not designed for operation at the SOFAR

channel depths (500-1200 meters) required for this research. If a safe, reliable, and inexpensive source could be developed for operation at these depths, it could be used to:

- Calibrate long-range propagation travel-time predictions
- Assess the importance of horizontal refraction for long-range propagation
- Study T-wave coupling at continental margins
- Investigate the nature of acoustic scattering at bathymetric features
- Look for reflected arrivals from events which occur in predicted shadow zones
- Determine whether or not shadow zones behind islands are filled in by diffraction

The need for an inexpensive source that would operate in the SOFAR channel and does not have the hazard and safety procedure problems of explosives was recognized in the recent International Workshop on Hydroacoustic Monitoring for the CTBT that met in Tahiti in late September 1999 (Massinon, 1999). The workshop findings identify acoustic source development as a technical issue and advocate an approach to the problem that addresses the safety issue and the need for low-cost expendable sources.

RESEARCH ACCOMPLISHED

Background

Implosion sources have been used in specialized oceanographic studies for nearly 50 years. In 1952, 0.01-liter glass floats were imploded as an acoustical signal for indicating that a sediment corer reached the ocean bottom (Isaacs and Maxwell, 1952). In 1976, a study used weakened glass spheres to vary the depth of implosion (Orr and Schoenberg, 1976). More recently (1996), a project to develop a deep-water ocean bottom implosive source using a 20-liter cylinder was conducted (Sauter et al., 1996). Light bulbs with lead sinkers are often used today in shallow water experiments to test hydrophone operation. We do not know of an existing implosion system suited to the hydroacoustic monitoring needs at SOFAR channel depths. Any development of such a system must show its utility by demonstrating good source properties (amplitude and frequency content), implosion depth control, reliability, repeatability, and long-range propagation of the signal.

Acoustic Properties of Imploding Spheres

An imploding source exploits the pressure difference between an enclosed volume of gas at nominal atmospheric pressure and the external water pressure at the implosion depth. A sudden catastrophic failure of the containing vessel leaves the relatively low-pressure gas bubble exposed to relatively high-pressure water and a rapid implosion ensues. The implosion momentum collapses the bubble radius to less than that required for an equilibrium pressure balance. At the instant of minimum bubble radius, the bubble begins expanding and radiates a positive acoustic pressure spike. This oscillation can continue for a few cycles, each with successively reduced pressure spikes as energy is dissipated and the bubble approaches a static equilibrium pressure. One distinct difference in the case of underwater explosions is the initial shock wave caused by ignition of the explosive and creation of the expanding gas globe, which consists of explosion gas products. There is no such analogue in an implosion. Another important difference is the relatively cold low-pressure gas inside the sphere compared to the high temperature dense explosive gas products in the gas bubble. The bubble collapse details of the two cases cannot be directly compared.

The Spherecracker

If a glass sphere is of sufficient volume to produce the desired source signal level and has sufficient wall thickness to survive the water pressures in the operational depth range, then sphere failure must be initiated by some controlled method at a predetermined depth. Such a device was designed and built for this study and is termed by us the *Spherecracker* (Harben et al., 2000).

The *Spherecracker*, shown in Figure 1, was designed to be rugged enough to be reusable, heavy enough to sink the whole assembly loaded with the sphere, and not dependent on stored energy at the surface (i.e. no electricity or

compressed air). The device consists of two orthogonal cutout plates that hold the sphere and a cylinder-piston-ram assembly that punches a hole in the sphere. The system firmly holds the sphere in place and in contact with a 4-inch-diameter piston. A 1/4-inch diameter ram is connected to the center of the piston and passes through a small O-ring sealed hole in the cap confining the piston and abutting the glass sphere. The ram initiates failure by punching a hole through the glass sphere. The end-cap on the cylinder confining the piston and opposing the ram end-cap tapers to a one-inch diameter opening with a rupture disk seated to it. The rupture disk is calibrated to fail within 5% of the calibrated failure pressure of 1000 psi. Failure of the rupture disk results in an inrush of high-pressure water into the air-filled piston chamber, driving the piston - and attached ram - towards the glass sphere.

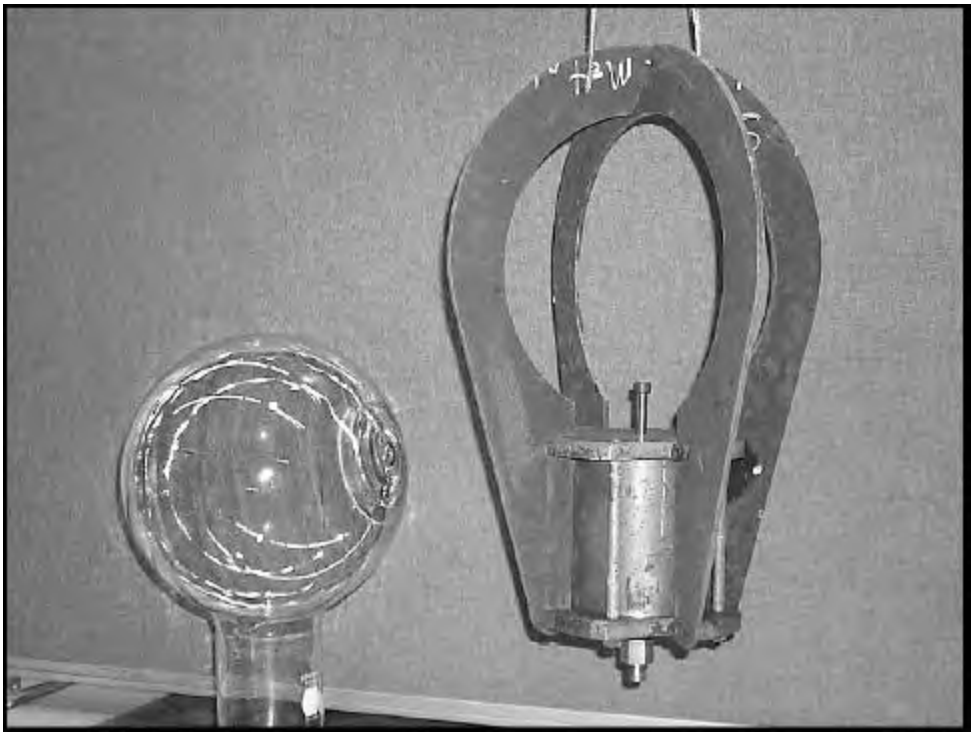


Figure 1. The *Spherecracker* is shown on the right in the lowering position. The piston assembly, shown in detail in Figure 2, is at the bottom of the mechanism. A Kontes glass sphere is shown on the left atop a laboratory beaker.

The operational concept is illustrated in Figure 2. Note that as the cylinder is lowered in the water, the water pressure on the ram serves to "cock" or position the piston near the rupture disk. When the disk fails, the water pressure on the relatively large area of the piston results in a force much greater than that on the small area opposing it. The net force drives the piston and the ram downward.

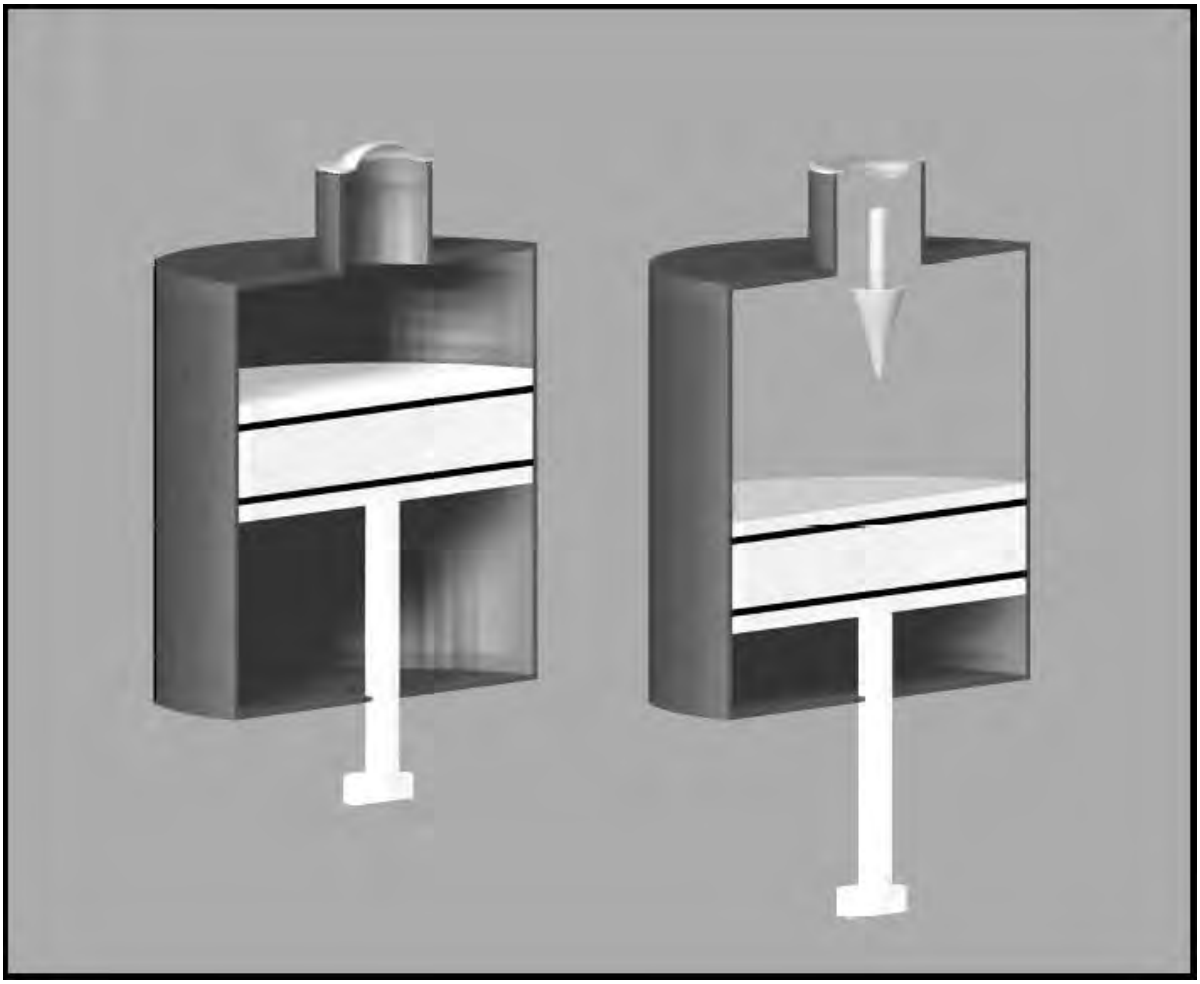


Figure 2. Conceptual view of the *Spherecracker* piston assembly. The rupture disk at the top keeps the cylinder volume above the piston at nominal atmospheric pressure (left). When the disk fails (right), high-pressure seawater rushes into the cylinder, driving the piston and ram downward.

Field Test at Dabob Bay, WA - March 1999

In March 1999 we conducted a test of an imploding glass sphere at Dabob Bay, WA. The purpose of this test was to record the source signal generated by the implosion and to estimate its source level. We used a 10-inch-diameter thin walled glass sphere that was lowered to a depth of 450 ft from a test barge (see Figure 3). Sandbags were used to sink the sphere to the test depth. The water depth at this site was 600 ft. Two hydrophones were used to record the implosion: one at a depth of 90 ft and one at a depth of 150 ft. A steel pipe was then slide down the tether line as a simple means of smashing the sphere and initiating the implosion (the *Spherecracker* was not available for this test). A Metrum tape recorder operating at 150,000 samples per second was used to record the implosion signal.

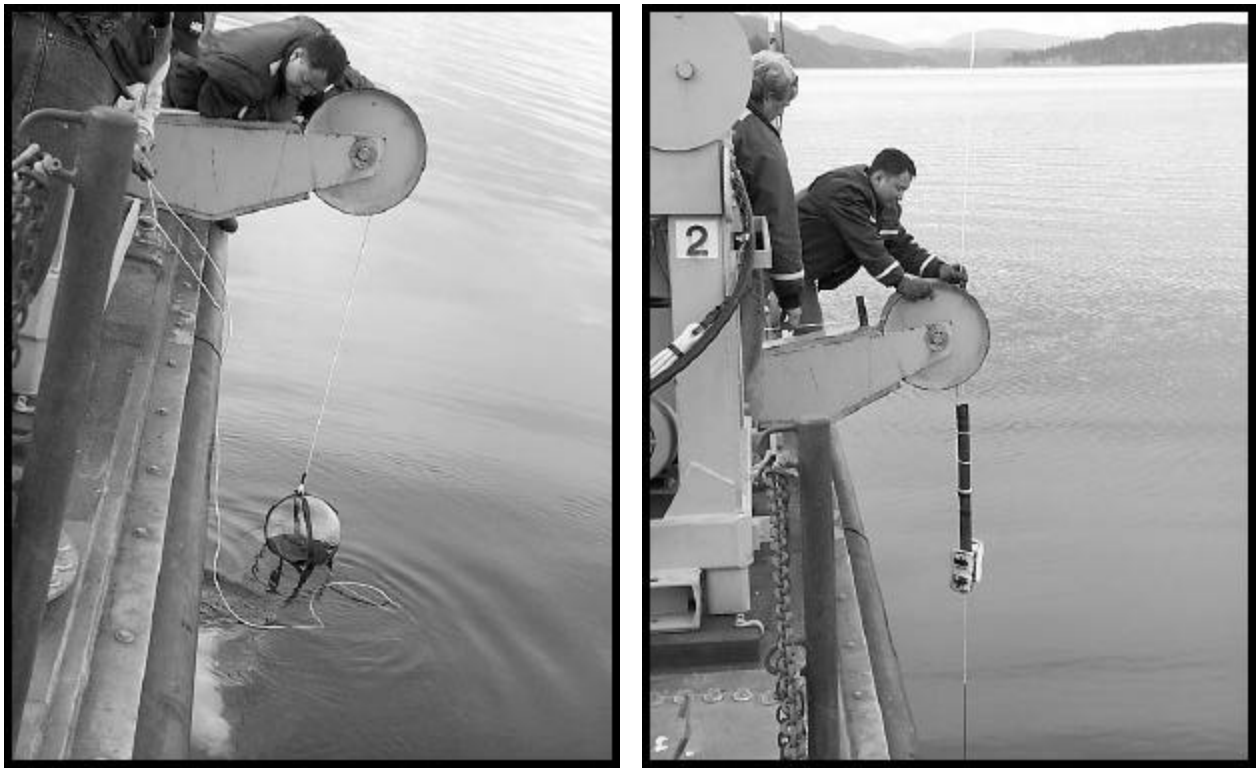


Figure 3. A 14-inch-diameter glass sphere is lowered into the water (left) during the March 1999 test conducted at Dabob Bay, WA. The sphere was lowered to a depth of 450 ft. A metal pipe was then slid down the tether line (right) in order to initiate failure. The water depth was 600-ft. Photos © by Ted Farrell.

The signal at the 150-ft hydrophone was clipped but the 90-ft hydrophone produced excellent data for analysis (see Figure 4). The recording, which was made at a horizontal offset of 33 meters from the source, shows three groups of arrivals: the sphere implosion followed by its bubble pulse, the inverted surface reflection of these signals, and finally the bottom bounce. Measured arrival time differences confirmed the implosion depth and hydrophone location. Figure 5 shows a blowup of the initial implosion signal. Note the precursor before the main signal, which appears in both the implosion and the bubble pulse. This may indicate that the sphere imploded in two steps. The width of the main signal is approximately 1/2 msec. The bubble pulse period is 4 msec.

The spectrum of the main implosion signal and the pre-event noise is shown in Figure 6. Ambient noise at this site is very low, so the signal-to-noise ratio is nearly 60 dB from 10-1000 Hz. Corrected to a source distance of 1-meter, the source level at 10 Hz is approximately 200 dB re 1-uPa.

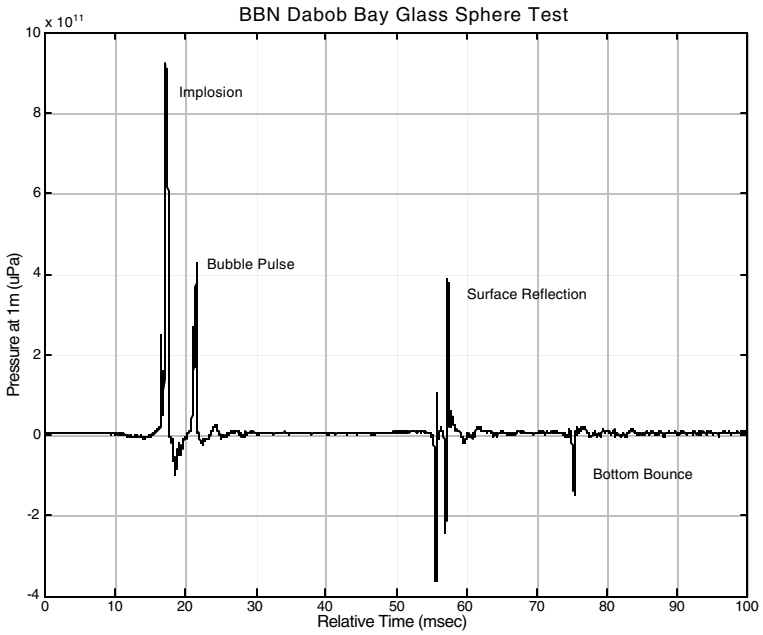


Figure 4. Recording of the glass sphere implosion test at Dabob Bay on the 90-ft hydrophone. Note the impulsive signal of the implosion, followed by the bubble pulse, then the surface reflection of the implosion and bubble pulse, and then the bottom reflection.

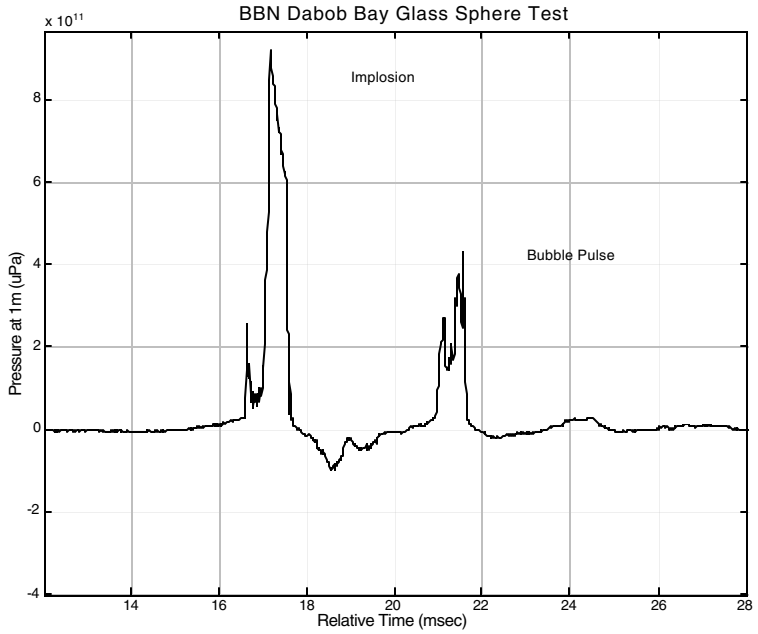


Figure 5. Blow-up of the sphere implosion waveform and its bubble pulse. Note the precursor before the main signal, which appears in both the implosion and the bubble pulse. The bubble pulse period is 4 msec.

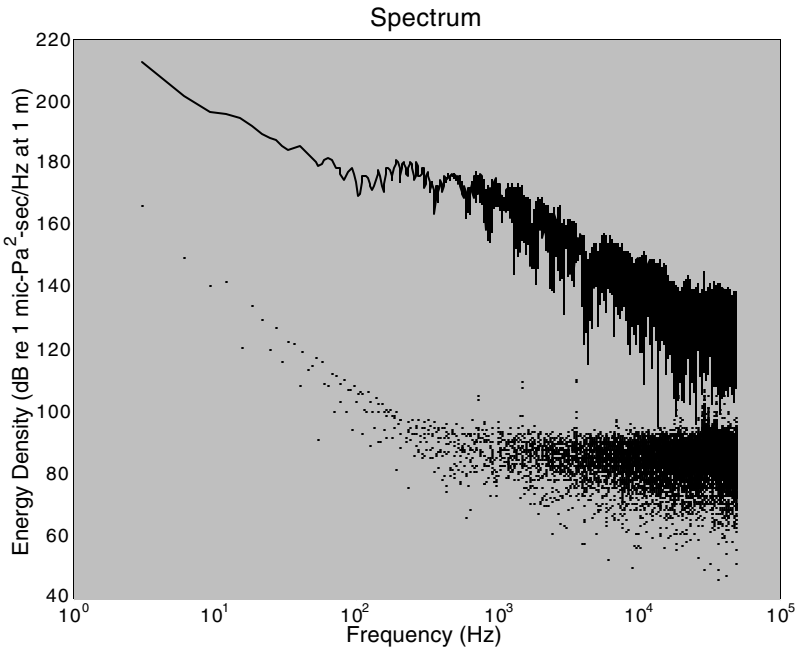


Figure 6. Spectrum of the Dabob Bay glass sphere implosion signal and pre-event noise corrected to a source distance of 1-meter. The source level at 10 Hz is approximately 200 dB re 1-uPa.

Field Test West of San Diego - February 2000

An opportunity to conduct a field test of a CGS sphere and the *Spherecracker* came in February 2000. The *Spherecracker* was loaded aboard the Research Vessel Sproul and tested west of San Diego at a water depth of around 1200 meters. The *Spherecracker* was loaded with a 22-liter CGS glass sphere and was lowered until a 1000 psi rupture disk failed. After initiating a successful implosion, the *Spherecracker* was recovered undamaged. By reloading the device with a new pressure disk and glass sphere, it could be used repeatedly.

The impulsive signal recorded from the implosion allowed accurate determinations of hydrophone depth, implosion depth and water depth from the surface reflected, bottom reflected, and 2nd bottom reflected phases. The implosion occurred at 685 meters depth. The implosion signal was felt on the ship and recorded by a calibrated hydrophone suspended 12 meters deep. The recorded signal, shown in Figure 7, was of short duration (less than 5 msec) and with a small bubble pulse about 2 msec after the main collapse. The event starts with a rarefaction as the sphere shatters and collapses. The large compressional pressure spike following the rarefaction occurs when the collapse reaches a minimum volume and reverses (begins expanding).

The spectrum of the implosion and the pre-event noise is shown in Figure 8. The source does not show any appreciable acoustic energy above background noise for frequencies below about 50 Hz. Above 50 Hz the source amplitude rises to a broad maximum for frequencies between 200 and 800 Hz. There is a relatively shallow high-frequency roll-off of the source energy between 1 kHz and 10 kHz, whereas the noise rolls off more steeply in this band. The consequence is that the signal-to-noise ratio is highest at the highest frequency shown.

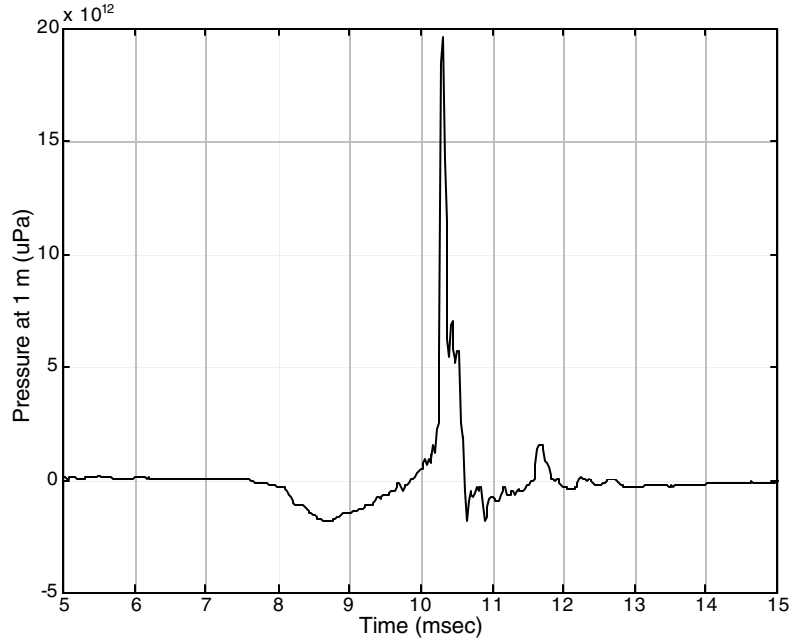


Figure 7. Waveform (left) recorded for the glass sphere implosion test off San Diego. The event starts with a rarefaction as the sphere shatters and collapses. The large compressional pressure spike following the rarefaction occurs when the collapse reaches a minimum volume and reverses (begins expanding).

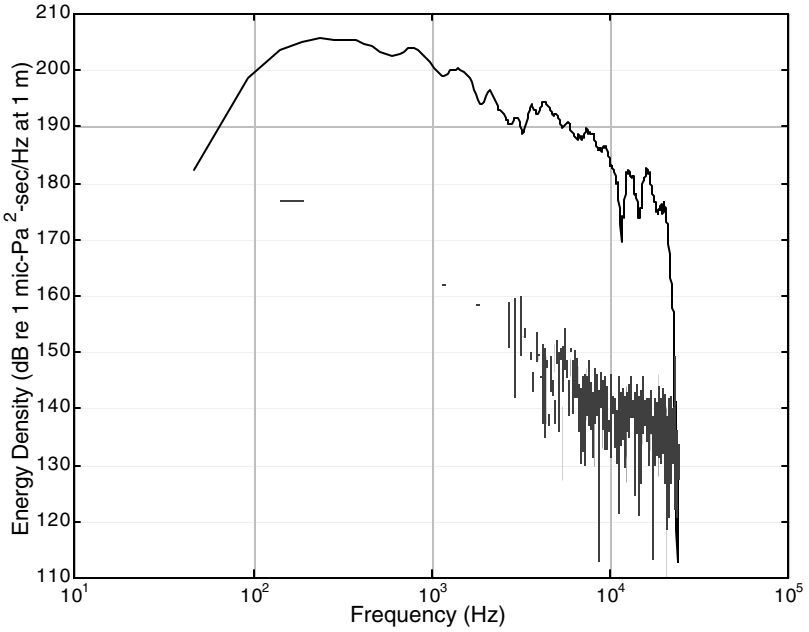


Figure 8. Spectrum of the glass sphere implosion test off San Diego. The peak of the spectrum is shifted toward the higher frequencies with respect to that seen for the Dabob Bay test. Source levels are on the order of 205 dB re 1-uPa at 200 Hz.

Potential Use as Calibration Sources

At the beginning of this paper we listed a number of potential experiments that could be conducted with imploding glass sphere sources. Using the source measurements made in this study, we now calculate how far acoustic energy would travel in the SOFAR channel from an imploding glass sphere. The calculation, shown in Figure 9, used an imploding glass sphere in the SOFAR channel near Ascension Island in the South Atlantic Ocean. Propagation characteristics were calculated for a frequency of 10 Hz. A source level of 205 dB re 1-uPa was used. The figure shows transmission loss calculated out to a level of 125 dB, which would attenuate the source level from 205 to 80 dB re 1-uPa, which is the average background noise level in the Atlantic Ocean. The calculation demonstrates that the imploding glass sphere signal could be recorded above the background noise level across the entire Atlantic Ocean, making it an appropriate source for travel time calibration.

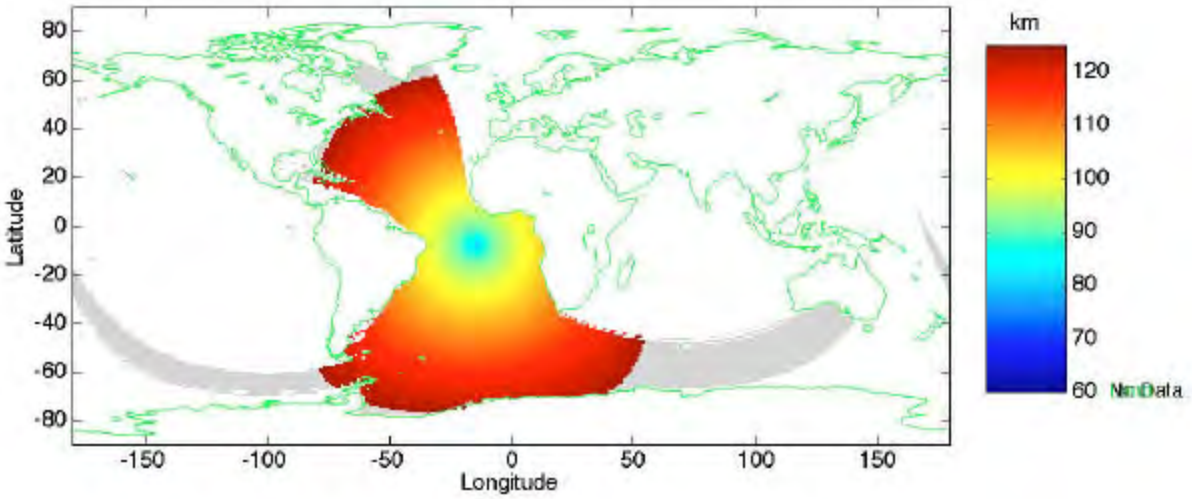


Figure 9. Model calculation of the attenuation of acoustic energy in the SOFAR channel from a 10-inch diameter glass sphere implosion near Ascension Island. Using a source strength of 205 dB re 1-uPa at 10 Hz, we used the program HydroCAM to compute the propagation out to a distance where the signal-to-noise ratio is 1:1 (based on average noise measurements of 80 dB re 1-uPa in the ocean). The calculation shows that the acoustic energy produced by the sphere implosion would be recorded across the Atlantic Ocean.

CONCLUSIONS AND RECOMMENDATIONS

We have demonstrated the utility of using imploding glass spheres as calibration sources for the hydroacoustic component of nuclear monitoring. We conducted two experiments, one in Dabob Bay, WA and another off the coast of San Diego CA, where the source signals from the implosions were recorded and analyzed. A device termed a *Spherecracker* was designed and built to initiate failure of the glass sphere at a preset depth. Source levels of approximately 200 dB re 1-uPa were measured for the sources. In the Dabob Bay experiment, the imploding glass sphere produced sufficient low frequency energy to be useful for calibration experiments in the frequency range of interest to nuclear explosion monitoring. In the deeper water test off San Diego, the source spectrum was shifted to higher frequencies. Further work on the implosion phenomenology and field-testing is needed to understand this difference and make the source a productive tool for hydroacoustic research.

ACKNOWLEDGMENTS

Ted Farrell, formerly of BBN Technologies and now at Johnson & Johnson, conducted the glass sphere test at Dabob Bay, WA. Charles Chassaing provided the shell theory background in order to assess whether or not a glass sphere would survive to SOFAR channel depths. We are also indebted to Donna Blackman and Tim Minshull for support of some early field tests. Support for the field test aboard the Research Vessel Sproul was provided by the National Science Foundation under grant OCE 97-12605.

REFERENCES

Harben, P.E., C. Boro, L.Dorman, and J. Pulli (2000), Use of Imploding Spheres: an Alternative to Explosives as Acoustic Sources at Mid-Latitude SOFAR Channel Depths, *Lawrence Livermore National Laboratory Report UCRL-ID-139032*.

Isaacs, J.D. and A.E. Maxwell (1952), The Ball-breaker: a Deep Water Signaling Device, *J. Marine Res., 11*, 63-68.

Massinon, B. (1999), Proceedings from the Informal Workshop on Hydroacoustics, Papeete, Tahiti.

Orr, M. and M. Schoenberg (1976), Acoustic signatures from Deep Water Implosions of Spherical cavities, *JASA*, *59*, No. 5, 1155-1159.

Sauter, A., L. Dorman and E. Canuteson (1996), Development of a Seismo-Acoustic Implosive Source, (abstract), Fall AGU Meeting, also at www.mpl.ucsd.edu/obs/reports/ABM/implosive.agu.html .

MODELING LONG-RANGE HYDROACOUSTIC REFLECTIONS IN THE ATLANTIC AND PACIFIC OCEANS

Jay J. Pulli, Zachary Upton, Rob Gibson, and Ted Farrell
BBN Technologies

Sponsored by the Defense Threat Reduction Agency
Arms Control Technology Division
Nuclear Treaties Branch

Contract Number DSWA01-97-C-0164

ABSTRACT

It is well known that acoustic energy that is trapped in the ocean's SOFAR channel can propagate for thousands of kilometers with little attenuation. When this energy encounters bathymetric features that intersect the SOFAR channel (e.g. islands, seamounts, and continental margins), it can be scattered and reflected back into the ocean. Historical data from many underwater explosions show large reflections arriving at receivers tens of minutes or hours after the direct arrival. If the sources of the bathymetric reflections can be identified, these reflected raypaths could then be used to improve the source localization. Spectral characteristics of the reflected signals are also similar to those of the direct arrivals and hence contain valuable information about the source. In some cases, such as when the direct source-receiver path is blocked by bathymetry, the only observable arrivals may be reflections.

Here we present a model for predicting long-range hydroacoustic reflections in the ocean. For a given source location, we use the program HydroCAM to predict ray paths, travel times and propagation losses to each potential scattering patch in the ocean. We then perform a second prediction where rays are computed from the receiver location to the scattering patches. These two results are combined to produce predictions of the bistatic ray path characteristics from the source to the scattering regions to the receiver location. We sort these calculations by time, starting with the direct arrival and extending in constant travel time ellipses out to a given time delay (e.g. 60 minutes past the direct arrival). For each travel time ellipse, we select the bathymetric features along that ellipse with slopes in the direction of propagation greater than a prescribed minimum. If these features intersect the SOFAR channel, their times and locations are stored and used to form an impulse response model of the ocean. Amplitudes are scaled by both propagation loss and an approximation to bathymetric scattering strength. This impulse response is then convolved with a model of the source time envelope to produce a synthetic waveform.

The model has been compared with recorded data for events in both the Pacific and Atlantic Oceans. For the Pacific, we modeled the signal from the IITRI underwater explosion, conducted off the coast of California on February 16, 1968. Recordings of this explosion from hydrophones off Midway Island show a prominent reflected arrival 20 minutes after the direct arrival. This corresponds with the model prediction of a reflection from the Aleutian Islands. For the Atlantic, we modeled the signal from the Chase 21 explosion off the coast of New Jersey in 1970 and recorded off Ascension Island. The reflected arrival seen in the data 9 minutes after the direct arrival corresponds with the model prediction of a reflection from the Guiana Plateau.

OBJECTIVE

Historical and contemporary hydroacoustic data from many underwater explosions and sub-sea earthquakes show large reflections arriving at receivers tens of minutes or hours after the direct arrival (Northrop, 1968). These reflections can be used for localization purposes as long as the sources of the bathymetric reflections can be identified. Spectral characteristics of the reflected signals are also similar to those of the direct arrivals and hence contain valuable information about the source. In some cases, such as when the

direct source-receiver path is blocked by bathymetry, the only observable arrivals may be reflections. The objective of this work is to provide a model basis for interpreting these reflected arrivals.

The need for an understanding of hydroacoustic reflections was recognized in the recent International Workshop on Hydroacoustic Monitoring for the Comprehensive Nuclear-Test-Ban Treaty that met in Tahiti in September 1999 (Massinon, 1999). The workshop findings identify research on hydroacoustic reflections as a technical issue and recommend that an assessment be made of their utility for the hydroacoustic localization problem.

RESEARCH ACCOMPLISHED

Overview of the Model

The model we have developed can best be described as a sequence of applied steps:

- For a given source location, we use the program HydroCAM (Farrell et al, 1997) to predict ray paths, travel times, and propagation losses to each potential scattering patch for a given ocean basin.
- Then, a second prediction is made where rays are computed from the receiver to each of these scattering patches.
- These two calculations are combined to produce predictions of the bistatic ray path characteristics from the source to the scattering regions and then to the receiver location.
- Next we sort these calculations by time, starting with the direct arrival and extending in constant travel time ellipses out to a given time delay (e.g. 60 minutes past the direct arrival).
- For each travel time ellipse, we select the bathymetric features along that ellipse with slopes in the direction of propagation greater than a prescribed minimum. The determination of slope, although simple in concept, was actually rather difficult to implement because of the relatively low resolution of available bathymetry for an entire ocean. We settled on a measure of the total relief (difference between maximum and minimum depths) of a given patch as an approximation to the actual slope.
- By combining the ray paths that correspond to the selected patches, we obtain an impulse response model of the ocean for the given source-receiver configuration.
- Each bathymetric feature will only reflect hydroacoustic energy if it penetrates the SOFAR channel axis where the energy is propagating. This is illustrated conceptually in Figure 1. The measure we use of this scattering strength is the difference between the bathymetric feature depth and the depth of the sound channel axis at this point. An arctangent function is used for the model (Figure 2). SOFAR channel depths were obtained from the "Database Description for the Master Generalized Digital Environment Model (GDEM), Version 5.0". SOFAR channel data are generally not available at the same resolution as bathymetry data, so a 2-D interpolation must be made before the two databases can be compared.
- Amplitudes for each path are then scaled by both propagation loss and attenuation.
- Finally, the impulse response model is convolved with a source model based on the envelope of the direct arrival.

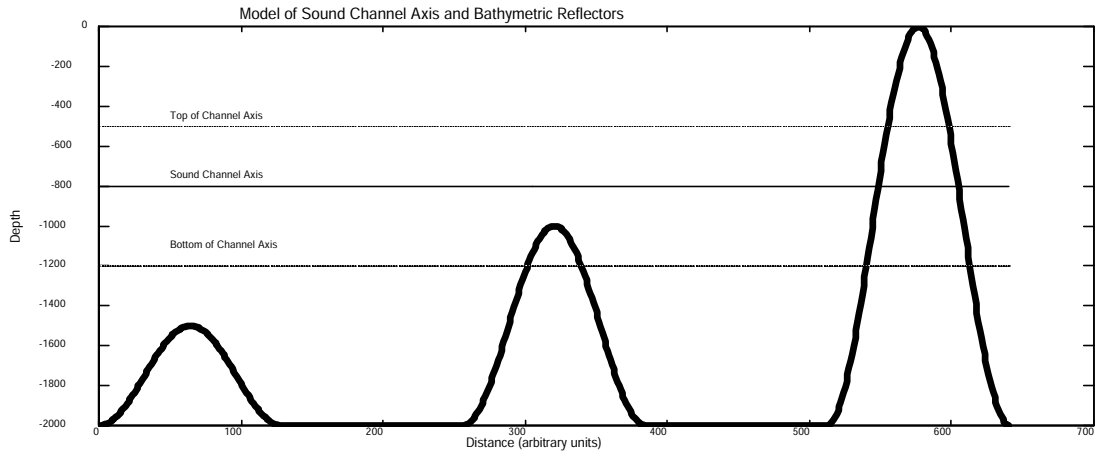


Figure 1. Conceptual model of three bathymetric features and their relationship to the sound channel axis (SCA). The feature on the left is below the sound channel and will not reflect energy in the sound channel. The feature in the middle penetrates the lower range of the sound channel and will reflect some energy. The feature on the right (e.g. an island) spans the entire sound channel and will efficiently reflect the energy.

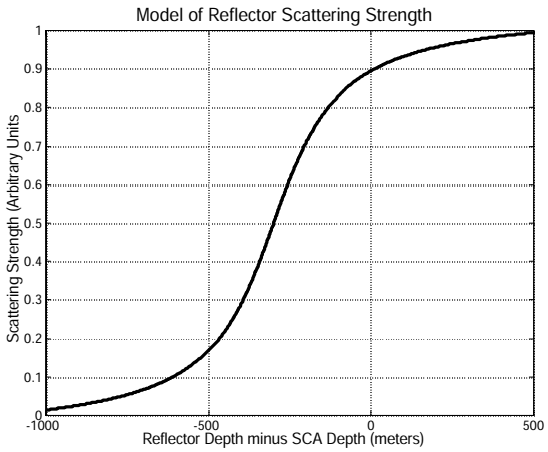


Figure 2. Model for scattering strength of a bathymetric feature versus its depth with respect to the SCA. Features which are well below the SCA will not reflect hydroacoustic energy, whereas features near or above the SCA will reflect energy. This is modeled with an arctangent function.

Pacific Example

Our first application of the model will be for the IITRI underwater explosion recorded at the hydrophone off Midway Island (see Figure 3). This explosion occurred on February 16, 1968 and was located in deep water off the coast of San Diego. The direct arrival is recorded at Midway at a travel time of 60 minutes; a prominent reflection can be seen arriving 15 minutes later.

The bathymetric feature finder was run for a travel time window of between 55 and 100 minutes, which should include reflected arrivals corresponding to the available data. The algorithm identified 241 possible bathymetric features, shown on the map in Figure 4. A histogram of the feature depth is shown in Figure 5. Most features are located at depths of between 750 and 1500 meters. A histogram of the sound channel axis depth in the Pacific is shown in Figure 5, where it can be seen that the sound channel axis occurs mostly at

depths of between 600 and 1200 meters. Hence many of the identified bathymetric features should reflect hydroacoustic energy from the SOFAR channel.

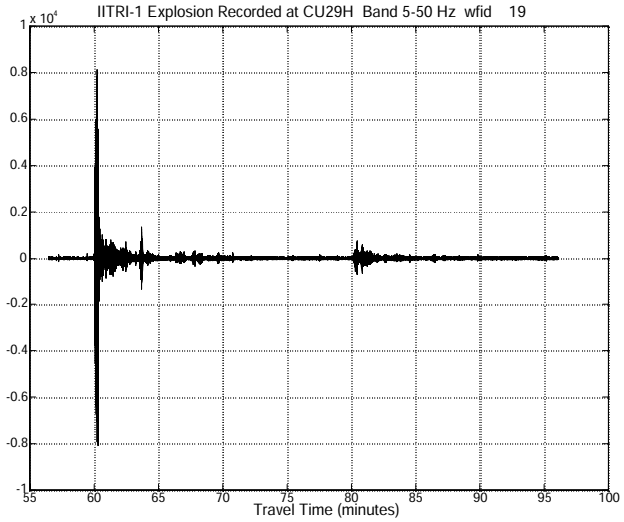


Figure 3. Recording of the IITRI underwater explosion at station Midway.

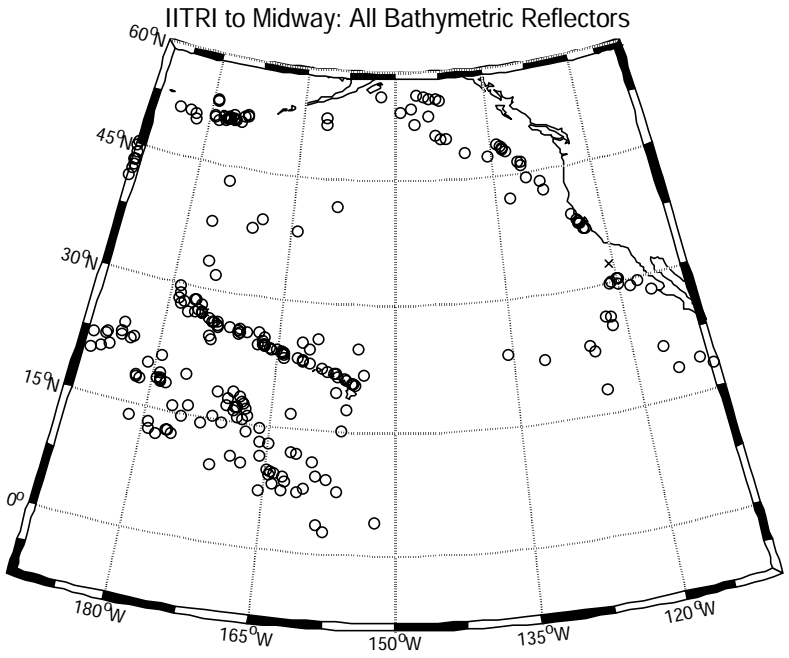


Figure 4. Map of bathymetric reflectors for the case the IITRI explosion recorded at Midway.

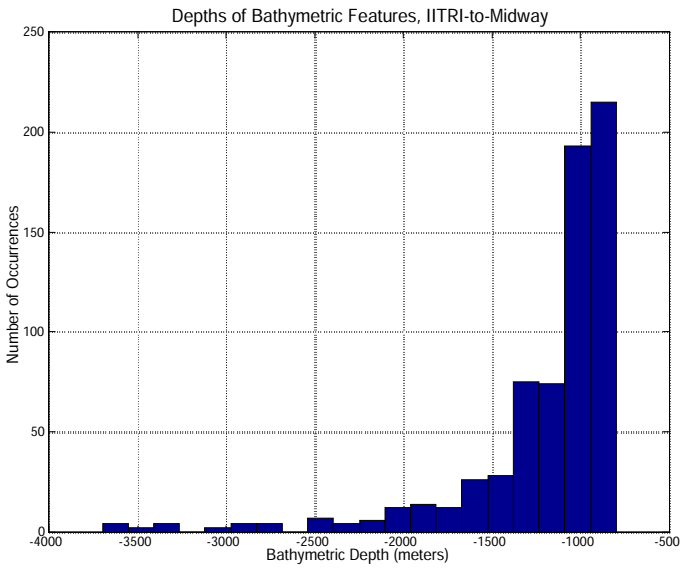


Figure 5. Histogram of bathymetric feature depths in the Pacific for the IITRI to Midway case.

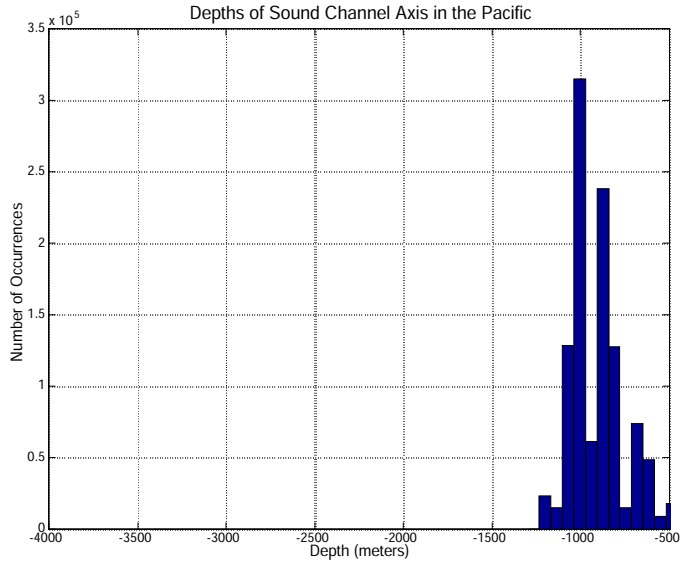


Figure 6. Histogram of sound channel axis depths in the Pacific.

Figure 7 shows the impulse response model derived from the bathymetry analysis. The amplitude corresponding to each scatterer has been scaled with the function shown in Figure 2 as well as with geometrical spreading and attenuation. After the direct arrival at 60 minutes, there is a decaying sequence of impulses with large reflections at 64 minutes and 80 minutes. Figure 8 shows the final output of the model where the impulse response has been convolved with a source envelope model.

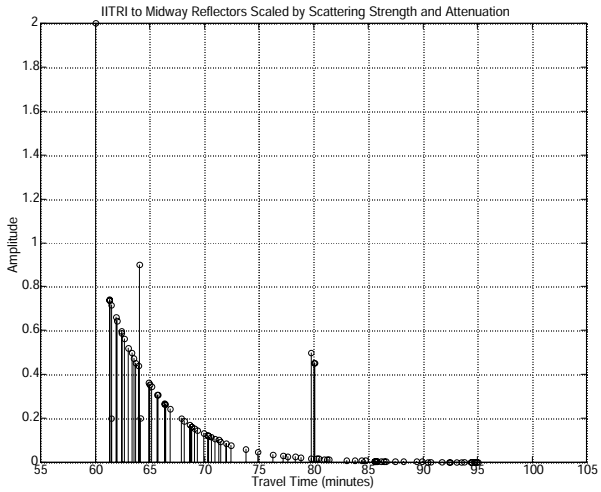


Figure 7. Impulse response model of the Pacific for the case of IITRI to Midway Island.

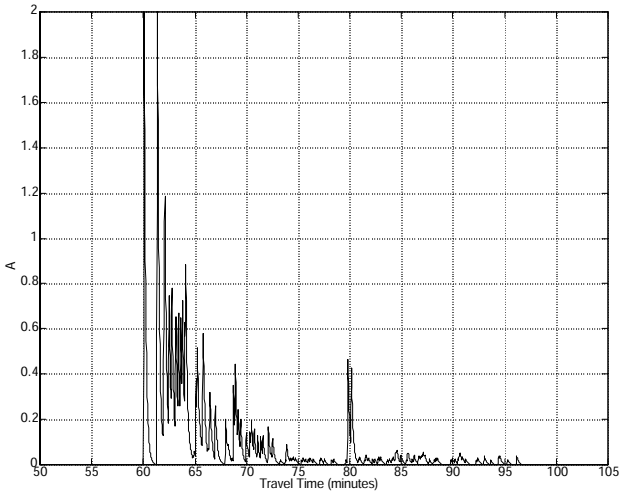


Figure 8. Impulse response model convolved with a model of the source

Atlantic Example

Our second application of the model is for the Chase21 explosion recorded at Ascension Island. This event, which occurred on June 25, 1970, was a ship-scuttling explosion on the continental shelf off the coast of New Jersey at a depth of 540 ft. The explosive charge was 614.5 tons. Although the explosion occurred above the SOFAR channel depth, energy was trapped in the channel and excellent recordings were obtained at the Ascension hydrophone array. The recording made at Ascension station FS27 is shown in Figure 9. A prominent feature of this signal is the presumed set of reflected arrivals, which are seen at a travel time of between 95 and 97 minutes. Our previous studies of this arrival indicate that the Guiana Plateau, a bathymetric feature off the northeast coast of South America, is the source of this reflected energy. A smaller reflection arrives at a travel time of approximately 102 minutes.

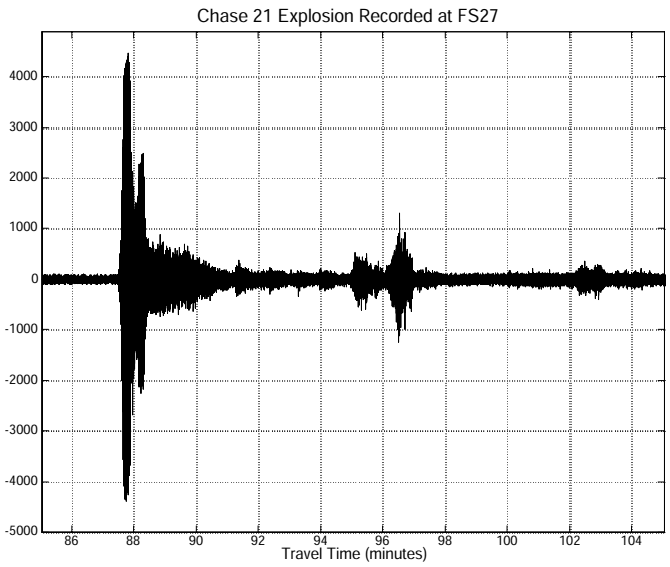


Figure 9. Hydroacoustic recording of the Chase 21 explosion at Ascension Island

The bathymetric feature finder was run for a travel time window of between 85 and 115 minutes, which should include reflected arrivals corresponding to the available data. The algorithm identified 309 possible bathymetric features, shown on the map in Figure 10. A histogram of the feature depth is also shown in Figure 11. Most features are located at depths of between 2000 and 4000 meters. A histogram of the sound channel axis depth in the Atlantic is shown in Figure 12, where it can be seen that the sound channel axis occurs mostly at depths of between 500 and 1200 meters. Hence only a few of the identified bathymetric features will reflect hydroacoustic energy from the SOFAR channel.

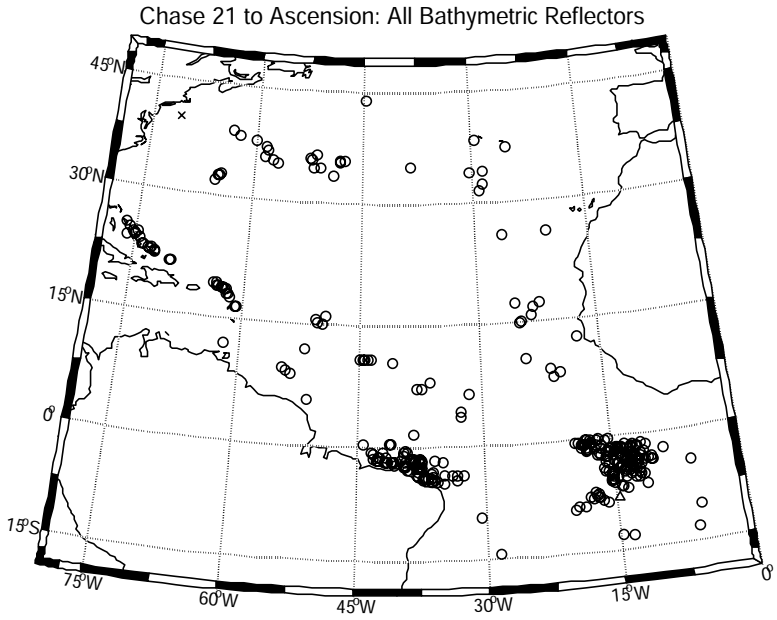


Figure 10. Bathymetric features in the equatorial Atlantic Ocean for the case of Chase21 to Ascension Island.

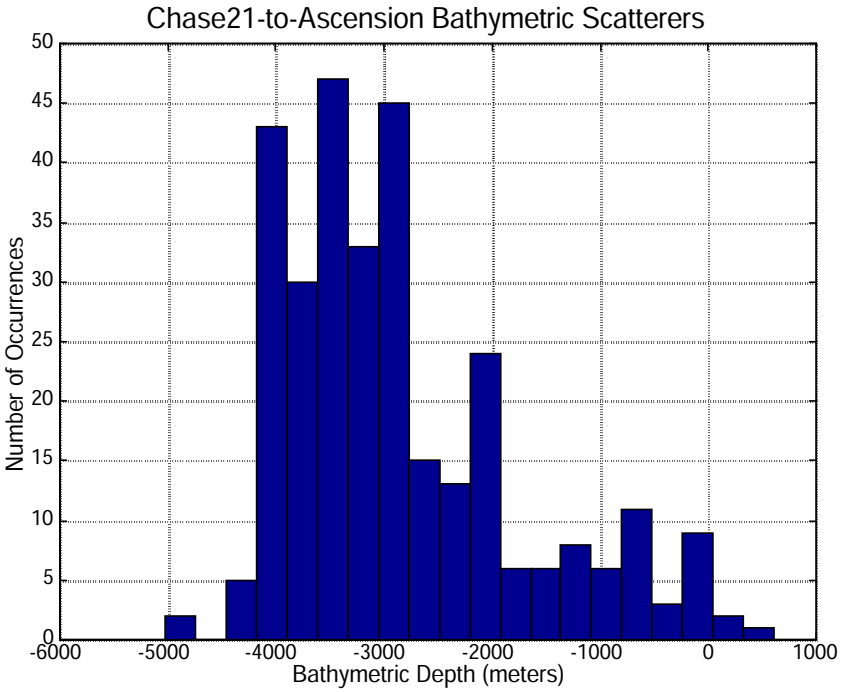


Figure 11. Histogram of bathymetric feature depth in the equatorial Atlantic for the Chase21 to Ascension case.

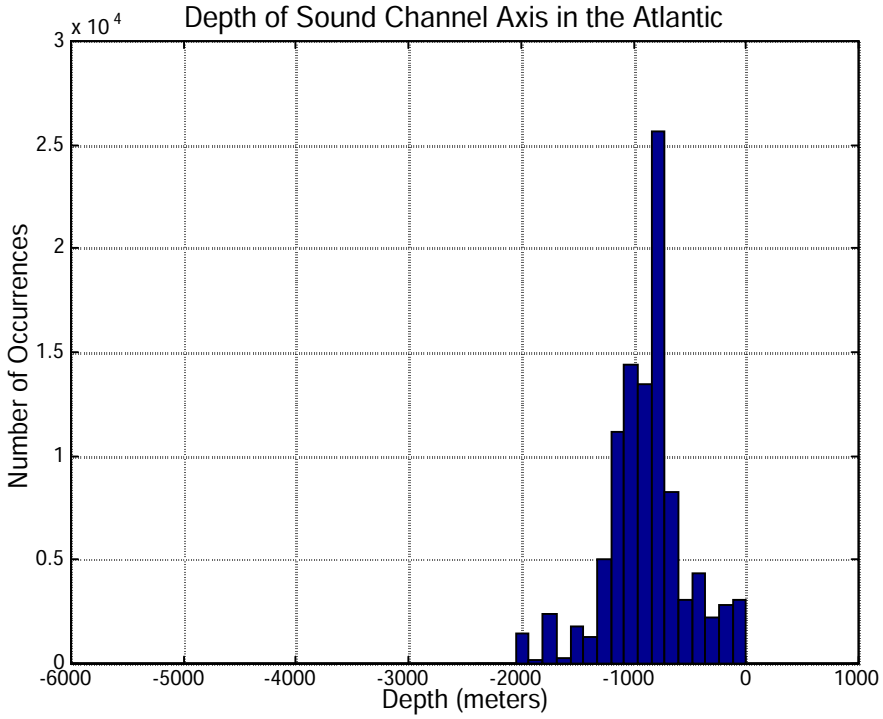


Figure 12. Histogram of sound channel axis depths in the equatorial Atlantic.

Figure 12 shows the impulse response model derived from the bathymetry analysis. The amplitude corresponding to each scatterer has been scaled with the function shown in Figure 2 as well as with geometrical spreading and attenuation. After the direct arrival at 88 minutes, there is a sequence of six large impulses which are not seen in the data. At 95 minutes there is a cluster of arrivals which correspond to scatterers at the Guiana Plateau (Angell et al. 1998, Pulli et al. 1999). This site has been identified, using bearing analysis, as the source of the reflected arrival at Ascension. At 100 minutes there is an additional arrival, however the data show an arrival two minutes later. Figure 13 shows the final output of the model where the impulse response has been convolved with a source envelope model.

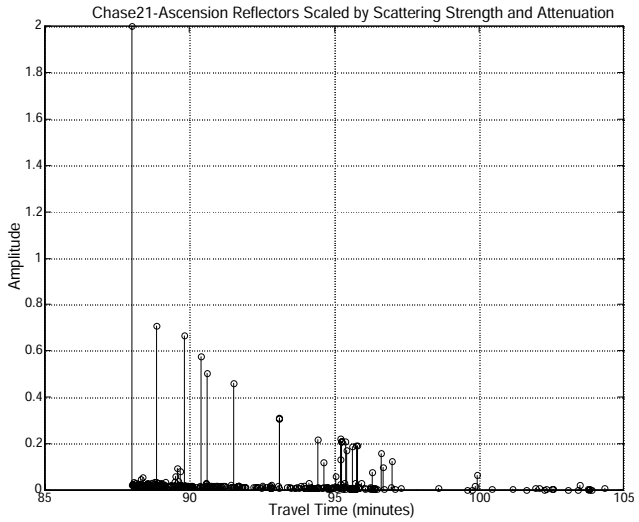


Figure 13. Impulse response model of the equatorial Atlantic for the case of Chase21 to Ascension Island. Note the cluster of arrivals at 95-96 minutes which matches those seen in the data shown in Figure 8.

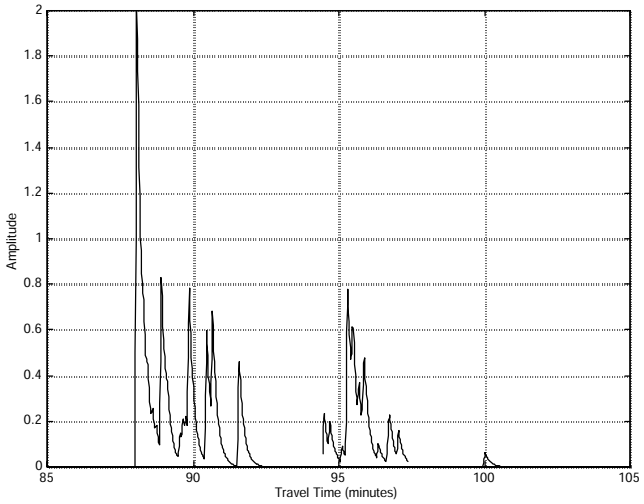


Figure 14. Impulse response model convolved with a model of the source.

CONCLUSIONS AND RECOMMENDATIONS

We have presented a model for long-range hydroacoustic reflections based on an analysis of bathymetry, slope, sound channel axis depth, travel time, and propagation loss. The model has been successfully applied to events in the Pacific and Atlantic Ocean basins. The model does not agree entirely with the data in that the model predicts more reflections than are actually observed. This is probably due to our imperfect knowledge of the actual scattering process. Improvements to the model can be accomplished with:

- Use of higher resolution bathymetry, especially in areas of known features as identified in this study.
- An analysis of slope and surface area calculations with these higher resolution bathymetric databases.
- A modeling study of reflections from bathymetric features as a function of frequency.

Key Words: Hydroacoustics, reflections, modeling, long-range propagation

REFERENCES

Angell, J., T. Farrell, and J. Pulli (1998), Characterization of reflected hydroacoustic signals, Proc. 20th Annual Seismic Research Symposium, Dept. of Defense, NTP, 650-659.

GDEM, Database Description for the Master Generalized Digital Environment Model (GDEM) Version 5.0, OAML DBD-20F, Naval Oceanographic Office, Stennis Space Center MS. September 1995

Farrell, T., K. LePage, C. Barklay, J. Angell, M. Barger (1997), Users Guide for the Hydroacoustic Coverage Assessment Model (HydroCAM), BBN Technical Memorandum W1309

Massinon, B. (1999), Proceedings from the Informal Workshop on Hydroacoustics Technology for the CTBT, Papeete, Tahiti.

Northrop, J. (1968) Submarine Topographic Echoes from Chase V, J. Geophys. Res., 73, No. 12

Pulli, J.J., T. Farrell, and R. Gibson (1999), Characterization and utilization of hydroacoustic signals reflected from continents and bathymetric features, 21st Seismic Research Symposium, Las Vegas, NV

T-PHASE OBSERVATIONS FROM THE MAY 1999 ASCENSION ISLAND EXPERIMENT

Arthur Rodgers and Philip Harben
Lawrence Livermore National Laboratory

Sponsored by U.S. Department of Energy
Office of Nonproliferation Research and Engineering
Office of Defense Nuclear Nonproliferation
National Nuclear Security Administration

Contract No. W-7405-ENG-48

ABSTRACT

The Comprehensive Nuclear-Test-Ban Treaty (CTBT) specifies that an International Monitoring System (IMS) will be used to detect and locate disturbances that could be related to nuclear testing. In order to monitor disturbances in and near the world's oceans, the IMS will rely on a network of 11 hydroacoustic stations. This hydroacoustic network will be composed of 6 hydrophone stations and 5 T-phase seismic stations. The hydrophone stations will record pressure variations in the ocean. The T-phase stations will record the seismic waves in the solid earth that are excited when a hydroacoustic wave strikes an island or continental margin. The coupling of hydroacoustic-to-seismic energy is currently an active area of research for CTBT monitoring.

We report observations of hydroacoustic waves and their conversion to seismic waves (T-waves) at the volcanic edifice of Ascension Island. An earthquake to the south of Ascension Island was recorded by International Monitoring System (IMS) hydrophones and temporary seismic stations deployed on Ascension Island by Lawrence Livermore National Laboratory (LLNL). The hydrophone recordings are rich in high-frequency (10-40 Hz) energy. However, the converted seismic waves are dominated by much lower frequencies (2-8 Hz). The T-waves demonstrate amplitude and travel-time variations on the Island. In addition to the earthquake records, off-shore airgun shots were recorded as part of a crustal structure study. These shots also produced hydroacoustic-to-seismic conversions. We performed two-dimensional finite difference simulations to investigate the T-phase conversion process at ocean-island margins. The point of these calculations will be to model the transfer function of the conversion process and to determine if T-phase amplitude variability is the result of conversion along the complex bathymetry of the island, propagation on the island or a site effect.

These observations suggest that the T-phase stations of the IMS may be useful for detecting and locating events in support of the CTBT provided that T-phase travel times are appropriately calibrated. However on volcanic islands, event identification based on T-phase data, which relies on high frequencies, may be inhibited by strong attenuation and low signal-to-noise.

Key Words: hydroacoustics, T-phases

Research performed under the auspices of the U.S. Department of Energy by the Lawrence Livermore National Laboratory under contract W-7405-ENG-48. LLNL contribution UCRL-JC-138996.

OBJECTIVE

The objective of this study is to understand the conversion of hydroacoustic-to-seismic energy at an island using both empirical data and theoretical modeling. Seismic data from the May 1999 Ascension Island Experiment were analyzed to study the variability of on-shore T-phase amplitudes and frequency content. Theoretical investigations of the conversion of hydroacoustic-to-seismic energy were also performed.

RESEARCH ACCOMPLISHED

During the last year we have extended our analysis of on-shore T-phase recordings of a moderately large earthquake to the south of Ascension Island. We performed additional investigations of T-phase conversion with two-

dimensional finite difference simulations. We are currently modeling T-phases from offshore airgun shots performed as part of a crustal structure study.

The May 1999 Ascension Island Experiment

One of the IMS hydrophone stations is located at Ascension Island in the south central Atlantic Ocean. During a five-day period in May 1999, an offshore airgun survey was conducted around Ascension Island to image the volcanic edifice. Lawrence Livermore National Laboratory (LLNL) deployed ten temporary seismic stations on Ascension Island to study the acoustic coupling and seismic propagation on the island. The goal was to simultaneously record acoustic waves in the ocean (denoted here as H-waves) on the IMS hydrophones and their conversion to seismic waves in the solid earth (T-phases) generated by the airgun shots. Additional airgun shots were used to precisely locate and calibrate the amplitude response of the hydrophones (Harben, et al., 1999; Harben et al., 2000). Figure 1 shows the locations of the hydrophone and seismic stations, the ship track and bathymetry around Ascension Island.

May 14, 1999 Earthquake Recordings

During the temporary seismic station deployment, an earthquake occurred to the south of Ascension Island and was recorded by both the hydrophones and seismic stations. Figure 2 shows the event location, the paths, and recording hydrophone and seismic stations. The hydrophone and vertical component seismic recordings of the event are shown in Figure 3. This event was reported by the United States Geologic Survey (USGS) Preliminary Determination of Epicenters (PDE) (Table 1).

Table 1. Event parameters from the USGS-PDE.

DATE	TIME (GMT)	LATITUDE	LONGITUDE	DEPTH	M_B
1999, May 14 (134)	17:10:09.03	-35.71	-15.89	10 km	4.8

Note in Figure 3 that the H-wave arrival timing is consistent with the source lying to the south of Ascension Island. One of the goals of the experiment was to calibrate the responses of the hydrophones to pressure (Harben et al., 2000). It was not possible to estimate the full frequency-dependent responses because of the placement of the hydrophones on the ocean floor. Nonetheless, the gain of the hydrophones was determined at 10 Hz and the roll-off of the nominal instrument was assumed to be valid for the passband 2-50 Hz. The hydrophone data were then converted to pressure in Pascals (Pa). The seismic instruments (Sprengnerther S-6000, 2-Hz free period) were calibrated and the raw seismic data was converted to absolute ground velocity in nanometers/second. Hydrophone and seismic data were recorded at 120 and 250 samples/second, respectively.

Comparison of Hydrophone and Seismic Spectra

Using the instrument corrections described above, we computed amplitude spectra of time series of equal length for windows around the T-phase arrivals. Figure 4 shows the waveform segments and the spectra of the signals and pre-event noise. The hydrophone record is well above the noise level for the entire band shown (1-30 Hz), while the seismic T-phase signal merges with the noise at about 12 Hz. This is presumed to be due to both inefficient conversion of hydroacoustic-to-seismic energy at the island edifice as well as high seismic noise levels on the island. Additionally, the fall-off of the seismic spectrum is more rapid than that of the hydroacoustic signal in the band 4-10 Hz. This suggests that attenuation along the island portion of the path is high. All these factors result in lower signal detection thresholds at island T-phase stations. Furthermore, event identification methods that rely on analysis of the high-frequency content will be inhibited by inefficient conversion, attenuation and low signal-to-noise.

T-phase Amplitude Variability: Path or Site Effect?

Several previous studies have documented the variability in T-phase amplitudes and character and related this to source-side and/or receiver-side conversion effects (Talandier and Okal, 1998; Piserchia et al, 1999; de Groot-Hedlin and Orcutt, 1999). The T-phases for the earthquake considered were well recorded at five LLNL-deployed

seismic stations. Figure 5 shows the envelopes of the T-phase records (filtered 2-6 Hz) and the peak envelope amplitudes plotted at their station locations. The envelopes show considerable differences given small inter-station spacing of a few kilometers (the island is only 10 km across). The peak envelope amplitudes vary by a factor of five between stations OBG and APS. The along-path bathymetry and topography are shown in Figure 5. Note that the path to station OBG shows that a seamount intersects the SOFAR channel at 800-m depth. This bathymetric feature could disrupt the guided hydroacoustic wave. The profile to station APS intersects an undersea canyon (not shown), which could focus incoming hydroacoustic energy and lead to amplification. Alternatively, site effects due to emplacement of the seismometers on different geologic structures could lead to the variability in the observed T-phase amplitudes. The fact that the amplitudes vary over such short spatial scales suggests that site effects play an important role in controlling T-phase amplitudes.

Modeling T-phase Conversions

We performed simulations of the propagation and subsequent conversion of hydroacoustic waves to seismic waves using an acoustic/elastic finite difference code (Larsen and Schultz, 1995). These calculations are done to investigate the T-phase conversion process. The ocean environment was simulated with the nominal sound speed profile for the Ascension Island region (Levitus et al., 1984). A soft sediment layer and solid crust with a velocity gradient were used below the ocean (Figure 6). Various scenarios were simulated. The simulation shown in Figure 6 shows the bathymetric profile from the earthquake to seismic station APS. An explosion source at the SOFAR axis depth (800 m) provided the excitation of the hydroacoustic wave. The synthetic response is also shown in Figure 6. Analysis of the particle motions provides insight into the wave-types. The large amplitude pulse has retrograde elliptical particle motion and propagates as a Rayleigh wave. The later portion of the trace shows linearly polarized waves with vertical particle motions, associated with compressional body-waves (P-waves). This behavior was first noted by Stevens et al. (2000) and suggests that the hydroacoustic energy is converted to Rayleigh waves along the sloping interface well off-shore. When the hydroacoustic energy traveling along the SOFAR axis strikes the island, it is converted mostly to P-wave energy. The Rayleigh wave energy travels faster than the acoustic wave and arrives before the converted hydroacoustic-to-P-wave energy. We saw similar, but more ambiguous, behavior in the observed T-phases.

We will perform additional calculations to model the offshore airgun shots and investigate the causes of T-phase amplitude variability on the island. Figure 6c shows three vertical component seismic records of two offshore airgun shots. The shot was just a few kilometers north of Ascension Island. We will attempt to model these data with our finite-difference simulations.

CONCLUSIONS AND RECOMMENDATIONS

The May 1999 Ascension Island Experiment provided valuable data for studying the conversion of hydroacoustic-to-seismic energy and seismic T-phase variability. Inefficient conversion, high attenuation and high noise levels on island T-phase stations will reduce the sensitivity of seismic T-phase sensors relative to in-ocean hydroacoustic sensors. Poor signal-to-noise for high-frequency (>10 Hz) T-phases will lower signal detection thresholds and the use of T-phases for event screening and identification. The variability of T-phase amplitudes over short distances suggests that site effects play an important role in controlling T-phase amplitudes. Amplitude variability must be accounted for if T-phase amplitudes are to be used to estimate event size.

REFERENCES

de Groot-Hedlin, C. and J. Orcutt, Synthesis of earthquake-generated T-waves, *Geophys. Res. Lett*., 26, 1227-1230, 1999.

Harben, P., J. Hollfelder and A. Rodgers, Experimentally determined coordinates for three MILS hydrophones near Ascension Island, UCRL-ID-136507, 1999.

Harben, P. E., D.K. Blackman, A. Rodgers, C. Turpin, J.R. Hollfelder, Calibration factors for three MILS Hydrophones near Ascension Island, UCRL-ID-138036, 2000.

Larsen, S., and C. Schultz, ELAS3D: 2D/3D elastic finite-difference wave propagation code, UCRL-MA-121792, 18 p., 1995.

Levitus, S., T. Boyer, J. Antonov, R. Burgett. and M. Conkright, World Ocean Atlas 1994, NOAA/NESDIS, Silver Springs, Maryland, 1994.

Piserchia, P.-F., J. Virieux, D. Rodrigues, S. Gaffet and J. Talandier, Hybrid numerical modeling of T-wave propagation: application to the Midplate experiment, *Geophys. J. Int*., 133, 789-800, 1999.

Stevens, J., G. E. Baker, R. Cook, G. D-Spain, L. Berger and S. Day, Empirical and numerical modeling of T-phase propagation from ocean to land, submitted to *Pure and Appl. Geophys.*, 2000.

Talandier, J. and E. Okal, On the mechanism of conversion of seismic waves to and from T waves in the vicinity of island shores, *Bull. Seism. Soc. Am*., 88, 621-632, 1998.

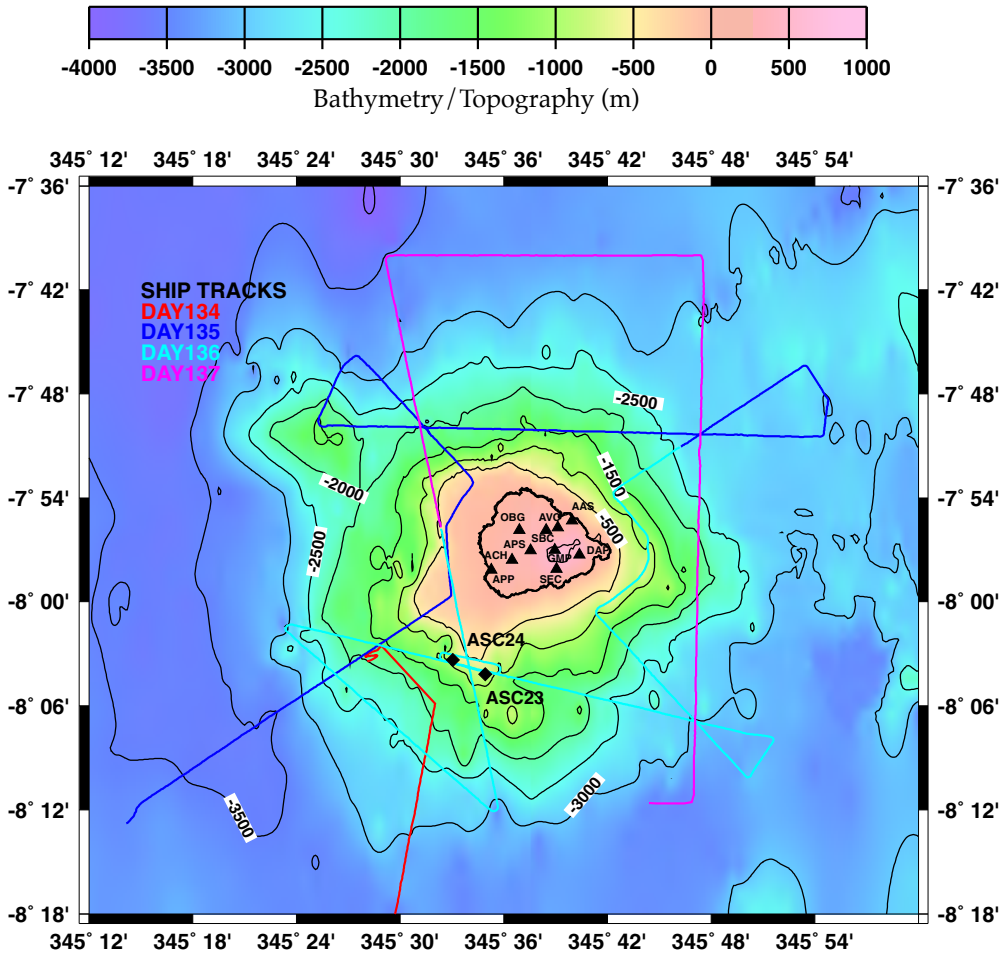


Figure 1. Map of Ascension Island with bathymetry. LLNL seismic stations (triangles) and MILS hydrophones (diamonds) are also shown. The ship tracks indicate the path of the towed airgun used for imaging crustal structure and hydrophone location and calibration.

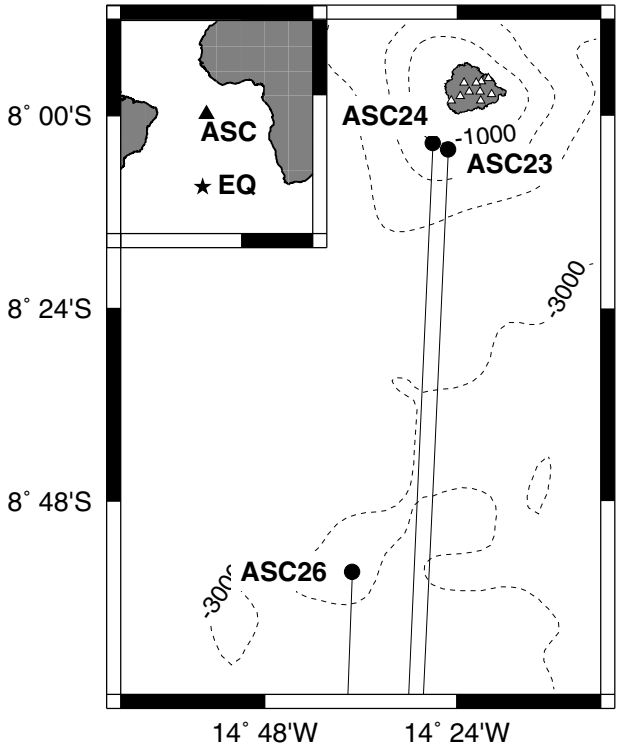


Figure 2. Map of Ascension Island, the MILS hydrophones and paths studied. The earthquake location is shown in the inset.

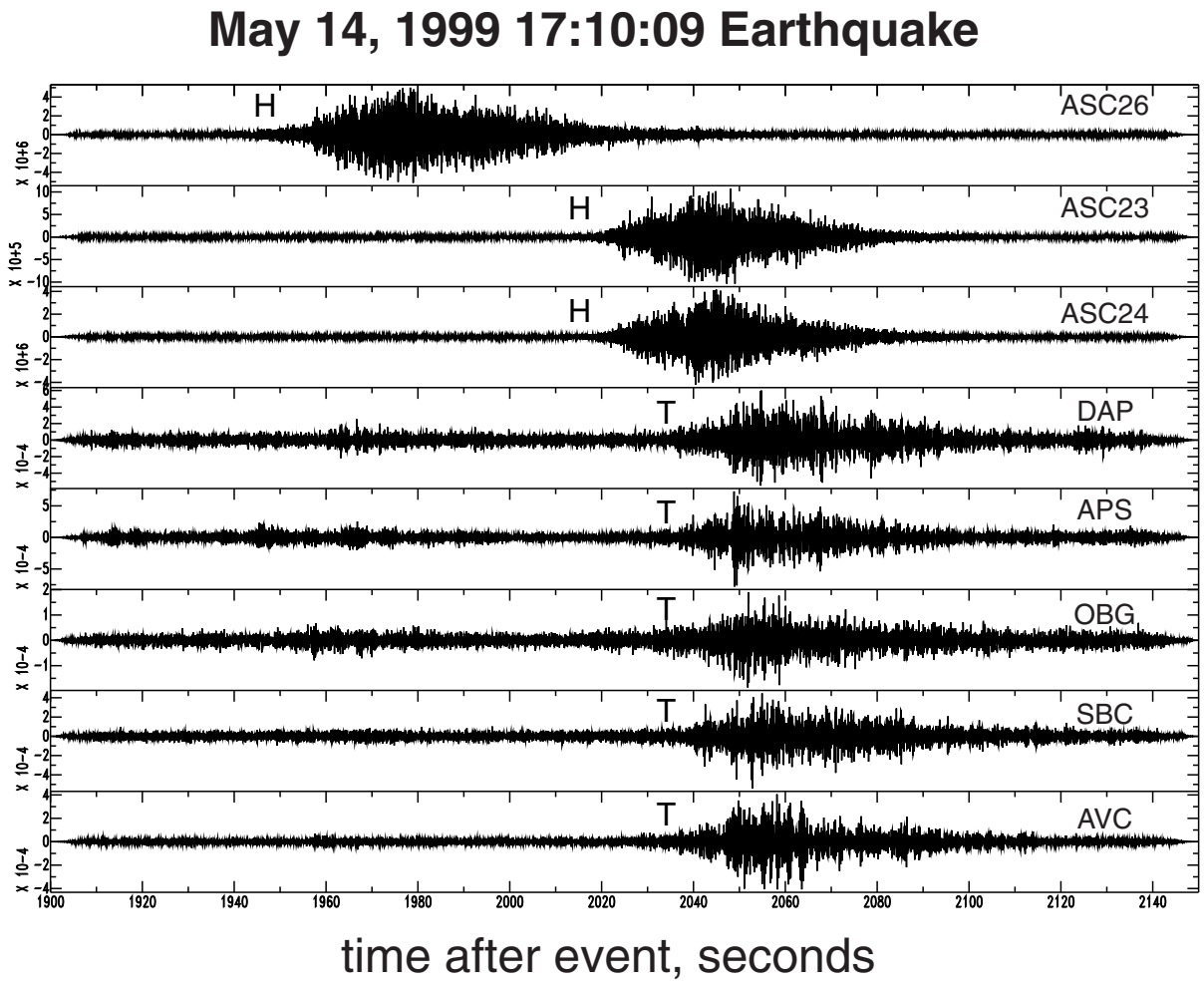


Figure 3. Waveforms for the May 14, 1999 earthquake. The hydrophones ASC26, ASC23 and ASC24 (top) and the vertical component on-shore seismic stations (bottom). Traces were high-pass filtered with a corner frequency of 2 Hz. Hydroacoustic and seismic T-phases are denoted by H and T, resprectively.

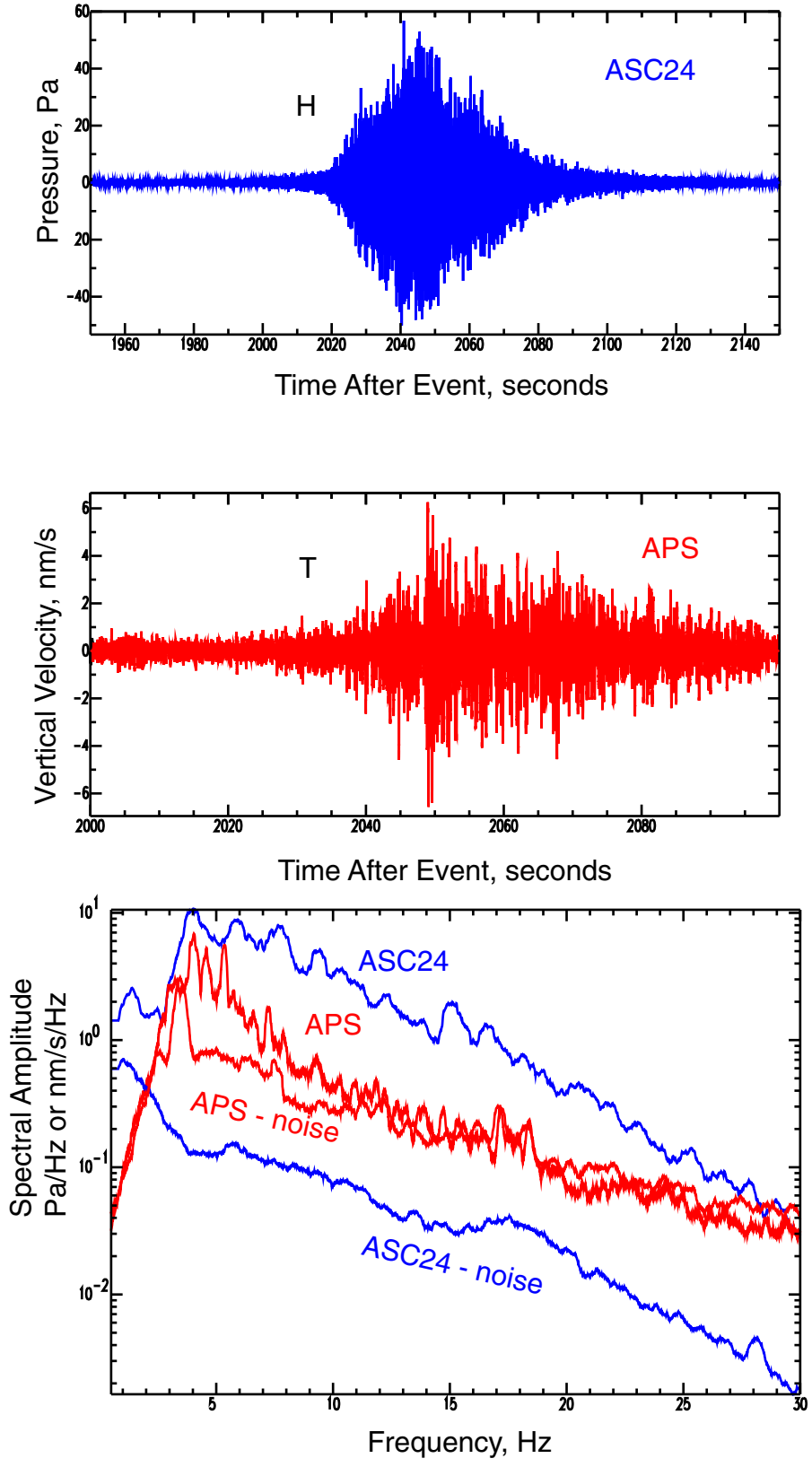


Figure 4. Waveforms of the May 14, 1999 earthquake, corrected for the respective instrument responses, for the ASC24 hydrophone (top) and the APS seismic station (middle). Signal and pre-event noise spectra for the traces are shown (bottom).

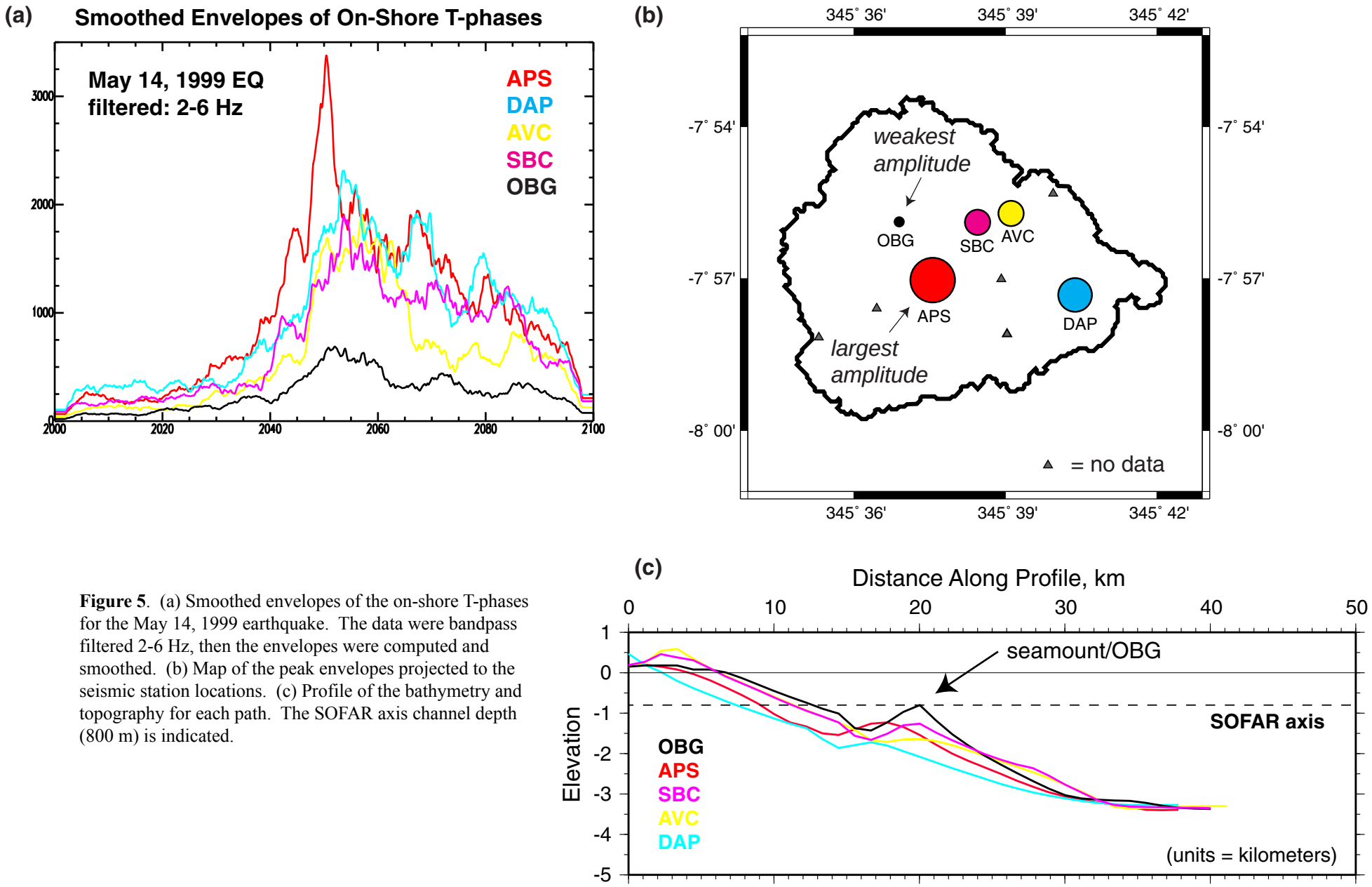


Figure 5. (a) Smoothed envelopes of the on-shore T-phases for the May 14, 1999 earthquake. The data were bandpass filtered 2-6 Hz, then the envelopes were computed and smoothed. (b) Map of the peak envelopes projected to the seismic station locations. (c) Profile of the bathymetry and topography for each path. The SOFAR axis channel depth (800 m) is indicated.

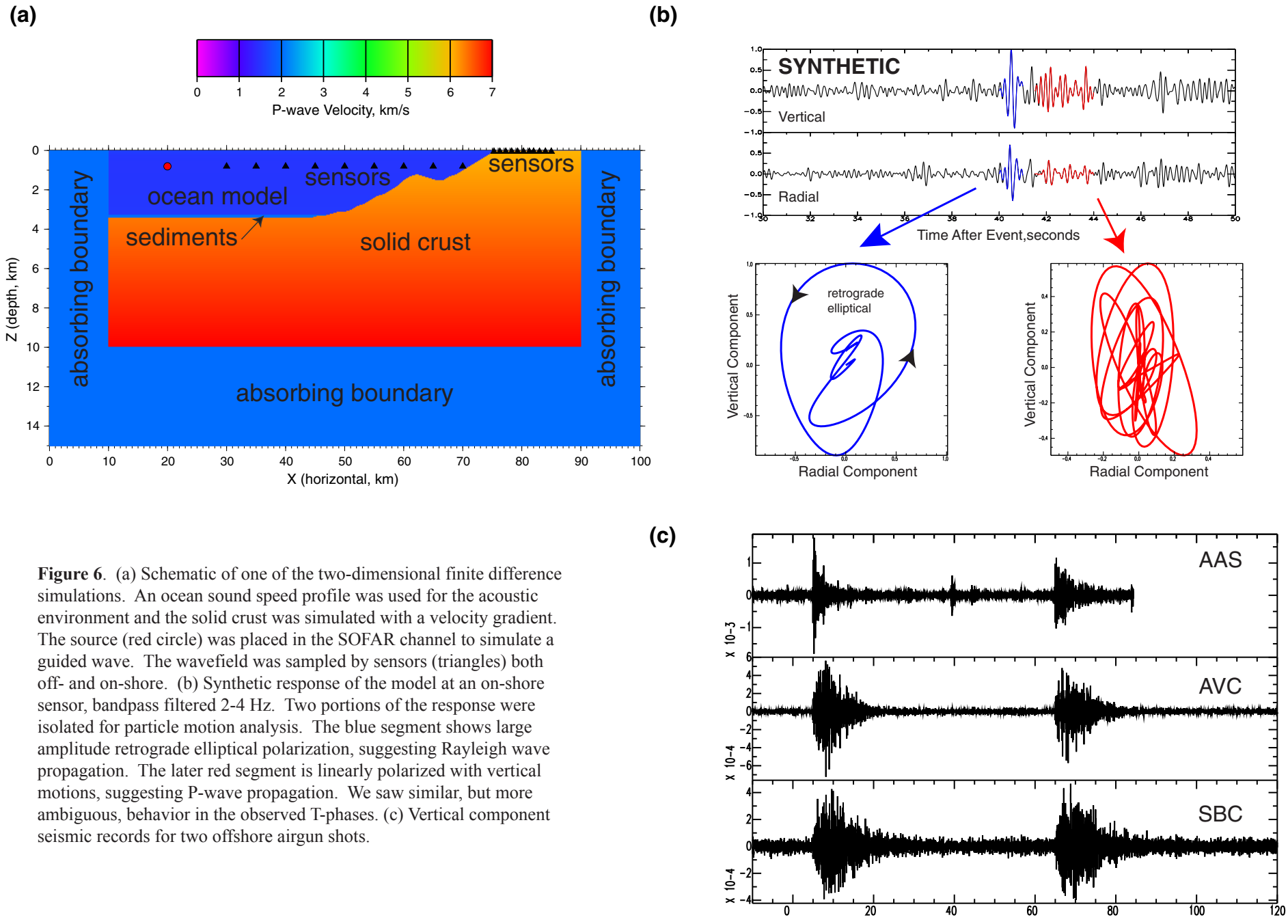


Figure 6. (a) Schematic of one of the two-dimensional finite difference simulations. An ocean sound speed profile was used for the acoustic environment and the solid crust was simulated with a velocity gradient. The source (red circle) was placed in the SOFAR channel to simulate a guided wave. The wavefield was sampled by sensors (triangles) both off- and on-shore. (b) Synthetic response of the model at an on-shore sensor, bandpass filtered 2-4 Hz. Two portions of the response were isolated for particle motion analysis. The blue segment shows large amplitude retrograde elliptical polarization, suggesting Rayleigh wave propagation. The later red segment is linearly polarized with vertical motions, suggesting P-wave propagation. We saw similar, but more ambiguous, behavior in the observed T-phases. (c) Vertical component seismic records for two offshore airgun shots.

FINITE DIFFERENCE MODELING OF T-PHASE PROPAGATION FROM OCEAN TO LAND

Jeffry L. Stevens, G. Eli Baker, Heming Xu
Maxwell Technologies, Systems Division

Gerald D'Spain and Lewis P. Berger
Marine Physical Laboratory, Scripps Institution of Oceanography

Sponsored by U. S. Department of Defense
Defense Threat Reduction Agency
Contract No. DSWA01-97-C-0166

ABSTRACT

We model the T-Phase transition from ocean to land and evolution of the seismic signal through this process. We model the transition with a composite technique using normal mode based numerical propagation codes to calculate the hydroacoustic pressure field in the ocean, and use this pressure field as input for the elastic finite difference code TRES to calculate the seismic propagation to land-based stations. Animations are created from the finite difference calculations to help visualize the complex conversion process. We have performed a detailed study of the transition from the Point Sur interim IMS station to seismic stations along the California coast. The numerical calculations performed to date are accurate to 9 Hz.

An unusual result of the analysis that is observed both in the data and the calculations is that converted surface waves arrive at coastal stations earlier than body waves. This occurs because conversion to surface waves occurs farther offshore than conversion to body waves. For a typical coastal structure, the P-waves arrive in the middle of the surface wavetrain and are obscured at stations near the coast. T-phases propagate primarily as P-waves once they are well inland from the coast and the surface waves have been attenuated.

We have performed a number of test cases to assess the robustness of these results. Calculations for slopes varying from 10 degrees to 30 degrees show little difference in the results. Other studies have reported stronger effects for steeper slopes. All of the IMS T-Phase stations, however, are located in areas where the offshore slope is less than 30 degrees. The California calculations have a low velocity surface layer, so we performed a set of calculations with the ocean embedded in a uniform structure. Again, the results are similar with coastal waveforms dominated by surface waves. In a faster, more uniform structure, however, the P-wave may appear ahead of the surface wave for slopes of 30 degrees or higher.

We are continuing this research by performing calculations for paths to the IMS T-Phase stations, using the bathymetry along selected paths to those stations.

OBJECTIVE

The objective of this project is to better understand the propagation of T-phases from ocean to land, and the performance of T-phase International Monitoring System (IMS) stations, through empirical and numerical methods. The empirical study uses data from pressure sensors in the ocean and coastal and island seismometers to examine the T-phase transfer function. The numerical study uses finite difference calculations to model propagation of T-phases from ocean to land.

RESEARCH ACCOMPLISHED

The International Monitoring System (IMS) hydroacoustic network is a relatively sparse network consisting of 6 underwater hydroacoustic stations and 5 land-based seismic T-phase stations as shown in Figure 1. The hydroacoustic stations are much more sensitive to underwater signals than the T-phase stations and have a higher sampling rate and broader frequency range. The broader frequency range is important for identifying explosions, which are characterized by higher frequency content than other sources. Because of these limitations of T-phase stations, it is important to understand the efficiency of T-phase conversion in order to assess the capabilities of the IMS network for detection and identification of underwater sources. We are in the third year of a three year project to investigate these issues. In our presentations over the past two years, we described the following research:

1. Empirical estimates of T-phase transfer functions using T-phases from earthquakes at Hawaii/Loihi recorded on the Point Sur hydroacoustic station and seismometers in the UC Berkeley and PG&E networks.
2. Numerical modeling of these T-phases, and analysis of the waveforms. A movie of one of the calculations is available on the Internet at http://www.maxwell.com/products/geop/Movies/hydro.htm .

Our earlier papers (Stevens et al., 1998; Stevens et al., 1999) also described research into H-phases from small explosions off the California coast observed at IMS stations, research into far inland T-phases observed at distances as great as 1000 km from the coast, and research into modal decomposition of T-phases. This work is also described in two papers to be published in the special CTBT volume of Pure and Applied Geophysics (Stevens, et al, 2000; D'Spain et al, 2000). In addition, we have performed work under this contract on analysis of a large Russian hydroacoustic data set which we used to analyze the coupling of shallow explosion sources. This work has been presented at last year's symposium (Eneva et al, 1999) and in a third paper in the Pure and Applied Geophysics special issue (Eneva et al, 2000a) The most recent results are described in a paper in this symposium (Eneva et al, 2000b).

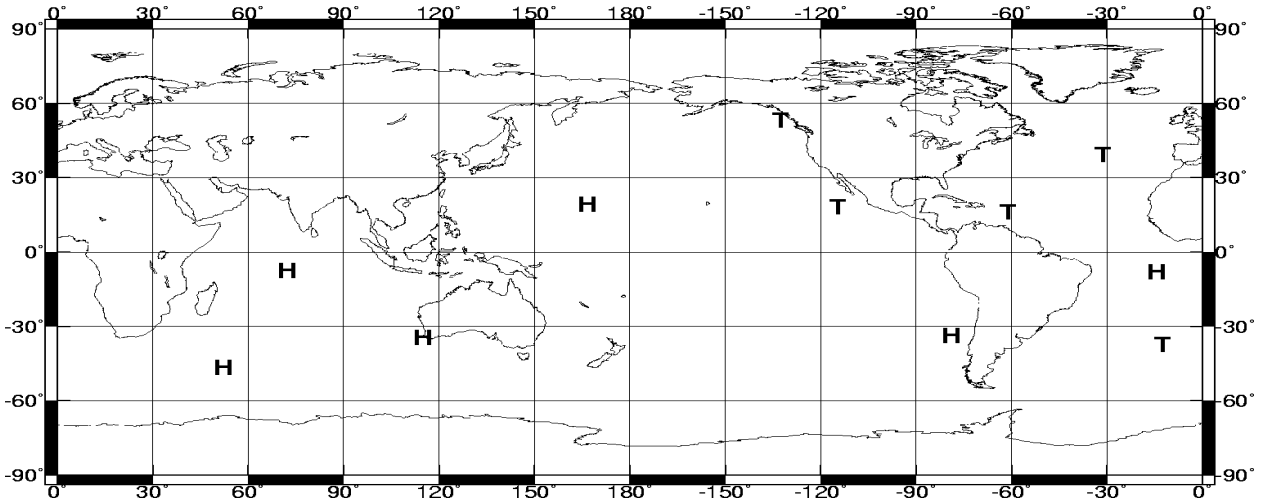


Figure 1. Hydroacoustic (H) and T-phase (T) stations in the future IMS network.

In the third year of this contract, most of the work on T-phase transfer functions has been directed towards extending the calculations to higher frequencies (from 4 Hz to 9 Hz), assessing the sensitivity of the results to a variety of physical parameters, and evaluating the implications of the results for IMS T-phase stations. In this paper, we first present a summary of the earlier work on T-phase transfer functions described in points 1 and 2 above, and then present the results of more recent work.

Observations of T-phase Transmission from the Ocean onto Land

We gathered data sets from events that were recorded on both underwater and coastal seismic stations for the purpose of directly measuring T-phase conversion. Four earthquakes from the emerging seamount Loihi and on the island of Hawaii generated very strong T-phases that impacted the California coast. We collected recordings of these events from the Point Sur (PSUR) hydroacoustic station, the Pacific Gas and Electric Central Coast seismic network (PG&E), and the Berkeley broadband digital seismic network (BDSN). The location of these stations and the bathymetry of the California continental shelf are shown in Figure 2. This is a nearly optimal situation for study of T-phase conversion because the hydroacoustic waves impact the coastline almost perpendicular to the coast as shown by the ray path on Figure 2.

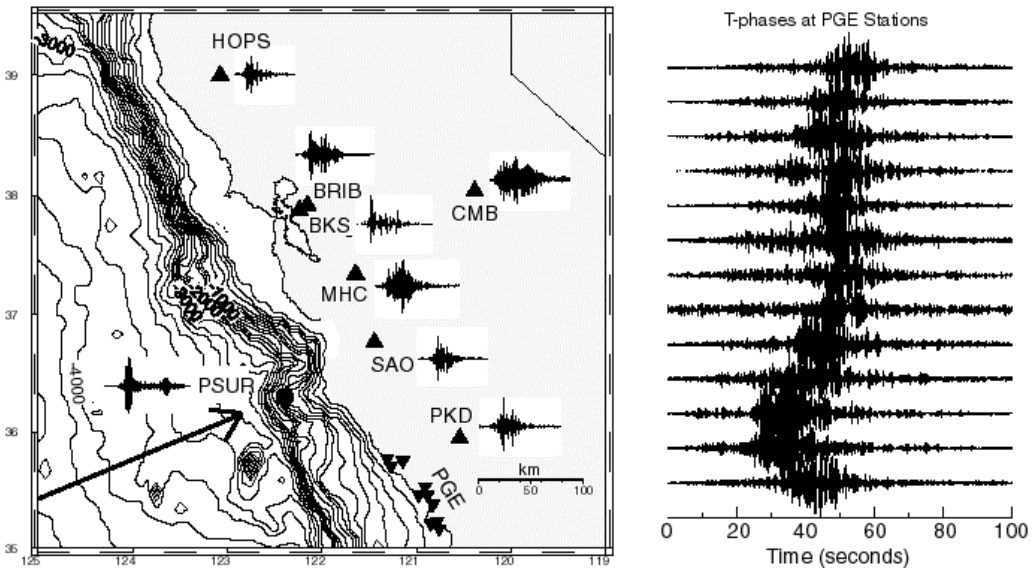


FIGURE 2. RECORDS FROM THE JUNE 30, 1997 LOIHI EVENT AND STATION LOCATIONS. THE PROPAGATION DIRECTION IS INDICATED BY THE ARROW, WHICH POINTS TO THE HYDROACOUSTIC STATION PSUR (INDICATED BY THE CIRCLE). 150 SECONDS OF THE T-PHASE RECORD IS SHOWN TO THE STATION'S LEFT. THE BDSN STATIONS (LARGE TRIANGLES) AND CORRESPONDING RECORDS ARE INCLUDED ON THE MAP ON THE SAME SCALE. THE PG&E STATION LOCATIONS ARE INDICATED BY INVERTED TRIANGLES AND THEIR WAVEFORMS ARE SHOWN TO THE RIGHT, IN ORDER OF INCREASING DISTANCE FROM BOTTOM TO TOP. THE ARRIVAL TIMES DO NOT CORRESPOND WELL TO TOTAL DISTANCE BECAUSE THE DISTANCE FROM THE CONVERSION POINT VARIES. THE BATHYMETRY IS CONTOURED IN 200 METER INTERVALS.

We calculated T-phase transfer functions for this data set by taking the ratio of the instrument corrected spectral amplitudes of the seismic stations to the Point Sur station for all good quality data at the PG&E stations and the 6 coastal BDSN stations (CMB was excluded because it is much farther inland). The spectral ratios were averaged for all events for each station. Two stations recorded all four events, 7 stations recorded 3, 9 stations recorded 2, and two stations recorded only 1 event. The resulting spectral ratios are shown in Figure 3. There is a clear decline in amplitude with frequency for both networks, but it is particularly pronounced for the BDSN network. This is likely due to greater attenuation of the higher frequencies because of the longer paths to the BDSN stations. Simulations discussed later in this paper indicate that much of the energy in the hydroacoustic wave is transmitted to land at approximately 200 m bathymetry, which corresponds to the contour line (Figure 2) nearest the coast. The crustal paths from the conversion point to the PG&E stations are only 5 to 20 km long, while paths to the BDSN stations are 40-75 km. Also shown in Figure 3 is an approximate upper bound on the transfer function derived from the simple case of a plane acoustic wave travelling in the ocean and propagating into a solid at normal incidence.

The ocean hydroacoustic phase may convert to a variety of complex phases due to the interaction with the coast. We can get some insight into the type of conversion that occurs by looking at far inland T-phases, and examining the propagation speeds of these waves. The T-phase from the 1997/06/30 event is large enough to be seen well inland from the California coast. Figure 4 shows two sets of seismograms recorded along the two (approximate) great circle paths. The paths are from SAO to KCC and from JRSC to MHC to CMB. Since the waveform is dispersed, there is some uncertainty about when to pick the arrival, however if we use the peaks of each wave train, then we get a velocity between SAO and KCC of 6.8 km/sec, and a velocity along the path of the other three stations of 5.6 km/sec. These velocities correspond to P-wave speeds, so the T-phases must be travelling as P-waves over this range.

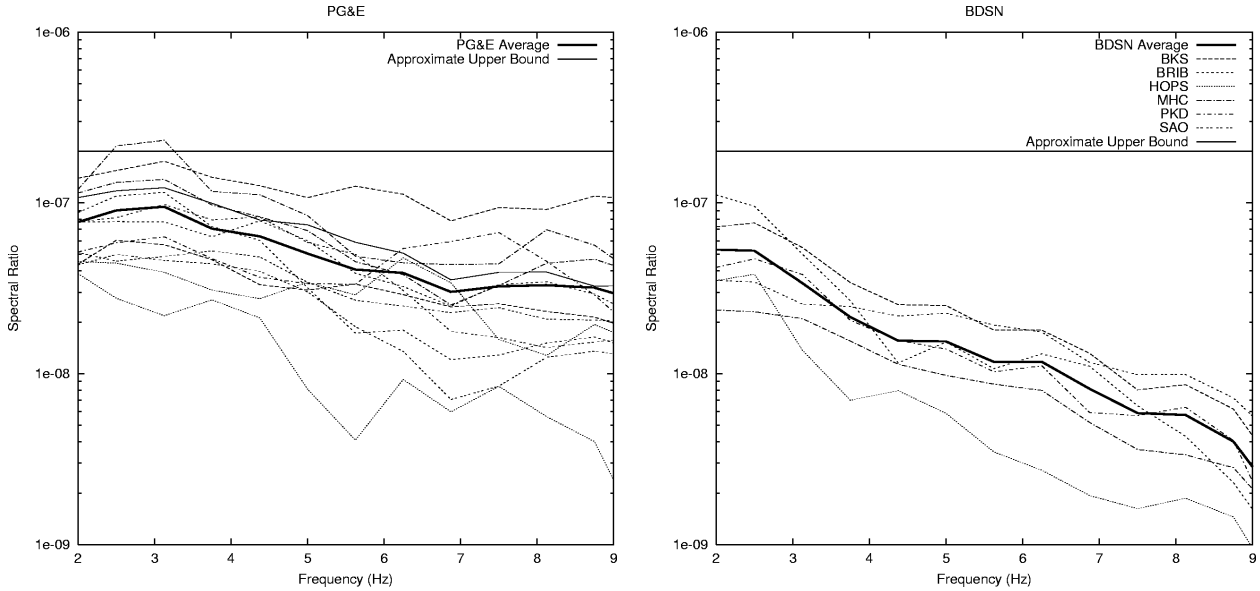


Figure 3. Ratios of seismic spectra at stations in California that recorded the Loihi events, divided by the Point Sur spectra. These are T-phase transfer functions converting pressure to vertical velocity. The frequency band shown here is from 2 to 9 Hz. The left plot shows PG&E stations and the right plot shows BDSN stations. The absolute amplitude of the PG&E records is uncertain, however the amplitude of the BDSN records, and the spectral shape of both sets of curves, are accurate. Also shown is the approximate upper bound for conversion from pressure in the ocean to particle velocity on land. The heavy line is the average log spectral ratio for all stations except far inland stations. Spectral ratios are in MKS units (meters/second/Pascal).

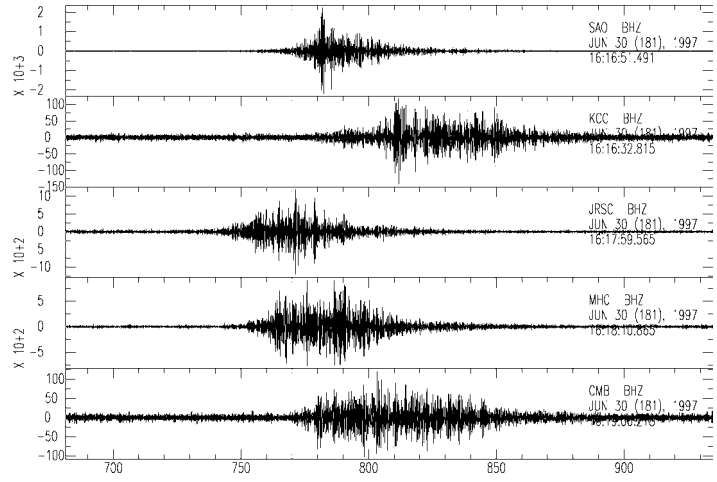


Figure 4. T-phases recorded near the coast and far inland from the 1997 June 30 Loihi event. The top two seismograms and the bottom three seismograms were recorded at stations along approximately the same great circle path. The horizontal axis is time in seconds. The data has been high pass filtered at 2 Hz.

Particle motion provides an independent means of assessing wave type. Figure 5 shows that the particle motion for the largest part of the record, near the front of the T-phase, is strongly linear. This part of the record is clearly dominated by body waves, most likely P-waves, in agreement with the conclusion from travel times. Linearity decreases later in the record, although it's not clear whether that is due to the arrival of later scattered P-wave energy, surface wave arrivals, or a mixture of phases. The particle motion of the earliest part of the T-phase is elliptical and retrograde, suggesting that this part of the wave train is composed of Rayleigh waves. This is consistent with the simulations later in this paper, which indicate that surface waves can precede the P-wave near the coast, due to earlier conversion of the T-phase in water to surface waves.

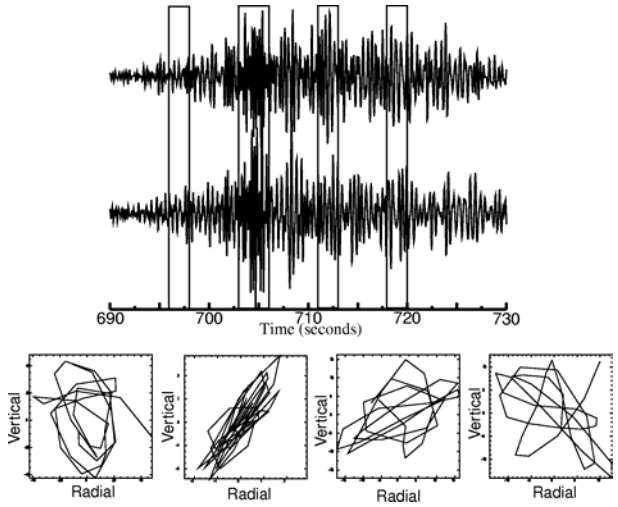


Figure 5. Vertical (top trace) and radial (lower trace) component seismograms from SAO for the 1997 June 30 event. Particle motions for four outlined time windows are shown below the seismograms. The very linear motion of the second time window indicates dominance there by body waves, and the elliptical motion of the first time window suggests that the early part of the wave train is composed of surface waves.

Two-dimensional finite difference calculation of propagation onto land

We use the two-dimensional finite difference code TRES2D to model the propagation of hydroacoustic waves onto the coast. TRES is a finite difference code developed at Maxwell Technologies (S-Cubed) with 2D and 3D versions that are used to model wave propagation. In this case we model a 2D slice of the propagation path. The normal mode code Kraken (Kraken can be obtained through the Ocean Acoustics Library web site at http://oalib.njit.edu/) was used to calculate the acoustic wave field in the ocean at a distance of 3710 km from Loihi. This solution was used as the source in the finite difference calculation using the representation theorem (see Stevens et al, 2000 for implementation details). Even though this is a two-dimensional problem, it requires a very large calculation because the distances of interest are large, about 100 km, the wave speed in the water is slow, and we are interested in frequencies higher than 1 Hz. We used recursive grid refinement (McLaughlin and Day, 1994), with the top 5 km portion (including ocean and the upper oceanic crust) covered with uniform grid cells of 16.75m x 16.75m and the remaining grid with cells of 67m x 67m. The calculation is accurate to 9 Hz throughout all the grids and the simulation time is 100 seconds. The time step is 0.005s for 67m spacing and 0.00125s for 16.75m spacing.

Velocities for the full grid were saved for each second of time in the calculation, and these were used to create images and animations of the velocity fields to help visualize the evolution of the velocity field. There is a gradual decay of the hydroacoustic wave as it travels upslope, with body waves emitted continuously with varying amplitudes into the earth below, and a surface wave that gradually forms along the ocean bottom. At sharper bathymetric gradients the transmission is increased, and when the hydroacoustic wave reaches an ocean depth of 200 meters, there is a burst of energy much larger than anywhere else along the path. Strong surface waves are generated on land from the edge of the ocean to the boundary of the calculation. Figure 6 shows a snapshot of the horizontal displacement field at 65 seconds. The figure shows the burst of energy at 200 meter depth. Color animations of this calculation can be viewed online at http://www.maxwell.com/products/geop/Movies/hydro.htm. The calculated T-phases have some very odd properties. As can be seen in Figure 6, a strong surface wave develops quite early and

can be seen on land at 65 seconds, which is the same time that the burst of body waves occurs. Consequently the surface wave appears in the wave train before, and simultaneous with, the body waves generated by the final decay of the hydroacoustic wave. The T-phase near the coast is therefore a mixture of seismic phases.

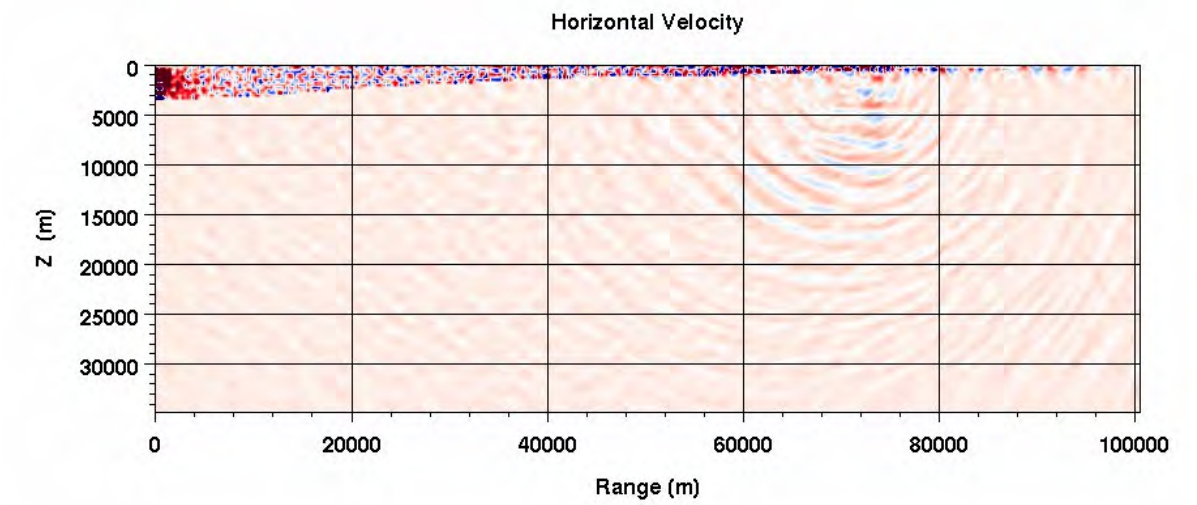


Figure 6. Snapshot of the calculation at 65 seconds. The dominant hydroacoustic arrival has reached a depth of 200 meters. At this point there is a burst of energy transferred as body waves from the ocean into land. Zero range corresponds to the point 3710 km from Loihi. The ocean/land interface at the surface is at location 87368.

The results of the calculation were saved with a much finer time resolution at selected locations along the surface, and at a depth of 740 meters in the center of the sound channel. Figure 7 shows the calculated horizontal velocity in the water at 47235 m, which corresponds approximately to the location of the Point Sur hydroacoustic station. Also shown are the horizontal and vertical components of the waveform on the surface at location 87904 m, which is on land close to the coast. The amplitude ratios between the velocity on land and in the water are about 0.2, which is consistent with our earlier estimates of the upper bound of the transfer function (note the earlier discussion was for pressure to velocity which adds a factor of about 10^{-7}). The waveforms on land are complex and longer in duration than the underwater waveform. From travel times and particle motion it is clear that the dominant energy is traveling at surface wave speeds. The complexity of the waveforms arises from the complex way the waves are generated over an extended region of the ocean bottom.

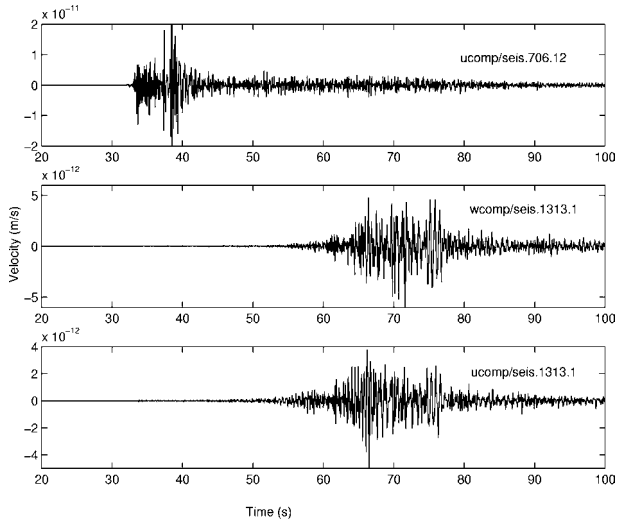


Figure 7. Calculated horizontal velocity at a depth of 740 meters in water at the location of the Point Sur station (top) and vertical (mid) and horizontal (bottom) components of the velocity on land close to the coast. The horizontal axis is time in seconds since the start of the calculation.

Figure 8 shows the spectral amplitude of the horizontal velocity in the 1-9 Hz frequency band underwater at the Point Sur location and the vertical velocity at a station on land close to the coast. The underwater spectrum is nearly flat across this frequency band. The spectra on land, however, exhibit a significant decline in amplitude with frequency, similar to the spectral decline observed for the coastal California stations. This suggests that during transmission from water to land, the higher frequencies scatter more strongly than the lower frequencies, leading to a decline in high frequency content in the coastal waveforms.

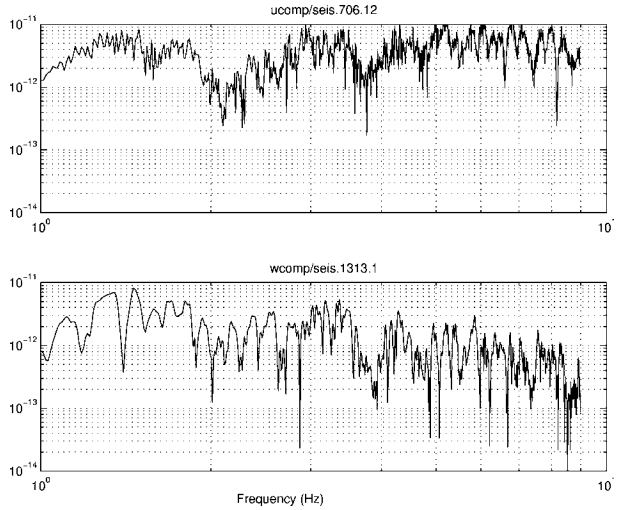


Figure 8. Calculated spectral amplitudes of the horizontal velocity at a depth of 740 meters underwater (top) and the vertical velocity at the surface on land near the coast (bottom).

We have used T-phase observations in water and on land together with numerical calculations of T-phase propagation from water to land in order to understand the nature of T-phase conversion. The results are complex and at first glance contradictory. Whereas T-phases are observed to travel at P-wave speeds on land, the calculations show strong surface waves near the coast. However, the calculations also show lower amplitude body wave arrivals even very close to the coast, and strong body waves propagated away from conversion points along the ocean bottom. Some of this body wave energy will return farther inland as P_g and P_n phases. The high frequency surface waves, on the other hand, can be expected to attenuate away very quickly and will not propagate to large distances. We therefore expect to see stronger surface waves than P-wave arrivals near the coast, with the surface waves dying out and the P-waves becoming dominant as the wave travels inland.

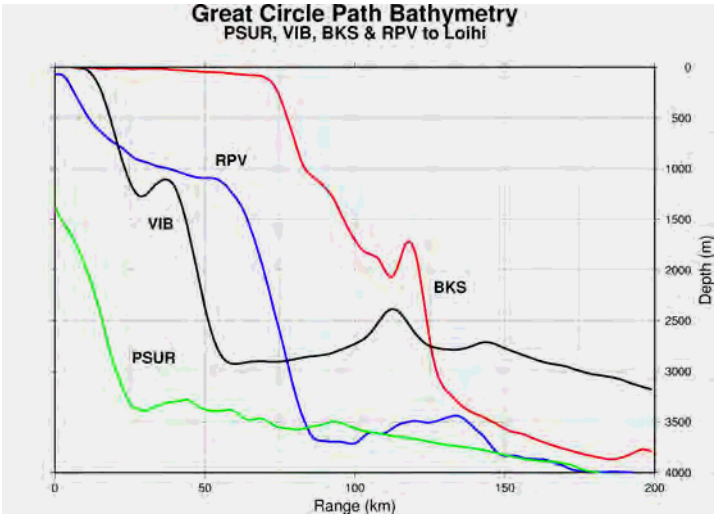


Figure 9. Great circle path showing bathymetry to PSUR, RPV, BKS, and VIB along the direction to Loihi from each station. Zero range corresponds to the station location. Vertical exaggeration makes the slopes appear steeper.

A similar study was performed by Piserchia et al (1998), in which they modeled T-phase conversion from an explosive source in the ocean, observed on the islands of Mururoa and Fangataufa in the South Pacific Ocean. They used ray tracing instead of a modal solution, and calculated Green's functions along a vertical boundary in order to propagate the source onto the islands. They found that the T-phase on land consisted of two P waves followed by two Rayleigh waves, where the multiple arrivals are identified as coming from different conversion points. The calculation was performed for a dominant frequency of 6 Hz, and in this case the calculated P and Rayleigh waves were found to be comparable in size. Cansi and Bethoux (1985) modeled far inland T-phases as converted T-P and T-S phases along a curve corresponding to a fixed depth in the ocean. They found good agreement with observed waveforms with synthetics composed only of P and S waves. Talandier and Okal (1998) studied conversion of T-phases on steep island slopes using data from the Polynesian Seismic Network and found from the observations and ray tracing arguments that the T-phase consisted primarily of P-waves at distances greater than 9 km from the conversion point. At closer distances, they found that the T-phase was more complex and composed primarily of S-waves and surface waves. They also suggested that only surface wave conversion would occur for slopes with angles of less than 16 degrees.

We have modeled propagation onto the California coast in considerable detail because of the availability of a good data set for comparison, and because we have stations both underwater and on land. The question arises as to how closely this models propagation onto the IMS T-phase stations which have different bathymetric profiles. Also, we would like to know how sensitive the calculations are to the details of the profile, and in particular to the slope of the ocean bottom on the approach to the coast. Figure 9 shows the bathymetric profiles off the coast of California in the direction of Loihi passing through the Point Sur, RPV, and BKS stations. Also shown for comparison is the profile in the direction of Loihi off the coast of VIB. Although they differ in detail, the structures are comparable in general features. The slope off the coast of VIB is similar to the slope off of BKS, although VIB is much closer to the coast. The slope through RPV is smaller. The slope used in the calculations is intermediate between these slopes. Note that there is considerable vertical exaggeration in these figures. Even the steepest part of the slope at VIB decreases by 1000 meters over a distance of 10 km, which corresponds to an angle of about 6 degrees. The steepest slopes off of the island T-phase stations change by 1000 meters over a distance of four km, an angle of about 14 degrees. To assess how much difference this caused, we ran three additional finite difference calculations, using the same ocean structure and modes as in the calculations above, but with constant slopes of 10, 20, and 30 degrees. In each case, the coastal boundary was fixed at 80 km from the left edge of the grid. The resulting vertical displacements at a point 7 km inland from the coast are shown in Figure 10. The waveforms are remarkably similar to each other and to the earlier calculations. The waveforms consist primarily of surface waves of comparable amplitude. The main difference is in the timing of the body wave which close examination shows arrives earlier than the surface wave for the 30 degree slope, and is within the surface wave wavetrain for the shallower slopes.

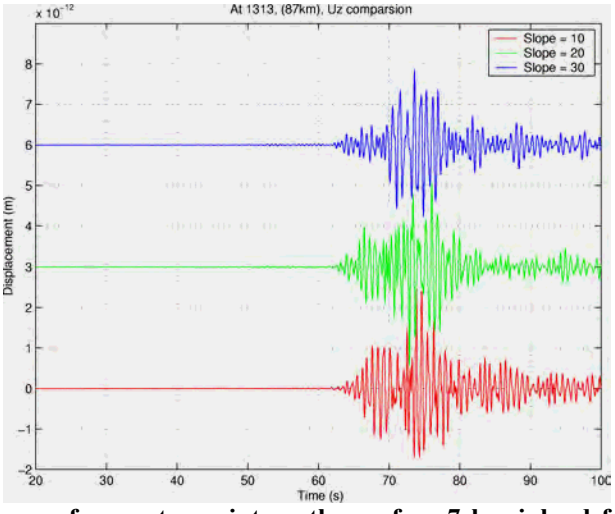


Figure 10. Vertical velocity waveforms at a point on the surface 7 km inland from the coast for the three calculations with slopes of 10 (bottom), 20 (middle), and 30 (top) degrees.

One of the conclusions that can be drawn from the calculations is that T-phases observed close to the conversion point should be dominated by surface waves. The calculations discussed above all had a low velocity layer near the surface, which could amplify the surface waves. To assess the magnitude of this effect, we performed another calculation with a uniform structure. The ocean was modeled as having a depth of 3500 meters and then a slope of 30 degrees up to the coast. Figure 11 shows the vertical component of velocity at a point 7 km from the coast for the two calculations with the uniform structure and the full structure including the low velocity layer. As expected, surface waves are smaller, however the wavetrain is still dominated by the surface waves which are much larger than the body waves at this distance. Body waves arrive at about 62 seconds. They are difficult to see, but can be identified by their particle motion.

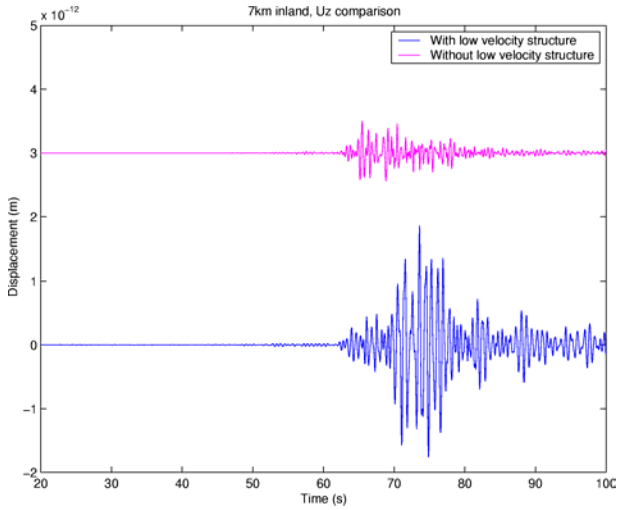


Figure 11. Vertical component of velocity on the free surface for calculations with a low velocity surface layer (bottom) and without (top).

Conclusions and Recommendations

We have used observations of T-phases underwater and on land to directly measure the transmission of energy from ocean to land, and have performed numerical simulations of T-phase propagation from ocean to land to obtain a better understanding of this process. The observations show that there is a significant decline in spectral amplitude with frequency on land compared to observations in the ocean. The observations also show that T-phases propagate primarily as P-waves once they are far enough inland. The numerical simulations provide considerable insight into the phenomena that occur when hydroacoustic waves propagate onto land. The calculations reproduce the spectral degradation observed in Coastal California stations. Both the calculations and the observations show that T-phases observed near the coast are composed primarily of surface waves. Because the surface waves are generated over a more extended region than body waves, they may arrive at near coastal stations earlier than the body wave and obscure any body wave arrivals.

Continuing research is needed to evaluate the response of the IMS T-phase stations. The calculations and parameter studies performed to date provide considerable insight into the expected response at these stations. The calculations cover the range of slopes offshore of the IMS stations, so we believe the effect of slope in general has been adequately modeled. However, specific calculations of T-phase conversion should be performed for each station along different angles of approach. Three dimensional calculations may be required to model the response of the island T-phase stations.

Acknowledgement
We thank Marcia McLaren of Pacific Gas and Electric for the use of her data and for pointing out to us the large T-phases from the Loihi events.

Key Words: hydroacoustic, T-phase, finite difference, IMS

References

Achenbach (1973), Wave Propagation in Elastic Solids, North-Holland Publishing Company, New York. Cansi, Y. and N. Bethoux (1985), "T waves with long inland paths: synthetic seismograms," J. Geophys. Res., V. 90, pp. 5459-5465.

D'Spain, G. L., L. P. Berger, W. A. Kuperman, J. L. Stevens, and G. E. Baker (1999), "Normal mode composition of earthquake T-phases," submitted to Pure and Appl. Geophys.

Eneva, M., J. L. Stevens, J. R. Murphy, and B. D. Khristoforov (2000b), "Effect of charge depth in Russian hydroacoustic data from nuclear and HE explosions," Proceedings of the 22nd Annual DOD/DOE Seismic Research Symposium, 12-15 September, 2000.

Eneva, M., J. L. Stevens, B. D. Khristoforov, J. R. Murphy, and V. V. Adushkin (2000a), "Analysis of Russian Hydroacoustic Data for CTBT Verification", Pure and Applied Geophysics, in press.

Eneva, M., J. L. Stevens, J. Murphy, B. D. Khristoforov and V. V. Adushkin (1999), "Analysis of Russian Hydroacoustic Data for CTBT Verification", Proceedings of the 21st Seismic Research Symposium on Monitoring a Comprehensive Test Ban Treaty, 21-24 September, 1999.

McLaughlin, K. L. and S. M. Day (1994). "3D Elastic Finite-Difference Seismic-Wave Simulations, Computers in Physics," 8, #6, pp 656-663.

Piserchia, P. F., J. Virieux, D. Rodrigues, S. Gaffet and J. Talandier (1998), "Hybrid numerical modelling of T-wave propagation: application to the Midplate experiment," Geophys. J. Int., V. 133, pp 789-800.

Stevens, Jeffry L., G. Eli Baker, Ron W. Cook, Gerald D'Spain, Lewis P. Berger, and Steven M. Day (2000), "Empirical and Numerical Modeling of T-Phase Propagation from Ocean to Land", Pure and Applied Geophysics, in press.

Stevens, Jeffry L., G. Eli Baker, Ron W. Cook, Gerald D'Spain, Lewis P. Berger, and Steven M. Day (1999), "Empirical and Numerical Modeling of T-Phase Propagation From Ocean to Land", Proceedings of the 21st Seismic Research Symposium on Monitoring a Comprehensive Test Ban Treaty, 21-24 September, 1999.

Stevens, J. L., G. E. Baker, J. R. Murphy, R. W. Cook, G. D'Spain, L. P. Berger, and B. D. Khristoforov (1998), "T-Phase Excitation and Transfer Function Research," Proceedings of the 20th Seismic Research Symposium on Monitoring a Comprehensive Test Ban Treaty, 21-23 September.

Talandier, J. and E. A. Okal (1998), "On the mechanism of conversion of seismic waves to and from T waves in the vicinity of island shores," Bull. Seism. Soc. Am., V.88, pp. 621-632.

6. Radionuclide Monitoring

THE DOE AUTOMATED RADIOXENON SAMPLER-ANALYZER (ARSA) BETA-GAMMA COINCIDENCE SPECTROMETER DATA ANALYZER

T.R. Heimbigner, T.W. Bowyer, J.I. McIntyre, K.H. Abel, J.C. Hayes, M.E. Panisko, and W.K. Pitts
Pacific Northwest National Laboratory

Sponsored by U. S. Department of Energy
Office of Nonproliferation and National Security
Office of Research and Development.
National Nuclear Security Administration

Contract No. DE-AC06-76RLO 1830

ABSTRACT

The Automated Radioxenon Sampler/Analyzer (ARSA) developed at the Pacific Northwest National Laboratory for the Comprehensive Nuclear-Test-Ban Treaty (CTBT) measures four radioxenon isotopes, ^{131m}Xe, ^{133m}Xe, ^{133g}Xe, and ^{135g}Xe. The system produces three sample histograms and three background histograms daily. The analysis of the sample histograms in conjunction with the background histograms is accomplished with a data analyzer that displays various one- and two-dimensional beta-gamma histograms. It also calculates the radioxenon concentrations and the minimum-detectable-concentrations (MDC) for each sample. This paper will describe the software program along with data formats, various software controllable parameters, and calculations.

Key Words: xenon, beta-gamma, software, analysis, CTBT

OBJECTIVE

The remote detection of clandestine nuclear explosions via a nuclear signature is possible due to the large amount of radioactive xenon isotopes generated from fission processes. Because of the very low chemical reactivity of xenon, it can escape the underground blast site through fissures in the ground and be detected hundreds and even thousands of miles from the test site. This feature is the basis behind the radionuclide monitoring portion of the International Monitoring System (IMS) mandated by the Comprehensive Nuclear-Test-Ban Treaty Organization (PrepCom 2000). The IMS has been tasked to establish several global networks for measurement of seismic, hydroacoustic, infrasound, radioactive particulates, and radioxenon concentrations.

To fulfill the CTBT requirement, Pacific Northwest National Lab (PNNL) developed an Automated Radioxenon Sampler-Analyzer (ARSA) to detect the four radioxenon fission products of interest (^{131m}Xe, ^{133g}Xe, ^{133m}Xe and ^{135g}Xe). As the name suggests, the ARSA is an automated system that can operate unattended in remote locations. The system separates and concentrates the ambient and radioxenon from the air and uses a beta-gamma coincidence counting system to determine the activity levels of each of the four isotopes. The collection xenon gas and beta-gamma coincidence counting systems are characterized in detail in several references and hence will not be described in this paper (Reeder et al 1998, Reeder and Bowyer 1998, Bowyer et al 1999a, Hayes et al, 1999).

The ARSA has been deployed in four locations to date; Richland, Washington; the Environmental Measurements Laboratory, located in New York City, during the fall of 1997; DME in Florida during September 1999; and the Institute for Atmospheric Research in Freiburg, Germany, during the fall of 1999 and winter and spring of 2000 (Bowyer et al, 1999b, McIntyre et al 2000). Its most recent performance in Freiburg has been very good and a large data set of radioxenon samples have been collected and analyzed.

Nuclide	^{131m}Xe	^{133m}Xe	^{133g}Xe	^{135g}Xe
Half-life	11.93 d	2.19 d	5.25 d	9.14 h
Gamma-rays				
Energy (keV)	163.9	233.2	81.0	249.8
Abundance (%)	1.96	10.3	37.0	90.0
X-rays (K-shell)				
Energy (keV)	30.	30.	31.	31.
Abundance (%)	54.1	56.3	48.9	5.2
Beta Spectrum				
Max. Energy (keV)			346.	905.
Abundance (%)			99.	97.
CE (K-shell)				
Energy (keV)	129.	199.	45.	214.
Abundance (%)	60.7	63.1	54.1	5.7

Table 1. Half-lives, principal radiations and abundances of Xe fission products.

Xenon Beta and Gamma Spectroscopy

Before discussing the ARSA Data Analyzer it is first necessary to discuss the salient features of the beta-gamma coincidence spectrum obtained from each of the radioxenon isotopes. Table 1 lists the half-life, prominent gamma-rays, beta endpoint energy, and important conversion electrons (CE) for ^{131m}Xe, ^{133g}Xe, ^{133m}Xe and ^{135}Xe (Browne and Firestone 1986, National Nuclear Data Center). The two meta-stable xenon isotopes, ^{131m}Xe and ^{133m}Xe, appear in the two-dimensional beta-gamma energy phase space on top of the 30-keV x-ray distribution of ^{133g}Xe. Without beta energy resolution, it would be difficult to unfold these two isotopes from their gamma rays that are not in coincidence with a beta particle or conversion electron (CE). The x-ray and gamma ray of ^{133g}Xe provide two measurements of this isotope, the only one that is specifically called out by the CTBT to have a minimum detectable concentration (MDC, see below) of less than 1.0 mBq/SCM.

Two-Dimensional b-g Spectrum

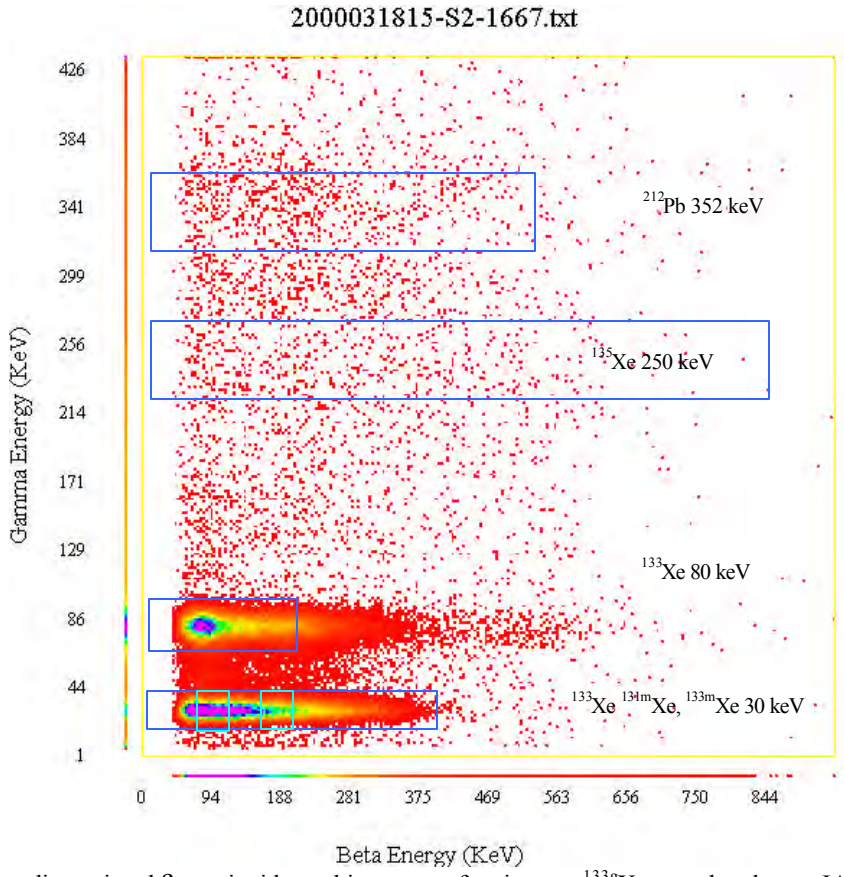


Figure 1. A two-dimensional β-γ coincidence histogram of an intense ^{133g}Xe sample taken at IAR. The outlined regions designate 5 radioxenon regions and one region for ^{214}Pb.

The data acquisition computer bins the pulse height data from the beta and gamma Analog-to-Digital-Converters (ADC) in a two-dimensional histogram (see Figure 1). This histogram clearly shows the presence of ^{133g}Xe via its 30-keV x-rays and 81-keV gamma-ray. Also indicated are the beta-gamma boxes that outline the regions of interest (ROI's) for each of the four radioisotopes and one region for ^{214}Pb (a short-lived daughter of ^{222}Rn). It is from this histogram and a previous 8-hour background histogram that calculations for the concentration of the four radioxenon isotopes are made as well as calculations for the various MDC values.

The 30-keV gamma ROI has the possibility for ^{131m}Xe, ^{133m}Xe and ^{133g}Xe to be present. By carefully gain matching the two beta cell PMT's it is possible to resolve the two conversion electron (CE) peaks of ^{131m}Xe (129-keV) and ^{133m}Xe (199-keV) from ^{133g}Xe (beta plus 45-keV CE). Though it is not present in Figure 1, the radon daughter, ^{214}Pb, interferes strongly with the 81- and 250-keV ROI's (^{214}Pb has x-rays at 79 keV and gamma rays at 242, 295 and 352 keV in coincident with beta particles). The ratio of counts in the 352-keV ROI to those in the 81- and 250-keV regions is constant and therefore it is possible to subtract out the ^{214}Pb contribution in the concentration calculations. The ratios are calibrated by injecting a ^{222}Rn gas sample into the beta cell and measuring the observed ratios.

ARSA Beta/Gamma Analyzer

The ARSA Beta/Gamma Analyzer was designed as a visual basic software tool to evaluate beta-gamma coincidence data produced by the ARSA system. The analyzer is designed to be as flexible as possible, thereby allowing the operator a great deal of freedom in determining how the information is to be presented and utilized. It is based on data files adhering to the RMS 3.0 data format for Beta Gamma systems (Biegalski 2000), and is capable of viewing any file written in this format. However, some capabilities of the analyzer, such as MDC and concentration calculations, have been tailored toward the ARSA system. The analyzer allows two files, a primary (sample) and secondary (background), to be opened at any one time, although the user can elect to open and view any file type described in the RMS 3.0 format (SAMPLEPHD, GASBKPHD, QCPHD, etc.).

The primary form for the analyzer is the Histogram form (see figure 2). This form shows a graphical representation of the detector data and is comprised of 3 main areas:

1. A (upper left panel in Figure 2) two-dimensional, false-color representation of the data with beta energy and gamma energy axes displayed. This image's colors can be scaled linearly or logarithmically to accentuate the structure of the image. Experienced users can immediately determine from this image if further investigation of the data is required. Additionally, potential interference from sources such as Radon will be evident in this image. Both the primary and secondary data files can be displayed.
2. Two one-dimensional histograms that display the Gamma (lower right panel in Figure 2) and the Beta (upper right panel in Figure 2) spectrum on two separate graph controls. A wide range of customization options is available including axis scaling, plotting method, line types, and more. Each graph has zoom-in and zoom-out capability. The graphs can be maximized to aid in viewing the data. Each graph supports multiple traces

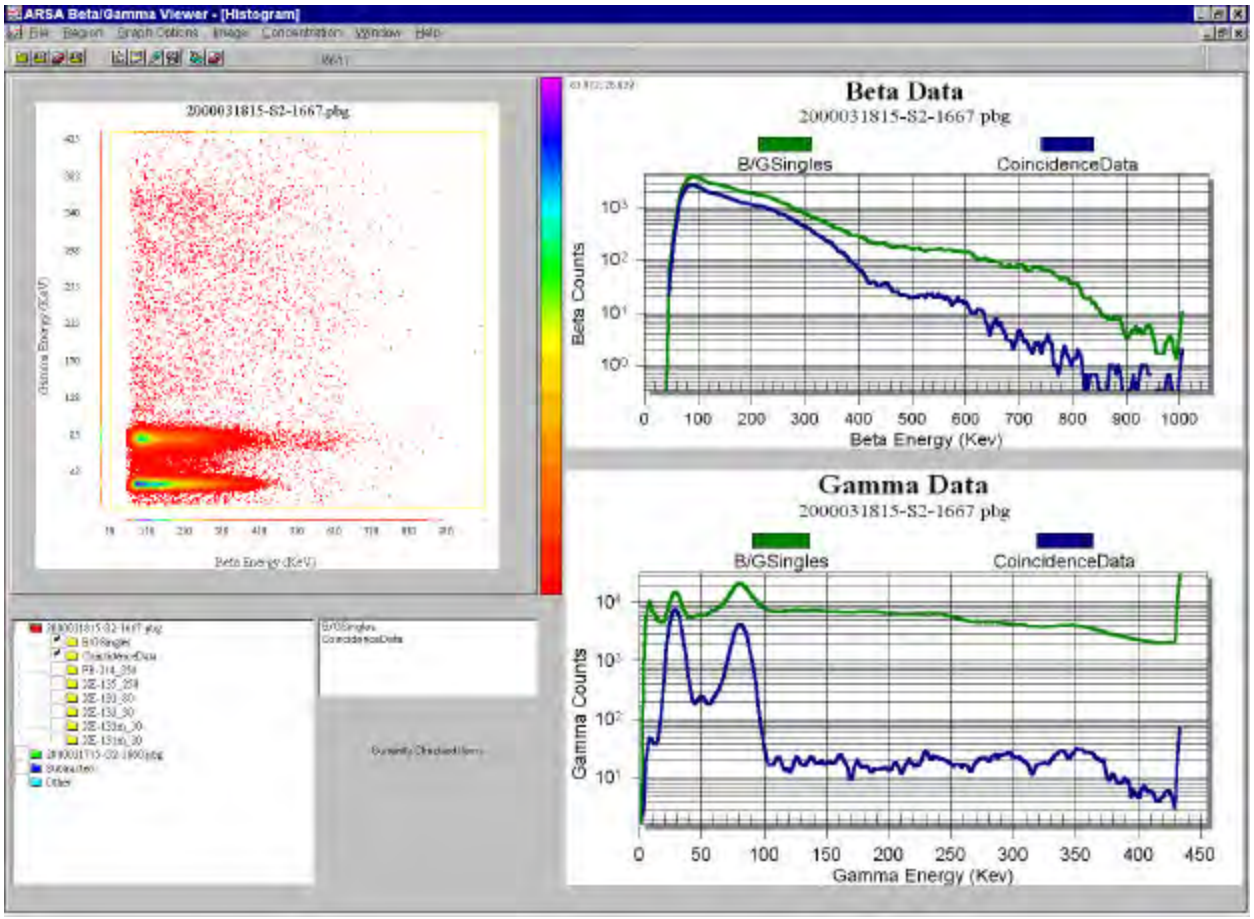


Figure 2. Screen image of the ARSA data Analyzer. See the text for a description.

and allows primary, secondary and subtracted data to be displayed simultaneously. Additionally, the user can select any combination of regions to be graphed. Typically, the entire coincidence spectrum or the Beta/Gamma singles data are displayed.

3. A "region definition area" (lower right panel in Figure 2) displays the filenames that are currently open as well as the regions described in the files. This area of the form is used to determine those regions that are to be graphed. Supplementary regions added by the user are noted in this area and can be graphed as well. Additional menu options allow the user to: switch between primary, secondary, and subtracted views; view /hide the regions of interest; add new regions; and change between grayscale and color.

Additional forms are the header form and the data grid form. The RMS 3.0 data format structures pertinent detector data in blocks and the header form essentially reconstructs these blocks on a tab control so the operator can immediately access pertinent information in the file. If desired, however, the user can elect to view the entire file in raw RMS 3.0 format. Occasionally, the data analysis personnel need to modify specific information contained in the file. These changes are then reflected in this file. The data grid form displays the primary file two-dimensional data in a grid. Additional options have been included to allow the user to add a new region from this form. This form is most useful when the operator is interested in viewing individual counts or is interested in additional information.

Radioxenon Concentration Calculations

The two-dimensional beta-gamma spectrum for the sample and the previous eight-hour background spectrum are used to determine the concentrations of all four radioxenons. The equation takes into account the half-life decay from the beginning of the sampling period, gamma and beta detection efficiencies, possible interferences from ^{222}Rn daughters and other xenon isotopes, the appropriate gamma and beta branching ratios, and the xenon gas collection efficiency. The background spectrum provides information on the ubiquitous background as well as the residual xenon and radon gases that adhere to the walls of the plastic scintillator. The background spectrum is subtracted from the sample spectrum for each β-γ bin, accounting for the difference in spectrum collection times (8-hours versus 24-hours). Each ROI is then summed over the beta-gamma energy range that it encompasses to give the total number of counts for that ROI. The radon interference in the 81- and 250-keV ROI's is removed by multiplying the number of counts in the 352-keV ROI by the previously determined radon ratios.

Below is a sample calculation for the ^{135g}Xe ROI and typical values used:

$$^{135}Xe_{Conc}\left(\frac{mBq}{m^3 air}\right) = \frac{C_2}{\varepsilon_g \varepsilon_b \gamma_{BR} \beta_{BR}} \frac{\lambda^2}{(1-\exp(-\lambda T_C))\exp(-\lambda T_P)(1-\exp(-\lambda T_A))} \frac{T_C}{V_{Air}} 1000$$

where:

C_2	=	*Counts - background and radon contamination*	→	100.0
ε_g	=	γ *Efficiency*	→	49.4%
ε_b	=	β *Efficiency*	→	80.6%
γ_{BR}	=	γ *BranchingRatio*	→	90.0%
β_{BR}	=	β *BranchingRatio*	→	100.0%
λ	=	$Ln(2)/^{135}Xe\ Half-life\ (\sec^{-1})$	→	$2.11*10^{-5}$
T_C	=	*CollectionTime* (sec)	→	28800
T_P	=	*ProcessingTime* (sec)	→	19640
T_A	=	*Acquisition Time* (sec)	→	86400
V_{Air}	=	*cc of Xenon*/0.087 *cc of Xenon per SCA*	→	~ 20.0

Using the above numbers and equation would yield $0.7 \pm 0.07\left(\frac{mBq^{135}Xe}{SCM}\right)$ for ^{135g}Xe and assumes no background counts or ^{222}Rn contamination. The factor of 1000 converts from Becquerels to milli-Becquerels.

Calculation of Minimum Detectable Concentration

The minimum detectable concentration (MDC) is a measure of the sensitivity of a particular detector system, and, for the ARSA system, is defined as the lowest amount of activity that can be detected using the counting system given the daily fluctuations in Radon gas interference, the background counts, the memory effect of previous samples on subsequent samples and the detector operations. A good general explanation for the determination of minimum detection limits can be found in reference (Curie 1968), which explains a variety of different measurement scenarios.

For the ARSA system the minimum detectable concentrations calculated assume that a 5% confidence level for measuring a false positive (radioxenon isotopes detected when none are present in the sample) and a 5% confidence level for measuring false negatives (reporting that no radioxenon isotopes are present in the sample when they are) (McIntyre et al 1999). Using these limits, it then is possible to determine the variance of the various backgrounds and interference terms in the absence of the radioxenon isotope and use them to calculate an MDC for the radioxenon isotope in question. Since the previous background count is subtracted from each sample spectrum, its variance must be included. The relevant MDC equation for any of the radioxenons:

$$MDC\left(\frac{mBq}{SC<MA}\right)=\frac{2.71+3.21s_0}{e_g e_b g_{BR} b_{BR}}\frac{l^2}{(1-\exp(-lT_C))\exp(-lT_P)(1-\exp(-lT_A))}\frac{T_C*1000}{V_{Air}}$$

where $s_0 = \sqrt{2*BackgroundCounts+(s_{Interfences})^2}$, and all other terms were defined in the concentration calculation equation. MDC values for ^{133g}Xe from field tests in Germany and New York were typically less than 0.15 mBq/SCA which is well below the 1.0 mBq/SCA requirement for radioxenon monitoring systems. See PrepCom (2000) for a thorough treatment of the MDCs calculated for the ARSA system.

Summary

A software package has been developed to analyze the two-dimensional spectra produced by the ARSA system. This software has proven to be very useful for analyzing data from ARSA systems (and other beta-gamma systems conforming to the RMS 3.0 format) during routine operation and allows operators to calculate concentrations for all of the radioxenons of interest to the CTBT (^{131m}Xe, ^{133g}Xe, ^{133m}Xe and ^{135g}Xe), as well as determining MDCs, and displaying data in raw and graphical forms. The software is flexible and allows significant operator intervention to modify regions of interest, energy calibrations, etc., if desired. The development of this software package was sponsored by the U. S. Department of Energy, Office of Nonproliferation Research and Engineering, Office of Research and Development.

REFERENCES

Biegaliski, K., (October 1999), Proposal for Release 3 Formats and Protocols: Full Incorporation of Noble Gas Data into Pulse Height Data Messages, Prototype International Data Centre, Rev. 10.

Biegalski K. and S. Biegalski (2000), Determining Detection Limits and Minimum Detectable Concentrations for Noble Gas Detectors Utilizing Beta-Gamma Coincidence Systems, MARC-V Conference, Kailua-Kona HI, 9-14 April 2000.

Bowyer, T., J. McIntyre, and P. Reeder (1999a), High Sensitivity Detection of Xe Isotopes via Beta-Gamma Coincidence Counting, 21st Seismic Research Symposium: Technologies for Monitoring the CTBT, Las Vegas NV 21-24 September, PNNL-SA-32048.

Bowyer, T., K. Abel, C. Hubbard, M. Panisko, P. Reeder, R. Thompson, and R. Warner (1999b), Field Testing of Collection and Measurement of Radioxenon for the Comprehensive Test Ban Treaty, J. Radioanal. Nucl. Chem., 240, 109.

Browne, E. and R. Firestone (1986), Table of Radioactive Isotopes, John Wiley and Sons, Inc., New York.

Curie, L. (1968), Analytical Chemistry 40, 586.

Hayes, J., K. Abel, T. Bowyer, T. Heimbigner, M. Panisko, P. Reeder, R. Thompson, L. Todd, and R. Warner (1999), Operations of the Automated Radioxenon Sampler/Analyzer -- ARSA, 21st Seismic Research Symposium, 21-24 September 1999, Las Vegas NV, PNNL-SA-32064.

McIntyre, J., K. Abel, C. Hubbard, M. Panisko, P. Reeder, and R. Thompson (2000), Measurements of Ambient Radioxenon Levels Using the Automated Radioxenon Sampler-Analyzer (ARSA), MARC-V Conference, Kailua-Kona HI, 9-14 April 2000.

McIntyre, J., T. Bowyer, and P. Reeder (1999), Calculations of Minimum-Detectable Concentration Levels of Radioxenon Isotopes Using the PNNL ARSA System, PNNL-13102.

National Nuclear Data Center, ENDF/B-VI, Brookhaven NY.

PrepCom (2000), Operational Manual for Radionuclide Monitoring and the International Exchange of Radionuclide Data, CTBT/WGB/TL-11/5/Rev.8, February 2000.

Reeder, P., T. Bowyer, and R. Perkins (1998), J. Radioanal. Nucl. Chem., 235, 89.

Reeder, P. and T. Bowyer (1998), Nucl. Instr. Meth. Phys. Res. A408, 582.

Radionuclide Laboratory Support for the Comprehensive Nuclear-Test-Ban Treaty International Monitoring System

Pamela D. Greenlaw, Colin G. Sanderson
Environmental Measurements Laboratory

Sponsored by The Defense Threat Reduction Agency
Arms Control Technology Division
Nuclear Treaty Branch

ABSTRACT

The protocol to the Comprehensive Nuclear-Test-Ban Treaty (CTBT) provides for the designation of a number of radionuclide laboratories to support the radionuclide monitoring network of the International Monitoring System (IMS). These laboratories, after being certified and when requested by the Technical Secretariat, are to provide additional analytical services, such as confirmatory gamma-ray spectrometry, quality control and intra laboratory exercises. The Environmental Measurements Laboratory (EML) has been designated as the U. S. CTBT Radionuclide Laboratory. EML is developing a separate secure facility for performing the required CTBT analyses and is currently set up for gamma-ray spectrometry with two, 120%, HPGe detectors. The laboratory will undergo a preliminary certification exercise with the CTBT Technical Secretariat which will included verification of the laboratory's quality assurance plan as well as it's current analytical capability. EML's CTBT laboratory is in the process of expanding its radiochemistry and counting capabilities to include both alpha and beta emitting radionuclides. This paper presents EML's continuing development of a radionuclide laboratory to corroborate the results of the routine analysis of a sample from an IMS radionuclide station, achieve a greater sensitivity for fission product analysis than can be achieved at the radionuclide stations and clarify the presence or otherwise of fission products in the case of a suspect or irregular analytical result from a particular radionuclide station.

KEY WORDS: Radionuclide Laboratory, International Monitoring System, Laboratory Certification

OBJECTIVE

The objective of this project is to establish the United States Comprehensive Nuclear-Test-Ban Treaty Radionuclide Laboratory to support the radionuclide monitoring network of the International Monitoring System.

Introduction

Since 1963 EML has maintained a world wide network of surface air sampling stations to monitor and inventory nuclear fallout. After collection, these filters are returned to EML and are analyzed for gamma-ray emitting radionuclides. Because of this long history of measuring aerosol particulates for radioactivity and the laboratory's active role in providing quality assurance for the Department of Energy's (DOE) Environmental Management programs, EML was selected by AFTAC to provide the United State's laboratory support for the CTBT radionuclide International Monitoring System (IMS) stations.

Requirements called forth in the treaty specify that a the network of radionuclide monitoring stations shall be supported by laboratories, which shall be certified by the Technical Secretariat in accordance with the relevant operational manual for the performance, on contract to the Organization and on a fee-for-service basis, of the analysis of samples from radionuclide monitoring stations. These laboratories shall, as required, also be drawn upon by the Technical Secretariat to perform additional analysis of samples from radionuclide monitoring stations. Additional requirements have been developed by the Comprehensive Nuclear-Test-Ban Treaty Organization (CTBTO), the Radionuclide Task Group 11/5 of Working Group B of the Preparatory Commission and at informal radionuclide workshops.

The US CTBT Laboratory

In order to meet the requirements of the treaty and the Operational Manual for Radionuclide Monitoring and the International Exchange of Radionuclide Data (CTBT/WGB/TL-11/5/Rev.8), EML chose to dedicate space within the laboratory for a secure CTBT laboratory comprised of three existing interconnecting laboratories. Each laboratory has a designated function; the first is used for sample receipt, log in and sample preparation for gamma counting; the second is a radiochemistry laboratory; and the third will be the counting laboratory.

Security

In order to maintain security, access to the laboratory will require a personalized card key. Entry into laboratory with the card key will be recorded in the CTBT laboratory's communications and analysis computer.

Five identical workstations will exist on their own independent LAN and will only be accessible after an operator has had the bar code on their DOE ID badge read and verified.

The Laboratory has documented plans and facilities for receipt of samples 24 hours a day, 7 days a week. SOPs to maintain sample chain of custody from time of receipt until final dispatch are in place and bar code readers are installed at appropriate locations in order to automate the chain of custody.

VSAT Communications with the Technical Secretariat and International Data Center
The CTBT requires secure and authenticated communications between the CTBTO Technical Secretariat, the International Data Center (IDC) and the IMS supporting Radionuclide Laboratories. The types of notifications from the Technical Secretariat and IDC to the laboratory and the required acknowledgments from the laboratories to the Technical Secretariat and IDC are listed below. These messages are authenticated and transmitted via Technical Secretariat installed VSAT e-mail and FTP. A backup communication system is also be available in the event that the GCI VSAT in unavailable. For either incoming or out going messages a dial-up connection to the EML LAN or a dial-up connection to a commercial ISP will be used to communicate with the Technical Secretariat/IDC.

Types of Messages

From the Technical Secretariat or IDC to the Laboratory	From the Laboratory to the Technical Secretariat or IDC
1. Initial notification of intent to dispatch a sample	1. Acknowledgment of intent to dispatch a sample and agreement to accept the sample
2. Notification of sample dispatch	2. Acknowledgment of sample dispatch notification
3. Sample collection information	3. Acknowledgment of sample receipt
4. Analysis required and any other information available about the sample	4. Report of preliminary results
5. Acknowledgment of receipt of preliminary results report	5. Report of intermediate counting results
6. Acknowledgment of receipt of intermediate counting results and possible request to terminate analysis	6. Final report of sample analysis

Sample Receipt, Inspection and Log-in
All samples sent to the CTBT Laboratory are received, inspected and logged in by the CTBT sample custodian. As an aid for this process each sample will have a unique printed bar code. The EML guard or the GSA Building guard notifies the sample custodian when shipping containers arrive.

Initial inspection of the shipping containers takes place in the CTBT Sample Receipt Laboratory. The shipping containers are placed in a hood and screened for external radiation before being opened. After all sample information has been verified and the sample bar code read into the computer, the samples are logged in, then transferred to the sample preparation area and either prepared for gamma counting or transferred to a locked storage cabinet.

Filter Sample Preparation (including sample splitting)
The CTBT Sample Preparation Laboratory is equipped with a heated manual hydraulic press capable of achieving over 10 metric tons and 650 degrees F. With the availability of a low temperature muffle furnace aerosol filter

samples can be pressed, heat pressed or melted into standard geometries for gamma counting. Sample identification is maintained with the use of the sample preparation bar code reader.

Tests performed with the US RASA filters indicated that equivalent counting efficiencies are achieved with either the unprocessed filters wrapped around the side of the detector or the filter melt in a 600 ml beaker on the detector end cap.

If required, the laboratory will be prepared to split any samples received

System Requirements for Gamma-Ray Sample Analysis
The radionuclide operational manual gives these gamma-ray analysis specifications for the IMS stations:

1.	*Air flow*	500 m^3 /hour
2.	*Collection time*	24 hours
3.	*Measurement time*	>20 hours
4.	*Measurement mode*	HPGe high-resolution gamma spectrometry
5.	*HPGe relative efficiency*	Equal to or greater than 40%
6.	*HPGE resolution*	< 2.5 keV at 1332 keV
7.	*Baseline sensitivity*	10 to 30 □Bq/m^3 for ^{140}Ba
8.	*Calibration range*	88 to 1836 keV

The requirements in the radionuclide operational manual for laboratories supporting the IMS require lower limits of detection for ^{140}Ba. These minimum laboratory requirements are:

Property	**Minimum Requirement**
Detector type	High resolution HPGe
Detector relative efficiency	40 %
MDA for ^{140}Ba for cylindrical sample geometry with a diameter of 70 mm and height of 5 mm with decay correction to start of spectral acquisition (not to exceed a 7 day count)	24 mBq
FWHM at 1333 keV	2.3
FWHM at 122 keV	1.3
Report format	IMS current version

The radionuclide operational manual specifies the requirement for a minimum detectable concentration (MDC) at radionuclide stations as a concentration range for ^{140}Ba of 10 to 30 □Bq m^{-3} for a 24-hour count and a laboratory requirement for a better minimum detectable activity (MDA). Accordingly, the MDA requirement for Laboratories is calculated from the low end of the station requirement range using a total air sample flow of 12,000 m^3. Laboratory measurement systems must, therefore be capable of achieving a MDA of 24 mBq for ^{140}Ba using the counting efficiency for a compressed cylindrical geometry of 70mm diameter and 5mm height and a count time of 7 days or less.

In order to minimize the possibility of down tine, two high efficiency p-type HPGe detectors have been installed in the EML CTBT counting laboratory. One detector has a relative efficiency of 120% and a FWHM resolution of 1.92 keV at 1333 keV. The second detector has a relative efficiency of 114% and a FWHM resolution of 1.82 keV at 1333 keV . Both detector are housed in low background cryostats and are shielded with copper, cadmium and 10 cm of very old lead. The ^{140}Ba MDAs for these detectors with different count times are shown below:

Gamma Detection MDA (^{140}Ba @ 537.27 keV)

Detector	MDA and Count Time		
CTBT 1	19.4 mBq - 7 days	25.6 mBq - 4 days	24 mBq - 4.55 days
CTBT 2	20.4 mBq - 7 days	27.0 mBq - 4 days	24 mBq - 5.06 days

The data above show that the CTBT Laboratory HPGe gamma-ray detectors can achieve the required ^{140}Ba MDA in less than the limiting 7 day count time restriction.

Radiochemical Analysis and Counting
The following excerpts from the Treaty can be interpreted to indicate that the CTBT Laboratories may be called upon to perform additional analyses beyond the initial nondestructive gamma-ray analysis. These additional analyses could be for alpha or beta emitting radionuclides and possibly noble gasses.

11. ...as required, also be drawn upon by the Technical Secretariat to perform additional analysis of samples from radionuclide monitoring stations.

98. ...The inspection team shall have the right to transfer samples for off-site analysis at laboratories designated by the Organization only if it demonstrates that the necessary sample analysis cannot be performed on-site.

101. The designated laboratories shall conduct chemical and physical analysis of the samples transferred for off-site analysis....

The EML CTBT Laboratory has been equipped with a fully functional radiochemistry laboratory, containing a chemical fume hood, muffle furnace, centrifuges, balance, glass ware and filtering apparatus. The counting laboratory has been equipped with a bank of 8 solid state alpha detectors and 4 EML beta scintillation counters. A beta-gamma coincidence gas counting system is planned for the future.

Chain of Custody
All samples received by the CTBT Laboratory shall have a legal chain of custody (COC) established, which records a continuous record of the physical possession, storage and analysis of samples. The COC at EML begins when the samples arrive at the fifth floor guard station. The three laboratory work stations (in the sample receipt, sample preparation and sample counting/communications area) have bar code readers which provides input to the CTBT laboratory information management system (LIMS). The LIMS provides a means for sample tracking and COC.

Laboratory Operational Manual
All laboratory operations, written as standard operating procedures (SOP), are maintained in the Laboratory Operational Manual. This manual also contains copies of the EML Institutional Quality Assurance Plan, CTBT Laboratory Quality Assurance Plan, ISO 17025, all equipment manuals and calibration certificates.

The Certification Process
The Comprehensive Nuclear-Test-Ban-Treaty states in its:
Protocol to The Comprehensive Nuclear Test-ban Treaty, Part I, A. General Provisions,
C. Radionuclide Monitoring, Section 11;

The network of radionuclide monitoring stations shall be supported by laboratories, which shall be certified by the Technical Secretariat...

These laboratories are certified in accordance with the radionuclide operational manual. The process of certification takes place in several steps, involving preparation and evaluation at both the Technical Secretariat in Vienna and the Radionuclide Laboratory and can be summarized in the following steps:

1. Formal Arrangement:
All certification procedures begin with a formal Memorandum of Understanding (MOU) and/or other arrangements as initiated by the respective National Authority with the Technical Secretariat to commence the process of

certification.

2. Document Review:
The laboratory supplies the Technical Secretariat with all quality documentation including the quality manual, SOPs and equipment manuals (with certification, specification and QC data sheets) , and all quality control documentation.

3. Confirmation of the Quality of Documented Analysis Results by Gamma Spectrometry:
The Technical Secretariat reviews the documentation of any intercomparison exercises in which the laboratory has participated.

4. Functional Test of Communications:
The laboratories GCI terminal should successfully test their communication link by exchanging information text messages described in the IDC Operations Manual.

5. Functional Test of Data Authentication:
The radionuclide laboratories conduct a test to ensure authentic data is transferred from the analysis system to the communication system with the IDC.

6. Test of Data/Report Format and Transfer to the IDC:
The radionuclide laboratories must send sample test data and sample reports to the IDC to allow review for correctness of format.

7. Certification Visit by Technical Secretariat Staff to Examine Equipment and Laboratory:

7.1. Physical Facilities
The Technical Secretariat will confirm that the conditions at the laboratory correspond to the information provided and reviewed prior to the visit and confirm that the Quality System is executed as documented.

7.2. Equipment and Reference Materials
Sample preparation equipment including laboratory press, balance and oven will be inspected. Review calibration and decontamination procedures and maintenance record. Inspect reference materials to confirm traceability documentation and storage adequacy.

7.3. Gamma Spectrometer
Instrument serial numbers will be compared to serial numbers on manufacturer's specification sheets. A Technical Secretariat radionuclide source in calibrated geometry will be counted to compare results as reported by same gamma spectrometer and software used to determine CTBT samples.

A background filter supplied by Technical Secretariat will be counted in same geometry as the Technical Secretariat source to confirm MDA calculation.

8. Issue of Certificate
When the laboratory meets IMS specifications and certification criteria the Technical Secretariat will issue a certificate to the Laboratory to formally recognize it as a laboratory supporting the IMS. If the laboratory does not fulfil the certification criteria on the first visit of the Technical Secretariat, the Technical Secretariat will issue a report delineating deficiencies and revaluation criteria. The Technical Secretariat will schedule a reinspection and/or review required corrective action documentation to complete the certification process.

9. Long Term Quality Assurance
The Technical Secretariat will establish a long-term program of quality assurance including intercomparison exercises between laboratories. Criteria will be established to evaluate the results of the intercomparison exercises. The results of Technical Secretariat sponsored and other international intercomparison exercises will be used by the Technical Secretariat to monitor the laboratory performance as available.

When changes occur in the laboratory to facilities, personnel or equipment, the Technical Secretariat shall be

notified and supplied with new documentation. If the change is deemed substantial (i.e., relocation of laboratory, replacement of gamma detectors) the Technical Secretariat will perform a re-certification of the laboratory. The results of other international intercomparison exercises will be used by the Technical Secretariat to monitor the laboratory performance.

To be certified a laboratory must establish and maintain a quality system based on ISO 17025. However, if a particular Radionuclide Laboratory is nationally or internationally accredited, then meeting the quality system requirements should require no more than a review of the existing quality documentation related to CTBT operations.

All measuring and testing equipment having an effect on the accuracy or validity of sample analyses should be calibrated so as to ensure measurements are traceable to national standards.

The requirements for the physical topology of the Global Communications Infrastructure (GCI) are the same for the laboratories as they are for the radionuclide stations. This means each laboratory will be connected to the IDC via the GCI using the basic topology or other permitted configuration.

During the certification process the laboratory is required to demonstrate to the Technical Secretariat that the environment in which IMS samples are processed and analyzed is maintained to sufficiently high standards.

SOPs for preparation of samples for gamma analysis have been prepared and are available. If different procedures are to be used for samples of different matrices/ geometries, these SOPs shall be available with validation data. If requested and authorized by the Technical Secretariat, other concentration, separation and radiochemical analysis methods can be used. SOPs and validation data for other preparation methods will be prepared and made available to the Technical Secretariat.

EML will work with the Technical Secretariat to finalize implementation plans for lab certification during the coming months.

RADIONUCLIDE OPERATIONAL RESEARCH & DEVELOPMENT

Harry S. Miley, Dale N. Anderson, Richard J. Arthur, J. Edward Ellis
Tom W. Heimbigner, Gary R. Kiebel, Robert C. Thompson
Pacific Northwest National Laboratory

Sponsored by US Department of Energy
Office of Nonproliferation Research and Engineering
Office of Defense Nuclear Nonproliferation
National Nuclear Security Adminstration

Contract DE-AC06-76RLO 1830

ABSTRACT

The development team responsible for creation of the automated aerosol and xenon sampling systems is continuing to solve problems related to the operation of automated systems for nuclear explosion monitoring. Several typical problems are presented here to characterize that effort. First, the development of tools for the efficient use of state-of-health information is in progress. Second, first-generation code segments useful for authenticating data have been developed and are discussed. Finally, the computations and experiments quantifying the effects of cascade summing in the operation of aerosol monitoring radiation detectors are discussed.

Both the Radionuclide Aerosol Sampler/Analyzer (RASA) and the Automatic Radioxenon Sampler/Analyzer (ARSA) gather state-of-health data (Miley, 1998; Bowyer, 1999). These data are stored and forwarded to a data center, such as the US National Data Center. Tools to simply visualize (with template eye guides) have been constructed. State-of-heath data from operational RASA units and specially designed experiments have been analyzed to demonstrate the ability to detect minute trends leading to failure. This analysis should allow systems maintenance staff some predictive capability.

Providing a digital signature on a data transmission serves to authenticate both that the message comes from a trusted source and that it has not been altered in any way. In addition, digital signature also makes the message undeniable: that is, it cannot be disputed that this message came from some other source or was fabricated. Authentication software has been produced in collaboration with Sandia National Laboratories and has undergone extensive testing on operational and test RASA units. Authentication code must implement the policy logic of an overall authentication infrastructure. Policy decisions for data authentication have not been completely set at this time. Because of this and the rapidly changing standards environment for authentication code today, this work will likely require extension to cover other authentication standards.

Cascade summing occurs when two gamma-rays emitted in the decay of a single nucleus both deposit energy in a detector. In addition to (or instead of) the familiar set of peaks and continuum usually uniquely associated with an isotope, higher energy peaks and continuum are observed. This effect occurs predominantly where the source is located close to the detector for maximum sensitivity, as in the International Monitoring System aerosol stations, including the RASA. The size of the effect may be computed by various means, including Monte Carlo simulation. Computations have been compared to experiment to show that in most cases the effect of summing is modest but perceptible. Certain extreme cases can show dramatic effect. The impact on efficiency measurements and certain fission products will be shown.

Key words: radionuclide, aerosol, SOH, cascade summing, authentication

OBJECTIVE

State-of Health Data

The general goals of State-of-Health (SOH) data gathering are to detect failures in the monitored process and to predict failures sufficiently ahead of time to minimize downtime. These goals can be separated into three distinct components: bounds checking on current SOH values, trend detection in SOH values, and fault detection/prediction based on detailed system knowledge. The philosophy of SOH development taken at Pacific Northwest National Laboratory (PNNL) is first to facilitate development, then to gradually analyze SOH parameters for failure-prediction capability. Finally, the production of tools to automatically examine SOH data will greatly reduce staffing needs while maximizing uptime. Because of the limited field experience with the RASA and ARSA, it is not well known what the most likely failure modes will be. Thus, as the operational experience base expands, more SOH parameters can be studied meaningfully.

Bounds checking of SOH values can be implemented relatively easily by creating a software process that compares each new SOH value to a pre-established range. This function in the RASA, for instance, automatically generates an alert e-mail to a pre-specified e-mail address describing the anomaly. The bounds range was originally established by histogramming a one-year sample of 5-minute resolution values. The 4 sigma limits of these values were chosen to limit false alarm alerts. This approach created a fairly narrow operation range. Unfortunately, conditions such as extreme weather, air conditioning failure, or other factors unrelated to the RASA directly have the ability to force the SOH values out of a narrowly defined range.

After a single system generated 600 alert e-mails in one weekend, it became generally acknowledged that the SOH value range needed to be sufficiently broad to limit alerts to obvious problems. The current idea for setting this range is to specify the nominal range of values (temperatures, currents, etc.) specified by subsystem suppliers. This is less sensitive to excursions but does not produce too many false alarms.

While bounds checking can and should be done on the monitored system, trend analysis need not be done on the RASA or ARSA. It may be sufficient to operate well-known process control software at the Data Center to examine these data. However, many of the SOH parameters are not naturally steady: for example diurnal variations are found in all RASA SOH temperatures. ARSA components normally undergo sizeable temperature swings every eight hours (Fig. 1). Thus, strong recurring patterns need to be mathematically nulled or accounted for in the mathematical trend model. Nulling can be accomplished effectively by taking the difference of two similar SOH parameters. It is preferable that one is not dependent on system performance. Outdoor air temperature or room temperature would be good examples of independent parameters.

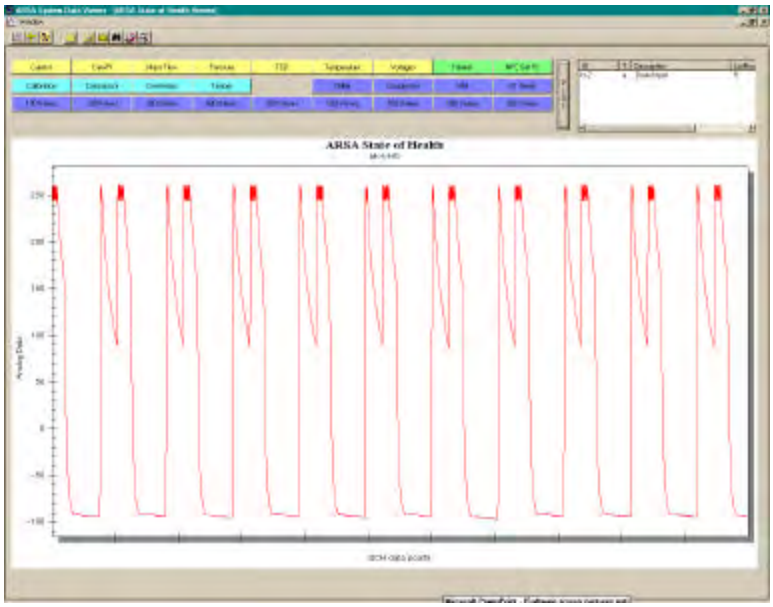


Figure 1. ARSA SOH Viewer

Because the development teams of the RASA and ARSA are still involved with the successful technology transfer to industry, it is possible to combine the RASA and ARSA development experience with mathematical and statistical methods to explore system failure predictions. Exploratory work of this sort has begun with the analysis of the temperature of the RASA blower motor and the current drawn by the RASA filter advance motor. Although the germanium detector seems to be the most failure-prone item, these motors are the critical mechanical components of the RASA. The goal of the SOH analysis is to predict failures far enough in advance to allow a service call that eliminates or minimizes downtime.

Blower Motor Thermal Test

To produce unambiguous data for the blower motor temperature analysis, researchers agreed that the commercially produced RASA would be left undisturbed for one month. In the fourth week, heat would be gradually applied to the motor to simulate or perhaps cause a bearing failure. Fortunately or unfortunately, a real failure occurred about 450 hours into the test (Fig. 2). The failure was of a type unknown on the PNNL prototype: when one or more filter strips terminates unexpectedly and the RASA continues to draw air, the blower motor can rapidly increase in temperature and emit a hot smell. After a cool-down period and replacement of the filter strip, the motor will return to normal operation.

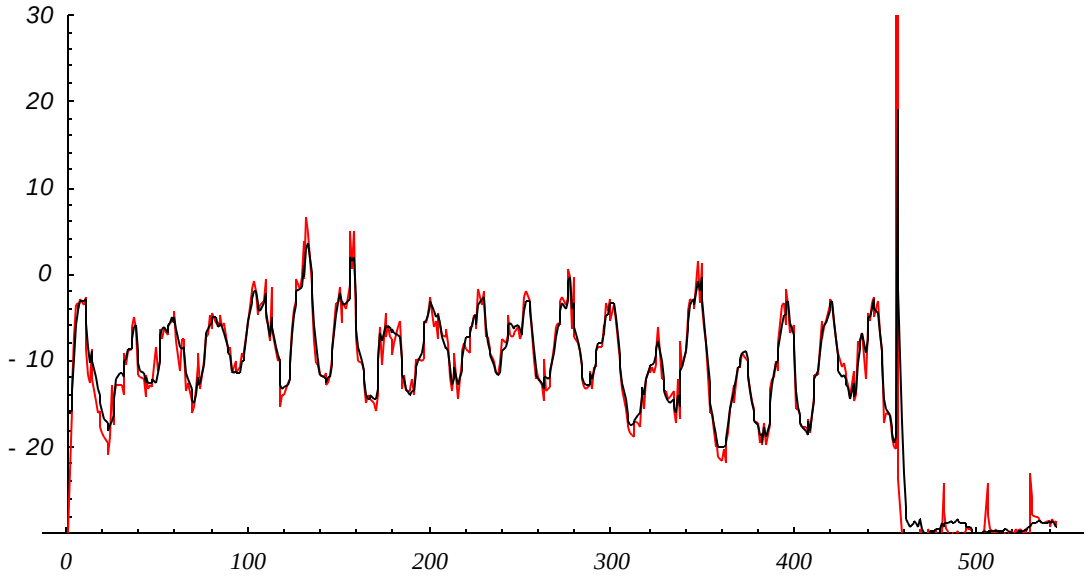


Figure 2. Temperature difference in degrees Celsius (black) vs. SARIMA predictions (red). Model was trained on first 240 hours data.

The strong diurnal variation in the raw blower temperature was suppressed by subtracting the inlet air temperature. Multiplying the inlet air temperature by some factor and also subtracting a fixed offset could have nulled the remaining diurnal variation more effectively. However, models were selected which naturally included diurnal variations. The time series models employed are formally known a seasonal autoregressive integrated moving average (SARIMA) models.

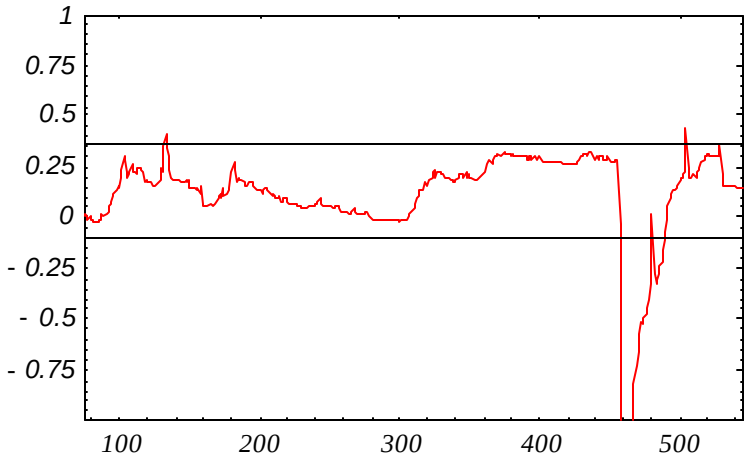


Figure 3. Cuscore statistic showing blower failure detection.

Obviously, this method has excellent predictive power, but the predictions are not sufficiently far out in the future to say that we have reached our goal of failure prediction, at least for this sudden-onset phenomenon. However, this model can be tuned to find patterns super-imposed on normal diurnal variation and to generate an alarm. As a crude example, the cuscore statistic is

shown for the blower failure example below. The failure is seen in figure 3 as a dramatic excursion of the cuscore with a minor accidental excursion at about 133 hours. The bounds on the cuscore represent a much tighter bound than that in the simple alerts. Furthermore, the cuscore can be tuned to be sensitive to expected failure onset patterns.

Advance Motor Current Analysis

As a surrogate indicator for RASA filter paper jams, advance motor current can be used to identify excessive motor load. Minimum, maximum, and average current during motor operation comprise the SOH monitoring data (Fig. 4). These three measurements should be used since the range of motor current can be indicative of filter paper jam as

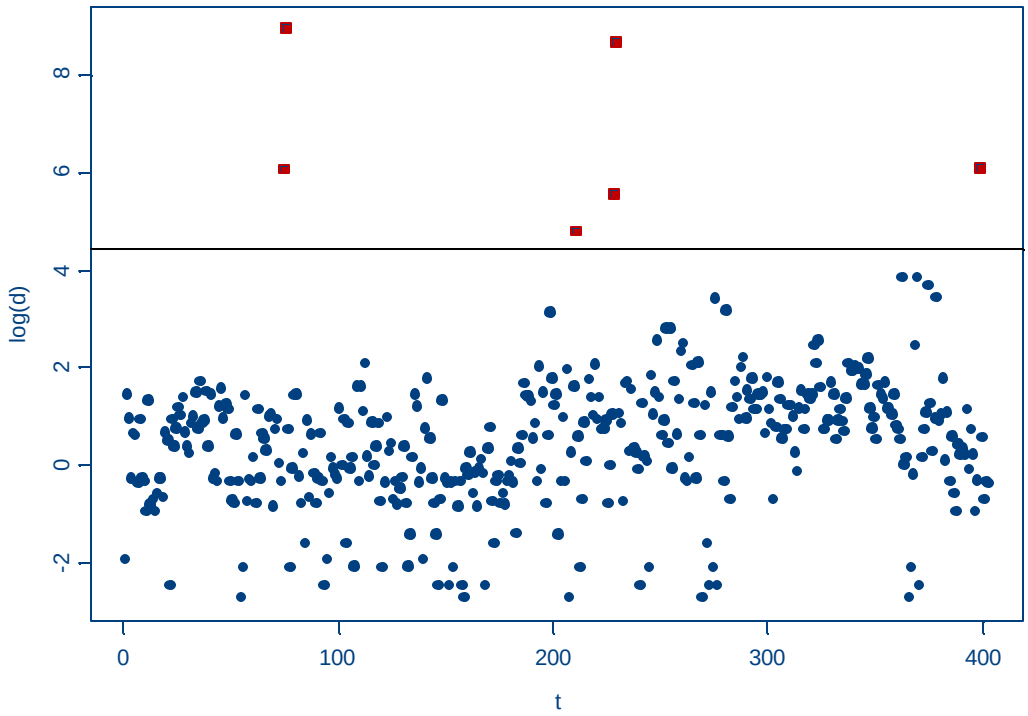


Figure 4. Advance motor SOH measurements (Mahalanobis distance) derived from advance motor current data. Extreme SOH measurements correspond to filter paper jams. Extreme SOH measurements serve as surrogate indicator for filter paper jams.

well as the average motor current. Outlier data from the USX01 advance motor were identified as real failures or false failures (maintenance activities can produce unusual advance motor current). Once the real and false failures were determined, the false failures were removed from the data set.

The Mahalanobis distance (relative to the nominal data) of the 403 observations are plotted versus time (Fig. 4). The known failures for the USX01 advanced motor stand apart from the nominal data in an obvious manner. We have found that all three SOH measures (minimum, maximum, and average current) are necessary to identify excessive motor load. If only one metric had been used, the entire behavior of the data would have never surfaced.

Based on this preliminary analysis, a simple rule can be used to identify excessive advance motor load (which has a strong possibility of being a filter paper jam):

If $(\mathbf{x} - \mu_{Nominal})' \Sigma^{-1}_{Nominal} (\mathbf{x} - \mu_{Nominal}) > c^2$, where

- $\mathbf{x}$ is the vector of SOH measurements (min, max, and average current)
- $\mu_{Nominal}$ and $\Sigma_{Nominal}$ are the mean vector and covariance matrix computed from a large number of nominal SOH measurements
- $c^2 = (\mu_{Nominal} - \mu_{Failure})' \Sigma^{-1}_{Nominal} (\mu_{Nominal} - \mu_{Failure}) / 4$

In reality, most of these advance motor failures were the result of allowing the polyester sealing tape to run out, which causes the filter to wind around the drive rollers. This particular failure mode should be quite rare in real monitoring use. However, it stands to reason that increased motor current over a few days may indicate an imminent jam or other maintenance condition.

These two exploratory analyses show that there is real potential in a mathematical/statistical approach to system management. The future of SOH operation research for the radionuclide systems includes about 50 more parameters and their interdependency. However, the approach of choice is to determine the first few most likely failure modes, as they become apparent, then design detection and then prediction tools for them. A list of analog SOH parameters for the ARSA and RASA can be found Miley (1998) and Bowyer (1999).

Authentication

RASA Authentication Software applies a digital signature to all normal outgoing messages that are e-mailed from a RASA system on which it is installed. This digital signature can be used to verify that the message actually came from the source that it claims to have, and that the contents of the message have not been altered.

The digital signature conforms to the S/MIME (Secure/Multipurpose Internet Mail Extensions) standard, version 2. It specifies adding a digital signature and public key certificate as a MIME attachment to the e-mail message. S/MIME is a developing standard of the Internet Engineering Task Force (IETF) S/MIME working group that has been widely adopted in industry. S/MIME specifies procedures for signed and/or encrypted data and X.509 public key certificates to be transmitted as MIME data types. All public key information needed to verify digital signatures is embodied within ISO (International Standards Organization) X.509 certificates.

The signature function is performed by a tamper-evident hardware cryptographic token (the U.S.-Government-developed Fortezza Card) in the form of a PC Card processor card obtained from a commercial supplier (Spyrus, http://www.spyrus.com/). The card is configured to use the Digital Signature Standard (DSS) with a public key size of 1024 bits and is capable of self-generating a private key and communicating the new public key.

The Authentication Software is constructed on the client-server model. There is one authentication server program. It manages interactions with a Fortezza card, X.509 certificate handling and PKCS #7 (Public-Key Cryptography Standards) signature generation, and maintains a database of public key certificates for use in verifying signed messages. Other RASA programs connect to the authentication server using a socket interface and can request that operations be performed. The OpenSSL (http://www.openssl.org/) software package is used as the basis library for certificate processing

The authentication software operates as a plug-in to existing RASA control software (version 2.2). When properly installed, the authentication software is automatically recognized by the RASA control software and is used to sign outgoing e-mail messages. When the authentication plug-in is not present, or is removed, the RASA control software automatically reverts to sending unsigned messages. A hardware interface card to receive the Fortezza PC Card processor card must be installed on the RASA control computer.

Implementation to Date

The original work on the authentication software was performed at Sandia National Laboratories (SNL). A prototype version of the software that could operate on a RASA system was constructed in collaboration with PNNL and demonstrated in the third quarter of 1999 (Harris 1999). Subsequently, the demonstration prototype was further modified by PNNL to operate in a production mode with RASA control software.

Modifications for the demonstration included porting the Sandia software to the operating system that RASA uses (QNX, http://www.qnx.com). The standard driver software for the Fortezza card (the CI Library) was also ported to QNX. This allowed software that already uses the Fortezza card with CI Library calls to be easily ported and used on the RASA.

Subsequent modifications focused on reliable operation of the software under actual operating conditions and upon the "plug-in" interface that allows it to be easily added to or removed from an existing RASA installation. Most of the modifications needed to achieve reliable operations were due to the differences between QNX and Unix (for example, a limitation on the maximum size of a message sent via a socket connection).

Version 1.0 of the RASA Authentication Software has been tested on the two RASA stations at Hanford (USX01 and USX03) using a Spyrus Fortezza card. The software was installed and used to sign normal outgoing RASA e-mail messages. Results were observed for several days of operation. The e-mail reader functions of both Netscape and Internet Explorer browsers were used to verify that the signatures for the e-mail messages would authenticate. Only the initial self-signed X509 certificates have been used for these tests. Third-party signed certificates have not been tested.

Future work being considered includes: Modifying the software to work with hardware tokens that conform to the PKCS #11 token interface standard; testing the system with authentication-only hardware tokens (subject to lesser cryptographic export regulation); and fully supporting X509 certificate management (signature by approved certificate authority using approved methods).

Cascade Summing

Cascade summing was brought up in Working Group B as an important issue that could stall efforts to implement final software at the International Data Centre for automatic radionuclide analysis (Miley et al, 1999). Cascade summing can be an important consideration for measuring isotopes that decay by emitting two or more gamma-rays in succession. Many important fission products and calibration isotopes have this property. Cascade summing is negligible when the source of radiation is at a reasonable distance from the detector, say as little as 10 cm for a point-like source and a 10-cm diameter detector. However, systems designed for detection of trace levels of radiation usually have maximal contact between the source and detector.

Table 1. Measured cascade summing effect for some fission products of interest.

Fission Product	Energy (keV)	Gammas /sec @ 10 cm	Gammas /sec @ 0 cm	Expt Ratio
Zr-95	756.7	203.0	196.0	0.966
Nb-95	765.8	64.0	62.6	0.978
Mo-99/Tc-99m	140.5	1388.0	1035.0	0.746
Ru-103	497.1	288.7	270.9	0.938
Rh-105	319.1			N/A
Ag-111	342.1	-	-	-
Cd-115m	933.8	-	-	-
Sn-125	1067.1	-	-	-
Sb-125	427.9	-	-	-
I-131	364.5	569.9	486.5	0.854
Ba-140	537.0	355.7	340.5	0.957
La-140	1596.2	1343.0	1030.0	0.767
Ce-141	145.4			N/A
Ce-143	293.3	114.4	86.5	0.756
Nd-147	531.0	84.7	80.5	0.951
Pm-149	286.0	-	-	-
Pm-151	340.1	-	-	-
Sm-153	103.2			N/A

An experiment was carried out to estimate the size of the summing effect in several geometries. A point-like fission product source was made and measured at 0 cm and 10 cm from the front face of a RASA gamma-ray detector.

The fission product spectra were analyzed in the usual way with an automated spectral analysis code and with human analyst review. The comparison of 0 cm and 10 cm results is found in Table 1. The significant (~25%) effect in Mo-99, La-140, and Ce-143 would be less in the RASA because of the lower gamma-ray efficiency, particularly at low energies.

Interestingly, gamma-ray detectors with good efficiency at low energies can have a significant problem with Ba-140. Every decay of Ba-140 which emits the characteristic 537 keV gamma-ray has to emit another 43 keV worth of

gamma-rays. If the source is at the front face of the detector and if the detector has essentially no absorber on its front face, many or most of the 537-keV gamma-rays will sum with all or part of the 43 keV, thereby greatly diminishing the 537-keV line. This can be easily rectified by adding absorber material to replace the normal 0.7 mm of useless Ge on a P-type detector.

The effect of cascade summing on calibration data has been estimated by use of the Monte Carlo code, CraZy (Miley, 1993). These computations show that the effect of summing at 10 cm is negligible, at 0 cm is worthy of consideration, and for the RASA geometry is one-half to one-third as large as at 0 cm. It should be noted that the 1-sigma statistical uncertainties in the 10-cm values are of the order of 30% because of the relatively low efficiency of that geometry. Around 10 million histories each for 8 scenarios were required to compute the 10-cm values even that well.

Table 2. Simulated corrections in calibration lines

Energy	0 cm	RASA	10 cm
898	29%	12%	2.6%
1173	31%	10%	3.4%
1332	32%	12%	1.6%
1836	32%	12%	2.4%

CONCLUSIONS AND RECOMMENDATIONS

The authentication work done to date will likely require follow-up to extend the cryptological hardware supported. In addition, reasonable structures for key management need to be addressed throughout the International Monitority System. This will be observed as an evolving process of standard selection and adoption, with trickle down occurring into the field hardware over a period of years. Command authentication will also likely require investment and will have a similar implementation profile.

Analysis of state-of-health parameters has great potential rewards in uptime and effective cost of ownership of the radionuclide systems. Additional development in SOH data management is required to allow the SOH data to be useful. In particular, the payoff in germanium detector uptime alone is worth a considerable investment into the understanding of its failure modes.

Finally, it will likely be necessary to revisit basic topics in gamma-ray spectrometry several more times before the small errors, approximations, and short-cuts in the analysis of the radionuclide data are ironed out. The best approach to take when these events occur is to seek expert guidance, perform simple experiments and calculations, and to engage the expert community as early as possible to prevent wildly non-optimal procedures and policies from being posited.

References

Bowyer, et al. (1999), JRNC, Vol. 240, No. 1 (1999) 109-122, (ARSA).

Harris, et al. (1999), Proceedings of 21st Seismic Research Symposium: Technologies for Monitoring the Comprehensive Nuclear Test Ban Treaty, 21-24 Sept 1999, Las Vegas, NV Vol. II LA -UR-99-4700. 331-337.

Miley, et al. (1998), JRNC, Vol. 235, Nos 1-2, 83-87, (RASA).

Miley, H., R. Arthur, S.Biegalski, (1999), Coincidence Summing in the IMS, PNNL-13278.

Miley, H., (1993), Conf Record Nucl. Sci. Symposium & Medical Imaging Conf. Oct. 31- Nov. 6, San Francisco, Ca USA Vol. 1 240-243.

AUTOMATIC AND INTERACTIVE ANALYSIS SOFTWARE FOR BETA-GAMMA COINCIDENCE SYSTEMS USED IN CTBT MONITORING

J. Rynes, K.M.F. Biegalski, P. Donohoe, and S. Biegalski
Veridian – Pacific-Sierra Research Corporation

Sponsored by the U.S. Department of Defense
Defense Threat Reduction Agency

Contract No. DTRA01-99-C-0031

ABSTRACT

A suite of software has been developed by Veridian Systems as part of the Prototype International Data Center (PIDC) to assist in the analysis of noble gas monitoring data for the Comprehensive Nuclear-Test-Ban Treaty (CTBT). There are two acceptable noble gas monitoring methods for CTBT verification purposes: high-resolution gamma-ray (□) spectrometry and beta-gamma (□-□) coincidence. Data from □-spectrometry systems can be analyzed with the existing software at the PIDC and the International Data Center (IDC). Because commercially available software did not exist to analyze data from the □-□ coincidence systems, this software has been developed at the PIDC for eventual deployment at the IDC.

The suite of software consists of automatic analysis software and CORIANT (COincident Radiation Interactive ANalysis Tool). The automatic analysis software automatically identifies and quantifies radionuclides present in the sample and categorizes the sample based on the type and quantity of radionuclides present. CORIANT is a graphical user interface that gives an analyst the capability to view three-dimensional β-γ coincidence data, view automatic analysis results, view temporal trends in the data, generate reports, and override the automatic analysis if needed. A general description of the automatic analysis software and CORIANT, and the implementation of this software at the PIDC are discussed in this paper.

1. OVERVIEW

Eventually 80 radionuclide monitoring stations will be deployed as part of the Comprehensive Nuclear-Test-Ban Treaty (CTBT) verification. All of these stations are required to monitor the atmosphere for the presence particulate radionuclides. Half of these stations are also required to monitor the atmosphere for the presence of gaseous radionuclides. Two acceptable noble gas monitoring methods are defined in the CTBT text: high-resolution gamma-ray (γ) spectrometry and beta-gamma (β-γ) coincidence. Noble gas data from γ-spectrometry systems can be analyzed with the existing software that is currently being used to analyze particulate station data at the Prototype International Data Center (PIDC) and the International Data Center (IDC). Because commercially available software did not exist to analyze β-γ coincidence data, a suite of software has been developed and installed at the PIDC to analyze these data both automatically and interactively.

This paper begins with a general description of the β-γ coincidence data used in CTBT monitoring. This is followed with a detailed description of the developed software suite that includes an automatic analysis package and a stand-alone interactive tool. The automatic analysis software automatically identifies and quantifies radionuclides present in the sample. It also categorizes the sample based on the type and quantity of radionuclides present. A general description of the automated analysis software and the implementation of this software at the PIDC will be discussed here. A detailed description of the analysis algorithms is given in references 1 and 2. The interactive tool, CORIANT (COincident Radiation Interactive ANalysis Tool), is a graphical user interface that gives an analyst the capability to view and manipulate three-dimensional β-γ coincidence data, view automatic analysis results, view temporal data trends, and generate reports. CORIANT also provides the analyst with a tool to override the automatic analysis if needed. The capabilities of CORAINT will be demonstrated in this paper.

2. β-γ COINCIDENCE DATA

Currently only two prototype systems are available to measure three-dimensional □-□ coincidence data useful for CTBT monitoring. These are the Automated Radioxenon Sampler Analyzer (ARSA) designed by PNNL, USA and SAUNA designed by FOA, Sweden. A detailed description of the ARSA system can be found in reference 3. A general description of data from □-□□coincidence systems will be presented here.

The β-γ coincidence data are generated in the following manner. A large quantity of air is collected over an extended period of time (typically 8-12 hours). The four gaseous radionuclides relevant in CTBT monitoring are ^{131}Xe, ^{131m}Xe, ^{133}Xe, and ^{133m}Xe. In order to reduce background signals, predominantly

Table 1 [(a)]

ROIs in β-γ Coincidence Spectra Relevant in CTBT Monitoring

ROI	Nuclides Possible	Quantification Nuclide	Centroid γ-Energy (keV)	Centroid β-Energy (keV)
1	^{214}Pb	[(b)]	352	-
2	^{214}Pb, ^{135}Xe	^{135}Xe	250	-
3	^{214}Pb, ^{133}Xe	^{133}Xe	81	-
4	^{131m}Xe, ^{133m}Xe, ^{133}Xe, ^{135}Xe	^{133}Xe [(c)]	30	-
5	^{131m}Xe, ^{133}Xe, ^{135}Xe	^{131m}Xe	30	130
6	^{133m}Xe, ^{133}Xe, ^{135}Xe	^{133m}Xe	30	199

(a) From Ref. 1

(b) Only used for determining interference from ^{214}Pb in ROIs #2 and #3.

(c) Not currently being used for quantification purposes.

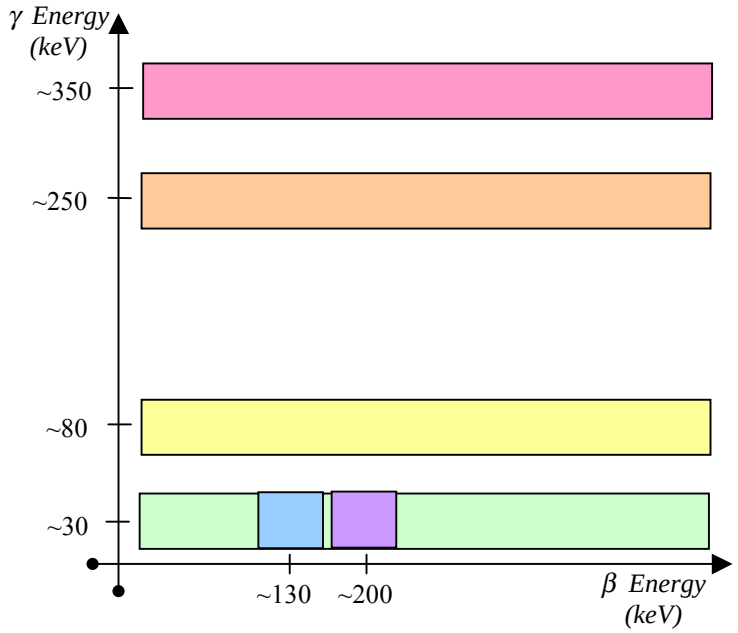


Figure 1: Required Regions of Interest with ROI Number
(not to scale – from Ref. 1)

from naturally occurring radon and its daughters, xenon gas is separated from the sampled air. The pure xenon gas is automatically placed in a scintillation chamber that can measure the energy and arrival time of electrons and photons emitted by a nucleus. The electrons can be either beta particles or conversion electrons and will be collectively called betas in this paper. Likewise, the photons can be either x rays or gamma rays and will collectively be called gammas. A three-dimensional spectrum is created by only storing the events in which an electron and a photon are detected in coincidence. The three axes of the spectrum are beta energy, gamma energy, and number of coincidence events. Each relevant decay event produces a gamma at a discrete energy and a beta over a range of energies. By summing the number of counts within each gamma and beta energy range, it is possible to calculate the activity of the radionuclides present. The gamma and beta energy range for each radionuclide is called a region-of-interest (ROI). Table 1 summarizes the important characteristics of the relevant ROIs and Figure 1 shows a graphical depiction of the ROIs.

2. AUTOMATIC ANALYSIS

3.1 Radionuclide Monitoring System Pipeline

Figure 2 shows the radionuclide monitoring system data pipeline. The four main components are *Input*,

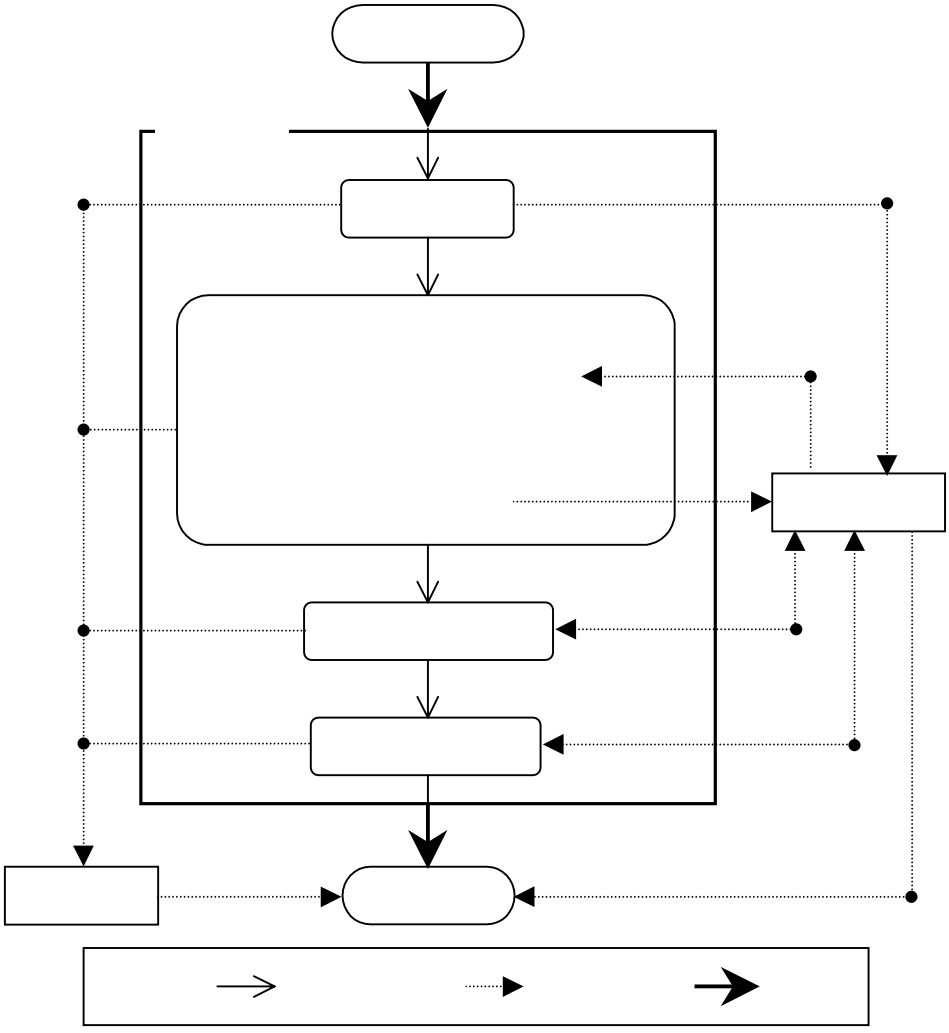


Figure 2: Radionuclide Monitoring System Data Pipeline

Analyze, *Categorize*, and *Flag*. The same pipeline is used for particulate systems, γ-spectroscopy gas systems, and β-γ coincidence gas systems except that the functionality the *Analyze* component is different. Each component of the process stores its results to an Oracle database and writes errors to an error log file. The pipeline automatically begins when a pulse height data (PHD) message is emailed into the system. The PHD message is a text file that contains the spectral data along with the sample, station, and detector parameters required in data processing. The *Input* software automatically parses the PHD file and stores the appropriate data in the database. Next, the pipeline calls the *Analyze* software. The *Analyze* software identifies which radionuclides are present in the spectrum and calculates the concentration of the identified radionuclides that are relevant in CTBT verification. The *Analyze* software is described in more detail in the following section.

After successful completion of the *Analyze* software, the pipeline next calls the *Categorize* software. This software automatically categorizes the sample based on the identified radionuclides. Each sample is assigned a category level based on whether the automatic analysis identified natural and/or man-made radionuclides at normal or abnormal levels. Only man-made radionuclides or radionuclides with a statistical filter are considered. The category levels are

- Level 1 indicates no radionuclides identified or only natural radionuclides identified,
- Level 2 indicates abnormal levels of natural radionuclides identified (not used for noble gas data),
- Level 3 indicates normal levels of man-made radionuclides identified,
- Level 4 indicates abnormal levels of a single man-made radionuclide identified, and
- Level 5 indicates abnormal levels of multiple man-made radionuclides identified.

In the final step of the *Categorize* software, the categorization results are saved to the database.

The pipeline next calls the *Flag* software. The *Flag* software determines whether the sample parameters, the *Analyze* results, and the *Categorize* results are within normal specifications. The *Flag* results are saved to the database and the program control returns to the pipeline. Before termination, the pipeline sends various emails to any user subscribing to that type of data product. The content of these emails includes the results, the error messages, and the warring messages generated in the spectral data processing. A user can view the automatic analysis results by using interactive tools such as CORIANT, subscribing to the emails, viewing the log file, or by directly accessing the database.

3.2 Analyze Software

The *Analyze* software begins by extracting three-dimensional β-γ coincidence data and the associated processing and sample parameters from the database. The spectral data are stored in channels whereas the ROI boundary definitions are stored in energy units. The ROI boundaries are converted to channels by calibrating the gamma axis and the beta axis (see Figure 1) using calibration data contained in the PHD file.

The gross counts are calculated by summing the counts per channel within the ROI boundaries. Because the calculated boundary channels are real numbers, not integers, a boundary typically falls within the middle of a channel. Hence, the boundary channel counts are weighted by the percentage of the boundary channel located within the ROI. The net counts are calculated by correcting the gross counts for the affects of Compton continuum background, gas cell background (i.e., "memory effect"), detector background, and interference from other nuclides.

The Compton continuum counts are background counts that exist in the absence of the associated radionuclide of the ROI. The Compton background is only a concern along the gamma axis and not along the beta axis. Two Compton regions are defined per ROI: one at higher gamma channels (the upper region) and one at lower gamma channels (the lower region).

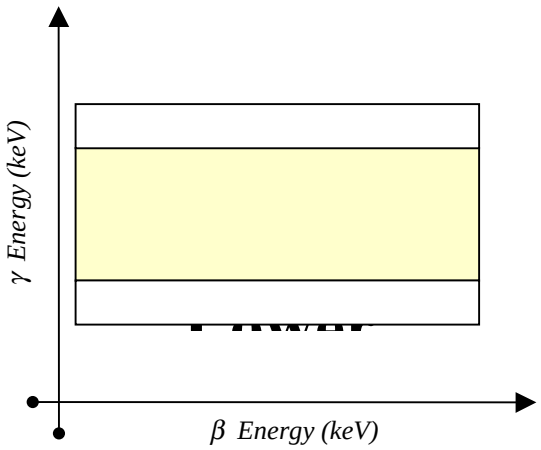


Figure 3: Compton and Gross Regions

Figure 3 shows an example of the upper and lower Compton regions. The boundaries of the upper Compton region are the ROI beta boundaries, the upper ROI gamma boundary, and the upper ROI gamma boundary plus three channels. Likewise, the boundaries of the lower Compton region are the ROI beta boundaries, the lower ROI gamma boundary, and the lower ROI gamma boundary minus three channels. Using the Compton region boundaries, the counts in each region are calculated in the same manner as the gross counts. The Compton counts are then calculated by adding the counts from the upper and lower Compton regions and multiplying the resulting sum by the ratio of the ROI area to Compton area. The ROI area is defined as the number of channels within the ROI boundaries and the Compton area is defined as the number of channels within the upper and lower Compton boundaries.

The gas cell background is any signal that would be present in a purged gas cell after a sample has been counted. It is often called the memory effect because is caused by the adsorption of radionuclides from the previous sample on the detector cell wall. The gas background counts are calculated by multiplying the net counts of the most recent prior (MRP) gas background sample by a decay factor. The decay factor accounts for differences in live time between the two samples and for the decay of the radionuclide associated with the ROI between acquisitions. A gas background sample is measured prior to every sample measurement.

The detector background is any signal that would be present in a purged gas cell with no memory effect. The detector background counts are calculated by multiplying the net counts of the MRP detector background sample by the ratio of the live time of the current sample to the live time of the MRP detector background sample. A detector background sample is measured only occasionally with relatively long acquisition times and with a new gas cell or one that has not been used in a sufficient amount of time for the memory effect to be significant.

A decaying radionuclide may produce counts in multiple ROIs (see Table 1). A ROI, by definition, can only be associated with one radionuclide. The current ROI to radionuclide association is shown in Table 1. The counts in a ROI not from its associated radionuclide are called the interference counts. The interference counts are calculated by multiplying the counts of the interfering radionuclide's associated ROI by the interference ratio. The interference ratio (from the PHD file) is equal to the ratio of counts in the current ROI to counts in the associated ROI of the interfering radionuclide. The interference ratio is a calibration parameter that is determined experimentally before the current measurement and depends on the ROI boundaries.

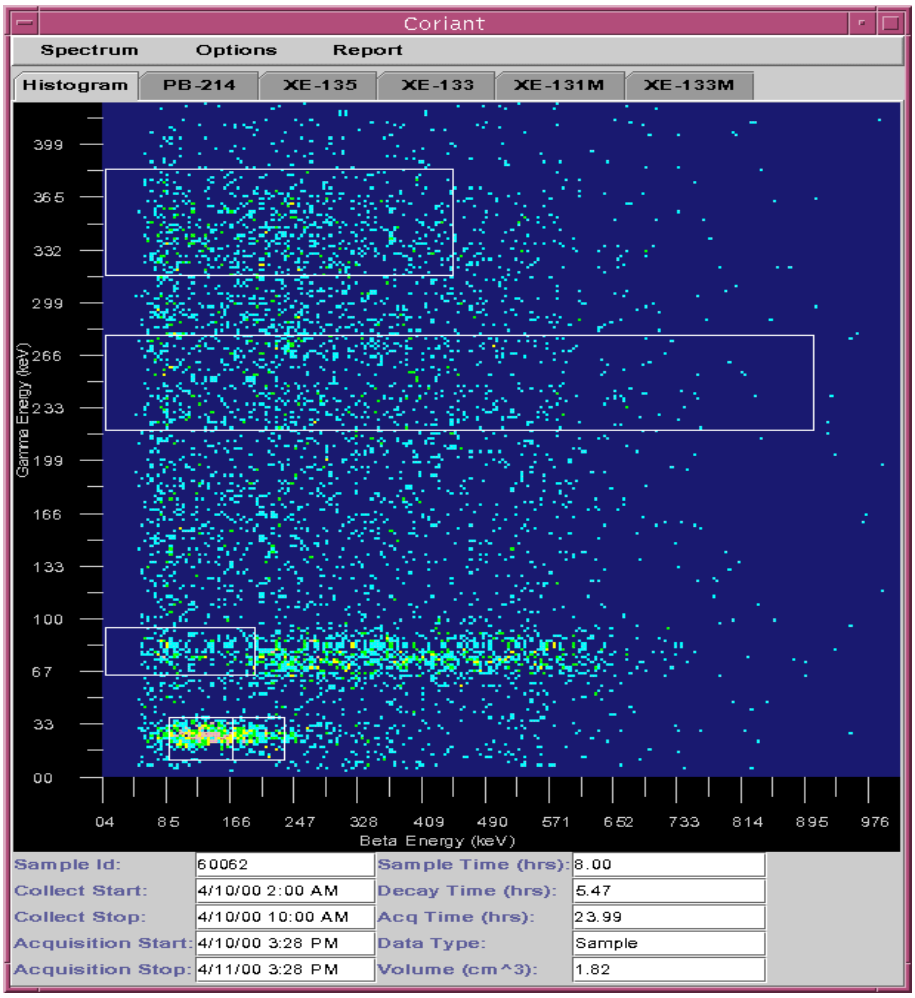
The critical level (Lc) is calculated for each ROI with an associated radionuclide as described in references 1 and 2. A radionuclide is declared identified if the net counts in its associated ROI are greater than its Lc value. The concentration is calculated as described in reference 1 for each radioxenon that was identified. The minimum detectable concentration (MDC) is calculated for each radioxenon, regardless of whether it was identified, as described in reference 2. All analysis results are then saved to the database.

3. INTERACTIVE ANALYSIS

CORIANT is the new interactive review tool for three-dimensional β-γ coincidence data used in CTBT monitoring. CORIANT graphically displays the β-γ coincidence data and allows an analyst to verify the automatic analysis results, add comments to samples, view temporal trends in the data, and generate reports. The main CORIANT window displays six tabbed windows, see Figure 4. The first tab is the Histogram window, which shows the sample data currently under review; the other five tab windows are called ROI tabs. Each ROI tab shows detailed information about the possible nuclides found in the sample. The five ROI tabs are ^{214}Pb, ^{135}Xe, ^{133}Xe, ^{133m}Xe, and ^{131m}Xe. In addition to the tabbed windows, there are multiple pop-up windows accessible through the pull down menu. The tabbed and pop-up windows are described separately below.

4.1 Histogram Window

The Histogram window, see Figure 4, shows a color-coded three-dimensional (third dimension in color) representation of the β-γ coincidence data. Each dot on the display represents a β-γ coincidence event



detected at that particular beta and gamma energy. The dot color indicates the number of events detected (counts) at that beta/gamma channel. ROI boxes can be overlaid on the histogram to show the exact locations of the five ROIs used for nuclide identification and quantification. The ROI overlays help an analyst determine if the energy/channel calibration equations are correct. At the bottom of the Histogram window, a text area displays important sample parameters including the sample id, decay time, collection start time, collection stop time, acquisition time, xenon gas volume.

5.2 ROI Tab Windows

Each ROI tab window represents one of the nuclides that can be found in β-γ coincidence data: ^{214}Pb, ^{135}Xe, ^{133}Xe, ^{133m}Xe, and ^{131m}Xe. Figure 5 shows the ROI tab window for ^{131m}Xe. The four sub-windows on each ROI tab window are

- Beta-Gated Gamma graph – shows a plot of the beta-gated gamma spectrum over that ROI,
- Gamma-Gated Beta graph – shows a plot of the gamma-gated beta spectrum over that ROI,
- Count summary pie chart – graphically represents how the gross counts are distributed between interference, memory (gas background), Compton, (detector) background, and net counts, and
- Information summary – displays the nuclide half-life, coincidence event abundance, coincidence event detection efficiency, gamma energy range, beta energy range, and if the nuclide was identified.

5.3 ROI Table Window

The ROI Table window, see Figure 6, is a tabular display that has one row for each of six ROIs shown in Table 1. This window is accessible through the pull-down menu. ROI 4 is not currently being used for nuclide identification or quantification; however, it may be used in future versions of the *Analyze* software.

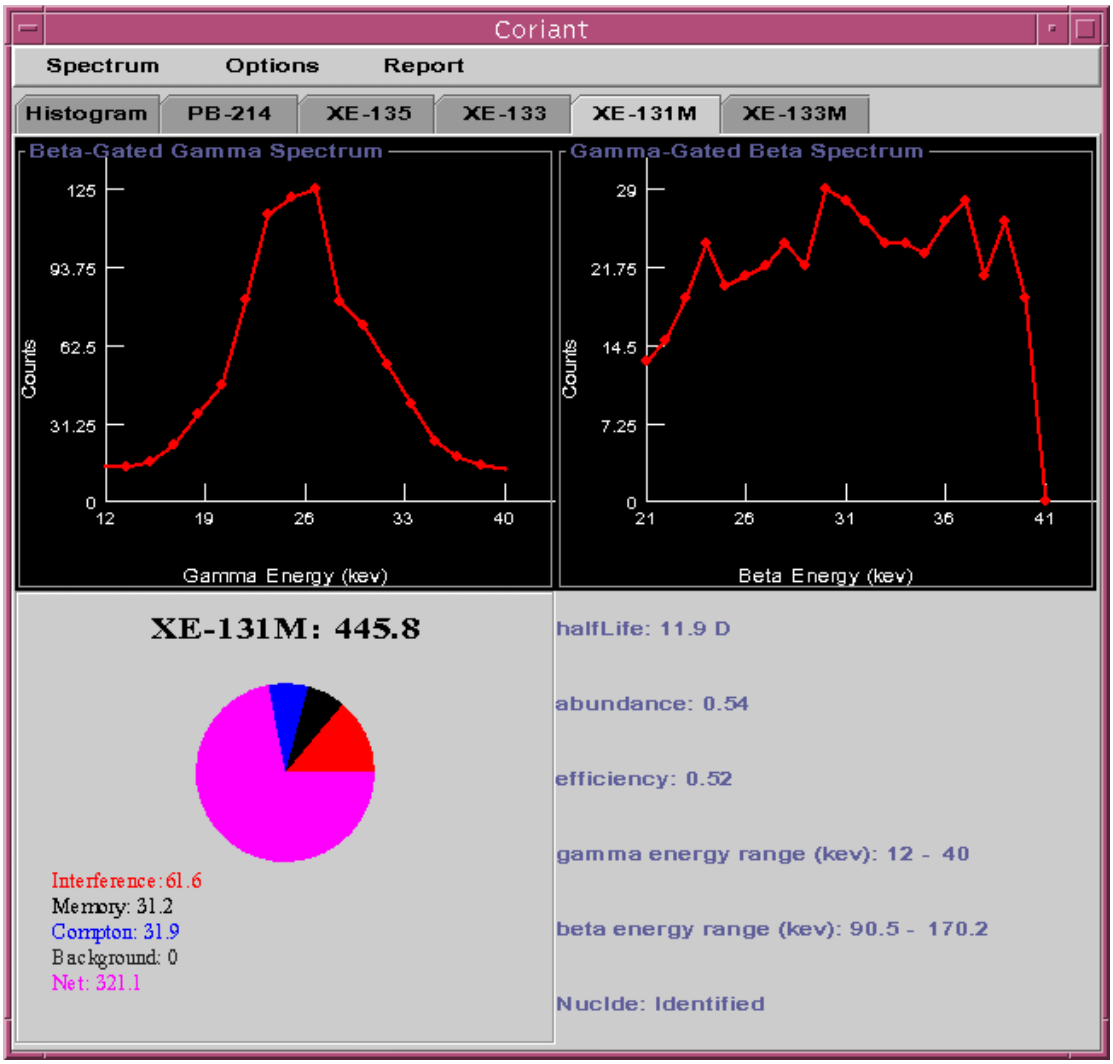


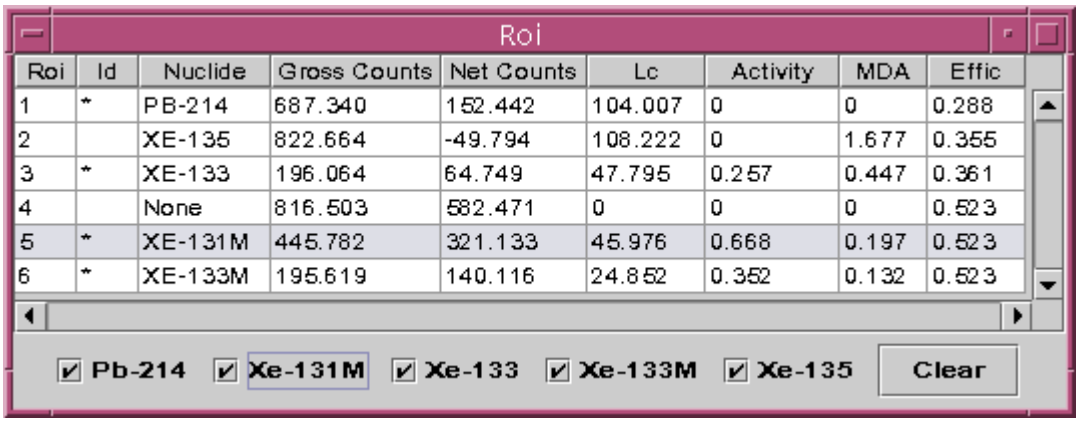
Figure 5: CORIANT Window Displaying the ^{131m}Xe Tab

The columns in the table include ROI number, nuclide identification flag, nuclide name, gross counts, net counts, Lc, activity, MDC, and ROI β-γ coincidence efficiency. Right-clicking the mouse on a row in the ROI window displays a pop-up menu. This menu allows an analyst to add a comment for the selected ROI, add a general comment for the sample, or plot the activity or MDC of that nuclide over the last 30 days, see Figure 7. Along the bottom row of this window are five check boxes that toggle the ROI box displays on the Histogram window.

4.4 Other Pop-up Windows

There are multiple pop-up windows accessible through the pull-down menu bar. A description of several of these windows is given below.

- *Assignment Window* is a tabular display that allows analysts to view the samples in the sample assignment queue that require review.
- *Beta Graph Window* shows a plot of the gamma-gated beta spectrum over the entire beta energy range.
- *Comment Window* displays all comments added to the current sample. These comments are



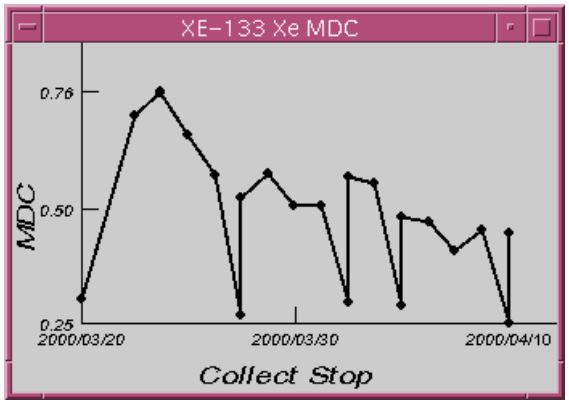


Figure 7: Historic MDC Values for ^{133}Xe

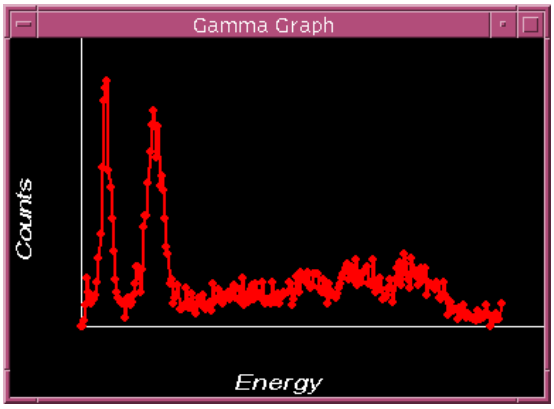


Figure 8: CORIANT Gamma Graph Window

included in the report that is distributed when the sample is released.

- *Count Summary Window* displays the "Count summary pie chart" described in Section 5.2 for each ROI.
- *ECR Window* shows the energy to channel calibration for both the gamma and beta axes.
- *Gamma Graph Window* shows a plot of the beta-gated gamma spectrum over the entire gamma energy range, see Figure 8.
- *Library Window* is a tabular display that has one row for each of the five radionuclides of interest. The table columns are the name, coincidence event abundance, and half-life of each nuclide.
- *Release Window* allows an analyst to mark a sample "released" or "viewed." A sample marked "released" indicates that the analyst agreed with the results of final analysis. The final analysis includes the automatic analysis plus any changes made by the analyst during the interactive review. A sample marked as "viewed" indicates the analyst reviewed the sample but that in the analyst's opinion, the final analysis results were flawed.
- *Station/Detector Window* is a report that displays the name, location, station type, and detector type.

SUMMARY

A suite of software has been developed at the PIDC to assist in the analysis of noble gas monitoring data for the CTBT. There are two acceptable noble gas monitoring methods for CTBT verification purposes: high-resolution γ-spectrometry and β-γ coincidence. Data from γ-spectrometry systems can be analyzed with the existing software at the PIDC and the IDC. Data from β-γ coincidence systems can be analyzed

with this newly developed software. This software is currently installed and is used in daily operations at the PIDC and is scheduled to be installed at the IDC in fall 2000.

The software suite consists of an automatic analysis package and a stand-alone interactive tool. The automatic analysis software automatically identifies and quantifies radionuclides present in the sample. It also categorizes the sample based on the type and quantity of radionuclides present. The interactive tool, CORIANT, is a graphical user interface that gives an analyst the capability to view three-dimensional β-γ coincidence data, view automatic analysis results, view temporal trends in the data, generate reports, and override the automatic analysis if needed. A general description of the automatic analysis software and CORIANT, and the implementation of this software at the PIDC were discussed in this paper.

Key Words: beta-gamma coincidence, radionuclide monitoring, noble gas, CTBT, PIDC, IDC

REFERENCES

[1] Biegalski, K.M.F. "Automatic Analysis Algorithm for Radionuclide Pulse Height Data from Beta-Gamma Coincidence Systems." MARC V Conference. Submitted for publication in the Journal of Radioanalytical and Nuclear Chemistry, April 2000.

[2] Biegalski, K.M.F. and Biegalski, S. "Determining Minimum Detectable Concentrations for Noble Gas Detectors Utilizing Beta-Gamma Coincidence Systems." MARC V Conference. Submitted for publication in the Journal of Radioanalytical and Nuclear Chemistry, April 2000.

[3] Reeder, P.L., Bowyer, T.W., and Perkins, R.W. "Analysis of Beta-Gamma Spectra for the PNNL ARSA and Estimate of Minimum Detectable Activities for (^{131m}Xe + ^{133m}Xe), ^{133g}Xe and ^{135g}Xe." PNNL-11784

TESTING FOR OUTLIERS IN RADIONUCLIDE DATA

Barbara Zhao, Wayne A. Woodward, H.L. Gray, and Mark D. Fisk
Southern Methodist University

Sponsored by U.S. Department of Defense
Defense Threat Reduction Agency

DTRA01-99-C-0018

ABSTRACT

The problem of monitoring atmospheric radionuclides over time is investigated. Such monitoring is desirable for both natural and anthropogenic radionuclides. The statistical problem is one of testing for a time series outlier, and the problem is complicated by the fact that often several observations may be missing. In fact it may be the case that several missing observations may occur immediately prior to a data value that is to be tested as an outlier. Evans (1996) proposes an exponentially weighted moving average (EWMA) approach for detecting these outliers. The EWMA approach is one that is quite popular in practice, but it is restricted to some extent by the fact that it is based on the assumption that the autoregressive integrated moving average model, ARIMA(0,1,1), is a good fit to the data. Evans presents simulation results based on simulated radionuclide data obtained from a model that he fit to Kuwait Be7 data consisting of a sinusoidal component with long period plus an autoregressive component. One problem with Evans' approach is that false alarm rates tend to be high when the data value to be tested as an outlier is preceded by a string of missing observations. In this paper we describe several alternative approaches for outlier detection, and we compare these with the Evans method using a simulation study. In this study, outlier detection capabilities are compared in the case in which no data are missing immediately prior to the data value to be tested as an outlier as well as in the more difficult case in which several data values are missing immediately prior to this value. Our results indicate that an autoregressive-based procedure suggested here has much better control over the false alarm rates than does the Evans procedure, and it has detection capability that is comparable to and sometimes better than that obtained by the Evans approach.

OBJECTIVE

The objective of this research is to investigate the problem of testing for outliers in radionuclide data. Such testing is used for detecting leakage from underground nuclear explosions, and it is also useful for equipment monitoring using natural radionuclides. In particular we develop techniques for testing for outliers in data structures typical of those encountered when monitoring natural radionuclide concentrations. Specifically, we assume that such data are collected at equal time increments but will sometimes involve missing observations. We compare our results with those obtained using the method of Evans (1996).

RESEARCH ACCOMPLISHED

Introduction

We have investigated outlier detection in time series data with the specific application being that of monitoring natural atmospheric radionuclide concentrations. Since these radionuclide concentrations are monitored regularly over time, the problem is that of detecting an outlier in a time series. Consequently, any technique for outlier detection must account for the correlation structure in the data. The radionuclide data sets often have several missing observations, sometimes resulting in contiguous strings of missing observations. Our goal is to develop outlier detection procedures capable of providing acceptable results in the presence of these missing observations. It will also be desirable that those involved in the actual monitoring will not be required to perform the sometimes difficult task of time series modeling as part of the monitoring procedure. In the following we discuss strategies for outlier detection and we compare results using our methods with those obtained using the EWMA technique of Evans (1996) via a simulation study.

Detecting Jumps

Obviously, an outlier should be detected at time *k* whenever the radionuclide observation at time *k* is "unusually large". Outlier detection techniques differ on the basis of how they define "unusually large". Letting y_k denote the radionuclide concentration detected at time *k*, then an outlier should be detected whenever the jump, $y_k - y_{k-1}$, is sufficiently large. If sufficient historical data are available, then a simple outlier detection procedure could be based on the empirical distribution of these "jumps". That is, we can empirically determine the values these jumps typically assume when no outlier is present in historical data. Then for a given level of significance, the 100α% upper critical value of these historical jumps can be estimated and compared with an observed "jump."

A problem occurs whenever it is desired to test whether y_k is an outlier when one or more values directly prior to time *k* are missing. In this case we can again obtain an appropriate empirical distribution based on historical data. For example, if an observation is to be tested as an outlier and the two preceding values are missing, then the relevant question concerns what type of "jump" typically occurs between the observation at time $k-3$ (i.e. the most recently observed data value in this case) and the observation at time *k*. Again, based on historical data we can obtain the 100α% upper critical value on the 3-step ahead differences. Obviously, the above procedure can be used in general for *k* step-ahead differences. In this report, the outlier detection technique based on these historical jump distributions will be called the "jump test".

AR-Based Prediction Method

Another common method of measuring whether an observation, y_k, is unusual is to compare it with the value of the time series at time *k* that is predicted to occur based on the other data. See Fox (1972) and Ljung (1989, 1993). If the observed value is sufficiently higher than the predicted value, then it is considered to be an outlier. In our implementation, predictions will be based on an autoregressive fit to the data. More generally, a time series is said to be an autoregressive moving average process of orders *p* and *q* , denoted ARMA(*p*, *q*), if

$$y_t = \varphi_1 y_{t-1} + \cdots + \varphi_p y_{t-p} + a_t - \theta_1 a_{t-1} - \cdots - \theta_q a_{t-q}$$

where a_t is a zero-mean white noise process with constant variance σ_a^2. Suppose that *m* successive observations $Y_{(T,m)} = (y_{T+1},...,y_{T+m-1})'$ are missing from a time series $Y = (y_1, y_2,..., y_n)'$. Consider the vector $Y_0 = (y_1,..., y_{T-1}, 0,...,0, y_{T+m},..., y_n)'$ that consists of all the actual observations and with zeros placed in the missing positions. The expression

$$Y = Y_0 + XY_{(T,m)}, \tag{1}$$

where *X* is an $n \times m$ matrix of 1s and 0s, leads to a formula for estimating the missing values, i.e.,

$$\hat{Y}_{(T,m)} = -(X'\Sigma^{-1}X)^{-1}X'\Sigma^{-1}Y_0 \tag{2}$$

where Σ is the covariance matrix associated with $(y_1, y_2,..., y_n)'$. Formula (2) also holds in the situation where the missing observations are not successive, say missing at $y_{t_1}, y_{t_2},..., y_{t_m}$. At time *k*, the difference between observed value y_K and its interpolated value $\hat{y}_k$, which is obtained from (2), can be measured by

$$\frac{(y_k - \hat{y}_k)'\Sigma_{kk}^{-1}(y_k - \hat{y}_k)}{\hat{\sigma}^2}, \tag{3}$$

which has an $F(1, n-1)$ distribution if y_k is not an outlier, where Σ^{-1}_{kk} is the kth diagonal element of Σ^{-1}, and $\hat{\sigma}^2$ is the estimate of the variance of the noise σ^2 in a time series model. Note that Ljung and Box (1979) give a formula for calculating Σ^{-1} based on known parameters in an *ARMA(p,q)* model. In our implementation we follow the suggestion of Ljung (1993), and use the estimates of the auotoregressive parameters to obtain the estimate of Σ. In any autoregressive analysis, model selection is often a key component. In the simulation results shown here, we use an AR(5) to fit the observed series. This allows for flexibility in the autoregressive model chosen and seems to work well. However, further research is needed on the impact of more careful model selection.

Model-Free Prediction Method

In order to avoid any distributional assumptions, we have considered a modification of Ljung's method that is applicable when a "large" number (N) of historical observations are available of which a% are randomly missing. The (current) data set on which an outlier is to be tested is of length n, and we assume that the observation to be tested as an outlier is preceded by m missing observations.

The method has three steps:

Step 1. Use an iterative algorithm to estimate the missing observations. At each step of the iteration, the missing observations are estimated using the formula in (2). Note also that at each step we estimate Σ directly from the definition and not based on a fitted model.

Step 2. Suppose we want to predict y_k and that some values proceeding y_k are missing. Using (2) we obtain $\hat{y}_k$ and find the difference $| y_k - \hat{y}_k |$. Using the historical data, we obtain an empirical distribution for $| y_k - \hat{y}_k |$ based upon the missing data structure present in the current realization.

Step 3. If the observed difference $| y_k - \hat{y}_k |$ is larger than the upper αth percentile of the empirical distribution obtained in Step 2, then y_k is found to be an outlier.

Evans' Method

Evans (1996) considered the problem of testing for outliers in the setting considered in this paper. He proposed a technique that is similar to the prediction-based methods presented here, but in this case the prediction is based on an exponentially-weighted moving average (EWMA) model. EWMA prediction is based on an ARIMA(0,1,1) fit to the data. A time series is said to follow an ARIMA(0,1,1) model if $y_t = y_{t-1} + a_t - \theta_1 a_{t-1}$. Evans' method is based on the computation of two prediction-interval filters that measure the average (location or level) and the variability of a process at time t. The extent to which the EWMA procedure provides satisfactory predictions depends to some extent on how well an ARIMA(0,1,1) model represents a reasonable fit to the data. However, this model is fairly restrictive and does not well represent many types of time series behavior. Evans reported some simulation evidence concerning the performance of his proposed outlier detector.

Simulation Procedure

We have used a simulation study to compare these four outlier detection methods. Simulations are made to compare the three methods for different time series models and different missing data structures. The details are as follows:

(a) We generate N observations $\{ y_k, t = 1,2,\cdots, N \}$. In the simulations reported here, we used N = 200. In this study we consider several different models for the data:

(i) AR(1) with $\varphi_1 = .6$

(II) AR(1) with $\varphi_1 = .6$ plus a sinusoid, f_t, of period six months where

$f_t = 11\sin(\frac{2\pi t}{180} + U)$ and U is a random uniform between -2π and 2π.

Note: this is Evans' simulation model based on Kuwait Be7 data.

(iii) AR(1) with $\varphi_1 = .9$

(iv) AR(1) with $\varphi_1 = .9$ + sin term as in (ii)

(v) AR(2) with $\varphi_1 = 1.41$ and $\varphi_2 = -.5$.

(vi) AR(4) with $\varphi_1 = 1.41, \varphi_2 = -1, \varphi_3 = .705,$ and $\varphi_4 = -.25$.

In all cases, we use $\sigma_a^2 = 81$. In Figure 1 we show typical realizations of length 200 from each of these models.

(b) The last observation, i.e. the 200th generated observation, is tested as a potential outlier. In our simulations, we consider the case in which the number of missing values immediately preceding the outlier to be tested is m = 0, 1, 3, 6, or 12. In the AR prediction approach the historical values are taken to be all observed data up to but not including the outlier. That is, the number of historical data values is $N - m - 1$. These historical observations are used for model identification and estimation of model parameters. In the case of the model-free and jump procedures, the historical data are taken to be the first $N - m - 11$ data values. In these cases, the historical data are used for obtaining empirical distributions of distributions of interest. In the simulations reported here, the historical data contain no missing values. However, our simulation code allows for missing data in the historical series. Results shown here are similar to those obtained when the historical data contained a moderate amount of missing data, i.e. 10% - 20% missing. If missing data do occur in the historical series, these missing values are "filled in" using the procedure outlined in Step 1 of the discussion of the model-free prediction method. Analysis then proceeds as in the no missing data case.

(c) Critical values for the model-free prediction method and for the jump method are obtained for the significance level of interest. In these simulations we used α = 0.05.

(d) We test an augmented version, $x_{200}^{(0)}$, of the last data value as an outlier. Specifically, we consider $x_{200}^{(0)} = x_{200} + h\sigma_x$ where σ_x denotes the estimated standard deviation of the data and where h = 0, 1, 2, 3, and 4.

Simulation Results

In Tables 1-6 we give simulation results. In each case, 1000 realizations of length N = 200 are generated and the tabled value is the proportion of times out of the 1000 replications that $x_{200}^{(0)}$ is detected as an outlier. It should be noted that for $h > 0$ this provides information concerning the detection capability of the test, and when h = 0 the proportion tabled provides for a check on the false alarm rate of the testing procedure. In the tables it can be seen that the AR-based prediction methods tend to outperform the EWMA approach recommended by Evans (1996). One serious problem with the Evans method is the fact that the false alarm rate rises above the .05 level whenever several values are missing prior to a potential outlier. Even with the higher false alarm rate, the Evans method tended to have lower power than the AR-based method for values of h greater than zero. It should be noted that the model-free method has performance similar to that of the AR-based method, although our more extensive simulation experience has shown that modeling of the data is probably preferable. It should be noted that the jump method maintains the desired false alarm rates but has a tendency to have lower detection probability than the more sophisticated methods.

Conclusions

Results shown here indicate that the AR-based prediction method is superior to the Evans approach for outlier detection in the setting considered here, particularly when missing data values occur immediately prior to the data value to be tested as an outlier. Specifically, methods discussed here are appropriate for monitoring radionuclide data which is collected at regular time intervals and for which an actual reading is obtained at most of the collection times. In the case of anthropogenic radionuclides where it is not uncommon for the atmospheric concentrations to be below a minimum detectable level the majority of the time, other outlier detection techniques must be developed.

Key Words: radionuclide monitoring, outlier testing, time series, autocorrelation

References

Evans, William C. (1996). Automated Categorization of Airborne Radioactivity Measurements for CTBT Monitoring. *Pacific-Sierra Research Corporation Technical Note 1091*, June 1996.

Fox, A.J. (1972). Outliers in time series. *J. R. Statist. Soc*. **B 34**, 350-363.

Ljung, G.M.(1989). A note on the estimation of missing values on time series. *Commun*. *Statist.-Simula.***18**, 459-465.

Ljung, G.M.(1993). On outlier detection in time series. *J. R. Statist. Soc*. **B 55**, 559-567

Ljung, G.M. and Box, G.E.P. (1979). The likelihood function of stationary autoregressive moving average models. *Biometrika* **66**, 265-270.

Table 1: Outlier Detection Results using the Six Models Listed in Simulation Section

		(i)					(ii)			
	h	Evans	AR	M-F	Jump	h	Evans	AR	M-F	Jump
	0.0	0.044	0.068	0.070	0.048	0.0	0.045	0.062	0.068	0.061
No	1.0	0.158	0.217	0.237	0.184	1.0	0.243	0.306	0.313	0.260
missing	2.0	0.536	0.679	0.690	0.600	2.0	0.691	0.832	0.837	0.759
value	3.0	0.860	0.954	0.954	0.903	3.0	0.945	0.989	0.991	0.978
	4.0	0.978	0.999	0.999	0.990	4.0	0.996	1.000	1.000	0.998
	0.0	0.046	0.054	0.062	0.046	0.0	0.040	0.055	0.064	0.061
One	1.0	0.173	0.196	0.211	0.152	1.0	0.250	0.259	0.264	0.192
missing	2.0	0.537	0.570	0.586	0.419	2.0	0.706	0.685	0.702	0.563
value	3.0	0.837	0.886	0.889	0.745	3.0	0.956	0.954	0.953	0.886
	4.0	0.972	0.992	0.990	0.932	4.0	0.997	0.997	0.997	0.990
	0.0	0.092	0.076	0.085	0.060	0.0	0.100	0.054	0.068	0.042
Three	1.0	0.197	0.176	0.198	0.110	1.0	0.267	0.197	0.218	0.153
missing	2.0	0.505	0.516	0.536	0.328	2.0	0.650	0.584	0.623	0.417
values	3.0	0.803	0.832	0.839	0.603	3.0	0.923	0.907	0.917	0.761
	4.0	0.945	0.963	0.969	0.844	4.0	0.993	0.995	0.995	0.955
	0.0	0.112	0.052	0.061	0.050	0.0	0.112	0.038	0.057	0.049
Six	1.0	0.240	0.186	0.196	0.115	1.0	0.264	0.157	0.177	0.135
missing	2.0	0.528	0.519	0.531	0.315	2.0	0.655	0.548	0.583	0.406
values	3.0	0.812	0.854	0.851	0.559	3.0	0.918	0.890	0.910	0.745
	4.0	0.949	0.978	0.978	0.800	4.0	0.990	0.993	0.994	0.929
	0.0	0.125	0.057	0.076	0.053	0.0	0.130	0.047	0.069	0.050
Twelve	1.0	0.246	0.169	0.195	0.124	1.0	0.299	0.152	0.204	0.153
missing	2.0	0.525	0.484	0.514	0.298	2.0	0.638	0.520	0.574	0.386
values	3.0	0.805	0.831	0.845	0.560	3.0	0.903	0.853	0.888	0.699
	4.0	0.950	0.976	0.978	0.802	4.0	0.979	0.981	0.988	0.904

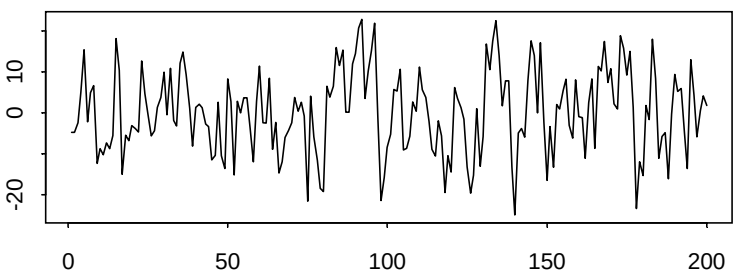
Table 1 Continued

		(iii)					(iv)		
	h	Evans AR	M-F	Jump	h	Evans AR	M-F	Jump	
	0.0	0.042	0.069	0.081	0.061	0.0	0.048	0.052	0.069	0.045
No	1.0	0.330	0.545	0.552	0.523	1.0	0.378	0.648	0.641	0.599
missing	2.0	0.808	0.979	0.979	0.974	2.0	0.865	0.987	0.984	0.985
value	3.0	0.969	1.000	1.000	1.000	3.0	0.982	1.000	1.000	1.000
	4.0	0.997	1.000	1.000	1.000	4.0	0.998	1.000	1.000	1.000
	0.0	0.043	0.056	0.066	0.049	0.0	0.049	0.057	0.076	0.055
One	1.0	0.347	0.399	0.422	0.338	1.0	0.386	0.419	0.436	0.361
missing	2.0	0.835	0.889	0.890	0.851	2.0	0.846	0.887	0.892	0.867
value	3.0	0.972	0.995	0.990	0.989	3.0	0.982	0.997	0.995	0.993
	4.0	0.998	1.000	1.000	1.000	4.0	1.000	1.000	1.000	1.000
	0.0	0.146	0.089	0.101	0.076	0.0	0.138	0.054	0.074	0.051
Three	1.0	0.362	0.267	0.281	0.214	1.0	0.382	0.264	0.292	0.222
missing	2.0	0.752	0.698	0.707	0.594	2.0	0.783	0.720	0.734	0.655
values	3.0	0.938	0.933	0.938	0.882	3.0	0.959	0.958	0.958	0.917
	4.0	0.992	0.996	0.996	0.982	4.0	0.999	0.994	0.993	0.988
	0.0	0.222	0.074	0.089	0.055	0.0	0.223	0.077	0.085	0.060
Six	1.0	0.399	0.211	0.234	0.154	1.0	0.424	0.250	0.252	0.187
missing	2.0	0.732	0.611	0.609	0.466	2.0	0.752	0.619	0.626	0.501
values	3.0	0.932	0.893	0.887	0.781	3.0	0.937	0.910	0.904	0.801
	4.0	0.984	0.981	0.979	0.951	4.0	0.992	0.982	0.981	0.947
	0.0	0.294	0.084	0.114	0.072	0.0	0.314	0.085	0.107	0.068
Twelve	1.0	0.428	0.218	0.240	0.140	1.0	0.445	0.218	0.234	0.159
missing	2.0	0.715	0.534	0.549	0.348	2.0	0.716	0.527	0.539	0.380
values	3.0	0.908	0.844	0.847	0.643	3.0	0.911	0.849	0.857	0.673
	4.0	0.975	0.969	0.975	0.865	4.0	0.979	0.967	0.968	0.868

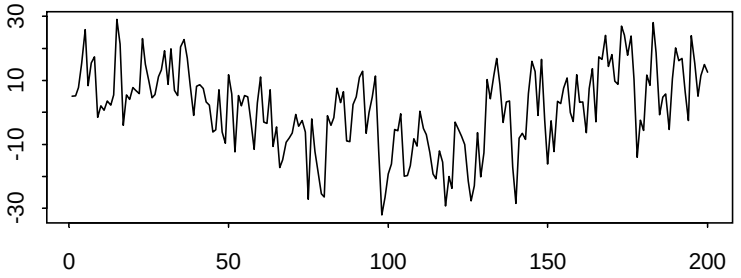
Table 1 Continued

	h	Evans	(v) AR	M-F	Jump	h	Evans	(vi) AR	M-F	Jump
	0.0	0.035	0.066	0.072	0.051	0.0	0.048	0.068	0.069	0.051
No	1.0	0.356	0.875	0.878	0.761	1.0	0.280	0.659	0.665	0.469
missing	2.0	0.784	0.999	0.999	0.997	2.0	0.722	0.989	0.989	0.957
value	3.0	0.958	1.000	1.000	1.000	3.0	0.948	1.000	1.000	1.000
	4.0	0.995	1.000	1.000	1.000	4.0	0.994	1.000	1.000	1.000
	0.0	0.035	0.070	0.080	0.052	0.0	0.048	0.070	0.078	0.055
One	1.0	0.354	0.471	0.487	0.379	1.0	0.279	0.306	0.312	0.241
missing	2.0	0.785	0.949	0.954	0.895	2.0	0.721	0.779	0.788	0.659
value	3.0	0.957	0.997	0.997	0.992	3.0	0.949	0.975	0.976	0.946
	4.0	0.995	1.000	1.000	1.000	4.0	0.994	0.998	0.997	0.995
	0.0	0.175	0.065	0.077	0.053	0.0	0.142	0.065	0.078	0.052
Three	1.0	0.388	0.239	0.253	0.195	1.0	0.335	0.211	0.218	0.158
missing	2.0	0.721	0.694	0.694	0.537	2.0	0.668	0.611	0.627	0.477
values	3.0	0.930	0.950	0.953	0.863	3.0	0.910	0.917	0.925	0.821
	4.0	0.988	0.999	0.998	0.982	4.0	0.991	0.991	0.992	0.969
	0.0	0.267	0.060	0.076	0.071	0.0	0.237	0.069	0.083	0.075
Six	1.0	0.428	0.202	0.208	0.159	1.0	0.371	0.199	0.211	0.145
missing	2.0	0.695	0.551	0.568	0.388	2.0	0.654	0.535	0.553	0.384
values	3.0	0.891	0.867	0.867	0.685	3.0	0.868	0.848	0.855	0.665
	4.0	0.971	0.979	0.980	0.890	4.0	0.973	0.977	0.975	0.874
	0.0	0.287	0.064	0.088	0.062	0.0	0.249	0.072	0.095	0.060
Twelve	1.0	0.428	0.180	0.212	0.129	1.0	0.384	0.178	0.207	0.114
missing	2.0	0.682	0.511	0.541	0.298	2.0	0.651	0.509	0.544	0.308
values	3.0	0.875	0.833	0.847	0.566	3.0	0.856	0.833	0.846	0.561
	4.0	0.958	0.973	0.979	0.799	4.0	0.958	0.971	0.975	0.789

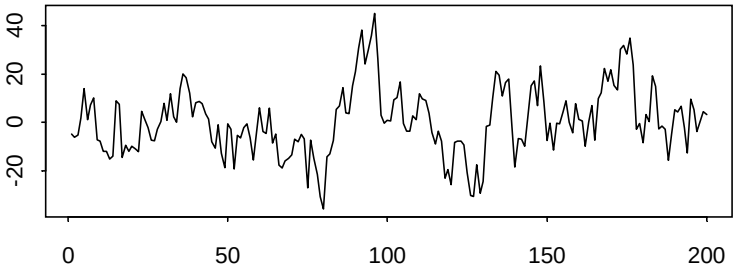
Figure 1. Typical Time Series Realizations for Simulation Models



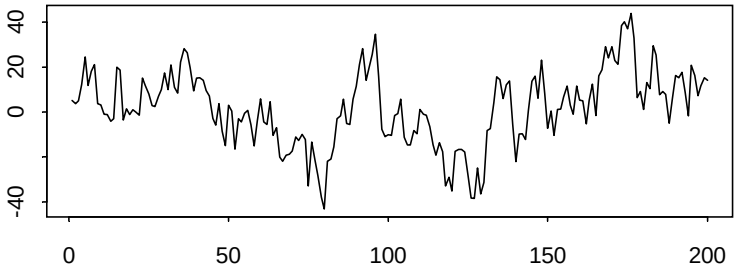
(i)



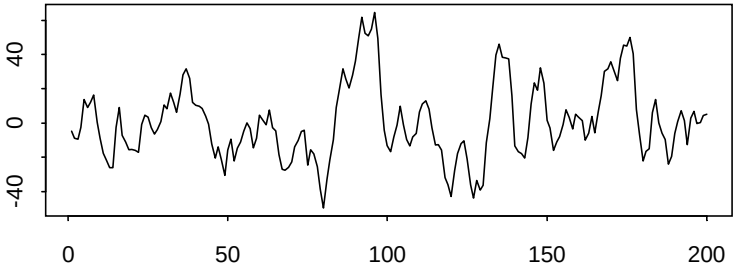
(ii)



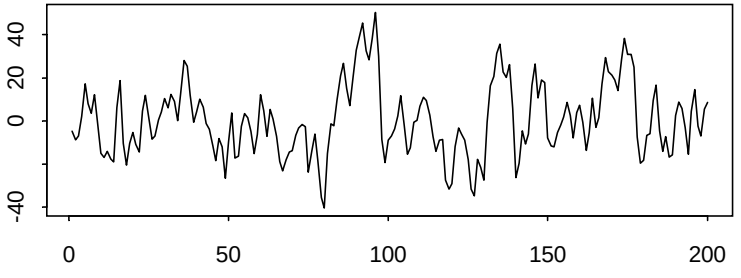
(iii)



(iv)



(v)



(vi)

7. Infrasound Monitoring

AN ALTERNATIVE CTBT INFRASOUND SENSOR USING PVDF PIEZOCABLE

Steven Africk
Physical Sciences Inc.

Sponsored by the Defense Threat Reduction Agency
Arms Control Technology Division
Nuclear Treaties Branch

SBIR Contract

ABSTRACT

We are exploring the feasibility of a novel infrasound sensor array employing piezoelectric cable. Piezocable is a coaxial cable with a center conductor, an outer shield, and a "dielectric" consisting of radially poled polyvinylidene fluoride (PVDF) which can be manufactured in almost arbitrary lengths and which is continuously piezoelectric. The infrasound sensor array consists of several lines of length on the order of up to hundreds of meters of piezocable, each of which is coupled individually and electronically to an on-site central processor. This design has several advantages over the usual concept in which the in-air pressure enters the porous hoses and is carried to a manifold in which signals from all hoses are added and input to the microbarograph where transduction takes place. Direct electronic transduction eliminates the air paths and the microbarograph making for a much simpler system which should be more reliable and less sensitive to environmental factors. It would also be less visible. In addition, in the piezocable system the output from each subarray line can be recorded and processed independently. This can support several novel processing options including real-time selection of those sensors with the best signal, noise, or signal to noise ratio, identification of incidence direction by array steering (by selection of those lines with the greatest signal), exclusion of signals from lines which are overly noisy (which could be due to animal activity, for example), or formation of superdirective (e.g. dipole) patterns at the subarray level. Geometries other than the "octopus" concept may also be desirable. Work is now focussed on a characterization of sensor noise which is expected to be dominated by electronic noise, pyroelectric effects, and wind noise. Theoretically, line array rejection of wind turbulence noise will be comparable to or better than that of a porous hose if the length of the piezocable line is comparable to the characteristic length of the porous hose. Current efforts in this program are focused on characterizing peizocable line noise both in the laboratory and outdoors in various meteorological conditions.

TUNING OF AUTOMATIC SIGNAL DETECTION ALGORITHMS FOR IMS STYLE INFRASOUND ARRAYS

David J. Brown[1], Charles N. Katz[1], Jin Wang[1], Rodney W. Whitaker[2]
Center for Monitoring Research[1]
Los Alamos National Laboratory[2]

Sponsored by the U.S. Department of Energy
Office of Nonproliferation Research and Engineering
Office of Defense Nuclear Nonproliferation
National Nuclear Security Administration

Sponsored by the Defense Threat Reduction Agency
Arms Control Technology Division
Nuclear Treaties Branch

Contract No. DTRA-01-99-C-0025

ABSTRACT

Design specifications for infrasonic arrays that comply with IMS requirements stipulate at least 4 sensors in a centered triangle configuration with maximal separation between sensors of between 1 to 3 km. Such a design is considered to be optimal for the detection of infrasound signals from explosive sources with yield down to around 1kT that are within a distance of around 3000km from the receiver. Automatic algorithms used for signal detection need to be optimized for both the signals of interest and the particular geometry of the IMS style array.

A research program nearing completion at the Center For Monitoring Research has been designed to produce automatic algorithms that are optimal with respect to signals and array geometry. Synthetic waveforms generated using Pierce's normal mode algorithm, designed to be representative of the infrasound signal from a 1-kT blast several thousand km from the receiver, were used to establish the Receiver Operator Curves (ROC curves) for the infrasonic signal detection algorithm in use at the Prototype International Data Centre (PIDC) in Arlington Virginia. The synthetic signals were implanted into conventional array channel data using an implant strategy that allowed the signal to noise ratio (SNR) of the signal to be specified in a fashion that accounts for the spectral composition of the background. SNR values ranging from 0.01 to 100 were used in the study to map out the ROC curves.

The PIDC infrasonic detection algorithm is known as a 'coincidence-detector' which relies on both the Fstat (Fischer Statistic), and the ratio of the L1 norms of a Short Term Average (STA) data window to that of a Long Term Average (LTA) data window, exceeding pre-determined threshold values simultaneously before a detection is declared. Such a detection algorithm provides a number of tunable parameters, such as three independent thresholds, STA and LTA times and the gap time separating the two, that can be used to explore the tradeoff between detection and false alarm rates necessary to generate ROC curves. The False Alarm Rate (FAR) places a control on all ROC curves, and the FAR value chosen for this exercise was set at 30 per day.

OBJECTIVE

Automatic signal detection algorithms of the variety in use at the Prototype International Data Centre (PIDC) for the processing of infrasound data have a number of 'tunable' parameters that can be chosen to enhance the Detector performance on signals considered to be of interest from a CTBT monitoring perspective; it may also be possible, by manipulating these parameters, to reduce the detection rate on signals generally not of interest, such as microbaroms and other natural forms of clutter. The main objective of this exercise, therefore, is to determine the optimal set of detector parameters for the automatic infrasound signal detector in use at the PIDC. The analysis will, for the present, be confined to data that conforms to IMS specifications, i.e., it is recorded on a 4-sensor centered-triangle infrasound array with sensor spacings of between 1 to 3 km on each side, and the sensor response will be assumed to be flat from 0.02 to 4.0 Hz.

The PIDC infrasound detector is known as a coincidence detector and has two major components. The first is a slowness-plane discretization that calculates two beams, an Fstat beam and a traditional beam directed at each point in the slowness plane. Both the Fstat, and the ratio of the L1 norm of a Short Term Average (STA) window to that of a Long Term Average (LTA) window on the traditional beam are required to achieve threshold values simultaneously before a detection can be declared. The second component of the Detector is a vernier-fk module that refines the slowness plane location of the signal. An additional threshold is placed on the coherent signal to noise ratio at the back-end of the vernier-fk module. Any signal is required to achieve this threshold value before a detection is declared. With such a Detector design, it becomes possible to devise a strategy that will reveal the optimal set of detection parameters for signals of interest. A tuning exercise of this kind culminates in the determination of Receiver Operator Curves (ROC) that provides a measure of the Probability of Detection (PD) as s function of Signal to Noise Ratio (SNR).

RESEARCH ACCOMPLISHED

In meeting this objective it was determined that the following steps constitute a workable Detector tuning strategy:

1. A suitable signal, representative of the acoustic signal generated by a 1-kt explosion located several thousand kilometers from the receiver is acquired.
2. One hundred hours of IMS-style array data, representative of a variety of ambient conditions, is chosen in which to implant the signal.
3. A method for implanting the signal time-series data into the background time-series data such that a pre-determined Signal to Noise Ratio (SNR) is achieved is determined.
4. Suitable definitions of Probability of Detection and False Alarm Rate are found
5. A method of parameter-variation is developed and executed to determine the tuned parameter list.
6. A method for establishing the ROC curves that provides Probability of Detection as a function of Signal to Noise ratio is determined.

Each of these tasks will be considered individually.

SignalData

The signal chosen for the tuning/implant exercise is a synthetic signal generated using the Pierce nomal-mode algorithm (Pierce, 1970) and was created via the InfraMAP toolkit (Gibson, et al., 1999). Six hundred modes were used to generate a signal that is considered to be representative of the acoustic signal generated by a 1-kt explosion nominally 1000 km from the receiver. The signal waveform is shown in Figure 1, and the Power Spectral Density is shown in Figure 2.

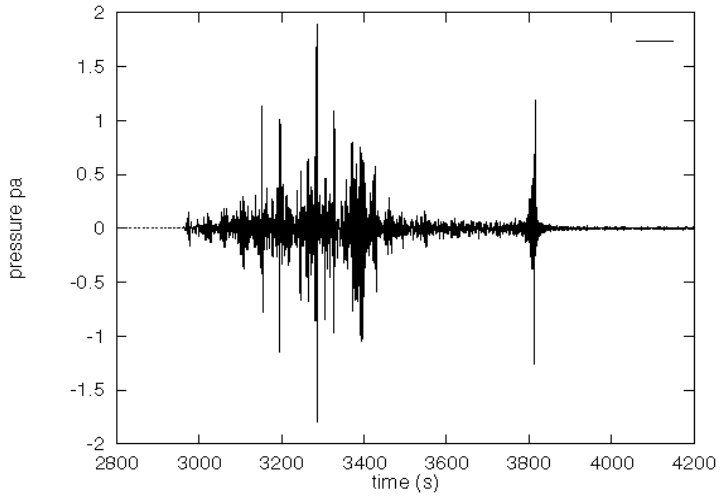


Figure 1: Synthetic signal representative of 1-kt source, nominally 1000 km from receiver.

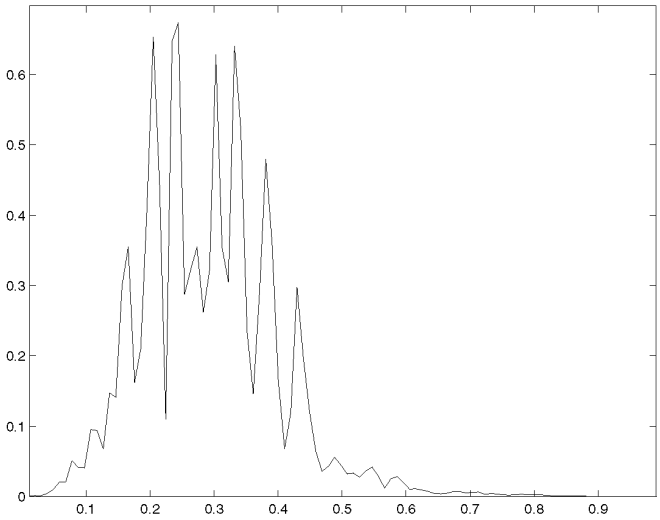


Figure2: Power Spectra of signal displayed in Figure 1.

Background Data

Ninety-Six hours of DLIAR array data were chosen as background data in which to implant the signal. The DLIAR array is an IMS-style array located in New Mexico and has 4 sensors in a centered triangle arrangement with approximately 1.2 km sensor separation along each side. Data from February 21 through 24, 1998 were chosen as background data as it represented a variety of ambient conditions. Additionally, analyst review indicated that few natural or man-made signals were present although some significant microbarom activity occurred. The extent to which microbaroms are present is revealed in Figure 3, which shows the speed, azimuth, and *Fstat* as a function of time for the four-day interval for periods ranging from 3.0 to 8.0 seconds. Days 1 and 4 have strong microbarom activity, while day 3 is almost completely devoid of activity. It is if interest to note that, even on kilometer-size arrays, microbaroms can routinely achieve Fstats of 10 or more, suggesting that they will often trigger the detector unless thresholds are placed on the energy of the signal.

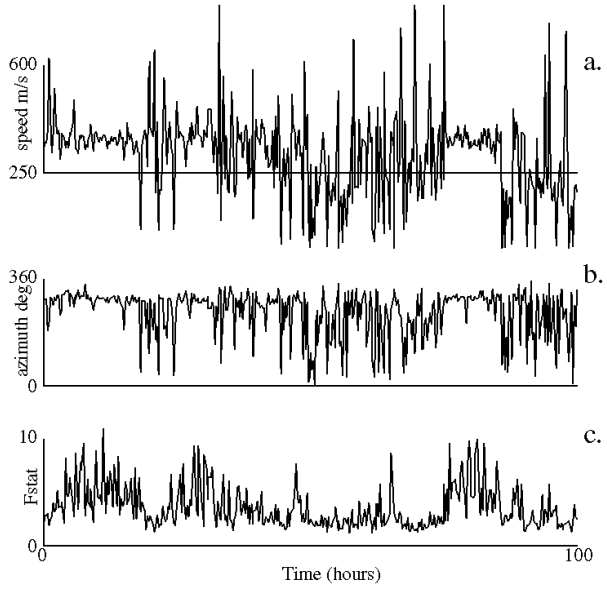


Figure 3: *speed, azimuth* and *fstat* for the 4 day period. Data filtered between 3 and 8 seconds.

A total of 42 man-made or naturally occurring signals with fstat > 2.0 were found to exist in the data and were excised in the subsequent analysis.

Signal Implantation

Signal implantation is always done so as to avoid the dominant microbarom direction. Typically, an arrival azimuth in the first quadrant, with azimuth less than 90degrees from north, is chosen. The signal is divided into three slowness regions with the intention of accommodating multipathing. An implanted signal is shown in Figure 4 with the three slowness regions indicated.

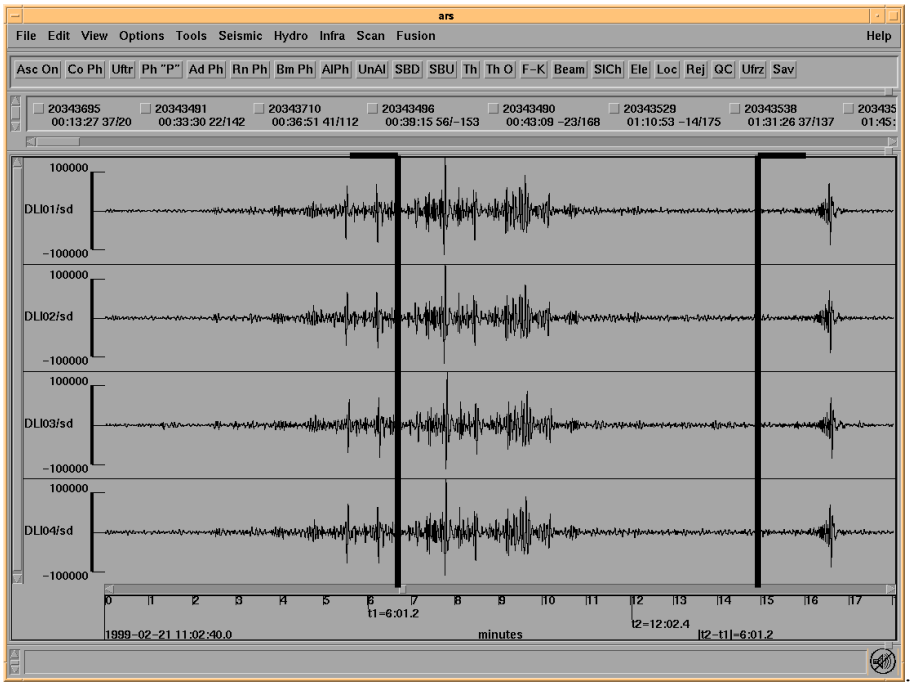


Figure 4: Example of implanted signal + backround data. Implant SNR = 25.0 . The three different phases have been indicated.

The signal is implanted according to the following prescription:

1. Assume there are $N = 2k$ points in the signal $\{S_1, \ldots, S_N\}$
2. Separate the signal into $N/2$ frequency pickets and calculate the power in each: $\{P_1, \ldots, P_{N/2}\}$
3. Call the total power T where $T = \sum_{i=1}^{N/2} P_i$
4. Sort the pickets into descending order of power: $\{U_1, \ldots, U_{N/2}\}$ and determine the index M at which 95% of the total power is obtained: $R = 0.95T = \sum_{i=1}^{M} U_i$
5. Extract the N-samples of background data where the signal is to be implanted, call these $\{X_1, \ldots, X_N\}$. Calculate the power in the $N/2$ pickets, call it $\{W_1, \ldots, W_{N/2}\}$, call $S = \sum_{i=1}^{N/2} W_i$
6. Sort the pickets into descending order of power: $\{V_1, \ldots, V_{N/2}\}$ and determine the 95% index K $Q = 0.95S = \sum_{i=1}^{K} V_i$

7. Specify the scale factor g as $g = \sqrt{\frac{Q}{R} SNR}$ where SNR is the desired implant SNR.
8. Create the new waveform as $Y_{J+i} = X_{J+\Delta+i} + gS_i$ where J is the insertion point and Δ is the delay.

PD

In specifying Probability of Detection, three different possible definitions were considered, viz:

1. 'Energy Packet' detection
2. 'Individual Phase' detection
3. 'Signal' detection

It is important to decide on an appropriate definition of PD as this definition can significantly alter the final arrangement of detector parameters. For example, it was found that long gap and LTA times strongly promote individual packet detection, but at the expense of detecting natural signals such as microbaroms.

Analyst inspection indicates that approximately 21 individual energy packets exist within the signal. Although it may be aesthetically pleasing to consider individual packet detection as a basis for PD, one must remember that an analyst will always inspect the signal, and whether two Energy Packets close together in time are detected together is not as significant as just one of the pair being detected. In addition, it is probably more appropriate to consider detecting individual phases (tropospheric, stratospheric and thermospheric) than just a single implanted signal. The signals of interest, as shown in Figure 1, can be at least 15 minutes in duration, and it may be possible for an analyst to simply miss one of the phases since it may not be in their analysis time period. The definition of PD used throughout this analysis, therefore, is the phase detection definition. With ninety-six implants, and three phases per implant, a PD can be determined for each phase and then for the signal as a whole.

FAR

False Alarm Rate controls detector performance. If infinite FAR were allowed, then the Detector would always be 'on' and a PD value of 1.0 would always be obtained. Conversely, if the FAR were zero, no false alarms would be tolerated and a PD value of 0.0 would always prevail; the detector would always be in the 'off' position. It is necessary, therefore, to establish definition of False Alarm Rate, and then settle on a reasonable value for FAR.

The general philosophy adopted here when defining False Alarm is that False Alarm Rate must be independent of the implantation strategy, i.e., False Alarms can only originate outside the implant region. By examining three features of each detection, namely azimuth, θ, speed |***s***|, time of arrival, and whether the detection is likely to be generated by microbaroms, it is possible to devise the following 'truth-table' for each detection. Here, θ indicates that the detection is, within a small error, coming from the implant azimuth; |***s***| indicates that the speed corresponds to one of the specified slownesses; time indicates that the detection occurs within an implant; and microbarom indicates that the detection is considered to be a microbarom. The θ designation and microbarom designation are mutually exclusive.

θ	T	F	F	T	F	F	F	F	T	T
|***s***|	T	T	F	F	F	F	T	T	F	T
time	T	T	T	T	F	T	T	F	F	F
microbarom	F	F	F	F	T	T	T	F	F	F

Genuine signals
Spatial aliasing
microbaroms
False Alarms

With this definition of FAR, it was decided that a FAR value of 30 per day would be acceptable.

Parameter Variation

The major parameters affecting Detector performance are listed in Table 1, along with a brief description of each parameter.

sta-time	Length in seconds of the Short Term Average window
gap-time	Length in seconds of the gap between the STA and LTA windows
lta-time	Length in seconds of the lagged Long Term Average Window
coherent-threshold	Threshold in the Primary Detect Space which the coherence has to achieve before a detection is allowed.
sta-lta-threshold	Threshold in the Primary Detect Space which the ratio of the *L1* norm of the STA window to that of the LTA window has to achieve before a detection is declared..
slowness_criterion	Radius around a given 'detection' in the slowness plane inside which all other detection will be considered to be in the same cluster.
beam_recip_snr	Back-end coherence threshold in the Coincidence Detect Space that needs to be exceeded before a detection is declared.

Table 1: Detector parameters considered in the tuning exercise.

The tuning strategy decided on here was the following. Signals of varying SNR were implanted into the background channel data. A suite of DFX detection runs were performed in which a single parameter is varied until a peak in the PD versus parameter-value curve is achieved, -for the specified FAR. For some parameters, the curve obtained proved to be somewhat insensitive to changes in the parameter value. In these situations it was possible to minimize total microbarom count. Indeed, the microbarom count often proved to be quite sensitive to the particular choice of parameter value. The parameter is then assigned this value, which will be held constant for all future runs. The next parameter is then varied in the same manner, maintaining the same FAR.

An example, showing results obtained for the variation of the ***sta-lta-threshold*** parameter is shown in Figure 5.

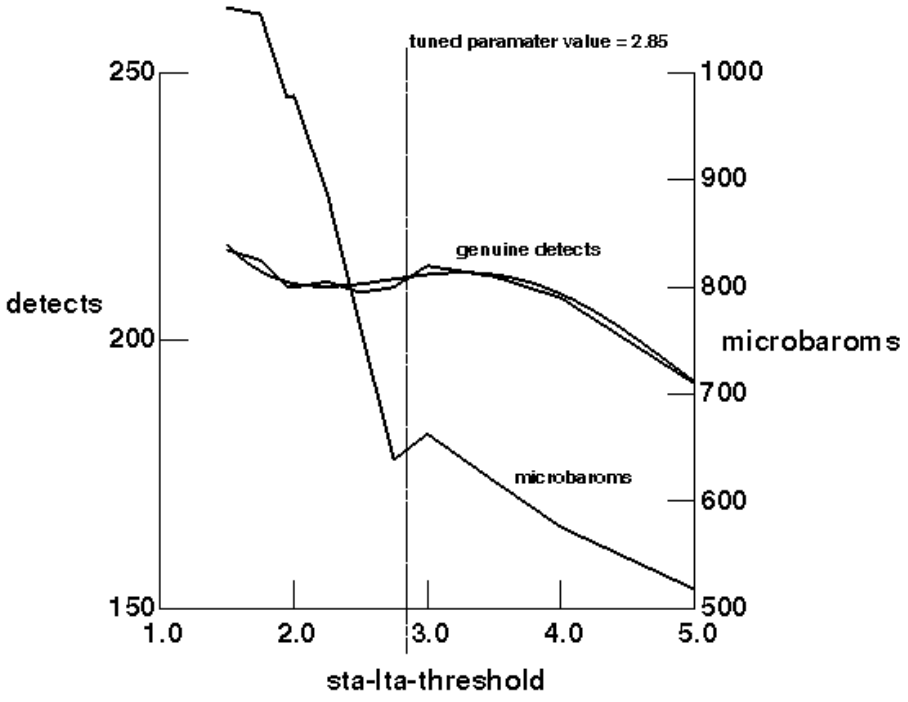


Figure 5: Variation of detect count with sta-lta-threshold. A 4-th order polynomial interpolation is shown as well as the variations in microbarom detections.

In this case, the genuine detection count is observed to be weakly-dependent on the ***sta-lta-threshold*** parameter. Microbaroms, however, appear to be strongly-dependent on the choice of parameter and it is therefore prudent to choose the parameter value near the crest of the genuine detect curve and near the local minimum in the microbarom count.

Final values for the 7 parameters considered in this exercise are shown in Table 2.

sta-time	8
gap-time	120
lta-time	45
coherent-threshold	1.765
sta-lta-threshold	2.85
slowness_criterion	0.38
beam_recip_snr	1.5

Roc Curves

Determination of the ROC curves for this Detector is the final task in this project and are currently being generated.

CONCLUSIONS AND RECOMMENDATIONS

Detector tuning exercises of this kind need to be performed to establish optimal Detector performance for the signals of interest. To achieve this goal, it was found necessary to rigorously define concepts like 'Probability of Detection' and 'False Alarm Rate'. With these definitions in place, and using synthetic signals that closely resemble the signals of interest, a tuning exercise has been performed that has allowed us to maximize the detection rate for the signals of interest, and reduce the detection rate for signals such as microbaroms that are not of interest. A recommendation must be that these exercise be expanded to include other representative signals, with different ambient noise conditions and geographic locations.

REFERENCES

Gibson, R., Norris, D., Farrell, T. (1999): *Development and Application of an Integrated Infrasound Propagation Modeling Tool Kit.*, Proc. 21st Seismic Research Symposium, DTRA, U.S Dept. of Defense, Las Vegas, Nevada.

Pierce, A.D., and Posey, J.W., 1970: *Theoretical Prediction of Acoustic-Gravity Pressure Waveforms Generated by Large Explosions in the Atmosphere*. Technical Report AFCRL-70-0134, Air Force Cambridge Research Laboratories, Bedford, Mass.

Key Words: Infrasonic signal detection, ROC curves, False Alarm Rate, Probability of Detection, IMS infrasound array

STATISTICAL PERFORMANCE MEASURES OF THE HWM-93 AND MSISE-90 EMPIRICAL ATMOSPHERIC MODELS AND THE RELATION TO INFRASONIC CTBT MONITORING

Douglas P. Drob and J. M. Picone, Upper Atmospheric Physics Branch,
E.O. Hulburt Center for Space Research, Naval Research Laboratory

Sponsored by the U.S. Department of Energy
Office of Nonproliferation Research and Engineering
Office of Defense Nuclear Nonproliferation
National Nuclear Security Administration
Contract No. DE-AT04-99AL66330

ABSTRACT

An enforceable Comprehensive Nuclear-Test-Ban Treaty (CTBT) will require accurate detection and location of low-yield nuclear detonations. Thorough knowledge of the upper atmosphere and advanced modeling techniques are required for reliable infrasonic detection and location of clandestine events. The purpose of this paper is to document a statistical performance measures study of the Naval Research Laboratory's (NRL) empirical upper atmospheric models. These models known as the MSISE-90 and HWM-93 models were originally developed at the NASA Goddard Space Flight Center and made freely available to the public and scientific research communities. The Upper Atmospheric Physics branch at NRL is working toward the production of improved versions of these empirical upper atmospheric models for use in verification and compliance with the CTBT. This study identifies weak areas in the current models for planning and implementation of future upgrades. In this report, we detail model performance in two atmospheric regions; 0 to 50 km and 50 to 120 km. This report primarily focuses on systematic biases in the wind model (HWM).

Key Words: infrasound, atmospheric models, statistical performance

OBJECTIVE

The Comprehensive Nuclear-Test-Ban Treaty (CTBT) global infrasonic network will permit the detection, identification, and location of natural and man-made impulsive events. The ability to characterize and locate sources with infrasound data is related to the accuracy of atmospheric state estimates used in the propagation calculations. Conversely, because infrasound propagation depends on the atmospheric conditions, signals from naturally occurring (e.g. mirco-baroms, volcanic activity) and man-made infrasonic sources (e.g. mining blasts) can be used to improve and validate local atmospheric conditions later used to investigate a clandestine event.

The atmosphere is variable on all length and time scales making it challenging to measure and model. Of the available atmospheric models, the Horizontal Wind Model (HWM-93) and Mass Spectrometer and Incoherent Scatter Radar Extended Model (MSISE-90) provide the best and most readily available time-dependent global specification of the atmosphere from the ground to the thermosphere for infrasound propagation modeling. The HWM-93 model provides vector winds and the MSISE-90 model provides density and temperature. This report highlights the statistical performance of HWM-93 and MSISE-90 empirical atmospheric models and explores how atmospheric variability and modeling biases can influence infrasound-modeling calculations.

To provide global specifications of the atmospheric state variables over the entire infrasonic propagation domain the HWM-93 and MSISE-90 models draw upon a forty-year, multi-instrument database of satellite- and ground-based atmospheric measurements. The models internal mathematical formulations, sets of spherical and vector spherical harmonic basis functions and corresponding empirical coefficients are used to provide statistical estimates of the atmospheric state variables at any given location, day-of-year, time-

of-day, and level of solar and geomagnetic activity. The two models, FORTRAN source codes, are available for download at http://uap-www.nrl.navy.mil/models_web.

We performed this study to determine if the current NRL empirical models provide sufficiently accurate atmospheric specifications for CTBT verification purposes. The limitations of these two atmospheric models stem from two kinds of uncertainty – one is statistical and one systematic. The statistical uncertainties are caused by unresolved random fluctuations in the upper atmosphere such as gravity waves, planetary waves, and turbulence. The systematic errors are caused by observation and modeling biases.

RESEARCH ACCOMPLISHED

Atmospheric model performance evaluation can be divided into two categories; objective statistical measures and consistency checks against physical laws. For this investigation, a database of standard deviations and mean biases was created to identify systematic model errors and tendencies. In addition, this database can be used in a number of ways to supplement the empirical models.

Model bias $<\varepsilon>$ describes whether a model is over- or under-predicting atmospheric behavior. Bias is defined as the average of the difference between a subset of N observations (d_i) and the corresponding model predictions (m_i). The subset of observations $\{d_0 \ldots d_N\}$ are chosen from a larger set over some arbitrary, yet statistically meaningful sample space (a bin). Although bias is an easy measure to compute and understand, it is often necessary to make an objective statement as to whether a given bias is significant. Additional measures must, therefore be considered. RMSE is defined as the positive square root of the mean square error (σ^2_ε). This is also called the standard error of estimate and written as:

$$\sigma^2{}_\varepsilon = <(d_i - m_i)^2> = \frac{1}{N-1}\sum_{i=1}^{N}(d_i - m_i)^2 . \quad (1)$$

Here $< >$ denotes the ensemble average of N observations and model predictions. RMSE is straightforward to calculate, but is sometimes difficult to interpret. This is especially true in the upper atmosphere where spatial and temporal variability is significant and tends to dominate the measure. In other words, RMSE is sensitive to the natural variability of the observed field. The natural variability of the upper atmosphere is also highly dependent on geographic region and season. Standard deviation is a statistical measure of the variability about the mean in a series of observations. It is the positive square root of the variance σ^2_d, which is defined as:

$$\sigma^2{}_d = <(d_i - <d>_i)^2> = \frac{1}{N-1}\sum_{i=1}^{N}(d_i - <d>_i)^2 = <d_i^2> - <d>_i^2 . \quad (2)$$

Other statistical analysis techniques such as anomaly correlation, principal component analysis, and multidimensional spectral analysis are useful in evaluating and improving the atmospheric models. As part of this project, we developed software tools to calculate, investigate, and utilize these statistical performance measures. These analysis tools will be utilized in our ongoing research activities.

STRATOSPHERIC STATISTICS (0 – 50 km)

The first set of statistical performance measures for the HWM/MSIS models was calculated in the 0 to 50 km region of the atmosphere using eight years of near-real-time global meteorological specifications produced by the United Kingdom Meteorology Office. These specifications include winds (U, V), temperature (T), and geopotential height (z) at 12:00 UT on a 73 x 96 degree horizontal grid on 18 pressure levels from 1000 to 0.4 millibars (mb). The 0.4 mb upper pressure level occurs at an approximate altitude of 50 km in the winter hemisphere and 55 km in the summer hemisphere. Our first step was to regrid the data from a pressure grid to an altitude grid that ranged from 0 to 50 km at 2.5 km intervals (21 levels). Then from these results model bias, RMSE, and standard deviation were calculated at 15-day intervals. Measures of RMSE were not calculated for the entire data set because the synoptic and sub-synoptic variability contained within the UKMO analysis were found to dominate RMSE.

It is known that a quasi-biennial oscillation (QBO) exists in the zonal (east-west) wind component of the equatorial stratosphere (*Naujokat*, 1986). The role that this oscillation plays in the general circulation and random variability of the atmosphere is an active area of upper atmospheric research. This feature is currently not included within the HWM wind model. As a result, a coherent model bias in the zonal wind field, with average magnitudes around 20 m/s, exists over a broad altitude region roughly ± 15° around the equator. This is shown in Figure 1.

In addition to biases caused by the QBO, other biases were discovered in the 0 to 55 km portion of the HWM model. Figure 2 shows two slices of the zonal mean wind bias over the same time span for two latitudes (45° S and 45° N). These results show that HWM does a reasonable job of predicting 15-day averages of the stratospheric winds in the northern hemisphere. However, localized stratospheric jet enhancements and planetary wave modulation can introduce significant model biases, especially in the southern hemisphere.

Atmospheric wave variance is a function of latitude, longitude, altitude, and season. In the stratosphere, the majority of wave energy resides in disturbances with horizontal wave numbers from 1 to 5 that migrating eastward or westward with periods ranging from 2 to 45 days. These waves have vertical wavelengths of 4 to 25 km and tend to grow exponentially with altitude. These waves are more frequent and intense in the northern hemisphere. Figure 3 shows the average 15-day standard deviations (1993-1995) of the zonal wind in m/s for four representative months. The temperature, pressure, and meridional wind fields also exhibit similar characteristics. The causes of these features are the mid-latitude jet stream fluctuations, the wintertime stratospheric zonal jet fluctuations, and wave growth with altitude.

In addition to the latitudinal and altitudinal variations of planetary waves, a fair amount of longitudinal variation also exists due to topology. Figure 5 shows representative months of a five-year average of 15-day standard deviations for the 50 km zonal wind field. The other geophysical fields exhibit behaviors

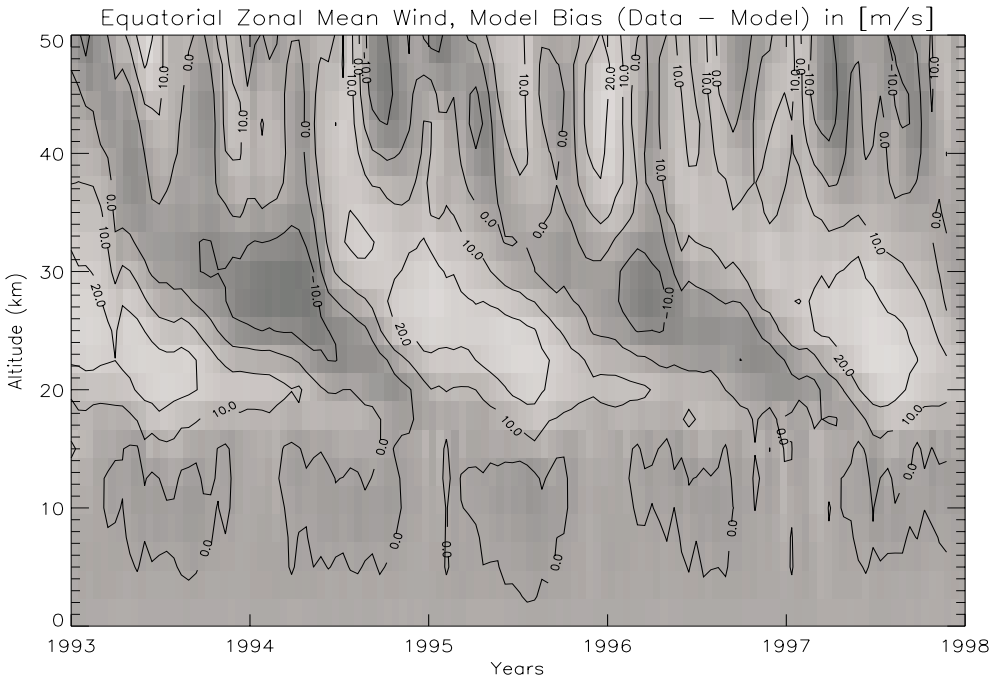


Fig. 1 – The equatorial zonal mean wind bias in m/s showing the effect of the missing stratospheric quasi-biennial oscillation (QBO).

similar to those in figure 4. The NRL-HWM/MSIS statistical performance database contains these fields at 15-day interval over the years 1993 to 1997, for the wind, temperature, and pressure fields from 0 to 50 km at 2.5 km intervals.

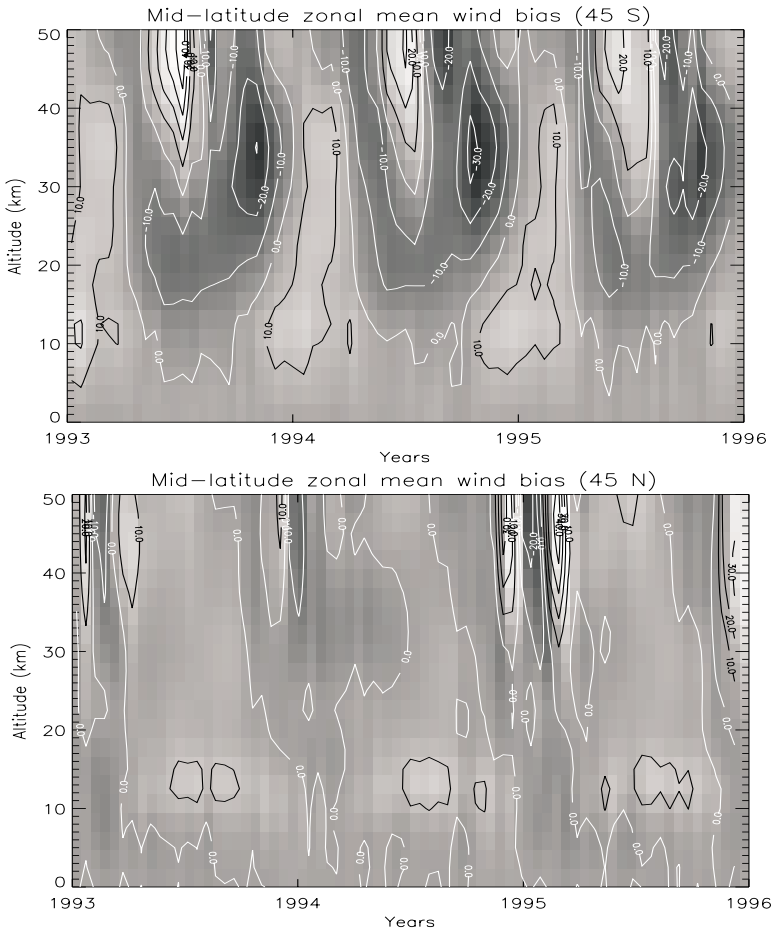


Fig. 2. – Zonal mean winds biases at 45° S (upper panel) and 45° N (lower panel).

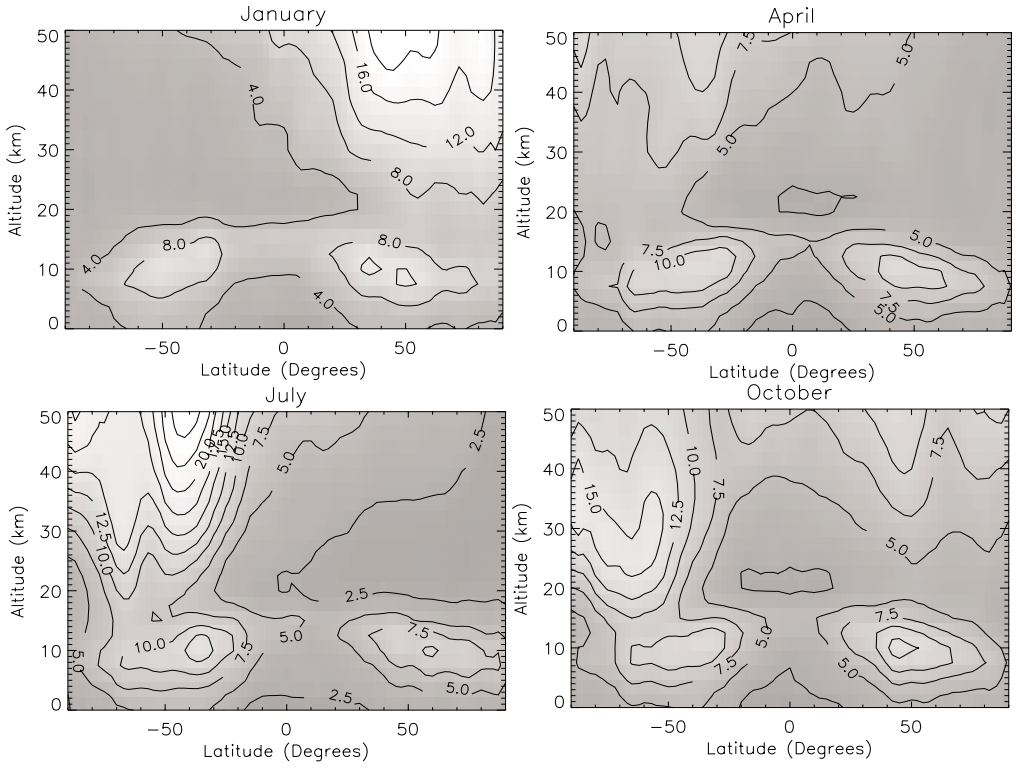


Fig. 3 – Representative months for 5-year climatological averages of the 15-day zonal wind standard deviations in units of m/s.

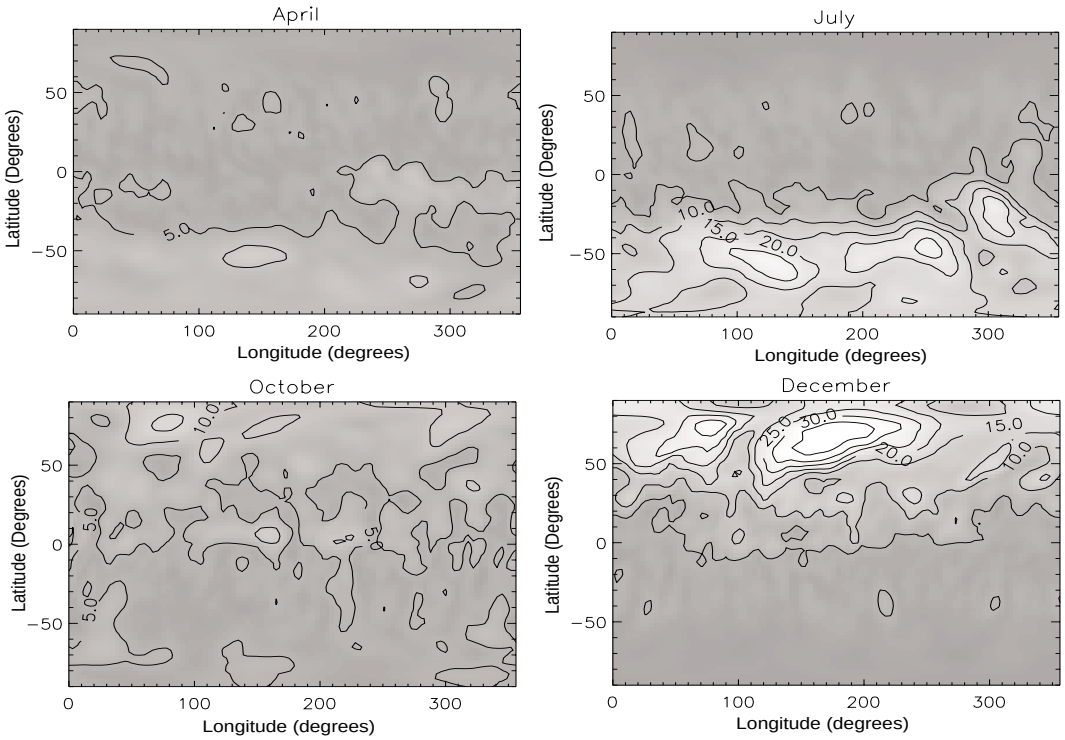


Fig. 4 – Climatological averages of the 15-day merdional wind, standard deviations in m/s at an altitude of 50 km. Four representative months are shown.

MESOSPHERE AND LOWER THERMOSPHERE STATISTICS (60 – 120 km)

The predominant variations in the Mesosphere and Lower Thermosphere (henceforth, MLT) are caused by direct diurnal solar heating of atmospheric ozone and water vapor. The resulting oscillations have harmonics of 24 (diurnal), 12 (semidiurnal), and 8 hours (terdirunal). The amplitudes and phases of these oscillations can vary significantly with latitude and season. On seasonal time scales, changes in the global general circulation pattern are also important. In addition, global scale planetary- and sub-synoptic gravity-waves are superimposed on the atmospheric general circulation and tidal oscillations. Reviews of upper atmospheric dynamics may be found in *Andrews et al.* (1987) and *Rees et al.* (1989).

Compared to the amount of data obtained daily for the atmosphere below 50 km, only a small amount of MLT data is available on a routine basis. Furthermore, the statistical uncertainties of these data are large, the sampling sparse, and the inherent natural variability large. No 'operational' weather monitoring systems currently exist for specifying the state of the MLT region.

Since the last update of the HWM and MSIS models, however, the NASA Upper Atmospheric Research Satellite (UARS) has significantly advanced our understanding of the dynamics in the MLT region. The UARS – High Resolution Doppler Interferometer (HRDI) was the first research instrument to measure global wind profiles throughout the MLT region (*Hays et al.*, 1994). The WINDII instrument onboard the UARS satellite also measured atmospheric wind profiles in the 85 to 180 km region (*Shepard et al.*, 1993). The UARS data provides a good opportunity to evaluate and improve the performance of the HWM model. In addition to obtaining the HRDI data set, we also obtained over one year of ground-based wind measurements from the Bribe Island, MF-radar (28º S, 153º E).

HWM-93 Performance

For the HWM model, the HRDI level 2-B wind measurements (version 11) from 1993 to 1996 were used to calculate a large set of monthly statistical performance measures. Point-for-point HWM wind estimates were first generated. Then zonally averaged, monthly-mean model biases and RMSE estimates where calculated on a 5° latitude by 2.5 km altitude grid that ranged from ± 65° and covered an altitude range from 52.5 to 117 km.

Meridional (north-south) wind biases between the HWM model and HRDI data for 1993 are shown in Figure 5. The model does a good job of reproducing the merdional wind measurements on a monthly-

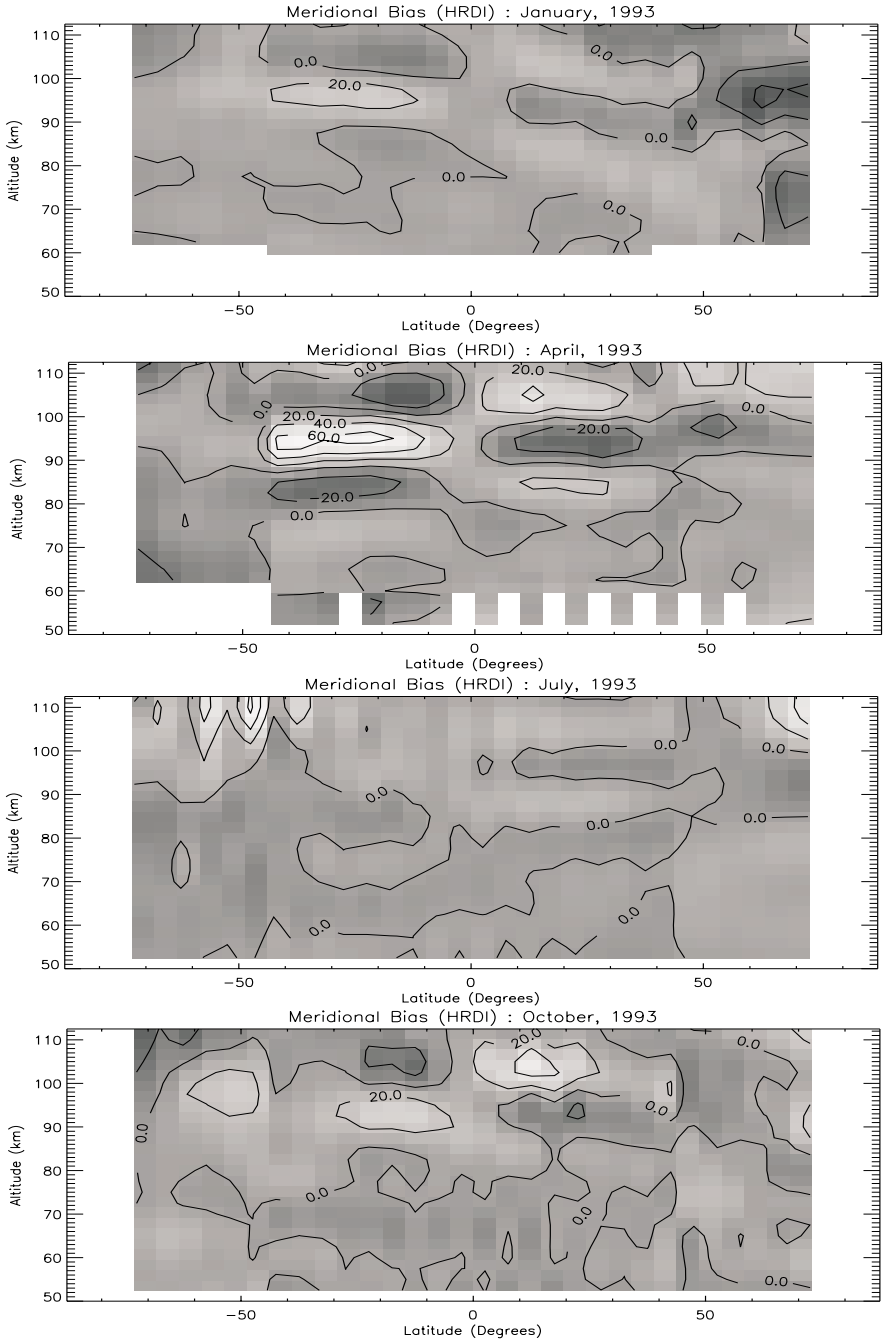


Fig 5. – Average meridional wind biases between the HRDI measurements and HWM model for representative months in 1993.

average basis, but there are notable exceptions. Systematic discrepancies appear in the sub-tropics during the equinox periods with magnitudes approaching 60 m/s near 90 km. These biases are caused by the misrepresentation of the diurnal (1-1) migrating solar tide within the model. Further analysis of the Bribe Island MF data tends to support this conclusion. While the HWM-93 mathematical formulation is capable of representing this component, the early data sets used to estimate diurnal tidal amplitudes coefficients in the MLT region of the model was somewhat limited.

Calculations of RMSE provide additional information on the performance and functionality of the HWM model. In general, this measure reflects atmospheric wave variances not represented in the empirical models. Between the altitudes of 50 and 90 km, typical RMSE magnitudes range from 20 to 30 m/s. Above 90 km, RMSE grows rapidly to 60 m/s. Regions of high RMSE at these altitudes also appear to be clustered around the equator and subtropics. In addition, there are several episodic RMSE enhancements at mid-latitudes near 70 km in the zonal wind field. These are observed at random times throughout the analysis period.

MSISE-90 Performance

It is now accepted that the MSISE-90 model, as well as the CIRA-86 international reference atmosphere (*Fleming et al.*, 1988), both underestimate the mesopause region (80 – 100) temperatures by 15 K at mid-latitudes and overestimate high-latitude mesopause region temperatures by about the same amount (*She and von Zahn*, 1998, *Lubken et al.*, 1999). We used two ground-based instruments and the HRDI temperatures measurements to perform an evaluation of the MSISE-90 model near the mesopause region (80 to 110 km). Because our findings are consistent with those published in the literature, we will not discuss the MSISE-90 mesopause region temperature biases in any detail here.

More importantly, we have recently completed the generation of NRLMSIS-00. In this new version of the MSIS model, we have added a significant amount of new data to the 120 to 600 km region. Changes to the model formulation were made at 120 km and several new physical constraints were used during the model generation process. These adjustments had several positive consequences on model accuracy as far down as 70 km. Using the data collected for this study, initial analysis indicates that NRLMSIS-00 is significantly better than MSISE-90 for CTBT verification and compliance applications. We anticipate a public release of the new model by the end of this year.

CONCLUSIONS AND RECOMMENDATIONS

The objective of this study was to: 1) define weaknesses in the current models for planning and implementation of future upgrades, 2) provide users with information about the models, and 3) develop a set of statistical uncertainties to supplement the models.

The dominant fluctuations of the upper atmosphere are primarily driven by direct solar heating. Because the resulting periodic wave processes are statistically repeatable from day to day and year to year, they can be parameterized with empirical models. The atmosphere also contains significant random and pseudo-random components. In the absence of direct observations, these components cannot be deterministically resolved or predicted with an empirical model. Their occurrence frequency and net influence, however can be parameterized with a statistical measure like standard deviation. This work represents the first step toward a global parameterization of atmospheric random variability that will extend from the ground to 120 km.

The systematic errors we discovered in the two models can exist for a number of reasons. For example, there are regions of the atmosphere were only a handful of data are available. In these regions, the model output represents an interpolation or extrapolation of data from other regions in space and time. While the use of physical constraints such as hydrostatic equilibrium and geostrophic balance can help reduce uncertainties, errors in the model predictions can still be significant. Additionally, the spectral fidelity of the models is determined by the density of the available data. Using our new database this can be subsequent improved in future model versions.

The set of finite basis functions used in the models to represent the atmosphere provides another source of error. While a given feature may be parameterized mathematically and resolved with the data, the feature may be unknown or simply ignored for computational reasons. Adjustment of the model formulation and assimilation of available data can rectify these errors.

A final source of systematic errors in our models comes from the data themselves. Almost 99.99% of all upper atmospheric measurements are made by indirect means, i.e. remote sensing techniques. Errors associated with instrumentation and poor data inversion procedures all contribute to the possibility of systematic, nonphysical errors in the observations. Owing to the fact that the upper atmospheric measurements are difficult to make, there are often no other coincident measurements available to provide consistency checks, especially where they are most needed.

Based on our findings there is a need for HWM model improvements. When compared to the recently available data sets, the historical database used to determine the present HWM empirical model coefficients was limited. For this reason, and minor limitations in the present model formulation, tidal amplitudes in the HWM-93 model have been underestimated in certain regions and seasons. Due to the lack of a parameterization of the equatorial quasi-biennial oscillation, systematic errors in the zonal wind field from 35 to 120 km ranging from 20 to 50 m/s are also present. Unlike random errors due to transient wave phenomena, these two errors have large temporal and spatial coherence. Under a significantly broad range of conditions, these errors will impact science and engineering calculations that use current versions of the HWM model to provide wind estimates.

This study illustrates that from 0 to 55 km, the models are inferior to operational data products available from a number of national and international Numerical Weather Prediction (NWP) centers. However, for analysis of early historical data, or in situations where NWP estimates and/or direct meteorological observations are not available, these models are extremely useful. Furthermore, these models are superior to other public domain atmospheric climatologies owing to their extension to higher altitudes and the ability to be directly embedded into engineering and scientific codes to produce estimates with minimal computation requirements.

The effect of the above mentioned limitations on infrasound propagation calculations for CTBT monitoring was recently illustrated in a study by *Garces et al*. (1999). In this study, we produced atmospheric estimates from the ground to 150 km for the entire year of 1996 over the Alaska and Hawaii CTBT infrasound sites by carefully merging the UKMO analysis data with the HWM and MSIS models. To do this we developed a methodology called the NRL-CAMPFIRE procedure (Combined Atmosphere Measurement Profiles For Infrasound Range Estimation). This method works well under most conditions; however, where large differences between the empirical models and the stratospheric analysis products occur, spurious ringing at the model boundaries can result. This is particularly true at high latitudes, where HWM often underestimates the localized velocity of the winter polar stratospheric jets by as much as 60 m/s. As expected, this is less of a problem over Hawaii, where the upper-stratosphere wind velocities are smaller.

Given the lack of accuracy of the HWM model in the stratosphere and the lack of operational meteorological specifications into the thermosphere, the above effects could be viewed as a minor inconvenience. However, this problem occurs close to the region where stratospheric infrasound reflections take place. Because infrasound rays are sensitive to errors and perturbations near their turning points, errors in the procedure will translate in to errors in infrasound propagation calculations. The rectification of the systematic biases in the current models would suppress these effects in the CAMPFIRE procedure by greatly reducing the differences between the current HWM model and NWP stratospheric analyses. We are now in the process of using our modeling tools to address this problem.

In this document, we have alerted current and potential HWM/MSIS users to weaknesses in the models. For those users that require additional information we have created a performance measures database. Having now identified several problematic areas, this information can be used to develop and add missing parameterizations to the models. Additionally, the new database of standard deviations can be used to

weight the various datasets during the model building process. Furthermore, these new measures will be useful as a-priori statistics in making improvements to the CAMPFIRE procedure.

REFERENCES

Andrews, D. G., J. R. Holton, and C. B. Holton, "Middle Atmospheric Dynamics", Academic Press, Orlando, Florida, 1987.

Burrage, M. D., M. E. Hagan, W. Skinner, D. L. Wu, P. B. Hays, Long-term variability in the solar diurnal tide observed by HRDI and simulated by GSWM, *Geophys. Res. Lett.*, **22**, 2641-2644, 1995.

Burrage, M. D., R. A. Vincent, H. G. Mayr, W. R. Skinner, N. F. Arnold, and P. B. Hays, Long-term variability in the equatorial middle atmosphere zonal wind, *J. Geophys. Res.*, **101**, 12847-12854, 1996.

Burrage, M. D. *et al.*, Validation of mesosphere and lower thermosphere winds from the high resolution Doppler imager on UARS**,** *J. Geophys. Res.*, **101**, 10365-10392, 1996.

Fleming, E.S., S. Chandra M.R. Schoeberl, and J.J. Barnett, Monthly mean global climatology of temperature, wind, geopotential height and pressure for 0-120 km, NASA technical memorandum, 100697, 1988.

Forbes, J. M., M. Kilpatrick, D. C. Fritts, A. H. Manson, and R. A. Vincent, Zonal mean and tidal dynamics from space: an empirical examination of aliasing and sampling issues, *Ann. Geophys.*, **15**, 1158-1164, 1997.

Garces, M, R. Hansen, K. Lindquist, D. P. Drob, and J. M. Picone, Variability of the lower atmosphere and its effects on infrasonic waves, Proc. 21 Annual Seismic Symposium on Monitoring the CTBT, 1999.

Garces, H. D. P. Drob, J. M. Picone, A theoretical study of the effects of geomagnetic fluctuations and and solar tides on the propagation of infrasounic waves in the atmosphere, *Geophys. J. Int.*, submitted, 1999.

Hays, P. B., D. L. Wu, Observations of the Diurnal Tide from Space, J. Atmos. Sci., **51**, 3077-3093, 1994.

Hedin, A. E., N. W. Spencer, and T. L. Killeen, Empirical global model of the upper thermopshere winds based on Atmopshere and Dynamics Explorer satellite data, *J. Geophys. Res.*, **93**, 9959-9978, 1988.

Hedin, A. E., M. A. Biondi, R. G. Burnside, G. Hernandez, R. M. Johnson, T. L. Killeen, C. Mazaudier, J. W. Meriwether, J. E. Salah, R. J. Sica, R. W. Smith, N. W. Spencer, V. B. Wickwar, and T. S. Virdi, Reviesed global model of upper thermospheric winds using satellite and ground-based observations, *J. Geophys. Res.*, **96**, 7657-7688, 1991.

Hedin, A. E., E. L. Fleming, A. H. manson, F. J. Schmidln, S. K. Avery, R. R. Clark, S. J. Franke, G. L. Fraser, T. Tsuda, F. Vial, and R. A. Vincent, Empirical wind model for the upper, middle and lower atmosphere, *J. Atmos. Terr. Phys.*, **58**, 1421-1447, 1996.

Hedin, A. E., M. J. Buonsanto, M. Cordrescu, M.-L. Duboin, C. G. Fesen, M. E. Hagan, K. L. Miller, and D. P. Sipler, Solar activity variations in mid-latitude thermospheric meridional winds, *J. Geophys. Res.*, **99**, 17601-17608, 1994.

Lubken, F. J., Thermal Structure of the Artic Summer Mesopause, J. Geophys. Res., **104**, 9135-9149, 1999.

Naujokat, B., An update of the observed quasi-biennial oscillation of the stratospheric winds over the tropics, *J. Atmos. Sci.,* **43**, 1873-1877, 1986.

Rees, M. H., "Physics and chemistry of the upper atmosphere", Cambridge University Press, New York, NY, 1989.

She, C.Y., U. von Zahn, Concept of a two-level mesopause: Support through new lidar observations, *J. Geophys. Res.*, **103**, 5855, 1998.

Shepard, G. et al., WINDII, the Wind Imaging Interferometer on the Upper-Atmosphere Research Satellite, *J. Geophys. Res.*, **98**, 10725-10750, 1993.

INSTALLATION AND PRE-CERTIFICATION OF CTBT STATION IS59, HAWAII

Milton Garcés[1]
Infrasound Laboratory, University of Hawaii, Manoa
[1]Also at the University of Alaska, Fairbanks

Henry Bass
National Center for Physical Acoustics, University of Mississippi

Sponsored by the U.S. Department of Defense

Contract No.: DASG60-99-0018

ABSTRACT

The IS59 site survey took place on June 2-16, 1999. The site survey report recommended the installation of IS59 in an exceptionally quiet and well forested area in the Western side of the island of Hawaii. After the September PTS acceptance of the proposed array location, lease and land use agreements were executed and site work began on December 1999. The acceptance test for the integrated data acquisition system took place on May 15-18. On May 25, 2000, IS59 began collecting and archiving pressure data, and since June 1 the CD-1 data frames have been continuously sent to the PIDC.

The IS59 array consists of four Chaparral 5 pressure sensors deployed in a tripartite configuration with a 1.9 km aperture. Each sensor feeds into Science Horizons digitizers and authentication boxes, which are powered via ground cables from a central solar panel array. Communication cables run from the concrete vaults that house the equipment to a central site with a 120 ft mast that support the telemetry antennas above the forest line. Continuous pressure, state of health, and meteorological data is sent via radio telemetry to the Infrasound Laboratory, which will act as the central facility that archives data and routes CD frames to the IDC through a VSAT link. This paper outlines the installation and ongoing pre-certification process of the Hawaii station, and shows various signals that have been observed during its operation.

Key Words: Hawaii, certification, IS59, infrasound

OBJECTIVE

The aim of this stage of the project is to complete the installation of IS59 and streamline its operation so that it will meet the certification requirements of the CTBT International Monitoring System. An additional objective is to identify enhancements that may optimize the performance of IS59.

RESEARCH ACCOMPLISHED

Introduction

IMS infrasound array IS59 is located in the Western side of island of Hawaii, also known as the Big Island (Figure 1). The array site is completely blocked from the trade winds by Mauna Kea, Mauna Loa and Hualalai volcanoes, and thus the site is exceptionally quiet (Garces and Bass, 1999). The array (Figure 2) has a 1.9 km baseline with a central power and communication system, and each element is connected to the central area via ground cables. Data is sent via radio telemetry to the Infrasound Laboratory (ISLA), which acts as the recording facility and archives data in CSS format. The first field station began recording pressure data on May 25, 2000 at 06:34:16 UT. The array began recording pressure data on May 26 at 02:15:43 UT, and the PIDC began receiving CD-1 frames on June 1, 2000. Various regional and distant events have been recorded, and the low self-noise and high sensitivity of the hand-tuned Chaparral 5 sensors have yielded a low threshold of detection. However, spatial aliasing reduces the detection capabilities of the array for small signal-to-noise ratio events with frequencies above 0.3 Hz.

Equipment and Installation

The equipment installed at IS59 is shown in Figure 3. The digitizer is the Science Horizons, Inc. (SHI) single-channel Analogue Input Module 24-bit Slimline (AIM24S-1), with the attached sealed Authentication box AIMA. Each of the four elements elements has a GPS time stamp and is connected via cable modems to a multidrop box, which ties in to a FreeWave 900 MHz spread-spectrum radio. A meteorological Handar station is connected to a separate but parallel telemetry line, also with a FreeWave. The two telemetry channels are brought into a 2-port Communications Interface Module (CIM II, bottom black box in Figure 4), which forwards the data to a Remote Processing Computer (RPC, upper black box). The RPC can assemble and forward CD-1 frames to three IP addresses, and also sends the data to the Science Horizons Acquisition and Viewing Executive (XAVE) software package (screen in Figure 4) which archives the data in CSS format and is used to display the real-time data stream. The RPC and XAVE software runs on separate Sun Ultra 5 machines running under the Solaris 7 OS and connected through an ethernet hub. AutoDRM commands are hardware-signed by a Spyrus box with a PC card. All mission-critical systems at the ISLA have Best Power Ferrus Series UPS for backup power.

To protect the equipment against falling hardwood trees, each sensor, AIM, and AIMA are housed inside a concrete vault with 6'" walls and steel lids (Figure 5). A levering system was developed to allow a single person to lift the heavy steel lids. Each site is fenced to discourage visits from pigs, cows, goats, and sheep. Each fence gate and vault is locked. The vaults of the corner elements have internal dimensions of 3'x3', and the central element and the battery vault have dimensions of 4'x4' (Figure 6). The vault of the central element has additional space for the deployment of other equipment.

Power to all elements is provided by a central solar panel array (Figure 7), with a battery bank that will provide backup power for 14 days. The solar panels provide 48 V DC, which is dropped down to 12 V and regulated at each vault. Barbed wire surrounds the battery vault for added security. All elements are connected for power and communications through ground cables. The power cables terminate at the battery vault, and the communication cables terminate at the fenced antenna enclosure, which also contains the Handar meteorological station (Figure 8). A 120' crank-up aluminum tower rises two 10dB Yagis above the rainforest treeline. The Yagis shoot directly to a smaller mast on the roof of the ISLA.

At the time of this writing, two tasks remained unfinished: the construction of the wind-noise-reducing filters and the completion of the VSAT installation. By the time of this publication, both tasks will be completed. The proposed wind-noise reducing filter is a variation of the French star design, but with the addition of more ports. As shown in Figure 9, 120 ports will be deployed in a symmetric 18m diameter array configuration. The central summing manifold is encased in the concrete foundation of the vault, and each port and central manifold intake will have mechanical valves which may be closed for calibration tests and for investigating the response of the pipe arrays.

Access to the conservation/agricultural district that contains the array site is regulated by the landowner through a series of locked gates and by a permit request procedure. No hunting is allowed in the area, and no problems with vandalism have been encountered to date. The ISLA is contained within a fenced facility that is closed and patrolled after work hours. The room that will contain the RPC and XAVE computers as well as the GCI hub will have restricted access and an alarm system. Backup generator power will be enabled after 20 minutes of a major AC power shutdown. However, all mission critical systems for IS59 have at least 1 hour of UPS backup.

Infrasonic Array Data

Array data has been archived since May 26, 2000, and regional and distant events have been observed. Figure 10 shows the channels recorded by IS59. The Chaparral pressure data is sampled at 20 Hz and all auxiliary, SOH, and met data is sampled at 1 Hz. Regional infrasonic events are generated by the slamming of surf along the cliffs, airplanes taking off and landing (Figure 11), and man-made explosions. The archived CSS data is post-processed using Matseis. In Figure 11, moving from top to bottom, the upper four waveforms (I59HxBDO) show the raw data, with a bandpass of approximately 0.01-8 Hz. The next four waveforms (I59HxBDObp) are band-passed filtered (two-pole, zero-phase Butterworth window) between 0.1-1 Hz, where microbarom signals dominate. The next four waveforms (I59HxBDOhp) are high-passed filtered for frequencies above 1 Hz. The last trace is an STA/LTA filter on I59H4BDOhp, with STA = 1 and LTA = 100. This signal can be clearly seen even in the raw data. The FK analysis for the band-passed signal contained within the dashed lines in the upper panel of Figure 11 is shown in the lower left panel. The arrival azimuth of 325^{o} apparent phase velocity of 360 m/s across the array suggests that this signal originated from an aircraft departing from the Kona airport, at a range of ~20 km. Later arrivals (Figure 11, lower right hand panel) have smaller amplitudes and higher frequencies, and are more typical of

the aircraft signals observed by IS59. However, sometimes the aircraft signals are not detected, suggesting that these arrivals may be dependent on the boundary layer conditions. Because the airstrip is aligned in the N-S direction and the predominant winds are in the E-W direction, the takeoff and landing direction may be varied throughout the day according to the predominant wind component along the N-S direction. Accordingly, aircraft signals may appear either slightly North or South of the airport.

In contrast to the MB2000, the Chaparral 5 sensors appear to be fairly insensitive to seismic events and may be tuned to have very low self-noise levels. Acoustic events that were not observed during the site survey (utilizing the MB2000) are now routinely observed by the Chaparrals, and similarly, seismic events are seldom observed. Some discrete events appear to come from distant sources because they exhibit dispersion. Positive identification of unknown distant sources is difficult without another array. However, various microbarom signals can be associated with well-defined storm systems in the Pacific Ocean, such as Typhoon Kirogi in Japan (Garcés et al., 2000).

CONCLUSIONS AND RECOMMENDATIONS

IS59 is operational, and efforts are under way to complete the installation so as to comply with the CTBT certification standards. IS59 is recording various intriguing signals that are difficult to identify and locate. Some of our event identification problems may be alleviated as the other IMS infrasound arrays are deployed and as other sources of data are integrated in the analysis. However, regional events may be difficult to identify and locate without an additional array on the island. It may be possible to enhance the array's ability to locate events by including seismic data in the analysis, although this improvement would be limited earthquake identification and to the analysis of acoustic signals that couple well into the ground. An additional limitation is the significant spatial aliasing above ~0.3 Hz induced by the 1.9 km aperture of the array. For these higher frequencies, our array processing capabilities are restricted to signals with a large signal-to-noise ratio. The aliasing problem can be solved by the addition of three elements near the center of the array.

REFERENCES

Garcés, M., and H. Bass (1999). *Results of the infrasonic site survey for CTBT station IS59, Hawaii*. Proceedings of the 21st Annual Research Symposium on Monitoring a Comprehensive Test Ban Treaty.

Garcés, M, D. Drob, M. Picone, K. Lindquist, and R. Hansen (2000). *Characterization Of Infrasonic Waves Observed In Hawaii During Summer.* 22nd Seismic Research Symposium: Planning for Verification of and Compliance with The Comprehensive Nuclear-Test-Ban Treaty, New Orleans (this issue).

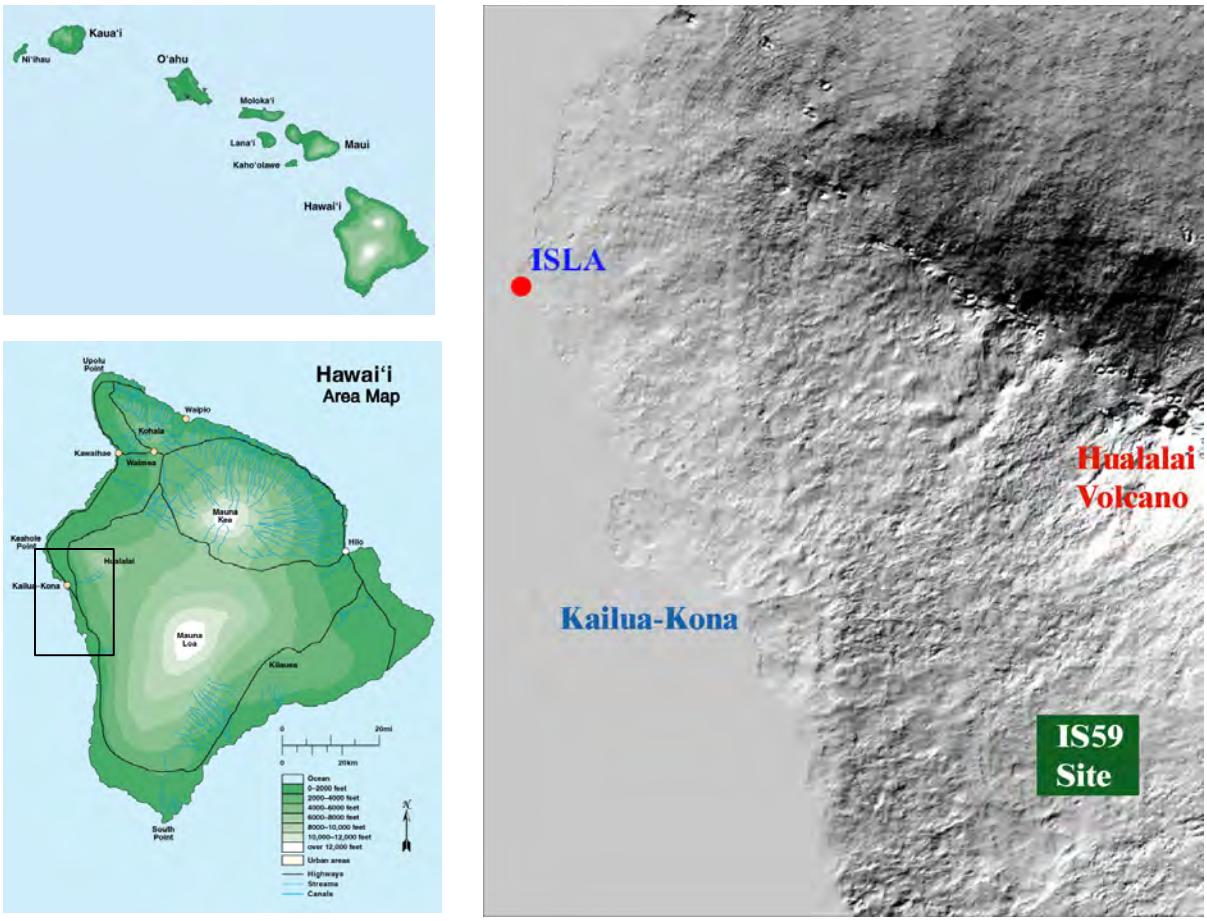


Figure 1. Location of IS59 and Infrasound Laboratory (ISLA) on the island of Hawaii.

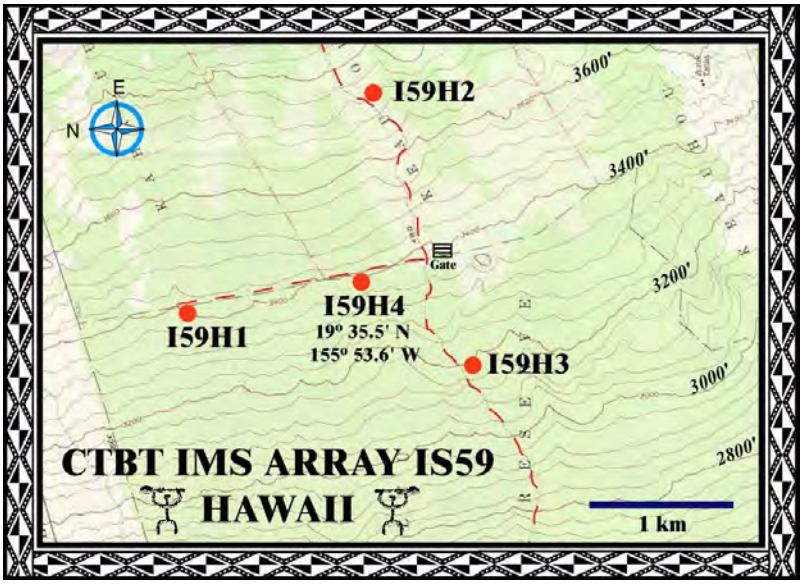


Figure 2. Infrasonic array geometry.

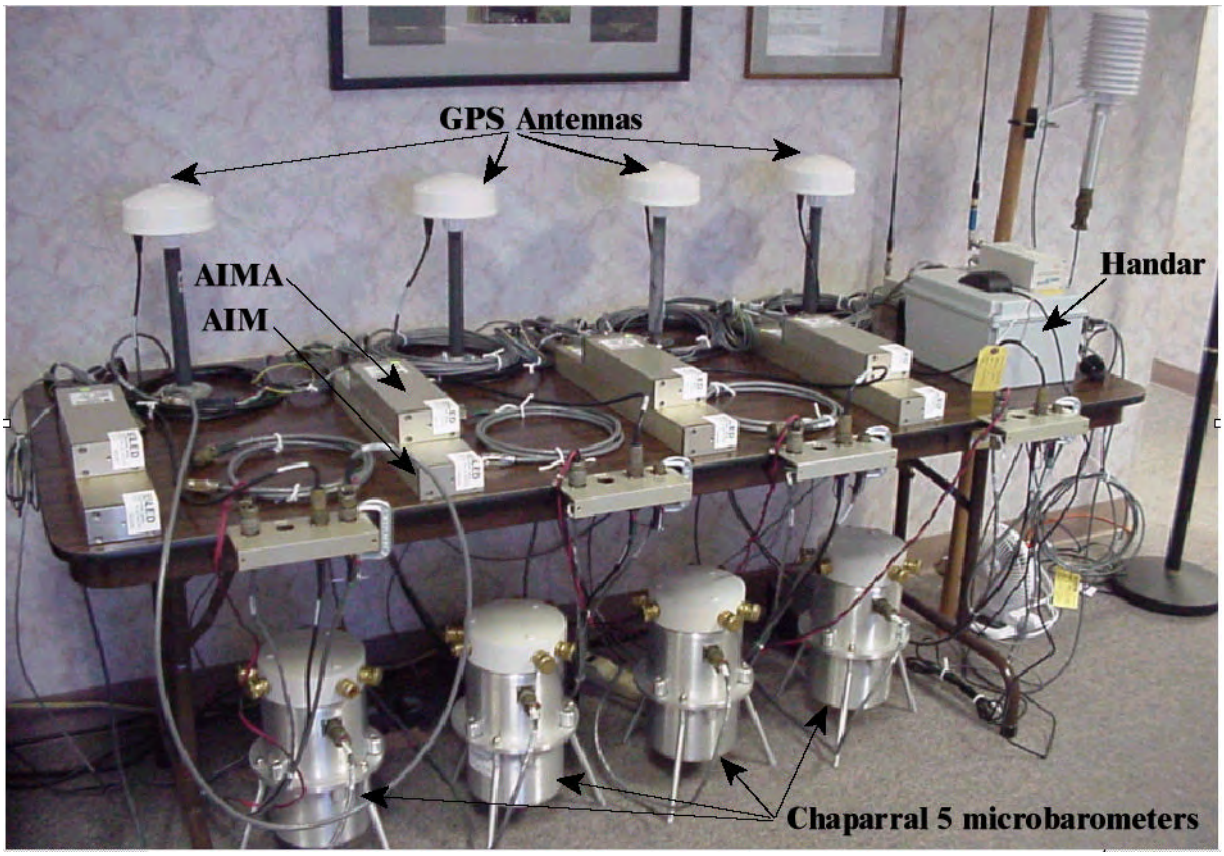


Figure 3. Data acquisition hardware.



Figure 4. Real-time data manager. The Xave workstation is shown on the left, and the RPC (top) and CIM (bottom) are shown on the left.







Figure 5. Instrument vaults. Six-inch concrete walls and steel lids ensure the equipment's survival in the case of a tree fall. Each vault is locked. Pipes for connecting the wind-noise reducing filters are connected to a summing manifold imbedded in the vault's foundation.

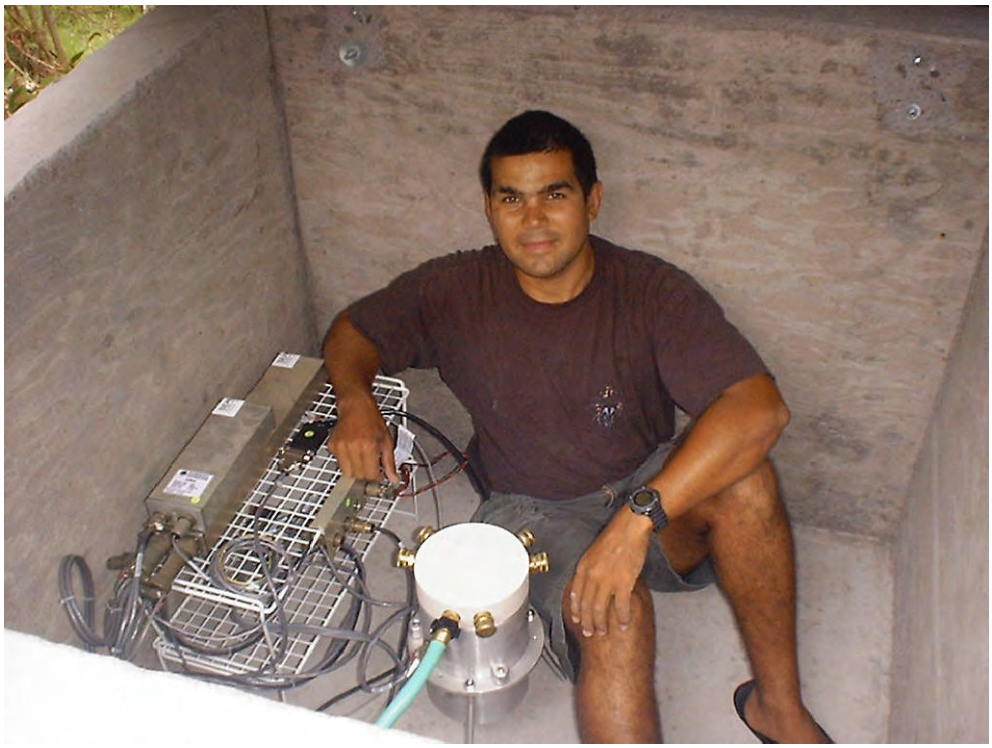


Figure 6. Vault's interior.



Figure 7. Central photovoltaic power system.



Figure 8. Weather station at antenna site.

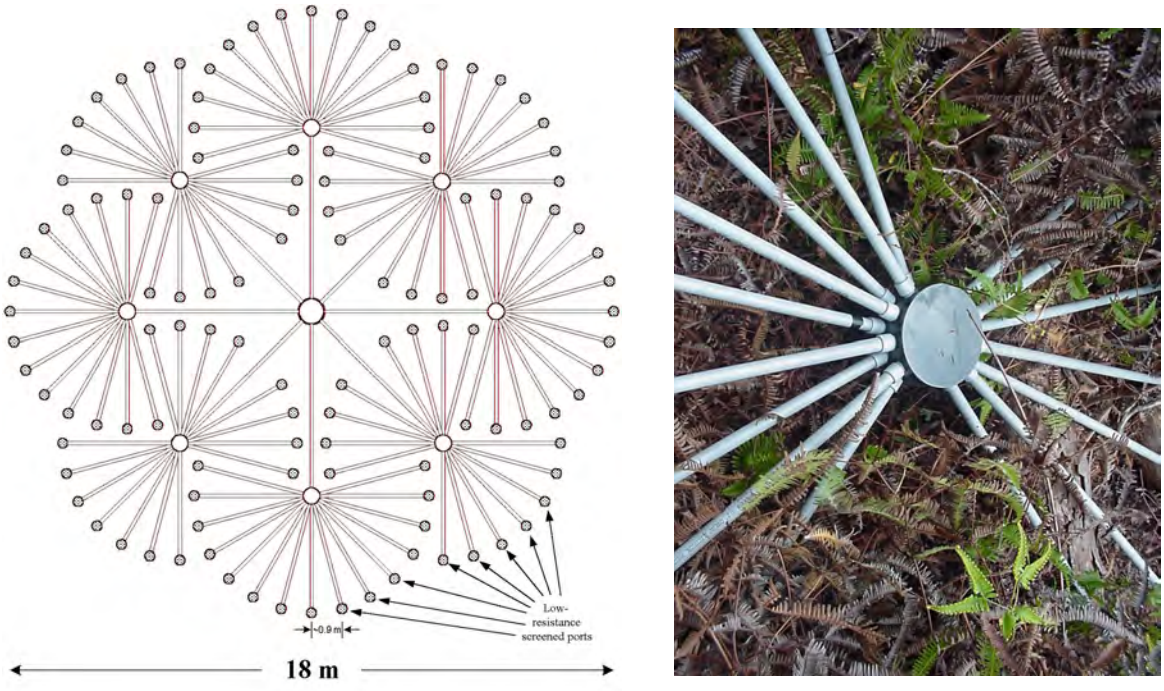


Figure 9. Wind-noise-reducing pipe array design (left) and PVC implementation (right).

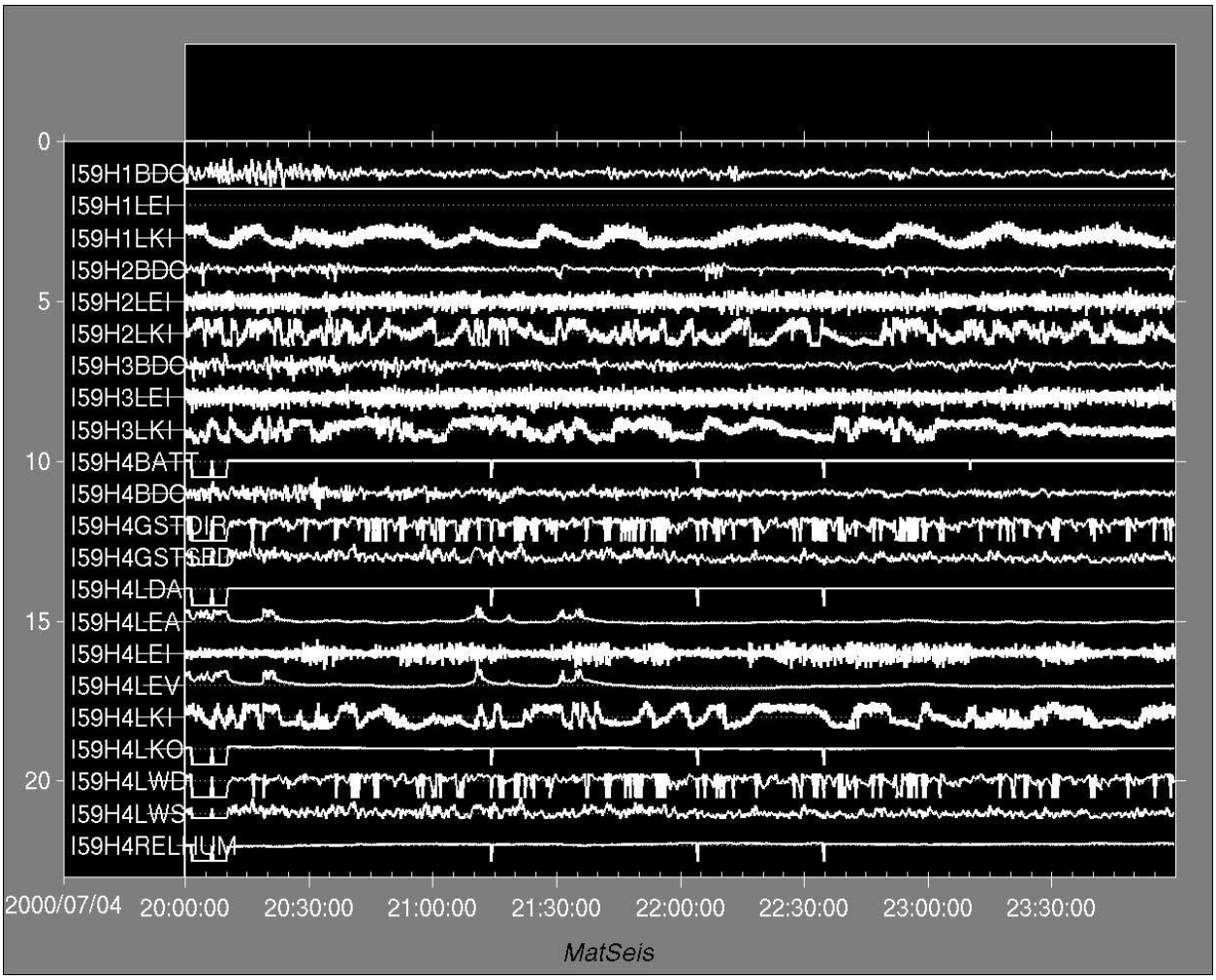
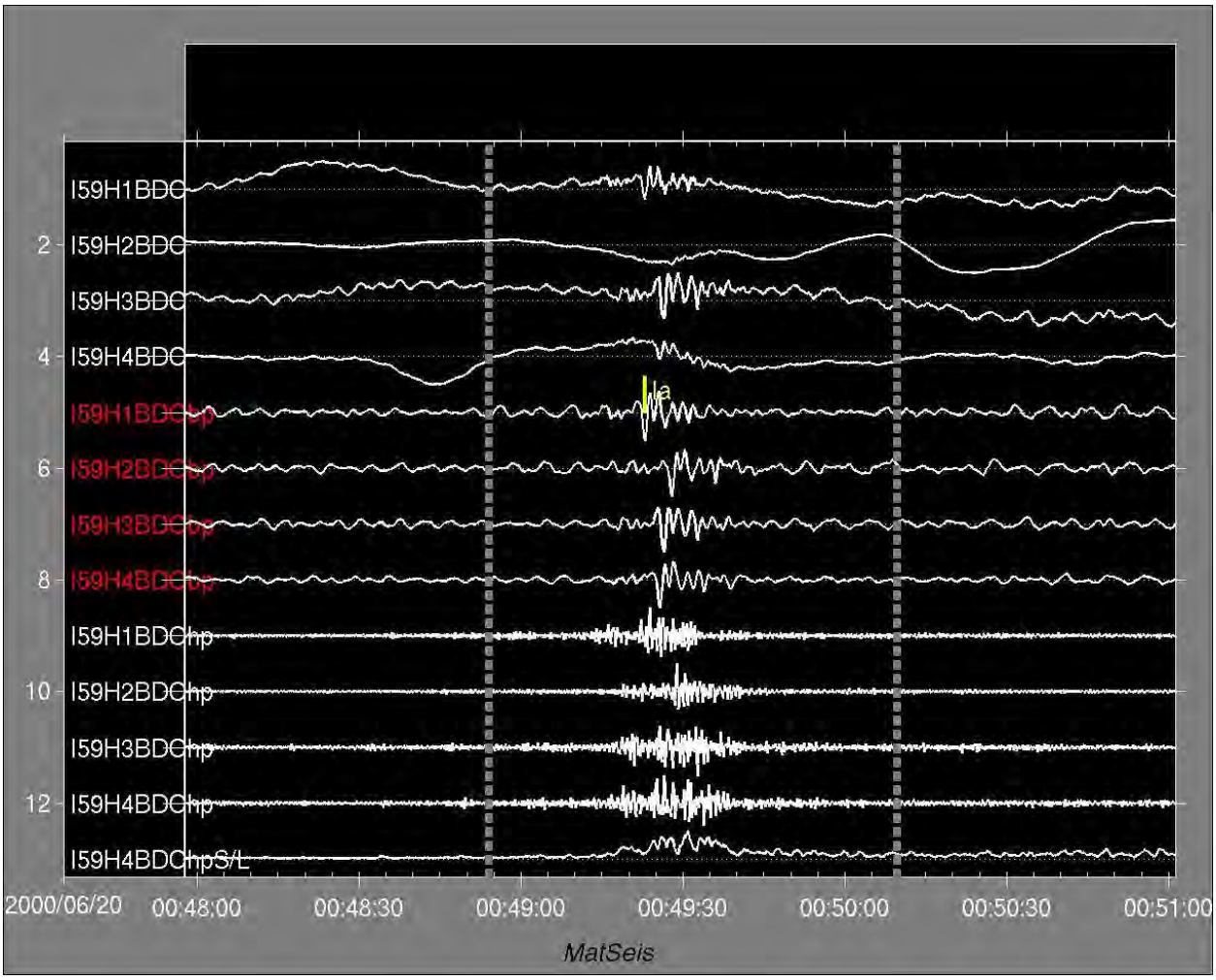
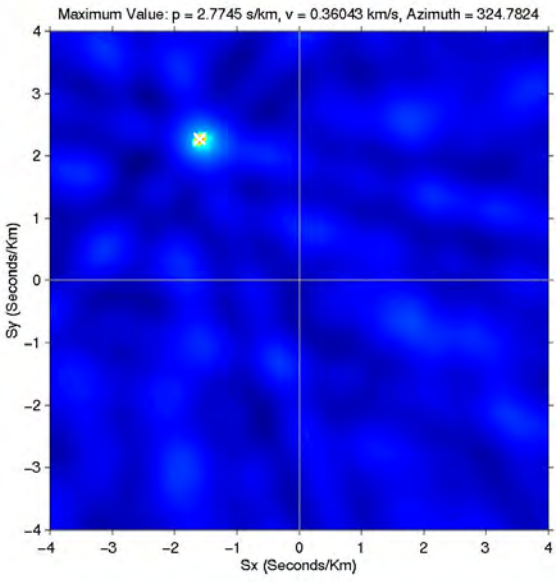


Figure 10. Pressure, meteorological, and state-of-health (SOH) channel data for IS59. All digitizers (IS59H1-4, as shown in Figure 2) have the Chaparral 5 pressure data (BDO, sampled at 20Hz) and two SOH channels sampled at 1 Hz: LEI is the voltage to the digitizer inside the vault, and LKI is the vault temperature. Associated with IS59H4 (central element) are two additional auxiliary channels and the all the Handar meteorological station channels. All of these additional channels are sampled at 1 Hz. LEA is the current and LEV is the voltage at the solar panel battery vault, which provides the power to the array. These two channels are connected as auxiliary channels to the AIM of H4. For the met station, BATT is the battery voltage, GSTDIR is the wind gust direction, GSTSPD is the wind gust speed, LDA is the barometric pressure, LKO is the outside temperature, LWD is the wind direction, LWS is the wind speed, and RELHUM is the relative humidity. The met station and digitizer data are telemetered on separate but parallel radio links to ISLA, where all data is assembled into CD-1 frames. The pressure channel will be renamed to BFO and I59H4 will be renamed I59H0, but at the time of this writing these changes have not been implemented.





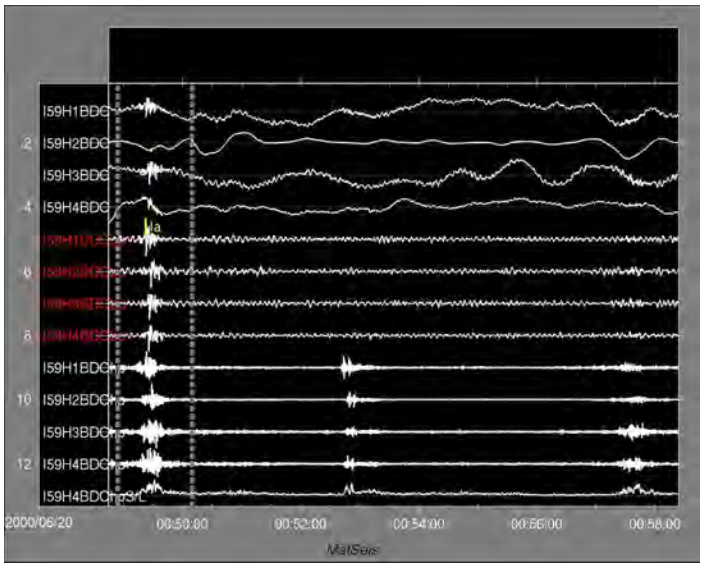


Figure 11. Pressure signal originating from the direction of the Kona International Airport.

CHARACTERIZATION OF PREDICTED INFRASONIC PHASES FOR IS59, HAWAII

Milton Garcés[1] and Colin Potter
Infrasound Laboratory, University of Hawaii, Manoa
[1]Also at the University of Alaska, Fairbanks

Douglas Drob and Michael Picone
Naval Research Laboratory, Upper Atmospheric Physics Branch

Roger Hansen and Kent Lindquist
Geophysical Institute, University of Alaska, Fairbanks

Sponsored by U.S. Department of Energy
Office of Nonproliferation Research and Engineering
Office of Defense Nuclear Nonproliferation
National Nuclear Security Administration

Contract No. DE-FC04-98AL79801

ABSTRACT

The atmosphere is a dynamic and complex medium, and infrasonic waves traveling through this medium will be strongly affected by its properties. The wind field, temperature, and composition of the atmosphere up to heights of 150 km will determine how sound waves are propagated between a source and a receiver. We integrate acoustic wave propagation models, the Naval Research Laboratory (NRL) Horizontal Wind Model (HWM93), the NRL Mass Spectrometer and Incoherent Scatter (MSIS90) atmospheric model, and the United Kingdom Meteorological Office (UKMO) Correlative Analyses to investigate the effects of atmospheric variability on the types of infrasonic phases that may be observed at CTBT array IS59 in Hawaii. Array IS59 [*Garcés and Bass*, 2000 (this issue)] started recording and archiving infrasonic data in May 25, 2000, and has recorded a variety of regional and distant events. We use the results of our theoretical and data assimilation work to characterize the response of IS59 so that it possible to associate and locate events using multiple arrays.

Key Words: Hawaii, infrasound, travel times, atmospheric models, phase identification, source location

OBJECTIVE

The objective of this work is to characterize the predicted phases and azimuth deviations of signals that can be observed with the Hawaii CTBT infrasonic array. This objective is fulfilled by integrating detailed atmospheric and acoustic propagation models and comparing the predicted results to recorded array data. This research addresses the need for accurate infrasonic source locations, which are essential to CTBT enforcement.

RESEARCH ACCOMPLISHED

1. Introduction

Infrasonic waves with frequencies between 0.02 and 10 Hz can travel thousands of kilometers before being significantly attenuated by viscosity and thermal conduction. Atmospheric wind, temperature, and composition fields from the ground to 160 km determine how these waves propagate. Between 60 km and 160 km infrasonic waves are strongly affected by solar tides (hourly), geomagnetic storms (daily), and solar EUV radiation (monthly). Below the stratospause (60 km) meteorological waves may eliminate or encourage waveguide propagation, depending on their strength and position. The acoustic propagation medium and therefore the predicted phases, travel time curves and azimuth deviations change significantly throughout the day and the seasons. Our studies (*Garcés et al*., 2000a-b, 1999a-c) show that in order to optimize phase identification and source location accuracy, infrasonic wave propagation models should access reliable atmospheric profiles evaluated within several hours of a suspect event. Ground truth validation of our approach is provided by the analysis of Concorde signals by *LePichon*

et al. (2000). In this study we use daily numerical weather prediction nowcasts from UKMO (< 50 km) and 6-hour climatological estimates from the NRL-HWM-93 and NRL-MSISE00 empirical atmospheric models (*Hedin*, 1991; *Hedin et al*., 1996; *Drob and Picone*, 2000) to evaluate the climatology over Hawaii for the whole of 1996 and for selected days of 1999. We compute the trajectories for acoustic rays propagating in these backgrounds using the formulation of *Garcés et al*., 1998. The effects of vertical winds, horizontal gradients, and spherical geometry are ignored.

2. Model results

Previous work (*Garcés et al*., 2000a-b, 1999a-c) has shown that the solar tides introduce significant hourly variability in the wind field of the Mesosphere and Lower Thermosphere (MLT). Figure 1 shows the zonal (E-W) and meridional wind (N-S) for 1996. The solar tides have dominant diurnal and semidiurnal periods, and thus each panel is separated by three hours so that we can observe the changes in phase. At this latitude (19^o 35.5' N), the zonal winds are more variable than the meridional winds, and geomagnetic effects not as significant as in the higher latitudes. Planetary waves in the troposphere introduce significant daily variability in the zonal winds. The clearest seasonal change is the reversal of the thermospheric winds and the zonal stratospheric winds. The seasonal thermospheric reversal is affected by the solar tides, which have high amplitudes above 100 km heights. Figure 2 shows the sound speed at Hawaii for 1996. Except in cases of extreme solar activity or near the thin boundary layer near the ground, at the lower latitudes the variability in the sound speed is negligible compared to the variability of the wind.

We now trace rays through the atmospheric models shown in Figures 1-2. Figure 3 illustrates the hourly time-dependence of thermospheric ducting caused by the solar tides in the MLT. Each color corresponds to a different local time separated by 6-hours. It is clear that the turning height of a ray may vary throughout the day, and that this change in path will affect the amplitude and frequency content of a received signal. Figure 4 shows the height in the atmosphere at which rays turn before arriving at the Hawaii array from an azimuth of 0^o. Since the stratospheric meridional winds are weak, there are no predicted stratospheric arrivals expected from either the North or the South (180^o). Thus, barring anomalously strong storms, all phases arriving in Hawaii from the North or South are thermospheric. Figure 5 shows the azimuth deviation for waves arriving from the North. The azimuth deviation for this arrival angle is determined by the zonal winds, which are strongly affected by meteorological waves in the troposphere. In general, the arrival azimuth needs to be corrected towards the left in Winter and towards the right in Summer. This means that an arrival detected near 16 h Hawaii Time with a slowness of 2.5 s/km arriving from the North in middle of Summer has a true azimuth of ~5^o East of North. However, the exact value of the azimuth deviation will depend on the strength and location of storm systems in the Pacific.

The turning heights of waves propagating along the E-W direction may vary significantly because of the dependence of the zonal winds on meteorological disturbances and because of the marked reversal in the stratospheric zonal wind. Figure 6 shows that stratospheric phases may be expected to arrive from the East (90^o azimuth) during Summer. If a sufficiently strong weather system were to appear in Spring and Fall, it may also be possible to induce stratospheric phases. Due to the relatively mild meridional winds, the azimuth deviation along the E-W direction (Figure 7) is slight and seldom exceeds a few degrees. The azimuth deviations of waves arriving from the South are also determined by the zonal winds. Figure 8 shows that the deviation trends for Southerly arrivals are the reverse of those for Northerly arrivals, as expected. As in Figure 4, all Southerly turning heights are in the thermosphere, and most of the variability is induced by the tides. Figure 9 shows the turning height of Westerly waves, showing the presence of stratospheric phases during Winter. The slowness range corresponding to the stratospheric phases depends on the state of the troposphere and stratosphere during that day, and thus a phase identification scheme based on static slowness ranges would lead to an incorrect ID. It follows that for certain arrival directions phase ID should be performed dynamically by using the most recent atmospheric data. Even if phase ID is not in question (as in N-S propagation), it is important to know at which level a ray turned in order to infer the source amplitude. Thus the daily variability of solar tides must be taken into consideration if precise estimates of the magnitude and location of an event need to be produced.

Our present line of research is moving towards providing meteorological nowcasts that can be ingested into the infrasonic propagation models to analyze specific events. For the July 4, 2000 reentry of the Compton Gamma Ray Observatory (CGRO) we used the atmospheric conditions of June 4, 1999 to estimate the expected propagation characteristics in Hawaii (Figure 10). No clear signals from the CGRO were detected by IS59, possibly due to the distant impact (~4000 km) and highly directional radiation pattern of the hypersonic reentry. However, in addition to various regional infrasonic events (*Garces and Bass*, 2000), continuous microbarom signals are recorded by IS59. Figure 11 shows a microbarom signal recorded on July 8 at IS59. The main coherent energy peak in the 0.1-0.5 Hz

band arrives from an azimuth of 292^{o} with an apparent horizontal velocity of 0.348 km/s, or a slowness of 2.87 s/km. This azimuth points towards Typhoon Kirogi, which took 27 lives in the Philippines and two in Japan. Very small azimuth deviations are expected for Westerly arrivals, and the slowness corresponds to a turning height that is near 120 km in the thermosphere. Although acoustic generation near the source will be evidently affected by the powerful typhoon winds, propagation near Hawaii will be unaffected by the distant disturbance and is likely to fall near the predicted values. With the addition of other infrasonic arrays within the Pacific Rim, it would be possible to associate and track pressure disturbances across the Pacific and use this ongoing endeavor to validate atmospheric models and maintain readiness in the monitoring of the CTBT.

CONCLUSIONS AND RECOMMENDATIONS

Only thermospheric arrivals are expected to arrive in Hawaii from the North or South throughout the year. The height in the atmosphere at which these rays turn in the thermosphere will be primarily determined by the solar tides. However, for propagation along the meridian, the azimuth deviation will be strongly affected by meteorological disturbances in the stratosphere and troposphere. Arrivals from the East will consist of thermospheric arrivals in Winter and both thermospheric and stratospheric arrivals in Summer. The slowness and turning height values of these arrivals are strongly influenced by the solar tides and by meteorological disturbances in the lower atmosphere. However, the azimuth deviations along the E-W direction are expected to be only a few degrees. In order to produce unambiguous phase identifications and accurate source locations, it is necessary to have access to recent and reliable atmospheric data. It is recommended that integrated global meteorological nowcasts ranging from sea level to heights of 150 km be developed for ingestion into infrasonic data analysis and interpretation programs.

REFERENCES

Drob, D., and J. Picone (2000). *Statistical performance measures of the HWM-93 and MSISE-90 empirical atmospheric models and the relation to infrasonic CTBT monitoring*. Proceedings of the 22nd Seismic Research Symposium: Planning for Verification of and Compliance with the Comprehensive Nuclear-Test-Ban Treaty (this issue).

Garcés, M., and H. Bass (2000). *Installation and pre-certification of CTBT station IS59, Hawaii*. Proceedings of the 22nd Seismic Research Symposium: Planning for Verification of and Compliance with the Comprehensive Nuclear-Test-Ban Treaty (this issue).

Garces, M, D. Drob, M. Picone, K. Lindquist, and R. Hansen (2000a). *Infrasonic CTBT monitoring and the atmosphere.* EOS, Trans. Am. Geophys. Union, 81, S5.

Garcés, M., D. Drob, and M. Picone (2000b). *A theoretical study of the effect of geomagnetic fluctuations and solar tides on the propagation of infrasonic waves in the atmosphere*. Geophys. J. International (accepted).

Garcés, M., R. Hansen, K. Lindquist, D. Drob, and M. Picone (1999a). *Variability of the lower atmosphere and its effect on the propagation of infrasonic waves.* Proceedings of the 21st Annual Research Symposium on Monitoring a Comprehensive Test Ban Treaty.

Garcés, M., D. Drob, and M. Picone (1999b). *Geomagnetic and solar effects on thermospheric phases during Winter*. EOS, Trans. Am. Geophys. Union, 80, S71.

Garcés, M., K. Lindquist, R. Hansen, D. Drob, and M. Picone (1999c). *Temporal variability in the propagation on infrasonic waves over Hawaii and Alaska during Winter*. J. Acous. Soc. Am., 105, 1104.

Garcés, M. A., R. A. Hansen, K. Lindquist (1998). *Travel times for infrasonic waves propagating in a stratified atmosphere*. Geophys. J. International, 135, 255-263.

Hedin, A.E., (1991). *Extension of the MSIS thermosphere model into the middle and lower atmosphere*. J. Geophys. Res. 96, 1159.

Hedin, A.E., M. A. Biondi, R. G. Burnside, G. Hernandez, R. M. Johnson, T. L. Killeen, C. Mazaudier, J. W. Meriwether, J. E. Salah, R. J. Sica, R. W. Smith, N. W. Spencer, V. B. Wickwar and T. S. Virdi, (1996). *Revised global model of upper thermospheric winds using satellite and ground-based observations*. J. Geophys. Res. 96, 7657-7688.

Le Pichon, A. M. Garcés, E. Blanc, M. Barthélémy, D. Drob (2000). *Acoustic propagation and atmosphere characteristics derived from infrasonic waves generated by the Concorde*. J. Acoust. Soc. Am. (submitted).

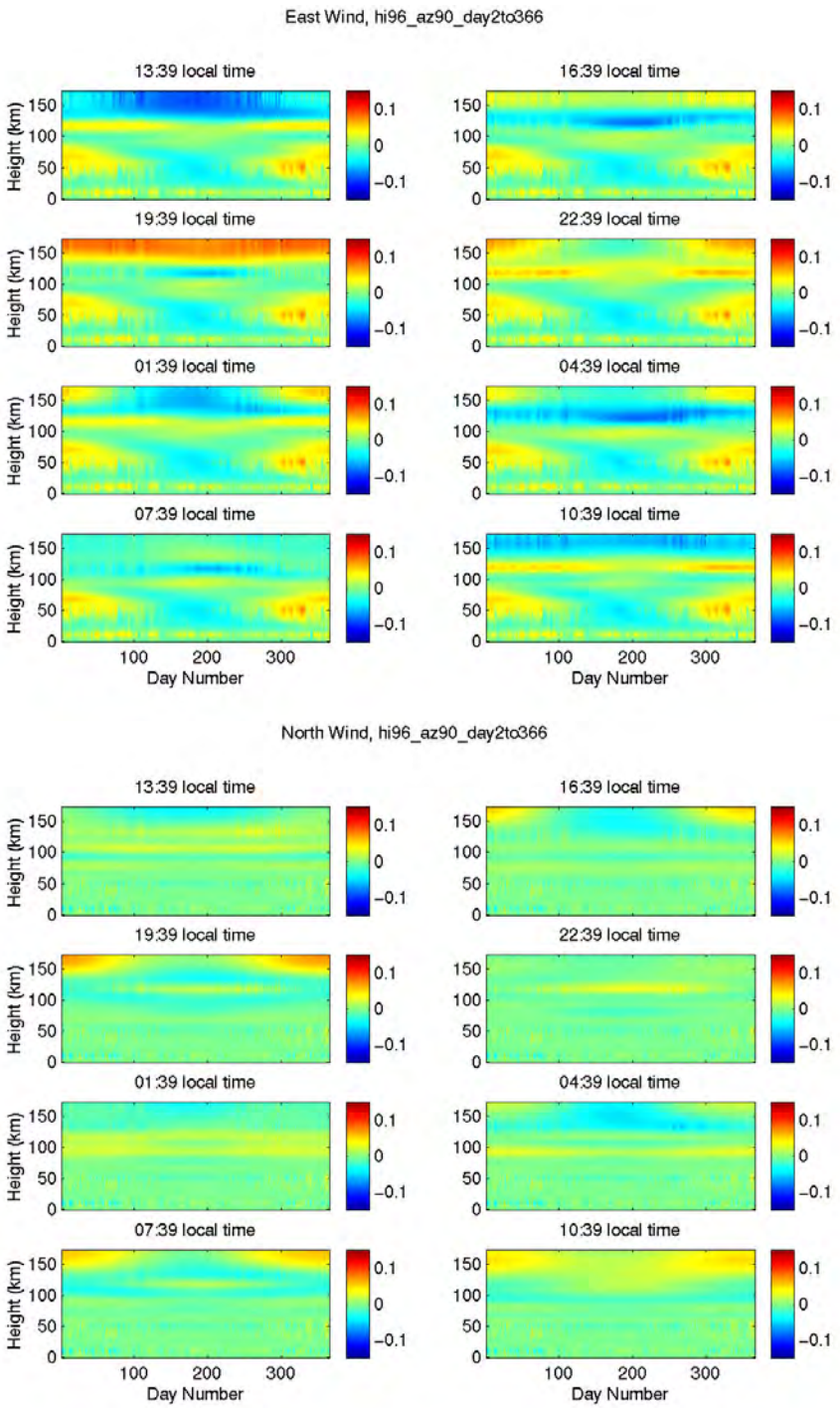


Figure 1. Zonal (upper panel) and Meridional (lower panel) winds (km/s) at Hilo, Hawaii, as a function of height, calendar day number and local time of day. Wind is positive towards the East and the North. Planetary waves produce daily variability up to 50 km, tides dominate diurnal changes in the mesosphere, and geomagnetic storms determine the daily variability of the lower thermosphere. Seasonal changes are visible at all levels in the atmosphere, and are particularly stable in the stratosphere reversal.

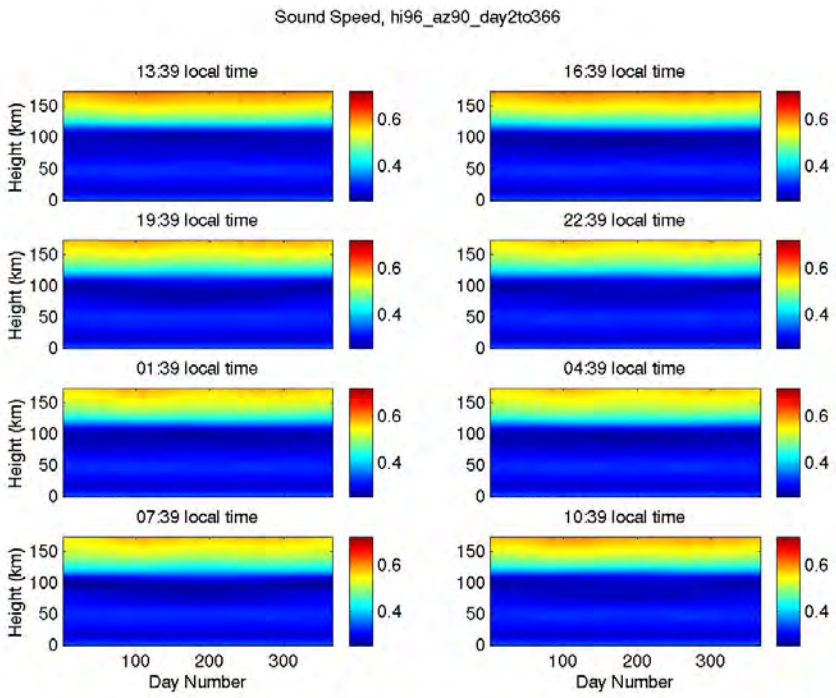


Figure 2. Sound speed (km/s) at Hawaii as a function of height, calendar year and local time of day. The variability is weak compared to that of the wind field. There is a slight increase of the sound speed in the thermosphere due to geomagnetic storms, and Summer cooling in the mesosphere is quite mild.

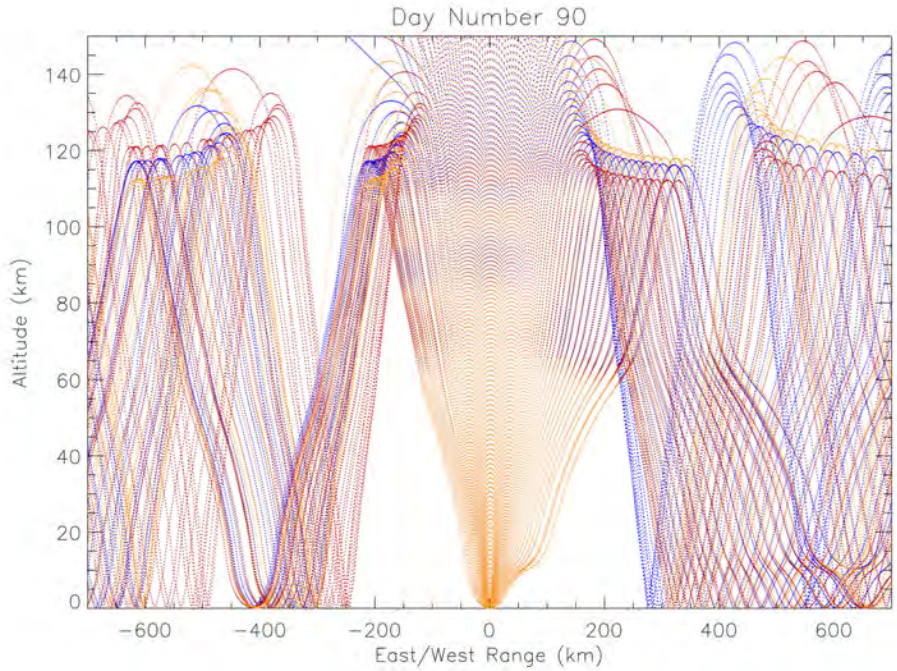


Figure 3. Hourly time-dependence of propagation due to thermosphere ducting over Hawaii. This variability is caused by thermal migrating tides in the middle and upper atmosphere. Each color corresponds to a different local time separated by 6-hours.

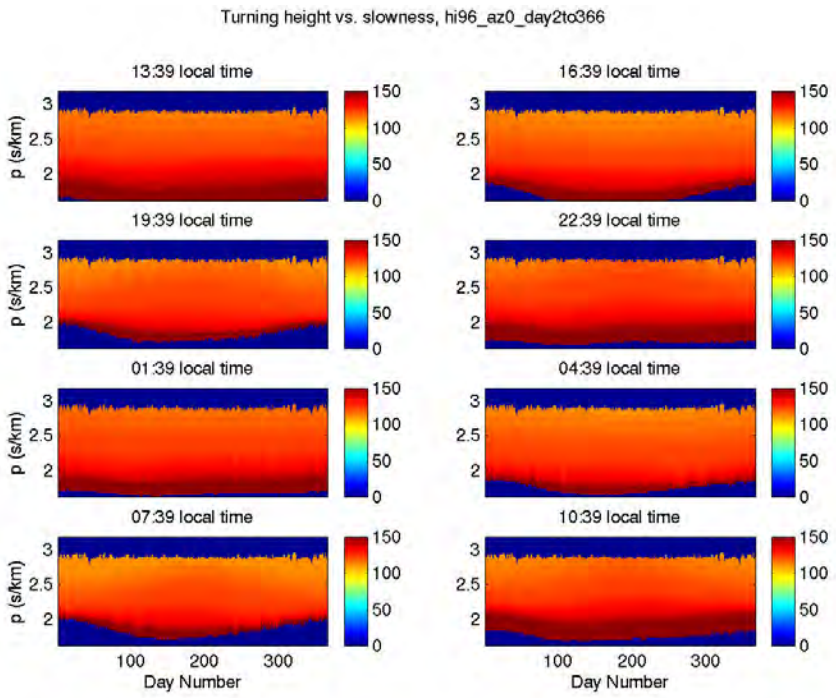


Figure 4. Turning height (km) of rays at Hawaii as a function of slowness (s/km), calendar year and local time of day for an arrival azimuth of 0 degrees. All predicted phases are thermospheric, and their variability is primarily determined by the solar tides and the seasonal changes in the thermosphere.

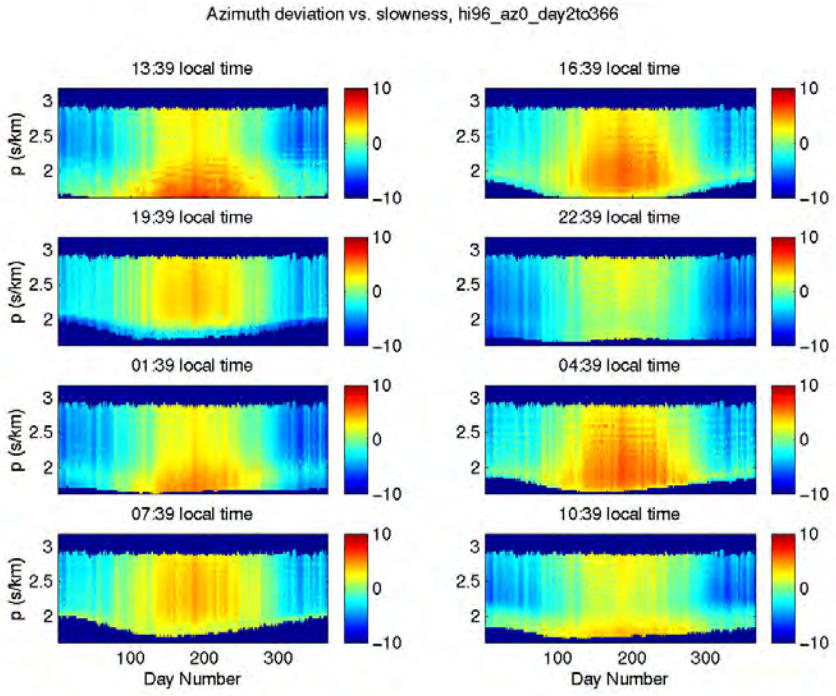


Figure 5. Azimuth deviation (degrees) at Hawaii as a function of slowness (s/km), calendar year and local time of day for an arrival azimuth of 0 degrees. A deviation of +5 degrees means that the arrival azimuth has to be corrected by adding 5 degrees towards the right of the arrival direction. The deviation, which for this azimuth is determined by the zonal wind, is strongly affected by planetary waves in the stratosphere.

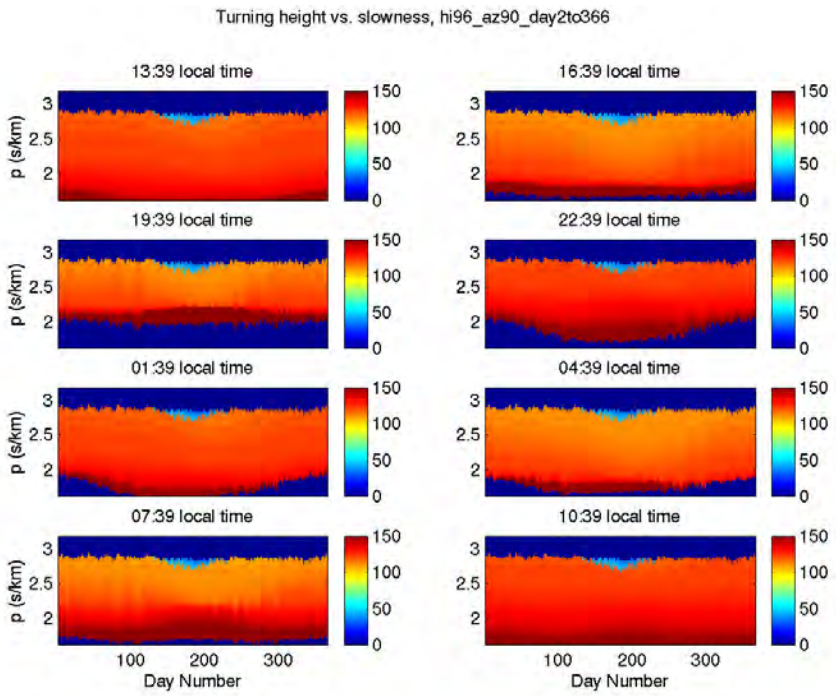


Figure 6. Turning height at Hawaii as a function of slowness, calendar year and local time of day for an arrival azimuth of 90 degrees. Stratospheric phases arrive from the East during Summer. The effects of the tides and the seasonal changes in the thermosphere are clearly seen in the turning heights of the thermospheric phases.

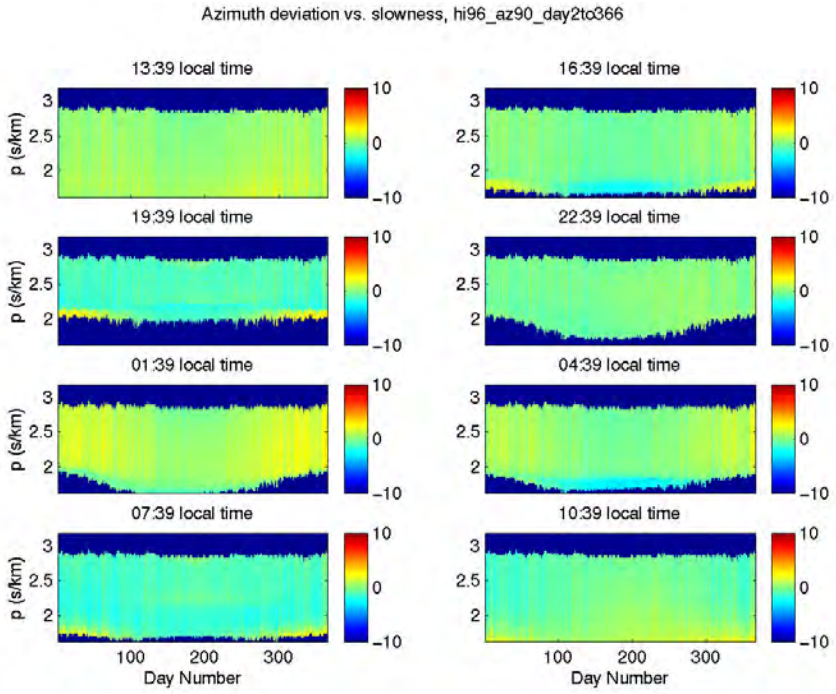


Figure 7. Azimuth deviation at Hawaii as a function of slowness, calendar year and local time of day for an arrival azimuth of 90 degrees. The deviation for this arrival angle is governed by the meridional wind, which is relatively stable and mild. Thus small deviations are expected for arrivals incident from both 90 and 270 degrees azimuth.

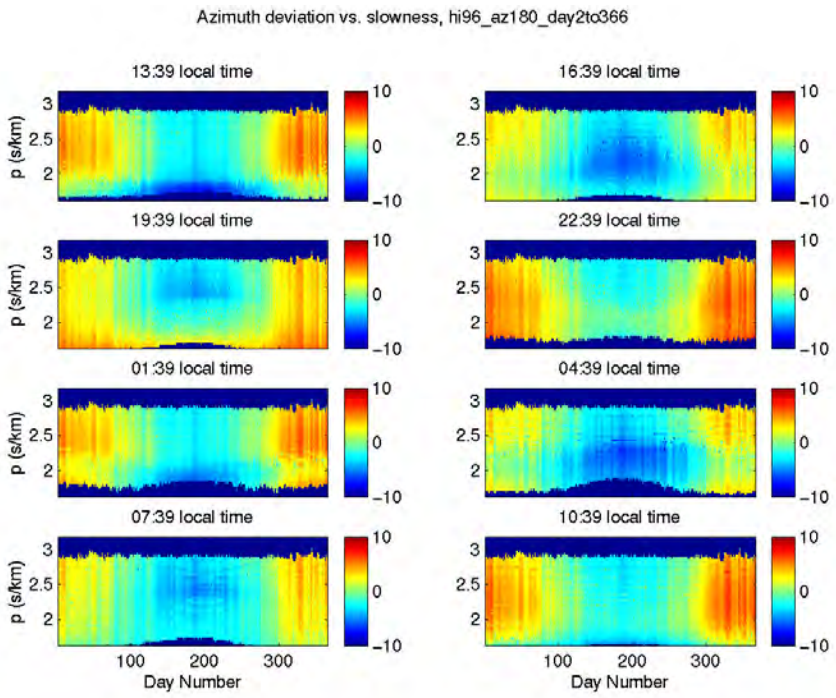


Figure 8. Azimuth deviation at Hawaii as a function of slowness, calendar year and local time of day for an arrival azimuth of 180 degrees. Planetary waves in the zonal wind introduce significant daily variability.

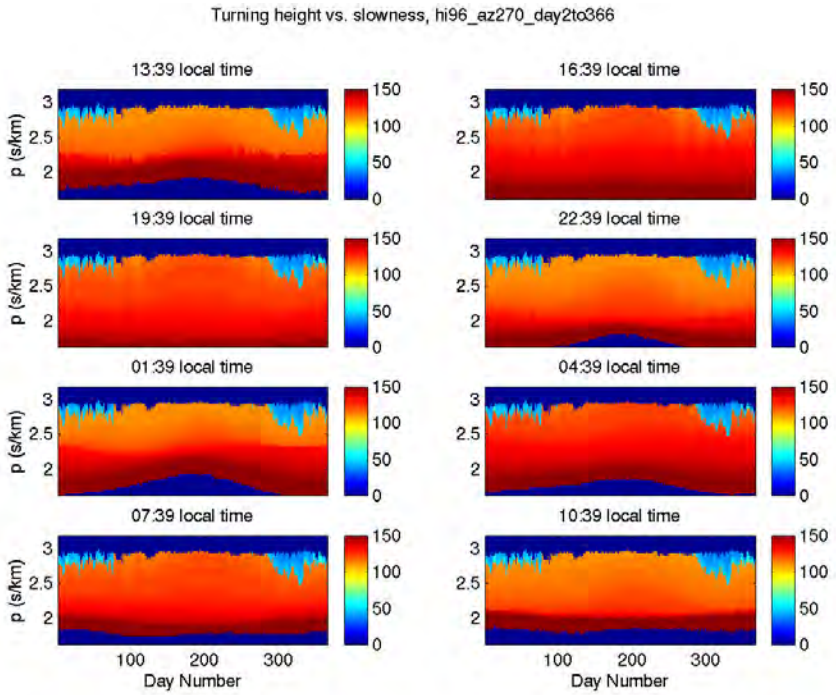


Figure 9. Turning height at Hawaii as a function of slowness, calendar year and local time of day for an arrival azimuth of 270 degrees. Stratospheric phases arrive from the West primarily during Winter.

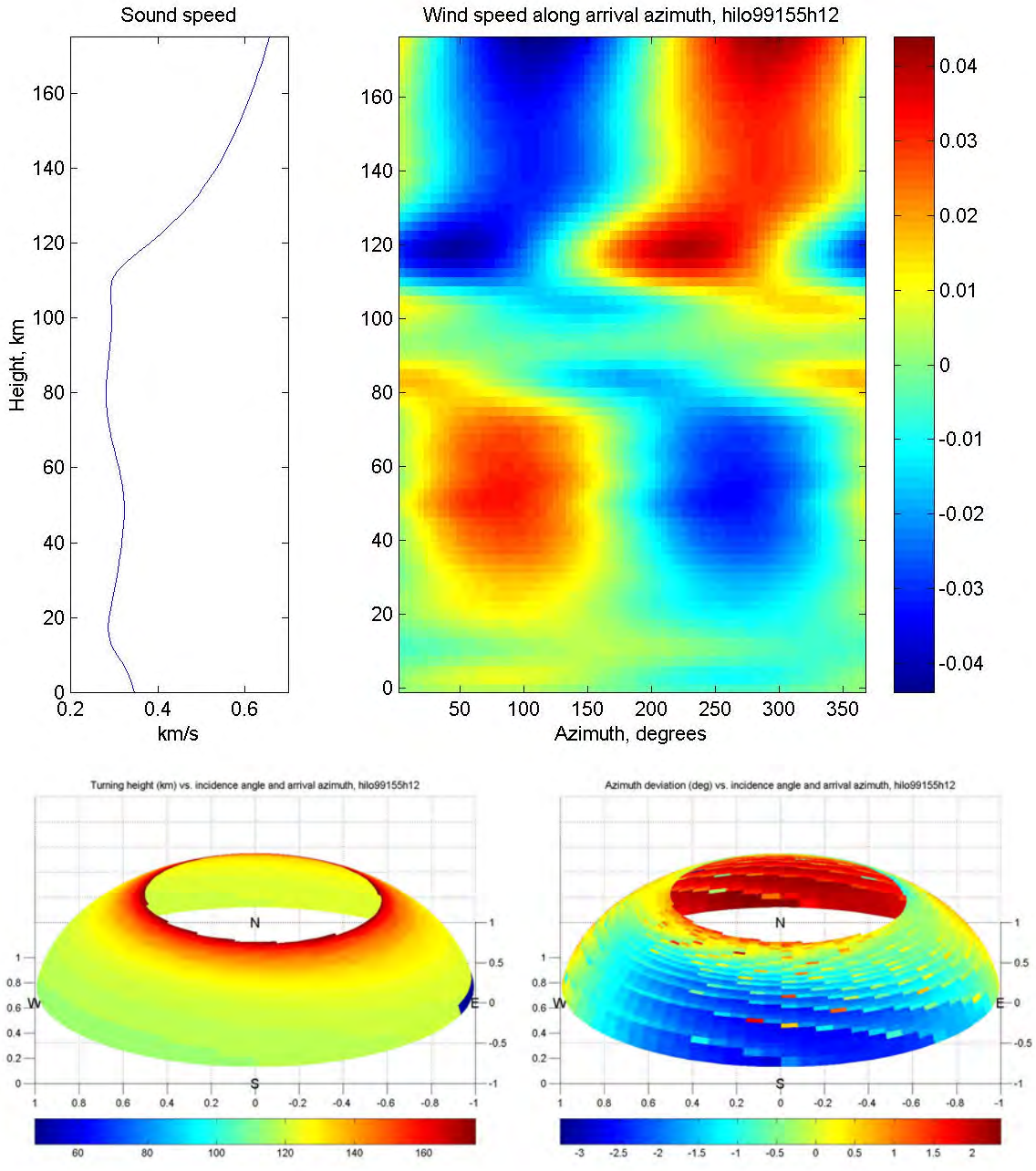


Figure 10. The upper panel show the sound speed and wind speed at Hilo for 12:00 UT on June 4, 1999. The wind speed is plotted as a function of height and arrival azimuth. In this frame a wave launched towards the South would have an arrival azimuth of 0° (N), and a positive wind along this direction would correspond to a Southward, or Northerly wind. The lower panels show the turning height and azimuth deviation of incident rays as a function of arrival azimuth and incidence angle for acoustic energy originating from a source located at the Earth's surface. The truncated hemisphere would be centered at the CTBT array location, and would allow immediate phase recognition. A detected arrival would correspond to a specific azimuth and incidence angle, and the color map on the surface of the sphere would indicate in what height of the atmosphere this ray has turned and its azimuth deviation. The truncated upper part of the hemisphere corresponds to rays which are lost to space.

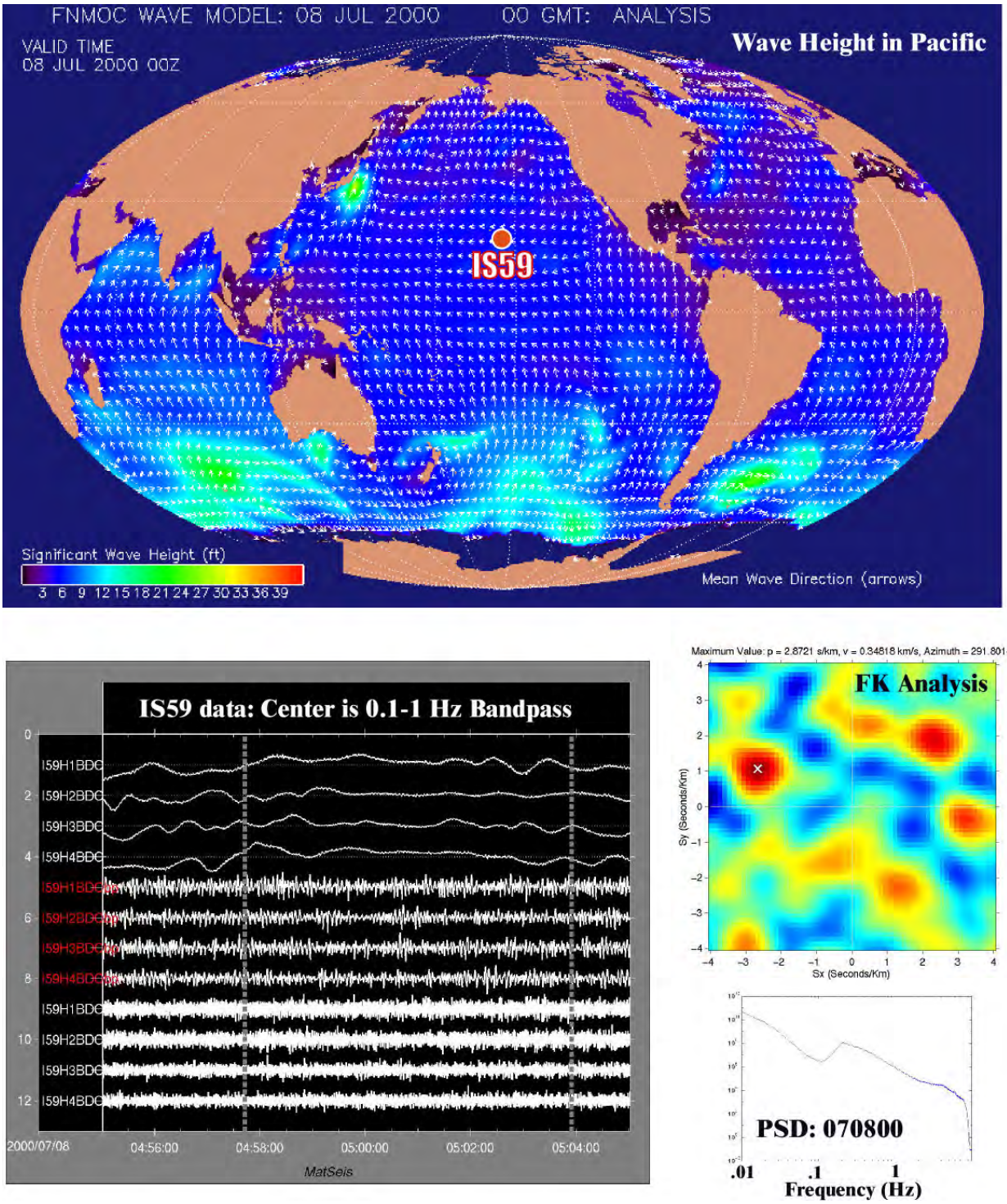


Figure 11. Microbarom signals recorded at IS59 on July 8, 2000. The dominant FK peak may be associated with a region of large significant wave heights generated by Typhoon Kirogi near Japan.

THE INFRASOUND ANALYSIS TOOL KIT *INFRAMAP*: CAPABILITIES, ENHANCEMENTS AND APPLICATIONS

Robert Gibson and David Norris
BBN Technologies, a part of GTE

Sponsored by the U.S. Defense Threat Reduction Agency
Arms Control Technology Division
Nuclear Treaties Branch

Contract No. DSWA01-97-C-0160

ABSTRACT

The analysis tool kit *InfraMAP* (*Infra*sonic *M*odeling of *A*tmospheric *P*ropagation) consists of three infrasound propagation models (3-D ray trace, normal mode, and parabolic equation), two atmospheric characterizations (HWM and MSIS), a global topography database, and user interfaces for model execution and data visualization. Software features have been implemented that allow improvements in both fidelity and functionality over previously available infrasound modeling capabilities. The ability to predict propagation characteristics that affect localization is therefore enhanced. *InfraMAP* has been delivered to DTRA and is currently being utilized by CTBT researchers and analysts.

Understanding variability in propagation paths is a necessary step in the development of an infrasound network performance model. *InfraMAP* includes a Propagation Variability module that uses a stochastic approach to assess variability in travel time and arrival azimuth. Environmental perturbation fields are defined using a 1-D vertical wave number spectrum of the horizontal wind. A Monte Carlo simulation is executed where rays are traced through multiple environmental realizations, consisting of the sum of mean and perturbed profiles. Ray parameters are calculated for each realization, and the sensitivity of ray tracing calculations to variability in wind profiles can be stochastically quantified. The modeled distributions of propagation variables can be used in assessing areas of uncertainty in source location. *InfraMAP* provides the infrastructure for incorporation of a localization capability as well as the existing propagation and variability modeling capabilities.

Systematic sensitivity analyses have been conducted to understand the effect of temporal, spatial and environmental parameters on accurate modeling of long-range infrasound propagation. These sensitivity investigations, along with comparisons of model predictions with measured data, serve to identify specific areas where additional infrasound research and further development of modeling techniques are needed.

OBJECTIVE

Verification of the Comprehensive Nuclear-Test-Ban Treaty (CTBT) will require the ability to detect, localize, and discriminate nuclear events on a global scale. Monitoring systems such as the International Monitoring System (IMS) rely on several sensor technologies to perform these functions. The current IMS infrasound system design includes a network of low-frequency atmospheric acoustic sensor arrays, which contribute primarily to the detection and localization of atmospheric nuclear events.

The dynamic nature of the atmosphere, the uncertainties involved in characterizing high-altitude temperatures and winds, and the long ranges over which infrasound signals propagate combine to make accurate predictions of infrasound propagation difficult. Reliable models are needed in order to predict infrasound propagation paths from potential event locations worldwide. Existing model implementations can be difficult to use and often neglect dynamic atmospheric forcing.

The purpose of this effort was to develop a tool that allows infrasound analysts and researchers to easily model propagation through realistic characterizations of the atmosphere. The tool should provide environmental integration and execution capabilities for a baseline set of acoustic propagation models. Development of such an integrated set of models should allow for high fidelity propagation modeling by offering features such as range-dependent temperature and winds. The ability to predict the critical infrasound propagation characteristics (travel time, azimuth, amplitude) that affect localization and network performance would therefore be enhanced.

The functionality of the software tool developed during this effort addresses these needs and the problems of interest in CTBT monitoring. The tool allows the research community to model or evaluate the performance of infrasound localization and detection algorithms. Use of the software is anticipated to lead to increased efficiency and effectiveness of CTBT operational and research components.

Using the modeling tool, systematic sensitivity analyses and validation studies can be carried out to understand the effect of environmental and model parameters on accurate modeling of long range propagation. These investigations serve to identify specific areas where additional infrasound research and further development of modeling capabilities are needed. They will also help to define requirements for an infrasound knowledge database. The CTBT research community will benefit from improved understanding of modeling issues, e.g., confidence bounds on predictions, the relative importance of temporal and spatial variability in the environment, and the need for *in situ* atmospheric data or synoptic models.

RESEARCH ACCOMPLISHED

InfraMAP Software Delivery

An integrated software package for infrasound modeling was developed and delivered during this effort. The software contains tools for modeling infrasound propagation through a dynamic atmosphere and for visualizing modeled propagation results and atmospheric characteristics. The atmospheric models, acoustic propagation codes, and display functions are integrated in a common software environment that allows for user-friendly data access and model execution. The tool kit, called *InfraMAP*, for *Infra*sonic *M*odeling of *A*tmospheric *P*ropagation, is a systems analysis tool that enables the user to perform propagation studies over global scales and at infrasonic frequencies. It can be applied to predict travel times, bearings, and amplitudes from potential event locations worldwide.

The baseline set of acoustic propagation models contained in *InfraMAP* consists of:

- *Ray Tracing:* a three-dimensional ray theory model [Jones *et al.*, 1986],
- *Normal Modes:* a WKB version [Dighe *et al*., 1998; Hunter and Whitaker, 1997] of the normal mode model [Pierce and Kinney, 1976; Pierce *et al.*, 1973; Pierce and Posey, 1970], and
- *PE:* a continuous-wave, two-dimensional parabolic equation (PE) model [Jensen *et al.*, 1994; West *et al.*, 1992].

InfraMAP provides integration of these three models with the following baseline environmental characterizations:

- the Horizontal Wind Model (HWM) [Hedin *et al.*, 1996] and
- the Extended Mass Spectrometer - Incoherent Scatter Radar (MSIS or MSISE) model [Picone *et al.*, 1997].

HWM provides zonal and meridional wind components, and MSISE provides temperature, density and atmospheric composition.

Topographic and bathymetric databases in *InfraMAP* are based on standard products from NOAA. The primary database is known as ETOPO (Earth TOPOgraphy) and is available at two resolutions (30 minute and 5 minute).

A software users' manual [Norris *et al.*, 1999] was also developed and delivered during this effort. The user interface runs as a MATLAB application on UNIX-based workstations. Figure 1 shows the main window of the *InfraMAP* user interface.

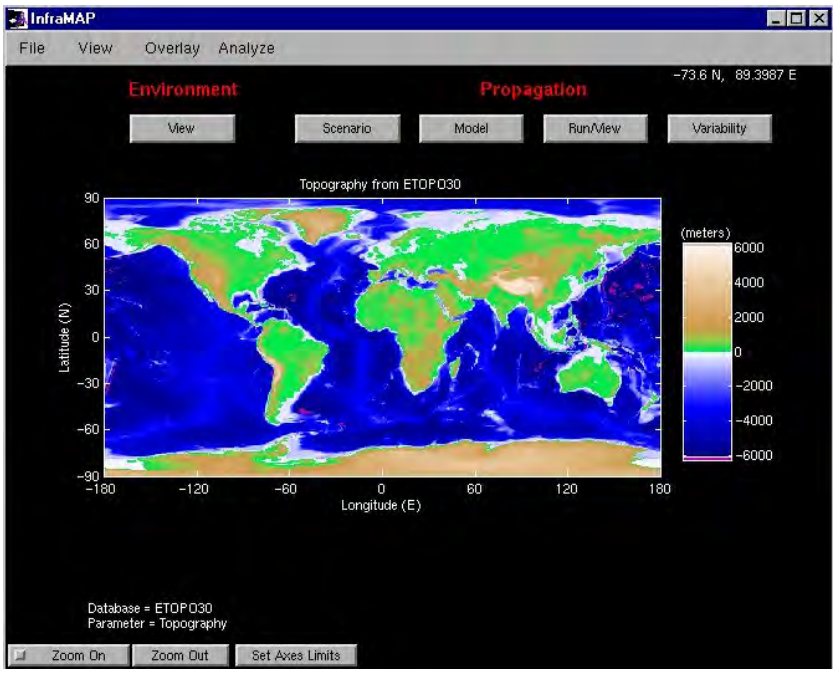


Figure 1: Main *InfraMAP* Window

Enhanced Capabilities

During the development of *InfraMAP*, a number of enhancements were made to the baseline functionality of the propagation models. Several of these capabilities are described in this section.

Various options are available for tracing rays. A single ray or a "fan" of rays can be launched from any given point. The ray tracing technique is capable of stepping either forward from a source or backward from a receiver. An option for "Reversing Propagation from a Receiver" is included in *InfraMAP*; when this option is selected, rays are "launched" from the receiver through an inverted propagation environment. During this effort, an algorithm for finding eigenrays, rays that connect a source and a receiver to within a specified tolerance, was developed and implemented. In the eigenray mode, an iterative algorithm is employed to search for rays that connect a source and receiver location to within a tolerance of a user-defined distance. The algorithm utilizes a shooting method to launch rays at various elevations and azimuths until eigenrays are identified. An example of a set of eigenrays identified for a 1000 km path is shown in Figure 2. Both stratospheric and thermospheric rays are shown.

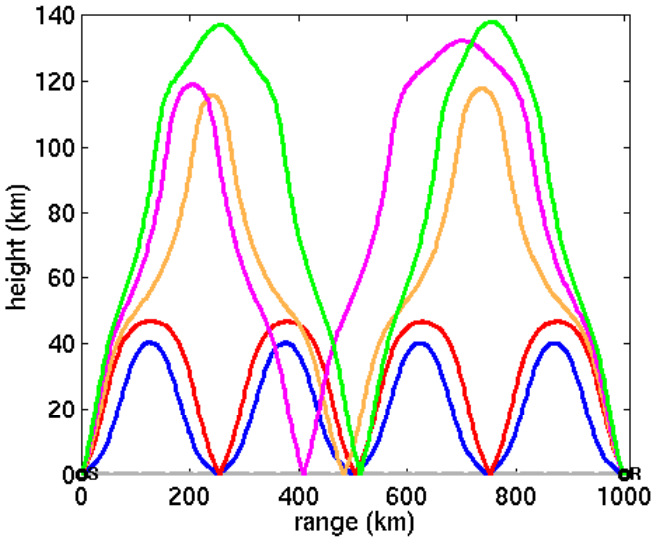


Figure 2: Eigenrays over a 1000 km path

Both range dependence and time dependence of the atmosphere are automated during ray tracing. At each step along a ray path, the local sound speed and wind components are determined from the environmental characterizations evaluated at the corresponding location and time. Time stamps can be displayed at user-selected intervals along ray paths. A plotting option was also developed for the display of ray paths on an azimuthally equidistant projection of the earth's topography.

For normal modes, *InfraMAP* automates the selection of the waveform time window, based on the signal velocity and range. In addition, the special case of dual-duct propagation is identified and automatically processed, in which case the full waveform solution is the sum of the upper and lower duct solutions.

Propagation Variability

InfraMAP incorporates propagation variability tools that support the assessment of localization performance of an infrasound network. Understanding variability in propagation paths is a necessary step in the development of a complete infrasound network model. The uncertainty bounds in a propagation model prediction depend to a large degree on uncertainties in the environmental characteristics.

A Monte Carlo approach to assessing the variability of both bearing and travel time was developed for infrasound propagation paths, based on application of ray tracing through a perturbed set of atmospheric profiles. This stochastic approach has the advantage of allowing flexibility in the choice of wind perturbation spectra, so the sensitivity of localization parameters to realistic characterizations of environmental variability can be assessed. The technique has been implemented so that it can be applied to any infrasound station in a user-defined network or at another location of interest.

InfraMAP's Propagation Variability menu provides the capability of performing a Monte Carlo perturbation analysis about a reference eigenray. There is a choice of analysis variables: either azimuth deviation or travel time. This analysis approach allows assessment of (a) the sensitivity of ray tracing calculations to variability in wind profiles, and (b) the resulting effect on the key parameters that affect source localization. The resulting distributions of propagation variables can be used in assessing areas of uncertainty in source location.

In the Propagation Variability analysis, the environmental perturbation fields are defined using a 1-D vertical wave number spectrum of the horizontal wind, and individual realizations of spatial fields are generated through a random-phase technique [Peitgen and Saupe, 1998]. Wind profiles are perturbed over multiple realizations. A Monte Carlo simulation is executed where rays are traced through each realization, consisting of the sum of a mean and a perturbed profile. Ray parameters are then calculated for each realization, and a statistical analysis is done over the entire set of realizations.

- If azimuth deviation is chosen, then the wind component normal to the great circle path (crosswind) is perturbed.
- If travel time is chosen, then the wind component along the great circle path (headwind or tailwind) is perturbed.

The wind perturbation is based on a power spectral density (PSD). Default values of the power law exponent, the perturbation wavelength range (in km), and the PSD magnitude are provided. The user must specify the number of realizations in the Monte Carlo simulation.

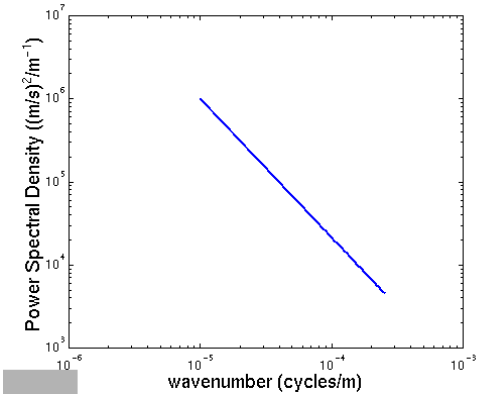


Figure 3: Wind perturbation spectrum

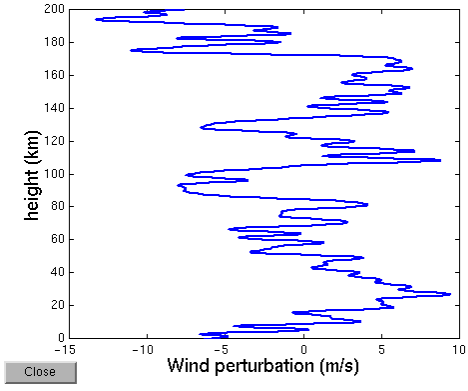


Figure 4: Wind perturbation profile

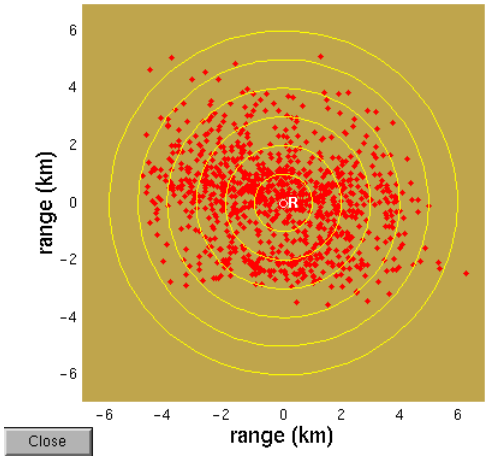


Figure 5: Ground hit points of multiple rays

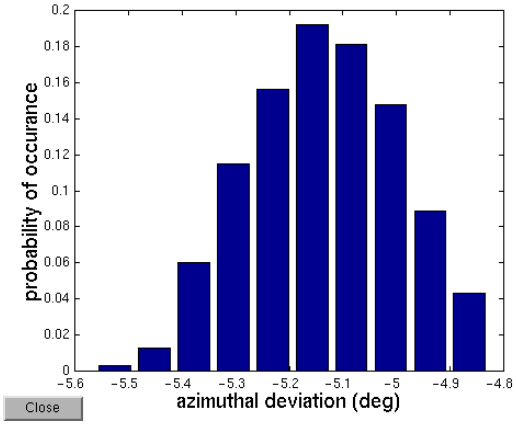


Figure 6: Probability density estimate

Three output displays of analysis results are presented:

- Probability density function estimate,
- Density of calculated ray ground hit points as a function of range, and
- Locations of ray ground hit points (overlaid on an azimuthally equidistant projection of topography). Perturbed ray endpoints are shown compared to the ground hit point of the unperturbed reference ray.

Examples are shown in Figures 3 through 6. Figure 3 depicts a wind perturbation spectrum, and Figure 4 shows a realization of a perturbation profile calculated using this spectrum. Figure 5 is a plot of ray ground hit points resulting from a Monte Carlo simulation, and Figure 6 is the corresponding probability density function estimate.

The software provides the infrastructure to add additional capabilities to support network performance evaluation, for example, station detection characteristics, estimates of noise levels, area of uncertainty estimates, etc.

Sensitivity Analyses

The *InfraMAP* tool kit allows sensitivity analyses to be conducted readily. Model parameters can be varied systematically in order to compare results from a range of propagation scenarios. Analyses have been presented that address temporal sensitivity of propagation [Gibson *et al.*, 1999; Norris and Gibson, 1999]. Other studies have been conducted to address spatial or environmental sensitivity; one such study is summarized here.

InfraMAP was used to evaluate the effect of variability in solar magnetic activity on ray paths. Geomagnetic disturbances from solar activity influence atmospheric temperature and winds at high altitudes. The planetary equivalent daily disturbance amplitude, A_P, is used as an input parameter in the wind and temperature models and it affects the modeled environment at altitudes above 100 km.

Archived values of A_P over a six-year period were reviewed to determine a realistic parameter range for the study.

- Values of A_P ranged from approximately 1 to 100.
- Approximately 97% of the days had A_P values of less than 50.

- 10% of the days had A_P equal to 4.

The values of A_P chosen for the study were: 4, 8, 16, 32, 64, and 128.

In the modeled scenarios, the source was located in Central Asia (50.5° N, 78.0° E), and the receivers were due West and due North at a range of 2500 km. The time of year was mid-September and the time of day was 12 UT. Five eigenrays were identified and all had turning points in the thermosphere at altitudes in the range 110-125 km. At these altitudes, modeled temperatures and winds are sensitive to solar effects.

The effects on travel time and azimuth deviation of the eigenrays are shown in Figures 7 and 8, respectively, for the northward path. Over the A_P range of the sensitivity study, the travel time variability was up to 2% for each ray path. This effect due to A_P is small compared to the range of travel times among the five rays. The change in azimuth deviation was up to 2 degrees, which is of the same order as the range among the five rays.

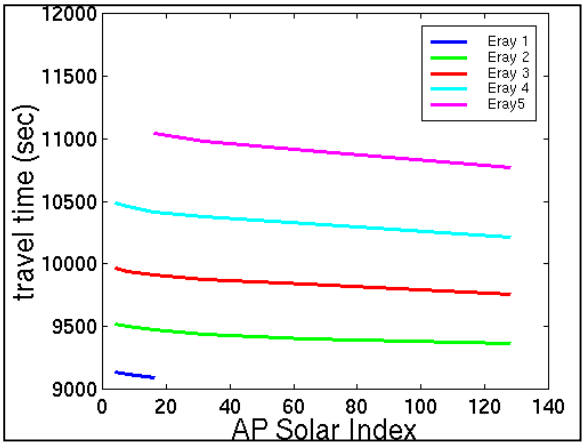


Figure 7: Travel time variability due to solar magnetic disturbance

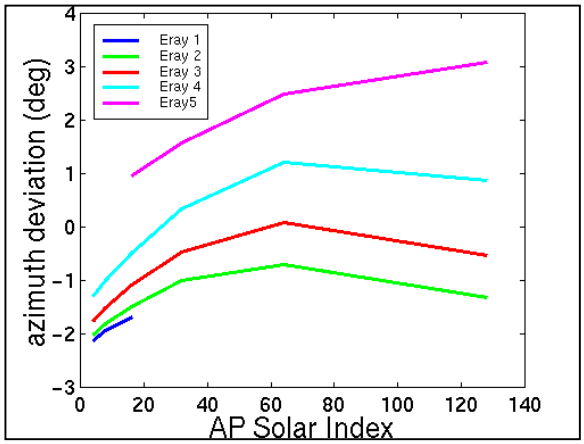


Figure 8: Azimuth deviation variability due to solar magnetic disturbance

For this particular modeled event scenario, it is concluded that solar magnetic disturbance effects may result in observable changes to thermospheric ray paths but are unlikely to represent a large source of variability in propagation. However, the effect of A_P variability may be more prominent in other geographic regions or in other event scenarios.

CONCLUSIONS AND RECOMMENDATIONS

A user-friendly software tool kit has been developed to predict the critical propagation characteristics that affect localization and detection performance of an infrasound monitoring network. The integrated set of models allows for higher fidelity propagation modeling than has previously been available to the infrasound monitoring community. It has been shown via modeling that significant biases in travel time and azimuth over ranges of CTBT interest are anticipated, and that these biases must be corrected for in order to avoid large location errors.

A perturbation approach to model propagation variability has been developed and is included in the software. Further investigations of environmental variability and its effect on propagation should be conducted. Additional development of network performance models incorporating these variability effects should also be performed.

Model-to-model comparisons are planned, during a subsequent effort, in order to validate the modeling techniques and to define confidence levels. Further enhancements to the functionality and efficiency of the baseline models will be incorporated into an updated version of the software. As higher fidelity

environmental characterizations become available, they should be integrated into a next-generation version of the software. Efforts should also be made to incorporate near-real-time updates to the propagation environment, based on updated measurements or synoptic models, and to evaluate resulting improvements over the current environmental models.

Key Words: infrasound, long-range propagation, database, atmosphere

REFERENCES

Dighe, K. A., R. W. Whitaker, and W. T. Armstrong, 1998: Modeling study of infrasonic detection of a 1 kT atmospheric blast, *Proceedings of the 20th Annual Seismic Research Symposium*, Santa Fe, New Mex.

Gibson, R., D. Norris, and T. Farrell, 1999: Development and application of an integrated infrasound propagation modeling tool kit, *Proceedings of the 21st Annual Seismic Research Symposium*, Las Vegas, NV.

Hedin, A. E, E. L. Fleming, A. H. Manson, F. J. Schmidlin, S. K. Avery, R. R. Clark, S. J. Franke, G. J. Fraser, T. Tsuda, F. Vial, and R. A. Vincent, 1996: Empirical wind model for the upper, middle, and lower atmosphere, *J. Atmos. Terr. Phys.*, **58**, 1421-1447.

Hunter, J. H. and R. W. Whitaker, 1997: Numerical modeling of long range infrasonic propagation, *Infrasound Workshop for CTBT monitoring*, Santa Fe, New Mex.

Jensen, F. B., W. A. Kuperman, M. B. Porter, and H. Schmidt, 1994: *Computational Ocean Acoustics*, AIP Press, New York.

Jones, M. J., J. P. Riley, and T. M. Georges, 1986: *A Versatile Three-Dimensional Hamiltonian Ray-Tracing Program for Acoustic Waves in the Atmosphere above Irregular Terrain*, NOAA Special Report, Wave Propagation Laboratory, Boulder, Co.

Norris, D. E. and R. Gibson, 1999: Seasonal variability and its effect on ray paths, *J. Acoust. Soc. Am.*, **106**, No. 4, Pt. 2, 2144.

Norris, D., R. Nadel, and R. Gibson, 1999: *User's Guide for InfraMAP (Infrasonic Modeling of Atmospheric Propagation*, BBN Technical Memorandum No. W1353, Arlington, Va.

Picone, J. M., A. E. Hedin, S. L. Coffey, J. Lean, D. P. Drob, H. Neal, D. J. Melendez-Alvira, R. R. Meier, and J. T. Mariska, 1997: The Naval Research Laboratory program on empirical models of the neutral upper atmosphere, in *Astrodynamics: Advances in the Astronautical Sciences*, Vol. 97, edited by F. R. Hoots, B. Kaufman, P. J. Cefola, and D. B. Spencer, American Astronautical Society, San Diego, Ca.

Peitgen, H. and D. Saupe, eds., 1998: *The Science of Fractal Images*, Springer-Verlag.

Pierce, A. D. and J. W. Posey, 1970: *Theoretical Prediction of Acoustic-Gravity Pressure Waveforms Generated by Large Explosions in the Atmosphere*, Technical Report AFCRL-70-0134, Air Force Cambridge Research Laboratories, Bedford, Mass.

Pierce, A. D., C. A. Moo, and J. W. Posey, 1973: *Generation and Propagation of Infrasonic Waves*, Technical Report AFCRL-TR-73-0135, Air Force Cambridge Research Laboratories, Bedford, Mass.

Pierce, A. D. and W. A. Kinney, 1976: *Computational Techniques for the Study of Infrasound Propagation in the Atmosphere*, Technical Report AFGL-TR-76-56, Air Force Geophysics Laboratories, Hanscom AFB, Mass.

West, M., K. E. Gilbert, and R. A. Sack, 1992: A tutorial on the Parabolic Equation (PE) model used for long range sound propagation in the atmosphere, *Applied Acoustics*, **37**, 31-49.

EVALUATION OF INFRASONIC SPATIAL FILTERS

Michael A.H. Hedlin, Jon Berger and Mark Zumberge

Institute of Geophysics and Planetary Physics
University of California, San Diego

Sponsored by Defense Threat Reduction Agency

ABSTRACT

The infrasound element of the global International Monitoring System (IMS) will consist of 60 stations. Each station in the global network will consist of an array of sensors. As the local surface wind strongly influences ambient infrasonic noise levels in the band of interest to the nuclear treaty monitoring community (between 0.05 and 4 Hz), each of these sensors will include a spatial filter designed to reduce the effects of wind noise. There are, however, many different design suggestions for spatial filtering system. In order to maximize the signal-to-noise ratio of signals of interest, it is essential that the spatial noise reduction systems be optimized to provide the most significant noise power reduction over the broadest band possible. We believe that substantial progress in these areas requires the comparative testing of the major noise reducing systems exposed to the same meteorological conditions.

Under our new DTRA contract we will construct and test several spatial filtering systems by simultaneous operation at the Pinon Flat Observatory (PFO) in southern California. These systems include the wind fence, microporous pipes, and a recent design in which a large number of open ports are connected to a summing manifold, and then to the microbarometer, by solid pipes. We will also compare these mechanical noise suppression schemes with a new design based on light-speed pressure averaging via optical fibres. The observatory is an ideal test site as it is subjected to winds that come from all azimuths at speeds ranging from 0 to over10 m/s.

Key Words: spatial averaging, turbulence

OBJECTIVE

Our objective is to evaluate several infrasonic noise reducing devices together at the Pinon Flat Observatory in southern California to identify which devices appear to be most effective under what circumstances.

BACKGROUND

Wind and Infrasonic Noise

The turbulent flow of wind is the most significant source of infrasonic noise in the band from .01 to 1 Hz (McDonald et al., 1971). The relationship between wind and infrasonic noise is given by Bernoulli s principle

$$p + (\rho v^2)/2 = C$$

where p is pressure, ρ is density, v is wind velocity and C is a constant. Differentiation of this formula shows that there is a simple linear scaling between variations in wind speed and pressure. Understanding the frequency dependence of infrasonic noise requires knowledge of the interaction of wind with topographic irregularities that cause the turbulence. In general terms, atmospheric turbulence is concentrated near the Earth s surface in the Atmospheric Boundary Layer (ABL; Kaimal and Finnigan, 1994) - a region of high Reynolds-number flow. The upper extent of the ABL is limited by the capping inversion which is highest (at 1 to 2 km) during the day when the Earth s surface radiates heat and lowest (10 s of meters) or nonexistent during the night (Panofsky and Dutton, 1984; Kaimal and Finnigan, 1994). The thickness of the boundary layer is also governed to some extent by topography as the turbulence of wind flow over the ground is increased by ground roughness. Large-scale atmospheric turbulence is maintained by thermal plumes and thus is most evident during the day. Wind shear introduces smaller eddies and cascades ener gy from the low to the higher frequencies (Kaimal and Finnigan, 1994). There is no universal statistical characterization of atmospheric turbulence at large scales (Wilson et al., 1999). The turbulence depends on the velocity and density profiles of the atmosphere as well as boundary effects such as topography and ground cover. The spatial structure of the atmospheric turbulence is dependent on the interaction of the wind with topography and can be modeled using one of a number of models including Gaussian, von Karman or Kolmogorov spectral models (Wilson et al., 1999). Wind noise is known to be incoherent at spacing of 10s of meters (e.g. Priestley, 1966). There exists a direct scaling between the size of the wind eddies and the time-frequency of the noise they produce. At 0.25 Hz, the scale of the turbulence is ~ 25 m (Grover, 1971). At comparable time frequencies, signals from remote sources have wavelengths that are considerably longer than any noise suppression device currently being considered. Thus, spatial averaging is expected to attenuate local sources of infrasonic noise while leaving signals from remote sources relatively unaltered.

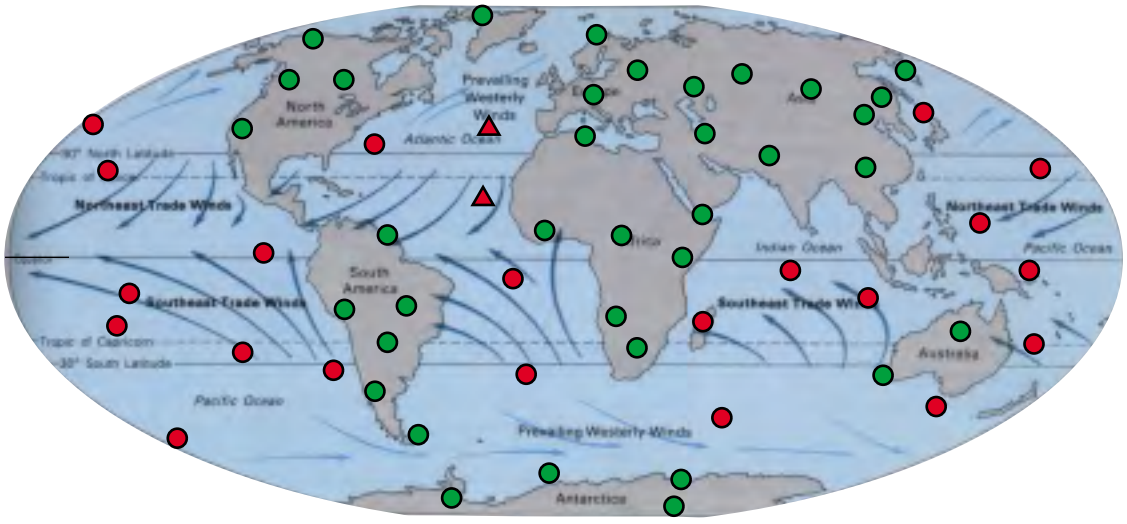


FIGURE 1. The planned global IMS infrasound network. Stations located on islands will, in general, be subject to strong winds and thus high infrasonic noise levels. Strong trade winds dominate in the tropics. In latitudes above 30°N and below 30°S the prevailing westerly winds dominate although local winds can be strongly influenced by local pressure cells. The 2 triangles in the Atlantic from north to south are the Azores and Cape Verde. Data from these sites is used in this paper. The background display of oceanic winds is adapted from the World Book. Encyclopedia.

Our group at IGPP recently collected infrasound and meteorological data on 3 islands in the Atlantic; Sao Miguel, Azores, Maio, Cape Verde and Ascension island. The experiments were conducted to collect infrasonic noise data required to make an informed recommendation about which site on each of these islands would be most suitable for a permanent IMS infrasound array. The experiments provided an abundance of data that is relevant to the issue of wind and infrasonic noise. Rudimentary spatial filters constructed with "spider" arms of perforated hose as illustrated in Figure 2 were used in these experiments.

In Figure 3 we display meteorological and infrasonic pressure data recorded in the Azores during a 15 minute time span in one mid-afternoon in October, 1998. The unfiltered pressure time series from the station at this site exhibits 30 second period fluctuations superimposed on substantially longer period energy. The shorter period variations dominate the filtered record (second panel from top). In this time period, minor wind velocity fluctuations are constant. The temperature and humidity vary relatively slowly. The detailed structure of the filtered pressure record results from the superposed contributions of myriad atmospheric phenomena.

The spectral content of the filtered data is displayed in Figure 4 which shows the decay in power levels from the peak at 30 second to the corner of the anti-aliasing filter at 9 Hz. A strong microbarom peak is centered at 0.2 Hz. The overall spectral shape is due to a well known phenomena in the atmosphere which receives a major input of energy at ~ 0.1 to 1 mHz. Energy from large scale eddies cascades into smaller eddies, and thus into higher frequencies, as the large eddies are broken up (Kaimal and Finnigan, 1994). The fall-off of energy below 0.01 Hz is due to the sensor filter.

From the spectral estimates taken over ~3 week time spans on each of the islands in the Atlantic we were able to investigate the dependence of infrasonic noise on wind speed at frequencies from 0.02 to 5 Hz. In the left panel of Figure 5 we display average power spectral density as a function of wind speed at a site on Maio, Cape Verde (Figure 1). Each curve from lowest to highest comes from a wind speed bin that spans 0.5 m/s. The first bin includes data from 0 to 0.5 m/s, the second from 0.5 to 1.0, and so on up to 3 m/s. When the wind speed is below 0.5 m/s the microbarom peak is obvious. At higher wind conditions the peak becomes obscured. At all frequencies the infrasonic power increases with increasing wind speed; the power increase is most evident at the long periods.

The right panel of this figure shows power spectral estimates from narrow frequency bands centered at the frequencies listed at the extreme right. The dependence of infrasonic power on wind speed and on frequency is clear. At this location in the northern trades, the wind is from the northeast and as a result the dependence of infrasound power on wind speed is relatively simple.

As wind speeds at Cape Verde are relatively constant, the most significant source of variability in infrasonic noise levels is the diurnal effect (Figure 6; left panel) which is predominantly due to day-night variations in the speed of the trade winds. Infrasonic noise levels are highly correlated with this effect and thus at any time of day, noise levels are quite easily predicted. Significant wind speed and noise level variations are common in the Azores in the early winter. The experiment in November and December of 1999 occurred at a time of advancing inclement weather. Toward the end of the experiment wind speed on Sao Miguel could increase from 1 to 6 m/s in a few hours. Commensurate noise power increases of 40 to 50 dB occurred.

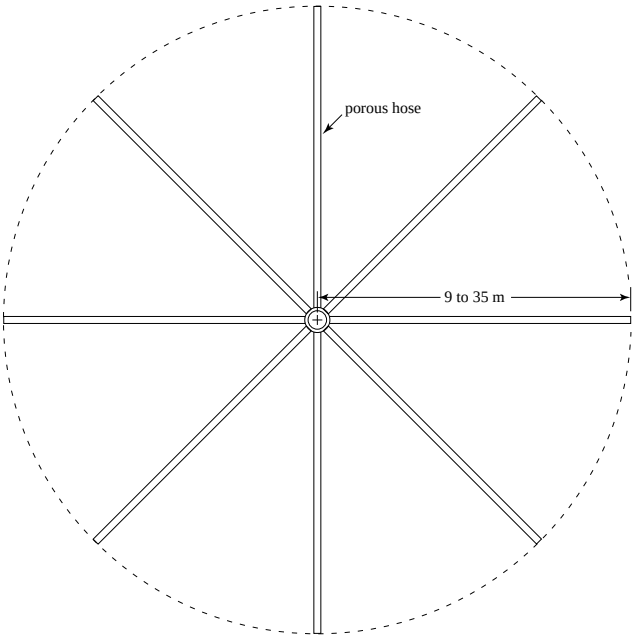


FIGURE 2. A "spider" Daniels filter. This filter is the simplest to construct and has a number of shortcomings. For example, the porosity is concentrated near the microbarometer at the center.

The Daniels Noise Space Filter

Daniels (1959) demonstrated that it is possible to increase the signal-to-noise ratio below 1 Hz by as much as 20 dB by averaging atmospheric pressure along a line. Daniels used a 1980 foot long tapered pipe along which pressure was sampled at 100 points. The success of this approach depends on the relatively small correlation lengths of infrasonic noise, which are due to local small-scale atmospheric turbulence, relative to the longer correlation lengths of infrasonic signals at the same frequencies. The linear porous pipe was useful for increasing signal to noise along a single azimuth perpendicular to the pipe.

Recent Approaches to Noise Reduction

The current monitoring situation is more complex than the one that existed in the 1950 s as we must now consider suspicious sources of any yield that occur at any location above or below ground. The global IMS network (Figure 1) will be used to detect weak signals detected with ever changing noise. The emphasis is on omnidirectional sensors and therefore the linear pipe arrangement is no longer adequate however the basic idea of sampling pressure over an area introduced by Daniels is still the basis of many modern noise reducing systems.

Various noise reducing devices have thus been recently proposed. A hexagonal arrangement of microporous pipes (Figure 7) was proposed in Paris at the 1998 infrasound workshop. Any system that employs micro-porous pipes averages pressure variations at a large number of points distributed along the pipes. The spatial extent of these systems is limited by the propagation of the signals from all ports to the summing manifold. These designs introduce phase delays and are limited to an aperture of ~ 1/4 of the wavelength (or ~75 m at 1 Hz). The hexagon design strives to overcome one limitation of the spider which concentrates most of the microporosity near the microphone. As illustrated in Figure 7, some hexagonal filters include several rings of porous pipe.

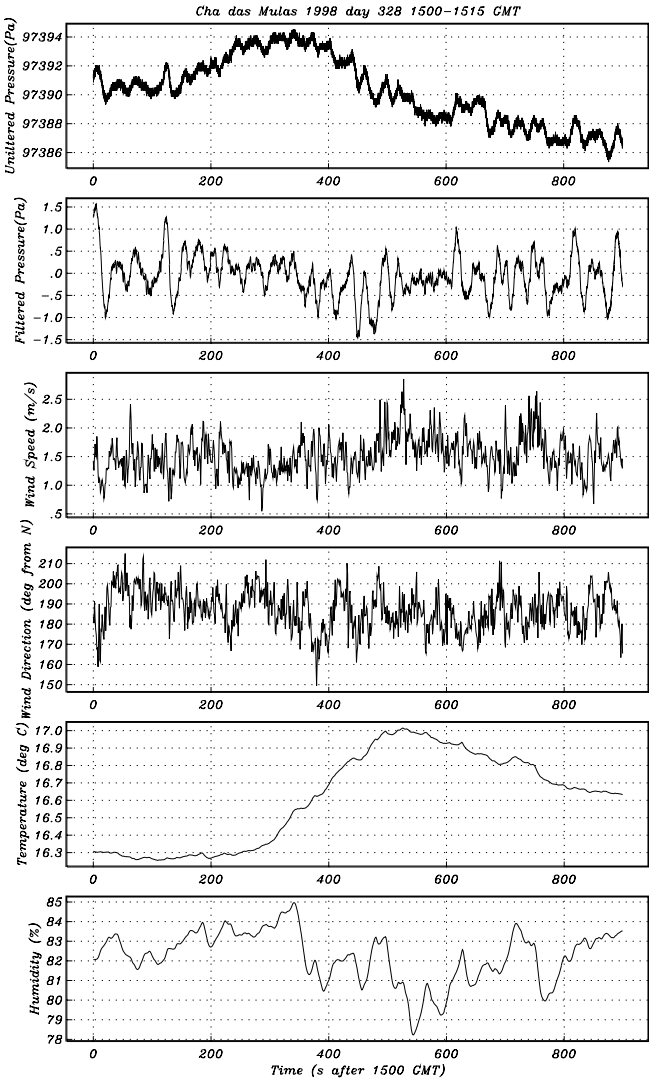


FIGURE 3. Atmospheric pressure and meteorological data from a 15 minute interval starting at 15:00 GMT at a site on Sao Miguel, Azores (Hedlin et al., 1999). Raw and filtered pressure data are shown in the upper two panels. Wind speed, direction, temperature and humidity are shown below. As shown in the next figure, this is a time of relatively low infrasonic noise.

A new design which involves discrete ports was conceived by Benoit Alcoverro at the Departement d'Analyse et de Surveillance de l'Environnement (DASE). This space filter distributes low-impedance ports spatially and signals are summed at a central manifold after propagation through impermeable pipes (Figures 8 and 9). The key features of this design is that the propagation distance, and thus the time delay, from each port to the summing manifold is equal and thus phase delays are eliminated. The impedances between the ports and the primary summing manifold are the same for all ports. Doug Christie (PTS, CTBTO) has proposed several innovative space filters based on this idea. The space filters range from 92 ports distributed over an area 18 m across (Figure 8) to 144 ports covering an area 70 m across (Figure 9). The narrower filter is considered to be effective at high frequencies. The 70 m aperture filter is considered appropriate for windy sites that require long-period noise suppression.

The Wind Shelter**.**

An example of a wind shelter is shown in Figure 10. These drawings are courtesy of Ludwik Liszka at the Swedish Institute of Space Physics. The wind shelter is akin to a forest as it reduces wind speeds inside the shelter and reduces the scale of the atmospheric turbulence so that much of the acoustic energy that results is displaced beyond the frequency band of interest. The design features of a filter (including the shelter height and porosity) are dependent on conditions at the site (Doug Revelle, personal communication). For example, the height of the shelter is dependent on the roughness of the surrounding topography and local mean wind speeds. We are currently building a wind fence that is 2 m tall.

An Optical Fiber Sensor.

Work on an entirely new kind of infrasound sensor - an Optical Fiber Infrasound Sensor (OFIS)- is now underway at IGPP funded under a separate program by DTRA. The aim of all mechanical filters is to sample the atmosphere at a series of points and add their pressure signals mechanically by joining

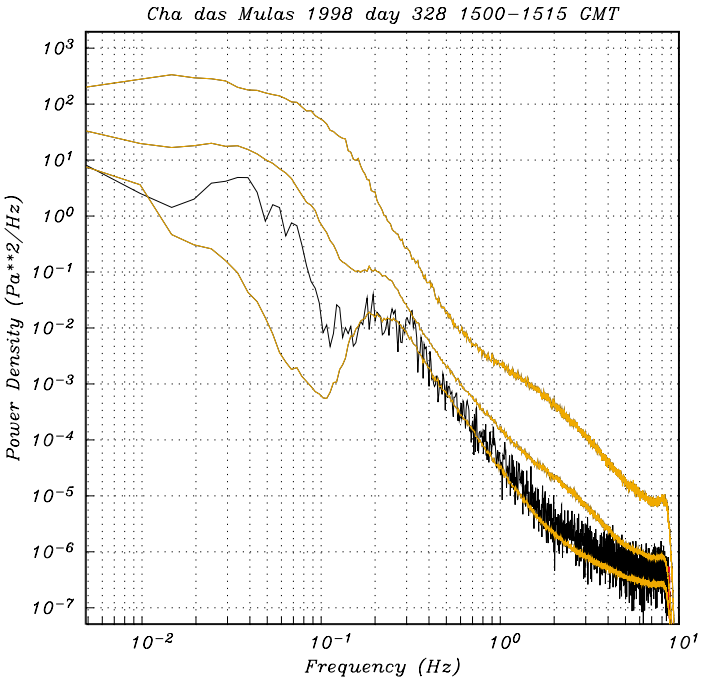


FIGURE 4. Noise power density at the Azores site. In black is shown a single power density estimate taken from the filtered pressure data displayed in the previous figure. The colored curves are the 10th, 50th and 90th percentile noise levels from the entire experiment. These curves are based on 454 noise level estimates taken at 1 hour intervals. Each estimate is taken from 15 minutes of data. The 5 second microbarom is not observed at times of high noise.

many tubes to a single microbarograph. Because of the finite sound velocity, there are phase delays along the lengths of the pipes, limiting the area that can be averaged over with mechanical filters. Further, because of the size of these spatial filters there is no practical way of measuring their response.

The Optical Fiber Infrasound Sensor (OFIS) consists of a long optical fiber whose optical path length is sensitive to the ambient atmospheric pressure. The OFIS integrates pressure variations that occur along the line in space defined by the optical fiber s path. The averaging characteristics are governed by the speed of light, so we can make the line over which pressure is averaged extremely long (many km). The distributed sensor approach has many advantages.

Figure 11 shows a schematic view of an OFIS. The optical path of a sensor fiber is interferometrically compared to that of a fiber shielded from the atmosphere. We have built two short test versions of the system. In one, we have added a mechanical element to the fiber which enhances its response to pressure changes.

In the context of the study proposed here, we have funding already to build an OFIS and deploy one version of it at Pinon Flat. The flexibility of an OFIS will allow us to readily rearrange it to sample over a configuration similar to one of the pipe arrays. Comparing records will allow us to assess the advantages of each and provide a method for determining the response of the acoustic filters.

OUTLINE OF OUR EXPERIMENT PLAN

The noise reduction systems we will investigate under our new DTRA contract are:

¥The porous hose spider (Figure 2).
¥The hexagonal porous pipe filter. (Figure 7)
¥An 18 m aperture multi-port filter. (Figure 8)
¥A 70 m aperture multi-port filter. (Figure 9)
¥A wind shelter. (Figure 10)
¥The Optical Fibre Infrasound Sensor (Figure 11)

All designs strive to provide omnidirectional noise reduction. The "Spider" design displayed in Figure 2 is commonly used in IMS infrasound surveys (e.g. those discussed in Hedlin et al., 2000). This is regarded as an inferior design. It is included to assess the performance of this simple filter relative to the more extensive, much costlier, filters. We are interested in constraining the performance jump the other (relatively expensive) systems will presumably provide over this simple filter and over a microbarometer that is not attached to any noise reduction device.

The hexagonal filter we will deploy at Pinon Flat will include ring at a radius of 9 m and two closely spaced rings at a radius of 35 m.

Theoretical work

The theory of sound propagation in pipes and networks of pipes is well developed through a combination of electrical analogs and the thermodynamics of air. The propagation properties of sound waves in enclosures such as pipes or volumes have a strong frequency dependence, due to the thermal and viscous boundary layers. This is in contrast to propagation properties in free air. The currently available accurate approximations of sound propagation in pipes and volumes span the entire frequency range of interest.

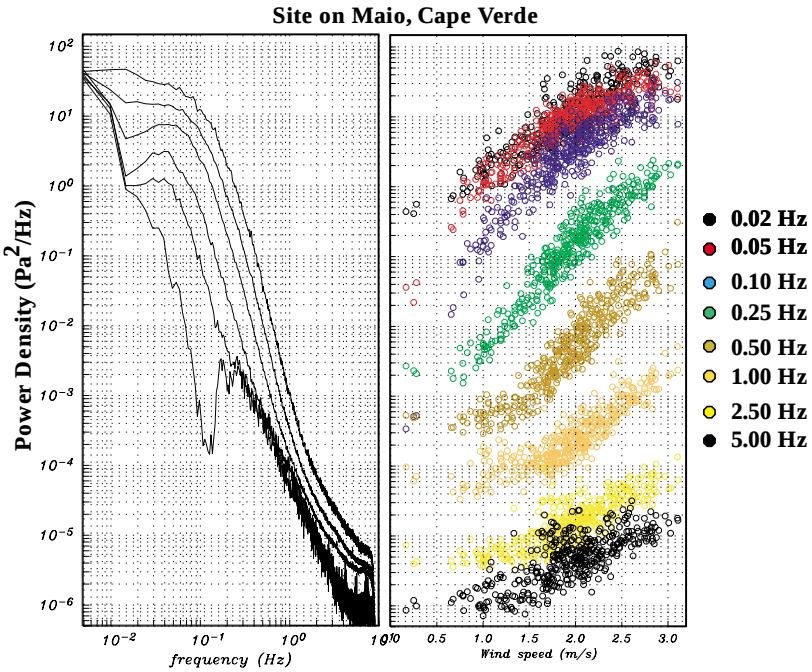


FIGURE 5. The panels to the left show the dependence of infrasonic noise power on frequency and wind speed at a site on Maio, Cape Verde. On the left we display average power spectral density as a function of wind speed. Infrasonic noise estimates were binned by wind speed into 0.5 m/s intervals starting at 0.0 m/s and then stacked. The curves on the left from lowest to highest are from the wind speed intervals from 0 to 0.5 m/s (lowest), 0.5 to 1.0 m/s (second lowest) up to 2.5 to 3.0 m/s (highest). On the right we display power spectral density from narrow frequency bands from the individual estimates. From top to bottom in each panel is noise power at 0.02 Hz (black); 0.05 Hz (red); 0.1 Hz (green); 0.25 Hz (dark blue); 0.5 Hz (light blue); 1.0 Hz (pink); 2.5 Hz (yellow); and 5.0 Hz (black).

In many of the earlier designs of noise-reducing structures at frequencies corresponding to the overall dimensions of the system, strong resonances occurred due to standing waves. Only through detailed impedance matching such resonances can be avoided. At higher frequencies the directional properties of most noise-reducers are increased, leading to an undesired departure from the omnidirectional angular response. In designing noise reducers one has to find a trade off between frequency response, angular response and the overall dimension of the system for the frequency band of interest (0.01 and 5 Hz).

Facilities.

The Pinon Flat Observatory is located about 100 miles from San Diego in the mountains that separate the coastal plain from the Imperial Valley (Figure 12). A section (1 square mile) is owned by the University of California as so provides plenty of space to deploy all of these systems simultaneously. It also provides basic infrastructure support such a lab space, accommodations, power, Internet connectivity, and security. An on-site caretaker is augmented by weekly visits by IGPP technicians.

As an environment for testing the efficacy of the various spatial filters, PFO offers a variety of wide wind conditions. As Figure 13 indicates we can expect a preponderance of wind speeds below 3 m/s however we can expect instantaneous wind speeds between 0 and 10+ m/s. Further there is a fairly uniform distribution of wind direction.

REFERENCES

Daniels, F.B. (1959), Noise-Reducing Line Microphone for Frequencies Below cps, J. Acoust. Soc. Am., **31**, 529.

Grover, F.H. (1971), Experimental Noise Reducers for an Active Microbarograph Array, Geophys. J.R. astr. Soc., **26**, 41.

Hedlin, M.A.H., Berger, J. and Vernon, F.L. (2000), Surveying Infrasonic Noise on Oceanic Islands, article in review with PAGEOPH.

Kaimal, J.C., and Finnigan, J.J. (1994), Atmospheric Boundary Layer Flows: Their Structure and Measurement, *Oxford University Press.*

McDonald, J.A., Douze, E.J., and Herrin, E. (1971), The structure of atmospheric turbulence and its application to the design of pipe arrays, *Geophys. J.R. astr. Soc.*, **26**, 99-109.

Panofsky, H.A., and Dutton, J.A. (1984) Atmospheric Turbulence: Models and Methods for Engineering Applications, *John Wiley and Sons Inc.*

Priestley, J.T. (1966), Correlation studies of pressure fluctuatinos on the ground beneath a turbulent boundary layer, Washington D.C., National Bureau of Standards Report No. 8942, U.S. Dept. of Commerce, National Bureau of Standard.

Wilson, D.K., Brasseur, J.G., and Gilbert, K.E. (1999), Acoustic scattering and the spectrum of atmospheric turbulence, *Journal of the Acoustical Society of America,* **105**, 30-34.

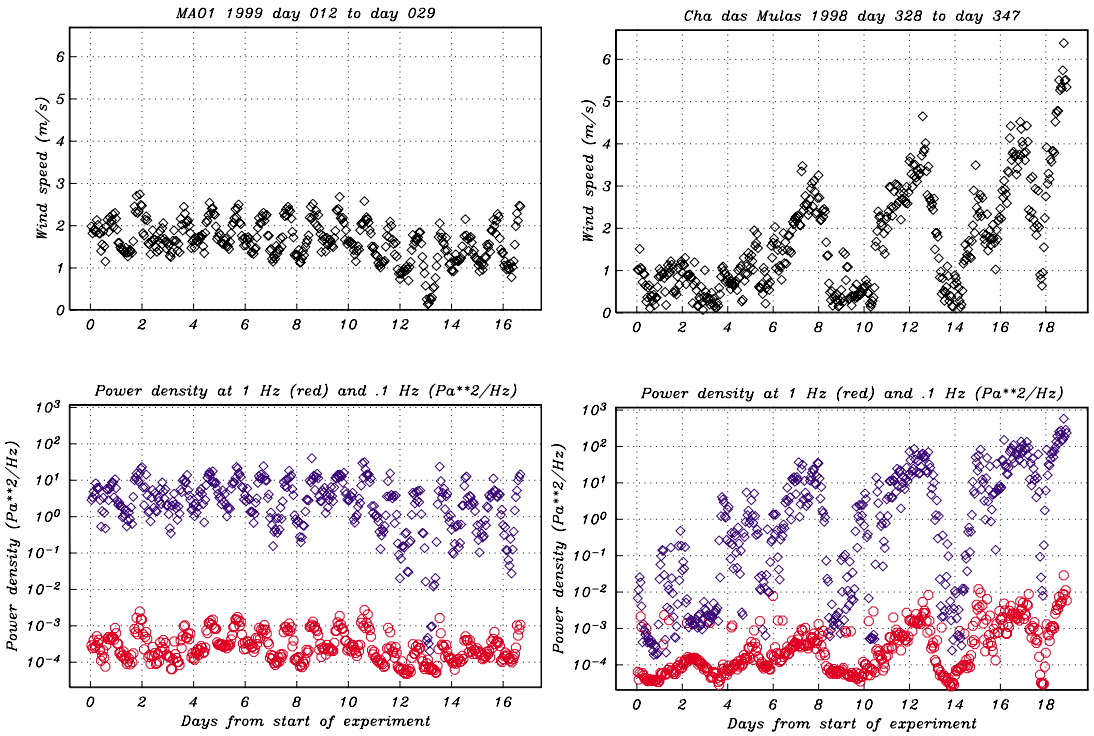


FIGURE 6. Noise power and wind speed as a function of time at one station in the Azores (left) and in Cape Verde. In the Azores, wind noise at 0.1 Hz (upper sequence of points in the lower panel) and at 1.0 Hz track closely the wind speed. Severe winds during a storm near the conclusion of the Azores experiment lead to wild swings in the noise level. At times, any infrasound station on the island will be deafened by the wind. In Cape Verde, diurnal variations are relatively slight.

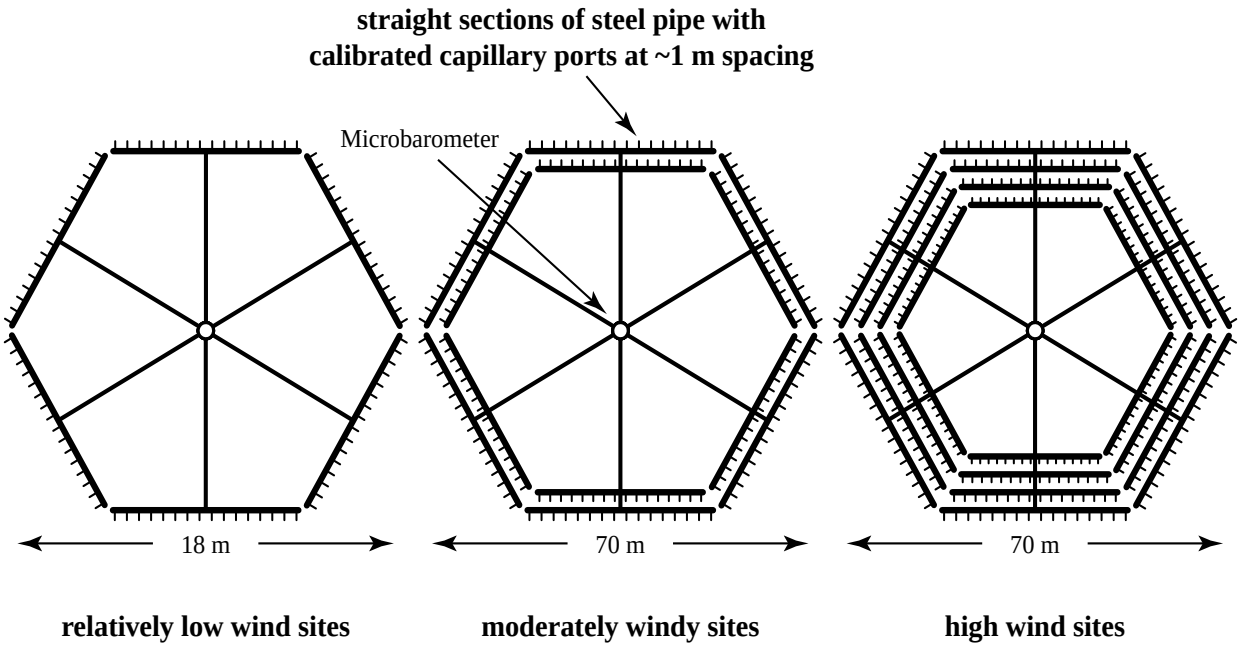


FIGURE 7. Three filters that use a hexagonal arrangement of porous pipes.

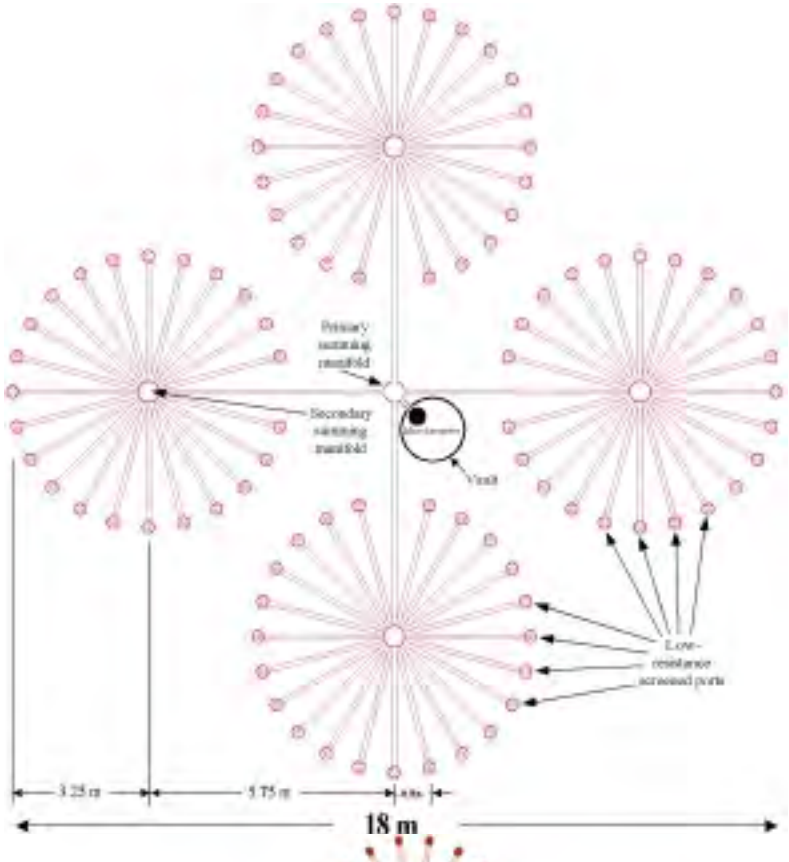


FIGURE 8. 92-port 18 m diameter wind-noise-reducing pipe array with high-frequency capability for use at short-period-optimized array elements at stations located in higher wind areas or at all array elements at stations located in low wind areas. This figure and caption are courtesy of Doug Christie.

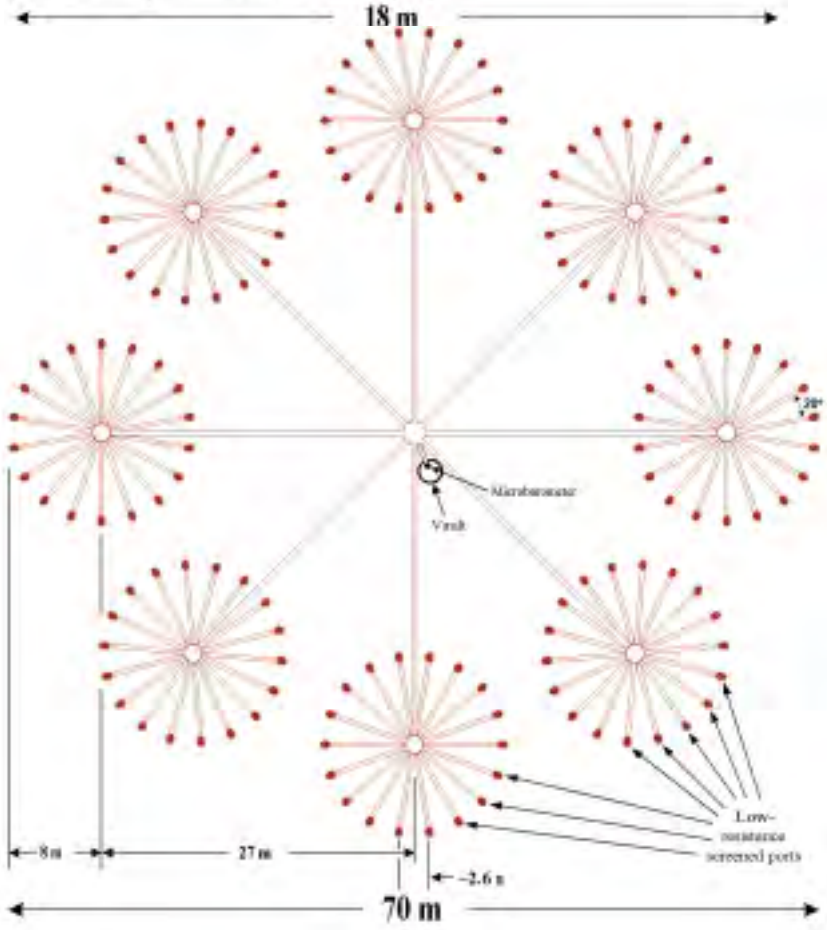


FIGURE 9. 144-port 70-m diameter wind-noise-reducing pipe array for use at long-period-optimized array elements at stations subject to high-wind conditions. Array and caption courtesy of Doug Christie.

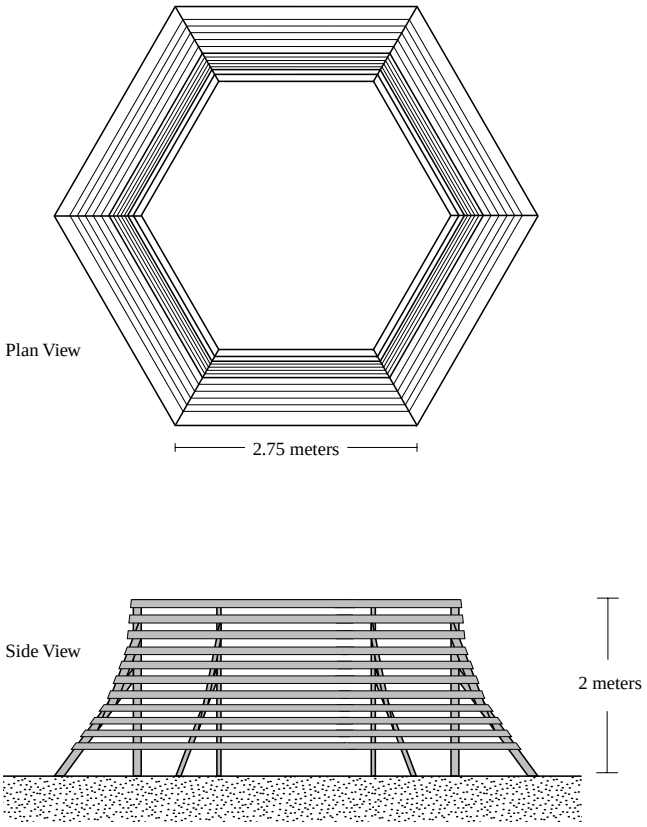


FIGURE 10. A wind shelter. This drawing was adapted from a sketch by Ludwik Liszka.

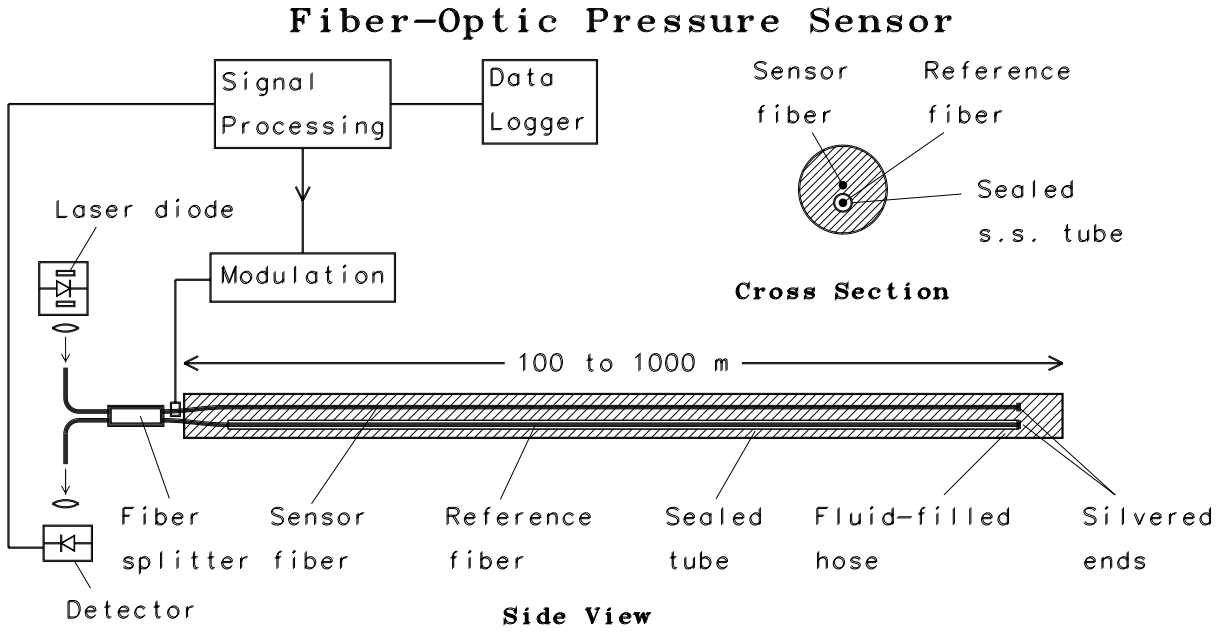


FIGURE 11. A schematic diagram of an Optical Fiber Infrasound Sensor (OFIS). Two optical fibers--one exposed to ambient pressure--form an interferometer. The integrated optical path length change caused by pressure variation along the sensor fiber is determined by the phase change of laser light traveling along the fiber. Temperature and laser wavelength fluctuations are common to both arms and largely cancel. Various schemes to increase the fiber's response to pressure changes and minimize response to strain and temperature are being investigated in our lab.



FIGURE 12. Pinon Flat Observatory . The photo, taken from the south shows a portion of one of the laser strainemeters

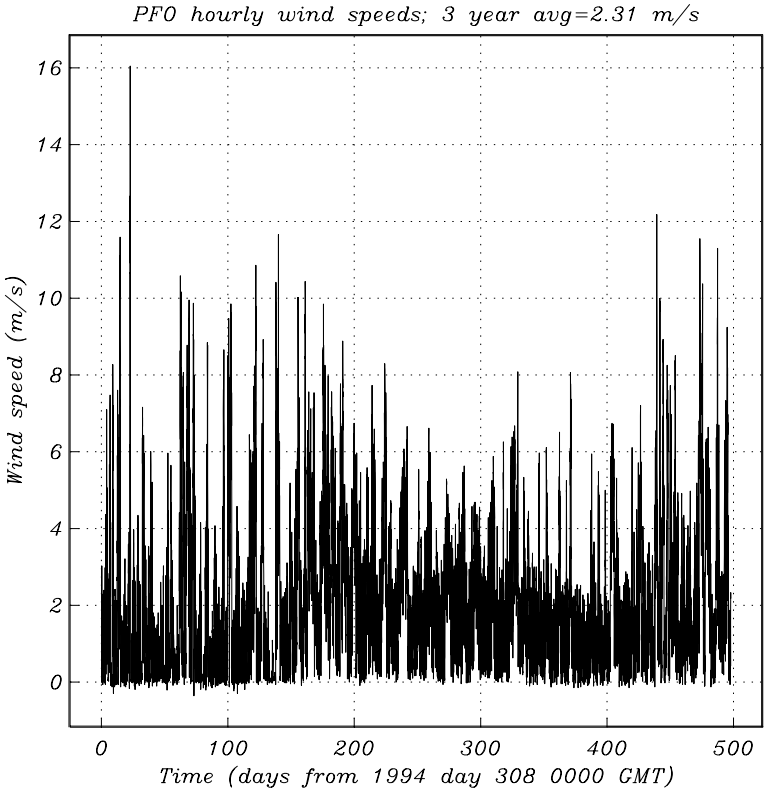


FIGURE 13. Instantaneous wind speed at an elevation of 2 m at the Pinon Flat Observatory for a 500 day time span starting on day 308 in 1994. These wind speed observations were taken once an hour.

INFRASOUND SENSOR MODELS AND EVALUATION

Richard P. Kromer and Timothy S. McDonald
Sandia National Laboratories

Sponsored by U.S. Department of Energy
Office of Nonproliferation and National Security
Office of Research and Development
National Nuclear Security Administration

Contract No. DE-AC04-94AL85000

ABSTRACT

Sandia National Laboratories has continued to evaluate the performance of infrasound sensors that are candidates for use by the International Monitoring System (IMS) for the Comprehensive Nuclear-Test-Ban Treaty Organization. The performance criteria against which these sensors are assessed are specified in *Operational Manual for Infrasound Monitoring and the International Exchange of Infrasound Data* (CTBT/WGB/TL-11/4/Rev8/Appendix I[1]).

This presentation includes the results of efforts concerning two of these sensors:
- Chaparral Physics Model 5
- CEA MB2000

Sandia is working with Chaparral Physics in order to improve the capability of the Model 5 (a prototype sensor) to be calibrated and evaluated. With the assistance of the Scripps Institution of Oceanography, Sandia is also conducting tests to evaluate the performance of the CEA MB2000. Sensor models based on theoretical transfer functions and manufacturer specifications for these two devices have been developed. This presentation will feature the results of coherence-based data analysis of signals from a "huddle" test, utilizing several sensors of both types, in order to verify the sensor performance.

Key Words: infrasound, sensor, evaluation, instrumentation

OBJECTIVE

The infrasound sensor evaluation task has the following objectives:
- Define characteristics of the Chaparral Physics Model 5 microbarograph.
- Evaluate the performance of the Chaparral 5 sensor with respect to IMS requirements using the IS-59 sensors deployed on Hawaii.
- Perform side-by-side testing of both CEA MB2000 and Chaparral Physics Model 5 infrasound sensors to compare relative sensor responses.

RESEARCH ACCOMPLISHED

Chaparral Physics Model 5 Microbarograph

Characteristics
- Smaller backing volume and leak than the Chaparral 4 to minimize effects from regional barometric pressure changes.
- Sensitivity of 100 mV/Pa (10 mV/(Bar) to maximize dynamic range and improve matching to 24-bit digitizers.
- Wide-range DC power supply (9-18 Vdc) to allow the sensor to operate directly from solar panels or unregulated power.
- Diagnostic capability to enable measurement of sensor self-noise and electronics gain.

Sensor Performance and IMS Requirements:

A comparison of Key Infrasound IMS requirements (Table 1) to Chaparral 5 sensor performance was performed.

Characteristics	Minimum Requirements
Sensor Noise	≤18 dB below minimum acoustic noise[1]
Calibration	≤5 % in absolute amplitude[2]
Dynamic Range	≥108 dB

[1] Minimum noise level at 1 Hz: ~ 5mPa(RMS√Hz)
[2] Periodicity: once per year (minimum)

Table 1- Key Infrasound Requirements (CTBT/WGB/TL-11/4/Rev8/Appendix I[1])

Sensor Noise Requirement: ≤18 dB below minimum acoustic noise of 5mPa(RMS√Hz) at 1 Hz

The specification of 18 dB below 5 mPa(RMS√Hz) at 1 Hz is 0.63 mPa(RMS√Hz) is equivalent to -64 dB relative to 1 Pa^2/Hz.

The Chaparral 5 sensor has the capability to substitute a fixed reference capacitor in place of the microphone element using an internal relay. In this mode, sensor self-noise can be accurately measured, even in a field environment. This technique was used in measuring sensor self-noise of the Chaparral 5 sensors installed in IS-59, Hawaii. A PDS of the IS-59 sensor noise with respect to IS-59 background is shown in Figure 1.

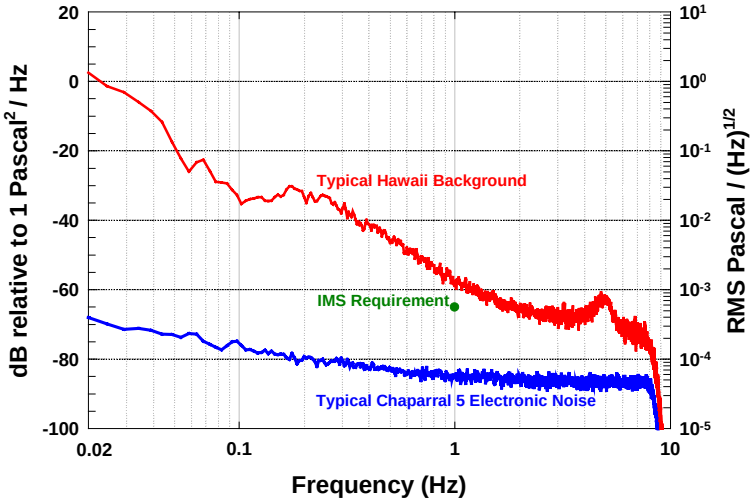


Figure 1 - Sensor Noise – IS-59 Chaparral 5 Sensors

Calibration Requirement: ≤5 % in absolute amplitude

Sensor Pressure Calibration

For a differential sensor, 5% absolute amplitude calibration is difficult to perform, especially in a field environment. Static pressure calibrations (typical 100 hPa (mBar)) such as those used on absolute barometric sensors (CEA MB2000) are not useable with differential ac-coupled sensors such as the Chaparral 5. A pressure source capable of generating small, accurate, sinusoidal signals is difficult to build, calibrate and operate. Signals are affected by ambient pressure, temperature and local atmospheric pressure changes. A process to perform 5% absolute calibration of a Chaparral 5 in a lab environment is being developed jointly by Sandia and Los Alamos National Laboratories.

The calibration solution for the Chaparral 5 is to calibrate a reference Chaparral 5 in the lab and use it as a

Secondary Standard to calibrate the production sensors. Calibration signals using piston-phone generated sinusoids provide a common stimulus to both reference and production sensors. This technique, as shown in Figure 2, was used in calibrating the Chaparral 5 sensors for installation in IS-59, Hawaii.



Figure 2 – Reference Sensor (left) and Five IS-59 Acoustically Paralleled Chaparral 5 Production Sensors

Sine-fit calculations provided a relative amplitude measurement from the reference sensor. Unfortunately, the reference sensor was not calibrated to <5%. The IS-59 sensors will have to be re-calibrated when this technique is perfected. Sensitivity of the IS-59 sensors relative to the reference sensor is shown in Table 2.

C5 Sensor Serial Number	C5_1272 Reference	C5_1322	C5_1323	C5_1324	C5_1325	C5_1326
Sensitivity Using Sinusoids	100mV/Pa	97.8mV/Pa	99.3mV/Pa	96.9mV/Pa	99.0mV/Pa	97.2mV/Pa

Table 2 – Sensitivity of IS-59 Chaparral 5 Sensors Using a Reference Sensor

Sensor Electronics Calibration

In the Chaparral 5 sensor, an electronics module provides a mechanism for converting pressure changes on the microphone element to electrical signals. The electronics module provides filtering to control the bandwidth of the sensor and amplification to set the sensitivity of these signals. A spike (similar to a step-calibration) circuit provides an indication of sensor electronics bandwidth and amplifier gain. Performing a spike calibration on a regular basis can detect changes in the electronics module performance over time and allow a form of sensor state-of-health. The amplitude of this spike is set in the Chaparral 5 to the equivalent signal of 10 Pascal. The spike can be performed with either the microphone element or a fixed reference capacitor substituted in the circuit. A change in the step-calibration with the microphone element in the circuit can indicate a defect in the microphone element. A change in the step-calibration with the fixed reference capacitor in the circuit can indicate gain or filter changes.

Dynamic Range Requirement: ≥108 dB

The Dynamic Range of a sensor usually refers to the ratio of some maximum output value to some minimum output value, usually RMS noise. For microbarograph dynamic range, Sandia uses the ratio of the peak value of the maximum sensor output to the RMS value of the sensor self-noise in a two-octave passband centered at 1 Hz (0.5 - 2 Hz). The dynamic range is measured at 1 Hz because the sensor noise limit is specified at 1 Hz. The IS-59 Chaparral 5 sensors dynamic range values are shown in Table 3.

Chaparral 5 S/N	RMS of Noise (0.5 to 2 Hz)	Dynamic Range (Peak/RMS)
1322	10.6 µv	119.5 dB
1324	7.0 µv	123.1 dB
1325	14.4 µv	116.8 dB
1326	8.1 µv	121.8 dB
1323 (spare)	3.5 µv	129.1 dB

Table 3 - IS-59 Chaparral 5 Dynamic Range

Sensor Response

The response of the Chaparral 5 is controlled by two features. An acoustical high-pass filter, determined by the combination of backing volume and leak-tube, passes the signals of interest and attenuates low-frequency barometric pressure changes. The time constant of the leak/volume is given by the expression $K=rv/\gamma P_a$ [3]. For the Chaparral 5, K= 13.3 for sea level; this is the equivalent to an electronic RC filter.

An electrical high-pass filter adds additional filtering to reduce the effect of unwanted low frequencies. For the IS-59 sensors, two pole/zeroes are contributed by the sensor electronics. One pole/zero is set by the amplifier board to a nominal RC value of 23.1; this is a nominal value as R is a function of amplifier gain and is not easily measured. A second pole/zero is set by the electronics de-coupling/output capacitor/resistor to a RC value of 110; this value assumes that the digitizer connected to the sensor has an input impedance of greater than 1 meg ohms. Low-impedance input digitizers can have significant impact on the Chaparral 5 low-frequency response.

The IS-59 and CEA MB2000 [2] sensors have an overall response (Figure 3) of:

Sensitivity: 0.100 V/Pa
Zeroes: 3 at s-plane origin
Poles: -7.52e-2, -4.33e-2, -9.1e-3

Sensitivity: 0.020 V/Pa
Zeroes: 1 at s-plane origin
Poles: -6.21e-2, -2.13e+2, -2.152e+2, -2.52e+2

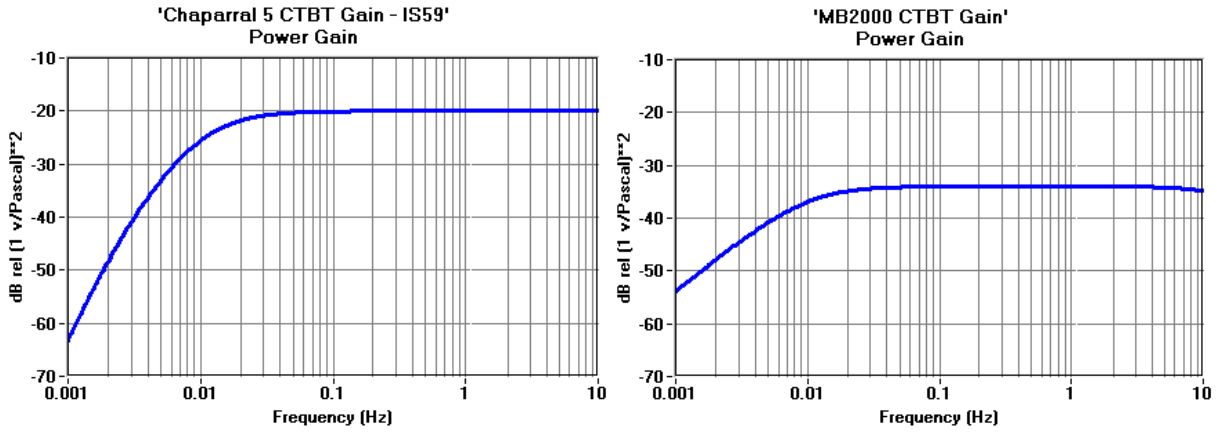


Figure 3 – IS-59 Chaparral 5 Sensor Power Gain and CEA CTBT MB2000 Power Gain

Side-by-side Comparison of CEA MB2000 and Chaparral Model 5 Sensors

A series of tests was performed at the Sandia Facility for Acceptance, Calibration and Testing (FACT) Site to compare the performance of the CEA MB2000 and Chaparral 5 sensors. Three MB2000 sensors were provided by University California San Diego/Scripps Institute of Oceanography and three Chaparral 5 sensors were provided by Southern Methodist University. The MB2000 sensors were set to a sensitivity of 20 mV/Pa. [2]; the Chaparral 5 sensors were set to a sensitivity of 400 mV/Pa. The six sensors were acoustically paralleled and connected to four porous hoses (Figure 4). Sensors were connected to a Quanterra Q4128 data acquisition system. Data were acquired over a one-week period.



Figure 4 – MB2000 and Chaparral 5 Comparison Test at Sandia FACT Site

Side-by-side coherence analysis indicated a coherence of >0.99 between the MB2000 sensors (Figure 5). The Chaparral 5 sensors showed coherence of approx. 0.8 – 0.9 between sensors (Figure 6). Coherence between the MB2000 and the Chaparral 5 sensors indicated >0.95 coherence above 0.2 Hz and <0.1 coherence below 0.1 Hz (Figure 7). A review of the data showed a diurnal cycle for coherence; it appears that the Chaparral 5 sensors are temperature and/or wind sensitive. This sensitivity appears to affect low-frequency signals (<0.2 Hz) the most.

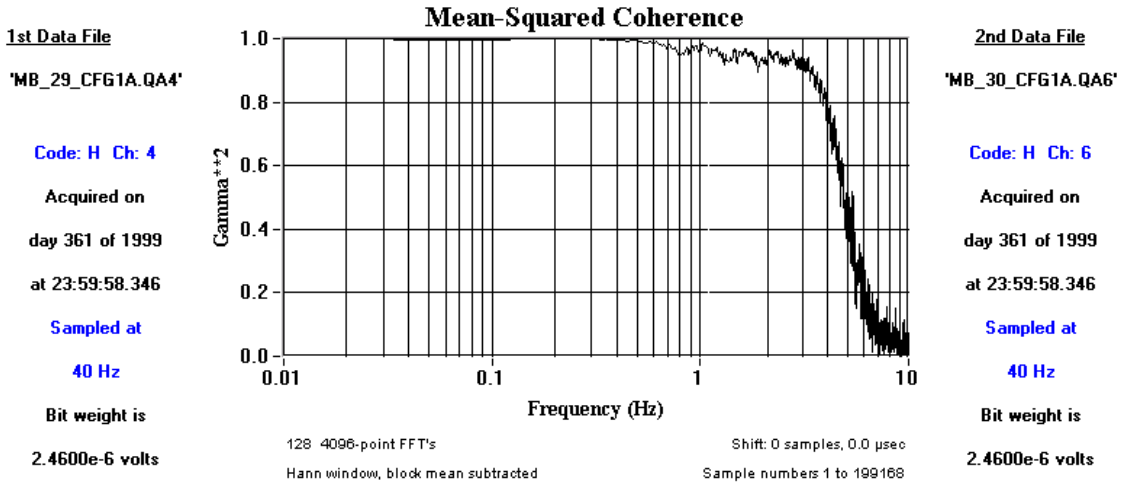


Figure 5 – Coherence Between MB2000 Sensors

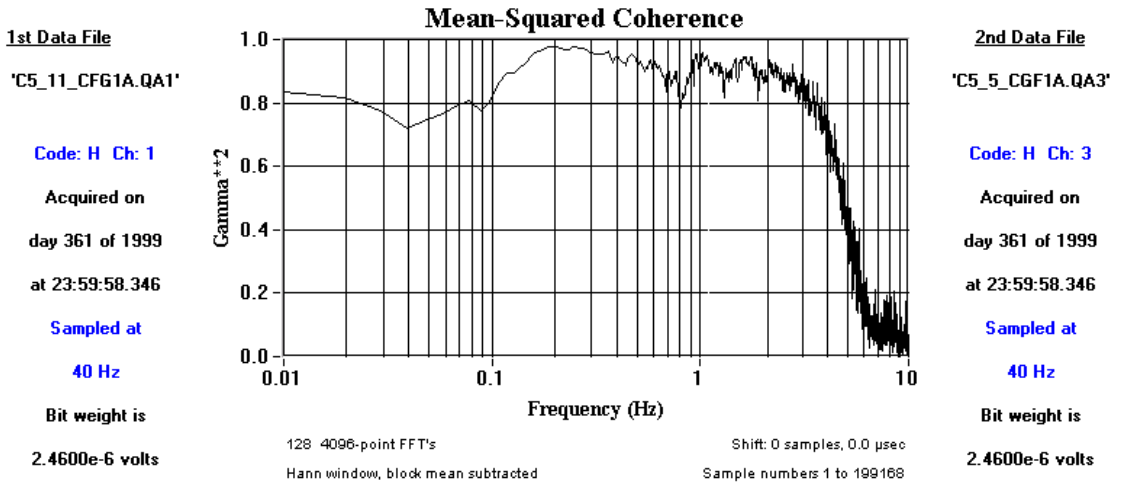


Figure 6 – Coherence Between Chaparral 5 Sensors

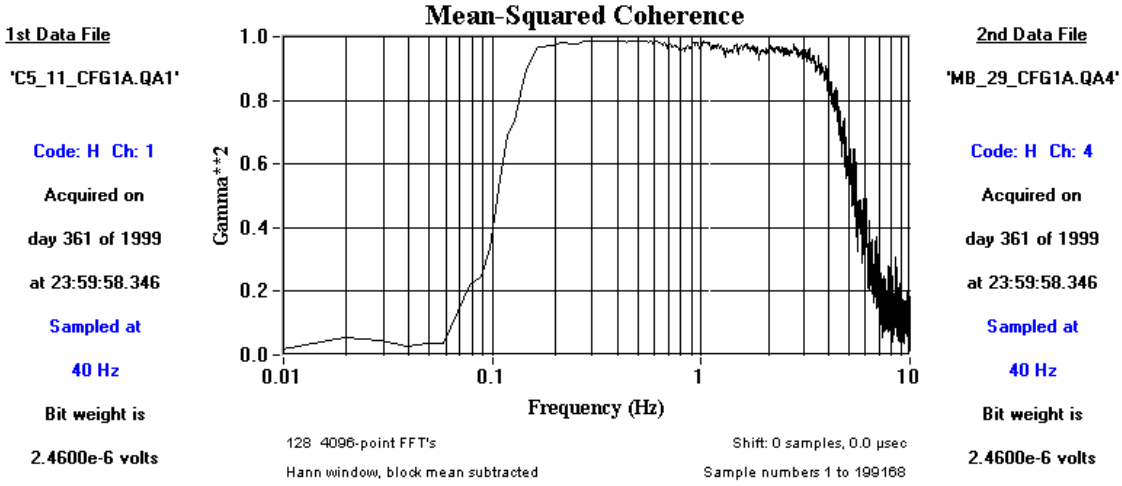


Figure 7 – Coherence Between Chaparral 5 and MB2000 Sensors

To minimize temperature effects, the Chaparral 5 sensors were packed in sand to provide thermal mass and isolate the sensors from wind (Figure 8). Data were acquired over a one-week period.



Figure 8 – MB2000 and Chaparral 5 Comparison Test at Sandia FACT Site

Side-by-side coherence analysis indicated a coherence of >0.99 between the MB2000 sensors (Figure 9). The Chaparral 5 sensors showed coherence of >0.98 between sensors (Figure 10). Coherence between the MB2000 and the Chaparral 5 sensors indicated >0.98 coherence above 0.02 Hz (Figure 11). Stabilizing the Chaparral 5 temperature and isolating the sensor from the wind corrected sensor variation. Since most applications require the sensors to be located in a buried vault, this sensitivity will not impact IMS performance. If this sensor is used for site surveys, care must be taken to insulate the sensor.

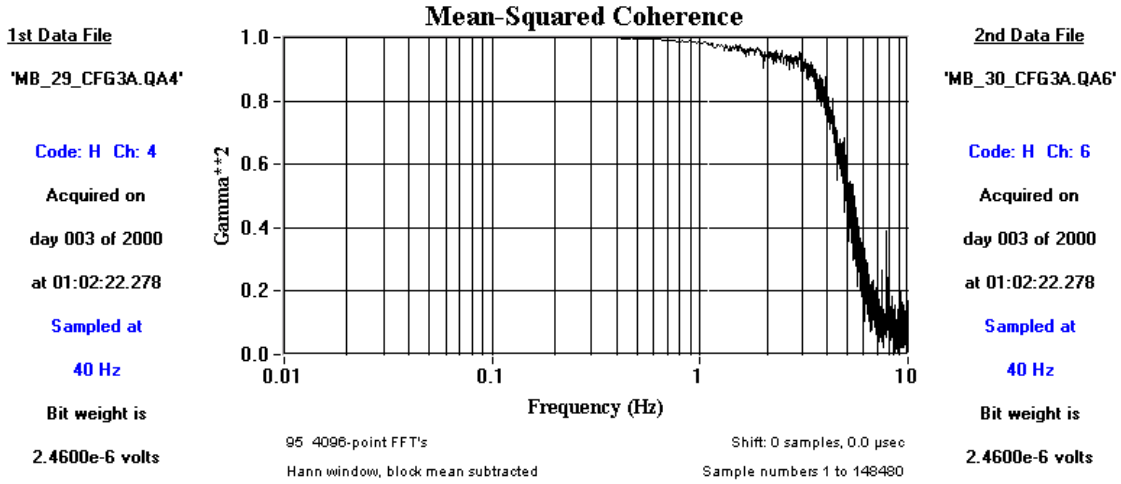


Figure 9 – Coherence Between MB2000 Sensors

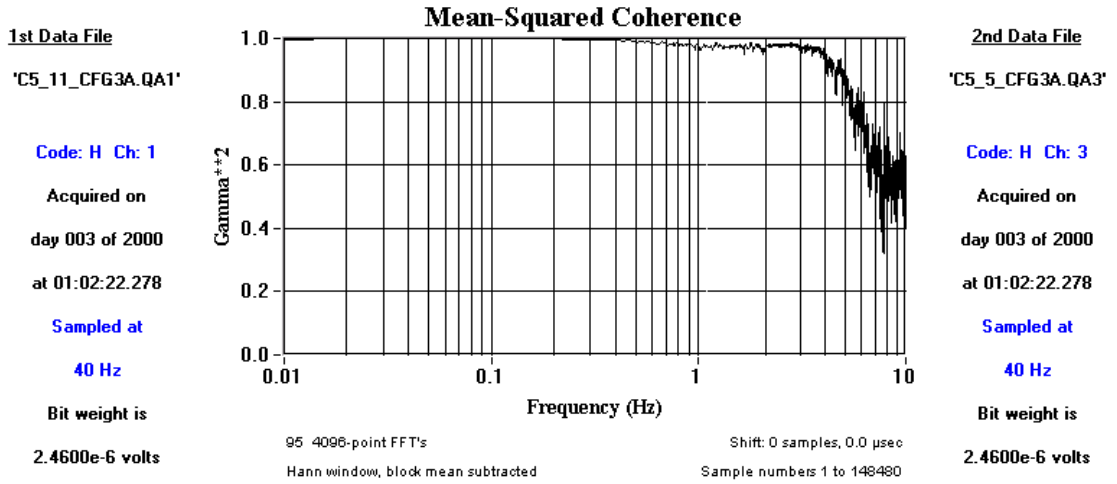


Figure 10 – Coherence Between Chaparral 5 Sensors

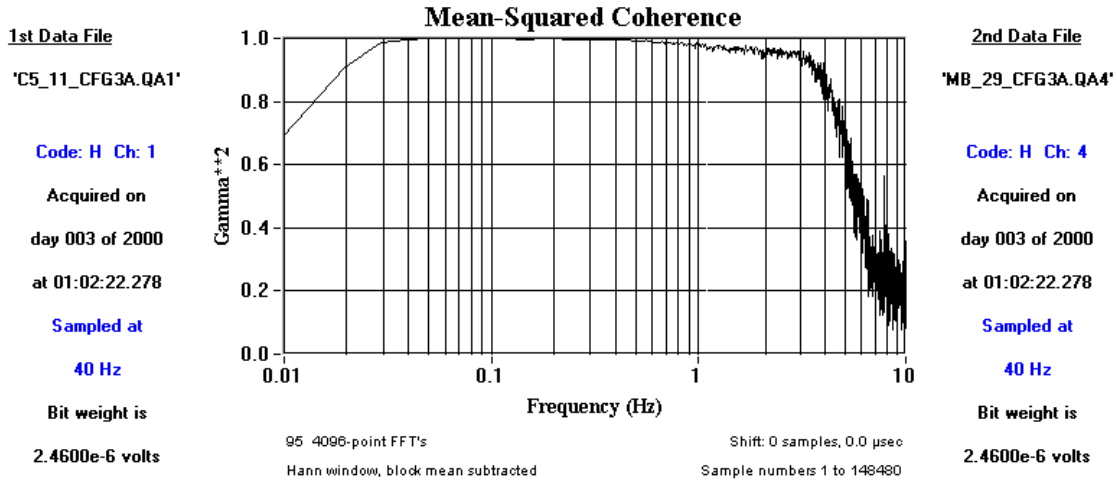


Figure 11 – Coherence Between Chaparral 5 and MB2000 Sensors

Side-by-side coherence analysis between the MB2000 and Chaparral 5 sensors indicated a relative gain difference of 26 dB. This corresponded to the gain difference of X20 between the sensors. Difference in sensitivity and phase between sensors was readily observed (Figure 12). It would appear that using the acoustical background as a common signal source for paralleled calibrated reference sensor and an installed sensor is a viable calibration technique.

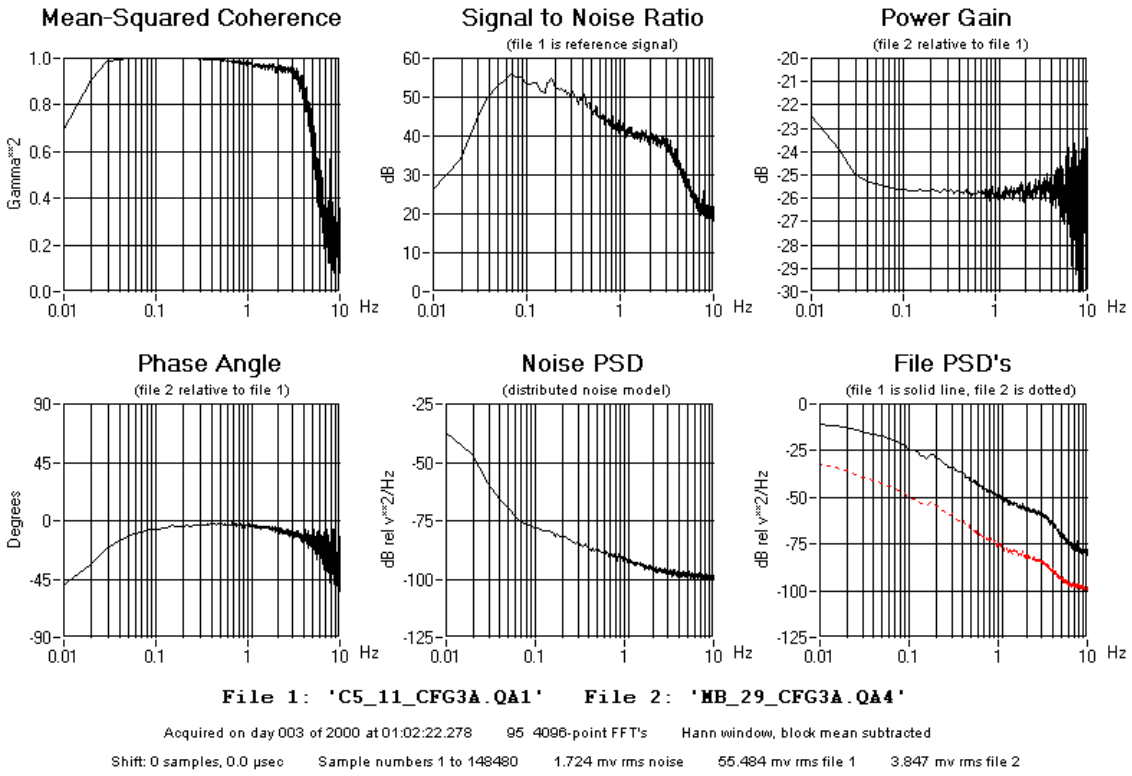


Figure 12 – Coherence Analysis Results Between Chaparral 5 and MB2000 Sensors

CONCLUSIONS AND RECOMMENDATIONS

The Chaparral Physics Model 5 is an improved version of the Chaparral 4. It met all IMS requirements tested. A response model was developed for the Chaparral 5 sensors used at IS-59, Hawaii. Sensitivity to temperature/wind was observed in the Chaparral 5. An installation technique to minimize these temperature effects was demonstrated at the Sandia FACT site. A technique to laboratory/field calibrate infrasonic sensors using a reference sensor was demonstrated using both the MB2000 and Chaparral 5 sensors. Techniques developed for sensor testing can be used for determining sensor conformance to IMS requirements.

REFERENCES

1. *Operational Manual for Infrasound Monitoring and the International Exchange of Infrasound Data*, CTBT/WGB/TL-11/4/Rev.8, 16 February 2000.

2. *MB2000 Microbarometer Product Manual;* CEA/Departement Analyse et Surveillance de l'Environnment, October 1997.

3. *The Design and Operation of Infrasonic Microphones*, Los Alamos National Laboratories Report #LA13257, J. Paul Mutschlecner and Rodney W. Whitaker, May 1997.

INFRASOUND DETECTION OF ROCKET LAUNCHES

Keith L. McLaughlin, Anna Gault, David J. Brown
SAIC, Center for Monitoring Research

Sponsored by US Army Space and Missile Defense Command
Contract No. DASG60-96-C-0064

ABSTRACT

The satellite launch industry is a multi billion-dollar international industry with over 100 commercial and military satellite launches conducted in 1999 alone. Rocket launches from both Cape Canaveral Air Force Station (CCAFS) and Vandenburg Air Force Base (VAFB) have been observed at operational infrasound stations monitored by the Prototype International Data Center (PIDC). As more IMS infrasound stations are installed worldwide, we can expect to more frequently observe rocket launches. Rocket launches may serve as useful "ground truth" data and/or Confidence Building Measures (CBM) to test and demonstrate IMS infrasound capabilities. Commercial and military launch facilities include Baykonyr in Kazakhstan, Plesetsk in Russia, Jinyu, Wuzhsi, Jiuquan, Xichang, and Taiyuan in China, Kourou in French Guinea, Alcantara in Brazil, Tanegashima in Japan, Vandenburg AFB and Cape Canaveral AFS in US, and the new Boeing ocean-going launch platform in the Pacific Ocean.

"Summer season" Space Shuttle launches are seen at the experimental DLIAR (2550 km) infrasound array in New Mexico and the more recently installed infrasound array, ISM (2780 km), in Canada. These long-range observations are strongly correlated with the geometry of stratospheric winds across North America. The 1-4 Hz signals arrive within 5 degrees of the nominal azimuth.

In order to take advantage of favorable West-to-East propagation, waveforms were examined for 14 VAFB launches in 1999 at SGAR (680 km) and DLIAR (1300 km). Detections were seen for a Titan IVB launched 5/22/99 and a Delta II launched 04/15/99. Interestingly, the Delta II of 02/22/99 and the Atlas IIA of 12/18/99 were not detected although these two rockets are of similar size. Upper atmospheric wind conditions should have been favorable for several of the detections, however noise levels were often high at SGAR and DLIAR. Relative amplitudes of the signals are consistent with relative thrusts (700 vs. 1700 thousand lbs). Observed arrival azimuths were within 5 degrees of nominal. Detailed analysis of DLIAR signals indicate azimuth can be tracked down-range from the launch site for two minutes. Arrival times and phase velocities are consistent with stratospheric propagation and nominal infrasound travel times to SGAR (2340 s) and DLIAR (4440 s). The signals were best observed between 0.1-2 Hz.

Long-range detections of Space Shuttle, Titan IVB, and Delta II launches are very encouraging. The Space Shuttle burns about 1 KT of liquid oxygen and hydrogen per minute. Therefore the equivalent explosive yield of the extended infrasound source is between one and two orders of magnitude smaller than 1 KT. The Titan IVB and Delta II launch vehicles are an order of magnitude smaller than the Space Shuttle.

OBJECTIVE

This work examines rocket launches as potential ground truth events to demonstrate long-range IMS infrasound capabilities such as detection and azimuth estimation as a function of changing atmospheric conditions.

REVIEW

Man-made low-frequency infrasound (less than ~20 Hz) may be excited by large strip-mine blasts, atmospheric explosions, gas pipeline ruptures, rocket launches, orbital (and sub-orbital) vehicle reentry sonic booms, and aircraft sonic booms. Some sources are point like (explosions) and others are distributed along a trajectory (meteors, sonic booms and rocket launches). The literature contains several examples of infrasound from missile launches in the late 1960's and early 1970's. Most results were an off-shoot of infrasonic research done for long-range atmospheric nuclear test detection. Interest in the topic diminshed as nuclear powers shifted to underground testing. Publications by Fehr (1967), Donn et al (1968), Kaschak (1969), Kaschak et al. (1970), Donn et al. (1971), Cotton and Donn (1971), Balachandran et al. (1971a), Balachandran et al. (1971b), and Posmentier (1971) provided an analysis of the frequent and large rocket launches of the early manned space program.

- Intensity was found to depend on thrust, trajectory, and sound speed and wind along the path. Rockets as small as 50 Klbs thrust and as large as 7,500 Klbs thrust (Saturn-V) were observed at long-range (900-1500 km). Amplitudes for the largest Saturn-V rockets ranged from 1 to 20 microbar near 1 Hz.
- Strong seasonal effects on detection were observed. For paths from Cape Canaveral Air Force Station, Florida, to stations in New Jersey and New York over a 12-month period (298 launches) the monthly detection percentages ranged from 10 to 80%. It was found that long-range rocket infrasound propagates primarily in the stratospheric waveguide (below 50km) and the existence of this waveguide depends strongly on the presence/absence, geometry, and direction of the jet streams at about 50 km altitude. Temperature and wind soundings coupled to 2D and 3D ray tracing was found to adequately explain the observed seasonal behavior.
- In situations where rockets were launched "toward" the receiver, first arriving waves were often "apparently supersonic" generated by the re-entry phase of the 1st stage booster entering the atmosphere closer to the station than the initial launch site. Waves with "apparently sonic" velocities were observed to arrive at azimuths from the launch site and the ascent trajectory.
- Dominant frequencies were generally between 0.1 and 1 Hz (although the infrasound systems of the time severely attenuated frequencies above 1 Hz). Dominant frequencies appeared to be related to solid vs. liquid fuel with solid rocket missiles having high somewhat frequencies, 0.1-2 Hz. It was noted that solid fuel missiles have higher accelerations and reach Mach 1 sooner.
- It was argued the infrasound source mechanism was aerodynamic (sonic booms) rather than rocket exhaust and that the largest signals were excited at altitudes near the tropopause and velocities above Mach 1. A) The frequency content of the supersonic re-entry phase was similar to the ascent phase. B) Recordings in the vicinity of a launch or static firings (Fehr 1967) were broadband (above 4 Hz to audible) with peak values in the 8-16 Hz frequency bandwidth and differed from lower frequency long-range infrasound. C) Saturn rocket engine static firings at ground level in both Florida and Huntsville, Alabama, were never observed in New Jersey or New York despite often-favorable propagation conditions and orientations of the static firings.
- Long-range infrasound arrived within 5-8 degrees of expected azimuths (when corrected for launch path) consistent with cross wind effects predicted by 3D ray tracing.
- Near-range infrasound observations of static firings of individual Saturn-V "F1" engines (1,500 Klbs thrust) are consistent with an equivalent far-field source of 75,000 microbars at 1m peaked near 8 Hz during continuous runs (171 DB). During startup and shutdown, the source was more broadband and showed peaks at 4 and 16 Hz.

Long-Range Attenuation Models and Equivalent Explosive Yield

Stevens et al. (1999) recently conducted a review of long range explosion generated infrasound propagation. They found the Whitaker (1995) relationship generally the most robust for low yields.

$$\text{Log}(P) = 3.37 + 0.68\ \text{Log}(W) - 1.36\ \text{Log}(R) + 0.019\ v,$$

where P is pressure in Pa (1 Pa = 10 microbar), W is yield in kiloton, R is range in km, R is range in degrees, v stratospheric wind velocity in m/sec. The relation has a strong dependence on atmospheric winds where v is positive if the wind is in the direction of propagation and negative if the wind is in the opposite direction of propagation. Upper atmospheric winds often attain velocities of over 50 m/s causing variations in amplitude of a factor of 20 or more. The attenuation relationships are all for surface source and receiver and are not generally considered valid for short-range propagation (< 200 km). If we apply the Whitaker attenuation relation to the Saturn-V historical literature data (0.1-2 Pa at 1500km, 0.1-1 Hz) we can estimate equivalent yield ranges of 0.07-6 tons (no wind), 1.7-150 tons (50 m/s head winds), 0.003-0.25 tons (50 m/s tail winds). These "equivalent" yield levels in the 1 Hz band are consistent with the rate of energy expended by the Saturn-V.

The total propellant (oxidizer plus fuel) available in a Saturn-V first stage (7,600 Klbs thrust) was about 2.3 Kt burned over a period of about 150 seconds or roughly equivalent to a 15-ton explosion every second for 150 seconds. The rate of energy release for the Space Shuttle (maximum thrust of 7,700 Klbs) is similar. The shuttle's three main engines (375 Klbs. thrust each) and 2 solid rocket boosters (SRB's) (3,300 Klbs thrust) burn between 1-1.3 Kt of propellant in 120 seconds to attain an altitude of about 50 km. The main engines then consume a maximum of 600 tons of propellant for another 5-6 minutes. If we assume the chemical efficiency of rocket fuel is close to

TNT, this is equivalent to a 10-ton chemical explosion every second. This is analogous to the ripple-fire problem in seismology where a strip mine may fire a series of smaller explosions spread out over time. For comparison, the first stage of a theater ballistic missile (TBM) (34-50 Klbs thrust) burns ~3 tons of fuel in ~90 seconds which is about 1/400th the amount of the shuttle in 80% of the total time. The actual infrasound excitation mechanism is uncertain. While the far-field mechanism may be supersonic shock waves, the expanding transonic exhaust plume may also contribute to infrasound radiation. In either case, the energy available for infrasound excitation is bounded by the rate at which fuel is burned and should be roughly proportional to the total rated thrust of the rocket.

Recent Observations

Recent infrasound observations were collected from waveform data available in the Center for Monitoring Research (CMR) and the IRIS data center. These data serve to provide some insights, source calibration, and ground truth validation. Most of the infrasound data is by necessity very long range (> 1000 km) from large rockets. Observations have been made at infrasound stations, SGAR, DLIAR, and ISM from Space Shuttle Launches at Cape Canaveral and Vandenburg Air Force Station at distances of 100's to 1000's of km. Seismic records of infrasound at distances of under 100 km were also collected at broadband seismic stations (Figure 1, Table 1 and Table 2.).

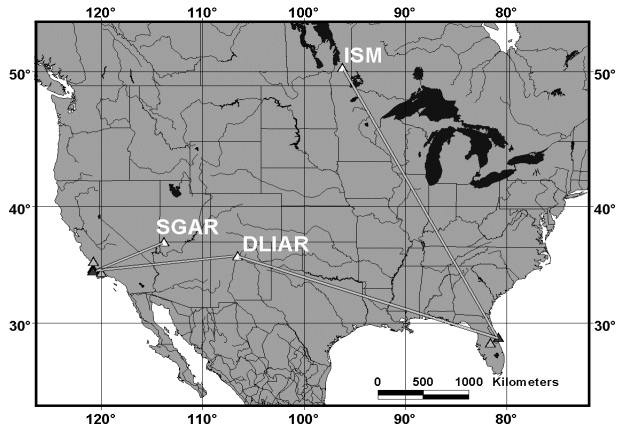


Figure 1. Infrasound arrays DLIAR, SGAR, and ISM detected launches from Cape Canaveral Air Force Station (CCAFS) and Vandenburg Air Force Base (VAFB).

Table 1. 1999 Space Shuttle Launches from Cape Canaveral Air Force Station

	Date GMT	Time GMT	Observed
STS-96	05/27/99	11:49:00	DLIAR
STS-93	07/24/99	04:31:00	DLIAR
STS-103	12/19/99	00:50:00	None

Table 2. 1999 VAFB Launches with rated thrust greater than 200 Klbs.

Date GMT		Rocket	VAFB Location	Thrust Klbs	Detect
1/10/99	08:06	MINUTE-0MAN III	NVAFB	200	No
2/22/99	10:39	DELTA II	SLC2	700	No
3/10/99	08:01	PEACE-KEEPER	NVAFB	500	No
4/15/99	18:32	DELTA II	SLC2	700	DLIAR, SGAR
4/27/99	18:22	ATHENA II	SLC2	400	No
5/22/99	09:36	TITAN IVB	SLC4E	1700	DLIAR, SGAR
6/20/99	02:15	TITAN II	SLC4W	430	No
8/20/99	08:45	MINUTE-MAN III	NVAFB	200	No
8/20/99	11:27	MINUTE-MAN III	NVAFB	200	No
9/24/99	18:22	ATHENA II	SLC6	400	No
10/3/99	02:01	MINUTE-MAN III	NVAFB	200	No
12/12/99	17:38	TITAN II	SLC4W	430	No
12/18/99	18:57	ATLAS IIAS	LC3E/W	700	No

NVAFB=North VAFB, LC2=Launch Complex 2, SLC4E =Space Launch Complex 4 East, SLC4W =Space Launch Complex 4 West, SLC6=Space Launch Complex 6.

Space Shuttle Launches in 1999. It has been observed that "summer season" Space Shuttle launches can be seen at the DLIAR infrasound array in New Mexico (2550 km with nominal travel time of 8500 seconds) and at the more recently installed ISM infrasound array in Canada (2780 km with nominal travel time of 9300 seconds). These low SNR detections (Figure 2) are possible only because signal processing can see coherent signals within the otherwise incoherent background noise. During the favorable summer season, observed peak amplitudes of a few Pa are seen with durations of ~400-500 seconds. It is not possible to determine the actual dominant frequency since the dominant frequency of the recorded signals are at or above the upper end of the of the system bandwidth (~4 Hz). The observations are consistent with the historic long-range Saturn-V signals cited in the literature given the rate of energy release of the Space Shuttle is about the same as a Saturn-V. While we expect propagation effects to extend the duration of the signals, it is not clear to what extent the signal duration is determined by the total burn time of the shuttle engines (~400 seconds) and the fact that the rocket is traveling away from the stations at supersonic speeds. "Winter-season" launches have not been detected at DLIAR or ISM. These seasonal effects are clearly related to the geometry of the winter/summer jet streams. The Whitaker attenuation formula predicts greater than an order of magnitude reduction in the amplitude due to a jet stream core of 50 m/s. Assuming, the already low SNR "summer-season" launch signals are enhanced by a "tail-wind", the "winter-season" launch signals must be two orders of magnitude below the noise.

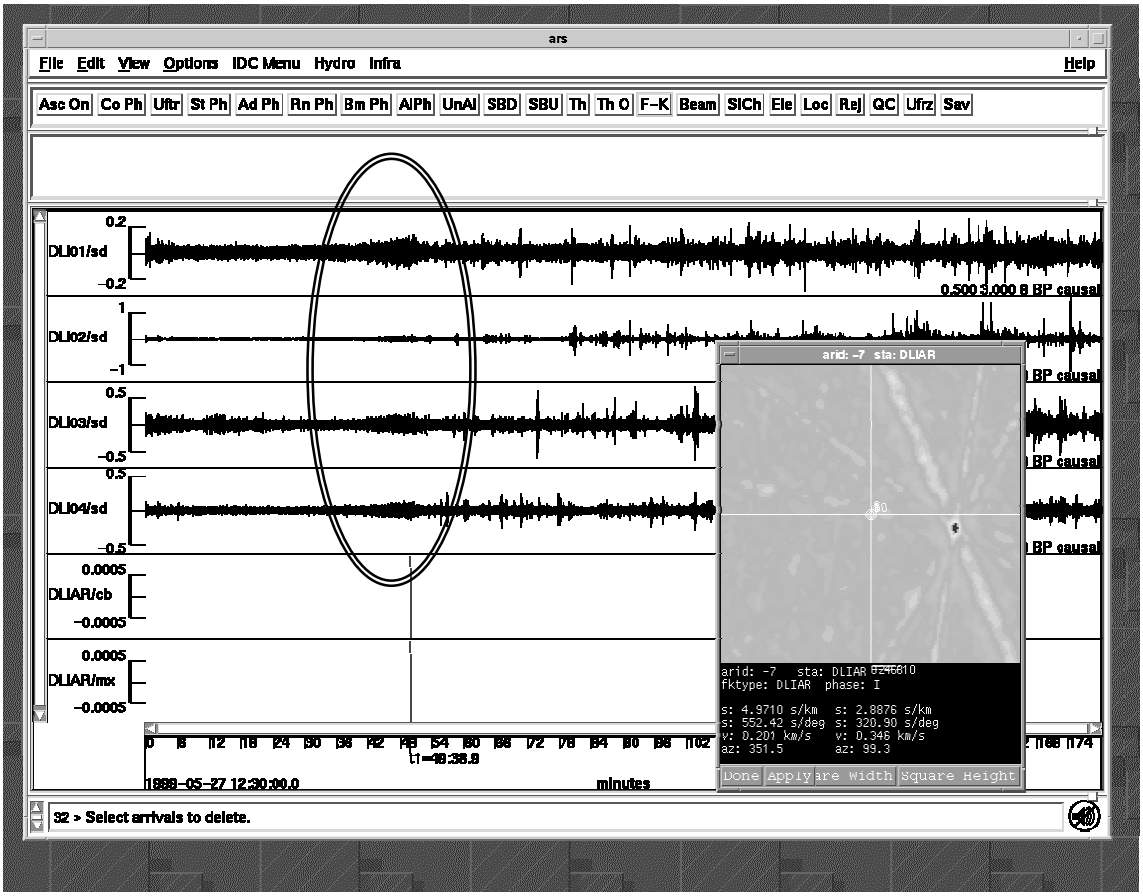


Figure 2. Low SNR arrival recorded at DLIAR in New Mexico from STS-96 launched on 27 May 1999 at 10:49 GMT. The inset frequency wavenumber plot shows a clear stratospheric infrasound arrival (apparent velocity 346 m/s) at the expected back azimuth (99.3 degrees) to CCAFS. Numerous incoherent and unrelated noise bursts can also be seen on the individual traces following the arrival.

A seismometer may serve as a noisy microbarograph. The seismometer responds to pressure waves pushing down on the earth's surface with a conversion efficiency of about one nanometer of vertical ground motion for each microbar of atmospheric pressure variation. Sorrells and Der (1970) give the relation, v = u2πf= c P(λ + 2 μ)/2μ/(λ+μ), where v is the ground velocity, u the ground displacement, c is the infrasound phase velocity, P is the infrasound pressure, and λ and μ are the Lame and shear modulii. Seismic data was available from the IRIS data center for the seismic station DWPF (installed in June 1999) for one shuttle launch (Figure 3). The instrument response is flat to ground velocity (and hence infrasound pressure) across the bandwidth of interest. Figure 4 shows a recording of STS-93 (07/24/99 04:31:00GMT) at DWPF (97 km). The largest seismic amplitudes are consistent with peak infrasound pressures of about 200 microbars. A small signal consistent with a seismic P-wave arrival (P at LO+15s) and S-wave arrival (S at LO+25s) can be seen soon after lift off (LO). The first infrasound arrival (I1 at LO+300s) is consistent with direct tropospheric propagation of the lift off transient at ~320-330 m/s with a sustained amplitude of ~50 nm/s. The larger infrasound signals I2 and I3 probably originate later, higher, and farther down range with peak amplitudes of ~200 nm. The seismic P & S waves as well as the infrasound signals I1 and I2 are peaked near 4 Hz. The infrasound signal I3 is more broadband. No signal is observable below 1 Hz due to high ground noise levels at low frequencies. The total infrasound signal lasts ~400 seconds. The dominant frequency (~4 Hz) at DWPF is consistent with the long-range infrasound signals observed at DLIAR.

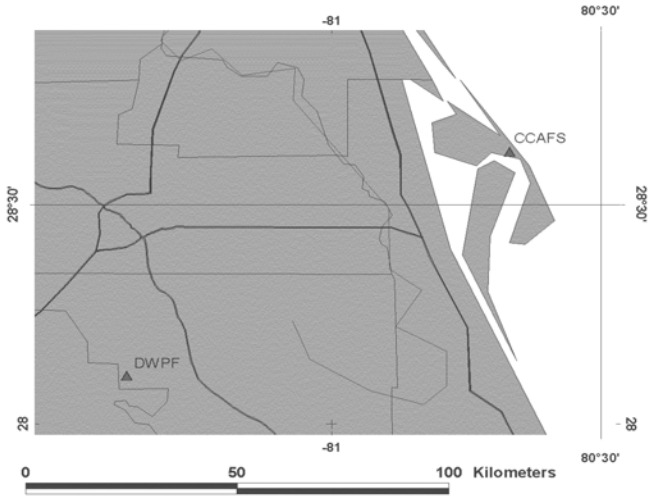


Figure 3. Seismic station, DWPF, is 97 km from the Shuttle Launch pads at Cape Canaveral Air Force Station CCAFS.

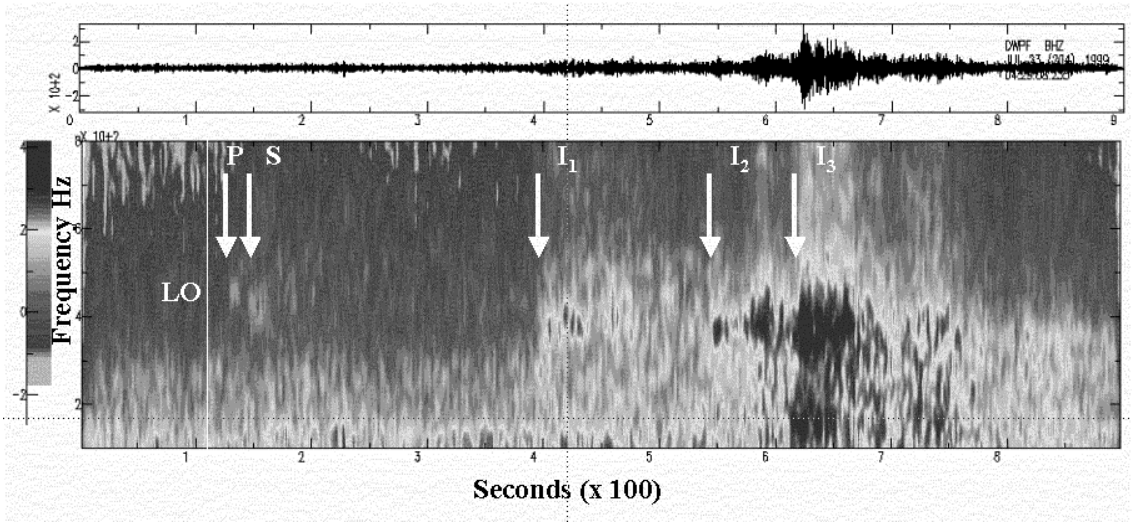


Figure 4. STS-93 (07/24/99 04:31:00GMT) at seismic station DWPF in central Florida (97 km from the launch pad). Sonogram below the seismogram shows frequency content as a function of time. A small signal consistent with a seismic P-wave arrival (P) and S-wave arrival (S) can be seen soon after lift off (LO). The first infrasound arrival (I1) is consistent with direct tropospheric propagation at 330 m/s.

VAFB Launches in 1999. In order to take advantage of favorable West-to-East propagation, waveform data was examined for signals from Vandenburg AFB launches during 1999 (Table 2). Data from eight of 14 launches were examined at SGAR (680 km) and DLIAR (1300 km). Detections were only seen for the Titan IVB of 5/22/99 (see Figures 5A & 5B) and the Delta II of 04/15/99. Interestingly, the Delta II of 02/22/99 and the Atlas IIA of 12/18/99 were not detected although these two rockets are of similar size. No rockets rated less than 700 Klbs thrust were detected. Relative amplitudes of the Delta II and Titan IVB are consistent with the relative thrusts (700 vs. 1700 Klbs). All observed azimuths of arrival were within 5 degrees of nominal (250 and 269 degrees at SGAR and DLIAR respectively). Arrival times and phase velocities are consistent with stratospheric propagation and nominal infrasound travel times to SGAR and DLIAR of 2340 and 4440 seconds respectively. The signals were best observed between 0.1 and 2 Hz. The Infratool analysis in Figure 6 demonstrates the back-azimuths are consistent and within 5 degrees of the launch site although there is evidence that the back-azimuth does decrease with time consistent with the trajectory of the rocket to the southwest of the launch site.

Seismic data was examined from two Caltech seismic stations PHL (65 - 85 km from VAFB launch facilities) and SBC (84 - 91 km from VAFB launch facilities) available from the IRIS data center. Four launches recorded at PHL are shown in Figure 7. The dominant frequencies of all signals are at the upper end of the bandwidth (7-8 Hz) and well above the long-range infrasound bandwidth observed at SGAR and DLIAR (0.1-2 Hz). Peak amplitudes vary from ~300 to 600 microbars, however, the amplitudes do not correlate well with range or thrust. A couple of the infrasound signals appear to arrive early (assuming 340 m/s propagation) suggesting that the launches were not exactly on the minute. Data dropouts produce spikes on two recordings and should not be confused with real arrivals. The set of five launches show extreme variability in onset and duration. The rockets were traveling away from the station and the signal durations are very extended lasting 400-500 seconds. Three of the signals show large transients near the end (a Delta II and two Minuteman III's). The two bottom traces in Figure 7 are Minuteman III's launched from the same area (NVAFB) separated by only 2 hours 42 minutes. These two records demonstrate the strong dependence of infrasound on meteorological conditions. While there are some similarities between the two records and the launch times may be uncertain, the timing between the arrivals is not reproduced. The spectral character of the signals at this range is quite different from the long-range signals recorded at SGAR and DLIAR. Sonograms of these records (Figure 8) show arrivals are characterized by 2-8 Hz broadband impulses and 4-8 Hz continuous coda.

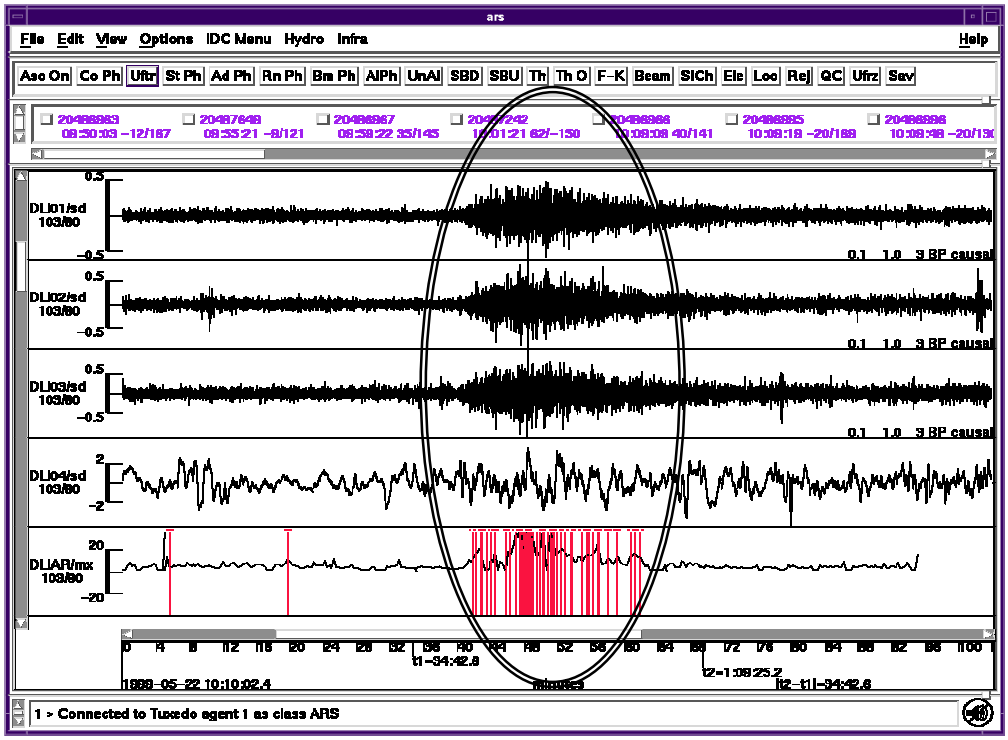


Figure 5A. Titan IVB 05/22/99 recording at DLIAR (1300 km).

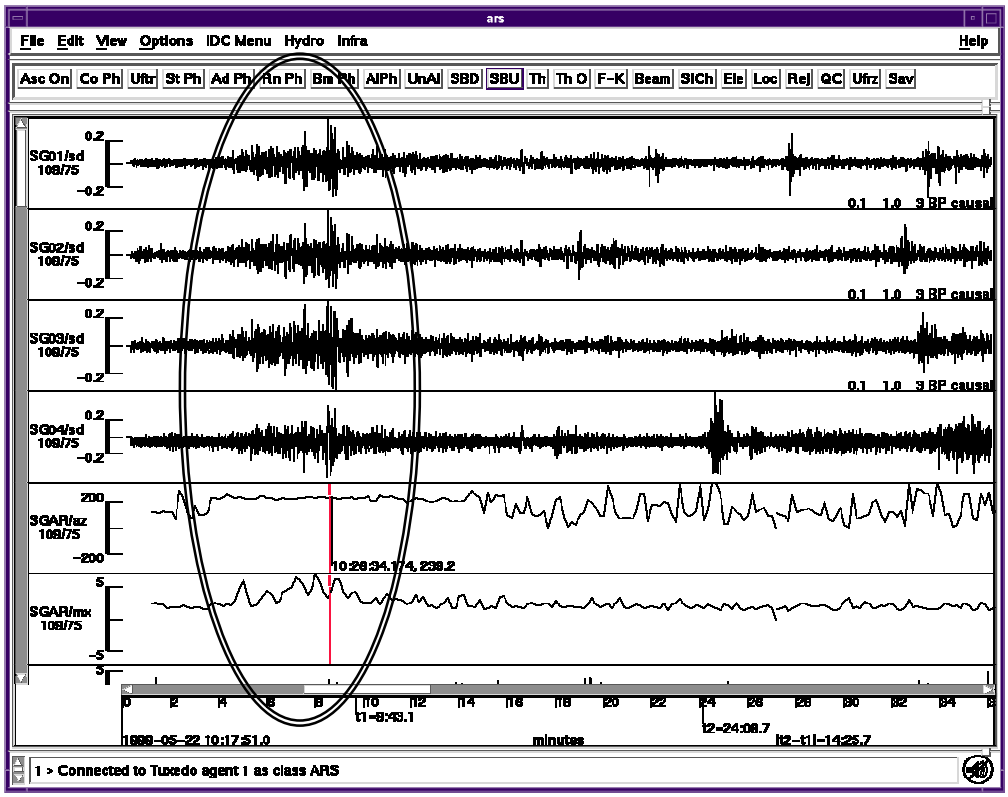


Figure 5B. Titan IVB 05/22/99 recording at SGAR (680 km).

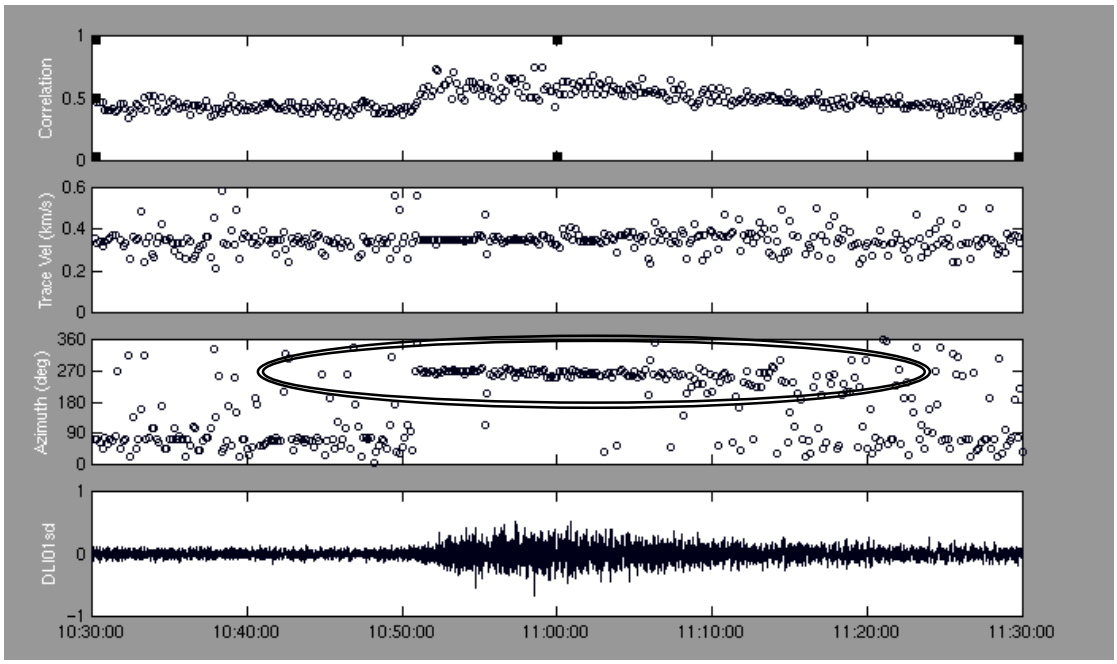


Figure 6. Infratool (SANDIA, DoE 1999) analysis of the Titan IVB recording at DLIAR (1300 km) shows azimuth of arriving energy is initially constant and within 5 degrees of nominal for ~5 minutes and then slowly decreases consistent with the rocket's trajectory to the southwest of VAFB.

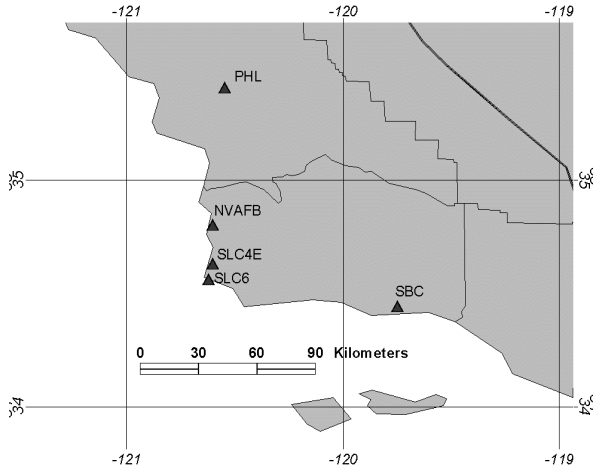


Figure 7A. Caltech station PHL is available from IRIS and between 65 and 85 km of launch facilities at VAFB. Signals were also observed at SBC.

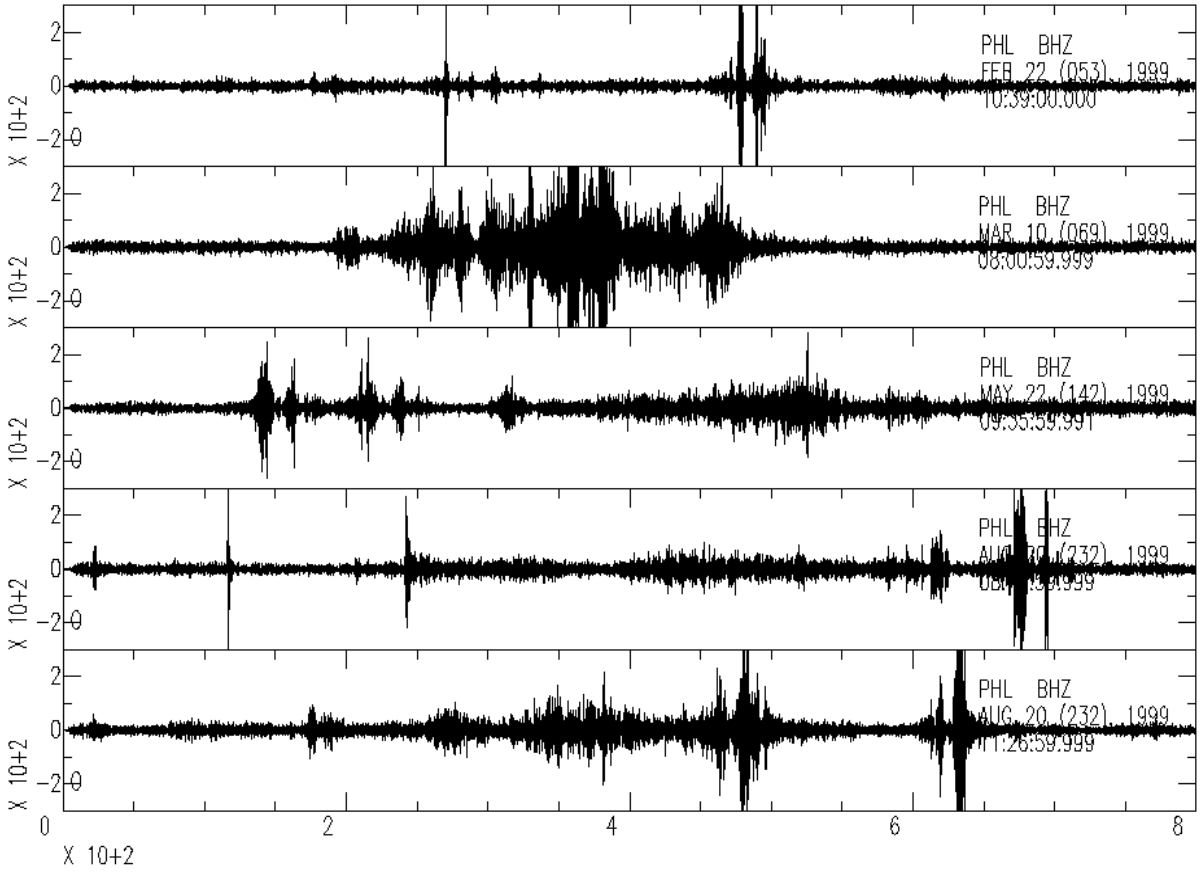


Figure 7B. Seismic recordings of five launches from VAFB at station PHL (1-8 Hz). All traces are aligned on announced lift off times (given to the minute) and plotted on the same time and amplitude scales. Ranges to the launch facilities vary from 65 to 85 km. A couple of the infrasound signals appear to arrive early suggesting launches were not exactly on the minute. Data dropouts produce spikes on two recordings. The set of five launches show extreme variability in onset, amplitude, and duration. Three of the signals show large transients near the end of the record. The two bottom traces are Minuteman III's launched from NVAFB separated by only 2 hours 42 minutes.

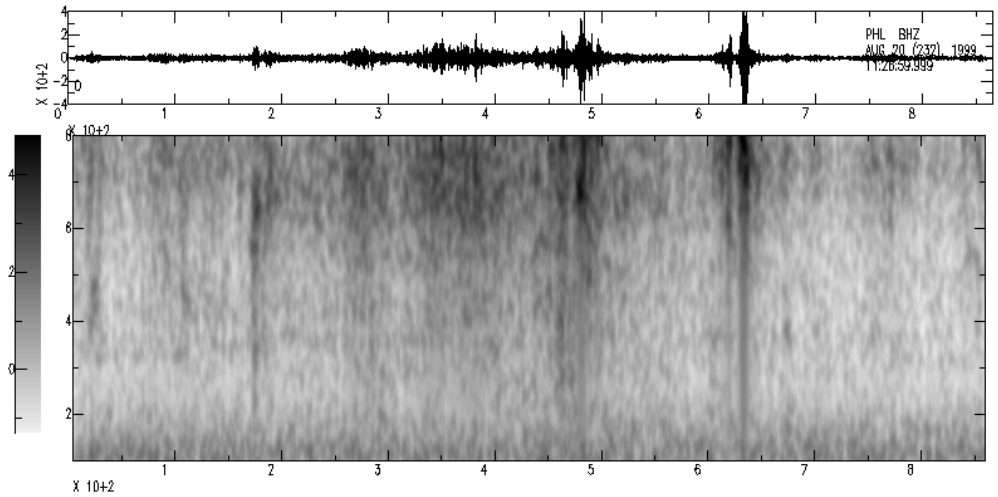


Figure 8. Spectrogram of 11:27 Mar 20, 1999 MINUTEMAN III launch from NVAFB at seismic station PHL (~68 km). Acoustic arrivals are characterized by broadband (2-8 Hz) impulses superimposed upon more continuous 4-8 Hz coda.

Propagation

Both climatological and daily meteorological models are available to compare with infrasound observations. Figure 9 contrasts the 200 mb wind (~10 km) velocities for May 27, 1999 (Space Shuttle detection at DLIAR) and December 19, 1999 (no Space Shuttle detection at DLIAR). The high altitude winds (10 Km) differ over a factor of two between these two dates. Figure 10 shows predicted ray paths for two simpler climatological models. The presence of a strong west to east mid-latitude jet stream inhibits propagation from east to west during the winter. During "summer" periods when the jet stream is weak or absent across the United States, a stratospheric waveguide may support east to west propagation. Obviously, more detailed 3D analysis of specific days for which long-range detections (and non-detections) are observed should be used to test numerical infrasound propagation predictions.

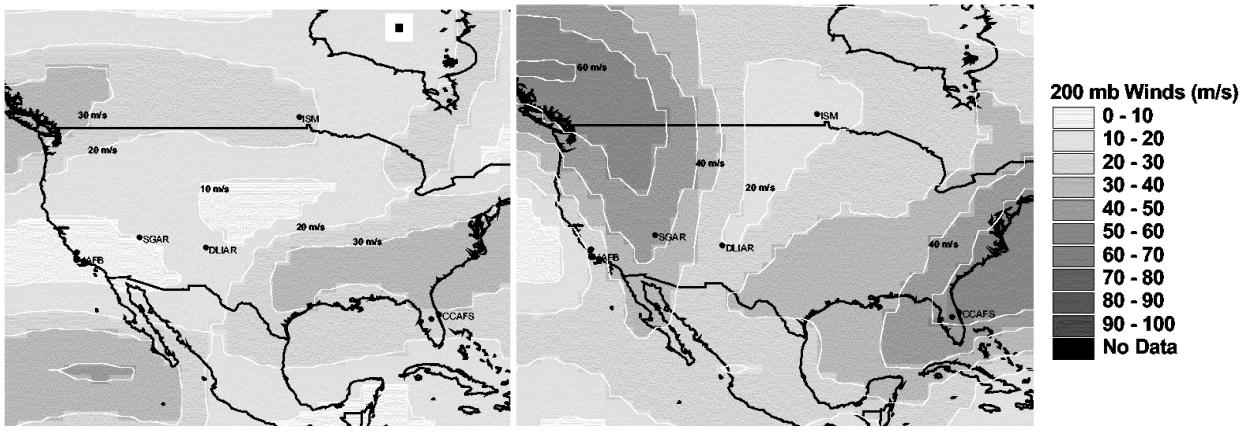


Figure 9. Contours for winds at 200 mb for May 27, 1999 (LEFT) and December 19, 1999 (RIGHT). Stratospheric winds between CCAFS and DLIAR or between CCAFS and IMS for the May 27 Space Shuttle launch (positive detection) were light in contrast to December 19 (no detection).

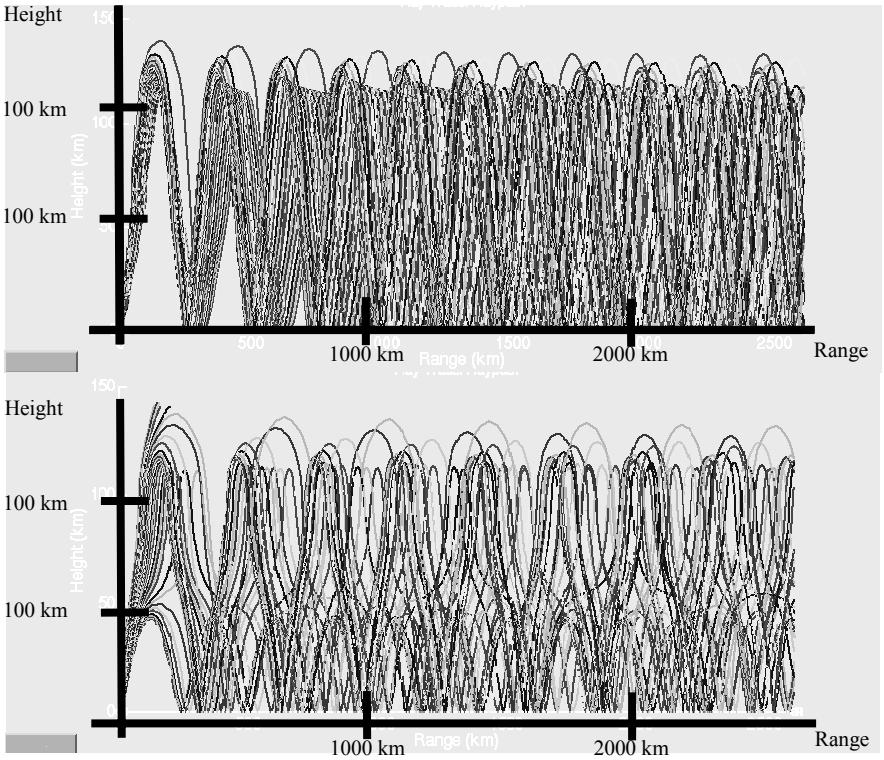


Figure 10. Ray paths predicted by "Inframap" (Norris et al. 1999 and Gibson et al. 1999) for the path from CCAFS to DLIAR for January (TOP) and July (BOTTOM) climatological models. Only a thermosphere return exists in the "winter" due to a dominant east to west mid latitude jet stream. During the "summer", a stratospheric return is present.

CONCLUSIONS AND RECOMMENDATIONS

The satellite launch industry is a multibillion-dollar international industry with over 100 commercial and military satellite launches conducted in 1999 alone. These diverse rocket launches may serve as useful future "ground truth" data to test and calibrate IMS infrasound system capabilities. Potential commercial and military launch facilities include Baykonyr in Kazakhstan, Plesetsk in Russia, Jinyu, Wuzhsi, Jiuquan, Xichang, and Taiyuan in China, Woomera in Australia, Kourou in French Guinea, Tenegashima in Japan, Vandenburg AFB, Cape Canaveral AFS, and the new Boeing ocean-going Sea Launch platform (Figure 11.). While IMS class arrays are not necessarily optimal for detecting rocket launches, observations demonstrate very low-yield atmospheric detection thresholds (~0.1-1 tons) at over 1000 km under favorable atmospheric conditions. Routine observations of announced launches also provide opportunities to further study dependence of long-range infrasound amplitudes with respect to stratospheric winds. As the IMS infrasound network becomes denser, it should be possible to test and validate 3D propagation codes.

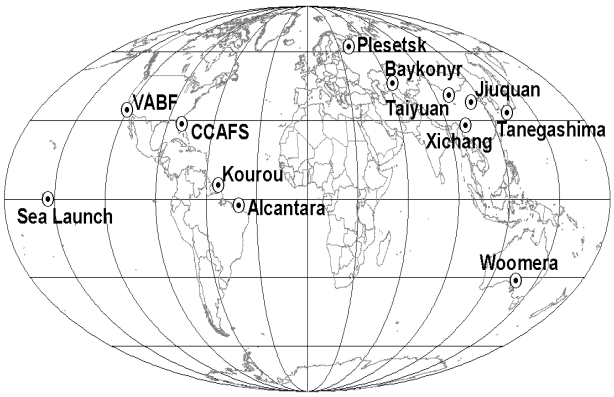


Figure 11. The future IMS infrasound system should observe orbital rocket launches from a dozen potential commercial sites worldwide.

Observations in this report of short-range infrasound (< 100km) recorded on seismic systems compared to long-range recordings on microbarograph systems indicate that the short-range frequency content may be much different than long-range frequency content. This may be due to propagation effects or it may be due to different effective source (excitation) mechanisms and propagation. Researchers in the 1960's concluded that long-range infrasound was generated by the supersonic shock waves. At closer distances, engine exhaust may also be a significant source of infrasound.

A comprehensive search of rocket-generated long-range infrasound on systems archived at the PIDC should be made so that automatic detectors could be tuned for these valuable signals. Amplitudes and azimuths of arrival should be compared to nominal values for each launch site and launch vehicle. Noise levels for non-detections of announced launches should be routinely measured and documented. These observations should then be compared with theoretical predictions based on climatological and specific daily meteorological models.

Acknowledgements

We wish to thank Rod Whitaker of LANL and Bob Blandford of AFTAC for helpful comments.

REFERENCES

Balachandran, N. W. Donn (1971b). Characteristics of acoustic signals from rockets, Geophys. J. Roy. Astr. Soc. 26, 135-148.

Balachandran, N., W. Donn, and G. Kashak (1971a). On the propagation of infrasound from rocket – effects of the winds, J. acoustic. Soc. Am., 50, #2 pg 397.

Cotton, D., W. Donn (1971). Sound from Apollo Rockets in Space, Science 171, 565-567.

Donn, W., E. Posmentier, U. Fehr, N. Balachandran (1968). Infrasound at long-range from Saturn-V, Science 162, 1116-1120.

Donn, W. L., I. Dalins, V. McCarty, M. Ewing, and G. Kaschak (1971). Air-coupled seismic waves at long-range from Apollo launchings, Geophys. J. Roy. Astr. Soc. 26, 161-171.

Fehr, U. (1967). Instrumental role in the observation of geoacoustical phenomena from artificial sources, J. acoustic. Soc. Am. 42, #5, pg 991-1007.

Gibson, R., D. Norris, & T. Farrell (1999). Development and Application of an Integrated Infrasound propagation Modeling Toolkit, 21st Seismic Research Symposium, Las Vegas, NV, 1999.

Kaschak, G. (1969) Long-range supersonic propagation of infrasound noise generated by missiles, J. Geophys. Res. (Space Phys.) 74, 914-918.

Kaschak, G. W. Donn, and U. Frehr (1970). Long-range infrasound from rockets, J. acoustic. Soc. Am., 48, 12-20.

Klass, P. (1964). Infrasound Detection technique May Serve as ICBM Warning, Aviation Week and Space Technology, Jan 13, 1964, pg 31.

Norris, D., R. Nadel, and R. Gibson (1999). "User's Guide for InfraMap", BBN Technical Memorandum W1353, BBN Technologies, 1300 N 17th St. Arlingt9on, VA 22209.

Pierce, A. D. and J. W. Posey (1971). Theory of the Excitation and Propagation of Lamb's Atmospheric Edge Mode from Nuclear Explosions, Geophys. J. R. Astr. Soc., 26, 341-368.

Posmentier, E. S. (1971). Preliminary Observations of 1-16 Hz Natural Background Infrasound and Signals from Apollo 14 and Aircraft, Geophys. J. R. Astr. Soc. 26. 173-177.

Sorrels, G. and Z. Der (1970). Long-range Seismic Noise and Atmospheric pressure Variations, Teledyne Geotech Report. # 70-12, Teledyne Geotech, Garland TX.

Stevens, J. L. D. A. Adams, G. E. Baker, H. Xu, J. R. Murphy (1999). Infrasound Scaling And Attenuation Relations From Soviet Explosion Data And Instrument Design Criteria From Experiments And Simulations. Proceedings Of The 21st Seismic Research Symposium, Las Vegas, NV.

Whitaker, R. W. (1995), "Infrasonic Monitoring," Proceedings of the 17th annual Seismic Research Symposium in Scottsdale, AZ, September 12-155, 1995, 997-1000.

Keith McLaughlin (scatter@cmr.gov), Anna Gault (gault@cmr.gov), David Brown (djb@cmr.gov).

Key Words: Infrasound, rocket launches

OPERATION OF A PROTOTYPE CTBT INFRASOUND ARRAY IN ARCTIC ALASKA

John V. Olson and Charles R. Wilson
Geophysical Institute, University of Alaska

Sponsored by the U.S. Department of Energy
Contract No. DE-FC04-98AL79802

ABSTRACT

A prototype Comprehensive Nuclear-Test-Ban-Treaty (CTBT) infrasound array was established in Fairbanks, Alaska in a wooded area on the campus of the University of Alaska in December 1999. The implementation of the array was carried out as part of the second phase of our studies of natural infrasound in arctic regions. A report on the earlier phase of our contract can be found in the Proceedings of the 21st Seismic Research Symposium[1] and on our web site: http://maxwell.gi.alaska.edu/~infra. In our implementation of the array four microphones were placed in the form of a triangle with one microphone placed near the center. During the winter months we also continued to monitor the response of three co-located microphones attached to different noise reducers to follow the relative effectiveness of the noise reducers in arctic conditions. These conditions ranged from severe winter cold with deep snow pack to the mild days of summer.

During the period of operation we detected several examples of naturally occurring infrasound as well as many man-made sounds. The naturally occurring infrasound signals of greatest interest are the 2-5 second period waves produced by marine storms that are termed microbaroms. We are studying these signals in order to estimate their spatial coherence. We believe that they can be identified and eliminated as a contaminating signal for CTBT arrays worldwide based upon their coherence properties. Other natural signals received included auroral infrasound, mountain-associated waves, thunder from summer storms and the eruption of the Japanese volcano, Mount Usu on March 31, 2000. A bolide that passed over central Alaska and exploded over Whitehorse, Canada on January 18, 2000 produced no detectable signal in our array. Man-made signals detected on our array are plentiful and varied. We witness every jet aircraft departure from the international airport located several miles away. Also recorded were the reports of military howitzers at the local army base as well as firework displays during holiday celebrations. Of special interest was the infrasound produced by two rockets launched from the University's Poker Flat Rocket Range located approximately 35 km from the array.

We present here an analysis of some of the signals mentioned above focusing on the properties that will help identify and eliminate these from CTBT analyses. We also include a summary of the effectiveness of the noise reducing arrays tested throughout the year.

Key Words: infrasound arrays, wind-noise reduction, microbaroms

[1] Olson, John V. and Charles R. Wilson, Simultaneous Comparison of Three Co-located Pipe Systems for Wind-Noise reduction for use with Model #4 Chaparral Infrasonic Microphones at Fairbanks, Alaska, Proceedings of the 21st Seismic Research Symposium, Vol. 2, p. 169, 1999.

OBJECTIVE

Infrasonic arrays have been identified as one of the four basic sensors to be used as part of the Comprehensive Nuclear-Test-Ban-Treaty (CTBT) program. The geometry of an individual infrasound array has been specified and is to be comprised of four microphones, with three placed in an equilateral triangle and the fourth located at the center. Other more complex patterns of microphones have also been proposed to provide redundancy and additional noise reduction. Each microphone in the array has attached to it a "noise reduction array" composed of a series of vented pipes in various configurations. The pipes serve to average the local turbulent pressure field that is generated by local winds.

In the first phase of our contract work with the Department of Energy (DOE) we studied the effectiveness of three wind-noise reducing arrays. They were: 1) a 305 meter long Daniels tapered steel pipe vented with hypodermic needles every 1.5 meters; 2) a system of twelve radial porous "soaker" hoses, each with a length of 15 meters; 3) a hexagonal array of six 30-meter long sections of 2-inch diameter rigid pipe. The three arrays were attached to three microphones at the same site and data was collected continuously throughout 1999. The reports of this test were reported at the 21st Seismic Symposium. We have continued to monitor the effectiveness of each wind-noise reducer to the present time.

We are now in the second phase of our work in which we have deployed four microphones in the CTBT configuration in order to test the array itself in high-latitude, arctic conditions. A wealth of natural and man-made infrasound is present in the interior of Alaska and we are compiling a summary of the various types in order to be able to learn how to discriminate against them in the analysis of infrasound data used to detect man-made explosions. The principal contaminant of the spectrum of signals is the microbarom signal. Ubiquitous world-wide these signals have periods that are in the same range of that expected from man-made explosions.

RESEARCH ACCOMPLISHED

1. Phase 1: Investigation of the effectiveness of three noise reduction arrays

Our first research task was to gather information on the relative effectiveness of three noise reducers. We installed three noise-reduction arrays on three co-located microphones and began to log data continuously at a 100 sample/second rate. The unprocessed data has a Nyquist frequency of 50 hertz, well beyond the requirements of the CTBT. For analysis the field data are low-pass filtered and decimated 10:1 to give a 5 hertz upper band limit. The original unprocessed data and the decimated data are archived to cd-rom for convenience.

The first noise-reduction array is a 305 meter long Daniels tapered steel pipe that is vented with a hypodermic needle every 1.5 meters. The pipe axis lies roughly east-west. The second array is the Los Alamos National Laboratory/Comprehensive Nuclear-Test-Ban-Treaty (LANL/CTBT) prototype. This array is comprised of a series of radial porous "soaker" hoses, each 15 meters long giving a total aperture of 30 meters. The third system is a hexagonal array of six 30 meter long linear sections of 2 inch diameter rigid pipe. The six chords of the hexagon are vented every 1.5 meters with hypodermic needles and each chord is separately connected to the microphone by a ¾ inch diameter rigid pipe from the center of the chord. The total aperture of this array is 70 meters. While a detailed report on the effectiveness of the three arrays used was given previously[2] we will summarize the results here.

In Figure 1 we show a 24 hour segment from a very quiet day (July 24, 1999) in which the rms variation of the data is computed over 10 minute segments from each microphone. In this figure it can be seen that there is a diurnal variation in the rms signal level from each sensor. During the quietest interval near 1500 UT the rms levels for all noise reducers falls to levels near 0.01 Pascals. This is typical of the quiet conditions that prevail in the early morning hours (0800 UT is local midnight). The data shown in Figure 1, although representing one of the quietest days recorded, is typical in the diurnal variation in wind noise

[2] Ibid.

levels with the quietest levels occurring between local midnight and dawn. Also typical is the fact that the hexagonal array shows the smallest response to wind noise.

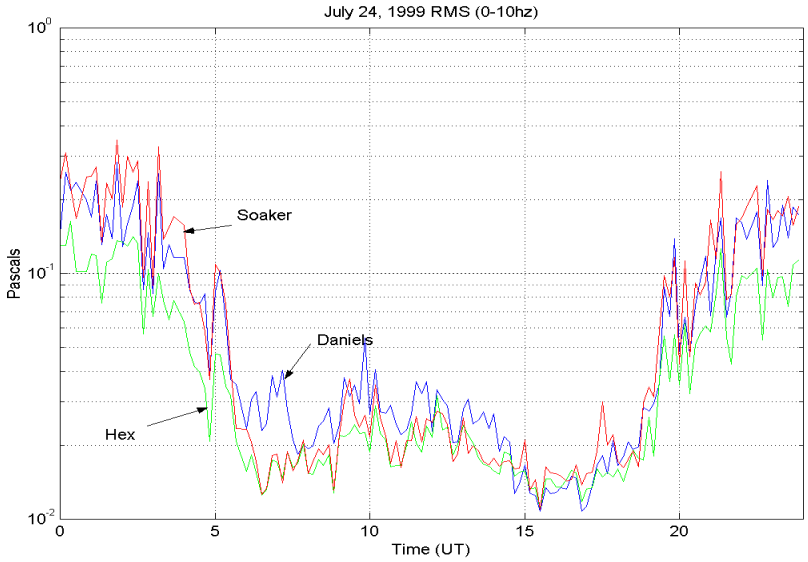


Figure 1. This figure shows the rms fluctuation levels from three co-located microphones for a quiet 24 hour interval on July 24, 1999. Typically quietest conditions occur near 1500 UT (0800 UT is local midnight). The relative wind-noise suppression of each of the noise reducers is shown. Note that the Hex array shows the lowest response to wind turbulence.

It is interesting to look at the power spectra computed from the data in Figure 1. In Figure 2 we show the power spectra of the three microphone outputs during the interval 1500-1510 UT. The data have been low-pass filtered and decimated to produce a sample interval of 1/10 second and a corresponding Nyquist frequency of 5 hertz. Notice that all three spectra are similar with relative minima near 1 hertz and a small peak between 2.5 and 3 hertz; the source of the peak is unknown but probably local and man-made. Also note that the hexagonal array is the quietest across the band of frequencies shown.

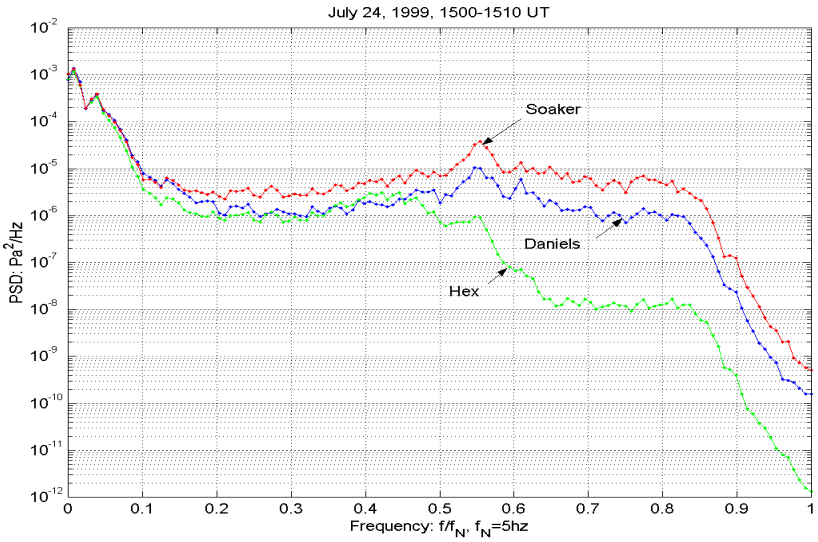


Figure 2. The power spectral density computed for the interval between 1500 and 1510 UT of July 24, 1999 (see Figure 1). During this quiet interval the hexagonal array shows the lowest response across the frequency band.

2. Phase 2: Analysis of data from a prototype CTBT array

In mid-December 1999 we began to assemble a prototype CTBT array. By the spring of 2000 four microphones were in place and operating. Data from the array continues to be logged at the 100 sample/second rage from each of the microphones with GPS time accuracy. The array is located in a wooded region located behind the Geophysical Institute on the University of Alaska campus. Figure 3 shows a map of the array and the exact locations are given in Table 1.

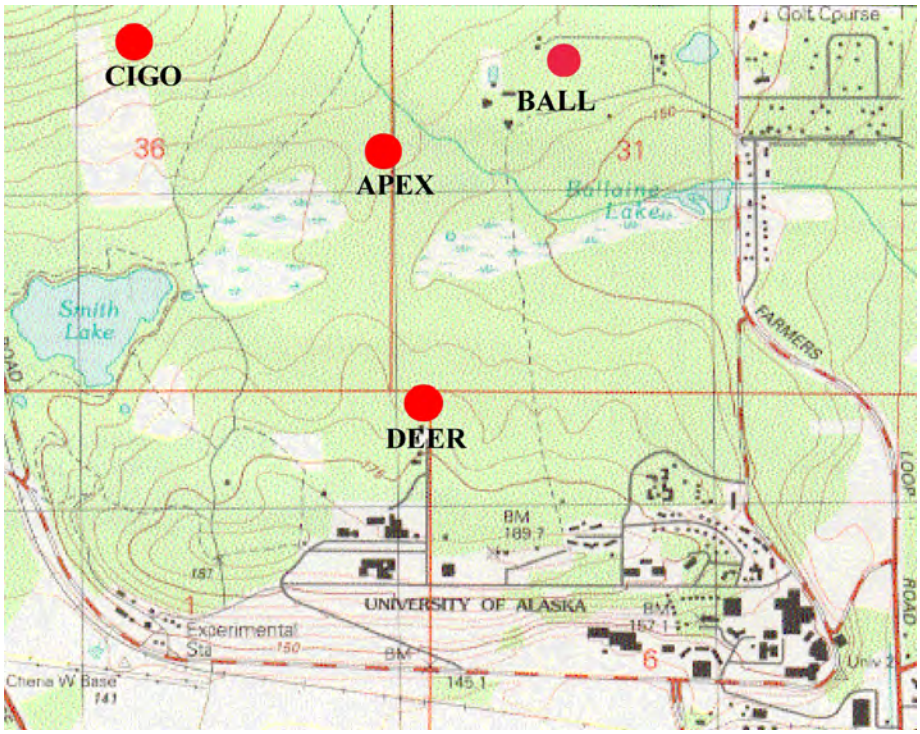


Figure 4. On the left, a map showing the locations of the four microphones that comprise the Geophysical Institute infrasound array. The microphones are located in a wooded area north of Institute on the campus of the University of Alaska. On the right, the impulse response of the array.

Table 1. Microphone Locations

Station	Latitude	Longitude	X (east) offset	Y(north) offset
Apex (APEX}	64° 52’ 19.3”	147° 50’ 41.3”	0.0	0.0
Ballaine Lake (BALL)	64° 52’ 27.2”	147° 50’ 03.3”	0.4978	0.2587
College Observatory (CIGO)	64° 52’ 30.6”	147° 51’ 30.7”	-0.6468	0.3486
Deer Yard (DEER)	64° 51’ 49.1”	147° 50’ 31.1”	0.1339	-0.9314

The impulse response of the array is shown in Figure 5. The principal images of the central lobes occur at wavenumbers with magnitudes greater than 8 which corresponds to frequencies greater than 0.5 hertz for acoustic waves propagating horizontally. This is important since if there were images of the central lobe at smaller values of the wavenumber then spatial aliasing would be possible for signals in the microbarom band between 0.1 and 0.5 hertz. Such aliasing would lead to biases and errors in the estimation of signal velocity and direction.

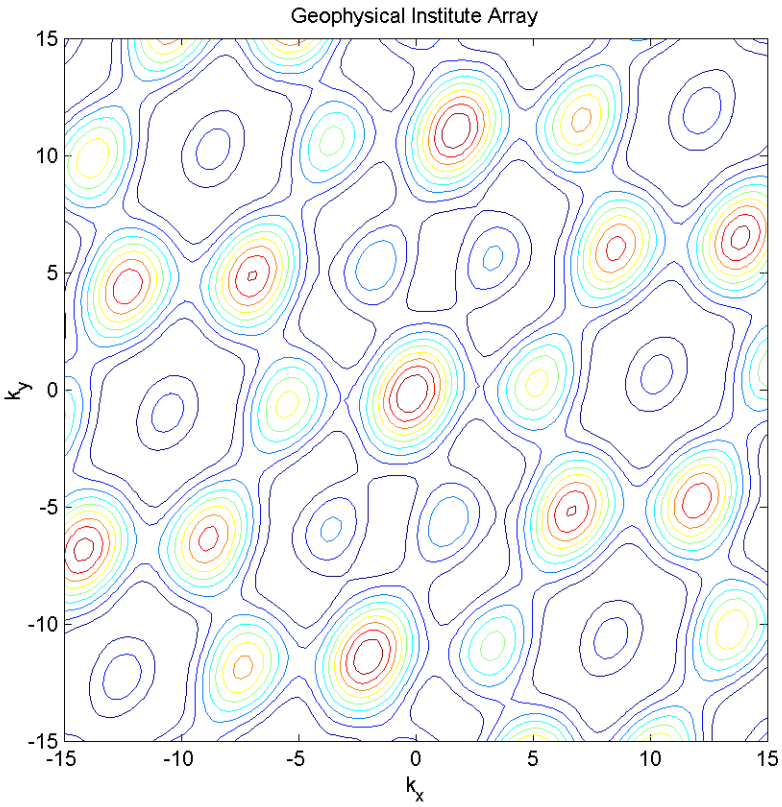


Figure 5. This figure shows the impulse response of the Geophysical Institute infrasound array shown in Figure 4. This impulse response is effectively the Fourier transform of the microphone array. The central lobe is surrounded by images determined by the symmetry properties of the array. Note the closest image lies at a distance of approximately k=10 corresponding to a frequency 0.53 hertz.

The impulse response of an array is important since it indicates the presence of spatial aliasing. The CTBT infrasound array is specified to have a fixed geometry and to operate over a frequency band from dc to 5 hertz. However, spatial aliasing can occur within this band. This can be seen by considering two microphones spaced at a certain distance. A sinsusoidal wave whose wavelength is equal to the microphone spacing will present the same phase to each microphone and so will not show any time delay as it moves across the two microphones giving, in effect, the appearance of an infinite velocity or of a wave incident from above. Now for a wave with wavelength slightly shorter than the microphone spacing the apparent phase speed is over estimated since the time delay measured between arrivals of points of constant phase is shortened due to aliasing. Thus, operation of an array at frequencies that have corresponding acoustic wavelengths shorter than the array can lead to inaccurate and biased estimates of the wave phase speed.

For a two dimensional array the information concerning spatial aliasing is contained in the impulse response. The various lobes in the impulse response are images of the central lobe in exactly the same sense that images of the spectrum of a signal are repeated for frequency aliased temporal data. Thus each lobe presents the wavenumber, or equivalently the frequency, of the wave whose wavelength will produce ambiguous simultaneous arrivals at the sensors in the array. For the target frequency band of the CTBT

program that lies between 0.1 and 1 hertz, the corresponding wave numbers for acoustic waves range between 1.88 km^{-1} and 18.8 km^{-1}. Clearly there is the possibility of aliasing in the prototype CTBT array. In order to avoid aliasing we band-pass filter the data from each microphone prior to making estimates based upon array correlations.

As an example of the signals observed by the array we show in Figure 6 a set of microbaroms that were observed on July 15, 2000. The five minute segment of data displayed in Figure 5 shows the four microphone signals in the top four panels and a phase-aligned plot that is a result of the least-squares analysis of the data to determine the apparent horizontal speed and the direction of arrival. The analysis shows these signals to be acoustic: they have an apparent horizontal speed of 0.331 km/sec and an azimuth of arrival of 231 degrees.

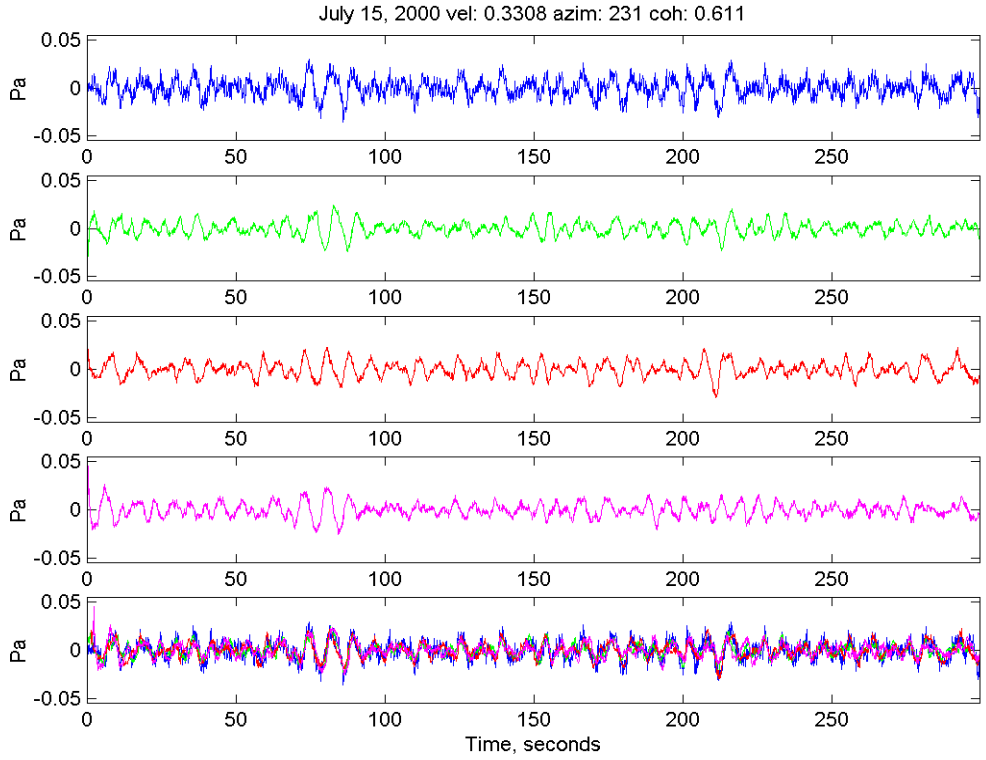


Figure 6. This plot shows microbarom data from July 15, 2000. The top four traces are the individual microphone output signals. The bottom trace shows a phase-aligned overlay as a result of the least-squares estimation of phase speed and direction of arrival.

The wavetrain displayed in Figure 5 is part of a nearly continuous train of signals from the same azimuth. In Figure 7 we show the least-squares estimation of the wave speed and azimuth of arrival for the entire day of July 15, 2000. There it can be seen that a coherent set of waves was present for several hours between 1100 UT and 1500 UT. The azimuth of arrival indicates that these waves were produced by a marine storm moving along the Pacific in near the Aleutian islands southwest of mainland Alaska. Although microbarom wavetrains are most prominent in the winter months they do occur throughout the year. A detailed description of the properties of microbaroms as well as other natural infrasound detected in polar regions is given on our web site http://maxwell.gi.alaska.edu/~infra.

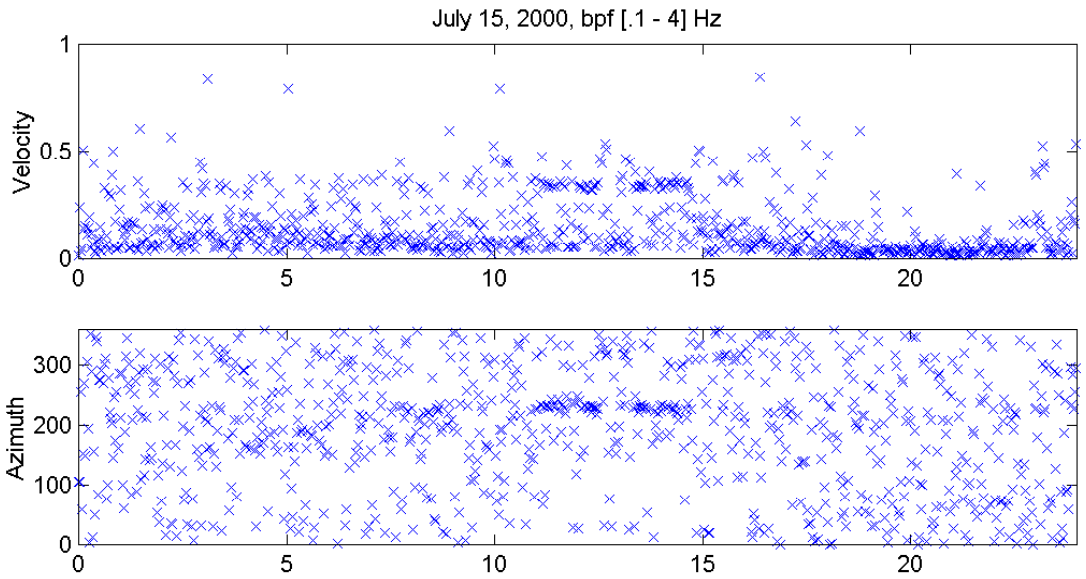


Figure 7. This figure shows the least-squares estimation of phase speed and azimuth of arrival for data from July 15, 2000. Each point in the diagram corresponds to an estimate made over a 100 second window located at that time. The interval between 1100 UT and 1500 UT represents the arrival of a microbarom wavetrain.

CONCLUSIONS AND RECOMMENDATIONS

We have operated a set of Chaparral microphones in Alaska for nearly two years as a test of the microphones, wind-noise reducing arrays and the prototype CTBT array configuration. Our research has been carried out in several stages and some questions are still being pursued. Nevertheless, our principal conclusions are as follows.

1. The hexagonal noise reducing array is the most effective at reducing the wind induced noise present at a microphone. Although pipes do have resonances it is possible to design the array so that the resonance occurs above the CTBT passband.
2. The prototype CTBT array using Chaparral microphones has operated successfully in central Alaska under the temperate weather of summer as well as the frigid climate of an Alaskan winter. We continued to log and analyze data through the year, even during periods when the ambient temperatures plunged below –40^{o} F.
3. The inclusion of a broad frequency band in the CTBT microphone and array specifications can lead to errors in estimation of signal parameters due to spatial aliasing. It is essential to band-pass filter data prior to subjecting them to array analyses that depend upon correlations between sensors.
4. We are studying the spatial coherence of microbarom signals. These signals, with periods near 5 seconds, are the principal contaminant of the frequency band in the range of the CTBT target signals. We have indications that the spatial coherence is not much greater than 1 km and so arrays larger than 1 km in aperture may be useful in discriminating against microbarom contamination.

ON THE ANALYSIS OF THE SPATIAL AND TEMPORAL STRUCTURE OF NATURAL INFRASOUND SIGNALS

John V. Olson, Charles R. Wilson and Curt A. L. Szuberla
Geophysical Institute, University of Alaska Fairbanks

Sponsored by the U.S. Department of Energy
Contract No. DE-FC04-98AL79802

ABSTRACT

The principal contaminant of the infrasound spectrum in the band between 0.2 – 0.5 hertz is the acoustic radiation associated with marine storms termed microbaroms.[1] These signals appear worldwide and, during winter months, can be the dominant signal during quiet periods. They tend to persist as collections of wavelets that last for hours and days. It is primarily against the spectral clutter presented by microbaroms that the detection of low-yield, man-made explosions must be made.

We have made the hypothesis that the spatial coherence of microbarom wavelets is limited to scales of approximately 1km. This is based upon previous experience operating arrays of various sizes at the Geophysical Institute, University of Alaska Fairbanks. In order to test this hypothesis we are conducting two experiments. In the first experiment we have begun to operate a single microphone at various distances from the permanent, four-microphone infrasound array located on the campus of the University of Alaska. By performing simple coherence tests as a function of the spacing of the microphone from the array we intend to make estimates of the mean coherence length. In the second experiment we are estimating the coherence length of microbarom wavelets in the time-series recorded by the microphones in the permanent array using Hilbert transform techniques. Preliminary estimates indicate that the microbarom has a spatial coherence of only a few wavelengths. Studies of historical data sets at Fairbanks indicate an average periods in the range of 3 – 7 seconds indicating a spatial coherence of the order of 5km.

The properties of the microbaroms and other coherent infrasound signals can be easily extracted from the broadband spectrum of incoherent signals through the use of the Pure-State filter. This is a coherence-based filter that, as distinct from other coherence-based analysis techniques, is not biased by the detector array geometry.

Key Words: infrasound microbarom coherence, signal discrimination

[1] A complete description of microbaroms and other natural infrasonic waves and a bibliography can be found on our web site: http://maxwell.gi.alaska.edu/~crw or http://maxwell.gi.alaska.edu/~infra

OBJECTIVE

The objective of this study is to describe the spatial coherence of microbarom signals with the expectation that such a description will enhance the ability to discriminate against these signals when detecting man-made explosions in the same frequency band. Microbaroms are small-amplitude fluctuations in atmospheric pressure that are apparently generated by marine storms. Lying in a frequency band between 0.1 and 0.5 hertz, they constitute the primary contaminant of the frequency band and they are ubiquitous. During winter months they are the dominant signal detected by infrasound arrays during quiet periods.

Previous experience has led us to hypothesize that the spatial coherence of packets of microbarom waveforms is limited to a few kilometers. The basis for this is the observations by the Geophysical Institute infrasound program that operated a large-aperture as well as a small aperture infrasound array for many years. Microbaroms are limited in frequency band and do not register as coherent signals across an array of large aperture.

We are pursuing this objective in two ways. The first is to perform actual measurements of microbarom coherence as a function of microphone spacing. We have one microphone that is not committed to array operation that can be moved to sites at varying distances from the normal array. Data from this microphone can then be used to study the variation of coherence as a function of distance. The second technique is based upon the analytic description of the waveforms as we detected them with the various array microphones. By characterizing the distribution of waveform coherence lengths we expect to translate this into an estimate of spatial coherence.

RESEARCH ACCOMPLISHED

In order to appreciate the complexity of the microbarom signal we show in Figure 1 a brief, five-minute, segment of data taken on July 15, 2000 during a period when microbarom signals were present in the array data. In most cases these signals are only apparent during quiet intervals. If there is significant wind driven pressure "noise" in the data it is necessary to band-pass filter the data near the microbarom passband. The top four panels in Figure 1 show the waveforms from each of the microphones. The bottom panel shows the data overlaid after signal time delays from station to station have been estimated using cross-correlation techniques. The time lags developed from cross-correlations of the microphone data are used to produce a least-squares estimate of velocity and azimuth of arrival. The estimators are the standard least-squares estimators as described in many textbooks. The details of our estimators are given in reports included on our web site http://maxwell.gi.alaska.edu/~infra.

As can be seen from Figure 1 the microbarom amplitudes are quite variable and there is the appearance of a sequence of superposed packets and noise that make up each microphone output. The fact that a single phase adjustment produces coherence across all packets for the entire five minute interval is an indication that the packets all move with acoustic speeds and are arriving from a common direction. In the case of these data the source appears to have been a marine storm off the Aleutian Islands southwest of the mainland of Alaska. The persistence of frequency, apparent velocity and azimuth of arrival for a sequence of microbaroms is not unusual. In fact wave trains can persist for hours or days. Figure 2 shows an analysis of the entire day of July 15, 2000. Each point on the plot represents the least-squares estimate of velocity and azimuth during a 100 second window. The data shown in Figure 1 have been taken from the sequence that lasts at least four hours between 1100 UT and 1500 UT. Finally, in Figure 3 we show the periodogram of the data from Figure 1. It is a simple Fourier transform that shows that most of the signal variance is contained between 0.1 and 0.3 hertz.

Since the microbarom wavetrain is persistent in its characteristics and narrow-band in frequency content we have turned to techniques based upon the Hilbert transform to extract some estimate of temporal coherence. From that estimate and the mid-band frequency under the assumption of acoustic propagation the spatial coherence, or packet size, can be inferred.

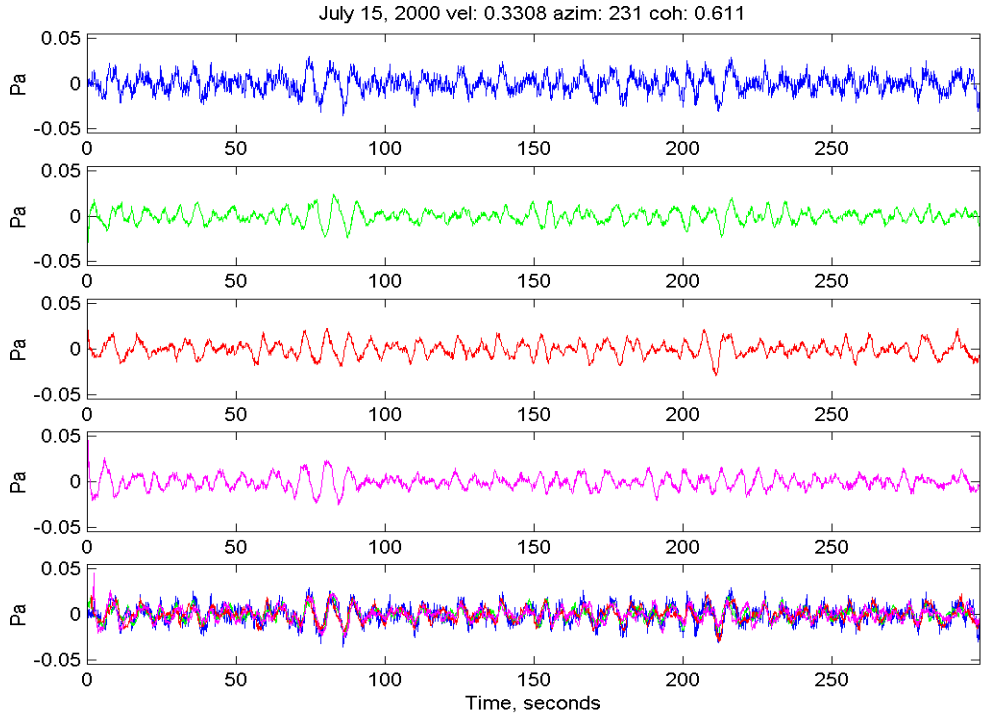


Figure 1. This plot shows a typical set of microbarom waves. Note the amplitude modulation. The top four panels show the data from individual microphones in the Geophysical Institute array. The bottom panel shows the phase-aligned data based upon a least-squares estimation of azimuth and velocity.

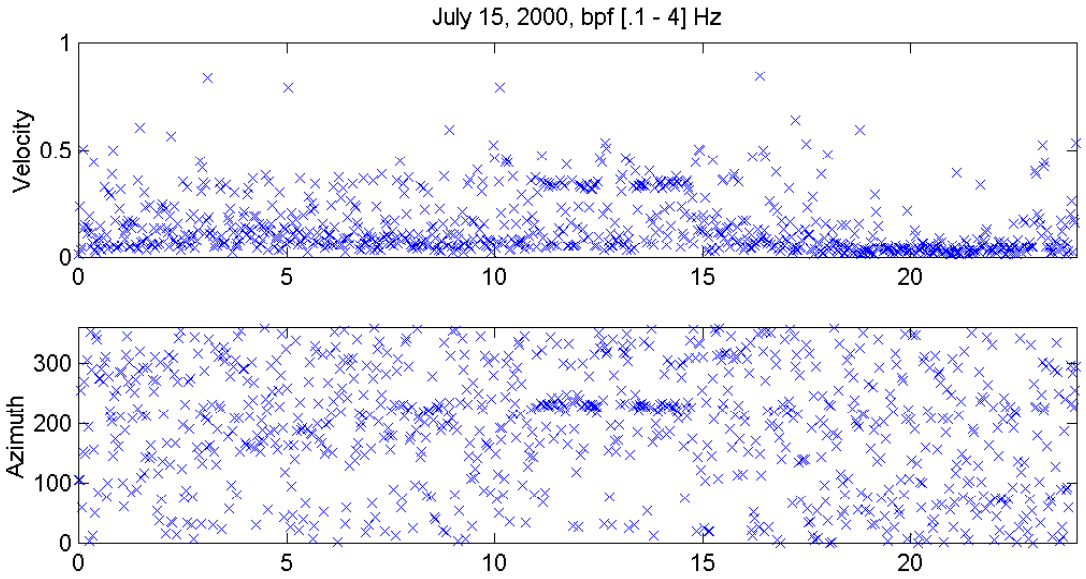


Figure 2. This plot shows the result of a least-squares estimation of azimuth and velocity for 24 hours of infrasound array data. Each data point represents the analysis of 100 seconds of data. Note the persistent azimuth and acoustic velocity trend between 1100 UT and 1500 UT. This is a microbarom wavetrain.

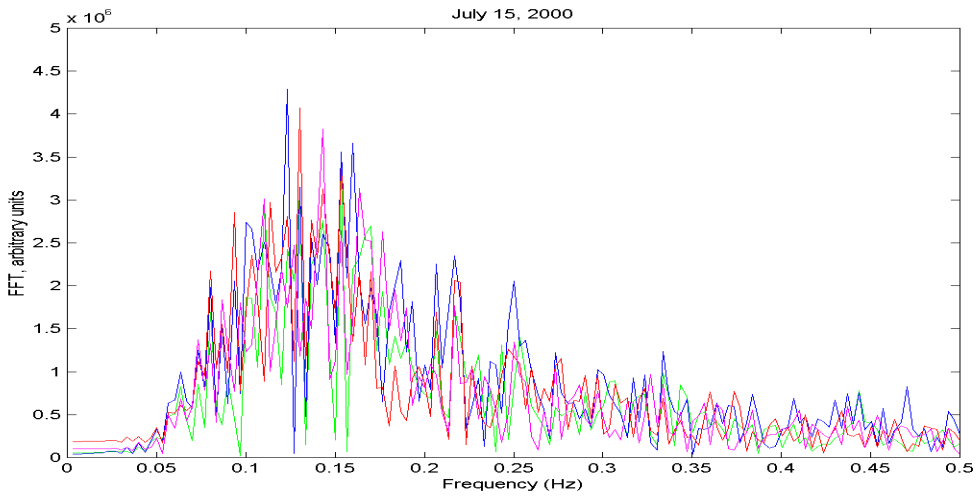


Figure 3. This figure is the periodogram showing the Fourier transform of the data in Figure 1. Notice that the waveform is relatively narrow band with most of the variance captured between 0.1 and 0.3 hertz.

With the expectation that the microbarom signals are narrowband with a persistent source azimuth we turn to the Hilbert transform to develop the analytic signal that represents the data from each microphone. Details of the Hilbert transform and the analytic signal are available in many textbooks such as, for example, the fine book by Bracewell, 1986. For a narrow-band function of one dimension the Hilbert transform produces a complex function called the "analytic signal". The amplitude of the analytic signal is the envelope of the waveform showing what one might think of as the shape of the group of waves or the wave packet. The instantaneous phase of the transform is the frequency-time product so that the instantaneous frequency may be obtained from the time derivative of the phase. Sudden changes in instantaneous frequency are taken to be the sudden phase changes that are expected to occur at the boundary between two coherent wave packets.

We have begun the analysis of microbarom data in order to estimate the most likely packet length. Our estimation is based upon the following process. The steps in this process are illustrated in Figure 4. First we compute the Hilbert transform of the data and extract the envelope and phase. The top panel in Figure 4 shows the waveform from the Ballaine Lake (BALL) microphone on July 15, 2000 as taken from Figure 1. Also plotted in the top panel is the magnitude of the analytic signal to indicate the packet envelope. From the time derivative of the phase of the analytic signal we extract the instantaneous frequency of the signal. This is displayed in the second panel of Figure 4. The instantaneous frequency varies with time throughout the interval. In the bottom left panel we show the derived distribution of instantaneous frequencies. From this distribution we extract a mean (which characterizes the mean frequency of the entire wave train) and an estimate of the 95% limits. These values are transcribed onto the second panel (the dashed lines) as an indication of the expected variation of the instantaneous frequency. We then identify any values of the instantaneous frequency that are larger than the 95% confidence limits as phase breaks in the wave train. These locations are transcribed to the top panel as vertical dashed lines to show the phase breaks in the wave train. Finally, we are in a position to estimate the distribution of wave packet lengths in the time domain by measuring the distances between the vertical lines representing phase breaks.

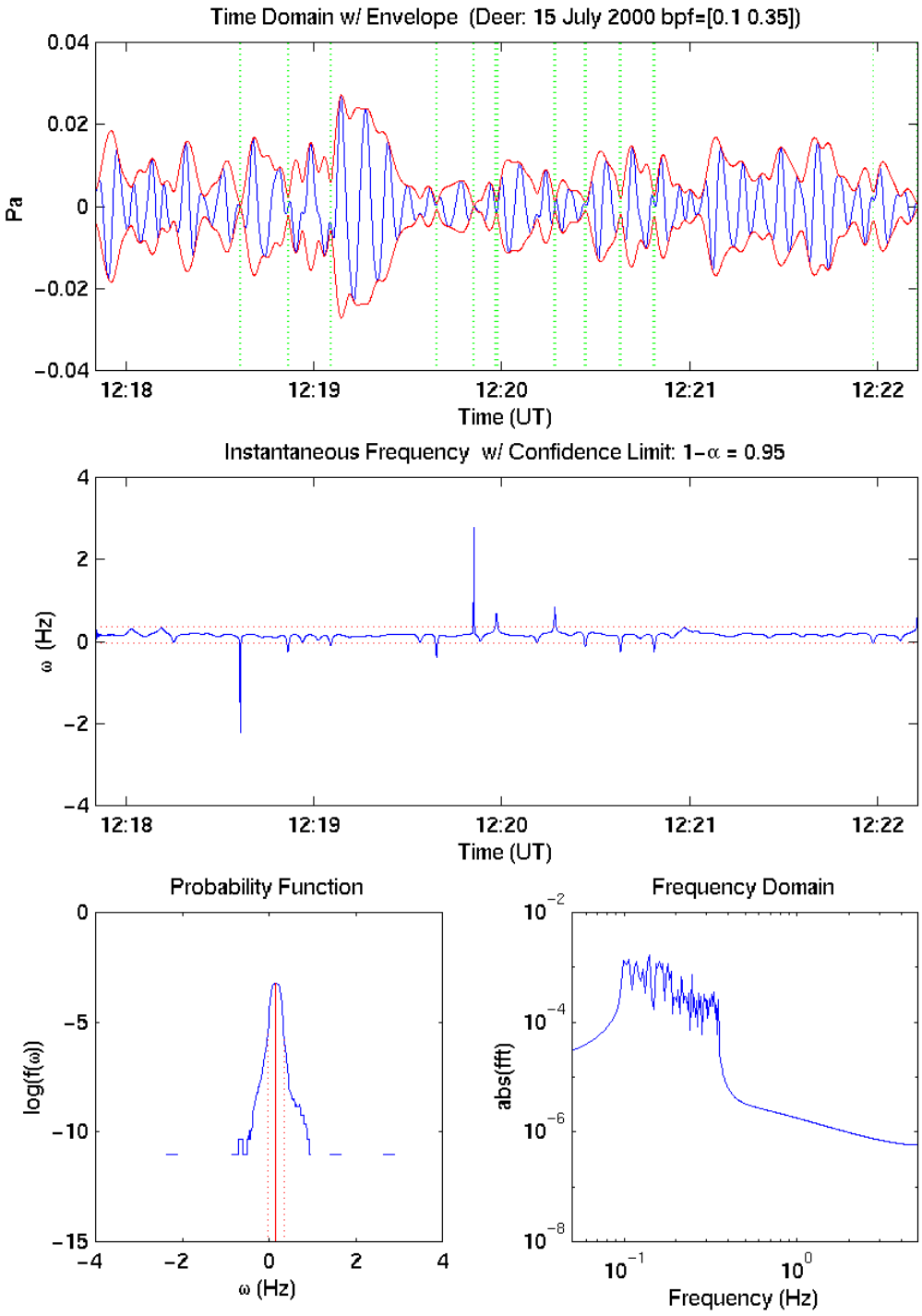


Figure 4. The top panel shows the waveform surrounded by the envelope derived from the analytic signal. The middle panel shows the variation in analytic signal phase along with 95% confidence limits derived from the distribution of amplitudes in the bottom left panel.

The distribution of distances between phase breaks calculated for the entire four hour interval between 1100 UT and 1500 UT on July 15, 2000 is shown in Figure 5. The four panels indicate the distribution in duration intervals obtained from each microphone. We have chosen to limit our search to intervals that are multiples of the mean period of the microbarom wave train. The distribution can be seen to be skewed towards low values in each case. The mean packet duration for each microphone is given in the plot panel for that distribution. We see that the means are all consistent and in the range between 22 and 25 seconds with variances that are fairly wide at approximately 20 seconds. With a mean wave period of about 6 seconds this indicates approximately four periods constitute the average packet length in time with a variance of the same order. At acoustic speeds these four periods span approximately 11 kilometers with a variance of the same order.

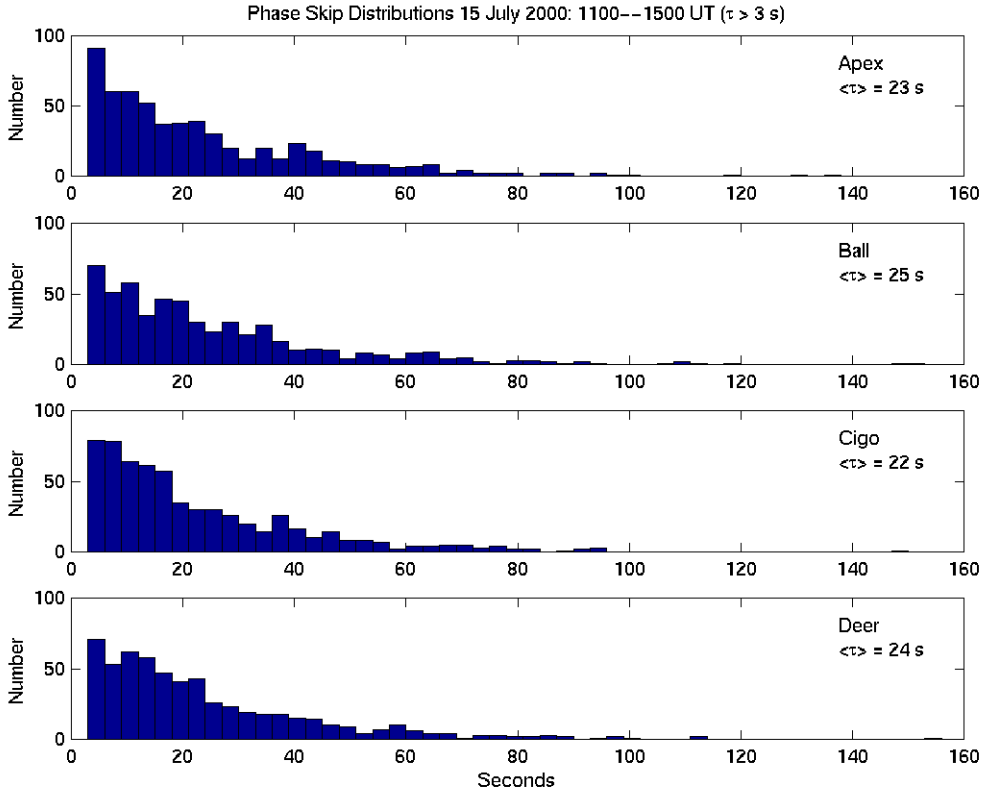


Figure 5. This plot shows the distribution of the intervals between phase jumps in the analytic signal for each microphone during the July 15, 2000 interval. Note the distributions have nearly the same mean and variances.

CONCLUSIONS AND RECOMMENDATIONS

Our analysis of the coherence time of the microbarom wave packets using analytic signal techniques based upon the Hilbert transform results in an estimate of the temporal coherence at about eight wave periods. Translated to distance by assuming acoustic speeds these eight wavelengths correspond to about 8 kilometers. The fact that the distribution of characteristic lengths is skewed and very broad compared to a basic wave period indicates that a simple one-microphone discriminate to be used to separate large-scale coherent signals in the band from microbaroms may not be as effective as hoped. The next step in the analysis will be the investigation of array apertures that allow discrimination to be made. In the meantime we plan to continue to investigate microbarom coherence extending our analysis to the cross-coherence between array elements.

REFERENCES

Bracewell, R., The Fourier Transform and Its Applications, McGraw-Hill, 2nd Edition, 1986.

DETECTION AND LOCATION CAPABILITIES OF MULTIPLE INFRASOUND ARRAYS

Robert H. Shumway

Sponsored by The Defense Threat Reduction Agency
Arms Control Technology Division
Nuclear Treaties Branch

Contract No. DTRA01-00-C0082

ABSTRACT

We develop an integrated approach to estimating wave-number parameters form a collection of local arrays and fusing these estimators to obtain an accurate location, along with its uncertainty ellipse. A small-array theory has been given in previous work that characterizes the detection probabilities and large sample variances of the local optimal detectors and we show how to incorporate the results of the local-array performance into a global network assessment. The wave-number estimators and their uncertainties are used as input to a Bayesian nonlinear regression that produces fusion ellipses for event locations using probable configurations of detecting stations in the global infrasound array proposed by the Prototype International Data Center (PIDC). The network capability is characterized as a function of separate local-array characteristics, including signal-to-noise ratios, bandwidth, array geometry, local correlation and coherent interfering signals.

Key Words: *Maximum likelihood, Bayes, signal estimation and detection, nonlinear estimation, regression, F-Statistics.*

OBJECTIVE

We are beginning a study to characterize the detection and location capabilities of the world-wide infrasound arrays configured for the Prototype International Data Center (PIDC) network. The study will utilize results of our previous work (see, for example, Blandford, 1997, Shumway et al, 1999) to characterize the detection and wave-number estimation capabilities of local arrays. In that study (Shumway and Kim, 1999), we have also developed *fusion posterior probability ellipses* for location that incorporate the two dimensional covariance matrices of the wave-number vector, e.g., velocity and azimuth, for each of the local arrays. The theory allows prediction of of a fusion ellipse for arbitrary configurations of recording arrays, under assumed local signal-to-noise ratios, array geometry and signal decorrelations. Extending these results to a full analysis of the detection and location capabilities of the PIDC network requires a two-stage approach, consisting first of characterizing local-array detection and estimation uncertainty and then incorporating these results into a detailed study of the detection and estimation capabilities of the full network.

Note that the theory is in place for following the above procedure through for perfectly correlated signals and uncorrelated noise. A generalization being developed in this study is the extension of the local-array performance capabilities to the case where there are coherent interfering signals or noises generated by such local features as wind or microbaroms or by multiple arrivals occurring in the same time window. If the local features are not readily available, this requires a *multiple stochastic signal* approach, where the interfering signals may have either known or unknown coherence properties. We are covering both the case where the interfering signals propagate according to some unknown velocity and azimuth and the case where the coherence structure must be estimated from the currently observed data. Extension of conventional stochastic signal models to the multiple signal case has been considered by Shumway (1983, 1988) and Shumway and Stoffer (2000). The above study should complete the characterization of *local-array performance* for infrasound.

The second stage will incorporate the results of the local-array performance into a summary *global-network performance* in terms of the uncertainty regions predicted by fusion ellipses. Usually, only a few arrays will record any given event so that local detection probabilities must be combined to develop an overall average fusion ellipse. In this study, we are expanding conventional network detection, as set out in Wirth (1976), to develop an *expected location contour map* of the world that could be expected for the proposed PIDC network. The network capability will be a function of separate inputs for each array, involving signal-to-noise ratios, bandwidth parameters, array geometry, local correlation and coherent interfering signals.

RESEARCH ACCOMPLISHED

Local-Array Estimation and Detection

In the case of a local array measuring a propagating plane wave from an infrasonic signal, we are generally dealing with a small number of sensors and a model of the form

$$y_j(t) = s_j[t - T_j(\boldsymbol{\theta})] + n_j(t), \tag{1}$$

corresponding to expressing the received process $y_j(t)$ as a signal $s_j(t)$ imbedded in in a noise series $n_j(t)$ on each of $j = 1, 2, \ldots, N$ sensors. The signal incurs a time delay $T_j(\boldsymbol{\theta})$ at the j^{th} sensor where $\boldsymbol{\theta} = (\theta_1, \theta_2)'$ is a vector of wave-number parameters that are nonlinearly related to velocity and azimuth and to the source location of the signal, say $\boldsymbol{x} = (x_1, x_2)'$. It is the vector $\boldsymbol{x}$ that we are primarily interested in estimating, where x_1 and x_2 will denote latitude and longitude in km, based on some arbitrary origin. In Shumway et al (1999), we have assumed that the signals had some correlation structure that could either be estimated from data or could conform to the distance, frequency correlation structure advanced by Mack and Flinn (1971). If the signals in (1) were perfectly correlated, replacing $s_j(t)$ by the common signal $s(t)$ simplifies

results considerably, as shown in Shumway et al (1999).

As we will see later, what is needed is a theory that will lead to an optimum detector and a signal detection probability for each local array. We also need an estimator for the wave-number vector $\boldsymbol{\theta}$ (velocity and azimuth) and a variance-covariance matrix that will depend on bandwidth, signal-to-noise ratio and the geometry of the local array. This has been done in Shumway et al (1999) under the two signal-correlation structures mentioned above. Then, noting that the true wave-number vector is a known nonlinear function of location, say $\boldsymbol{\theta}_k(\boldsymbol{x})$ for the k^{th} array, $k = 1, 2, \ldots, n$ gives a set of values from which we may infer location and a confidence or posterior probability ellipse for that location. This is covered in Shumway and Kim (1999) for the case of a perfectly correlated signal.

In the new work, we are extending the above theory to the case where one or more interfering signals are present. They may be generated by consistent wind effects (see Hedlin, 1998) or by ground, atmospheric, stratospheric or thermispheric reflections (see Armstrong, 1998). Many times, separate phases can be analyzed in isolation but it is also possible that more information will accrue from a broad time window that increases the time-bandwidth product. For a simple double-signal example, suppose that the received process is of the form

$$y_j(t) = s[(t - T_j(\boldsymbol{\theta})] + u[t - D_j(\boldsymbol{\gamma})] + n_j(t), \tag{2}$$

where $u(t)$ represents a second interfering signal with an unknown set of time delays, depending on a second set of wave-numbers $\boldsymbol{\gamma} = (\gamma_1, \gamma_2)'$ corresponding to an interfering signal, possibly generated by wind (see Hedlin et al, 1998). While there there are models and computer code available (see, for example, Dighe et al, 1998) for generating wind profiles at a given site as a function of weather conditions, the development of a theory for a general interfering signal with unknown velocity and azimuth characteristics would still be a useful exercise. In this proposal, we discuss isolating either a propagating signal or a signal with completely unknown coherence structure. It should be noted that the restriction in (2) to just two unknown signals is not necessary.

Signal Detection

In order to handle the optimum signal detection problem, we review the results for a single signal with unknown wave-number parameters that obtains when $s_j(t) = s(t)$ in (1), namely, the case of a perfectly correlated signal. The requisite theory follows from writing the model in the frequency domain and applying the Whittle likelihood to obtain the optimum detector for testing the absence of a signal (see Shumway et al, 1999) for details. For the likelihood ratio detector, we obtain a ratio of beam-power to noise power in the neighborhood of a center frequency that is expressed as an F-Statistic of the form

$$F(\hat{\boldsymbol{\theta}}) = \frac{N^{-1}B(\hat{\boldsymbol{\theta}})}{SSE(\hat{\boldsymbol{\theta}})}, \tag{3}$$

introduced by Shumway (1983), where the numerator has the well-known beam-power and the denominator is an estimated noise power, obtained by summing the squared deviations of each channel from the overall beam. The parameter $\hat{\boldsymbol{\theta}}$ is the maximizer of the beam-power and the log likelihood. It is commonly computed by searching over the two-dimensional space spanned by the vector or over some suitable restricted space. The distribution of the detector (3) is proportional to an F-statistic with $2BT$ and $2BT(N-1)$ degrees of freedom, where BT is the time-bandwidth product. That is

$$F(\hat{\boldsymbol{\theta}}) \sim (1 + rN)F_{2BT,2BT(N-1)}, \tag{4}$$

where $\sim$ denotes *is distributed as* and

$$r = \frac{P_s}{P_n} \tag{5}$$

denotes the signal-to noise ratio, computed as the ratio of the signal power spectrum P_s to the noise power spectrum P_n.

In the sequel, we propose extending the above theory to the model (2), possibly containing the interfering signal. Portions of the requisite theory are available in Shumway and Stoffer (2000), where tests of hypotheses involving multiple signals are developed from classical regression theory. It is clear that a stepwise approach will be involved, with searches over $\boldsymbol{\theta}$ and $\boldsymbol{\gamma}$ needed to find maximum likelihood estimators for those two parameter vectors. An approach proposed for the fixed multiple-signal case is given in Shumway (1983) and it is proposed that the approach be extended to the random signal case.

In the case that the simpler model (2) does not hold, we are also investigating the possibility of estimating the propagation structure of the interfering interfering signals, using models of the form

$$y_j(t) = s[(t - T_j(\boldsymbol{\theta})] + \sum_{k=1}^{q} \lambda_{jk}(t-\tau)u_k(\tau) + n_j(t), \tag{6}$$

where the unknown filters $\lambda_{jk}(t)$ can be estimated using a generalization of factor analysis in the frequency domain. For example, taking discrete Fourier transforms on both sides of (6) and vectorizing leads to a frequency domain model of the form

$$\boldsymbol{Y} = \boldsymbol{A}S + \Lambda \boldsymbol{U} + N, \tag{7}$$

which can be recognized as factor analysis in the frequency domain and the estimated Λ may be a reasonable approximation to some generalized modal structure in the frequency domain. The vector

$$\boldsymbol{A} = (e^{2\pi i \nu T_1(\boldsymbol{\theta})}, \ldots, e^{2\pi i \nu T_N(\boldsymbol{\theta})})'$$

still contains the propagating plane wave. Of course, the bandwidth requirements of such a procedure are fairly stringent and a limited number of *modal* components U_j can be fitted for a small array.

Optimal Estimation of Wave-number Parameters

Although the signal detection solution discussed in the previous section required maximum likelihood estimators for the wave-number parameters, obtained by maximizing the beam-power in the uncorrelated signal case, it is convenient to give a separate discussion of the problem of estimating the wave-number (velocity and azimuth) parameters of a given local array. The main reason for needing this additional discussion is to specify the array-dependent uncertainty of the estimated wave-number parameters which serve as critical inputs for the location procedure. For any given source, it is clear that different recording arrays will have wave-number estimators with different variances and covariances. Providing estimators of the differential that can be attributed to differing values for signal-to-noise ratios, bandwidth and geometry of the array will be important for determining the uncertainty region of the location procedure. It should be noted here that additional variability due to geophysical causes other than those given above will be incorporated later, in part, through a variance scaling factor introduced in the location model.

For the uncorrelated signal case, Shumway et al (1999) have obtained the large-sample covariance matrix (Cramer-Rao Lower Bound) of the two-dimensional estimated wave-number vector $\hat{\boldsymbol{\theta}}$ as

$$\Sigma \approx \frac{1}{(2\pi)^2}\frac{1}{2BT}\frac{1}{rN}\left(1 + \frac{1}{rN}\right)R^{-1}, \tag{8}$$

where, in addition to depending on the signal-to-noise ratio r, the covariance matrix depends on the geometry of the array, as determined by the sample covariance matrix of the sensor coordinates $\boldsymbol{r}_j = (r_{j1}, r_{j2})', j - 1, \ldots, N$, say

$$R = \frac{1}{N}\sum_{j=1}^{N}(\boldsymbol{r}_j - \bar{\boldsymbol{r}})(\boldsymbol{r}_j - \bar{\boldsymbol{r}})'. \tag{9}$$

Equations (8) and (9) exhibit several advantages that accrue when formulating location in terms of the wave-number parameters θ_1 and θ_2 rather than in terms of velocity and azimuth, which are more complicated nonlinear functions of the location. Furthermore, for typical arrays, such as the ones illustrated later, coordinates can be chosen so that the off-diagonal elements of R are zero, leading to uncorrelated estimators for the two wave-number parameters. In the case of a correlated signal, this is not the case and Shumway et al (1999) show what (8) becomes when one specifies the coherence matrix of the signals in (1) but still uses the simple beam-forming estimator for $\boldsymbol{\theta}$. Detailed estimators for the variances of the azimuth estimators as a function of array-baseline size have been computed in Shumway et al (1999). Those computations show that the increase in variance attributable to signal decorrelation is not very substantial over the frequency and array baseline distances contemplated for PIDC (see, also Armstrong, 1998).

In order to cover wave-number estimation and uncertainty for multiple signal models of the form (2), we will need to extend the approach in Shumway et al (1999) to that more complicated model. The benefits from such an extension will be estimators for the wave-number vector $\boldsymbol{\theta}$ that are uncontaminated by the interfering signal $u(t)$. We will also obtain estimators for the variance-covariance matrix of $\hat{\boldsymbol{\theta}}$. As a by-product of the estimation, there will be separate estimators of the wave-number parameters of the interfering signal and its waveform. it should be noted that the estimator for the primary signal will no longer be the straight beam and that the test statistic will no longer be a monotone function of the the beam power. Some examples of multiple signal estimation in the deterministic signal case are given in Shumway (1983) and extensions to the stochastic signal case are discussed in Shumway and Stoffer (2000).

RESEARCH ACCOMPLISHED

Global Location Capabilities

Integrating or fusing data from the single-array sources into a best overall location, with an uncertainty region provided, will be an important aspect of evaluating the predicted performance of the PIDC network. Hence, we consider a methodology for using the information developed in the detection and estimation portions of this paper for estimating the location vector $\boldsymbol{x} = (x_1, x_2 2)'$. In general, we propose a model of the form

$$\hat{\boldsymbol{\theta}}_k = \boldsymbol{\theta}_k(\boldsymbol{x}) + \boldsymbol{e}_k, \tag{10}$$

where $\hat{\boldsymbol{\theta}}_k = (\hat{\theta}_{1k}, \hat{\theta}_{2k})', k = 1, \ldots, n$ is the estimated wave-number vector, as computed from maximizing the beam-power, or F-statistic (3) at the k^{th} array and

$$\boldsymbol{\theta}_k(\boldsymbol{x}) = \frac{\nu}{V} \frac{\boldsymbol{x} - \boldsymbol{c}_k}{\|\boldsymbol{x} - \boldsymbol{c}_k\|} \tag{11}$$

gives the theoretical connection between the wave-number parameters and location. In (11), ν is the center frequency, V is velocity and $\boldsymbol{c}_k = (c_{1k}, c_{2k})'$ denote the coordinates of the k^{th} array ($\|\boldsymbol{a}\| = \sqrt{a_1^2 + a_2^2}$ is the norm of the vector $\boldsymbol{a}$). It can generally be assumed that velocity is known or can be inferred from the wave-number plot. It should be noted that there are often separate phases at the same array that may have their own estimated $\hat{\boldsymbol{\theta}}_k$ and these are included under those that possibly contribute to the model (11). Under certain conditions, there may also be estimators of travel times $\hat{t}_k$, where $t_k(\boldsymbol{x}) = \|\boldsymbol{x} - \boldsymbol{c}_k\|/V$, perhaps from cross-correlation or other means, that could be added to the observations on location $\boldsymbol{x}$.

A possible assumption for the bivariate error terms in (10) is that they are independent and identically distributed with mean zero and 2×2 covariance matrix

$$\text{cov } \boldsymbol{e}_k = \sigma^2 \Sigma_k, \tag{12}$$

where the matrix Σ_k comes from (8), specialized to the k^{th} array. Note that the components of (8) will vary according to the array size and geometry, signal-to-noise ratio and the time-bandwidth product. The scaling

variance σ^2 is to account for additional variability from geophysical sources or from the observed error in a particular event location. If there are consistent biases associated with particular regions or subsets of arrays, constant correction terms can be added to the defining Equation (10). If a number of events are available, the correction terms may even be estimated by least squares using consistent source-receiver pairs.

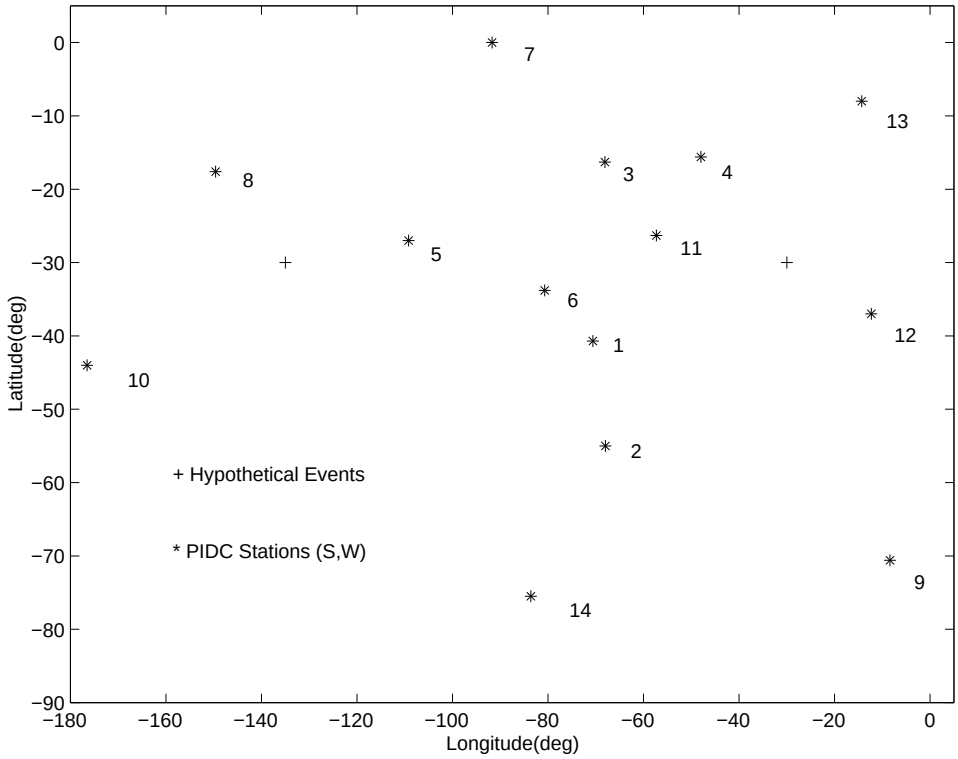


Figure 1: Proposed PIDC infrasound arrays in the southwest quadrant and two hypothetical event locations

As an example of a small demonstration set, we consider Figure 1, which shows the 14 PIDC array centers $\boldsymbol{c}_k$ proposed for the southwest quadrant of the world-wide network. For purposes of illustration, we also show two hypothetical events that might generate observed wave-number parameters $\hat{\boldsymbol{\theta}}_k, k = 1, \ldots, n$ for incorporation into the location model defined in (11) and (12). Later, we discuss an approach to combining or fusing the wave-number parameters into an overall location, based on a given fixed set of recording arrays and their characteristics, as defined by the signal-to-noise ratio r, the time-bandwidth product BT and the array geometry, as it is expressed in terms of R and N in (8).

The solution for a fixed configuration of recording arrays is not the only factor of interest since there will be multiple possible recording configurations possible for any given event. That is, the capability of the network will be an expected value, accumulated over possible recording configurations, weighted by the probability of each particular configuration. The resulting network capability can be contoured by setting an event at each location on the world-wide grid and then computing the probability that each station detects the event, given by (4). We may then compute a weighted average of some parameter reflecting the location capability. For this discussion, we assume that the area of the 90% ellipse is of interest, where the ellipse may be a confidence ellipse under classical assumptions or a posterior probability ellipse under the Bayesian paradigm. We are estimating this kind of network capability using a method that essentially parallel the *Networth* calculations made by Wirth et al (1976) in the case of seismic arrays.

We extend the classical methods first to the case where we observe wave-number parameters and their covariance matrix from n arrays and wish to combine or *fuse* the information into an overall location. The nonlinear model (10) and (11) can be treated in the usual way. That is, expand $\boldsymbol{\theta}_k(\boldsymbol{x})$ around some initial value, say $\boldsymbol{x} = \boldsymbol{x}_0$ and write a linearization as

$$\hat{\boldsymbol{\theta}}_k - \boldsymbol{\theta}_k(\boldsymbol{x}_0) = A_k(\boldsymbol{x}_0)(\boldsymbol{x} - \boldsymbol{x}_0) + \boldsymbol{e}_k, \tag{13}$$

where

$$A_k(\boldsymbol{x}) = \frac{\partial \boldsymbol{\theta}_k(\boldsymbol{x})}{\partial \boldsymbol{x}} \tag{14}$$

is the usual 2×2 matrix of partial derivatives of $\boldsymbol{\theta}_k(\boldsymbol{x})$. Then, stacking the n, 2×1 wave-number vectors and minimizing the weighted sum of squared errors can be done by successively estimating $\boldsymbol{\beta} = \boldsymbol{x} - \boldsymbol{x}_0$. This leads to

$$\hat{\boldsymbol{x}} = \hat{\boldsymbol{x}}_0 + C^{-1}(\boldsymbol{x}_0) \sum_{k=1}^{n} A_k(\boldsymbol{x}_0)' \; \Sigma_k^{-1} [\hat{\boldsymbol{\theta}}_k - \boldsymbol{\theta}_k(\boldsymbol{x}_0)], \tag{15}$$

where

$$C(\boldsymbol{x}_0) = \sum_{k=1}^{n} A_k(\boldsymbol{x}_0)' \; \Sigma_k^{-1} A_k(\boldsymbol{x}_0). \tag{16}$$

It follows that the estimated covariance matrix of the final estimator is

$$\widehat{\text{cov}}\; \hat{\boldsymbol{x}} = \sigma^2 C^{-1}(\hat{\boldsymbol{x}}). \tag{17}$$

Equations (10) and (11) exhibit the *fusion estimators* at each stage as pooled estimators over the n arrays as long as the variances are known. We may also develop a confidence ellipse for the fusion estimators under assumptions (A), (B) and (C), as given below.

(A) **Variance Known:** We may assume that the variance σ^2 is known, either from the statistical variances of the computed wave-number estimators or from a combination of factors including the statistical wave-number variances. In this case, the generalization of the usual chi-squared ellipse considered by Evernden (1969) can be computed from the fact that

$$\big(\boldsymbol{x} - \hat{\boldsymbol{x}}\big)' C(\hat{\boldsymbol{x}}) \big(\boldsymbol{x} - \hat{\boldsymbol{x}}\big) \sim \sigma^2 \chi_2^2, \tag{18}$$

where $\sim$ denotes *is distributed as* and χ_2^2 denotes a chi-squared distribution with 2 degrees of freedom. Note that the statistical uncertainty of the wave-number estimators is already in the matrix Σ_k so that a plausible estimator for σ^2 in the absence of other factors might by unity.

(B) **Variance Unknown:** If variances are known only up to the constant σ^2, this scaling variance may be estimated from the set of arrays that record the event. For the Gaussian case, the maximum likelihood estimator is proportional to the unbiased estimator

$$s^2 = \frac{1}{2(n-1)} \sum_{k=1}^{n} \big(\hat{\boldsymbol{\theta}}_k - \boldsymbol{\theta}_k(\hat{\boldsymbol{x}})\big)' \; \Sigma_k^{-1} \big(\hat{\boldsymbol{\theta}}_k - \boldsymbol{\theta}_k(\hat{\boldsymbol{x}})\big). \tag{19}$$

This case, originally considered in Flinn(1965), leads to a confidence interval based on the F-distribution, namely

$$\big(\boldsymbol{x} - \hat{\boldsymbol{x}}\big)' C(\hat{\boldsymbol{x}}) \big(\boldsymbol{x} - \hat{\boldsymbol{x}}\big) \sim 2 s^2 F_{2,2(n-1)}, \tag{20}$$

where $F_{2,2(n-1)}$ denotes the F-distribution with 2 and $2(n-1)$ degrees of freedom.

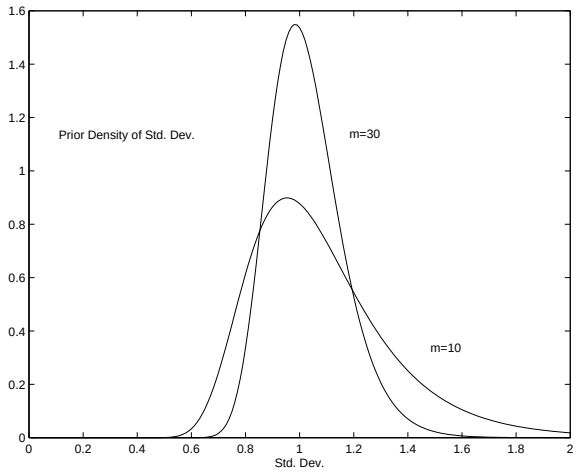


Figure 2: Possible prior distributions for standard deviations of measured wave-number estimates

(C) **Variance Subject to Prior Distribution:** It is often the case that it is unrealistic to assume that the variance is known exactly because (18) becomes too small. For a small number of arrays, the ellipse based on the F-statistic (20) is often much too large. A useful compromise, introduced by Jordan and Sverdrup (1981)and continued by Bratt and Bache (1988), is to quantify the initial uncertainty about σ^2 by assigning it a prior distribution with density function $\pi(\sigma^2)$. It is convenient to use the inverted chi-squared distribution with parameters m, representing the equivalent sample size embodied in the prior information and σ_0^2, representing a prior centering value for the variance. Figure 2 plots the density function for the standard deviation σ for $\sigma_0 = 1$ and $m = 10, 30$. We note that the two values put the standard deviation between .4 and 2 for $m = 10$ and between .6 and 1.6 for $m = 30$ For a fully Bayesian approach, we assume a non-informative prior on $(-\infty < x_1, x_2 < \infty)$ for the location $\boldsymbol{x}$ and compute the posterior distribution, given the wave-number observations, as a bivariate t-distribution with 2 and $2(n-1)+m$ degrees of freedom. The posterior estimator for the variance is

$$\sigma'^2 = \frac{2(n-1)s^2 + m\sigma_0^2}{2(n-1)+m} \tag{21}$$

implying that the best approach is simply to pool the initial variance σ_0^2 and the sample variance s^2, weighted by their degrees of freedom. The quadratic form involving the location vector $\boldsymbol{x}$ in the multivariate t has an F-distribution, making the 95% posterior probability ellipse for the location expressible as

$$(\boldsymbol{x} - \hat{\boldsymbol{x}})' C(\hat{\boldsymbol{x}})(\boldsymbol{x} - \hat{\boldsymbol{x}}) \sim 2\sigma'^2 F_{2,2(n-1)+m} \tag{22}$$

It is interesting that the form of the posterior probability ellipse (18) is similar to (20) but will be tighter because of the additional degrees of freedom for the F-statistic. Hence, the Bayesian solution represents a compromise between (18) and (20), the methods of (A) and (B).

CONCLUSIONS AND RECOMMENDATIONS

Development of Global Network Performance Measures

We are proposing to combine the theoretical information available from the previous sections into an overall assessment of expected global network performance. Since there will likely be relatively few stations recording each event, we will make computations based on the Bayesian posterior probability interval given by (22).

The natural measure to use for the overall analysis will be the area of the ellipse, taken here to be the area of the 90% posterior probability ellipse.

First, consider the area for a fixed event location and a specified set of detecting arrays. Crucial inputs are as follows:

Signal-to-Noise Ratio

The signal-to-noise ratio r should be determined for each array recording a signal from that particular location. One option is to just assume a value, based on experience, or to sample randomly from an assumed distribution of values. Given an observed event and a recording station, estimation of the signal and noise spectra by maximum likelihood is solved in Shumway et al (1999) for both perfectly correlated and decorrelated signals. These estimators can be used directly if events and recordings are available. In the example given here, we arbitrarily take signal-to-noise ratios of $r = 2, 3$.

Array Geometry

The geometry of each array affects the detection probability for that array and the accuracy of the input wave-number $\hat{\boldsymbol{\theta}}_k(\boldsymbol{x})$, large through N, the number of sensors and R, the sample covariance matrix of the array. Again, Shumway et al (1999) show expressions for the estimated variance under the two different assumptions for correlation. In the example that comes next we used two array geometries; the first was a triangle with baseline 1km and a center element; the second was the first triangular array with an additional inverted inner triangle with baseline distance .2km (see Blandford, 1997).

Time-Bandwidth Product, Center frequency, velocity

The time-bandwidth product BT will depend on the assumed frequency band containing the signal and the length of the signal window. We assumed here a center frequency of 1 Hz and a time-bandwidth product of $BT = 17$, which represented a reasonable compromise from our earlier work (Shumway et all, 1999) with a Pacific Islands event. Velocity was assumed to be .3 km/sec in the example.

Note that the values of r and N in the preceding discussion are sufficient for computing the detection probability at a fixed false alarm rate from the F-distribution given by (4). The input covariance matrix Σ_k can be computed from (8), using an array assumption and a configuration of recording stations. For the posterior probability ellipse (22) we require an assumed location $\boldsymbol{x}$ which we took as the two events marked with + in Figure 1. This leads to a value for the matrix $C(\boldsymbol{x})$ in (16). As assumptions for the prior scaling variance and its uncertainty, we took $\sigma_0^2 = 1$ and $m = 10$, assuming the sample variance $s^2 = 1$.

Figure 3 shows the predicted posterior 90 and 95% ellipses for the locations of the two events, assuming various recording array configurations (see also Table 1). We note that ellipses produce reasonably satisfactory regions for a small number of arrays detecting but that the areas are still not up to the often-mentioned standard of areas less than 1000 km^2 at 90% confidence. Of course, this could be achieved by increasing the assumed time-bandwidth product or the signal-to-noise ratio or by changing the nature of the recording array. Table 1 gives a short introduction to what might happen under various scenarios. Increasing the number of elements in the array decreases the area by approximately 10%; increasing the signal-to-noise ratio 2 to 3 leads to reductions of about 40%. Assuming that there are more detecting arrays also has a fairly substantial effect.

Finally, we plan to develop an expression for the average area expected over all possible configurations of detecting arrays. That is, define a detection indicator D_k that is one if the array detects and is zero otherwise, for the full set of possible detecting arrays, say, for $k = 1, 2, \ldots, K$ of them. If we define $p_k = Pr\{D_k = 1\}$,

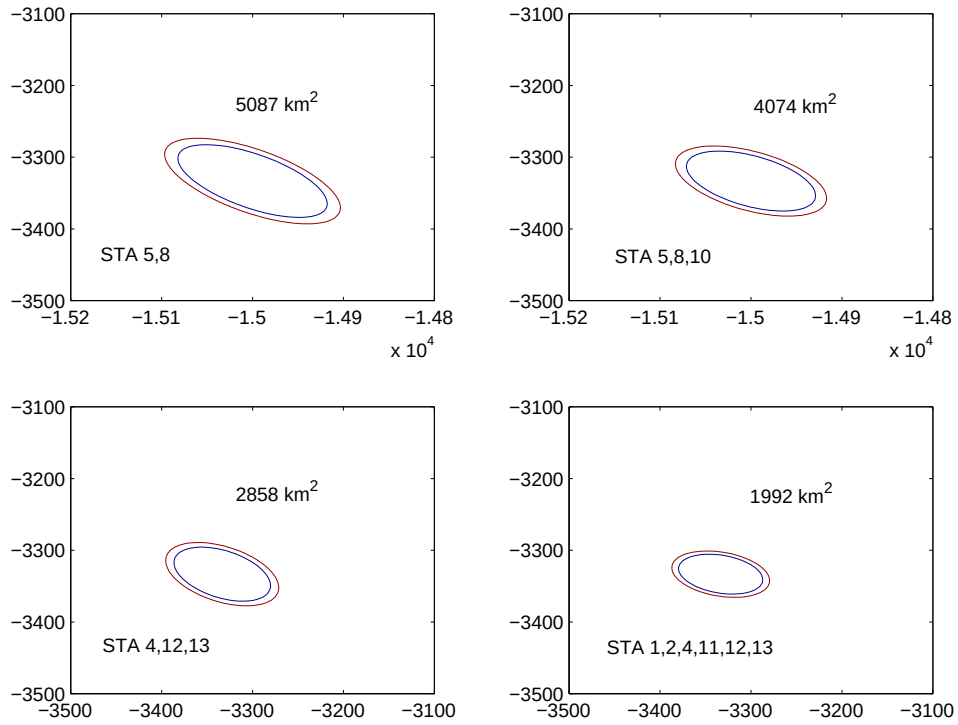


Figure 3: Posterior probability (90 and 95%) ellipses for various array detection configurations assuming 7-element arrays, perfect signal correlation and a single channel $S/N = 2$.

the joint density of the random variables $D_1, D_2, \ldots, D_K$ would be

$$P(D_1, \ldots, D_k) = \prod_{k=1}^{K} p_k^{D_k} (1 - p_k)^{1 - D_k}. \tag{23}$$

The probabilities can be arbitrary for each station, based on recorded data, but our preferred approach is to use the estimated probabilities computed from the result (4). Now, for any given event, we can observe 2^K possible configurations of detecting stations and each one of them will give a predicted area. We can multiply each configuration probability by its area and add them up to get the average areas of location for that particular source. Alternately, and perhaps, easier would be to simulate values of $D_1, \ldots, D_K$ repeatedly and simply average the resulting areas. In either case, it is clear that a relatively small computing effort will yield an average predicted 90% uncertainty area for each location. Plotting contours on the map will give us an index of global network performance.

Table 1: Areas (km^2) of 90% Posterior Probability Ellipses for Simple and Extended Triangular Arrays

	Triangular	Array	Extended	Array
Stations/Event	$S_N = 2$	$S_N = 3$	$S_N = 2$	$S_N = 3$
5,8/1	5554	3566	5087	3316
5,8,10/1	4448	2856	4074	2656
4,12,13/2	3129	2002	2858	1863
1,2,4,11,12,13/2	2176	1397	1992	1299

REFERENCES

Armstrong, W.T. (1998). Comparison of infrasound correlation over differing array baseline. In *Proceedings of 21st Annual Seismic Research Symposium on Monitoring a Comprehensive Test Ban Treaty (CTBT).* 543-554

Blandford, R.R. (1997). Design of infrasonic arrays. *AFTAC Report AF-TR-97-013*, Headquarters, Air Force Technical Applications Center, Patrick AFB FL 32925-3002.

Bratt, S.R. and T.C. Bache (1988). Locating events with a sparse network of regional arrays. *Bull. Seismolog. Soc. Amer*, **78**, 780-798.

Dighe, K.A., R.W. Whitaker and W.T. Armstrong (1998). Modeling study of infrasonic detection of 1 kt atmospheric blast. In *Proceedings of 21st Annual Seismic Research Symposium on Monitoring a Comprehensive Test Ban Treaty (CTBT).* 571-585.

Evernden, J.F. (1969). Precision of epicenters obtained by small numbers of world-wide stations. *Bull Seismolog. Soc. Amer.*, **59**, 1365-1398.

Flinn, E.A. (1965). Confidence regions and error determinations for seismic event location. *Rev. Geophys.*, **3**, 157-185.

Hedlin, M.H., F.L. Vernon and J. Berger (1998). Surveying infrasonic noise on oceanic islands. In *Proceedings of 20th Annual Seismic Research Symposium on Monitoring a Comprehensive Test Ban Treaty (CTBT)*, 586-595.

Jordan, T.H. and K.A. Sverdrup (1981). Teleseismic location techniques and their application to earthquake clusters in the South-Central Pacific, *Bull Seismolog. Soc. Amer*, **71**, 1105-1130.

Shumway, R.H.(1983). Replicated time series regression: An approach to signal estimation and detection. *Handbook of Statistics Vol. 3*, Chapt. 18, 383-408, Time Series in the Frequency Domain. D.R. Brillinger and P.R. Krishnaiah ed., North Holland.

Shumway, R.H., S.E. Kim and R.R. Blandford (1999). Nonlinear estimation for time series observed on arrays. Chapter 7, Ghosh ed. *Asymptotics, Nonparametrics and Time Series*, 227-258. New York: Marcel Dekker.

Shumway, R.H. and D.S. Stoffer (2000). *Time Series Analysis and Its Applications.* New York: Springer-Verlag. Forthcoming.

Shumway, R.H. and S.E. Kim (1998). Detection and estimation on small infrasonic arrays. *Proceedings of 20th Annual Seismic Research Symposium on Monitoring a Comprehensive Test Ban Treaty (CTBT)*, 628-637.

Shumway, R.H. and S.E. Kim (1999). Estimation and location using multiple infrasound arrays. *Proceedings of 21st Annual Seismic Research Symposium on Monitoring a Comprehensive Test Ban Treaty (CTBT).*

Wirth, M.H. R.R. Blandford and R.H. Shumway(1976). Automatic seismic array and network detection. *Bull. Seismolog. Soc. Amer.*, **66**, 1375-1380.

INFRASOUND MODELING USING SOVIET EXPLOSION DATA AND INSTRUMENT DESIGN CRITERIA FROM EXPERIMENTS AND SIMULATIONS

Jeffry L. Stevens, David A. Adams, G. Eli Baker, Heming Xu, and John R. Murphy
Maxwell Technologies, Systems Division

Igor Divnov and V. N. Bourchik
Institute for the Dynamics of the Geospheres, Moscow, Russia

Sponsored by U. S. Department of Defense
Defense Threat Reduction Agency
Contract No. DSWA01-97-C-0129

ABSTRACT

This project has two distinct parts:

1. modeling of infrasound signals from atmospheric explosions and evaluation of International Monitoring System network performance using data from historic Russian nuclear tests and other infrasound data sources; and
2. analysis of infrasound instrumentation through a program of experimentation and theoretical modeling.

The Institute for the Dynamics of the Geospheres (IDG) in Moscow, Russia, has an archive of infrasound recordings from Soviet atmospheric nuclear tests that were conducted in 1957 and 1961. IDG has digitized a total of 238 infrasound waveforms from 27 atmospheric nuclear tests. Two events were high altitude explosions at Kapoustin Yar, 12 others were at the Shagan River Test Site, and the other 13 were at Novaya Zemlya. 138 of the waveforms have measurable, unclipped signals, known instrument responses, yields, and calibrations. We have been modeling this data in two ways: first, by using the data to place constraints on infrasound scaling relations; and second, by numerical modeling of the infrasound signals. Scaling relations estimate the pressure as a function of yield and range. Several scaling relations exist in the literature, and the differences between them lead to large differences in estimates of the detection threshold of the International Monitoring System (IMS). We find that a scaling relation developed by Los Alamos is most consistent with the data set. We are modeling the waveforms using modal superposition and finite difference calculations, and are also using the Inframap package developed by BBN.

IMS network detection capability is predicted using the network simulation programs NetSim and XNICE. NetSim uses joint probabilities together with a scaling relation to calculate the detection threshold. XNICE has the additional capability of estimating the detection threshold for non-Gaussian noise distributions. We find that IMS noise levels have a distribution that is non-Gaussian and time-dependent. The noise is characterized by a fairly well-defined minimum level, but highly variable maxima. The two-station 90% probability IMS detection threshold is found to be about one kiloton with higher thresholds in ocean regions and lower thresholds on land.

A typical infrasound recording instrument uses an array of pipes connected to a central manifold to spatially filter random pressure fluctuations along the ground and so enhance the signal-to-noise ratio (S/N). We present a rapid, accurate, method of estimating the performance of any pipe configuration used for infrasound recording. We first describe experimental work that provides the physical basis for simulations and permits estimation of parameter values. We then describe the propagator method used for the calculations. The performance of a pipe array depends on the character of the noise, and so meaningful modeling of infrasound pipe array performance hinges on accurate knowledge of the temporal and spatial distribution of pressure fluctuations over the array. We discuss the physical basis for the noise model, and limitations imposed by necessary simplifications. We present the amplitude and phase responses, and their sensitivities to different parameters, of two different types of pipes used to construct the arrays: closed-ended pipes with acoustic inlets along their lengths versus open ended, otherwise impermeable pipes. Finally, we simulate the S/N enhancement for six different pipe configurations, and discuss the results' implications for instrument design.

OBJECTIVE

The objective of this project is to develop a better understanding of infrasound excitation, propagation, and recording in order to be able to predict the capability of the IMS network to detect and identify atmospheric explosions. To accomplish this, we are gathering a data set of infrasound recordings from historical Soviet explosions, modeling these data and using them to develop improved scaling and attenuation relations. In addition, we are using experimental and numerical methods to model the response of infrasound recording instrumentation.

RESEARCH ACCOMPLISHED

Part 1: Infrasound scaling and attenuation relations and IMS detection capability

The International Monitoring System (IMS) required by the Comprehensive Nuclear Test Ban Treaty (CTBT) will include sixty infrasound stations designed to detect atmospheric nuclear explosions. A design goal is that the system be able to detect and locate explosions as small as one kiloton anywhere in the world. In order to estimate the capability of the infrasound network, it is necessary to be able to predict the amplitude of an infrasound signal at any location, and to evaluate whether the signal would be detectable above noise levels at the recording stations. Scaling and attenuation relations are empirical and/or theoretical equations that relate the amplitude and period of infrasound signals to the explosion yield and source to receiver distance. Several different relations have been developed based on theoretical infrasound modeling, and on recordings of atmospheric nuclear and chemical explosions. The different scaling relations, however, imply very different detection threshold levels. In last year's report, we discussed several scaling relations and showed that some were unrealistic, and that two scaling relations developed by Whitaker (1995) and Clauter and Blandford (1998) were consistent with the data. These scaling relations are given by the expressions:

$$\log P = 0.92 + 0.5 \log W - 1.47 \log \Delta \qquad \text{AFTAC (Clauter and Blandford, 1998)} \qquad (1)$$

$$\log P_c = 3.37 + 0.68 \log W - 1.36 \log R \qquad \text{LANL (Whitaker, 1995)} \qquad (2)$$

where W is the explosion yield in kilotons, delta is distance in degrees, R is distance in kilometers, P is pressure in Pascals and P_c is wind corrected pressure given by $P_c = 10^{-0.19V}$ where V is the component of the stratospheric wind velocity in meters/second in the direction of wave motion.

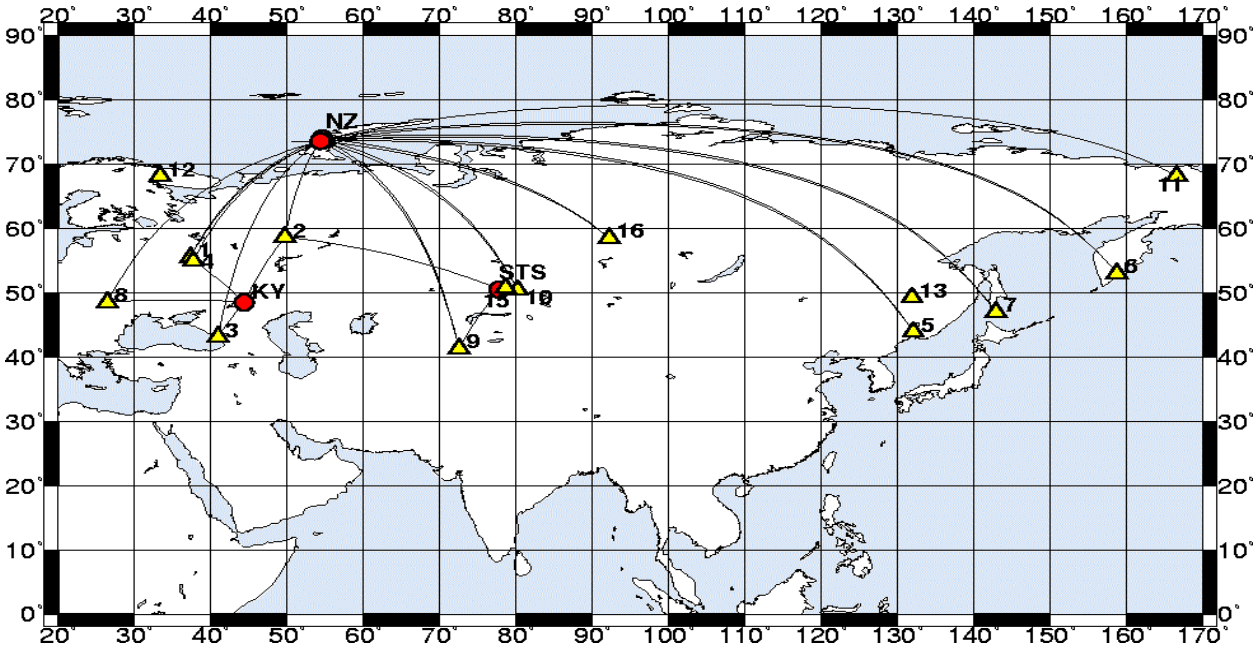


Figure 1. Stations recording infrasound signals from atmospheric explosions at three Soviet nuclear test sites Semipalatinsk (STS), Kapoustin Yar (KY), and Novaya Zemlya (NZ).

SOVIET INFRASOUND DATA

We now have a much more extensive data set of infrasound records from Soviet atmospheric explosions. IDG has an archive of approximately 300 recordings from 34 Soviet atmospheric nuclear tests that were conducted in 1957 and 1961. 20 of these explosions were located at the Novaya Zemlya test site, 12 at Semipalatinsk, and 2 at Kapoustin Yar (see Figure 1). Of these, 233 recordings from 27 of the tests recorded at stations from 1000 to 5000 km were found to be of adequate quality for digitization. The yields of these tests range from 0.4 KT to 58 MT. The data set includes two high altitude explosions and the largest (58 megaton) atmospheric explosion ever detonated. The explosions corresponding to this data set are listed in Table 1. The number of records listed in the table is the total number of records digitized for each event.

Test Site	Explosion Number	Date	Time (Moscow)	Latitude	Longitude	Height of Burst (m)	Yield (KT)	Number Records
STS	088	1961/09/04	08:00:27	50.45	77.74	725	9	2
STS	089	1961/09/05	09:00:05	50.45	77.74	500	16	3
KY	091	1961/09/06		48.45	44.30	22700	11	6
STS	094	1961/09/10				390	12	2
NZ	095	1961/09/10	12:00:14	73.52	54.30	2000	2700	23
NZ	099	1961/09/12	13:08:00	73.52	54.30	1190	1150	23
STS	100	1961/09/13	08:01:55.8	50.45	77.75	710	14	1
NZ	102	1961/09/14	12:56:16	73.52	54.3	1700	1200	17
STS	103	1961/09/14	08:59:59.4	50.35	77.82	0.5	0.4	1
STS	105	1961/09/17	10:00:46.6	50.45	77.75	695	21	1
NZ	111	1961/09/20	11:12:12	73.52	54.30	1600	2000	6
STS	112	1961/09/21	17:01:01.6	50.33	77.70	110	0.8	2
NZ	113	1961/09/22	11:11:00	73.52	54.30	1300	260	4
STS	114	1961/09/26	10:01:19.8	50.45	77.75	665	1.2	2
NZ	116	1961/10/02	13:30:50	73.92	54.55	1500	250	13
STS	117	1961/10/04	10:01:19.9	50.44	77.76	605	13	1
NZ	118	1961/10/04	10:30:55	73.52	54.30	2100	3000	13
KY	119	1961/10/06		48.45	44.30	41300	40	4
NZ	120	1961/10/06	10:00:08	73.52	54.30	2700	4000	20
STS	122	1961/10/12	08:31:03.6	50.45	77.75	670	15	1
STS	123	1961/10/17	10:00:00.8	50.45	77.75	505	6.6	2
STS	124	1961/10/19	08:30:42.6	50.45	77.73	710	10	2
NZ	125	1961/10/20	11:07:03	73.52	54.30		1450	17
NZ	126	1961/10/23	11:31:22	73.5	54.3	3500	12500	21
NZ	128	1961/10/25	11:31:05	73.52	54.3	1450	300	10
NZ	133	1961/10/30	11:33:27	73.52	54.30	4000	58000	21
NZ	147	1961/11/04	10:20:23	73.5	54.3	1750	150-1500	20

Table 1. Soviet atmospheric nuclear explosions and the number of records for each event that have been digitized by IDG. STS is the Semipalatinsk test site, KY is Kapoustin Yar, and NZ is Novaya Zemlya.

Seventeen stations recorded data from these tests. Figure 1 shows the paths from each event to each station in the data set. Data were recorded on instruments with varying low and high pass filters. IDG has put considerable effort into identifying the instrument parameters that were in use at each of the recording stations. Some information about the data is not available. Absolute times are not known for any of the waveforms. For two of the stations, the source to receiver distance is known, but only the general area is known for the station location.

Measurement of Russian data

All of the Russian data were carefully measured in a consistent manner. The data were first filtered to remove long and short period noise outside the frequency band of the data. A Butterworth filter was used with corner frequencies of .01 and .2 Hz for events with yield less than 100 kilotons, .002 and .1 Hz for events with yields between 100 kilotons and 2 megatons, and .001 and .1 Hz for events with yield greater than 2 megatons. The

amplitude and period were measured as half the maximum peak to peak amplitude and twice the time difference between the peak and trough, respectively. Measurements were made on both the acoustic wave and the low frequency Lamb wave if possible. Only data with known instrument responses were measured, and a digital correction for the instrument response was made at the observed period. A few signals with apparent calibration errors were not used. The final result is that measurements were made on a total of 133 waveforms. 107 acoustic waves from 17 events and 96 Lamb waves from 9 events were measured.

Figure 2 shows a comparison between pressure measurements made from the Russian data and equations 1 and 2. All pressures are zero to peak amplitudes in Pascals. Also shown on the figure are measurements from the US Project Dominic tests. The AFTAC relation (equation 1) fits the lower yield data quite well. The LANL relation (equation 2) appears to fit the data very well over the entire scaled range, although there is considerable scatter about the line. The pressure measurements have not been wind corrected since we have only limited information about wind conditions at the time of the tests. The data are consistent with the slopes of 0.5-0.68 of the AFTAC and LANL relations, with the LANL relation fitting the data over the widest range.

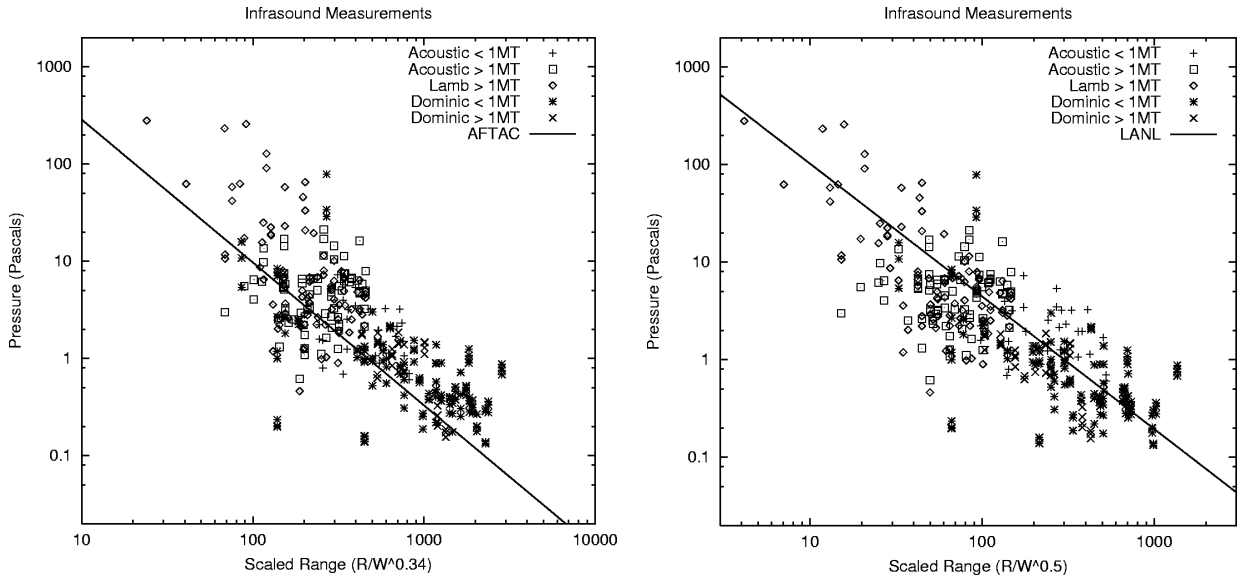


Figure 2. Comparison of Russian data with scaling relations. Left is the AFTAC relation (Clauter and Blandford) equation 1, and right is the LANL relation (Whitaker) equation 2.

Infrasound Magnitudes

In the analysis above, we used a data set of infrasound waveforms from Soviet atmospheric tests ranging in yield from 6 kilotons to 58 megatons to place constraints on infrasound scaling relations and to estimate the detection threshold of the future International Monitoring System. Analysis of 133 waveforms shows that measured pressures are consistent with yield and attenuation scaling relations developed at LANL for HE tests, and also fairly consistent with a scaling relation developed by AFTAC. Because the LANL relation is consistent with data over a very wide yield range, it has recently been adopted as the basis for an infrasound magnitude by the International Data Center (IDC) (Brown, 1999). A magnitude is a useful quantity for giving an estimate of source size that is independent of the distance at which the signal is measured. The magnitude equation is:

$$M_l = \log_{10} P + 1.36 \log_{10} R - 0.019v \qquad (3)$$

where the last term corrects for wind as discussed earlier. Infrasound magnitudes for the Russian data set (without wind correction), are listed in Table 2. Magnitudes for the acoustic wave and Lamb wave are listed separately. Figure 3 shows M_l plotted vs. Yield for the seven Soviet explosions. Also shown is the LANL relation, equation 2, rewritten as a magnitude/yield relation:

$$M_I = 0.68 \log W + 3.37 \quad (4)$$

As can be seen in Figure 3, equation 4 fits the data over this very wide yield range very well. An exception is the low yield, high altitude explosion at Kapoustin Yar which lies above the curve by about 0.5 magnitude units.

Test Site	Explosion	M_I Acoustic	$\sigma(M_I)$ Acoustic	Number Acoustic	M_I Lamb	$\sigma(M_I)$ Lamb	Number Lamb
STS	088	4.44		1			
STS	089	4.31	0.05	3			
KY	091	4.53	0.18	5			
NZ	095	5.52	0.26	16	5.50	0.25	16
NZ	099	5.29	0.46	18	5.26	0.37	20
NZ	102	5.29	0.34	13	5.13	0.31	9
NZ	111	5.56	0.40	5	5.42	0.13	3
NZ	113	4.94	0.37	2			
NZ	116	4.98	0.32	6			
STS	117	4.52		1			
KY	119	4.45	0.48	4			
NZ	120	5.38	0.48	11	5.36	0.53	12
STS	123	4.46		1			
STS	124	4.47	0.40	2			
NZ	125	5.43	0.56	9	5.24	0.41	10
NZ	126	5.33	0.35	4	6.15	0.43	14
NZ	128	5.04	0.38	6	4.92	0.38	2
NZ	133				6.69	0.40	10

Table 2. Infrasound magnitude for eighteen Soviet explosions.

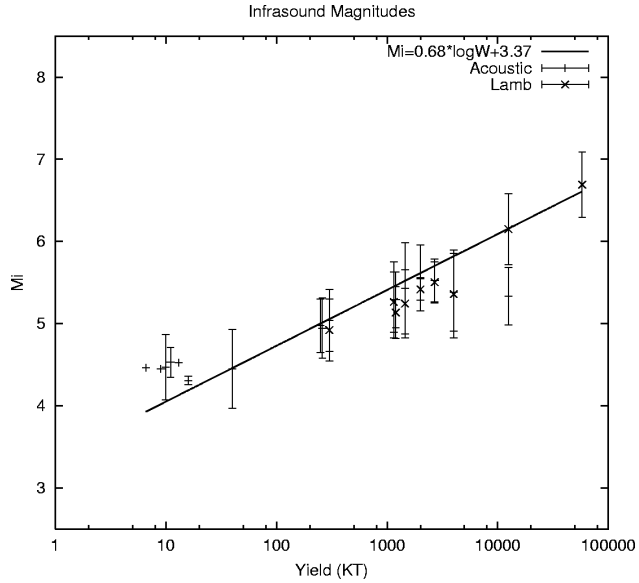


Figure 3. Infrasound magnitude plotted vs. yield for eighteen Soviet explosions.

Network Detection Simulations

In order to predict the performance of the proposed 60 station IMS infrasound network, we modified the network simulation program NetSim (Sereno et al., 1990) to include the models of infrasound propagation described in equations 1 and 2. NetSim uses these equations to calculate the pressures as a function of yield

and range. These are used together with station locations, a noise model, a minimum signal to noise ratio for reliable measurement, and the number of stations required for a signal to be reported, to determine the network detection threshold as a function of position on the earth. We have calculated detection thresholds for the proposed IMS network using station dependent noise level estimates. The calculations were performed using the following parameters:

1. We used noise estimates from Blandford, et al (1995), which are based on wind measurements. The log noise levels varied from –1.37 to –0.09 (Pascals), with the highest levels being in oceanic regions. Log standard deviation was again taken to be 0.37.
2. The minimum signal to noise ratio for detection is 2.
3. Two stations detect infrasound signals at a 90% confidence level.
4. Four element infrasound arrays increase signal to noise ratio by a factor of 2.
5. Propagation error has a log standard deviation in log signal of 0.3.
6. Station reliability is 95%.

Detection threshold maps were calculated for the AFTAC and LANL scaling relations. The results are shown in Figures 4 and 5. For the LANL model (Figure 4), the detection threshold is between 0.5 and 2 KT. For the AFTAC model (Figure 5), the detection threshold ranges from about 0.2 KT to about 1 KT. These scaling relations predict, therefore, that the infrasound detection threshold for the IMS network is less than the design goal of one kiloton in most locations, but higher in some regions, particularly in broad ocean areas.

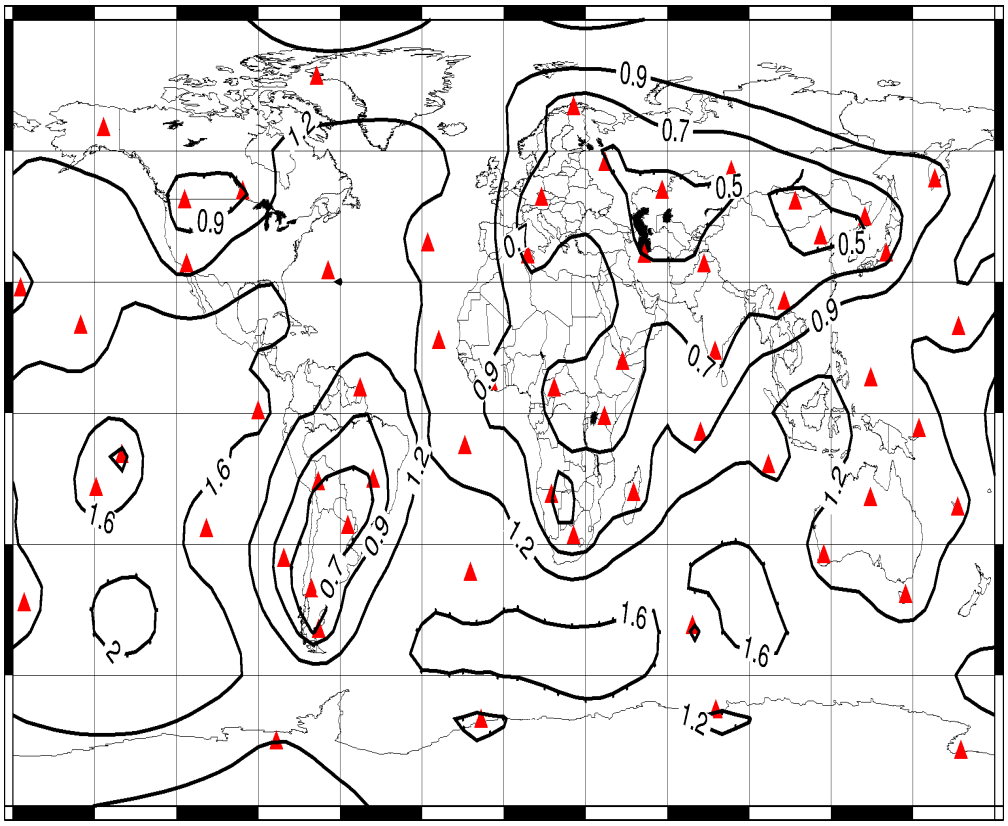


Figure 4. Contours showing detection thresholds with a 90% level of confidence for detection at 2 infrasound stations with station dependent noise levels using the LANL scaling relation (equation 2). The intervals are logarithmically spaced with labels in kilotons.

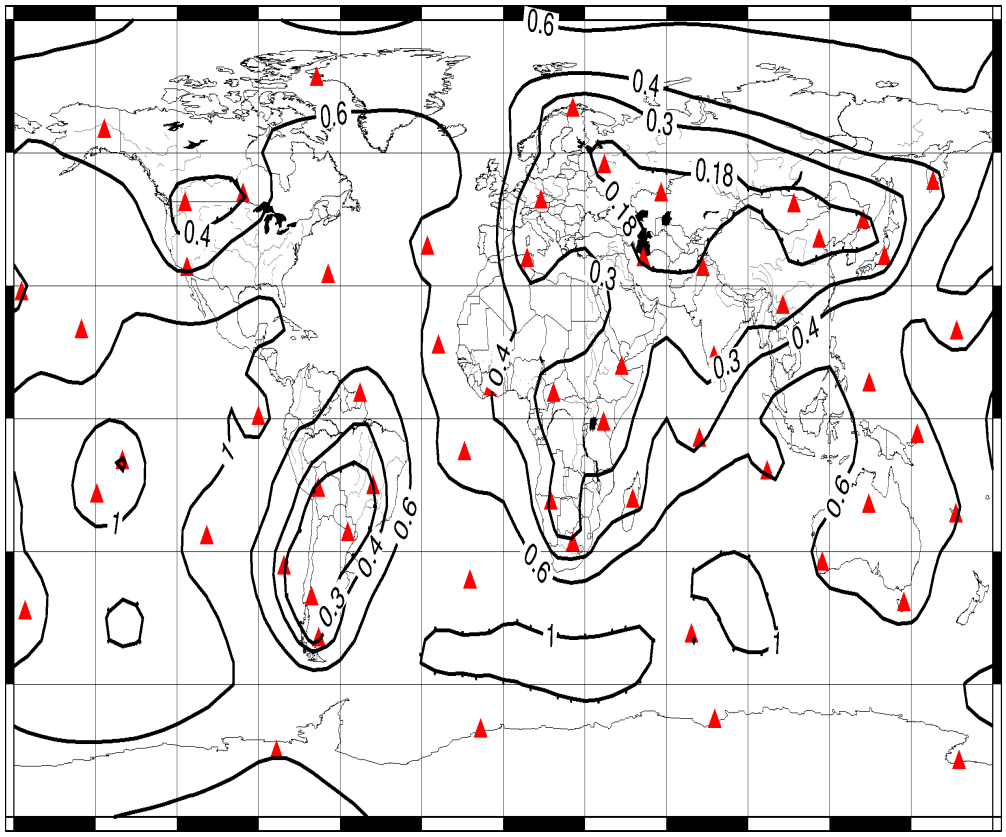


Figure 5. Contours showing detection thresholds with a 90% level of confidence for detection at 2 infrasound stations with station dependent noise levels using the AFTAC scaling relation (equation 1). The intervals are logarithmically spaced with labels in kilotons.

The network simulation results indicate that the detection threshold of the future IMS infrasound network may be somewhat higher than the one-kiloton design goal in some locations. This result depends, of course, on a number of assumptions that went into the simulations. We made the assumptions that a four element array leads to a factor of two improvement in signal/noise ratio, that the noise levels at all stations are independent, and that a signal will be identified with a signal to noise ratio of 2. In general, these assumptions are optimistic, although experienced analysts may be able to detect a signal at lower S/N ratios. Improvements could also be made in the signal and noise modeling. Two improvements in particular which would make the simulations more realistic are:

1. including stratospheric winds, which would have the effect of improving detection in some directions and degrading it in others.
2. Including actual noise distributions at each station instead of an average with a Gaussian distribution.

Figure 6, for example, shows the measured noise levels as a function of time over a seven month period since the start of 1999 as a time series and as a frequency distribution. Clearly the noise distribution is skewed, and much higher than average noise levels are common.

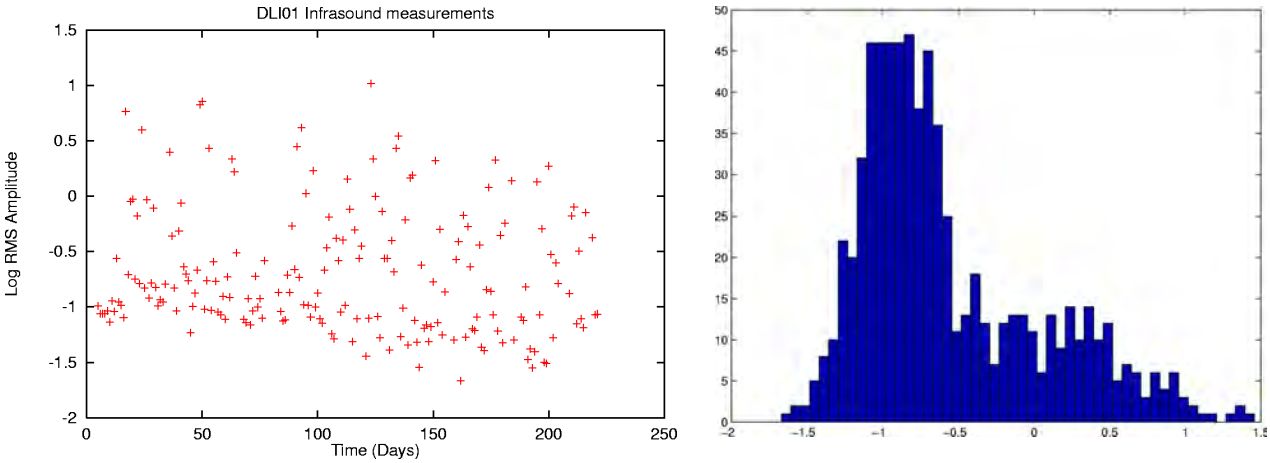


Figure 6. Noise measurements at the Los Alamos infrasound station since January, 1999. The left figure shows the logarithm of the RMS noise amplitude taken at noon each day since the beginning of 1999. The right figure shows the frequency distribution of the noise measurements. The distribution of noise is both skewed and time dependent.

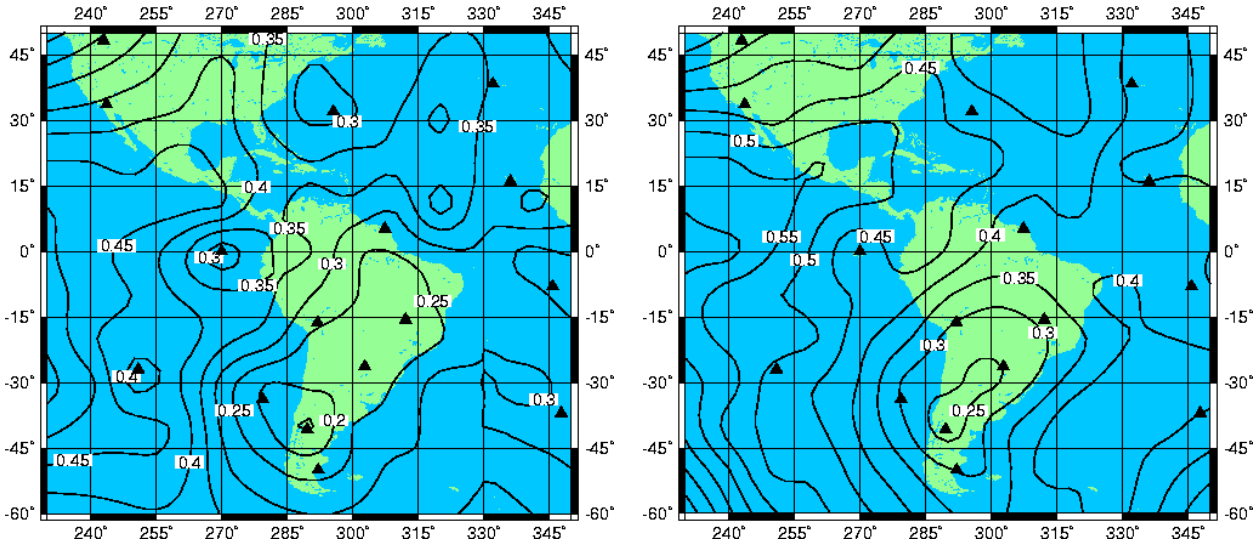


Figure 7: Threshold contours of yield in kilotons for 90% detection at 2 or more stations for the Gaussian noise model (left) and for the non-Gaussian noise model (right). Simulations were performed with XNICE.

NetSim does not have the capability to model non-Gaussian distributions, but they can be modeled with XNICE (Barker, 1996; Barker et al, 1994) (XNICE stands for the X Window version of the Network Identification Capability Estimation system, which can model network identification as well as detection capability). We modified XNICE to handle infrasound as well as seismic data, and did a test case to assess the difference caused by a realistic noise distribution such as that shown in Figure 6. We used a constant mean noise level at all stations of 0.1 Pascals and a minimum S/N of 1.5, and performed two test cases: one with a Gaussian distribution with a standard deviation of 0.64 (derived from the distribution in Figure 6), and one with the noise distribution modified to have the same shape as the distribution in Figure 6 at all stations. Figures 7 and 8 show the results for South America. The absolute numbers are lower than was shown in Figure 3 because the parameters used in the calculation, particularly the lower minimum S/N, are different. However, the effect of including the actual noise distribution is to increase the threshold level by about 50%,

which is a significant difference. The IMS thresholds should be reevaluated as actual noise data becomes available for the IMS infrasound stations.

Simulations of Pipe Array Amplitude and Phase Response and S/N Improvement

We have developed a numerical model with a sound physical basis, and used it to simulate the response of arrays of pipes used as spatial filters in recording infrasonic signals. We reported (Stevens et al, 1999) on experiments to determine the physical basis for the model and to provide empirical measures of dispersion and attenuation, and on the numerical method used to simulate the amplitude and phase response of any configuration. Here we present results of simulations for various pipe configurations (Figure 8), including amplitude and phase responses (Figures 9 and 10) of open and closed ended pipe arrays, and S/N improvement under various noise conditions (Figure 11).

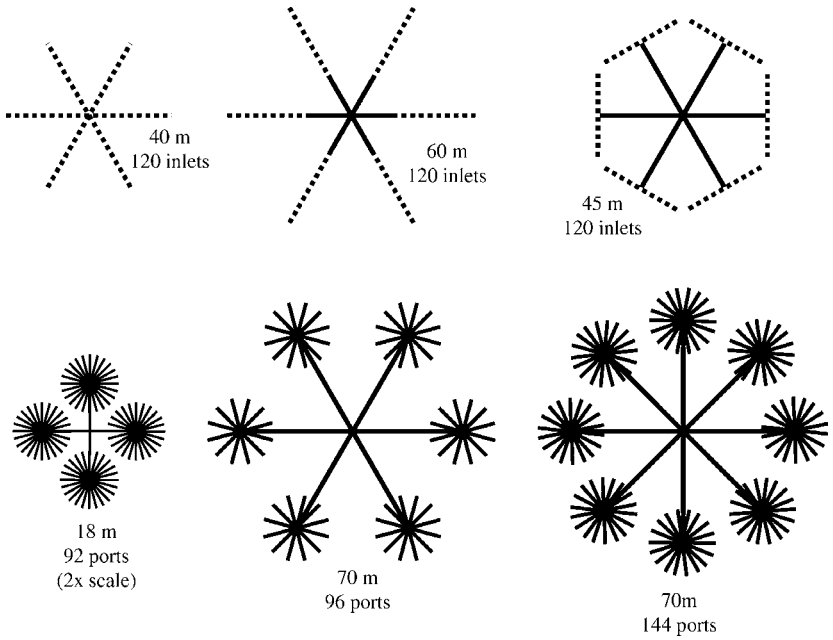


Figure 8. Designs for which we perform simulations (from Noel and Whitaker, 1991; Christie, 1999; Alcoverro, 1998). Close-ended arrays (top row) use 2.5 cm radius pipes with 100 acoustic ohm inlets every meter (dotted lines) connected to impermeable pipe (solid lines). Pressure is measured at a summing manifold at the center of each configuration. The long radial arms of the open-ended impermeable pipe arrays (bottom row) are 0.95 cm radius, and the shorter arms (and all pipes in the 18 m diameter configuration) are 0.64 cm radius. Summing manifolds are at the center of each set of radial arms, which are then connected by the long radial pipes to a central summing manifold where the pressure is measured.

The signal-to-noise improvement of a pipe array depends on the character of the noise, as well as on the spatial configuration. We assume that noise is due to slowly evolving eddies, with a zeroth order Von Karmann distribution, advected past the instrument at the mean wind speed. We perform simulations for wind speeds of 1 and 6 m/s, and correlation lengths of 1 and 10 m (Figure11).

We conclude that open-ended pipes hold most of the advantages over closed-ended pipes with high impedance acoustic inlets, as they have essentially flat amplitude responses while the closed-ended pipes act as lowpass filters. The open-ended pipes also have flat phase responses. The phase response of the closed-ended pipes varies much more across the spectrum of interest. The most important design criterion for enhancing S/N is sufficient spatial sampling. Extra ports spaced at less distance than the noise correlation length provide no advantage. Differences in performance are very significant at lower frequencies, with the two 70 m diameter configurations providing the best S/N enhancement. Their performances were nearly identical even though one had 144 ports and the other had only 96. The 18 m diameter configuration performed the worst at low frequency.

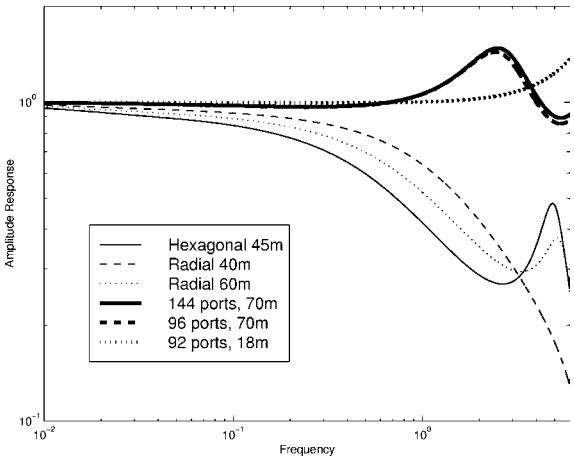


Figure 9. Amplitude responses of configurations shown in Figure 8. Open-ended pipes provide a flat response but lower resonance frequency. In the closed-ended pipe arrays, narrower pipes could provide a somewhat flatter response.

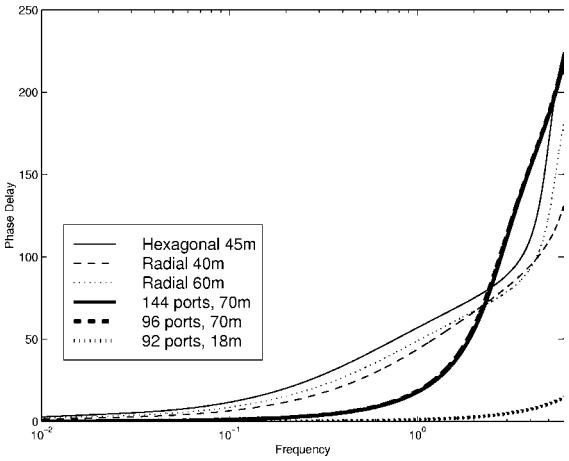


Figure 10. Phase responses of configurations shown in Figure 8. Up to resonance frequency, the open-ended pipe arrays responses are flatter. Wider pipes would produce a flatter phase response for the close-ended pipes.

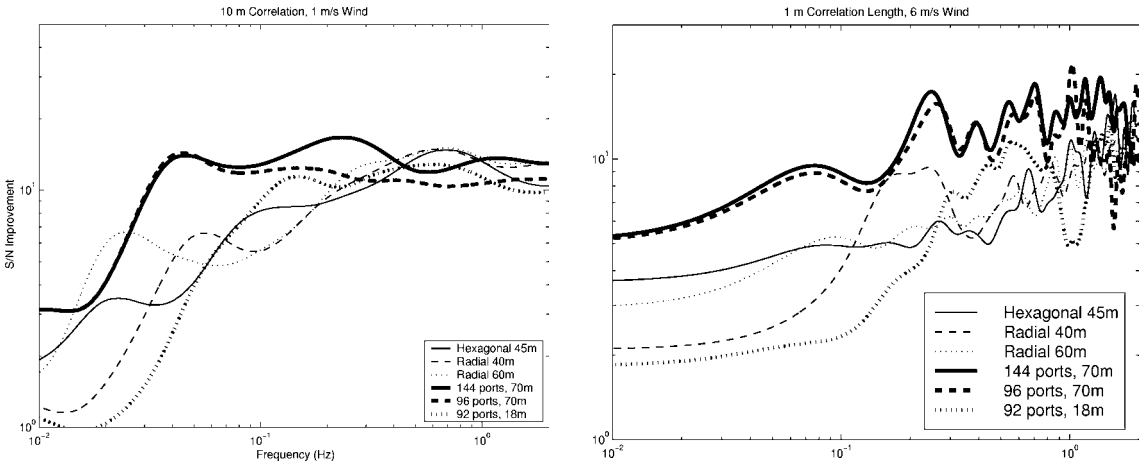


Figure 11. S/N improvement for six different configurations (Figure 8), for 10 m correlation length self-similar noise carried past the instruments by 1 m/s wind (left) and 1 m correlatation length noise advected by 6 m/s wind (right). Maximum radius spanned and number of ports (for open-ended pipes) are listed. Each of the close-ended pipe configurations has 120 inlets.

CONCLUSIONS AND RECOMMENDATIONS

In the analysis above, we used a data set of infrasound waveforms from 27 Soviet atmospheric tests to place constraints on infrasound scaling relations and to estimate the detection threshold of the future International Monitoring System. Analysis of 138 waveforms shows that measured pressures are consistent with yield and attenuation scaling relations developed at LANL for HE tests, and also fairly consistent with a scaling relation developed by AFTAC. The network simulation results indicate that the detection threshold of the future IMS infrasound network may be somewhat higher than the one-kiloton design goal in some locations, particularly in broad ocean regions. Measured infrasound noise distributions are found to be skewed and inconsistent with a Gaussian distribution. Infrasound noise measurements should be made at each IMS station location and the detection thresholds reevaluated using actual noise distributions.

We have developed a rapid, accurate, method of estimating the performance of any pipe configuration used for infrasound recording, and used it to model the response of instrument configurations being considered for the IMS infrasound network. The method is based on appropriate physics, the computations are based on propagator matrices, and results match experimental data. This will permit numerical simulation-based optimization of new designs before deployment, speeding up development and testing of new designs. It will also enable optimization of configurations where noise conditions are well known, and estimation of response curves for existing instruments. The most important step that can be taken next to improve instrument performance is to obtain, and utilize in such modeling, more complete and accurate noise models.

Acknowledgement

We thank Bob Blandford and Dean Clauter for helpful discussions and for providing the station dependent noise estimates.

Key Words: infrasound, scaling relation, attenuation, atmospheric explosion, instrument

REFERENCES

Alcoverro, B. (1998), Acoustic filters design and experimental results, *Proceeding: Workshop on Infrasound*, Commissarriat à l'Énergie Atomique, Bruyères le Châtel, France

Barker, T.G. (1996), "Xnice: A System for Assessing Network Identification Performance," Maxwell Laboratories Scientific Report to Phillips Laboratory, PL-TR-96-2087.

Barker, T. G., K. L. McLaughlin, and J. L. Stevens (1994), "Network Identification Capability Evaluation (NICE)", S-CUBED Technical Report to the Advanced Research Projects Agency SSS-TR-94-14701, July.

Blandford, R. R., D. A. Clauter, R. W. Whitaker, and T. Armstrong (1995), "Infrasound Network Options," AFTAC/DOE White Paper.

Brown, D. J. (1999) "Summary of Infrasound Source Location Meeting: San Diego, November 9-10, 1998, Center for Monitoring Research Technical Report CMR-99/02, January.

Christie, D.R. (1999), Wind-noise reducing pipe arrays, memo of the Provisional Technical Secretariat, CTBTO, Vienna, Austria

Clauter, D. A. and R. R. Blandford (1998), "Capability Modeling of the Proposed International Monitoring System 60-Station Infrasonic Network," proceedings of the Infrasound workshop for CTBT monitoring, Santa Fe, New Mexico, August 25-28, 1997, LANL report number LA-UR-98-56.

Kaimal, J.C. and J.J. Finnigan (1994), Atmospheric Boundary Layer Flows: Their Structure and Measurement, Oxford Univ. Press

Noel, S.D. and Whitaker, R.W. (1991), Comparison of noise reduction systems, LANL report LA-12008-MS UC-700

Sereno, T. J., S. R. Bratt, and G. Yee (1990), "NetSim: A computer program for simulating detection and location capability of regional seismic networks," SAIC Annual Technical Report to DARPA, SAIC 90/1163, March.

Stevens, J.L., D. Adams, G.E. Baker, H. Xu, J. Morris, I. Divnov, V. Bourchik, and I. Kitov, (1999), Infrasound scaling and sttenuation relations from Soviet explosion data and instrument design criteria from experiments and simulations, *Proceedings 21th Annual Seismic Research Symposium on monitoring a CTBT*, 185-194

Whitaker, R. W. (1995), "Infrasonic Monitoring," proceedings of the 17th annual Seismic Research Symposium in Scottsdale, AZ, September 12-155, 1995, 997-1000.

THE ROLE OF GROUND TRUTH IN IMPROVED IDENTIFICATION OF MINING EXPLOSION SIGNALS
UTILIZATION OF CALIBRATION EXPLOSIONS AND ACOUSTIC SIGNALS

Brian Stump and Chris Hayward, Southern Methodist University

Sponsored by the Defense Threat Reduction Agency
Contract No. DSWA01-98-C-0176

ABSTRACT

The characterization and identification of small magnitude seismic sources using regional observations involves the analysis of signals from natural and man made sources. Proper event classification will depend upon the appropriate assessment of source and propagation path effects. Our work is intended to investigate supplementary procedures and data sets that can improve source characterization procedures. Several approaches to improved source identification procedures have been investigated including: (1) Execution of contained calibration explosions; (2) Utilization of regional array data for improved separation of source and propagation path effects; (3) Development of in-mine ground truth through mine records or on site instrumentation; (4) Combining seismic and infrasound data for source characterization.

A series of single-fired calibration shots were detonated in a mine in NE Wyoming for the purpose of developing source scaling relations and comparison to typical delay-fired explosions. Regional data from these explosions are consistent with a simple Mueller-Murphy source model.

The variation in seismograms across regional arrays is used to contrast local site effects with source and regional propagation contributions. The three IMS arrays in the western US - TXAR, PDAR and NVAR- were used in the study. TXAR with its homogeneous geology shows the least variability and NVAR with instruments in seven different rock types shows the greatest variation in both amplitudes and wave shapes.

Ground truth from controlled mining explosions can be obtained from typical blasting records maintained by the mines or more directly from close-in seismic and acoustic observations from within the mine. Mines in the Iron Range (IR) of Minnesota, the Powder River Basin (PRB) in Wyoming, and the Porphyry Copper District (PCD) of east central Arizona and south west New Mexico were used in gathering ground truth ranging from mine records (IR) to in-mine monitoring (PRB and PCD). The contribution of this information to regional monitoring is compared and contrasted.

The focus of this paper will be on the in-mine ground truth developed in the PCD and applied to to regional seismic and infrasonic signals. Seismic and infrasonic signals both in-mine and at regional distances will be used in characterizing the source and propagation path effects.

Key Words: ground truth, mining explosion, seismo-acoustic, infrasound, regional, and calibration

OBJECTIVE

Regional arrays designed for monitoring purposes will detect both natural and man made sources. Many of the artificial sources can be associated with mining operations (Heuze and Stump, 2000). It is important that these sources be properly characterized and found distinct from a nuclear explosion. This discrimination process has historically depended upon seismic data. Recent work (Sorrells *et al.*, 1997; Hsu and Stump, 1997; Hagerty *et al.*, 1999; Sorrells *et. al*, 2000; Stump *et al.*, 2000) has suggested that the association of infrasonic signals with seismic might be useful in the characterization of a source as a near-surface mining explosion with its accompanying infrasound signal.

The efficiency of infrasonic wave propagation is well known to be strongly affected by the direction and magnitude of atmospheric winds. Seasonal variations in detection thresholds for infrasonic waves associated with mining explosions have been documented (Sorrells *et al.*, 1997; Hsu and Stump, 1997). Average atmospheric models predict no infrasonic returns until a distance range of several hundred

kilometers. Several researchers (Hagerty *et al*, 1999; Stump *et al.*, 2000; and Sorrells *et al*, 2000) have reported robust observations in the 50 - 250 km range indicating that seasonal winds may be important to these observations.

The work reported in this paper is motivated by a need to understand atmospheric effects on infrasonic propagation and the possibility of using infrasound and seismic waves to identify mining explosions. The approach we have taken is empirical in that the first step has been the design, construction and installation of monitoring equipment that can produce a comprehensive data set. A regional size network of seismic and infrasound sensors, some of which are arrays, has been designed using a combination of new and existing facilities (Figure 1).

Key to the success of this operation is the development of ground truth information pertinent to the mining sources. Based upon previous studies of large coal cast blasting operations in Wyoming that trigger the IMS (Hedlin *et al. 2000*), the porphyry copper region of Arizona and New Mexico was chosen for the study. Mining explosions for hard rock mining are primarily designed to fracture the material but not move the rock. This blasting practice is in strong contrast to coal cast blasting where the primary goal is to move the overburden into the pit.

This mining region is bounded by the two arrays, NVAR and TXAR, providing the link to the IMS. Critical to the success of the experiment has been cooperation with the local mines producing the sources. Close cooperation has been developed with the Phelps Dodge mines in Morenci, Arizona and Tyrone, New Mexico where in-mine seismic and acoustic systems have been deployed and are operated for ground truth. Additional cooperation is ongoing with the Black Mesa Coal Mine in NE Arizona providing data from large scale cast blasts. Additional cooperating organizations in this regional study include Los Alamos National Laboratory (Rod Whitaker, LANL and ST. GEORGE), University of Arizona (Terry Wallace, TUC and WUAZ) and University of Texas, El Paso (Diane Doser).

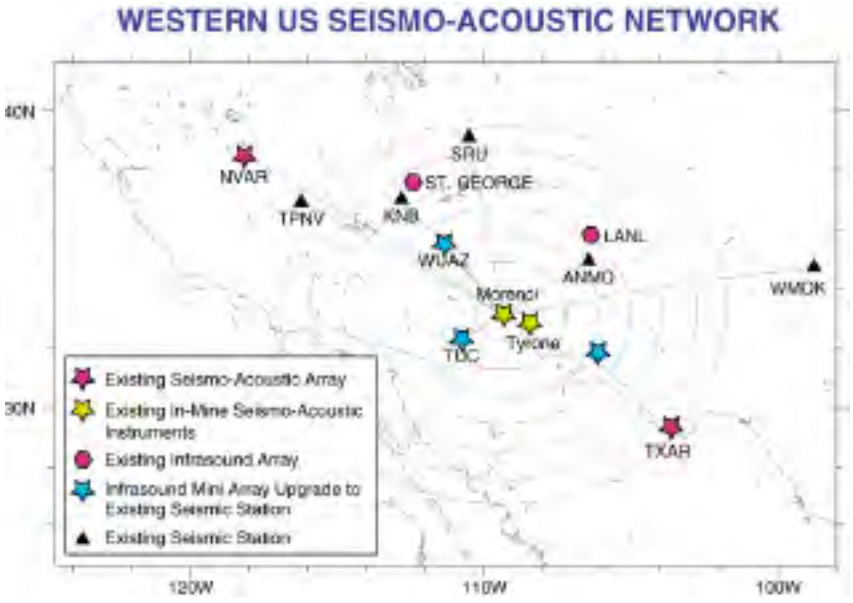


Figure 1: Map depicting the seismo-acoustic array that is being used to study the effect of mining practices and atmospheric models on the generation and propagation of seismic and infrasound signals.

The resources in this seismic and infrasonic network (Figure 1) will provide the opportunity to study seismo-acoustic signals (and seismic alone) from a large number of blasts in order to constrain both source and propagation path effects. In addition to this permanent array, a set of five portable seismo-acoustic

data acquisition systems have been constructed for the purposes of filling in the details of propagation path effects between the network stations.

Installation of the infrasound components to TUC and WUAZ are continuing in the summer of 2000 as well as the establishment of the seismo-acoustic site near El Paso, Texas. Parallel with this installation has been the construction of a ground truth data base from the majority of the resources in the network including the ground truth stations in the mines. We report on preliminary findings from this data set.

RESEARCH ACCOMPLISHMENTS

In-Mine Monitoring Systems for Ground Truth. The in-mine monitoring systems consist of a three-component broadband STS-2 (Figure 2) sensor and RefTek digitizing and archival system and small aperture acoustic array.

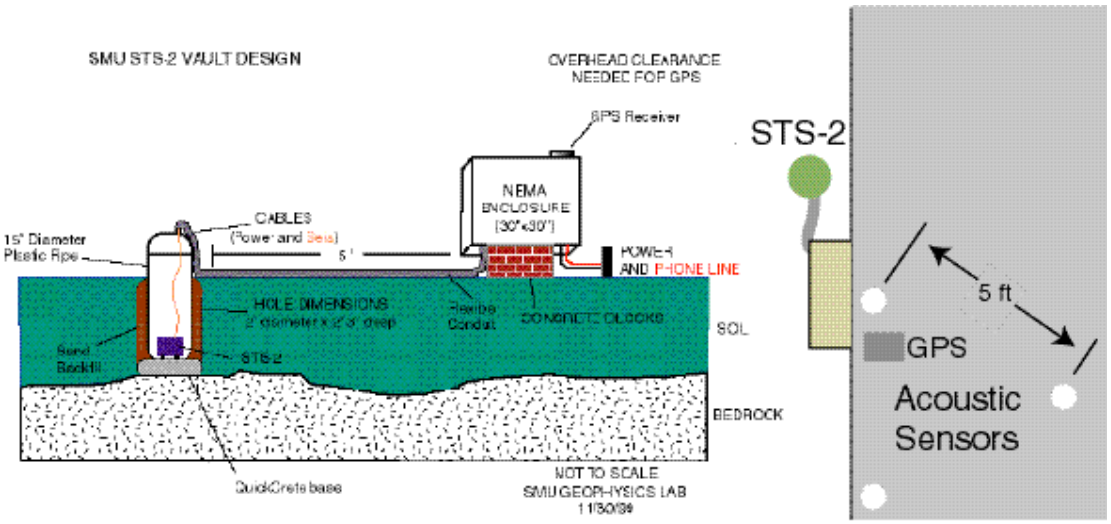


Figure 2. Schematic of the vault design and NEMA enclosure for in-mine deployments. The relative locations of the seismometer and acoustic gauges are shown to the right.

The recording devices for the system are housed in a 30" X 30" standard NEMA (Figure 3) enclosure. The RefTek 72A-08 digitizer is attached to a 4GB hard disk by a SCSI cable. Also, monitoring the data flowing into the hard drive is another computer-- the RefTek 114. This unit analyzes the data for triggered events and either dials out with event information or can be accessed for remote inquiry. Raw data from the hard drive can be transferred from the station to SMU where analysis for start time, shot size, and additional parameters occurs. Electrical power for each station is provided by a 12-volt car battery recharged by a trickle charger connected to 110 VAC. The total system amperage draw is 1.2 amps facilitating the use of commercial power as opposed to solar power. Accurate timing information at each station is obtained via GPS satellite clocks mounted to the top of the enclosure.

The instrument deployment in the Morenci Mine is illustrated in Figure 4 with similar equipment at Tyrone, NM. The site is centrally located in the main pit of the mine and provides coverage for the entire mine. The ore body at the Morenci mine is a large granite/granodiorite complex that has undergone hypogene alteration during the Laramide orogeny. The ore body is bounded on all sides by normal faulting. The current blasting method used at Morenci is designed to fragment the material and does not involve material casting. The 62' holes (that includes 50' for the bench and 12' subgrade) are drilled with a 12.25" or 13.75" drill bit. The drilling is conducted on a 24 hour operations schedule, while blasting is limited to daylight hours. An ANFO slurry is then loaded into the holes to a depth of 28-30'. Above the ANFO, the hole is stemmed with drill cuttings. The production at Morenci calls for approximately 300-400 holes per day with between 1500-2000 lbs/hole. The blasting engineers use 17-40 msec non-electric

surface delays between each hole firing, and approximately 80% of the shots are designed in a Chevron pattern with the remainder being fired en echelon.

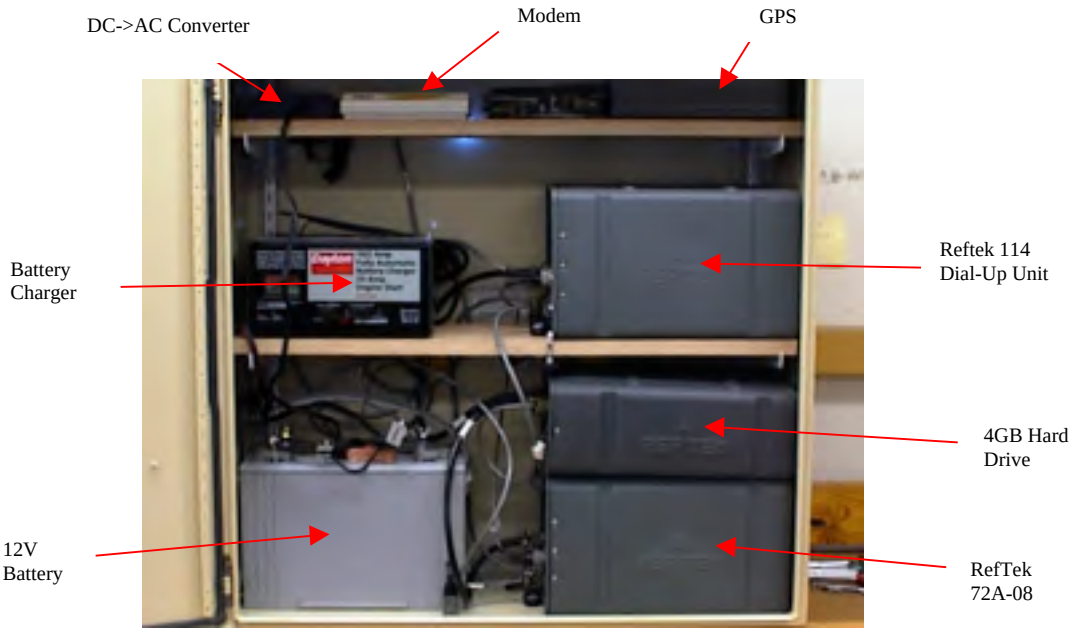


Figure 3. NEMA enclosure housing RefTek data acquisition equipment, including the RefTek 114 dial-up unit.

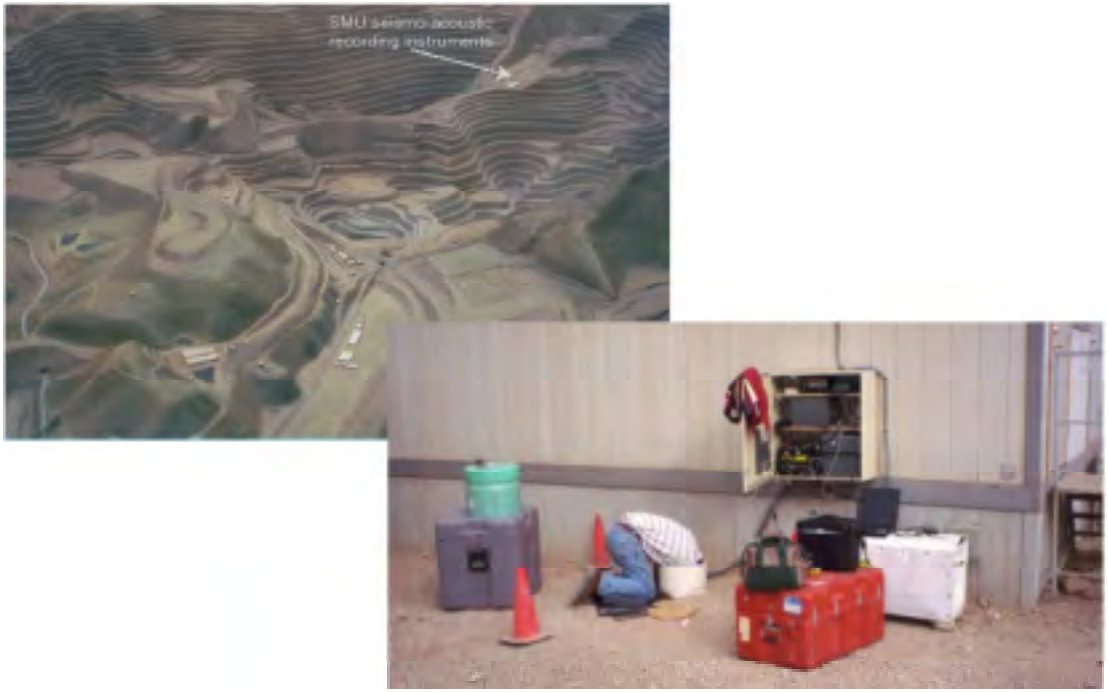


Figure 4: The pit location of the in-mine system at Morenci is illustrated in the upper left. The actual system during installation is pictured in the lower right.

Regional Seismic and Infrasonic Installations. The regional instrumentation that is being installed under this work is designed much like the in-mine system based upon Ref Tek data loggers and Ref Tek 114 where there is telephone service. The power system is solar at the remote sites. The infrasonic component consists of three, Chapparel Model 2 microphones modified to operate at 12 volts. The three sensors are arranged in a triangular pattern with 100 m separation. Eight, 25' porous hoses as illustrated in Figure 5, provide noise reduction.



Figure 5: One element of a regional infrasound array. The porous hoses are summed by the manifold shown in the lower right, which is connected to the Chapparel Model 2 microphone.

Seismo-Acoustic Network Results. The in-mine stations were deployed in January 2000 followed by the initial regional infrasound stations. A preliminary data base of ground truth events has been built and provides the basis for the analysis reported. An example event is reproduced in Figure 6 including the in-mine and regional data. This particular explosion is from Morenci and illustrates the types of regional signals that this blasting generates.

For purposes of this preliminary summary we have focused on a limited collection of events with ground truth from the mine. The events and their characteristics are summarized in Table 1. There are several interesting conclusions that can be drawn from this ground truth data set. Shot sizes ranged from 10,980 to 605,820 lbs, almost two orders of magnitude. It is also worth noting that it is often the case that multiple patterns or arrays of explosions may be simultaneously or nearly simultaneously detonated producing a complex interaction that may be seen at local and regional distances. The source duration, as quantified by the shot delay times, span a relative narrow range between 0.30 to 2.19 s. Two of the patterns (Events 6 and 8) were composed of shots that included no delay times. A wide-range of blasting practices is reflected in this tabulation providing an opportunity to quantify the effect of these source parameters on the seismic and infrasonic signals.

The in-mine acoustic signals that accompany the events listed in Table 1 are reproduced in Figure 7a. One can identify a range of amplitudes and wave shapes reflective of the variation in blasting practices. Event 1, which is also reproduced in Figure 6, consisted of the detonation of three distinct explosive patterns. This source characteristic is reflected in the complex pattern in the acoustic waveform. A filter panel for Event 1 (Figure 7b) further illustrates the complexity of the waveform produced by the detonation of the three patterns. The in-mine acoustic frequency content is quite broadband extending from several seconds to tens of Hertz.

Contrasting the acoustic signal from Event 1 with that from Event 3 (single pattern), illustrates that the single source produces a simple acoustic pulse that might be used to interpret the more complicated detonations. These results also suggest that the in-mine observations can be used in developing ground truth from the blasts and identifying multiple pattern shots. One can also imagine that a combination of

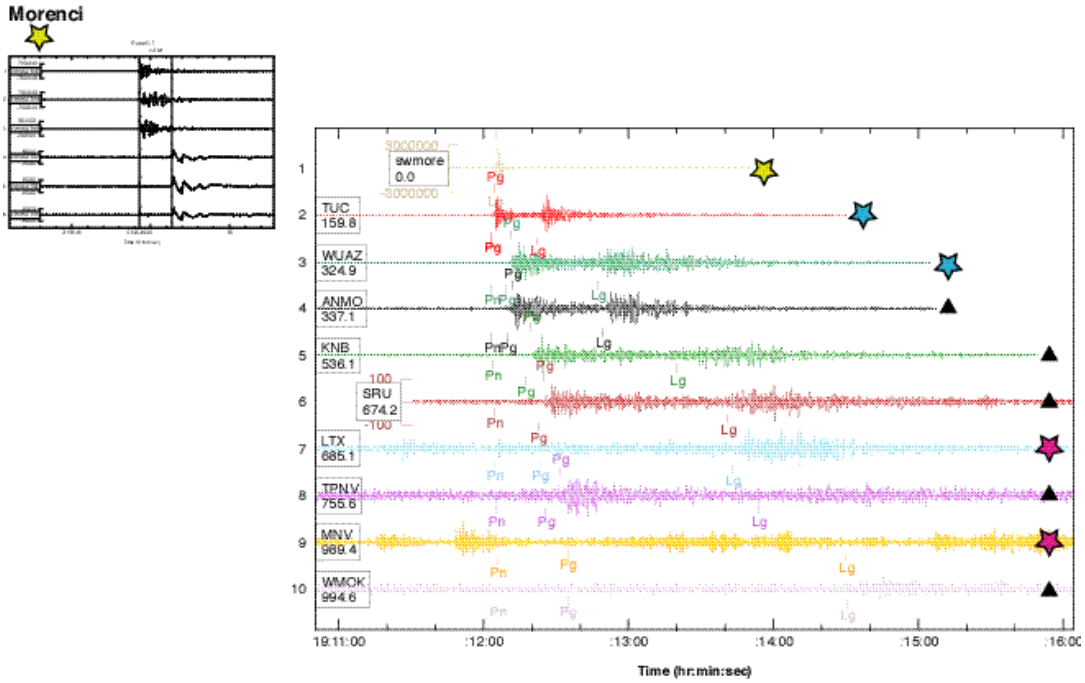


Figure 6: The in-mine seismic (first 3 waveforms) and acoustic data (second 3 waveforms) (upper left) and regional network data (seismic) (lower right) from a Morenci blast. The symbols to the right of each waveform correspond to the station types illustrated in Figure 1.

Table 1: Blast Parameters

Event #	Date	Number of Patterns	Total Charge in lbs.	Shot Duration (s)
1	3/13/00	3	184320 90850 50750	0.88 0.65 0.30
2	3/13/00	2	108620	0.43
3	3/10/00	1	31450	0.83
4	3/10/00	1		
5	3/10/00	1	102620	0.54
6	3/09/00	2	10980	0.00
7	3/08/00	1	385070	1.13
8	3/07/00	2	170870 18640	0.80 0.00
9	3/06/00	1	36110	0.95
10	3/03/00	3	141030	0.25
11	3/03/00	1	83100	1.29
12	3/02/00	1	55930	0.85
13	3/02/00	2	35170 125730	0.93 0.78
14	3/02/00	1	19070	0.69
15	3/01/00	2	241180 286330	0.84 0.85
16	2/25/00	1	605820	2.19
17				
18	2/24/00	3	32400 50790 23710	0.45 0.79 0.61

seismic and acoustic observations could be used for locating events within the mine. As Figure 4 illustrates, the mine is quite large with blasting in number of different areas.

The peak amplitude of the acoustic signal from the detonation of each pattern listed in Table 1 was plotted against the total amount of explosives (Figure 8a). The data indicates a strong correlation between peak amplitude in the acoustic signal and the total amount of explosives. There are three data points that fall outside this positive correlation which warrant further study.

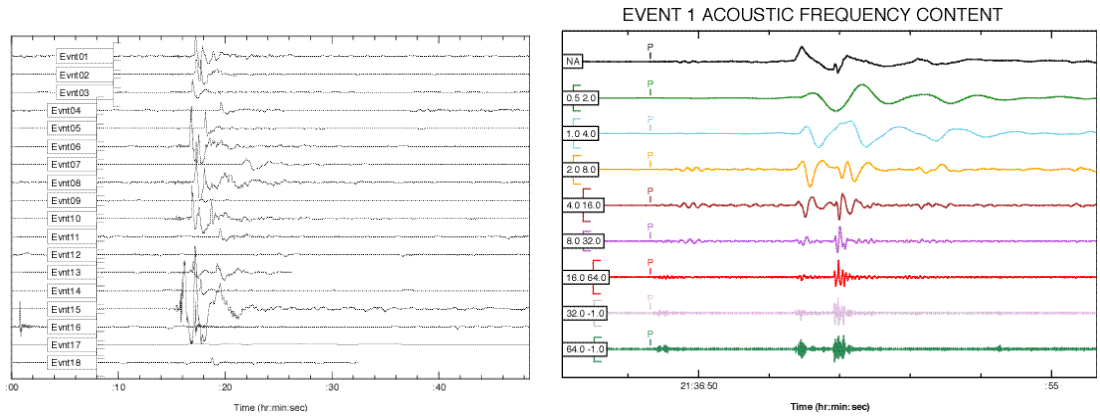


Figure 7: a-left) Acoustic signals from the in-mine instrumentation illustrated in Figure 4. The signals from the eighteen events for which ground truth information is listed in Table 1 are included. b-right)Bandpass filter panel for the in-mine acoustic data from Event 1.

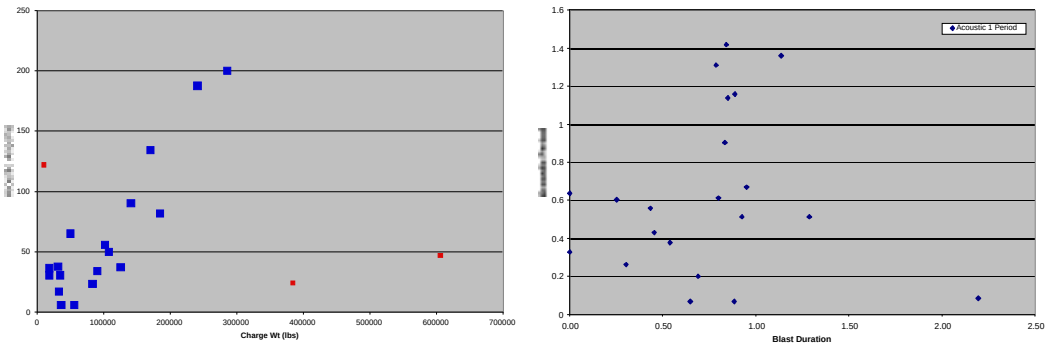


Figure 8: a-left) Peak acoustic amplitude from the in-mine data is plotted against the total explosive yield for the shots listed in Table 1. b-right) The pulse width of the acoustic signal is plotted against explosive source duration as defined by the shot delay times.

There is not as clear of a relationship between the period of the acoustic signal and the duration of the blast. Signal period does increase with source duration although it appears from the data in Figure 8b that there is more than just blast delay times that are contributing. Little is known about these individual shots other than information gathered from the blasting log.

A complementary analysis of the in-mine seismic data for the events in Table 1 was also undertaken. The vertical waveforms from the STS-2 for the same events is reproduced in Figure 9a. The STS-2 was installed in hopes of exploring the long period part of the signal at close ranges. Careful examination of the data suggests that clipping is experienced for the largest of the signals. A filter panel of the vertical waveform from Event 1 (unclipped) is reproduced in Figure 9b. This plot illustrates that the signals have significant long period energy, particularly for the shear arrivals. The compressive energy dominates the highest frequencies.

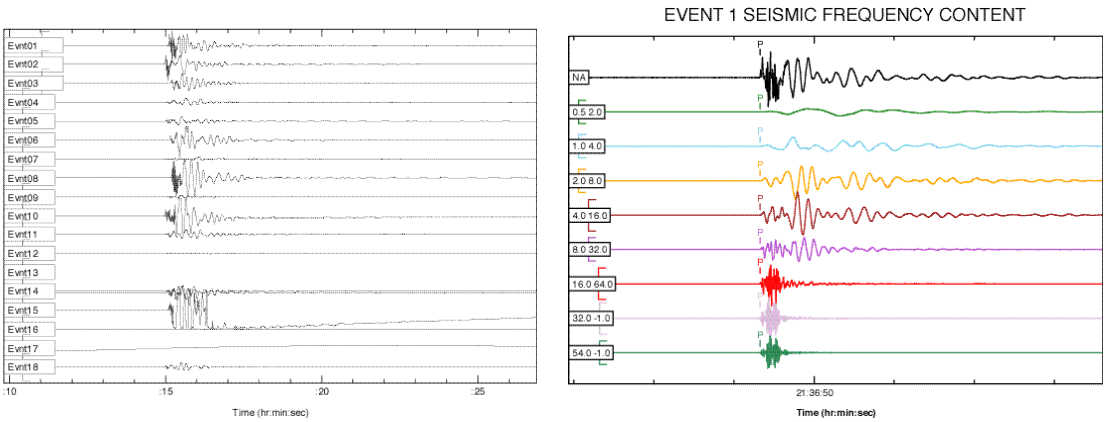


Figure 9: a-left) Vertical seismic signals from the in-mine instrumentation illustrated in Figure 4. The signals from the eighteen events for which ground truth information is listed in Table 1 are included. b-right)Bandpass filter panel for in-mine seismic data from Event 1.

Unlike the acoustic data, there appears to be little relationship between peak seismic amplitude and total amount of explosives. Typically the delay patterns developed for mining blasts are designed to maximize rock fragmentation and minimize ground motion within the mine and the surrounding area at frequencies above several Hertz. The peak amplitude data reproduced in Figure 10 supports this interpretation in contrast to the acoustic signal. It appears that the in-mine acoustic signals may better reflect the total size of the mining explosion whereas the seismic data may be constrained by the something like the maximum amount of explosives per borehole or per delay period. The in-mine data developed during this study will provide the opportunity to further explore these effects. No attempt has been made to correct for spatial decay at this preliminary stage which can also be an important effect for sources in a mine as big as that illustrated in Figure 4.

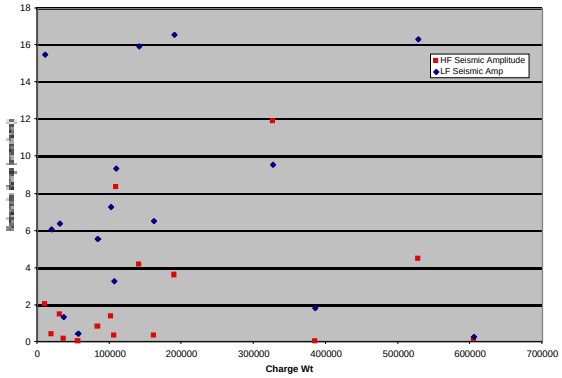


Figure 10: Peak amplitudes from the in-mine seismic data were measured in two bands, high frequency (HF - red symbol) at 20 Hz and wide band (LF - blue symbol) centered near 5 Hz.

The regional seismic data from one of the regional seismic stations (TUC) is summarized and compared to the ground truth information. Time domain peak amplitudes for the three regional phases, P_g, L_g and R_g were measured and plotted against total charge weight in Figure 11. The amplitudes for each phase vary by an approximate order of magnitude. Generally the L_g amplitudes are the largest. The data indicates a general increase in amplitude with total explosive yield.

Subsequent analysis of the complete network of regional data will provide a quantification of regional variations in amplitude and frequency content of the signals. Relating this to ground truth information such as that reproduced in Table 1 will provide the basis to assess important monitoring issues for small size

explosions. Although unanalyzed at this point, the explosions fired with no delays provide an important control in this analysis.

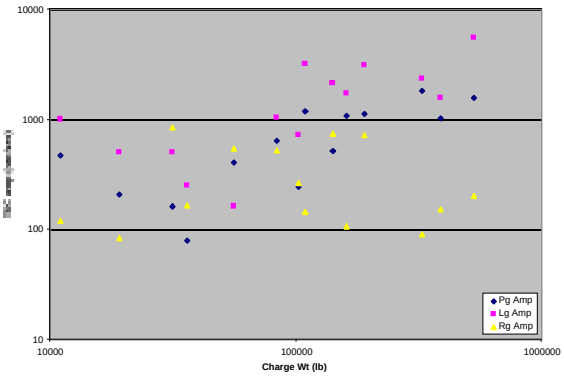


Figure 11: Peak amplitudes of the regional phases P_g, L_g and R_g measured at the regional station TUC (Figure 1) for the events listed in Table 1.

CONCLUSIONS AND RECOMMENDATIONS

The development of an integrated data set of ground truthed explosions that include multiple seismic and infrasonic observations across a regional network is underway. Critical to this study is the development of the ground truth information which has motivated the installation of seismic and acoustic instruments in two hard rock copper mines. Preliminary analysis of this data indicates that the blasting practices from such mines are quite different from coal cast blasting (Pearson *et al.*, 1995) including the near-simultaneous detonation of multiple explosive patterns and shots with no delays. Since these explosions are primarily designed to fracture rock, there is little casting or horizontal movement of the material. Figure 12 includes four frames from a video of a hard rock mining explosions and captures the relatively short time duration and the minimal post shot displacement.

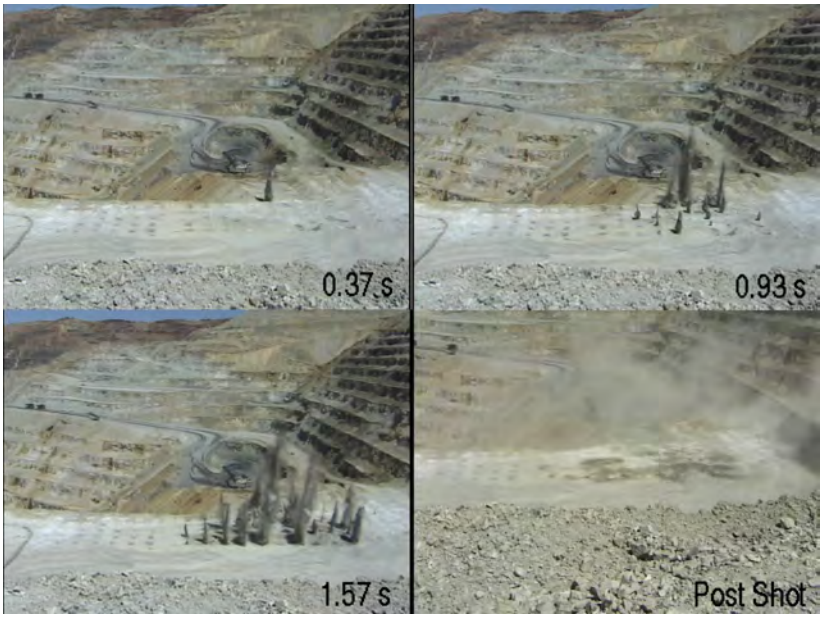


Figure 12: Four video frames from a hard rock mining explosion designed to fragment the material. The relative source time is designated in the lower right of each image.

The completion of the regional network is anticipated in the summer of 2000 providing the opportunity to extend the data base further. The network will remain in place in order to document the effects of seasonal variations in the atmosphere on the infrasound signals generated by these mines. This data set is intended to support a modeling effort to quantify infrasonic wave propagation effects as well as investigate source information that may be retained in these regional signals.

Preliminary analysis of the combined in-mine and regional data sets illustrates the utility of such studies in quantifying source and propagation path effects. The in-mine acoustic data suggests a strong source contribution that must be compared to the regional data. This data is also useful in identifying complex blasting practices that may include the detonation of multiple explosive patterns over time periods of a second or less. The implication of such a blasting practice on regional seismic and infrasonic signals will be explored. The time separation between patterns could be responsible for low frequency spectral scalloping that has been observed by other researchers.

Portable seismic and infrasonic stations will be deployed to quantify the effects of range on the infrasonic signals filling in between the semi-permanent stations diagramed in Figure 1. This data along with atmospheric models in the region will provide the basis for extension of an infrasonic modeling effort.

REFERENCES

Hagerty, M. T., W.-Y. Kim and P. Martysevich, 1999. Characteristics of Infrasound Signals Produced by Large Mining Explosions in Kazakhstan, *Proceedings of the 21st Seismic Research Symposium Technologies for Monitoring the Comprehensive Nuclear-Test-Ban Treaty,* p.123-132.

Hedlin, M. A. H., B. W. Stump, D. C. Pearson and X. Yang, 2000. Identification of Mining Blasts at Mid- to Far-Regional Distances Using Low Frequency Seismic Signals, accepted *Pageoph.*

Heuze, F. and B. Stump , Editors, 1999. Mine Seismicity and the Comprehensive Nuclear-Test-ban Treaty, Report of a Working Group from Government, Industry and National Laboratories, *LA-UR-99-384 Los Alamos National Laboratory, UCRL-ID-132897 Lawrence Livermore National Laboratory,* 70 pp.

Hsu, V. and B. W. Stump, 1997. Seismic and Infrasonic Arrays at Pinedale Seismic Research Facility (PSRF), Wyoming: Synergy of Infrasonic and Seismic Signals from Mining Explosions, *Seismological Research Letters, 68,* p. 320.

Pearson, D.C., B. W. Stump, D. F. Baker, C. L. Edwards, 1995. The LANL/LLNL/AFTACK Black Thunder Mine Regional Mining Blast Experiment, *17th Annual PL/AFOSR/DOE Seismic Research Symposium,* 562-571.

Sorrells, G. G., E. Herrin and J. L. Bonner, 1997. Construction of Regional Ground-Truth Data Base, *Seismological Research Letters, 68,* 743-752.

Sorrells, G.G., J.G. Swanson, and I Tibuleac, 2000. Seismo-Acoustic Studies at the Nevada Seismic Array, *Proceedings of the 22nd Seismic Research Symposium*(this volume).

Stump, B., C. Hayward and S. M. House, 2000. A Small Aperture Seismo-Acoustic Array - Signal Assessment, *Proceedings of the 22nd Seismic Research Symposium*(this volume).

AKNOWLEDGEMENTS Jessie Bonner for his ideas and contributions to the early stages of this work. Nick Hickson, James Hanson and Lia Lowry of PD Morenci have provided valuable support for the first in-mine system. Colin Sharpe, Joe Ortega and John Gregory of PD Tyrone made the second in-mine system possible. The regional network data is being made available with the cooperation of Rod Whitaker (LANL), Terry Wallace (U of A) n and Diane Doser (UT, El Paso). Craig Pearson, C.L. Edwards and Diane Baker (LANL) have provided help with instrumentation issues. The contributions of our engineer, Karl Thomason, who passed away recently, will be greatly missed.

A SMALL APERTURE SEISMO-ACOUSTIC ARRAY
Signal Assessment

Brian Stump,Chris Hayward, and Sara Mihan House, Southern Methodist University
Myung-Soon Jun and Jeong-Soo Jeon, Korea Institute of Geology, Mining and Materials

Sponsored by Defense Threat Reduction Agency
Contract No. DSWA01-98-C-0131

ABSTRACT

The Korea Institute of Geology, Mining, and Materials and Southern Methodist University jointly designed, installed, and operated a 1-km aperture four-element seismo-acoustic array northeast of Seoul, Korea. Joint analysis of the seismic and acoustic recordings can be particularly important in identifying and locating industrial blasting sources. Results from this research array are being used to assess the importance of co-located seismic and acoustic sensors and to determine the utility of small aperture arrays for regional monitoring. In the two months analyzed, there were many more acoustic signals than seismic. Approximately 1/4 of all seismic signals is associated with an acoustic arrival and is presumed to be from mining regions. The vast majority of seismo-acoustic observations come from sources in the 30 - 200 km range in contrast with the shadow zone of no acoustic returns predicted by average atmospheric models. Event location is based upon regional phase identification using the array and back azimuth estimates from both the seismic and acoustic data. Despite the small size of the array, event clusters are identified at regional distances. Waveform comparisons of these clusters indicate that the events are from common source areas. Within the event clusters, there is more event-to-event variation in the acoustic than the seismic signals suggesting the importance of variable atmospheric propagation. The high-Q path of the Korean Peninsula results in regional seismograms that have significant energy to frequencies as high as 16 Hz. The results from this study suggest that small aperture seismo-acoustic arrays such as those similar arrays at Lajitas, Texas (TXAR) and at Mina, Nevada (NVAR) can be important tools in improving

Key Words: Seismo-acoustic, array, regional monitoring, infrasound

OBJECTIVE

The objective of this joint Southern Methodist University (SMU) and Korea Institute of Geology, Mining and Materials (KIGAM) program is to design, procure, integrate, test, install and operate a seismo-acoustic array in the Republic of Korea in order to create a ground truth database as has been done for Lajitas, Texas (TXAR).

RESEARCH ACCOMPLISHMENTS

Array Description The Korean Peninsula provides a unique laboratory for studying regional seismic wave propagation problems in the context of the Comprehensive Nuclear-Test-Ban Treaty (CTBT). There are numerous three-component 40 or 100 samples/s broadband seismic stations in the region operated by KIGAM (Figure 1, closed triangles) as well as the new seismo-acoustic array (CHNAR) jointly operated by SMU and KIGAM. A variety of natural and man-made sources provide ample opportunity for characterizing both wave propagation and source effects within the region (Figure 1, circles and x's).

The focus of this current work is on the analysis of the seismo-acoustic data gathered from the recently installed seismo-acoustic array, CHNAR, in the far north of the Republic of Korea (Figure 1). The array has four-sites about 1 km apart (Figure 2a). Each site has a vertical GS-13 seismometer and a surface acoustic hose array. Data is transmitted from the sites using 2.4 GHz spread-spectrum radios to the central hub. There at the array hub, the data from all the stations are combined, formatted into an Alpha protocol data stream, and then transmitted to the Korea National Data Center by an additional set of spread spectrum radios and a leased telephone line. At the Data Center, CHNAR data is forwarded to SMU.

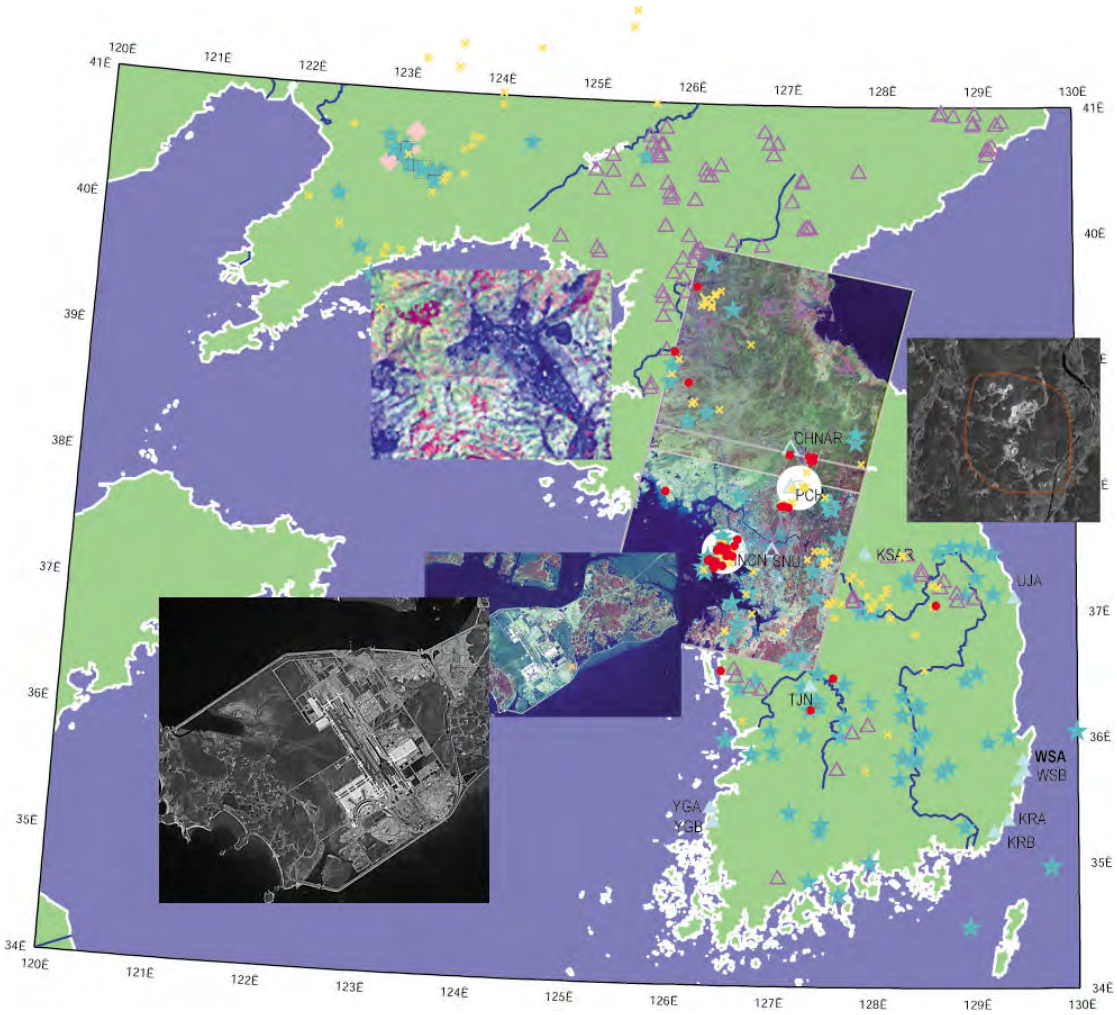


Figure 1. Map of Korean Peninsula that includes the new seismo-acoustic array, CHNAR, the IMS array, KSAR, as well as a number of broadband stations. Superimposed on the map are a number of events including those from this study designated as closed -red circles (seismo-acoustic) and yellow x's (seismic only). Events from KNDC bulletin are marked as blue stars. Ground truth studies based on event locations are highlighted as white circles. Accompanying Landsat images for these regions are also plotted.

The array central element (CHN00) is shown in Figure 2-right. The seismometer is emplaced at the bottom of a 10 m cased borehole. An eleven-element hose array (25' each hose) is deployed at the surface for the purpose of reducing wind noise. At most sites, the hose arrays are covered by low growing grasses. A 1-meter fence to protect the array from intrusion surrounds each hose array (not shown in the figure). The area around the array experiences little cultural activity other than rice farming. The hose array is connected to an acoustic sensor suspended in the borehole. All sites operate on solar charged batteries and telemeter the data to the central hub. Seismic and infrasound channels are sampled at 40 Hz thus providing high-frequency data for regional analysis. A weather station at the hub records local temperature, wind speed and direction.

At sites CHN00, CHN01 and CHN02, the seismometer boreholes are grouted into competent Proterozoic mica schists. Site CHN03 is in a localized weathered Quaternary Basalt flow that appears to affect the regional signals above 10 Hz. .

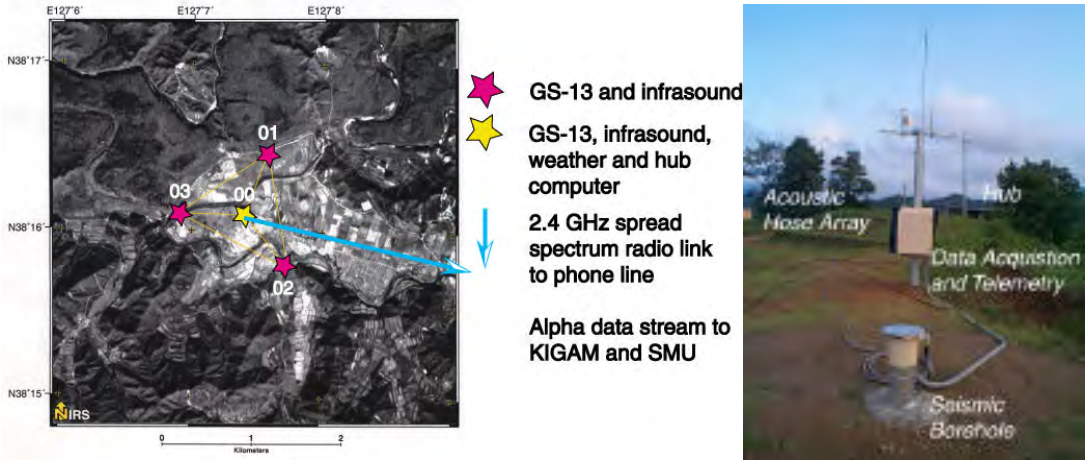


Figure 2 Left: The three outlying sites (CHN01, CHN02, CHN03) are shown in pink. The central site (CHN00) includes the array hub. The blue arrow indicates a radio link to a commercial phone line. Right: The annotated picture of the central site shows a typical site. The borehole contains the GS-13 and the acoustic sensor. The acoustic hose array is on the surface (middle left). The pole-mounted enclosure includes batteries, solar panels, digitizer, and spread spectrum radio. The radio antenna and GPS antenna are mounted on the left of the top crosspiece. The thin finger-like pole at the top is for lightning protection. In the background the mast for the array hub and weather station is positioned just outside the hub building.

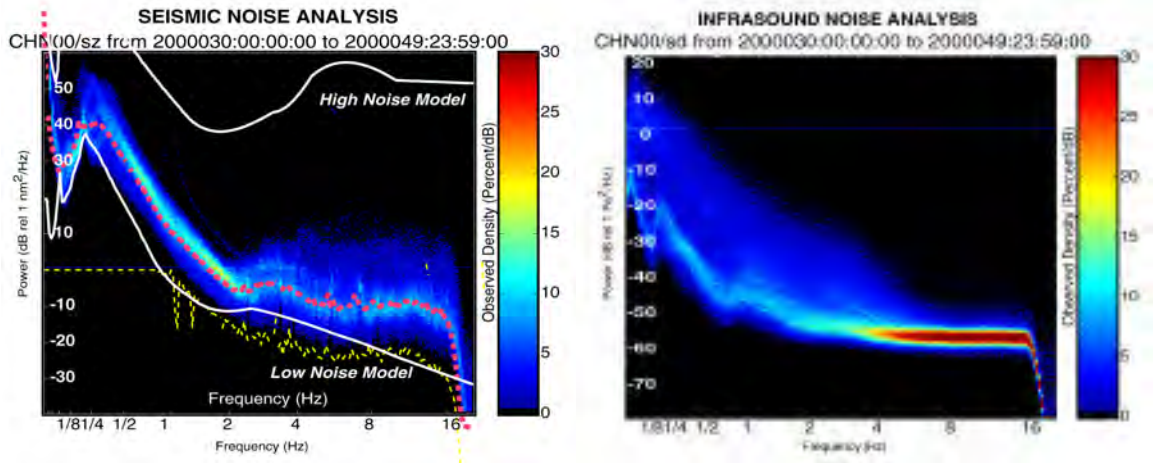


Figure 3: Seismic and acoustic noise estimates from array element CHN00. Colors in the plot represent the observed power-normalized probability density at each frequency from the 20-day analysis. The median for the seismic noise is represented by the red dotted line. The left image is for the seismic data and the right image is for the infrasound data.

Seismic and infrasound noise analysis was done for the twenty-day period from Jan 30, 2000 to Feb 18, 2000, while the site was snow covered. This time period was divided into 10-minute non-overlapping blocks. In each 10 minute block, a 50% overlapped, 104.8s block Welch method was used to estimate the noise spectrum. The resulting noise estimates for one site after instrument correction are shown in Figure 3. Some seismic noise blocks approach the low noise model (as shown by the range of blue values) but the most frequently observed noise level (shown by the red dotted line) is 10 or more dB above this model. Seismic noise levels at CHNAR are well below the high noise model (the upper white line in Figure 3) consistent with competent rock at a remote inland location. The infrasonic noise varies over a much broader range than the seismic noise. Microbarom noise shows as a peak between 1/4 and 1/8 Hz. Above 4 Hz, the infrasound noise spectrum flattens into instrument noise, probably due to the 50-foot aperture of the noise reduction hose array. The effect of the anti-alias filters at 16 Hz is apparent in both plots.

For this time period, the seismic noise spectral variance increases with frequency while the infrasound noise spectral variance decreases with frequency. For seismic noise, the high frequency variance probably reflects local noise sources. For infrasound noise, the reduced high frequency variance is due in part to the effects of the hose arrays. The general characteristics of the noise data for the entire array are well represented with the results from site CHN00. There are additional inter-array variations reflective of the local effects. For example, CHN03 shows increased noise levels above 10 Hz resulting from the emplacement of the seismometer in the shallow (~15 m thick) volcanic layer.

Types of Signals The CHNAR array has contributed significantly to the accurate location and identification of local, regional, and teleseismic signals from a variety of seismic and infrasound sources.

An example of seismo-acoustic signals is given in Figure 4. In this case, the event was first located using the seismic data; distance was determined from the L_g-P time and back azimuth from FK analysis. The acoustic data was then searched for an associated arrival at 414.7s (the expected acoustic arrival time) and a similar back azimuth. This particular event comes from the NE at an approximate distance of 130 km.

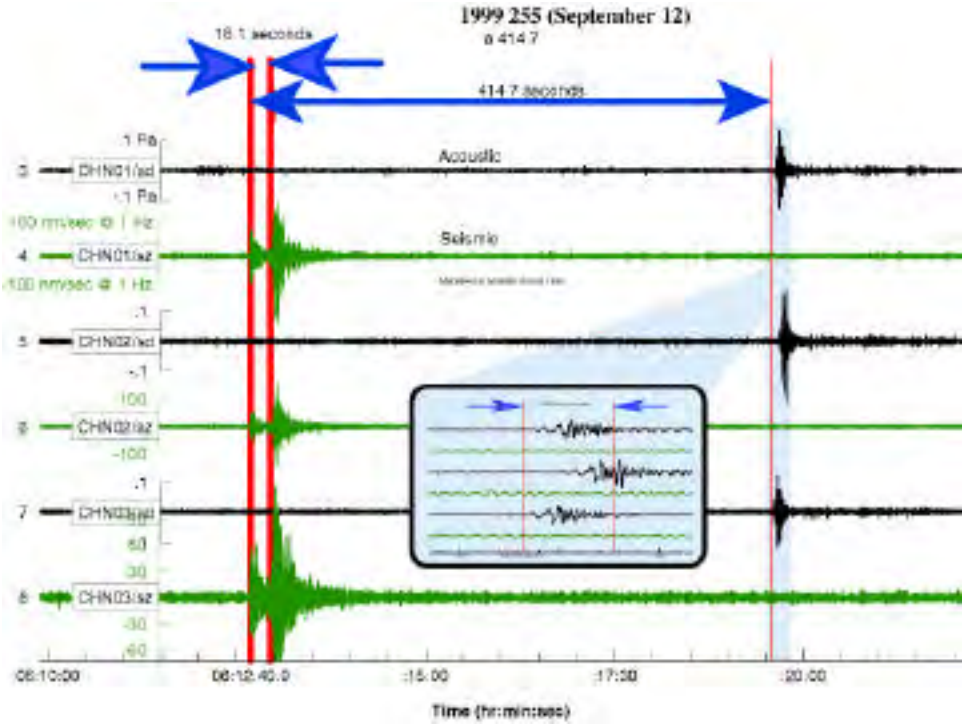


Figure 4: A regional seismo-acoustic signal recorded at CHNAR. The green traces are the seismic channels and the black traces are the infrasound signals. The infrasound arrivals are expanded in the small inset at the center of the figure. Black traces (acoustic) have be shifted relative to absolute time to fit them on the plot. All traces have been filtered in the 0.5 to 5 Hz band.

There are many more infrasound signals than there are seismic or seismo-acoustic. Many of these are distinct and easily recognizable from their waveform although their source or location is unknown. As an example, Figure 5, is a narrow band exponentially decaying signal with a 3.3 Hz frequency. Coupled with its FK direction, it would be easily recognizable should it repeat. In this example, there are no associated seismic signals.

Seismic, Seismo-Acoustic and Acoustic Event Statistics The two month period from January 1 to February 29, 2000 was chosen for a reconnaissance analysis of all seismic and seismo-acoustic signals. This time period overlaps with the period used for the noise analysis (Figure 3). This signal analysis was done to quantify the CHNAR's utility to detect and associate seismic and infrasound signals. One of the primary goals was to assess the identification of man-made signals from mining operations. Since regional

signals were the primary interest, both the seismic and infrasonic data were filtered from 1 to 5 Hz matching the expected best SNR and the flat part of the noise spectra (Figure 3). An analyst reviewed the data to form events.

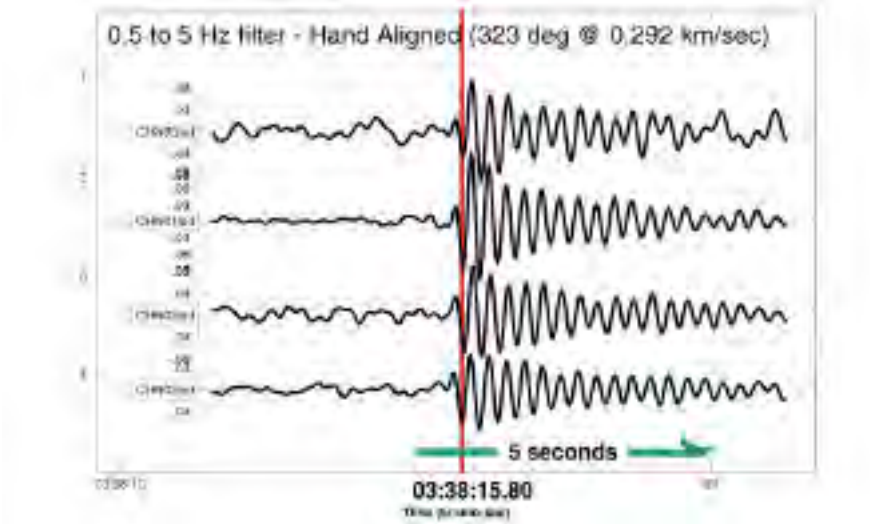


Figure 5: An example of a narrow band infrasound signal recorded at CHNAR. The signals have been time aligned in an attempt to estimate phase velocity and back azimuth.

The analyst formed events based on an interpretable seismic arrival. Regional phases such as P_g, P_n, PmP, L_g and R_g were identified based on arrival order, frequency content and FK phase velocity estimates. For each of the associated phases, FK back azimuth estimates had to be consistent. A crude distance estimate was made using L_g-P time and multiplying by 8 km/s. This procedure provided an initial event location that then triggered a search for associated infrasound arrivals in a window defined by with group velocities of 250 to 400 m/s. If a coherent infrasonic signal was found in this window with a FK back azimuth consistent with the seismic estimates, then a seismo-acoustic event was formed.

The number of seismic events averages about 4 per day with as many as 12 in any one day (Figure 6). There are few events from day 35 to 41 (Feb 4-10) during the Spring Festival, a Korean national holiday. This seismic lull and the dramatic activity increase for the week prior to the holiday suggests that many of these seismic events may be man-made.

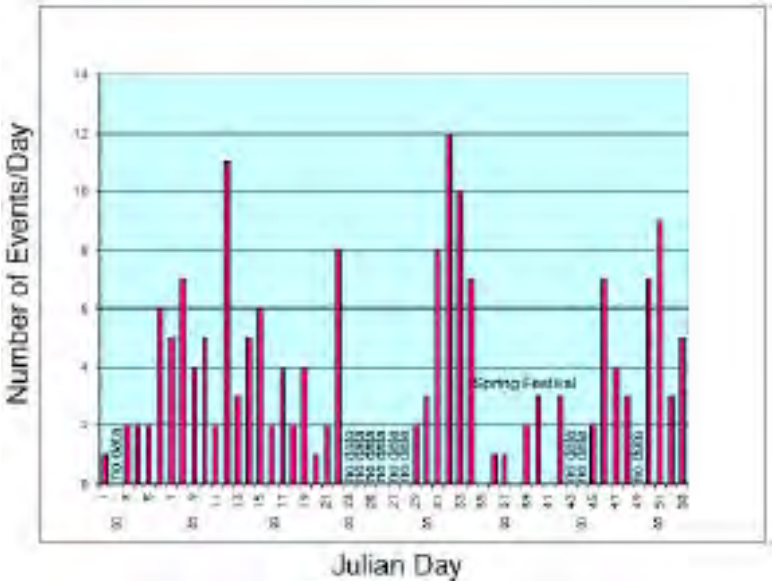


Figure 6: Number of seismic events as a function of Julian Day for the time period of the study, January-February 2000.

The man-made source is further supported by the origin time of day. An hourly binned histogram (Figure 7a) shows that the maximum number of seismic events, 25, occurs during the noon hour local time. The number of events increases dramatically in the mid-morning hours and then stops abruptly after 6 pm local time. A similar plot was made for the seismo-acoustic events and is reproduced in Figure 7b. All but one of the seismo-acoustic events identified during this study occurred during daylight working hours, 7am until 6 pm local time. These observations indicate that most of the signals received from CHNAR are associated with industrial operations such as mining.

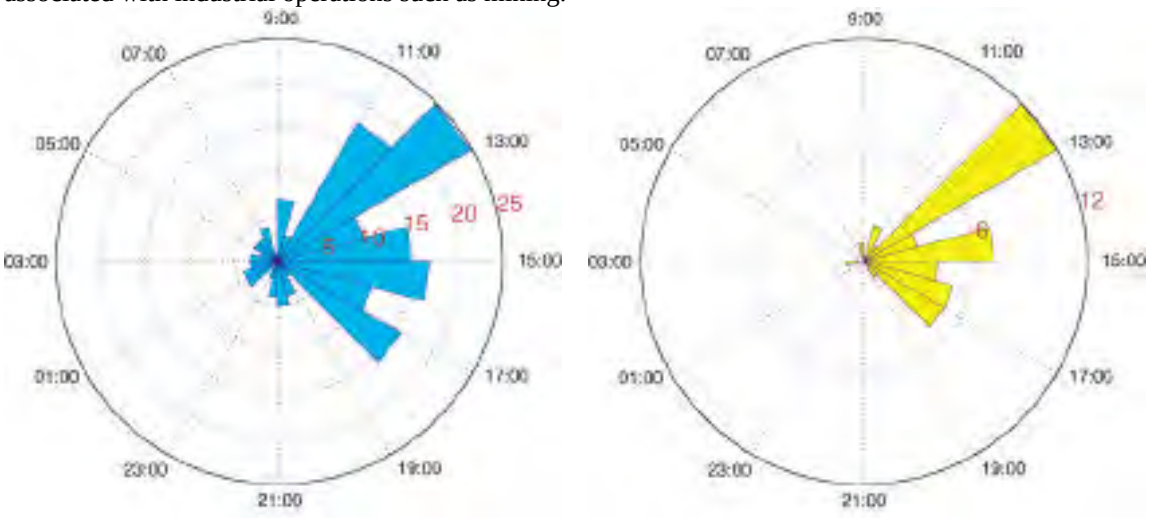


Figure 7: a) The number of seismic events identified using CHNAR during January and February are plotted as a function of local time in the image to the left (blue). b) The total number of seismo-acoustic events identified during this study as a function of local time is plotted to the right (yellow). Both plots indicated a concentration of events during local working hours.

The spatial distribution of seismic (red x) and seismo-acoustic (yellow o) events identified in the study are plotted as a function of average azimuth from CHNAR and L_g-P time (range ~ [L_g-P time] x 8 km/s) in Figure 8. Although all interpretation is based only on CHNAR, a single small-aperture array, the events cluster into a number of well-defined groups. Groups 1,4,5,6, and 11 include seismo-acoustic events constrained to day time hours and therefore suggest either a mining or construction source. Group 2 events occur at all hours but include no seismo-acoustic signals. Therefore they are probably associated with natural seismicity.

An average of 4 events/day (157 total events) occurred during the period-analyzed (Figure 8). Only 22% (35 events) are seismo-acoustic and have associated infrasound signals. Only one of the seismo-acoustic signal occurs at night and it is a local high frequency event.

It was obvious on even a casual perusal that on any day, there are many more infrasound signals than seismic. One week (19-25 February 2000) of infrasound data was comprehensively reviewed with the analyst examining all of the recorded infrasound data. An infrasound event was defined as visually correlated coherent signals across the array. For each infrasound event the analyst made an FK measurement of back azimuth and phase velocity summarized in Figure 9. 263 infrasound events were observed for this seven day period where the number of events a day ranged from 13 to 84, four to ten times higher than the number of seismic events. Like the seismo-acoustic events, the acoustic only events mostly occur during normal workday hours. The observed azimuths are from a very narrow range, primarily from the northwest, which is the direction of the prevailing winds during this time period.

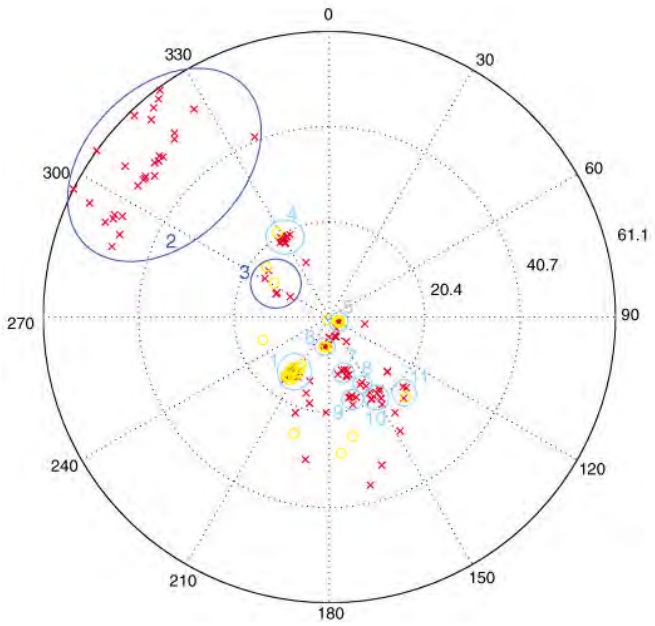


Figure 8: Event groups and locations for January-February 2000 using CHNAR. Average azimuth was determined from all associated arrivals. The distance (radius) is plotted as L_g-P time in seconds. A rough distance conversion may be calculated made by multiplying the plotted L_g-P time by 8km/s. The red x's are seismic events while the yellow o's are seismo-acoustic events. The events are subjectively divided into 11 groups. Dark blue ellipses indicate that some events within the group occurred during the night. Light blue ellipses indicate all events in the group occur during the day.

Event Clusters Event location and time-of-day clusters provide an opportunity to characterize seismic waveforms and infer the characteristics of sources. Clusters such as #1 in Figure 8 with the high number of seismo-acoustic events might be construction or mine related. Clusters such as #2 with no associated infrasound signals, and day and night occurrence might be earthquakes. In order to investigate these clusters further, waveforms for each cluster may be examined.

Events in Group 2, over 400 km to the NW of CHNAR, occur at all hours and have no associated infrasound signals. Waveforms for these events (Figure 10a) are very similar although the peak amplitudes span a factor of five. The modest P_g arrival and the following large L_g wave packet arrival are easily identified. At this distance an emergent P_n is the first arrival and can barely be seen in the second seismogram. For smaller events it is not discernable above background noise. For smaller events the range estimate is too near, when P_g is mistaken for the P_n first arrival. Inspection of the locations in Figure 8 suggests two linear trends in the locations for Group 2. The closer events are those for which P_g was mistakenly interpreted as a first arrival. When these mislocated events are moved to the correct range, the events form a single linear trend that overlaps the Tan Lu Fault in SE China. This further supports earthquake (non-industrial) source hypothesis.

The regional seismograms were bandpass filtered to investigate the frequency content of the regional arrivals. Figure 10b illustrates one of the events filtered into bands 0.05-0.5 Hz, 0.5-1 Hz, 1-2 Hz, 2-4 Hz, 4-8 Hz, 8-16 Hz. Similar results were found for the other events in the group. This display illustrates the relative spectral energy of Pg and Lg. The shear energy dominates the P energy at in all filter bands. This is consistent with an explosion source.

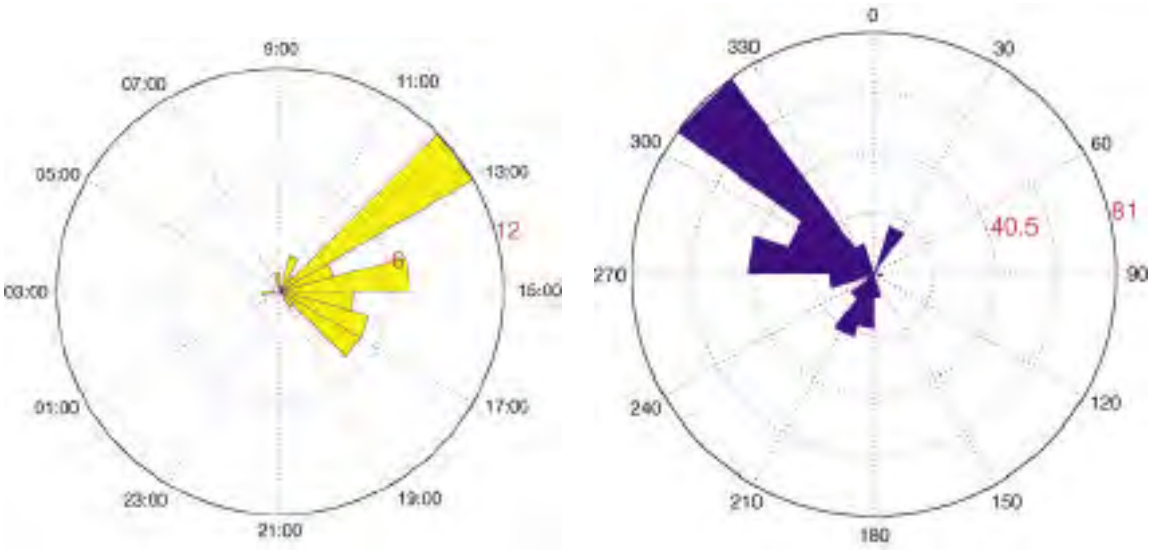


Figure 9: Summary results from the analysis of the infrasound data. (a)The left figure plots the number of events in hour bins (local time). (b)The right figure plots the number of events coming from different azimuths with respect to CHNAR.

An example from Group 1 (Figure 11a) compares vertical seismograms for signals hypothesized to be industrial or construction explosions. Most of the events in this group have associated infrasound signals (the seismo-acoustic source case). The source is approximately 120 km away and the waveforms include P_g, PmP and L_g arrivals. Although seismograms are similar, subtle differences in arrival time and waveshapes within the group warrant further study. The event-to-event amplitude range is small, no more than 6 dB.

The example Group 1 bandpass filtered seismogram (Figure 11b) show strong high frequency P waves and indications of an intermediate frequency surface wave. Both observations are consistent with an explosion source. Based on these observations the estimated source location was investigated for possible sources (ground truth investigation). In this region, construction is in progress for a new international airport to serve Seoul. At either end of the airport are two small mountains that are being explosively removed. Close-in measurements of one of these explosions validated them as the source of events for Group 1. This location is shown in Figure 1 along with the overhead imagery of the new airport.

Infrasound waveforms for all sites and three of the Group 1 events in Figure 11 are displayed in Figure 12. The move-out across the array and strong visual coherence is apparent and is used to identify an infrasound event within the predicted time window. Signal amplitude covers a narrow range of 0.1 to 0.2 Pascals. Although there is significant event-to-event waveform variation, single events show good correlation across the array event at relatively high frequencies. The signals are relatively high frequency (Figure 12b) with energy centered from 1 to 8 Hz. Similar spectra were found for the other infrasound signals from this and other clusters.

A similar investigation of the signals in Group 6, which included many seismo-acoustic signals, suggested a mining or construction sources. Investigation in this region followed by local measurements validated the source of signals from Group 6 as a granite quarry. The overhead imagery for this location is also included in Figure 1.

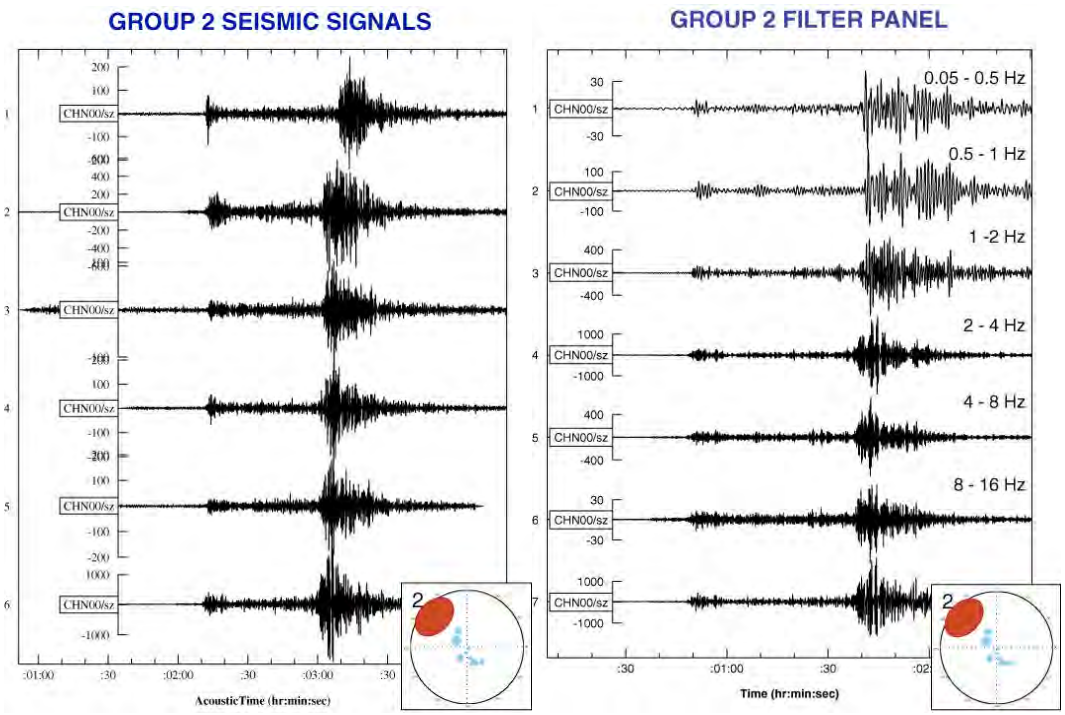


Figure 10: (a) Comparison of vertical seismograms recorded at Site CHN00 for six events from Group 2 in Figure 8. (b) Bandpass filtered seismograms of one event from Group 2.

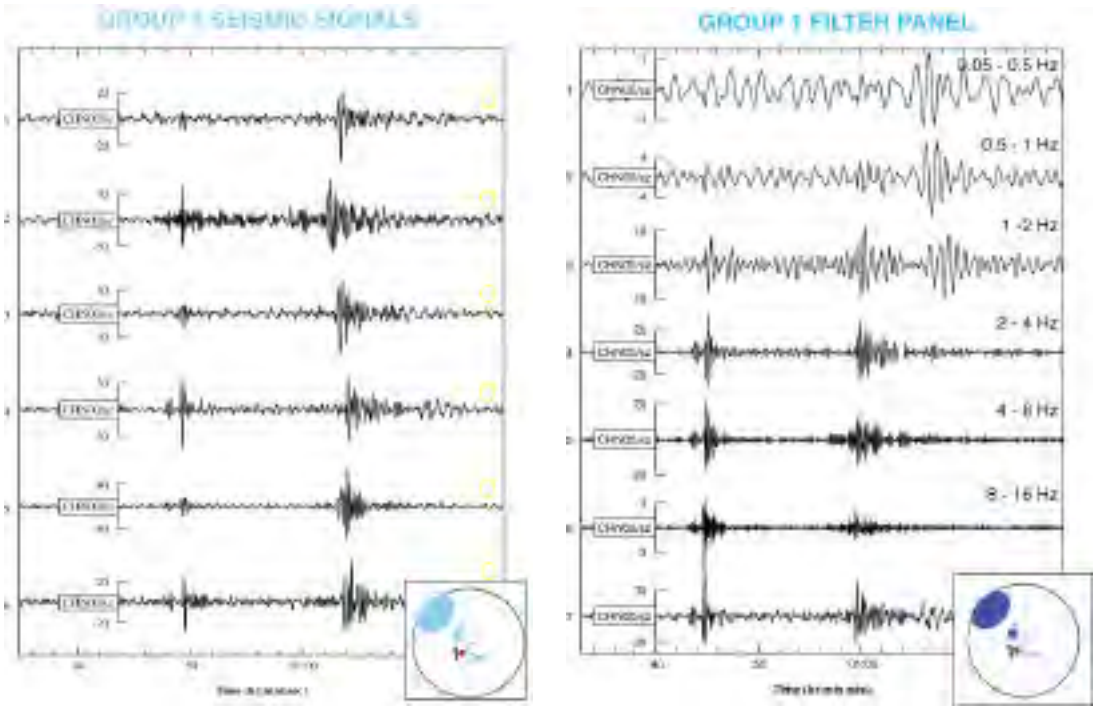


Figure 11: (a) Comparison of vertical seismograms recorded at Site 00 for six events from Group 1 in Figure 8. (b) Bandpass filtered seismograms of one event from Group 1.

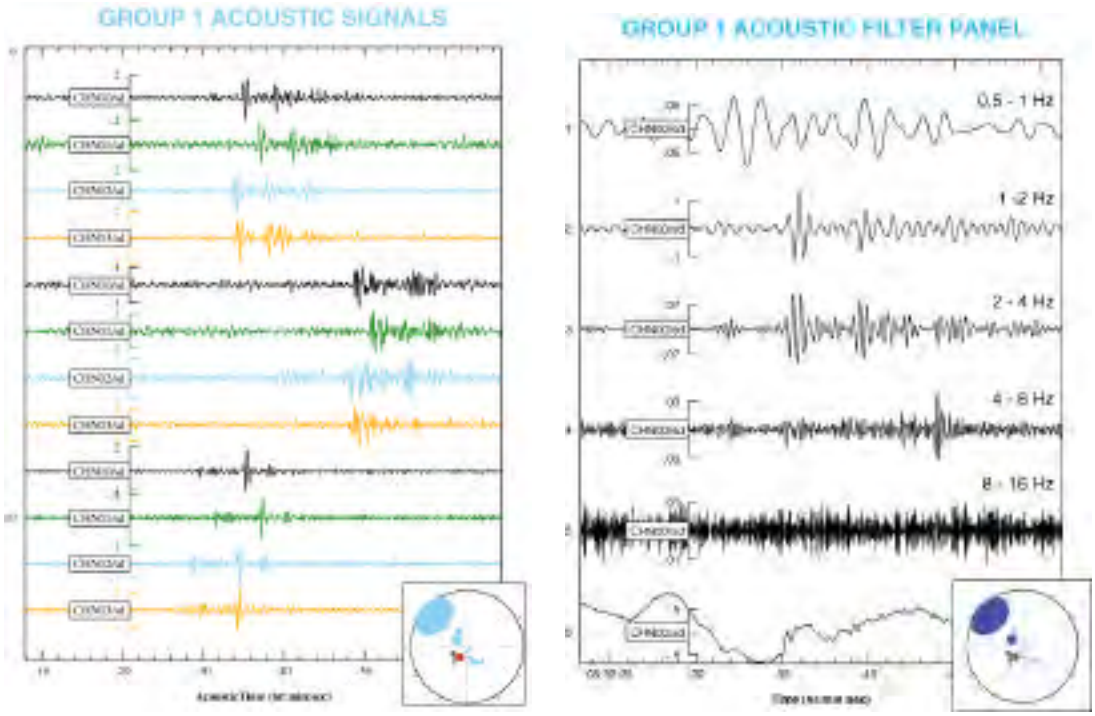


Figure 12: (a) Comparison of infrasound signals recorded across CHNAR from three Group 1 events (b) Bandpass filtered infrasound signal from one of these events.

CONCLUSIONS AND RECOMMENDATIONS

A small aperture array for seismo-acoustic signals has been designed, constructed and installed. Many seismic and infrasonic signals are observed daily. Nearly a quarter of all seismic signals has associated infrasonic arrivals. Most occur during normal local working hours. There are many more infrasonic signals than there are seismic. These observations suggest that a great deal of the activity observed is manmade.

Event locations based upon data from CHNAR cluster. Investigation of these clusters indicates great similarity in seismic waveforms. Two clusters of seismo-acoustic events were used to trigger a successful search for ground truth information. One source region was associated with construction blasting at a new airport and the second was a granite quarry.

Many of the seismo-acoustic signals are observed in the distance range of 50 to 200 km. Average atmospheric velocity models do not predict ray paths that return in this distance range. This observation and the correlation of the wind direction and predominant direction of low altitude winds suggest that local ducting may be important for these signals.

Additional work is needed in the interpretation and modeling of seismic and infrasound signals. Emphasis will be placed on gathering additional ground truth information to aid in this study.

ACKNOWLEDGEMENTS

The work of Karl Thomason, Nin-Chul Shin, Jason McKenna, Il-Young Che, Paul Golden, Dong Kyun Kim, Yong-Sung Kim, and Jung-Ho Park in the design, installation and operation of the array are acknowledged. This work could not have been completed without this enthusiastic and cooperative team not to mention significant helpings of kimchi.

PROGRESS ON THE ESTABLISHMENT OF THE CTBT IMS INFRASOUND NETWORK

A. Veloso, D. Christie, P. Campus, M. Bell, A. Langlois, E. Demirovic and P. Martysevich.
International Monitoring System Division, Provisional Technical Secretariat
Comprehensive Nuclear-Test-Ban Treaty Organization

ABSTRACT

The Comprehensive Nuclear-Test-Ban Treaty Organization has now been in operation for a period of three years. During this time, considerable progress has been made on the establishment of the IMS Infrasound Monitoring Network. This network consists of 60 array stations, none of which existed when the Treaty was opened for signature in September 1996. The network is designed to detect and locate all atmospheric nuclear explosions at any point on the globe with yields of 1 kt or more.

As of today, 60% of the site surveys has been completed and 10% of the stations in the network are sending data to the IDC in Vienna. By the end of 2000 it is expected that 70% of the site surveys will be finished and about 18% of the infrasound global network will be operation. Programs for site surveys and site preparation are in progress at Antarctic stations and preparations for the certification of a number of stations are underway. Infrasound stations will be certified after it has been demonstrated during a period of testing and evaluation that the station substantially meets PrepCom approved technical specifications and the stations operational performance is in accord with the requirements for an IMS monitoring station.

This presentation will be primarily concerned with an overview of progress to date on the establishment of the global infrasound network. In addition, this presentation will focus on the intrinsic difficulties that the IMS is faced with in the establishment of the infrasound network. This will be illustrated by examples from site surveys and station installations that have recently been completed.

Key Words: infrasound stations, International Monitoring System

An Optical Fiber Infrasound Sensor

Jonathan Berger, Richard Hilt, Eric Husmann,
Scott Nooner, Ruedi Widmer-Schnidrig and Mark Zumberge

Institute of Geophysics and Planetary Physics
Scripps Institution of Oceanography
University of California San Diego

Abstract We have designed a new type of infrasonic sensor using optical fibers as distributed sensing elements. The design addresses the limitations of mechanical spatial filters used to average wind-generated, turbulent pressure fluctuations.

We have built two styles of prototype. In the first design of an OFIS (optical fiber infrasound sensor), we rely on the change in optical path that results from an optical fiber's strain-optic coefficient (i.e., the index of refraction is pressure dependent). In the second design, the optical fiber is attached to and strained by a compliant tube, which deforms under pressure. In both types, the optical fiber path length is monitored interferometrically. The second type has proven to have a better signal-to-noise ratio and is currently the primary focus of our developments.

These devices lend themselves to deployment in long, continuous lines, effectively integrating the pressure variations along their lengths. The response over the length of the sensor is governed by the speed of light rather than the speed of sound (as is the case for conventional infrasound filters). Since our sensors can readily be made kilometers long and deployed as spatial filters in arbitrary geometries, they potentially are a significant improvement over conventional systems.

Introduction

The basic specifications of infrasonic monitoring stations for the International Monitoring System of the CTBTO have been established but the ultimate goal of infrasonic monitoring is to maximize the detection capability for signals of interest. The task is to record accurately small changes in ambient air pressure from frequencies of a few hertz to periods of 50 seconds. The measurement of infrasonic signals in this band presents a classical problem of maximizing the signal-to-noise ratio while maintaining some capacity to estimate accurately event azimuth by recording in an array configuration with a spatial separation determined by the wavenumber of interest. The principal source of noise in the frequency band of interest is turbulence in the wind field.

Infrasonic signals are observed from events at all distance ranges, with the dominant period of the signal being a function of source size. Propagation characteristics of acoustic gravity waves in the atmosphere at long-range distances are well known (e.g., Press and Harkrider, 1962), and infrasonic signals have been seen from various large natural events and man-made events. These include great earthquakes (e.g., Mikumo, 1968), explosive volcanoes (Eissler, 1986), atmospheric nuclear explosions (Donn and Ewing, 1962), and smaller conventional explosions (Hedlin *et al*., 1996).

Typical variations in wind speed cause pressure variations of hundreds of μbar, while the signals of interest are typically a few μbar or less. This principal component of the noise field is caused by small-scale turbulence, and travels essentially with the wind speed, on the order of a few m/s to a few tens of m/s. Infrasonic signals, on the other hand, travel as acoustic-gravity waves with group velocities around 280-340 m/s, reducing to acoustic pressure waves traveling with the velocity of sound at high frequencies (Press and Harkrider, 1962).

Studies in infrasound detection often center on techniques of noise reduction. Almost all work to date consists of recording pressure at a single point while an attempt is made to force the pressure at that point to be representative of the pressure averaged along a line or over an area. Typically, a series of perforated pipes or permeable hoses are connected to a microphonic sensor. Pressure noise along the pipe's length is partially incoherent while, for pipe lengths less than the wavelength of interest (typically a few hundred meters), the signal is coherent. The aim of the mechanical filter is to add pressure variations at discrete inlets along its length so that the incoherent noise will average away while the signal is enhanced. Conceptually, one can envision the ideal case of many sensors in an array separately recorded and their signals added together electronically.

Significant efforts have gone into the designs of these mechanical filters. One of the more venerable devices is the Daniels filter (Daniels, 1959), which relies on pipes of varying diameter to create a series of acoustic impedance changes with the hope of reducing acoustic reflections in the pipe. Burridge (1971) analyzed this type of "pipe-microbarograph" and similar configurations. When added acoustically in the filter pipe, there exists a phase delay for each element caused by the finite speed of sound. Burridge modeled pipes with varying dimensions, numbers of inlets, and acoustic impedances to find the best compromise of response flattening and attenuation minimization. In all cases, however, the response clearly is a compromise. The difficulty becomes greater as the frequency increases. As Burridge showed, flat response above 0.1 or 1 Hz is not attainable.

A new approach

Through the use of optical fiber technology we have constructed an infrasound pressure sensor capable of averaging infrasonic signals along km-scale line lengths with an averaging phase-delay governed by the speed of light rather than the speed of sound as is the case with existing infrasonic filters. We have constructed prototype fiber-optic infrasound sensors in our La Jolla labs and deployed a small-scale field version at the University of California San Diego's Piñon Flat Observatory (PFO) in southern California which has been designated in the CTBT as the site of an IMS infrasound monitoring station.

Our new sensor, described here and shown in Figure 1, we call an OFIS (for Optical Fiber Infrasound Sensor). We use a compliant, sealed tube helically wrapped with an optical fiber. As the ambient pressure around the tube changes, it's diameter changes in response and strains the optical fiber (this strain is monitored interferometrically). This technique is sensitive to the *integrated* pressure along the tube, and we can build the tube arbitrarily long. The apparent pressure change P inferred from the observed optical path change along a fiber wrapped around a tube of length L is governed by

$$P = (1/L) \int_0^L P(x)\, dx.$$

Thus pressure variations $P(x)$ (at position x along the tube) having a spatial scale shorter than the total length of the sensor L will be averaged away. An optical fiber is a true, linear, integrator whose incremental step-size is the order of the tube diameter (2.5 cm). Because the phase delay variation along the fiber is governed by the speed of light rather than the speed of sound as in the mechanical filters, the response is flat up to very high frequencies.

To obtain immunity from slight wavelength fluctuations in the laser which illuminates the interferometer, we use an equal-arm Mach-Zender interferometer. In such a device, the difference in the optical path lengths of two identical optical fibers is sensed. We optimize the sensor by configuring the coupling between the optical fibers and the compliant tube such that the signal of interest affects one fiber more than the other while sources of noise have the same effect on both fibers (a.k.a. common mode rejection). For example, the fibers themselves have temperature coefficients, but to a good approximation, both experience the same temperature environment, and—being differential—the interferometer is unaffected. By spacing the wraps of the two fibers as shown in Figure 1, one fiber experiences approximately twice the strain as the other as the tube deforms from pressure changes. The fibers wound close together strengthen one another and hence strain less (for a given pressure difference) than the two isolated fibers.

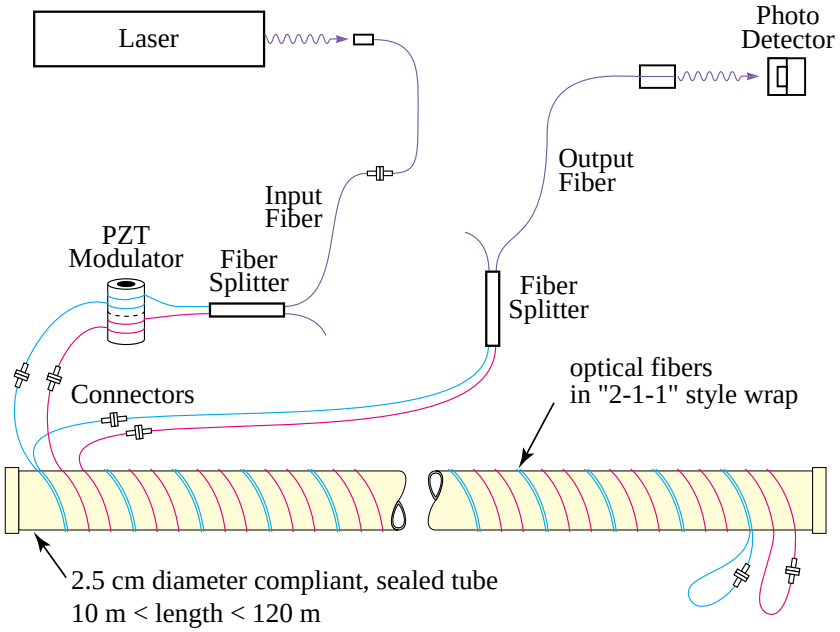


Figure 1. The Optical fiber Infrasound Sensor (OFIS) is constructed from a compliant, sealed tube wrapped with optical fibers to interferometrically sense deformations in the tube caused by pressure fluctuations. The spacing of the optical fiber wraps assures that one of the two fibers experiences greater strain than the other as the tube expands from pressure changes. Other disturbances like temperature and vibration are common to both fibers and hence cancel.

We should mention that our original design did not include a compliant tube, rather we had hoped to rely on an optical fiber's inherent response to pressure changes (via it's strain-optic effect). Our plan was to place two optical fibers side-by-side and encase one of them (the

reference fiber) inside a stiff sealed tube to shield it from pressure fluctuations. Early experiments revealed, however, that strains in the loose fibers caused noise larger than the small pressure signals we hoped to detect. This led us to the compliant tube as a means of increasing the pressure-induced strain in the fiber. We further found that it was necessary to constrain the reference arm fiber on the same compliant tube to avoid these same strains that occur along a loose fiber. After finding that this style of wrapping (which we have dubbed a 2-1-1 style) appears to be the most favorable of those we have tried, we built a machine to wrap fibers with this spacing (repeat length is 5.4 cm) on continuous lengths of tubing.

Lab experiments

We experimented with dozens of materials and winding configurations before settling on the type of device shown in Figure 1. This uses silicon tubing having 25 mm outside diameter and 3 mm wall thickness. The optical fibers are tight buffered (900 μm diameter) Corning SMF28 illuminated with a 1310 nm DFB diode laser. Standard optical fiber splitters are used to separate the light into the two arms and re-combine them into a detector where the interference fringes are formed. A piezo-electric cylinder modulates the optical path length difference at 250 kHz and a phase sensitive detector extracts a second fringe signal in quadrature to the direct one. These two analog signals are recorded at 500 Hz and the optical phase (which is proportional to strain and, hence, to pressure) is calculated in post-processing. The sensitivity is empirically determined by noting the interferometer's response to a known pressure difference instilled by pumping air into the inside of the tube. This coefficient, expressed in optical phase shift per μbar of pressure difference per meter of tubing is typically around 0.05 radian $\mu bar^{-1}\ m^{-1}$ for the dimensions listed above.

The sensors are evaluated with spectral analysis. A pair of identical sensors is constructed and ambient pressure fluctuations are recorded with the two lying side-by-side. We assume that self-noise in each instrument is not correlated with the other and that pressure variations are common to both. Power spectral densities of each sensor and the coherency are computed. The incoherent portion of the recording is taken as noise (the incoherent spectrum is the spectrum of the difference between the two time series).

We performed a test of two 10-m-long sensors recording ambient pressure fluctuations in our lab. We put the two fiber-wrapped tubes in a wooden box (20 cm by 40 cm in cross section) lined with woven fiberglass insulation 9 cm thick. Figure 2 is an example of results. Figure 2a shows the time series of each; Figure 2b shows their individual spectra and the spectrum of the difference (or the self-noise). On the bottom of 2b is a graph of the coherency. Clearly the self-noise in these sensors is very low and their ability to detect sub-μbar pressure signals in the band of interest (0.02 Hz to 20 Hz) is promising.

Field experiments

Our first test of these sensors in a more practical environment took place at Piñon Flat Observatory, the University of California's geophysical test site located 180 km northeast of San Diego. We built a 120-m-long wooden enclosure (with vent holes to allow infrasonic pressure variations to be freely passed) identical to the short one used in our lab experiment and placed it along the ground surface. We assembled four 30-m-long segments of the sensor tube with connectorized terminations of the optical fibers to facilitate either linking the segments in series or operating them individually.

In our first experiment, we compared the records from two 60-m-long sensors operating side-by-side in the test enclosure. Figure 3 shows the results both in the time domain and the frequency domain. Again the two records are highly coherent, although the noise is somewhat higher than seen in our lab. Figure 4 is a similar plot comparing a 120-m-long sensor with a 10-m-long sensor, taken during an especially quiet period. The microbarom peak is coherently seen.

Conclusions

We have designed and tested a new style of infrasonic pressure sensor that can be deployed in lengths up to several km. Tests of the design in the laboratory indicate that the self-noise of the sensor is at least 20 dB below the expected ambient noise level over the band 0.02 to 1 Hz. Side-by-side test of two 60-m prototypes installed in the field show highly coherent noise levels across the band of interest. These sensors are expected to improve significantly the ability to average over wind induced noise and thereby increase the observed signal-to-noise ratio of propagating infrasound signals.

Acknowledgements This research was supported by DTRA contract DTRA01-99-C-0056 and by Kinemetrics, Inc.

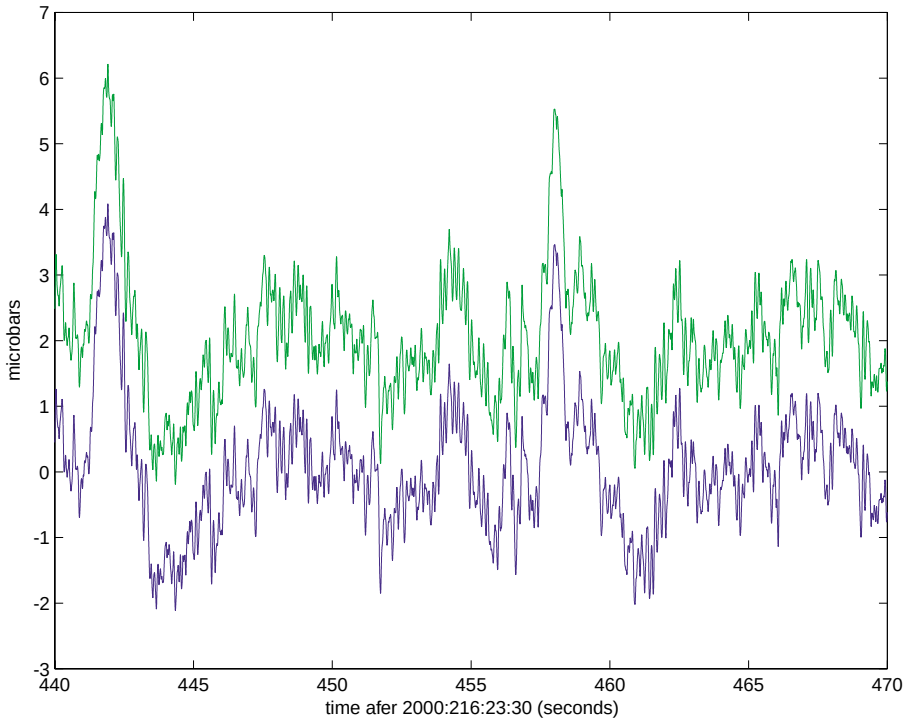


Figure 2a. Pressure variations recorded by two identical 10-m-long OFIS elements placed side-by-side in our basement lab. (The data have been band-pass filtered between 0.1 and 10 Hz).

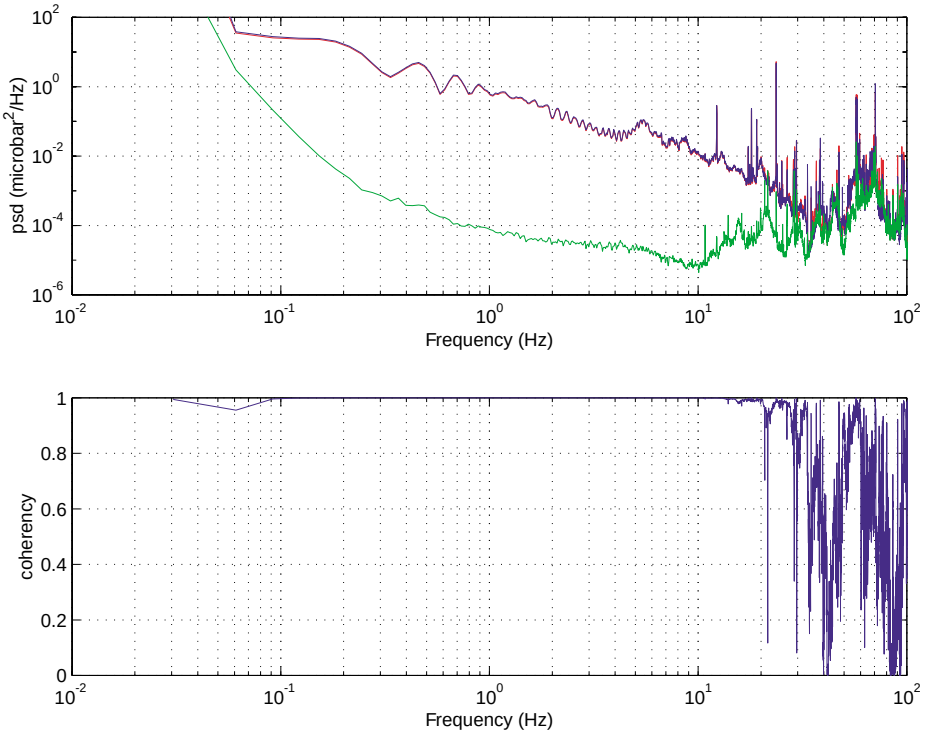


Figure 2b. Spectra taken from longer versions of the records shown in Figure 2a. The red and blue plots are the spectra of the individual records, the green plot is the incoherent noise (since they're nearly identical, it's difficult to see much of the red trace).

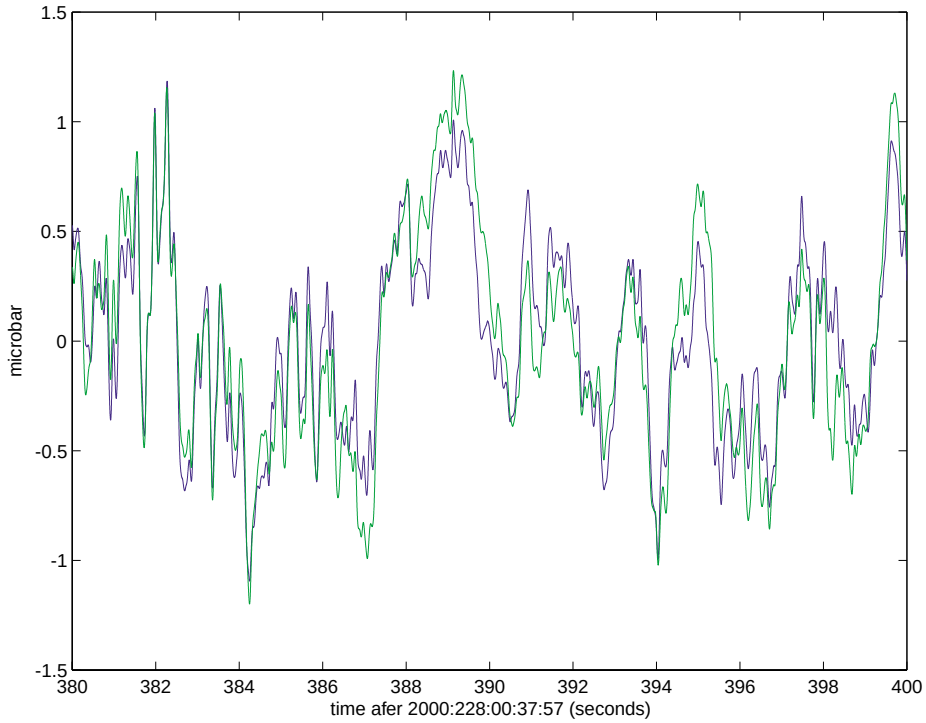


Figure 3a. Pressure variations recorded by two identical 60-m-long OFIS elements placed side-by-side at Piñon Flat Observatory. (The data have been band-pass filtered between 0.1 and 10 Hz).

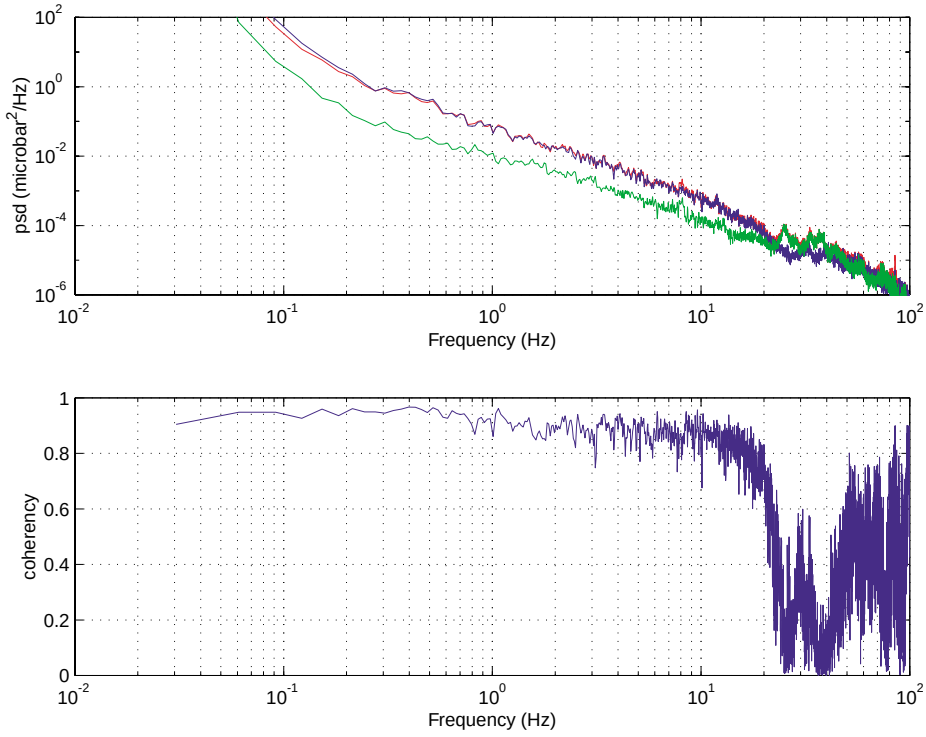


Figure 3b. Spectra taken from the 60-m sensors during operation in the field. The red and blue traces are the spectra of the individual records, the green plot is the incoherent noise.

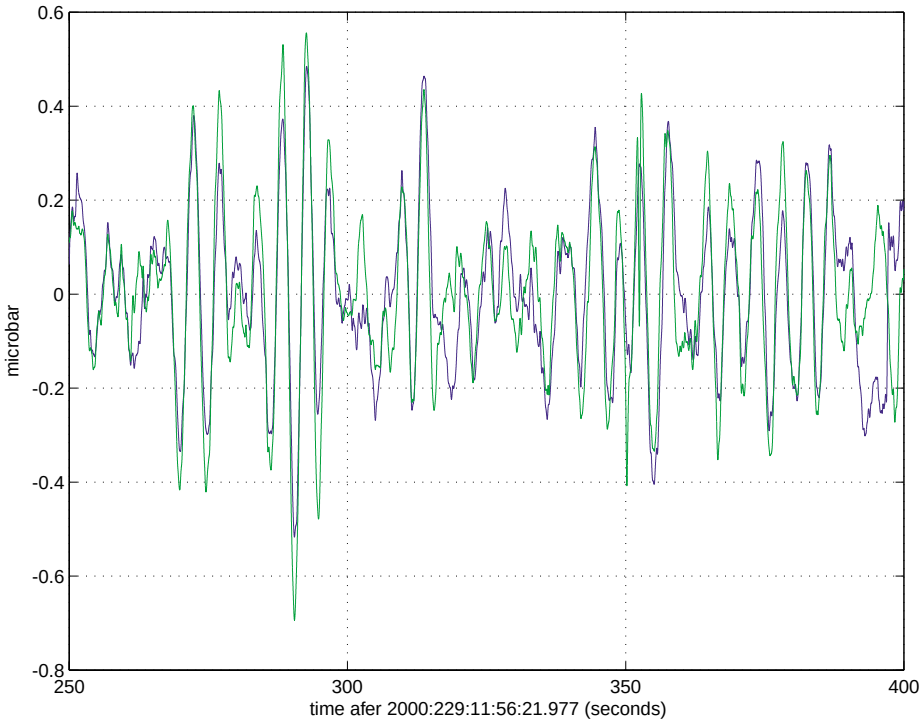


Figure 4a. Pressure variations recorded with a 10-m-long OFIS element placed adjacent to one end of a 120-m-long OFIS element. (As in the other plots, the data have been band-pass filtered between 0.1 and 10 Hz).

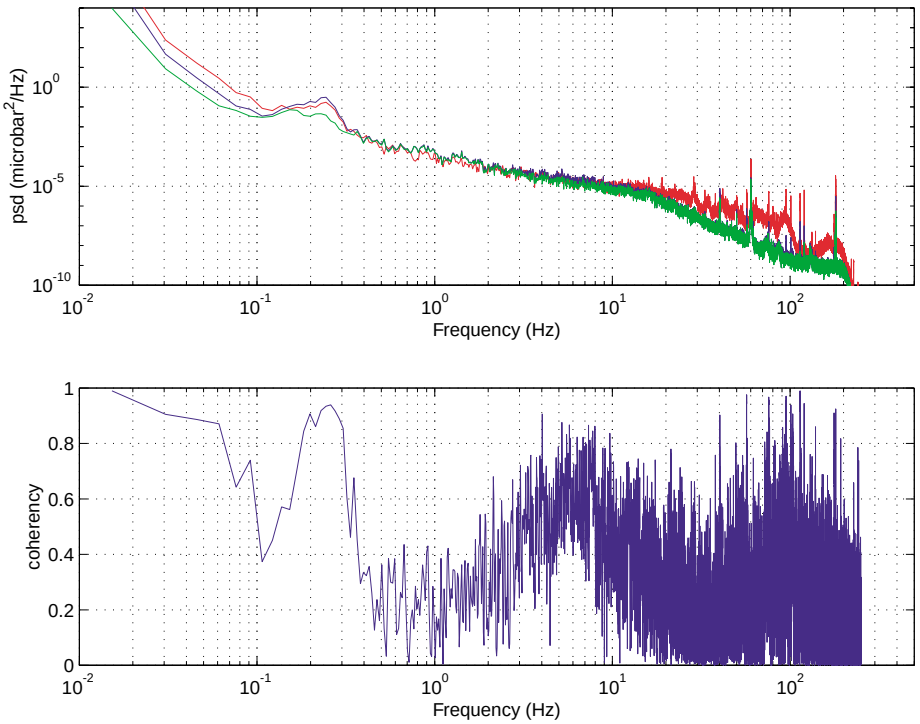


Figure 4b. Spectra taken from the 10-m (red) and 120-m (blue) sensors during operation in the field. The green plot is the incoherent part of the spectrum.

References

Burridge, R., The acoustics of pipe arrays, *Geophys. J. R. Astr. Soc.* 26, 53-69, 1971.

Daniels, F.B., Noise reducing line microphone for frequencies below 1 c.p.s., *J. Acoust. Soc. Am.* 31, 529-531, 1959.

Donn, W.L. and M. Ewing, Atmospheric waves from nuclear explosions, *J. Geophys. Res.* 67, 1855-1866, 1962.

Eissler, H.K., Investigations of earthquakes and other seismic sources in regions of volcanism: Chapter 3, Investigations of global seismic and atmospheric signals associated with explosive volcanic eruptions, Ph.D. Thesis, California Institute of Technology, 174 pp., 1986.

Hedlin, M.A.H., F.L. Vernon, J.B. Minster, and J.A. Orcutt, Experiments in regional monitoring of small seismo/acoustic events, in *Proceedings of the 18th Annual Seismic Research Symposium on Monitoring a Comprehensive Test Ban Treaty, 4-6 September 1996,* PL-TR-96-2153, Environmental Research Papers, No. 1195, J.F. Lewkowicz, J.M. McPhetres, and D.T. Reiter, eds., 515-523, 1996.

Mikumo, T., Atmospheric pressure waves and tectonic deformation associated with the Alaskan earthquake of March 28, 1964, *J. Geophys. Res.* 73, 2009-2025, 1968.

Press, F., and D.G. Harkrider, Propagation of acoustic-gravity waves in the atmosphere, J. *Geophys. Res.* 67, 3889-3908, 1962.

8. Data Processing and Analysis

MIDDLE EAST AND NORTH AFRICA DATABASE DEVELOPMENT AND RESEARCH TO POPULATE THE DOE KNOWLEDGE BASE

Muawia Barazangi, Dogan Seber, Eric Sandvol, Francisco Gomez, Christine Sandvol, and Carrie Brindisi
Institute for the Study of the Continents (INSTOC), Cornell University

Sponsored by U.S. Department of Energy
Office of Nonproliferation Research and Engineering
Office of Defense Nuclear Nonproliferation
National Nuclear Security Administration

Cooperative Agreement No. DE-FC04-99AL66045

ABSTRACT

The objective of this work is to update, analyze, and document data for the Middle East and North Africa regions in order to provide accurate input to the DOE's Knowledge Base system. Specifically, we aim to provide assessments and comparison of different geophysical databases, such as Moho and basement maps, for the region of study, in an effort to document the accuracy and the extent and magnitude of the discrepancies. Additional "ground truth" information, primarily based on satellite information, for distinguishing mine-related activity are also to be provided, both through analysis of existing data at Cornell, and where possible, through in-country sources. Another objective is to map characteristics of regional seismic wave propagation and to document velocity models for the Middle East using data available to Cornell University.

To date, we have developed and delivered to DOE authorities (1) a complete crustal structure including detailed topography, sediment thickness, and Moho depth values for the entire Middle East and North Africa regions, (2) our regional seismic waveform attenuation characteristics results in the Middle East region, and (3) a comprehensive study of Moho and basement depth models for the region.

We developed a new complete crustal model for the Middle East and North Africa regions. The final model includes topography, basement depth, and Moho depth values for the entire region. These models are justifiable and better represent the crustal structure in the Middle East and North Africa regions. These models will serve as a good starting point in geophysical studies in this region. We also conducted a comparative study of available Moho and basement data sets developed by different groups in these regions.

We also determined the regional seismic wave (Sn and Lg) attenuation characteristics using a ratioing technique. We obtained tomographic images of efficient and inefficient Lg and Sn phases using data from local seismic networks in the region. We specifically utilized waveform data from the Turkish National Seismic Network, Syrian National Seismic Network, and all available permanent and temporary broadband stations in these regions.

Our future work will include developing a detailed tomographic upper mantle velocity images in the region. We will modify and improve existing Pn velocity models in the region by making use of local station data and readings.

Key Words: Databases, Moho, basement, Middle East, North Africa, GIS, CTBT

OBJECTIVE

The objective of this work is to update, analyze, and document data for the Middle East and North Africa in order to provide accurate input to the DOE Knowledge Base system. Specifically, we aim to provide assessments and comparison of different geophysical databases, such as Moho and basement maps, for the region of study, in an effort to document the accuracy and the extent and magnitude of the discrepancies. Additional "ground truth" information, primarily based on satellite information, for distinguishing mine-related activity are also to be provided, both through analysis of existing data at Cornell, and where possible, through in-country sources. Another objective is to map characteristics of regional seismic wave propagation and to document velocity models for the Middle East using data available to Cornell University. We will also provide metadata and the appropriate references for the above work.

The work under this Cooperative Agreement is being coordinated with scientists at the Lawrence Livermore National Laboratory (LLNL) and the Sandia National Laboratory (SNL).

RESEARCH ACCOMPLISHED

A. MIDDLE EAST AND NORTH AFRICA CRUSTAL STRUCTURE

Currently, there are several data sets that provide information about the crustal structure in the Middle East and North Africa regions. These data sets vary in quality and resolution. Utilization of these data sets in seismological research efforts will likely produce different results. In order to determine and document variations in data sets for a given region we analyzed each data set individually and then calculated differences and determined statistical correlations among data sets. All data were entered into ArcInfo GIS software and processed using the surface processing tools provided in that software.

We have analyzed the following data sets: Cornell Moho, LLNL Moho, CRUST 5.1, IPE Moho, Cornell basement, LLNL basement, UC basement, CRUST 5.1 basement, IPE basement.

A.1. Moho Data Sets

- Cornell University Moho Map

The Cornell University Moho map was developed by us over several years (Figure 1). The data set covers a significant portion of the Middle East and North Africa region. It was compiled from several different data sources. These sources include crustal scale refraction and reflection profiles, receiver function depth estimations, gravity modeling, and surface wave dispersion curve inversion results.

The majority of the Middle East data sets were compiled from about 50 refraction and gravity profiles in the region. The complete set of profiles and their interpretations are available in our web site at *http://atlas.geo.cornell.edu/htmls/fin2/figmain.html*. We digitized all these crustal cross section interpretations and marked the basement and Moho interfaces in each cross section. . We also used the receiver function results from our previous seismological studies in the region (e.g., Sandvol et al., 1998a; Sandvol et al., 1998b). Later, we used them in the interpolation to obtain a gridded Moho map for the region.

Several contour maps were also digitized to provide constraints in the gridding. We collected contour maps for Iran, Afar triangle, Egypt, Aegean Sea, Greece, Italy, and the eastern Mediterranean Sea (see refs). In addition, some Moho values were digitized from interpretations of low resolution refraction profiles with PmP measurements as points for North Africa.

Collectively, these data sets were used to obtain the Cornell University Moho map for the region. In order to provide constraining points in regions with sparse data coverage, we added pseudo Moho depth values based on known tectonic units. Using 3 km resolution bathymetry maps we outlined the edge of the continental shelf and assigned a Moho thickness of 15 km to these contours. The 15 km Moho depth was chosen arbitrarily to approximate the crustal thinning from the continental regions to oceanic regions. We also added pseudo contours in inland areas of the continents to allow a rapid transition to continental Moho depth just after the shelf margin.

-LLNL MENA 1.0 Moho Map

The MENA 1.0 crustal model of Sweeney and Walter (1998) is a modified version of the CRUST 5.1 velocity model. The details of the models are provided in the mentioned report and will not be discussed here in detail. However, it is important to note that this model is a regionalized model. The entire region is divided into 28 distinct tectonic units, and each tectonic unit is assigned a uniform crustal thickness and velocity structure. These values are mainly adopted from the CRUST 5.1 global model with some modifications.

-IPE Moho Map

The IPE Moho map actually covers all of Eurasia. The coverage in the Middle East and North Africa, however, is not complete. The data set covers the region from about 24.5N to north. For this reason, it is not possible to make a full comparison with other data sets.

This data set is also the least known among the Moho maps. The depth-to-Moho contour maps published by the Soviet IPE (Institute for the Physics of the Earth) were digitized by the Cornell group, and a gridded map was obtained. However, the accuracy of the contours is not known. It is speculated that the contours were based on interpretations of refraction, gravity, and surface wave studies in the region. Currently, there is no information available about the data sampling and resolution. However, the contour values, at continental scales, are consistent with known crustal thicknesses in the region. At larger scales this correlation is lost, indicating that data used in contouring were sparse.

-CRUST 5.1 Moho

The CRUST 5.1 model is a global data set with 5x5 degree resolution (Mooney et al., 1998). The biggest disadvantage of this model is its low resolution. Areas more than 500 km in width and length are assigned only one average value. However, the model also consists of velocities that could help in forming a complete crustal structure. The details of this model are described in Mooney et al. (1998) and will not be discussed here.

A. 2. Comparisons of Moho data sets

All these Moho data sets were imported into ArcInfo software and calculations were done within the ArcInfo environment. We gridded all data to 10 km cell size, even though none of the data sets has 10 km resolution. To determine how these four different Moho data sets compare with each other, we calculated the correlation matrix for the four data sets.

Table 1. Correlation Matrix for Moho Data Sets

	Cornell	**MENA 1.0**	**IPE**	**CRUST 5.1**
Cornell	1.00000	0.67289	0.51157	0.58360
MENA 1.0	0.67289	1.00000	0.63023	0.79576
IPE	0.51157	0.63023	1.00000	0.58733
CRUST 5.1	0.58360	0.79576	0.58733	1.00000

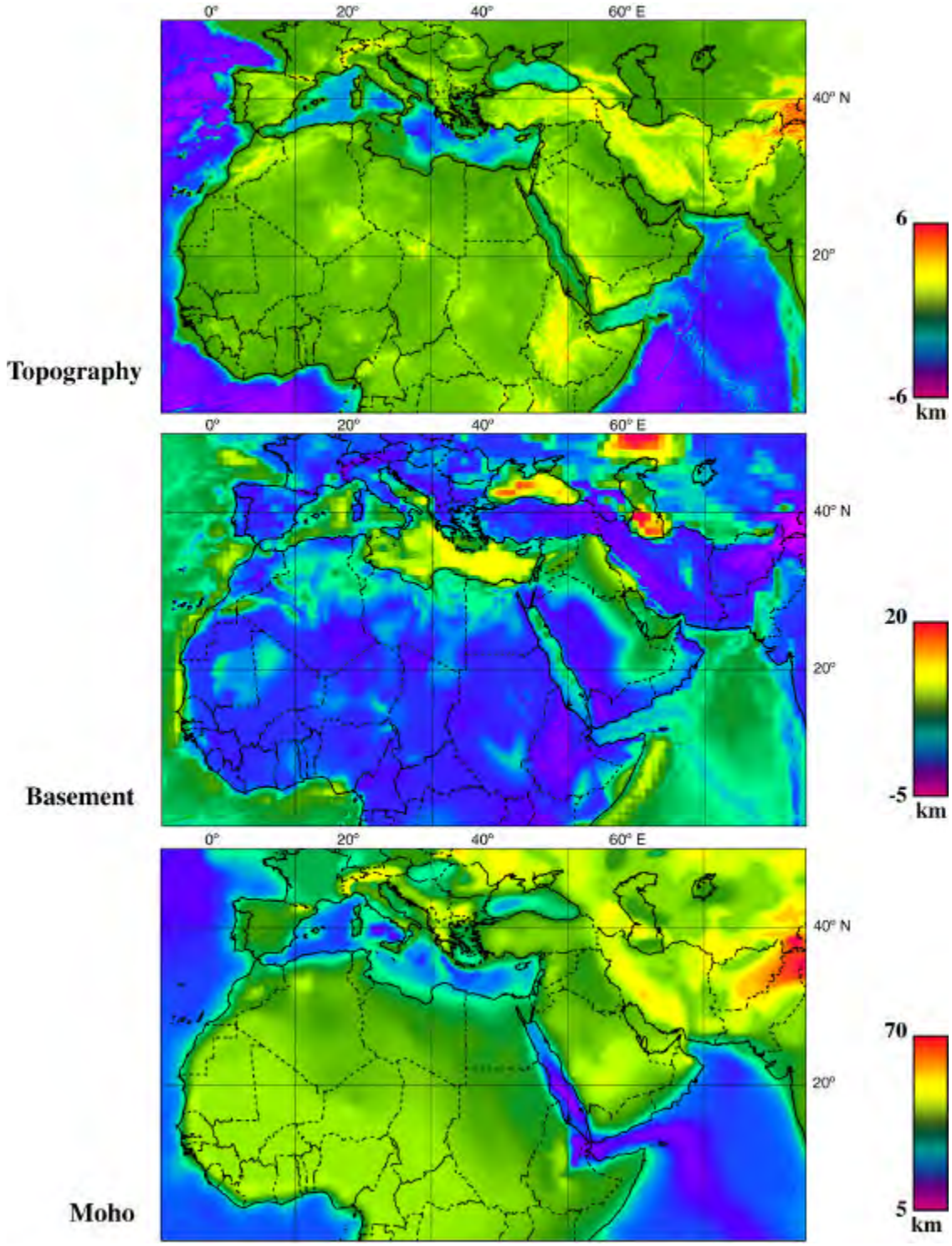


Figure 1. Maps showing the final crustal structure for the Middle East and North Africa region. Cornell basement and Moho depth data sets represent the best known structure for the Middle East and North.

Cornell Moho vs MENA 1.0

The differences between the two data sets are at relatively short length scales (Figure 2). This is expected because of the nature of the MENA 1.0 data set. Since this data set is generalized, and the Moho depth varies within a tectonic unit, most of the differences reflect variations occurring within a tectonic zone identified in the MENA 1.0 model. In a few places such as the Red Sea, the Alps, the Zagros, and the East African rift, longer wavelength variations are observed.

The majority of short wavelength variations are observed near the continental margins where a sudden change in crustal thickness occurs. Since none of the data sets has "measured" depth-to-Moho along the continental margins, these changes are expected and cannot really be constrained. However, there are significant differences in Moho depth values of the two data sets in certain regions, such as the Pyrenees, and beneath the Sardinia and Corsica Islands. These short period, but high magnitude variations are probably due to the generalization process of the MENA 1.0 data set. It is known that the Pyrenees are underlain by thicker crust due to continental subduction. Similarly, the Moho beneath the Corsica and Sardinia Islands is deeper than beneath the adjacent oceanic areas. This is not observed in the MENA 1.0 map.

We believe the longer period variations are also a result of over simplification of the tectonic boundaries. For example, the large variations in Moho depth along the Red Sea are due to the assumption in the MENA 1.0 data set that the entire Red Sea is underlain by a uniform crustal thickness. However, geophysical and geological studies suggest that the rifting and oceanic spreading in the southern part of the Red Sea is much more mature. The northern Red Sea is still in its early rifting stages and no oceanic crust yet exists there. This along strike variation is reflected in Moho depth as well.

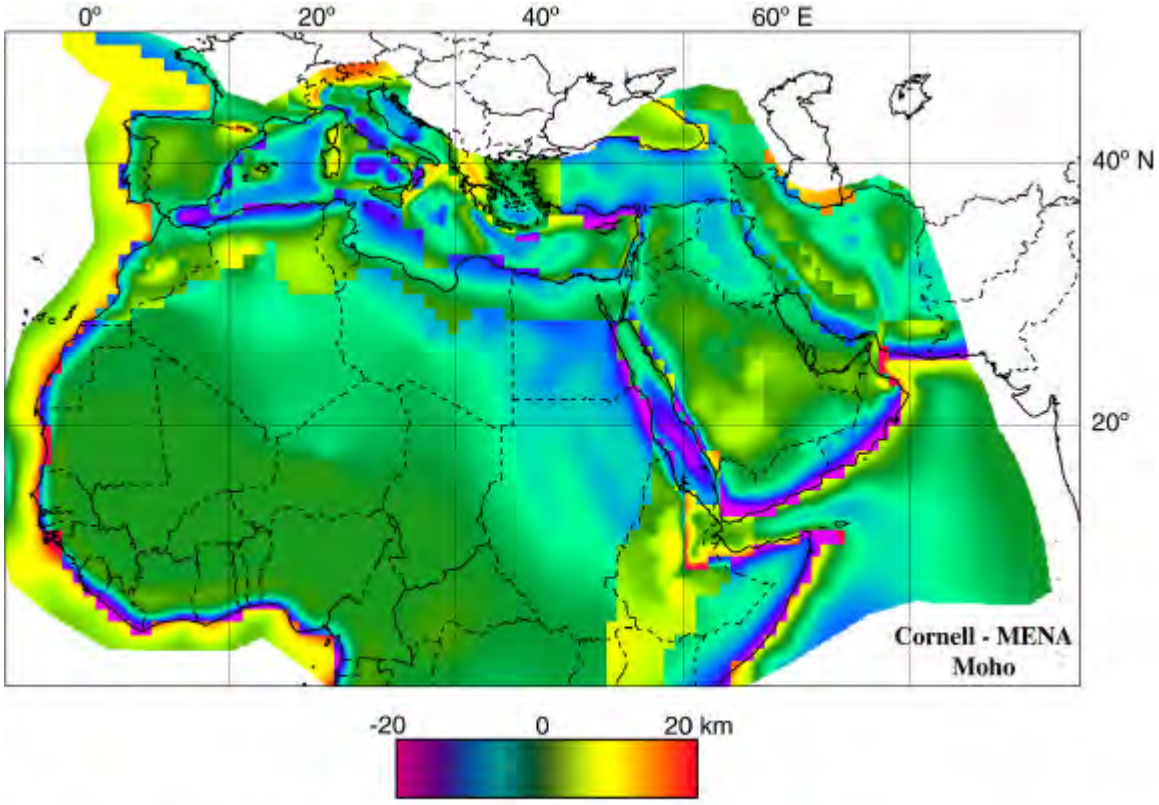


Figure 2. Map showing the differences between the Cornell Moho and the MENA 1.0 Moho data sets.

Comparisons of Other Moho Data Sets

The overlap between the Cornell Moho and the IPE Moho maps is quite limited; only about ¼ of the region is covered by the overlap between the two data sets. The differences in Moho values span a wide range of values, the majority of the variations are in the ± 9 km range.

The Cornell Moho and the CRUST 5.1 maps also show strong variation in the Middle East and North Africa region. This is an expected phenomenon because of the extremely low resolution of the CRUST 5.1 data set. Very large (up to ±20 km) variations exist at the margins of the continents. A 5-degree cell size in the CRUST 5.1 data set does not provide enough resolution to meaningfully analyze the Moho structure in this region.

The MENA 1.0 and the IPE maps overlap in the northern half of the area of interest. The largest variations between the data sets are in Pakistan, Afghanistan, and the southern Caspian Sea. The IPE values in these regions are much larger (~ 10km) than the Moho depth values in the MENA 1.0 data set. Additional differences occur along the continental margins, where the resolution of the MENA 1.0 data set plays an important role.

Tthe MENA 1.0 and the CRUST 5.1 model correlate reasonably well since the MENA 1.0 is based on the CRUST 5.1 model, and the differences reflect the modifications made to the CRUST 5.1 model in order to obtain the MENA 1.0 crustal model. More than 30% of the values in the two data sets are within ±1 km range.

The mismatches between the CRUST 5.1 and IPE data sets are quite strong. The variations in this case are not limited to continental margins; they are distributed over the entire region. The strong variations to note are in the Bay of Biscay, the Pyrenees, the Alps, the entire Mediterranean basin, northwest Arabia, the Persian Gulf, and the Hindu Kush mountains.

A. 3. Basement Data Sets

- Cornell University Basement Map

The basement structure shown in Figure 1 was obtained by merging the Cornell's older version basement map, which covers mostly the land areas in the Middle East and North Africa regions, with the UCSD basement map. The UCSD map is used to supplement the sediment thickness in oceanic areas. We chose the UCSD sediment map for the compilation, because of the good correlation between the two data sets as well as the consistency of models with known tectonic units. In order to account for the topographic and bathymetric changes, we also added the topography/bathymetry data shown in Figure 1 to this basement map. By doing so, we obtained a basement depth data set that includes topography and the water level.

- LLNL MENA 1.0 Basement Map

The MENA 1.0 Basement values were extracted from the MENA 1.0 crustal model based on P wave velocity values. A P wave velocity of 6 km/s was selected as the basement identifier in the velocity model. The depth where P wave velocity jumps over 6.0 km/s was taken to represent the basement depth in that region.

This data set is a revised version of the CRUST 5.1 model. The details of these data are described in Sweeney and Walter (1998). The model has 28 different tectonic units, and each unit is assigned a unique depth to basement value.

- IPE Basement Map

The IPE basement map is similar to the IPE Moho map in its geographic extent, covering only the northern part of the Middle East and North Africa region. This data set was digitized from the Soviet IPE basement map contours. The reliability of the contour values remains as a problem. There is currently no information about how these contours were drawn and what the resolution limits are in this data set. This basement map shows very deep basins in the Caspian Sea, the eastern Mediterranean Sea, and the Black Sea regions. It is known that the southern Caspian Sea is underlain by very thick sedimentary cover (about 20 km).

Similarly, the Black Sea is known to be underlain by a deep basin. For these known areas, the IPE basement values appear consistent with known structures. However, the IPE map also shows zero sediment thickness in most parts of the Middle East where it is known that there are thick sedimentary covers. For example, parts of Morocco, Syria, and Turkey are shown in this map as regions with no sedimentary cover. However, based on recent studies we know that there are several sedimentary basins in these regions.

- University of California Basement Map

The UC basement map is a compilation from several sources and it provides global sediment thickness estimations at 1x1 degree resolution. The details for this model can be obtained from http://mahi.ucsd.edu/Gabi/sediment.html. We cropped the global data set to show only the Middle East and North Africa region. This map also shows the large basins in the regions, such as the southern Caspian, the Black Sea, and the eastern Mediterranean. Smaller size variations in sediment thickness will be less accurate, since the sample size is more than 100 km in this map.

-CRUST 5.1 Basement Map

Due to extremely large sample spacing, it is almost impossible to evaluate this data set for sediment thickness. Very few tectonic units show distinct sediment thickness values. The Black Sea and parts of the eastern Mediterranean Sea and southern Caspian Sea regions are examples of these units. However, the sampling size precludes a meaningful analysis of the basement depth values.

A. 4. Comparisons of Basement Data Sets

In order to compare the data sets mentioned above, we performed statistical correlation calculations among the data sets. Table 2 shows the correlation coefficients for each data pairs. The highest correlation is between the UCSD and CRUST 5.1 models. The lowest correlation is between the Cornell and IPE basement data sets. The high correlation between CRUST 5.1 and UCSD models is likely to be a function of the underlying data used in each model. Since the CRUST 5.1 model has low resolution, this correlation is almost meaningless. In the following sections, we analyze each data set against the others and try to bring some constraints on which ones are more reliable.

Table 2. Correlation Matrix for Basement Data Sets

	Cornell	**MENA 1.0**	**UC**	**IPE**	**CRUST 5.1**
Cornell	1.00000	0.42071	0.47555	0.28747	0.35394
MENA 1.0	0.42071	1.00000	0.60434	0.55753	0.56240
UC	0.47555	0.60434	1.00000	0.56820	0.63596
IPE	0.28747	0.55753	0.56820	1.00000	0.47460
CRUST 5.1	0.35394	0.56240	0.63596	0.47460	1.00000

- Cornell vs. MENA 1.0 basement maps

Figure 3 shows the difference map between these two data sets. These two data sets differ strongly in the Arabian peninsula, except in the shield region. The two deep basins in the northern Arabian peninsula, in the Palmyrides and the Rutbah regions, are absent from the MENA 1.0 data set. Similarly, the depth to basement in the Mesopotamian foredeep also shows variations. Since the gradual thickening of the sediments from the shield region to the Zagros is not represented in the MENA 1.0 data set, basement depth variations in this region reach 10 km. Other basins in Africa are also oversimplified in the MENA 1.0 data set and several kilometer thick basins are not adequately represented in the MENA 1.0 data set. This results in the differences seen between these two data sets. The variations in basement depth values mostly range from -2 km to about 6 km.

There are also larger variations in the data sets but with fewer occurrences.

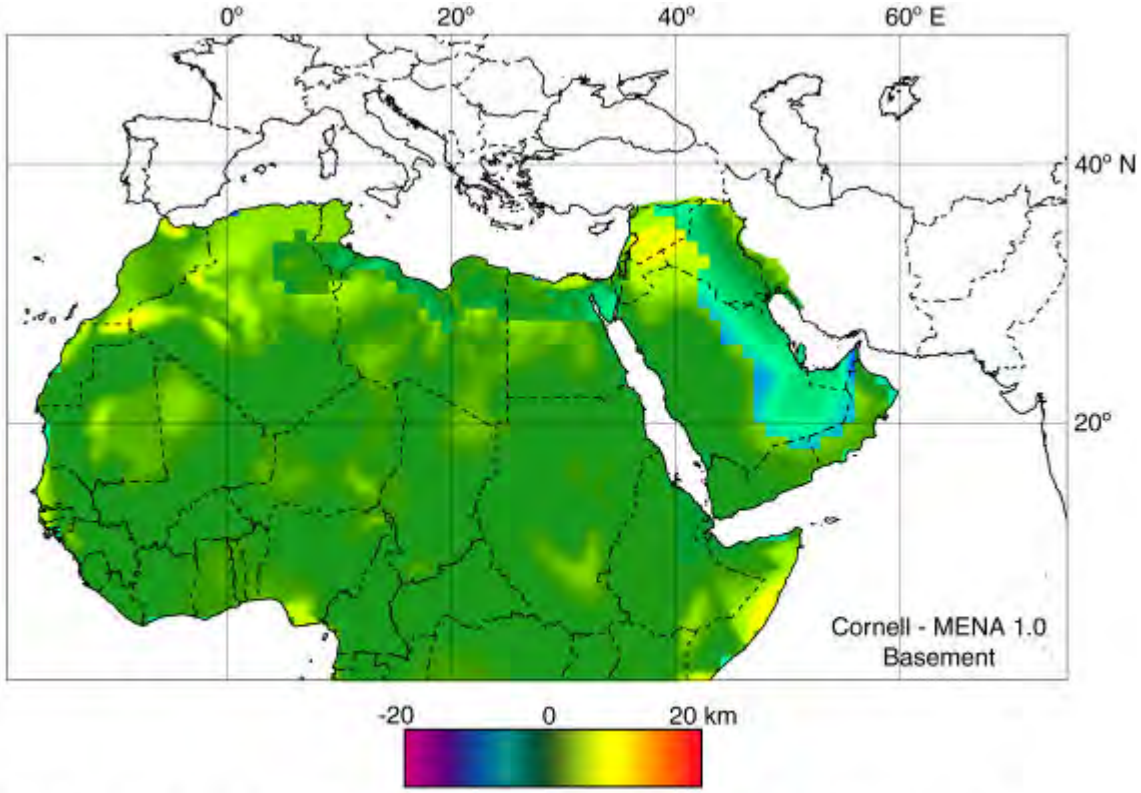


Figure 3. Map showing the differences between the Cornell basement model and MENA 1.0 model.

Comparisons of Other Basement Data Sets

The overlap between the IPE and Cornell basement maps is quite limited. However, in regions where they do overlap the variations between the two data sets are within ± 2 km. The variations are mostly at shorter wavelength scales. Important basins, such as the Rif basin in northern Morocco and the deep sedimentary rocks in Syria, are not represented in the IPE data set.

The Cornell and UCSD basement data sets are reasonably well correlated. Most of the basement depth values agree within about two kilometers in these data sets. However, in some cases they disagree about the depth of these basins. Extreme variations reach a value as high as 12 km at locations.

The differences in basement depth values between the Cornell and CRUST 5.1 data sets are due to large cell size of the CRUST 5.1 basement model. It is practically impossible to have a meaningful comparison between these two data sets due to cell size variations.

The MENA 1.0 and IPE basement maps vary strongly. The largest variations are observed in the Caspian Sea and the western Mediterranean Sea regions. The magnitude of these variations reaches 20 km. The basement depth in the Caspian Sea basin is under-estimated by the MENA 1.0 model, and it is overestimated in the western Mediterranean region relative to the IPE data set. Other regions of significant deviations in these data sets are in southern Cyprus, central Arabia, and the Adriatic Sea regions.

There are quite large variations between the MENA 1.0 and UCSD basement data sets in the Caspian Sea and western Mediterranean Sea regions. Significant variations are also observed in central Africa where deep basins exist. The differences are related to the same problem of generalization as in the MENA 1.0 data set. Within a tectonic unit depth-to-basement values vary quite significantly, and these are not accounted for in the MENA 1.0 data set. The UCSD data set does take into account variations within tectonic units with about 100 km resolution.

The differences between the MENA 1.0 and CRUST 5.1 show that in the Mediterranean and eastern Arabia regions basement depth values exhibit large variations. The overall variations are within the ± 5 km limits. However, in the Mediterranean Sea region and Arabia these differences reach 20 km.

The variations between the IPE and UCSD data sets are seen in the Caspian Sea region and near the Zagros fold belt, the western coast of Africa, and the southern Aegean Sea. The differences reach 20 km in some of these regions.

The IPE and CRUST 5.1 basement maps show the variations mainly due to the aforementioned problem of large sampling size in the CRUST 5.1 model. The variations reach large magnitudes, in several regions, such as the Caspian Sea, they reach high values.

The largest differences between the UCSD and CRUST 5.1 data sets are seen in the Caspian Sea and Black Sea areas. The majority of difference values are within ± 5 km of each other. The difference map shows numerous smaller regions where significant deviations exist in the basement depth values. This is also simply related to the large sample size in the CRUST 5.1 data set.

B. WORK IN PROGRESS

Seismic Velocity in the Middle East

Currently our efforts are focused on developing a detailed velocity structure for the Middle East region. We are utilizing local seismic networks in Turkey and Syria and make phase readings on digital short period station recordings. These data will then be merged with the ISC catalogue readings and a detailed phase reading database will be developed. These data then will be used to obtain an accurate and detailed velocity structure for the Middle East region. Figure 4 shows seismic stations used in Turkey and Syria along with other stations that report seismic phase readings to ISC.

Acquiring Ground Truth for Seismic Discrimination

Another effort that is currently underway is to develop a ground truth database using high resolution satellite imagery. Based on collaborations with the LLNL research group, recently we ordered four Landsat 7 TM scenes in Syria, Jordan, and Iran. We will register these TM scenes and determine mining sites within them and their location to be used in LLNL's discrimination efforts.

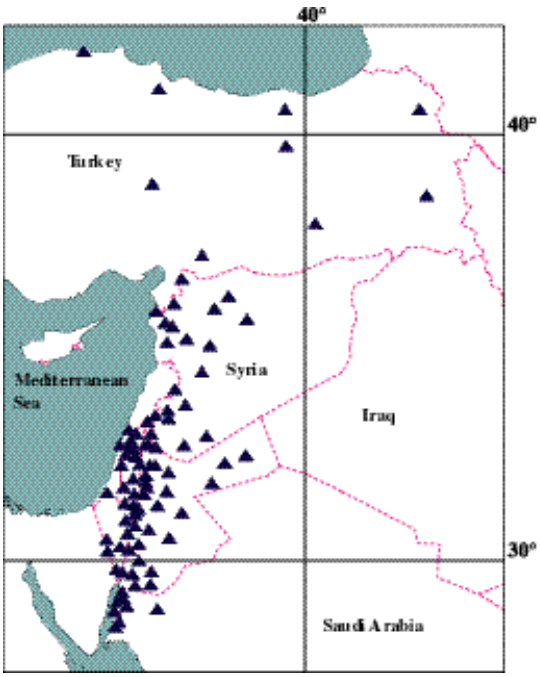


Figure 4. Map showing seismic stations in Turkey and Syria along with stations that report to ISC in the Middle East region.

CONCLUSIONS AND RECOMMENDATIONS

Our efforts under this Cooperative Agreement are of direct relevance to the comprehensive development of the DOE Knowledge Base. It is essential to provide the Knowledge Base with the most accurate available information; but also, as important, to compare and contrast the final selection of data sets with other data sets available and widely used by researchers in the CTBT community. The revised Cornell basement and Moho depth data sets that we have recently delivered to DOE/LLNL is the most complete and accurate for the Middle East and North Africa regions.

Beyond the scope of this ongoing Cooperative Agreement, we recommend that a second agreement be negotiated between Cornell and DOE in order for Cornell to provide DOE labs with "ground truth" information (based on data available at Cornell) to better strengthen and expand the ongoing calibration efforts in the Middle East and North Africa regions.

REFERENCES

Khair, K., and G. N. Tsokas, Nature of the Levantine (eastern Mediterranean) crust from multiple-source Werner deconvolution of Bouguer gravity anomalies, J. Geophy. Res., 104, 25,469-25,478, 1999.

Mooney, W.D., G. Laske, and T.G. Masters, CRUST 5.1: A global crustal model at 5ºx5º: J. Geophy. Res., 103, 727-747, 1998.

Makris, J., Geophysical and geodynamic implications for the evolution of the Hellenides, *Geological evolution of the Mediterranean Basin, Advanced Research Institute conference on the Geological evolution of the Mediterranean Basin Conference. Sicily, Italy: Nov. 19-27,* 1982, 231-248, 1985.

Nicolich, R., Crustal structures from seismic studies in the frame of the European geotraverse (southern segment) and crop projects, The lithosphere of Italy: Advances in earth science research, Edited by A. Boriani, M. Bonafede, G.B. Piccardo, and G.B. Vai, 41-61, 1989.

Sandvol, E., Dogan Seber, Alexander Calvert, and Muawia Barazangi, Grid search modeling of receiver functions: implications for crustal structure in the Middle East and North Africa, J. Geophy. Res., 103, 26,899-26,917, 1998a.

Sandvol, E., Dogan Seber, Muawia Barazangi, Frank Vernon, Robert J. Mellors,. And Abdullah M. Al-Amri, Lithospheric seismic velocity discontinuities beneath the Arabian Shield, Geophysical Research Letters, 25, 2,873-2,876, 1998b.

Sweeney, J., and B. Walter, Preliminary Definition of Geophysical Regions for the Middle East and North Africa, LLNL report # UCRL-ID-132899, 1998.

van der Beek, P. A., and S. Cloetingh, Lithospheric flexure and the tectonic evolution of the Betic Cordilleras (SE Spain), Tectonophysics, 203, 325-344, 1992.

Vidal, N., J. Gallart, and J. Danobeitia, A deep seismic crustal transect from the NE Iberian Peninsula to the western Mediterranean, J. Geophy. Res., 103, 12,381-12,396, 1998.

Yarmolyuk, V.A., and Y. Y. Kuznetsov, Geological Map of Africa, 1:5,000,000 scale, Ministry of Geology of the USSR, 1977.

Yegorova, T.P., V.I. Starostenko, V. G. Kozlenko, and N.I. Pavlenkova, Three-dimensional gravity modelling of the European Mediterranean lithosphere, Geophy. J. Int., 129, 355-367, 1997.

AUTOMATIC INTERPRETATION OF REGIONAL SHORT PERIOD SEISMIC SIGNALS USING THE CUSUM-SA ALGORITHMS

Zoltan A.Der[1] , Matthew W. McGarvey[1], and Robert H. Shumway[2]
[1] Ensco Inc, Springfield VA.
[2] University of California at Davis, Davis CA.

Sponsored by the Defense Threat Reduction Agency
Contract DSWA01-98-C-0155

1.0. ABSTRACT

Automatic seismogram interpretation and onset estimation are desirable goals facilitating the rapid location and discrimination of seismic events, automation also relieves the human operator from onerous repetitive tasks. At regional distances the onsets of seismic phases are associated with gradual, rather than sudden, changes in the statistical properties of the seismic time series, i.e. changes in autoregressive models and mean square amplitudes. The work presented combines two aspects of the onset time estimation, the detection of the onset as a change in the trend of the cumulative sum (CUSUM) of a suitable test statistic, and a randomized search for its location, simulated annealing (SA). The latter is applied repeatedly, thus, resulting in multiple onset time estimates. These typically form clusters around the arrival times of the known seismic phases, but there are some scattered values as well, that have to be discarded. The uncertainties in the onset times estimated can be quantified in terms of the spread in the values of the best defined clusters. Various standard cluster analysis methods can be applied to define individual clusters. The system is presently developed using MATLAB, utilizing its graphical user interface capabilities.

2.0. OBJECTIVES

The objective of this work is to develop automated methods for interpreting regional and teleseismic short period seismograms using ideas and algorithms from the statistical literature. In the analyses of seismic data, onset times of the various seismic arrivals are of great importance, because they are used in locating the sources and segmenting the seismograms into wave groups used in discrimination of various types of events. Although various onset time (or change point) estimation methods have been tested in the past, with success, for time series where the properties (amplitudes and frequency spectra) suddenly change, actual seismograms are more complex. Amplitudes increase and decrease and spectra of various arrivals may be different. Because of the great variability of the seismic data, it is necessary to make the methodology work reliably under varying conditions. It is likely that several approaches that have been tried may have to be combined to achieve reliability and robustness to achieve these goals.

3.0. RESEARCH ACCOMPLISHED

3.1. Background.

Automatic phase arrival time estimation for regional arrivals is of considerable interest because of the need for rapid location and identification of numerous seismic events by networks monitoring natural and man-made seismic activity. Times of seismic 'phase' arrivals can be defined as time instants, where some visible characteristic, such as amplitude, frequency content or wave polarization changes in some recording. Typically, regional arrivals are high frequency, broadband, emergent wave groups containing numerous cycles. Generally, later arrivals have no clear, impulsive waveforms and are preceded by the codas of earlier ones and their onset times can only be defined to within a few cycles. Besides locating events from multiple *Pn* times at several stations, onset time estimation is useful in facilitating location using multiple arrivals in the same seismogram and in automated application time and frequency domain discriminants.

The methods developed in this paper differ from the semi-automatic computer guided onset time determination methods presently used by analysts in current systems, in which preliminary phase onset predictions suggest picks to the analysts. We find that these suggested onset times often take precedence over what the analysts actually sees in the seismogram leading to biased or censored onset times. What we are trying to do is to teach

the computer to pick multiple phase onsets based on the seismograms only, as if it were the first time in an unknown region.

There are numerous statistical approaches in the literature to determining the arrival time of 'phases'. Onsets of packets of seismic energy associated with various paths, i.e. seismic phases, are usually associated with sudden changes in amplitudes, spectra, polarization and slowness. Generally it is assumed that it is known that the change occurs somewhere in a predefined time interval and that the statistical model of the time series changes abruptly. It is also assumed that the time series are stationary before and after such a change and that the statistical distributions are multivariate Gaussian (e.g. Basseville and Nikiforov 1993).

Depending on the autoregressive models applied one may test for spectral and amplitude changes (single channnel model), slowness changes (multichannel model applied to array sensor outputs) or polarization (three-channel model) as described by several workers (Kushnir 1996, Leonard and Kennett 1999). The model fitting can be performed for each guess of the onset time (Taylor et al 1992, Takanami 1991) or the fit to two fixed models fitted at each side of the possible arrival times may be used (Kvaerna 1966a,b). The minimum of the summed squared residuals occurs when two models are fitted such that the boundary of the fitting regions correspond to the onset time. In any case, the estimation process decreases the degrees of freedom in the process, thus decreasing the stability and its sensitivity. Common to all these methods is the assumption that the time interval where the phase onset occurs is known and there are sufficient segments of the time series preceding and following the onset for effect the estimation models. The approach described above is quite general and is applicable to many kinds of problems involving changes in time series.

Subtle changes in the frequency content in noisy records often give clue to a human indicating the onset of a seismic phase arrival. On the other hand, when such human capabilities are needed it simply indicates a failure of applying appropriate frequency domain prefiltering that could produce an enhanced amplitude contrast between the noise and the arrival. Appropriate prefiltering in frequency is a prerequisite for further onset time determination regardless of the method (Kvaerna 1996a,b). Various schemes for optimum pre-filtering were suggested and most of these seem to work well in practice and the exact nature of filter is not critical as long as they are reasonably close to the optimum S/N^2 shape (averages of signal amplitude spectrum divided by the squared noise amplitude spectrum). Minimum phase filters based on Kvaerna 's definition of "usable bandwidth" (Kvaerna 1995, 1996a), as well as those shaped according to S/N^2 , $S^2/(S^2+N^2)$ the latter is a Wiener filter (Whalen 1971), where S and N are signal and noise spectral amplitudes respectively, or noise-adaptive predictive filtering all enhance the amplitude contrast between the noise background preceding the onset of the signal.

This happens because both regional seismic signals and noise have similar spectral shapes in the 3-10 Hz band, in which they both fall off with frequency. These statements seem to be generally true for typical regional seismograms. Thus after suitable prefiltering has been performed, the problem reduces to, for most practical purposes, to a detection of a sudden or gradual change in trace amplitude levels.

3.2. Some CUSUM-based onset time estimation methods.

A step-like change in amplitude levels can be detected easier if a cumulative sum (CUSUM) of the squared or absolute amplitudes it is computed (Der and Shumway 1999, Iclan and Tiao 1994, Basseville and Nikiforov 1993, Shumway 1998). After imposing a linear trend to the CUSUM, a repetitive onset time estimation is performed, locating the minima or maxima of various chosen functions, by simulated annealing. The clustering in the multiple onset time estimates provides a means to assess the reliability of the process and the significance of each major arrival. In practical tests, the method has outperformed those based on testing for changes in autoregressive models.

The approaches based on the cumulative sum statistics are simple to apply and can be automated for applications in a CTBT monitoring environment. Inclán and Tiao (1996) developed a properly centered and normalized CUSUM test statistic and tabulated critical points for testing of significance. Furthermore, they developed an Iterative Cumulative Sum of Squares (ICSS) algorithm that allows sequential identification of multiple changepoints in a white noise series. In this work we have tested their approach on a set of regional seismic data.

Suppose first that a single channel time series x_κ, $\kappa=1,2,\ldots n$ is observed and we have a possible change point that is to be detected using a CUSUM type statistic. Assume that the time series x has been prewhitened and has a zero mean, so that the change in regime can be modeled simply by a change in the variance of the white noise process. Inclán and Tiao (1996) proposed using the centered and scaled cumulative sum of the squared amplitudes. First define the sum of squares function over the interval $[1\ \kappa]$ of length points as

$$C_k = \sum_{i=1}^{k} x_i^2 \qquad (1)$$

The scaled and normalized CUSUM statistic over the interval $[1,T]$ at the point $1<\kappa<T$ is defined as

$$D_\kappa = \frac{C_k}{C_T} - \frac{\kappa}{T} \qquad (2)$$

The F statistic for testing for a change of variance at time κ is

$$F_{T-\kappa,\kappa} = \left(\left(C_T - C_\kappa\right)/\left(T-\kappa\right)\right)/\left(C_\kappa/\kappa\right) \qquad (3)$$

This is, of course the standard power detector. With no change in variance in the time interval $1<\kappa<T$, $D(\kappa)$ is a monotone function of t. If the variance increases $D(\kappa)$ will have a maximum at the change point.

If we assume that the x_i are normally distributed with mean 0 and variances σ then we can obtain the likelihoods for testing one change against no change and let $NT=1$ represent one change. The likelihood for $NT=0$ is

$$l\left(N_T=0;x\right) = -\frac{T}{2}\log(2\pi) - \frac{T}{2}\log\left[C_T/T\right] - \frac{T}{2} \qquad (4)$$

The likelihood function for $NT=1$, change at point t is

$$l\left(t,N_T=1;x\right) = -\frac{T}{2}\log(2\pi) - \frac{\kappa}{2}\log\left[C_\kappa/\kappa\right] - \frac{T-\kappa}{2}\log\left[\frac{C_T-C_\kappa}{T-\kappa}\right] - \frac{T}{2} \qquad (5)$$

The best estimate of the change point is where the likelihood ratio is maximized

$$\log L\left(\kappa,\sigma_1^2,\sigma_2^2\right) \approx -\max\left\{-\frac{\kappa}{2}\log\left(1+\frac{T}{\kappa}D_\kappa\right) - \frac{T-\kappa}{\kappa}\log\left(1-\frac{T}{T-\kappa}D_\kappa\right)\right\} \qquad (6)$$

The function puts more weight on the middle of the time series. This is not a serious disadvantage since prior to applying the algorithm one has a fairly good idea where the main regional phases are (from standard detection algorithms and F-K analyses). All the previous formulas assume that the time series were pre-whitened. In doing F-tests with bandwidth limited data the degrees of freedom used in the assumed F distributions should be appropriately reduced to account for the limited bandwidth.

The paper by Chen and Gupta (1997) uses a corrected form of AIC, say

$$AIC(C(\kappa)) = -2\log L(\kappa, \sigma_1^2, \sigma_2^2) + \frac{4(T\kappa - \kappa^2 - T)}{(\kappa - 2)(T - \kappa - 2)} \quad (7)$$

for $2<\kappa<T-2$, and chooses τ as a minimizer of $AIC(C(\kappa))$ by introducing the second, penalty function term. Constructing an unbiased estimator leads to equation (7) above (Hurvich and Tsai 1989). The AIC likelihood is claimed to perform better if the break point is close to the ends of the segment, a situation that we try to avoid, however.

A binary iterative version of the CUSUM algorithm was proposed by Inclan and Tiao (1994) and Chen and Gupta (1997) which uses repetitive applications of the approach described above for subintervals of the first time interval. The method applies the following steps;

1) Calculate D(κ) from the start to the endpoint of the initial time segment
2) Search for a significant maximum as defined by equation (3). If one is found at κ_1 then
3) Search the time interval $1<\kappa<\kappa_1$ for another significant maxima (that pass an F-test)
4) Similarly search the $\kappa_1<\kappa<T$ intervals for a significant maximum
5) Continue the same procedure in each subinterval until no more significant maxima are found.

3.3. Basic building blocks of the CUSUM-based onset time estimation system

In order to apply any of the search methods for locating onsets, first one needs to segment the seismograms such that each of the segments contain only one arrival. Typically, a regional seismogram contains multiple arrivals followed by either a coda where the amplitude decays with time or remains nearly constant.

Moreover, the minima of the variants of the CUSUM functions described above will provide reasonable onset time estimates, additional refinements can greatly improve the results. The exact locations of such absolute minima may be accidental and thus may be of lesser importance than the overall layout of the regions of minima, whether they are narrowly localized or broad. The latter case implies greater uncertainties in the onset times, while the former a lesser uncertainty. It is therefore desirable to use stochastic, randomized search methods repeatedly and use the multiple onset time picks to estimate more stable onset times and their uncertainties.

3.3.1. Leaky integration

Applying leaky integration to the absolute trace amplitude generates a function which has maxima close to the trace maxima but delayed in time. This function is useful, therefore, for segmenting the seismogram between such maxiam such that each segment will contain one sudden increase of trace amplitude envelopes (a phase onset).

3.3.2. F tests.

F tests are standard tools for verifying the arrival of a new package of energy from the source, i. e. a phase arrival. In this work we pick the arrival time from the modified CUSUM $D(\kappa)$ and test whether the variances on both sides of this arrival are indeed different. In performing an F test on seismic data that has not been prewhitened one must make sure that the number of degrees of freedom is adjusted appropriately. F statistics for the assumed phase onset within one segment must pass a significance test before the onset is accepted. Otherwise the segment is declared as containing no onsets.

3.3.3. Simulated annealing.

Simulated annealing (SA) was designed to find global minima of irregular functions where many local minima may exist. It tends to disregard minor local minima and converge to the lowest points. It uses the randomized Metropolis search algorithm which is based on a thermodynamic analogy (Press et al 1986). Initially, it allows a

search using large steps in the independent variables, which may even be associated with increased values of the function. This allows the solution to "jump out" from local minima and resume searching for other minima. As "cooling" occurs such steps are accepted less and less and finally the solution will settle in broad global minima. Repeated application of SA with random starting points will give rise to *populations* of onset time estimates that can be used for evaluation of the efficiency and accuracy of the method.

3.3.4. Cluster analysis

The multiple application of SA searches automatically provides means for assessing the stability and accuracy of the onset estimates derived from the SA method. Starting out with numerous randomly chosen positions for the onset time within a search window these will converge into positions of prominent CUSUM minima and form a varying number of tight clusters. Besides these there will be hopefully much fewer scattered 'solutions' that are obviously spurious and thus must be discarded. This approach was not pursued much in our recent work but it has a considerable potential (Der and Shumway 1999). We apply the well known K-means clustering algorithm (Tou and Gonzalez 1974, Theodoris and Koutroumbas 1999) for finding the clusters in a population of SA onset times or trace amplitude maxima in this report.

3.4 Flow diagram of the process.

Figure 1 shows two ways such a process may be put together from its building blocks. One applies the SA algorithm, the other does not. The F-test makes the decision whether in a given segment a phase onset is declared or not. The one involving SA is more refined, but it takes more time for computations. The optimization of the whole process requires optimum choices in the numerous parameters required. Such are those appropriate to the prefiltering methods, the leaky integration constants, the temperatures and cooling rates and number of trials for SA, specifications needed for cluster analysis. Optimizing such parameters requires the testing of the algorithms on large amounts of data and minimizing the number of false or missed onset times

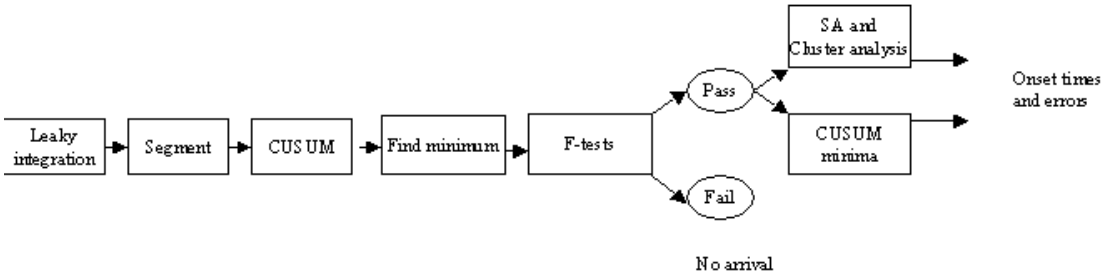


Figure 1. Flow diagram of the process.

3.4. PRACTICAL EXAMPLES OF THE APPLICATIONS OF THE METHODOLOGIES DESCRIBED ABOVE.

3. 4.1. Performance of the CUSUM Procedure for Estimating Pn Onset Times.

During the early phase of this work we have made evaluations of the performance of the CUSUM minimum and the combined CUSUM-SA procedure for picking onset times of first-arriving Pn phases under various S/N scenarios. The evaluation was based on comparing the performance of **a)** human analysts **b)** picking the absolute minimum of normalized CUSUM and keeping the arrival if the F tests is passed **c)** picking the median of multiple picks using SA on the CUSUM and taking the median of these, but discarding the result if the SA arrivals are highly scattered.

The results, reported at the annual research review meeting last year and in a subsequent annual report, will not be repeated here. We simply state that the performance of the second of these options was comparable to a human analysts picking the initial Pn arrival times. The module for Pn onset time estimation will be tested more

extensively in the near future.

3.4.2. Application of the binary iterative version of normalized CUSUM method to Segment Complete Regional Seismograms.

The iterative binary segmentation method method of Inclán and Tiao (1996) was applied to many regional seismograms. Typically, three iterations were used. During the first iteration, the largest arrival was commonly picked. In the succeeding iterations the smaller arrivals were identified. Although this binary segmentation approach works well for events where the various arrivals have grossly unequal amplitudes, it fails in many cases where there are several arrivals with comparable amplitudes. Therefore, we need more general segmentation methods while retaining much of the statistical testing machinery contained in the papers of Inclán and Tiao (1996) and Chen and Gupta (1997).

3.4.3. Methods based on seismogram segmentation.

The approach proposed below seems to work much better than the binary segmentation methods. In order to find the rapid increases in amplitude we have leaky-integrated the absolute trace amplitudes of the seismogram. The maxima of traces thus processed will be located at times later than the maximum amplitude portions of the respective phases due to the time delay introduced by the leaky integral low-pass filter. If we segment the seismogram from beginning to end using these maxima as the intermediate point then the actual onsets will be interior to these segments. If we locate the minima of the functions $D(\kappa)$ within these initial segments then we shall have the approximate locations of the phase onsets. Now, if we create windows that are centered on this preliminary onset time with the end points at the maxima of the leaky-integrated absolute amplitudes.

We have tested two methods for finding the broad maxima. One method consisted of the monitoring the amplitude differential (gradient) in the leaky-integrated absolute amplitude trace over a set time interval (typically tied to the time constant of the leaky integrator), finding a maximum and set the segment separation such that this gradient decreased by a set factor (typically 0.9). Automatic onset time picks for seismograms segmented this way are shown in **Figure 2**. The examples shown were taken from the Ground Truth data base compiled by Multimax Inc. and downloaded through the Internet. Many of these seismograms are not strictly regional, some distances are teleseismic. Consequently some broader bandpass prefiltering was needed to enhance these arrivals.

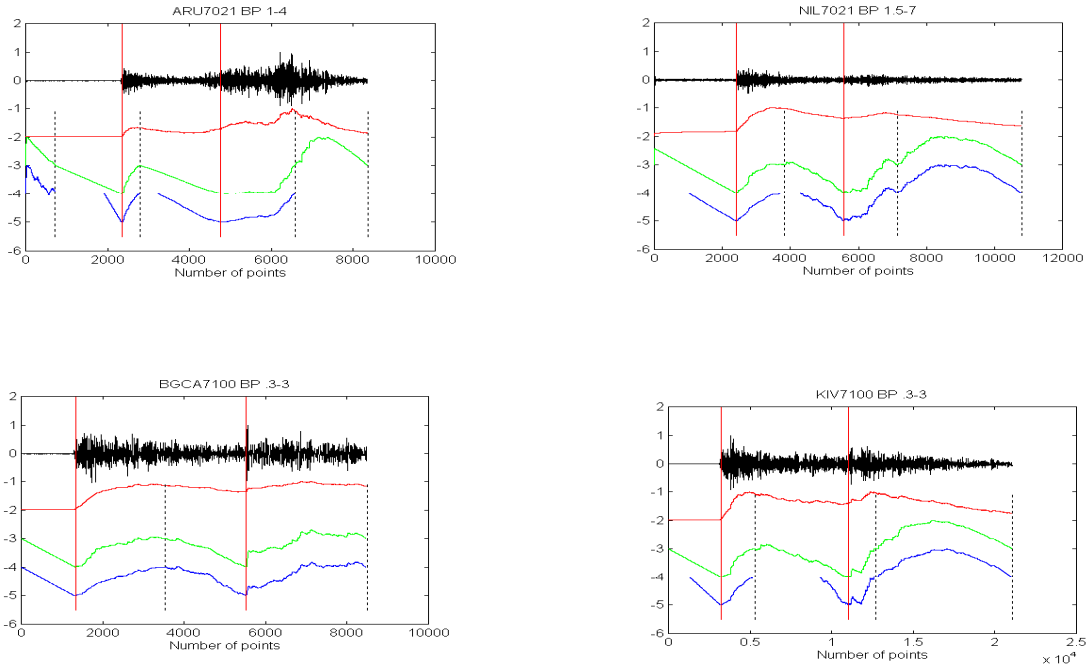


Figure 2 continued

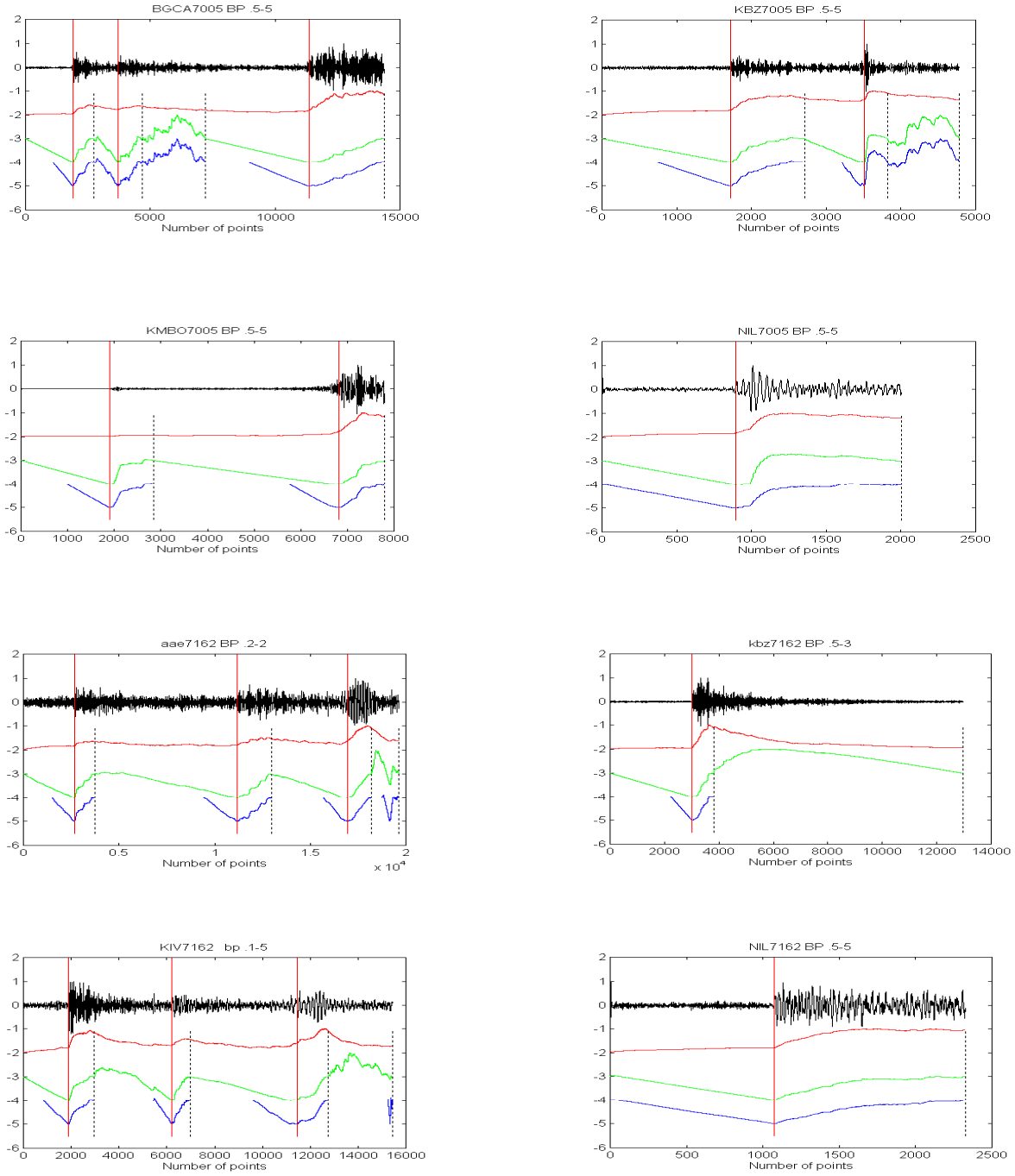


Figure 2. Examples of the decomposition of seismograms into segments bounded by the decreasing portions of the maxima of the leaky-integrated absolute amplitudes (second trace. This is followed by looking for the minima in the function D(t) of Incl□n and Tiao (1994) in each segment (third trace). This is followed by the redefinition of shorter segments designed to be centered on this minimum be bounded by the previous right side of the segment (shorter segments below). This is followed by an F-test around the minimum to determine whether the change in amplitudes is significant. An onset (vertical lines) is declared if this is the case. Such onsets can be further refined by actually defining the onsets as maxima of F or the statistics of Chan and Gupta (1997).

Another approach we have tried for finding the broad maxima was based on a cluster analysis of multiple solutions produced by simulated annealing (SA) . Since our SA program was designed for finding minima, we have simply reversed the sign of the leaky-integrated trace for such computations. The centers of the clusters for the picks of minima thus produced can be used as limits of the segments to be searched for single increases in amplitude. Note that this procedure is the same as the one we have applied for finding onset times previously (Der and Shumway 1999). Illustrations of the results of such procedures are shown in **Figure 3**. We have found that this method was somewhat more robust than the previous one.

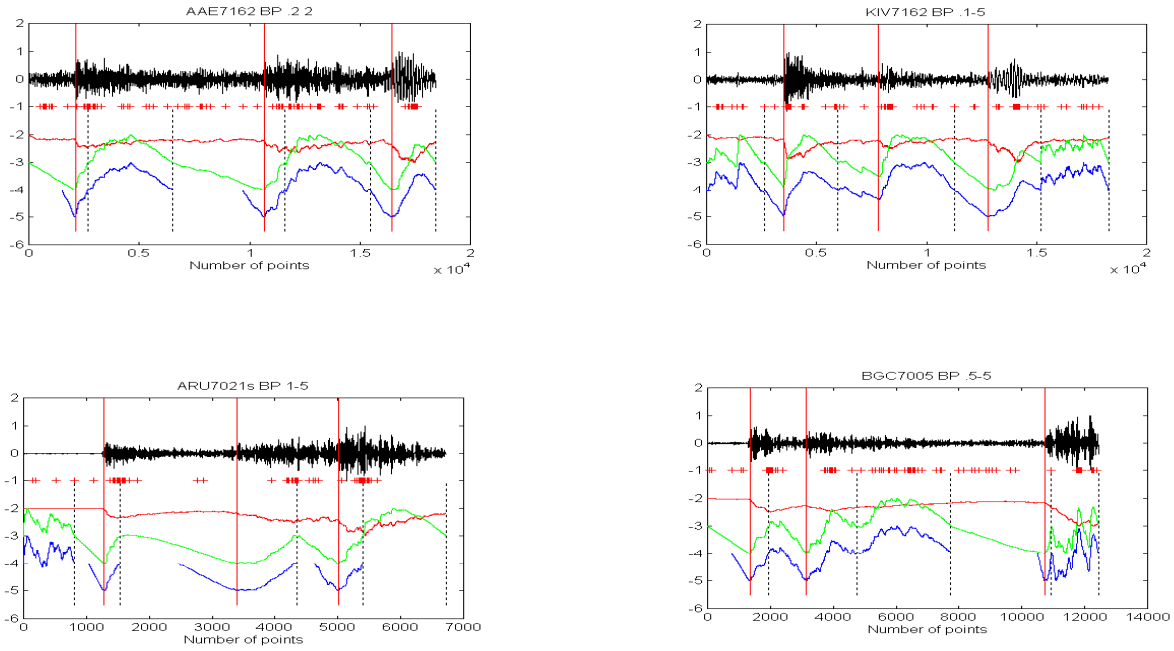


Figure 3. Examples of the decomposition of seismograms (top trace) into segments bounded by the clusters of the SA picks (plus signs) of the mimima of the sign-inverted leaky-integrated absolute amplitudes (second trace), followed by looking for the minima in the function D(t) of Inclán and Tiao (1994) in each segment (third trace). This is followed by the redefinition of shorter segments designed to be centered on this minimum be bounded by the previous right side of the segment (shorter segments below). The next step is an F-test around the minimum to determine whether the change in amplitudes is significant. An onsets (vertical lines) are declared if this is the case. The first letters in the titles are the station names and the following digits are the event 'orid'-s (see data base Schema 3.0 Manual), referring to Table I. The band-pass filters used are indicated in the rest of the title.

It appears, however, that reliable segmentation of high frequency seismograms and the automatic determination of the onset times of the various arrivals will require sophisticated algorithms. The algorithms need to have sufficient flexibility to recognize arrivals with quite different amplitudes, impulsive arrivals without codas, phases with long codas and phases where the seismogram essentially consists of a series of increases in amplitude without much decrease until the Lg coda. The latter is typical of Kola peninsula quarry blasts and the binary iterative segmentation procedures of Inclán and Tiao (1994) and Chen and Gupta (1997) seem to work well for these. For seismograms containing phases with codas the segmentation methods using SA work better. In actual implementation of such methods more than a single approach may have to be employed in interpreting seismograms in the automatic mode.

Since the methods have been tested in the interpretative MATLAB computing environment they run slow under MATLAB. This is misleading, however. According to our previous experience (Der and Shumway 1999), when implemented as compiled codes all the algorithms tested will run much faster than any human analyst could read the seismograms. SA is a very fast algorithm because it mostly involves comparisons of the magnitudes of various quantities (Press et al 1986) . In this prototyping stage we have not taken the pains, either, to fully exploit the efficient vectorized computation features in MATLAB. In the actual implementation MATLAB codes can also be compiled or linked to compiled C or FORTRAN modules.

4.0. CONCLUSIONS AND RECOMMENDATIONS.

CUSUM-based methods seem to be quite suitable for processing regional seismograms since these consist of long wavetrains and have emergent phase onsets. Since CUSUM methods emphasize changes in the properties of signals over several cycles this kinds of methods can be used to segment regional seismograms. CUSUM-based methods to pick seismic phase onset times can also be developed based on a variety of statistics that are diagnostic of polarization, slowness, and spectral changes (Jurkevics 1988, Der et al 1993). Other candidates may include instantaneous relative phase differences among components, adaptive slowness estimates or their combination.

During the course of previous work described in Der and Shumway (1999), and in the work summarized in this report, we have developed the essential building blocks for a practical implementation of an automatic seismogram interpretation algorithm. As stated above, not all the approaches that we have tried worked equally well for segmentation of seismograms and onset estimation under the various scenarios encountered in practice. For seismograms that contain steplike increases in the amplitudes of the successive phases binary iterative segmentation procedures of Inclán and Tiao (1994) and Chen and Gupta (1997) seem to work well. For seismograms containing phases with codas and variable amplitudes the segmentation methods using SA work better. Once the segments are defined numerous, previously developed approaches for the determination of the onset times described described in the literature can be applied (Inclán and Tiao 1994, Chen and Gupta 1997, Basseville and Nikiforov 1993).

Any practical algorithm package for the automatic interpretation of high frequency seismograms will have to possess sufficient intelligence to recognize various situations and chose the best algorithms. We shall implement the final code in a MATLAB environment complete with a suitable graphical user interface (Marchard 1990). Most of the algorithms described have been programmed as MATLAB M-files during the work described.

Key Words; onset times, change points, location, discrimination

5.0. REFERENCES

Basseville, M. and I.V. Nikiforov (1993), Detection of Abrupt Changes: Theory and Application. Prentice Hall Information and System Science Series, Prentice Hall, Englewood Cliffs, NJ.

Bendat, J. S., and Piersol, A. G. (1986), Random Data; Analysis and Measurement Procedures. John Wiley & Sons.

Chen, J. and Gupta, A. K. (1997), Testing and locating change points with applications to stock prices. J. Amer. Statist. Assoc., 92, 739-747.

Der, Z.A., Baumgardt,D.R. and R.H. Shumway (1993), The nature of particle motion in regional seismograms and its utilization for phase identification. Geophys. J. Int., 115, 1012-1024.

Der, Z. A. and R. H. Shumway (1999), Phase onset time estimation at regional distances using the CUSUM-SA algorithm. Phys. Earth and Planet. Int., 113,227-246.

Hurvich, C. M., and Tsai, C-L (1989, Regression and time series model selection in small samples. Biometrika, 76, 297-307.

Inclán, C., and G. C. Tiao (1994), Use of cumulative sums of squares for retrospective detection in the changes of variance. J. Amer. Statist. Assoc., 89,, 913-923.

Jurkevics, A. (1988), Polarization analysis of three-component array data. Bull. Seism. Soc. Am., 78, 1725-1743.

Kushnir, A. F. (1996), Algorithms for adaptive statistical processing of seismic array data. In 'Monitoring a Comprehensive Test Ban treaty', E. S. Husebye and A. M. Dainty Eds., Kluwer Academic Publishers.

Kvaerna, T. (1995), Automatic onset time estimation based on autoregressive processing. Semiannual Technical Summary, 1 April-30 September 1995. NORSAR, Sci. Report No. 1-95/96, Kjeller, Norway.

Kvaerna, T. (1996a), Quality assessment of automatic onset times estimated by the autoregressive method. Semiannual Technical Summary, 1 April-30 September 1995. NORSAR, Sci. Report No. 1-95/96, Kjeller, Norway.

Kvaerna, T. (1996b), Time shifts of phase onsets caused by SNR variations, Semiannual Technical Summary, 1 October 1995-31 March 1996. NORSAR, Sci. Report No. 2-95/96, Kjeller, Norway. Leonard, M., and Kennett, B. L. N. (199), Mul;ti-component autoregressive techniques for the analysis of seismograms. Phys. Earth Planet. Int., 113, 247-264.

Leonard, M., and Kennett, B. L. N. (1999), Multi-component autoregressive techniques for the analysis of seismograms. Phys. Earth. Planet. Int., 113, 247-264.

Maeda, N. (1985), A method for reading and checking phase time in auto-processing ssystem of seismic wave data (in Japanese with English abstract), J. Seismol. Soc. Jpn., 38, 365-379.

Marchard, P. (1996), Graphics and GUIs with MATLAB. CRC Press.

Press, W.H., Flannery, B.P., Teukolsky, S.A. and W.T. Vetterling (1986), Numerical Recipes: The Art of Scientific Computing. Cambridge University Press.

Shumway, R. H. (1998), An iterative cumulative sum of squares algorithm for phase onset estimation. ENSCO Technical Memo.

Takanami, T. (1991), A study of detection and extraction methods for earthquake waves by autoregressive models. J. Fac. Sci. Hokkaido, U., Ser VII, 9, 67-196.

Taylor, D. W. A., Ghalib, H. A. A. and Kimmel, R. H. (1992), Autoregressive analysis for seismic signal detection and onset time estimation. ENSCO Inc. Technical Report DCS-92-90 prepared for AFTAC.

Theodoris, S., and Koutroumbas, K. (1999), Pattern Recognition, Addison-Wesley.

Tou, J. T., and Gonzalez, R. C. (1974), Pattern Recognition Principles. Addison-Wesley.

Yokota, T., Zhou, S., Mizoue, M., and Nakamura, I. (1981), An automatic measurement of arrival time of seismic waves and its application to an on-line processing system (in Japanese with English abstract), Bull. Earthquake. Res. Inst. Univ. Tokyo, 55, 449-484.

Whalen, A. D., (1971), Detection of Signals in Noise. Academic Press.

REDUCING INFORMATION OVERLOAD IN LARGE SEISMIC DATA SETS

Jeff Hampton, Chris Young, John Merchant, Dorthe Carr and Julio Aguilar-Chang[1]

Sandia National Laboratories and [1]Los Alamos National Laboratory

Sponsored by U.S. Department of Energy
Office of Nonproliferation Research and Engineering
Office of Defense Nuclear Nonproliferation
National Nuclear Security Administration

Contract No. DE-AC04-94AL85000

ABSTRACT

Event catalogs for seismic data can become very large. Furthermore, as researchers collect multiple catalogs and reconcile them into a single catalog that is stored in a relational database, the reconciled set becomes even larger. The sheer number of these events makes searching for relevant events to compare with events of interest problematic. Information overload in this form can lead to the data sets being under-utilized and/or used incorrectly or inconsistently. Thus, efforts have been initiated to research techniques and strategies for helping researchers to make better use of large data sets. In this paper, we present our efforts to do so in two ways: 1) the Event Search Engine, which is a waveform correlation tool and 2) some content analysis tools, which are a combination of custom-built and commercial off-the-shelf tools for accessing, managing, and querying seismic data stored in a relational database.

The current Event Search Engine is based on a hierarchical clustering tool known as the dendrogram tool, which is written as a MatSeis graphical user interface. The dendrogram tool allows the user to build dendrogram diagrams for a set of waveforms by controlling phase windowing, down-sampling, filtering, enveloping, and the clustering method (e.g. single linkage, complete linkage, flexible method). It also allows the clustering to be based on two or more stations simultaneously, which is important to bridge gaps in the sparsely recorded event sets anticipated in such a large reconciled event set. Current efforts are focusing on tools to help the researcher winnow the clusters defined using the dendrogram tool down to the minimum optimal identification set. This will become critical as the number of reference events in the reconciled event set continually grows. The dendrogram tool is part of the MatSeis analysis package, which is available on the Nuclear Explosion Monitoring Research & Engineering Program Web Site (http://www.ctbt.rnd.doe.gov/ctbt/data/matseis/matseis.html).

As part of the research into how to winnow the reference events in these large reconciled event sets, additional database query approaches have been developed to provide windows into these datasets. These custom built content analysis tools help identify dataset characteristics that can potentially aid in providing a basis for comparing similar reference events in these large reconciled event sets. Once these characteristics can be identified, algorithms can be developed to create and add to the reduced set of events used by the Event Search Engine. These content analysis tools have already been useful in providing information on station coverage of the referenced events and basic statistical information on events in the research datasets. The tools can also provide researchers with a quick way to find interesting and useful events within the research datasets. The tools could also be used as a means to review reference event datasets as part of a dataset delivery verification process. There has also been an effort to explore the usefulness of commercially available web-based software to help with this problem. The advantages of using off-the-shelf software applications, such as Oracle's WebDB, to manipulate, customize and manage research data are being investigated. These types of applications are being examined to provide access to large integrated data sets for regional seismic research in Asia. All of these software tools would provide the researcher with unprecedented power without having to learn the intricacies and complexities of relational database systems.

Key Words: information overload, Event Search Engine, winnowing, dendrogram, tools, database, WebDB.

OBJECTIVE

The main objective of our research is to provide tools and techniques that can help seismic event monitoring researchers make better use of large event catalogues. One part of our effort focuses on developing a method to identify similar waveforms in a large archived set. Another aspect of our research involves improved methods for accessing event catalog data stored in a relational database system. We feel that proper use of relational database systems will greatly improve the researchers' ability to utilize and understand the data in their catalogs.

RESEARCH ACCOMPLISHED

Below we discuss three technologies that have been developed or are being researched in order to fulfill the objectives described above. These are: 1) Event Search Engine, 2) Content Analysis Tools, and 3) WebDB.

1) *Event Search Engine*:

We are developing a set of tools known as the Event Search Engine (ESE) to provide a way to search large seismic data sets in an optimized and faster way based on a waveform correlation. The use of waveform correlation to identify similar events is well-established (e.g. Israelsson, 1990; Harris, 1991; Aster and Scott, 1993; Riviere-Barbier and Grant, 1993), but there are problems with applying it to large data sets. If a researcher has a catalog of several thousand events or more, the time it would take to compare all the catalog waveforms with a waveform of interest could be prohibitive, at least for common use. The ESE is being developed to deal with this problem.

One component of the ESE is a hierarchical clustering tool known as the dendrogram tool, which is written as a MatSeis graphical user interface (GUI). The dendrogram tool allows the user to build dendrogram diagrams for a set of waveforms, which would typically be an archived set plus one from a current event of interest. These diagrams can be used to establish any groupings of similar waveforms within the set. Dendrograms are built as an iterative process in which the most similar set of waveforms is found first and formed into a group, and the next most similar pair is found, with the group considered in the same way as individual waveforms. The trick to this method is in the way the correlations are calculated between the individual waveforms and the group. There are many methods to do this (e.g. single linkage, complete linkage, flexible method – see Krzanowski, 1988), and our tool allows the user to choose which method they want to use. Prior to calculating the dendrogram, the user can apply various signal-processing parameters to improve the correlation including phase windowing, down-sampling, filtering, and enveloping. We also allow the clustering to be based on two or more stations simultaneously, which is important to bridge gaps in sparsely recorded regional events. Based on the settings the user selects, dendrograms can be quickly and easily generated for a variety of clustering techniques in combination with different waveform filtering and down-sampling choices. This allows the researcher to find the optimal combination for his research goals.

The dendrogram picture that is produced as a result of the waveform comparison shows the researcher in a concise visual way the clusters of similar waveforms. (See Figure 1) The waveform of interest that was selected is highlighted so the researcher can see at a glance how it fits in with the other waveforms. For example, if the waveform of interest joins to a group at a low correlation level, then there is a clear indication that the waveform of interest is not like any of the other waveforms compared.

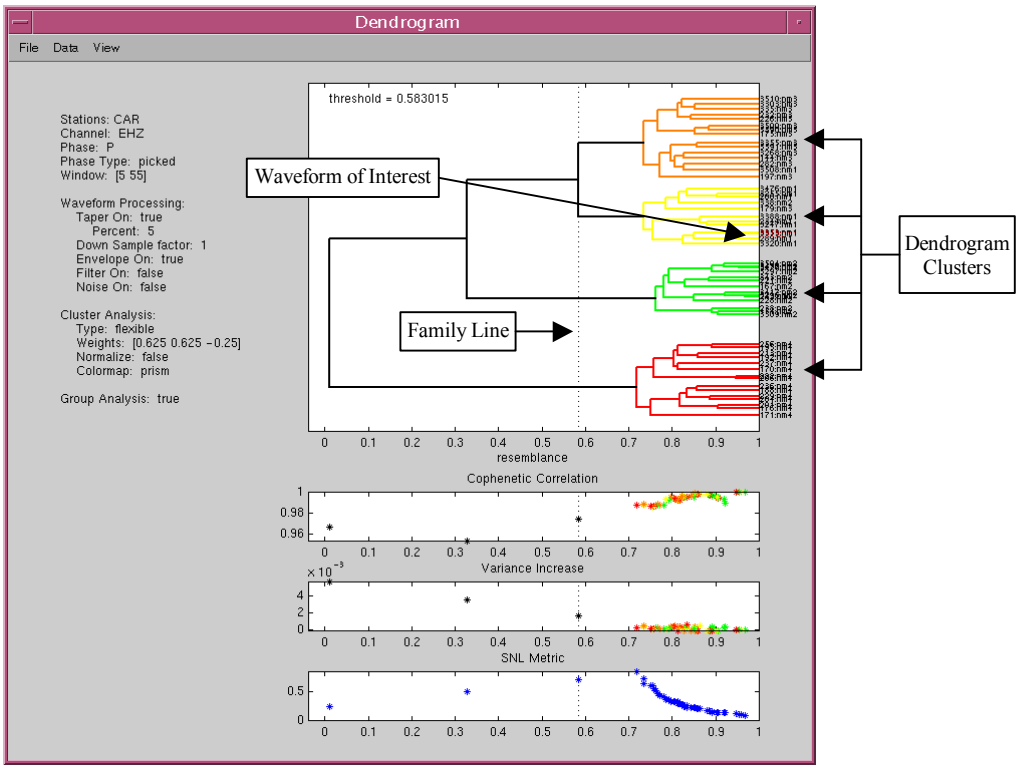


Figure 1. Example Dendrogram Cluster.

Perhaps the least understood aspect of dendrogram analysis is where to draw the vertical line that establishes the resulting clusters, which we call families. Our default location for this line is where the largest drop between successive cophenetic correlations occur (Ludwig and Reynolds, 1988). Cophenetic correlation is a measure of the correlation between the actual waveform correlations and those predicted by the dendrogram. A cophenetic correlation value can be calculated after each join in the iterative dendrogram formation process, comparing actual and theoretical values for only the waveforms that have been clustered to that point. Note that cophenetic correlations must be exactly 1.0 until a waveform is joined to a group, because the actual and theoretical correlations of a waveform to another waveform are the same. As a method of automatically establishing the family line, we have found that cophenetic correlation works a relatively small amount of the time. However, we continue to use it because we have found no better method and because the plot of cophenetic correlation sometimes proves useful in understanding the dendrogram. In fact, the automatically chosen location of the family line is not particularly important as the user can move the line to any position and see how this affects the families. To make this clearer, whenever the line is moved, we assign a different color to each family to the right of the line and redraw the dendrogram.

This coloring is also used for plots of the waveforms and of the locations of the events. The waveforms can be sent to the MatSeis utility Freeplot, where they will appear in the same order as in the dendrogram with each waveform correctly shifted for the best correlation with the waveform immediately above it. (See Figure 2) This allows the user to quickly evaluate whether the families in the dendrogram are grouping waveforms with useful characteristics. If the data is sent to the map, the result is a plot of the locations of each event with the symbol assigned the same color as from the dendrogram. (See Figure 3) This is a very useful option which, when combined with the waveform plot, can be used to evaluate the locations of a set of similar events. To facilitate this, the user can draw a box around any set of origins in the map and highlight this same set back in the dendrogram to see whether or not they have been grouped.

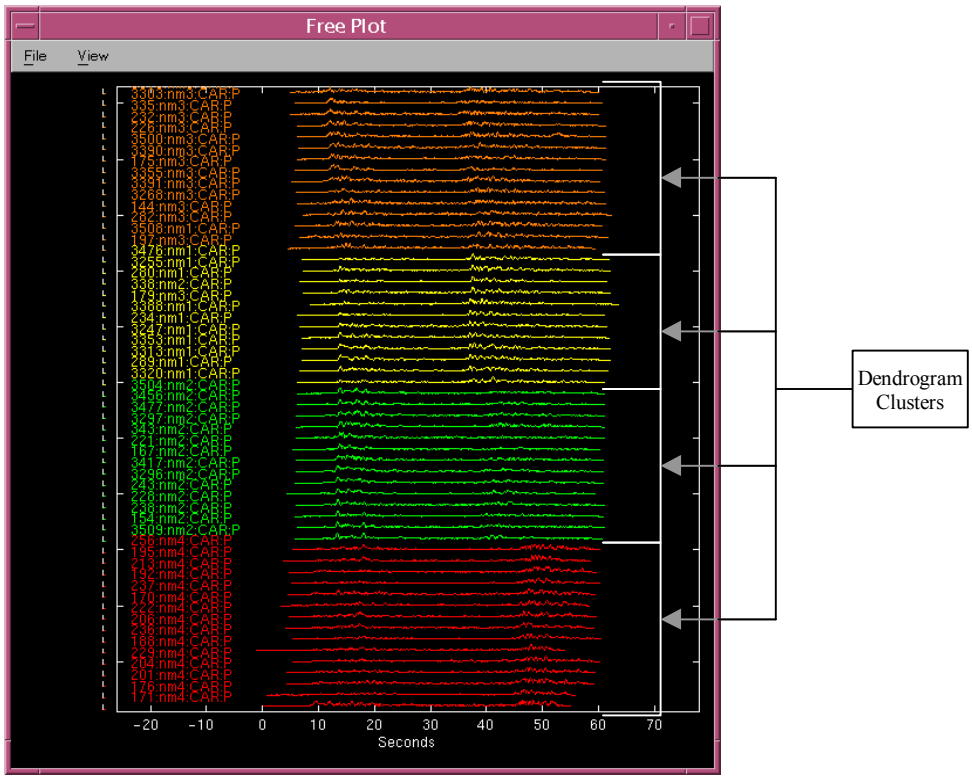


Figure 2. Freeplot Sample Screen.

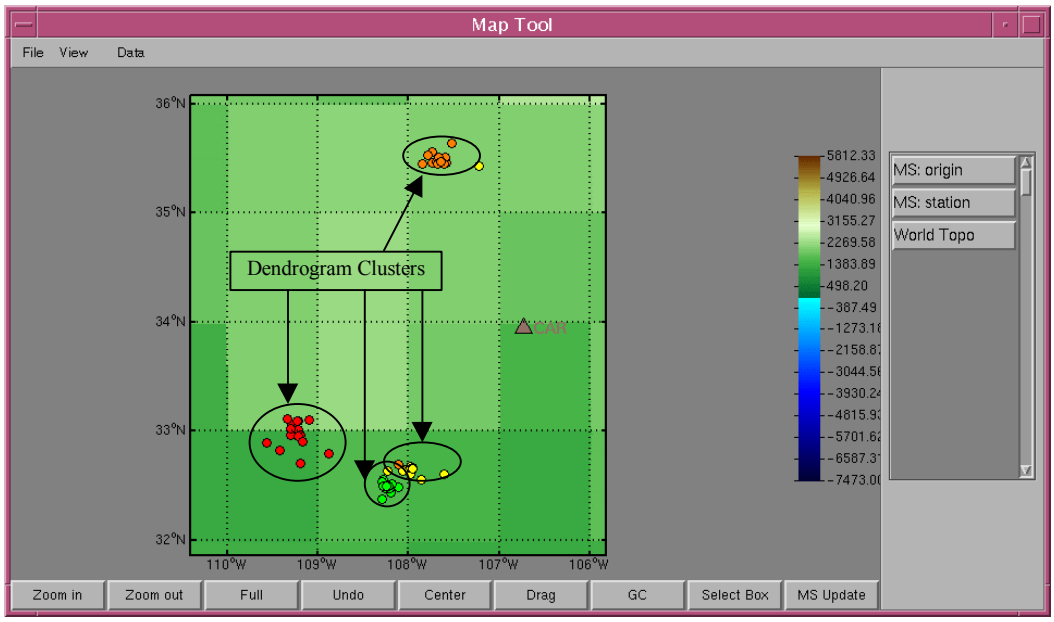


Figure 3. Map Tool Sample Screen.

2) *Content Analysis Tools*:

One of the problems faced by us in order to begin using the dendrogram tool with large data sets was how to find the stations with good waveform coverage, which would lead to meaningful dendrograms. Requesting a set of waveforms for a large list of origins is a time-consuming process even if they are managed with a relational

database, so proceeding with one station after another can be tedious. A better solution is to provide some means to see which of the stations is best represented in the data set, and to work on these first. This was one of the springboards that started us thinking about ways of visualizing summary information about the data sets that we were using. If we had a dynamic way of summarizing the content of our data sets, we could considerably improve the process of creating a dendrogram. Therefore, several web-based tools were developed to produce detailed listings and several choices of charts that would help us to understand our data sets better.

The web-based tools we developed allow the user to query the database data sets based on several criteria such as station, channel, latitude range, longitude range, and date range. (See Figure 4) These tools also distinguish between querying against origins with waveforms and origins with arrivals. These content analysis tools allow the researcher to quickly visualize their data sets given a set of user-supplied values. All the while, the researcher hasn't had to deal with the database directly or learn SQL, a database query language, to formulate their queries.

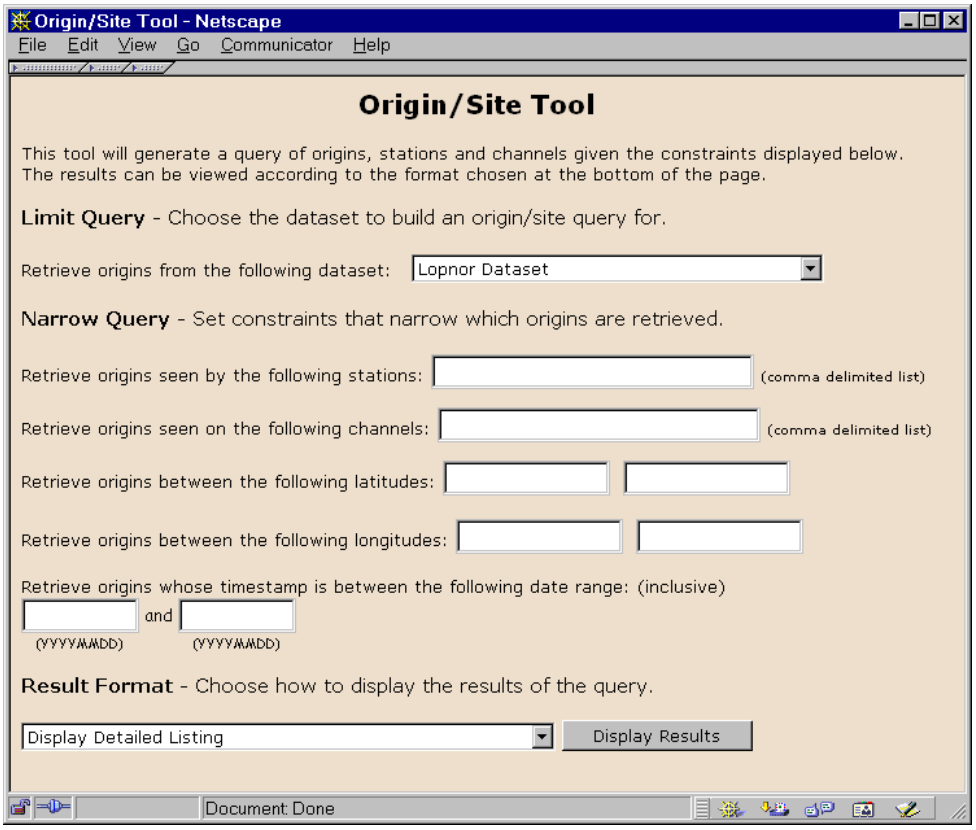


Figure 4. Content Analysis Tools Query Screen.

The results of these queries can be displayed in different user-selectable ways. The detailed listing for origins with waveforms produces a table containing the origins with their associated stations. In the corresponding table cells, waveform or arrival availability is noted by channel. The listing provides researchers with specific information about the origins that the charts don't include. The charts, however, include information on 1) total number of origins per station ranked from most to least origins seen, 2) total number of origins per station broken down by year when seen ranked from most to least total origins (See Figure 5), 3) total number of origins per year, 4) number of origins per number of stations, and 5) number of origins per number of stations broken down by year when seen. The charts are extremely useful to the researchers in presenting the "big picture" aspects for the data set being queried. These aspects include such things as the distribution of origins to stations, origin coverage, yearly coverage, etc.

Like the dendrogram tool, it helps to visualize the results based on the location of the origins on a map. Thus an ArcView based version of the query interface was built to complement the web-based applications. Using this interface, the researcher can perform the exact same query they used for the web-based tools to present the resulting origins geo-located on a map. The origins are also color-coded based on the year of the event. This makes it easier to compare with the plots broken down by year. (See Figure 6)

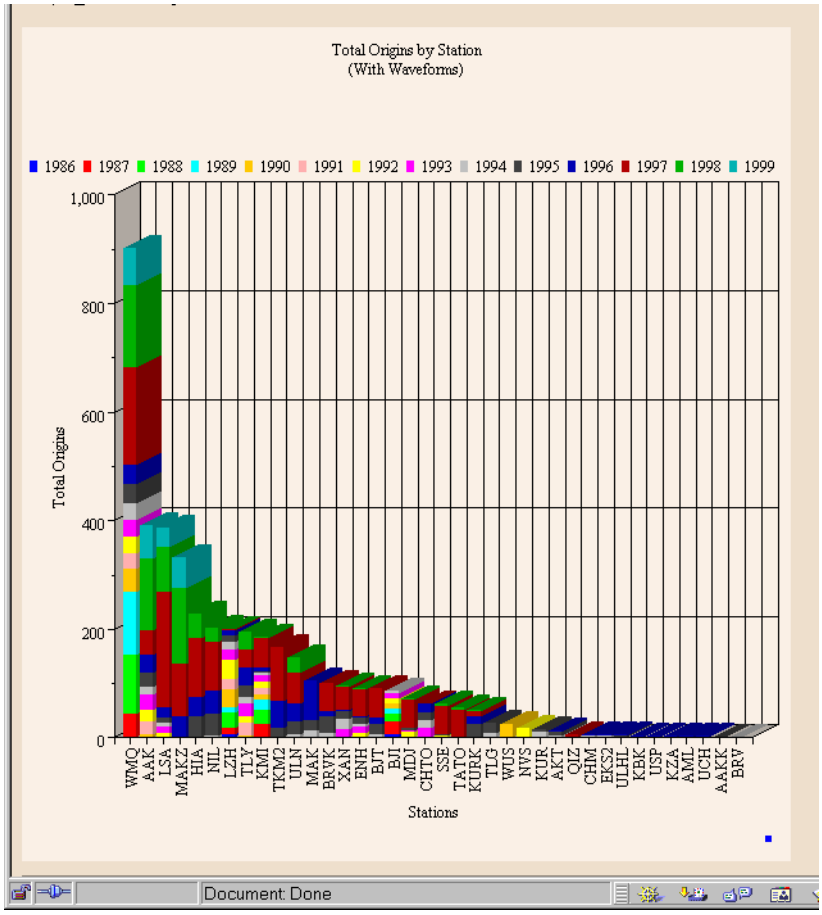


Figure 5. Sample Total Origin Plot by Station broken down by year.

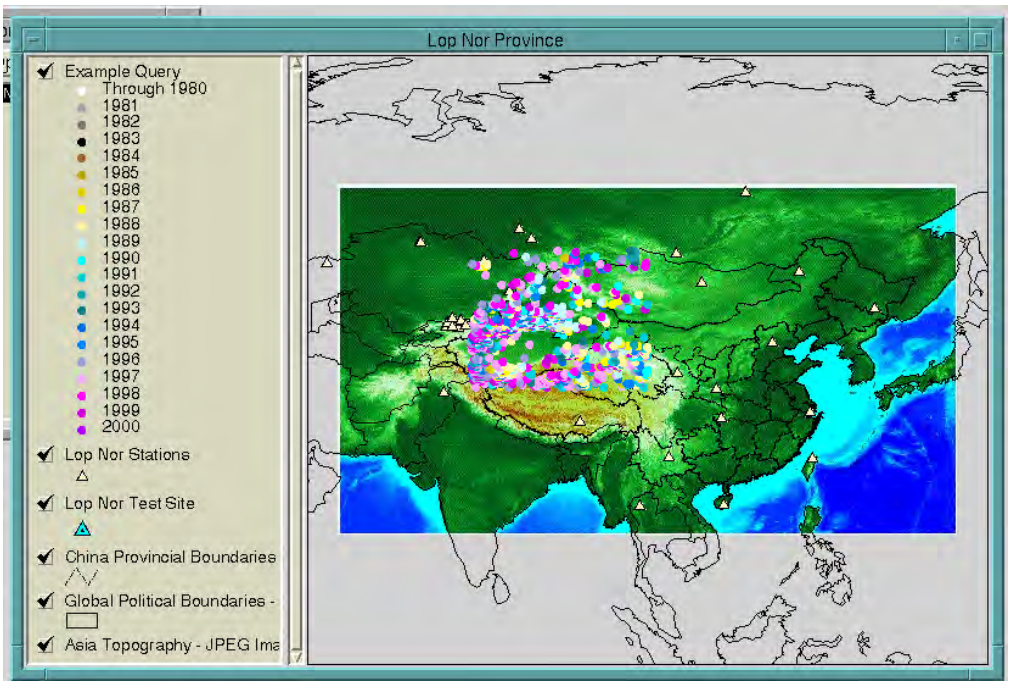


Figure 6. ArcView Sample Results Screen.

3) *WebDB*:

In the same way the web-based Content Analysis tools allow the researcher to query the database without having to know much, if anything, about SQL, Oracle's WebDB can be used by researchers to manage, explore, and manipulate seismic data in their research databases. WebDB provides an out-of-the-box web-based interface to look at the data contained within the database. All that is required from the researcher to use this tool is a web browser, such as Netscape® Navigator or Microsoft® Internet Explorer.

One of the major problems associated with storing seismic data in a sophisticated relational database management system is knowing how to efficiently access and use this data. Until now researchers had to learn SQL in order to access and display the data contained in a relational database system. WebDB is an off-the-shelf software application that gives researchers the ability to access reports that dynamically query the database tables containing seismic data using selection criteria specified by the researcher. The researcher can run a report and specify, for example, a latitude-longitude window and a time range and see the results displayed in either html, plain text ASCII, or MS Excel formats. Researchers with an intimate knowledge of the underlying database structure can create their own reports and make them available to other researchers. One of the useful features of WebDB is that these reports can contain links to other WebDB components, such as other reports with more detailed information and their associated charts, which can be used to graphically display the results of the pre-created query. The ability to display results in a graphical manner using WebDB is not as advanced as the graphical capabilities of the Content Analysis Tools described above; however, it provides charting options at a more basic level.

<u>How can WebDB help a seismic researcher?</u>

Following is a simple example of the practical application of using WebDB to look at the contents of a seismic research database.

A researcher accesses via a web browser a report that contains a summary list of events found in a given area of interest. The researcher creates this report by simply providing a latitude range and longitude range in a parameter entry form similar to the one shown in Figure 7.

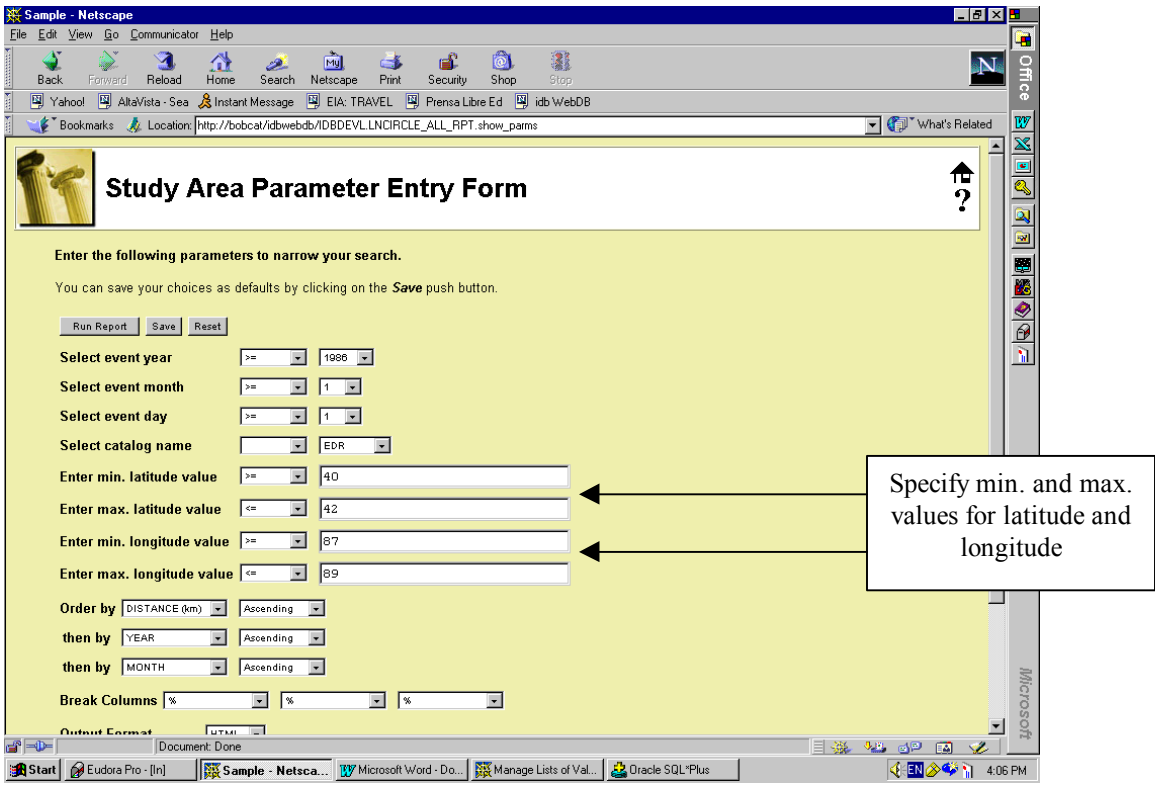


Figure 7. WebDB Create Report Sample Sceen.

This report contains event summary information such as the origin identification number (origin id), latitude, longitude, depth, magnitude, and time of the events. (See Figure 8)

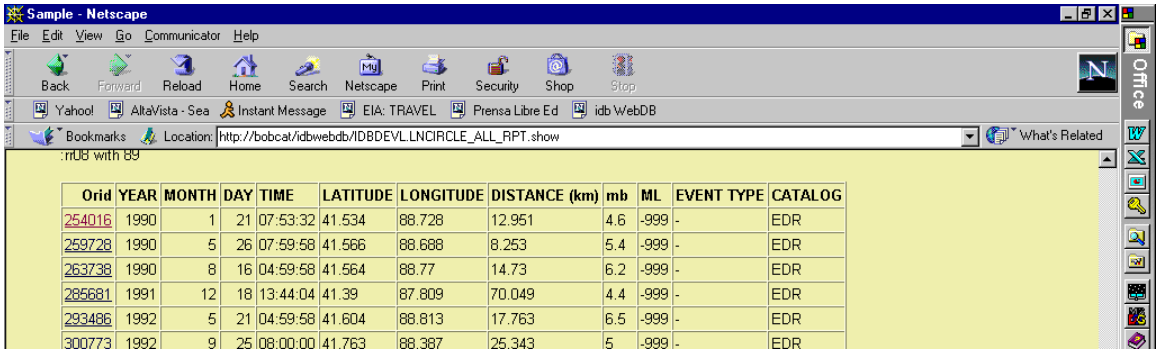


Figure 8. WebDB Sample Report.

By clicking on the origin id link, the researcher will then be presented a report that contains a deeper level of detail regarding the chosen event, such as Julian date and epoch time, number of associated phases, number of locating phases, geographic region number, seismic region number, estimated depth from depth phases, and much more event-specific information. (See Figure 9)

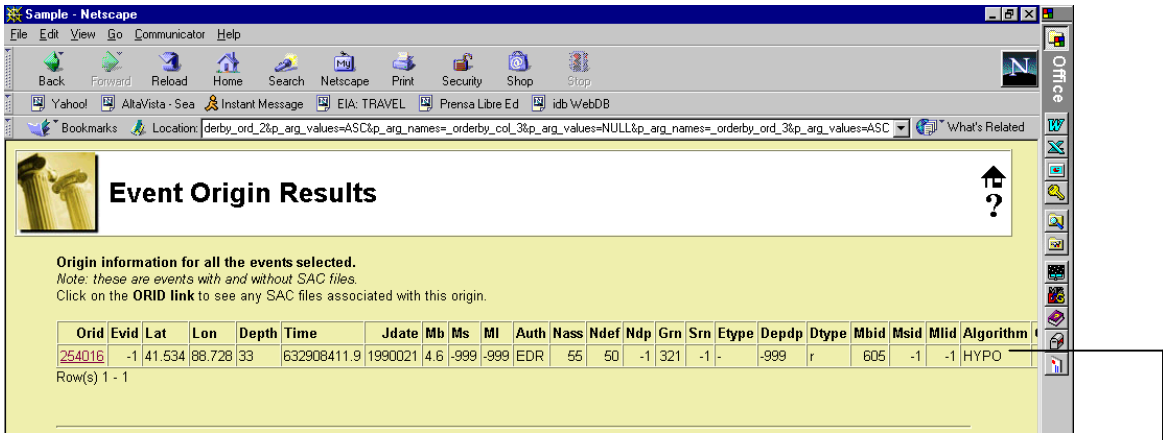


Figure 9. WebDB Linked Report Sample.

The researcher can then continue the drill-down process and, by clicking on the event link from this more-detailed report, he can see a third report which contains a listing of all the waveform files associated with the chosen event. (See Figure 10) This waveform file report can then be formatted and saved as a plain text ASCII file, which can in turn be used as data input to other applications, such as SAC (Seismic Analysis Code).

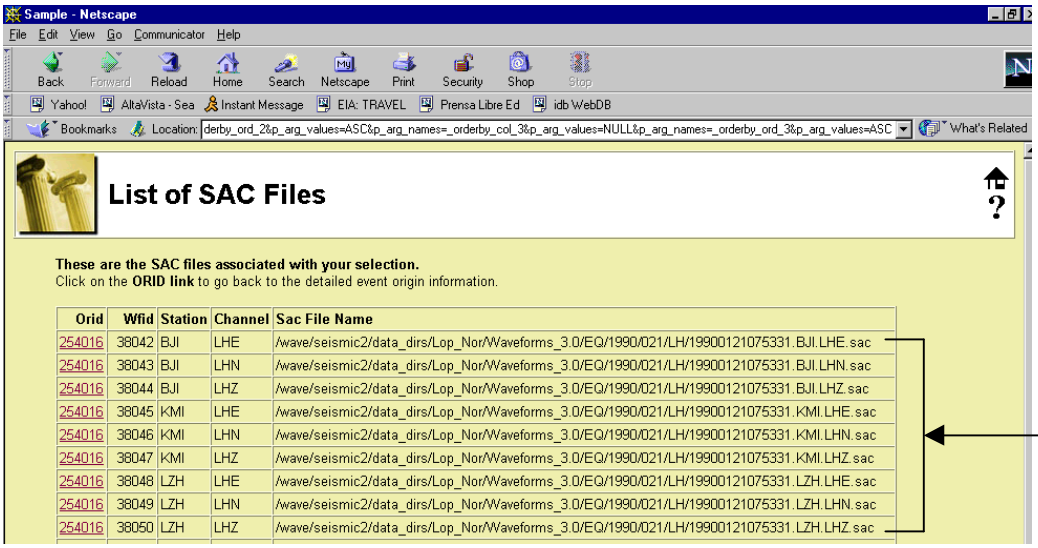


Figure 10. WebDB Drill-Down Example.

Alternatively, the origin id link can take the researcher to a different report which shows information pertaining to all the arrivals recorded for this event, such as station names that recorded the event, channels, phases recorded with those channels, arrival times, signal type, azimuth, amplitude of measurement, period, signal to noise ratio, and many more parameters.

CONCLUSIONS AND RECOMMENDATIONS

Each of the tools presented in this paper deal with different aspects of information overload. The Event Search Engine via the dendrogram tool can be used to find similar waveforms from which a possible reduced set can be generated. The content analysis tools help the researcher to ask “big picture” type questions about their data sets and present the results in various forms. Oracle’s WebDB provides a simple wizard-style approach to creating interfaces for viewing, using, and managing relational database data.

For the Event Search Engine, our future work will focus on necessary modifications to process very large (>500) sets of waveforms. We believe that to do this, the data set must be broken down into subsets, which can then be processed sequentially. As each subset is processed, all redundant, sufficiently similar, waveforms are winnowed and the resulting set is passed on to process with the next subset. Because many of the waveforms may have been automatically collected and thus may not contain good signals, we will also need to build in a mechanism to weed out low quality waveforms which add nothing to the resultant dendrogram.

We believe that we have just scratched the surface on the kinds of listings and plots that can be provided by the content analysis tools. We think these other listings and plots will be even more useful in providing insight into a researcher's data set. However, even at this early stage of development, we have found these tools to be useful for various purposes. On the one hand, the researchers will find it a useful tool to find holes in their data sets where they might need to do more data gathering to build a more complete data set. While on the other hand, the researcher who wants to use a data set will find it a useful tool for browsing the data set content to get a feel for what is in the particular data set they are interested in. In the near future we would like to expand the plotting capability to multiple dimensions, such as plotting total origins by number of stations by magnitude, or total origins by station broken down by depth, etc. We will also be increasing the number of constraints by which a query can be limited by, such as station distance, azimuth gap, depth, magnitude, etc. All of these enhancements should combine to give the researcher tremendous power and accessibility to their database stored data sets.

REFERENCES

Aster, R. C. and J. Scott (1993). Comprehensive characterization of waveform similarity in microearthquake data sets, Bull. Seism. Soc. Amer., 83, 1307-1314.

Harris, D. B. (1991). A waveform correlation method for identifying quarry explosions, Bull. Seism. Soc. Amer., 81, 2395-2418.

Israelsson, H. (1990). Correlation of waveforms from closely spaced regional events, Bull. Seism. Soc. Amer., 80, 2177-2193.

Krzanowski, W. J. (1988). Principles of multivariate analysis: a user's perspective, Oxford Univ. Press, Oxford.

Ludwig, J. A., and J. F. Reynolds (1988). Statistical ecology, a primer on methods and computing, John Wiley & sons, New York, NY, 337 pp.

Riviere-Barbier, F. and L. T. Grant (1993). Identification and location of closely spaced mining events, Bull. Seism. Soc. Amer., 83, 1527-1546.

FORMATION OF GROUND TRUTH DATABASES AND OTHER STUDIES FOR REGIONAL SEISMIC RESEARCH

Ivan Henson, Indra Gupta, and Robert Wagner
Multimax, Inc.

Sponsored by The Defense Threat Reduction Agency
Arms Control Technology Division
Nuclear Treaties Branch

Contract No. DSWA01-98-C-0156

ABSTRACT

In the second year of this project, the main objective continues to be the formation of databases providing ground truth for regional seismic research conforming to the latest Center for Monitoring Research (CMR) schema. The effort focuses on events in the CMR Calibration Event Bulletin (CEB) from China, the former Soviet Union, and North America. Selected CEB events are re-analyzed using the seismic analysis software *geotool* starting with the Reviewed Event Bulletin (REB) solutions. Modifications to the original REB results include mostly arrival phase re-timings and adding missed phases, including depth phases. New waveform data are retrieved and analyzed from available IRIS stations mostly within 25 degrees distance. A modified version of *LocSAT*, called *Locate*, which uses a graphical user interface and allows interactive processing to generate location results, is used to locate the CEB events. Two sets of location results per event are derived: the first by using only the revised IDC arrivals, and the second by using both the IRIS and revised IDC data.

Analysis of datasets of 70 CEB events in China and 80 CEB events in the former Soviet Union (FSU) has been completed. Re-analysis of the Chinese data included using waveforms from over 140 IDC stations contributing over 4000 arrivals, supplemented by nearly 3800 waveforms from over 130 IRIS stations providing nearly 2300 additional arrivals. Similarly, the FSU data included not only waveforms from about 130 IDC stations contributing over 4000 arrivals, but also nearly 4000 waveforms from more than 160 IRIS stations providing over 2300 new arrivals. The most important contribution of the IRIS data is the addition of a large number of arrivals from regional phases. Similar analysis of CEB events in North America, based on the use of both IDC and IRIS stations, is in progress.

An examination of the travel time residuals versus epicentral distance, based on the use of IASPEI91 travel time tables, for both the Chinese and FSU datasets indicated that the residuals for all phases, derived from the combined use of the IRIS and revised IDC data, show both positive and negative scatter which increases with distance. The residuals are small for P, Pn, and Pg, with average values less than 0.5 sec. But for both Sn and Lg, the residuals are large and mostly negative (average values several sec negative), suggesting that the IASPEI91 tables for these two phases are not strictly valid for these two regions.

Other studies included an examination of aftershock activity due to a 100 ton chemical explosion at the Degelen, Kazakh Test Site on 22 August 1998. Analysis of aftershock data from a suspected nuclear event is one of the principal technologies employed for the on-site inspection part of CTBT monitoring. All available aftershock data for 25 days after the explosion were first retrieved and scanned. Seismic events recorded by a local network of six three-component stations indicate at least 669 possible aftershocks that were recorded at two or more stations. The events show strong attenuation with distance and no clear evidence of diminished activity after 25 days. Locations of 14 well recorded aftershocks, obtained by using a closely spaced network of recording stations, showed all epicenters to lie within less than 200 m of the 100-ton shot. This implies that aftershock locations determined within several days of the detonation time of an explosion may provide a fairly accurate location of ground zero.

OBJECTIVE

The overall objective of this project is to improve monitoring of the Comprehensive Test Ban Treaty (CTBT), which requires the ability to detect, locate and identify seismic events. Once a suspicious event has been detected, its location must be accurately determined as a precursor to event identification and potential on-site inspections. Following last year's effort (Henson *et al*., 1999), the main objective continues to be the formation of databases which provide improved ground truth for events in China, former Soviet Union (FSU), and North America, as selected from the Calibration Event Bulletin (CEB) established at the Center for Monitoring Research (CMR). Re-analysis of the International Data Center (IDC) data combined with retrieval and analysis of selected Incorporated Research Institutions for Seismology (IRIS) data leads to improved location and depth estimates of CEB events. Additional work included an examination of aftershock activity due to a 100 ton chemical explosion at the Degelen, Kazakh Test Site; this is useful because analysis of aftershock data from a suspected nuclear event is one of the principal technologies employed for the on-site inspection part of CTBT monitoring.

RESEARCH ACCOMPLISHED

(a) Formation of Databases and Related Study

Selected CEB events from China, the former Soviet Union, and North America are re-analyzed using the seismic analysis software *geotool,* starting with the Reviewed Event Bulletin (REB) solutions. The original REB results are improved by re-timing phase arrivals and adding missed phases, including depth phases. New waveform data from IRIS stations are retrieved and the arrival times of various phases are determined. Note that the IRIS stations are selectively retrieved so that mostly regional and near teleseismic distances are represented (up to 25 degrees), with additional data for teleseismic stations which fall within the largest azimuthal gap (up to about 50-70 degrees) and near the PKP caustic. The CEB events are re-located by using a modified version of *LocSAT*, called *Locate*, which uses a graphical user interface and allows interactive processing to generate location results. For each event, two sets of location results are derived: the first by using only the revised IDC arrivals, and the second by using both the IRIS and revised IDC data.

Analysis of datasets of 70 CEB events in China and 80 CEB events in FSU has been completed. Waveforms from over 140 IDC stations contributing over 4000 arrivals, supplemented by nearly 3800 waveforms from over 130 IRIS stations providing nearly 2300 additional arrivals, contributed to the re-analysis of the Chinese data (Henson *et al*., 1999). The FSU data included waveforms from about 130 IDC stations contributing over 4000 arrivals, and nearly 4000 waveforms from more than 160 IRIS stations providing over 2300 new arrivals. The REB epicentral locations of these 80 FSU events are shown in Figure 1 along with the locations of both IDC and IRIS stations that recorded these events. Note the large number of IRIS stations at regional distances for most of these events. A comparison of the propagation paths available in the original REB dataset and the IRIS and revised IDC dataset for Pn and Lg, shown in Figures 2 and 3, respectively, clearly demonstrates the significant contribution the IRIS data have made in providing additional regional phases.

The results obtained from analysis of all 80 CEB events in FSU were delivered to the CMR. Each event location consists of four CSS3.0 files, including the origin, origerr, arrival, and assoc database tables. Therefore, a total of 640 such database files were delivered to CMR ready for installation into their CEB database. All IRIS waveform data that contributed to the 80 CEB events in FSU were also delivered to the CMR on one 8 mm archive tape in CSS3.0 format. Analysis, similar to that carried out for the Chinese and FSU events, has been completed for about 100 CEB events in North America by using waveform data from both IDC and IRIS stations.

The *Locate* software uses the IASPEI91 tables in order to obtain predicted travel times for a suite of seismic phases at various distance and depth ranges. Frequently, the arrival time residuals for various phases were observed to be too large to be selected as defining phases. In order to determine whether these residuals show any systematic trends, we made plots of the dependence of observed arrival time residuals with distance for P and the four regional phases, Pn, Pg, Sn, and Lg for both the China and FSU data. The residuals for all phases, based on the "revised IDC + IRIS" arrival times, show generally larger scatter (both positive and negative) with increasing distance. The residuals are small for P, Pn, and Pg, with average values less than 0.5 sec. But for both Sn and Lg, the residuals are large and mostly negative (average values several sec negative), suggesting that the IASPEI91 travel time tables for

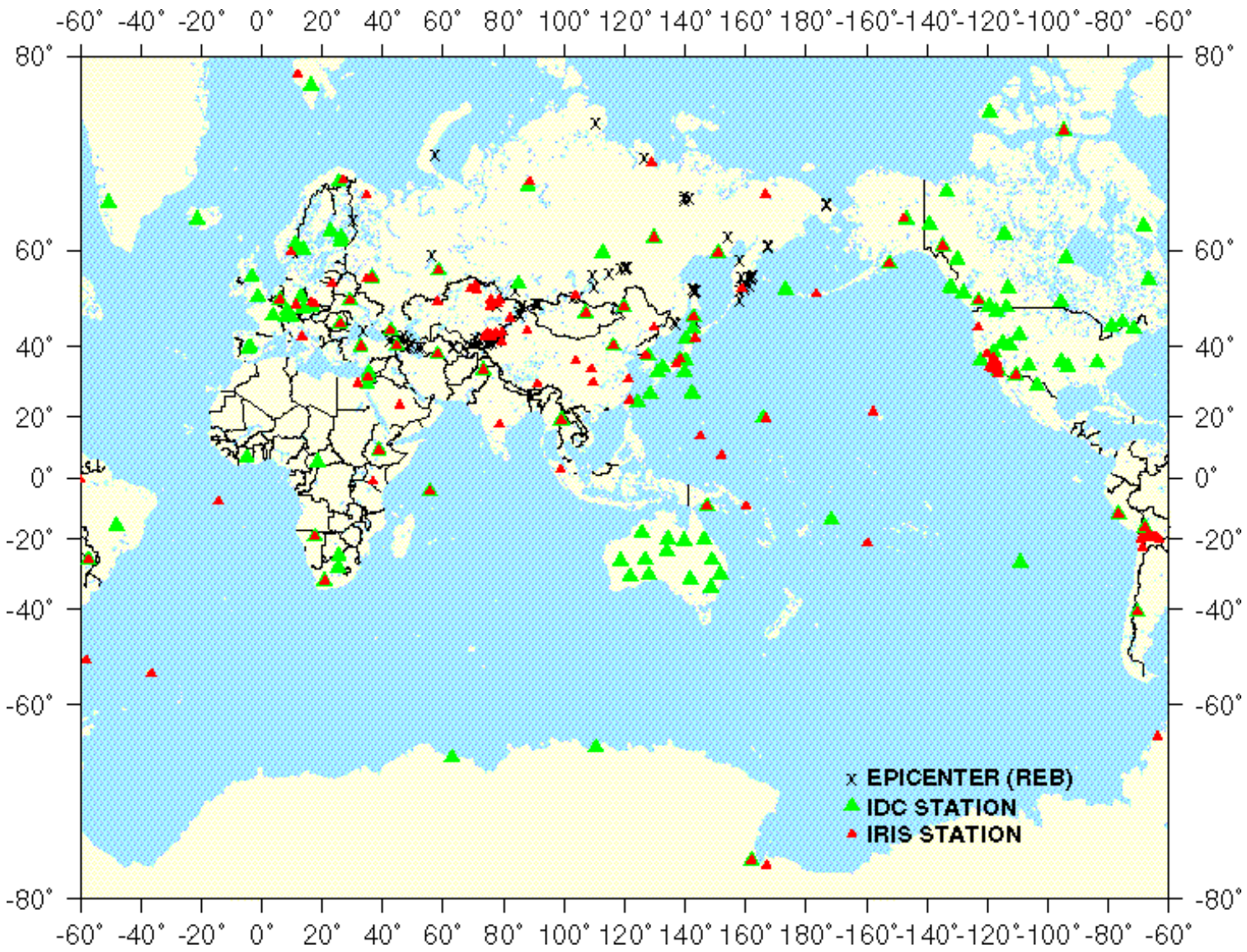


Figure 1. REB epicentral locations of 80 events in the former Soviet Union (FSU) and the IDC and IRIS recording stations which provided waveform data analyzed in this project. Note the large number of IRIS stations at regional distances for most of the 80 FSU events.

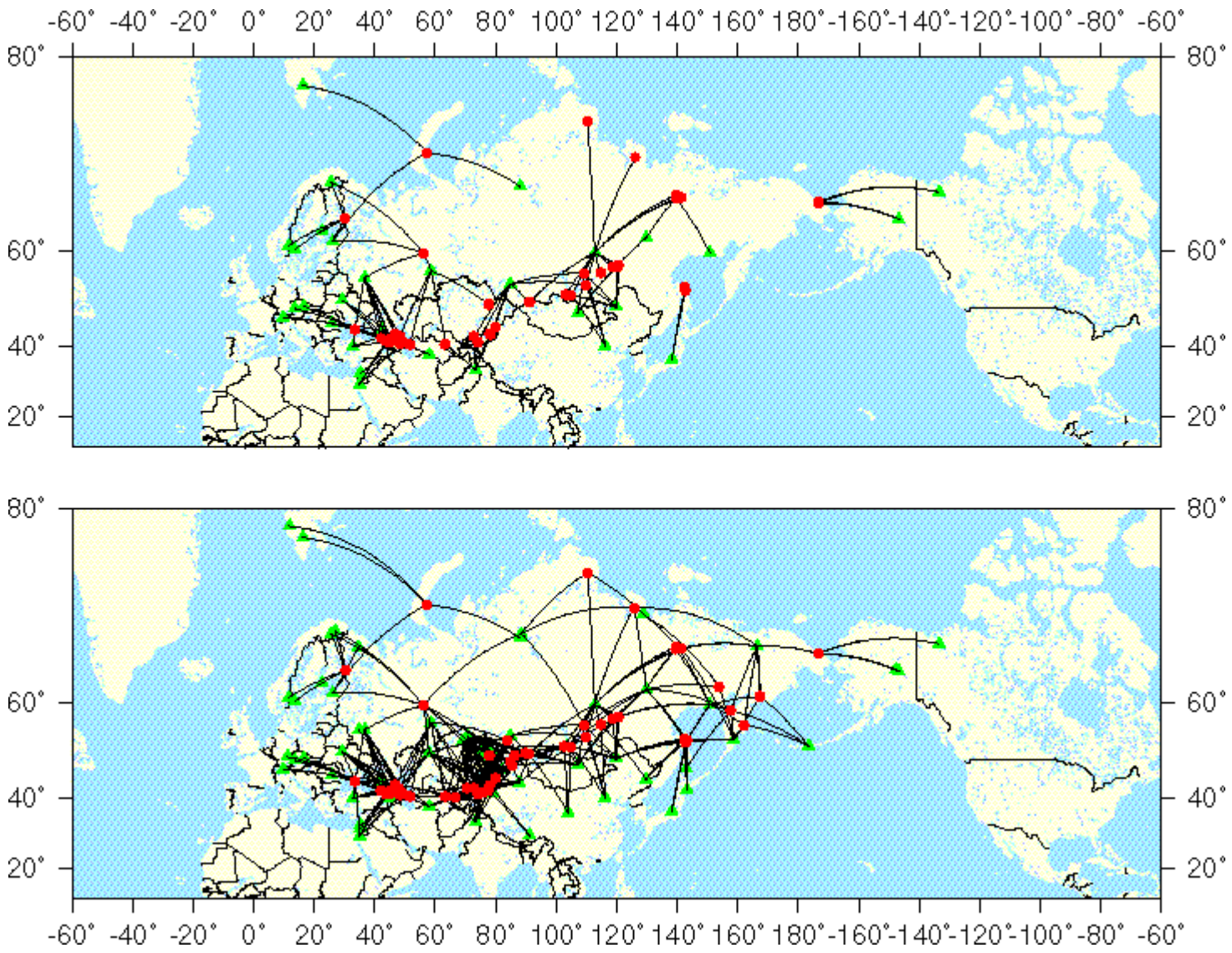


Figure 2. Comparison of Pn phases and corresponding propagation paths for the FSU available in (a) original REB dataset showing 45 events and 111 paths, and (b) IRIS and revised IDC dataset showing 65 events with 479 paths. The IRIS data provide a large number of additional Pn arrivals.

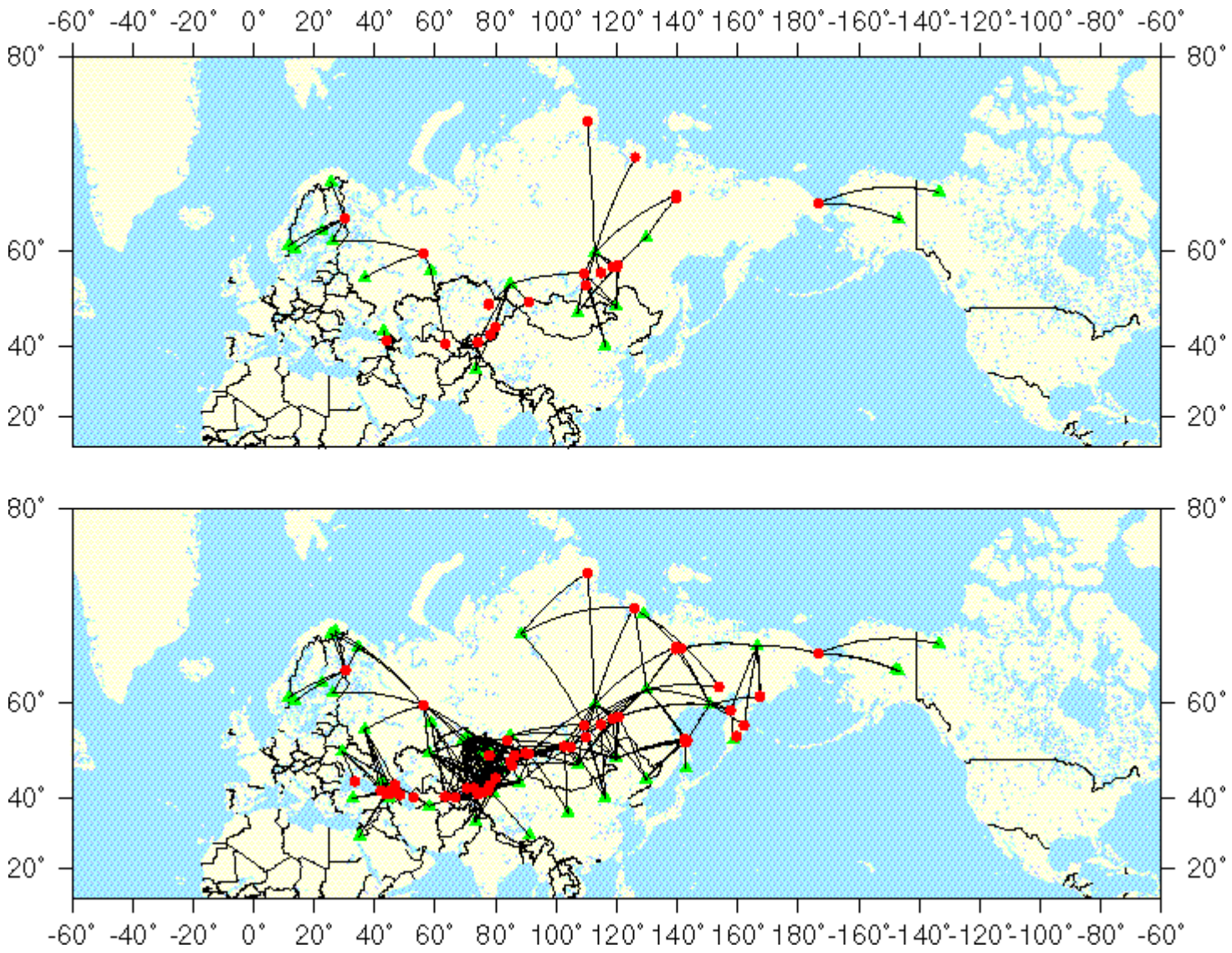


Figure 3. Comparison of Lg phases and corresponding propagation paths for the FSU available in (a) original REB dataset showing 21 events and 41 paths, and (b) IRIS and revised IDC dataset showing 63 events with 438 paths. The IRIS data provide a large number of additional Lg arrivals.

Sn and Lg are probably not applicable to either of the two regions. Figure 4 shows the results for Pn and Sn for epicentral distances up to 15 degrees. All data points are shown along with the moving medians (each with a window length of 2 degrees and shift of 0.5 degrees). For distances up to about 10 degrees, a comparison of the residuals for China and FSU shows significant differences. The residual medians for China and FSU differ by about 0.7 and 2.8 sec for Pn and Sn, respectively, indicating that both Pn and Sn arrive relatively later for events in China than those in FSU. A possible reason is generally deeper Moho for most seismic events in China as compared to those in the FSU, as indicated by the global crustal model of Mooney *et al*. (1998; see Plate 1d, p. 733).

(b) Analysis of Aftershock Data from a 100-ton Calibration Shot

Under the CTBT, the initial detection capability for a treaty violation will come from the International Monitoring System (IMS). However, in some cases, the IMS may not be able to provide conclusive evidence and an on-site inspection (OSI) may be used to gather evidence to determine the nature of the event. Aftershock monitoring can be used to accomplish two main goals: (1) to reduce the OSI search radius by locating the aftershocks, and (2) to help determine the source type of the event (*e.g*. explosion or earthquake). Several early studies (*e.g*. Hamilton and Healy, 1969; Ryall and Savage, 1969) indicated that explosions can stimulate significant seismic activity and that post-shot seismicity is constrained to the vicinity of the explosion in both space and time. Numerous studies *(e.g*., Jarpe *et al*., 1994; Sweeney *et al*., 1996; Gross, 1996) noted differences in the spectral characteristics of aftershocks from various natural and man-made seismic sources, including the Non-Proliferation Experiment of 22 September 1993, consisting of about 1 kt of chemical explosives.

We investigated the characteristics of seismic events following a 100-ton chemical explosion detonated at the FSU's nuclear test site at Degelen, eastern Kazakhstan on 22 August 1998 and examined their usefulness for on-site inspection. This explosion was carried out as a calibration experiment for the CTBT verification as a part of the closing of nuclear test tunnels under the Nunn-Lugar Cooperative Threat Reduction Program (Leith and Kluchko, 1998). The engineering and geological characteristics of the tunnel in which this experiment was carried out have been described by Leith *et al*. (1997). A topographic map of the Degelen Mountain region can be seen in Figure 1 of Gupta and Wagner (1992) and Figure 2 of Leith *et al*. (1997).

Analysis of high-frequency seismic data from a local network of six three-component stations monitoring the chemical explosion at the Degelen test site was started by first retrieving and scanning all available waveform data covering a period of 25 days. One of the stations was at ground zero, whereas the other five were within a distance of about 2.5 km. As many as 669 possible aftershocks were observed between 22 August to 15 September 1998 at two or more stations during 25 days of monitoring. Figure 5 shows a histogram displaying the distribution of 669 events, starting at the detonation time (05:00 hrs) of the calibration shot. No data were available for the first four hours. The distribution of events is uneven, with a significant increase in the number of seismic events after 16 days. This large increase in the number of seismic events after Day 16 is unexpected and appears to be in conflict with earlier studies of aftershocks from chemical and nuclear explosions which show seismic activity generally decaying with time (Jarpe *et al*., 1994; Smith, 1997). A possible reason could be delayed collapse of a portion of the tunnel weakened by the explosion, especially because the tunnel is located in a region of complex geology, including faults and fracture zones (Leith *et al*., 1997). Several man-made activities, such as removal of collapsed debris (mucking) and installation of ventilation and electrical systems, are known to occur at this site; these provide other possible explanations. An examination of amplitude data from various stations also indicated that the amplitudes of aftershock recordings attenuate strongly with distance and there was no evidence of reduced activity after 25 days.

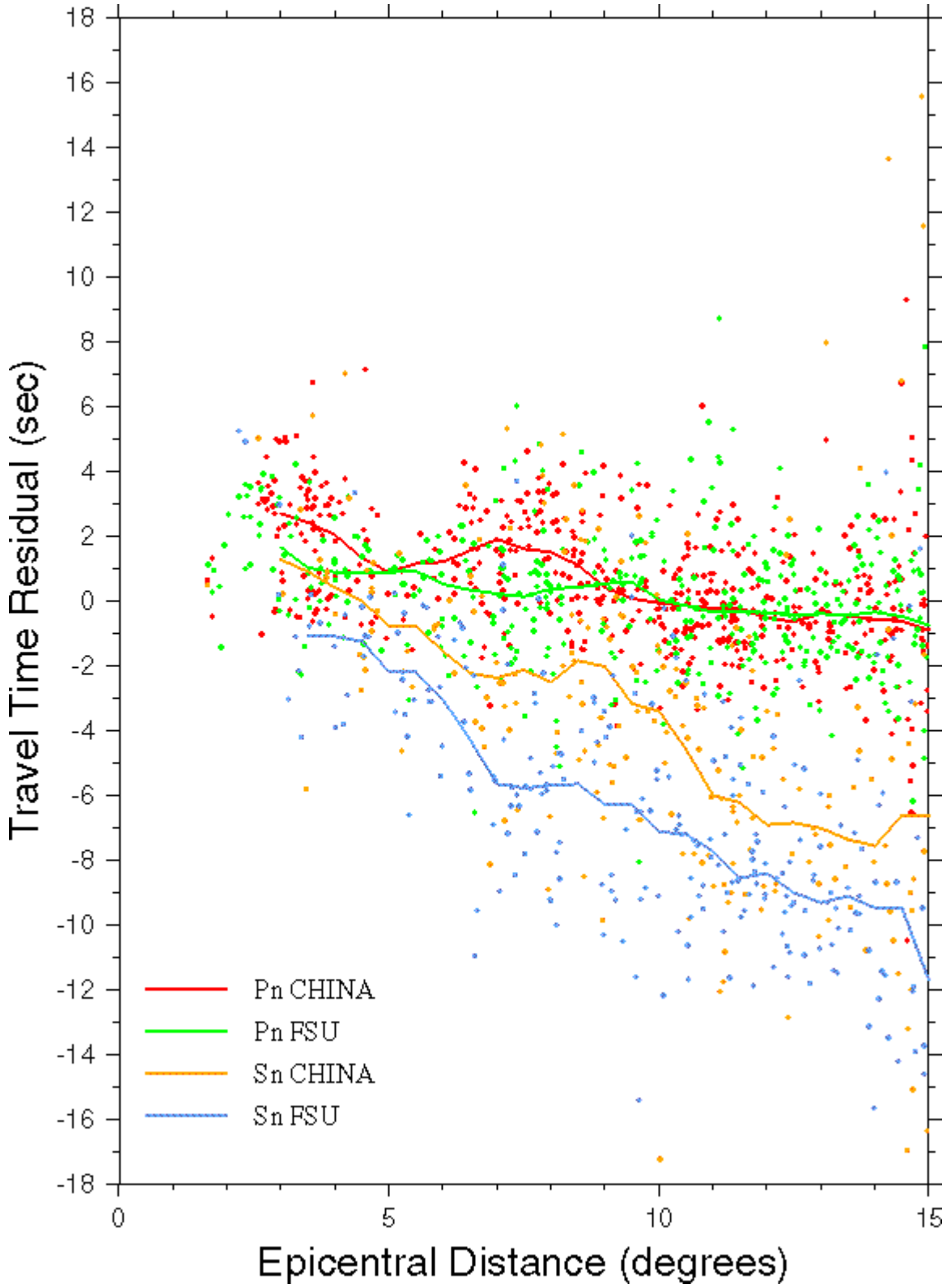


Figure 4. Travel time residuals for Pn and Sn for China and FSU showing data points and moving medians. For distances up to 10 degrees, the residuals indicate that both Pn and Sn arrive relatively later for events in China than those in FSU; a possible reason is a relatively deeper Moho under

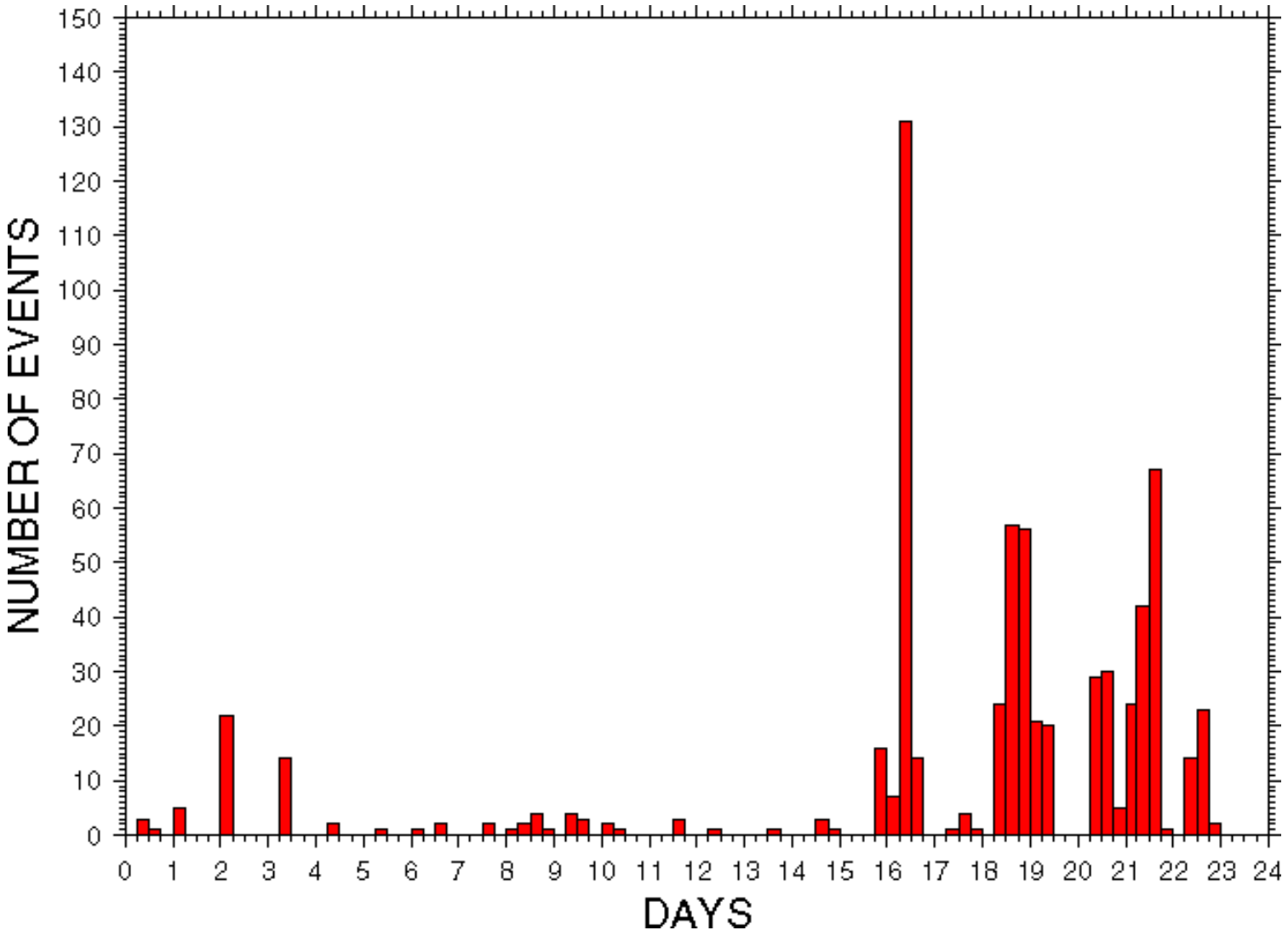


Figure 5. Histogram showing the distribution of 669 aftershocks between 22 August and 15 September 1998 (25 days), starting at the detonation time of the calibration shot. No data were available for the first four hours. The distribution of events is uneven and a significant increase in the number of seismic events is observed after 16 days, perhaps due to tunnel collapse or some man-made activity.

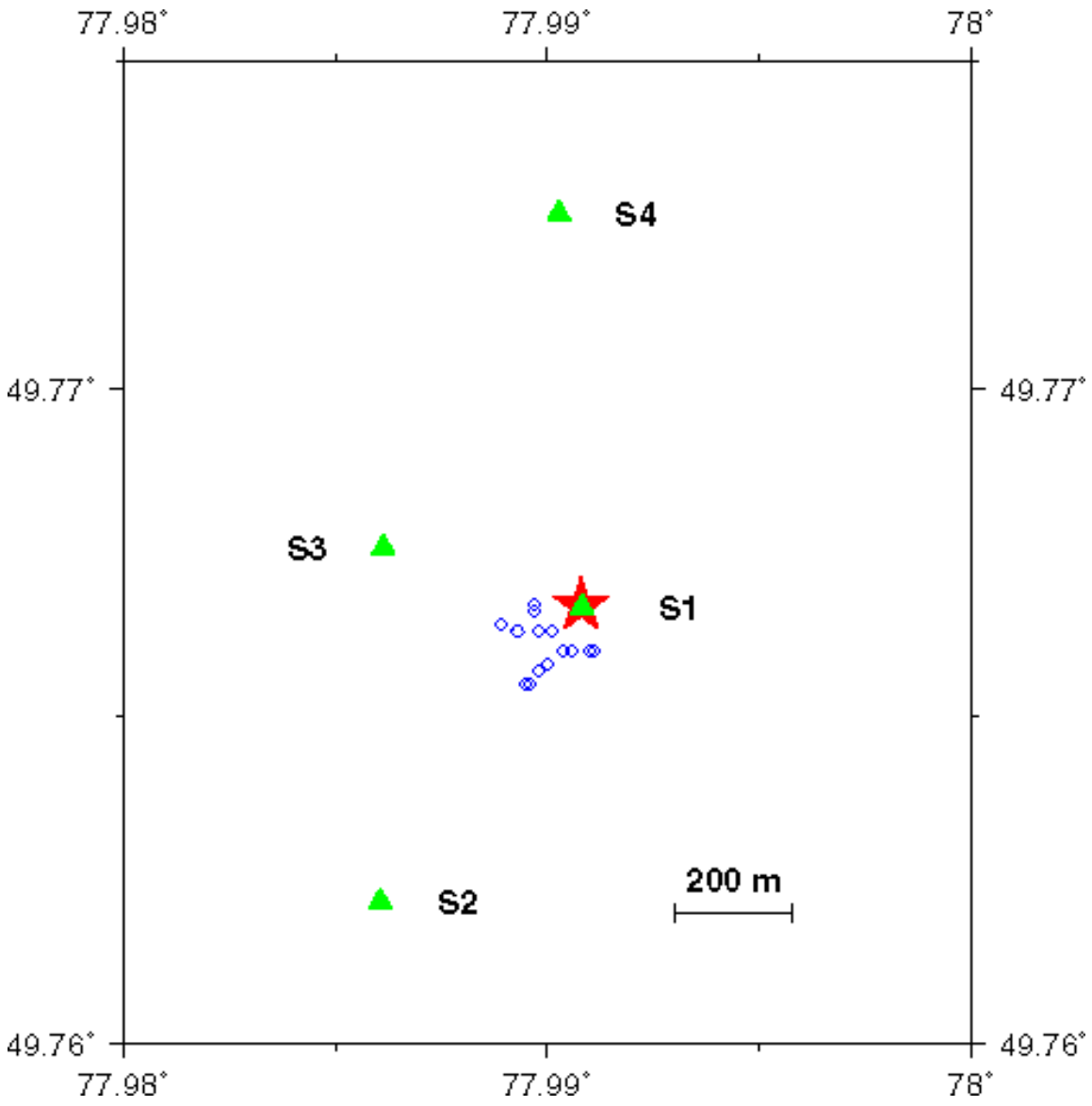


Figure 6. Epicentral locations of 14 aftershocks of the 22 August 1998 Degelen shot. Station S1 is at ground zero, whereas the other five stations lie within a distance of about 2.5 km (only four stations are shown here). All epicenters plot within less than 200 m of the main event, suggesting that aftershock locations may provide a fairly accurate location of the main shot.

Fourteen (14) aftershocks were found to be well recorded at four or more stations. Their epicentral locations, based on P-wave arrivals, showed all epicenters to lie within less than 200 m of ground zero of the 100-ton shot (Figure 6). These aftershocks, distributed over a period of about 20 days, suggest that aftershock locations determined within several days of the detonation time, may provide a fairly accurate epicentral location of the explosion. It seems therefore that monitoring of aftershock activity, even if initiated several days after an explosion, can be useful for on-site inspection of a region in which a suspicious event has occurred.

CONCLUSIONS AND RECOMMENDATIONS

Formation of databases with significantly improved ground truth can be accomplished by a combination of re-analysis of the IDC data and retrieval and examination of data from other available sources such as the IRIS. Similar to the Chinese dataset, the most important contribution of the IRIS data to the FSU dataset is the addition of a large number of arrivals from regional phases, so that solutions based on the combined use of both IRIS and IDC data provide improved estimates of both epicentral location and depth in comparison to the original REB solution. Such analysis should also be carried out for other regions of the world. Analysis of aftershock data from a 100 ton chemical explosion at the Degelen, Kazakh Test Site demonstrates that monitoring of aftershock activity from a suspected nuclear event within several days of its detonation may provide a fairly accurate location of ground zero. It will be useful to carry out similar studies of possible aftershocks from large explosions at other test sites.

Key Words: Database, ground truth, explosion aftershocks, CTBT, regional seismic research

REFERENCES

Gross, S. (1996). Aftershocks of nuclear explosions compared to natural aftershocks, Bull. Seism. Soc. Am. 86, 1054-1060.

Gupta, I. N. and R. A. Wagner (1992). Evidence for Rg-to-P scattering in teleseismic P coda of East Kazakh explosions, Bull. Seism. Soc. Am. 82, 2139-2152.

Hamilton, R. M. and J. H. Healy (1969). Aftershocks of the Benham nuclear explosion, Bull. Seism. Soc. Am. 59, 2271-2281.

Henson, I., I. Gupta, and R. Wagner (1999). A ground truth database for regional seismic research, Proc. of the 21st Seismic Research Symposium: Technologies for Monitoring the Comprehensive Nuclear-Test-Ban Treaty, Vol. II, U. S. Department of Energy, Washington, 338-347.

Jarpe, S., P. Goldstein, and J. J. Zucca (1994). Comparison of the non-proliferation event aftershocks with other Nevada Test Site events, in Proc. Symposium on the Non-Proliferation Experiment: Results and Implications for the Test Ban Treaties, DOE Conf-9404100, 8-34 to 8-40.

Leith, W., V. V. Adushkin, E. M. Gorbunova, A. A. Spivak, and V. G. Spungin (1997). Engineering-geologic characteristics of Tunnel 214, Degelen Mountain, USGS Technical Report, DSWA/PMRC IACRO 96-8609 (Dec. 31, 1997).

Leith, W. and L. J. Kluchko (1998). Seismic experiments, nuclear dismantlement go hand in hand in Kazakhstan, EOS, Transactions AGU 79, 437-444.

Mooney, W. D., G. Laske, and T. G. Masters (1998). CRUST 5.1: A global crustal model at 5° X 5°, J. Geophys. Res. 103, 727-747.

Ryall, A. and W. U. Savage (1969). A comparison of seismological effects for the Nevada underground test Boxcar with natural earthquakes in the Nevada region, Jour. Geophys. Res. 74, 4281-4289.

Smith, A. T. (1997). Application of aftershock monitoring to an on-site inspection: location and equipment requirements, UCRL-ID-128849, Lawrence Livermore National Laboratory.

Sweeney, J. J., C. Carrigan, W. Pickles, C. Schultz, and A. Smith (1996). Results of the LLNL on site inspection research project, PL-TR-96-2153, Phillips Laboratory, Hanscom AFB, MA.

REGIONAL SEISMIC THRESHOLD MONITORING

T. Kværna, F. Ringdal, J. Schweitzer and L. Taylor
NORSAR, Kjeller, Norway

Sponsored by The Defense Threat Reduction Agency
Arms Control Technology Division
Nuclear Treaties Branch

ABSTRACT

We are starting a project to develop an optimized, automatic capability to monitor seismic events originating in an extended geographical region, using data from a sparse network of regional arrays and three-component stations. The work will build on the site-specific threshold monitoring technique developed under previous contracts. As an integral part of the method development, we plan to apply and evaluate the method in several practical applications. Our focus will be on using IMS and selected non-IMS stations to experimentally investigate the performance of regional threshold monitoring of a grid system covering the entire Novaya Zemlya region, and an area with high mining activity (e.g. the Kola Peninsula).

The basic approach in the project will be:

- To apply a regional travel time model for the paths between each station and grid node, possibly with source-station specific corrections.
- To apply wave attenuation relationships based primarily on regional calibration events, as available.
- To apply optimized bandpass filters for the grid nodes to be monitored, also considering the use of several bandpass filters in parallel if sufficient calibration information is not available.
- To provide automatic "explanation facilities" to assist the analyst in assessing the results.

An important consideration in the project work will be to lay the foundation for its actual implementation in an operational monitoring system. Thus, the software will be developed using the general framework already provided by the prototype IDC, and the examples of applications will to a large extent (although not exclusively) be based on data from the emerging IMS. To facilitate a possible future implementation of this method in the IDC operational environment, the data formats will be made compatible with those of the global Threshold Monitoring system now operational at the Vienna International Data Centre.

OBJECTIVE

The objective of this work has been to assess the applicability of a temporary three-component network for Threshold Monitoring (Kværna and Ringdal, 1999; Ringdal and Kværna, 1989, 1992) of a small mining area located within local/regional distances. In particular, we have focused on comparing the performance of such a network with the performance of a single IMS array with respect to background noise levels and suppression of signals from interfering events. These results will be important when considering strategies for permanent monitoring of a larger region.

RESEARCH ACCOMPLISHED

Station network and data

In the time period May-October 1999, 13 Lennartz MARSlite data loggers equipped with three-component LE-3D/5s were deployed in Finnmark, northern Norway. This was a cooperative project between NORSAR and the University in Potsdam, Germany, primarily initiated for studying the local seismicity of the neotectonic Masi fault system (Schweitzer, 1999). This instrument deployment, denoted the "MASI network", provided continuous data for the entire period of operation. A map with the sensor sites is shown in **Figure 1**. Within the same area we also find the ARCES array (IMS station PS 28) and the IRIS three-component station Kevo (KEV) in northern Finland that is also a part of the Finnish national seismic network. Continuous data from both ARCES and KEV were stored together with the data from the MASI network on CDs for subsequent analysis.

A quarry with a size of approximately 2 km across is located on the Kola Peninsula, between the towns of Nikel and Zapolarnyi near the Russian-Norwegian border. Relatively large blasts (~100 tons) are regularly detonated in this quarry, providing strong signals at the nearby stations. An example of such an event as recorded at three of the MASI stations and at ARCES is shown in **Figures 2** and **3**. Clear P, S, and Rg phases are observed at many of the closest stations.

For the purpose of optimizing the SNR of the phases to be used for threshold monitoring, the three-component observations were rotated into the L, Q, and T ray oriented coordinate system, where P generally had the largest SNR in the L direction and S in the Q or T directions, as seen from **Figure 2**. For ARCES, the best SNRs were found on array beams steered with either P or S velocities, But as seen from **Figure 3,** where the center three-component ARA0 has been rotated into the L, Q, T coordinate system, the largest P amplitude is found on the L component and the largest S amplitude is found on the T component. Most of the P energy on the horizontal components is in this way projected into the L component. This effect will usually be observable for local and regional P phases where the rays approach the Earth's surface at relatively large incidence angles.

For the purpose of testing the performance of the MASI network for monitoring of the quarry near Nikel, we derived processing parameters for Threshold Monitoring from the event shown in **Figures 2** and **3**. This event had an announced yield of 98 tons and was assigned a local magnitude of 1.97 based on the S phase recordings at ARCES and Apatity. Details of the processing parameters are given in **Table 1**.

Threshold monitoring of the mine near Nikel, Russia

In a practical monitoring situation, a variety of seismic stations at local distances may be available for monitoring a given target site of interest. Usually, such local networks are of a lower quality and sensitivity than IMS stations, but this is to some extent compensated for by the proximity of the network stations to the target site. This tradeoff is in fact one of the main topics for study under the present project.
The IMS network in Fennoscandia is composed of high-quality regional arrays. In addition, we have access to experimental data from local stations such as the MASI network, and this gives us the possibility to test the concept of optimized site-specific seismic monitoring using dense local networks and comparing the results to monitoring using a sparse network of high-quality seismic arrays.

We have carried out a monitoring experiment focusing on the mining site near Nikel, Kola Peninsula. Our purpose has been to compare the results from site-specific monitoring in the following two cases:

- Optimized threshold monitoring using P and S waves from the ARCES array
- Optimized threshold monitoring using P and S waves a local network composed of the MASI stations supplemented by the Kevo station in Finland

We note that the ARCES array is at a distance of about 200 km from the target site, whereas the local network stations are at distances ranging from 30 km to about 300 km. The closest station (MA05) should in theory be able to provide the best recording of mining events at Nikel. In practice, this station is not ideally situated, and its capability is therefore not quite as good as expected. We will return to this point in the following discussion.

Monitoring example for 2 June 1999

Figures 4 and **5** show the results from optimized site-specific threshold monitoring for the two cases mentioned above (ARCES array and the local network) for a typical 24-hour period (2 June 1999). In the following, we provide some comments to these plots, which in fact illustrate many of the most important conclusions from this preliminary study:

The ARCES plot (**Figure 4**) shows three traces: The two bottom traces correspond to the P phase and the S phase. We note that the threshold monitoring technique can be used on individual phases as well as on a combination of phases from one or several stations. In this particular case, the ARCES P phase monitoring result shows a general "background" noise level of about magnitude 0. This simply means that the background noise level for an ARCES P

beam steered to the Nikel site, with an optimized filter setting, and compensated for wave attenuation, is close to magnitude 0. We can easily translate this to a detectability estimate, simply by adding a detection threshold (typically a factor of 4.0 in SNR, or 0.5 in magnitude units). In a detectability context, it would thus mean that the ARCES P wave detectability for this site is around magnitude 0.5.

The S phase plot for ARCES (**Figure 4**) is interpreted in the same way as the P wave trace. The background level for the S phase is slightly lower than for the P phase (about magnitude -0.5). This reflects the fact that the ARCES S phase is stronger than the P phase for events from this mine. We recall that the threshold monitoring trace shows the "upper limit" of an event that could possibly have occurred at a given instance in time. Thus the "absence" of an S phase on the recorded trace is a stronger indication of a low upper limit than the "absence" of a P phase.

The combined P and S threshold trace for ARCES (upper trace in **Figure 4**) shows the overall threshold monitoring result using all the available information from the ARCES array. The background level is about magnitude -0.6, and the number of "spurious" peaks due to interfering events and other noise bursts is reduced compared to either the P wave trace or the S wave trace. The actual events at the mining sites, as well as the other main peaks on the trace, are indicated. Note that all the peaks exceeding magnitude 0 can be either associated with events in the mine or explained as a result of other causes. Thus, the monitoring capability of the ARCES array for the Nikel mining site is close to magnitude 0.

Figure 5 is a threshold plot for the local network defined earlier. In this case, 5 station traces are shown (5 bottom traces), with the combined network trace on the top. Note that each of the 5 station traces have been generated using a combination of the P and S phase for that station, so that we have not displayed the individual phase traces in each case.

First we will briefly comment on the performance of the individual stations. The best station is the "permanent" station Kevo, which has a background threshold of about magnitude 0. Kevo is known to be an excellent station for local as well as regional/teleseismic recording, and is situated on hard rock in a low-noise environment. It is therefore not surprising that it is performing well, especially taken into account that the temporary MASI stations were, due to logistic considerations, placed near populated areas, and some also on sediments. Nevertheless, the performance of Kevo is encouraging. KEV is at about the same distance from the target site as ARCES (actually slightly nearer). The fact that ARCES has a better performance than KEV is not surprising, since the ARCES array has the advantage of noise suppression through beamforming of 25 sensors. This is sufficient to explain the performance difference of about 0.6 magnitude units.

For the stations in the MASI network, the most pronounced feature is the high variability of the background noise. While we have not attempted to study this in detail, we attribute it to the siting of the instruments and the proximity to man-made noise sources (roads, buildings etc.). Nevertheless, these stations have a threshold (background noise level) between 0 and 1 on the magnitude scale, which means that they will contribute to lowering the overall network threshold. Thus, the combined thresholds (top of **Figure 5**) are well below magnitude 0, although not quite as low as for the ARCES array. The number of spurious peaks is reduced compared to the ARCES plot, and this is in fact one of the main benefits of having a distributed network available rather than a concentrated array. The geographical distribution of the network enables spurious noise bursts or interfering signals to be more effectively suppressed.

Monitoring example for 17 August 1999

Our second example is from 17 August 1999 (**Figures 6** and **7**). This is the day of the large Turkey earthquake (occurring early in the morning GMT), and during the same day (at about 4.40 GMT) a relatively large earthquake occurred in Revda, Kola Peninsula. These "interfering" events naturally stand out on the plots, both for the ARCES array (**Figure 6**) and the network (**Figure 7**). Otherwise, the same considerations as were previously made for the 2 June example also apply in this case: The ARCES threshold is slightly lower than the network threshold, but the network has a reduced occurrence of spurious peaks on the combined threshold trace.

We note that the closest network station (MA05) was not in operation on 17 August 1999. This seems to have had little effect on the network threshold. This is encouraging, since it indicates robustness to failure of one or a few individual network stations.

CONCLUSIONS AND RECOMMENDATIONS

The main objective of the research described here is to develop and test a new, advanced method for applying regional seismic array technology to the field of nuclear test ban monitoring. To that end, we have addressed the development and testing of a method for optimized seismic monitoring of an extended geographical region, using a sparse network of regional arrays and three-component stations. We have applied the method to a temporary local network in northern Norway, and demonstrated that such a network can in certain cases be processed with a threshold monitoring capability that approaches that of a high-quality regional array (ARCES). We emphasize that the experiments undertaken so far address the monitoring of a site that is within local distance (0-300 km) of the network, and that a high-quality regional array will become progressively more capable than the network as the distance from the network to the target site increases.

We believe that the results described in this paper as well as in earlier contributions demonstrate that the optimized threshold monitoring method has the potential to become an important tool in day-to-day monitoring of seismic activity. By this method, the full resources of the monitoring network will be brought to bear to focus on a specific target site in order to enable monitoring of this target site with as high a capability as the network and available calibration information will allow.

In future research we plan to develop the site-specific method further to enable monitoring of a larger area, and it will then be necessary to apply a number of "optimized" beams. This is simple in principle, but in practice, the number of such beams may easily become too large to be reasonably manageable by the analyst, calling for an additional level of data reduction. We will develop a semi-automated method to form a (potentially large) number of optimized beams to cover a given region, and to process jointly, by automatic means, the resulting threshold traces so as to provide the analyst with a suitable "composite" result for review. We believe that in this way the threshold monitoring technique can be developed into a powerful tool for practical seismic CTBT monitoring.

ACKNOWLEDGEMENTS

We would like to acknowledge Frank Krüger and Daniel Vollmer of the Institute for Geosciences at the University of Potsdam, Germany for their extensive support during planning and fieldwork of the MASI experiment. The University of Potsdam also provided the 13 mobile stations of the temporary network.

Key Words: Data Processing and Analysis

REFERENCES

Kværna, T. and F. Ringdal (1999): Seismic Threshold Monitoring for Continuous Assessment of Global Detection Capability. *Bull. Seism. Soc. Am.*, 89, 946-959.

Kværna, T., J. Schweitzer, L. Taylor and F. Ringdal (1999): Monitoring of the European Arctic using regional generalized beamforming. In: *NORSAR Semiannual Tech. Summ. 1 October 1998 - 31 March 1999, NORSAR Sci. Rep. 2-98/99*, Kjeller, Norway

Ringdal, F. & T. Kværna (1989): A multichannel processing approach to real time network detection, phase association and threshold monitoring. *Bull. Seism. Soc. Am.*, 79, 1927-1940.

Ringdal, F. & T. Kværna (1992): Continuous seismic threshold monitoring. *Geophys. J. Int.*, 111, 505-514.

Schweitzer, J. (1999): The MASI-1999 field experiment. In: *NORSAR Semiannual Tech. Summ. 1 April - 30 September 1999, NORSAR Sci. Rep. 1-1999/2000*, Kjeller, Norway

Table 1: Parameters processing for Threshold Monitoring of the mine near Nikel

Station	Phase	Flow	Fhigh	Azimuth	Inc/ Vel	Comp.	STA len	Travel time	STA calib	Distance (km)
MA05	P	3.0	8.0	89.0	84.2	l	0.6	5.46	-2.016	27.58
MA05	S	3.0	8.0	89.0	-	t	0.5	8.86	-2.856	27.58
MA04	P	4.5	9.0	109.09	34.42	l	1.0	12.95	-0.835	59.01
MA04	S	3.0	6.0	110.23	60.87	t	1.0	17.76	-1.661	59.01
MA03	P	4.0	8.0	88.2	78.3	l	0.5	25.06	-1.283	146.50
MA03	S	4.0	8.0	88.2	78.3	t	1.0	42.33	-1.883	146.50
KEV	P	3.0	6.0	95.75	42.18	l	1.0	28.14	-1.308	150.40
KEV	S	3.0	8.0	110.17	63.70	t	1.0	45.14	-1.634	150.40
MA02	P	4.5	9.0	83.69	73.46	l	1.0	33.68	-1.447	199.96
MA02	S	3.5	7.0	124.06	62.56	t	1.0	57.54	-1.531	199.96
ARCES	P	4.0	8.0	92.70	7.99	z	1.0	34.75	-1.737	205.23
ARCES	S	4.0	8.0	94.12	4.81	z	1.0	60.31	-2.183	205.23
MA12	P	4.0	8.0	98.3	65.0	l	0.5	37.39	-1.728	225.01
MA12	S	4.0	8.0	98.3	65.0	q	1.5	64.23	-2.486	225.01
MA13	S	2.0	4.0	103.84	65.62	q	1.0	64.43	-1.221	225.11
MA06	P	3.5	8.0	126.99	27.72	l	1.0	41.00	-0.873	248.46
MA06	S	1.5	3.0	124.06	62.56	t	1.0	69.46	-1.198	248.46
MA10	P	2.0	5.0	71.63	60.18	l	1.0	46.57	-0.858	282.62
MA10	S	1.5	5.0	60.59	63.18	t	1.0	78.45	-1.305	282.62
MA08	P	4.0	8.0	75.0	53.0	l	1.0	49.01	-0.686	295.58
MA08	S	4.0	8.0	75.0	53.0	q	1.0	81.61	-1.210	295.58

Figure 1. Map showing the locations of the stations of the MASI network, the ARCES array, and the KEV station. Also shown are the locations of the quarry near Nikel and the epicenter of an M_s 4.2 earthquake occurring near Revda on the Kola Peninsula.

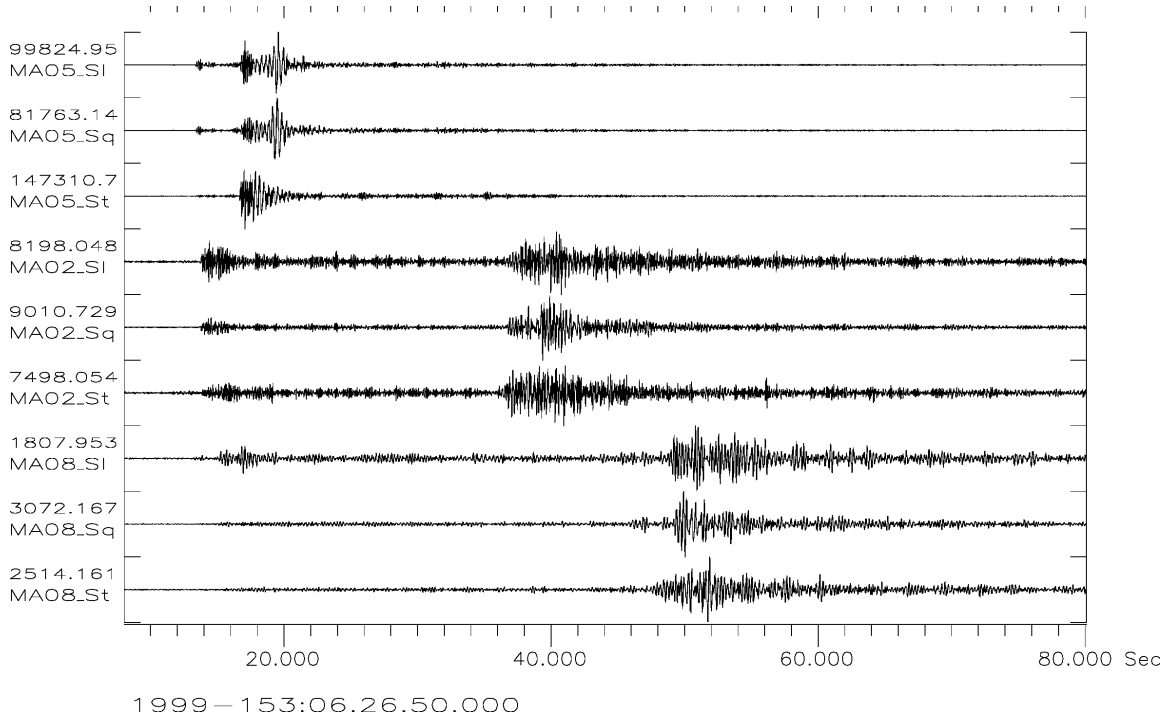


Figure 2. Recordings of the quarry blast near Nikel (2 June1999, M_L 1.97) at three of the MASI stations. The traces were rotated into the L, Q, T components and bandpass filtered between 3 and 10 Hz.

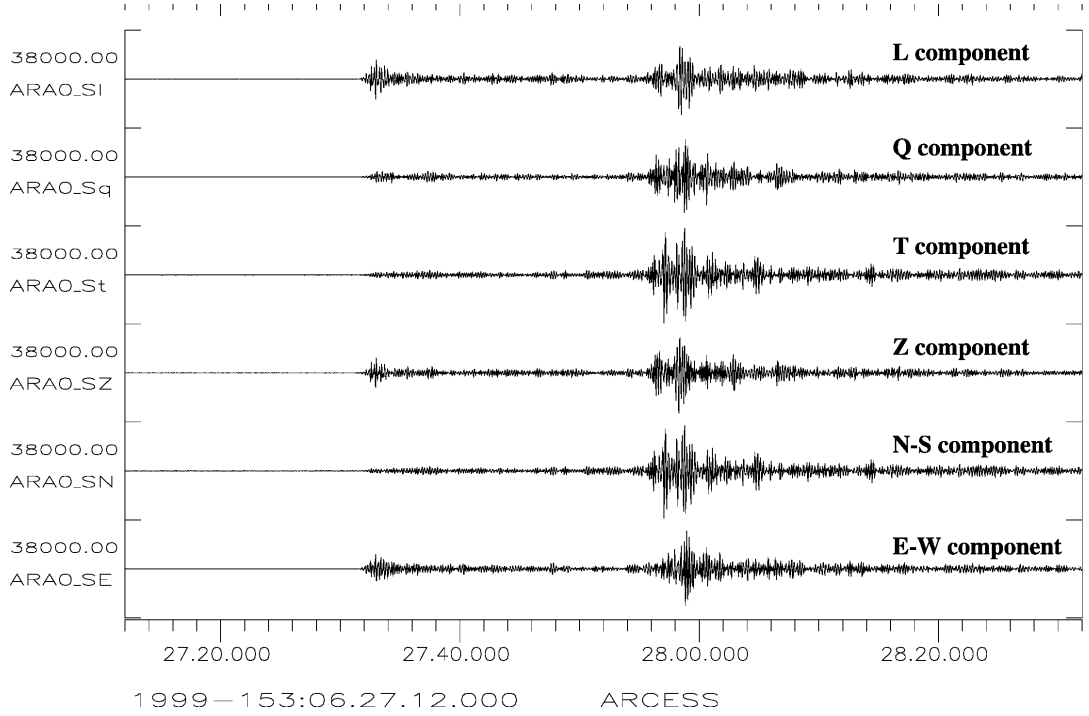


Figure 3. Recordings of the quarry blast near Nikel (2 June1999, M_L 1.97) at ARA0, the central three-component element of the ARCES array. The upper three traces show the L, Q, T components and all traces were bandpass

filtered between 4 and 10 Hz.

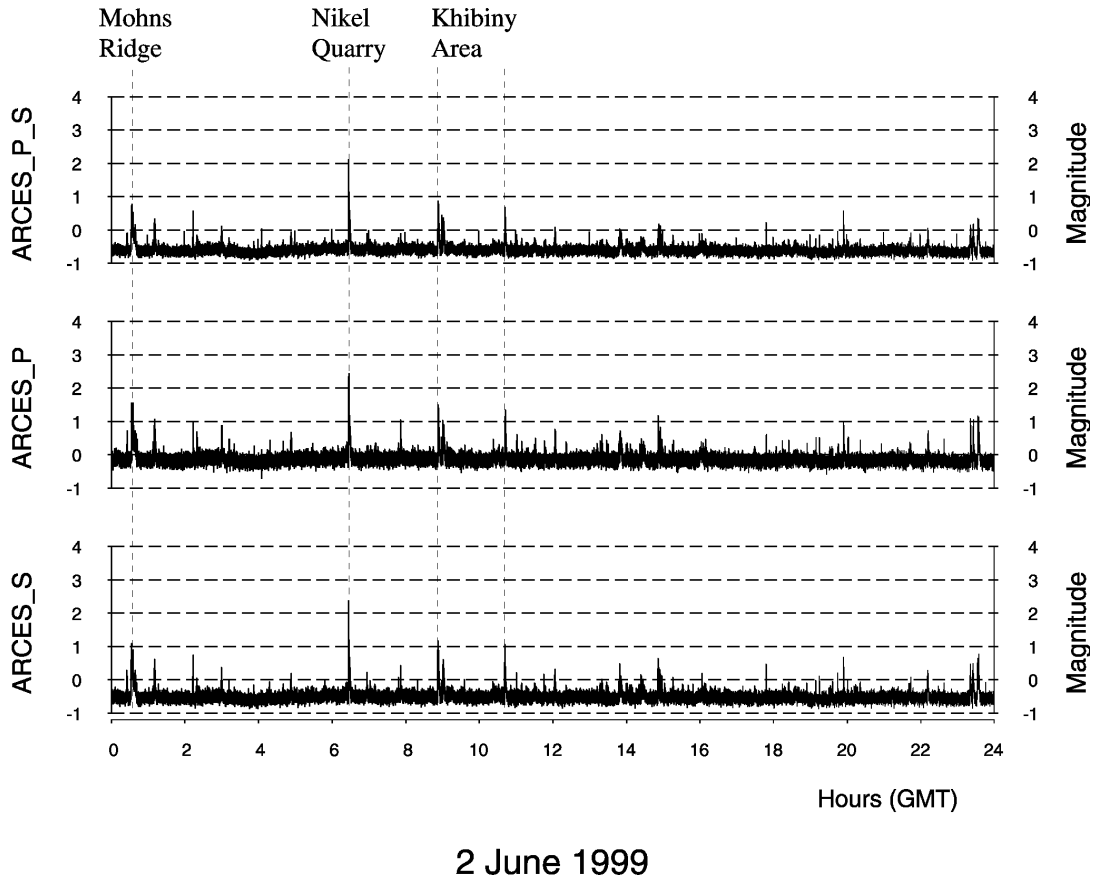


Figure 4. Results from threshold monitoring of the quarry near Nikel for 2 June 1999, using the ARCES array. The combined P and S phase threshold trace is shown on top, whereas the two lower traces show the thresholds for the P and S phases individually. The locations of the events causing the threshold peaks are given above the upper trace.

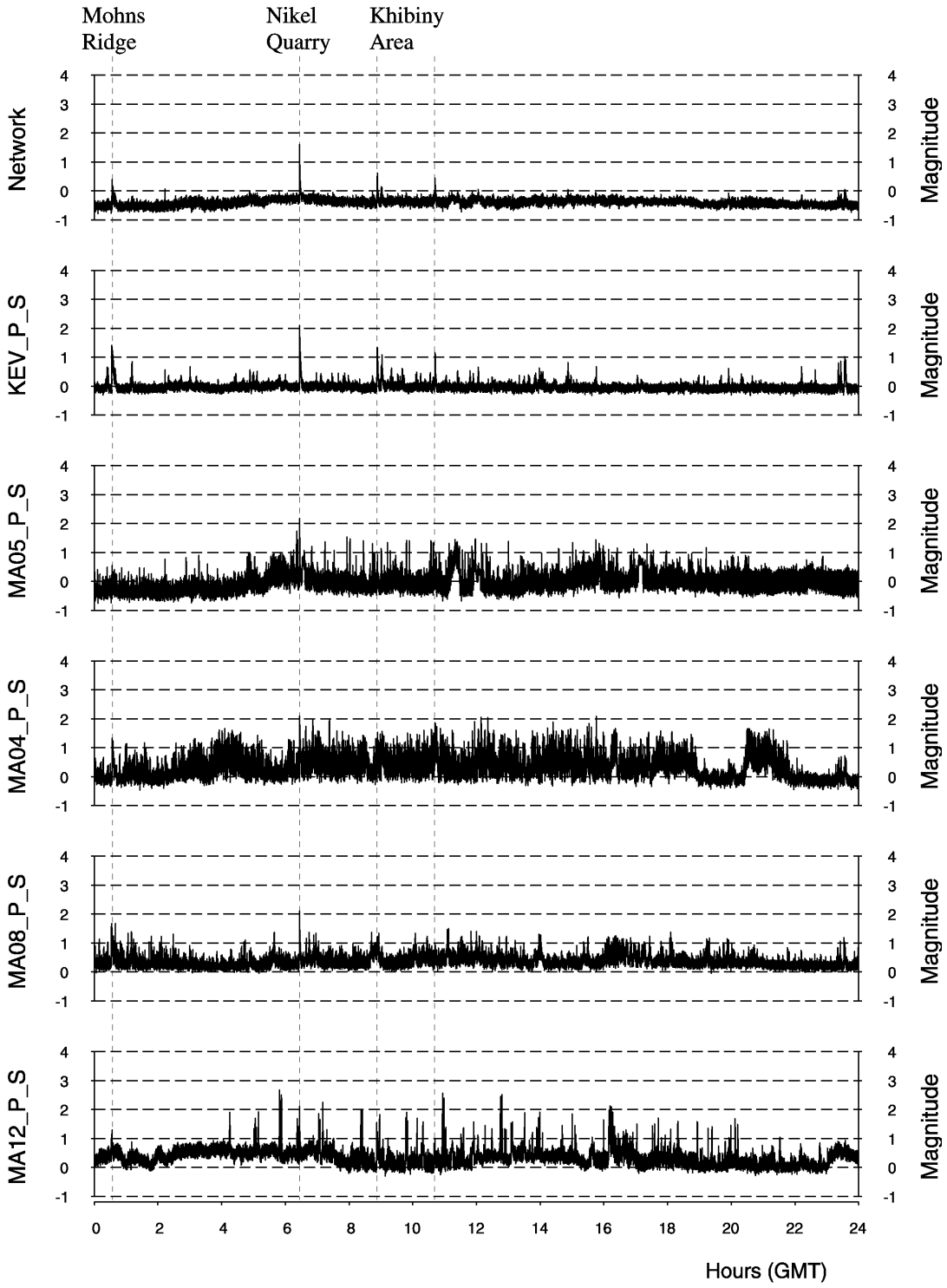


Figure 5. Results from threshold monitoring of the quarry near Nikel for 2 June 1999, using the MASI network. The combined P and S phase threshold trace for the network is shown on top, whereas the other traces show the combined P and S phase thresholds for selected stations. The locations of the events causing the threshold peaks are given above the upper trace.

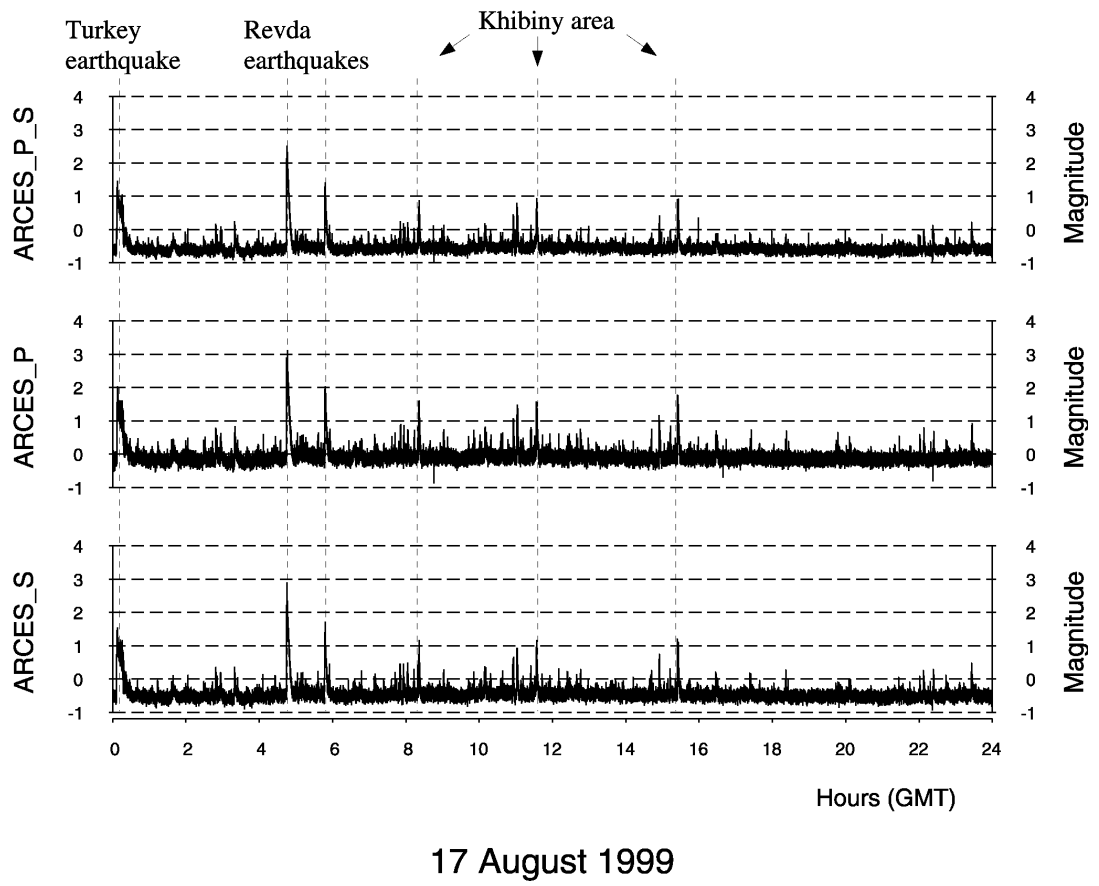


Figure 6. Results from threshold monitoring of the quarry near Nikel for 17 August 1999, using the ARCES array. The combined P and S phase threshold trace is shown on top, whereas the two lower traces show the thresholds for the P and S phases individually. The locations of the events causing the threshold peaks are given above the upper trace.

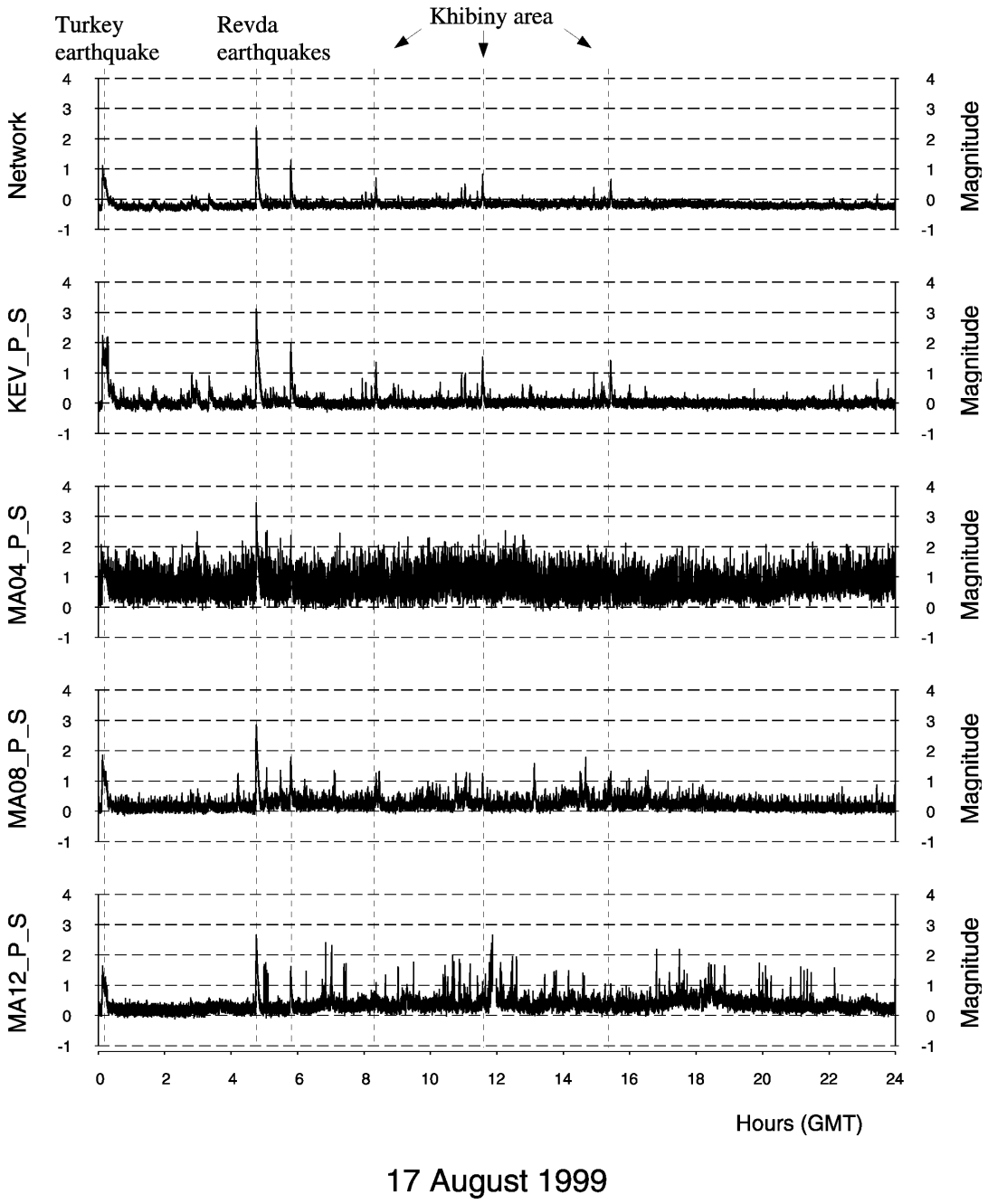


Figure 7. Results from threshold monitoring of the quarry near Nikel for 17 August 1999, using the MASI network. The combined P and S phase threshold trace for the network is shown on top, whereas the other traces show the combined P and S phase thresholds for selected stations. The locations of the events causing the threshold peaks are given above the upper trace.

THE GSETT-3 EXPERIMENT AND THE PROTOTYPE INTERNATIONAL DATA CENTER

Robert G. North and Richard J. Stead

Science Applications International Corporation
Center for Monitoring Research

Sponsored by The Defense Threat Reduction Agency
Arms Control Technology Division
Nuclear Treaties Branch

Contract No. DTRA-01-99-C-0025

ABSTRACT

On February 20, 2000 the International Data Center (IDC) operated by the Provisional Technical Secretariat of the CTBT Organization in Vienna assumed responsibility for the generation of IDC products and the distribution of IDC products and International Monitoring System (IMS) data. This marked the end of the Group of Scientific Experts third Technical Test (GSETT-3) that started continuous operation on January 1, 1995. During the five years of GSETT-3 the Prototype IDC (PIDC) at the Center for Monitoring Research (CMR) acquired data from over 200 seismic, hydroacoustic, infrasonic and radionuclide facilities worldwide. Automatic processing and subsequent analysis of these data led to Reviewed Event Bulletins (REB) that were issued for every single day, except May 8-14, 1995, between January 1995 and February 2000 and that contained 99,212 events. Over 50 nations participated in GSETT-3 through the operation of sensor facilities, provision of data and bulletins, and staffing the PIDC.

During GSETT-3 participation steadily increased and new functionality was added to the PIDC every few months. Many new features were provided by a variety of DTRA contractors and several foreign agencies. A visiting scientist program brought scientists from many countries to participate in the development, operation and evaluation of the PIDC. Initially only seismic data were processed and analyzed, but hydroacoustic and radionuclide data were incorporated in 1996 and infrasonic data in 1998. Both automatic and reviewed bulletins include signal detections from all three acoustic technologies, and over 15% of REB events have associated hydroacoustic T-phases; infrasonic associations are much rarer. The history of participation in GSETT-3, and improvements in, and additions of new features to, processing and analysis are summarized.

GSETT-3 bulletins have been used by the USGS National Earthquake Information Center and the International Seismological Centre (ISC), and have markedly improved the products of these two agencies. The standardized and centralized processing and analysis of data at the PIDC from a global network of high-quality stations have reduced event detection thresholds in many parts of the world, increased the number of magnitude estimates, and added to the percentage of events for which secondary phases, particularly core and depth phases, are reported. The ISC has noted a significant decline in the number of events that they find for the first time, particularly in the oceans and the Southern Hemisphere.

The software developed for, and tested at, the PIDC is being transferred to the IDC in Vienna in a series of software releases of which the third is being delivered in September 2000. These software deliveries will be completed early in 2002. Until then the PIDC will continue to acquire and process data, and produce reviewed bulletins at a frequency sufficient to test and evaluate improvements to software and operational parameters such as improved detection and association “recipes”, event characterization measurements, and corrections to improve location and magnitude determinations.

Key Words:

Seismic, hydroacoustic, infrasonic, international participation, bulletins, global seismicity

Introduction

The Group of Scientific Experts (GSE) of the United Nations Conference on Disarmament met in Geneva for one or two sessions each year from 1976 to 1996. Its primary function was to discuss, develop and test the procedures that would be needed to verify compliance with a CTBT. During two decades, over 50 countries participated in the work of the GSE, which operated by consensus – all reports and the procedures, formats and tests that they developed had to have unanimous agreement. The work of the GSE provides the basis of the verification system that is described in the Treaty and is now being implemented in the International Monitoring System, which includes the International Data Centre in Vienna. The procedures developed by the GSE were thoroughly tested in a series of experiments called Technical Tests. The initial test, GSETT-1 – GSE Technical Test number 1 - was conducted in 1984 and involved the exchange of phase readings over the telex-based World Meteorological Organization (WMO) Global Telecommunications System (GTS). A much more ambitious test (GSETT-2), involving the exchange of both phase readings and the corresponding waveform segments (in the first of the "GSE" formats) by both WMO/GTS and email, and the processing of these data by four International Data Centres (IDCs) located in Canberra, Moscow, Stockholm and Arlington (Center for Monitoring Research - CMR) was carried out over a six-week period in 1992. This experiment established the superiority of email over the telex system, demonstrated that many countries could implement the quite complex procedures, and acted as a starting point for the development of the basis of the future IDC. It proved a very complex task to reconcile the output of the four IDCs, and one major conclusion was that one IDC would be preferable.

Discussions on the next generation of the system began almost immediately after the conclusion of GSETT-2. Rapid political changes removed long-standing objections to the exchange of real-time continuous waveform data. Detailed procedures for the IDC were developed, and a number of small experiments conducted in data exchange. The CMR was designated as the single prototype IDC (PIDC) and significant extra funding permitted its rapid development, with initial data receipt from northern Europe (Norway, Germany and a few others) during 1993 and 1994 testing data acquisition and the processing of data from regional arrays. This signified the start of GSETT-3, and the PIDC produced and distributed sporadic bulletins on a trial basis. The full-scale phase of GSETT-3 began on January 1, 1995, with continuous waveform data from over 50 stations being received, processed and analyzed on a daily basis. Analysis and bulletin production and distribution was carried out on a 7-day per week basis, with bulletins being distributed within 48 hours after the end of the data day. The capability of the PIDC improved rapidly over the next few years. The number of stations providing data to the PIDC increased quite rapidly over the first six months, and much more slowly thereafter.

This paper describes the history of GSETT-3, largely from the perspective of the PIDC. The changes in station data processing and analysis are given in a series of tables. The PIDC was very much an international effort, with participation in its development, operation and evaluation by visitors to CMR from over 30 countries.

Contributing Data Network

The number of seismic stations whose data were used by the PIDC peaked in mid-1996. The drop thereafter was primarily due to discontinuing use of non-IMS stations in Europe, North America and Australia. The number of auxiliary stations used fluctuated as cost of telephone calls to non-AutoDRM sites became a concern. In late 1998 auxiliary station access was restricted to those for which data retrieval was by AutoDRM. The first hydroacoustic and infrasonic sites came online in late 1995, and radionuclide data were first received in 1996.

Since 1997 there has been some change in the mix of stations of a particular technology reporting to the PIDC, but little change in the overall station count, except for a modest increase in the number of infrasound stations.

Detection Processing

This includes both detection and phase identification. For arrays, phase identification is established from the observed slowness, while for three component stations, neural nets use a variety of signal features. Tuning of both processes has been carried out as more data accumulated.

1993 –May 3 GSETT-3 begins, primary data detection processing at NDCs, retrieved by PIDC
–May 5 auxiliary data detection processing at PIDC
1994 –Mar 4 tune detection processing for auxiliary stations in Germany
–Apr 16 neural net phase identification (NNPI)
–Jun 26 primary data detection processing at PIDC
1995 –Jun 2, Aug 10, Oct 25, Nov 24 tune detection processing 1996 –Jan 27 new detection processing software (DFX)
–Jan 27, Feb 27, Apr 9, May 2, Aug 25, Oct tune detection processing
–Aug 19 hydroacoustic detection processing
–Oct 14 tune P/Pn crossover in phase identification
1997 –Apr 18, May 28 tune detection processing
–Jun 6 tune NNPI
–Jul 25 improved error estimates for detection times
1998 –Jan 1 large array detection processing (NORSAR)
–Feb 24 tune detection processing
–Apr 3 tune NNPI
–Apr 8 infrasonic detection processing, probabilistic times for hydroacoustic detections
–Oct 23 NNPI for hydroacoustic detections
2000 July Hydroacoustic azimth estimation, depth-phase SNR

Hydroacoustic Processing

Only two IMS hydrophone stations, and one T-phase station, are operating at present. This, combined with the lack of data from explosive underwater sources, has hampered tuning efforts, but considerable success has been achieved with the detection and association of T-phases from earthquakes. T-phases are associated with approximately 20% of all events in the REBs.

1995 –Sep 1 First continuous hydroacoustic data (PSUR)
1996 –Apr 8 Operational hydroacoustic processing
–Apr 15 Retrieve T-phase data from island auxiliary stations
–Apr 22 hydroacoustic analysis
–May 5 hydroacoustic associations in published REB
–Aug 19 automated hydroacoustic processing
1997 –Apr 30 hydroacoustic fusion with seismic bulletin, time-defining H phase
1998 –Oct 23 Neural net phase identification for hydroacoustic arrivals
–Apr 8 probabilistic arrival times, 2D travel times

Infrasound Processing

As for hydroacoustic, shortages of data, particularly from arrays with configurations close to that required for the IMS, plus a lack of "ground truth" (signals from confirmed sources at known locations) have led to slow progress. Neverthless, infrasonic signals associated with earthquakes in the REB have been detected, along with a number of rocket (shuttle, etc) launches and a number of events whose occurrence could not be independently confirmed.

1995 –Nov 12 First continuous infrasound data (WRAI)
1998 –Apr 8 infrasound processing
–Dec 1 infrasound arrivals in automated bulletins and REB
1999 –Dec 1 First IMS infrasound array (ISM, Canada)
2000 July Laterally and seasonally-varying travel times

Network Processing

The association of signals from seismic, hydroacoustic and infrasound stations is a difficult problem, particularly since the low detection levels used result in frequent overlapping of signals from different events. The criteria for event definition are more liberal than those of other agencies such as the USGS NEIC and the ISC. Laterally varying seismic travel times for regional phases are used in Northern Europe and North America, and the travel times for both hydroacoustic and infrasonic signals are both laterally and seasonally dependent.

1993	–May 3	GSETT3 begins, PIDC uses ESAL for network processing, Travel times are IASPEI
1994	–Jul 27, Oct 29	modify event-definition criteria
-	-Oct 4	M8.2 Kurile Islands event: scaling problem with ESAL
1995	–Jan 20	tune network processing
1996	–Jan 21	tune network processing
	–Mar 1	new network processing software (GA)
1997	–May 19	fusion of hydroacoustic data and seismic data
	–Aug 22	first regional travel times: Fennoscandia
1998	–Jan 5	Slowness-Azimuth Source Corrections (SASCs)
	–Apr 8	hydroacoustic 2D travel times
	–Dec 1	fusion of infrasonic data
1999	–Jan 19	GSASC - global (all ranges and azimuths) SASCs
	–Apr 1	Single-Station Source Corrections (SSSCs), Northern Europe
2000	–Jan 11	SSSCs, North America
2000	July	Updated SASCs; corrections for station misorientation

Analysis

The goal of the IDC system is to automate detection, phase identification and association as much as possible, so the work of the analysts consists of confirming, correcting and adding to the automatic results. The starting point for analysis is the last of three successive automatic event lists. At the present time, parameters for detection, phase identification and association are set so that approximately half of all events are rejected by the analysts, and roughly ten percent of the events in the REB are not created by the automatic processing and have to be added during analysis. Feedback from the analysts has proved extremely important in guiding the improvement of the prior automatic processes.

1993	–May 15	analysis begins, 2 days/week, 2 analysts. Primary data is only event segments, northern Europe.
1994	–Feb 5	Primary network and REB now global
	–May 14	First continuous primary data (continuous analyst scan)
	–Sep 3	Analysis increased to 3 days/week
	–Oct 29	Analysis increased to 4 days/week
1995	–Jan 1	Continuous analysis (7 days/week), 9 - 12 analysts, 7 days. REB released within 48 hours.
	–May 10	database failure (5 days), no REB May 8 - May 14
1996	–Jan 7	Severe winter storms on Jan 7 and 12 shut down DC area. REB is produced on schedule
	–May 1	Two-team independent analysis experiment demonstrates variation in REB is primarily near threshold of system.
	–May 5	hydroacoustic analysis
	–Jun 15	7-day analysis in 5-day work week, REB in 48 - 120 hours
	–Jun 25	end of daily scanning
	–Jul 8	Two-pass auxiliary data analysis experiment demonstrates only minor improvements with much more auxiliary data
1997	–Mar 28	database failure (4 days), REB produced every day.
1998	-Dec 1	infrasonic analysis
2000	–Feb 20	Full-scale operation of IDC, end of 7-day REB at PIDC, 3 analysts

Magnitude Estimation

The PIDC has broken new ground in magnitude estimation, with the routine operational use of path-dependent Ms, maximum likelihood magnitudes, and most recently with "generalized" mb – mb extended to short distances. Most of this development has been carried out by Maxwell Technologies

1993 - May 3 GSETT-3 begins with only simple ML
1994 - Mar 19 reliable amplitude measurements for mb
- May 20 tune mb
1995 - Apr 9, Oct 31 tune ML
- May 18 first MS
1996 - Apr 17 Tune Ms
- Dec 18 Recall processing adds magnitudes for analyst-added arrivals
1997 - Jan 12 Maximum Likelihood Ms
1998 - Apr 12 Maximum likelihood and upper bound mb and Ms in REB
2000 -.July "Generalized mb, including station corrections; Ms station corrections

Event Characterization

The IDC will not identify events, but does compute event characterization parameter and uses them to "screen" events. This work has been largely carried out by Mission Research Corporation and the Australian NDC

1994 –Mar 19 reliable amplitude measurements for mb
1995 –May 18 Ms first available
1996 –Jul 10 first two event characterization computations available:
origin-based frequency-dependent amplitudes, short-period/long-period ratio
–Aug 1 additional computations: - spectral variance, cepstral quefrencies and peak amplitudes, complexity
1997 –Mar 14 Event Characterization Bulletin
1998 –Apr 8 further computations - third moment of frequency,time-frequency parameters
first-motion
2000 July Screening based on hydraocoustic signal properties and regional P/S amplitudes

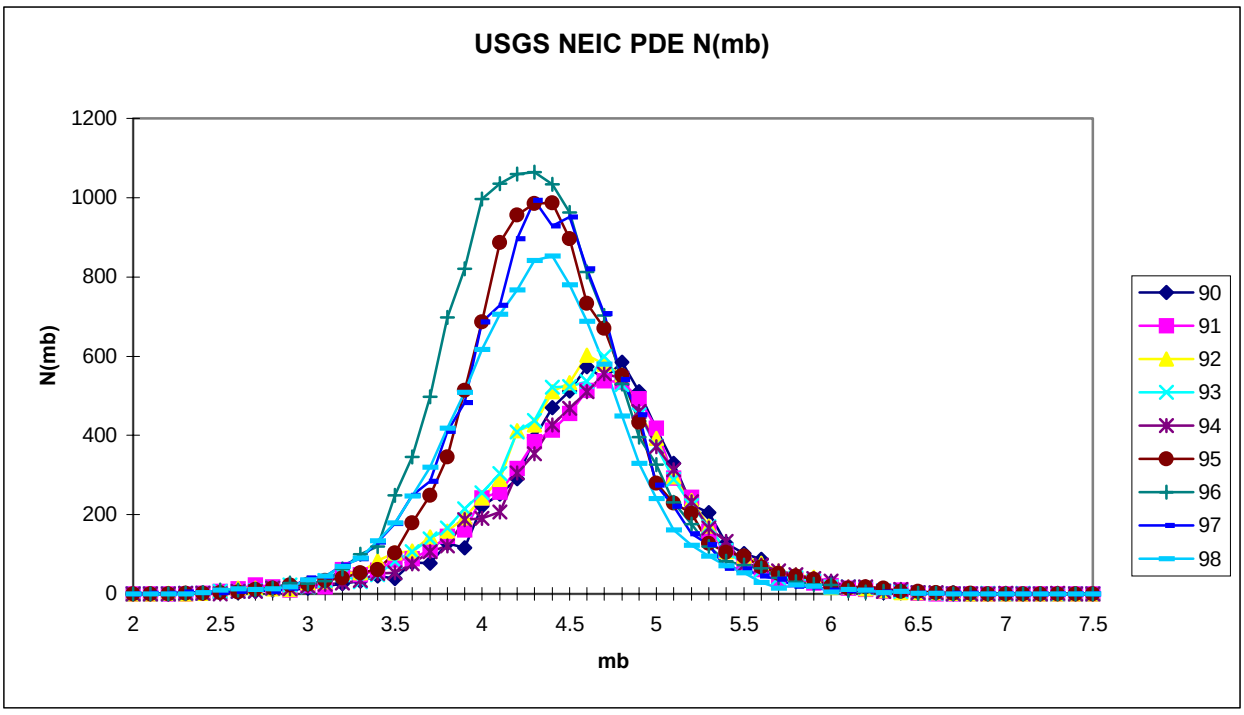
Product and Data Distribution

Rapid dissemination of results and the contributing raw data is a key element of the system. Both results and data have been made available through a web page, subscriptions (automatic delivery of products/data as they are generated/received) and AutoDRM (mail-based request system).

1993 –May 15 REB 2 days/week. REB distributed in GSETT2 format.
1994 –Jun 16 First continuous primary data. forwarding available.
–Dec 1 AutoDRM
1995 –Jan 1 Continuous REB
–Jan 13 PIDC web page, version 2 (web available to all)
–May 22 constrained subscriptions
1996 –Jan 4 near-realtime AutoDRM.
–Dec 2 automated subscription requests, "immediate" subscriptions
1997 –Mar 14 event characterization bulletin
–Mar 26 arrival and detection subscriptions, Jul 17 waveform subscriptions
–Oct 24 flat-file product subscriptions
1998 –Apr 8 GSE2.1 (IMS1.0) message formats
–Jul 31 event screening
1999 –Jan 6 Threshold monitoring maps on web
2000 –Apr 14 Secure web server available for products after 2000 Feb 20.
-Apr 21 Auto DRM restricted for products after 2000 Feb 20.
July Validation/signing of messages; forwarded auxiliary data requests

Impact of PIDC Products on Other Bulletins

The PIDC REBs have been quite extensively used by both the NEIS and the ISC as input to their bulletin products. The phase readings included in the REBs are used as part of the data input for the NEIS and the ISC, and have significantly increased the numbers of events located by both. Because nearly every REB teleseismic P-wave detection is accompanied by amplitude and period readings, the proportion of events with associated m_b magnitudes has increased sharply. The special effort by the PIDC analysts to identify and report depth phases has similarly improved the proportion of events to which depths other than a default value, such as 33km, can be assigned. The ISC has noted that the number of "new" events that they create, mainly in the southern oceans, from unassociated teleseismic observations has decreased significantly as the PIDC does particularly well in this area. The figure below shows magnitude-frequency curves for events with mb magnitudes in the USGS NEIC bulletin, by year. Note the sudden increase in the number of events in 1995, when NEIC started using PIDC phase reports.



The five lower curves (peaking at about mb 4.7) are for the years 1990, 1991, 1992, 1993, and 1994. The other four curves are for 1996 to 1998. The increased reporting of events with mb is a combination of events that could only be formed with phase data from the PIDC, and magnitudes provided only by the PIDC for teleseismic events.

International Participation

Foreign visitors and contributors have played a key role in the development, testing and operation of the PIDC. Norway and Australia have contributed software for Threshold Monitoring, large array processing, and event characterization. Areas in which foreign contributions have been made include–location calibration

–event characterization
–radionuclide processing development
–infrasound processing development
–hydroacoustic system evaluation
–magnitude studies
–operations (analysis, "pipeline" operation, QC)

Summary

The development and operation of the Prototype IDC

–helped establish the technical capability to monitor the treaty
–served as the platform for international technical cooperation
–advanced the state of monitoring technology
–demonstrated performance that corroborates theoretical predictions
–had a pronounced, beneficial, collateral effect on global monitoring
–serves as the operational test and evaluation platform for transition to the Treaty IDC
–will provide an on-going testbed for research and development in nuclear test-ban monitoring

DEVELOPMENT OF AUTOMATED MOMENT TENSOR SOFTWARE AT THE PROTOTYPE INTERNATIONAL DATA CENTER

*Douglas Dreger, Barbara Romanowicz, and Jeffry Stevens**
Seismological Laboratory
281 McCone Hall
University of California, Berkeley
Berkeley, CA 94720

*Maxwell Technologies
9210 Sky Park Court
San Diego, CA 92123

Contract No.: DTRA01-00-C-0038

ABSTRACT

We are porting automatic seismic moment tensor software used by the Berkeley Seismological Laboratory to the Prototype International Data Center (PIDC). This software package utilizes a surface wave spectral amplitude and phase method coupled with a three-component waveform inverse method that is scaleable from teleseismic to regional distances. The objective is to initially develop automatic software for the analysis of Mw5.5 and greater events on a global scale utilizing the International Monitoring System (IMS). For regions of specific interest we will utilize crustal structure calibration information from other DTRA projects to refine capabilities to Mw4.5 and greater. Currently version 0.1 is ported to the PIDC, and several examples of its use are presented. During the course of this project a staged testing program will be employed to refine the software and to provide robust code suitable for operations at the PIDC.

KEY WORDS:

Source parameters, seismic moment tensor, automated seismic analysis, discrimination

OBJECTIVE

On a global scale approximately 10,000 magnitude 4 events occur annually and therefore automated seismic analysis systems are needed to quickly review the seismicity to monitor the CTBT. The objective of this project is to adapt and port to the Prototype International Data Center (PIDC) a set of codes developed and routinely used at UC Berkeley (Romanowicz et al., 1993; Dreger and Romanowicz, 1994; Pasyanos et al., 1996) to determine seismic moment tensors and source depth of seismic events automatically and close to real-time. While these codes are being used at UC Berkeley to monitor the strain release in natural earthquakes in northern California, the moment tensor inversion approach provides a potentially powerful discrimination procedure in several ways: (1) by providing estimates of M_w (moment magnitude), a more accurate measure of event size than Ms which can then be used along with M_L to construct magnitude ratio discriminants (e.g. Woods et al., 1993); (2) by providing estimates of source depth, which will help distinguish natural events (depths typically >> 1km) from nuclear explosions and (3) by providing estimates of radiation pattern characteristics (i.e. deviations from the typical double-couple radiation of earthquakes).

The initial performance goal of the ported software is the automated determination of moment tensors on a global scale for larger events (M>5.5-6.0) with a reduced threshold in a specifically targeted region. Later releases of the software will incorporate calibration information for several regions of interest, allowing moment tensor determinations at a lower magnitude threshold of approximately M~4-4.5.

RESEARCH ACCOMPLISHED

The two moment tensor codes used at UC Berkeley to monitor central and northern California earthquakes have been adapted to run at the PIDC, extracting all waveform data, event information, and instrument responses from the PIDC database (version v. 0.1). The adaptation of the codes to their current functionality, illustrated below, has met with several challenges, which required the development of signal processing code to remove SAC2000 dependency, and code to handle different instrument response formats that are used at the PIDC.

Two seismic moment tensor methodologies are run in parallel for two primary reasons; 1) to provide redundancy in the event that circumstances detrimental to any one methodology does not preclude the determination of a seismic moment tensor; 2) and to provide a means of automatically checking solutions for quality (e.g. Pasyanos et al., 1996).

The first methodology we use is a frequency domain, surface wave approach, adapted from the two-step method of Romanowicz (1982), for which calibrated fundamental mode surface wave phase velocities, in the period range 10-60 sec, are used for propagation corrections (Pasyanos et al., 1996). This method utilizes surface waves, which are the largest of the regional phases allowing for the analysis of smaller seismic events, and inverts the observed azimuthal variation in surface wave amplitude and phase for specific periods. We are able to analyze events to a magnitude of 3.5 using Berkeley Digital Seismic Network stations in the 100 to 500 km distance range. With sufficient azimuthal coverage this method is found to perform quite well.

The second methodology we employ is a time domain waveform fitting procedure that utilizes the entire long-period (T>20 seconds) wavefield (P_{nl}, S_n, Love and Rayleigh) (Dreger and Romanowicz, 1994; Pasyanos et al., 1996; Fukuyama et al., 1998; Fukuyama and Dreger, 2000). For the majority of events in northern and central California, two 1D crustal/upper-mantle velocity models are adequate. The operation of the code in Japan (NIED) is accomplished with a

single calibrated velocity model for the entire region (Fukuyama et al., 1998; Fukuyama and Dreger, 2000). With this method data from a single station is often sufficient, however in practice we use three-component data from 2 to 3 stations to improve the azimuthal coverage of the focal sphere (Pasyanos et al., 1996).

Examples of the Execution of the Moment Tensor Codes at the PIDC

Example #1: 06/01/98 event in Kamchatka

The analysis of surface wave spectra at seven stations for the 06/01/98 event in Kamchatka (Figure 1a) yields a thrust event (M6.4) consistent with the convergent tectonics of the region. A depth minimum exists at roughly 40 kilometers, similar to the reported Harvard CMT centroid depth of 35 kilometers.

Two primary stations were available within 5000 kilometers, BJT and HIA (2800 & 3600 km respectively). For this example, we have concentrated on the body wave portion of the record. The spherical reference model Green's functions used (IASP91) have difficulty matching the dispersion of surface waves for short paths and the relatively short periods used. We have also used the instrument responses from the PIDC database. Although the similar azimuth of the two stations essentially reduces the problem to a single-station analysis, the inversion retrieves an M6.4 thrust event (Figure 1b) with an optimal depth of 40-50 kilometers, consistent with the surface wave results. Close examination of the waveform fits indicates additional errors in the Green's functions; the early and late body wave arrivals cannot both be aligned with the kernels used.

Example #2: 06/14/98 event in Honshu, Japan

For a moderate event in Japan both the surface wave analysis (Figure 2a) and the complete waveform inversion (Figure 2b) retrieve a normal-type event. The surface wave inversion identifies a depth minimum of roughly 40 kilometers, in contrast to the shallow centroid value of 15 reported by Harvard. JMA reports a depth of 50 km and the moment tensor solution of the Japanese National Research Institute for Earth Science and Disaster Prevention (NIED) yielded 26 km. The body wave inversion utilized two stations BJT and HIA at distances of 2200 and 2300 km respectively. There is difficulty explaining the vertical component data but a mechanism consistent with the surface wave analysis was obtained. The estimated moment magnitude is roughly a quarter of a unit lower than that estimated using surface waves, but is only 0.1 magnitude unit different than the solution reported by NIED (http://argent.geo.bosai.go.jp/freesia/event/hypo/joho.html). The normal mechanism obtained by the three-component body waveform inversion (Figure 2b) compares quite well with the NIED result.

Examples of Events with Volumetric Source Components

The moment tensor inversion at regional distances offers promising possibilities of distinguishing primarily double-couple solutions, typical of tectonic earthquakes, from solutions with significant non-double-couple or isotropic components, as would be expected from man-made explosions (or in some cases, of volcanic earthquakes). Figure 3 is adapted from Dreger and Woods (2000) and shows a comparison of moment tensor solutions obtained for the Little Skull Mountain earthquake (06/29/1992; M_W=5.6) and the Bexar nuclear explosion at the Nevada Test Site (04/04/1991; M_W=4.5). Both events were observed at two TERRAscope broadband stations at distances greater than 300 km. At the time of the Little Skull Mountain earthquake it was possible to use the four broadband stations shown in Figure 3a. At the time of the Bexar explosion only the PAS and PFO stations were available. We were able to demonstrate for the Little Skull Mountain earthquake that the solution obtained using only PAS and PFO was essentially identical to the solution obtained with greater than two stations (Dreger and Woods,

2000). Figure 3b shows that a full moment tensor inversion (one that allows for an isotropic component) of the tectonic Little Skull Mt. earthquake results in only a nominal isotropic component (88% double-couple, 5% CLVD, 7% isotropic). In contrast the full moment tensor inversion for the Bexar nuclear explosion yields a very anomalous radiation pattern that is only 6% double couple (Figure 3c). The moment tensor solution is dominated by a CLVD component and has a 28% isotropic component that indicates volumetric expansion. It may be surprising that the isotropic component is as small as it is however Patton (1988) demonstrated that for nuclear explosions it is not possible to distinguish between an isotropic component and a vertically oriented CLVD (both do not radiate significant SH waves) using long-period surface wave data. Several other NTS nuclear explosions with different levels of tectonic release were studied and it was found that the complete three-component waveform method yielded relatively shallow source depth and anomalous radiation characteristics that identified the events as suspect.

In a recent study of Mammoth Lakes, California seismicity (Dreger et al., 2000) statistically significant evidence of volumetric sources has been observed. Figure 4 shows the locations of broadband stations used in the analysis, and seismic moment tensors that were determined from the five closest Berkeley Digital Seismic Network stations. These stations provide more than 100 degrees of azimuthal coverage, which is an adequate sampling of the focal sphere using three-component records. We have performed a significance test on the improvement in fit afforded by both deviatoric non-double-couple and full moment tensor solutions including an isotropic component compared to a pure double-couple null hypothesis. In this analysis we have found that the improvement in fit that is obtained by the full moment tensor is significant at the 99% level using the F statistic to evaluate the difference in variance for two models. Furthermore a 'Jackknife' test demonstrates that solutions are extremely stable and are not biased by specific stations or station geometry. This study showed that noise in the inversion can produce isotropic components at the 10% level, however for the anomalous events the isotropic component (>30%) is shown to be statistically significant demonstrating that volcanic regions with relatively shallow seismicity may present substantial challenges in the monitoring of the CTBT.

CONCLUSIONS AND RESEARCH PLAN

We have successfully ported the UCB seismic moment tensor codes to the PIDC (v. 0.1) and have demonstrated their application to a number of far-regionally recorded moderate earthquakes. In addition, we have investigated the resolution of non-double-couple components of the seismic moment tensor, particularly the isotropic component for a number of western US earthquakes and NTS nuclear explosions. The results for the nuclear explosions indicates that recovery of a pure isotropic solution is not possible (e.g. Patton, 1988) and because of the presence of tectonic release. For a swarm of M4.5 earthquakes in the Long Valley Caldera we have recovered statistically significant volumetric components (Dreger et al., 2000).

The current project was initiated on July 20, 2000 and involves the stepwise development and refinement of automated seismic moment tensor software at the PIDC. The stages involve the testing of the present version (v. 0.1) on seismicity recorded by the IMS for a period of 3 months. Results from the test will be used to refine the algorithms, and Maxwell Technologies will provide software development support to port the system into the PIDC computing environment, yielding v. 1.0. v 1.0 will be 'frozen' and tested in an operational testbed environment for a period of 3 months. Results from the test will be used to further refine the algorithms, and Green's functions will be tuned for regions of specific interest resulting in v. 2.0 of the software, for which we will submit a Configuration Control Board (CCB) proposal for implementation.

References

Dreger, D. S., H. Tkalcic, and M. Johnston (2000). Dilational processes accompanying earthquakes in the Long Valley Caldera, *Science*, 288, 122-125.

Dreger, D. and B. Woods (2000) Regional moment tensors as discriminants?, in revision.

Dreger, D. and B. Romanowicz (1994) Source characteristics of events in the San Francisco Bay Region, USGS Open-file report, 94-176, 301-309.

Fukuyama, E., M. Ishida, D. Dreger, and H. Kawai (1998). Automated seismic moment tensor determination by using on-line broadband seismic waveforms, *Jishin*, 51, 149-156.

Fukuyama, E. and D. Dreger (2000). Stress test of automated moment tensor determination system for the future 'Tokai' earthquake, *In press Geophys. Journ. Int*.

Pasyanos, M., D. Dreger and B. Romanowicz (1996) Toward real-time estimation of regional moment tensors, Bull. Seism. Soc. Amer., 86, 1255-1269.

Patton, H. J. (1988). Source models of the Harzer explosion from regional observations of fundamental-mode and higher mode surface waves, *Bull. Seism. Soc. Am.,* 78, 1133-1157.

Romanowicz, B. (1982) Moment tensor inversion of long period Rayleigh waves: a new approach, J. Geophys. Res., 87, 5395-5407.

Romanowicz, B. and Ph. Guillemant (1984) An experiment in the retrieval of depth and source parameters of large earthquakes using very long period Rayleigh wave data, Bull. Seism. Soc. Am., 74, 417-437.

Romanowicz, B., M. Pasyanos, D. Dreger and R. Uhrhammer (1993) Monitoring of strain release in central and northern California using broadband data, Geophys. Res. Lett., 20, 1643-1646.

Woods, B. B., S. Kedar, and D. V. Helmberger (1993). ML:M0 as a regional seismic discriminant, *Bull. Seism. Soc. Am.,* **83**, 1167-1183.

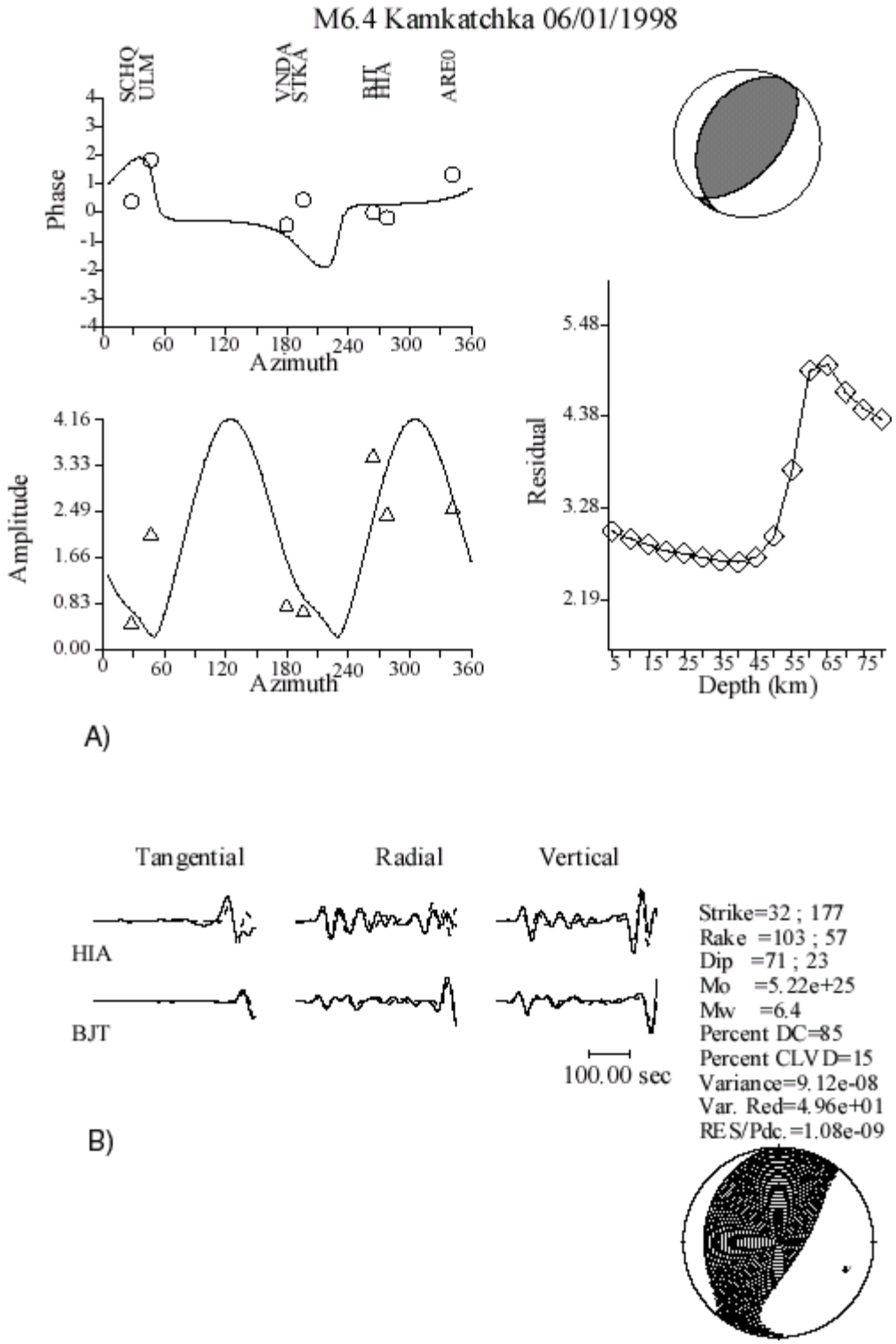


Figure 1. Example of inversion results for a Mw6.4 event in Kamchatka on 06/01/1998. A) Surface wave spectral amplitude & phase observations (circles) are compared to predictions for the shown mechanism. The resolution of the event depth is shown. B) Example of a two station, three-component body waveform inversion for the same event. Data is solid and synthetic is dashed. Only IMS stations were used in these analyses.

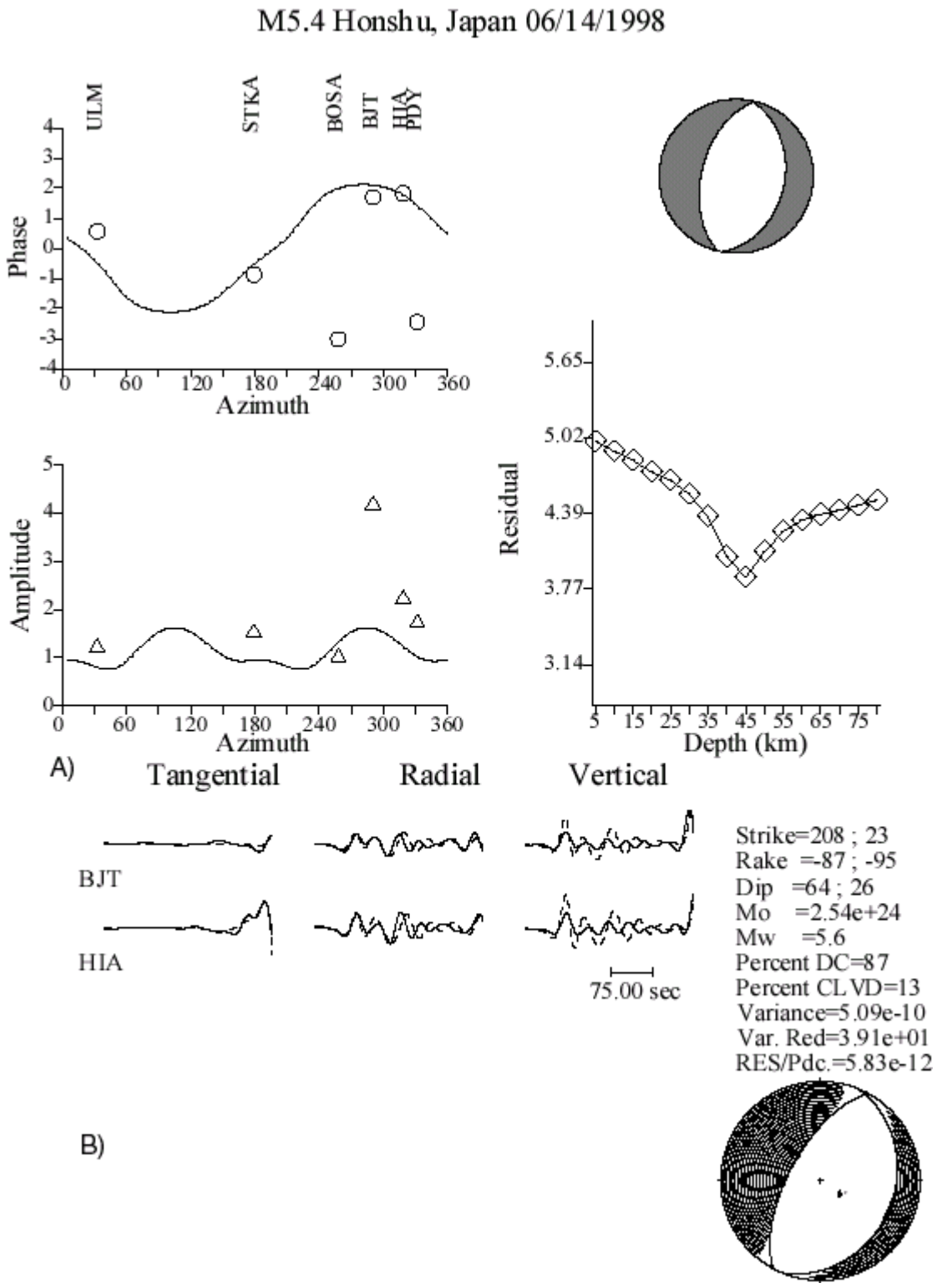


Figure 2. Example of inversion results for a Mw5.6 event in Honshu, Japan on 06/14/1998. A) Surface wave spectral amplitude & phase observations (circles) are compared to predictions for the shown mechanism. The resolution of the event depth is shown. B) Example of a two station, three-component body waveform inversion for the same event. Data is solid and synthetic is dashed. Only IMS stations were used in these analyses.

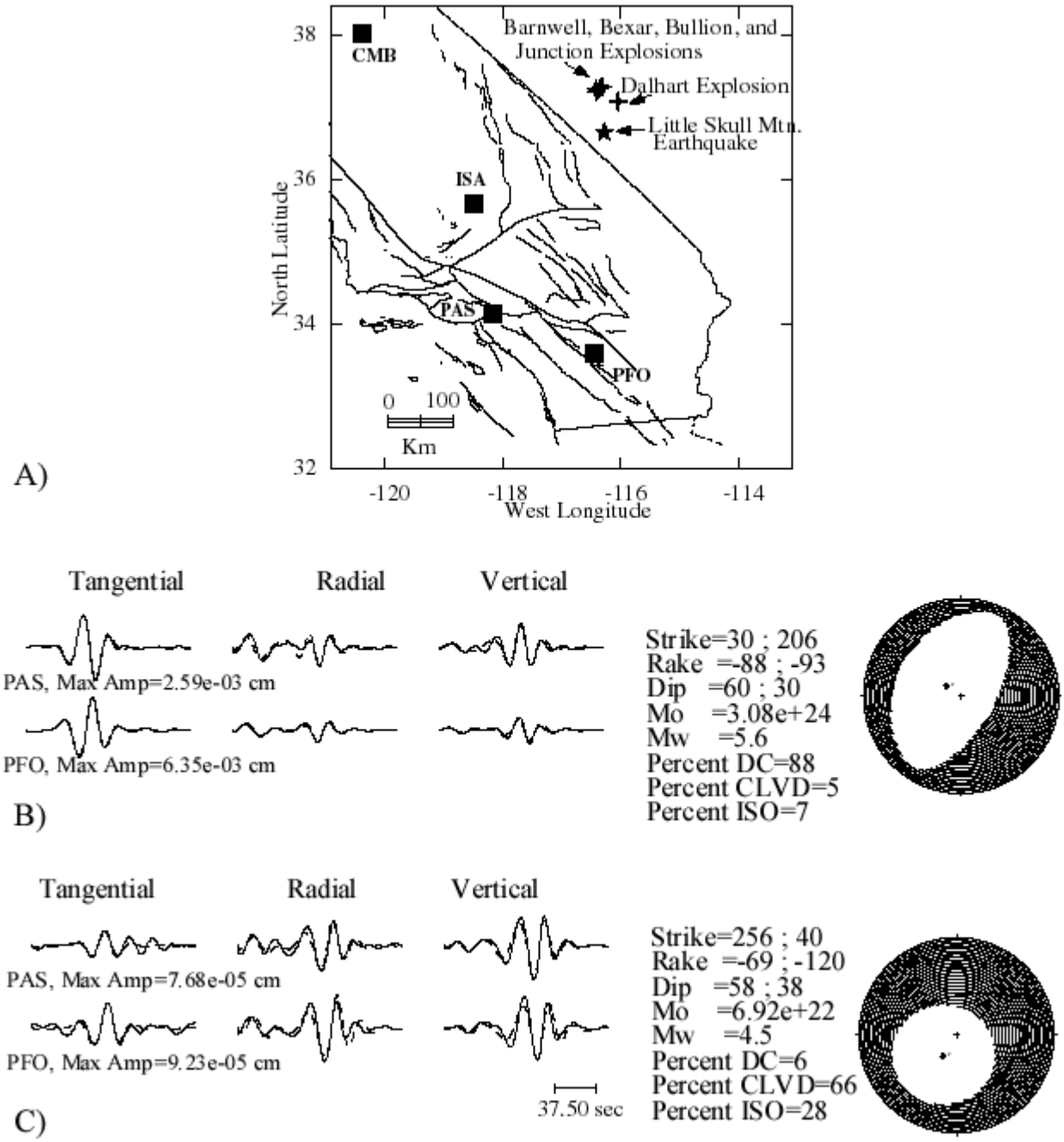


Figure 3. A) map showing the locations of broadband stations (squares), Little Skull Mt. Reference earthquake (star) and NTS explosions studied by Dreger and Woods (2000) (plusses). B) Complete moment tensor inversion of broadband displacement data for the Little Skull Mt. Earthquake. Note the nominal isotropic component. C) Complete moment tensor inversion for the BEXAR nuclear explosion. Note the unusually small double-couple component.

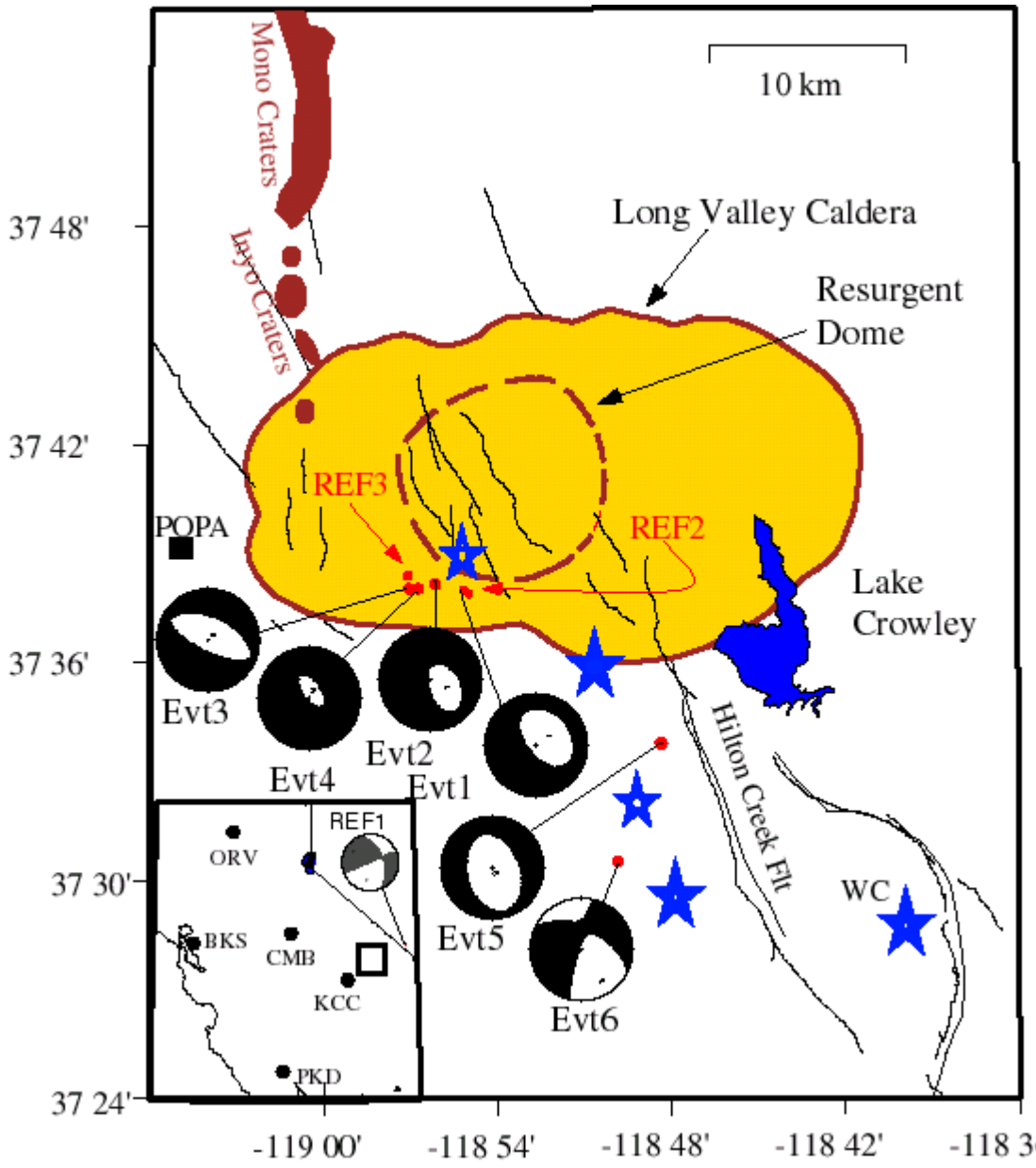


Figure 4. Map showing the Berkeley Digital Seismic Network, the Long Valley Caldera region (square) and a western Nevada reference earthquake (inset). The map of the Long Valley Caldera shows the locations of 1997 seismicity (red dots) in relation to caldera structure such as the resurgent dome, mapped faults, and the Inyo Craters chain. The blue stars show the locations of non-double-couple (filled) and double-couple (open) events of the 1978-1980 Long Valley swarm. The P-wave radiation pattern for the full moment tensor solutions for the 1997 events are shown. REF1, EVT5 & EVT6 are events located outside the caldera margin that have small, statistically insignificant volumetric components. The moment tensors for these events are primarily double-couple. EVT1-4 have anomalous seismic moment tensors with statistically significant volumetric components.

LLNL MIDDLE EAST AND NORTH AFRICA AND FORMER SOVIET UNION RESEARCH DATABASE

Jennifer L. O'Boyle, Stanley D. Ruppert, Teresa F. Hauk, Doug Dodge, Mike Firpo
Lawrence Livermore National Laboratory

Sponsored by U.S. Department of Energy
Office of Nonproliferation Research and Engineering
Office of Defense Nuclear Nonproliferation
National Nuclear Security Administration

Contract No. W-7405-ENG-48

ABSTRACT:
The Lawrence Livermore National Laboratory (LLNL) Ground-Based Nuclear Explosion Monitoring (GNEM) R&D program has made significant progress populating a comprehensive Seismic Research Knowledge Base (SRKB) and deriving calibration parameters for the Middle East and North Africa (ME/NA) and Former Soviet Union (FSU) regions. The LLNL SRKB provides not only a coherent framework in which to store and organize very large volumes of collected seismic waveforms, associated event parameter information, and spatial contextual data, but also provides an efficient data processing/research environment for deriving location and discrimination correction surfaces. The SRKB is a flexible and extensible framework consisting of a relational database (RDB), Geographical Information System (GIS), and associated product/data visualization and data management tools. This SRKB framework is designed to accommodate large volumes of data (over 2 million waveforms from 20,000 events) in diverse formats from many sources (both LLNL derived research and integrated contractor products) in addition to maintaining detailed quality control and metadata. Using the SRKB framework, we are combining travel-time observations, event characterization studies, and regional tectonic models to assemble a library of ground truth information and phenomenology (e.g. travel-time and amplitude) correction surfaces required for support of the ME/NA and FSU regionalization program. Corrections and parameters distilled from the LLNL SRKB provide needed contributions to the DOE Knowledge Base (DOE KB) for the ME/NA and FSU regions and will help improve monitoring for underground nuclear testing. The LLNL research products will facilitate calibration of International Monitoring System (IMS) stations (primary and auxiliary), their surrogates (if not yet installed) and selected gamma stations necessary to complete the above tasks in the ME/NA and FSU regions. We present expanded lookup tables for critical station parameter information (including location and response) and a new integrated and reconciled event catalog dataset, including specification of preferred origin solutions and associated phase arrivals for the complete PDE, EDR, CMT, ISC bulletins and selected regional catalogs. In addition to an overview of selected datasets and individual research products, we present an overview of our visualization, integration, and organizational processes. Development of these processes and the LLNL SRKB was necessitated by both the very large amount of data and information involved (over 1.5 TB) and the varied data and research result formats utilized. Products contained and organized within the LLNL SRKB are grouped in 5 major categories:

1) Reference contextual information and lookup tables
2) Ground truth and regionalization data
3) Event location products
4) Event identification products
5) Visualization and data manipulation processes

Keywords: MENA, FSU, seismic, database, Knowledge Base, GIS, visualization

OBJECTIVE

The primary objective of the Lawrence Livermore National Laboratory (LLNL) Seismic Research Knowledge Base (SRKB) is to help coordinate the LLNL Ground-Based Nuclear Explosion Monitoring (GNEM) Middle East, North Africa (ME/NA) and Former Soviet Union (FSU) regionalization program. The LLNL SRKB provides efficient access to, and organization of, thousands of seismic events and associated waveforms, while also providing the framework to store, organize, and disseminate research results for delivery into the DOE KB. Reference event libraries and ground truth datasets showing space and time clustering of natural earthquake and mine events, phase blockage maps, and event characterization parameters are compiled from the SRKB. Sufficient metadata (including measurement procedures, codes, comments and measurement errors) are stored at each step in the analysis process to allow recreation or verification of results at any stage in the processing flow. Corrections and parameters distilled from the LLNL SRKB provide needed contributions to the Department of Energy (DOE) Knowledge Base (KB) for the ME/NA and FSU regions and will enable the United States National Data Center (USNDC) to effectively verify Comprehensive Nuclear-Test-Ban Treaty (CTBT) compliance. The LLNL contributions support critical USNDC pipeline functions in detection, location, feature extraction, discrimination, and analyst review. Figure 1 outlines the LLNL GNEM research processes and integration of research into the DOE KB.

LLNL research products created using the SRKB may be grouped under two major categories: primary data products and derived products. The primary products are those developed in the process of collecting the raw materials for calibration: ground truth data, waveform data, event catalogs, phase pick information, regional station information and instrument responses. The derived products (distilled from the organized raw seismological data) are models and corrections that improve detection, location and discrimination functions. To calibrate International Monitoring System (IMS) stations (primary and auxiliary), as well as a variety of gamma stations that experience has shown to be useful, the LLNL SRKB must incorporate and organize the following categories of primary and derived measurements, data and metadata:

Contextual and Reference Datasets

1) Station Parameter Tables and Instrument Responses
2) Global and Regional Earthquake Catalogs
3) Selected Calibration Events
4) Geologic/Geophysical Datasets
5) MENA 1.1 Geophysical Model

Measurements and Raw Data

1) Event Waveform Data
2) Phase Picks
3) Travel-time and Velocity Models
4) Rayleigh and Love Surface Wave Group Velocity Measurements
5) Phase Amplitude Measurements and Magnitude Calibrations
6) Middle East Mine Atlas and Reference Waveforms

In order to efficiently organize this information within the SRKB, it was necessary to automate procedures needed to create and update database tables. This need prompted the development of custom tables to track additional information created by or related to loading data. We are also in the process of developing custom database tables (where existing defined tables are inadequate) in order to organize and store research results in a manner that will allow these results to be accessible to the research team and to track metadata related to table entries.

RESEARCH ACCOMPLISHED

Contextual Data Acquisition

Data collection for the LLNL SRKB began in 1996 and continues today. The LLNL study area surrounding the Middle East and North Africa including Europe, part of the Former Soviet Union, and Central Africa, has been termed the ME/NA and FSU regions (between latitudes 10° South and 90° North and longitudes -20° West and 85° East). Most of the archived waveforms in the LLNL SRKB are from events located within this region and occurring between 1976 and 2000. Special datasets are compiled for specific areas of interest or special events, such as the Novaya Zemlya test site and the 1998 India and Pakistan nuclear tests. The SRKB is organized in CSS3.0 (Center for Seismic Studies Version 3.0) format with USNDC and LLNL extensions.

Station Parameters

Development of travel-time corrections requires not only accurate source locations, origin times and quality-controlled waveform data, but also accurate knowledge of station locations. Seismic station information is a metadata requirement needed to support all stages of seismic waveform analysis. These metadata include such parameters as station operation dates, location and elevation, type of channels and instruments, sampling rates, and instrument responses. Our main source of this information is Incorporated Research Institute for Seismology (IRIS) "dataless" SEED files, which are provided by each of the networks affiliated with IRIS. These files contain all station parameters and response information and are updated periodically by the networks. Other station information has been obtained through Internet station books and AutoDRM systems. CSS3.0 **site** and **sitechan** table entries (listing station location, available channels, sensor orientations, operation dates, etc.) were created for almost all IRIS affiliated networks as well as many other stations with waveforms in the SRKB (Figure 2).

As networks become more expansive and install more instruments, we have encountered some confusion over seismic stations with multiple operators and duplication of channels or simpler cases where two stations were given the same code. To resolve these problems of non-uniqueness in our database tables, we have appended a network code to some of the station codes. We attempt to standardize the channel names based on the FDSN naming convention used at IRIS. However, consistent adherence to the FDSN naming convention was not possible in all cases. In the future, we intend to append a 2-character location code that is now being utilized by some IRIS networks to the channel code. This is necessary to distinguish between multiple channels of the same type operating simultaneously at a single station.

We reviewed all new station and channel information and existing database entries for completeness and coherency before updating the SRKB tables. Over 1800 station and array element table entries have been updated, but we still have not located reliable parameter data for some stations. Minimal or inconsistent information restricts the reliability of some entries. Often discrepancies arise between multiple information sources for the same station, but IRIS or the network operator is assumed to offer the most complete information in most cases. We maintain a list of sources for each station parameter in custom database tables**,** since each parameter may be obtained from a different source. **Network** and **affiliation** tables have been created to track the network(s) to which each station is associated.

Instrument and **sensor** tables are used to document instrument type and response for each station and channel. The IRIS "dataless" SEED files are used to generate instrument response (RESP) files for each station/network/channel/time combination delineated by calibration periods. The **sensor** table references the response file through the **instrument** table, which contains pointers to the online flatfiles. Frequency-amplitude-phase (FAP) files have been provided by some other networks and are similarly stored with database pointers. The Seismic Analysis Code (SAC) has been modified to interpret either response information type (RESP or FAP) for use in performing instrument response corrections on waveform data by using the EVALRESP software library available from IRIS.

To manage and update the large number of response files for stations maintained in the LLNL SRKB, we have automated the required processing and quality control steps. As we load information into the **instrument** and **sensor** tables, the automated system separates the RESP file into individual epochs, removes overlapping epochs and verifies that the epochs correspond to those in the station parameter tables. New RESP files are created from these results with the station and channel names modified if necessary. If the "frequency of sensitivity" is provided in the RESP file, the inverse value is inserted as the calibration period; otherwise, the "normalization frequency" is used. If neither value is found, the file is not processed. The IRIS EVALRESP program is used to calculate a transfer function to supply a displacement amplitude response.

Event Bulletins

Reference event locations and origin time information are necessary in most stages of our seismic processing and research. Bulletin information from many global, local, and regional earthquake catalogs has been incorporated into the LLNL SRKB and provides a much larger source for event selection. This combined and reconciled source facilitates comparison of event parameters provided by multiple networks with different degrees of location quality and accuracy for a wider range of magnitudes in comparison to the single global catalog used in the past. The global catalogs include: USGS Monthly (Final) Preliminary Determination of Epicenters (PDE) catalog, USGS Earthquake Data Report (EDR) catalog with phase arrival information, Bulletin of the International Seismological Centre (ISC) with phase arrival information, Harvard Centroid Moment Tensor (CMT) catalog, and the Multimax Ground Truth

dataset. We have also compiled numerous regional and local catalogs from countries in the ME/NA region, including Jordan, Israel, Morocco, and the Joint Seismic Observing Program (JSOP). A special catalog was compiled for events in the European Arctic and at Novaya Zemlya in collaboration with NORSAR. Figure 3 shows a global map of the event location coverage provided by several of the bulletins. We have established a number of collaborative agreements with countries and institutes in our study region that are yielding both local seismic catalogs and ground truth information as well as seismic waveform data.

We have developed an automated method to load various bulletins of different formats into native-format database tables, which retain many of the fields provided in the original bulletin, as well as assign a unique origin identifier (*orid*) to each event. Individual bulletins are then merged into a single CSS3.0 **origin** table retaining the author of the original bulletin. The event type and depth determination method are remapped to a common set of designators. A space-time correlation algorithm is used to reconcile events between individual catalogs. Events common to multiple bulletins will be assigned common event identifiers (*evid*) while retaining unique *orid*s. The **event** table stores the preferred origin for each event based on a ranked list of catalog preferences. Phase arrivals provided with native catalogs are loaded into the **assoc** and **arrival** tables. The arrivals can be used to check the event reconciliation.

Phase Information

LLNL researchers and analysts have made phase picks for over 1800 events to yield over 20,000 travel-time observations available to the LLNL research team for location and discrimination projects. Phase analysis is an ongoing effort, since new events and waveforms are continually being added to the SRKB. Phase information is recorded in the **arrival** and **assoc** tables, along with pick and waveform quality and other comments that are recorded in a **remark** table. Augmenting the LLNL picks, we added ~5.5 million USGS Earthquake Data Report (EDR) catalog phase pick observations to the SRKB to be used for travel-time correction studies and correction surface generation. Since the EDR picks are available only for 1990-1997, we supplemented the EDR picks with the complete Bulletin of the International Seismological Centre (ISC) phase arrival measurements from 1964-1996, which includes 28 million picks. Phase picks have also been entered into the SRKB from the Joint Seismic Observing Program (JSOP) and a reviewed subset of the ISC bulletin (Engdahl *et al*., 1998).

Waveforms

We are collecting seismic data from IMS primary and auxiliary stations, as well as surrogate stations (for IMS stations not yet installed) and other stations needed to support calibration in the region of study. We have obtained up to 10 years of continuous data for important ME/NA and FSU stations from IRIS, Institut de Physique du Globe de Paris GEOSCOPE program, the GEO-Forschungs Zentrum/Potsdam, Germany GEOFON program and other data centers. Current data are being supplied by an LLNL joint project with the Jordan Natural Resources Authority from two seismometers deployed in Jordan. Data for particular events has been obtained from the prototype International Data Center (PIDC) and the USNDC. The Center for Monitoring Research (CMR) and NORSAR have provided waveforms for special regions/events, such as the Novaya Zemlya test site.

Our current data collection emphasis is on events recorded between 1990 and present, except for IMS surrogate stations no longer in operation or for special events such as nuclear tests. All available channels and components are requested from each station or array. Data from IRIS, GEOSCOPE, and GEOFON are provided in SEED format, waveforms from USNDC, NORSAR and CMR are organized in CSS format, and data from LLNL deployments are recorded in REFTEK format. Additionally, although the continuous data remain archived on tapes, seismic events are extracted from the continuous waveforms. This process is outlined in Figure 4. We are augmenting the open historic station data with seismic data from LLNL field deployments, such as the Jordanian stations, and collaborative research efforts established in ME/NA countries.

To generate the event waveforms for the SRKB, we have developed an automated way of extracting waveforms based on events selected from an **origin** table and adding entries for these waveforms into the appropriate database tables. Waveforms are extracted from continuous data in the native format and then converted to CSS3.0 format. Currently, we can perform waveform extraction on data in SAC, SEED, CSS, SEGY and GSE formats. Information already in the database is used to determine station parameters and event origins which are then used in determining the appropriate time window of data to extract. The extracted waveforms are entered into staging database tables and then are reconciled and loaded into the main database tables. At this time, waveforms are checked for poor or missing signals, which are then recorded in a metadata table. If waveforms for a specific event are segmented, the

segments will be merged together; if a gap exists between segments, the space will be filled with zero-value data points. If two segments overlap, a correlation test is done before the two segments are joined.

The number of waveforms in the SRKB is now over 2 million, which corresponds to 20,000 seismic events. In addition to individual event waveform segments and continuous data traces managed by the SRKB, we also maintain an archive of active and passive seismic data from various field deployments, which include IRIS/PASSCAL experiments in Tanzania, Pakistan, Caspian Sea, and Turkmenistan. We are also archiving the very long FSU Peaceful Nuclear Explosion (PNE) refraction profiles collected under contract to LLNL by the US Geological Survey (USGS).

SRKB waveforms may contain dropouts, glitches, timing errors or other problems affecting waveform analysis. We have developed an algorithm that analyzes and reports on 18 separate problems in the categories of timing errors, zero slope detection, discontinuity detection, and median filtering. This automated procedure measures waveform quality in a consistent manner and generates custom database tables which describe the types of problems encountered along with the location and frequency of these problems. These tables allow researchers to quickly identify sets of quality reviewed waveforms, thus minimizing the laborious process of previewing each trace.

Other Reference Datasets

Collaborations with Cornell University, USGS and other organizations allow us to obtain reference datasets useful as background and supporting information for research. Most of these datasets are provided as Geographic Information System (GIS) products, which allow us to integrate them with LLNL datasets. The datasets include geographic, geopolitical, mining industry, geologic and tectonic information.

Database Organization

The LLNL SRKB is a framework consisting of a relational database (RDB), Geographical Information System (GIS), and associated product/data visualization and data management tools, as outlined in Figure 5. The SRKB is necessary for the storage and organization of very large volumes of collected seismic waveforms, associated event parameter information, and spatial contextual data, but also provides an efficient data processing/research environment for deriving location and discrimination correction surfaces.

Database Format

The LLNL SRKB is designed to be flexible and extensible in order to accommodate large volumes of data in diverse formats from many sources in addition to maintaining detailed quality control and metadata. The SRKB is comprised of ORACLE relational database software running on a SUN UNIX Server accessible from researcher workstations. Data are stored in CSS3.0 format (Center for Seismic Studies Version 3.0 database structure) with USNDC and LLNL extensions. These formats provide parameter defined tables for different elements of seismic data, such as event and station information, as well as allowing for customized tables to be developed for specific research needs or results. The CSS3.0 format offers the ability to organize data in a standard format, store metadata necessary for documenting research methods and deliver compatible data to DOE and other researchers.

Class Libraries

We have written a set of C++ classes designed primarily as components of computer programs for use by the LLNL GNEM program, which consists of about 130 classes. Of these, about 10 are service classes with no specific seismological capability, *e.g.* time class, architecture class, etc. All the remaining classes are specialized to some degree for use in seismological applications. All of the collection classes have database-aware specializations as well, since most of the programs developed with the classes interact extensively with the SRKB database. The class library has built-in support for the CSS3.0, SAC, GSE2.0, and PC-SUDS data formats.

Using the classes has proven to be an effective means of building the utility programs required to support the SRKB. In most cases, nearly all the required functionality exists within the classes, so the program only needs to collect user input and manage a few object interactions. Since the developer is shielded from the intricacies of data formats, embedded SQL, and the like, programs can usually be constructed quickly, and can be easily maintained and augmented. In addition, when improvements are made to any of the classes, all programs using those classes can benefit just by recompiling.

Data Access

Different researcher needs for data and metadata require that subsets of data be provided in a format easily accessible to many diverse types of software and analysis tools. Therefore, the SRKB access tools have been designed to utilize the power of the relational database to facilitate efficient queries and data retrieval. The Seismic Analysis Code (SAC) software used by LLNL researchers provides direct access to database table information and waveforms and uses the response files to perform instrument response corrections. PL/SQL language can be used to make database queries on contents of any of the available database tables.

For spatial queries and organization, we have adopted a Geographic Information System (GIS), which provides a framework to store and manipulate spatially-defined data. The GIS is linked with the ORACLE database to provide joint spatial and relational queries. We have integrated a large number of our research products and contextual datasets into the GIS, as shown in Figure 6. A customized framework provides an organized menu system for accessing the datasets and also includes additional functionality developed in collaboration with Sandia National Laboratories. The GIS is organized by geographic regions, seismic stations and research product types to provide easy access to a large number of products developed in various formats. Links are established for related non-spatial data, such as photographs or graphs, and metadata are provided for each dataset. Researchers can use the GIS to browse many of their research products and also to perform basic comparisons, queries, and analyses. It also provides a way to use LLNL products in conjunction with other datasets, including integrated contractor products.

CONCLUSIONS AND RECOMMENDATIONS

Corrections and parameters distilled from the LLNL SRKB provide needed contributions to the DOE Knowledge Base for the ME/NA and FSU regions and will enable the USNDC to effectively verify CTBT compliance. The LLNL portion of the DOE KB supports critical USNDC pipeline functions in detection, location, feature extraction, discrimination, and analyst review in the Middle East, North Africa and portions of the Former Soviet Union. A wide range of research products required to support the ME/NA and FSU regionalization program are being derived from waveforms, station parameters, and bulletin information contained in the LLNL SRKB. The derived products (distilled from the organized raw seismological data) include: models, calibrations and correction surfaces that improve detection, location, discrimination and event characterization functions, and capability studies to help guide our research efforts.

We have made a major effort to provide a product development environment that encourages the natural synergies among each of the separate research efforts of the LLNL GNEM researchers. The derivation of reference and ground truth datasets and location and identification products takes place in an integrated environment with changes and improvements in one area being used to facilitate development of the remaining areas. We utilize the LLNL SRKB as an integrating framework to provide the basis for synergistic development of all LLNL GNEM research. By combining travel-time observations, event characterization studies, and regional wave-propagation studies of the LLNL GNEM research team for ground truth and regional events, we have assembled a substantial library of ground truth information (origin times, locations, depths, magnitudes), event location correction surfaces, tomographic models and mine explosion statistics.

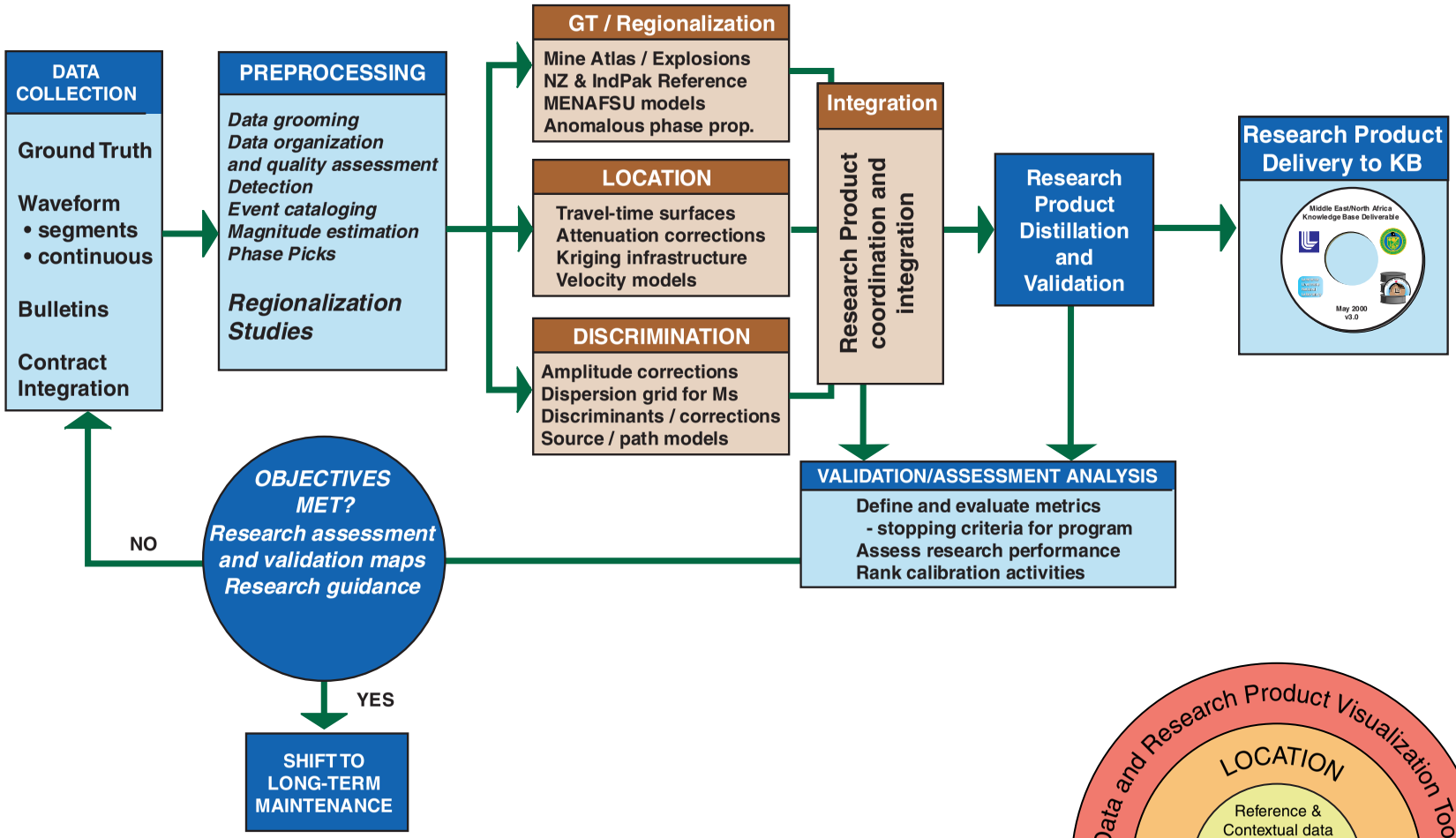
The datasets and research products contained and organized within the LLNL SRKB may be grouped under 5 major categories:

1) Reference contextual information and lookup tables
2) Ground truth and regionalization data
3) Event location products
4) Event identification products
5) Visualization and data manipulation processes

Given the large quantity of data now managed by the SRKB, emphasis has shifted to create the efficient "production" level seismic data selection, processing and visualization tools necessary to meet programmatic and DOE KB needs. These tools, along with data browsers to allow visualization and quick access to both data and delivered research products, are under development in collaboration with Sandia National Laboratories. The tools provide such functionality as deriving location corrections, making amplitude and magnitude measurements, and developing discriminants.

REFERENCES

Engdahl, R., R. van der Hilst and R. Buland (1998). Global teleseismic earthquake relocation with improved travel-times and procedures for depth determination, *Bull. Seismol. Soc. Am.*, **88**, 722-743.



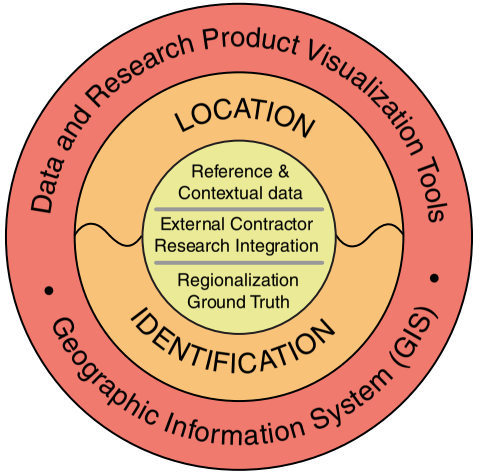


Figure 1. LLNL Seismic Research Knowledge Base process flow. The SRKB is the framework that supports and integrates the LLNL GNEM seismic calibration research. Integration and synergy of data, research and visualization tools are made possible through the LLNL SRKB.

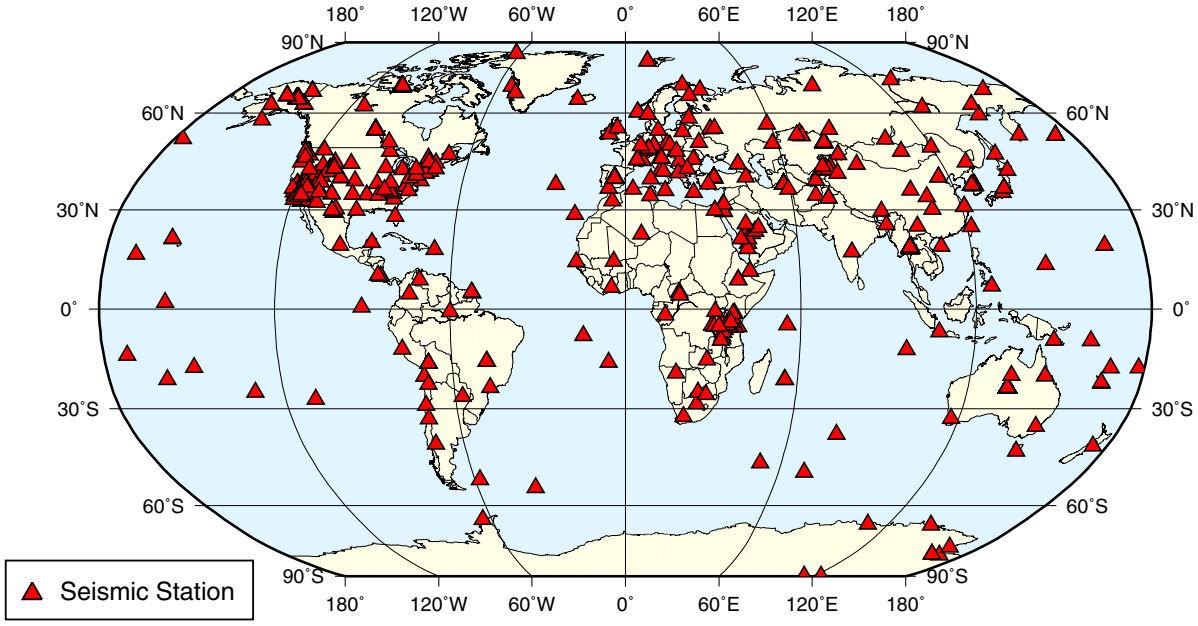


Figure 2. Distribution of seismic stations contained in the LLNL SRKB database tables. Station parameters have been reviewed and updated for most stations.

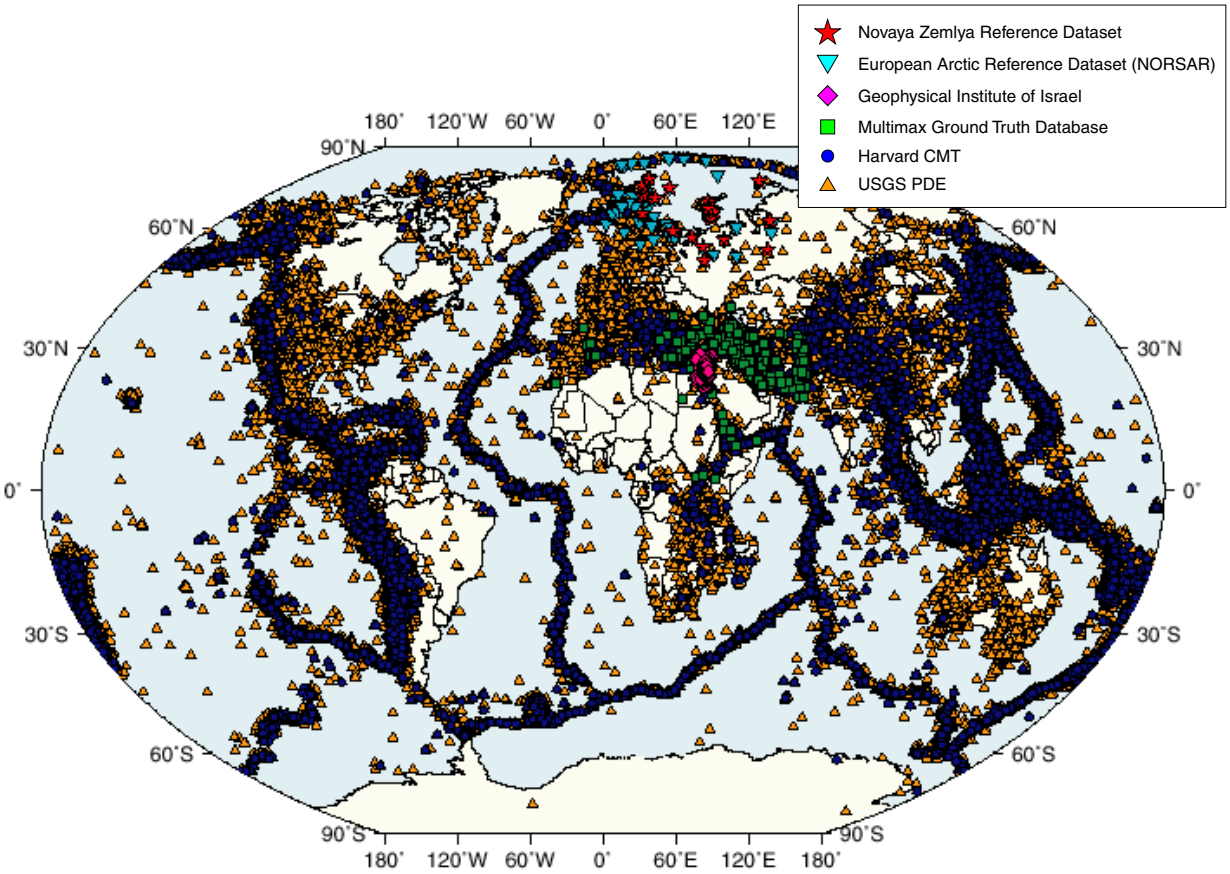


Figure 3. Events from many of the global, regional and local bulletins incorporated in the LLNL SRKB reconciled event database tables.

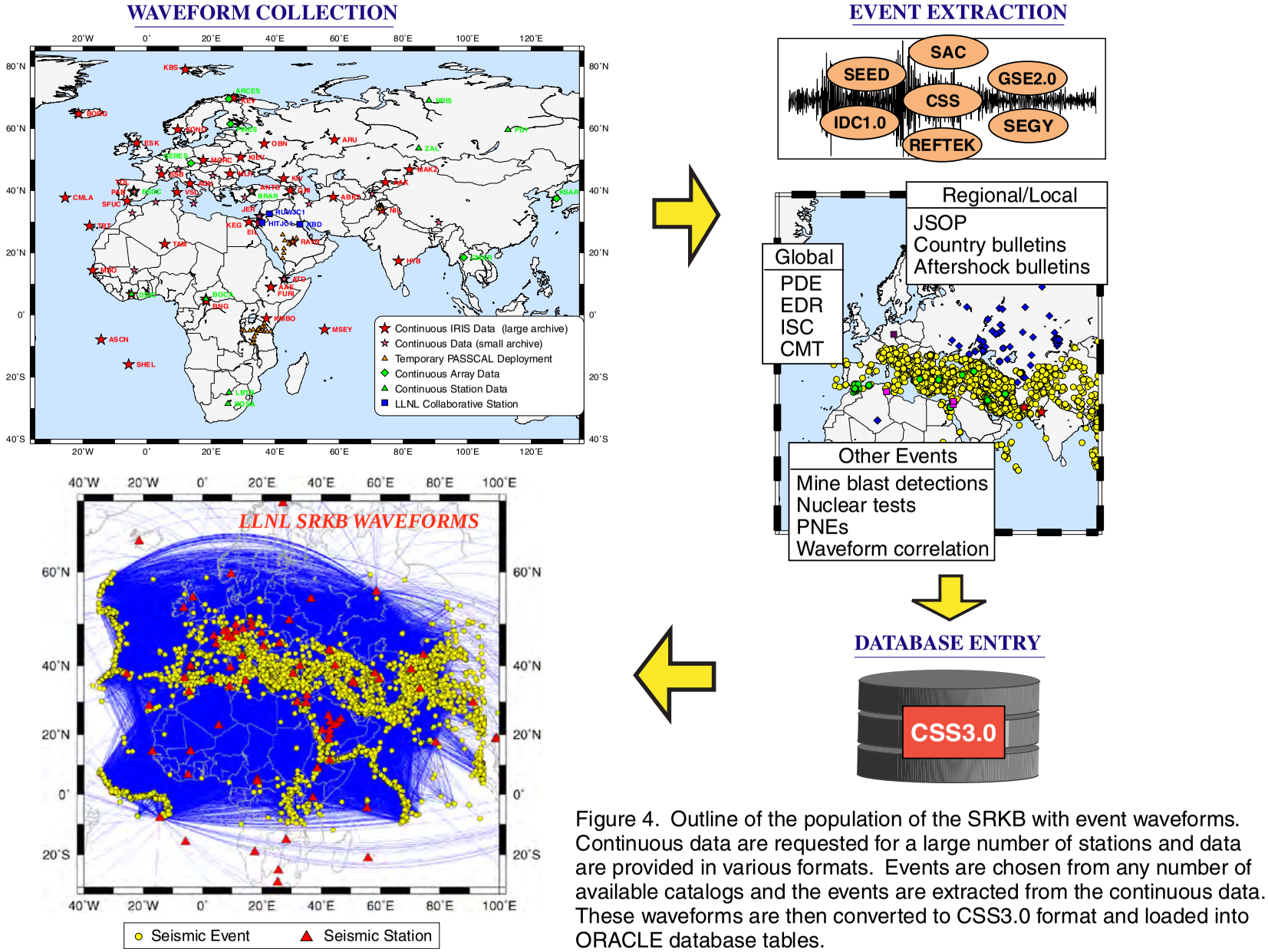


Figure 4. Outline of the population of the SRKB with event waveforms. Continuous data are requested for a large number of stations and data are provided in various formats. Events are chosen from any number of available catalogs and the events are extracted from the continuous data. These waveforms are then converted to CSS3.0 format and loaded into ORACLE database tables.

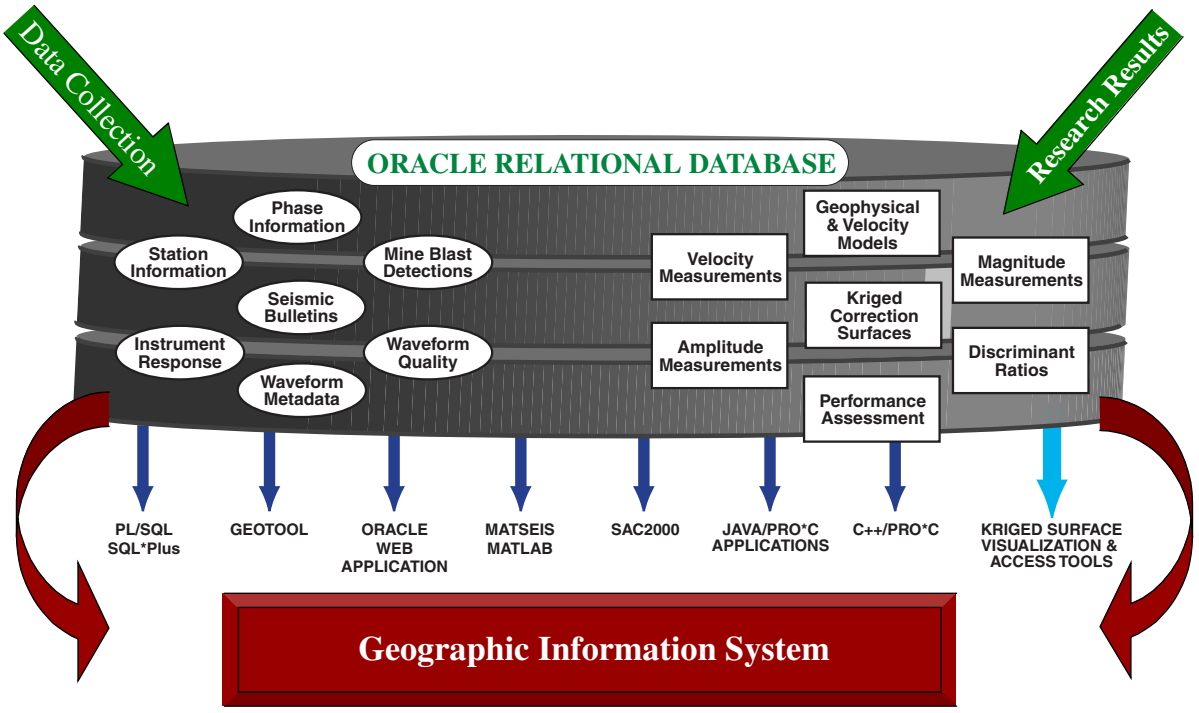


Figure 5. The LLNL SRKB integrates a relational database, a Geographic Information System (GIS) and visualization/data management processes.

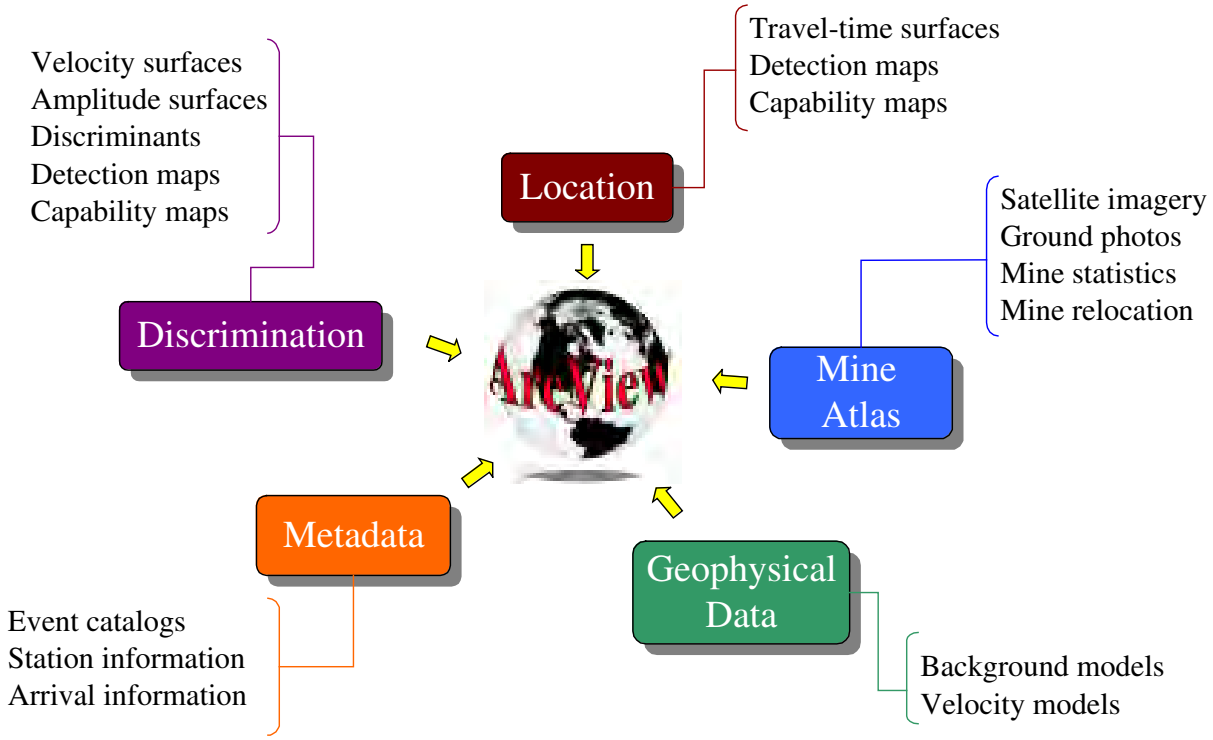


Figure 6. A large portion of raw and derived data and research products is incorporated into a GIS system. ESRI ArcView software is used to create this integrated framework for SRKB datasets.

SURFACE WAVE SIMULATION AND PROCESSING WITH MATSEIS

Beverly D. Thompson, Eric P. Chael, Chris J. Young, William R. Walter[1], and Michael E. Pasyanos[1]

Sandia National Laboratories and [1]Lawrence Livermore National Laboratory

Sponsored by U.S. Department of Energy
Office of Nonproliferation Research and Engineering
Office of Defense Nuclear Nonproliferation
National Nuclear Security Administration

Contract No. DE-AC04-94AL85000

ABSTRACT

In order to exploit the information on surface wave propagation that is stored in large seismic event datasets, Sandia and Lawrence Livermore National Laboratories have developed a MatSeis interface for performing phase-matched filtering of Rayleigh wave arrivals. MatSeis is a MATLAB-based seismic processing toolkit which provides graphical tools for analyzing seismic data from a network of stations. Tools are available for spectral and polarization measurements, as well as beam forming and f-k analysis with array data, to name just a few. Additionally, one has full access to the MATLAB environment and any functions available there. Previously we reported the development of new MatSeis tools for calculating regional discrimination measurements. The first of these performs Lg coda analysis as developed by Mayeda and coworkers at Lawrence Livermore National Laboratory. A second tool measures regional phase amplitude ratios for an event and compares the results to ratios from known earthquakes and explosions.

Release 1.5 of MatSeis includes the new interface for the analysis of surface wave arrivals. This effort involves the use of regionalized dispersion models from a repository of surface wave data and the construction of phase-matched filters to improve surface wave identification, detection, and magnitude calculation. The tool works as follows. First, a ray is traced from source to receiver through a user-defined grid containing different group velocity versus period values to determine the composite group velocity curve for the path. This curve is shown along with the upper and lower group velocity bounds for reference. Next, the curve is used to create a phase-matched filter, apply the filter, and show the resultant waveform. The application of the filter allows obscured Rayleigh arrivals to be more easily identified. Finally, after screening information outside the range of the phase-matched filter, an inverse version of the filter is applied to obtain a cleaned "raw" waveform which can be used for amplitude measurements.

Because all the MatSeis tools have been written as MATLAB functions, they can be easily modified to experiment with different processing details. The performance of the propagation models can be evaluated using any event available in the repository of surface wave events.

Key Words: data processing, data analysis, surface waves

OBJECTIVE

Though improved regional discriminants are desirable for identifying small seismic events, Ms:mb remains as a preferred method when Rayleigh arrivals are recognizable. Phase-matched filtering (Herrin and Goforth, 1977) is a well-established method for enhancing and extracting Rayleigh waves from records of located events. This technique requires a reasonably accurate estimate of the Rayleigh dispersion along the path from event to station. Better models of surface-wave propagation at global and regional scales are now available (eg, Stevens and Adams, 1999; Pasyanos et al., 1999). These models have become sufficiently mature to enable the routine use of phase-matched filtering, which should permit reliable Ms measurements down to lower magnitudes.

To facilitate surface-wave analysis and Ms estimation, we have added an interactive phase-matched filtering capability to MatSeis, a seismic toolkit based on MATLAB. Graphical interfaces make the surface wave analysis routines easier to use and accessible to a wider audience. The user can select among different surface-wave propagation models to evaluate their appropriateness for an observed Rayleigh arrival. In addition, the inherent flexibility and openness of MATLAB simplifies the process of developing and modifying the algorithms. MatSeis provides connections to a repository of surface wave data so that phase-matched filtering can be performed for any events and waveforms stored there.

BACKGROUND

The MatSeis seismic processing toolkit was originally developed at Sandia to support Comprehensive Test Ban Treaty (CTBT) R&D on improving event association and location (Harris and Young, 1997). Through menus in the MatSeis user interface, a researcher can connect to a repository of surface wave data and select events, arrivals and waveforms for analysis. Once the desired data have been obtained, the waveforms can be displayed as a record section for any event, with signals from the various stations organized vertically based on their epicentral distance (Figure 1).

Selected travel-time curves may be overlaid on the plot, to assist in identifying phases. The package provides a wide assortment of functions to help the user interpret the signals and hence characterize the event. A variety of filters can be applied to the signals. Arrivals can be picked or retimed, then their amplitude and period may be measured. The user may relocate the event using an interface to a location routine descended from TTAZLOC (Bratt and Bache, 1988), and display station and event positions on a map through a connection to the M_Map mapping toolbox (Pawlowicz, 1998).

Modules are included for spectrum estimation, waveform correlation, polarization analysis, beamforming and frequency-wavenumber analysis. MatSeis serves as a key tool for developing and testing the DOE Knowledge Base, a system for storing and accessing region-specific information. Thus the analysis functions in MatSeis can exploit the contents of the Knowledge Base for optimal performance in a given geographic area.

Written in the MATLAB® language, MatSeis can be readily modified or extended to include new functionality, so it serves as a convenient platform for prototyping new algorithms. Because of this inherent flexibility, and the access to region-specific information in the DOE Knowledge Base, we believe that MatSeis provides a suitable environment for analyzing long-period surface-wave arrivals as well. Previously we reported the development of MatSeis tools for calculating regional discrimination measurements (Chael et al., 1999). The first of these performs Lg coda analysis as developed by Mayeda and coworkers at Lawrence Livermore National Laboratory. The second measures amplitude ratios among regional arrivals for an event and compares the results to those from known earthquakes and explosions.

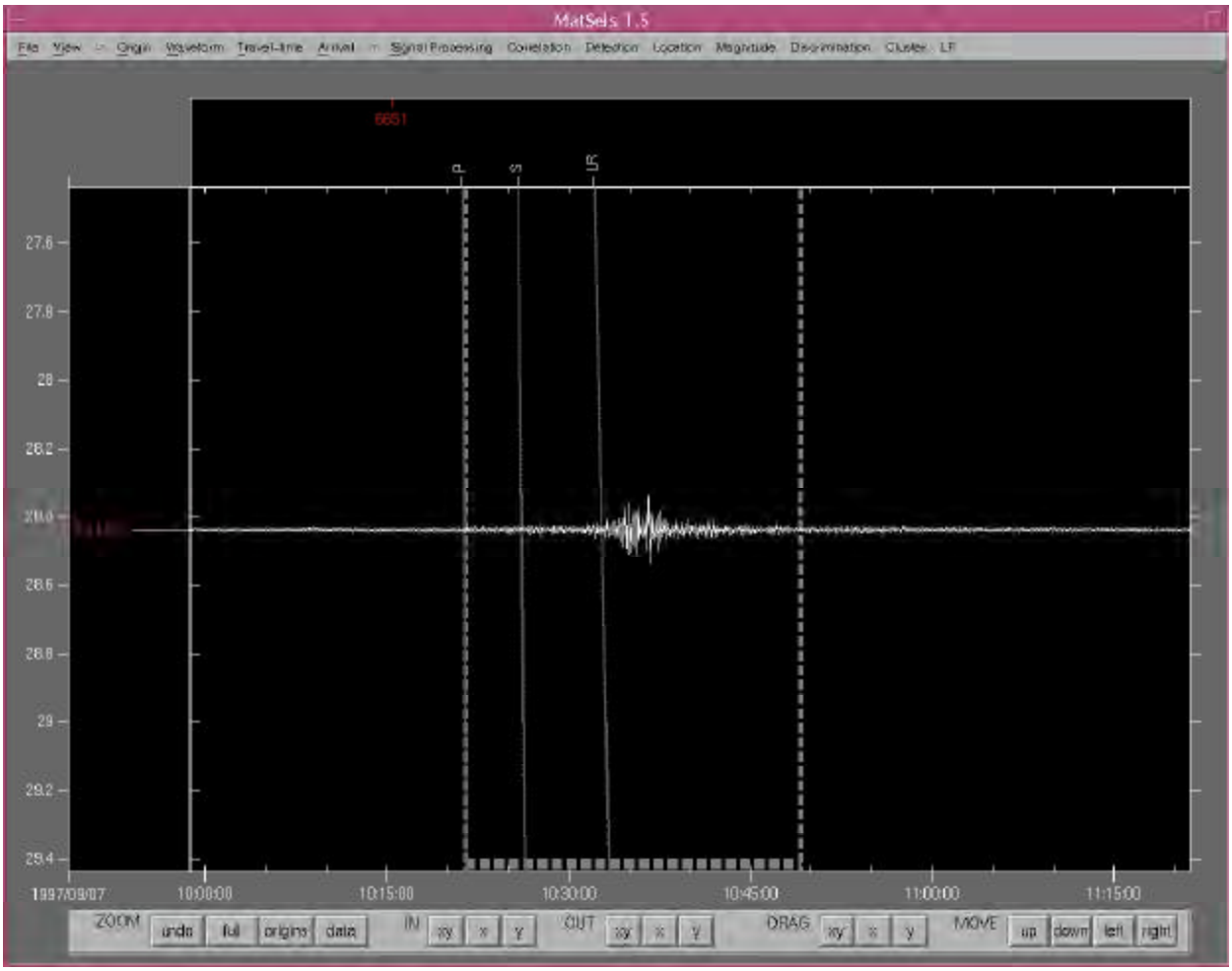


Figure 1. MatSeis Main Window Display

RESEARCH ACCOMPLISHED

The current Release 1.5 of the MatSeis package includes new tools for the analysis of surface wave arrivals. These routines can generate phase-matched filters for any desired path, given a 2D model of Rayleigh group velocity distribution. So far we have incorporated a regionalized model of the whole earth (Stevens and Adams, 1999), a tomographic model for the Middle East and North Africa (Pasyanos, 1999), as well as individual dispersion curves for some specific paths from the Lop Nor (China) test site. For each frequency available in the chosen model, the travel time over the great circle from source to receiver is determined by following the path through the model grid, and looking up the tabulated group velocity for each cell traversed. The resulting path-average dispersion curve is plotted along with the maximum and minimum group velocities in the grid at any frequency. Next, the path-average curve is used to create a phase-matched filter, using Equation 4b of Herrin and Goforth (1977). We chose to calculate the correlation form of this filter, so that its waveform is effectively a unit-amplitude synthetic, which can be directly compared to the recorded signal. Correlating this filter with the seismogram should result in a peak near zero lag if the synthetic and observed waveforms agree, assuming there is sufficient signal energy relative to the noise in the data. Finally, a window around the peak in the cross-correlation function can be extracted, then convolved with the phase-matched filter. This redisperses the energy, which should produce a restored version of the original signal with reduced noise, and hence a cleaner Rayleigh arrival.

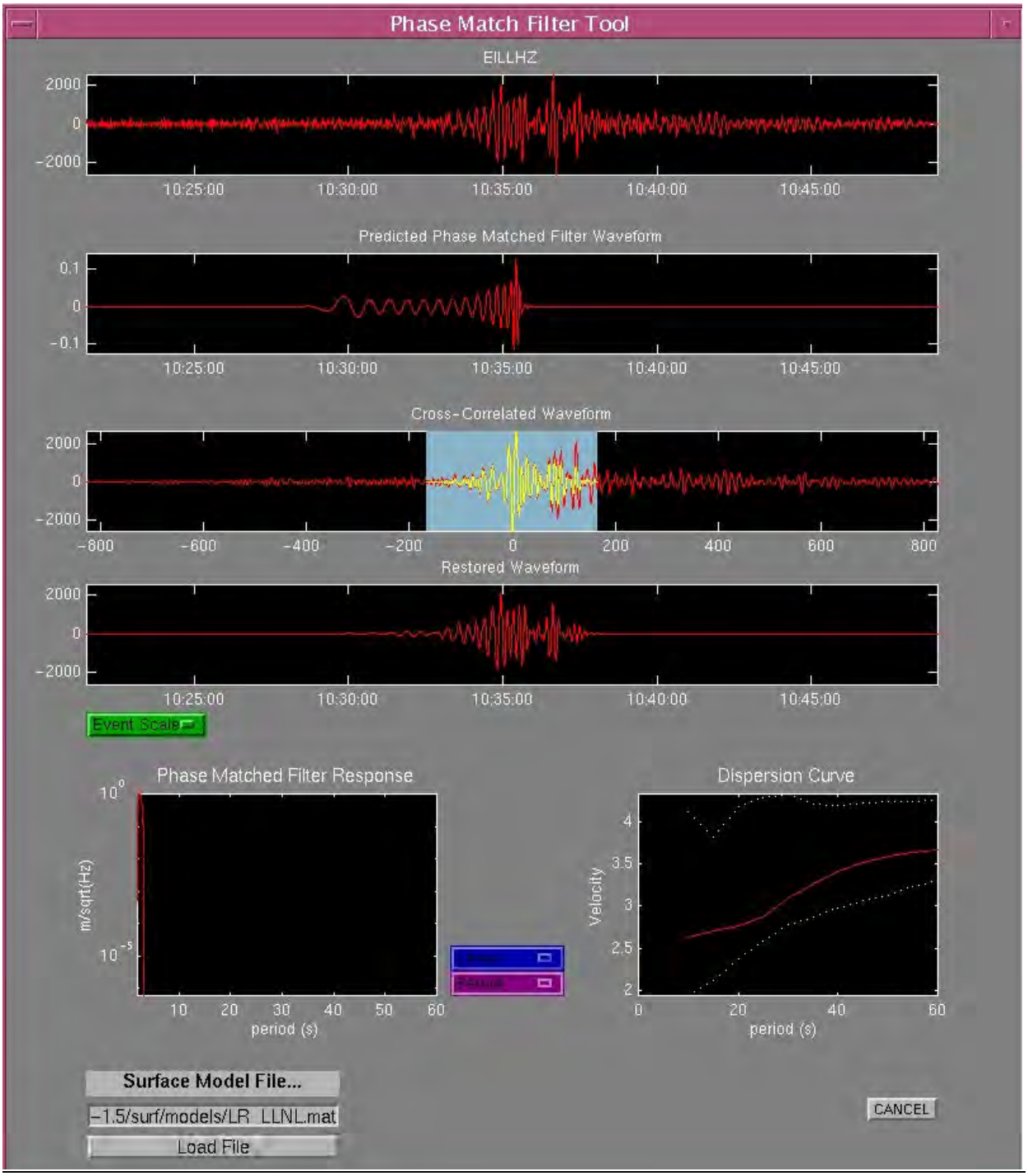


Figure 2. Phase Match Tool with ray traced path using LLNL Model.

To begin surface wave analysis in MatSeis, the user first selects from the main display one event and one long-period waveform, identified by its station and channel codes. Next a time window spanning the expected Rayleigh arrival is marked (the vertical dashed lines in Figure 1). When the 'Phase Match Tool' is chosen under the 'LP' menu, the user interface shown in Figure 2 appears. The topmost waveform displays the selected seismogram of the event from the main MatSeis window. The phase-matched filter for this source-station path is shown below this, plotted on the same time axis. The third waveform represents the cross-correlogram of the data and the filter, centered on a lag

time of zero. The blue box on this plot highlights the segment of the correlogram to be extracted and redispersed. By clicking and dragging with the mouse, the user can move and resize the blue box to extract any desired portion of the trace. The restored waveform, fourth from the top, shows the result of convolving the correlogram segment within the blue selection box with the phase-matched filter.

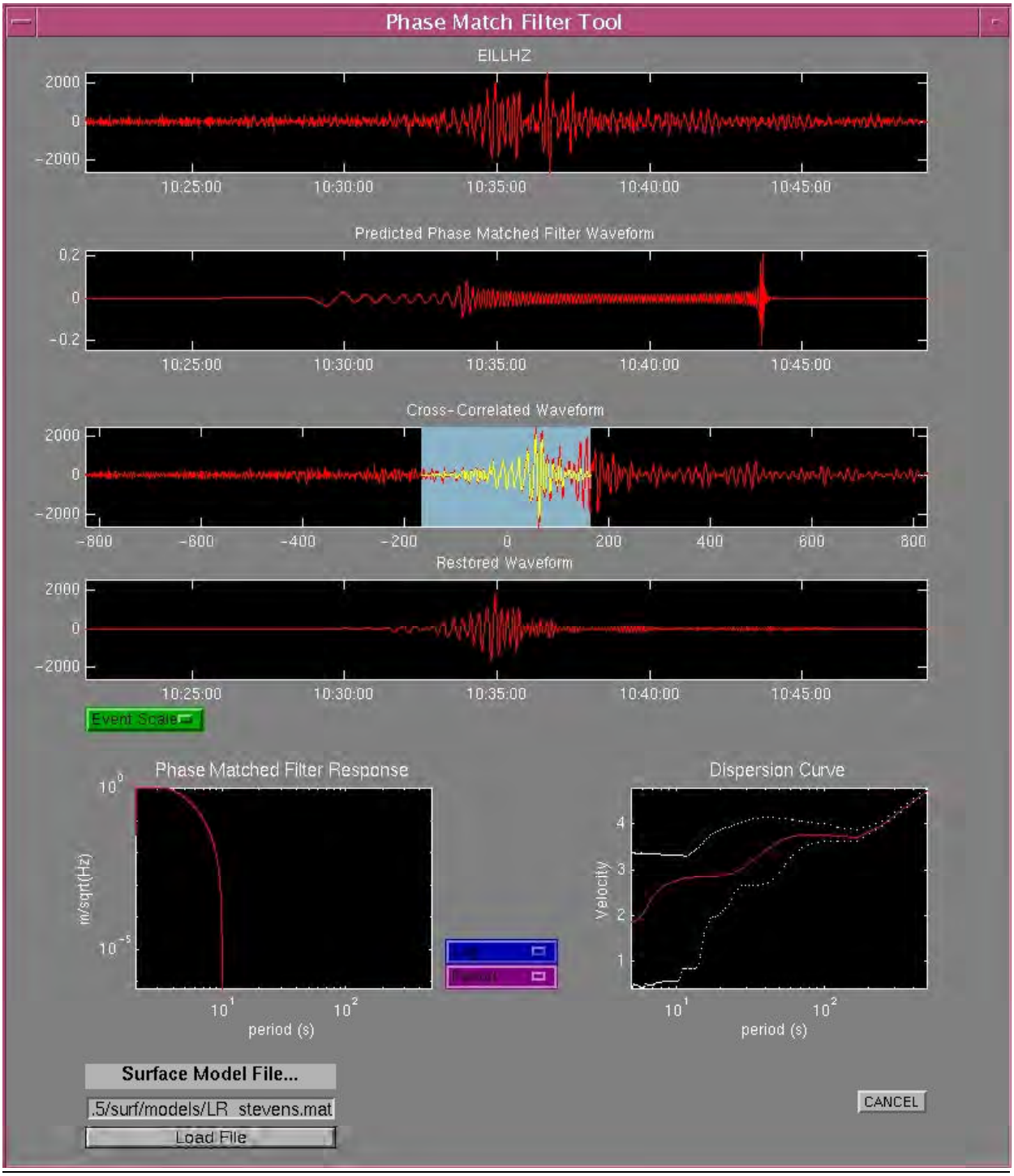


Figure 3. Phase Match Tool with ray traced path using Stevens Model.

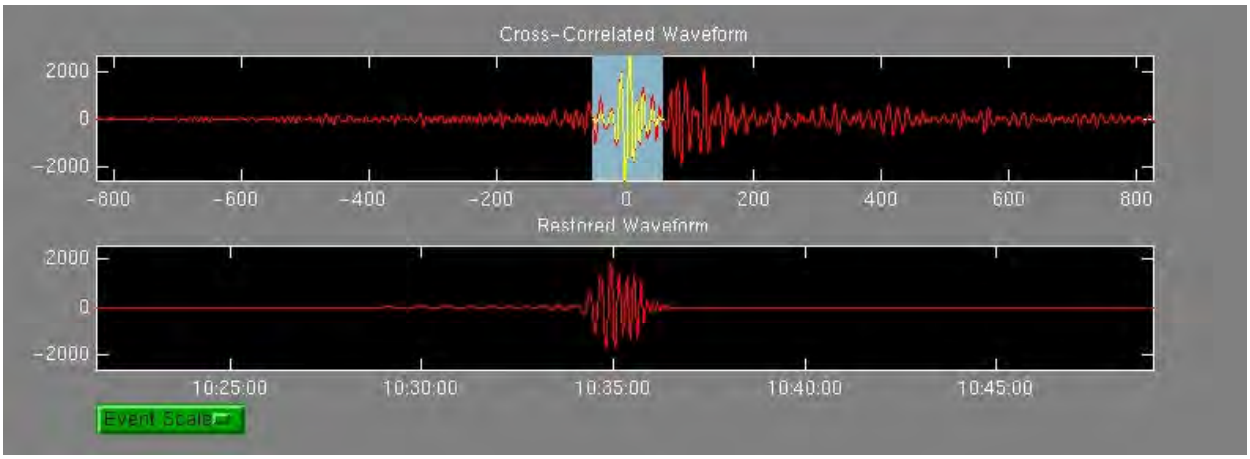


Figure 4. Restored Waveform for 100 sec window

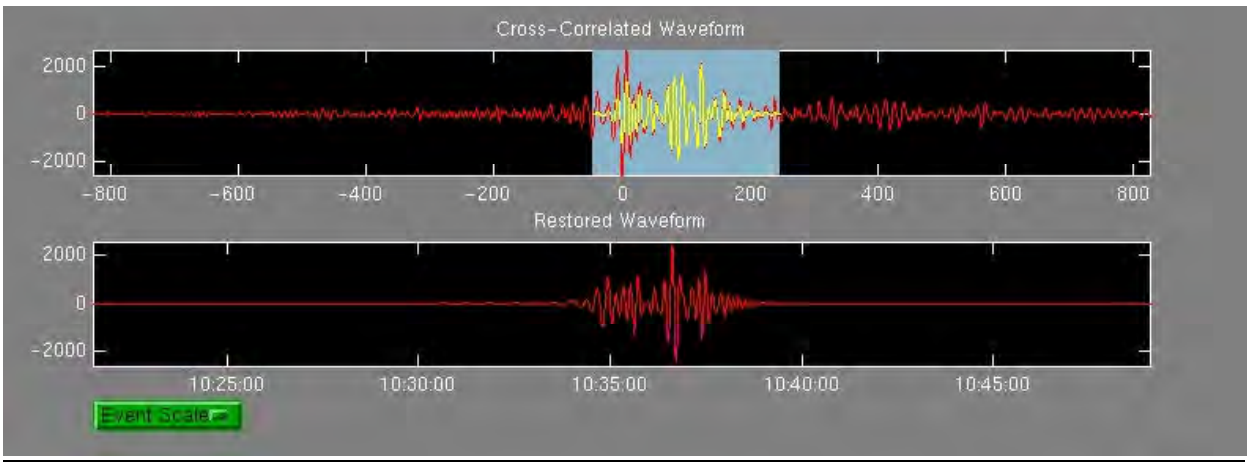


Figure 5. Restored Waveform for 300 sec window

The dispersion curve used to construct the phase-matched filter is shown in the bottom right corner of Figure 2. The dashed lines in the dispersion curve window indicate the maximum and minimum values among all cells in the model at each frequency. At this point, the dispersion curve and synthetic signal have been created. The phase-matched filter's frequency response spectrum is shown in the lower left corner window of the figure. The filter has an amplitude response of one across the frequencies tabulated in the model, and tapers to zero outside this band. The menu at the bottom of the interface allows the user to choose any available gridded dispersion model to test the effect of each on the performance of the matched filter. Figures 2 and 3 illustrate the results obtained using two different models with the same seismogram.

Figure 4 and Figure 5 demonstrate the effect of selecting different length segments of the correlogram. To restore the original Rayleigh arrival and eliminate extraneous noise, the highlighted segment is convolved with the phase-matched filter waveform to produce the restored waveform, shown at the bottom. As the selection box gets wider, the restored trace more closely resembles the original seismogram, but may reintroduce more noise or multipathed energy.

CONCLUSIONS AND RECOMMENDATIONS

We have implemented phase-matched filtering as MATLAB functions, and developed an easy-to-use graphical interface, which can be invoked from the MatSeis toolkit. As a result, a user can apply these techniques to any event in the database, and can select an appropriate Rayleigh propagation model. We will soon add the capability to measure amplitudes and periods from either the original or restored waveforms, then compute Ms magnitudes. Additionally, we plan to update the interface to allow the user to control the frequency response of the phase-matched filter.

REFERENCES

Chael, E., M. Harris, C. Young, K. Mayeda, W. Walter, S. Taylor, A. Velasco, Prototyping regional discrimination tools with MatSeis, *Proceedings of the 21st Annual Seismic Research Symposium*, Sept. 1999, 294-299.

Harris, M. and C. Young, MatSeis: a seismic GUI and toolbox for MATLAB, *Seism. Res. Lett.*, **68**, 267-269, 1997.

Herrin, E. and T. Goforth, Phase-matched filters: application to the study of Rayleigh waves, *Bull. Seism. Soc. Am.*, **67**, 1259-1275, 1977.

Pasyanos, M. E., W. R. Walter and S. Hazler, Improving mb:Ms discrimination using phase matched filters derived from regional group velocity tomography, *Proceedings of the 21st Annual Seismic Research Symposium*, Sept. 1999, 565-571.

Pawlowicz, R., M_Map: a mapping package for MATLAB, http://www.ocgy.ubc.ca/~rich/map.html, 1998.

Rezapour, M. and R. G. Pearce, Bias in surface-wave magnitude Ms due to inadequate distance corrections, *Bull. Seism. Soc. Am.*, **88**, 43-61, 1998.

Stevens, J. L. and D. A. Adams, Improved methods for regionalized surface wave analysis, *Proceedings of the 21st Annual Seismic Research Symposium*, Sept. 1999, 274-282.

9. International Monitoring System

THE PRIMARY SEISMIC NETWORK, INTERNATIONAL MONITORING SYSTEM: STATUS AND PLANS

H. Given, L. Astiz, S. Barrientos, S. Bereza, C. Ebeling, M. Hfaiedh,
G. Perez, R. Stewart, Y. Starovoit, N. Tavener, M. Yamamoto
Seismic Monitoring Section, International Monitoring System Division, Provisional Technical Secretariat,
Preparatory Commission for the Comprehensive Nuclear-Test-Ban Treaty

ABSTRACT

The primary seismic network is one of five monitoring networks of the International Monitoring System (IMS) established under the Comprehensive Nuclear-Test-Ban Treaty. The Signatory States of the Comprehensive Nuclear-Test-Ban Treaty have formed a Preparatory Commission to oversee Treaty-related activities until the Treaty enters into force. The Preparatory Commission has established technical requirements, certification standards, and draft operational practices for the primary seismic network. The Seismic Monitoring Section of the International Monitoring System Division of the Preparatory Commission's Provisional Technical Secretariat (PTS) is responsible for the establishment, certification, and operation of the seismic stations according to Commission's requirements and standards.

The primary seismic network comprises 31 arrays and 19 3-component seismic stations, including 12 new arrays and two new 3-component stations that did not exist prior to signature of the Treaty in 1996. Site surveys have been completed for all but 5 of these "new" stations. Although uniform network requirements and standards apply, the primary seismic network in fact has a diverse set of station equipment. About 30% of the primary seismic stations have some affiliation with the US nuclear test monitoring program through national or international agreements. Most new stations built during the next 24 months with direct funding from the Preparatory Commission will use integrated seismic data acquisition systems provided by the company Nanometrics. These systems use Nanometrics HRD-24 digitizers with an incorporated authentication token recording either Geotech GS-13 or Guralp Systems CMG-3ESPV sensors for short-period channels for vault/posthole or deep borehole deployments respectively. Three-component stations will use a seismometer covering the IMS passband of 0.02-16 Hz that is appropriate for the sensor environment at the station. A Sun Microsystems Unix workstation will provide data reformatting and buffering, command interpretation, and onward communications to the Global Communication Infrastructure. Stations will have a standard channel sensitivity appropriate for either low or moderate background noise profiles.

The Preparatory Commission has stated that stations may be certified when the PTS is assured that the site, the station equipment, and the infrastructure substantially meet the technical specifications for IMS stations; when data authentication devices, including anti-tampering devices, are in place and have been demonstrated to function properly; and when the existing and proper functioning of the station interface to the Global Communications Structure is confirmed. Certification status indicates that an IMS monitoring station is complete and ready to be used in the global monitoring mission. With current projections and staffing, at least 30% of the stations of the primary seismic network are expected to be certified by the end of 2001.

CERTIFICATION OF U.S.INTERNATIONAL MONITORING SYSTEM STATIONS

Preston B. Herrington, Randy K. Rembold, J. Mark Harris, and Richard P. Kromer
Sandia National Laboratories

Sponsored by
U. S. Department of Energy
Office of Nonproliferation and National Security
Office of Research and Development
National Nuclear Security Administration

Contract No. DE-AC04-94AL85000

Defense Threat Reduction Agency
under DTRA IACRO 00-3421

ABSTRACT

All stations planned for the International Monitoring System (IMS) must be certified by the Provisional Technical Secretariat (PTS) prior to acceptance to ensure that the monitoring stations initially meet the required specifications. Working Group B of the Preparatory Commission for the Comprehensive Nuclear-Test-Ban Treaty has established requirements for the quality, availability, and surety of data received at the International Data Centre (IDC). These requirements are verified by the PTS during a 3-component process that includes initial station assessment, testing and evaluation, and certification.

Sandia National Laboratories has developed procedures, facilities, and tools that can be used to assist in evaluating IMS stations for compliance with certification requirements. System evaluation includes station design reviews, component testing, and operational testing of station equipment. Station design is evaluated for security and reliability considerations, and to ensure that operational procedures and documentation are adequate. Components of the station are tested for compliance with technical specifications, such as timing and noise levels of sampled data, and monitoring of tamper detection equipment. Data sent from the station in an IMS-standard format (CD-1 or IMS-1) are analyzed for compliance with the specified protocol and to ensure that the station data (sensor and state-of-health) are accurately transmitted. Data availability and authentication statistics are compiled and examined for problems.

OBJECTIVE

The Provisional Technical Secretariat (PTS) has established procedures for certifying monitoring stations in the International Monitoring System (IMS) [1]. Each station operator is responsible for supporting PTS certification activities. The objective of this work was to assist U. S. station operators in meeting IMS certification requirements.

RESEARCH ACCOMPLISHED

IMS Station Certification Overview

The PTS may certify a station once it has been demonstrated that the site, station equipment, and infrastructure substantially meet the minimum technical requirements for IMS stations [1]. The station operator is responsible for preparing the station to meet these requirements. To accomplish certification, the PTS forms a technical Certification Team for each station under consideration. The Certification Team evaluates the station and recommends corrective actions if needed. Once satisfied that the station meets IMS requirements, the Certification Team presents its recommendation to the PTS Certification Group, which reviews the certification request and approves the certification.

For U. S. IMS stations, Sandia National Laboratories (SNL) serves as a common point of contact for the PTS Certification Teams. SNL works with the station operator to compile the needed documentation and evaluates station components and station design to ensure that IMS requirements are met. SNL conducts a mock certification visit to ensure readiness of the station and prepares a Certification Manual for the station. The U. S. Department of

Defense, Nuclear Treaty Program Office delivers the Certification Manual to the PTS for review and schedules the PTS Certification Team site visit. The flow chart shown in Figure 1 illustrates the steps required for each station. Note that many of these steps may be underway concurrently.

Compilation of Station Documentation

The PTS has written a series *Operational Manuals* and *Guidelines for Station Operators on Certification of IMS Stations* for each type of IMS station [2-9]. SNL reviews these two types of documents and develops both a Documentation Checklist and a Station Compliance Checklist. Because the two types of PTS documents are subject to change, SNL frequently reviews the documents and adapts the checklists to reflect changes. These checklists are then sent to the station operators along with a description of the needed documentation. When possible, this is done during station installation so that the operators can begin gathering the documentation while much of the work is being done.

The documentation required by the PTS to support certification is comprehensive. It includes:

1. General station information
   - IMS Station Questionnaire
   - land ownership/leases and any restrictions
   - ownership of equipment
2. Infrastructure
   - site surveys
   - maps of the area and of the site layout, sensor coordinates
   - block diagrams of both the equipment and facility
   - descriptions and diagrams of the power supply systems
   - descriptions and diagrams of the physical security systems
3. Data Acquisition System information
   - sensor specifications
   - digitizer specifications
   - data authentication
   - equipment specifications
   - noise plots
   - user manuals
   - meteorological sensor information
4. Central Processing Facility information
   - software descriptions and commands
   - data format and protocols
   - command authentication
   - data authentication
   - environmental control of the facility
5. Communications
   - descriptions and specifications on all communications equipment (for both intra-site and external communications)
   - any licensing required
   - a layout of the system including cabling
6. Station Inventory
   - listing of all equipment
   - spare sensors and their calibration sensitivities

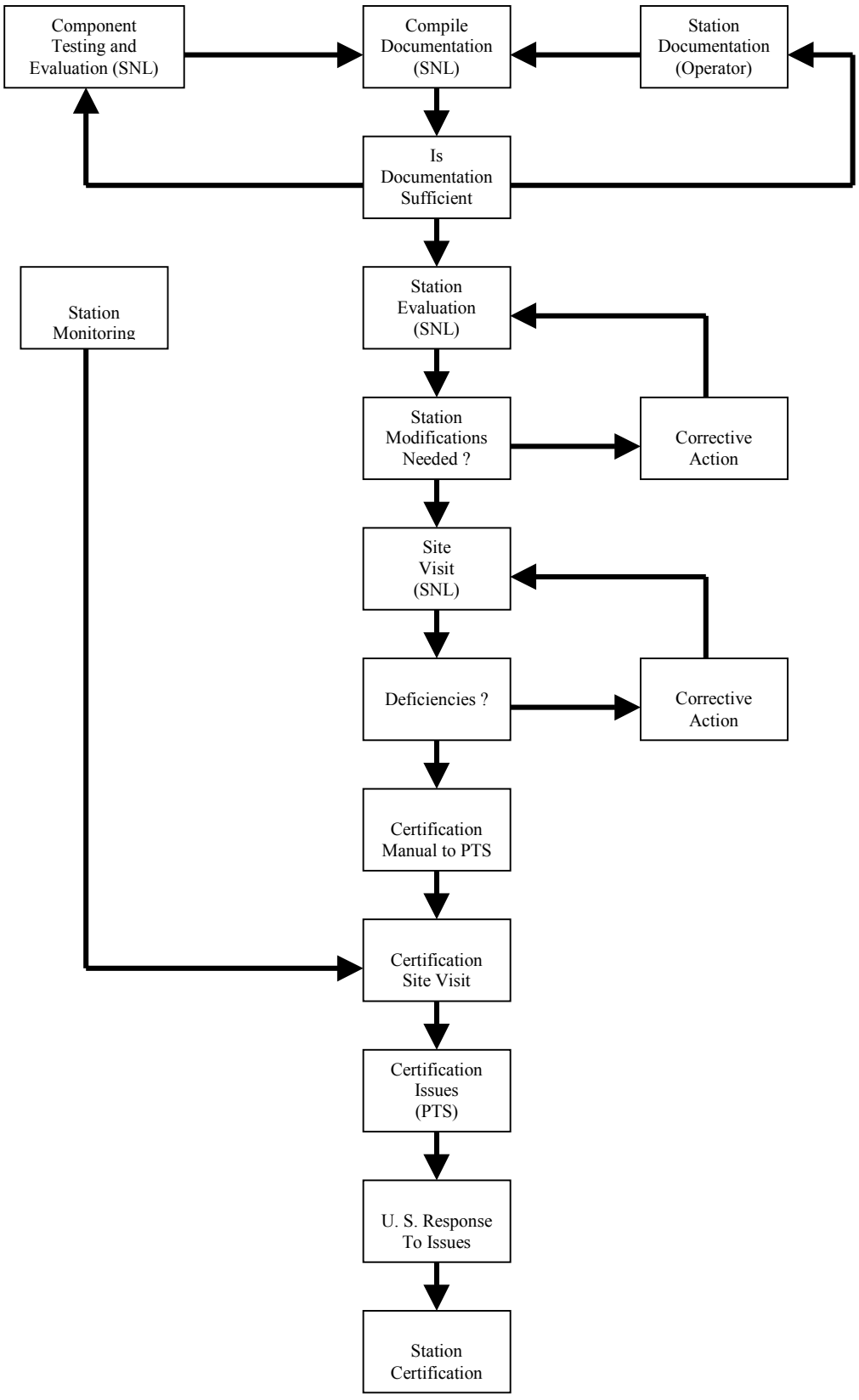


Figure 1. U. S. Station Certification Process.

7. Operation and Maintenance documentation
    - data and state-of-health monitoring
    - staff members and their experience
    - procedures for troubleshooting and repairing equipment
    - calibration procedures and schedules
    - preventive maintenance procedures and schedules
    - record keeping procedures
    - equipment failures and system outages
    - data availability.

Once the documentation is received at SNL, it is checked for completeness and thoroughness. Everything listed on the checklist must be addressed and the information must answer the questions posed by the PTS. The station operator is consulted to resolve any problems.

Component Testing

The testing required for hardware components to determine compliance with IMS requirements for station certification is performed in three parts: sensor performance, data acquisition system performance, and station performance. The tests used by SNL are described here.

IMS Sensor Testing

Information on sensor performance (sensitivity and self-noise) is obtained from the manufacturer's data sheets and/or sensor testing.

Sensor testing is performed by comparing the IMS sensor to a known calibrated sensor using side-by-side coherence testing between the two sensors. Using this technique, the relative gain and phase of the IMS sensor to reference the sensor is determined. Sensor self-noise is determined by using side-by-side coherence testing between the two IMS sensors to determine an average self-noise.

IMS Data Acquisition System (DAS) Testing

Information on data acquisition system performance is obtained from the manufacturer's data sheets and/or system testing.

An assortment of tests is performed to measure the conformance of the DAS to IMS requirements:

- Digitizer DC Accuracy (Sensitivity)
  This test determines the counts/volt or digitizer bit-weight using a Standard Voltage Source as a stimulus to the DAS input(s).
- Digitizer Input Terminated Noise (Self-noise)
  This test determines DAS self-noise by terminating DAS input(s) with appropriate resistor termination.
- Digitizer Time-Tag Accuracy
  This test determines DAS sample timing accuracy by using a GPS synchronized signal generator as a stimulus to the DAS input(s).

IMS System Performance

Information on station performance is obtained from historical data and the results of sensor and data acquisition system testing.

System resolution and noise are determined by converting the data acquisition system characteristics to sensor units using the sensor transfer function. System noise, in geophysical units, is compared to historical backgrounds to determine the system's ability to measure signals to the required resolution.

Station Evaluation and Testing

SNL examines the station documentation for compliance with the specifications listed in the *Operational Manual*. The complete system is evaluated for reliability and security as well. Station design problems may be discovered and corrected at this time.

Testing the integrated station equipment is also very important. The preferred method to verify that station operation will meet IMS operating requirements is to test the completed station, including the communications network, in a monitoring environment.

SNL has developed a system to receive and analyze data from a station in CD-1 format. This software stores all of the CD-1 data frames on disk in a human-readable format. These files are searched for particular problems or conditions. For example, the occurrence of short data segments, indicating a data dropout at some point, can be found and examined. The handshaking and configuration frames are examined to ensure correct connection. The sensor data values are examined for problems. Also, this system allows the raw protocol frames to be stored on disk for later review or playback. This system was used to receive data from PS47 (forwarded through the U. S. National Data Center) to support testing of the data availability, status flags, and authentication for the PS47 certification.

Data Surety and Authentication

Correct implementation of data and command authentication at monitoring stations has been problematic, at least in part, because detailed PTS authentication specifications have not been available to station operators and equipment manufacturers. SNL has demonstrated authentication technology applied to various station configurations [10,11]. These activities helped clarify the station requirements for authentication.

Authentication equipment that will meet certification requirements is now available commercially. SNL has performed detailed, formal evaluations on some authentication devices to support use at U. S. stations [e.g. 12]. For these evaluations, test plans were developed, the equipment was tested in a simulated station environment, and results were documented in detail. The tests included evaluation of the station design, physical security of the authentication device, intrusion monitoring, data and command authentication, remote key change operation, and a software security review.

SNL developed software tools and procedures to support this testing, including a CD-1 data receiver with digital signature verification and X.509 key management software. This software has been under development for a number of years. It has been used for authentication demonstrations as well as device testing. Also, SNL has developed tools to demonstrate and test S/MIME authentication techniques as required by Radionuclide and Auxiliary Seismic stations.

Since many data surety requirements are system oriented, data surety must be evaluated in the context of a complete monitoring system. In addition to the secure operation of specific authentication equipment, station security and access authorization are important to data surety and are thoroughly reviewed.

Station Monitoring

The PTS requires long-term operation of the station (at least three months for some stations) prior to certification. The station is monitored for outages, data gaps, spikes, state-of-health, and overall station operability. Data availability statistics are calculated for data received at the data center. SNL monitors these quantities with assistance from the U. S. NDC and the pIDC. Station configuration changes during this evaluation period may cause a delay in the evaluation process.

Mock Certification

Upon completion of the documentation process and initial evaluations, SNL conducts a mock certification site visit. The site visit allows SNL to verify station documentation and perform station testing. First, station configuration is examined to confirm that the collected station documentation is accurate. Block diagrams and circuit drawings are checked against actual configurations, the station inventory is compared with that given in the documentation, and on-site measurements are taken to determine if any changes in the system have occurred. Next, SNL conducts tests that the PTS has identified (e.g. power failure recovery, system reboot, loss of GPS, security system performance, partial loss of data, parallel recording of data, command authentication and remote key change, and system calibration). During this process SNL collects data to determine if the data are formatted correctly, that status is reported correctly, that authentication is functioning, and that data are buffered and retransmitted during communication outages. On completion of the site visit, SNL coordinates correction of any deficiencies discovered with the station operator. Finally, SNL writes a report detailing tests and tasks completed.

PTS Certification Site Visit and Response

Following the completion of the station monitoring process and the correction of any deficiencies discovered during the mock certification site visit, the U. S. sends the Certification Manual to the PTS Certification Team and schedules a certification site visit. SNL serves as U. S. Team Leader during the certification site visit. The certification visit begins with a meeting of U. S. representatives, SNL, the Station Operator, and the PTS Certification Team to discuss any questions the PTS may have concerning the documentation or the station itself. The PTS Certification Team may present the U. S. with a schedule of events, or inform the group of the next task they would like to complete as the visit progresses. During the station site visit, the PTS and U. S. teams complete a variety of tests as requested by the PTS Certification Team.

At the conclusion of the certification site visit, a closeout meeting is held to discuss any issues that surfaced either during the visit or with the Certification Manual. Later, the PTS Certification Team presents any certification issues in a formal document to the U. S. These may be presented in four categories: Actions Required Before Certification, Strong Recommendations, Additional Information Required, and Documentation Corrections. SNL and the Station Operator coordinate the resolution of the issues raised by the PTS Certification Team. The U. S. then provides a Response to Issues to the PTS Certification Team. Discussions may continue until the PTS Certification Team feels that all of their concerns have been resolved. At that time the PTS Certification Team will present its recommendation to the PTS Certification Group. If the Certification Group concurs with the Certification Team recommendation, it will notify all parties that the station is certified for operation in the IMS.

CONCLUSIONS AND RECOMMENDATIONS

Sandia National Laboratories has developed processes and procedures to assist operators of U. S. IMS stations in preparing for PTS certification activities. SNL has developed test and evaluation techniques to ensure station components are acceptable and system properties are adequate. These techniques were used in the successful certification process of PS47 (NVAR, Mina, Nevada) and it is expected that the techniques will be used in the certification processes of all remaining U. S. IMS stations.

Key Words: certification, IMS, authentication, station assessment

REFERENCES

1. *Procedures for IMS Station Certification*, CTBT/PTS/INF.144/Rev.1, 13 May 1999.
2. *Operational Manual for Seismological Monitoring and the International Exchange of Seismological Data*, CTBT/WGB/TL-11/2/Rev.8, 16 February 2000.
3. *Operational Manual for Hydroacoustic Monitoring and the International Exchange of Hydroacoustic Data*, CTBT/WGB/TL-11/3/Rev.8, 16 February 2000.
4. *Operational Manual for Infrasound Monitoring and the International Exchange of Infrasound Data*, CTBT/WGB/TL-11/4/Rev.8, 16 February 2000.
5. *Operational Manual for Radionuclide Monitoring and the International Exchange of Radionuclide Data*, CTBT/WGB/TL-11/5/Rev.8, 18 February 2000.
6. *Guidelines for Station Operators on Certification of IMS Seismic Stations*, PTS.
7. *Guidelines for Station Operators on Certification of IMS Hydroacoustic Stations*, PTS.
8. *Guidelines for Station Operators on Certification of IMS Infrasound Stations*, PTS.
9. *Guidelines for Station Operators on Certification of IMS Radionuclide Stations*, CTBT/PTS/INF.234, 12 January 2000.
10. Draelos, T., M. Harris, P. Herrington, and R. Kromer, Data Surety Demonstrations, *20th Seismic Research Symposium on Monitoring a CTBT*, September 1998.
11. Harris, M., P. Herrington, H. Miley, J. E. Ellis, D. McKinnon, and D. St. Pierre, Data Authentication Demonstrations for Radionuclide Stations, *21st Seismic Research Symposium: Technologies for Monitoring the Comprehensive Nuclear-Test-Ban Treaty*, September 1999.
12. Harris, M., *PS47 Authentication Equipment Evaluation*, Sandia National Laboratories, February 2000.

COMPARISON OF PIDC AND IDC EVENT BULLETINS

Hans Israelsson
Center for Monitoring Research

Sponsored by the Defense Threat Reduction Agency
Arms Control Technology Division
Nuclear Treaties Branch

Contract No. DTRA01-99-C-0025

ABSTRACT

We compare event lists and bulletins between March 7 and July 6, 2000 of the International Data Centre (IDC) of the Preparatory Commission for the Comprehensive Nuclear-Test-Ban Treaty Organization (CTBTO PrepCom) in Vienna and of the Prototype International Data Centre (PIDC) operated at the Center for Monitoring Research (CMR), Arlington, VA.

Automatic events lists and reviewed bulletins of the PIDC and IDC show good overall agreement for this period. Differences in automatic event lists, which appear somewhat larger than the previous period, February 20-March 6, can be related to differences in data available at the two data centers and linked directly to a few discrepancies in software configurations. The daily variation of difference in data availability correlates, as expected, with the degree to which daily automatic bulletins of the two data centers match. The matched events of the automatic event lists depend strongly on the number of defining phases, ndef. For the whole period the percentage of matched events is over 90% for ndef larger than five. Hydroacoustic and infrasonic associated automatic arrival data had, compared with seismic data, very high matching rates, which, however, were based on a small number of observations.

The agreement of the REBs, compared for 35 data days during the period, showed a slight increase compared with the previous period with about 80% matched events. The consistent scanning at the PIDC of all REB data days during this period, as opposed to the previous period, could have contributed to the improvement. About 25% of the events that were unique to one of the data centers in the two REBs were also built from SEL3 events that were unique to that data center. Another 25% of the unique events were added in the analyst review. A large portion of the added events, in particular those added by the IDC (55%), depended, however, on phases added in the analyst review to meet the minimum event definition criteria of the REB. The remaining 50% of the unique events in the REBs started out from events that existed, in some version, in the SEL3s of both data centers. However, the versions of the events in the two SEL3s were identical only in a small number of cases.

As for the previous period some of the differences in associated arrivals of the REB events suggest differences in analyst procedures. The IDC REB has a larger number of added time defining phases than that of the PIDC at about the same rate as the previous period. The two data centers identify and use depth phases differently to constrain focal depth. This difference is, however, less pronounced than for the previous period - the PIDC used depth phases to constrain depth for about 50% as many events as the IDC, compared with 100% more for the previous period. Some of the manually picked arrival times in the PIDC REB are, on average, late compared with those in the IDC REB.

OBJECTIVE

Since February 20, 2000, the International Data Centre (IDC) of the Preparatory Commission for the Comprehensive Nuclear-Test-Ban Treaty Organization (CTBTO PrepCom) in Vienna has routinely distributed data and derived products (automatic event lists, SEL1, SEL2, SEL3 and reviewed bulletins, REB). While the Prototype International Data Centre (PIDC) operated at the Center for Monitoring Research (CMR), Arlington, VA has ended its distribution, it has continued to operate and produce automatic products on a full time basis, whereas reviewed bulletins are prepared only intermittently.

Here we compare event lists and bulletins of the two data centers for a 122 day period, March 7 –July 6, 2000. A previous comparison covered the initial 16 days of IDC data product distribution, February 20–March 6, 2000 (Israelsson, 2000a). The study period for this report goes up to the implementation at the PIDC of Release 3 of the IDC application software. While standard event lists cover the entire study period, REBs are compared for 35 data days. In addition, Standard Event Bulletins (SEB), which include event screening results, are analyzed for 13 data days and daily station status reports for the entire period are also compared.

The comparisons are based on data extracted from CMR databases. The PIDC data were retrieved directly from PIDC database accounts while the IDC data were retrieved from a PIDC account filled with parsed AutoDRM messages (format IMS1.0) of the IDC event lists and bulletins. Formatted messages were used for SEBs and station status reports. Detailed results from the comparisons can be found in Israelsson (2000b).

RESEARCH ACCOMPLISHED

Ideally PIDC and IDC event lists and bulletins should be equal - nominally, the same software was used and the same data were shared between the two data centers. In practice, several circumstances contribute to differences. As a premise for the comparisons we comment at the outset briefly on two factors – data availability and software configuration - for the study period. In the comparisons we are accounting for differences in neither of these factors. For example, if there were large differences in data availability for a particular day, that day is still included in the statistics, which thus represent *operational* agreement.

Data Availability

The station status reports are compiled on a daily basis about 5 hours after the end of a data day. Thus, late incoming data are not included and possible differences between the status reports at the two data centers may, for example, not reflect differences in data availability at the time a particular event list or bulletin was prepared. However, differences in station data availability at an early stage in event processing (SEL1) might propagate into differences in the resulting event list at a later stage, even if there were no differences in data availability at that later stage. This is because of the non-linearity of the event association program, *GA*.

For a given station and data day the difference in data availability between the two data centers, as reported in station status messages, is used as a metric. There were occasional dramatic differences in this metric throughout the study period; stations, for which data are forwarded from the IDC to the PIDC have all occasionally low data availability at the PIDC, whereas stations, for which data are forwarded from the US NDC to the PIDC have occasional low data availability at the IDC. For 23 out of the 122 data days the difference in data availability was larger than 10% for three or more of the 16 array stations. WRA was omitted in this statistic as it was not used in the processing at the two data centers.

The differences for hydro acoustic and infra sonic stations follow the pattern of the seismic stations. For two of the infra sonic stations (ISM and IS59) data was only available at the PIDC during the study period.

Software Configuration Discrepancies

Several changes, so called software patches, to improve software or software configurations, were implemented at the IDC and PIDC at different times during the study period. However, implementation of patches at the two data center is usually not synchronized; often, a change in the PIDC operations is not be implemented in the IDC operations until months later. Two such changes at the PIDC affecting the event bulletins can be noted. One of the changes concerns the so called grid file for the event association program *GA* (Global Association Algorithm) which automatically generates event lists (SEL1–SEL3), which in turn are used as starting point in analyst review. The seismic array station PDYAR and the infrasonic station ISM were added to the PIDC grid file. Past experience with changes, ever so marginal, to the grid file have shown marked effects on resulting automatic event lists. The other change was made for the so called beam recipe of one of the seismic arrays (ARCES). Both changes were implemented at the PIDC towards the end of March, 2000, without corresponding changes at the IDC during the study period. These two examples of configuration differences may not be the only ones with impact on processing results. It appears, for example, that the PIDC and IDC lists of auxiliary stations to be requested for waveform data differed in varying degree throughout the study period. While the IDC appears to have used the same list throughout the study period, the PIDC list was updated from time to time to include only those auxiliary stations that were actually in operation.

Automatic Standard Event Lists

This section on Automatic Standard Event Lists first compares associated arrivals in the standard event lists. This facilitates interpretation of possible differences between events, as differences in station detections propagate into event solutions. Ideally, a comparison of station detections should be based on all arrivals – associated and un-associated – but only associated arrivals were obtained as formatted products from the IDC. We relate differences in associated arrivals to differences in data availability, discussed above, but take only limited advantage of full access of all PIDC station detections for the comparisons.

Associated Arrivals

For a given event list type (e.g., SEL3) the lists of the two data centers were searched for matching arrivals. Two arrivals at a given station were considered matched if their arrival times agreed within 4.0 secs.

The statistics were analyzed for matched and unique *events* separately as matching of arrivals can not usually be expected for events unique to the two data centers. The definition of matched events is given in the following section "*Events*". The summary matched percentages of the SEL3 arrivals (defined as number of matched/(number of matched + number of unique), for matched events)) for primary, hydroacoustic, and infrasonic stations are all high. However, the statistics are based on only a small number of detections for the hydroacoustic and infrasonic stations. The matching percentage for the auxiliary stations, about 49%, is clearly lower than that for the primary stations, about 90%.

The matching percentages for both primary and auxiliary networks are slightly lower than corresponding percentages for the previous study period, February 20–March 6. There is a small percentage (about 1%) of the time-defining arrivals that are cross associated, i.e, matched arrivals are associated with different events unique to the two data centers.

A data availability metric is defined as the mean of the absolute values of the differences in data availability for the seismic array stations (WRA omitted correlates, as one would expect, with matched arrival percentages for the primary stations as a function of data day; drops in data availability coincide with lower matched rates. The matched percentages change with time for the primary network and vary with data day between 62% and 95%. The auxiliary network shows more drastic variations – between 0% and 80%.

Although the data do not show large differences for most primary stations, a few have matching percentages clearly below 90% (e.g., ARCES, BRAR, ILAR, NVAR, PDYAR). At the time of the change in beam recipe for ARCES at the PIDC its matched arrival rate drops from almost 100% to about 80%, where it stays for the remainder of the study period. The appearance of PDYAR in only the PIDC grid file might explain the low matching rate for this array.

The statistics by station shows that the discrepancy for auxiliary stations is probably also related to differences in data availability, which in turn stems from differences in the set of stations for which requests were issued, as discussed above. For example, there are no arrival data at all for the three Russian stations ARU, KVAR, and OBN in the IDC SEL3 bulletin as these stations were probably missing from the set of requested stations at the IDC. As data from these stations were not requested by the IDC one would expect more arrivals at the IDC than at the PIDC for other auxiliary stations that would be requested instead of the Russian stations. Indeed, there are several such stations, for which the rate of unique arrivals is higher for the IDC than for the PIDC in the SEL3 (DAVOS, LBTB, NIL, SPITS). However, the statistics for the auxiliary stations in SEL3 do not indicate that one of the data centers was requesting systematically more data from auxiliary stations than the other data center. Statistics for *associated*, i.e., non-defining arrivals showed that matching percentages for primary and auxiliary stations overall are clearly lower for the associated phases than those of the time-defining arrivals above.

Values of some signal attributes (arrival time, azimuth, slowness, signal-to-noise ratio, amplitude and period) used in the formation of events and event location were compared for matched arrivals. A value of 0.1 (in relevant unit – , sec, degrees, sec/degree, SNR, nm, sec) was used as a threshold to declare differences for the attributes. Most stations had no or only marginal differences. There were 8 stations (INK, JKA, JNU, ARCES, NVAR, PDAR, PDYAR and TXAR) with more than 100 matched arrivals for which the differences in one or more of arrival time, azimuth, slowness ratio measurements or signal-to-noise ratio exceeded 0.1 for 10% or more of the arrivals. The reason for the differences for ARCES in is probably the recipe change mentioned earlier. Differences for NVAR,

PDAR and TXAR, were also noted for the previous period, February 20–March 6 and was then related to updates in station information (database tables site, sensor, and instrument) for NVAR and TXAR, which were implemented only at the PIDC. There is no obvious explanation at this time for the other stations.

Events

Events were matched on the basis of overlap of associated arrivals; the comparison required that either two or more arrivals be common and at the same time the events be within 20 degrees, or at least half of the time-defining arrivals of both events be common. Matched events with epicenters within 10 km and depth differences within 10 km are classified as "equal"; otherwise matched events are considered to be only "similar".

The percentages of matched events are slightly smaller than or similar to values for the previous period, February 20–March 6. The percentage of matched events as a function of data day for the SEL3, correlates closely with the data availability; low data availability usually results in low matching percentages. The daily matched percentages for SEL1 and SEL2 correlates, as expected, closely with those of the SEL3.

Matching percentages is a strong function of the number of defining phases, ndef. With ndef larger than five, the percentage of matched events is 90% or more. Most events – matched as well as unique – are based on three defining observations, and most of the unique events are based on ndef=3 or less..

Magnitudes

mb and ML network magnitudes were compared for matched events defined as "equal", i.e., with epicenters within 10 km and with depths within 10 km. Network magnitudes are considered "equal" if corresponding network values in the two bulletins are within 0.1 magnitude units, the associated uncertainties are within 0.1 magnitude units, and the difference in number of stations is less than 2.

Differences, which exceed 0.1 magnitude unit, occur for about 15% of the mb and 9% for the ML, which are clearly larger than for the previous period, February 20–March 6. The differences occur when the number of stations used for the network magnitudes differ, in particular for small number of stations.

Reviewed Event Bulletins

The comparison of the REBs begins with a comparison of events, followed by comparisons of the supporting arrival data, focal depths and magnitudes.

Matched Events

The same criteria used to match automatic events lists were used to match REB events. As before, matched events with epicenters within 10 km and depth differences within 10 km are classified as "equal"; otherwise matched events are only considered "similar". Scanning was performed at both data centers for all REBs .

As for the automatic event lists, the percent of matched events as a function of data day correlates with availability of station data. The percentages of matched events (similar and equal) for the REB as a function of the number of defining phases, ndef, are lower than those for the SEL3; the 90% level of matched events occurs for ndef=10 for the REB and ndef=6 for the SEL3. The percentage of "equal" events is much lower for the REB than for automatic events. Analyst review results in changes in station arrival data (see section "*Associated Arrivals*") to the automatically generated events in the SEL3 from which the review starts and these changes contribute to differences in REB solutions.

Distances between epicenters and differences in origin times of matched events depend strongly on ndef. The differences are also larger than for the automatic SEL3. Differences in depth follow the usual trade-off with differences in origin times.

Unique Events

The percentages of events that are unique to the two data centers are similar (about 10% of all events in the PIDC and IDC REBs) with a slightly larger number of events unique to the IDC. The geographical distribution of the unique events appears to follow the pattern of seismicity with most events concentrated to the most active seismic regions around the Pacific.

The unique events have been divided into several groups. Added events refer to those events in the REB with no corresponding event in the SEL3 (i.e., no common event identification number, *evid*); revised events refer to REB events that also appear in the SEL3. The revised events unique to one data center are also grouped into events for which their version in the SEL3 does or does not have a matched event in the SEL3 of the other data center. We refer to these categories as "revised-unique SEL3" and "revised-common SEL3". For all unique events in the PIDC and IDC REBs combined about 25% were added, another 25% were in the category "revised-unique SEL3", and, the remaining 50% were of the "revised-common SEL3" type. This means that approximately half of the unique events appeared in only one of the REBs because no version of it appeared in the SEL3 of the other data center. For the other half of the unique events ("revised-common SEL3"), a version did exist in the SEL3 of the other data center, but was not included by the other data center for various reasons Quite a few events appearing in the SEL3 of both data centers ("revised-common SEL3") and having sufficient support of automatic detections to satisfy event definition criteria were interpreted differently; they were accepted for the REB by one data center and rejected by the other. Most of these unique events had some significant modification of the SEL3 – mostly data for a station was added in the analyst review. In a small number of instances, the SEL3 and REB solutions had almost identical or only marginal differences.

The unique events of the IDC include a much larger portion of added events than that of the PIDC (40% compared with 12%); this explains the somewhat larger percentage of events unique to the IDC. The difference in added events between the two data centers is, however, smaller for this period than in the previous study period. The systematic scanning for all of the REB data days at the PIDC for this period probably contributed to a smaller difference in added events.

For each of the three main sub-groups of the unique event a further distinction is made between events depending on whether or not they satisfy the minimum event definition criteria (defining phases at three or more primary stations and a weight count of 4.6 or more) if only automatically detected phases are counted (i.e. excluding phases added by analyst). The latter sub-groups are indicated with "above criteria" and "below criteria". The IDC unique events also have a larger percentage of "below criteria" events (55% compared with 30%), that is, events that were pushed above the threshold of the event definition criteria by phases added in analyst review.

Associated Arrivals

Time-defining and associated arrivals in the REBs consist of automatic detections and phases added by the analysts. The data are grouped into matched and unique events. The time-defining arrivals belonging to matched events show an overall matching percentage of about 79% for primary stations and about 55% for auxiliary stations. While the percent for auxiliary stations is similar to that for the SEL3, the percentage for primary stations is clearly lower. The lower value for the REB is primarily due to the phases added manually. The IDC has a consistently higher proportion of analyst-added phases. As for time-defining phases, the IDC has a higher proportion of added phases for associated (non-defining) arrivals.

A comparison of signal attributes for matched arrivals in the REB show a high percentage of the arrivals with differences in arrival time, which in turn often leads to differences in azimuth and slowness. Time differences for those matched arrivals, which are not identical, show a small systematic bias in arrival times, with an average PIDC arrival time being about 0.3 sec late. The difference could be due to different practices at the two data centers of band pass filtering during analyst review. At the PIDC standard practice it to read arrival times from band pass filtered (casual) traces, while unfiltered traces are used at the IDC if possible. Willemann (1999) found that PIDC arrivals at some stations were, on average, *early* compared with picks by station operators. The differences in this case were probably due to reasons unrelated to the differences observed between PIDC and IDC.

Surface Wave Associations

Surface wave arrivals are considered matched if arrival times agree within 80 seconds. The overall matching percentage of arrivals for matched events is about 83%, which is higher than for time defining phases. Some differences are to be expected in the association of surface waves as matched events often have slightly different locations, and the surface wave associations for an event are dictated by the 2–100 degree epicentral distance interval. A review of statistics by station showed a low matching average for station NVAR (about 50%) that could not be directly related to station availability. The low value for NVAR might be related to updates in station configuration in February, 2000 as previously mentioned.

Focal Depths

Differences in focal depth estimates are, as differences in origin times, more pronounced for events based on a smaller number of defining phases. Differences in depth and origin time follow the well known trade-off between the two parameters . Some of the differences in depth can also be related to the use of depth phases. Compared with statistics for other time defining and associated phases, the PIDC REB contains a much higher proportion of depth phases. As a result of the more extensive use of depth phases at the PIDC, focal depths in the PIDC REB also have a larger portion of events with depth constrained by depth phases. However, the difference of about 50% more events in the PIDC REB is less pronounced compared with the previous study period, when there were about twice as many events.

Magnitudes

Network magnitudes are considered equal if corresponding network values in the two bulletins are within 0.1 magnitude units, associated uncertainties are within 0.1 magnitude units, and the difference in the number of magnitude defining stations is less than two. For "equal" events differences larger than 0.1 magnitude unit occur frequently, mostly because the magnitudes are based on different number of stations. For example, mb magnitudes agree within 0.1 magnitude units for only 55% of the matched equal events, which is similar to the percentage for the previous study period, February 20–March 6. Differences in magnitude larger than 0.1 occur predominantly when the magnitudes are based on a small number of stations. For matched events that are not "equal", but only "similar", differences are larger, as expected. Ms magnitudes show the closest agreement among magnitude types.

IDC did not report maximum likelihood estimates (magnitude types mbmle and Msmle). This was due to a temporary change in the program GSEBull at the IDC that suppressed all maximum likelihood magnitudes in the event bulletins. The IDC maximum likelihood magnitudes are, however, still in the IDC database.

Standard Event Bulletins

Standard Event Bulletins, SEB, were obtained at the PIDC towards the end of the study period for 13 data days. Event screening into categories for matched (equal and similar) events for this 13 day period were compared.

About 70% of all events were screened in the same category. About 38% of all events (or 182 events) were screened *out* by both data centers, while 45% were screened out by at least one data center (22 and 17 events by the PIDC and IDC respectively About 82% of events that were screened out by at least one data center were also screened out by both data centers. About half of the events that were screened out by only one of the data centers were screened out on the basis of the Ms:mb score. This, in turn, can be attributed to differences in mb (see preceding section on Magnitudes). Use of maximum likelihood magnitudes in the future might give more robust Ms:mb score and thereby provide more consistent screening between the two data centers. The IDC screened out a few more events by itself on the basis of Ms:mb, which agrees with its somewhat higher reporting of Ms magnitudes.

CONCLUSIONS AND RECOMMENDATIONS

Automatic events lists and reviewed bulletins of the PIDC and IDC show good overall agreement between March 7-July 6, 2000. Differences in automatic event lists, which appear somewhat larger than for the previous period, February 20-March 6, can be related to differences in data available at the two data centers and to a few discrepancies in software configurations.

Differences in data availability as reflected in daily station status reports varied during the period; for example, the difference in data availability was larger than 10% for three or more of the 16 primary array stations during 23 out of 122 data days. The daily variation of difference in data availability correlates, as expected, with the degree to which daily automatic bulletins of the two data centers matches.

There were configuration differences for almost the entire study period in the grid file for the Global Association program, GA, in the beam recipe for the seismic array station ARCES, and in the list of auxiliary stations, for which waveform data were requested. Time defining arrivals of auxiliary stations showed also a much lower matched percentages than for primary stations for the event lists and bulletins of the two data centers. A low matching percentage for the primary array station PDYAR could be due to differences in grid files. The time of the beam recipe change at ARCES could be correlated with a change in the matching of its arrivals in the automatic bulletins. Apart from these effects that could be observed directly, the configuration discrepancies have other, indirect, effects

on the automatic bulletins, which are difficult to untangle and gauge. Some observed differences in the automatic bulletins had no obvious explanation; a low matching arrival rate for the seismic array station BRAR, differences in signal attributes at several stations.

Hydroacoustic and infrasonic associated arrival data had, compared with seismic data, very high matching rates, which, however, were based on a smaller number of observations.

Differences in automatic event lists, SEL3s, which are the starting point for analyst review are almost bound to lead to differences in the reviewed event lists, REB, in particular if differences in the automatic event lists are due to differences in available station data. About 25% of the events that were unique to one of the data centers in the two REBs were also built from SEL3 events that were unique to that data center. Another 25% of the unique events were added in the analyst review. A large portion of the added events, in particular those added by the IDC (55%), depended, however, on phases added in the analyst review to meet the minimum event definition criteria of the REB. The remaining 50% of the unique events in the REBs started out from events that existed, in some version, in the SEL3s of both data centers. However, the versions of the events in the two SEL3s were identical only in a small number of cases. About 20% of all the events in the REBs of the two data centers combined were unique to one of the data centers (9% unique PIDC and 11% unique IDC events). Most of the unique events were based on 4 or less defining phases. The 80% matched REB events represents a slight increase compared with the previous period. The consistent scanning at the PIDC of all REBs during this period, as opposed to the previous period, could have contributed to the improved matching.

As for the previous period some of the differences in associated arrivals of the REB events suggest differences in analyst procedures. The IDC REB has a larger number of added time defining phases than that of the PIDC at about the same rate as the previous period. The two data centers identify and use depth phases differently to constrain focal depth. This difference is, however, less pronounced than for the previous period - the PIDC used depth phases to constrain depth for about 50% as many events as the IDC, compared with 100% as many for the previous period. Manually picked arrival times in the PIDC REB are, on average, late compared with those in the IDC REB. Indeed, measurement standard errors derived from common manually picked arrivals in the REB clearly depart from the a *priori error* used in the event location algorithm. This suggests that a review and re-estimate of REB measurement errors should be considered, in particular as modeling errors are being reduced as a result of location calibration.

The event screening as reported in Standard Event Bulletins SEB for 13 days of the study period for matched events showed some differences between the data centers (SEBs not available for previous study period). For example, about 82% of all the matched events that were screened out by one or both data centers, were also screened out by both data centers. Most events that were screened out by only PIDC were screened out of on the basis of the depth score, which might be expected in the light of differences in use of depth phases for depth estimation. However, almost half of the events that were screened out by only one data center were screened out on the basis of the Ms:mb score. Differences in the Ms:mb score are most likely due to differences in mb magnitudes. Almost half of matched events in the REB with hypocenters within 10 km had mb values that differed with more than 0.1 magnitude unit. Use of maximum likelihood magnitudes in the future might provide more robust Ms:mb scores for event screening.

The high percentage of identical event solutions typical of the automatic events lists for the two data centers is not retained for the REBs; events are slightly diverging from automatic to reviewed results. With the revision of automatic results, differences in the supporting station data are introduced, which result in increased differences between event solutions. This effect is well known and has been documented during the early phase of GSETT-3 from a comparison of the independent analyses of the same data by two analyst teams (GSE/WGO, 1996). Differences between the REBs were, perhaps, also due to a general difference in the review process; the limited staff at the PIDC (about 4 versus12 analysts) did not allow the two-step review carried out at the IDC, where all events reviewed by individual analysts are scrutinized by a lead analyst in a final step.

The element of subjectivity of reviewed bulletins raises issues of rules and procedures guiding analyst review. Can changes *vis a vis* automatic solutions that are common to more than one analyst be identified? Only such changes would be useful in tuning automatic processing. Do some of the changes merely introduce "random noise"? Should revision of automatic events be limited to instances when the reviewed and automatic solutions, in some sense, are significantly different? These and related questions warrant further consideration to make reviewed bulletins less dependent on analyst interpretation.

ACKNOWLEDGMENTS

I would like to thank Manochehr Bahavar, David Mason, Bob North, and Victoria Oancea at the CMR for suggestions and explanations of PIDC procedures and Alexander Boresch and Ronan Lebras with SAIC in Vienna for helpful comments on IDC procedures.

.Keywords: Seismic processing, seismic bulletin

REFERENCES

GSE/WGO (1996), Analysis evaluation experiment: simultaneous independent analysis by two teams, Working Group Paper GSE/WGO/24.

Israelsson, H. (2000a), Comparison of PIDC and IDC Event Lists and Bulletins February 20 - March 6, 2000, Center for Monitoring Research, Technical Report, CMR-00/08.

Israelsson, H. (2000b), Comparison of PIDC and IDC Event Lists and Bulletins March 7 - July 6, 2000, Center for Monitoring Research, Technical Report, CMR-00/XX (in preparation).

Willemann, R. (1999), Differences between Independent Arrival Time Picks, http:// www.isc.ac.uk.

10. Other Topics

MIGRATION OF RESEARCH RESULTS INTO OPERATIONAL MONITORING SYSTEMS

Leslie A. Casey, Ellen R. Shepherd,[1] Aaron A. Velasco,[2] and Stan D. Ruppert[3]
U.S. Department of Energy, [1]Sandia National Laboratories, [2]Los Alamos National Laboratory, and
[3]Lawrence Livermore National Laboratory

Sponsored by U.S. Department of Energy
Office of Nonproliferation Research and Engineering
Office of Defense Nuclear Nonproliferation
National Nuclear Security Administration

Contract No. DE-AC04-94AL85000

ABSTRACT

For the Department of Energy (DOE) Knowledge Base to support activities for monitoring nuclear explosions consistent with eventual verification activities under the Comprehensive Nuclear-Test-Ban Treaty (CTBT), a process is defined to ensure the integrity and utility of research results during the migration into information products for use in operational monitoring systems.

The process of validating, verifying, and managing the information products ensures deliveries of high-quality Knowledge Base releases to the United States National Data Center (USNDC). These activities are critical to the successful integration of scientific research to support operational monitoring systems at the USNDC. A by-product of this process is that data sets, or components of information products, that have undergone the validation and verification process may be distributed as operational calibration products to the International Data Centre. All contributors to information products, whether DOE-funded or not, will benefit from transparency of the integration process to effect successful participation in the process.

As an information product passes through the steps necessary to become part of a delivery to the USNDC, domain experts, including the end-users, will provide *validation* -- a determination of relevance and scientific quality. The integration process continues with *verification* -- an assessment of completeness and correctness, provided by the Knowledge Base integrator, the information product coordinator, and the contributing organization. The information products and their constituent data sets are systematically tracked through the integration portion of their life cycle (Moore, et al, 2000; Carr et al, 2000).

Finally, the proposed delivery of the Knowledge Base and its constituent information products is reviewed by an Integration Board. The integration process is presented in this paper, with details described in Moore et al., (2000).

Key Words: DOE Knowledge Base, information product, integration, verification, validation

OBJECTIVE

A well-defined process ensures the integrity and utility of research results during the migration into information products for use in the DOE Knowledge Base to support activities for monitoring nuclear explosions consistent with eventual verification activities under the Comprehensive Nuclear-Test-Ban Treaty (CTBT). The process of validating, verifying, and managing the information products ensures high-quality deliveries to the United States National Data Center (USNDC).

RESEARCH ACCOMPLISHMENTS

The process for migrating research results into information products for use in the DOE Knowledge Base has been defined and implemented. This process and its implementation ensure that the delivery of a DOE Knowledge Base comprises verified, validated, and well-managed information products. If any process is to retain its effectiveness, it must be refined over the course of its use; thus, this process is also undergoing refinement. This paper describes the integration process as documented in Moore et al. (2000) with refinements developed during its most recent

implementation. This paper serves the purpose of offering transparency of the integration process to facilitate effective participation in the process by all contributors to information products.

Motivation and benefits of the integration process

For the DOE Knowledge Base to be useful as a tool for improving U.S. monitoring capabilities, the contents of the Knowledge Base must be subjected to a well-defined set of procedures to ensure integrity and relevance. The integration process addresses the following issues:

1. What do end-users want and need?
2. How do researchers collaborate to address those needs?
3. How is research integrated into a useful and reliable product?

These questions drove the development of the integration process and are answered explicitly at the end of this paper after the process is described.

In addition to ensuring integrity, relevance, and usefulness of the information products, the integration process provides additional benefits:

- Evidence that the process was followed. All steps in the process are logged.
- Direction for interactions. Procedural guidance provided by the process ensures effective, purposeful interactions.
- Programmatic benefits. The procedure provides a basis for scheduling and offers periodic status reports.

Description of the process

Figure 1 summarizes the state changes for information products (IP).

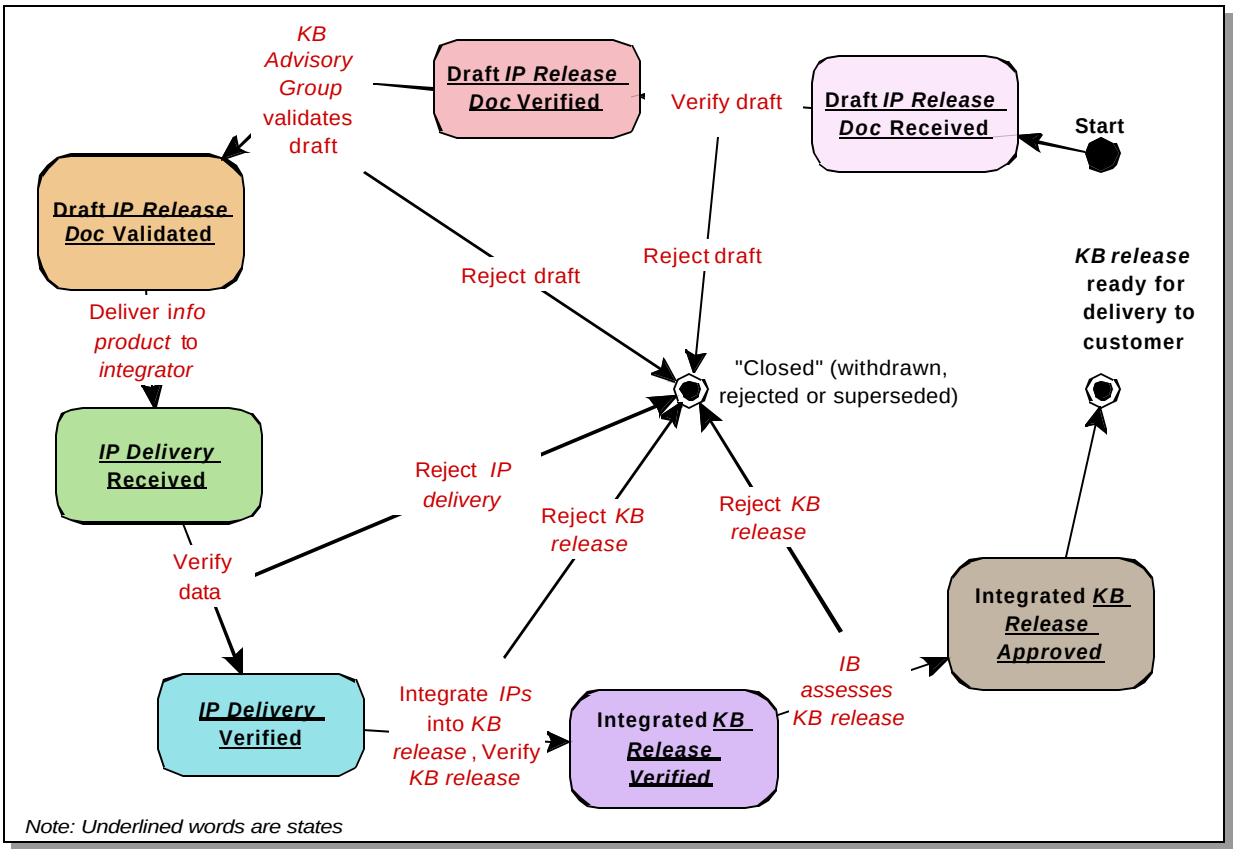


Fig. 1. State transition diagram for Information Product integration into the Knowledge Base.

The following nomenclature is used for the integration process and Knowledge Base releases. An *information product* comprises

- one or more conceptually related data sets
- metadata corresponding to each data set
- an information product release document (described in state 1 below)
- any associated models, interface tools, or visualization tools.

A *data set* is a collection of data usually all of the same kind; examples include event data, contextual data, or parametric grid data. *Metadata* describes the content, source, quality and condition of a data set.

The integration process defines *states* through which an information product passes as it migrates from the research environment into the Knowledge Base. Though the integration process is a joint effort, Sandia National Laboratories (SNL) holds the primary responsibility for integrating information products into the Knowledge Base, so the states in the diagram are defined relative to SNL's role. As the Knowledge Base integrator, SNL systematically tracks each of the states for each of the information products offered for inclusion in the Knowledge Base.

1. The initial state of the process is Draft Information Product (IP) Release Document Received. A *release document* is developed by a contributor (a research organization, typically) and contains at a minimum:
   - information product identification
   - content description
   - changes since prior versions
   - installation instructions.

When the draft version of the release document is received, it indicates that the contributor intends to submit an information product for inclusion in the Knowledge Base, so the Knowledge Base integrator begins tracking that proposed information product. The Knowledge Base integrator also identifies two points of contact for this specific information product:

- An *information product coordinator* who represents the contributing organization.
- An *information product integrator (*representing the Knowledge Base integrator organization) who will work with this particular information product. This paper will continue to refer to the Knowledge Base integrator for clarity in process description, but it is a specific person, the information product integrator, who performs the integration and tracking for a particular information product.

The Knowledge Base integrator reviews the draft release document for completeness. If unsatisfactory, the draft release document is returned to the contributor with feedback. If the draft release document is found to be satisfactory, the information product is promoted to the next state.

2. In this state, Draft Information Product Document Verified, the proposed information product represented by the draft release document is subjected to technical review via the Knowledge Base Advisory Group for that information product. The Advisory Group comprises
   - domain experts from peer organizations and
   - one or more representatives from the end-user organization.

The Advisory Group provides *validation*, a determination of relevance and scientific quality, of the information product proposed for inclusion in the Knowledge Base. The assessment is based on whether or not the proposed information product supports the defined monitoring goals. Written assessment and recommendations are provided to the contributor and to the Knowledge Base integrator.

If the Advisory Group deems the information product (represented by its draft release document) unsuitable, then the draft release document is returned to the contributor with feedback. If satisfactory, the information product is promoted to the next state.

3. At this point, Draft Information Product Release Document Validated, the contributor prepares the delivery of the information product by
   - finalizing the release document,
   - synthesizing the research data,
   - completing the associated metadata, and

- completing associated interface tools.

Meanwhile, the Knowledge Base integrator (SNL) uses the validated draft release document as a basis for integrating the information product into the Knowledge Base. For example, the release document provides information about quantity and format of the forthcoming data, which helps with system configuration, both in the integration test bed and at the end-user site. Also, the release document provides information about testing and verifying the forthcoming information product, which aids in the verification process. It provides information about associated process tools and interface tools, which helps coordinate tool development and testing.

4. The integration process continues when the contributor delivers the comprehensive information product for integration; SNL logs this state as Information Product Delivery Received.

The information product is considered received when all data sets comprising the information product have been received, all metadata received, the final release document received, and any interface tools for process or visualization have been received.

The Knowledge Base integrator performs extensive verification of the information product for completeness, consistency, and correctness, based on the preparation using the release document. The integrator tracks each data set contained in the information product and its associated metadata for both receipt and verification. The integrator may return the information product to the contributor with feedback if the information product or one or more of its data sets are found to be unacceptable, incomplete, or missing. If acceptable, the information product is promoted to the next state.

5. This state, Information Product Delivery Verified, indicates the information product is ready to be integrated into a Knowledge Base release.

At this point, several verified information products are integrated into a potential Knowledge Base release. The combined release is verified at a system level, appropriate classification issues are addressed, and the Knowledge Base integrator develops a Knowledge Base release document. The Knowledge Base integrator synthesizes the following to complete the integration into the potential Knowledge Base release:

- the comprehensive potential release and its release document,
- information product release documents,
- Advisory Group recommendations, and
- tracking reports demonstrating the verification, validation, and management of the information products.

6. With verification activities completed, the state now becomes Integrated Knowledge Base Release Verified, which means the proposed Knowledge Base release and its supporting documentation are ready to be presented to the Integration Board for approval.

In addition to the potential release and its supporting documentation presented to the Integration Board, contributors are encouraged to present an overview of their respective information products during the Integration Board meeting.

The purpose of the Integration Board is to provide high-level approval that the information products have been verified, validated, and properly integrated based on recommendations by the Knowledge Base Advisory Groups, which have accepted the information products after technical review. The Integration Board comprises, at a minimum, a program leader from each contributing organization, the DOE sponsor, and a technical representative from the end-users' site. Specifically, the purpose of the Integration Board is to

- review the contents of the potential Knowledge Base release
- be advised by the Knowledge Base Advisory Groups' reports
- be informed by the information product status reports from the tracking tool used in the integration process
- accept or deny all or part of the potential Knowledge Base release.

7. If the Integration Board approves the potential release, then the state becomes Integrated Knowledge Base Release Approved, and the approved Knowledge Base release is delivered to the USNDC. Integration of specific

information products into a Knowledge Base release does not guarantee acceptance by the USNDC, which exercises its own review process after receipt of a release.

This integration process can also be summarized in terms of data flow, as shown in Figure 2.

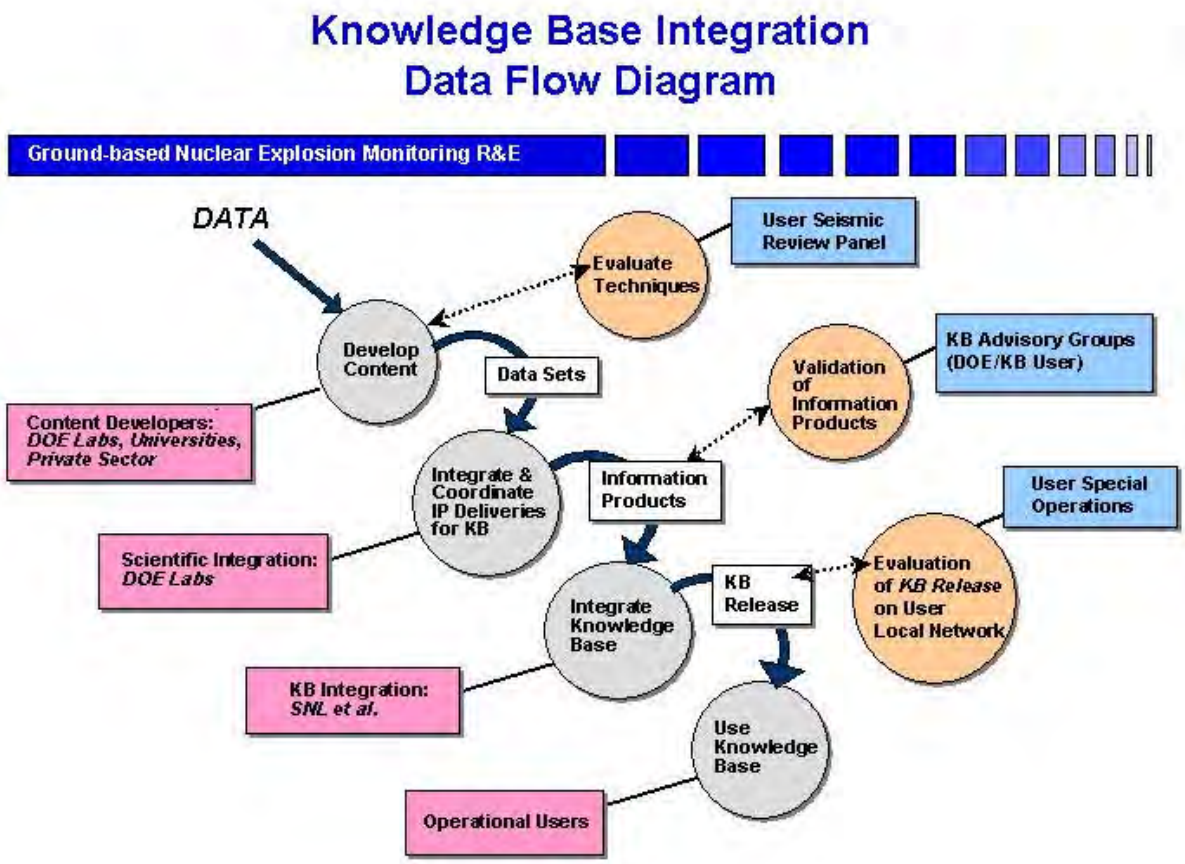


Figure 2. Basic data flow for Knowledge Base Development and Integration (shown relative to parallel user evaluation process).

How the process addresses the original issues

The integration process was developed to address three issues mentioned early in this paper. Those issues are explicitly addressed here.

What do end-users want and need?

The integration process includes end-users early on with their participation in the Advisory Group review of the draft release document for validity or relevance of a proposed information product. The needs of end-users are addressed even earlier by the contributing organizations with their interactions with end-users. These interactions, while outside the scope of the integration process, form the basis for the research and any resulting information products. Further, the end-users are represented on the Integration Board to ensure their needs are met.

How do researchers collaborate to address those needs?
The integration process provides guidance in collaborating by establishing the roles of information product integrator and information product coordinator. These two roles must work closely together using a well-defined process to ensure successful integration of scientific research results into a useful information product. In addition, the integration process provides evidence, or documentation, of the collaborations to support the usefulness and reliability of the information products.

How is research integrated into a useful and reliable product?
One of the original and enduring requirements in developing a process to integrate research results into information products for use within the Knowledge Base is that the process may not prescribe the type or amount of data developed by the researchers. That is, the process must integrate a wide range of data types, data complexity, and data volume. The purpose for this requirement is to accommodate, not constrain, the researchers in their work so that the full utility of their research is maintained during its integration into the Knowledge Base.

CONCLUSIONS AND RECOMMENDATIONS

The process of validating, verifying, and managing the information products is critical to the successful integration of scientific research to support operational monitoring systems at the USNDC. We have defined and implemented a successful process to date.

Continued success of the integration process relies on the following:

- The integration process is rigorous and well-defined.
- All contributors, whether DOE-funded or not, are knowledgeable about the process.
- The process continues to be refined as USNDC requirements emerge and as various types of research evolve.
- We get and incorporate feedback from the end-users concerning the usefulness of the format and functionality.
- We get and incorporate feedback from the end-users regarding the validity of the content and functionality.

Near-term work on the integration process includes the following:

- Evolution of process tools. The tracking tool will be modified to incorporate refinements to the process and enhanced to generate various types of reports such as tracking by information product or tracking by contributor.
- Refinements of process. As the number, complexity, and type of information products expand, the process will need to be refined to accommodate the growth. For example, as research interface tools are developed and included with information products, they will be integrated with equally rigorous and well-defined processes to ensure integrity and utility.

REFERENCES

Moore, S., et al., (2000). *The Integration Process Design for Incorporating Information Products into the Department of Energy Knowledge Base*, SAND2000-0597.

Carr, D., et al., (2000). *Knowledge Base Contributor's Guide*, SAND2000-0442.

DELIVERING RESEARCH RESULTS TO THE DTRA CMR R&D TESTBED

David H. Salzberg, Robert L. Woodward, Robert G. North
Science Applications International Corporation/Center for Monitoring Research

Sponsored by the Defense Threat Reduction Agency
Arms Control Technology Division
Nuclear Treaties Branch
Contract No. DTRA01-99-C-0025

ABSTRACT

The purpose of the Research and Development Testbed (R&D Testbed) at the Defense Threat Reduction Agency's (DTRA) Center for Monitoring Research (CMR) is to improve nuclear explosion monitoring capability by supporting the R&D community with a wide range of activities and resources and providing environments for testing and evaluating promising research results at a wide range of scales. For certain deliverables, DTRA directs its sponsored researchers to deliver their research results to the R&D Testbed. Results delivered to the R&D Testbed are permanently archived in a manner that facilitates access by other researchers. In addition, the R&D Testbed provides a facility to evaluate such research results and, if desired, integrate them into other software systems and subsystems. For example deliverables are both integrated into software for delivery to the Comprehensive Test Ban Treaty Organization's International Data Centre and also transitioned to the US Air Force Technical Applications Center (AFTAC) at Patrick Air Force Base in Florida for routine worldwide nuclear explosion test monitoring. The purpose of this paper is to formally document the established procedures of the DTRA CMR R&D Testbed.

A key component for success of the R&D Testbed is the delivery, test, and acceptance of results from the R&D community. In general, the R&D Testbed expects four types of deliveries: technical reports, data to receive and store, software components to evaluate and possibly integrate, and parametric results (such as Source Specific Station Corrections) to evaluate and integrate. Separate procedures are required for the different types of deliveries:

- Technical reports only need to be delivered to the R&D Testbed, preferably electronically.
- Data deliveries:
  - Data must be delivered in electronic form, by FTP or tape submission.
  - A description of the data format will aid the delivery; the preferred format is CSS 3.0.
    - Other formats require discussion to ensure the format is properly defined.
- Deliveries that are to be evaluated and/or integrated (software components and parametric results):
  - Optimally, a delivery schedule is defined early in a research contract.
  - The R&D Testbed staff can assist the researcher in defining the software interfaces.
  - A test plan with evaluation criteria is generated by the researcher in collaboration with R&D Testbed staff.
  - The component to be evaluated is delivered.
  - The component is evaluated at the R&D Testbed.
  - The R&D Testbed provides feedback to researcher regarding the testing.
  - A test report is generated by the R&D Testbed with collaboration from the researcher.
  - DTRA will direct the subsequent activity: the component may be developed further or integrated into the operational test and evaluation system at CMR.

The procedure for delivery and evaluation of data and components requires coordination between the R&D Testbed and the sponsored researcher. For data deliveries, the primary issue is ensuring that the R&D Testbed is able to integrate the delivery into its archive database. For deliveries that are to be evaluated and/or integrated, the process is more detailed and requires contact early in the research and development cycle and continuing beyond the component delivery. Historically, the duration of the test and integration cycle has been 3-6 months, and after product delivery has required significant effort by both the R&D Testbed staff and the researcher.

As of June 2000, the R&D Testbed expects deliveries over the next 3 years from: 23 projects that require evaluation, 36 that require only archiving of final reports, and 32 that require integration of data. Given the resources required to properly evaluate deliveries, every effort should be made to define a realistic delivery and testing schedule that works for both the researcher and the R&D Testbed.

Key Words:

Nuclear explosion monitoring, evaluation, testing, delivery, monitoring capability, research and development

OBJECTIVE

One of the primary objectives of the Research and Development Testbed at the DTRA Center for Monitoring Research is to provide a central delivery point for test, evaluation and storage of the results of DTRA sponsored Nuclear Monitoring research and development. The focus of this paper is to outline the procedures established for interacting with the R&D Testbed for the purposes of accepting, integrating, testing, and evaluating research results.

RESEARCH AND DEVELOPMENT TESTBED PROCEDURES

The R&D Testbed was designed to handle deliveries ranging in complexity from technical reports to software components that are to be evaluated for potential use in an integrated operational environment. Procedures have been developed and refined over time to facilitate delivery and testing of various types of deliverables, where the level of procedure is dependent on the type of delivery. For delivery of reports, all that is required is an electronic copy of the report in a known format. Other types of delivery require a delivery plan, which includes descriptions of what is to be delivered, its format, how it is to be installed, and a schedule. In addition, delivery of items that are to be evaluated must include a test plan that describes suggested test procedures and expected results. Templates for delivery and test plans are being published on the R&D Testbed web site (http://www.cmr.gov/rdtb).

Research Reports

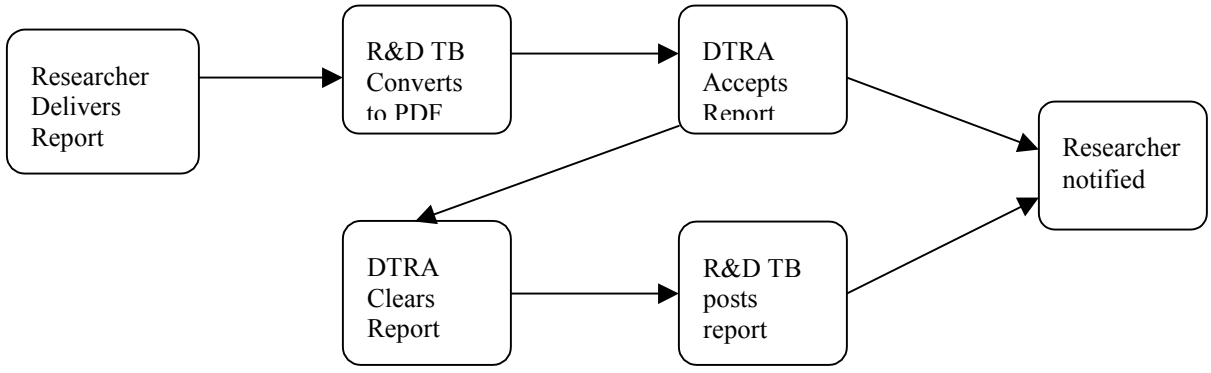
Delivery of final research reports requires minimal procedure. One notifies the R&D Testbed regarding the delivery, specifying a proposed delivery method and product format. The preferred delivery method is electronic distribution, with the format specified (e.g., MS Word, Frame 5.5, PDF.).

Once the report is delivered, the report will (with DTRA approval) be made available via the R&D Testbed web page or ftp site. In addition, a hardcopy of the report will be archived at CMR.

Table 1 Actions for Report Deliveries

Contributor	**R&D TB**	**DTRA**
1. Electronic delivery formatted in: • PDF • Word • FM • Postscript	1. Convert to PDF 2. Post on R&D Testbed web site as PDF 3. Reply to sender	1. Acceptance of deliverable 2. Clearance as needed -- prior to posting 3. Receive copy of report

Figure 1 : The process flow for delivering reports:



Data and Parametric Products

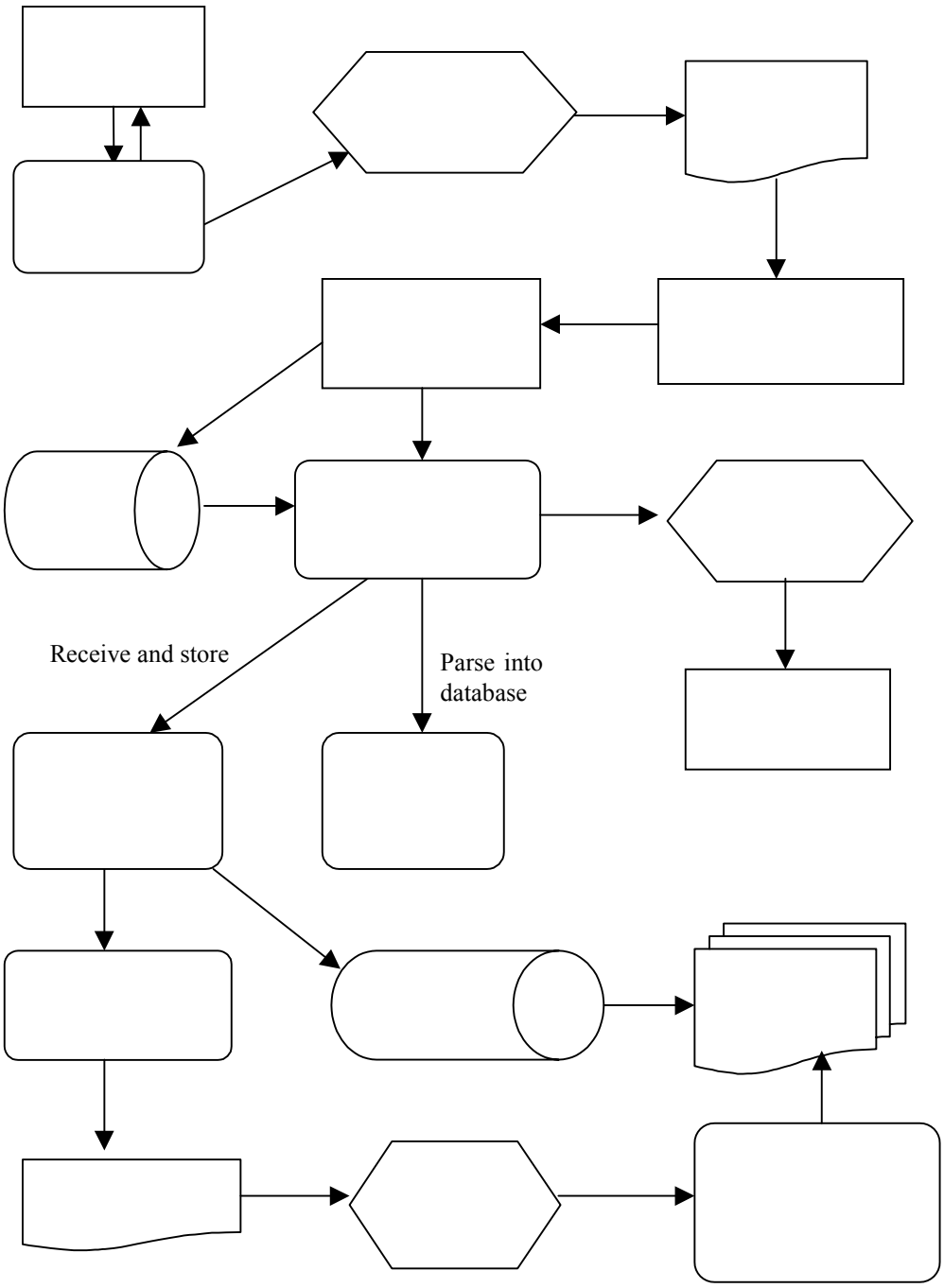
Some deliveries to the R&D Testbed can be described as 'Receive and Store' deliveries. That is, such items are received by the R&D Testbed; they are subjected to basic acceptance tests, and are then stored with the intent of making them available to other researchers. Previous examples of such deliveries would be waveform data sets, earthquake catalogs, velocity models, and so forth.

Receive and Store deliveries to the R&D Testbed require special preparation to ensure that the R&D Testbed will be able to interpret formats, have sufficient metadata to enable the product's use, and be ready to successfully integrate the data set into the R&D Testbed databases and storage system. There are a number of general actions by the contributor, the R&D Testbed, and DTRA, which apply to any product which will be stored on the R&D Testbed and which will subsequently be used by others. Such actions are outlined in Table 2 below, with specific examples provided for waveform and event catalog deliveries. In addition, Figure 2 illustrates the process flow.

Table 2 : Actions for Data Deliveries

	Contributor	**R&D TB**	**DTRA**
Generic Receive and Store	1. Abbreviated delivery plan 1.1. Type of information to store 1.2. Expected delivery size 1.3. Limits on redistribution (DTRA may overrule) 1.4. Expected delivery date 2. Electronic delivery in documented format	1. Verify readability 2. Store as delivered 3. Delivery report	1. Acceptance of deliverable 2. Clearance as needed -- prior to posting 3. Assessment of future action on deliverable 4. Resolution of disputes
Example 1: Waveform data	1. Abbreviated delivery plan 1.1. Expected delivery size 1.1.1. Bytes of data 1.1.2. Number of waveform segments 1.2. Delivered format 1.2.1. CSS 3.0 is preferred 1.2.2. GSE, SEED, SAC, or AH acceptable 1.3. Description of supplementary data (origins, arrivals, etc.) 1.4. Limits on redistribution 1.5. Expected delivery date 2. Electronic delivery of waveforms in expected format	1. Review delivery plan 2. Verify readability 3. Load into R&D Testbed database 3.1. Convert to CSS 3.0 format 3.2. Add any new stations to R&D Testbed station listing 3.3. Load waveform onto mass storage device 3.4. Load waveform description and associated data into the R&D Testbed database 4. Prepare delivery report and submit to DTRA 5. Post for export	
Example 2: Event Catalog	1. Abbreviated delivery plan 1.1. Expected delivery size 1.1.1. Bytes of data 1.1.2. Number of events 1.2. Delivered format 1.2.1. CSS 3.0 is preferred 1.2.2. Any format with metadata is acceptable 1.3. Limits on redistribution 1.4. Expected delivery date 2. Catalogs in ASCII (DB ready) and including metadata	1. Review delivery plan 2. Verify readability 3. Load into R&D Testbed database 3.1. Convert to CSS 3.0 format 3.2. Load origin, event, arrival, etc. tables to R&D Testbed database 4. Prepare delivery report and submit to DTRA 5. Post for export	

Figure 2 : The process for delivering data to the R&D Testbed



Software to be evaluated

Procedures for delivering software to the R&D Testbed are similar to that required for data deliveries. The primary differences involve the need for additional information in the delivery plan such as configuration issues (e.g., a list of files required to execute the code), and hardware and software requirements (e.g., the type of computer system required by the component and the expected version of the operating system). Of particular importance to the process are steps ensuring that the delivered component can run on the R&D Testbed, that the R&D Testbed staff understand what is required to install and evaluate the component, and that the delivery timing allows for sufficient evaluation of the component during the performance period of the contributor's contract. To mitigate potential issues, a delivery plan and a stand-alone test plan are to be submitted to the R&D Testbed by the contributor. In addition, the R&D Testbed can supply a compatibility list of software, hardware, and commercial off the shelf (COTS) products.

It is important that a realistic schedule, mutually agreeable to the contributor and the R&D Testbed, be negotiated with R&D Testbed staff as soon as possible in the overall process. The schedule should contain, at minimum, the expected date of submission for the delivery and test plans, the expected delivery date of the component, the evaluation period, and a final report date. The schedule is critical because any deviation in the schedule (by either party) may result in scheduling conflicts with other submissions to the R&D Testbed.

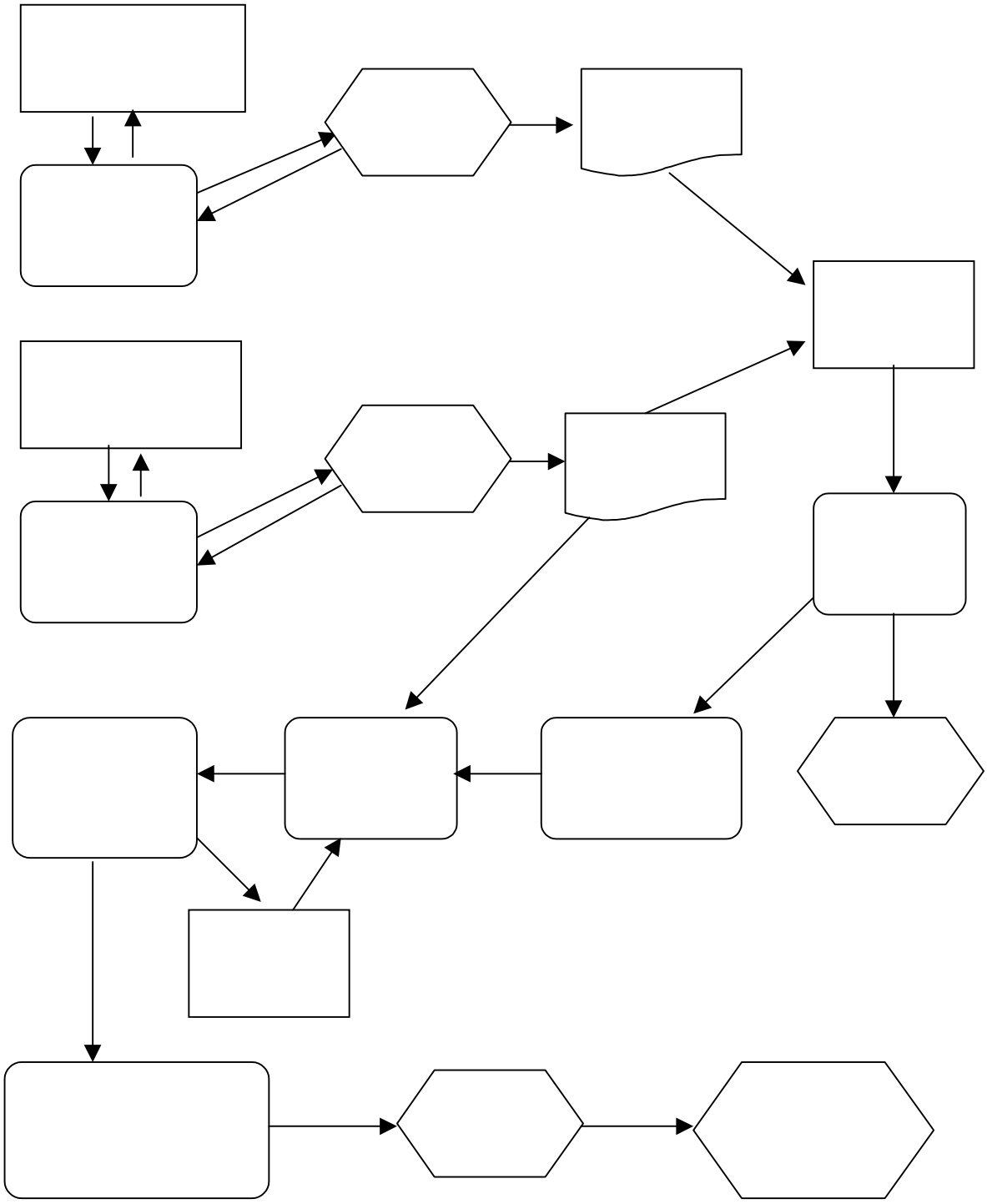
The stand-alone test plan focuses on the procedures for testing, the test criteria, and test cases. Researchers shall submit a test plan that provides comprehensive information on testing the product. This shall include features to be tested, pass/fail criteria, testing approach, resource requirements, and schedules. Test plans should clearly detail all procedures for test cases. Delivery and Test Plan templates are available from the R&D Testbed web site.

Specifications for each party are outlined in Table 3 below. In addition, Figure 3 on the following page illustrates the process for delivery and evaluating software components.

Table 3 : Actions for Software Deliveries to be Evaluated

Contributor	R&D TB	DTRA
1. Prepare delivery plan 1.1. System impact 1.1.1. What does the component do? 1.1.2. What are the inputs and outputs? 1.1.3. How is the software started? 1.2. System requirements 1.2.1. Hardware needed by software 1.2.2. Software requirements (deviations from the COTS list) 1.3. Configuration issues 1.4. Support requirements: what R&D Testbed staff support will be required for delivery 1.5. Delivery schedule 1.6. Installation instructions 2. Prepare stand-alone test plan 2.1. Procedures to execute test 2.2. Test cases 2.3. Evaluation criteria 2.4. Sample results 3. Deliver software 3.1. Complete source code 3.2. Consistent with COTS list 3.3. Documentation	1. Maintain COTS list 2. Supply metadata guidelines 3. Review delivery and test plan 4. Install and test software in stand-alone mode 5. Prepare delivery report and submit to DTRA 6. Evaluate parametric information 7. Prepare evaluation report and submit to DTRA	1. Acceptance of deliverable 2. Clearance as needed -- prior to posting 3. Assessment of future action on deliverable 4. Resolution of disputes

Figure 3 : Process Flow for the Delivery and Evaluation of Software at the R&D Testbed



Components to be Evaluated in the Context of a Full-Scale Monitoring System

Components that are to be tested and evaluated after integration into a full-scale monitoring system environment, for example the CTBT Monitoring Software System (CMSS), require additional steps than components that are to be evaluated in a stand-alone environment.

The delivered components must be compatible with the applications in the full-scale test environment. For example, while R&D Testbed facilities include Intel-based machines, the full-scale environment uses the SUN SPARC family processors. Special attention must be placed on how the component is to be integrated; that is, what process will initiate the component, where the component retrieves data, and where it writes output. As such, an integration plan is added to the delivery requirements. In addition, developers of these components are encouraged to work with the R&D Testbed software and systems engineers as early as possible in their development process to ensure compatibility with the environment of the R&D Testbed. These additional requirements have significant implications regarding the delivery schedule. The test and evaluation schedule is tighter for full-scale testing, due to competition for access to the integrated environment.

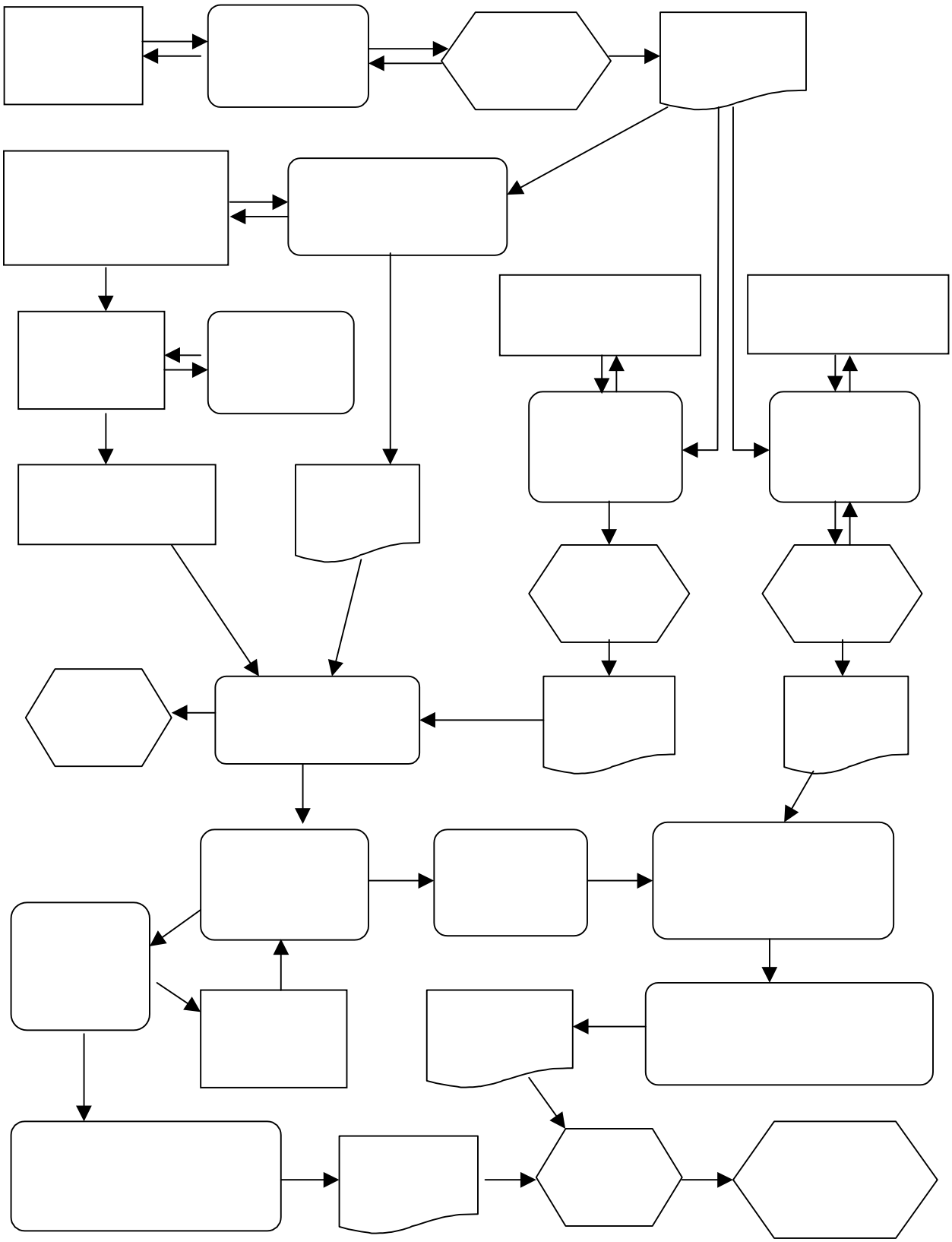
An integration test plan is required for components which will be integrated and evaluated in the context of a larger system. Integration tests differ from the stand-alone tests in that the stand-alone test is primarily focused on the function of the delivered application, whereas integration focuses on the operation of the system as a whole with the delivered component installed. As such, the Integration Test Plan provides the procedures for evaluating the delivered component within the context of the full-scale test environment. The primary issues in the Integration Test Plan are the instructions for determining and assessing correct interaction between the system and the specific application, and the basis for estimating overall system impact. The performance of the application and the integrated system, in terms of monitoring capability criteria, are assessed in the context of the final system output. For example, improvements in event location precision and accuracy would be performance criteria for location algorithms or location calibration parameters. Templates for both the Integration Plan and the Integration Test Plan are available on the R&D Testbed web site.

There are specific actions for the contributor, the R&D Testbed, and DTRA, as outlined in Table 4 below. In addition, Figure 4 illustrates the process for delivery and evaluating software components.

Table 4 : Actions for Software Deliveries to be Integrated

Contributor	R&D TB	DTRA
1. Delivery plan [See Table 3] 2. Integration plan 2.1. List the application that initializes the component 2.2. Explain all interfaces 2.2.1. Input interfaces 2.2.2. Component output 2.2.3. Controlling the component 2.3. Integration instructions 3. Stand-alone test plan [See Table 3] 4. Integration test plan 4.1. Procedures to execute test 4.2. Evaluation methodology 4.3. Expected system impact 5. Deliver software 5.1. Complete source code 5.2. Consistent with COTS list 5.3. Documentation	1. Maintain COTS list 2. Supply metadata guidelines 3. Review delivery and test plans 4. Install and test software in stand alone mode 5. Integrate component according the integration plan 6. Prepare delivery report and submit to DTRA 7. Prepare evaluation plan and submit to DTRA 8. Evaluate parametric information 9. Prepare evaluation report and submit to DTRA	1. Acceptance of deliverable 2. Clearance as needed -- prior to posting 3. Assessment of future action on deliverable 4. Resolution of disputes

Figure 4: Process for Delivering Integrated Products



SUMMARY

The DTRA CMR Research and Development Testbed is a designated testing and archival delivery point for DTRA sponsored research efforts. The R&D Testbed has the capability to test and evaluate deliveries in stand-alone mode, and in the context of the CTBT Monitoring System Software. Because of the complexity of receiving, storing, distributing, and evaluating a wide range of research products, a basic level of procedure is essential and is proportional to the complexity of the delivery:

1. Research report deliveries require:
    - Using an acceptable electronic format
2. Deliveries of data and parametric information require:
    - Prepare an abbreviated delivery plan
3. Deliveries of stand-alone components require:
    - A delivery plan
    - A stand-alone-test plan
4. Deliveries of components, information, or systems intended for integration require:
    - A delivery plan
    - An integration plan
    - A stand-alone test plan
    - An integration test plan

GLOBAL AND REGIONAL GIS DATABASE DEVELOPMENT IN SUPPORT OF CTBT MONITORING

Dogan Seber, Eric Sandvol, Christine Sandvol, Carrie Brindisi, and Muawia Barazangi
Institute for the Study of the Continents (INSTOC), Cornell University

Sponsored by The Defense Threat Reduction Agency
Arms Control Technology Division
Nuclear Treaties Branch

Grant No. DSWA01-97-1-0006

ABSTRACT

One of our main goals is to facilitate and enhance the capability of the US NDC and the IMS to accurately locate, calibrate, and evaluate seismic events in the Middle East, North Africa, and the United States. We achieve this by developing interactive, diversified geophysical, geological, and geographical digital databases to assist in the compliance and verification of the CTBT treaty. We are developing and testing an information system with a menu-driven, easy to use access tools. Currently, the information system includes large volumes of geophysical, geological, and geographical data sets relevant for research in CTBT monitoring. Newly collected data sets in the Middle East, North Africa, and the United States include detailed Moho and basement structures, velocity information, fault maps, Lg Q values, and many other geological and geophysical data sets. All these data sets are geo-referenced, formatted to allow simultaneous utilization and accessible with custom tailored tools.

For easy access to the information system we have developed two different mechanisms. The first is a menu-driven internal system that is run on UNIX and NT platforms. The second access mechanism is based on World Wide Web and easily accessible by any web browsers. The menu-driven system provides effective and efficient access to large volumes of data sets as well as the tools to manipulate them. Users can select any region on Earth and determine what relevant data sets are available and utilize them based on their objectives. Further information about this system can be accessed at http://atlas.geo.cornell.edu/ctbt/geoid.html. The web-based access is universal and allows any person to access and utilize the information systems with a JAVA enabled web browser. The web server is interactive and allows access to the core information system via a dynamic mapping interface developed for this purpose. The web site is accessible at http://atlas.geo.cornell.edu/ima.html.

All of the compiled data sets are also accompanied by related metadata. The metadata provide the necessary information about the quality, resolution, accuracy, and techniques that were used in collecting the original data. Refer to http://atlas.geo.cornell.edu/ for further information.

Key Words: Databases, Middle East, North Africa, United States, GIS, CTBT

OBJECTIVE

Our main objective is to facilitate and enhance the capability of the US NDC and the IMS to accurately locate, calibrate, and evaluate seismic events in the Middle East, North Africa, and the United States, by developing an interactive, diversified geophysical, geological, and geographical digital databases to assist in the compliance and verification of the CTBT treaty. We are also developing and improving the design of menu driven, easy to use, custom made tools as well as metadata for all developed data sets. The metadata will provide the necessary information about the quality, resolution, accuracy, and techniques that were used in collecting the original data. Another objective is to deliver results of the original research on crustal and upper mantle structures of the Middle East and North Africa, and the character of regional seismic wave propagation for the purpose of obtaining a better understanding of high frequency wave propagation in this region.

RESEARCH ACCOMPLISHED

Our efforts in global and regional GIS database development in support of CTBT monitoring have been going on successfully. We have added significant new data sets to our digital library, and revised our data access tools in the past year. We have added the following data sets to our data library.

Geographical	Geologic	Geophysical	Gridded/Image
US State boundaries	*US Aquifers*	*US CNSS Seismicity*	*US Moho*
US County boundaries	*US Mines*		*US Pn Velocity*
US Cities	*Global Tectonic Provinces*		*US Pg Velocity*
US Lakes	*Geology of Former Soviet Union*		*US Bouguer Gravity*
US Rivers	*Geology of Asia Pacific*		*US Magnetic Anomaly*
US Roads	*Plate Boundaries*		*Updated Middle East and North Africa Moho*
US Rail Roads	*US Tectonic Boundaries*		*Updated Middle East and North Africa Basement*
US Urban Araes			*Landsat TM*

We have added the recently released USA National Atlas data to our system. The USA Atlas is published by the USGS and includes many different data layers for the United States including all geographic data sets listed in the above table (first column) and additional data sets. In addition, we have developed our own new data sets both at the regional and global scales.

Tectonic boundary map of the US is one data set that was developed by us to provide a reliable and high resolution tectonic boundaries of the US (Figure 1). This map was digitized from analog maps and the results were compared with known tectonic units and digital elevation models at 90m resolution. In this map each tectonic unit is represented by a polygon with unique attributes and each unit can be used individually and/or as a whole.

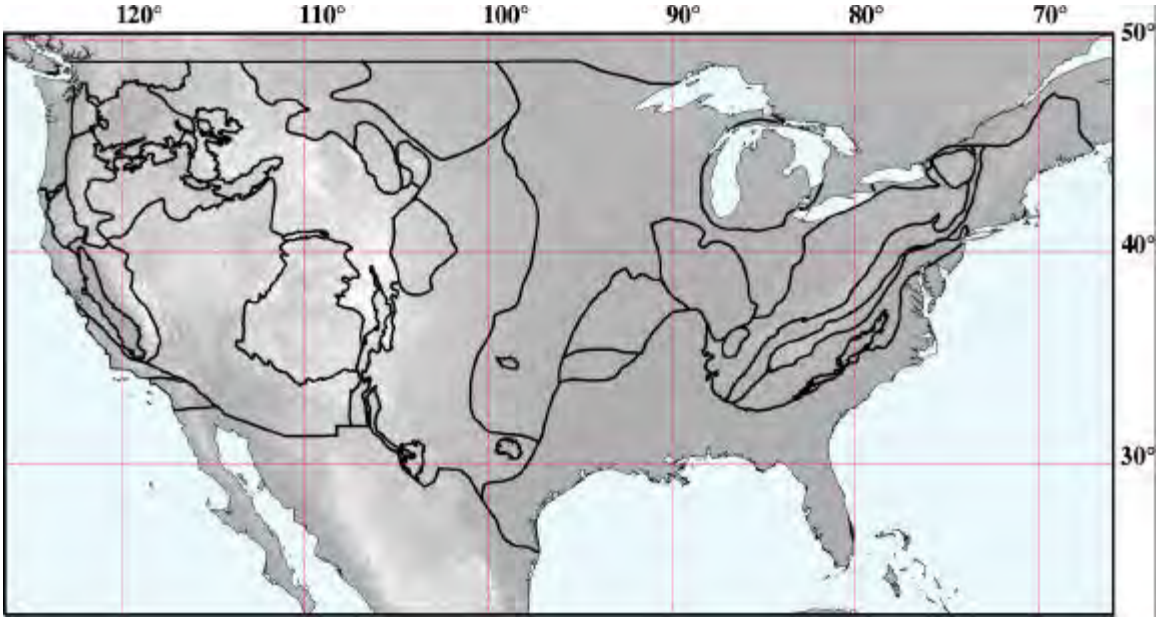


Figure 1. Tectonic boundary map of the United States.

Currently, we are developing detailed Moho and basement maps for the United States. The Moho map being developed is a collection of all published information about the depth of Moho anywhere in the US. This is a time consuming effort. However, the majority of available data have been entered into our system (Figure 2). Soon, this information will be used to make a detailed gridded Moho map for the US.

In our efforts to compile a comprehensive Moho depth data set, we not only record the point and the corresponding depth value, but also record all other relevant information such as the author names, publication source, the method used in obtaining the Moho point (Figure 3). This is extremely useful for researchers as they will always want to know about the details, resolution, and accuracy of the final gridded Moho map. These original point/contour information will be critical in judging the accuracy of the Moho map of the US. Results of this work will be essential to improve event locations and IMS calibration for the USA.

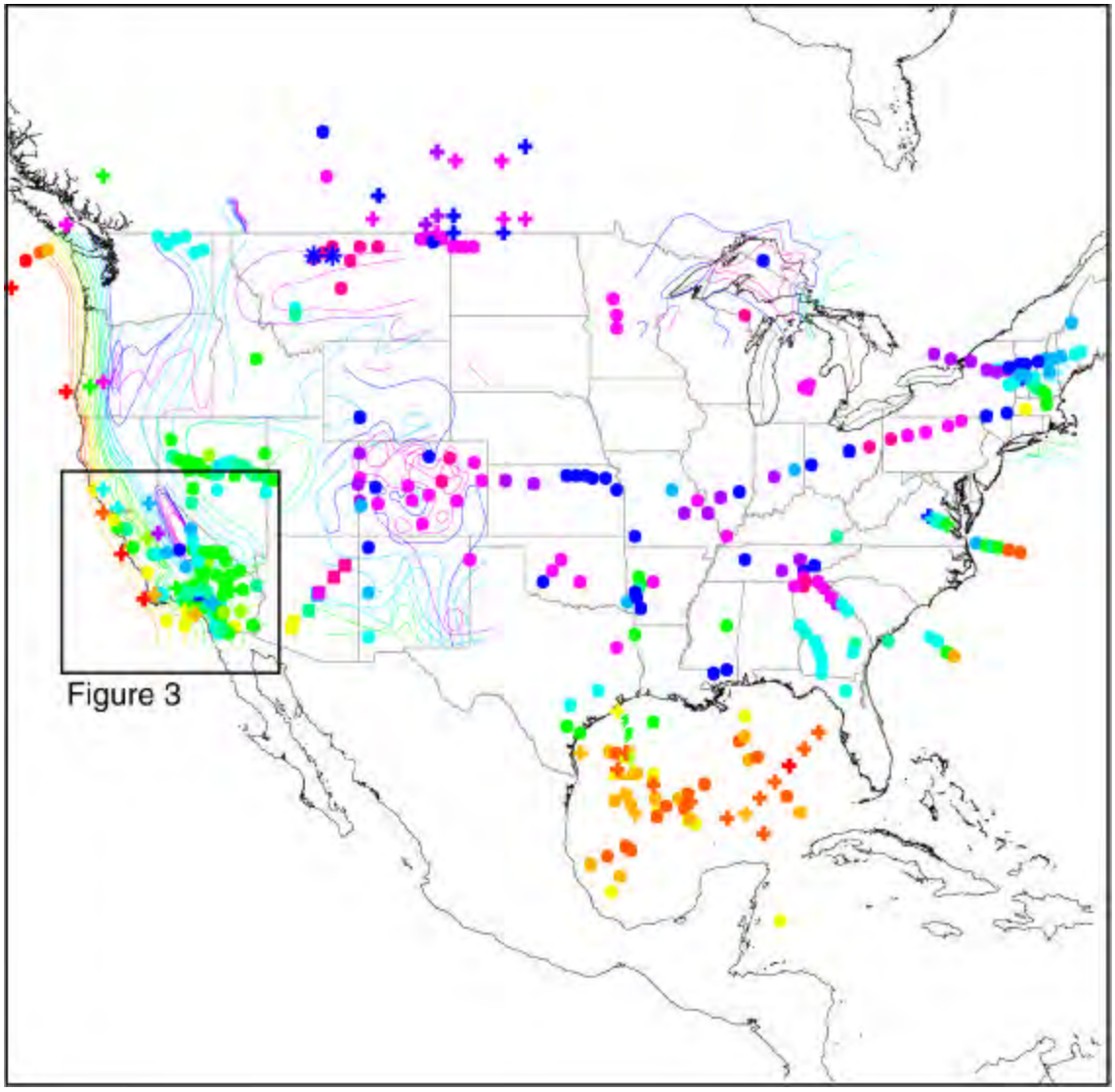


Figure 2. Map showing collected depth to Moho measurements in the US. Each point/contour represents locations where a Moho depth measurement exists. Each point/line shown also includes information about the source, author name, journal that the data were published in, and the method used in measuring the Moho depth. This work is in progress.

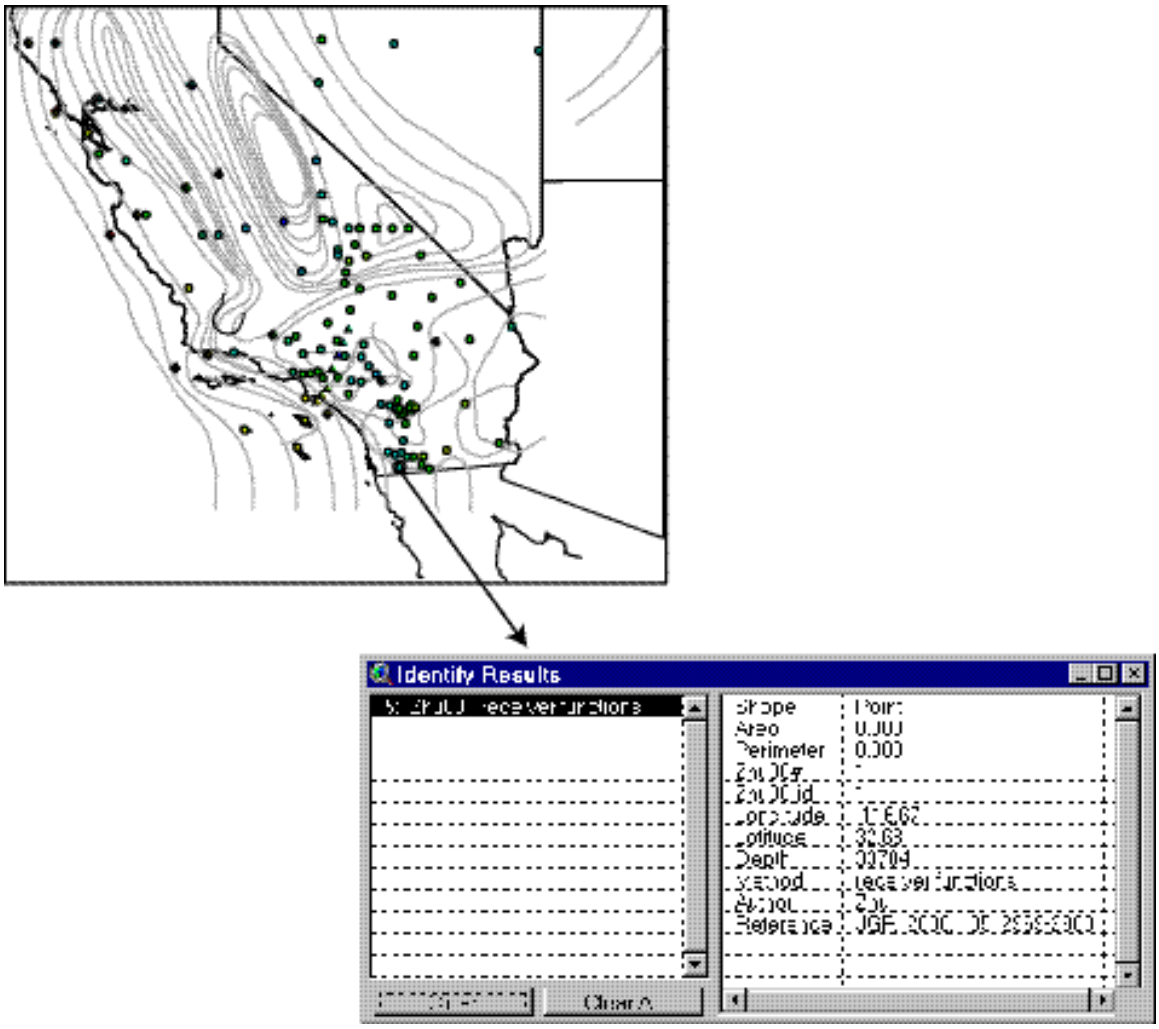


Figure 3. Detailed view of the inset map shown in Figure 2. Users of this data set can click on any of the points/contours in the map and display the information regarding that measurement.

We are also collecting all available sediment thickness maps at state levels. We have completed about ¾ of the US. The remaining ¼ coverage will be completed in the coming months.

In the Middle East and North Africa region we have improved our data coverage extent of the Moho and basement maps by collecting more data sets. We have now a complete crustal model for the entire Middle East and North Africa (Figure 4). This model is now being evaluated with independent data sources such as Bouguer gravity data and three-dimensional gravity modeling to determine which regions have reliable depth-to-Moho values, and which regions might need additional revisions.

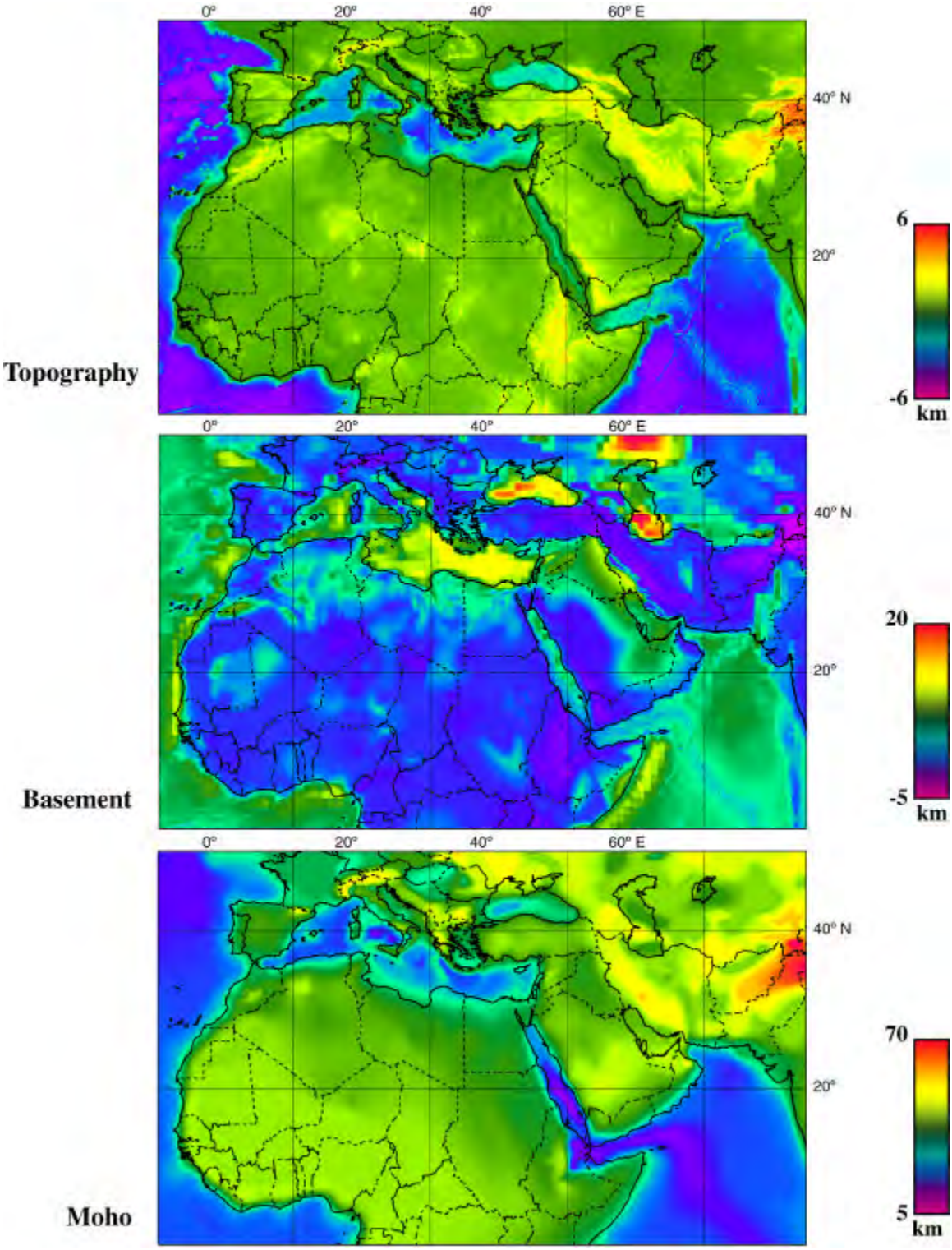


Figure 4. Maps showing the new crustal model for the Middle East and North Africa region. The model includes topography, sediment thickness, and Moho depth at the same scales.

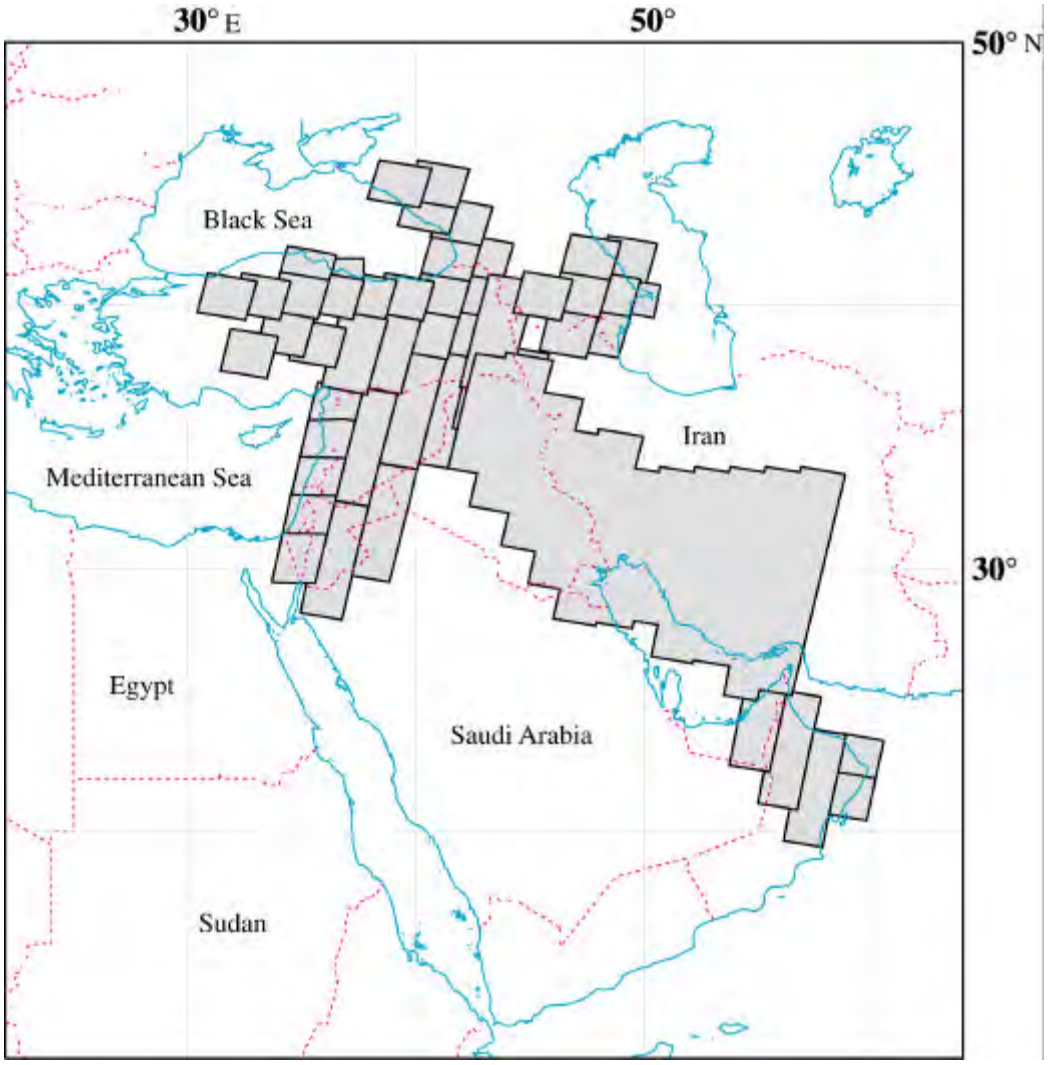


Figure 5. Landsat TM locations available in the Cornell database.

Also, for the Middle East and North Africa regions we continue to georeference our Landsat TM imagery (Figure 5). It is expected that this process will be completed within a couple of months and all these TM scenes will be made available online at full resolution via our main web server.

Data sets mentioned in this article and others covering the Middle East, North Africa, and the US along with their respective metadata can be accessed via our main web server at http://atlas.geo.cornell.edu (Figure 6).

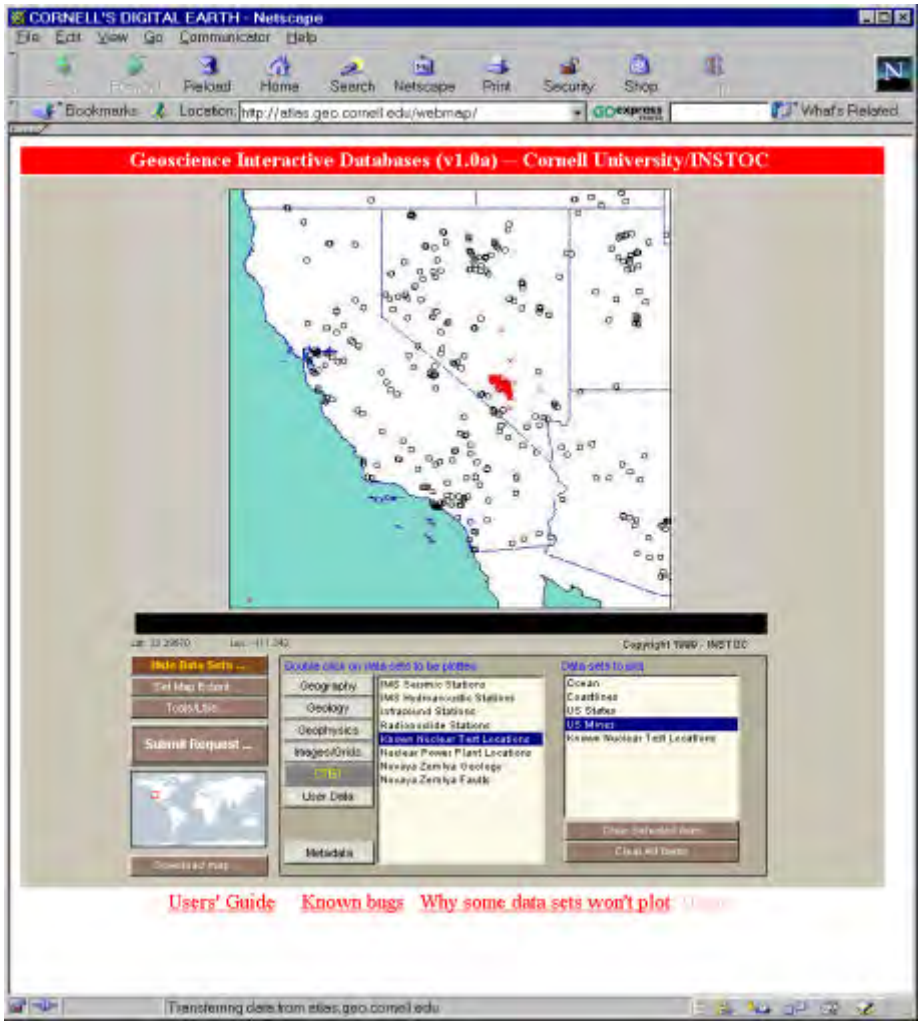


Figure 6. Web mapping applet available in our web site allows access to all data sets with an easy-to-use interactive application. Users can select any data sets and display it at any scales. Here, we selected US mines and known nuclear test locations. The application is available at http://atlas.geo.cornell.edu/.

CONCLUSIONS AND RECOMMENDATIONS

We have been collecting and organizing available seismological, geophysical, and geological data sets for the Middle East, North Africa and the United States into a comprehensive Geographic Information System (GIS). In addition to the GIS databases and tools, we have been developing a special World Wide Web (WWW) site to allow restricted access to our databases. All the data sets in our GIS system are documented with a standard metadata format in order to explain the source and nature of the data, their resolution, and their accuracy. The developed system and its efficiency in using and analyzing information will help CTBT researchers and decision makers to fuse and integrate the results of the four established monitoring technologies to reach a conclusion in a very short time. The system also significantly contributes to the better location and calibration of suspect events for any given region. This system will also help in On Site Inspection efforts.

We recommend that ongoing efforts to develop databases be expanded to include higher resolution data sets not only for the regions of the Middle East and North Africa but also to most regions on Earth. Such

developed information system and data sets will help to achieve better event locations with the required accuracy as stated in the CTBT.

SEISMIC CATALOGUE COMPLETENESS AND ACCURACY

Terry Wallace[1], Frank Vernon[2], and Gary Pavlis[3]

[1]SASO, Department of Geosciences,
University of Arizona
[2]IGPP, University of San Diego
[3]Department of Geological Sciences
University of Indiana

Sponsored by the Defense Threat Reduction Agency
Arms Control Technology Division
Nuclear Treaties Branch

Contract No. DTRA01-00-C-0069

ABSTRACT

The single most important goal of seismic monitoring of a nuclear weapons treaty is the detection and accurate location of seismic events of various origins (natural and man made) globally. However, the metric for evaluating the performance of the IMS or other monitoring networks is not easily established since global catalogues, such are the ISC and PDE, have been shown to be incomplete, with large regional variability. Further, the event parameters (location, origin time and magnitudes) are often quite different from catalogue to catalogue. We propose a collaborative research project between three universities to construct an as accurate as possible catalogue for the time period of 1995 to the present in a region of monitoring interest. This is an *intensive* project and will require both a data collection effort and a substantial research effort. The data collection effort will include the concatenation of a large number of disparate data sources (IMS, GSN and Geoscope stations, temporary, portable seismic experiments, various national networks and independently operated stations). This psuedonetwork will have temporally changing capability, and establishing seismic phase correlation with regional data will be a primary task. A significant part of the research effort will focus on improving the location of seismic events which are detected on a limited number of stations, primarily at regional distances (and a very small number of teleseismic stations). We will also investigate strategies for optimizing detection capabilities on particular subregions.

The area of focus stretches from Saudi Arabia to the eastern Tien Shan in northwestern China. The data sources include 12 different networks and experiments: much of the data is not readily available to the research community at large. The various research groups (UCSD, IU and UofA) bring different expertise to the project, and the collaborative effort will provide the following: (1) a detailed catalogue that will provide a test bed for comparison of performance, (2) research on strategies for regional event location and quantification, (3) investigation on establishing realistic errors in earthquake parameters reported, and (4) investigation of optimizing detection capability by using temporally or intermittently deployed seismic assets.

A TESTBED FOR NUCLEAR EXPLOSION MONITORING RESEARCH AND DEVELOPMENT

Robert L. Woodward, David H. Salzberg, Robert G. North
Center for Monitoring Research
Science Applications International Corporation

Sponsored by The Defense Threat Reduction Agency
Arms Control Technology Division
Nuclear Treaties Branch

Contract No. DTRA01-99-C-0025

ABSTRACT

The Research and Development Testbed (R&D Testbed), developed within the Defense Threat Reduction Agency's (DTRA) Center for Monitoring Research (CMR), is designed to support US national and international nuclear test monitoring and verification needs by providing several key functions to the R&D community. First, the R&D Testbed supports the Department of Defense (DoD) sponsored research and development community by providing an interface to the wide range of resources available at CMR. For example, the R&D Testbed provides access to CMR resources such as: near-real time waveform data from International Monitoring System (IMS) and GSETT3 stations, multi-terabyte seismic, hydroacoustic and infrasonic waveform archives, specialty ground-truth calibration databases, research archives, high resolution gamma-ray spectroscopy and beta-gamma coincidence spectroscopy radionuclide databases, and past and present products of both the Prototype International Data Center and the International Data Centre (IDC).

A second R&D Testbed function is to provide a centralized repository and exchange mechanism for research results generated by DoD sponsored researchers, facilitating the exchange of results among the R&D community. Uniform acceptance criteria and validation testing are applied to all results delivered to the R&D Testbed, thus ensuring easy and reliable use of these results by others. Further, centralized storage ensures that valuable research results accumulate through time--preventing their loss and avoiding their duplication. Deliveries to the R&D Testbed can take a variety of forms such as: technical reports, waveform data, event catalogues, parametric information, algorithms, and software. The mechanics of delivering results to the R&D Testbed is the subject of another symposium presentation.

Finally, R&D Testbed facilities provide researchers with the tools to evaluate R&D results to assess their impact on monitoring capability by providing test environments at whatever scale is appropriate to the evaluation. Testing can range from the full data load of the IMS stations and the full processing environment of the IDC, to highly specific tests confined to special data sets. This wide range of testing environments provides unique testing opportunities for the R&D community. In particular, testing at operational-like scales allows issues to be identified which can go unnoticed in more limited-scale testing. The evaluations of R&D results will be passed to DTRA so that the most promising R&D products can be identified for appropriate action, such as further development or integration into larger systems.

The R&D Testbed is a collaboration between DTRA, the R&D community, and CMR. A wide range of CMR staff, including scientific, software development, testing, and infrastructure support teams are available to support all phases of R&D Testbed activity. Although for many DTRA contractors the delivery of results to the R&D Testbed is mandatory, the R&D Testbed staff will work with contributors on advance planning, scheduling, assisting with test plans and other activities to make the delivery and acceptance process as smooth as possible. Such coordination among all participants is crucial, as the R&D Testbed will be receiving deliveries of various types from nearly ninety different research contracts over the next three years.

Key Words:

Nuclear explosion monitoring, evaluation, testing, monitoring capability, research and development

MISSION

The mission of the DTRA CMR R&D Testbed is to provide a research and development environment with test and evaluation facilities at appropriate scales to enable advances, measure progress, and focus resources on the important issues in monitoring and verification. To achieve this mission, a wide range of resources and experience at CMR are available to the nuclear monitoring research community. In the remainder of this paper we highlight some of these resources and how they may be utilized to support both research and development efforts, as well as the test, evaluation, and transition of subsequent research results.

BACKGROUND

The R&D Testbed at the Defense Threat Reduction Agency's Center for Monitoring Research provides a valuable resource to the nuclear monitoring R&D community. The CMR facility has a long record of research and development activities, supporting both in-house and external research. Further, the processes and procedures utilized by CMR are based on a history of moving solutions from basic R&D to integrated systems. For example, over the past several years CMR has been developing, testing, and transitioning systems to both US government and multi-lateral monitoring organizations (e.g. the US National Data Center located in Florida at Patrick Air Force Base

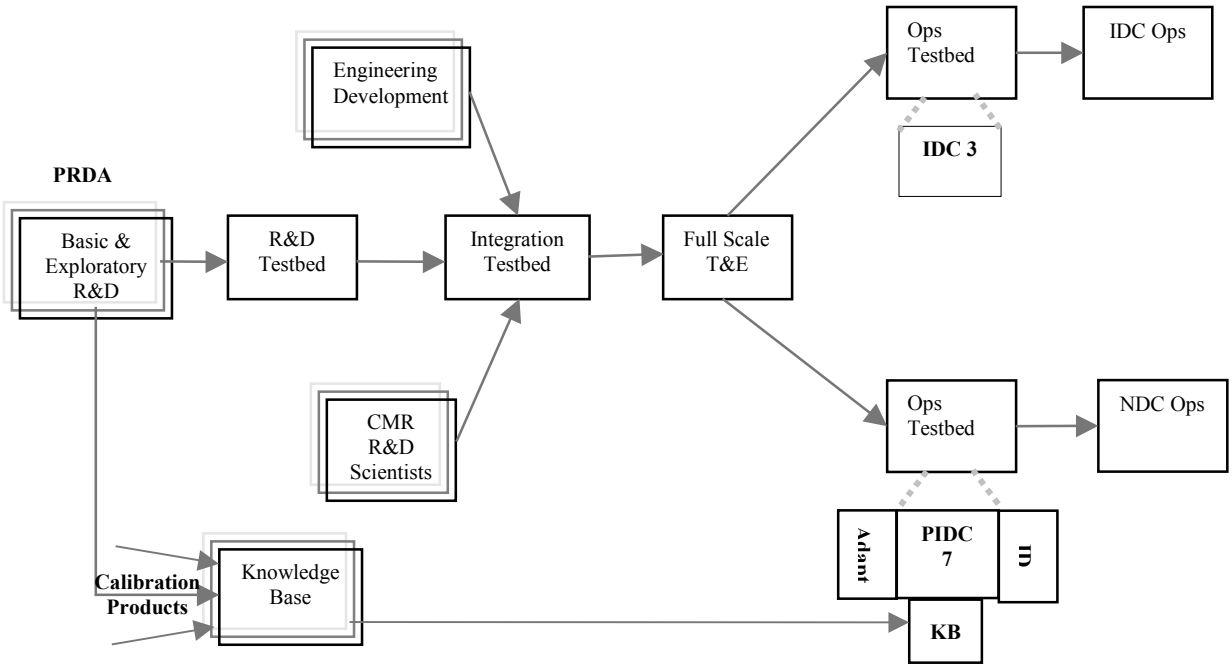


Figure 1. Illustration of the process for moving from basic and exploratory R&D work, on the left of the figure, to final operational systems, on the right side of the figure. As one moves from basic R&D testing to the full-scale test environment, the formalism of the procedures increases, proportional to the scale of the testing. In addition, this figure illustrates how the PIDC 7.0 software release feeds into the NDC operations environment, and Release 3 software (based on PIDC 7.0) feeds into IDC operations environment.

(NDC), and the International Data Centre located in Vienna, Austria (IDC). As illustrated in Figure 1, these efforts have resulted in refined procedures for all stages of the process required to move basic R&D results from the research stage through to operational systems. Extensive testing is conducted at all scales as a routine part of the development and transition process. These tests range from stand-alone and unit tests of individual software components and parametric information, to integration testing on an isolated testbed, up to operational test and evaluation in a full-scale environment.

DATA AND ANALYSIS RESOURCES

The R&D Testbed provides access to a variety of data and products, many of which are produced by the Prototype International Data Center (PIDC) at CMR. A brief listing of some of the more important data resources includes:

- Waveform data (seismic, infrasound, hydroacoustic)
- Radionuclide data
- Event bulletins (from both the PIDC and IDC)
- Special-purpose event and waveform databases
- Web pages

Most data and results can be accessed remotely using AutoDRM or web-based interfaces. See the R&D Testbed web site (http://www.cmr.gov/rdtb) for more details and additional links. In addition, open international facilities are available for visiting scientists who wish to directly access research, operations, and development expertise, as well as interact closely with the CMR data archives and databases. Computer and database accounts are also available for direct access to R&D Testbed resources.

CMR currently receives over three gigabytes of data from the IMS and other networks each day and has over five years of archived data. Continuous time series data arrive in near-real-time from primary seismic stations and arrays, as well as from hydroacoustic and infrasound stations. Waveform segments are requested from auxiliary seismic stations, and radionuclide stations send in observations as discrete messages. Figure 2 illustrates the quantity of seismic, hydroacoustic and infrasound data received since 1995. The R&D Testbed provides complete access to the data archives, as well as current data arriving via the International Monitoring System (IMS), though the latter are subject to some restriction.

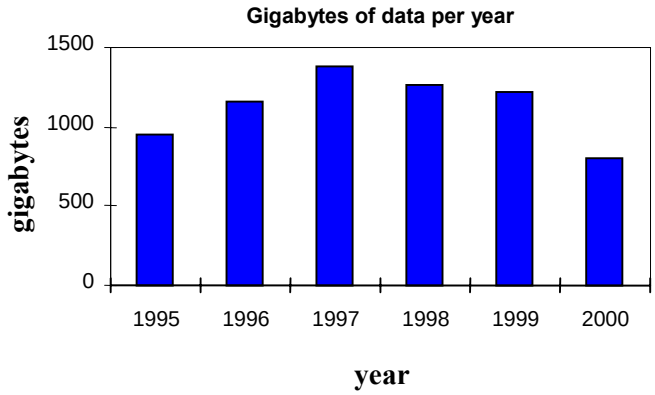


Figure 2. Gigabytes of data in the CMR data archive. The majority of the data, in terms of volume, are comprised of continuous time series data from seismic, hyrdoacoustic, and infrasound sensors.

Processing results from the PIDC for all of the data collected since 1995 are available on-line and by remote access. These results include preliminary automated event bulletins as well as the analyst Reviewed Event Bulletin (REB). As the IDC has assumed production of daily REBs since February 20, 2000, the PIDC has scaled back to an average of two REBs produced each week. The R&D Testbed provides the research community with access to both PIDC and IDC REBs for every day, from the present back to January 1, 1995, comprising over 100,000 events.

A variety of databases have been assembled for research purposes, and these are best accessed via the web (see the R&D Testbed web site, www.cmr.gov/rdtb, for links and instructions). For example, the Nuclear Explosion Database contains a large set of seismic recordings of nuclear tests. The Ground Truth Database contains an extensive catalog of events for which seismic ground truth information, to various levels of certainty, are known. Although the seismic R&D databases are most numerous at CMR, it is important to note that databases exist for all four monitoring technologies: There are hydroacoustic and infrasound research databases, as well as high resolution

gamma-ray spectroscopy and beta-gamma coincidence spectroscopy radionuclide databases. Reports are available to accompany most of the special databases and augment the detail provided on the web site.

DELIVERIES TO THE R&D TESTBED

The principal investigators of DTRA-sponsored nuclear monitoring research have been instructed to deliver the results of their research to the R&D Testbed. Deliveries take a number of forms, such as reports, raw data (e.g. seismic waveforms), parametric information (e.g. velocity models, station correction tables), and software. The R&D TB verifies that all deliveries meet appropriate acceptance criteria and pass validation tests. Such screening of contributions ensures that deliveries have been made successfully and increases the probability that these results may be successfully used by others. In addition, the R&D Testbed acts as an archive of research results, to prevent their loss and facilitate their distribution within the R&D community. Finally, the accumulation of results through time, and across projects and disciplines, provides the users of the R&D Testbed with a unique research tool.

Various procedures have been established for making deliveries to the R&D Testbed, as well as using the testbed for other purposes, such as testing and evaluating research results (Salzberg, et al, this issue). Test and evaluation procedures are scaled to the level necessary to achieve meaningful results. For example, the most stringent criteria are applied to the use of the full-scale testing environment, while more relaxed criteria are appropriate for limited-scale tests or the test and evaluation of stand-alone applications. An oversight committee prioritizes R&D Testbed activities, as well as reviewing schedules, plans and results.

TEST ENVIRONMENTS

Multiple test environments are available as part of the R&D Testbed. The smallest-scale test environments are readily reconfigured and adapted to the specific needs of a given test. At the largest scale is the capability for full-scale testing under heavy, real-time, data-flow and processing loads. The key benefit of the R&D Testbed's overall test capability is illustrated in Figure 3. Tests can be flexible enough to provide direct R&D interaction and experimentation, yet can be structured enough to simulate a full-scale, mission-critical operational environment.

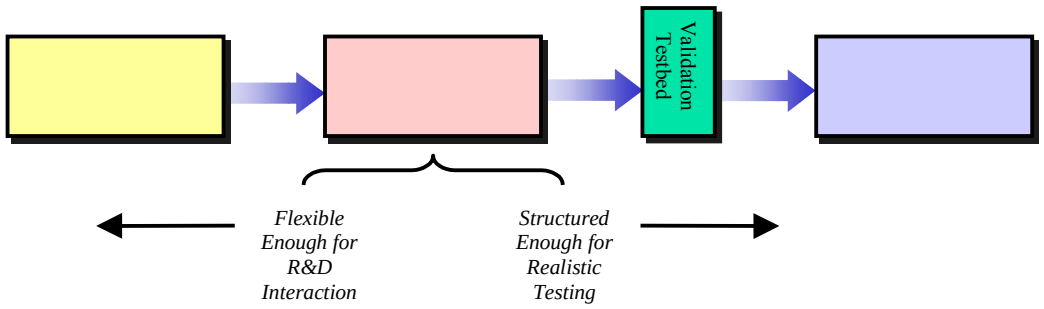


Figure 3. Illustration of the range of test environments available within the R&D Testbed.

Full-scale testing capability is provided by the Prototype Data Center (PDC), which comprises a superset of the functionality of the PIDC. Tests using the PDC are subjected to the full data load and timeliness pressures of a system receiving and processing continuous data running on a high availability basis. Strict configuration control is applied to the full-scale system, with changes subject to the approval of the Configuration Control Board. Such control ensures that changes in behavior of the system, or system output, are well understood, predictable, and repeatable.

A second full-scale, but more configurable, system is provided by the integration testbed. The integration testbed system completely replicates the PDC full-scale system (with the exception of the mass storage system), and provides an environment which can be configured for specific tests. Currently, the integration testbed is used for integrating and testing the full CTBT Monitoring Software System releases for the PIDC, as well as other tests which are incompatible with the more formal PDC environment or where special configurations are required.

Finally, the R&D Testbed provides a broad range of environments for unit tests and stand-alone tests. These tests take advantage of the available resources and processing results and range in scope from single desktops to complete systems.

FACILITIES

A comprehensive infrastructure environment exists at CMR to support the R&D Testbed user community and the R&D Testbed itself. A substantial Commercial Off the Shelf (COTS) software and hardware environment is maintained and documented on the R&D Testbed web site, and is highlighted here:

- Over 60 servers
- Over 90 workstations
- Mass storage systems (DLT, CD-ROM)
- Multiple Oracle instances
- Multiple web sites (open and secure)
- Multiple networks
- Firewall security

A number of these resources can be utilized directly by the R&D community (e.g. accounts are available for direct use of the Oracle database), while others are used to provide community support (e.g. the mass storage system is used to archive and serve data).

R&D Testbed contributors can conduct software demonstrations, as well as train others in the use of their software, in the training and briefing facility. There are multiple large-screen computer projections, from both Sun UNIX and PC hardware platforms, with access to the complete CMR COTS software environment.

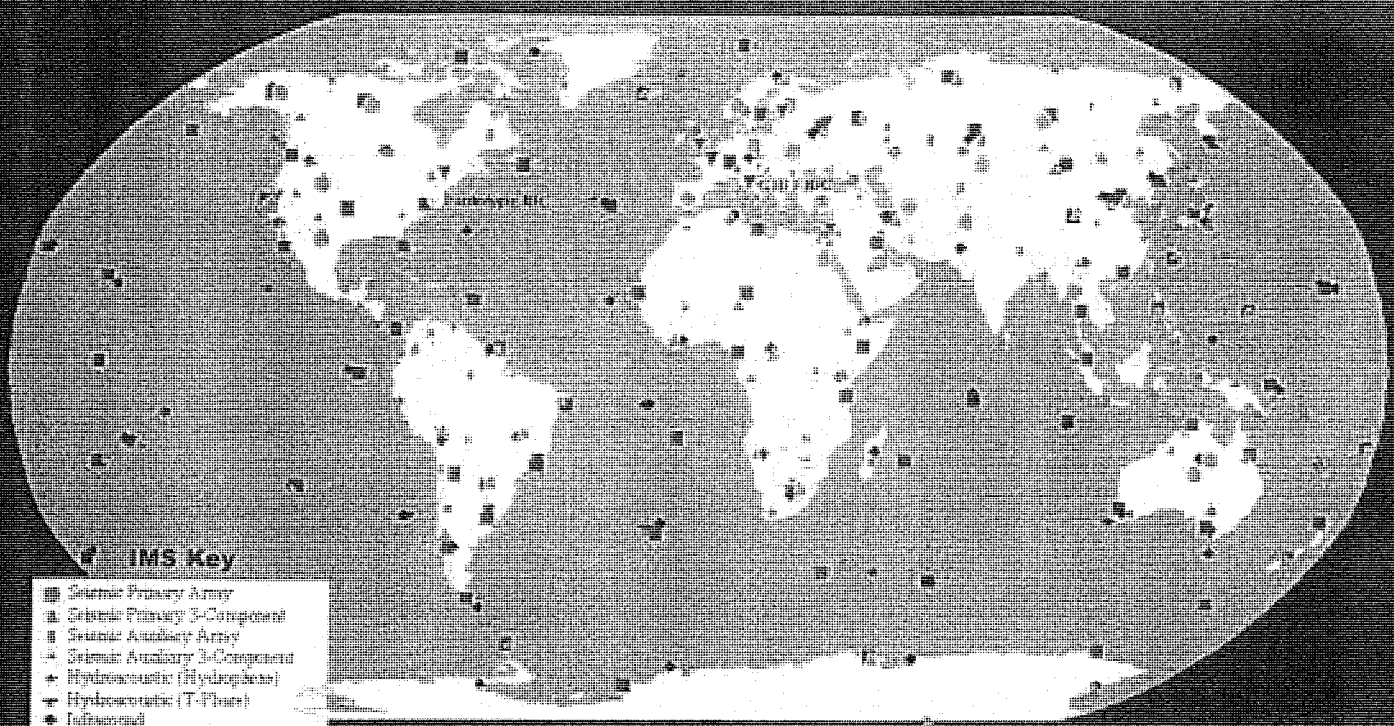
SUMMARY

The R&D Testbed makes use of all the facilities, resources, and expertise of CMR for the purpose of improving nuclear monitoring and verification capabilities. This role can be summarized in terms of the following broadly stated goals:

- The R&D Testbed supports the R&D community, from the inception of research through to testing and archiving of results on the R&D testbed itself. Such support can take the form of providing access to current IMS data, production results, IDC results, data archives, and more.

- The R&D Testbed archives research results to ensure important work is not lost and can be shared readily amongst the R&D community.

- The R&D Testbed provides a mechanism for the test, evaluation, and integration of R&D results. Testing can be conducted at various scales, ensuring proper test environments. Such test and evaluation provides the US government with quantitative measures of current monitoring capability, identifying obstacles and establishing expectations for achieving improved capability.



Hosted by:
U.S. Department of Defense
U.S. Department of Energy

September 12-15, 2000
New Orleans, LA